

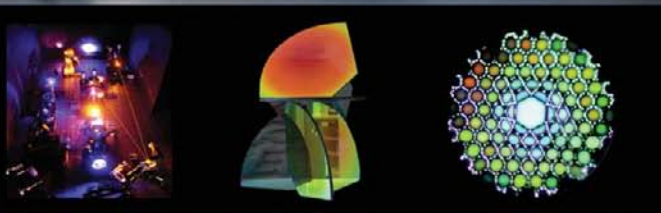
Third Edition

Sponsored by the Optical Society of America

# HANDBOOK OF OPTICS

## **Volume IV**

*Optical Properties of Materials, Nonlinear Optics,  
Quantum Optics*



*Editor-in-Chief:*  
**Michael Bass**

*Associate Editors:*  
Casimer M. DeCusatis  
Jay M. Enoch  
Vasudevan Lakshminarayanan  
Guifang Li  
Carolyn MacDonald  
Virendra N. Mahajan  
Eric Van Stryland

OSA<sup>®</sup>

# HANDBOOK OF OPTICS

---

## ABOUT THE EDITORS

---

**Editor-in-Chief:** Dr. Michael Bass is professor emeritus at CREOL, The College of Optics and Photonics, University of Central Florida, Orlando, Florida.

**Associate Editors:**

Dr. Casimer M. DeCusatis is a distinguished engineer and technical executive with IBM Corporation, Poughkeepsie, New York.

Dr. Jay M. Enoch is dean emeritus and professor at the School of Optometry at the University of California, Berkeley.

Dr. Vasudevan Lakshminarayanan is professor of Optometry, Physics, and Electrical Engineering at the University of Waterloo, Ontario, Canada.

Dr. Guifang Li is a professor at CREOL, The College of Optics and Photonics, University of Central Florida, Orlando, Florida.

Dr. Carolyn MacDonald is professor and chair of physics at the University at Albany, SUNY, and the director of the Albany Center for X-Ray Optics.

Dr. Virendra N. Mahajan is a distinguished scientist at The Aerospace Corporation.

Dr. Eric Van Stryland is a professor at CREOL, The College of Optics and Photonics, University of Central Florida, Orlando, Florida.

# HANDBOOK OF OPTICS

---

Volume IV  
Optical Properties of Materials,  
Nonlinear Optics, Quantum Optics

---

THIRD EDITION

---

Sponsored by the  
OPTICAL SOCIETY OF AMERICA

**Michael Bass** Editor-in-Chief  
*CREOL, The College of Optics and Photonics  
University of Central Florida  
Orlando, Florida*

**Guifang Li** Associate Editor  
*CREOL, The College of Optics and Photonics  
University of Central Florida  
Orlando, Florida*

**Eric Van Stryland** Associate Editor  
*CREOL, The College of Optics and Photonics  
University of Central Florida  
Orlando, Florida*



New York Chicago San Francisco Lisbon London Madrid  
Mexico City Milan New Delhi San Juan Seoul  
Singapore Sydney Toronto

Copyright © 2010 by The McGraw-Hill Companies, Inc. All rights reserved. Except as permitted under the United States Copyright Act of 1976, no part of this publication may be reproduced or distributed in any form or by any means, or stored in a database or retrieval system, without the prior written permission of the publisher.

ISBN: 978-0-07-162929-4

MHID: 0-07-162929-7

The material in this eBook also appears in the print version of this title: ISBN: 978-0-07-149892-0, MHID: 0-07-149892-3.

All trademarks are trademarks of their respective owners. Rather than put a trademark symbol after every occurrence of a trademarked name, we use names in an editorial fashion only, and to the benefit of the trademark owner, with no intention of infringement of the trademark. Where such designations appear in this book, they have been printed with initial caps.

McGraw-Hill eBooks are available at special quantity discounts to use as premiums and sales promotions, or for use in corporate training programs. To contact a representative please e-mail us at [bulksales@mcgraw-hill.com](mailto:bulksales@mcgraw-hill.com).

Information contained in this work has been obtained by The McGraw-Hill Companies, Inc. (“McGraw-Hill”) from sources believed to be reliable. However, neither McGraw-Hill nor its authors guarantee the accuracy or completeness of any information published herein, and neither McGraw-Hill nor its authors shall be responsible for any errors, omissions, or damages arising out of use of this information. This work is published with the understanding that McGraw-Hill and its authors are supplying information but are not attempting to render engineering or other professional services. If such services are required, the assistance of an appropriate professional should be sought.

#### TERMS OF USE

This is a copyrighted work and The McGraw-Hill Companies, Inc. (“McGraw-Hill”) and its licensors reserve all rights in and to the work. Use of this work is subject to these terms. Except as permitted under the Copyright Act of 1976 and the right to store and retrieve one copy of the work, you may not decompile, disassemble, reverse engineer, reproduce, modify, create derivative works based upon, transmit, distribute, disseminate, sell, publish or sublicense the work or any part of it without McGraw-Hill’s prior consent. You may use the work for your own noncommercial and personal use; any other use of the work is strictly prohibited. Your right to use the work may be terminated if you fail to comply with these terms.

THE WORK IS PROVIDED “AS IS.” MCGRAW-HILL AND ITS LICENSORS MAKE NO GUARANTEES OR WARRANTIES AS TO THE ACCURACY, ADEQUACY OR COMPLETENESS OF OR RESULTS TO BE OBTAINED FROM USING THE WORK, INCLUDING ANY INFORMATION THAT CAN BE ACCESSED THROUGH THE WORK VIA HYPERLINK OR OTHERWISE, AND EXPRESSLY DISCLAIM ANY WARRANTY, EXPRESS OR IMPLIED, INCLUDING BUT NOT LIMITED TO IMPLIED WARRANTIES OF MERCHANTABILITY OR FITNESS FOR A PARTICULAR PURPOSE. McGraw-Hill and its licensors do not warrant or guarantee that the functions contained in the work will meet your requirements or that its operation will be uninterrupted or error free. Neither McGraw-Hill nor its licensors shall be liable to you or anyone else for any inaccuracy, error or omission, regardless of cause, in the work or for any damages resulting therefrom. McGraw-Hill has no responsibility for the content of any information accessed through the work. Under no circumstances shall McGraw-Hill and/or its licensors be liable for any indirect, incidental, special, punitive, consequential or similar damages that result from the use of or inability to use the work, even if any of them has been advised of the possibility of such damages. This limitation of liability shall apply to any claim or cause whatsoever whether such claim or cause arises in contract, tort or otherwise.

## COVER ILLUSTRATIONS

---

**Left:** Photograph of a femtosecond optical parametric oscillator pumped in the blue by the second harmonic of a Ti:sapphire laser and operating in the orange. The oscillator can deliver femtosecond pulses across the entire visible range from the blue-green to yellow-red by simple rotation of the nonlinear crystal. (*Courtesy of Radiantis, S. L., Barcelona, Spain.*) See Chapter 19.

**Middle:** Photograph of a thin-film-based sculpture showing the beautiful colors of thin films seen in reflection and transmission. The variety of properties one may achieve with optical thin films is demonstrated in this photo by the different colors of reflected and transmitted light seen as a result of different coating design and angle of incidence. See Chapter 7.

**Right:** This is an optical micrograph of the end face of a hollow core photonic crystal fiber with super continuum white light launched at the far end. It shows the separation of colors according to the lifetimes of Mie resonances in the hollow channels. This illustrates nonlinear optical phenomena as discussed in several chapters of this volume, but also uses fibers as discussed in Chapter 11 of Vol. V.

*This page intentionally left blank*

---

# CONTENTS

---

<b>Contributors</b>	<b>xiii</b>
<b>Brief Contents of All Volumes</b>	<b>xv</b>
<b>Editors' Preface</b>	<b>xxi</b>
<b>Preface to Volume IV</b>	<b>xxiii</b>
<b>Glossary and Fundamental Constants</b>	<b>xxv</b>

## Part 1. Properties

---

<b>Chapter 1. Optical Properties of Water</b>	<i>Curtis D. Mobley</i>	<b>1.3</b>
---	-------------------------	------------

---

1.1	Introduction / 1.3
1.2	Terminology, Notation, and Definitions / 1.3
1.3	Radiometric Quantities Useful in Hydrologic Optics / 1.4
1.4	Inherent Optical Properties / 1.9
1.5	Apparent Optical Properties / 1.12
1.6	The Optically Significant Constituents of Natural Waters / 1.13
1.7	Particle Size Distributions / 1.15
1.8	Electromagnetic Properties of Water / 1.16
1.9	Index of Refraction / 1.18
1.10	Measurement of Absorption / 1.20
1.11	Absorption by Pure Sea Water / 1.21
1.12	Absorption by Dissolved Organic Matter / 1.22
1.13	Absorption by Phytoplankton / 1.23
1.14	Absorption by Organic Detritus / 1.25
1.15	Bio-Optical Models for Absorption / 1.27
1.16	Measurement of Scattering / 1.29
1.17	Scattering by Pure Water and by Pure Sea Water / 1.30
1.18	Scattering by Particles / 1.30
1.19	Wavelength Dependence of Scattering: Bio-Optical Models / 1.35
1.20	Beam Attenuation / 1.40
1.21	Diffuse Attenuation and Jerlov Water Types / 1.42
1.22	Irradiance Reflectance and Remote Sensing / 1.46
1.23	Inelastic Scattering and Polarization / 1.47
1.24	Acknowledgments / 1.50
1.25	References / 1.50

---

<b>Chapter 2. Properties of Crystals and Glasses</b>	<i>William J. Tropf, Michael E. Thomas, and Eric W. Rogala</i>	<b>2.1</b>
--	--	------------

---

2.1	Glossary / 2.1
2.2	Introduction / 2.3
2.3	Optical Materials / 2.4
2.4	Properties of Materials / 2.5
2.5	Properties Tables / 2.36
2.6	References / 2.77

---

<b>Chapter 3. Polymeric Optics</b>	<i>John D. Lytle</i>	<b>3.1</b>
------------------------------------	----------------------	------------

---

3.1	Glossary / 3.1
3.2	Introduction / 3.1



- 3.3 Forms / 3.2
- 3.4 Physical Properties / 3.2
- 3.5 Optical Properties / 3.5
- 3.6 Optical Design / 3.7
- 3.7 Processing / 3.11
- 3.8 Coatings / 3.17
- 3.9 References / 3.18

---

**Chapter 4. Properties of Metals** *Roger A. Paquin* **4.1**

---

- 4.1 Glossary / 4.1
- 4.2 Introduction / 4.2
- 4.3 Summary Data / 4.11
- 4.4 References / 4.70

---

**Chapter 5. Optical Properties of Semiconductors**  
*David G. Seiler, Stefan Zollner, Alain C. Diebold,  
and Paul M. Amirtharaj* **5.1**

---

- 5.1 Glossary / 5.1
- 5.2 Introduction / 5.3
- 5.3 Optical Properties / 5.8
- 5.4 Measurement Techniques / 5.56
- 5.5 Acknowledgments / 5.83
- 5.6 Summary and Conclusions / 5.83
- 5.7 References / 5.91

---

**Chapter 6. Characterization and Use of Black Surfaces for Optical Systems** *Stephen M. Pompea and Robert P. Breault* **6.1**

---

- 6.1 Introduction / 6.1
- 6.2 Selection Process for Black Baffle Surfaces in Optical Systems / 6.10
- 6.3 The Creation of Black Surfaces for Specific Applications / 6.13
- 6.4 Environmental Degradation of Black Surfaces / 6.16
- 6.5 Optical Characterization of Black Surfaces / 6.18
- 6.6 Surfaces for Ultraviolet and Far-Infrared Applications / 6.21
- 6.7 Survey of Surfaces with Optical Data / 6.34
- 6.8 Paints / 6.35
- 6.9 Conclusions / 6.59
- 6.10 Acknowledgments / 6.59
- 6.11 References / 6.60
- 6.12 Further Readings / 6.67

---

**Chapter 7. Optical Properties of Films and Coatings**  
*Jerzy A. Dobrowolski* **7.1**

---

- 7.1 Introduction / 7.1
- 7.2 Theory and Design of Optical Thin-Film Coatings / 7.5
- 7.3 Thin-Film Manufacturing Considerations / 7.10
- 7.4 Measurements on Optical Coatings / 7.12
- 7.5 Antireflection Coatings / 7.15
- 7.6 Two-Material Periodic Multilayers Theory / 7.32
- 7.7 Multilayer Reflectors—Experimental Results / 7.39
- 7.8 Cutoff, Heat-Control, and Solar-Cell Cover Filters / 7.53
- 7.9 Beam Splitters and Neutral Filters / 7.61
- 7.10 Interference Polarizers and Polarizing Beam Splitters / 7.69

- 7.11 Bandpass Filters / 7.73
- 7.12 High Performance Optical Multilayer Coatings / 7.96
- 7.13 Multilayers for Two or Three Spectral Regions / 7.98
- 7.14 Phase Coatings / 7.101
- 7.15 Interference Filters with Low Reflection / 7.104
- 7.16 Reflection Filters and Coatings / 7.106
- 7.17 Special Purpose Coatings / 7.113
- 7.18 References / 7.114

---

## Chapter 8. Fundamental Optical Properties of Solids *Alan Miller* 8.1

- 8.1 Glossary / 8.1
- 8.2 Introduction / 8.3
- 8.3 Propagation of Light in Solids / 8.4
- 8.4 Dispersion Relations / 8.14
- 8.5 Lattice Interactions / 8.16
- 8.6 Free Electron Properties / 8.21
- 8.7 Band Structures and Interband Transitions / 8.24
- 8.8 References / 8.32

---

## Chapter 9. Photonic Bandgap Materials *Pierre R. Villeneuve* 9.1

- 9.1 Glossary / 9.1
- 9.2 Introduction / 9.2
- 9.3 Maxwell's Equations / 9.2
- 9.4 Three-Dimensional Photonic Crystals / 9.4
- 9.5 Microcavities in Three-Dimensional Photonic Crystals / 9.6
- 9.6 Microcavities in Photonic Crystals with Two-Dimensional Periodicity / 9.8
- 9.7 Waveguides / 9.12
- 9.8 Conclusion / 9.17
- 9.9 References / 9.18

## Part 2. Nonlinear Optics

---

### Chapter 10. Nonlinear Optics *Chung L. Tang* 10.3

- 10.1 Glossary / 10.3
- 10.2 Introduction / 10.4
- 10.3 Basic Concepts / 10.5
- 10.4 Material Considerations / 10.19
- 10.5 Appendix / 10.21
- 10.6 References / 10.23

---

### Chapter 11. Coherent Optical Transients *Paul R. Berman and Duncan G. Steel* 11.1

- 11.1 Glossary / 11.1
- 11.2 Introduction / 11.2
- 11.3 Optical Bloch Equations / 11.3
- 11.4 Maxwell-Bloch Equations / 11.6
- 11.5 Free Polarization Decay / 11.7
- 11.6 Photon Echo / 11.11
- 11.7 Stimulated Photon Echo / 11.15
- 11.8 Phase Conjugate Geometry and Optical Ramsey Fringes / 11.19
- 11.9 Two-Photon Transitions and Atom Interferometry / 11.22
- 11.10 Chirped Pulse Excitation / 11.25
- 11.11 Experimental Considerations / 11.26
- 11.12 Conclusion / 11.28
- 11.13 References / 11.28

<b>Chapter 12. Photorefractive Materials and Devices</b> <i>Mark Cronin-Golomb and Marvin Klein</i>	<b>12.1</b>
<hr/>	
12.1 Introduction / 12.1	
12.2 Materials / 12.10	
12.3 Devices / 12.28	
12.4 References / 12.38	
12.5 Further Reading / 12.45	
<b>Chapter 13. Optical Limiting</b> <i>David J. Hagan</i>	<b>13.1</b>
<hr/>	
13.1 Introduction / 13.1	
13.2 Basic Principles of Passive Optical Limiting / 13.4	
13.3 Examples of Passive Optical Limiting in Specific Materials / 13.9	
13.4 References / 13.13	
<b>Chapter 14. Electromagnetically Induced Transparency</b> <i>Jonathan P. Marangos and Thomas Halfmann</i>	<b>14.1</b>
<hr/>	
14.1 Glossary / 14.1	
14.2 Introduction / 14.2	
14.3 Coherence in Two- and Three-Level Atomic Systems / 14.4	
14.4 The Basic Physical Concept of Electromagnetically Induced Transparency / 14.5	
14.5 Manipulation of Optical Properties by Electromagnetically Induced Transparency / 14.10	
14.6 Electromagnetically Induced Transparency, Driven by Pulsed Lasers / 14.15	
14.7 Steady State Electromagnetically Induced Transparency, Driven by CW Lasers / 14.16	
14.8 Gain without Inversion and Lasing without Inversion / 14.18	
14.9 Manipulation of the Index of Refraction in Dressed Atoms / 14.19	
14.10 Pulse Propagation Effects / 14.20	
14.11 Ultraslow Light Pulses / 14.22	
14.12 Nonlinear Optical Frequency Conversion / 14.24	
14.13 Nonlinear Optics at Maximal Atomic Coherence / 14.28	
14.14 Nonlinear Optics at the Few Photon Level / 14.32	
14.15 Electromagnetically Induced Transparency in Solids / 14.33	
14.16 Conclusion / 14.36	
14.17 Further Reading / 14.36	
14.18 References / 14.37	
<b>Chapter 15. Stimulated Raman and Brillouin Scattering</b> <i>John Reintjes and Mark Bashkansky</i>	<b>15.1</b>
<hr/>	
15.1 Introduction / 15.1	
15.2 Raman Scattering / 15.1	
15.3 Stimulated Brillouin Scattering / 15.43	
15.4 References / 15.54	
15.5 Additional References / 15.60	
<b>Chapter 16. Third-Order Optical Nonlinearities</b> <i>Mansoor Sheik-Bahae and Michael P. Hasselbeck</i>	<b>16.1</b>
<hr/>	
16.1 Introduction / 16.1	
16.2 Quantum Mechanical Picture / 16.4	
16.3 Nonlinear Absorption and Nonlinear Refraction / 16.7	
16.4 Kramers-Kronig Dispersion Relations / 16.9	
16.5 Optical Kerr Effect / 16.11	
16.6 Third-Harmonic Generation / 16.14	
16.7 Stimulated Scattering / 16.14	
16.8 Two-Photon Absorption / 16.19	
16.9 Effective Third-Order Nonlinearities; Cascaded $\chi^1; \chi^1$ Processes / 16.20	
16.10 Effective Third-Order Nonlinearities; Cascaded $\chi^2; \chi^2$ Processes / 16.22	

- 16.11 Propagation Effects / 16.24  
 16.12 Common Experimental Techniques and Applications / 16.26  
 16.13 References / 16.31

---

**Chapter 17. Continuous-Wave Optical Parametric Oscillators** **17.1**  
*Majid Ebrahim-Zadeh*

---

- 17.1 Introduction / 17.1  
 17.2 Continuous-Wave Optical Parametric Oscillators / 17.2  
 17.3 Applications / 17.21  
 17.4 Summary / 17.29  
 17.5 References / 17.31

---

**Chapter 18. Nonlinear Optical Processes for Ultrashort Pulse Generation** **18.1**  
*Uwe Siegner and Ursula Keller*

---

- 18.1 Glossary / 18.1  
 18.2 Abbreviations / 18.3  
 18.3 Introduction / 18.3  
 18.4 Saturable Absorbers: Macroscopic Description / 18.5  
 18.5 Kerr Effect / 18.11  
 18.6 Semiconductor Ultrafast Nonlinearities: Microscopic Processes / 18.15  
 18.7 References / 18.23

---

**Chapter 19. Laser-Induced Damage to Optical Materials** **19.1**  
*Marion J. Soileau*

---

- 19.1 Introduction / 19.1  
 19.2 Practical Estimates / 19.2  
 19.3 Surface Damage / 19.2  
 19.4 Package-Induced Damage / 19.4  
 19.5 Nonlinear Optical Effects / 19.5  
 19.6 Avoidance of Damage / 19.5  
 19.7 Fundamental Mechanisms / 19.6  
 19.8 Progress in Measurements of Critical NLO Parameters / 19.9  
 19.9 References / 19.11

### Part 3. Quantum and Molecular Optics

---

**Chapter 20. Laser Cooling and Trapping of Atoms** **20.3**  
*Harold J. Metcalf and Peter van der Straten*

---

- 20.1 Introduction / 20.3  
 20.2 General Properties Concerning Laser Cooling / 20.4  
 20.3 Theoretical Description / 20.6  
 20.4 Slowing Atomic Beams / 20.11  
 20.5 Optical Molasses / 20.13  
 20.6 Cooling Below the Doppler Limit / 20.17  
 20.7 Trapping of Neutral Atoms / 20.21  
 20.8 Applications / 20.26  
 20.9 References / 20.39

---

**Chapter 21. Strong Field Physics** **21.1**  
*Todd Ditmire*

---

- 21.1 Glossary / 21.1  
 21.2 Introduction and History / 21.2  
 21.3 Laser Technology Used in Strong Field Physics / 21.4  
 21.4 Strong Field Interactions with Single Electrons / 21.5  
 21.5 Strong Field Interactions with Atoms / 21.10

21.6 Strong Field Interactions with Molecules / 21.22  
21.7 Strong Field Nonlinear Optics in Gases / 21.27  
21.8 Strong Field Interactions with Clusters / 21.31  
21.9 Strong Field Physics in Underdense Plasmas / 21.36  
21.10 Strong Field Physics at Surfaces of Overdense Plasmas / 21.46  
21.11 Applications of Strong Field Interactions with Plasmas / 21.52  
21.12 References / 21.55

---

**Chapter 22. Slow Light Propagation in Atomic  
and Photonic Media** *Jacob B. Khurgin* **22.1**

---

22.1 Glossary / 22.1  
22.2 Introduction / 22.2  
22.3 Atomic Resonance / 22.2  
22.4 Bandwidth Limitations in Atomic Schemes / 22.9  
22.5 Photonic Resonance / 22.9  
22.6 Slow Light in Optical Fibers / 22.13  
22.7 Conclusion / 22.15  
22.8 References / 22.16

---

**Chapter 23. Quantum Entanglement in Optical Interferometry**  
*Hwang Lee, Christoph F. Wildfeuer, Sean D. Huver,  
and Jonathan P. Dowling* **23.1**

---

23.1 Introduction / 23.1  
23.2 Shot-Noise Limit / 23.4  
23.3 Heisenberg Limit / 23.6  
23.4 “Digital” Approaches / 23.7  
23.5 Noon State / 23.9  
23.6 Quantum Imaging / 23.13  
23.7 Toward Quantum Remote Sensing / 23.14  
23.8 References / 23.15

**Index** **I.1**

---

# CONTRIBUTORS

---

**Paul M. Amirtharaj** *Sensors and Electron Devices Directorate, U.S. Army Research Laboratory, Adelphi, Maryland (CHAP. 5)*

**Mark Bashkansky** *Optical Sciences Division, Naval Research Laboratory, Washington, D.C. (CHAP. 15)*

**Paul R. Berman** *Physics Department, University of Michigan, Ann Arbor, Michigan (CHAP. 11)*

**Robert P. Breault** *Breault Research Organization, Inc., Tucson, Arizona (CHAP. 6)*

**Mark Cronin-Golomb** *Department of Biomedical Engineering, Tufts University, Medford, Massachusetts (CHAP. 12)*

**Alain C. Diebold** *College of Nanoscale Science and Engineering, University at Albany, Albany, New York (CHAP. 5)*

**Todd Ditmire** *Texas Center for High Intensity Laser Science, Department of Physics, The University of Texas at Austin, Austin, Texas (CHAP. 21)*

**Jerzy A. Dobrowolski** *Institute for Microstructural Sciences, National Research Council of Canada, Ottawa, Ontario, Canada (CHAP. 7)*

**Jonathan P. Dowling** *Hearne Institute for Theoretical Physics, Department of Physics and Astronomy, Louisiana State University, Baton Rouge, Louisiana (CHAP. 23)*

**Majid Ebrahim-Zadeh** *ICFO—Institut de Ciències Fotòniques, Mediterranean Technology Park, Barcelona, Spain, and Institutio Catalana de Recerca i Estudis Avancats (ICREA), Passeig Lluís Companys, Barcelona, Spain (CHAP. 17)*

**David J. Hagan** *CREOL, The College of Optics and Photonics, University of Central Florida, Orlando, Florida (CHAP. 13)*

**Thomas Halfmann** *Institute of Applied Physics, Technical University of Darmstadt, Darmstadt, Germany (CHAP. 14)*

**Michael P. Hasselbeck** *Department of Physics and Astronomy, University of New Mexico, Albuquerque, New Mexico (CHAP. 16)*

**Sean D. Huver** *Hearne Institute for Theoretical Physics, Department of Physics and Astronomy, Louisiana State University, Baton Rouge, Louisiana (CHAP. 23)*

**Ursula Keller** *Institute of Quantum Electronics, Physics Department, Swiss Federal Institute of Technology (ETH), Zurich, Switzerland (CHAP. 18)*

**Jacob B. Khurgin** *Department of Electrical and Computer Engineering, Johns Hopkins University, Baltimore, Maryland (CHAP. 22)*

**Marvin Klein** *Intelligent Optical Systems, Inc., Torrance, California (CHAP. 12)*

**Hwang Lee** *Hearne Institute for Theoretical Physics, Department of Physics and Astronomy, Louisiana State University, Baton Rouge, Louisiana (CHAP. 23)*

**John D. Lytle** *Advanced Optical Concepts, Santa Cruz, California (CHAP. 3)*

**Jonathan P. Marangos** *Quantum Optics and Laser Science Group, Blackett Laboratory, Imperial College, London, United Kingdom (CHAP. 14)*

**Harold J. Metcalf** *Department of Physics, State University of New York, Stony Brook, New York (CHAP. 20)*

**Alan Miller** *Scottish Universities Physics Alliance, School of Engineering and Physical Sciences, Heriot-Watt University, Edinburgh, Scotland (CHAP. 8)*

**Curtis D. Mobley** *Applied Electromagnetics and Optics Laboratory, SRI International, Menlo Park, California (CHAP. 1)*

**Roger A. Paquin** *Advanced Materials Consultant, Tucson, Arizona, and Optical Sciences Center, University of Arizona, Tucson (CHAP. 4)*

**Stephen M. Pompea** *National Optical Astronomy Observatory, Tucson, Arizona (CHAP. 6)*

**John Reintjes** *Optical Sciences Division, Naval Research Laboratory, Washington, D.C. (CHAP. 15)*

**Eric W. Rogala** *Raytheon Missile Systems, Tucson, Arizona* (CHAP. 2)

**David G. Seiler** *Semiconductor Electronics Division, National Institute of Standards and Technology, Gaithersburg, Maryland* (CHAP. 5)

**Mansoor Sheik-Bahae** *Department of Physics and Astronomy, University of New Mexico, Albuquerque, New Mexico* (CHAP. 16)

**Uwe Siegner** *Institute of Quantum Electronics, Physics Department, Swiss Federal Institute of Technology (ETH), Zurich, Switzerland* (CHAP. 18)

**Marion J. Soileau** *CREOL, The College of Optics and Photonics, University of Central Florida, Orlando, Florida* (CHAP. 19)

**Duncan G. Steel** *Physics Department, University of Michigan, Ann Arbor, Michigan* (CHAP. 11)

**Chung L. Tang** *School of Electrical and Computer Engineering, Cornell University, Ithaca, New York* (CHAP. 10)

**Michael E. Thomas** *Applied Physics Laboratory, Johns Hopkins University, Laurel, Maryland* (CHAP. 2)

**William J. Tropf** *Applied Physics Laboratory, Johns Hopkins University, Laurel, Maryland* (CHAP. 2)

**Peter van der Straten** *Debye Institute, Department of Atomic and Interface Physics, Utrecht University, Utrecht, The Netherlands* (CHAP. 20)

**Pierre R. Villeneuve** *Department of Physics, Massachusetts Institute of Technology, Cambridge, Massachusetts* (CHAP. 9)

**Christoph F. Wildfeuer** *Hearne Institute for Theoretical Physics, Department of Physics and Astronomy, Louisiana State University, Baton Rouge, Louisiana* (CHAP. 23)

**Stefan Zollner** *Freescale Semiconductor, Inc., Hopewell Junction, New York* (CHAP. 5)

---

# BRIEF CONTENTS OF ALL VOLUMES

---

## VOLUME I. GEOMETRICAL AND PHYSICAL OPTICS, POLARIZED LIGHT, COMPONENTS AND INSTRUMENTS

---

### PART 1. GEOMETRICAL OPTICS

---

Chapter 1. General Principles of Geometrical Optics *Douglas S. Goodman*

### PART 2. PHYSICAL OPTICS

---

Chapter 2. Interference *John E. Greivenkamp*

Chapter 3. Diffraction *Arvind S. Marathay and John F. McCalmont*

Chapter 4. Transfer Function Techniques *Glenn D. Boreman*

Chapter 5. Coherence Theory *William H. Carter*

Chapter 6. Coherence Theory: Tools and Applications *Gisele Bennett, William T. Rhodes, and J. Christopher James*

Chapter 7. Scattering by Particles *Craig F. Bohren*

Chapter 8. Surface Scattering *Eugene L. Church and Peter Z. Takacs*

Chapter 9. Volume Scattering in Random Media *Aristide Dogariu and Jeremy Ellis*

Chapter 10. Optical Spectroscopy and Spectroscopic Lineshapes *Brian Henderson*

Chapter 11. Analog Optical Signal and Image Processing *Joseph W. Goodman*

### PART 3. POLARIZED LIGHT

---

Chapter 12. Polarization *Jean M. Bennett*

Chapter 13. Polarizers *Jean M. Bennett*

Chapter 14. Mueller Matrices *Russell A. Chipman*

Chapter 15. Polarimetry *Russell A. Chipman*

Chapter 16. Ellipsometry *Rasheed M. A. Azzam*

### PART 4. COMPONENTS

---

Chapter 17. Lenses *R. Barry Johnson*

Chapter 18. Afocal Systems *William B. Wetherell*

Chapter 19. Nondispersive Prisms *William L. Wolfe*

Chapter 20. Dispersive Prisms and Gratings *George J. Zissis*

Chapter 21. Integrated Optics *Thomas L. Koch, Frederick J. Leonberger, and Paul G. Suchoski*

Chapter 22. Miniature and Micro-Optics *Tom D. Milster and Tomasz S. Tkaczyk*

Chapter 23. Binary Optics *Michael W. Farn and Wilfrid B. Veldkamp*

Chapter 24. Gradient Index Optics *Duncan T. Moore*

### PART 5. INSTRUMENTS

---

Chapter 25. Cameras *Norman Goldberg*

Chapter 26. Solid-State Cameras *Gerald C. Holst*

Chapter 27. Camera Lenses *Ellis Betensky, Melvin H. Kreitzer, and Jacob Moskovich*

Chapter 28. Microscopes *Rudolf Oldenbourg and Michael Shribak*

Chapter 29. Reflective and Catadioptric Objectives *Lloyd Jones*



- Chapter 30. Scanners *Leo Beiser and R. Barry Johnson*
- Chapter 31. Optical Spectrometers *Brian Henderson*
- Chapter 32. Interferometers *Parameswaran Hariharan*
- Chapter 33. Holography and Holographic Instruments *Lloyd Huff*
- Chapter 34. Xerographic Systems *Howard Stark*
- Chapter 35. Principles of Optical Disk Data Storage *Masud Mansuripur*

## VOLUME II. DESIGN, FABRICATION, AND TESTING; SOURCES AND DETECTORS; RADIOMETRY AND PHOTOMETRY

---

### PART 1. DESIGN

---

- Chapter 1. Techniques of First-Order Layout *Warren J. Smith*
- Chapter 2. Aberration Curves in Lens Design *Donald C. O'Shea and Michael E. Harrigan*
- Chapter 3. Optical Design Software *Douglas C. Sinclair*
- Chapter 4. Optical Specifications *Robert R. Shannon*
- Chapter 5. Tolerancing Techniques *Robert R. Shannon*
- Chapter 6. Mounting Optical Components *Paul R. Yoder, Jr.*
- Chapter 7. Control of Stray Light *Robert P. Breault*
- Chapter 8. Thermal Compensation Techniques *Philip J. Rogers and Michael Roberts*

### PART 2. FABRICATION

---

- Chapter 9. Optical Fabrication *Michael P. Mandina*
- Chapter 10. Fabrication of Optics by Diamond Turning *Richard L. Rhorer and Chris J. Evans*

### PART 3. TESTING

---

- Chapter 11. Orthonormal Polynomials in Wavefront Analysis *Virendra N. Mahajan*
- Chapter 12. Optical Metrology *Zacarias Malacara and Daniel Malacara-Hernández*
- Chapter 13. Optical Testing *Daniel Malacara-Hernández*
- Chapter 14. Use of Computer-Generated Holograms in Optical Testing *Katherine Creath and James C. Wyant*

### PART 4. SOURCES

---

- Chapter 15. Artificial Sources *Anthony LaRocca*
- Chapter 16. Lasers *William T. Silfvast*
- Chapter 17. Light-Emitting Diodes *Roland H. Haitz, M. George Craford, and Robert H. Weissman*
- Chapter 18. High-Brightness Visible LEDs *Winston V. Schoenfeld*
- Chapter 19. Semiconductor Lasers *Pamela L. Derry, Luis Figueroa, and Chi-shain Hong*
- Chapter 20. Ultrashort Optical Sources and Applications *Jean-Claude Diels and Ladan Arissian*
- Chapter 21. Attosecond Optics *Zenghu Chang*
- Chapter 22. Laser Stabilization *John L. Hall, Matthew S. Taubman, and Jun Ye*
- Chapter 23. Quantum Theory of the Laser *János A. Bergou, Berthold-Georg Englert, Melvin Lax, Marian O. Scully, Herbert Walther, and M. Suhail Zubairy*

### PART 5. DETECTORS

---

- Chapter 24. Photodetectors *Paul R. Norton*
- Chapter 25. Photodetection *Abhay M. Joshi and Gregory H. Olsen*
- Chapter 26. High-Speed Photodetectors *John E. Bowers and Yih G. Wey*
- Chapter 27. Signal Detection and Analysis *John R. Willison*
- Chapter 28. Thermal Detectors *William L. Wolfe and Paul W. Kruse*

### PART 6. IMAGING DETECTORS

---

- Chapter 29. Photographic Films *Joseph H. Altman*
- Chapter 30. Photographic Materials *John D. Baloga*

- Chapter 31. Image Tube Intensified Electronic Imaging *C. Bruce Johnson and Larry D. Owen*  
 Chapter 32. Visible Array Detectors *Timothy J. Tredwell*  
 Chapter 33. Infrared Detector Arrays *Lester J. Kozlowski and Walter F. Kosonocky*

---

## PART 7. RADIOMETRY AND PHOTOMETRY

- Chapter 34. Radiometry and Photometry *Edward F. Zalewski*  
 Chapter 35. Measurement of Transmission, Absorption, Emission, and Reflection *James M. Palmer*  
 Chapter 36. Radiometry and Photometry: Units and Conversions *James M. Palmer*  
 Chapter 37. Radiometry and Photometry for Vision Optics *Yoshi Ohno*  
 Chapter 38. Spectroradiometry *Carolyn J. Sher DeCusatis*  
 Chapter 39. Nonimaging Optics: Concentration and Illumination *William Cassarly*  
 Chapter 40. Lighting and Applications *Anurag Gupta and R. John Koschel*

---

## VOLUME III. VISION AND VISION OPTICS

- Chapter 1. Optics of the Eye *Neil Charman*  
 Chapter 2. Visual Performance *Wilson S. Geisler and Martin S. Banks*  
 Chapter 3. Psychophysical Methods *Denis G. Pelli and Bart Farell*  
 Chapter 4. Visual Acuity and Hyperacuity *Gerald Westheimer*  
 Chapter 5. Optical Generation of the Visual Stimulus *Stephen A. Burns and Robert H. Webb*  
 Chapter 6. The Maxwellian View with an Addendum on Apodization *Gerald Westheimer*  
 Chapter 7. Ocular Radiation Hazards *David H. Sliney*  
 Chapter 8. Biological Waveguides *Vasudevan Lakshminarayanan and Jay M. Enoch*  
 Chapter 9. The Problem of Correction for the Stiles-Crawford Effect of the First Kind in Radiometry and Photometry, a Solution *Jay M. Enoch and Vasudevan Lakshminarayanan*  
 Chapter 10. Colorimetry *David H. Brainard and Andrew Stockman*  
 Chapter 11. Color Vision Mechanisms *Andrew Stockman and David H. Brainard*  
 Chapter 12. Assessment of Refraction and Refractive Errors and Their Influence on Optical Design *B. Ralph Chou*  
 Chapter 13. Binocular Vision Factors That Influence Optical Design *Clifton Schor*  
 Chapter 14. Optics and Vision of the Aging Eye *John S. Werner, Brooke E. Scheffrin, and Arthur Bradley*  
 Chapter 15. Adaptive Optics in Retinal Microscopy and Vision *Donald T. Miller and Austin Roorda*  
 Chapter 16. Refractive Surgery, Correction of Vision, PRK, and LASIK *L. Diaz-Santana and Harilaos Giniis*  
 Chapter 17. Three-Dimensional Confocal Microscopy of the Living Human Cornea *Barry R. Masters*  
 Chapter 18. Diagnostic Use of Optical Coherence Tomography in the Eye *Johannes F. de Boer*  
 Chapter 19. Gradient Index Optics in the Eye *Barbara K. Pierscionek*  
 Chapter 20. Optics of Contact Lenses *Edward S. Bennett*  
 Chapter 21. Intraocular Lenses *Jim Schwiegerling*  
 Chapter 22. Displays for Vision Research *William Cowan*  
 Chapter 23. Vision Problems at Computers *Jeffrey Anshel and James E. Sheedy*  
 Chapter 24. Human Vision and Electronic Imaging *Bernice E. Rogowitz, Thrasyvoulos N. Pappas, and Jan P. Allebach*  
 Chapter 25. Visual Factors Associated with Head-Mounted Displays *Brian H. Tsou and Martin Shenker*

---

## VOLUME IV. OPTICAL PROPERTIES OF MATERIALS, NONLINEAR OPTICS, QUANTUM OPTICS

---

### PART 1. PROPERTIES

- Chapter 1. Optical Properties of Water *Curtis D. Mobley*  
 Chapter 2. Properties of Crystals and Glasses *William J. Tropf, Michael E. Thomas, and Eric W. Rogala*  
 Chapter 3. Polymeric Optics *John D. Lytle*  
 Chapter 4. Properties of Metals *Roger A. Paquin*

- Chapter 5. Optical Properties of Semiconductors *David G. Seiler, Stefan Zollner, Alain C. Diebold, and Paul M. Amiritharaj*
- Chapter 6. Characterization and Use of Black Surfaces for Optical Systems *Stephen M. Pompea and Robert P. Breault*
- Chapter 7. Optical Properties of Films and Coatings *Jerzy A. Dobrowolski*
- Chapter 8. Fundamental Optical Properties of Solids *Alan Miller*
- Chapter 9. Photonic Bandgap Materials *Pierre R. Villeneuve*

---

## PART 2. NONLINEAR OPTICS

- Chapter 10. Nonlinear Optics *Chung L. Tang*
- Chapter 11. Coherent Optical Transients *Paul R. Berman and Duncan G. Steel*
- Chapter 12. Photorefractive Materials and Devices *Mark Cronin-Golomb and Marvin Klein*
- Chapter 13. Optical Limiting *David J. Hagan*
- Chapter 14. Electromagnetically Induced Transparency *Jonathan P. Marangos and Thomas Halfmann*
- Chapter 15. Stimulated Raman and Brillouin Scattering *John Reintjes and Mark Bashkansky*
- Chapter 16. Third-Order Optical Nonlinearities *Mansoor Sheik-Bahae and Michael P. Hasselbeck*
- Chapter 17. Continuous-Wave Optical Parametric Oscillators *Majid Ebrahim-Zadeh*
- Chapter 18. Nonlinear Optical Processes for Ultrashort Pulse Generation *Uwe Siegner and Ursula Keller*
- Chapter 19. Laser-Induced Damage to Optical Materials *Marion J. Soileau*

---

## PART 3. QUANTUM AND MOLECULAR OPTICS

- Chapter 20. Laser Cooling and Trapping of Atoms *Harold J. Metcalf and Peter van der Straten*
- Chapter 21. Strong Field Physics *Todd Ditmire*
- Chapter 22. Slow Light Propagation in Atomic and Photonic Media *Jacob B. Khurgin*
- Chapter 23. Quantum Entanglement in Optical Interferometry *Hwang Lee, Christoph F. Wildfeuer, Sean D. Huver, and Jonathan P. Dowling*

---

# VOLUME V. ATMOSPHERIC OPTICS, MODULATORS, FIBER OPTICS, X-RAY AND NEUTRON OPTICS

---

---

## PART 1. MEASUREMENTS

- Chapter 1. Scatterometers *John C. Stover*
- Chapter 2. Spectroscopic Measurements *Brian Henderson*

---

## PART 2. ATMOSPHERIC OPTICS

- Chapter 3. Atmospheric Optics *Dennis K. Killinger, James H. Churnside, and Laurence S. Rothman*
- Chapter 4. Imaging through Atmospheric Turbulence *Virendra N. Mahajan and Guang-ming Dai*
- Chapter 5. Adaptive Optics *Robert Q. Fugate*

---

## PART 3. MODULATORS

- Chapter 6. Acousto-Optic Devices *I-Cheng Chang*
- Chapter 7. Electro-Optic Modulators *Georgeanne M. Purvinis and Theresa A. Maldonado*
- Chapter 8. Liquid Crystals *Sebastian Gauza and Shin-Tson Wu*

---

## PART 4. FIBER OPTICS

- Chapter 9. Optical Fiber Communication Technology and System Overview *Ira Jacobs*
- Chapter 10. Nonlinear Effects in Optical Fibers *John A. Buck*
- Chapter 11. Photonic Crystal Fibers *Philip St. J. Russell and G. J. Pearce*
- Chapter 12. Infrared Fibers *James A. Harrington*
- Chapter 13. Sources, Modulators, and Detectors for Fiber Optic Communication Systems *Elsa Garmire*
- Chapter 14. Optical Fiber Amplifiers *John A. Buck*
- Chapter 15. Fiber Optic Communication Links (Telecom, Datacom, and Analog) *Casimer DeCusatis and Guifang Li*

- Chapter 16. Fiber-Based Couplers *Daniel Nolan*  
 Chapter 17. Fiber Bragg Gratings *Kenneth O. Hill*  
 Chapter 18. Micro-Optics-Based Components for Networking *Joseph C. Palais*  
 Chapter 19. Semiconductor Optical Amplifiers *Jay M. Wiesenfeld and Leo H. Spiekman*  
 Chapter 20. Optical Time-Division Multiplexed Communication Networks *Peter J. Delfyett*  
 Chapter 21. WDM Fiber-Optic Communication Networks *Alan E. Willner, Changyuan Yu, Zhongqi Pan, and Yong Xie*  
 Chapter 22. Solitons in Optical Fiber Communication Systems *Pavel V. Mamyshev*  
 Chapter 23. Fiber-Optic Communication Standards *Casimer DeCusatis*  
 Chapter 24. Optical Fiber Sensors *Richard O. Claus, Ignacio Matias, and Francisco Arregui*  
 Chapter 25. High-Power Fiber Lasers and Amplifiers *Timothy S. McComb, Martin C. Richardson, and Michael Bass*

---

## PART 5. X-RAY AND NEUTRON OPTICS

---

### Subpart 5.1. Introduction and Applications

- Chapter 26. An Introduction to X-Ray and Neutron Optics *Carolyn MacDonald*  
 Chapter 27. Coherent X-Ray Optics and Microscopy *Qun Shen*  
 Chapter 28. Requirements for X-Ray Diffraction *Scott T. Misture*  
 Chapter 29. Requirements for X-Ray Fluorescence *George J. Havrilla*  
 Chapter 30. Requirements for X-Ray Spectroscopy *Dirk Lützenkirchen-Hecht and Ronald Frahm*  
 Chapter 31. Requirements for Medical Imaging and X-Ray Inspection *Douglas Pfeiffer*  
 Chapter 32. Requirements for Nuclear Medicine *Lars R. Furenlid*  
 Chapter 33. Requirements for X-Ray Astronomy *Scott O. Rohrbach*  
 Chapter 34. Extreme Ultraviolet Lithography *Franco Cerrina and Fan Jiang*  
 Chapter 35. Ray Tracing of X-Ray Optical Systems *Franco Cerrina and Manuel Sanchez del Rio*  
 Chapter 36. X-Ray Properties of Materials *Eric M. Gullikson*

### Subpart 5.2. Refractive and Interference Optics

- Chapter 37. Refractive X-Ray Lenses *Bruno Lengeler and Christian G. Schroer*  
 Chapter 38. Gratings and Monochromators in the VUV and Soft X-Ray Spectral Region *Malcolm R. Howells*  
 Chapter 39. Crystal Monochromators and Bent Crystals *Peter Siddons*  
 Chapter 40. Zone Plates *Alan Michette*  
 Chapter 41. Multilayers *Eberhard Spiller*  
 Chapter 42. Nanofocusing of Hard X-Rays with Multilayer Laue Lenses *Albert T. Macrander, Hanfei Yan, Hyon Chol Kang, Jörg Maser, Chian Liu, Ray Conley, and G. Brian Stephenson*  
 Chapter 43. Polarizing Crystal Optics *Qun Shen*

### Subpart 5.3. Reflective Optics

- Chapter 44. Reflective Optics *James Harvey*  
 Chapter 45. Aberrations for Grazing Incidence Optics *Timo T. Saha*  
 Chapter 46. X-Ray Mirror Metrology *Peter Z. Takacs*  
 Chapter 47. Astronomical X-Ray Optics *Marshall K. Joy and Brian D. Ramsey*  
 Chapter 48. Multifoil X-Ray Optics *Ladislav Pina*  
 Chapter 49. Pore Optics *Marco Beijersbergen*  
 Chapter 50. Adaptive X-Ray Optics *Ali Khounsary*  
 Chapter 51. The Schwarzschild Objective *Franco Cerrina*  
 Chapter 52. Single Capillaries *Donald H. Bilderback and Sterling W. Cornaby*  
 Chapter 53. Polycapillary X-Ray Optics *Carolyn MacDonald and Walter Gibson*

### Subpart 5.4. X-Ray Sources

- Chapter 54. X-Ray Tube Sources *Susanne M. Lee and Carolyn MacDonald*  
 Chapter 55. Synchrotron Sources *Steven L. Hulbert and Gwyn P. Williams*  
 Chapter 56. Laser Generated Plasmas *Alan Michette*

- Chapter 57. Pinch Plasma Sources *Victor Kantsyrev*  
Chapter 58. X-Ray Lasers *Greg Tallents*  
Chapter 59. Inverse Compton X-Ray Sources *Frank Carroll*

**Subpart 5.5. X-Ray Detectors**

- Chapter 60. Introduction to X-Ray Detectors *Walter Gibson and Peter Siddons*  
Chapter 61. Advances in Imaging Detectors *Aaron Couture*  
Chapter 62. X-Ray Spectral Detection and Imaging *Eric Lifshin*

**Subpart 5.6. Neutron Optics and Applications**

- Chapter 63. Neutron Optics *David Mildner*  
Chapter 64. Grazing-Incidence Neutron Optics *Mikhail Gubarev and Brian Ramsey*

---

# EDITORS' PREFACE

---

The third edition of the *Handbook of Optics* is designed to pull together the dramatic developments in both the basic and applied aspects of the field while retaining the archival, reference book value of a handbook. This means that it is much more extensive than either the first edition, published in 1978, or the second edition, with Volumes I and II appearing in 1995 and Volumes III and IV in 2001. To cover the greatly expanded field of optics, the *Handbook* now appears in five volumes. Over 100 authors or author teams have contributed to this work.

Volume I is devoted to the fundamentals, components, and instruments that make optics possible. Volume II contains chapters on design, fabrication, testing, sources of light, detection, and a new section devoted to radiometry and photometry. Volume III concerns vision optics only and is printed entirely in color. In Volume IV there are chapters on the optical properties of materials, nonlinear, quantum and molecular optics. Volume V has extensive sections on fiber optics and x ray and neutron optics, along with shorter sections on measurements, modulators, and atmospheric optical properties and turbulence. Several pages of color inserts are provided where appropriate to aid the reader. A purchaser of the print version of any volume of the *Handbook* will be able to download a digital version containing all of the material in that volume in PDF format to one computer (see download instructions on bound-in card). The combined index for all five volumes can be downloaded from [www.HandbookofOpticsOnline.com](http://www.HandbookofOpticsOnline.com).

It is possible by careful selection of what and how to present that the third edition of the *Handbook* could serve as a text for a comprehensive course in optics. In addition, students who take such a course would have the *Handbook* as a career-long reference.

Topics were selected by the editors so that the *Handbook* could be a desktop (bookshelf) general reference for the parts of optics that had matured enough to warrant archival presentation. New chapters were included on topics that had reached this stage since the second edition, and existing chapters from the second edition were updated where necessary to provide this compendium. In selecting subjects to include, we also had to select which subjects to leave out. The criteria we applied were: (1) was it a specific application of optics rather than a core science or technology and (2) was it a subject in which the role of optics was peripheral to the central issue addressed. Thus, such topics as medical optics, laser surgery, and laser materials processing were not included. While applications of optics are mentioned in the chapters there is no space in the *Handbook* to include separate chapters devoted to all of the myriad uses of optics in today's world. If we had, the third edition would be much longer than it is and much of it would soon be outdated. We designed the third edition of the *Handbook of Optics* so that it concentrates on the principles of optics that make applications possible.

Authors were asked to try to achieve the dual purpose of preparing a chapter that was a worthwhile reference for someone working in the field and that could be used as a starting point to become acquainted with that aspect of optics. They did that and we thank them for the outstanding results seen throughout the *Handbook*. We also thank Mr. Taisuke Soda of McGraw-Hill for his help in putting this complex project together and Mr. Alan Tourtlotte and Ms. Susannah Lehman of the Optical Society of America for logistical help that made this effort possible.

We dedicate the third edition of the *Handbook of Optics* to all of the OSA volunteers who, since OSA's founding in 1916, give their time and energy to promoting the generation, application, archiving, and worldwide dissemination of knowledge in optics and photonics.

*Michael Bass, Editor-in-Chief*

*Associate Editors:*

*Casimer M. DeCusatis*

*Jay M. Enoch*

*Vasudevan Lakshminarayanan*

*Guifang Li*

*Carolyn MacDonald*

*Virendra N. Mahajan*

*Eric Van Stryland*

*This page intentionally left blank*

---

# PREFACE TO VOLUME IV

---

Volume IV is a compendium of articles on properties (Chapters 1 to 9), nonlinear optics (Chapters 10 to 19), and quantum and molecular optics (Chapters 20 to 23). As with the rest of the *Handbook*, articles were chosen for their archival nature. Clearly, optical properties of materials fit into the archival category well. This volume devotes a large number of pages to explain and describe the optical properties of water, crystals and glasses, metals, semiconductors, solids in general, thin films and coatings including optical blacks, and photonic bandgap materials. These articles have been updated to include new materials and understanding developed since the previous edition including, among other things, advances in thin-film materials. Nonlinear optics is a mature field, but with many relatively new applications, much of them driven by advances in optical materials. Areas covered here are frequency conversion via second-order nonlinearities including optical parametric oscillators, third-order nonlinearities of two-photon absorption and nonlinear refraction, as well as stimulated Raman and Brillouin scattering, photorefractive materials and devices, coherent optical transients, electromagnetically induced transparency, optical limiting, and laser-induced damage. Nonlinear optical processes for ultrashort pulses is included here and has been a major part of the revolution in sources for obtaining laser pulses now down to attoseconds; however, other chapters on these ultrashort pulses are included in Volume II. Clearly, advances in fiber optic telecommunications have been greatly impacted by nonlinear optics, thus much work in this field is included in the fiber optics chapters in Volume V. The new chapter on laser-induced damage is a much needed addition to the *Handbook* covering a problem from the earliest days of the laser. Chapters on quantum optics in general cover some more modern aspects of optics that have become archival: laser cooling and trapping, where multiple Nobel prizes have recently been awarded; high-field physics that result from the availability of the extreme irradiance produced by lasers; slow light, topics related to being able to slow and even stop light propagation in materials; and correlated states or quantum entanglement, the unusual behavior of quantum systems where optics has played a pivotal role in its understanding as well as some interesting applications in secure communication/cryptography. The chapter on the quantum theory of lasers is, however, included in Volume II. We thank all of the many authors who gave their input to this volume of the *Handbook of Optics*.

Guifang Li and Eric Van Stryland  
*Associate Editors*



*This page intentionally left blank*

---

# GLOSSARY AND FUNDAMENTAL CONSTANTS

---

## Introduction

This glossary of the terms used in the *Handbook* represents to a large extent the language of optics. The symbols are representations of numbers, variables, and concepts. Although the basic list was compiled by the author of this section, all the editors have contributed and agreed to this set of symbols and definitions. Every attempt has been made to use the same symbols for the same concepts throughout the entire *Handbook*, although there are exceptions. Some symbols seem to be used for many concepts. The symbol  $\alpha$  is a prime example, as it is used for absorptivity, absorption coefficient, coefficient of linear thermal expansion, and more. Although we have tried to limit this kind of redundancy, we have also bowed deeply to custom.

## Units

The abbreviations for the most common units are given first. They are consistent with most of the established lists of symbols, such as given by the International Standards Organization ISO<sup>1</sup> and the International Union of Pure and Applied Physics, IUPAP.<sup>2</sup>

## Prefixes

Similarly, a list of the numerical prefixes<sup>1</sup> that are most frequently used is given, along with both the common names (where they exist) and the multiples of ten that they represent.

## Fundamental Constants

The values of the fundamental constants<sup>3</sup> are listed following the sections on SI units.

## Symbols

The most commonly used symbols are then given. Most chapters of the *Handbook* also have a glossary of the terms and symbols specific to them for the convenience of the reader. In the following list, the symbol is given, its meaning is next, and the most customary unit of measure for the quantity is presented in brackets. A bracket with a dash in it indicates that the quantity is unitless. Note that there is a difference between units and dimensions. An angle has units of degrees or radians and a solid angle square degrees or steradians, but both are pure ratios and are dimensionless. The unit symbols as recommended in the SI system are used, but decimal multiples of some of the dimensions are sometimes given. The symbols chosen, with some cited exceptions, are also those of the first two references.

---

## RATIONALE FOR SOME DISPUTED SYMBOLS

---

The choice of symbols is a personal decision, but commonality improves communication. This section explains why the editors have chosen the preferred symbols for the *Handbook*. We hope that this will encourage more agreement.

## Fundamental Constants

It is encouraging that there is almost universal agreement for the symbols for the fundamental constants. We have taken one small exception by adding a subscript  $B$  to the  $k$  for Boltzmann's constant.

## Mathematics

We have chosen  $i$  as the imaginary almost arbitrarily. IUPAP lists both  $i$  and  $j$ , while ISO does not report on these.

## Spectral Variables

These include expressions for the wavelength  $\lambda$ , frequency  $\nu$ , wave number  $\sigma$ ,  $\omega$  for circular or radian frequency,  $k$  for circular or radian wave number and dimensionless frequency  $x$ . Although some use  $f$  for frequency, it can be easily confused with electronic or spatial frequency. Some use  $\bar{\nu}$  for wave number, but, because of typography problems and agreement with ISO and IUPAP, we have chosen  $\sigma$ ; it should not be confused with the Stefan-Boltzmann constant. For spatial frequencies we have chosen  $\xi$  and  $\eta$ , although  $f_x$  and  $f_y$  are sometimes used. ISO and IUPAP do not report on these.

## Radiometry

Radiometric terms are contentious. The most recent set of recommendations by ISO and IUPAP are  $L$  for radiance [ $\text{Wcm}^{-2}\text{sr}^{-1}$ ],  $M$  for radiant emittance or exitance [ $\text{Wcm}^{-2}$ ],  $E$  for irradiance or incidence [ $\text{Wcm}^{-2}$ ], and  $I$  for intensity [ $\text{Wsr}^{-2}$ ]. The previous terms,  $W$ ,  $H$ ,  $N$ , and  $J$ , respectively, are still in many texts, notably Smith<sup>4</sup> and Lloyd<sup>5</sup> but we have used the revised set, although there are still shortcomings. We have tried to deal with the vexatious term *intensity* by using *specific intensity* when the units are  $\text{Wcm}^{-2}\text{sr}^{-1}$ , *field intensity* when they are  $\text{Wcm}^{-2}$ , and *radiometric intensity* when they are  $\text{Wsr}^{-1}$ .

There are two sets to terms for these radiometric quantities, which arise in part from the terms for different types of reflection, transmission, absorption, and emission. It has been proposed that the *ion* ending indicate a process, that the *ance* ending indicate a value associated with a particular sample, and that the *ivity* ending indicate a generic value for a "pure" substance. Then one also has reflectance, transmittance, absorptance, and emittance as well as reflectivity, transmissivity, absorptivity, and emissivity. There are now two different uses of the word emissivity. Thus the words *exitance*, *incidence*, and *sterance* were coined to be used in place of emittance, irradiance, and radiance. It is interesting that ISO uses radiance, exitance, and irradiance whereas IUPAP uses radiance, exitance [*sic*], and irradiance. We have chosen to use them both, i.e., emittance, irradiance, and radiance will be followed in square brackets by exitance, incidence, and sterance (or vice versa). Individual authors will use the different endings for transmission, reflection, absorption, and emission as they see fit.

We are still troubled by the use of the symbol  $E$  for irradiance, as it is so close in meaning to electric field, but we have maintained that accepted use. The spectral concentrations of these quantities, indicated by a wavelength, wave number, or frequency subscript (e.g.,  $L_\lambda$ ) represent partial differentiations; a subscript  $q$  represents a photon quantity; and a subscript  $\nu$  indicates a quantity normalized to the response of the eye. Thereby,  $L_\nu$  is luminance,  $E_\nu$  illuminance, and  $M_\nu$  and  $I_\nu$  luminous emittance and luminous intensity. The symbols we have chosen are consistent with ISO and IUPAP.

The refractive index may be considered a radiometric quantity. It is generally complex and is indicated by  $\bar{n} = n - ik$ . The real part is the relative refractive index and  $k$  is the extinction coefficient. These are consistent with ISO and IUPAP, but they do not address the complex index or extinction coefficient.

## Optical Design

For the most part ISO and IUPAP do not address the symbols that are important in this area.

There were at least 20 different ways to indicate focal ratio; we have chosen FN as symmetrical with NA; we chose  $f$  and  $e\text{fl}$  to indicate the effective focal length. Object and image distance, although given many different symbols, were finally called  $s_o$  and  $s_i$  since  $s$  is an almost universal symbol for distance. Field angles are  $\theta$  and  $\phi$ ; angles that measure the slope of a ray to the optical axis are  $u$ ;  $u$  can also be  $\sin u$ . Wave aberrations are indicated by  $W_{ijk}$ , while third-order ray aberrations are indicated by  $\sigma_i$  and more mnemonic symbols.

## Electromagnetic Fields

There is no argument about  $\mathbf{E}$  and  $\mathbf{H}$  for the electric and magnetic field strengths,  $Q$  for quantity of charge,  $\rho$  for volume charge density,  $\sigma$  for surface charge density, etc. There is no guidance from Refs. 1 and 2 on polarization indication. We chose  $\perp$  and  $\parallel$  rather than  $p$  and  $s$ , partly because  $s$  is sometimes also used to indicate scattered light.

There are several sets of symbols used for reflection transmission, and (sometimes) absorption, each with good logic. The versions of these quantities dealing with field amplitudes are usually specified with lower case symbols:  $r$ ,  $t$ , and  $a$ . The versions dealing with power are alternately given by the uppercase symbols or the corresponding Greek symbols:  $R$  and  $T$  versus  $\rho$  and  $\tau$ . We have chosen to use the Greek, mainly because these quantities are also closely associated with Kirchhoff's law that is usually stated symbolically as  $\alpha = \epsilon$ . The law of conservation of energy for light on a surface is also usually written as  $\alpha + \rho + \tau = 1$ .

## Base SI Quantities

length	m	meter
time	s	second
mass	kg	kilogram
electric current	A	ampere
temperature	K	kelvin
amount of substance	mol	mole
luminous intensity	cd	candela

## Derived SI Quantities

energy	J	joule
electric charge	C	coulomb
electric potential	V	volt
electric capacitance	F	farad
electric resistance	$\Omega$	ohm
electric conductance	S	siemens
magnetic flux	Wb	weber
inductance	H	henry
pressure	Pa	pascal
magnetic flux density	T	tesla
frequency	Hz	hertz
power	W	watt
force	N	newton
angle	rad	radian
angle	sr	steradian

## Prefixes

<i>Symbol</i>	<i>Name</i>	<i>Common name</i>	<i>Exponent of ten</i>
F	exa		18
P	peta		15
T	tera	trillion	12
G	giga	billion	9
M	mega	million	6
k	kilo	thousand	3
h	hecto	hundred	2
da	deca	ten	1
d	deci	tenth	-1
c	centi	hundredth	-2
m	milli	thousandth	-3
$\mu$	micro	millionth	-6
n	nano	billionth	-9
p	pico	trillionth	-12
f	femto		-15
a	atto		-18

## Constants

$c$	speed of light vacuo [ $299792458 \text{ ms}^{-1}$ ]
$c_1$	first radiation constant = $2\pi c^2 h = 3.7417749 \times 10^{-16} [\text{Wm}^2]$
$c_2$	second radiation constant = $hc/k = 0.014838769 [\text{mK}]$
$e$	elementary charge [ $1.60217733 \times 10^{-19} \text{ C}$ ]
$g_n$	free fall constant [ $9.80665 \text{ ms}^{-2}$ ]
$h$	Planck's constant [ $6.6260755 \times 10^{-34} \text{ Js}$ ]
$k_B$	Boltzmann constant [ $1.380658 \times 10^{-23} \text{ JK}^{-1}$ ]
$m_e$	mass of the electron [ $9.1093897 \times 10^{-31} \text{ kg}$ ]
$N_A$	Avogadro constant [ $6.0221367 \times 10^{23} \text{ mol}^{-1}$ ]
$R_\infty$	Rydberg constant [ $10973731.534 \text{ m}^{-1}$ ]
$\epsilon_0$	vacuum permittivity [ $\mu_0^{-1} \text{ c}^{-2}$ ]
$\sigma$	Stefan-Boltzmann constant [ $5.67051 \times 10^{-8} \text{ Wm}^{-1} \text{ K}^{-4}$ ]
$\mu_0$	vacuum permeability [ $4\pi \times 10^{-7} \text{ NA}^{-2}$ ]
$\mu_B$	Bohr magneton [ $9.2740154 \times 10^{-24} \text{ JT}^{-1}$ ]

## General

<b>B</b>	magnetic induction [ $\text{Wbm}^{-2}, \text{kgs}^{-1} \text{ C}^{-1}$ ]
$C$	capacitance [ $\text{f}, \text{C}^2 \text{ s}^2 \text{ m}^{-2} \text{ kg}^{-1}$ ]
$C$	curvature [ $\text{m}^{-1}$ ]
$c$	speed of light in vacuo [ $\text{ms}^{-1}$ ]
$c_1$	first radiation constant [ $\text{Wm}^2$ ]
$c_2$	second radiation constant [ $\text{mK}$ ]
<b>D</b>	electric displacement [ $\text{Cm}^{-2}$ ]
$E$	incidence [irradiance] [ $\text{Wm}^{-2}$ ]
$e$	electronic charge [coulomb]
$E_v$	illuminance [lux, $\text{lmm}^{-2}$ ]
<b>E</b>	electrical field strength [ $\text{Vm}^{-1}$ ]
$E$	transition energy [J]
$E^g$	band-gap energy [eV]
$f^g$	focal length [m]
$f_c$	Fermi occupation function, conduction band
$f_v$	Fermi occupation function, valence band

FN	focal ratio ( $f$ /number) [—]
$g$	gain per unit length [ $\text{m}^{-1}$ ]
$g_{\text{th}}$	gain threshold per unit length [ $\text{m}^{-1}$ ]
$\mathbf{H}$	magnetic field strength [ $\text{Am}^{-1}$ , $\text{Cs}^{-1} \text{m}^{-1}$ ]
$h$	height [m]
$I$	irradiance (see also $E$ ) [ $\text{Wm}^{-2}$ ]
$I$	radiant intensity [ $\text{Wsr}^{-1}$ ]
$I$	nuclear spin quantum number [—]
$I$	current [A]
$i$	$\sqrt{-1}$
$\text{Im}()$	imaginary part of
$J$	current density [ $\text{Am}^{-2}$ ]
$\mathbf{j}$	total angular momentum [ $\text{kg m}^2 \text{s}^{-1}$ ]
$J_1()$	Bessel function of the first kind [—]
$k$	radian wave number $=2\pi/\lambda$ [ $\text{rad cm}^{-1}$ ]
$\mathbf{k}$	wave vector [ $\text{rad cm}^{-1}$ ]
$k$	extinction coefficient [—]
$L$	sterance [radiance] [ $\text{Wm}^{-2} \text{sr}^{-1}$ ]
$L_v$	luminance [ $\text{cdm}^{-2}$ ]
$L^v$	inductance [h, $\text{m}^2 \text{kg C}^2$ ]
$L$	laser cavity length
$L, M, N$	direction cosines [—]
$M$	angular magnification [—]
$M$	radiant exitance [radiant emittance] [ $\text{Wm}^{-2}$ ]
$m$	linear magnification [—]
$m$	effective mass [kg]
MTF	modulation transfer function [—]
$N$	photon flux [ $\text{s}^{-1}$ ]
$N$	carrier (number) density [ $\text{m}^{-3}$ ]
$n$	real part of the relative refractive index [—]
$\tilde{n}$	complex index of refraction [—]
NA	numerical aperture [—]
OPD	optical path difference [m]
$P$	macroscopic polarization [ $\text{C m}^{-2}$ ]
$\text{Re}()$	real part of [—]
$R$	resistance [ $\Omega$ ]
$\mathbf{r}$	position vector [m]
$S$	Seebeck coefficient [ $\text{VK}^{-1}$ ]
$s$	spin quantum number [—]
$s$	path length [m]
$S_o$	object distance [m]
$S_i$	image distance [m]
$T$	temperature [K, C]
$t$	time [s]
$t$	thickness [m]
$u$	slope of ray with the optical axis [rad]
$V$	Abbe reciprocal dispersion [—]
$V$	voltage [V, $\text{m}^2 \text{kg s}^{-2} \text{C}^{-1}$ ]
$x, y, z$	rectangular coordinates [m]
$Z$	atomic number [—]

## Greek Symbols

$\alpha$	absorption coefficient [ $\text{cm}^{-1}$ ]
$\alpha$	(power) absorptance (absorptivity)

$\epsilon$	dielectric coefficient (constant) [—]
$\epsilon$	emittance (emissivity) [—]
$\epsilon$	eccentricity [—]
$\epsilon_1$	Re ( $\epsilon$ )
$\epsilon_2$	Im ( $\epsilon$ )
$\tau$	(power) transmittance (transmissivity) [—]
$\nu$	radiation frequency [Hz]
$\omega$	circular frequency = $2\pi\nu$ [rads <sup>-1</sup> ]
$\omega$	plasma frequency [Hz]
$\lambda$	wavelength [ $\mu\text{m}$ , nm]
$\sigma$	wave number = $1/\lambda$ [cm <sup>-1</sup> ]
$\sigma$	Stefan Boltzmann constant [Wm <sup>-2</sup> K <sup>-1</sup> ]
$\rho$	reflectance (reflectivity) [—]
$\theta, \phi$	angular coordinates [rad, °]
$\xi, \eta$	rectangular spatial frequencies [m <sup>-1</sup> , r <sup>-1</sup> ]
$\phi$	phase [rad, °]
$\phi$	lens power [m <sup>-2</sup> ]
$\Phi$	flux [W]
$\chi$	electric susceptibility tensor [—]
$\Omega$	solid angle [sr]

## Other

$\mathfrak{R}$	responsivity
$\exp(x)$	$e^x$
$\log_a(x)$	log to the base $a$ of $x$
$\ln(x)$	natural log of $x$
$\log(x)$	standard log of $x$ : $\log_{10}(x)$
$\Sigma$	summation
$\Pi$	product
$\Delta$	finite difference
$\delta x$	variation in $x$
$dx$	total differential
$\partial x$	partial derivative of $x$
$\delta(x)$	Dirac delta function of $x$
$\delta_{ij}$	Kronecker delta

## REFERENCES

---

1. Anonymous, *ISO Standards Handbook 2: Units of Measurement*, 2nd ed., International Organization for Standardization, 1982.
2. Anonymous, *Symbols, Units and Nomenclature in Physics*, Document U.I.P. 20, International Union of Pure and Applied Physics, 1978.
3. E. Cohen and B. Taylor, "The Fundamental Physical Constants," *Physics Today*, 9 August 1990.
4. W. J. Smith, *Modern Optical Engineering*, 2nd ed., McGraw-Hill, 1990.
5. J. M. Lloyd, *Thermal Imaging Systems*, Plenum Press, 1972.

**William L. Wolfe**  
College of Optical Sciences  
University of Arizona  
Tucson, Arizona

**PART**

---

**1**

---

**PROPERTIES**

---



*This page intentionally left blank*

---

# OPTICAL PROPERTIES OF WATER

---

Curtis D. Mobley

*Applied Electromagnetics and Optics Laboratory  
SRI International  
Menlo Park, California*

---

## 1.1 INTRODUCTION

---

This article discusses the optical properties of three substances: pure water, pure sea water, and natural water. Pure water (i.e., water molecules only) without any dissolved substances, ions, bubbles, or other impurities, is exceptionally difficult to produce in the laboratory. For this and other reasons, definitive direct measurements of its optical properties at visible wavelengths have not yet been made. Pure sea water—pure water plus various dissolved salts—has optical properties close to those of pure water. Neither pure water nor pure sea water ever occur in nature. Natural waters, both fresh and saline, are a witch's brew of dissolved and particulate matter. These solutes and particulates are both optically significant and highly variable in kind and concentration. Consequently, the optical properties of natural waters show large temporal and spatial variations and seldom resemble those of pure water.

The great variability of the optical properties of natural water is the bane of those who desire precise and easily tabulated data. However, it is the connections between the optical properties and the biological, chemical, and geological constituents of natural water and the physical environment that define the critical role of optics in aquatic research. For just as optics utilizes results from the biological, chemical, geological, and physical subdisciplines of limnology and oceanography, so do those subdisciplines incorporate optics. This synergism is seen in such areas as bio-optical oceanography, marine photochemistry, mixed-layer dynamics, laser bathymetry, and remote sensing of biological productivity, sediment load, or pollutants.

---

## 1.2 TERMINOLOGY, NOTATION, AND DEFINITIONS

---

*Hydrologic optics* is the quantitative study of the interactions of radiant energy with the earth's oceans, estuaries, lakes, rivers, and other water bodies. Most past and current research within hydrologic optics has been within the subfield of oceanic optics, in particular the optics of deep ocean waters, as opposed to coastal or estuarine areas. This emphasis is reflected in our uneven understanding of the optical properties of various water types.

Although the optical properties of different water bodies can vary greatly, there is an overall similarity that is quite distinct from, say, the optical properties of the atmosphere. Therefore, hydrologic and atmospheric optics have developed considerably different theoretical formulations, experimental methodologies, and instrumentation as suited to each field's specific scientific issues. Chapter 3, "Atmospheric Optics," by Dennis K. Killinger, James H. Churnside, and Laurence S. Rothman in Vol. V discusses atmospheric optics. The text by Mobley<sup>1</sup> gives a comprehensive treatment of hydrologic optics.

Radiative transfer theory is the framework that connects the optical properties of water with the ambient light field. A rigorous mathematical formulation of radiative transfer theory as applicable to hydrologic optics has been developed by Preisendorfer<sup>2</sup> and others. Preisendorfer found it convenient to divide the optical properties of water into two classes: inherent and apparent. *Inherent optical properties* (IOPs) are those properties that depend only upon the medium and therefore are independent of the ambient light field within the medium. The two fundamental IOPs are the absorption coefficient and the volume scattering function (VSF). Other IOPs include the attenuation coefficient and the single-scattering albedo. *Apparent optical properties* (AOPs) are those properties that depend both on the medium (the IOPs) and on the geometric (directional) structure of the ambient light field and that display enough regular features and stability to be useful descriptors of the water body. Commonly used AOPs are the irradiance reflectance, the average cosines, and the various attenuation functions ( $K$  functions). (All of these quantities are defined below.) The radiative transfer equation provides the connection between the IOPs and the AOPs. The physical environment of a water body—waves on its surface, the character of its bottom, the incident radiance from the sky—enters the theory via the boundary conditions necessary for solution of the radiative transfer equation.

The IOPs are easily defined but they can be exceptionally difficult to measure, especially in situ. The AOPs are generally much easier to measure, but they are difficult to interpret because of the confounding environmental effects. (A change in the sea surface wave state or in the sun's position changes the radiance distribution, and hence the AOPs, even though the IOPs are unchanged.)

Hydrologic optics employs standard radiometric concepts and terminology, although the notation adopted by the International Association for Physical Sciences of the Ocean (IAPSO<sup>3</sup>) differs somewhat from that used in other fields. Table 1 summarizes the terms, units, and symbols for those quantities that have proven most useful in hydrologic optics. These quantities are defined and discussed in Secs. 1.3 to 1.5. Figure 1 summarizes the relationships among the various inherent and apparent optical properties. In this figure, note the central unifying role of radiative transfer theory. Note also that the spectral absorption coefficient and the spectral volume scattering function are the fundamental inherent optical properties in the sense that all inherent optical properties are derivable from those two. Likewise, spectral radiance is the parent of all radiometric quantities and apparent optical properties. The source term  $S$  in the radiative transfer equation accounts both for true internal sources such as bioluminescence and for radiance appearing at the wavelength of interest owing to inelastic scattering from other wavelengths.

Most radiative transfer theory assumes the radiant energy to be monochromatic. In this case the associated optical properties and radiometric quantities are termed *spectral* and carry a wavelength ( $\lambda$ ) argument or subscript [e.g., the spectral absorption coefficient  $a(\lambda)$  or  $a_\lambda$ , or the spectral downward irradiance  $E_d(\lambda)$ ]. Spectral radiometric quantities have the SI unit  $\text{nm}^{-1}$  added to the units shown in Table 1 [e.g.,  $E_d(\lambda)$  has units  $\text{W m}^{-2} \text{nm}^{-1}$ ]. Many radiometric on the other hand, respond to a fairly wide bandwidth, which complicates the comparison of data and theory.

### 1.3 RADIOMETRIC QUANTITIES USEFUL IN HYDROLOGIC OPTICS

Consider an amount  $\Delta Q$  of radiant energy incident in a time interval  $\Delta t$  centered on time  $t$ , onto a surface of area  $\Delta A$  located at  $(x, y, z)$ . The energy arrives through a set of directions contained in a solid angle  $\Delta\Omega$  about the direction  $(\theta, \phi)$  normal to the area  $\Delta A$  and is produced by photons in

**TABLE 1** Terms, Units, and Symbols for Quantities Commonly Used in Hydrologic Optics

Quantity	SI Units	IAPSO Recommended Symbol*	Historic Symbol† (if different)
Fundamental quantities			
Most of the fundamental quantities are not defined by IAPSO, in which case common usage is given.			
geometric depth below water surface	m	$z$	
polar angle of photon travel	radian or degree	$\theta$	
wavelength of light (in vacuo)	nm	$\lambda$	
cosine of polar angle	dimensionless	$\mu \equiv \cos \theta$	
optical depth below water surface	dimensionless	$\tau$	
azimuthal angle of photon travel	radian or degree	$\phi$	
scattering angle	radian or degree	$\psi, \gamma$ or $\Theta$	$\theta$
solid angle	sr	$\Omega$ or $\omega$	$\Omega$
Radiometric quantities			
The quantities as shown represent broadband measurements. For narrowband (monochromatic) measurements add the adjective “spectral” to the term, add $\text{nm}^{-1}$ to the units, and add a wavelength index $\lambda$ to the symbol [e.g., spectral radiance, $L_\lambda$ or $L(\lambda)$ ] with units $\text{W m}^{-2} \text{sr}^{-1} \text{nm}^{-1}$ . PAR is always broadband.			
(plane) irradiance	$\text{W m}^{-2}$	$E$	$H$
downward irradiance	$\text{W m}^{-2}$	$E_d$	$H(-)$
upward irradiance	$\text{W m}^{-2}$	$E_v$	$H(+)$
net (vertical) irradiance	$\text{W m}^{-2}$	$\bar{E}$	$\bar{H}$
scalar irradiance	$\text{W m}^{-2}$	$E_0$	$h$
downward scalar irradiance	$\text{W m}^{-2}$	$E_{0d}$	$h(-)$
upward scalar irradiance	$\text{W m}^{-2}$	$E_{0u}$	$h(+)$
radiant intensity	$\text{W sr}^{-1}$	$I$	$J$
radiance	$\text{W m}^{-2} \text{sr}^{-1}$	$L$	$N$
radiant exitance	$\text{W m}^{-2}$	$M$	$W$
photosynthetically available radiation	photons $\text{s}^{-1} \text{m}^{-2}$	PAR or $E_{\text{PAR}}$	
quantity of radiant energy	J	$Q$	$U$
radiant power	W	$\Phi$	$P$
Inherent optical properties			
absorptance	dimensionless	$A$	
absorption coefficient	$\text{m}^{-1}$	$a$	
scattering	dimensionless	$B$	
scattering coefficient	$\text{m}^{-1}$	$b$	$s$
backward scattering coefficient	$\text{m}^{-1}$	$b_b$	$b$
forward scattering coefficient	$\text{m}^{-1}$	$b_f$	$f$
attenuance	dimensionless	$C$	
attenuation coefficient	$\text{m}^{-1}$	$c$	$\alpha$
(real) index of refraction	dimensionless	$n$	
transmittance	dimensionless	$T$	
volume scattering function	$\text{m}^{-1} \text{sr}^{-1}$	$\beta$	$\sigma$
scattering phase function	$\text{sr}^{-1}$	$\beta$	$P$
single-scattering albedo	dimensionless	$\omega_0$ or $\tilde{\omega}$	
Apparent optical properties			
(vertical) attenuation coefficients			
of downward irradiance $E_d(z)$	$\text{m}^{-1}$	$K_d$	$K(-)$
of total scalar irradiance $E_0(z)$	$\text{m}^{-1}$	$K_0$	$k$

(Continued)

**TABLE 1** Terms, Units, and Symbols for Quantities Commonly Used in Hydrologic Optics (*Continued*)

Quantity	SI Units	IAPSO Recommended Symbol*	Historic Symbol† (if different)
Apparent optical properties			
of downward scalar irradiance $E_{0d}(z)$	$\text{m}^{-1}$	$K_{0d}$	$k(-)$
of upward scalar irradiance $E_{0u}(z)$	$\text{m}^{-1}$	$K_{0u}$	$k(+)$
of PAR	$\text{m}^{-1}$	$K_{\text{PAR}}$	
of upward irradiance $E_u(z)$	$\text{m}^{-1}$	$K_u$	$K(+)$
of radiance $L(z, \theta, \phi)$	$\text{m}^{-1}$	$K(\theta, \phi)$	
irradiance reflectance (ratio)	dimensionless	$R$	$R(-)$
average cosine of light field	dimensionless	$\bar{\mu}$	
of downwelling light	dimensionless	$\bar{\mu}_d$	$D(-) = 1/\bar{\mu}_d$
of upwelling light	dimensionless	$\bar{\mu}_u$	$D(+) = 1/\bar{\mu}_u$
distribution function	dimensionless		$D = 1/\bar{\mu}$

\*References 1 and 3.

†Reference 2.

a wavelength interval  $\Delta\lambda$  centered on wavelength  $\lambda$ . Then an *operational* definition of the *spectral radiance* is

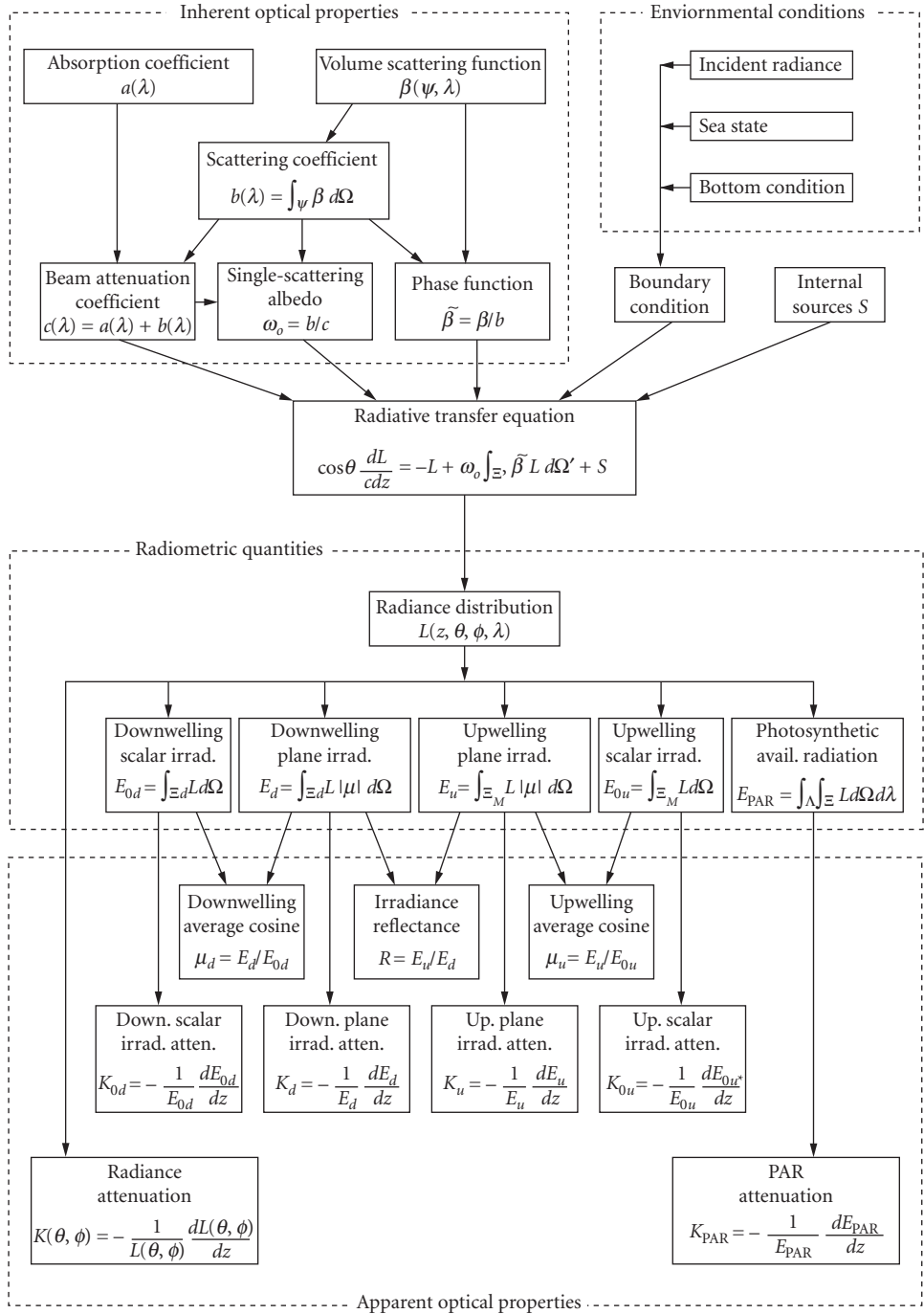
$$L(x, y, z, t, \theta, \phi, \lambda) \equiv \frac{\Delta Q}{\Delta t \Delta A \Delta \Omega \Delta \lambda} \quad \text{Js}^{-1} \text{m}^{-2} \text{sr}^{-1} \text{nm}^{-1}$$

In practice, one takes  $\Delta t$ ,  $\Delta A$ ,  $\Delta \Omega$ , and  $\Delta \lambda$  small enough to get a useful resolution of radiance over the four parameter domains but not so small as to encounter diffraction effects or fluctuations from photon shot noise at very low light levels. Typical values are  $\Delta t \sim 10^{-3}$  to  $10^3$  s (depending on whether or not one wishes to average out sea surface wave effects),  $\Delta A \sim 10^{-3}$  m<sup>2</sup>,  $\Delta \Omega \sim 10^{-2}$  sr, and  $\Delta \lambda \sim 10$  nm. In the conceptual limit of infinitesimal parameter intervals, the spectral radiance is defined as

$$L(x, y, z, t, \theta, \phi, \lambda) \equiv \frac{\partial^4 Q}{\partial t \partial A \partial \Omega \partial \lambda} \quad \text{Js}^{-1} \text{m}^{-2} \text{sr}^{-1} \text{nm}^{-1}$$

Spectral radiance is the fundamental radiometric quantity of interest in hydrologic optics: it specifies the positional ( $x, y, z$ ), temporal ( $t$ ), directional ( $\theta, \phi$ ) and spectral ( $\lambda$ ) structure of the light field. For typical oceanic environments, horizontal variations (on a scale of tens to thousands of meters) of inherent and apparent optical properties are much less than variations with depth, and it is usually assumed that these properties vary only with depth  $z$ . Moreover, since the time scales for changes in IOPs or in the environment (seconds to seasons) are much greater than the time required for the radiance field to reach steady state (microseconds) after a change in IOPs or boundary conditions, time-independent radiative transfer theory is adequate for most hydrologic optics studies. The spectral radiance therefore usually is written  $L(z, \theta, \phi, \lambda)$ . The exceptions are applications such as time-of-flight lidar.

There are few conventions on the choice of coordinate systems. Oceanographers usually measure the depth  $z$  positive downward from  $z = 0$  at the mean water surface. In radiative transfer theory it is convenient to let  $(\theta, \phi)$  denote the direction of photon travel (especially when doing Monte Carlo simulations). When displaying data it is convenient to let  $(\theta, \phi)$  represent the direction in which the instrument was pointed (the viewing direction) in order to detect photons traveling in



**FIGURE 1** Relationships between the various quantities commonly used in hydrologic optics.

the opposite direction. Some authors measure the polar angle  $\theta$  from the zenith (upward) direction, even when  $z$  is taken as positive downward; others measure  $\theta$  from the  $+z$  axis (nadir, or downward, direction). In the following discussion  $\Xi_u$  denotes the hemisphere of *upward* directions (i.e., the set of directions  $(\theta, \phi)$  such that  $0 \leq \theta \leq \pi/2$  and  $0 \leq \phi \leq 2\pi$  if  $\theta$  is measured from the zenith direction) and  $\Xi_d$  denotes the hemisphere of *downward* directions. The element of solid angle is  $d\Omega = \sin\theta d\theta d\phi$  with units of steradian. The solid angle measure of the set of directions  $\Xi_u$  or  $\Xi_d$  is  $\Omega(\Xi_u) = \Omega(\Xi_d) = 2\pi$  sr.

Although the spectral radiance completely specifies the light field, it is seldom measured both because of instrumental difficulties and because such complete information often is not needed for specific applications. The most commonly measured radiometric quantities are various *irradiances*.

Consider a light detector constructed so as to be equally sensitive to photons of a given wavelength  $\lambda$  traveling in any direction  $(\theta, \phi)$  within a *hemisphere* of directions.<sup>4</sup> If the detector is located at depth  $z$  and is oriented facing *upward*, so as to collect photons traveling *downward*, then the detector output is a measure of the *spectral downward scalar irradiance* at depth  $z$ ,  $E_{0d}(z, \lambda)$ . Such an instrument is summing radiance over all the directions (elements of solid angle) in the downward hemisphere  $\Xi_d$ . Thus  $E_{0d}(z, \lambda)$  is related to  $L(z, \theta, \phi, \lambda)$  by

$$E_{0d}(z, \lambda) = \int_{\Xi_d} L(z, \theta, \phi, \lambda) d\Omega \quad \text{W m}^{-2} \text{ nm}^{-1}$$

The symbolic integral over  $\Xi_d$  can be evaluated as a double integral over  $\theta$  and  $\phi$  after a specific coordinate system is chosen.

If the same instrument is oriented facing *downward*, so as to detect photons traveling *upward*, then the quantity measured is the *spectral upward scalar irradiance*  $E_{0u}(z, \lambda)$ :

$$E_{0u}(z, \lambda) = \int_{\Xi_u} L(z, \theta, \phi, \lambda) d\Omega \quad \text{W m}^{-2} \text{ nm}^{-1}$$

The *spectral scalar irradiance*  $E_0(z, \lambda)$  is just the sum of the downward and upward components:

$$E_0(z, \lambda) \equiv E_{0d}(z, \lambda) + E_{0u}(z, \lambda) = \int_{\Xi} L(z, \theta, \phi, \lambda) d\Omega \quad \text{W m}^{-2} \text{ nm}^{-1}$$

Here  $\Xi = \Xi_d \cup \Xi_u$  is the set of all directions;  $\Omega(\Xi) = 4\pi$  sr.  $E_0(z, \lambda)$  is useful<sup>2</sup> because it is proportional to the spectral radiant energy density ( $\text{J m}^{-3} \text{ nm}^{-1}$ ) at depth  $z$ .

Now consider a detector designed<sup>4</sup> so that its sensitivity is proportional to  $|\cos\theta|$ , where  $\theta$  is the angle between the photon direction and the normal to the surface of the detector. This is the ideal response of a “flat plate” collector of area  $\Delta A$ , which when viewed at an angle  $\theta$  to its normal appears to have an area of  $\Delta A |\cos\theta|$ . If such a detector is located at depth  $z$  and is oriented facing *upward*, so as to detect photons traveling *downward*, then its output is proportional to the *spectral downward plane irradiance*  $E_d(z, \lambda)$  (usually called *spectral downwelling irradiance*). This instrument is summing the downwelling radiance weighted by the cosine of the photon direction:

$$E_d(z, \lambda) = \int_{\Xi_d} L(z, \theta, \phi, \lambda) |\cos\theta| d\Omega \quad \text{W m}^{-2} \text{ nm}^{-1}$$

Turning this instrument upside down gives the *spectral upward plane irradiance* (*spectral upwelling irradiance*)  $E_u(z, \lambda)$ :

$$E_u(z, \lambda) = \int_{\Xi_u} L(z, \theta, \phi, \lambda) |\cos\theta| d\Omega \quad \text{W m}^{-2} \text{ nm}^{-1}$$

$E_d$  and  $E_u$  are useful because they give the energy flux (power per unit area) across the horizontal surface at depth  $z$  owing to downwelling and upwelling photons, respectively.

The *spectral net irradiance* at depth  $z$ ,  $\bar{E}(z, \lambda)$  is the difference in the downwelling and upwelling plane irradiances:

$$\bar{E}(z, \lambda) = E_d(z, \lambda) - E_u(z, \lambda)$$

Photosynthesis is a quantum phenomenon (i.e., it is the *number* of available photons rather than the *amount* of radiant energy that is relevant to the chemical transformations). This is because if a photon of, say,  $\lambda = 350$  nm, is absorbed by chlorophyll it induces the same chemical change as does a photon of  $\lambda = 700$  nm, even though the 350-nm photon has twice the energy of the 700-nm photon. Only a part of the photon energy goes into photosynthesis; the excess is converted to heat or reradiated. Moreover, chlorophyll is equally able to absorb and utilize a photon regardless of the photon's direction of travel. Therefore, in studies of phytoplankton biology the relevant measure of the light field is the *photosynthetically available radiation*, PAR or  $E_{\text{PAR}}$ , defined by

$$\text{PAR}(z) \equiv \int_{350 \text{ nm}}^{700 \text{ nm}} \frac{\lambda}{hc} E_0(z, \lambda) d\lambda \quad \text{photons s}^{-1} \text{ m}^{-2}$$

where  $h = 6.6255 \times 10^{-34}$  J s is Planck's constant and  $c = 3.0 \times 10^{17}$  nm s<sup>-1</sup> is the speed of light. The factor  $\lambda/hc$  converts the energy units of  $E_0$  (watts) to quantum units (photons per second). Bio-optical literature often states PAR values in units of mol photons s<sup>-1</sup> m<sup>-2</sup> or einst s<sup>-1</sup> m<sup>-2</sup>. Morel and Smith<sup>5</sup> found that over a wide variety of water types from very clear to turbid, with corresponding variations in the spectral nature of the irradiance, the conversion factor for energy to quanta varied by only  $\pm 10$  percent about the value  $2.5 \times 10^{18}$  photons s<sup>-1</sup> W<sup>-1</sup> ( $4.2 \mu\text{einst s}^{-1} \text{ W}^{-1}$ ).

For practical reasons related to instrument design, PAR is sometimes estimated using the spectral downwelling plane irradiance and the visible wavelengths only:

$$\text{PAR}(z) \approx \int_{400 \text{ nm}}^{700 \text{ nm}} \frac{\lambda}{hc} E_d(z, \lambda) d\lambda \quad \text{photons s}^{-1} \text{ m}^{-2}$$

However, it is now recognized<sup>6,7</sup> that the use of  $E_d$  rather than  $E_0$  can lead to errors of 20 to 100 percent in computations of PAR. Omission of the 350–400-nm band is less troublesome since those wavelengths are rapidly absorbed near the water surface, except in very clear waters.

## 1.4 INHERENT OPTICAL PROPERTIES

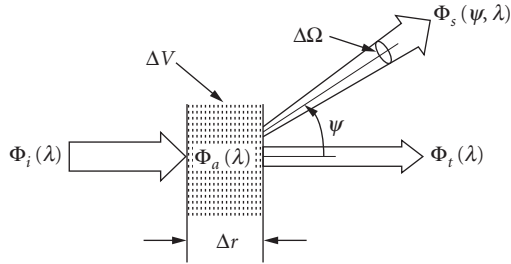
Consider a small volume  $\Delta V$  of water of thickness  $\Delta r$  as seen by a narrow collimated beam of monochromatic light of spectral radiant power  $\Phi_i(\lambda)$  W nm<sup>-1</sup> as schematically illustrated in Fig. 2. Some part  $\Phi_a(\lambda)$  of the incident power  $\Phi_i(\lambda)$  is absorbed within the volume of water. Some part  $\Phi_s(\psi, \lambda)$  is scattered out of the beam at an angle  $\psi$ , and the remaining power  $\Phi_t(\lambda)$  is transmitted through the volume with no change in direction. Let  $\Phi_s(\lambda)$  be the total power that is scattered into all directions. Furthermore, assume that no inelastic scattering occurs (i.e., assume that no photons undergo a change in wavelength during the scattering process). Then by conservation of energy,

$$\Phi_i(\lambda) = \Phi_a(\lambda) + \Phi_s(\lambda) + \Phi_t(\lambda)$$

The *spectral absorbance*  $A(\lambda)$  is the fraction of incident power that is absorbed within the volume:

$$A(\lambda) \equiv \frac{\Phi_a(\lambda)}{\Phi_i(\lambda)}$$





**FIGURE 2** Geometry used to define inherent optical properties.

Likewise the *spectral scatterance*  $B(\lambda)$  is the fractional part of the incident power that is scattered out of the beam,

$$B(\lambda) \equiv \frac{\Phi_s(\lambda)}{\Phi_i(\lambda)}$$

and the *spectral transmittance*  $T(\lambda)$  is

$$T(\lambda) \equiv \frac{\Phi_t(\lambda)}{\Phi_i(\lambda)}$$

Clearly,  $A(\lambda) + B(\lambda) + T(\lambda) = 1$ . A quantity easily confused with the absorptance  $A(\lambda)$  is the absorbance  $D(\lambda)$  (also called *optical density*) defined as<sup>8</sup>

$$D(\lambda) \equiv \log_{10} \frac{\Phi_i(\lambda)}{\Phi_s(\lambda) + \Phi_t(\lambda)} = -\log_{10}[1 - A(\lambda)]$$

$D(\lambda)$  is the quantity actually measured in a spectrophotometer.

The inherent optical properties usually employed in hydrologic optics are the spectral absorption and scattering coefficients which are, respectively, the spectral absorptance and scatterance *per unit distance* in the medium. In the geometry of Fig. 2, the *spectral absorption coefficient*  $a(\lambda)$  is defined as

$$a(\lambda) \equiv \lim_{\Delta r \rightarrow 0} \frac{A(\lambda)}{\Delta r} \quad \text{m}^{-1}$$

and the *spectral scattering coefficient*  $b(\lambda)$  is

$$b(\lambda) \equiv \lim_{\Delta r \rightarrow 0} \frac{B(\lambda)}{\Delta r} \quad \text{m}^{-1}$$

The *spectral beam attenuation coefficient*  $c(\lambda)$  is defined as

$$c(\lambda) \equiv a(\lambda) + b(\lambda)$$

Hydrologic optics uses the term attenuation rather than extinction.

Now take into account the angular distribution of the scattered power, with  $B(\psi, \lambda)$  being the fraction of incident power scattered out of the beam through an angle  $\psi$  into a solid angle

$\Delta\Omega$  centered on  $\psi$  as shown in Fig. 2. Then the angular scatterance per unit distance and unit solid angle,  $\beta(\psi, \lambda)$ , is

$$\beta(\psi, \lambda) \equiv \lim_{\Delta r \rightarrow 0} \lim_{\Delta\Omega \rightarrow 0} \frac{B(\psi, \lambda)}{\Delta r \Delta\Omega} = \lim_{\Delta r \rightarrow 0} \lim_{\Delta\Omega \rightarrow 0} \frac{\Phi_s(\psi, \lambda)}{\Phi_i(\lambda) \Delta r \Delta\Omega} \quad \text{m}^{-1} \text{sr}^{-1}$$

The spectral power scattered into the given solid angle  $\Delta\Omega$  is just the spectral radiant intensity scattered into direction  $\psi$  times the solid angle:  $\Phi_s(\psi, \lambda) = I_s(\psi, \lambda) \Delta\Omega$ . Moreover, if the incident power  $\Phi_i(\lambda)$  falls on an area  $\Delta A$ , then the corresponding incident irradiance  $E_i(\lambda) = \Phi_i(\lambda) / \Delta A$ . Noting that  $\Delta V = \Delta r \Delta A$  is the volume of water that is illuminated by the incident beam gives

$$\beta(\psi, \lambda) = \lim_{\Delta V \rightarrow 0} \frac{I_s(\psi, \lambda)}{E_i(\lambda) \Delta V}$$

This form of  $\beta(\psi, \lambda)$  suggests the name *spectral volume scattering function* and the physical interpretation of scattered intensity per unit incident irradiance per unit volume of water;  $\beta(\psi, \lambda)$  also can be interpreted as the differential scattering cross section per unit volume. Integrating  $\beta(\psi, \lambda)$  over all directions (solid angles) gives the total scattered power per unit incident irradiance and unit volume of water or, in other words, the spectral scattering coefficient:

$$b(\lambda) = \int_{\Xi} \beta(\psi, \lambda) d\Omega = 2\pi \int_0^\pi \beta(\psi, \lambda) \sin\psi \, d\psi$$

The last equation follows because scattering in natural waters is azimuthally symmetric about the incident direction (for unpolarized sources and for randomly oriented scatterers). This integration is often divided into forward scattering,  $0 \leq \psi \leq \pi/2$ , and backward scattering,  $\pi/2 \leq \psi \leq \pi$ , parts. The corresponding spectral forward and backward scattering coefficients are, respectively,

$$b_f(\lambda) \equiv 2\pi \int_0^{\pi/2} \beta(\psi, \lambda) \sin\psi \, d\psi$$

$$b_b(\lambda) \equiv 2\pi \int_{\pi/2}^\pi \beta(\psi, \lambda) \sin\psi \, d\psi$$

The preceding discussion has assumed that no inelastic (transpectral) scattering processes are present. However, transpectral scattering does occur in natural waters attributable to fluorescence by dissolved matter or chlorophyll and to Raman or Brillouin scattering by the water molecules themselves (see Sec. 1.23). Power lost from wavelength  $\lambda$  by scattering into wavelength  $\lambda' \neq \lambda$  appears in the above formalism as an increase in the spectral absorption.<sup>9</sup> In this case,  $a(\lambda)$  accounts for “true” absorption (e.g., conversion of radiant energy into heat) as well as for the loss of power at wavelength  $\lambda$  by inelastic scattering to another wavelength. The gain in power at  $\lambda'$  appears as a source term in the radiative transfer formalism.

Two more inherent optical properties are commonly used in hydrologic optics. The *spectral single-scattering albedo*  $\omega_0(\lambda)$  is

$$\omega_0(\lambda) \equiv \frac{b(\lambda)}{c(\lambda)}$$

The single-scattering albedo is the probability that a photon will be scattered (rather than absorbed) in any given interaction; hence,  $\omega_0(\lambda)$  is also known as the *probability of photon survival*. The *spectral volume scattering phase function*,  $\tilde{\beta}(\psi, \lambda)$  is defined by

$$\tilde{\beta}(\psi, \lambda) \equiv \frac{\beta(\psi, \lambda)}{b(\lambda)} \quad \text{sr}^{-1}$$

Writing the volume scattering function  $\beta(\psi, \lambda)$  as the product of the scattering coefficient  $b(\lambda)$  and the phase function  $\beta(\psi, \lambda)$  partitions  $\beta(\psi, \lambda)$  into a factor giving the *strength* of the scattering,  $b(\lambda)$  with units of  $\text{m}^{-1}$ , and a factor giving the *angular distribution* of the scattered photons,  $\beta(\psi, \lambda)$  with units of  $\text{sr}^{-1}$ .

## 1.5 APPARENT OPTICAL PROPERTIES

The quantity

$$\bar{\mu}_d(z, \lambda) \equiv \frac{\int_{\Xi_d} L(z, \theta, \phi, \lambda) |\cos\theta| d\Omega}{\int_{\Xi_u} L(z, \theta, \phi, \lambda) d\Omega} \equiv \frac{E_d(z, \lambda)}{E_{0d}(z, \lambda)}$$

is called the *spectral downwelling average cosine*. The definition shows that  $\bar{\mu}_d(z, \lambda)$  is the average value of the cosine of the polar angle of all the photons contributing to the downwelling radiance at the given depth and wavelength. The *spectral upwelling average cosine* is defined analogously:

$$\bar{\mu}_u(z, \lambda) \equiv \frac{E_u(z, \lambda)}{E_{0u}(z, \lambda)}$$

The average cosines are useful one-parameter measures of the directional structures of the downwelling and upwelling light fields. For example, if the downwelling light field (radiance distribution) is collimated in direction  $(\theta_0, \phi_0)$  so  $L(\theta, \phi) = L_0 \delta(\theta - \theta_0) \delta(\phi - \phi_0)$ , where  $\delta$  is the Dirac  $\delta$  function, then  $\bar{\mu}_d = |\cos\theta_0|$ . If the downwelling radiance is completely diffuse (isotropic),  $L(\theta, \phi) = L_0$  and  $\bar{\mu}_d = \frac{1}{2}$ . Typical values of the average cosines for waters illuminated by the sun and sky are  $\bar{\mu}_d \approx \frac{3}{4}$  and  $\bar{\mu}_u \approx \frac{3}{8}$ . Older literature generally refers to *distribution functions*,  $D_d$  and  $D_u$ , rather than to average cosines. The distribution functions are just reciprocals of the average cosines:

$$D_d(z, \lambda) = \frac{1}{\bar{\mu}_d(z, \lambda)} \quad \text{and} \quad D_u(z, \lambda) = \frac{1}{\bar{\mu}_u(z, \lambda)}$$

The *spectral irradiance reflectance* (or *irradiance ratio*)  $R(z, \lambda)$  is the ratio of spectral upwelling to downwelling plane irradiances:

$$R(z, \lambda) \equiv \frac{E_u(z, \lambda)}{E_d(z, \lambda)}$$

$R(z, \lambda)$  just beneath the sea surface is of great importance in remote sensing (see Sec. 1.22).

Under typical oceanic conditions for which the incident lighting is provided by the sun and sky, the various radiances and irradiances all decrease approximately exponentially with depth, at least when far enough below the surface (and far enough above the bottom, in shallow water) to be free of boundary effects. For example, it is convenient to write the depth dependence of  $E_d(z, \lambda)$  as

$$E_d(z, \lambda) \equiv E_d(0, \lambda) \exp\left[-\int_0^z K_d(z', \lambda) dz'\right] \equiv E_d(0, \lambda) \exp[-\bar{K}_d(z, \lambda)z]$$

where  $K_d(z, \lambda)$  is the *spectral diffuse attenuation coefficient* for spectral downwelling plane irradiance and  $\bar{K}_d(z, \lambda)$  is the average value of  $K_d(z, \lambda)$  over the depth interval 0 to  $z$ . Solving for  $K_d(z, \lambda)$  gives

$$K_d(z, \lambda) = -\frac{d \ln E_d(z, \lambda)}{dz} = -\frac{1}{E_d(z, \lambda)} \frac{dE_d(z, \lambda)}{dz} \quad \text{m}^{-1}$$

The distinction between *beam* and *diffuse* attenuation coefficients is important. The beam attenuation coefficient  $c(\lambda)$  is defined in terms of the radiant power lost from a single, narrow, collimated beam of photons. The downwelling diffuse attenuation coefficient  $K_d(z, \lambda)$  is defined in terms of the decrease with depth of the ambient downwelling irradiance  $E_d(z, \lambda)$ , which comprises photons heading in all downward directions (a diffuse or uncollimated light field).  $K_d(z, \lambda)$  clearly depends on the directional structure of the ambient light field and so is classified as an apparent optical property. Other diffuse attenuation coefficients, e.g.,  $K_t$ ,  $K_{0.6}$ ,  $K_{0.4}$ ,  $K_{PAR}$ , and  $K(\theta, \phi)$  are defined in an analogous manner, using the corresponding radiometric quantities.

In *homogeneous* waters, these “ $K$  functions” depend only weakly on depth and therefore can serve as convenient, if imperfect, descriptors of the water body. Smith and Baker<sup>10</sup> have pointed out other reasons why  $K$  functions are useful:

1. The  $K$ 's are defined as ratios and therefore do not require absolute radiometric measurements.
2. The  $K$ 's are strongly correlated with chlorophyll concentration (i.e., they provide a connection between biology and optics).
3. About 90 percent of the diffusely reflected light from a water body comes from a layer of water of depth  $1/K_d(0, \lambda)$  (i.e.,  $K_d$  has implications for remote sensing).
4. Radiative transfer theory provides several useful relations between the  $K$ 's and other quantities of interest, such as absorption and beam attenuation coefficients, the irradiance reflectance, and the average cosines.
5. Instruments are available for routine measurement of the  $K$ 's.

It must be remembered, however, that in spite of their utility  $K$  functions are apparent optical properties—a change in the environment (e.g., solar angle or sea state) changes their value, sometimes by a negligible amount but sometimes greatly. However, numerical simulations by Gordon<sup>11</sup> show how with a few additional but easily made measurements measured values of  $K_d(z, \lambda)$  and  $\bar{K}_d(\lambda)$  can be “normalized” to remove the effects of solar angle and sea state. The normalized  $K_d$  and  $\bar{K}_d$  are equal to the values that would be obtained if the sun were at the zenith and the sea surface were calm. If this normalization is performed, the resulting  $K_d(z, \lambda)$  and  $\bar{K}_d(\lambda)$  can be regarded as *inherent* optical properties for all practical purposes. It is strongly recommended that Gordon's procedure be routinely followed by experimentalists.

## 1.6 THE OPTICALLY SIGNIFICANT CONSTITUENTS OF NATURAL WATERS

### Dissolved Substances

Pure sea water consists of pure water plus various dissolved salts, which average about 35 parts per thousand (%) by weight. These salts increase scattering above that of pure water by 30 percent (see Table 10 in Sec. 1.17). It is not well established what, if any, effect these salts have on absorption, but it is likely that they increase absorption somewhat at ultraviolet wavelengths.

Both fresh and saline waters contain varying concentrations of dissolved organic compounds. These compounds are produced during the decay of plant matter and consist mostly of various humic and fulvic acids.<sup>8</sup> These compounds are generally brown in color and in sufficient concentrations can color the water yellowish brown. For this reason the compounds are generically referred to as *yellow matter*, *Gelbstoff*, or *gilvin*. Yellow matter absorbs very little in the red, but absorption increases rapidly with decreasing wavelength. Since the main source of yellow matter is decayed terrestrial vegetation, concentrations are generally greatest in lakes, rivers, and coastal waters influenced by river runoff. In such waters yellow matter can be the dominant absorber at the blue end of the spectrum. In mid-ocean waters absorption by yellow matter is usually small compared to absorption by other constituents, but some yellow matter is likely to be present as the result of decaying phytoplankton, especially at the end of a bloom.

## Particulate Matter

Particulate matter in the oceans has two distinct origins: biological and physical. The organic particles of optical importance are created as bacteria, phytoplankton, and zooplankton grow and reproduce by photosynthesis or by eating their neighbors. Particles of a given size are destroyed by breaking apart after death, by flocculation into larger aggregate particles, or by settling out of the water column. Inorganic particles are created primarily by weathering of terrestrial rocks and soils. These particles can enter the water as wind-blown dust settles on the sea surface, as rivers carry eroded soil to the sea, or as currents resuspend bottom sediments. Inorganic particles are removed from the water by settling, aggregating, or dissolving. This particulate matter usually is the major determiner of both the absorption and scattering properties of natural waters and is responsible for most of the temporal and spatial variability in these optical properties.

**Organic Particles** These occur in many forms.

**Viruses** Natural marine waters contain virus particles<sup>12</sup> in concentrations of  $10^{12}$  to  $10^{15}$  particles  $m^{-3}$ . These particles are generally much smaller (2–200 nm) than the wavelength of visible light, and it is not known what, if any, direct effect viruses have on the optical properties of sea water.

**Colloids** Nonliving colloidal particles in the size range 0.4–1.0  $\mu m$  are found<sup>13</sup> in typical number concentrations of  $10^{13} m^{-3}$  and colloids of size  $\leq 0.1 \mu m$  are found<sup>14</sup> in abundances of  $10^{15} m^{-3}$ . Some of the absorption traditionally attributed to dissolved matter may be due to colloids, some of which strongly resemble fulvic acids in electron micrographs.<sup>14</sup>

**Bacteria** Living bacteria in the size range 0.2–1.0  $\mu m$  occur in typical number concentrations of  $10^{11}$ – $10^{13} m^{-3}$ . It only recently has been recognized<sup>15–17</sup> that bacteria can be significant scatterers and absorbers of light, especially at blue wavelengths and in clean oceanic waters where the larger phytoplankton are relatively scarce.

**Phytoplankton** These ubiquitous microscopic plants occur with incredible diversity of species, size, shape, and concentration. They range in cell size from less than 1  $\mu m$  to more than 200  $\mu m$ , and some species form even larger chains of individual cells. It has long been recognized that phytoplankton are the particles primarily responsible for determining the optical properties of most oceanic waters. Their chlorophyll and related pigments strongly absorb light in the blue and red and thus when concentrations are high determine the spectral absorption of sea water. These particles are generally much larger than the wavelength of visible light and are efficient scatterers, especially via diffraction, thus influencing the scattering properties of sea water.

**Organic detritus** Nonliving organic particles of various sizes are produced, for example, when phytoplankton die and their cells break apart. They may also be formed when zooplankton graze on phytoplankton and leave behind cell fragments and fecal pellets. Even if these detrital particles contain pigments at the time of their production, they can be rapidly photo-oxidized and lose the characteristic absorption spectrum of living phytoplankton, leaving significant absorption only at blue wavelengths.

**Large particles** Particles larger than 100  $\mu m$  include zooplankton (living animals with sizes from tens of micrometers to two centimeters) and fragile amorphous aggregates<sup>18</sup> of smaller particles (“marine snow,” with sizes from 0.5 mm to tens of centimeters). Such particles occur in highly variable numbers from almost none to thousands per cubic meter. Even at relatively large concentrations these large particles tend to be missed by optical instruments that randomly sample only a few cubic centimeters of water or that mechanically break apart the aggregates. However, these large particles can be efficient diffuse scatterers of light and therefore may significantly affect the optical properties (especially backscatter) of large volumes of water, e.g., as seen by remote sensing instruments. Although such optical effects are recognized, they have not been quantified.

**Inorganic Particles** These generally consist of finely ground quartz sand, clay minerals, or metal oxides in the size range from much less than 1  $\mu m$  to several tens of micrometers. Insufficient attention has been paid to the optical effects of such particles in sea water, although it is recognized that inorganic particles are sometimes optically more important than organic particles. Such situations can occur both in turbid coastal waters carrying a heavy sediment load and in very clear oceanic waters which are receiving wind-blown dust.<sup>19</sup>

At certain stages of its life, the phytoplankton coccolithophore species *Emiliania huxleyi* is a most remarkable source of crystalline particles. During blooms *E. huxleyi* produces and sheds enormous numbers of small (2–4  $\mu\text{m}$ ) calcite plates; concentrations of  $3 \times 10^{11}$  plates  $\text{m}^{-3}$  have been observed.<sup>20</sup> Although they have a negligible effect on light absorption, these calcite plates are extremely efficient light scatterers: irradiance reflectances of  $R = 0.39$  have been observed<sup>20</sup> at blue wavelengths during blooms (compared with  $R = 0.02$  to  $0.05$  in the blue for typical ocean waters, discussed in Sec. 1.22). Such coccolithophore blooms give the ocean a milky white or turquoise appearance.

## 1.7 PARTICLE SIZE DISTRIBUTIONS

In spite of the diverse mechanisms for particle production and removal, observation shows that a single family of particle size distributions often suffices to describe oceanic particulate matter in the optically important size range from 0.1 to 100  $\mu\text{m}$ . Let  $N(x)$  be the number of particles per unit volume with size greater than  $x$  in a sample of particles;  $x$  usually represents equivalent spherical diameter computed from particle volume, but also can represent particle volume or surface area. The Junge (also called *hyperbolic*) cumulative size distribution<sup>21</sup> is then

$$N(x) = k \left( \frac{x}{x_0} \right)^{-m}$$

where  $k$  sets the scale,  $x_0$  is a reference size, and  $-m$  is the slope of the distribution when  $\log N$  is plotted versus  $\log x$ ;  $k$ ,  $x_0$ , and  $m$  are positive constants.

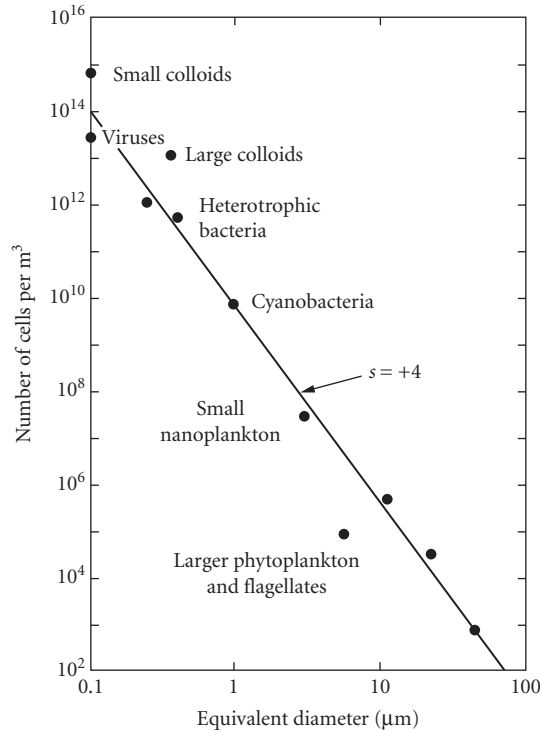
Oceanic particle size distributions usually have  $m$  values between 2 and 5, with  $m = 3$  to 4 being typical; such spectra can be seen in McCave,<sup>22</sup> Fig. 7. It often occurs that oceanic particle size spectra are best described by a segmented distribution in which a smaller value of  $m$  is used for  $x$  less than a certain value and a larger value of  $m$  is used for  $x$  greater than that value. Such segmented spectra can be seen in Bader,<sup>21</sup> and in McCave,<sup>22</sup> Fig. 8.

The quantity most relevant to optics, e.g., in Mie scattering computations for polydisperse systems, is not the *cumulative* size distribution  $N(x)$ , but rather the *number* size distribution  $n(x)$ . The number distribution is defined such that  $n(x) dx$  is the number of particles in the size interval from  $x$  to  $x + dx$ . The number distribution is related to the cumulative distribution by  $n(x) = |dN(x)/dx|$ , so that for the Junge distribution

$$n(x) = kmx_0^{-m}x^{-m-1} \equiv Kx^{-s}$$

where  $K \equiv kmx_0^{-m}$  and  $s \equiv m + 1$ ;  $s$  is commonly referred to as the slope of the distribution. Figure 3 shows the number distribution of biological particles typical of open ocean waters; note that a value of  $s = 4$  gives a reasonable fit to the plotted points.

It should be noted, however, that the Junge distribution sometimes fails to represent oceanic conditions. For example, during the growth phase of a phytoplankton bloom the rapid increase in population of a particular species may give abnormally large numbers of particles in a particular size range. Such bloom conditions therefore give a “bump” in  $n(x)$  that is not well modeled by the simple Junge distribution. Moreover, Lambert et al.<sup>23</sup> found that a log-normal distribution sometimes better described the distributions of inorganic particles found in water samples taken from near the bottom at deep ocean locations. These particles were principally aluminosilicates in the 0.2- to 10.0- $\mu\text{m}$  size range but included quartz grains, metal oxides, and phytoplankton skeletal parts such as coccolithophore plates. Based on the sampling location it was assumed that the inorganic particles were resuspended sediments. Lambert et al. found that the size distributions of the individual particle types (e.g., aluminosilicates or metal oxides) obeyed log-normal distributions which “flattened out” below 1  $\mu\text{m}$ . For particles larger than  $\sim 1 \mu\text{m}$ , log-normal and Junge distributions gave nearly



**FIGURE 3** Number size distribution typical of biological particles in the open ocean. (Based on Stramski and Kiefer,<sup>17</sup> with permission.)

equivalent descriptions of the data. Biological particles were not as well described by the log-normal distribution, especially for sizes greater than 5  $\mu\text{m}$ .

## 1.8 ELECTROMAGNETIC PROPERTIES OF WATER

In studies of electromagnetic wave propagation at the level of Maxwell's equations it is convenient to specify the bulk electromagnetic properties of the medium via the electrical permittivity  $\epsilon$ , the magnetic permeability  $\mu$ , and the electrical conductivity  $\sigma$ . Since water displays no significant magnetic properties, the permeability can be taken equal to the free-space (in vacuo) value at all frequencies:  $\mu = \mu_0 = 4\pi \times 10^{-7} \text{ N A}^{-2}$ . Both  $\epsilon$  and  $\sigma$  depend on the frequency  $\omega$  of the propagating electromagnetic wave as well as on the water temperature, pressure, and salinity. Low-frequency ( $\omega \rightarrow 0$ ) values for the permittivity are of order  $\epsilon \approx 80\epsilon_0$ , where  $\epsilon_0 = 8.85 \times 10^{-12} \text{ A}^2 \text{ s}^2 \text{ N}^{-1} \text{ m}^{-2}$  is the free-space value. This value decreases to  $\epsilon \approx 1.8\epsilon_0$  at optical frequencies. Extensive tabulations of  $\epsilon/\epsilon_0$  as a function of temperature and pressure are given for pure water in Archer and Wang.<sup>24</sup> The low-frequency conductivity ranges from  $\sigma \approx 4 \times 10^{-6} \text{ siemen m}^{-1}$  for pure water to  $\sigma \approx 4.4 \text{ siemen m}^{-1}$  for sea water.

The effects of  $\epsilon$ ,  $\mu$ , and  $\sigma$  on electromagnetic wave propagation are compactly summarized in terms of the complex index of refraction,  $m = n - ik$ , where  $n$  is the real index of refraction,

$k$  is the dimensionless electrodynamic absorption coefficient, and  $i = \sqrt{-1}$ ;  $n$  and  $k$  are collectively called the *optical constants* of water (a time dependence convention of  $\exp(+i\omega t)$  is used in deriving wave equations from Maxwell's equations). The explicit dependence of  $m$  on  $\epsilon$ ,  $\mu$ , and  $\sigma$  is given by<sup>25</sup>

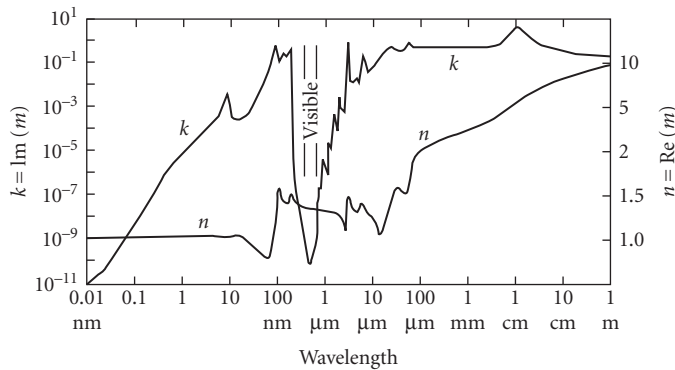
$$\begin{aligned} m^2 &= \mu\epsilon c^2 - i \frac{\mu\sigma c^2}{\omega} \\ &= (n - ik)^2 = n^2 - k^2 - i2nk \end{aligned}$$

where  $c = (\epsilon_0\mu_0)^{-1/2}$  is the speed of light in vacuo. These equations can be used to relate  $n$  and  $k$  to the bulk electromagnetic properties. The optical constants are convenient because they are directly related to the scattering and absorbing properties of water. The real index of refraction  $n(\lambda)$  governs scattering both at interfaces (via the laws of reflection and refraction) and within the medium (via thermal or other fluctuations of  $n(\lambda)$  at molecular and larger scales). The spectral absorption coefficient  $a(\lambda)$  is related to  $k(\lambda)$  by<sup>25</sup>

$$a(\lambda) = \frac{4\pi k(\lambda)}{\lambda}$$

Here  $\lambda$  refers to the in vacuo wavelength of light corresponding to a given frequency  $\omega$  of electromagnetic wave.

Figure 4 shows the wavelength dependence of the optical constants  $n$  and  $k$  for pure water. The extraordinary feature seen in this figure is the narrow “window” in  $k(\lambda)$ , where  $k(\lambda)$  decreases by over nine orders of magnitude between the near ultraviolet and the visible and then quickly rises again in the near infrared. This behavior in  $k(\lambda)$  gives a corresponding window in the spectral absorption coefficient  $a(\lambda)$  as seen in Table 2. Because of the opaqueness of water outside the near-UV to near-IR wavelengths, hydrologic optics is concerned only with this small part of the electromagnetic spectrum. These wavelengths overlap nicely with the wavelengths of the sun's maximum energy output and with a corresponding window in atmospheric absorption, much to the benefit of life on earth.



**FIGURE 4** The optical constants of pure water. The left axis gives  $k = \text{Im}(m)$  and the right axis gives  $n = \text{Re}(m)$  where  $m$  is the complex index of refraction. (Redrawn from Zoloratev and Demin,<sup>26</sup> with permission.)



**TABLE 2** Absorption Coefficient  $a$  of Pure Water As a Function of Wavelength  $\lambda^a$

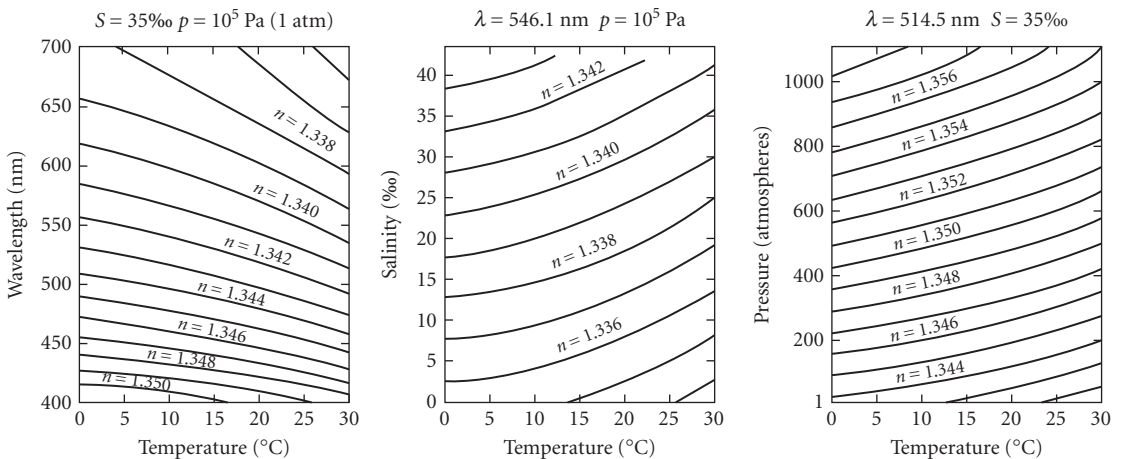
$\lambda$	$a$ ( $m^{-1}$ )	$\lambda$	$a$ ( $m^{-1}$ )
0.01 nm	$1.3 \times 10^1$	700 nm	0.650
0.1	$6.5 \times 10^2$	800	2.07
1	$9.4 \times 10^4$	900 nm	7.0
10	$3.5 \times 10^6$	1 $\mu m$	$3.3 \times 10^1$
100	$5.0 \times 10^7$	10	$7.0 \times 10^4$
200	3.07	100 $\mu m$	$6.5 \times 10^4$
300	0.141	0.001 m	$1.3 \times 10^4$
400	0.0171	0.01	$3.6 \times 10^3$
500	0.0257	0.1	$5.0 \times 10^1$
600 nm	0.244	1 m	2.5

<sup>a</sup>Data for 200 nm  $\leq \lambda \leq$  800 nm taken from Table 6. Data for other wavelengths computed from Fig. 4.

## 1.9 INDEX OF REFRACTION

### Seawater

Austin and Halikas<sup>27</sup> exhaustively reviewed the literature on measurements of the real index of refraction of sea water. Their report contains extensive tables and interpolation algorithms for the index of refraction (relative to air),  $n(\lambda, S, T, p)$ , as a function of wavelength ( $\lambda = 400$  to 700 nm), salinity ( $S = 0$  to 43‰), temperature ( $T = 0$  to 30°C), and pressure ( $p = 10^5$  to  $10^8$  Pa, or 1 to 1080 atm). Figure 5 illustrates the general dependence of  $n$  on these four parameters:  $n$  decreases with increasing wavelength or temperature and increases with increasing salinity or pressure. Table 3 gives the values of  $n$  for the extreme values of each parameter. The extreme values of  $n$ , 1.329128 and 1.366885, show that  $n$  varies by less than 3 percent over the entire parameter range relevant to hydrologic optics. Table 4 gives selected values of  $n(\lambda, T)$  for fresh water ( $S = 0$ ) and for typical sea water ( $S = 35$ ‰) at atmospheric pressure ( $p = 10^5$  Pa). The values in Table 4 can be multiplied by 1.000293 (the index of refraction of dry air at STP and  $\lambda = 538$  nm) if values relative to vacuum are



**FIGURE 5** Real index of refraction of water for selected values of pressure, temperature, and salinity. (Adapted from Austin and Halikas.<sup>27</sup>)

**TABLE 3** Index of Refraction of Water  $n$  for the Extreme Values of Pressure  $p$ , Temperature  $T$ , Salinity  $S$ , and Wavelength  $\lambda$  Encountered in Hydrologic Optics\*

$p$ (Pa)	$T$ (°C)	$S$ (‰)	$\lambda$ (nm)	$n$
$1.01 \times 10^5$	0	0	400	1.344186
1.01	0	0	700	1.331084
1.01	0	35	400	1.351415
1.01	0	35	700	1.337906
1.01	30	0	400	1.342081
1.01	30	0	700	1.329128
1.01	30	35	400	1.348752
1.01	30	35	700	1.335316
$1.08 \times 10^8$	0	0	400	1.360076
1.08	0	0	700	1.346604
1.08	0	35	400	1.366885
1.08	0	35	700	1.352956
1.08	30	0	400	1.356281
1.08	30	0	700	1.342958
1.08	30	35	400	1.362842
1.08	30	35	700	1.348986

\*Reproduced from Austin and Halikas.<sup>27</sup>**TABLE 4** Index of Refraction of Fresh Water and of Sea Water at Atmospheric Pressure for Selected Temperatures and Wavelengths\*

Temp (°C)	Fresh water ( $S = 0$ ) wavelength (nm)							
	400	420	440	460	480	500	520	540
0	1.34419	1.34243	1.34092	1.33960	1.33844	1.33741	1.33649	1.33567
10	1.34390	1.34215	1.34064	1.33933	1.33817	1.33714	1.33623	1.33541
20	1.34317	1.34142	1.33992	1.33860	1.33745	1.33643	1.33551	1.33469
30	1.34208	1.34034	1.33884	1.33753	1.33638	1.33537	1.33445	1.33363
Temp (°C)	Wavelength (nm)							
	560	580	600	620	640	660	680	700
0	1.33494	1.33424	1.33362	1.33305	1.33251	1.33200	1.33153	1.33108
10	1.33466	1.33399	1.33336	1.33279	1.33225	1.33174	1.33127	1.33084
20	1.33397	1.33328	1.33267	1.33210	1.33156	1.33105	1.33059	1.33016
30	1.33292	1.33223	1.33162	1.33106	1.33052	1.33001	1.32955	1.32913
Temp (°C)	Sea water ( $S = 35\text{‰}$ ) wavelength (nm)							
	400	420	440	460	480	500	520	540
0	1.35141	1.34961	1.34804	1.34667	1.34548	1.34442	1.34347	1.34263
10	1.35084	1.34903	1.34747	1.34612	1.34492	1.34385	1.34291	1.34207
20	1.34994	1.34814	1.34657	1.34519	1.34401	1.34295	1.34200	1.34116
30	1.34875	1.34694	1.34539	1.34404	1.34284	1.34179	1.34085	1.34000
Temp (°C)	Wavelength (nm)							
	560	580	600	620	640	660	680	700
0	1.34186	1.34115	1.34050	1.33992	1.33937	1.33885	1.33836	1.33791
10	1.34129	1.34061	1.33997	1.33938	1.33882	1.33830	1.33782	1.33738
20	1.34039	1.33969	1.33904	1.33845	1.33791	1.33739	1.33690	1.33644
30	1.33925	1.33855	1.33790	1.33731	1.33676	1.33624	1.33576	1.33532

\*Data extracted from Austin and Halikas.

**TABLE 5** Index of Refraction Relative to Water,  $n$ , of Inorganic Particles Found in Sea Water

Substance	$n$
Quartz	1.16
Kaolinite	1.17
Montmorillonite	1.14
Hydrated mica	1.19
Calcite	1.11/1.24

desired. Millard and Seaver<sup>28</sup> have developed a 27-term formula that gives the index of refraction to part-per-million accuracy over most of the oceanographic parameter range.

## Particles

Suspended particulate matter in sea water often has a bimodal index of refraction distribution. Living phytoplankton typically have “low” indices of refraction in the range 1.01 to 1.09 relative to the index of refraction of seawater. Detritus and inorganic particles generally have “high” indices in the range of 1.15 to 1.20 relative to seawater.<sup>29</sup> Typical values are 1.05 for phytoplankton and 1.16 for inorganic particles.

Table 5 gives the relative index of refraction of terrigenous minerals commonly found in river runoff and wind-blown dust. Only recently has it become possible to measure the refractive indices of individual phytoplankton cells.<sup>30</sup> Consequently, little is yet known about the dependence of refractive index on phytoplankton species, or on the physiological state of the plankton within a given species, although it appears that the dependence can be significant.<sup>31</sup>

## 1.10 MEASUREMENT OF ABSORPTION

Determination of the spectral absorption coefficient  $a(\lambda)$  for natural waters is a difficult task for several reasons. First, water absorbs only weakly at near-UV to blue wavelengths so that very sensitive instruments are required. More importantly, scattering is never negligible so that careful consideration must be made of the possible aliasing of the absorption measurements by scattering effects. In pure water at wavelengths of  $\lambda = 370$  to 450 nm, molecular scattering provides 20 to 25 percent (Table 10) of the total beam attenuation,  $c(\lambda) = a(\lambda) + b(\lambda)$ . Scattering effects can dominate absorption at all visible wavelengths in waters with high particulate loads. Additional complications arise in determining the absorption of pure water because of the difficulty of preparing uncontaminated samples.

Many techniques have been employed in attempts to determine the spectral absorption coefficient for pure water,  $a_w(\lambda)$ ; these are reviewed in Smith and Baker.<sup>32</sup> The most commonly employed technique for routine determination of  $a(\lambda)$  for oceanic waters consists of filtering a sample of water to retain the particulate matter on a filter pad. The spectral absorption of the particulate matter,  $a_p(\lambda)$ , is then determined in a spectrophotometer. The absorption of pure water,  $a_w(\lambda)$ , must be added to  $a_p(\lambda)$  to obtain the total absorption of the oceanic water sample. Even though this technique for determining absorption has been in use for many years, the methodology is still evolving<sup>33–35</sup> because of the many types of errors inherent in the  $a_p(\lambda)$  measurements (e.g., inability of filters to retain all particulates, scattering effects within the sample cell, absorption by dissolved matter retained on the filter pad, and decomposition of pigments during the filtration process).

Moreover, this methodology for determining total absorption assumes that absorption by dissolved organic matter (yellow substances) is negligible, which is not always the case. If the absorption by yellow matter,  $a_y(\lambda)$ , is desired, then the absorption of the *filtrate* is measured, and  $a_y(\lambda)$  is taken to be  $a_{\text{filtrate}}(\lambda) - a_w(\lambda)$ . Several novel instruments under development<sup>36–38</sup> show promise for circumventing the problems inherent in the filter-pad technique as well as for making in situ measurements of total absorption which at present is difficult.<sup>39</sup>

## 1.11 ABSORPTION BY PURE SEA WATER

Table 2 showed the absorption for pure water over the wavelength range from 0.01 nm (x-rays) to 1 m (radio waves). As is seen in the table, only the near-UV to near-IR wavelengths are of interest in hydrologic optics. Smith and Baker<sup>32</sup> made a careful but indirect determination of the *upper bound* of the spectral absorption coefficient of pure sea water,  $a_w(\lambda)$ , in the wavelength range of oceanographic interest,  $200 \text{ nm} \leq \lambda \leq 800 \text{ nm}$ . Their work assumed that for the clearest natural waters (1) absorption by salt or other dissolved substances was negligible, (2) the only scattering was by water molecules and salt ions, and (3) there was no inelastic scattering (i.e., no fluorescence or Raman scattering). With these assumptions the inequality (derived from radiative transfer theory)

$$a_w(\lambda) \leq K_d(\lambda) - \frac{1}{2}b_m^{\text{sw}}(\lambda)$$

holds. Here  $b_m^{\text{sw}}(\lambda)$  is the spectral scattering coefficient for pure sea water;  $b_m^{\text{sw}}(\lambda)$  was taken as known (Table 10). Smith and Baker then used measured values of the diffuse attenuation function  $K_d(\lambda)$  from very clear waters (e.g., Crater Lake, Oregon, U.S.A., and the Sargasso Sea) to estimate  $a_w(\lambda)$ . Table 6 gives their self-consistent values of  $a_w(\lambda)$ ,  $K_d(\lambda)$ ,  $b_m^{\text{sw}}(\lambda)$ .

The Smith and Baker absorption values are widely used. However, it must be remembered that the values of  $a_w(\lambda)$  in Table 6 are upper bounds; the true absorption of pure water is likely to be somewhat lower, at least at violet and blue wavelengths.<sup>40</sup> Smith and Baker pointed out that there are uncertainties because  $K_p$ , an apparent optical property, is influenced by environmental conditions. They also commented that at wavelengths below 300 nm, their values are “merely an educated guess.” They estimated the accuracy of  $a_w(\lambda)$  to be within +25 and –5 percent between 300 and 480 nm and +10 to –15 percent between 480 and 800 nm. Numerical simulations by Gordon<sup>11</sup> indicate that a more restrictive inequality,

$$a_w(\lambda) \leq \frac{K_d(\lambda)}{D_0(\lambda)} - 0.62b_m^{\text{sw}}(\lambda)$$

could be used. Here  $D_0(\lambda)$  is a measurable distribution function [ $D_0(\lambda) > 1$ ] that corrects for the effects of sun angle and sea state on  $K_d(\lambda)$  (discussed earlier). Use of the Gordon inequality could reduce the Smith and Baker absorption values by up to 20 percent at blue wavelengths. And finally, the Smith and Baker measurements were not made in optically pure water but rather in the “clearest natural waters.” Even these waters contain a small amount of dissolved and particulate matter which will contribute something to both absorption and scattering.

There is evidence<sup>41</sup> that absorption is weakly dependent on temperature, at least in the red and near infrared ( $\partial a/\partial T \sim 0.0015 \text{ m}^{-1} \text{ }^\circ\text{C}^{-1}$  at  $\lambda = 600 \text{ nm}$  and  $\partial a/\partial T \sim 0.01 \text{ m}^{-1} \text{ }^\circ\text{C}^{-1}$  at  $\lambda = 750 \text{ nm}$ ) and perhaps also slightly dependent on salinity; these matters are under investigation.

**TABLE 6** Spectral Absorption Coefficient of Pure Sea Water,  $a_w$ , As Determined by Smith and Baker (Values of the molecular scattering coefficient of pure sea water,  $b_m^{sw}$ , and of the diffuse attenuation coefficient  $K_d$  used in their computation of  $a_w$  are also shown.\*)

$\lambda$ (nm)	$a_w$ ( $m^{-1}$ )	$b_m^{sw}$ ( $m^{-1}$ )	$K_d$ ( $m^{-1}$ )	$\lambda$ (nm)	$a_w$ ( $m^{-1}$ )	$b_m^{sw}$ ( $m^{-1}$ )	$K_d$ ( $m^{-1}$ )
200	3.07	0.151	3.14	500	0.0257	0.0029	0.0271
210	1.99	0.119	2.05	510	0.0357	0.0026	0.0370
220	1.31	0.0995	1.36	520	0.0477	0.0024	0.0489
230	0.927	0.0820	0.968	530	0.0507	0.0022	0.0519
240	0.720	0.0685	0.754	540	0.0558	0.0021	0.0568
250	0.559	0.0575	0.588	550	0.0638	0.0019	0.0648
260	0.457	0.0485	0.481	560	0.0708	0.0018	0.0717
270	0.373	0.0415	0.394	570	0.0799	0.0017	0.0807
280	0.288	0.0353	0.306	580	0.108	0.0016	0.109
290	0.215	0.0305	0.230	590	0.157	0.0015	0.158
300	0.141	0.0262	0.154	600	0.244	0.0014	0.245
310	0.105	0.0229	0.116	610	0.289	0.0013	0.290
320	0.0844	0.0200	0.0944	620	0.309	0.0012	0.310
330	0.0678	0.0175	0.0765	630	0.319	0.0011	0.320
340	0.0561	0.0153	0.0637	640	0.329	0.0010	0.330
350	0.0463	0.0134	0.0530	650	0.349	0.0010	0.350
360	0.0379	0.0120	0.0439	660	0.400	0.0008	0.400
370	0.0300	0.0106	0.0353	670	0.430	0.0008	0.430
380	0.0220	0.0094	0.0267	680	0.450	0.0007	0.450
390	0.0191	0.0084	0.0233	690	0.500	0.0007	0.500
400	0.0171	0.0076	0.0209	700	0.650	0.0007	0.650
410	0.0162	0.0068	0.0196	710	0.839	0.0007	0.834
420	0.0153	0.0061	0.0184	720	1.169	0.0006	1.170
430	0.0144	0.0055	0.0172	730	1.799	0.0006	1.800
440	0.0145	0.0049	0.0170	740	2.38	0.0006	2.380
450	0.0145	0.0045	0.0168	750	2.47	0.0005	2.47
460	0.0156	0.0041	0.0176	760	2.55	0.0005	2.55
470	0.0156	0.0037	0.0175	770	2.51	0.0005	2.51
480	0.0176	0.0034	0.0194	780	2.36	0.0004	2.36
490	0.0196	0.0031	0.0212	790	2.16	0.0004	2.16
				800	2.07	0.0004	2.07

\*Reproduced from Smith and Baker,<sup>32</sup> with permission.

## 1.12 ABSORPTION BY DISSOLVED ORGANIC MATTER

Absorption by yellow matter is reasonably well described by the model<sup>42</sup>

$$a_y(\lambda) = a_y(\lambda_0) \exp[-0.014(\lambda - \lambda_0)]$$

over the range  $350 \text{ nm} \leq \lambda \leq 700 \text{ nm}$ . Here  $\lambda_0$  is a reference wavelength usually chosen to be  $\lambda_0 = 440 \text{ nm}$  and  $a_y(\lambda_0)$  is the absorption due to yellow matter at the reference wavelength. The value of  $a_y(\lambda)$  of course depends on the concentration of yellow matter in the water. The exponential decay constant depends on the relative proportion of specific types of yellow matter; other studies have found exponents of  $-0.014$  to  $-0.019$  (Roesler et al.,<sup>43</sup> table 1). Both total concentration and proportions are highly variable. Table 7 gives measured values of  $a_y(440)$  for selected waters. Because of the variability in yellow matter concentrations, the values found in Table 7 have little general

**TABLE 7** Measured Absorption Coefficient at  $\lambda = 440$  nm Due to Yellow Matter,  $a_y(440 \text{ nm})$ , for Selected Waters\*

Water Body	$a_y(440 \text{ nm})$ ( $\text{m}^{-1}$ )
Oceanic waters	
Sargasso Sea	$\approx 0$
off Bermuda	0.01
Gulf of Guinea	0.024–0.113
oligotrophic Indian Ocean	0.02
mesotrophic Indian Ocean	0.03
eutrophic Indian Ocean	0.09
Coastal and estuarine waters	
North Sea	0.07
Baltic Sea	0.24
Rhone River mouth, France	0.086–0.572
Clyde River estuary, Australia	0.64
Lakes and rivers	
Crystal Lake, Wisconsin, U.S.A.	0.16
Lake George, Australia	0.69–3.04
Lake George, Uganda	3.7
Carrao River, Venezuela	12.44
Lough Napeast, Ireland	19.1

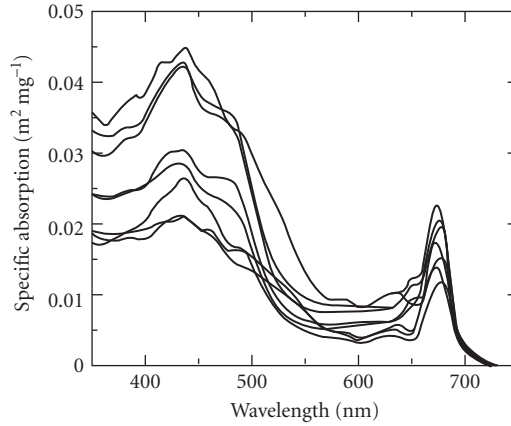
\*Condensed from Kirk,<sup>8</sup> with permission.

validity even for the particular water bodies sampled, but they do serve to show representative values and the range of influence of yellow matter in determining the total absorption. Although the above model allows the determination of spectral absorption by yellow matter if the absorption is known at one wavelength, no model yet exists that allows for the direct determination of  $a_y(\lambda)$  from given concentrations of yellow matter constituents.

### 1.13 ABSORPTION BY PHYTOPLANKTON

Phytoplankton cells are strong absorbers of visible light and therefore play a major role in determining the absorption properties of natural waters. Absorption by phytoplankton occurs in various photosynthetic pigments of which the chlorophylls are best known to nonspecialists. Absorption by chlorophyll itself is characterized by strong absorption bands in the blue and in the red (peaking at  $\lambda \approx 430$  and  $665$  nm, respectively, for chlorophyll *a*), with very little absorption in the green. Chlorophyll occurs in all plants, and its concentration in milligrams of chlorophyll per cubic meter of water is commonly used as the relevant optical measure of phytoplankton abundance. (The term “chlorophyll concentration” usually refers to the sum of chlorophyll *a*, the main pigment in phytoplankton cells, and the related pigment pheophytin *a*.) Chlorophyll concentrations for various waters range from  $0.01 \text{ mg m}^{-3}$  in the clearest open ocean waters to  $10 \text{ mg m}^{-3}$  in productive coastal upwelling regions to  $100 \text{ mg m}^{-3}$  in eutrophic estuaries or lakes. The globally averaged, near-surface, open-ocean value is in the neighborhood of  $0.5 \text{ mg m}^{-3}$ .

The absorbing pigments are not evenly distributed within phytoplankton cells but are localized into small “packages” (chloroplasts) which are distributed nonrandomly throughout the cell. This localized distribution of pigments means<sup>8</sup> that the spectral absorption by a phytoplankton cell or by a collection of cells in water is “flatter” (has less-pronounced peaks and reduced overall absorption) than if the pigments were uniformly distributed throughout the cell or throughout the water. This so-called “pigment packaging effect” is a major source of both inter- and intraspecies variability in spectral absorption by phytoplankton. This is because the details of the pigment



**FIGURE 6** Chlorophyll-specific spectral absorption coefficients for eight species of phytoplankton. (Redrawn from Sathyendranath *et al.*,<sup>44</sup> with permission.)

packaging within cells depend not only on species but also on a cell's size and physiological state (which in turn depends on environmental factors such as ambient lighting and nutrient availability). Another source of variability in addition to chlorophyll *a* concentration and packaging is changes in pigment composition (the relative proportions of accessory pigments, namely, chlorophylls *b* and *c*, pheopigments, biliproteins, and carotenoids) since each pigment displays a characteristic absorption curve.

A qualitative feel for the nature of phytoplankton absorption can be obtained from Fig. 6 which is based on absorption measurements from eight different single-species laboratory phytoplankton cultures.<sup>44</sup> Measured spectral absorption coefficients for the eight cultures,  $a_i(\lambda)$ ,  $i = 1$  to 8, were first reduced by subtracting  $a_i(737)$  to remove the effects of absorption by detritus and cell constituents other than pigments: the assumption is that pigments do not absorb at  $\lambda = 737$  nm and that the residual absorption is wavelength independent (which is a crude approximation). The resulting curves were then normalized by the chlorophyll concentrations of the respective cultures to generate the *chlorophyll-specific spectral absorption* curves for phytoplankton,  $a_i^*(\lambda)$ .

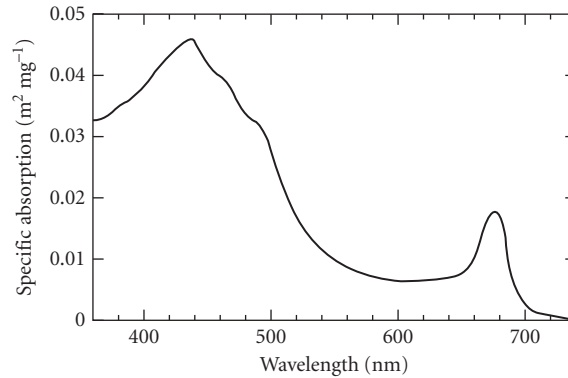
$$a_i^*(\lambda) = \frac{a_i(\lambda) - a_i(737)}{C_i} \quad \frac{\text{m}^{-1}}{\text{mg m}^{-3}} = \text{m}^2 \text{mg}^{-1}$$

which are plotted in Fig. 6.

Several general features of phytoplankton absorption are seen in Fig. 6:

1. There are distinct absorption peaks at  $\lambda \approx 440$  and 675 nm.
2. The blue peak is one to three times as high as the red one (for a given species) due to the contribution of accessory pigments to absorption in the blue.
3. There is relatively little absorption between 550 and 650 nm, with the absorption minimum near 600 nm being 10 to 30 percent of the value at 440 nm.

Similar analysis by Morel<sup>45</sup> yielded the average specific absorption curve shown in Fig. 7. Morel's curve is an average of spectra from 14 cultured phytoplankton species. The Morel curve is qualitatively the same as the curves of Fig. 6 and is as good a candidate as any for being called a "typical" phytoplankton specific absorption curve. The  $a^*(\lambda)$  values of Fig. 7 are tabulated in Table 8 for reference.



**FIGURE 7** Average chlorophyll-specific spectral absorption coefficient for 14 species of phytoplankton. (Redrawn from Morel,<sup>45</sup> with permission.)

## 1.14 ABSORPTION BY ORGANIC DETRITUS

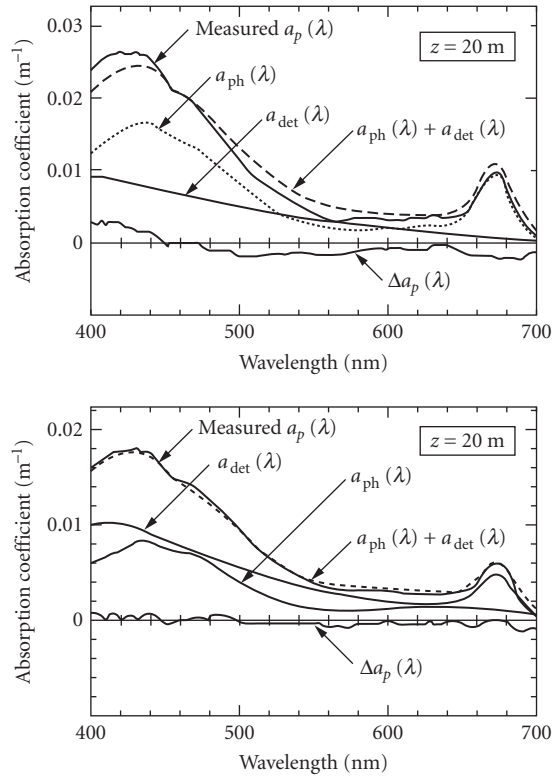
Only recently has it become possible to determine the relative contributions of living phytoplankton and nonliving detritus to the total absorption by particulates. Iturriaga and Siegel<sup>46</sup> used micro-spectrophotometric techniques capable of measuring the spectral absorption of individual particles as small as 3  $\mu\text{m}$  diameter to examine the absorption properties of particulates from Sargasso sea waters. Roesler et al.<sup>43</sup> employed a standard filter-pad technique with measurements made before

**TABLE 8** Average Chlorophyll-Specific Spectral Absorption Coefficient  $a^*$  for 14 Species of Phytoplankton As Plotted in Fig. 7 (The standard deviation is  $\sim 30\%$  of the mean except in the vicinity of 400 nm, where it is  $\sim 50\%$ .\*)

$\lambda$ (nm)	$a^*$ ( $\text{m}^2 \text{mg}^{-1}$ )	$\lambda$ (nm)	$a^*$ ( $\text{m}^2 \text{mg}^{-1}$ )	$\lambda$ (nm)	$a^*$ ( $\text{m}^2 \text{mg}^{-1}$ )
400	0.0394	500	0.0274	600	0.0053
405	0.0395	505	0.0246	605	0.0053
410	0.0403	510	0.0216	610	0.0054
415	0.0417	515	0.0190	615	0.0057
420	0.0429	520	0.0168	620	0.0059
425	0.0439	525	0.0151	625	0.0061
430	0.0448	530	0.0137	630	0.0063
435	0.0452	535	0.0125	635	0.0064
440	0.0448	540	0.0115	640	0.0064
445	0.0436	545	0.0106	645	0.0066
450	0.0419	550	0.0098	650	0.0071
455	0.0405	555	0.0090	655	0.0084
460	0.0392	560	0.0084	660	0.0106
465	0.0379	565	0.0078	665	0.0136
470	0.0363	570	0.0073	670	0.0161
475	0.0347	575	0.0068	675	0.0170
480	0.0333	580	0.0064	680	0.0154
485	0.0322	585	0.0061	685	0.0118
490	0.0312	590	0.0058	690	0.0077
495	0.0297	595	0.0055	695	0.0046
				700	0.0027

\*Data courtesy of A. Morel.<sup>45</sup>





**FIGURE 8** Examples of the relative contributions of absorption by phytoplankton  $a_{\text{ph}}(\lambda)$ , and by organic detritus  $a_{\text{det}}(\lambda)$ , to the total particulate absorption  $a_p(\lambda)$ , from Sargasso Sea waters. (Redrawn from Iturriaga and Siegel,<sup>46</sup> with permission.)

and after pigments were chemically extracted to distinguish between absorption by pigmented and nonpigmented particles from fjord waters in the San Juan Islands, Washington, U.S.A. Each of these dissimilar techniques applied to particles from greatly different waters found very similar absorption spectra for nonpigmented organic particles derived from phytoplankton.

Figure 8 shows the microspectrophotometrically determined contributions of absorption by phytoplankton,  $a_{\text{ph}}(\lambda)$ , and of absorption by detritus,  $a_{\text{det}}(\lambda)$ , to the independently measured (by the filter-pad technique) total particulate absorption,  $a_p(\lambda)$ , for two depths at the same Atlantic location. The small residual,  $\Delta a_p(\lambda) = a_p(\lambda) - a_{\text{ph}}(\lambda) - a_{\text{det}}(\lambda)$  shown in the figure is attributed either to errors in the determination of the phytoplankton and detrital parts (particles smaller than  $\sim 3 \mu\text{m}$  were not analyzed) or to contamination by dissolved organic matter of the filter-pad measurements of total particulate absorption. Note that at the shallow depth the phytoplankton are relatively more important at blue wavelengths whereas the detritus is slightly more important at the deeper depth. There is no generality in this result (other locations showed the reverse)—it merely illustrates the variability possible in water samples taken only 60 vertical meters apart.

The important feature to note in Fig. 8 is the general shape of the spectral absorption curve for detritus. Roesler et al. found essentially identical curves in their determination of  $a_{\text{det}}(\lambda)$ . These curves are reminiscent of the absorption curves for yellow matter and, indeed, Roesler et al. found that the model

$$a_{\text{det}}(\lambda) = a_{\text{det}}(400) \exp[-0.011(\lambda - 400)]$$

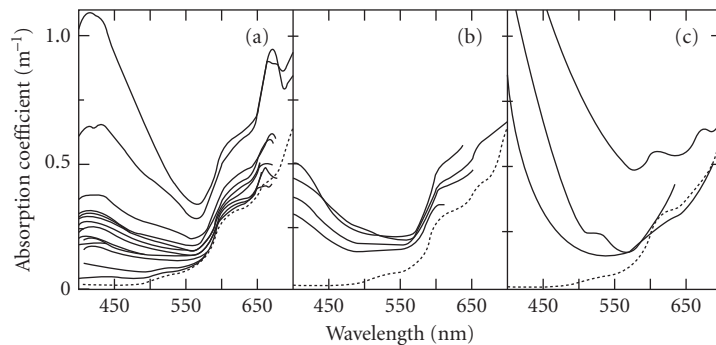
provides a satisfactory fit to detrital absorption curves. Other studies have found coefficients of  $-0.006$  to  $-0.014$  (Roesler et al.,<sup>43</sup> table 1) instead of  $-0.011$ .

## 1.15 BIO-OPTICAL MODELS FOR ABSORPTION

Depending on the concentrations of dissolved substances, phytoplankton, and detritus, the total spectral absorption coefficient of a given water sample can range from almost identical to that of pure water to one which shows orders-of-magnitude greater absorption than pure water, especially at blue wavelengths. Figure 9 shows some  $a(\lambda)$  profiles from various natural waters. Figure 9a shows absorption profiles measured in phytoplankton-dominated waters where chlorophyll concentrations ranged from  $C = 0.2$  to  $18.4 \text{ mg m}^{-3}$ . In essence, the absorption is high in the blue because of absorption by phytoplankton pigments and high in the red because of absorption by the water. Figure 9b shows the absorption at three locations where  $C \approx 2 \text{ mg m}^{-3}$  but where the scattering coefficient  $b$  varied from  $1.55$  to  $3.6 \text{ m}^{-1}$  indicating that nonpigmented particles were playing an important role in determining the shape of  $a(\lambda)$ . Figure 9c shows curves from waters rich in yellow matter, which is causing the high absorption in the blue. One of the goals of bio-optics is to develop predictive models for absorption curves such as those seen in Fig. 9.

*Case 1 waters* are waters in which the concentration of phytoplankton is high compared to non-biogenic particles.<sup>47</sup> Absorption by chlorophyll and related pigments therefore plays a major role in determining the total absorption coefficient in such waters, although detritus and dissolved organic matter derived from the phytoplankton also contribute to absorption in case 1 waters. Case 1 water can range from very clear (oligotrophic) water to very turbid (eutrophic) water, depending on the phytoplankton concentration. *Case 2 waters* are “everything else,” namely, waters where inorganic particles or dissolved organic matter from land drainage dominate so that absorption by pigments is relatively less important in determining the total absorption. (The cases 1 and 2 classifications must not be confused with the Jerlov water *types* 1 and 2, discussed later.) Roughly 98 percent of the world’s open ocean and coastal waters fall into the case 1 category, and therefore almost all bio-optical research has been directed toward these phytoplankton-dominated waters. However, near-shore and estuarine case 2 waters are disproportionately important to human interests such as recreation, fisheries, and military operations.

Prieur and Sathyendranath<sup>48</sup> developed a pioneering bio-optical model for the spectral absorption coefficient of case 1 waters. Their model was statistically derived from 90 sets of spectral absorption data taken in various case 1 waters and included absorption by phytoplankton pigments,



**FIGURE 9** Examples of spectral absorption coefficients  $a(\lambda)$  for various waters. Panel (a) shows  $a(\lambda)$  for waters dominated by phytoplankton, panel (b) is for waters with a high concentration of nonpigmented particles, and panel (c) is for waters rich in yellow matter. (Based on Prieur and Sathyendranath,<sup>48</sup> with permission.)

by nonpigmented organic particles derived from deceased phytoplankton, and by yellow matter derived from decayed phytoplankton. The contribution of phytoplankton to the total absorption was parametrized in terms of the chlorophyll concentration  $C$  (i.e., chlorophyll  $a$  plus pheophytin  $a$ ). The contributions of nonpigmented particles and of yellow matter were parametrized in terms of both the chlorophyll concentration and the total scattering coefficient at  $\lambda = 550$  nm,  $b(550)$ . The essence of the Prieur-Sathyendranath model is contained in a more recent and simpler variant given by Morel:<sup>6</sup>

$$a(\lambda) = [a_w(\lambda) + 0.06a_c^{**}(\lambda)C^{0.65}][1 + 0.2\exp(-0.014(\lambda - 440))] \quad (1)$$

Here  $a_w(\lambda)$  is the absorption coefficient of pure water and  $a_c^{**}(\lambda)$  is a nondimensional, statistically derived chlorophyll-specific absorption coefficient;  $a_w(\lambda)$  and  $a_c^{**}(\lambda)$  values are given in Table 9 [these  $a_w(\lambda)$  values are slightly different than those of Table 6]. When  $C$  is expressed in  $\text{mg m}^{-3}$  and  $\lambda$  is in nm, the resulting  $a(\lambda)$  is in  $\text{m}^{-1}$ .

Another simple bio-optical model for absorption has been developed independently by Kopelevich.<sup>49</sup> It has the form<sup>50</sup>

$$a(\lambda) = a_w(\lambda) + C[a_c^0(\lambda) + 0.1\exp[-0.015(\lambda - 400)]]$$

where  $a_c^0(\lambda)$  is the chlorophyll-specific absorption coefficient for phytoplankton ( $\text{m}^2 \text{mg}^{-1}$ ), and  $a_w(\lambda)$  and  $C$  are defined as for Eq. (1). The Kopelevich model as presently used<sup>49</sup> takes  $a_w(\lambda)$  from Smith and Baker<sup>32</sup> (Table 6) and takes  $a_c^0(\lambda)$  from Yentsch.<sup>51</sup>

Although these and similar bio-optical models for absorption are frequently used, caution is advised in their application. Both models assume that the absorption by yellow matter covaries with that due to phytoplankton; i.e., each implies that a fixed percentage of the total absorption at a given wavelength always comes from yellow matter. The general validity of this assumption is doubtful even for open ocean waters: Bricaud et al.<sup>42</sup> show data (Fig. 5) for which  $a(375)$ , used as an index for yellow matter concentration, is uncorrelated with chlorophyll concentration even in oceanic regions uninfluenced by freshwater runoff. Gordon<sup>52</sup> has developed a model that avoids assuming any relation between yellow matter and phytoplankton. However, his model becomes singular as  $C \rightarrow 0.01 \text{ mg m}^{-3}$  and cannot be expected to work well for  $C$  much less than  $0.1 \text{ mg m}^{-3}$ . The Kopelevich model has the chlorophyll contribution proportional to  $C$ , whereas the Morel model has  $C^{0.65}$ . The exponent of 0.65 is probably closer to reality, since it reflects a change in the relative contributions to absorption by phytoplankton and by detritus as the chlorophyll concentration changes (absorption by detritus is relatively more important at low chlorophyll concentrations<sup>52</sup>). Moreover, the chlorophyll-specific absorption curve of Yentsch<sup>51</sup> used in the Kopelevich

**TABLE 9** Absorption by Pure Sea Water,  $a_w$ , and the Nondimensional Chlorophyll-Specific Absorption Coefficient  $a_c^{**}$  Used in the Prieur-Sathyendranath-Morel Model for the Spectral Absorption Coefficient  $a(\lambda)$ \*

$\lambda$ (nm)	$a_w$ ( $\text{m}^{-1}$ )	$a_c^{**}$	$\lambda$ (nm)	$a_w$ ( $\text{m}^{-1}$ )	$a_c^{**}$	$\lambda$ (nm)	$a_w$ ( $\text{m}^{-1}$ )	$a_c^{**}$
400	0.018	0.687	500	0.026	0.668	600	0.245	0.236
410	0.017	0.828	510	0.036	0.618	610	0.290	0.252
420	0.016	0.913	520	0.048	0.528	620	0.310	0.276
430	0.015	0.973	530	0.051	0.474	630	0.320	0.317
440	0.015	1.000	540	0.056	0.416	640	0.330	0.334
450	0.015	0.944	550	0.064	0.357	650	0.350	0.356
460	0.016	0.917	560	0.071	0.294	660	0.410	0.441
470	0.016	0.870	570	0.080	0.276	670	0.430	0.595
480	0.018	0.798	580	0.108	0.291	680	0.450	0.502
490	0.020	0.750	590	0.157	0.282	690	0.500	0.329
						700	0.650	0.215

\*Condensed with permission from Prieur and Sathyendranath,<sup>48</sup> who give values every 5 nm.

model is based on laboratory cultures of phytoplankton, whereas the later work by Prieur and Sathyendranath used in situ observations to derive the  $a_c^*(\lambda)$  values of Table 9—an additional point in favor of Eq. (1). Either of these bio-optical models is useful but clearly imperfect. They may (or may not) give correct *average* values, but they give no information about the *variability* of  $a(\lambda)$ . It can be anticipated that the simple models now available will be replaced, perhaps by models designed for specific regions and seasons, as better understanding of the variability inherent in spectral absorption is achieved.

## 1.16 MEASUREMENT OF SCATTERING

Scattering in natural waters is caused both by small scale ( $\ll \lambda$ ) density fluctuations attributable to random molecular motions and by the ubiquitous large ( $> \lambda$ ) organic and inorganic particles. Scattering by water molecules (and salt ions, in seawater) determines the minimum values for the scattering properties. However, as is the case for absorption, the scattering properties of natural waters are greatly modified by the particulate matter that is always present.

Scattering measurements are even more difficult than absorption measurements. The conceptual design of an instrument for measuring the volume scattering function  $\beta(\psi, \lambda)$  is no more complicated than Fig. 2 and the defining equation  $\beta(\psi, \lambda) = I_s(\psi, \lambda) / [E_i(\lambda) \Delta V]$ : a collimated beam of known irradiance  $E_i$  illuminates a given volume of water  $\Delta V$  and the scattered intensity  $I_s$  is measured as a function of scattering angle and wavelength. However, the engineering of instruments capable of the in situ determination of  $\beta(\psi, \lambda)$  is quite difficult. The magnitude of the scattered intensity typically increases by five or six orders of magnitude in going from  $\psi = 90^\circ$  to  $\psi = 0.1^\circ$  for a given natural water sample, and scattering at a given angle  $\psi$  can vary by two orders of magnitude among water samples. The required dynamic range of an instrument is therefore great. Corrections must be made for absorption within the sample volume and also along the incident and scattered beam paths for in situ instruments. The rapid change in  $\beta(\psi, \lambda)$  at small scattering angles requires very precise alignment of the optical elements, but rolling ships seem designed to knock things out of alignment. Because of these design difficulties only a few one-of-a-kind instruments have been built for in situ measurement of the volume scattering function, and measurements of  $\beta(\psi, \lambda)$  are not routinely made. Petzold<sup>53</sup> gives the details of two such instruments, one for small scattering angles ( $\psi = 0.085, 0.17, \text{ and } 0.34^\circ$ ) and one for larger angles ( $10^\circ \leq \psi \leq 170^\circ$ ); these are the instruments used to obtain the data presented in Sec. 1.18. Other instruments are referenced in Kirk<sup>8</sup> and in Jerlov.<sup>29</sup>

Commercial instruments are available for laboratory measurement of  $\beta(\psi, \lambda)$  at fixed scattering angles (e.g.,  $\psi$  every  $5^\circ$  from  $\sim 20^\circ$  to  $\sim 160^\circ$ ). These instruments are subject to their own problems, such as degradation of samples between the times of collection and measurement. Moreover, measurements of  $\beta(\psi, \lambda)$  over a limited range of  $\psi$  are not sufficient for determination of  $b(\lambda)$  by integration. In practice, the scattering coefficient  $b(\lambda)$  is usually determined by the conservation of energy relation  $b(\lambda) = c(\lambda) - a(\lambda)$  after measurements of beam attenuation and absorption have been made.

Both in situ and laboratory instruments sample ( $\sim \text{cm}^3$ ) volumes of water and therefore may fail to detect the presence of optically significant large aggregates (marine snow) if such particles are too few in number to be reliably captured in the sample volume. However, such particles can affect the scattering properties of large volumes of water (e.g., as seen in remote sensing or underwater visibility studies).

Measurements at near forward ( $\psi < 1^\circ$ ) and near backward ( $\psi > 179^\circ$ ) angles are exceptionally difficult to make, yet the behavior of  $\beta(\psi, \lambda)$  at these extreme angles is of considerable interest. Accurate determination of  $\beta$  at small angles is crucial to the determination of  $b$  by integration since typically one-half of all scattering takes place at angles of less than a few degrees. Scattering at small angles is important in underwater imaging and it is of theoretical interest for its connections to scattering theory, particle optical properties, and particle size distributions. The behavior of  $\beta$  very near  $\psi = 180^\circ$  is important in laser remote-sensing applications.

Spinrad et al.<sup>54</sup> and Padmabandu and Fry<sup>55</sup> have reported measurements at very small angles on suspensions of polystyrene spheres but no such measurements have been published for natural water samples. The Padmabandu and Fry technique is notable in that it allows the measurement of  $\beta$  at  $\psi = 0^\circ$  exactly by use of the coupling of two coherent beams in a photorefractive crystal to measure the phase shift that corresponds to  $0^\circ$  scattering. Measurement of  $\beta(0, \lambda)$  is of theoretical interest because of its relation to attenuation via the optical theorem. Enhanced backscatter has been reported<sup>56</sup> in suspensions of latex spheres; a factor-of-two increase in scattered intensity between  $\psi = 179.5$  and  $180.0^\circ$  is typical. Whether or not such backscattering enhancement ever occurs in natural waters is a subject of heated debate.

## 1.17 SCATTERING BY PURE WATER AND BY PURE SEA WATER

Morel<sup>57</sup> has reviewed in detail the theory and observations pertaining to scattering by pure water and by pure sea water. In pure water random molecular motions give rise to rapid fluctuations in the number of molecules in a given volume  $\Delta V$ , where  $\Delta V$  is small compared to the wavelength of light but large compared to atomic scales (so that the liquid within the volume is adequately described by statistical thermodynamics). The Einstein-Smoluchowski theory of scattering relates these fluctuations in molecular number density to associated fluctuations in the index of refraction, which give rise to scattering. In sea water the basic theory is the same but random fluctuations in the concentrations of the various ions ( $\text{Cl}^-$ ,  $\text{Na}^+$ , etc.) give somewhat greater index of refraction fluctuations, and hence greater scattering. The net result of these considerations is that the volume scattering function for either pure water or for pure sea water has the form

$$\beta_w(\psi, \lambda) = \beta_w(90^\circ, \lambda_0) \left( \frac{\lambda_0}{\lambda} \right)^{4.32} (1 + 0.835 \cos^2 \psi) \quad \text{m}^{-1} \text{sr}^{-1} \quad (2)$$

which is reminiscent of the form for Rayleigh scattering. The wavelength dependence of  $\lambda^{-4.32}$  rather than  $\lambda^{-4}$  (for Rayleigh scattering) results from the wavelength dependence of the index of refraction. The 0.835 factor is attributable to the anisotropy of the water molecules. The corresponding phase function is

$$\tilde{\beta}_w(\psi) = 0.06225(1 + 0.835 \cos^2 \psi) \quad \text{sr}^{-1}$$

and the total scattering coefficient  $b_w(\lambda)$  is given by

$$b_w(\lambda) = 16.06 \left( \frac{\lambda_0}{\lambda} \right)^{4.32} \beta_w(90^\circ, \lambda_0) \quad \text{m}^{-1} \quad (3)$$

Table 10 gives values of  $\beta_w(90^\circ, \lambda)$  and  $b_w(\lambda)$  for selected wavelengths for both pure water and pure sea water ( $S = 35$  to  $39\%$ ). Note that the pure sea water values are about 30 percent greater than the pure water values at all wavelengths. Table 11 shows the dependence of  $b_w$ (546) on pressure, temperature, and salinity. Note that molecular scattering decreases as decreasing temperature or increasing pressure reduce the smallscale fluctuations.

## 1.18 SCATTERING BY PARTICLES

Heroic efforts are required to obtain water of sufficient purity that a Rayleigh-like volume scattering function is observed. As soon as there is a slight amount of particulate matter in the water—always the case for even the clearest natural water—the volume scattering function becomes highly peaked in the forward direction, and the scattering coefficient increases by at least a factor of 10.

**TABLE 10** The Volume Scattering Function at  $\psi = 90^\circ$ ,  $\beta_w(90^\circ, \lambda)$ , and the Scattering Coefficient  $b_w(\lambda)$  for Pure Water and for Pure Sea Water ( $S = 35\text{--}39\%$ )<sup>a</sup>

$\lambda$ (nm)	Pure water		Pure sea water	
	$\beta_w(90^\circ)$ ( $10^{-4} \text{ m}^{-1} \text{ sr}^{-1}$ )	$b_w^\dagger$ ( $10^{-4} \text{ m}^{-1}$ )	$\beta(90^\circ)$ ( $10^{-4} \text{ m}^{-1} \text{ sr}^{-1}$ )	$b_w^\dagger$ ( $10^{-4} \text{ m}^{-1}$ )
350	6.47	103.5	8.41	134.5
375	4.80	76.8	6.24	99.8
400	3.63	58.1	4.72	75.5
425	2.80	44.7	3.63	58.1
450	2.18	34.9	2.84	45.4
475	1.73	27.6	2.25	35.9
500	1.38	22.2	1.80	28.8
525	1.12	17.9	1.46	23.3
550	0.93	14.9	1.21	19.3
575	0.78	12.5	1.01	16.2
600	0.68	10.9	0.88	14.1

<sup>a</sup>Reproduced from Morel,<sup>57</sup> with permission.<sup>†</sup>Computed from  $b(\lambda) = 16.0\beta(90^\circ, \lambda)$ .

Even for the most numerous oceanic particles (e.g., colloids at a concentration of  $10^{15} \text{ m}^{-3}$ ) the average distance between particles is greater than ten wavelengths of visible light. For the optically most significant phytoplankton the average separation is thousands of wavelengths. Moreover, these particles usually are randomly distributed and oriented. Ocean water therefore can be treated as a very dilute suspension of random scatterers and consequently the intensity of light scattered by an ensemble of particles is given by the sum of the intensities due to the individual particles. Coherent scattering effects are negligible except perhaps at extremely small scattering angles.<sup>58</sup> An overview of scattering by particles is given in Chap. 7 “Scattering by Particles” by Craig F. Bohren in Vol. I.

The contribution of the particulate matter to the total volume scattering function  $\beta(\psi, \lambda)$  is obtained from

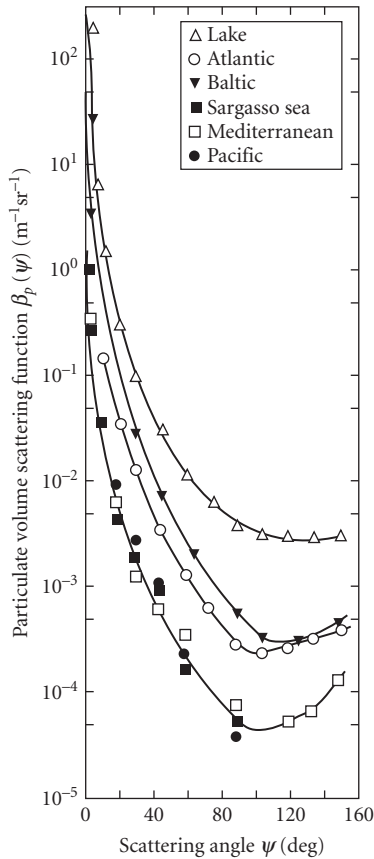
$$\beta_p(\psi, \lambda) \equiv \beta(\psi, \lambda) - \beta_w(\psi, \lambda)$$

Here the subscript p refers to particles, and w refers to pure water (if  $\beta$  is measured in fresh water) or pure sea water (for oceanic measurements). Figure 10 shows several particle volume scattering functions determined from in situ measurements of  $\beta(\psi, \lambda)$  in a variety of waters ranging from very clear to very turbid. The particles cause at least a four-order-of-magnitude increase in scattering between  $\psi \approx 90^\circ$  and  $\psi \approx 1^\circ$ . The contribution of molecular scattering to the total is therefore completely negligible except at backscattered directions ( $\psi \geq 90^\circ$ ) in the clearest natural waters. The top curve in Fig. 10 is shown for small scattering angles in Fig. 11. The scattering function shows

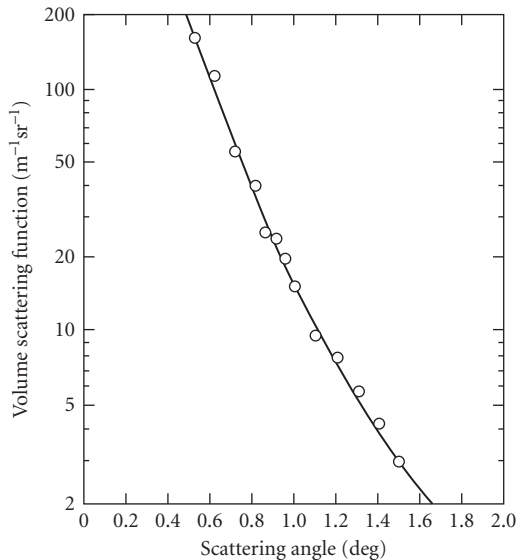
**TABLE 11** Computed Scattering Coefficient  $b$  of Pure Water ( $S = 0$ ) and of Pure Sea Water ( $S = 35\%$ ) at  $\lambda = 546 \text{ nm}$  as a Function of Temperature  $T$  and Pressure  $p$  (Numbers in the body of the table have units of  $\text{m}^{-1}$ .<sup>a</sup>)

$T$ ( $^\circ\text{C}$ )	$p = 10^5 \text{ Pa (1 atm)}$		$p = 10^7 \text{ Pa (100 atm)}$		$p = 10^8 \text{ Pa (1000 atm)}$	
	$S = 0$	$S = 35\%$	$S = 0$	$S = 35\%$	$S = 0$	$S = 35\%$
0	0.00145	0.00195	0.00140	0.00192	0.00110	0.00167
10	0.00148	0.00203	0.00143	0.00200	0.00119	0.00176
20	0.00149	0.00207	0.00147	0.00204	0.00125	0.00183
40	0.00150	0.00213	0.00149	0.00212	0.00136	0.00197

<sup>a</sup>Data extracted from the more extensive table of Shifrin,<sup>58</sup> with permission.



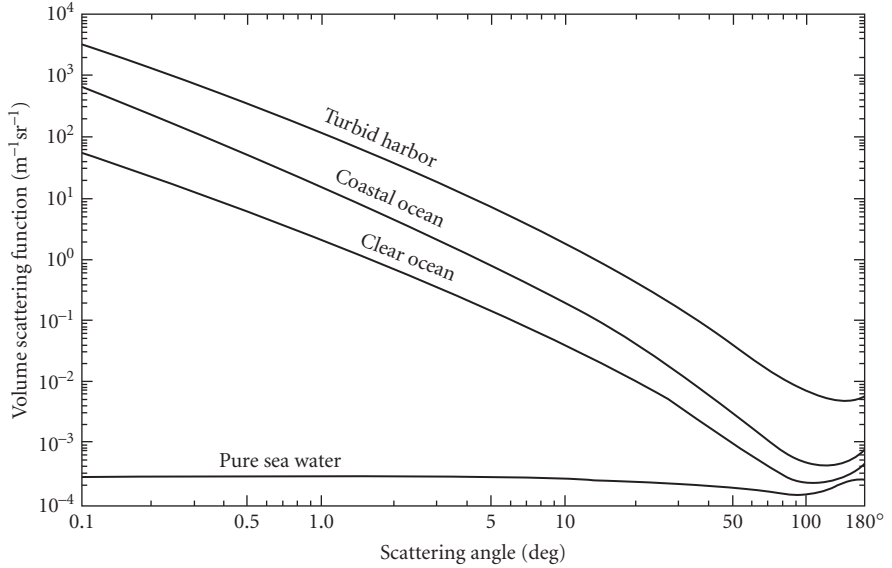
**FIGURE 10** Particulate volume scattering functions  $\beta_p(\psi, \lambda)$  determined from *in situ* measurements in various waters; wavelengths vary. (Redrawn from Kullenberg,<sup>59</sup> with permission.)



**FIGURE 11** Detail of the forward scattering values of the “lake” volume scattering function seen in the top curve of Fig. 10. (Redrawn from Preisendorfer.<sup>2</sup>)

no indication of “flattening out” even at angles as small as  $0.5^\circ$ . Note that the scattering function increases by a factor of 100 over only a one-degree range of scattering angle.

Highly peaked forward scattering such as that seen in Figs. 10 and 11 is characteristic of diffraction-dominated scattering in a polydisperse system. Scattering by refraction and reflection from particle surfaces becomes important at large scattering angles ( $\psi \geq 15^\circ$ ). Mie scattering calculations are well able to reproduce observed volume scattering functions given the proper optical properties and size distributions. Early efforts along these lines are seen in Kullenberg<sup>59</sup> and in Brown and Gordon.<sup>60</sup> Brown and Gordon were unable to reproduce observed backscattering values using measured particle size distributions. However, their instruments were unable to detect submicrometer particles. They found that the Mie theory properly predicted backscattering if they assumed the presence of numerous, submicrometer, low-index-of-refraction particles. It is reasonable to speculate that bacteria and the recently discovered colloidal particles are the particles whose existence was inferred by Brown and Gordon. Recent Mie scattering calculations<sup>61</sup> have used three-layered spheres to model the structure of phytoplankton (cell wall, chloroplasts, and cytoplasm core) and have used polydisperse mixtures of both organic and inorganic particles.



**FIGURE 12** Measured volume scattering functions from three different natural waters and the computed volume scattering function for pure sea water, all at  $\lambda = 514$  nm. (Redrawn from Petzold.<sup>53</sup>)

The most carefully made and widely cited scattering measurements are found in Petzold.<sup>53</sup> Figure 12 shows three of his  $\beta(\psi, \lambda)$  curves displayed on a log-log plot to emphasize the forward scattering angles. The instruments had a spectral response centered at  $\lambda = 514$  nm with an FWHM of 75 nm. The top curve was obtained in the very turbid water of San Diego Harbor, California; the center curve comes from near-shore coastal water in San Pedro Channel, California; and the bottom curve is from very clear water in the Tongue of the Ocean, Bahama Islands. The striking feature of these volume scattering functions (and those of Fig. 10) from very different waters is the similarity of their shapes. Although the scattering coefficients  $b$  of the curves in Fig. 12 vary by a factor of 50 (Table 13), the uniform shapes suggest that it is reasonable to define a “typical” particle phase  $\tilde{\beta}_p(\psi, \lambda)$ . This has been done<sup>62</sup> with three sets of Petzold’s data from waters with a high particulate load (one set being the top curve of Fig. 12), as follows: (1) subtract  $\beta_w(\psi, \lambda)$  from each curve to get three particle volume scattering functions  $\beta_p^i(\psi, \lambda)$ ,  $i = 1, 2, 3$ ; (2) compute three particle phase functions via  $\tilde{\beta}_p^i(\psi, \lambda) = \beta_p^i(\psi, \lambda) / b^i(\lambda)$ ; (3) average the three particle phase functions to define the typical particle phase function  $\tilde{\beta}_p(\psi, \lambda)$ . Table 12 displays the three Petzold volume scattering functions plotted in Fig. 12, the volume scattering function for pure sea water, and the average particle phase function computed as just described. This particle phase function satisfies the normalization  $2\pi \int_0^\pi \tilde{\beta}_p(\psi, \lambda) \sin \psi \, d\psi = 1$  if a behavior of  $\tilde{\beta}_p \sim \psi^{-m}$  is assumed for  $\psi < 0.1^\circ$  ( $m$  is a positive constant between zero and two, determined from  $\tilde{\beta}_p$  at the smallest measured angles), and a trapezoidal rule integration is used for  $\psi \geq 0.1^\circ$ , with linear interpolation used between the tabulated values. This average particle phase function is adequate for many radiative transfer calculations. However, the user must remember that significant deviations from the average can be expected in nature (e.g., in waters with abnormally high numbers of either large or small particles), although the details of such deviations have not been quantified.

Table 13 compares several inherent optical properties for pure sea water and for the three Petzold water samples of Fig. 12 and Table 12. These data show how greatly different even clear ocean water is from pure sea water. Note that natural water ranges from absorption-dominated ( $\omega_0 = 0.247$ ) to scattering-dominated ( $\omega_0 = 0.833$ ) at  $\lambda = 514$  nm. The ratio of backscattering to total scattering is typically a few percent in natural water. However, there is no clear relation between  $b_b/b$  and the water type, at least for the Petzold data of Table 13. This lack of an obvious relation is likely the result of



**TABLE 12** Volume Scattering Functions  $\beta(\psi, \lambda)$  for Three Oceanic Waters and for Pure Sea Water and a Typical Particle Phase  $\hat{\beta}_p(\psi, \lambda)$ , All at  $\lambda = 514$  nm

Scattering Angle (deg)	Volume scattering functions ( $\text{m}^{-1} \text{sr}^{-1}$ )				Particle Phase Function <sup>‡</sup> ( $\text{sr}^{-1}$ )
	Clear Ocean*	Coastal Ocean*	Turbid Harbor*	Pure Sea Water <sup>†</sup>	
0.100	$5.318 \times 10^1$	$6.533 \times 10^2$	$3.262 \times 10^3$	$2.936 \times 10^{-4}$	$1.767 \times 10^3$
0.126	4.042	4.577	2.397	2.936	1.296
0.158	3.073	3.206	1.757	2.936	$9.502 \times 10^2$
0.200	2.374	2.252	1.275	2.936	6.991
0.251	1.814	1.579	$9.260 \times 10^2$	2.936	5.140
0.316	1.360	1.104	6.764	2.936	3.764
0.398	$9.954 \times 10$	$7.731 \times 10^1$	5.027	2.936	2.763
0.501	7.179	5.371	3.705	2.936	2.012
0.631	5.110	3.675	2.676	2.936	1.444
0.794	3.591	2.481	1.897	2.936	1.022
1.000	2.498	1.662	1.329	2.936	$7.161 \times 10^1$
1.259	1.719	1.106	$9.191 \times 10^1$	2.935	4.958
1.585	1.171	$7.306 \times 10^0$	6.280	2.935	3.395
1.995	$7.758 \times 10^{-1}$	4.751	4.171	2.934	2.281
2.512	5.087	3.067	2.737	2.933	1.516
3.162	3.340	1.977	1.793	2.932	1.002
3.981	2.196	1.273	1.172	2.930	$6.580 \times 10^0$
5.012	1.446	$8.183 \times 10^{-1}$	$7.655 \times 10^0$	2.926	4.295
6.310	$9.522 \times 10^{-2}$	5.285	5.039	2.920	2.807
7.943	6.282	3.402	3.302	2.911	1.819
10.0	4.162	2.155	2.111	2.896	1.153
15.0	2.038	$9.283 \times 10^{-2}$	$9.041 \times 10^{-1}$	2.847	$4.893 \times 10^{-1}$
20.0	1.099	4.427	4.452	2.780	2.444
25.0	$6.166 \times 10^{-3}$	2.390	2.734	2.697	1.472
30.0	3.888	1.445	1.613	2.602	$8.609 \times 10^{-2}$
35.0	2.680	$9.063 \times 10^{-3}$	1.109	2.497	5.931
40.0	1.899	6.014	$7.913 \times 10^{-2}$	2.384	4.210
45.0	1.372	4.144	5.858	2.268	3.067
50.0	1.020	2.993	4.388	2.152	2.275
55.0	$7.683 \times 10^{-4}$	2.253	3.288	2.040	1.699
60.0	6.028	1.737	2.548	1.934	1.313
65.0	4.883	1.369	2.041	1.839	1.046
70.0	4.069	1.094	1.655	1.756	$8.488 \times 10^{-3}$
75.0	3.457	$8.782 \times 10^{-4}$	1.345	1.690	6.976
80.0	3.019	7.238	1.124	1.640	5.842
85.0	2.681	6.036	$9.637 \times 10^{-3}$	1.610	4.953
90.0	2.459	5.241	8.411	1.600	4.292
95.0	2.315	4.703	7.396	1.610	3.782
100.0	2.239	4.363	6.694	1.640	3.404
105.0	2.225	4.189	6.220	1.690	3.116
110.0	2.239	4.073	5.891	1.756	2.912
115.0	2.265	3.994	5.729	1.839	2.797
120.0	2.339	3.972	5.549	1.934	2.686
125.0	2.505	3.984	5.343	2.040	2.571
130.0	2.629	4.071	5.154	2.152	2.476
135.0	2.662	4.219	4.967	2.268	2.377
140.0	2.749	4.458	4.822	2.384	2.329
145.0	2.896	4.775	4.635	2.497	2.313

(Continued)

**TABLE 12** Volume Scattering Functions  $\beta(\psi, \lambda)$  for Three Oceanic Waters and for Pure Sea Water and a Typical Particle Phase  $\tilde{\beta}_p(\psi, \lambda)$ , All at  $\lambda = 514$  nm (*Continued*)

Scattering Angle (deg)	Volume scattering functions ( $\text{m}^{-1} \text{sr}^{-1}$ )				
	Clear Ocean*	Coastal Ocean*	Turbid Harbor*	Pure Sea Water†	Particle Phase Function‡ ( $\text{sr}^{-1}$ )
150.0	3.088	5.232	4.634	2.602	2.365
155.0	3.304	5.824	4.900	2.697	2.506
160.0	3.627	6.665	5.142	2.780	2.662
165.0	4.073	7.823	5.359	2.847	2.835
170.0	4.671	9.393	5.550	2.896	3.031
175.0	4.845	9.847	5.618	2.926	3.092
180.0	5.109	$1.030 \times 10^{-3}$	5.686	2.936	3.154

\*Data reproduced from Petzold.<sup>53</sup>

†Computed from Eq. (2) and Table 10.

‡Courtesy of H. R. Gordon; see also Ref. 62.

differing particle types in the three waters. Since refraction and reflection are important processes at large scattering angles, the particle indices of refraction are important in determining  $b_p$ . Total scattering is dominated by diffraction and so particle composition has little effect on  $b$  values. The last row of Table 13 gives the angle  $\psi$  such that one-half of the total scattering occurs at angles between  $0$  and  $\psi$ . This angle is rarely greater than  $10^\circ$  in natural waters.

## 1.19 WAVELENGTH DEPENDENCE OF SCATTERING: BIO-OPTICAL MODELS

The strong  $\lambda^{-4.32}$  wavelength dependence of pure-water scattering is not seen in natural waters. This is because scattering is dominated by diffraction from polydisperse particles that are usually much larger than the wavelength of visible light. Although diffraction depends on the particle size-to-wavelength ratio, the presence of particles of many sizes diminishes the wavelength effects that are seen in diffraction by a single particle. Moreover, diffraction does not depend on particle composition. However, some wavelength dependence is to be expected, especially at backward scattering angles where refraction, and hence particle composition, is important. Molecular scattering also contributes something to the total scattering and can even dominate the particle contribution at backscatter angles in clear water.<sup>63</sup>

Morel<sup>64</sup> presents several useful observations on the wavelength dependence of scattering. Figure 13 shows two sets of volume scattering functions, one from the very clear waters of the Tyrrhenian Sea and one from the turbid English Channel. Each set displays  $\beta(\psi, \lambda)/\beta(90^\circ, \lambda)$  for  $\lambda = 366, 436$ , and

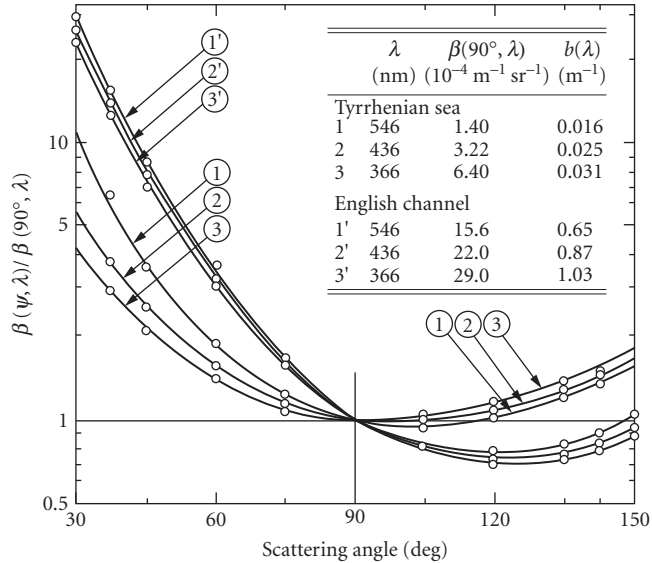
**TABLE 13** Selected Inherent Optical Properties for the Waters Presented in Fig. 12 and in Table 12 (All values are for  $\lambda = 514$  nm except as noted.)

Water	$a$ ( $\text{m}^{-1}$ )	$b$ ( $\text{m}^{-1}$ )	$c$ ( $\text{m}^{-1}$ )	$\omega_0$	$b_p/b$	$\psi$ for $\frac{1}{2}b$ (deg)
Pure sea water	0.0405*	0.0025†	0.043	0.058	0.500	90.00
Clear ocean	0.114‡	0.037	0.151§	0.247	0.044	6.25
Coastal ocean	0.179‡	0.219	0.398§	0.551	0.013	2.53
Turbid harbor	0.366‡	1.824	2.190§	0.833	0.020	4.68

\*Value obtained by interpolation in Table 6.

†Value obtained by interpolation in Table 10.

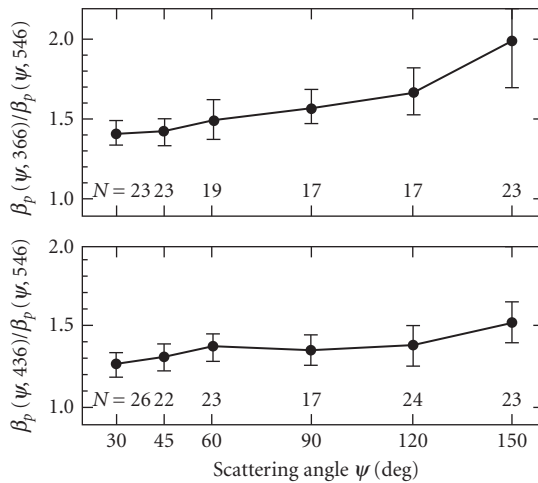
‡Estimated by Petzold<sup>53</sup> from  $c(530 \text{ nm}) - b(514 \text{ nm})$ .§Measured by Petzold at  $\lambda = 530$  nm.



**FIGURE 13** Wavelength dependence of total volume scattering functions measured in very clear (Tyrrhenian Sea) and in turbid (English Channel) waters. (Redrawn from Morel.<sup>64</sup>)

546 nm. The clear water shows a definite dependence of the shape of  $\beta(\psi, \lambda)$  on  $\lambda$  whereas the particle-rich turbid water shows much less wavelength dependence. In each case the volume scattering function of shortest wavelength is most nearly symmetric about  $\psi = 90^\circ$ , presumably because symmetric molecular scattering is contributing relatively more to the total scattering at short wavelengths.

Figure 14 shows a systematic wavelength dependence of particle volume scattering functions. Figure 14a shows average values of  $\beta_p(\psi, 366 \text{ nm})/\beta_p(\psi, 546 \text{ nm})$  for  $N$  samples as labeled in



**FIGURE 14** Wavelength dependence of particulate volume scattering functions.  $N$  is the number of samples. (Redrawn from Morel.<sup>64</sup>)

**TABLE 14** Exponents  $n$  Required to Fit the Data of Fig. 14 Assuming That  $\beta_p(\psi, \lambda) = \beta_p(\psi, 546)(546/\lambda)^n$

Wavelength $\lambda$ (nm)	Scattering angle $\psi$		
	30°	90°	150°
366	0.84	1.13	1.73
436	0.99	1.33	1.89

the figure. The vertical bars are one standard deviation of the observations. Figure 14b shows the ratio for  $\lambda = 436$  to 546 nm. These ratios clearly depend both on wavelength and scattering angle. Assuming that  $\beta_p(\psi, \lambda)$  has a wavelength dependence of

$$\beta_p(\psi, \lambda) = \beta_p(\psi, 546) \left( \frac{546 \text{ nm}}{\lambda} \right)^n$$

the data of Fig. 14 imply values for  $n$  as seen in Table 14. As anticipated, the wavelength dependence is strongest for backscatter ( $\psi = 150^\circ$ ) and weakest for forward scatter ( $\psi = 30^\circ$ ).

Kopelevich<sup>49,65</sup> has statistically derived a two-parameter model for spectral volume scattering functions (VSFs). This model separates the contributions by “small” and “large” particles to the particulate scattering. Small particles are taken to be mineral particles less than 1  $\mu\text{m}$  in size and having an index of refraction of  $n = 1.15$ ; large particles are biologic particles larger than 1  $\mu\text{m}$  in size and having an index refraction of  $n = 1.03$ . The model is defined by

$$\beta(\psi, \lambda) = \beta_w(\psi, \lambda) + v_s \beta_s^*(\psi) \left( \frac{550 \text{ nm}}{\lambda} \right)^{1.7} + v_\ell \beta_\ell^*(\psi) \left( \frac{550 \text{ nm}}{\lambda} \right)^{0.3} \quad (4)$$

with the following definitions:

- $\beta_w(\psi, \lambda)$  the VSF of pure sea water, given by Eq. (2) with  $\lambda_0 = 550$  nm and an exponent of 4.30
- $v_s$  the volume concentration of small particles, with units of  $\text{cm}^3$  of particles per  $\text{m}^3$  of water, i.e., parts per million (ppm)
- $v_\ell$  the analogous volume concentration of large particles
- $\beta_s^*(\psi)$  the small-particle VSF per unit volume concentration of small particles, with units of  $\text{m}^{-1} \text{sr}^{-1} \text{ppm}^{-1}$
- $\beta_\ell^*(\psi)$  the analogous large-particle concentration-specific VSF

The concentration-specific VSFs for small and large particles are given in Table 15. Equation (4) can be evaluated as if the two parameters  $v_s$  and  $v_\ell$  are known; the ranges of values for oceanic waters are  $0.01 \leq v_s \leq 0.20$  ppm  $0.01 \leq v_\ell \leq 0.40$  ppm. However, these two parameters are themselves parametrized in terms of the total volume scattering function measured at  $\lambda = 550$  nm for  $\psi = 1$  and  $45^\circ$ :

$$\begin{aligned} v_s &= -1.45 \times 10^{-4} \beta(1^\circ, 550 \text{ nm}) + 10.2 \beta(45^\circ, 550 \text{ nm}) - 0.002 \\ v_\ell &= 2.2 \times 10^{-2} \beta(1^\circ, 550 \text{ nm}) - 1.2 \beta(45^\circ, 550 \text{ nm}) \end{aligned} \quad (5)$$

Thus  $\beta(\psi, \lambda)$  can also be determined from two measurements of the total VSF.

The mathematical form of the Kopelevich model reveals its underlying physics. Large particles give diffractive scattering at very small angles; thus  $\beta_\ell^*(\psi)$  is highly peaked for small  $\psi$  and the wavelength dependence of the large particle term is weak ( $\lambda^{-0.3}$ ). Small particles contribute more to

**TABLE 15** The Concentration-Specific Volume Scattering Functions for Small ( $\beta_s^*$ ) and Large ( $\beta_\ell^*$ ) Particles As a Function of the Scattering Angle  $\psi$  for Use in the Kopelevich Model for Spectral Volume Scattering Functions, Eq. (4)\*

$\psi$ (deg)	$\beta_s^* \left( \frac{\text{m}^{-1} \text{sr}^{-1}}{\text{ppm}} \right)$	$\beta_\ell^* \left( \frac{\text{n}^{-1} \text{sr}^{-1}}{\text{ppm}} \right)$	$\psi$ (deg)	$\beta_s^* \left( \frac{\text{m}^{-1} \text{sr}^{-1}}{\text{ppm}} \right)$	$\beta_\ell^* \left( \frac{\text{m}^{-1} \text{sr}^{-1}}{\text{ppm}} \right)$
0	5.3	140	45	$9.8 \times 10^{-2}$	$6.2 \times 10^{-4}$
0.5	5.3	98	60	4.1	3.8
1	5.2	46	75	2.0	2.0
1.5	5.2	26	90	1.2	$6.3 \times 10^{-5}$
2	5.1	15	105	$8.6 \times 10^{-3}$	4.4
4	4.6	3.6	120	7.4	2.9
6	3.9	1.1	135	7.4	2.0
10	2.5	0.20	150	7.5	2.0
15	1.3	$5.0 \times 10^{-2}$	180	8.1	7.0
30	0.29	$2.8 \times 10^{-3}$	$b^* =$	$1.34 \text{ m}^{-1}/\text{ppm}$	$0.312 \text{ m}^{-1}/\text{ppm}$

\*Reproduced from Kopelevich.<sup>49</sup>

scattering at large angles and thus have a more symmetric VSF and a stronger wavelength dependence ( $\lambda^{-1.7}$ ). This model gives a reasonably good description of VSFs observed in a variety of waters (Shifrin,<sup>58</sup> fig. 5.20).

Several simple models are available for the scattering coefficient  $b(\lambda)$ . A commonly employed bio-optical model for  $b(\lambda)$  is that of Gordon and Morel<sup>66</sup> (see also Ref. 6):

$$b(\lambda) = b_w(\lambda) + \left( \frac{550 \text{ nm}}{\lambda} \right) 0.30C^{0.62} \quad \text{m}^{-1} \quad (6)$$

Here  $b_w(\lambda)$  is given by Eq. (3) and Table 10.  $\lambda$  is in nm and  $C$  is the chlorophyll concentration in  $\text{mg m}^{-3}$ . A related bio-optical model for the backscatter coefficient  $b_b(\lambda)$  is found in Morel.<sup>45</sup>

$$b_b(\lambda) = \frac{1}{2}b_w(\lambda) + \left[ 0.002 + 0.02 \left( \frac{1}{2} - \frac{1}{4} \log C \left( \frac{500 \text{ nm}}{\lambda} \right) \right) \right] 0.30C^{0.62}$$

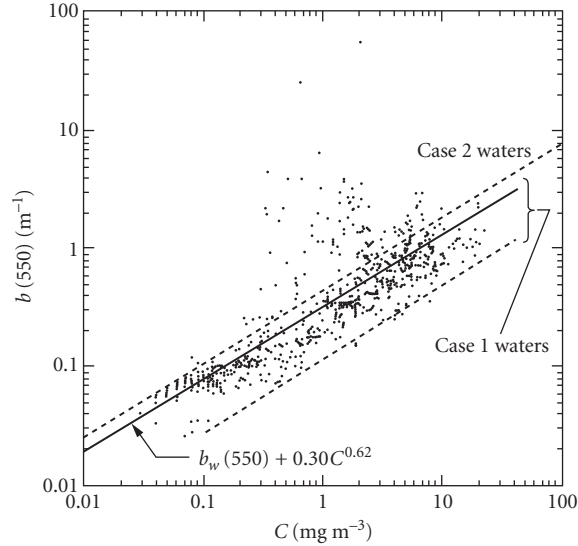
The  $\left( \frac{1}{2} - \frac{1}{4} \log C \right)$  factor gives  $b_b(\lambda)$  a  $\lambda^{-1}$  wavelength dependence in very clear ( $C = 0.01 \text{ mg m}^{-1}$ ) water and no wavelength dependence in very turbid ( $C = 100 \text{ mg m}^{-3}$ ) water. These empirically derived models are intended for use only in case 1 waters.

A feeling for the accuracy of the  $b(\lambda)$  model of Eq. (6) can be obtained from Fig. 15, which plots measured  $b(550 \text{ nm})$  values versus chlorophyll concentration  $C$  in both case 1 and case 2 waters. Note that even when the model is applied to the case 1 waters from which it was derived, the predicated  $b(550 \text{ nm})$  value easily can be wrong by a factor of 2. If the model is misapplied to case 2 waters, the error can be an order of magnitude. Note that for a given  $C$  value,  $b(550 \text{ nm})$  is higher in case 2 waters than in case 1 waters, presumably because of the presence of additional particles that do not contain chlorophyll.

Integration over  $\psi$  of the Kopelevich  $b(\psi, \lambda)$  model of Eq. (4) yields another model for  $b(\lambda)$ :

$$b(\lambda) = 0.0017 \left( \frac{500 \text{ nm}}{\lambda} \right)^{4.3} + 1.34\nu_s \left( \frac{550 \text{ nm}}{\lambda} \right)^{1.7} + 0.312\nu_\ell \left( \frac{550 \text{ nm}}{\lambda} \right)^{0.3} \quad \text{m}^{-1}$$

where  $\nu_s$  and  $\nu_\ell$  are given by Eq. (5). Kopelevich claims that the accuracy of this model is  $\sim 30$  percent.



**FIGURE 15** Measured scattering coefficients at  $\lambda = 550$  nm,  $b(550)$ , as a function of chlorophyll concentration  $C$ . Case 1 waters lie between the dashed lines. Case 2 waters lie above the upper dashed line, which is defined by  $b(550) = 0.45C^{0.62}$ . The solid line is the model of Eq. (6). (Redrawn from Gordon and Morel,<sup>66</sup> with permission.)

A bio-optical model related to the Kopelevich model is found in Haltrin and Kattawar<sup>50</sup> (their notation):

$$b(\lambda) = b_w(\lambda) + b_{ps}^0(\lambda)P_s + b_{pl}^0(\lambda)P_\ell$$

Here  $b_w(\lambda)$  is given by

$$b_w(\lambda) = 5.826 \times 10^{-3} \left( \frac{400}{\lambda} \right)^{4.322}$$

which is essentially the same as Eq. (3) and the data in Table 10. The terms  $b_{ps}^0(\lambda)$  and  $b_{pl}^0(\lambda)$  are the specific scattering coefficients for small and large particles, respectively, and are given by

$$b_{ps}^0(\lambda) = 1.1513 \left( \frac{400}{\lambda} \right)^{1.7} \quad \text{m}^2 \text{ g}^{-1}$$

$$b_{pl}^0(\lambda) = 0.3411 \left( \frac{400}{\lambda} \right)^{0.3} \quad \text{m}^2 \text{ g}^{-1}$$

$P_s$  and  $P_\ell$  are the concentrations in  $\text{g m}^{-3}$  of small and large particles, respectively. These quantities are parametrized in terms of the chlorophyll concentration  $C$ , as shown in Table 16. This work also presents a model for backscattering:

$$b_b(\lambda) = \frac{1}{2} b_w(\lambda) + B_s b_{ps}^0(\lambda)P_s + B_\ell b_{pl}^0(\lambda)P_\ell$$

**TABLE 16** Parameterization of Small ( $P_s$ ) and Large ( $P_l$ ) Particle Concentrations in Terms of the Chlorophyll Concentration  $C$  for Use in the Kopelevich-Haltrin-Kattawar Models for  $b(\lambda)$  and  $b_b(\lambda)$ <sup>a</sup>

$C$ (mg m <sup>-3</sup> )	$P_s$ (g m <sup>-3</sup> )	$P_l$ (g m <sup>-3</sup> )
0.00	0.000	0.000
0.03	0.001	0.035
0.05	0.002	0.051
0.12	0.004	0.098
0.30	0.009	0.194
0.60	0.016	0.325
1.00	0.024	0.476
3.00	0.062	1.078

<sup>a</sup>Reproduced from Haltrin and Kattawar,<sup>50</sup> with permission

Here  $B_s = 0.039$  is the backscattering probability for small particles and  $B_l = 0.00064$  is the backscattering probability for large particles.

The bio-optical models for scattering just discussed are useful but very approximate.

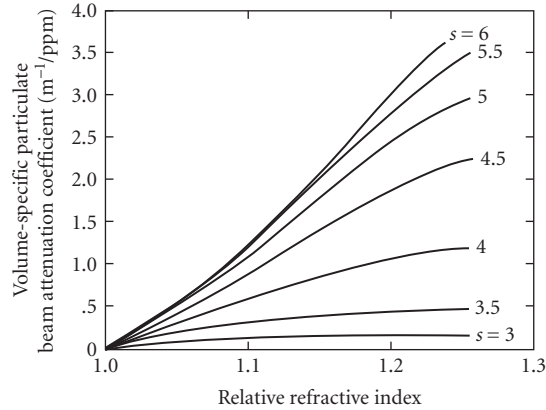
The reason for the frequent large discrepancies between model predictions and measured reality likely lies in the fact that scattering depends not just on particle concentration (as parameterized in terms of chlorophyll concentration), but also on the particle index of refraction and on the details of the particle size distribution which are not well parameterized in terms of the chlorophyll concentration alone. Whether or not the Kopelevich model or its derivative Haltrin-Kattawar form which partition the scattering into large and small particle components is in some sense better than the Gordon-Morel model is not known at present. Another consequence of the complexity of scattering is seen in the next section.

## 1.20 BEAM ATTENUATION

The spectral beam attenuation coefficient  $c(\lambda)$  is just the sum of the spectral absorption and scattering coefficients:  $c(\lambda) = a(\lambda) + b(\lambda)$ . Since both  $a(\lambda)$  and  $b(\lambda)$  are highly variable functions of the nature and concentration of the constituents of natural waters so is  $c(\lambda)$ . Beam attenuation near  $\lambda = 660$  nm is the only inherent optical property of water that is easily, accurately, and routinely measured. This wavelength is used both for engineering reasons (the availability of a stable LED light source) and because absorption by yellow matter is negligible in the red. Thus the quantity

$$c_p(660 \text{ nm}) \equiv c(660 \text{ nm}) - a_w(660 \text{ nm}) - b_w(660 \text{ nm}) \equiv c(660 \text{ nm}) - c_w(660 \text{ nm})$$

is determined by the nature of the suspended particulate matter. The particulate beam attenuation  $c_p(660 \text{ nm})$  is highly correlated with total particle volume concentration (usually expressed in parts per million), but it is much less well correlated with chlorophyll concentration.<sup>67</sup> The particulate beam attenuation can be used to estimate the total particulate load (often expressed as g m<sup>-3</sup>).<sup>68</sup> However, the dependence of the particulate beam attenuation on particle properties is not simple. Spinrad<sup>69</sup> used Mie theory to calculate the dependence of the volume-specific particulate beam attenuation (particulate beam attenuation coefficient  $c_p$  in m<sup>-1</sup> per unit suspended particulate volume in parts per million) on the relative refractive index and on the slope  $s$  of an assumed Junge size distribution for particles in the size range from 1 to 80  $\mu\text{m}$ ; the result is shown in Fig. 16. Although the details of the figure are sensitive to the choice of upper and lower size limits in the Mie calculations, the qualitative behavior of the curves is generally valid and supports the statements made in the closing paragraph of Sec. 1.19.



**FIGURE 16** Computed relationship between volume-specific particulate beam attenuation coefficient, relative refractive index, and slope  $s$  of a Junge number size distribution. (Reproduced from Spinrad,<sup>69</sup> with permission.)

Because of the complicated dependence of scattering and hence of beam attenuation on particle properties, the construction of bio-optical models for  $c(\lambda)$  is not easy. The reason is that chlorophyll concentration alone is not sufficient to parametrize scattering.<sup>70</sup> Figure 17 illustrates this insufficiency. The figure plots vertical profiles of  $c(665 \text{ nm})$ , water density (proportional to the oceanographic variable  $\sigma_t$ ), and chlorophyll concentration (proportional to fluorescence by chlorophyll and related pigments). Note that the maximum in beam attenuation at 46 m depth coincides with the interface (pycnocline) between less dense water above and more dense water below. Peaks in beam attenuation are commonly observed at density interfaces because particle concentrations are often greatest there. The maximum in chlorophyll concentration occurs at a depth of 87 m. The chlorophyll concentration depends not just on the number or volume of chlorophyll-bearing particles but also on their photoadaptive state, which depends on nutrient availability and ambient lighting. Thus chlorophyll concentration cannot be expected to correlate well with total scattering or with particulate beam attenuation  $c_p(\lambda)$ .

Voss<sup>71</sup> has developed an empirical model for  $c(\lambda)$  given a measurement of  $c$  at  $\lambda = 490 \text{ nm}$ :

$$c(\lambda) = c_w(\lambda) + [c(490 \text{ nm}) - c_w(490 \text{ nm})][1.563 - 1.149 \times 10^{-3} \lambda]$$

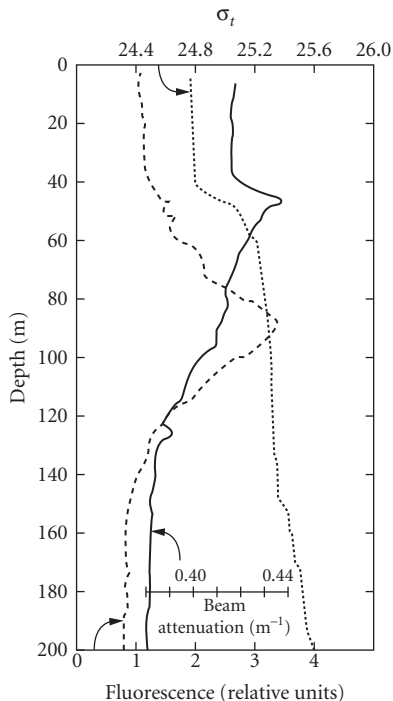
where  $\lambda$  is in nm and  $c$  is in  $\text{m}^{-1}$ . The attenuation coefficient for pure sea water,  $c_w = a_w + b_w$ , is given by the Smith-Baker data of Table 6. This model was statistically derived from data of global extent. Testing of the model with independent data usually gave errors of less than 5 percent, although occasional errors of  $\sim 20$  percent were found.

Voss also determined a least-squares fit of  $c(490 \text{ nm})$  to the chlorophyll concentration. The result

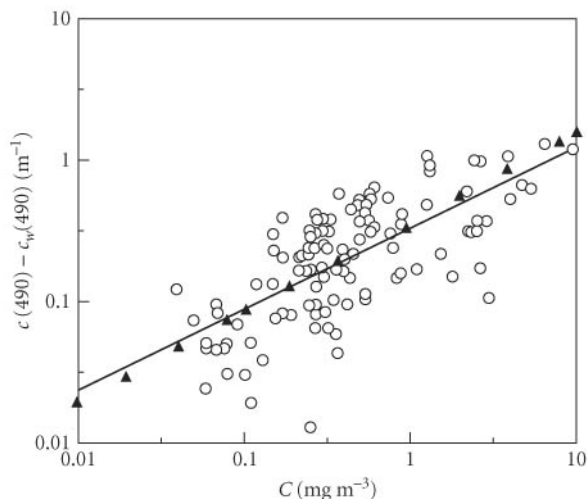
$$c(490 \text{ nm}) = 0.39C^{0.57} \quad (7)$$

is similar in form to the chlorophyll dependence of the  $a(\lambda)$  and  $b(\lambda)$  models seen in Eqs. (1) and (6), respectively. Figure 18 shows the spread of the data points used to determine Eq. (7). Note that for a given value of  $C$  there is an order-of-magnitude spread in values of  $c(490 \text{ nm})$ . The user of Eq. (7) or of the models for  $b(\lambda)$  must always keep in mind that large deviations from the predicted values will be found in natural waters.





**FIGURE 17** Example from the Pacific Ocean water of the depth dependence of beam attenuation (solid line), water density ( $\sigma_t$ , dashed line), and chlorophyll concentration (fluorescence, dotted line). (Reproduced from Kitchen and Zaneveld,<sup>70</sup> with permission.)



**FIGURE 18** Particulate beam attenuation at 490 nm (open circles) as a function of chlorophyll concentration  $C$  as used to determine Eq. (7) which is given by the solid line. Solid triangles give values as predicted by the sum of Eqs. (1) and (6). (Redrawn from Voss,<sup>71</sup> with permission.)

## 1.21 DIFFUSE ATTENUATION AND JERLOV WATER TYPES

As seen in Fig. 1 and in Table 1 there is a so-called diffuse attenuation coefficient for any radiometric variable. The most commonly used diffuse attenuation coefficients are those for downwelling plane irradiance,  $K_d(z, \lambda)$ , and for PAR,  $K_{\text{PAR}}(z)$ . Although the various diffuse attenuation coefficients are conceptually distinct, in practice they are often numerically similar and they all asymptotically approach a common value at great depths in homogeneous water.<sup>2</sup> The monograph by Tyler and Smith<sup>72</sup> gives tabulations and plots of  $E_d(z, \lambda)$ ,  $E_u(z, \lambda)$  and the associated  $K_d(z, \lambda)$ ,  $K_u(z, \lambda)$ , and  $R(z, \lambda)$  measured in a variety of waters.

Observation shows that  $K_d(z, \lambda)$  varies systematically with wavelength over a wide range of waters from very clear to very turbid. Moreover,  $K_d(z, \lambda)$  is often rather insensitive to environmental effects<sup>73</sup> except for extreme conditions<sup>74</sup> (such as the sun within  $10^\circ$  of the horizon) and in most cases correction can be made<sup>11</sup> for the environmental effects that are present in  $K_d$ .  $K_d$  therefore is regarded as a quasi-inherent optical property whose variability is governed primarily by changes in the inherent optical properties of the water body and not by changes in the external environment.

Jerlov<sup>29</sup> exploited this benign behavior of  $K_d$  to develop a frequently used classification scheme for oceanic waters based on the spectral shape of  $K_d$ . The *Jerlov water types* are in essence a classification based on water clarity as quantified by  $K_d(z_s, \lambda)$ , where  $z_s$  is a depth just below the sea surface.

This classification scheme can be contrasted with the case 1 and case 2 classification described earlier, which is based on the nature of the suspended matter within the water. The Jerlov water types are numbered I, IA, IB, II, and III for open ocean waters, and 1 through 9 for coastal waters. Type I is the clearest and type III is the most turbid open ocean water. Likewise, for coastal waters type 1 is clearest and type 9 is most turbid. The Jerlov types I to III generally correspond to case 1 water since phytoplankton predominate in the open ocean. Types 1 to 9 correspond to case 2 waters where yellow matter and terrigenous particulates dominate the optical properties. A rough correspondence between chlorophyll concentration and Jerlov oceanic water type is given by<sup>45</sup>

$$C: \quad 0-0.01 \sim 0.05 \sim 0.1 \sim 0.5 \sim 1.5-2.0 \text{ mg m}^{-3}$$

$$\text{water type:} \quad \text{I} \quad \text{IA} \quad \text{IB} \quad \text{II} \quad \text{III}$$

Austin and Petzold<sup>75</sup> reevaluated the Jerlov classification using an expanded database and slightly revised the  $K_d(\lambda)$  values used by Jerlov in his original definition of the water types. Table 17 gives the revised values for  $K_d(\lambda)$  for the water types commonly encountered in oceanography. These values are recommended over those found in Jerlov.<sup>29</sup> Figure 19 shows the percent transmittance of  $E_d(\lambda)$  per meter of water for selected Jerlov water types. Note how the wavelength of maximum transmittance shifts from blue in the clearest open ocean water (type I) to green (types III and 1) to yellow in the most turbid, yellow-matter-rich coastal water (type 9).

Austin and Petzold also presented a simple model that allows the determination of  $K_d(\lambda)$  at all wavelengths from a value of  $K_d$  measured at any single wavelength. This model is defined by

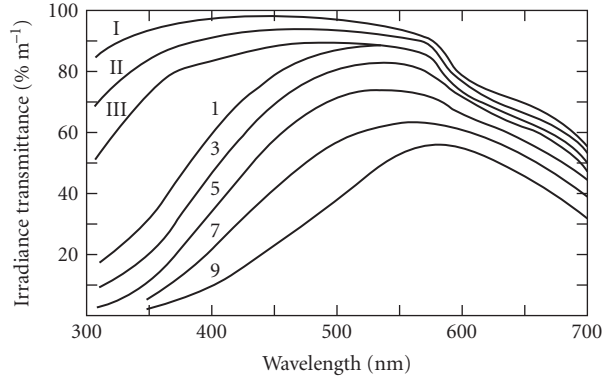
$$K_d(\lambda) = \frac{M(\lambda)}{M(\lambda_0)} [K_d(\lambda_0) - K_{\text{dw}}(\lambda_0)] + K_{\text{dw}}(\lambda)$$

Here  $\lambda_0$  is the wavelength at which  $K_d$  is measured and  $K_{\text{dw}}$  refers to values for pure sea water.  $K_{\text{dw}}(\lambda)$  and the statistically derived coefficients  $M(\lambda)$  are given in Table 18. (These  $K_{\text{dw}}$  values differ slightly from those seen in Table 6.) This model is valid in waters where  $K_d(490) \leq 0.16 \text{ m}^{-1}$  which corresponds to a chlorophyll concentration of  $C \leq 3 \text{ mg m}^{-3}$ .

**TABLE 17** Downwelling Irradiance Diffuse Attenuation Coefficients  $K_d(\lambda)$  Used to Define the Jerlov Water Types As Determined by Austin and Petzold\* (All quantities in the body of the table have units of  $\text{m}^{-1}$ .)

$\lambda$ (nm)	Jerlov water type					
	I	IA	IB	II	III	1
350	0.0510	0.0632	0.0782	0.1325	0.2335	0.3345
375	0.0302	0.0412	0.0546	0.1031	0.1935	0.2839
400	0.0217	0.0316	0.0438	0.0878	0.1697	0.2516
425	0.0185	0.0280	0.0395	0.0814	0.1594	0.2374
450	0.0176	0.0257	0.0355	0.0714	0.1381	0.2048
475	0.0184	0.0250	0.0330	0.0620	0.1160	0.1700
500	0.0280	0.0332	0.0396	0.0627	0.1056	0.1486
525	0.0504	0.0545	0.0596	0.0779	0.1120	0.1461
550	0.0640	0.0674	0.0715	0.0863	0.1139	0.1415
575	0.0931	0.0960	0.0995	0.1122	0.1359	0.1596
600	0.2408	0.2437	0.2471	0.2595	0.2826	0.3057
625	0.3174	0.3206	0.3245	0.3389	0.3655	0.3922
650	0.3559	0.3601	0.3652	0.3837	0.4181	0.4525
675	0.4372	0.4410	0.4457	0.4626	0.4942	0.5257
700	0.6513	0.6530	0.6550	0.6623	0.6760	0.6896

\*Reproduced from Austin and Petzold,<sup>75</sup> with permission.



**FIGURE 19** Percentage transmittance per meter of water of downwelling irradiance  $E_d$  as a function of wavelength for selected Jerlov water types. (Reproduced from Jerlov,<sup>29</sup> with permission.)

Unlike the beam attenuation coefficient  $c(\lambda)$ , the diffuse attenuation  $K_d(z, \lambda)$  is highly correlated with chlorophyll concentration. The reason is seen in the approximate formula<sup>11</sup>

$$K_d(\lambda) \approx \frac{a(\lambda) + b_b(\lambda)}{\cos \theta_{sw}}$$

where  $\theta_{sw}$  is the solar angle measured within the water. Since  $a(\lambda) \gg b_b(\lambda)$  for most waters,  $K_d(\lambda)$  is largely determined by the absorption properties of the water, which are fairly well parametrized by the chlorophyll concentration. Beam attenuation on the other hand is proportional to the total scattering which is not well parametrized by chlorophyll concentration. Observations show<sup>76</sup> that the beam attenuation at 660 nm is not in general correlated with diffuse attenuation.

A bio-optical model for  $K_d(\lambda)$  is given by Morel:<sup>45</sup>

$$K_d(\lambda) = K_{dw}(\lambda) + \chi(\lambda)C^{e(\lambda)}$$

Here  $K_{dw}(\lambda)$  is the diffuse attenuation for pure sea water, and  $\chi(\lambda)$  and  $e(\lambda)$  are statistically derived functions that convert the chlorophyll concentration  $C$  in  $\text{mg m}^{-3}$  into  $K_d$  values in  $\text{m}^{-1}$ . Table 19

**TABLE 18** Values of the Coefficient  $M(\lambda)$  and of the Downwelling Diffuse Attenuation Coefficient for Pure Sea Water,  $K_{dw}(\lambda)$ , for Use in the Austin and Petzold Model for  $K_d(\lambda)$ \*

$\lambda$ (nm)	$M$ ( $\text{m}^{-1}$ )	$K_{dw}$ ( $\text{m}^{-1}$ )	$\lambda$ (nm)	$M$ ( $\text{m}^{-1}$ )	$K_{dw}$ ( $\text{m}^{-1}$ )	$\lambda$ (nm)	$M$ ( $\text{m}^{-1}$ )	$K_{dw}$ ( $\text{m}^{-1}$ )
350	2.1442	0.0510	470	1.1982	0.0179	590	0.4840	0.1578
360	2.0504	0.0405	480	1.0955	0.0193	600	0.4903	0.2409
370	1.9610	0.0331	490	1.0000	0.0224	610	0.5090	0.2892
380	1.8772	0.0278	500	0.9118	0.0280	620	0.5380	0.3124
390	1.8009	0.0242	510	0.8310	0.0369	630	0.6231	0.3296
400	1.7383	0.0217	520	0.7578	0.0498	640	0.7001	0.3290
410	1.7591	0.0200	530	0.6924	0.0526	540	0.7300	0.3559
420	1.6974	0.0189	540	0.6350	0.0577	660	0.7301	0.4105
430	1.6108	0.0182	550	0.5860	0.0640	670	0.7008	0.4278
440	1.5169	0.0178	560	0.5457	0.0723	680	0.6245	0.4521
450	1.4158	0.0176	570	0.5146	0.0842	690	0.4901	0.5116
460	1.3077	0.0176	580	0.4935	1.1065	700	0.2891	0.6514

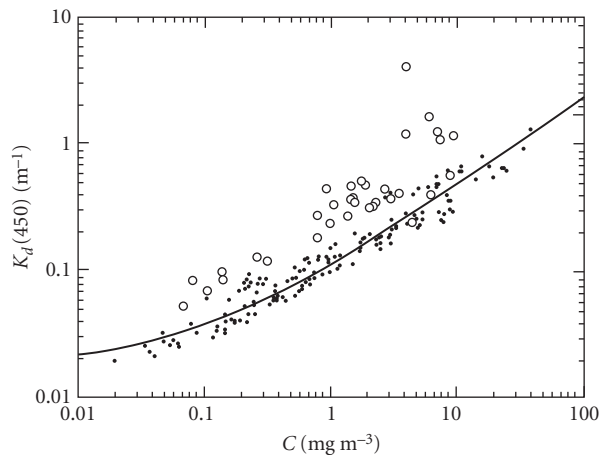
\*Condensed with permission from Austin and Petzold,<sup>75</sup> who give values every 5 nm.

**TABLE 19** Values of the Coefficients  $\chi(\lambda)$  and  $e(\lambda)$  and of the Downwelling Diffuse Attenuation Coefficient for Pure Sea Water,  $K_{dw}(\lambda)$ , for Use in the Morel Model for  $K_d(\lambda)$ \*

$\lambda$ (nm)	$\chi(\lambda)$	$e(\lambda)$	$K_{dw}(\lambda)$ ( $\text{m}^{-1}$ )	$\lambda$ (nm)	$\chi(\lambda)$	$e(\lambda)$	$K_{dw}(\lambda)$ ( $\text{m}^{-1}$ )
400	0.1100	0.668	0.0209	550	0.0410	0.650	0.0640
410	0.1125	0.680	0.0196	560	0.0390	0.640	0.0717
420	0.1126	0.693	0.0183	570	0.0360	0.623	0.0807
430	0.1078	0.707	0.0171	580	0.0330	0.610	0.1070
440	0.1041	0.707	0.0168	590	0.0325	0.618	0.1570
450	0.0971	0.701	0.0168	600	0.0340	0.626	0.2530
460	0.0896	0.700	0.0173	610	0.0360	0.634	0.2960
470	0.0823	0.703	0.0175	620	0.0385	0.642	0.3100
480	0.0746	0.703	0.0194	630	0.0420	0.653	0.3200
490	0.0690	0.702	0.0217	640	0.0440	0.663	0.3300
500	0.0636	0.700	0.0271	650	0.0450	0.672	0.3500
510	0.0578	0.690	0.0384	660	0.0475	0.682	0.4050
520	0.0498	0.680	0.0490	670	0.0515	0.695	0.4300
530	0.0467	0.670	0.0518	680	0.0505	0.693	0.4500
540	0.0440	0.660	0.0568	690	0.0390	0.640	0.5000
				700	0.0300	0.600	0.6500

\*Condensed with permission from Morel,<sup>45</sup> who gives values every 5 nm.

gives the  $K_{dw}$ ,  $\chi$ , and  $e$  values used in the Morel model. This model is applicable to case 1 waters with  $C \leq 30 \text{ mg m}^{-3}$ , although the  $\chi$  and  $e$  values are somewhat uncertain for  $\lambda > 650 \text{ nm}$  because of sparse data available for their determination. Some feeling for the accuracy of the Morel  $K_d(\lambda)$  model can be obtained from Fig. 20 which shows predicted (the line) and observed  $K_d(450)$  values as a function of  $C$ . Errors can be as large as a factor of 2 in case 1 waters (dots) and can be much larger if the model is misapplied to case 2 waters (open circles). The Morel model allows the determination of  $K_d(\lambda)$  if  $C$  is measured; the Austin and Petzold model determines  $K_d(\lambda)$  from a measurement at one wavelength.



**FIGURE 20** Measured  $K_d$  values at 450 nm as a function of chlorophyll concentration  $C$ . Dots are measurements from case 1 waters; open circles are from case 2 waters. The solid line gives  $K_d(450)$  as predicted by the Morel bio-optical model. (Redrawn from Morel,<sup>45</sup> with permission.)

**TABLE 20** Approximate Depth of the Euphotic Zone,  $z_{\text{eu}}$ , in Homogeneous Case 1 Water As a Function of Chlorophyll Concentration  $C$ .\*

$C$ ( $\text{mg m}^{-3}$ )	$z_{\text{eu}}$ (m)	$C$ ( $\text{mg m}^{-3}$ )	$z_{\text{eu}}$ (m)
0.0	183	1	39
0.01	153	2	29
0.03	129	3	24
0.05	115	5	19
0.1	95	10	14
0.2	75	20	10
0.3	64	30	8
0.5	52		

\*Data extracted from Morel,<sup>45</sup> with permission.

Morel<sup>45</sup> also presents a very simple bio-optical model for  $\bar{K}_{\text{PAR}}(0, z_{\text{eu}})$  the value of  $K_{\text{PAR}}(z)$  averaged over the euphotic zone  $0 \leq z \leq z_{\text{eu}}$ :

$$\bar{K}_{\text{PAR}}(0, z_{\text{eu}}) = 0.121C^{0.428}$$

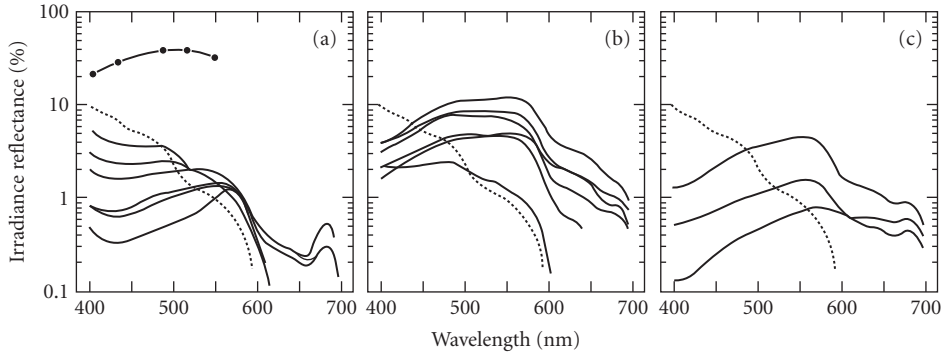
where  $C$  is the mean chlorophyll concentration in the euphotic zone in  $\text{mg m}^{-3}$  and  $\bar{K}_{\text{PAR}}$  is in  $\text{m}^{-1}$ . The euphotic zone is the region where there is sufficient light for photosynthesis to take place; it extends roughly to the depth where  $E_{\text{PAR}}(z)$  is 1 percent of its surface value [i.e.,  $E_{\text{PAR}}(z_{\text{eu}}) = 0.01 E_{\text{PAR}}(0)$ ]. Table 20 gives  $z_{\text{eu}}$  as a function of  $C$  as determined by the Morel model.

## 1.22 IRRADIANCE REFLECTANCE AND REMOTE SENSING

The spectral irradiance reflectant  $R(\lambda) \equiv E_u(\lambda)/E_d(\lambda)$  is an important apparent optical property. Measurements of  $R(z, \lambda)$  within the water have been used<sup>77</sup> to estimate water quality parameters such as the chlorophyll concentration, the particle backscattering coefficient, and the absorption coefficient of yellow matter. More importantly,  $R(\lambda)$  just below the water surface can be related to the radiance leaving the water;<sup>78</sup> this radiance is available for detection by aircraft- or satellite-borne instruments. Understanding the dependence of  $R(\lambda)$  upon the constituents of natural waters is therefore one of the central problems in remote sensing of water bodies.

Figure 21 illustrates the variability of  $R(\lambda)$  in natural waters. Figure 21a shows  $R(\lambda)$  in percent for various case 1 waters. For low-chlorophyll concentrations  $R(\lambda)$  is highest at blue wavelengths, hence the blue color of clean ocean water. As the chlorophyll concentration increases, the maximum in  $R(\lambda)$  shifts to green wavelengths. The enhanced reflectance near  $\lambda = 685$  nm is due to chlorophyll fluorescence. Also note the exceptionally high values measured<sup>20</sup> within a coccolithophore bloom;  $R(\lambda)$  is high there because of the strong scattering by the numerous calcite particles (see Sec. 1.6). Figure 21b shows  $R(\lambda)$  from waters dominated by suspended sediments (i.e., by nonpigmented particles). For high-sediment concentrations  $R(\lambda)$  is nearly flat from blue to yellow wavelengths, and therefore the water appears brown. Figure 21c is from waters with high concentrations of yellow substances; the peak in  $R(\lambda)$  lies in the yellow. With good reason the term “ocean color” is often used as a synonym for  $R(\lambda)$ .

One of the main goals of oceanic remote sensing is the determination of chlorophyll concentrations in near-surface waters because of the fundamental role played by phytoplankton in the global ecosystem. Gordon et al.<sup>78</sup> define the *normalized water-leaving radiance*  $[L_w(\lambda)]_N$  as the radiance that would leave the sea surface if the sun were at the zenith and the atmosphere were absent; this



**FIGURE 21** Measured spectral irradiance reflectances  $R(\lambda)$  from various waters. Panel (a) is from case waters with different quantities of phytoplankton; the dotted line is  $R(\lambda)$  for pure sea water. The heavy dots give values measured within a coccolithophore bloom.<sup>20</sup> Panel (b) is from case 2 waters dominated by suspended sediments and panel (c) is from case 2 waters dominated by yellow matter. (Redrawn from Sathyendranath and Morel,<sup>79</sup> with permission.)

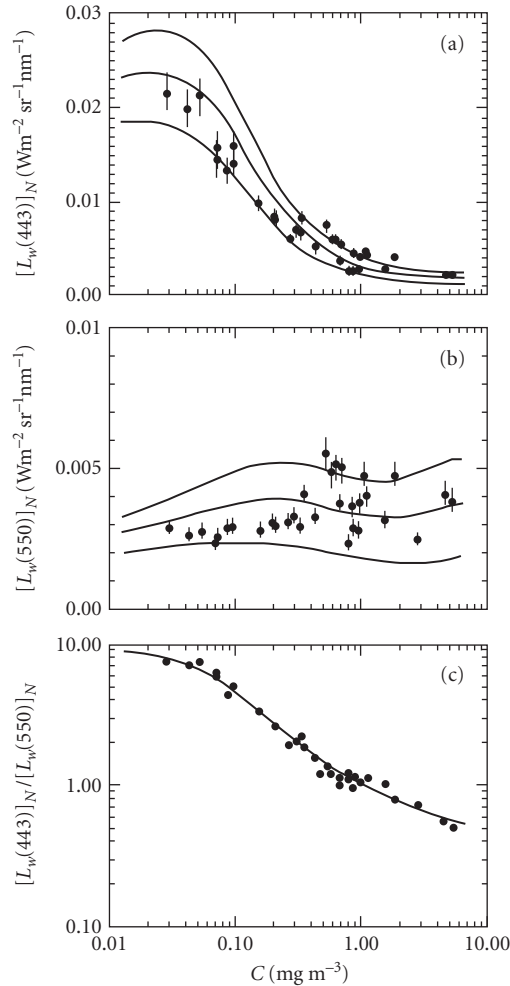
quantity is fundamental to remote sensing. They then show that  $[L_w]_N$  is directly proportional to  $R$  and that  $R$  is proportional to  $b_b/(a + b_b)$  (i.e., to  $b_b/K_d$ ). Although  $a$  or  $K_d$  are reasonably well modeled in terms of chlorophyll concentration  $C$  in case 1 waters,  $b_b$  is not well described in terms of  $C$ . Thus poor agreement is to be expected between observed values of  $[L_w(\lambda)]_N$  and values predicted by a model parametrized in terms of  $C$ . This is indeed the case as is seen in Fig. 22a and b which shows observed and predicted  $[L_w(443 \text{ nm})]_N$  and  $[L_w(550 \text{ nm})]_N$  values as a function of chlorophyll concentration. Based on these figures there seems to be little hope of being able to reliably retrieve  $C$  from a remotely sensed  $[L_w(\lambda)]_N$  value. However, in spite of the noise seen in Fig. 22a and b, the ratios of normalized water-leaving radiances for different wavelengths can be remarkably well-behaved functions of  $C$ . Figure 22c shows predicted (the line) and observed (dots) values of  $[L_w(443 \text{ nm})]_N/[L_w(550 \text{ nm})]_N$ ; the agreement between prediction and observation is now rather good. Thus, measurement of  $[L_w(\lambda)]_N$  at two (carefully chosen) wavelengths along with application of a bio-optical model for their ratio can yield a useful estimate of chlorophyll concentration. Such models are the basis of much remote sensing.

### 1.23 INELASTIC SCATTERING AND POLARIZATION

Although the basic physics of inelastic scattering and polarization is well understood, only recently has it become computationally practicable to incorporate these effects into predictive numerical models of underwater radiance distributions. For this reason as well as because of the difficulty of making needed measurements, quantitative knowledge about the significance of inelastic scattering and polarization in the underwater environment is incomplete.

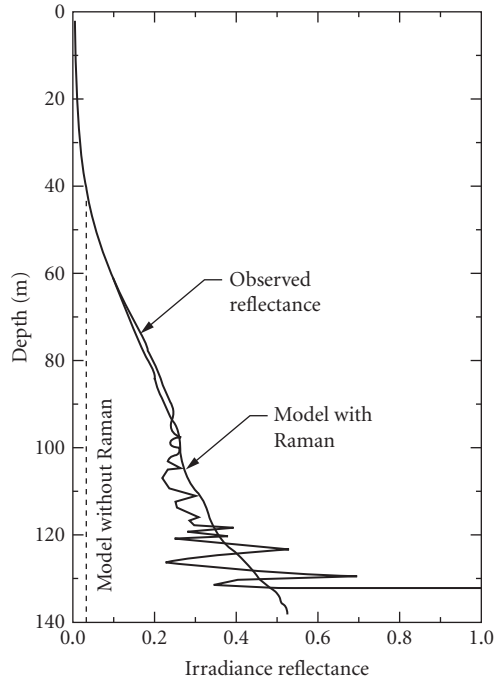
Inelastic scattering processes are often negligible in comparison to sunlight or artificial lights as sources of underwater light of a given wavelength. However, in certain circumstances transpectral scatter is the dominant source of underwater light at some wavelengths. Figure 23 illustrates just such a circumstance.

Figure 23 shows a measured depth profile from the Sargasso Sea of irradiance reflectance at  $\lambda = 589 \text{ nm}$  (yellow-orange light); note that  $R(589 \text{ nm})$  increases with depth. Because of the fairly high absorption of water at this wavelength [ $a_w(589 \text{ nm}) = 0.152 \text{ m}^{-1}$ ] most of the yellow-orange component of the incident solar radiation is absorbed near the surface and monochromatic radiative transfer theory shows that the reflectance should approach a value of  $R(589 \text{ nm}) \approx 0.04$  for the



**FIGURE 22** In panels (a) and (b) the solid lines are values of the normalized water-leaving radiances  $[L_w(\lambda)]_N$  at  $\lambda = 443$  and  $550$  nm, respectively, as predicted by various models that relate  $[L_w(\lambda)]_N$  to the chlorophyll concentration  $C$ . The dots are measured values of  $[L_w(\lambda)]_N$ . Panel (c) shows the predicted (line) and observed ratio of the  $[L_w(\lambda)]_N$  values of panels (a) and (b). (Redrawn from Gordon et al.,<sup>78</sup> with permission.)

water body of Fig. 22. Calculations by Marshall and Smith<sup>80</sup> explain the paradox. Light of blue-green wavelengths ( $\lambda \sim 500$  nm) can penetrate to great depth in the clear Sargasso Sea water [ $a_w(500 \text{ nm}) \approx 0.026 \text{ m}^{-1}$ ]. Some of this light is then Raman scattered from blue-green to yellow-orange wavelengths providing a source of yellow-orange light at depth. Moreover, since the phase function for Raman scattering is symmetric in the forward and backward hemispheres Raman scattered photons are equally likely to be heading upward [and thus contribute to  $E_u(589 \text{ nm})$ ] or downward [and thus contribute to  $E_d(589 \text{ nm})$ ] even though most of the blue-green light at depth is heading downward [e.g.,  $E_d(500 \text{ nm}) \gg E_u(500 \text{ nm})$ ].



**FIGURE 23** Observed irradiance reflectance  $R$  at 589 nm (light line) and values predicted by a model including Raman scattering (heavy line) and omitting Raman scattering (dashed line). (Redrawn from Marshall and Smith,<sup>80</sup> with permission.)

Thus as depth increases and Raman scattering becomes increasingly important relative to transmitted sunlight as a source of ambient yellow-orange light,  $E_u(589\text{ nm})$  and  $E_d(589\text{ nm})$  become more nearly equal and the irradiance reflectance  $R(589\text{ nm})$  increases. Such an increase is not seen at blue-green wavelengths since  $E_d$  transmitted from the surface remains much greater than  $E_u$  at great depths. Since Raman scattering is by the water molecules themselves this process is present (and indeed relatively more important) even in the clearest waters. Another oceanographic effect of Raman scattering occurs in the filling of Fraunhofer lines in the solar spectrum as seen underwater; this matter is just now coming under detailed investigation.<sup>81</sup>

Fluorescence by chlorophyll or other substances can be significant if the fluorescing material is present in sufficient quantity. Chlorophyll fluoresces strongly near  $\lambda = 685\text{ nm}$ ; this source of red light is responsible<sup>82</sup> for the enhanced reflectance near 685 nm noted in Fig. 21a. The spectral signature of fluorescence is a useful tool for analyzing many of the constituents of natural waters.<sup>83</sup>

Relatively little attention has been paid to the state of polarization of underwater light fields.<sup>84</sup> Some use of polarized light has been made in enhancing underwater visibility<sup>85</sup> and it is well established that many oceanic organisms sense polarized light when navigating.<sup>86</sup> Voss and Fry<sup>87</sup> measured the Mueller matrix for ocean water and Quinby-Hunt et al.<sup>88</sup> have studied the propensity of certain phytoplankton to induce circular polarization in unpolarized or linearly polarized light. Kattawar and Adams<sup>89</sup> have shown that errors of up to 15 percent can occur in calculations of underwater radiance if scalar (unpolarized) radiative transfer theory is used instead of vector (polarized) theory.



## 1.24 ACKNOWLEDGMENTS

---

This paper was written while the author held a National Research Council Resident Research Associateship (Senior Level) at the Jet Propulsion Laboratory, California Institute of Technology. This associateship was supported by the Ocean Biochemistry Program at NASA Headquarters. Final proofing was supported by SRI. Karen Baker, Annick Bricaud, Howard Gordon, Richard Honey, Rodolpho Iturriaga, George Kattawar, Scott Pegau, Mary Jane Perry, Collin Roesler, Shubha Sathyendranath, Richard Spinrad, and Kenneth Voss all made helpful comments on a draft of the paper; their efforts are greatly appreciated.

## 1.25 REFERENCES

---

1. C. D. Mobley, *Light and Water: Radiative Transfer in Natural Waters*, Academic Press, San Diego, 1994, 592 pp.
2. R. W. Preisendorfer, *Hydrologic Optics*, 6 volumes, U.S. Dept. of Commerce, NOAA, Pacific Marine Environmental Lab., Seattle, 1976, 1757 pp. Available from National Technical Information Service, 5285 Port Royal Road, Springfield, Virginia 22161.
3. A. Morel and R. C. Smith, "Terminology and Units in Optical Oceanography," *Marine Geodesy* **5**(4):335 (1982).
4. N. Højerslev, "A Spectral Light Absorption Meter for Measurements in the Sea," *Limnol. Oceanogr.* **20**(6):1024 (1975).
5. A. Morel and R. C. Smith, "Relation between Total Quanta and Total Energy for Aquatic Photosynthesis," *Limnol. Oceanogr.* **19**(4):591 (1974).
6. A. Morel, "Light and Marine Photosynthesis: A Spectral Model with Geochemical and Climatological Implications," *Prog. Oceanogr.* **26**:263 (1991).
7. J. T. O. Kirk, "The Upwelling Light Stream in Natural Waters," *Limnol. Oceanogr.* **34**(8):1410 (1989).
8. J. T. O. Kirk, *Light and Photosynthesis in Aquatic Ecosystems*, Cambridge Univ. Press, New York, 1983, 410 pp.
9. R. W. Preisendorfer and C. D. Mobley, "Theory of Fluorescent Irradiance Fields in Natural Waters," *J. Geophys. Res.* **93**(D9):10831 (1988).
10. R. C. Smith and K. Baker, "The Bio-Optical State of Ocean Waters and Remote Sensing," *Limnol. Oceanogr.* **23**(2):247 (1978).
11. H. Gordon, "Can the Lambert-Beer Law Be Applied to the Diffuse Attenuation Coefficient of Ocean Water?," *Limnol. Oceanogr.* **34**(8):1389 (1989).
12. C. A. Suttle, A. M. Chan, and M. T. Cottrell, "Infection of Phytoplankton by Viruses and Reduction of Primary Productivity," *Nature* **347**:467 (1990).
13. I. Koike, S. Hara, K. Terauchi, and K. Kogure, "Role of Submicrometer Particles in the Ocean," *Nature* **345**:242 (1990).
14. M. L. Wells and E. D. Goldberg, "Occurrence of Small Colloids in Sea Water," *Nature* **353**:342 (1991).
15. R. W. Spinrad, H. Glover, B. B. Ward, L. A. Codispoti, and G. Kullenberg, "Suspended Particle and Bacterial Maxima in Peruvian Coastal Water during a Cold Water Anomaly," *Deep-Sea Res.* **36**(5):715 (1989).
16. A. Morel and Y.-H. Ahn, "Optical Efficiency Factors of Free-Living Marine Bacteria: Influence of Bacterioplankton upon the Optical Properties and Particulate Organic Carbon in Oceanic Waters," *J. Marine Res.* **48**:145 (1990).
17. D. Stramski and D. A. Kiefer, "Light Scattering by Microorganisms in the Open Ocean," *Prog. Oceanogr.* **28**:343 (1991).
18. A. Alldredge and M. W. Silver, "Characteristics, Dynamics and Significance of Marine Snow," *Prog. Oceanogr.* **20**:41 (1988).
19. K. L. Carder, R. G. Steward, P. R. Betzer, D. L. Johnson, and J. M. Prospero, "Dynamics and Composition of Particles from an Aeolian Input Event to the Sargasso Sea," *J. Geophys. Res.* **91**(D1):1055 (1986).
20. W. M. Balch, P. M. Holligan, S. G. Ackleson, and K. J. Voss, "Biological and Optical Properties of Mesoscale Cocolithophore Blooms in the Gulf of Maine," *Limnol. Oceanogr.* **36**(4):629 (1991).

21. H. Bader, "The Hyperbolic Distribution of Particle Sizes," *J. Geophys. Res.* **75**(15):2822 (1970).
22. I. N. McCave, "Particulate Size Spectra, Behavior, and Origin of Nepheloid Layers over the Nova Scotian Continental Rise," *J. Geophys. Res.* **88**(C12):7647 (1983).
23. C. E. Lambert, C. Jehanno, N. Silverberg, J. C. Brun-Cottan, and R. Chesselet, "Log-Normal Distributions of Suspended Particles in the Open Ocean," *J. Marine Res.* **39**(1):77 (1981).
24. D. G. Archer and P. Wang, "The Dielectric Constant of Water and Debye-Hückel Limiting Law Slopes," *J. Phys. Chem. Ref. Data* **19**:371 (1990).
25. M. Kerker, *The Scattering of Light and Other Electromagnetic Radiation*, Academic Press, New York, 1969, 666 pp.
26. V. M. Zolotarev and A. V. Demin, "Optical Constants of Water over a Broad Range of Wavelengths, 0.1 Å-1 m," *Opt. Spectrosc. (U.S.S.R.)* **43**(2):157 (Aug. 1977).
27. R. W. Austin and G. Halikas, "The Index of Refraction of Seawater," SIO ref. no. 76-1, Scripps Inst. Oceanogr., San Diego, 1976, 121 pp.
28. R. C. Millard and G. Seaver, "An Index of Refraction Algorithm over Temperature, Pressure, Salinity, Density, and Wavelength," *Deep-Sea Res.* **37**(12):1909 (1990).
29. N. G. Jerlov, *Marine Optics*, Elsevier, Amsterdam, 1976, 231 pp.
30. R. W. Spinrad and J. F. Brown, "Relative Real Refractive Index of Marine Micro-Organisms: A Technique for Flow Cytometric Measurement," *Appl. Optics* **25**(2):1930 (1986).
31. S. G. Ackleson, R. W. Spinrad, C. M. Yentsch, J. Brown, and W. Korjef-Bellows, "Phytoplankton Optical Properties: Flow Cytometric Examinations of Dilution-Induced Effects," *Appl. Optics* **27**(7):1262 (1988).
32. R. C. Smith and K. S. Baker, "Optical Properties of the Clearest Natural Waters," *Appl. Optics* **20**(2):177 (1981).
33. T. T. Bannister, "Estimation of Absorption Coefficients of Scattering Suspensions Using Opal Glass," *Limnol. Oceanogr.* **33**(4, part 1):607 (1988).
34. B. G. Mitchell, "Algorithms for Determining the Absorption Coefficient of Aquatic Particles Using the Quantitative Filter Technique (QFT)," *Ocean Optics X*, R. W. Spinrad (ed.), *Proc. SPIE* **1302**:137 (1990).
35. D. Stramski, "Artifacts in Measuring Absorption Spectra of Phytoplankton Collected on a Filter," *Limnol. Oceanogr.* **35**(8):1804 (1990).
36. J. R. V. Zaneveld, R. Bartz, and J. C. Kitchen, "Reflective-Tube Absorption Meter," *Ocean Optics X*, R. W. Spinrad (ed.), *Proc. SPIE* **1302**:124 (1990).
37. E. S. Fry, G. W. Kattawar, and R. M. Pope, "Integrating Cavity Absorption Meter," *Appl. Optics* **31**(12):2025 (1992).
38. W. Doss and W. Wells, "Radiometer for Light in the Sea," *Ocean Optics X*, R. W. Spinrad (ed.), *Proc. SPIE* **1302**:363 (1990).
39. K. J. Voss, "Use of the Radiance Distribution to Measure the Optical Absorption Coefficient in the Ocean," *Limnol. Oceanogr.* **34**(8):1614 (1989).
40. F. Sogandares, Z.-F. Qi, and E. S. Fry, "Spectral Absorption of Water," presentation at the Optical Society of America Annual Meeting, San Jose, Calif., 1991.
41. W. S. Pegau and J. R. V. Zaneveld, "Temperature Dependent Absorption of Water in the Red and Near Infrared Portions of the Spectrum," *Limnol. Oceanogr.* **38**(1):188 (1993).
42. A. Bricaud, A. Morel, and L. Prieur, "Absorption by Dissolved Organic Matter of the Sea (Yellow Substance) in the UV and Visible Domains," *Limnol. Oceanogr.* **26**(1):43 (1981).
43. C. S. Roesler, M. J. Perry, and K. L. Carder, "Modeling in situ Phytoplankton Absorption from Total Absorption Spectra in Productive Inland Marine Waters," *Limnol. Oceanogr.* **34**(8):1510 (1989).
44. S. Sathyendranath, L. Lazzara, and L. Prieur, "Variations in the Spectral Values of Specific Absorption of Phytoplankton," *Limnol. Oceanogr.* **32**(2):403 (1987).
45. A. Morel, "Optical Modeling of the Upper Ocean in Relation to Its Biogenous Matter Content (Case 1 Waters)," *J. Geophys. Res.* **93**(C9):10749 (1988).
46. R. Iturriaga and D. Siegel, "Microphotometric Characterization of Phytoplankton and Detrital Absorption Properties in the Sargasso Sea," *Limnol. Oceanogr.* **34**(8):1706 (1989).
47. A. Morel and L. Prieur, "Analysis of Variations in Ocean Color," *Limnol. Oceanogr.* **22**(4):709 (1977).
48. L. Prieur and S. Sathyendranath, "An Optical Classification of Coastal and Oceanic Waters Based on the Specific Spectral Absorption Curves of Phytoplankton Pigments, Dissolved Organic Matter, and Other Particulate Materials," *Limnol. Oceanogr.* **26**(4):671 (1981).

49. O. V. Kopelevich, "Small-Parameter Model of Optical Properties of Sea Water," *Ocean Optics*, vol 1, *Physical Ocean Optics*, A. S. Monin (ed.), Nauka Pub., Moscow, 1983, chap. 8 (in Russian).
50. V. I. Haltrin and G. Kattawar, "Light Fields with Raman Scattering and Fluorescence in Sea Water," Tech. Rept., Dept. of Physics, Texas A&M Univ., College Station, 1991, 74 pp.
51. C. S. Yentsch, "The Influence of Phytoplankton Pigments on the Color of Sea Water," *Deep-Sea Res.* 7:1 (1960).
52. H. Gordon, "Diffuse Reflectance of the Ocean: Influence of Nonuniform Pigment Profile," *Appl. Optics* 31(12):2116 (1992).
53. T. J. Petzold, "Volume Scattering Functions for Selected Ocean Waters," SIO Ref. 72-78, Scripps Inst. Oceanogr., La Jolla, 1972 (79 pp). Condensed in *Light in the Sea*, J. E. Tyler (ed.), Dowden, Hutchinson & Ross, Stroudsburg, 1977, chap. 12, pp. 150-174.
54. R. W. Spinrad, J. R. V. Zaneveld, and H. Pak, "Volume Scattering Function of Suspended Particulate Matter at Near-Forward Angles: A Comparison of Experimental and Theoretical Values," *Appl. Optics* 17(7):1125 (1978).
55. G. G. Padmabandu and E. S. Fry, "Measurement of Light Scattering at 0° by Small Particle Suspensions," *Ocean Optics X*, R. W. Spinrad (ed.), *Proc. SPIE* 1302:191 (1990).
56. Y. Kuga and A. Ishimaru, "Backscattering Enhancement by Randomly Distributed Very Large Particles," *Appl. Optics* 28(11):2165 (1989).
57. A. Morel, "Optical Properties of Pure Water and Pure Sea Water," *Optical Aspects of Oceanography*, N. G. Jerlov and E. S. Nielsen (eds.), Academic Press, New York, 1974, chap. 1, pp 1-24.
58. K. S. Shifrin, *Physical Optics of Ocean Water*, AIP Translation Series, Amer. Inst. Physics, New York, 1988, 285 pp.
59. G. Kullenberg, "Observed and Computed Scattering Functions," *Optical Aspects of Oceanography*, N. G. Jerlov and E. S. Nielsen (eds.), Academic Press, New York, 1974, chap. 2, pp 25-49.
60. O. B. Brown and H. R. Gordon, "Size-Refractive Index Distribution of Clear Coastal Water Particulates from Scattering," *Appl. Optics* 13:2874 (1974).
61. J. C. Kitchen and J. R. V. Zaneveld, "A Three-Layer Sphere, Mie-Scattering Model of Oceanic Phytoplankton Populations," presented at Amer. Geophys. Union/Amer. Soc. Limnol. Oceanogr. Annual Meeting, New Orleans, 1990.
62. C. D. Mobley, B. Gentili, H. R. Gordon, Z. Jin, G. W. Kattawar, A. Morel, P. Reinersman, K. Stamnes, and R. H. Starn, "Comparison of Numerical Models for Computing Underwater Light Fields," *Appl. Optics* 32(36):7484 (1993).
63. A. Morel and B. Gentili, "Diffuse Reflectance of Ocean Waters: Its Dependence on Sun Angle As Influenced by the Molecular Scattering Contribution," *Appl. Optics* 30(30):4427 (1991).
64. A. Morel, "Diffusion de la lumière par les eaux de mer. Résultats expérimentaux et approach théorique," NATO AGARD lecture series no. 61, *Optics of the Sea*, chap. 3.1, pp. 1-76 (1973), G. Halikas (trans.), Scripps Inst. Oceanogr., La Jolla, 1975, 161 pp.
65. O. V. Kopelevich and E. M. Mezhericher, "Calculation of Spectral Characteristics of Light Scattering by Sea Water," *Izvestiya, Atmos. Oceanic Phys.* 19(2):144 (1983).
66. H. R. Gordon and A. Morel, "Remote Assessment of Ocean Color for Interpretation of Satellite Visible Imagery, A Review," *Lecture Notes on Coastal and Estuarine Studies*, vol. 4, Springer-Verlag, New York, 1983, 114 pp.
67. J. C. Kitchen, J. R. V. Zaneveld, and H. Pak, "Effect of Particle Size Distribution and Chlorophyll Content on Beam Attenuation Spectra," *Appl. Optics* 21(21):3913 (1982).
68. J. K. Bishop, "The Correction and Suspended Particulate Matter Calibration of Sea Tech Transmissometer Data," *Deep-Sea Res.* 33:121 (1986).
69. R. W. Spinrad, "A Calibration Diagram of Specific Beam Attenuation," *J. Geophys. Res.* 91(C6):7761 (1986).
70. J. C. Kitchen and J. R. V. Zaneveld, "On the Noncorrelation of the Vertical Structure of Light Scattering and Chlorophyll *a* in Case 1 Water," *J. Geophys. Res.* 95(C11):20237 (1990).
71. K. J. Voss, "A Spectral Model of the Beam Attenuation Coefficient in the Ocean and Coastal Areas," *Limnol. Oceanogr.* 37(3):501 (1992).

72. J. E. Tyler and R. C. Smith, *Measurements of Spectral Irradiance Underwater*, Gordon and Breach, New York, 1970, 103 pp.
73. K. S. Baker and R. C. Smith, "Quasi-Inherent Characteristics of the Diffuse Attenuation Coefficient for Irradiance," *Ocean Optics VI*, S. Q. Duntley (ed.), *Proc. SPIE* **208**:60 (1979).
74. C. D. Mobley, "A Numerical Model for the Computation of Radiance Distributions in Natural Waters with Wind-Blown Surfaces," *Limnol. Oceanogr.* **34**(8):1473 (1989).
75. R. W. Austin and T. J. Petzold, "Spectral Dependence of the Diffuse Attenuation Coefficient of Light in Ocean Water," *Opt. Eng.* **25**(3):471 (1986).
76. D. A. Siegel and T. D. Dickey, "Observations of the Vertical Structure of the Diffuse Attenuation Coefficient Spectrum," *Deep-Sea Res.* **34**(4):547 (1987).
77. S. Sugihara and M. Kishino, "An Algorithm for Estimating the Water Quality Parameters from Irradiance Just below the Sea Surface," *J. Geophys. Res.* **93**(D9):10857 (1988).
78. H. R. Gordon, O. B. Brown, R. E. Evans, J. W. Brown, R. C. Smith, K. S. Baker, and D. C. Clark, "A Semianalytic Model of Ocean Color," *J. Geophys. Res.* **93**(D9):10909 (1988).
79. S. Sathyendranath and A. Morel, "Light Emerging from the Sea—Interpretation and Uses in Remote Sensing," *Remote Sensing Applications in Marine Science and Technology*, A. P. Cracknell (ed.), D. Reidel, Dordrecht, 1983, chap. 16, pp. 323–357.
80. B. R. Marshall and R. C. Smith, "Raman Scattering and In-Water Ocean Optical Properties," *Appl. Optics* **29**:71 (1990).
81. G. W. Kattawar and X. Xu, "Filling-in of Fraunhofer Lines in the Ocean by Raman Scattering," *Appl. Optics* **31**(30):6491 (1992).
82. H. Gordon, "Diffuse Reflectance of the Ocean: The Theory of Its Augmentation by Chlorophyll *a* Fluorescence at 685 nm," *Appl. Optics* **18**:1161 (1979).
83. J. J. Cullen, C. M. Yentsch, T. L. Cucci, and H. L. MacIntyre, "Autofluorescence and Other Optical Properties As Tools in Biological Oceanography," *Ocean Optics IX*, M. A. Blizard (ed.), *Proc. SPIE* **925**:149 (1988).
84. A. Ivanoff, "Polarization Measurements in the Sea," *Optical Aspects of Oceanography*, N. G. Jerlov and E. S. Nielsen (eds.), Academic Press, New York, 1974, chap. 8, pp. 151–175.
85. G. D. Gilbert and J. C. Pernicka, "Improvement of Underwater Visibility by Reduction of Backscatter with a Circular Polarization Technique," *SPIE Underwater Photo-Optics Seminar Proc*, Santa Barbara, Oct. 1966.
86. T. H. Waterman, "Polarization of Marine Light Fields and Animal Orientation," *Ocean Optics X*, M. A. Blizard (ed.), *Proc. SPIE* **925**:431 (1988).
87. K. J. Voss and E. S. Fry, "Measurement of the Mueller Matrix for Ocean Water," *Appl. Optics* **23**:4427 (1984).
88. M. S. Quinby-Hunt, A. J. Hunt, K. Lofftus, and D. Shapiro, "Polarized Light Studies of Marine *Chlorella*," *Limnol. Oceanogr.* **34**(8):1589 (1989).
89. G. W. Kattawar and C. N. Adams, "Stokes Vector Calculations of the Submarine Light Field in an Atmosphere–Ocean with Scattering According to a Rayleigh Phase Matrix: Effect of Interface Refractive Index on Radiance and Polarization," *Limnol. Oceanogr.* **34**(8):1453 (1989).

*This page intentionally left blank*

---

# PROPERTIES OF CRYSTALS AND GLASSES

---

William J. Tروف and Michael E. Thomas

*Applied Physics Laboratory  
Johns Hopkins University  
Laurel, Maryland*

Eric W. Rogala

*Raytheon Missile Systems  
Tucson, Arizona*

---

## 2.1 GLOSSARY

---

$A, B, C, D, E, G$	dispersion equation constants
$a, b$	partial dispersion equation constants
$a, b, c$	crystal axes
$B$	inverse dielectric constant ( $=1/\epsilon = 1/n^2$ )
$B$	bulk modulus
$C$	heat capacity
$c$	speed of light
$c$	elastic stiffness tensor
$D$	electric displacement
$D$	dispersion
$d$	piezoelectric coefficient
$d_{ij}^{(2)}$	nonlinear optical coefficient
$E$	Young's modulus
$E$	energy
$E$	electric field
$e$	strain
$G$	shear modulus
$G$	thermal optical constant
$g$	degeneracy
Hi	Hilbert transform
$h$	heat flow
$k$	Index of absorption
$k_B$	Boltzmann constant
$\ell$	phonon mean free path
$L$	length
MW	molecular weight
$m$	Integer, mass
$N()$	occupation number density
$n$	refractive index

$\tilde{n}$	complex refractive index = $n + ik$
$\mathbf{P}$	electric polarization
$P$	relative air pressure = air pressure/one atmosphere (dimensionless)
$P$	pyroelectric constant
$P_{x,y}$	relative partial dispersion
$\mathbf{p}$	elasto-optic tensor
$\mathbf{q}$	piezo-optic tensor
$r$	electro-optic coefficient
$r$	amplitude reflection coefficient
$r_{ij}$	electro-optic coefficient
$S(\ )$	oscillator strength
$\mathbf{s}$	elastic compliance tensor
$T$	temperature
$t$	amplitude transmission coefficient
$U$	enthalpy
$u$	atomic mass unit
$V$	Volume
$v$	velocity of sound
$x$	displacement
$x$	variable of integration
$Z$	formulas per unit cell
$\alpha$	linear thermal expansion coefficient
$\alpha$	intensity (power) absorptance
$\alpha_m$	macroscopic polarizability
$\alpha, \beta, \gamma$	crystal angles
$\beta$	power absorption coefficient
$\gamma(\ )$	line width
$\gamma$	Gruneisen parameter
$\epsilon$	relative dielectric constant, permittivity
$\epsilon$	emittance
$\theta_D$	Debye temperature
$\kappa$	thermal conductivity
$\lambda$	wavelength
$\Lambda(\ )$	complex function
$\mu$	permeability
$\nu$	wave number ( $\omega/2\pi c$ )
$\nu_d$	Abbe number (constringence)
$\rho$	density
$\rho$	intensity reflectance
$\sigma$	stress
$\tau$	intensity (power) transmittance
$\chi$	susceptibility
$\chi^{(2)}$	second-order susceptibility
$\Omega$	solid angle
$\omega$	frequency

### Subscripts

ABS	absorptance
abs	absolute
bb	blackbody
C	656.3 nm
d	587.6 nm
EXT	extinctance

$F$	486.1 nm
$i$	integers
$P$	constant pressure
$r$	relative
SCA	scatterance
$V$	constant volume
0	vacuum or constant terms (or $T = 0$ )
1, 2, 3	principal axes

## 2.2 INTRODUCTION

Nearly every nonmetallic crystalline and glassy material has potential use in transparent optics. If a nonmetal is sufficiently dense and homogeneous, it will have good optical properties. Generally, a combination of desirable optical properties, good thermal and mechanical properties, and cost and ease of manufacture dictate the number of readily available materials. In practice, glasses dominate the available optical materials for several important reasons. Glasses are easily made of inexpensive materials, and glass manufacturing technology is mature and well-established. The resultant glass products can have very high optical quality and meet most design requirements.

Common glasses, however, are composed of low-atomic-weight oxides and therefore will not transmit beyond about 2.5  $\mu\text{m}$  or below 0.3  $\mu\text{m}$ . Some crystalline materials transmit at wavelengths longer (e.g., heavy-metal halides and chalcogenides) or shorter (e.g., fluorides) than common, oxide-based glasses. Crystalline materials are also used for situations that require the material to have very low scatter, high thermal conductivity, or exceptionally high hardness and strength, especially at high temperature. Other applications of crystalline optical materials make use of their directional properties, particularly those of noncubic (uni- or biaxial) crystals. Phase matching (e.g., in wave mixing) and polarization (e.g., in wave plates) are example applications. For these reasons, crystalline solids are used for a wide variety of specialized applications.

Polycrystalline materials form an intermediate class. Typically engineered from powders, polycrystalline materials approach the properties of crystals with reduced cost, particularly when made into complex shapes. Most polycrystalline materials are made with large grains ( $\gg \lambda$ ) to reduce scatter, and the properties of crystalline materials in this chapter are obtained from samples with large grains or single crystals. Recent work has produced materials with sub-micrometer grains ( $\ll \lambda$ ) for applications such as laser gain media and highly durable windows.

This chapter gives the physical, mechanical, thermal, and optical properties of selected crystalline, polycrystalline, and glassy materials. Crystals are chosen based on availability of property data and usefulness of the material. Unfortunately, for many materials, property data are imprecise, incomplete, or not wholly applicable to optical-quality material. Glasses are more accurately and uniformly characterized, but their optical property data are usually limited to wavelengths below 1.06  $\mu\text{m}$ . Owing to the preponderance of glasses, only a small, representative fraction of available glasses are included below. SI-derived units, as commonly applied in material characterization, are used.

Property data are accompanied with brief explanations and useful functional relationships. We have updated the previous version of this chapter<sup>1</sup> by extracting property data from standard compilations<sup>2-12</sup> as well as recent literature. Unfortunately, property data are often sparse. For example, refractive index data may be available for only a portion of the transparent region or the temperature dependence of the index may not be known. Strength of many materials is poorly characterized. Thermal conductivity is frequently unavailable and other thermal properties are usually sketchy.

For brevity, we have reduced the number of materials in this chapter. Many seldom-used or no-longer-produced materials have been eliminated. New materials, principally used for laser gain media or wave mixing were added. Glasses have been updated to their new arsenic- and lead-free analogs.



## 2.3 OPTICAL MATERIALS

Crystalline and amorphous (including glass) materials are differentiated by their structural (crystallographic) order. The distinguishing structural characteristic of amorphous substances is the absence of long-range order; the distinguishing characteristic of crystals is the presence of long-range order. This order, in the form of a periodic structure, can cause directional-dependent (anisotropic) properties that require a more complex description than needed for isotropic, amorphous materials. The periodic structure of crystals are used to classify them into six crystal systems,\* and further arrange them into 14 (Bravais) space lattices, 32 point groups, and 230 space groups based on the characteristic symmetries found in a crystal.

Glass is by far the most widely used optical material, accounting for more than 90 percent of all optical elements manufactured. Traditionally, glass has been the material of choice for optical systems designers, owing to its high transmittance in the visible-wavelength region, high degree of homogeneity, ease of molding, shaping, and machining, relatively low cost, and the wide variety of index and dispersion characteristics available.

Under proper conditions, glass can be formed from many different inorganic mixtures. Primary glass-forming compounds include oxides, halides, and chalcogenides with the most common mixtures being the oxides of silicon, boron, and phosphorous used for glasses transmitting in the visible spectrum. By varying the chemical composition of glasses (glasses are not fixed stoichiometrically), the properties of the glass can be modified. For optical applications, glass compositions are altered to vary the refractive index, dispersion, and thermo-optic coefficient, allowing glasses to be used in combination to make optics with excellent performance over wide spectral and temperature ranges.

Historically, emphasis was placed on optimizing optics for the visible spectrum. The approach was to produce a wide variety of glass and selecting the best combination of glasses to optimize a design. Early glass technologists found that adding BaO offered a high-refractive-index glass with lower than normal dispersion, B<sub>2</sub>O<sub>3</sub> offered low index and very low dispersion, and by replacing oxides with fluorides, glasses could be obtained with very low index and very low dispersion. Later, others developed very high index glasses with relatively low dispersions by introducing rare-earth elements, especially lanthanum, to glass compositions. Other compounds are added to silica-based glass mixtures to help with chemical stabilization, typically the alkaline earth oxides and in particular Al<sub>2</sub>O<sub>3</sub> to improve the resistance to attack by water.

Advances in detector and source technology pushed the design spectrum into both the UV and IR. To extend the transmission range of glasses into the ultraviolet, a number of fluoride and fluorophosphate glasses were developed. Nonoxide glasses are used for infrared applications requiring transmission beyond the transmission limit of typical optical glasses (cf., 2.4 to 2.7 μm for an absorption coefficient of <1 cm<sup>-1</sup>). These materials include chalcogenides such as As<sub>2</sub>S<sub>3</sub> glass and heavy-metal fluorides such as ZrF<sub>4</sub>-based glasses.

With today's computing power, optical designs are becoming far more elegant and simple, and require fewer optical glass types. Advances in polishing and use of aspheres have introduced a new design variable, reducing the dependence on a continuous range material properties. An increased awareness of the environment has led to the elimination of many hazardous materials from optical glasses. These factors lead to a major reduction of the glass library available from manufacturers.

Crystalline materials include naturally occurring minerals and manufactured crystals. Both single crystals and polycrystalline forms are available for many materials. Polycrystalline optical materials are typically composed of many small (cf., 50 to 200 μm) individual crystals ("grains") with random orientations and *grain boundaries* between them. These grain boundaries are a form of material defect arising from the lattice mismatch between individual grains. Polycrystalline materials are made by diverse means such as pressing powders (usually with heat applied), sintering, or chemical vapor deposition. Single crystals are typically grown from dissolved or molten material using a variety of techniques. Usually, polycrystalline materials offer greater hardness and strength at the expense of increased scatter and reduced thermal conductivity.

\*Cubic (or isometric), hexagonal (including rhombohedral), tetragonal, orthorhombic, monoclinic, and triclinic are the crystallographic systems.

Uniformity of the refractive index throughout an optical element is a prime consideration in selecting materials for high-performance lenses, elements for coherent optics, laser harmonic generation, and acousto-optical devices. In general, highly pure, single crystals achieve the best uniformity, followed by glasses (especially those specially manufactured for homogeneity), and lastly polycrystalline materials. Similarly, high-quality single crystals have very low scatter, typically one-tenth that of the best glasses.

Applications requiring optical elements with direction-dependent properties, such as polarizers and phase-matching materials for harmonic generation, frequently use single crystals.

Purity of starting materials is a prime factor in determining the quality of the final product. High material quality and uniformity of processing is required to avoid impurity absorption, index non-uniformity, voids, cracks, and bubbles, and excess scatter. Practical manufacturing techniques limit the size of optics produced from a given material (glasses are typically limited by the moduli, i.e., deformation caused by the weight of the piece). Some manufacturing methods, such as hot pressing, also produce significantly lower quality material when size becomes large (especially when the thinnest dimension is significantly increased). Cost of finished optical elements is a function of size, raw material cost, and the difficulty of machining, polishing, and coating the material. Any one of these factors can dominate cost.

Information on general optical glass properties and classification can be found on select manufacturer's websites<sup>13-15</sup> and in the literature.<sup>16,17</sup> General information on the manufacturing methods for glasses and crystalline materials is available in several sources.<sup>10,12,18,19</sup> Information on cutting and polishing of optical elements can be found in the literature.<sup>3,20,21</sup> Further information on applications of optical material are found in this section of this *Handbook* and a variety of sources.<sup>2,18,22,23</sup>

## 2.4 PROPERTIES OF MATERIALS

### Symmetry Properties

The description of the properties of solids depends on structural symmetry. The structural symmetry of crystalline materials dictates the number of appropriate directional-dependent terms that describe a property.<sup>24</sup> *Neumann's principle* states that physical properties of a crystal must possess at least the symmetry of the point group of the crystal. Amorphous (glassy) materials, having no long-range symmetry, are generally considered isotropic,\* and require the least number of property terms. Macroscopic material properties are best described in tensor notation; the rank of the property tensors can range from zero (scalar property) up to large rank. Table 1 summarizes common material properties and the rank of the tensor that describes them.

The rank of the property tensor and the symmetry of the material (as determined by the point group for crystals) determine the number of terms needed to describe a property. Table 2 summarizes both the number of terms needed to describe a property and the number of unique terms as a function of property tensor rank and point group. Another important term in the definition of tensor characteristics is the *principal values* of a second-rank tensor property. The principal values of a property are those values referenced to (measured along) the crystal axes as defined in Table 2. For example, a second-rank tensor of a triclinic crystal has nine nonzero coefficients, and because of symmetry, six independent coefficients. These six coefficients can be separated into (1) three principal values of the quantity (e.g., thermal expansion coefficient, dielectric constant, refractive index, and stress), and (2) the three angles describing the orientation of the crystal axes ( $\alpha$ ,  $\beta$ ,  $\gamma$ ).

Properties of materials depend on several fundamental constants that are listed in Table 3.<sup>25</sup> These constants are defined as follows.

\*Glass properties are dependent on cooling rate. Nonuniform cooling will result in density variation and residual stress which cause anisotropy in all properties. Such nonisotropic behavior is different from that of crystals in that it arises from thermal gradients rather than periodic structure order. Hence, the nature of anisotropy in glasses varies from sample to sample.

**TABLE 1** Tensor Characteristics and Definitions of Properties

Tensor rank	Property	Symbol	Units	Relationship	
0	Enthalpy (energy)	$U$	J/mole	—	
	Temperature	$T$	K	—	
	Heat capacity	$C$	J/(mole · K)	$C = \partial U / \partial T$	
1	Displacement	$x$	m	—	
	Heat flow	$h$	W/m <sup>2</sup>	—	
	Electric field	$\mathbf{E}$	V/m	—	
	Electric polarization	$\mathbf{P}$	C/m <sup>2</sup>	$\mathbf{P} = \epsilon_0 \chi \mathbf{E}$	
	Electric displacement	$\mathbf{D}$	C/m <sup>2</sup>	$\mathbf{D} = \epsilon_0 \mathbf{E} + \mathbf{P}$	
	Pyroelectric constant	$p$	C/(m <sup>2</sup> · K)	$\Delta \mathbf{P} = p \Delta T$	
	2	Stress	$\sigma$	Pa	—
Strain		$e$	—	—	
Thermal expansion		$\alpha$	K <sup>-1</sup>	$e = \alpha T$	
Thermal conductivity		$k$	W/(m · K)	$h = -k (\partial T / \partial x)$	
Dielectric constant (relative permittivity)		$\epsilon$	—	$\mathbf{D} = \epsilon_0 \epsilon_r \mathbf{E}$	
Inverse dielectric tensor		$\mathbf{B}$	—	$\mathbf{B} = \epsilon_r^{-1}$	
Susceptibility		$\chi$	—	$\epsilon_r = \chi + 1$	
3		Piezoelectric coefficient (modulus)	$d$	m/V $\equiv$ C/N	$\mathbf{P} = d \cdot \sigma$
		(converse piezoelectric effect)	$d$	m/V $\equiv$ C/N	$e = d \cdot \mathbf{E}$
4		Electro-optic coefficient (linear)	$r$	m/V	$\Delta \mathbf{B} = r \cdot \mathbf{E}$
	Second-order susceptibility	$\chi^{(2)}$	m/V	$\mathbf{P} = \epsilon_0 \chi^{(2)} \mathbf{E}_1 \mathbf{E}_2$	
	Elastic stiffness	$\mathbf{c}$	Pa	$\sigma = \mathbf{c} \cdot \mathbf{e}$ ; $\mathbf{c} = 1/\mathbf{s}$	
4	Elastic compliance	$\mathbf{s}$	Pa <sup>-1</sup>	$\mathbf{e} = \mathbf{s} \cdot \sigma$ ; $\mathbf{s} = 1/\mathbf{c}$	
	Elasto-optic tensor	$\mathbf{p}$	—	$\Delta \mathbf{B} = \mathbf{p} \cdot \mathbf{e}$ ; $\mathbf{p} = q \cdot \mathbf{c}$	
	Piezo-optic tensor	$\mathbf{q}$	Pa <sup>-1</sup>	$\Delta \mathbf{B} = \mathbf{q} \cdot \sigma$ ; $\mathbf{q} = \mathbf{p} \cdot \mathbf{s}$	

## Optical Properties: Introduction

**Refractive Index** Important optical properties, definitions, formulas, and basic concepts are derived from a classical description of propagation based on the macroscopic Maxwell's equations.<sup>22</sup> The standard wave equation for the electric field  $\mathbf{E}$  is obtained from Faraday, Gauss, and Ampere laws in Maxwell's form:\*

$$\nabla^2 \mathbf{E} = (-i\omega\mu\sigma - \omega^2\mu\epsilon)\mathbf{E} \quad (1)$$

where  $\sigma$ ,  $\epsilon$ , and  $\mu$  are the frequency-dependent conductivity, permittivity, and permeability, respectively. These quantities are scalars in an isotropic medium. To simplify notation, a generalized permittivity is sometimes defined as:

$$\epsilon_c(\omega) = \epsilon_r(\omega) \left[ 1 + i \frac{\sigma(\omega)}{\omega\epsilon(\omega)} \right] \quad (2)$$

where  $\epsilon_c(\omega)$  is a generalized relative permittivity of dielectric constant (i.e., with  $\epsilon_0$  removed from  $\epsilon = \epsilon_0 \epsilon_c$ ) that includes contributions from free charges [via the conductivity  $\sigma(\omega)$ ] and bound charges [via the relative permittivity,  $\epsilon_r(\omega)$ ]. Assuming a nonmagnetic material ( $\mu_r = 1$ ), and using the preceding generalized dielectric constant, the plane-wave solution to the wave equation is

$$\mathbf{E}(z, \omega) = \mathbf{E}(0) \exp \left[ i(\omega z / c) \sqrt{\epsilon_c(\omega)} \right] \quad (3)$$

\*The definition of the dielectric constant and refractive index in this section is based on a harmonic field of the form  $\exp(-i\omega t)$ . Other definitions lead to different sign conventions (e.g.,  $\bar{n} = n - ik$ ) and care must be taken to ensure consistency.

**TABLE 2** Crystal Classes and Symmetries

Crystal System	Crystal Axes	Space lattice		Point group		Space Group Nos.	Tensor coefficients*						
		Types	Symmetry	Schönflies	Internat'l		Rank 1	Rank 2	Rank 3	Rank 4			
Triclinic (—)	$a \neq b \neq c$	P	$\bar{1}$	$C_1$	$\bar{1}$	1	3 (3)	9 (6)	18(18)	36 (21)			
	$\alpha \neq \beta \neq \gamma$			$C_1$	$\bar{1}$	2	0	9 (6)	0	36 (21)			
Monoclinic (2-fold axis)	$a \neq b \neq c$	P, I (or C)	2/m	$C_2$	2	3–5	1 (1)	5 (4)	8 (8)	20 (13)			
	$\alpha = \beta = 90^\circ$			$C_s$	m	6–9	2 (2)	5 (4)	10 (10)	20 (13)			
	$\gamma \neq 90^\circ$			$C_{2h}$	2/m	10–15	0	5 (4)	0	20 (13)			
Orthorhombic (3 $\perp$ 2-fold axes)	$a \neq b \neq c$	P, I, C, F	mmm	$D_2$	222	16–24	0	3 (3)	3 (3)	12 (9)			
	$\alpha = \beta = \gamma = 90^\circ$			$C_{2v}$	2mm	25–46	1 (1)	3 (3)	5 (5)	12 (9)			
				$D_{2h}$	mmm	47–74	0	3 (3)	0	12 (9)			
Tetragonal (4-fold axis)	$a = b \neq c$	P, I	4/m	$C_4$	$\frac{4}{4}$	75–80	1 (1)	3 (2)	7 (4)	16 (7)			
	$\alpha = \beta = \gamma = 90^\circ$			$S_4$	$\frac{4}{4}$	81–82	0	3 (2)	7 (4)	16 (7)			
				$C_{4h}$	4/m	83–88	0	3 (2)	0	16 (7)			
				$D_4$	422	89–98	0	3 (2)	2 (1)	12 (6)			
				$C_{4v}$	4mm	99–110	1 (1)	3 (2)	5 (3)	12 (6)			
				$D_{2d}$	$\frac{4}{4}$	111–122	0	3 (2)	3 (2)	12 (6)			
				$D_{4h}$	4/mmm	123–142	0	3 (2)	0	12 (6)			
Hexagonal (3-fold axis)	$a = b \neq c$	P, R	$\bar{3}$	$C_3$	$\frac{3}{3}$	143–146	1 (1)	3 (2)	13 (6)	24 (7)			
	$\alpha = \beta = 90^\circ$			$C_{3i}$	$\frac{3}{3}$	147–148	0	3 (2)	0	24 (7)			
	$\gamma = 120^\circ$			$D_3$	32	149–155	0	3 (2)	5 (2)	18 (6)			
				$D_{3v}$	3m	156–161	1 (1)	3 (2)	8 (4)	18 (6)			
				$D_{3h}$	$\frac{3}{3}$	162–167	0	3 (2)	0	18 (6)			
	(6-fold axis)				P	6/m	$C_6$	$\frac{6}{6}$	168–173	1 (1)	3 (2)	7 (4)	12 (5)
							$C_{3h}$	$\frac{6}{6}$	174	0	3 (2)	6 (2)	12 (5)
		$C_{6h}$	6/m	175–176			0	3 (2)	0	12 (5)			
		$D_6$	622	177–182			0	3 (2)	2 (1)	12 (5)			
		$C_{6v}$	6mm	183–186			1 (1)	3 (2)	5 (3)	12 (5)			
		$D_{3h}$	$\bar{6}2M$	187–190			0	3 (2)	3 (1)	12 (5)			
		$D_{6h}$	6/mmm	191–194			0	3 (2)	0	12 (5)			
Cubic (isometric) (Four 3-fold axes)	$a = b = c$	P, I, F	m3	T	23	195–199	0	3 (1)	3 (1)	12 (3)			
	$\alpha = \beta = \gamma = 90^\circ$			$T_h$	m3	200–206	0	3 (1)	0	12 (3)			
				O	432	207–224	0	3 (1)	0	12 (3)			
				$T_d$	$\bar{4}3m$	215–220	0	3 (1)	3 (1)	12 (3)			
				$O_h$	m3m	221–230	0	3 (1)	0	12 (3)			
Isotropic	Amorphous	—	$\infty\infty m$	—	—	—	0	3 (1)	0	12 (2)			

\*Values are the number of nonzero coefficients in (equilibrium) property tensors and the values in parentheses are the numbers of independent coefficients in the tensor. Note that the elasto-optic and piezo-optic tensors have lower symmetry than the rank-4 tensors defined in this table and therefore have more independent coefficients than shown. Second-, third-, and fourth-rank tensors are given in the usual reduced index format (see text).

**TABLE 3** Fundamental Physical Constants (2006 CODATA Values<sup>25</sup>)

Constant	Symbol	Value	Unit
Atomic mass unit (amu)	$u$	$1.660\,538\,782(83) \times 10^{-27}$	kg
Avogadro constant	$N_A$	$6.022\,141\,79(30) \times 10^{23}$	mole <sup>-1</sup>
Boltzmann constant	$k_B$	$1.380\,6504(24) \times 10^{-23}$	J/K
Elementary charge	$e$	$1.602\,176\,487(40) \times 10^{-19}$	C
Permeability of vacuum	$\mu_0$	$4\pi \cdot 10^{-7} = 12.566\,370\,614 \times 10^{-7}$	N/A <sup>2</sup> or H/m
Permittivity of vacuum	$\epsilon_0$	$8.854\,187\,187 \times 10^{-12}$	F/m
Planck constant	$h$	$6.626\,068\,96(33) \times 10^{-34}$	J · s
Speed of light	$c$	299 792 458	m/s

In optics, it is frequently convenient to define a *complex refractive index*,  $\bar{n}$ , the square root of the complex dielectric constant (henceforth, the symbol  $\epsilon$  will be used for the relative complex dielectric constant):

$$\begin{aligned}\bar{n} &= n + ik = \sqrt{\epsilon} = \sqrt{\epsilon' + i\epsilon''} \\ \epsilon' &= n^2 - k^2; & \epsilon'' &= 2nk \\ n^2 &= \frac{1}{2} \left[ \epsilon' + \sqrt{\epsilon'^2 + \epsilon''^2} \right] \\ k^2 &= \frac{1}{2} \left[ -\epsilon' + \sqrt{\epsilon'^2 + \epsilon''^2} \right] = \left( \frac{\epsilon''}{2n} \right)^2\end{aligned}\quad (4)$$

where  $n$  is the (real) *index of refraction* and  $k$  is the *index of absorption* (or imaginary part of the complex refractive index). (The index of absorption is also called the absorption constant, index of extinction, or some other combination of these terms.) Using this definition of the complex index of refraction and the solution of the wave equation [Eq. (3)], the optical power density (proportional to  $1/2|\mathbf{E}|^2$  from Poynting's vector) is

$$\text{Power density} = \frac{1}{2} n \sqrt{\mu_0/\epsilon_0} |\mathbf{E}(z)|^2 = \frac{1}{2} n \sqrt{\mu_0/\epsilon_0} |\mathbf{E}(0)|^2 \exp(-2\omega k z/c) \quad (5)$$

where the exponential function represents the attenuation of the wave. The meanings of  $n$  and  $k$  are clear:  $n$  contributes to phase effects (time delay or variable velocity) and  $k$  contributes to attenuation by absorption. In practice, attenuation is conveniently described by a power absorption coefficient,  $\beta_{\text{ABS}}$ , which describes the internal transmittance over a distance  $z$ , i.e.,

$$\tau = \frac{|\mathbf{E}(z)|^2}{|\mathbf{E}(z=0)|^2} = e^{-2\omega k z/c} = e^{-\beta_{\text{ABS}} z} \quad (6a)$$

and  $\beta_{\text{ABS}}$  (with units of reciprocal length, usually  $\text{cm}^{-1}$ ) is

$$\beta_{\text{ABS}} = 2\omega k/c = 4\pi\nu k \quad (6b)$$

where  $\nu$  is the wave number in reciprocal length, usually  $\text{cm}^{-1}$ .

**Kramers–Krönig and Sum Rule Relationships** The principal of causality—that a material cannot respond until acted upon—when applied to optics, produces important symmetry properties and relationships that are very useful in modeling and analyzing optical properties. As a consequence of these symmetry properties, the real and imaginary parts of the dielectric constant (and of the complex index of refraction) are Hilbert transforms of each other. The Hilbert transform,  $\text{Hi}[\Lambda(\omega)]$ , of the complex function  $\Lambda(\omega)$  is defined as (the symbol  $P$  denotes the principal value of the integral)

$$\text{Hi}[\Lambda(\omega)] = \frac{i}{\pi} P \int_{-\infty}^{\infty} \frac{\Lambda(\omega')}{\omega - \omega'} d\omega' \quad (7)$$

and the relationships between the components of the dielectric constant or index of refraction are

$$\begin{aligned}\varepsilon' - 1 &= \text{Hi}[\varepsilon''] \\ \varepsilon'' &= \text{Hi}^{-1}[\varepsilon' - 1] \\ n - 1 &= \text{Hi}[k] \\ k &= \text{Hi}^{-1}[n - 1]\end{aligned}\quad (8)$$

These are the *Kramers–Krönig relationships* (abbreviated KK). Usually the Hilbert transforms for the refractive index are written in single-sided form:

$$n(\omega) - 1 = \frac{2}{\pi} P \int_0^{\infty} \frac{\omega' k(\omega')}{\omega'^2 - \omega^2} d\omega' \quad (9a)$$

with the inverse transform given by

$$k(\omega) = \frac{2\omega}{\pi} P \int_0^{\infty} \frac{n(\omega') - 1}{\omega'^2 - \omega^2} d\omega' \quad (9b)$$

These are fundamental relationships of any causal system.

A number of useful integral relationships, or *sum rules* result from Fourier transforms and the Kramers–Krönig relationship.<sup>26</sup> For example, the real part of the refractive index satisfies

$$\int_0^{\infty} [n(\omega) - 1] d\omega = 0 \quad (10a)$$

and

$$\begin{aligned}n(\omega=0) - 1 &= \frac{2}{\pi} \int_0^{\infty} \frac{k(\omega')}{\omega'} d\omega' \\ &= \frac{c}{\pi} \int_0^{\infty} \frac{\beta_{\text{ABS}}(\omega')}{\omega'^2} d\omega'\end{aligned}\quad (10b)$$

The dielectric constant and the refractive index also have the following symmetry properties:

$$\begin{aligned}\varepsilon(\omega) &= \varepsilon^*(-\omega) \\ \bar{n}(\omega) &= \bar{n}^*(-\omega)\end{aligned}\quad (10c)$$

Practical models of the dielectric constant or refractive index must satisfy these fundamental symmetries and integral relationships.

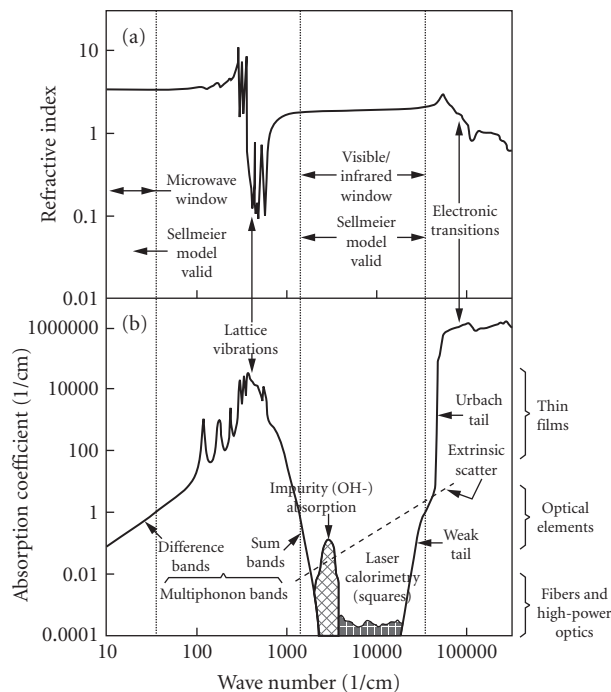
## Optical Properties: Origin and Models

Intrinsic optical properties of a material are determined by three basic physical processes: electronic transitions, lattice vibrations, and free-carrier effects.<sup>5-7,27,28</sup> However, the dominant physical process depends on the material and spectral region of interest. All materials have contributions to the complex index of refraction from electronic transitions. Insulators and semiconductors also require the characterization of the lattice vibrations (or phonons) to fully understand the optical properties. Transparency of semiconductors, particularly those with small bandgaps, is additionally influenced by free-carrier effects. The strength of the free-carrier influence on transmission and absorption depends on the free-carrier concentration; thus free-carrier effects dominate the optical properties of metals in the visible and infrared.

In the range of transparency of a bulk material, more subtle effects such as multiphonon processes (see later discussion; also refer to Chap. 16, “Third-Order Nonlinearities,” by Mansoor Sheik-Bahae

and Michael P. Hasselbeck), impurity and defect absorption, and scattering become the important loss mechanisms. Intrinsic atomic (Rayleigh) scattering is a very weak effect, but is important in long-path optical fibers and ultraviolet materials (refer to Chap. 9, “Volume Scattering in Random Media,” by Aristide Dogariu and Jeremy Ellis in Vol. I). Extrinsic scattering, caused by density (local composition) variations, defects, or grains in polycrystalline solids, is typically much larger than intrinsic scattering in the visible and infrared spectral regions. Impurity and defect (electronic or vibrational) absorption features can be of great concern depending on the spectral region, incident radiation intensity, or material temperature required by the application.

Figure 1 illustrates the frequency dependence of  $n$  and  $k$  for an insulating polar crystal.<sup>29</sup> The value of  $n(\omega, T)$  is essentially the sum of the contributions of all electronic and lattice vibration resonances, and is dominated by those with fundamental oscillation frequencies above  $\omega$ . Figure 1a indicates regions of validity for the popular Sellmeier model (see discussion under “Electronic Transitions”). The frequency dependence of the imaginary part of the index of refraction  $k(\omega, T)$  requires consideration of



**FIGURE 1** The wave number (frequency) dependence of the complex refractive index of Yttria<sup>29</sup> (a) shows the real part of the refractive index,  $n(\omega)$ . The real part is high at low frequency and monotonically increases, becomes oscillatory in the lattice vibration (phonon) absorption bands, increases monotonically (normal dispersion) in the optical transparent region, and again becomes oscillatory in the electronic absorption region; (b) shows the imaginary part of the refractive index, in terms of the absorption coefficient,  $\beta(\nu) = 4\pi\nu k(\nu)$ . The absorption coefficient is small in the transparent regions and very high in the electronic and vibrational (phonon) absorption bands. The optical transparent region is bounded by the “Urbach tail” absorption at high frequency and by multiphonon absorption at low frequency (wave number). In between, loss is primarily due to impurities and scatter. (Reprinted by permission of McGraw-Hill, Inc.)

not only the dominant physical processes but also higher-order processes, impurities, and defects as illustrated in Fig. 1b. The spectral regions of the fundamental resonances are opaque. The infrared edge of transparency is controlled by multiphonon transitions. Transparent regions for insulators are divided in two regions: microwave and visible/infrared.

**Lattice Vibrations** Atomic motion, or lattice vibrations, accounts for many material properties, including heat capacity, thermal conductivity, elastic constants, and optical and dielectric properties. Lattice vibrations are quantized; the quantum of lattice vibration is called a *phonon*. In crystals, the number of lattice vibrations is equal to three times the number of atoms in the primitive unit cell (see further discussion); three of these are acoustic vibrations (translational modes in the form of sound waves), the remainder are optical vibrations (or modes or phonons) for materials with more than one type atom per unit cell. For most practical temperatures, only the acoustic phonons are thermally excited because optical phonons are typically of much higher frequency, hence acoustic modes play a dominant role in thermal and elastic properties. There are three types of optical modes: infrared-active, Raman-active, and optically inactive. Infrared-active modes, typically occurring in the spectral region from 100 to 1000  $\text{cm}^{-1}$ , are those that (elastically) absorb light (photon converted to phonon) through an interaction between the electric field and the light and the dipole moment of the crystal. Raman modes\* (caused by phonons that modulate the polarizability of the crystal to induce a dipole moment) weakly absorb light through an inelastic mechanism (photon converted to phonon and scattered photon) and are best observed with intense (e.g., laser) light. Optically inactive modes have no permanent or induced dipole moment and therefore do not interact with light. Optically active modes can be simultaneously infrared- and Raman-active and are experimentally observed by either infrared or Raman spectroscopy, as well as by x-ray or neutron scattering.

Crystal symmetries reduce the number of unique lattice vibrations (i.e., introduce vibrational degeneracies). Group theory analysis determines the number of optical modes of each type for an ideal material. Defects and impurities will increase the number of observed infrared-active and Raman-active modes in a real material. As structural disorder increases (nonstoichiometry, defects, variable composition), the optical modes broaden and additional modes appear. Optical modes in noncrystalline (amorphous) materials such as glasses are very broad compared to those of crystals.

Lattice vibration contributions to the static dielectric constant,  $\epsilon(0)$ , are determined from the longitudinal-mode (LO) and transverse-mode (TO) frequencies of the optical modes using the Lyddane-Sachs-Teller (LST) relationship<sup>30</sup> as extended by Cochran and Cowley<sup>31</sup> for materials with multiple optical modes:

$$\epsilon(0) = \epsilon(\infty) \prod_j^{j_{\max}} \frac{\omega_j^2(\text{LO})}{\omega_j^2(\text{TO})} \quad (11)$$

where  $\omega$  is frequency (also expressible in wave numbers) and  $\epsilon(\infty)$  is the high-frequency (electronic transition) contribution to the dielectric constant (not the dielectric constant at infinite frequency). This relationship holds individually for each principal axis. The index  $j$  denotes infrared-active lattice vibrations with minimum value usually found from group theory (discussed later). This LST relationship has been extended to include the frequency dependence of the real dielectric constant (in transparent, i.e., nonabsorbing, spectral regions):

$$\epsilon(\omega) = \epsilon(\infty) \prod_j^{j_{\max}} \frac{\omega_j^2(\text{LO}) - \omega^2}{\omega_j^2(\text{TO}) - \omega^2} \quad (12a)$$

A modified form of this fundamental equation, including absorption, is used by Gervais and Piriou<sup>32</sup> and others to model the complete dielectric constant in the infrared:

$$\epsilon(\omega) = \epsilon(\infty) \prod_j^{j_{\max}} \frac{\omega_j^2(\text{LO}) - \omega^2 - i\omega\gamma_j(\text{LO})}{\omega_j^2(\text{TO}) - \omega^2 - i\omega\gamma_j(\text{TO})} \quad (12b)$$

\*Brillouin scattering is a term applied to inelastic scattering of photons by acoustic phonons.



where  $\gamma$  is the line width of the longitudinal and transverse modes as denoted by the symbol in parentheses. This form of the dielectric constant is known as the *semiquantum* four-parameter model.

Frequently, the infrared dielectric constant is modeled in a three-parameter classical oscillator form (or Maxwell–Helmholtz–Drude<sup>33</sup> dispersion formula), namely

$$\varepsilon(\omega) = \varepsilon(\infty) + \sum_j^{\text{jmax}} \frac{S_j \omega_j^2(\text{TO})}{\omega_j^2(\text{TO}) - \omega^2 - i\omega\gamma_j} \quad (13)$$

where  $S_j$  ( $=\Delta\varepsilon_j$ ) is the oscillator strength and  $\gamma_j$  is the full width of the  $j$ th mode. This model assumes no coupling between modes and provides a good representation of the dielectric constant, especially if the modes are weak [small separation between  $\omega(\text{TO})$  and  $\omega(\text{LO})$ ] and uncoupled. The static dielectric constant  $\varepsilon(0)$  is merely the sum of the high-frequency dielectric constant  $\varepsilon(\infty)$  and strengths  $S_j$  of the individual, IR-active modes. This formulation has been widely used to model infrared dispersion. This model can also be used to represent the high-frequency dielectric constant using additional modes [i.e.,  $\varepsilon(\infty)$  is replaced by 1, the dielectric constant of free space, plus the contribution of electronic modes; see later discussion in this chapter]. Strengths and line widths for the classical dispersion model can be derived from the values of the four-parameter model.<sup>34</sup>

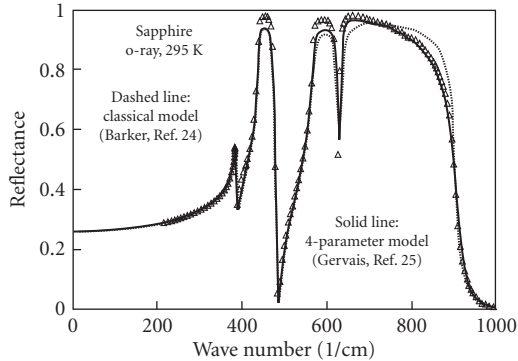
Both the classical and four-parameter dispersion models satisfy the Kramers–Krönig relationship [Eqs. (7) and (8)] and are therefore physically realizable. The frequencies  $\omega(\text{TO})$  and  $\omega(\text{LO})$  arise from the interaction of light with the material, correspond to solutions of the Maxwell wave equation,  $\mathbf{V} \cdot \mathbf{D} = 0$  (no free charges), and are obtained from measurements. A transverse field corresponds to an electromagnetic wave with  $\mathbf{E}$  perpendicular to the wave vector. At higher frequencies [ $\omega > \omega(\text{TO})$ ], the external electric field counters the internal polarization field of the material until the real part of the dielectric constant is zero, hence  $\mathbf{D} = 0$  at  $\omega(\text{LO})$ . The longitudinal frequency  $\omega(\text{LO})$  is always greater than the transverse frequency  $\omega(\text{TO})$ . The separation of  $\omega(\text{LO})$  and  $\omega(\text{TO})$  is a measure of the strength ( $S_j$  or  $\Delta\varepsilon_j$ ) of the optical mode. Raman modes are, by their nature, very weak and therefore  $\omega(\text{LO}) \approx \omega(\text{TO})$ , hence Raman modes do not contribute appreciably to dielectric properties.

In Eq. (12a), the  $\omega(\text{TO})$  frequencies correspond to the poles and the  $\omega(\text{LO})$  frequencies correspond to the zeros of the dielectric constant. The real part of the dielectric constant continuously rises with frequency [except for a discontinuity at  $\omega(\text{TO})$ ] and the dielectric constant is real and negative [i.e., highly absorbing, Eq. (3)] between the transverse and longitudinal frequencies. When damping is added to the dielectric constant model to represent the response of real materials [e.g., Eq. (12b) or (13)], the transverse and longitudinal frequencies become the maxima and minima of the dielectric constant. With damping, a negative dielectric constant is not a necessary condition for absorption, and the material will also absorb outside the region bounded by  $\omega(\text{TO})$  and  $\omega(\text{LO})$ . Furthermore, damping allows the real part of the dielectric constant (and also the refractive index) to decrease with frequency near  $\omega(\text{TO})$ . This dispersive condition is called *anomalous dispersion* and can only occur in absorptive regions.

As an example of lattice vibrations, consider the simple case of crystalline sodium chloride (NaCl) which has four molecules (eight atoms) per unit cell. Since the sodium chloride structure is face-centered cubic, a primitive cell has one molecule or two atoms. The number of unique vibrations is further reduced by symmetry: for sodium chloride, the lattice vibrations consist of one (triply degenerate) acoustic mode and one (triply degenerate) optical mode. Many metals have one atom per primitive unit cell and therefore have no optical modes. Group IV cubic materials (diamond, silicon, germanium) have two atoms per unit cell with one (triply degenerate) optical mode that is Raman-active only. Therefore, to first order, these nonpolar materials are transparent from their bandgap to very low frequencies. In practice, multiphonon vibrations, defects, impurities, and free carriers introduce significant absorption.

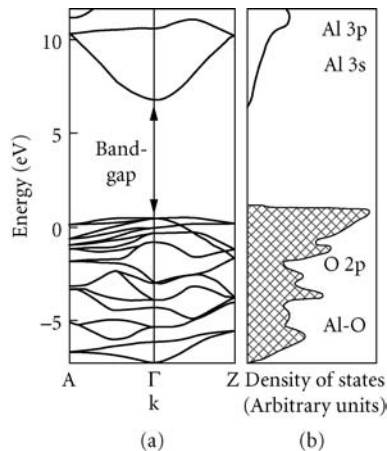
Figure 2 shows a typical crystal infrared spectrum and the corresponding classical oscillator<sup>35</sup> and four parameter model<sup>36</sup> fits to the data. Parameters for both the extended LST [Eq. (12)] and classical oscillator [Eq. (13)] vibration models are given at the end of this chapter for many materials.

**Electronic Transitions** Electronic transitions in a solid begin at the material's bandgap. This point generally marks the end (upper frequency) of a material's useful transparency. Above the bandgap, the



**FIGURE 2** The infrared spectrum of sapphire ( $\text{Al}_2\text{O}_3$ ) showing the fit to data of the three-parameter classic oscillator model of Barker (dashed line<sup>35</sup>) and the four-parameter model of Gervais (solid line<sup>36</sup>). The four-parameter model better fits experimental data (triangles) in the  $650$  to  $900\text{-cm}^{-1}$  region.

material is highly reflective. The large number of possible electronic transitions produces broad-featured spectra. However, electronic structure is fundamental to understanding the nature of the bonds forming the solid and thus many of the material properties. In three dimensions, the band structure becomes more complicated, because it varies with direction just as lattice vibrations do. This point is illustrated in Fig. 3 for the case of the electronic  $k$ -space diagram for sapphire.<sup>37</sup> Also included in this figure is the corresponding electronic density of states that determines the strength of the absorption.



**FIGURE 3** Electronic energy band diagram for sapphire at room temperature<sup>37</sup> (a) shows the complex  $k$ -space energy levels of the electrons of sapphire. The arrow denotes the direct bandgap transition and (b) shows the density of electronic states as a function of energy level. The many direct and indirect electronic transitions give rise to a broad electronic absorption with few features. (Reprinted by permission of the American Ceramic Society.)

In polar insulators, no intraband electronic transitions are allowed, and the lowest frequency electronic absorption is often caused by creation of an *exciton*, a bound electron-hole pair. The photon energy required to create this bound pair is lower than the bandgap energy. Excitons have many properties similar to that of a hydrogen atom. The absorption spectrum of an exciton is similar to that of hydrogen and occurs near the bandgap of the host material. The bond length between the electron-hole pair, hence the energy required to create the exciton, depends on the host medium. Long bond lengths are found in semiconductors (low-energy exciton) and short bond lengths are found in insulating materials.

Other lower-frequency transitions are caused by interband transitions between the anion valence band and the cation conduction band. For sapphire (see Fig. 3), the lowest energy transitions are from the upper valence band of oxygen ( $2p^6$ ) to the conduction band of aluminum ( $3s + 3p$ ). There are typically many of these transitions which appear as a strong, broad absorption feature. Higher energy absorption is caused by surface and bulk plasmons (quanta of collective electronic waves), and still higher energy absorption is attributable to promotion of inner electrons to the conduction band and ultimately liberation of electrons from the material (photoemission).

Classical electronic polarization theory produces a model of the real part of the dielectric constant similar to the model used for the real dielectric constant of lattice vibrations [Eq. (13)]. General properties of the real dielectric constant (and real refractive index) can be deduced from this model. Bound electrons oscillate at a frequency proportional to the square root of the binding energy divided by the electronic mass. Oscillator strength is proportional to the inverse of binding energy. This means that insulators with light atoms and strong bonding have large bandgaps, hence good UV transmission (cf., LiF). Furthermore, high bonding energy (hence high-energy bandgap) means low refractive index (e.g., fluorides).

When both electronic and lattice vibrational contributions to the dielectric constant are modeled as oscillations, the dielectric constant in the transparent region between electronic and vibrational absorption is (mostly) real and the real part takes the form

$$\epsilon'(\omega) - 1 = n^2(\omega) - 1 = \sum_j \frac{S_j \omega_j^2}{\omega_j^2 - \omega^2} \quad (14)$$

which is the widely used *Sellmeier dispersion formula*.<sup>38</sup> The sum includes both electronic (UV) and vibrational (IR or *polar* or *ionic*) contributions. Most other dispersion formulas (such as the Schott glass power series) are recast, series expanded, or simplified forms of the Sellmeier model. The refractive index of most materials with good homogeneity can be modeled to a few parts in  $10^5$  over their entire transparent region with a Sellmeier fit of a few terms. The frequency ( $\omega_j$ ) term(s) in a Sellmeier fit are not necessarily TO modes, but are correlated to the strong TOs nearest the transparent region, with adjustments to the constants made to account for weaker modes, multiphonon effects, and impurities. The Sellmeier model works well because it is (1) based on a reasonable physical model and (2) adjusts constants to match data. The relationship between the Sellmeier equation and other dispersion formulas is discussed later.

The *Urbach tail* model is successfully applied to model the frequency and temperature dependence of the ultraviolet absorption edge in a number of materials, particularly those with a direct bandgap, over several orders of magnitude in absorption. Urbach<sup>39</sup> observed an exponential absorption edge in silver halide materials (which have an indirect bandgap). Further development added temperature dependence in the form

$$\beta_{\text{ABS}}(E, T) = \beta_0 \exp \left[ -\sigma(T) \frac{(E_0 - E)}{k_B T} \right] \quad (15a)$$

where

$$\sigma(T) = \sigma_0(T) \frac{2k_B T}{E_p} \tanh \frac{E_p}{2k_B T} \quad (15b)$$

where  $E_0$  is the bandgap energy (typically the energy of an exciton) at  $T = 0$  K,  $T$  temperature in kelvins, and  $E_p$  a characteristic phonon energy. The interpretation of the Urbach tail is a broadening of the electronic bandgap by phonon interactions, and several detailed theories have been proposed.<sup>28,40</sup>

Below the Urbach tail, absorption continues to decrease exponentially, albeit much slower than predicted by the Urbach formula. This region of slowly decreasing absorption is sometimes called the “weak tail,” and has been observed in both semiconductor<sup>41</sup> and crystalline materials.<sup>42,43</sup> Typically, the weak tail begins at the point when the absorption coefficient falls to  $0.1 \text{ cm}^{-1}$ .

Unfortunately, the optical properties of the electronic transitions, which drive optoelectronic device performance, can not be modeled in a straightforward manner like the vibrational transition models because most electronic transitions are coupled together to form broad homogeneous absorption bands. Thus, the shape of the density-of-states function that determines the spectral response is seldom in the simple functional form of a classical oscillator model.

Adachi<sup>44</sup> has developed models that successfully represent the complex permittivity of electronic transitions as a function of both frequency and temperature by considering the effect of various electronic interband transitions from valence to conduction band. These transitions peak at various critical point locations (e.g.,  $\Gamma$  and L) and include energy level shifts caused by spin-orbit coupling. Various density-of-state models are used, including the classical oscillator to represent several closely spaced transitions.

The Adachi model accounts for first-order electronic transitions, and represents the complex refractive index over a wide frequency and temperature range. Model predictions agree well with experimental complex index of refraction data in transparent spectral regions ending at the bandgap. Model parameters are available for CdTe, GaAs, GaP, GaSb, InAs, InP, InSb, ZnTe, AlGaAs, InGaAsP, and others.<sup>44-51</sup>

The electronic transitions have a very different functional form than the vibrational modes, yet a Sellmeier model, an approximate form to the classical oscillator model, is commonly used to represent the real part of the relative permittivity in transparent spectral regions ending at the bandgap. However, a polynomial expansion of the electronic susceptibility functions shows similar structure to an expansion of the Sellmeier equation. It is expected that when high precision is needed (e.g.,  $<10^{-5}$ ) in the refractive index, the more physically correct (Adachi) model should be used. This is certainly the case for absorption near the bandgap.

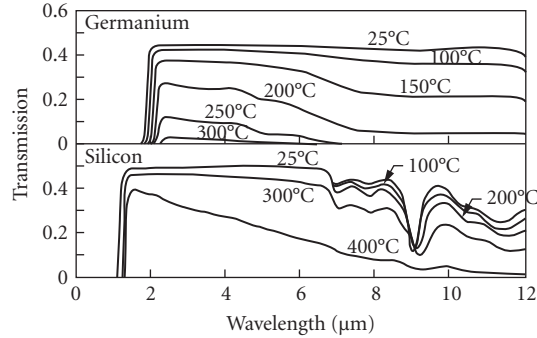
**Free Carriers** Free carriers, such as electrons in metals, or electrons and holes in semiconductors, also affect the optical properties of materials. For insulators or wide-bandgap semiconductors (i.e., bandgap greater than 0.5 eV) with a low number of free carriers at room temperature (low conductivity), the effect of free carriers on optical absorption is small [see Eq. (2)]. For nonmetals, the free-carrier concentration grows with temperature so that even an “insulator” has measurable conductivity (and free-carrier absorption) at very high temperature. Commonly used optical materials such as silicon and germanium have a significant increase in free-carrier absorption at moderately high temperature as illustrated in Fig. 4.<sup>52</sup>

Free-carrier effects can be modeled as an additional contribution to the dielectric constant model. For example, the classical model [Eq. (13)] takes the form

$$\epsilon(\omega) = \epsilon(\infty) + \sum_j^{\max} \frac{S_j \omega_j^2(\text{TO})}{\omega_j^2(\text{TO}) - \omega^2 - i\omega\gamma_j} - \frac{\omega_p^2}{\omega^2 + i\omega\gamma_c} \quad (16)$$

where  $\omega_p$  is the plasma frequency, proportional to the square root of the free-carrier density, and  $\gamma_c$  is the damping frequency (i.e., determines the effective width of the free-carrier influence). Such a model is well known to accurately predict the far-infrared ( $\geq 10 \mu\text{m}$ ) refractive index of metals<sup>53</sup> and also has been used to model the free-carrier contribution to the optical properties of semiconductors.

**Multiphonon Absorption and Refraction** Absorption at the infrared edge of insulators is principally caused by anharmonic terms in the lattice potential leading to higher harmonics of the lattice resonances. This phenomenon is called multiphonon absorption because the frequencies are harmonics



**FIGURE 4** Decreased transmission of germanium and silicon with temperature is attributable to an increase in free-carrier concentration resulting in increased absorption.<sup>52</sup> The absorption is greater at longer wave lengths; see Eq. (16). (Reprinted by permission of the Optical Society of America.)

of the characteristic lattice phonons (vibrations). For absorption in the infrared, each successively higher multiple of the fundamental frequency is weaker (and broader) leading to decreasing absorption beyond the highest fundamental absorption frequency (maximum transverse optical frequency). At about three times  $\omega(\text{TO})$  the absorption coefficient becomes small and a material with thickness of 1 to 10  $\mu\text{m}$  is reasonably transparent. The infrared absorption coefficient of materials (especially highly ionic insulators) can be characterized by an exponential absorption coefficient,<sup>54</sup>  $\beta_{\text{ABS}}$ , of the form

$$\beta_{\text{ABS}} = \beta_0 \exp\left(-\gamma \frac{\omega}{\omega_0}\right) \quad (17a)$$

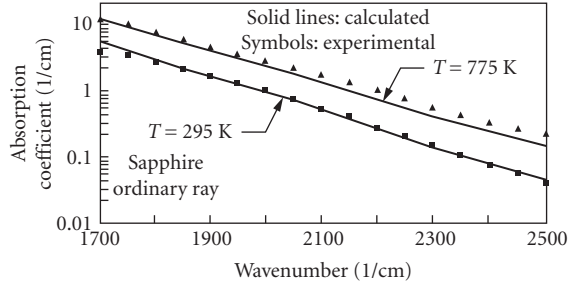
where  $\beta_0$  is a constant (dimensions same as the absorption coefficient, typically  $\text{cm}^{-1}$ ),  $\gamma$  is a dimensionless constant (typically found to be near 4),  $\omega_0$  is frequency or wave number of the maximum transverse optical frequency (units are  $\text{cm}^{-1}$  for wave numbers; values are given in the property data tables), and  $\omega$  is the frequency or wave number of interest. This formula works reasonably well for ionic materials at room temperature for the range of absorption coefficients from 0.001 to 10  $\text{cm}^{-1}$ .

In the classical (continuum) limit, the temperature dependence of multiphonon absorption has a  $T^{n-1}$  dependence, where  $n$  is the order of the multiphonon process,<sup>55</sup> that is  $n \approx \omega/\omega_0$ . At low temperature, there is no temperature dependence since only transitions from the ground state occur. Once the temperature is sufficiently high (e.g., approaching the Debye temperature), transitions that originate from excited states become important and the classical temperature dependence is observed. Bendow et al.<sup>56</sup> has developed a simple model of the temperature dependence of multiphonon absorption based on a Bose–Einstein distribution of states:

$$\beta_{\text{ABS}}(\omega, T) = \beta_0 \frac{[N(\omega_0, T) + 1]^{\omega/\omega_0}}{N(\omega, T) + 1} \exp(-A\omega/\omega_0) \quad (17b)$$

where  $N(\omega, T)$  is the phonon occupation density from Bose–Einstein statistics.

Thomas et al.<sup>57</sup> have successfully developed a semiempirical, quantum mechanical model of (sum band) multiphonon absorption based on the Morse interatomic potential and a gaussian function for the phonon density of states. Use of the Morse potential leads to an exact solution to the Schrödinger equation and includes anharmonic effects to all orders. The model contains parameters derived from room-temperature measurements of absorption, is computationally efficient, and has been applied to many ionic substances. Figure 5 shows a typical result compared to experimental data. Model parameters are available for oxides,<sup>57</sup> diamond,<sup>58</sup> glasses,<sup>59</sup> and semiconductors.<sup>60</sup>



**FIGURE 5** Temperature-dependent change of absorption in insulators is principally confined to the absorption edges, especially the infrared multiphonon absorption edge. This figure shows measured and predicted absorption coefficients at the infrared edge of transparency for the ordinary ray of crystalline sapphire. Increasing temperature activates higher multiphonon processes, resulting in a rapid increase in absorption. The multiphonon model of Thomas et al.<sup>57-59</sup> accurately predicts the frequency- and temperature-dependence of infrared absorption in highly ionic materials such as oxides and halides.

Multiphonon absorption modeling also contributes to the real refractive index. Although multiphonon contributions to the real index are small compared to one-phonon contributions, they are important for two cases in the infrared: (1) when the refractive index must be known beyond two decimal places, or (2) at high temperature. In the first case, multiphonon contributions to the index are significant over a large spectral region. In the second case, the contribution of multiphonon modes to the real refractive index grows rapidly at high temperature because of the  $T^{n-1}$  dependence of the  $n$ th mode strength.

**Absorption in the Transparent Region** In the transparent region, away from the electronic and vibrational resonances, absorption is governed by impurities and defects. The level of absorption is highly dependent on the purity of the starting materials, conditions of manufacture, and subsequent machining and polishing. For example, OH impurities are common in oxides,\* occurring at frequencies below the fundamental (nonbonded) OH vibration at  $3735\text{ cm}^{-1}$ . OH can be removed by appropriate heat treatment.

Low-level absorption coefficient measurements are typically made by laser calorimetry or photoacoustic techniques. Data are available for a number of materials in the visible,<sup>42,61</sup> at  $1.3\text{ }\mu\text{m}$ ,<sup>62</sup> and at  $2.7$  and  $3.8\text{ }\mu\text{m}$ .<sup>63</sup>

## Optical Properties: Applications

**Dielectric Tensor and Optical Indicatrix** Many important materials are nonisotropic (e.g., the crystals  $\text{Al}_2\text{O}_3$ ,  $\text{SiO}_2$ , and  $\text{MgF}_2$ ), and their optical properties are described by tensor relationships (see earlier section, "Symmetry Properties"). The dielectric constant,  $\epsilon$ , a second-rank tensor, relates the electric field  $\mathbf{E}$  to the electric displacement  $\mathbf{D}$ :

$$\begin{pmatrix} \mathbf{D}_x \\ \mathbf{D}_y \\ \mathbf{D}_z \end{pmatrix} = \epsilon_0 \cdot \begin{pmatrix} \epsilon_{xx} & \epsilon_{xy} & \epsilon_{xz} \\ \epsilon_{yx} & \epsilon_{yy} & \epsilon_{yz} \\ \epsilon_{zx} & \epsilon_{zy} & \epsilon_{zz} \end{pmatrix} \cdot \begin{pmatrix} \mathbf{E}_x \\ \mathbf{E}_y \\ \mathbf{E}_z \end{pmatrix} \quad (18a)$$

\*The OH vibrational impurity absorption in oxides is known for  $\text{Al}_2\text{O}_3$ , ALON,  $\text{MgAl}_2\text{O}_4$ ,  $\text{MgO}$ ,  $\text{SiO}_2$ ,  $\text{Y}_2\text{O}_3$ , and  $\text{Yb}_2\text{O}_3$ .

From the symmetry of properties, this is a symmetric tensor with  $\epsilon_{ab} = \epsilon_{ba}$ . Usually, the dielectric constant components are given as principal values, that is, those values along the unit cell of the appropriate crystal class. In this case, the principal dielectric constants are

$$\begin{aligned}\epsilon_{x'x'} &\equiv \epsilon_1 \\ \epsilon_{y'y'} &\equiv \epsilon_2 \\ \epsilon_{z'z'} &\equiv \epsilon_3\end{aligned}\tag{18b}$$

where the primes on the subscripts denote principal values (i.e., along the crystallographic axes, possible in a nonorthogonal coordinate system) and the subscripts 1, 2, and 3 denote reduced notation for these values (see "Elastic Properties"). The relationship between dielectric constant and refractive index, Eq. (4), means there are similarly three principal values for the (complex) refractive index. Also, the components of the dielectric tensor are individually related to the corresponding components of the refractive index. (Subscripts  $a$ ,  $b$ , and  $c$  or  $x$ ,  $y$ , and  $z$  as well as others may be used for the principal values of the dielectric constant or refractive index.)

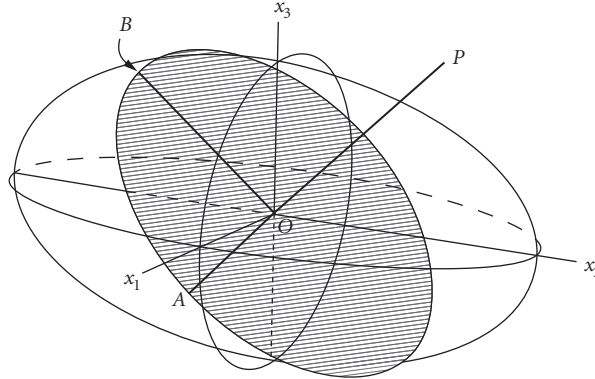
Three important cases arise:

1. Isotropic and cubic materials have only one dielectric constant,  $\epsilon$ , (hence one refractive  $\bar{n}$ ). Therefore  $\epsilon_1 = \epsilon_2 = \epsilon_3 = \epsilon \bar{n}^2$ .
2. Hexagonal (including trigonal) and tetragonal crystals have two principal dielectric constants,  $\epsilon_1$  and  $\epsilon_3$ , (hence two refractive indices,  $\bar{n}$  and  $\bar{n}_3$ ). Therefore  $\epsilon_1 = \epsilon_2 \neq \epsilon_3$ . Such materials are called *uniaxial*; the unique crystallographic axis is the  $c$  axis, which is also called the *optical axis*. One method of denoting the two unique principal axes is to state the orientation of the electric field relative to the optical axis. The dielectric constant for the  $E \perp c$  situation is  $\epsilon_1$  or  $\epsilon_{\perp}$ . This circumstance is also called the *ordinary ray*, and the corresponding symbol for the refractive index is  $\bar{n}_1, \bar{n}_{\perp}, \bar{n}_o$  (for ordinary ray), and  $\bar{n}_\omega$  or  $\omega$  (primarily in the older literature). The dielectric constant for  $E \parallel c$  situation is  $\epsilon_3$  or  $\epsilon_{\parallel}$ . This condition is called the *extraordinary ray*, and the corresponding symbol for the refractive index is  $\bar{n}_3, \bar{n}_{\parallel}, \bar{n}_e$  (for extraordinary ray), and  $\bar{n}_e$  or  $\epsilon$  (again, primarily in the older literature). Crystals are called *positive uniaxial* when  $n_e - n_o > 0$ , and *negative uniaxial* otherwise. Since the dispersions of the ordinary and extraordinary wave are different, a crystal can be positive uniaxial in one wavelength region and negative uniaxial in another (AgGaS<sub>2</sub> is an example).
3. Orthorhombic, monoclinic, and triclinic crystals have three principal dielectric constants,  $\epsilon_1, \epsilon_2$ , and  $\epsilon_3$  (hence, three refractive indices,  $\bar{n}_1, \bar{n}_2$ , and  $\bar{n}_3$ ). Therefore  $\epsilon_1 \neq \epsilon_2 \neq \epsilon_3 \neq \epsilon_1$ . These crystals are called *biaxial*. Confusion sometimes arises from the correlation of the principal dielectric constants with the crystallographic orientation owing to several conventions in selecting the crystal axes. [The optical indicatrix (see following discussion) of a biaxial material has two circular sections that define optical axes. The orientation of these axes are then used to assign a positive- or negative-biaxial designation.]

The existence of more than one dielectric constant or refractive index means that, for radiation with arbitrary orientation with respect to the crystal axes, two plane-polarized waves, of different speed, propagate in the crystal. Hence, for light propagating at a random orientation to the principal axes, a uniaxial or biaxial crystal exhibits two effective refractive indices different from the individual principal values. The refractive index of the two waves is determined from the *optical indicatrix* or *index ellipsoid*, a triaxial ellipsoidal surface defined by

$$\frac{x_1^2}{n_1^2} + \frac{x_2^2}{n_2^2} + \frac{x_3^2}{n_3^2} = 1\tag{19a}$$

where the  $x_1, x_2$ , and  $x_3$  are the principal axes of the dielectric constant. The indicatrix is illustrated in Fig. 6: for a wave normal in an arbitrary direction (OP), the two waves have refraction indices equal to the axes of the ellipse perpendicular to the wave normal (OA and OB). The directions



**FIGURE 6** The *optical indicatrix* or *index ellipsoid* used to determine the effective refractive index for an arbitrary wave normal in a crystal. The axes of the ellipsoid correspond to the principal axes of the crystal, and the radii of the ellipsoid along the axes are the principal values of the refractive indices. For propagation along an arbitrary wave normal (OP), the effective refractive indices are the axes of the ellipse whose normal is parallel to the wave normal. In the illustrated case, the directions OA and OB define the effective refractive indices.<sup>24</sup> (Reprinted by permission of Oxford University Press.)

represented by OA and OB are the vibrational planes of the electric displacement vector  $\mathbf{D}$  of the two waves. When the wave normal is parallel to an optic axis, the two waves propagate with principal refractive indices. For uniaxial materials and the wave normal parallel to the  $x_3$  (or  $z$  or  $c$  crystallographic or optical) axis, the vibrational ellipsoid is circular and the two waves have the same refractive index ( $n_o$ ), and there is no double refraction. Equation (19a) can also be written

$$B_1 x_1^2 + B_2 x_2^2 + B_3 x_3^2 = 1 \quad (19b)$$

where  $B_i = 1/\bar{n}_i^2 = 1/\epsilon_i$  is called the *inverse dielectric tensor*. The inverse dielectric tensor is used in defining electro-optic, piezo-optic, and elasto-optic relationships (see Table 1).

Fresnel formulas, found elsewhere in this *Handbook*, use the complex refractive index to calculate reflection and transmission at a material boundary as a function of incident angle, polarization, and (crystal) orientation (for uni- and biaxial crystals).

**Total Power Law** Incident light on a material is reflected, transmitted, or absorbed. Scattering is a term used to describe diffuse reflectance (surface scatter) and diffuse transmittance (bulk scatter). Conservation of energy dictates that the fractional amount reflected  $\rho$ , absorbed  $\alpha_{\text{ABS}}$ , transmitted  $\tau$ , and scattered  $\alpha_{\text{SCA}}$  total to unity, hence

$$1 = \rho(\Omega_i, \omega) + \alpha_{\text{SCA}}(\Omega_i, \omega) + \alpha_{\text{ABS}}(\Omega_i, \omega) + \tau(\Omega_i, \omega) \quad (20)$$

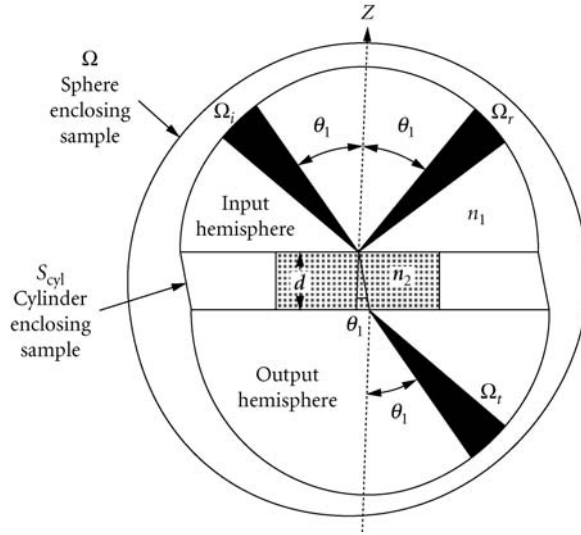
where these time-averaged quantities, illustrated in Fig. 7, are

$$\rho(\Omega_i, \omega) = \frac{\Phi_r(\Omega_i, \omega)}{\Phi_i(\omega)} = \text{total integrated reflectance} \quad (21a)$$

$$\alpha_{\text{SCA}}(\Omega_i, \omega) = \frac{\Phi_s(\Omega_i, \omega)}{\Phi_i(\omega)} = \text{total integrated scatterance} \quad (21b)$$

$$\alpha_{\text{ABS}}(\Omega_i, \omega) = \frac{\Phi_a(\Omega_i, \omega)}{\Phi_i(\omega)} = \text{total integrated absorbance} \quad (21c)$$





**FIGURE 7** Geometry of incident, transmitted, and reflected beams for a plane transparent slab of thickness  $d$ . The power equals the reflected, refracted, and absorbed components, assuming no scatter.

and

$$\tau(\Omega_i, \omega) = \frac{\Phi_t(\Omega_t, \omega)}{\Phi_i(\omega)} = \text{total integrated transmittance} \quad (21d)$$

Notice that these quantities are functions of the angle of incidence and frequency only.

The sum of total integrated scatterance and total integrated absorbance can be defined as the total integrated extintance  $\alpha_{\text{EXT}}$

$$\alpha_{\text{EXT}}(\Omega_i, \omega) = \alpha_{\text{ABS}}(\Omega_i, \omega) + \alpha_{\text{SCA}}(\Omega_i, \omega) \quad (22)$$

and the total power law becomes

$$1 = \rho(\Omega_i, \omega) + \alpha_{\text{EXT}}(\Omega_i, \omega) + \tau(\Omega_i, \omega) \quad (23)$$

Another useful quantity is emittance, which is defined as

$$\varepsilon(\Omega_i, \omega) = \frac{\Phi_e(\Omega_i, \omega)}{\Phi_{\text{bb}}(\omega)} = \text{total integrated emittance} \quad (24a)$$

where  $\Phi_{\text{bb}}$  is the blackbody function representing the spectral emission of a medium which totally absorbs all light at all frequencies. When  $\Phi_i(\omega) = \Phi_{\text{bb}}(\omega)$ , then the total integrated emittance equals the total integrated absorbance:

$$\varepsilon(\Omega_i, \omega) = \alpha_{\text{ABS}}(\Omega_i, \omega) \quad (24b)$$

**Dispersion Formulas for Refractive Index** The dielectric constant and refractive index are functions of frequency, hence wavelength. The frequency or wavelength variation of refractive index is called *dispersion*. Dispersion is an important property for optical design (i.e., correction of chromatic aberration) and in the transmission of information (i.e., pulse spreading). Other optical properties are derived from the change in refractive index with other properties such as temperature (*thermo-optic* coefficient), stress or strain (*piezo-optic* or *elasto-optic* coefficients), or applied field (*electro-optic* or *piezo-electric* coefficients). Since the dielectric constant is a second-order tensor with three principal values, the coefficients defined here are also tensor properties (see Table 1).

Precise refractive index measurements give values as functions of wavelength. Frequently, it is desirable to have a functional form for the dispersion of the refractive index (i.e., for calculations and value interpolation). There are many formulas used for representing the refractive index. One of the most widely used is the Sellmeier (or Drude or Maxwell-Helmholtz-Drude) dispersion model [Eq. (14)], which arises from treating the absorption like simple mechanical or electrical resonances. Sellmeier<sup>38</sup> proposed the following dispersion formula in 1871–1872 (although Maxwell had also considered the same derivation in 1869). The usual form of this equation for optical applications gives refractive index as a function of wavelength rather than wave number, frequency, or energy. In this form, the Sellmeier equation is

$$n^2(\lambda) - 1 = \sum_{i=1} \frac{A_i \cdot \lambda^2}{\lambda^2 - \lambda_i^2} \quad (25a)$$

The Sellmeier formula has the appropriate physical basis to accurately represent the refractive index throughout the transparent region in the simplest manner. The Sellmeier constants have physical meaning, particularly for simple substances. Most other dispersion formulas are closely related to (or are a disguised form of) the Sellmeier equation. Many of these other dispersion formulas are unable to cover as wide a spectral region, and unlike the Sellmeier form, do not lend themselves to extrapolation outside the interval of available measurements. For these reasons, we strongly urge that the Sellmeier model be universally used as the standard representation of the refractive index.

Modifications of the Sellmeier terms that include composition variation<sup>64,65</sup> and temperature dependence<sup>66</sup> have been applied to successfully model refractive index. The variation of the Sellmeier  $A_i$  and  $\lambda_i$  constants is usually modeled as linearly dependent on the mole fraction of the components and temperature.

An often-used, slight modification of this formula puts the wavelength of the shortest wavelength resonance at zero ( $\lambda_1 = 0$ ), that is, the first term is a constant. This constant term represents contributions to refractive index from electronic transitions at energies far above the bandgap. Sellmeier terms with small  $\lambda_i$  (representing electronic transitions) can be expanded as a power series,

$$\frac{A_i \cdot \lambda^2}{\lambda^2 - \lambda_i^2} = A_i \cdot \sum_{i=0}^{\infty} (\lambda_i^2 / \lambda^2)^j = A_i + \frac{A_i \cdot \lambda_i^2}{\lambda^2} + \frac{A_i \cdot \lambda_i^4}{\lambda^4} + \dots \quad (25b)$$

and the terms with large  $\lambda_i$  (representing vibrational transitions) are expanded as:

$$\frac{A_i \cdot \lambda^2}{\lambda^2 - \lambda_i^2} = -A_i \cdot \sum_{j=1}^{\infty} (\lambda^2 / \lambda_i^2)^j = -A_i \cdot \frac{\lambda^2}{\lambda_i^2} - A_i \cdot \frac{\lambda^4}{\lambda_i^4} - \dots \quad (25c)$$

The first term of this expansion is occasionally used to represent the long-wavelength (infrared) contribution to the index of refraction (instead of the Sellmeier term).

A generalized form of the short-wavelength approximation to the Sellmeier equation is the Cauchy formula, developed in 1836. This was the first successful attempt to represent dispersion by an equation:

$$n = A_0 + \sum_{i=1} \frac{A_i}{\lambda^{2i}} \quad \text{or} \quad n^2 = A'_0 + \sum_{i=1} \frac{A'_i}{\lambda^{2i}} \quad (26)$$

Power series approximations to the Sellmeier equation are expressed in many forms. One common form is the Schott glass formula used for glasses:

$$n^2 = A_0 + A_1\lambda^2 + A_2\lambda^{-2} + A_3\lambda^{-4} + A_4\lambda^{-6} + A_5\lambda^{-8} + \dots \quad (27)$$

For typical high-quality glasses, this equation is accurate to  $\pm 3 \cdot 10^{-6}$  in the visible (400–765 nm) and within  $\pm 5 \cdot 10^{-6}$  from 365 to 1014 nm. A comparison of the Schott power series formula with a three-term Sellmeier formula showed equivalent accuracy of the range of the Schott fit, but that the Sellmeier model was accurate over a much wider wavelength range.<sup>67</sup> A number of other power series dispersion formulas (e.g., Ketteler–Neumann<sup>68</sup>) are occasionally used.

Frequently, Sellmeier terms are written in altered fashion such as this form used by Li<sup>69</sup> and others:

$$\frac{A_i}{(\lambda^2 - \lambda_i^2)} = \frac{A_i(\lambda^2 / \lambda_i^2)}{(\lambda^2 - \lambda_i^2)} - \frac{A_i}{\lambda_i^2} \quad (28a)$$

which is the equivalent of the combination of two Sellmeier terms, one located at zero wavelength and the other at  $\lambda_i$ . The Zernike formula<sup>70</sup> also uses a term in this form. Another way to modify Sellmeier terms is to convert the wavelength of the resonances to wave number or energy [see Eq. (14)].

Another common formula for the index of refraction is the Hartmann<sup>45</sup> or Cornu equation:

$$n = A + \frac{B}{\lambda - \lambda_0} \quad (28b)$$

This equation is more distantly related to the Sellmeier formulation. Note that a two-term Sellmeier formula (with  $\lambda_i = 0$ ) can be written as

$$(n^2 - n_0^2) \cdot (\lambda^2 - \lambda_0^2) = (n - n_0) \cdot (\lambda - \lambda_0) \cdot (n + n_0) \cdot (\lambda + \lambda_0) = \text{constant} \quad (28c)$$

and the Hartmann formula can be written as a hyperbola

$$(n - n_0) \cdot (\lambda - \lambda_0) = \text{constant} \quad (28d)$$

Note that in a limited spectral region, the difference terms of the Sellmeier formula of Eq. (28c) vary much more rapidly than do the sum terms, hence the Hartmann and Sellmeier forms will have nearly the same shape in a limited spectral range.

Other equations that combine Sellmeier and power series terms (cf., Wemple formula) are often used. One such formulation is the Herzberger equation, first developed for glasses<sup>71</sup> and later applied to infrared crystalline materials:<sup>72</sup>

$$n = A + \frac{B}{(\lambda^2 - 0.028)} + \frac{C}{(\lambda^2 - 0.028)^2} + D\lambda^2 + E\lambda^4 \quad (28e)$$

where the choice of the constant  $\lambda_0^2 = 0.028$  is arbitrary in that it is applied to all materials.

The Pikhtin-Yas'kov formula<sup>73</sup> is nearly the same as the Sellmeier form with the addition of another term representing a broadband electronic contribution (which is equal to the real part of one of the terms in Adachi's model<sup>44</sup>):

$$n^2 - 1 = \frac{A}{\pi} \ln \frac{E_1^2 - (\hbar\omega)^2}{E_0^2 - (\hbar\omega)^2} + \sum_i \frac{G_i}{E_i^2 - (\hbar\omega)^2} \quad (28f)$$

This formulation has been applied to some semiconductor materials. The unique term arises from assuming that the imaginary part of the dielectric constant is a constant between energies  $E_0$  and  $E_1$ , and that infinitely narrow resonances occur at  $E_i$ . The formula is then derived by applying the Kramers–Krönig relationship to this model.

**Dispersion Formulas Used for Glasses** Dispersion in glasses (and most other materials) is accurately represented by a Sellmeier model [Eq. (25a)] with three terms, two representing electronic (short wavelength) absorption and one representing lattice vibration (long wavelength) absorption contribution to the refractive index. Typically for glasses, the *Abbe number*, or constringence  $\nu_d$ , is also given. The Abbe number is a measure of dispersion in the visible and is defined as  $\nu_d = (n_d - 1)/(n_F - n_C)$ , where  $n_d$ ,  $n_F$ , and  $n_C$  are refractive indices at 587.6, 486.1, and 656.3 nm, respectively. The quantity  $(n_F - n_C)$  is known as the *principle dispersion*. A relative partial dispersion  $P_{x,y}$  can be calculated at any wavelengths  $x$  and  $y$  from

$$P_{x,y} = \frac{(n_x - n_y)}{(n_F - n_C)} \quad (29a)$$

For so-called “normal” glasses, the partial dispersions obey a linear relationship, namely

$$P_{x,y} = a_{x,y} + b_{x,y} \nu_d \quad (29b)$$

where  $a_{x,y}$  and  $b_{x,y}$  are empirical constant characteristics of normal glasses. However, for correction of secondary spectrum in an optical system (i.e., achromatization for more than two wavelengths), it is necessary to employ a glass that does not follow the glass line. Glass manufacturers usually list  $\Delta P_{x,y}$  for a number of wavelength pairs as defined by:

$$P_{x,y} = a_{x,y} + b_{x,y} \nu_d + \Delta P_{x,y} \quad (29c)$$

The deviation term  $\Delta P_{x,y}$  is a measure of the dispersion characteristics differing from the normal glasses. Schott glasses F2 and K7 define the normal glass line.

In the transparent region, refractive index decreases with increasing wavelength, and the magnitude of  $dn/d\lambda$  is a minimum between the electronic and vibrational absorptions. The wavelength ( $\lambda_0$ ) of minimum  $dn/d\lambda$ , called the “zero”-dispersion point, is given by

$$\left. \frac{d^2n(\lambda)}{d\lambda^2} \right|_{\lambda=\lambda_0} = 0 \quad (30)$$

which is the desired operating point for high-bandwidth, information-carrying optical fibers, as well as the optimum wavelength for single-element refractive optical systems. For glassy silica fibers, the zero dispersion point is 1.272  $\mu\text{m}$ .

The equation for the dispersion in a standard single-mode fiber is

$$D_{\text{chromatic}} = \frac{S_0}{4} \left( \lambda - \frac{\lambda_0^4}{\lambda^3} \right) \quad (31)$$

where the operating wavelength is  $\lambda$ , the zero-dispersion wavelength is  $\lambda_0$ , and  $S_0$  is the slope of the dispersion curve. The dispersion units are picoseconds per wavelength bandwidth (nm) per unit length of fiber (km).

One approach to reducing both dispersion and loss is to use a material with a wide transparent region, that is, widely separated electronic and vibrational absorptions, hence the interest in materials such as heavy-metal fluoride glasses for fiber applications. Recent work in photonic bandgap (PBG) fibers and micro-structured optical fibers demonstrates that light can be guided in hollow cores. Index-guided fibers can operate below 800 nm but the effective mode area is small. PBG fibers have been theorized to work below 800 nm with an order of magnitude larger effective mode area.<sup>74</sup> Hence, dispersionless transmission of short pulses in the near visible range is achieved.<sup>75-77</sup>

**Thermo-Optic and Photoelastic Coefficients** Temperature is one of the main factors influencing the refractive index of solids. The thermo-optical coefficients  $\partial n/\partial T$  (or  $\partial \epsilon/\partial T$ ) can be estimated from a derivation of the Clausius–Mossotti relationship:<sup>78</sup>

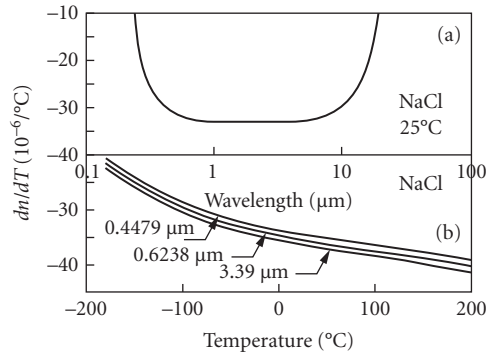
$$\frac{1}{(\epsilon-1)(\epsilon+2)}\left(\frac{\partial \epsilon}{\partial T}\right) = -\alpha \left[ 1 - \frac{V}{\alpha_m} \left( \frac{\partial \alpha_m}{\partial V} \right)_T \right] + \frac{1}{3\alpha_m} \left( \frac{\partial \alpha_m}{\partial T} \right)_V \quad (32)$$

where  $\alpha_m$  is the macroscopic polarizability. The first two terms are the principal contributors in ionic materials: a positive thermal expansion coefficient results in a negative thermo-optic coefficient and a positive change in polarizability with volume results in a positive thermo-optic coefficient. In ionic materials with a low melting point, thermal expansion is high and the thermo-optic coefficient is negative (typical of alkali halides); when thermal expansion is small (indicated by high melting point, hardness, and high elastic moduli), the thermo-optic coefficient is positive, dominated by the volume change in polarizability (typical of the high-temperature oxides).

Thermal expansion has no frequency dependence but polarizability does. At frequencies (wavelengths) near the edge of transparency, the polarizability (and  $\partial \alpha_m/\partial V$ ) rises, and  $\partial n/\partial T$  becomes more positive (or less negative). Figure 8 shows the variation of refractive index for sodium chloride as a function of frequency and temperature.

An approach similar to that for the thermo-optic coefficient, above, can be used to estimate the photoelastic constants of a material. The simplest photoelastic constant is that produced by uniform pressure, that is,  $dn/dP$ . More complex photoelastic constants are tensors whose components define the effect of individual strain (elasto-optic coefficients) or stress (piezo-optic coefficients) tensor terms. Bendow et al.<sup>79</sup> calculate  $dn/dP$  and the elasto-optic coefficients for a number of cubic crystals and compare the results to experiment.

**Thermo-Optic Coefficients for Glasses** The effect of temperature on the refractive index is dependent upon several factors, including the material and wavelength. The refractive index also changes as a function of air pressure. A distinction is therefore made between absolute refractive index, which is measured in vacuum, and refractive index relative to normal air, which is defined as the refractive index at normal air pressure (1 atmosphere = 101.325 kPa). The standard temperature



**FIGURE 8** The thermo-optic coefficient ( $dn/dT$ ) of sodium chloride (NaCl): (a) shows the wavelength dependence of room-temperature thermo-optic coefficient. The thermo-optic coefficient is nearly constant in the transparent region, but increases significantly at the edges of the transparent region and (b) illustrates the temperature dependence of the thermo-optic coefficient. The thermo-optic coefficient decreases (becomes more negative) with increasing temperature, primarily as the density decreases.

for refractive index measurements is 22°C, and manufacturer's quoted index of refraction values are always relative to normal air pressure.

The change in the absolute refractive index as a function of temperature is modeled as a first-order or linear change with temperature,

$$n_{\text{abs}}(\lambda, T) = n_{\text{abs}}(\lambda, T_0) + \frac{dn_{\text{abs}}(\lambda, T)}{dT} \Delta T \quad (33)$$

In the visible, the absolute refractive index as a function of wavelength can be well-approximated by a single-term Sellmeier model, Eq. (25a), and the temperature derivative of refractive index is then

$$\frac{dn_{\text{abs}}}{dT} = \frac{1}{2n_{\text{abs}}} \frac{d(n_{\text{abs}}^2 - 1)}{dT} = \frac{n_{\text{abs}}^2 - 1}{2n_{\text{abs}}} \left[ \frac{1}{A} \frac{dA}{dT} + \frac{2\lambda_{\text{K}}}{\lambda^2 - \lambda_{\text{K}}^2} \frac{d\lambda_{\text{K}}}{dT} \right] \quad (34)$$

a function of the temperature dependence of the mode strength ( $A$ ) and its location ( $\lambda_{\text{K}}$ ). The mode strength is the product of the strength (polarizability) of the individual absorption oscillators and the density of those oscillators (i.e., is a function of the volume expansion).

The change in  $n$  with respect to  $T$  is then modeled by using constants  $D_0$ ,  $D_1$ , and  $D_2$  to represent the temperature dependence of mode strength, and constants  $E_0$  and  $E_1$  to represent the temperature dependence of mode location, namely,

$$\frac{dn_{\text{abs}}(\lambda, T)}{dT} = \frac{n^2(\lambda, T_0) - 1}{2n(\lambda, T_0)} \left[ D_0 + 2D_1 \Delta T + 3D_2 \Delta T^2 + \frac{E_0 + 2E_1 \Delta T}{\lambda^2 - \lambda_{\text{K}}^2} \right] \quad (35)$$

$T_0$  is the reference temperature, generally 20°C.  $T$  is the temperature of interest, and  $\Delta T$  is the difference,  $T - T_0$ . The wavelength of interest is  $\lambda$ . The terms  $D_0$ ,  $D_1$ ,  $D_2$ ,  $E_0$ ,  $E_1$ , and  $\lambda_{\text{K}}$  are all constants dependent upon the glass type and are found by fitting to measurements. The relative index values found in catalogs can be used in Eq. (35) without loss of accuracy. This is why the abs subscript was dropped from the  $n$  terms on the right-hand side of the equation. Using Eq. (35) in Eq. (33) allows for the calculation of the change in the refractive index, as well as the new refractive index as a function of temperature.

The refractive index relative to air as a function of temperature, and the change itself as a function of temperature can be computed from the relationships<sup>13</sup>

$$n_{\text{rel}}(\lambda, T) = \frac{n_{\text{abs}}(\lambda, T)}{n_{\text{air}}(\lambda, T, P)} \quad (36a)$$

$$\frac{dn_{\text{rel}}(\lambda, T)}{dT} = \frac{\frac{dn_{\text{abs}}(\lambda, T)}{dT} - n_{\text{rel}}(\lambda, T) \frac{dn_{\text{air}}(\lambda, T, P)}{dT}}{n_{\text{air}}(\lambda, T, P)} \quad (36b)$$

The approximation that  $n_{\text{rel}}(\lambda, T_0)$  can be substituted for  $n_{\text{rel}}(\lambda, T)$  maintains sufficient accuracy, and simplifies the calculation.

The widely accepted equations for  $n_{\text{air}}$  and  $dn_{\text{air}}/dT$  of dry air are

$$n_{\text{air}}(\lambda, T, P) = 1 + \frac{n_{\text{air}}(\lambda, T_{15^\circ\text{C}}, P_0) - 1}{1 + 3.4785 \cdot 10^{-3}(T - 15^\circ\text{C})} P \quad (37a)$$

$$\frac{dn_{\text{air}}(\lambda, T, P)}{dT} = \frac{-0.00367 n_{\text{air}}(\lambda, T, P) - 1}{1 + 0.00367 T} \quad (37b)$$

where  $P$  is the atmospheric pressure divided by the reference pressure ( $P_0 = 1$  atmosphere).

The index of refraction in air at 15°C and 1 atmosphere of pressure is given by

$$n_{\text{air}}(\lambda, T_{15^\circ\text{C}}, P_0) = 1 + \left[ 6432.8 + \frac{2949810\lambda^2}{146\lambda^2 - 1} + \frac{25540\lambda^2}{41\lambda^2 - 1} \right] \times 10^{-8} \quad (37c)$$

The wavelength  $\lambda$  is in units of micrometers, and temperature is in units of degrees Celsius.  $P$  is the relative air pressure and is dimensionless. This completes the equations necessary to compute the absolute and relative index of refraction at any temperature and pressure, provided the proportionality constants in Eq. (33) and the parameters of Eq. (35) are available for the glass of interest. These equations are typically valid for temperature ranges of  $-100^\circ\text{C}$  to  $140^\circ\text{C}$ , and a wavelength range of 0.3650 to 1.014  $\mu\text{m}$ .

**Athermal Glasses** The environmental temperature affects glass in terms of thermal expansion coefficient [ $\alpha$ , see Eq. (46a)] and the variation of the index of refraction,  $dn_{\text{rel}}/dT$ . Both effects deteriorate the wavefront due to the changed optical path and the change in the index of refraction. To mitigate the effect of temperature variations, the glass should ideally compensate for any thermal expansion effects by the refractive index change. Since all glasses exhibit a positive thermal expansion coefficient (increase in size with increased temperature), the ideal glass would have a negative temperature coefficient. This can be expressed in terms of the thermo-optical constant,  $G$ :

$$G = \alpha(n_{\text{rel}}(\lambda, T) - 1) + \frac{dn_{\text{rel}}(\lambda, T)}{dT} \quad (38)$$

Any glass with  $G$  near zero (e.g.,  $|G| < 1 \cdot 10^{-6} \text{ K}^{-1}$ ) is referred to as athermal. Not all glasses with negative relative index temperature coefficients are athermal. Schott glasses N-PK51, N-FK51A, and N-PK52A show athermal behavior.

**Nonlinear Optical Coefficients** One of the most important higher-order optical coefficients is the nonlinear (or second-order) susceptibility. With the high electric fields generated by lasers, the nonlinear susceptibility gives rise to important processes such as second-harmonic generation, optical rectification, parametric mixing, and the linear electro-optic (Pockels) effect. The second-order susceptibility,  $\chi^{(2)}$ , is related to the polarization vector  $\mathbf{P}$  by

$$\mathbf{P}_i(\omega) = \varepsilon_0 [\chi_{ij} \mathbf{E}_j + g\chi_{ijk}^{(2)} \mathbf{E}_j(\omega_1) \mathbf{E}_k(\omega_2)] \quad (39)$$

where  $g$  is a degeneracy factor arising from the nature of the electric fields applied. If the two frequencies are equal, the condition of optical rectification and second-harmonic generation (SHG) arises, and  $g = 1/2$ . When the frequencies of  $\mathbf{E}_j$  and  $\mathbf{E}_k$  are different, parametric mixing occurs and  $g = 1$ . If  $\mathbf{E}_k$  is a dc field, the situation is the same as the linear electro-optic (or Pockels) effect, and  $g = 2$ . The value of nonlinear susceptibility is a function of the frequencies of both the input fields and the output polarization ( $\omega = \omega_1 \pm \omega_2$ ).

The nonlinear susceptibility is a third-order (3 by 3 by 3) tensor. A nonlinear optical coefficient  $d^{(2)}$ , frequently used to describe these nonlinear properties, is equal to one-half of the second-order nonlinear susceptibility, that is,  $d^{(2)} = 1/2\chi^{(2)}$ . Nonlinear optical coefficients are universally written in reduced (matrix) notation,  $d_{ij}^{(2)}$ , where the index  $i = 1, 2, \text{ or } 3$  and the index  $j$  runs from 1 to 6.<sup>80</sup> (Both the piezo-electric coefficient and the nonlinear optical coefficient are given the symbol  $d$ , and the resulting confusion is enhanced because both coefficients have the same units.) The relationship between the electro-optic coefficient  $r$  and the nonlinear optical coefficient  $d^{(2)}$  is

$$r_{ij} = \frac{2gd_{ij}^{(2)}}{\varepsilon^2} \quad (40)$$

Units of the second-order nonlinear optical coefficient are m/V (or pm/V, where pm =  $10^{-12}$ ) in mks units.

**TABLE 4** Typical Nonlinear Optical Coefficients

Crystal	Nonlinear Optical Coefficient (pm/V)
$\beta$ -BaB <sub>2</sub> O <sub>4</sub>	$d_{11} = 1.60$
KH <sub>2</sub> PO <sub>4</sub>	$d_{36} = 0.39$
LiB <sub>3</sub> O <sub>5</sub>	$d_{32} = 1.21$
LiNbO <sub>3</sub>	$d_{31} = 5.07$
LiIO <sub>3</sub>	$d_{31} = 3.90$
KTiOPO <sub>4</sub>	$d_{31} = 5.85$
Urea	$d_{14} = 1.17$

Typical values of the nonlinear optical coefficients are listed in Table 4.<sup>81</sup> Additional nonlinear optical coefficients are given in reviews (also refer to Chap. 10, "Nonlinear Optics" by Chung L. Tang).<sup>80-83</sup>

**Scatter** Scatter is both an intrinsic and extrinsic property. Rayleigh, Brillouin, Raman, and stoichiometric (index variation) contributions to scatter have been derived in simple form and used to estimate scatter loss in several fiber-optic materials.<sup>84</sup> Rayleigh scattering refers to elastic scatter from features small compared to the wavelength of light. In highly pure and defect-free optical crystals, Rayleigh scatter is caused by atomic scale inhomogeneities (much smaller than the wavelength) in analogy to Rayleigh scatter from molecules in the atmosphere. In most materials, including glasses, Rayleigh scatter is augmented by extrinsic contributions arising from localized density variations (which also limit the uniformity of the refractive index). Attenuation in high-quality optical materials is frequently limited by Rayleigh scatter rather than absorption.

Brillouin and Raman scatter are forms of inelastic scattering from acoustic and optical phonons (vibrations). The frequency of the scattered light is shifted by the phonon frequency. Creation of phonons results in longer-wavelength (low-frequency) scattered light (Stokes case) and annihilation of phonons results in higher-frequency scattered light (anti-Stokes case). Rayleigh, Brillouin, and Raman scatter all have  $\lambda^{-4}$  wavelength dependence. Polycrystalline and translucent materials have features such as grain boundaries and voids whose size is larger than the wavelength of light. This type of scatter is often called Mie scatter because the scattering features are larger than the wavelength of the light. Mie scatter typically has a measured  $\lambda^{-m}$  dependence where the parameter  $m$  typically lies between 1 and 2.<sup>85,86</sup> Rayleigh and Mie scatter may arise from either surface roughness or bulk nonuniformities.

## Other Properties of Materials

**Naming of Crystals and Glasses** All materials are characterized by name(s) for identification, a chemical formula (crystalline materials) or approximate composition (glasses, amorphous substances), and a density ( $\rho$ , in kg/m<sup>3</sup>). Crystalline materials are further identified by crystal class, space group, unit-cell lattice parameters, molecular weight (of a formula unit in atomic mass units, amu), and number of formula units per unit cell ( $Z$ ). (See standard compilations of crystallographic data.<sup>87,88</sup>)

**Material Designation and Composition** Crystals are completely identified by both the chemical formulation and the space group. Chemical formulation alone is insufficient for identification because many substances have several structures (called *polymorphs*) with different properties. Properties in the data tables pertain only to the specific structure listed. Materials in the data tables having several stable polymorphs at room temperature include SiO<sub>2</sub> (eight polymorphs), C (diamond, graphite, and amorphous forms), and SiC and ZnS (both have cubic and hexagonal forms).

The space group also identifies the appropriate number of independent terms (see Tables 1 and 2) that describe a physical quantity. Noncubic crystals require two or more values to fully describe thermal expansion, thermal conductivity, refractive index, and other properties. Often, scalar quantities are



given in the literature when a tensor characterization is needed. Such a characterization may be adequate for polycrystalline materials, but is unsatisfactory for single crystals that require knowledge of directional properties.

Historically, optical glasses have been identified by traditional names derived from their composition and their dispersion relative to their index of refraction. This dates back to the 1880s when low dispersion crown glasses (typically with Abbe number  $\nu_d > 50$ ) and higher dispersion flint glasses (typically,  $\nu_d < 50$ ) dominated the glass map.<sup>89</sup> It took Ernst Abbe, Carl Zeiss, and the work of Otto Schott to expand the glass by developing two new glass formers, fluorine and boron.<sup>90,91</sup> In addition, Schott's work with BaO network modifiers pioneered new variations in index of refraction within the same groups. This gave rise to classifications of "heavy" and "light" (index of refraction designation), in addition to crown and flint (Abbe number classification).

The next major advancement in glass technology came in the 1930s when rare earth elements and network-former phosphorous became readily available.<sup>92,93</sup> These new glass types were named by adding the compounds chemical symbol to the traditional nomenclature of crown or flint, heavy or light. This led to various groups evolving on the Abbe diagram, groups whose position gave strong indication of the chemical composition of the glass. This distinction and borders in the Abbe diagram remains till the present day. However the traditional nomenclature is rapidly ending as manufacturers, primarily in Japan, are adopting new naming conventions for their glasses.

The primary reason for this nomenclature change is advances in manufacturing techniques, raw material supply and purity, and the evolution of new materials have all led to new compositional families of glasses that cross traditional borders. So a given glass family name such as PSK may have glasses without any phosphorous. Furthermore, different manufacturers producing a glass with identical index of refraction and Abbe numbers may in fact have entirely different physical and chemical properties (e.g., Schott N-LaSF31A, Hikari's E-LaSF08, and Hoya's TaFD30.) A single name would be disingenuous.

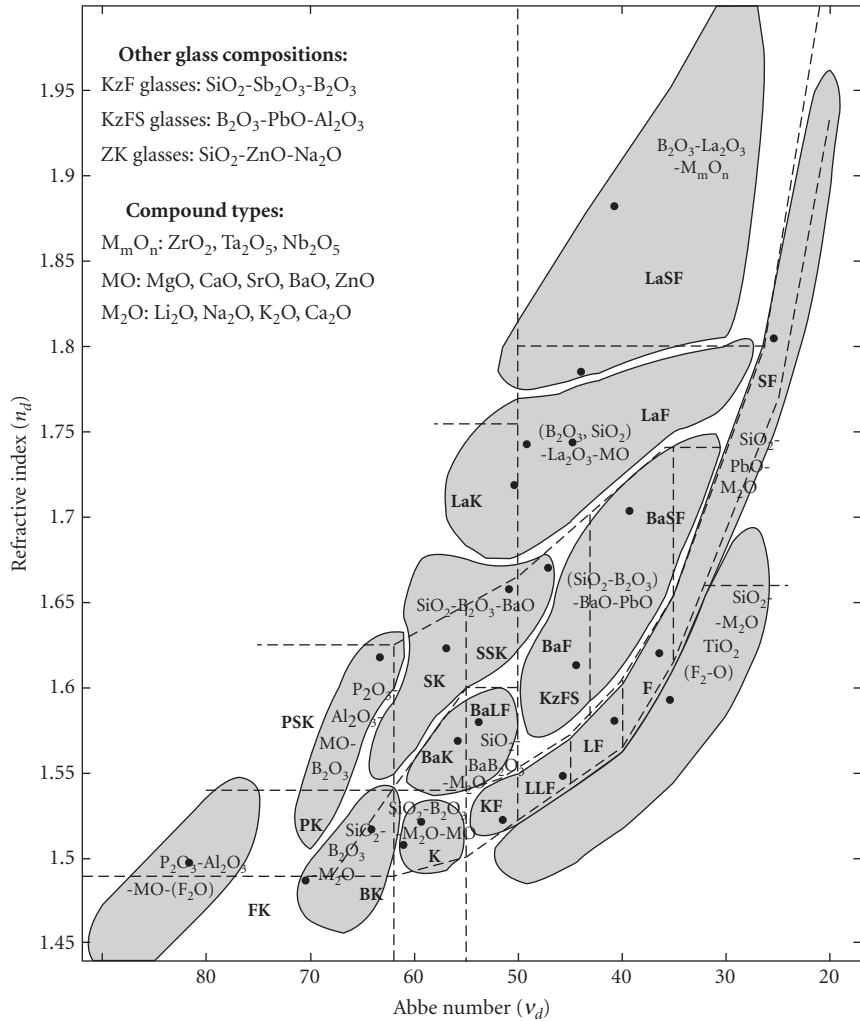
The main classical groups are listed in Table 8, and a representative glass from each is shown. Figure 9 shows the classic Abbe diagram with traditional nomenclature and the newer style showing glass systems based more on constituent materials. A thorough discussion of the various glass systems is found in the literature.<sup>17</sup>

Regardless of the categorizing and naming of glasses and glass systems or groups, a specific glass identifier scheme, as defined in military standard MIL-G-174, remains in use today. This convention uses a six-digit number representing the first three digits of  $(n_d - 1)$  and the first three digits of  $\nu_d$ . Each manufacturer also has its own designator, usually based on traditional or new names, that uniquely identifies each glass. For example, the glass with code 517624 has the following manufacturer's designations:

Manufacturer	Designation for Glass 517642
Schott	N-BK7
Corning	B-16-64
Pilkington	BSC-517642B
Hoya	BSC-7
Ohara	S-BSL 7 (closest value 516641)

Properties of glass are primarily determined from the compositions, but also depend on the manufacturing process, specifically the thermal history. In fact, refractive index specifications in a glass catalog should be interpreted as those obtained with a particular annealing schedule. Annealing removes stress (and minimizes stress-induced birefringence) and minimizes the effect of thermal history, producing high refractive-index uniformity. Special (*precision*) annealing designed to maximize refractive index homogeneity may, however, increase refractive index slightly above a nominal (catalog) value. A complete discussion of the annealing process can be found in literature.<sup>16,94</sup>

In general, both glass composition and thermal processing are proprietary (so the compositions given are only illustrative). However, manufacturers' data sheets on individual glasses can provide detailed and specific information on optical and mechanical properties. Also, the data sheets supply useful details on index homogeneity, climate resistance, stain resistance, and chemical (acid and



**FIGURE 9** The Abbe diagram (refractive index,  $n_d$ , versus Abbe number,  $v_d$ ) showing the composition of common glass systems, the Schott glass classifications, and the sample glasses (dots) included in this chapter. (Reprinted by permission of Springer-Verlag.)

alkaline) resistance for a particular glass type. For very detailed work or demanding applications, a glass manufacturer can supply a *melt data sheet* providing accurate optical properties for a specific glass lot.

A driving force in the recent breaking of traditional glass manufacture practices has been a growing movement for environmentally responsible glass. The primary elements of contention were arsenic and lead, and other toxic elements. For example, thorium oxide use has been discontinued, and cadmium oxide is restricted to colored glass manufacture. The principal concerns lie not in the end user, despite the negative connotation lead and lead-based products have incurred the past few decades. In fact, lead-containing glass is still available and labeled as such. The concern rests in the manufacture and disposal of hazardous waste. No guarantee could be made that the workplace would be safe, and the waste disposed of properly.

The replacements for PbO are typically  $\text{TiO}_2$ ,  $\text{Nb}_2\text{O}_5$ ,  $\text{ZrO}_2$ , and  $\text{WO}_3$ . The replacement for  $\text{As}_2\text{O}_3$  as a refining agent has been  $\text{Sb}_2\text{O}_3$ . For approximately 50 percent of the glasses containing  $\text{As}_2\text{O}_3$  and no PbO, the use of  $\text{Sb}_2\text{O}_3$  has not changed the properties of the glass. Using substitute materials for Glasses formerly containing PbO and  $\text{As}_2\text{O}_3$  has modified the properties of the glass, sometimes significantly. One by-product of lead removal has been lighter weight. Manufacturers have begun to denote the reformulated glasses by specific designations. Schott uses “N-” to prefix the new glass materials, Hikari uses “E-”, and Ohara uses “S-”. References to environmental concerns are included in the reference section.<sup>10,95</sup>

**Unit Cell Parameters, Molecular Weight, and Density** The structure and composition of crystals can be used to calculate density. This calculated (theoretical or x-ray) density should closely match that of optical-quality materials. Density,  $\rho$ , is mass divided by volume:

$$\rho = \frac{Z \cdot (\text{MW}) \cdot u}{a \cdot b \cdot c \sqrt{\sin^2 \alpha + \sin^2 \beta + \sin^2 \gamma - 2(1 - \cos \alpha \cdot \cos \beta \cdot \cos \gamma)}} \quad (41)$$

where  $Z$  is the number of formula units in a crystal unit cell,  $\text{MW}$  is the molecular weight of a formula unit in amu,  $u$  is weight of an amu (Table 3),  $a$ ,  $b$ , and  $c$  are unit cell axes lengths, and  $\alpha$ ,  $\beta$ , and  $\gamma$  are unit cell axes angles.

Typically, pure amorphous materials have lower density than the corresponding crystalline materials. Density of glasses and other amorphous materials is derived from measurements.

**Elastic Properties** Elastic properties of materials can be described with a hierarchy of terms. On the atomic scale, interatomic force constants or potential energies can be used to predict the vibrational modes, thermal expansion, and elastic properties of a material. On the macroscopic scale, elastic properties are described using elastic moduli (or constants) related to the directional properties of a material. The tensor relationships between stress ( $\sigma$ , a second-order tensor) and strain ( $e$ , a second-order tensor) are

$$\begin{aligned} \sigma_{ij} &= c_{ijkl} \cdot e_{kl} \\ e_{ij} &= s_{ijkl} \cdot \sigma_{kl} \end{aligned} \quad (42a)$$

where the fourth-rank tensors  $c_{ijkl}$  and  $s_{ijkl}$  are named elastic stiffness  $c$  and elastic compliance  $s$ , respectively. This is the tensor form of Hooke's law. Each index ( $i$ ,  $j$ ,  $k$ , and  $l$ ) has three values (i.e.,  $x$ ,  $y$ , and  $z$ ), hence the  $c$  and  $s$  tensors have 81 terms.

The stiffness and compliance tensors are usually written in a matrix notation made possible by the symmetry relationship of the stress and strain tensors. Symmetry reduces the number of independent terms in the stiffness and compliance tensors from 81 to 36. The usual notation for the reduced (matrix) notation form of the stiffness and compliance tensors is

$$\begin{aligned} \sigma_i &= c_{ij} \cdot e_j \\ e_i &= s_{ij} \cdot \sigma_j \end{aligned} \quad (42b)$$

where the indices, an abbreviation of the  $ij$  or  $kl$  components, run from 1 to 6. Table 5 shows the conversion from tensor to matrix notation. Thus, the stiffness and compliance tensors are written as 6 by 6 matrices which can again be shown to be symmetric, given 21 independent terms. Virtually all data will be found in matrix notation. These tensors (matrices) that relate stress and strain are sometimes called *second-order* stiffness and compliance. Higher-order tensors are used to describe nonlinear elastic behavior (i.e., third-order stiffness determines the stress tensor from the square of the strain tensor).

Stiffness and compliance tensors are needed to completely describe the linear elastic properties of a crystal. Even a completely amorphous material has two independent constants that describe the relationship between stress and strain. Usually, the elastic properties of materials are expressed in terms of engineering (or technical) moduli: Young's modulus ( $E$ ), shear modulus (or modulus

**TABLE 5** Matrix Notation for Stress, Strian, Stiffness, and Compliance Tensors

Tensor-to-matrix index conversion		Tensor-to-matrix element conversion	
Tensor Indices ij or kl	Matrix Indices $m$ or $n$	Notation	Condition
11	1	$\sigma_m = \sigma_{ij}$ $e_m = \sigma_{ij}$	$m = 1, 2, 3$
22	2	$\sigma_m = \sigma_{ij}$ $e_m = 2e_{ij}$	$m = 4, 5, 6$
33	3	$c_{mn} = c_{ijkl}$	all $m, n$
23 or 32	4	$s_{mn} = s_{ijkl}$	$m, n = 1, 2, 3$
13 or 31	5	$s_{mn} = 2s_{ijkl}$	$m = 1, 2, 3$ and $n = 4, 5, 6$ $m = 4, 5, 6$ and $n = 1, 2, 3$
12 or 21	6	$s_{mn} = 4s_{ijkl}$	$m, n = 4, 5, 6$

of rigidity  $G$ ), bulk modulus ( $B$ , compressibility<sup>-1</sup>), and Poisson's ratio ( $\nu$ ). For example, Young's modulus is defined as the ratio of the longitudinal tension to the longitudinal strain for tension, a quantity which is anisotropic (i.e., directionally dependent) for all crystal classes (but is isotropic for amorphous materials). Therefore the engineering moduli only accurately describe the elastic behavior of isotropic materials. The engineering moduli also approximately describe the elastic behavior of polycrystalline materials (assuming small, randomly distributed grains). Various methods are available to estimate the engineering moduli of crystals.

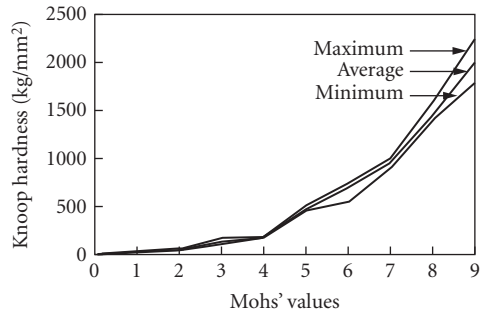
Values of the engineering moduli for crystalline materials given in the data tables are estimated from elastic moduli using the Voigt and Reuss methods (noncubic materials) or the Haskin and Shtrikman method<sup>96</sup> (cubic materials) to give shear ( $G$ ) and bulk ( $B$ ) moduli. Young's modulus ( $E$ ) and Poisson's ratio ( $\nu$ ) are then calculated assuming isotropy using the following relationships:

$$E = \frac{9 \cdot G \cdot B}{G + 3 \cdot B} \quad \nu = \frac{3 \cdot B - 2 \cdot G}{6 \cdot B + 2 \cdot G} \quad (43)$$

**Hardness and Strength** Hardness is an empirical and relative measure of a material's resistance to wear (mechanical abrasion). Despite the qualitative nature of the result, hardness testing is quantitative, repeatable, and easy to measure. The first measure of hardness was the Mohs scale which compares the hardness of materials to one of 10 minerals. Usually, the Knoop indent test is used to measure hardness of optical materials. The test determines the resistance of a surface to penetration by a diamond indenter with a fixed load (usually 50 to 200 g). The Knoop hardness number (usually measured in  $\text{kg}/\text{mm}^2 = 9.8 \text{ MPa}$ ) is the indenter mass (proportional to load) divided by the area of the indent. Figure 10 compares the Mohs and Knoop scales.<sup>9</sup>

Materials with Knoop values less than  $100 \text{ kg}/\text{mm}^2$  are very soft, difficult to polish, and susceptible to handling damage. Knoop hardness values greater than 750 are quite hard. Typical glasses have hardness values of 350 to  $600 \text{ kg}/\text{mm}^2$ . Hardness qualitatively correlates to Young's modulus and to strength. Hardness of crystals is dependent on the orientation of the crystal axes with respect to the tested surface. Coatings can significantly alter hardness.

Strength is a measure of a material's resistance to fracture (or onset of plastic deformation). Strength is highly dependent on material flaws and therefore on the method of manufacture, as well as the method of measurement. For optical materials, strength is most conveniently measured in flexure; tensile strengths are typically 50 to 90 percent of those measured in flexure. Because of high variability in strength values, quoted strength values should only be used as a guide for comparison of materials. Strength of crystals also is dependent on the orientation of the crystal axes with respect to the applied stress. Applications requiring high strength to avoid failure should use large safety margins (typically a factor of four) over average strength whenever possible.



**FIGURE 10** A comparison of Mohs and Knoop hardness scales.<sup>12</sup> The Mohs scale is qualitative, comparing the hardness of a material to one of 10 minerals: talc (Moh  $\equiv$  1), gypsum ( $\equiv$  2), calcite ( $\equiv$  3), fluorite ( $\equiv$  4), apatite ( $\equiv$  5), orthoclase ( $\equiv$  6), quartz ( $\equiv$  7), topaz ( $\equiv$  8), sapphire ( $\equiv$  9), and diamond (Moh  $\equiv$  10). The Knoop scale is determined by area of a mark caused by an indenter; the Knoop value is the indenter mass divided by the indented area. The mass of the indenter (load) is usually specified; 200 or 500 g are typical. (Reprinted by permission of Ashlee Publishing Company.)

Fracture toughness is another measure of strength, specifically, a material's ability to resist crack propagation. Fracture toughness measures the applied stress required to enlarge a flaw (crack) of given size and has units of  $\text{MPa} \cdot \text{m}^{1/2}$ . Values for representative materials are given in Table 6.

**Characteristic Temperatures** Characteristic temperatures of crystalline materials are those of melting (or vaporization or decomposition) and phase transitions. Of particular importance are the phase-transition temperatures. These temperatures mark the boundaries of a particular structure. A phase transition can mean a marked change in properties. One important phase-transition point is the Curie temperature of ferroelectric materials. Below the Curie temperature, the material is ferroelectric; above this temperature it is paraelectric. The Curie temperature phase transition is particularly significant because the change in structure is accompanied by drastic changes in some properties such as the static dielectric constant which approaches infinity as temperature nears the Curie temperature. This transition is associated with the lowest transverse optical frequency (the soft mode) approaching zero [hence the static dielectric constant approaches infinity from the Lyddane-Sachs-Teller relationship, Eq. (11)].

**TABLE 6** Fracture Toughness of Some Materials

Fracture toughness		Fracture toughness	
Material	$\text{MPa} \cdot \text{m}^{1/2}$	Material	$\text{MPa} \cdot \text{m}^{1/2}$
$\text{Al}_2\text{O}_3$	3	$\text{MgAl}_2\text{O}_4$	1.5
ALON	1.4	$\text{MgF}_2$	1.0
AlN	3	$\text{PbTiO}_3$	1.1
N-BK7 glass	1.1	SF58 glass	0.38
C, diamond	2.0	Si	0.95
$\text{CaF}_2$	0.5	fused $\text{SiO}_2$	0.8
$\text{CaLa}_2\text{S}_4$	0.68	$\text{Y}_2\text{O}_3$	0.7
F2 glass	0.55	ZnS	0.5 (crystal) 0.8 (CVD)
GaP	0.9	ZnSe	0.33
Ge	0.66	$\text{ZrO}_2\text{:Y}_2\text{O}_3$	2.0
LaK10 glass	0.95	Zerodur	0.9

The term *glass* applies to a material that retains an amorphous state upon solidification. More accurately, glass is an undercooled, inorganic liquid with a very high viscosity at room temperature and is characterized by a gradual softening with temperature and a hysteresis between glass and crystalline properties. The gradual change in viscosity with temperature is characterized by several temperatures, especially the glass transition temperature and the softening-point temperature. The glass transition temperature defines a second-order phase transition analogous to melting. At this temperature, the temperature dependence of various properties changes (in particular, the linear thermal expansion coefficient) as the material transitions from a liquid to glassy state. Glasses can crystallize if held above the transition temperature for sufficient time. The annealing point is defined as the temperature resulting in a glass viscosity of  $10^{13}$  poise and at which typical glasses can be annealed within an hour or so. In many glasses, the annealing point and the glass transition temperature are close. In an optical system, glass elements need to be kept 150 to 200°C below the glass transition temperature to avoid significant surface distortion. At the *softening temperature*, viscosity is  $10^{7.6}$  poise and glass will rapidly deform under its own weight; glasses are typically molded at this temperature. Glasses do not have a true melting point; they become progressively softer (more viscous) with increased temperature. Other amorphous materials may not have a well-defined glass transition; instead they may have a conventional melting point. Glasses that crystallize at elevated temperature also have a well-defined melting point.

Glass-ceramics have been developed which are materials with both glasslike and crystalline phases. In particular, low-thermal-expansion ceramics comprise a crystalline phase with a negative thermal expansion and a vitreous phase with a positive thermal expansion. Combined, the two phases result in very high dimensional stability. Typically, the ceramics are made like other glasses, but after stresses are removed from a blank, a special heat-treatment step forms the nuclei for the growth of the crystalline component of the ceramic. Although not strictly ceramics, similar attributes can be found in some two-phase glasses.

**Heat Capacity and Debye Temperature** Heat capacity, or specific heat, a scalar quantity, is the change in thermal energy with a change in temperature. Units are typically J/(gm · K). Debye developed a theory of heat capacity assuming that the energy was stored in acoustical phonons. This theory, which assumes a particular density of states, results in a Debye molar heat capacity [units J/(mole · K)] of the form

$$C_V(T) = 9mN_A k_B \left( \frac{T}{\theta_D} \right)^3 \int_0^{\theta_D/T} \frac{x^4 e^x}{(e^x - 1)^2} dx \quad (44a)$$

where  $C_V$  is the molar heat capacity in J/(mole · K) per unit volume,  $\theta_D$  is the Debye temperature,  $m$  the number of atoms per formula unit,  $N_A$  is Avogadro's number, and  $k_B$  is Boltzmann's constant. At low temperatures ( $T \rightarrow 0$  K), heat capacity closely follows the  $T^3$  law of Debye theory

$$C_V(T) = \frac{12\pi^4}{5} mN_A k_B \left( \frac{T}{\theta_D} \right)^3 = 1943.76 \cdot m \left( \frac{T}{\theta_D} \right)^3 \text{ J/(mole} \cdot \text{K)} \quad (T \ll \theta_D) \quad (44b)$$

and the high-temperature (classical) limit is

$$C_V(T) = 3mN_A k_B = 24.943 \cdot m \text{ J/(mole} \cdot \text{K)} \quad (T > \theta_D) \quad (44c)$$

If heat capacity data are fit piecewise to the Debye equation, a temperature-dependent  $\theta_D$  can be found. Frequently, a Debye temperature is determined from room-temperature elastic constants, and is therefore different from the low-temperature value. The Debye temperature given in the tables is, when possible, derived from low-temperature heat capacity data.

The Debye equations can be used to estimate heat capacity  $C_V$  over the entire temperature range, typically to within 5 percent of the true value using a single Debye temperature value. Usually, however,  $C_p$ , the constant pressure heat capacity, rather than  $C_V$ , is desired. At low temperatures, thermal

expansion is small, and  $C_p \approx C_v$ . At elevated temperature, the relationship between  $C_v$  and  $C_p$  is given by the thermodynamic relationship

$$C_p(T) = C_v(T) + 9\alpha^2 TVB \quad (45)$$

where  $T$  is temperature (K),  $V$  is the molar volume ( $\text{m}^3/\text{mole}$ ),  $\alpha$  is the thermal expansion coefficient, and  $B$  is the bulk modulus ( $\text{Pa} = \text{Nt}/\text{m}^2$ ).

Molar heat capacity can be converted to usual units by dividing by the molecular weight (see the physical property tables for crystals) in g/mole. Since molar heat capacity approaches the value of  $24.943 \text{ J}/(\text{mole} \cdot \text{K})$  the heat capacity per unit weight is inversely proportional to molecular weight at high temperature (i.e., above the Debye temperature).

**Thermal Expansion** The linear thermal expansion coefficient  $\alpha$  is the fractional change in length with a change in temperature as defined by

$$\alpha(T) = \frac{1}{L} \frac{dL}{dT} \quad (46a)$$

and units are  $1/\text{K}$ . The units of length are arbitrary. Thermal expansion is a second-rank tensor; nonisometric crystals have a different thermal expansion coefficient for each principal direction. At low temperature, thermal expansion is low, and the coefficient of thermal expansion approaches zero as  $T \rightarrow 0 \text{ K}$ . The expansion coefficient generally rises with increasing temperature; Fig. 11 shows temperature dependence of the expansion coefficient for several materials. Several compilations of data exist.<sup>97,98</sup>

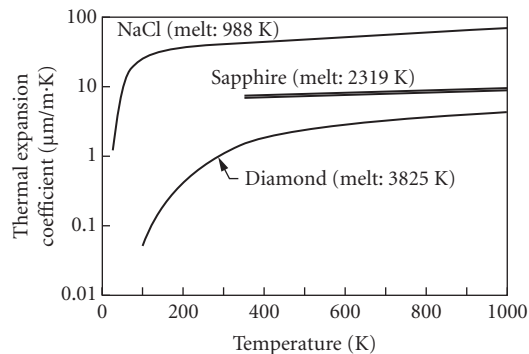
The volume expansion coefficient  $\alpha_v$  is the fractional change in volume with an increase in temperature. For a cubic or isotropic material with a single linear thermal expansion coefficient

$$\alpha_v(T) = \frac{1}{V} \frac{dV}{dT} = 3\alpha \quad (46b)$$

can be used to estimate the temperature change of density.

The Grüneisen relationship relates the thermal expansion coefficient to molar heat capacity

$$\alpha(T) = \frac{\gamma C_v(T)}{3B_0 V_0} \quad (46c)$$



**FIGURE 11** Thermal expansion of several materials. Expansion arises from the anharmonicity of the interatomic potential. At low temperature, expansion is very low and the expansion coefficient is low. As temperature increases, the expansion coefficient rises, first quickly, then less rapidly.

where  $B_0$  is the bulk modulus at  $T = 0$  K,  $V_0$  is the volume at  $T = 0$  K, and  $\gamma$  is the Grüneisen parameter. This relationship shows that thermal expansion has the same temperature dependence as the heat capacity. Typical values of  $\gamma$  lie between 1 and 2.

**Thermal Conductivity** Thermal conductivity  $\kappa$  determines the rate of heat flow through a material with a given thermal gradient. Conductivity is a second-rank tensor with up to three principal values. This property is especially important in relieving thermal stress and optical distortions caused by rapid heating or cooling. Units are  $\text{W}/(\text{m}\cdot\text{K})$

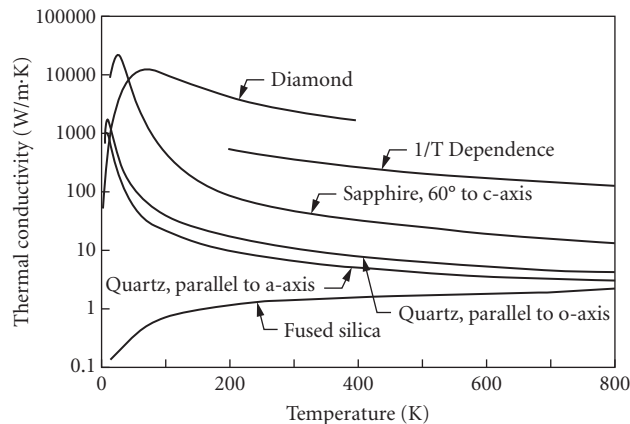
Kinetic theory gives the following expression for thermal conductivity,  $\kappa$

$$\kappa = \frac{1}{3} C_v v \ell \quad (47)$$

where  $v$  is the phonon (sound) velocity and  $\ell$  is the phonon mean free path. At very low temperature ( $T < \theta_D/20$ ), the temperature dependence of thermal conductivity is governed by  $C_v$ , which rises as  $T^3$  [see Eq. (36b)]. At high temperature ( $T > \theta_D/10$ ), the phonon mean free path is limited by several mechanisms. In crystals, scattering by other phonons usually  $\ell$ . In the high-temperature limit, the phonon density rises proportional to  $T$  and thermal conductivity is inversely proportional to  $T$ . Figure 12 illustrates the temperature dependence of thermal conductivity of several crystalline materials.

Thermal conductivity in amorphous substances is quite different compared to crystals. The phonon mean free path in glasses is significantly less than in crystals, limited by structural disorder. The mean free path of amorphous materials is typically the size of the fundamental structural units (e.g., 10 Å) and has little temperature dependence; hence the temperature dependence of thermal conductivity is primarily governed by the temperature dependence of heat capacity. At room temperature, the thermal conductivity of oxide glasses is a factor of 10 below typical oxide crystals. Figure 12 compares the thermal conductivity of fused silica to crystalline silica (quartz).

Thermal conductivity of crystals is highly dependent on purity and order. Mixed crystals, second-phase inclusion, nonstoichiometry, voids, and defects can all lower the thermal conductivity



**FIGURE 12** Thermal conductivity of several materials. Conductivity initially rises rapidly as the heat capacity increases. Peak thermal conductivity of crystals is high due to the long phonon mean free path of the periodic structure which falls with increasing temperature as the phonon free path length decreases ( $\approx 1/T$ ). The phonon mean free path of amorphous materials (e.g., fused silica) is small and nearly independent of temperature, hence thermal conductivity rises monotonically and approaches the crystalline value at high temperature.



of a material. Values given in the data table are for the highest-quality material. Thermal conductivity data are found in compilations<sup>98</sup> and reviews.<sup>99</sup>

**Correlation of Properties** All material properties are correlated to a relatively few factors, for example, constituent atoms, the bonding between the atoms, and the structural symmetry. The binding forces, or chemical bonds, play a major role in properties. Tightly bonded materials have high moduli, high hardness and strength, and high Debye temperature (hence high room-temperature thermal conductivity). Strong bonds also mean lower thermal expansion, lower refractive index, higher-frequency optical vibrational modes (hence less infrared transparency), and higher energy bandgaps (hence more ultraviolet transparency). Increased mass of the constituent atoms lowers the frequency of both electronic and ionic resonances. Similarly, high structural symmetry can increase hardness and eliminate (to first order) ionic vibrations (cf., diamond, silicon, and germanium).

**Combinations of Properties** A given material property is influenced by many factors. For example, the length of a specimen is affected by stress (producing strain), by electric fields (piezo-electric effect), and by temperature (thermal expansion). The total strain is then a combination of these linear effects and can be written as

$$\Delta e_{ij} = \left( \frac{\partial e_{ij}}{\partial \sigma_{kl}} \right)_{E,T} \Delta \sigma_{kl} + \left( \frac{\partial e_{ij}}{\partial \mathbf{E}_k} \right)_{\sigma,T} \Delta \mathbf{E}_k + \left( \frac{\partial e_{ij}}{\partial T} \right)_{\sigma,E} \Delta T \quad (48)$$

$$\Delta e_{ij} = s_{ijkl} \Delta \sigma_{kl} + d_{ijk} \Delta \mathbf{E}_k + \alpha_{ij} \Delta T$$

Often, these effects are interrelated, and frequently dependent on measurement conditions. Some properties of some materials are very sensitive to measurement conditions (the subscripts in the preceding equation denote the variable held constant for each term). For example, if the measurement conditions for the elastic contribution were adiabatic, stress will cause temperature to fall, which, in turn, decreases strain (assuming positive thermal expansion coefficient). Thus the elastic contribution to strain is measured under isothermal (and constant  $\mathbf{E}$  field) conditions so as not to include the temperature effects already included in the thermal expansion term.

The conditions of measurement are given a variety of names that may cause confusion. For example, the mechanical state of “clamped,” constant volume, and constant strain all refer to the same measurement condition which is paired with the corresponding condition of “free,” “unclamped,” constant pressure, or constant stress. In many cases, the condition of measurement is not reported and probably unimportant (i.e., different conditions give essentially the same result). Another common measurement condition is constant  $\mathbf{E}$  field (“electrically free”) or constant  $\mathbf{D}$  field (“electrically clamped”).

Some materials, particularly ferroelectrics, have large property variation with temperature and pressure, hence measurement conditions may greatly alter the data. The piezoelectric effect contributes significantly to the clamped dielectric constant of ferroelectrics. The difference between the isothermal clamped and free dielectric constants is

$$\epsilon_0 \cdot (\epsilon_i^e - \epsilon_i^\sigma) = -d_{ij} d_{ik} c_{jk}^E \quad (49)$$

where  $d_{ij}$  is the piezo-electric coefficient and  $c_{jk}^E$  is the (electrically free) elastic stiffness. If the material structure is centrosymmetric, all components of  $d_{ij}$  vanish, and the two dielectric constants are the same.

## 2.5 PROPERTIES TABLES

The following tables summarize the basic properties for representative crystals and glasses. In general, the presented materials are (1) of general interest, (2) well-characterized (within the limitations imposed by general paucity of data and conflicting property values), and (3) represent a wide

range of representative types and properties. Few materials can be regarded as well-characterized. Crystalline materials are represented by alkali halides, oxides, chalcogenides, and a variety of crystals with nonlinear optical, ferroelectric, piezoelectric, and photorefractive properties.

A number of materials in the previous edition have been removed for the sake of brevity. Properties of the following crystals and glasses are found in this chapter:<sup>1</sup>

$\beta$ -AgI (iodyrite)	InAs	PbS
AlAs	InP	PbSe
AlN	KCl	Se
BN	KF	$\beta$ -SiC
BP	LaF <sub>3</sub>	$\alpha$ -SiC
CaLa <sub>2</sub> S <sub>4</sub>	NaBr	Te
CsBr	NaF (valliaumite)	Tl <sub>3</sub> AsSe <sub>3</sub> (TAS)
CsCl	NaI	TlCl
CuCl (nantokite)	PbF <sub>2</sub>	ZnO (zincite)
TiK1	TiF1	PK2
BaLK1	KzF6	ZK1
PSK3	BaK1	LgSK2
SK4	SSK4	BaSF10
TaC2	TaD5	ULTRAN 30 (548743)
CORTRAN 9753	ZBL	ZBLA
ZBT	HBL	HBLA
HBT		

The physical property tables define the composition, density, and structure (of crystalline materials). Table 7 gives data for 71 crystalline materials. Table 8 compares glasses from different manufacturers and selects 24 representative “optical” glasses intended for visible and near-infrared use (typically to 2.5  $\mu\text{m}$ ). Table 9 gives physical property data for 17 specialty glasses and substrate materials. The specialty glasses include fused silica and germania, calcium aluminate, fluoride, germanium-, and chalcogenide-based glasses, many of which are intended for use at longer wavelengths. The three substrate materials, Pyrex, Zerodur, and ULE, are included because of their widespread use for mirror blanks.

Mechanical properties for crystals are given in two forms, room-temperature elastic constants (or moduli) for crystals (Tables 10 through 16), and engineering moduli, flexure strength, and hardness for both crystals (Table 17) and glasses (Table 18). Engineering moduli for crystalline materials should only be applied to the polycrystalline forms of these materials. Accurate representation of the elastic properties of single crystals requires the use of elastic constants in tensor form. Strength is highly dependent on manufacture method and many have significant sample-to-sample variability. These characteristics account for the lack of strength data. For these reasons, the provided strength data is intended only as a guide. Glasses and glass-ceramics flexure strengths typically range from 30 to 200 MPa, although glass fibers with strength exceeding 1000 MPa have been reported.

Thermal properties are given in Tables 19 and 20 for crystals and glasses, respectively. Characteristic temperatures (Debye, phase change, and melt for crystals; glass transitions, soften, and melt temperatures for glasses), heat capacity, thermal expansion, and thermal conductivity data are included. Directional thermal properties of crystals are given when available. Only room-temperature properties are reported except for thermal conductivity of crystals, which is also given for temperatures above and below ambient, if available.

Optical properties are summarized in Tables 21 and 22 for crystals and glasses, respectively. These tables give the wavelength boundaries of the optical transparent region (based on a  $1\text{ cm}^{-1}$  absorption coefficient), characteristic refractive index ( $\bar{n}_\infty$ , the asymptote of the electronic contribution to the refractive index for crystals), or  $n_d$  and  $v_d$  for glasses), and values of  $dn/dT$  at various wavelengths. Tables 23 and 24 give dispersion formulas for crystals and glasses, respectively.

**TABLE 7** Composition, Structure, and Density of Crystals

Material	Crystal System and Space Group	Unit Cell Dimension (Å)	Molecular Weight (amu)	Formulae/ Unit Cell	Density (g/cm <sup>3</sup> )
Ag <sub>3</sub> AsS <sub>3</sub> (proustite)	Hexagonal R3c (C <sub>3v</sub> <sup>6</sup> ) #161	a = 10.756 c = 8.652	494.72	6	5.686
AgBr (bromyrite)	Cubic Fm3m (O <sub>h</sub> <sup>5</sup> ) #225	5.7745	187.77	4	6.477
AgCl (cerargyrite)	Cubic Fm3m (O <sub>h</sub> <sup>5</sup> ) #225	5.547	143.32	4	5.578
AgGaS <sub>2</sub> (AGS)	Tetragonal I42d (D <sub>2d</sub> <sup>12</sup> ) #122	a = 5.757 c = 10.304	241.72	4	4.701
AgGaSe <sub>2</sub>	Tetragonal I42d (D <sub>2d</sub> <sup>12</sup> ) #122	a = 5.992 c = 10.886	335.51	4	5.702
Al <sub>2</sub> O <sub>3</sub> (sapphire, alumina)	Hexagonal R3c (D <sub>3d</sub> <sup>6</sup> ) #167	a = 4.759 c = 12.989	101.96	6	3.987
Al <sub>23</sub> O <sub>27</sub> N <sub>5</sub> , ALON	Cubic Fd3m (O <sub>h</sub> <sup>7</sup> ) #227	7.948	1122.59	1	3.713
Ba <sub>3</sub> [B <sub>3</sub> O <sub>6</sub> ] <sub>2</sub> , BBO	Hexagonal R3 (C <sub>3</sub> <sup>4</sup> ) #146	a = 12.532 c = 12.726	668.84	6	3.850
BaF <sub>2</sub>	Cubic Fm3m (O <sub>h</sub> <sup>5</sup> ) #225	6.2001	175.32	4	4.886
BaTiO <sub>3</sub>	Tetragonal P4 <sub>2</sub> /mmn (D <sub>4h</sub> <sup>14</sup> ) #136	a = 39920 c = 4.0361	233.19	1	6.020
BeO (bromellite)	Hexagonal P6 <sub>3</sub> mc (C <sub>6v</sub> <sup>4</sup> ) #186	a = 2.693 c = 4.395	25.012	2	3.009
Bi <sub>12</sub> GeO <sub>20</sub> , BGO	Cubic I23 (T <sup>3</sup> ) # 197	10.143	2900.39	2	9.231
Bi <sub>12</sub> SiO <sub>20</sub> , BSO (selenite)	Cubic I23 (T <sup>3</sup> ) # 197	10.1043	2855.84	2	9.194
BiB <sub>3</sub> O <sub>6</sub> , BIBO	Monoclinic C2 (C <sub>2</sub> <sup>3</sup> ) #5	a = 7.1203 b = 4.9948 c = 6.5077 γ = 105.59°	337.41	2	5.027
C (diamond)	Cubic Fd3m (O <sub>h</sub> <sup>7</sup> ) #227	3.56696	12.011	8	3.516
CaCO <sub>3</sub> (calcite)	Hexagonal R3c (D <sub>3d</sub> <sup>6</sup> ) #167	a = 4.9898 c = 17.060	100.09	6	2.711
CaF <sub>2</sub> (fluorite)	Cubic Fm3m (O <sub>h</sub> <sup>5</sup> ) #225	5.46295	78.07	4	3.181
CaMoO <sub>4</sub> (powellite)	Tetragonal I4 <sub>1</sub> /a (C <sub>4h</sub> <sup>6</sup> ) #88	a = 5.23 c = 11.44	200.04	4	4.246
CaWO <sub>4</sub> (scheelite)	Tetragonal I4 <sub>1</sub> /a (C <sub>4h</sub> <sup>6</sup> ) #88	a = 5.243 c = 11.376	287.92	4	6.115
CdGeAs <sub>2</sub>	Tetragonal I42d (D <sub>2d</sub> <sup>12</sup> ) #122	a = 5.9432 c = 11.216	334.89	4	5.615
CdS (greenockite)	Hexagonal P6 <sub>3</sub> mc (C <sub>6v</sub> <sup>4</sup> ) #186	a = 4.1367 c = 6.7161	144.48	2	4.821
CdSe	Hexagonal P6 <sub>3</sub> mc (C <sub>6v</sub> <sup>4</sup> ) #186	a = 4.2972 c = 7.0064	191.37	2	5.672

**TABLE 7** Composition, Structure, and Density of Crystals (*Continued*)

Material	Crystal System and Space Group	Unit Cell Dimension (Å)	Molecular Weight (amu)	Formulae/ Unit Cell	Density (g/cm <sup>3</sup> )
CdTe	Cubic F43m (T <sub>d</sub> <sup>2</sup> ) #216	6.4830	240.01	4	5.851
CsLiB <sub>6</sub> O <sub>10</sub> , CLBO	Tetragonal I42d (D <sub>2d</sub> <sup>12</sup> ) #122	a = 10.494 c = 8.939	492.70	4	2.461
CsI	Cubic Pm3m (O <sub>h</sub> <sup>5</sup> ) #221	4.566	259.81	1	4.532
CuGaS <sub>2</sub>	Tetragonal I42d (D <sub>2d</sub> <sup>12</sup> ) #122	a = 5.351 c = 10.480	197.40	4	4.369
GaAs	Cubic F43m (T <sub>d</sub> <sup>2</sup> ) #216	5.65325	144.64	4	5.317
GaN	Hexagonal P6 <sub>3</sub> mc (C <sub>6v</sub> <sup>4</sup> ) #186	a = 3.186 c = 5.178	83.73	2	6.109
GaP	Cubic F43m (T <sub>d</sub> <sup>2</sup> ) #216	5.4495	100.70	4	4.133
Ge	Cubic Fd3m (O <sub>h</sub> <sup>7</sup> ) #227	5.65741	72.64	8	5.329
KBr	Cubic Fm3m (O <sub>h</sub> <sup>5</sup> ) #225	6.600	119.00	4	2.749
KH <sub>2</sub> PO <sub>4</sub> , KDP	Tetragonal I42d (D <sub>2d</sub> <sup>12</sup> ) #122	a = 7.4529 c = 6.9751	136.09	4	2.338
KI	Cubic Fm3m (O <sub>h</sub> <sup>5</sup> ) #225	7.065	166.00	4	3.127
KNbO <sub>3</sub>	Orthorhombic Bmm2 (C <sub>2v</sub> <sup>14</sup> ) #38	a = 5.6896 b = 3.9692 c = 5.7256	180.00	2	4.623
KTaO <sub>3</sub>	Cubic Pm3m (O <sub>h</sub> <sup>5</sup> ) #221	3.9885	268.04	1	7.015
KTiOPO <sub>4</sub> , KTP	Orthorhombic Pna2 <sub>1</sub> (C <sub>2v</sub> <sup>9</sup> ) #33	a = 12.8164 b = 6.4033 c = 10.5897	197.94	8	3.026
LiB <sub>3</sub> O <sub>5</sub> , LBO	Orthorhombic Pna2 <sub>1</sub> (C <sub>2v</sub> <sup>9</sup> ) #33	a = 8.4473 b = 7.3788 c = 5.1395	119.37	4	2.475
LiCaAlF <sub>6</sub> , LiCAF	Hexagonal P31c (D <sub>3d</sub> <sup>2</sup> ) #163	a = 5.008 c = 9.643	187.99	2	2.981
LiF	Cubic Fm3m (O <sub>h</sub> <sup>5</sup> ) #225	4.0173	25.939	4	2.657
α-LiIO <sub>3</sub>	Hexagonal P6 <sub>3</sub> (C <sub>6</sub> <sup>6</sup> ) #173	a = 5.4815 c = 5.1709	181.84	2	4.488
LiNbO <sub>3</sub>	Hexagonal R3c (C <sub>3v</sub> <sup>6</sup> ) #161	a = 5.1483 c = 13.8631	147.85	6	4.629
LiYF <sub>4</sub> , YLF	Tetragonal 14 <sub>1</sub> /a (C <sub>4h</sub> <sup>6</sup> ) #88	a = 5.175 c = 10.74	171.84	4	3.968
MgAl <sub>2</sub> O <sub>4</sub> (spinel)	Cubic Fd3m (O <sub>h</sub> <sup>7</sup> ) #227	8.084	142.27	8	3.577

(Continued)

**TABLE 7** Composition, Structure, and Density of Crystals (*Continued*)

Material	Crystal System and Space Group	Unit Cell Dimension (Å)	Molecular Weight (amu)	Formulae/ Unit Cell	Density (g/cm <sup>3</sup> )
MgF <sub>2</sub> (sellaite)	Tetragonal P4 <sub>2</sub> /mnm (D <sub>4h</sub> <sup>14</sup> ) #136	a = 4.623 c = 3.053	62.302	2	3.171
MgO (periclase)	Cubic Fm3m (O <sub>h</sub> <sup>5</sup> ) #225	4.2117	40.304	4	3.583
NaCl (halite, rock salt)	Cubic Fm3m (O <sub>h</sub> <sup>5</sup> ) #225	5.63978	58.44	4	2.164
[NH <sub>4</sub> ] <sub>2</sub> CO (urea, carbamide)	Tetragonal I4 <sub>2</sub> m (D <sub>2d</sub> <sup>3</sup> ) #113	a = 5.661 c = 4.712	60.055	2	1.321
NH <sub>4</sub> H <sub>2</sub> PO <sub>4</sub> , ADP	Tetragonal I4 <sub>2</sub> d (D <sub>2d</sub> <sup>12</sup> ) #122	a = 7.4991 c = 7.5493	115.03	4	1.800
PbMoO <sub>4</sub> (wulfenite)	Tetragonal I4 <sub>1</sub> /a (C <sub>4h</sub> <sup>6</sup> ) #88	a = 5.4312 c = 12.1065	367.16	4	6.829
PbTe (altaite)	Cubic Fm3m (O <sub>h</sub> <sup>5</sup> ) #225	6.443	334.80	4	8.314
PbTiO <sub>3</sub>	Tetragonal P4 <sub>2</sub> /mnm (D <sub>4h</sub> <sup>14</sup> ) #136	a = 3.8966 c = 4.1440	303.07	1	7.998
RbTiOPO <sub>4</sub> , RTP	Orthorhombic Pna2 <sub>1</sub> (C <sub>2v</sub> <sup>9</sup> ) #33	a = 12.948 b = 6.494 c = 10.551	244.31	8	3.654
Si	Cubic Fd3m (O <sub>h</sub> <sup>7</sup> ) #227	5.43085	28.0855	8	2.329
SiO <sub>2</sub> (α-quartz)	Hexagonal P3 <sub>2</sub> 21 (D <sub>3</sub> <sup>6</sup> ) #154	a = 4.9136 c = 5.4051	60.084	3	2.648
SrF <sub>2</sub>	Cubic Fm3m (O <sub>h</sub> <sup>5</sup> ) #225	5.7996	125.62	4	4.277
SrMoO <sub>4</sub>	Tetragonal I4 <sub>1</sub> /a (C <sub>4h</sub> <sup>6</sup> ) #88	a = 5.380 c = 11.97	247.58	4	4.746
SrTiO <sub>3</sub>	Cubic Pm3m (O <sub>h</sub> <sup>5</sup> ) #221	3.9049	183.49	1	5.117
TeO <sub>2</sub> (paratellurite)	Tetragonal P4 <sub>1</sub> 2 <sub>1</sub> 2 (D <sub>4</sub> <sup>4</sup> ) #92	a = 4.810 c = 7.613	159.60	4	6.019
TiO <sub>2</sub> (rutile)	Tetragonal P4 <sub>2</sub> /mnm (D <sub>4h</sub> <sup>14</sup> ) #136	a = 4.5937 c = 2.9618	79.866	2	4.244
TlBr	Cubic Pm3m (O <sub>h</sub> <sup>5</sup> ) #221	3.9846	284.29	1	7.462
Tl[0.46Br, 0.54I], KRS-5	Cubic Pm3m (O <sub>h</sub> <sup>5</sup> ) #221	4.108	307.79	1	7.372
Tl[0.7Cl, 0.3Br], KRS-6	Cubic Pm3m (O <sub>h</sub> <sup>5</sup> ) #221	3.907	253.17	1	7.049
Y <sub>3</sub> Al <sub>5</sub> O <sub>12</sub> , YAG	Cubic Ia3d (O <sub>h</sub> <sup>10</sup> ) #230	12.008	593.62	8	4.554
Y <sub>2</sub> O <sub>3</sub> (yttria)	Cubic Ia3 (T <sub>h</sub> <sup>7</sup> ) #206	10.603	225.81	16	5.033
YVO <sub>4</sub>	Tetragonal I4 <sub>1</sub> /amd (D <sub>4h</sub> <sup>19</sup> ) #141	a = 7.1192 c = 6.2898	203.84	2	4.247

**TABLE 7** Composition, Structure, and Density of Crystals (Continued)

Material	Crystal System and Space Group	Unit Cell Dimension (Å)	Molecular Weight (amu)	Formulae/ Unit Cell	Density (g/cm <sup>3</sup> )
ZnGeP <sub>2</sub>	Tetragonal I42d (D <sub>2d</sub> <sup>12</sup> ) #122	a = 5.466 c = 10.722	199.97	4	4.146
β-ZnS (zincblende)	Cubic F43m (T <sub>d</sub> <sup>2</sup> ) #216	5.4094	97.445	4	4.089
α-ZnS (wurtzite)	Hexagonal P6 <sub>3</sub> mc (C <sub>6v</sub> <sup>4</sup> ) #186	a = 3.8218 c = 6.2587	97.445	2	4.088
ZnSe	Cubic F43m (T <sub>d</sub> <sup>2</sup> ) #216	5.6685	144.34	4	5.264
ZnTe	Cubic F43m (T <sub>d</sub> <sup>2</sup> ) #216	6.1034	192.98	4	5.638
ZrO <sub>2</sub> :0.12Y <sub>2</sub> O <sub>3</sub> (cubic zirconia)	Cubic Fm3m (O <sub>h</sub> <sup>5</sup> ) #225	5.148	121.98	4	5.939

**TABLE 8** Optical Glass Reference Table [Cross-referenced glass examples, including 6-digit glass code and density (ρ, g/cm<sup>3</sup>)]

Common Name	Manufacturer			
	Schott	Ohara	Hoya	Pilkington
Fluor crown	FK	FSL	FC, FCD <sup>1</sup>	
	N-FK5 (487704)	S-FSL5 (487702)	FC5 (487704)	—
	ρ = 2.45	ρ = 2.46	ρ = 2.45	
Phosphate crown	PK	FPL	PC, PCS <sup>2</sup>	
	N-PK52A (497816)	S-FPL51 (497816)	FCD1 (497816)	—
	ρ = 3.70	ρ = 3.62	ρ = 3.70	
Zinc crown	ZK		ZnC	ZC
	N-ZK7 (508612)	—	—	ZC508612A
	ρ = 2.49			ρ = 2.50
Borosilicate crown	BK	BSL	BSC	BSC
	N-BK7 (517642)	S-BSL7(516614)	BSC7 (517642)	BSC517642B
	ρ = 2.51	ρ = 2.52	ρ = 2.52	ρ = 2.50
Crown	K	NSL	C	HC <sup>3</sup>
	N-K5 (522595)	S-NSL5 (522598)	—	HC522595A
	ρ = 2.59	ρ = 2.49		ρ = 2.54
Crown flint	KF	NSL	CF	
	N-KF9 (523515)	—	—	—
	ρ = 2.50			
Very light flint	LLF	TIL	FEL <sup>4</sup>	ELF <sup>4</sup>
	LLF1 (548457)	S-TIL1 (548458)	E-FEL1 (548458)	—
	ρ = 2.94	ρ = 2.49	ρ = 2.54	
Dense phosphate crown	PSK	BAL, PHM	PCD	
	N-PSK53A (618634)	S-PHM52 (618634)	PCD4 (618634)	—
	ρ = 3.57	ρ = 3.67	ρ = 3.52	
Barium crown	BaK	BAL	BaC	MBC <sup>5</sup>
	N-BaK4 (569560)	S-BAL14 (569563)	BAC4 (569560)	MBC569561A
	ρ = 3.05	ρ = 2.89	ρ = 2.85	ρ = 3.06

(Continued)

**TABLE 8** Optical Glass Reference Table [Cross-referenced glass examples, including 6-digit glass code and density ( $\rho$ , g/cm<sup>3</sup>)] (Continued)

Common Name	Manufacturer			
	Schott	Ohara	Hoya	Pilkington
Barium light flint	BaLF	BAL	BaFL <sup>6</sup>	
	N-BaLF4 (580540) $\rho = 3.11$	S-BAL3 (571530) $\rho = 2.98$	BaFL3 (571530) $\rho = 2.98$	—
Light flint	LF	TIL	FL	LF
	LF5 (581409) $\rho = 3.22$	S-TIL25 (581407) $\rho = 2.59$	E-FL5 (581409) $\rho = 2.59$	LF581409A $\rho = 3.23$
Fluoro flint	TiF	TIM	FF	—
	TiF1 (511510) $\rho = 2.479$ (obsolete)	S-FTM16 (593353) $\rho = 2.64$	*FF5 (593354) $\rho = 2.64$	—
Special short flint	KzFS	BAH, BAM	ADF <sup>7</sup>	
	N-KzFS4 (613445) $\rho = 3.00$	S-NBM51 (613443) $\rho = 2.93$	E-ADF10 (613443) $\rho = 3.04$	—
Dense crown	SK	BAL, BSM	BaCD <sup>8</sup>	DBC <sup>8</sup>
	N-SK10 (623570) $\rho = 3.67$ (obsolete)	S-BSM10 (623570) $\rho = 3.60$	E-BACD10 (623569) $\rho = 3.66$	DBC623569A $\rho = 3.66$
Flint	F	TIM	F	DF <sup>9</sup>
	N-F2 (620364) $\rho = 2.65$	S-TIM1 (626357) $\rho = 2.71$	E-F2 (620363) $\rho = 2.67$	DF620364A $\rho = 3.61$
Very dense crown	SSK	BSM	BaCED <sup>10</sup>	DBC
	N-SSK5 (658509) $\rho = 3.71$	S-BSM25 (658509) $\rho = 3.50$	BaCED5 (658509) $\rho = 3.64$	DBC658509A $\rho = 3.56$
Barium flint	BaF	BAH, BAF	BaF	
	N-BaF10 (670471) $\rho = 3.75$	S-BAH10 (670473) $\rho = 3.48$	BAF10 (670472) $\rho = 3.61$	—
Barium dense flint	BaSF	BAH	BaFD	
	N-BaSF64 (704394) $\rho = 3.20$	—	BAFD15 (702402) $\rho = 2.99$	—
Lanthanum crown	LaK	LAL, YGH	LaC, LaCL <sup>11</sup>	LAC
	N-LaK10 (720506) $\rho = 3.69$	S-LAL10 (720502) $\rho = 3.86$	LAC10 (720503) $\rho = 3.87$	LAC720504B $\rho = 3.86$
Tantalum crown	LaK	LAL, YGH	TaC	
	N-LaK33A (754523) $\rho = 4.22$	S-YGH51 (755523) $\rho = 4.40$	TAC6 (755523) $\rho = 4.27$	—
Niobium flint	LaF	LAM	NbF, NbFD	
	N-LaF35 (743494) $\rho = 4.12$	S-LAM60 (743493) $\rho = 4.06$	NbF1 (743492) $\rho = 4.17$	—
Light lanthanum flint	N-LaF33 (786441) $\rho = 4.36$	S-LAH51 (786442) $\rho = 4.40$	NBFD11 (786439) $\rho = 4.43$	—
	LaF	LAM	LaF	LAF
Lanthanum flint	N-LaF2 (744449) $\rho = 4.30$	S-LAM2 (744448) $\rho = 4.32$	LaF2 (744449) $\rho = 4.39$	LAF744447B $\rho = 4.32$
	LaF	LAM	LaFL	LAF
	LaF2 (744447) $\rho = 4.34$ (obsolete)	S-LAM59 (697485) $\rho = 3.77$	LAFL2 (697485) $\rho = 4.05$	—

**TABLE 8** Optical Glass Reference Table [Cross-referenced glass examples, including 6-digit glass code and density ( $\rho$ , g/cm<sup>3</sup>)] (Continued)

Common Name	Manufacturer			
	Schott	Ohara	Hoya	Pilkington
Dense flint	SF	TIM, TIH	FD, FDS <sup>12</sup>	EDF, DEDF, LDF
	SF2 (648338)	S-TIM22 (648338)	E-FD2 (648338)	EDF648339A
	$\rho=3.86$	$\rho = 2.79$	$\rho = 2.77$	$\rho = 3.86$
	N-SF10 (728285)	S-TIH10 (728285)	E-FD10 (728283)	DEDF728284A
	$\rho = 3.05$	$\rho = 3.06$	$\rho = 3.07$	$\rho = 4.27$
Lanthanum dense flint	N-SF6 (805254)	S-TIH6 (805254)	FD60 (805255)	LDF805254A
	$\rho = 3.37$	$\rho = 3.37$	$\rho = 3.36$	$\rho = 3.37$
	LaSF	LAH	TaF <sup>13</sup> , TaFD <sup>14</sup>	—
	N-LaSF44 (804465)	S-LAH65 (804466)	TaF3 (804465)	—
	$\rho = 4.44$	$\rho = 4.76$	$\rho = 4.65$	—
Antimony flint	N-LaSF31A (883408)	S-LAH58 (883408)	TaFD30 (883408)	—
	$\rho = 5.51$	$\rho = 5.52$	$\rho = 5.51$	—
	KzF	—	SbF	—
Fused silica (UV)	KzFN1 (551496)	—	SbF1 (551495)	—
	$\rho = 2.71$ (obsolete)	—	$\rho = 2.72$	—
	Lithosil-Q	—	—	—
	Lithosil-Q (458678)	—	—	—
	$\rho = 2.20$	—	—	—

<sup>1</sup>FCD = dense fluor crown; <sup>2</sup>PCS = special phosphate crown; <sup>3</sup>HC = hard crown; <sup>4</sup>FEL = ELF = extra light flint; <sup>5</sup>MBC = medium barium crown; <sup>6</sup>BaFL = light barium flint; <sup>7</sup>ADF = abnormal dispersion flint; <sup>8</sup>BACD = DBC = dense barium crown; <sup>9</sup>DF = dense flint; <sup>10</sup>BaCED = extra dense barium crown; <sup>11</sup>LaCL = light lanthanum crown; <sup>12</sup>FDS = special dense flint; <sup>13</sup>TaF = tantalum flint; <sup>14</sup>TaFD = tantalum dense flint.

**TABLE 9** Physical Properties of Specialty Glasses and Substrate Materials

Glass type	Density (g/cm <sup>3</sup> )	Typical composition
Fused silica (SiO <sub>2</sub> ) (e.g., Corning 7940 or Schott Lithosil-Q)	2.202	100%SiO <sub>2</sub>
Fused germania (GeO <sub>2</sub> )	3.604	100%GeO <sub>2</sub>
BS-39B (Barr and Stroud)	3.1	50%CaO, 34%Al <sub>2</sub> O <sub>3</sub> , 9%MgO
CORTRAN 9754 (Corning)	3.581	33%GeO <sub>2</sub> , 20%CaO, 37%Al <sub>2</sub> O <sub>3</sub> , 5%BaO, 5%ZnO
IRG 2 (Schott)	5.00	Germanium glass
IRG 9 (Schott)	3.63	Fluorophosphate glass
IRG 11 (Schott)	3.12	Calcium aluminate glass
IRG 100 (Schott)	4.67	Chalcogenide glass
HTF-1 (Ohara) [443930]	3.94	Heavy metal fluoride glass
ZBLAN	4.52	56%ZrF <sub>4</sub> , 14%BaF <sub>2</sub> , 6%LaF <sub>3</sub> , 4%AlF <sub>3</sub> , 20%NaF
Arsenic trisulfide (As <sub>2</sub> S <sub>3</sub> )	3.198	100%As <sub>2</sub> S <sub>3</sub>
Arsenic triselenide (As <sub>2</sub> Se <sub>3</sub> )	4.69	100%As <sub>2</sub> Se <sub>3</sub>
AMTRI-1/TI-20	4.41	55%Se, 33%Ge, 12%As
AMTIR-3/TI-1173	4.70	60%Se, 28%Ge, 12%Sb
Pyrex (e.g., Corning 7740)	2.23	81%SiO <sub>2</sub> , 13%B <sub>2</sub> O <sub>3</sub> , 4%Na <sub>2</sub> O, 2%Al <sub>2</sub> O <sub>3</sub> [two-phase glass]
Zerodur (Schott)	2.53	56%SiO <sub>2</sub> , 25%Al <sub>2</sub> O <sub>3</sub> , 8%P <sub>2</sub> O <sub>5</sub> , 4%Li <sub>2</sub> O, 2%TiO <sub>2</sub> 2%ZrO <sub>2</sub> , ZnO/MgO/Na <sub>2</sub> O/As <sub>2</sub> O <sub>3</sub> [glass ceramic]
ULE (Corning 7971)	2.205	92.5%SiO <sub>2</sub> , 7.5%TiO <sub>2</sub> [glass ceramic]



**TABLE 10** Room-Temperature Elastic Constants of Cubic Crystals

Material	Stiffness (GPa)			Compliance (TPa <sup>-1</sup> )			Ref.
	$c_{11}$	$c_{12}$	$c_{44}$	$s_{11}$	$s_{12}$	$s_{44}$	
AgBr	56.3	32.8	7.25	31.1	-11.5	138	83, 100
AgCl	59.6	36.1	6.22	31.1	-11.7	161	83, 101
ALON	393	108	119	2.89	-0.62	8.40	102
BaF <sub>2</sub>	91.1	41.2	25.3	15.3	-4.8	39.5	83
Bi <sub>12</sub> GeO <sub>20</sub> (BGO)	125.0	32.4	24.9	8.96	-1.84	40.4	103
Bi <sub>12</sub> SiO <sub>20</sub> (BSO)	129.8	29.7	24.7	8.42	-1.57	40.2	104
C (diamond)	1077	124.7	557	0.95	-0.099	1.73	83
CaF <sub>2</sub>	165	46	33.9	6.94	-1.53	29.5	83
CdTe	53.5	36.9	20.2	42.6	-17.4	49.4	83, 105
CsI	24.5	6.6	6.31	46.1	-9.7	158	83
GaAs	118	53.5	59.4	11.75	-3.66	16.8	83
GaP	141	62.4	71.2	9.70	-2.97	14.0	83
Ge	129	48	67.1	9.73	-2.64	14.9	83
KBr	34.5	5.5	5.10	30.3	-4.2	196	83
KI	27.4	4.3	3.70	38.2	-5.2	270	83
KTaO <sub>3</sub>	431	103	109	2.7	-0.63	9.2	83
LiF	112	46	63.5	11.6	-3.35	15.8	83
MgAl <sub>2</sub> O <sub>4</sub>	282.9	155.4	154.8	5.79	-2.05	6.46	106
MgO	297.8	95.1	155.8	3.97	-0.96	6.42	106
NaCl	49.1	12.8	12.8	22.9	-4.8	78.3	83
PbTe	107	8	13.2	9.46	-0.64	75.8	83, 107
Si	165	63	79.1	7.68	-2.12	12.6	83
SrF <sub>2</sub>	124	44	31.8	9.86	-2.57	31.5	83
SrTiO <sub>3</sub>	315.6	102.7	121.5	3.77	-0.93	8.23	108
TlBr	37.6	14.8	7.54	34.2	-9.6	133	83
Tl[Br:I], (KRS-5)	34.1	13.6	5.79	38.0	-10.8	173	83
Tl[Cl:Br], (KRS-6)	39.7	14.9	7.23	31.9	-8.8	139	83
Y <sub>3</sub> Al <sub>5</sub> O <sub>12</sub> (YAG)	328.1	106.4	113.7	3.62	-0.89	8.80	109
Y <sub>2</sub> O <sub>3</sub>	223.7	112.4	74.6	6.73	-2.25	13.4	110
ZnS	102	64.6	44.6	19.5	-7.6	22.5	83
ZnSe	86.4	51.5	40.2	21.0	-7.9	24.9	83
ZnTe	71.5	40.8	31.1	23.9	-8.5	32.5	83
ZrO <sub>2</sub> :Y <sub>2</sub> O <sub>3</sub>	405.1	105.3	61.8	2.77	-0.57	16.18	111

**TABLE 11** Room-Temperature Elastic Constants of Tetragonal Crystals (Point groups 4mm,  $\bar{4}2m$ , 422, and 4/mmm)

Material	c or s	Subscript of stiffness (GPa) or compliance (TPa <sup>-1</sup> )						Ref.	
		11	12	13	33	44	66		
AgGaS <sub>2</sub>	c	87.9	58.4	59.2	75.8	24.1	30.8	83, 112	
	s	26.2	-7.7	-14.5	35.9	41.5	32.5		
AgGaSe <sub>2</sub>	c	80.1	51.6	52.6	70.7	21.2	24.7	113	
	s	26.9	-8.2	-13.9	34.9	47.2	40.5		
BaTiO <sub>3</sub>	c <sup>E</sup>	275	179	152	165	54.4	113	83	
	s <sup>E</sup>	8.05	-2.35	-5.24	15.7	18.4	8.84		
	c <sup>E</sup>	211	107	114	160	56.2	127		114
	s <sup>E</sup>	8.01	-1.57	4.60	12.8	17.8	7.91		

**TABLE 11** Room-Temperature Elastic Constants of Tetragonal Crystals (Point groups  $4mm$ ,  $\bar{4}2m$ ,  $422$ , and  $4/mmm$ ) (Continued)

Material	c or s	Subscript of stiffness (GPa) or compliance (TPa <sup>-1</sup> )						Refs.
		11	12	13	33	44	66	
CdGeAs <sub>2</sub>	c	94.5	59.6	59.7	83.4	42.1	40.8	83, 115
	s	21.6	-7.04	-10.4	26.9	23.8	24.5	
CsLiB <sub>5</sub> O <sub>10</sub>	c	62.79	-16.74	23.86	37.4	33.31	26.7	116
	s	38.33	25.75	-40.88	78.90	44.82	37.45	
CuGaS <sub>2</sub>	c							
	s							
KH <sub>2</sub> PO <sub>4</sub> (KDP)	c	71.2	-5.0	14.1	56.8	12.6	6.22	83
	s	14.9	1.9	-4.2	19.7	78.4	161	
MgF <sub>2</sub>	c	138	88	62	201	56.5	95.6	83
	s	12.6	-7.2	-1.65	6.01	17.7	10.5	
[NH <sub>4</sub> ] <sub>2</sub> CO (Urea)	c	21.7	8.9	24	53.2	6.26	0.45	117
	s	95	16	-50	64	160	2220	
NH <sub>4</sub> H <sub>2</sub> PO <sub>4</sub> (ADP)	c	67.3	5.0	19.8	33.7	8.57	6.02	83
	s	18.3	2.2	-12.0	43.7	117	166	
PbTiO <sub>3</sub>	c <sup>E</sup>	235	101	98.8	105	65.1	104	118
	s <sup>E</sup>	7.06	-0.40	-6.27	21.3	15.5	9.62	
TeO <sub>2</sub>	c	56.12	51.55	23.03	105.71	26.68	66.14	119, 120
	s	114.5	-104.3	-2.3	10.5	37.5	15.1	
TiO <sub>2</sub>	c	269	177	146	480	124	192	83
	s	6.80	-4.01	-0.85	2.60	8.06	5.21	
YVO <sub>4</sub>	c	244.51	48.93	81.09	313.7	24.18	16.18	121
	s	4.54	-0.57	-1.03	3.72	20.76	61.6	
ZnGeP <sub>2</sub>	c	(87)	(66)	(64)	(81)	(20)	(23)	122
	s	(33.5)	(-14.2)	(-15.2)	(36.4)	(50)	(43.5)	

**TABLE 12** Room-Temperature Elastic Constants of Tetragonal Crystals (Point groups  $4$ ,  $\bar{4}$ , and  $4/m$ )

Material	c or s	Subscript of stiffness (GPa) or compliance (TPa <sup>-1</sup> )							Ref.
		11	12	13	16	33	44	66	
CaMoO <sub>4</sub>	c	144	65	47	-13.5	127	36.8	45.8	83, 123
	s	9.90	-4.2	2.1	4.4	9.48	27.1	24.4	
CaWO <sub>4</sub>	c	141	61	41	-17	125	33.7	40.7	83, 124
	s	10.5	-4.7	-1.9	6.4	9.3	29.7	30.2	
PbMoO <sub>4</sub>	c	107.2	61.9	52.0	-15.8	93.2	26.4	34.8	83, 125
	s	20.8	-11.8	-5.0	14.9	16.3	37.9	42.3	
SrMoO <sub>4</sub>	c	117.3	58.7	46.8	-10.8	103.8	34.9	46.6	83, 126
	s	13.2	-5.7	-3.3	4.5	12.6	28.7	23.7	
YLiF <sub>4</sub>	c	121	60.9	52.6	-7.7	156	40.9	17.7	83, 127
	s	12.8	-6.0	-2.3	8.16	7.96	24.4	63.6	

**TABLE 13** Room-Temperature Elastic Constants of Hexagonal Crystals (Point groups  $6$ ,  $\bar{6}$ ,  $6/m$ ,  $622$ ,  $6mm$ ,  $\bar{6}2m$  and  $6/mmm$ )

Material	c or s	Subscript of stiffness (GPa) or compliance (TPa <sup>-1</sup> )					Ref.
		11	12	13	33	44	
BeO	c	470	168	119	494	153	83
	s	2.52	-0.80	-0.41	2.22	6.53	
CdS	c	88.4	55.4	48.0	95.2	15.0	83
	s	20.5	-9.9	-5.3	15.9	66.7	
CdSe	c	74.1	45.2	38.9	84.3	13.4	83
	s	23.2	-11.2	-5.5	16.9	74.7	
GaN	c	296	130	158	267	241	128
	s	5.10	-0.92	-2.48	6.68	4.15	
LiIO <sub>3</sub>	c <sup>E</sup>	81.24	31.84	9.25	52.9	17.83	129
	s <sup>E</sup>	14.7	-5.6	-1.6	19.5	56.1	
ZnS	c	122	58	43	138	28.7	83
	s	11.0	-4.5	-2.1	8.6	34.8	

**TABLE 14** Room-Temperature Elastic Constants of Hexagonal (Trigonal) Crystals (Point groups  $32$ ,  $3m$ ,  $\bar{3}m$ )

Material	c or s	Subscript of stiffness (GPa) or compliance (TPa <sup>-1</sup> )						Ref.
		11	12	13	14	33	44	
Ag <sub>3</sub> AsS <sub>3</sub>	c	59.5	31.7	29.6	0.18	39.8	9.97	83, 130
	s	28.6	-7.3	-15.9	-0.6	48.8	100	
Al <sub>2</sub> O <sub>3</sub>	c	496	159	114	-23	499	146	83
	s	2.35	-0.69	-0.38	0.47	2.18	7.0	
$\beta$ -Ba <sub>3</sub> B <sub>6</sub> O <sub>12</sub> (BBO)	c	123.8	60.3	49.4	12.3	53.3	7.8	131
	s	25.63	-14.85	-9.97	-63.97	37.21	331.3	
CaCO <sub>3</sub> (Calcite)	c	144	54.2	51.2	-20.5	84.3	33.5	83
	s	11.4	-4.0	-4.5	9.5	17.3	41.4	
LiCaAlF <sub>6</sub> (LiCAF)	c	118	42	54	$\pm 19$	107	50	132
	s	12.9	-3.4	-4.8	$\pm 6.2$	-14.2	24.7	
LiNbO <sub>3</sub>	c	202	55	72	8.5	244	60.2	83
	s	5.81	-1.12	-1.38	-0.98	4.93	16.9	
$\alpha$ -SiO <sub>2</sub>	c	86.6	6.74	12.4	-17.8	106.4	58.0	83
	s	12.8	-1.75	-1.30	4.47	9.73	20.0	

**TABLE 15** Room-Temperature Elastic Constants of Orthorhombic Crystals

Material	c or s	Subscript of stiffness (GPa) or compliance (TPa <sup>-1</sup> )									Ref.
		11	12	13	22	23	33	44	55	66	
KNbO <sub>3</sub>	c <sup>E</sup>	224	102	182	273	130	245	75	28.5	95	133
	s <sup>E</sup>	11.3	-0.3	-8.2	4.9	-2.4	11.5	13.3	35.1	10.5	
KTiOPO <sub>4</sub> (KTP)	c	166	37	54	164	51	181	56	54	45	134
	s	6.8	-1	-1.8	6.8	-1.6	6.5	17.9	18.5	22.2	
LiB <sub>3</sub> O <sub>5</sub> (LBO)	c <sup>E</sup>	127.1	126.6	52.0	237.7	57.6	65.5	109.3	86.7	17.8	135
	s <sup>E</sup>	19.64	-8.49	-8.13	9.01	-1.18	22.76	9.15	11.53	56.25	
RbTiOPO <sub>4</sub> RTP	c	163	45	35	165	63	178	58	57	50	136
	s	6.73	-1.54	-0.78	7.36	-2.30	6.59	17.24	17.54	20.0	

**TABLE 16** Room-Temperature Elastic Constants for Monoclinic Crystals

Material	c or s	Subscript of stiffness (GPa) or compliance (TPa <sup>-1</sup> )							Ref.
		11	12	13	15	22	23	25	
BiB <sub>3</sub> O <sub>6</sub>	c	159.7	74.2	60.0	-49.7	52.5	13.4	-4.3	137
	s	34.3	-46.8	-0.03	20.1	83.2	-1.27	-27.56	
Material	c or s	33	35	44	46	55	66	—	Ref.
BiB <sub>3</sub> O <sub>6</sub>	c	205.2	-70.8	23.3	-18.6	74.6	66.9	—	137
	s	7.33	6.87	55.2	15.3	31.7	19.2	—	

**TABLE 17** Mechanical Properties of Crystals

Material	Moduli (GPa)			Poisson's Ratio	Flexure Strength (MPa)	Knoop Hardness (kg/mm <sup>2</sup> )
	Elastic	Shear	Bulk			
Ag <sub>3</sub> AsS <sub>3</sub>	30	11	36.8	0.36		
AgBr	24.7	8.8	40.5	0.39 <sub>9</sub>		7.0
AgCl	22.9	8.1	44.0	0.41	26	9.5
AgGaS <sub>2</sub>	53	19	67	0.37		320
AgGaSe <sub>2</sub>	47.8	17.5	60.4	0.37		230
Al <sub>2</sub> O <sub>3</sub>	402	163	252	0.23	1200	2250
ALON	317	128	203	0.24	310	1850
Ba <sub>3</sub> B <sub>6</sub> O <sub>12</sub> , BBO	30	11	60.6	0.41		
BaF <sub>2</sub>	65.9	25.2	57.8	0.31	27	78
BaTiO <sub>3</sub>	145	53	174	0.36		580
BeO	395	162	240	0.23	275	1250
Bi <sub>12</sub> GeO <sub>20</sub> , BGO	82	32	63.3	0.28		
Bi <sub>12</sub> SiO <sub>20</sub> , BSO	84	33	63.1	0.28		
BiB <sub>3</sub> O <sub>6</sub> , BIBO	91	37.5	52.5	0.21		
C, diamond	1142	534	442	0.069	2940	9000
CaCO <sub>3</sub> , calcite	83	32	73.2	0.31		100
CaF <sub>2</sub>	110	42.5	85.7	0.29	90	170
CaMoO <sub>4</sub>	103	40	80	0.29		250
CaWO <sub>4</sub>	96	37	77	0.29		300
CdGeAs <sub>2</sub>	74	28	70	0.32		470
CdS	47.3	17.2	64.0	0.38	28	122
CdSe	42	15.3	53	0.37	21	65
CdTe	38.4	14.2	42.4	0.35	26	50
CsLiB <sub>6</sub> O <sub>10</sub> , CLBO	70.3	27.5	52.5	0.28		
CsI	18	7.3	12.6	0.26	5.6	12
CuGaS <sub>2</sub>			95.8			430
GaAs	116	46.6	75.0	0.24	55	710
GaN	294	118	195	0.25	70	750
GaP	139	56.2	88.6	0.24	100	875
Ge	132	54.8	75.0	0.20 <sub>6</sub>	100	850

(Continued)

**TABLE 17** Mechanical Properties of Crystals (*Continued*)

Material	Moduli (GPa)			Poisson's Ratio	Flexure Strength (MPa)	Knoop Hardness (kg/mm <sup>2</sup> )
	Elastic	Shear	Bulk			
KBr	18	7.2	15.2	0.30	11	6.5
KH <sub>2</sub> PO <sub>4</sub> , KDP	38	15.1	27	0.27		
KI	14	5.5	11.9	0.30		5
KNbO <sub>3</sub>	144	53	173	0.36		500
KTaO <sub>3</sub>	316	124	230	0.27		
KTiOPO <sub>4</sub> , KTP	137	55	88	0.24		700
LiB <sub>3</sub> O <sub>5</sub> , LBO	104	41	80	0.28		600
LiCaAlF <sub>6</sub> , LiCAF	93	36	71	0.28		
LiF	110	45	65.0	0.22 <sub>5</sub>	27	115
LiIO <sub>3</sub>	55	22.4	33.5	0.23		
LiNbO <sub>3</sub>	170	68	112	0.25		630
LiYF <sub>4</sub> , YLF	85	32	81	0.32	35	300
MgAlO <sub>4</sub>	276	109	198	0.26 <sub>8</sub>	170	1650
MgF <sub>2</sub>	137	54	99.7	0.27	100	500
MgO	310	131	163	0.18	130	675
NaCl	37	14.5	25.3	0.26	9.6	16.5
[NH <sub>4</sub> ] <sub>2</sub> CO, urea	~9	~3	17	0.41		
NH <sub>4</sub> H <sub>2</sub> PO <sub>4</sub> , ADP	29	11	27.9	0.32 <sub>5</sub>		
PbMoO <sub>4</sub>	66	24.6	71	0.34		
PbTe	57.3	22.6	41.9	0.27		
PbTiO <sub>3</sub>	144	56	117	0.20	98	
RbTiOPO <sub>4</sub> , RTP	140	56.8	87.7	0.23		(500)
Si	165	66.4	97.0	0.221	130	1150
SiO <sub>2</sub> , $\alpha$ -quartz	95	44	38	0.08		740
SrF <sub>2</sub>	89.2	34.6	70.7	0.29		150
SrMoO <sub>4</sub>	89	35	71	0.29		
SrTiO <sub>3</sub>	283	115	174	0.23		600
TeO <sub>2</sub>	45	17	46	0.33		
TiO <sub>2</sub>	293	115	215	0.27		880
TlBr	24	8.9	22.4	0.32		12
Tl[Br, I], KRS-5	19.6	7.3	20.4	0.34	26	40
Tl[0.7Cl, 0.3Br], KRS-6	24	9.0	32.2	0.33	21	30
Y <sub>3</sub> Al <sub>5</sub> O <sub>12</sub> , YAG	280	113	180	0.24	150	1350
Y <sub>2</sub> O <sub>3</sub>	173	66.4	149.5	0.31	150	700
YVO <sub>4</sub>	133	50	134	0.33		
ZnGeP <sub>2</sub>	[44]	[16]	86	[0.39]		980
$\beta$ -ZnS	83.5	31.6	77.1	0.32	60	175
$\alpha$ -ZnS	87	33	74	0.30	69	
ZnSe	75.2	28.9	63.1	0.30	55	115
ZnTe	61.1	23.5	51.0	0.30	24	82
ZrO <sub>2</sub> : 12%Y <sub>2</sub> O <sub>3</sub>	23.3	88.6	205	0.31	(200)	1150

**TABLE 18** Mechanical Properties of Optical and Specialty Glasses and Substrate Materials

Selected Glass Code or Designation	Moduli (GPa)			Poisson's Ratio	Flexure Strength (MPa)	Knoop Hardness (kg/mm <sup>2</sup> )
	Elastic	Shear	Bulk			
487704 N-FK5	62	25	39	0.232		520
497816 N-PK52A	71	27	59	0.298		355
508612 N-ZK7	70	29	41	0.214		530
517642 N-BK7	82	34	46	0.206		610
522595 N-K5	71	29	43	0.224		530
523515 N-KF9	66	27	40	0.225		480
548458 LLF1	60	25	34	0.208		450
618634 N-PSK53A	76	30	60	0.288		415
569560 N-BaK4	77	31	49	0.24		550
580537 N-BaLF4	77	31	49	0.245		540
581409 LF5	59	24	36	0.223		450
593355 FF5	[65]	[26]	[41]	[0.238]		500
613443 N-KzFS4	78	31	50	0.241		520
623570 N-SK10	82	32	60	0.273		570
620364 N-F2	82	33	50	0.228		600
658509 N-SSK5	88	34	66	0.278		590
670472 N-BaF10	89	35	65	0.271		620
704394 N-BaSF64	105	42	74	0.264		650
720504 N-LaK10	116	45	90	0.286		780
754523 N-LaF33	111	43	93	0.301		740
743492 NbF1	109	42	95	0.31		790
744447 N-LaF2	94	36	74	0.288		530
805254 N-SF6	93	37	65	0.262		550
883409 N-LaSF31A	126	48	105	0.301		650
Fused silica	72.6	31	36	0.164	110	635
Fused germania	43.1	18	23	0.192		
BS-39B	104	40	83	0.29	90	760
CORTRAN 9754	84.1	33	67	0.290	44	560
IRG 2	95.9	37	73	0.282		481
IRG 9	77.0	30	61	0.288		346
IRG 11	107.5	42	83	0.284		610
IRG 100	21	8	15	0.261		150
HTF-1	64.2	25	49	0.28		320
ZBLAN	60	23	53	0.31		225
Arsenic trisulfide	15.8	6	13	0.295	16.5	180
Arsenic triselenide	18.3	7	14	0.288	16.2	120
AMTIR-1/TI-20	21.9	9	16	0.266	18.6	170
AMTIR-3/TI-1173	21.7	9	15	0.265	17.2	150
Pyrex	62.8	26	35	0.200		
Zerodur	91	37	58	0.24		630
ULE	67.3	29	34	0.17	50	460

**TABLE 19** Thermal Properties of Crystals

Material	CC*	Temperature (K)		Heat Capacity (J/g · K)	Thermal Expansion (10 <sup>-6</sup> /K)	Thermal conductivity (W/m · K)		
		Debye	Melt†			@ 250 K	@ 300 K	@ 500 K
Ag <sub>3</sub> AsS <sub>3</sub>	H		769 m		16    a 12    c		0.092    a 0.110    c	
AgBr	C	145	705 m	0.279	33.8	1.11	0.93	0.57
AgCl	C	162	728 m	0.3544	32.4	1.25	1.19	
AgGaS <sub>2</sub>	T	193	1269 m	0.404	12.7    a -13.2    c		1.5    a 1.4    c	
AgGaSe <sub>2</sub>	T	156	1269 m	0.297	19.8    a -8.1    c 4.15    c		1.1    a 1.0    c	
Al <sub>2</sub> O <sub>3</sub>	H	1030	2319	0.777	6.65    a 7.15    c	58	46	24.2
ALON	C		2323 m	0.830	5.66		12.6	7.0
Ba <sub>3</sub> B <sub>6</sub> O <sub>12</sub> , BBO	H	112	900 p 1368 m	0.490	4.0    a 36.0    c		1.2    a 1.6    c	
BaF <sub>2</sub>	C	283	1553 m	0.4474	18.4	11	7.5	
BaTiO <sub>3</sub>	T	345	267 p 406 p 1898 m	0.439	16.8    a -9.07    c	—	1.3	—
BeO	H	1280	2373 p 2725 m	1.028	5.64    a 7.47    c	420	350	200
Bi <sub>12</sub> GeO <sub>20</sub> (BGO)	C	580	1203	0.242	16.8			
Bi <sub>12</sub> SiO <sub>20</sub> (BSO)	C	350	1274	0.180	15.0			
BiB <sub>3</sub> O <sub>6</sub> , BIBO	M		999 m	0.500	-25.6    a 50.4    b 7.7    c			
C, diamond	C	2240	1770 p	0.5169	1.25	2800	2200	1300
CaCO <sub>3</sub> , calcite	H		323 p 3825 m	0.8820	-3.7    a 25.1    c	5.1    a 6.2    c	4.5    a 5.4    c	(3.4)    a (4.2)    c
CaF <sub>2</sub>	C	510	1424 p	0.9113	18.9	13	9.7	5.5
CaMoO <sub>4</sub>	T	300	1730 m	0.573	7.6    a 11.8    c		4.0    a 3.8    c	

CaWO <sub>4</sub>	T	245	1855 m	0.396	6.35  a 12.38  c		16	9.5
CdGeAs <sub>2</sub>	T	253	900 p 943 m		8.4  a 0.25  c			
CdS	H	215	1560 m	0.3814	4.6  a 2.5  c		14  a 16  c	
CdSe	H	181	1580 m	0.258	4.40  a 2.45  c		6.2  a 6.9  c	
CdTe	C	160	1320 m	0.210	5.0	8.2	6.3	
CsLiB <sub>6</sub> O <sub>10</sub> , CLBO	T		1118 m	0.93	21  a -17  c		2.0  a 2.2  c	
CsI	C	124	898 m	0.2032	48.6		1.05	
CuGaS <sub>2</sub>	T	356	1553 m	0.452	11.2  a 6.9  c		17.9	
GaAs	C	344	1511 m	0.318	5.8	(65)	54	27
GaN	H	365	1160 d		3.17  a 5.59  c		130  c	
GaP	C	460	1740 m	0.435	5.3	120	100	(45)
Ge	C	380	1211 m	0.3230	5.7	74.9	59.9	33.8
KBr	C	174	1007 m	0.4400	38.5	5.5	4.8	2.4
KH <sub>2</sub> PO <sub>4</sub> , KDP	T		123 p 450 p 526 m	0.879	26.8  a 42.4  c		1.3  a 1.2  c	1.7  a 1.3  c
KI	C	132	954 m	0.3192	40.3		2.1	
KNbO <sub>3</sub>	O	—	223 p 476 p 1333 m	0.767	(37)		~4	
KTaO <sub>3</sub>	C	311		0.366	5.3	0.2	0.17	
KTiOPO <sub>4</sub> , KTP	O	365	1148 m 1423 d	0.727	11  a 9  b 0.  c		2.0  a 3.0  b 3.3  c	
LiB <sub>3</sub> O <sub>5</sub> , LBO	O	1115 (@300K)	1107 p	1.020	107.1  a -95.4  b 33.7  c		2.7  a 3.1  b 4.5  c	
LiCaAlF <sub>6</sub> , LiCAF	H		1083 m	0.935	22  a 3.6  c		4.58  a 5.14  c	

(Continued)



**TABLE 19** Thermal Properties of Crystals (*Continued*)

Material	CC*	Temperature (K)		Heat Capacity (J/g · K)	Thermal Expansion (10 <sup>-6</sup> /K)	Thermal conductivity (W/m · K)		
		Debye	Melt <sup>†</sup>			@ 250 K	@ 300 K	@ 500 K
LiNbO <sub>3</sub>	H	560	1470 c 1530 m	0.648	15.4  a 5.3  c		5.4  a 5.3  c	
LiYF <sub>4</sub> , YLF	T	460	1092 m	0.79	14.3  a 10.1  c	6.3  a 8.8  c	5.3  a 7.2  c	
MgAlO <sub>4</sub>	C	850	2408 m	0.8191	6.97	30	25	
MgF <sub>2</sub>	T	535	1536 m	1.0236	9.4  a 13.6  c		30  a 21  c	
MgO	C	950	3073 m	0.9235	10.6	73	59	32
NaCl	C	321	1074 m	0.8699	41.1	8	6.5	4
[NH <sub>4</sub> ] <sub>2</sub> CO, urea	T	135	408 m	1.553	52.7  a 11.4  c			
NH <sub>4</sub> H <sub>2</sub> PO <sub>4</sub> , ADP	T		148 p 463 m	1.236	32  a 4.2  c		1.26  a 0.71  c	
PbMoO <sub>4</sub>	T	190	1338 m	0.326	8.7  a 20.3  c			
PbTe	C	175	1190 m	0.151	19.8	2.5	2.3	1.8
PbTiO <sub>3</sub>	T	337	763 p 1563 m	0.462			4	2.8
RbTiOPO <sub>4</sub> , RTP	O		1213 m 1374 d		10.1  a 13.7  b -4.2  c			
Si	C	645	1680 m	0.7139	2.62	191	140	73.6
SiO <sub>2</sub> , α-quartz	H	271	845 p	0.7400	12.38  a 6.88  c	7.5  a 12.7  c	6.2  a 10.4  c	3.9  a 6.0  c
SrF <sub>2</sub>	C	378	1710 m	0.6200	18.1	11	8.3	
SrMoO <sub>4</sub>	T	260	1763 m	0.619	9.6  a 21.7  c		4.0  a 4.2  c	
SrTiO <sub>3</sub>	C	—	110 p 2358 m	0.536	8.3	12.5	11.2	
TeO <sub>2</sub>	T	~100	1006 m	[0.41]	15.0  a 4.9  c	3.2  a 1.9  c	2.6  a 1.7  c	

TiO <sub>2</sub>	T	760	2128 m	0.6910	6.86  a 8.97  c	8.3  a 11.8  c	7.4  a 10.4  c	(5.5)  a (8.0)  c
TlBr	C	116	740 m	0.1778	51		0.53	
Tl[Br, I] KRS-5	C	(110)	687 m	(0.16)	58		0.32	
Tl[Cl, Br], KRS-6	C	(120)	697 m	0.201	51		0.50	
Y <sub>3</sub> Al <sub>5</sub> O <sub>12</sub> , YAG	C	754	2193 p	0.625	7.7		13.4	
Y <sub>2</sub> O <sub>3</sub>	C	465	2640 p	0.4567	6.56		13.5	
YVO <sub>4</sub>	T	443	2083	0.56	2.2  a 8.4  c		8.9  a 12.1  c	
ZnGeP <sub>2</sub>	T	428	1225 p 1300 m		7.8  a 5.0  c	60	35  a 36  c	16
$\beta$ -ZnS	C	340	1293 p	0.4732	6.8		16.7	10
$\alpha$ -ZnS	H	351	2100 m	0.4723	6.54  a 4.59  c			
ZnSe	C	270	1790 m	0.339	7.1		13	8
ZnTe	C	225	1510 m	0.218	8.4		10	
ZrO <sub>2</sub> :12%Y <sub>2</sub> O <sub>3</sub>	C	563	3110 m	0.46	8.6		1.8	1.9

\*CC = crystal class; C = cubic; H = hexagonal; M = monoclinic; O = orthorhombic; T = tetragonal.

†Temperature codes: m = melt temperature; c = Curie temperature; d = decomposition temperature; p = phase change (to different structure) temperature; v = vaporization (sublimation) temperature.

**TABLE 20** Thermal Properties of Optical and Specialty Glasses and Substrate Materials

Selected Glass Code	Temperature (K)			Heat Capacity (J/g · K)	Thermal Expansion (10 <sup>-6</sup> /K)	Thermal Conductivity (W/m · K)
	Glass	Soften	Melt*			
487704 N-FK5	739	945		0.808	9.2	0.925
497816 N-PK52A	740	811		0.67	13.01	0.73
508612 N-ZK7	812	994		0.77	4.5	1.042
517642 N-BK7	830	992		0.858	7.1	1.114
522595 N-K5	819	993		0.783	8.2	0.95
523515 N-KF9	749	913		[0.75]	9.61	1.04
548458 LLF1	704	901		0.65	8.1	[0.960]
618634 N-PSK53A	879	972		0.590	9.56	0.64
569560 N-BaK4	854	998		0.680	6.99	0.88
580537 N-BaLF4	851	934		0.69	6.52	0.827
581409 LF5	692	858		0.657	9.1	0.866
593355 FF5	788	843		[0.80]	8.6	[0.937]
613445 N-KzFS4	820	948		0.76	7.3	0.84
623570 N-SK10	905	1017		0.55	7.0	0.88
620364 N-F2	842	959		0.81	7.84	1.05
658509 N-SSK5	918	1024		0.574	6.8	[0.806]
670472 N-BaF10	933	1063		0.56	6.18	0.78
704394 N-BaSF64	855	985		[0.70]	7.3	[0.90]
720504 N-LaK10	909	987		0.64	5.68	0.86
754523 LaF33	873	946		0.57	5.6	0.8
743492 NbF1	863	898		[0.48]	5.3	[0.845]
744447 N-LaF2	926	1015		0.51	8.06	0.67
805254 N-SF6	862	956		0.69	9.03	0.96
883409 N-LaSF31A	992	1103		0.44	6.74	0.79
Fused silica	1273		1983	0.746	0.51	1.38
Fused germania	800		1388		6.3	
BS-39B		[970]		0.865	8.0	1.23
CORTRAN 9754	1008	1147		0.54	6.2	0.81
IRG 2	975			0.495	8.8	0.91
IRG 9	696			0.695	16.1	0.88
IRG 11	1075			0.749	8.2	1.13
IRG 100	550	624			15.0	0.3
HTF-1	658				16.1	
ZBLAN	543		745	0.520	17.5	0.4
Arsenic trisulfide	460	573		0.473	26.1	0.17
Arsenic triselenide	375	345		0.349	24.6	0.205
AMTIR-1/TI-20	635	678		0.293	12.0	0.25
AMTIR-3/TI-1173	550	570		0.276	14.0	0.22
Zerodur				0.821	0.5	1.46
					(20–300°C)	
Pyrex	560	821		1.05	3.25	1.13
ULE	1000	1490		0.776	±0.03	1.31
					(5–35°C)	

\*Or liquidus temperature.

**TABLE 21** Summary Optical Properties of Crystals

Material	Transparency ( $\mu\text{m}$ )		Refractive Index ( $n_{\omega}$ )	Thermo-optic coefficient ( $10^{-6}/\text{K}$ )						Ref.
	UV	IR		$\lambda(\mu\text{m})$	$dn/dT$	$\lambda(\mu\text{m})$	$dn/dT$	$\lambda(\mu\text{m})$	$dn/dT$	
Ag <sub>3</sub> AsS <sub>3</sub>	0.63(o) 0.61(e)	12.5(o) 13.3(e)	2.736(o) 2.519(e)	0.65	150					130
AgBr	0.49	35	2.116			3.39	-61	10.6	-50	139
AgCl	0.42	23	2.002	0.633	-61	3.39	-58	10.6	-35	139, 140
AgGaS <sub>2</sub>	0.50(o) 0.52(e)	11.4(o) 12.0(e)	2.408(o) 2.354 (e)	0.6	258(o) 255(e)	1.0	176(o) 179(e)	10.0	153(o) 155(e)	141 142
AgGaSe <sub>2</sub>	0.75	17.0	2.617(o) 2.584(e)			1.0	75.6(o) 80.5(o)	10.0	79.7(o) 85.9(e)	143
Al <sub>2</sub> O <sub>3</sub>	0.19(o)	5.0(o) 5.2(e)	1.7555(o) 1.7478(e)	0.458	11.7(o) 12.8(e)	3.39	11.3(o) 12.4(e)	5.0	14.1(o) 15.6(e)	144, 145, 146, 147
ALON	0.23	4.8	1.771	0.633	11.7					148
BBO	0.19	2.6	1.656 (o) 1.501(e)	0.4047	-16.6(o) -9.8(e)	0.5790	-16.4(o) -9.4(e)	1.014	-16.8(o) -8.8(e)	131
BaF <sub>2</sub>	0.14	12.2	1.4663	0.633 0.365	-16.0 -15.2	3.39 3.30	-15.9 -15.6	10.6	-14.5	145 149
BaTiO <sub>3</sub>			2.277(o) 2.250(e)							
BeO	0.21	3.5	1.710(o) 1.723(e)	0.458	8.2(o) 13.4(e)	0.633	8.2(o) 13.4(e)			150
BGO	0.50	3.1	2.367	0.51	-34.5	0.65	-34.9			151
BSO	0.52		2.397							
BiB <sub>3</sub> O <sub>6</sub> , BIBO	0.27	2.7	1.433(x) 1.450(y) 1.509(z)	0.5	69.6(x) 63.9(y) 85.6(z)	1.0	53.8(x) 48.1(y) 74.0(z)	3.0	45.5(x) 43.0(y) 61.1(z)	152
Diamond	0.24	2.7	2.380	0.546	10.1			30	9.6	153, 154
CaCO <sub>3</sub>	0.24(o) 0.21(e)	2.2(o) 3.3(e)	1.642(o) 1.478(e)	0.365	3.6(o) 14.4(e)	0.458	3.2(o) 13.1(e)	0.633	2.1(o) 11.9(e)	2
CaF <sub>2</sub>	0.135	9.4	1.4278	0.254 0.365	-7.5 -10.6	0.663	-10.4	3.39 3.30	-8.1 -10.8	149 155
CaMoO <sub>4</sub>			1.945(o) 1.951(e)	0.588	-9.6(o) -10.0(e)					156

(Continued)

**TABLE 21** Summary Optical Properties of Crystals (*Continued*)

Material	Transparency ( $\mu\text{m}$ )		Refractive Index ( $n_{\infty}$ )	Thermo-optic coefficient ( $10^{-6}/\text{K}$ )						Ref.
	UV	IR		$\lambda(\mu\text{m})$	$dn/dT$	$\lambda(\mu\text{m})$	$dn/dT$	$\lambda(\mu\text{m})$	$dn/dT$	
CaWO <sub>4</sub>	(0.2)	5.3	1.884(o) 1.898(e)	0.546	-7.1(o) -10.2(e)					157
CdGeAs <sub>2</sub>	2.5	15	3.522(o) 3.608(e)							
CdS	0.52(o) 0.51(e)	14.8(o) 14.8(e)	2.276(o) 2.293(e)	10.6	58.6(o) 62.4(e)					158
CdSe	0.75	20	2.448(o) 2.467(e)							
CdTe	0.85	29.9	2.6829	1.15	147	3.39	98.2	10.6	98.0	159
CsI	0.245	62	1.743	0.365	-87.5	0.633	-99.3	30.0	-88.0	160
CsLiB <sub>6</sub> O <sub>10</sub> , CLBO	0.18	2.75	1.487(o) 1.435(e)	0.532	-1.9(o) -0.5(e)					161, 162
CuGaS <sub>2</sub>			2.493(o) 2.487(e)	0.55	130(o) 173(e)	1.0	59(o) 60(e)	10.0	56(o) 57(e)	163 164
GaAs	0.90	17.3	3.32	1.15	250	3.39	200	10.6	200	165
GaN			2.31(o) 2.31(e)	1.15	61					
GaP	0.54	10.5	3.014	0.546	200	0.633	160			166
Ge	1.8	15	4.0017	2.5	462	5.0	416	20.0	401	167
HfO <sub>2</sub> :Y <sub>2</sub> O <sub>3</sub>	0.35	6.5	2.074	0.365	14.1	0.436	11.0	1.01	5.8	168
KBr	0.200	30.2	1.537	0.458	-39.3	1.15	-41.9	10.6	-41.1	145
KH <sub>2</sub> PO <sub>4</sub>	0.176	1.42	1.503(o) 1.460(e)	0.624	-39.6(o) -38.2(e)					169
KI	0.250	38.5	1.629	0.458	-41.5	1.15	-44.7	30	-30.8	145
KNbO <sub>3</sub>	0.4	5.0	2.103(x) 2.199(y) 2.233(z)	0.436	67(x) -26(y) 125(z)	1.064	23(x) -34(y) 63(z)	3.00	21(x) -23(y) 55(z)	170
KTaO <sub>3</sub>			2.14							
KTiOPO <sub>4</sub>	0.35	4.5	1.814(x) 1.857(y) 2.143(z)	0.5	10.8(x) 15.5(y) 28.3(z)	1.5	5.3(x) 7.6(y) 12.3(z)			171, 172
LiB <sub>3</sub> O <sub>5</sub>	0.16	3.6	1.568(x) 1.589(y) 1.608(z)	0.532	-0.9 -13.5 -7.4	1.064	-1.9 -13.0 -8.3			173

LiCaAlF <sub>6</sub> , LiCAF	0.11		1.388(o) 1.386(e)	0.546	-4.2(o) -4.6(e)					174
LiF	0.120	6.60	1.388	0.458 0.365	-16.0 -15.0	1.15 1.53	-16.9 -15.6	3.39	-14.5	145 149
LiIO <sub>3</sub>	0.38	5.5	1.846(o) 1.708(e)	0.4	-74.5(o) -63.5(e)	1.0	-84.9(o) -69.2(e)			80
LiNbO <sub>3</sub>	0.35	5.0	2.282(o) 2.006(e)	0.66	4.4(o) 37.9(e)	3.39	0.3(o) 28.9(e)			175
LiYF <sub>4</sub>	0.18	6.7	1.447(o) 1.469(e)	0.436	-0.54(o) -2.44(e)	0.546	-0.67(o) -2.30(e)	0.578	-0.91(o) -2.86(e)	176
MgAl <sub>2</sub> O <sub>4</sub>	0.2	5.3	1.701	0.589	9.0					144
MgF <sub>2</sub>	0.13(o) 0.13(e)	7.7(o) 7.7(e)	1.3734(o) 1.3851(e)	0.633	1.12(o) 0.58(e)	1.15	0.88(o) 0.32(e)	3.39	1.19(o) 0.6(e)	145
MgO	0.35	6.8	1.720	0.365	19.5	0.546	16.5	0.768	13.6	177, 178
NaCl	0.174	18.2	1.526	0.458	-34.2	0.633	-35.4	3.39	-36.3	145
[NH <sub>4</sub> ] <sub>2</sub> CO	0.21	1.4	1.477(o) 1.586(e)							
NH <sub>4</sub> H <sub>2</sub> PO <sub>4</sub>	0.185	1.45	1.518(o) 1.471(e)	0.624	-47.1(o) -4.3(e)					169
PbMoO <sub>4</sub>	0.5	5.4	2.265(o) 2.175(e)	0.588	-75(o) -41(e)					156
PbTe	4.0	20	5.57	3.39	-2100	5.0	-1500	10.6	-1200	179
PbTiO <sub>3</sub>			2.52(o) 2.52(e)							
RbTiOPO <sub>4</sub> , RTP	0.34	4.5	1.763(x) 1.768(y) 1.8478(z)	0.633	56(x) 91(y) 66(z)					180
Si	1.1	6.5	3.4159	2.5	166	5.0	159	10.6	157	167
α-SiO <sub>2</sub>	0.155	4.0	1.5352(o) 1.5440(e)	0.254	-2.9(o) -4.0(e)	0.365	-5.4(o) -6.2(e)	0.546	-6.2(o) -7.0(e)	178
SrF <sub>2</sub>	0.13	11.0	1.4316	0.633	-16.0	1.15	-16.2	10.6	-14.5	145
SrMoO <sub>4</sub>			1.867(o) 1.869(e)							
SrTiO <sub>3</sub>	0.5	5.1	2.283							

(Continued)

**TABLE 21** Summary Optical Properties of Crystals (*Continued*)

Material	Transparency ( $\mu\text{m}$ )		Refractive Index ( $n_\infty$ )	Thermo-optic coefficient ( $10^{-6}/\text{K}$ )						Ref.
	UV	IR		$\lambda(\mu\text{m})$	$dn/dT$	$\lambda(\mu\text{m})$	$dn/dT$	$\lambda(\mu\text{m})$	$dn/dT$	
TeO <sub>2</sub>	0.34	4.5	2.177(o) 2.316(e)	0.436	30(o) 25(e)	0.644	9(o) 8(e)			181
TiO <sub>2</sub>	0.42	4.0	2.432(o) 2.683(e)	0.405	4(o) -9(e)					182
TlBr	0.44	38	2.271							
KRS-5	0.58	42	2.380	0.633 1.014	-250 -237	10.6	-233	30	-195	183 149
KRS-6	0.42	27	2.196							
Y <sub>3</sub> Al <sub>5</sub> O <sub>12</sub>	0.21	5.2	1.812	0.458	11.9	0.633	9.4	1.06	9.1	184
Y <sub>2</sub> O <sub>3</sub>	0.29	7.1	1.892	0.663	8.3					148
YVO <sub>4</sub>	0.4	5.0	1.944(o) 2.146(5)	0.488	27.7(o) 22.9(e)	0.633	19.7(o) 12.7(e)	1.34	16.6(o) 10.3(e)	185
ZnGeP <sub>2</sub>	0.8	12.5	3.119(o) 3.156(e)	0.64	359(o) 376(e)	1.0	212(o) 230(e)	10	165(o) 170(e)	164, 186
$\beta$ -ZnS	0.4	12.5	2.258	0.633	63.5	1.15	49.8	10.6	46.3	159
$\alpha$ -ZnS			2.271(o) 2.275(e)							
ZnSe	0.51	19.0	2.435	0.633	91.1	1.15	59.7	10.6	52.0	159
ZnTe	0.6	25	3.15							
ZrO <sub>2</sub> :Y <sub>2</sub> O <sub>3</sub>	0.38	6.0	2.113	0.365	16.0	0.458	10.0	0.633	7.9	187

**TABLE 22** Summary Optical Properties of Optical and Specialty Glasses

Material	Transparency ( $\mu\text{m}$ )		Refractive Index ( $n_d$ )	Abbe Number ( $v_d$ )	Thermo-optic coeff. ( $10^{-6}/\text{K}$ )*				Ref.
	UV	IR			$\lambda(\mu\text{m})$	$dn/dT$	$\lambda(\mu\text{m})$	$dn/dT$	
N-FK5	0.279	2.78	1.48749	70.41	0.4358	-0.6	1.060	-1.4	188
N-PK52A	0.306		1.49700	81.61	0.4358	-6.0	1.060	-5.7	188
N-ZK7	0.306	2.77	1.50847	61.19	0.4358	7.6	1.060	6.7	188
N-BK7	0.303	2.91	1.51680	64.17	0.4358	3.5	1.060	2.4	188
N-K5	0.313	3.30	1.52249	59.48	0.4358	2.7	1.060	1.4	188
N-KF9	0.346	2.90	1.52346	51.54	0.4358	2.6	1.060	0.9	188
LLF1	0.310	3.30	1.54814	45.75	0.4358	3.9	1.060	2.1	188
N-PSK53A	0.326	2.84	1.61800	63.39	0.4358	-1.8	1.060	-2.9	188
N-BaK4	0.335	3.21	1.56883	55.98	0.4358	4.7	1.060	3.1	188
N-BaLF4	0.340	3.22	1.57956	53.87	0.4358	6.0	1.060	4.2	188
LF5	0.321	3.30	1.58144	40.85	0.4358	3.4	1.060	0.8	188
FF5	0.346		1.59270	35.45	0.6328	0.8			189
N-KzFSN4	0.332	2.65	1.61336	44.49	0.4358	4.7	1.060	2.5	188
N-SK10	0.333	2.74	1.62280	56.90	0.4358	3.5	1.060	2.1	188
N-F2	0.364	3.08	1.62004	36.37	0.4358	5.1	1.060	2.7	188
N-SSK5	0.351	2.93	1.65844	50.88	0.4358	4.2	1.060	2.2	188
N-BaF10	0.356	2.92	1.67003	47.20	0.4358	6.0	1.060	3.8	188
N-BaSF64	0.359	2.98	1.70400	39.38	0.4358	5.9	1.060	2.8	188
N-LaK10	0.346	2.56	1.72000	50.41	0.4358	6.1	1.060	4.2	188
N-LaF33	0.337	2.61	1.78582	44.05	0.4358	10.0	1.060	7.0	188
NbF1	0.313		1.74330	49.22	0.6328	7.9			189
N-LaF2	0.354	2.83	1.74397	44.85	0.4358	2.3	1.060	-0.1	188
N-SF6	0.378	3.21	1.80518	25.43	0.4358	4.8	1.060	-0.8	188
N-LaSF31A	0.344	2.78	1.88300	40.76	0.4358	6.6	1.060	3.3	188
SiO <sub>2</sub>	0.16	3.8	1.45857	67.7	0.5893	10			190
					0.3650	9.3	1.53	8.0	149
GeO <sub>2</sub>	0.30	4.9	$n_D = 1.60832$	41.2					191
BS-39B	0.38	4.9	$n_D = 1.6764$	44.5	0.5893	7.4			192
Corning 9754	0.36	4.8	$n_D = 1.6601$	46.5					193
Schott IRG 2	0.44	5.1	1.8918	30.03	0.436	10.4	3.30	4.4	149, 188
Schott IRG9	0.38	4.1	1.4861	81.02					188
Schott IRG 11	0.44	4.75	1.6809	44.21					188
Schott IRG 100	0.93	13	$n_1 = 2.7235$	—	2,5	103	10.6	56	188
Ohara HTF-1	0.21	6.9	1.44296	92.46					194
ZBLAN	0.25	6.9	$n_D = 1.480$	64	0.6328	-14.5			195, 196
As <sub>2</sub> S <sub>3</sub>	0.62	11.0	$n_1 = 2.4777$	—	0.6	85	1.0	17	197, 198
As <sub>2</sub> Se <sub>3</sub>	0.87	17.2	$n_{12} = 2.7728$	—	0.83	55	1.15	33	199, 200
AMTIR-1/TI-20	0.75	(14.5)	$n_1 = 2.6055$	—	1.0	101	10.0	72	200, 201
AMTIR-3/ TI-1173	0.93	16.5	$n_3 = 2.6366$	—	3.0	98	12.0	93	200, 201

\*Thermo-optic coefficient in air:  $(dn/dT)_{rel}$ .



**TABLE 23** Room-Temperature Dispersion Formulas for Crystals

Material	Dispersion Formula (Wavelength, $\lambda$ , in $\mu\text{m}$ )	Range ( $\mu\text{m}$ )	Ref.
$\text{Ag}_3\text{AsS}_3$	$n_o^2 = 7.483 + \frac{0.474}{\lambda^2 - 0.09} - 0.0019\lambda^2$ ; $n_e^2 = 6.346 + \frac{0.342}{\lambda^2 - 0.09} - 0.0011\lambda^2$	0.63–4.6(o) 0.59–4.6(e)	202
AgBr	$\frac{n^2 - 1}{n^2 + 2} = 0.453505 + \frac{0.09929\lambda^2}{\lambda^2 - 0.070537} - 0.00150\lambda^2$	0.49–0.67	203
AgCl	$n^2 - 1 = \frac{2.062508\lambda^2}{\lambda^2 - (0.1039054)^2} + \frac{0.9461465\lambda^2}{\lambda^2 - (0.2438691)^2} + \frac{4.300785\lambda^2}{\lambda^2 - (70.85723)^2}$	0.54–21.0	140
AgGaS <sub>2</sub>	$n_o^2 = 5.7975 + \frac{0.2311}{\lambda^2 - 0.0688} - 0.00257\lambda^2$ $n_e^2 = 5.5436 + \frac{0.2230}{\lambda^2 - 0.0946} - 0.00261\lambda^2$	0.58–10.6	142
AgGaSe <sub>2</sub>	$n_o^2 = 6.8507 + \frac{0.4297}{\lambda^2 - 0.1584} - 0.00125\lambda^2$ $n_e^2 = 6.6792 + \frac{0.4597}{\lambda^2 - 0.2122} - 0.00126\lambda^2$	0.73–13.5	143
$\text{Al}_2\text{O}_3$ , sapphire	$n_o^2 - 1 = \frac{1.4313493\lambda^2}{\lambda^2 - (0.0726631)^2} + \frac{0.65054713\lambda^2}{\lambda^2 - (0.1193242)^2} + \frac{5.3414021\lambda^2}{\lambda^2 - (18.028251)^2}$ $n_e^2 - 1 = \frac{1.5039759\lambda^2}{\lambda^2 - (0.0740288)^2} + \frac{0.55069141\lambda^2}{\lambda^2 - (0.1216529)^2} + \frac{6.5927379\lambda^2}{\lambda^2 - (20.072248)^2}$	0.2–5.5	204
ALON	$n^2 - 1 = \frac{2.1375\lambda^2}{\lambda^2 - 0.10256^2} + \frac{4.582\lambda^2}{\lambda^2 - 18.868^2}$	0.4–2.3	205
BBO	$n_o^2 = 2.7405 + \frac{0.0184}{\lambda^2 - 0.0179} - 0.0155\lambda^2$ $n_e^2 = 2.3730 + \frac{0.0128}{\lambda^2 - 0.0156} - 0.0044\lambda^2$	0.22–1.06	131
$\text{BaF}_2$	$n^2 - 1 = \frac{0.643356\lambda^2}{\lambda^2 - (0.057789)^2} + \frac{0.506762\lambda^2}{\lambda^2 - (0.10968)^2} + \frac{3.8261\lambda^2}{\lambda^2 - (46.3864)^2}$	0.27–10.3	206
$\text{BaTiO}_3$	$n_o^2 - 1 = \frac{4.187\lambda^2}{\lambda^2 - (0.223)^2}$ ; $n_e^2 - 1 = \frac{4.064\lambda^2}{\lambda^2 - (0.211)^2}$	0.4–0.7	207
BeO	$n_o^2 - 1 = \frac{1.92274\lambda^2}{\lambda^2 - (0.07908)^2} + \frac{1.24209\lambda^2}{\lambda^2 - (9.7131)^2}$ $n_e^2 - 1 = \frac{1.96939\lambda^2}{\lambda^2 - (0.08590)^2} + \frac{1.67389\lambda^2}{\lambda^2 - (10.4797)^2}$	0.44–7.0	208
$\text{BiB}_3\text{O}_6$ , BIBO	$n_x^2 = 3.07403 + \frac{0.03231}{\lambda^2 - 0.03163} - 0.013376\lambda^2$ $n_y^2 = 3.16940 + \frac{0.03717}{\lambda^2 - 0.03483} - 0.01827\lambda^2$ $n_z^2 = 3.6545 + \frac{0.05112}{\lambda^2 - 0.03713} - 0.02261\lambda^2$	0.48–3.1	152
$\text{Bi}_{12}\text{GeO}_{20}$ , BGO	$n^2 - 1 = 2.165 + \frac{2.655\lambda^2}{\lambda^2 - 0.07891}$	0.4–0.7	151 209

**TABLE 23** Room-Temperature Dispersion Formulas for Crystals (*Continued*)

Material	Dispersion Formula (Wavelength, $\lambda$ , in $\mu\text{m}$ )	Range ( $\mu\text{m}$ )	Ref.
$\text{Bi}_{12}\text{SiO}_{20}$ , BSO	$n^2 = 2.72777 + \frac{3.01705\lambda^2}{\lambda^2 - (0.2661)^2}$	0.48–0.7	104 210
C, diamond	$n^2 - 1 = \frac{4.3356\lambda^2}{\lambda^2 - (0.1060)^2} + \frac{0.3306\lambda^2}{\lambda^2 - (0.1750)^2}$	0.225– $\infty$	211
$\text{CaCO}_3$ , calcite	$n_o - 1 = \frac{0.8559\lambda^2}{\lambda^2 - (0.0588)^2} + \frac{0.8391\lambda^2}{\lambda^2 - (0.141)^2} + \frac{0.0009\lambda^2}{\lambda^2 - (0.197)^2} + \frac{0.6845\lambda^2}{\lambda^2 - (7.005)^2}$ $n_e - 1 = \frac{1.0856\lambda^2}{\lambda^2 - (0.07897)^2} + \frac{0.0988\lambda^2}{\lambda^2 - (0.142)^2} + \frac{0.317\lambda^2}{\lambda^2 - (11.468)^2}$	0.2–2.2	2
$\text{CaF}_2$	$n^2 - 1 = \frac{0.5675888\lambda^2}{\lambda^2 - (0.050263605)^2} + \frac{0.4710914\lambda^2}{\lambda^2 - (0.1003909)^2} + \frac{3.8484923\lambda^2}{\lambda^2 - (34.649040)^2}$	0.23–9.7	155
	$n^2 - 1 = \frac{0.443749998\lambda^2}{\lambda^2 - (0.00178027854)^2} + \frac{0.444930066\lambda^2}{\lambda^2 - (0.00788536061)^2}$ $+ \frac{0.150133991\lambda^2}{\lambda^2 - (0.0124119491)^2} + \frac{8.85319946\lambda^2}{\lambda^2 - (2752.28175)^2}$	0.14–2.3	212
$\text{CaMoO}_4$	$n_o^2 - 1 = \frac{2.7840\lambda^2}{\lambda^2 - (0.1483)^2} + \frac{1.2425\lambda^2}{\lambda^2 - (11.576)^2}$ $n_e^2 - 1 = \frac{2.8045\lambda^2}{\lambda^2 - (0.1542)^2} + \frac{1.0055\lambda^2}{\lambda^2 - (10.522)^2}$	0.45–3.8	213
$\text{CaWO}_4$	$n_o^2 - 1 = \frac{2.5493\lambda^2}{\lambda^2 - (0.1347)^2} + \frac{0.9200\lambda^2}{\lambda^2 - (10.815)^2}$ $n_e^2 - 1 = \frac{2.6041\lambda^2}{\lambda^2 - (0.1379)^2} + \frac{4.1237\lambda^2}{\lambda^2 - (21.371)^2}$	0.45–4.0	213
$\text{CdGeAs}_2$	$n_o^2 = 10.1064 + \frac{2.2988\lambda^2}{\lambda^2 - 1.0872} + \frac{1.6247\lambda^2}{\lambda^2 - 1370}$ $n_e^2 = 11.8018 + \frac{1.2152\lambda^2}{\lambda^2 - 2.6971} + \frac{1.6922\lambda^2}{\lambda^2 - 1370}$	2.4–11.5	214
CdS	$n_o^2 = 5.1792 + \frac{0.23504}{\lambda^2 - 0.083591} + \frac{0.036927}{\lambda^2 - 0.23504}$ $n_e^2 = 5.2599 + \frac{0.20865}{\lambda^2 - 0.10799} + \frac{0.027527}{\lambda^2 - 0.23305}$	0.51–1.4	215
CdSe	$n_o^2 = 4.2243 + \frac{1.7680\lambda^2}{\lambda^2 - 0.2270} + \frac{3.1200\lambda^2}{\lambda^2 - 3380}$ $n_e^2 = 4.2009 + \frac{1.8875\lambda^2}{\lambda^2 - 0.2171} + \frac{3.6461\lambda^2}{\lambda^2 - 3629}$	1–22	214
CdTe	$n^2 - 1 = \frac{6.1977889\lambda^2}{\lambda^2 - (0.317069)^2} + \frac{3.2243821\lambda^2}{\lambda^2 - (72.0663)^2}$	6–22	216

(Continued)

**TABLE 23** Room-Temperature Dispersion Formulas for Crystals (*Continued*)

Material	Dispersion Formula (Wavelength, $\lambda$ , in $\mu\text{m}$ )	Range ( $\mu\text{m}$ )	Ref.
CsLiB <sub>6</sub> O <sub>10</sub> , CLBO	$n_o^2 = 2.2104 + \frac{0.01018}{\lambda^2 - 0.01424} - 0.01258\lambda^2$ $n_e^2 = 2.0588 + \frac{0.00838}{\lambda^2 - 0.01363} - 0.00607\lambda^2$	0.19–2.75	161
CsI	$n^2 - 1 = \frac{0.34617251\lambda^2}{\lambda^2 - (0.229567)^2} + \frac{1.0080886\lambda^2}{\lambda^2 - (0.1466)^2} + \frac{0.28551800\lambda^2}{\lambda^2 - (0.1810)^2}$ $+ \frac{0.39743178\lambda^2}{\lambda^2 - (0.2120)^2} + \frac{3.3605359\lambda^2}{\lambda^2 - (161.0)^2}$	0.29–50	160
CuGaS <sub>2</sub>	$n_o^2 = 3.9064 + \frac{2.3065\lambda^2}{\lambda^2 - 0.1149} + \frac{1.5479\lambda^2}{\lambda^2 - 738.43}$ $n_e^2 = 4.3165 + \frac{1.8692\lambda^2}{\lambda^2 - 0.1364} + \frac{1.7575\lambda^2}{\lambda^2 - 738.43}$	0.55–11.5	163 164
GaAs	$n^2 = 3.5 + \frac{7.4969\lambda^2}{\lambda^2 - (0.4082)^2} + \frac{1.9347\lambda^2}{\lambda^2 - (37.17)^2}$	1.4–11	217
GaN	$n_o^2 = 3.60 + \frac{1.75\lambda^2}{\lambda^2 - (0.256)^2} + \frac{4.1\lambda^2}{\lambda^2 - (17.86)^2}$ $n_e^2 = 5.35 + \frac{5.08\lambda^2}{\lambda^2 - (18.76)^2}$	<10	218
GaP	$n^2 = 4.1705 + \frac{4.9113\lambda^2}{\lambda^2 - 0.1174} + \frac{1.9928\lambda^2}{\lambda^2 - 756.46}$	0.2–22	219
Ge	$n^2 = 9.28156 + \frac{6.72880\lambda^2}{\lambda^2 - 0.44105} + \frac{0.21307\lambda^2}{\lambda^2 - 3870.1}$	2–12	220
HfO <sub>2</sub> : 9.8%Y <sub>2</sub> O <sub>3</sub>	$n^2 - 1 = \frac{1.9558\lambda^2}{\lambda^2 - (0.15494)^2} + \frac{1.345\lambda^2}{\lambda^2 - (0.0634)^2} + \frac{10.41\lambda^2}{\lambda^2 - (27.12)^2}$	0.365–5	168
KBr	$n^2 = 1.39408 + \frac{0.79221\lambda^2}{\lambda^2 - (0.146)^2} + \frac{0.01981\lambda^2}{\lambda^2 - (0.173)^2}$ $+ \frac{0.15587\lambda^2}{\lambda^2 - (0.187)^2} + \frac{0.17673\lambda^2}{\lambda^2 - (60.61)^2} + \frac{2.06217\lambda^2}{\lambda^2 - (87.72)^2}$	0.2–40	221
KH <sub>2</sub> PO <sub>4</sub> , KDP	$n_o^2 = 2.259276 + \frac{0.01008956}{\lambda^2 - 0.0129426} + \frac{13.00522\lambda^2}{\lambda^2 - 400}$ $n_e^2 = 2.132668 + \frac{0.008637494}{\lambda^2 - 0.0122810} + \frac{3.2279924\lambda^2}{\lambda^2 - 400}$	0.2–15	70
KI	$n^2 = 1.47285 + \frac{0.16512\lambda^2}{\lambda^2 - (0.129)^2} + \frac{0.41222\lambda^2}{\lambda^2 - (0.175)^2} + \frac{0.44163\lambda^2}{\lambda^2 - (0.187)^2}$ $+ \frac{0.16076\lambda^2}{\lambda^2 - (0.219)^2} + \frac{0.33571\lambda^2}{\lambda^2 - (69.44)^2} + \frac{1.92474\lambda^2}{\lambda^2 - (98.04)^2}$	0.25–50	221
KNbO <sub>3</sub>	$n_x^2 = 4.4222 + \frac{0.09972}{\lambda^2 - 0.05496} - 0.01976\lambda^2$ $n_y^2 = 4.8353 + \frac{0.12808}{\lambda^2 - 0.05674} - 0.02528\lambda^2 + 1.8590 \cdot 10^{-6} \lambda^4 - 1.0689 \cdot 10^{-6} \lambda^6$ $n_z^2 = 4.9856 + \frac{0.15266}{\lambda^2 - 0.06331} - 0.02831\lambda^2 + 2.0754 \cdot 10^{-6} \lambda^4 - 1.2131 \cdot 10^{-6} \lambda^6$	0.40–5.3	222

**TABLE 23** Room-Temperature Dispersion Formulas for Crystals (*Continued*)

Material	Dispersion Formula (Wavelength, $\lambda$ , in $\mu\text{m}$ )	Range ( $\mu\text{m}$ )	Ref.
KTaO <sub>3</sub>	$n^2 - 1 = \frac{3.591\lambda^2}{\lambda^2 - (0.193)^2}$	0.4–1.06	223
KTiOPO <sub>4</sub> KTP	$n_x^2 = 3.29100 + \frac{0.04140}{\lambda^2 - 0.03978} + \frac{9.35522}{\lambda^2 - 31.45571}$ $n_y^2 = 3.45018 + \frac{0.04341}{\lambda^2 - 0.04597} + \frac{16.98825}{\lambda^2 - 39.43799}$ $n_z^2 = 4.59423 + \frac{0.06206}{\lambda^2 - 0.04763} + \frac{110.80672}{\lambda^2 - 86.12171}$	0.43–3.54	172
LiB <sub>3</sub> O <sub>5</sub> , LBO	$n_x^2 = 2.45768 + \frac{0.0098877}{\lambda^2 - 0.026095} - 0.013847\lambda^2$ $n_y^2 = 2.52500 + \frac{0.017123}{\lambda^2 - 0.0060517} - 0.0087838\lambda^2$ $n_z^2 = 2.58488 + \frac{0.012737}{\lambda^2 - 0.016293} - 0.016293\lambda^2$	0.29–1.06	224
LiCaAlF <sub>6</sub> , LiCAF	$n_o^2 = 1.92552 + \frac{0.00492}{\lambda^2 - 0.00569} - 0.00421 \cdot \lambda^2$ $n_e^2 = 1.92155 + \frac{0.00494}{\lambda^2 - 0.00617} - 0.00373 \cdot \lambda^2$	0.4–1.0	174
LiF	$n^2 - 1 = \frac{0.92549\lambda^2}{\lambda^2 - (0.07376)^2} + \frac{6.96747\lambda^2}{\lambda^2 - (32.79)^2}$	0.1–10	221
LiIO <sub>3</sub>	$n_o^2 = 2.03132 + \frac{1.37623\lambda^2}{\lambda^2 - 0.0350823} + \frac{1.06745\lambda^2}{\lambda^2 - 169.0}$ $n_e^2 = 1.83086 + \frac{1.08807\lambda^2}{\lambda^2 - 0.0313810} + \frac{0.554582\lambda^2}{\lambda^2 - 158.76}$	0.5–5	82
LiNbO <sub>3</sub>	$n_o^2 - 1 = \frac{2.9804\lambda^2}{\lambda^2 - 0.01764} + \frac{1.2290\lambda^2}{\lambda^2 - 0.05914} + \frac{12.614\lambda^2}{\lambda^2 - 474.60}$ $n_e^2 - 1 = \frac{2.4272\lambda^2}{\lambda^2 - 0.02047} + \frac{0.5981\lambda^2}{\lambda^2 - 0.06660} + \frac{8.9543\lambda^2}{\lambda^2 - 416.08}$	0.4–5.0	225
LiYF <sub>4</sub>	$n_o^2 = 1.38757 + \frac{0.70757\lambda^2}{\lambda^2 - 0.00931} + \frac{0.18849\lambda^2}{\lambda^2 - 50.99741}$ $n_e^2 = 1.31021 + \frac{0.84903\lambda^2}{\lambda^2 - 0.00876} + \frac{0.53607\lambda^2}{\lambda^2 - 134.9566}$	0.23–2.6	176
MgAl <sub>2</sub> O <sub>4</sub>	$n^2 - 1 = \frac{1.8938\lambda^2}{\lambda^2 - (0.09942)^2} + \frac{3.0755\lambda^2}{\lambda^2 - (15.826)^2}$	0.35–5.5	226
MgF <sub>2</sub>	$n_o^2 - 1 = \frac{0.48755708\lambda^2}{\lambda^2 - (0.04338408)^2} + \frac{0.39875031\lambda^2}{\lambda^2 - (0.09461442)^2} + \frac{2.3120353\lambda^2}{\lambda^2 - (23.793604)^2}$ $n_e^2 - 1 = \frac{0.41344023\lambda^2}{\lambda^2 - (0.03684262)^2} + \frac{0.50497499\lambda^2}{\lambda^2 - (0.09076162)^2} + \frac{2.4904862\lambda^2}{\lambda^2 - (23.771995)^2}$	0.20–7.04	227
MgO	$n^2 - 1 = \frac{1.111033\lambda^2}{\lambda^2 - (0.0712465)^2} + \frac{0.8460085\lambda^2}{\lambda^2 - (0.1375204)^2} + \frac{7.808527\lambda^2}{\lambda^2 - (26.89302)^2}$	0.36–5.4	177

(Continued)

**TABLE 23** Room-Temperature Dispersion Formulas for Crystals (*Continued*)

Material	Dispersion Formula (Wavelength, $\lambda$ , in $\mu\text{m}$ )	Range ( $\mu\text{m}$ )	Ref.
NaCl	$n^2 = 1.00055 + \frac{0.19800\lambda^2}{\lambda^2 - (0.050)^2} + \frac{0.48398\lambda^2}{\lambda^2 - (0.100)^2} + \frac{0.38696\lambda^2}{\lambda^2 - (0.128)^2}$ $+ \frac{0.25998\lambda^2}{\lambda^2 - (0.158)^2} + \frac{0.08796\lambda^2}{\lambda^2 - (40.50)^2} + \frac{3.17064\lambda^2}{\lambda^2 - (60.98)^2} + \frac{0.30038\lambda^2}{\lambda^2 - (120.34)^2}$	0.2–30	221
[NH <sub>4</sub> ] <sub>2</sub> CO <sub>3</sub> Urea	$n_o^2 = 2.1823 + \frac{0.0125}{\lambda^2 - 0.0300}$ $n_e^2 = 2.51527 + \frac{0.0240}{\lambda^2 - 0.0300} + \frac{0.020(\lambda - 1.52)}{(\lambda - 1.52)^2 + 0.8771}$	0.3–1.06	228
NH <sub>4</sub> H <sub>2</sub> PO <sub>4</sub> ADP	$n_o^2 = 2.302842 + \frac{0.011125165}{\lambda^2 - 0.01325366} + \frac{15.102464\lambda^2}{\lambda^2 - 400}$ $n_e^2 = 2.163510 + \frac{0.009616676}{\lambda^2 - 0.01298912} + \frac{5.919896\lambda^2}{\lambda^2 - 400}$	0.2–1.5	229
PbMoO <sub>4</sub>	$n_o^2 - 1 = \frac{3.54642\lambda^2}{\lambda^2 - (0.18518)^2} + \frac{0.58270\lambda^2}{\lambda^2 - (0.33764)^2}$ $n_e^2 - 1 = \frac{3.52555\lambda^2}{\lambda^2 - (0.17950)^2} + \frac{0.20660\lambda^2}{\lambda^2 - (0.32537)^2}$	0.44–1.08	230
PbTe	$n^2 - 1 = \frac{30.046\lambda^2}{\lambda^2 - (1.563)^2}$	4.0–12.5	231
PbTiO <sub>3</sub>	$n_o^2 - 1 = \frac{5.363\lambda^2}{\lambda^2 - (0.224)^2}; \quad n_e^2 - 1 = \frac{5.366\lambda^2}{\lambda^2 - (0.217)^2}$	0.45–1.15	232
RbTiOPO <sub>4</sub> , RTP	$n_x^2 = 1.6795 + \frac{1.4281\lambda^2}{\lambda^2 - 0.0325} - 0.0119\lambda^2$ $n_y^2 = 2.0360 + \frac{1.0883\lambda^2}{\lambda^2 - 0.0437} - 0.0090\lambda^2$ $n_z^2 = 2.2864 + \frac{1.1280\lambda^2}{\lambda^2 - 0.0562} - 0.0188\lambda^2$	0.4–1.5	180
Si	$n_2 - 1 = \frac{10.6684293\lambda^2}{\lambda^2 - (0.301516485)^2} + \frac{0.003043475\lambda^2}{\lambda^2 - (1.13475115)^2} + \frac{1.54133408\lambda^2}{\lambda^2 - (1104.0)^2}$	1.36–11	67
$\alpha$ -SiO <sub>2</sub> quartz	$n_o^2 - 1 = \frac{0.663044\lambda^2}{\lambda^2 - (0.060)^2} + \frac{0.517852\lambda^2}{\lambda^2 - (0.106)^2} + \frac{0.175912\lambda^2}{\lambda^2 - (0.119)^2}$ $+ \frac{0.565380\lambda^2}{\lambda^2 - (8.844)^2} + \frac{1.675299\lambda^2}{\lambda^2 - (20.742)^2}$ $n_e^2 - 1 = \frac{0.665721\lambda^2}{\lambda^2 - (0.060)^2} + \frac{0.503511\lambda^2}{\lambda^2 - (0.106)^2} + \frac{0.214792\lambda^2}{\lambda^2 - (0.119)^2}$ $+ \frac{0.539173\lambda^2}{\lambda^2 - (8.792)^2} + \frac{1.807613\lambda^2}{\lambda^2 - (197.70)^2}$	0.18–0.71	178
SrF <sub>2</sub>	$n^2 - 1 = \frac{0.67805894\lambda^2}{\lambda^2 - (0.05628989)^2} + \frac{0.37140533\lambda^2}{\lambda^2 - (0.10801027)^2} + \frac{3.8484723\lambda^2}{\lambda^2 - (34.649040)^2}$	0.21–11.5	145

**TABLE 23** Room-Temperature Dispersion Formulas for Crystals (*Continued*)

Material	Dispersion Formula (Wavelength, $\lambda$ , in $\mu\text{m}$ )	Range ( $\mu\text{m}$ )	Ref.
SrMoO <sub>4</sub>	$n_o^2 - 1 = \frac{2.4839\lambda^2}{\lambda^2 - (0.1451)^2} + \frac{0.1015\lambda^2}{\lambda^2 - (4.603)^2}$ $n_e^2 - 1 = \frac{2.4923\lambda^2}{\lambda^2 - (0.1488)^2} + \frac{0.1050\lambda^2}{\lambda^2 - (4.544)^2}$	0.45–2.4	213
SrTiO <sub>3</sub>	$n^2 - 1 = \frac{3.042143\lambda^2}{\lambda^2 - (0.1475902)^2} + \frac{1.170065\lambda^2}{\lambda^2 - (0.2953086)^2} + \frac{30.83326\lambda^2}{\lambda^2 - (33.18606)^2}$	0.43–3.8	156
TeO <sub>2</sub>	$n_o^2 - 1 = \frac{2.584\lambda^2}{\lambda^2 - (0.1342)^2} + \frac{1.157\lambda^2}{\lambda^2 - (0.2638)^2}$ $n_e^2 - 1 = \frac{2.823\lambda^2}{\lambda^2 - (0.1342)^2} + \frac{1.542\lambda^2}{\lambda^2 - (0.2631)^2}$	0.4–1.0	181
TiO <sub>2</sub>	$n_o^2 = 5.913 + \frac{0.2441}{\lambda^2 - 0.0803}; \quad n_e^2 = 7.197 + \frac{0.3322}{\lambda^2 - 0.0843}$	0.43–1.5	182
TlBr	$\frac{n^2 - 1}{n^2 + 2} = 0.48484 + \frac{0.10279\lambda^2}{\lambda^2 - 0.90000} - 0.0047896\lambda^2$	0.54–0.65	203
Tl[Br, I], KRS-5	$n^2 - 1 = \frac{1.8293958\lambda^2}{\lambda^2 - (0.150)^2} + \frac{1.6675593\lambda^2}{\lambda^2 - (0.250)^2} + \frac{1.1210424\lambda^2}{\lambda^2 - (0.350)^2}$ $+ \frac{0.04513366\lambda^2}{\lambda^2 - (0.450)^2} + \frac{12.380234\lambda^2}{\lambda^2 - (164.59)^2}$	0.58–39.4	183
TlCl	$\frac{n^2 - 1}{n^2 + 2} = 0.47856 + \frac{0.07858\lambda^2}{\lambda^2 - 0.08377} - 0.00881\lambda^2$	0.43–0.66	203
Tl[Cl, Br], KRS-6	$n^2 - 1 = \frac{3.821\lambda^2}{\lambda^2 - (0.02234)^2} - 0.000877\lambda^2$	0.6–24	233
Y <sub>3</sub> Al <sub>5</sub> O <sub>12</sub> , YAG	$n^2 - 1 = \frac{2.28200\lambda^2}{\lambda^2 - 0.01185} + \frac{3.27644\lambda^2}{\lambda^2 - 282.734}$	0.4–5.5	234
Y <sub>2</sub> O <sub>3</sub>	$n^2 - 1 = \frac{2.578\lambda^2}{\lambda^2 - (0.1387)^2} + \frac{3.935\lambda^2}{\lambda^2 - (22.936)^2}$	0.2–12	235
YVO <sub>4</sub>	$n_o^2 = 3.778790 + \frac{0.07479}{\lambda^2 - 0.045731} - 0.009701\lambda^2$ $n_e^2 = 4.607200 + \frac{0.108087}{\lambda^2 - 0.052495} - 0.014305\lambda^2$	0.48–1.34	185
ZnGeP <sub>2</sub>	$n_o^2 = 8.0409 + \frac{1.68625\lambda^2}{\lambda^2 - 0.40824} + \frac{1.2880\lambda^2}{\lambda^2 - 611.05}$ $n_e^2 = 8.0929 + \frac{1.8649\lambda^2}{\lambda^2 - 0.41468} + \frac{0.84052\lambda^2}{\lambda^2 - 452.05}$	2.5–9.5	236
$\beta$ -ZnS	$n^2 - 1 = \frac{0.33904026\lambda^2}{\lambda^2 - (0.31423026)^2} + \frac{3.7606868\lambda^2}{\lambda^2 - (0.1759417)^2} + \frac{2.7312353\lambda^2}{\lambda^2 - (33.886560)^2}$	0.55–10.5	144

(Continued)

**TABLE 23** Room-Temperature Dispersion Formulas for Crystals (*Continued*)

Material	Dispersion Formula (Wavelength, $\lambda$ , in $\mu\text{m}$ )	Range ( $\mu\text{m}$ )	Ref.
$\alpha$ -ZnS	$n_o^2 - 1 = 3.4175 + \frac{1.7396\lambda^2}{\lambda^2 - (0.2677)^2}$ ; $n_e^2 - 1 = 3.4264 + \frac{1.7491\lambda^2}{\lambda^2 - (0.2674)^2}$	0.36–1.4	237
ZnSe	$n^2 - 1 = \frac{4.2980149\lambda^2}{\lambda^2 - (0.1920630)^2} + \frac{0.62776557\lambda^2}{\lambda^2 - 0.37878260^2} + \frac{2.8955633\lambda^2}{\lambda^2 - 46.994595^2}$	0.55–18	145
ZnTe	$n^2 = 9.92 \frac{0.42530}{\lambda^2 - (0.37766)^2} + \frac{2.63580}{\lambda^2 / (56.5)^2 - 1}$	0.55–30	238
ZrO <sub>2</sub> : 12%Y <sub>2</sub> O <sub>3</sub>	$n^2 - 1 = \frac{1.347091\lambda^2}{\lambda^2 - (0.166739)^2} + \frac{2.117788\lambda^2}{\lambda^2 - (0.166739)^2} + \frac{9.452943\lambda^2}{\lambda^2 - (24.320570)^2}$	0.36–5.1	186

**TABLE 24** Room-Temperature Dispersion Formula for Glasses

Material	Dispersion Formula (Wavelength, $\lambda$ , in $\mu\text{m}$ )	Range ( $\mu\text{m}$ )	Ref.
N-FK5	$n^2 = 1 + \frac{1.07715032\lambda^2}{\lambda^2 - 0.00676601657} + \frac{0.168079109\lambda^2}{\lambda^2 - 0.0230642817} + \frac{0.851889892\lambda^2}{\lambda^2 - 89.0498778}$	0.28–2.4	188
N-PK52A	$n^2 = 1 + \frac{1.029607\lambda^2}{\lambda^2 - 0.00516800155} + \frac{0.1880506\lambda^2}{\lambda^2 - 0.0166658798} + \frac{0.736488165\lambda^2}{\lambda^2 - 138.964129}$	0.3–2.4	188
N-ZK7	$n^2 = 1 + \frac{1.07715032\lambda^2}{\lambda^2 - 0.00676601657} + \frac{0.168079109\lambda^2}{\lambda^2 - 0.0230642817} + \frac{0.851889892\lambda^2}{\lambda^2 - 89.0498778}$	0.3–2.4	188
N-BK7	$n^2 = 1 + \frac{1.03961212\lambda^2}{\lambda^2 - 0.00600069867} + \frac{0.231792344\lambda^2}{\lambda^2 - 0.0200179144} + \frac{1.01046945\lambda^2}{\lambda^2 - 103.560653}$	0.3–2.4	188
N-K5	$n^2 = 1 + \frac{1.08511833\lambda^2}{\lambda^2 - 0.00661099503} + \frac{0.199562005\lambda^2}{\lambda^2 - 0.024110866} + \frac{0.930511663\lambda^2}{\lambda^2 - 111.982777}$	0.3–2.4	188
N-KF9	$n^2 = 1 + \frac{1.19286778\lambda^2}{\lambda^2 - 0.00839154696} + \frac{0.0893346571\lambda^2}{\lambda^2 - 0.0404010786} + \frac{0.920819805\lambda^2}{\lambda^2 - 112.572446}$	0.36–2.4	188
LLF1	$n^2 = 1 + \frac{1.21640125\lambda^2}{\lambda^2 - 0.00857807248} + \frac{0.13366454\lambda^2}{\lambda^2 - 0.0420143003} + \frac{0.883399468\lambda^2}{\lambda^2 - 107.593060}$	0.37–1.01 <sup>†</sup>	188
N-PSK53A	$n^2 = 1 + \frac{1.38121836\lambda^2}{\lambda^2 - 0.00706416337} + \frac{0.196745645\lambda^2}{\lambda^2 - 0.0233251345} + \frac{0.886089205\lambda^2}{\lambda^2 - 97.4847345}$	0.31–2.5	188
N-BaK4	$n^2 = 1 + \frac{1.28834642\lambda^2}{\lambda^2 - 0.00779980626} + \frac{0.132817724\lambda^2}{\lambda^2 - 0.0315631177} + \frac{0.945395373\lambda^2}{\lambda^2 - 105.965875}$	0.334–2.5	188
N-BaLF4	$n^2 = 1 + \frac{1.31004128\lambda^2}{\lambda^2 - 0.0079659645} + \frac{0.142038259\lambda^2}{\lambda^2 - 0.0330672072} + \frac{0.964929351\lambda^2}{\lambda^2 - 109.19732}$	0.36–2.4	188
LF5	$n^2 = 1 + \frac{1.28035628\lambda^2}{\lambda^2 - 0.00929854416} + \frac{0.163505973\lambda^2}{\lambda^2 - 0.0449135769} + \frac{0.893930112\lambda^2}{\lambda^2 - 110.493685}$	0.33–2.4	188
FF5	$n^2 = 1 + \frac{1.3241093\lambda^2}{\lambda^2 - 0.01004} + \frac{0.147104\lambda^2}{\lambda^2 - 0.05705} - 0.0095123\lambda^2$	0.37–1.01	189*
N-KzFSN4	$n^2 = 1 + \frac{1.35055424\lambda^2}{\lambda^2 - 0.0087628207} + \frac{0.197575506\lambda^2}{\lambda^2 - 0.0371767201} + \frac{1.09962992\lambda^2}{\lambda^2 - 90.3866994}$	0.36–2.4	188

**TABLE 24** Room-Temperature Dispersion Formula for Glasses (*Continued*)

Material	Dispersion Formula (Wavelength, $\lambda$ , in $\mu\text{m}$ )	Range ( $\mu\text{m}$ )	Ref.
N-SK10	$n^2 = 1 + \frac{1.34972093\lambda^2}{\lambda^2 - 0.00736272269} + \frac{0.238587973\lambda^2}{\lambda^2 - 0.0253765327} + \frac{0.966733600\lambda^2}{\lambda^2 - 103.502909}$	0.334–2.5	188
N-F2	$n^2 = 1 + \frac{1.39757037\lambda^2}{\lambda^2 - 0.00995906143} + \frac{0.159201403\lambda^2}{\lambda^2 - 0.0546931752} + \frac{1.26865430\lambda^2}{\lambda^2 - 119.248346}$	0.33–2.4	188
N-SSK5	$n^2 = 1 + \frac{1.59222659\lambda^2}{\lambda^2 - 0.00920284626} + \frac{0.103520774\lambda^2}{\lambda^2 - 0.0423530072} + \frac{1.05174016\lambda^2}{\lambda^2 - 106.927374}$	0.36–2.4	188
N-BaF10	$n^2 = 1 + \frac{1.58514950\lambda^2}{\lambda^2 - 0.00926681282} + \frac{0.143559385\lambda^2}{\lambda^2 - 0.0424489805} + \frac{1.08521269\lambda^2}{\lambda^2 - 105.613573}$	0.37–1.01	188
N-BaSF64	$n^2 = 1 + \frac{1.6554268\lambda^2}{\lambda^2 - 0.00104485644} + \frac{1.71319770\lambda^2}{\lambda^2 - 0.0499394756} + \frac{1.33664448\lambda^2}{\lambda^2 - 118.961472}$	0.365–2.5	188
N-LaK10	$n^2 = 1 + \frac{1.72878017\lambda^2}{\lambda^2 - 0.00886014635} + \frac{0.169257825\lambda^2}{\lambda^2 - 0.0363416509} + \frac{1.19386956\lambda^2}{\lambda^2 - 82.9009069}$	0.36–2.4	188
N-LaF33	$n^2 = 1 + \frac{1.79653417\lambda^2}{\lambda^2 - 0.00927313493} + \frac{0.311577903\lambda^2}{\lambda^2 - 0.0358201181} + \frac{1.15981863\lambda^2}{\lambda^2 - 87.3448712}$	0.32–2.5	188
NbF1	$n^2 = 1 + \frac{1.9550984\lambda^2}{\lambda^2 - 0.011628} + \frac{0.0165083\lambda^2}{\lambda^2 - 0.064357} - 0.012813\lambda^2$	0.37–1.01	189*
N-LaF2	$n^2 = 1 + \frac{1.80984227\lambda^2}{\lambda^2 - 0.0101711622} + \frac{0.15729555\lambda^2}{\lambda^2 - 0.0442431765} + \frac{1.0930037\lambda^2}{\lambda^2 - 100.687748}$	0.35–2.4	188
N-SF6	$n^2 = 1 + \frac{1.77931763\lambda^2}{\lambda^2 - 0.0133714182} + \frac{0.338149866\lambda^2}{\lambda^2 - 0.0617533621} + \frac{2.08734474\lambda^2}{\lambda^2 - 174.01759}$	0.40–2.4	188
N-LASF31A	$n^2 = 1 + \frac{1.96485075\lambda^2}{\lambda^2 - 0.00982060155} + \frac{0.475231259\lambda^2}{\lambda^2 - 0.0344713438} + \frac{1.48360109\lambda^2}{\lambda^2 - 110.739863}$	0.334–2.5	188
Fused silica	$n^2 - 1 = \frac{0.6961663\lambda^2}{\lambda^2 - (0.0684043)^2} + \frac{0.4079426\lambda^2}{\lambda^2 - (0.1162414)^2} + \frac{0.8974794\lambda^2}{\lambda^2 - (9.896161)^2}$	0.21–3.71	190
Fused germania	$n^2 - 1 = \frac{0.80686642\lambda^2}{\lambda^2 - (0.06897261)^2} + \frac{0.71815848\lambda^2}{\lambda^2 - (0.1539661)^2} + \frac{0.85416831\lambda^2}{\lambda^2 - (11.841931)^2}$	0.43–4.5	191*
BS-93B	$n^2 - 1 = \frac{1.7441\lambda^2}{\lambda^2 - (0.1155)^2} + \frac{1.6465\lambda^2}{\lambda^2 - (14.981)^2}$	0.43–4.5	192
CORTAN 9754	$n^2 - 1 = \frac{1.66570\lambda^2}{\lambda^2 - (0.10832)^2} + \frac{0.04059\lambda^2}{\lambda^2 - (0.23813)^2} + \frac{1.31792\lambda^2}{\lambda^2 - (13.57622)^2}$	0.4–5.5	193
IRG 2	$n^2 - 1 = \frac{2.07670\lambda^2}{\lambda^2 - (0.11492)^2} + \frac{0.35738\lambda^2}{\lambda^2 - (0.23114)^2} + \frac{2.88166\lambda^2}{\lambda^2 - (17.48306)^2}$	0.365–4.6	188*
IRG 9	$n^2 - 1 = \frac{2.07670\lambda^2}{\lambda^2 - (0.11492)^2} + \frac{0.35738\lambda^2}{\lambda^2 - (0.23114)^2} + \frac{2.88166\lambda^2}{\lambda^2 - (17.48306)^2}$	0.365–4.6	188*

(Continued)



**TABLE 24** Room-Temperature Dispersion Formula for Glasses (*Continued*)

Material	Dispersion Formula (Wavelength, $\lambda$ , in $\mu\text{m}$ )	Range ( $\mu\text{m}$ )	Ref.
IRG 11	$n^2 - 1 = \frac{1.7531\lambda^2}{\lambda^2 - (0.1185)^2} + \frac{0.4346\lambda^2}{\lambda^2 - (8.356)^2}$	0.48–3.3	188*
IRG 100	$n^2 = 4.5819 + \frac{2.2693\lambda^2}{\lambda^2 - (0.447)^2} - 0.000928\lambda^2$	1–14	188*
HTF-1	$n^2 - 1 = \frac{1.06375\lambda^2}{\lambda^2 - (0.078958)^2} + \frac{0.80098\lambda^2}{\lambda^2 - (15.1579)^2}$	0.37–5	194*
ZBLAN	$n^2 - 1 = \frac{1.168\lambda^2}{\lambda^2 - (0.0954)^2} + \frac{2.77\lambda^2}{\lambda^2 - (25.0)^2}$	0.50–48	195
AMTIR-1/ TI-20	$n^2 - 1 = \frac{5.298\lambda^2}{\lambda^2 - (0.29007)^2} + \frac{0.6039\lambda^2}{\lambda^2 - (32.022)^2}$	1–14	201*
AMTIR-3/ TI-1173	$n^2 - 1 = \frac{5.8505\lambda^2}{\lambda^2 - (0.29192)^2} + \frac{1.4536\lambda^2}{\lambda^2 - (42.714)^2}$	3–14	201*
	$n^2 - 1 = \frac{5.8357\lambda^2}{\lambda^2 - (0.29952)^2} + \frac{1.064\lambda^2}{\lambda^2 - (38.353)^2}$	0.9–14	239

\*Our dispersion equation from referenced data.

†Schott dispersion formula range; data available to 2–3  $\mu\text{m}$ .

Vibrational modes of many optical materials are summarized in Tables 25 through 40 for a number of common optical crystal types. These tables give number and type of zone-center (i.e., the wave vector  $\approx 0$ , where  $\Gamma$  is the usual symbol denoting the center of the Brillouin zone) optical modes predicted by group theory (and observed in practice) as well as the frequency (in wave number) of the infrared-active and Raman modes. Mulliken notation is used. Table 41 summarizes the available lattice vibration dispersion models for many crystals.

Parameters for ultraviolet and infrared absorption models for crystals and glasses are not included in this edition. Please refer to the previous edition<sup>1</sup> for these parameters.

**TABLE 25** Optical Modes of Crystals with Diamond Structure; Space Group:  $Fd\bar{3}m$  ( $O_h^7$ ) #227;  $\Gamma = F_{2g}$ (R)

Material	Raman Mode Location ( $\text{cm}^{-1}$ )	Ref.
C (diamond)	1332.4	240
Si	519.5	241
Ge	300.6	242

**TABLE 26** Optical Modes of Crystals with Cesium Chloride Structure; Space Group:  $Pm\bar{3}m$  ( $O_h^5$ ) #221;  $= F_{1u}$ (IR)

Material	Mode location ( $\text{cm}^{-1}$ )			Material	Mode location ( $\text{cm}^{-1}$ )		
	$\omega_{\text{TO}}$	$\omega_{\text{LO}}$	Ref.		$\omega_{\text{TO}}$	$\omega_{\text{LO}}$	Ref.
CsBr	75	113	243	TlBr	43	101	245
CsCl	99	160	243, 244	TlCl	63	158	245
CsI	62	88	243	TlI	40	87	246

**TABLE 27** Optical Modes of Crystals with Sodium Chloride Structure; Space Group:  $Fm\bar{3}m (O_h^1) \#225$ ;  $\Gamma = F_{1u}(\text{IR})$ 

Material	Mode location ( $\text{cm}^{-1}$ )			Material	Mode location ( $\text{cm}^{-1}$ )		
	$\omega_{\text{TO}}$	$\omega_{\text{LO}}$	Ref.		$\omega_{\text{TO}}$	$\omega_{\text{LO}}$	Ref.
AgBr	79	138	245	MgO	401	718	245, 251
AgCl	106	196	245	MgS	237	430	248
BaO	132	425	247	NaBr	134	209	245
BaS	158	230	248	NaCl	164	264	245
CaO	295	557	247, 249	NaF	244	418	245
CaS	256	376	248	NaI	117	176	245
CdO	270	380	250	NiO	401	580	245
KBr	113	165	245	SrO	227	487	247, 249
KCl	142	214	245	SrS	194	284	248
KF	190	326	245	PbS	71	212	252
KI	101	139	245	PbSe	39	116	253
LiF	306	659	245, 251	PbTe	32	112	254

**TABLE 28** Optical Modes of Crystals with Zinblende Structure; Space Group:  $F\bar{4}3m (T_d^2) \#216$ ;  $\Gamma = F_2(\text{R, IR})$ 

Material	Mode location ( $\text{cm}^{-1}$ )			Material	Mode location ( $\text{cm}^{-1}$ )		
	$\omega_{\text{TO}}$	$\omega_{\text{LO}}$	Ref.		$\omega_{\text{TO}}$	$\omega_{\text{LO}}$	Ref.
AlAs	364	402	255	GaSb	230	240	262
AlSb	319	340	256	InAs	217	239	262, 263
BN	1055	1305	257, 258	InP	304	345	256
BP	799	829	257, 258	InSb	179	191	263, 264
CdTe	141	169	259	-SiC	793	970	242, 265
CuCl	172	210	260	ZnS	282	352	259, 266
GaAs	269	292	256	ZnSe	206	252	259
GaP	367	403	256, 261	ZnTe	178	208	259, 267

**TABLE 29** Optical Modes of Crystals with Fluorite Structure; Space Group:  $Fm\bar{3}m (O_h^1) \#225$ ;  $\Gamma = F_{1u}(\text{IR}) + F_{2g}(\text{R})$ 

Material	Mode locations ( $\text{cm}^{-1}$ )			Ref.
	$F_{1u}(\omega_{\text{TO}})$	$F_{1u}(\omega_{\text{LO}})$	$F_{2g}$	
BaCl <sub>2</sub>			185	268
BaF <sub>2</sub>	184	319	241	269, 270, 271
CaF <sub>2</sub>	258	473	322	269, 270, 271
CdF <sub>2</sub>	202	384	317	271, 272
EuF <sub>2</sub>	194	347	287	268
$\beta$ -PbF <sub>2</sub>	102	337	256	268, 272
SrCl <sub>2</sub>	147	243	182	268, 273, 274
SrF <sub>2</sub>	217	366	286	269, 270, 271
ThO <sub>2</sub>	281	568		275
UO <sub>2</sub>	281	555	445	275, 276
ZrO <sub>2</sub>	354	680	605	277

**TABLE 30** Optical Modes of Crystals with Corundum Structure; Space Group: ( $R\bar{3}c(D_{3d}^6)$ ) #167);  $\Gamma = 2A_{1g}(R) + 2A_{1u}(-) + 3A_{2g}(-) + 2A_{2u}(IR, E \parallel c) + 5E_g(R) + 4E_u(IR, E \perp c)$

Material	Mode locations ( $cm^{-1}$ )												
	Infrared modes (LO in parentheses)						Raman modes						
	$E_u$	$E_u$	$E_u$	$E_u$	$A_{1u}$	$A_{1u}$	$E_g$	$E_g$	$E_g$	$E_g$	$E_g$	$A_{1g}$	$A_{1g}$
$Al_2O_3$ (Refs. 35, 278)	385 (388)	422 (480)	569 (625)	635 (900)	400 (512)	583 (871)	378	432	451	578	751	418	645
$Cr_2O_3$ (Refs. 279, 280)	417 (420)	444 (446)	532 (602)	613 (766)	538 (602)	613 (759)	—	351	397	530	609	303	551
$Fe_2O_3$ (Refs. 280, 281)	227 (230)	286 (368)	437 (494)	524 (662)	299 (414)	526 (662)	245	293	298	413	612	226	500

**TABLE 31** Optical Modes of Crystals with Wurtzite Structure; Space Group:  $P6_3mc(C_{6v}^4)$  #186;  $\Gamma = A_1(R, IR E \parallel c) + 2B_1(-) + E_1(R, IR E \perp c) + 2E_2(R)$

Material	Mode locations ( $cm^{-1}$ )				
	IR modes TO & (LO)		Raman modes		Ref.
	$E_1$	$A_1$	$E_2$	$E_2$	
$\beta$ -AgI	106 (124)	106 (124)	17	112	282
AlN	673 (916)	614 (893)	252	660	283
BeO	725 (1095)	684 (1085)	340	684	284, 285
CdS	235 (305)	228 (305)	44	252	285, 286
CdSe	172 (210)	166 (211)	34	176	287
GaN	560 (746)	533 (744)	145	568	218, 288
$\alpha$ -SiC	797 (970)	788 (964)	149	788	289
ZnO	407 (583)	381 (574)	101	437	285, 290
ZnS	274 (352)	274 (352)	55	280	285

**TABLE 32** Optical Modes of Crystals with Trigonal Selenium Structure; Space Group:  $P3_1 21(D_3^4)$  #152;  $\Gamma = A_1(R) + A_2(IR, E \parallel c) + 2E(IR, E \perp c, R)$

Material	Mode locations ( $cm^{-1}$ )				
	Raman	Infrared, $E \perp c$		Infrared, $E \parallel c$	Ref.
	$A_1$	E	E	$A_2$	
Se	237	144 (150)	225 (225)	102 (106)	291, 292
Te	120	92 (106)	144 (145)	90 (96)	293

**TABLE 33** Optical Modes of Crystals with  $\alpha$ -Quartz Structure; Space Group:  $P3_221$  ( $D_3^6$ ) #154;  $\Gamma = 4A_1(R) + 4A_2(IR, E \parallel c) + 8E(IR, E \perp c, R)$

Material	Infrared modes, $E \perp c$							
	E	E	E	E	E	E	E	E
SiO <sub>2</sub> (Refs. 294, 295, 296)	128 (128)	265 (270)	394 (403)	451 (511)	697 (699)	796 (809)	1067 (1159)	1164 (1230)
GeO <sub>2</sub> (Refs. 297)	121 (121)	166 (166)	326 (372)	385 (456)	492 (512)	583 (595)	857 (919)	961 (972)
Material	Infrared modes, $E \parallel c$				Raman modes			
	A <sub>2</sub>	A <sub>2</sub>	A <sub>2</sub>	A <sub>2</sub>	A <sub>1</sub>	A <sub>1</sub>	A <sub>1</sub>	A <sub>1</sub>
SiO <sub>2</sub> (Refs. 294, 295, 296)	364 (388)	500 (552)	777 (789)	1080 (1239)	207	356	464	1085
GeO <sub>2</sub> (Ref. 297)					212	261	440	880

**TABLE 34** Optical Modes of Crystals with Rutile Structure; Space Group:  $P4_2/mnm$  ( $D_{2h}^{14}$ ) #136;  $\Gamma = A_{1g}(R) + A_{2g}(-) + A_{2u}(IR, E \parallel c) + B_{1g}(R) + B_{2g}(R) + 2B_{1u}(-) + E_g(R) + 3E_u(IR, E \perp c)$

Material	Mode locations (cm <sup>-1</sup> )							
	Infrared modes (LO in parentheses)				Raman modes			
	E <sub>u</sub>	E <sub>u</sub>	E <sub>u</sub>	A <sub>2u</sub>	B <sub>1g</sub>	E <sub>g</sub>	A <sub>1g</sub>	B <sub>2g</sub>
CoF <sub>2</sub> (Refs. 298, 299, 230)	190 (234)	270 (276)	405 (529)	345 (506)	68	246	366	494
FeF <sub>2</sub> (Refs. 299, 300, 301)	173 (231)	244 (248)	405 (530)	307 (487)	73	257	340	496
GeO <sub>2</sub> (Refs. 297, 303, 304)	300 (345)	370 (470)	635 (815)	455 (755)	97	680	702	870
MgF <sub>2</sub> (Refs. 301, 302, 305, 306, 307)	247 (303)	410 (415)	450 (617)	399 (625)	92	295	410	515
SnO <sub>2</sub> (Refs. 308, 309, 310)	243 (273)	284 (368)	605 (757)	465 (703)	123	475	634	776
TiO <sub>2</sub> (Refs. 32, 36, 301, 311)	189 (367)	382 (444)	508 (831)	172 (796)	143	447	612	826
ZnF <sub>2</sub> (Refs. 299, 300, 303, 305)	173 (227)	244 (264)	380 (498)	294 (488)	70	253	350	522

**TABLE 35** Optical Modes of Crystals with Scheelite Structure; Space Group:  $I4_1/a(C_{4h}^6)$  #88;  $\Gamma = 3A_g(R) + 4A_u(IR, E \parallel c) + 5B_g(R) + 3B_u(-) + 5E_g(R) + 4E_u(IR, E \perp c)$

Material	Ref.	Infrared modes, $E \perp c$				Infrared modes, $E \parallel c$			
		$E_u$	$E_u$	$E_u$	$E_u$	$A_u$	$A_u$	$A_u$	$A_u$
CaMoO <sub>4</sub>	312, 313, 314	146 (161)	197 (258)	322 (359)	790 (910)	193 (202)	247 (317)	420 (450)	772 (898)
CaWO <sub>4</sub>	312, 313, 314	142 (153)	200 (248)	313 (364)	786 (906)	177 (181)	237 (323)	420 (450)	776 (896)
SrMoO <sub>4</sub>	313	125	[181]	[327]	[830]	153	[282]	[404]	[830]
SrWO <sub>4</sub>	313	[140]	[168]	[320]	[833]	[150]	[278]	[410]	[833]
PbMoO <sub>4</sub>	313, 314	90 (99)	105 (160)	301 (318)	744 (886)	86 (132)	258 (278)	373 (387)	745 (865)
PbWO <sub>4</sub>	313, 314, 315	73 (101)	104 (137)	288 (314)	756 (869)	58 (109)	251 (278)	384 (393)	764 (866)
LiYF <sub>4</sub>	316, 317	143 (173)	292 (303)	326 (367)	424 (566)	195 (224)	252 (283)	396	490

Material	Ref.	Raman modes												
		$A_g$	$A_g$	$A_g$	$B_g$	$B_g$	$B_g$	$B_g$	$B_g$	$B_g$	$E_g$	$E_g$	$E_g$	$E_g$
CaMoO <sub>4</sub>	318	205	333	878	110	219	339	393	844	145	189	263	401	797
CaWO <sub>4</sub>	318, 319	218	336	912	84	210	336	401	838	117	195	275	409	797
SrMoO <sub>4</sub>	318	181	327	887	94	157	327	367	842	111	137	231	381	797
SrWO <sub>4</sub>	318, 319	187	334	925	75		334	370	839	101	131	238	378	797
PbMoO <sub>4</sub>	320	164	314	868	64	75	317	348	764	61	100	190	356	744
PbWO <sub>4</sub>	320	178	328	905	54	78	328	358	766	63	78	192	358	753
LiYF <sub>4</sub>	316, 317	[150]	264	425	177	248	329	382	427	153	199	329	368	446

**TABLE 36** Optical Modes of Crystals with Spinel Structure; Space Group:  $Fd\bar{3}m (O_h^7) \#227$ ;  $\Gamma = A_{1g}(R) + E_g(R) + F_{1g}(-) + 3F_{2g}(R) + 2A_{2u}(-) + 2E_u(-) + 4F_{1u}(IR) + 2F_{2u}(-)$ 

Material	Ref.	Mode locations ( $\text{cm}^{-1}$ )								
		Infrared modes				Raman modes				
		$F_{1u}$	$F_{1u}$	$F_{1u}$	$F_{1u}$	$F_{2g}$	$F_{2g}$	$F_{2g}$	$E_g$	$A_{1g}$
$\text{MgAl}_2\text{O}_4$	226, 321, 322	305 (311)	428	485 (497)	670 (800)	311	492	611	410	722
$\text{CdIn}_2\text{S}_4$	323, 324	68 (69)	171 (172)	215 (270)	307 (311)	93	247	312	185	366
$\text{ZnCr}_2\text{O}_4$	325	186 (194)	372 (377)	506 (522)	624 (711)	186	515	610	457	692
$\text{ZnCr}_2\text{S}_4$	326, 327, 328	115 (117)	249 (250)	340 (360)	388 (403)	116	[290]	361	249	403

**TABLE 37** Optical Modes of Crystals with Cubic Perovskite Structure; Space Group:  $Pm\bar{3}m (O_h^h) \#221$ ;  $\Gamma = 3F_{1u}(IR) + F_{2u}(-)$ 

Material	Infrared mode locations ( $\text{cm}^{-1}$ )			
	$F_{1u}^*$	$F_{1u}$	$F_{1u}$	Ref.
$\text{KTaO}_3$	85 (88)	199 (200)	549 (550)	329
$\text{SrTiO}_3$	88 (173)	178 (473)	544 (804)	329, 330, 331
$\text{KMgF}_3$	168 (197)	299 (362)	458 (551)	332, 333
$\text{KMnF}_3$	119 (144)	193 (270)	399 (483)	332, 333

\*"Soft" mode with strong temperature dependence.

**TABLE 38** Optical Modes of Crystals with Tetragonal Perovskite Structure; Space Group:  $P4_2/mnm (D_{4h}^{14}) \#136$ ;  $\Gamma = 3A_1(IR, E \parallel c, R) + B_1(R) + 4E(IR, E \perp c, R)$ 

Material	Mode locations ( $\text{cm}^{-1}$ )								
	Infrared ( $E \perp c$ )				Raman	Infrared ( $E \parallel c$ )			
	E	E	E	E	$B_1$	$A_1$	$A_1$	$A_1$	Ref.
$\text{BaTiO}_3$	34 (180)	181 (306)	306 (465)	482 (706)	305	180 (187)	280 (469)	507 (729)	329, 333, 334
$\text{PbTiO}_3$	89 (128)	221	250 (445)	508 (717)	415	127 (215)	351 (445)	613 (794)	335

**TABLE 39** Optical Modes of Crystals with the Chalcopyrite Structure; Space Group:  $\bar{1}\bar{4}2d$  ( $D_{2d}^{12}$ ) #122;  $\Gamma = A_1(R) + 2A_2(-) + 3B_1(R) + 3B_2(IR, E \parallel c, R) + 6E(IR, E \perp c, R)$ 

Material	Ref.	Mode locations ( $\text{cm}^{-1}$ )						
		Raman modes				Infrared modes ( $E \parallel c$ )		
		$A_1$	$B_1$	$B_1$	$B_1$	$B_2$	$B_2$	$B_2$
AgGaS <sub>2</sub>	336 337	295	118	179	334	195 (199)	215 (239)	366 (400)
AgGaSe <sub>2</sub>	113	181	56	160	253	58 (58)	155 (161)	252 (275)
CdGeAs <sub>2</sub>	338	[185]	[105]	[169]	[242]	[108] [(109)]	203 (210)	270 (278)
CuGaS <sub>2</sub>	336	312	138	203	243	259 (284)	339 (369)	371 (402)
ZnGeP <sub>2</sub>	339 340	328	120	247	389	[140]	361 (341)	411 (401)
ZnSiP <sub>2</sub>	341	344	131				352 (362)	511 (535)

Material	Ref.	Infrared mode location ( $E \perp c$ )					
		E	E	E	E	E	E
AgGaS <sub>2</sub>	336, 337	63 (64)	93 (96)	158 (160)	225 (230)	323 (347)	368 (392)
AgGaSe <sub>2</sub>	336, 342	78 (78)	133 (135)	112 (112)	160 (163)	208 (213)	247 (274)
CdGeAs <sub>2</sub>	338, 343, 344	95 (95)	[114] [(114)]	159 (161)	200 (206)	255 (258)	272 (280)
CuGaS <sub>2</sub>	336	75 (76)	95 (98)	147 (167)	260 (278)	335 (352)	365 (387)
ZnGeP <sub>2</sub>	339, 340	94 (94)	141 (141)	201 (206)	328 (330)	369 (375)	386 (406)
ZnSiP <sub>2</sub>	341	105 (105)	185 (185)	270 (270)	335 (362)	477 (477)	511 (535)

**TABLE 40** Optical Modes of Other Crystals

Material/Space Group	Irreducible Optical Representation and Optical Modes Locations ( $\text{cm}^{-1}$ )
Orpiment, As <sub>2</sub> S <sub>3</sub> P2 <sub>1</sub> /b( $C_{2h}^5$ ) #14 (Ref. 345)	$\Gamma = 15A_g(R) + 15B_g(R) + 14A_u(IR, E \parallel b) + 13B_u(IR, E \parallel a, E \parallel c)$ [7A <sub>g</sub> (IR, E $\parallel$ c, R) + 7A <sub>2</sub> (R) + 7B <sub>1</sub> (IR, E $\parallel$ b, R) + 6B <sub>2</sub> (IR, E $\parallel$ a, R)] for a noninteracting molecular layer structure A <sub>g</sub> = 136, 154, 204, 311, 355, 382 B <sub>g</sub> = 140, 159, 198, 278, 311, 354, 383
Calcite, CaCO <sub>3</sub> R $\bar{3}c$ ( $D_{3d}^6$ ) #167 (Refs. 346, 347)	$\Gamma = A_{1g}(R) + 2A_{1u}(-) + 3A_{2u}(IR, E \parallel c) + 4E_g(R) + 5E_u(IR, E \perp c)$ A <sub>1g</sub> = 1088 E <sub>g</sub> = 156, 283, 714, 1432 A <sub>2u</sub> = 92(136), 303(387), 872(890) E <sub>u</sub> = 102(123), 223(239), 297(381), 712(715), 1407(1549)

**TABLE 40** Optical Modes of Other Crystals (*Continued*)

Material/Space Group	Irreducible Optical Representation and Optical Modes Locations (cm <sup>-1</sup> )
BBO, Ba <sub>3</sub> [B <sub>3</sub> O <sub>6</sub> ] <sub>2</sub> R3(C <sub>3</sub> <sup>4</sup> ) #146 (Ref. 348)	$\Gamma = 41A(\text{IR}, E \parallel c, R) + 41E(\text{IE}, E \perp c, R)$ (See reference)
BSO, selenite, Bi <sub>12</sub> SiO <sub>20</sub> I23 (T <sup>3</sup> ) #197 (Ref. 349)	$\Gamma = 8A(\text{R}) + 8E(\text{R}) + 24F(\text{IR})$ A = 92, 149, 171, 282, 331, 546, 785 E = 68, 88, 132, 252, —, 464, 626 F = 44, 51, 59, 89, 99, 106, —, 115, 136, 175, 195, 208, 237, 288, 314, 353, 367, 462, 496, 509, 531, 579, 609, 825
BIBO, BiB <sub>3</sub> O <sub>6</sub> C2(C <sub>2</sub> <sup>3</sup> ) #5 (Refs. 350, 351)	$\Gamma = 13A + 14B$ (See references)
Iron pyrite, FeS <sub>2</sub> Pa3 (T <sup>6</sup> ) #205 (Refs. 352, 353)	$\Gamma = A_g(\text{R}) + E_g(\text{R}) + 3F_g(\text{R}) + 2A_u(-) + 2E_u(-) + 5F_u(\text{IR})$ A <sub>g</sub> = 379 E <sub>g</sub> = 343 F <sub>g</sub> = 435, 350, 377 F <sub>u</sub> = 293(294), 348(350), 401(411), 412(421), 422(349)
KDP, KH <sub>2</sub> PO <sub>4</sub> I42d (D <sub>2d</sub> <sup>12</sup> ) #122 (Ref. 354)	$\Gamma = 4A_1(\text{R}) + 5S_2(-) + 6B_1(\text{R}) + 6B_2(\text{IR}, E \parallel c, R) + 12E(\text{IR}, E \perp c, R)$ A <sub>1</sub> = 360, 514, 918, 2700 B <sub>1</sub> = 156, 479, 570, 1366, 1806, 2390 B <sub>2</sub> = 80, 174, —, 386, 510, 1350 E = 75, 95, 113, 190, 320, 490, 530, 568, 960, 1145, —, 1325
KTP Pna2 <sub>1</sub> (C <sub>2v</sub> <sup>9</sup> ) #33 (Refs. 355, 356)	$\Gamma = 47A_1(\text{IR}, E \parallel c, R) + 48A_2(\text{R}) + 47B_1(\text{IR}, E \parallel a, R) + 47B_2(\text{IR}, E \parallel b, R)$
Lanthanum fluoride, LaF <sub>3</sub> P3c1 (D <sub>3d</sub> <sup>4</sup> ) #165 (Refs. 357, 358, 359)	$\Gamma = 5A_{1g}(\text{R}) + 12E_g(\text{R}) + 6A_{2u}(\text{IR}, E \parallel c)$ A <sub>1g</sub> = 120, 231, 283, 305, 390 E <sub>g</sub> = 79, 145, 145, 163, 203, 226, 281, 290, 301, 315, 325, 366 A <sub>2u</sub> = 142(143), 168(176), 194(239), —, 275(296), 323(468) E <sub>u</sub> = 100(108), 128(130), 144(145), 168(183), 193(195), 208(222), 245(268), 272(316), 354(364), 356(457)
LBO LiB <sub>3</sub> O <sub>5</sub> Pna2 <sub>1</sub> (C <sub>2v</sub> <sup>9</sup> ) #33 (Ref. 360)	$\Gamma = 26A_1(\text{IR}, E \parallel z, R) + 27A_2(\text{R}) + 26B_1(\text{IR}, E \parallel x, R) + 26B_2(\text{IR}, E \parallel y, R)$ (See reference)
Lithium iodate, LiIO <sub>3</sub> P6 <sub>3</sub> (C <sub>6</sub> <sup>6</sup> ) #173 (Refs. 361, 362)	$\Gamma = 4A(\text{IR}, E \parallel c, R) + 5B(-) + 4E_1(\text{IR}, E \perp c, R) + 5E_2(\text{R})$ A = 148(148), 238(238), 358(468), 795(817) E <sub>1</sub> = 180(180), 330(340), 370(460), 764(848) E <sub>2</sub> = 98, 200, 332, 347, 765
Lithium niobate, LiNbO <sub>3</sub> R3c (C <sub>3v</sub> <sup>6</sup> ) #161 (Refs. 363, 364)	$\Gamma = 4A_1(\text{IR}, E \parallel c, R) + 5A_2(+ 9E(\text{IR}, E \perp c, R))$ A <sub>1</sub> = 255(275), 276(333), 334(436), 633(876) E = 155(198), 238(243), 265(295), 325(371), 371(428), 431(454), 582(668), 668(739), 743(880)
Potassium niobate, KNbO <sub>3</sub> Bmm2 (C <sub>2v</sub> <sup>14</sup> ) #38 (Ref. 365)	$\Gamma = 4A_1(\text{IR}, E \parallel z, R) + 4B_1(\text{IR}, E \parallel x, R) + 3B_2(\text{IR}, E \parallel y, R) + A_2(\text{R})$ A <sub>1</sub> = 190(193), 290(296), 299(417), 607(827) B <sub>1</sub> = 187(190), 243(294), 267(413), 534(842) B <sub>2</sub> = 56(189), 195(425), 511(838) A <sub>2</sub> = 283
Tl <sub>3</sub> AsSe <sub>3</sub> , TAS R3m (C <sub>3v</sub> <sup>6</sup> ) #160 (Ref. 366)	$\Gamma = 4A_1(\text{IR}, E \parallel c, R) + 4A_2(-) + 6E(\text{IR}, E \perp c, R)$ A <sub>1</sub> = 62(66), 93(97), 119(132), 239(247) E = 64.1(67.5), 78.1(82), 92.6(96), 125 (133), 240(250)

(Continued)



**TABLE 40** Optical Modes of Other Crystals (*Continued*)

Material/Space Group	Irreducible Optical Representation and Optical Modes Locations (cm <sup>-1</sup> )
Paratellurite, TeO <sub>2</sub> P4 <sub>1</sub> 2 <sub>1</sub> 2 (D <sub>4</sub> <sup>+</sup> ) #92 (Refs. 367, 368)	$\Gamma = 4A_1(\text{R}) + 4A_2(\text{IR, E} \parallel \text{c}) + 5B_1(\text{R}) + 4B_2(\text{R}) + 8E(\text{IR, E} \perp \text{c, R})$ $A_1 = 148, 393, 648$ $A_2 = 82(110), 259(263), 315(375), 575(775)$ $B_1 = 62, 175, 216, 233, 591$ $B_2 = 155, 287, 414, 784$ $E = 121(123), 174(197), 210(237), 297(327), 330(379), 379(415), 643(720), 769(812)$
Yttria, Y <sub>2</sub> O <sub>3</sub> Ia3 (T <sub>h</sub> <sup>7</sup> ) #206 (Ref. 369)	$\Gamma = 4E_g(\text{R}) + 4A_g^s(\text{R}) + 14F_g(\text{R}) + 5E_u(-) + 5A_u(-) + 16F_u(\text{IR})$ $E_g = 333, 830, 948$ $A_g^s = 1184$ $F_g = (131), 431, 469, 596$ $F_u = 120(121), 172(173), 182(183), 241(242), 303(315), 335(359), 371(412), 415(456), 461(486), 490(535), 555(620)$
Yttrium Vanadate, YVO <sub>4</sub> I4 <sub>1</sub> /amd (D <sub>4h</sub> <sup>19</sup> ) #141 (Refs. 370, 371)	$\Gamma = 2A_{1g}(\text{R}) + 5E_g(\text{R}) + 4B_{1g}(\text{R}) + 1B_{2g}(-) + 3A_{2u}(\text{IR} \parallel \text{c}) + 4E_u(\text{IR} \perp \text{c}) + 1A_{2g}(-) + 1A_{1u}(-) + 1B_{1u}(-) + 2B_{2u}(-)$ $E_u = 195(222), 263(309), 309(311), 780(930)$ $A_{2u} = 310, 455, 803$
Yttrium aluminum garnet (YAG), Y <sub>3</sub> Al <sub>2</sub> (AlO <sub>4</sub> ) <sub>3</sub> Ia3d (O <sub>h</sub> <sup>10</sup> ) #230 (Refs. 372, 373)	$\Gamma = 5A_{1u}(-) + 3A_{1g}(-) + 5A_{2g}(-) + 10E_u(-) + 8E_g(\text{R}) + 14F_{1g}(-) + 17F_{1u}(\text{IR}) + 14F_{2g}(\text{R}) + 16F_{2u}(-)$ $A_{1g} = 373, 561, 783$ $E_g = 162, 310, 340, 403, 531, 537, 714, 758$ $F_{2g} = 144, 218, 243, 259, 296, 408, 436, 544, 690, 719, 857$ $F_{1u} = 122(123), 163(172), 177(180), 219(224), 290(296), 330(340), 373(378), 387(388), 395(403), 428(438), 446(472), 472(511), 516(549), 569(585), 692(712), 723(765), 782(841)$

**TABLE 41** Summary of Available Lattice Vibration Model Parameters

Material	Dispersion model reference		Material	Dispersion model reference	
	Classical	Four-Parameter		Classical	Four-Parameter
AgBr		374	KNbO <sub>3</sub>	365	
AgCl		374	KTaO <sub>3</sub>	329	
AgGaS <sub>2</sub>	336		KTiOPO <sub>4</sub>	355	
AgGaSe <sub>2</sub>	342		LaF <sub>3</sub>		358
Al <sub>2</sub> O <sub>3</sub>	35	36	La <sub>2</sub> O <sub>3</sub>	384	
ALON	205		LiF	251	
As <sub>2</sub> S <sub>3</sub> (cryst)	345		LiIO <sub>3</sub>	361, 362	
As <sub>2</sub> S <sub>3</sub> (glass)	375		LiNbO <sub>3</sub>	385	
As <sub>2</sub> S <sub>3</sub> (cryst)	345		YLiF <sub>4</sub>	316	
As <sub>2</sub> Se <sub>3</sub> (glass)	375		MgAl <sub>2</sub> O <sub>4</sub>	226	
BaF <sub>2</sub>	269		MgF <sub>2</sub>	305, 307	302
BaTiO <sub>3</sub>	329, 376	334	MgO	251	
BeO	284		NaF	386	
BN	257		PbF <sub>2</sub>	272	

**TABLE 41** Summary of Available Lattice Vibration Model Parameters (*Continued*)

Material	Dispersion model reference		Material	Dispersion model reference	
	Classical	Four-Parameter		Classical	Four-Parameter
CaCO <sub>3</sub>	347		PbSe	387	
CaF <sub>2</sub>	269		PbWO <sub>4</sub>	315	
CaMoO <sub>4</sub>	312		Se	291, 377	
CaWO <sub>4</sub>	312		SiO <sub>2</sub>	296, 388	
CdGeP <sub>2</sub>	343		SrF <sub>2</sub>	269	
CdS	259		SrTiO <sub>3</sub>	329	331
CdSe	287		Te	293	
CdTe	259, 377		TeO <sub>2</sub>	368, 389	389
CsBr	243		TiO <sub>2</sub>	372	32
CsCl	243, 244		TlBr		374
CsI	242		TlCl		374
FeS <sub>2</sub>	378, 379		Y <sub>3</sub> Al <sub>5</sub> O <sub>12</sub>	390	373
GaAs	380		Y <sub>2</sub> O <sub>3</sub>	369	
GaN	217, 287		YVO <sub>4</sub>	371	370
GaP	260, 381		ZnGeP <sub>2</sub>	339	
GeO <sub>2</sub>	302		ZnS	259	
HfO <sub>2</sub> :Y <sub>2</sub> O <sub>3</sub>	167		ZnSe	259	
KBr	382		ZnTe	259	
KI	383				

## 2.6 REFERENCES

1. W. J. Tropf, M. E. Thomas, and T. J. Harris, "Properties of Crystals and Glasses," Chap. 33, in M. Bass (ed.), *Handbook of Optics, Second Edition, Vol. 2: Devices, Measurements, and Properties*, McGraw-Hill, New York, 1994.
2. D. E. Gray (ed.), *American Institute of Physics Handbook*, 3d ed., McGraw-Hill, New York, 1972.
3. W. L. Wolfe and G. J. Zissis (eds.), *The Infrared Handbook*, Environmental Research Institute of Michigan, 1985.
4. M. J. Weber (ed.), *Handbook of Laser Science and Technology*, CRC Press, Boca Raton, 1986.
5. E. D. Palik (ed.), *Handbook of Optical Constants of Solids*, Academic Press, Orlando, 1985.
6. E. D. Palik (ed.), *Handbook of Optical Constants of Solids II*, Academic Press, Orlando, 1991.
7. E. D. Palik (ed.), *Handbook of Optical Constants of Solids III*, Academic Press, Orlando, 1997.
8. David N. Nikogosyan, *Nonlinear Optical Crystals: A Complete Survey*, Springer, New York, 2005.
9. N. P. Bansal and R. H. Doremus, *Handbook of Glass Properties*, Academic Press, Orlando, 1986.
10. H. Bach and N. Neuroth, *The Properties of Optical Glass*, Springer-Verlag, Berlin, 1995.
11. B. O. Seraphin and H. E. Bennett, "Optical Constants," in R. K. Willardson and A. C. Beer (eds.), *Semiconductors and Semimetals, Vol. 3: Optical Properties of III-V Compounds*, Academic Press, New York, 1967.
12. F. V. Tooley (ed.), *The Handbook of Glass Manufacture*, Ashlee Publishing Co., New York, 1985.
13. Schott North America, Advanced Optic Home. Contains the optical glass catalog and technical information. [http://www.us.schott.com/advanced\\_optics/english/index.html](http://www.us.schott.com/advanced_optics/english/index.html), accessed Feb 26, 2008.

14. Hoya Corporation USA. <http://www.hoyaoptics.com>, accessed May 21, 2008.
15. Ohara Inc., Products and Services. <http://www.ohara-inc.co.jp/en/product/optical/opticalglass/01000.html>, accessed Sep 11, 2008.
16. D. Krause, "Glasses," in W. Martienssen and H. Warlimont (eds.), *Springer Handbook of Condensed Matter and Materials Data*, Springer, Berlin and Heidelberg, 2005.
17. M. Brinkmann, J. Hayden, M. Letz, et al., "Optical Materials and Their Properties," in F. Trager (ed.), *Springer Handbook of Lasers and Optics*, Springer, New York, 2007.
18. S. Musikant, *Optical Materials: An Introduction to Selection and Application*, Marcel Dekker, New York, 1985.
19. P. Klocek (ed.), *Handbook of Infrared Optical Materials*, Marcel Dekker, New York, 1991.
20. G. W. Fynn and W. J. A. Powell, *Cutting and Polishing Optical and Electronic Materials*, 2d ed., Adam Hilger, Bristol, 1988.
21. W. Zschommler, *Precision Optical Glassworking*, SPIE, Bellingham, WA, 1986.
22. M. E. Thomas, *Optical Propagation in Linear Media: Atmospheric Gases and Particles, Solid-State Components, and Water*, Oxford University Press, USA, 2006.
23. D. C. Harris, *Materials for Infrared Windows and Domes: Properties and Performance*, SPIE Press, Bellingham WA, 1999.
24. J. F. Nye, *Physical Properties of Crystals*, Oxford University Press, Oxford, 1985.
25. P. J. Mohr, B. N. Taylor, and D. B. Newell, "CODATA Recommended Values for the Fundamental Physical Constants: 2006," *J. Phys. Chem. Ref. Data* **37**:1187–1284 (2006).
26. D. Y. Smith, "Dispersion Theory, Sum Rules, and Their Application to the Analysis of Optical Data," in E. D. Palik (ed.), *Handbook of Optical Constants of Solids*, Academic Press, New York, 1985.
27. T. Skettrup, "Urbach's Rule Derived from Thermal Fluctuations in the Band Gap Energy," *Phys. Rev. B* **18**:2622–2631 (1978).
28. F. K. Kneubühl, "Review of the Theory of the Dielectric Dispersion of Insulators," *Infrared Phys.* **29**:925–942 (1989).
29. W. J. Tropf, T. J. Harris, and M. E. Thomas, "Optical Materials: Visible and Infrared," in R. Waynant and W. Ediger (eds.), *Electro-optics Handbook*, McGraw-Hill, New York, 1993.
30. R. H. Lyddane, R. G. Sachs, and E. Teller, "On the Polar Vibrations of Alkali Halides," *Phys. Rev.* **59**:673–676 (1941).
31. W. Cochran and R. A. Cowley, "Dielectric Constants and Lattice Vibrations," *J. Phys. Chem. Solids* **23**:447–450 (1962).
32. F. Gervais and B. Piriou, "Temperature Dependence of Transverse- and Longitudinal-optic Modes in TiO<sub>2</sub> (Rutile)," *Phys. Rev. B* **10**:1642–1654 (1974).
33. J. W. S. Rayleigh, "The Theory of Anomalous Dispersion," *Phil. Mag.* **48**:151–152 (1889).
34. L. Merten and G. Lamprecht, "Directional Dependence of Extraordinary Infrared Oscillator Parameters of Uniaxial Crystals," *Phys. Stat. Sol. (b)* **39**:573–580 (1970). [Also see J. L. Servoin, F. Gervais, A. M. Quittet, and Y. Luspín, "Infrared and Raman Response in Ferroelectric Perovskite Crystals: Apparent Inconsistencies," *Phys. Rev. B* **21**:2038–2041 (1980).]
35. A. S. Barker, "Infrared Lattice Vibrations and Dielectric Dispersion in Corundum," *Phys. Rev.* **132**:1474–1481 (1963).
36. F. Gervais and B. Piriou, "Anharmonicity in Several-Polar-Mode Crystals: Adjusting Phonon Self-Energy of LO and TO Modes in Al<sub>2</sub>O<sub>3</sub> and TiO<sub>2</sub> to Fit Infrared Reflectivity," *J. Phys. C* **7**:2374–2386 (1974).
37. R. H. French, "Electronic Band Structure of Al<sub>2</sub>O<sub>3</sub> with Comparison to ALON and AlN," *J. Am. Ceram. Soc.* **73**:477–489 (1990).
38. W. Sellmeier, "Zur Erklärung der abnormen Farbenfolge im Spectrum einiger Substanzen," *Ann. Phys. Chem.* **219**(Series 2, **143**):272–282 (1871). [Also see W. Sellmeier, "II. Ueber die durch Aetherschwingungen erregten Mitschwingungen der Körpertheilchen und deren Rückwirkung auf die ersteren, besonders zur Erklärung der Dispersion und ihrer Anomalien," *Ann. Phys. Chem.* **221**:520–549 (1872).]
39. F. Urbach, "The Long-Wavelength Edge of Photographic Sensitivity and the Electronic Absorption of Solids," *Phys. Rev.* **92**:1324 (1953).
40. H. Sumi and A. Sumi, "The Urbach–Martienssen Rule Revisited," *J. Phys. Soc. Japan* **56**:2211–2220 (1987).
41. D. L. Wood and J. Tauc, "Weak Absorption Tails in Amorphous Semiconductors," *Phys. Rev. B* **5**:3144–3151 (1972).

42. H. Mori and T. Izawa, "A New Loss Mechanism in Ultra-Low Loss Optical Fiber Materials," *J. Appl. Phys.* **51**:2270–2271 (1980).
43. M. E. Innocenzi, R. T. Swimm, M. Bass, R. H. French, A. B. Villaverde, and M. R. Kokta, "Room-Temperature Optical Absorption in Undoped  $\alpha$ -Al<sub>2</sub>O<sub>3</sub>," *J. Appl. Phys.* **67**:7542–7546 (1990).
44. S. Adachi, "Model Dielectric Constants of GaP, GaAs, GaSb, InSb, InAs, and InSb," *Phys. Rev. B* **35**:7454–7463 (1987).
45. S. Adachi, "Optical Properties of Al<sub>x</sub>Ga<sub>1-x</sub>As Alloys," *Phys. Rev. B* **38**:12345–12352 (1988).
46. S. Adachi, "Optical Properties of In<sub>1-x</sub>Ga<sub>x</sub>As<sub>y</sub>P<sub>1-y</sub> Alloys," *Phys. Rev. B* **39**:12612–12621 (1989).
47. S. Adachi, "Excitonic Effects in the Optical Spectrum of GaAs," *Phys. Rev. B* **41**:1003–1013 (1990).
48. S. Adachi, "Effects of the Indirect Transitions on Optical Dispersion Relations," *Phys. Rev. B* **41**:3504–3508 (1990).
49. S. Adachi, *Physical Properties of III-V Semiconductor Compounds: InP, InAs, GaAs, GaP, InGaAs, and InGaAsP*, Wiley-Interscience, New York, 1992.
50. S. Adachi, T. Kimura, and N. Suzuki. "Optical Properties of CdTe: Experiment and Modeling," *J. Appl. Phys.* **74**:3435–3441 (1993).
51. K. Sato and S. Adachi, "Optical Properties of ZnTe," *J. Appl. Phys.* **73**:926–931 (1993).
52. D. T. Gillespie, A. L. Olsen, and L. W. Nichols, "Transmittance of Optical Materials at High Temperature," *Appl. Opt.* **4**:1488–1493 (1965).
53. M. A. Ordal, R. J. Bell, R. W. Alexander, L. L. Long, and M. R. Querry, "Optical Properties of Fourteen Metals in the Infrared and Far Infrared: Al, Co, Cu, Au, Fe, Pb, Mo, Ni, Pd, Pt, Ag, Ti, V, and W," *Appl. Opt.* **24**:4493–4499 (1985).
54. T. F. Deutsch, "Absorption Coefficient of Infrared Laser Window Materials," *J. Phys. Chem. Solids* **34**:2091–2104 (1973). [Also see T. F. Deutsch, "Laser Window Materials—An Overview," *J. Electron. Mater.* **4**:663–719 (1975).]
55. D. L. Mills and A. A. Maradudin, "Theory of Infrared Absorption by Crystals in the High Frequency Wing of Their Fundamental Lattice Absorption," *Phys. Rev. B* **8**:1617–1630 (1973). [Also see A. A. Maradudin and D. L. Mills, "Temperature Dependence of the Absorption Coefficient of Alkali Halides in the Multiphonon Regime," *Phys. Rev. Lett.* **31**:718–721 (1973).]
56. H. G. Lipson, B. Bendow, N. E. Massa, and S. S. Mitra, "Multiphonon Infrared Absorption in the Transparent Regime of Alkaline-Earth Fluorides," *Phys. Rev. B* **13**:2614–2619 (1976).
57. M. E. Thomas, R. I. Joseph, and W. J. Tropf, "Infrared Transmission Properties of Sapphire, Spinel, Yttria, and ALON as a Function of Frequency and Temperature," *Appl. Opt.* **27**:239–245 (1988).
58. M. E. Thomas, W. J. Tropf, and A. Szpak, "Optical Properties of Diamond," *Diamond and Films and Technology* **5**:159–180 (1995).
59. D. Yanga, M. E. Thomas, S. Andersson, and Bob Podgurski, "Infrared Optical Properties of Eight Different Schott Glasses," *Proc. SPIE* **4102**:134–143 (2000).
60. D. V. Hahn, M. E. Thomas, and D. W. Blodgett, "Modeling of the Frequency- and Temperature-Dependent Absorption Coefficient of Long-Wave-Infrared (2–25  $\mu$ m) Transmitting Materials," *Appl. Opt.* **44**:6913–6920 (2005).
61. J. A. Harrington, B. L. Bobbs, M. Braunstein, R. K. Kim, R. Stearns, and R. Braunstein, "Ultraviolet-Visible Absorption in Highly Transparent Solids by Laser Calorimetry and Wavelength Modulation Spectroscopy," *Appl. Opt.* **17**:1541–1546 (1978).
62. N. C. Frenelius, R. J. Harris, D. B. O'Quinn, M. E. Gangl, D. V. Dempsey, and W. L. Knecht, "Some Optical Properties of Materials Measured at 1.3  $\mu$ m," *Opt. Eng.* **22**:411–418 (1983).
63. J. A. Harrington, D. A. Gregory, and W. F. Ott, "Infrared Absorption in Chemical Laser Window Materials," *Appl. Opt.* **15**:1953–1959 (1976).
64. J. W. Fleming, "Dispersion in GeO<sub>2</sub>-SiO<sub>2</sub> Glasses," *Appl. Opt.* **23**:4486–4493 (1984).
65. D. L. Wood, K. Nassau, and T. Y. Kometani, "Refractive Index of Y<sub>2</sub>O<sub>3</sub> Stabilized Zirconia: Variation with Composition and Wavelength," *Appl. Opt.* **29**:2485–2488 (1990).

66. N. P. Barnes and M. S. Piltch, "Temperature-Dependent Sellmeier Coefficients and Nonlinear Optics Average Power Limit for Germanium," *J. Opt. Soc. Am.* **69**:178–180 (1979).
67. B. Tatian, "Fitting Refractive-Index Data with the Sellmeier Dispersion Formula," *Appl. Opt.* **23**:4477–4485 (1984).
68. P. G. Nutting, "Dispersion Formulas Applicable to Glass," *J. Opt. Soc. Am.* **2–3**:61–65 (1919).
69. H. H. Li, "Refractive Index of ZnS, ZnSe, and ZnTe and Its Wavelength and Temperature Derivatives," *J. Phys. Chem. Ref. Data* **13**:103–150 (1984).
70. F. Zernike, "Refractive Indices of Ammonium Dihydrogen Phosphate and Potassium Dihydrogen Phosphate between 2000 Å and 1.5,  $\mu$ ," *J. Opt. Soc. Am.* **54**:1215–1220 (1964). [Errata: *J. Opt. Soc. Am.* **55**:210E (1965)]
71. M. Herzberger, "Colour Correction in Optical Systems and a New Dispersion Formula," *Opt. Acta* **6**:197–215 (1959).
72. M. Herzberger and C. D. Salzberg, "Refractive Indices of Infrared Optical Materials and Color Correction of Infrared Lenses," *J. Opt. Soc. Am.* **52**:420–427 (1962).
73. A. N. Pikhtin and A. D. Yas'kov, "Dispersion of the Refractive Index of Semiconductors with Diamond and Zinc-Blende Structures," *Sov. Phys. Semicond.* **12**:622–626 (1978).
74. J. Riishede, J. Lægsgaard, J. Broeng, and A. Bjarklev, "All-Silica Photonic Bandgap Fibre with Zero Dispersion and Large Mode Area at 730 nm," *J. Optics A* **6**:667–670 (2004).
75. J. Riishede, N.A. Mortensen, and J. Lægsgaard, "A 'Poor Man's Approach' to Modeling Micro-Structured Optical Fibers," *J. Optics A* **5**:534–538 (2003).
76. J. Lægsgaard, P. J. Roberts, and M. Bache, "Tailoring the Dispersion Properties of Photonic Crystal Fibers," *Opt. Quant. Electron.* **39**:995–1008 (2007).
77. N. A. Mortensen, "Photonic Crystal Fibres: Mapping Maxwell's Equations onto a Schrödinger Equation Eigenvalue Problem," *J. Europ. Opt. Soc. Rapid Public.* **1**:06009 (2006).
78. A. J. Bosman and E. E. Havinga, "Temperature Dependence of Dielectric Constants of Cubic Ionic Compounds," *Phys. Rev.* **129**:1593–1600 (1963).
79. B. Bendow, P. D. Gianino, Y-F. Tsay, and S. S. Mitra, "Pressure and Stress Dependence of the Refractive Index of Transparent Crystals," *Appl. Opt.* **13**:2382–2396 (1974).
80. S. Singh, "Nonlinear Optical Properties," in *Handbook of Laser Science and Technology, Volume III Optical Materials: Part I*, CRC Press, Boca Raton, 1986, pp. 3–228.
81. D. F. Eaton, "Nonlinear Optical Materials," *Science* **253**:281–287 (1991).
82. M. M. Choy and R. L. Byer, "Accurate Second-Order Susceptibility Measurements of Visible and Infrared Nonlinear Crystals," *Phys. Rev. B* **14**:1693–1706 (1976).
83. A. G. Every and A. K. McCurdy, Landolt-Börnstein Numerical Data and Functional Relationships in Science and Technology, New Series, Group III: *Crystal and Solid State Physics, Volume 29A: Low Frequency Properties of Dielectric Crystals*, Springer-Verlag, Berlin, 1993.
84. M. E. Lines, "Scattering Loss in Optic Fiber Materials. I. A New Parametrization," *J. Appl. Phys.* **55**:4052–4057 (1984); "II. Numerical Estimates," *J. Appl. Phys.* **55**:4058–4063 (1984).
85. J. A. Harrington and M. Sparks, "Inverse-Square Wavelength Dependence of Attenuation in Infrared Polycrystalline Fibers," *Opt. Lett.* **8**:223–225 (1983).
86. D. D. Duncan and C. H. Lange, "Imaging Performance of Crystalline and Polycrystalline Oxides," *Proc. SPIE* **1326**:59–70 (1990).
87. J. D. H. Donnay and H. M. Ondik (eds.), *Crystal Data Determination Tables*, 3d ed., U. S. Department of Commerce, 1973.
88. R. W. G. Wyckoff, *Crystal Structures*, John Wiley & Sons, New York, 1963.
89. N. J. Kreidl, "Optical Properties," in F. V. Tooley (ed.), *Handbook of Glass Manufacture*, Books for Industry, New York, 1974, pp. 957–997.
90. H. G. Pfänder, "Geschichte des Glases," Schott Glaslexikon (mvg, Landsberg 1997) pp. 13–23.
91. M. K. Th. Clement, "The Chemical Composition of Optical Glasses and Its Influence on the Optical Properties," in H. Bach, N. Neuroth (eds.), *The Properties of Optical Glass*, Springer, Berlin, Heidelberg, 1998, pp. 58–81.

92. G. F. Brewster, N. J. Kreidl, T. G. Pett, "Lanthanum and Barium in Glass-forming System," *J. Soc. Glass Technol.* **31**:153–169 (1947).
93. W. Jahn, "Mehrstoffsysteme zum Aufbau Optischer Gläser," *Glastechn. Ber.* **43**:107–120 (1961).
94. Schott North America, "Refractive Index and Dispersion," Technical Information 29, (Schott North America Advanced Optics, Duryea, PA 18642, January 2007).
95. S. Wolff and U. Kolberg, "Environmental Friendly Optical Glasses," in H. Bach, N. Neuroth (eds.), *The Properties of Optical Glass*, Springer, Berlin, Heidelberg 1998, pp. 144–148.
96. G. Simmons and H. Wang, *Single Crystal Elastic Constants and Calculated Aggregate Properties: A Handbook*, MIT Press, Cambridge, MA, 1971.
97. R. S. Krishnan, R. Srinivasan, and S. Devanarayanan, *Thermal Expansion of Crystals*, Pergamon Press, Oxford, 1979.
98. Y. S. Touloukian (ed.), *Thermophysical Properties of Matter*, IFI/Plenum, New York, 1970.
99. G. A. Slack, "The Thermal Conductivity of Nonmetallic Crystals," in H. Ehrenreich, F. Seitz, and D. Turnbull (eds.), *Solid State Physics, Vol. 34*, Academic Press, New York, 1979.
100. K. F. Loje and D. E. Schuele, "The Pressure and Temperature Derivative of the Elastic Constants of AgBr and AgCl," *J. Phys. Chem. Solids* **31**:2051–2067 (1970).
101. W. Hidshaw, J. T. Lewis, and C. V. Briscoe, "Elastic Constants of Silver Chloride from 4.2 to 300 K," *Phys. Rev.* **163**:876–881 (1967).
102. Stiffness and compliance of ALON are estimated from the engineering moduli.
103. M. Gospodinov, P. Sveshtarov, N. Petkov, T. Milenov, V. Tassev, and A. Nikolov, "Growth of Large Crystals of Bismuth-Germanium Oxide and Their Physical Properties," *Bulgarian J. Phys.* **16**:520–522 (1989).
104. M. Gospodinov, S. Haussühl, P. Sveshtarov, V. Tassev, and N. Petkov, "Physical Properties of Cubic Bi<sub>12</sub>SiO<sub>20</sub>," *Bulgarian J. Phys.* **15**:140–143 (1988).
105. R. D. Greenough and S. B. Palmer, "The Elastic Constants and Thermal Expansion of Single-Crystal CdTe," *J. Phys. D* **6**:587–592 (1973).
106. A. Yoneda, "Pressure Derivatives of Elastic Constants of Single Crystal MgO and MgAl<sub>2</sub>O<sub>4</sub>," *J. Phys. Earth* **38**:19–55 (1990).
107. A. J. Miller, G. A. Saunders, and Y. K. Yoğurtçu, "Pressure Dependence of the Elastic Constants of PbTe, SnTe and Ge<sub>0.08</sub>Sn<sub>0.92</sub>Te," *J. Phys. C* **14**:1569–1584 (1981).
108. J. B. Wachtman, M. L. Wheat, and S. Marzullo, "A Method for Determining the Elastic Constants of a Cubic Crystal from Velocity Measurements in a Single Arbitrary Direction: Application to SrTiO<sub>3</sub>," *J. Res. Nat. Bur. Stand.* **67A**:193–204 (1963).
109. Y. K. Yoğurtçu, A. J. Miller, and G. A. Saunders, "Elastic Behavior of YAG Under Pressure," *J. Phys. C* **13**:6585–6597 (1980).
110. J. W. Palko, W. M. Kriven, S. V. Sinogeikin, J. D. Bassn, and A. Sayir, "Elastic Constants of Yttria Y<sub>2</sub>O<sub>3</sub> Monocrystals to High Temperatures," *J. Appl. Phys.* **89**:7791–7796 (2001).
111. H. M. Kandil, J. D. Greiner, and J. F. Smith, "Single Crystal Elastic Constants of Yttria-Stabilized Zirconia in the Range 20 to 700°C," *J. Am. Ceram. Soc.* **67**:341–346 (1984).
112. M. H. Grimsditch and G. D. Holah, "Brillouin Scattering and Elastic Moduli of Silver Thiogallate (AgGaS<sub>2</sub>)," *Phys. Rev. B* **12**:4377–4382 (1975). [Also see N. S. Orlova, "X-Ray Diffuse Scattering Study of Anisotropy of Elastic Properties in Silver Thiogallate," *Cryst. Res. Technol.* **33**:87–99 (1998).]
113. R. Fourret, P. Derollez, A. Laamyem, B. Hennion, and J. Gonzalez, "Phonons in Silver Gallium Diselenide," *J. Phys.: Condens. Matter* **9**:6579–6589 (1997).
114. Z. Li, S. -K. Chan, M. H. Grimsditch, and E. S. Zouboulis, "The Elastic and Electromechanical Properties of Tetragonal BaTiO<sub>3</sub> Single Crystals," *J. Appl. Phys.* **70**:7327–7332 (1991).
115. T. Hailing, G. A. Saunders, W. A. Lambson, and R. S. Feigelson, "Elastic Behavior of the Chalcopyrite CdGeAs<sub>2</sub>," *J. Phys. C* **15**:1399–1418 (1982).
116. I. Martynyuk-Lototska, O. Mys, O. Krupych, V. Adamiv, Ya. Burak, R. Vlokh, and W. Schranz, "Elastic, Piezooptic and Acoustooptic Properties of Borate Crystals (Ba<sub>2</sub>O<sub>4</sub>, Li<sub>2</sub>B<sub>4</sub>O<sub>7</sub>, and CsLiB<sub>6</sub>O<sub>10</sub>)," *Integrated Ferroelectrics* **63**:99–103 (2004).

117. G. Fischer and J. Zarembowitch, "Elastic Properties of Single-Crystal Urea," *C. R. Acad. Sc. Paris* **270B**:852–855 (1970).
118. Z. Li, M. Grimsditch, C. M. Foster, and S.-K. Chan, "Dielectric and Elastic Properties of Ferroelectric Materials at Elevated Temperature," *J. Phys. Chem. Solids* **57**:1433–1438 (1996).
119. Y. Ohmachi and N. Uchida, "Temperature Dependence of Elastic, Dielectric, and Piezoelectric Constants in TeO<sub>2</sub> Single Crystals," *J. Appl. Phys.* **41**:2307–2311 (1970).
120. I. M. Silvestrova, Y. V. Pisarevskii, P. A. Senyushenkov, A. I. Krupny, R. Vozska, I. F. Földvári, and J. Janszky, "Temperature Dependence of the Elastic Constants of Paratellurite," *Phys. Stat. Sol. (a)* **101**:437–444 (1987).
121. W. Ruju, L. Fengying, W. Xing, and Y. Huaguang, "Ultrasonic Study on Nd:YVO<sub>4</sub> Crystals," *Chinese J. Lasers* **27**:449–454 (2000).
122. A. V. Kopytov and A. S. Poplavnoi, "Crystal Lattice Dynamics of ZnGeP<sub>2</sub> and AgGaS<sub>2</sub> in Hard Ion Model," *Sov. Phys. J.* **23**:353–360 (1980).
123. W. J. Alton and A. J. Barlow, "Acoustic-Wave Propagation in Tetragonal Crystals and Measurements of the Elastic Constants of Calcium Molybdate," *J. Appl. Phys.* **38**:3817–3820 (1967).
124. J. M. Farley and G. A. Saunders, "Ultrasonic Study of the Elastic Behavior of Calcium Tungstate between 1.5 K and 300 K," *J. Phys. C* **5**:3021–3037 (1972). [Also see J. M. Farley and G. A. Saunders, "The Elastic Constants of CaWO<sub>4</sub>," *Solid State Commun.* **9**:965–969 (1971); and M. Gluyas, F. D. Hughes, and B. W. James, "The Elastic Constants of Calcium Tungstate, 4.2–300 K," *J. Phys. D: Appl. Phys.* **6**:2025–2037 (1973)]
125. J. M. Farley, G. A. Saunders, and D. Y. Chung, "Elastic Properties of Scheelite Structure Molybdates and Tungstates," *J. Phys. C* **8**:780–786 (1975).
126. J. M. Farley, G. A. Saunders, and D. Y. Chung, "Elastic Properties of Strontium Molybdate," *J. Phys. C* **6**:2010–2019 (1973).
127. P. Blanchfield and G. A. Saunders, "The Elastic Constants and Acoustic Symmetry of LiYF<sub>4</sub>," *J. Phys. C* **12**:4673–4689 (1979). [Also see P. Blanchfield, T. Hailing, A. J. Miller, G. A. Saunders, and B. Chapman, "Vibrational Anharmonicity of Oxide and Fluoride Scheelites," *J. Phys. C* **20**:3851–3859 (1983).]
128. V. A. Savastenko and A. U. Sheleg, "Study of the Elastic Properties of Gallium Nitride," *Phys. Stat. Sol. (a)* **48**:K135–K139 (1978).
129. S. Haussühl, "The Propagation of Elastic Waves in Hexagonal Lithium Iodate," *Acustica* **23**:165–169 (1970).
130. I. I. Zubrinov, V. I. Semenov, and D. V. Sheloput, "Elastic and Photoelastic Properties of Proustite," *Sov. Phys. Solid State* **15**:1921–1922 (1974).
131. D. Eimerl, L. Davis, and S. Velsko, "Optical, Mechanical, and Thermal Properties of Barium Borate," *J. Appl. Phys.* **62**:1968–1983 (1987).
132. B. W. Woods, S. A. Payne, J. E. Marion, R. S. Hughes, and L. E. Davis, "Thermomechanical and Thermo-optical Properties of the LiCaAlF<sub>6</sub>: Cr<sup>3+</sup> Laser Material," *J. Opt. Soc. Am.* **B8**:970–977 (1991).
133. A. G. Kalinichev, J. D. Bass, C. S. Zha, P. D. Han, and D. A. Payne, "Elastic Properties of Orthorhombic KNbO<sub>3</sub> Single Crystals by Brillouin Scattering," *J. Appl. Phys.* **74**:6603–6608 (1993).
134. L. Glasser and C. R. A. Catlow, "Modelling Phase Changes in the Potassium Titanyl Phosphate System," *J. Mater. Chem.* **7**:2537–2542 (1997). [Also see I. I. Zubrinov, V. K. Sapozhnikov, E. V. Pestrykov, and V. V. Atuchin, "Elastic and Elastooptic Properties of KTiOPO<sub>4</sub>," *Proc. SPIE* **5129**:249–254 (2003).]
135. R. Guo, S.A. Markgraf, Y. Furukawa, M. Sato, and A. S. Bhalla, "Pyroelectric, Dielectric, and Piezoelectric Properties of LiB<sub>3</sub>O<sub>5</sub>," *J. Appl. Phys.* **78**:7234–7239 (1995).
136. M. Serhane and P. Moch, "Brillouin Scattering in KTiOPO<sub>4</sub>, RbTiOPO<sub>4</sub> and TlTiOPO<sub>4</sub>: A Study of the Ferroelectric-Paraelectric Phase Transition," *J. Phys.: Condens. Matter* **6**:3821–3830 (1994).
137. S. Haussühl, L. Bohaty, and P. Becker, "Piezoelectric and Elastic Properties of the Nonlinear Optical Material Bismuth Triborate, BiB<sub>3</sub>O<sub>6</sub>," *Appl. Phys.* **A82**:495–502 (2006).
138. M. V. Hobden, "The Dispersion of the Refractive Indices of Proustite (Ag<sub>3</sub>AsS<sub>3</sub>)," *Opto-Electronics* **1**:159 (1969).
139. Y. Tsay, B. Bendow, and S. S. Mitra, "Theory of the Temperature Derivative of the Refractive Index in Transparent Crystals," *Phys. Rev. B* **5**:2688–2696 (1972).

140. L. W. Tilton, E. K. Plyler, and R. E. Stephens, "Refractive Index of Silver Chloride for Visible and Infra-Red Radiant Energy," *J. Opt. Soc. Am.* **40**:540–543 (1950).
141. G. C. Bhar, D. K. Ghosh, P. S. Ghosh, and D. Schmitt, "Temperature Effects in AgGaS<sub>2</sub> Nonlinear Devices," *Appl. Opt.* **22**:2492–2494 (1983).
142. E. Takaoka and K. Kato, "Thermo-Optic Dispersion Formula for AgGaS<sub>2</sub>," *Appl. Opt.* **38**:4577–4580 (1999).
143. E. Takaoka and K. Kato, "Thermo-Optic Dispersion Formula of AgGaSe<sub>2</sub> and Its Practical Applications," *Appl. Opt.* **37**:561–564 (1998).
144. K. Vedam, J. L. Kirk, and B. N. N. Achar, "Piezo- and Thermo-Optic Behavior of Spinel (MgAl<sub>2</sub>O<sub>4</sub>)," *J. Solid State Chem.* **12**:213–218 (1975).
145. A. Feldman, D. Horowitz, R. M. Walker, and M. J. Dodge, "Optical Materials Characterization Final Technical Report, February 1, 1978–September 30, 1978," NBS Technical Note 993, February 1979.
146. J. Tapping and M. L. Reilly, "Index of Refraction of Sapphire between 24 and 1060°C for Wavelengths of 633 and 799 nm," *J. Opt. Soc. Am. A* **3**:610–616 (1986).
147. D. Yang, M. E. Thomas, and S. G. Kaplan, "Measurement of the Infrared Refractive Index of Sapphire as Function of Temperature," *Proc. SPIE* **4375**:53–63 (2001).
148. C. H. Lange and D. D. Duncan, "Temperature Coefficient of Refractive Index for Candidate Optical Windows," *SPIE Proc.* **1326**:71–78 (1990).
149. T. Yamamuro, S. Sato, T. Zenno, N. Takeyama, H. Matsuhara, I. Maeda, Y. Matsueda, "Measurement of Refractive Indices of 20 Optical Materials at Low Temperatures," *Optical Engineering* **45**(8):083401 (2006).
150. H. W. Newkirk, D. K. Smith, and J. S. Kahn, "Synthetic Bromellite. III. Some Optical Properties," *Am. Mineralogist* **51**:141–151 (1966).
151. K. Vedam and P. Hennessey, "Piezo- and Thermo-Optical Properties of Bi<sub>12</sub>GeO<sub>20</sub>, II. Refractive Index," *J. Opt. Soc. Am.* **65**:442–445 (1975).
152. N. Umemura, K. Miyata, and K. Kato, "New Data on the Optical Properties of BiB<sub>3</sub>O<sub>6</sub>," *Opt. Matl.* **30**:532–534 (2007).
153. G. N. Ramachandran, "Thermo-Optic Behavior of Solids, I. Diamond," *Proc. Ind. Acad. Sci.* **A25**:266–279 (1947).
154. J. Fontanella, R. L. Johnston, J. H. Colwell, and C. Andeen, "Temperature and Pressure Variation of the Refractive Index of Diamond," *Appl. Opt.* **16**:2949–2951 (1977).
155. I. H. Malitson, "A Redetermination of Some Optical Properties of Calcium Fluoride," *Appl. Opt.* **2**:1103–1107 (1963).
156. M. J. Dodge, "Refractive Index," in M. J. Weber (ed.), *Handbook of Laser Science and Technology, Volume IV, Optical Material: Part 2*, CRC Press, Boca Raton, 1986.
157. T. W. Houston, L. F. Johnson, P. Kisiuk, and D. J. Walsh, "Temperature Dependence of the Refractive Index of Optical Maser Crystals," *J. Opt. Soc. Am.* **53**:1286–1291 (1963).
158. R. Weil and D. Neshmit, "Temperature Coefficient of the Indices of Refraction and the Birefringence in Cadmium Sulfide," *J. Opt. Soc. Am.* **67**:190–195 (1977).
159. R. J. Harris, G. T. Johnson, G. A. Kepple, P. C. Krok, and H. Mukai, "Infrared Thermo-optic Coefficient Measurement of Polycrystalline ZnSe, ZnS, CdTe, CaF<sub>2</sub> and BaF<sub>2</sub>, Single Crystal KCl, and TI-20 Glass," *Appl. Opt.* **16**:436–438 (1977).
160. W. S. Rodney, "Optical Properties of Cesium Iodide," *J. Opt. Soc. Am.* **45**:987–992 (1955).
161. T. Sasaki, Y. Mori, and M. Yoshimura, "Progress in the Growth of a CsLiB<sub>6</sub>O<sub>10</sub> Crystal and Its Application to Ultraviolet Light Generation," *Opt. Matl.* **23**:343–351 (2003). [Also see G. C. Bhar, P. Kumbhakar, and A. K. Chaudhary, "Generation of Ultraviolet Radiation with Wide Angular Tolerance in Cesium Lithium Borate Crystal," *PRAMANA J. Phys.* **55**:413–421 (2000).]
162. N. Umemura and K. Kato, "Ultraviolet Generation Tunable to 0.185 μm in CsLiB<sub>6</sub>O<sub>10</sub>," *Appl. Opt.* **36**:6794–6796 (1997).
163. G. D. Boyd, H. Kasper, and J. H. McFee, "Linear and Nonlinear Optical Properties of AgGaS<sub>2</sub>, CuGaS<sub>2</sub>, and CuInS<sub>2</sub>, and Theory of the Wedge Technique for the Measurement of Nonlinear Coefficients," *IEEE J. Quantum Electr.* **7**:563–573 (1971).



164. G. C. Bhar and G. Ghosh, "Temperature-Dependent Sellmeier Coefficients and Coherence Lengths for Some Chalcopyrite Crystals," *J. Opt. Soc. Am.* **69**:730–733 (1979). [Also see G. C. Bhar, "Refractive Index Dispersion of Chalcopyrite Crystals," *J. Phys. D* **13**:455–460 (1980).]
165. M. Bertolotti, V. Bogdanov, A. Ferrari, A. Jascow, N. Nazorova, A. Pikhtin, and L. Schirone, "Temperature Dependence of the Refractive Index in Semiconductors," *J. Opt. Soc. Am. B* **7**:918–922 (1990).
166. D. A. Yas'kov and A. N. Pikhtin, "Optical Properties of Gallium Phosphide Grown by Float Zone. I. Refractive Index and Reflection Coefficient," *Mat. Res. Bull.* **4**:781–788 (1969). [Also see D. A. Yas'kov and A. N. Pikhtin, "Dispersion of the Index of Refraction of Gallium Phosphide," *Sov. Phys. Sol. State* **9**:107–110 (1967).]
167. H. H. Li, "Refractive Index of Silicon and Germanium and Its Wavelength and Temperature Derivatives," *J. Phys. Chem. Ref. Data* **9**:561–658 (1980).
168. D. L. Wood, K. Nassau, T. Y. Kometani, and D. L. Nash, "Optical Properties of Cubic Hafnia Stabilized with Yttria," *Appl. Opt.* **29**:604–607 (1990).
169. C. S. Hofer, "Thermal Variations of the Refractive Index in Optical Materials," *Proc. SPIE* **681**:135–142 (1986).
170. B. Zysset, I. Biaggio, and P. Günter, "Refractive Indices of Orthorhombic  $\text{KNbO}_3$ . I. Dispersion and Temperature Dependence," *J. Opt. Soc. Am. B* **9**:380–386 (1992). [Also see Y. Uematsu, "Nonlinear Optical Properties of  $\text{KNbO}_3$  Single Crystal in the Orthorhombic Phase," *Jap. J. Appl. Phys.* **13**:1362–1368 (1974).]
171. J. D. Bierlein and H. Vanherzeele, "Potassium Titanyl Phosphate: Properties and New Applications," *J. Opt. Soc. Am. B* **6**:622–633 (1989).
172. K. Kato and E. Takaoka, "Sellmeier and Thermo-Optic Dispersion Formulas for KTP," *Appl. Opt.* **41**:5040–5044 (2002).
173. S. P. Velsko, M. Webb, L. Davis, and C. Huang, "Phase-Matched Harmonic Generation in Lithium Triborate (LBO)," *IEEE J. Quantum Electron.* **27**:2182–2192 (1991).
174. B. W. Woods, S. A. Payne, J. E. Marion, R. S. Hughes, and L. E. Davis, "Thermomechanical and Thermo-Optical Properties of the  $\text{LiCaAlF}_6:\text{Cr}^{3+}$  Laser Material," *J. Opt. Soc. Am.* **B8**:970–977 (1991).
175. D. S. Smith, H. D. Riccius, and R. P. Edwin, "Refractive Indices of Lithium Niobate," *Opt. Commun.* **17**:332–335 (1976).
176. N. P. Barnes and D. J. Gettemy, "Temperature Variation of the Refractive Indices of Yttrium Lithium Fluoride," *J. Opt. Soc. Am.* **70**:1244–1247 (1980).
177. R. E. Stephens and I. H. Malitson, "Index of Refraction of Magnesium Oxide," *J. Nat. Bur. Stand.* **49**:249–252 (1952).
178. T. Radhakrishnan, "Further Studies on the Temperature Variation of the Refractive Index of Crystals," *Proc. Indian Acad. Sci.* **A33**:22–34 (1951).
179. J. N. Zemel, J. D. Jensen, and R. B. Schoolar, "Electrical and Optical Properties of Epitaxial Films of PbS, PbSe, PbTe, and SnTe," *Phys. Rev.* **140A**:330–342 (1965).
180. J. J. Carvajal, P. Segonds, A. Peña, J. Zaccaro, B. Boulanger, F. Diaz, and M. Aguil, "Structural and Optical Properties of  $\text{RbTiOPO}_4:\text{Nb}$  Crystals," *J. Phys.: Condens. Matter* **19**:116214 (2007).
181. N. Uchida, "Optical Properties of Single Crystal Paratellurite ( $\text{TeO}_2$ )," *Phys. Rev. B* **4**:3736–3745 (1971).
182. J. R. DeVore, "Refractive Index of Rutile and Sphalerite," *J. Opt. Soc. Am.* **41**:416–419 (1951).
183. W. S. Rodney and I. H. Malitson, "Refraction and Dispersion of Thallium Bromide Iodide," *J. Opt. Soc. Am.* **46**:956–961 (1956).
184. L. G. DeShazer, S. C. Rand, and B. A. Wechsler, "Laser Crystals," in M. J. Weber (ed.), *Handbook of Laser Science and Technology, Volume V, Optical Material: Part 3*, CRC Press, Boca Raton, 1986.
185. H. S. Shi, G. Zhang, and H. Y. Shen, "Measurement of Refractive Indices and Thermal Refractive Index Coefficients of  $\text{YVO}_4$  Crystal," *J. Synthetic Cryst.* **30**:85–88 (2001).
186. G. D. Boyd, E. Beuhler, and F. G. Storz, "Linear and Nonlinear Optical Properties of  $\text{ZnGeP}_2$  and  $\text{CdSe}$ ," *Appl. Phys. Lett.* **18**:301–304 (1971).
187. D. L. Wood and K. Nassau, "Refractive Index of Cubic Zirconia Stabilized with Yttria," *Appl. Opt.* **21**:2978–2981 (1982).

188. Schott Glass Technologies, Duryea, Pa.
189. Hoya Optics, Inc., Fremont, Calif.
190. W. S. Rodney and R. J. Spindler, "Index of Refraction of Fused-Quartz Glass for Ultraviolet, Visible, and Infrared Wavelengths," *J. Res. Nat. Bur. Stand.* **53**:185–189 (1954). [Also see I. H. Malitson, "Interspecimen Comparison of the Refractive Index of Fused Silica," *J. Opt. Soc. Am.* **55**:1205–1209 (1965).]
191. J. W. Fleming, "Dispersion in  $\text{GeO}_2$ - $\text{SiO}_2$  Glasses," *Appl. Opt.* **23**:4486–4493 (1984).
192. Barr & Stroud, Ltd., Glasgow, Scotland (UK).
193. Corning, Inc., Corning, N. Y. [Also see W. H. Dumbaugh, "Infrared Transmitting Germanate Glasses," *Proc. SPIE* **297**:80–85 (1981).]
194. Ohara Corporation, Somerville, N. J.
195. R. N. Brown and J. J. Hutta, "Material Dispersion in High Optical Quality Heavy Metal Fluoride Glasses," *Appl. Opt.* **24**:4500–4503 (1985).
196. J. M. Jewell, C. Askins, and I. D. Aggarwal, "Interferometric Method for Concurrent Measurement of Thermo-Optic and Thermal Expansion Coefficients," *Appl. Opt.* **30**:3656–3660 (1991).
197. W. S. Rodney, I. H. Malitson, and T. A. King, "Refractive Index of Arsenic Trisulfide," *J. Opt. Soc. Am.* **48**:633–636 (1958).
198. A. R. Hilton and C. E. Jones, "The Thermal Change in the Nondispersive Infrared Refractive Index of Optical Materials," *Appl. Opt.* **6**:1513–1517 (1967).
199. Y. Ohmachi, "Refractive Index of Vitreous  $\text{As}_2\text{Se}_3$ ," *J. Opt. Soc. Am.* **63**:630–631 (1973).
200. J. A. Savage, "Optical Properties of Chalcogenide Glasses," *J. Non - Cryst. Solids* **47**:101–116 (1982).
201. Amorphous Materials, Inc., Garland, Tex.
202. K. F. Hulme, O. Jones, P. H. Davies, and M. V. Hobden, "Synthetic Proustite ( $\text{Ag}_3\text{AsS}_3$ ): A New Crystal for Optical Mixing," *Appl. Phys. Lett.* **10**:133–135 (1967).
203. H. Schröter, "On the Refractive Indices of Some Heavy-Metal Halides in the Visible and Calculation of Interpolation Formulas for Dispersion," *Z. Phys.* **67**:24–36 (1931) [in German].
204. I. H. Malitson and M. J. Dodge, "Refractive Index and Birefringence of Synthetic Sapphire," *J. Opt. Soc. Am.* **62**:1405A (1972). [Also see M. J. Dodge, "Refractive Index," in *Handbook of Laser Science and Technology, Volume IV, Optical Materials: Part 2*, CRC Press, Boca Raton, 1986, p. 30.]
205. W. J. Tropf and M. E. Thomas, "Aluminum Oxynitride (ALON) Spinel," in E. D. Palik (ed.), *Handbook of Optical Constants of Solids II*, Academic Press, Orlando, 1991, pp. 775–785.
206. I. H. Malitson, "Refractive Properties of Barium Fluoride," *J. Opt. Soc. Am.* **54**:628–632 (1964).
207. S. H. Wemple, M. Didomenico, and I. Camlibel, "Dielectric and Optical Properties of Melt-Grown  $\text{BaTiO}_3$ ," *J. Phys. Chem. Solids* **29**:1797–1803 (1968).
208. D. F. Edwards and R. H. White, "Beryllium Oxide," in E. D. Palik (ed.), *Handbook of Optical Constants of Solids II*, Academic Press, Orlando, 1991, pp. 805–814.
209. M. Simon, F. Mersch, C. Kuper, S. Mendricks, S. Wevering, J. Imbrock, and E. Krätzig, "Refractive Indices of Photorefractive Bismuth Titanate, Barium-Calcium Titanate, Bismuth Germanium Oxide, and Lead Germinate," *Phys. Stat. Sol. (a)* **159**:559–562 (1997). [Also see E. Burattini, G. Cappuccio, M. Grandolfo, P. Vecchia, and Sh. M. Efendiev, "Near-Infrared Refractive Index of Bismuth Germanium Oxide ( $\text{Bi}_{12}\text{GeO}_{20}$ )," *J. Opt. Soc. Am.* **73**:495–497 (1983).]
210. R. E. Aldrich, S. O. Hou, and M. L. Harvill, "Electrical and Optical Properties of  $\text{Bi}_{12}\text{SiO}_{20}$ ," *J. Appl. Phys.* **42**:493–494 (1971).
211. F. Peter, "In Refractive Indices and Absorption Coefficients of Diamond between 644 and 226 Micrometers," *Z. Phys.* **15**:358–368 (1923) [In German].
212. M. Daimon and A. Masumura, "High-Accuracy Measurements of the Refractive Index and Its Temperature Coefficient of Calcium Fluoride in a Wide Wavelength Range from 138 to 2326 nm," *Appl. Opt.* **41**:5275–5281 (2002).
213. W. L. Bond, "Measurement of the Refractive Index of Several Crystals," *J. Appl. Phys.* **36**:1674–1677 (1965). [Our fit to the dispersion data.]

214. G. C. Bhar, "Refractive Index Interpolation in Phase-matching," *Appl. Opt.* **15**:305–307 (1976).
215. M. S. Gomez, J. M. Guerra, and F. Vilches, "Weighted Nonlinear Regression Analysis of a Sellmeier Expansion: Comparison of Several Nonlinear Fits of CdS Dispersion," *Appl. Opt.* **24**:1147–1150 (1985).
216. A. G. DeBell, E. L. Dereniak, J. Harvey, J. Nissley, J. Palmer, A. Selvarajan, and W. L. Wolfe, "Cryogenic Refractive Indices and Temperature Coefficients of Cadmium Telluride from 6  $\mu\text{m}$  to 22  $\mu\text{m}$ ," *Appl. Opt.* **18**:3114–3115 (1979).
217. A. H. Kachare, W. G. Spitzer, and J. E. Fredrickson, "Refractive Index of Ion-Implanted GaAs," *J. Appl. Phys.* **47**:4209–4212 (1976).
218. A. S. Barker and M. Ilegems, "Infrared Lattice Vibrations and Free-Electron Dispersion in GaN," *Phys. Rev. B* **7**:743–750 (1973).
219. F. L. Madarasz, J. O. Dimmock, N. Dietz, and K. J. Bachmann, "Sellmeier Parameters for ZnGaP<sub>2</sub> and GaP" *J. Appl. Phys.* **87**:1564–1565 (2000). [Erratum: *J. Appl. Phys.* **87**:7597 (2000).]
220. N. P. Barnes and M. S. Piltch, "Temperature-Dependent Sellmeier Coefficients and Nonlinear Optics Average Power Limit for Germanium," *J. Opt. Soc. Am.* **69**:178–180 (1979).
221. H. H. Li, "Refractive Index of Alkali Halides and Its Wavelength and Temperature Derivatives," *J. Phys. Chem. Ref. Data* **5**:329–528 (1976).
222. N. Umemura, K. Yoshida, and K. Kato, "Phase-Matching Properties of KNbO<sub>3</sub> in the Mid-Infrared," *Appl. Opt.* **38**:991–994 (1999).
223. Y. Fujii and T. Sakudo, "Dielectric and Optical Properties of KTaO<sub>3</sub>," *J. Phys. Soc. Japan* **41**:888–893 (1976).
224. F. Hanson and D. Dick, "Blue Parametric Generation from Temperature-Tuned LiB<sub>3</sub>O<sub>5</sub>," *Opt. Lett.* **16**:205–207 (1991). [Also see C. Chen, Y. Wu, A. Jiang, B. Wu, G. You, R. Li, and S. Lin, "New Nonlinear-Optical Crystal: LiB<sub>3</sub>O<sub>5</sub>," *J. Opt. Soc. Am. B* **6**:616–621 (1989); K. Kato, "Tunable UV Generation to 0.2325  $\mu\text{m}$  in LiB<sub>3</sub>O<sub>5</sub>," *IEEE J. Quantum Electron.* **QE-26**:1173–1175 (1990); and S. P. Velsko, M. Webb, L. Davis, and C. Huang, "Phase-Matched Harmonic Generation in Lithium Triborate (LBO)," *IEEE J. Quantum Electron.* **QE-27**:2182–2192 (1991).]
225. D. E. Zelmon, D. L. Small, and D. Jundt, "Infrared Corrected Sellmeier Coefficients for Congruently Grown Lithium Niobate and 5 mol% Magnesium Oxide-Doped Lithium Niobate," *J. Opt. Soc. Am.* **B14**:3319–3322 (1997). [Also see D. F. Nelson and R. M. Mikulyak, "Refractive Indices of Congruently Melting Lithium Niobate," *J. Appl. Phys.* **45**:3688–3689 (1974).]
226. W. J. Tropf and M. E. Thomas, "Magnesium Aluminum Spinel (MgAlO<sub>4</sub>), in E. D. Palik (ed.), *Handbook of Optical Constants of Solids II*, Academic Press, Orlando, 1991, pp. 881–895. [Improved fit with additional data.]
227. M. J. Dodge, "Refractive Properties of Magnesium Fluoride," *Appl. Opt.* **23**:1980–1985 (1984).
228. M. J. Rosker, K. Cheng, and C. L. Tang, "Practical Urea Optical Parametric Oscillator for Tunable Generation throughout the Visible and Near-infrared," *IEEE J. Quantum Electron.* **QE-21**:1600–1606 (1985).
229. G. E. Jellison, Jr., I. Paulauskas, L. A. Boatner, and D. J. Singh, "Optical Functions of KTaO<sub>3</sub> as Determined by Spectroscopic Ellipsometry and Comparison with Band Structure Calculations," *Phys. Rev.* **B74**:155130 (2006).
230. I. H. Malitson, as quoted by W. L. Wolfe in W. G. Driscoll (ed.), *Handbook of Optics*, 1st ed., McGraw-Hill, New York, 1978. [Our fit to the dispersion data.]
231. F. Weiting and Y. Yixun, "Temperature Effects on the Refractive Index of Lead Telluride and Zinc Sulfide," *Infrared Phys.* **30**:371–373 (1990).
232. S. Singh, J. P. Remeika, and J. R. Potopowicz, "Nonlinear Optical Properties of Ferroelectric Lead Titanate," *Appl. Phys. Lett.* **20**:135–137 (1972).
233. G. Hettner and G. Leisegang, "Dispersion of the Mixed Crystals TlBr-TlI (KRS-5) and TlCl-TlBr (KRS-6) in the Infrared," *Optik* **3**:305–314 (1948) [in German]. [Our fit to the dispersion data.]
234. D. E. Zelmon, D. L. Small, and R. Page, "Refractive-index Measurements of Undoped Yttrium Aluminum Garnet from 0.4 to 5.0  $\mu\text{m}$ ," *Appl. Opt.* **37**:4933–4935 (1998).
235. Y. Nigara, "Measurement of the Optical Constants of Yttrium Oxide," *Jap. J. Appl. Phys.* **7**:404–408 (1968).

236. D. E. Zelmon, E. A. Hanning, and Peter G. Schunemann, "Refractive-Index Measurements and Sellmeier Coefficients for Zinc Germanium Phosphide from 2 to 9 mm with Implications for Phase Matching in Optical Frequency-Conversion Devices," *J. Opt. Soc. Am.* **B18**:1307–1310 (2001).
237. T. M. Bieniewski and S. J. Czyzak, "Refractive Indexes of Single Hexagonal ZnS and CdS Crystals," *J. Opt. Soc. Am.* **53**:496–497 (1963). [Our fit to the dispersion data.]
238. H. H. Li, "Refractive Index of ZnS, ZnSe, and ZnTe and Its Wavelength and Temperature Derivatives," *J. Phys. Chem. Ref. Data* **13**:103–150 (1984).
239. P. Kloock and L. Colombo, "Index of Refraction, Dispersion, Bandgap and Light Scattering in GeSe and GeSbSe Glasses," *J. Non-Cryst. Solids* **93**:1–16 (1987).
240. S. A. Solin and A. K. Ramdas, "Raman Spectrum of Diamond," *Phys. Rev. B* **1**:1687–1698 (1970). [Also see B. J. Parsons, "Spectroscopic Mode Grüneisen Parameters for Diamond," *Proc. Royal Soc. Lond. A* **352**:397–417 (1977).]
241. B. A. Weinstein and G. J. Piermarini, "Raman Scattering and Phonon Dispersion in Si and GaP at Very High Pressure," *Phys. Rev. B* **12**:1172–1186 (1975).
242. D. Olego and M. Cardona, "Pressure Dependence of Raman Phonons of Ge and 3C-SiC," *Phys. Rev. B* **25**:1151–1160 (1982).
243. P. Vergnat, J. Claudel, A. Hadni, P. Strimer, and F. Vermillard, "Far Infrared Optical Constants of Cesium Halides at Low Temperatures," *J. Phys.* **30**:723–735 (1969) [in French].
244. H. Shimizu, Y. Ohbayashi, K. Yamamoto, K. Abe, M. Midorikawa, and Y. Ishibashi, "Far-Infrared Reflection Spectra of CsCl Single Crystals," *J. Phys. Soc. Japan* **39**:448–450 (1975).
245. S. S. Mitra, "Infrared and Raman Spectra Due to Lattice Vibrations," in *Optical Properties of Solids*, Plenum Press, New York, 1969.
246. R. P. Lowndes and C. H. Perry, "Molecular Structure and Anharmonicity in Thallium Iodide," *J. Chem. Phys.* **58**:271:278 (1973).
247. M. Galtier, A. Montaner, and G. Vidal, "Optical Phonons of CaO, SrO, BaO at the Center of the Brillouin Zone at 300 and 17 K," *J. Phys. Chem. Solids* **33**:2295–2302 (1972) [in French].
248. R. Ramnarine and W. F. Sherman, "The Far-Infrared Investigation of the Mode Frequencies of Some Alkaline Earth Sulfides," *Infrared Phys.* **26**:17–21 (1986).
249. J. L. Jacobson and E. R. Nixon, "Infrared Dielectric Response and Lattice Vibrations of Calcium and Strontium Oxides," *J. Phys. Chem. Solids* **29**:967–976 (1968).
250. Z. V. Popović, G. Stanišić, D. Stojanović, and R. Kostić, "Infrared and Raman Spectral of CdO," *Phys. Stat. Sol. (b)* **165**:K109–K112 (1991).
251. J. R. Jasperse, A. Kahan, J. N. Plendl, and S. S. Mitra, "Temperature Dependence of Infrared Dispersion in Ionic Crystals LiF and MgO," *Phys. Rev.* **146**:526–542 (1966). [Also see A. Kachare, G. Andermann, and L. R. Brantley, "Reliability of Classical Dispersion Analysis of LiF and MgO Reflectance Data," *J. Phys. Chem. Solids* **33**:467–475 (1972).]
252. R. Geick, "Measurement and Analysis of the Fundamental Lattice Vibration Spectrum of PbS," *Phys. Lett.* **10**:51–52 (1964).
253. H. Birkhard, R. Geick, P. Kästner, and K. -H. Unkelback, "Lattice Vibrations and Free Carrier Dispersion in PbSe," *Phys. Stat. Sol. (b)* **63**:89–96 (1974).
254. E. G. Bylander and M. Hass, "Dielectric Constant and Fundamental Lattice Frequency of Lead Telluride," *Solid State Commun.* **4**:51–52 (1966).
255. M. Ilegems and G. L. Pearson, "Infrared Reflection Spectra of Ga<sub>1-x</sub>Al<sub>x</sub>As Mixed Crystals," *Phys. Rev. B* **1**:1576–1582 (1970).
256. A. Mooradian and G. B. Wright, "First Order Raman Effect in III-V Compounds," *Solid State Commun.* **4**:431–434 (1966). [Also see W. J. Turner and W. E. Reese, "Infrared Lattice Bands in AlSb," *Phys. Rev.* **127**:126–131 (1962).]
257. P. J. Gielisse, S. S. Mitra, J. N. Plendl, R. D. Griffis, L. C. Mansur, R. Marshall, and E. A. Pascoe, "Lattice Infrared Spectra of Boron Nitride and Boron Monophosphide," *Phys. Rev.* **155**:1039–1046 (1967).
258. J. A. Sanjurjo, E. López-Cruz, P. Vogl, and M. Cardona, "Dependence on Volume of the Phonon Frequencies and the IR Effective Charges of Several III-V Semiconductors," *Phys. Rev.* **B28**:4579–4584 (1983).

259. A. Manabe, A. Mitsuishi, and H. Yoshinga, "Infrared Lattice Reflection Spectra of II-VI Compounds," *Jap. J. Appl. Phys.* **6**:593–600 (1967).
260. G. R. Wilkenson, "Raman Spectra of Ionic, Covalent, and Metallic Crystals," in A. Anderson (ed.), *The Raman effect, Vol. 2: Applications*, Marcel Dekker, New York, 1973.
261. A. S. Barker, "Dielectric Dispersion and Phonon Line Shape in Gallium Phosphide," *Phys. Rev.* **165**:917–922 (1968).
262. M. Hass and B. W. Hennis, "Infrared Lattice Reflection Spectra of III-V Compound Semiconductors," *J. Phys. Chem. Solids* **23**:1099–1104 (1962).
263. R. Carles, N. Saint-Cricq, J. B. Renucci, M. A. Renucci, and A. Zwick, "Second-Order Raman Scattering in InAs," *Phys. Rev.* **B22**:4804–4815 (1980).
264. R. B. Sanderson, "Far Infrared Optical Properties of Indium Antimonide," *J. Phys. Chem. Solids* **26**:803–810 (1965).
265. L. Patrick and W. J. Choyke, "Lattice Absorption Bands in SiC," *Phys. Rev.* **123**:813–815 (1965).
266. W. G. Nilsen, "Raman Spectrum of Cubic ZnS," *Phys. Rev.* **182**:838–850 (1969).
267. J. C. Irwin and J. LaCombe, "Raman Scattering in ZnTe," *J. Appl. Phys.* **41**:1444–1450 (1970).
268. R. Shivastava, H. V. Lauer, L. L. Chase, and W. E. Bron, "Raman Frequencies of Fluorite Crystals," *Phys. Lett.* **36A**:333–334 (1971).
269. W. Kaiser, W. G. Spitzer, R. H. Kaiser, and L. E. Howarth, "Infrared Properties of CaF<sub>2</sub>, SrF<sub>2</sub>, and BaF<sub>2</sub>," *Phys. Rev.* **127**:1950–1954 (1962).
270. I. Richman, "Longitudinal Optical Phonons in CaF<sub>2</sub>, SrF<sub>2</sub>, and BaF<sub>2</sub>," *J. Chem. Phys.* **41**:2836–2837 (1966).
271. D. R. Bosomworth, "Far-Infrared Optical Properties of CaF<sub>2</sub>, SrF<sub>2</sub>, BaF<sub>2</sub>, and CdF<sub>2</sub>," *Phys. Rev.* **157**:709–715 (1967).
272. J. D. Axe, J. W. Gaglianella, and J. E. Scardefield, "Infrared Dielectric Properties of Cadmium Fluoride and Lead Fluoride," *Phys. Rev.* **139**:A1211–A1215 (1965).
273. R. Droste and R. Geick, "Investigation of the Infrared-Active Lattice Vibration in SrCl<sub>2</sub>," *Phys. Stat. Sol. (b)* **62**:511–517 (1974).
274. A. Sadoc, F. Moussa, and G. Pepy, "The Lattice Dynamics of SrCl<sub>2</sub>," *J. Phys. Chem. Solids* **37**:197–199 (1976).
275. J. D. Axe and G. D. Pettit, "Infrared Dielectric Dispersion and Lattice Dynamics of Uranium Dioxide and Thorium Dioxide," *Phys. Rev.* **151**:676–679 (1966).
276. P. G. Marlowe and J. P. Russell, "Raman Scattering in Uranium Dioxide," *Phil. Mag.* **14**:409–410 (1966).
277. S. Shin and M. Ishigame, "Defect-Induced Hyper-Raman Spectra in Cubic Zirconia," *Phys. Rev. B* **34**:8875–8882 (1986).
278. S. P. S. Porto and R. S. Krishnan, "Raman Effect of Corundum," *J. Chem. Phys.* **47**:1009–1012 (1967).
279. D. R. Renneke and D. W. Lynch, "Infrared Lattice Vibrations and Dielectric Dispersion in Single-Crystal Cr<sub>2</sub>O<sub>3</sub>," *Phys. Rev.* **138**:A530–A533 (1965).
280. I. R. Beattie and T. R. Gibson, "The Single-Crystal Raman Spectra of Nearly Opaque Materials. Iron(III) Oxide and Chromium(III) Oxide," *J. Chem. Soc. (A)*, 980–986 (1970). DOI: 10.1039/J19700000980.
281. S. Onari, T. Arai, and K. Kudo, "Infrared Lattice Vibrations and Dielectric Dispersion in  $\alpha$ -Fe<sub>2</sub>O<sub>3</sub>," *Phys. Rev. B* **16**:1717–1721 (1977).
282. G. L. Bottger and C. V. Damsgard, "Raman Scattering in Wurtzite-Type AgI Crystals," *J. Chem. Phys.* **57**:1215–1218 (1972).
283. L. E. McNeil, M. Grimsditch, and R. H. French, "Vibrational Spectroscopy of Aluminum Nitride," *J. Am. Ceram. Soc.* **76**:1132–1136 (1993).
284. E. Loh, "Optical Phonons in BeO Crystals," *Phys. Rev.* **166**:673–678 (1967).
285. C. A. Arguello, D. L. Rousseau, and S. P. S. Porto, "First-Order Raman Effect in Wurtzite-Type Crystals," *Phys. Rev.* **181**:1351–1363 (1969).
286. B. Tell, T. C. Damen, and S. P. S. Porto, "Raman Effect in Cadmium Sulfide," *Phys. Rev.* **144**:771–774 (1966).
287. R. Geick, C. H. Perry, and S. S. Mitra, "Lattice Vibrational Properties of Hexagonal CdSe," *J. Appl. Phys.* **37**:1994–1997 (1966).

288. D. D. Manchon, A. S. Barker, P. J. Dean, and R. B. Zetterstrom, "Optical Studies of the Phonons and Electrons in Gallium Nitride," *Solid State Commun.* **8**:1227–1231 (1970).
289. D. W. Feldman, J. H. Parker, W. J. Choyee, and L. Patrick, "Raman Scattering in 6H SiC," *Phys. Rev.* **170**:698–704 (1968).
290. T. C. Damen, S. P. S. Porto, and B. Tell, "Raman Effect in Zinc Oxide," *Phys. Rev.* **142**:570–574 (1966).
291. R. Geick, U. Schröder, and J. Stuke, "Lattice Vibrational Properties of Trigonal Selenium," *Phys. Stat. Sol.* **24**:99–108 (1967).
292. G. Locovsky, A. Mooradian, W. Taylor, G. B. Wright, and R. C. Keezer, "Identification of the Fundamental Vibrational Modes of Trigonal,  $\alpha$ -monoclinic, and Amorphous Selenium," *Solid State Commun.* **5**:113–117 (1967).
293. E. D. Palik, "Tellurium (Te)," in E. D. Palik (ed.), *Handbook of Optical Constants of Solids II*, Academic Press, Orlando, 1991, pp. 709–723.
294. B. D. Saksena, "Analysis of the Raman and Infra-Red Spectra of  $\alpha$ -Quartz," *Proc. Ind. Acad. Sci.* **12A**:93–139 (1940).
295. J. F. Scott and S. P. S. Porto, "Longitudinal and Transverse Optical Lattice Vibrations in Quartz," *Phys. Rev.* **161**:903–910 (1967).
296. S. M. Shapiro and J. D. Axe, "Raman Scattering from Polar Phonons," *Phys. Rev. B* **6**:2420–2427 (1972).
297. J. F. Scott, "Raman Spectra of GeO<sub>2</sub>," *Phys. Rev. B* **8**:3488–3493 (1970).
298. A. S. Barker and J. A. Detzenberger, "Infrared Lattice Vibrations in CoF<sub>2</sub>," *Solid State Commun.* **3**:131–132 (1965).
299. M. Balkanski, P. Moch, and G. Parisot, "Infrared Lattice-Vibration Spectra in NiF<sub>2</sub>, CoF<sub>2</sub>, and FeF<sub>2</sub>," *J. Chem. Phys.* **44**:940–944 (1966).
300. R. M. Macfarlane and S. Ushioda, "Light Scattering from Phonons in CoF<sub>2</sub>," *Solid State Commun.* **8**:1081–1083 (1970).
301. S. P. S. Porto, P. A. Fleury, and T. C. Damen, "Raman Spectra of TiO<sub>2</sub>, MgF<sub>2</sub>, ZnF<sub>2</sub>, FeF<sub>2</sub>, and MnF<sub>2</sub>," *Phys. Rev.* **154**:522–526 (1967).
302. J. Giordano and C. Benoit, "Infrared Spectra of Iron, Zinc, and Magnesium Fluorides: I. Analysis of Results," *J. Phys. C* **21**:2749–2770 (1988). [Also see C. Benoit and J. Giordano, "Dynamical Properties of Crystals of MgF<sub>2</sub>, ZnF<sub>2</sub>, and FeF<sub>2</sub>: II. Lattice Dynamics and Infrared Spectral," *J. Phys. C* **21**:5209–5227 (1988).]
303. A. Kahan, J. W. Goodrum, R. S. Singh, and S. S. Mitra, "Polarized Reflectivity Spectra of Tetragonal GeO<sub>2</sub>," *J. Appl. Phys.* **42**:4444–4446 (1971).
304. D. M. Roessler and W. A. Albers, "Infrared Reflectance of Single Crystal Tetragonal GeO<sub>2</sub>," *J. Phys. Chem. Solids* **33**:293–296 (1972).
305. A. S. Barker, "Transverse and Longitudinal Optic Mode Study in MgF<sub>2</sub> and ZnF<sub>2</sub>," *Phys. Rev.* **136**:A1290–A1295 (1964).
306. R. S. Krishnan and J. P. Russell, "The First-Order Raman Spectrum of Magnesium Fluoride," *Brit. J. Appl. Phys.* **17**:501–503 (1966).
307. J. Giordano, "Temperature Dependence of IR Spectra of Zinc and Magnesium Fluoride," *J. Phys. C* **20**:1547–1562 (1987).
308. R. Summit, "Infrared Absorption in Single-Crystal Stannic Oxide: Optical Lattice-Vibration Modes," *J. Appl. Phys.* **39**:3762–3767 (1967).
309. J. F. Scott, "Raman Spectrum of SnO<sub>2</sub>," *J. Chem. Phys.* **53**:852–853 (1970).
310. R. S. Katiyar, P. Dawson, M. M. Hargreave, and G. R. Wilkerson, "Dynamics of the Rutile Structure III. Lattice Dynamics, Infrared and Raman Spectra of SnO<sub>2</sub>," *J. Phys. C* **4**:2421–2431 (1971).
311. R. S. Katiyar and R. S. Krishnan, "The Vibrational Spectrum of Rutile," *Phys. Lett.* **25A**:525–526 (1967).
312. A. S. Barker, "Infrared Lattice Vibrations in Calcium Tungstate and Calcium Molybdate," *Phys. Rev.* **135**:A742–A747 (1964).
313. P. Tarte and M. Liegeois-Duyckaerts, "Vibrational Studies of Molybdates, Tungstates and Related Compounds—I. New Infrared Data and Assignments for the Scheelite-Type Compounds X<sup>II</sup>MoO<sub>4</sub> and X<sup>II</sup>WO<sub>4</sub>," *Spectrochim. Acta* **28A**:2029–2036.

314. V. M. Nagiev, Sh. M. Efendiev, and V. M. Burlakov, "Vibrational Spectra of Crystals with Scheelite Structure and Solid Solutions on Their Basis," *Phys. Stat. Sol. (b)* **125**:467–475 (1984).
315. J. M. Stencel, E. Silberman, and J. Springer, "Temperature-Dependent Reflectivity, Dispersion Parameters, and Optical Constants for  $\text{PbWO}_4$ ," *Phys. Rev. B* **12**:5435–5441 (1976).
316. S. A. Miller, H. E. Rast, and H. H. Caspers, "Lattice Vibrations of  $\text{LiF}_4$ ," *J. Chem. Phys.* **53**:4172–4175 (1970).
317. E. Schultheiss, A. Scharmann, and D. Schwabe, "Lattice Vibrations in  $\text{BiLiF}_4$  and  $\text{YLiF}_4$ ," *Phys. Stat. Sol. (b)* **138**:465–475 (1986).
318. S. P. S. Porto and J. F. Scott, "Raman Spectra of  $\text{CaWO}_4$ ,  $\text{SrWO}_4$ ,  $\text{CaMoO}_4$ , and  $\text{SrMoO}_4$ ," *Phys. Rev.* **157**:716–719 (1967).
319. S. Desgreniers, S. Jandl, and C. Carlone, "Temperature Dependence of the Raman Active Phonons in  $\text{CaWO}_4$ ,  $\text{SrWO}_4$ , and  $\text{BaWO}_4$ ," *J. Phys. Chem. Solids* **45**:1105–1109 (1984).
320. R. K. Khanna, W. S. Brower, B. R. Guscott, and E. R. Lippincott, "Laser Induced Raman Spectra of Some Tungstates and Molybdates," *J. Res. Nat. Bur. Std.* **72A**:81–84 (1968).
321. M. P. O'Horo, A. L. Frisillo, and W. B. White, "Lattice Vibrations of  $\text{MgAl}_2\text{O}_4$  Spinel," *J. Phys. Chem. Solids* **34**:23–28 (1973).
322. M. E. Strifler and S. I. Boldish, "Transverse and Longitudinal Optic Mode Frequencies of Spinel  $\text{MgAl}_2\text{O}_4$ ," *J. Phys. C* **11**:L237–L241 (1978).
323. K. Yamamoto, T. Murakawa, Y. Ohbayashi, H. Shimizu, and K. Abe, "Lattice Vibrations in  $\text{CdIn}_2\text{S}_4$ ," *J. Phys. Soc. Japan* **35**:1258 (1973).
324. H. Shimizu, Y. Ohbayashi, K. Yamamoto, and K. Abe, "Lattice Vibrations in Spinel-Type  $\text{CdIn}_2\text{S}_4$ ," *J. Phys. Soc. Japan* **38**:750–754 (1975).
325. H. D. Lutz, B. Müller, and H. J. Steiner, "Lattice Vibration Spectra. LIX. Single Crystal Infrared and Raman Studies of Spinel Type Oxides," *J. Solid State Chem.* **90**:54–60 (1991).
326. H. D. Lutz, G. Wäschenbach, G. Kliche, and H. Haeuseler, "Lattice Vibrational Spectra, XXXIII: Far-Infrared Reflection Spectra, TO and LO Phonon Frequencies, Optical and Dielectric Constants, and Effective Changes of the Spinel-Type Compounds  $\text{MCr}_2\text{S}_4$  ( $M = \text{Mn, Fe, Co, Zn, Cd, Hg}$ ),  $\text{MCr}_2\text{Se}_4$  ( $M = \text{Zn, Cd, Hg}$ ), and  $\text{MIn}_2\text{S}_4$  ( $M = \text{Mn, Fe, Co, Zn, Cd, Hg}$ )," *J. Solid State Chem.* **48**:196–208 (1983).
327. K. Wakamura, H. Iwatani, and K. Takarabe, "Vibrational Properties of One- and Two-Mode Behavior in Spinel Type Mixed Systems  $\text{Zn}_{1-x}\text{Cd}_x\text{Cr}_2\text{S}_4$ ," *J. Phys. Chem. Solids* **48**:857–861 (1987).
328. H. C. Gupta, G. Sood, A. Parashar, and B. B. Tripathi, "Long Wavelength Optical Lattice Vibrations in Mixed Chalcogenide Spinel  $\text{Zn}_{1-x}\text{Cd}_x\text{Cr}_2\text{S}_4$  and  $\text{CdCr}_2(\text{S}_{1-x}\text{Se}_x)_4$ ," *J. Phys. Chem. Solids* **50**:925–929 (1989).
329. A. S. Barker and J. H. Hopfield, "Coupled-Optical-Phonon-Mode Theory of the Infrared Dispersion in  $\text{BaTiO}_3$ ,  $\text{SrTiO}_3$ , and  $\text{KTaO}_3$ ," *Phys. Rev.* **135**:A1732–A1737 (1964).
330. A. S. Barker, "Temperature Dependence of the Transverse and Longitudinal Optic Mode Frequencies and Charges in  $\text{SrTiO}_3$  and  $\text{BaTiO}_3$ ," *Phys. Rev.* **145**:391–399 (1966).
331. J. L. Servoin, Y. Luspin, and F. Gervais, "Infrared Dispersion in  $\text{SrTiO}_3$  at High Temperature," *Phys. Rev. B* **22**:5501–5506 (1980).
332. C. H. Perry and E. F. Young, "Infrared Studies of Some Perovskite Fluorides. I. Fundamental Lattice Vibrations," *J. Appl. Phys.* **38**:4616–4624 (1967).
333. A. Scalabrin, A. S. Chaves, D. S. Shim, and S. P. S. Porto, "Temperature Dependence of the  $A_1$  and E Optical Phonons in  $\text{BaTiO}_3$ ," *Phys. Stat. Sol. (b)* **79**:731–742 (1977).
334. J. L. Servoin, F. Gervais, A. M. Quittet, and Y. Luspin, "Infrared and Raman Responses in Ferroelectric Perovskite Crystals," *Phys. Rev. B* **21**:2038–2041 (1980).
335. G. Burns and B. A. Scott, "Lattice Modes in Ferroelectric Perovskites:  $\text{PbTiO}_3$ ," *Phys. Rev. B* **7**:3088–3101 (1973).
336. J. P. van der Ziel, A. E. Meixner, H. M. Kasper, and J. A. Ditzberger, "Lattice Vibrations of  $\text{AgGaS}_2$ ,  $\text{AgGaSe}_2$ , and  $\text{CuGaS}_2$ ," *Phys. Rev. B* **9**:4286–4294 (1974).
337. W. H. Koschel and M. Bettini, "Zone-Centered Phonons in  $\text{A}^1\text{B}^{\text{III}}\text{S}_2$  Chalcopyrites," *Phys. Stat. Sol. (b)* **72**:729–737 (1975).

338. V. G. Tyuterev and S. I. Skachkov, "Lattice Dynamics, Thermodynamic and Elastic Properties of  $\text{AgGaS}_2$ ," *Nuovo Cimento* **14D**:1097–1103 (1992).
339. A. Miller, G. D. Holah, and W. C. Clark, "Infrared Dielectric Dispersion of  $\text{ZnGeP}_2$  and  $\text{CdGeP}_2$ ," *J. Phys. Chem. Solids* **35**:685–693 (1974).
340. M. Bettini and A. Miller, "Optical Phonons and  $\text{ZnGeP}_2$  and  $\text{CdGeP}_2$ ," *Phys. Stat. Sol. (b)* **66**:579–586 (1974).
341. I. P. Kaminow, E. Buehler, and J. H. Wernick, "Vibrational Modes in  $\text{ZnSiP}_2$ ," *Phys. Rev. B* **2**:960–966 (1970).
342. L. Artus, J. Pascual, A. Gouillet, and J. Camassel, "Polarized Infrared Spectra of  $\text{AgGaS}_2$ ," *Solid State Commun.* **69**:753–756 (1989).
343. G. D. Holah, A. Miller, W. D. Dunnett, and G. W. Isler, "Polarised Infrared Reflectivity of  $\text{CdGeAs}_2$ ," *Solid State Commun.* **23**:75–78 (1977).
344. E. V. Antropova, A. V. Kopytov, and A. S. Poplavnoi, "Phonon Spectrum and IR Optical Properties of  $\text{CdGeAs}_2$ ," *Opt. Spectrosc.* **64**:766–768 (1988).
345. R. Zallen, M. L. Slade, and A. T. Ward, "Lattice Vibrations and Interlayer Interactions in Crystalline  $\text{As}_2\text{S}_3$  and  $\text{As}_2\text{Se}_3$ ," *Phys. Rev. B* **3**:4257–4273 (1971).
346. S. P. S. Porto, J. A. Giordmaine, and T. C. Damen, "Depolarization of Raman Scattering in Calcite," *Phys. Rev.* **147**:608–611 (1966).
347. K. H. Hellwege, W. Lesch, M. Plihal, and G. Schaack, "Two Phonon Absorption Spectra and Dispersion of Phonon Branches in Crystals of Calcite Structure," *Z. Physik* **232**:61–86 (1970). [Also see R. K. Vincent, "Emission Polarization Study on Quartz and Calcite," *Appl. Opt.* **11**:1942–1945 (1972).]
348. J. Q. Lu, G. X. Lan, B. Li, Y. Y. Yang, and H. F. Wang, "Raman Scattering Study of the Single Crystal  $\beta\text{-BaB}_2\text{O}_4$  under High Pressure," *J. Phys. Chem. Solids* **49**:519–527 (1988).
349. W. Wojdowski, "Vibrational Modes in  $\text{Bi}_{12}\text{GeO}_{20}$  and  $\text{Bi}_{12}\text{SiO}_{20}$  Crystals," *Phys. Stat. Sol. (b)* **130**:121–130 (1985).
350. X. Hu, J. Wang, B. Teng, C-K. Loong, and M. Grimsditch, "Raman Study of Phonons in Bismuth Triborate  $\text{BiB}_3\text{O}_6$  Crystal," *J. Appl. Phys.* **97**:033501 (2005).
351. D. Kasprowicz, T. Runka, M. Szybowicz, P. Ziobrowski, A. Majchrowski, E. Michalski, and M. Drozdowski, "Characterization of Bismuth Triborate Single Crystal Using Brillouin and Raman Spectroscopy," *Cryst. Res. Technol.* **40**:459–465 (2005).
352. H. Vogt, T. Chattopadhyay, and H. J. Stolz, "Complete First-Order Raman Spectra of the Pyrite Structure Compounds  $\text{FeS}_2$ ,  $\text{MnS}_2$ , and  $\text{SiP}_2$ ," *J. Phys. Chem. Solids* **44**:869–873 (1983).
353. H. D. Lutz, G. Schneider, and G. Kliche, "Far-Infrared Reflection Spectra, TO- and LO-Phonon Frequencies, Coupled and Decoupled Plasmon-Phonon Modes, Dielectric Constants, and Effective Dynamical Charges of Manganese, Iron, and Platinum Group Pyrite Type Compounds," *J. Phys. Chem. Solids* **46**:437–443 (1985).
354. D. K. Agrawal and C. H. Perry, "The Temperature Dependent Raman Spectra of KDP,  $\text{KD}^*\text{P}$ , KDA, and ADP," in M. Balkanski (ed.), *Proceedings of the Second International Conference on Light Scattering in Solids*, Flammarion Sciences, Paris, 1971, pp. 429–435.
355. G. E. Kugel, F. Bréhat, B. Wyncke, M. D. Fontana, G. Marnier, C. Carabatos-Nedelec, and J. Mangin, "The Vibrational Spectrum of  $\text{KTiOPO}_4$  Single Crystal Studied by Raman and Infrared Reflective Spectroscopy," *J. Phys. C* **21**:5565–5583 (1988).
356. B. Mohamadou, G. E. Kugel, F. Brehat, B. Wyncke, G. Marnier, P. Simon, "High-Temperature Vibrational Spectra, Relaxation, and Ionic Conductivity Effects in  $\text{KTiOPO}_4$ ," *J. Phys. Condens. Matter* **3**:9489–9501 (1991).
357. R. P. Bauman and S. P. S. Porto, "Lattice Vibrations and Structure of Rare-Earth Fluorides," *Phys. Rev.* **161**:842–847 (1967).
358. R. P. Lowndes, J. F. Parrish, and C. H. Perry, "Optical Phonons and Symmetry of Tysonite Lanthanide Fluorides," *Phys. Rev.* **182**:913–922 (1969).
359. E. Liarokapis, E. Anastassakis, and G. A. Kourouklis, "Raman Study of Phonon Anharmonicity in  $\text{LaF}_3$ ," *Phys. Rev. B* **32**:8346–8355 (1985).



360. H. R. Xia, L. X. Li, H. Yu, S. M. Dong, J. Y. Wang, Q. M. Lu, C. Q. Ma, and X. N. Wang, "Structure and the Nonlinearity of Lithium Triborate Studied by Raman and Infrared Reflectivity Spectroscopy," *J. Mater. Res.* **16**:3465–3470 (2001).
361. W. Otaguro, E. Weiner-Avnera, C. A. Arguello, and S. P. S. Porto, "Phonons, Polaritrons, and Oblique Phonons in  $\text{LiIO}_3$  by Raman Scattering and Infrared Reflection," *Phys. Rev. B* **4**:4542–4551 (1971).
362. J. L. Duarte, J. A. Sanjurjo, and R. S. Katiyar, "Off-Normal Infrared Reflectivity in Uniaxial Crystals:  $\alpha$ - $\text{LiIO}_3$  and  $\alpha$ -quartz," *Phys. Rev. B* **36**:3368–3372 (1987).
363. R. Claus, G. Borstel, E. Wiesendanger, and L. Steffan, "Directional Dispersion and Assignment of Optical Phonons in  $\text{LiNbO}_3$ ," *Z. Naturforsch.* **27a**:1187–1192 (1972).
364. X. Yang, G. Lan, B. Li, and H. Wang, "Raman Spectra and Directional Dispersion in  $\text{LiNbO}_3$  and  $\text{LiTaO}_3$ ," *Phys. Stat. Sol. (b)* **141**:287–300 (1987).
365. D. G. Boziniš and J. P. Hurrell, "Optical Modes and Dielectric Properties of Ferroelectric Orthorhombic  $\text{KNbO}_3$ ," *Phys. Rev. B* **13**:3109–3120 (1976).
366. N. N. Syrbu, V. T. Krasovsky, and I. N. Grincheshen, "Infrared Vibrational Modes in  $\text{Ti}_3\text{SbS}_3$ ,  $\text{Ti}_3\text{AsS}_3$ , and  $\text{Ti}_3\text{AsSe}_3$  Crystals," *Cryst. Res. Technol.* **29**:1095–1102 (1994).
367. A. S. Pine and G. Dresselhaus, "Raman Scattering in Paratellurite," *Phys. Rev. B* **5**:4087–4093 (1972).
368. D. M. Korn, A. S. Pine, G. Dresselhaus, and T. B. Reed, "Infrared Reflectivity of Paratellurite,  $\text{TeO}_2$ ," *Phys. Rev. B* **8**:768–772 (1973).
369. W. J. Tropf and M. E. Thomas, "Yttrium Oxide ( $\text{Y}_2\text{O}_3$ )," in E. D. Palik (ed.), *Handbook of Optical Constants of Solids II*, Academic Press, Orlando, 1991, pp. 1081–1098.
370. C. Z. Bi, J. Y. Ma, J. Yan, X. Fang, D. Z. Yao, B. R. Zhao, and X. G. Qiu, "Far-Infrared Optical Properties of  $\text{YVO}_4$  Single Crystal," *Eur. Phys. J.* **B51**:167–171 (2006).
371. S. A. Miller, H. H. Caspers, and H. E. "Rast, Lattice Vibrations of Yttrium Vanadate," *Phys. Rev.* **168**:964–969 (1968). [Also see H. E. Rast, H. H. Caspers, and S. A. Miller, "Infrared Spectral Emittance and Optical Properties of Yttrium Vanadate," *Phys. Rev.* **169**:705–709 (1968).]
372. M. Thirumavalavan, J. Kumar, F. D. Gnanam, and P. Ramasamy, "Vibrational Spectra of  $\text{Y}_3\text{Al}_5\text{O}_{12}$  Crystals Grown from Ba- and Pb-Based Flux Systems," *Infrared Phys.* **26**:101–103 (1986).
373. G. A. Gledhill, P. M. Nikolić, A. Hamilton, S. Stojilković, V. Blagojević, P. Mihajlovic, and S. Djurić, "FIR Optical Properties of Single Crystal  $\text{Y}_3\text{Al}_5\text{O}_{12}$  (YAG)," *Phys. Stat. Sol. (b)* **163**:K123–K128 (1991).
374. R. P. Lowndes, "Anharmonicity in the Silver and Thallium Halides: Far-Infrared Dielectric Response," *Phys. Rev. B* **6**:1490–1498 (1972).
375. G. Lucovsky, "Optic Modes in Amorphous  $\text{As}_2\text{S}_3$  and  $\text{As}_2\text{Se}_3$ ," *Phys. Rev. B* **6**:1480–1489 (1972).
376. W. G. Spitzer, R. C. Miller, D. A. Kleinman, and L. E. Howarth, "Far Infrared Dielectric Dispersion in  $\text{BaTiO}_3$ ,  $\text{SrTiO}_3$ , and  $\text{TiO}_2$ ," *Phys. Rev.* **126**:1710–1721 (1962).
377. E. J. Danielewicz and P. D. Coleman, "Far Infrared Optical Properties of Selenium and Cadmium Telluride," *Appl. Opt.* **13**:1164–1170 (1974).
378. J. L. Verble and R. F. Wallis, "Infrared Studies of the Lattice Vibrations in Iron Pyrite," *Phys. Rev.* **182**:783–789 (1969).
379. H. D. Lutz, G. Kliche, and H. Haeuseler, "Lattice Vibrational Spectra XXIV: Far-infrared Reflection Spectra, Optical and Dielectric Constants, and Effective Charges of Pyrite Type Compounds  $\text{FeS}_2$ ,  $\text{MnS}_2$ ,  $\text{MnSe}_2$ , and  $\text{MnTe}_2$ ," *Z. Naturforsch.* **86a**:184–190 (1981).
380. C. J. Johnson, G. H. Sherman, and R. Weil, "Far Infrared Measurement of the Dielectric Properties of GaAs and CdTe at 300 K and 8 K," *Appl. Opt.* **8**:1667–1671 (1969).
381. D. A. Kleinman and W. G. Spitzer, "Infrared Lattice Absorption of GaP" *Phys. Rev.* **118**:110–117 (1960).
382. A. Hadni, J. Claudel, D. Chanal, P. Strimer, and P. Vergnat, "Optical Constants of Potassium Bromide in the Far Infrared," *Phys. Rev.* **163**:836–843 (1967).
383. A. Hadni, J. Claudel, G. Morlot, and P. Strimer, "Transmission and Reflection Spectra of Pure and Doped Potassium Iodide at Low Temperature," *Appl. Opt.* **7**:161–165 (1968) [in French].
384. J. Zarembowitch, J. Gouteron, and A. M. Lejus, "Raman Spectra of Lanthanide Sesquioxide Single Crystals with A-type Structure," *Phys. Stat. Sol. (b)* **94**:249–256 (1979).

385. A. S. Barker and R. Loudon, "Dielectric Properties and Optical Phonons in  $\text{LiNbO}_3$ ," *Phys. Rev.* **158**:433–445 (1967).
386. I. F. Chang and S. S. Mitra, "Temperature Dependence of Long-Wavelength Optic Phonons of NaF Single Crystals," *Phys. Rev. B* **5**:4094–4100 (1972).
387. H. Burkhard, R. Geick, P. Kästner, and K. -H. Unkelbach, "Lattice Vibrations and Free Carrier Dispersion in PbSe," *Phys. Stat. Sol. (b)* **63**:89–96 (1974).
388. W. G. Spitzer and D. A. Kleinman, "Infrared Lattice Bands of Quartz," *Phys. Rev.* **121**:1324–1335 (1961).
389. B. Orel and V. Moissenko, "A Vibrational Study of Piezoelectric  $\text{TeO}_2$  Crystals," *Phys. Stat. Sol.(b)* **165**:K37–K41 (1991).
390. A. M. Hofmeister and K. R. Campbell, "Infrared Spectroscopy of Yttrium Aluminum, Yttrium Gallium, and Yttrium Iron Garnets," *J. Appl. Phys.* **72**:638–646 (1992).

*This page intentionally left blank*

---

# POLYMERIC OPTICS

---

John D. Lytle

*Advanced Optical Concepts  
Santa Cruz, California*

---

## 3.1 GLOSSARY

---

$A_{\text{H}_2\text{O}}$	water absorption
$K$	thermal conductivity
$T_s$	maximum service temperature
$\alpha$	thermal expansion coefficient
$\rho$	density

---

## 3.2 INTRODUCTION

---

A small number of carbon-based polymeric materials possesses some of those qualities which have made glass an attractive optical material. Most of these polymeric materials do exhibit certain physical deficiencies compared to glass. But, despite the fact that “plastic optics” has acquired an image as a low-end technology, it may nonetheless be a better choice, or even the best choice, in certain applications.

### Selection Factors

Virtually all of the polymers having useful optical properties are much less dense than any of the optical glasses, making them worthy of consideration in applications where weight-saving is of paramount importance. Many of them exhibit impact resistance properties which exceed those of any silicate glass, rendering them well-suited to military applications (wherein high “g” loads may be encountered), or ideal for some consumer products in which safety may be a critical consideration.

Though the physical properties of the polymers may make them better matched to certain design requirements than glass, by far the most important advantage of polymeric optics is the considerable creative freedom they make available to the optical and mechanical design effort.<sup>1</sup> While the design constraints and guidelines governing glass optics design and fabrication are fairly well defined, the various replication processes which may be put to use in polymer optics fabrication make available unique

opportunities for the creation of novel optical components and systems which would be unthinkable or unworkable in glass. Oftentimes, the differences in the engineering approach, or in the production processes themselves, may make possible very significant cost reductions in high-volume situations.<sup>2</sup>

## 3.3 FORMS

---

### Thermoset Resins

Optical polymers fall into basically two categories—the *thermoset* resins and the *thermoplastic* resins. The thermoset resin group consists of chemistries in which the polymerization reaction takes place during the creation of the part, which may be produced by casting, or by transfer replication. The part which has been created at completion of the reaction may then be postprocessed, if desired, by machining. In general, the thermoset resins cannot be melted and re-formed.

The most commonly encountered thermoset optical resin is that used to produce ophthalmic lenses for eyewear.<sup>3</sup> The monomer, which is stored in liquid form at reduced temperature, is introduced into a mold, where the polymerization reaction takes place, forming a part which assumes the shape of the cavity containing it. Alternatively, epoxy-based chemistries have been used with some success to form replicated reflecting surface shapes by a transfer process, and to produce aspheric figuring (at relatively modest expense) upon spherical refractive or reflective substrates.

### Thermoplastic Resins

With the possible exception of eyewear, most polymeric optics are executed in thermoplastic materials which are supplied in already polymerized form.<sup>4</sup> These materials are normally purchased in bulk as small pellets. These pellets are heated to a temperature beyond the softening point, so that they flow to become a single viscous mass. This mass is then formed to assume the shape desired in the final part.

Parts may be created by the injection molding process, in which the heated polymer is squirted into a mold at high pressure and allowed to cool in the shape of the desired component. Or the pellets may be directly heated between the two halves of a compression mold, and the mold closed to effect formation of the part. Hybrid molding technologies combining these two processes are recently experiencing increasing popularity in optical molding applications, and have produced optical surface figures of very high quality.

The capability of modern molding technology to produce optics having very good surface-figure quality has made possible the creation of polymeric optical components for a wide variety of applications. Among these are medical disposables, intraocular lenses, a host of consumer products, military optics, and a number of articles in which optical, mechanical, and electrical functions are combined in a single part.<sup>5</sup>

## 3.4 PHYSICAL PROPERTIES

---

### Density

Optical glass types number in the hundreds (if all manufacturers worldwide are counted). The glass types available from the catalogs cover a wide range of optical, physical, thermal, and chemical properties. The density of these materials varies from about  $2.3 \text{ g/cm}^3$  to about  $6.3 \text{ g/cm}^3$ . The heaviest optically viable polymer possesses a density of only about  $1.4 \text{ g/cm}^3$ , whereas the lightest of these materials will readily float in water, having a density of  $0.83 \text{ g/cm}^3$ .<sup>6</sup> All other things being equal, the total element count in an optical system may often be reduced (at modest cost penalty) by the inclusion of nonspherical surfaces. All things considered, then, polymeric optical systems may be made much less massive than their glass counterparts, especially if aspheric technology is applied to the polymer optical trains.

### Hardness

Although cosmetic blemishes rarely impact final image quality (except in the cases of field lenses or reticles), optical surfaces are customarily expected to be relatively free of scratches, pits, and

the like. Ordinary usage, especially cleaning procedures, are likely to result in some scratching with the passage of time. Most common optical glasses possess sufficient hardness that they are relatively immune to damage, if some modest amount of care is exercised.

The polymeric optical materials, on the other hand, are often so soft that a determined thumb-nail will permanently indent them. The hardness of polymeric optics is difficult to quantify (in comparison to glass), since this parameter is not only material-dependent, but also dependent upon the processing. Suffice it to say that handling procedures which would result in little or no damage to a glass element may produce considerable evidence of abrasion in a polymeric surface, particularly in a thermoplastic. In fact, the compressibility of most thermoplastic polymers is such that the support for hard surface coatings is sufficiently low that protection provides immunity against only superficial abrasion. These deficiencies are of no particular consequence, however, if the questionable surfaces are internal, and thereby inaccessible.

## Rigidity

A property closely related to hardness is the elastic modulus, or Young's modulus. This quantity, and the elongation factor at yield, are determinants of the impact resistance, a performance parameter in which the polymers outshine the glasses. These properties are, again, dependent upon the specified polymeric alloy, any additives which may be present, and processing history of the polymer, and cannot be dependably quoted.<sup>7,8</sup> The reader is referred to any of several comprehensive references listed herein for mechanical properties data. Those properties which create good impact resistance become liabilities if an optical part is subjected to some torsion or compressive stress. Since optical surface profiles must often be maintained to subwavelength accuracy, improper choice of the thickness/diameter ratio, or excessive compression by retaining rings, may produce unacceptable optical figure deformations.

Polymer chemistry is a complex subject probably best avoided in a discussion of polymer optics. Carbon-based polymers have been synthesized to include an extensive variety of chemical subgroups, however. Unfortunately, relatively few of these materials are actually in regular production, and only a handful of those possess useful optical properties for imaging purposes.

## Service Temperature

Any decision involving a glass/plastic tradeoff should include some consideration of the anticipated thermal environment. While the optical glasses may exhibit upper service temperature limits of from 400 to 700°C, many of the glass types having the most interesting optical properties are quite fragile, and prone to failure if cooled too quickly. These failures are mostly attributable to cooling-induced shrinkage of the skin layer, which shatters because the insulating properties of the material prevent cooling (and shrinkage) of the bulk material at the same rate.

The polymeric materials, on the other hand, have much lower service temperature limits, in some cases no higher than about 60°C.<sup>9</sup> The limit may approach 250°C for some of the fluoropolymers. The thermal conductivity of many of these polymers may be as much as an order of magnitude lower than for the glasses and the thermal expansion coefficients characterizing the polymers are often an order of magnitude larger than those associated with optical glasses. Consequently, subjecting any polymeric optical element to a significant thermal transient is likely to create more severe thermal gradients in the material, and result in significant thermally induced optical figure errors.<sup>10</sup> Again, it is suggested that the interested reader consult the plastic handbooks and manufacturer's literature for a complete listing of this behavior, as additives and variation in molecular weight distribution may significantly affect all of these properties. Some of the most important physical properties of the more readily available optical polymers are tabulated in Table 1.

## Conductivity (Thermal, Electrical)

Most materials which exhibit poor thermal conductivity are also poor electrical conductors. Since many unfilled polymers are very effective electrical insulators, they acquire static surface charge

**TABLE 1** Physical Properties

Material	$\rho$	$\alpha$	$T_s$	$K$	$A_{\text{H}_2\text{O}}$
P-methylmethacrylate	1.18	6.0	85	4–6	0.3
P-styrene	1.05	6.4–6.7	80	2.4–3.3	0.03
NAS	1.13	5.6	85	4.5	0.15
Styrene acrylonitrile (SAN)	1.07	6.4	75	2.8	0.28
P-carbonate	1.25	6.7	120	4.7	0.2–0.3
P-methyl pentene	0.835	11.7	115	4.0	0.01
P-amide (Nylon)	1.185	8.2	80	5.1–5.8	1.5–3.0
P-arylate	1.21	6.3		7.1	0.26
P-sulfone	1.24	2.5	160	2.8	0.1–0.6
P-styrene co-butadiene	1.01	7.8–12			0.08
P-cyclohexyl methacrylate	1.11				
P-allyl diglycol carbonate	1.32		100	4.9	
Cellulose acetate butyrate	1.20			4.0–8.0	
P-ethersulfone	1.37	5.5	200	3.2–4.4	
P-chloro-trifluoroethylene	2.2	4.7	200	6.2	0.003
P-vinylidene fluoride	1.78	7.4–13	150		0.05
P-etherimide	1.27	5.6	170		0.25

fairly easily, and dissipate it very slowly. Not surprisingly, these areas of surface charge quickly attract oppositely charged contaminants, most of which are harder than the plastic. Attempts to clear the accumulated particles from the surfaces by cleaning can, and usually do, result in superficial damage. Application of inorganic coatings to these surfaces may do double duty by providing a more conductive surface (less likely to attract contaminants), while improving the abrasion resistance.

## Outgassing

In contrast to glass optical parts, which normally have very low vapor pressure when properly cleaned, most polymers contain lubricants, colorants, stabilizers, and so on, which may outgas throughout the life of the part. This behavior disqualifies most plastic optical elements from serving in space-borne instrumentation, since the gaseous products, once lost, surround the spacecraft, depositing upon solar panels and other critical surfaces. Some, but few, thermoset resins may be clean enough for space applications if their reaction stoichiometry is very carefully controlled in the creation of the part.

## Water Absorption

Most polymers, particularly the thermoplastics, are hygroscopic. They absorb and retain water, which must, in most cases, be driven off by heating prior to processing. Following processing, the water will be reabsorbed if the surfaces are not treated to inhibit absorption. Whereas only a very small amount of water will normally attach to the surfaces of a glass optical element, the polymer materials used for optics may absorb from about 0.003 to about 2 percent water by weight. Needless to say, the trapped water may produce dimensional changes, as well as some minor alterations of the spectral transmission. Physical properties of some of the more familiar optical polymers are listed in Table 1. Density =  $\rho$  ( $\text{g}/\text{cm}^3$ ); thermal expansion coefficient =  $\alpha$  ( $\text{cm}/\text{cm} \text{ } ^\circ\text{C} \times 10^{-5}$ ); max. service temperature =  $T_s$  ( $^\circ\text{C}$ ); thermal conductivity =  $K$  ( $\text{cal}/\text{sec cm } ^\circ\text{C} \times 10^4$ ); and water absorption (24 h) =  $A_{\text{H}_2\text{O}}$  (%). Values are to be considered approximate, and may vary with supplier and processing variations.

## Additives

Polymers are normally available in a variety of “melt flow” grades—each of which possesses viscosity properties best suited to use in parts having specific form factors. A number of additives are commonly present in these materials. Such additives may, or may not, be appropriate in an optical application. Additives for such things as flame retardancy, lubricants, lubrication, and mold release are best avoided if not included to address a specific requirement. Frequently, colorants are added for the purpose of neutralizing the naturally occurring coloration of the material. These additives create an artificial, but “clear,” appearance. The colorants must, of course, absorb energy to accomplish this, resulting in a net reduction in total spectral transmission.

## Radiation Resistance

Most of the optical polymers will be seen to exhibit some amount of fluorescence if irradiated by sufficiently intense high-energy radiation.<sup>11</sup> High-energy radiation of the ultraviolet and ionizing varieties will, in addition, produce varying amounts of polymer chain crosslinking, depending upon the specific polymer chemistry. Crosslinking typically results in discoloration of the material, and some amount of nonuniform energy absorption. Inhibitors may be added to the polymeric material to retard crosslinking, although, oddly enough, the polymers most susceptible to UV-induced discoloration are generally the least likely to be affected by ionizing radiation, and vice versa.

## Documentation

Although polymeric materials suffer some shortcomings in comparison to glass (for optical applications), distinct advantages do exist. The major obstacle to the use of polymers, however, is the spotty and imprecise documentation of many of those properties required for good engineering and design. In general, the resin producers supply these materials in large quantity to markets wherein a knowledge of the optical properties is of little or no importance. With luck, the documentation of optical properties may consist of a statement that the material is “clear.” In the rare case where refractive index is documented, the accuracy may be only two decimal places. In these circumstances, the optical designer or molder is left to investigate these properties independently—a complex task, since the processing itself may affect those properties to a substantial degree.

Unfortunately, optical applications may represent only a small fraction of a percent of the total market for a given resin formulation, and since these materials are sold at prices ranging from less than two dollars to a few dollars per pound, the market opportunity represented by optical applications seems minuscule to most polymer vendors.

---

## 3.5 OPTICAL PROPERTIES

### Variations

It is only a fortuitous accident that some of the polymers exhibit useful optical behavior, since most all of these materials were originally developed for other end uses. The possible exceptions are the materials used for eyeglass applications (poly-diallylglycol), and the materials for optical information storage (specially formulated polycarbonate). Citation of optical properties for any polymeric material must be done with some caution and qualification, as different melt flow grades (having different molecular weight distribution) may exhibit slightly different refractive index properties. Additives to regulate lubricity, color, and so on can also produce subtle alterations in the spectral transmission properties.



## Spectral Transmission

In general, the carbon-based optical polymers are visible-wavelength materials, absorbing fairly strongly in the ultraviolet and throughout the infrared.<sup>12–14</sup> This is not readily apparent from the absorption spectra published in numerous references, though. Such data are normally generated by spectroscopists for the purpose of identifying chemical structure, and are representative of very thin samples. One can easily develop the impression from this information that the polymers transmit well over a wide spectral range. Parenthetically, most of these polymers, while they have been characterized in the laboratory, are not commercially available. What is needed for optical design purposes is transmission data (for available polymers) taken from samples having sufficient thickness to be useful for imaging purposes.

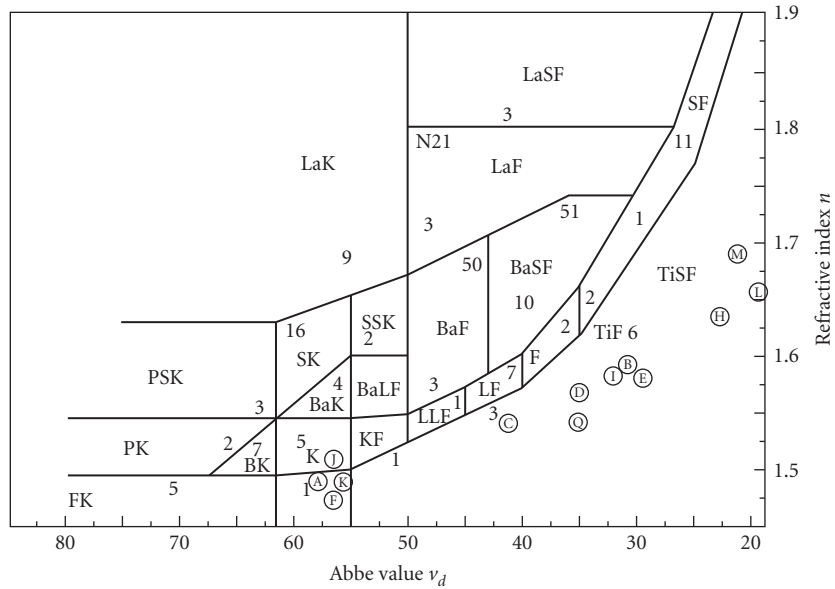
Some specially formulated variants of poly-methylmethacrylate have useful transmission down to 300 nm.<sup>15</sup> Most optical polymers, however, begin to absorb in the blue portion of the visible spectrum, and have additional absorption regions at about 900 nm, 1150 nm, 1350 nm, finally becoming totally opaque at about 2100 nm. The chemical structure which results in these absorption regions is common to almost all carbon-based polymers, thus the internal transmittance characteristics of these materials are remarkably similar, with the possible exception of the blue and near-UV regions. A scant few polymers do exhibit some spotty narrowband transmission leakage in the far-infrared portion of the spectrum, but in thicknesses suitable only for use in filter applications.

## Refractive Index

The chemistry of carbon-based polymers is markedly different from that of silicate glasses and inorganic crystals in common use as optical materials. Consequently, the refractive properties differ significantly. In general, the refractive indices are lower, extending to about 1.73 on the high end, and down to a lower limit of about 1.3. In practice, those materials which are readily available for purchase exhibit a more limited index range—from about 1.42 to 1.65. The Abbe values for these materials vary considerably, though, from about 100 to something less than 20. Refractive index data for a few of these polymers, compiled from a number of sources, is displayed in Table 2. In the chart, PMMA signifies polymethylmethacrylate; P-styr, polystyrene; P-carb, polycarbonate; SAN, styrene acrylonitrile; PEI, polyetherimide; PCHMA, polycyclohexylmethacrylate. The thermo-optic coefficients at room temperature (change in refractive index with temperature) are also listed. Note that these materials, unlike most glasses, experience a reduction in refractive index with increasing temperature. Figure 1, a simplified rendition of the

**TABLE 2** Refractive Index of Some Optical Polymers

Line ID	Wavl., nm	PMMA	P-styr	P-carb	SAN	PEI	PCHMA
	1014.0	1.4831	1.5726	1.5672	1.5519		
s	852.1	1.4850	1.5762	1.5710	1.5551		
r	706.5	1.4878	1.5820	1.5768	1.5601		
C	656.3	1.4892	1.5849	1.5799	1.5627		1.502
C'	643.9	1.4896	1.5858	1.5807	1.5634	1.651	
D	589.3	1.4917	1.5903	1.5853	1.5673		
d	587.6	1.4918	1.5905	1.5855	1.5674	1.660	1.505
e	546.1	1.4938	1.5950	1.5901	1.5713	1.668	
F	486.1	1.4978	1.6041	1.5994	1.5790		1.511
F'	480.0	1.4983	1.6052	1.6007	1.5800	1.687	
g	435.8	1.5026	1.6154	1.6115	1.5886		
h	404.7	1.5066	1.6253	1.6224	1.5971		
i	365.0	1.5136	1.6431	1.6432	1.6125		
Abbe number		57.4	30.9	29.9	34.8	18.3	56.1
$dn/dT \times 10^{-4}/^{\circ}\text{C}$		-1.05	-1.4	-1.07	-1.1		



**FIGURE 1** Optical glasses and polymers: (a) polymethylmethacrylate; (b) polystyrene; (c) NAS; (d) styrene acrylonitrile; (e) polycarbonate; (f) polymethyl pentene; (g) acrylonitrile-butadiene styrene (ABS); (h) polysulfone; (i) polystyrene co-maleic anhydride; (j) polycyclohexylmethacrylate (PCHMA); (k) polyallyl diglycol carbonte; (l) polyetherimide (PEI); and (m) polyvinyl naphthalene.

familiar glass map ( $n$  vs.  $\nu$ ), shows the locations of some of the more familiar polymers. Note that these materials all occupy the lower and right-hand regions of the map. In the Schott classification system, the polymers populate mostly the FK, TiK, and TiF regions of the map.<sup>16</sup>

## Homogeneity

It must be kept constantly in mind that polymeric optics are molded and not mechanically shaped. The exact optical properties of a piece cannot, therefore, be quantified prior to manufacture of the element. In fact, the precise optical properties of the bulk material in an optical element are virtually certain to be a function of both the material itself, and of the process which produced the part. Some materials, notably styrene and butyrate resins, are crystalline to some degree, and therefore inherently birefringent. Birefringence may develop in amorphous materials, though, if the injection mold and process parameters are not optimized to prevent this occurrence. Likewise, the bulk scatter properties of a molded optical element are a function of the inherent properties of the material, but are also strongly related to the cleanliness of the processing and the heat history of the finished part.

## 3.6 OPTICAL DESIGN

### Design Strategy

Virtually all optical design techniques which have evolved for use with glass materials work well with polymeric optics. Ray-tracing formulary, optimization approaches, and fundamental optical construction principles are equally suitable for glass or plastic. The generalized approach to optical design with polymeric materials should be strongly medium-oriented, though. That is, every

effort must be made to capitalize upon the design flexibility which the materials and manufacturing processes afford. Integration of form and function should be relentlessly pursued, since mechanical features may be molded integral with the optics to reduce the metal part count and assembly labor content in many systems.

## Aberration Control

The basic optical design task normally entails the simultaneous satisfaction of several first-order constraints, the correction of the monochromatic aberrations, and the control of the chromatic variation of both first-order quantities and higher-order aberrations. It is well known that management of the Petzval sum, while maintaining control of the chromatic defects, may be the most difficult aspect of this effort.<sup>17,18</sup> It is also widely recognized that the choice of optical materials is key to success. While the available polymer choices cover a wide range of Abbe values, ensuring that achromatization may be accomplished in an all-polymer system, the refractive index values for these materials are not well-positioned on the “glass” map to permit low Petzval sums to be easily achieved.

## Material Selection

Simultaneous correction of the Petzval sum and the first-order chromatic aberration may, however, be nicely accomplished if the materials employed possess similar ratios of Abbe number to central refractive index. This implies that the *best* material combinations (involving polymers) should probably include an optical glass. Also implied is the fact that these hybrid material combinations may be inherently superior (in this respect) to all-glass combinations. Ideally, the chosen materials should be well-separated (in Abbe value) on the glass map, so that the component powers required for achromatization do not become unduly high. This condition is satisfied most completely with polymers which lie in the TiF sector of the glass map, coupled with glasses of the LaK, LaF, and LaSF families.

Most lens designers would prefer to utilize high-refractive-index materials almost exclusively in their work. Optical power must be generated in order to form images, and because the combination of optical surface curvature and refractive index creates this refractive power, these two variables may be traded in the lens design process. Since it is well known that curvature generates aberration more readily than does a refractive index discontinuity, one generally prefers to achieve a specified amount of refractive power through the use of low curvature and high-refractive index. From this perspective, the polymers are at a distinct disadvantage, most of them being low-index materials.

## Aspheric Surfaces

An offsetting consideration in the use of polymeric optical materials is the freedom to employ nonspherical surfaces. While these may be awkward (and very expensive) to produce in glass, the replication processes which create plastic optical parts do not differentiate between spherical and nonspherical surfaces.

As any lens designer can attest, the flexibility that aspheric surfaces make available is quite remarkable.<sup>19,20</sup> Spherical surfaces, while convenient to manufacture by grinding and polishing, may generate substantial amounts of high-order aberration if used in any optical geometry which departs significantly from the aplanatic condition. These high-order aberrations are often somewhat insensitive to substantial changes in the optical prescription. Thus, profound configurational alterations may be necessary to effect a reduction in these image defects.

On the other hand, the ability to utilize surface shapes which are more complex than simple spheres permits these high-order aberration components to be moderated at their point of origin, which may in turn reduce the amount of “transferred aberration” imparted to surfaces downstream in the optical train. In a multielement optical system, especially one employing cascaded aspheric surfaces, the required imagery performance may be achieved using fewer total elements. And due to

the fact that the surface aberration contributions are diminished, the sensitivity to positioning errors may also be reduced, with the result that an aspheric optical system may actually be more forgiving to manufacture than its spherical counterpart.

In practice, the use of aspheric surfaces in polymer optical elements appears to more than compensate for the handicap imposed by low-refractive index values. Using aspheric surfaces, it is possible to bend, if not break, many of the rules which limit design with spherical surfaces. Aspherics create extra leverage to deal with the monochromatic aberrations, and with the chromatic variation of these image defects. A designer experienced with aspherics, given a capable set of software tools, can frequently create optical constructions which deliver high performance, despite the fact that they appear odd to those accustomed to the more "classical" spherical surface configurations. Quite often, unfavorable design constraints such as an inconvenient aperture stop location, may be handled with less difficulty using aspherics.

## Athermalization

The thermal behavior of the polymers, mentioned previously, may cast a shadow upon some applications where the temperature is expected to vary over a significant range, but the focal surface location must be fixed in space. In such cases, the variation of refractive index usually accounts for the largest share of the variation, with the dimensional changes playing a secondary role. In such situations, the thermally induced excursions of the focal surface may be compensated by modeling these functions and designing mechanical spacers of the proper material to stabilize the detector/image location.

Alternatively, the optical system may be designed to exhibit inherently athermal behavior over the operational temperature range.<sup>21</sup> Unfortunately, this is not strictly possible using only polymeric materials, as the thermo-optic coefficients display so little variation among themselves that the component powers would be absurdly high.

In combination with one or more glass elements, however, very nicely athermalized design solutions may be obtained with polymer elements.<sup>22</sup> Athermal designs may be generated by modeling the optical system in multiconfiguration mode in the lens design software, much as one would develop a zoom lens. The parameters to be "zoomed" in this case are the refractive indices at two or more temperatures within the operating range. The resulting designs frequently concentrate most of the refractive power in the glass elements, with the polymer elements functioning to achieve achromatism and control of the monochromatic aberrations. See also Chap. 8, "Thermal Compensation Techniques," by Philip J. Rogers and Michael Roberts in Vol. II of this *Handbook*.

## Processing Considerations

In much the same manner that optical design with polymer materials is different from optical design with glass, the treatment of the fabrication and assembly issues are also quite different matters. The major issues requiring examination are those related to the materials themselves. While it is possible to characterize the glass for an optical system with complete certainty prior to performing any fabrication operations, with polymers, one's knowledge of the starting materials is only a rough indication of the properties of the finished optical parts.

When optical properties data are offered by the polymer supplier, it should be realized that these numbers apply *only* to measurement samples which have been predried to specification, have experienced a specified residence time in the extrusion barrel under specific temperature conditions, have been injected into the mold cavity at specific rates and pressures, and so on. Consequently, it is unlikely that the refractive properties of a polymer element will conform closely to catalog values (if such values are indeed supplied). Moreover, homogeneity, bubble content, scatter properties, and so on, are all process-dependent. So while the melt sheets may fix the optical properties of glass materials very precisely, the uncertainty associated with the polymers demands that refractive variations be allocated a significant portion of the fabrication and assembly error budget.

## Manufacturing Error Budget

Other constructional parameters, conversely, may be implemented with great precision and repeatability in plastic. The molding process, executed by means of modern equipment, can be exceedingly stable. Vertex thickness, curvature, and wedge may often be maintained to a greater level of precision, with greater economy than is possible with glass fabrication technology. It is not unusual to see part-to-part variations in vertex thickness of less than 0.01 to 0.02 mm over a run of thousands of parts from a single cavity.

## Multiple Cavities

The economic appeal of injection molding is the ability to create several parts in one molding cycle. In a multicavity scenario, the parts from different cavities may exhibit some small dimensional differences, depending upon the level of sophistication of the tool design and the quality of its construction. Cavity variations in axial thickness, fortunately, may be permanently minimized by implementing small tooling adjustments after the mold has been exercised. Consequently, part thickness variation rarely consumes a significant fraction of the constructional error budget.

## Dimensional Variations

Surface radii, like axial thickness, may be replicated with great repeatability *if* the molding process is adjusted to a stable optimum. Radius errors, if they are present, are usually attributable to incorrect predictions of shrinkage, and may be biased out by correcting the radii of the mold inserts. Thus, the consistency of surface radii achievable with glass may often be equaled in plastic. Thus, radius errors, as well as axial thickness errors, frequently constitute a small portion of the polymer optics manufacturing error budget.

Element wedge, like axial thickness, may be minimized by careful attention to precision in the tool design and construction. It is quite possible to achieve edge-to-edge thickness variations of less than 0.01 mm in molded plastic lenses. With polymer lenses, the azimuthal location of the part gate may be used, if necessary, to define rotational orientation of the element in the optical train. Consequently, rotational alignment of plastic optical parts may be easily indexed.

## Optical Figure Variations

Control of optical figure quality is obviously key to the successful execution of a good optical design. In glass, achievement of subfringe of figure conformance is accomplished routinely, albeit at some cost penalty. In polymeric optics, the nonlinear shrinkage, surface tension, and other processing-related effects cause surface figure errors to scale with part size, sometimes at a rate proportional to some exponent of diameter. This limits the practical size range for polymeric optics, although capable optics molders may routinely produce elements in the 10-mm-diameter range to subfringe accuracy.<sup>23</sup>

On one hand, it can probably be stated that processing-induced variations in properties, and a dearth of dependable optical data, preclude any serious discussions of such things as apochromatic polymeric optics, or of large polymeric optics operating at the diffraction limit. On the other hand, the consistency with which some dimensional parameters may be reproduced in quantity, and the design freedom and flexibility afforded by molded aspherics, make possible the satisfaction of some design requirements which would be out of range for conventional glass optics.<sup>24,25</sup>

## Specification

Given the fact that the guidelines and restrictions for design and implementation are very different for glass and polymeric optics, it is not surprising that the approach to specification of polymer optical parts and systems should be tailored to the materials and processes of polymer optics. Attempts

to convert a glass optics concept to plastic are frequently unsuccessful if the translation overlooks the fundamental themes of the molding and tooling technologies involved. Much as optimum tube and solid-state electrical circuit topologies should be significantly different, so must the execution of a conceptual optical system, depending upon whether glass or polymer material is the medium.

It follows naturally that manufacturing drawings for polymer optics may contain annotations which seem unfamiliar to those versed in glass optics manufacture. Furthermore, some specifications which are universally present on all glass optics drawings may be conspicuously absent from a polymer optics print.

For example, thermal and cosmetic damage considerations preclude the use of the familiar test glasses in the certification of polymeric optics. Figure conformance, then, need only be specified in “irregularity” or asphericity terms, since the alternative method, use of a noncontacting interferometer, implies that the focus error (*fringe power* in test plate language) will be automatically removed in the adjustment of the test setup.

References to ground surfaces may be omitted from polymer optics drawings, since no such operation takes place. Discussions of “chips” inside the clear aperture, staining, and the like are also superfluous. Beauty defect specifications do apply, although such imperfections are almost always present in every sample from a specific cavity, probably implying the need to rework a master surface.

In general, the lexicon of optics, and that of the molding industry, do not overlap to a great extent. Molding terms like *flash* and *splay* are meaningless to most optical engineers. Those endeavoring to create a sophisticated polymeric optical system, anticipating a successful outcome, are advised to devote some time to the study of molding, and to discussions with the few experts in the arcane field of optics molding, before releasing a drawing package which may be unintelligible to or misunderstood by the vendor.

## 3.7 PROCESSING

### Casting

As mentioned above, polymeric optics may be produced by any of several processes. These include fabrication, transfer replication, casting, compression molding, injection molding, and some combinations of the aforementioned.<sup>26</sup> The earliest polymeric optical parts were probably produced by fabrication or precipitation from solution. Large military tank prisms have been made by both processes. In the latter case, the polymer (typically PMMA) was dissolved, and the solvent then evaporated to produce a residue of polymer material in the shape of the mold—a very inefficient technique indeed.

Many of the polymers may be fabricated by cutting, grinding, and polishing, much as one would deal with glass materials. The thermoset resin tradenamed CR-39 (poly-diallylglycol) was formulated specifically to be processed using the same techniques and materials as those used to fabricate glass optics. And this material does indeed produce good results when processed in this manner. It is used extensively in the ophthalmic industry to produce spectacle lenses. The processing, in fact, usually involves casting the thermoset resin to create a lens blank which emerges from the mold with the optical surfaces polished to final form. More conventional fabrication techniques may then be utilized to edge the lens, or perhaps to add a bifocal portion.

### Abrasive Forming

Unfortunately, the softness of most of the polymers, coupled with their poor thermal conductivity, complicates the achievement of a truly high quality polish using conventional methods. Even in the case of CR-39, which is relatively hard for a polymer material, some amount of “orange peel” in the polished surface seems unavoidable. Many thermoplastics, most of them softer than CR-39, may be conventionally ground and polished to give the appearance of an acceptable optical surface. Closer

examination, however, reveals surface microstructure which probably does not fall within the standards normally associated with precision optics. Nonetheless, fabrication of optical elements from large slabs of plastic is often the only viable approach to the creation of large, lightweight refractive lenses, especially if cost is an issue.

In general, the harder, more brittle polymers produce better optical surfaces when ground and polished. PMMA and others seem to fare better than, say, polycarbonate, which is quite soft, exhibits considerable elongation at the mechanical yield point, but is in great demand due to its impact resistance.

### Single-Point Turning

An alternative approach to fabrication, one that is especially useful for the production of aspheric surfaces, is the computer numerical control (CNC) lathe turning of the bulk material using a carefully shaped and polished tool bit of single-crystal diamond or cubic boron nitride. See also Chap. 10, "Fabrication of Optics by Diamond Turning," by Richard L. Rhorer and Chris J. Evans in Vol. II of this *Handbook*. The lathe required to produce a good result is an exceedingly high precision tool, having vibration isolation, temperature control, hydrostatic or air bearings, and so on. On the best substrate materials (PMMA is again a good candidate), very good microroughness qualities may be achieved. With other materials, a somewhat gummy character (once more, polycarbonate comes to mind) may result in microscopic tearing of the surface, and the expected scatter of the incident radiation.

The diamond-turning process is often applied in conjunction with other techniques in order to speed progress and reduce cost. Parts which would be too large or too thick for economical stand-alone injection molding are frequently produced more efficiently by diamond-turning injection molded, stress-relieved preforms, which require minimal material removal and lathe time for finishing. Postpolishing, asymmetric edging, and other postoperations may be performed as necessary to create the finished part. Optics for illumination and TV projection applications are often produced by some combination of these techniques. Given the fact that the technology in most widespread use for the production of plastic optics involves some form of molding (a front-loaded process, where cost is concerned), diamond-turning is often the preferred production method for short production runs and prototype quantities.

### Compression Molding

Most high-volume polymeric optics programs employ a manufacturing technology involving some form of molding to produce the optical surfaces, if not the entire finished part.<sup>27</sup> Of the two most widely used approaches, compression molding is best suited to the creation of large parts having a thin cross section. In general, any optical surface possessing relief structure having high spatial frequency is not amenable to injection molding, due to the difficulty of forcing the material through the cavity, and due to the fact that the relief structure in the mold disrupts the flow of the polymer. In addition, the relief structure in the master surfaces may be quite delicate, and prone to damage at the high pressures often present in the mold cavity.

The compression molding process is capable of producing results at considerably lower surface pressure than injection molding, and as long as the amount of material to be formed is small, this molding technology can replicate fine structure and sharp edge contours with amazing fidelity. Since the platens of a compression molding press are normally heated using steam or electrical heaters, most compression molded parts are designed to be executed in polymers having a relatively low temperature softening point, and materials like polyethersulfone are rarely utilized.

### Injection Molding

Optical parts having somewhat smaller dimensions may be better suited to production by the injection molding process.<sup>28</sup> This is probably the preferred polymer manufacturing technology for optical elements having a diameter smaller than 0.1 m and a thickness not greater than 3 cm. Not only do the economics favor this approach in high production volume, but if properly applied, superior optical surfaces may be produced.<sup>29</sup>

It should be kept firmly in mind that the basic injection molded process (as it is known to most practitioners) requires a great deal of refinement and enhancement in order to produce credible optical parts.<sup>30</sup> Unfortunately, very few molders possess either the molding know-how, or the testing and measurement sophistication to do the job correctly. Given a supply of quality polymer material, the molding machine itself must be properly configured and qualified. Relatively new machinery is a must. The platens to which the mold halves are mounted must be very rigid and properly aligned. And this alignment must be maintainable on a shot-to-shot basis for long periods. The screw and barrel must be kept scrupulously clean, and must be carefully cleaned and purged when switching materials. The shot capacity, in ideal circumstances, should be more carefully matched to the part volume than for non-optical parts. The process control computer must be an inordinately flexible and accurate device, able to profile and servo a number of operational functions that might be of little importance if the molded part were not optical in nature.<sup>31</sup>

Since much of the heating of the injected polymer resin occurs as a result of physical shear and compression (due to a variable pitch screw), the selection of these machine characteristics is critical to success. In addition, the energy supplied to the machine barrel by external electric heaters must be controlled with more care than in standard industrial applications. A failure of a single heater, or a failure of one of the thermal measurement devices which close that servo loop, may result in many defective parts.

## Vendor Selection

The injection mold itself requires special attention in both design and execution in order to produce state-of-the-art molded lenses. A number of closely held “trade tricks” normally characterize a mold designed to produce optical parts, and these subtle variations must be implemented with considerably greater accuracy than is normally necessary in ordinary molding. The mold and molding machine are often designed to operate more symbiotically than would be the case in producing non-optical parts. Control of the mold temperature and temperature gradients is extremely critical, as is the control bandwidth of those temperatures and the temperature of the molding room itself. The most important conclusion to be drawn from the preceding paragraphs is that *the molding vendor for polymer optical parts must be selected with great care*. A molding shop, no matter how sophisticated and experienced with medical parts, precision parts for electronics, and so on, will probably consume much time and many dollars before conceding defeat with optical parts.

Although success in molding optical elements is a strong function of equipment, process control, and engineering acumen, *attention to detail in the optical and mechanical design phases will consistently reduce the overall difficulty of manufacturing these items*. An awareness of the basic principles of injection molding procedures and materials is very helpful here, but it is necessary to be aware that, in the optical domain, we are dealing with micrometer-scale deformations in the optical surfaces. Thus, errors or oversights in design and/or molding technique which would totally escape notice in conventional parts can easily create scrap optics.

## Geometry Considerations

The lens design effort, for best results, must be guided by an awareness of the basic physics of creating an injection molded part, and of the impact of part cross section, edge configuration, asymmetry, and so on. In general, any lens having refractive power will possess a varying thickness across its diameter. Unfortunately, meniscus-shaped elements may mold best due to the more uniform nature of the heat transfer from the bulk.<sup>32</sup> Positive-powered lens elements will naturally shrink toward their center of mass as they cool, and it may be difficult to fill the mold cavity efficiently if the edge cross section is only a small fraction of the center thickness.

Negative lenses, on the other hand, tend to fill in the outer zones more readily, since the thinner portion of the section (the center) tends to obstruct flow directly across the piece from the part gate. In extreme circumstances, it is possible that the outer zones of the lens element will be first to



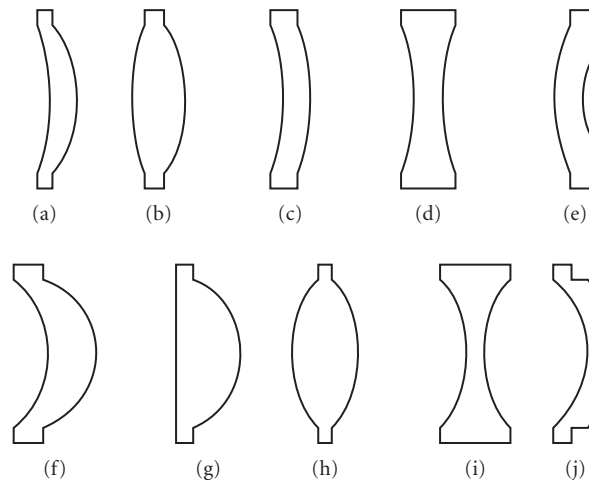
fill, trapping gases in the center, forming an obvious *sink* in molding terminology. Parts designed with molded-in bores may exhibit the ‘*weld-line*’ phenomenon, which is a visible line in the part where the flow front of the molten plastic is divided by the mold cavity obstruction forming the bore. In the case of both negative and positive lens elements, it is good policy to avoid element forms wherein the center-to-edge thickness ratio exceeds three for positive elements, or is smaller than 0.3 for negative elements.

## Shrinkage

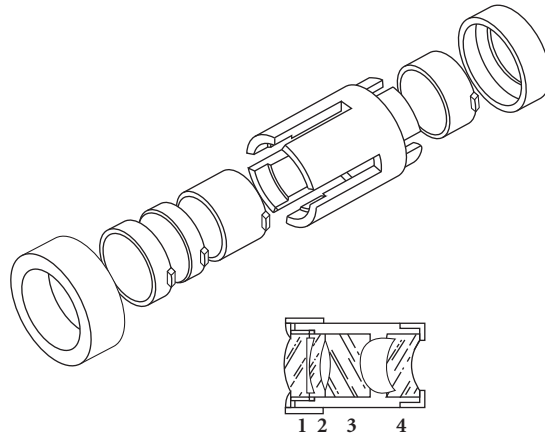
Surface-tension effects may play a significant role in the accuracy to which a precision optical surface may be molded.<sup>33,34</sup> Particularly in areas of the part where the ratio of surface area/volume is locally high (corners, edges), surface tension may create nonuniform shrinkage which propagates inward into the clear aperture, resulting in an edge rollback condition similar to that which is familiar to glass opticians. Surface tension and volumetric shrinkage may, however, actually aid in the production of accurate surfaces. Strongly curved surfaces are frequently easier to mold to interferometric tolerances than those having little or no curvature. These phenomena provide motivation to oversize optical elements, if possible, to a dimension considerably beyond the clear apertures. A buffer region, or an integrally molded flange provides the additional benefit of harmlessly absorbing optical inhomogeneities which typically form near the injection gate. Figure 2 depicts several optical element forms exhibiting favorable (*a–e*) and unfavorable (*f–j*) molding geometries. In some cases, a process combining injection and compression molding may be used to improve optical figure quality. Several variants of this hybrid process are in use worldwide, with some injection molding presses being specifically fitted at the factory to implement this procedure.<sup>35</sup>

## Mechanical Assembly

In order to appreciate fully the design flexibility and cost-saving potential of polymer optics, it is necessary to modify one’s approach to both optical and mechanical design. A fully optimized polymeric optical system not only makes use of aspheric technology and integrally molded features in the optical elements, but embodies an extension of this design philosophy into the lens housing concept and assembly strategy. These issues should ideally be considered in concert from the very



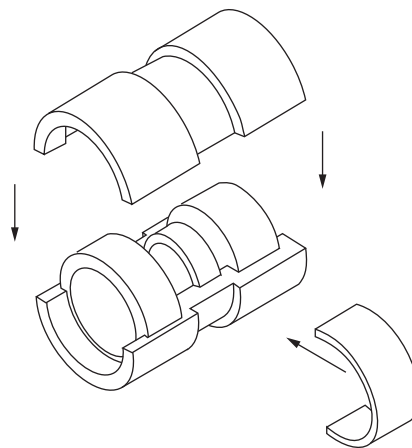
**FIGURE 2** Some polymer lens element cross-sectional configurations.



**FIGURE 3** Collet-type lens housing. Joining by ultrasound eliminates the possibility of pinching lens elements.

beginning, so that design progress in one aspect does not preclude parallel innovation in other facets of the development process.

It is important to resist the urge to emulate glass-based optomechanical design approaches, since the polymer technology permits design features to be implemented which would be prohibitively expensive (or even impossible) in metal and glass. Spacers required to separate elements may be molded as part of the elements (Fig. 2), reducing the metal part total and simplifying assembly operations. See also Chap. 6, "Mounting Optical Components," by Paul R. Yoder, Jr. in Vol II of this *Handbook*. Housings may be configurations which would be either improbable or unmanufacturable using machine tool technology. The collet-and-cap design shown in Fig. 3 is one such example. Joining might be accomplished by ultrasonic bonding. The clamshell concept shown in Fig. 4 may be designed so that the two halves of the housing are actually the same part, aligned by molded-in locating pins. Joining might be performed by a simple slip-on C ring.



**FIGURE 4** Clamshell lens housing. Possibility of lens jamming during assembly is minimized.

Whereas lens assemblies in glass and metal are normally completed by seating threaded retaining rings, their plastic counterparts may be joined by snap-together pieces, ultrasonic bonding, ultraviolet-curing epoxies, expansion C rings, or even solvent bonding.<sup>36</sup> Solvent bonding is dangerous, however, since the errant vapors may actually attack the polymer optical surfaces.

Following the basic polymeric optics philosophy, the lens element containment and assembly approach should probably not even consider the disassembly option in the event of a problem. In order to maximize assembly precision and minimize unit cost, the design of the lens cell should evolve alongside that of the optical system, and this cell should be visualized as an extension of a fixture conceived to minimize the labor content of the assembly.

An in-depth treatment of optical mold design and tooling technology is obviously beyond the scope of this discussion. Many of the methods and procedures parallel those in use in the molding industry at large. However, a number of subtle and very important detail differences do exist, and these are not extensively documented in the literature. Issues having to do with metallurgy, heat treatment, chemical passivation, metal polishing, and so on, have little to do with the actual design and engineering of a polymeric optical system. In a modern tool design exercise, though, the flow behavior of the polymer material in the mold, and the thermal behavior of that mold, are carefully modeled in multinode fashion, so that part quality may be maximized, and cycle time minimized.<sup>37</sup> A nodding awareness of these methods, and the underlying physics, may be helpful to the person responsible for the engineering of the polymer optical system.

## Testing and Qualification

In the process of implementing any optical system design, the matters of testing and certification become key issues. In molded optics, the master surfaces, whose shapes are ultimately transferred to the polymer optical parts, must be measured and documented. A convenient testing procedure for the optical elements replicated from these surfaces must likewise be contrived, in order to optimize the molding process and ensure that the finished assembly will perform to specification. The performance of that assembly must itself be verified, and any disparities from specification diagnosed.

In general, mechanical dimensions of the polymer parts may be verified by common inspection tools and techniques used in the glass optics realm. The possibility of inflicting surface damage, however, dictates that noncontact interferometric techniques be used in lieu of test glasses for optical figure diagnosis. This is a straightforward matter in the case of spherical surfaces, but requires some extra effort in the case of aspherics. See also Chap. 13, "Optical Testing," by Daniel Malacara-Hernández in Vol. II of this *Handbook*.

Obviously, aspheric master surfaces must be scrupulously checked and documented, lest the molder struggle in vain to replicate a contour which is inherently incorrect. The verification of the aspheric masters and their molded counterparts may be accomplished in a variety of ways. Mechanical gauging, if properly implemented, works well, but provides reliable information through only one azimuthal section of the part. Measurement at a sufficient number of points to detect astigmatism is awkward, very time consuming, and expensive. And this is not exactly consistent with the spirit of polymer optics.

## Null Optics

An optical *null corrector* permits the aspheric surface to be viewed in its entirety by the interferometer as if it were a simple spherical surface.<sup>38,39</sup> This is a rapid and convenient procedure. The null optics consist of very accurately manufactured (and precisely aligned) spherical glass elements designed to introduce aberration in an amount equal to, but of opposite sign from, that of the tested aspheric. Thus, interspersing this device permits aspherics to be viewed as if they were spherical. Since there exists no simple independent test of the null compensator, one must depend heavily upon the computed predictions of correction and upon the skill of the fabricator of the corrective optics. See also Chap. 14, "Use of Computer-Generated Holograms in Optical Testing," by Katherine Creath and James C. Wyant in Vol. II of this *Handbook*.

The concept of greatest importance regarding the use of aspheric surfaces is that *successful production of the total system is cast into considerable doubt if a surface is present which is not amenable to convenient testing*. While some aspheric optics may be nulled fairly easily, those which appear in polymer optical systems are frequently strong, exhibiting significant high-order derivatives. If the base curves are strong, especially strongly convex, there may exist no practical geometry in which to create a nulling optical system. And if a favorable geometry does exist, several optical elements may be necessary to effect adequate correction. One can easily approach a practical limit in this situation, since the manufacturing and assembly tolerances of the cascaded spherical elements may themselves (in superposition) exceed the theoretical correction requirement. The bottom line is that one should not proceed with cell design, or any other hardware design and construction, until the aspheric testing issues have been completely resolved.

## 3.8 COATINGS

### Reflective Coatings

Given the fact that optical polymers exhibit specular properties similar to those of glass, it is not surprising that optical coatings are often necessary in polymeric optical systems. The coatings deposited upon polymer substrates fall mostly into four general categories. These include coatings to improve reflectivity, to suppress specular reflection, to improve abrasion resistance, and to retard accumulation of electrostatic charge.

Reflective coatings may be applied by solution plating, or by vacuum-deposition. These are most often metallic coatings, usually aluminum if vacuum-deposited, and normally chromium if applied by plating. The abrasion resistance and general durability of such coatings is rather poor, and susceptibility to oxidation quite high, if no protective coating is applied over the metal film. In some applications, especially involving vacuum deposition, the overcoat may be a thin dielectric layer, deposited during the same process which applies the metal film. If the reflective coating has been applied by plating, the overcoat may be an organic material, perhaps lacquer, and may be deposited separately by spraying or dipping. Not surprisingly, the quality of a surface so treated will be poor by optical standards, and probably suitable only for toy or similar applications.

### Antireflection Coatings

Antireflection coatings are frequently utilized on polymer substrates, and may consist of a single layer or a rudimentary multilayer stack yielding better reflection-suppression performance. Due to the stringent requirements for control of the layer thicknesses, such coating formulations may be successfully deposited only in high-vacuum conditions, and only if temperatures in the chamber remain well below the service temperature of the substrate material. Elevated temperatures, necessary for baking the coatings to achieve good adhesion and abrasion resistance, may drive off plasticizing agents, limiting the "hardness" of the chamber vacuum. Such temperatures can ultimately soften the optical elements, so that their optical figure qualities are compromised. Relatively recent developments in the area of ion beam-assisted deposition have made possible improvements in the durability of coatings on polymer materials without having to resort to significantly elevated chamber temperatures.<sup>40</sup> See also Chap. 7, "Optical Properties of Films and Coatings," by Jerzy A. Dobrowolski in this volume of *Handbook*.

### Antiabrasion Coatings

In general, many polymeric optical systems which could benefit from application of coatings are left uncoated. This happens because the expense incurred in cleaning, loading, coating, unloading, and inspecting the optical elements may often exceed that of molding the part itself. Some optics, particularly those intended for ophthalmic applications, are constantly exposed to abuse by abrasion,

and must be protected, cost notwithstanding. Antiabrasion coatings intended to provide immunity to scratching may be of inorganic materials (normally vacuum-deposited), or may be organic formulations.<sup>41</sup>

Inorganic antiabrasion coatings may be similar to those used for simple antireflection requirements, except that they may be deposited in thicknesses which amount to several quarter-wavelengths. The practical thickness is usually limited by internal stress buildup, and by differential thermal expansion between coating and substrate. In general, the inorganic coatings derive their effectiveness by virtue of their hardness, and provide protection only superficially, since sufficient pressure will collapse the underlying substrate, allowing the coating to fracture.

Organic coatings for abrasion resistance normally derive their effectiveness from reduction of the surface frictional coefficient, thereby minimizing the opportunity for a hard contaminant to gain the purchase required to initiate a scratch. These coatings are often applied by dipping, spraying, or spinning. Coatings thus deposited usually destroy the smoothness which is required if the piece is to be qualified as a precision optical element.

### Antistatic Coatings

Coatings applied for the purpose of immunization against abrasion, or suppression of specular reflection, often provide a secondary benefit. They may improve the electrical conductivity of the host surface, thus promoting the dissipation of surface static charge, and the accumulation of oppositely charged contaminants. In circumstances where antireflection or antiabrasion coating costs cannot be justified, chemical treatments may be applied which increase conductivity. These materials typically leave a residue sufficiently thin that they are undetectable, even in interferometric testing.

## 3.9 REFERENCES

---

1. R. M. Altman and J. D. Lytle, "Optical Design Techniques for Polymer Optics," *S.P.I.E. Proc.* **237**:380–385 (1980).
2. C. Teyssier and C. Tribastone, *Lasers & Optronics* **Dec**:50–53 (1990).
3. PPG Ind., Inc., Tech Bulletin-CR-39.
4. H. Dislich, *Angew. Chem. Int. Ed. Engl.* **18**:49–59 (1979).
5. H. D. Wolpert, *Photonics Spectra* **Feb**:68–71 (1983).
6. *Plastics Desk Top Data Bank*, pp. 803–837 (1986).
7. *Modern Plastics Encyclopedia—Eng. Data Bank*, McGraw-Hill, New York, 1977, pp. 453–708.
8. *Plastics Technology Manufacturing Hdbk. and Buyer's Guide*, 1986, pp. 358–740.
9. *C.R.C. Hdbk. of Laser Science & Technology*, vol. IV, pp. 85–91.
10. *Encyclopedia of Polymer Science and Technology*, vol. 1, John Wiley & Sons, 1976.
11. *Space Materials Hdbk*, Lockheed Missiles and Space Corp., 1975.
12. J. D. Lytle, G. W. Wilkerson, and J. G. Jaramillo, *Appl. Opt.* **18**:1842–1846 (1979).
13. D. C. Smith, Alpert et al., *N.R.L. Report* 3924, 1951.
14. R. E. Kagarise and L. A. Weinberger, *N.R.L. Report* 4369, 1954.
15. Rohm & Haas Product Bulletin-PL 612d, 1979.
16. *Catalogue of Optical Glasses*, Schott Glass Technologies, 1989.
17. J. D. Lytle, *S.P.I.E. Proc.* **1354**:388–394 (1990).
18. J. Hoogland, *S.P.I.E. Proc.* **237**:216–221 (1980).
19. A. Osawa et al., *S.P.I.E. Proc.* **1354**:337–343 (1990).
20. E. I. Betensky, *S.P.I.E. Proc.* **1354**:663–668 (1990).

21. L. R. Estelle, *S.P.I.E. Proc.* **237**:392–401 (1980).
22. K. Straw, *S.P.I.E. Proc.* **237**:386–391 (1980).
23. M. Muranaka, M. Takagi, and T. Maruyama, *S.P.I.E. Proc.* **896**:123–131 (1988).
24. J. D. Lytle, *S.P.I.E. Proc.* **181**:93–102 (1979).
25. A. L. Palmer, “Practical Design Considerations for Polymer Optical Systems,” *S.P.I.E. Proc.* **306** (1981).
26. D. F. Horne, *Optical Production Technology*, 2d. ed., Adam Hilger, Ltd., 1983 pp. 167–170.
27. J. R. Egger, *S.P.I.E. Proc.* **193**:63–69 (1979).
28. R. Benjamin, *Plastics Design and Processing* **19**(3):39–49 (1979).
29. R. F. Weeks, *Optical Workshop Notebook*, vol. I., O.S.A., 1974–1975, sect. XVII.
30. D. F. Horne, “Lens Mechanism Technology,” Crane, Russack & Co., New York, 1975.
31. J. Sneller, *Modern Plastics Intl.* **11**(6):30–33 (1981).
32. J. D. Lytle, “Workshop on Optical Fabrication and Testing,” *Tech. Digest*, O.S.A., pp. 54–57 (1980).
33. E. C. Bernhardt and G. Bertacchi, *Plastics Technology Jan*:81–85 (1986).
34. G. R. Smoluk, *Plastics Engineering Jul*:107 (1966).
35. *Plastics News*, Aug. 1989, pp. 8–9.
36. *Plastics World*, July 1979, p. 34.
37. M. H. Naitove, *Plastics Technology Apr.* (1984).
38. D. Malacara (ed.), *Optical Shop Testing*, John Wiley & Sons, New York, 1978, chaps. 9, 14.
39. G. W. Hopkins and R. N. Shagam, *Appl. Opt.* **16**(10):2602 (1977).
40. J. D. Rancourt, *Optical Thin Films-User’s Hdbk.*, MacMillan, New York, 1987, pp. 197–199.
41. J. W. Prane, *Polymer News* **6**(4):178–181 (1980).

*This page intentionally left blank*

---

# PROPERTIES OF METALS

---

Roger A. Paquin

*Advanced Materials Consultant  
Tucson, Arizona, and  
Optical Sciences Center  
University of Arizona  
Tucson, Arizona*

---

## 4.1 GLOSSARY

---

- $a$  absorptance, absorptivity
- $a$  plate radius (m)
- $B$  support condition
- $C_{ij}$  elastic stiffness constants (N/m<sup>2</sup>)
- $C_p$  specific heat (J/kg K)
- CTE coefficient of thermal expansion (K<sup>-1</sup>)
- $D$  flexural rigidity (N m<sup>2</sup>)
- $D$  thermal diffusivity (m<sup>2</sup>/s)
- $E$  elastic modulus (Young's) (N/m<sup>2</sup>)
- $\mathbf{E}$  electromagnetic wave vector (J)
- $e$  electron charge (C)
- $E_o$  amplitude of electromagnetic wave at  $x = 0$  (J)
- $G$  load factor (N/kg)
- $G$  shear modulus, modulus of rigidity (N/m<sup>2</sup>)
- $g$  acceleration due to gravity (m/s<sup>2</sup>)
- $I$  light intensity in medium (W/m<sup>2</sup>)
- $i$   $(-1)^{1/2}$
- $I_o$  light intensity at interface (W/m<sup>2</sup>)
- $I_o$  section moment of inertia (m<sup>4</sup>/m)
- $K$  bulk modulus (N/m<sup>2</sup>)
- $k$  extinction coefficient
- $k$  thermal conductivity (W/mK)
- $L$  length (m)
- $M$  materials parameter (kg/Nm)
- $m$  electron mass (kg)
- $\mathbf{N}$  complex index of refraction



$N$	number of dipoles per unit volume ( $\text{m}^{-3}$ )
$n$	index of refraction
$P$	plate size ( $\text{m}^4$ )
$q$	load ( $\text{N}/\text{m}^2$ )
$r$	Reflectance, reflectivity
$R_I$	intensity reflection coefficient
$S$	structural efficiency ( $\text{m}^{-2}$ )
$T$	temperature (K)
$t$	time (s)
$t$	transmittance, transmissivity
$V_0$	volume per unit area of surface (m)
$x$	distance (m)
$\alpha$	coefficient of thermal expansion ( $\text{K}^{-1}$ )
$\alpha$	absorption coefficient ( $\text{m}^{-1}$ )
$\beta$	deflection coefficient
$\beta$	dynamic deflection coefficient
$\Gamma$	damping constant
$\delta$	skin depth (nm)
$\delta$	deflection (m)
$\delta_{\text{DYN}}$	dynamic deflection (m)
$\epsilon$	emittance, emissivity ( $\text{W}/\text{m}^2$ )
$\epsilon$	complex dielectric constant
$\epsilon_0$	permittivity of free space (F/m)
$\epsilon_1$	real part of dielectric constant
$\epsilon_2$	imaginary part of dielectric constant
$\theta$	angular acceleration ( $\text{s}^2$ )
$\lambda$	wavelength (m)
$\lambda_0$	wavelength in vacuum (m)
$\mu$	magnetic susceptibility (H/m)
$\nu$	frequency ( $\text{s}^{-1}$ )
$\nu$	Poisson' ratio
$\rho$	mass density ( $\text{kg}/\text{m}^3$ )
$\sigma$	conductivity (S/m)
$\omega$	radian frequency ( $\text{s}^{-1}$ )

---

## 4.2 INTRODUCTION

Metals are commonly used in optical systems in three forms: (1) structures, (2) mirrors, and (3) optical thin films. In this article, properties are given for metal mirror substrate and structural materials used in modern optical systems. Many other materials have not been included due to their limited applicability. Metal film properties are discussed in the context of thick films (claddings) rather than optical thin films that are covered in Chap. 7, "Optical Properties of Films and Coatings." Since mirrors are structural elements, the structural properties are equally important as the optical properties to the designer of an optical system. Therefore, the properties addressed here include physical, mechanical, and thermal properties in addition to optical properties. Mechanical and thermal properties of silicon (Si) and silicon carbide (SiC) are included, but not their optical properties since they are given in Chap. 5, "Optical Properties of Semiconductors."

After brief discussions of optical properties, mirror design, and dimensional stability, curves and tables of properties are presented, as a function of temperature and wavelength, where available. For more complete discussions or listings, the reader should consult the references and/or one of the available databases.<sup>1-3</sup> A concise theoretical overview of the physical properties of materials is given by Lines.<sup>4</sup>

## Nomenclature

The symbols and units used in this subsection are consistent with usage in other sections of this *Handbook* although there are some unavoidable duplications in the usage of symbols between categories of optical, physical, thermal, and mechanical properties. Definitions of symbols with the appropriate units are contained in the table at the beginning of this chapter.

## Optical Properties

The definitions for optical properties given in this section are primarily in the geometric optics realm and do not go into the depth considered in many texts dealing with optical properties of solids.<sup>5-8</sup>

There is obviously a thickness continuum between thin films and bulk, but for this presentation, bulk is considered to be any thickness of material that has bulk properties. Typically, thin films have lower density, thermal conductivity, and refractive index than bulk; however, current deposition techniques are narrowing the differences. Optical properties of thin films are presented only when bulk properties have not been found in the literature.

The interaction between light and metals takes place between the optical electric field and the conduction band electrons of the metal.<sup>9</sup> Some of the light energy can be transferred to the lattice by collisions in the form of heat. The optical properties of metals are normally characterized by the two optical constants: index of refraction  $n$  and extinction coefficient  $k$  that make up the complex refractive index  $N$  where:

$$N = n + ik \quad (1)$$

The refractive index is defined as the ratio of phase velocity of light in vacuum to the phase velocity of light in the medium. The extinction coefficient is related to the exponential decay of the wave as it passes through the medium. Note, however, that these “constants” vary with wavelength and temperature. The expression for an electromagnetic wave in an absorbing medium contains both of these parameters:

$$\mathbf{E} = E_0 e^{-2\pi kx/\lambda_0} e^{-i(2\pi nx/\lambda_0 - \omega t)} \quad (2)$$

where  $E_0$  is the amplitude of the wave measured at the point  $x = 0$  in the medium,  $E$  is the instantaneous value of the electric vector measured at a distance  $x$  from the first point and at some time  $t$ ,  $\omega$  is the angular frequency of the source, and  $\lambda_0$  is the wavelength in vacuum.

The absorption coefficient  $\alpha$  is related to the extinction coefficient by:

$$\alpha = 4k/\lambda_0 \quad (3)$$

and for the general case, the absorption coefficient also appears in the absorption equation:

$$I = I_0 e^{-\alpha x} \quad (4)$$

However, this equation implies that the intensities  $I$  and  $I_0$  are measured within the absorbing medium. The complex dielectric constant  $\epsilon$  for such a material is:

$$\epsilon = \epsilon_1 + i\epsilon_2 \quad (5)$$

where the dielectric constants are related to the optical constants by:

$$\epsilon_1 = n^2 - k^2 \quad (6)$$

$$\epsilon_2 = 2nk \quad (7)$$

Two additional materials properties that influence the light-material interaction are magnetic susceptibility  $\mu$  and conductivity  $\sigma$  that are further discussed later.

The equations describing the reflection phenomena, including polarization effects for metals, will not be presented here but are explained in detail elsewhere.<sup>5-8,10,11</sup> After a brief description of Lorentz and Drude theories and their implications for metals, and particularly for absorption, the relationship among reflection, transmission, and absorption is discussed.<sup>9</sup>

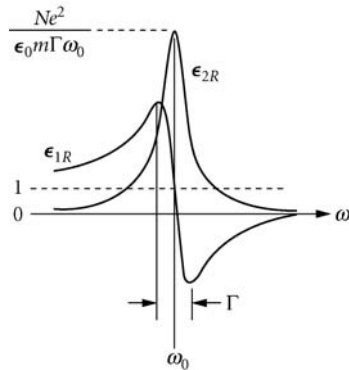
The classical theory of absorption in dielectrics is due to H. A. Lorentz<sup>12</sup> and in metals to P. K. L. Drude.<sup>13</sup> Both models treat the optically active electrons in a material as classical oscillators. In the Lorentz model, the electron is considered to be bound to the nucleus by a harmonic restoring force. In this manner, Lorentz's picture is that of the nonconductive dielectric. Drude considered the electrons to be free, and set the restoring force in the Lorentz model equal to zero. Both models include a damping term in the electron's equation of motion that in more modern terms is recognized as a result of electron-phonon collisions.

These models solve for the electron's motion in the presence of the electromagnetic field as a driving force. From this, it is possible to write an expression for the polarization induced in the medium and from that to derive the dielectric constant. The Lorentz model for dielectrics gives the relative real and imaginary parts of the dielectric constant  $\epsilon_{1R}$  and  $\epsilon_{2R}$  in terms of  $N$ , the number of dipoles per unit volume;  $e$  and  $m$ , the electron charge and mass;  $\Gamma$ , the damping constant;  $\omega$  and  $\omega_0$ , the radian frequencies of the field and the harmonically bound electron; and  $\epsilon_0$ , the permittivity of free space. These functions are shown in Fig. 1. The range of frequencies where  $\epsilon_1$  increases with frequency is referred to as the *range of normal dispersion*, and the region near  $\omega = \omega_0$ , where it decreases with frequency is called the *range of anomalous dispersion*.

Since the ionic polarizability is much smaller than the electronic polarizability at optical frequencies, only the electronic terms are considered when evaluating optical absorption using the Lorentz model for dielectrics. The Drude model for metals assumes that the electrons are free to move. This means that it is identical to the Lorentz model except that  $\omega_0$  is set equal to zero. The real and imaginary parts of the dielectric constant are then given by

$$\epsilon_{1R} = 1 - (Ne^2\epsilon_0 m) \frac{1}{\omega^2 + \Gamma^2} \quad (8)$$

$$\epsilon_{2R} = (Ne^2\epsilon_0 m) \frac{\Gamma}{\omega(\omega^2 + \Gamma^2)} \quad (9)$$



**FIGURE 1** Frequency dependences of  $\epsilon_{1R}$  and  $\epsilon_{2R}$ .<sup>9</sup>

The quantity  $\Gamma$  is related to the mean time between electron collisions with lattice vibrations, and by considering electronic motion in an electric field  $E$  having radian frequency  $\omega$ , an expression for the average velocity can be obtained. An expression for the conductivity  $\sigma$  is then obtained and the parts of the dielectric constant can be restated. At electromagnetic field frequencies that are low, it can be shown that  $\epsilon_2 \gg \epsilon_1$  and therefore it follows that:

$$\alpha = (\omega\mu\sigma/2)^{1/2} \quad (10)$$

In other words, the optical properties and the conductivity of a perfect metal are related through the fact that each is determined by the motion of free electrons. At high frequencies, transitions involving bound or valence band electrons are possible and there will be a noticeable deviation from this simple result of the Drude model. However, the experimental data reported for most metals are in good agreement with the Drude prediction at wavelengths as short as 1  $\mu\text{m}$ .

From Eq. (10) it is clear that a field propagating in a metal will be attenuated by a factor of  $1/e$  when it has traveled a distance:

$$\delta = (2/\omega\mu\sigma)^{1/2} \quad (11)$$

This quantity is called the *skin depth*, and at optical frequencies for most metals it is  $\sim 50$  nm. After a light beam has propagated one skin depth into a metal, its intensity is reduced to 0.135 of its value at the surface.

Another aspect of the absorption of light energy by metals that should be noted is the fact that it increases with temperature. This is important because during laser irradiation the temperature of a metal will increase and so will the absorption. The coupling of energy into the metal is therefore dependent on the temperature dependence of the absorption. For most metals, all the light that gets into the metal is absorbed. If the Fresnel expression for the electric field reflectance is applied to the real and imaginary parts of the complex index for a metal-air interface, the field reflectivity can be obtained. When multiplied by its complex conjugate, the expression for the intensity reflection coefficient is obtained:

$$R_I = 1 - 2\mu\epsilon_0\omega/\sigma \quad (12)$$

Since the conductivity  $\sigma$  decreases with increasing temperature,  $R_I$  decreases with increasing temperature, and at higher temperatures more of the incident energy is absorbed.

Since reflection methods are used in determining the optical constants, they are strongly dependent on the characteristics of the metallic surface. These characteristics vary considerably with chemical and mechanical treatment, and these treatments have not always been accurately defined. Not all measurements have been made on freshly polished surfaces but in many cases on freshly deposited thin films. The best available data are presented in the tables and figures, and the reader is advised to consult the appropriate references for specifics.

In this article, an ending of *-ance* denotes a property of a specific sample (i.e., including effects of surface finish), while the ending *-ivity* refers to an intrinsic material property. For most of the discussion, the endings are interchangeable.

Reflectance  $r$  is the ratio of radiant flux reflected from a surface to the total incident radiant flux. Since  $r$  is a function of the optical constants, it varies with wavelength and temperature. The relationship between reflectance and optical constants is:<sup>5</sup>

$$r = \frac{(n-1)^2 + k^2}{(n+1)^2 + k^2} \quad (13)$$

The reflectance of a good, freshly deposited mirror coating is almost always higher than that of a polished or electroplated surface of the same material. The reflectance is normally less than unity—some transmission and absorption, no matter how small, are always present. The relationship between these three properties is:

$$r + t + a = 1 \quad (14)$$

Transmittance  $t$  is the ratio of radiant flux transmitted through a surface to the total incident radiant flux and absorptance  $a$  is the ratio of the radiant flux lost by absorption to the total incident radiant flux. Since  $t$  and  $a$  are functions of the optical constants, they vary with wavelength and temperature. Transmittance is normally very small for metals except in special cases (e.g., beryllium at x-ray wavelengths). Absorptance is affected by surface condition as well as the intrinsic contribution of the material.

The thermal radiative properties are descriptive of a radiant energy-matter interaction that can be described by other properties such as the optical constants and/or complex dielectric constant, each of which is especially convenient for studying various aspects of the interaction. However, the thermal radiative properties are particularly useful since metallic materials are strongly influenced by surface effects, particularly oxide films, and therefore in many cases they are not readily calculated by simple means from the other properties.

For opaque materials, the transmission is near zero, so Eq. (14) becomes:

$$r + a = 1 \quad (15)$$

but since Kirchoff's law states that absorptance equals emittance,  $\epsilon$ , this becomes:

$$r + \epsilon = 1 \quad (16)$$

and the thermal radiative properties of an opaque body are fully described by either the reflectance or the emittance. Emittance is the ratio of radiated emitted power (in  $W/m^2$ ) of a surface to the emissive power of a blackbody at the same temperature. Emittance can therefore be expressed as either *spectral* (emittance as a function of wavelength at constant temperature) or *total* (the integrated emittance over all wavelengths as a function of temperature).

## Physical Properties

The physical properties of interest for metals in optical applications include density, electrical conductivity, and electrical resistivity (the reciprocal of conductivity), as well as crystal structure. Chemical composition of alloys is also included with physical properties.

For density, mass density is reported with units of  $kg/m^3$ . Electrical conductivity is related to electrical resistivity, but for some materials, one or the other is normally reported. Both properties vary with temperature.

Crystal structure is extremely important for stability since anisotropy of the elastic, electric, and magnetic properties and thermal expansion depend on the type of structure.<sup>14</sup> Single crystals of cubic metals have completely isotropic coefficient of thermal expansion (CTE), but are anisotropic in elastic properties—modulus and Poisson's ratio. Materials with hexagonal structures have anisotropic expansion and elastic properties. While polycrystalline metals with randomly oriented small grains do not exhibit these anisotropies they can easily have local areas that are inhomogeneous or can have overall oriented crystal structure induced by fabrication methods.

The combined influence of physical, thermal, and mechanical properties on optical system performance is described under "Properties Important in Mirror Design," later in this chapter.

## Thermal Properties

Thermal properties of metals that are important in optical systems design include: coefficient of thermal expansion  $\alpha$ , referred to in this section as CTE; thermal conductivity  $k$ ; and specific heat  $C_p$ . All of these properties vary with temperature; usually they tend to decrease with decreasing temperature. Although not strictly a thermal property, the maximum usable temperature is also included as a guide for the optical designer.

*Thermal expansion* is a generic term for change in length for a specific temperature change, but there are precise terms that describe specific aspects of this material property. ASTM E338 Committee recommends the following nomenclature:<sup>15</sup>

Coefficient of linear thermal expansion (CTE or thermal expansivity):

$$\alpha \equiv \frac{1}{L} \frac{\Delta L}{\Delta T} \quad (17)$$

Instantaneous coefficient of linear thermal expansion:

$$\alpha' \equiv \lim_{\Delta T \rightarrow 0} \left( \frac{1}{L} \frac{\Delta L}{\Delta T} \right) \quad (18)$$

Mean coefficient of linear thermal expansion:

$$\bar{\alpha} \equiv \frac{1}{T_2 - T_1} \int_{T_1}^{T_2} \alpha' dT \quad (19)$$

In general, lower thermal expansion is better for optical system performance, as it minimizes the effect of thermal gradients on component dimensional changes. CTE is the prime parameter in materials selection for cooled mirrors.

*Thermal conductivity* is the quantity of heat transmitted per unit of time through a unit of area per unit of temperature gradient with units of W/mK. Higher thermal conductivity is desirable to minimize temperature gradients when there is a heat source to the optical system.

*Specific heat*, also called heat capacity per unit mass, is the quantity of heat required to change the temperature of a unit mass of material one degree under conditions of constant pressure. A material with high specific heat requires more heat to cause a temperature change that might cause a distortion. High specific heat also means that more energy is required to force a temperature change (e.g., in cooling an infrared telescope assembly to cryogenic temperatures).

Maximum usable temperature is not a hard number. It is more loosely defined as the temperature at which there is a significant change in the material due to one or more of a number of things, such as significant softening or change in strength, melting, recrystallization, and crystallographic phase change.

## Mechanical Properties

Mechanical properties are divided into elastic/plastic properties and strength, and fracture properties. The elastic properties of a metal can be described by a  $6 \times 6$  matrix of constants called the elastic stiffness constants.<sup>16–18</sup> Because of symmetry considerations, there are a maximum of 21 independent constants that are further reduced for more symmetrical crystal types. For cubic materials there are three constants,  $C_{11}$ ,  $C_{12}$ , and  $C_{44}$ , and for hexagonal five constants,  $C_{11}$ ,  $C_{12}$ ,  $C_{13}$ ,  $C_{33}$ , and  $C_{44}$ . From these, the elastic properties of the material, Young's modulus  $E$  (the elastic modulus in tension), bulk modulus  $K$ , modulus of rigidity  $G$  (also called shear modulus), and Poisson's ratio  $\nu$  can be calculated. The constants, and consequently the properties, vary as functions of temperature. The properties vary with crystallographic direction in single crystals,<sup>14</sup> but in randomly oriented polycrystalline materials the macroproperties are usually isotropic.

Young's modulus of elasticity  $E$  is the measure of stiffness or rigidity of a metal—the ratio of stress, in the completely elastic region, to the corresponding strain. Bulk modulus  $K$  is the measure of resistance to change in volume—the ratio of hydrostatic stress to the corresponding change in volume. Shear modulus, or modulus of rigidity,  $G$  is the ratio of shear stress to the corresponding shear strain under completely elastic conditions.

Poisson's ratio  $\nu$  is the ratio of the absolute value of the rate of transverse (lateral) strain to the corresponding axial strain resulting from uniformly distributed axial stress in the elastic deformation region.

For isotropic materials the properties are interrelated by the following equations:<sup>18</sup>

$$G = \frac{E}{2(1+\nu)} \quad (20)$$

$$K = \frac{E}{3(1-2\nu)} \quad (21)$$

The mechanical strength and fracture properties are important for the structural aspect of the optical system. The components in the system must be able to support loads with no permanent deformation within limits set by the error budget and certainly with no fracture. For ductile materials such as copper, the yield and/or microyield strength may be the important parameters. On the other hand, for brittle or near-brittle metals such as beryllium, fracture toughness may be more important. For ceramic materials such as silicon carbide, fracture toughness and modulus of rupture are the important fracture criteria. A listing of definitions for each of these terms<sup>19</sup> follows:

*creep strength*: the stress that will cause a given time-dependent plastic strain in a creep test for a given time.

*ductility*: the ability of a material to deform plastically before fracture.

*fatigue strength*: the maximum stress that can be sustained for a specific number of cycles without failure.

*fracture toughness*: a generic term for measures of resistance to extension of a crack.

*hardness*: a measure of the resistance of a material to surface indentation.

*microcreep strength*: the stress that will cause 1 ppm of permanent strain in a given time; usually less than the microyield strength.

*microstrain*: a deformation of  $10^{-6}$  m/m (1 ppm).

*microyield strength*: the stress that will cause 1 ppm of permanent strain in a short time; also called precision elastic limit (PEL).

*ultimate strength*: the maximum stress a material can withstand without fracture.

*yield strength*: the stress at which a material exhibits a specified deviation from elastic behavior (proportionality of stress and strain), usually  $2 \times 10^{-3}$  m/m (0.2 percent).

## Properties Important in Mirror Design

There are many factors that enter into the design of a mirror or mirror system, but the most important requirement is optical performance. Dimensional stability, weight, durability, and cost are some of the factors to be traded off before an effective design can be established.<sup>20-23</sup> The loading conditions during fabrication, transportation, and use and the thermal environment play a substantial role in materials selection. To satisfy the end-use requirements, the optical, structural, and thermal performance must be predictable. Each of these factors has a set of parameters and associated material properties that can be used to design an optic to meet performance goals.

For optical performance, the shape or optical figure is the key performance factor followed by the optical properties of reflectance, absorptance, and complex refractive index. The optical properties of a mirror substrate material are only important when the mirror is to be used bare (i.e., with no optical coating).

To design for structural performance goals, deflections due to static (or inertial) and dynamic loads are usually calculated as a first estimate.<sup>24</sup> For this purpose, the well-known plate equations<sup>25</sup> are invoked. For the static case,

$$\delta = \beta qa^4/D \quad (22)$$

where  $\delta$  = deflection

$\beta$  = deflection coefficient (depends on support condition)

$q$  = normal loading (uniform load example)

$a$  = plate radius (semidiameter)

$D$  = flexural rigidity, defined as:

$$D = EI_0/(1-\nu^2) \quad (23)$$

where, in turn  $E$  = Young's modulus of elasticity

$I_0$  = moment of inertia of the section

$\nu$  = Poisson's ratio

But

$$q = \rho V_0 G \quad (24)$$

where  $\rho$  = material density

$V_0$  = volume of material per unit area of plate surface

$G$  = load factor (g's)

After substitution and regrouping the terms:

$$\delta = \beta \frac{\rho(1-\nu^2)}{E} \frac{V_0}{I_0} a^4 G \quad (25)$$

or

$$\delta \times B = M \times S \times P \times G \quad (26)$$

where  $B$  = support condition

$M$  = materials parameters

$S$  = structural efficiency

$P$  = plate size

$G$  = load factor

This shows five terms, each representing a parameter to be optimized for mirror performance.  $B$ ,  $P$ , and  $G$  will be determined from system requirements;  $S$  is related to the geometric design of the part; and  $M$  is the materials term showing that  $\rho$ ,  $\nu$ , and  $E$  are the important material properties for optimizing structural performance.

For the dynamic case of deflection due to a local angular acceleration  $\ddot{\theta}$  about a diameter (scanning applications), the equation becomes:

$$\delta_{\text{DYN}} = \beta_D \frac{\rho(1-\nu^2)}{E} \frac{V_0}{I_0} a^5 \frac{\ddot{\theta}}{g} \quad (27)$$

The same structural optimization parameters prevail as in the static case. Note that in both cases maximizing the term  $E/\rho$  (specific stiffness) minimizes deflection.

The determination of thermal performance<sup>26,27</sup> is dependent on the thermal environment and thermal properties of the mirror material. For most applications, the most significant properties are the coefficient of thermal expansion CTE or  $\alpha$ , and thermal conductivity  $k$ . Also important are the specific heat  $C_p$ , and thermal diffusivity  $D$ , a property related to dissipation of thermal gradients that is a combination of properties and equal to  $k/\rho C_p$ . There are two important thermal figures of merit, the coefficients of thermal distortion  $\alpha/k$  and  $\alpha/D$ . The former expresses steady-state distortion per unit of input power, while the latter is related to transient distortions.

Typical room-temperature values for many of the important properties mentioned here are listed for a number of mirror materials in Table 1. It should be clear from the wide range of properties and figures of merit that no one material can satisfy all applications. A selection process is required and a tradeoff study has to be made for each individual application.<sup>20</sup>

Metal optical components can be designed and fabricated to meet system requirements. However, unless they remain within specifications throughout their intended lifetime, they have failed. The most often noted changes that occur to degrade performance are dimensional instability and/or environment-related optical property degradation. Dimensional instabilities can take many forms with many causes, and there are any number of ways to minimize them. Dimensional instabilities can only be discussed briefly here; for a more complete discussion, consult Refs. 28 to 31. The instabilities most often observed are:

- temporal instability: a change in dimensions with time in a uniform environment (e.g., a mirror stored in a laboratory environment with no applied loads changes figure over a period of time)



**TABLE 1** Properties of Selected Mirror Materials

	$\rho$ Density ( $10^3 \text{ kg/m}^3$ )	$E$ Young's Modulus (GN/m <sup>2</sup> )	$E/\rho$ Specific Stiffness (arb. units)	CTE Thermal Expansion ( $10^{-6}/\text{K}$ )	$k$ Thermal Conductivity (W/m K)	$C_p$ Specific Heat (J/kg K)	$D$ Thermal Diffusivity ( $10^{-6} \text{ m}^2/\text{s}$ )	Distortion coefficient	
								CTE/ $k$ Steady State ( $\mu\text{m}/\text{W}$ )	CTE/ $D$ Transient ( $\text{s}/\text{m}^2 \text{ K}$ )
Preferred	small	large	large	small	large	large	large	small	small
Fused silica	2.19	72	33	0.50	1.4	750	0.85	0.36	0.59
Beryllium: 1–70	1.85	287	155	11.3	216	1925	57.2	0.05	0.20
Aluminum: 6061	2.70	68	25	22.5	167	896	69	0.13	0.33
Copper	8.94	117	13	16.5	391	385	115.5	0.53	0.14
304 stainless steel	8.00	193	24	14.7	16.2	500	4.0	0.91	3.68
Invar 36	8.05	141	18	1.0	10.4	515	2.6	0.10	0.38
Silicon	2.33	131	56	2.6	156	710	89.2	0.02	0.03
SiC: RB-30% Si	2.89	330	114	2.6	155	670	81.0	0.02	0.03
SiC: CVD	3.21	465	145	2.4	198	733	82.0	0.01	0.03

- thermal/mechanical cycling or hysteresis instability: a change in dimensions when the environment is changed and then restored, where the measurements are made under the same conditions before and after the exposure (e.g., a mirror with a measured figure is cycled between high and low temperatures and, when remeasured under the original conditions, the figure has changed)
- thermal instability: a change in dimensions when the environment is changed, but completely reversible when the original environment is restored (e.g., a mirror is measured at room temperature, again at low temperature where the figure is different, and finally at the original conditions with the original figure restored)

There are other types of instabilities, but they are less common, particularly in metals. The sources of the dimensional changes cited here can be attributed to one or more of the following:

- externally applied stress
- changes in internal stress
- microstructural changes
- inhomogeneity/anisotropy of properties

In general, temporal and cycling/hysteresis instabilities are primarily caused by changes in internal stress (i.e., stress relaxation). If the temperature is high enough, microstructural changes can take place as in annealing, recrystallization, or second-phase precipitation. Thermal instability is a result of inhomogeneity and/or anisotropy of thermal expansion within the component, is completely reversible, and cannot be eliminated by nondestructive methods.

To eliminate potential instabilities, care must be taken in the selection of materials and fabrication methods to avoid anisotropy and inhomogeneity. Further care is necessary to avoid any undue applied loads that could cause part deformation and subsequent residual stress. The fabrication methods should include stress-relief steps such as thermal annealing, chemical removal of damaged surfaces, and thermal or mechanical cycling. These steps become more critical for larger and more complex component geometries.

Instabilities can also be induced by attachments and amounts. Careful design to minimize induced stresses and selection of dissimilar materials with close thermal expansion matching is essential.<sup>32</sup>

### 4.3 SUMMARY DATA

The properties presented here are representative for the materials and are not a complete presentation. For more complete compilations, the references should be consulted.

#### Optical Properties

Thin films and their properties are discussed in Chap. 7, "Optical Properties of Films and Coatings," and therefore are not presented here except in the case where bulk (surface) optical properties are not available.

**Index of Refraction and Extinction Coefficient** The data for the optical constants of metals are substantial, with the most complete listing available in the two volumes of *Optical Constants of Metals*,<sup>33,34</sup> from which most of the data presented here have been taken. Earlier compilations<sup>35,36</sup> are also available. While most of the data are for deposited films, the references discuss properties of polished polycrystalline surfaces where available. Table 2 lists room-temperature values for  $n$  and  $k$  of Al,<sup>37</sup> Be,<sup>38</sup> Cu,<sup>39</sup> Cr,<sup>40</sup> Au,<sup>39</sup> Fe,<sup>40</sup> Mo,<sup>39</sup> Ni,<sup>39</sup> Pt,<sup>39</sup> Ag,<sup>39</sup> W,<sup>39</sup> and  $\alpha$ -SiC.<sup>41</sup> Figures 2 to 14 graphically show these constants with the absorption edges shown in most cases.

Extensive reviews of the properties of aluminum<sup>37</sup> and beryllium<sup>38</sup> also discuss the effects of oxide layers on optical constants and reflectance. Oxide layers on aluminum typically reduce the optical constant values by 25 percent in the infrared, 10 to 15 percent in the visible, and very little in the ultraviolet.<sup>37</sup> As a result of the high values of  $n$  and  $k$  for aluminum in the visible and infrared, there are relatively large variations of optical constants with temperature, but they result in only small changes in reflectance.<sup>37</sup> The beryllium review<sup>38</sup> does not mention any variation of properties with temperature. The optical properties of beryllium and all hexagonal metals vary substantially with crystallographic direction. This variation with crystallography is shown for the dielectric constants of beryllium in Fig. 15.<sup>42</sup> The optical constants can be obtained from the dielectric constants using the following equations:<sup>9</sup>

$$n = \left\{ \left[ (\epsilon_1^2 + \epsilon_2^2)^{1/2} + \epsilon_1 \right] / 2 \right\}^{1/2} \quad (28)$$

$$k = \left\{ \left[ (\epsilon_1^2 + \epsilon_2^2)^{1/2} - \epsilon_1 \right] / 2 \right\}^{1/2} \quad (29)$$

This variation in optical properties results in related variations in reflectance and absorptance that may be the main contributors to a phenomenon called *anomalous scatter*, where the measured scatter from polished surfaces does not scale with wavelength when compared to the measured surface roughness.<sup>43-47</sup>

The optical constants reported for SiC are for single-crystal hexagonal material.

#### Reflectance and Absorptance

Reflectance data in the literature are extensive. Summaries have been published for most metals<sup>35-36</sup> primarily at normal incidence, both as deposited films and polished bulk material. Reflectance as a function of angle is presented for a number of metals in Refs. 48 and 49. Selected data are also included in Ref. 50. Temperature dependence of reflectance is discussed in a number of articles, but little measured data are available. Absorption data summaries are not as readily available, with one summary<sup>35</sup> and many articles for specific materials, primarily at laser wavelengths and often as a function of temperature. Table 3 lists values of room-temperature normal-incidence reflectance as a function of wavelength, and Figs. 16 to 26 show  $r$  and  $a$  calculated from  $\eta$  and  $k$  in the range of 0.015 to 10  $\mu\text{m}$ .<sup>35</sup> Figure 27<sup>35</sup> shows reflectance for polarized radiation as a function of incidence angle for three combinations of  $n$  and  $k$ , illustrating the tendency toward total external reflectance for angles greater than about 80°.

**TABLE 2**  $n$  and  $k$  of Selected Metals at Room Temperature

Metal	eV	Wavelength Å	$\mu\text{m}$	$n$	$k$
Aluminum <sup>37</sup>	300.0	41.3		1.00	0.00
	180.0	68.9		0.99	0.01
	130.0	95.4		0.99	0.02
	110.0	113.0		0.99	0.03
	100.0	124.0		0.99	0.03
	95.0	131.0		1.00	0.04
	80.0	155.0		1.01	0.02
	75.0	165.0		1.01	0.02
	72.0	172.0		1.02	0.00
	50.0	248.0		0.97	0.01
	25.0	496.0		0.81	0.02
	17.0	729.0		0.47	0.04
	12.0	1,033.0	0.10	0.03	0.79
	6.00	2,066.0	0.21	0.13	2.39
	4.00	3,100.0	0.31	0.29	3.74
	3.10	4,000.0	0.40	0.49	4.86
	2.48	5,000.0	0.50	0.77	6.08
	2.07	6,000.0	0.60	1.02	7.26
	1.91	6,500.0	0.65	1.47	7.79
	1.77	7,000.0	0.70	1.83	8.31
	1.55	8,000.0	0.80	2.80	8.45
	1.10		1.13	1.20	11.2
	0.827		1.50	1.38	15.4
	0.620		2.00	2.15	20.7
	0.310		4.00	6.43	39.8
0.177		7.00	14.0	66.2	
0.124		10.0	25.3	89.8	
0.062		20.0	60.7	147.0	
0.039		32.0	103.0	208.0	
Beryllium <sup>38</sup>	300.0	41.3		1.00	0.00
	200.0	62.0		0.99	0.00
	150.0	82.7		0.99	0.01
	119.0	104.0		1.00	0.02
	100.0	124.0		0.99	0.00
	50.0	248.0		0.93	0.01
	25.0	496.0		0.71	0.10
	17.0	729.0		0.34	0.42
	12.0	1,033.0	0.10	0.30	1.07
	6.00	2,066.0	0.21	0.85	2.64
	4.00	3,100.0	0.31	2.47	3.08
		4,133.0	0.41	2.95	3.14
		5,166.0	0.52	3.03	3.18
		6,888.0	0.69	3.47	3.23
			1.03	3.26	3.96
			3.10	2.07	12.6
			6.20	3.66	26.7
		12.0	11.3	50.1	
		21.0	19.9	77.1	
		31.0	37.4	110.0	
		62.0	86.1	157.0	
Copper <sup>39</sup>	9,000.0	1.38		1.00	0.00
	4,000.0	3.10		1.00	0.00

**TABLE 2**  $n$  and  $k$  of Selected Metals at Room Temperature (*Continued*)

Metal	eV	Wavelength Å	$\mu\text{m}$	$n$	$k$
Copper <sup>39</sup>	1,500.0	8.27		1.00	0.00
	1,000.0	12.4		1.00	0.00
	900.0	13.8		1.00	0.00
	500.0	24.8		1.00	0.00
	300.0	41.3		0.99	0.01
	200.0	62.0		0.98	0.02
	150.0	82.7		0.97	0.03
	120.0	103.0		0.97	0.05
	100.0	124.0		0.97	0.07
	50.0	248.0		0.95	0.13
	29.0	428.0		0.85	0.30
	26.0	477.0		0.92	0.40
	24.0	517.0		0.96	0.37
	23.0	539.0		0.94	0.37
	20.0	620.0		0.88	0.46
	15.0	827.0		1.01	0.71
	12.0	1,033.0	0.10	1.09	0.73
	6.50	1,907.0	0.19	0.96	1.37
	5.20	2,384.0	0.24	1.38	1.80
	4.80	2,583.0	0.26	1.53	1.71
	4.30	2,885.0	0.29	1.46	1.64
	2.60	4,768.0	0.48	1.15	2.5
	2.30	5,390.0	0.54	1.04	2.59
	2.10	5,904.0	0.59	0.47	2.81
	1.80	6,888.0	0.69	0.21	4.05
	1.50	8,265.0	0.83	0.26	5.26
	0.950		1.30	0.51	6.92
	0.620		2.00	0.85	10.6
0.400		3.10	1.59	16.5	
0.200		6.20	5.23	33.0	
0.130		9.54	10.8	47.5	
Chromium <sup>40</sup>	10,000.0	1.24		1.00	0.00
	6,015.0	2.06		1.00	0.00
	5,878.0	2.11		1.00	0.00
	3,008.0	4.12		1.00	0.00
	1,504.0	8.24		1.00	0.00
	992.0	12.5		1.00	0.00
	735.0	16.9		1.00	0.00
	702.0	17.7		1.00	0.00
	686.0	18.1		1.00	0.00
	403.0	30.8		1.00	0.00
	202.0	61.5		0.98	0.00
	100.0	124.0		0.94	0.03
	62.0	200.0		0.88	0.12
	52.0	238.0		0.92	0.18
	29.5	420.0		0.78	0.21
	24.3	510.0		0.67	0.39
	18.0	689.0		0.87	0.70
	14.3	867.0		1.06	0.82
	12.8	969.0		1.15	0.75
	11.4	1,088.0	0.109	1.08	0.69
7.61	1,629.0	0.163	0.66	1.23	

(Continued)

**TABLE 2**  $n$  and  $k$  of Selected Metals at Room Temperature (*Continued*)

Metal	eV	Wavelength Å	μm	$n$	$k$
Chromium <sup>40</sup>	5.75	2,156.0	0.216	0.97	1.74
	4.80	2,583.0	0.258	0.86	2.13
	3.03	4,092.0	0.409	1.54	3.71
	2.42	5,123.0	0.512	2.75	4.46
	1.77	7,005.0	0.700	3.84	4.37
	1.26	9,843.0	0.984	4.50	4.28
	1.12		1.11	4.53	4.30
	0.66		1.88	3.96	5.95
	0.60		2.07	4.01	6.48
	0.34		3.65	2.89	12.0
	0.18		6.89	8.73	25.4
	0.09		13.8	11.8	33.9
	0.06		20.7	21.2	42.0
	0.04		31.0	14.9	65.2
	Gold <sup>39</sup>	8,266.0	1.50		1.00
2,480.0		5.00		1.00	0.00
2,066.0		6.00		1.00	0.00
1,012.0		12.25		1.00	0.00
573.0		21.6		1.00	0.00
220.0		56.4		0.99	0.01
150.0		82.7		0.96	0.01
86.0		144.0		0.89	0.06
84.5		147.0		0.89	0.07
84.0		148.0		0.89	0.06
68.0		182.0		0.86	0.12
60.0		207.0		0.86	0.16
34.0		365.0		0.78	0.47
30.0		413.0		0.89	0.60
29.0		428.0		0.91	0.60
27.0		459.0		0.90	0.64
26.0		480.0		0.85	0.56
21.8		570.0		1.02	0.85
19.4		640.0		1.16	0.73
17.7		700.0		1.08	0.68
15.8		785.0		1.03	0.74
12.4		1,000.0	0.10	1.20	0.84
8.27		1,550.0	0.15	1.45	1.11
7.29		1,700.0	0.17	1.52	1.07
6.36		1,950.0	0.20	1.42	1.12
4.10		3,024.0	0.30	1.81	1.92
3.90		3,179.0	0.32	1.84	1.90
3.60		3,444.0	0.34	1.77	1.85
3.00		4,133.0	0.41	1.64	1.96
2.60		4,769.0	0.48	1.24	1.80
2.20	5,636.0	0.56	0.31	2.88	
1.80	6,888.0	0.69	0.16	3.80	
1.40	8,856.0	0.89	0.21	5.88	
1.20		1.03	0.27	7.07	
0.82		1.51	0.54	9.58	
0.40		3.10	1.73	19.2	
0.20		6.20	5.42	37.5	
0.125		9.92	12.2	54.7	

**TABLE 2**  $n$  and  $k$  of Selected Metals at Room Temperature (*Continued*)

Metal	eV	Wavelength Å	μm	$n$	$k$
Iron <sup>36,40</sup>	10,000.0	1.24		1.00	0.00
	7,071.0	1.75		1.00	0.00
	3,619.0	3.43		1.00	0.00
	1,575.0	7.87		1.00	0.00
	884.0	14.0		1.00	0.00
	825.0	15.0		1.00	0.00
	320.0	38.8		0.99	0.00
	211.0	58.7		0.98	0.01
	153.0	81.2		0.97	0.02
	94.0	132.0		0.94	0.05
	65.0	191.0		0.90	0.12
	56.6	219.0		0.98	0.19
	54.0	230.0		1.11	0.18
	51.6	240.0		0.97	0.05
	30.0	413.0		0.82	0.13
	22.2	559.0		0.71	0.35
	20.5	606.0		0.74	0.42
	18.0	689.0		0.78	0.51
	15.8	785.0		0.77	0.61
	11.5	1,078.0	0.11	0.93	0.84
	11.0	1,127.0	0.11	0.91	0.83
	10.3	1,200.0	0.12	0.87	0.91
	8.00	1,550.0	0.15	0.94	1.18
	5.00	2,480.0	0.25	1.14	1.87
	3.00	4,133.0	0.41	1.88	3.12
	2.30	5,390.0	0.54	2.65	3.34
	2.10	5,903.0	0.59	2.80	3.34
	1.50	8,265.0	0.83	3.05	3.77
	1.24		1.00	3.23	4.35
	0.496		2.50	4.13	8.59
	0.248		5.00	4.59	15.4
	0.124		10.0	5.81	30.4
	0.062		20.0	9.87	60.1
	0.037		33.3	22.5	100.0
	0.025		50.0	45.7	141.0
	0.015		80.0	75.2	158.0
0.010		125.0	120.0	207.0	
0.006		200.0	183.0	260.0	
0.004		287.0	238.0	306.0	
Molybdenum <sup>39</sup>	2,000.0	6.19		1.00	0.00
	1,041.0	11.6		1.00	0.00
	396.0	31.3		1.00	0.01
	303.0	40.9		1.00	0.01
	211.0	58.8		0.99	0.00
	100.0	124.0		0.93	0.01
	60.0	207.0		0.90	0.11
	37.5	331.0		0.81	0.29
	35.0	354.0		0.87	0.38
	33.8	367.0		0.91	0.33
	33.0	376.0		0.90	0.33
	31.4	394.0		0.92	0.31

(Continued)

**TABLE 2**  $n$  and  $k$  of Selected Metals at Room Temperature (*Continued*)

Metal	eV	Wavelength Å	$\mu\text{m}$	$n$	$k$
Molybdenum <sup>39</sup>	29.2	424.0		0.84	0.26
	23.4	530.0		0.58	0.55
	17.6	704.0		0.94	1.14
	15.6	795.0		1.15	1.01
	15.0	827.0		1.14	0.99
	14.4	861.0		1.13	1.00
	13.2	939.0		1.20	1.03
	12.0	1,033.0	0.10	1.26	0.92
	11.0	1,127.0	0.11	1.05	0.77
	8.80	1,409.0	0.14	0.65	1.41
	6.20	2,000.0	0.20	0.81	2.50
	4.40	2,818.0	0.28	2.39	3.88
	3.30	3,757.0	0.38	3.06	3.18
	3.10	4,000.0	0.40	3.03	3.22
	2.40	5,166.0	0.52	3.59	3.78
	2.30	5,391.0	0.54	3.79	3.61
	2.20	5,636.0	0.56	3.76	3.41
	2.05	6,052.0	0.61	3.68	3.49
	1.90	6,526.0	0.65	3.74	3.58
	1.70	7,293.0	0.73	3.84	3.51
	1.50	8,266.0	0.83	3.53	3.30
	1.20		1.03	2.44	4.22
	0.58		2.14	1.34	11.3
	0.24		5.17	3.61	30.0
	0.12		10.3	13.4	58.4
0.10		12.4	18.5	68.5	
Nickel <sup>39</sup>	9,919.0	1.25		1.00	0.00
	4,133.0	3.00		1.00	0.00
	1,771.0	7.00		1.00	0.00
	929.0	13.3		1.00	0.00
	500.0	24.8		1.00	0.00
	300.0	41.3		0.99	0.01
	180.0	68.9		0.98	0.02
	120.0	103.0		0.96	0.05
	84.0	148.0		0.93	0.11
	68.0	182.0		0.98	0.17
	66.0	188.0		1.01	0.16
	64.0	194.0		0.98	0.11
	50.0	248.0		0.93	0.15
	45.0	276.0		0.88	0.13
	35.0	354.0		0.86	0.24
	23.0	539.0		0.92	0.44
	20.5	605.0		0.89	0.49
	13.0	954.0		1.08	0.71
	10.0	1,240.0	0.12	0.95	0.87
	7.20	1,722.0	0.17	1.03	1.27
6.20	2,000.0	0.20	1.00	1.54	
4.80	2,583.0	0.26	1.53	2.11	
4.15	2,988.0	0.30	1.74	2.00	
3.95	3,140.0	0.31	1.72	1.98	
3.15	3,938.0	0.39	1.61	2.33	
2.40	5,166.0	0.52	1.71	3.06	

**TABLE 2**  $n$  and  $k$  of Selected Metals at Room Temperature (*Continued*)

Metal	eV	Wavelength Å	$\mu\text{m}$	$n$	$k$
Nickel <sup>39</sup>	1.80	6,888.0	0.69	2.14	4.00
	1.20		1.03	2.85	5.10
	0.45		2.76	4.20	10.2
	0.40		3.10	3.84	11.4
	0.28		4.43	4.30	16.0
	0.22		5.64	4.11	20.2
	0.12		10.3	7.11	38.3
	0.10		12.4	9.54	45.8
Platinum <sup>39</sup>	2,000.0	6.20		1.00	0.00
	1,016.0	12.2		1.00	0.00
	504.0	24.6		0.99	0.00
	244.0	50.8		0.99	0.01
	121.0	102.0		0.95	0.02
	83.7	150.0		0.88	0.08
	72.9	170.0		0.89	0.10
	53.9	230.0		0.86	0.20
	51.7	240.0		0.88	0.22
	45.6	250.0		0.87	0.16
	32.6	380.0		0.66	0.45
	30.2	410.0		0.70	0.58
	29.5	420.0		0.71	0.57
	28.8	430.0		0.72	0.65
	28.2	440.0		0.72	0.58
	24.8	500.0		0.71	0.72
	20.7	600.0		0.84	0.94
	16.8	740.0		1.05	0.82
	13.2	940.0		1.20	0.93
	12.7	980.0		1.17	0.96
	10.1	1,230.0	0.12	1.36	1.18
	9.05	1,370.0	0.14	1.43	1.14
	8.38	1,480.0	0.15	1.47	1.15
	7.87	1,575.0	0.16	1.46	1.19
	7.29	1,700.0	0.17	1.49	1.22
	6.05	2,050.0	0.20	1.19	1.40
	5.40	2,296.0	0.23	1.36	1.61
	3.00	4,133.0	0.41	1.75	2.92
	2.30	5,390.0	0.54	2.10	3.67
	1.80	6,888.0	0.69	2.51	4.43
1.20		1.03	3.55	5.92	
0.78		1.55	5.38	7.04	
0.70		1.77	5.71	6.83	
0.65		1.91	5.52	6.66	
0.40		3.10	2.81	11.4	
0.20		6.20	5.90	24.0	
0.13		9.54	9.91	36.7	
0.10		12.4	13.2	44.7	
Silver <sup>39</sup>	10,000.0	1.24		1.00	0.00
	6,000.0	2.07		1.00	0.00
	3,000.0	4.13		1.00	0.00
	1,500.0	8.26		1.00	0.00
	800.0	15.5		1.00	0.00
	370.0	33.5		1.01	0.01

 (*Continued*)



**TABLE 2**  $n$  and  $k$  of Selected Metals at Room Temperature (*Continued*)

Metal	eV	Wavelength Å	$\mu\text{m}$	$n$	$k$
Silver <sup>39</sup>	350.0	35.4		1.00	0.00
	170.0	72.9		0.97	0.00
	110.0	113.0		0.90	0.02
	95.0	131.0		0.86	0.06
	85.0	146.0		0.85	0.11
	64.0	194.0		0.89	0.21
	50.0	248.0		0.88	0.29
	44.0	282.0		0.90	0.33
	35.0	354.0		0.87	0.45
	31.0	400.0		0.93	0.53
	27.5	451.0		0.85	0.62
	22.5	551.0		1.03	0.62
	21.0	590.0		1.11	0.56
	20.0	620.0		1.10	0.55
	15.0	827.0		1.24	0.69
	13.0	954.0		1.32	0.60
	10.9	1,137.0	0.11	1.28	0.56
	10.0	1,240.0	0.12	1.24	0.57
	9.20	1,348.0	0.13	1.18	0.55
	7.60	1,631.0	0.16	0.94	0.83
	4.85	2,556.0	0.26	1.34	1.35
	4.15	2,988.0	0.30	1.52	0.99
	3.90	3,179.0	0.32	0.93	0.50
	3.10	4,000.0	0.40	0.17	1.95
	2.20	5,636.0	0.56	0.12	3.45
	1.80	6,888.0	0.69	0.14	4.44
	1.20		1.03	0.23	6.99
0.62		2.00	0.65	12.2	
0.24		5.17	3.73	31.3	
0.125		9.92	13.1	53.7	
Tungsten <sup>39</sup>	2,000.0	6.20		1.00	0.00
	1,016.0	12.2		1.00	0.00
	516.0	24.0		0.99	0.00
	244.0	50.8		0.99	0.02
	100.0	124.0		0.94	0.04
	43.0	288.0		0.74	0.27
	38.5	322.0		0.82	0.33
	35.0	354.0		0.85	0.31
	33.0	376.0		0.82	0.28
	32.0	388.0		0.79	0.30
	30.5	406.0		0.77	0.29
	23.8	521.0		0.48	0.60
	22.9	541.0		0.49	0.69
	22.1	561.0		0.49	0.76
	16.0	775.0		0.98	1.14
	15.5	800.0		0.96	1.12
	14.6	849.0		0.90	1.20
	11.8	1,051.0	0.11	1.18	1.48
	10.8	1,148.0	0.11	1.29	1.39
	10.3	1,204.0	0.12	1.22	1.33
7.80	1,590.0	0.16	0.93	2.06	
5.60	2,214.0	0.22	2.43	3.70	

**TABLE 2**  $n$  and  $k$  of Selected Metals at Room Temperature (*Continued*)

Metal	eV	Wavelength Å	$\mu\text{m}$	$n$	$k$
Tungsten <sup>39</sup>	5.00	2,480.0	0.25	3.40	2.85
	4.30	2,883.0	0.29	3.07	2.31
	4.00	3,100.0	0.31	2.95	2.43
	3.45	3,594.0	0.36	3.32	2.70
	3.25	3,815.0	0.38	3.45	2.49
	3.10	4,000.0	0.40	3.39	2.41
	2.80	4,428.0	0.44	3.30	2.49
	1.85	6,702.0	0.67	3.76	2.95
	1.75	7,085.0	0.71	3.85	2.86
	1.60	7,749.0	0.77	3.67	2.68
	1.20		1.03	3.00	3.64
	0.96		1.29	3.15	4.41
	0.92		1.35	3.14	4.45
	0.85		1.46	2.80	4.33
	0.58		2.14	1.18	8.44
	0.40		3.10	1.94	13.2
	0.34		3.65	1.71	15.7
	0.18		6.89	4.72	31.5
	0.12		10.3	10.1	46.4
	0.07		17.7	26.5	73.8
0.05		24.8	46.5	93.7	
Silicon carbide <sup>41</sup>	30.0	413.0		0.74	0.11
	20.5	605.0		0.35	0.53
	13.1	946.0		0.68	1.41
	9.50	1,305.0	0.13	1.46	2.21
	9.00	1,378.0	0.14	1.60	2.15
	7.60	1,631.0	0.16	2.59	2.87
	6.40	1,937.0	0.19	4.05	1.42
	5.00	2,480.0	0.25	3.16	0.26
	3.90	3,179.0	0.32	2.92	0.01
	3.00	4,133.0	0.41	2.75	0.00
	2.50	4,959.0	0.50	2.68	0.00
	1.79	6,911.0	0.69	2.62	—
	1.50	8,266.0	0.83	2.60	—
	0.62		2.00	2.57	0.00
	0.31		4.00	2.52	0.00
	0.12		6.67	2.33	0.02
	0.11		9.80	1.29	0.01
	0.10		10.40	0.09	0.63
	0.10		10.81	0.06	1.57
	0.10		11.9	0.16	4.51
0.09		12.6	8.74	18.4	
0.08		12.7	17.7	6.03	
0.05		13.1	7.35	0.27	
		15.4	4.09	0.02	
		25.0	3.34	—	

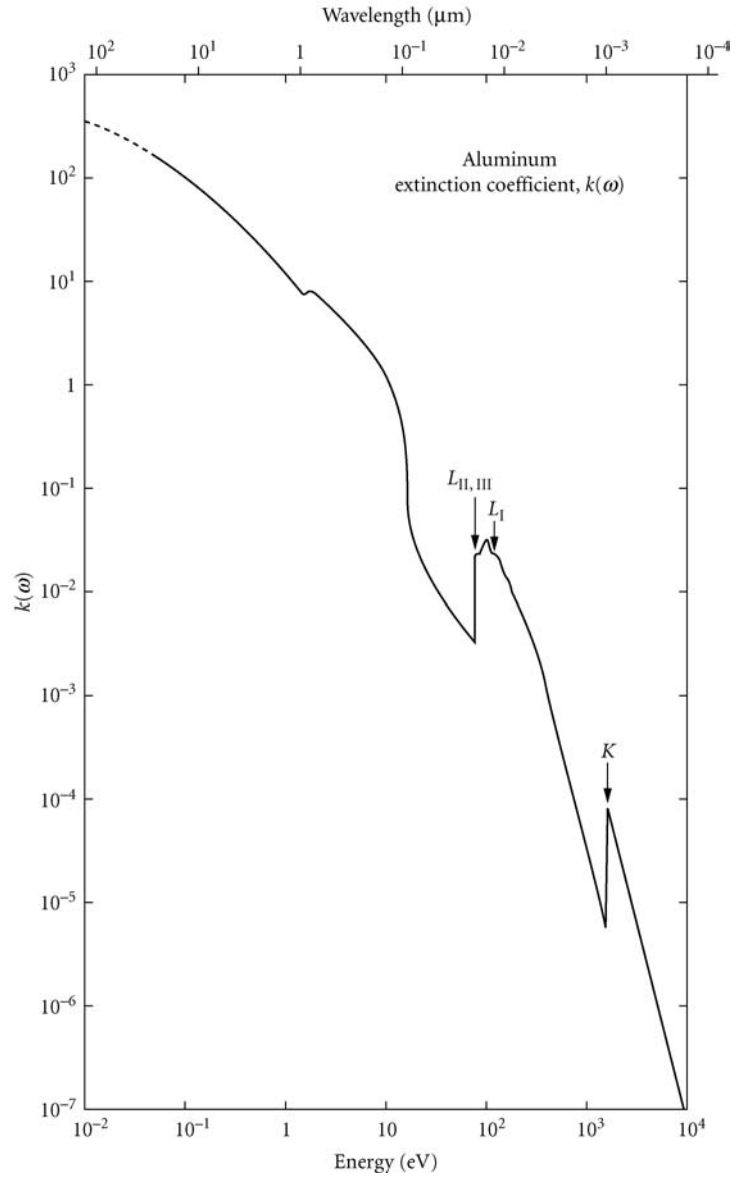


FIGURE 2  $k$  for aluminum vs. photon energy.<sup>37</sup>

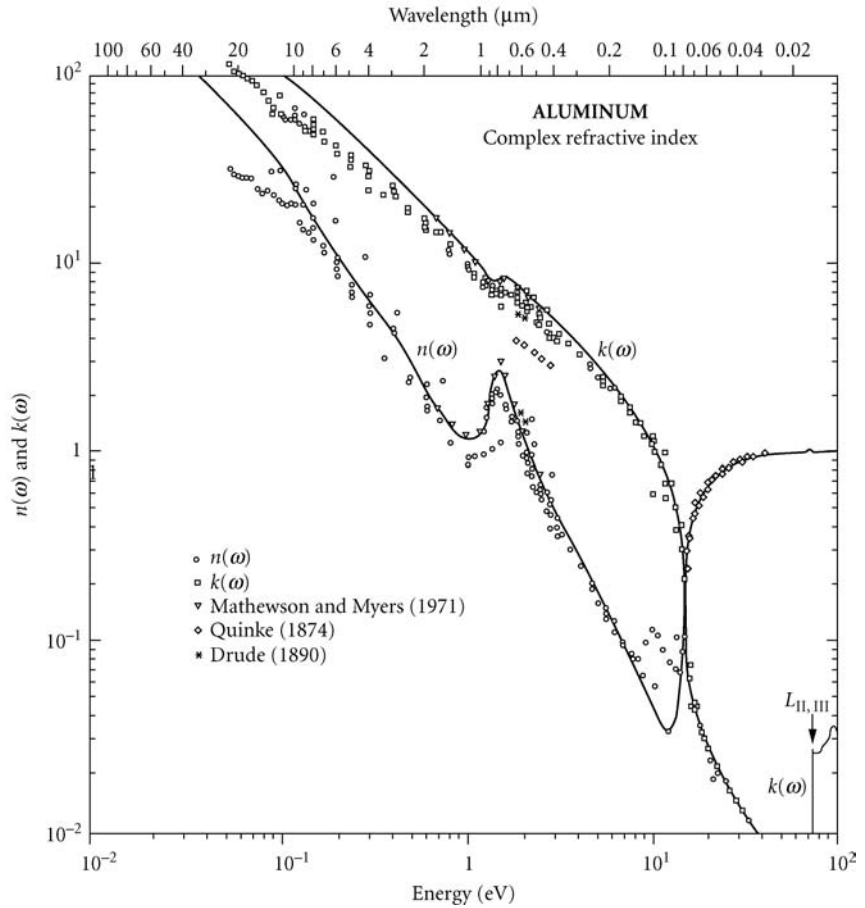


FIGURE 3  $n$  and  $k$  for aluminum vs. photon energy.<sup>37</sup>

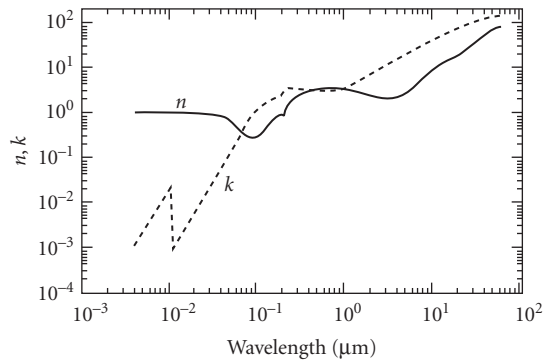


FIGURE 4  $n$  and  $k$  for beryllium vs. wavelength.<sup>38</sup>

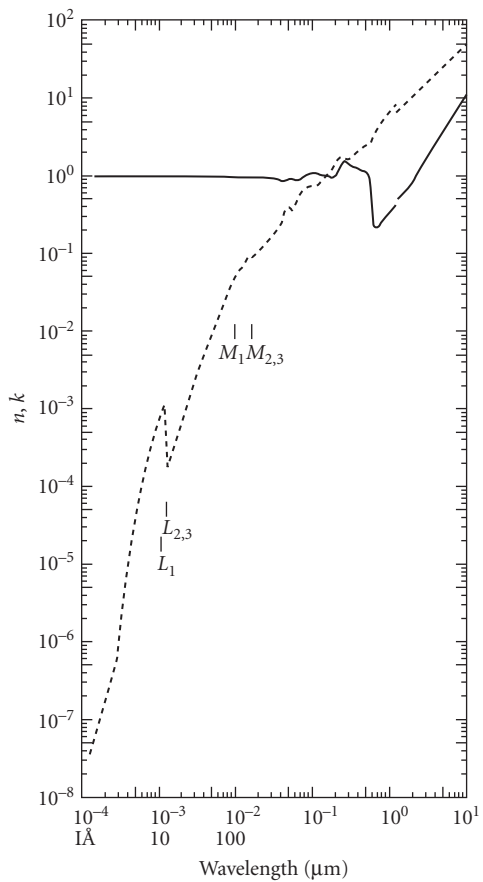


FIGURE 5  $n$  and  $k$  for copper vs. wavelength.<sup>39</sup>

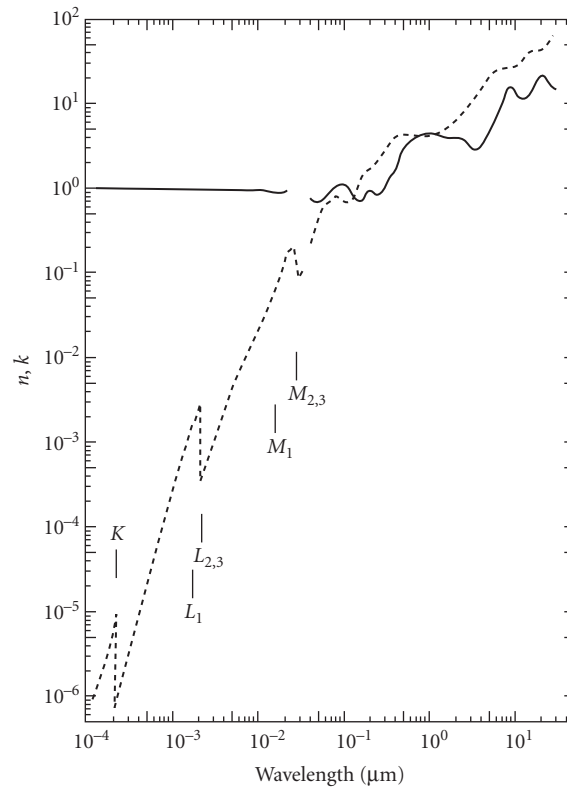


FIGURE 6  $n$  and  $k$  for chromium vs. wavelength.<sup>40</sup>

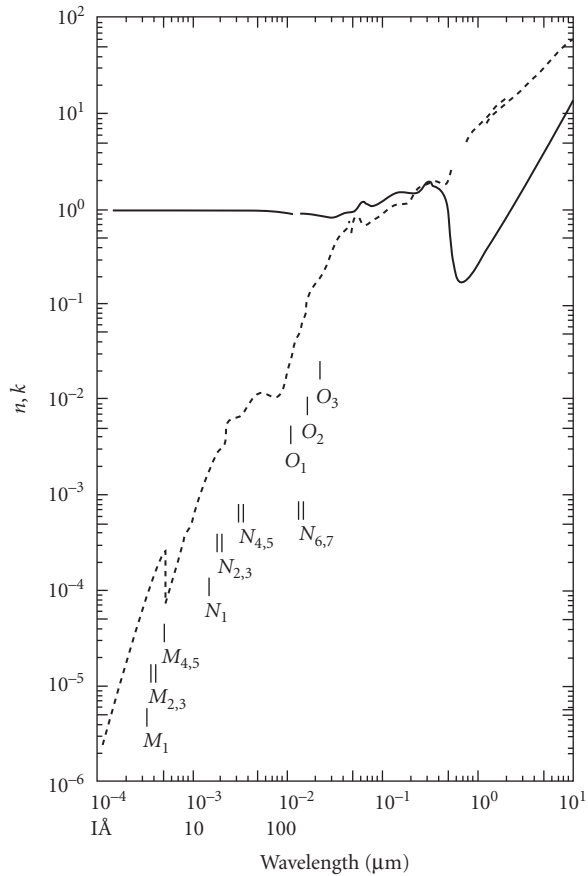


FIGURE 7  $n$  and  $k$  for gold vs. wavelength.<sup>39</sup>

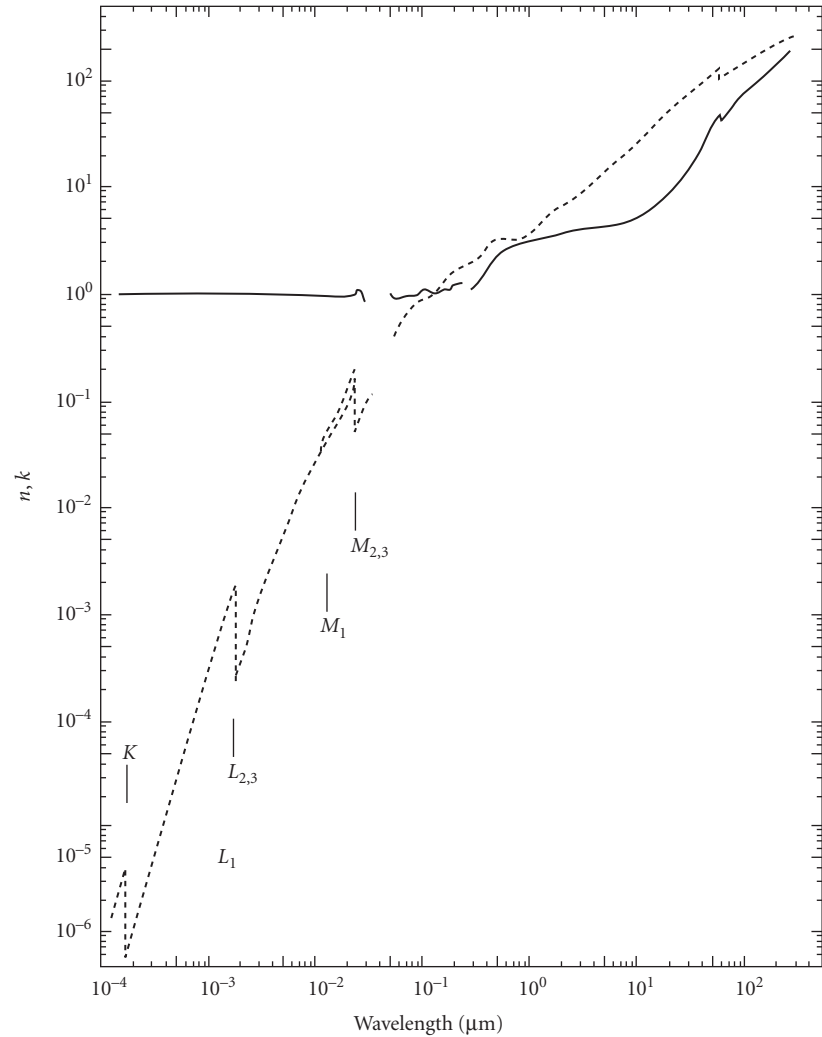


FIGURE 8  $n$  and  $k$  for iron vs. wavelength.<sup>40</sup>

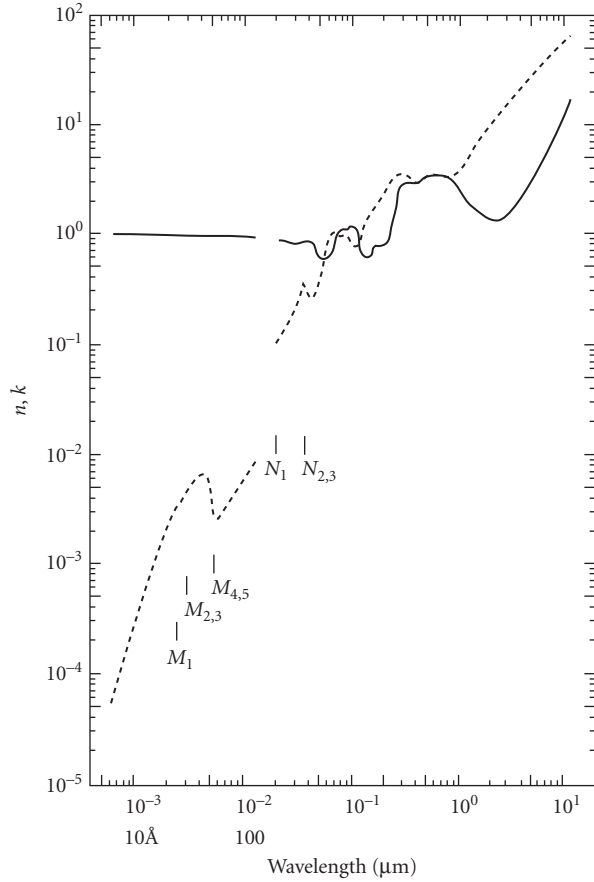


FIGURE 9  $n$  and  $k$  for molybdenum vs. wavelength.<sup>39</sup>

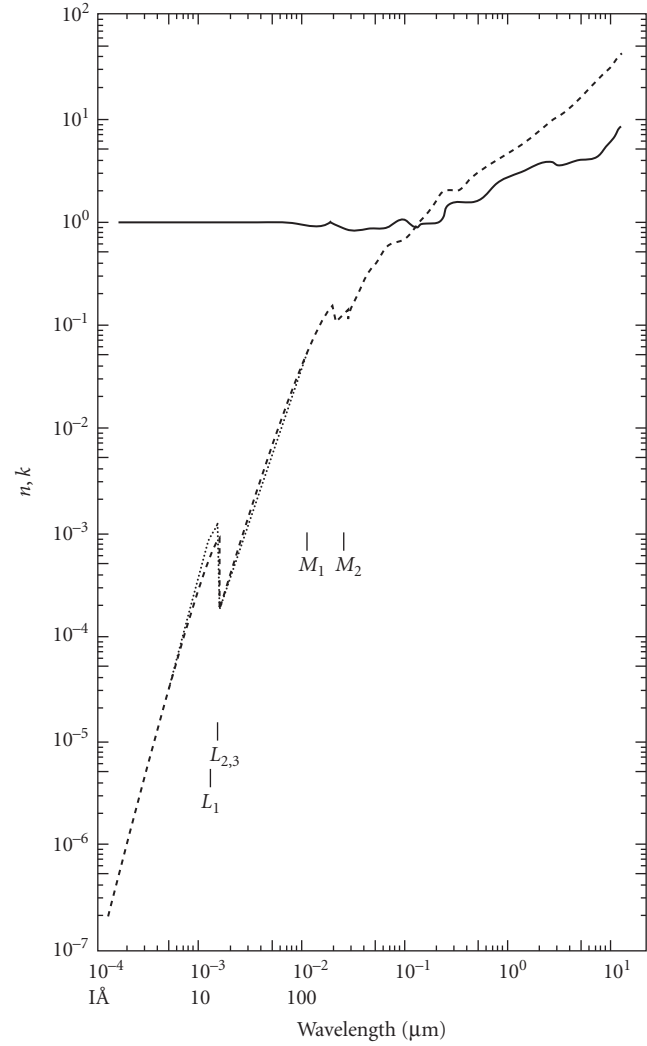


FIGURE 10  $n$  and  $k$  for nickel vs. wavelength.<sup>39</sup>

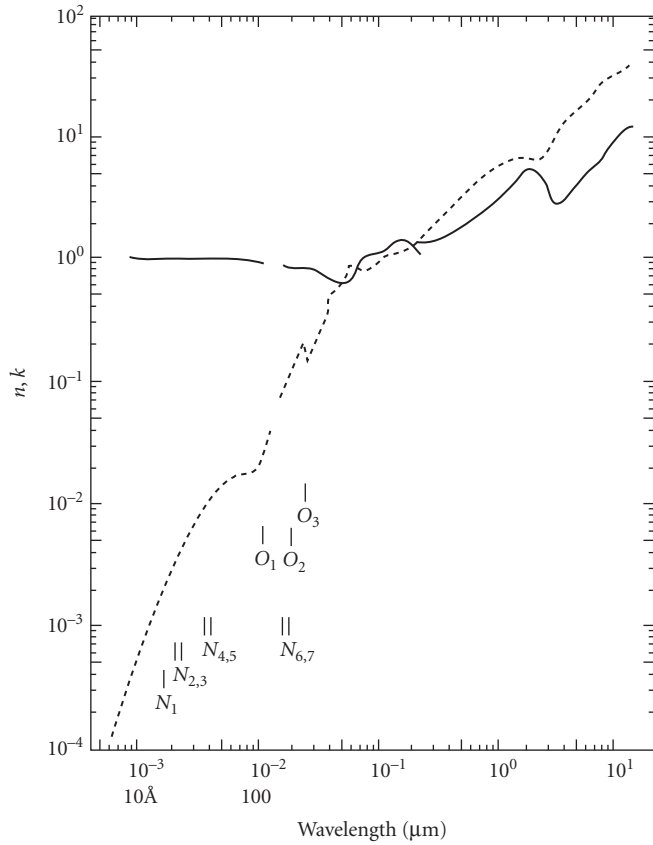


FIGURE 11  $n$  and  $k$  for platinum vs. wavelength.<sup>39</sup>

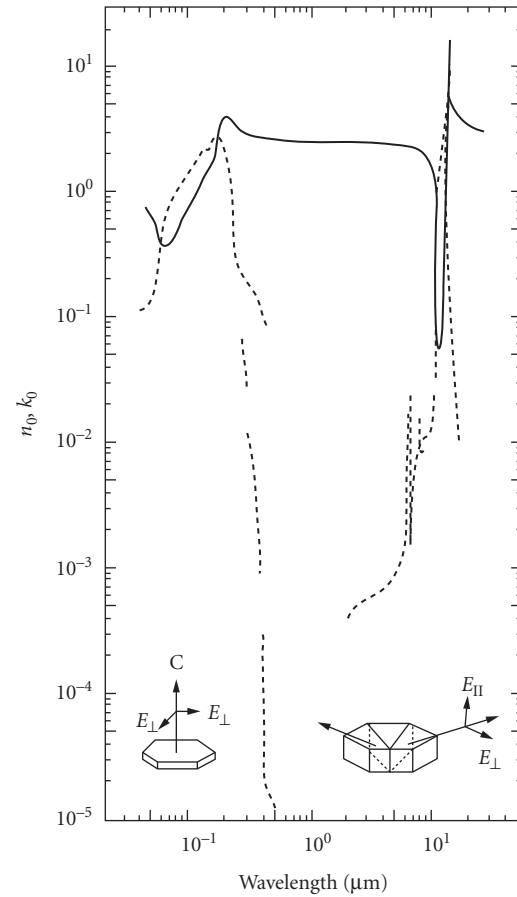
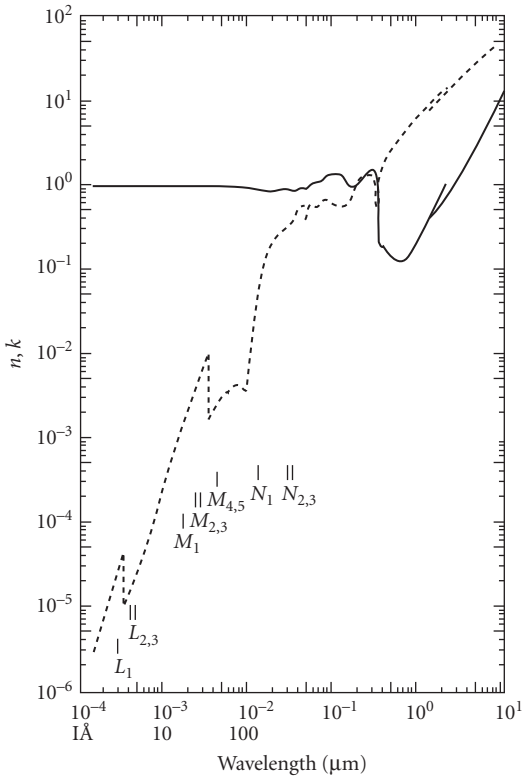
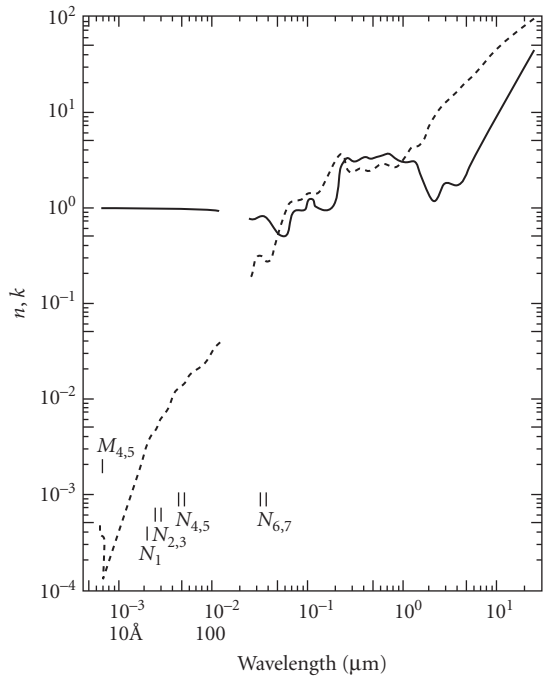


FIGURE 12  $n$  and  $k$  for silicon carbide vs. wavelength.<sup>41</sup>

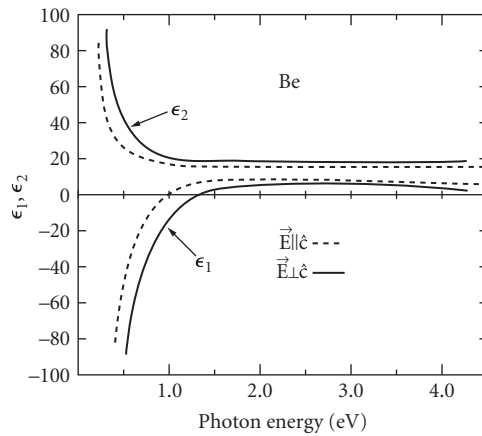




**FIGURE 13**  $n$  and  $k$  for silver as a function of wavelength.<sup>39</sup>



**FIGURE 14**  $n$  and  $k$  for tungsten vs. wavelength.<sup>39</sup>



**FIGURE 15** Dielectric function for beryllium vs. photon energy showing variation with crystallographic direction.<sup>42</sup>

**TABLE 3** Reflectance of Selected Metals at Normal Incidence

Metal	eV	Wavelength Å	μm	R	
Aluminum <sup>36</sup>	0.040		31.0	0.9923	
	0.050		24.8	0.9915	
	0.060		20.7	0.9906	
	0.070		17.7	0.9899	
	0.080		15.5	0.9895	
	0.090		13.8	0.9892	
	0.100		12.4	0.9889	
	0.125		9.92	0.9884	
	0.175		7.08	0.9879	
	0.200		6.20	0.9873	
	0.250		4.96	0.9858	
	0.300		4.13	0.9844	
	0.400		3.10	0.9826	
	0.600		2.07	0.9806	
	0.800		1.55	0.9778	
	0.900		1.38	0.9749	
	1.00		1.24	0.9697	
	1.10		1.13	0.9630	
	1.20		1.03	0.9521	
	1.30	9,537.0		0.95	0.9318
	1.40	8,856.0		0.89	0.8852
	1.50	8,265.0		0.83	0.8678
	1.60	7,749.0		0.77	0.8794
	1.70	7,293.0		0.73	0.8972
	1.80	6,888.0		0.69	0.9069
	2.00	6,199.0		0.62	0.9148
	2.40	5,166.0		0.52	0.9228
	2.80	4,428.0		0.44	0.9242
	3.20	3,874.0		0.39	0.9243
	3.60	3,444.0		0.34	0.9246
	4.00	3,100.0		0.31	0.9248
	4.60	2,695.0		0.27	0.9249
	5.00	2,497.0		0.25	0.9244
	6.00	2,066.0		0.21	0.9257
	8.00	1,550.0		0.15	0.9269
	10.00	1,240.0		0.12	0.9286
	11.00	1,127.0		0.11	0.9298
	13.00	954.0			0.8960
	13.50	918.0			0.8789
	14.00	886.0			0.8486
	14.40	861.0			0.8102
	14.60	849.0			0.7802
	14.80	838.0			0.7202
	15.00	827.0			0.6119
	15.20	816.0			0.4903
15.40	805.0			0.3881	
15.60	795.0			0.3182	
15.80	785.0			0.2694	
16.00	775.0			0.2326	
16.20	765.0			0.2031	
16.40	756.0			0.1789	
16.75	740.0			0.1460	

(Continued)

**TABLE 3** Reflectance of Selected Metals at Normal Incidence (*Continued*)

Metal	eV	Wavelength Å	μm	R
Aluminum <sup>39</sup>	17.00	729.0		0.1278
	17.50	708.0		0.1005
	18.00	689.0		0.0809
	19.00	653.0		0.0554
	20.0	620.0		0.0398
	21.0	590.0		0.0296
	22.0	564.0		0.0226
	23.0	539.0		0.0177
	24.0	517.0		0.0140
	25.0	496.0		0.0113
	26.0	477.0		0.0092
	27.0	459.0		0.0076
	28.0	443.0		0.0063
	30.0	413.0		0.0044
	35.0	354.0		0.0020
	40.0	310.0		0.0010
	45.0	276.0		0.0005
	50.0	248.0		0.0003
	55.0	225.0		0.0001
	60.0	206.0		0.0000
	70.0	177.0		0.0000
	72.5	171.0		0.0002
	75.0	165.0		0.0002
	80.0	155.0		0.0002
	85.0	146.0		0.0002
	95.0	131.0		0.0003
	100.0	124.0		0.0002
	120.0	103.0		0.0002
	130.0	95.4		0.0001
	150.0	82.7		0.0001
170.0	72.9		0.0001	
180.0	68.9		0.0000	
200.0	62.0		0.0000	
300.0	41.3		0.0000	
Beryllium <sup>38</sup>	0.020		61.99	0.989
	0.040		31.00	0.989
	0.060		20.66	0.988
	0.080		15.50	0.985
	0.100		12.40	0.983
	0.120		10.33	0.982
	0.160		7.75	0.981
	0.200		6.20	0.980
	0.240		5.17	0.978
	0.280		4.43	0.972
	0.320		3.87	0.966
	0.380		3.26	0.955
	0.440		2.82	0.940
	0.500		2.48	0.917
	0.560		2.21	0.887
0.600		2.07	0.869	
0.660		1.88	0.841	
0.720		1.72	0.810	

**TABLE 3** Reflectance of Selected Metals at Normal Incidence (*Continued*)

Metal	eV	Wavelength Å	μm	R
Beryllium <sup>38</sup>	0.780		1.59	0.775
	0.860		1.44	0.736
	0.940		1.32	0.694
	1.00		1.24	0.667
	1.10		1.13	0.640
	1.20		1.03	0.615
	1.40	8,856.0	0.89	0.575
	1.60	7,749.0	0.77	0.555
	1.90	6,525.0	0.65	0.540
	2.40	5,166.0	0.52	0.538
	2.80	4,428.0	0.44	0.537
	3.00	4,133.0	0.41	0.537
	3.30	3,757.0	0.38	0.536
	3.60	3,444.0	0.34	0.536
	3.80	3,263.0	0.33	0.538
	4.00	3,100.0	0.31	0.541
	4.20	2,952.0	0.30	0.547
4.40	2,818.0	0.28	0.558	
4.60	2,695.0	0.27	0.575	
Copper <sup>36</sup>	0.10		12.4	0.980
	0.50		2.48	0.979
	1.00		1.24	0.976
	1.50	8,265.0	0.83	0.965
	1.70	7,293.0	0.73	0.958
	1.80	6,888.0	0.69	0.952
	1.90	6,525.0	0.65	0.943
	2.00	6,199.0	0.62	0.910
	2.10	5,904.0	0.59	0.814
	2.20	5,635.0	0.56	0.673
	2.30	5,390.0	0.54	0.618
	2.40	5,166.0	0.52	0.602
	2.60	4,768.0	0.48	0.577
	2.80	4,428.0	0.44	0.545
	3.00	4,133.0	0.41	0.509
	3.20	3,874.0	0.39	0.468
	3.40	3,646.0	0.36	0.434
	3.60	3,444.0	0.34	0.407
	3.80	3,263.0	0.33	0.387
	4.00	3,100.0	0.31	0.364
	4.20	2,952.0	0.30	0.336
	4.40	2,818.0	0.28	0.329
	4.60	2,695.0	0.27	0.334
	4.80	2,583.0	0.26	0.345
	5.00	2,497.0	0.25	0.366
	5.20	2,384.0	0.24	0.380
	5.40	2,296.0	0.23	0.389
5.60	2,214.0	0.22	0.391	
5.80	2,138.0	0.21	0.389	
6.00	2,066.0	0.21	0.380	
6.50	1,907.0	0.19	0.329	
7.00	1,771.0	0.18	0.271	
7.50	1,653.0	0.17	0.230	

(Continued)

**TABLE 3** Reflectance of Selected Metals at Normal Incidence (*Continued*)

Metal	eV	Wavelength Å	μm	R
Copper <sup>36</sup>	8.00	1,550.0	0.15	0.206
	8.50	1,459.0	0.15	0.189
	9.00	1,378.0	0.14	0.171
	9.50	1,305.0	0.13	0.154
	10.00	1,240.0	0.12	0.139
	11.00	1,127.0	0.11	0.118
	12.00	1,033.0	0.10	0.111
	13.00	954.0		0.109
	14.00	886.0		0.111
	15.00	827.0		0.111
	16.00	775.0		0.106
	17.00	729.0		0.097
	18.00	689.0		0.084
	19.00	653.0		0.071
	20.00	620.0		0.059
	21.00	590.0		0.048
	22.00	564.0		0.040
	23.00	539.0		0.035
	24.00	517.0		0.035
	25.00	496.0		0.040
	26.00	477.0		0.044
	27.00	459.0		0.043
	28.00	443.0		0.039
	29.00	428.0		0.032
	30.00	413.0		0.025
	32.00	387.0		0.017
	34.00	365.0		0.014
	36.00	344.0		0.012
	38.00	326.0		0.010
	40.00	310.0		0.009
45.00	276.0		0.006	
50.00	248.0		0.005	
55.00	225.0		0.004	
60.00	206.0		0.003	
70.00	177.0		0.002	
90.00	138.0		0.002	
Chromium <sup>36</sup>	0.06		20.70	0.962
	0.10		12.40	0.955
	0.14		8.86	0.936
	0.18		6.89	0.953
	0.22		5.64	0.954
	0.26		4.77	0.951
	0.30		4.13	0.943
	0.42		2.95	0.862
	0.54		2.30	0.788
	0.66		1.88	0.736
	0.78		1.59	0.680
	0.90		1.38	0.650
	1.00		1.24	0.639
1.12		1.11	0.631	
1.24	9,998.0	1.00	0.629	
1.36	9,116.0	0.91	0.631	

**TABLE 3** Reflectance of Selected Metals at Normal Incidence (*Continued*)

Metal	eV	Wavelength Å	μm	R
Chromium <sup>36</sup>	1.46	8,492.0	0.85	0.632
	1.77	7,005.0	0.70	0.639
	2.00	6,199.0	0.62	0.644
	2.20	5,635.0	0.56	0.656
	2.40	5,166.0	0.52	0.677
	2.60	4,768.0	0.48	0.698
	2.80	4,428.0	0.44	0.703
	3.00	4,133.0	0.41	0.695
	4.00	3,100.0	0.31	0.651
	4.40	2,818.0	0.28	0.620
	4.80	2,583.0	0.26	0.572
	5.20	2,384.0	0.24	0.503
	5.60	2,214.0	0.22	0.443
	6.00	2,066.0	0.21	0.444
	7.00	1,771.0	0.18	0.425
	7.60	1,631.0	0.16	0.378
	8.00	1,550.0	0.15	0.315
	8.50	1,459.0	0.15	0.235
	9.00	1,378.0	0.14	0.170
	10.00	1,240.0	0.12	0.120
	11.00	1,127.0	0.11	0.103
	11.50	1,078.0	0.11	0.100
	12.00	1,033.0	0.10	0.101
	13.00	954.0		0.119
	14.00	886.0		0.135
	15.00	827.0		0.143
	16.00	775.0		0.139
	18.00	689.0		0.129
	19.00	653.0		0.131
	20.00	620.0		0.130
22.00	563.0		0.112	
24.00	517.0		0.096	
26.00	477.0		0.063	
28.00	443.0		0.037	
30.00	413.0		0.030	
Gold (electropolished) <sup>36</sup>	0.10		12.40	0.995
	0.20		6.20	0.995
	0.40		3.10	0.995
	0.60		2.07	0.994
	0.80		1.55	0.993
	1.00		1.24	0.992
	1.20		1.03	0.991
	1.40	8,856.0	0.89	0.989
	1.60	7,749.0	0.77	0.986
	1.80	6,888.0	0.69	0.979
	2.00	6,199.0	0.62	0.953
	2.10	5,904.0	0.59	0.925
	2.20	5,635.0	0.56	0.880
	2.30	5,390.0	0.54	0.807
	2.40	5,166.0	0.52	0.647
2.50	4,959.0	0.50	0.438	
2.60	4,768.0	0.48	0.331	

(Continued)

**TABLE 3** Reflectance of Selected Metals at Normal Incidence (*Continued*)

Metal	eV	Wavelength Å	μm	R
Gold (electropolished) <sup>36</sup>	2.70	4,592.0	0.46	0.356
	2.80	4,428.0	0.44	0.368
	2.90	4,275.0	0.43	0.368
	3.00	4,133.0	0.41	0.369
	3.10	3,999.0	0.40	0.371
	3.20	3,874.0	0.39	0.368
	3.40	3,646.0	0.36	0.356
	3.60	3,444.0	0.34	0.346
	3.80	3,263.0	0.33	0.360
	4.00	3,100.0	0.31	0.369
	4.20	2,952.0	0.30	0.367
	4.40	2,818.0	0.28	0.370
	4.60	2,695.0	0.27	0.364
	4.80	2,583.0	0.26	0.344
	5.00	2,497.0	0.25	0.319
	5.40	2,296.0	0.23	0.275
	5.80	2,138.0	0.21	0.236
	6.20	2,000.0	0.20	0.203
	6.60	1,878.0	0.19	0.177
	7.00	1,771.0	0.18	0.162
	7.40	1,675.0	0.17	0.164
	7.80	1,589.0	0.16	0.171
	8.20	1,512.0	0.15	0.155
	8.60	1,442.0	0.14	0.144
	9.00	1,378.0	0.14	0.133
	9.40	1,319.0	0.13	0.122
	9.80	1,265.0	0.13	0.124
	10.20	1,215.0	0.12	0.127
	11.00	1,127.0	0.11	0.116
	12.00	1,033.0	0.10	0.109
14.00	886.0		0.140	
16.00	775.0		0.123	
18.00	689.0		0.109	
20.00	620.0		0.133	
22.00	563.0		0.164	
24.00	517.0		0.125	
26.00	477.0		0.079	
28.00	443.0		0.063	
30.00	413.0		0.064	
Iron <sup>36</sup>	0.10		12.40	0.978
	0.15		8.27	0.956
	0.20		6.20	0.958
	0.26		4.77	0.911
	0.30		4.13	0.892
	0.36		3.44	0.867
	0.40		3.10	0.858
	0.50		2.48	0.817
	0.60		2.07	0.783
	0.70		1.77	0.752
0.80		1.55	0.725	
0.90		1.38	0.700	
1.00		1.24	0.678	
1.10		1.13	0.660	

**TABLE 3** Reflectance of Selected Metals at Normal Incidence (*Continued*)

Metal	eV	Wavelength Å	μm	R
Iron <sup>36</sup>	1.20		1.03	0.641
	1.30	9,537.0	0.95	0.626
	1.40	8,856.0	0.89	0.609
	1.50	8,265.0	0.83	0.601
	1.60	7,749.0	0.77	0.585
	1.70	7,293.0	0.73	0.577
	1.80	6,888.0	0.69	0.573
	1.90	6,525.0	0.65	0.563
	2.00	6,199.0	0.62	0.563
	2.20	5,635.0	0.56	0.563
	2.40	5,166.0	0.52	0.567
	2.60	4,768.0	0.48	0.576
	2.80	4,428.0	0.44	0.580
	3.00	4,133.0	0.41	0.583
	3.20	3,874.0	0.39	0.576
	3.40	3,646.0	0.36	0.565
	3.60	3,444.0	0.34	0.548
	4.00	3,100.0	0.31	0.527
	4.33	2,863.0	0.29	0.494
	4.67	2,655.0	0.27	0.470
	5.00	2,497.0	0.25	0.435
	5.50	2,254.0	0.23	0.401
	6.00	2,066.0	0.21	0.366
	6.50	1,907.0	0.19	0.358
	7.00	1,771.0	0.18	0.333
	7.50	1,653.0	0.17	0.298
	8.00	1,550.0	0.15	0.272
	8.50	1,459.0	0.15	0.251
	9.00	1,378.0	0.14	0.236
	9.50	1,305.0	0.13	0.226
10.00	1,240.0	0.12	0.213	
11.00	1,127.0	0.11	0.162	
11.17	1,110.0	0.11	0.159	
11.33	1,094.0	0.11	0.159	
11.50	1,078.0	0.11	0.160	
12.00	1,033.0	0.10	0.163	
12.50	992.0		0.165	
13.00	954.0		0.162	
13.50	918.0		0.159	
14.00	886.0		0.151	
15.00	827.0		0.135	
16.00	775.0		0.116	
17.00	729.0		0.102	
18.00	689.0		0.091	
20.00	620.0		0.083	
22.00	563.0		0.068	
24.00	517.0		0.045	
26.00	477.0		0.031	
28.00	443.0		0.021	
30.00	413.0		0.014	
Molybdenum <sup>36</sup>	0.10		12.40	0.985
	0.20		6.20	0.985
	0.30		4.13	0.983

(Continued)



**TABLE 3** Reflectance of Selected Metals at Normal Incidence (*Continued*)

Metal	eV	Wavelength Å	μm	R
Molybdenum <sup>36</sup>	0.50		2.70	0.971
	0.70		1.77	0.932
	0.90		1.38	0.859
	1.00		1.24	0.805
	1.10		1.13	0.743
	1.20		1.03	0.671
	1.30	9,537.0	0.95	0.608
	1.40	8,856.0	0.89	0.562
	1.50	8,265.0	0.83	0.550
	1.60	7,749.0	0.77	0.562
	1.70	7,293.0	0.73	0.570
	1.80	6,888.0	0.69	0.576
	2.00	6,199.0	0.62	0.571
	2.20	5,635.0	0.56	0.562
	2.40	5,166.0	0.52	0.594
	2.60	4,768.0	0.48	0.582
	2.80	4,428.0	0.44	0.565
	3.00	4,133.0	0.41	0.550
	3.20	3,874.0	0.39	0.540
	3.40	3,646.0	0.36	0.541
	3.60	3,444.0	0.34	0.546
	3.80	3,263.0	0.33	0.554
	4.00	3,100.0	0.31	0.576
	4.20	2,952.0	0.30	0.610
	4.40	2,818.0	0.28	0.640
	4.60	2,695.0	0.27	0.658
	4.80	2,583.0	0.26	0.678
	5.00	2,497.0	0.25	0.695
	5.20	2,384.0	0.24	0.706
	5.40	2,296.0	0.23	0.706
	5.60	2,214.0	0.22	0.700
	6.00	2,066.0	0.21	0.674
	6.40	1,937.0	0.19	0.641
	6.80	1,823.0	0.18	0.592
	7.20	1,722.0	0.17	0.548
	7.40	1,675.0	0.17	0.542
7.60	1,631.0	0.16	0.552	
7.80	1,589.0	0.16	0.542	
8.00	1,550.0	0.15	0.530	
8.40	1,476.0	0.15	0.495	
8.80	1,409.0	0.14	0.450	
9.20	1,348.0	0.13	0.385	
9.60	1,291.0	0.13	0.320	
10.00	1,240.0	0.12	0.250	
10.40	1,192.0	0.12	0.188	
10.60	1,170.0	0.12	0.138	
11.20	1,107.0	0.11	0.123	
11.60	1,069.0	0.11	0.135	
12.00	1,033.0	0.10	0.154	
12.80	969.0		0.178	
13.60	912.0		0.187	
14.40	861.0		0.182	

**TABLE 3** Reflectance of Selected Metals at Normal Incidence (*Continued*)

Metal	eV	Wavelength Å	μm	R
Molybdenum <sup>36</sup>	14.80	838.0		0.179
	15.00	827.0		0.179
	16.00	775.0		0.194
	17.00	729.0		0.233
	18.00	689.0		0.270
	19.00	653.0		0.284
	20.00	620.0		0.264
	22.00	563.0		0.207
	24.00	517.0		0.151
	26.00	477.0		0.071
	28.00	443.0		0.036
	30.00	413.0		0.023
	32.00	387.0		0.030
	34.00	365.0		0.034
	36.00	344.0		0.043
	38.00	326.0		0.033
40.00	310.0		0.025	
Nickel <sup>36</sup>	0.10		12.40	0.983
	0.15		8.27	0.978
	0.20		6.20	0.969
	0.30		4.13	0.934
	0.40		3.10	0.900
	0.60		2.07	0.835
	0.80		1.55	0.794
	1.00		1.24	0.753
	1.20		1.03	0.721
	1.40	8,856.0	0.89	0.695
	1.60	7,749.0	0.77	0.679
	1.80	6,888.0	0.69	0.670
	2.00	6,199.0	0.62	0.649
	2.40	5,166.0	0.52	0.590
	2.80	4,428.0	0.44	0.525
	3.20	3,874.0	0.39	0.467
	3.60	3,444.0	0.34	0.416
	3.80	3,263.0	0.33	0.397
	4.00	3,100.0	0.31	0.392
	4.20	2,952.0	0.30	0.396
	4.60	2,695.0	0.27	0.421
	5.00	2,497.0	0.25	0.449
	5.20	2,384.0	0.24	0.454
	5.40	2,296.0	0.23	0.449
5.80	2,138.0	0.21	0.417	
6.20	2,000.0	0.20	0.371	
6.60	1,878.0	0.19	0.325	
7.00	1,771.0	0.18	0.291	
8.00	1,550.0	0.15	0.248	
9.00	1,378.0	0.14	0.211	
10.00	1,240.0	0.12	0.166	
11.00	1,127.0	0.11	0.115	
12.00	1,033.0	0.10	0.108	
13.00	954.0		0.105	
14.00	886.0		0.106	

*(Continued)*

**TABLE 3** Reflectance of Selected Metals at Normal Incidence (*Continued*)

Metal	eV	Wavelength Å	μm	R
Nickel <sup>36</sup>	15.00	827.0		0.107
	16.00	775.0		0.103
	18.00	689.0		0.092
	20.00	620.0		0.071
	22.00	564.0		0.055
	24.00	517.0		0.051
	27.00	459.0		0.042
	30.00	413.0		0.034
	35.00	354.0		0.022
	40.00	310.0		0.014
	50.00	248.0		0.004
	60.00	206.0		0.002
	65.00	191.0		0.002
	70.00	177.0		0.004
90.00	138.0		0.002	
Platinum <sup>36</sup>	0.10		12.40	0.976
	0.15		8.27	0.969
	0.20		6.20	0.962
	0.30		4.13	0.945
	0.40		3.10	0.922
	0.45		2.76	0.882
	0.50		2.50	0.813
	0.55		2.25	0.777
	0.60		2.07	0.753
	0.65		1.91	0.746
	0.70		1.77	0.751
	0.80		1.55	0.762
	0.90		1.38	0.765
	1.00		1.24	0.762
	1.20		1.03	0.746
	1.40	8,856.0	0.89	0.725
	1.60	7,749.0	0.77	0.706
	1.80	6,888.0	0.69	0.686
	2.00	6,199.0	0.62	0.664
	2.50	4,959.0	0.50	0.616
	3.00	4,133.0	0.41	0.565
	4.00	3,100.0	0.31	0.472
	5.00	2,497.0	0.25	0.372
	6.00	2,066.0	0.21	0.276
	7.00	1,771.0	0.18	0.230
	8.00	1,550.0	0.15	0.216
	9.00	1,378.0	0.14	0.200
	9.20	1,348.0	0.13	0.198
9.40	1,319.0	0.13	0.200	
10.20	1,215.0	0.12	0.211	
11.00	1,127.0	0.11	0.199	
12.00	1,033.0	0.10	0.173	
12.80	969.0		0.158	
13.60	912.0		0.155	
14.80	838.0		0.157	
15.20	816.0		0.155	
16.00	775.0		0.146	

**TABLE 3** Reflectance of Selected Metals at Normal Incidence (*Continued*)

Metal	eV	Wavelength Å	µm	R
Platinum <sup>36</sup>	17.50	708.0		0.135
	18.00	689.0		0.142
	20.00	620.0		0.197
	21.00	590.0		0.226
	22.00	564.0		0.240
	23.00	539.0		0.226
	24.00	517.0		0.201
	26.00	477.0		0.150
	28.00	443.0		0.125
	29.00	428.0		0.118
	30.00	413.0		0.124
Silver <sup>36</sup>	0.10		12.40	0.995
	0.20		6.20	0.995
	0.30		4.13	0.994
	0.40		3.10	0.993
	0.50		2.48	0.992
	1.00		1.24	0.987
	1.50	8,265.0	0.83	0.960
	2.00	6,199.0	0.62	0.944
	2.50	4,959.0	0.50	0.914
	3.00	4,133.0	0.41	0.864
	3.25	3,815.0	0.38	0.816
	3.50	3,542.0	0.35	0.756
	3.60	3,444.0	0.34	0.671
	3.70	3,351.0	0.34	0.475
	3.77	3,289.0	0.33	0.154
	3.80	3,263.0	0.33	0.053
	3.90	3,179.0	0.32	0.040
	4.00	3,100.0	0.31	0.103
	4.10	3,024.0	0.30	0.153
	4.20	2,952.0	0.30	0.194
	4.30	2,883.0	0.29	0.208
	4.50	2,755.0	0.28	0.238
	4.75	2,610.0	0.26	0.252
	5.00	2,497.0	0.25	0.257
	5.50	2,254.0	0.23	0.257
	6.00	2,066.0	0.21	0.246
	6.50	1,907.0	0.19	0.225
	7.00	1,771.0	0.18	0.196
7.50	1,653.0	0.17	0.157	
8.00	1,550.0	0.15	0.114	
9.00	1,378.0	0.14	0.074	
10.00	1,240.0	0.12	0.082	
11.00	1,127.0	0.11	0.088	
12.00	1,033.0	0.10	0.100	
13.00	954.0		0.112	
14.00	886.0		0.141	
15.00	827.0		0.156	
16.00	775.0		0.151	
17.00	729.0		0.139	
18.00	689.0		0.124	
19.00	653.0		0.111	

(Continued)

**TABLE 3** Reflectance of Selected Metals at Normal Incidence (*Continued*)

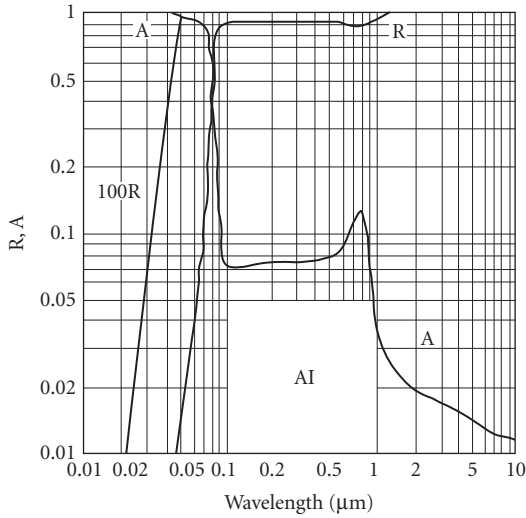
Metal	eV	Wavelength Å	μm	R
Silver <sup>36</sup>	20.00	620.0		0.103
	21.00	590.0		0.112
	21.50	577.0		0.124
	22.00	564.0		0.141
	22.50	551.0		0.157
	23.00	539.0		0.163
	24.00	517.0		0.165
	25.00	496.0		0.154
	26.00	477.0		0.133
	28.00	443.0		0.090
	30.00	413.0		0.074
	34.00	365.0		0.067
	38.00	326.0		0.043
	42.00	295.0		0.036
	46.00	270.0		0.031
	50.00	248.0		0.027
	56.00	221.0		0.024
	62.00	200.0		0.016
	66.00	188.0		0.016
	70.00	177.0		0.021
76.00	163.0		0.013	
80.00	155.0		0.012	
90.00	138.0		0.009	
100.00	124.0		0.005	
Tungsten <sup>36</sup>	0.10		12.40	0.983
	0.20		6.20	0.981
	0.30		4.13	0.979
	0.38		3.26	0.963
	0.46		2.70	0.952
	0.54		2.30	0.948
	0.62		2.00	0.917
	0.70		1.77	0.856
	0.74		1.68	0.810
	0.78		1.59	0.759
	0.82		1.51	0.710
	0.86		1.44	0.661
	0.98		1.27	0.653
	1.10		1.13	0.627
	1.20		1.03	0.590
	1.30	9,537.0	0.95	0.545
	1.40	8,856.0	0.89	0.515
	1.50	8,265.0	0.83	0.500
	1.60	7,749.0	0.77	0.494
	1.70	7,293.0	0.73	0.507
1.80	6,888.0	0.69	0.518	
1.90	6,525.0	0.65	0.518	
2.10	5,904.0	0.59	0.506	
2.50	4,959.0	0.50	0.487	
3.00	4,133.0	0.41	0.459	
3.50	3,542.0	0.35	0.488	
4.00	3,100.0	0.31	0.451	
4.20	2,952.0	0.30	0.440	

**TABLE 3** Reflectance of Selected Metals at Normal Incidence (*Continued*)

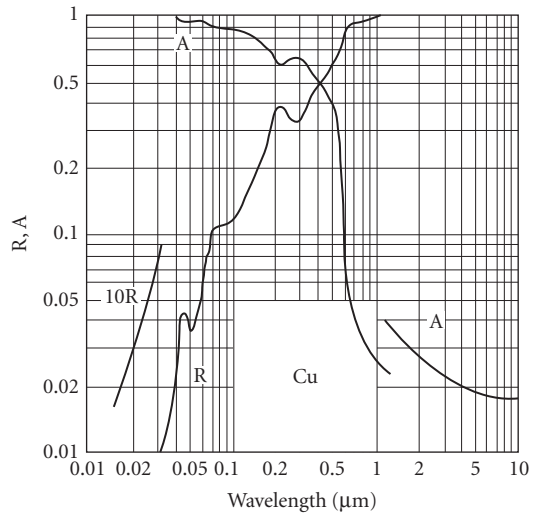
Metal	eV	Wavelength Å	μm	R
Tungsten <sup>36</sup>	4.60	2,695.0	0.27	0.455
	5.00	2,497.0	0.25	0.505
	5.40	2,296.0	0.23	0.586
	5.80	2,138.0	0.21	0.637
	6.20	2,000.0	0.20	0.646
	6.60	1,878.0	0.19	0.631
	7.00	1,771.0	0.18	0.607
	7.60	1,631.0	0.16	0.556
	8.00	1,550.0	0.15	0.505
	8.40	1,476.0	0.15	0.449
	9.00	1,378.0	0.14	0.388
	10.00	1,240.0	0.12	0.287
	10.40	1,192.0	0.12	0.270
	11.00	1,127.0	0.11	0.290
	11.80	1,051.0	0.11	0.318
	12.80	969.0		0.333
	13.60	912.0		0.325
	14.80	838.0		0.276
	15.60	795.0		0.246
	16.00	775.0		0.249
	16.80	738.0		0.273
	17.60	704.0		0.304
	18.80	659.0		0.340
	20.00	620.0		0.354
	21.20	585.0		0.331
	22.40	553.0		0.287
	23.60	525.0		0.252
	24.00	517.0		0.234
	24.80	500.0		0.191
	25.60	484.0		0.150
	26.80	463.0		0.105
	28.00	443.0		0.073
	30.00	413.0		0.047
	34.00	365.0		0.032
	36.00	344.0		0.036
	40.00	310.0		0.045

Figures 28 to 34 show reflectance for polished surfaces and thin films of Al, Be, SiC, and Ni, including effects of oxide films on the surface.<sup>51</sup> One effect of absorption is to limit the penetration depth of incident radiation. Penetration depth is shown in Fig. 35 as a function of wavelength for Al, Be, and Ni.<sup>51</sup>

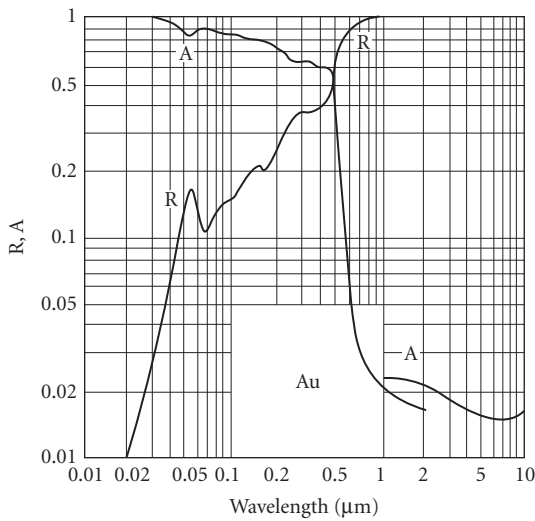
Absorption is a critical parameter for high-energy laser components, and is discussed in hundreds of papers as a function of surface morphology, angle of incidence, polarization state, and temperature. Only a few representative examples of this body of work can be cited here. When absorptance measurements were made of metal mirrors as a function of angle of incidence, polarization state, and wavelength,<sup>52</sup> it was found that measured values agreed with theory except at high angles of incidence where surface condition plays an undefined role. With the advent of diamond-turning as a mirror-finishing method, many papers have addressed absorptance characteristics of these unique surfaces as a function of surface morphology and angle of incidence, particularly on Ag and Cu mirrors.<sup>53,54</sup> It has been observed that mirrors have the lowest absorptance when the light is s-polarized and the grooves are oriented parallel to the plane of incidence.<sup>54</sup> The temperature dependence of optical absorption



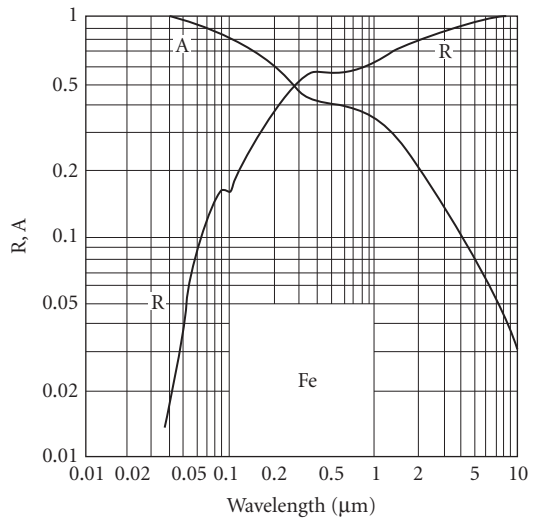
**FIGURE 16** Reflectance and absorptance for aluminum vs. wavelength calculated for normal incidence.<sup>35</sup> (With permission.)



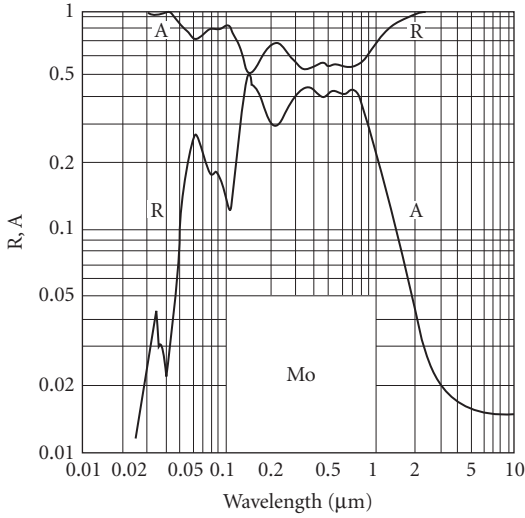
**FIGURE 17** Reflectance and absorptance for copper vs. wavelength calculated for normal incidence.<sup>35</sup> (With permission.)



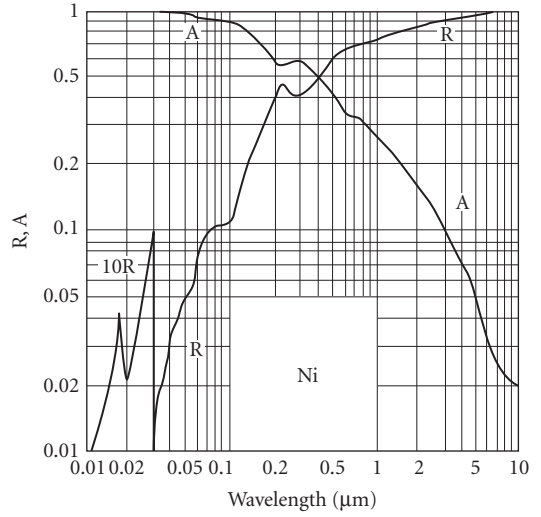
**FIGURE 18** Reflectance and absorptance for gold vs. wavelength calculated for normal incidence.<sup>35</sup> (With permission.)



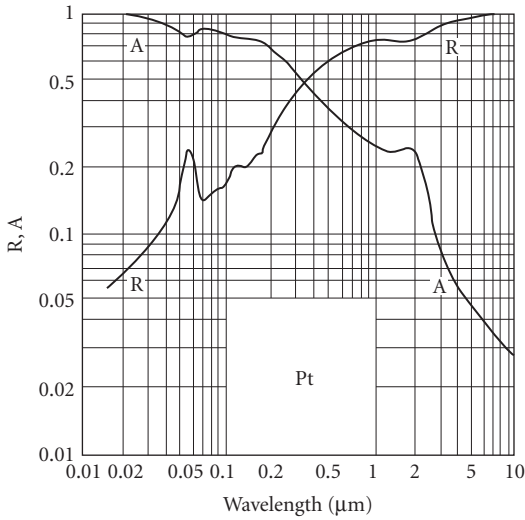
**FIGURE 19** Reflectance and absorptance for iron vs. wavelength calculated for normal incidence.<sup>35</sup> (With permission.)



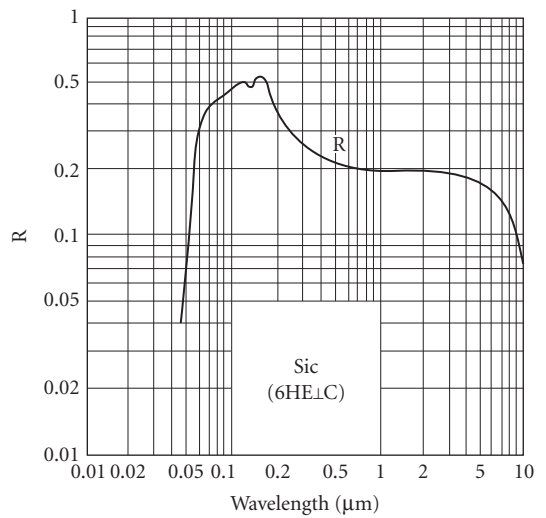
**FIGURE 20** Reflectance and absorptance for molybdenum vs. wavelength calculated for normal incidence.<sup>35</sup> (With permission.)



**FIGURE 21** Reflectance and absorptance for nickel vs. wavelength calculated for normal incidence.<sup>35</sup> (With permission.)

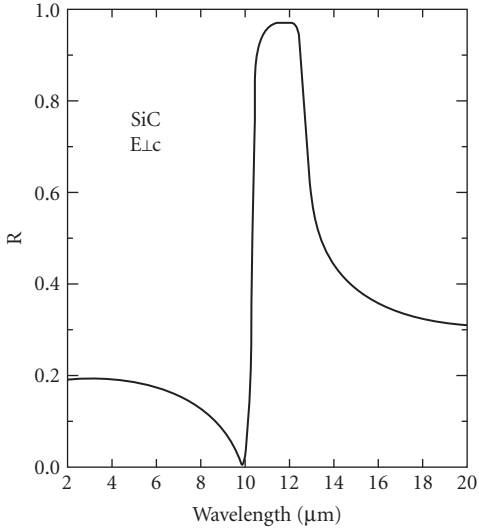


**FIGURE 22** Reflectance and absorptance for platinum vs. wavelength calculated for normal incidence.<sup>35</sup> (With permission.)

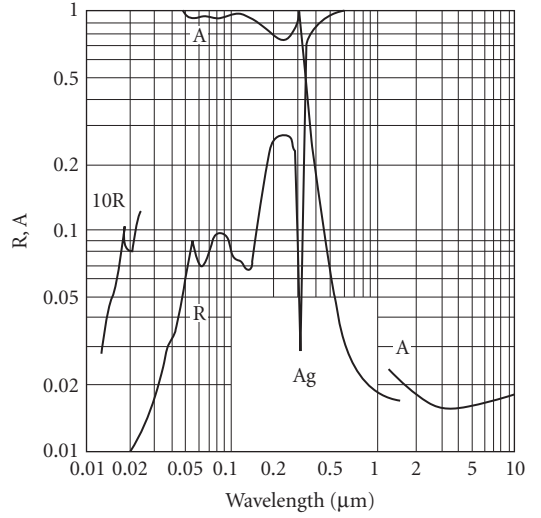


**FIGURE 23** Reflectance for the basal plane of hexagonal silicon carbide vs. wavelength calculated for normal incidence.<sup>35</sup> (With permission.)

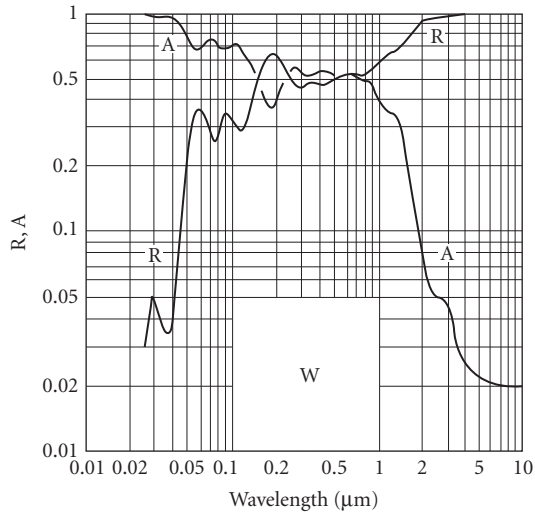




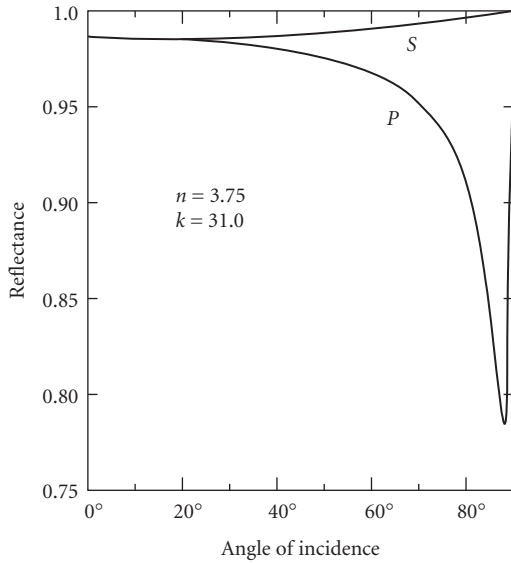
**FIGURE 24** Infrared reflectance for the basal plane of hexagonal silicon carbide vs. wavelength calculated for normal incidence.<sup>35</sup> (With permission.)



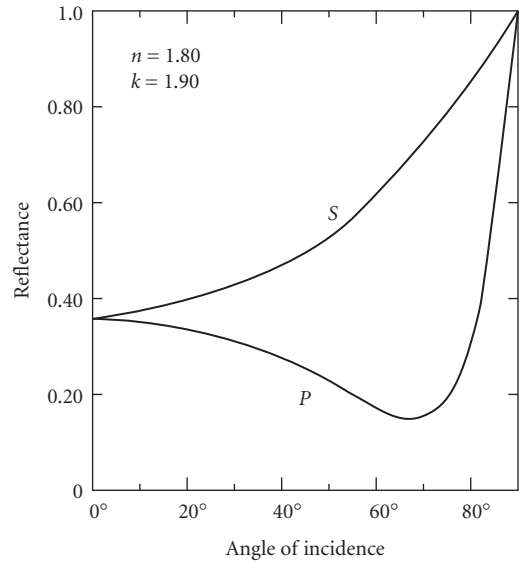
**FIGURE 25** Reflectance and absorptance for silver vs. wavelength calculated for normal incidence.<sup>35</sup> (With permission.)



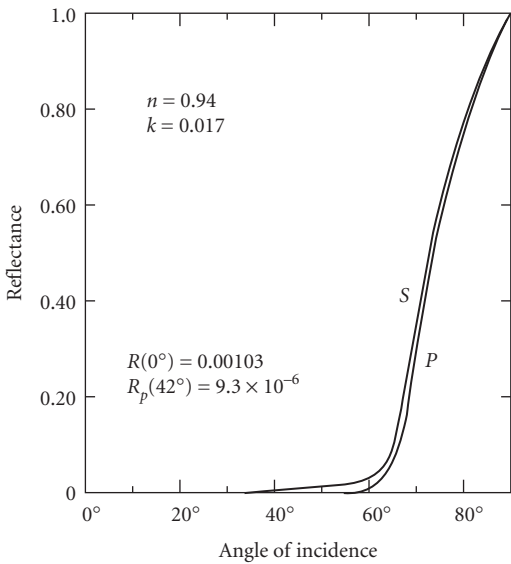
**FIGURE 26** Reflectance and absorptance for tungsten vs. wavelength calculated for normal incidence.<sup>35</sup> (With permission.)



(a)

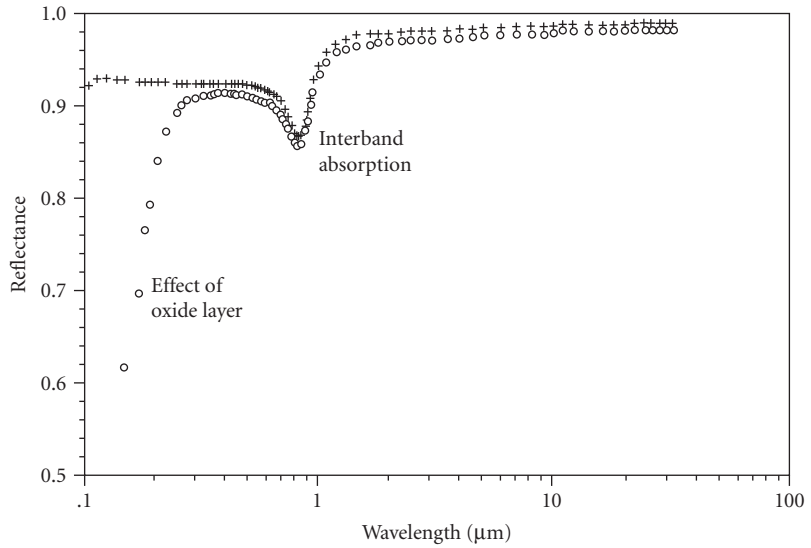


(b)

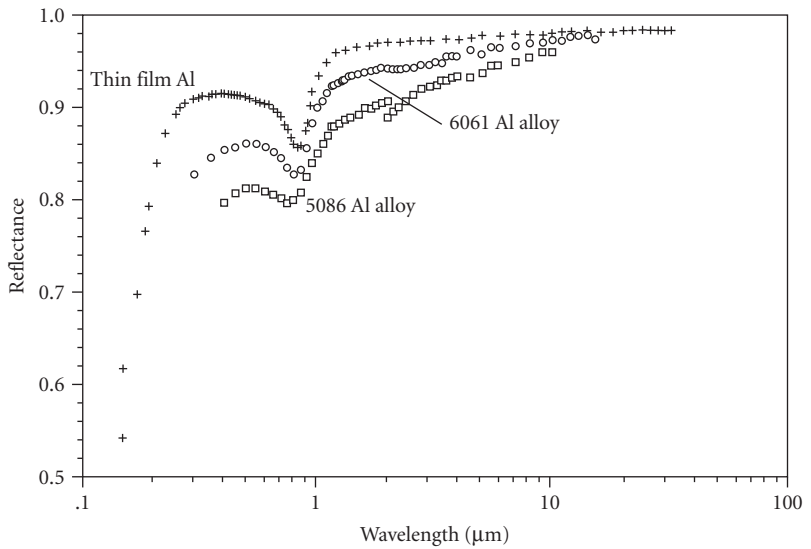


(c)

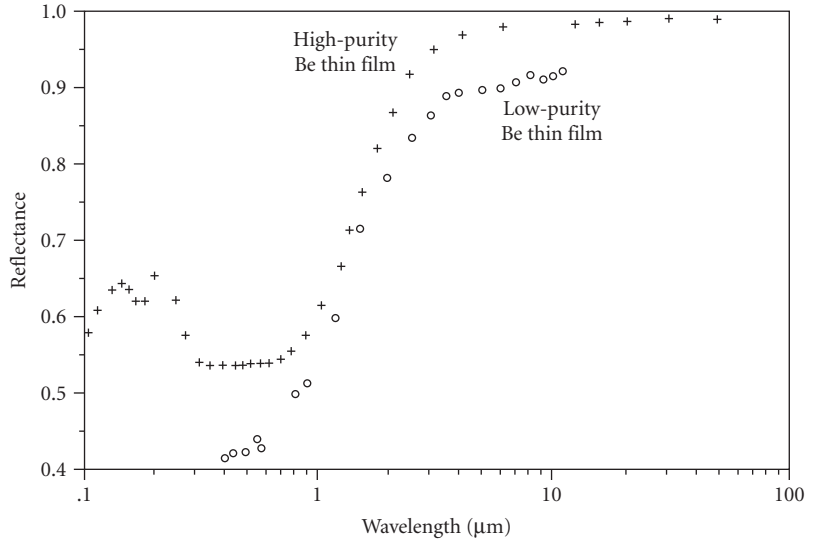
**FIGURE 27** Reflectance for polarized radiation vs. angle of incidence for a vacuum-metal interface.<sup>35</sup> (With permission.) (a)  $n = 3.75$ ,  $k = 31.0$ , approximate values for gold at  $\lambda = 5 \mu\text{m}$ ; (b)  $n = 1.80$ ,  $k = 1.90$ ,  $\lambda = 0.3 \mu\text{m}$ ; and (c)  $n = 0.94$ ,  $k = 0.017$ , approximate values for gold at  $\lambda = 0.01 \mu\text{m}$ . Note the tendency toward total external reflectance for angle  $\geq 80^\circ$ .



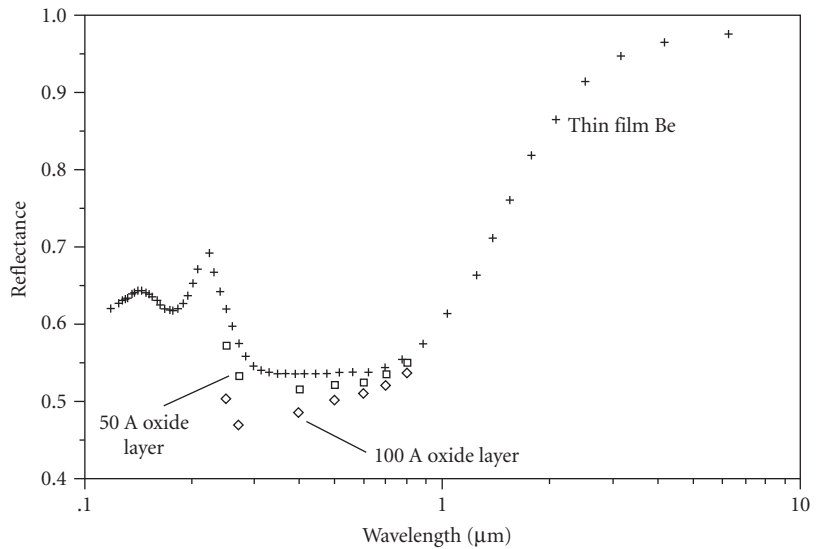
**FIGURE 28** Effect of oxide layer on the reflectivity of aluminum vs. wavelength<sup>51</sup> calculated from  $n$  and  $k$ .<sup>37</sup>



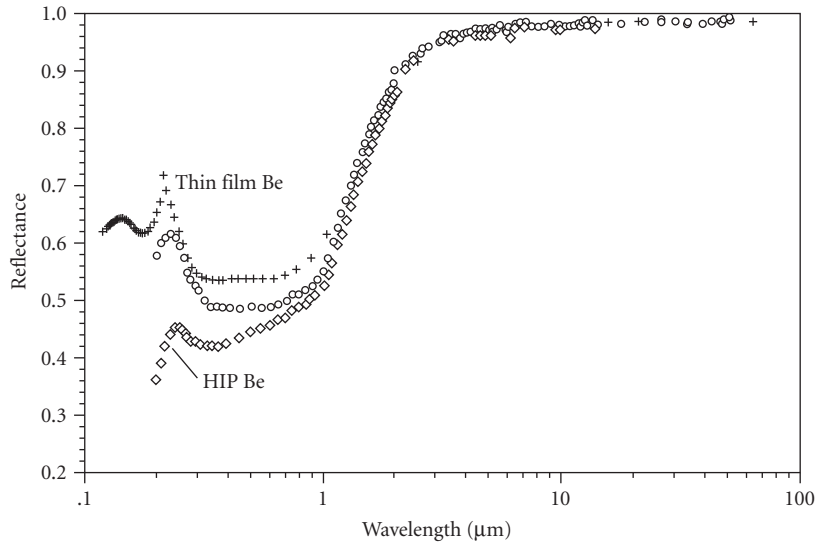
**FIGURE 29** Reflectance of optical-grade aluminum alloys vs. wavelength.<sup>51</sup>



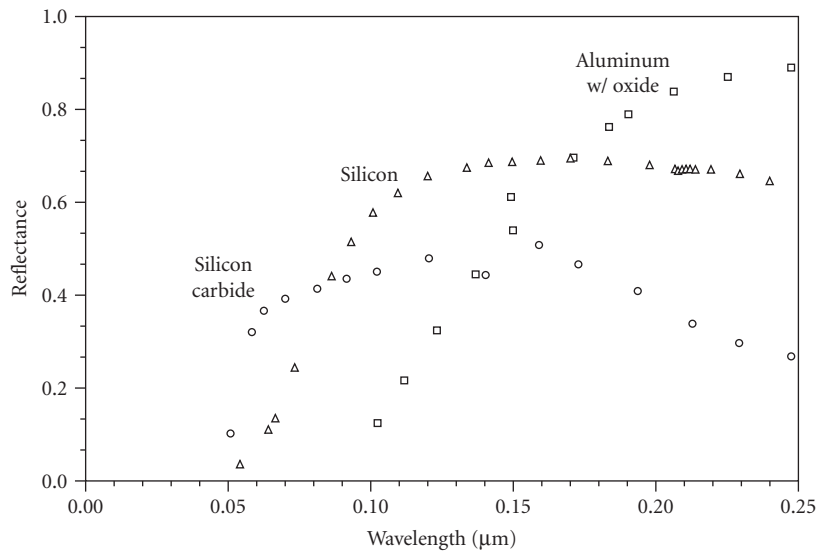
**FIGURE 30** Effect of impurities on the reflectance of beryllium thin films vs. wavelength.<sup>51</sup>



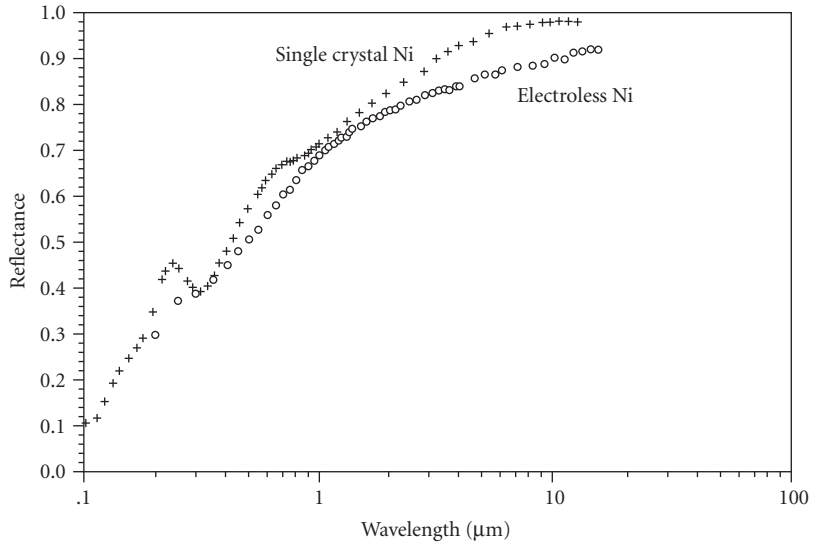
**FIGURE 31** Effect of oxide layer thickness on the reflectance of beryllium vs. wavelength<sup>51</sup> calculated from  $n$  and  $k$ .<sup>38</sup>



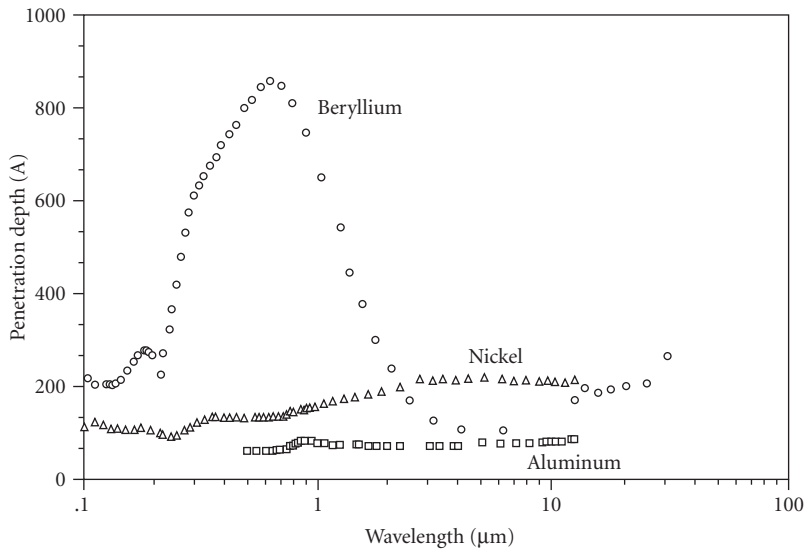
**FIGURE 32** Reflectance of polished and evaporated beryllium vs. wavelength;<sup>51</sup> comparison of evaporated high-purity thin film,<sup>38</sup> polished high-purity thick film, and polished bulk beryllium (2 percent BeO).



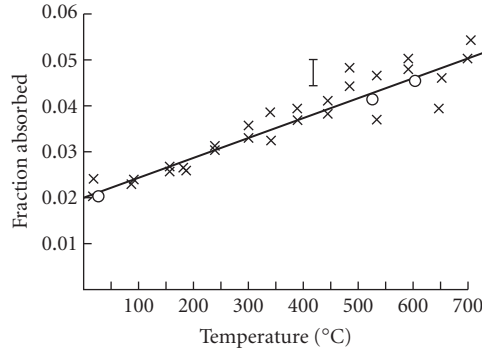
**FIGURE 33** Ultraviolet reflectance of aluminum, silicon, and silicon carbide vs. wavelength.<sup>51</sup>



**FIGURE 34** Reflectance of pure nickel<sup>39</sup> and electroless nickel (Ni-P alloy)<sup>51</sup> vs. wavelength calculated from  $n$  and  $k$ .



**FIGURE 35** Penetration depth in Ångströms vs. wavelength for aluminum, beryllium, and nickel.<sup>51</sup>



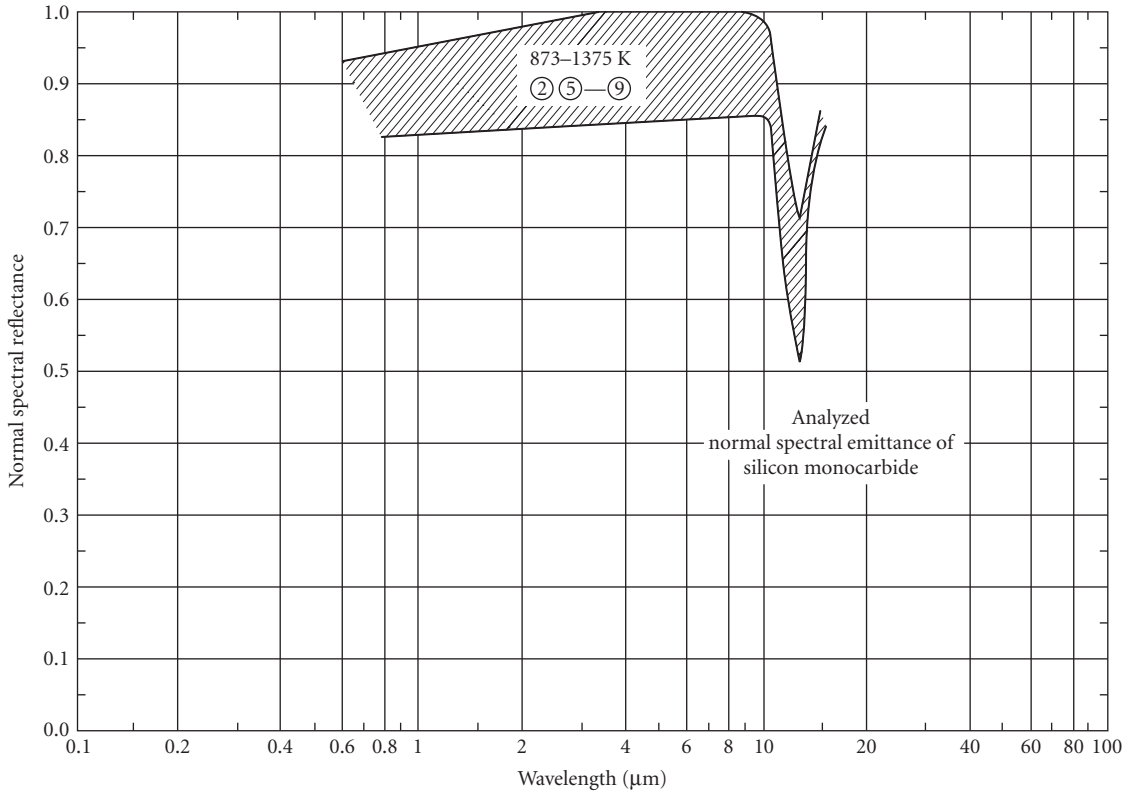
**FIGURE 36** The 10.6- $\mu\text{m}$  absorbance of Mo vs. temperature.<sup>53</sup>  $\times$  is heating and O is cooling. The straight line is a least-squares fit to the data.

has long been known,<sup>55</sup> but measurements and theory do not always agree, particularly at shorter wavelengths. Figure 36 shows absorbance of Mo as a function of temperature at a wavelength of 10.6  $\mu\text{m}$ .<sup>55</sup>

Mass absorption of energetic photons<sup>56</sup> follows the same relationship as described in Eq. (4), but with the product mass attenuation coefficient  $\mu$  and mass density  $\rho$  substituted for absorption coefficient  $\alpha$ . Table 4 lists mass attenuation coefficients for selected elements at energies between 1 keV (soft x rays) and 1 GeV (hard gamma rays). Units for the coefficient are  $\text{m}^2/\text{kg}$ , so that when multiplied by mass density in  $\text{kg}/\text{m}^3$ , and depth  $x$  in m, the exponent in the equation is dimensionless. To a

**TABLE 4** Mass Attenuation Coefficients for Photons<sup>56</sup>

		Mass attenuation coefficient ( $\text{m}^2/\text{kg}$ )						
		Photon energy (MeV)						
Atomic No.		0.001	0.01	0.1	1.0	10.0	100.0	1000.0
Be	4	$6.04 \times 10^1$	$6.47 \times 10^{-2}$	$1.33 \times 10^{-2}$	$5.65 \times 10^{-3}$	$1.63 \times 10^{-3}$	$9.94 \times 10^{-4}$	$1.12 \times 10^{-3}$
C	6	$2.21 \times 10^{-2}$	$2.37 \times 10^{-1}$	$1.51 \times 10^{-2}$	$6.36 \times 10^{-3}$	$1.96 \times 10^{-3}$	$1.46 \times 10^{-3}$	$1.70 \times 10^{-3}$
O	8	$4.59 \times 10^2$	$5.95 \times 10^{-1}$	$1.55 \times 10^{-2}$	$6.37 \times 10^{-3}$	$2.09 \times 10^{-3}$	$1.79 \times 10^{-3}$	$2.13 \times 10^{-3}$
Mg	12	$9.22 \times 10^1$	2.11	$1.69 \times 10^{-2}$	$6.30 \times 10^{-3}$	$2.31 \times 10^{-3}$	$2.42 \times 10^{-3}$	$2.90 \times 10^{-3}$
Al	13	$1.19 \times 10^2$	2.62	$1.70 \times 10^{-2}$	$6.15 \times 10^{-3}$	$2.32 \times 10^{-3}$	$2.52 \times 10^{-3}$	$3.03 \times 10^{-3}$
Si	14	$1.57 \times 10^2$	3.39	$1.84 \times 10^{-2}$	$6.36 \times 10^{-3}$	$2.46 \times 10^{-3}$	$2.76 \times 10^{-3}$	$3.34 \times 10^{-3}$
P	15	$1.91 \times 10^2$	4.04	$1.87 \times 10^{-2}$	$6.18 \times 10^{-3}$	$2.45 \times 10^{-3}$	$2.84 \times 10^{-3}$	$3.45 \times 10^{-3}$
Ti	22	$5.87 \times 10^2$	$1.11 \times 10^1$	$2.72 \times 10^{-2}$	$5.89 \times 10^{-3}$	$2.73 \times 10^{-3}$	$3.71 \times 10^{-3}$	$4.56 \times 10^{-3}$
Cr	24	$7.40 \times 10^2$	$1.39 \times 10^1$	$3.17 \times 10^{-2}$	$5.93 \times 10^{-3}$	$2.86 \times 10^{-3}$	$4.01 \times 10^{-3}$	$4.93 \times 10^{-3}$
Fe	26	$9.09 \times 10^2$	$1.71 \times 10^1$	$3.72 \times 10^{-2}$	$5.99 \times 10^{-3}$	$2.99 \times 10^{-3}$	$4.33 \times 10^{-3}$	$5.33 \times 10^{-3}$
Ni	28	$9.86 \times 10^2$	$2.09 \times 10^1$	$4.44 \times 10^{-2}$	$6.16 \times 10^{-3}$	$3.18 \times 10^{-3}$	$4.73 \times 10^{-3}$	$5.81 \times 10^{-3}$
Cu	29	$1.06 \times 10^3$	$2.16 \times 10^1$	$4.58 \times 10^{-2}$	$5.90 \times 10^{-3}$	$3.10 \times 10^{-3}$	$4.66 \times 10^{-3}$	$5.72 \times 10^{-3}$
Zn	30	$1.55 \times 10^2$	$2.33 \times 10^1$	$4.97 \times 10^{-2}$	$5.94 \times 10^{-3}$	$3.18 \times 10^{-3}$	$4.82 \times 10^{-3}$	$5.91 \times 10^{-3}$
Ge	32	$1.89 \times 10^2$	3.74	$5.55 \times 10^{-2}$	$5.73 \times 10^{-3}$	$3.16 \times 10^{-3}$	$4.89 \times 10^{-3}$	$6.00 \times 10^{-3}$
Mo	42	$4.94 \times 10^2$	8.58	$1.10 \times 10^{-1}$	$5.84 \times 10^{-3}$	$3.65 \times 10^{-3}$	$6.10 \times 10^{-3}$	$7.51 \times 10^{-3}$
Ag	47	$7.04 \times 10^2$	$1.19 \times 10^1$	$1.47 \times 10^{-1}$	$5.92 \times 10^{-3}$	$3.88 \times 10^{-3}$	$6.67 \times 10^{-3}$	$8.20 \times 10^{-3}$
W	74	$3.68 \times 10^2$	9.69	$4.44 \times 10^{-1}$	$6.62 \times 10^{-3}$	$4.75 \times 10^{-3}$	$8.80 \times 10^{-3}$	$1.08 \times 10^{-2}$
Pt	78	$4.43 \times 10^2$	$1.13 \times 10^1$	$4.99 \times 10^{-1}$	$6.86 \times 10^{-3}$	$4.87 \times 10^{-3}$	$9.08 \times 10^{-3}$	$1.12 \times 10^{-2}$
Au	79	$4.65 \times 10^2$	$1.18 \times 10^1$	$5.16 \times 10^{-1}$	$6.95 \times 10^{-3}$	$4.93 \times 10^{-3}$	$9.19 \times 10^{-3}$	$1.13 \times 10^{-2}$



**FIGURE 37** Analyzed normal spectral emittance of silicon carbide vs. wavelength.<sup>57</sup>

high approximation, mass attenuation is additive for elements present in a body, independent of the way in which they are bound in chemical compounds. Table 4 is highly abridged; the original<sup>56</sup> shows all elements and absorption edges.

**Emittance** Where the transmittance of a material is essentially zero, the absorptance equals the emittance as described above and expressed in Eqs. (15) and (16). Spectral emittance  $\epsilon_s$  is the emittance as a function of wavelength at constant temperature. These data have been presented as absorptance curves in Figs. 16 to 22, 25, and 26. For SiC,  $\epsilon_s$  is given in Fig. 37.<sup>57</sup> Spectral emittance of unoxidized surfaces at a wavelength of 0.65 μm is given for selected materials in Table 5.<sup>58</sup>

Total emittance  $\epsilon_t$  is the emittance integrated over all wavelengths and usually given as a function of temperature. The total emittance of SiC is given in Fig. 38,<sup>59</sup> and for selected materials in Table 6.<sup>60</sup> Numerous papers by groups at the University of New Orleans (Ramanathan et al.<sup>61-65</sup>) and at Cornell University (Sievers et al.<sup>66,67</sup>) give high- and low-temperature data for the total hemispherical emittance of a number of metals including Ag, Al, Cu, Mo, W, and AISI 304 stainless steel.

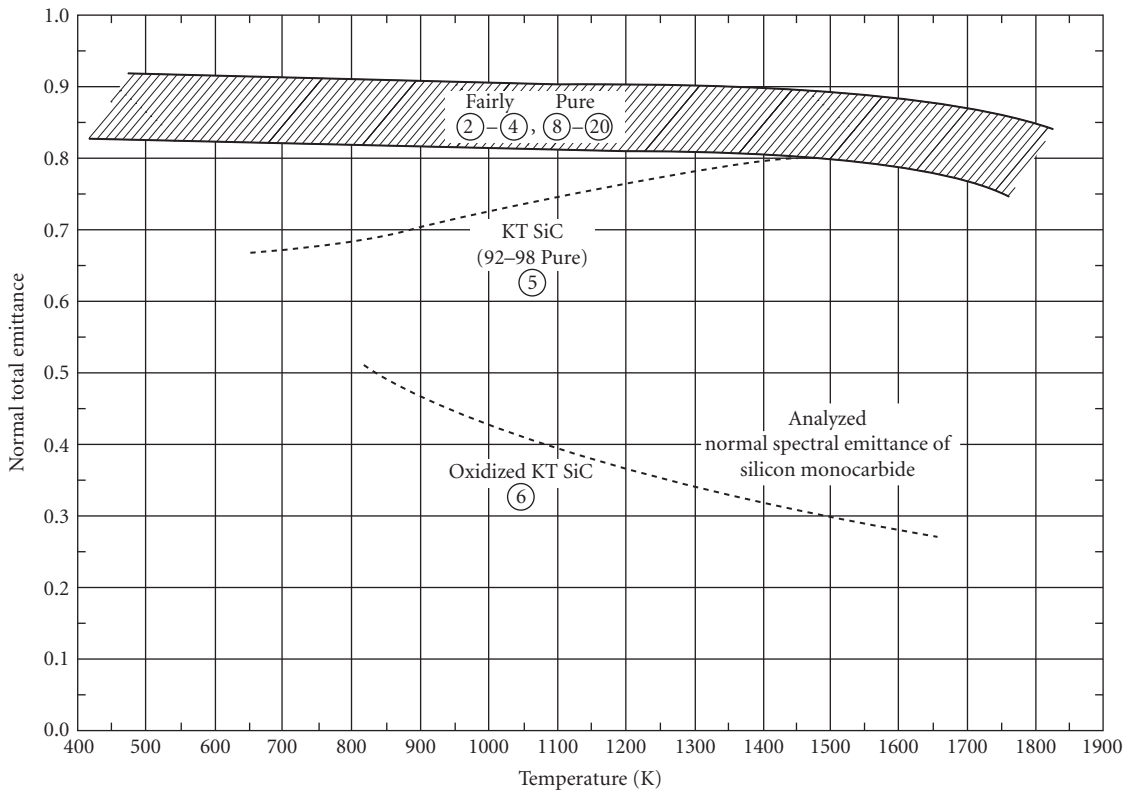
## Physical Properties

The physical properties at room temperature of a number of metals are listed in Table 7. The crystal form does not appreciably affect the physical properties, but is a factor in the isotropy of thermal and mechanical properties. For most metals, resistivity is directly proportional to temperature and



**TABLE 5** Normal Spectral Emittance of Selected Metals ( $\lambda = 0.65 \mu\text{m}$ )<sup>58</sup>

Metal	Emissivity
Beryllium	0.61
Chromium	0.34
Copper	0.10
Gold	0.14
Iron	0.35
Cast iron	0.37
Molybdenum	0.37
Nickel	0.36
80Ni-20Cr	0.35
Palladium	0.33
Platinum	0.30
Silver	0.07
Steel	0.35
Tantalum	0.49
Titanium	0.63
Tungsten	0.43



**FIGURE 38** Analyzed normal total emittance of silicon carbide vs. temperature.<sup>59</sup>

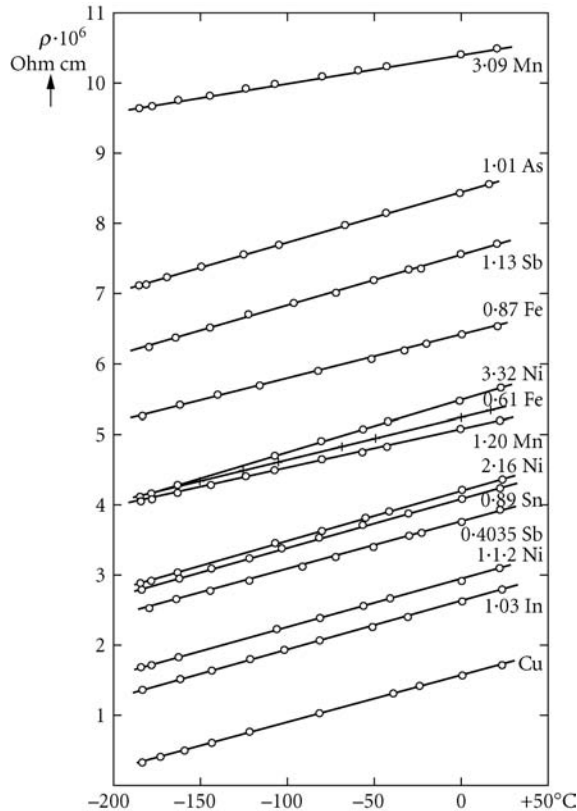
**TABLE 6** Total Emittance of Selected Materials<sup>60</sup>

Metal	Temperature (°C)	Emissivity	
80 Ni-20 Cr	100	0.87	
	600	0.87	
	1300	0.89	
Aluminum	50–500	0.04–0.06	
	Polished	200	0.11
Oxidized	600	0.19	
Chromium	50	0.1	
	Polished	500–1000	0.28–0.38
Copper Oxidized	50	0.6–0.7	
	500	0.88	
Polished	50–100	0.02	
Unoxidized	100	0.02	
Glass	20–100	0.94–0.91	
	250–1000	0.87–0.72	
	1100–1500	0.7–0.67	
Gold			
Carefully polished	200–600	0.02–0.03	
Unoxidized	100	0.02	
Iron, cast	Oxidized	200	0.64
	600	0.78	
Unoxidized	100	0.21	
Molybdenum	600–1000	0.08–0.13	
	1500–2200	0.19–0.26	
Nickel			
Polished	200–400	0.07–0.09	
Unoxidized	25	0.045	
	100	0.06	
	500	0.12	
	1000	0.19	
Platinum			
Polished	200–600	0.05–0.1	
Unoxidized	25	0.017	
	100	0.047	
	500	0.096	
	1000	0.152	
Silver			
Polished	200–600	0.02–0.03	
Unoxidized	100	0.02	
	500	0.035	
Steel			
304 SS	500	0.35	
Unoxidized	100	0.08	
Tantalum, unoxidized	1500	0.21	
	2000	0.26	
Tungsten, unoxidized	25	0.024	
	100	0.032	
	500	0.071	
	1000	0.15	

**TABLE 7** Composition and Physical Properties of Metals

Metal	Mass Density 10 <sup>3</sup> kg/m <sup>3</sup>	Electrical Conductivity % IACS <sup>a</sup>	Electrical Resistivity Nohm m <sup>b</sup>	Crystal Form <sup>c</sup>	Chemical Composition Weight %, Typical	Reference
Aluminum: 5086-O	2.66	31	56	fcc	4.0 Mg, 0.4 Mn, 0.15 Cr, bal. Al	84
Aluminum: 6061-T6	2.70	43	40	fcc	1.0 Mg, 0.6 Si, 0.3 Cu, 0.2 Cr, bal. Al	84
Beryllium: I-70-H	1.85	43	40	cph	99.0 Be min., 0.6 BeO, 0.08 Fe, 0.05 C, 0.03 Al, 0.02 Mg	85
Copper: OFC	8.94	101	17	fcc	99.95 Cu min.	84
Gold	19.3	73	24	fcc	99.99 Au min.	84
Invar 36	8.1	<sup>d</sup>	820	bcc	36.0 Ni, 0.35 Mn, 0.2 Si, 0.02 C, bal. Fe	86
Molybdenum	10.22	34 <sup>e</sup>	52 <sup>e</sup>	bcc	99.9 Mo min., 0.015 C max.	84
Nickel: 200	8.9	18	95	fcc	99.0 Ni min.	84
Nickel: electroless plate	7.75	<sup>d</sup>	900	fcc	10.5 P, bal. Ni	87
Silicon	2.33	<sup>f</sup>	<sup>f</sup>	dia. cubic	99.99 Si	84
Silicon carbide (SiC): CVD	3.21	<sup>f</sup>	<sup>f</sup>	cubic	99.99 SiC (beta)	88
SiC: reaction sintered	2.91	<sup>f</sup>	<sup>f</sup>	cph + dia. cubic	74.0 SiC (alpha), 26.0 Si	88
Silver	10.49	103	15 <sup>e</sup>	fcc	99.9 Ag min.	84
Stainless steel: 304	8.00	<sup>d</sup>	720	fcc	19.0 Cr, 9.0 Ni, 1.0 Mn, 0.5 Si, bal. Fe	89
Stainless steel: 416	7.80	<sup>d</sup>	570	distorted bcc	13.0 Cr, 0.6 Mn, 0.6 Mo, 0.5 Si, bal. Fe	89
Stainless steel: 430	7.80	<sup>d</sup>	600	bcc	17.0 Cr, 0.5 Mn, 0.5 Si, bal. Fe	89
Titanium: 6A14V	4.43	<sup>d</sup>	1710	bcc + cph	6.0 Al, 4.0 V, bal. Ti	90

<sup>a</sup>For equal volume at 293 K.<sup>b</sup>At 293 K.<sup>c</sup>fcc = face-centered cubic; cph = close-packed hexagonal; bcc = body-centered cubic.<sup>d</sup>Not available.<sup>e</sup>At 273 K.<sup>f</sup>Depends on impurity content.



**FIGURE 39** Electrical resistance of Cu and Cu alloys vs. temperature;<sup>68</sup> composition is in atomic percent.

pure metals generally have increased resistivity with increasing amounts of alloying elements. This is shown graphically for copper in Fig. 39.<sup>68</sup> Resistivity for a number of pure, polycrystalline metals is listed as a function of temperature in Table 8.<sup>69</sup>

## Thermal Properties

The thermal properties of materials were documented in 1970 through 1977 in the 13-volume series edited by Touloukian et al.<sup>70</sup> of the Thermophysical Properties Research Center at Purdue University. The properties database continues to be updated by the Center for Information and Numerical Data Analysis and Synthesis (CINDAS).<sup>1</sup>

Selected properties of coefficient of thermal expansion, CTE, thermal conductivity  $k$ , and specific heat  $C_p$  at room temperature, are listed in Table 9. Maximum usable temperatures are also listed in the table.

The CTE of a material is a measure of length change at a specific temperature, useful for determining dimensional sensitivity to local temperature gradients. The total expansion (contraction) per unit length  $\Delta L/L$  for a temperature change  $\Delta T$  is the area under the CTE vs.  $T$  curve between the temperature extremes. Table 10 and Figs. 40 through 42 show recommended<sup>71,72</sup> CTE vs.  $T$  relationships for a number of materials. More recent expansion data have been published for many

**TABLE 8** Electrical Resistivity (nohm m) of Pure, Polycrystalline Metals<sup>69</sup>

Temp. (K)	Aluminium	Beryllium	Chromium	Copper	Gold	Iron	Molybdenum	Nickel	Platinum	Silver	Tungsten
1	0.0010	0.332		0.020	0.220	0.225	0.0070	0.032	0.02	0.010	0.0002
10	0.0019	0.332		0.020	0.226	0.238	0.0089	0.057	0.154	0.012	0.0014
20	0.0076	0.336		0.028	0.350	0.287	0.0261	0.140	0.484	0.042	0.012
40	0.181	0.367		0.239	1.41	0.758	0.457	0.68	4.09	0.539	0.544
60	0.959	0.67		0.971	3.08	2.71	2.06	2.42	11.07	1.62	2.66
80	2.45	0.75		2.15	4.81	6.93	4.82	5.45	19.22	2.89	6.06
100	4.42	1.33	16.0	3.48	6.50	12.8	8.58	9.6	27.55	4.18	10.2
150	10.06	5.10	45.0	6.99	10.61	31.5	19.9	22.1	47.6	7.26	20.9
200	15.87	12.9	77.0	10.46	14.62	52.0	31.3	36.7	67.7	10.29	31.8
273	24.17	30.2	118.0	15.43	20.51	85.7	48.5	61.6	96.0	14.67	48.2
293	26.50	35.6	125.0	16.78	22.14	96.1	53.4	69.3	105.0	15.87	52.8
298	27.09	37.0	126.0	17.12	22.55	98.7	54.7	71.2	107.0	16.17	53.9
300	27.33	37.6	127.0	17.25	22.71	99.8	55.2	72.0	108.0	16.29	54.4
400	38.7	67.6	158.0	24.02	31.07	161.0	80.2	118.0	146.0	22.41	78.3
500	49.9	99.0	201.0	30.90	39.70	237.0	106.0	177.0	183.0	28.7	103.0
600	61.3	132.0	247.0	37.92	48.70	329.0	131.0	255.0	219.0	35.3	130.0
700	73.5	165.0	295.0	45.14	58.20	440.0	158.0	321.0	254.0	42.1	157.0
800	87.0	200.0	346.0	52.62	68.10	571.0	184.0	355.0	287.0	49.1	186.0
900	101.8	237.0	399.0	60.41	78.60		212.0	386.0	320.0	56.4	215.0

**TABLE 9** Thermal Properties of Metals at Room Temperature

Metal	Coeff. of Thermal Expansion (ppm/K)	Thermal Conductivity (W/m K)	Specific Heat (J/kg K)	Maximum Temperature (K)	Reference
Aluminum: 5086-O	22.6	127	900	475	84
Aluminum: 6061-T6	22.5	167	896	425	84
Beryllium: I-70-H	11.3	216	1925	800	85
Copper: OFC	16.5	391	385	400	84
Gold	14.2	300	130	400	84
Iron	11.8	81	450	900	84
Invar 36	1.0	10	515	475	86
Molybdenum	4.8	142	276	1100	84
Nickel: 200	13.4	70	456	650	84
Nickel: Electroless plate (11% P)	11.0	7	460	425	87
(8% P)	12.8			450	91
Silicon	2.6	156	710	725	84
Silicon Carbide (SiC): CVD	2.2	198	733	1200	88
	2.4	250	700		92
SiC: Reaction sintered	2.6	155	670	1100	92
Silver	19.0	428	235	400	84
Stainless steel: 304	14.7	16	500	700	89
Stainless steel: 416	9.5	25	460	500	89
Stainless steel: 430	10.4	26	460	870	89
Titanium: 6A14V	8.6	7	520	650	84

materials that are too numerous to list here, but those for beryllium<sup>73</sup> and beta silicon carbide<sup>74</sup> are included in Table 10.

Thermal conductivities of many pure polycrystalline materials have been published by the National Bureau of Standards<sup>75,76</sup> (now National Institute for Science and Technology) as part of the National Standard Reference Data System. Selected portions of these data, along with data from Touloukian et al.,<sup>77,78</sup> and specific data for beryllium<sup>79</sup> and beta silicon carbide,<sup>80</sup> are listed in Table 11 and shown in Figs. 43 through 46.

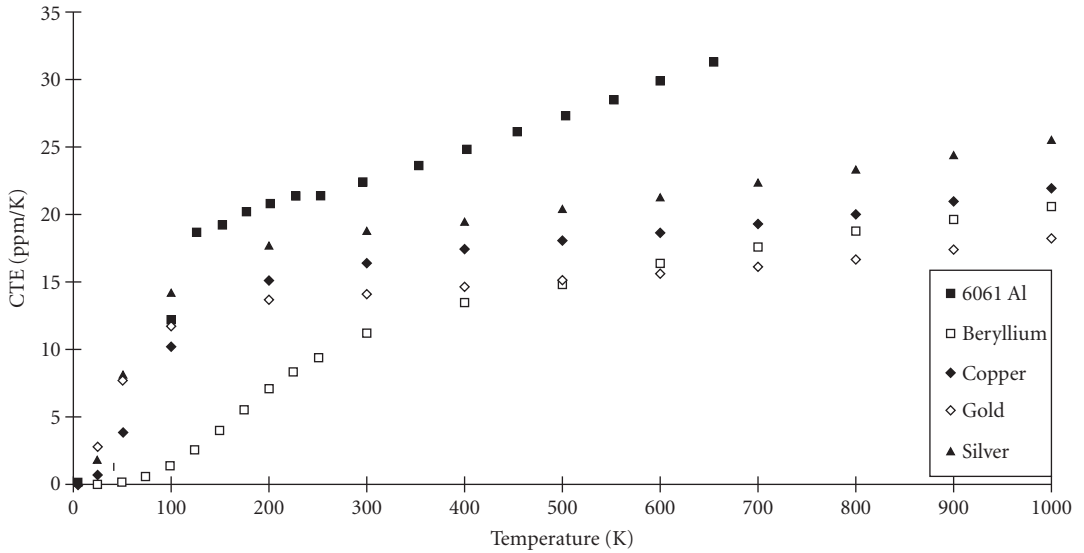
The specific heat of metals is very well documented.<sup>73,81–83</sup> Table 12 and Figs. 47 through 49 show the temperature dependence of this property. Table values are cited in J/kg K, numerically equal to W s/kg K.

## Mechanical Properties

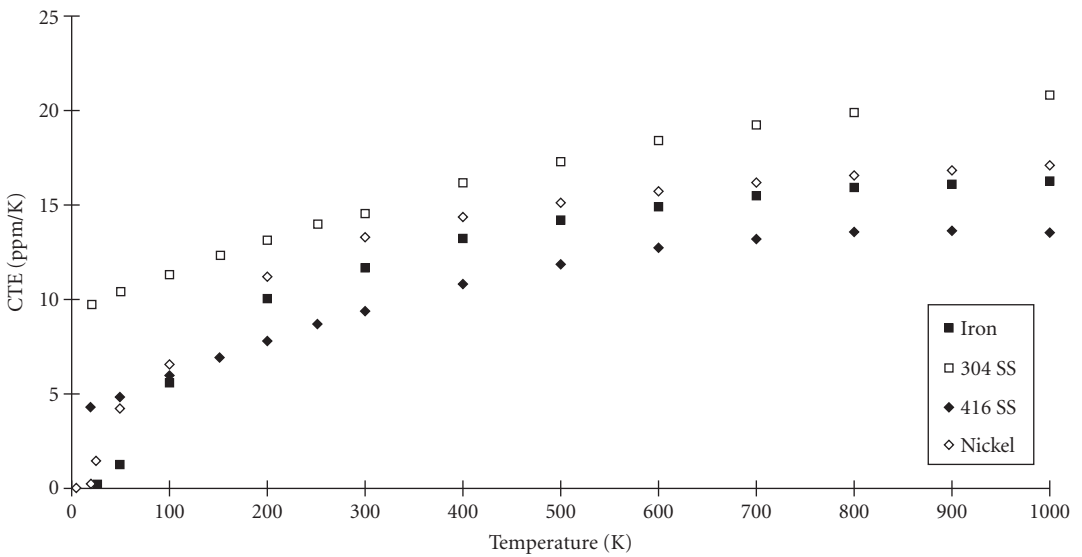
Mechanical properties are arbitrarily divided between the elastic properties of moduli, Poisson's ratio, and elastic stiffness, and the strength and fracture properties. All of these properties can be anisotropic as described by the elastic stiffness constants, but that level of detail is not included here. In general, cubic materials are isotropic in thermal properties and anisotropic in elastic properties. Materials of any of the other crystalline forms will be anisotropic in both thermal and elastic properties. For an in-depth treatment of this subject see, for example, Ref. 4.

**TABLE 10** Temperature Dependence of the Coefficient of Linear Thermal Expansion (ppm/K) of Selected Materials

Temp. (K)	6061 Al	Be	Cu	Au	Fe	304 SS	416 SS	Mo	Ni	Ag	Si	Alpha SiC	Beta SiC
5		0.0003	0.005	0.03	0.01				0.02	0.015		0.01	
10		0.001										0.02	
20		0.005				9.8	4.3	0.3			0		
25		0.009	0.63	2.8	0.2			0.4	0.25	1.9	0	0.03	
50		0.096	3.87	7.7	1.3	10.5	4.9	1	1.5	8.2	-0.2	0.06	
75		0.47							4.3		-0.5	0.09	
100	12.2	1.32	10.3	11.8	5.6	11.4	6	2.8	6.6	14.2	-0.4	0.14	
125	18.7	2.55											
150	19.3	4.01				12.4	7				0.5	0.4	
175	20.3	5.54											
200	20.9	7.00	15.2	13.7	10.1	13.2	7.9	4.6	11.3	17.8	1.5	1.5	
225	21.5	8.32											
250	21.5	9.50				14.1	8.8				2.2	2.8	
293	22.5	11.3	16.5	14.2	11.8	14.7	9.5	4.8	13.4	18.9	2.6	3.3	3.26
300		11.5										3.4	3.29
350	23.8												3.46
400	25.0	13.6	17.6	14.8	13.4	16.3	10.9	4.9	14.5	19.7	3.2	4	3.62
450	26.3												3.77
500	27.5	15.1	18.3	15.4	14.4	17.5	12.1	5.1	15.3	20.6	3.5	4.2	3.92
600	30.1	16.6	18.9	15.9	15.1	18.6	12.9	5.3	15.9	21.5	3.7	4.5	4.19
700		17.8	19.5	16.4	15.7	19.5	13.5	5.5	16.4	22.6	3.9	4.7	4.42
800		19.1	20.3	17	16.2	20.2	13.8	5.7	16.8	23.7	4.1	4.9	4.62
900		20.0	21.3	17.7	16.4		13.9	6	17.1	24.8	4.3	5.1	4.79
1000		20.9	22.4	18.6	16.6	21.1	13.9	6.2	17.4	25.9	4.4	5.3	4.92
Reference	71	73	71	71	71	71	71	71	71	71	72	72	74



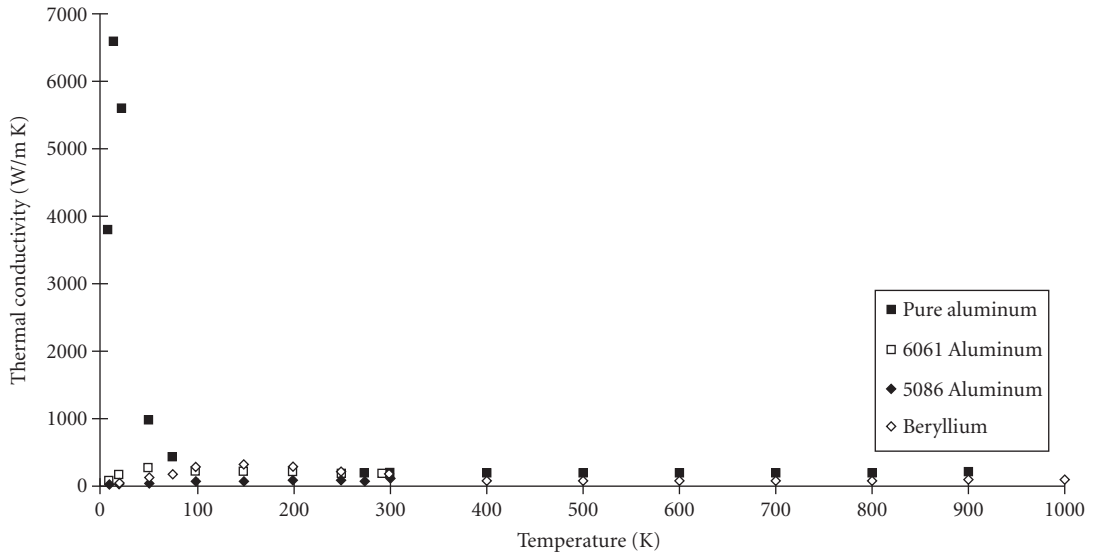
**FIGURE 40** Coefficient of linear thermal expansion of 6061 aluminum alloy,<sup>71</sup> beryllium,<sup>73</sup> copper,<sup>71</sup> gold,<sup>71</sup> and silver<sup>71</sup> vs. temperature.



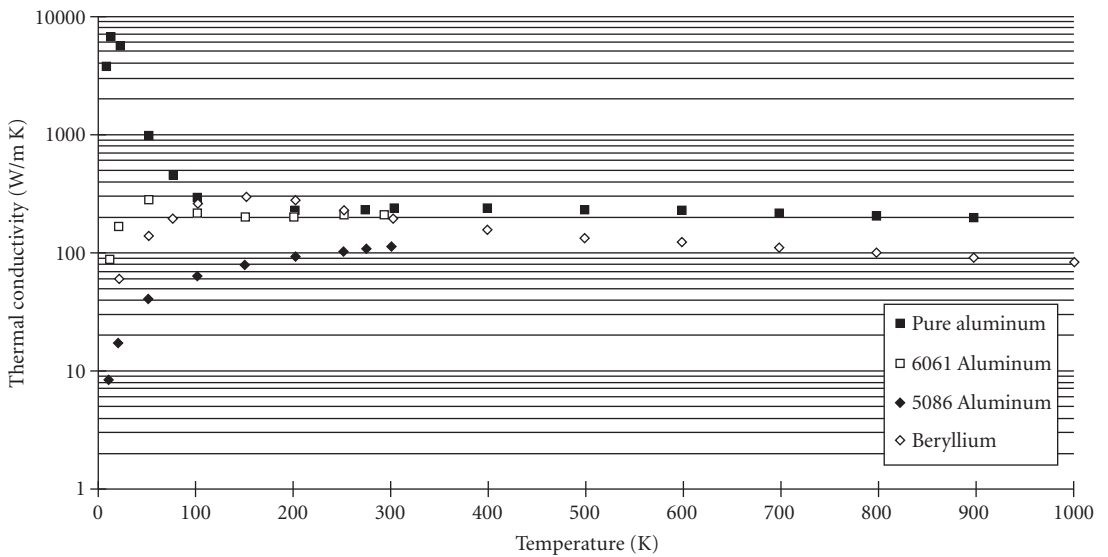
**FIGURE 41** Coefficient of linear thermal expansion of iron,<sup>71</sup> stainless steel types 304<sup>71</sup> and 416,<sup>71</sup> and nickel<sup>71</sup> vs. temperature.







(a)



(b)

**FIGURE 43** Thermal conductivity of three aluminum alloys<sup>75-77</sup> and beryllium<sup>79</sup> vs. temperature.

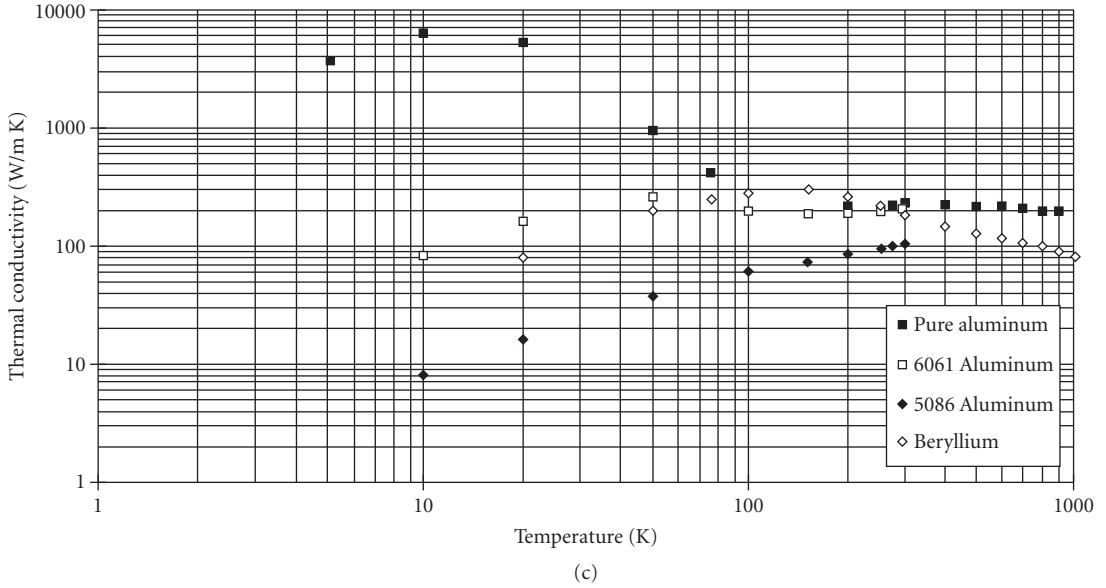


FIGURE 43 (Continued)

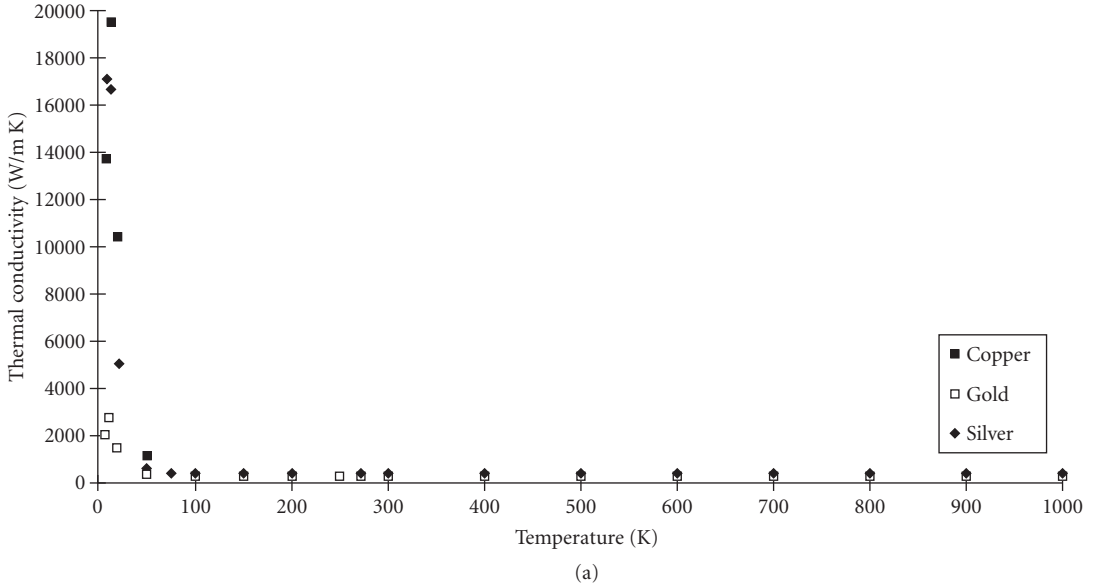


FIGURE 44 Thermal conductivity of copper,<sup>77</sup> gold,<sup>77</sup> and silver<sup>77</sup> vs. temperature.

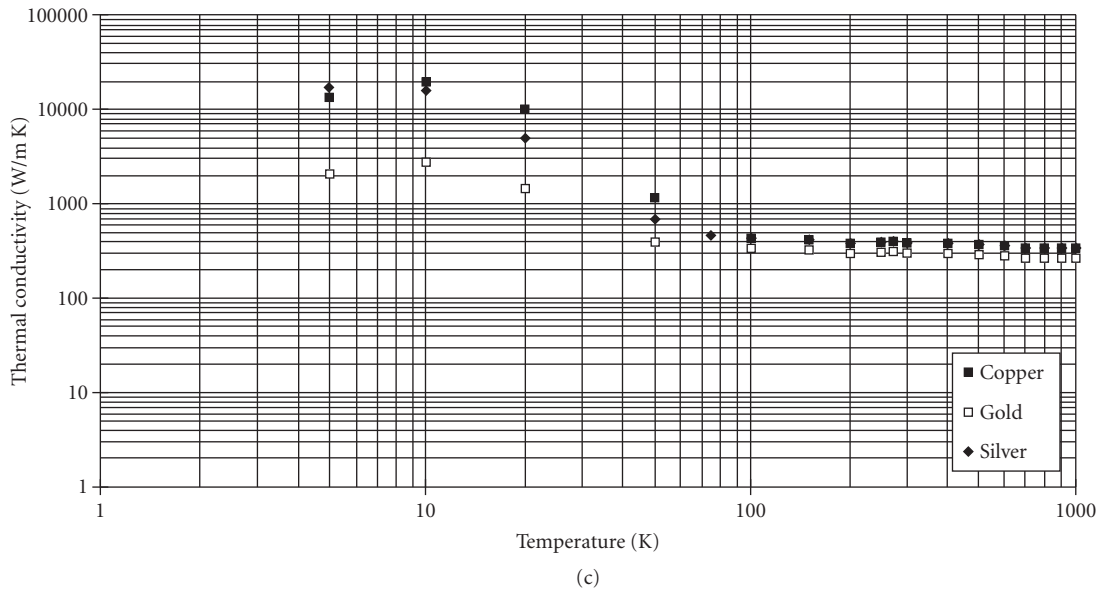
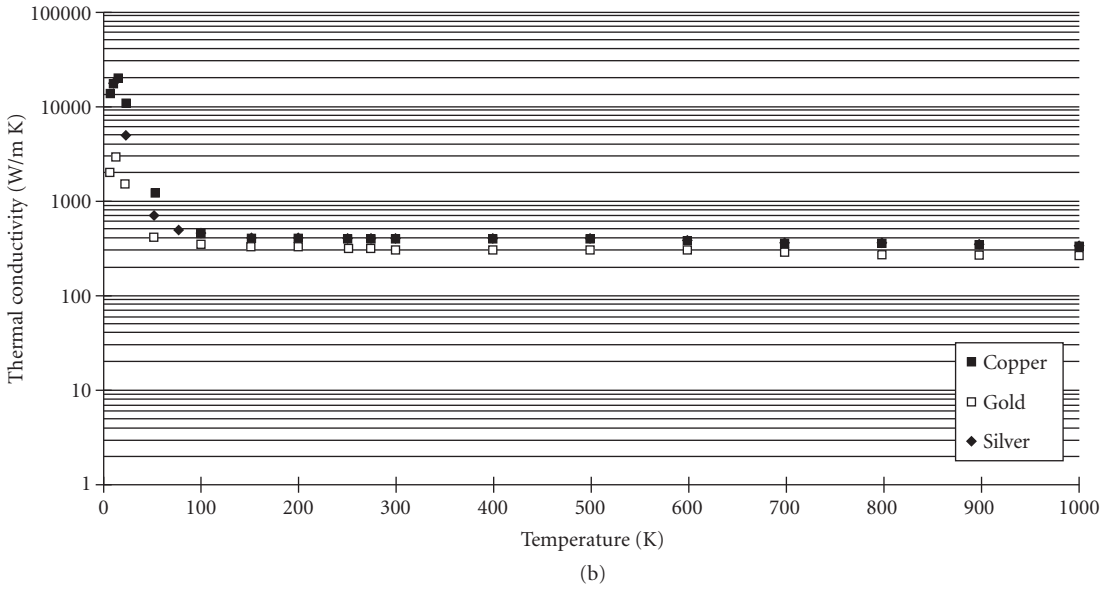


FIGURE 44 (Continued)

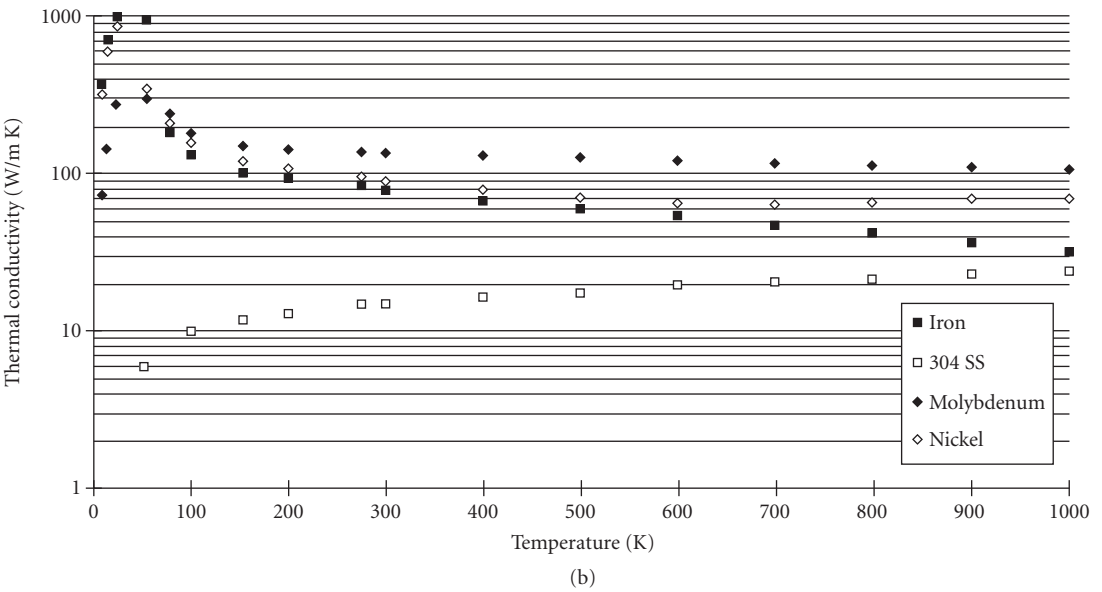
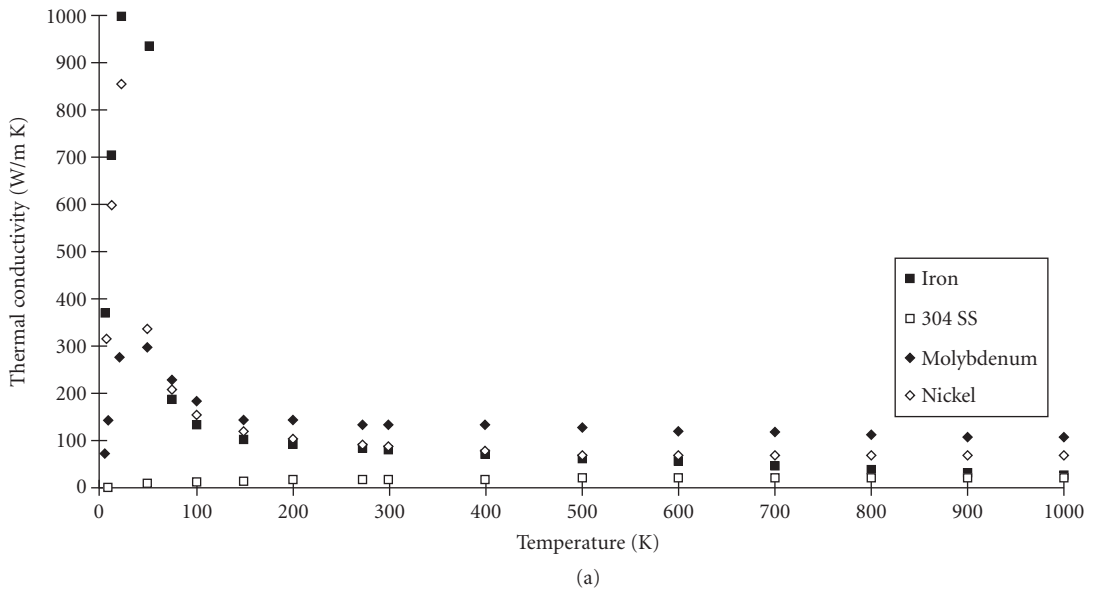


FIGURE 45 Thermal conductivity of iron,<sup>77</sup> type 304 stainless steel,<sup>77</sup> molybdenum,<sup>77</sup> and nickel<sup>77</sup> vs. temperature.

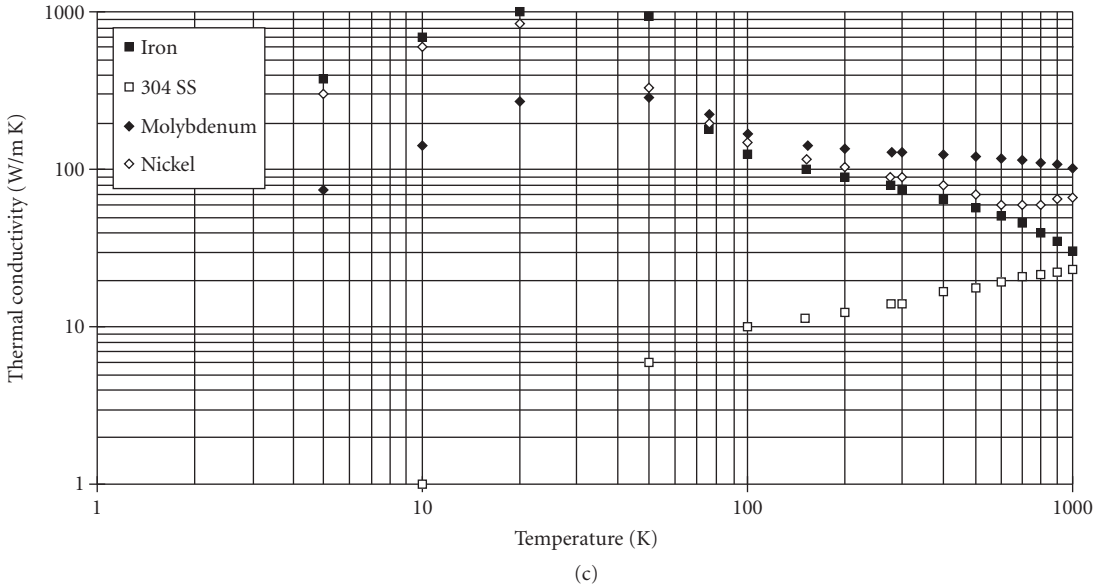


FIGURE 45 (Continued)

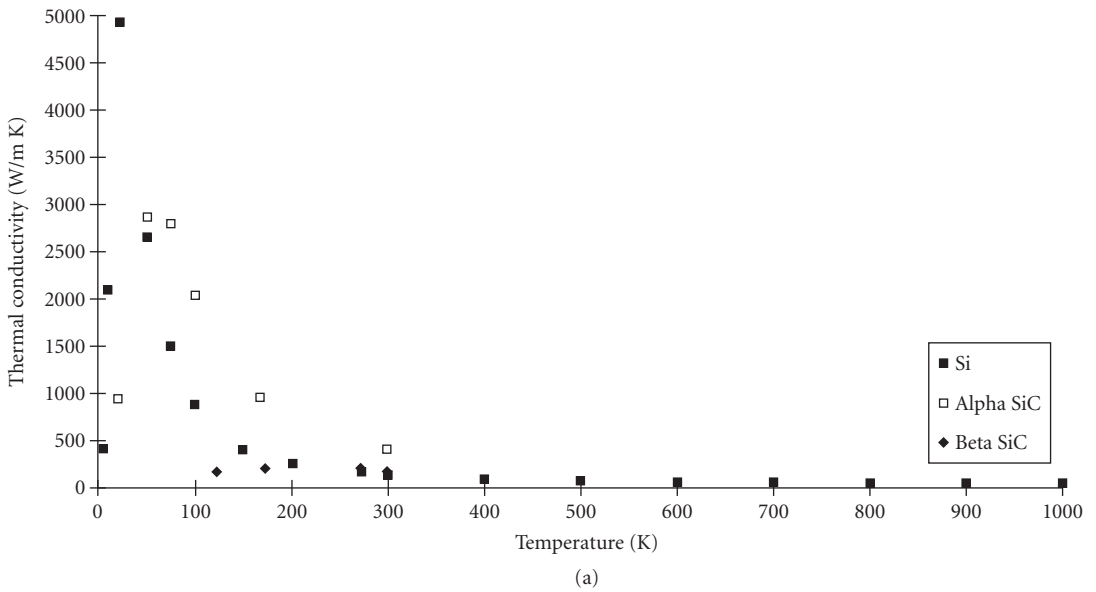


FIGURE 46 Thermal conductivity of silicon<sup>77</sup> and alpha<sup>78</sup> and beta<sup>80</sup> silicon carbide vs. temperature.

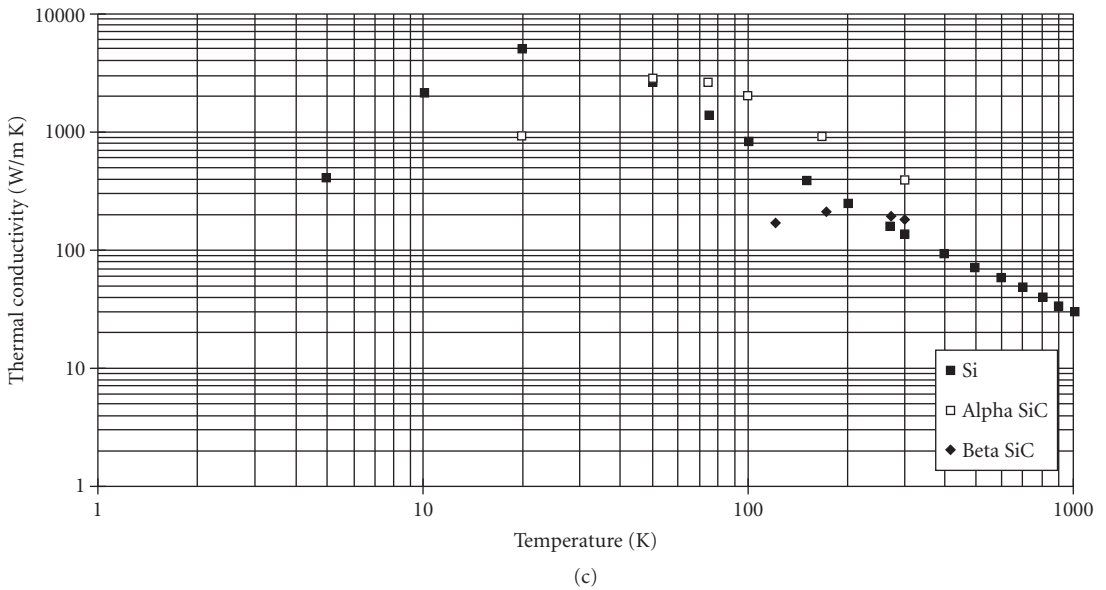
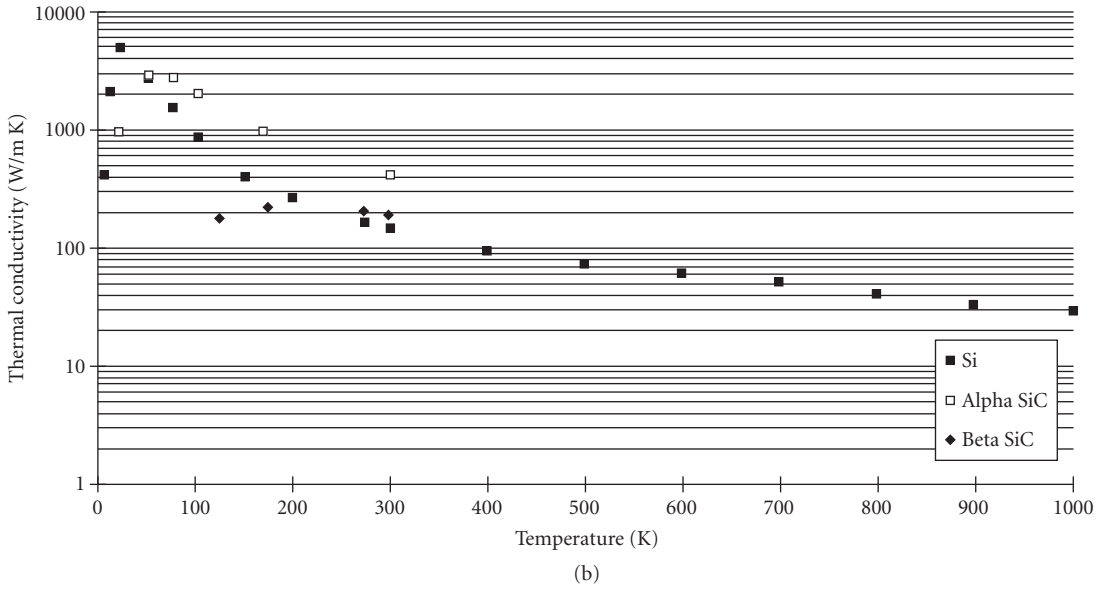
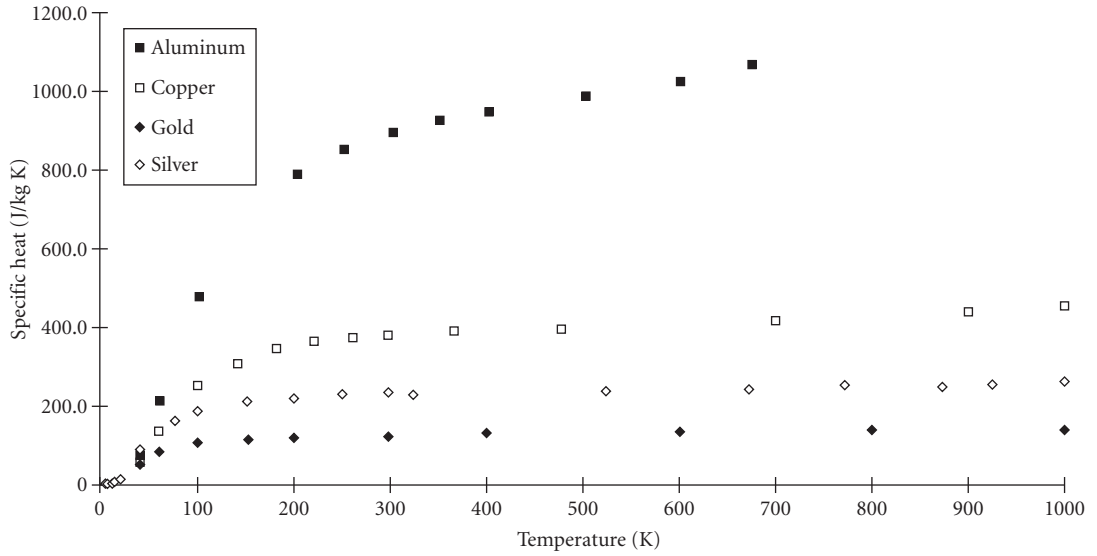


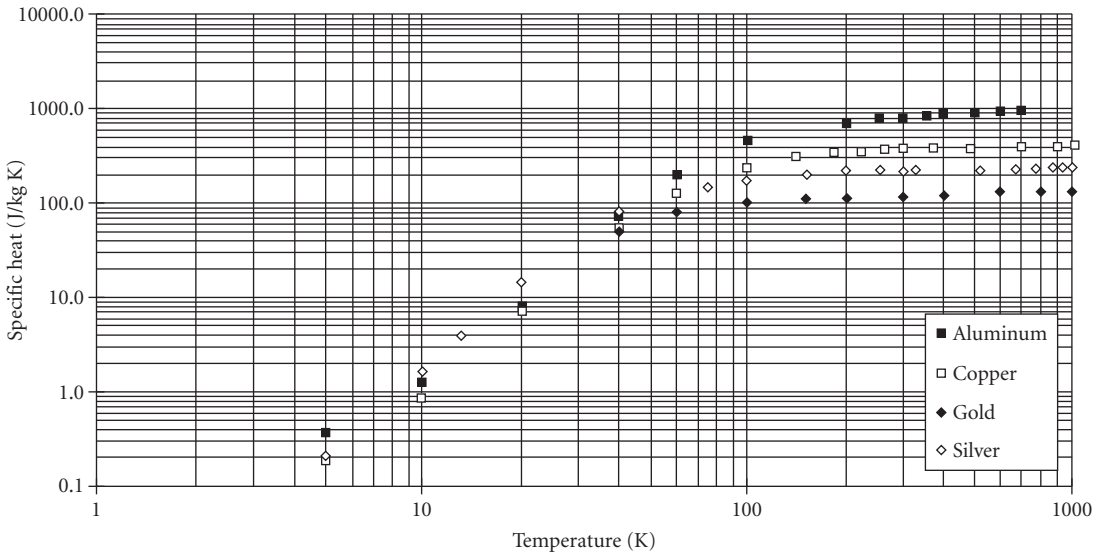
FIGURE 46 (Continued)





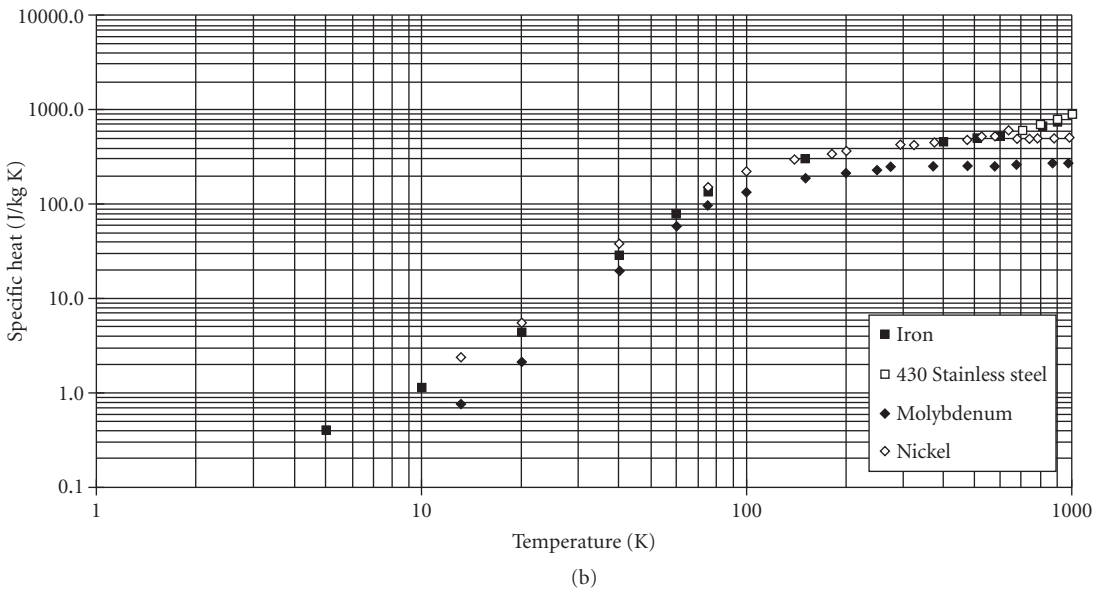
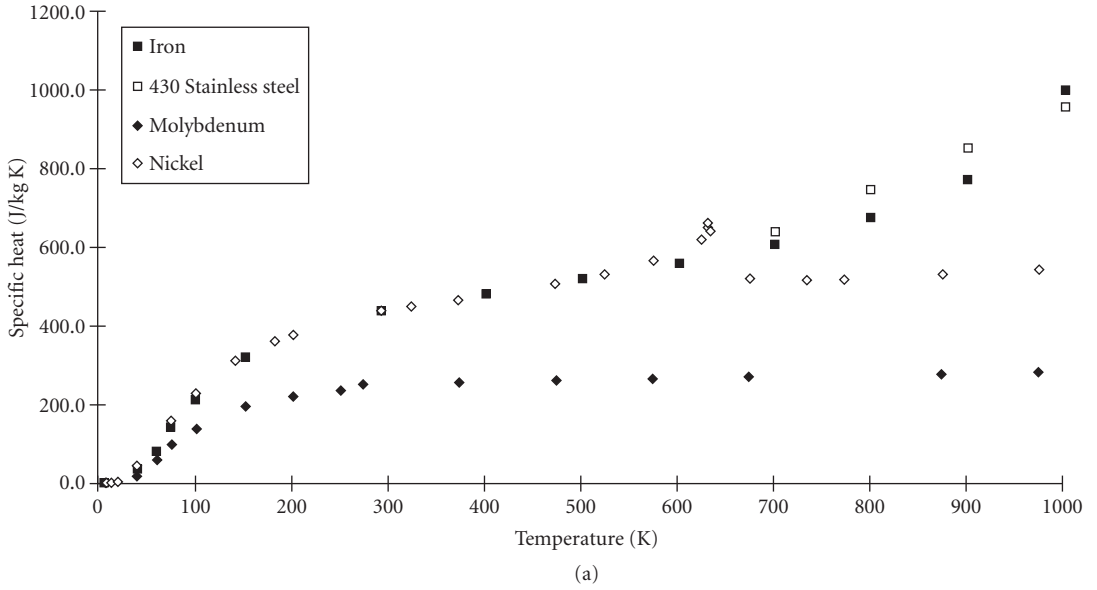


(a)



(b)

**FIGURE 47** Specific heat of aluminum,<sup>81,82</sup> copper,<sup>83</sup> gold,<sup>83</sup> and silver<sup>83</sup> vs. temperature.



**FIGURE 48** Specific heat of iron,<sup>83</sup> type 430 stainless steel,<sup>83</sup> molybdenum,<sup>83</sup> and nickel<sup>83</sup> vs. temperature.

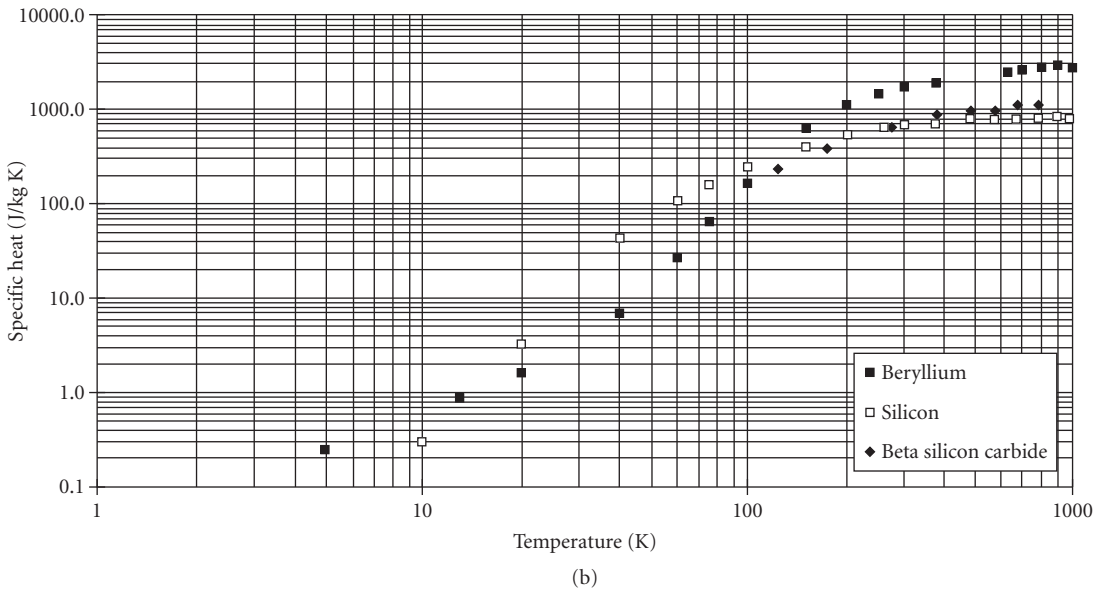
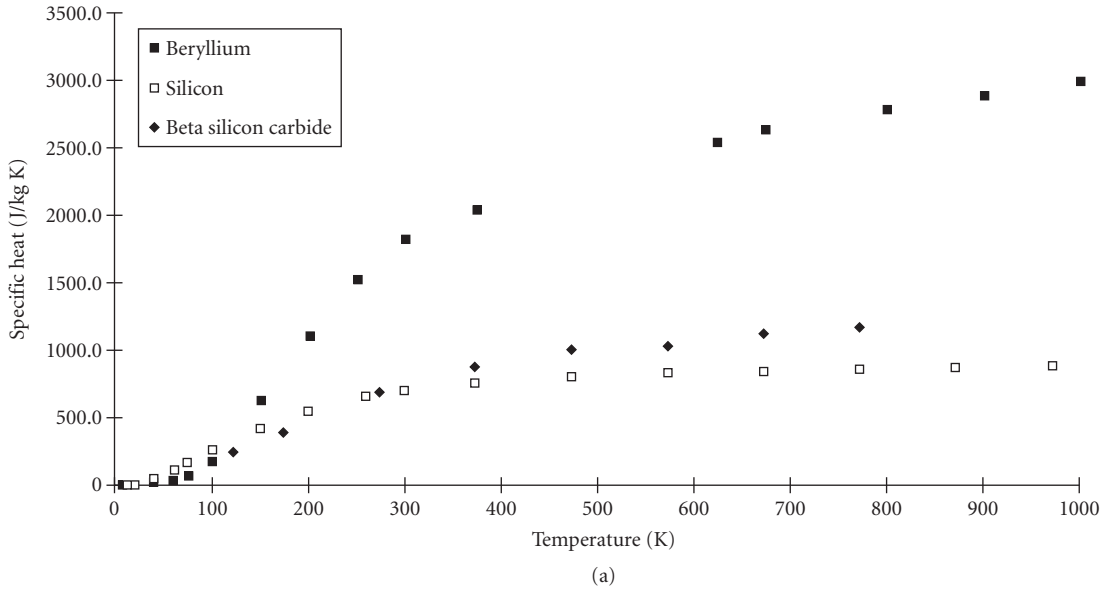


FIGURE 49 Specific heat of beryllium,<sup>73,83</sup> silicon,<sup>83</sup> and beta silicon carbide<sup>80</sup> vs. temperature.

**TABLE 13** Elastic Stiffness Constants for Selected Single Crystal Metals

Cubic Metals <sup>93</sup>	Elastic stiffness (GN/m <sup>2</sup> )				
	$C_{11}$	$C_{44}$	$C_{12}$		
Aluminum	108.0	28.3	62.0		
Chromium	346.0	100.0	66.0		
Copper	169.0	75.3	122.0		
Germanium	129.0	67.1	48.0		
Gold	190.0	42.3	161.0		
Iron	230.0	117.0	135.0		
Molybdenum	459.0	111.0	168.0		
Nickel	247.0	122.0	153.0		
Silicon	165.0	79.2	64.0		
Silicon carbide <sup>94</sup>	352.0	233.0	140.0		
Silver	123.0	45.3	92.0		
Tantalum	262.0	82.6	156.0		
Tungsten	517.0	157.0	203.0		
Hexagonal Metals	$C_{11}$	$C_{33}$	$C_{44}$	$C_{12}$	$C_{13}$
Beryllium <sup>95</sup>	288.8	354.2	154.9	21.1	4.7
Magnesium <sup>93</sup>	22.0	19.7	60.9	-7.8	-5.0
Silicon carbide <sup>94</sup>	500.0	521.0	168.0	98.0	

**Elastic Properties** The principal elastic stiffnesses  $C_{ij}$  of single crystals of some materials are given in Table 13. The three moduli and Poisson's ratio for polycrystalline materials are given in Table 14. These properties vary little with temperature, increasing temperature causing a gradual decrease in the moduli.

**TABLE 14** Elastic Moduli and Poisson's Ratio for Selected Polycrystalline Materials

Materials	Young's Modulus (GN/m <sup>2</sup> )	Shear Modulus (GN/m <sup>2</sup> )	Bulk Modulus (GN/m <sup>2</sup> )	Poisson's Ratio	Reference
Aluminum: 5086-O	71.0	26.4		0.33	84
Aluminum: 6061-T6	68.9	25.9		0.33	84
Beryllium: I-701-H	315.4	148.4	115.0	0.043	96
Copper	129.8	48.3	137.8	0.343	97
Germanium	79.9	29.6		0.32	97
Gold	78.5	26.0	171.0	0.42	97
Invar 36	144.0	57.2	99.4	0.259	97
Iron	211.4	81.6	169.8	0.293	97
Molybdenum	324.8	125.6	261.2	0.293	97
Nickel	199.5	76.0	177.3	0.312	97
Platinum	170.0	60.9	276.0	0.39	97
Silicon	113.0	39.7		0.42	97
Silicon carbide: CVD	461.0			0.21	80
Silicon carbide: reaction sintered	413.0			0.24	88
Silver	82.7	30.3	103.6	0.367	97
Stainless steel: 304	193.0	77.0		0.27	97
Stainless steel: 416	215.0	83.9	166.0	0.283	97
Stainless steel: 430	200.0	80.0		0.27	97
Tantalum	185.7	62.2	196.3	0.342	97
Tungsten	411.0	160.6	311.0	0.28	97

**TABLE 15** Strength and Fracture Properties for Selected Materials

Material	Yield Strength (MN/m <sup>2</sup> )	Microyield Strength (MN/m <sup>2</sup> )	Elongation (in 50 mm) %	Fracture Toughness (MN m <sup>-3/2</sup> )	Flexural Strength (MN/m <sup>2</sup> )	Hardness*	Reference
Aluminum: 5086-O	115.0	40.0	22.0	>25.0	—	55 HRB	84
Aluminum: 6061-T6	276.0	160.0	15.0	<25.0	—	95 HRB	84
Beryllium: I-70-H	276.0	30.0	4.0	12.0	—	80 HRB	84,85
Copper	195.0	12.0	42.0	—	—	10 HRB	84
Germanium	—	—	—	1.0	110.0	800 HK	84
Gold	125.0	—	30.0	—	—	30 HK	84
Invar 36	276.0	37.0	35.0	—	—	70 HRB	86
Molybdenum	600.0	—	40.0	—	—	150 HK	84
Nickel	148.0	—	47.0	—	—	109 HRB	84
Platinum	150.0	—	35.0	—	—	40 HK	84
Silicon	—	—	—	1.0	207.0	1150 HK	84
Silicon carbide: CVD	—	—	—	3.0	595.0	2500 HK	80
Silicon carbide: reaction sintered	—	—	—	2.0	290.0	2326 HK	88
Silver	130.0	—	47.0	—	—	32 HK	84
Stainless steel: 304	241.0	—	60.0	—	—	80 HRB	89
Stainless steel: 416	950.0	—	12.0	—	—	41 HRC	89
Stainless steel: 430	380.0	—	25.0	—	—	86 HRB	89
Tantalum	220.0	—	30.0	—	—	120 HK	84
Tungsten	780.0	—	2.0	—	—	350 HK	84

\*HK = Knoop (kg/mm<sup>2</sup>); HRB = Rockwell B; HRC = Rockwell C.

**Strength and Fracture Properties** The properties of tensile yield (at 0.2 percent offset), microyield strength, ductility (expressed as percent elongation in 50 mm), fracture toughness, flexural strength, and mechanical hardness are listed in Table 15. Most of these properties vary with temperature: strength and hardness decreasing, and fracture toughness and ductility increasing with temperature.

## 4.4 REFERENCES

- Center for Information and Numerical Data Analysis and Synthesis (CINDAS), Purdue Univ., 2595 Yeager Rd., W. Lafayette, IN 47906, (800) 428-7675.
- Optical Properties of Solids and Liquids (OPTROP), Sandia National Laboratory, Div. 1824, P.O. Box 5800, Albuquerque, NM 87185, (505) 844-2109.
- H. Wawrousek, J. H. Westbrook, and W. Grattideg (eds.), "Data Sources of Mechanical and Physical Properties of Engineering Materials," *Physik Daten/Physics Data*, No. 30-1, Fachinformationszentrum Karlsruhe, 1989.
- M. E. Lines, "Physical Properties of Materials: Theoretical Overview," in Paul Kloczek (ed.), *Handbook of Infrared Optical Materials*, Marcel Dekker, New York, 1991, pp. 1-69.
- N. F. Mott and H. Jones, *The Theory of The Properties of Metals and Alloys*, Dover, New York, 1958, pp. 105-125.
- A. V. Sokolov, *Optical Properties of Metals*, American Elsevier, New York, 1967.
- F. Wooten, *Optical Properties of Solids*, Academic Press, New York, 1972.
- M. Born and E. Wolf, *Principles of Optics*, 5th ed., Pergamon Press, London, 1975, pp. 611-627.

9. This discussion is adapted with permission from M. Bass, "Laser-Materials Interactions," in *Encyclopedia of Physical Science and Technology* **8**, Academic Press, New York, 1992, pp. 415–418.
10. F. Stern in F. Seitz and D. Turnbull (eds.), *Solid State Physics*, vol. 15, Academic Press, New York, 1963, pp. 300–324.
11. L. D. Landau and E. M. Lifshitz, *Electrodynamics of Continuous Media*, Addison-Wesley, Reading, Mass., 1965, pp. 257–284.
12. H. A. Lorentz, *The Theory of Electrons*, Dover, New York, 1952.
13. P. K. L. Drude, *Theory of Optics*, Dover, New York, 1959.
14. C. S. Barrett, *Structure of Metals*, 2d ed., McGraw-Hill, New York, 1952, pp. 521–537.
15. As reported by S. F. Jacobs in "Variable Invariables—Dimensional Instability with Time and Temperature," P. R. Yoder, Jr. (ed.), *Optomechanical Design*, Critical Reviews of Optical Science and Technology, **CR43**, SPIE Optical Engineering Press, Bellingham, Wash., 1992, p. 201.
16. C. Kittel, *Introduction to Solid State Physics*, 3d ed., Wiley, New York, 1966, pp. 111–129.
17. H. Reisman and P. S. Pawlik, *Elasticity*, Wiley, New York, 1980, pp. 128–135.
18. A. Kelly and N. H. Macmillan, *Strong Solids*, 3d ed., Clarendon Press, Oxford, 1986, pp. 382–393.
19. For more complete descriptions see, for example, *Metals Handbook*, 9th ed., **8**, Mechanical Testing, American Society for Metals, Metals Park, OH, 1985, pp. 1–15.
20. R. A. Paquin, "Selection of Materials and Processes for Metal Optics," in *Selected Papers on Optomechanical Design*, Proc. SPIE, Milestone Series, **770**:27–34 (1987).
21. D. Janeczko, "Metal Mirror Review," in R. Hartmann and W. J. Smith (eds.), *Infrared Optical Design*, Critical Reviews of Optical Science and Technology, **CR38**, SPIE Optical Engineering Press, Bellingham, Wash., 1991, pp. 258–280.
22. M. H. Krim, "Mechanical Design of Optical Systems for Space Operation," in P. R. Yoder, Jr. (ed.), *Optomechanical Design*, Critical Reviews of Optical Science and Technology, **CR43**, SPIE Optical Engineering Press, Bellingham, Wash., 1992, pp. 3–17.
23. P. R. Yoder, Jr. *Opto-Mechanical Systems Design*, 2d ed., Marcel Dekker, New York, 1993, pp. 1–41.
24. This analysis is the same as that used by many structural engineers such as the late G. E. Seibert of Perkin-Elmer and Hughes Danbury Optical Systems.
25. S. Timoshenko and S. Woinowsky-Kreiger, *Theory of Plates and Shells*, 2d ed., McGraw-Hill, New York, 1959, pp. 51–78.
26. P. K. Mehta, "Nonsymmetric Thermal Bowing of Curved Circular Plates," in A. E. Hatheway (ed.), *Structural Mechanics of Optical Systems II*, Proc. SPIE **748** (1987).
27. E. Pearson, "Thermo-elastic Analysis of Large Optical Systems," in P. R. Yoder, Jr. (ed.), *Optomechanical Design*, Critical Reviews of Optical Science and Technology, **CR43**, SPIE Optical Engineering Press, Bellingham, Wash., 1992, pp. 123–130.
28. C. W. Marschall and R. E. Maringer, *Dimensional Instability, an Introduction*, Pergamon, New York, 1977.
29. R. A. Paquin (ed.), "Dimensional Stability," Proc. SPIE **1335** (1990).
30. R. A. Paquin and D. Vukobratovich (eds.), "Optomechanics and Dimensional Stability," Proc. SPIE **1533** (1991).
31. R. A. Paquin, "Dimensional Instability of Materials; How Critical Is It in the Design of Optical Instruments?," in P. R. Yoder (ed.), *Optomechanical Design*, Critical Reviews of Optical Science and Technology, **CR43**, SPIE Optical Engineering Press, Bellingham, Wash., 1992, pp. 160–180.
32. Op. cit. Ref 23, pp. 271–320, 567–584.
33. E. D. Palik (ed.), *Handbook of Optical Constants of Solids*, Academic Press, Orlando, 1985.
34. E. D. Palik (ed.), *Handbook of Optical Constants of Solids II*, Academic Press, Orlando, 1991.
35. D. W. Lynch, "Mirror and Reflector Materials," in M. J. Weber (ed.), *CRC Handbook of Laser Science and Technology*, **IV**, Optical Materials, Part 2: Properties, CRC Press, Boca Raton, Florida, 1986.
36. J. H. Weaver, C. Krafka, D. W. Lynch, and E. E. Koch (eds.), "Optical Properties of Metals," Pts. 1 and 2, *Physik Daten/Physics Data*, Nos. 18-1 and 18-2, Fachinformationszentrum Karlsruhe, 1981.
37. D. Y. Smith, E. Shiles, and Mitio Inokuti, "The Optical Properties of Aluminum," in E. D. Palik (ed.), *Handbook of Optical Constants of Solids*, Academic Press, Orlando, 1985, pp. 369–406.

38. E. T. Arakawa, T. A. Callcott, and Y.-C. Chang, "Beryllium," in E. D. Palik (ed.), *Handbook of Optical Constants of Solids II*, Academic Press, Orlando, 1991, pp. 421–433.
39. D. W. Lynch and W. R. Hunter, in E. D. Palik (ed.), *Handbook of Optical Constants of Solids*, Academic Press, Orlando, 1985, pp. 275–367.
40. D. W. Lynch and W. R. Hunter, in E. D. Palik (ed.), *Handbook of Optical Constants of Solids II*, Academic Press, Orlando, 1991, pp. 341–419.
41. W. J. Choyke and E. D. Palik, "Silicon Carbide," in E. D. Palik (ed.), *Handbook of Optical Constants of Solids*, Academic Press, Orlando, 1985, pp. 587–595.
42. J. H. Weaver, D. W. Lynch, and R. Rossi, "Optical Properties of Single-Crystal Be from 0.12 to 4.5 eV," *Phys. Rev. B* **7**:3537–3541 (1973).
43. J. C. Stover, J. Rifkin, D. R. Cheever, K. H. Kirchner, and T. F. Schiff, "Comparison of Wavelength Scaling Data to Experiment," in R. P. Breault (ed.), *Stray Light and Contamination in Optical Systems*, *Proc. SPIE* **967**:44–49 (1988).
44. C. L. Vernold, "Application and Verification of Wavelength Scaling for Near Specular Scatter Predictions," in J. C. Stover (ed.), *Scatter from Optical Components*, *Proc. SPIE* **1165**:18–25 (1989).
45. J. E. Harvey, "Surface Scatter Phenomena: A Linear, Shift-Invariant Process," in J. C. Stover (ed.), *Scatter from Optical Components*, *Proc. SPIE* **1165**:87–99 (1989).
46. J. C. Stover, M. L. Bernst, D. E. McGary, and J. Rifkin, "An Investigation of Anomalous Scatter from Beryllium Mirrors," in J. C. Stover (ed.), *Scatter from Optical Components*, *Proc. SPIE* **1165**:100–109 (1989).
47. See also papers in the "Scatter from Be Mirrors" session in J. C. Stover (ed.), *Optical Scatter: Applications, Measurement, and Theory*, *Proc. SPIE* **1530**:130–230 (1991).
48. Y. S. Touloukian and D. P. DeWitt, "Thermal Radiative Properties, Metallic Elements and Alloys," vol. 7 in Y. S. Touloukian and C. Y. Ho (eds.), *Thermophysical Properties of Matter*, IFI/Plenum, New York, 1970.
49. Y. S. Touloukian and D. P. DeWitt, "Thermal Radiative Properties, Nonmetallic Solids," vol. 8 in Y. S. Touloukian and C. Y. Ho (eds.), *Thermophysical Properties of Matter*, IFI/Plenum, New York, 1971.
50. J. S. Browder, S. J. Ballard, and P. Klocek in Paul Klocek (ed.), *Handbook of Infrared Optical Materials*, Marcel Dekker, New York, 1991, pp. 155–426.
51. C. M. Egert, "Optical Properties of Aluminum, Beryllium, Silicon Carbide (and more)" in *Proc. of Al, Be, and SiC Optics Technologies Seminar*, MODIL, Oak Ridge National Lab., 1993.
52. W. D. Kimura and D. H. Ford, "Absorptance Measurement of Metal Mirrors at Glancing Incidence," *Appl. Optics* **25**:3740–3750 (1986).
53. M. Bass and L. Liou, "Calorimetric Studies of Light Absorption by Diamond Turned Ag and Cu Surfaces and Analyses Including Surface Roughness Contributions," *J. Appl. Phys.* **56**:184–189 (1984).
54. W. D. Kimura and T. T. Saito, "Glancing Incidence Measurements of Diamond Turned Copper Mirrors," *Appl. Optics* **26**:723–728 (1987).
55. M. Bass, D. Gallant, and S. D. Allen, "The Temperature Dependence of the Optical Absorption of Metals," in *Basic Optical Properties of Materials*, NBS SP574, U.S. Govt. Printing Office, Wash. D.C., 1980, pp. 48–50.
56. This discussion and Table 4 are based on the article: M. J. Berger and J. H. Hubbell, "Photon Attenuation Coefficients," in D. R. Lide (editor-in-chief), *CRC Handbook of Chemistry and Physics*, 74th ed., CRC Press, Boca Raton, Fla., 1993, pp. 10-282-10-286.
57. Op. cit., Ref. 49, p. 798.
58. D. R. Lide (editor-in-chief), *CRC Handbook of Chemistry and Physics*, 74th ed., CRC Press, Boca Raton, Fla., 1993, p. 10–299.
59. Op. cit., Ref. 49, p. 792.
60. Op. cit., Ref. 58, p. 10–298.
61. K. O. Ramanathan and S. H. Yen, "High-Temperature Emissivities of Copper, Aluminum, and Silver," *J. Opt. Soc. Am.* **67**:32–38 (1977).
62. E. A. Estalote and K. O. Ramanathan, "Low-Temperature Emissivities of Copper and Aluminum," *J. Opt. Soc. Am.* **67**:39–44 (1977).
63. K. O. Ramanathan, S. H. Yen, and E. A. Estalote, "Total Hemispherical Emissivities of Copper, Aluminum, and Silver," *Appl. Optics* **16**:2810–2817 (1977).

64. D. P. Verret and K. O. Ramanathan, "Total Hemispherical Emissivity of Tungsten," *J. Opt. Soc. Am.* **68**:1167–1172 (1978).
65. C. R. Roger, S. H. Yen, and K. O. Ramanathan, "Temperature Variation of Total Hemispherical Emissivity of Stainless Steel AISI 304," *J. Opt. Soc. Am.* **69**:1384–1390 (1979).
66. R. Smalley and A. J. Sievers, "The Total Hemispherical Emissivity of Copper," *J. Opt. Soc. Am.* **68**:1516–1518 (1978).
67. S. X. Cheng, P. Cebe, L. M. Hanssen, D. M. Riffe, and A. J. Sievers, "Hemispherical Emissivity of V, Nb, Ta, Mo, and W from 300 to 1000 K," *J. Opt. Soc. Am. B* **4**:351–356 (1987).
68. Op. cit. Ref. 5, p. 287.
69. Op. cit. Ref. 58, pp. 12–32–12–33.
70. Y. S. Touloukian et al. (eds.), *Thermophysical Properties of Matter, 1–13*, IFI/Plenum, New York, 1970–1977.
71. Y. S. Touloukian, R. K. Kirby, R. E. Taylor, and P. D. Desai, "Thermal Expansion, Metallic Elements and Alloys," vol. 12 in Y. S. Touloukian and C. Y. Ho (eds.), *Thermophysical Properties of Matter*, IFI/Plenum, New York, 1975, pp. 23 (Be), 77 (Cu), 125 (Au), 157 (Fe), 208 (Mo), 225 (Ni), 298 (Ag), 1028 (Al), 1138 (SS).
72. Y. S. Touloukian, R. K. Kirby, R. E. Taylor, and T. Y. R. Lee, "Thermal Expansion, Nonmetallic Solids," vol. 13 in Y. S. Touloukian and C. Y. Ho (eds.), *Thermophysical Properties of Matter*, IFI/Plenum, New York, 1977, pp. 154 (Si), 873 (SiC).
73. C. A. Swenson, "HIP Beryllium: Thermal Expansivity from 4 to 300 K and Heat Capacity from 1 to 108 K," *J. Appl. Phys.* **70**(6):3046–3051 (Sep 1991).
74. Z. Li and C. Bradt, "Thermal Expansion of the Cubic (3C) Polytype of SiC," *J. Mater. Sci.* **21**:4366–4368 (1986).
75. C. Y. Ho, R. W. Powell, and P. E. Liley, *Thermal Conductivity of Selected Materials*, NSRDS-NBS-8, National Standard Reference Data System—National Bureau of Standards, Part 1 (1966).
76. C. Y. Ho, R. W. Powell, and P. E. Liley, *Thermal Conductivity of Selected Materials*, NSRDS-NBS-16, National Standard Reference Data System—National Bureau of Standards, part 2 (1968).
77. Y. S. Touloukian, R. W. Powell, C. Y. Ho, and P. G. Klemens, "Thermal Conductivity, Metallic Elements and Alloys," vol. 1 in Y. S. Touloukian and C. Y. Ho (eds.), *Thermophysical Properties of Matter*, IFI/Plenum, New York, 1970.
78. Y. S. Touloukian, R. W. Powell, C. Y. Ho, and P. G. Klemens, "Thermal Conductivity, Nonmetallic Solids," vol. 2 in Y. S. Touloukian and C. Y. Ho (eds.), *Thermophysical Properties of Matter*, IFI/Plenum, New York, 1970.
79. D. H. Killpatrick, private communication, Feb. 1993.
80. "CVD Silicon Carbide," Technical Bulletin #107, Morton International Advanced Materials, 1991.
81. Op. cit. Ref. 58, p. 12–133.
82. E. A. Brandes and G. B. Brook (eds.), *Smithell's Metals Reference Book*, 7th ed., Butterworth Heinmann, Oxford, 1992, pp. 14–3–14–5.
83. Y. S. Touloukian and E. H. Buyco, "Specific Heat, Metallic Elements and Alloys," vol. 4 in Y. S. Touloukian and C. Y. Ho (eds.), *Thermophysical Properties of Matter*, IFI/Plenum, New York, 1970.
84. *Metals Handbook*, 2, 10th ed., Properties and Selection: Nonferrous Alloys and Special-Purpose Materials, ASM International, Metals Park, OH, 1990, pp. 93–94 and 102–103 (Al), 265 (Cu), 704–705 (Au), 1118–1129 (Fe), 1140–1143 (Mo), 441 (Ni), 1154–1156 (Si), and 699–700 & 1156–1158 (Ag).
85. I-70-H Optical Grade Beryllium Block, Preliminary Material Spec, Brush Wellman Inc., Nov. 1990.
86. *Carpenter Invar "36"*, Technical Data Sheet, Carpenter Technology Corp., Nov. 1980.
87. *Metals Handbook*, 5, 9th ed., Surface Cleaning, Finishing, and Coating, American Society for Metals, Metals Park, OH, 1982, pp. 223–229.
88. *Engineered Materials Handbook*, 4, Ceramics and Glasses, ASM International, Metals Park, OH, 1991, pp. 677, 806–808.
89. *Metals Handbook*, 1, 10th ed., Properties and Selection: Irons, Steels, and High Performance Alloys, ASM International, Metals Park, OH, 1990, p. 871.
90. *Materials Engineering, Materials Selector 1993*, Dec. 1992, p. 104.
91. D. L. Hibbard, "Dimensional Stability of Electroless Nickel Coatings," in R. A. Paquin (ed.), *Dimensional Stability, Proc. SPIE* **1335**:180–185 (1990).



92. G. A. Graves, private communication, Feb. 1993.
93. Op. cit. Ref. 82, pp. 15-5–15-7.
94. Z. Li and R. C. Bradt, "Thermal Expansion and Elastic Anisotropies of SiC as Related to Polytype Structure," in C. E. Selmer (ed.), *Proceedings of the Silicon Carbide 1987 Symposium 2*, Amer. Ceram. Soc, Westerville, OH, 1989, pp. 313–339.
95. W. D. Rowland and J. S. White, "The Determination of the Elastic Constants of Beryllium in the Temperature Range 25 to 300°C," *J. Phys. F: Metal Phys.* 2:231–236 (1972).
96. H. Ledbetter, private communication, Oct. 1987.
97. Op. cit., Ref. 82, pp. 15-2–15-3.

---

# OPTICAL PROPERTIES OF SEMICONDUCTORS

---

David G. Seiler

*Semiconductor Electronics Division  
National Institute of Standards and Technology  
Gaithersburg, Maryland*

Stefan Zollner

*Freescale Semiconductor, Inc.  
Hopewell Junction, New York*

Alain C. Diebold

*College of Nanoscale Science and Engineering  
University at Albany  
Albany, New York*

Paul M. Amirtharaj

*Sensors and Electron Devices Directorate  
U.S. Army Research Laboratory  
Adelphi, Maryland*

---

## 5.1 GLOSSARY

---

<b>A</b>	power absorption
<b>B</b>	magnetic field
<i>c</i>	velocity of light
<b>D</b>	displacement field
<i>d</i>	film thickness
<b>E</b>	applied electric field
$E_c$	energy, conduction band
$E_{ex}$	exciton binding energy
$E_g$	energy band gap
$E_H$	hydrogen atom ionization energy = 13.6 eV
<b>E</b>	electric field

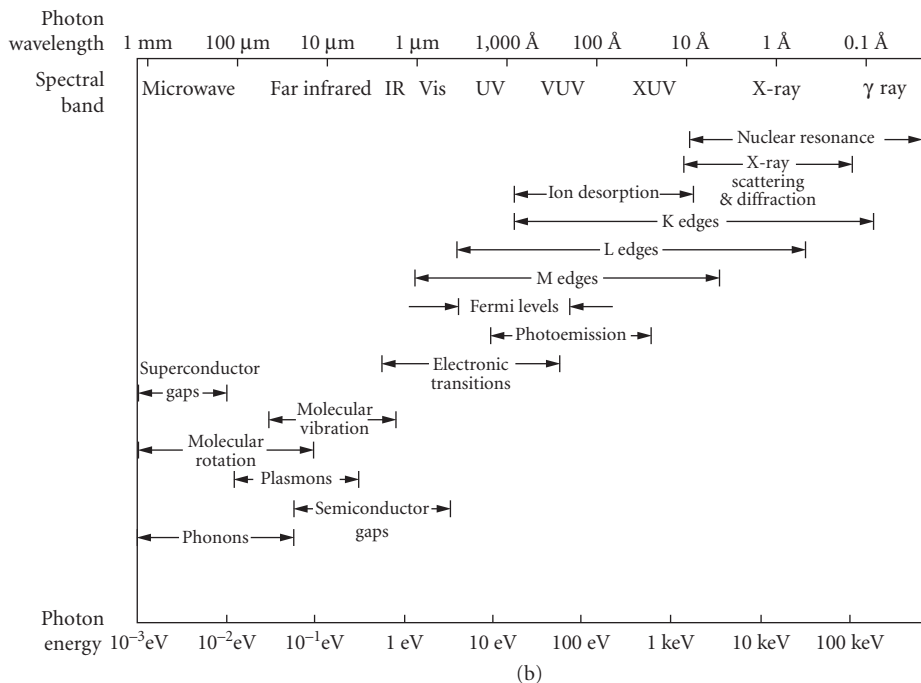
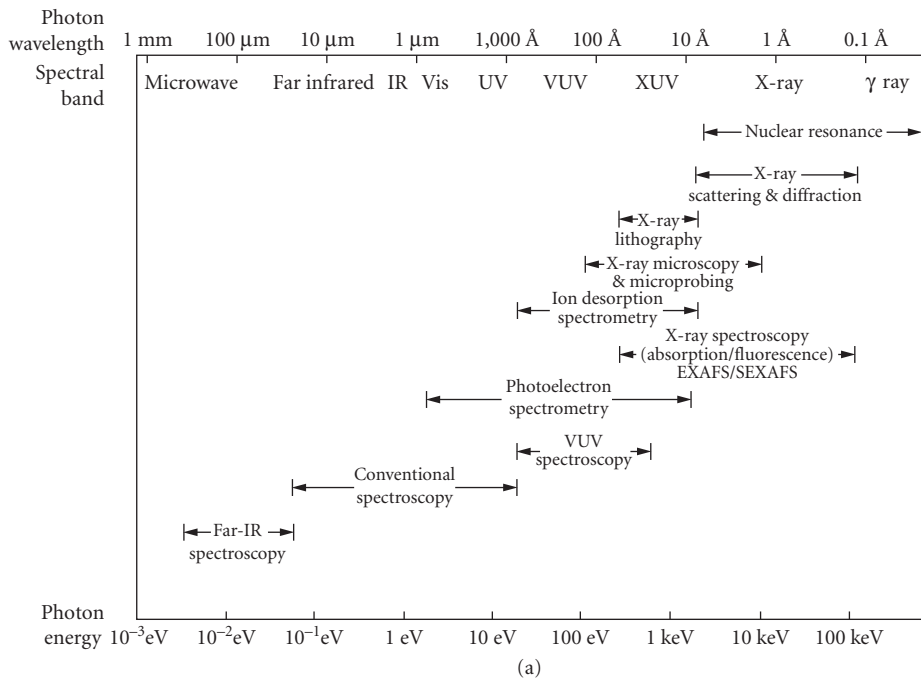
$E_n^\pm$	Landau level energy
$E_v$	energy, valence band
$e_I$	ionic charge
$g^*$	effective $g$ -factor
$\mathbf{K}$	phonon wave vector
$k$	extinction coefficient
$k_B$	Boltzmann's constant
$\mathbf{k}$	electron/hole wave vector
$L_\pm$	coupled LO phonon — plasmon frequency
$m_e^*$	electron effective mass
$m_h^*$	hole effective mass
$m_i$	ionic mass
$m_i'$	reduced ionic mass
$m_{\text{imp}}$	impurity ion mass
$m_l^*$	longitudinal effective mass
$m_o$	electron rest mass
$m_r$	electron-hole reduced mass
$m_t^*$	transverse effective mass
$N$	volume density
$n$	refractive index (real part)
$\tilde{n} = (n + ik)$	complex index of refraction
$\mathbf{P}$	polarization field
$\mathbf{q}$	photon wave vector
$R$	power reflection
$R_y$	effective Rydberg
$S$	oscillator strength
$T$	power transmission
$T$	temperature
$V$	Verdet coefficient
$\alpha$	absorption coefficient
$\alpha_{\text{AD}}$	absorption coefficient, allowed-direct transitions
$\alpha_{\text{AI}}$	absorption coefficient, allowed-indirect transitions
$\delta$	skin depth or penetration depth
$\gamma$	phenomenological damping parameter
$\Delta$	spin-orbit splitting energy
$\Gamma$	Brillouin zone center
$\epsilon$	dielectric function
$\epsilon_{\text{fc}}(\omega)$	free-carrier dielectric function
$\epsilon_{\text{imp}}(\omega)$	impurity dielectric function
$\epsilon_{\text{int}}(\omega)$	intrinsic dielectric function
$\epsilon_{\text{lat}}(\omega)$	lattice dielectric function
$\epsilon(0)$	static dielectric constant
$\epsilon_0$	free-space permittivity
$\epsilon_1$	Real( $\epsilon$ )
$\epsilon_2$	Im( $\epsilon$ )

$\epsilon_{\infty}$	high-frequency limit of dielectric function
$\eta$	impurity ion charge
$\lambda$	wavelength
$\lambda_c$	cut-off wavelength
$\mu$	mobility
$\mu_B$	Bohr magneton
$\nu$	frequency
$\sigma$	conductivity
$\tau$	scattering time
$\phi$	work function
$\chi$	susceptibility
$\chi^{(n)}$	induced nonlinear susceptibility
$\Omega$	phonon frequency
$\omega$	angular frequency
$\omega_c$	cyclotron resonance frequency
$\omega_{LO}$	longitudinal optical phonon frequency
$\omega_p$	free-carrier plasma frequency
$\omega_{pv}$	valence band plasma frequency
$\omega_{TO}$	transverse optical phonon frequency

## 5.2 INTRODUCTION

Rapid advances in semiconductor manufacturing and associated technologies have increased the need for optical characterization techniques for materials analysis and in situ monitoring/control applications. Optical measurements have many unique and attractive features for studying and characterizing semiconductor properties: (1) they are contactless, nondestructive, and compatible with any transparent ambient including high-vacuum environments; (2) they are capable of remote sensing, and hence are useful for in situ analysis on growth and processing systems; (3) the high lateral resolution inherent in optical systems may be harnessed to obtain spatial maps of important properties of the semiconductor wafers or devices; (4) combined with the submonolayer sensitivity of a technique such as ellipsometry, optical measurements lead to unsurpassed analytical details; (5) the resolution in time obtainable using short laser pulses allows ultrafast phenomena to be investigated; (6) the use of multichannel detection and high-speed computers can be harnessed for extremely rapid data acquisition and reduction which is crucial for real-time monitoring applications such as in situ sensing; (7) they provide information that complements transport analyses of impurity or defect and electrical behavior; (8) they possess the ability to provide long-range, crystal-like properties and hence support and complement chemical and elemental analyses; and (9) finally, most optical techniques are “table-top” procedures that can be implemented by semiconductor device manufacturers at a reasonable cost. All optical measurements of semiconductors rely on a fundamental understanding of their optical properties. In this chapter, a broad overview of the optical properties of semiconductors is given, along with numerous specific examples.

The optical properties of a semiconductor can be defined as any property that involves the interaction between electromagnetic radiation or light and the semiconductor, including absorption, diffraction, polarization, reflection, refraction, and scattering effects. The electromagnetic spectrum is an important vehicle for giving an overview of the types of measurements and physical processes characteristic of various regions of interest involving the optical properties of semiconductors. The electromagnetic spectrum accessible for studies by optical radiation is depicted in Fig. 1, where both the photon wavelengths and photon energies, as well as the common designations for



**FIGURE 1** The electromagnetic spectrum comprising the optical and adjacent regions of interest: (a) characterization techniques using optical spectroscopy and synchrotron radiation and (b) molecular, atomic, and electronic processes characteristic in various parts of the electromagnetic spectrum plotted as a function of photon energy.<sup>1</sup>

the spectral bands, are given.<sup>1</sup> Figure 1a shows the various techniques and spectroscopies and their spectral regions of applicability. Molecular, atomic, and electronic processes characteristic of various parts of the spectrum are shown in Fig. 1b. The high-energy x-ray, photoelectron, and ion desorption processes are important to show because they overlap the region of vacuum ultraviolet (VUV) spectroscopy. The ultraviolet (UV) region of the spectrum has often been divided into three rough regions: (1) the near-UV, between 2000 and 4500 Å; (2) the VUV, 2000 Å down to about 400 Å; and (3) the region below 400 Å covering the range of soft x-rays, 400 to 10 Å.<sup>2</sup> The spectrum thus covers a broad frequency range which is limited at the high-frequency end by the condition that  $\lambda \gg a$ , where  $\lambda$  is the wavelength of the light wave in the material and  $a$  is the interatomic distance. This limits the optical range to somewhere in the soft x-ray region. Technical difficulties become severe in the ultraviolet region (less than 100 nm wavelength, or greater than 12.3 eV photon energies), and synchrotron radiation produced by accelerators can be utilized effectively for ultraviolet and x-ray spectroscopy without the limitations of conventional laboratory sources. A lower limit of the optical frequency range might correspond to wavelengths of about 1 mm (photon energy of  $1.23 \times 10^{-3}$  eV). This effectively excludes the microwave and radio-frequency ranges from being discussed in a chapter on the optical properties of semiconductors.

From the macroscopic viewpoint, the interaction of matter with electromagnetic radiation is described by Maxwell's equations. The optical properties of matter are introduced into these equations as the constants characterizing the medium such as the dielectric constant, magnetic permeability, and electrical conductivity. (They are not actually "constants" since they vary with frequency.) From our optical viewpoint, we choose to describe the solid by the complex dielectric constant or complex dielectric function  $\epsilon(\omega)$ . This dielectric constant is a function of the space and time variables and should be considered as a response function or linear integral operator. The complex index of refractive index  $\tilde{n}$  is the complex square root of the dielectric function. Its real and imaginary parts are the refractive index  $n$  and the extinction coefficient  $k$ .

There are a number of methods for determining the optical constants of a semiconductor as a function of wavelength. Some of the most common techniques are as follows:

1. Measure the reflectivity at normal incidence *or* the transmission of a thin slab of known thickness over a wide wavelength range and use a Kramers-Kronig dispersion relation.
2. Measure the transmission of a thin slab of known thickness *and* the absolute reflectivity at normal incidence for a uniform bulk isotropic thin slab of known thickness with smooth surfaces (front and back).
3. Use a polarimetric method like ellipsometry which involves finding the ratio of reflectivities for polarizations perpendicular and parallel to the plane of incidence at a nonnormal incidence together with the difference of phase shifts upon reflection. With recent advancements in the availability of commercial ellipsometers, this is the most common method in use today.
4. Use detailed computer modeling and fitting of reflection, transmission, and/or ellipsometric measurements over a sufficiently large energy range. This method can also be applied in many circumstances to obtain the optical constants of anisotropic materials or thin films.
5. Calculate the band structure of a crystalline material using ab initio methods employing the local density approximation (LDA) with GW corrections (to correct the bandgap error usually found in LDA calculations). Integrate this band structure to determine the joint density of states weighted with the probability of optical transitions by the dipole operator matrix elements. If this technique is used, the Bethe-Salpeter equations need to be solved to take into account many-body excitonic effects (electron-hole interactions). Due to recent advances in computer technology, the accuracy of this method approaches the accuracy of measurements, especially if large samples with high quality cannot be obtained.

These optical constants describe an electromagnetic wave in the medium of propagation; the refractive index  $n$  gives the phase shift of the wave, and the extinction coefficient  $k$  gives the attenuation of the wave. In practice, one often uses the absorption coefficient  $\alpha$  instead of  $k$  because of Beer's law formalism describing the absorption.

The field of optical spectroscopy is a very important area of science and technology since most of our knowledge about the structure of atoms, molecules, and solids is based upon spectroscopic investigations. For example, studies of the line spectra of atoms in the late 1800s and early 1900s revolutionized our understanding of the atomic structure by elucidating the nature of their electronic energy levels. Similarly for the case of semiconductors, optical spectroscopy has proven essential to acquiring a systematic and fundamental understanding of the nature of semiconductors. Since the early 1950s, detailed knowledge about the various eigenstates present in semiconductors has emerged including energy bands, excitonic levels, impurity and defect levels, densities of states, energy-level widths (lifetimes), symmetries, and changes in these conditions with temperature, pressure, magnetic field, electric field, etc. One of the purposes of this chapter is to review and summarize the major optical measurement techniques that have been used to investigate the optical properties of semiconductors related to these features. Specific attention is paid to the types of information that can be extracted from such measurements of the optical properties.

Most optical properties of semiconductors are integrally related to the particular nature of their electronic and vibrational structures.<sup>3</sup> These electronic and vibrational dispersion relations are in turn related to the type of crystallographic structure, the particular atoms, and their bonding. The full symmetry of the space groups is also essential in determining the structure of the energy bands and vibrational modes. Group theory makes it possible to classify energy eigenstates, determine essential degeneracies, derive selection rules, and reduce the order of the secular determinants which must be diagonalized in order to compute approximate eigenvalues. Often, experimental measurements must be carried out to provide quantitative numbers for these eigenvalues. A full understanding of the optical properties of semiconductors is thus deeply rooted in the foundations of modern solid-state physics. In writing this chapter, the authors have assumed that the readers are familiar with some aspects of solid-state physics such as can be obtained from an advanced undergraduate course.

Most semiconductors have a diamond, zincblende, wurtzite, or rock-salt crystal structure. Elements and binary compounds, which average four valence electrons per atom, preferentially form tetrahedral bonds. A tetrahedral lattice site in a compound AB is one in which each atom A is surrounded symmetrically by four nearest neighboring B atoms. The most important lattices with a tetrahedral arrangement are the diamond, zincblende, and wurtzite lattices. In the diamond structure, all atoms are identical, whereas the zincblende structure contains two different atoms. The wurtzite structure is in the hexagonal crystal class, whereas the diamond and zincblende structures are cubic. Other lattices exist which are distorted forms of these, and many lattices have no relation to the tetrahedral structures.

Band structure calculations show that only the valence band states are important for predicting the following crystal ground-state properties: charge density, Compton profile, compressibility, cohesive energy, lattice parameter, x-ray emission spectra, and hole effective masses. In contrast, both the valence band and conduction band states are important for predicting the following properties: optical dielectric constant or refractive index, optical absorption spectrum, and electron effective masses. Further complexities arise because of the many-body nature of the particle interactions which necessitates understanding excitons, electron-hole droplets, polarons, polaritons, etc.

The optical properties of semiconductors cover a wide range of phenomena which are impossible to do justice to in just one short chapter in this *Handbook*. We have thus chosen to present an extensive, systematic overview of the field, with as many details given as possible. The definitions of the various optical properties, the figures chosen, the tables presented, and the references given all help to orient the reader to appreciate various principles and measurements that form the foundations of the optical properties of semiconductors.

The optical properties of semiconductors are often subdivided into those that are electronic and those that are vibrational (lattice related) in nature. The electronic properties concern processes involving the electronic states of the semiconductor, while the lattice properties involve vibrations of the lattice (absorption and creation of phonons). Lattice properties are of considerable interest for heat dissipation, electronic transport, and lifetimes (broadenings) of electronic states, but it is the electronic properties which receive the most attention in semiconductors

because of the technological importance of their practical applications. Modern-day semiconductor optoelectronic technologies include lasers, light-emitting diodes, photodetectors, optical amplifiers, modulators, switches, etc., all of which exploit specific aspects of the electronic optical properties.

Almost all of the transitions that contribute to the optical properties of semiconductors can be described as one-electron transitions. Most of these transitions conserve the crystal momentum and thus measure the vertical energy differences between the conduction and valence bands. In the one-electron approximation, each valence electron is considered as a single particle, moving in a potential which is the sum of the core potentials and a self-consistent Hartree potential of the other valence electrons.

The phenomena usually studied to obtain information on the optical properties of semiconductors are (1) absorption, (2) reflection or ellipsometry, (3) photoconductivity, (4) emission, (5) light scattering, and (6) modulation techniques. Most of the early information on the optical properties of semiconductors was obtained from measurements of photoconductivity, but these measurements can be complicated by carrier trapping, making interpretation of the results sometimes difficult. Thus, most quantitative measurements are of the type (1), (2), (4), or (5). For example, the most direct way of obtaining information about the energy gaps between band extrema and about impurity levels is by measuring the optical absorption over a wide range of wavelengths. This information can also be obtained by (2) and (4).

The transient nature of the optical properties of semiconductors is important to establish because it gives insight to the various relaxation processes that occur after optical excitation. Because of the basic limitations of semiconductor devices on speed and operational capacity, ultrafast studies have become an extremely important research topic to pursue. The push to extend the technologies in the optoelectronic and telecommunication fields has also led to an explosion in the development and rise of ultrafast laser pulses to probe many of the optical properties of semiconductors: electrons, holes, optical phonons, acoustic phonons, plasmons, magnons, excitons, and the various coupled modes (polaritons, polarons, excitonic molecules, etc.). The time scale for many of these excitations is measured in femtoseconds ( $10^{-15}$ ) or picoseconds ( $10^{-12}$ ). Direct time measurements on ultrafast time scales provide basic information on the mechanisms, interactions, and dynamics related to the various optical properties. Some of the processes that have been investigated are the carrier lifetime, the formation time of excitons, the cooling and thermalization rates of hot carriers, the lifetime of phonons, the screening of optical-phonon-carrier interactions, the dynamics of ballistic transport, the mechanism of laser annealing, dephasing processes of electrons and excitons, optical Stark effect, etc. It is not possible in this short review chapter to cover these ultrafast optical properties of semiconductors. We refer the reader to the many fine review articles and books devoted to this field.<sup>4,5</sup>

The advent of the growth of artificially structured materials by epitaxial methods such as molecular beam epitaxy (MBE) has made possible the development of a new class of materials and heterojunctions with unique electronic and optical properties. Most prominent among these are heterojunction quantum wells and superlattices. The field of microstructural physics has thus been one of the most active areas of research in the past decades. The novel properties of nanostructures fabricated from ultrathin layers of semiconductors of thicknesses  $<100 \text{ \AA}$  stem from microscopic quantum mechanical effects. The simplest case to visualize is that of a particle confined in a box which displays distinct quantum energy states, the equivalent of which are electrons and holes confined to a thin layer of a material such as GaAs sandwiched between two thick layers of AlAs. The new energy states produced by the confinement of the charges in the artificially produced potential well can be manipulated, by tailoring the size and shape of the well, to produce a wide variety of effects that are not present in conventional semiconductors. Microstructures formed from alternating thin layers of two semiconductors are called superlattices. They also lead to novel electronic and optical behaviors, most notable of which are large anisotropic properties. The ability to “engineer” the behavior of these nanostructures has led to an explosion of research and applications that is too large to be dealt with in this short review. The reader is referred to several review articles on their optical behavior.<sup>6,7</sup>



## 5.3 OPTICAL PROPERTIES

### Background

The interaction of the semiconductor with electromagnetic radiation can be described, in the semiclassical regime, using response functions such as  $\epsilon$  and  $\chi$  which are defined in the following section. The task of the description is then reduced to that of building a suitable model of  $\chi$  and  $\epsilon$  that takes into account the knowledge of the physical characteristics of the semiconductor and the experimentally observed optical behavior. One example of a particularly simple and elegant, yet surprisingly accurate and successful, model of  $\epsilon$  for most semiconductors is the linear-chain description of lattice vibrations.<sup>8</sup> This model treats the optical phonons (i.e., the vibrations that have an associated dipole moment) as damped simple harmonic motions. Even though the crystal is made up of  $\approx 10^{23}$  atoms, such a description with only a few resonant frequencies and phenomenological terms, such as the damping and the ionic charge, accurately accounts for the optical behavior in the far-infrared region. The details of the model are discussed in the following section “Optical/Dielectric Response.” Such simple models are very useful and illuminating, but they are applicable only in a limited number of cases, and hence such a description is incomplete.

A complete and accurate description will require a self-consistent quantum mechanical approach that accounts for the microscopic details of the interaction of the incident photon with the specimen and a summation over all possible interactions subject to relevant thermodynamical and statistical mechanical constraints. For example, the absorption of light near the fundamental gap can be described by the process of photon absorption resulting in the excitation of a valence band electron to the conduction band. In order to obtain the total absorption at a given energy, a summation has to be performed over all the possible states that can participate, such as from multiple valence bands. Many-body effects (the Coulomb attraction between the photoexcited electron and hole) also need to be considered for an accurate description. Thermodynamic considerations such as the population of the initial and final states have to be taken into consideration in the calculation as well. Hence, a detailed knowledge of the specimen and the photon-specimen interaction can, in principle, lead to a satisfactory description.

### Optical/Dielectric Response

*Optical Constants and the Dielectric Function* In the linear regime for an isotropic solid, the dielectric function  $\epsilon$  and the susceptibility  $\chi$  are defined by the following relations:<sup>9</sup>

$$\mathbf{D} = \epsilon_0 \mathbf{E} + \mathbf{P} \quad (1)$$

$$\mathbf{D} = \epsilon_0 (1 + \chi) \mathbf{E} \quad (2)$$

$$\mathbf{D} = \epsilon \mathbf{E} = (\epsilon_1 + i\epsilon_2) \mathbf{E} \quad (3)$$

where  $\mathbf{E}$ ,  $\mathbf{D}$ , and  $\mathbf{P}$  are the free-space electric field, the displacement field, and the polarization field inside the semiconductor;  $\epsilon_0$  is the permittivity of free space; and  $\epsilon$  and  $\chi$  are dimensionless quantities, each of which can completely describe the optical properties of semiconductors. The refractive index  $\tilde{n}$  of the material is related to  $\epsilon$  as shown below:

$$\tilde{n} = \sqrt{\epsilon} = n + ik \quad (4)$$

The real and imaginary parts of the refractive index,  $n$  and  $k$ , which are also referred to as the optical constants, embody the linear optical property of the material. The presence of  $k$ , the imaginary component, denotes absorption of optical energy by the semiconductor. Its relationship to the absorption Coefficient is discussed in the following section. “Reflection, Transmission, and Absorption coefficients.” In the spectral regions where absorptive processes are weak or absent, as in the case of the sub-bandgap range,  $k$  is very small, whereas in regions of strong absorption, the magnitude of  $k$  is large. The optical constants for a large number of semiconductors may be found in Refs. 10 and 11. The variation in the real part  $n$  is usually much smaller. For example, in GaAs, at room temperature, in the visible and near-visible region extending from 1.4 to 6 eV,  $k$  varies from  $<10^{-3}$  at 1.41 eV which is just below the gap, to a maximum of 4.1 at 4.94 eV.<sup>12</sup> In comparison,  $n$  remains nearly constant in the near-gap region extending from 3.61 at 1.4 eV to 3.8 at 1.9 eV, with the maximum and minimum values of 1.26 at 6 eV and 5.1 at 2.88 eV, respectively. The real and imaginary components are related by causal relationships that are also discussed in the following sections.

**Reflection, Transmission, and Absorption Coefficients** The reflection and transmission from a surface at normal incidence are given by

$$\tilde{r} = \frac{(\tilde{n}-1)}{(\tilde{n}+1)} = |\tilde{r}| \cdot \exp(i\theta) \quad (5)$$

$$R = |\tilde{r}|^2 \quad (6)$$

$$T = (1-R) \quad (7)$$

where  $\tilde{r}$  is the complex (Fresnel) reflection coefficient (consisting of a magnitude and a phase  $\theta$ ) and  $R$  and  $T$  are the reflectance and transmission, describing the ratio of the reflected and transmitted intensity relative to the incident intensity. For a thin slab, in free space, with thickness  $d$  and complex refractive index  $\tilde{n}$ , the appropriate expressions are:<sup>13</sup>

$$\tilde{r} = \frac{\tilde{r}_1 + \tilde{r}_2 \cdot \exp(i4\pi\tilde{n}d/\lambda)}{1 + \tilde{r}_1 \cdot \tilde{r}_2 \cdot \exp(i4\pi\tilde{n}d/\lambda)} \quad (8)$$

where  $\tilde{r}_1$  and  $\tilde{r}_2$  are the Fresnel reflection coefficients at the first and second interfaces, respectively, and  $\lambda$  is the free-space wavelength.

For most cases of optical absorption, the energy absorbed is proportional to the thickness of the specimen. The variation of intensity inside the absorptive medium is given by the following relationship:

$$I(x) = I(0) \cdot \exp(-\alpha \cdot x) \quad (9)$$

and the absorption coefficient  $\alpha$  is related to the optical constants by

$$\alpha = 4\pi k/\lambda \quad (10)$$

Here we note that  $\alpha$  (measured in  $\text{cm}^{-1}$ ) describes the attenuation of the radiation intensity rather than that of the electric field.

In spectral regions of intense absorption, all the energy that enters the medium is absorbed. The only part of the incident energy that remains is that which is reflected at the surface. In such a case, it is useful to define a characteristic “skin” thickness that is subject to an appreciable density of optical energy. A convenient form used widely is simply the inverse of  $\alpha$ ; that is,  $1/\alpha$ . This skin depth (or penetration length) is usually denoted by  $\delta$ :

$$\delta = \frac{1}{\alpha} \quad (11)$$

The skin depths in semiconductors range from  $>100$  nm near the bandgap to  $<5$  nm at the higher energies of  $\approx 6$  eV.

**Kramers-Kronig Relationships** A general relationship exists for linear systems between the real and imaginary parts of a response function as shown in the following:

$$\varepsilon_1(\omega) = 1 + \frac{2}{\pi} P \int_0^{\infty} \frac{\omega' \varepsilon_2(\omega')}{\omega'^2 - \omega^2} d\omega' \quad (12)$$

$$\varepsilon_2(\omega) = -\frac{2\omega}{\pi} P \int_0^{\infty} \frac{\varepsilon_1(\omega') d\omega'}{\omega'^2 - \omega^2} + \frac{\sigma_0}{\varepsilon_0 \cdot \omega} \quad (13)$$

where  $\sigma_0$  is the dc conductivity.

$$n(\omega) = 1 + \frac{2}{\pi} P \int_0^{\infty} \frac{\omega' k(\omega')}{\omega'^2 - \omega^2} d\omega' \quad (14)$$

$$k(\omega) = -\frac{2}{\pi} P \int_0^{\infty} \frac{n(\omega')}{\omega'^2 - \omega^2} d\omega' \quad (15)$$

where  $P$  denotes the principal part of the integral. These are referred to as the Kramers-Kronig dispersion relationships.<sup>14,15</sup> An expression of practical utility is one in which the experimentally measured reflectance  $R$  at normal incidence is explicitly displayed as shown:

$$\theta(\omega) = -\frac{\omega}{\pi} P \int_0^{\infty} \frac{\ln(R(\omega'))}{\omega'^2 - \omega^2} d\omega' \quad (16)$$

This is useful since it shows that if  $R$  is known for all frequencies, the phase  $\theta$  of the Fresnel reflection coefficient can be deduced, and hence a complete determination of both  $n$  and  $k$  can be accomplished. In practice,  $R$  can be measured only over a limited energy range, but approximate extrapolations can be made to establish reasonable values of  $n$  and  $k$ .

The measurement of the reflectivity over a large energy range spanning the infrared to the vacuum ultraviolet, 0.5 to 12 eV range, followed by a Kramers-Kronig analysis, used to be the main method of establishing  $n$  and  $k$ .<sup>16</sup> However, the advances in spectroscopic ellipsometry in the past 20 years have made this obsolete in all but the highest energy region. A Kramers-Kronig analysis of reflectance data also has experimental difficulties related to surface roughness and native oxides, which are more easily corrected with ellipsometry than with reflectivity measurements. The Kramers-Kronig relations are still important today, since they place consistency conditions on optical constants determined from ellipsometry.

Above 12 eV, the higher energy reflectance is dominated by the valence band plasma edge  $\omega_{pV}$  and, hence, takes the following forms for  $\varepsilon(\omega)$ ,  $\tilde{n}(\omega)$ , and  $R(\omega)$ :

$$\tilde{n} = \sqrt{\varepsilon(\omega)} \approx -\frac{1}{2} \cdot \left( \frac{\omega_{\text{PV}}^2}{\omega^2} \right) \quad (17)$$

$$R(\omega) = \frac{(n(\omega)-1)}{(n(\omega)+1)} = \frac{1}{16} \cdot \left( \frac{\omega_{\text{PV}}^4}{\omega^4} \right) \quad (18)$$

**Sum Rules** Having realized the interrelationships between the real and imaginary parts of the response functions, one may extend them further using a knowledge of the physical properties of the semiconductor to arrive at specific equations, commonly referred to as sum rules.<sup>14,15</sup> These equations are useful in cross-checking calculations and measurements for internal consistency or reducing the computational effort. Some of the often-used relations are shown below:

$$\int_0^{\infty} \omega \varepsilon_2(\omega) d\omega = \frac{\pi}{2} \omega_{\text{PV}}^2 \quad (19)$$

$$\int_0^{\infty} \omega \operatorname{Im} \left[ \frac{-1}{\varepsilon(\omega)} \right] d\omega = \frac{\pi}{2} \omega_{\text{PV}}^2 \quad (20)$$

$$\int_0^{\infty} \omega k(\omega) \cdot d\omega = \frac{\pi}{4} \omega_{\text{PV}}^2 \quad (21)$$

$$\int_0^{\infty} [n(\omega) - 1] d\omega = 0 \quad (22)$$

where  $\omega_{\text{PV}}$  is the valence band plasma frequency.

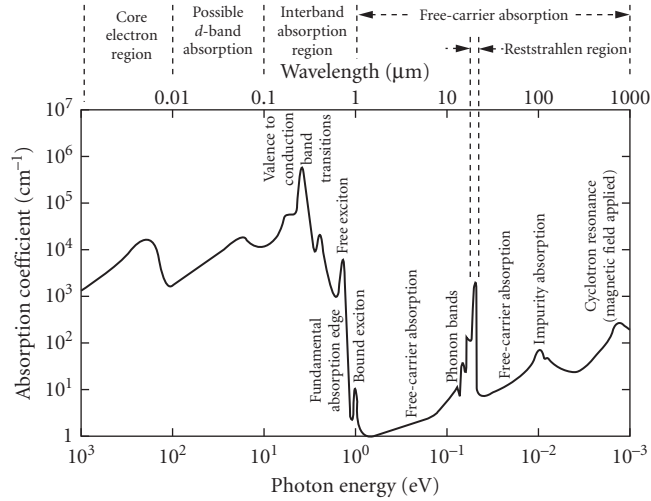
The dc static dielectric constant,  $\varepsilon(0)$ , may be expressed as

$$\varepsilon(0) = 1 + \frac{2}{\pi} \int_0^{\infty} \frac{\varepsilon_2(\omega)}{\omega} \cdot d\omega \quad (23)$$

The reader is referred to Refs. 14 and 15 for more details.

## Linear Optical Properties

**Overview** The optical properties of semiconductors at low enough light levels are often referred to as linear properties in contrast to the nonlinear optical properties described later. There are many physical processes that control the amount of absorption or other optical properties of a semiconductor. In turn, these processes depend upon the wavelength of radiation, the specific properties of the individual semiconductor being studied, and other external parameters such as pressure, temperature, etc. Just as the electrical properties of a semiconductor can be controlled by purposely introducing impurity dopants (both *p* and *n* type) or affected by unwanted impurities or defects, so too are the optical properties affected by them. Thus, one can talk about *intrinsic* optical properties of semiconductors that depend upon their perfect crystalline nature and *extrinsic* properties that are introduced by impurities or defects. Many types of defects exist in real solids: point defects, macroscopic structural defects, etc. In this section we review and summarize intrinsic linear optical properties related to lattice effects, interband transitions, and free-carrier or intraband transitions. Impurity- and defect-related extrinsic optical properties are also covered in a separate section and in the discussion of lattice properties affected by them. Figure 2 schematically depicts



**FIGURE 2** Absorption spectrum of a typical semiconductor showing a wide variety of optical processes.

various contributions to the absorption spectrum of a typical semiconductor as functions of wavelength (top axis) and photon energy (bottom axis). Data for a real semiconductor may show more structure than shown here. On the other hand, some of the structure shown may be reduced or not actually present in a particular semiconductor (e.g., impurity absorption, bound excitons,  $d$ -band absorption). Table 1 shows the classification of the optical responses of the semiconductor to light in various wavelength regions showing the typical origin of the response and how the measurements are usually carried out. At the longest wavelengths shown in Fig. 2, cyclotron resonance (CR) may occur for a semiconductor in a magnetic field, giving rise to an absorption peak corresponding to a transition of a few meV energy between Landau levels. Shallow impurities may give rise to additional absorption at low temperatures, and here a 10 meV ionization energy has been assumed. If the temperature was high enough so that  $k_B T$  was greater than the ionization energy, the absorption peak would be washed out. At wavelengths between 5 and 50  $\mu\text{m}$ , a new set of absorption peaks arises due to the vibrational modes of the lattice. In ionic crystals, the absorption coefficient in the reststrahlen region may reach  $10^5 \text{ cm}^{-1}$ , whereas in homopolar semiconductors like Si and Ge, only multiphonon features with lower absorption coefficients are present (around 5 to 50  $\text{cm}^{-1}$ ).

*Models of the dielectric function* The interaction of light with semiconductors can be completely described by the dielectric function,  $\epsilon(\omega)$ . The dielectric function  $\epsilon(\omega)$  may be divided into independent parts to describe various physical mechanisms so long as the processes do not interact strongly with each other; this is an approximation, referred to as the adiabatic approximation which simplifies the task at hand considerably.<sup>17</sup> The major players that determine the optical behavior of an intrinsic semiconductor are the lattice, particularly in a nonelemental semiconductor; the free carriers (i.e., mobile electrons and holes) and the interband transitions between the energy states available to the electrons. These three mechanisms account for the intrinsic linear properties that lead to a dielectric function as shown:

$$\epsilon_{\text{int}}(\omega) = \epsilon_{\text{lat}}(\omega) + \epsilon_{\text{fc}}(\omega) + \epsilon_{\text{inter}}(\omega) \quad (24)$$

The addition of impurities and dopants that are critical to controlling the electronic properties leads to an additional contribution, and the total dielectric response may then be described as shown:

$$\epsilon(\omega) = \epsilon_{\text{int}}(\omega) + \epsilon_{\text{imp}}(\omega) \quad (25)$$

**TABLE 1** Classification by Wavelength of the Optical Responses for Common Semiconductors

Wavelength (nm)	Responses	Physical Origin	Application	Measurement Tech.
$\lambda > \lambda_{\text{TO}}$ Far-IR and micro wave region	Microwave <i>R</i> and <i>T</i> Plasma <i>R</i> and <i>T</i>	Free-carrier plasma	Detectors Switches	<i>R</i> , <i>T</i> , and <i>A</i> * Microwave techniques Fourier Transform Spectrometry (FTS), FT-SE
$\lambda_{\text{LO}} < \lambda < \lambda_{\text{TO}}$ Reststrahlen region	Reststrahlen <i>R</i>	Optical phonons in ionic crystals	Absorbers Filters	<i>R</i> , <i>T</i> , and <i>A</i> FTS & Dispersion spectrometry (DS), FT-SE
$\lambda \sim \lambda_{\text{LO}}, \lambda_{\text{TO}}, \lambda_{\text{P}}$ Far-IR region	Far-IR <i>A</i>	Optical phonons, impurities (vibrational and electronic), free carriers, intervalence transitions	Absorbers Filters	<i>R</i> , <i>T</i> , and <i>A</i> FTS, DS, and FT-SE
$\lambda_{\text{LO}} > \lambda > \lambda_{\text{G}}$ Mid-IR region	Mid-IR <i>T</i> and <i>A</i>	Multiphonon, multiphoton transitions, impurities (vibrational and electronic), intervalence transitions excitons, Urbach tail	Detectors Switches Absorbers Filters	<i>R</i> , <i>T</i> , and <i>A</i> Ellipsometry FTS and DS
$\lambda < \lambda_{\text{G}}$ IR, visible, and UV	<i>R</i> , <i>T</i> , and <i>A</i>	Electronic interband transitions	Reflectors Detectors	Reflection Ellipsometry
$\lambda \sim \lambda_{\text{W}}$ UV, far-UV	Photoemission	Fermi energy to vacuum-level electronic transitions	Photocathodes Detectors	High-vacuum spectroscopy techniques, UV ellipsometry
$\lambda_{\text{W}} > \lambda > \geq a$	<i>R</i> , <i>T</i> , and <i>A</i>  Diffraction	Ionic-core transitions  Photo—ionic-core interactions	Detectors  X-ray optics and monochromators	Soft x-ray and synchrotron- based analyses  X-ray techniques

\**R*, *T*, and *A*—Reflection, transmission, and absorption. SE—Spectroscopic ellipsometry.

Note: P—Plasma; G—Energy gap; W—Work functions; *a*—lattice constant.

TO, LO—Transverse and longitudinal optical phonons.

### Lattice Absorption

**Phonons** The dc static response of a semiconductor lattice devoid of free charges to an external electromagnetic field may be described by the single real quantity  $\epsilon(0)$ . As the frequency of the electromagnetic radiation increases and approaches the characteristic vibrational frequencies associated with the lattice, strong interactions can occur and modify the dielectric function substantially. The main mechanism of the interaction is the coupling between the electromagnetic field with the oscillating dipoles associated with vibrations of an ionic lattice.<sup>8</sup> The interactions may be described, quite successfully, by treating the solid to be a collection of damped harmonic oscillators with a characteristic vibrational frequency  $\omega_{\text{TO}}$  and damping constant  $\gamma$ . The resultant dielectric function may be written in the widely used CGS units as:

$$\epsilon_{\text{lat}}(\omega) = \epsilon(\infty) + \frac{S\omega_{\text{TO}}^2}{(\omega_{\text{TO}}^2 - \omega^2 - i\omega\gamma)} \quad (26)$$

where *S* is called the oscillator strength and may be related to the phenomenological ionic charge  $e_p$ , reduced mass  $m'_i$ , and volume density *N*, through the equation

$$S\omega_{\text{TO}}^2 = \frac{4\pi N e_i^2}{m'_i} \quad (27)$$

In the high frequency limit of  $\varepsilon(\omega)$ , for  $\omega \gg \omega_{\text{TO}}$ , (but well below the onset of interband absorption)

$$\varepsilon(\omega) \rightarrow \varepsilon_{\infty} \quad (28)$$

The relationship may be easily extended to accommodate more than one characteristic vibrational frequency by summing over all phonon modes  $i$ :

$$\varepsilon_{\text{lat}}(\omega) = \varepsilon_{\infty} + \sum_i \frac{S_i (\omega_{\text{TO}}^i)^2}{[(\omega_{\text{TO}}^i)^2 - \omega^2 - i\omega\gamma^i]} \quad (29)$$

It is worth noting some important physical implications and interrelations of the various parameters in Eq. (26).

For a lattice with no damping, it is obvious that  $\varepsilon(\omega)$  displays a pole at  $\omega_{\text{TO}}$  and a zero at a well-defined frequency, usually referred to by  $\omega_{\text{LO}}$ . A simple but elegant and useful relationship exists between these parameters as shown by

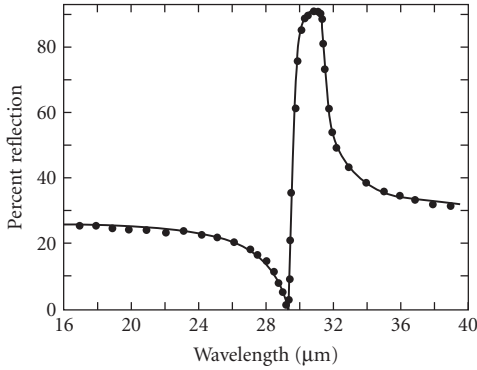
$$\frac{\varepsilon(0)}{\varepsilon_{\infty}} = \left( \frac{\omega_{\text{LO}}}{\omega_{\text{TO}}} \right)^2 \quad (30)$$

which is known as the Lyddane-Sachs-Teller relation.<sup>18</sup>

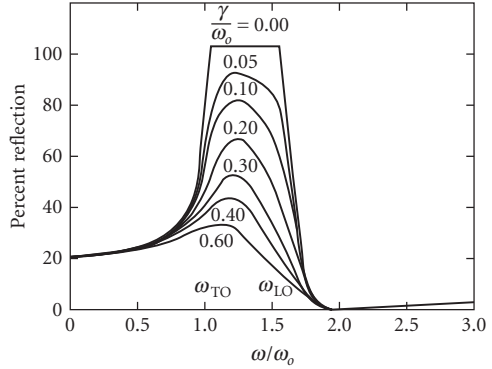
The physical significance of  $\omega_{\text{TO}}$  and  $\omega_{\text{LO}}$  is that these are the transverse and longitudinal optical phonon frequencies with zero wave vector,  $\mathbf{K}$ , supported by the crystal lattice. The optical vibrations are similar to standing waves on a string. The wave pattern, combined with the ionic charge distribution, leads to oscillating dipoles that can interact with the incident radiation and, hence, the name optical phonons.  $\varepsilon(\omega)$  is negative for  $\omega_{\text{TO}} \geq \omega \geq \omega_{\text{LO}}$ , which implies no light propagation inside the crystal and, hence, total reflection of the incident light. The band of frequencies spanned by  $\omega_{\text{TO}}$  and  $\omega_{\text{LO}}$  is referred to as the reststrahlen band.

The reflectivity spectrum of AlSb<sup>19</sup> is shown in Fig. 3. It is representative of the behavior of most semiconductors. Note that the reflectivity is greater than 90 percent at  $\approx 31 \mu\text{m}$  in the reststrahlen band spanned by the longitudinal and transverse optical phonons. The two asymptotic limits of the reflection tend to  $[(\sqrt{\varepsilon(0)}-1)/(\sqrt{\varepsilon(0)}+1)]^2$  and  $[(\sqrt{\varepsilon_{\infty}}-1)/(\sqrt{\varepsilon_{\infty}}+1)]^2$ , respectively, compare Eqs. (5) and (6). The effects of the phonon damping are illustrated in Fig. 4.<sup>20</sup> For the ideal case with zero damping, the reflection in the reststrahlen band is 100 percent. Since absolute reflectance measurements are very difficult to carry out experimentally, the reststrahlen region is nowadays often investigated with infrared ellipsometry. Note that for the elemental semiconductors such as Si and Ge, the lack of a dipole moment associated with the optical vibrations of the lattice leads to the absence of any oscillator strength and hence no interaction with the radiation. The reflection spectrum will, therefore, show no change at or near the optical phonon frequencies. The optical phonon frequencies ( $\omega_{\text{LO}}$  and  $\omega_{\text{TO}}$ ) and wavelengths and  $\varepsilon(0)$  and  $\varepsilon_{\infty}$  for the commonly known semiconductors are presented at the end of this chapter in Table 11. For elemental semiconductors,  $\varepsilon(0) = \varepsilon_{\infty}$ .

The optical phonons  $\omega_{\text{LO}}$  and  $\omega_{\text{TO}}$  are the frequencies of interest for describing the optical interactions with the lattice. In addition, the lattice is capable of supporting vibrational modes over a wide range of frequencies extending from 0 to  $\omega_{\text{LO}}(\Gamma)$ , the LO phonon frequency at the center of the Brillouin zone,  $\Gamma$ , as discussed by Cochran in Ref. 21. The vibrational modes can be subdivided into two major categories. The first are optical phonons that possess an oscillating dipole moment and therefore can interact with light. The second group is the acoustic phonons; that is, sound-like vibrations that do not possess a dipole moment and hence are not of primary importance in



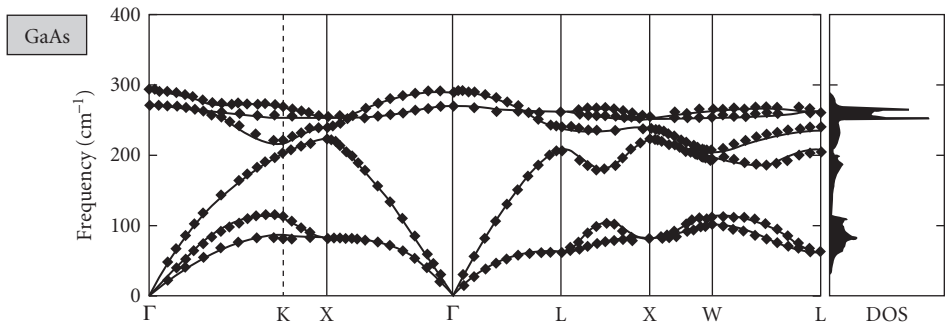
**FIGURE 3** Reststrahlen reflection spectrum of AlSb.<sup>19</sup>



**FIGURE 4** Reflection spectra of a damped oscillator for various values of the damping factor.<sup>20</sup>

determining the optical properties. For the optical band, only the  $\mathbf{K} \approx 0$  modes are important since a strong interaction is precluded for other modes due to the large mismatch in the wave vectors associated with the light and vibrational disturbances.

The simple treatment so far, though very useful, is limited to the most obvious and strongest aspect of the interaction of light with the lattice. However, many weaker but important interaction mechanisms have not yet been accounted for. An attempt to produce a complete description starts with the consideration of the total number of atoms  $N$  that makes up the crystal. Each atom possesses three degrees of freedom, and hence one obtains  $3N$  degrees of freedom for the crystal, a very large number of magnitude,  $\approx 10^{24}$ . The complexity of the description can be readily reduced when one realizes the severe restriction imposed by the internal symmetry of the crystal. The vibrational characteristics now break up into easily understandable normal modes with well-defined physical characteristics. The translational symmetry associated with the crystal makes it possible to assign a definite wave vector to each lattice mode. In addition, the phonons can be divided into two major classes: the optical vibrations, which we have already discussed, and the acoustic vibrations, which, as the name implies, are sound-like vibrations. The acoustic phonons for  $|\mathbf{K}| \rightarrow 0$  are identical to the sound waves. Hence, specifying the type of phonon, energy, wave vector, and polarization uniquely describes each vibrational mode of the crystal. The conventional description of phonons is achieved by graphically displaying these properties in a frequency versus  $\mathbf{K}$  plot, as shown in Fig. 5 for GaAs.<sup>22</sup>



**FIGURE 5** Phonon dispersion curves of GaAs. Experimental data are represented by symbols. Solid lines show the results of the calculation of Gianozzi et al.<sup>22</sup>



The energies of the phonons are plotted as a function of the wave vector along the high-symmetry directions for each acoustic and optical branch. It can be shown that the number of acoustic branches is always three, two of transverse polarization and one longitudinal, leaving  $3p-3$  optical branches, where  $p$  is the number of atoms in the primitive cell. The majority of the most important semiconductors fall into the three cubic classes of crystals—namely, the diamond, zincblende, and the rock-salt structures that contain two atoms per primitive cell and hence possess three acoustic and three optical branches each.<sup>23</sup> However, more complicated structures with additional optical phonon branches can be found. The most important group among the second category is the wurtzite structure displayed by CdS, CdSe, GaN, InN, AlN, etc., which contains four atoms in the primitive cell and hence two additional sets of optical phonon branches.<sup>23</sup> The specific symmetry associated with the vibrational characteristics of each mode is used to distinguish them as well as their energies at the high-symmetry points in the phonon dispersion curves.

*Multiphonon absorption* It has already been pointed out that the interaction of light with phonons is restricted to those with  $\mathbf{K} \approx 0$ . This is true only when single-phonon interactions are considered in ideal crystals. Higher-order processes, such as multiphonon absorption, can activate phonons with  $\mathbf{K} \neq 0$ .<sup>23,24</sup> Symmetry considerations and their implication on the multiphonon absorption are discussed by Birman in Ref. 25. In multiphonon processes, the total momentum of the interacting phonons will be 0, but many modes with  $\mathbf{K} \neq 0$  can participate in the interaction.

The energy and momentum conservation conditions may be expressed as follows:

$$\hbar\omega = \sum_i \hbar\Omega_i \quad (31)$$

$$\hbar\mathbf{q} = \sum_i \hbar\mathbf{K}_i \approx 0 \quad (32)$$

where  $\hbar\omega$  is the energy of the absorbed photon,  $\hbar\Omega_i$  is the energy of the phonons, and  $\hbar\mathbf{q}$  and  $\hbar\mathbf{K}_i$  are the corresponding momenta. Any number of phonons can participate in the process. However, the strength of interaction between the incident photon and the higher-order processes falls off rapidly with increasing order, making only the two- or three-phonon processes noteworthy in most semiconductors. The well-defined range that spans the phonon energies in most semiconductors, extending from 0 to the LO phonon energy at the center of the zone  $\Gamma$ , restricts the  $n$ -phonon process to a maximum energy of  $n\hbar\omega_{\text{LO}}(\Gamma)$ . Among the participating phonons, those with large values of  $\mathbf{K}$  and those in the vicinity of the critical points are the most important owing to their larger populations. These factors are important in understanding the multiphonon absorption behavior, as we now discuss.<sup>23,24</sup>

Multiphonon processes may be subdivided into two major categories: (1) sum processes where multiple phonons are created, and (2) difference processes in which both phonon creation and annihilation occur with a net absorption in energy. The former process is more probable at higher-incident photon energies and the converse is true for the latter. The reduction of the equilibrium phonon population at low temperatures leads to a lower probability for the difference process, and hence it is highly temperature dependent.

The multiphonon interactions are governed by symmetry selection rules in addition to the energy and momentum conservation laws stated earlier. A list of the possible combination processes is presented in Table 2 for the diamond structure and Table 3 for the zincblende structure. Representative multiphonon absorption spectra are presented in Figs. 6 and 7 for Si<sup>26</sup> and GaAs.<sup>27</sup> The Si  $\omega_{\text{TO}}$  and  $\omega_{\text{LO}}$  frequency of  $\sim 522 \text{ cm}^{-1}$  is indicated in the spectrum for reference. Note that the absence of a dipole moment implies that  $\omega_{\text{TO}}$  and  $\omega_{\text{LO}}$  are degenerate, and no first-order absorption is present. In contrast, for GaAs the very large absorption associated with the one-phonon absorption precludes the possibility of obtaining meaningful multiphonon absorption data in the reststrahlen band that spans the  $\sim 269$  to  $295 \text{ cm}^{-1}$  ( $\sim 34$ – $37 \text{ meV}$ ) spectral region. The multiphonon spectra obtained from GaAs are displayed in Fig. 7a and b. The absorption associated with the multiphonon processes is much smaller than the single-phonon process. However, the rich structure displayed by the spectra is extremely useful in analyzing the lattice dynamics of the material. In

**TABLE 2** Infrared Allowed Processes in the Diamond Structure<sup>24</sup>

Two-Phonon Processes
TO(X) + L(X)
TO(X) + TA(X)
L(X) + TA(X)
TO(L) + LO(L)
TO(L) + TA(L)
LO(L) + LA(L)
LA(L) + TA(L)
TO(W) + L(W)
TO(W) + TA(W)
L(W) + TA(W)

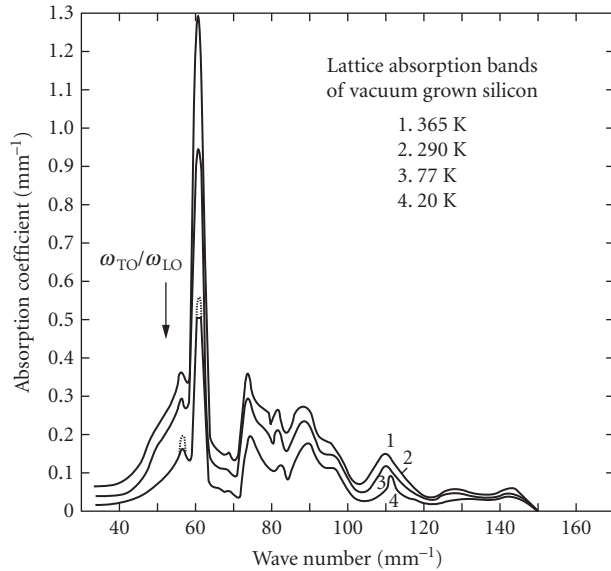
addition, in applications such as windows for high-power lasers, even the small absorption levels can lead to paths of catastrophic failure.

*Impurity-related vibrational optical effects* The role of impurities is of primary importance in the control of the electrical characteristics of semiconductors and hence their technological applications. This section outlines the main vibrational features of impurities and the resulting modification of the optical properties of these semiconductors. Impurities can either lead to additional vibrational modes over and beyond that supported by the unperturbed lattice or they can activate normally inactive vibrational modes.<sup>28</sup> The perturbation of the lattice by a substitutional impurity is a change in the mass of one of the constituents and a modification of the bonding forces in its vicinity. If the impurity is much lighter than the host atom it replaces, high-frequency vibrational modes above  $\omega_{LO}(\Gamma)$ , the maximum frequency supported by the unperturbed lattice, are introduced. These vibrational amplitudes are localized in the vicinity of the impurity and hence are known as local vibrational modes (LVM). For heavier impurities, the impurity-related vibrations can occur within the phonon band or in the gap between the acoustic and optical bands. These modes are referred to as resonant modes (RM) or gap modes (GM).<sup>28</sup>

The qualitative features of an impurity vibrational mode can be understood by considering a simple case of a substitutional impurity atom in a linear chain. The results of a numerical calculation of a 48-atom chain of GaP are presented in Figs. 8 and 9.<sup>28</sup> The highly localized character can be seen from Fig. 9. Note that the degree of localization reduces with increasing defect mass for a fixed bonding strength.

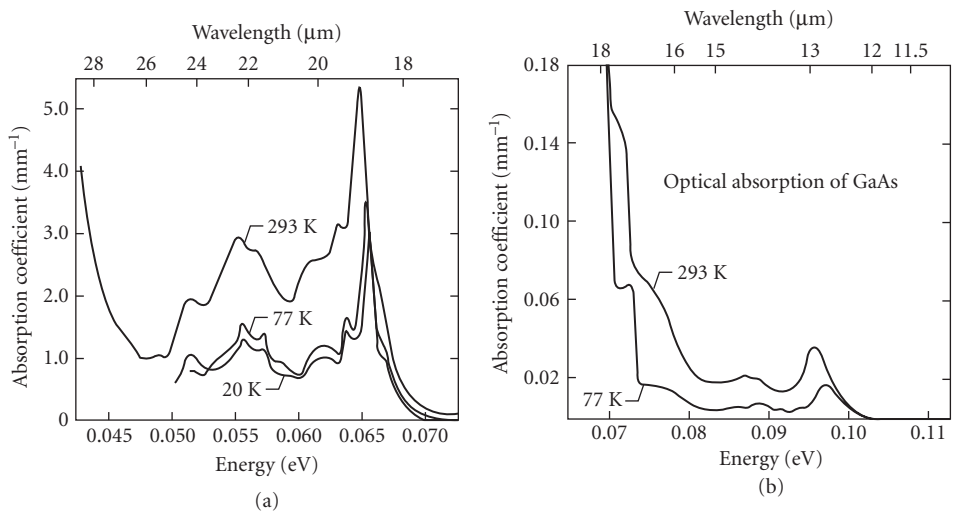
**TABLE 3** Infrared Allowed Processes in the Zincblende Structure<sup>24</sup>

Two-Phonon Processes
2LO( $\Gamma$ ), LO( $\Gamma$ ) + TO( $\Gamma$ ), 2TO( $\Gamma$ )
2TO(X), TO(X) + LO(X), TO(X) + LA(X), TO(X) + TA(X)
LO(X) + LA(X), LO(X) + TA(X)
LA(X) + TA(X)
2TA(X)
2TO(L), TO(L) + LO(L), TO(L) + LA(L), TO(L) + TA(L)
2LO(L), LO(L) + LA(L), LO(L) + TA(L)
2LA(L), LA(L) + TA(L)
2TA(L)
TO <sub>1</sub> (W) + LO(W), TO <sub>1</sub> (W) + LA(W)
TO <sub>2</sub> (W) + LO(W), TO <sub>2</sub> (W) + LA(W)
LO(W) + LA(W), LO(W) + TA <sub>1</sub> (W), LO(W) + TA <sub>2</sub> (W)
LA(W) + TA <sub>1</sub> (W), LA(W) + TA <sub>2</sub> (W)

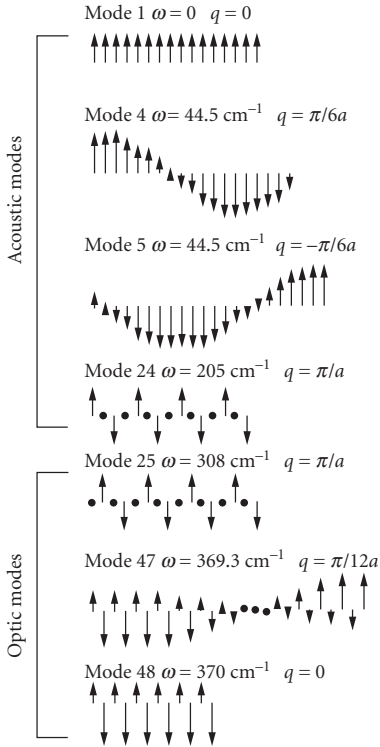


**FIGURE 6** Multiphonon absorption of vacuum-grown Si.<sup>26</sup>

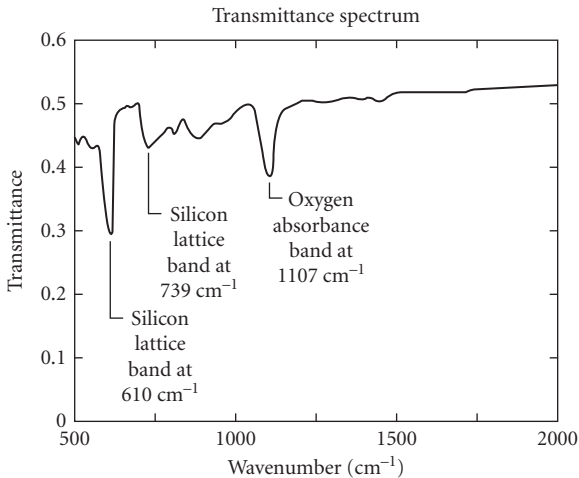
The absorption band produced by the LVM has been successfully used in impurity analyses. Figure 10 shows the IR absorption spectrum associated with interstitial oxygen in Si taken at the National Institute of Standards and Technology (NIST), and Fig. 11 displays the absorption spectrum from a carbon-related LVM in GaAs.<sup>29,30</sup> Note that the multiple peaks in the high-resolution spectrum are a consequence of the mass perturbations to the local environment resulting from the



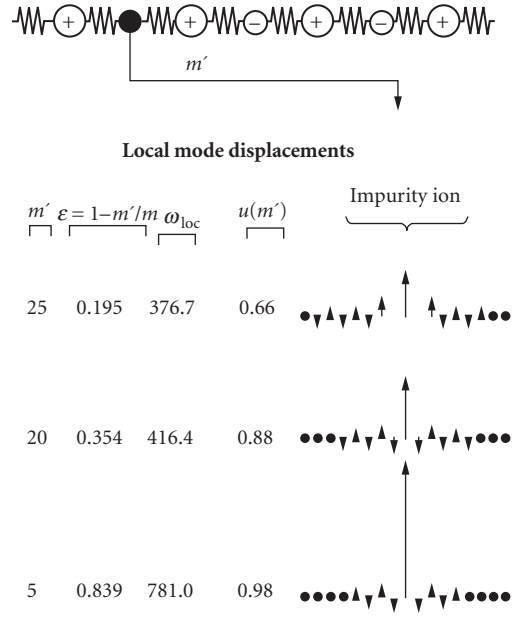
**FIGURE 7** Lattice absorption coefficient of high-resistivity *n*-type GaAs vs. wavelength from (a) 18 to 28  $\mu\text{m}$  and (b) 10 to 18  $\mu\text{m}$  at 77 and 293 K.<sup>27</sup>



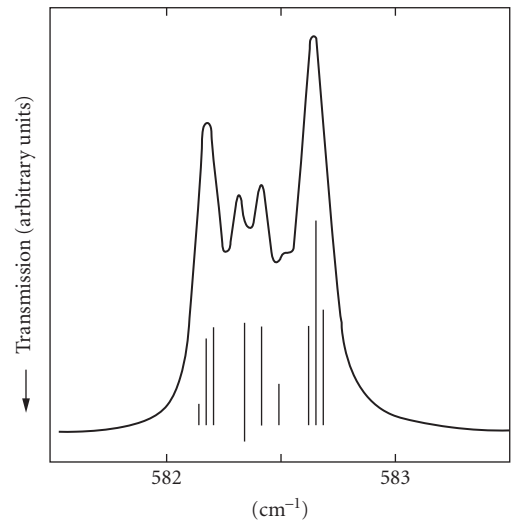
**FIGURE 8** Linear-chain model calculations for GaP. A 48-atom chain is considered. Position along the chain is plotted horizontally and ion displacement vertically. Modes 24 and 25 occur on either side of the gap between the acoustic and optic bands.<sup>28</sup>



**FIGURE 10** IR absorption due to interstitial oxygen in Si.



**FIGURE 9** Eigenvectors for the highest-frequency (localized) mode for three isotopic substitutions on the  $m = 31$  site. Note the extreme localization for a substituent of mass 5.<sup>28</sup>



**FIGURE 11**  $^{12}\text{C}$  local modes in GaAs and the predicted fine structure. The height of each line is proportional to the strength of each mode.<sup>30</sup>

**TABLE 4** Localized Modes in Semiconductors<sup>28</sup>

Host and Impurity	Mode Frequency (temp. K)	Defect Symmetry; Method of Observation
<i>Diamond</i> N	1340(300)	$T_d, A^*$
<i>Silicon</i>		
<sup>10</sup> B	644(300), 646(80)	$T_d; A$
<sup>11</sup> B	620(300), 622(80)	$T_d; A$
As	366(80) Reson.	$T_d; A$
P	441 Reson, 491(80) Reson.	$T_d; A$
<sup>14</sup> C	570(300), 573(80)	$T_d; A$
<sup>13</sup> C	586(300), 589(80)	$T_d; A$
<sup>12</sup> C	605(300), 680(80)	$T_d; A$
O	Bands near 30, 500, 1100, 1200	<i>Complex; A, R, T</i>
<i>GaAs</i>		
Al	362(80), $\approx$ 371(4.2)	$T_d; A, R, T$
P	355(80), 353(300), $\approx$ 363(4.2)	$T_d; A, R, T$
Si <sub>Ga</sub>	384(80)	$T_d; A$
Si <sub>As</sub>	399(80)	$T_d; A$

\*A—absorption; T—transmission; R—reflection; Reson. —resonant mode.

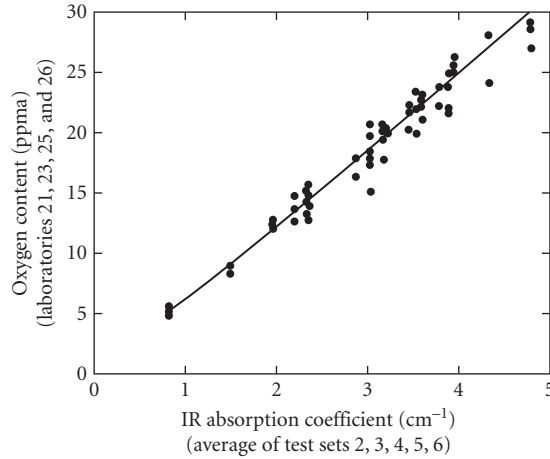
two naturally occurring isotopes of Ga. The fine structure in the spectrum helps identify the site occupied by C as belonging to the As sublattice. When accurate calibration curves are available, the concentration of the impurity can be determined from the integrated intensity of the LVM band. The LVM frequencies of a number of hosts and impurities are presented in Table 4.<sup>28</sup> The symmetry of the point group associated with the defect is  $T_d$ . The use of LVM in the study of complex defects, particularly those that involve hydrogen, has led to a wealth of microscopic information not easily attainable by any other means.<sup>31</sup>

The quantitative accuracy obtainable from LVM analysis may be illustrated by a simple harmonic model calculation. In such an approximation, the total integrated absorption over the entire band may be expressed as:<sup>32</sup>

$$\int \alpha d\omega = \frac{2\pi^2 N \eta^2}{n m_{\text{imp}} c} \quad (33)$$

where  $N$  is the volume density of the impurity and  $\eta$  and  $m_{\text{imp}}$  are the apparent charge and mass of the impurity ion;  $c$  is the velocity of light.  $n$  is the refractive index of the host crystal.  $\eta$  is an empirically derived parameter that is specific to each center, that is, a specific impurity at a specific lattice location. Once calibration curves are established, measurement of the intensity of absorption can be used to determine  $N$ . Figure 12 displays a calibration used to establish the density of interstitial oxygen.<sup>33</sup> Such analyses are routinely used in various segments of the electronic industry for materials characterization.

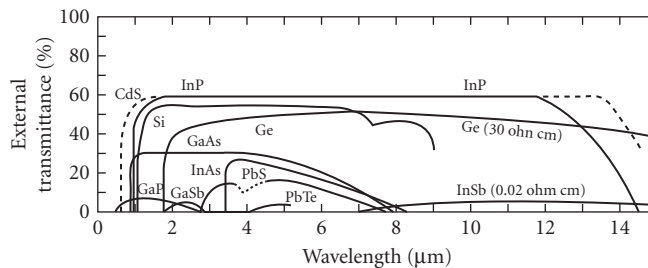
The effect of the impurities can alter the optical behavior in an indirect fashion as well. The presence of the impurity destroys translational symmetry in its vicinity and hence can lead to relaxation of the wave-vector conservation condition presented earlier in Eq. (32). Hence, the entire acoustic and optical band of phonons can be activated, leading to absorption bands that extend from zero frequency to the maximum  $\omega_{\text{LO}}(\Gamma)$ . The spectral distribution of the absorption will depend on the phonon density-of-states modulated by the effect of the induced dipole moment.<sup>28</sup> The latter is a consequence of the perturbation of the charge distribution by the impurity. The perturbation due to defects may be viewed in a qualitatively similar fashion. For instance, a vacancy may be described as an impurity with zero mass.



**FIGURE 12** The absorption coefficient dependence on the concentration of interstitial oxygen in Si.<sup>33</sup>

### Interband Absorption

*Absorption near the fundamental edge* The fundamental absorption edge is one of the most striking features of the absorption spectrum of a semiconductor. Within a small fraction of an electron volt at an energy about equal to the energy gap  $E_g$  of the material, the semiconductor changes from being practically transparent to completely opaque—the absorption coefficient changing by a factor of  $10^4$  or more. This increased absorption is caused by transitions of electrons from the valence band to the conduction band. This characteristic optical property is clearly illustrated in Fig. 13, which shows the transmission versus wavelength for a number of major semiconductors.<sup>34</sup> At the lower wavelengths, the transmission approaches zero which defines a cutoff wavelength  $\lambda_c$  for each material. For example,  $\lambda_c \approx 7.1 \mu\text{m}$  for InSb;  $\lambda_c \approx 4.2 \mu\text{m}$ , PbTe;  $\lambda_c \approx 3.5 \mu\text{m}$ , InAs;  $\lambda_c \approx 1.8 \mu\text{m}$ , GaSb and Ge;  $\lambda_c \approx 1 \mu\text{m}$ , Si; and  $\lambda_c \approx 0.7 \mu\text{m}$  for CdS. At much longer wavelengths than the edge at  $\lambda_c$ , lattice and free-carrier absorption become appreciable and the transmission drops. Studies of the fundamental absorption edge thus give values for the energy gap and information about the states just above the edge in the conduction band and below it in the valence band. Properties of these states are important to know since they are responsible for electrical conduction. Details of the band structure near the band extrema can be determined from the position and shape of the absorption edge and from its temperature, magnetic field, pressure, impurity concentration, and other parameters' dependence. Finally, this fundamental gap



**FIGURE 13** The transmission of CdS, InP, Si, Ge, GaAs, GaP, GaSb, InAs, InSb, PbTe, and PbS.<sup>34</sup>

region is important because usually it is only near the energy gap that phenomena such as excitons (both free and bound), electron-hole drops, donor-acceptor pairs, etc., are seen.

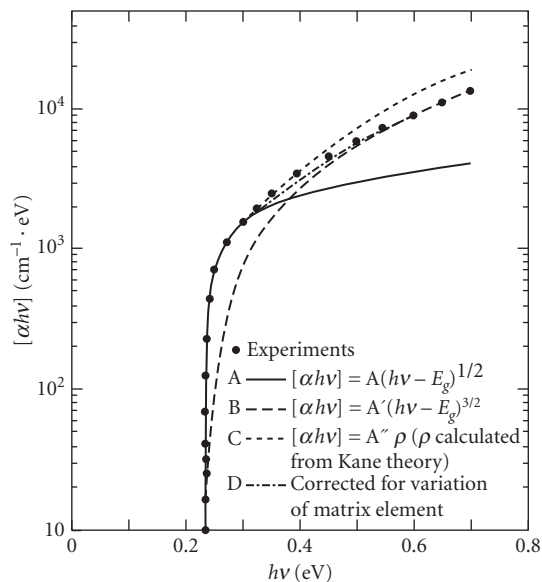
Interband transitions near the fundamental absorption edge are classified as (1) direct or vertical or (2) indirect or nonvertical. The momentum of light ( $\hbar q = \hbar m \omega / c$ ) is negligible compared to the momentum of a  $\mathbf{k}$ -vector state at the edge of the Brillouin zone. Thus, because of momentum conservation, electrons with a given wave vector in a band can only make transitions to states in a higher band having essentially the same wave vector. Such transitions are called vertical transitions. A nonvertical transition can take place, but only with the assistance of phonons or other entities which help preserve momentum.

*Direct transitions* The interband absorption coefficient depends upon the band structure and photon energy  $\hbar \omega$ . Use of quantum mechanics and, in particular, time-dependent perturbation theory becomes necessary.<sup>35</sup> For a nonzero momentum (dipole) matrix element, a simple model gives for allowed direct transitions

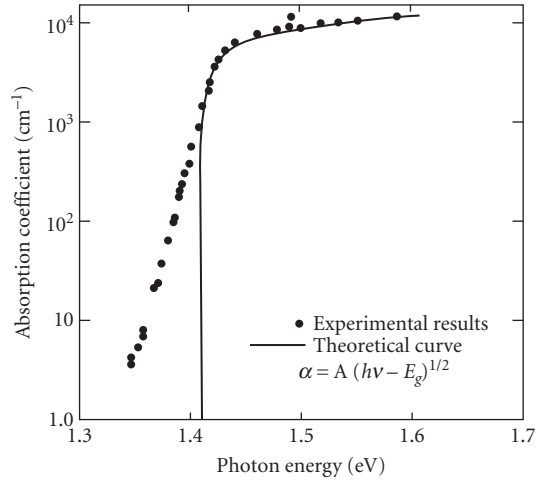
$$\alpha_{AD} = C_{AD} (\hbar \omega - E_g)^{1/2} \quad (34)$$

The coefficient  $C_{AD}$  involves constants, valence and conduction band effective masses, matrix elements, and only a slight dependence on photon energy. The absorption strengths of direct-gap semiconductors are related to their density of states and the momentum matrix element that couples the bands of interest. Many semiconductors such as AlAs, AlP, GaAs, InSb, CdS, ZnTe, and others have allowed direct transitions; many complex oxides, such as  $\text{Cu}_2\text{O}$ ,  $\text{SiO}_2$ , and rutile, have forbidden direct absorption.

Figure 14 shows the spectral variation of the absorption coefficient for pure InSb at a temperature of 5 K compared to various theoretical predictions.<sup>36</sup> We note the extremely sharp absorption edge which is fit best by the  $(\hbar \omega - E_g)^{1/2}$  dependence near the edge. However, a big deviation from the experimental data occurs at higher photon energies. Consideration of two more details allows a better



**FIGURE 14** Theoretical fit to the experimental absorption edge of InSb at  $\approx 5$  K.<sup>36</sup>



**FIGURE 15** Absorption edge of GaAs at room temperature.<sup>38</sup>

fit: (1) use of a more complicated band model from Kane<sup>37</sup> which predicts a more rapidly increasing density of states than for the simple bands, and (2) taking into account a decrease in the optical matrix element at the higher photon energies because of the  $\mathbf{k}$ -dependence of the wave functions. The calculated curves in Fig. 14 were arbitrarily shifted so that they look like a better fit than they are. The actual calculated absorption is a factor of about 15 too low at high energies. This discrepancy was attributed to the neglect of exciton effects which can greatly affect the absorption as discussed later. Modern calculations (including the Bethe-Salpeter corrections for many-body effects to the local density approximation) have much better accuracy in describing the optical absorption due to excitons.

Figure 15 shows the absorption behavior of GaAs at room temperature compared with calculations based on Kane's theory.<sup>38</sup> Below about  $10^3 \text{ cm}^{-1}$ , the absorption decreases much more slowly than predicted and absorption is even present for energies below  $E_g$ . In practice, there seems to exist an exponentially increasing absorption edge rule (called Urbach's<sup>39</sup> rule) in most direct transition materials which is found to correlate reasonably well with transitions involving band tails. These band tails seem to be related to disorder, such as doping effects, phonon-assisted transitions, and the broadening of electronic states due to electron-phonon interactions.

*Indirect transitions* Semiconductors such as GaP, Ge, and Si have indirect gaps where the maximum valence band energy and minimum conduction band energy do not occur at the same  $\mathbf{k}$  value. In this case, the electron cannot make a direct transition from the top of the valence band to the bottom of the conduction band because this would violate conservation of momentum. Such a transition can still take place but as a two-step process requiring the cooperation of another particle and which can then be described by second-order perturbation theory. The particle most frequently involved is an intervalley phonon of energy  $\hbar\Omega_{\mathbf{k}}$  which can be either generated or absorbed in the transition. (In some cases, elastic scattering processes due to impurity atoms or dislocations must be considered; they are less frequent than the phonon interactions in high-purity crystals.) The photon supplies the needed energy, while the phonon supplies the required momentum. The transition probability depends not only on the density of states and the electron-phonon matrix elements as in the direct case, but also on the electron-phonon interaction which is temperature dependent.

Calculations of the indirect-gap absorption coefficient give for the allowed indirect transitions

$$\alpha_{\text{AI}} = C_{\text{AI}}^{(\text{abs})} (\hbar\omega + \hbar\Omega_q - E_g)^2 + C_{\text{AI}}^{(\text{em})} (\hbar\omega - \hbar\Omega_q - E_g)^2 \quad (35)$$



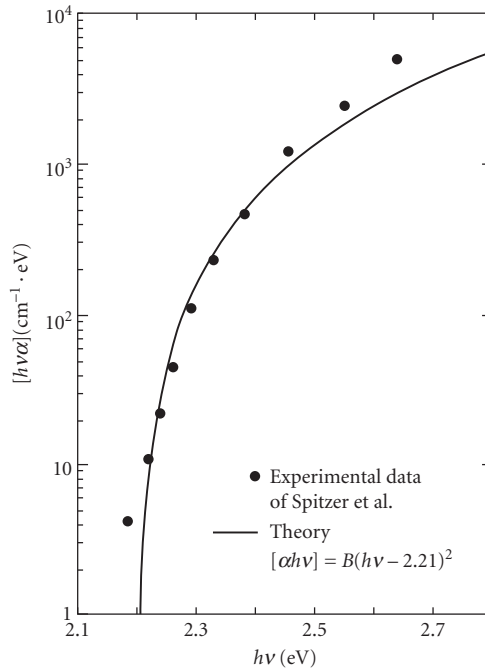
where the superscripts (abs) and (em) refer to phonon absorption and emission, respectively. This expression is only nonzero when the quantities in parentheses are positive, that is, when  $\hbar\omega \pm \hbar\Omega q > E_g$ . We note that the phonon energies are usually small ( $\leq 0.05$  eV) compared to the photon energy of about 1 eV and thus for the case of allowed indirect transitions with phonon absorption

$$\alpha_{\text{AI}} \approx C_{\text{AI}}^{(\text{abs})} (\hbar\omega - E_g)^2$$

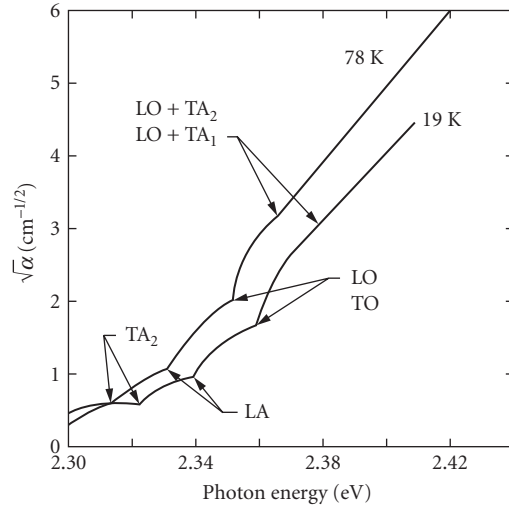
dependence of the direct transition as seen in Eq. (34).  $\hbar\omega - E_g$ ), much faster than the half-power

Figure 16 shows the variation of the absorption coefficient of GaP with photon energy at room temperature near the indirect edge.<sup>39</sup> A reasonable fit to the experimental data of Spitzer et al.<sup>40</sup> is obtained indicating that, for GaP, allowed indirect transitions dominate. Further complications arise because there can be more than one type of phonon emitted or absorbed in the absorption process. Transverse acoustic (TA), longitudinal acoustic (LA), transverse optic (TO), and longitudinal optic (LO) phonons can be involved as shown in the absorption edge data of GaP, as seen in Fig. 17.<sup>41</sup> The phonon energies deduced from these types of experimental absorption edge studies agree with those found from neutron scattering.

Both indirect and direct absorption edge data for Ge are shown in Fig. 18, while the analysis of the 300 K data is plotted in part *b*.<sup>42</sup> At the lowest energies,  $\alpha$  rises due to the onset of indirect absorption as seen by the  $\alpha^{1/2}$  dependence on photon energy. At higher energies, a sharper rise is found where direct transitions occur at the zone center and an  $\alpha^2$  dependence on energy is then seen. Note the large shifts of  $E_g$  with temperature for both the direct and indirect gaps. Also, the direct-gap absorption is much stronger than that of the indirect-gap absorption.

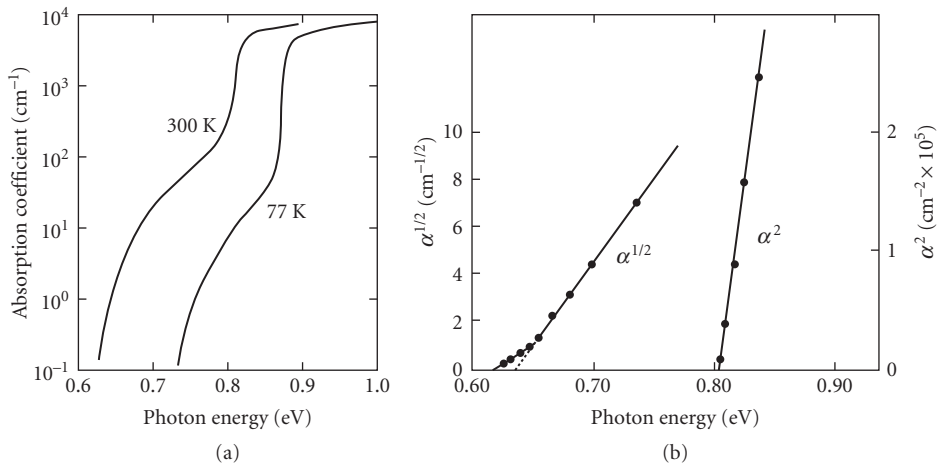


**FIGURE 16** Comparison of the experimental data at room temperature for the absorption edge of GaP with the theory for an indirect edge.<sup>39</sup>



**FIGURE 17** Absorption spectra at the edge of GaP, showing thresholds associated with the emission of each of several different phonons.<sup>41</sup>

*Excitons* Among the various optical properties of semiconductors, the subject of excitons has one of the dominant places because of their remarkable and diverse properties. Studies of exciton properties represent one of the most important aspects of scientific research among various solid-state properties. According to Cho,<sup>43</sup> there are a number of reasons for this: (1) excitonic phenomena are quite common to all the nonmetallic solids—semiconductors, ionic crystals, rare gas crystals, molecular crystals, etc.; (2) the optical spectra often consist of sharp structure, which allows a detailed theoretical analysis; (3) theories are not so simple as to be understood by a simple application of atomic theory or the Bloch band scheme, but still can be represented by a quasi-hydrogen-like level scheme; (4) sample quality and experimental techniques have continually been improved



**FIGURE 18** (a)  $\alpha$  vs.  $\hbar\omega$  for Ge and (b) the analysis of the 300 K experimental data.<sup>42</sup>

**TABLE 5** A Glossary of the Main Species of Excitons<sup>44</sup>

Exciton	In essence, an electron and hole moving with a correlated motion as an electron-hole pair
Wannier exciton	Electron and hole both move in extended orbits; energy levels related to hydrogen-atom levels by scaling, using effective masses and dielectric constant; occurs in covalent solids such as silicon
Frenkel exciton	Electron and hole both move in compact orbits, usually essentially localized on adjacent ions; seen in ionic solids, such as KCl, in absorption
Self-trapped exciton	One or both carriers localized by the lattice distortion they cause; observed in ionic solids, such as KCl, in emission
Bound exciton	Only a useful idea when a defect merely prevents translational motion of an exciton and does not otherwise cause significant perturbation
Core exciton	Lowest-energy electronic excitation from a core state, leaving an unoccupied core orbital (e.g., the 1 s level of a heavy atom) and an electron in the conduction band whose motion is correlated with that of the core hole
Excitonic molecule	Complex involving two holes and two electrons
Multiple bound excitons	Complex of many holes and a similar number of electrons, apparently localized near impurities; some controversy exists, but up to six pairs of localized carriers have been suggested
Exciton gas	High concentration of electrons and holes in which each electron remains strongly associated with one of the holes (as insulating phase)
Electron-hole drops	High concentration of electrons and holes in which the motions are plasma-like (a metallic phase), not strongly correlated as in excitons

with subsequent experiments proving existing theories and giving rise to new ones; and (5) the exciton is an elementary excitation of nonmetallic solids, a quantum of electronic polarization. It has a two-particle (electron and hole) nature having many degrees of freedom, and, along with the variety of energy-band structures, this leads to a lot of different properties from material to material or from experiment to experiment. Table 5 gives a definition of the major types of excitons in a glossary obtained from Hayes and Stoneham.<sup>44</sup> Many examples exist in the literature involving work on excitons in semiconductors to understand their nature and to determine their properties. Besides the references cited in this chapter, the authors refer the reader to the more detailed work presented in Refs. 45 and 46.

An electron, excited from the valence band to a higher energy state in the conduction band, can still be bound by the Coulomb attraction to the hole that the electron leaves in the valence band. This neutral bound-electron hole pair is called an exciton which can move throughout the crystal. Excitons are most easily observed at energies just below  $E_g$  using optical absorption or photoluminescence measurements. There are two models used for describing excitons in solids, named after Frenkel and Wannier. In a solid consisting of weakly interacting atoms, Frenkel considered excitons as described by excitations of a single atom or molecule.<sup>47</sup> An excited electron describes an orbit of atomic dimensions around an atom with a vacant valence state. The empty valence state acts as a mobile hole since the excitation can move from one atom to another. These tightly bound excitons are similar to an ordinary excited state of the atom, except that the excitation can propagate through the solid. The radius of the Frenkel exciton is on the order of the lattice constant. Frenkel excitons are useful to describe optical properties of solids like alkali halides and organic phosphors.

Wannier (or also called Mott-Wannier) excitons are also electrons and holes bound by Coulomb attraction.<sup>48,49</sup> In contrast to the Frenkel exciton, the electron and hole are separated by many lattice spacings producing a weakly bound exciton which is remarkably similar to a hydrogen-atom-like system. Since the electron and hole are, on the average, several unit cells apart, their Coulomb interaction is screened by the average macroscopic dielectric constant,  $\epsilon_\infty$ , and electron and hole effective masses can be used. Their potential energy  $-e^2/\epsilon_\infty r$  is just that of the hydrogen atom (except for  $\epsilon_\infty$ ). The binding energy of the free exciton (relative to a free electron and free hole) is then given by the hydrogen-atom-like discrete energy levels plus a kinetic energy term due to the motion of the exciton:

$$E_{\text{ex}} = \frac{R_y}{n^2} - \frac{\hbar^2 k^2}{2(m_e^* + m_h^*)} \quad (37)$$

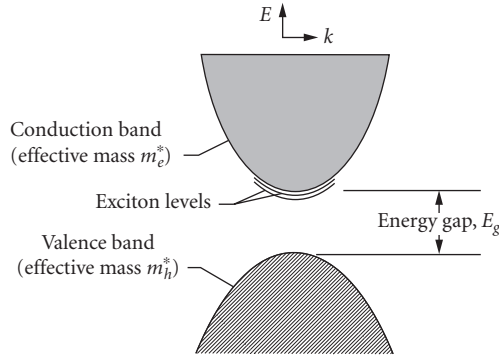
$$R_y = \left( \frac{m_r}{\epsilon_\infty^2} \right) \left( \frac{e^4}{2\hbar^2} \right) = \left( \frac{m_r}{m_H \epsilon_\infty^2} \right) E_H \quad (38)$$

where

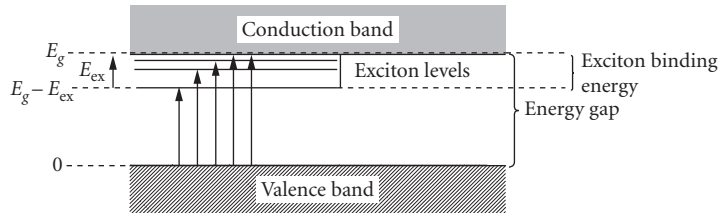
$$m_r = \left( \frac{1}{m_e^*} + \frac{1}{m_h^*} \right)^{-1} \quad (39)$$

$m_e^* \approx 0.21 m_0$ ,  $m_h^* \approx 0.64 m_0$ , and  $\epsilon_\infty \approx 8.9$ ; here  $m_r \approx 0.158 m_0$  and  $R \approx 27$  meV. The Bohr radius for the  $n = 1$  ground state is about  $30 \text{ \AA}$ .

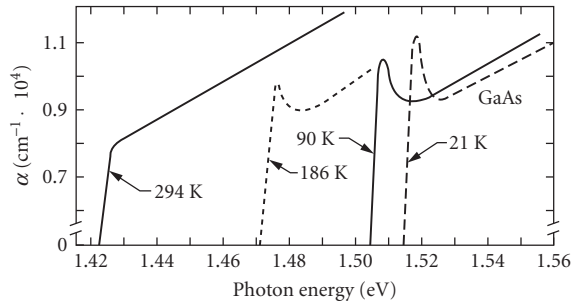
A series of excitonic energy levels thus exists just below the conduction band whose values increase parabolically with  $k$  and whose separation is controlled by  $n$ . Excitons are unstable with respect to radiative recombination whereby an electron recombines with a hole in the valence band, with the emission of a photon or phonons. These excitonic levels are shown in Figs. 19 and 20. For



**FIGURE 19** Exciton levels in relation to the conduction-band edge, for a simple band structure with both conduction and valence band edges at near  $k = 0$ .



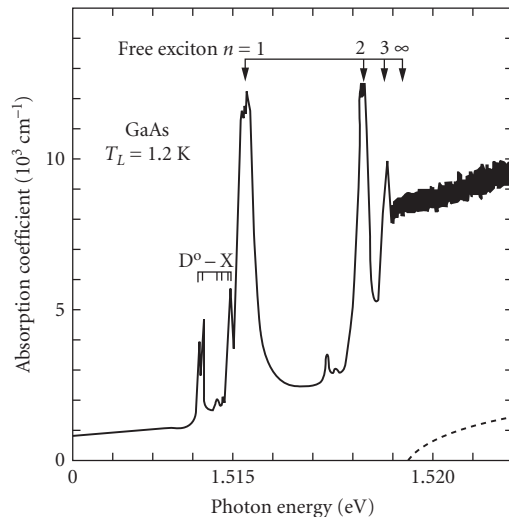
**FIGURE 20** Energy levels of a free exciton created in a direct process. Optical transitions from the top of the valence band are shown by the arrows; the longest arrow corresponds to the energy gap.



**FIGURE 21** Observed exciton absorption spectra in GaAs at various temperatures between 21 and 294 K. Note the decrease in the band edge with increasing temperatures.<sup>50</sup>

many semiconductors only a single peak is observed, as shown in Fig. 21 for GaAs.<sup>50</sup> However, even though only one line is observed, the exciton states make a sizable contribution to the magnitude of the absorption near and above the edge. At room temperatures, the exciton peak can be completely missing since the binding energy is readily supplied by phonons. In semiconductors with large enough carrier concentrations, no excitons exist because free carriers tend to shield the electron-hole interaction. Neutral impurities can also cause a broadening of the exciton lines and, at large enough concentrations, cause their disappearance.

Extremely sharp exciton states can often be seen as shown in Fig. 22, which shows the absorption spectrum of a very thin, very pure epitaxial crystal of GaAs.<sup>51</sup> The  $n = 1, 2,$  and  $3$  excitons are clearly



**FIGURE 22** Absorption spectrum at 1.2 K of ultra-pure GaAs near the band edge. The  $n = 1, 2, 3$  free exciton peaks are shown; also the bandgap  $E_g$ , determined by extrapolation to  $n = \infty$ , and impurity lines ( $D_0X$ ) from the excitons bound to  $\approx 10^{15} \text{ cm}^{-3}$  donors. (The rise at high energy is due to substrate absorption.) The dashed line shows the  $(E - E_g)$  behavior expected in the absence of electron-hole interaction (the absolute magnitude is chosen to fit the absorption far from the band edge).<sup>51</sup>

seen followed by excited states with  $n > 3$  leading smoothly into the continuum. The dashed line, calculated neglecting the effects of excitons, illustrates how important exciton effects are in understanding the optical properties of semiconductors and confirms the qualitative picture of exciton absorption.

Excitons in direct-gap semiconductors such as GaAs are called direct excitons. For indirect-gap semiconductors like Si or GaP, the absorption edge is determined by the influence of indirect excitons as revealed by the shape of the absorption. Such indirect-exciton transitions have been observed in several materials including Ge, Si, diamond, GaP, and SiC.

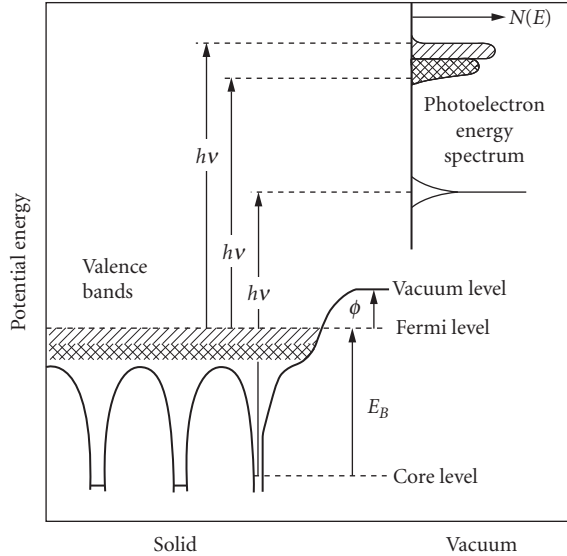
Real semiconductor crystals contain impurities and defects which also can affect the optical properties related to excitonic features, in addition to their causing impurity/defect absorption. A bound exciton (or bound-exciton complex) is formed by binding a free exciton to a chemical impurity atom (ion), complex, or a host lattice defect. The binding energy of the exciton to the defect or impurity is generally weak compared to the free-exciton binding energy. These bound excitons are extrinsic properties of the semiconductor; the centers to which the free excitons are bound can be either neutral donors or acceptors or ionized donors or acceptors. They are observed as sharp-line (width  $\approx 0.1$  meV) optical transitions in both absorption and photoluminescence spectra. The absorption or emission energies of these bound-exciton transitions always appear below those of the corresponding free-exciton transitions. Bound excitons are very commonly observed because semiconductors contain significant quantities of impurities or defects which produce the required binding. These complexes are also of practical interest because they characterize the impurities often used to control the electrical properties of semiconductors as well as being able to promote radiative recombination near the band gap. Bound excitons exhibit a polarization dependence similar to the free-exciton states from which they originated.

At higher densities of free excitons and low temperatures, they can form an electron-hole droplet by condensing into a “liquid” phase. This condensed phase occurs for electron-hole concentrations of about  $2 \times 10^{17} \text{ cm}^{-3}$  and can be thought of as an electron-hole plasma with a binding energy of several meV with respect to the free excitons.<sup>52</sup>

*Polaritons* Interesting optical effects arise when one considers explicitly the influence of longitudinal and transverse optical phonons on a transverse electromagnetic wave propagating through the semiconductor. This influence can be taken into account via the dielectric function of the medium. Dispersion curves that arise do not conform either to the photon or to the phonon. The coupling between the photon and phonon becomes so strong that neither can continue to be regarded as an independent elementary excitation, but as a photon-phonon mixture! This mixture can be regarded as a single quantity which can be interpreted as a new elementary excitation, the *polariton*.<sup>53</sup> Similar couplings exist between an exciton and the photon. It is an important consideration for interpreting some optical processes involving Raman and luminescence measurements.

*High-energy transitions above the fundamental edge* The optical properties of most semiconductors have been thoroughly investigated throughout the visible and ultraviolet regions where transitions above the fundamental gap energy give rise to properties strongly dependent upon photon energy. This regime is dominated by optical absorption and reflection of a photon arising from both valence and core electron transitions from the ground state of the system into various bound, autoionizing, continuum, or other excited states. The sum of all excitations—both bound (nonionizing) and ionizing—gives the total absorption coefficient and the complex dielectric constant at each photon energy  $h\nu$ . Photoemission or photoelectron spectroscopy measurements in this high-energy regime provide an alternative to ultraviolet spectroscopy for providing detailed information on the semiconductor. (See the electromagnetic spectrum in Fig. 1 in the Introduction for a reminder that photoemission measurements overlap UV measurements.) Electrons may be ejected from the semiconductor by high-energy photons as shown in Fig. 23.<sup>54</sup> Their kinetic energies are measured and analyzed to obtain information about the initial electron states. Ionizing excitations involve electron excitations into unbound states above the vacuum level. These excitations result in photoemissions depicted for the two valence bands and the core level shown. For photoemission involving one-electron excitations (usually dominant), binding energies  $E_B$  of valence and core levels are given directly by the measured kinetic energies  $E$  (from  $N(E)$  in the figure and energy conservation):

$$E_B = h\nu - E - \phi \quad (40)$$



**FIGURE 23** A schematic energy-level diagram showing photoemission from the valence bands and a core level in a solid.<sup>54</sup>

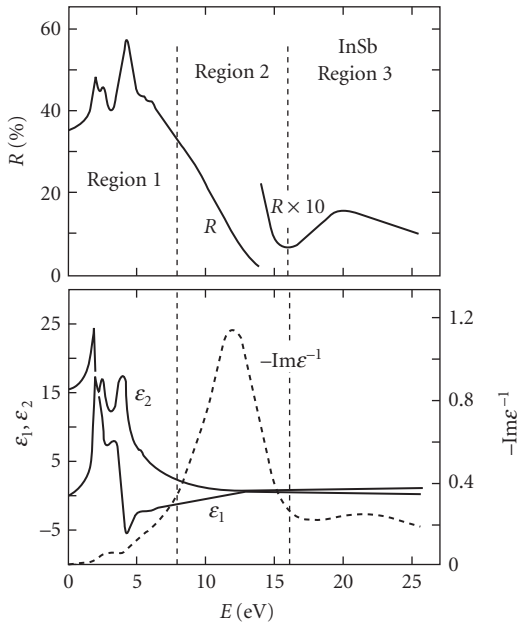
Here  $\phi$  is the work function (usually about 2 to 5 eV for most clean solids) which is known or easily measured. X-ray photoemission spectroscopy (XPS) is usually used to study core states and ultraviolet photoemission spectroscopy (UPS) to study valence band states. Photoemission techniques are also used for the study of surface states. Synchrotron radiation provides an intense source of light over a large spectral region. By measuring the angular distribution of the emitted UPS electrons, a direct determination of the  $E$  versus  $k$  relation for the valence band of GaAs can be made.

There are several regions of importance that must be considered in describing the optical properties of this high-energy region. Figure 24 shows the regions for InSb that are representative of the results for other semiconductors.<sup>55</sup> InSb is a narrow gap material with a direct bandgap of 0.17 eV at room temperature, so what is shown is at much greater energies than  $E_g$ . Sharp structure associated with transitions from the valence band to higher levels in the conduction band characterize the first region that extends to about 8 to 10 eV. This behavior is also characteristic for group-IV and other III-V compound semiconductors, see Fig. 25 which displays the imaginary part of the dielectric function for Si and GaAs. To show how this type of optical spectra can be interpreted in terms of the materials energy band structure, consider Fig. 26 which shows the spectral features of  $\epsilon_2$  for Ge in *a* and the calculated energy bands for Ge in *b*.<sup>57,58</sup> Electronic transitions can take place between filled and empty bands subject to conservation of energy and wave vector. The initial and final electron wave vectors are essentially equal, and only vertical transitions between points separated in energy by  $\hbar\omega = E_c(k) - E_v(k)$  are allowed.

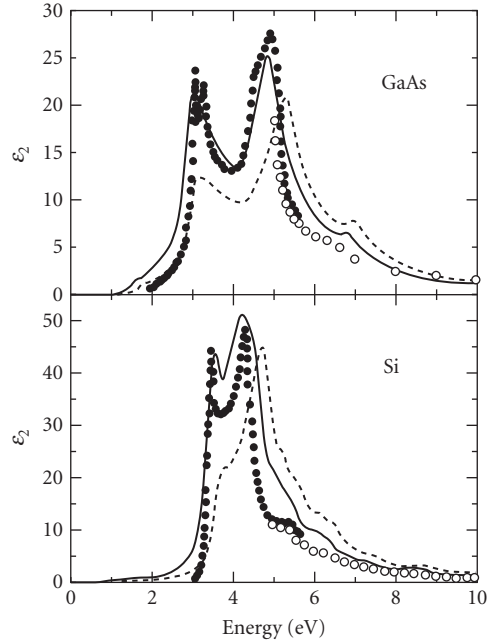
The intensity of the absorption is proportional to the number of initial and final states and usually peaks when the conduction and valence bands are parallel in  $k$ -space. This condition is expressed by

$$\nabla_k [E_c(k) - E_v(k)] = 0 \quad (41)$$

Places in  $k$ -space where this is true are called critical points or Van Hove singularities. The experimental peaks can be sharp as shown in Fig. 26*a* because interband transitions in very pure crystals are not appreciably broadened by damping, and thus the lineshapes are determined primarily by the density of states, especially at low temperature. At room temperature, the broadening is dominated by electron-phonon scattering. Much information is available from the data if a good theory is used.



**FIGURE 24** The spectral dependence of the reflectance  $R$ , the real and imaginary parts of the dielectric constant  $\epsilon_1$  and  $\epsilon_2$ , and the energy-loss function  $-\text{Im}(\epsilon^{-1})$  for InSb.<sup>55,56</sup>



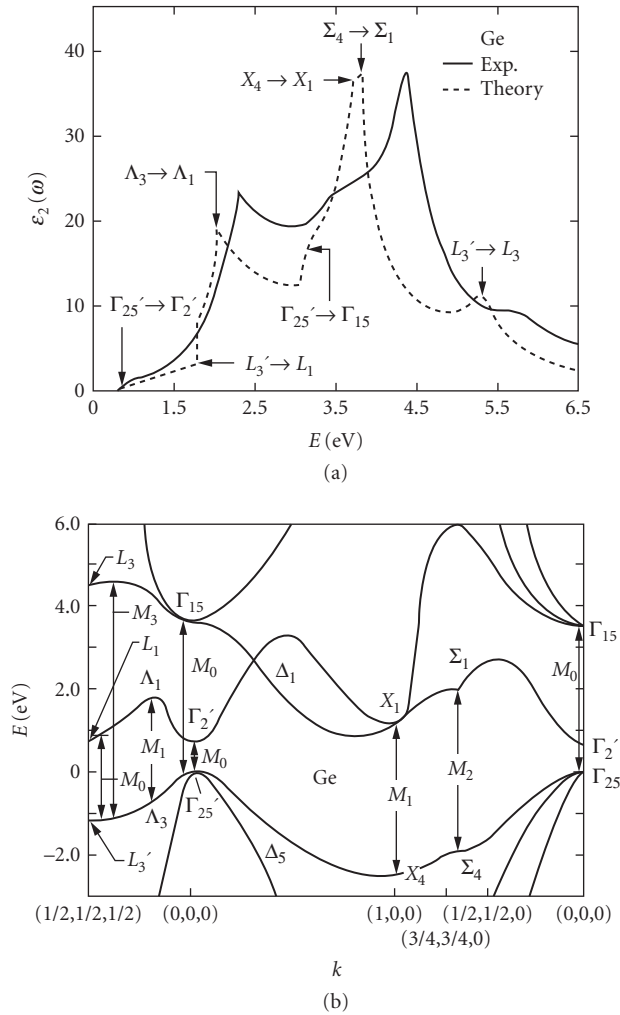
**FIGURE 25** Imaginary part of the dielectric function for GaAs and Si. The symbols show experimental results. The dashed line is the result of a calculation based on the local-density approximation with GW corrections. The calculation shown by the solid line also takes into account excitonic effects using the Bethe-Salpeter equations.<sup>59</sup>

Figure 26*b* shows pseudopotential energy-band calculations that show the special points and special lines in the Brillouin zone that give rise to the data shown in *a*. Band structure calculations using the local density approximation (see Fig. 26) are unable to predict the correct location of the peaks in the dielectric function. In general, the calculated gap is lower than the experimentally observed one (see Fig. 26). Considerable improvement to the accuracy of the excited states is possible when employing GW corrections to the band structure. While these corrections give an accurate band structure (Fig. 25, dashed line), they still ignore the excitonic interactions between the electron and hole participating in the interband transition and thus underestimate the magnitude of the absorption. Quite recently, a number of groups have been successful in considering excitonic Coulomb effects in their calculations using the Bethe-Salpeter equations. Modern calculations of the band structure and the dielectric function are almost as accurate as the best experimental methods, see Fig. 25.<sup>59</sup>

The second region in Fig. 24 extends to about 16 eV and shows a rapid decrease of reflectance due to the excitation of collective plasma oscillations of the valence electrons. The behavior in this second “metallic” region is typical of the behavior of certain metals in the ultraviolet. One can think of the valence electrons as being essentially unbound and able to perform collective oscillations. Sharp maxima in the function  $-\text{Im} \epsilon^{-1}$ , which describes the energy loss of fast electrons traversing the material, have been frequently associated with the existence of plasma oscillations.

In the third region, the onset of additional optical absorption is indicated by the rise in reflectance. This structure is identified with transitions between filled *d* bands below the valence band and empty conduction band states. As shown in Fig. 27, the structure in region three is present in other III-V compounds, but is absent in Si which does not have a *d*-band transition in this region.<sup>60</sup>

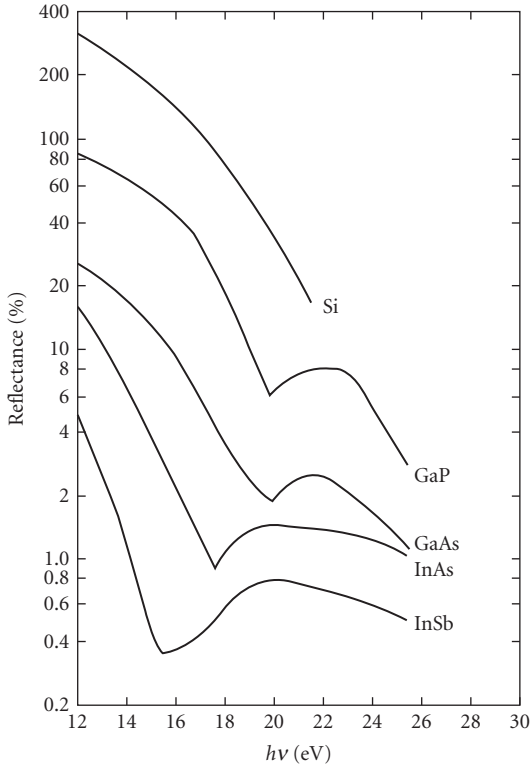




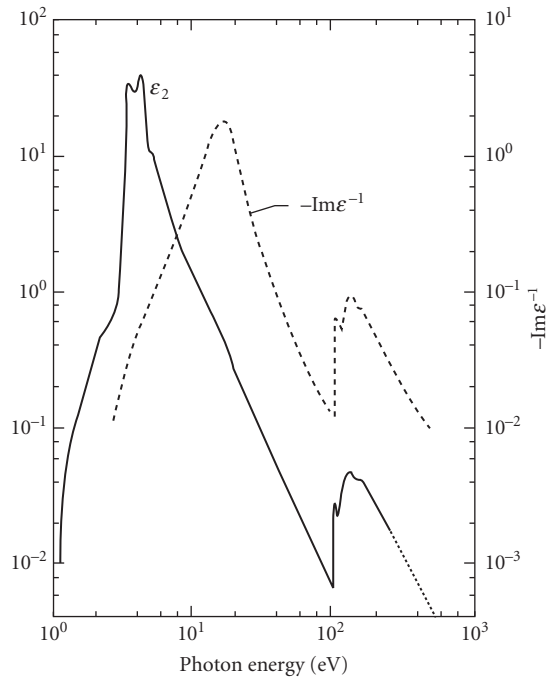
**FIGURE 26** (a) Spectral features of  $\epsilon_2$  for Ge; (b) the calculated pseudopotential energy bands for Ge along some of the principal axes.<sup>57,58</sup>

Other structure at higher photon energies is observed for Si as shown in Fig. 28 which shows the imaginary part of the dielectric constant of Si from 1 to 1000 eV.<sup>56,61</sup> The large peaks on the left are due to excitations of valence electrons, whereas the peaks on the right are caused by excitation of core electrons from L shell states. K shell electrons are excited at energies beyond the right edge of the graph (beyond 1000 eV).

Elemental and compound semiconductors can often be mixed to form mixed-crystal alloys, such as  $\text{Al}_{1-x}\text{Ga}_x\text{As}$  or  $\text{Si}_{1-x}\text{Ge}_x$ . The former alloy is used for optoelectronic applications (e.g., CD players), while the latter is found in high-end microprocessors or cellular telephones. The vibrational spectra of such alloys show multimode behavior (i.e., Si-Si, Ge-Ge, and Si-Ge vibrations in  $\text{Si}_{1-x}\text{Ge}_x$  alloys) with phonon mode energies depending on the masses of the atoms. In the visible and UV spectral range, on the other hand, the peaks in the dielectric function given by the energy of the critical



**FIGURE 27** Reflectance of several semiconductors at intermediate energies. Starting from 12 eV the reflectance decreases, representing the exhaustion of bonding  $\rightarrow$  anti-bonding oscillator strength at energies greater than  $2E_g$ . The rise in reflectivity in the 15 to 20 eV range in the Ga and In compounds is caused by excitation of electrons from Ga cores (3d states) or In cores (4d states). The ordinate should be multiplied by 2 for InSb, 1 for InAs, 1/2 for GaAs, 1/4 for GaP, and 1/10 for Si.<sup>60</sup>



**FIGURE 28** Imaginary part of the dielectric function for Si from 1 to 1000 eV.<sup>2</sup> (From reflectivity measurements of H.R. Philipp and H. Ehrenreich, Ref. 60, out to 20 eV and from transmission measurements of C. Gahwiller and F. C. Brown, Ref. 61, from 40 eV to 200 eV.)

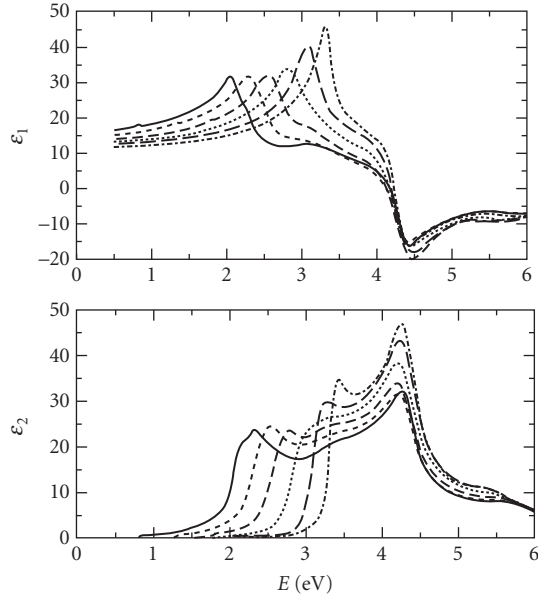
points shift roughly linear with composition as shown in Fig. 29. The dielectric function of such alloys is known with very high accuracy (often also as a function of strain) and used in the production of modern microelectronic circuits to measure thickness and composition of semiconductor alloy films.<sup>62,63</sup>

### Free Carriers

*Plasmons* Semiconductors, in addition to a crystal lattice that may be ionic, may contain free charges as well.

The free-carrier contribution to the dielectric function is given by Maxwell's equation in CGS (Centimeter, Gram, Second) system of units

$$\epsilon_{fc}(\omega) = -i \frac{4\pi\sigma}{\omega} \quad (42)$$



**FIGURE 29** Real and imaginary parts of the dielectric function of  $\text{Si}_{1-x}\text{Ge}_x$  alloys (bulk polycrystals) for  $x$  from 0 to 1 in steps of 0.2. Ge and Si are shown by the solid and long-dashed lines, respectively. The  $E_1$  peak shifts from near 2 eV in Ge to about 3.4 eV in Si. Thin-film effects and strain modify these values in epitaxial films.<sup>62</sup>

The task of establishing the functional form of  $\epsilon(\omega)$  hence reduces to one of determining the conductivity at the appropriate optical frequencies.

The response of a charge to an externally applied field may be described by classical methods, assuming a damping or resistive force to the charge that is proportional to the velocity of the charge. This simplification is known as the Drude approximation,<sup>64</sup> and it leads to the following relationship:

$$\sigma = \frac{Ne^2\tau}{m^*} \frac{1}{1 - i\omega\tau} \quad (43)$$

and is related to the dc conductivity by the relationship:

$$\sigma(0) = Ne^2\tau/m^* \quad (44)$$

where  $N$  is the free-carrier density,  $1/\tau$  is the constant of proportionality for the damping force, and  $\tau$  is a measure of the electron-electron collision time. Now,

$$\epsilon_{fc}(\omega) = -\frac{i\omega^2\epsilon_\infty}{\omega\left(\omega + \frac{i}{\tau}\right)} \quad (45)$$

$\omega_p$  is the plasma frequency that describes oscillations of the plasma, that is, the delocalized charge cloud

$$\omega_p^2 = \frac{4\pi N e^2}{m^* \epsilon_\infty} \quad (46)$$

against the fixed crystal lattice.

In an ideal plasma with no damping, the  $\epsilon(\omega)$  reduces to

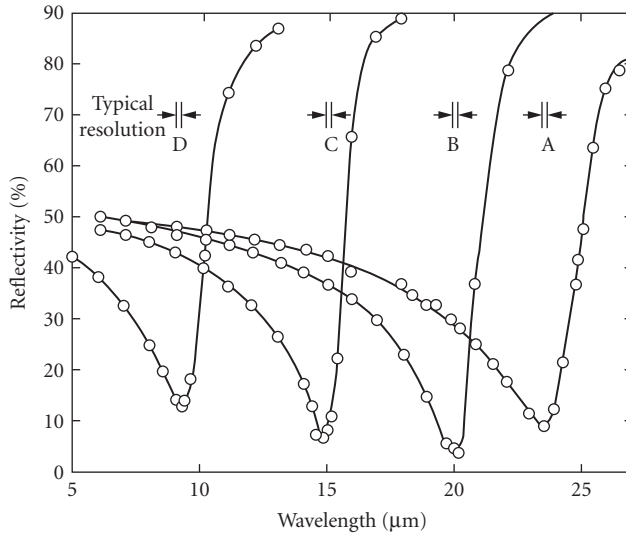
$$\epsilon(\omega) = 1 - \frac{\omega_p^2}{\omega^2} \quad (47)$$

$\epsilon(\omega)$  is negative for  $\omega < \omega_p$ , which leads to total reflection and, hence, the term plasma reflectivity.

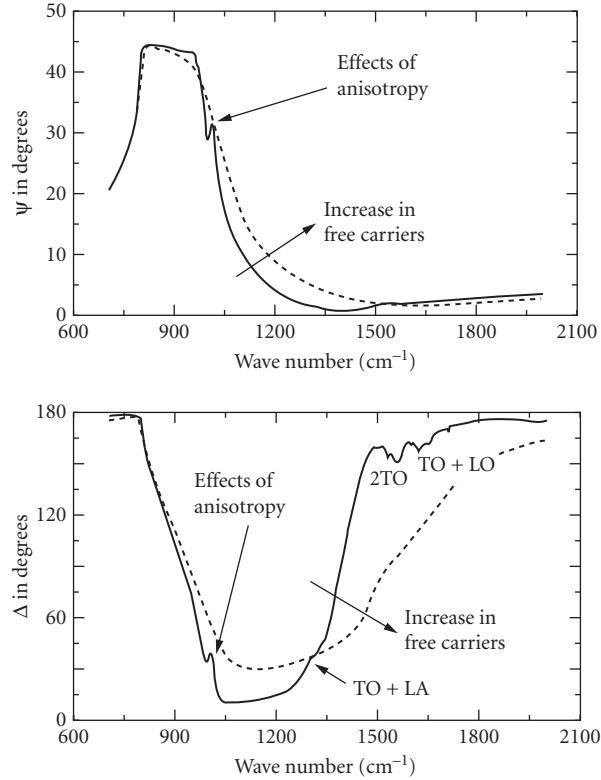
The phenomenon of optical reflection from a plasma reflection and the relationship to the free-carrier density are illustrated in Fig. 30 using the far-infrared reflection spectrum from a series of PbTe samples with hole densities extending from  $3.5 \times 10^{18} \text{ cm}^{-3}$  to  $4.8 \times 10^{19} \text{ cm}^{-3}$ .<sup>65</sup> The plasma frequency increases with increasing carrier density as described by Eq. (46).

*Coupled plasmon-phonon behavior* Most semiconductor samples contain free carriers and phonons, and the frequencies of both are comparable. Hence, a complete description of the far-infrared optical properties has to take both into account. This can be achieved readily using Eq. (45) to describe the free carriers. The combined  $\epsilon(\omega)$  may then be expressed as

$$\epsilon(\omega) = \epsilon_\infty + \frac{S\omega_{\text{TO}}^2}{\omega_{\text{TO}}^2 - \omega^2 - i\omega\gamma} - \frac{i\omega_p^2\epsilon_\infty}{\omega(\omega + i/\tau)} \quad (48)$$



**FIGURE 30** Reflectivity at 81 K and normal incidence of variously doped samples of *p*-type PbTe, showing the plasma resonance. Hole concentrations: A,  $3.5 \times 10^{18} \text{ cm}^{-3}$ ; B,  $5.7 \times 10^{18} \text{ cm}^{-3}$ ; C,  $1.5 \times 10^{19}$ ; D,  $4.8 \times 10^{19} \text{ cm}^{-3}$ .<sup>65</sup>



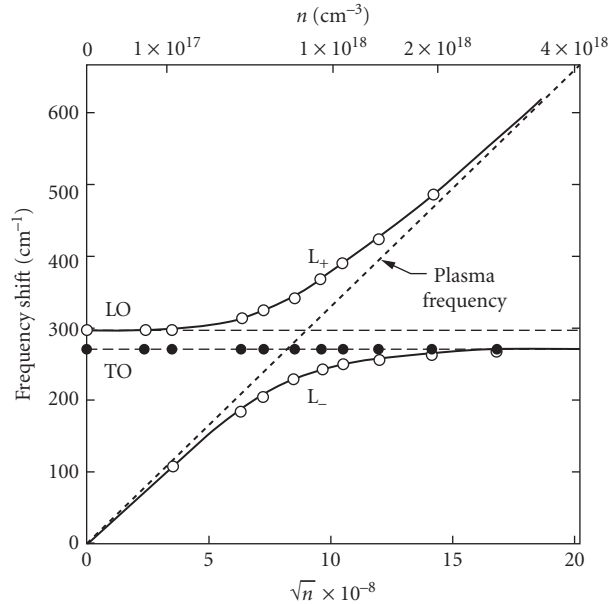
**FIGURE 31** Mid-infrared ellipsometry spectra for 4H SiC. The reststrahlen band in the phonon absorption region (near  $900\text{ cm}^{-1}$ ) is affected by free carriers and the crystal anisotropy. Two-phonon absorption is also visible.<sup>66</sup>

A good example of the accurate description of the far-infrared behavior of a semiconductor is presented in Fig. 31.<sup>66</sup> The ellipsometric angles  $\Psi$  (related to reflectivity) and  $\Delta$  (related to the polarization phase shift) of 4H SiC in the vicinity of the reststrahlen band (phonon absorption near  $900\text{ cm}^{-1}$ ) are affected by the free-carrier effects and the anisotropy of the crystal. All the major features in the complicated spectrum can be well described using the simple oscillatory models described.

The coexistence of phonons and plasmons leads to a coupling between the two participants.<sup>67</sup> Of particular interest are the coupled plasmon-LO phonon modes denoted by  $L_+$  and  $L_-$  that are exhibited as minimas in the reflection spectra. As explained earlier, the LO phonon frequencies occur at the zeros of the dielectric function  $\epsilon(\omega)$ . In the presence of plasmons, the zeros are shifted to the coupled mode frequencies  $L_+$  and  $L_-$ . These frequencies can be determined directly for the case of no damping for both the phonon and the plasmon as shown below:

$$L_{\pm} = \frac{1}{2} \{ (\omega_{\text{LO}}^2 + \omega_p^2) \pm [(\omega_{\text{LO}}^2 - \omega_p^2)^2 + 4\omega_{\text{LO}}^2 \omega_p^2 (1 - \epsilon_{\infty} / \epsilon(0))]^{1/2} \} \quad (49)$$

Note that the presence of the plasmon introduces an additional low frequency zero at  $L_-$ . The relationship of the  $L_+$  and  $L_-$  frequencies with the carrier density is presented in Fig. 32.<sup>69</sup> The existence of the coupled modes were predicted by Varga<sup>67</sup> and later observed using Raman scattering<sup>68,69</sup> and far-infrared reflectivity.<sup>70</sup>



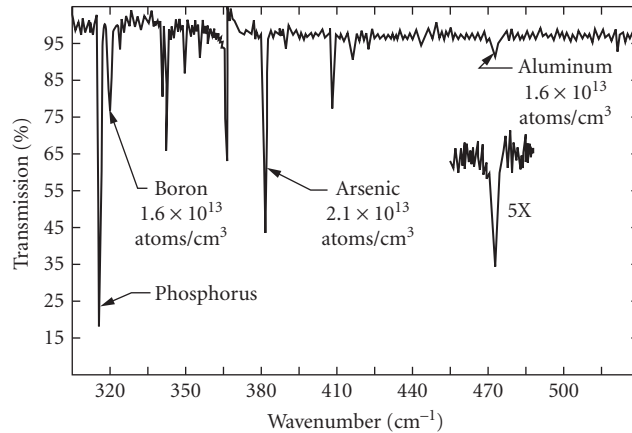
**FIGURE 32** The solid curves labeled  $L_+$  and  $L_-$  give the calculated frequencies of the coupled longitudinal plasmon-phonon modes, and the measured frequencies are denoted by the open circles.<sup>69</sup>

**Impurity and Defect Absorption** The extended electronic states, excitons, lattice vibrations, and free carriers discussed thus far are all intrinsic to the pure and perfect crystal. In practice, real-life specimens contain imperfections and impurities. The characteristic optical properties associated with impurities and defects are the subject of discussion in this section. Two representative examples of the most widely observed effects, namely, shallow levels and deep levels in the forbidden gap, are considered in the following discussion.

Some of the effects due to impurities are considered in other parts of this chapter: impurity-related vibrational effects were considered under “Lattice”; excitons bound to impurity states were discussed under “Excitons”; and impurity-related effects in magneto-optical behavior are dealt with under “Magnetic-Optical Properties.” In addition to these effects, optical absorption due to electronic transitions between impurity-related electronic levels may also be observed in semiconductors.

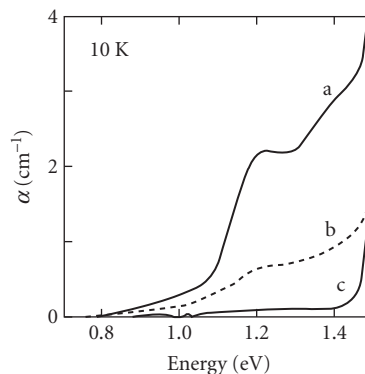
The presence of impurities in a semiconductor matrix leads to both a perturbation of the intrinsic electronic quantum states and the introduction of new states, particularly in the forbidden energy gap. The major classes of electronic levels are the shallow levels that form the acceptor and donor states and lie close to the valence and conduction band extremes, respectively, and those that occur deep in the forbidden gap. The former are well known and are critical in controlling the electrical behavior of the crystal, and the latter are less well known but are, nevertheless, important in determining the sub-bandgap optical behavior.

Direct transitions from the shallow levels to the closest band extrema can be observed in the far-infrared transmission spectra of many semiconductors. An elegant example of this property is illustrated with the spectrum obtained from a high-purity Si wafer<sup>71</sup> as displayed in Fig. 33. Sharp, well-resolved absorption features from electronic transitions due to B, P, As, and Al are present, as are additional features perhaps from unidentified impurities. Note that both acceptors and donor bands are observable due to the highly nonequilibrium state in which the specimen was maintained through the use of intense photoexcitation.

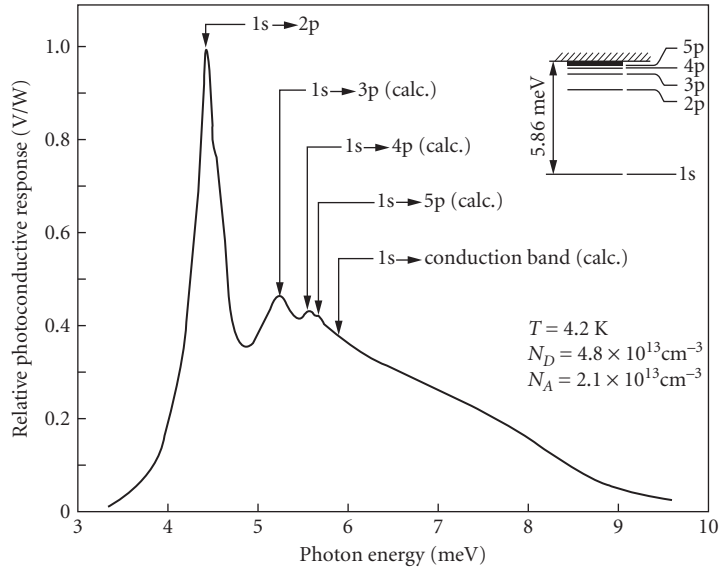


**FIGURE 33** Total impurity spectrum of a 265- $\Omega$ -cm *n*-type Si sample obtained by the simultaneous illumination method. The input power to the illumination source was about 50 W.<sup>71</sup>

Electronic transitions from impurity- and defect-related levels deep in the forbidden gap can significantly alter the sub-bandgap behavior. One of the best known examples of this is the native defect level known as EL2 in GaAs. The level occurs 0.75 eV below the conduction band extremum, and, when present, it can completely dominate the subband gap absorption. The absorption spectrum recorded from a GaAs sample containing EL2 is presented in Fig. 34.<sup>72</sup> The onset of the absorption at 0.75 eV is due to transitions to the conduction band extremum at the direct gap, and the features at 1.2 and 1.4 eV are due to transitions to higher-lying extrema.<sup>72</sup> The figure also shows two spectra that exhibit the well-known photoquenching effect associated with EL2. When the specimen is subjected to intense white light radiation, the EL2 absorption is quenched, leaving only the band-to-band transitions with an onset at  $E_g$  which occurs at  $\approx 1.5$  eV at 10 K.



**FIGURE 34** EL2 optical absorption spectra recorded at 10 K in the same undoped semi-insulating GaAs material. Curve a: after cooling in the dark; curves b and c: after white light illumination for 1 min and 10 min, respectively.<sup>72</sup>



**FIGURE 35** Far-infrared photoconductivity spectrum of a high-purity GaAs sample showing the measured transition energies and those calculated from the hydrogenic model using the ( $1s \rightarrow 2p$ ) transition energy. The hydrogenic energy level diagram is shown in the inset.<sup>73</sup>

Optical measurements of shallow impurities in semiconductors have been carried out by absorption (transmission) and photoconductivity techniques. The photoconductivity method is a particularly powerful tool for studying the properties of shallow impurity states, especially in samples which are too pure or too thin for precise absorption measurements. In most cases, this type of photoconductivity can only be observed in a specific temperature range, usually at liquid helium temperatures. Figure 35 shows the photoconductivity response of a high-purity GaAs sample with specific transition energies that correspond to hydrogenic-like transitions.<sup>73</sup> If the excited states of the impurity were really bound states, electrons in these states could not contribute to the conductivity of the sample, and the excited state absorption would not result in peaks in the photoconductivity spectrum. However, there have been several suggestions as to how the electrons that are excited from the ground state to higher bound excited states can contribute to the sample's conductivity. First, if the excited state is broadened significantly by interactions with neighboring ionized donor and acceptor states, it is essentially unbound or merged with the conduction band. Other mechanisms for impurity excited-state photoconductivity all involve the subsequent transfer of the electron into the conduction band after its excitation to the excited state by the absorption of a photon. Mechanisms that have been considered for this transfer include (1) impact ionization of the electrons in the excited state by energetic free electrons, (2) thermal ionization by the absorption of one or more phonons, (3) photoionization by the absorption of a second photon, and (4) field-induced tunneling from the excited state into the conduction band. All of these mechanisms are difficult to describe theoretically.

## Magneto-Optical Properties

**Background** Phenomena occurring as a result of the interaction of electromagnetic radiation with solids situated in a magnetic field are called magneto-optical (MO) phenomena. Studies of MO phenomena began in 1845 when Michael Faraday observed that the plane of vibration of polarized light rotated as it propagated through a block of glass in a strong magnetic field. By the 1920s, most



MO effects were fairly well understood in terms of the classical dynamics of an electron in a magnetic field. However, when semiconductors were first investigated in the early 1950s, a quantum mechanical interpretation of the MO data in terms of the energy-band structure was found to be necessary. MO spectroscopy was developed in the 1950s and 1960s as a powerful tool for characterizing the fundamental electronic properties of semiconductors. Cyclotron resonance experiments using microwaves, interband studies using broadband visible and infrared sources, and finally lasers were used to characterize the symmetry of band structures, as well as properties such as energy gaps, effective masses, and other band parameters. The two major limitations of the classical theory are that no effects depending on the density of states are predicted and no effects of electron spin are included.

Table 6 presents an overview of the typical types of magneto-optical phenomena observed in semiconductors and the information that can be determined from the experimental measurements. Four classes of MO phenomena can be distinguished: those arising from (1) interband effects, (2) excitonic effects, (3) intraband or free-carrier effects, and (4) impurity magnetoabsorption effects. Further clarification can then be made by determining whether the effect is absorptive or dispersive, resonant or nonresonant, and upon the relative orientation of the magnetic field to the direction of propagation of the electromagnetic radiation and its polarization components. Resonant experiments usually provide more detailed information about the band structure of a semiconductor and often are easier to interpret. There is thus a wide variety of effects as shown which can give different types of information about the crystal's energy-band structure, excitonic properties, and impurity levels. Before summarizing and discussing each of these magneto-optical effects, it is necessary to briefly describe the effects of a magnetic field on the energy-band structure of a semiconductor.

**Effect of a Magnetic Field on the Energy Bands** Magneto-optical experiments must be analyzed with specific energy-band models in order to extract the related band parameters and to emphasize the underlying physical concepts with a minimum of mathematical complexity. Most often, one deals with only the highest valence bands and the lowest conduction bands near the forbidden energy-gap region. If simple parabolic bands are assumed, a fairly complete analysis of the MO experiments is usually possible, including both the resonant transition frequencies and their line shapes. On the other hand, if more complicated energy bands (e.g., degenerate, non-parabolic) are needed to describe the solid, the detailed analysis of a particular experiment can be complicated.

The effect of a magnetic field on a free electron of mass  $m^*$  was determined in 1930 by Landau, who solved the Schrodinger equation. The free electrons experience a transverse Lorentz force which causes them to travel in orbits perpendicular to the magnetic field. The resulting energy eigenvalues corresponding to the transverse components of the wave vector are quantized in terms of harmonic oscillator states of frequency  $\omega_c$ , while a plane-wave description characterizes the motion along the magnetic field. The allowed energy levels, referred to as Landau levels, are given by

$$E_n^\pm = \left( n + \frac{1}{2} \right) \hbar \omega_c + \frac{\hbar^2 k_z^2}{2m^*} \pm \frac{1}{2} g^* \mu_B B \quad (50)$$

where  $n$  is the Landau level number (0, 1, 2, . . .),  $\omega_c$  (the cyclotron frequency) is equal to  $eB/m_c^*$ , and  $m_c^*$  is the cyclotron effective mass. The middle term represents the energy of an electron moving along the direction of the  $\mathbf{B}$  field in the  $z$  direction; it is not quantized. The first term represents the quantized energy of motion in a plane perpendicular to the field. The last term represents the effect of the electron's spin;  $g^*$  is the effective spectroscopic  $g$ -factor or spin-splitting factor and

$$\mu_B = e\hbar/2m_0 = 5.77 \times 10^{-2} \text{ meV/T} \quad (51)$$

is the Bohr magneton. The  $g$ -factor in a semiconductor has values quite different from the usual value of two found for atomic systems (e.g., for narrow-energy gaps and a strong spin-orbit interaction,  $g^*$  can be large and negative).

**TABLE 6** Magneto-Optical Phenomena and Typical Information Obtainable

Magneto-Optical Effect	Some Information or Properties Obtainable
<b>Interband effects</b>	
<i>In transmission</i>	
Band-to-band magnetoabsorption.....	Energy gaps, effective masses, g-factors, higher band parameters
Faraday rotation (resonant and nonresonant).....	Energy gaps, effective masses
Faraday ellipticity (nonresonant).....	Relaxation times
Voigt effect (resonant and nonresonant).....	Effective masses
Cross-field magnetoabsorption	
<i>In reflection</i>	
Magnetoreflexion.....	Studies of very deep levels or where absorption is high, similar information as in transmission magnetoabsorption
Kerr rotation	
Kerr ellipticity	
<b>Magneto-excitonic effects</b>	
In transmission, reflection, and photoconductivity	Diamagnetic and Zeeman shifts and splittings; energy gap; effective reduced-mass tensor; effective Rydberg; anisotropy parameter; dielectric tensor components; effective g-factors; effective masses; quality of materials, structures, alloys and interfaces
<b>Intraband or free-carrier effects</b>	
<i>In transmission</i>	
Cyclotron resonance (resonant).....	Effective masses, relaxation times, nonparabolicity
Combined resonance.....	Same information as cyclotron resonance plus g-factors
Spin resonance.....	g-factors
Phonon-assisted cyclotron resonance harmonics.....	Same information as cyclotron resonance plus phonon information
Faraday rotation (resonant and nonresonant).....	Carrier concentration, effective masses; use for impure materials, flexible, can be used at high temperature
Faraday ellipticity (nonresonant)	
Voigt effect (nonresonant)	
Interference fringe shift (nonresonant)	
Oscillatory variation of the Shubnikov-de Haas type.....	Carrier concentration
<i>In reflection</i>	
Magnetoplasma reflection.....	Effective masses, carrier concentration
Magnetoplasma rotation (Kerr effect)	
Magnetoplasma ellipticity	
<b>Impurity magneto-absorption</b>	
Zeeman and diamagnetic effect-type behavior of impurities	Hydrogenic impurity information, binding energy, effective masses, effective Rydberg, central cell corrections, static dielectric constant; both impurity and Landau level information; impurity information as above plus Landau-level information related to effective masses and g-factors
Photoionization behavior (transitions from ground state of impurity to Landau levels).....	

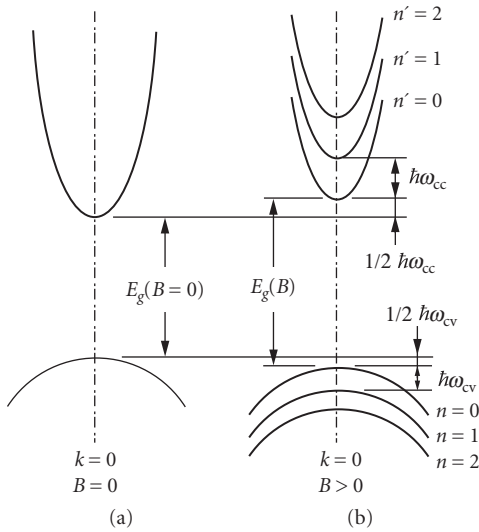


FIGURE 36 Landau levels for simple bands.

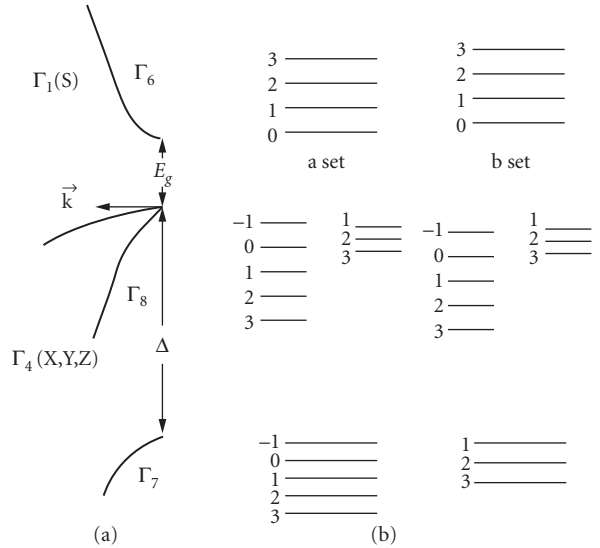


FIGURE 37 (a) Zincblende semiconductor energy bands ( $\mathbf{H} = 0$ ) and (b) in an applied magnetic field  $\mathbf{H}$ .<sup>74</sup>

Figure 36 shows schematically the effect of a magnetic field on a simple parabolic direct gap extrema at  $k = 0$ . The quasi-continuous parabolic behavior of the nondegenerate conduction and valence bands at  $\mathbf{B} = 0$  (shown in *a*) is modified by the application of a magnetic field into Landau levels as shown in *b*. Each Landau level is designated by an integer  $n = 0, 1, 2, 3, \dots$ . Finally, in Fig. 37, the Landau effects are shown schematically for zincblende energy bands when both spin and valence band degeneracy are taken into account for both  $\mathbf{B} = 0$  (*a*) and  $\mathbf{B} \neq 0$  (*b*).<sup>74</sup> With spin included, the valence band splits into the  $\Gamma_8$  and  $\Gamma_7$  bands with spin-orbit splitting energy  $\Delta$ . The quantization of the bands into Landau levels is illustrated in the right-hand side of the figure. The Pidgeon and Brown<sup>75</sup> model has been successfully used to describe the magnetic field situation in many semiconductors, since it includes both the quantum effects resulting from the partial degeneracy of the p-like bands and the nonparabolic nature of the energy bands. The *a*-set levels are spin-up states, and the *b*-set, the spin-down states. These large changes in the  $\mathbf{E}$  versus  $k$  relations of the bands when a magnetic field is applied also means large changes in the density of states which become periodic with a series of peaks at energies corresponding to the bottom of each Landau level. This oscillatory variation in the density of states is important for understanding the various oscillatory phenomena in a magnetic field and is a key advantage of using magnetic fields to study semiconductors.

**Interband Magneto-Optical Effects** Interband transitions in a magnetic field connect Landau-level states in the valence band to corresponding states in the conduction band. Thus, they yield direct information concerning energy gaps, effective masses, effective g-factors, and higher band parameters. The strongest allowed transitions are those that are proportional to the interband matrix element  $p = - (i \hbar / m_0) \langle s | p_j | x \rangle$ , where  $j = x, y, z$ .

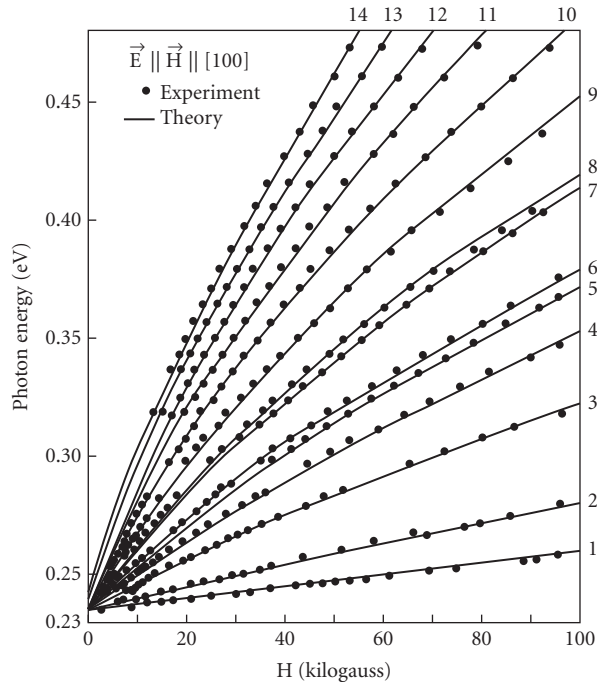
This matrix element directly connects the p-like valence band ( $x, y, z$ ) which is triply degenerate with the s-like conduction band through the momentum operator  $p_j$ . The transition energies can be calculated directly from a knowledge of the selection rules and use of an energy-band model. The selection rules are given by<sup>76</sup>

$$\begin{aligned} \sigma_L: a(n) &\rightarrow a(n-1), b(n) \rightarrow b(n-1) \\ \sigma_R: a(n) &\rightarrow a(n+1), b(n) \rightarrow b(n+1) \\ \pi: a(n) &\rightarrow b(n+1), b(n) \rightarrow a(n-1) \end{aligned}$$

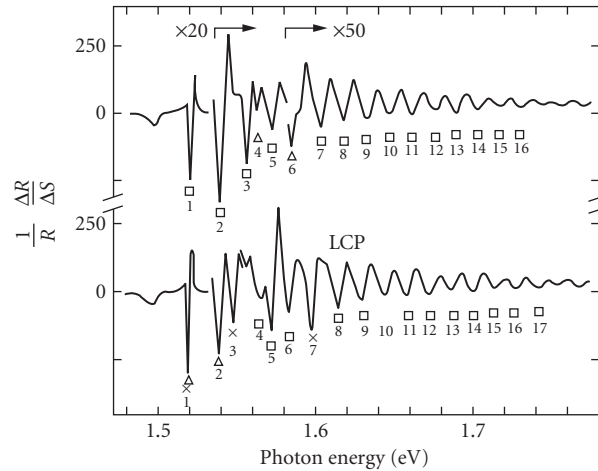
where  $\sigma_L$ ,  $\sigma_R$ , and  $\pi$  are left circular, right circular, and linear ( $\mathbf{e} \parallel \mathbf{B}$ ) polarizations. As discussed earlier,  $a$  and  $b$  denote the spin-up and spin-down states, and  $n$  the Landau-level number. Often, sharp optical transitions between the Landau levels are observed, providing highly accurate information about the fundamental band parameters such as the energy gap  $E_g$ , effective masses of the electrons and holes, higher band parameters, etc.

InSb is a material in which interband effects have been studied very extensively; thus, it is a good representative example. Even though it is a narrow-gap semiconductor and thus has a small exciton binding energy, Weiler<sup>77</sup> has shown that excitonic corrections must be made to properly interpret the magnetic-field-dependent data. This shall be discussed in more detail in the next section. The band models discussed earlier predict that there is an increase in the energy of the absorption edge with magnetic field because of the zero point energy  $1/2\hbar\omega_c$  of the lowest conduction band. At larger photon energies, transmission minima (absorption maxima) which are dependent upon magnetic field are observed. By plotting the photon energy positions of the transmission minima against magnetic field, converging, almost linear plots are obtained as shown in Fig. 38.<sup>75</sup> Extrapolation of the lines to zero field gives an accurate value for the energy gap. Use of a band model and specific transition assignments further allow the determination of other important band parameters, such as effective masses and  $g$ -factors.

*Magnetoreflexion* Besides the changes in absorption brought about by the magnetic field, there are changes in the refractive index. Since the reflectivity depends upon both the real and imaginary



**FIGURE 38** Energy values of transmission minima versus magnetic field for electron transitions between Landau levels of valence and conduction bands in InSb. Plot of the photon energy of the principal transmission minima as a function of magnetic field for  $\mathbf{E} \parallel \mathbf{H} \parallel [100]$ . The solid lines represent the best theoretical fit to the experimental data. The numeral next to each line identifies the quantum assignment.<sup>75</sup>



**FIGURE 39** Stress-modulated magnetorefectance spectra for the fundamental edge in epitaxially grown high-purity (211) GaAs at  $T \approx 30$  K, with  $\Delta S = 5 \times 10^{-5}$ , observed in the Faraday configuration with magnetic field  $\mathbf{H} \parallel [11\bar{2}]$  and  $H = 88.6$  kG. The number directly below each prominent transition refers to the identification of the transitions,  $\Delta$ , LHa;  $\times$ , LHb;  $\square$ , HH(AV).<sup>78</sup>

parts of the index, clearly it is affected by the field. Interband transitions are often observed in reflection because of the high absorption coefficients. In addition, modulation spectroscopy techniques, in which a parameter such as stress, electric field, wavelength, magnetic field, etc. is periodically varied and the signal synchronously detected, provide several orders of magnitude enhancement in the sensitivity for observing resonant transitions. This is especially important for the observation of higher energy transitions lying far away from the energy of the fundamental gap. Figure 39<sup>78</sup> shows the stress-modulated magnetorefectance spectra for the fundamental edge region, the interpretation of which must involve the effect of excitons on the transitions. Quantitative information about the split-off valence to conduction band edge in GaAs is also obtainable from magnetoreflexion.<sup>79</sup>

*Faraday rotation* A plane-polarized wave can be decomposed into two circularly polarized waves. The rotation of the plane of polarization of light as it propagates through the semiconductor in a direction parallel to an applied magnetic field is called the Faraday effect, or Faraday rotation. The amount of rotation is usually given by the empirical law  $\Theta = VB_l$ , where  $\Theta$  is the angle of rotation,  $V$  is the Verdet coefficient,  $\mathbf{B}$  is the magnetic field value, and  $l$  is the thickness. The Verdet coefficient is temperature, wavelength, and sometimes field dependent. The Faraday effect can then be understood in terms of space anisotropy effects introduced by the magnetic field upon the right and left circularly polarized components. The refractive indices and propagation constants are different for each sense of polarization, and a rotation of the plane of polarization of the linearly polarized wave is observed. The sense of rotation depends on the direction of the magnetic field. Consequently, if the beam is reflected back and forth through the sample, the Faraday rotation is progressively increased. When measurements are thus made, care must be taken to avoid errors caused by multiple reflections. Faraday rotation may also be considered as birefringence of circularly polarized light.

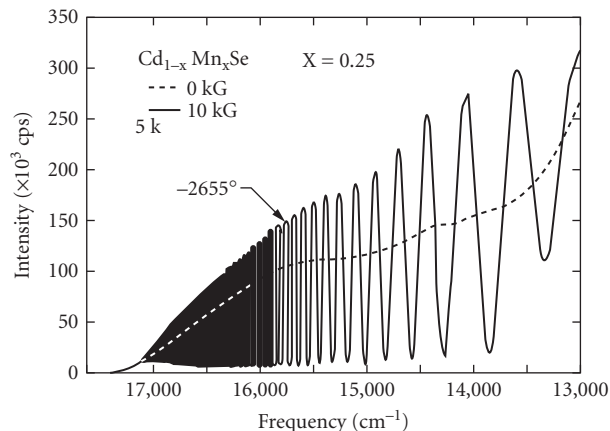
If absorption is present, then the absorption coefficient will also be different for each sense of circular polarization, and the emerging beam will be elliptically polarized. Faraday ellipticity specifies the ratio of the axes of the ellipse.

Faraday rotation can be observed in the Faraday configuration with the light beam propagating longitudinally along the  $\mathbf{B}$ -field direction. Light propagating transverse to the field direction is

designated as the Voigt configuration. Two cases must be distinguished—the incident beam may be polarized so that its  $\mathbf{E}$  field is either parallel or perpendicular to  $\mathbf{B}$ . The Voigt effect is birefringence induced by the magnetic field and arises from the difference between the parallel and perpendicular indices of refraction in the transverse configuration. It is usually observed by inclining the incident plane-polarized radiation with the electric vector at  $45^\circ$  to the direction of  $\mathbf{B}$ . The components resolved parallel and perpendicular to  $\mathbf{B}$  then have different phase velocities and recombine at the end of the sample to give emerging radiation which is elliptically polarized. Measurements of this ellipticity then determine the Voigt effect.

The interband Faraday effect is a large effect and is therefore useful for characterizing semiconductors. For frequencies smaller than the frequency corresponding to the energy gap, the interband Faraday effect arises from the dispersion associated with the interband magnetoabsorption. In this region, it has been used to determine energy gaps and their pressure and temperature dependence. Since the beam propagates through the crystal in a transparent region of the spectrum, it may be attractive to use in certain applications. For example, in GaAs,<sup>80</sup> at long wavelengths the Faraday effect has a positive rotation, while near the gap the Verdet coefficient becomes negative. For frequencies equal to or larger than the frequency corresponding to the energy gap, the Faraday rotation is dominated by the nearest magneto-optical transition. Oscillatory behavior, like that seen in the magnetoabsorption, is also often observed.

Diluted magnetic semiconductors (DMS) are a class of materials that have attracted considerable scientific attention. Any known semiconductor with a fraction of its constituent ions replaced by some species of magnetic ions (i.e., ions bearing a net magnetic moment) can be defined as a member of this group. The majority of DMS studied so far have involved  $\text{Mn}^{+2}$  ions embedded in various II–VI hosts. The optical properties of DMS are controlled by the interaction between the localized magnetic moments of  $\text{Mn}^{+2}$  and the conduction and/or valence band electrons (referred to as the sp-d interaction), which results in features unique to DMS. The best known (and quite spectacular) of these are the huge Faraday rotations of the visible and near-infrared light in wide-gap DMS. The origin of the large rotations is the sp-d exchange interaction which makes the band structure much more sensitive to the strength of external magnetic fields than in ordinary semiconductors. Figure 40 shows the Faraday effect in  $\text{Cd}_{1-x}\text{Mn}_x\text{Se}$  ( $x = 0.25$ ) at  $T = 5$  K.<sup>81</sup> Each successive peak represents an additional Faraday rotation of  $180^\circ$ .



**FIGURE 40** Faraday effect in  $\text{Cd}_{1-x}\text{Mn}_x\text{Se}$  ( $x = 0.25$ ),  $T = 5$  K. The dashed line represents the transmission of light as a function of its frequency for a 3-mm-thick sample located between two polaroids with their axes at  $45^\circ$  and at zero magnetic field. The light propagates along the optic axis,  $\hat{c}$ . The oscillations occur when a 10-kG magnetic field is applied along  $\hat{c}$ .<sup>81</sup>

*Excitonic magneto-optical effects* As described earlier, a free exciton consists of an electron and hole bound together electrostatically. When the pair has an energy less than that of the energy gap, they orbit around each other. If the orbital radius is large compared with the lattice constant, they can be approximately treated as two point charges having effective masses and being bound together by a Coulomb potential that gives rise to a hydrogen-atom-like behavior. In the presence of a magnetic field, excitons give rise to Zeeman and diamagnetic effects analogous to those in atomic spectra. Fine structure can occur due to motions other than the simple orbiting of an electron and hole—the carriers can have intrinsic motion, motion around an atom, spin motion, and motion of the complete exciton through the lattice. Some of these motions may even be coupled together.

Bound excitons (or bound-exciton complexes) or impurity-exciton complexes are extrinsic properties of materials. Bound excitons are observed as sharp-line optical transitions in both photoluminescence and absorption. The bound exciton is formed by binding a free exciton to a chemical impurity atom (or ion), a complex, or a host lattice defect. The binding energy of the exciton to the impurity or defect is generally smaller than the free-exciton binding energy. The resulting complex is molecular-like (hydrogen-molecule-like), and bound excitons have many spectral properties analogous to those of simple diatomic molecules.

The application of a magnetic field to samples where excitonic features are observed in the absorption spectra results in line splittings, energy shifts, and changes in linewidths. These arise from diamagnetic and Zeeman effects just as in atomic or molecular spectroscopy. The treatment of the problem of an exciton in a magnetic field in zincblende-type structures is difficult due to the complexity of the degenerate valence band. Often a practical solution is adopted that corrects the interband model calculations for exciton binding energies that are different for each Landau level. Elliott and Loudon showed that the absorption spectrum has a peak corresponding to the lowest  $N = 0$  hydrogen-like bound state of the free exciton, which occurs below the free interband transition by the exciton binding energy  $E_B$ .<sup>82</sup> Weiler suggests that for transitions to the conduction band Landau level  $n$ , the exciton binding energy  $E_B$  can be approximated by<sup>74</sup>

$$E_B(n) \approx 1.6R[\gamma_B/(2n+1)]^{1/3} \quad (52)$$

where  $R$  is the effective Rydberg,

$$R = R_0 \mu / m_0 \epsilon(0) \quad (53)$$

$R_0 = 13.6$  eV,  $\epsilon(0)$  is the static-dielectric constant,  $\mu$  is the reduced effective mass for the transition, and  $\gamma_B$  is the reduced magnetic field

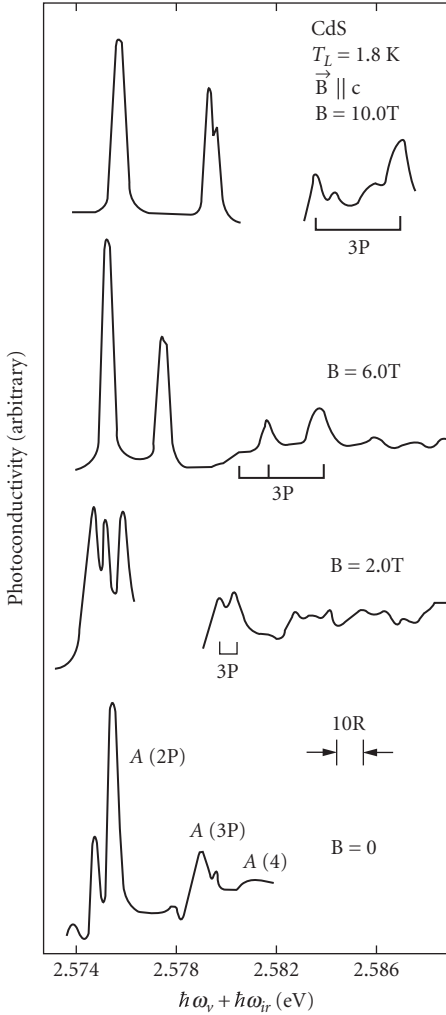
$$\gamma_B = m_0 S / 2\mu R \quad (54)$$

and

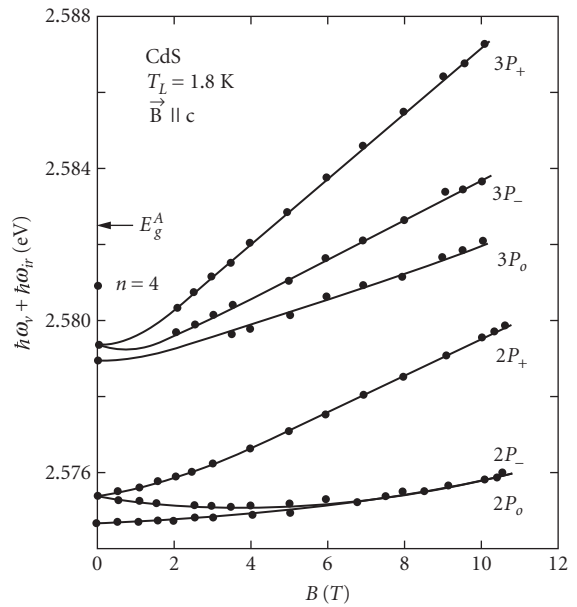
$$S = \hbar eB / m_0 \quad (55)$$

Thus after calculating the interband transition energy for a particular conduction band Landau level  $n$ , one subtracts the above binding energy to correct for exciton effects.

Nondegenerate semiconductors, in particular, materials belonging to the wurtzite crystal structure, have been extensively studied both with and without a magnetic field. Exciton states in CdS have been studied by high-resolution two-photon spectroscopy in a magnetic field using a fixed near-infrared beam and a tunable visible dye laser.<sup>83,84</sup> Figure 41 shows the photoconductive response versus total photon energy near the A-exciton region.<sup>83</sup> The two-photon transitions involve P states, and both 2P and 3P states are clearly seen. As the field is increased, both Zeeman splittings and diamagnetic shifts occur. Figure 42 shows both experimental and theoretical transition energies versus  $\mathbf{B}$  field.<sup>83</sup> Excellent agreement is obtained by using variational calculations that have been successfully used to describe impurity atoms in a magnetic field.



**FIGURE 41** Photoconductivity vs. total photon energy  $\hbar\omega_v + \hbar\omega_{ir}$  near the A-exciton region in CdS platelets for various magnetic fields. The magnetic field was parallel to the hexagonal  $c$  axis in a Voigt configuration with  $E$  perpendicular to  $c$  for the two photons at a lattice temperature of  $T_L = 1.8$  K. The instrumental resolution  $R = 0.1$  meV is narrower than the intrinsic linewidths.<sup>83</sup>

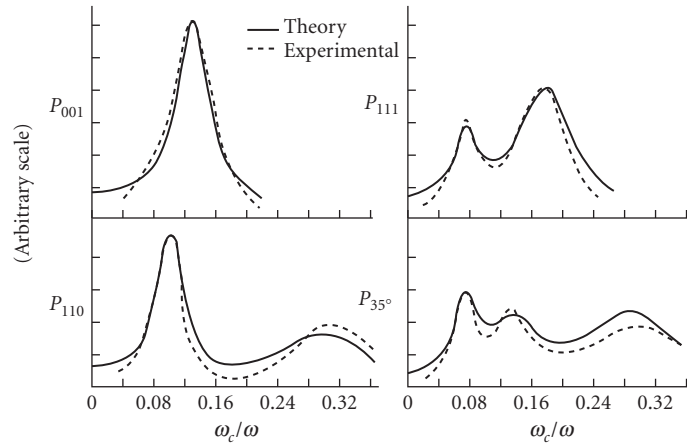


**FIGURE 42** Peak positions, in total photon energy  $\hbar\omega_v + \hbar\omega_{ir}$ , for the 2P and 3P A excitons in CdS platelets as a function of applied  $B$  field. The solid points were determined experimentally, and the solid curves are theoretically obtained from variational calculations of the diamagnetic shifts along with use of the experimental  $g$ -factors.<sup>83</sup>

### Intraband or Free-Carrier Effects

**Cyclotron resonance** Cyclotron resonance absorption of free carriers is the simplest and most fundamental magneto-optical effect and provides a direct determination of carrier effective masses. Classically, it is a simple phenomenon—charged particles move in circular orbits (in planes perpendicular to the direction of the magnetic field) whose radii increase as energy is absorbed from the applied electric fields at infrared or microwave frequencies. After a time  $\tau$ , a collision takes place and





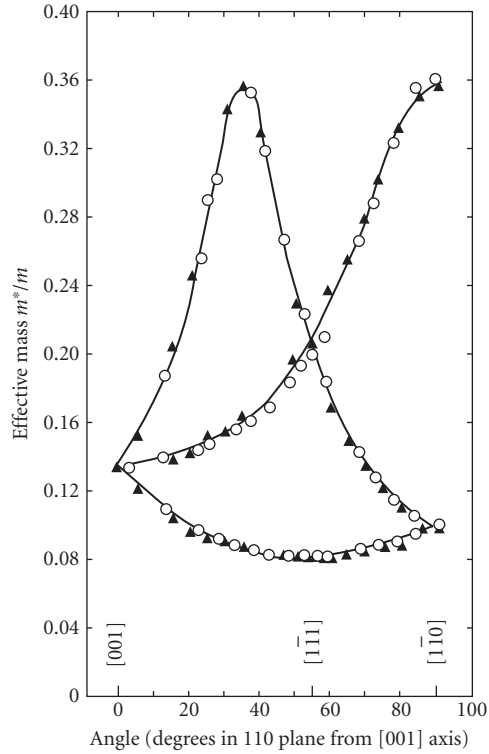
**FIGURE 43** Microwave absorption in intrinsic  $n$ -type Ge at 4.2 K for four different directions of  $\mathbf{B}$  in the (110) plane as a function of the magnetic field.  $P_{35^\circ}$  represents the absorption with  $\mathbf{B}$  at  $35^\circ$  to the [001] axis.<sup>88</sup>

the absorption process begins again. From the resonance relation  $\omega_c = e\mathbf{B}/m^*$ , extensive and explicit information about the effective masses and the shape of energy surfaces near the band extrema can be obtained. Excellent reviews of cyclotron resonance have been previously published by McCombe and Wagner<sup>85,86</sup> and Kobori et al.<sup>87</sup>

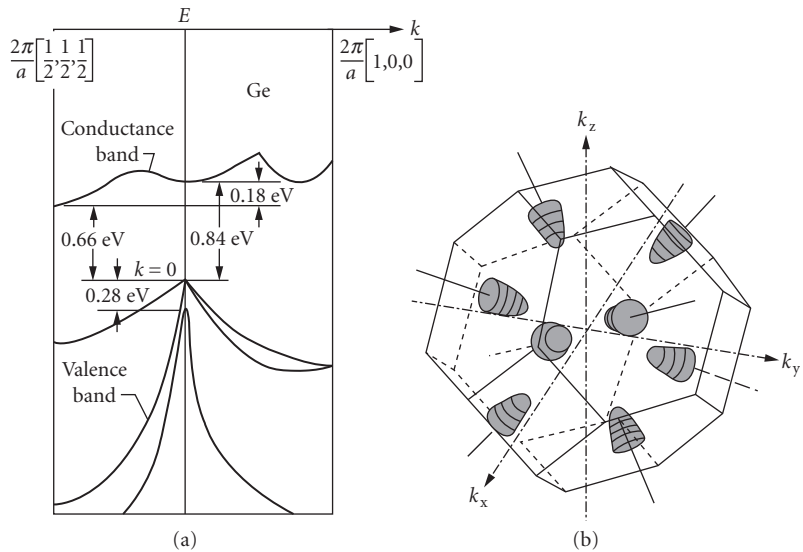
A classical example of the explicit band structure information that can be obtained from cyclotron resonance experiments is given for Ge. Figure 43 shows the microwave absorption for  $n$ -type germanium at 4.2 K for four different  $\mathbf{B}$ -field directions, each peak corresponding to a specific electron effective mass.<sup>88</sup> Figure 44 shows the orientation dependence of the effective masses obtained from the cyclotron resonance experiments which demonstrates that there is a set of crystallographically equivalent ellipsoids oriented along all  $\langle 111 \rangle$  directions in the Brillouin zone.<sup>89</sup> Figure 45 shows the band structure of Ge that these measurements helped to establish<sup>90</sup>:  $a$  illustrates the conduction band minima along the  $\langle 111 \rangle$  direction at the zone edge and  $b$ , the eight half-prolate ellipsoids of revolution or four full ellipsoids. The longitudinal and transverse masses are  $m_l^* = 1.6m_0$  and  $m_t^* = 0.082m_0$ , respectively. Both holes and electrons could be studied by using light to excite extra carriers. This illustrates the use of cyclotron resonance methods to obtain band structure information. Since that time, numerous experiments have been carried out to measure effective mass values for carriers in various materials.

The beginning of modern magneto-optics in which “optical” as opposed to “microwave” techniques were used, began in 1956 with the use of infrared frequencies at high magnetic fields. Far-infrared lasers are extremely important for modern-day measurements of cyclotron resonance as seen in Fig. 46 for  $n$ -type InSb.<sup>91</sup> At low temperatures, only the lowest CR transition  $C_1$  ( $0^+ \rightarrow 1^+$ ) is seen. Raising the temperature populates the higher-lying Landau levels, and other CR transitions are seen at different fields because of the nonparabolicity of the conduction band which gives rise to an energy-dependent effective mass. At 13 K, a second transition  $C_2$  ( $0^- \rightarrow 1^-$ ) is seen and at 92 K,  $C_3$  ( $1^+ \rightarrow 2^+$ ). The low field feature denoted by  $I$  is called impurity cyclotron resonance because, although it is a neutral donor excitation, its appearance resembles that of the regular CR magnetoabsorption. It results from neutral donors exhibiting a Zeeman transition ( $1s \rightarrow 2p^+$ ), the transition energy of which is much larger than the ionization energy. The  $I$  signal gradually disappears as the temperature increases because the donors become ionized.

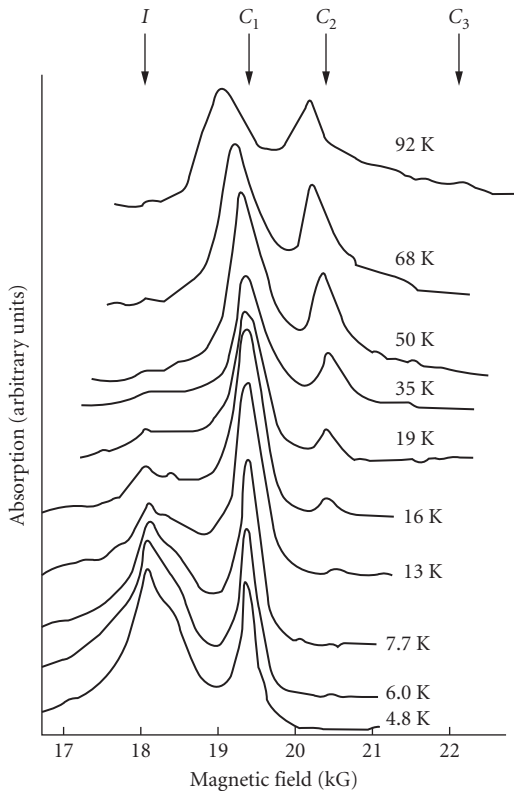
Cyclotron resonance also serves as a valuable tool for materials characterization through making use of the cyclotron resonance linewidth and intensity. Resonance linewidths can differ considerably from sample to sample. This difference in linewidth is attributed to differences in impurity content, with the higher-purity samples having the narrowest linewidths and largest intensities. Figure 47 shows the electron CR signals for both  $n$ -type and  $p$ -type GaAs crystals with low compensation.<sup>87</sup>



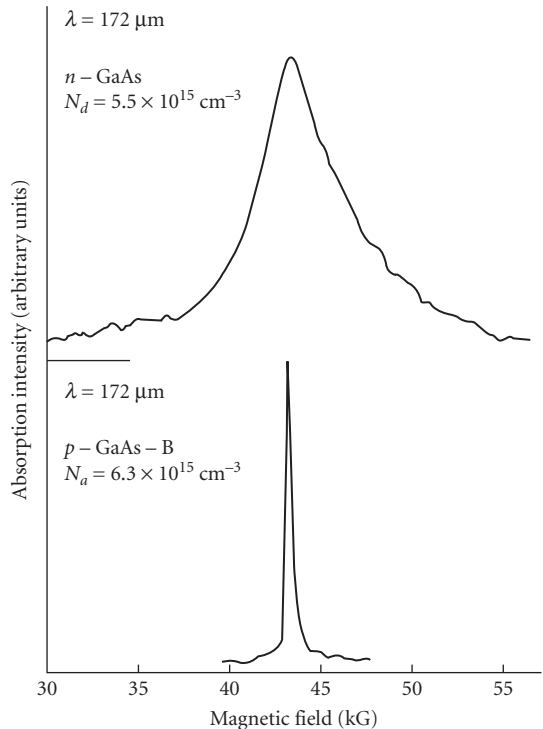
**FIGURE 44** Effective mass of electrons in Ge at 4 K for magnetic field directions in a (110) plane.<sup>89</sup>



**FIGURE 45** (a) Band structure of Ge plotted along the [100] and [111] directions and (b) ellipsoidal energy surface corresponding to primary valleys along the  $\langle 111 \rangle$  directions.<sup>90</sup>



**FIGURE 46** Thermal equilibrium resonance traces in  $n$ -type InSb at various temperatures. At 4.8 K, only the lowest cyclotron transition  $C_1(0^+ \rightarrow 1^+)$  and impurity cyclotron resonance  $I$  are visible. On raising the temperature, the signal  $I$  disappears on complete ionization of donors, while the second and third cyclotron transitions  $C_2(0^- \rightarrow 1^-)$  and  $C_3(1^+ \rightarrow 2^+)$  start to show up.<sup>91</sup>



**FIGURE 47** Difference in electron cyclotron resonance linewidth between  $n$ - and  $p$ -type GaAs crystals, having the same order of donor or acceptor concentrations.<sup>87</sup>

The observed large difference in linewidths is primarily considered to reflect the difference in the electron-donor and electron-acceptor scattering rates.

An electron placed in the conduction band of a polar insulator or semiconductor surrounds itself with an induced lattice-polarization charge. The particle called a polaron consists of the electron with its surrounding lattice-polarization charge. The term *magnetopolaron* is also often referred to as a polaron in a magnetic field. Landau-level energies of these magnetopolarons are shifted relative to those predicted for band electrons. These energy shifts give rise to polaron effects that are most clearly evident in optical experiments such as cyclotron resonance. The review by Larsen provides an annotated guide to the literature on polaron effects in cyclotron resonance.<sup>92</sup>

*Free-carrier Faraday rotation and other effects* Observation of free-carrier rotation was first reported in 1958. It is best understood as the differential dispersion of the cyclotron resonance absorption, and, as such, it is an accurate method for determining carrier effective masses. It can be measured off resonance and detected under conditions which preclude the actual observations of cyclotron resonance absorption. Cyclotron resonance is a more explicit technique which enables carriers of different mass to be determined by measuring different resonant frequencies. The Faraday effect is an easier and

more flexible technique, but is less explicit, since the dispersion involves the integral of all CR absorption. Also, it is unable to detect any anisotropy of the effective mass in a cubic crystal.

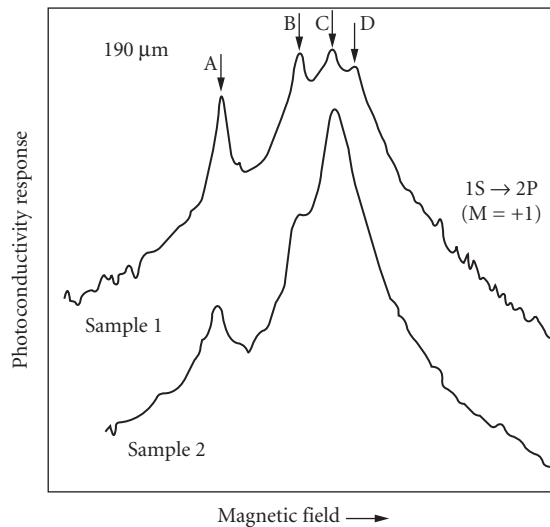
Other free-carrier effects are ellipticity associated with the Faraday rotation, the Voigt effect, and the magnetoplasma effect on the reflectivity minimum.

*Impurity magnetoabsorption* Impurity states forming shallow levels (i.e., those levels separated from the nearest band by an energy much less than the gap  $E_g$ ) can be described by the effective mass approximation. This simple model for impurities is that of the hydrogen atom with an electron which has an effective mass  $m^*$  and the nuclear charge reduced to  $e/\epsilon_\infty$ , by the high-frequency dielectric constant of the crystal. This hydrogen-atom-like model leads to a series of energy levels leading up to a photoionization continuum commencing at an energy such that the electron (hole) is excited into the conduction (or valence) band.

The effect of a magnetic field on impurity levels and the related optical transitions is one of the most important tools for the study of the electronic states in semiconductors. The reason for this is that a magnetic field removes all degeneracies including the Kramers' degeneracy due to time reversal. It can produce new quantization rules, and it is a strong perturbation which is not screened like the Coulomb interactions.

For donor states with an isotropic conduction band minimum, as in GaAs or InSb, the hamiltonian acquires terms which are linear (Zeeman term) and quadratic (diamagnetic) in magnetic field. In this case, perturbation theory is appropriate to use until one considers transitions to very high quantum numbers or very high fields. Often complicated variational procedures must be used for accurate solutions. In the high field limit where  $\hbar\omega_c/R \gg 1$  or for high energies, the impurity level quantum numbers do not provide a proper classification, and, instead, the states should be related to the continuum Landau levels. The effect of a magnetic field on acceptor impurity states is more complicated because of band degeneracy and of spin-orbit coupling. Also for acceptors, one can be in the high field limit at relatively small values of the field for shallow levels and for excited states.

High-resolution photoconductivity measurements in high-purity GaAs indicate that the behavior of shallow donors in GaAs deviates from that predicted by the simple hydrogenic model. Figure 48



**FIGURE 48** The photoconductivity due to the ( $1s \rightarrow 2p$ ,  $m = +1$ ) transition as a function of magnetic field for two different samples when excited by  $190 \mu\text{m}$  laser radiation. For sample 1,  $N_D = 2.0 \times 10^{14} \text{ cm}^{-3}$ ,  $N_A = 4.0 \times 10^{13} \text{ cm}^{-3}$ , and  $\mu_{77\text{K}} = 153,000 \text{ cm}^2/\text{V} \cdot \text{s}$ . For sample 2,  $N_D = 4.3 \times 10^{13} \text{ cm}^{-3}$ ,  $N_A = 2.5 \times 10^{13} \text{ cm}^{-3}$ , and  $\mu_{77\text{K}} = 180,000 \text{ cm}^2/\text{V} \cdot \text{s}$ .<sup>93</sup>

shows that, under high resolution, the single ( $1s \rightarrow 2p$ ) transition observed at lower resolution actually consists of several different unresolved transitions.<sup>93</sup> The photoconductive response is shown for two different high-purity GaAs samples. The magnetic field range shown covers about 1 kG at around 15 kG. The different transitions labeled A, B, C, and D each correspond to a different donor species, and variation of the amplitude of these transitions in different samples results from the different relative concentrations of the particular donor species. Thus, the use of magnetic fields in studying the absorption properties of shallow impurities provides an analytical method of characterizing impurities. Because of the central-cell corrections (chemical shifts), different impurities of the same type (donor or acceptors) can be distinguished and identified by back-doping experiments.

**Semiconductor Nanostructures: Low Dimensional Systems** Development of growth techniques such as molecular beam epitaxy and metal organic chemical vapor deposition have made possible the precise growth of high-quality, layered, semiconductor heterostructures. Various sequences of thin film layers can be grown to form quantum wells, wires, and dots as well as superlattices and heterojunctions. In these low dimensional systems, the quantization effect of the magnetic field is significantly enhanced, leading to a wealth of new ways to characterize these structures. We refer the readers to recent books that review these systems.<sup>94,95</sup>

## Nonlinear Optical Properties of Semiconductors

**Background** The study and characterization of nonlinear optical properties of semiconductors are increasingly important topics for research and development, with new effects being discovered and useful nonlinear optical devices being constructed. The underlying cause of these nonlinear optical effects lies in the interaction of electromagnetic radiation with matter. Each nonlinear optical process may be thought to consist of the intense light first inducing a nonlinear response in a medium and then the medium in reacting, modifying the optical fields in a nonlinear way. There is a wide variety of nonlinear optical phenomena in semiconductors, leading to many papers on the subject of nonlinear properties. It is thus not possible here to do justice to this field. We refer the reader to Chap. 10, "Nonlinear Optics."<sup>96</sup> Here, we give a brief overview of the nonlinear optical processes starting from Maxwell's equations and describe and categorize some important second- and third-order nonlinear processes and properties.

### Theoretical Overview of Nonlinear Optical Processes and Properties

**Maxwell's equations and polarization power series expansion** All electromagnetic phenomena are governed by Maxwell's equations for the electric and magnetic fields  $\mathbf{E}(\mathbf{r}, t)$  and  $\mathbf{B}(\mathbf{r}, t)$  or by the resulting wave equations

$$\left[ \nabla \cdot \nabla + \frac{1}{c^2} \frac{\partial^2}{\partial t^2} \right] \mathbf{E}(\mathbf{r}, t) = \frac{-4\pi}{c^2} \frac{\partial^2}{\partial t^2} \mathbf{P}(\mathbf{r}, t) \quad (56)$$

$$\nabla \cdot \mathbf{E}(\mathbf{r}, t) = -4\pi \nabla \cdot \mathbf{P}(\mathbf{r}, t)$$

Here,  $\mathbf{P}$  is the generalized electric polarization which includes not only the electric dipole part but all the multiple contributions. In general,  $\mathbf{P}$  is a function of  $\mathbf{E}$  which describes fully the response of the medium to the field. It is often known as the constitutive equation since all optical phenomena would be predictable and easily understood from it and its solution for the resulting set of Maxwell's equations with appropriate boundary conditions. Unfortunately, this equation is almost never possible to solve exactly, and physically reasonable approximations must be resorted to for progress to occur.

Most nonlinear optical properties can be described in terms of a power series expansion for the induced polarization. (This assumes that  $\mathbf{E}$  is sufficiently weak.) Since lasers are most often used to observe nonlinear optical effects, one usually deals with the interaction of several monochromatic or quasi-monochromatic field components, and  $\mathbf{E}$  and  $\mathbf{P}$  can be expanded into their Fourier components as

$$\mathbf{E}(\mathbf{r}, t) = \sum_i \mathbf{E}(\mathbf{q}_i, \omega_i), \quad \mathbf{P}(\mathbf{r}, t) = \sum_i \mathbf{P}(\mathbf{q}_i, \omega_i) \quad (57)$$

where

$$\mathbf{E}(\mathbf{q}_i, \omega_i) = \mathbf{E}(\omega_i) \exp(i\mathbf{q}_i \cdot \mathbf{r} - i\omega_i t) + \text{c.c.} \quad (58)$$

The induced polarization is usually written as

$$\begin{aligned} \mathbf{P}(\mathbf{q}_i, \omega_i) = & \chi^{(1)}(\mathbf{q}_i, \omega_i) \cdot \mathbf{E}(\mathbf{q}_i, \omega_i) + \sum_{j,k} \chi^{(2)}(\mathbf{q}_i = \mathbf{q}_j + \mathbf{q}_k, \omega_i = \omega_j + \omega_k) : \mathbf{E}(\mathbf{q}_j, \omega_j) \mathbf{E}(\mathbf{q}_k, \omega_k) \\ & + \sum_{j,k,l} \chi^{(3)}(\mathbf{q}_i = \mathbf{q}_j + \mathbf{q}_k + \mathbf{q}_l, \omega_i = \omega_j + \omega_k + \omega_l) : \mathbf{E}(\mathbf{q}_j, \omega_j) \mathbf{E}(\mathbf{q}_k, \omega_k) \mathbf{E}(\mathbf{q}_l, \omega_l) + \dots \quad (59) \end{aligned}$$

It is, however, sometimes more convenient to use  $\mathbf{E}(\mathbf{r}, t)$  and  $\mathbf{P}(\mathbf{r}, t)$  directly instead of their Fourier components, especially when dealing with transient nonlinear phenomena.

In the electric dipole approximation,  $\chi^{(n)}(\mathbf{r}, t)$  is independent of  $\mathbf{r}$ , or  $\chi^{(n)}(\mathbf{k}, \omega)$  is independent of  $\mathbf{q}$ , and the equations become simpler to write and to work with. These  $\chi^{(n)}$  are the susceptibilities, with  $\chi^{(1)}$  = linear electric dipole susceptibility and  $\chi^{(2)}$  ( $\chi^{(3)}$ ) = nonlinear second-order (third-order) susceptibility tensor. Both absorptive and refractive effects can be described in terms of these complex electric susceptibilities, which have real and imaginary parts for each tensor element. These linear and nonlinear susceptibilities characterize the optical properties of the medium and are related to the microscopic structure of the medium. Knowledge of  $\chi^{(n)}$  allows, at least in principle, to predict the  $n$ th-order nonlinear optical effects from Maxwell's equations. Consequently, much effort (both experimentally and theoretically) has gone into determining the  $\chi^{(n)}$ .

The definitions of the nonlinear susceptibilities in the literature vary and have led to some confusion. Shen reviews these definitions and the reasons for the confusion.<sup>97</sup> In addition to some intrinsic symmetries, the susceptibilities must obey crystallographic symmetry requirements. The spatial symmetry of the nonlinear medium imposes restrictions upon the form of the various  $\chi^{(n)}$  tensors. Butcher has determined the structure of the second- and third-order tensors for all crystals.<sup>98</sup> One important consequence is that, for media with inversion symmetry,  $\chi^{(2)} \equiv 0$ , and thus  $\chi^{(3)}$  represents the lowest-order nonlinearity in the electric-dipole approximation. Of the 12 nonzero elements, only 3 are independent. These susceptibility tensors must transform into themselves under the point group symmetry operations of the medium.

It is often convenient to discuss the various optical processes which might occur in terms of whether they are active or passive. Passive processes involve energy or frequency conservation, and the material medium acts basically as a catalyst. The susceptibilities are predominantly real for passive processes. Of course, as resonances are approached, susceptibilities become complex and may even become totally imaginary. These passive nonlinear optical phenomena are listed in Table 7.<sup>99</sup> Active nonlinear optical phenomena are listed in Table 8.<sup>99</sup> In general, energy is exchanged between the radiation and the material only for the active processes. We also note that second-order effects are always passive.

*Second-order nonlinear optical properties* Most existing nonlinear optical devices are based upon second-order nonlinear optical effects that are quite well understood. Here, we assume the presence of only three quasi-monochromatic fields

$$\mathbf{E} = \mathbf{E}(\omega_1) + \mathbf{E}(\omega_2) + \mathbf{E}(\omega_3) \quad (60)$$

**TABLE 7** Passive Nonlinear Optical Phenomena<sup>99</sup>

Frequencies of Incident Fields	Frequencies of Fields Generated by the Polarization of the Medium	Susceptibility	Process (Acronym)
$\omega_1$	No polarization	$0(\epsilon = 1)$	Vacuum propagation (VP)
$\omega_1$	$\omega_1$	$\chi^{(1)}(\omega_1; \omega_1)$	Linear dispersion (LD)
$\omega_1, \omega_2$	$\omega_3[\omega_3 = \omega_1 + \omega_2]$	$\chi^{(2)}(\omega_3; \omega_1, \omega_2)$	Sum mixing (SM)
$\omega_1$	$\omega_3[\omega_3 = 2\omega_1]$	$\chi^{(2)}(\omega_3; \omega_1, \omega_1)$	Second-harmonic generation (SHG)
$\omega_1, 0$	$\omega_1$	$\chi^{(2)}(\omega_1; \omega_1, 0)$	Electro-optic linear Kerr effect (EOLKE)
$\omega_1$	$\omega_2, \omega_3[\omega_1 = \omega_2 + \omega_3]$	$\chi^{(2)}(\omega_2; -\omega_3, \omega_1)$	Difference-frequency mixing (DFM)
$\omega_1$	$\omega_2[\omega_1 = 2\omega_2]$	$\chi^{(2)}(\omega_2; -\omega_2, \omega_1)$	Degenerate difference-frequency (DDF)
$\omega_1$	0	$\chi^{(2)}(0; -\omega_1, \omega_1)$	Inverse electro-optic effect (IEOE)
$\omega_1, \omega_2, \omega_3$	$\omega_4[\omega_4 = \omega_1 + \omega_2 + \omega_3]$	$\chi^{(3)}(\omega_4; \omega_1, \omega_2, \omega_3)$	Third-harmonic generation (THG)
$\omega_1, \omega_2$	$\omega_3, \omega_4[\omega_1 + \omega_2 = \omega_3 + \omega_4]$	$\chi^{(3)}(\omega_3; -\omega_4, \omega_1, \omega_2)$ $\chi^{(3)}(\omega_3; -\omega_3, \omega_1, \omega_2)$	Four-wave difference-frequency mixing processes (FWDFMP)
$\omega_1$	$\omega_2, \omega_3, \omega_4[\omega_1 = \omega_2 + \omega_3 + \omega_4]$	$\chi^{(3)}(\omega_2; -\omega_3, -\omega_4, \omega_1)$	Intensity-dependent refractive index (IDRI)
$\omega_1$	$\omega_1$	$\chi^{(3)}(\omega_1; \omega_1, -\omega_1, \omega_1)$	
$\omega_1, 0$	$\omega_1$	$\chi^{(3)}(\omega_1; 0, 0, \omega_1)$	Quadratic Kerr effect (QKE)

$\omega = 0$  indicates the presence of a uniform electric field.

and

$$\omega_1 = |\omega_2 \mp \omega_3| \quad (61)$$

Thus, Eq. (56) can be decomposed into three sets of equations for each  $\mathbf{E}(\omega_i)$ . They are then nonlinearly coupled with one another through the polarizations

$$\mathbf{P}(\omega_1) = \chi^{(1)}(\omega_1) \cdot \mathbf{E}(\omega_1) + \chi^{(2)}(\omega_1 = |\omega_2 \pm \omega_3|) : \mathbf{E}(\omega_2)\mathbf{E}(\omega_3) \quad (62)$$

The second-order nonlinear processes are then described by the solutions of the coupled-wave equations with the proper boundary conditions.  $\chi^{(2)} = 0$  for materials with a center of inversion. The coefficient  $\chi^{(2)}$  is a third-rank tensor. Some second-order processes include sum- and difference-frequency mixing, the electro-optic linear Kerr effect, the inverse electro-optic effect, parametric amplification and oscillation, and second-harmonic generation. The past emphasis has been

**TABLE 8** Active Nonlinear Optical Phenomena<sup>99</sup>

Susceptibility	Process
$\chi^{(1)}(\omega_1; \omega_1)$	Linear absorption ( $\omega_1 \approx \omega_{10}$ )
$\chi^{(3)}(\omega_2; \omega_1, -\omega_1, \omega_2)$	Raman scattering ( $\omega_2 \approx \omega_1 \mp \omega_{10}$ )
$\chi^{(3)}(\omega_1; \omega_1, -\omega_1, \omega_1)$	Two-photon absorption ( $2\omega_1 \approx \omega_{10}$ ) or saturable absorption ( $\omega_1 \approx \omega_{10}$ )
$\chi^{(5)}(\omega_2; \omega_1, \omega_1, -\omega_1, -\omega_1, \omega_2)$	Hyper-Raman scattering ( $\omega_2 \approx 2\omega_1 \mp \omega_{10}$ )

on finding new nonlinear crystals with a large  $\chi^{(2)}$ . Semiconductor crystals have received much attention: III-V compounds like GaAs and InSb, II-VI compounds like ZnS and CdSe, I-III-VI compounds like AgGaS<sub>2</sub> and CuInS<sub>2</sub>, and II-IV-V compounds like CdSiAs<sub>2</sub> and ZnGeP<sub>2</sub>.

In most applications of second-order nonlinear optical effects, it is important to achieve phase-matching conditions

$$\Delta\mathbf{q} = \mathbf{q}_1 - \mathbf{q}_2 - \mathbf{q}_3 = 0 \quad (63)$$

where  $\mathbf{q}_i$  is the wave vector of  $\mathbf{E}(\omega_i)$ . This ensures an efficient energy conversion between the pump field(s) and the signal field.

The intensity of the electric field of a laser can produce photons at multiples of the frequency of the probing light signal ( $\omega_0$ ). Second harmonic generation has been widely used to characterize interfaces between silicon and thin dielectric films as well as thin metal films.<sup>100</sup> There are two sources of second harmonic light at the interface between dielectric films and centro-symmetric crystals such as silicon. One is due to the weak electric quadrupole contribution, and the second is due to a surface dipole contribution.<sup>101,102</sup> The dipole contribution is stronger than the second harmonic signal from the quadrupole one. The detailed crystalline symmetry along the probe beam direction results in a rotational dependence to the quadrupole signal. The surface dipole contribution is strongly affected by chemical changes in the interface making it an ideal means of characterizing subtle process-induced changes in the dielectric film stack used for transistor applications.<sup>101</sup> The second harmonic intensity,  $I$ , from a  $p$ - or  $s$ -polarized probe and a  $p$ - or  $s$ -polarized SHG signal for the Si(100) crystal face are

$$I_{pp}(2\omega) = |a_{pp}^{(0)} + a_{pp}^{(4)} \cos(4\Phi)|^2$$

$$I_{ps}(2\omega) = |a_{ps}^{(4)} \sin(4\Phi)|^2$$

$$I_{sp}(2\omega) = |a_{sp}^{(0)} + a_{sp}^{(4)} \cos(4\Phi)|^2$$

$$I_{ss}(2\omega) = |a_{ss}^{(4)} \sin(4\Phi)|^2$$

Here, the  $a$  coefficients are due to either a surface dipole contribution  $a^{(0)}$  or a bulk quadrupole  $a^{(4)}$  contribution.  $\Phi$  is the angle between the  $[0\bar{1}0]$  crystal axis and the projection of the wave vector of the second harmonic light on the surface. The SHG signal is also strongly influenced by electric fields present in the sample. Changes in the electric field due to trapped charge in hafnium oxide have been characterized using the changes in  $a^{(0)}$  due to annealing temperature.<sup>101</sup> Both the phase and amplitude of the second harmonic signal from Si(100) surfaces have been measured by SHG.<sup>102</sup>

*Third-order nonlinear optical properties* In materials with inversion symmetry, third-order processes are the dominant nonlinearity. These processes are described by a fourth-rank nonlinear susceptibility tensor  $\chi^{(3)}$  whose contribution to the polarization is given according to Eq. (59) by

$$\mathbf{P}(\omega_i) = \sum_{j,k,l} \omega^{(3)}(\omega_i = \omega_j + \omega_k + \omega_l) : \mathbf{E}(\omega_j) \mathbf{E}(\omega_k) \mathbf{E}(\omega_l) \quad (64)$$

In general, this nonlinearity will provide a coupling between four electromagnetic waves. Depending on whether the susceptibility tensor elements are real or imaginary and on whether some of the frequencies are identical or different, a large variety of physical phenomena can be understood and accounted for: third-harmonic generation, two-photon absorption, saturable absorption, intensity-dependent index of refraction, stimulated Raman effect, anti-Stokes generation, stimulated Rayleigh scattering, modulation of the index of refraction, and self-focusing of light. We concentrate on discussing only a few of the most pertinent cases of interest.



*Third-harmonic generation* Here, the output frequency  $\omega_4 = \omega_1 + \omega_2 + \omega_3 = 3\omega_1$ , since  $\omega_1 = \omega_2 = \omega_3$ . The polarization at the frequency  $\omega_4$  will generate radiation at the third-harmonic frequency. The quantum process responsible for the harmonic generation may be described as a scattering process in which three quanta at the fundamental frequency are annihilated and one quantum at the third-harmonic frequency is created. The system remains in the ground state, although three virtually excited states are involved in the scattering process. Since the phases are important, the process is actually an interference between many four-photon scattering processes.

*Two-photon absorption* Here, for example,  $\omega_1 = -\omega_2 = \omega_3 = \omega_4$  and  $\Delta\mathbf{k} = 0$ , and the nonlinear polarization has components described by

$$\mathbf{P}(\omega_4) = \chi^{(3)}(\omega_4 = +\omega_1 - \omega_2 + \omega_3) : \mathbf{E}(\omega_1)\mathbf{E}^*(\omega_2)\mathbf{E}(\omega_3) \quad (65)$$

The nonlinear susceptibility  $\chi^{(3)}$  is purely imaginary, but positive. One can define an absorption coefficient proportional to the intensity itself. In the important case of resonance, the sum of two frequencies of the exciting field is approximately equal to a transition frequency of the medium,  $\omega_{ab} = 2\omega_1$ , where  $\hbar\omega_{ab}$  is the energy difference between two levels  $|a\rangle$  and  $|b\rangle$  with the same parity.

The TPA coefficient can be expressed in terms of a third-order nonlinear susceptibility tensor by solving the wave equation using the slowly varying amplitude approximation. The explicit expression for  $\beta$  is related to the imaginary part of the third-order electric dipole susceptibility tensor which depends upon the crystal class and laser electric field direction, for example, in crystals with  $\bar{4}3m$  symmetry (e.g.,  $\text{Hg}_{1-x}\text{Cd}_x\text{Te}$ , GaAs, InSb, etc.) and the electric field along the [001] direction,<sup>103</sup>

$$\beta = \frac{32\pi^2\omega}{n^2c^2} \left[ 3\text{Im}\chi_{1111}^{(3)}(-\omega, \omega, \omega, -\omega) \right] \quad (66)$$

where the convention used is that of Maker and Terhune (1965).<sup>104</sup>

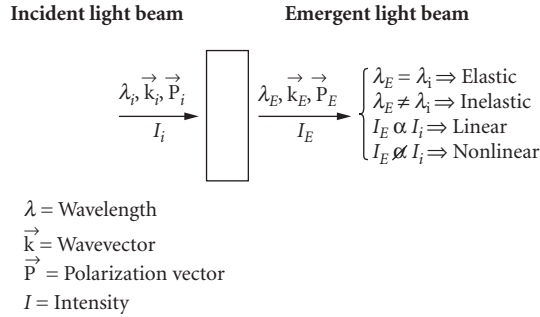
Since  $\chi^{(3)}$  is a second-rank tensor, there are, in general, nine terms contributing to  $\beta$  with magnitudes which vary with orientation. However, in most systems the symmetry is such that there are relations between some of the terms. For example, in crystals with  $\bar{4}3m$  symmetry, there are three possible values of  $\chi$  for each  $\beta$ , and for crystals with  $m\bar{3}m$  symmetry, there are four possible values. These can, in general, be measured by using both linearly and circularly polarized light. It is not always possible to sort out all the different TPA spectra simply by changing the sample orientation or the light polarization because of the competing process of absorption by second-harmonic-produced light.

## 5.4 MEASUREMENT TECHNIQUES

### Overview

The ability to measure the optical response of a semiconductor specimen precisely under well-controlled environmental conditions is of obvious importance in the determination of the optical properties of semiconductors. The significant resolution with which optical spectra can be measured makes it possible to perform precise determinations of the intrinsic properties such as the energy separation between electronic states, lattice vibration frequencies, as well as extrinsic properties due to impurities. The wealth of information that can be obtained and the direct relevance to device-related issues has led to much effort being expended in developing techniques and apparatus to perform a wide range of measurements. This chapter reviews the most widely used procedures and optical components employed in these investigations.

Optical studies, except in rare instances, are contactless and noninvasive. These attractive features have led to widespread use of the techniques in both scientific analyses and, more recently,



**FIGURE 49** Schematic of interaction of light with semiconductors showing the linear, nonlinear, elastic, and inelastic processes.

in manufacturing environments. Specific procedures and experimental apparatus and variations of them are too numerous to be dealt with in this brief chapter. The motivation here is, therefore, to set forth the essentials and dwell on the major aspects of each technique covered, as well as to provide some references which contain more details than could be given here.

The essence of spectroscopic investigations is to determine the interaction of a light beam, with a well-defined wavelength, intensity, polarization, and direction, with a semiconductor specimen, in most cases from the point of view of the light beam. Figure 49 schematically displays this light-specimen interaction. Upon interacting, both the specimen and the light beam will change, and the experimental task is to precisely measure the change in the properties of the light beam. The changes may be classified into the linear and nonlinear regimes based on whether or not the response of the specimen is linear with respect to the incident power. The interactions may be elastic or inelastic; the light beam may also undergo a change in all aspects except its wavelength or photon energy in the former, and the wavelength can also be modified in the latter. These terms arise from the elastic or inelastic interaction of the photon with the specimen where the incident photon energy is preserved or modified in the process. The incident light beam may be reflected, scattered, and transmitted by the specimen. In addition to these processes, a properly excited specimen may emit light as well. The last process, known as luminescence, may also be exploited to gain an insight into the physical behavior of the material.

The linear, elastic regime covers most of the procedures used to elucidate the equilibrium properties related to the optical constants,  $n$  and  $k$ , introduced previously. The techniques used are comprised of reflection and transmission spectroscopies where the energy reflection  $R$  and transmission  $T$  of the specimen are studied as function of the wavelength, polarization, and angle of incidence. The net energy absorption  $A$  may be determined from  $R$  and  $T$  as follows:  $A = (1 - R - T)$ .

As discussed earlier, a complete knowledge of  $R$  or  $T$  over a large range of energies is required to determine both  $n$  and  $k$ . Such a task is usually difficult. A more convenient and accurate procedure is to measure the change in polarization properties of an obliquely incident plane-polarized light beam after it interacts with the specimen. This procedure, called ellipsometry, uses the polarization change of the incident beam in the material to extract  $n$  and  $k$  as well as the thickness of each layer of a multilayer structure.<sup>105,106</sup> The underlying principles and a more detailed discussion follow.

The nonlinear and inelastic spectroscopic procedures have been popular since the advent of lasers. The very large power densities achievable using lasers over the wide range of energies extending from the far-infrared (FIR) to the UV have driven the rapid developments in this field. At high excitation powers, the absorption of light energy can become superlinear due to the presence of higher-order interactions as discussed previously. Exploitation of these specific interactions as a means of gaining information regarding the specimen is the content of nonlinear spectroscopic techniques. On the other hand, the high degree of wavelength purity and coherence offered by lasers is exploited to perform inelastic spectroscopic analyses such as Raman<sup>107</sup> and Brillouin<sup>107</sup> spectroscopies. The crux of these techniques is to project a high-power highly coherent laser beam onto a

specimen and observe the scattered part of the intensity. The scattered part will be dominated by light with the same wavelength as the incident laser beam; that is, the elastic part, but a small part, usually  $<10^{-8}$  of the original intensity, can be observed with well-defined frequency shifts. These additional frequency bands, similar to the sidebands that arise as a consequence of intensity modulation, can be analyzed to provide crucial information regarding the specimen. For instance, optical phonons can interact with the incoming laser photon and energy-shift it by an amount equal to a multiple of the phonon energy. Hence, an analysis of the frequency-shifted bands in the Raman spectrum can be used to establish phonon energies. The major task of Raman spectroscopy is to isolate the very weak frequency-shifted component in the scattered beam.<sup>107</sup>

Light emission is important for both spectroscopic analysis and device applications and, hence, has commanded a large amount of attention.<sup>108,109</sup> Any excited semiconductor will emit light as a means of relaxing to its equilibrium state. Under proper excitation, such as with above-bandgap radiation, the light emission can be made quite intense and can then be easily recorded and subjected to spectroscopic analyses. Within the specimen, the above-bandgap photoexcitation leads to a transition of the electron from a valence band to the conduction band, followed by a rapid process of thermalization whereby the excited electron and hole reach their respective band extrema and recombine from there radiatively; that is, by emitting the potential energy in the form of a photon. The photoexcited free electrons and holes may also form an exciton, or interact with the impurity states in the forbidden band, or both. The final recombination can be mediated by a large number of such intermediate processes, and, hence, the luminescence spectra can display a very rich and complicated structure. The most important aspect of the luminescence spectrum is the fact that nearly all the interactions involve impurity and defect states in the forbidden band. Add to this the rapid thermalization and large self-absorption effects for emission of light with energies greater than the gap, and luminescence is almost entirely a sub-bandgap tool dominated by the impurities and defects present in the semiconductor.

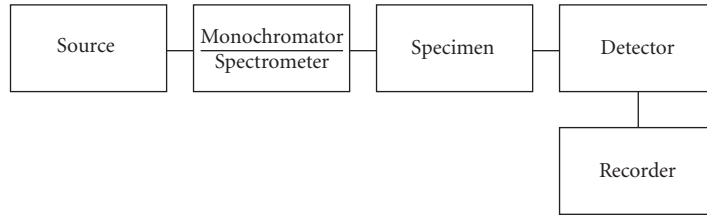
The major categories of spectroscopic procedures are grouped by the energy range of photons used. The commonality of the instrumentation for a given wavelength range accounts for this categorization. The lowest energy region in the FIR spans the phonon energies and a variety of other possible excitations such as plasmons (free-carrier oscillations), magnons, and impurity-related electronic and vibrational excitations. The energy-bandgap of semiconductors ranges from 0 for HgTe to  $>5$  eV<sup>110</sup> in diamond and can hence occur anywhere from the far-infrared to the vacuum ultraviolet. For two of the most important electronic materials, namely Si and GaAs, the gaps occur in the near-infrared at 0.8 and 1.5 eV,<sup>110</sup> respectively. Hence, the mid- and near-infrared investigations have largely been confined to the study of impurity states within the forbidden gap. The electronic band transitions dominate the higher energies.

## Instrumentation

The major components of a spectroscopic system are schematically displayed in Fig. 50. Light from the broadband source enters a monochromator fitted with a dispersion element that separates the various wavelength components and allows a chosen narrow spectral band of light to interact with the specimen. A detector converts the intensity information in the beam to an electrical or digital signal that can then be recorded by a computer or other recording device and then analyzed. Passive components such as lenses and mirrors, filters, polarizers, light pipes, and optical fibers, etc., that are needed to tailor the behavior of the system also form an integral part of the experimental apparatus. A short discussion of each of the major components follows.

### Sources

*Broadband* The ideal broadband source should emit light with sufficient intensity in the wavelength band of interest, possess a stable output and exhibit a minimum amount of noise, and display a slowly varying spectral character; that is, the source should not possess intense spectral features that will interfere with the measurement procedure.<sup>111</sup> All these characteristics can be



**FIGURE 50** Schematic of a spectroscopic measurement apparatus.

satisfied by blackbodies, and, if blackbodies with high enough temperatures can be fabricated, they would be ideal sources for any wavelength region. However, this is not possible since the operating temperatures required to obtain workable energy densities in the ultraviolet are extremely large. Hence, blackbody sources are usually restricted to wavelengths in the red-yellow region starting at  $\approx 500$  nm or larger and ending at  $\approx 2000$   $\mu\text{m}$  in the FIR. The incandescent lamp with a hot filament is the best known BB source. Gas emission lamps such as high-pressure arc lamps and low-pressure discharge lamps are useful in the visible and ultraviolet region. Their main feature is the ability to produce a large intensity in the upper energy regions. However, the inherent atomic processes and associated line spectra that are present make using these somewhat complicated. Care should be exercised to avoid wavelength regions where intense spectroscopic features arise from the discharge medium. The unavoidable electronic activity in the discharge media can also be a source of noise.

*Laser* Laser sources are required in applications where large intensities are essential, as in the studies of nonlinear optical phenomena using Raman scattering or photoluminescence techniques. Lasers are currently available from the UV to the FIR, and often both cw and pulsed operations are possible.<sup>112</sup> The argon and krypton ion lasers with emissions in the visible and near-infrared regions, the Nd:YAG with a 1.06  $\mu\text{m}$  emission, and the  $\text{CO}_2$  laser with emission in the 9.2 to 10.8  $\mu\text{m}$  range have been the workhorses for a wide variety of semiconductor investigations.

Since efficient laser operation requires a set of excitable electronic or vibrational levels properly arranged to produce population inversion and sufficient amplification, intense laser emission is usually confined to specific wavelengths. However, the use of optically excited dye lasers and tunable solid-state lasers such as the Ti:sapphire lasers can be used to fill the wavelength regions in between most of the visible and near-infrared regions.

The semiconductor lasers that are currently available extend in wavelength from the red to the far-infrared. The III-V alloy-based double heterostructure lasers, fabricated from  $\text{Al}_x\text{Ga}_{1-x}\text{As}$  and  $\text{In}_{1-x}\text{Ga}_x\text{As}$ , are particularly efficient in the near-infrared region. The IV-VI alloy-based lasers, fabricated from  $\text{Pb}_{1-x}\text{Sn}_x\text{Te}$ , operate at considerably longer wavelengths of  $\approx 10$   $\mu\text{m}$ ; a small range of emission wavelength tunability has been achieved based on the change of the band gap with the temperature. The intense interest in the development of blue-green laser emission is now having substantial influence.

### *Spectrometers and Monochromators*

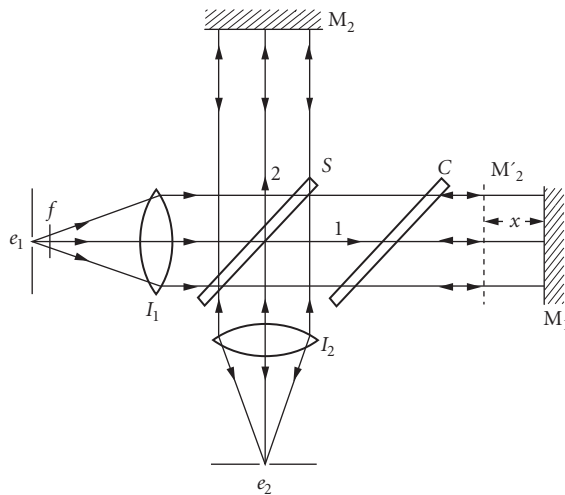
*Dispersion spectrometers* The monochromator or the spectrometer is the heart of the spectroscopic apparatus, and the dispersion element that analyzes the light is the main component of the monochromator.<sup>113</sup> The simplest and best known dispersion unit is the transparent prism. The physical mechanism that leads to the dispersion is the inherent dispersion in the optical refractive index  $n$  of the prism material over the wavelength range of interest. Prism-based monochromators work very well and are still employed. They possess a large throughput; that is, they transmit a large fraction of the incident intensity but suffer from limited resolution since the degree of dispersion is restricted by the characteristics of the prism material.

The most widely used dispersion element is the diffraction grating which is a collection of finely spaced grooves or slits. Diffraction from the multiple slits leads to a dispersive action. The dispersion is given by the following relationship:  $n\lambda = d \sin(\theta)$ .

The fact that the degree of dispersion can be controlled by the slit spacing reduces the complexity of design and fabrication when compared to the prism. Gratings have a drawback in that they display multiple orders, and hence the throughput at any given order is likely to be very high. Blazing (i.e., control of the shape of the groove) can be used to increase energy in a given band in a particular order to reduce this shortcoming. Both transmission and reflection gratings can be fabricated as well as concave gratings that both disperse and focus the light beam. The major manufacturing flaw in grating fabrication that used mechanical devices was that groove spacing was not well controlled and hence the flawed grating led to the appearance of spectroscopic artifacts that were called "ghosts." The advent of holographic grating fabrication procedures has eliminated these difficulties.

*Fourier-transform spectrometers* An alternate method for performing spectroscopic measurements is the use of Michelson's interferometer.<sup>114</sup> Figure 51 displays the layout of the interferometer. The approach in this procedure is to divide the white-light beam from the source into two wavefronts, introduce a path difference  $x$  between the two, recombine them, and record the interference-modulated intensity as a function of  $x$ . The recorded intensity variation  $\mathbf{B}(x)$  is known as the interferogram, and a Fourier transformation of  $I(x)$  will yield the spectral distribution of the white light. Experimentally, this is achieved as shown in Fig. 51. The incident beam from the source is collimated by lens  $I_1$ , split into two wavefronts by the beam splitter  $S$ . The two wave fronts are directed to a movable mirror,  $M_1$ , and a fixed mirror,  $M_2$ . The reflected beams are combined at the detector where the intensity is recorded as a function of  $x$ , the path difference between  $M_1$  and  $M_2$ . The spectrum  $\mathbf{B}(\omega)$  is related to  $I(x)$  by the following relationship:

$$\mathbf{B}(\omega) = \int_0^\infty [I(x) - I(\infty)] \cos(2\pi\omega x) dx \tag{67}$$



$$B(\omega) = \int_0^\infty [I(x) - I(\infty)] \cos(2\pi\omega x) dx$$

**FIGURE 51** Schematic of the Fourier-transform interferometer.

This procedure of measuring the spectra is referred to as Fourier-transform spectroscopy and contains two major advantages: the throughput advantage and the multiplex advantage, both of which greatly add to the ultimate signal-to-noise ratios that can be achieved as compared to measurements performed with grating spectrometers under comparable conditions of illumination and recording times. The throughput advantage arises from the fact that improved resolution is not achieved at the expense of reducing slits and reduced throughput, and the multiplex advantage is a consequence of the fact that all wavelength channels are observed all the time as opposed to a one-channel-at-a-time measurement constriction in the dispersion-based instruments.

These significant advantages come with a price. The much larger signal intensities are likely to be seen by the detector and place stringent conditions on the detector performance in its dynamic range and linearity. Less-than-optimum performance may lead to significant distortions in the transformed spectrum that are not intuitively evident. The FT spectrometer was used first in the far-infrared, soon after the advent of high-speed computers that were capable of performing the Fourier transformations. However, the advances in the technology of designing and fabricating complicated optical elements and computer hardware have contributed greatly to the advancement of the field, and FT spectrometers are now available that cover a wide spectral region extending from FIR to the VUV.

**Detectors** The photomultiplier (PMT)<sup>115</sup> is a widely used light detector that is a vacuum-tube-based device that uses a photoemitter followed by a large ( $>10^5$ ) amplification stage so that very low signal levels can be detected. The wavelength band that the detector responds to is determined by the photocathode and window characteristics. Photomultipliers are particularly useful when low-light-level detection is needed as in Raman spectroscopy, but their use is largely confined to the visible and near-infrared as a consequence of the limitation in obtaining photoemitters for lower energies. Use of fluorescent phosphors can extend the upper working region of the PMTs to the VUV and beyond. Since they are vacuum-based devices, they are fragile and have to be handled with care.

Solid-state detectors<sup>115</sup> which are almost entirely fabricated from semiconductors have advanced to a state where, in many applications, they are preferable to PMTs. The simplest semiconductor detector is the photoconductor (PC), where absorption of an above-band-gap photon leads to an increase in conductivity. Semiconducting PC detectors are, therefore, sensitive to any radiation with an energy larger than the bandgap. Since the bandgap of semiconductors extends all the way from 0 in HgTe to  $>5$  eV in diamond,<sup>110</sup> detectors that function over a very large energy range can be fabricated. Photovoltaic detectors, as the name implies, employ the photovoltaic effect in a p-n junction and can also detect above-bandgap radiation.

The explosive growth in semiconductor technology that has led to large-scale integration has benefited spectroscopic experimenters directly in the field of detectors. Imaging devices such as the CCD (charge-coupled device) array have been incorporated in spectroscopy. The array detectors combined with a dispersion spectrometer can be used for observing multiple channels simultaneously. This has led to an advantage similar to the multiplex advantage in the Fourier spectrometer. In addition, the low noise levels present in these detectors, particularly when they are cooled, have had a large impact on high-sensitivity spectroscopic analysis. Commercially available CCDs are fabricated and, hence, have a lower energy limit of 0.8 eV, the bandgap of Si. However, some linear and 2D arrays, fabricated from InSb and HgCdTe, with longer wavelength response are also available.

## Major Optical Techniques

Advances in semiconductor physics have relied on measuring fundamental material and device properties, measuring the quality of the material, and accurately determining the details of thin films, quantum wells, and other microstructures that control or affect device performance. Properties that need to be determined therefore include basic band structure properties such as energy gaps, the presence and concentration of impurities and defects, alloy parameters, layer thicknesses, homogeneity, and uniformity. A very practical review, "Optical Characterization in Microelectronics Manufacturing" describes in detail six techniques: ellipsometry, infrared spectroscopy, microscopy, modulation spectroscopy, photoluminescence, and Raman scattering.<sup>116</sup> The

discussion of each technique indicates the basic semiconductor quantities measured, gives the scientific basis of the technique, and indicates how the measurement is made. Illustrative examples from the literature are discussed in detail, showing applications to important semiconductor materials.

Much of the basic physics concerning the optical functions of silicon and related materials has been known since the 1950s. Jellison has reviewed the understanding of the physics of optical measurements in the interest of providing the background required for understanding the many optical techniques.<sup>117</sup> The practical value of spectroscopic ellipsometry in gate dielectric metrology for the semiconductor industry is well known and has been documented by Clive Hayzelden.<sup>118</sup> Finally, we point out that there are important applications in real-time monitoring of film growth, etching, and surface modification using spectroscopic ellipsometry measurements with monolayer precision.<sup>119</sup>

**Reflection and Transmission/Absorption** Measurements of the power reflection, transmission, and absorption,  $R$ ,  $T$ , and  $A$ , respectively, are the simplest and most direct methods of spectroscopic analyses of semiconductor materials. The measurements are simple to perform so long as satisfactory spectroscopic apparatus is available in the wavelength region of interest. The major drawback is the less-than-satisfactory absolute accuracies with which the measurements can be performed.

The measurements are usually conducted at near-normal incidence for convenience; normal incidence measurements are difficult to perform and oblique incidence measurements are difficult to analyze. Once the major elements of the spectroscopic system—namely, the source, monochromator, and detector—have been chosen, the  $R$  measurements are obtained by directing the light beam on the specimen and measuring the incident and reflected intensities with the detector. The experimental  $R$  is determined by ratioing the incident and reflected power,  $I_0$  and  $I_R$ , respectively.

$$R = \frac{I_R}{I_0} \quad (68)$$

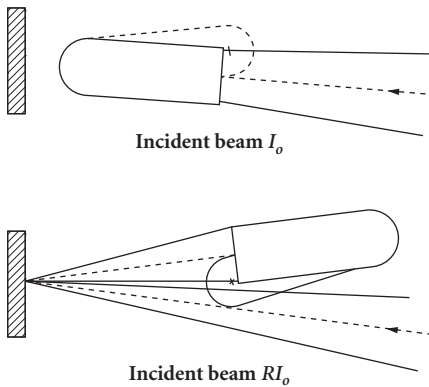
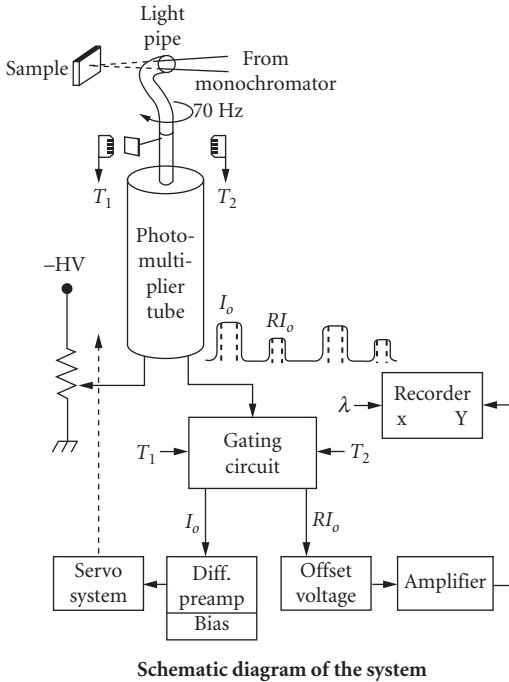
The spectral behavior of the measurement apparatus will not affect the final result so long as they remain fixed during the observation of  $I_0$  and  $I_R$ . A change in the source intensity or the response of the detector will be reflected in the measurement. Since the measurement conditions cannot be identical in the two measurements, this is an unavoidable source of error.

Several arrangements have been attempted to minimize such an error. The most direct approach is to hold the optical path fixed and instead of measuring  $I_0$  and  $I_R$ , one measures  $I_{\text{REF}}$  and  $I_R$ , where  $I_{\text{REF}}$  is the reflected intensity from a well-calibrated reference surface. A ratio of these two measurements leads to the following relationship:

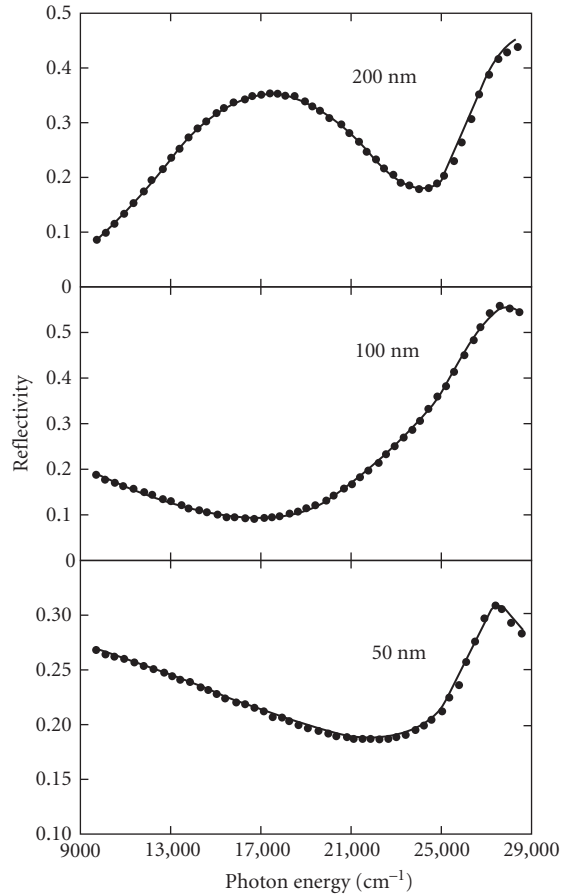
$$\frac{I_R}{I_{\text{REF}}} = \frac{R}{R_{\text{REF}}} \quad (69)$$

A knowledge of  $R_{\text{REF}}$ , the known reflectivity of the reference surface, may then be used to extract  $R$ . This procedure works well and has been employed widely in the infrared region, where reference surfaces from metal mirrors with  $\approx 100$  percent reflectivity and stable blackbody sources are available. For the visible and higher-energy regions that use gas lamp sources that tend to be not as stable as blackbody sources, the reference method is not satisfactory. The procedure used to overcome the short-term variations in the lamp intensity was to perform the ratioing at each measurement wavelength. Such a “real-time” ratioing arrangement used a dynamical arrangement with a rotating optical element that directed the light beam alternately to the reference and the sample. Many such configurations were used, and a good example of a particularly ingenious arrangement is presented in Fig. 52. The essence of this rotating light pipe reflectometer<sup>120</sup> was the rotating light pipe that sampled the incident and reflected beam alternately at a frequency of  $\approx 70$  Hz, a frequency large enough to remove any errors due to variations in the lamp intensity.

The use of reflectometers for the spectroscopic analysis of semiconductors in the visible and near-visible regions has been limited since the advent of the spectroscopic ellipsometer. However, they are still used at higher energies and in applications where their simplicity makes them attractive, for example, to monitor thin films in semiconductor device fabrication.



**FIGURE 52** Schematic diagram of the rotating light pipe reflectometer and expanded top view showing the geometry of the sample and bent light pipe.<sup>120</sup>



**FIGURE 53** Measured (points) and calculated (line) optical reflectivity spectra of silicon dioxide films on silicon.<sup>121</sup>

Recent advances in optics have pushed the energy range of commercial reflectometers to just beyond 10 eV (120 nm) and ellipsometers to just beyond 8 eV (150 nm). Reflectometers and ellipsometers are both currently used for measurement of dielectric film thickness during the manufacture of integrated circuits and other semiconducting multilayer film measurements. The reflectivity spectrum obtained from three  $\text{SiO}_2$  films on Si is presented in Fig. 53.<sup>121</sup> The results of the computer fit are also displayed. The thicknesses determined from the reflection analyses agree to within  $\approx 0.5$  percent of the values obtained from ellipsometric values. As illustrated in the figure, the change in the spectral shape from the 200-nm-thick film to 100 nm is much greater than that between the



100- and the 50-nm films which points to reducing sensitivity to film thickness determination as the films get thinner. The ultra-precise measurement of film thickness for dielectric films less than 2 nm in thickness requires use of ellipsometry.

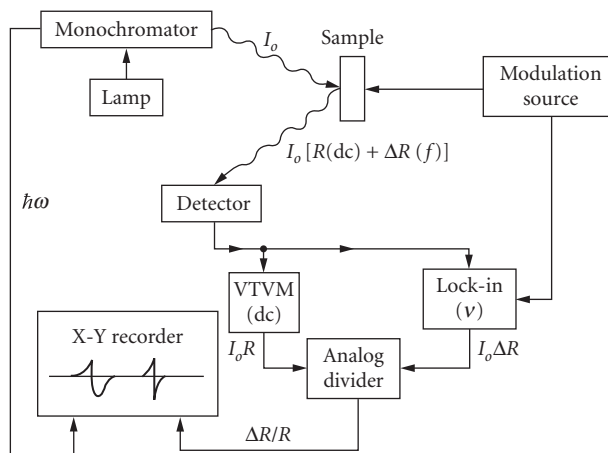
The techniques used to measure the transmission spectra are almost identical to those used for reflection except that nature provides a perfect reference, namely, the absence of the sample in the beam. The sample-in/sample-out reference intensity ratioing works satisfactorily. Since transmission measurements are mainly confined to energies below the forbidden gap and hence lower energies covered by blackbody sources, the difficulties faced by high-energy reflectivity analysis have not been as keenly felt.

The absorption of energy of a specimen may be determined from a knowledge of  $R$  and  $T$ . The most important absorption mechanism is that associated with the electronic transitions discussed previously. The absorption edge spectra for a number of semiconductors were reproduced in Fig. 13. The sub-bandgap region has been studied extensively using absorption spectroscopy where the spectra are dominated by impurity-related effects. The absorption from the electronic transitions associated with a number of impurities in Si was presented earlier in Fig. 33. The impurity-related vibrational features and the lattice phonon bands can be observed as discussed under the section, "Lattice." The collective charge carrier oscillations and impurity to band-type transitions may also be observed in this region.

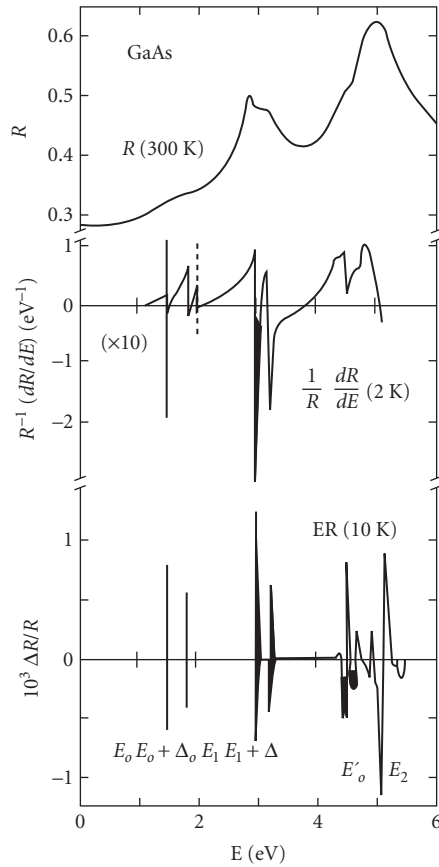
**Modulation Spectroscopy** A very useful variation of the reflection and transmission analysis is the use of modulation techniques that produce a periodic perturbation of a property of the specimen or the light beam and detect in-phase changes in  $R$  and  $T$ . The schematic diagram of a measurement apparatus is presented in Fig. 54.<sup>122</sup> The capacity of lock-in amplifiers for very large amplifications of  $> 10^5$  with a concomitant reduction in broadband noise is the heart of the procedure. Modulations in  $R$  and  $T$ , namely,  $\Delta R$  and  $\Delta T$ , of  $10^{-5}$  can be easily detected. This means the modulating perturbation can be quite small and accessible in routine experimental systems. In the simplest cases, the modulation response of a specimen to a property  $x$  may be expressed as follows:

$$\Delta R = \frac{dR}{dx} \cdot \Delta x \quad (70)$$

where  $\Delta x$  is the intensity of modulation. The modulated property may be internal to the specimen, such as the temperature and pressure, or external, such as the wavelength or polarization of the probe. The most attractive feature, from a measurement point of view, is the fact that modulation



**FIGURE 54** Block diagram of a typical modulation spectrometer.<sup>122</sup>



**FIGURE 55** A comparison of three types of spectra from 0 to 6 eV for a typical semiconductor, GaAs. *Top*: reflectance  $R$ ; *middle*: energy-derivative reflectance; and *bottom*: low-field electroreflectance.<sup>123</sup>

spectra are derivative-like and hence suppress slowly varying background structure and emphasize features in the vicinity of the critical points in the electronic band structure. Figure 55 presents a comparison of the reflective spectrum of GaAs in the 0 to 6 eV region and a wavelength-modulated spectrum and an electric-field-modulated spectrum.<sup>123</sup> Note the narrow linewidths and larger signal-to-noise ratios in both the WMR (wavelength modulation reflectance) and ER (electroreflectance) spectra. For instance, the  $E_0 + \Delta_0$ , indistinguishable in  $R$ , is clearly observable in both WMR and ER. These techniques are crucial in providing accurate values of the interband transition energies, which result in a better understanding of the electronic band structure of a material.

A variety of modulation procedures, underlying mechanisms, measured specimen properties, and other salient features are presented in Table 9.<sup>123</sup> The techniques are broadly classified as internal or external modulation to signify if the perturbation is intrinsic to the measurement approach, as in the case of WMR, or is external, as in the case of ER where an externally applied electric-field modulation is needed at the specimen surface. Temperature, stress, and magnetic-field modulation are included for completion. Compositional modulation that compares two nearly identical alloy samples is less frequently used to investigate semiconductors. Spectroscopic ellipsometry, to be discussed later, may

**TABLE 9** Characteristics of Some Commonly Used Modulation Techniques<sup>123</sup>

Technique	Name	Type	Variable	Sample Parameters Affected	Lineshape Type	Principal Parameters Measured	Principal Advantages	Disadvantages
Wavelength modulation: energy derivative reflectance	Internal	Scalar	Wavelength $\lambda$ ; energy $\hbar\omega$	—	1st derivative	$E_g, \gamma$	Universal applicability; minimal sample preparation; fast, convenient	Measurement system can generate intrinsic structure, not easy to eliminate
Spectroscopic ellipsometry	Internal	Scalar	Wavelength $\lambda$ ; energy $\hbar\omega$	—	Absolute	Dielectric function	As energy derivative reflectance but on $\epsilon_1, \epsilon_2$ directly	Strongly influenced by surface preparation and thin films
Composition modulation	Internal	Scalar	Sample compared to control sample	—	Complicated	Doping, alloying effects	Obtains differences for parameters impossible to vary cyclically	Two samples/beam motion involved; alignment and surface preparation critical
Thermomodulation	External	Scalar	Temperature $T$	Threshold $E_g$ ; broadening parameters $\gamma$	1st derivative	$E_g, \gamma, dE_g/dT, d\gamma/dT$	Wide applicability; identifies Fermi-level transitions in metals	Slow response (1–40 Hz); broad spectra
Hydrostatic pressure	External	Scalar	Pressure $P$	Threshold $E_g$	1st derivative	Deformation potentials		Cannot be modulated; must be used in conjunction with another technique
Light modulation (photoreflectance) (photovoltage)	External	Scalar or tensor	Intensity $I$ of secondary beam	Carrier concentration or surface electric field	Complicated	$E_g$	Convenient; minimal sample preparation required	Effect on material usually not well-defined
Uniaxial stress	External	Tensor	Stress $X$	Threshold $E_g$ ; matrix elements	1st derivative	$E_g, \gamma$ symmetries; deformation potentials	Symmetry determination	Difficult to modulate; limited to high fracture/yield stress materials
Electric field	External	Tensor	Field $\mathbf{E}$	Electron energy $E(k)$ oscillations	3rd derivative (low) Franz-Keldysh symmetries (high)	$E_g, \gamma$ Effective masses in VUV; impurity concentrations	Very high resolution; only high-resolution technique usable	Requires certain resistivity ranges
Magnetic field	External	Tensor	Field $\mathbf{H}$	Election energy levels	Landau levels	$E_g$ , effective masses	Extremely high resolution	Advantages realized only for lower conduction band minima

also be considered to be a polarization-modulation technique. Modulation techniques are useful in yielding crystal properties such as the electronic transition energies as well as information regarding the perturbation mechanism such as the electro-optic or magneto-optic effects.

A widely used and very useful form of a modulation technique for the study of semiconductors is the electric-field-modulated reflection spectroscopy, referred to as electroreflectance. The basis of the procedure is the electric-field-induced changes in the optical response.

The electric-field-induced perturbations can be treated in detail by considering the effects of the applied potential on the electronic band structure. For relatively weak fields (i.e., for field strengths not large enough to modify the band structure significantly), the major perturbation mechanism may be considered to be the acceleration of the electron to a successive set of momentum states. The perturbation to  $\epsilon(\mathbf{E}, \mathbf{E})$ , for such a simple case may be expressed as:<sup>123</sup>

$$\Delta\epsilon = \frac{(\hbar\Omega)^3}{3E^2} \frac{\partial^3}{\partial E^3} [E^2 \cdot \epsilon(E)] \quad (71)$$

where  $E$  is the energy and

$$(\hbar\Omega)^3 = (e^2 \mathbf{E}^2 \hbar^2) / (8\mu_{\parallel}) \quad (72)$$

$e$  is the electronic charge, and  $\mu_{\parallel}$  the effective mass parallel to  $\mathbf{E}$ .

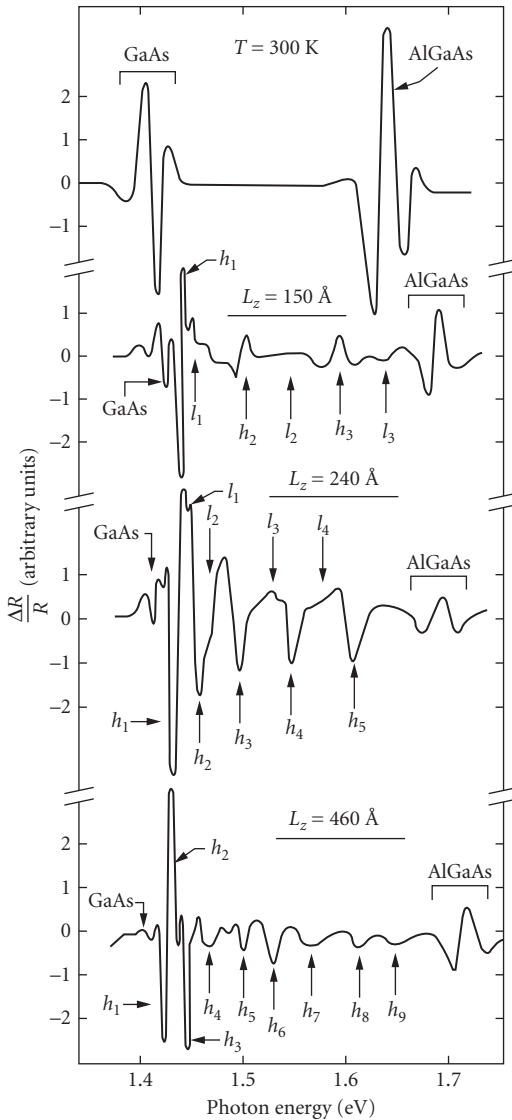
When the field is large, the electroreflectance spectra display oscillatory structure, known as Franz-Keldysh oscillations, and  $\Delta R/R$  has a more complicated functional form that can be found in Ref. 124.

In practical terms, the oscillations may be analyzed to determine  $\hbar\Omega$  and, hence, the strength of the electric field that causes the perturbation.

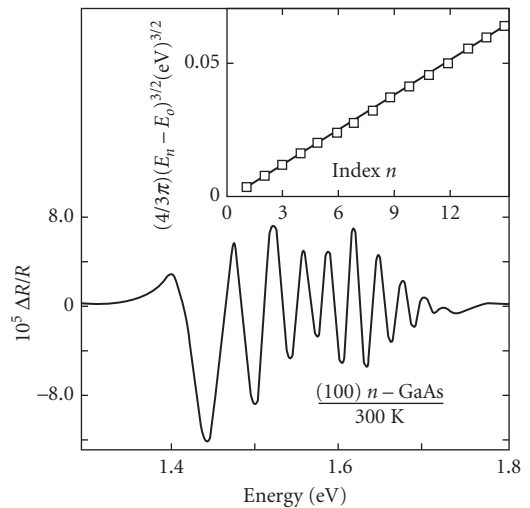
A particularly attractive and widely used form of electroreflectance is the contactless form of electric-field-modulated reflectivity known as photorefectance (PR).<sup>125</sup> In this procedure, one uses the electric-field modulation produced near the surface of the specimen by a chopped laser beam to modulate the reflectivity of a weak probe beam. PR is observable when there is band bending at the surface of the semiconductor such as that observed in damaged oxide layers on silicon.<sup>126,127</sup>

The sharp features in the PR spectrum associated with the critical points in the electronic density of states including the direct gap  $E_g$  may be employed to determine the transition's energies accurately. The information obtained using ER and PR was instrumental in leading to a detailed understanding of the band structure of semiconductors. The variation of the critical point energies with alloy composition has been used to understand the electronic behavior as well as characterize semiconductor alloys.<sup>128</sup> Similar studies have been used extensively in the study of microstructures, where PR is particularly useful since it allows the observation of the gap as well as several additional higher-energy transitions as shown in Fig. 56.<sup>129</sup> Distinct transition from both the well and the barrier region can be observed, and, hence, a complete picture of the microstructure can be obtained. The electric-field-induced Franz-Keldysh oscillations in the ER and PR line shapes have been used to establish the electric field strengths,<sup>124,130</sup> and, more recently, a similar technique has been used to measure the electric field strength in the surface region of GaAs and the effects of passivation<sup>130</sup> as shown in Fig. 57. The electric field strength can be determined from the slope of the inset in Fig. 57. Since PR measurements can be performed at room temperature with minimal sample preparation, it is attractive for routine characterization. Commercial PR spectrometers are now available for use in semiconductor fabrication. Several excellent reviews of the applications of PR are available. A compilation of activity may be found in the Proceedings of the 1990 International Conference on Modulation Spectroscopy<sup>131</sup> and the review by Glembocki and Shanabrook,<sup>132</sup> and the reader is referred to them for more details. A more recent reference is the third International Workshop on Modulation Spectroscopy of Semiconductor Structures, July 3–5, 2008, Wrocław, Poland.

**Ellipsometry** The reflection and transmission measurements discussed in the previous section consider the ratio of the incident to the reflected or transmitted optical power and hence ignore

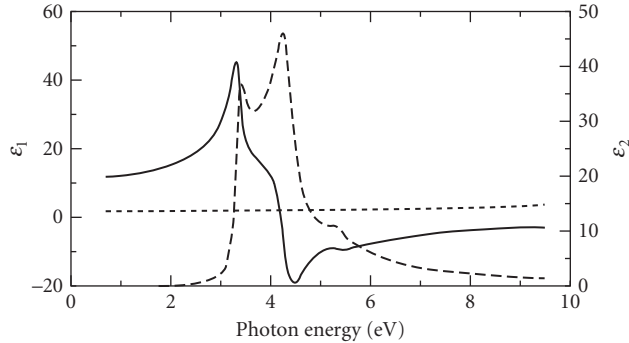


**FIGURE 56** Room-temperature PR spectra for an undoped GaAs/Al<sub>x</sub>Ga<sub>1-x</sub>As heterojunction and three multiple quantum-well samples with  $x \approx 0.2$ ,  $L_z$  is the well thickness, and arrows labeled  $h_1, h_2, \dots$  ( $l_1, l_2, \dots$ ) correspond to calculated values of interband transitions involving heavy (light) hole valence bands.<sup>129</sup>



**FIGURE 57** Photoreflectance spectrum at room temperature with  $I_{\text{pump}} = 3 \mu\text{W}/\text{cm}^2$  and  $I_{\text{probe}} = 2 \mu\text{W}/\text{cm}^2$ . The inset shows a plot of  $(4/3\pi)(E_n - E_0)^{3/2}$  as a function of index  $n$ . The slope of the line in the inset yields the electrical field strength.<sup>130</sup>

any information carried by the phase change suffered by the incident beam. A complete description of the reflection or transmission process will have to include the phase information as well. Ellipsometry attempts to obtain part of the phase information by measuring the phase difference, introduced upon reflection, between the normal components of obliquely incident plane-polarized



**FIGURE 58** Real (solid) and imaginary (dashed) parts of the dielectric function of Si determined using VUV spectroscopic ellipsometry. For comparison, the real part of the dielectric function of  $\text{SiO}_2$  is given by the short-dashed line.<sup>138</sup>

light. Even though the absolute phase suffered by each component is not measured, the phase difference may be measured easily as an ellipticity in the polarization state of the reflected light, hence, the name ellipsometry. Recent developments in ellipsometry as well as handbooks covering practical applications can be found in Refs. 133, 134, 135, 136, and 137.

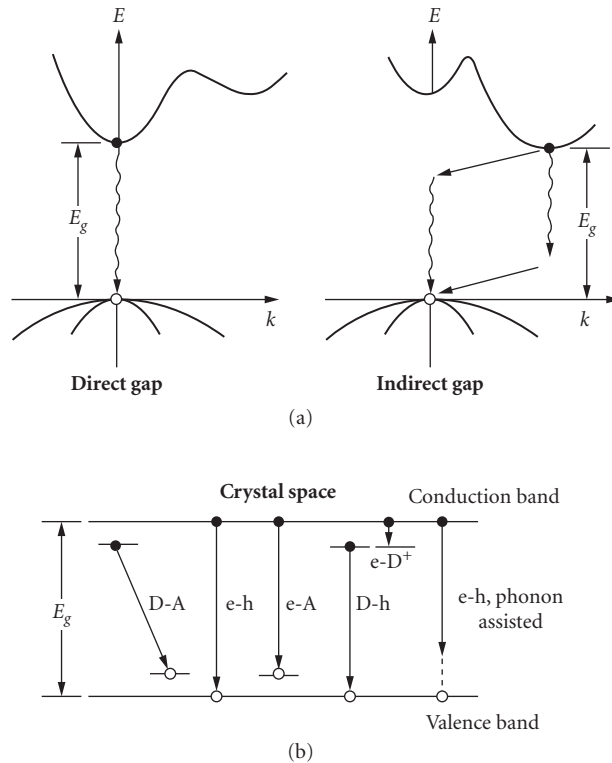
The intrinsic sensitivity of ellipsometry may be illustrated by considering a thin film with thickness  $d$ , refractive index  $n$ , and measurement wavelength  $\lambda$ . The phase change in the reflected component can be measured to a precision of  $0.001^\circ$  in ellipsometers which translates to a sensitivity of approximately  $10^{-4}\lambda$  in thickness. Such extraordinary precision may be used for the study of sub-monolayer films or as a real-time monitor for measuring very small changes in materials' properties. With recent advances in instrumentation, the lower wavelength limit has been extended to below 135 nm (9.5 eV). As an example, Figure 58 shows the dielectric functions of Si and  $\text{SiO}_2$  between 0.7 eV and 9.5 eV. Due to the extended spectral limit into the VUV, ellipsometry has become attractive to study wide-bandgap semiconductors, insulators, oxides, and very thin films.<sup>138</sup>

Recent extensions of ellipsometry to long wavelength now permit investigation of lattice vibrations (phonons) and free-charge carriers (plasmons) in complex semiconductor layer structures.<sup>139</sup> The infrared dielectric function is sensitive to strain, composition, and ordering. Furthermore, concentration, mobility, and effective mass parameters can be determined from far-infrared magneto-optic generalized ellipsometry measurements.<sup>140–143</sup> Even the sign of the free-charge carrier can be determined, just as in an electrical Hall effect measurement. Finally, magneto-optic generalized ellipsometry has even been extended into the terahertz frequency domain using an intense terahertz synchrotron source at wavelengths from approximately  $30$  to  $270\text{ cm}^{-1}$  (0.9–8.1 THz).<sup>144</sup> Even Landau transitions could be seen in a two-dimensionally confined electron system in a grapheme sample.

**Luminescence** The process of luminescence, as described earlier, occurs in a suitably excited specimen. It is a mechanism through which the excited specimen relaxes to the equilibrium state.<sup>108,109</sup> Hence, unlike reflection and transmission spectroscopies, luminescence procedures concentrate on the relaxation of the specimen and often lead to complementary information. For instance, impurities in semiconductors (particularly at low concentrations) are impossible to detect through reflection and more difficult to detect by absorption than by luminescence. Luminescence spectroscopy is thus an important part of the analysis of the optical behavior of semiconductors.<sup>108</sup> Moreover, since one of the main applications of semiconductors is in the arena of light emitters including lasers, the study of luminescence provides direct access to device optoelectronic information.

Luminescence processes may be induced by excitations that produce free electron-hole (e-h) pairs that may recombine across the bandgap or through defect- and impurity-related intermediate steps and emit a photon. The excitations employed most often are (1) an incident intense above-bandgap radiation such as from a laser source, (2) an incident electron beam, (3) electrical injection of electrons and/or holes through an appropriate contact, and (4) thermal excitation. These procedures are known as photoluminescence (PL), cathodoluminescence (CL),<sup>145</sup> electroluminescence (EL),<sup>146</sup> and thermoluminescence (TL), respectively. The most widely used technique for the analysis of semiconductor materials is PL. Cathodoluminescence measurements are usually conducted in a scanning electron microscope (SEM). The SEM electron beam can be focused to a spot size 1000 Å and can be scanned over the area of the sample. Hence, much work has been performed in CL imaging of wafers where one can obtain not only spectroscopic information but also spatial details. Electroluminescence is the most difficult to obtain because of the complexity of producing appropriate contacts. However, in terms of application, EL is the most important since a light emitter has to be able to produce light in an efficient manner under electrical excitation. Thermoluminescence is a technique used with insulators and wide-gap materials and is not widely employed in the analysis of the commercially important materials such as GaAs and Si. The principles of luminescence and the optical information regarding the semiconductor that can be obtained are discussed in the next section using PL.

*Photoluminescence* Luminescence processes may be excited using an above-bandgap-beam of light that leads to the creation of an electron-hole pair that may recombine across the gap and emit a photon with energy equal to the gap  $E_g$ . This process is schematically displayed in Fig. 59.<sup>109</sup> Two



**FIGURE 59** Schematic of photoexcitation and relaxation in semiconductors.<sup>109</sup>

possibilities are shown: namely, the direct-gap and the indirect-gap semiconductors. The recombination will be direct in the former and will have to involve an additional participant, mostly a phonon, to conserve momentum in the latter. This is the simplest possible recombination mechanism. Several additional routes exist for the relaxation that involves impurities. The photoexcited charges may recombine with ionized acceptors (A) and donors (D) with or without involving a phonon. The process may also be more complicated where, for example, an electron may be trapped by an ionized donor which may subsequently recombine with a hole at a neutral acceptor, leading to a donor-acceptor pair (DAP) transition. In addition, recombination may also occur through the annihilation of excitons considered further in this section.

Excitons, as discussed earlier, are hydrogen-like two-particle electron-hole combinations that are not included in the one-electron energy band description of the solid. The strong Coulomb interaction between the electron and the hole leads to the excitonic coupling.

As the excitation intensity increases, so does the population of the excitons. Higher-order interactions can occur between excitons and entities, such as biexcitons, and may be observed. Under intense excitation, the electrons and holes form a liquid state known as the electron-hole liquid. The presence of impurities and defects can also significantly alter the nature of the luminescence spectra, in particular the excitonic behavior. The electric field in the vicinity of the impurity can trap and localize excitons. Such an interaction leads to bound excitons; the binding energy of the bound exciton  $E_{BE}$  will, in addition to  $E_{ex}$  given in Eq. (37), contain a localization part as shown:

$$E_{BE} = E_{ex} + \delta \quad (73)$$

The impurity potential that confines an exciton to a given center depends on both the impurity and its local environment. Hence, the impurity-bound excitonic features can be very rich and informative. A detailed knowledge of the PL excitonic spectrum may be used to identify both the chemical species and its environment, as is demonstrated later on. The observed luminescent photon energy at low temperatures may be written as

$$E = E_g - E_{BE} \quad (74)$$

Transitions from a free electron or hole to a neutral acceptor or donor, respectively, will occur at the following energies:

$$E = E_g - E_{ion} \quad (75)$$

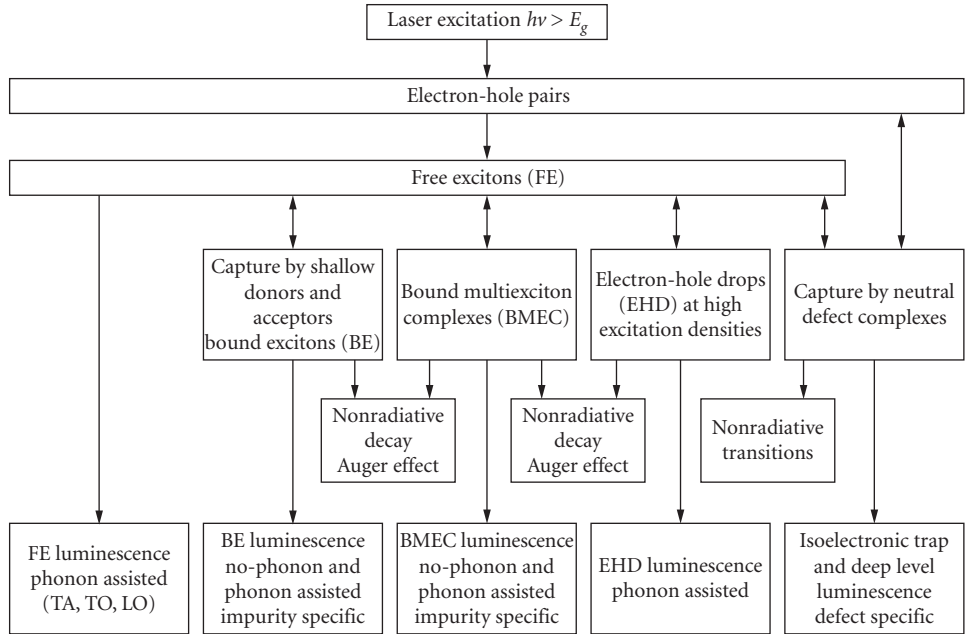
where  $E_{ion}$  is the relevant ionization energy. A complete description of the free-to-bound transition will have to take into account both the dispersion of the band in the vicinity of the minima and the population distribution. For the donor-to-acceptor transition, an additional electrostatic energy term  $e^2/\epsilon(0)r_{sep}$  will have to be accounted for as shown:

$$E = E_g - (E_A + E_D) + \frac{e^2}{\epsilon(0)}r_{sep} \quad (76)$$

where  $r_{sep}$  is the distance that separates the two participating centers. The last term is needed to account for the electrostatic energy of the final ionized state of both centers. All of the transitions discussed may occur with phonon participation, and hence the emission energies should be reduced by the quantum of the energy of the phonon; multiple phonons may also be involved in more complex spectra.

The measurement of PL is, in most cases, routine and straightforward, which partly accounts for its popularity as a materials characterization technique. The laser provides the excitation and the



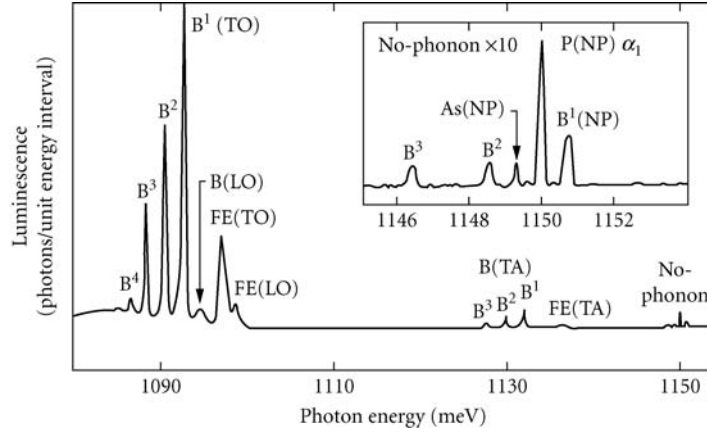


**FIGURE 60** Luminescence decay processes stimulated by above-bandgap photoexcitation in high-purity Si.<sup>147</sup>

dispersive spectrometer along with a sensitive detector, the detection. The sample should be cooled to  $\approx 5$  K so that the temperature-induced broadening is kept to a minimum and the population of the processes with a small activation energy, such as the excitons, is sufficiently high to perform accurate measurements. Photoluminescence measurements may also be performed using Fourier transform (FT) spectrometers. The main advantage is the extraordinary resolution that can be achieved with the FT systems.

The extension of PL into a tool with quantitative accuracy, particularly in very high-purity Si, has demonstrated the versatility of the analysis.<sup>147</sup> The paths of luminescence decay in high-purity Si are schematically presented in Fig. 60. The first step in the excitation process is the creation of electron-hole pairs, which subsequently can undergo a wide variety of processes before recombination. Figure 60 represents the possible intermediate states that eventually lead to radiative recombinations. A typical spectrum obtained from a sample containing  $1.3 \times 10^{13} \text{ cm}^{-3}$  B,  $1.8 \times 10^{12} \text{ cm}^{-3}$  P, and  $3 \times 10^{11} \text{ cm}^{-3}$  As is presented in Fig. 61.<sup>147</sup> The spectrum displays both the no-phonon (NP) component (shown as an inset) and TA, TO, and LO phonon-assisted features for the free exciton (FE) and the impurity-related bound exciton features. The measurement was performed at 4.2 K. Since B is an acceptor and P and As are donors in Si, electrical transport analyses are not sufficient to fully analyze the impurities. In contrast, all three impurities can be unambiguously identified using PL. In addition, when dependable calibration curves are available, the concentration of each species can also be established. A representative calibration curve is presented in Fig. 62 for the impurities B, Al, and P.<sup>147</sup> Note that quantitative measurements can be performed down to  $10^{12} \text{ cm}^{-3}$  for all three impurities. In the case of B, in ultrapure samples, measurements can be performed to levels as low as  $\sim 10^{10} \text{ cm}^{-3}$ .

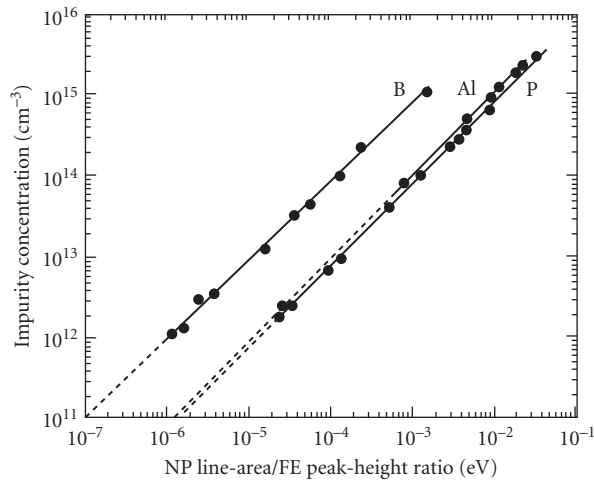
Next, we turn our attention to GaAs, which is a direct-bandgap material and hence exhibits efficient luminescence. Figure 63a displays a representative spectrum from a high-quality MOCVD-grown sample doped with C and Zn measured using an FT spectrometer.<sup>148</sup> The spectra shown are intense, sharp, and well-resolved near the band edge, with excitonic features appearing slightly below



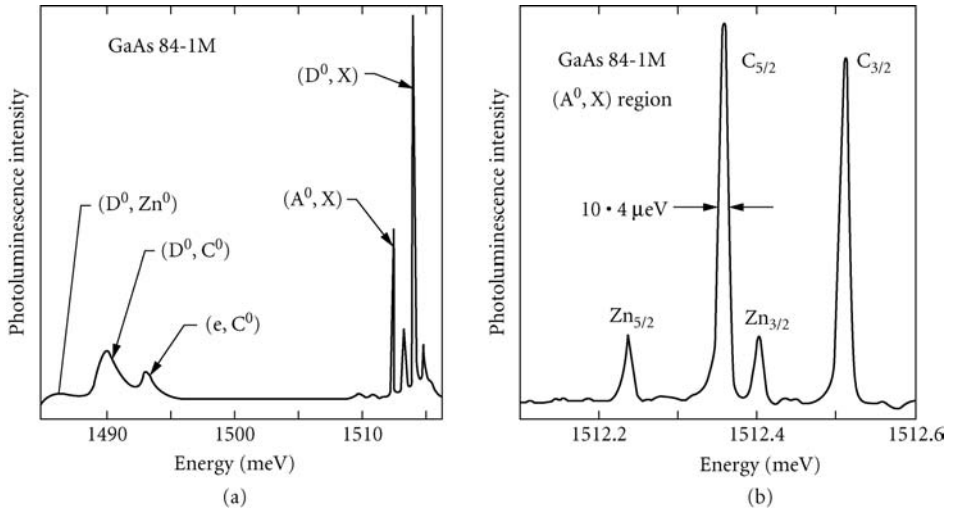
**FIGURE 61** Photoluminescence spectrum from a Si sample doped with  $1.3 \times 10^{13} \text{ cm}^{-3}$  B, contaminated with  $1.8 \times 10^{12} \text{ cm}^{-3}$  P, and  $3 \times 10^{11} \text{ cm}^{-3}$  As.<sup>147</sup>

the band gap of  $\approx 1.519 \text{ eV}$  at 4.2 K. The near-edge features, labeled ( $A^0, X$ ) and ( $D^0, X$ ), are due to excitons bound to neutral donors and acceptors, and the deeper-lying features are the free-to-bound transition to the C acceptor, ( $e, C^0$ ) and the donor-acceptor-pair transitions, ( $D^0, Zn^0$ ), and ( $D^0, C^0$ ), to the Zn and C centers, respectively. An expanded high-resolution version of the same spectrum, in the vicinity of ( $A^0, X$ ) region, is displayed in Fig. 63b.<sup>148</sup> Note the impressive resolution obtainable in the FT system and the clear resolution of the excited states associated with the bound exciton.

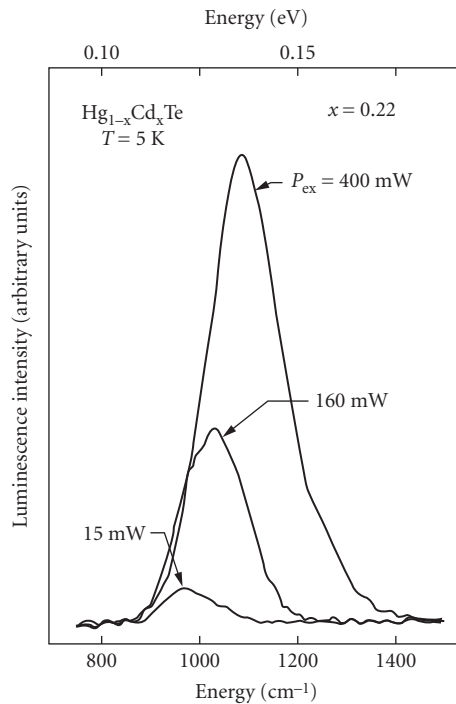
The use of PL techniques may be extended deeper in the infrared region as well. Deep levels associated with impurities such as Fe, Cr, and Ag in GaAs are known to produce luminescence bands at  $\sim 0.35$ ,  $\sim 0.6$ , and  $\sim 1.2 \text{ eV}$ .<sup>149</sup> The narrow-gap semiconductors such as InAs, InSb, and HgCdTe luminesce in the 100 to 200 meV region farther into the infrared region. An example of the PL spectra observed from  $\text{Hg}_{0.78}\text{Cd}_{0.22}$  Te narrow-gap alloy<sup>150</sup> is displayed in Fig. 64. The spectra, in comparison to those presented earlier, are rather featureless due to the fact that the effective masses in the



**FIGURE 62** Calibration of the photoluminescence technique for measuring B, P, and Al concentrations in Si.<sup>147</sup>



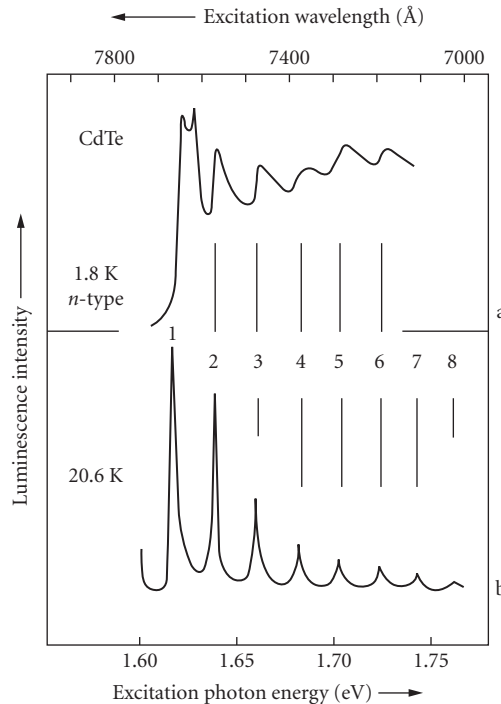
**FIGURE 63** (a) Representative PL spectrum from MOCVD-grown GaAs.<sup>148</sup> (b) High-resolution, near-band edge spectrum of the same sample as in (a).<sup>148</sup>



**FIGURE 64** Luminescence spectra from  $\text{Hg}_{0.78}\text{-Cd}_{0.22}\text{Te}$  measured at 6 K for different 1.06  $\mu\text{m}$  excitation power.<sup>150</sup>

narrow-gap semiconductors tend to be small, and hence the excitonic binding energies are small as well. Therefore, sharp, well-resolved spectra are not normally observed. The observation of luminescence is much more difficult in narrow-gap semiconductors.

The luminescence processes described provide information on the relaxation mechanisms and hence are heavily weighted toward transitions that involve only the first excited state and the final ground state of a system. A complete study of a recombination process, for instance the FE, requires information regarding the higher excited states. This can be achieved by a variation of the PL procedure known as photoluminescence excitation (PLE) spectroscopy. The crux of this technique is to concentrate on the PL response with respect to the excitation wavelength and thereby to determine the excitation resonances. Since the resonances occur when the excitation photon energy matches the excited energies, information regarding the excited states may be elucidated. The principle is illustrated with Fig. 65, where an attempt is made to determine the process that the photoexcited electron-hole pair undergoes before the formation of a free exciton in high-purity CdTe.<sup>151</sup> The spectrometer was set to the FE energy of 1.596 eV, and the excitation photon energy was scanned from 1.6 to ~1.8 eV. The excitation wavelength may be scanned using a dye laser as shown in Fig. 65. Two PLE spectra obtained at 1.8 and 20.6 K are displayed in Fig. 65. The strong oscillatory behavior, with spacing of 21 meV, demonstrates a cascade process through intermediate states separated by the LO phonon energy of 21 meV. This study illustrates the importance of the LO phonon in the electron-hole relaxation process and yields information regarding electronic states that lie above the conduction band extremum, involving the hot electron behavior.

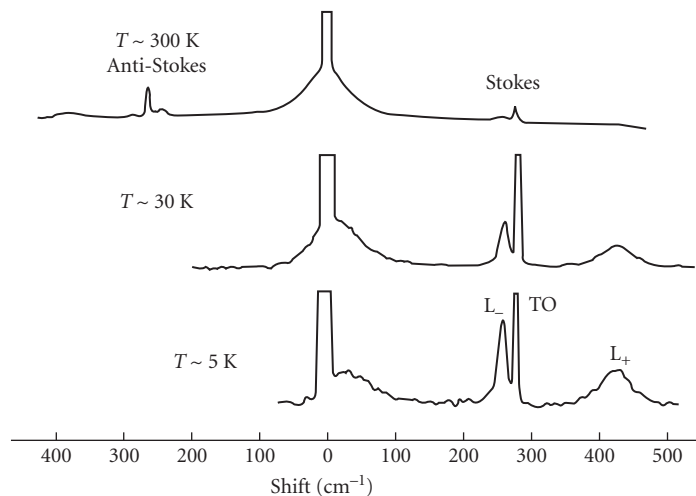


**FIGURE 65** Excitation spectra of exciton luminescence of the emission line at 1.596 eV in the energy region higher than the bandgap of CdTe: (a) a pure *n*-type sample at 1.8 K and (b) the sample at 20.6 K.<sup>151</sup>

**Inelastic Light Scattering (Raman and Brillouin)** The elastic interaction of the incident photon with the specimen implies a process where the energy or wavelength of the photon is preserved. For instance, reflection and transmission spectroscopies involve the measurement of the fraction of the incident beam that is reflected or transmitted with no change in the incident wavelength. The vast majority of the incident photons undergo only elastic interactions, but a tiny fraction, of the order of  $\sim 10^{-8}$ , are subjected to inelastic scattering. Inelastic interactions, though very few, are extremely important as probes of the properties of the specimen. The advent of high-powered coherent laser sources and sensitive detectors has made the measurement of the scattered spectra straightforward, leading to an explosive growth in the last 20 years. Several excellent reviews may be found in the five volumes on light scattering, edited by Cardona and Guntherodt.<sup>152</sup> A good introduction to the procedure and theory may be found in Ref. 153.

The experimental procedure involves projecting a high-power laser beam onto a specimen, collecting the back-scattered light, and performing a spectrum analysis and detection. Multiple-dispersion stages are needed for improved resolution and filtering out of the unwanted elastically scattered beam. A typical set of spectra measured from GaAs<sup>68</sup> is presented in Fig. 66. The axes for the spectra are the detected intensity and the frequency shift suffered by the incident light. The intense peak at  $0 \text{ cm}^{-1}$  is the elastically scattered peak. The spectrum at the room temperature of  $\sim 300 \text{ K}$  displays both the frequency up-shifted and down-shifted components labeled as Stokes and anti-Stokes features corresponding to the TO phonon interaction; these correspond to microscopic processes where the incident photon loses or gains energy due to TO phonon emission or absorption, respectively. At lower temperatures, additional features labeled  $L_+$  and  $L_-$  appear near the TO peak as well as a broad feature in the  $0$  to  $100 \text{ cm}^{-1}$  region. These features originate from charge carriers and were discussed in earlier sections.

The inelastic scattering techniques are usually divided into two categories, namely, Brillouin and Raman scattering. The former covers low frequencies extending from  $0$  to  $\sim 10 \text{ cm}^{-1}$ , while the latter spans the higher frequencies. The low-frequency Brillouin scattering measurements provide access to information on properties of acoustic phonons, spin waves, etc., and involve the use of specialized spectrometers needed to remove the very intense elastic peak.<sup>154</sup> The position of the elastic peak is taken to be the reference zero position, and the scattered spectrum is measured with respect to the zero position; that is, the spectrum is recorded as a function of the frequency shift and not the absolute frequency. Raman scattering is, in general, easier to perform and more informative for the study of semiconductors and hence is emphasized in this section.



**FIGURE 66** Typical Raman spectrum in GaAs, with  $n = 1.4 \times 10^{18} \text{ cm}^{-3}$ , at 300, 30, and 5 K showing the lineshape change with temperature.<sup>69</sup>

The techniques reviewed so far all involve first-order interactions that provide direct information regarding the electronic, vibrational, and impurity-related behavior of semiconductors. In contrast, inelastic light scattering such as Raman and Brillouin scattering involves the electron-phonon or other quasi-particle interactions and hence can provide additional information regarding these interactions. In addition, since inelastic scattering involves a higher-order interaction, processes that are inactive in first-order may be investigated. For instance, the optical phonons in Si do not possess a dipole moment and therefore do not interact with infrared radiation but can be clearly observed in Raman scattering.

The response of the specimen may be expressed, through the susceptibility  $\chi$ .<sup>155</sup> However, the presence of the inelastic interactions will give rise to additional contributions. Consider the example of lattice vibrations and their influence on  $\chi$  in the visible-frequency range. Since the lattice vibrational frequencies correspond to far-infrared light frequencies, no direct contribution is expected. However, the lattice vibrations can influence  $\chi$  even in the visible-frequency range in an indirect fashion by a small amount. The influence of this interaction may be expressed as follows:

$$\begin{aligned}\chi &= \chi_0 + \sum_i \frac{\partial \chi}{\partial u_i} \cdot \mathbf{u}_i \\ &+ \sum_{i,j} \frac{\partial^2 \chi}{\partial u_i \partial u_j} \mathbf{u}_i \mathbf{u}_j \\ &+ \dots\end{aligned}\quad (77)$$

where  $\mathbf{u}_i$  and  $\mathbf{u}_j$  are the displacements associated with the normal modes of lattice vibrations or phonons. The first term contains the elastic term, and the second and third terms denote the second- and third-order inelastic interactions with the phonons. Note that the form of  $\chi$  shown here differs from that used previously in nonlinear optics because it is expressed explicitly in terms of the phonon coordinates. Assuming sinusoidal oscillations for the incident radiation  $\mathbf{E}$  and the phonons  $\mathbf{u}_j$ , the polarization induced in the specimen may be expressed as follows:

$$\mathbf{P} = \chi_0 \mathbf{E}_0 \exp(i\omega_0 t) + \sum_i \chi' u_{i0} \exp\{i(\omega_0 \pm \omega_i)t\} + \sum_{ij} \chi'' u_{i0} u_{j0} \exp\{i(\omega_0 \pm \omega_i \pm \omega_j)t\} \quad (78)$$

The source of the inelastically scattered or frequency-shifted components is immediately apparent.

The scattered intensity, assuming only second-order interactions, is usually expressed in terms of a differential cross section; that is, scattered energy per unit time in the solid angle  $d\Omega$  as follows:

$$\begin{aligned}\frac{d\sigma}{d\Omega} &= V^2 \left(\frac{\omega_s}{c}\right)^4 \hat{\mathbf{e}}_i \chi' \hat{\mathbf{e}}_s n_j && \text{Stokes} \\ &(n_j + 1) && \text{Anti-Stokes}\end{aligned}\quad (79)$$

where  $\hat{\mathbf{e}}_i$  and  $\hat{\mathbf{e}}_s$  denote the polarization state of the scattered and incident light,  $\omega_s$  the frequency of the scattered beam, and  $V$  the scattering volume.

$\chi'$  and  $\chi''$  are Raman tensors whose symmetry properties may be calculated from a knowledge of the structure of the crystals.<sup>156</sup> The notation used to express the combination of incident and scattered beam directions and polarizations is as follows:  $a(b, c)d$ , where  $a$  and  $d$  denote the incident and scattered directions, and  $b$  and  $c$  denote the respective polarizations. Using the cubic crystal axes  $x$ ,  $y$ , and  $z$ , the selection rules may be expressed as follows.

Back scattering from (100) surface:

TO—disallowed for any combination of incident and scattered beam configurations

LO—allowed only for crossed polarizations; that is,  $z(x, y) \bar{z}$  and  $z(y, x) \bar{z}$ , where  $\bar{z}$  is the opposite direction to  $z$ .

Similar selection rules may be derived for other orientations and crystal structures.

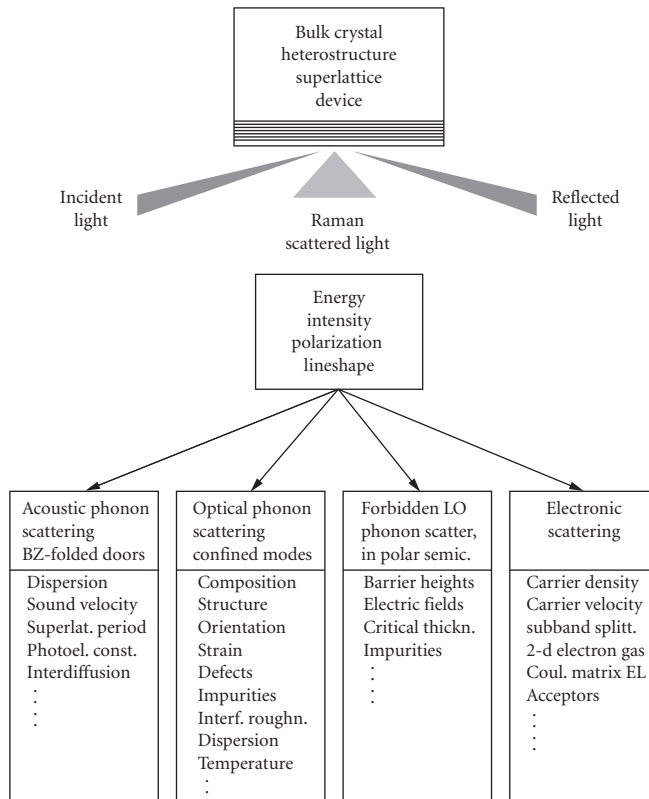
A microscopic description of the scattering event considers quantum mechanical details using perturbation theory. The incident photon with frequency  $\omega_i$  and wave vector  $\mathbf{k}_i$  produces a transition from the initial state  $i$  to a virtual state  $b$  where the incident photon is annihilated, followed by a transition to the final state  $f$ , accompanied by the emission of the “scattered” photon with frequency and wave vector  $\omega_s$  and  $\mathbf{q}_s$ , respectively. The entire process is part of a complete quantum mechanical event and will be governed by momentum, energy, and symmetry conservation rules shown as

$$\begin{aligned} \hbar \omega_i &= \hbar \omega_s \pm \hbar \Omega \\ \hbar \mathbf{q}_i &= \hbar \mathbf{q}_s \pm \hbar \mathbf{K} \end{aligned} \tag{80}$$

where  $\Omega$  and  $\mathbf{K}$  denote the frequency and wave vector of the participating phonon. The exact forms of the scattering cross section will depend on the details of the interactions and are reviewed in Ref. 153.

One of the most powerful aspects of Raman scattering is the ability to perform resonance excitation. When the incident photon energy or the scattered photon energy matches an intrinsic excitation energy, a substantial increase in the scattered intensity is observed. This ability to resonate has been used for both an understanding of the details of the scattering process and applications in which the source of the scattering can be selected. For instance, the study of a particular impurity in a large matrix may be conducted by tuning the resonance to match that of the impurity. Examples of resonance studies are discussed in the following sections.

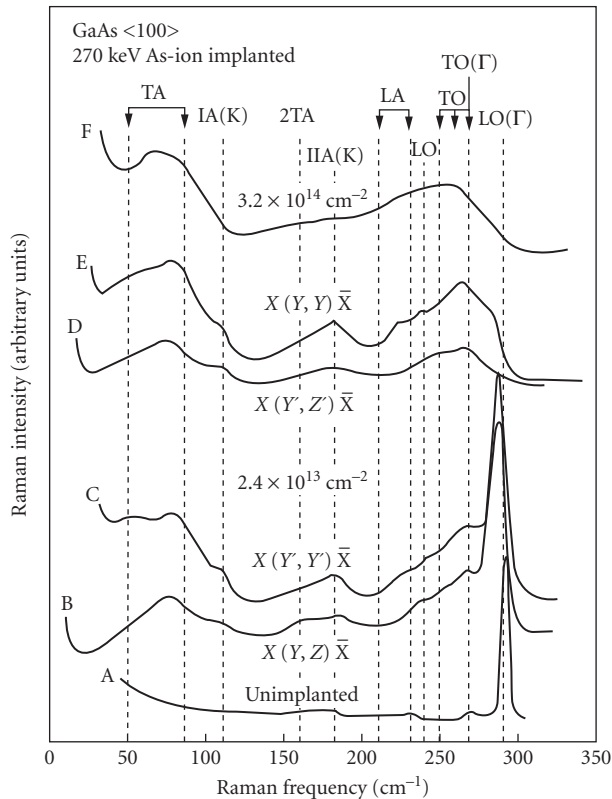
The power and versatility of Raman scattering to probe many important properties of semiconductors have been exploited for a wide variety of characterizations. Figure 67 schematically displays



**FIGURE 67** Schematics of inelastic light scattering and information which can be extracted from such measurements.<sup>157</sup>

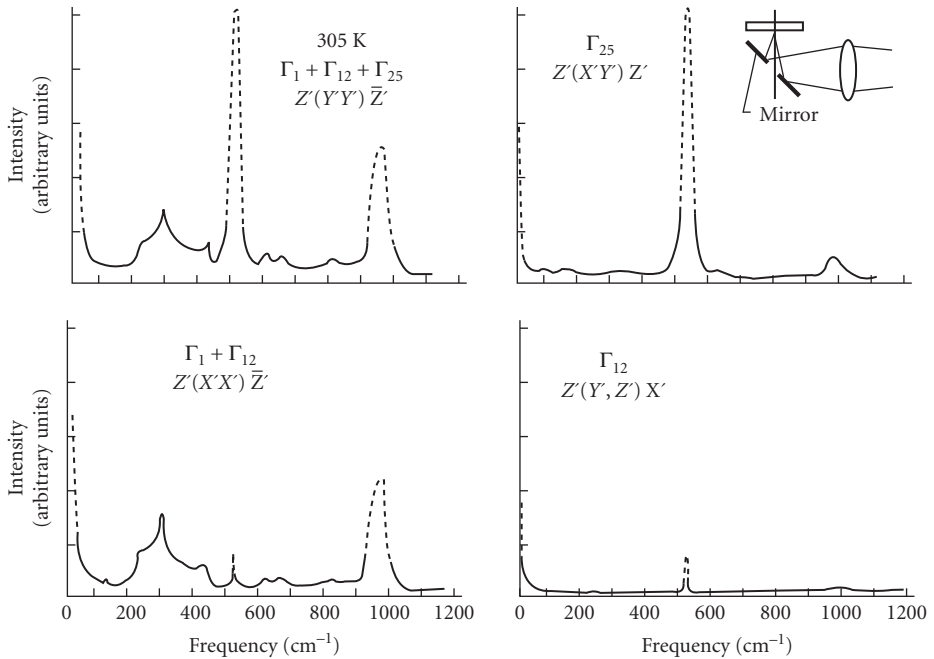
the broad areas where Raman scattering has been employed.<sup>157</sup> The study of materials, devices, and microstructural properties include chemical, structural, and electronic properties. The developments in microscopic measurements and analysis have opened up new applications as well. The measurement of the temperature in a spot  $\approx 1 \mu\text{m}$  in diameter is one such example that is discussed in the following sections.

The most dominant Raman-scattering mechanism in semiconductors is that due to phonons—in particular, the optical phonons at the center of the Brillouin zone—namely, TO ( $\Gamma$ ) and LO ( $\Gamma$ ). Even though a semiconductor crystal can support a variety of vibrations, the momentum conservation requirements restrict the interaction of the incident photon to only the TO ( $\Gamma$ ) and LO ( $\Gamma$ ). The position and shape of the spectra contain important information regarding the structural state of the material: the presence of strain will be reflected as shifts in the line position; degraded crystal quality due to multiple grains and concomitant distributed strain will lead to a broadening of the lineshape. The effects of crystal damage on the Raman spectrum as a result of ion implantation in GaAs is displayed in Fig. 68.<sup>158</sup> Note the large increase in the linewidth of the LO ( $\Gamma$ ) feature. In addition, a series of new structures, not present in the undamaged sample, can also be observed. These have been interpreted to be the result of relaxing the momentum conservation laws and hence the activation of phonon-scattering processes not normally allowed in a good crystal. A simple interpretation of the broadening of the LO lineshape was provided using a phonon confinement model, where the LO phonon is described as being confined to small damage-free regions. The shift



**FIGURE 68** Raman spectra of  $\langle 100 \rangle$  GaAs before implantation (A), implanted to a fluence of  $2.4 \times 10^{13} \text{ cm}^{-2}$  for various polarization configurations (B, C, D, and E) and a fluence of  $3.2 \times 10^{14} \text{ cm}^{-2}$  (F).<sup>158</sup>



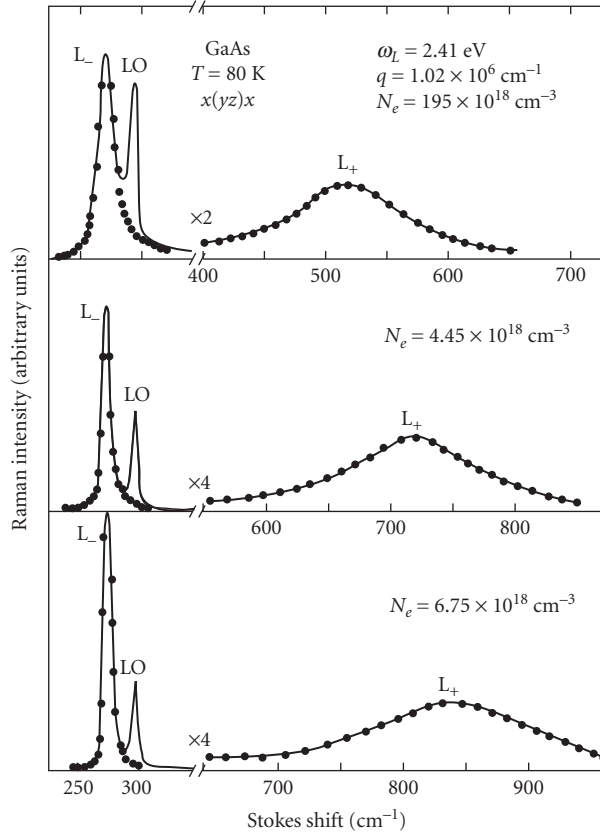


**FIGURE 69** The Raman spectra of Si at room temperature showing the multiphonon contributions. The polarization configuration and the representations which were possible contributors to the spectra are shown for each of the four spectra.<sup>159</sup>

in the position of the LO peak and the full-width-at-half-maximum were related to the diameter of the undamaged region. The information obtained is useful in characterizing lattice damage, amorphous materials, and degrees of recovery during annealing.

As explained earlier, Raman processes can involve higher-order interactions that involve more than one phonon. Hence, multiphonon scattering can be performed, and information complementary to that discussed in the section entitled “Lattice” on the infrared absorption properties can be obtained. The Raman spectra obtained from Si<sup>159</sup> are displayed in Fig. 69. The spectra were recorded at room temperature where  $X' = (100)$ ,  $Y' = (011)$ , and  $Z' = (0\bar{1}1)$ . The irreducible representation of the phonons involved is also noted in the figure. Note the strong peak at  $\sim 522 \text{ cm}^{-1}$  which is due to the degenerate TO( $\Gamma$ )/LO( $\Gamma$ ) phonons that are not observable in infrared absorption measurements. Additional bands present in the 200 to 400  $\text{cm}^{-1}$  and the 600 to 1000  $\text{cm}^{-1}$  range are due to multiphonon scattering processes. The ability to employ polarization selection rules has been used effectively to isolate the symmetry character of the underlying vibrational features and can be used to eventually identify the source of the various features. Such studies are useful both in understanding the optical behavior of Si and in illuminating the lattice dynamical properties of the material.

In crystals that contain a substantial number of free carriers, the incident photon can scatter off collective charge oscillations, known as plasmons, as discussed earlier. The Raman spectra measured from three GaAs samples<sup>160</sup> with electron densities ranging from  $1.95 \times 10^{18}$  to  $6.75 \times 10^{18} \text{ cm}^{-3}$  are presented in Fig. 70. The observed features in addition to the LO phonon peak at  $\sim 293 \text{ cm}^{-1}$  are due to the coupled LO phonon-plasmon features, also discussed earlier. The variation of the  $L_+$  mode frequencies with the carrier density may be calculated and compared to measurements, as was shown in Fig. 32. The shape of the  $L_+$  and the  $L_-$  features can be used to deduce the mobility of the carriers as well. The uniqueness of the Raman results is that they can be employed to study the behavior of carriers near the

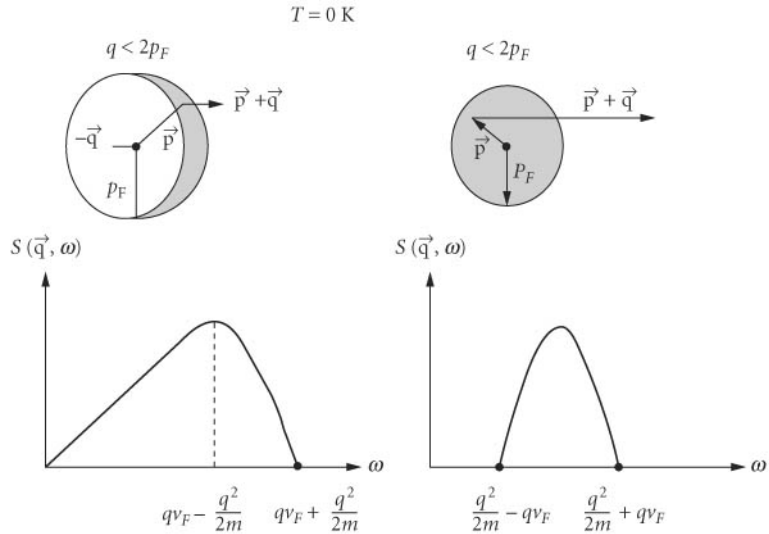


**FIGURE 70** Raman spectra of three different  $n$ -GaAs samples obtained in backscattering geometry from (100) surfaces showing the coupled plasmon-LO phonon modes.<sup>160</sup>

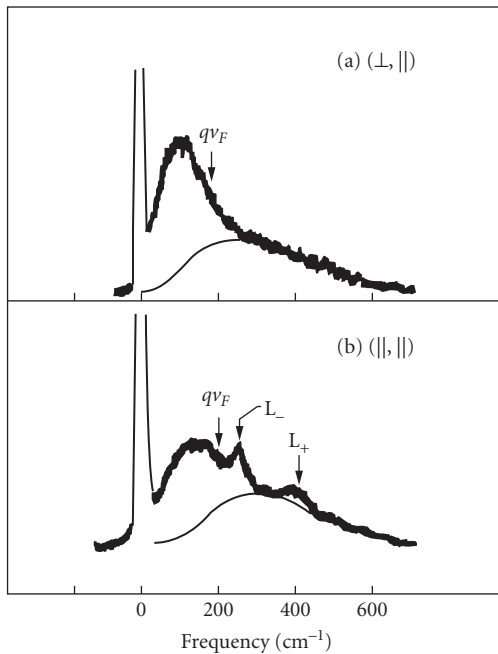
surface. Since the incident laser light with a photon energy of  $\sim 2.5$  eV penetrates only 1000 Å into the sample, the Raman results represent only the behavior of this near-surface region.

The single-particle nature of the free carriers can also be probed by Raman scattering.<sup>69</sup> The mechanism responsible for the interaction is the scattering of the carriers from inside the Fermi-surface to momentum states that lie outside, the total change in momentum being equal to that imparted by the photons. The integrated effect in the case of the spherical Fermi-surface in GaAs is displayed in Fig. 71. The Fermi wave vector is denoted by  $\mathbf{p}_F$  and that of the electron is  $\mathbf{p}$ . The wave-vector change as a result of the scattering is  $\mathbf{q}$ . Two cases of small and large  $\mathbf{q}$  and the resultant single-particle spectrum at 0 K are shown. The net effect in the first case will be a linear increase followed by a rapid fall, and, when  $\mathbf{q}$  is large, the spectrum displays a band-like behavior as shown. The single-particle spectrum measured from a sample of  $n$ -GaAs<sup>161</sup> is presented in Fig. 72. The measurements were performed using the 6471 Å line of the  $\text{Kr}^+$  laser at 10 K. The ability to probe the Fermi sphere directly, using a spectroscopic technique, can lead to valuable insights into the electronic distributions that are complementary to those obtained from transport studies that usually provide only information regarding integrated effects of all the carriers.

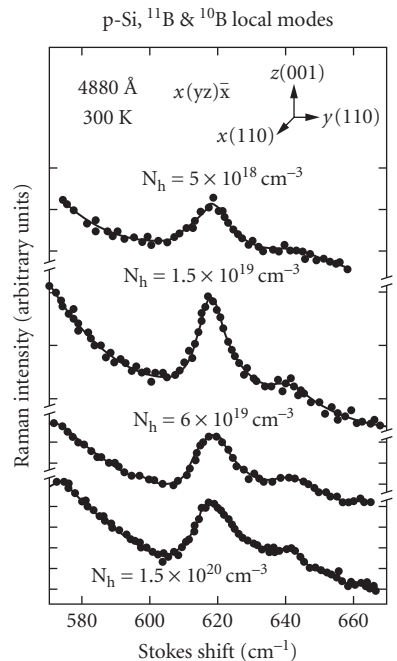
The effect of resonance enhancement, as mentioned earlier, is one of the most powerful features of Raman scattering. The effect can be illustrated with the variation of the scattering intensity of the



**FIGURE 71** Single-particle excitation spectrum at 0 K.<sup>69</sup>



**FIGURE 72** Single-particle spectra and coupled LO phonon-plasmon modes ( $L_{\pm}$ ) for  $n$ -GaAs,  $n = 1.3 \times 10^{18} \text{ cm}^{-3}$ . Temperature: 10 K. Excitation: 6471 Å. The interband transition energy from the split-off valence band to the Fermi level is very close to the laser photon energy. Estimated luminescence background is shown by the dashed line.<sup>161</sup>



**FIGURE 73** Scattering by local modes of boron (isotopes  $\text{B}^{10}$  and  $\text{B}^{11}$ ) in  $p$ -type silicon.<sup>163</sup>

optical phonons in CdS with the incident photon energy as discussed in Ref. 162. An order-of-magnitude enhancement was observed as the excitation energy approached the energy gap at  $\sim 2.6$  eV for all the observed phonon modes. In addition, the TO modes both displayed a reduction before a large enhancement as  $E_g$  was approached. The reduction was interpreted as the result of a destructive interference between the resonant and nonresonant terms that contribute to the scattering cross section. Resonance Raman-scattering studies can therefore shed light on the microscopic details of the scattering process.

The application of Raman scattering to the localized vibration due to impurities is illustrated in Fig. 73 which presents the data obtained from B-doped Si.<sup>163</sup> In most cases, the density of the impurities needs to be quite high to be observable in Raman scattering. However, rapid advances in the measurement procedures may improve the sensitivities. Direct measurement of the electronic transitions related to dopant ions can also be observed in Raman scattering. A good example is the electronic interbound state transitions from three donors in GaP.<sup>164</sup> The normally symmetric, threefold degenerate 1S state of the donor, split into a 1S(A<sub>1</sub>) singlet and a 1S(E) doublet due to the interaction with the conduction band valleys in the indirect-gap GaP was clearly observed as well-resolved peaks.<sup>164</sup> The Raman spectra are sensitive to the impurity electronic states and provide a tool to probe them as well.

## 5.5 ACKNOWLEDGMENTS

The authors express their deep appreciation for the help rendered by Erik Secula in preparing the manuscript.

## 5.6 SUMMARY AND CONCLUSIONS

An overview of the optical properties of semiconductors has been presented in this chapter. These properties form the foundation for understanding and utilizing the wide variety of optical devices manufactured today. A number of materials can be used together with electronic circuits to generate, detect, and manipulate light signals leading to the field of optoelectronics. Semiconductor materials are becoming increasingly important for use in optoelectronic devices: devices can be made very small, leading to a high degree of compactness and compatibility with other electronic and optical functions; they are robust and highly reliable; they are highly efficient as light-generating sources with internal efficiencies sometimes approaching 100 percent; they are capable of large power dissipation, of very high frequency performance, and can access an enormous range of wavelengths; and performances can be tuned over wavelength, frequency, and efficiency.<sup>165</sup> Table 10 lists some of the most important materials and their applications for optoelectronics.<sup>165</sup>

In conclusion, Table 11 presents some of the important parameters for the most common semiconductors that determine the optical behavior of each material. The forbidden-energy gap and higher-energy critical point energies are listed along with optical phonon energies, dielectric constants, refractive index at energies below the energy gap, and free exciton binding energy. Closely related transport parameters such as the charge carrier effective masses and the mobilities are also included for completion. The reader is referred to Palik's compilation in Refs. 10 and 11 for refractive indices for several semiconductors over a wide range of energies. Additional information may also be obtained from many comprehensive collections of physical parameters such as those presented in the Landolt and Bornstein Tables,<sup>166-169</sup> which are now available on the Internet.<sup>170</sup> A more concise semiconductor data handbook was recently published by O. Madelung, and much of the data, figures, references, and more detailed information were shifted to an accompanying CD-ROM.<sup>171</sup>

**TABLE 10** Some Important Semiconductor Materials and Applications for Optoelectronics<sup>165</sup>

Material	Type	Substrate	Devices	Wavelength Range ( $\mu\text{m}$ )	Applications
Si	IV	Si	Detectors, solar cells	0.5–1	Solar energy conversion, e.g., watches, calculators, heating, cooling, detectors
SiC	IV	SiC	Blue LEDs	0.4	Displays, optical disk memories, etc.
Ge	IV	Ge	Detectors	1–1.8	Spectroscopy
GaAs	III–V	GaAs	LEDs, lasers, detectors, solar cells, imagers, intensifiers, electro-optic modulators, optoisolators	0.85	Remote control TV, etc., video disk players, range-finding, solar energy conversion, optical fiber communication systems (local networks), image intensifiers
AlGaAs	III–V	GaAs	LEDs, lasers, solar cells, imagers	0.67–0.98	
GaInP	III–V	GaAs	Visible lasers, LEDs	0.5–0.7	Displays, control, compact disk players, laser printers/scanners, optical disk memories, laser medical equipment
GaAlInP	III–V	GaAs	Visible lasers, LEDs	0.5–0.7	
GaP	III–V	GaP	Visible LEDs	0.5–0.7	
GaAsP	III–V	GaP	Visible LEDs, optoisolators	0.5–0.7	
InP	III–V	InP	Solar cells	0.9	Space solar cells
InGaAs	III–V	InP	Detectors	1–1.67	Optical fiber communications (long-haul and local loop)
InGaAsP	III–V	InP	Lasers, LEDs	1–1.6	
InAlAs	III–V	InP	Lasers, detectors	1–2.5	
InAlGaAs	III–V	InP	Lasers, detectors	1–2.5	
GaSb/GaAlSb	III–V	GaSb	Detectors, lasers	2–3.5	Imaging
GaAlInN	III–V	Quartz, GaN, AlN	IR to UV source and detector	0.25–0.7	Displays, optical disk memories, bio detectors, solar cells, photochemistry, traffic lights, etc.
CdHgTe	II–VI	CdTe	IR detectors	3–5 and 8–12	Infrared imaging, night vision sights, missile seekers, and many other military applications
ZnSe	II–VI	ZnSe	Short LED, lasers	0.4–0.6	Commercial applications (R&D stage only)
ZnS	II–VI	ZnS	Short LED, lasers	0.4–0.6	
Pb compounds	IV–VI	Pb Compounds	IR lasers, detectors	3–30	Spectroscopy, pollution monitoring

**TABLE 11** Material Parameters<sup>1</sup>

Material	Type (I/D)	$E_g$				Higher-Energy Transitions ( $\approx 300$ K)			
		300 K (eV)	77 K (eV)	$\approx 0$ K (eV)	$dE_g/dT$ ( $10^{-2}$ eV/K)	$E_0$ (eV)	$E_0 + \Delta_0$ (eV)	$E_1$ (eV)	$E_1 + \Delta_1$ (eV)
Si	I	1.1242 <sup>(a-1)</sup>	1.169 <sup>(a-1)</sup>	1.170 <sup>(a-1)</sup>	-2.8 <sup>(a-2)</sup>	4.185(4.2 K) <sup>(a-3)</sup>	4.229(4.2 K) <sup>(a-3)</sup>	3.40 <sup>(a-4)</sup>	
Ge	I	0.664 <sup>(b-1)</sup>	0.734 <sup>(b-1)</sup>	0.744 <sup>(b-2)</sup>	-3.7 <sup>(b-3)</sup>	0.888(10 K) <sup>(b-4)</sup>	1.184(10 K) <sup>(b-4)</sup>	2.05 <sup>(b-5)</sup>	2.298 <sup>(b-6)</sup>
$\alpha$ -Sn	D	0 <sup>(c-1)</sup>	0 <sup>(c-1)</sup>	0 <sup>(c-1)</sup>	0	-0.42(85 K) <sup>(c-2)</sup>	0.8(10 K) <sup>(c-2)</sup>	1.316 <sup>(c-3)</sup>	1.798 <sup>(c-3)</sup>
GaAs	D	1.424 <sup>(d-1)</sup>	1.5115 <sup>(d-2)</sup>	1.51914 <sup>(d-3)</sup>	-3.9 <sup>(d-4)</sup>	$E_g$	1.760 <sup>(d-5)</sup>	2.915 <sup>(d-6)</sup>	3.139 <sup>(d-6)</sup>
AlAs	I	2.153 <sup>(e-1)</sup>	2.223 <sup>(e-1)</sup>	2.229 <sup>(e-1)</sup>	-3.6 <sup>(e-1)</sup>	3.02 <sup>(e-2)</sup>	3.32 <sup>(e-2)</sup>	$\sim 3.9$ <sup>(e-2)</sup>	$\sim 4.1$ <sup>(e-2)</sup>
InAs	D	0.354 <sup>(f-1)</sup>	0.404 <sup>(f-2)</sup>	0.418 <sup>(f-3)</sup>	-3.5 <sup>(f-4)</sup>	$E_g$	0.725 <sup>(f-1)</sup>	2.5 <sup>(f-5)</sup>	2.75 <sup>(f-5)</sup>
InP	D	1.344 <sup>(g-1)</sup>	1.4135 <sup>(g-2)</sup>	1.4236 <sup>(g-3)</sup>	-2.9 <sup>(g-2)</sup>	$E_g$	1.45 <sup>(g-4)</sup>	3.158 <sup>(g-5)</sup>	3.28 <sup>(g-6)</sup>
InSb	D	0.18 <sup>(h-1)</sup>	0.23 <sup>(h-2)</sup>	0.2368 <sup>(h-2)</sup>	-2.7 <sup>(h-2)</sup>	$E_g$	1.16 <sup>(h-3)</sup>	1.88 <sup>(h-4)</sup>	2.38 <sup>(h-4)</sup>
GaP	I	2.272 <sup>(i-1)</sup>	2.338 <sup>(i-2)</sup>	2.350 <sup>(i-1)</sup>	-3.7 <sup>(i-2)</sup>	2.780 <sup>(i-3)</sup>	2.860 <sup>(i-3)</sup>	3.785(10 K) <sup>(i-3)</sup>	3.835(10 K) <sup>(i-3)</sup>
ZnS (cubic)	D	3.68 <sup>(j-1)</sup>		3.78 <sup>(j-1)</sup>	-4.7 <sup>(j-2)</sup>	$E_g$	3.752(15 K) <sup>(j-3)</sup>	5.73 <sup>(j-1)</sup>	
ZnSe	D	2.70 <sup>(k-1)</sup>		2.8215 <sup>(k-2)</sup>	-4.8 <sup>(k-3)</sup>	$E_g$	3.12 <sup>(k-1)</sup>	4.77 <sup>(k-1)</sup>	4.97 <sup>(k-1)</sup>
ZnTe	D	2.30 <sup>(l-1)</sup>		2.3941 <sup>(l-2)</sup>	-4.1 <sup>(l-1)</sup>	$E_g$	3.18 <sup>(l-3)</sup>	3.64 <sup>(l-3)</sup>	4.22 <sup>(l-3)</sup>
CdTe	D	1.505 <sup>(m-1)</sup>	1.583 <sup>(m-2)</sup>	1.6063 <sup>(m-3)</sup>	-2.9 <sup>(m-4)</sup>	$E_g$	2.1 <sup>(m-5)</sup>	3.31 <sup>(m-6)</sup>	3.87 <sup>(m-5)</sup>
HgTe	D	0 <sup>(n-1)</sup>	0 <sup>(n-1)</sup>	0 <sup>(n-1)</sup>	0	-0.106 <sup>(n-1)</sup>	1.08 <sup>(n-2)</sup>	2.12 <sup>(n-2)</sup>	2.78 <sup>(n-2)</sup>
CdS (Hexagonal)	D	2.485 <sup>(o-1)</sup>	2.573 <sup>(o-1)</sup>	2.5825 <sup>(o-2)</sup>	+4.1 <sup>(o-1)</sup>	$E_g$			
PbS	D	0.42 <sup>(p-1)</sup>	0.307 <sup>(p-2)</sup>	0.286 <sup>(p-3)</sup>	+5.2 <sup>(p-3)</sup>	$E_g$		1.85 <sup>(p-4)</sup>	
PbTe	D	0.311 <sup>(q-1)</sup>	0.217 <sup>(q-2)</sup>	0.188 <sup>(q-1)</sup>	+4.5 <sup>(q-3)</sup>	$E_g$		1.24 <sup>(q-4)</sup>	
PbSe	D	0.278 <sup>(r-1)</sup>	0.176 <sup>(r-2)</sup>	0.1463 <sup>(r-3)</sup>	+4.0 <sup>(r-4)</sup>	$E_g$		1.59 <sup>(r-5)</sup>	
GaN (hexagonal)	D	3.39 <sup>(s-1)</sup>		3.503 <sup>(s-2)</sup>		$E_g$			
AlN (hexagonal)	D	6.13 <sup>(t-1)</sup>		6.19 <sup>(t-1,2)</sup>		$E_g$			
InN (hexagonal)	D			1.89 <sup>(u-1)</sup>		$E_g$			

Material	$E_{cx}$ (FE) (eV)	$\epsilon(0)$	$\epsilon_\infty$	$n(\lambda)$ $\lambda > \lambda_c$	$dn/dT$ ( $10^{-4}$ /K)	$\hbar\omega_{TO}$ (eV)	$\hbar\omega_{LO}$ (eV)	$\mu_e^2$ (cm <sup>2</sup> / V·s)	$\mu_h^2$ (cm <sup>2</sup> / V·s)	$m^*/m_0^2$	$m_h^*/m_0^2$
Si	0.014 <sup>(a-5)</sup>	11.9 <sup>(a-6)</sup>	11.9 <sup>(a-6)</sup>	3.4179(10 $\mu$ m) <sup>(a-7)</sup>	1.3 <sup>(a-8)</sup>	0.0642 <sup>(a-9)</sup>	0.0642 <sup>(a-9)</sup>	1,500 <sup>(a-10)</sup>	450 <sup>(a-10)</sup>	0.98 <sup>3(a-10)</sup>	0.16 <sup>5(a-10)</sup>
Ge	0.00415 <sup>(b-7)</sup>	16.2 <sup>(b-8)</sup>	16.2 <sup>(b-8)</sup>	4.00319(10 $\mu$ m) <sup>(b-9)</sup>	4.0 <sup>(b-10)</sup>	0.0373 <sup>(b-11)</sup>	0.0373 <sup>(b-11)</sup>	3,900 <sup>(b-12)</sup>	1900 <sup>(b-12)</sup>	1.64 <sup>3(b-12)</sup>	0.04 <sup>5(b-12)</sup>
$\alpha$ -Sn	0	24 <sup>(c-4)</sup>	24 <sup>(c-4)</sup>	—	—	0.0244 <sup>(c-5)</sup>	0.0244 <sup>(c-5)</sup>	1,400 <sup>(c-6)</sup>	1200 <sup>(c-6)</sup>	0.028 <sup>(c-2)</sup>	0.195 <sup>(c-2)</sup>
GaAs	0.0042 <sup>(d-7)</sup>	13.18 <sup>(d-8)</sup>	10.89 <sup>(d-8)</sup>	3.298(5 $\mu$ m) <sup>(d-9)</sup>	1.5 <sup>(d-10)</sup>	0.0333 <sup>(d-11)</sup>	0.0362 <sup>(d-11)</sup>	8,500 <sup>(d-12)</sup>	400 <sup>(d-12)</sup>	0.067 <sup>(d-12)</sup>	0.082 <sup>(d-12)</sup>
AlAs	0.02 <sup>(e-1)</sup>	10.06 <sup>(e-3)</sup>	8.16 <sup>(e-3)</sup>	2.87(2 $\mu$ m) <sup>(e-4)</sup>	1.2 <sup>(e-5)</sup>	0.04488 <sup>(e-6)</sup>	0.05009 <sup>(e-6)</sup>	300 <sup>(e-7)</sup>	200 <sup>(e-8)</sup>	1.1 <sup>3(e-2)</sup>	0.153 <sup>5(e-9)</sup>
InAs	0.0017 <sup>(f-3)</sup>	15.15 <sup>(f-6)</sup>	12.25 <sup>(f-6)</sup>	3.42(10 $\mu$ m) <sup>(f-7)</sup>		0.0269 <sup>(f-8)</sup>	0.0296 <sup>(f-8)</sup>	3,300 <sup>(f-8)</sup>	460 <sup>(f-8)</sup>	0.19 <sup>4(e-2)</sup>	0.409 <sup>6(e-9)</sup>
InP	0.0051 <sup>(g-3)</sup>	12.61 <sup>(g-7)</sup>	9.61 <sup>(g-7)</sup>	3.08(5 $\mu$ m) <sup>(g-8)</sup>	0.83 <sup>(g-9)</sup>	0.0377 <sup>(g-10)</sup>	0.0428 <sup>(g-10)</sup>	4,600 <sup>(g-11)</sup>	150 <sup>(g-11)</sup>	0.023 <sup>(f-8)</sup>	0.4 <sup>(f-8)</sup>
										0.077 <sup>(g-11)</sup>	0.64 <sup>(g-11)</sup>

(Continued)

Material	$E_{\text{ex}}$ (FE) (eV)	$\epsilon(0)$	$\epsilon_{\infty}$	$n(\lambda)$ $\lambda > \lambda_c$	$dn/dT$ ( $10^{-4}/\text{K}$ )	$\hbar\omega_{\text{TO}}$ (eV)	$\hbar\omega_{\text{LO}}$ (eV)	$\mu_c^2(\text{cm}^2/\text{V}\cdot\text{s})$	$\mu_h^2(\text{cm}^2/\text{V}\cdot\text{s})$	$m_c^*/m_0^*$	$m_h^*/m_0^*$
InSb	0.00052 <sup>(h-5)</sup>	16.8 <sup>(h-6)</sup>	15.68 <sup>(h-7)</sup>	3.953(10 $\mu\text{m}$ ) <sup>(h-8)</sup>	4.7 <sup>(h-9)</sup>	0.0223 <sup>(h-10)</sup>	0.0237 <sup>(h-10)</sup>	80,000 <sup>(h-11)</sup>	1250 <sup>(h-11)</sup>	0.0145 <sup>(h-11)</sup>	0.40 <sup>(h-11)</sup>
GaP	$\approx 0.02$ <sup>(i-1)</sup>	11.11 <sup>(i-4)</sup>	9.11 <sup>(i-4)</sup>	2.90(10 $\mu\text{m}$ ) <sup>(i-5)</sup>		0.0455 <sup>(i-6)</sup>	0.050 <sup>(i-6)</sup>	110 <sup>(i-7)</sup>	75 <sup>(i-7)</sup>	0.82 <sup>(i-7)</sup>	0.60 <sup>(i-7)</sup>
ZnS (cubic)	0.036 <sup>(j-4)</sup>	5.1 <sup>(j-5)</sup>	2.95 <sup>(j-6)</sup>	2.2014(10 $\mu\text{m}$ ) <sup>(j-7)</sup>	0.46 <sup>(j-8)</sup>	0.03397 <sup>(j-9)</sup>	0.04364 <sup>(j-10)</sup>	165 <sup>(j-10)</sup>	5 <sup>(j-11)</sup>	0.28 <sup>(j-12)</sup>	0.49 <sup>(j-12)</sup>
ZnSe	0.018 <sup>(k-4)</sup>	9.6 <sup>(k-5)</sup>	6.3 <sup>(k-5)</sup>	2.410(10 $\mu\text{m}$ ) <sup>(k-6)</sup>	0.52 <sup>(k-7)</sup>	0.02542 <sup>(k-8)</sup>	0.03099 <sup>(k-8)</sup>	600 <sup>(k-9)</sup>	100 <sup>(k-10)</sup>	0.142 <sup>(k-11)</sup>	0.57 <sup>(k-12)</sup>
ZnTe	0.0132 <sup>(l-2)</sup>	10.1 <sup>(l-4)</sup>	7.28 <sup>(l-5)</sup>	2.64(5 $\mu\text{m}$ ) <sup>(l-6)</sup>		0.02194 <sup>(l-7)</sup>	0.02542 <sup>(l-7)</sup>	330 <sup>(l-8)</sup>		0.11 <sup>(l-9)</sup>	0.6 <sup>(l-10)</sup>
CdTe	0.0132 <sup>(m-3)</sup>	10.2 <sup>(m-7)</sup>	7.1 <sup>(m-7)</sup>	2.684(5 $\mu\text{m}$ ) <sup>(m-8)</sup>		0.0174 <sup>(m-7)</sup>	0.0208 <sup>(m-9)</sup>	1,050 <sup>(m-10)</sup>	100 <sup>(m-10)</sup>	0.1 <sup>(m-11)</sup>	0.4 <sup>(m-12)</sup>
HgTe	0	21.0 <sup>(n-3)</sup>	15.2 <sup>(n-3)</sup>	—		0.01463 <sup>(n-4)</sup>	0.0171 <sup>(n-4)</sup>	35,000 <sup>(n-5)</sup>		0.031 <sup>(n-6)</sup>	0.42 <sup>(m-7)</sup>
CdS (Hexagonal)	0.0274 <sup>(o-3)</sup>	8.7( $\epsilon_{11}(0)$ ) <sup>(o-4)</sup>	5.53( $\epsilon_{1\infty}$ ) <sup>(o-4)</sup>	2.227(10 $\mu\text{m}$ ) $\perp$ c <sup>(o-5)</sup>	0.6 <sup>(o-5)</sup>	see(o-6)	see(o-6)	340 <sup>(o-7)</sup>	50 <sup>(o-7)</sup>	0.21 <sup>(o-7)</sup>	0.8 <sup>(o-7)</sup>
		9.25( $\epsilon_{33}(0)$ ) <sup>(o-4)</sup>	5.5( $\epsilon_{3\infty}$ ) <sup>(o-4)</sup>	2.245(10 $\mu\text{m}$ ) $\parallel$ c <sup>(o-5)</sup>	0.62 <sup>(o-5)</sup>						
PbS		169 <sup>(p-5)</sup>	17.2 <sup>(p-5)</sup>	3.68(16 $\mu\text{m}$ ) <sup>(p-6)</sup>		0.00810 <sup>(p-7)</sup>	0.02539 <sup>(p-7)</sup>	600 <sup>(p-8)</sup>	700 <sup>(p-8)</sup>	0.105 <sup>3(p-9)</sup>	0.105 <sup>3(p-9)</sup>
										0.080 <sup>4(p-9)</sup>	0.075 <sup>4(p-9)</sup>
PbTe		414 <sup>(q-5)</sup>	33 <sup>(q-6)</sup>	5.66(10 $\mu\text{m}$ ) <sup>(q-7)</sup>		0.00399 <sup>(q-5)</sup>	0.01414 <sup>(q-8)</sup>	6,000 <sup>(q-9)</sup>	4000 <sup>(q-9)</sup>	0.24 <sup>3(q-10)</sup>	0.31 <sup>3(q-10)</sup>
										0.024 <sup>4(q-10)</sup>	0.024 <sup>4(q-10)</sup>
PbSe		210 <sup>(r-6)</sup>	22.9 <sup>(r-7)</sup>	4.75(10 $\mu\text{m}$ ) <sup>(r-8)</sup>		0.00546 <sup>(r-9)</sup>	0.0165 <sup>(r-10)</sup>	1,000 <sup>(r-11)</sup>	800 <sup>(r-12)</sup>	0.07 <sup>3(r-13)</sup>	0.068 <sup>3(r-13)</sup>
										0.04 <sup>4(r-13)</sup>	0.034 <sup>4(r-13)</sup>
GaN (Hexagonal)		8.9 <sup>(s-3)</sup>	5.35 <sup>(s-3)</sup>			0.0661 ( $A_1$ ) <sup>(s-1)</sup>	0.0911 ( $A_1$ ) <sup>(s-1)</sup>	1000 <sup>(s-4)</sup>	30 <sup>(s-5)</sup>	0.19 (transverse);	
						0.0694 ( $E_1$ ) <sup>(s-1)</sup>	0.092 ( $E_1$ ) <sup>(s-1)</sup>			0.23	
										(longitudinal) <sup>(s-6)</sup>	
AlN (Hexagonal)		8.5 <sup>(t-3)</sup>	4.77 <sup>(t-3)</sup>			0.075 ( $A_1$ ) <sup>(t-1)</sup>	0.110 ( $A_1$ ) <sup>(t-1)</sup>	135 <sup>(t-4)</sup>	14 <sup>(s-5)</sup>	0.33 (transverse);	
						0.0832 ( $E_1$ ) <sup>(t-1)</sup>	0.113 ( $A_1$ ) <sup>(t-1)</sup>			0.33	
										(longitudinal) <sup>(t-5)</sup>	
InN (Hexagonal)		15.3 <sup>(s-3)</sup>	8.4 <sup>(s-3)</sup>			0.0496 ( $A_1$ ) <sup>(u-2)</sup>	0.0707 ( $E_1$ ) <sup>(u-2)</sup>	3200 <sup>(u-3)</sup>			
						0.060 ( $E_1$ ) <sup>(u-2)</sup>					

<sup>1</sup>Most values quoted are at  $\approx 300$  K, except where indicated.

<sup>2</sup>Highest values reported.

<sup>3</sup>Longitudinal effective mass.

<sup>4</sup>Transverse effective mass.

<sup>5</sup>Light-hole effective mass.

<sup>6</sup>Heavy-hole effective mass.

<sup>7</sup>Band extrema effective masses are obtained from low-temperature measurements. See quoted references for more details.

#### a-Si

<sup>(a-1)</sup>W. Bludau, A. Onton, and W. Heinke, *J. Appl. Phys.* **45**:1846 (1974).

<sup>(a-2)</sup>H. D. Barber, *Sol. St. Electronics* **10**:1039 (1967).

<sup>(a-3)</sup>D. E. Aspnes and A. A. Studna, *Solid State Communications* **11**:1375 (1972).

<sup>(a-4)</sup>A. Duanois and D. E. Aspnes, *Phys. Rev. B.* **18**:1824 (1978).

<sup>(a-5)</sup>K. L. Shaklee and R. E. Nahory, *Phys. Rev. Lett.* **24**:942 (1970).

<sup>(a-6)</sup>K. V. Rao and A. Smakula, *J. Appl. Phys.* **37**:2840 (1966).

<sup>(a-7)</sup>C. D. Salzberg and J. J. Villa, *J. Opt. Soc. Am.* **47**:244 (1957).

<sup>(a-8)</sup>M. Cardona, W. Paul, and H. Brooks, *J. Phys. Chem. Solids* **8**:204 (1959).

<sup>(a-9)</sup>G. Dolling, *Inelastic Scattering of Neutrons in Solids and Liquids*, vol. II, IAEA, Vienna, 1963, p. 37.

<sup>(a-10)</sup>S. M. Sze, *Physics of Semiconductor Devices*, 2nd ed., John Wiley, New York, 1981, p. 849.

#### b-Ge

<sup>(b-1)</sup>G. G. Macfarlane, T. P. McLean, J. E. Quarinaton, and V. Roberts, *Phys. Rev.* **108**:1377 (1957).

<sup>(b-2)</sup>S. Zwerdling, B. Lax, L. M. Roth, and K. J. Button, *Phys. Rev.* **114**:80 (1959).

<sup>(b-3)</sup>T. P. McLean, in *Progress in Semiconductors*, vol. 5, A. F. Gibson (ed.), Heywood, London, 1960.

<sup>(b-4)</sup>D. E. Aspnes, *Phys. Rev. B* **12**:2297 (1975).

- (b-5) A. K. Gosh, *Phys. Rev.* **165**:888 (1968).
- (b-6) L. Vina and M. Cardona, *Physica* **117B** and **118B**:356 (1983).
- (b-7) V. I. Sidorov and Ya. E. Pokrovski, *Sov. Phys. Semicond.* **6**:2015 (1973).
- (b-8) F. A. D'Altroy and H. Y. Fan, *Phys. Rev.* **103**:671 (1956).
- (b-9) R. P. Edwin, M. T. Dudermeil, and M. Lamare, *Appl. Opt.* **21**:878 (1982).
- (b-10) See (a-8).
- (b-11) G. Nilsson and G. Nelin, *Phys. Rev. B* **6**:3777 (1972).
- (b-12) See (a-10).

#### c- $\alpha$ Sn

- (c-1) J. R. Chelikowsky and M. L. Cohen, *Phys. Rev. B* **14**:556 (1976).
- (c-2) S. H. Groves, C. R. Pidgeon, A. W. Ewald, and R. J. Wagner, *J. Phys. Chem. Solids* **31**:2031 (1970).
- (c-3) L. Vina, H. Hockst, and M. Cardona, *Phys. Rev. B* **31**:958 (1985).
- (c-4) R. E. Lindquist and A. W. Ewald, *Phys. Rev.* **135**:A191 (1964).
- (c-5) C. J. Buchenauer, M. Cardona, and F. H. Pollak, *Phys. Rev. B* **3**:1243 (1971).
- (c-6) See (a-10).

#### d-GaAs

- (d-1) D. D. Sell, H. C. Casey, and K. W. Wecht, *J. Appl. Phys.* **45**:2650 (1974).
- (d-2) M. B. Panish and H. C. Casey, *J. Appl. Phys.* **40**:163 (1969).
- (d-3) B. J. Skromme and G. E. Stillman, *Phys. Rev. B* **29**:1982 (1984).
- (d-4) J. Camassel, D. Auvergne, and H. Mathieu, *J. Appl. Phys.* **46**:2683 (1975).
- (d-5) C. Alibert, S. Gaillard, M. Erman, and P. M. Frijlink, *J. Phys. Paris* **44**:C10-229 (1983).
- (d-6) P. Lautenschlager, M. Garriga, S. Logothetidis, and M. Cardona, *Phys. Rev. B* **35**:9174 (1987).
- (d-7) D. D. Sell, *Phys. Rev. B* **6**:3750 (1972).
- (d-8) G. A. Samara, *Phys. Rev. B* **27**:3494 (1983).
- (d-9) K. G. Hambleton, C. Hilsun, and B. R. Holeman, *Proc. Phys. Soc.* **77**:1147 (1961).
- (d-10) M. Cardona, *Proc. Int. Conf. Phys. Semicond.*, Prague, 1960, Publ. House of the Czech. Acad. of Sciences, Prague, 1960, p. 388.
- (d-11) A. Mooradian and G. B. Wright, *Solid State Communications* **4**:431 (1966).
- (d-12) See (a-10).

#### e-AlAs

- (e-1) B. Monemar, *Phys. Rev. B* **8**:5711 (1983).
- (e-2) S. Adachi, *J. Appl. Phys.* **58**:R1 (1985).
- (e-3) R. E. Fern and A. Onton, *J. Appl. Phys.* **42**:3499 (1971).
- (e-4) M. Hoch and K. S. Hinge, *J. Chem. Phys.* **35**:451 (1961).
- (e-5) H. G. Grimmeiss and B. Monemar, *Phys. Stat. Sol. (a)* **5**:109 (1971).
- (e-6) O. K. Kim and W. G. Spitzer, *J. Appl. Phys.* **50**:4362 (1979).
- (e-7) M. Ettenberg, A. G. Sigai, A. Dreeben, and S. L. Gilbert, *J. Electrochem. Soc.* **119**:1355 (1971).
- (e-8) J. D. Wiley, in *Semiconductors and Semimetals*, vol. 10, R. K. Willardson and A. C. Beer (eds.), Academic Press, New York, 1975, p. 91.
- (e-9) M. Huang and W. Y. Ching, *J. Phys. Chem. Solids* **46**:977 (1985).

#### f-InAs

- (f-1) F. Lukes, *Phys. Stat. Sol. (b)* **84**:K113 (1977).
- (f-2) E. Adachi, *J. Phys. Soc. Jpn.* **2**:1178 (1968).
- (f-3) A. V. Varfolomeev, R. P. Seisyan, and R. N. Yakimova, *Sov. Phys. Semicond.* **9**:560 (1975).
- (f-4) F. Matossi and F. Stern, *Phys. Rev.* **111**:472 (1958).
- (f-5) M. Cardona and G. Harbeke, *J. Appl. Phys.* **34**:813 (1963).
- (f-6) M. Haas and B. W. Hennis, *J. Phys. Chem. Solids* **23**:1099 (1962).
- (f-7) O. G. Lorimor and W. G. Spitzer, *J. Appl. Phys.* **36**:1841 (1965).
- (f-8) R. Carles, N. Saint-Cricq, J. B. Renucci, M. A. Renucci, and A. Zwick, *Phys. Rev. B* **22**:4804 (1980).

#### g-InP

- (g-1) M. Bugaski and W. Lewandowski, *J. Appl. Phys.* **57**:521 (1985).
- (g-2) W. J. Turner, W. E. Reese, and G. D. Pettit, *Phys. Rev.* **136**:A1467 (1964).



- <sup>(g-3)</sup>H. Mathieu, Y. Chen, J. Camassel, J. Allegre, and D. S. Robertson, *Phys. Rev. B* **32**:4042 (1985).  
<sup>(g-4)</sup>K. L. Shaklee, M. Cardona, and F. H. Pollak, *Phys. Rev. Lett.* **16**:48 (1966).  
<sup>(g-5)</sup>S. M. Kelso, D. E. Aspnes, M. A. Pollak, and R. E. Nahory, *Phys. Rev. B* **26**:6669 (1982).  
<sup>(g-6)</sup>E. Matatagui, A. E. Thompson, and M. Cardona, *Phys. Rev.* **176**:950 (1968).  
<sup>(g-7)</sup>See (f-6).  
<sup>(g-8)</sup>F. Oswald, *Z. Naturforsch* **9a**:181 (1954).  
<sup>(g-9)</sup>See (d-10).  
<sup>(g-10)</sup>A. Mooradian and G. B. Wright, *Solid State Communications* **4**:431 (1966).  
<sup>(g-11)</sup>See (a-10).

### h-InSb

- <sup>(h-1)</sup>F. Lukes and E. Schmidt, *Proc. Int. Conf. Phys. Semicond.*, Exeter, 1962, Inst. of Physics, London, 1962, p. 389.  
<sup>(h-2)</sup>C. L. Littler and D. G. Seiler, *Appl. Phys. Lett.* **46**:986 (1985).  
<sup>(h-3)</sup>S. Zwerdling, W. H. Kleiner, and J. P. Theriault, *MIT Lincoln Laboratory Report 8G-00M*, 1961.  
<sup>(h-4)</sup>M. Cardona, K. L. Shaklee, and F. H. Pollak, *Phys. Rev.* **154**:696 (1967).  
<sup>(h-5)</sup>A. Baldereschi and N. O. Lipari, *Phys. Rev. B* **3**:439 (1971).  
<sup>(h-6)</sup>J. R. Dixon and J. K. Furdyna, *Solid State Communications* **35**:195 (1980).  
<sup>(h-7)</sup>See (f-6).  
<sup>(h-8)</sup>T. S. Moss, S. D. Smith, and T. D. F. Hawkins, *Proc. Phys. Soc. B* **70**:776 (1957).  
<sup>(h-9)</sup>See (g-9).  
<sup>(h-10)</sup>W. Keifer, W. Richter, and M. Cardona, *Phys. Rev. B* **12**:2346 (1975).  
<sup>(h-11)</sup>See (a-10).

### i-GaP

- <sup>(i-1)</sup>R. G. Humphreys, U. Rossler, and M. Cardona, *Phys. Rev. B* **18**:5590 (1978).  
<sup>(i-2)</sup>D. Auvergne, P. Merle, and H. Mathieu, *Phys. Rev. B* **12**:1371 (1975).  
<sup>(i-3)</sup>S. E. Stokowski and D. D. Sell, *Phys. Rev. B* **5**:1636 (1972).  
<sup>(i-4)</sup>G. A. Samara, *Phys. Rev. B* **27**:3494 (1983).  
<sup>(i-5)</sup>H. Welker, *J. Electron* **1**:181 (1955).  
<sup>(i-6)</sup>See (g-10).  
<sup>(i-7)</sup>See (a-10).

### j-ZnS

- <sup>(j-1)</sup>D. Theis, *Phys. Stat. Sol. (b)* **79**:125 (1977).  
<sup>(j-2)</sup>J. Camassel and D. Auvergne, *Phys. Rev. B* **12**:3258 (1975).  
<sup>(j-3)</sup>B. Segall and D. T. F. Marple, *Physics and Chemistry of II-VI Compounds*, M. Aven and J. S. Prener (eds.), North-Holland, Amsterdam, 1967, p. 318.  
<sup>(j-4)</sup>W. Walter and J. L. Birman, *Proc. Int. Conf. on II-VI Semiconducting Compounds*, 1967, D. G. Thomas (ed.), W. A. Benjamin, New York, 1967, p. 89.  
<sup>(j-5)</sup>G. Martinez, in *Handbook on Semiconductors*, vol. 2, T. S. Moss (ed.), North-Holland, Amsterdam, 1980, p. 210.  
<sup>(j-6)</sup>M. Balkanski and Y. Petroff, *Proc. 7th Intl. Conf. Physics of Semicond.* Paris, 1964, Dunod, Paris, 1964, p. 245.  
<sup>(j-7)</sup>W. L. Wolfe, A. G. DeBell, and J. M. Palmer, *Proc. SPIE* **245**:164 (1980).  
<sup>(j-8)</sup>R. J. Harris, G. T. Johnston, G. A. Kepple, P. C. Krock, and M. Mukai, *Appl. Opt.* **16**:436 (1977).  
<sup>(j-9)</sup>M. Balkanski, M. Nusimovici, and R. Letoullec, *J. Phys. Paris* **25**:305 (1964).  
<sup>(j-10)</sup>C. A. Klein and R. N. Donadio, *J. Appl. Phys.* **51**:797 (1980).  
<sup>(j-11)</sup>See (a-10).  
<sup>(j-12)</sup>J. C. Miklosz and R. G. Wheeler, *Phys. Rev.* **153**:913 (1967).

### k-ZnSe

- <sup>(k-1)</sup>See (j-1).  
<sup>(k-2)</sup>P. J. Dean, D. C. Herbert, C. J. Werkhoven, B. J. Fitzpatrick, and R. M. Bhargava, *Phys. Rev. B* **23**:4888 (1981).  
<sup>(k-3)</sup>J. Baillou, J. Daunay, P. Bugnet, Jac Daunay, C. Auzary, and P. Poindessault, *J. Phys. Chem. Solids* **41**:295 (1980).  
<sup>(k-4)</sup>A. K. Ray and F. A. Kroger, *J. Appl. Phys.* **50**:4208 (1979).  
<sup>(k-5)</sup>A. Hadni, J. Claudel, and P. Strimer, *Phys. Stat. Sol.* **26**:241 (1968).  
<sup>(k-6)</sup>X. J. Jiang, T. Hisamura, Y. Nosua, and T. Goto, *J. Phys. Soc. Jpn* **52**:4008 (1983).  
<sup>(k-7)</sup>See (j-8).

- (k-8) M. Cardona, *J. Phys. Paris* **C8**:29 (1984).  
 (k-9) T. Yao, M. Ogura, S. Matsuoka, and T. Morishita, *J. Appl. Phys.* **43**:499 (1983).  
 (k-10) G. Jones and J. Woods, *J. Phys. D* **9**:799 (1976).  
 (k-11) T. Ohyama, E. Otsuka, T. Yoshida, M. Isshiki, and K. Igaki, *Jpn. J. Appl. Phys.* **23**:L382 (1984).  
 (k-12) M. Sondergeld, *Phys. Sta. Sol. (b)* **81**:253 (1977).

#### **l-ZnTe**

- (l-1) See (j-1).  
 (l-2) M. Venghaus and P. J. Dean, *Phys. Rev. B* **21**:1596 (1980).  
 (l-3) See (h-5).  
 (l-4) D. Berlincourt, M. Jaffe, and L. R. Shiozawa, *Phys. Rev.* **129**:1009 (1983).  
 (l-5) D. T. F. Marple, *J. Appl. Phys.* **35**:539 (1964).  
 (l-6) T. L. Chu, S. S. Chu, F. Firszt, and C. Herrington, *J. Appl. Phys.* **59**:1259 (1986).  
 (l-7) See (k-8).  
 (l-8) A. G. Fisher, J. N. Carides, and J. Dresner, *Solid State Commun.* **2**:157 (1964).  
 (l-9) H. Venghaus, P. J. Dean, P. E. Simmonds, and J. C. Pfister, *Z. Phys. B* **30**:125 (1978).  
 (l-10) M. Aven and B. Segall, *Phys. Rev.* **130**:81 (1963).

#### **m-CdTe**

- (m-1) P. M. Amirtharaj and D. Chandler-Horowitz, (unpublished).  
 (m-2) P. M. Amirtharaj, R. C. Bowman, Jr., and R. L. Alt, *Proc. SPIE* **946**:57 (1988).  
 (m-3) N. Nawrocki and A. Twardowski, *Phys. Stat. Sol. (b)* **97**:K61 (1980).  
 (m-4) See (j-2).  
 (m-5) See (l-3).  
 (m-6) A. Moritani, K. Tamiguchi, C. Hamaguchi, and J. Nakai, *J. Phys. Soc. Jpn.* **34**:79 (1973).  
 (m-7) T. J. Parker, J. R. Birch, and C. L. Mok, *Solid State Communications* **36**:581 (1980).  
 (m-8) L. S. Ladd, *Infrared Phys.* **6**:145 (1966).  
 (m-9) J. R. Birch and D. K. Murray, *Infrared Phys.* **18**:283 (1978).  
 (m-10) See (a-10).  
 (m-11) K. K. Kanazawa and F. C. Brown, *Phys. Rev.* **135**:A1757 (1964).  
 (m-12) See (j-3).

#### **n-HgTe**

- (n-1) W. Szuszkiewicz, *Phys. Stat. Sol. (b)* **81**:K119 (1977).  
 (n-2) See (m-6).  
 (n-3) J. Baars and F. Sorger, *Solid State Commun.* **10**:875 (1972).  
 (n-4) H. Kepa, T. Giebultowicz, B. Buras, B. Lebech, and K. Clausen, *Physica Scripta* **25**:807 (1982).  
 (n-5) T. C. Harmon, in *Physics and Chemistry of II-VI Compounds*, M. Aven and J. S. Prener (eds), North Holland Publishing, Amsterdam, 1967, p. 767.  
 (n-6) Y. Guldner, C. Rigaux, M. Grynberg, and A. Mycielski, *Phys. Rev. B* **8**:3875 (1973).  
 (n-7) K. Shinizu, S. Narita, Y. Nisida, and V. I. Ivanov-Omskii, *Solid State Commun.* (eds.), **32**:327 (1979).

#### **o-CdS**

- (o-1) V. V. Sobolev, V. I. Donetskina, and E. F. Zagainov, *Sov. Phys. Semicond.* **12**:646 (1978).  
 (o-2) D. G. Seiler, D. Heiman, and B. S. Wherrett, *Phys. Rev. B* **27**:2355 (1983).  
 (o-3) A series excitons: D. G. Seiler, D. Heiman, R. Fiegenblatt, R. Aggarwal, and B. Lax, *Phys. Rev. B* **25**:7666 (1982); B series excitons: see (o-2).  
 (o-4) A. S. Barker and C. J. Summers, *J. Appl. Phys.* **41**:3552 (1970).  
 (o-5) R. Weil and D. Neshmit, *J. Opt. Soc. Am.* **67**:190 (1977).  
 (o-6) Complex Phonon Structure with Nine Allowed Optical Modes. See B. Tel, T. C. Damen, and S. P. S. Porto, *Phys. Rev.* **144**:771 (1966).  
 (o-7) See (a-10).

#### **p-PbS**

- (p-1) R. B. Schoolar and J. R. Dixon, *Phys. Rev. A* **137**:667 (1965).  
 (p-2) D. L. Mitchell, E. D. Palik, and J. N. Zemel, *Proc. 7th Int. Conf. Phys. Semicond.*, Paris, 1964, Dunod, Paris, 1964, p. 325.  
 (p-3) G. Nimtz and B. Schlicht, *Springer Tracts in Modern Physics*, vol. 98, Springer-Verlag, Berlin, 1983, p. 1.

<sup>(p-4)</sup>M. Cardona and D. L. Greenaway, *Phys. Rev. A* **133**:1685 (1964).

<sup>(p-5)</sup>R. Dalven, in *Solid State Physics*, vol. 28, H. Ehrenreich, F. Seitz, and D. Turnbull (eds.), Academic, NY, 1973, p. 179.

<sup>(p-6)</sup>R. B. Schoolar and J. N. Zemel, *J. Appl. Phys.* **35**:1848 (1964).

<sup>(p-7)</sup>M. M. Elcombe, *Proc. Soc. London*, **A300**:210 (1967).

<sup>(p-8)</sup>See (a-10).

<sup>(p-9)</sup>K. F. Cuff, M. R. Ellet, C. D. Kulgin, and L. R. Williams, in *Proc. 7th Int. Conf. Phys. Semicond.*, Paris, 1964, M. Hulin (ed.), Dunod, Paris, 1964, p. 677.

#### q-PbTe

<sup>(q-1)</sup>M. Preier, *Appl. Phys.* **20**:189 (1979).

<sup>(q-2)</sup>C. R. Hewes, M. S. Adler, and S. D. Senturia, *Phys. Rev. B* **7**:5195 (1973).

<sup>(q-3)</sup>See (p-3).

<sup>(q-4)</sup>See (p-4).

<sup>(q-5)</sup>W. E. Tennant, *Solid State Communications* **20**:613 (1976).

<sup>(q-6)</sup>J. R. Lowney and S. D. Senturia, *J. Appl. Phys.* **47**:1773 (1976).

<sup>(q-7)</sup>N. Piccioli, J. B. Beson, and M. Balkanski, *J. Phys. Chem. Solids* **35**:971 (1974).

<sup>(q-8)</sup>W. Cochran, R. A. Cowley, G. Dolling, and M. M. Elcombe, *Proc. R. Soc. London*, **A293**:433 (1966).

<sup>(q-9)</sup>See (a-10).

<sup>(q-10)</sup>See (p-9).

#### r-PbSe

<sup>(r-1)</sup>U. Schlichting, Dissertation Technische Universität Berlin, 1970.

<sup>(r-2)</sup>D. L. Mitchell, E. D. Palik, and J. N. Zemel, *Proc. 7th Int. Conf. Phys. Semicond.*, Paris, 1964, M. Hulin (ed.), Dunod, Paris, 1964, p. 325.

<sup>(r-3)</sup>H. Pasher, G. Bauer, and R. Grisar, *Phys. Rev. B* **38**:3383 (1988).

<sup>(r-4)</sup>A. F. Gibson, *Proc. Phys. Soc. (London)* **B65**:378 (1952).

<sup>(r-5)</sup>See (p-4).

<sup>(r-6)</sup>See (p-5).

<sup>(r-7)</sup>J. N. Zemel, J. D. Jensen, and R. B. Schoolar, *Phys. Rev. A* **140**:330 (1965).

<sup>(r-8)</sup>H. Burkhard, R. Geick, P. Kastner, and K. H. Unkelbach, *Phys. Stat. Sol. (b)* **63**:89 (1974).

<sup>(r-9)</sup>E. Burstein, R. Wheeler, and J. Zemel, *Proc. 7th Int. Conf. Phys. Semicond.*, Paris, 1964, M. Hulin (ed.), Dunod, Paris, 1964, p. 1065.

<sup>(r-10)</sup>R. N. Hall and J. H. Racette, *J. Appl. Phys.* **32**:2078 (1961).

<sup>(r-11)</sup>J. N. Zemel, J. D. Jensen, and R. B. Schoolar, *Phys. Rev. A* **140**:330 (1965).

<sup>(r-12)</sup>U. Schlichting and K. H. Gobrecht, *J. Phys. Chem. Solids* **34**:753 (1973).

<sup>(r-13)</sup>See (p-9).

#### s-GaN

<sup>(s-1)</sup>H. P. Maruska and J. J. Tietjen, *Appl. Phys. Lett.* **15**: 327 (1969); For a discussion of band parameters in III-Nitrides, see also I. Vurgaftman and J. R. Meyer, *J. Appl. Phys.* **94**: 3675 (2003).

<sup>(s-2)</sup>O. Madelung, *Semiconductor Data Handbook*, 3rd ed., Springer, New York, 2004, p. 103.

<sup>(s-3)</sup>S. N. Mohammad and H. Morkoc, *Prog. Quant. Electron.* **20**: 361 (1996).

<sup>(s-4)</sup>U. V. Bhapkar and M. S. Shur, *J. Appl. Phys.* **82**: 1649 (1997).

<sup>(s-5)</sup>M. S. Shur and M. Asif Khan, *MRS. Bull.* **22**: 44 (1997).

<sup>(s-6)</sup>W. R. L. Lambrecht, K. Kim, S. N. Rashkeev, and B. Segall, Electronic and Optical Properties Group-III Nitrides, their Heterostructures and Alloys, *Mat. Res. Soc. Symp. Proc.* **395**: 455–466 (1996).

#### t-AlN

<sup>(t-1)</sup>O. Madelung, *Semiconductor Data Handbook*, 3rd ed., Springer, New York, 2004, p. 88.

<sup>(t-2)</sup>W. M. Yim, E. J. Stofko, P. J. Zanzucchi, J. I. Pankove, M. Ettenburg, and S. L. Gilbert, *J. Appl. Phys.* **44**: 292 (1973).

<sup>(t-3)</sup>V. W. L. Chin, T. L. Tansley, and T. Osotchan, *J. Appl. Phys.* **75**: 7365 (1994).

<sup>(t-4)</sup>S. K. O'Leary, B. E. Foutz, M. S. Shur, U. V. Bhapkar, and L. F. Eastman, *Solid State Comm.* **105**: 621 (1998).

<sup>(t-5)</sup>J. A. Majewski, M. Stadele, and P. Vogl, Electronic Structure of Biaxially Strained Wurtzite Crystals GaN and AlN, *Mat. Res. Soc. Symp. Proc.* **449**: 887–892 (1997).

#### u-InN

<sup>(u-1)</sup>T. L. Tansley and C. P. Foley, *J. Appl. Phys.* **59**: 3241 (1986).

<sup>(u-2)</sup>O. Madelung, *Semiconductor Data Handbook*, 3rd ed., Springer, New York, 2004, p. 137.

<sup>(u-3)</sup>S. K. O'Leary, B. E. Foutz, M. S. Shur, U. V. Bhapkar, and L. F. Eastman, *J. Appl. Phys.* **83**: 826 (1998).

## 5.7 REFERENCES

1. D. Attwood, B. Hartline, and R. Johnson, *The Advanced Light Source: Scientific Opportunities*, Lawrence Berkeley Laboratory Publication 5111, 1984, pp.331–389.
2. F. C. Brown, “Ultraviolet Spectroscopy of Solids with the Use of Synchrotron Radiation,” in *Solid State Physics*, vol. 29, H. Ehrenreich, F. Seitz, and D. Turnbull (eds.), Academic Press, New York, 1974, pp. 1–73.
3. P. Y. Yu and M. Cardona, *Fundamentals of Semiconductors*, Springer, Berlin, 1996.
4. A. V. Nurmikko, in *Semiconductors and Semimetals*, vol. 36, D. G. Seiler and C. L. Littler (eds.), Academic Press, New York, 1992, p. 85.
5. R. R. Alfano, (ed.), *Semiconductors Probed by Ultrafast Laser Spectroscopy*, vols. I and II, Academic Press, New York, 1984.
6. G. Bastard, C. Delalande, Y. Guldner, and P. Voisin, in *Advances in Electronics and Electron Physics*, vol. 72, P. W. Hawkes (ed.), Academic Press, New York, 1988, p. 1.
7. C. Weisbuch and B. Vinter, *Quantum Semiconductor Structures, Fundamentals and Applications*, Academic Press, New York, 1991, p. 57.
8. M. Born and K. Huang, *Dynamical Theory of Crystal Lattices*, chap. 2, Oxford University Press, London, 1954, p. 38.
9. W. K. H. Panofsky and M. Phillips, *Classical Electricity and Magnetism*, Addison-Wesley, New York, 1962, p. 29.
10. E. D. Palik (ed.), *Handbook of Optical Constants of Solids*, vol. 1, Academic Press, New York, 1985.
11. E. D. Palik (ed.), *Handbook of Optical Constants of Solids*, vol. 2, Academic Press, New York, 1991.
12. E. D. Palik (ed.), *Handbook of Optical Constants of Solids*, vol. 1, Academic Press, New York, 1985, p. 429.
13. M. Born and E. Wolf, *Principles of Optics*, Pergamon, London, 1970, p. 61.
14. J. S. Toll, “Causality and the Dispersion Relation: Logical Foundations,” *Phys. Rev.* **104**:1760–1770 (1956).
15. D. Y. Smith, “Comments on the Dispersion Relations for the Complex Refractive Index of Circularly and Elliptically Polarized Light,” *J. Opt. Soc. Am.*, **66**(5):454–460 (1976).
16. D. L. Greenaway and G. Harbeke, *Optical Properties and Band Structure of Semiconductors*, Pergamon, London, 1968, p. 9.
17. J. M. Ziman, *Principles of the Theory of Solids*, Cambridge University Press, London, 1972, p. 200.
18. C. Kittel, *Introduction to Solid State Physics*, 4th ed., John Wiley, New York, 1971, p. 184.
19. W. J. Turner and W. E. Reese, “Infrared Lattice Bands in AlSb,” *Phys. Rev.* **127**:126–131 (1962).
20. S. S. Mitra, in *Optical Properties of Solids*, S. Nudelman and S. S. Mitra (eds.), Plenum Press, New York, 1979, p. 333.
21. W. Cochran, *The Dynamics of Atoms in Crystals*, Crane, Rusak and Co., New York, 1973.
22. P. Gianozzi, S. de Gironcoli, P. Pavone, and S. Baroni, “*Ab initio* Calculation of Phonon Dispersions in Semiconductors,” *Phys. Rev. B* **43**:7231–7242 (1991).
23. S. S. Mitra and N. E. Massa, in *Handbook on Semiconductors*, T. S. Moss and W. Paul (eds.), North Holland, Amsterdam, 1982, p. 81.
24. W. G. Spitzer, in *Semiconductors and Semimetals*, vol. 3., R. K. Willardson and A. C. Beer (eds.), Academic Press, New York, 1967, p. 17.
25. J. L. Birman, *Theory of Crystal Space Groups and Lattice Dynamics*, Springer-Verlag, Berlin, 1974, p. 271.
26. F. A. Johnson, “Lattice Absorption Bands in Silicon,” *Proc. Phys. Soc. (London)* **73**:265 (1959).
27. W. Cochran, S. J. Fray, F. A. Johnson, J. E. Quarrington, and N. Williams, “Lattice Absorption in Gallium Arsenide,” *J. Appl. Phys.* **32**:2102 (1961).
28. A. S. Barker and A. J. Sievers, “Optical Studies of the Vibrational Properties of Disordered Solids,” *Rev. Mod. Phys.* **47**(2):S1–S179 (1975).
29. W. M. Theis, K. K. Bajaj, C. W. Litton, and W. G. Spitzer, “Direct Evidence for the Site of Substitutional Carbon Impurity in GaAs,” *Appl. Phys. Lett.* **41**:70 (1982).
30. R. S. Leigh and R. C. Newman, “Host Isotope Fine Structure of Local Modes: C and Si in GaAs,” *J. Phys. C: Solid State Phys.* **15**:L1045 (1982).

31. M. Stavola and S. J. Pearton, in *Semiconductors and Semimetals*, vol. 34, J. I. Pankove and N. M. Johnson (eds.), Academic Press, New York, 1991, p. 139.
32. R. C. Newman, in *Growth and Characterization of Semiconductors*, R. A. Stradling and P. C. Klipstein (eds.), Adam Hilger, Bristol, 1990, p. 105.
33. A. Baghdadi, W. M. Bullis, M. C. Croarkin, Y. Li, R. I. Scace, R. W. Series, P. Stallhofer, and M. Watanabe, "Interlaboratory Determination of the Calibration Factor for the Measurement of the Interstitial Oxygen Content of Silicon by Infrared Absorption," *J. Electrochem. Soc.* **136**:2015 (1989).
34. W. L. Wolfe, in *The Infrared Handbook*, W. L. Wolfe and G. J. Zeiss (eds.), Environmental Research Institute, Ann Arbor, 1978, pp. 7–39.
35. A. Miller, *Handbook of Optics*, 2nd ed., vol. I, chap. 9, McGraw-Hill, New York, 1994.
36. E. J. Johnson, in *Semiconductors and Semimetals*, vol. 3, R. K. Willardson and A. C. Beer (eds.), Academic Press, New York, 1967, p. 153.
37. E. O. Kane, "Band Structure of Indium Antimonide," *J. Phys. Chem. Solids* **1**:249 (1957).
38. T. S. Moss and T. D. F. Hawkins, "Infrared Absorption in Gallium Arsenide," *Infrared Phys.* **1**:111 (1961).
39. (op. cit.) E. J. Johnson, p. 191.
40. W. G. Spitzer, M. Gershenson, C. J. Frosch, and D. F. Gibbs, "Optical Absorption in n-Type Gallium Phosphide," *J. Phys. Chem. Solids* **11**:339 (1959).
41. M. Gershenson, D. G. Thomas, and R. E. Dietz, *Proc. Int. Conf. Phys. Semicond. Exeter*, Inst. of Physics, London, 1962, p. 752.
42. W. C. Dash and R. Newman, "Intrinsic Optical Absorption in Single-Crystal Germanium and Silicon at 77°K and 300°K," *Phys. Rev.* **99**:1151 (1955). See also G. Burns, *Solid State Physics*, Academic Press, New York, 1985, p. 505.
43. K. Cho, *Excitons*, vol. 14 of *Topics in Current Physics*, K. Cho (ed.), Springer-Verlag, New York, 1979, p. 1.
44. W. Hayes and A. M. Stoneham, *Defects and Defect Processes in Nonmetallic Solids*, John Wiley and Sons, New York, 1985, p. 40.
45. D. C. Reynolds and T. C. Collins, *Excitons: Their Properties and Uses*, Academic Press, New York, 1981, pp. 1–291.
46. E. I. Rashba and M. D. Sturge (eds.), *Excitons*, North Holland, Amsterdam, 1982, pp. 1–865.
47. J. Frenkel, "On the Transformation of Light into Heat in Solids II," *Phys. Rev.* **37**:1276–1294 (1931).
48. G. H. Wannier, "The Structure of Electronic Excitation Levels in Insulating Crystals," *Phys. Rev.* **52**:191–197 (1937).
49. N. F. Mott, "On the Absorption of Light by Crystals," *Proc. Roy. Soc. A* **167**:384 (1938).
50. M. D. Sturge, "Optical Absorption of Gallium Arsenide between 0.6 and 2.75 eV," *Phys. Rev.* **127**:768–773 (1962). For an excellent discussion of theoretical aspects see article by M. Sturge, "Advances in Semiconductor Spectroscopy," in B. DiBartolo (ed.), *Spectroscopy of Laser-Type Materials*, Plenum Press, New York, 1987, p. 267.
51. Adapted by permission from R. G. Ulbrich and C. Weisbuch, Contribution to the study of optical pumping in III-V Semiconductors, These de doctorat d'Etat, Univ. Paris 7, 1977 (Unpublished).
52. (op. cit.) W. Hayes and A. M. Stoneham, p. 51.
53. O. Madelung, *Introduction to Solid-State Theory*, Springer-Verlag, New York, 1978, p. 254.
54. G. Burns, *Solid State Physics*, Academic Press, New York, 1985, p. 969.
55. H. R. Philipp and H. Ehrenreich, in *Semiconductors and Semimetals*, vol. 3, R. K. Willardson and A. C. Beer (eds.), Academic Press, New York, 1967, p. 93. For a review of interband transitions in Semiconductors see M. L. Cohen and J. R. Chelikowski, *Electronic Structure and Optical Properties of Semiconductors*, Springer-Verlag, Berlin, 1988.
56. H. R. Philipp and H. Ehrenreich, "Optical Properties of Semiconductors," *Phys. Rev.* **129**:1550–1560 (1963).
57. D. Brust, J. C. Phillips, and F. Bassani, "Critical Points and Ultraviolet Reflectivity of Semiconductors," *Phys. Rev. Lett.* **9**:94–97 (1962).
58. D. Brust, "Electronic Spectra of Crystalline Germanium and Silicon," *Phys. Rev.* **134**:A1337–A1353 (1964).
59. M. Rohlffing and S. G. Louie, "Electron-hole Excitations and Optical Spectra from First Principles," *Phys. Rev. B* **62**:4927–4944 (2000).

60. H. R. Philipp and H. Ehrenreich, "Observation of  $d$  Bands in 3-5 Semiconductors," *Phys. Rev. Lett.* **8**:92–94 (1962).
61. C. Gahwiller and F. C. Brown, "Photoabsorption near the  $L_{\text{III}}$  Edge of Silicon and Aluminum," *Phys. Rev. B* **2**:1918–1925 (1970).
62. S. Zollner, in *Silicon-Germanium Carbon Alloys: Growth, Properties, and Applications*, S. T. Pantelides and S. Zollner (eds.), Taylor & Francis, New York, 2001, p. 387.
63. J. Humlicek, M. Garriga, M. I. Alonso, and M. Cardona, "Optical Spectra of  $\text{Si}_x\text{Ge}_{1-x}$  Alloys," *J. Appl. Phys.* **65**, 2827–2832, 1989.
64. S. Perkowitz, in *Infrared and Millimeter Waves*, vol. 8, K. J. Button (ed.), Academic Press, New York, 1983, p. 71.
65. J. R. Dixon and H. R. Riedl, "Electric-Susceptibility Hole Mass of Lead Telluride," *Phys. Rev.* **138**:A873–A881 (1965).
66. T. E. Tiwald, J. A. Woollam, S. Zollner, J. Christiansen, R. B. Gregory, T. Wetteroth, S. R. Wilson, and A. R. Powell, "Carrier Concentration and Lattice Absorption in Bulk and Epitaxial Silicon Carbide Determined using Infrared Ellipsometry," *Phys. Rev. B* **60**:11464–11474 (1999).
67. B. B. Varga, "Coupling of Plasmons to Polar Phonons in Degenerate Semiconductors," *Phys. Rev.* **137**: A1896–A1902 (1965).
68. A. Mooradian and G. B. Wright, "Observation of the Interaction of Plasmons with Longitudinal Optical Phonons in GaAs," *Phys. Rev. Lett.* **16**:999–1001 (1966).
69. A. Mooradian, in *Advances in Solid State Physics*, vol. 9, O. Madelung (ed.), Pergamon Press, London, 1969, p. 74.
70. C. G. Olson and D. W. Lynch, "Longitudinal-Optical-Phonon-Plasmon Coupling in GaAs," *Phys. Rev.* **177**:1231–1234 (1969).
71. S. C. Baber, "Net and Total Shallow Impurity Analysis of Silicon by Low Temperature Fourier Transform Infrared Spectroscopy," *Thin Solid Films* **72**:201–210 (1980).
72. G. M. Martin, "Optical Assessment of the Main Electron Trap in Bulk Semi-Insulating GaAs," *Appl. Phys. Lett.* **39**: 747 (1981).
73. C. M. Wolfe and G. E. Stillman, *Gallium Arsenide and Related Compounds*, Inst. Phys., London, 1971, p. 3.
74. M. H. Weiler, *Semiconductors and Semimetals*, vol. 16, R. K. Willardson and A. C. Beer (eds.), Academic Press, New York, 1981, p. 119.
75. C. R. Pidgeon and R. N. Brown, "Interband Magneto-Absorption and Faraday Rotation in InSb," *Phys. Rev.* **146**:575 (1966).
76. M. H. Weiler, R. L. Aggarwal, and B. Lax, "Warping- and Inversion-Asymmetry-Induced Cyclotron-Harmonic Transitions in InSb," *Phys. Rev. B* **17**:3269 (1978).
77. M. H. Weiler, "Conduction and Valence Band Effective Mass Parameters in InSb," *J. Magn. Magn. Mater.* **11**:131–135 (1979).
78. M. Reine, R. L. Aggarwal, and B. Lax, "Stress-Modulated Magnetorefectivity of Gallium Antimonide and Gallium Arsenide," *Phys. Rev. B* **5**:3033 (1972).
79. M. Reine, R. L. Aggarwal, B. Lax, and C. M. Wolfe, "Split-Off Valence-Band Parameters for GaAs from Stress-Modulated Magnetorefectivity," *Phys. Rev. B* **2**:458 (1970).
80. H. Piller, *Proc. 7th Int. Conf. Phys. Semicond.*, Dunod, Paris, 1964, p. 297.
81. E. Oh, D. U. Bartholomew, A. K. Ramdas, J. K. Furdyna, and U. Debska, "Interband Faraday Effect in  $\text{Cd}_{1-x}\text{Mn}_x\text{Se}$ ," *Phys. Rev. B* **38**:13183 (1988).
82. R. J. Elliott and R. Loudon, "Theory of the Absorption Edge in Semiconductors in a High Magnetic Field," *J. Phys. Chem. Solids* **15**:196–207 (1960).
83. D. G. Seiler, D. Heiman, R. Feigenblatt, R. L. Aggarwal, and B. Lax, "Two-Photon Magnetospectroscopy of A-Exciton States in CdS," *Phys. Rev. B* **25**:7666 (1982).
84. D. G. Seiler, D. Heiman, and B. S. Wherrett, "Two-Photon Spectroscopy of B Excitons in CdS," *Phys. Rev. B* **27**:2355 (1983).
85. B. D. McCombe and R. J. Wagner, *Adv. Electron. and Electron. Phys.* **37**:1 (1975).
86. B. D. McCombe and R. J. Wagner, *Adv. Electron. and Electron. Phys.* **38**:1 (1975).

87. H. Kobori, T. Ohyama, and E. Otsuka, "Line-Width of Quantum Limit Cyclotron Resonance. II. Impurity and Carrier-Carrier Scatterings in Ge, InSb and GaAs," *J. Phys. Soc. Jpn.* **59**:2164–2178 (1990).
88. B. Lax, H. J. Zeiger, and R. N. Dexter, "Anisotropy of Cyclotron Resonance in Germanium," *Physica* **20**:818–828 (1954).
89. G. Dresselhaus, A. F. Kip, and C. Kittel, "Cyclotron Resonance of Electrons and Holes in Silicon and Germanium Crystals," *Phys. Rev.* **98**:368 (1955).
90. M. A. Omar, *Elementary Solid State Physics*, Addison-Wesley, Reading, 1975, p. 285.
91. O. Matsuda and E. Otsuka, "Cyclotron Resonance Study of Conduction Electrons in n-Type Indium Antimonide under a Strong Magnetic Field—I: Thermal Equilibrium Case," *J. Phys. Chem. Solids* **40**:809–817 (1979).
92. D. Larsen, in *Landau Level Spectroscopy*, vol. 27.1, chap. 3, G. Landwehr and E. I. Rashba (eds.), North Holland, Amsterdam, 1991, p. 109.
93. H. R. Fetterman, D. M. Larsen, G. E. Stillman, P. E. Tannenwald, and J. Waldman, "Field-Dependent Central-Cell Corrections in GaAs by Laser Spectroscopy," *Phys. Rev. Lett.* **26**:975–978 (1971).
94. G. W. Bryant and G. S. Solomon, *Optics of Quantum Dots and Wires*, Artech House, Boston, 2005.
95. T. N. Muiira, *Physics of Semiconductors in High Magnetic Fields*, Oxford University Press, Oxford, 2008.
96. C. L. Tang, *Handbook of Optics*, 3rd ed., vol. IV, chap. 10, McGraw-Hill, New York, 2009.
97. Y. R. Shen, *The Principles of Nonlinear Optics*, John Wiley and Sons, New York, 1984, p. 38.
98. P. N. Butcher, *Nonlinear Optical Phenomena*, Ohio State University Engineering Publications, Columbus, 1965, p. 1.
99. B. S. Wherrett, *Nonlinear Optics*, P. G. Harper and B. S. Wherrett (eds.), Academic Press, New York, 1977, p. 4.
100. M. C. Downer, D. S. Mendoza, and V. I. Gavrilenko, "Optical Second Harmonic Spectroscopy of Semiconductor Surfaces: Advances in Microscopic Understanding," *Surf. Intef. Anal.* **31**:966–986 (2001).
101. R. Carriles, J. Kwon, Y. Q. An, J. C. Miller, M. C. Downer, J. Price, and A. C. Diebold, "Second-harmonic Generation from Si/SiO<sub>2</sub>/Hf<sub>(1-x)</sub>Si<sub>x</sub>O<sub>2</sub> Structures," *Appl. Phys. Lett.* **88**:161120 (2006).
102. Y. Q. An, R. Carriles, and M. C. Downer, "Absolute Phase and Amplitude of Second-Order Nonlinear Optical Susceptibility Components at Si(001) Interfaces," *Phys. Rev. B* **75**:241307 (2007).
103. J. H. Bechtal and W. L. Smith, "Two-Photon Absorption in Semiconductors with Picosecond Laser Pulses," *Phys. Rev. B* **13**:3515–3522 (1976).
104. P. D. Maker and R. H. Terhune, "Study of Optical Effects Due to an Induced Polarization Third Order in the Electric Field Strength," *Phys. Rev.* **137**:A801–A818 (1965).
105. R. M. A. Azzam and N. M. Bashara, *Ellipsometry and Polarized Light*, North-Holland, Amsterdam, 1987, p. 153. See also Azzam in *Handbook of Optics*, 2nd ed., vol. II, chap. 27, McGraw-Hill, New York, 1994.
106. D. E. Aspnes, "Analysis of Semiconductor Materials and Structures by Spectroellipsometry," *Proc. SPIE* **946**:84 (1988).
107. W. Hayes and R. Loudon, *Scattering of Light by Crystals*, John-Wiley, New York, 1978, p. 53.
108. P. J. Dean, "Photoluminescence as a Diagnostic of Semiconductors," *Prog. Crystal Growth and Characterization* **5**:89 (1982).
109. M. Voos, R. F. Lehney, and J. Shah, in *Handbook of Semiconductors*, vol. 2, T. S. Moss and M. Balkanski (eds.), North-Holland, Amsterdam, 1980, p. 329.
110. See Table 11.
111. A. J. LaRocca, in *Handbook of Optics*, 3rd ed., vol. II, chap. 15, McGraw-McGraw-Hill, New York, 2009.
112. W. T. Silfvast, in *Handbook of Optics*, 3rd ed., vol. II, chap. 16, McGraw-Hill, New York, 2009.
113. B. Henderson in *Handbook of Optics*, 3rd ed., vol. I, chap. 31, McGraw-Hill, New York, 2009.
114. P. Hariharan, in *Handbook of Optics*, 3rd ed., vol. I, chap. 32, McGraw-Hill, New York, 2009.
115. P. R. Norton in *Handbook of Optics*, 3rd ed., vol. II, chap. 24, McGraw-Hill, New York, 2009.
116. S. Perkowitz, D. G. Seiler, and W. M. Duncan, "Optical Characterization in Semiconductor Manufacturing," *J. Res. Natl. Inst. Stand. Technol.* **99**:605 (1994).
117. G. E. Jellison, Jr, "Physics of Optical Metrology of Silicon-Based Semiconductor Devices," in *Handbook of Silicon Semiconductor Metrology*, A. C. Diebold (ed.) Marcel Dekker, Inc., New York, 2001, p. 723.

118. Clive Hayzelden, "Gate Dielectric Metrology," in *Handbook of Silicon Semiconductor Metrology*, A. C. Diebold (ed.), Marcel Dekker, Inc., New York, 2001, p. 17.
119. R. W. Collins, "Automatic Rotating Element Ellipsometers: Calibration, Operation, and Real-Time Applications," *Rev. Sci. Instrum.* **61**:2029 (1990).
120. U. Gerhardt and G. Rubloff, "A Normal Incidence Scanning Reflectometer of High Precision," *Appl. Opt.* **8**:305 (1969).
121. M. I. Bell and D. A. McKeown, "High-Precision Optical Reflectometer for the Study of Semiconductor Materials and Structures," *Rev. Sci. Instrum.* **61**:2542 (1990).
122. D. E. Aspnes and J. E. Fischer, in *Encyclopaedic Dictionary of Physics*, suppl. vol. 5, Thewlis (ed.), Pergamon, Oxford, 1975, p. 176.
123. D. E. Aspnes, in *Handbook on Semiconductors*, vol. 1, T. S. Moss and M. Balkanski (eds.), North-Holland, Amsterdam, 1980, p. 109.
124. D. E. Aspnes and A. A. Studna, "Schottky-Barrier Electroreflectance: Application to GaAs," *Phys. Rev. B* **7**:4605–4625 (1973).
125. R. E. Nahory and J. L. Shay, "Reflectance Modulation by the Surface Field in GaAs," *Phys. Rev. Lett.* **21**:1569–1571 (1968).
126. K. Dev, M. Y. L. Jung, R. Gunawan, R. D. Braatz, and E. G. Seebauer, "Mechanism for Coupling between Properties of Interfaces and Bulk Semiconductors," *Phys. Rev. B* **68**:195311 (2003).
127. K. Dev and E. G. Seebauer, "Band Bending at the Si(1 1 1)–SiO<sub>2</sub> Interface Induced by Low-Energy Ion Bombardment," *Surf. Sci.* **550**:185–191 (2004).
128. F. H. Pollak, "Modulation Spectroscopy as a Technique for Semiconductor Characterization," *Proc. SPIE* **276**:142–156 (1981).
129. O. J. Glembocki, B. V. Shanabrook, N. Bottka, W. T. Beard, and J. Comas, "Photoreflectance Characterization of Interband Transitions in GaAs/AlGaAs Multiple Quantum Wells and Modulation-Doped Heterojunctions," *Appl. Phys. Lett.* **46**:970 (1985).
130. X. Yin, H. M. Chen, F. Pollak, Y. Chan, P. A. Montano, P. D. Kichner, G. D. Pettit, and J. M. Woodall, "Photoreflectance Study of Surface Photovoltage Effects at (100) GaAs Surfaces/Interfaces," *Appl. Phys. Lett.* **58**:260 (1991).
131. F. H. Pollak, M. Cardona, and D. E. Aspnes (eds.), *Proc. Int. Conf. on Modulation Spectroscopy*, Proc. SPIE Bellingham, 1990, p. 1286.
132. O. J. Glembocki and B. V. Shanabrook, in *Semiconductors and Semimetals*, vol. 36, D. G. Seiler and C. L. Littler (eds.), Academic Press, New York, 1992, p. 221.
133. H. G. Tompkins and W. A. McGahan, *Spectroscopic Ellipsometry and Reflectometry*, Wiley, New York, 1999.
134. *The Proc. 2007 Int. Conf. on Spectroscopic Ellipsometry IV*, in *Phys. Stat. Sol. (a)* **205**:4 (2008).
135. H. G. Tompkins and E. A. Irene, *Handbook of Ellipsometry*, Springer, New York, 2005.
136. R. M. A. Azzam, "Ellipsometry," in M. Bass (ed.), *Handbook of Optics*, 3rd ed., vol. V, chap. 2, McGraw-Hill, New York, 2009.
137. R. W. Collins, Ellipsometry, in *The Optics Encyclopedia*, Wiley-VCH, Weinheim, 2004, p. 609.
138. N.V. Edwards, in *Characterization and Metrology for ULSI Technology*, D. G. Seiler A. C. Diebold, Th. J. Shaffner, R. McDonald, S. Zollner, R. P. Khosla, and E. M. Secula (eds.), AIP, Melville, 2003, p. 723.
139. M. Schubert, *Infrared Ellipsometry on Semiconductor Layer Structures*, Springer-Verlag, Berlin, 2004.
140. M. Schubert, T. Hofmann, and C. M. Herzinger, "Generalized Far-Infrared Magneto-Optic Ellipsometry for Semiconductor Layer Structures: Determination of Free-Carrier Effective-Mass, Mobility, and Concentration Parameters in *n*-Type GaAs," *J. Opt. Soc. Am. A* (**20**):347–356 (2003).
141. T. Hofmann, M. Schubert, C. M. Herzinger, and I. Pietzonka, "Far-Infrared-Magneto-Optic Ellipsometry Characterization of Free-Charge-Carrier Properties in Highly Disordered *n*-Type Al<sub>0.19</sub>Ga<sub>0.33</sub>In<sub>0.48</sub>P," *Appl. Phys. Lett.* **82**:3463 (2003).
142. T. Hofmann, U. Schade, K. Agarwal, B. Daniel, C. Klingshirn, M. Hetterich, C. Herzinger, and M. Schubert, "Conduction-Band Electron Effective Mass in Zn<sub>0.87</sub>Mn<sub>0.13</sub>Se Measured by Terahertz and Far-Infrared Magneto-optic Ellipsometry," *Appl. Phys. Lett.* **88**: 42105 (2006).
143. T. Hofmann, C. M. Herzinger, C. Krahmer, K. Streubel, and M. Schubert, "The Optical Hall Effect," *Phys. Stat. Sol. (a)* **205**(4): 779–783 (2008).



144. T. Hofmann, U. Schade, C. M. Herzinger, P. Esquinazi, and M. Schubert, "Terahertz Magneto-Optic Generalized Ellipsometry Using Synchrotron and Blackbody Radiation," *Rev. Sci. Instr.* **77**:063902 (2006).
145. D. B. Holt and B. G. Yacobi, in *SEM Microcharacterization of Semiconductors*, D. B. Holt and D. C. Joy (eds.), Academic Press, New York, 1989, p. 373.
146. J. I. Pankove, in *Electroluminescence*, J. I. Pankove (ed.), Springer-Verlag, Berlin, 1977, p. 1.
147. E. C. Lightowers, in *Growth and Characterization of Semiconductors*, R. A. Stradling and P. C. Klipstein (eds.), Adam Hilger, Bristol, 1990, p. 135.
148. M. L. W. Thewalt, M. K. Nissen, D. J. S. Beckett, and K. R. Lundgren, "High Performance Photoluminescence Spectroscopy Using Fourier Transform Interferometry," *Mat. Res. Soc. Symp.* **163**:221 (1990).
149. D. E. Aspnes, in *Properties of GaAs*, EMIS Data Reviews, Series #2, p. 229 INSPEC, London, 1990.
150. F. Fuchs, A. Lusson, P. Koidl, and R. Triboulet, "Fourier Transform Infrared Photoluminescence of  $\text{Hg}_{1-x}\text{Cd}_x\text{Te}$ ," *J. Crystal Growth* **101**:722 (1990).
151. P. Hiesinger, S. Suga, F. Willmann, and W. Dreybrodt, "Excitation Spectra of Exciton Luminescence in CdTe," *Phys. Stat. Sol. (b)* **67**:641–652 (1975).
152. *Light Scattering in Solids*, M. Cardona (ed.), vol. 1., Springer-Verlag, Berlin, 1983; *Light Scattering in Solids*, vol. 2, M. Cardona and G. Guntherodt (eds.), Springer-Verlag, Berlin, 1982; *Light Scattering in Solids*, vol. 3, M. Cardona and G. Guntherodt (eds.), Springer-Verlag, Berlin, 1982; *Light Scattering in Solids*, vol. 4, M. Cardona and G. Guntherodt (eds.), Springer-Verlag, Berlin, 1984; *Light Scattering in Solids*, vol. 5, M. Cardona and G. Guntherodt (eds.), Springer-Verlag, Berlin, 1989.
153. (op. cit.) W. Hayes and R. Loudon, pp. 1–360.
154. A. S. Pine, in *Light Scattering of Solids*, vol. 1, M. Cardona (ed.), Springer-Verlag, Berlin, 1982, p. 253.
155. (op. cit.) W. Hayes and R. Loudon, p. 16.
156. (op. cit.) W. Hayes and R. Loudon, p. 44.
157. G. Abstreiter, "Micro-Raman Spectroscopy for Characterization of Semiconductor Devices," *Applied Surface Science* **50**:73–78 (1991).
158. K. K. Tiong, P. M. Amiratharaj, F. H. Pollak, and D. E. Aspnes, "Effects of As<sup>+</sup> Ion Implantation on the Raman Spectra of GaAs: 'Spatial Correlation' Interpretation," *Appl. Phys. Lett.* **44**:122 (1984).
159. P. A. Temple and C. E. Hathaway, "Multiphonon Raman Spectrum of Silicon," *Phys. Rev. B* **7**:3685–3697 (1973).
160. G. Abstreiter, R. Trommer, M. Cardona, and A. Pinczuk, "Coupled Plasmon-LO Phonon Modes and Lindhard-Mermin Dielectric Function of n-GaAs," *Solid State Communications* **30**:703–707 (1979).
161. A. Pinczuk, L. Brillson, E. Burstein, and E. Anastassakis, "Resonant Light Scattering by Single-Particle Electronic Excitations in n-GaAs," *Phys. Rev. Lett.* **27**:317–320 (1971).
162. J. M. Ralston, R. L. Wadsack, and R. K. Chang, "Resonant Cancellation of Raman Scattering from CdS and Si," *Phys. Rev. Lett.* **25**:814–818 (1970).
163. M. Chandrasekhar, H. R. Chandrasekhar, M. Grimsditch, and M. Cardona, "Study of the Localized Vibrations of Boron in Heavily Doped Si," *Phys. Rev. B* **22**:4825–4833 (1980).
164. D. D. Manchon, Jr., and P. J. Dean, *Proc. 10th Int. Conf. on Physics of Semiconductors*, S. P. Keller, J. C. Hensel, and F. Stern (eds.), USAEC, Cambridge, 1970, p. 760.
165. A. W. Nelson, in *Electronic Materials from Silicon to Organics*, L. S. Miller and J. B. Mullin (eds.), Plenum Press, New York, 1991, p. 67.
166. O. Madelung, M. Schulz, and H. Weiss (eds.), *Landolt-Bornstein Numerical Data and Functional Relationships in Science and Technology, Group III—Crystal and Solid State Physics*, vol. 17a, Springer-Verlag, Berlin, 1982.
167. O. Madelung, M. Schulz, and H. Weiss (eds.), *Landolt-Bornstein Numerical Data and Functional Relationships in Science and Technology, Group III—Crystal and Solid State Physics*, vol. 17b, Springer-Verlag, Berlin, 1982.
168. O. Madelung, M. Schulz, and H. Weiss (eds.), *Landolt-Bornstein Numerical Data and Functional Relationships in Science and Technology, Group III—Crystal and Solid State Physics*, vol. 17f, Springer-Verlag, Berlin, 1982.
169. O. Madelung and M. Schulz (eds.), *Landolt-Bornstein Numerical Data and Functional Relationships in Science and Technology, Group III—Crystal and Solid State Physics*, vol. 22a, Springer-Verlag, Berlin, 1987.
170. <http://lb.chemie.uni-hamburg.de/search/index.php>, accessed May 21, 2009.
171. O. Madelung, *Semiconductors: Data Handbook*, 3rd ed., Springer-Verlag, Berlin, 2004.

---

# CHARACTERIZATION AND USE OF BLACK SURFACES FOR OPTICAL SYSTEMS

---

Stephen M. Pompea

*National Optical Astronomy Observatory  
Tucson, Arizona*

Robert P. Breault

*Breault Research Organization, Inc.  
Tucson, Arizona*

---

## 6.1 INTRODUCTION

---

Optical instruments and telescopes rely on black baffle and vane surfaces to minimize the effect of stray light on overall system performance. For well-designed and well-baffled systems, the black surfaces chosen for the baffles and vanes can play a significant role in reducing the stray light on the detector.<sup>1-8</sup> In space-borne systems, a large number of black surfaces play an important role. An excellent and comprehensive review of infrared surfaces is given by Persky.<sup>9</sup> Additional infrared measurements of materials are given by Miller<sup>10</sup> and Persky and Szczesniak.<sup>11</sup> Black surfaces are also used extensively in solar collector applications. Excellent reviews of spectrally selective surfaces for heating and cooling applications are found in Hahn and Seraphim<sup>12</sup> and in Granqvist.<sup>13</sup> In many solar applications, high solar absorptance is desired along with low thermal emittance.<sup>14</sup> In general, surfaces for solar applications will not be addressed in this chapter.

Black coatings are also used in radiometric detectors.<sup>15</sup> Because the surface needed is often small, these surfaces may be even more specialized than the black coatings used for stray light reduction in optical instruments. This chapter will concentrate on the selection and characterization of black surfaces chosen for stray light suppression and suitable for application to relatively large areas of an optical system or optical test bed. Some examples of these uses are seen in Table 1.

The optical system designer has a wide repertoire of baffle surfaces from which to choose. Summaries of optical properties of materials were given by Wolfe,<sup>16</sup> Pompea et al.,<sup>4</sup> and McCall et al.<sup>17</sup> Reviews of materials by McCall<sup>18</sup> and Smith and Howitt<sup>19</sup> emphasized the ultraviolet/visible and infrared properties, respectively. A number of company databases of scattering data are available, including one using the same instrument (for bidirectional scatter distribution function or BSDF measurements at 0.5145  $\mu\text{m}$ ) for approximately 15,000 data runs.<sup>20</sup> Large amounts of BSDF data are at Breault Research Organization and a BSDF database format has been proposed by Klicker et al.<sup>21</sup> An organized effort to create specialized databases of optical properties of surfaces applicable to both ground- and space-based instruments has been undertaken and is proving to have great utility.<sup>22</sup>

The choices of optical black surfaces are usually first narrowed by the nature of the application, the substrates available or possible, the wavelength or bandpasses of interest, the angles at which the surfaces must be nonreflective, and a host of system issues and environmental factors.<sup>5</sup> As the system performance requirements have become more stringent, an array of surfaces has become available to meet these requirements. Many paints (e.g., Chemglaze Z306, SolarChem) (Table 2); anodized surfaces (e.g., Martin Black, Infrablack, Tiodize) (Table 3); etched, electrodeposited, and

## 6.2 PROPERTIES

**TABLE 1** Possible Uses for Black Surfaces in Optical Systems and Test Beds

Apertures and field stops	Baffles	Barrels	Blackbodies	Choppers	Cold shields	Detector housings
Dewar interiors	Enclosures and testing structures	Lens edges	Laser light traps	Radiometers	Radiators	Simulators and targets

**TABLE 2** Painted Surfaces

Surface Name or Designation	Manufacturer and/or Distributor (contact person)	Historical Notes	Surface Type	Main Literature References
Aeroglaze L300	Lord Corporation Chemical Products Division Industrial Coatings 2000 West Grandview Boulevard P.O. Box 10038 Erie, PA 16514-0038	Formerly called Chemglaze L300	Paint	24
Chemglaze Z004	Lord Corporation Erie, Pa.		Paint	24
Aeroglaze Z302	Lord Corporation Erie, Pa.	Formerly called Chemglaze Z302	Paint	25, 26, 24
Aeroglaze Z306	Lord Corporation Erie, Pa.	Formerly called Chemglaze Z306	Paint	27, 24, 28, 29, 30, 31, 20, 32, 33, 19, 34, 35, 36, 37, 38, 39, 40, 41, 42
Aeroglaze Z306 with microspheres	Lord Corporation Erie, Pa.	Formerly called Chemglaze Z306 with microspheres	Paint	43, 44, 45, 28, 24
Aeroglaze Z307	Lord Corporation Erie, Pa.	Formerly called Chemglaze Z307 (conductive)	Paint	24
Aeroglaze Z313	Lord Corporation Erie, Pa.	Formerly called Chemglaze Z313	Paint	35, 24
Ames 24E Ames 24E2	NASA Ames Research Center Moffet Field, Calif. S. Smith Sterling Software 1121 San Antonio Rd. Palo Alto, CA 94303		Paint	4, 46, 47, 34
Cardinal 6450	Cardinal Industrial Finishes 1329 Potrero Ave., So. El Monte, CA 91733-3088	Formerly called "Cardinal 6550"	Paint	48, 35
Cornell Black	Prof. J. Houck Department of Astronomy Cornell University Ithaca, NY 14853		Paint	39, 32, 33, 19, 49
DeSoto Flat Black	PRC-Desoto International, Inc. 5454 San Fernando Rd. Glendale, CA 91203		Paint	50, 35
Electrically Conductive Black Optical Paint	Jet Propulsion Laboratory, Caltech, 4800 Oak Grove Dr. Pasadena, CA 91109	Has no tradename	Paint	51, 52, 53

(Continued)

**TABLE 2** Painted Surfaces (*Continued*)

Surface Name or Designation	Manufacturer and/or Distributor (contact person)	Historical Notes	Surface Type	Main Literature References
IITRI Bone Black D-111 (IITRI D111)	IIT Research Institute 10 West 35th Street Chicago, IL 60616		Paint	25, 54, 32, 34, 55, 38
LMSC Black	Lockheed Palo Alto Research Lab		Painted multi-player coating	32, 33, 19, 55
MH21-1	IIT Research Institute Chicago, Ill.		Paint	54
MH55	IIT Research Institute Chicago, Ill.		Paint	54
MH2200	IIT Research Institute Chicago, Ill.	Formerly 3M's ECP 2200 paint, but sold to IIT	Paint	26, 27, 56, 54, 57, 33, 19, 35, 58
Solarchem	Eastern Chem Lac Corporation 1080-T Eastern Ave. Malden, MA 02148		Paint	4
463-3-8	Akzo Nobel Coatings, Inc. 434 W. Meats Avenue Orange, CA 92665	Formerly called "Cat-a-lac 463-3-8" diffuse black paint	Paint	27, 56, 59, 60, 30, 58, 42, 55, 41
443-3-8	Akzo Nobel Coatings, Inc. Orange, Calif.	Formerly called "Cat-a-lac 443-3-8"	Paint	61, 25, 56, 59, 60, 58, 55, 41
443-3-17	Akzo Nobel Coatings, Inc. Orange, Calif.	Formerly called "Sikkens 443-3-17" glossy black	Paint	26, 60

*Source:* Adapted from McCall.<sup>23</sup>

**TABLE 3** Anodized Surfaces

Surface Name	Manufacturer	Notes	Surface Type	Main Literature References
Infrablack	Lockheed Martin, Denver CO 80201	For Al substrates only	Anodization process	43, 62, 63, 3, 64, 4, 46
Martin Black	Lockheed Martin Denver, CO	For Al substrates only	Anodization process	43, 25, 65, 62, 66, 63, 67, 3, 45, 68, 59, 69, 70, 32, 33, 46, 34, 35, 58, 55, 29, 38, 31, 64, 4, 20, 71, 39, 72, 37, 41, 38
Martin Black, enhanced	Lockheed Martin Denver, Colo.	For Al substrates only	Anodization process	63, 31, 4
Martin Black, posttreated	Lockheed Martin Denver, Colo.	For Al substrates only	Anodization process	63

*Source:* Adapted from McCall.<sup>23</sup>

plasma-sprayed metal surfaces (Table 4) are now available to meet quite specific optical and system performance and environmental requirements.

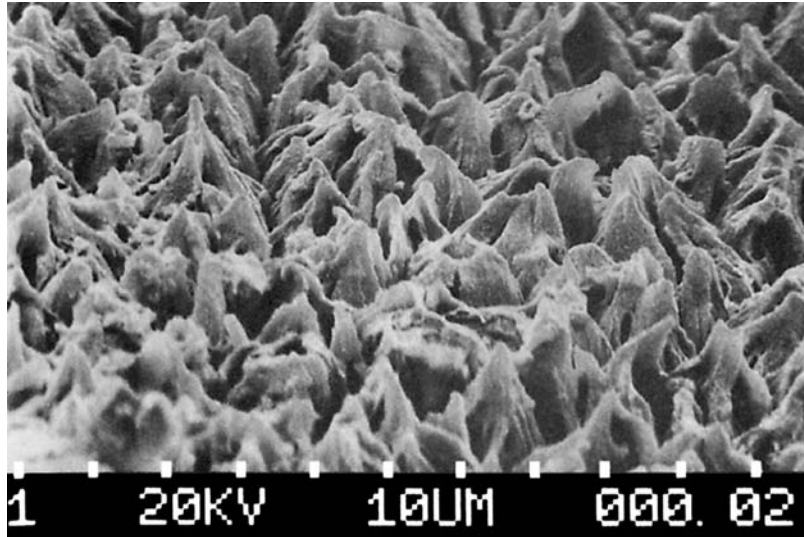
New classes of surfaces are also being developed to give selected performance at specific angles and wavelengths. Other materials are being developed for applications where "hardened" laser-resistant or radiation-resistant materials are needed. A third area where much development is currently taking place is in the area of materials that are able to withstand severe and unusual forms of environmental exposure for long periods.

**TABLE 4** Other Processes

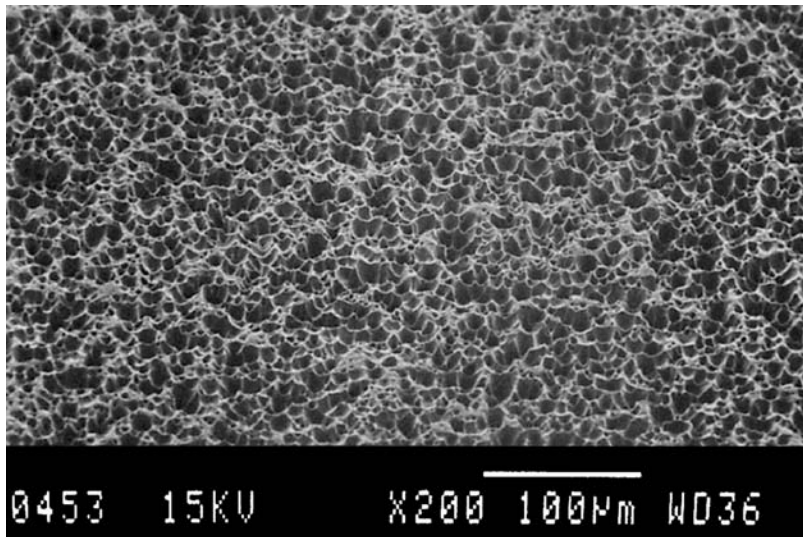
Surface Name	Manufacturer	Notes	Surface Type	Main Literature References
Black chrome-type surfaces	Lockheed Martin Denver, Colo.	For many kinds of metal substrates	Electrodeposition process	63, 4, 41
Black cobalt-type surfaces (Cobalt black)	Lockheed Martin Denver, Colo. And many more companies	For many kinds of metal substrates; references to black copper, black, steel, etc., are covered by black cobalt	Electrodeposition processes, and can be followed by chemical or thermal oxidation	63, 4, 73, 74
Black nickel (NBS black) (Ball black)	Ball Aerospace Electro-Optics Engineering Dept. P.O. Box 1062 Boulder CO 80306 and many others	For many kinds of metal substrate; Ball improved the patent developed by NBS	Deposition and etching process	65, 19, 29, 50, 37, 75, 76
Black Kapton film	DuPont Wilmington, DE 19898		Foil	35
Black Tedlar film	DuPont TEDLAR / Declar PPD, D-12082 1007 Market Street Wilmington, DE 19898		Foil	35
Boron black	Lockheed Martin Denver, Colo.	For many kinds of metals	Plasma spray deposition process	4, 63
Boron carbide	Lockheed Martin Denver, Colo.	For Ti substrates only	Proprietary process	4
Silicon carbide	Lockheed Martin Denver, Colo. And more companies	For many kinds of metals	Chemical vapor deposition	4
Textured surfaces	NASA Ames Research Center Moffet Field, Calif. (Sheldon Smith) Spire Corporation Patriots Park, Bedford, MA 01730 Optics MODIL, Oak Ridge National Lab Oak Ridge, TN 37831-8039	For many kinds of metal substrates	Either: —sputtered coated —ion beametched —sputter coated then etched	77, 78, 79, 29, 80, 37, 81, 82, 79, 83
Black optical thin-film interference coatings	National Research Council of Canada Thin Films, Institute for Microstructural Sciences Montreal Road, Building M-36 Ottawa, Ontario, Canada, K1A OR6	For metal, dielectric, or other substrates	Vacuum deposition techniques: —sputter deposition —ion vapor deposition —resistance-heated source —electron-beam gun deposition	84, 85, 86, 87

*Source:* Adapted from McCall.<sup>23</sup>

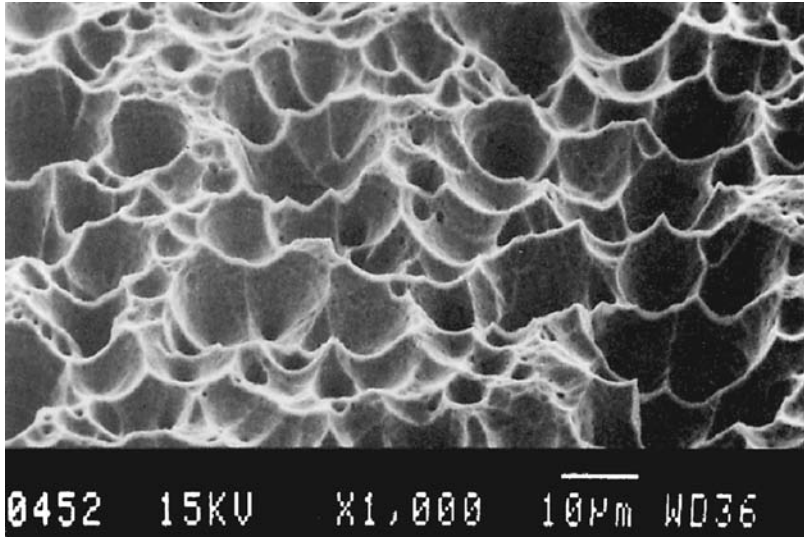
The surface morphology of a “black” or diffusely scattering surface is only one determinant of its complex optical properties. However, for many surfaces, surface roughness plays a most significant role. This can be illustrated in Figs. 1 to 8, scanning electron micrographs of some important black or diffuse surfaces. The size and shapes of the surface features provide a valuable indication of how light will be absorbed and scattered or diffracted by such a surface. The creation and design of new



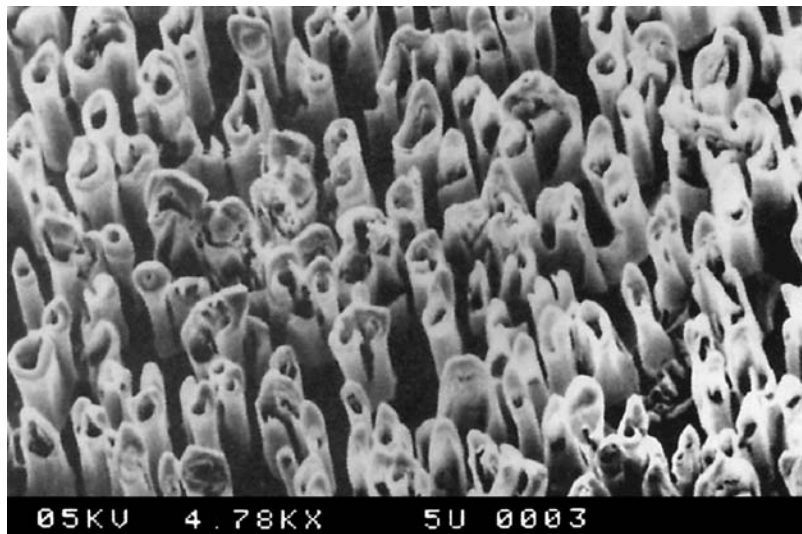
**FIGURE 1** Scanning electron micrograph of Martin Optical Black, an anodized aluminum surface for ultraviolet, visible, and infrared use. (Photo courtesy of Don Shepard, Lockheed Martin, Denver.)



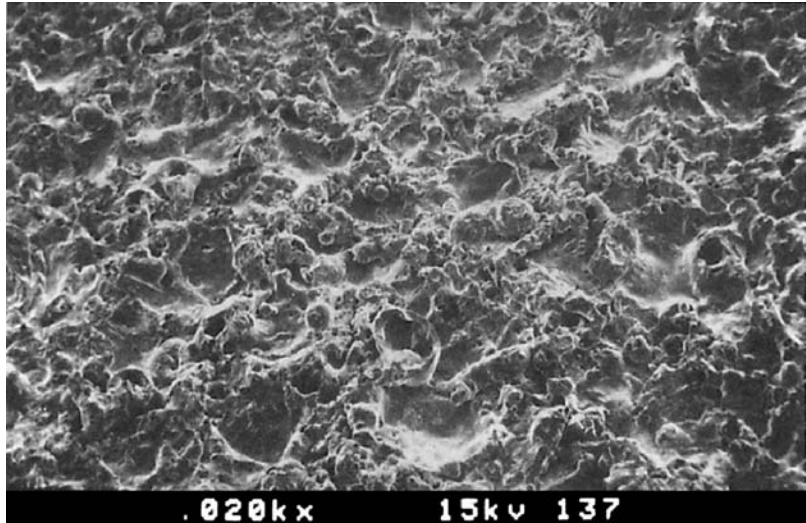
**FIGURE 2** Scanning electron micrograph of Ball Black, an etched electroless nickel surface applicable to a variety of substrates. (Photo courtesy of Arthur Olson, Ball Aerospace Systems Group, Boulder, Colorado.)



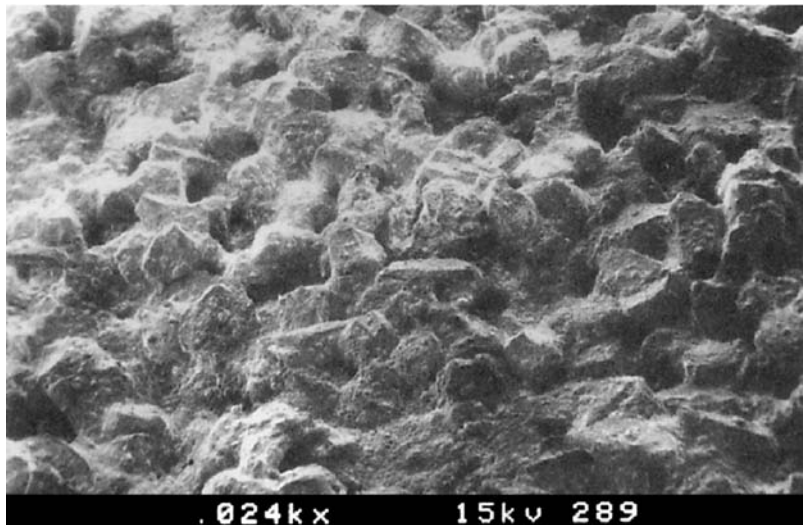
**FIGURE 3** Scanning electron micrographs of Ball Black, an etched electroless nickel surface applicable to a variety of substrates. This surface is representative of a class of etched electroless nickel surfaces. (Photo courtesy of Arthur Olson, Ball Aerospace Systems Group, Boulder, Colorado.)



**FIGURE 4** Scanning electron micrograph of a sputtered beryllium surface. (Photo courtesy of Roland Seals, Optics MODIL, Oak Ridge National Laboratory.)

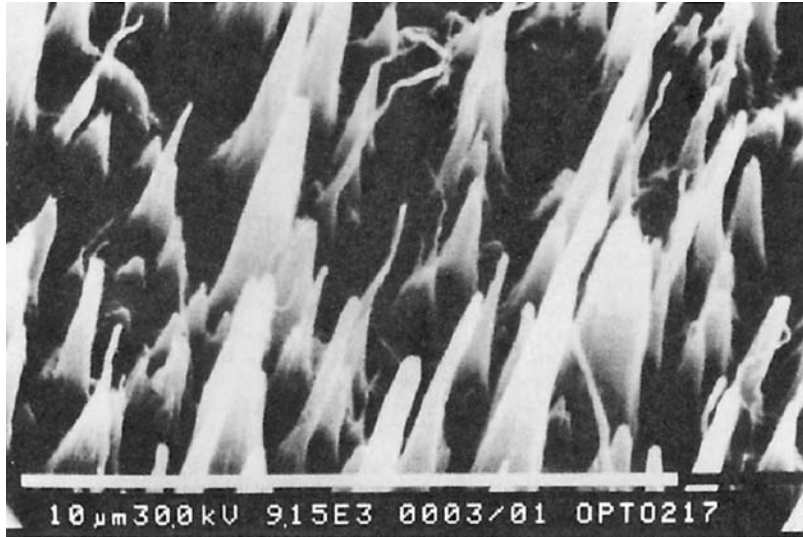


**FIGURE 5** Scanning electron micrographs of Ames Perfect Diffuse Reflector (PDR) at 24 magnification. (Photo courtesy of Sheldon Smith, NASA Ames Research Center and Sterling Federal Systems, Palo Alto, Calif.)

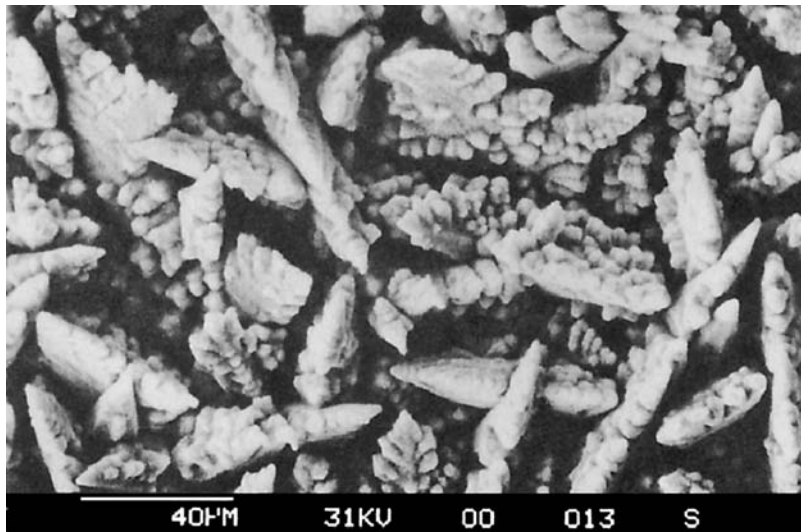


**FIGURE 6** Scanning electron micrographs of Ames 24E at 24 $\times$  magnification. (Photo courtesy of Sheldon Smith, NASA Ames Research Center and Sterling Federal Systems, Palo Alto, Calif.)





**FIGURE 7** Scanning electron micrograph of a textured graphite surface created by bombarding a carbon surface with positive argon ions. (Photo courtesy of Chuck Bowers, Hughes Aircraft, El Segundo, Calif.)



**FIGURE 8** Scanning electron micrograph of Orlando Black surface, produced by electrodeposition of copper and subsequent oxidation in a proprietary process. (Photo courtesy of D. Janeczko, Martin Marietta Electronic Systems, Orlando, Fla.)

surfaces will be touched upon later, in the section on design techniques for creating new surfaces for specific applications.

This chapter gives a summary of the materials used in a variety of optical systems (with an emphasis on those that are currently available) and describes their optical and material properties so that the optical designer can begin the material selection process. As such, it is rather an extreme condensation of the data available. However, even the data presented here cannot be considered very definitive. There are a number of reasons for inconsistencies and ambiguities in the data presented. First, many of these surfaces and the processes that create them are evolving, and improving continuously. Even though the actual surface may change, the name may not. Thus, optical measurements of the same named surface that are separated by several years may not be consistent, even if the measurement techniques are consistent.

A second cause of inconsistency among data sets comes from the remeasurement of "archival" samples. When new measurement techniques or improved instruments become available, or the needs of a program demand new measurements, archival samples are retrieved and remeasured. Sometimes these archival samples may not have been stored properly and may not be in pristine or original condition. Other times, these samples may never have been archival in quality. They may have been marketing samples made without specific quality control and distributed widely. These measurements still enter the body of literature with the reader usually unaware of the important circumstances. For robust samples, poor storage may be of little importance. For more exotic materials (e.g., specialized baffles for space applications) that must be handled carefully, lack of proper handling can be of great importance. In this latter case, the measurements made on these degraded surfaces may not be representative.

Wolfe<sup>88</sup> compares the theory and experiments for bidirectional reflectance distribution function (BRDF) measurements of microrough surfaces. The BRDF of a surface is very useful in understanding the optical performance of a surface and is defined as the ratio of scattered radiance [ $W/(cm^2sr)$ ] to surface irradiance ( $W/cm^2$ ). Its units are inverse steradians. Radiance is used in the definition of BRDF in order to make the BRDF independent of the parameters of the measuring instrument, such as the detector aperture and distance to the detector. BRDF measurements can be made by a variety of instruments and can be made for any number of wavelengths. For example, BRDF measurements of surfaces have been made in vacuum ultraviolet to far-infrared wavelengths. However, the most common BRDF measurements that are made on black surfaces are probably made at convenient laser wavelengths of 0.6328 and 10.6  $\mu m$ . It is important to keep in mind that these measurements may be of less predictive value if the system is operating at a substantially different wavelengths than where the measurements were made.

To make a BRDF measurement requires a light source, a sample mounted and illuminated by that source from a variety of angles, a detector to measure the scatter from the sample, and the computer/electronics package to accurately record the detection of the scattered light as a function of angle of incidence and detection angle.

While the optical properties of surfaces can be described or characterized through the use of specular and diffuse reflectance measurements, the use of BRDF measurements are very useful in characterizing both highly specular and highly diffuse surfaces and provide an excellent way to characterize the optical properties of any surface. The BRDF can be used to describe the angle-dependent optical scatter from any surfaces. The angular distribution of scatter can be used, in conjunction with computer modeling to calculate if the scatter from a black surface will be a limiting factor in the resolution or noise level of an optical system. BRDF measurements of surfaces are also used in computer graphics visualization programs to illustrate what a surface may look like under various illumination conditions. For some types of black surfaces, the angular distribution of scatter can be used to calculate a variety of surface parameters (e.g., surface roughness) if certain assumptions about the surface can be made. For opaque black surfaces, appropriate BRDF measurements in the wavelengths, angles, polarizations, and so on of interest have proven to be one of the best overall descriptors of the optical properties of the surface.

Measurements of optical quantities such as the BRDF, that are by definition measurement-device-independent, can also show large variations.<sup>89,90</sup> No attempt has been made in this chapter to reconcile measurement discrepancies; indeed, no attempt to even identify the areas where conflicting data

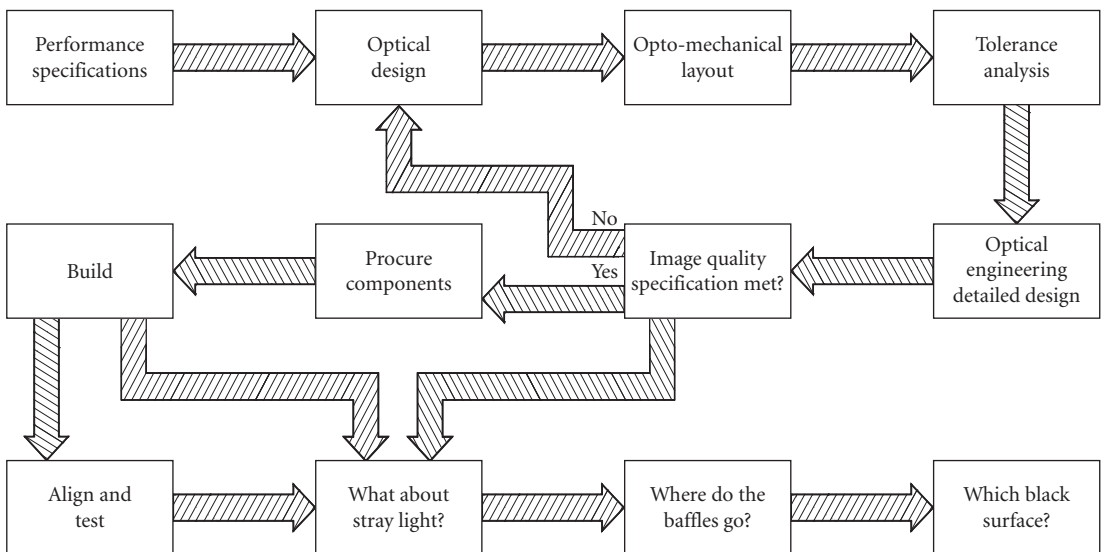
occur is made. This would be a herculean task, but more importantly, it is probably unnecessary. The variations in the measurement process ensure that the optical description of black surfaces is still an order-of-magnitude science, or, at best, a half-an-order-of-magnitude science. Optical practitioners should use their own safety factor or better yet, have their own measurements made.<sup>5,17</sup>

## 6.2 SELECTION PROCESS FOR BLACK BAFFLE SURFACES IN OPTICAL SYSTEMS

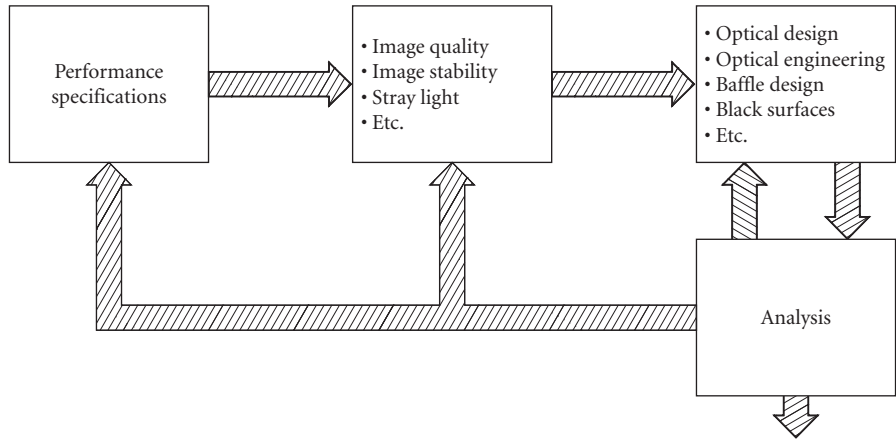
The selection of black surfaces is a systems issue; it must be addressed early and consider all aspects of system design and performance. It must also be examined from a total system performance perspective. Cost and schedule considerations have important effects on the decision and need to be taken seriously. A baffle structure that cannot be built with surfaces that cannot be coated is not a desirable state of affairs!

Similarly, proper financial and schedule support must be present. Black surfaces need to be taken as seriously as any other optical components, such as mirror surfaces or the thin films that act as filters. They deserve serious treatment in their design, fabrication, procurement, and testing. They are not last-minute design decisions or items to be created at the last minute. Since the baffle design and choice of surfaces often sets the final system performance (especially in infrared systems), it makes little sense to expend great energy and money to optimize other more traditional system components while ignoring stray light design and the surfaces so important in the design.

Figures 9 and 10 are a comparison of two processes that could lead to the selection of surfaces for an application. Figure 9 shows a process where design activities are done sequentially. In this process, stray light issues (including black surface issues) are left to the end of the program. In practice, with limited budgets, stray light and other fundamental system engineering issues are often not addressed at all in this process, or are addressed only at stages in the program where the system design is frozen, or cannot be changed without great expense. At this stage, when fundamental problems are found, they often have severe performance, budget, and schedule penalties. That many stray light and black surface problems are rectified (with severe penalties to schedule and budget) at late stages in programs attests to the overall importance of black surfaces to the ultimate success of a system.



**FIGURE 9** When selection of black surfaces is left to the end of a program, serious risks to the program are likely. (From Pompea and McCall.<sup>5</sup>)



**FIGURE 10** The most effective context for black surface selection is near the beginning of the program. This flowchart illustrates the early phase of a system-oriented design process. (From Pompea and McCall.<sup>5</sup>)

In an integrated systems engineering or concurrent engineering environment, illustrated in Fig. 10, the selection process begins early. There are many iterations of the design in the early stages, and close work among designers of different disciplines is essential. The level of detail increases with time, but no fundamental issues are decided without addressing their implication for the system and for each subsystem. This process is far superior to the one in the first flowchart, in which the surface selection process is treated as a trivial one and one waits until the end of the program to evaluate candidate surfaces. A review of general aspects of selection with emphasis on the system level issues inherent in the selection process is given by Pompea and McCall,<sup>5</sup> McCall et al.,<sup>17</sup> and Pompea.<sup>91</sup>

Once it has been decided to use black surfaces in an optical system, a whole host of system-level issues must be addressed to determine an appropriate coating or coatings. The high-level items include (1) purpose and position of the surface in the instrument, (2) wavelength(s) and waveband(s) of interest, (3) general robustness of the surface, (4) nature of the installation process, (5) environment of the optical system, (6) availability, (7) cost, (8) substrate, and (9) other mission or system requirements.

For systems that operate over a wide wavelength range, the selection process may be difficult because data may not be available over the entire wavelength range of interest. For example, the next generation of infrared and submillimeter telescopes are being designed for wavelengths between about 10 and 800  $\mu\text{m}$ . Baffle coatings must be adequate over this entire wavelength range.

The position of the coating in the system and its function at that location is a critical item. For positions where the incident radiation is nearly normal to the surface, the optical considerations become less critical, since the reflectance at near-normal incidence does not vary as significantly at this angle for the most often used surfaces. Also, the BRDF is usually at its lowest value. There is a wealth of data at these near-normal incident angles.<sup>4</sup>

The corollary is that if surfaces must be used close to grazing incidence, the optical properties become extremely important to understand (and quantify for system predictions) just as the amount of data becomes vanishingly small.<sup>6</sup> Although there is sufficient optical data on specular reflections from specular surfaces, there is relatively little information on specular reflections from diffuse surfaces, let alone BRDFs at large angles of incidence. For these reasons, optical designers try to use lambertian-like surfaces at near to normal incidence light paths as possible.

The robustness of the surface in its environment is a complex subject. Some specific areas that will be addressed here are the atomic oxygen environment of low earth orbit, outgassing in the vacuum of space, and particle generation by surfaces. The practical considerations of expense, schedule, ease of

cleaning, exportability, and availability of specialized surfaces all play important roles. For a unique space instrument, there are different manufacturing considerations than for a large-volume production process. The installation process is often overlooked. It often plays a key role in the successful use of many surfaces.

Exposed spacecraft surfaces often must not contribute to spacecraft charging problems. Some nonconductive surfaces support the buildup of charges that can create large electrical potentials between spacecraft components, or the spacecraft and the plasma and subsequent damage may result. This is particularly important in the region near a detector, which is often very charge-sensitive. Surfaces such as Martin Black do not support charges in excess of 200 V, since the coating can leak charge to the aluminum substrate. Textured metallic coatings, as a general rule, do not have surface charging problems. Some paints as well (e.g., Aeroglaze Z307) are designed to be conductive. Table 5 describes several surfaces used for thermal control in space craft. Some of these surfaces are designed to be conductive, to avoid charging effects. For space applications where charge buildup is not critical, nonconductive surfaces may be used.

Other considerations are the ability of a surface to withstand vibration, acceleration, elevated temperatures, thermal cycling, chemical attack (including atomic oxygen), solar and nuclear radiation, micrometeoroids, and moisture.

For the coating of baffle and (particularly) vane surfaces in ground-based telescopes, a further consideration may often be important. The baffle and vane surfaces in telescopes often have a large view angle or geometrical configuration factor (GCF) with the sky. This is particularly true for telescopes that operate without an enclosure or with a very large slit or opening to the night sky. In this case, the black baffle and vane surfaces must not radiatively couple strongly to the night sky. If there is a substantial view to the sky, and the emissivity of the surface is high, it will cool below the air temperature. This can create temperature-induced “seeing” effects which degrade image quality. The requirement that a surface be strongly absorbing of visible light, yet a poor emitter in the infrared is often a difficult one to meet. Table 6 gives the absorptivity and emissivity of some widely used surfaces.

In many laboratory or instrument applications, the use of one of a few standard black coatings or surfaces (such as the now unavailable 3M Black Velvet 101-C10) was entirely adequate to achieve the necessary performance of the optical system. In these applications, if the stray light performance was inadequate, it usually indicated that the stray light design, not the choice of black surface, was in error. The explanation was that the ignorance of some of the principles of stray light design could produce system performance five orders of magnitude worse than a poor choice of surfaces. The visibility of surfaces from the detector and the paths from those surfaces to the front of the instrument (not the optical properties or blackness of the surface) largely determine the total system performance. In stray light terminology, the GCF (geometrical configuration factor of surfaces) is more important than the BRDF (bidirectional scatter characteristics of surfaces).

**TABLE 5** Black Nonconductive and Electrically Conductive Paints and Coatings for Space Use

Name	Type of Coating	Binder	Solar Absorptivity	Thermal Emittance
ML-210-IB	Thermal control	Inorganic	0.98±0.02	0.91±0.02
RM-550-IB	Thermal control	Inorganic	0.97±0.02	0.91±0.02
TMD-560-IB	Thermal control	Inorganic	0.95±0.02	0.91±0.02
AZ-1000-ECB	Thermal control conductive	Inorganic	0.97±0.02	0.89±0.02
MLS-85-SB	Thermal control	Organic	0.98±0.02	0.91±0.02
MLS-85-SB-c	Thermal control conductive	Organic	0.98±0.02	0.91±0.02

**Source:** Courtesy of J. Zweiner, AZ Technology, Huntsville, Alabama.

**TABLE 6** Black Coatings

	$\overline{\alpha}_s$	$\overline{\epsilon}_n$
Anodize Black	0.88	0.88
Carbon Black Paint NS-7	0.96	0.88
Cat-a-lac Black Paint	0.96	0.88
Chemglaze Black Paint Z306	0.96	0.91
Delrin Black Plastic	0.96	0.87
Ebanol C Black	0.97	0.73
Ebanol C Black-384 ESH* UV	0.97	0.75
GSFC Black Silicate MS-94	0.96	0.89
GSFC Black Paint 313-1	0.96	0.86
Hughson Black Paint H322	0.96	0.86
Hughson Black Paint L-300	0.95	0.84
Martin Black Paint N-150-1	0.94	0.94
Martin Black Velvet Paint	0.91	0.94
3M Black Velvet Paint	0.97	0.91
Paladin Black Lacquer	0.95	0.75
Parsons Black Paint	0.98	0.91
Polyethylene Black Plastic	0.93	0.92
Pyramil Black on Beryllium Copper	0.92	0.72
Tedlar Black Plastic	0.94	0.90
Velestat Black Plastic	0.96	0.85

\*Note: Solar absorptivity (0.3 to 2.4  $\mu\text{m}$ ) and normal emittance (5 to 35  $\mu\text{m}$ ) of black coatings.

Source: From Henniger.<sup>92</sup>

### 6.3 THE CREATION OF BLACK SURFACES FOR SPECIFIC APPLICATIONS

The optical properties in the visible (e.g., BRDF at 0.6328  $\mu\text{m}$ ) at near-normal incidence between painted black surfaces and more specialized high-performance black surfaces usually do not differ by more than a factor of 10. For infrared and ultraviolet wavelengths, the performance of more specialized surfaces is far superior to many paints by a much larger factor. The optical designer must take care not to overspecify the optical performance properties required for a baffle surface. The lowest reflectance surface is not necessary for all applications. On the other hand, the choice of low-performance coatings has important consequences.

Some systems have been designed with an excessive number of vanes on their baffles. In these cases, the baffle system is probably too heavy, costs more than necessary to manufacture, and the excessive number of vane edges may be introducing extra diffraction effects that degrade the performance. The advantage of the high-performance coatings often lies not only in their optical properties, but in the considerable experience of their manufacturers in working on baffle systems, the reliability and consistency in the application process, and the superior documentation of the optical performance characteristics. The environmental resistance of the high-performance coatings is generally much better and much better documented than paints that are used for a wide variety of applications.

## Black Surfaces as Optical Design Elements

The systems approach to the choice of black surfaces in optical systems that has been stressed here has led to the rule of thumb in stray light design that the choice of a black surface's optical properties should not be the first design issue considered. If the performance of the preliminary design is inadequate, the designer should look at the design carefully, rather than look for a better black surface to boost the performance. A flaw in the general system design is probably more responsible for the performance than the "blackness" of surfaces.

One reason for this approach is that the choice of a different black surface may not improve the performance, if the surface is used in the system in certain ways (e.g., grazing incidence). An important equalizing factor among many black surfaces is that they become highly specular when used at angles significantly different from normal incidence. This optical performance characteristic makes it critical for the baffle designer to conceptualize the paths and ranges of angles that are required, and to avoid using a surface where its performance is required at grazing incidence or close to it. The writing of scatter specifications is discussed by Stover,<sup>93</sup> and Breault<sup>2</sup> discusses sources of BRDF data and facilities where BRDF measurements are routinely made.

Black surfaces can be contaminated and their absorbing or diffuse structure can be destroyed by improper handling. This can lead to a significant degradation in their optical properties. A margin of safety should always be included in the performance estimates.

Many specific high-performance applications today require that black surfaces must become critical design elements that are used with only small "safety" factors. First, all of the principles of stray light design are used. If the required performance is barely achievable without optimizing the choice of black surfaces, then considerable attention must be paid to the choice of surfaces. Sometimes, designers must often use several black surfaces in an instrument or telescope; each particular black surface is used where its performance is optimal. In the past few years, a variety of black surfaces have become available to supplement the old standbys such as 3M Black Velvet (the mainstay of laboratories 10 years ago), and Chemglaze Z306 (now called Aeroglaze Z306) and Martin Black (the standard bearers for space instruments in the 1980s). Since the applications for these blacks are so specific, we refer to them as *designer blacks*. This term refers not only to new classes of surfaces that have been developed, but also to the creativity of optical and material scientists in modifying existing surfaces to create special properties for specific applications.

This new array of designer optical blacks can still be subdivided into the traditional categories of specular blacks and diffuse (lambertian) blacks. Glossy or specular black surfaces have been used for vane cavities and their use is reviewed by Freniere<sup>94</sup> and Freniere and Skelton.<sup>61</sup> The approach is to reflect unwanted radiation out of the system or to attenuate it while tightly controlling its reflected direction. The use of specular baffles (reflective black or shiny) requires considerable care to avoid sending specular beams further into the instrument at some particular narrow angles.<sup>59,95</sup> The increasing sophistication of stray light analysis programs makes this analysis much more complete. The most widely used specular black surfaces are Chemglaze Z302 and a paint formerly called Cat-a-lac Glossy Black, now available from Akzo as 463-3-8.

The lambertian black surface is often the most desirable type of surface to use in baffled telescopes and instruments. However, there is no *true* lambertian black, though several are extremely close for a near-normal angle of incidence. All diffuse blacks have larger BRDFs at large angles of incidence. Furthermore, these black surfaces can be further categorized by the wavelengths where they absorb best, the general categories being the ultraviolet, visible, near-infrared, middle-infrared, and far-infrared. They can also be distinguished by their degree of resistance to the atomic oxygen found in low earth orbit, their resilience under laser illumination, and their performance at narrow laser wavelengths or specific angles of incidence. The method of manufacture and the performance of these specialized surfaces may be proprietary or classified. Even if the general qualities of these surfaces that perform in these areas are known, the full range of test results on them often are not readily available.

## Design Techniques for Creating Black Surfaces

Four general tools are available to the black surface designer to tailor the optical properties. Many highly absorbing surfaces use several of these effects to good advantage. The first tool is to use absorbing compounds in the surface. Examples of this are the organic black dye, which is a good visible absorber, in the Martin Black anodized surface and the carbon black particles found in many paints. Similarly, for the infrared paints, the addition of silicon carbide particles provides good absorption near 12  $\mu\text{m}$ . The addition of compounds may create quite different properties at visible and infrared wavelengths; a visual observation of blackness is no guarantee of its infrared properties. The converse is also true. Titanium dioxide is a good infrared absorber, but is very reflective in the visible region. "Black," therefore, means absorptive in the wavelength region being discussed.

The addition of large (relative to the wavelength of interest) cavities, craters, or fissures in the surface can aid in the absorption process by requiring the radiation to make multiple reflections within the material before it leaves the surface. The same effect is achieved by growing large angular projections from a flat substrate. Each reflection allows more of the radiation to be absorbed. For example, a surface with a reflectivity of 15 percent (a rather poor black) becomes a very good black if the light can scatter or reflect three times within the surface before it exits. After three internal reflections, the 15 percent reflectivity black has become a  $(0.15)^3$  or 0.34 percent reflective surface. The NBS Black and Ball Black surfaces are good examples of this; they are shiny electroless nickel surfaces until etched. After etching, the surface is filled with a plethora of microscopic, cavities that absorb enough light to create a surface that is black to the eye.

Black appliqués can also be used to create rough absorbing surfaces.<sup>96</sup> These surfaces can be "tuned" for different wavelengths or for maximum absorptance at certain angles of incidence. This can be done by angling fibers or surface structure to provide cavities that are oriented normal to the angle of incidence. These materials have low reflectance at a variety of incident angles.<sup>96-98</sup>

Aerogels can also be used to create very black surfaces. Aerogels are highly porous materials nanometer-scale structures that can be synthesized through the removal of the pore-filling liquid. Of particular interest are carbon aerogels consist of 10-nm-sized particles, which are amorphous, connected in an interconnected network with approximately 10- to 50-nm pores and a pore volume of over 80 percent. Since carbon has inherent absorption in the infrared, this innately rough surface can have extremely low reflectivities over a broad wavelength range (e.g., 2 to 14  $\mu\text{m}$ ).<sup>99</sup>

The third phenomenon is the use of scattering from the surface structure, from particles in the surface coating, or from the substrate to diffuse the incoming beam over a hemispherical solid angle. Even without any absorption, this dilution factor can be very important in destroying specular paths, particularly in the far-infrared, where broad wavelength absorption is difficult. For an introduction to surface roughness and scattering phenomena, see Refs. 33, 46, 93, and 100. An in-depth, very readable, treatment of scattering by small particles is given by Bohren and Huffman.<sup>101</sup>

The fourth phenomenon is based on optical interference of light in thin films. A black optical thin-film multilayer structure can significantly enhance, through optical interference, the amount of absorption of light in a multilayer structure over that of intrinsic absorption alone.<sup>87</sup> The black layer system technology has been used successfully in a range of applications.<sup>84-87,102,103</sup> Optical thin films provide tremendous design flexibility. The reflectance, absorptance, and transmittance can be tailored as a function of angle and wavelength. Black multilayers may have a higher cost per unit of surface area, are generally limited to small surfaces, and have a strong angular sensitivity. This last characteristic can be used to great advantage for specialized applications. The films (especially those deposited by ion-beam process) are durable and are suitable for space use.

There is no ideal black surface. For good absorption across a wide wavelength band (e.g., 0.5 to 20  $\mu\text{m}$ ), the surface might be excessively thicker than is needed for a narrowband application. Even a "perfect" absorbing surface has disadvantages associated with higher emissivity (e.g., the surface radiates to the detector). In practice, even specular surfaces can be acceptable as black baffle surfaces under the right circumstances, although they are much more difficult to use. By design, they must direct the energy out of the system or in a direction that is not harmful to the system performance.<sup>95,104,105</sup> Their alignment is critical and there are caveats for their use.<sup>59</sup> The "blackest" surface is not necessarily the best for a specific application.



In some other applications, a combination of low absorptance and high emittance are desirable. High emittance-low absorptance coatings are possible using a combination of techniques or surfaces. For example, a potassium silicate binder with zinc oxide or zinc orthotitanate particles can be applied to an anodized aluminum surface. In this case, the absorptance is less than 0.16 and the emittance is about 0.92.<sup>106</sup>

## 6.4 ENVIRONMENTAL DEGRADATION OF BLACK SURFACES

---

Contamination control for terrestrial and spaceborne sensors is a very rapidly developing and important area. A good introduction to the field with extensive references is given in Refs. 2, 107 to 109. A good review of contamination assessment techniques given by Heaney<sup>110</sup> and Nahm et al.<sup>111</sup> discusses scattering from contaminated surfaces. The prevention, detection, and removal of contamination should be important considerations early in the design of the sensor.

Three areas of great interest for spaceborne sensors are the effects of atomic oxygen, outgassing effects, and particle generation by surfaces. A large number of other effects can also influence the performance of surfaces or of the systems where those surfaces are installed over short or long periods. These include adhesion of coatings, radiation effects on coatings, thermal cycling effects, vacuum ultraviolet effects, and electrostatic charging effects, to name a few. It would be helpful if each new coating developed could be tested by a suite of tests relevant to the area of concern, similar to what was done in cryomechanical tests of Ames 24E2 infrared black coating.<sup>34</sup> All too often, the tests are done on different formulations at different labs and with different degrees of care. This makes it extremely difficult for the optical designer to have the data necessary to make good decisions.

The surface contamination of a black surface as well as aging effects can affect its optical properties. However, the effect of contaminants from black surfaces on mirror scatter in the optical system is much more pronounced. Williams and Lockie<sup>112</sup> use the BRDF as the sensitive parameter to judge the effects of dust, hydrocarbon oil, acrylic, and peelable coating residue on low-scatter mirror surfaces. Young<sup>113</sup> describes the effect of particle scatter on mirrors. Shepard et al.<sup>71</sup> have suggested that scattering properties of black baffle surfaces may be temperature-dependent. This may be a result of chemical changes in the surface or in changes to the surface as absorbed molecules are released at increased temperatures. Further work should be done at the temperatures of interest.

A large number of studies have been done to describe the behavior of black baffle surfaces to intense exposure to high-powered lasers and radiation, where damage to the surface is widespread. Accurate results can often be obtained using other vehicles to deliver energy into the surface. For example, rapid pulsed, low-energy electron beam irradiation of optical surfaces is described by Murray and Johnson<sup>114</sup> as a cost effective way to test for radiation hardness. Black baffle surfaces are vulnerable even at low fluences because of their great absorptivity. The damage mechanisms are not well understood. Many of the damage mechanisms are related to the thermal shocks produced by rapid heating of a surface of thin layers on different materials. The destruction of surfaces not only reduces the ability of the surface to absorb stray radiation, but often also creates a contaminating cloud of particles that can greatly affect the optical system.

### Atomic Oxygen Effects

Spacecraft surfaces on the early space-shuttle flights showed significant weight loss and aging effects. For example, on STS-1 the forward bulkhead camera blanket was milky yellow after the flight and the white paints on the shuttle exhibited exposure-related degradation effects. On later flights, surfaces such as Kapton showed significant mass losses. These effects were attributed to the interaction of the surfaces with the atomic oxygen present in low earth orbit.<sup>115</sup> The atomic oxygen attacks the binder materials in paints, thus removing mass, and causes glossy surfaces to become more lambertian.<sup>116</sup> Carbon particles are released when the binder is removed. The weight loss is due both to chemical processes and to erosional (kinetic energy) processes.

A second problem is that many surfaces have a glow associated with them when exposed to the atomic oxygen. Both of these phenomena undermine the effectiveness of baffle surfaces on space instruments. The effect of exposure to atomic oxygen on anodized black surfaces (Martin Black and Enhanced Martin Black) has been measured and simulations of atomic oxygen exposure on Chemglaze (now called Aeroglaze) Z306 paint has been done with a plasma etch chamber.<sup>64</sup>

These tests showed that a carbon-black-based paint could be significantly degraded by atomic oxygen over time while anodized surfaces exhibited only small changes in their surface morphologies or in their visible and near-infrared reflectances. The graying of some smooth painted black surfaces is somewhat compensated for by an etching process that roughens these surfaces. If the exposure times are short, the etching action of the atomic oxygen may even improve the scattering properties of paints. However, removed material may show up on optical surfaces, degrading the optical performance, and it should be obvious that long exposure times would remove too much of the coating.

In general, however, the optical properties of surfaces degrade during longer exposure times and at higher atomic oxygen flux levels. Experiments in space on the long duration exposure facility (LDEF) have indicated how the properties of materials change after nearly six years of exposure to atomic oxygen. For Chemglaze (now called Aeroglaze) Z306 paint, for example, this exposure has led to a loss of the binder material<sup>117</sup> and to loss of pigment. Some ion-textured surfaces were also flown as part of this experiment and showed high stability in the space environment.<sup>79</sup> The effects of space exposure on infrared baffle coatings were described by Blue and Perkowitz<sup>118</sup> who showed that long-term exposure decreased the reflectance of these surfaces.

## Outgassing

For space applications, the amount of outgassed material and its composition are of great importance. One of the primary dangers is that the outgassed products may form a film with undesirable properties on optical components. This hazard of space exposure is particularly relevant for cooled systems. For cryogenic systems, the continued outgassing of materials as they break down after long exposure to the space environment becomes an additional source of contamination on optical surfaces. Outgassing is also of concern for severe environments on the ground, though the correlation between vacuum testing and a behavior of black surfaces under severe heat in air is not well understood. For the context of this chapter, only vacuum outgassing measures will be considered. In either case, the condensation of volatile materials on optical components can lead to catastrophic system failure.

The two primary measures or tests of outgassing are the *total mass loss* (TML) and the percent *collected volatile condensable materials* (CVCN). An American Society for Testing and Materials (ASTM) Standard Test Method was developed for this purpose and is called E 595-77/84. Several NASA publications give values for TML and CVCN (Ref. 119 gives the most extensive listing; see also Ref. 120). For example, measurements at Goddard Space Flight Center of Chemglaze (now Aeroglaze) Z306 black urethane paint give a TML of 0.92 percent and a CVCN of 0.03 percent. Wood et al. shows the near-infrared absorption due to the outgassing products of Aeroglaze Z306 black paint. For the paint, the total mass loss was 2.07 percent. Ames<sup>28</sup> reports outgassing problems with Aeroglaze Z306 if exposed to temperatures greater than 40°C after a room temperature cure. However, many potential space material outgassing problems with this and other surfaces can be avoided completely with proper bakeout procedures. In 1993, a low volatile version of Z306 was being developed.

A third measure of outgassing relates to the water content of the material or surface. The *water vapor regained* (WVR) is a measure of the amount of water reabsorbed/reabsorbed in 24 hours, while the sample is exposed to 25°C and 50 percent relative humidity (for extensive listings, see Ref. 119). This determination is done after the vacuum tests for TML and CVCN.

## Particle Generation

Materials for space use must be able to withstand launch vibration without generating an excessive number of particles. This is not simply a coating or surface problem—it is a dynamics and substrate problem as well. The details of the baffle design and assembly play an important role in the generation

of particles. If a baffle surface is grossly distorted by the launch vibration, the adhesion of the black surface should not be blamed for the failure; the baffle design failed. A common source of particle generation is abrasion between coated baffle surfaces. For severe vibration environments and for fragile surfaces, special considerations are necessary.<sup>70</sup> Similarly, surfaces must be able to withstand thermal cycling without producing particles. As painted materials outgas and their composition is altered, particles in the paint can become dislodged.

Materials used in baffles can also get dusty or contaminated by exposure to outgassing products from the spacecraft. For an accessible ground-based black surface, normal cleaning procedures appropriate to the surface may be used, if they do not damage the texture or optical properties of the surface. For a baffle system already in space, the cleaning procedures developed to clean mirrors in situ may apply. These techniques include laser cleaning, plasma or ion cleaning, and jet snow cleaning (see, e.g., Ref. 121, and other papers in Ref. 109).

### **Baffle Material for Extreme Environments**

One important form of degradation for earth-based materials involves the exposure of the surface to the elements of temperature cycling, sunlight, humidity, and other factors of its operating environment. This combination is a severe test of many surfaces. Unfortunately, there is very little data published on the environmental degradation of black surfaces that are exposed to the outdoor environment, or to high temperatures, such as might be found in a closed automobile in the summer. Often, a black surface that is very ordinary in its optical properties is chosen for use in an extreme environment. The reason is that it was the first surface that did not peel or fade significantly.

Space-based surfaces must withstand severe launch vibrations, temperature extremes, collisions with space debris and micrometeoroids, and exposure to ultraviolet radiation. Military missions have also added the requirement that these materials be hardened against nuclear or laser threats. For example, these baffle surfaces and their associated optics must still perform after exposure to high-power lasers.

In the simplest sense, these black surfaces must be able to either selectively reject laser radiation (a difficult requirement) or be able to absorb significant amounts of energy and not degrade. Most of the coatings have been developed for application to substrates, which can survive high temperatures, such as molybdenum, beryllium, tungsten, carbon/carbon, and titanium, because of their ability to withstand high flux densities of laser light. Generally, painted surfaces are completely inadequate. Even anodized surfaces on aluminum may not be adequate at these flux densities.

## **6.5 OPTICAL CHARACTERIZATION OF BLACK SURFACES**

---

The baffle designer must be concerned about the optical properties of black surfaces over a large range of wavelengths and angles of incidence. Wolfe<sup>16</sup> summarizes the relevant design data. Performance measurements, such as measurements of the specular reflectance and total hemispherical reflectance over a range of wavelengths are now supplemented by a more complete characterization of these optical surfaces: the bidirectional reflectance distribution function (BRDF).<sup>122</sup> BRDF has units of inverse steradians and is usually measured at several discrete wavelengths, which are easily generated by the most common lasers. In particular, measurements at the HeNe laser wavelengths of 0.6328  $\mu\text{m}$  and at the  $\text{CO}_2$  wavelength of 10.6  $\mu\text{m}$  are particularly valuable for visible and infrared applications. There is a notable shortage of BRDF data in the ultraviolet, from 1 to 4  $\mu\text{m}$ , and for far-infrared wavelengths.

BRDF measurements at the same wavelength have the additional advantage that they are directly comparable. As Smith and Wolfe<sup>123</sup> point out, the directional reflectivity of a surface is convolved with the instrument function (a weighted mean of the detector solid angle), a unique characteristic of each reflectometer. An approximate deconvolution of the instrument function can be easily

performed by dividing the measured reflectance by the projected measurements, which are instrument independent as mentioned in ASTM Standard E12.09. However, simple specular reflectance measurements and spectra made on different instruments must first be divided by the projected detector solid angle before being compared. Several studies<sup>89,90</sup> have detailed the variation between BRDF measurements made in different laboratories. With the advent of the ASTM standard, greater congruence among BRDF measurements in the future is probable.

Because of the value of BRDF measurements in comparing the scattering characteristics of surfaces, a large set of BRDF data of black baffle materials that have traditionally been used in optical devices of all types, as well as the scattering functions of some new materials are presented in this chapter. These measurements may be compared to previous measurements made on other instruments.<sup>67</sup>

The specular and total hemispherical reflectance data thus become most valuable in describing some general characteristics of a surface over a wide wavelength range, while the BRDF data at a wavelength of particular interest allow the designer to characterize the angular scattering of the surface for angles of incidence of interest and for view angles from the detector. The total integrated scatter also is extremely useful for surface roughness determination.<sup>93</sup>

This chapter provides the optical designer a useful summary of data. Sufficient data are presented to allow a determination of which surfaces might be appropriate for a given task. The data generally can be divided into two forms, the first being specular and hemispherical reflectance data over a wavelength range. These data allow the designer to choose a surface with the right basic properties over the wavelength range of interest. BRDF measurement provides a second form of data. The data are usually presented for a few characteristic angles of incidence ( $5^\circ$ ,  $30^\circ$ ,  $45^\circ$ , and  $60^\circ$  are the most common) at each wavelength. These BRDF measurements are particularly useful as input to optical modeling or stray light modeling programs.

In stray light analysis programs such as APART,<sup>124</sup> ASAP,<sup>125</sup> and GUERAP,<sup>126</sup> as well as many other modeling programs, it is the mathematical value of the bidirectional reflectance distribution function that is used by the program models. In these programs, a library of BRDF functions for the most common surfaces is available for use by the analyst. For surfaces that do not explicitly have a BRDF associated with them in the code, the BRDF values can be input.

In most baffle designs, surfaces are used at angles not represented by the available BRDF measurements. Some surfaces are even used at angles close to grazing incidence where few measurements have been made. For these areas, the data available for the models are very limited, and often generous extrapolations are needed. A smooth transition between measurements at different angles or at very large angles of incidence, or from one wavelength to another is often assumed. The more unusual or nonrandom the surface, the more these assumptions or extrapolations should be questioned. Examples of how BRDF measurements are made and used in system designs and analysis are found in, for example, Refs. 3, 43, and 127 to 130.

Black surfaces are also used in radiators used for the thermal control of spacecraft. The hemispherical reflectivity can provide a general indication of the optical properties for a thermal analysis. The normal emittance at room temperature is also an important quantity for spacecraft design. Table 7 gives the hemispherical reflectance and normal emittance of some surfaces. Radiatively cooled surfaces are important for space infrared telescopes and, if designed properly, can provide a reliable means of reducing background radiation. Because of on-orbit degradation, the radiators must be sized for the appropriate performance at the end of the mission.

For these applications, the absorptivity and emissivity of surfaces as a function of wavelength and temperature must be well understood. Thus, room temperature measurements of normal emittance may not be very useful if the surface is to be used at cryogenic temperatures. Stierwalt<sup>41,132</sup> has contributed greatly to the measurement of far-infrared emissivity of black materials. Clarke and Larkin<sup>133</sup> describe measurements on a number of black surfaces suitable for radiometry detectors where a low reflectance is needed, independent of wavelength. For opaque surfaces, the spectral emittance at a given wavelength is equal to the spectral absorptance, which is equal to one minus the spectral reflectance.

These parameters are very sensitive to coating thickness and may change with exposure to ultraviolet radiation from the sun, with damage from solar electron and proton radiation, damage from space debris and micrometeoroids, and with outgassing. In practice, the solar absorptance is measured

**TABLE 7** Hemispherical Reflectance and Emittance of Some Common Spacecraft Surfaces

Surface	Thickness	Hemispherical reflectance at 546 nm (incidence angle, degrees)					Normal Emittance (300 K)
		20	40	60	70	80	
Cat-a-lac Black 463-3-8	0.002"	0.054	0.061	0.096	0.141	0.223	0.891
Black Velvet 401-C10	0.025"	0.035	0.036	0.047	0.058	0.085	0.911
Chemglaze Z306	0.005"	0.048	0.052	0.074	0.098	0.144	0.915
Chemglaze Z306 with silica powder		0.031	0.033	0.040	0.050	0.070	0.912
Chemglaze Z306 with 3M glass microballoons left on 20- $\mu$ m screen	0.006"	0.040	0.048	0.068	0.090	0.130	0.920
Chemglaze Z306 with 3M glass microballoons left on 44- $\mu$ m screen	0.010"	0.036	0.040	0.055	0.070	0.097	0.923
Chemglaze Z306 with 3M glass microballoons left on 63- $\mu$ m screen	0.011"	0.037	0.040	0.053	0.064	0.084	0.923
Scotchlite Brand Reflective Sheeting #3285 Black		0.059	0.062	0.095	0.156	0.318	0.909
Scotchlite Brand Reflective Sheeting "C" Black W/A #234		0.146	0.130	0.129	0.135	0.157	0.846
NiS-dyed Anodized Al from Light Metal Coloring Corp.		0.056	0.061	0.097	0.151	0.333	0.912
Sandoz-Bk Organic Black anodized Al from Almag Co.		0.041	0.048	0.064	0.082	0.129	0.884
Black Chrome anodized Al from Goddard SFC		0.028	0.031	0.053	0.083	0.156	0.625
NiS-dyed anodized Al from Langley Research Center		0.050	0.053	0.083	0.138	0.253	0.915
NiS-dyed anodized Al, substrate blasted with glass shot, from Light Metals Coloring Corp.		0.045	0.049	0.073	0.100	0.146	0.920

*Source:* Data courtesy of J. Heaney, Goddard Space Flight Center.<sup>131</sup>

by obtaining the reflectance from 0.3 to 2.4  $\mu\text{m}$ , the region containing 95 percent of the sun's energy. The normal emittance is determined using an infrared spectrophotometer over the wavelength range 5 to 35  $\mu\text{m}$ , where close to 90 percent of the energy of a 300 K blackbody is emitted (see Table 6). While these measurements are useful for design of radiators that operate near room temperature, further measurements are required in order to predict a surface's thermal emittance at lower operating temperature.

## 6.6 SURFACES FOR ULTRAVIOLET AND FAR-INFRARED APPLICATIONS

Many surfaces are multipurpose and are useful for a variety of wavelengths. Before discussing the properties of these surfaces, it may be instructive to look at several surfaces that are used for ultraviolet and far-infrared applications. In these wavelength regions, the performance of black surfaces is often critical to the performance of the optical instrument.

### Black Surfaces for Ultraviolet Applications

For space telescopes or instruments operating in the ultraviolet, surfaces such as Martin Black have been used successfully. However, very few measurements of candidate baffle material have been made at wavelengths less than 0.3  $\mu\text{m}$  (300 nm) and even fewer have been made at shorter ultraviolet wavelengths. Jelinsky and Jelinsky<sup>40</sup> studied the performance characteristics of a variety of surfaces and surface treatments for use on baffle materials in the Extreme Ultraviolet Explorer. They determined some scattering characteristics of several materials at 30.4, 58.4, and 121.6 nm.

Heaney<sup>131</sup> has made some pioneering bidirectional measurements at 15°, 45°, 75°, and 85° at 58.4 nm (584 Å) of candidate baffle materials for space instrument applications. Interestingly, two of his samples are "bare" aluminum with no applied coating. The natural oxide present on uncoated aluminum samples is strongly absorbing at this wavelength and, by itself, reduces the reflectances to below 5 percent at near-normal incidence. The baffle surface candidates are described here and their optical properties are presented in the figures.

*Roughened aluminum:* Aluminum 6061 alloy, sheet finish, sandblasted to an unspecified degree of surface roughness. Uncoated (Fig. 11).

*Gold iridite:* Aluminum with a chromate surface coating produced in a room temperature chemical conversion process (Fig. 12).

*Black nickel:* Aluminum with a black nickel surface that was produced in an electroplating process with NiS and ZnS (Fig. 13).

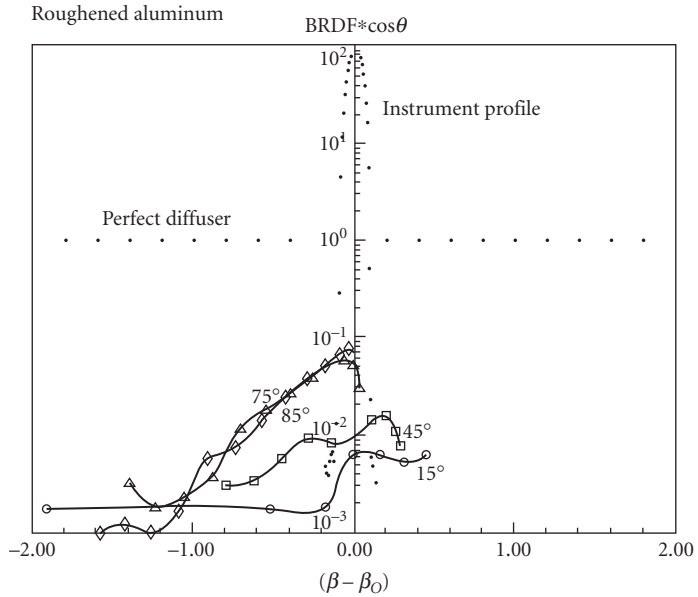
*Copper black:* An aluminum substrate coated with approximately 80 to 100 nanometers of evaporated Cu to provide a conductive layer and then overcoated with an evaporated Cu black deposited at a chamber pressure in the  $10^{-3}$  torr range (Fig. 14).

*Black paint:* An aluminum substrate painted with a carbon-loaded black silicone paint (NSB69-82) (Fig. 15).

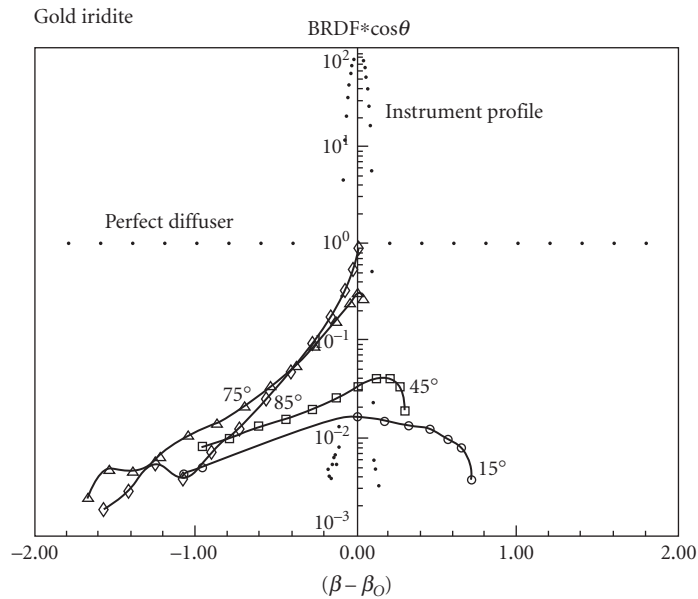
*Aluminum, grooved and blazed:* An aluminum plate, 6061 alloy, with grooves cut at a blaze angle of about 20°, with a period of 1.1 mm, a depth of 0.4 mm, and otherwise uncoated (Figs. 16, 17, and 18).

### Surfaces for Far-Infrared (>30 $\mu\text{m}$ ) Use

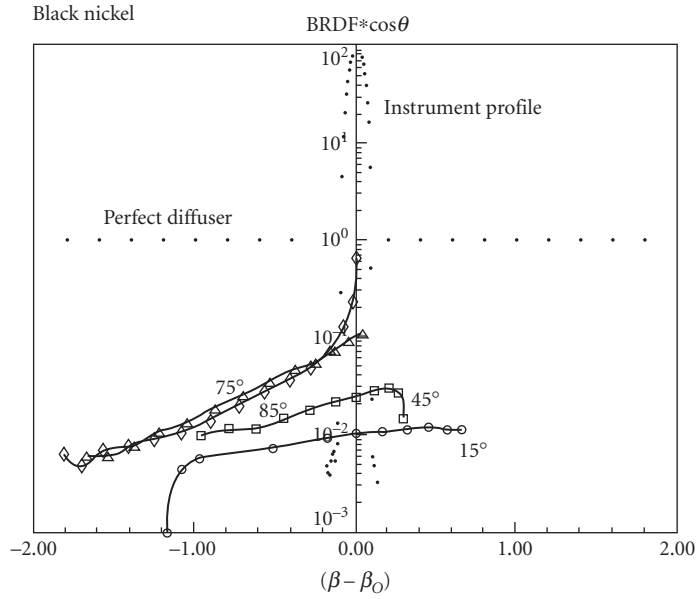
In the far-infrared wavebands, many surfaces such as paints, which have good visible absorptance, lose their absorbing and scattering characteristics. Although measurements have only been made at wavelengths longer than 15  $\mu\text{m}$  on a few surfaces, the data suggest that most surfaces do not



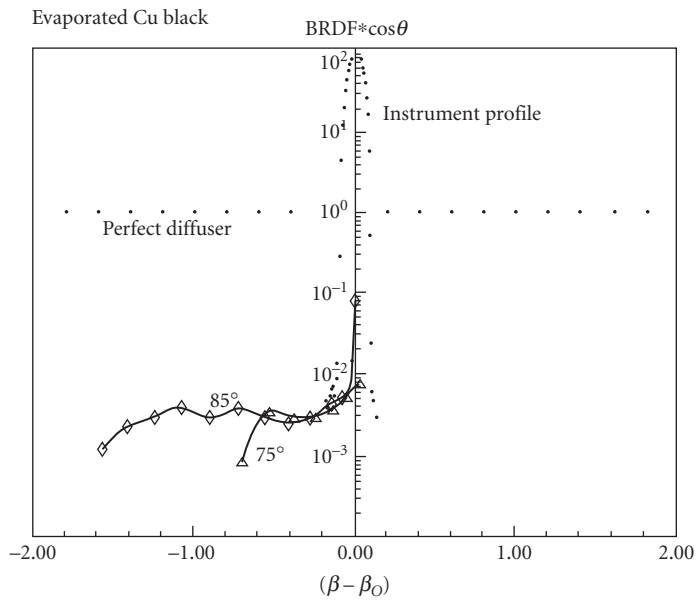
**FIGURE 11** BRDF of roughened aluminum. Instrument profile and perfect diffuse reflector shown for reference. Wavelength is 58.4 nm. (From Heaney.<sup>131</sup>)



**FIGURE 12** BRDF of gold iridite. Instrument profile and perfect diffuse reflector shown for reference. Wavelength is 58.4 nm. (From Heaney.<sup>131</sup>)

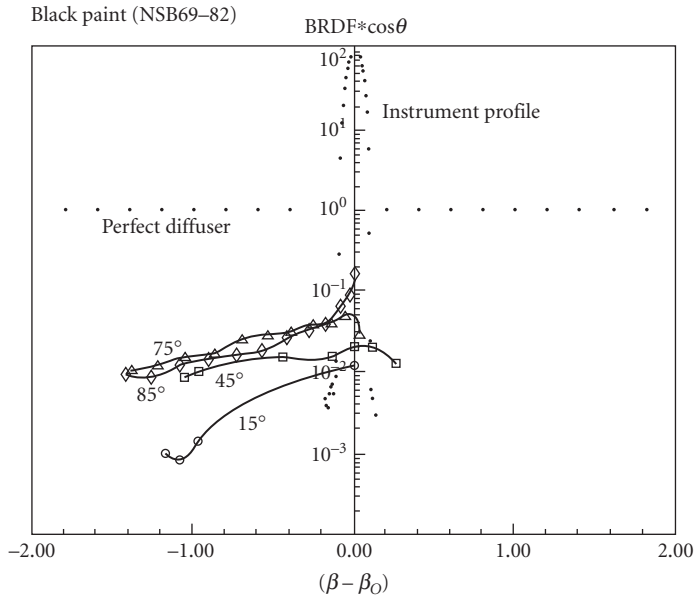


**FIGURE 13** BRDF of black nickel. Instrument profile and perfect diffuse reflector shown for reference. Wavelength is 58.4 nm. (From Heaney.<sup>131</sup>)

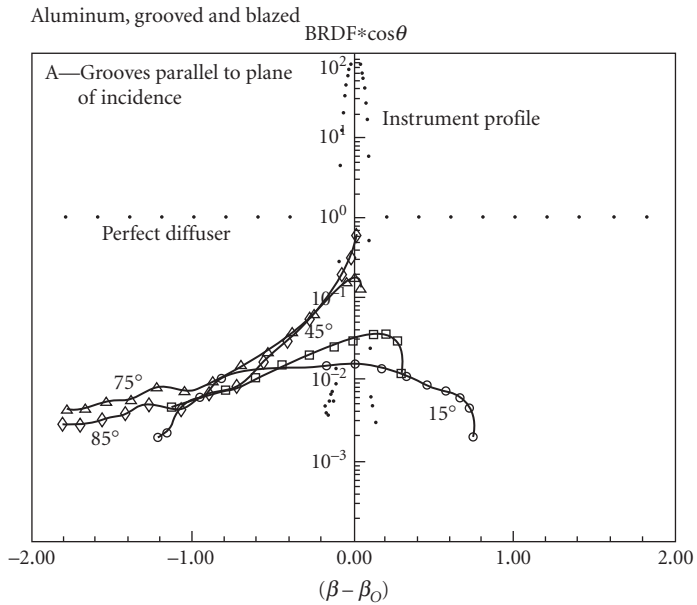


**FIGURE 14** BRDF of evaporated Cu black. Instrument profile and perfect diffuse reflector shown for reference. Wavelength is 58.4 nm. (From Heaney.<sup>131</sup>)

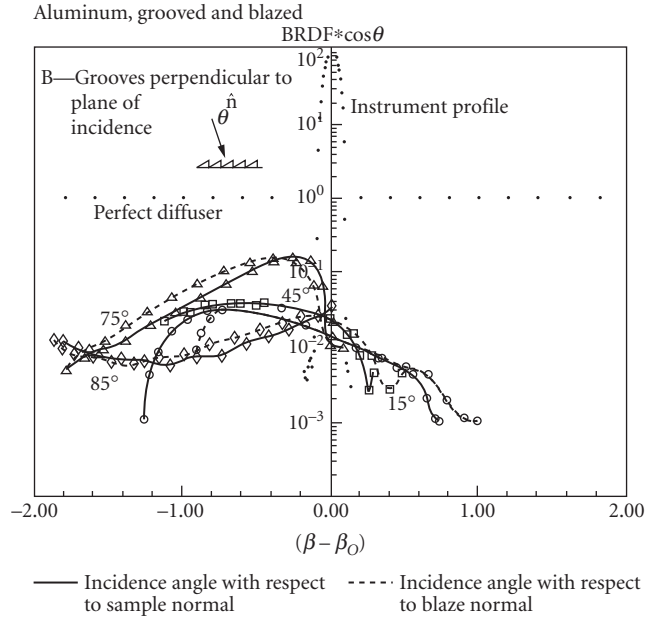




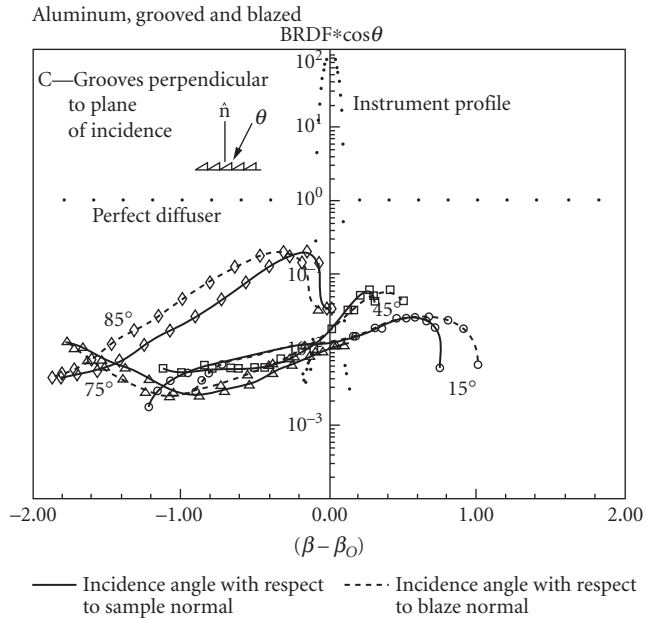
**FIGURE 15** BRDF of NSB69-82 black paint. Instrument profile and perfect diffuse reflector shown for reference. Wavelength is 58.4 nm. (From Heaney.<sup>131</sup>)



**FIGURE 16** BRDF of aluminum, grooved and blazed, with grooves parallel to angle of incidence. Instrument profile and perfect diffuse reflector shown for reference. Wavelength is 58.4 nm. (From Heaney.<sup>131</sup>)



**FIGURE 17** BRDF of aluminum, grooved and blazed, with grooves perpendicular to angle of incidence. Instrument profile and perfect diffuse reflector shown for reference. Wavelength is 58.4 nm. (From Heaney.<sup>131</sup>)



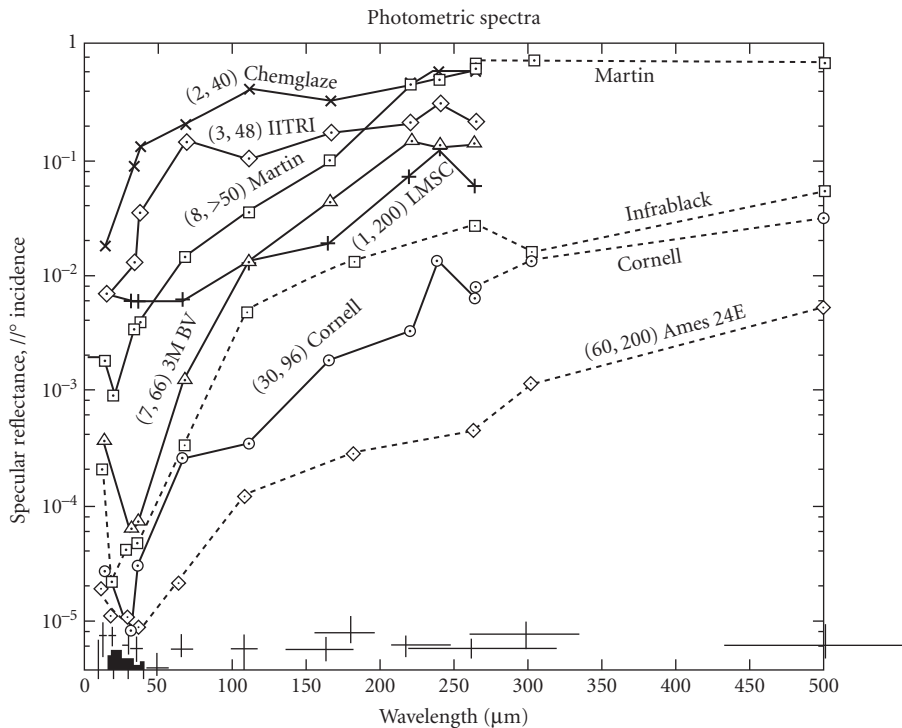
**FIGURE 18** BRDF of aluminum, grooved and blazed, with grooves perpendicular to angle of incidence. Instrument profile and perfect diffuse reflector shown for reference. Wavelength is 58.4 nm. (From Heaney.<sup>131</sup>)

perform well as “blacks” for long wavelength operation.<sup>41,133</sup> Smith<sup>32</sup> points out that many coatings become transparent at longer wavelength and the substrate roughness enters strongly into the scattering characteristics. An example of this is Infrablack, a rough anodized surface that was previously described. The approach has been carried further in Ames 24E.<sup>134</sup> A number of approaches and surfaces have been developed to create effective surfaces at these wavelengths.

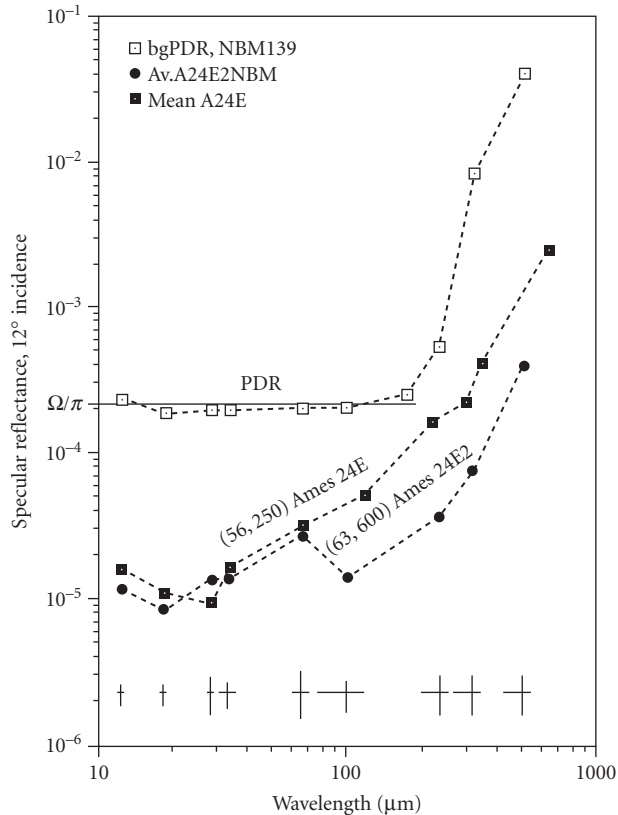
A model has been constructed<sup>33</sup> to describe the effect of coating roughness and thickness on the specular reflectance. Smith and Howitt<sup>19</sup> survey materials for infrared opaque coatings (2 to 700  $\mu\text{m}$ ). They highlight the value of silicon carbide and carbon black for far-infrared absorption. Smith<sup>32,33,39,46,57,72,134–137</sup> provides much of the reference work in this area.

The optical properties of the several infrared coatings and surfaces are given in Figs. 19 to 24. For applications in laboratories and in calibration facilities, surfaces like velvet, commando cloth, and even neoprene may be used. The long-wavelength measurements on these surfaces are given in Figs. 25 to 32. The long-wavelength coatings may be grouped into a few basic categories discussed here. As this area is one of rapid development for space infrared telescopes and space radiators, there will likely be many new approaches in the next few years.

**Multiple-Layer Approach** For reducing the far-infrared reflectance of baffles, a technique of using antireflection surfaces composed of multiple layers with a different refractive index in each layer was discussed by Grammar et al.<sup>55</sup> For such a coating to be effective, it must match the optical constants of free space with the large constants of the baffle substrate.



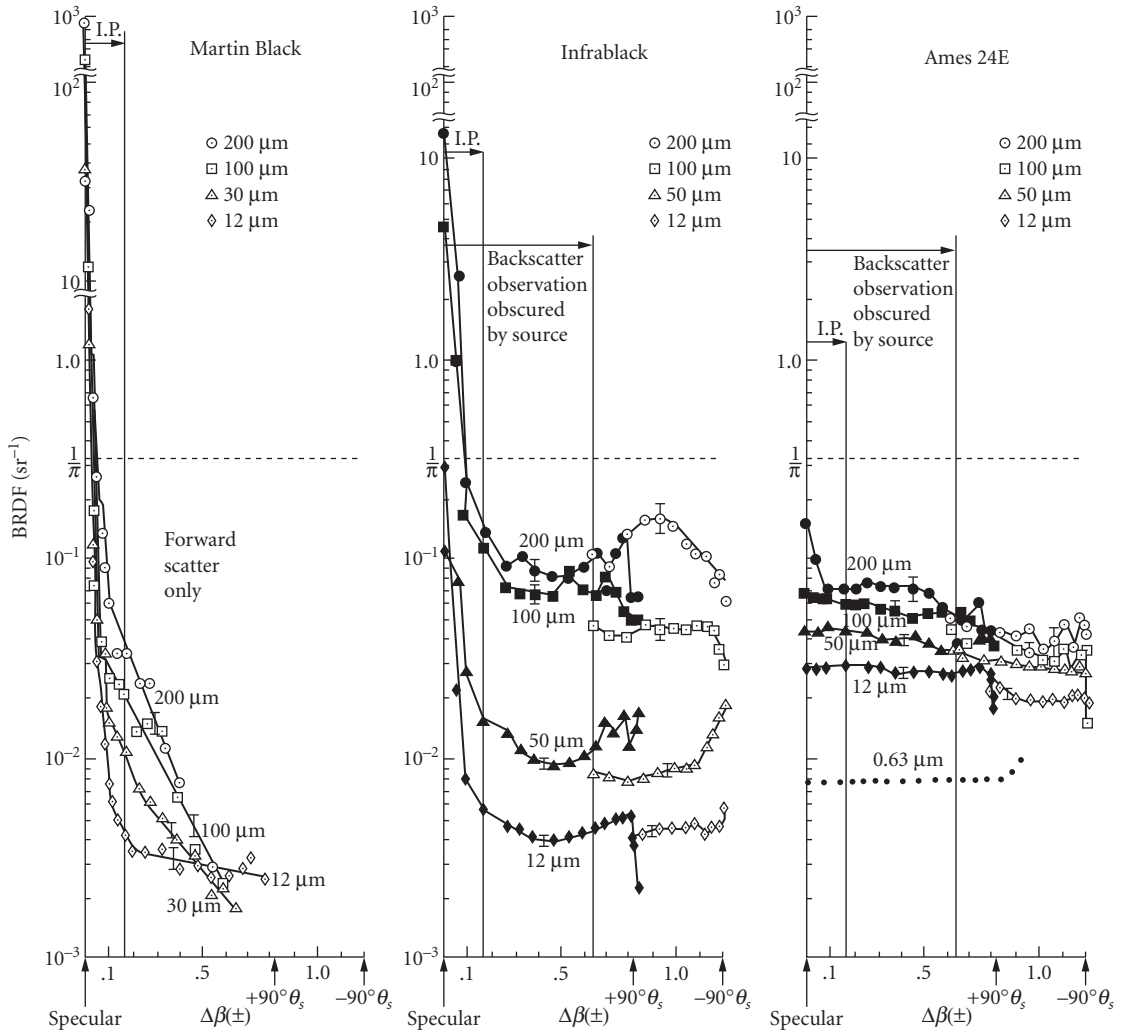
**FIGURE 19** Specular reflectance spectra of eight black coatings. Measurements of coating roughness and thickness in micrometers are shown in parentheses before the name of each coating. Filter passbands are shown by horizontal error bars. The absorption bands of amorphous silicates are indicated by the solid histogram in lower left end of the graph. (From Smith.<sup>32,33,46</sup>)



**FIGURE 20** Specular reflectance spectra of PDR surface and two infrared black coatings. Dashed lines connect data points of a set, and the solid line indicates the theoretical value of reflectance for a perfect lambertian surface. The coating roughness and thickness are given in parentheses, and filter passbands are indicated by horizontal error bars. (From Smith.<sup>136,137</sup>)

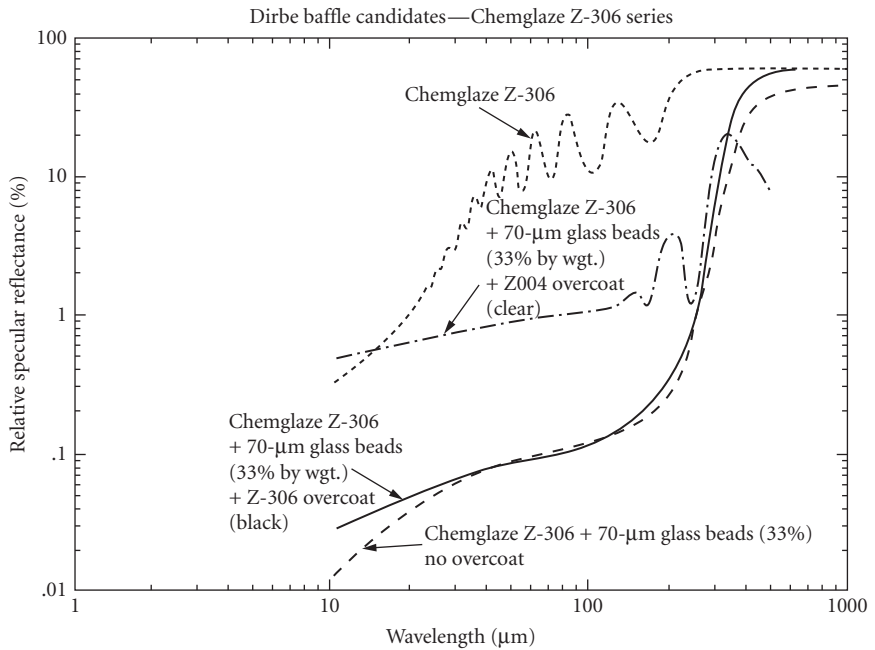
**Teflon Overcoat** A polytetrafluoroethylene (Teflon) spray-on lubricant was used as an antireflection overcoat for opaque baffle surfaces in the far-infrared and submillimeter by Smith.<sup>50</sup> A thick Teflon overcoat created by spraying Teflon Wet Lubricant reduced the specular reflectance at millimeter and infrared wavelengths by a factor of two. The refractive index of the coating plays a more significant role than the thickness.

**Cornell Black** Houck<sup>49</sup> created a far-infrared black paint based on adding large particles of grit (silicon carbide #80 and #180 grit) to 3M Black Velvet Nextel 101-C10. This paint could be repeatedly cycled to cryogenic temperatures with no flaking or peeling. The far-infrared properties of Cornell Black are described by Smith.<sup>32,33</sup> Since this 3M paint is no longer available, Cornell Black is not now generally used. The ECP-2200 (now called MH2200) replacement for 3M Black Velvet was studied by Smith and Howitt<sup>19</sup> in an effort to create a paint similar to Cornell Black. Houck<sup>49</sup> gives complete instructions for making the Cornell Black paint.

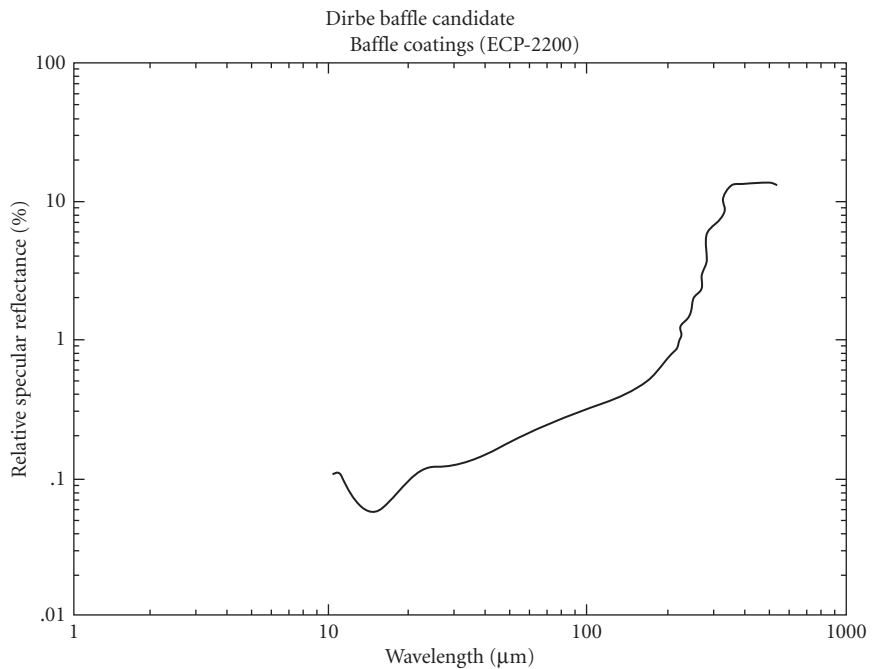


**FIGURE 21** BRDFs of Martin Black, Infrablack, and Ames 24E. Note the different breaks in the ordinate scale of the Martin Black measurements used to compress its specular reflectance to fit the scale of the figure. Forward scatter data are solid symbols; backscatter data are open symbols. Forward and backscatter measurements at  $0.6328 \mu\text{m}$  of Ames 24E are by D. Shepard of Martin Marietta (Denver) and are shown schematically by the dotted line in the right hand figure. (From Smith.<sup>46</sup>) Smith<sup>137</sup> recalibrated this data; the relative comparison of these coatings remained essentially unchanged.

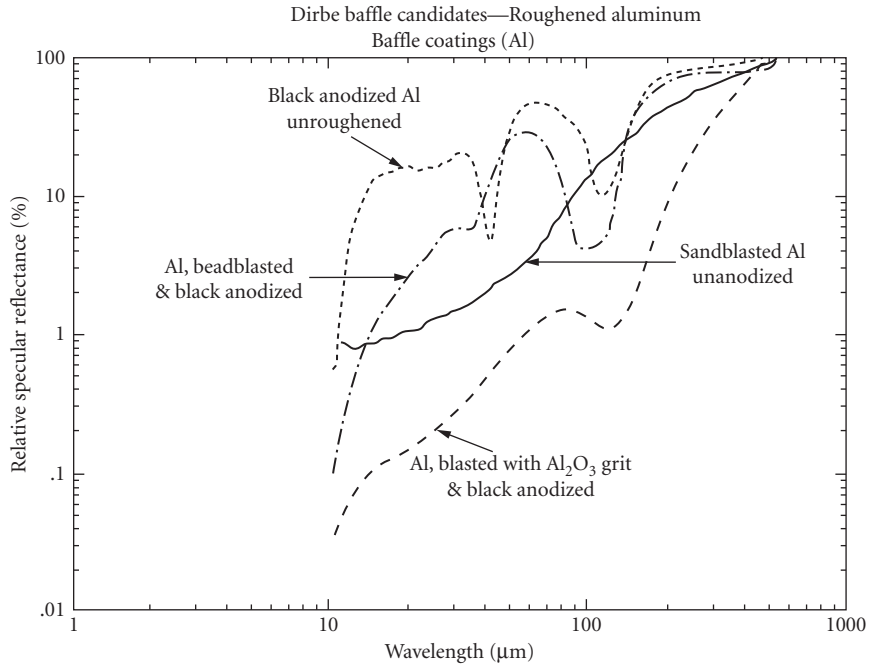
**Infrablack** Infrablack is a black anodized surface generally applied to 6061 Aluminum.<sup>31,64,138</sup> It is highly suitable for space radiators, infrared baffles, and for applications where a high emissivity is desired. The specular reflectance of the Infrablack is conservatively one order of magnitude less than that of Martin Black across the spectral region from 12 to 500  $\mu\text{m}$ . The reduced reflectance of Infrablack is attributed to a large increase in the roughness of its substrate prior to anodization. The diffuse reflectance characteristics of the Infrablack are different from Martin Black at the longer wavelengths. At 12 and 50  $\mu\text{m}$ , the BRDF of Infrablack is considerably less than that of Ames 24E, while at 100 and 200  $\mu\text{m}$  they are comparable.



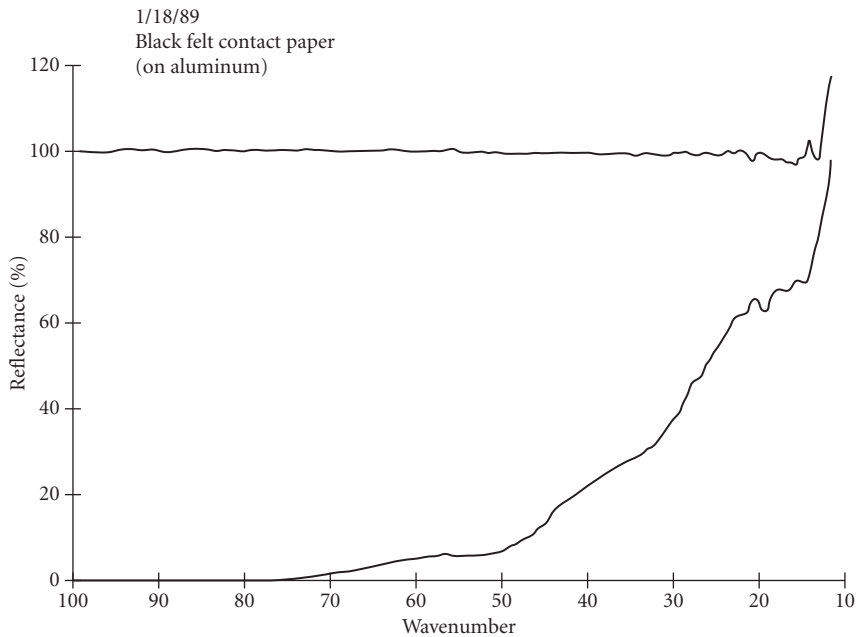
**FIGURE 22** Specular reflectances of Diffuse Infrared Background Explorer candidate baffle surfaces based on Chemglaze (now Aeroglaze) Z-306, over the wavelength range 1 to 1000  $\mu\text{m}$ . (From Heaney.<sup>131</sup>)



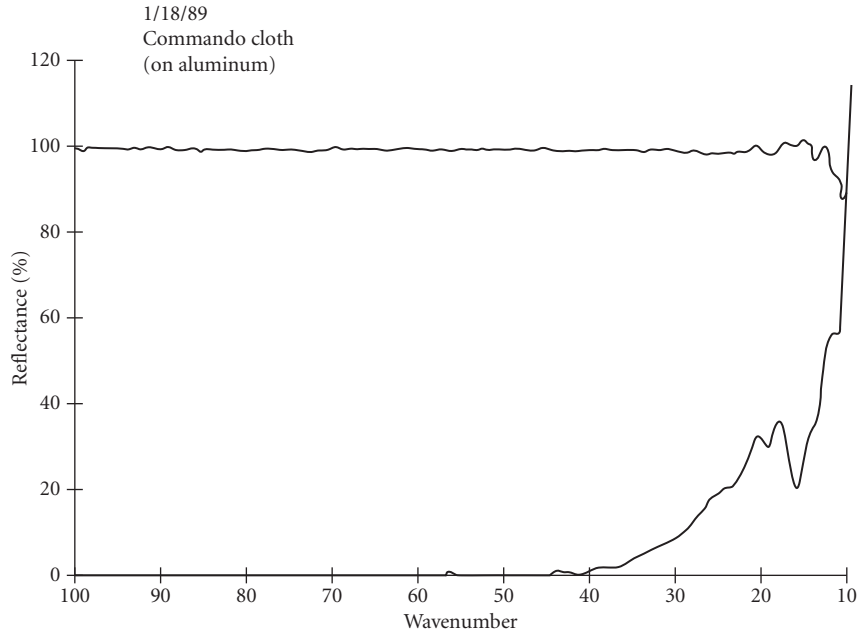
**FIGURE 23** Specular reflectance of Diffuse Infrared Background Explorer candidate baffle surface based on ECP-2200 (now MH2200) black paint over the wavelength range 1 to 1000  $\mu\text{m}$ . (From Heaney.<sup>131</sup>)



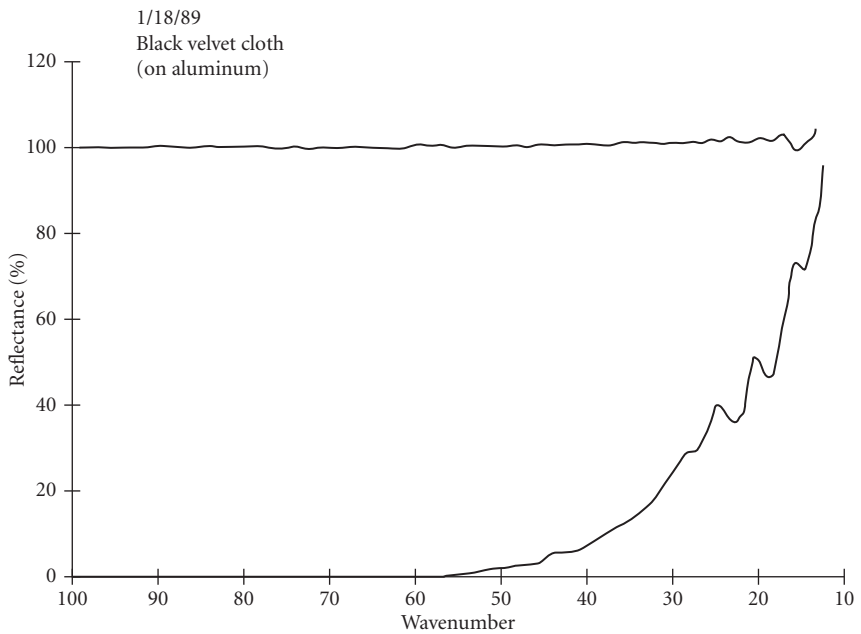
**FIGURE 24** Specular reflectance of Diffuse Infrared Background Explorer candidate baffle surface based on roughened aluminum surfaces over the wavelength range 1 to 1000  $\mu\text{m}$ . (From Heaney.<sup>131</sup>)



**FIGURE 25** Reflectance of black felt contact paper from 100 to 10 wave numbers (100 to 1000  $\mu\text{m}$ ). (From Heaney.<sup>131</sup>)

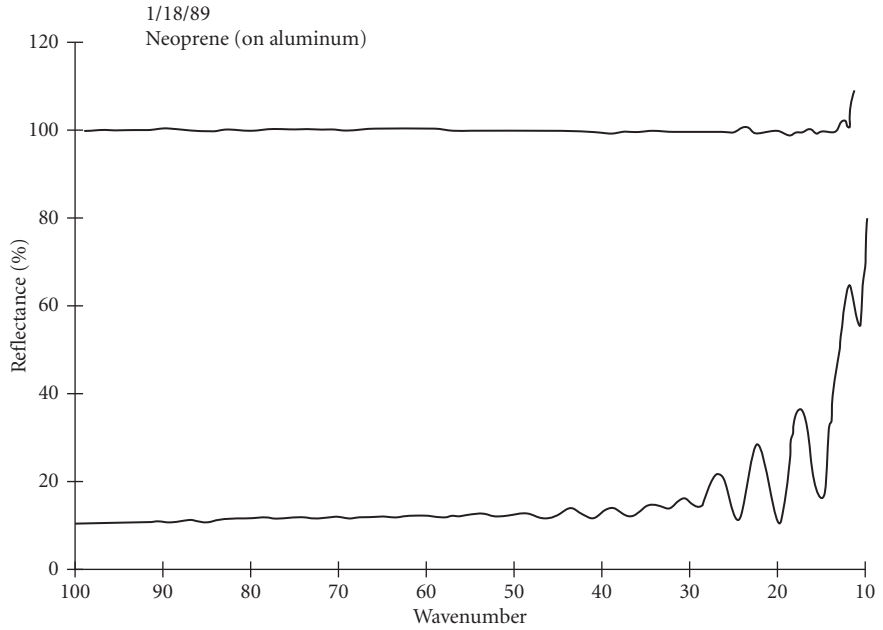


**FIGURE 26** Reflectance of commando cloth on aluminum from 100 to 10 wave numbers (100 to 1000  $\mu\text{m}$ ). (From Heaney.<sup>131</sup>)

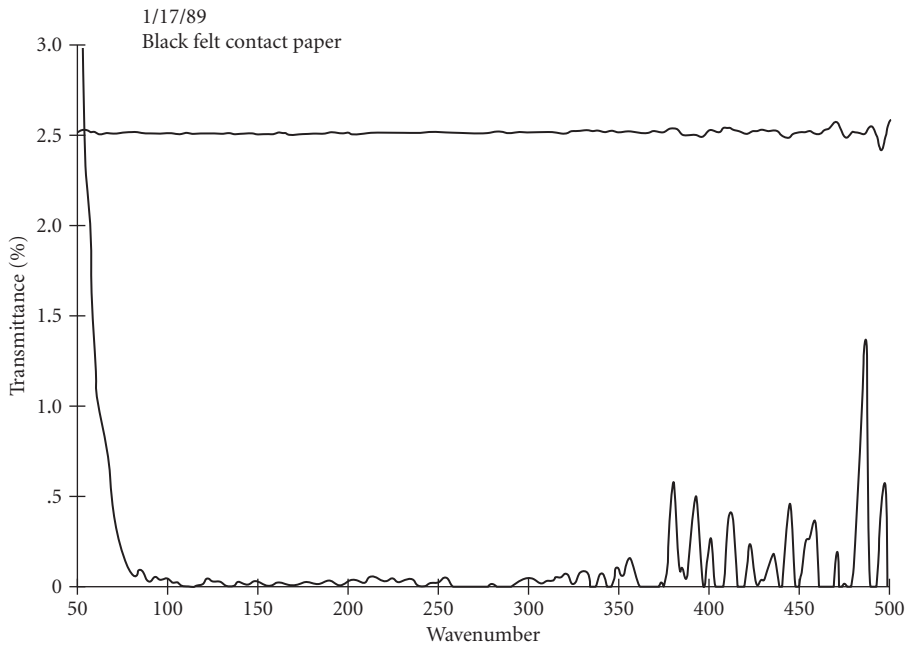


**FIGURE 27** Reflectance of black velvet cloth on aluminum from 100 to 10 wave numbers (100 to 1000  $\mu\text{m}$ ). (From Heaney.<sup>131</sup>)

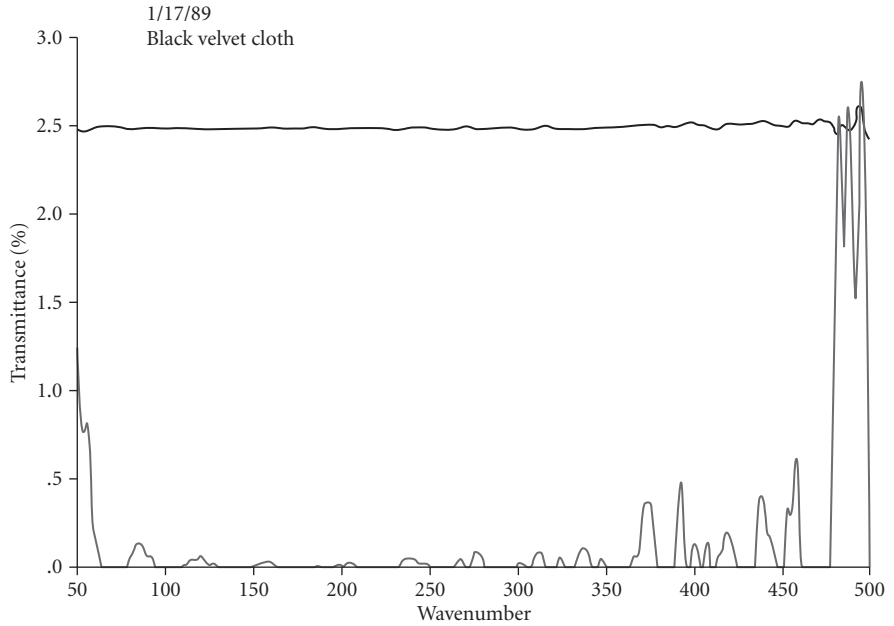




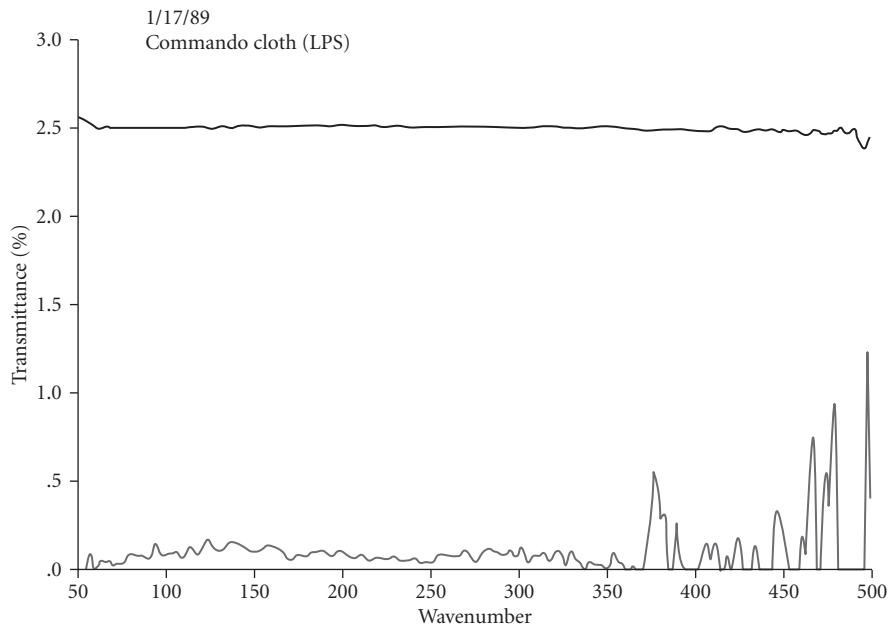
**FIGURE 28** Reflectance of neoprene on aluminum from 100 to 10 wave numbers (100 to 1000  $\mu\text{m}$ ). (From Heaney.<sup>131</sup>)



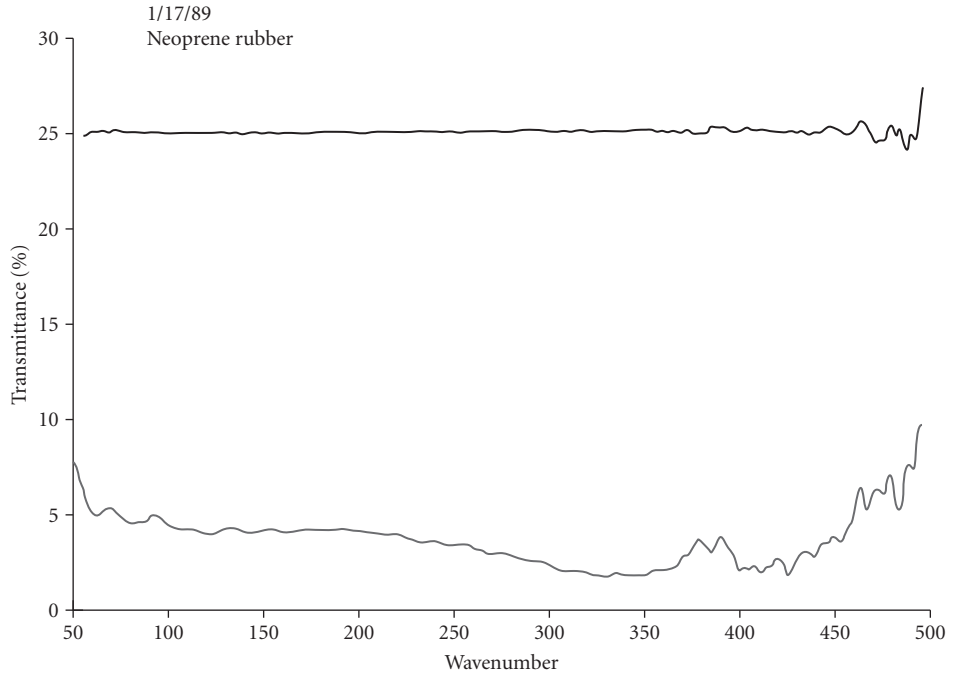
**FIGURE 29** Transmittance of black felt contact paper from 50 to 500 wave numbers (200 to 20  $\mu\text{m}$ ). (From Heaney.<sup>131</sup>)



**FIGURE 30** Transmittance of black velvet cloth from 50 to 500 wave numbers (200 to 20  $\mu\text{m}$ ). (From Heaney.<sup>131</sup>)



**FIGURE 31** Transmittance of commando cloth (lps) from 50 to 500 wave numbers (200 to 20  $\mu\text{m}$ ). (From Heaney.<sup>131</sup>)



**FIGURE 32** Transmittance of neoprene rubber from 50 to 500 wave numbers (200 to 20  $\mu\text{m}$ ). (From Heaney.<sup>131</sup>)

**Ames 24E and Ames 24E2** Ames 24E is a new coating developed at NASA's Ames Research Center.<sup>46</sup> The coating is a very rough, very thick, highly absorbing coating composed largely of SiC grit and carbon black, and has very low far-infrared reflectance.<sup>46</sup> BRDF measurements show that this surface is a model lambertian surface at a wavelength of 10.6  $\mu\text{m}$  at near-normal incidence. Ames 24E is nearly lambertian at longer wavelengths, even at 200  $\mu\text{m}$ .

Ames 24E2 is a formulation using ECP-2200, carbon black, silicone resin, and #80 silicon carbide grit. The coating was developed for far-infrared space telescopes and can pass severe cryogenic cycling and vibration tests.<sup>34</sup> The coating is considerably less reflective at 100  $\mu\text{m}$  than Ames 24E and has excellent absorption out to about 500  $\mu\text{m}$ . Smith<sup>137</sup> has also developed a highly lambertian, diffuse reflectance standard, which he calls PDR, for perfect diffuse reflector. It shows lambertian behavior from 10 to about 100  $\mu\text{m}$ .

## 6.7 SURVEY OF SURFACES WITH OPTICAL DATA

### A Note on Substrates and Types of Coatings

Many different substrates are employed for baffle and vane surfaces. In particular, for space or cryogenic use, the 6000 series of alloys of aluminum (particularly 6061) are popular. They represent the baseline by which other materials are judged. Titanium and graphite epoxy are also widely used, and beryllium and carbon fiber substrates are becoming more common. For high-temperature applications or for resistance to lasers, materials with high melting points such as nickel, molybdenum, and carbon/carbon are used.

The distinction between substrate and surface or surface coating is blurry. When paints or other coatings are applied to a substrate, the distinction between the two is very clear. However, many surfaces today involve an extensive alteration of the substrate before the “coating” is applied. They may chemically alter the substrate to create the surface coating, which is an integral part of the substrate. In these cases, the use of the word substrate only serves as a description of the material that must be altered to create the black surface.

The classification of surfaces by substrate and/or type of coating or surface treatment is only one of the many ways available. However, it is a very useful form of classification, and will be used here.

## 6.8 PAINTS

Paints are easy to apply and their availability and usually low price make them ideal for laboratory experiments and instruments. However, their high outgassing rates and, in some cases, the large number of particles that can be liberated from them compromise their use in space-based applications. However, there are many space-qualified paints that have been flown in space. Notable among them is Aeroglaze Z306, and the derivatives of this basic paint system that have been developed at Goddard Space Flight Center.

The way that paint may be applied can greatly affect the optical properties. The most obvious are the number of coats and the thickness; the substrate preparation also plays a critical role. Brown<sup>27</sup> describes the effects of number of coats on optical performance for three diffuse paints. The importance of developing a procedure for painting that incorporates the paint manufacturers' application recommendations cannot be overstated. This procedure must also include process control requirements, cleanliness requirements, application process and surface preparation requirements, safety requirements, quality assurance requirements, and storage shipping requirements, as McCall<sup>18</sup> describes in detail. A short description of a few of the more common paints is given here. Table 2 gives further reference data on these and other paints.

### *3M Paints and Their Current Derivatives*

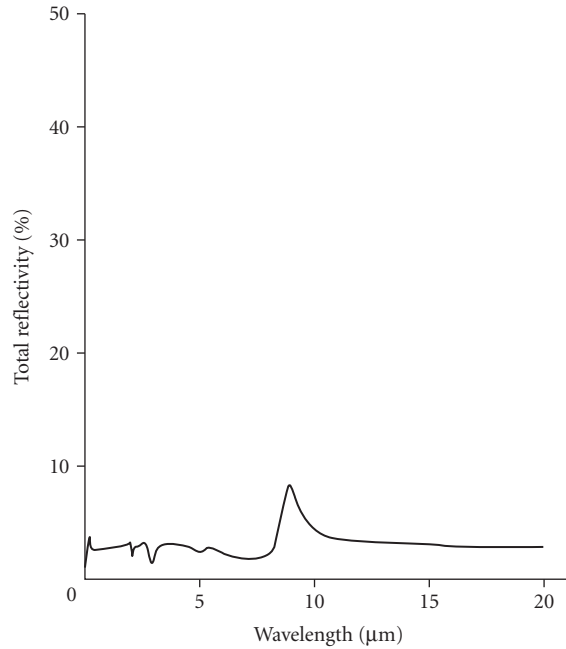
*3M Nextel Black Velvet* Several varieties of 3M Black Nextel paint from Minnesota Mining and Manufacturing Company have seen extensive use in ground-based instruments and were considered as standards for black coatings. These paints consisted of pigments with approximately 20 percent carbon black and 80 percent silicon dioxide. However, most of them are presently unavailable. Those that are available are manufactured under license by other companies. The optical properties of the original paint are given in Fig. 33.

The paint labeled 3M 101-C10 historically was one of the most widely used laboratory black paints; however, it is no longer made. Redspot Paint and Varnish (Evansville, Indiana) now makes a similar paint, but uses resin instead of glass microspheres, making it unsuitable for space applications according to Ames.<sup>28</sup> Two other paint varieties in the same line were 3M401-C10 and 3M3101 (see Figs. 34 and 35), apparently available from Red Spot Paint and Varnish.

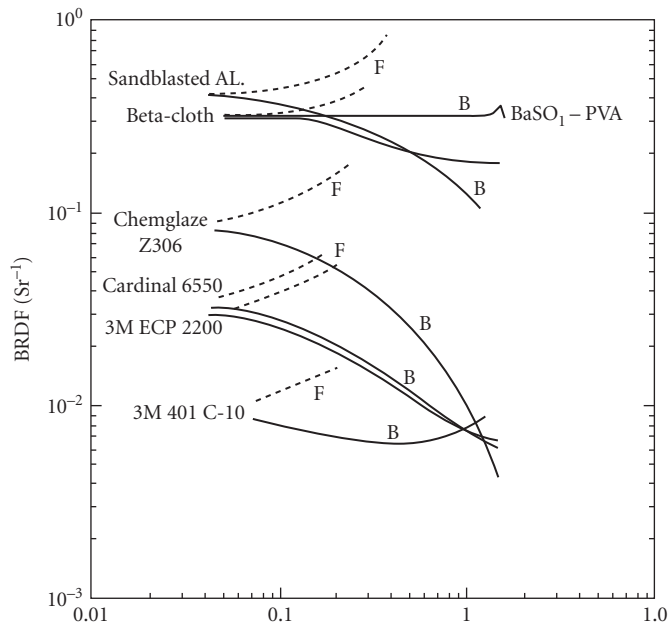
The 3M Nextel Black Velvet was replaced by 3M SCS-2200 (3M Brand ECP-2200) (see Fig. 35). The optical differences between the original and its replacement are discussed by Willey et al.<sup>42</sup> Illinois Institute of Technology now produces the ECP-2200 under the name MH2200 (see following).

*Nextel 2010* A sprayable Nextel 2010 Velvet paint is available from the German company Mankiewicz Gebr. & Co., Hamburg, and has been used on several ground-based astronomical instruments, where cryogenic cycling durability is important. The 2010 surface has an outgassing rate of  $1.3 \times 10^{-4}$  g/cm<sup>2</sup> at 84°F (29°C) in a 20-hour test at  $10^{-5}$  to  $10^{-6}$  torr. The solar alpha of this surface (from the company literature) is about 0.97 and the normal emittance is about 0.95.

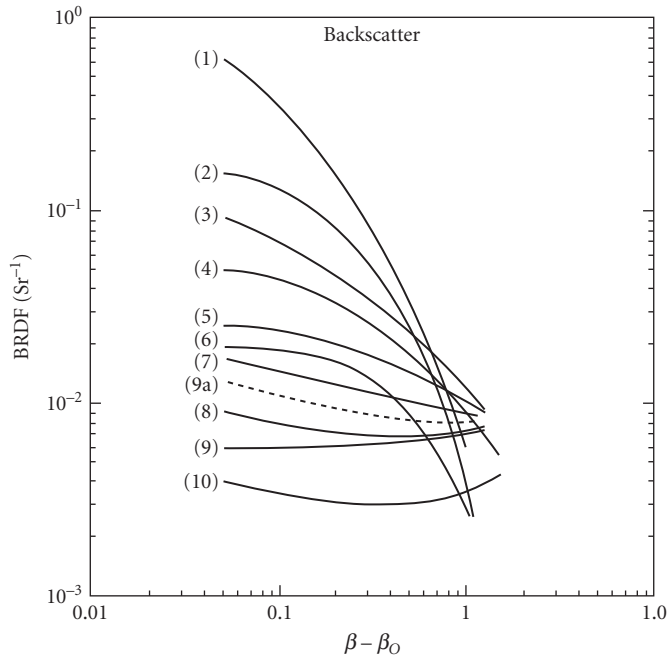
The total emissivity of different black surfaces was investigated with regard to their being used as a total radiation standard in the temperature range -60 to +180°C by Lohregel.<sup>139</sup> The investigations showed that the matte varnish Nextel Velvet Coating 2010 black with an emissivity of 0.951 was



**FIGURE 33** Total hemispherical reflectivity of 3M Nextel Black Velvet. (From Willey et al.<sup>42</sup>)



**FIGURE 34** Comparison of BRDF profiles at an angle of 45° and 633-nm wavelength. (From Viehmann and Predmore.<sup>35</sup>)



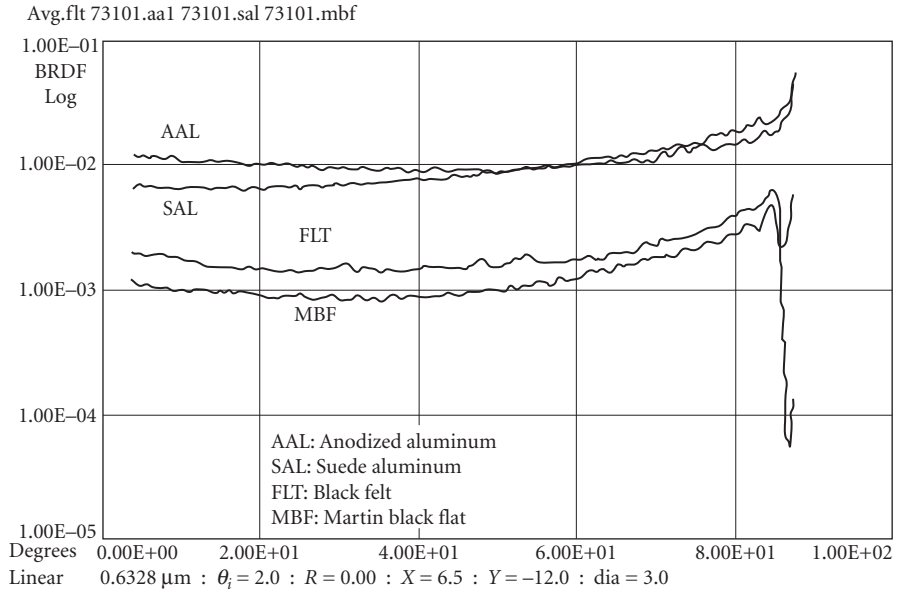
**FIGURE 35** Comparison of BRDF profiles at an angle of  $45^\circ$  and 254-nm wavelength: (1) Reynolds Tru Color Diffuse; (2) Chemglaze Z306; (3) Sikkens 443; (4) Sanodal Fast Black GL; (5) Chemglaze Z306 plus microballoons; (6) Sanodal deep black MLW; (7) 3M 401-C10; (8) Chemglaze Z313; (9) DeSoto Flat; (10) DeSoto Flat after EUVSH; (11) Martin Black anodize. (From Viehmann and Predmore.<sup>35</sup>)

best suited for these purposes. Additional changes to the surface (sprinkling of Cu globules, etching) could be made to increase the total emissivity by a further 0.007 or 0.016, respectively. The present availability of this paint from U.S. manufacturers is unknown.

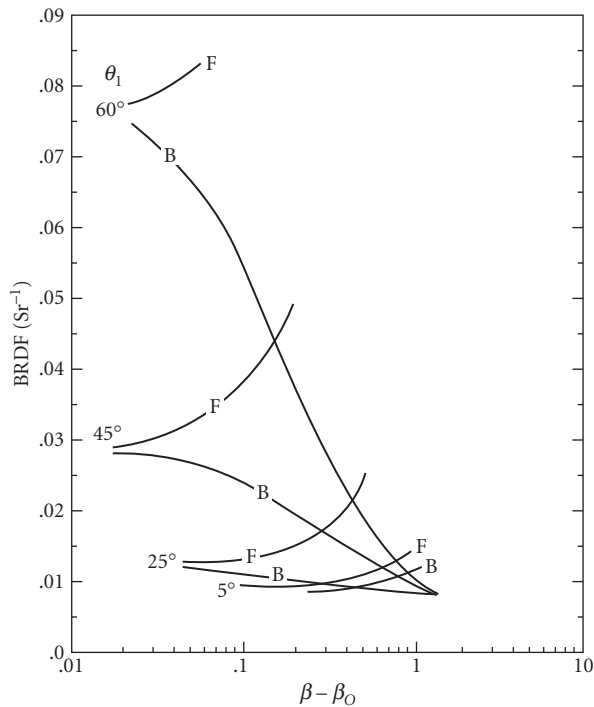
*Nextel Brand Suede Coating Series 3101-C10* C-10 is the black variety of this paint, available from Red Spot (see references). It is a low-gloss paint, with reasonable abrasion resistance (see Fig. 36). It has a soft-cushioned feel and suedelike appearance and was used on office equipment, furniture, and electronic equipment housings. The manufacturer recommends it for interior use only.

*MH 2200* MH2200 (formerly ECP-2200, which was derived from the original 3M Nextel Black Velvet) is a one-part, flat black, nonselective solar absorber coating designed for high-temperature service (Fig. 37). When applied to aluminum substrates, the coating integrity and its “solar absorption” of 0.96 are unaffected by temperatures to about  $500^\circ\text{C}$ . The coating is 43 percent solids in xylene and is intended for nonwear applications. ECP-2200 is available from IIT Research Institute. It is touted as the substitute for 3M Nextel Black, but does not have the low BRDF at visible wavelengths of its former relative. It has a normal emittance of 0.95 at  $10.6\ \mu\text{m}$  and an absorptance of 0.96 over the wavelength range of 0.35 to  $2.15\ \mu\text{m}$ . Its emittance is 0.86 on an aluminum substrate (normal emittance at  $75^\circ\text{F}$  from 2 to  $25\ \mu\text{m}$ ).

*Aeroglaze Z Series* Aeroglaze (formerly Chemglaze) Z306 diffuse black paints are part of the Z line of single-package, moisture-curing, ASTM Type II, oil-free polyurethanes.<sup>24</sup> This paint has excellent chemical, solvent, and (if used with a primer) salt-spray resistance. This is a popular paint for aerospace



**FIGURE 36** BRDF data for anodized aluminum, 3M Nextel Suede paint, black felt, and an aluminum flat with Martin Black wavelength is 633 nm, at near normal incidence. (From Cady *et al.*<sup>66</sup>)



**FIGURE 37** BRDF profiles of 3M ECP-2200 black paint 6550 at 633 nm. (From Viehmann and Predmore.<sup>35</sup>)

use, especially after the discontinuation of 3M's 401-C10 Black Velvet Nextel.<sup>28</sup> For space use, the Aeroglaze 9924 and Aeroglaze 9929 primers are recommended. The optical properties are given in Figs. 34 and 38 to 43.

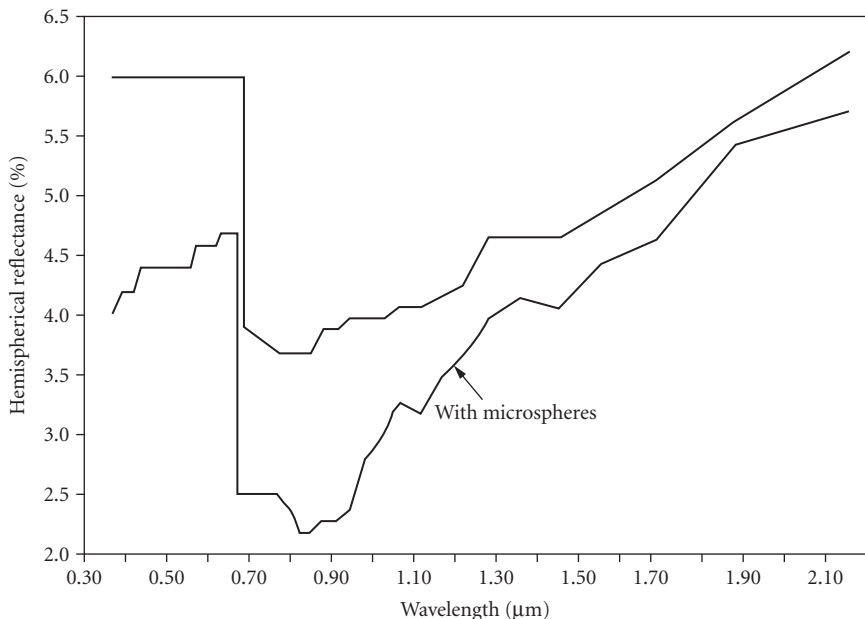
A low volatile version of the paint is being developed. In a version developed at Goddard Space Flight Center (based on the Z306)<sup>44</sup> glass microballoons are added to reduce the specular component, though the particles may be a source of particulate contamination. Other versions were developed at Goddard based on the Z004 paint. Goddard Black is a generic term for several paints of composition and optical properties different from Z306. This name is often incorrectly applied to the modified Z306 described here.

**Akzo Nobel Paints** Three paints sold formerly under the label Cat-a-lac are now known as Akzo 463-3-8 (formerly Cat-a-lac 463-3-8 diffuse black), 443-3-8 (formerly Cat-a-lac 443-3-8) (see Figs. 34 and 43 to 46) and 443-3-17 (formerly called Sikkens 443-3-17). The Bostic name is also formerly associated with these same paints. The 463-3-8 is the most diffuse of the three blacks, and the other two are considered "glossy." It is an epoxy-based system with low outgassing and low reflectance.

**Cardinal Black** From Cardinal Industrial Finishes. Optical data are given in Fig. 47.

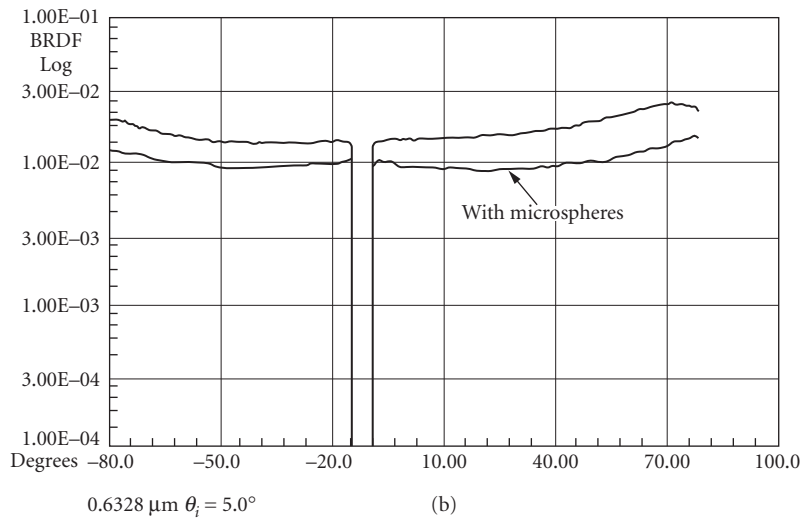
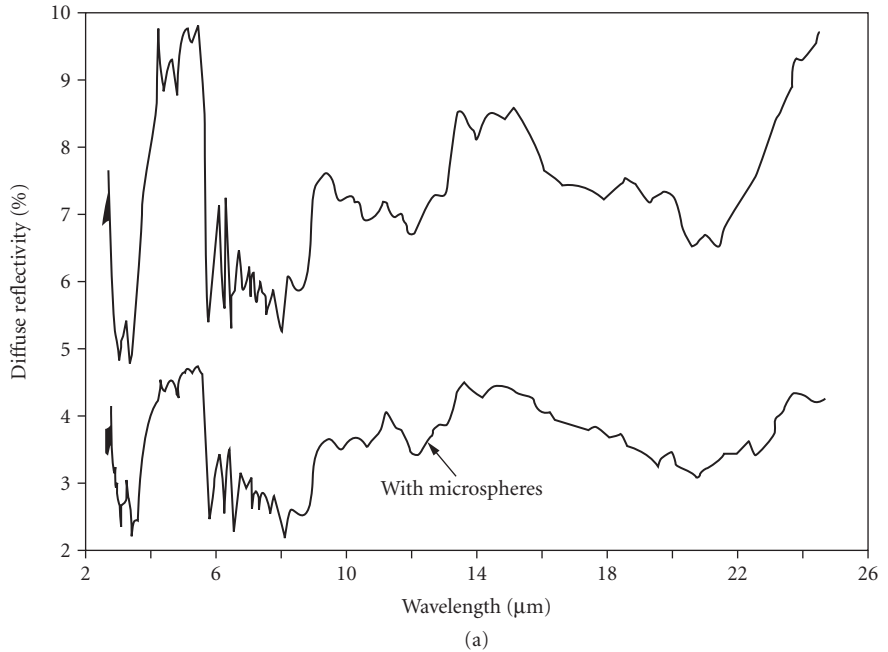
**Cat-a-lac Black (Former Name)** This is an epoxy system with low outgassing and low reflectance. It is now manufactured by Sikkens Aerospace Finishes (see Akzo in the tables for address) and is described here.

**DeSoto Black** The PRC DeSoto Black is a flat black paint most suitable for the range 0.2 to 2.5  $\mu\text{m}$ . It has a reflectance of between 2 and 3 percent over this range. Its emissivity is 0.960 compared to a 300 K blackbody, while its absorptivity over the solar spectrum is 0.924. DeSoto Black can meet outgassing requirements for space applications when vacuum baked. The weight loss is typically below 0.5 percent and the volatile condensable material is below 0.5 percent, similar to 3M Black Velvet.<sup>140</sup> A BRDF curve is given in Fig. 35.

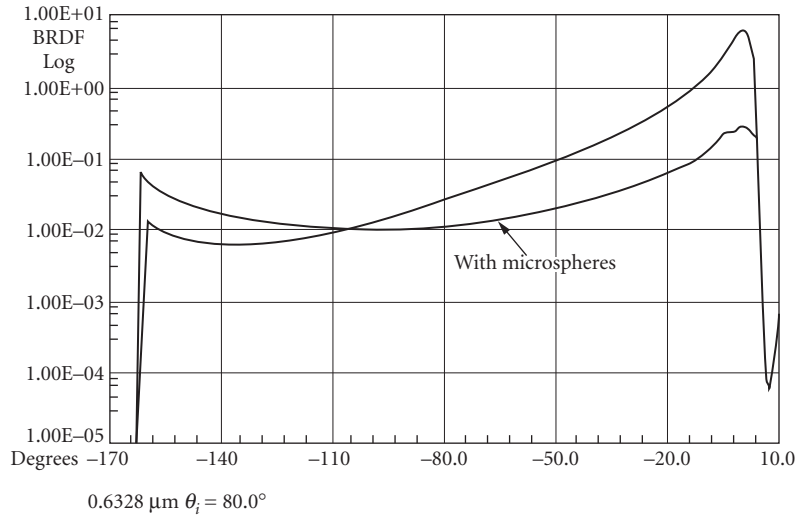


**FIGURE 38** Diffuse visible and near-infrared hemispherical reflectance of Chemglaze (now called Aeroglaze) Z306, and Z306 with microspheres. (From Ames.<sup>28</sup>)

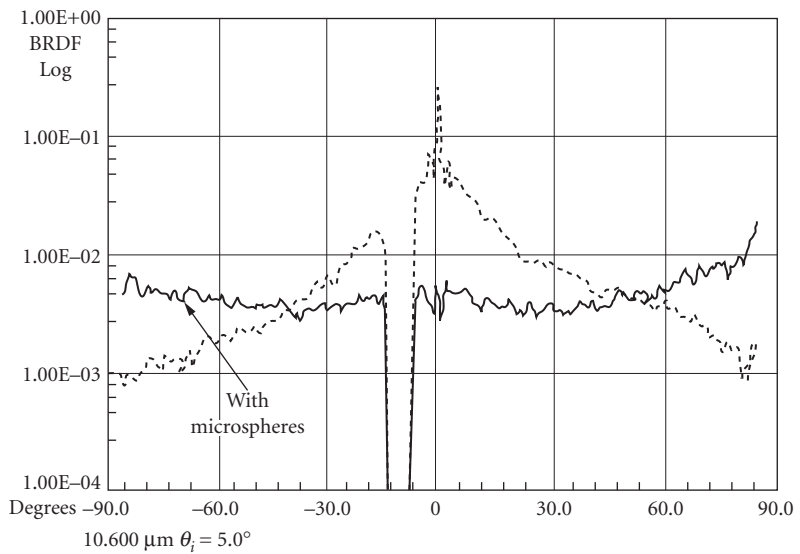




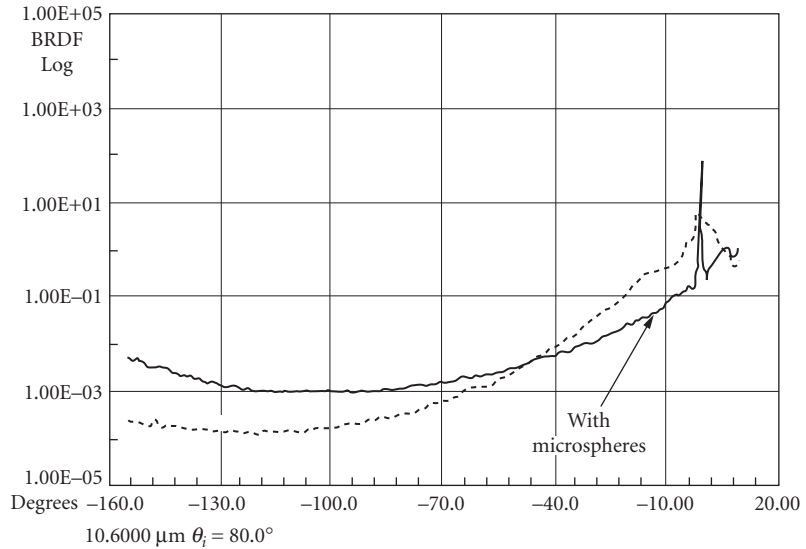
**FIGURE 39** (a) Infrared diffuse reflectivity of Chemglaze Z306 (now called Aeroglaze) and Z306 with microspheres. (b) BRDF for Chemglaze (now Aeroglaze) Z306 at near-normal incidence ( $5^\circ$ ) at a wavelength of  $0.6328 \mu\text{m}$ . (From Ames.<sup>28</sup>)



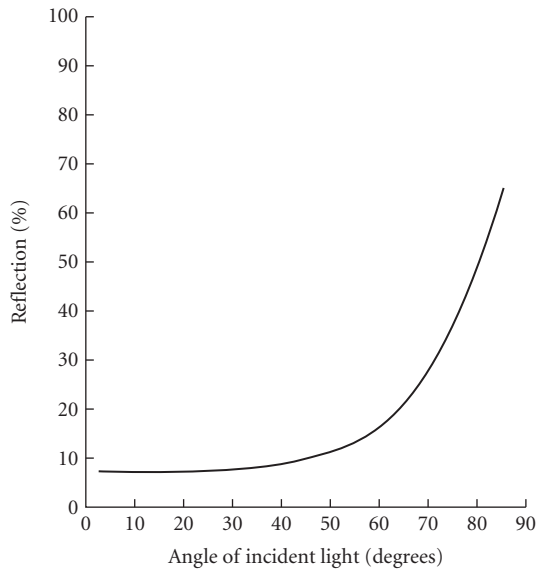
**FIGURE 40** BRDF for Chemglaze (now Aeroglaze) Z306 at near grazing incidence ( $80^\circ$ ) at a wavelength of  $0.6328 \mu\text{m}$ . (From Ames.<sup>28</sup>)



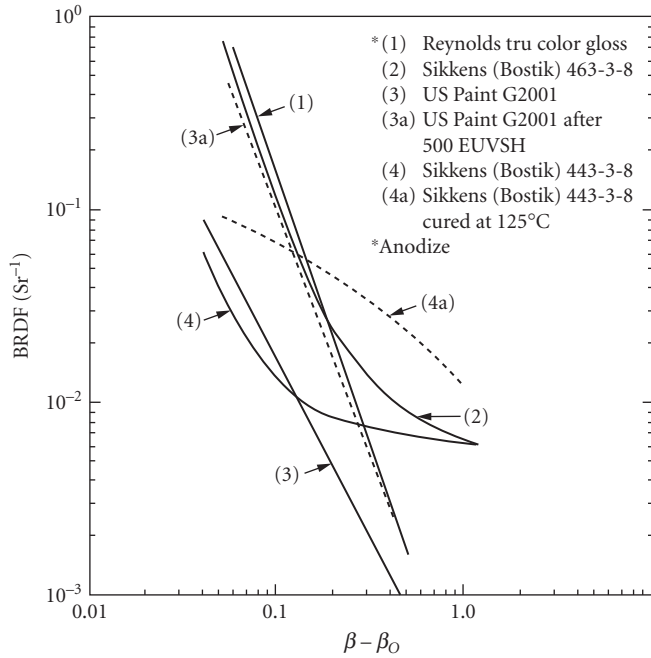
**FIGURE 41** BRDF for Chemglaze (now Aeroglaze) Z306 at near-normal incidence ( $5^\circ$ ) at a wavelength of  $10.60 \mu\text{m}$ . (From Ames.<sup>28</sup>)



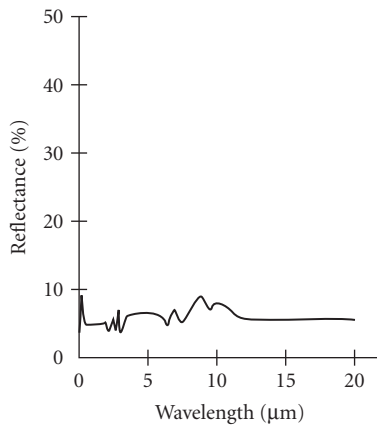
**FIGURE 42** BRDF for Chemglaze (now Aeroglaze) Z306 at near grazing incidence ( $80^\circ$ ) at a wavelength of  $10.60 \mu\text{m}$ . (From Ames.<sup>28</sup>)



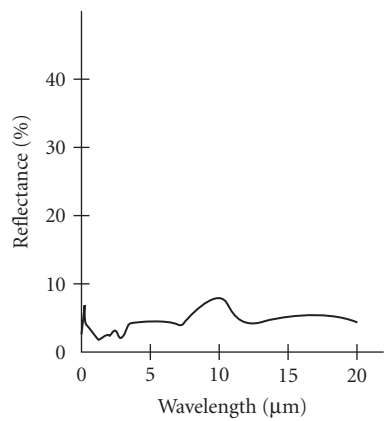
**FIGURE 43** Specular reflection measured for Cat-a-lac glossy (now called Akzo 443-3-8) and for Chemglaze glossy (now called Aeroglaze Z302). The wavelength is  $0.6328 \mu\text{m}$ . The two lines overlap. (From Griner.<sup>25</sup>)



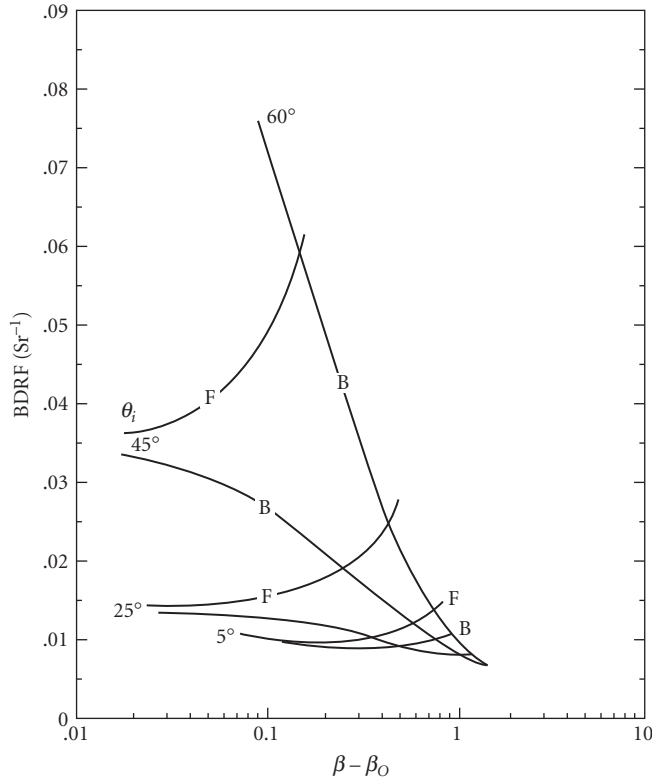
**FIGURE 44** BRDFs of glossy surfaces at 0.254  $\mu\text{m}$  and 45° angle of incidence. (From Viehmann and Predmore.<sup>35</sup>)



**FIGURE 45** Total hemispherical reflectivity of Bostic 463-3-8 (now called Akzo 463-3-8) on bare aluminum. (From Willey et al.<sup>42</sup>)



**FIGURE 46** Total hemispherical reflectivity of Bostic 463-3-8 (now called Akzo 463-3-8) on ZnCr primer. (From Willey et al.<sup>42</sup>)



**FIGURE 47** BRDF profiles of Cardinal black paint 6550 at 633 nm. (From Viehmann and Predmore.<sup>35</sup>)

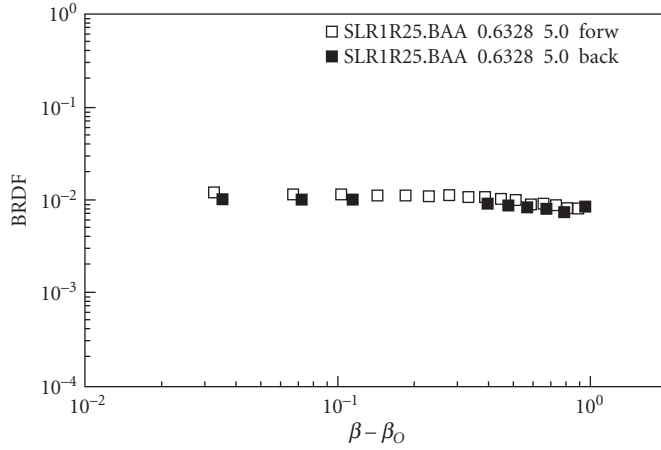
**Floquil: Black for Lens Edges** Lewis et al.<sup>141</sup> discuss experiments to find low-scatter blackening components for refractive elements. With index of refraction matching, gains of several magnitudes in lower BRDF can be achieved over other edge-blackening techniques. The paint Floquil (Polly S Corporation) has been used as an edge-blackening compound and is discussed by Lewis. Smith and Howitt<sup>19</sup> give a specular reflectance curve for Floquil in the infrared from 20 to 200  $\mu\text{m}$ .

**Parson's Black** Prior to 1970, Parson's Black was a standard black reference.

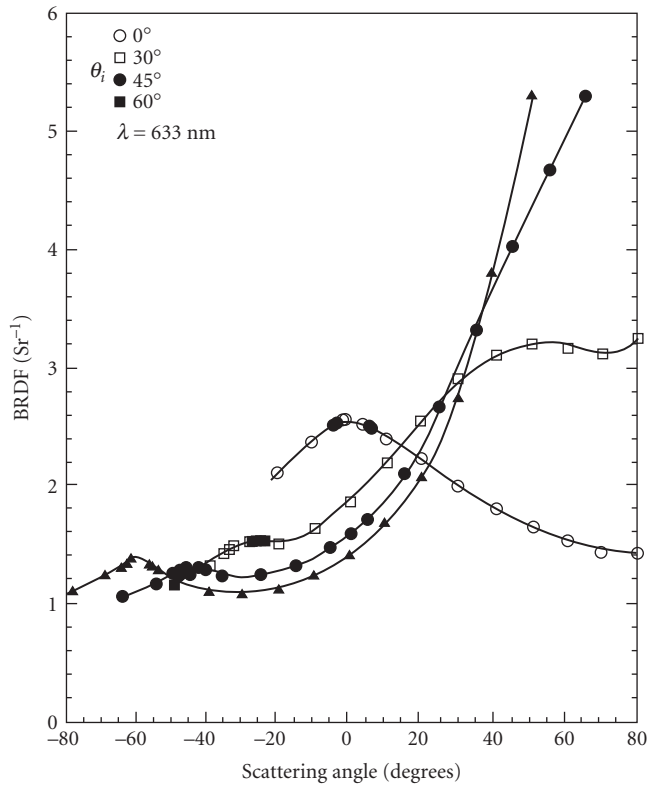
**SolarChem** SolarChem is a black paint with excellent visible absorbing properties and has been suggested as a replacement for the unavailable 3M Nextel Black. The visible BRDF of SolarChem has a flat profile at near-normal angles of incidence (Fig. 48), while the 10.6- $\mu\text{m}$  BRDF of SolarChem shows quite a different shape.<sup>88</sup> The surface is highly specular at 10.6  $\mu\text{m}$ .

## Anodized Processes

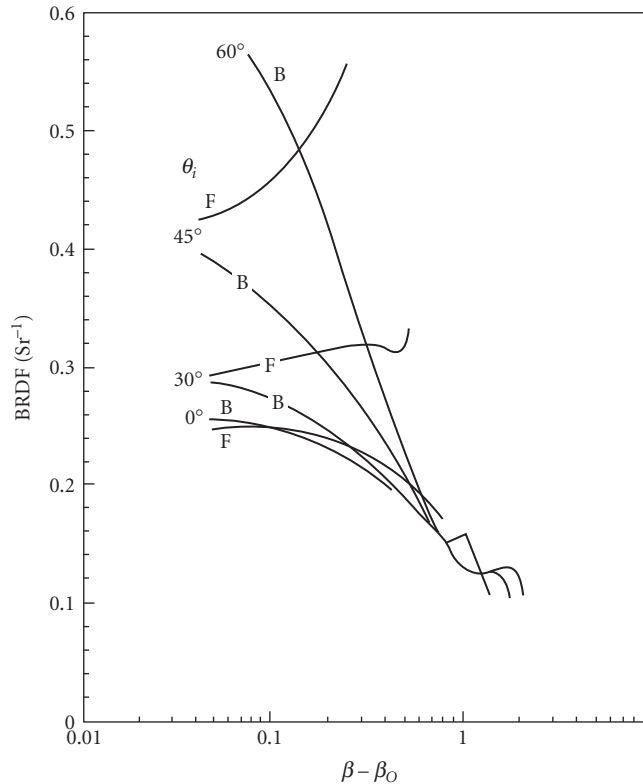
Anodized processes can produce fine black surfaces. The condition of the substrate plays an important role in the overall scattering properties of the surfaces. A common technique is to sandblast (vapor hone) the surface before anodization. Many varieties of grit may be used and each will produce a different kind of surface treatment. Sometimes, small pieces of grit can become embedded in the surface and this may affect the anodizing process. The BRDF of sandblasted aluminum surfaces are given in Figs. 49 and 50. Table 3 gives reference data on anodized surfaces.



**FIGURE 48** Visible (0.6328  $\mu\text{m}$ ) BRDF of SolarChem at  $5^\circ$  angle of incidence. (From Pompea *et al.*<sup>4</sup>)



**FIGURE 49** BRDF profiles of sandblasted aluminum. Open circle:  $0^\circ$  open square:  $30^\circ$  filled circle:  $45^\circ$  filled square:  $60^\circ$ ; wavelength of 633 nm. (From Viehmann and Predmore.<sup>35</sup>)



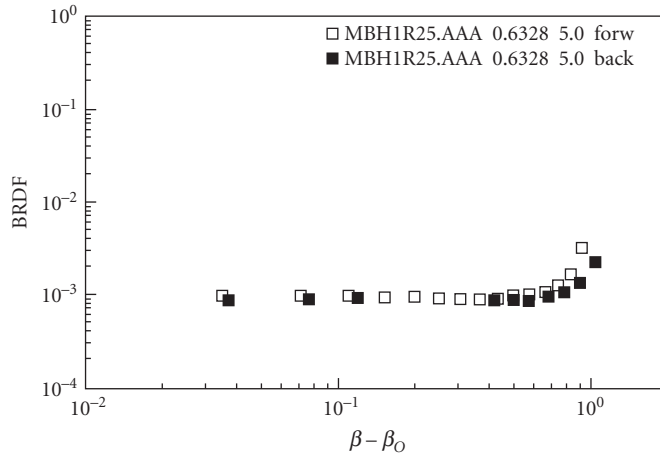
**FIGURE 50** Forward (F) and back (B) scatter profiles of sandblasted aluminum. Wavelength of 633 nm. (From Viehmann and Predmore.<sup>35</sup>)

**Martin Black** Martin Black is an anodized aluminum surface that is made microrough by a special anodization process developed by Lockheed Martin, Denver.<sup>142,143</sup> It is made black from the inclusion of an aniline dye that is sealed into the surface. It was developed for the Skylab program and has been used on a wide variety of space instruments operating at vacuum ultraviolet to far-infrared wavelengths. The surface is rough, and scattering at several fundamentally different scale lengths occurs.

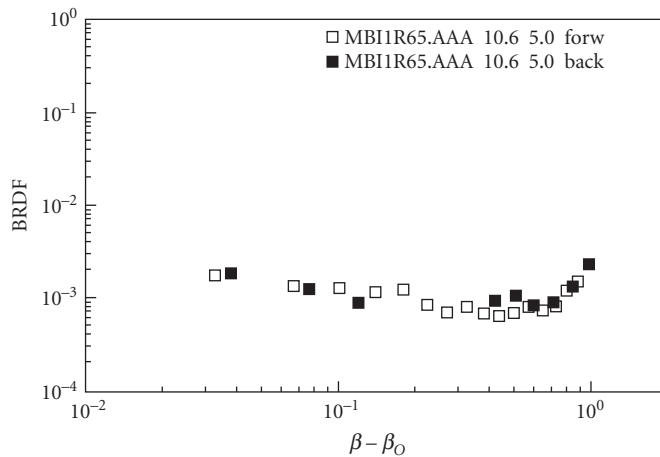
Special care in handling surfaces of this class is needed since the surface morphology consists of pyramids extending from the surface, and these features are easily crushed. The surface is still quite black, however, even if some surface damage occurs. The surface morphology works well for space applications as it does not support electrical potentials higher than 200 V, is not affected by temperatures as high as 450°C, by hard vacuum, or by ultraviolet radiation. It also has very low outgassing rates and will not delaminate even under severe environmental conditions.<sup>144</sup> It passes NASA SP-R-0022A specifications for outgassing.

The surface is also highly resistant to chemical attack by atomic oxygen prevalent in low earth orbit.<sup>64</sup> BRDF measurements of Martin Black show its lambertian character at 0.6328 and 10.6  $\mu\text{m}$ . The reflectance spectrum shows significant reflectances at about 2.5 and 5  $\mu\text{m}$ ; at other wavelengths, the reflectance is low. The optical data are given in Figs. 36, 51, and 52.

**Enhanced Martin Black** Enhanced Martin Black is similar in its properties to Martin Black, but was created to provide an even more durable surface for long exposure to atomic oxygen in low earth orbit. Experiments aboard the space shuttle confirm this superiority in the shuttle orbit environment.<sup>64</sup> The



**FIGURE 51** Visible ( $0.6328 \mu\text{m}$ ) BRDF of Martin Black at  $5^\circ$  angle of incidence. (From Pompea *et al.*<sup>4</sup>)



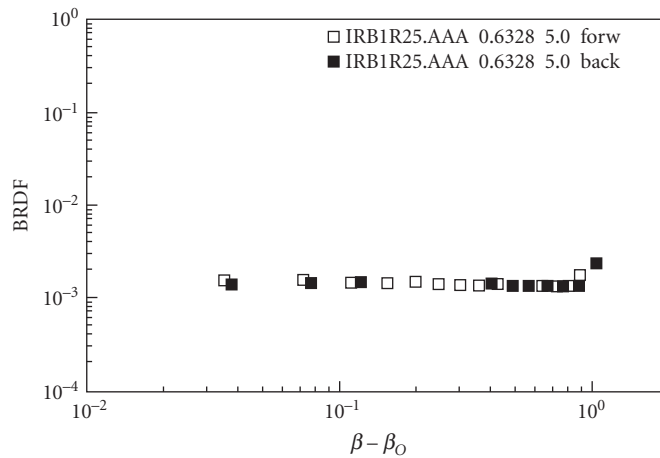
**FIGURE 52** Infrared ( $10.6 \mu\text{m}$ ) BRDF of Martin Black at  $5^\circ$  angle of incidence. (From Pompea *et al.*<sup>4</sup>)

process refinements also reduced the near- and middle-infrared reflectances from about 40 percent at  $2.3 \mu\text{m}$  to about 25 percent and from about 15 percent at  $5.5 \mu\text{m}$  to about 3.5 percent, while maintaining an absorption of about 99.6 percent in the visible region.

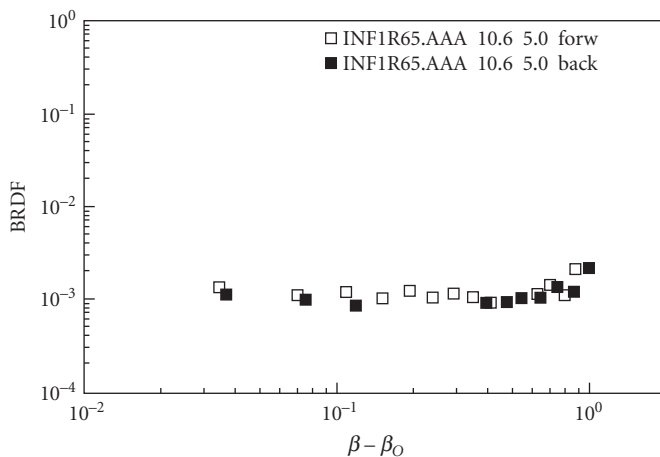
**Posttreated Martin Black** Another variation of the Martin Black surface is designed for near-infrared applications. Posttreated Martin Black uses hydrogen fluoride to further reduce the near-infrared reflectance peak and eliminate the middle-infrared reflectance peak of Martin Black. The area under the  $2.3\text{-}\mu\text{m}$  peak of Martin Black has been reduced by about two-thirds and the  $5.8\text{-}\mu\text{m}$  peak of Martin Black has been eliminated.



**Infrablack** Infrablack is another anodized surface from Martin Marietta, which relies upon a very rough substrate to produce a diffusing and absorbing surface for wavelengths up to  $750\ \mu\text{m}$ .<sup>138,145</sup> It was developed for the next generation of far-infrared NASA telescopes. It has also been used in experiments to measure the Stefan-Boltzmann constant where a “blackbody” surface with very high emissivity was needed. This type of surface can also be used in space radiators where high emissivity is beneficial. Like other anodized surfaces in this class, the Infrablack surface is fragile and care in handling is needed to avoid crushing the surface structure. As with Martin Black, even a mistreated or crushed surface will still be significantly more light absorbing than most other black surfaces. Infrablack can be tuned for maximum absorption between 100 and  $500\ \mu\text{m}$ . The BRDF in the visible and infrared for Infrablack is similar to Martin Black and Enhanced Martin Black; all exhibit relatively lambertian behavior in the visible at near-normal angles of incidence (Figs. 53 and 54).



**FIGURE 53** Visible ( $0.6328\ \mu\text{m}$ ) BRDF of Infrablack at  $5^\circ$  angle of incidence. (From Pompea et al.<sup>4</sup>)



**FIGURE 54** Infrared ( $10.6\ \mu\text{m}$ ) BRDF of Infrablack at  $5^\circ$  angle of incidence. (From Pompea et al.<sup>4</sup>)

**DEEP SPACE BLACK** DEEP SPACE BLACK (N-Science/Advanced Surface Technologies, Arvada, Colorado) shares many if not most characteristics of Martin Optical Black, a similar specialized anodization process. Like Martin Black it is extremely absorptive over a wide range of wavelengths from ultraviolet to the infrared and is best used on 6061 aluminum. The surface has good mechanical stability. The surface can be fine tuned for better performance in the near-infrared (1 to 5  $\mu\text{m}$ ) and for maximal durability in the low-earth orbit space environment. The total hemispherical reflectance in the 0.4- to 0.7- $\mu\text{m}$  range is 0.37 and 0.78 percent in the 0.4- to 1.0- $\mu\text{m}$  range. Like Martin Black, the surface does not support an electrical potential greater than 200 V and is robust under vibration and cryogenic cooling. When cryogenically cooled the surface has an emissivity in the far-infrared region (7 to 120  $\mu\text{m}$ ) of 0.985 or better.

This surface is used in controlling stray light or as black surface with high emissivity in a variety of optical systems such as detector cold shields and assemblies, detector calibration sources and blackbody cavities, thermal control and radiator surfaces, and spacecraft applications such as star trackers and cameras. DEEP SPACE BLACK is available in three variations:

DEEP SPACE BLACK-VIS: DSB-VIS is optimized for performance in the visible wavelength regime.

DEEP SPACE BLACK-Full Spectrum Basic: DSB-FSB is optimized to provide best performance over the largest wavelength regime possible. DEEP SPACE BLACK-Full Spectrum Enhanced: DSB-FSE is a special variant of DSB-FSB that has a more robust finish with the same outstanding optical characteristics of the FSB. DSB-FSE provides a somewhat improved optical performance in the near- and middle-IR. The performance in the visible region of the spectrum is maintained. This product is more suited to spacecraft applications, including those applications concerned with LEO environments.

**Tiodize V-E17 Surface** The Tiodize process is an electrolytic-conversion hard coating of titanium using an all-alkaline, room-temperature bath. It produces an antigall coating with good optical properties. The process can be used on all forms of titanium and its alloys and has been used in a wide variety of space vehicles and aircraft. The Ultra V-E17 coating is a black organic coating which changes the absorptivity and emissivity of titanium (0.62 and 0.89, respectively) to 0.89 and 0.91, respectively. The emittances were determined from a 25-point integration between 4.8 and 26.2  $\mu\text{m}$ . The absorptance was determined by a 19-point integration between 0.32 and 2.1  $\mu\text{m}$ . The surface has a total mass loss (TML) of 0.91 percent and no detectable volatile condensable material (VCM) in tests run at Ford Aerospace.<sup>146</sup> Its interaction with atomic oxygen is unknown.

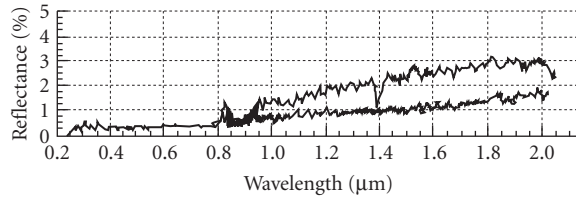
**TRU-Color Diffuse Black** An electrolytic coloring process from Reynolds Aluminum.

**Hughes Airborne Optical Adjunct Coating** A cleanable specular black for use at 1 to 10  $\mu\text{m}$ .

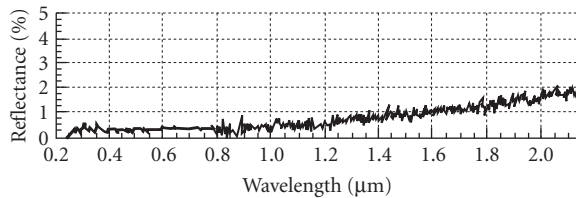
## Etching of Electroless Nickel

The etching of electroless nickel provides a black coating useful for many applications. Some reference data on several electroless nickel processes are presented in Table 4. Kodama et al.<sup>147</sup> developed optical absorbing black films of etched nickel-phosphorus alloy deposited on substrates using an electroless plating process. Results of varying the plating and etching bath components and conditions were studied. They produced an optical absorber with a spectral reflectance of about 0.1 to 0.2 percent in the wavelength range of 488 to 1550 nm. The absorber showed substantial immunity to degradation in two accelerated-aging environments: 2000 hours in a dry-heat environment at 100°C, and 2000 hours in a damp-heat environment at 85°C and 85 percent relative humidity.

**NBS Black** This is a blackened electroless nickel surface developed for use as a solar collector at the National Bureau of Standards (now NIST) in Gaithersburg, MD.<sup>75,76,148</sup> It consists of an electroless nickel-phosphorous coating that can be plated onto a wide variety of substrates such as metals, glass, ceramics, and plastics. This coating is subsequently etched using nitric acid, creating conically shaped holes into the surface, which act as light traps.



**FIGURE 55** Total integrated scatter of NBS Black. The substrates are magnesium AZ31B-F (upper curve) and magnesium ZK60A-T5. Substrate is silica sandblasted.  $\alpha = 0.978$ .  $\epsilon = 0.697$ . (From Geikas.<sup>65</sup>)



**FIGURE 56** Diffuse scatter of NBS Black. The substrates are magnesium AZ31B-F and magnesium ZK60A-T5. The plots are overlaid and are virtually identical. Substrate is silica sandblasted.  $\alpha = 0.978$ .  $\epsilon = 0.697$ . (From Geikas.<sup>65</sup>)

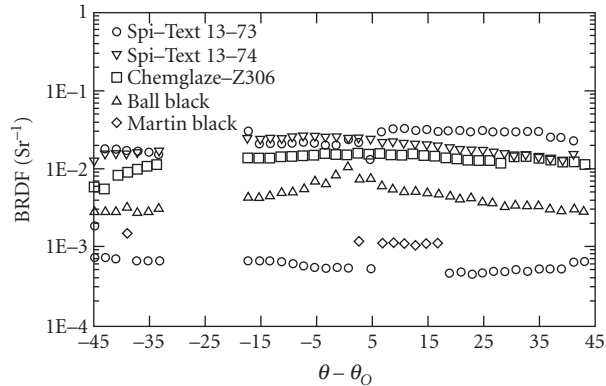
The specular reflectance is less than 1 percent over the range of 0.32 to 2.4  $\mu\text{m}$ , making it an extremely black coating (Figs. 55 and 56). As this surface finish was developed for solar collectors, the surface has a high value for absorptivity (0.978), but a low value for room-temperature emissivity (about 0.5). The surface is moderately durable as the surface's relief consists of conical holes into the surface. The NBS Black process has been modified resulting in the next surface, which has greater infrared absorption.

**Ball Black** Ball Black is an optical black surface produced with modifications to the techniques just described—the selective etching on an electroless nickel surface to produce a multiplicity of conical light traps in the surface.<sup>29,65</sup> The surface appears intensely black to the eye. The surface, however, is still an unaltered nickel-phosphorous deposit with the same chemical properties as the unetched surface, which was shiny. Ball Black can be plated on aluminum, beryllium, copper, stainless steel, invar, polycarbonate and ABS plastics, titanium, and some magnesium alloys. Since this process involves only deposition and etching of a metallic material, problems with outgassing or volatilization of the surface in a vacuum are minimal.

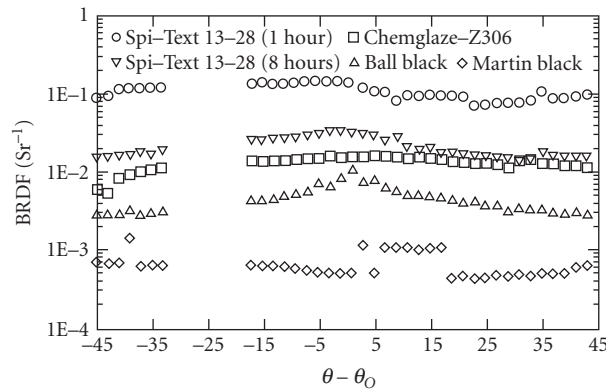
The surface is able to withstand rapid changes in temperature, with immersion into boiling water after being at liquid nitrogen temperature. The surface is sensitive to handling, though less so than surfaces like Martin Black. Small blemishes in the surface can be restored by re-etching without replating. The solar absorptivity can be made to vary between 0.71 and 0.995 and its room-temperature emissivity can be tailored to values between 0.35 and 0.94 by changes in the etching parameters. The directional reflectance increases by less than a factor of two from 1.5 to 12  $\mu\text{m}$ . It has a BRDF of about  $6 \times 10^{-2}$  at normal incidence at 0.6328  $\mu\text{m}$ . See Figs. 57 and 58 for optical data.

## Plasma-Sprayed Surfaces

**Boron Black** Martin Marietta Boron Black is a surface that is black in the visible (solar absorptivity between 0.89 and 0.97, and emissivity of at least 0.86) and black in the infrared<sup>149</sup> (Fig. 59). Boron



**FIGURE 57** BRDF measurements at 0.6328 μm of textured metal surfaces from Spire Corporation and Chemglaze Z306 paint, Ball Black electroless nickel coating, and Martin Black anodized coating. (From Lompadó et al.<sup>29</sup>)

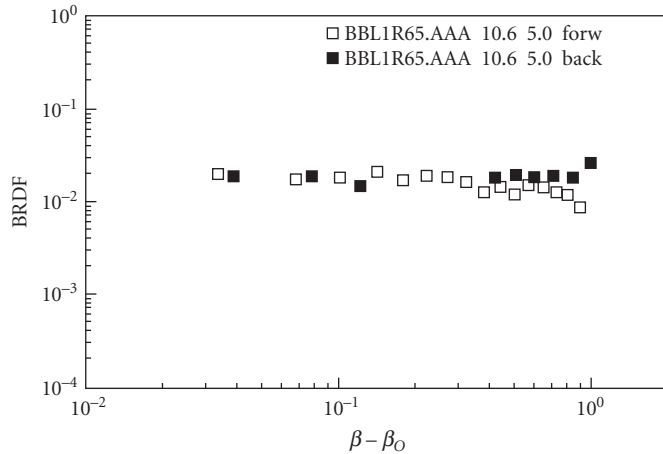


**FIGURE 58** BRDF measurements at 0.6328 μm of two textured metal surfaces from Spire Corporation and Chemglaze Z306 paint, Ball Black electroless nickel coating, and Martin Black anodized coating. (From Lompadó et al.<sup>29</sup>)

Black is a plasma-sprayed surface and can probably be applied to most metallic substrates. It has been applied to molybdenum, nickel, and titanium substrates. It offers a low-atomic-number surface with good optical properties and the ease of a plasma-spray deposition. The infrared BRDFs show a profile characteristic of a surface with lambertian profiles at near-normal angles of incidence.

**Boron Carbide** This is a Martin Marietta proprietary process. The boron carbide surface is applied to a titanium substrate. A 10- to 15-μm layer of B<sub>4</sub>C is applied in a proprietary plasma-spraying process. BRDF measurements at 30° angle of incidence at two wavelengths illustrate that this surface is more lambertian in the visible.

**Beryllium Surfaces** Porous surfaces or those with steep-walled features which can trap radiation have been developed using plasma-sprayed beryllium and sputter-deposited beryllium by workers at Oak Ridge<sup>82,150,151</sup> and at Spire Corp.<sup>152</sup> who are developing baffles that can operate in severe environments.

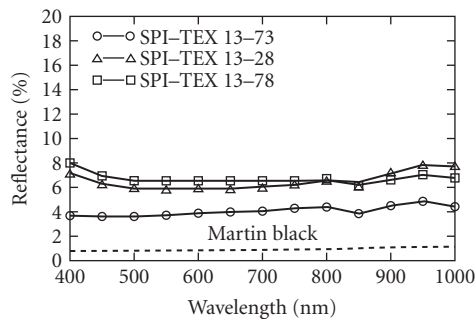


**FIGURE 59** Infrared ( $10.6 \mu\text{m}$ ) BRDF of Boron Black Black at  $5^\circ$  angle of incidence. (From Pompea et al.<sup>4</sup>)

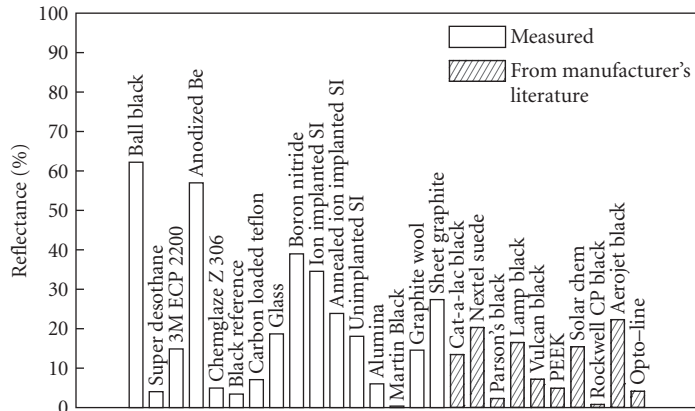
Plasma-sprayed beryllium samples appear visually rough with a matte gray finish. The specular reflectance is approximately constant at about 1.6 percent from 2 to  $50 \mu\text{m}$ , while the BRDF is lambertian in character at near-normal angles of incidence with a value of about  $5 \times 10^{-2} \text{ sr}^{-1}$ , equivalent to a total hemispherical reflectance of about 15 percent.

Beryllium surfaces with varying thicknesses and columnar grain sizes can also be created by low-temperature magnetron sputtering. The surfaces can then be chemically etched to enhance their absorptive properties. These surfaces exhibit less than 2 percent specular reflectance at near-infrared wavelengths. Very thick surfaces ( $350 \mu\text{m}$ ) exhibit specular reflectances of less than 0.5 percent up to  $50 \mu\text{m}$  wavelength.

A sputtered coating of Be on a Be surface can be made more absorptive through exposure to an oxygen plasma to form a layer of BeO on the surface of the coating.<sup>29</sup> Optical data are presented in Figs. 57, 58, 60, and 61.



**FIGURE 60** Total hemispherical reflectance in the visible bandpass for textured baffle materials from Spire Corp. The 13-73 surface is a textured aluminum surface. (From Spire.<sup>81</sup>)



**FIGURE 61** Total hemispherical reflectance data for baffle materials at 10.6  $\mu\text{m}$ . The shaded measurements are from the manufacturer's literature and have not been independently verified. (From Johnson.<sup>153</sup>)

## Ion Beam-Sputtered Surfaces

Ion beam-sputtering processes can roughen surfaces of a large variety of compositions. An excellent review is by Banks in Cuomo et al.<sup>77</sup> (see also Ref. 78). A variety of sputtering processes can create rough features of various geometries that decrease specular reflections and create a black-appearing surface from a light-appearing substrate. Since the roughness is integral to the surface, these surfaces often have desirable environmental resistance to atomic oxygen. However, these surfaces also have tremendous surface area for trapping of contaminants and thus a potential for large outgassing rates if preventative steps are not taken. These surfaces are expensive to make in large areas, though they are becoming less expensive as coating facilities are built to harness this technology. They do have tremendous potential as diffuse baffle surfaces and as high-emittance surfaces for high-temperature space radiators.<sup>154,155</sup> They are also cleanable and very durable.

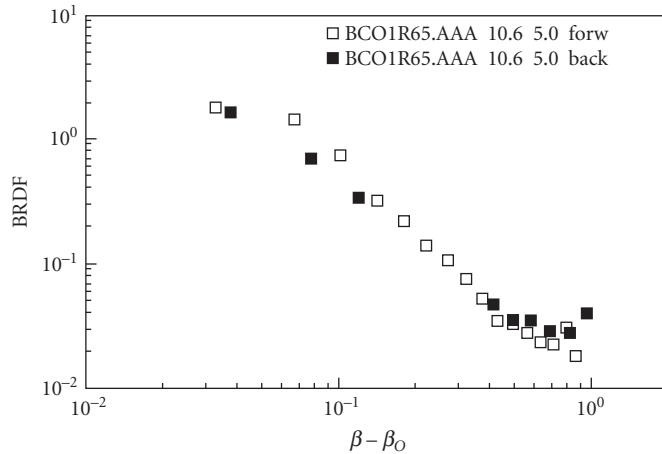
Lompado et al.<sup>29</sup> and Blatchley et al.<sup>83</sup> describe several textured aluminum surfaces and give plots of their total hemispherical reflectance in the 0.4- to 1.0- $\mu\text{m}$  range, as well as BRDF plots at 0.6328 and 10.6  $\mu\text{m}$  (Fig. 60).

## Electrodeposited Surfaces

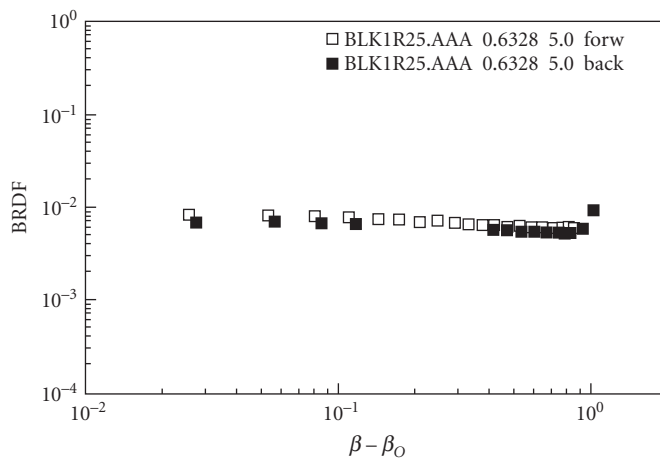
Refer to Table 4 for further reference data on these surfaces.

**Black Cobalt** Black cobalt is a patented surface developed at Martin Marietta<sup>156</sup> which appears black in the visible, with a solar absorptivity of at least 0.96 and emissivity of at least 0.6. It is applied by an electrodeposition process to a substrate of nickel, molybdenum, or titanium; other substrates are also expected to work. It can be used at higher temperatures than anodized aluminum surfaces such as Martin Black. It is stable against loss of absorptivity at temperatures greater than 450°C for prolonged periods. The surface is not a lambertian surface at 10.6  $\mu\text{m}$  (Fig. 62).

**Black Chrome** A black chrome surface developed for aerospace use<sup>157</sup> is black in the visible and is created by an electroplating process on a conducting substrate. Many metallic substrates can be used and samples on molybdenum, nickel, and titanium have been made. The preferred substrates are titanium and molybdenum. The coating process involves electrodeposition using chromium and chromium oxides. The visible BRDF is flat (Fig. 63), while the infrared profile shows the surface to



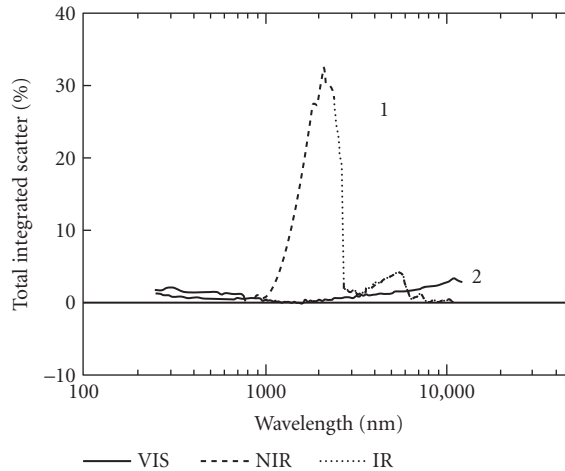
**FIGURE 62** Infrared (10.6  $\mu\text{m}$ ) BRDF of Black Cobalt at 5° angle of incidence. (From Pompea et al.<sup>4</sup>)



**FIGURE 63** Visible (0.6328  $\mu\text{m}$ ) BRDF of Black Chrome at 5° angle of incidence. (From Pompea et al.<sup>4</sup>)

be largely specular in its scattering profile. The solar absorptivity is at least 0.95 and the emissivity can be tailored in the range of 0.4 to 0.8. The surface has excellent adhesion to the substrate.

**Orlando Black Optical Coating** A dendritic surface is produced by the electrodeposition of copper in a proprietary copper-plating formulation (Janeczko<sup>158</sup>). The dendritic structure is then oxidized to form smaller structures superimposed on the larger ones. The surface has excellent broadband absorption properties from 0.4 to 14  $\mu\text{m}$  and good absorptance at nonnormal angles of incidence (Fig. 64). It may be suitable for use at shorter wavelengths. The surface is usable in vacuum environments as well as a thermal reference in FLIR systems. A wide variety of materials can be coated including ABS plastic, nylon, Ultem, Noryl, fiberglass-reinforced epoxy, glass, stainless steel, copper, brass, nickel, aluminum, gold, and beryllium oxide. Dimensional allowances must be made for the thickness of the finish (approximately 0.001 in).



**FIGURE 64** Total integrated scatter measurement of (1) and (2) Orlando Black commercially available anodized aluminum. (From Janeczko.<sup>158</sup>)

## Other Specialty Surfaces

Refer to Table 4 for further data on some of these surfaces.

**Acktar Black Coatings** (Acktar Ltd., Kiryat-Gat, Israel) Aktar makes a number of black coatings including Nano Black, Magic Black, Vacuum Black, Fractal Black, Ultra Black, and Metal Velvet. These inorganic coatings each have a wide range of working temperatures, very low outgassing (CVCN) in the 0.001 percent range and RML in the 0.167 percent range. Additionally the coatings have excellent adhesion to aluminum, copper, stainless steel, invar, kovar, glass, ceramics, polyimide, nickel, magnesium, titanium and other metals. There are options to make the coatings electrically conductive or nonconductive. The company also makes high emissivity foils.

**Carbon Nanotubes and Nanostructured Materials** Carbon nanotube arrays can also be used to create ultrablack surfaces. These surfaces are not yet practical for many applications but may have utility in specialized areas. For example, Yang et al.<sup>159</sup> have demonstrated that low-density vertically aligned carbon nanotube arrays can be engineered to have an extremely low index of refraction. The nanoscale surface roughness of the arrays contributes to an ultralow diffuse reflectance of  $1 \times 10^{-7}$ ; an order-of-magnitude lower compared to commercial low-reflectance standard carbon. The nanotube arrays can have an integrated total reflectance of 0.045 percent making it among the darkest materials ever fabricated.

Vorobyev and Guo<sup>160</sup> and Paivasaari et al.<sup>161</sup> have also showed that laser ablation and altering of metallic surfaces can lead to greatly enhance optical absorptance.

Nanostructuring alone can enhance the absorptance by a factor of about three or more. The physical mechanism of the increased absorption is due to several effects including nanostructural, microstructural, and macrostructural surface modifications. The value of femtosecond laser ablation techniques using high fluences with a large number of applied pulses in reducing surface reflectivity may be applicable for a wide variety of metallic surfaces. Currently the process is time consuming for large area surfaces.

**DURACON** (American IMEX Corporation, Monroe, CT) DURACON is another high emissivity (>0.98 over the 0.55- to 1.8- $\mu\text{m}$  range; >0.95 over the 2- to 20- $\mu\text{m}$  wavelength range) durable black coating used in applications that cover a variety of wavelengths, especially the middle-infrared. It has



good thermal diffusivity and the interesting property that its conductivity can be tailored from low resistivity (less than  $700 \Omega \text{ cm}$ ) to nearly an insulating surface. Thus, it can be used in environments where electrostatic discharge may be damaging to dielectric and insulating surfaces. It has good adherence and can be used on ceramic, glass, composite, plastic, and metal surfaces. It is durable to handling, unlike some anodized surfaces with surface structures that can be damaged by abrasion or direct compression. It also has very good ability to withstand wind shear at high Mach numbers and to withstand thermal cycling to  $1000^\circ\text{F}$ .

The surface can be applied by brush on, spray, or dip coating and any damaged areas can be repaired using a brushed on application of a fresh layer. The product is reported to be ready for normal regular use in 2 hours after this repair.

**Electrically Conductive Black Paint** Birnbaum et al.<sup>51</sup> developed an electrically conductive, flat black paint for space use in places such as Jupiter's radiation belts where spacecraft charging effects can be important. Its small resistivity prevents the buildup of charge on the surface. It has a visual reflectance of less than 5 percent and other desirable optical properties.

**Epner laser black** (Brooklyn, New York) This makes a well-known coating used in a variety of application. Laser Black is a multilayer metallic oxide that has a microdendritic structure susceptible to crushing. This inorganic coating does not outgas and when vibrated ultrasonically in acetone shows no flaking or chipping. It has good durability at cryogenic temperatures and can be applied to any metallic substrate and most plastics. It requires a deposition of copper approximately 10 to 12  $\mu\text{m}$  thick. Laser Black is used in cold shields for micro-bolometers and in baffles.

**Ebanol C** This specialty cupric oxide coating can be applied per MIL-C-14550 undercoat and MIL-F-495 processes: immersion in a zincate bath followed by a high cyanide, low copper bath, and copper strike and dip in an Ebanol C solution.<sup>9</sup>

**High-Resistivity Coatings** Strimer et al.<sup>162</sup> describe a number of black surfaces with high electrical resistivity for visible and infrared applications.

**Sputtered and CVD Surfaces** Carbon, quartz, and silicon surfaces have been modified by sputtering or by chemical vapor deposition<sup>163-165</sup> to create surfaces that are black over the wavelength range of 1 to 15  $\mu\text{m}$ . The textured surfaces are produced by sputtering with a low-energy (e.g., 500 eV) broadbeam ion source while adding impurities to the surface. The results from sputtering with this seeding process are structures in the form of cones, pyramids, and ridges. The exact nature of the surfaces created depends on the substrate temperature, ion and impurity fluxes, and the impurity species. The reflectivity of one modified silicon surface was below 1 percent throughout 1- to 25- $\mu\text{m}$  wavelength range.

**Silicon Carbide** A silicon carbide surface for high-temperature applications was developed at Martin Marietta for application to a carbon-carbon substrate. It is applied to a hot substrate by a chemical vapor deposition process. The visible BRDF is flat, while the infrared profiles show the surface's specular nature at the longer wavelength.<sup>4</sup>

**IBM Black (Tungsten Hexafluoride)** This is a surface being produced at Martin Marietta, Orlando, using a process licensed from IBM. Any material that can tolerate  $400^\circ\text{C}$  can be used as a substrate for this process which involves vapor deposition of tungsten. The surface has dendritic structures that form light-absorbing traps. The surface looks like a collection of obelisks, does not outgas, and is rugged to the touch. Optical properties and an SEM photograph of the surface are given by Willey et al.<sup>42</sup> The surface is very black in the 1- to 2- $\mu\text{m}$  wavelength range.

**ZO-MOD BLACK** ZO-MOD BLACK (ZYP Coatings, Oak Ridge, Tenn.) is a high-emissivity coating applied like paint to ceramic porous and fibrous structures. On heating, a hard abrasion- and chemical-resistant, calcia-stabilized zirconium oxide coating is formed. The coating has high emissivity. The coating has been used inside of ceramic furnaces.

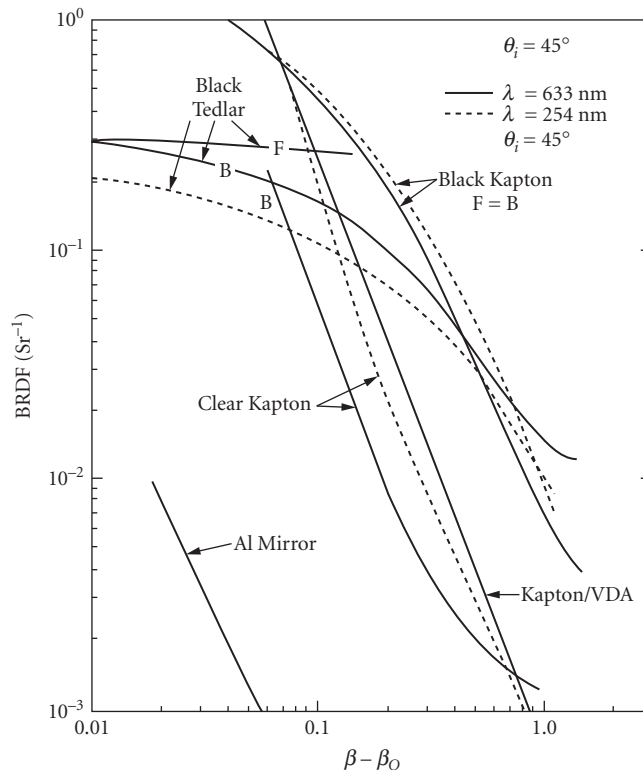
**Gold Black** Gold blacks are fragile surfaces made by evaporating gold in a low-pressure atmosphere of helium or nitrogen. The surface has good visible light absorption. The preparation and optical properties of gold blacks are given by Harris and McGinnies,<sup>166</sup> Blevin and Brown,<sup>167</sup> and Zaeschmar and Nedoluha.<sup>168</sup>

**Flame-Sprayed Aluminum** Flame-sprayed aluminum is a very durable and very rough surface that has uses as an infrared diffuse reflectance standard. The parameters of the flame-spray process must be tightly controlled to create a similar surface each time.

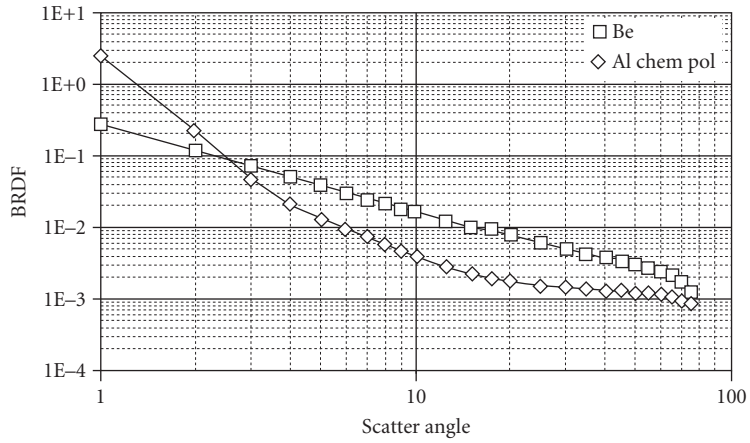
**Black Glass** Black glass is available from Schott Glass Technologies, Duryea, Pa., in a glass called UG1, which is an ionically colored glass. Star Instruments, Flagstaff, Ariz., produces a glossy black glass called LOX8. It is a low-expansion copper glass with a coefficient of expansion of about 30 times lower than Pyrex.

**Black Kapton** The optical properties of Black Kapton are given in Fig. 65.

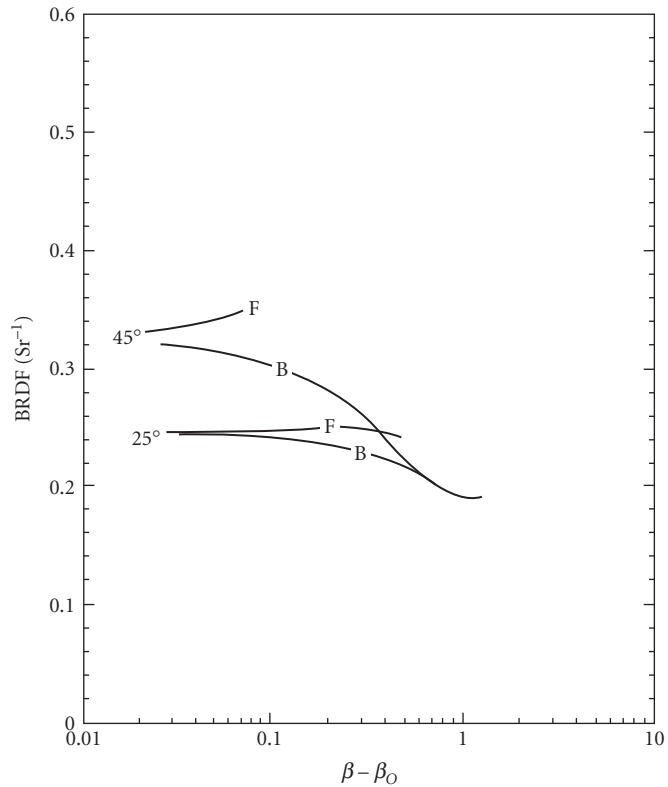
**Other Surfaces** Some other data is given for specular metallic anodized baffle surfaces (Fig. 66). This kind of basic treatment is adequate for some applications. The BRDF of Beta cloth is given in Fig. 67. Figure 68 shows the potential of various structured carbon surfaces to be highly absorbing over a wide range of angles. These kind of surfaces have great potential for the future.



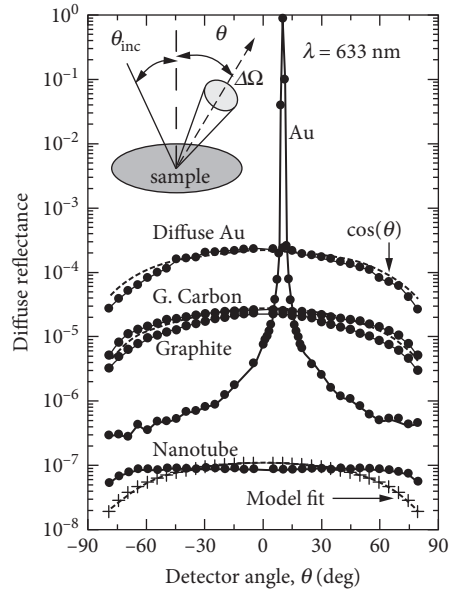
**FIGURE 65** BRDFs of black Kapton and black Tedlar films. (From Viehmann and Predmore.<sup>35</sup>)



**FIGURE 66** BRDF of specular baffle materials using Be and Al substrates that are polished and anodized. The measurements were made at 0.5145  $\mu\text{m}$ . (From Schaub et al.<sup>20</sup>)



**FIGURE 67** BRDF profiles of beta-cloth. Wavelength of 633 nm. (From Viehmann and Predmore.<sup>35</sup>)



**FIGURE 68** Diffuse reflectance of carbon nanotube samples compared to other carbon-based materials. (From Yang *et al.*<sup>159</sup>)

## 6.9 CONCLUSIONS

Black surfaces are used as optical elements in a variety of ways. There is a great choice of surfaces available, but the selection of the appropriate surface is often problematical. The consequences of choosing the wrong surface are often quite severe.

For the selection process to be most effective, it must be done as early as possible. While the optical data on surfaces is relatively extensive, the data are often inconsistent or are not available for the particular wavelength of interest. The creation of large databases of optical and material properties is a great aid to the optical designer and materials consultant. Of great concern for space materials is the lack of very long term environmental test data. The synergistic effect of a number of degrading influences (e.g., solar ultraviolet, charging effects, atomic oxygen) is unknown for many interesting and potentially effective space materials. The use of specialized surfaces that can be tailored for very specific applications is an emerging trend and is likely to continue.

When black surfaces are used effectively in optical systems, the performance of the system can be greatly enhanced. However, when other approaches to stray light control are not implemented, even the “blackest” possible surfaces cannot establish the desired system performance. This cruel fact is a persuasive basis for an integration of black surface selection into the general stray light design studies, which today are nearly mandatory for the design of high-performance optical devices.

## 6.10 ACKNOWLEDGMENTS

The National Optical Astronomy Observatory is operated by the Association of Universities for Research in Astronomy (AURA), Inc. under cooperative agreement with the National Science Foundation. Special thanks to J. Heaney (NASA Goddard Space Flight Center), S. H. C. P. McCall (Stellar Optics

Laboratory, Inc.), and S. Smith (NASA Ames Research Center) for the use of their unpublished data. Thanks to R. Bonaminio (Lord Corp.), C. Bowers (Hughes Aircraft Co.), B. Banks (NASA Lewis Research Center), R. Harada (IIT Research Institute), D. Janeczko (Martin Marietta Corp.), A. Olson (Ball Aerospace), R. Seals (Oak Ridge National Laboratory), D. Shepard (Lockheed Martin), and S. Smith (NASA Ames Research Center) for providing data and photographs. Thanks also to J. Martin, L. Bergquist, F. Bartko, R. Culver, and S. Russak for support in the early stages of this work, and to D. Shepard, S. McCall, S. Smith, and W. Wolfe for helpful suggestions on this manuscript.

## 6.11 REFERENCES

1. W. L. Wolfe, "Scattered Thoughts on Baffling Problems," *Proc. SPIE: Radiation Scattering in Optical Systems*, SPIE, Bellingham, Wash., **257**:2 (1980).
2. R. P. Breault, "Stray Light Technology Overview of the 1980 Decade (And a Peek into the Future)," *Proc. SPIE: Stray Radiation in Optical Systems*, R. P. Breault (ed.), SPIE, Bellingham, Wash., **1331**:2–11 (1990).
3. D. W. Bergener, S. M. Pompea, D. F. Shepard, and R. P. Breault, "Stray Light Performance of SIRTf: A Comparison," *Proc. SPIE: Stray Radiation IV*, R. P. Breault (ed.), SPIE, Bellingham, Wash., **511**:65–72 (1984).
4. S. M. Pompea, D. F. Shepard, and S. Anderson, "BRDF Measurements at 6328 Angstroms and 10.6 Micrometers of Optical Black Surfaces for Space Telescopes," *Proc. SPIE: Stray Light and Contamination in Optical Systems*, R. P. Breault (ed.), SPIE, Bellingham, Wash., **967**:236–248 (1988).
5. S. M. Pompea and S. H. C. P. McCall, "Outline of Selection Process for Black Baffle Surfaces in Optical Systems," *Proc. SPIE: Stray Radiation in Optical Systems II*, R. P. Breault (ed.), SPIE, Bellingham, Wash., **1753** (1992a).
6. S. M. Pompea, J. E. Mentzell, and W. A. Siegmund, "A Stray Light Analysis of the 2.5 Meter Telescope for the Sloan Digital Sky Survey," *Proc. SPIE: Stray Radiation in Optical Systems II*, R. P. Breault (ed.), SPIE, Bellingham, Wash., **1753** (1992b).
7. S. M. Pompea, R. Pfisterer, and J. Morgan, "A Stray Light Analysis of the Apache Point Observatory 3.5-Meter Telescope System," *Proc. SPIE*, SPIE, Bellingham, Wash., **4842**:128–138, (2003).
8. S. M. Pompea, "The Management of Stray Radiation Issues in Space Optical Systems," *Space Science Reviews* **74**:181–193 (1995).
9. M. J. Persky, "Review of Black Surfaces for Space-Borne Infrared Systems," *Rev. Sci. Instrum.* **70**:2193–2217 (1999).
10. John L. Miller, "Multispectral Infrared BRDF Forward-Scatter Measurements of Common Black Surface Preparations and Materials—or "how black is black in the IR?" *Proc. SPIE*, **5405**:25–35 (2004).
11. M. J. Persky and M. Szczesniak, "Infrared, Spectral, Directional-Hemispherical Reflectance of Fused Silica, Teflon Polytetrafluoroethylene Polymer, Chrome Oxide Ceramic Particle Surface, Pyromark 2500 Paint, Krylon 1602 Paint, and Duraflect Coating," *Appl. Opt.* **47**:1389–1396 (2008).
12. R. E. Hahn and B. O. Seraphin, "Spectrally Selective Surfaces for Photothermal Solar Energy Conversion," in *Physics of Thin Films*, vol. 10, Academic Press, Orlando, Fla., 1978.
13. C. G. Granqvist, *Spectrally Selective Surfaces for Heating and Cooling Applications*, vol. TT 1, SPIE Optical Engineering Text, Bellingham, Wash., 1989.
14. K. M. Yousif, B. E. Smith, and C. Jaynes, "Investigation of Microstructure of Molybdenum-Copper Black Electrodeposited Coatings with Reference to Solar Selectivity" *J. Mater. Sci.* **31**:185–191 (1996).
15. D. B. Betts, F. J. J. Clarke, L. J. Cox, and J. A. Larkin, "Infrared Reflection Properties of Five Types of Black Coating for Radiometric Detectors," *J. Phys. E: (London) Sci. Instrum.* **18**:689–696 (August, 1985).
16. W. L. Wolfe, "Optical Materials," Chap. 7, in *The Infrared Handbook*, W. L. Wolfe and G. J. Zissis (eds.), ERIM, Ann Arbor, Michigan, 1978.
17. S. H. C. P. McCall, S. M. Pompea, R. P. Breault, and N. L. Regens, "Reviews of Properties of Black Surfaces for Ground and Space-Based Optical Systems," *Proc. SPIE: Stray Radiation II*, R. P. Breault (ed.), SPIE, Bellingham, Wash., **1753** (1992).
18. S. H. C. P. McCall, "Optical Properties (UV and Visible) of Black Baffle Materials and Processes for Use in Space," *Proprietary Report from Stellar Optics Laboratories* (78 Normark Drive, Thornhill, Ontario, Canada, L3T 3R1) to *Space Astrophysics Laboratory*, ISTS, Ontario, Canada, June 17, 1992.

19. S. M. Smith and R. V. Howitt, "Survey of Materials for an Infrared-Opaque Coating," *Proc. SPIE: Infrared, Adaptive, and Synthetic Aperture Optical Systems*, SPIE, Bellingham, Wash., **643**:53–62 (1986).
20. C. Schaub, M. Davis, G. Inouye, and P. Schaller, "Visible Scatter Measurements of Various Materials," *Proc. SPIE: Stray Radiation in Optical Systems*, R. P. Breault (ed.), SPIE, Bellingham, Wash., **1331**:293–298 (1990).
21. K. A. Klicker, D. M. Fuhrman, D. R. Bjork, "A BSDF Database," *Proc. SPIE: Stray Radiation in Optical Systems*, R. P. Breault (ed.), SPIE, Bellingham, Wash., **1331**:270–279 (1990).
22. S. H. C. P. McCall, R. L. Sinclair, S. M. Pompea, and R. P. Breault, "Spectrally Selective Surfaces for Ground and Space-Based Instrumentation: Support for a Resource Base," *Proc. SPIE: Space Astronomical Telescopes and Instruments II*, P. Bely and J. B. Breckinridge (ed.), SPIE, Bellingham, Wash., **1945** (1993).
23. S. H. C. P. McCall, *Black Materials Database of Stellar Optics Laboratories*, 78 Normark Drive, Thornhill, Ontario, Canada, L3T 3R1, unpublished, 1992c.
24. Lord Chemical Products Division, Industrial Coatings Office, 845 Olive Avenue, Novato, CA 94945, 1992.
25. D. B. Griner, "BRDF Measurements of Stray Light Suppression Coatings for the Space Telescope," *Proc. SPIE*, SPIE, Bellingham, Wash., **183**:98 (1979).
26. R. Fernandez, R. G. Seasholtz, L. G. Oberle, and J. R. Kadambi, "Comparison of the Bidirectional Reflectance Distribution Function of Various Surfaces," *Proc. SPIE*, SPIE, Bellingham, Wash., **967**:292 (1988).
27. C. W. Brown and D. R. Smith, "High-Resolution Spectral Reflection Measurements on Selected Optical-Black Baffle Coatings in the 5–20 Micrometer Region," *Proc. SPIE: Stray Radiation in Optical Systems*, R. P. Breault (ed.), SPIE, Bellingham, Wash., **1331**:210–240 (1990).
28. A. J. Ames, "Z306 Black Paint Measurements," *Proc. SPIE: Stray Radiation in Optical Systems*, R. P. Breault (ed.), SPIE, Bellingham, Wash., **1331**:299–304 (1990).
29. A. Lompado, B. W. Murray, J. S. Wollam, and J. F. Meroth, "Characterization of Optical Baffle Materials," *Proc. SPIE: Scatter from Optical Components*, J. Stover (ed.), SPIE, Bellingham, Wash., **1165**:212–226 (1989).
30. J. A. Muscari and T. O'Donnell, "Mass Loss Parameters for Typical Shuttle Materials," *Proc. SPIE*, SPIE, Bellingham, Wash., **287**:20 (1981).
31. S. M. Pompea, D. E. Bergener, D. W. Shepard, S. Russak, and W. L. Wolfe, "Reflectance Measurements on an Improved Optical Black for Stray Light Rejection from 0.3 to 500 Micrometers," *J. Opt. Eng.* **23**:149–152 (1984).
32. S. M. Smith, "Far Infrared Reflectance Spectra of Optical Black Coatings," *Proc. SPIE: Scattering in Optical Materials*, S. Musikant (ed.) Optical Society of America, Washington, DC, **362**:57–59 (1982).
33. S. M. Smith, "Specular Reflectance of Optical-Black Coatings in the Far Infrared," *Appl. Opt.* **23**(14):2311–2326 (1984).
34. S. M. Smith, "Cryo-Mechanical Tests of Ames 24E2 IR-Black Coating," *Proc. SPIE: Stray Radiation in Optical Systems*, R. P. Breault (ed.), SPIE, Bellingham, Wash., **1331**:241–248 (1990).
35. W. Viehmann and R. E. Predmore, "Ultraviolet and visible BRDF Data on Spacecraft Thermal Control and Baffle Materials," *Proc. SPIE*, SPIE, Bellingham, Wash., **675**:67 (1986).
36. CAL, "Space Systems Process Procedure for the Preparation and Application of Chemglaze Z306 Black Paint for Space Applications," *Document PQ-CAL-SR-10333* from Canadian Astronautics Ltd., 1986.
37. M. M. Nordberg, C. Von Benken, and E. J. Johnson, "Reflectivity Changes in Optical Baffle Materials Following Pulsed Electron Bombardment," *Proc. SPIE*, SPIE, Bellingham, Wash., **1050**:185 (1989).
38. R. J. Noll, R. Harned, R. Breault, and R. Malugin, "Stray Radiation and Infrared Astronomical Satellite (IRAS) Telescope," *Proc. SPIE*, SPIE, Bellingham, Wash., **257**:119 (1980).
39. S. M. Smith, "Far Infrared (FIR) Optical Black Bidirectional Reflectance Distribution Function (BRDF)," *Proc. SPIE: Radiation Scattering in Optical Systems*, SPIE, Bellingham, Wash., **362**:161–168 (1980).
40. P. Jelinsky and S. Jelinsky, "Low Reflectance EUV Materials: A Comparative Study," *Appl. Opt.* **26**(4):613–615 (1987).
41. D. L. Stierwalt, "Infrared Absorption of Optical Blacks," *Opt. Eng.* **18**(2):147–151 (1979).
42. R. R. Willey, R. W. George, J. G. Ohmart, and J. W. Walvoord, "Total Reflectance Properties of Certain Black Coatings from 0.2 to 20 Micrometers," *Proc. SPIE: Generation, Measurement and Control of Stray Radiation III*, R. P. Breault (ed.), SPIE, Bellingham, Wash., **384**:19–26 (1983).
43. D. C. Evans and R. P. Breault, "APART/PADE Analytical Evaluation of the Diffuse Infrared Background Experiment for NASA's Cosmic Background Explorer," *Proc. SPIE: Stray Radiation IV*, R. P. Breault (ed.), SPIE, Bellingham, Wash., **511**:54–64 (1984).

44. T. Heslin, J. Heaney, and M. Harper, "The Effects of Particle Size on the Optical Properties and Surface Roughness of a Glass-Balloon-Filled Black Paint," *NASA Technical Note TND-7643*, Goddard Space Flight Center, Greenbelt, MD., May 1974.
45. D. C. Evans, "Principles of Stray Light Supp and Conceptual Application to the Design of the Diffuse Infrared Background Experiment for NASA's Cosmic Background Explorer," *Proc. SPIE*, SPIE, Bellingham, Wash., **384**:82 (1983).
46. S. M. Smith, "The Reflectance of Ames 24E, Infrablack, and Martin Black," *Proc. SPIE: Stray Radiation V*, R. P. Breault (ed.), SPIE, Bellingham, Wash., **967**:248–254 (1988).
47. S. M. Nee and H. E. Bennett, "Characterization of Optical Blacks by Infrared Ellipsometry and Reflectometry," *Proc. SPIE* **1331**:249 (1990).
48. Cardinal, product information and MSDSs on Velvathane and 6450-01 paints, El Monte, Calif., 1992.
49. J. R. Houck, "New Black Paint for Cryogenic Infrared Applications," *Proc. SPIE*, S. Musikant (ed.), SPIE, Bellingham, Wash., **362**:54–56 (1982).
50. S. M. Smith, "A Simple Antireflection Overcoat for Opaque Coatings in the Submillimeter Region," *Proc. SPIE: Stray Radiation V*, R. P. Breault (ed.), SPIE, Bellingham, Wash., **675**:55–60 (1986).
51. M. B. Birnbaum, E. C. Metzler, and E. L. Cleveland, "Electrically Conductive Black Optical Black Paint," *Proc. SPIE: Scattering in Optical Materials*, S. Musikant (ed.), SPIE, Bellingham, Wash., **362**:60–70 (1982).
52. E. C. Metzler, "Application of Temperature Control Paints," *JPL Doc. No. FS501424 D*, 21 March 1988.
53. R. P. Breault, "Stray Light Technology Overview in 1988," *Proc. SPIE*, SPIE, Bellingham, Wash., **967**:2 (1988).
54. IITRI, product information and MSDSs on paints MH-211, D111, and MH2200, from the Illinois Institute of Technology Research Institute, Chicago, Ill., 1992.
55. J. R. Grammar, L. J. Balin, M. D. Blue, and S. Perkowitz, "Absorbing Coatings for the Far Infrared," *Proc. SPIE: Radiation Scattering in Optical Systems*, G. Hunt (ed.) SPIE, Bellingham, Wash., **257**:192–195 (1980).
56. W. Driscoll, (ed.), and W. Vaughan (assoc. ed.), *Handbook of Optics*, McGraw-Hill, New York, 1978, pp. 7–112.
57. S. M. Smith, "Analysis of 12–700 Micrometer Reflectance Spectra of Three Optical Black Samples," *Proc. SPIE: Generation, Measurement, and Control of Stray Radiation III*, R. P. Breault (ed.), SPIE, Bellingham, Wash., **384**:32–36 (1983).
58. C. L. Wyman, D. B. Griner, G. H. Hunt, and G. B. Shelton, *Opt. Eng.* **14**(6):528 (1975).
59. R. P. Breault, "Specular Vane Cavities," *Proc. SPIE: Generation, Measurement, and Control of Stray Radiation III*, R. P. Breault (ed.), SPIE, Bellingham, Wash., **384**:90–97 (1983).
60. AKZO Coatings, Inc., product information and MSDSs on 443-3-17 and 443-3-8, Orange, Calif., 1992.
61. E. R. Freniere and D. L. Skelton, "Use of Specular Black Coatings in Well-Baffled Optical Systems," *Proc. SPIE: Stray Radiation V*, R. P. Breault (ed.), SPIE, Bellingham, Wash., **675**:126–132 (1986).
62. T. R. Gull, H. Hertzog, F. Osantowski, and A. R. Toft, "Low Orbit Effects on Optical Coatings and Materials as Noted on Early Shuttle Flights," *RAL Workshop on Advanced Technology Reflectors for Space Instrumentation*, M. Grande (ed.), SPIE, Bellingham, Wash., June 16–18, 1986.
63. Martin Marietta, product information from Martin Marietta, 1992.
64. S. M. Pompea, D. W. Bergener, D. F. Shepard, and K. S. Williams, "The Effects of Atomic Oxygen on Martin Black and Infrablack," *Proc. SPIE*, R. P. Breault (ed.), **511**:24–30 (1984).
65. G. Geikas, "Scattering Characteristics of Etched Electroless Nickel Coatings," *Proc. SPIE: Generation, Measurement, and Control of Stray Radiation III*, R. P. Breault (ed.), SPIE, Bellingham, Wash., **384**:10–18 (1983).
66. F. M. Cady, D. R. Cheever, K. A. Klicker, and J. C. Stover, "Comparison of Scatter Data from Various Beam Pumps," *Proc. SPIE*, SPIE, Bellingham, Wash., **818**:21 (1987).
67. F. O. Bartell, J. E. Hubbs, M. J. Nofziger, and W. L. Wolfe, *Appl. Opt.* **21**(17):3178 (1982).
68. L. D. Brooks, J. E. Hubbs, F. O. Bartell, and W. L. Wolfe, "Bidirectional Reflectance Distribution Function of the Infrared Astronomical Satellite Solar-Shield Material," *Appl. Opt.* **21**:2465 (1982).
69. R. P. Breault, "Specification of the Scattering Characteristics of Surfaces and Systems for Use in the Analysis of Stray Light," *Proc. SPIE*, SPIE, Bellingham, Wash., **181**:108 (1979).

70. P. J. Young, R. Noll, L. Andreozzi, and J. Hope, "Particle Contamination from Martin Optical Black," *Proc. SPIE*, SPIE, Bellingham, Wash., **257**:196 (1980).
71. D. F. Shepard, S. M. Pompea, and S. Anderson, "The Effect of Elevated Temperatures on the Scattering Properties of an Optical Black Surface at 0.6328 and 10.6 Micrometers," *Proc. SPIE: Stray Radiation V*, R. P. Breault (ed.), SPIE, Bellingham, Wash., **967**:286–291 (1988).
72. S. M. Smith, "Bidirectional Reflectance Distribution Function (BRDF) Measurements of Sunshield and Baffle Materials for the Infrared Astronomy Satellite (IRAS) Telescope," *Proc. SPIE: Modern Utilization of Infrared Technology VII*, SPIE, Bellingham, Wash., **304**:205–213 (1981).
73. B. Vitt, "Properties of Black Cobalt Coatings," *Proc. SPIE*, SPIE, Bellingham, Wash., **823**:218 (1987).
74. M. G. Hutchins, P. J. Wright, and P. D. Grebenik, "SnO<sub>2</sub>: Sb Dip Coated Films on Anodized Aluminium Selective Absorber Plates," *Proc. SPIE*, SPIE, Bellingham, Wash., **653**:188 (1986).
75. C. E. Johnson, "Unique Surface Morphology with Extremely High Light Absorption Capability," *Proc. Electro-less Nickel Conference*, No. 1, Cincinnati, Ohio, November 6–7, 1979.
76. C. E. Johnson, "Black Electroless Nickel Surface Morphologies with Extremely High Light Absorption Capacity," *Metal Finishing*, July, 1980.
77. J. J. Cuomo, S. M. Rossnagel, and H. R. Kaufman, *Handbook of Ion Beam Processing Technology: Principles, Deposition, Film Modification, and Synthesis*, Noyes Publications, Park Ridge, NJ, 1989. (See Chap. 17, Banks, B. A., "Topography Texturing Effects," 1989.)
78. B. A. Banks, "Ion Beam Applications Research—A 1981 Summary of Lewis Research Center Programs," *NASA Technical Memorandum 81721*, 1981.
79. M. J. Mirtich, S. K. Rutledge, N. Stevens, R. Olle, and J. Mellow, "Ion Beam Textured and Coated Surfaces Experiment (IBEX)," Presented at *LDEF First Postretrieval Symposium*, Orlando, Fla., June 3–8, 1991.
80. J. S. Wollam and B. W. Murray, *Proc. SPIE*, SPIE, Bellingham, Wash., **1118**:88 (1989).
81. Spire, product information from Spire Corporation (Appendix A–D of Spire Document FR 10106), Bedford, Mass., (1992).
82. C. M. Egert and D. D. Allred, "Diffuse Absorbing Beryllium Coatings Produced by Magnetron Sputtering," *Proc. SPIE: Stray Radiation in Optical Systems*, R. P. Breault (ed.), SPIE, Bellingham, Wash., **1331**:170–178 (1990).
83. C. C. Blatchley, E. A. Johnson, Y. K. Pu, and C. Von Benken, "Rugged Dark Materials for Stray Light Suppression by Seeded Ion Beam Texturing," *Proc. SPIE: Stray Radiation II*, R. P. Breault (ed.), SPIE, Bellingham, Wash., **1753** (1992).
84. G. Hass, H. H. Schroeder, and A. F. Turner, "Mirror Coatings for Low Visible and High Infrared Reflectance," *J. Opt. Soc. Am.* **46**:31–35 (1956).
85. J. A. Dobrowolski, "Versatile Computer Program for Absorbing Optical Thin Film Systems," *Appl. Opt.* **20** (1981).
86. J. A. Dobrowolski, F. C. Ho, and A. J. Waldorf, "Research on Thin Film Anticounterfeiting Coatings at the National Research Council of Canada," *Appl. Opt.* **28**:2702–2717 (1989).
87. J. A. Dobrowolski, B. T. Sullivan, and R. C. Bajcar, "An Optical Interference, Contrast Enhanced Electroluminescent Device," *Appl. Opt.* **31**:5988 (1992).
88. W. L. Wolfe and Y. Wang, "Comparison of Theory and Experiments for Bidirectional Reflectance Distribution Function (BRDF) of Microrough Surfaces," *Proc. SPIE: Scattering in Optical Materials*, S. Musikant (ed.), SPIE, Bellingham, Wash., **362**:40 (1982).
89. T. A. Leonard, T. A. and M. Pantoliano, "BRDF Round Robin," *Proc. SPIE: Stray Light and Contamination in Optical Systems*, R. P. Breault (ed.), SPIE, Bellingham, Wash., **967**:226–235 (1988).
90. T. A. Leonard, M. Pantoliano, and J. Reilly, "Results of a CO<sub>2</sub> BRDF Round Robin," *Proc. SPIE: Scatter from Optical Components*, J. Stover (ed.), SPIE, Bellingham, Wash., **1165**:444–449 (1989).
91. S. M. Pompea, "Stray Radiation Issues on Adaptive Optics Systems," in *Adaptive Optics for Astronomy*, D. Alloin and J.-M. Mariotti (eds.), Kluwer Academic Publishers, Dordrecht, 1994.
92. J. H. Henninger, "Solar Absorptance and Thermal Emittance of Some Common Spacecraft Thermal Control Coatings," *NASA Reference Publication 1121*, 1984, p. 7.
93. J. Stover, *Optical Scattering: Measurement and Analysis*, 2nd ed., SPIE Press, Bellingham, Wash., 1995.



94. E. R. Freniere, "First-Order Design of Optical Baffles," *Proc. SPIE: Radiation Scattering in Optical Systems*, G. Hunt (ed.), SPIE, Bellingham, Wash., **257**:19–22 (1980).
95. G. Peterson and S. Johnston, "Specular Baffles," *Proc. SPIE: Stray Radiation in Optical Systems II*, R. P. Breault (ed.), SPIE, Bellingham, Wash., **1753** (1992).
96. K. Snail, P. Brown, J. Costantino, W. C. Shemano, C. W. Schmidt, W. F. Lynn, C. L. Seaman, and T. R. Knowles, "Optical Characterization of Black Appliqués" *Proc. SPIE* **2864**:465 (1996).
97. S. R. Meier, "Characterization of Highly Absorbing Black Appliqués in the Infrared," *Appl. Opt.* **40**:2788–2795 (2001).
98. S. R. Meier, "Reflectance and Scattering Properties of Highly Absorbing Black Appliqués over a Broadband Spectral Region," *Appl. Opt.* **40**:6260–6264 (2001).
99. S. R. Meier, M. L. Korwin, and C. I. Merzbacher, "Carbon Aerogel: A New Nonreflective Material for the Infrared," *Appl. Opt.* **39**:3940–3944 (2000).
100. J. M. Bennett and L. Mattsson, *Introduction to Surface Roughness and Scattering*, Optical Society of America, 1989.
101. C. F. Bohren and D. F. Huffman, *Absorption and Scattering of Light by Small Particles*, John Wiley and Sons, New York, 1983.
102. R. Ludwig, "Antireflection Coating on a Surface With High Reflecting Power," U. S. Patent 4,425,022, Jan. 10, 1984.
103. J. A. Dobrowolski, E. H. Hara, B. T. Sullivan, and A. J. Waldorf, "A High Performance Optical Wavelength Multiplexer/Demultiplexer," *Appl. Opt.* **30** (1991).
104. W. I. Linlor, "Reflective Baffle System with Multiple Bounces," *Proc. SPIE: Stray Radiation IV*, R. P. Breault (ed.), SPIE, Bellingham, Wash., **675**:217–239 (1986).
105. A. W. Greynolds and R. K. Melugin, "Analysis of an All-Specular Linlor Baffle Design," *Proc. SPIE: Stray Radiation IV*, R. P. Breault (ed.), SPIE, Bellingham, Wash., **675**:240–248 (1986).
106. H. Babel and H. G. Lee, "High emittance low absorptance coatings," US Patent 5,296,285 (1994).
107. A. P. Glassford, (ed.), *Proc. SPIE: Optical System Contamination: Effects, Measurements, Control*, SPIE, Bellingham, Wash., **777** (1987). (Entire volume)
108. A. P. Glassford, (ed.), *Proc. SPIE: Optical System Contamination: Effects, Measurements, Control II*, SPIE, Bellingham, Wash., **1329** (1990). (Entire volume)
109. A. P. Glassford, (ed.), *Proc. SPIE: Optical System Contamination: Effects, Measurements, Control III*, SPIE, Bellingham, Wash., **1754** (1992). (Entire volume)
110. J. B. Heaney, "A Comparative Review of Optical Surface Contamination Assessment Techniques," *Proc. SPIE: Optical System Contamination: Effects, Measurements, Control*, P. A. Glassford (ed.), SPIE, Bellingham, Wash., **777**:179 (1987).
111. K. Nahm, P. Spyak, and W. Wolfe, "Scattering from Contaminated Surfaces," *Proc. SPIE: Scatter from Optical Components*, J. Stover (ed.), SPIE, Bellingham, Wash., **1165**:294–305 (1989).
112. V. L. Williams and R. T. Lockie, "Optical Contamination Assessment by Bidirectional Reflectance-Distribution Function (BRDF) Measurement," *Opt. Eng.* **18**(2):152–156 (1979).
113. R. P. Young, "Low Scatter Mirror Degradation by Particle Contamination," *Opt. Eng.* **15**(6):516–520 (1976).
114. B. W. Murray and Johnson, E. A., "Pulsed Electron Beam Testing of Optical Surfaces," *Proc. SPIE: Conference on Optical Surfaces Resistant to Severe Environments*, paper no. 1330-01, San Diego, July 11, 1990.
115. M. McCargo, R. E. Dammann, J. C. Robinson, and R. J. Milligan, "Erosion of Diamond Films and Graphite in Oxygen Plasma," *Proceedings of the International Symposium on Environmental and Thermal Control Systems for Space Vehicles*, Joulouse, France, European Space Agency, Noordwijk, The Netherlands, October, 1983, pp. 1–5.
116. A. F. Whittaker, "Atomic Oxygen Effects on Materials," *STS-8 Paint Data Summary*, Marshall Space Flight Center, January 1984.
117. J. L. Golden, "Results of an Examination of the A-276 White and Z-306 Black Thermal Control Paint Disks flown on LDEF," *NASA Conference Publication 10072*, First LDEF Post-Retrieval Symposium Abstracts, June 2–8, 1991.
118. M. D. Blue, and S. Perkowitz, "Space-Exposure Effects on Optical-Baffle Coatings at Far-Infrared Wavelengths," *Appl. Opt.* **31**:4305–4309 (1991).

119. W. A. Campbell and J. J. Scialdone, "Outgassing Data for Selecting Spacecraft Materials," *NASA Reference Publication 1134*, Revision 2, November 1990.
120. R. E. Predmore and E. W. Mielke, *Materials Selection Guide, Revision A*, Goddard Space Flight Center, August 1990.
121. R. V. Peterson, W. Krone-Schmidt, and W. V. Brandt, "Jet-Spray Cleaning of Optics," *Proc. SPIE: Optical System Contamination: Effects, Measurement, Control III*, A. P. Glassford (ed.), SPIE, Bellingham, Wash., **1754** (1992).
122. J. A. Gunderson, "Goniometric Reflection Scattering Measurements and Techniques at 10.6 Micrometers," Thesis, Univ. of Arizona, 1977.
123. S. M. Smith and W. L. Wolfe, "Comparison of Measurements by Different Instruments of the Far-Infrared Reflectance of Rough, Optically Black Coatings," *Proc. SPIE: Scattering of Optical Materials*, S. Musikant (ed.), SPIE, Bellingham, Wash., **362**:46–53 (1983).
124. R. P. Breault, A. Greynold, and S. Lange, "APART/PADE Version 7: A Deterministic Computer Program Used to Calculate Scattered and Diffracted Energy," *Proc. SPIE: Radiation Scattering in Optical Systems*, G. Hunt (ed.), SPIE, Bellingham, Wash., **257** (1980).
125. A. W. Greynolds, *Advanced Systems Analysis Package (ASAP) Users Manual*, Breault Research Organization, Inc., Tucson, Ariz., 1988.
126. S. S. Steadman and B. K. Likeness, "GUERAP III Simulation of Stray Light Phenomena," *Proc. SPIE: Stray Light Problems in Optical Systems*, SPIE, Bellingham, Wash., **107** (1977).
127. R. P. Breault, "Current Technology of Stray Light," *Proc. SPIE: Stray Radiation V*, R. P. Breault (ed.), SPIE, Bellingham, Wash., **675**:4–13 (1986).
128. F. D. Orazio, W. K. Stowell, and R. M. Silva, "Instrumentation of a Variable Angle Scatterometer (VAS)," *Proc. SPIE: Stray Radiation III*, R. P. Breault (ed.), SPIE, Bellingham, Wash., **384**:123–131 (1983).
129. F. O. Bartell, "BRDF Measurement Equipment: Intrinsic Design Considerations," *Proc. SPIE: Stray Radiation IV*, R. P. Breault (ed.) **511**:31–34 (1984).
130. R. M. Silva, F. D. Orazio, and R. B. Sledge, "A New Instrument for Constant (Beta-Beta<sub>g</sub>) Scatter Mapping of Contiguous Optical Surfaces of up to 25 Square Inches," *Proc. SPIE: Stray Radiation IV*, R. P. Breault (ed.), SPIE, Bellingham, Wash., **511**:38–43 (1984).
131. J. B. Heaney, Optics Branch, Code 717, Goddard Space Flight Center, Greenbelt, MD., private communication (unpublished data), 1992.
132. D. L. Stierwalt, J. B. Bernstein, and D. D. Kirk, "Measurements of the Infrared Spectral Absorptance of Optical Materials," *Appl. Opt.* **2**(11):1169–1173 (1963).
133. F. J. J. Clarke and J. A. Larkin, "Measurements of Total Reflectance, Transmittance and Emissivity over the Thermal IR Spectrum," *Infrared Physics* **25**:359–367 (1985).
134. S. M. Smith, "Formation of Ames 24E2 IR-Black Coatings," *NASA Tech. Memo 102864*, July (1991).
135. S. M. Smith, "BRDFs of Ames 24E, Ames 24E2, and Ames 47A at Photometric Wavelengths of 220 and 350 micrometers," *Sterling Technical Note TN-91-8441-000-74*, Sterling Software, Moffett Field, Calif., October 1991.
136. S. M. Smith, "An Almost "Perfectly" Diffuse, "Perfect" Reflector for Far-Infrared Reflectance Calibration," *Proc. SPIE: Stray Radiation in Optical Systems II*, Breault (ed.) **1753**:252–261 (1992).
137. S. M. Smith, Sterling Software, NASA Ames Research Center, private communication, April 1992.
138. S. M. Pompea, D. W. Bergener, D. F. Shepard, S. L. Russak, and W. L. Wolfe, "Preliminary Performance Data on an Improved Optical Black for Infrared Use," *Proc. SPIE: New Optical Materials*, SPIE, Bellingham, Wash., **400**:128 (1983).
139. J. Lohrengel, "Total Emissivity of Black Coatings," ("Gesamtemissionsgrad von Schwärzen"), *Wärme - Stoffübertrag* Springer-Verlag, Berlin, **21**(5):311–315 (27 July 1987).
140. V. Freibel, *Colorado, M & P Information Bulletin No. 82.21*, Ball Aerospace, Boulder, 7/27/82.
141. I. T. Lewis, A. R. Telkamp, and A. F. Ledebuhr, "Low Scatter Edge Blackening Compounds for Refractive Optical Elements," *Proc. SPIE: Scatter from Optical Components*, J. Stover (ed.), SPIE, Bellingham, Wash., **1165**:227–236 (1989).
142. J. F. Wade, J. E. Peyton, B. R. Klitzky, and R. E. Groff, "Optically Black Coating and Process for Forming It," U. S. Patent 4,111,762, September 5, 1978.

143. D. F. Shepard, Martin Black and Infrablack Contact at Lockheed Martin, P.O. Box 179, Denver, Colorado 80201.
144. J. F. Wade and W. R. Wilson, *Proc. SPIE*, SPIE, Bellingham, Wash., **67**:59 (1973).
145. S. M. Pompea, D. W. Bergener, and D. F. Shepard, "Reflectance Characteristics of an Infrared Absorbing Surface," *Proceedings 31st National Infrared Information Symposium*, National Bureau of Standards, Boulder, Colorado, 1983, p. 487.
146. W. Friedrichs, product literature from Tiodize Co., Inc., 5858 Engineer Drive, Huntington Beach, CA 92649.
147. S. Kodama, M. Horiuchi, T. Kunii, and K. Kuroda, "Ultra-Black Nickel-Phosphorus Alloy Optical Absorber," *Instrumentation and Measurement, IEEE Transactions* **39**:230–232 (1990).
148. C. Johnson, "Ultra-Black Coating due to Surface Morphology," U. S. Patent 4,361,630, 30, November 1982.
149. D. F. Shepard, R. J. Fenolia, D. C. Nagle, and M. E. Marousek, "High-Temperature, High-Emissivity, Optically Black Boron Surface," U. S. Patent 5,035,949, July 30, 1991, Martin Marietta Corporation.
150. R. D. Seals, C. M. Egert, and D. D. Allred, "Advanced Infrared Optically Black Baffle Materials," *Proc. SPIE: Optical Surfaces Resistant to Severe Environments*, SPIE, Bellingham, Wash., **1330**:164–177 (1990).
151. R. D. Seals, "Advanced Broadband Baffle Materials," *Proc. SPIE: Reflective and Refractive Materials for Earth and Space Applications*, SPIE, Bellingham, Wash., **1485**:78–87 (1991).
152. B. W. Murray and J. S. Wollam, "Space Durable Beryllium Baffle Materials," *SPIE Symposium on Aerospace Sensing*, Orlando, Fla., March 1989.
153. E. Johnson, Spire Corporation, Bedford, Mass., private communication, March 1992.
154. S. K. Rutledge, B. A. Banks, M. J. Mirtich, R. Lebed, J. Brady, D. Hotes, and M. Kussmaul, "High Temperature Radiator Materials for Applications in the Low Earth Orbital Environment," *NASA Technical Memorandum 100190*, 1987.
155. B. A. Banks, S. K. Rutledge, M. J. Mirtich, T. Behrend, D. Hotes, M. Kussmaul, J. Barry, C. Stidham, T. Stueber, and F. DiFillippo, "Arc-Textured Metal Surfaces for High Thermal Emittance Radiators," *NASA Technical Memorandum 100894*, 1988.
156. D. F. Shepard and R. J. Fenolia, "Optical Black Cobalt Surface," U. S. Patent 4,904,353, February 27, 1990, Martin Marietta Corporation.
157. R. J. Fenolia, D. F. Shepard, and S. L. Van Loon, "Optically Black Pliable Foils," U. S. Patent 4,894,125, January 16, 1990, Martin Marietta Corporation.
158. D. J. Janeczko, "Optics and Electro-Optics," Martin Marietta Corporation, Orlando, Fla., personal communication, 1992.
159. Z.-P. Yang, L. Ci, J. A. Bur, S.-Y. Lin, and P. M. Ajayan, "Experimental Observation of an Extremely Dark Material Made by a Low-Density Nanotube Array," *Nano Lett.* **8**:446–451 (2008).
160. A. Y. Vorobyev and G. Guo, "Effect of Nanostructure-Covered Femtosecond Laser-Induced Periodic Surface Structures on Optical Absorptance of Metals," *Appl. Phys. A* **86**:321–324 (2007).
161. K. Paivasaari, J. J. J. Kaakkunen, M. Kuittinen, and T. Jaaskelainen, "Enhanced Optical Absorptance of Metals Using Interferometric Femtosecond Ablation," *Optics Express*, **15**:13838–13843 (2007).
162. P. Strimer, X. Gerbaux, A. Hadni, T. Souel, "Black Coatings of Infrared and Visible, with High Electrical Resistivity," *Infrared Physics* **21**:7–39 (1981).
163. R. S. Robinson, and S. M. Rossnagel, "Ion-Beam Induced Topography and Surface Diffusion," *J. Vac. Sci. Technol.* **21**:790 (1982).
164. R. B. Culver, W. A. Solberg, R. S. Robinson, and I. L. Spain, "Optical Absorption of Microtextured Graphite Surfaces in the 1.1–2.4 Micrometer Wavelength Region," *Appl. Opt.* **24**:924 (1984).
165. C. W. Bowers, R. B. Culver, W. A. Solberg, and I. L. Spain, "Optical Absorption of Surfaces Modified by Carbon Filaments," *Appl. Opt.* **26**:4625 (1987).
166. L. Harris, R. T. McGinnies, and B. M. Siegel, "The Preparation and Optical Properties of Gold Black," *J. Opt. Soc. Am.* **38**(7) (1948).
167. W. R. Blevin, and W. J. Brown, "Black Coatings for Absolute Radiometers," *Int. J. Sci. Metrology* **2**(4):139–143 (October 1966).
168. G. Zaeschmar and A. Nedoluha, "Theory of the Optical Properties of Gold Blacks," *J. Opt. Soc. Am.* **62**(3):348–352 (1972).

## 6.12 FURTHER READINGS

- Anderson, S., S. M. Pompea, D. F. Shepard, and R. Castonguay, "Performance of a Fully Automated Scatterometer for BRDF and BTDF Measurements at Visible and Infrared Wavelengths," *Proc. SPIE: Stray Light and Contamination in Optical Systems* **967**:159 (1988).
- Banks, B. A., NASA Technical Memorandum 81721, Lewis Research Center, 1981.
- Bartell, F. O., E. L. Dereniak, and W. L. Wolfe, "The Theory and Measurement of BRDF and BTDF," *Proc. SPIE: Radiation Scattering in Optical Systems* **257**:154 (1980).
- Bennett, H. E. and E. L. Church, "Surface Roughness Measurement in the Submicrometer Range Using Laser Scattering," *Opt. Eng.* **18**:103 (1979).
- Bonnot, A. M., H. Belkhir, D. Pailharey, and P. Mathiez, *Proc. SPIE* **562**:209 (1985).
- Bonnot, A. M., H. Belkhir, and D. Pailharey, *Proc. SPIE: Optical Materials Technology for Energy Efficiency and Solar Energy Conversion V* **653**:215 (1986).
- Brooks, L. D. and W. L. Wolfe, "Microprocessor-Based Instrumentation for Bidirectional Reflectance Distribution Function (BRDF) Measurements from Visible to Far Infrared (FIR)," *Proc. SPIE: Radiation Scattering in Optical Systems* **257**:177 (1980).
- Davis, L. and J. G. Kepros, "Improved Facility for BRDF/BTDF Optical Scatter Measurements," *Proc. SPIE: Stray Radiation V* **675**:24 (1986).
- Duran, M. and C. Gricurt, "Hipparcos Telescope Stray Light Protection," *Proc. SPIE: Stray Radiation V* **675**:134 (1986).
- "Method of Forming Electrodeposited Anti-reflective Surface Coatings, U.S. Patent 5,326,454, Martin Marietta Corporation.
- Freniere, E. R., "Use of Specular Black Coatings in Well-Baffled Optical Systems," *Proc. SPIE: Stray Radiation V* **675**:126 (1986).
- Garrison, J. D., J. C. Haiad, and A. J. Averett, "Progress in the Commercialization of a Carbonaceous Solar Selective Absorber on a Glass Substrate," *Proc. SPIE: Optical Materials Technology for Energy Efficiency and Solar Energy Conversion VI* **823**:225 (1987).
- Hunt, P. J., R. Noll, L. Andreozzi, and J. Hope, "Particle Contamination from Martin Optical Black," *Proc. SPIE: Radiation Scattering in Optical Systems*, G. Hunt (ed.) **257**:196 (1980).
- LDEF, "The Long Duration Exposure Facility (LDEF) Mission I Experiments," NASA SP-473, NASA Langley Research Center, Washington, D.C., November 1986.
- Leger, L. J., J. T. Visentine, and J. F. Kuminecz, "Low Earth Orbit Oxygen Effects on Surfaces," presented at AIAA 22nd Aerospace Sciences Meeting, Reno, Nevada, January 9–12, 1984.
- Mende, S. B., P. M. Banks, and D. A. Klingelsmith III, "Observation of Orbiting Vehicle Induced Luminosities on the STS-8 Mission," *Geophys. Res. Lett.* **11**:527 (1984).
- Ranbar Technology, Inc., Glenshaw, Pa., product information and MSDSs on Ranbar G113 Paint, 1990.
- Redspot Paint and Varnish Co., Inc., product information on Nextel Suede, P.O. Box 418, Evansville, In., 47703, 1992.
- Schiff, T. F., J. C. Stover, D. R. Cheever, and D. R. Bjork, "Maximum and Minimum Limitations Imposed on BSDF Measurements," *Proc. SPIE* **967**:50 (1988).
- Seraphin, B. O., (ed.), "Solar Energy Conversion—Solid State Physics Aspects," in *Topics in Applied Physics*, vol. 31, Springer Verlag, 1979.
- Sikkens Aerospace Finishes Division of Akzo Coatings America, Inc., 434 W. Meats Avenue, Orange, CA 92665.
- Stover, J. C., and C. H. Gillespie, *Proc. SPIE* **362**:172 (1982).
- Stover, J. C., C. H. Gillespie, F. M. Cady, D. R. Cheever, and K. A. Klicker, *Proc. SPIE* **818**:62 (1987).
- Stover, J. C., C. Gillespie, F. M. Cady, D. R. Cheever, and K. A. Klicker, *Proc. SPIE* **818**:68 (1987).
- Visentine, J. T., (ed.), *Atomic Oxygen Effects Measurement for Shuttle Missions STS-8 and 41-G, Volume I-III*, NASA TM-100459, 1988.
- Wood, B. E., W. T. Bertrand, E. L. Kiech, J. D. Holt, and P. M. Falco, *Surface Effects of Satellite Material Outgassing Products*, Final Report AEDC-TR-89-2, Arnold Engineering Development Center, 1989.

*This page intentionally left blank*

---

# OPTICAL PROPERTIES OF FILMS AND COATINGS

---

Jerzy A. Dobrowolski

*Institute for Microstructural Sciences  
National Research Council of Canada  
Ottawa, Ontario, Canada*

---

## 7.1 INTRODUCTION

---

### Scope of Chapter

In the broadest sense of the term, an optical filter is any device or material which is deliberately used to change the spectral-intensity distribution or the state of polarization of the electromagnetic radiation incident upon it. The change in the spectral intensity distribution may or may not depend on the wavelength. The filter may act in transmission, in reflection, or in both.

Filters can be based on many different physical phenomena, including absorption, refraction, interference, diffraction, scattering, and polarization. For a comprehensive review of this broader topic the interested reader is referred to the chapter entitled “Coatings and Filters” which appeared in the first edition of the *Handbook of Optics*.<sup>1</sup> This chapter deals only with filters that are based on absorption and interference of electromagnetic radiation in thin films. Optical thin-film coatings have numerous applications in many branches of science and technology and there are also many consumer products that use them. The spectral region covered in this chapter extends from about 0.003 to 300  $\mu\text{m}$  ( $3$  to  $3 \times 10^5$  nm), although the main emphasis is on filters for the visible and adjacent spectral regions.

The discussion in this chapter is largely confined to generic thin-film filters, such as antireflection coatings, cutoff filters, narrowband transmission or rejection filters, reflectors, beam splitters, and so forth. Filters for very specific applications, such as filters for colorimeters and other scientific instruments, color correction filters, and architectural coatings, are, as a rule, not treated. Of the filters described, many are available commercially while others are only research laboratory prototypes. This review does not cover thin-film filters whose properties can be changed by external electric or magnetic fields, temperature, or illumination level.

In this introductory section some general considerations on the use of optical filters are presented. In the following sections, the theory of optical multilayers and the methods for their deposition and characterization are briefly discussed. These sections are useful for gaining a proper understanding of the operation, advantages, and limitations of optical coatings. The remaining sections then describe the properties of various generic thin-film filters.

For further information on this subject the interested reader is particularly encouraged to consult the books by Macleod,<sup>2</sup> Rancourt,<sup>3</sup> and Baumeister.<sup>4</sup>

## General Theory of Filters

There are many different ways of describing the performance of optical coatings and filters. For example, transmission and reflection filters intended for visual applications are adequately described by a color name alone, or by reference to one of the several existing color systems (see Chap. 10, Vol. III). There also exist other specialized filter specifications for specific applications. However, the most complete information on the performance of a filter is provided by spectral transmittance, reflectance, absorptance, and optical density curves. This is the method adopted in this chapter.

Referring to Fig. 1, at a wavelength  $\lambda$  the spectral transmittance  $T(\lambda)$  of a filter placed between two semi-infinite media is equal to the ratio of the light intensity of that wavelength transmitted  $I_T(\lambda)$  by the filter to that incident  $I_0(\lambda)$  upon it,

$$T(\lambda) = \frac{I_T(\lambda)}{I_0(\lambda)} \quad (1)$$

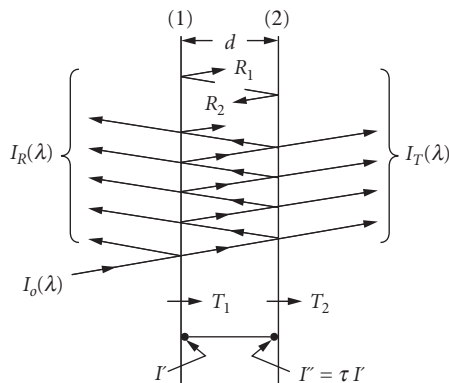
The spectral reflectance  $R(\lambda)$  of a filter is defined in a similar way,

$$R(\lambda) = \frac{I_R(\lambda)}{I_0(\lambda)} \quad (2)$$

At non-normal incidence the component of the intensity perpendicular to the interface must be used in the above equations.<sup>2</sup> The relationship between the transmittance  $T(\lambda)$  and the density  $D(\lambda)$  of a filter is given by

$$D(\lambda) = \log \frac{1}{T(\lambda)} \quad (3)$$

In this chapter, transmittances and reflectances will be plotted using either linear or logarithmic scales. The logarithmic scale is particularly well suited whenever accurate information about the low transmission or reflection region is to be conveyed. However, this is done at the expense of detail at the high end of the scale. A variant, the decibel scale, equal to  $-10D(\lambda)$ , is frequently used in the telecommunications field. Wavelengths are normally specified in micrometers ( $\mu\text{m}$ ) because this is the most convenient unit for the whole spectral range covered in this chapter. In the following discussions the dependence of the transmittance, reflectance, and absorptance on wavelength will be implicitly assumed.



**FIGURE 1** Specular transmission and reflection of light by a plane-parallel plate (see Sec. 7.1, subsection "General Theory of Filters").

## Transmission and Reflection of Coatings on a Substrate

Many multilayer coatings are deposited onto a transparent or partially transparent substrate. Both the multilayer and the substrate contribute to the overall performance of the filter. For example, absorption in the substrate is frequently used to limit the transmission range of the filter. Reflectances at the filter interfaces need also to be considered. However, they can be reduced by anti-reflection coatings, or by cementing several components together.

In general, a filter can consist of multilayer coatings deposited onto one or both sides of a substrate. The overall transmittance  $T_{\text{total}}$  of a filter can be expressed in terms of the internal, or intrinsic transmittance  $\tau$  of the substrate and the transmittances  $T_1$ ,  $T_2$  and internal reflectances  $R_1$ ,  $R_2$  of each surface of the substrate (Fig. 1).

The internal transmittance  $\tau$  of a substrate is defined to be the ratio of the light intensity  $I''$  just before reaching the second interface to the intensity  $I'$  just after entering the substrate (Fig. 1):

$$\tau = \frac{I''}{I'} \quad (4)$$

Expressions for the evaluation of the transmittance  $T$  and reflectance  $R$  of multilayer coatings are given in Sec. 7.2, subsection "Matrix Theory for the Analysis of Multilayer Systems."

Providing that the incident light is not coherent, there will be no interference between the beams reflected from the two surfaces of a substrate, even when the surfaces are plane parallel. A summation of all the partial reflections leads to the following expression for the overall spectral transmittance  $T_{\text{total}}$  of a filter:

$$T_{\text{total}} = \frac{T_1 T_2 \tau}{1 - R_1 R_2 \tau^2} \quad (5)$$

The reflection coefficients of uncoated interfaces can be calculated from Eq. (80), providing that the complex refractive indices of the substrate and of the medium are known. If all the materials in the filter are nonabsorbing, then

$$T_{\text{total}} = \frac{T_1 T_2}{1 - R_1 R_2} \quad (6)$$

If  $R_1$  is small, an appropriate expression for  $T_{\text{total}}$  is

$$T_{\text{total}} \approx [1 - R_1(1 - R_2)]T_2 \quad (7)$$

However, this last approximation is not valid in general; some infrared substrate materials have high-reflection coefficients and in such cases Eq. (6) must be used.

## Transmission Filters in Series and Parallel

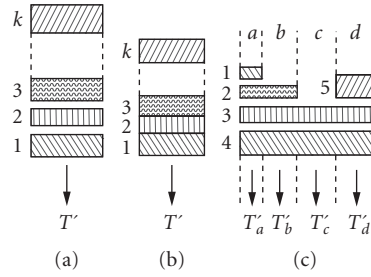
To obtain a desired spectral transmittance it is frequently necessary to combine several filters. One common approach is to place several filters in series (Fig. 2a).

Because of the many different partial reflections that may take place between the various surfaces, precise formulas for the resulting transmittance are complicated.<sup>5</sup> Accurate calculations are best carried out using matrix methods.<sup>6</sup>

To a first approximation, the resultant transmittance  $T'$  of a filter system consisting of  $k$  individual filters placed in series is given by

$$T' \approx T'_1 T'_2 T'_3 \dots T'_k \quad (8)$$





**FIGURE 2** Transmission filters arranged in series and in parallel. The filters can be air-spaced (a), (c) or cemented (b).

Here  $T'_i$  is the total transmittance of filter  $i$ . This expression is valid only if the reflectances of the individual filters are small or if the interference filters are slightly inclined to one another and the optics are arranged in such a way that the detector sees only the direct beam.

Under other circumstances the use of this expression with interference filters can lead to serious errors. Consider two separate filters placed in series and let  $T'_1$ ,  $T'_2$ ,  $R'_1$  and  $R'_2$  correspond to the transmittances and reflectances of the two filters. If  $T'_1 = T'_2 = R'_1 = R'_2 = 0.5$ , then according to Eq. (8), the resulting transmittance will be  $T' = 0.25$ . For this simple case the precise expression can be derived from Eq. (5) and is given by

$$T' = \frac{T'_1 T'_2}{1 - R'_1 R'_2} \quad (9)$$

Evaluating this expression one obtains  $T' = 0.33$ . This is significantly different from the result obtained from the application of Eq. (8).

Some spectral transmittance curves cannot be easily designed by placing filters in series alone. For certain applications it is quite acceptable to place filters not only in series, but also in parallel.<sup>7</sup> This introduces areas as additional design parameters. Thus, for example, the effective spectral transmittance  $T'$  of the filter shown in Fig. 2c would be given by

$$T' = \left( \frac{a}{A} T'_a + \frac{b}{A} T'_b + \frac{c}{A} T'_c + \frac{d}{A} T'_d \right) \quad (10)$$

where

$A$  = overall area of filter,

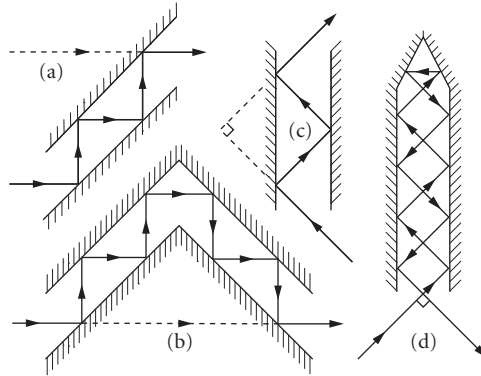
$a, b, c, d$  = areas of the four zones,

$T'_a, T'_b, T'_c, T'_d$  = transmittances of four zones

The latter are given by

$$\begin{aligned} T'_a &= T'_1 \cdot T'_2 \cdot T'_3 \cdot T'_4 \\ T'_b &= T'_1 \cdot T'_2 \cdot T'_3 \\ T'_c &= T'_1 \cdot T'_2 \\ T'_d &= T'_1 \cdot T'_2 \cdot T'_3 \cdot T'_5 \end{aligned} \quad (11)$$

Great care must be exercised when using such filters. Because the spectral transmittance of each zone of the filter is different, errors will result unless the incident radiation illuminates the filter uniformly.



**FIGURE 3** Various arrangements (a) to (d) for multiple-reflection filters.

Similar care must be used when employing the filtered radiation. One way proposed to alleviate these problems is to break the filter down into a large number of small, regular elements and to reassemble it in the form of a mosaic.<sup>8</sup>

### Reflection Filters in Series

If radiation is reflected from  $k$  different filters, the resultant reflectance  $R'$  will be given by

$$R' = R'_1 \cdot R'_2 \cdot R'_3 \cdots R'_k \quad (12)$$

which is analogous to Eq. (8) for the resultant transmittance of filters placed in series. Many of the considerations of that section also apply here. For instance,  $R'$  will be significant only at those wavelengths at which every one of the reflectors has a significant reflectance. Metal layers (Sec. 7.15, subsection “Reducing Reflection with a Thin Metal Film”) and thin-film interference coatings can be used exclusively or in combination.

For the sake of convenience the number of different reflecting surfaces used is normally restricted. The outlines of some possible reflector arrangements given in Fig. 3 are self-explanatory. The arrangement shown in Fig. 3b does not deviate or displace an incident parallel beam. The number of reflections depends in each case on the lengths of the plates and on the angle of incidence of the beam. Other arrangements are possible.

Clearly, reflection filters placed in series require more space and are more complicated to use than transmission filters. But if in a given application these shortcomings can be accepted, multiple-reflection filters offer great advantages, which stem mainly from the nature of the reflectors available for their construction (see Sec. 7.16, subsection “Multiple Reflection Filters”).

## 7.2 THEORY AND DESIGN OF OPTICAL THIN-FILM COATINGS

### Design Approaches

A thin-film designer may be asked to design a multilayer coating in which the transmittance, reflectance, and/or absorptance values are specified at a number of wavelengths, angles, and polarizations of the incident light. The designer may be required to provide a coating with many other more

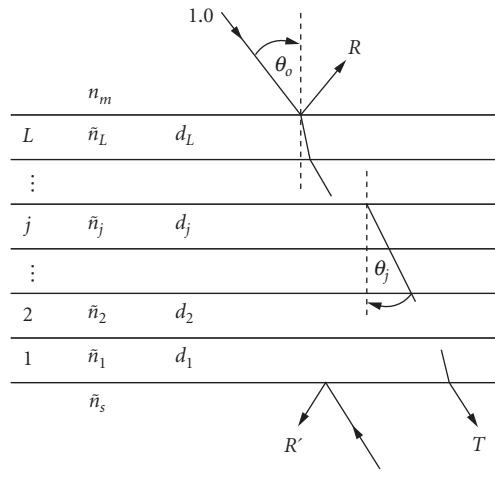
complicated properties, including integral quantities such as CIE color coordinates, solar absorptance, or emissivity.<sup>9</sup> The parameters that can be used to reach these goals are the number of layers in the multilayer, its overall thickness, the layer thicknesses and the refractive indices and extinction coefficients of the individual layers and of the surrounding media. Clearly, the more demanding the performance specifications, the more complex the resulting system. Many different methods have been developed for the design of multilayer coatings. For a good overview of this topic the interested reader is referred to the books by Macleod,<sup>2</sup> Knittl,<sup>10</sup> and by Furman and Tikhonravov.<sup>11</sup> Here only the most important methods will be mentioned.

Graphical vector methods provide the most understanding of the problem, but the necessary approximations limit them to the solution of problems in which the final reflectance is not too high. Admittance diagrams and similar chart methods do not suffer from this limitation, but they are best applied to problems in which the specifications are relatively simple.<sup>12</sup> Many problems can be solved using the known properties of periodic multilayer systems.<sup>13</sup> Analytical synthesis methods yield solutions to problems in which quite complex spectral transmittance or reflectance curves are specified.<sup>14,15</sup> However, solutions frequently obtained in this way call for the use of inhomogeneous layers that are often more difficult to deposit, or for homogeneous layers with optical constants that are outside the range of known materials. Numerical design methods are the most flexible of all because they can be applied to problems with very complex specifications requiring a large number of layers for their solution.<sup>16,17</sup> They are usually based on the matrix theory of optical multilayer systems and are particularly powerful for the solution of complicated spectral problems when combined with analytical methods.

## Matrix Theory for the Analysis of Multilayer Systems

If electromagnetic radiation falls onto a structure consisting of thin films of several different materials, multiple reflections will take place within the structure. Depending on the light source and the layer thicknesses, the reflected beams may be coherent and interfere with one another. This optical interference can be used to design optical multilayer filters with widely varying spectral characteristics. In this section the basic equations for thin-film calculations are presented and some general properties of interference filters are listed. For a thorough discussion of this topic the reader is referred to the work of Macleod<sup>2,18</sup> and Thelen.<sup>19</sup>

Consider the thin-film system consisting of  $L$  layers shown in Fig. 4. The construction parameters comprise not only the refractive indices  $n_j$  and the thicknesses  $d_j$  of the layers  $j = 1, 2, \dots, L$ , but also



**FIGURE 4** Construction parameters of a multilayer.

the refractive indices  $n_s$  and  $n_m$  of the substrate and the incident medium. The angle of incidence  $\theta$ , the wavelength  $\lambda$ , and the plane of polarization of the incident radiation are the external variables of the system. It should perhaps be mentioned here that in some application areas it is more customary to use the grazing angle of incidence  $\theta_g$ , where  $\theta_g = 90 - \theta$ .

The most general method of calculating the transmittance  $T$  and the reflectance  $R$  of a multilayer from the above quantities is based on a matrix formulation<sup>20,21</sup> of the boundary conditions at the film surfaces derived from Maxwell's equations.<sup>21</sup>

It can be shown that the amplitude reflection  $r$  and transmission  $t$  coefficients of a multilayer coating consisting of  $L$  layers bounded by semi-infinite media, for the general case of obliquely incident light, are given by

$$r = \frac{\eta_m E_m - H_m}{\eta_m E_m + H_m} \quad (13)$$

and

$$t = \frac{2\eta_m}{\eta_m E_m + H_m} \quad (14)$$

where

$$\begin{pmatrix} E_m \\ H_m \end{pmatrix} = \mathbf{M} \begin{pmatrix} 1 \\ \eta_s \end{pmatrix} \quad (15)$$

$E_m$  and  $H_m$  are the electric and magnetic vectors, respectively, in the incident medium, and  $\mathbf{M}$  is a product matrix given by

$$\mathbf{M} = \mathbf{M}_L \mathbf{M}_{L-1} \cdots \mathbf{M}_j \cdots \mathbf{M}_2 \mathbf{M}_1 \quad (16)$$

In the above equation  $\mathbf{M}_j$  is a  $2 \times 2$  matrix that represents the  $j$ th film of the system:

$$\mathbf{M}_j = \begin{pmatrix} m_{11} & im_{12} \\ im_{21} & m_{22} \end{pmatrix} = \begin{pmatrix} \cos\delta_j & \frac{i}{\eta_j} \sin\delta_j \\ i\eta_j \sin\delta_j & \cos\delta_j \end{pmatrix} \quad (17)$$

where

$$\delta_j = \frac{2\pi}{\lambda} (n_j d_j \cos\theta_j) \quad (18)$$

the quantity  $n_j d_j \cos\theta_j$  is the *effective optical thickness* of the layer  $j$  for an angle of refraction  $\theta_j$ . In Eqs. (13) to (17)  $\eta$  represents the admittance of the medium, substrate, or layer and is given by

$$\eta = \begin{cases} \frac{n}{\cos\theta} & p\text{-polarization} \\ n\cos\theta & s\text{-polarization} \end{cases} \quad (19)$$

depending on whether the incident radiation is polarized parallel ( $p$ ) or perpendicular ( $s$ ) to the plane of incidence. Clearly, for normal incidence of light, the value of the admittance is equal to the refractive index. The angle  $\theta_j$  is related to the angle of incidence  $\theta_0$  by Snell's law

$$n_m \sin\theta_0 = n_j \sin\theta_j \quad (20)$$

The intensity transmittance and reflectance are

$$T = \frac{\eta_s}{\eta_m} |t|^2 \quad (21)$$

$$R = |r|^2 \quad (22)$$

and the phase changes on transmission and reflection,  $\phi_T$  and  $\phi_R$ , are given by

$$\phi_T = \arg t \quad (23)$$

$$\phi_R = \arg r \quad (24)$$

More often than not, multilayer coatings are specified in terms of  $T$  and  $R$  and the phase changes on reflection and transmission are usually not of direct interest to the users. Exceptions are reflectors for interferometers.<sup>22</sup> It has also been found that specifying certain values of  $\phi_T$ ,  $\phi_r$  was useful in controlling the solution type obtained by some thin-film design methods.<sup>23</sup>

If the materials in a multilayer are all nonabsorbing, then  $T + R = 1$ . Should one or more materials absorb, then in the above equations the refractive indices of these materials must be replaced by their complex refractive indices  $\tilde{n}$ , defined by

$$\tilde{n} = n - ik \quad (25)$$

where  $k$  is the extinction coefficient of the material. Even though all the elements of the layer matrix for such a material are now complex, its determinant will still be unity. The absorptance of the multilayer is then calculated from

$$A = 1 - T - R \quad (26)$$

Certain important general conclusions about the properties of multilayer filters can be drawn from the above equations.

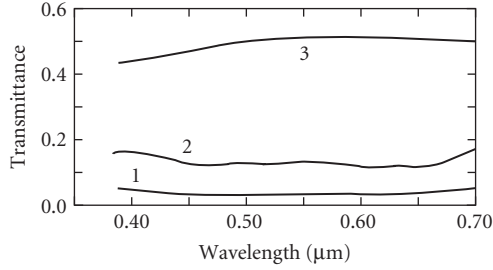
1. The properties of thin-film systems vary with angle of incidence [Eqs. (18), and (19)]. For some applications this is the major disadvantage of interference filters compared to absorption filters.
2. This variation depends on the polarization of the incident radiation [Eq. (19)]. The following equations define  $T$  and  $R$  for obliquely incident nonpolarized radiation:

$$T = \frac{1}{2}(T_p + T_s) \quad (27)$$

$$R = \frac{1}{2}(R_p + R_s) \quad (28)$$

The dependence of  $T$  and  $R$  on polarization has been used for the design of polarizers (see Chap. 13, Vol. I). However, like the angular variation, it is a disadvantage for most other applications. Many researchers have investigated ways of reducing these effects.<sup>13,24-27</sup>

3. Transmittance curves of nonabsorbing multilayers composed of layers whose optical thicknesses are all multiples of  $\lambda/4$  show symmetry about  $\lambda_0$  when plotted on a relative wavenumber scale  $\lambda_0/\lambda$  [Eqs. (17) and (18)].
4. A proportional change of all the thicknesses of a nonabsorbing multilayer results merely in a displacement of the transmittance curve on a wave-number scale [Eq. (18)]. Thus a thin-film design can be utilized in any part of the spectrum subject only to the limitations imposed by the dispersion of the optical constants of the materials used.
5. The reflectance and absorptance of a filter containing absorbing layers will depend, in general, on which side of the filter the radiation is incident (Fig. 5). However, the transmittance does not depend on the direction of the incident light.



**FIGURE 5** Spectral characteristics of a thin chromium alloy film on glass. Curve 1: transmittance; curves 2 and 3: reflectance from the glass and air sides, respectively. (After *Liberty Mirror*.<sup>28</sup>)

Layers	$n_m$	Sublayers
$L$	$n_L$	$L_{\text{sub}}$
		$L_{\text{sub}}^{-1}$
		$\vdots$
$\vdots$		
$j$	$n_j$	$\vdots$
		$j_{\text{sub}}$
		$\vdots$
$\vdots$		
$2$	$n_2$	$\vdots$
		$3$
		$2$
$1$	$n_1$	$1$
		$2$
		$3$
	$n_s$	

**FIGURE 6** Subdivision of layers for the evaluation of the electric field within a multilayer (see Sec. 7.2, subsection “Matrix Theory for the Analysis of Multilayer Systems”).

An important parameter is the electric field amplitude squared,  $|E|^2$ . The susceptibility of a multilayer to high-power laser damage is proportional to the highest value of this quantity within the multilayer. One way to evaluate  $E$  is to subdivide each layer of the system into  $L_{\text{sub}}$  sublayers (Fig. 6) and to evaluate the partial matrix products  $P_j$ ,

$$\mathbf{P}_j = \begin{pmatrix} p_{11} & ip_{12} \\ ip_{21} & p_{22} \end{pmatrix} = \prod_{k=1}^j (\mathbf{S}_k) \quad (29)$$

for all  $L$  sublayers, where  $S_k$  is the matrix of the  $k$ th sublayer. Then, the electric field amplitude at a point  $j$  in the multilayer is given in terms of the elements of the total and partial product matrices by the following expression:<sup>29</sup>

$$E_j = \frac{4[p_{11}^2 + (n_s p_{12})^2]}{[m_{11} + (n_s m_{22}/n_m)]^2 + [(m_{21}/n_m) + n_s m_{12}]^2} \quad (30)$$

The analysis of optical thin-film systems [with computer programs based on Eqs. (13) to (30)] is relatively simple. The design of filters with any but the simplest spectral characteristics is a more complicated problem and one of the methods listed in Sec. 7.2, subsection "Design Approaches" must be used.

### 7.3 THIN-FILM MANUFACTURING CONSIDERATIONS

The optical, mechanical, and environmental properties of multilayer coatings depend on the materials used, on the deposition process and on the surface quality of the substrate.

There are many different methods for the deposition of thin films.<sup>30-32</sup> Some of the more common processes are reviewed below. The deposition methods and process parameters used affect the microstructure of the resulting layers. The films can be dense with an amorphous or a microcrystalline structure, or they may exhibit a columnar growth with considerable voids. The optical constants clearly depend on this microstructure and films of the same materials may sometimes have very different properties, depending on how they were deposited (see, for example, Ref. 33). The individual films in a multilayer may be under tensile or compressive stress and, unless materials and film thicknesses are selected to compensate for these stresses, the overall stress may be large enough to distort the substrate or cause the multilayer to break up. The mechanical properties of multilayer coatings also critically depend on the microstructure of the films. An excellent discussion of the effects of microstructure on the various properties of optical coatings has been given by Macleod.<sup>18</sup>

#### Optical Coating Materials

Many different materials have been used in the past for the construction of optical multilayer coatings. Some of the compounds used for the deposition of nonabsorbing layers for the ultraviolet, visible, and infrared parts of the spectrum are cryolite (1.35), LiF (1.37), MgF<sub>2</sub> (1.39), ThF<sub>4</sub> (1.52), CeF<sub>3</sub> (1.62), PbF<sub>2</sub> (1.73), ZnS (2.30), ZnSe (2.55), Si (3.5), Ge (4.20), Te (4.80), PbTe (5.50), and the oxides SiO<sub>2</sub> (1.48), Al<sub>2</sub>O<sub>3</sub> (1.60), MgO (1.72), Y<sub>2</sub>O<sub>3</sub> (1.82), Sc<sub>2</sub>O<sub>3</sub> (1.86), SiO (1.95), HfO<sub>2</sub> (1.98), ZrO<sub>2</sub> (2.10), CeO<sub>2</sub> (2.20), Nb<sub>2</sub>O<sub>5</sub> (2.20), Ta<sub>2</sub>O<sub>5</sub> (2.10), and TiO<sub>2</sub> (2.45). The numbers in parenthesis represent the approximate refractive indices at the midpoints of the material transparency range. Some of the metals used in the same wavelength range for the deposition of reflecting or absorbing layers are Ag(0.12 - i3.45), Al(1.02 - i6.85), Au(0.31 - i2.88), Cu(0.83 - i2.60), Ni(1.80 - i3.33), Cr(3.18 - i4.41), Inconel(2.94 - i2.92), and Rh(2.00 - i5.11). The complex refractive indices of the metals given in the brackets correspond to a wavelength of 0.56 μm. The above values are approximate and are intended as a rough guide only. More extensive listings of coating materials are given, for example, by Macleod<sup>2</sup> and Costich.<sup>34</sup>

As already mentioned, the properties of multilayers depend on the materials used for their construction. For example, layers made of oxides are, as a rule, harder than those made of fluorides, sulphides, or semiconductors. They are therefore preferred for use on exposed surfaces. Semiconductor materials should be avoided in filters that are to be used over a wide range of temperatures because their optical constants can change significantly. Some metals are soft and easily damaged while others tarnish when exposed to the atmosphere. Such coatings require further protective coatings, or should be cemented between two transparent plates. Other materials require the precoating with adhesion layers to ensure a good bond to the substrate. For example, frequently a Ni adhesive layer is deposited onto glass before coating with Au.

## Evaporation

*Conventional (nonreactive) or reactive evaporation* from resistance, induction or electron beam gun sources is a low energy process ( $\sim 0.1$  eV) and the resulting films frequently have a porous structure. The porosity may vary with the material, the substrate temperature, the residual pressure in the deposition chamber, the deposition rate and angle of incidence of the vapour on the substrate. Values of porosities ranging from 0 to 40 percent have been observed. On exposure to the atmosphere some of the voids in the film may adsorb water vapor. This increases the effective refractive index of the films and results in a shift of the spectral features of the multilayer towards longer wavelengths ("ageing"). This shift is partially reversible—by placing the filter in an inert atmosphere or in a vacuum, or on heating, some of the adsorbed water vapor can be removed. Unless it has been allowed for at the design stage, such ageing can render some filters useless.

The microstructure of the films can be significantly affected by bombarding the substrate during deposition with energetic ions from an auxiliary ion beam source.<sup>35–37</sup> The additional energy ( $\sim 50$  to  $100$  eV) results in denser films. Hence, coatings produced by *ion-assisted deposition* have higher refractive indices and exhibit less or no ageing on exposure to the atmosphere.

The *ion-plating* process can result in even denser coatings.<sup>38–40</sup> In this high deposition rate process the starting material must be a good conductor and is usually a metal. Argon and a reactive gas species are introduced into the chamber and, together with the evaporant, are ionized. The ions are then accelerated to the substrate with energies of the order of  $10$  to  $50$  eV. Transparent films with near-bulklike densities and low temperature variation of refractive index can be obtained by this process. For most materials the layers are glasslike and the interfaces remain smooth. This results in a lower scatter. *Plasma-ion-assisted deposition* is a process that also produces such good quality coatings, but it has the advantage over the ion-plating process that it does not require a conducting evaporant, so that fluorides and other nonconducting materials can be deposited with it.<sup>41–43</sup>

Conventionally evaporated thin films can be under compressive or tensile stresses. If not controlled, these stresses can distort the substrate or cause the multilayer to break up. The magnitudes of the stresses depend on the material and on the deposition conditions. It is often possible to select the materials and process parameters so that the stresses of the various layers counteract each other. In contrast, almost all ion-plated layers are under compressive stress. It is therefore more difficult to produce stress-compensated multilayers by this process.

## Sputtering

*Reactive or nonreactive DC, RF, AC, or pulsed magnetron sputtering* are also used to deposit optical multilayer coatings. Very many variants of this process exist.<sup>44</sup> Most are significantly slower than evaporation and the targets can be quite expensive. Filters produced by magnetron sputtering may therefore also be more expensive. However, the process is stable, provides excellent control over the thicknesses of the layers and can be readily scaled to provide uniform coatings over large areas. Both metal and metal oxide layers can be produced. Sputtering is an energetic process and results in dense, bulklike layers that exhibit virtually no ageing.

In *ion-beam sputtering* an energetic beam of inert ions is aimed at a target made of the material that is to be deposited. Atoms or clusters of atoms of the material are dislodged from the target and land on the substrate with a high energy (about  $10$  to  $200$  eV). This is the slowest physical vapor thin-film deposition method described here and it cannot yet be readily scaled for the coating of large components. However, it yields the highest quality coatings. Many of the high reflectance coatings for laser gyros, in which no significant losses can be tolerated, are produced in this way.

## Deposition from Solutions

In this procedure the substrate is either dipped in an organo-metallic solution and withdrawn at a very steady rate from it, or the solution is applied from a pipette onto a spinning substrate. The substrate is then placed in an oven to drive off the solvent. The thickness of the film depends on the



concentration of the solvent and on the rate of withdrawal or spinning. Other factors that influence the process are temperature and humidity, as well as the freshness of the solution. Although it yields quite porous films, this method is of interest because many of the layers produced in this way have a high laser damage threshold. The process has also been adapted for the coating of quite large area substrates with multilayer antireflection coatings for picture frame glass and for display windows.

### Other Deposition Methods

Great strides have been made in the development of various *chemical vapor deposition methods* for the production of optical coatings.<sup>45</sup> These processes often take place in the presence of plasmas operating at microwave and/or radio frequencies. The advantage of this approach is that it is relatively easy to produce robust layers with intermediate optical constants through the use of appropriate mixtures of two or more reactant gases. However, most of the reactants used are toxic and their handling requires special care.

*Atomic layer deposition* is inherently a slow deposition process that is capable of depositing very precise, conformal layers onto irregular-shaped substrates. Recently it has been demonstrated that it can be a commercially viable process if large chambers that contain stacks of closely packed substrate holders are used for the simultaneous coating of hundreds of objects.<sup>46</sup>

### Thickness Control during Deposition

The performance of many optical multilayers depends critically on the thicknesses of the individual layers. The control of the layer thicknesses during their formation is therefore very important. Many different methods exist for the monitoring of layer thicknesses. For very steady deposition processes, such as sputtering, simple timing can give good results. However, the most common techniques used are quartz crystal and optical monitoring. The former is very sensitive and can be used for thin and thick films, as well as transparent and opaque films. However, it is an indirect method and requires careful calibration. This is usually not a problem whenever layers of established coating materials are formed using a standard geometry and deposition conditions. Optical monitoring can be performed directly on the substrate, or indirectly on a witness glass. The quantities measured are usually  $T$ ,  $R$ , or the ellipsometric parameters. One advantage of direct optical monitoring is that the parameters measured are usually closely related to the required performance. Furthermore, with optical monitoring, a real-time error determination and compensation is possible after the deposition of each layer, through the reoptimization of the remaining layers of the system.<sup>47</sup> With this method even quite complicated multilayer structures can be manufactured. This process is now used in many laboratories. Even better results should be possible in the future when the above process is combined with ion-beam etching to adjust the thicknesses of layers that exceed the intended value.<sup>48</sup>

## 7.4 MEASUREMENTS ON OPTICAL COATINGS

---

### Optical Properties

*Transmission, Reflection, and Absorption* The most commonly used instrument for the measurement of the optical performance of thin-film coatings is the spectrophotometer. The wavelength dispersion of commercial instruments for the 0.185 to 80.0  $\mu\text{m}$  spectral range is usually provided by prisms or by ruled or holographic gratings. Grazing incidence gratings, crystals, or multilayer coatings are used in the soft x-ray and extreme ultraviolet (XUV) spectral regions. Fourier transform spectrometers are capable of measurements from about 2 to 500  $\mu\text{m}$ . A variety of attachments are available for the measurement of specular and diffuse reflectance. Absolute measurements of  $T$  and  $R$  that are accurate to within  $\pm 0.1$  percent are difficult to make even in the visible part of the electromagnetic spectrum. Measurements at oblique angles of incidence are even more difficult.

Very small absorptions of single layers are normally measured with calorimeters.<sup>49</sup> The losses of high performance laser reflectors are obtained from measurements of the decay times of Fabry-Perot interferometer cavities formed from these mirrors.<sup>50</sup>

Roughness of the substrate and irregularities occurring within individual films and the layer interfaces give rise to light scattering in all directions.<sup>51–53</sup> For many applications it is important to minimize this scatter. Special instruments, called scatterometers, are used to measure the angular variation of the light scatter. Such data provides information about the substrate and multilayer.<sup>54</sup>

The transmittance, reflectance, and absorptance of some optical coatings are affected by exposure to atomic oxygen and by electron, proton, and ultraviolet irradiation. They also depend critically on the cleanliness of the components measured. In space contamination of optical components can also take place.<sup>55,56</sup>

**Optical Constants** A reliable knowledge of the optical constants of all the materials used in the construction of optical multilayer coatings is essential. There exist many different methods for their determination.<sup>57</sup> These include methods that are based on refractometry, photometric, and spectrophotometric measurements of  $R$  and/or  $T$ , polarimetry, singlewavelength or spectroscopic ellipsometry, various interferometric methods, attenuated total reflection, or on a combination of two or more of the above methods. Excellent monographs on the various methods will be found in Palik's *Handbook of Optical Constants of Solids*.<sup>58,59</sup> Some are suitable for measurements on bulk materials and the results are valid only for films produced by the more energetic deposition processes described above. The optical constants of porous films must be measured directly. They will depend on the deposition parameters and on the layer thickness, and may differ significantly from those of bulk materials.<sup>60</sup> Special methods have to be used for the determination of the optical constants in the x-ray, XUV, and sub-millimeter regions. The accurate measurement of very small, residual extinction coefficients of transparent coating materials is difficult. Generally it involves the use of laser calorimetry or the use of the film as a spacer layer in a bandpass filter. It is also very important to be able to measure the thickness of the film independently.

**Laser Damage** A measure of the ability of an optical component to withstand high laser irradiations is the laser damage threshold (LDT). There are several ways of defining this quantity. One frequently used definition is based on a plot of the percentage of components that are damaged when they are exposed to different laser fluences. The value of the fluence corresponding to the intersection of a mean curve through the experimental points with the ordinate is defined to be the LDT. It is thus the maximum fluence at which no damage is expected to the component.

Absorption is the main cause for laser damage. The incident radiation that is absorbed in the optical component will be converted into heat. If the thermal conductance of the optical component is too low, the temperature of the local hot spot on the mirror will rise to a value at which damage occurs. The damage will therefore depend on the thermal conduction of the materials of which the mirror blank is made. For example, some high reflectivity mirrors consist of coatings on Si or Cu substrates that are water-cooled during use.

Thermal conductivities of thin films are several orders of magnitude smaller than those of the corresponding bulk materials. (Exceptions to this are some fluoride layers.) This compounds the problem. To increase the LDT, the deposition methods are optimized to obtain thin films with more bulklike thermal conductivities.

Absorption damage usually initiates at defects and other imperfections. In the case of the substrate, it may occur at or below the surface, even when the substrate material is nonabsorbing. It is very important to avoid materials with color centers and subsurface damage and inclusions. The substrate surface must be very smooth and devoid of scratches, digs, and pores, otherwise polishing compounds and other contaminants can be trapped. It is imperative that the substrate be perfectly clean prior to coating. Electric fields associated with the above imperfections increase the absorption by an amount that is proportional to the refractive index of the material.

The coating materials used for the construction of high LDT multilayers must be very pure, with absorption edges far away from the wavelength of interest. As a rule, materials in thin-film form have

extinction coefficients that are orders of magnitude larger than those of the corresponding bulk materials. Currently the processes used to produce high LDT coatings include ion-beam sputtering, sol-gel deposition, and electron beam gun evaporation. To reduce the effects of the residual surface roughness, the thicknesses of the layers are often adjusted to shift the peaks of the electric field away from the layer boundaries.

The form that the damage takes depends to a large extent on the materials. Pitting of the coatings is probably due to the evaporation of the thin-film materials. Delamination may be due to poor adhesion of the layers to the substrate, to undue stresses in the films and/or to a poor match between the expansion coefficients of the layers and the substrate.

The LDT also depends on the laser pulse duration. For very short pulses ( $<10$  ns) thermal conductance does not play a role in the process. For higher values, the LDT is proportional to the square root of the pulse duration. For high repetition rates the LDT depends on the repetition rate. To achieve a long life (10,000 or 100,000 pulses) in an industrial environment, the laser should be operated at a fraction (say, 1/4 or 1/10) of the nominal LDT. In CW lasers it is not the LDT, but the power handling capability that is of essence. Long before damage takes place, the heating can cause a distortion of the surface that, in turn, can result in loss of power and in mode and focussing problems.

The development of high LDT of laser coatings is so important, that conferences have been held in Boulder, Colorado, on this topic every year since 1970. For more detail the reader is referred to the proceedings of these conferences,<sup>61</sup> as well as to an article written by Ristau.<sup>62</sup> There exists also a draft international standard on this topic. An increasing number of thin-film vendors include in their catalogues LDT information on all or some of their products. Independent LDT test services are provided by several commercial companies and publically funded institutions.

## Mechanical Properties

Optical multilayer coatings are frequently required to operate under severe mechanical and environmental conditions. Quite frequently meeting these requirements is more difficult than to achieve the necessary optical performance. A number of standards deal with the substrate and coating quality (MIL-0-13830B), the adhesion of coatings (MIL-M-13508C, MIL C 48497), their abrasion resistance (MIL-C-675A, MIL C 675C, MIL-C-14806-A, MIL C 48497), hardness (MIL-M-13508C), and resistance to humidity (MIL-C-675A, MIL-C-14806-A, MIL-810-C, MIL C 48497), salt solution (MIL-C-675-A) and salt spray (MIL-M-13508-C, MIL-C-14806-A). Most of these standards are reprinted in Rancourt's book.<sup>3</sup> Depending on the application, multilayer coatings may be required to meet one or more of the above standards. An overview of the subject of stresses and hardness of thin films on a substrate has been recently published by Baker and Nix.<sup>63</sup> Sapiha and her coworkers compared various mechanical properties of three commonly used oxide layers produced by different deposition processes.<sup>64</sup>

## Analytical Analysis Methods

In addition to optical and mechanical measurements, multilayer coatings can be subjected to a number of analytical measurements. These include Auger electron spectroscopy, energy dispersive x-ray analysis, Rutherford backscattering, secondary ion mass spectrometry, transmission electron microscopy and x-ray photoelectron spectroscopy.<sup>63,65</sup> Some of these tests are destructive. However, when a multilayer coating is subjected to these tests, they yield fairly accurate information about the number of layers in a system, and on the composition, thickness, and structure of the individual layers.<sup>66</sup>

## 7.5 ANTIREFLECTION COATINGS

### Effect of Surface Reflections on Performance of Optical Systems

The reflectance of an interface between two nonabsorbing media of refractive indices  $n_1$  and  $n_2$  is given by

$$R = \left[ \frac{n_1 - n_2}{n_1 + n_2} \right]^2 \quad (31)$$

An expression for the total transmittance  $T_0$  of a nonabsorbing plane-parallel plate that takes into account the effect of multiple internal reflections within the plate can be obtained from Eq. (9):

$$T_0 = \frac{1-R}{1+R} \quad (32)$$

Of this light only a fraction  $(1-R)^2$  passes through the plate without undergoing any reflections.

An expression for the transmission of a number of such plates placed in series is of interest. It helps to explain the effect of multiple reflections between the various plates on the performance of devices such as tripple glazings and photographic objectives. It can be shown<sup>6</sup> that the total transmittance  $T_{\text{total}}$  of  $m$  plates placed in series is given by

$$T_{\text{total}} = \frac{T_0}{m - T_0(m-1)} \quad (33)$$

The amount of light transmitted directly  $T_{\text{direct}}$  is

$$T_{\text{direct}} = (1-R)^{2m} \quad (34)$$

The light  $T_{\text{stray}}$  that undergoes multiple reflections before transmission is responsible for spurious images and stray light in the image plane. It is given by

$$T_{\text{stray}} = T_{\text{total}} - T_{\text{direct}} \quad (35)$$

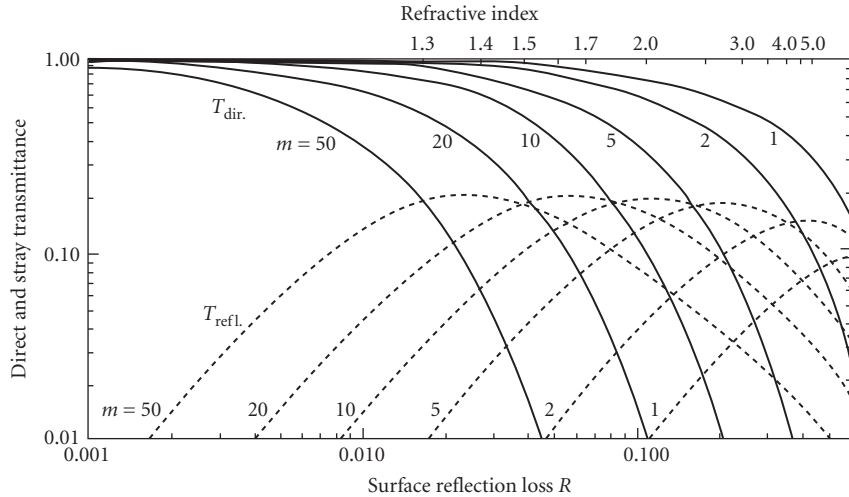
The variation of  $T_{\text{direct}}$  and  $T_{\text{stray}}$  with  $R$ , for several values of  $m$ , is shown in Fig. 7. The refractive indices of the plate material plotted against the upper  $x$  axis assume that the plates are in air.

It will be seen that even for a relatively small number of low-refractive-index plates the ratio  $T_{\text{stray}}/T_{\text{direct}}$  becomes significant. This means that in an image-forming system under unfavorable conditions the stray light can completely obscure the image.<sup>67</sup> Second, even in nonimaging optical systems the loss of light  $(1 - T_{\text{direct}} - T_{\text{stray}})$  can become quite prohibitive.

Both these problems can be overcome by reducing the surface reflection through the application of suitable antireflection coatings to the plate boundaries. Since antireflection coatings with zero reflectance across the whole spectrum cannot be constructed, the spectral reflectance  $R(\lambda)$  of antireflection coatings is usually chosen to minimise the integral

$$\int_{\lambda} R(\lambda) I(\lambda) S(\lambda) d\lambda \quad (36)$$

where  $I(\lambda)$  and  $S(\lambda)$  are the spectral-intensity distribution of the incident radiation and the spectral sensitivity of the detector, respectively. A low reflectance is thus needed only in the spectral region in



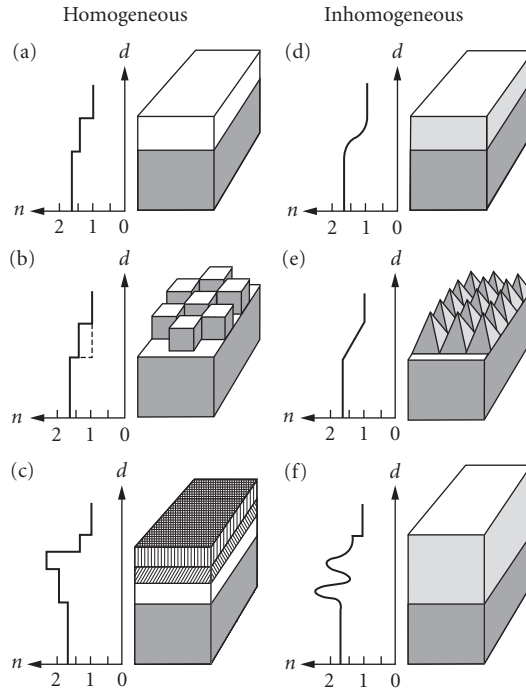
**FIGURE 7** Transmittance of a system of  $m$  parallel plates of surface reflectances  $R$  for directly transmitted radiation  $T_{\text{direct}}$  and for radiation that suffers multiple reflections before transmission  $T_{\text{stray}}$ . The upper x axis is calibrated in terms of the refractive index of the plates for the special case when the plates are in air.

which  $I(\lambda)S(\lambda)$  is significant. It should be emphasized here that in addition to this requirement, for most applications antireflection coatings must be mechanically very tough, withstand drastic climatic and thermal variations, and stand up to the usual lens-cleaning procedures. Some examples of improvements in the performance of image-forming and non-image-forming optical systems obtained through the use of antireflection coatings are given by Mussett and Thelen<sup>67</sup> and by Faber et al.<sup>68</sup>

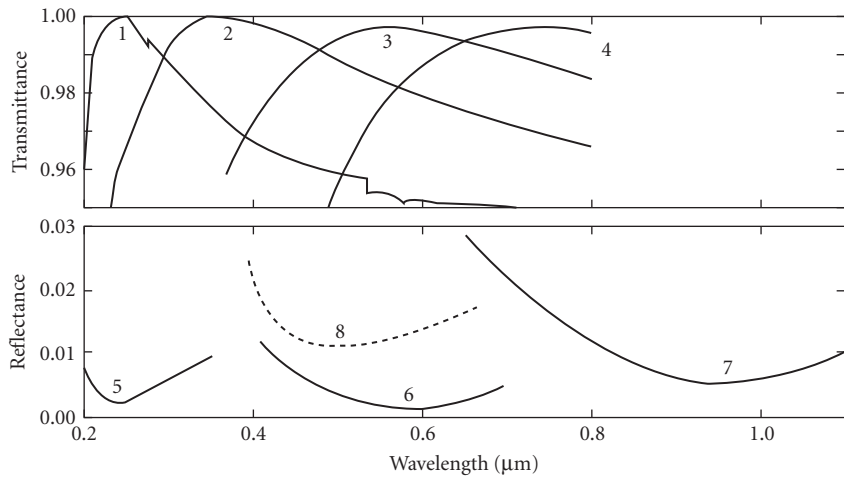
Antireflection coatings can be based on homogeneous layers or on inhomogeneous coatings. One can further classify them into single layer, digital, or structured, and homogeneous multilayer or complex inhomogeneous layer coatings (Fig. 8a to f). Because of their industrial importance, antireflection coatings for the visible and infrared spectral regions have been the subject of much research and development. Two books have been written on this topic<sup>69,70</sup> and there exists a very extensive literature in scientific and technical journals. For a review of this literature and for a systematic discussion of antireflection coatings, the reader is referred to the excellent review articles by Cox and Hass<sup>71</sup> and by Mussett and Thelen.<sup>67</sup> A recent report on the present state of the art has been published in the Japanese language. In this section, only a brief summary will be given of the results obtained thus far, intended to aid in the selection of antireflection coatings for particular applications. The calculated data is presented on a logarithmic scale. The relative wavenumber scale facilitates the calculations of the width of the effective region of a coating in different parts of the spectrum.

### Antireflection Coatings Made of Homogeneous Layers

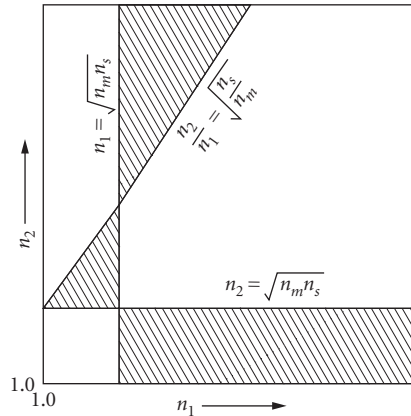
The single homogeneous-layer antireflection coating (Fig. 8a) was the first antireflection coating and perhaps is still the most widely used. Theoretically it should be possible to obtain a zero reflectance at one wavelength with single dense films. However, because of a lack of suitable low-index coating materials, this cannot be realized in practice for substrates with indexes less than about 1.9. Nevertheless, even with the available materials a very useful reduction in reflection in a broad spectral region is obtained for all common glass types, the reflectance never rising above that of the uncoated surface (Fig. 9, curve 8). With the sol-gel method it is possible to produce homogeneous porous oxide and fluoride films with very low refractive indices.<sup>72-75</sup> Such films have excellent optical characteristics



**FIGURE 8** Structure and effective refractive index profiles of various types of antireflection coatings. (a), (b), (c) homogeneous single layer, digital and multilayer AR coatings and (d), (e), (f) simple inhomogeneous layer, structured and more complex inhomogeneous layer AR coatings.



**FIGURE 9** Performance of single layer porous homogeneous antireflection coatings on various substrate surfaces. Porous silica on fused silica (1, 3, 5); on glass (6); on KDP (7);  $\text{SF}_8$  (4). Porous  $\text{MgF}_2$  on fused silica (2). A conventional single layer antireflection coating on glass is shown for comparison (8). (Curve 1 after Wilder;<sup>72</sup> curve 2 after Thomas;<sup>74</sup> curves 3 and 4 after Thomas;<sup>75</sup> curves 5–7 after O'Neill;<sup>73</sup> and curve 9 after Balzers.<sup>76</sup>)



**FIGURE 10** Refractive index combinations (*shaded areas*) of two-layer antireflection coatings with which a zero reflectance at one wavelength can be achieved.

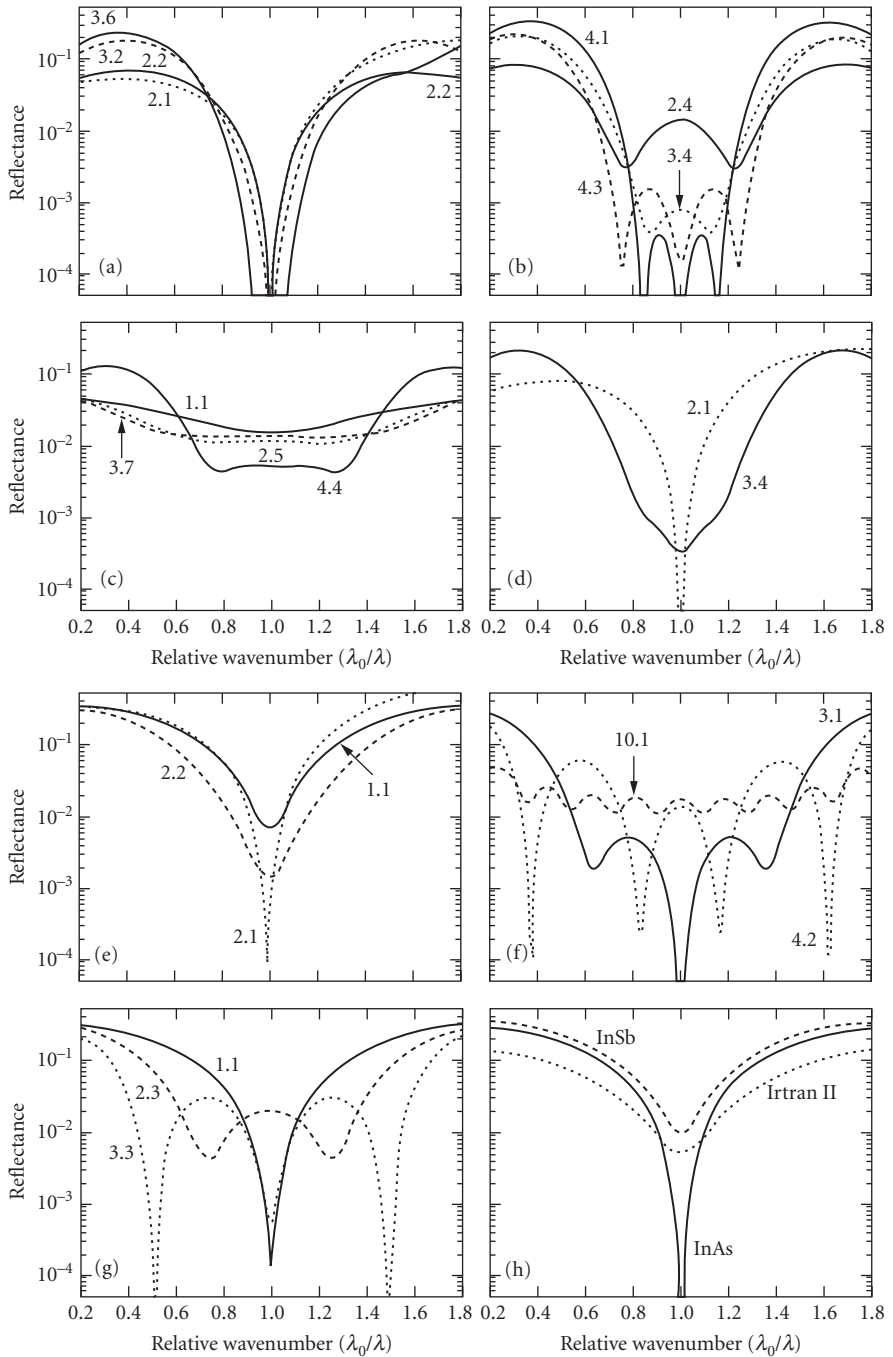
(Fig. 9) and have laser damage thresholds that are considerably higher than those produced by conventional means. However, these gains are at the expense of mechanical strength and long-term stability. Low-refractive index coating materials can also be simulated by the deposition or etching of subwavelength structures (Fig. 8*b, e*). The effective refractive index depends on the volume fraction occupied by the structures.<sup>77</sup>

If more than one layer is used, all the degrees of freedom could be used to either (1) obtain a more complete antireflection in one particular spectral region; (2) increase the width of the spectral region over which the reflectance is generally low; or (3) obtain a coating in which the low reflectance is very uniform across the spectrum.<sup>78,79</sup> Vlasov has shown with the aid of a diagram of the type shown in Fig. 10 that even for a two-layer antireflection coating there exists a large number of refractive index combinations which will yield zero reflectance at one wavelength.<sup>69</sup> As the number of layers and the overall thickness of the antireflection coating increases, it becomes possible to find solutions for a particular problem that not only fully meet the most important above desiderata and almost satisfy the others but are also based on the use of the mechanically most satisfactory coating materials.

The conditions that are satisfied by the refractive indexes and thicknesses of various types of antireflection coatings are given in Table 1. In a few cases where they are very complicated, reference is made to a paper in which they are set out in full. The calculated transmittance curves of antireflection-coated surfaces of glass (Fig. 11*a to c*), quartz (Fig. 11*d*), germanium (Fig. 11*e and f*), silicon (Fig. 11*g*), and other infrared materials (Fig. 11*h*) utilize refractive indexes that for the most part correspond to real coating materials, and hence the curves represent realistic solutions rather than the theoretically best possible ones. The actual refractive indices used in the calculations (and optical thicknesses where they do not correspond to a multiple of  $\lambda/4$ ) are given in Table 1.

Figure 11*a* shows the performance of several antireflection coatings on glass for applications which require the highest possible efficiency for a limited wavelength region. Of these the coating 2.1 has probably found the greatest acceptance. A typical measured performance curve for such a coating is shown in Fig. 12. Antireflection coatings with a low reflectance in a broad spectral region are shown in Fig. 11*b* and Fig. 13. Coatings of the type 3.4 probably find the widest application in practice. The performance of commercial coatings for quartz substrates are shown in Fig. 14.

Solutions listed in Table 1 presume that coating materials with the required refractive indices exist. This is frequently not the case and the thin-film designer must seek solutions based on available coating materials. For example, Furman<sup>89</sup> gives a series of practical two-, three-, and four-layer solutions for 10 different values of the substrate index ranging between 1.5 and 4.0, while Stolov provides<sup>90</sup> seven-layer solutions for 10 values of  $n_s$ ,  $1.46 \leq n_s \leq 1.82$ .



**FIGURE 11** Calculated performance of various antireflection coatings. The numbers identifying the individual curves refer to Table 1. (a) High-efficiency antireflection coatings for glass; (b) broadband antireflection coatings for glass; (c) highly achromatic antireflection coatings for glass; and (d) antireflection coatings for quartz. (e) Antireflection coatings for germanium; and (f) broadband antireflection coatings for germanium. (g) Antireflection coatings for silicon and (h) single-layer antireflection coatings for Irtran II, InAs, and InSb.



**TABLE 1** Some Antireflection Coatings<sup>80,81</sup> (*The incident medium in all cases is air.*)

Type	Conditions or Reference	Substrate Material	$n_s$	$n_1$ ( $n_1 d_1 / \lambda$ )	$n_2$ ( $n_2 d_2 / \lambda$ )	$n_3$ ( $n_3 d_3 / \lambda$ )	$n_4$ ( $n_4 d_4 / \lambda$ )	$n_m$
1.1	$n_1 = \sqrt{n_s n_m}; n_1 d_1 = \frac{\lambda}{4}$	Glass	1.51	1.38				1.00
		Irtran II	2.20	1.59				1.00
		InSb	4.00	2.20				1.00
		InAs	3.40	1.85				1.00
		Ge	4.10	2.20				1.00
		Si	3.50	1.85				1.00
2.1	$\tan^2 \delta_1 = \frac{(n_1^2(n_m - n_s)(n_s n_m - n_2^2))}{(n_s n_2^2 - n_m n_1^2)(n_s n_m - n_1^2)}$	Glass	1.51	2.30	1.38 (0.0524)			1.00
		Quartz	1.48	2.09	1.48 (0.0947)			1.00
		Ge	4.10	1.35	4.10 (0.0951)	4.10 (0.0586)		1.00
2.2	$\tan^2 \delta_2 = \frac{n_2^2(n_m - n_s)(n_s n_m - n_1^2)}{(n_s n_2^2 - n_m n_1^2)(n_s n_m - n_2^2)}$	Glass	1.51	1.70	1.38			1.00
		Ge	4.10	3.30	1.57			1.00
2.3	$n_2 n_s = n_1^2 n_m; n_1 d_1 = n_2 d_2 = \frac{\lambda}{4}$	Si	3.5	2.20	1.35			1.00
2.4	$n_1^2 - \frac{n_1 n_s}{2n_2 n_m}(n_2^2 + n_1^2)(n_1 + n_2) + n_2 n_s^2 = 0$ $\frac{1}{2}n_1 d_1 = n_2 d_2 = \frac{\lambda}{4}$	Glass	1.51	1.70	1.38			1.00
2.5	$n_1 d_1 = n_2 d_2 = \frac{\lambda}{4}$ (see Kard, Ref. 80)	Glass	1.55	1.484	1.32			1.00
3.1	$n_3 n_s = n_2^2 = n_m n_s;$ $n_1 d_1 = n_2 d_2 = n_3 d_3 = \frac{\lambda}{4}$	Ge	4.1	3.30	2.20	1.35		1.00
3.2	$n_1 n_3 = n_2 \sqrt{n_m n_s};$ $n_1 d_1 = n_2 d_2 = n_3 d_3 = \frac{\lambda}{4}$	Glass	1.53	1.80	2.14	1.47		1.00
3.3	$n_2^2 = n_m n_s, n_m n_1^2 = n_3^2 n_s;$ $n_1 d_1 = n_2 d_2 = n_3 d_3 = \frac{\lambda}{4}$	Si	3.45	2.56	1.86	1.38		1.00
3.4	$n_3^2 n_s = n_m n_1^2;$ $n_1 d_1 = \frac{1}{2}n_2 d_2 = n_3 d_3 = \frac{\lambda}{4}$	Glass	1.51	1.65	2.10	1.38		1.00
		Quartz	1.48	1.65	2.10	1.38		1.00
3.5	$n_3^2 n_s = n_m n_1^2,$ $\frac{1}{3}n_1 d_1 = \frac{1}{2}n_2 d_2 = n_3 d_3 = \frac{\lambda}{4}$	Glass	1.51	1.659	2.20	1.38		1.00

(Continued)

**TABLE 1** Some Antireflection Coatings<sup>80,81</sup> (*The incident medium in all cases is air.*) (Continued)

Type	Conditions or Reference	Substrate Material	$n_s$	$n_1$ ( $n_1 d_1 / \lambda$ )	$n_2$ ( $n_2 d_2 / \lambda$ )	$n_3$ ( $n_3 d_3 / \lambda$ )	$n_4$ ( $n_4 d_4 / \lambda$ )	$n_m$
3.6	(see Thetford Ref. 81)	Glass	1.52	1.80 (0.1799)	2.20 (0.4005)	1.38 (0.2402)		1.00
3.7	$n_1 d_1 = n_2 d_2 = n_3 d_3 = \frac{\lambda}{4}$ (see Kard, Ref. 80)	Glass	1.55	1.53	1.454	1.32		1.00
4.1	$n_1 n_4 = n_2 \sqrt{n_m n_3}$ ; $n_1 d_1 = n_2 d_2 = \frac{1}{2} n_3 d_3 = n_4 d_4 = \frac{\lambda}{4}$	Glass	1.51	1.38	1.548	2.35	1.38	1.00
4.2	$n_1 n_4 = n_2 n_3 = n_m n_5$ ; $n_1 d_1 = n_2 d_2 = n_3 d_3 = n_4 d_4 = \frac{\lambda}{4}$	Ge	4.0	2.96	2.20	1.82	1.38	1.00
4.3	$n_1 d_1 = n_2 d_2 = n_3 d_3 = n_4 d_4 = \frac{\lambda}{4}$ (see Kard, Ref. 80)	Glass	1.55	1.846	2.289	2.014	1.32	1.00
4.4	(Design derived from Kard, Ref. 82.)	Glass	1.55	1.656 (0.2417)	1.888 (0.2463)	1.832 (0.2390)	1.38 (0.2424)	1.00
10.1	$n_1 d_s = n_s - (11-l) \frac{n_s - n_9}{10}$ , $l = 1, 2, \dots, 10$ $n_1 d_1 = n_2 d_2 = \dots = n_{10} d_{10} = \frac{\lambda}{4}$ [see Kard, Ref. 80]	Ge	4.00	$n_1 = 3.735$ ...		$n_9 = 3.735$	$n_{10} = 1.35$	1.00

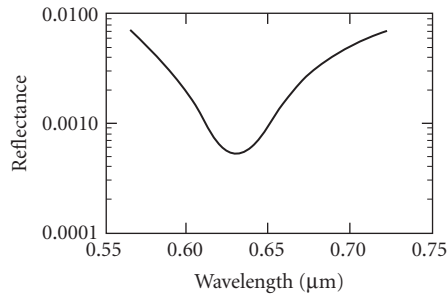
Willey has given a useful empirical expression which relates the average reflectance  $R_{\text{avg}}$  in the visible and near-infrared spectral region  $\lambda_{\text{min}} \leq \lambda \leq \lambda_{\text{max}}$  to the overall optical thickness  $\Sigma(nd)$  of an antireflection coating composed of layers of refractive indices  $n_M, n_H$  and a single, outermost layer of index  $n_L$ :<sup>91</sup>

$$R_{\text{avg}} = 0.01 \left[ \frac{\lambda_{\text{max}}}{\lambda_{\text{min}}} (n_L - 1) \right]^{3.4} \left( \frac{\lambda_{\text{max}}}{\Sigma(nd)} \right)^{0.63} [(1.2 - \Delta n)^2 + 0.42] \quad (37)$$

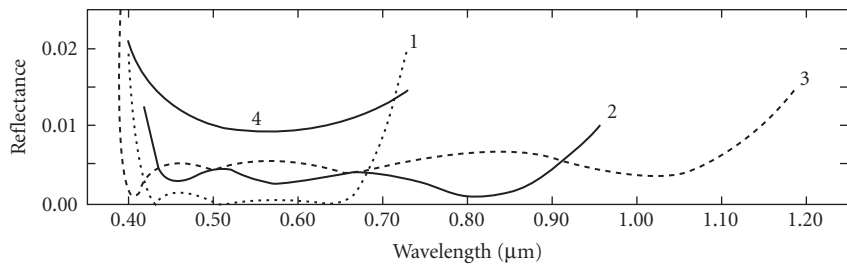
The above expression is valid for the following parameter values:

$$\begin{aligned} 1.5 \leq \frac{\lambda_{\text{max}}}{\lambda_{\text{min}}} \leq 3.0 & \quad 1.17 \leq n_L \leq 1.46 & \quad 1.38 \leq n_M, n_H \leq 2.58 \\ 1.0 \leq \frac{\Sigma(nd)}{\lambda_{\text{max}}} \leq 3.0 & \quad 0.4 \leq \Delta n = n_H - n_M \leq 1.2 \end{aligned} \quad (38)$$

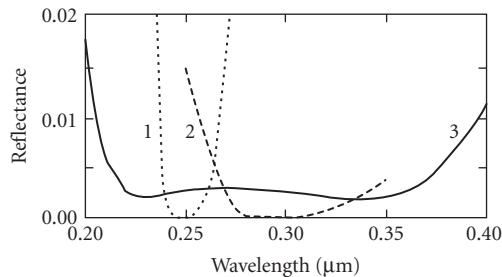
A method for the design of optimum or near-optimum two-material antireflection coatings for a given substrate, coating materials, and overall thickness has recently been described.<sup>92</sup>



**FIGURE 12** Reflectance of a high-efficiency antireflection coating on glass. (After Costich.<sup>172</sup>)



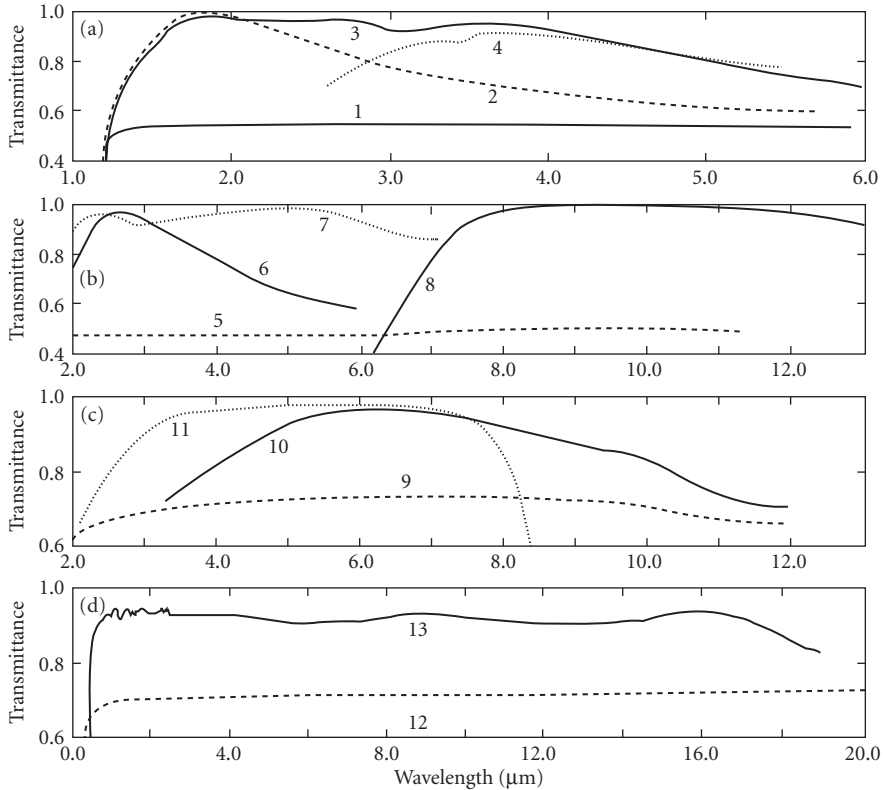
**FIGURE 13** Reflectances of three broadband antireflection coatings. (Curve 1 after Turner;<sup>173</sup> curve 2 after Optical Coating Laboratory;<sup>84</sup> curve 3 after Thin Film Lab;<sup>85</sup> and curve 4 after Balzers<sup>76</sup> corresponds to a single-layer AR coating on glass and is shown for comparison purposes.)



**FIGURE 14** Ultraviolet antireflection coatings on fused silica. (Curve 1 after TecOptics;<sup>83</sup> curve 2 after Reynard Corp.;<sup>87</sup> and curve 3 after Spindler & Hoyer.<sup>88</sup>)

Since for some applications the color introduced into an optical system by antireflection coatings is of paramount importance, it has been the subject of many studies.<sup>93–96</sup> One way to avoid the problem is to utilize coatings that are particularly achromatic (Fig. 11c). Thus, for example, 50 surfaces coated with antireflection coating 4.4 would have a transmittance of  $78 \pm 3$  percent across the whole visible spectrum. Nevertheless, of the coatings shown in Fig. 11c only the single-layer antireflection coating is being used extensively. Antireflection coatings can also be used to correct the residual color of lens systems.<sup>97</sup>

Often transmittance rather than reflectance measurements are performed to evaluate antireflection coatings. In general, it is incorrect to assume that  $T = 1 - R$ . For instance, the transmission of antireflection-coated infrared materials depends not only on the efficiency of the antireflection coating but

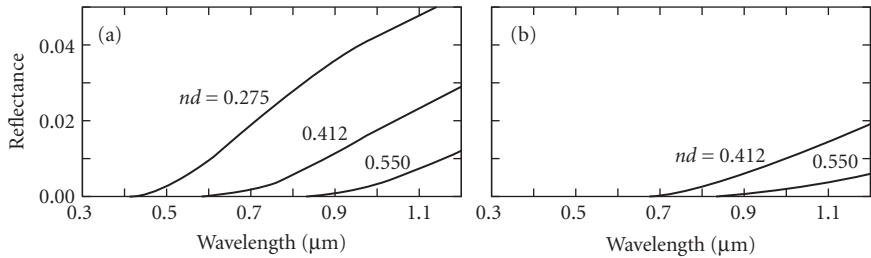


**FIGURE 15** Transmittance of plates of infrared materials antireflection-coated on both sides. (a) Silicon. Curve 1: uncoated plate of 1.5 mm thickness; curve 2: single  $\lambda_0/4$  layer of  $\text{SiO}_2$  ( $\lambda_0 = 1.8 \mu\text{m}$ ); curve 3:  $\lambda_0/4$  coatings of  $\text{MgF}_2$ , and  $\text{CeO}_2$  ( $\lambda_0 = 2.2 \mu\text{m}$ ); and curve 4: hard carbon layer. (b) Germanium. Curve 5: uncoated plate; curve 6: single  $\lambda_0/4$  layer of  $\text{SiO}$  ( $\lambda_0 = 2.7 \mu\text{m}$ ); and curve 7:  $\lambda_0/4$  coatings of  $\text{MgF}_2$ ,  $\text{CeO}_2$ , and  $\text{Si}$  ( $\lambda_0 = 3.5 \mu\text{m}$ ); and curve 8: environmentally stable, high laser damage threshold three-layer design based on  $\text{ThF}_4$  and  $\text{Ge}$ . (c) Irtran II. Curve 9: uncoated plate of 2 mm thickness; curve 10: single  $\lambda_0/4$  coating of  $\text{CeF}_3$ ; and curve 11:  $\lambda_0/4$  layers of  $\text{MgF}_2$  and  $\text{SiO}$  ( $\lambda_0 = 4.2 \mu\text{m}$ ). (d) Zinc selenide. Curve 12: uncoated plate and curve 13: extremely broadband AR coating composed of 398 layers produced by molecular beam deposition. (Curves 1–3, 5–7, 9–11 after Cox and Hass;<sup>71</sup> curve 4 after Balzers;<sup>76</sup> curve 8 after Oh<sup>98</sup>; and curve 13 after Fisher.<sup>99</sup>)

also on the thickness and temperature of the material. This is because of the finite scatter and absorption in such materials and because of the dependence, in some cases, of the latter on temperature. The measured spectral transmittances of three common antireflection-coated infrared materials at room temperature are shown in Fig. 15. Curves for other materials are given by Cox and Hass.<sup>71</sup>

## Inhomogeneous and Structured Antireflection Coatings

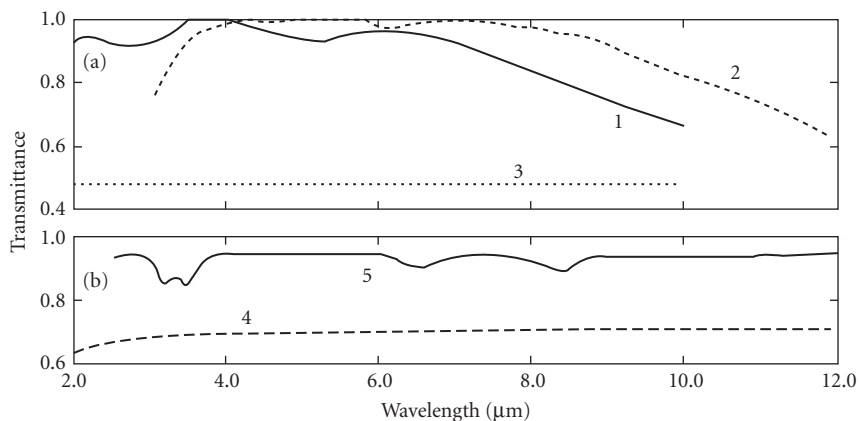
The interface between two media with refractive indices  $n_1$  and  $n_2$  can be antireflection coated over a very broad spectral region by the application of a transition layer with an index that changes continuously from  $n_1$  to  $n_2$  (Fig. 8d). Many different refractive index profiles have been investigated in the past.<sup>100–103</sup> Although some of these profiles are more effective than others, all reduce the reflectance to a fraction of a percent over the spectral region in which the coatings are transparent and do not



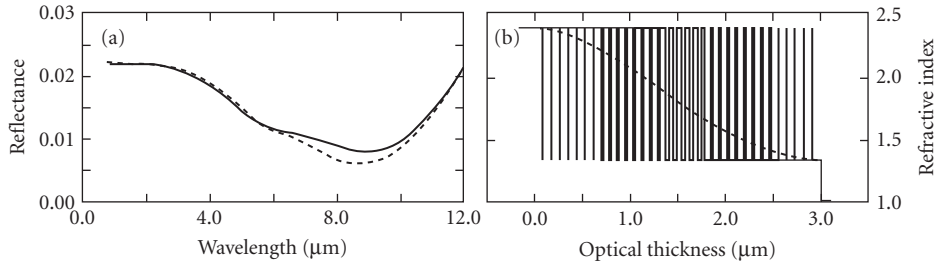
**FIGURE 16** Calculated reflectances of the interfaces between two media antireflection-coated with inhomogeneous layers of indicated thicknesses and (complex) refractive indexes that vary smoothly, from the index of one medium to that of the other. (a) Two nonabsorbing media of indexes 1.52 and 2.36. (b) Glass-chromium interface with refractive indexes 1.52 and  $2.26 - i0.43$ , respectively. (After Anders and Eichinger.<sup>107</sup>)

scatter excessively, and for which the optical thickness of the layer is at least one half wavelength (Fig. 16a). A further advantage of inhomogeneous antireflection coatings is that they are not sensitive to the angle of incidence.<sup>104</sup> Processes used for the production of inhomogeneous antireflection coatings include various additive, subtractive, additive/subtractive, and replication methods. Excellent reviews of this topic exist.<sup>105, 106</sup>

In the additive method relatively dense inhomogeneous layers of varying compositions of two or more compounds are formed on the substrate by physical or chemical deposition processes. Such coatings are mechanically more durable than any other described in this section. However, because of a lack of coating materials with refractive indexes lower than about 1.35, solid inhomogeneous layers are not very suitable for the antireflection coating of air-glass interfaces. The several different inhomogeneous antireflection coatings of this type described in the past do not offer any special advantages over those composed of homogeneous layers.<sup>70, 108, 109</sup> The situation is different in the case of high-index materials (Fig. 17). An even lower reflectance can be achieved by ending the inhomogeneous layer



**FIGURE 17** (a) Measured transmittance of a germanium plate coated on both sides with inhomogeneous antireflection coatings. Curve 1: 1.2- $\mu\text{m}$ -thick film with an index that changes gradually from that of Ge to that of  $\text{MgF}_2$  (after Jacobsson<sup>110</sup>); curve 2: 1.76- $\mu\text{m}$ -thick film with an index that varies from 4.0 to 1.5, overcoated with a 0.74- $\mu\text{m}$ -thick homogeneous  $\text{MgF}_2$  layer (after Scheuerman<sup>111</sup>); and curve 3: transmittance of an uncoated plate. (b) Measured transmittance of a TBI-5 plate. Curve 4: uncoated and curve 5: coated on both sides with ten 2.5- $\mu\text{m}$ -thick homogeneous layers with refractive indexes that vary between 1.3 and 2.29 and that are obtained through the evaporation of suitable NaF-CdTe mixtures. (After Kuznetsov and Perveyev.<sup>112</sup>)



**FIGURE 18** Calculated performances (a) and refractive index profiles (b) of an inhomogeneous layer coating and its two-material equivalent. (After Southwell.<sup>116</sup>)

when its index is equal to the square of that of the lowest-index coating material available. It is then possible to complete the coating by depositing an additional homogeneous quarter-wave-thick layer of that material (Fig. 17a).

A dense inhomogeneous layer can be approximated by a series of homogeneous layers of gradually decreasing refractive indexes (curve 10.1, Fig. 11f).<sup>113,114</sup> Such layers can be prepared by evaporating a series of appropriate mixtures of two coating materials or, without mixing, by using the Herpin equivalent-index concept<sup>115</sup> to simulate intermediate refractive indexes. An even more practical solution is to replace the inhomogeneous layer by a series of thin homogeneous layers of two materials only (Fig. 18).<sup>116</sup>

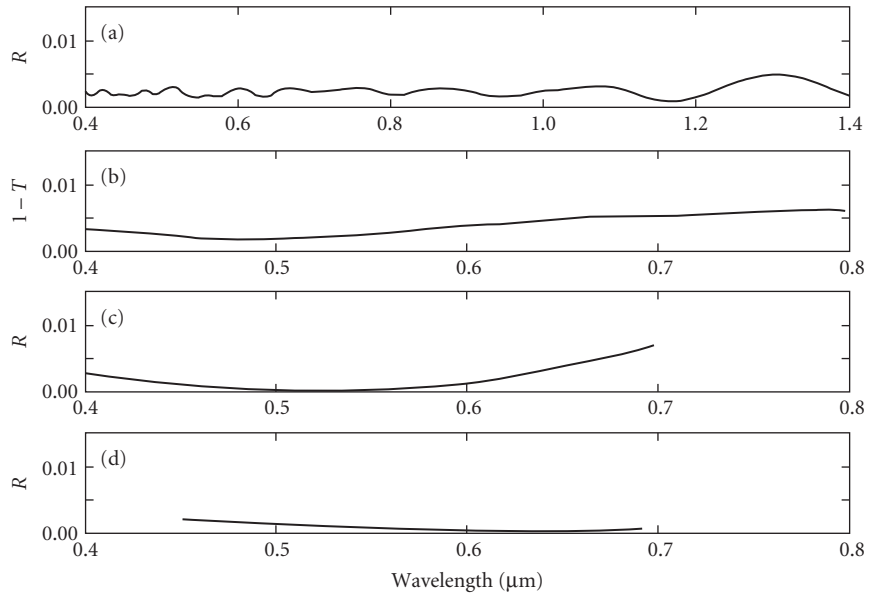
In another additive process a refractive index variation down to a value of 1.0 is achieved by depositing onto the substrate microspheres of transparent oxides or fluorides which form pyramid-like clumps (Fig. 8e).<sup>117</sup> If losses due to scattering are to be low, the average lateral size of the features of this structure must be a small fraction of the shortest wavelength for which the coating is to be effective. A reflectance of 0.3 percent can be achieved, but the films are fragile.

The subtractive methods are attractive because they do not require expensive deposition equipment. The surface to be antireflection coated is leached and/or etched to form a porous transition layer in which the index varies with thickness. Not all optical materials can be treated in this way. However, special phase-separable glasses have been developed that lend themselves well to this process.<sup>118–121</sup> Fairly durable antireflection coatings with a reflectance of less than 0.5 percent for the 0.35 to 2.5  $\mu\text{m}$  spectral region have been produced in this way (Fig. 19a). Some other materials, such as Lexan, Mylar, and CR-39 plastic, require an ion implantation pretreatment before the etching can be applied.<sup>101,122</sup>

In the technologically important additive/subtractive method, a single glasslike film is first deposited by a sol-gel process onto the surface that is to be antireflection coated. The composition of the film is such that, after phase separation, it can be readily leached and/or etched to form a porous microstructure with a controlled refractive index gradient.<sup>123,126</sup> This eliminates the need for the use of expensive phase separation glass components. Such coatings have reflectances as low as 0.13 percent and a laser damage threshold that is 4 times higher than that of coatings produced by conventional physical vapor deposition techniques (Fig. 19b).<sup>127</sup> Variants of this process exist.

Microstructured surfaces can also be produced in polymeric and similar materials by a replication process from a suitable cast. Average reflectances in the visible of the order of 0.3 percent have been reported for surfaces treated in this way (Fig. 19c).<sup>124</sup>

Recently there has been a renewed interest in antireflection coatings in which the variable porosities of leached or etched layers are simulated by dense regular shaped structures formed by photochemical or mechanical means. Clapham and coworkers appear to have been the first to demonstrate such devices.<sup>128</sup> They applied a photoresist to a surface, exposed it to two orthogonal sets of ultraviolet interference fringes, and then developed it to form a regular array of protuberances that could be optionally enlarged by additional ion-beam etching. Such surfaces can reduce the reflectance to less than 0.3 percent in the visible part of the spectrum (Fig. 19d).<sup>125</sup> The theory of such structures has been investigated by several workers<sup>129,130</sup> and devices for wavelengths extending into the micrometer



**FIGURE 19** Measured performance of various broadband inhomogeneous antireflection coatings. (a) Subtractive process—leached and etched phase separation glass (after Asahara<sup>120</sup>); (b) additive/subtractive process—leached and etched phase-separable film deposited onto fused silica (after Yoldas<sup>123</sup>); (c) replication process on a cellulose acetate butyrate surface (after Maffitt<sup>124</sup>); and (d) structured antireflection coating in photoresist (after Wilson<sup>125</sup>).

and sub-millimeter region have been fabricated.<sup>77,121</sup> Efficient laboratory prototype AR coatings produced by the glancing angle deposition process have been demonstrated by Kennedy and Brett.<sup>131</sup>

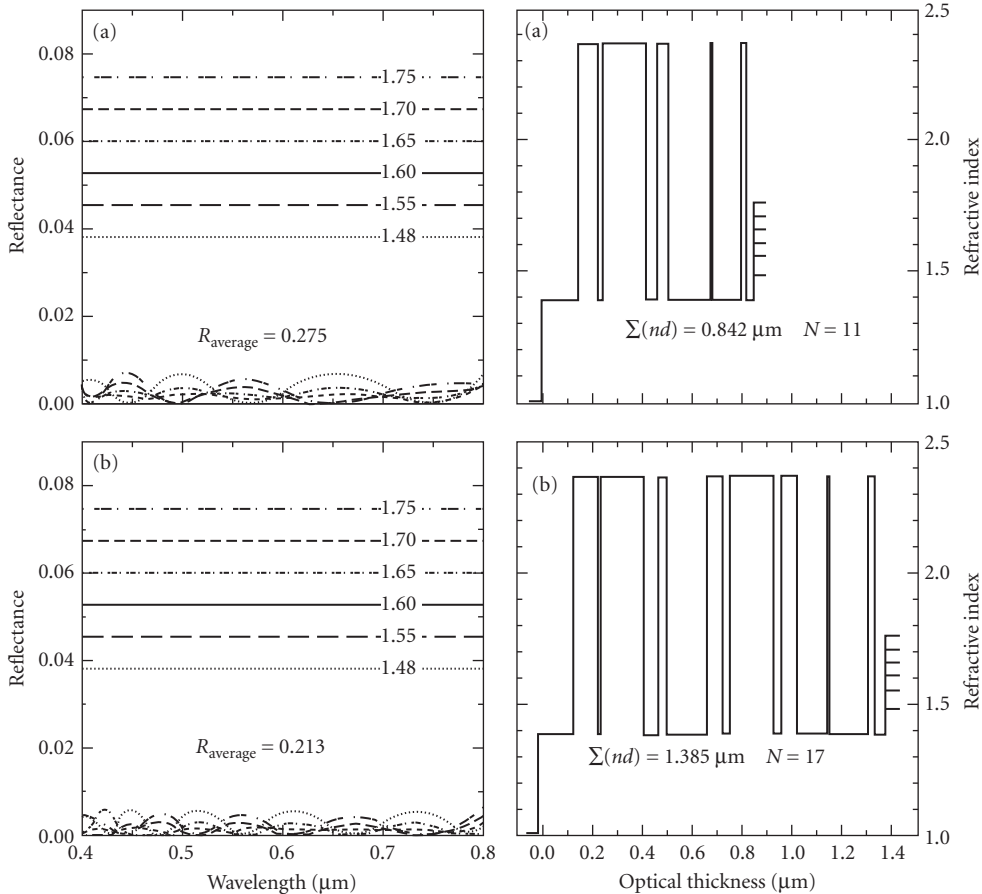
## Universal AR Coatings

The idea of a universal AR coating which would reduce the reflectances of a range of substrates with different refractive indices has been first proposed by Vvedenski et al.<sup>132</sup> Such an AR coating could simplify operations in a coating shop, because all substrates, regardless of the glass that they were made of, could be coated in one deposition run. The prize that one pays for this convenience is that the performance of an AR coating consisting of the same number of layers, but designed for one substrate only will be significantly better.

In Fig. 20 are shown the results obtained for two AR coatings of this type consisting of 11, 17 layers each (rows a, b, respectively). The coatings were designed to simultaneously reduce the reflectances of substrates of index 1.48, 1.55, 1.60, 1.65, 1.73, and 1.75. In column 1 the reflectances of the uncoated and of the coated substrates are shown. Also indicated are the average reflectances of all the coated substrates. The refractive index profiles of the six systems for the different substrate materials shown in a2, b2 differ only in the substrate refractive indices. Increasing the number of layers in the universal AR coatings shown in this figure will result in a diminishing return in the performance. Several papers on this topic have been published by Yeuch-Yeong Liou.<sup>134</sup>

## Antireflection Coating of Absorbing and Amplifying Media

Antireflection coatings for glasses and semiconductors in regions of weak absorption, and for present-day laser materials in which  $k_r$ , the imaginary part of the complex refractive index [Eq. (25)] is small and negative, differ little from those described above.<sup>135</sup>



**FIGURE 20** Universal AR coatings for substrates with refractive indices 1.48, 1.55, 1.60, 1.65, 1.70, and 1.75. Rows *a*, *b* depict solutions based on 11, 17 layers. Column 1 depicts the reflectances of the substrates before and after the application of the AR coating. In column 2 are shown the refractive index profiles of the solutions. (After Dobrowolski and Sullivan.<sup>133</sup>)

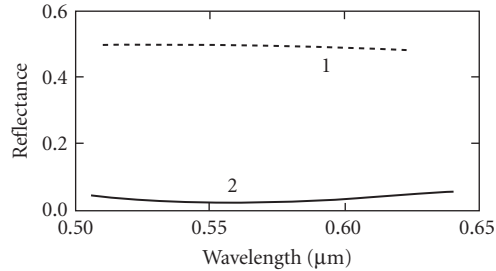
The reduction of the reflectance of opaque materials for architectural, decorative and technical purposes leads to a corresponding increase in the absorption.<sup>136,137</sup> This can be utilised to improve the efficiency of radiation detectors and to control the solar-absorptance and thermal-emittance characteristics of surfaces (see, for example, Ref. 138 and 139). A measured example of the reduction in the reflectance of a metal surface attainable with a homogeneous nonabsorbing layer is shown in Fig. 21.

Inhomogeneous transition layers whose refractive index and extinction coefficient change gradually from the values of one of the media to those of the other are also very effective.<sup>107</sup> The calculated reflectance of a glass-chromium interface coated in this way, useful for blackening of prism faces, lens edges, scales, and so on, is shown in Fig. 16*b*. Metal-air interfaces can be treated a little less effectively with single layers because of the lack of suitable low-index materials.

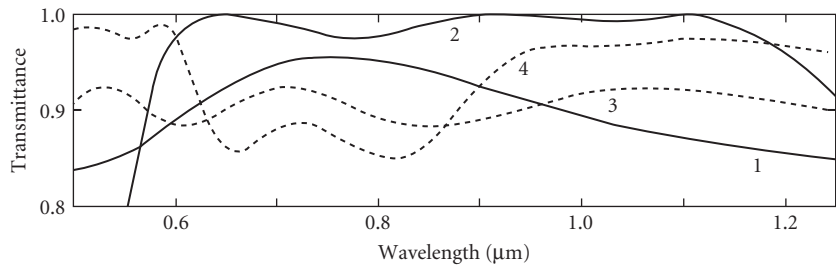
### Antireflection Coating of Surfaces Carrying a Thin Film

For some applications it is necessary to deposit a certain film onto a glass surface. The objectionable reflectance that such a film would normally introduce can be avoided by incorporating it into an





**FIGURE 21** Antireflection coating of opaque metals. Curves 1 and 2: reflectance of chromium and of chromium with a ZnS layer. (After Lupashko and Sklyarevskii.<sup>136</sup>).



**FIGURE 22** Calculated single-surface transmittance of antireflection coatings incorporating a conducting layer. Curves 1 and 2: glass of refractive index 1.755 coated with a 0.566- $\mu\text{m}$ -thick  $\text{SnO}_2$  layer before and after three dielectric layers were added to complete the antireflection coating and curves 3 and 4: as above except that the refractive index of the glass and the metric thickness of the  $\text{SnO}_2$  film are 1.516 and 0.200  $\mu\text{m}$ , respectively. (After Veremey and Gorbunova.<sup>142</sup>)

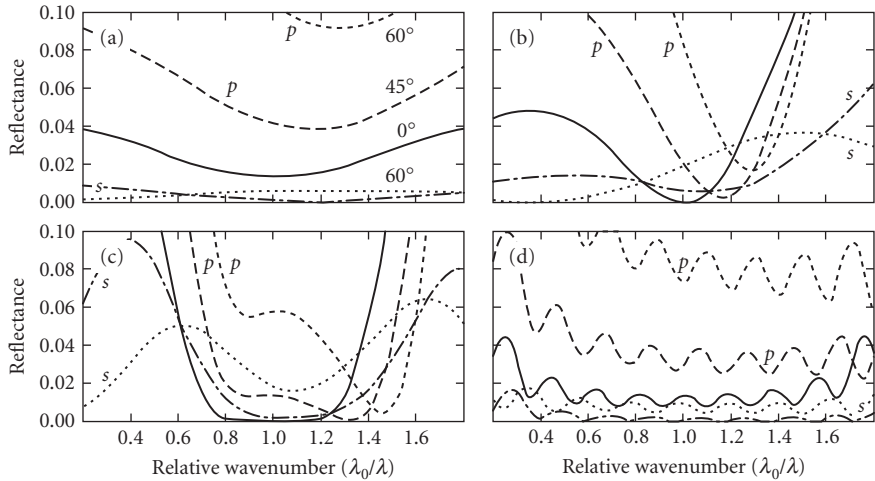
antireflection coating. Thus, for example, Fig. 22 shows the calculated transmittances of two conducting layers before and after inclusion in antireflection coatings. The use of homogeneous and of inhomogeneous antireflection coatings with absorbing layers for ophthalmic purposes is described by Katsube et al.<sup>140</sup> and Anders.<sup>141</sup>

### Antireflection Coatings at Nonnormal Angle of Incidence

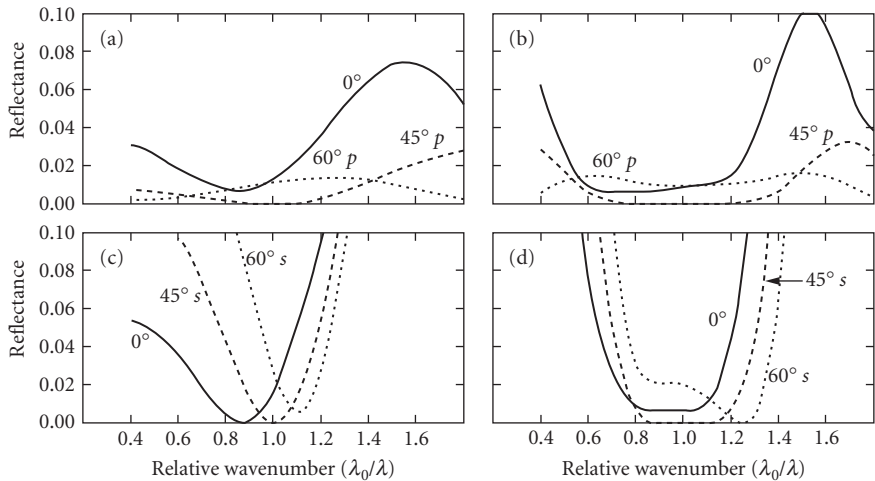
The calculated performances at  $0^\circ$ ,  $45^\circ$ , and  $60^\circ$  incidence of the three commercially most important antireflection coatings and of a 10-layer coating for germanium are shown in Fig. 23. The deterioration with angle of incidence is particularly severe for the narrowband high-efficiency antireflection coating. Figure 23d suggests that the closer the design of an antireflection coating approximates an inhomogeneous transition layer (Sec. 7.5, subsection “Inhomogeneous and Structured Antireflection Coatings”) the less angle-dependent is its performance.

To design an antireflection coating for one angle of incidence and one plane of polarization the effective thicknesses and refractive indexes [Eqs. (18) and (19)] of its layers should satisfy the relations set out in Table 1. In practice, small departures from those conditions are required to optimise the performance with good coating materials. Calculated curves for two sets of two- and three-layer coatings designed for use at  $45^\circ$  are shown in Fig. 24.

If the obliquely incident radiation is unpolarized, a compromise is necessary. The effective thicknesses are matched for the design angle, but the refractive-index conditions set out in Table 1



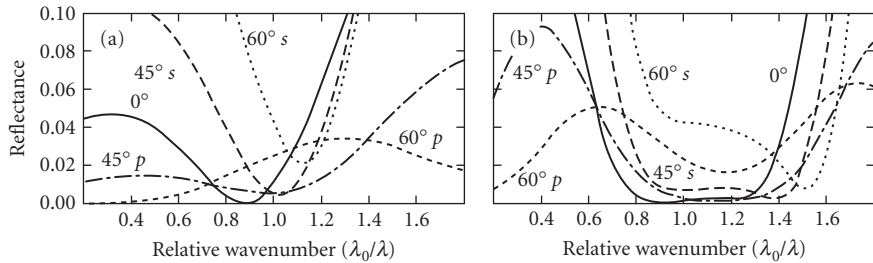
**FIGURE 23** Calculated reflectance of (a) one-, (b) two-, (c) three-, and (d) 10-layer antireflection coatings (systems 1.1, 2.1, 3.4, and 10.1 in Table 1) at angles of incidence of  $0^\circ$  (solid curve),  $45^\circ$  (dashed curve), and  $60^\circ$  (dotted curve) for light polarized parallel and perpendicular to the plane of incidence.



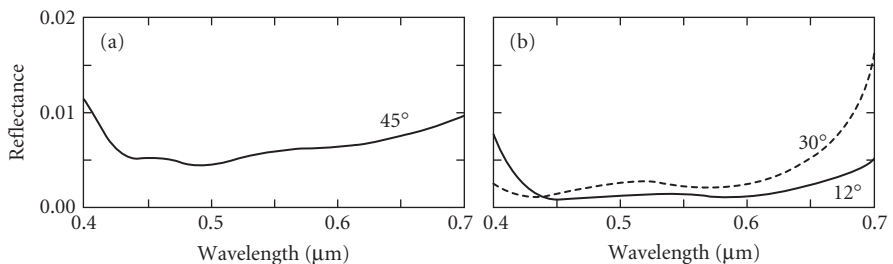
**FIGURE 24** Calculated reflectance at  $0^\circ$  (solid curve),  $45^\circ$  (dashed curve), and  $60^\circ$  (dotted curve) of (a) and (c) two-layer and (b) and (d) three-layer antireflection coatings designed for light incident at  $45^\circ$  and polarized parallel or perpendicular to the plane of incidence. (After Turbadar.<sup>143,144</sup>)

are satisfied for normal incidence since they cannot be satisfied for both polarizations at the same time (Fig. 25).

Achromatic antireflection coatings can be designed that are optimised for both polarizations at the same time or that are suitable for use over a range of angles of incidence (Fig. 26b).<sup>24,145</sup> But the problem becomes more difficult the greater the spectral and angular ranges required, especially if angles of incidence greater than  $60^\circ$  are involved.



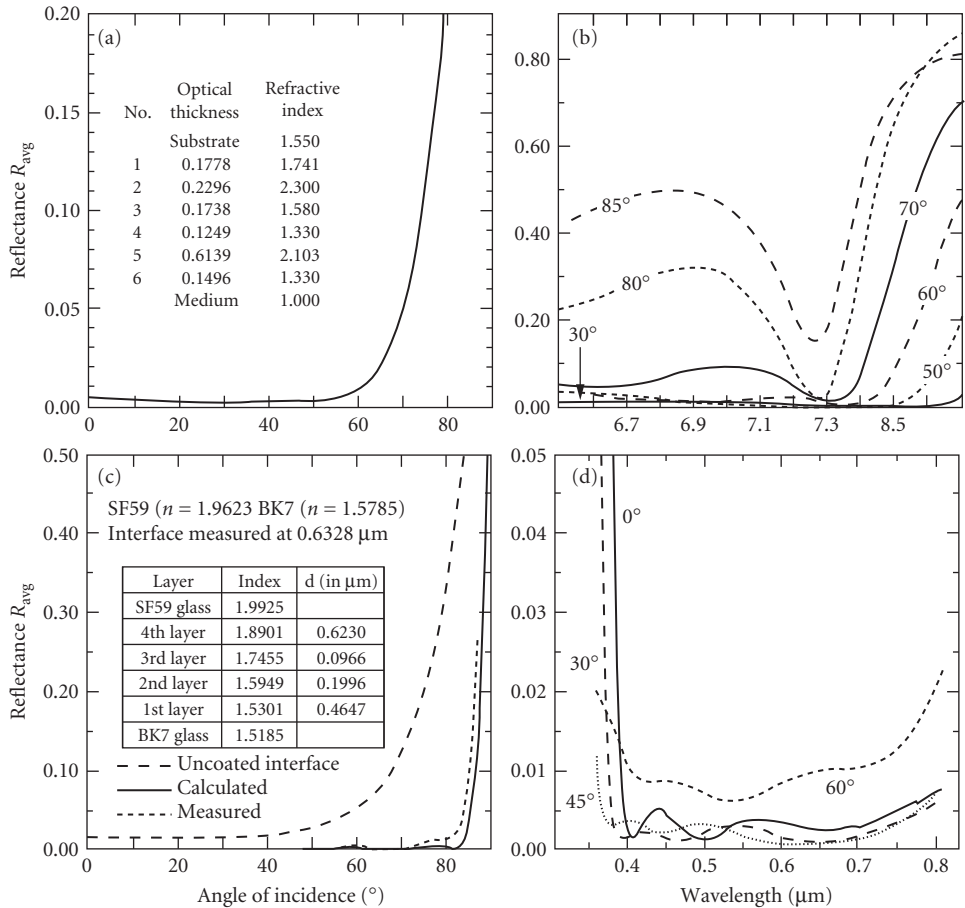
**FIGURE 25** Calculated reflectance at  $0^\circ$  (solid curve),  $45^\circ$  (dashed curve), and  $60^\circ$  (dotted curve) of (a) two-layer and (b) three-layer antireflection coatings (systems 2.1 and 3.4 in Table 1) for use with unpolarized light, with the thicknesses of the layers optimized for an angle of incidence of  $45^\circ$ .



**FIGURE 26** Average reflectances for unpolarized light of antireflection coatings designed (a) for  $45^\circ$  incidence and (b) for use with a convergent light cone of semi-angle of  $30^\circ$ . (*Optical Coating Laboratory*.<sup>84</sup>)

In Fig. 27a is shown the variation with angle of incidence of the calculated average reflectance of a six-layer AR coating system for the He-Ne laser wavelength. The reflectance is less than 1 percent for all angles smaller than  $60^\circ$ , but only for a narrow wavelength region around the design wavelength. The performance was limited by the lowest available refractive index at the time.

It has been shown previously (Fig. 19) that, for normal incidence of light, the reflectance from an interface between two media with refractive indices  $n_s$ ,  $n_m$  can be effectively removed over a broad spectral region by an inhomogeneous layer with a refractive index that changes gradually from  $n_s$  to  $n_m$ , providing that the optical thickness of this inhomogeneous layer is at least one half wavelength thick at the longest wavelength for which the reflectance is to be low. It has been shown numerically<sup>151</sup> and theoretically,<sup>152</sup> that this rule continues to hold for up to very high angles of incidence, providing that the *effective* optical thickness is at least one-half wavelength at the highest angle of interest. This means that broadband inhomogeneous layer AR coatings effective up to very high angles of incidence will be very thick. However, it is possible to transform such solutions to homogeneous layer systems with which, because of the additional thin-film interference effects, similar performances can be obtained with a small number of layers and much smaller overall optical thicknesses. Such solutions still call for the use of at least one layer with a refractive index that is very close to the medium index,  $n_m$ . Such solutions can be readily implemented for glass/glass interfaces (Fig. 27c). The angular measurements shown in this diagram were obtained with a laser light source, but the AR region was quite broad. When the medium is air and a maximum angle of incidence is  $85^\circ$  is stipulated, a refractive index of the outermost layer should be of the order of 1.02. In the infrared part of the spectrum there are a number of Reststrahlen materials with a refractive index that falls below unity. The measured average spectral reflectance for a number of angles of incidence of an AR coating based on such a material is shown in Fig. 27b. The antireflection region is narrow because the refractive index of the outermost layer has the required value only in a narrow wavelength band. In the visible part of the spectrum such indices can only be achieved with very porous or structured layers. Ways of producing such layers are



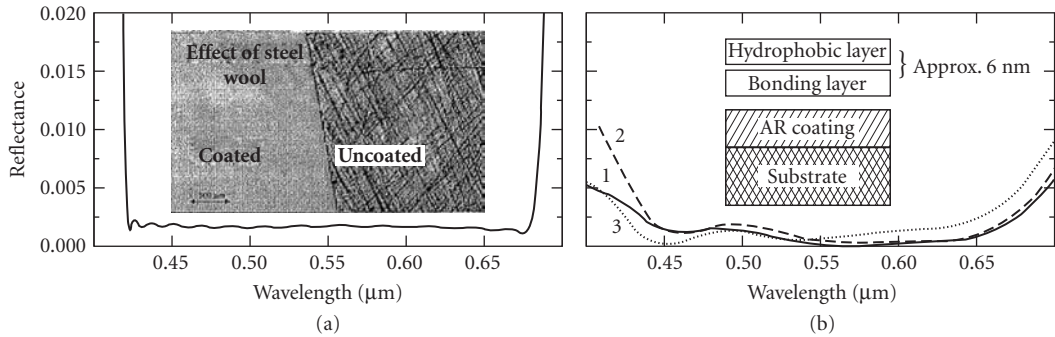
**FIGURE 27** Wide angle AR coatings. (a) Calculated average reflectance of a conventional AR coating for the He-Ne laser wavelength for angles of incidence up to 60° (after Dobrowolski *et al.*<sup>146,147</sup>); (b) measured average reflectance of a Si/air interface for angles of incidence up to 85° with an AR coating based on the use of a Reststrahlen material (after Dobrowolski *et al.*<sup>148</sup>); (c) measured average reflectance of a glass/glass interface for angles of incidence up to 85° (after Ma *et al.*<sup>149</sup>); and (d) predicted performance of a hybrid wide-band AR coating for angles of incidence up to 60° (after Schulz *et al.*<sup>150</sup>).

being investigated at many laboratories. The predicted average reflectance of a hybrid AR coating consisting of seven solid thin films and an outermost structured layer is shown in Fig. 27d. It is expected to be less than 1 percent over a broad spectral region for all angles of incidence smaller than 60°. This will be a huge improvement over the performance of the coating depicted in Fig. 27a.

The design of antireflection coatings for very high angles of incidence has been considered by Monga.<sup>153,154</sup>

## Nonoptical Properties of Antireflection Coatings

Antireflection coatings, in addition to optical specifications, often have to satisfy additional, nonoptical requirements. One such requirement may be to provide scratch resistance to soft, plastic surfaces. In Fig. 28a is shown the measured reflectance of an AR coating produced by Schulz *et al.* for



**FIGURE 28** Nonoptical properties of antireflection coatings. (a) Measured reflectance of a 27-layer, 3- $\mu\text{m}$ -thick  $\text{SiO}_2/\text{Ta}_2\text{O}_5$  AR coating. The insert illustrates the effect of steel wool on the coated and uncoated portions of the substrate (after Schulz et al.<sup>43</sup>). (b) Performance of a water- and dust-repellent AR coating. Curves 1 and 2 are the calculated and measured reflectances. Curve 3 is the performance after cleaning the coating with acetone (after Bruynoghe et al.<sup>155</sup>).

a PMMA surface.<sup>43</sup> It consists of 27 layers of  $\text{SiO}_2$  and  $\text{Ta}_2\text{O}_5$ , with an overall metric thickness of over 3  $\mu\text{m}$ , of which most corresponds to  $\text{SiO}_2$ . The inset shows, that the AR coating provides good protection from abrasion. Bruynoghe et al. describe an AR coating which repels water, oil, and dust (Fig. 28b).<sup>155</sup> This coating consists of a more or less conventional AR coating onto which is deposited a bilayer coating, the first part of which provides for good adhesion to the AR coating, and the second, the required hydrophobic properties. The total thickness of the bilayer is 0.006  $\mu\text{m}$ .

## 7.6 TWO-MATERIAL PERIODIC MULTILAYERS THEORY

### Nonabsorbing $[AB]^N$ and $[AB]^N A$ Multilayer Types

Let a periodic multilayer be composed of  $N$  periods  $AB$ , where  $A$ ,  $B$  represent layers of refractive indexes  $n_A$ ,  $n_B$  and optical thicknesses  $n_A d_A$ ,  $n_B d_B$ . The most general representation of the complete multilayer is

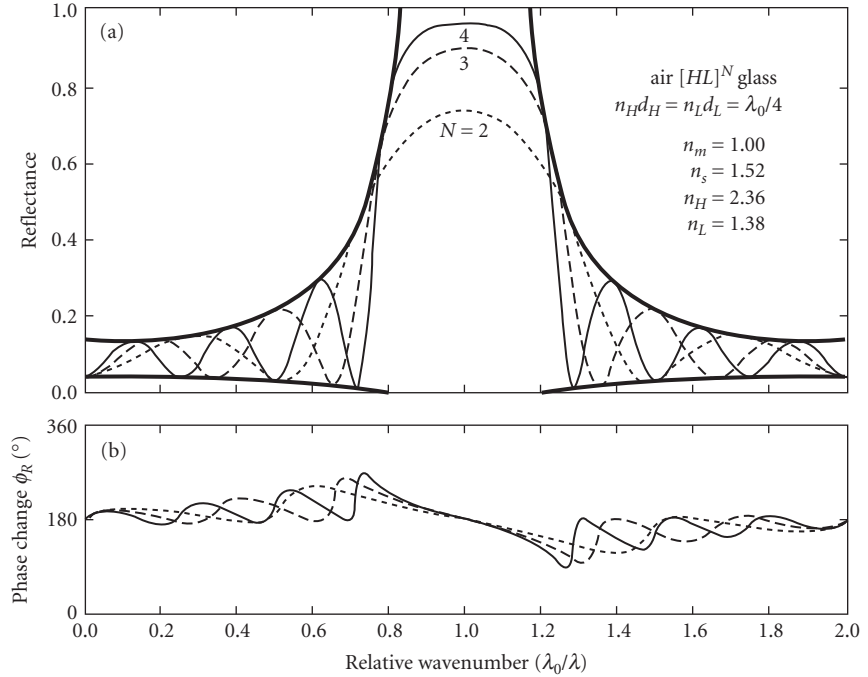
$$AB \cdot AB \cdot AB \cdots AB = [AB]^N \quad (39)$$

In practice it is customary to write  $[HL]^N$  or  $[LH]^N$ , depending on whether  $n_A$  is greater or less than  $n_B$ , respectively. The spectral-reflectance curve of the multilayer  $[AB]^N$  will lie within a pair of envelopes which, at normal incidence, depend only on  $n_A d_A$ ,  $n_B d_B$ ,  $n_A$ ,  $n_B$ ,  $n_s$ , and  $n_m$ .<sup>156,157</sup> For  $n_s = n_m$  the lower of the envelopes becomes  $R = 0$ . The envelopes contain high-reflectance zones within which the reflectance at each wavelength increases monotonically with the number of periods, approaching 1.0 as  $N$  tends to infinity (Fig. 29). Outside these high-reflectance zones the curves exhibit subsidiary maxima and minima whose number depends on  $n_A d_A / n_B d_B$  and which increases with  $N$ . The first-order high-reflectance zone occurs at a wavelength  $\lambda_1$  given by

$$n_A d_A + n_B d_B = \frac{\lambda_1}{2} \quad (40)$$

and subsequent zones occur at wavelengths  $\lambda_q$  ( $\lambda_1 > \lambda_2 > \lambda_3 \dots$ ) given by

$$N(n_A d_A + n_B d_B) = q \frac{\lambda_q}{2} \quad q=2,3,4 \dots \quad (41)$$



**FIGURE 29** (a) Calculated reflectance and (b) phase change on reflection of periodic multilayers of the type  $[HLH]^N$ .  $H$  and  $L$  stand for high- and low-refractive-index layers of quarter-wave thickness at  $\lambda_0 = 1.0 \mu\text{m}$ . The heavy lines are the envelopes of the reflectance curves.

providing that at these wavelengths

$$n_A d_A, n_B d_B \neq p \frac{\lambda_q}{2} \quad p=1,2,3 \dots \quad (42)$$

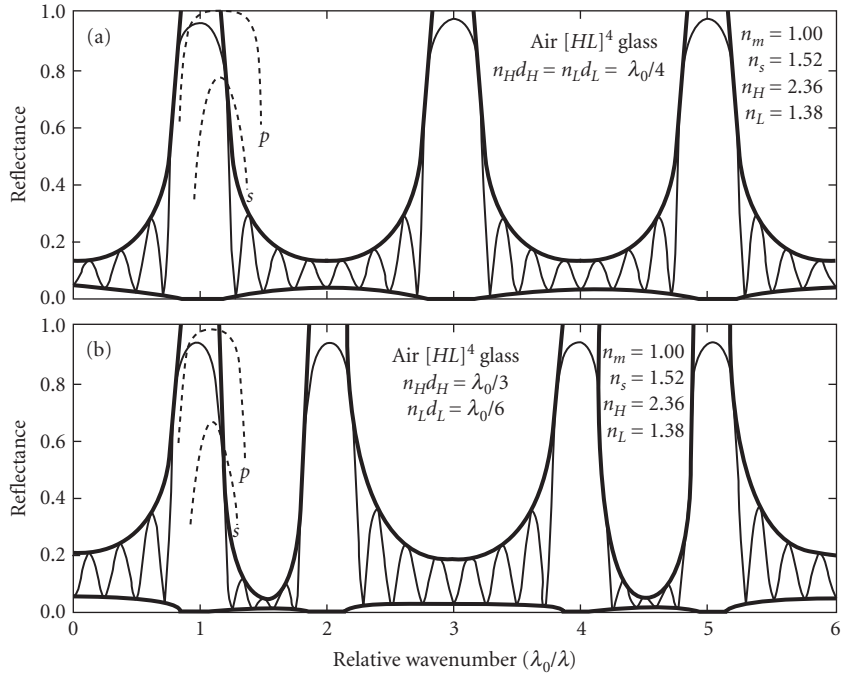
It is thus possible, by choosing suitable thickness ratios, to arrange for or to suppress high-reflectance zones in several spectral regions at the same time. This is useful in the design of broadband reflectors (Sec. 7.7, “Rejection Filters”), cutoff filters and hot- and cold mirrors (Sec. 7.8), laser reflectors, and so on. Typical curves for thickness ratios 1:1 and 2:1 are given in Fig. 30. Plotted on a  $\lambda_0/\lambda$  scale, they show symmetry about all wavelengths  $\lambda$  for which  $n_A d_A$  and  $n_B d_B$  are both equal to some integral multiple of  $\lambda/4$ .

**Maximum Reflectance** For a given refractive index ratio ( $n_A/n_B$ ) and number of periods  $N$  the highest reflectance occurs whenever  $n_A d_A$ ,  $n_B d_B$  are each equal to an odd multiple of  $\lambda/4$ . It is given by

$$R_{\max} = \left[ \frac{n_m/n_s - (n_A/n_B)^{2N}}{n_m/n_s + (n_A/n_B)^{2N}} \right]^2 \quad (43)$$

Intermediate reflectances are obtained for the related symmetrical multilayers  $[AB]^N A$ :

$$R_{\max} = \left[ \frac{n_m n_s / n_A^2 - (n_A/n_B)^{2N}}{n_m n_s / n_A^2 + (n_A/n_B)^{2N}} \right]^2 \quad (44)$$



**FIGURE 30** Calculated reflectance curves of periodic multilayers with (a) 1:1 and (b) 2:1 thickness ratios. The dotted curves represent the reflectance of polarized radiation incident at an angle of  $60^\circ$ .

Results for a number of such cases are given in Fig. 31. Intermediate reflectances can be obtained by changing the refractive index of any of the layers in the stack.

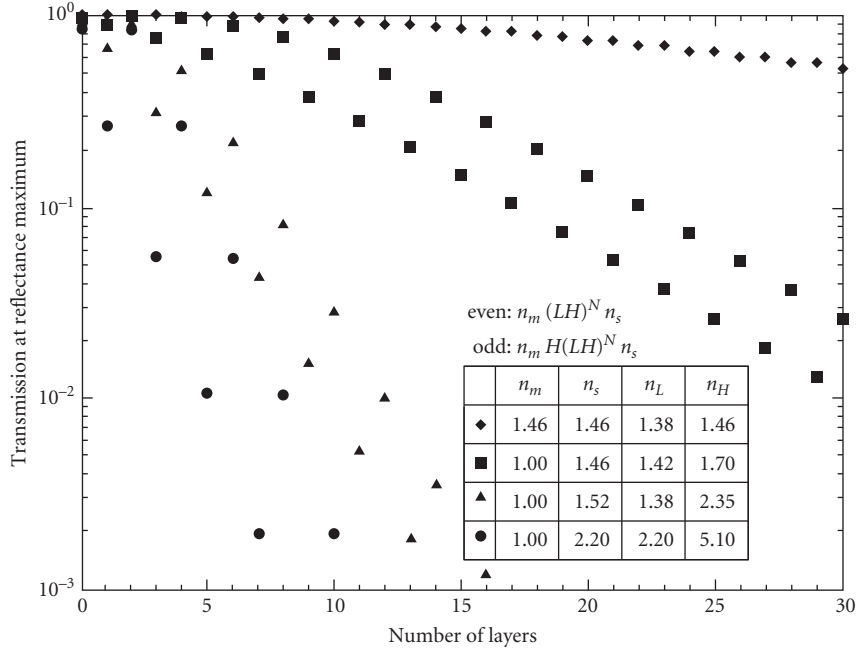
Explicit expressions for  $R$  for other thicknesses are complicated.

**Phase Change on Reflection** The dispersion of the phase change on reflection from periodic all-dielectric multilayers is much greater than that of metal reflectors. Unless corrected for, it will lead to errors in some metrological and interferometric applications. Like reflectance, it varies rapidly outside the high-reflection zone (Fig. 29b). Within the high-reflection zone it changes almost linearly with wavenumber and is  $180^\circ$  at  $\lambda_0/\lambda = 1$ . The slope of this portion of the graph increases and approaches a limiting value as  $N$  tends to infinity. The limiting value (in degrees per unit wavelength) is given by

$$\left[ \frac{d\phi}{d\lambda} \right]_{\lambda} = \left\{ \begin{array}{ll} \frac{180n_m}{\lambda_0(n_H - n_L)} & \text{for } n_H \\ \frac{180n_H n_L}{\lambda_0 n_m (n_H - n_L)} & \text{for } n_L \end{array} \right\} \quad (45)$$

depending on whether the light is first incident on a high- ( $n_H$ ) or low- ( $n_L$ ) refractive index layer.<sup>158</sup> The above values should be multiplied by 3, 5, ... in stacks composed of  $3\lambda/4$ ,  $5\lambda/4$ , ... layers.

Böhme has shown that, by changing the refractive index of one of the layers in a quarter-wave stack, it is possible to obtain a zero value of the phase change on reflection  $\phi$  at  $\lambda_0$ .<sup>159</sup>



**FIGURE 31** Transmittance at the reflection maximum of quarterwave stacks composed of  $\text{MgF}_2$  and  $\text{SiO}_2$  in the visible region (◆),  $\text{MgF}_2$  and  $\text{MgO}$  in the ultraviolet (■),  $\text{MgF}_2$  and  $\text{ZnS}$  in the visible region (▲), and  $\text{ZnS}$  and  $\text{PbTe}$  in the infrared (●).

### Periodic Multilayers of the $[(0.5A)B(0.5A)]^N$ Type

The construction of such multilayers differs from that of the type  $[AB]^N A$  discussed above by having outermost layers of only half the thickness of the remaining layers.<sup>115</sup> The position and width of the high-reflection zones are the same in both cases, but in coatings of the  $[(0.5A)B(0.5A)]^N$  type it is possible to reduce the height of the subsidiary maxima on either one or the other side of the main reflectance maximum if  $n_A t_A = n_B t_B$ . Kard et al. describe the optimum choice of all the construction parameters ( $N, n_A, n_B, n_s, n_m$ ) of such a coating.<sup>160</sup> If the refractive indices  $n_s$  and  $n_m$  of the surrounding media must be chosen on some other basis, then for maximum improvement of the short- and long-wavelength transmission the refractive indexes  $n_A$  and  $n_B$  of the coating materials must satisfy

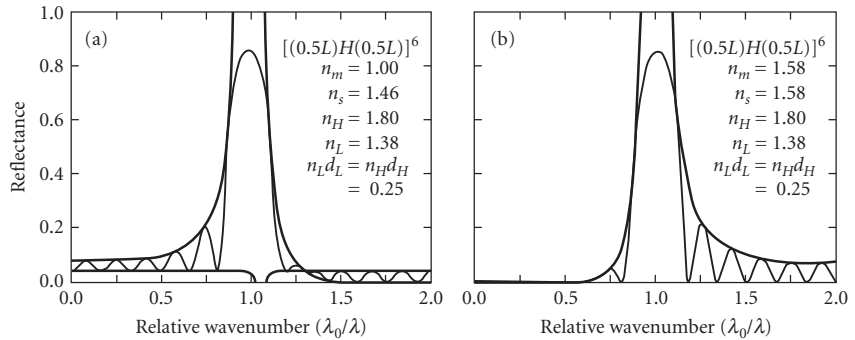
$$n_s n_m = \frac{n_A^3}{n_B} \quad (46)$$

or

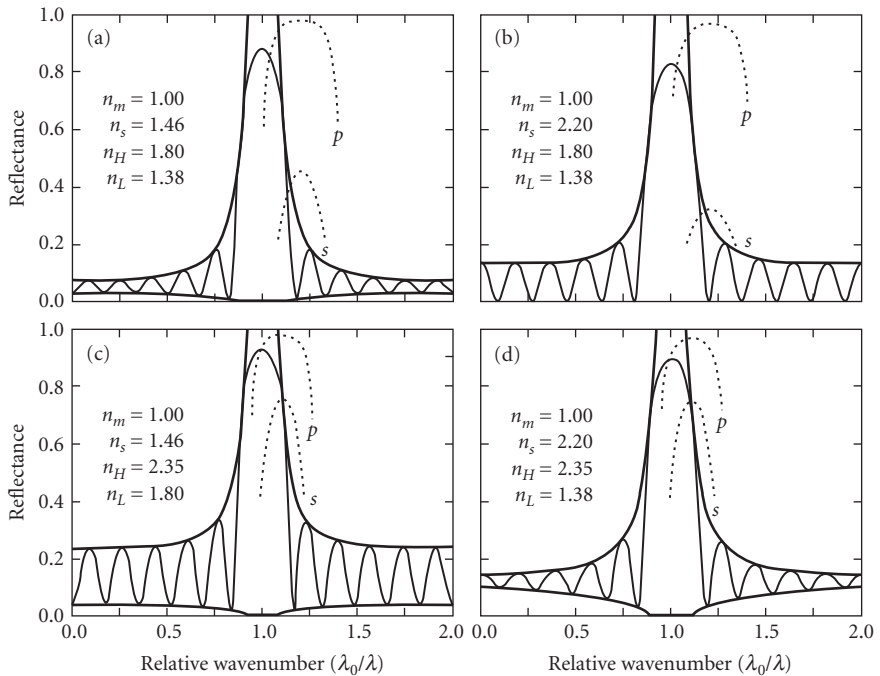
$$n_s n_m = n_A n_B \quad (47)$$

respectively. Estimates of the maximum reflectance for larger values of  $N$  can be obtained from Fig. 31. Multilayers of this type are of importance in the design of cutoff filters (Sec. 7.8), and are illustrated in Fig. 32, which should be compared with the curves of Fig. 33.





**FIGURE 32** Calculated reflectance curves of two periodic multilayers with symmetrical periods of the type  $[(0.5L)H(0.5L)]^6$  in which the subsidiary reflectance maxima on (a) the short- and (b) the long-wavelength side of the high-reflectance zone are reduced.

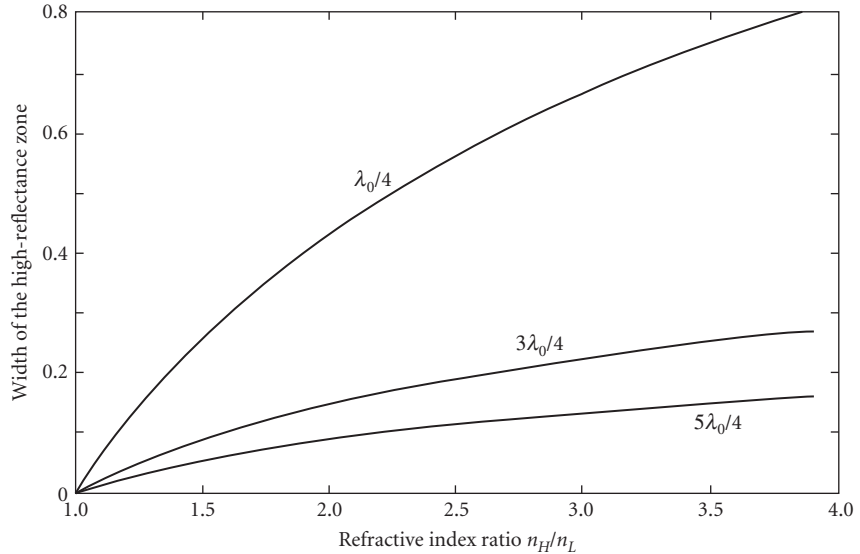


**FIGURE 33** Calculated reflectance curves of two quarter-wave stacks of the type  $H(LH)^N$  with different values of  $n_H$  and  $n_L$  but with the same ratio  $n_H/n_L$ , (rows 1, 2) deposited onto two different substrate materials (columns 1 and 2). The dotted curves represent the reflectances for light incident at  $60^\circ$ .

### Width of the High-Reflectance Zone

For a given value of  $(n_A/n_B)$ , the width  $\Delta\lambda_R/\lambda$  of the high-reflectance zone is greatest when  $n_A d_A = n_B d_B = \lambda/4$ , and it is then given by

$$\frac{\Delta\lambda_R}{\lambda} = \frac{4}{\pi} \sin^{-1} \left( \frac{1 - n_A/n_B}{1 + n_A/n_B} \right) \quad (48)$$



**FIGURE 34** Calculated widths of high-reflectance zones of two-material periodic stacks of layers of optical thicknesses  $\lambda_0/4$ ,  $3\lambda_0/4$ , and  $5\lambda_0/4$  for different refractive index ratios.

This width is reduced by a factor of  $2N-1$  if  $N$ th-order quarter-wavelength layers are used. Graphs of the widths of the high-reflectance zones versus refractive index ratio for  $\lambda_0/4$ ,  $3\lambda_0/4$ , and  $5\lambda_0/4$  layer stacks are given in Fig. 34. Periodic multilayers with equal refractive index ratios have high-reflectance zones of equal widths, but their reflectance curves will not be the same unless the refractive indexes of the surrounding media are also increased by the same ratio (Fig. 33).

### Periodic Multilayers of the $[xH \cdot (1-x)L]^N \cdot xH$ Type

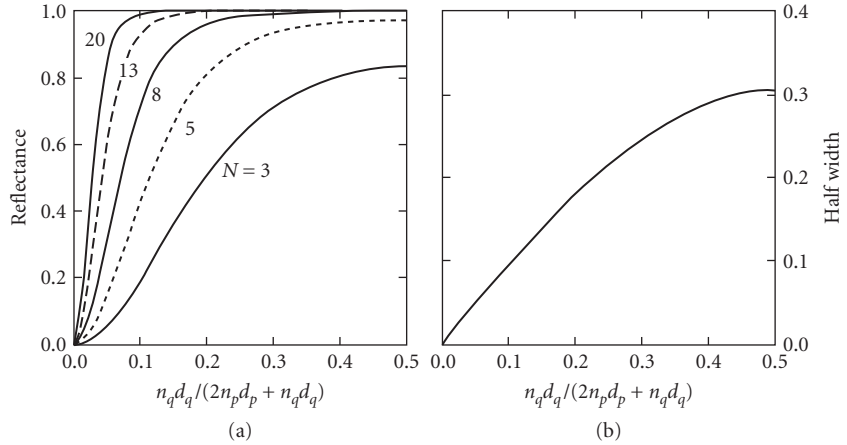
As already stated in Sec.7.6, subsection “Periodic Multilayers of the  $[(0.5A)B(0.5A)]^N$  Type” it is not necessary for the optical thicknesses of the layers of a periodic multilayer reflector to be equal to a quarter wave. A multilayer system of the type  $[xH \cdot (1-x)L]^N \cdot xH$ , where  $H, L$  correspond to quarter-wave layers of a high- and low-refractive index and where  $0 < x < 1.0$ , will have a high reflectance, providing that the number of periods  $N$  is high enough.<sup>161-164</sup> However, the smaller the value of  $x$ , the narrower the width of the high reflectance zone. Given two coating materials, it is thus possible to independently select the reflectance and the width of the rejection region. Figure 35a, and b shows the relationship between  $R_{\max}$ ,  $\Delta\lambda_R/\lambda$  and  $x$ ,  $N$  for values of  $n_H, n_L$ , corresponding to the refractive indices of ZnS and polyethylene at about 200  $\mu\text{m}$ .

### Angular Sensitivity

For some applications it is important to reduce the angular variation of the reflectance curve. This can be done by using materials with high refractive indexes (Fig. 33) (see also Sec. 7.8, subsection “Angle-of-Incidence Effects”). Another way is to use periods in which the high-index film is thicker than the low-index film (Fig. 30b and Fig. 60a).

### Multilayer Reflectors Made of Absorbing Materials

It is possible to achieve a high reflectance with multilayers of the  $[AB]^N A$  type even when  $A, B$  correspond to absorbing materials. This is of particular interest for spectral regions for which no nonabsorbing coating materials exist. The optical thicknesses of the periods of such systems are still



**FIGURE 35** Width of the high reflectance zone (a) and maximum reflectance (b) of periodic multilayers of the type  $[xH(1-x)L]^N x \cdot H$ . The curves were evaluated for refractive indices  $n_H = 2.4$  and  $n_L = 1.51$ . (After Shao.<sup>165</sup>)

approximately equal to  $\lambda/2$  but, for maximum reflectance, the individual thicknesses  $d_A$ ,  $d_B$  may be quite different, depending on the number of periods  $N$  and on the optical constants of the materials used. Reflectors with  $k_A > k_B$ , have structures that are intermediate to those of quarter-wave stacks (with  $k_A = k_B = 0$  and optical thicknesses of  $\lambda/4$ , in which constructive interference effects are maximized), and those of ideal Bragg crystals (with  $k_A \gg k_B$ , and in which  $d_A \ll d_B$  to minimize absorption losses).

In the extreme ultraviolet (XUV) and the soft x-ray regions ( $n - 1$ ),  $k$  is much smaller than 1 for most coating materials.<sup>165-167</sup> To design a periodic multilayer with a high normal incidence reflectance for a given wavelength, it is first necessary to choose a material ( $n_B - ik_B$ ) with the lowest possible extinction coefficient.<sup>166,168</sup> Next a second, chemically compatible material ( $n_A - ik_A$ ) is selected with the lowest extinction coefficient that will maximize the normal incidence Fresnel reflection coefficient of the interface between the two materials given by

$$r_{BA} = \frac{(n_B - n_A) - i(k_B - k_A)}{(n_B + n_A) + (k_B + k_A)} \quad (49)$$

Vinogradov and Zeldovich use a factor  $\beta_{\text{opt}}$  to relate the metric thicknesses of the layers  $A$  and  $B$  that yield a maximum reflectance to the overall thickness  $d_{\text{opt}}$  of the period:<sup>169</sup>

$$d_A = \beta_{\text{opt}} \cdot d_{\text{opt}} \quad \text{and} \quad d_B = (1 - \beta_{\text{opt}}) \cdot d_{\text{opt}} \quad (50)$$

where  $\beta_{\text{opt}}$  is obtained by the solution of the equation

$$\tan(\pi\beta_{\text{opt}}) = \pi \left[ \beta_{\text{opt}} + \frac{n_B k_B}{n_A k_A - n_B k_B} \right] \quad (51)$$

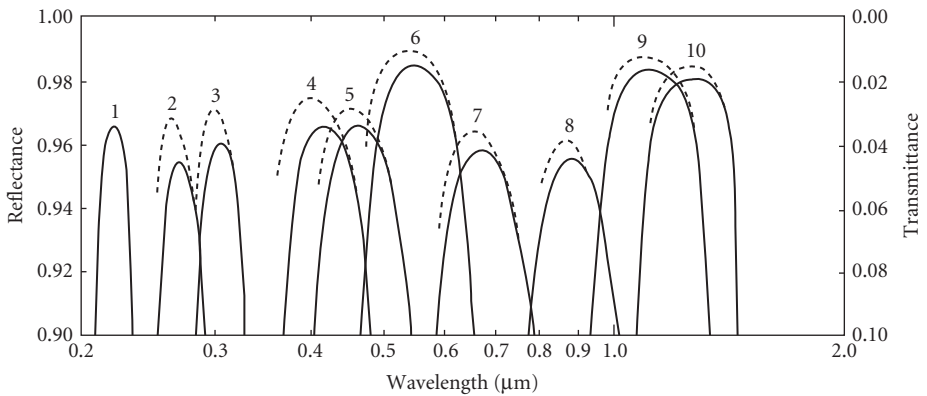
$d_{\text{opt}}$  is approximately equal to  $\lambda/2$ , but Vinogradov and Zeldovich give a more accurate expression for this quantity, as well as for the limiting reflectance  $R$  and the number of periods  $N$  required to reach that value.<sup>169</sup>

## 7.7 MULTILAYER REFLECTORS—EXPERIMENTAL RESULTS

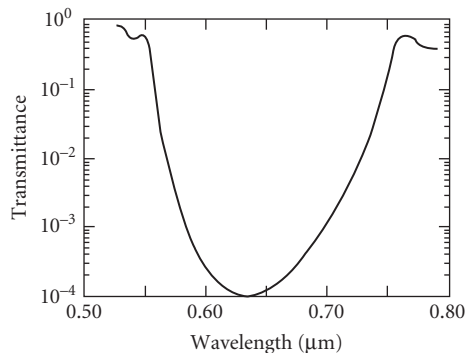
In the calculations of the data for Figs. 29 to 34, the dispersion of the optical constants of the materials was ignored, and it was assumed that the films were absorption and scatter free and that their thicknesses had precisely the required values. In practice, none of these assumptions is strictly valid, and hence there are departures from the calculated values. In general, the agreement is better within the high-reflectance zone than outside.

### Reflectors for Interferometers, Lasers, etc.

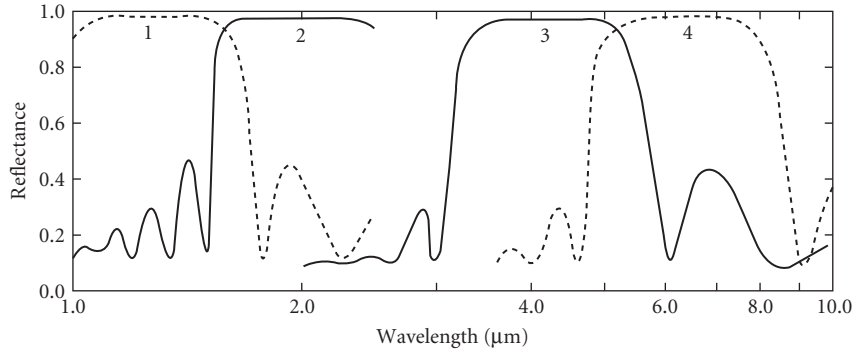
The measured reflectances and transmittances of a number of quarter-wave reflectors suitable for use in Fabry-Perot interferometers are shown in Fig. 36. The transmission of a typical commercial laser reflector for  $\lambda = 0.6328 \mu\text{m}$  is shown in Fig. 37. The measured reflectances of a number of highly reflecting coatings for the infrared spectral region are shown in Fig. 38.



**FIGURE 36** Measured spectral reflectance and transmittance curves of periodic all-dielectric reflectors of the type  $[HL]^N H$  for the ultraviolet, visible, and near-infrared parts of the spectrum. Curve 1: 27 layers of MgO and MgF<sub>2</sub>; curves 2 and 3: 11 and 13 layers of PbF<sub>2</sub> and cryolite, respectively; curves 4, 5, 7, and 8: 7 layers of ZnS and cryolite; curves 6, 9-, and 10: 9 layers of ZnS and cryolite. (Curve 1 after Apfel<sup>170</sup> and curves 2 to 10 after Hefft et al.<sup>171</sup>)



**FIGURE 37** Measured spectral transmittance of a laser reflector. (After Costich.<sup>172</sup>)



**FIGURE 38** Measured spectral-reflectance curves of all-dielectric reflectors for the infrared made of stibnite and chiolite. Curves 1 and 2: multilayers of the type  $[HL]^4H$  on glass; curves 3 and 4: type  $[(0.5L)H(0.5L)]^4$  on barium fluoride. (After Turner and Baumeister.<sup>173</sup>)

Both “soft” laser coatings that can be dissolved in weak acids and “hard” coatings that can be removed only through polishing are available commercially.

### Effects of Imperfections

**Thickness Errors** Small errors in the thickness of the layers of a quarter-wave stack have only a very small effect on the reflectance and on the phase change on reflection of the multilayer within the high-reflectance zone but they do affect the performance outside the zone.<sup>174,175</sup> In fact, the effect may be quite serious: thickness variations can give rise to an apparent lack of flatness of the substrate surface.<sup>176–178</sup>

**Dispersion** The most noticeable effects of dispersion of the optical constants in quarter-wave stacks of a given multilayer type are the increase in the peak reflectance with decrease in wavelength (see Fig. 36) and the asymmetry of the maxima on either side of the main reflectance maximum.

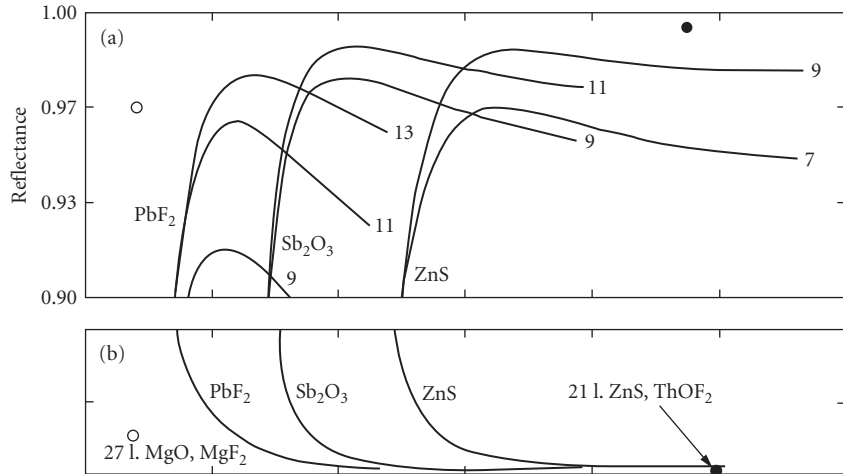
**Absorption** The separation between the transmission and reflectance curves in Fig. 36 is mostly due to absorption. These losses can limit the usefulness of the reflectors for some applications. Thus, for example, in interference filters and Fabry-Perot interferometers they lead to a reduction in the peak transmissions and limit the attainable half widths. In optical information-storage devices they set a limit to the highest reflectance attainable. In lasers the losses counteract directly the gain in the laser medium. In addition, absorption within the layers is responsible for damage to laser reflectors (see also Sec. 7.4, subsection “Laser Damage”).

If the two materials used for the construction of periodic quarter-wave stacks have small, but finite extinction coefficients, the resulting absorption at first reduces both the transmission and reflection coefficients.<sup>156,176,179,180</sup> With an increase in the reflectance of a multilayer of the  $[HL]^N H$  type the absorption occurs more and more at the expense of the reflection coefficient, approaching a limiting value of

$$A = -\delta R = \frac{2\pi n_m}{n_H^2 - n_L^2} (k_H + k_L) \quad (52)$$

that is independent of the number of layers.<sup>2</sup> The corresponding expression for a multilayer  $[HL]^N$  in which a low refractive index faces the incident medium is

$$A = -\delta R = \frac{2\pi(n_L^2 k_H + n_H^2 k_L)}{n_m(n_H^2 - n_L^2)} \quad (53)$$



**FIGURE 39** Variation with wavelength of the observed peak reflectance of 7-, 9-, 11-, and 13-layer quarter-wave stacks made of PbF<sub>2</sub>, Sb<sub>2</sub>O<sub>3</sub>, or ZnS with cryolite as the low-index material (a). The lower curves indicate the limiting value of the absorbance with these materials (b). (After Honcia and Krebs.<sup>181</sup> Results obtained by Apfel<sup>170</sup> (o) and Behrndt and Doughty<sup>182</sup> (•) with other materials are included for comparison.)

Figure 39 shows the spectral variation of experimentally determined maximum reflectances and limiting losses of various quarter-wave multilayer reflectors.

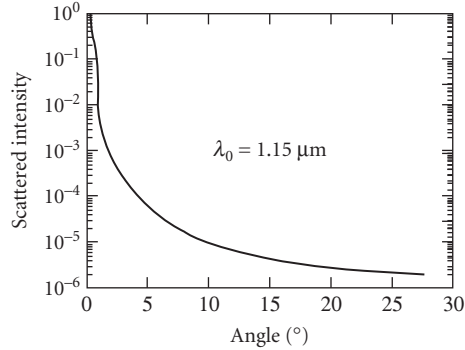
The absorption in periodic multilayers composed of materials having finite extinction coefficients can be reduced below the values given by Eqs. (52) and (53) if a structure of the  $[xH \cdot (1-x)L]^N \cdot xH$  type is used.<sup>163</sup>

**Surface and Interface Imperfections** In thin-film calculations it is usually assumed that substrate surfaces and interfaces between the layers are smooth and that the layers are homogeneous. In practice, substrate surfaces and interfaces have a certain roughness and, at times, thin uniform or inhomogeneous interface layers formed between the boundaries of two layers as a result of oxidation, chemical interactions, or interdiffusion of the two coating materials. The interface layers, as a rule, are different at the *AB* and *BA* boundaries and are typically 0.0003 or 0.0010  $\mu\text{m}$  thick. These and other imperfections of the layer system result in reduced reflection and/or in scatter. If ignored in the model used to represent the multilayer, they add to the discrepancies that are observed between the calculated and experimental data.

Scattering losses are particularly significant at shorter wavelengths. For this reason there have been many theoretical and experimental investigations of scattering of surfaces and thin films. Investigations have shown that when scatter does occur, most of the light is scattered in directions that are close to that of the specularly reflected light.<sup>156,183</sup> The experimental results for a typical mirror are shown in Fig. 40.

**Very low loss reflectors** Mirrors with very low losses are required for use in laser cavities and in ring lasers. Mirrors with a combined loss  $L$  (= transmission + absorption + scatter) of the order of  $5 \times 10^{-5}$  are commercially available. With special manufacturing techniques practically loss-free reflectors can now be made.

A 41 quarter-wave stack made of Ta<sub>2</sub>O<sub>5</sub> and SiO<sub>2</sub> layers with a combined loss of  $L = 1.6 \geq 10^{-6}$ , corresponding to a reflectance of 0.9999984 at 0.633  $\mu\text{m}$ , has been reported.<sup>185</sup> The absorption and scatter losses were estimated to be of the order of  $1.1 \geq 10^{-6}$ . The essential starting point for the manufacture of such coatings are superpolished substrates with a surface roughness of 0.5  $\text{\AA}$  rms or



**FIGURE 40** Measured intensity of the scattered radiation as a function of the angle away from the direction of specular reflection. (After Blazey.<sup>184</sup>)

less. The layers were deposited by reactive ion-beam sputtering from high purity oxide targets in a cryogenically pumped, fully automated deposition system.<sup>186</sup>

An even greater challenge will be the requirements of reflecting coatings for Michelson interferometers for the detection of gravitational waves.<sup>185,187</sup> For this application, not only must the absorption and scattering losses be less than 0.5 and 2 ppm, but in addition, to reduce the thermal noise arising from mechanical loss in the coatings, it will be necessary to match the thermal expansion coefficient and the Young's modulus of the coating materials to those of the substrates.

*Multilayers for the soft x-ray and XUV regions* The effect of roughness and of interface layers is particularly important in soft x-ray and XUV multilayers because the dimensions of these defects are comparable to the thicknesses of the individual layers and of the wavelength.<sup>165,166,168</sup> For this reason much attention has been focused on the proper modeling of such coatings. Many workers use several very thin layers and the matrix method outlined in Sec. 7.2, subsection "Matrix Theory for the Analysis of Multilayer Systems" to model the effects of roughness and interface layers.<sup>188,189</sup> Others make use of the following recursive formula for the amplitude reflectance  $r_j$  of the first  $j$  layers of the system:

$$r_j = \frac{r_{j-1} + r_{BA} \exp(2i\delta_j)}{1 + r_{j-1} r_{BA} \exp(2i\delta_j)} \quad (54)$$

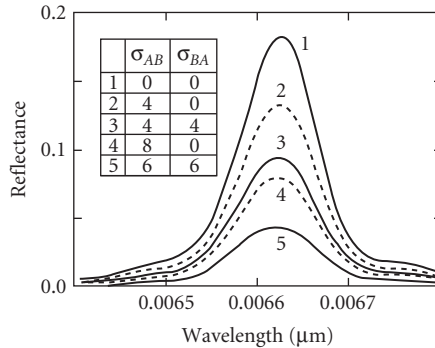
Here  $\delta_j$  is the effective optical thickness of the  $j$ th layer [Eq. (18)],  $r_{j-1}$  is the amplitude reflectance of the first  $(j-1)$  layers and  $r_{BA}$  is the amplitude reflectance of the interface between the  $j$ th and  $(j+1)$ th layers. In this approach, if the Fresnel amplitude reflection coefficient  $r_{BA}$  is replaced by

$$r_{BA} \exp \left\{ -\frac{1}{2} \left[ \frac{4\pi}{\lambda_0} \sigma \Re(\tilde{n} \cos \tilde{\theta}_0) \right]^2 \right\} \quad (55)$$

the combined effect of roughness and of interface layers  $\sigma$  can be allowed for.<sup>190</sup> In the hard x-ray region, where  $n \approx 1$ ,  $k \approx 0$  for all materials, the exponential term in the above expression reduces to the so-called Debye-Waller factor DW,

$$DW = \exp \left[ -\frac{1}{2} \left( \frac{4\pi}{\lambda_0} \sigma \cos \theta_j \right)^2 \right] \quad (56)$$

The calculated reflectance of a XUV mirror, with and without the effect of surface imperfections is shown in Fig. 41. These significant reflection losses can be reduced through interface engineering—a



**FIGURE 41** Calculated reflectances of 64-period x-ray mirrors with different imperfections  $\sigma$  (in Å) at the ReW-C and C-ReW interfaces. (Afer Spiller.<sup>191</sup>)

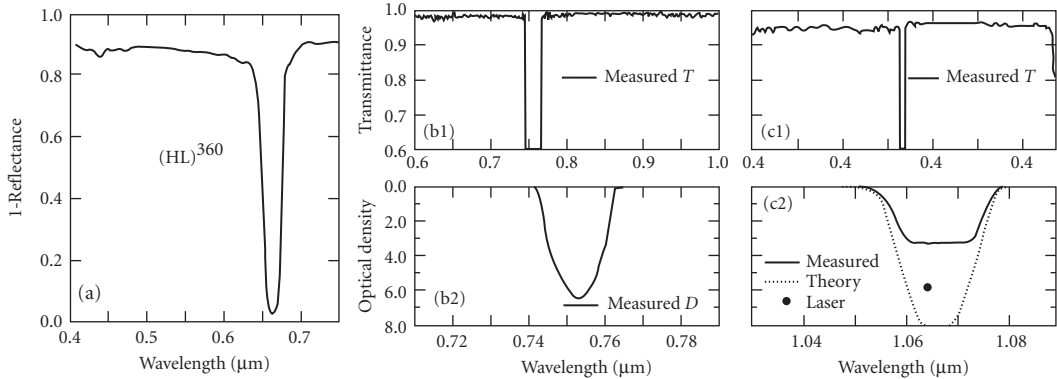
process in which interdiffusion or oxidation is inhibited by the deposition at the interfaces of thin barrier layers of materials such as C or  $B_4C$ .<sup>192</sup>

## Narrowband Reflection Coatings

Narrowband rejection (or notch, or minus) filters transmit freely all the radiation incident upon them except in one narrow spectral region in which the radiation is either wholly or partially reflected.<sup>193</sup> Lord Rayleigh observed a corresponding natural phenomenon in potassium chlorate crystals.<sup>194</sup> Subsequent experimenters reported crystals with rejection bands varying between 0.001 and 0.038  $\mu\text{m}$  in width and reflectances between 33 and 99.9 percent.<sup>195–197</sup> But, unfortunately, at present the size of the crystals that can be grown is insufficient, and the position and width of the rejection region cannot be controlled. The same comments can be made about coextruded polymer films made of the thermoplastic materials polypropylene ( $n = 1.49$ ) and polycarbonate ( $n = 1.59$ ).<sup>198,199</sup> With thin films the above limitations can be overcome, but until recently it has been difficult to achieve the extremely narrow widths and high rejections observed in the crystals.

A quarter-wave stack of the type  $[AB]^N A$  has been suggested as a model for the construction of such filters (see, for example, Refs. 196 and 200). It follows from Figs. 31 and 34 that the closer the refractive index ratio  $n_A/n_B$  is to unity, the narrower the width of the reflectance zone and the more layers required to achieve a certain rejection. Shown in Fig. 42a is  $(1 - \text{the measured reflectance})$  of a multilayer consisting of 760 layers that was produced by a plasma chemical deposition technique.<sup>201</sup> Unfortunately, that method could only deposit such coatings on the inside of a tube. To reduce the number of layers, films with higher  $n_A/n_B$  ratios could be utilized and the width reduced by using layers with thicknesses that are odd multiples of a quarter wavelength. But this can be done only at the expense of bringing the adjacent higher- and lower-order reflection peaks closer. Resonant reflectors are an extreme example of this. However, recent progress in the manufacture of multilayer systems (see Sec. 7.12) has made it possible to produce notch filters for Raman spectroscopy at any wavelength in the visible or near-infrared that exceed the reported performance of the naturally occurring crystals. Fig. 42b shows the measured transmittance and optical density of a filter that has a 0.020- $\mu\text{m}$ -wide rejection region and a very high transmittance with only a 1 to 2 percent ripple in the wavelength range  $0.6 < \lambda < 1.00 \mu\text{m}$ . The optical density at  $\lambda = 0.75$  is 6.0. The filter consists of 714 layers and it has a metric thickness of 51  $\mu\text{m}$ .<sup>202</sup> The measured width of the notch of the filter shown in Fig. 42c is about 0.024  $\mu\text{m}$  and it has an optical density of 5.9 at  $\lambda = 1.064 \mu\text{m}$ , as measured with a laser. The second surface of this filter was not antireflection coated, and so the transmittance is a little lower, but the high transmittance extends from 0.4 to 1.09  $\mu\text{m}$ . The metric thickness of this filter is 122.2  $\mu\text{m}$  and it consists of 4410 layers.<sup>203</sup>



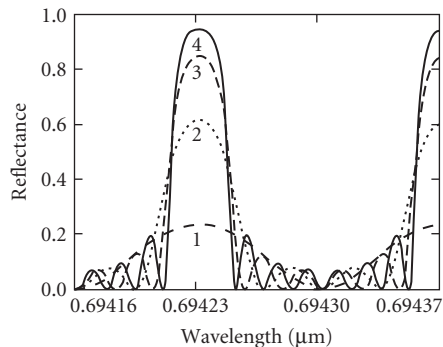


**FIGURE 42** Narrow band rejection filters. (a) Measured value of  $(1 - \text{reflectance})$  of a 760-layer quarterwave stack produced by chemical vapor deposition using materials with refractive indices of 1.575, 1.585 (after Edmonds *et al.*<sup>201</sup>); (b) measured reflectance and optical density a 714-layer, 51- $\mu\text{m}$ -thick filter (after Iridian Spectral Technologies<sup>202</sup>); and (c) measured reflectance and optical density a 4410-layer, 122.2- $\mu\text{m}$ -thick filter (after JDSU<sup>203</sup>).

## Resonant Reflectors

In the past, even “hard” evaporated coatings could not survive the power densities present in some high-power lasers. To overcome this problem, resonant reflectors were used.<sup>204–207</sup> They consisted of one or more accurately air-spaced plane-parallel plates of thicknesses of the order of millimeters made of a tough, high-optical-quality material. Because of the long coherence length of the laser radiation incident upon them, interference takes place in the same way as in thin films. Resonant reflectors may be regarded as being quarter-wave reflectors of enormously high order of interference, and all the equations given in Sec. 7.6 apply.

Resonant reflectors made of quartz and sapphire are commercially available. Since the refractive index of quartz is lower than that of sapphire, a larger number of plates is required to attain the same reflectance. On the other hand, quartz is much cheaper and is less temperature sensitive. The calculated reflectance of one-, two-, three-, and four-plate sapphire resonant reflectors are shown in Fig. 43. In another development diffusion-doped quartz plates are used in the construction of resonant



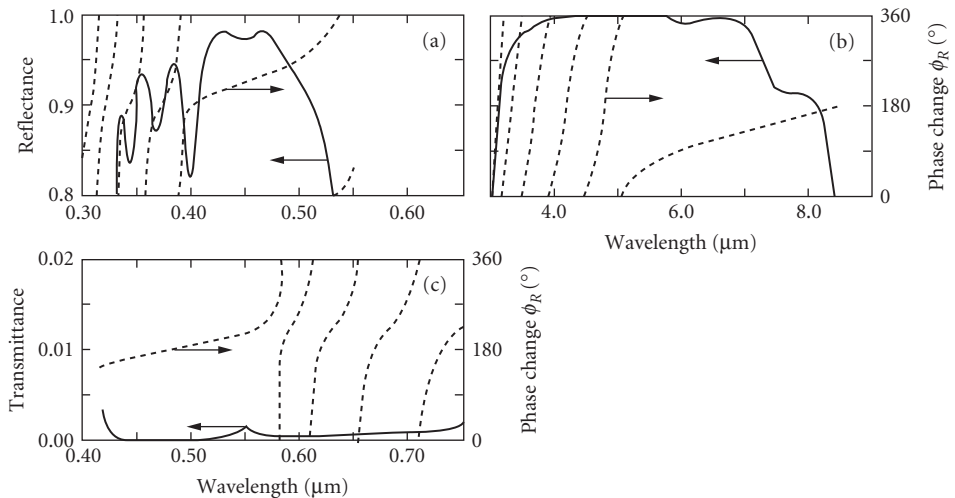
**FIGURE 43** Calculated spectral reflectance of resonant reflectors consisting of one, two, three, and four sapphire plates ( $n = 1.7$ ). The optical thicknesses of the plates and of the air spaces between them were assumed to be 1.7 mm.

reflectors.<sup>208</sup> The doping process causes the refractive index of the plate to increase smoothly in a 0.5- $\mu\text{m}$  region from that of quartz to about 2.0 at the surface. As a consequence fewer elements are needed to achieve a given reflectance.

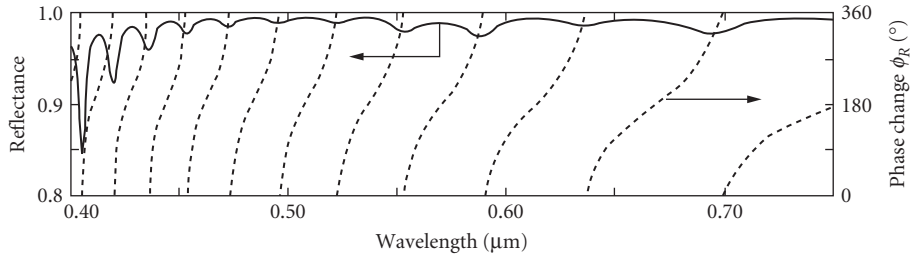
## All-Dielectric Broadband Reflectors

There are several ways of obtaining a coating with a broad high-reflection region should the width attainable with quarter-wave stacks be inadequate. For a broad region with a very high reflectance one can superimpose two quarter-wave stacks tuned to two different wavelengths. The widest continuous high-reflection region is attained when materials with the highest available refractive-index ratios are used and the thicknesses of the layers are so chosen that the two high-reflectance zones are contiguous (see Fig. 44c). For an even broader region further quarter-wave stacks can be superimposed. If high-reflection regions overlap, special precautions must be taken to prevent the appearance of sharp reflectance minima in the high-reflection region.<sup>173</sup> It is not easy to obtain a very uniform, moderately high reflectance in this way. Another approach is to deposit onto the substrate a series of alternating high- and low-refractive-index films of gradually increasing or decreasing thicknesses (Fig. 45). A broad high-reflection region can also be obtained with a multilayer in which the layers are different multiples of  $\lambda/4$  of a selected wavelength (see Fig. 46). Finally, it has been suggested that multilayers with 10:1 high reflectance regions might be produced by depositing hundreds of layers of random thicknesses made of two materials that are nonabsorbing throughout the spectral range of interest.<sup>209</sup> As yet experimental data for this approach have not been presented.

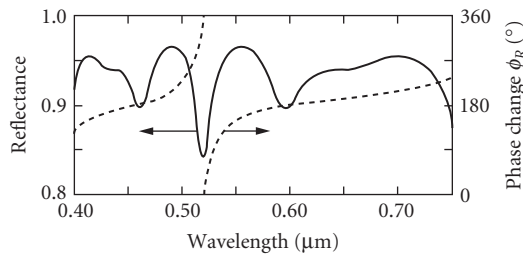
If only a relatively small increase in the high-reflection region is required, or if a uniform but only moderately high reflectance is required, the desired result can be achieved by modifying the thicknesses and refractive indexes of a quarter-wave stack using a computer refinement program or by the addition of achromatizing  $\lambda/2$  layers. The measured performances of several such reflectors are shown in Figs. 47 and 48. Broadband reflectors with moderate and high reflectances for the ultraviolet spectral region have been reported by Korolev,<sup>213</sup> Sokolova,<sup>214</sup> and Stolov.<sup>215</sup> A broadband reflector for the XUV spectral region is shown in Fig. 57b.



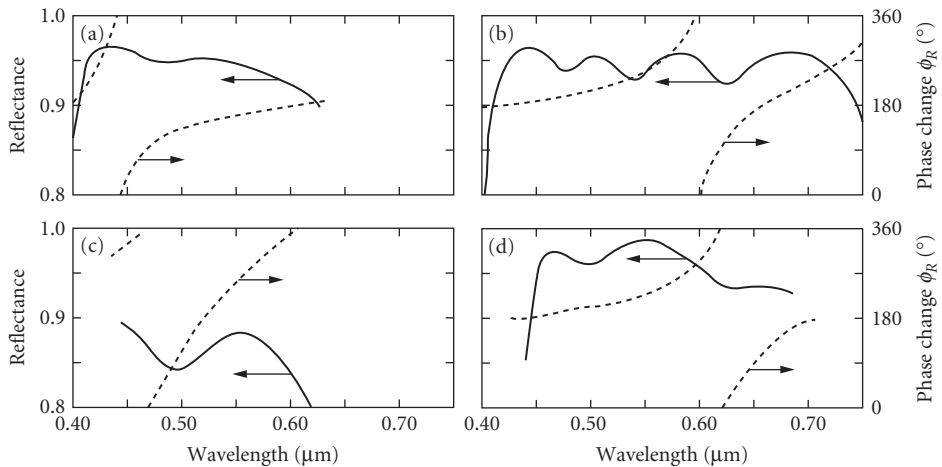
**FIGURE 44** Measured reflectance of all-dielectric broadband reflectors consisting of two superimposed quarter-wave stacks with contiguous high-reflectance zones. The dotted curves in Figs. 35 to 39 represent the calculated phase changes on reflection. [(a) and (b) after Turner and Baumeister;<sup>173</sup> (c) after Perry.<sup>210</sup>]



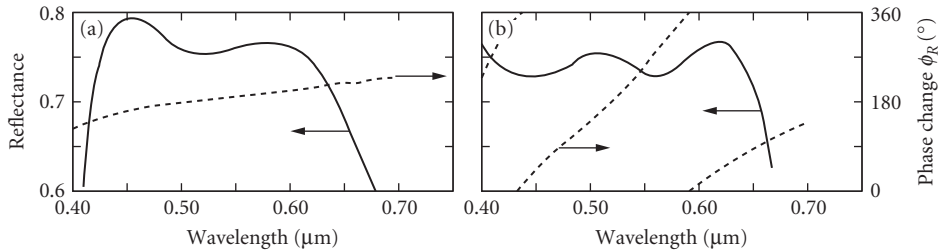
**FIGURE 45** Calculated reflectance of an all-dielectric broadband reflector consisting of 35 layers made of a low- and a high-index material and having optical thicknesses that vary in a geometric progression. (After Heavens and Liddell.<sup>211</sup>)



**FIGURE 46** Calculated reflectance of an all-dielectric broadband reflector consisting of 11 layers all of which have optical thicknesses that are various multiples of  $0.13 \mu\text{m}$ . (After Elsner.<sup>212</sup>)



**FIGURE 47** Measured reflectances of all-dielectric broadband reflectors designed with refinement programs. [(a) after Penselin and Steudel;<sup>216</sup> (b) after Baumeister and Stone;<sup>217</sup> (c) after Ciddor;<sup>218</sup> and (d) after Ramsay and Ciddor.<sup>178</sup>]



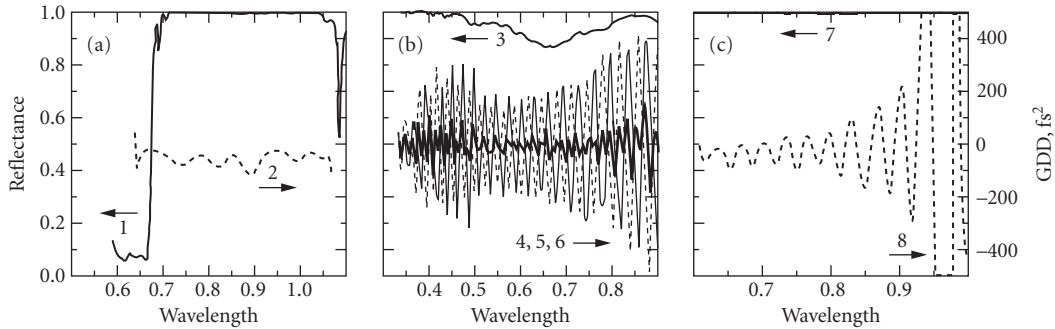
**FIGURE 48** Measured reflectances of achromatic all-dielectric reflectors with an intermediate reflectance derived from a quarter-wave stack through (a) the addition of half-wavelength achromatizing layers (after Turner<sup>219</sup>) and (b) designed with a refinement program (after Ciddor<sup>218</sup>).

**Broadband Reflectors Effective over a Wide Range of Angles (Perfect Mirrors)** At times it is required that the reflectance be high not only over a broad wavelength region, but also for a large range of angles of incidence. It was clear that if this is to be achieved, the superimposed periodic stacks (Fig. 44) must be contiguous at the highest angle required, and that they will therefore overlap at lower angles. This situation has been investigated at some length in a theoretical paper for visible reflectors effective for angles up to  $50^\circ$ .<sup>220</sup> Subsequently a number of workers outside the thin-film field rediscovered this possibility and described similar coatings working for all angles, which they called “perfect mirrors.”<sup>221–223</sup>

**Phase Change on Reflection from Broadband Reflectors** The phase change on reflection from broadband reflectors varies even more rapidly with wavelength (Figs. 44 to 47) than that from quarter-wave stacks (Fig. 29).<sup>224,225</sup> In fact, the phase change can be so large, that it has been proposed for the construction of spacerless transmission interference filters (see Fig. 93h). But a high phase change on reflection can also be a disadvantage in certain metrological applications. Another consequence of this rapid variation is that, in the presence of systematic thickness variations in the layers, it can give an impression of a lack of flatness in the substrate.<sup>178</sup> Figures 47d and 48a represent designs of broadband reflectors in which an effort was made to reduce this effect.

## Coatings for Ultrafast Optics

In all sections of this chapter, with the exception of this one, it is assumed that the intensity of the radiation that is falling onto a multilayer does not vary in time and that a steady state exists. However, there are applications in telecommunications, spectroscopy, and in other areas in which the use of very short pulses of light is a great advantage. But, for pulse durations shorter than 100 fs, the transient effects that can be ignored during steady-state operations become significant. In ultrafast optics the incident light can consist of very short Gaussian light pulses with a temporal bandwidth as short as 5 fs. Under these conditions the phase changes  $\phi_R$ ,  $\phi_T$  of a multilayer on reflection or transmission, and their first and second derivatives with respect to  $\omega$ , where  $\omega = 2\pi c/\lambda$  and where  $c$  is the speed of light in a vacuum, become very important. The first and second derivatives of the phase changes,  $-(d\phi/d\omega)$  and  $-(d^2\phi/d\omega^2)$ , are called the Group Delay (GD) and Group Delay Dispersion (GDD), respectively. Unless they are suitably controlled in a multilayer, the pulse length of the incident beam can be considerably broadened on reflection. In order to avoid this, the thicknesses of layer pairs in a coating are reduced in a systematic way, so that light of shorter wavelengths does not penetrate as deeply into the multilayer structure before a significant part of it is reflected. Such structures resemble those used in broadband reflectors (see, for example, Fig. 45) and are called by some “chirped multilayers.” At times it is useful to use “double chirped” structures in which, in addition to a gradual reduction of the bilayer thickness, the relative thicknesses of the high and low refractive index layers



**FIGURE 49** Measured reflectances  $R$  and the Group Delay Dispersions (GDD) of three different systems designed for femtosecond use. (a) Input coupler.<sup>228</sup> (b) The large fluctuations of the GDD values that occur in mirrors designed for a very wide spectral regions can be reduced by reflecting the light from a pair of mirrors designed to have oscillations that are complementary. In this diagram, the dotted and thin solid curves correspond to the individual GDD curves; the heavy solid curve corresponds to the GDD after reflection from both mirrors.<sup>229</sup> (c) Dispersive mirror designed by the time-domain method.<sup>230</sup>

within each pair are also varied. Of course, more degrees of freedom to obtain the required performance are obtained if in the final calculations the thicknesses of all layers of the system are allowed to vary independently.

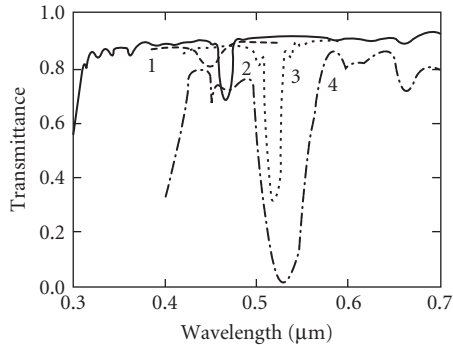
It has been shown that the temporal and spectral widths of the reflected pulses are related to one another through a Fourier transformation that uses a product of the complex spectrum of the incident pulse with the factor  $r_i(\omega)\exp[\phi_i(\omega)]$  for the reflecting coating (see, for example, Refs. 226 and 227). In the numerical design of such coatings,  $R$ ,  $GD$ , and  $GDD$ , or even the desired temporal pulse length, may need to be specified and they will depend on the particular problem on hand. A more detailed presentation of the design of such coatings is outside the scope of this chapter and the interested reader is referred to the reviews by MacLeod<sup>2</sup> and Tempea et al.<sup>226</sup>

Some of the multilayer reflector coating types that are required for ultrafast optics include input couplers (with a high  $R$  and a negative  $GDD$  and a high  $T$  in the gain and absorption region of the laser); output couplers (with a certain  $GDD$  and a rather low transmittance  $0.05 < T < 0.3$  in a wide spectral range of the laser oscillator); chirped mirrors with very large bandwidths. The measured performance of three reflecting coatings for femtosecond applications are shown in Fig. 49.

It should be stated that this is currently a very fast moving field. Tunable dispersion compensators<sup>202,231</sup> for femtosecond use are currently employed.<sup>232</sup> Compressors and stretchers for nonlinear optics amplifiers with negative and positive  $GDD$  as large as of 2000 fs<sup>2</sup> are being developed.<sup>233</sup> In addition to reflectors, the design of beam splitters<sup>234</sup> and antireflection coatings<sup>235</sup> for ultrafast optics have also been discussed in the literature.

## Rejection Filters

**Minus Filters** Minus filters are, in essence, multilayer reflectors in which the ripples in the transmission regions on either side of the high reflectance zone have been reduced or eliminated. Filters of this kind with various widths and attenuations find applications as correction filters.<sup>236</sup> Narrow minus filters with high attenuations have various scientific and technological uses, including protection of equipment and personnel from harmful laser radiation. Figure 50 shows the measured transmittances of a number of rejection filters of various widths and attenuations. Quite recently spectacular progress has been made in the deposition of narrowband rejection filters that find applications in Raman spectroscopy. The two commercial narrow band rejection filters shown in Fig. 42*b* and *c* consist of 713, 4410 layers each, have 0.02- and 0.025- $\mu\text{m}$ -wide rejection regions and measured transmittances of less than  $10^{-6}$  at the center of the notches.<sup>202,203</sup>



**FIGURE 50** Measured spectral transmittances of several narrowband rejection filters. (Curves 1 to 3 after Dobrowolski<sup>236</sup> and curve 4 after Optical Coating Laboratory.<sup>237</sup>)

Thelen has shown how to optimize the transmission on both sides of the rejection band of a minus filter simultaneously.<sup>238</sup> If the multilayer is surrounded on both sides by the same medium, it will be symmetrical and can be represented by  $C[AB]^NAC$ ,  $DAC[AB]^NACAD$ , . . . Here  $A$ ,  $B$ ,  $C$ ,  $D$ , . . . are layers of quarter-wave optical thickness at the design wavelength and

$$n_m = n_s = n_A \quad (57)$$

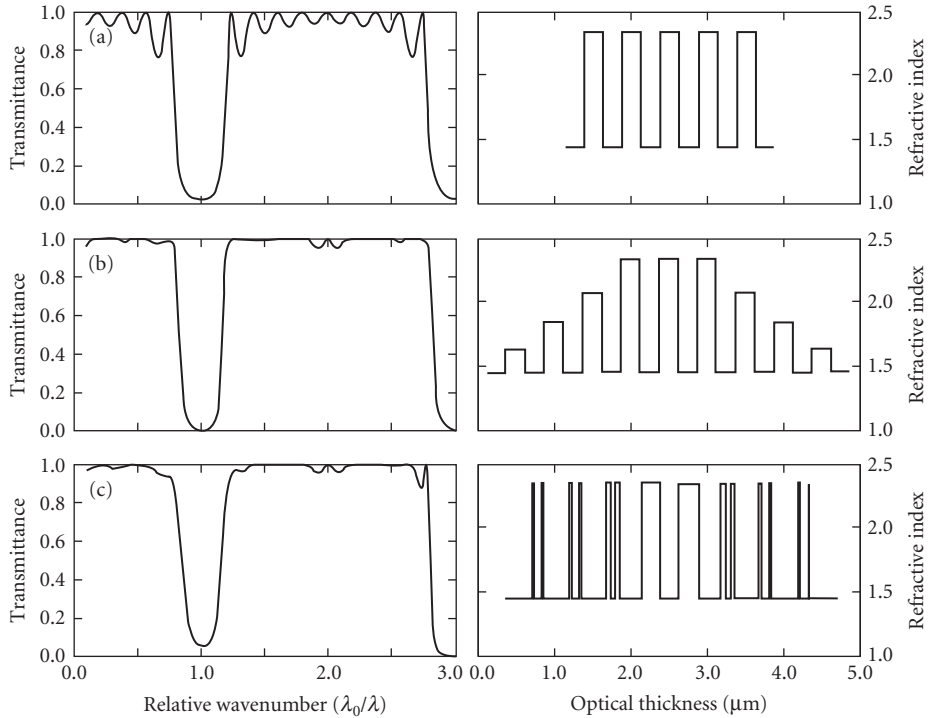
The refractive indices  $n_C$ ,  $n_D$ , . . . depend on  $n_A$  and  $n_B$  in a more complicated way. The larger the number of different materials used in the construction of these multilayers, the better the performance in the transmission region. Should the use of more than two coating materials not be convenient, it is a simple matter to find a two-material version of this solution. The above points are illustrated in Fig. 51.

Young<sup>193</sup> described two other design methods for narrowband rejection filters with improved transmission characteristics. The methods are based on analogies with antenna theory, and they yield nonperiodic equi-ripple designs in which all the layers either have equal thicknesses but different indexes or are made of two materials only but have many different thicknesses.

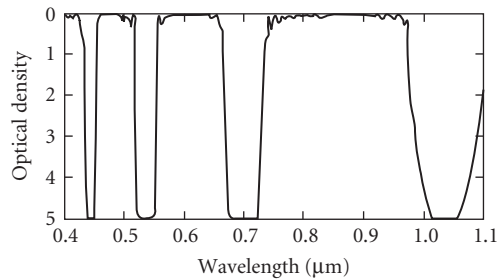
Should the simultaneous rejection of several wavelengths be required, it is possible to achieve this by depositing several minus filters on top of one another (Fig. 52).

**Rugate Filters** In inhomogeneous layers the refractive index varies continuously in the direction of the thickness of the layer.<sup>100,240,241</sup> If the refractive index varies in a periodic manner between two extreme values, it is possible to design a minus filter with a high transmission on either side of the rejection band (Fig. 53). Such periodic inhomogeneous layers are sometimes called rugate filters. The rejection wavelength corresponds to that wavelength for which the period of the index variation is equal to a half wavelength. The attenuation depends on the ratio of the highest to lowest refractive index in the design and on the number of periods. As in the multilayer minus filters, the width of the rejection region also depends on the refractive index ratio. Rugate filters do not have the higher-order reflection peaks that are characteristic of periodic multilayers and this is one reason for their attractiveness. Another reason—no sharp interfaces, less scatter, and better mechanical properties. However, they are more difficult to produce. If necessary, they can be approximated by a homogeneous multilayer system consisting of a few (three or four) materials.

As in the case of minus filters, it is possible to reject a number of wavelengths by depositing several rugate filters on top of each other. However, the combined overall thickness of the rugate filters will then be quite high. It is possible to find an inhomogeneous layer solution to this problem in which the refractive index profile is more complicated, but which requires a considerably thinner inhomogeneous layer (Fig. 54).<sup>242</sup>

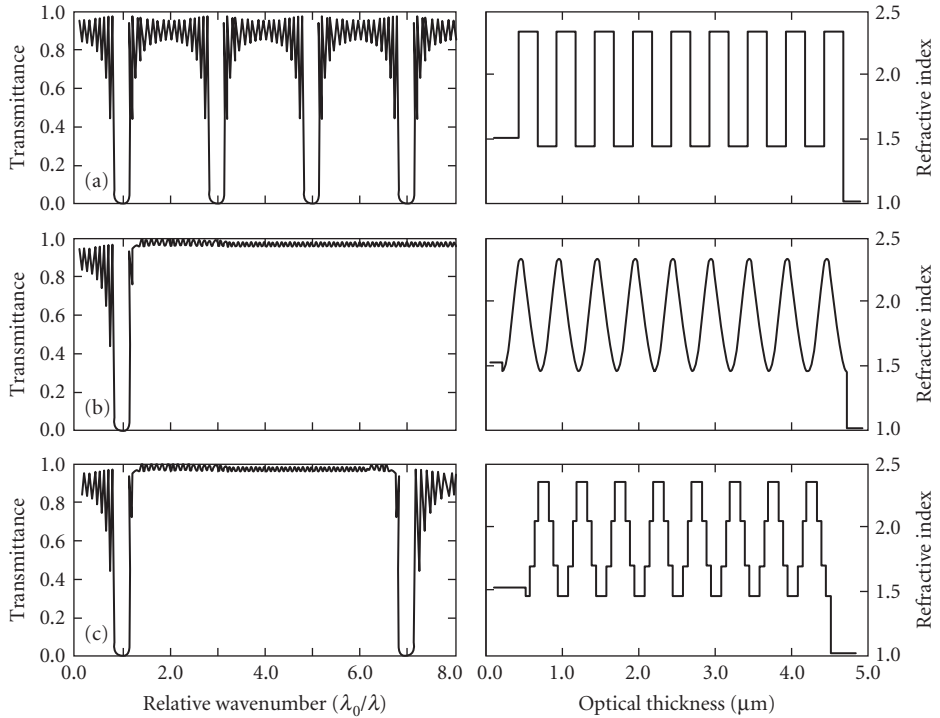


**FIGURE 51** Suppression of ripples in the transmission region of rejection filters. Calculated spectral transmittance curves and refractive index profiles of a 9-layer quarter-wave stack (a); a 17-layer, 5 material minus filter (b); and a two material equivalent of the minus filter (c).

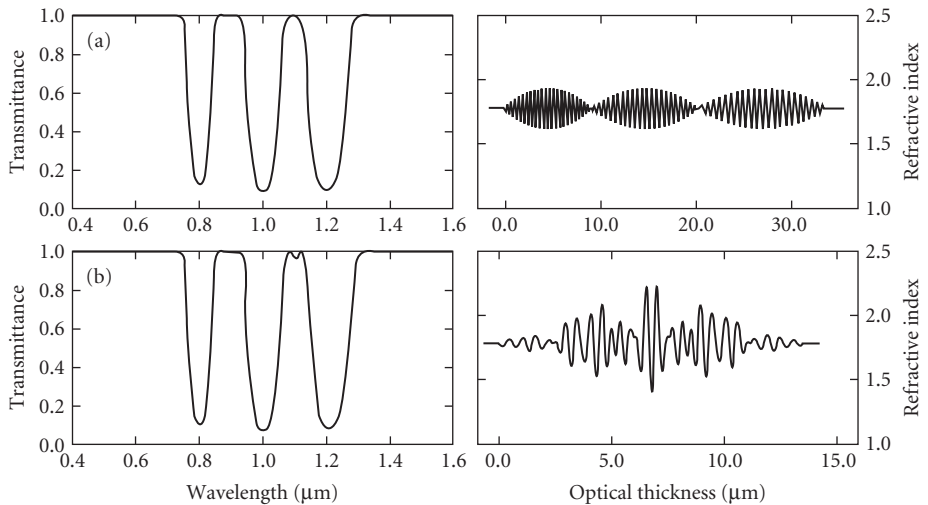


**FIGURE 52** Transmission of laser goggles for the rejection of the ruby (0.694  $\mu\text{m}$ ) and the NdYag (0.532 and 1.064  $\mu\text{m}$ ) laser lines. (After Omega Optical Inc.<sup>239</sup>)

In Lippmann-Bragg holographic mirrors the refractive index varies continuously in a direction perpendicular to the plane of the substrate. These devices behave like thin-film systems and have properties similar to those of rugate filters. Holographic edge and narrowband rejection filters are available commercially.<sup>244,245</sup>

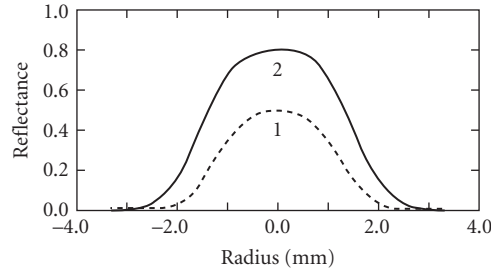


**FIGURE 53** Suppression of higher order reflectance peaks in rejection filters. Calculated spectral transmittance curves and refractive index profiles of a 17-layer quarter-wave stack (a); a 9-period rugate filter (b); and a 49-layer four material design (c) by Thelen.<sup>13</sup>



**FIGURE 54** Simultaneous suppression of several laser wavelengths. Calculated spectral transmittance curves and refractive index profiles of a series (a) and a parallel (b) solution to the problem (After Verly.<sup>243</sup>)





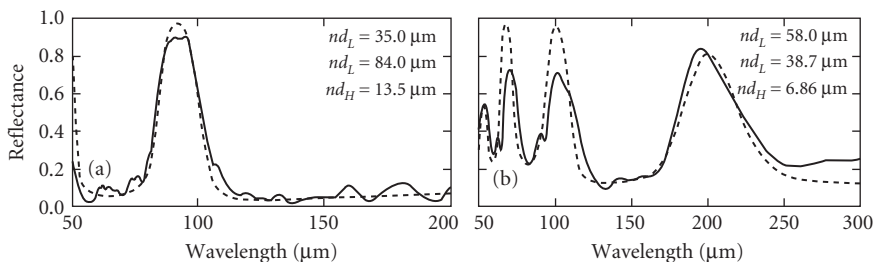
**FIGURE 55** Experimental results for two super-Gaussian graded reflectivity mirrors for  $\lambda = 1.064 \mu\text{m}$ . Curve 1: three layer system with one layer of varying thickness, with  $R_{\text{max}} = 0.5$  and  $\omega = 1.92 \text{ mm}$  (after Piegari<sup>250</sup>) and curve 2: fully shaped mirror with  $R_{\text{max}} = 0.85$  and  $\omega = 1.90 \text{ mm}$  (after Duplain<sup>248</sup>).

## Graded Reflectivity Mirrors

Mirrors in which the absorption or reflection varies radially have been proposed in the past for the control of modes and of edge diffraction effects in laser resonators.<sup>246,247</sup> In addition to meeting the reflectance specifications, graded reflectivity mirrors must have a sufficiently high laser damage threshold for use with high-power lasers. Graded reflectivity mirrors are produced by depositing thin films through a suitable mask. The substrate and the mask can be stationary, or one or both can rotate. A single shaped layer suffices for a maximum reflectance of intermediate values. For higher values the shaped layer can be inserted between a stack of layers of uniform thickness or, alternatively, all the layers can be deposited through the mask.<sup>248,249</sup> The experimentally measured reflections of two graded reflectivity mirrors are shown in Fig. 55.

## Multilayer Reflectors for the Far-Infrared Region

Thin film-filters cannot be produced by conventional deposition techniques for wavelengths greater than about  $80 \mu\text{m}$  because of a lack of low absorption coating materials that can be deposited in the form of thick, stable films. However, a hybrid process in which plastic sheets coated with relatively thin high refractive index materials are heat-bonded can be used to produce self-supporting optical multilayer filters.<sup>251,252,164</sup> As mentioned before (Sec. 7.6, subsection "Periodic Multilayers of the  $[xH \cdot (1-x)L]^N \cdot xH$  Type"), periodic multilayers of unequal optical thickness can have a high reflectance, providing that the number of periods is high enough. The measured reflectance curves of two typical hybrid multilayer filters are shown in Fig. 56.



**FIGURE 56** Measured and calculated performance of (a)  $L'(HL)^{16}$  and (b)  $L'(HL)^{16}$  reflectors made of ZnS and polyethylene of thicknesses indicated in the diagram. An instrumental resolution of  $3 \text{ cm}^{-1}$  was assumed in the calculations. (After Shao.<sup>164</sup>)

## Multilayer Reflectors for the Soft X-Ray and XUV Regions

There are two main obstacles to obtaining multilayers with a high normal incidence reflectance in the soft x-ray and in the XUV regions. First, at these wavelengths all materials absorb; this limits the number of layers that can contribute to the overall reflectance. Second, roughness and the interdiffusion and alloying of the materials degrade the individual interfaces; this reduces their contribution to the overall reflectance.<sup>189</sup>

XUV mirrors are normally produced from two chemically compatible materials by sputtering or by electron beam gun evaporation. As already discussed in Sec. 7.6, subsection “Multilayer Reflectors Made of Absorbing Materials” the XUV multilayers mirrors have a period of optical thickness  $\lambda/2$ . Within this period, the thickness of the less absorbing material is larger. This material usually has an absorption edge that is close to the design wavelength. Optical constants can vary widely in this region.<sup>167</sup> The second more absorbing material is therefore selected to maximize the Fresnel reflection coefficient of the interface.

Theoretically, the best results are obtained with pure elements. However, sometimes alloys are used because they result in multilayers with better interfaces. At other times,  $\text{MoSi}_2$  might be used in place of Mo, or  $\text{B}_4\text{C}$  instead of C or B. Examples of some more commonly used material pairs for near-normal incidence reflectors are (a) Mo/Si for the 130 to 250 Å region; (b) Mo/Y for the 90 to 130 Å region; (c)  $\text{W/B}_4\text{C}$ ,  $\text{Ru/B}_4\text{C}$ ,  $\text{Mo/B}_4\text{C}$ , etc. for the 70 to 130 Å region; and (d) Co/C, W/C, Re/C,  $\text{ReW/C}$ , Ni/C, etc. for the 45 to 70 Å. In the above, the second material in each pair has the lower extinction coefficient. A much more complete review of this topic will be found in the review article by Windt et al.<sup>253</sup> Also, an up-to-date list of material pairs and the measured peak reflectances achieved with them will be found on Henke’s website.<sup>254</sup>

There are many reasons why there are differences between the theoretical performance of a multilayer reflector and the reflectance measured on a synchrotron.<sup>165,166</sup> The highest near-normal reflectance achieved at 135 Å thus far is  $R \approx 0.70$  for an interface-engineered Mo/Si multilayer.<sup>255</sup> The measured reflectances of other experimentally produced x-ray and XUV mirrors are shown in Fig. 57. Curve 8 in this diagram shows that, as in the visible part of the spectrum (Figs. 44 to 48), by departing from periodic multilayer systems, it is possible to produce reflectors in this spectral region that have a comparatively wide spectral region with a constant reflectance.

In the XUV and soft x-ray regions, the reflectances that can be achieved with near-normal angles of incidence are not sufficient. For some imaging applications it is necessary to resort to near-grazing incidence mirrors. In Sec. 7.16 the reflectances of some metals, compounds, and two- or three-layer combinations at high angles, as well as periodic and nonperiodic multilayer interference reflectors consisting of tens or even thousands of layers, are presented.

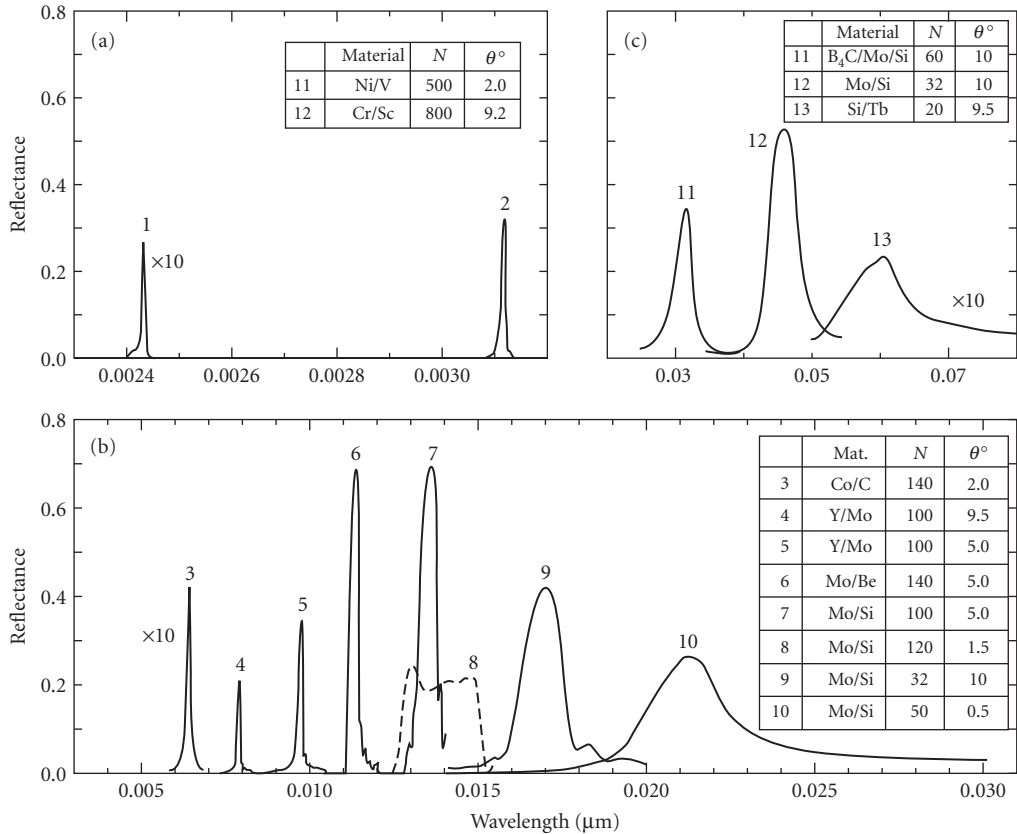
For more information on coatings for the XUV and soft x-ray region, the interested reader is referred to the review article by Yulin.<sup>266</sup>

## 7.8 CUTOFF, HEAT-CONTROL, AND SOLAR-CELL COVER FILTERS

Ideal cutoff filters would reject all the radiation below, and transmit all that above a certain wavelength, or vice versa. Real cutoff filters, of course, are not perfect and so, in addition to the cutoff wavelength, the slope of the transition region and the extent and average transmission values of the transmission and rejection regions must be specified. The tolerable departures of these quantities from the ideal values depend greatly on the application. Most all-dielectric cutoff filters are based on periodic multilayers, whose basic properties were described in Sec. 7.6.

### Transmission in the Passband Region

The usual way of avoiding the secondary transmission minima in the transmission band of a quarter-wave stack is through the use of eighth-wave layers on both sides of the stack (Sec. 7.6, subsection “Periodic Multilayers of the  $[(0.5A) B (0.5A)]^N$  Type”).

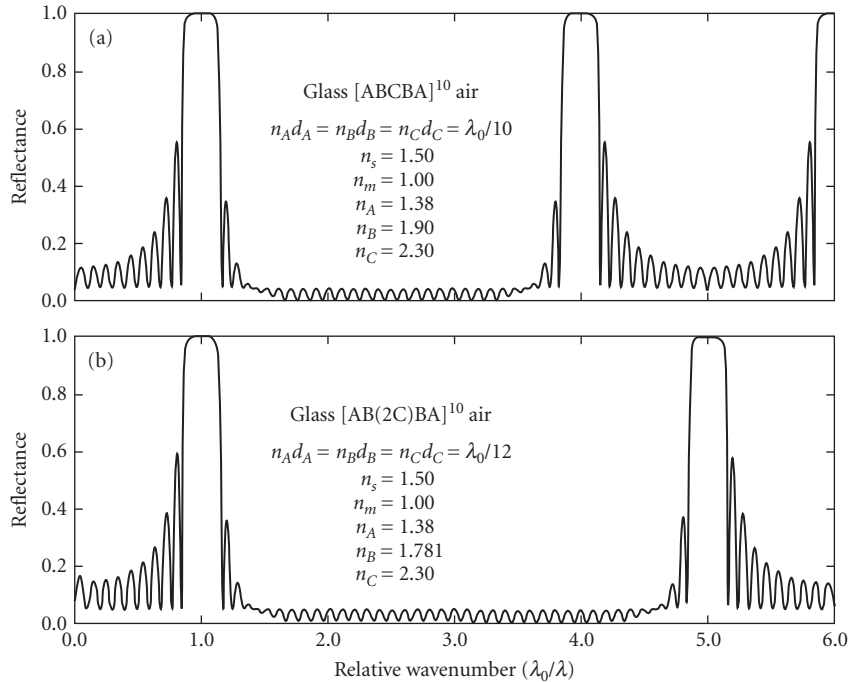


**FIGURE 57** Measured reflectance curves of some representative multilayer x-ray mirrors for the (a) 0.0022 to 0.0032  $\mu\text{m}$ ; (b) 0.003 to 0.0029  $\mu\text{m}$ ; and (c) 0.03 to 0.08  $\mu\text{m}$  spectral regions. The materials used, the number of layers  $N$  and the angles  $\theta_0$  at which the near-normal reflectance was measured are indicated in the tables. (Curve 1 after Eriksson;<sup>256</sup> curve 2 after Gullikson;<sup>257</sup> curve 3 after Spiller;<sup>258</sup> curves 4 and 5 after Montcalm;<sup>259</sup> curve 6 after Skulina;<sup>260</sup> curve 7 after Bajt;<sup>255</sup> curves 8 and 12 after Kaiser;<sup>261</sup> curve 9 after Ravet;<sup>262</sup> curve 10 after Ceglie;<sup>263</sup> curve 11 after Gautier;<sup>264</sup> and curve 13 after Kjornrattanawanich.<sup>265</sup>)

Other, less frequently used methods of smoothing the transmission in the passband are the adjustment of the thicknesses of all the layers of a quarter-wave stack,<sup>267</sup> the use of homogeneous<sup>268</sup> and inhomogeneous<sup>269</sup> layers on either side of the stack; the choice of an optimum set of refractive index values for the substrate and films,<sup>270</sup> and the use of an equi-ripple design<sup>193</sup> in which thicknesses are kept constant but the refractive indices are varied.

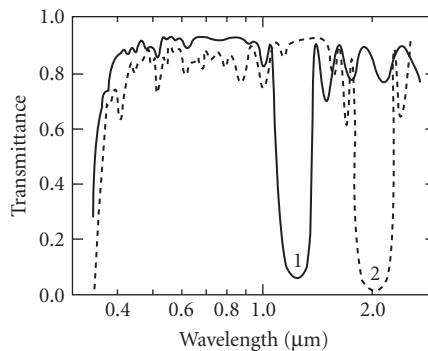
## The Width of the Transmission Region

For short-wavelength cutoff filters of the type described above, the transmission region is limited only by the transmission characteristics of the materials used for their construction. In long-wavelength cutoff filters the transmission regions can be limited by the appearance of higher-order reflectance maxima (Sec. 7.6, subsection “Nonabsorbing  $[\text{AB}]^N$  and  $[\text{AB}]^N\text{A}$  multilayer Types”). Should this be a serious limitation, it is possible to suppress a number of adjacent reflectance maxima by using multilayers with periods composed of three or more different materials (Fig. 58).



**FIGURE 58** Calculated reflectances (a), (b) of two different of three-material periodic multilayers with suppressed higher-order reflectance maxima. (After Thelen.<sup>271</sup>)

By using a period consisting of an inhomogeneous layer with a special refractive-index profile an even larger number of consecutive reflectance maxima can be suppressed (see also Fig. 53).<sup>269</sup> Figure 59 shows the measured results for two such experimental coatings in which reflectance maxima are suppressed at three and nine consecutive integer multiples of  $1/\lambda_0$ , a fact obscured in the case of the second filter by the absorption of the materials used.



**FIGURE 59** Measured transmittance of periodic multilayers in which higher-order reflectance maxima are suppressed through the use of periods that consist of an inhomogeneous layer. (After Scheuerman.<sup>111</sup>)

## Transmission in the Rejection Region

Figure 31 can be used for an estimate of the number of layers required to achieve a given transmission (Sec. 7.6, subsection “Maximum Reflectance”). Through the use of suitable substrate materials the transmittances throughout the rejection region can typically be below 0.01 and 0.1 percent for short- and long-wavelength cutoff filters, respectively. Rejection filters with higher rejections can be provided or, alternatively, two or more filters in series can be used if they are placed at a small angle to one another.

## The Width of the Rejection Region

The width of the high-reflection region of  $[(0.5A)B(0.5A)]^N$  coatings can be estimated from Fig. 34. There is no shortage of absorbing materials should it be necessary to extend the rejection region of shortwave cutoff filters. The number of suitable absorbing materials for long-wavelength cutoff filters is more restricted and often it is necessary to use thin films to extend the cutoff region. In addition to the superposition of two or more cutoff filters tuned to different wavelengths (Sec. 7.7, subsection “Rejection Filters”) one can deposit such coatings onto different substrates or onto the opposite sides of the same substrate.<sup>272</sup> The resulting transmission will be governed by the considerations of Sec. 7.1, subsection “Transmission Filters in Series and Parallel.”

## Slope of the Cutoff

This quantity is defined in a number of ways. One common definition is

$$\left| \frac{\lambda_{0.8} - \lambda_{0.05}}{\lambda_{0.5}} \right| \times 100\% \quad (58)$$

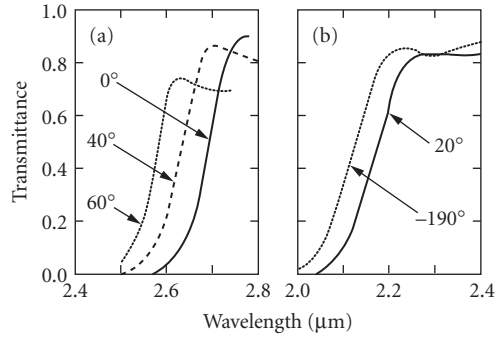
where  $\lambda_{0.8}$ ,  $\lambda_{0.5}$  and  $\lambda_{0.05}$  refer to the wavelengths at which the transmittances are 0.8, 0.5, and 0.05 of the maximum transmittance of the filter. Explicit formulas for the slope are complicated.<sup>160</sup> The slope increases with the number of periods and with the refractive index ratio. Slopes with values of the order of 5 percent are readily available in practice.

## Angle-of-Incidence Effects

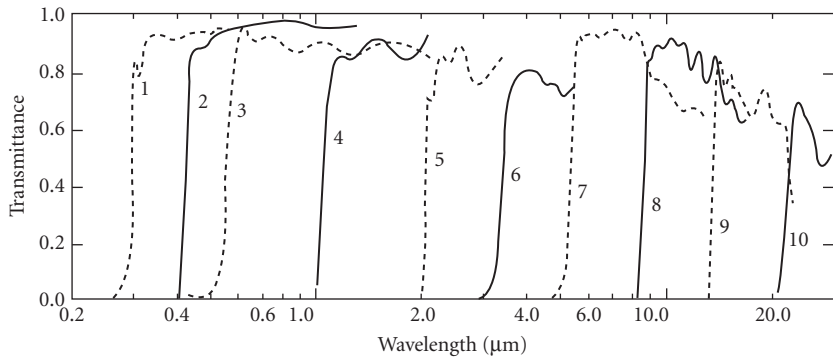
The edges of cutoff filters move toward shorter wavelengths as the angle of incidence is increased. The use of higher-index materials reduces the effect. Measured results for a cutoff filter in which the shift was reduced by using high-refractive-index layers that have 3 times the thickness of the low-index layers are shown in Fig. 60a. See also Sec. 7.9, subsection “Nonpolarizing Beam Splitters” on polarization independent color-selective beam splitters.

## Experimental Results

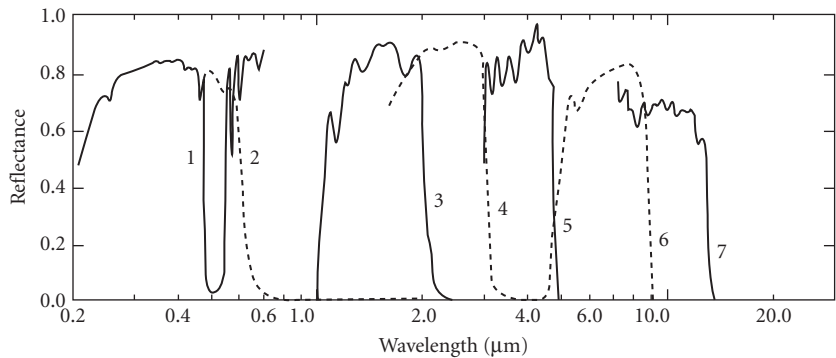
The spectral transmittance curves of a number of commercially available short- and long-wavelength cutoff filters are shown in Figs. 61 and 62. High performance long- and short-wavelength cutoff filters are depicted in Figs. 63, 104, and 115. Similar filters for intermediate wavelengths can, of course, be constructed. It is also possible to construct edge filters in which the thicknesses of all the layers vary in proportion around the circumference of the substrate (see also Sec. 7.11, subsection “Linear and Circular Wedge Filters”). A tuning of the cutoff wavelength is thus possible.



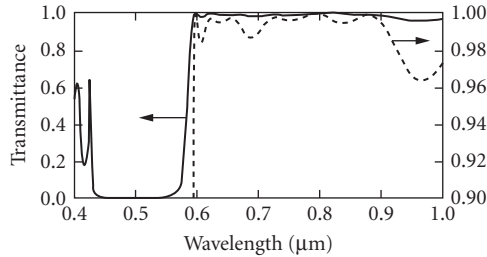
**FIGURE 60** Effect of (a) angle of incidence and (b) temperature on the performance of cutoff filters. (Optical Coating Laboratory.<sup>273</sup>)



**FIGURE 61** A series of commercial short-wavelength cutoff filters. (Curves 1, 5, 8, 9, and 10 after Optical Coating Laboratory;<sup>237,274</sup> curve 2 after Bausch & Lomb;<sup>275</sup> curves 3 and 6 after Turner;<sup>83</sup> curve 4 after Eastman Kodak;<sup>276</sup> and curve 5 after Infrared Industries.<sup>277</sup>)



**FIGURE 62** A series of commercial long-wavelength cutoff filters. (Curve 1 after Apfel;<sup>170</sup> curve 2 after Eastman Kodak;<sup>276</sup> curves 3, 4, and 7 after Optical Coating Laboratory;<sup>274</sup> and curves 5 and 6 after Infrared Industries.<sup>277</sup>)



**FIGURE 63** Measured transmittance of an unblocked short-wavelength cutoff filter. (After *Thin Film Lab*.<sup>85</sup>)

### Heat Reflectors, Cold Mirrors, and Infrared Suppressing Filters

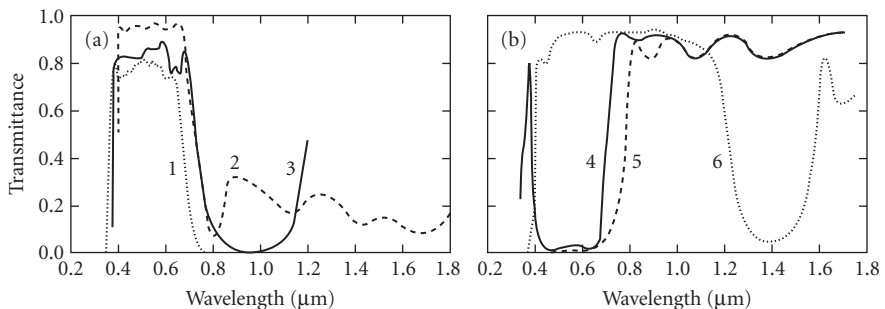
Only 39 percent of the total radiation from carbon arcs and 13 percent from tungsten lamps operated at 3250 K represent visible light. Most of the remaining energy is infrared radiation, which is converted into heat on absorption. The use of heat reflectors and cold mirrors in film projectors,<sup>278</sup> in spot lamps for television and film studios,<sup>279</sup> and other optical instruments can lead to a very significant reduction of this unwanted heat.

Heat reflectors (also called hot mirrors) are special long-wavelength cutoff filters with a cutoff at 0.7  $\mu\text{m}$  which transmit the visible radiation from 0.4 to 0.7  $\mu\text{m}$  without disturbing the color balance. The width of the rejection region depends on the light source to be used and on whether a heat absorbing glass is also to be used. The spectral-transmittance curves of three typical commercial heat reflectors are shown in Fig. 64a. The measured spectral transmittance and reflectance curves of two heat-reflecting coatings not based on periodic multilayers are shown in Fig. 65.

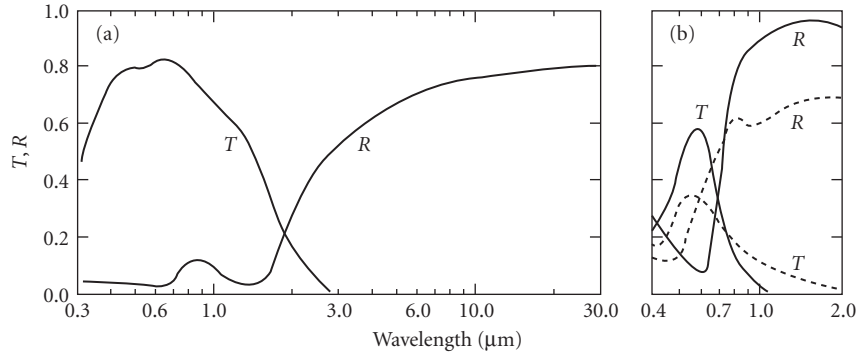
Cold mirrors reflect as much as possible of the visible light incident upon them and transmit the remaining radiation. The reflectance curves of two commercial cold mirrors are shown in Fig. 64b.

### Solar-Cell Covers

Solar-cell covers remove the incident solar energy that does not contribute to the electrical output of the cell and protect it from possible deterioration of its performance through the action of ultraviolet radiation.<sup>283,284</sup> The spectral transmittance of a blue-red solar-cell cover is shown in Fig. 64b. The earlier blue solar-cell covers (curve 2, Fig. 61) protected the cell only from the adverse effects of ultraviolet radiation.



**FIGURE 64** Measured performance of commercial multilayer coatings for heat control: (a) heat-reflecting coatings; (b) cold mirrors and blue-red solar-cell cover. (Curve 1 after Corion Corporation;<sup>280</sup> curve 2 after Bausch & Lomb;<sup>275</sup> curve 3 after Balzers;<sup>76</sup> curves 4 and 6 after Optical Coating Laboratory;<sup>257</sup> and curve 5 after Heliotek.<sup>281</sup>)



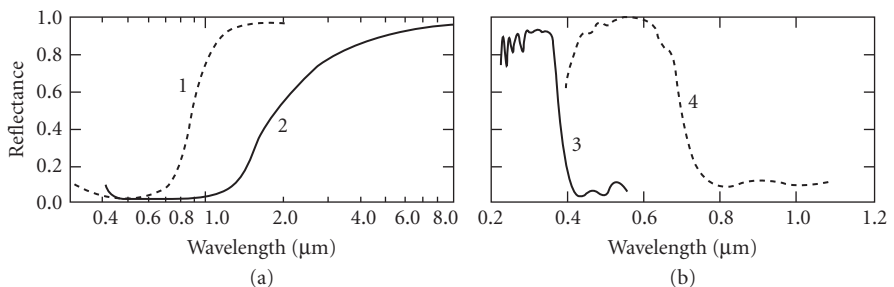
**FIGURE 65** Two nonperiodic coatings with heat-reflecting properties: (a) spray-deposited conducting coating of tin oxide and (b) transmittance and reflectance of a gold film (dotted curves) and of a broadband metal dielectric filter (solid curves) with semitransparent gold films of the same total thickness. (After Turner.<sup>282</sup>)

## Temperature Effects

Refractive indexes of optical materials increase almost linearly with increase in temperature thus causing cutoff edges to move toward longer wavelengths. In actual filters the fractional-wavelength shift varies between  $3 \times 10^{-3}$  and  $10^{-4}/^{\circ}\text{C}$ . Ion-plated films have a smaller temperature shift than films prepared by conventional e-beam evaporated layers.<sup>285</sup> Higher-index materials tend to be more temperature sensitive, thus making it difficult to construct filters that are insensitive both to angle of incidence and temperature changes.<sup>286</sup> The measured performance of a cutoff filter at two temperatures is shown in Fig. 60b.

## Metal-Dielectric Reflection Cutoff Filters

It is possible to construct metal dielectric cutoff filters that act in reflected light (Fig. 66). Short-wavelength cutoff filters consist of an opaque metal layer and one or more additional layers. The light is removed through absorption within the absorbing layers of the system. The thicknesses of the individual layers are adjusted to maximize the absorption and width of the rejection region. Long-wavelength cutoff filters consist of all-dielectric multilayer reflectors superimposed



**FIGURE 66** Short- and long-wavelength metal-dielectric reflection cutoff filters based on reflection. (a) Curves 1 and 2: three-layer coatings on aluminum (after Drummer and Hass<sup>138</sup>) and (b) curves 4 and 5: multilayer reflecting coatings deposited onto black absorber coatings (after Hoppert<sup>287</sup>).



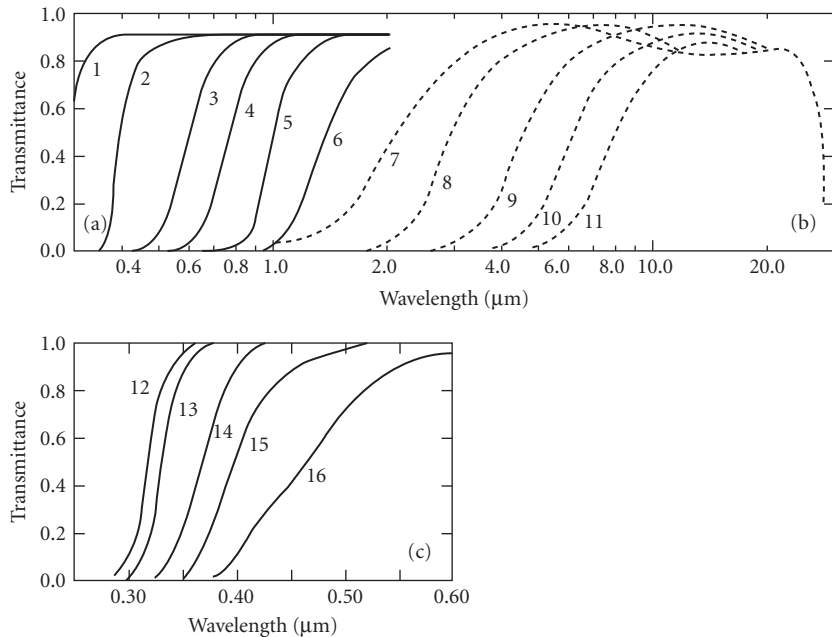
onto a black absorbing coating. A high attenuation of the unwanted radiation can be achieved by placing identical filters of either type in a multiple reflection arrangement of the kind depicted in Fig. 3.

### Cutoff Filters Based on Absorption

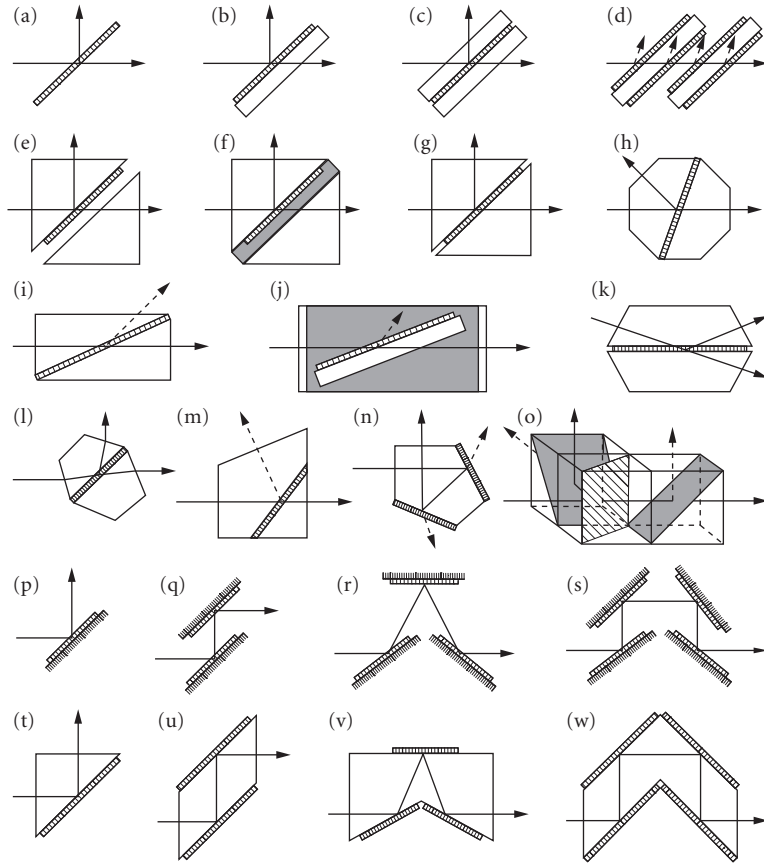
All materials used in multilayer interference coatings possess short- and long-wavelength absorption edges. These can often be used to assist in the blocking of such filters. The admixture of small amounts of absorbing materials to an evaporant or organic coating solution is used at times to tune this absorption edge (Fig. 67a and c). For example, antireflection coatings containing such ultraviolet-absorbing materials can be used to protect works of art.<sup>288</sup>

A series of commercial short-wavelength cutoff filters for the infrared spectral region consisting of chemically deposited silver sulfide coatings on silver chloride substrates are also shown in Fig. 67b. These filters are quite delicate. When protected with a polystyrene layer, their transmittance is reduced and sharp absorption bands appear. The filters should not be used outdoors unless additionally protected, nor should they be exposed to ultraviolet radiation or temperatures in excess of 110°C.

The greatest advantage of cutoff filters based on absorption in thin films is their much smaller angular dependence.



**FIGURE 67** Spectral transmittance of absorbing films produced in various ways. (a) Envelopes of the transmission maxima of thick evaporated films of ZnS (curve 2), Ge (curve 6), and various mixtures of ZnS and Ge (curves 3 to 5) on a glass substrate (curve 1) (after Chang<sup>289</sup>); (b) spectral transmittance of chemically deposited silver sulfide coatings on silver chloride substrates (curves 7 to 11) (Eastman Kodak<sup>276</sup>); and (c) intrinsic transmittance of thin films of titanium dioxide with admixtures of heavy metal oxides, deposited from organic solutions. Curve 12:  $\text{TiO}_2 + 1.5\text{SiO}_2$ ; curve 13:  $\text{TiO}_2$ ; curve 14:  $\text{TiO}_2 + 0.5\text{PbO}$ ; curve 15:  $\text{TiO}_2 + 0.15\text{Fe}_2\text{O}_3$ ; curve 16:  $\text{TiO}_2 + 5.7\text{UO}_3$  (after Schröder<sup>290</sup>).



**FIGURE 68** Schematic representations (*a* to *w*) of some arrangements for beam splitters, polarizers, phase retarders and multiple reflection devices. Thin films are represented in the diagrams by narrow shaded rectangles. Heavy lines ending in an arrow represent the path of the utilized radiation. Broken lines correspond to beams that are not used. The angles of incidence depend on the application.

## 7.9 BEAM SPLITTERS AND NEUTRAL FILTERS

### Geometrical Considerations

Several different physical forms of beam splitters are illustrated in Fig. 68. The simplest beam splitter (Fig. 68*b*) consists of a coating on a transparent plane-parallel substrate. If the two derived beams are to traverse identical paths, a cemented beam splitter is used (Fig. 68*c*). The lateral displacement of the transmitted beam introduced by the above forms can be avoided with a beam splitting cube (Fig. 68*f*). To reduce the stray reflected light in the system, the free surfaces of the above beam splitters can be antireflection coated. Alternatively the coatings can be deposited onto an approximately 2- $\mu\text{m}$ -thick nitrocellulose pellicle (Fig. 68*a*). The latter is an integral part of the multilayer and may introduce an interference pattern into the spectral reflectance and transmittance characteristics. Pellicle beam splitters are very light and yet quite sturdy.<sup>111,291,292</sup> They are, however, subject to vibrations

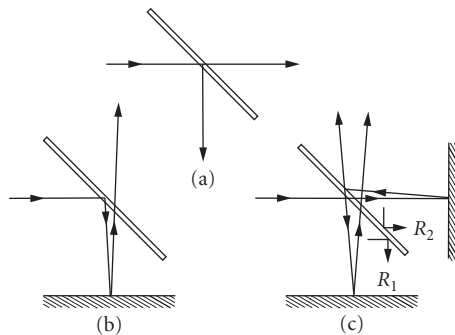
caused by air currents and acoustical waves. The mechanical design of rugged, environmentally stable mounts for the above types of beam splitters have been discussed by Heinrich et al., and Lipshutz.<sup>293,294</sup> Pellicles made of Mylar have been used at temperatures down to 4 K.<sup>295</sup>

In general, the transmission and reflection coefficients  $T$  and  $R$  will depend on the polarization of the incident radiation. The polarization effect can be reduced though the use of more complicated thin-film designs, but usually at the expense of other performance aspects. Achromatic or color-selective beam splitting arrangements have been described in which the two derived beams have intensities that are completely polarization-independent over a very wide spectral region.<sup>296</sup> They consist of three identical beam splitters arranged in such a way that each beam undergoes identical reflections and transmissions on passing through the system (Fig. 68*o*).

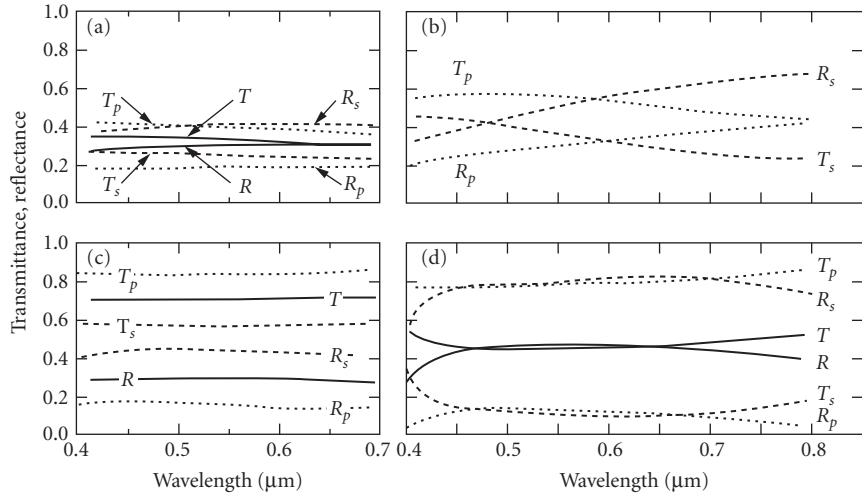
## Achromatic Beam Splitters

These devices are introduced into an incident beam of radiation when it is desired to divide it into two beams of approximately equal relative spectral composition but propagating in two different directions.<sup>297</sup> In neutral beam splitters the quantity  $0.5(R_p + R_s)_{\theta=45^\circ}$  is always close to the reflectance at normal incidence, even though the individual  $R_p$  and  $R_s$  values may be quite different. The reflectance of absorbing, uncemented beam splitters depends also on the direction of incidence (Sec. 7.2, subsection "Matrix Theory for the Analysis of Multilayer Systems"). The optimum values of  $T$  and  $R$  depend on the application. For example, for a binocular eye piece on a nonpolarizing microscope the most important requirement is  $T_p + T_s = R_p + R_s$  (Fig. 69*a*). For a vertical illuminator ( $R_p T_p + R_s T_s$ ) should be a maximum (Fig. 69*b*). The condition for maximum fringe contrast in some interferometers requires that  $R_{1,p} T_p = R_{2,p} T_p$  and  $R_{1,s} T_s = R_{2,s} T_s$  (Fig. 69*c*). This is satisfied automatically by all nonabsorbing and by absorbing cemented beam splitters. The occasional requirement that the phase change on reflection be the same for radiation incident onto the beam splitter from opposite sides is automatically satisfied at the design wavelength by all-dielectric coatings composed of  $\lambda/4$  layers, but not by uncemented metal beam splitters.<sup>298</sup>

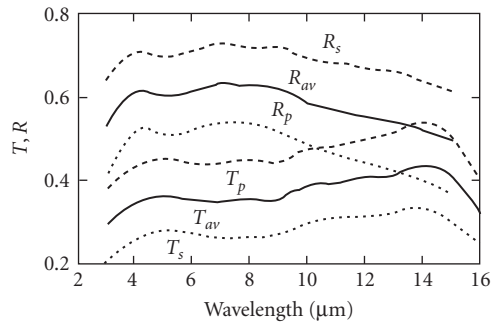
For maximum efficiency with unpolarized radiation  $R_p$ ,  $R_s$ ,  $T_p$ , and  $T_s$  should all approach 0.5. However, such a coating will not necessarily exhibit the best ratio of the intensities of the directly transmitted or reflected radiation to that which first undergoes multiple reflections.<sup>297</sup> Often beam splitters are required that are uniform over a broad spectral region. Inconel films satisfy this requirement although about one-third of the incident radiation is lost through absorption (see also Sec. 7.9, subsection "Neutral Filters"). The design of achromatic all-dielectric beam splitters has been discussed by many workers.<sup>299-304</sup> Knittl considered the design of beam splitters in which both the reflectance and the phase change on reflection are achromatized.<sup>305</sup> The measured performance of several beam splitters is shown in Figs. 70 and 71.



**FIGURE 69** Three different ways [(a), (b), and (c)] of using beam splitters.



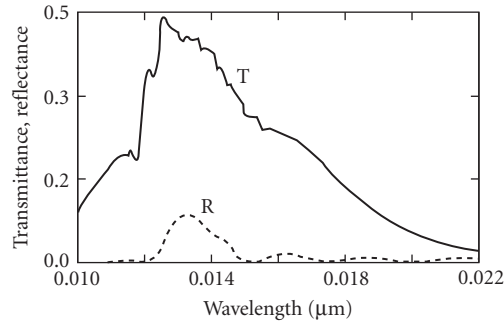
**FIGURE 70** Measured spectral transmittance for polarized and unpolarized light of (a) Inconel- and (c) dielectric-coated beam-splitting plates (Oriol<sup>306</sup>) and of (b) silver- and (d) dielectric-coated beam-splitting cubes (after Anders<sup>297</sup>).



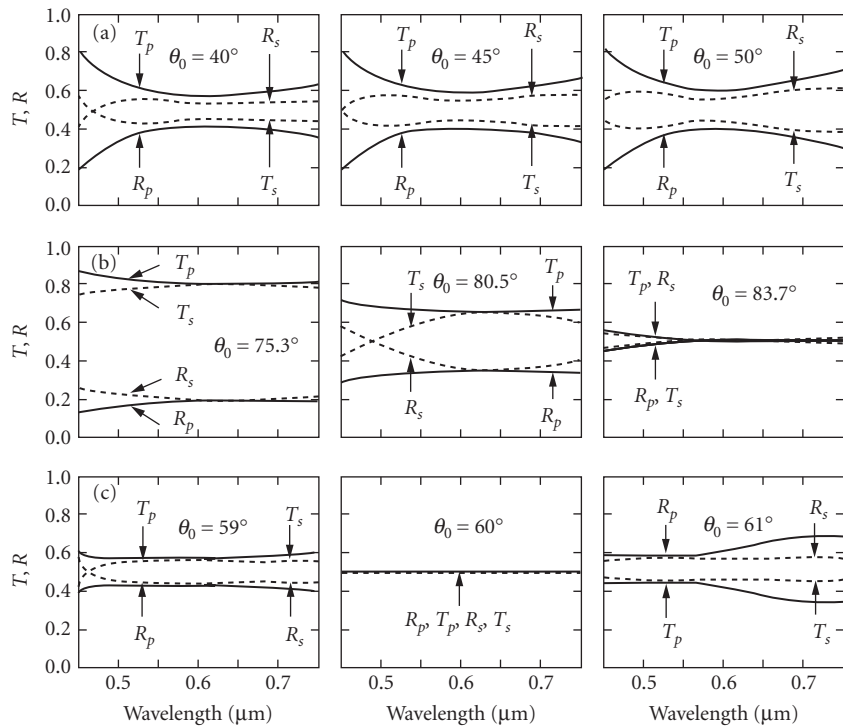
**FIGURE 71** Measured performance of a 45° infrared beam splitter consisting of a suitably coated ZnSe plate. (After Pellicori<sup>307</sup>)

Beam splitters for the x-ray region described so far operate at close to normal incidence and are effective only over a very narrow range of wavelengths. They consist of multilayer reflecting stacks (see Secs. 7.6, subsection “Multilayer Reflectors Made of Absorbing Materials” and 7.7, subsection “Multilayer Reflectors for the Soft X-Ray and XUV Regions”) deposited onto membranes or onto substrates that are thinned to enhance the transmitted component (Fig. 72).<sup>308</sup>

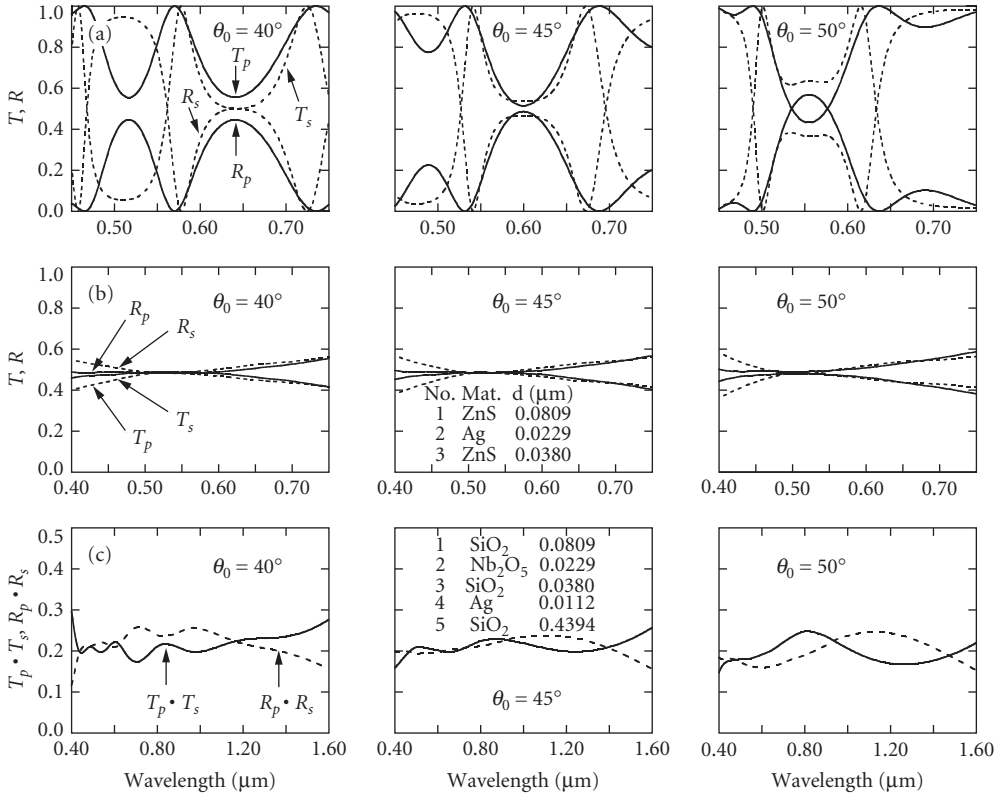
**Nonpolarizing Beam Splitters** For some applications it is important that the beam splitter introduce no polarization effects. Azzam has shown that, with the appropriate single layer on the face of a suitable high-refractive-index prism, it is possible to construct a polarization independent beam splitter.<sup>309</sup> This device is quite achromatic and, in addition, by changing the angle of incidence of the beam on the prism, the beam-splitting ratio can be tuned over a wide range of values (Fig. 73a). The principle of frustrated total internal reflection can also be used to design beam splitters that have a very good performance.<sup>310,311</sup> In these devices radiation is incident at a very oblique angle



**FIGURE 72** Measured performance of an x-ray beam splitter consisting of 11 pairs of Mo and Si layers on a 0.03- $\mu\text{m}$ -thick  $\text{Si}_3\text{N}_4$  membrane, operating at an angle of incidence of  $0.5^\circ$ . (After Ceglie.<sup>263</sup>)



**FIGURE 73** Calculated performance at three angles of incidence of beam splitters with an incident medium of air. (a) Beam splitter of the type glass  $(HL)^2$  air, where  $n_H = 2.35$ ,  $n_L = 1.38$ ; (b) single layer ( $n = 1.533$ ,  $d = 0.1356 \mu\text{m}$ ) on a prism ( $n_s = 2.35$ ) (after Azzam<sup>309</sup>); and (c) 15-layer frustrated total internal reflection beam splitter (after Macleod<sup>311</sup>). The last two systems are fairly polarization independent and yield different T/R ratios for different angles of incidence.



**FIGURE 74** Calculated performance of polarization insensitive achromatic beam splitters consisting of layer systems cemented between glass prisms. (a) All-dielectric system of the type  $n_s$  ( $LMHMHML$ )<sup>2</sup>, where  $n_s = 1.52$ ,  $n_L = 1.38$ ,  $n_M = 1.63$ ,  $n_H = 2.35$ ; the quarterwave layers are matched for 45° incidence. (after Thelen<sup>13</sup>); (b) three-layer metal/dielectric system (after Chang<sup>322</sup>); and (c) polarization independent beam splitting arrangement of the type of Figure 68o composed of three identical prisms (after Ho<sup>296</sup>).

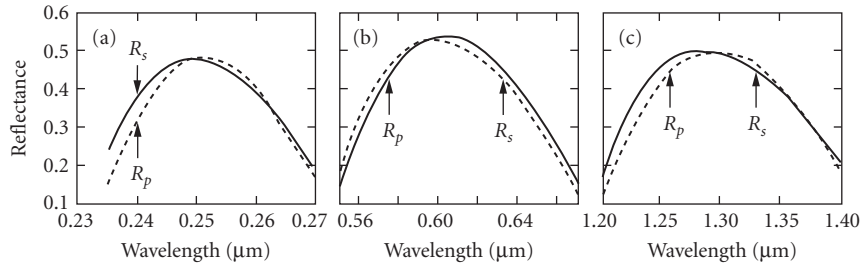
onto an air gap or low-refractive-index films at the interface between two prisms (Fig. 68e, and f). Unfortunately, the performance of such systems is very sensitive to the angle of incidence (Fig. 73c).

In many applications it is important that the beam splitter be relatively insensitive to the angle of incidence. One way is to reduce the angle of incidence as much as possible (Fig. 68h).<sup>312</sup> However, in many cases a 45° angle of incidence is mandatory. Relatively polarization insensitive beam splitters based on dielectric-metal-dielectric layer systems embedded between two prisms have been described.<sup>313,314</sup> Much work has been done to find solutions based on dielectric layers only.<sup>24,207,314–321</sup> However, the improvement is frequently at the expense of the width of the spectral region over which the beam splitter is effective. Some typical results are shown in Figs. 74 and 75.

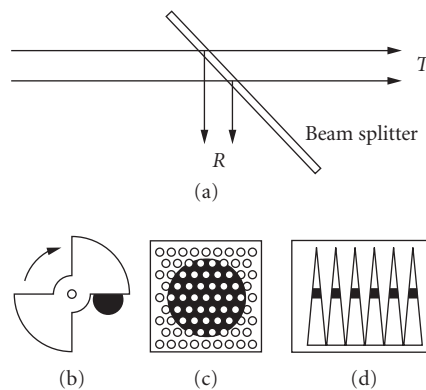
Simple angle- and polarization-insensitive mechanical solutions to the achromatic beamsplitting problem exist if the application can tolerate spacial or temporal beam sharing (Fig. 76).

## Color-Selective Beam Splitters

For various technological applications a beam of light must be divided into several components of different color. All-dielectric color selective beam splitters (*dichroics*) are used for this purpose



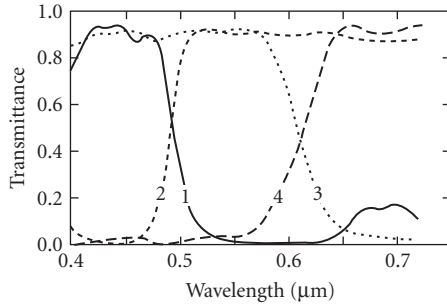
**FIGURE 75** Measured performances (a) to (c) of polarization insensitive beam splitters of the type of Fig. 74a produced for three different spectral regions. (After Konoplev.<sup>323</sup>)



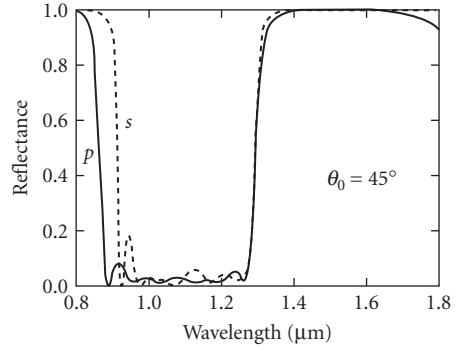
**FIGURE 76** Achromatic and angle-insensitive mechanical beam splitting arrangements. (a) and (b) Rotating aluminized blade which alternatively transmits and reflects the incident radiation. (c) Stationary transparent plate with a polka-dot pattern in which either the circles or the background (each of equal total area) are aluminized. (d) Aluminized saw-tooth pattern on a transparent substrate that can be displaced to reflect different fractions of the incident radiation that is collimated into a narrow beam.

because they are practically lossless and because their transition wavelengths can be selected at will. They are essentially cutoff filters (Sec. 7.8) usually designed for use at  $45^\circ$  incidence. Their spectral characteristics normally depend on the polarization of the incident radiation. The effect of this and of the variations in the angle of incidence and thickness of the coatings on the chromaticity coordinates of dichroic beam splitters for television cameras was investigated by Pohlack.<sup>324</sup> If necessary, the polarization of the derived beams can be reduced through the use of auxiliary normal incidence cutoff filters.<sup>219</sup> Typical transmittance curves of several color-selective beam splitters are shown in Fig. 77.

**Nonpolarizing Edge and Bandpass Filters** For more exacting applications, such as for use in multiplexers and demultiplexers, or for the separation of emission or absorption lines in atmospheric physics or Raman spectroscopy, it is possible to design and construct short- and long-wavelength color selective beam splitters in which the polarization splitting has been largely eliminated.<sup>13,325</sup> In the designs described the polarization splitting is usually removed for all angles smaller than the design angle, but the cutoff wavelength still shifts with the angle of incidence (Fig. 78). Some of the designs do not have a wide transmission region.



**FIGURE 77** Measured spectral transmittance of four color-selective beam splitters. (*Optical Coating Laboratory*.<sup>237</sup>)



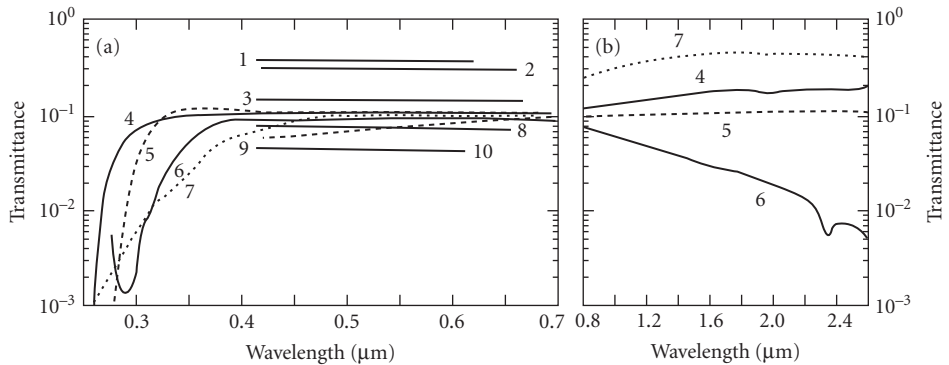
**FIGURE 78** Calculated transmittance of a polarization independent color selective beam splitter for several angles of incidence. (*After Thelen*.<sup>13</sup>)

## Neutral Filters

These devices are used whenever the intensity of the incident radiation is to be reduced uniformly throughout an extended part of the spectrum. The radiation usually traverses neutral filters at or near-normal incidence. A number of absorbing glasses and gelatin filters are suitable for making neutral-density filters with densities of up to 5.0. However, their spectral transmission curves are not very uniform.

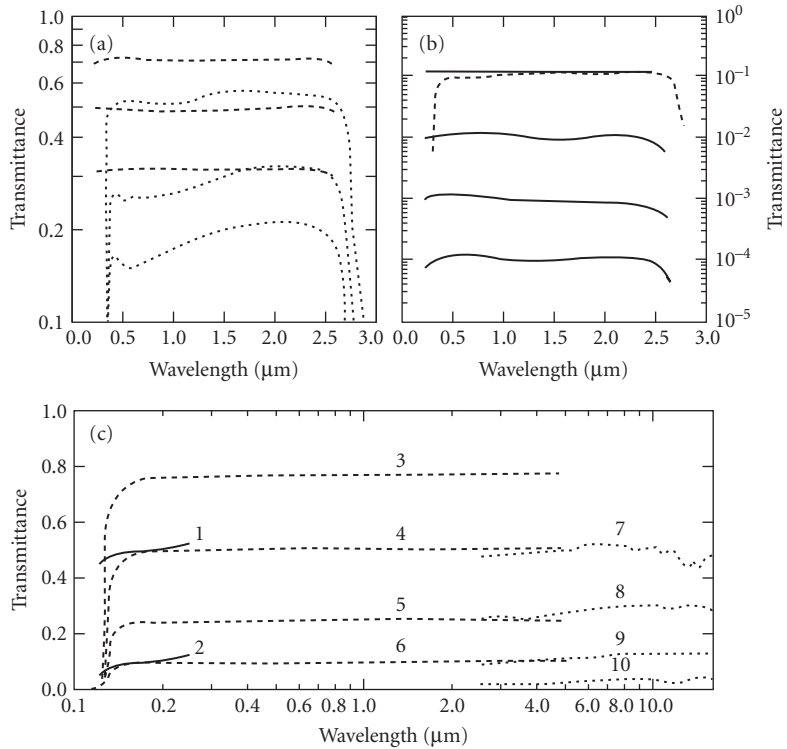
Evaporated films of metals such as aluminum, chromium, palladium, platinum, rhodium, tungsten, and alloys such as chromel, nichrome, and inconel have been used for a long time to produce filters with densities of up to 6.0. A disadvantage of such filters is their high specular reflection. At present inconel is commonly used for high-precision neutral-density filters. Chromium is favored when tough, unprotected coatings are required (Fig. 79). The operating range and neutrality depends on the substrate materials. The spectral-transmittance curves of neutral-density filters on magnesium fluoride, calcium fluoride, quartz, glass, sapphire, and germanium substrates are shown in Fig. 80. Linear and circular metal-film neutral-density wedges and step filters are also available commercially.

At times there may be a need for a neutral attenuation that is not based on absorption. Sets of all-dielectric multilayer coating designs have been published with uniform transmission levels for the ultraviolet,<sup>326</sup> visible,<sup>215,327</sup> and near-infrared<sup>328</sup> parts of the spectrum (Fig. 81).

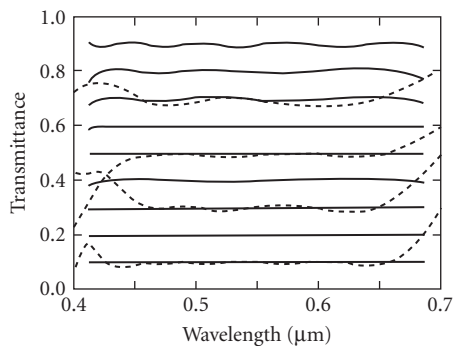


**FIGURE 79** (a), (b) Spectral transmittance of various neutral density materials. Curve 1: tungsten film on glass; curves 2 and 3: diffuse and specular transmittance of photographic emulsion; curve 4: M-type carbon suspension in gelatine; curve 5: Inconel film on glass; curve 6: photographic silver density; curve 7: Wratten 96 density filter; curve 8: chromium film; curves 9 and 10: chromel A film on glass evaporated at pressures of  $10^{-3}$  and  $10^{-4}$  Torr, respectively. (Curves 1 to 3, 9, and 10 after Banning;<sup>329</sup> curves 4 to 7 after Eastman Kodak Company;<sup>330</sup> and curve 8 after Optical Coating Laboratory.<sup>237</sup>)





**FIGURE 80** Neutral-density attenuators (a), (b) Inconel films on glass substrates (dotted curves, Bausch & Lomb<sup>275</sup>) and on quartz substrates (full and broken curves, Corion<sup>331</sup>). (c) Alloy films on  $\text{MgF}_2$  (solid curves, after Acton<sup>332</sup>); on  $\text{CaF}_2$  (broken curves, after Spindler & Hoyer<sup>88</sup>); and on Ge (dotted curves, after Oriol.<sup>306</sup>)



**FIGURE 81** Achromatic all-dielectric attenuators. The solid curves are calculated results (after Hodgkinson<sup>327</sup>) and the dotted curves represent the performance of commercial coatings (after TechOptics<sup>86</sup>).

## 7.10 INTERFERENCE POLARIZERS AND POLARIZING BEAM SPLITTERS

The dependence of the optical properties of thin-film systems on the plane of polarization of obliquely incident radiation<sup>24</sup> (Sec. 7.2, subsection “Matrix Theory for the Analysis of Multilayers Systems”) can be exploited to design interference polarizers and polarizing beam splitters with properties that augment those attainable by other means (Chap. 13, Vol. I). The main difference between a polarizer and a polarizing beam splitter is that in the former only one polarized beam is required, whereas in the latter both beams are to be utilized. A polarizing beam splitter can therefore also be used as a polarizer. The performance in transmission or reflection of both devices is usually characterized by their degree of polarization  $P$ , or by the extinction ratio ER, both of which are functions of the transmittance  $T$  and reflectance  $R$  for the desired and undesired polarizations:

$$\left. \begin{aligned} P &= \left| \frac{T_{\text{desired}} - T_{\text{undesired}}}{T_{\text{desired}} + T_{\text{undesired}}} \right| \quad \text{or} \quad P = \left| \frac{R_{\text{desired}} - R_{\text{undesired}}}{R_{\text{desired}} + R_{\text{undesired}}} \right| \\ \text{or by} \\ \text{ER} &= \frac{T_{\text{desired}}}{T_{\text{undesired}}} \quad \text{or} \quad \text{ER} = \frac{R_{\text{desired}}}{R_{\text{undesired}}} \end{aligned} \right\} \quad (59)$$

In a polarizing beam splitter a high degree of polarization is required in both beams and this is more difficult to achieve. Presently efficient interference polarizers and polarizing beam splitters can be constructed for the soft x-ray, ultraviolet, visible, and infrared spectral regions. Interference polarizers and polarizing beam splitters are of particular interest whenever large areas and low losses are required. Schematic representations of the geometries of some of the devices are given in Fig. 68.

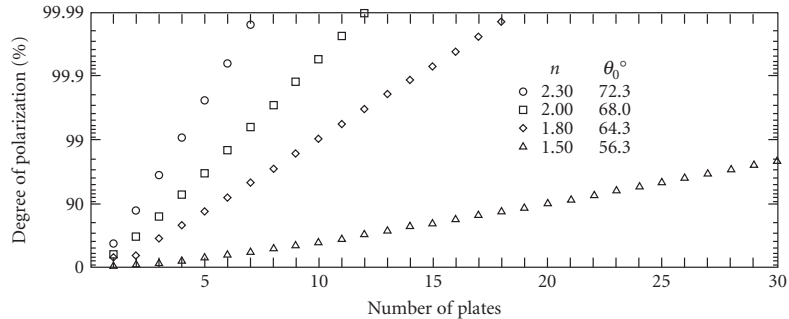
### Multicomponent Polarizers

It is always possible to find an angle of incidence at which a substrate coated with a film of quarter-wave effective thickness will reflect only  $s$ -polarized radiation which is polarized perpendicular to the plane of incidence.<sup>333</sup> This property can be used to construct efficient transmitting polarizers using far fewer plates than necessary in the conventional pile-of-plates polarizer of equal performance (Fig. 68*d*).<sup>334</sup> The calculated degree of polarization attainable with different numbers of plates is shown in Fig. 82 for a series of film indices and polarizing angles. Experimental results agree closely with the calculations. In polarizers of this type the variation of the degree of polarization is small over a wavelength span of 2:1 and for angular apertures of up to 10°.<sup>333</sup> Yet, because of its bulk, this type of polarizer is not frequently used. An exception is polarizers for the infrared, where it is more difficult to produce multilayers composed of many layers. Because of the high refractive indices available in that spectral region, it is possible to achieve a high degree of polarization even after a single transmission through a plate coated with one layer only.<sup>335</sup>

Several geometries of the reflection equivalent of the multiple plate polarizer exist (Fig. 68). The reflectors can consist of one or more dielectric layers deposited onto nonabsorbing parallel plates or prisms (Fig. 68 *t* to *w*). In other devices the substrates are made of metal, or are coated with an opaque metallic film (Fig. 68 *p* to *s*).<sup>336</sup> The angles of incidence on the various mirrors need not be the same. Polarizers of this type are particularly useful in the infrared<sup>337</sup> and vacuum ultraviolet (see subsection “Polarizers for the Extreme Ultraviolet and Soft X-Ray Regions”) spectral regions. Interesting variants are polarizers that are based on total internal reflection or frustrated total internal reflection (Fig. 68 *m* and *n*).

### Plate Polarizers

The number of coated plates in the transmission polarizers described above can be reduced without compromising the performance by depositing more than one high-refractive-index layer onto the surface



**FIGURE 82** Calculated degree of polarization of different numbers of plates of refractive index 1.5 coated on both sides with films of different refractive indexes  $n$ . The films have effective optical thicknesses of a quarter wavelength at the appropriate polarizing angle  $\theta$ .

of a plate and by spacing them with low-index films. In particular, it is possible to minimize the surface scatter, plate absorption, and lateral beam displacement by combining all the layers into one coating.

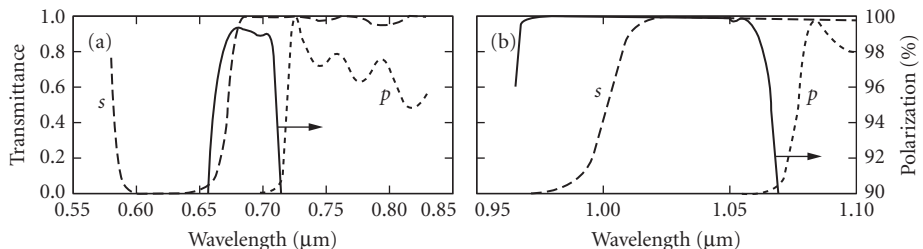
The most common solution for high-power laser applications are plate polarizers that are based on the polarization splitting that occurs at higher angles, for example, at the edges of quarter-wave stack reflectors (Fig. 68).<sup>338</sup> The plate on which the multilayer is deposited is held at Brewster's angle with respect to the incident light to avoid second surface reflections. Usually the long-wavelength edge of the reflector is used and the design is somewhat modified to remove the ripples in the transmission band of the  $p$ -polarized radiation (Fig. 83). The use of other multilayer structures, such as bandpass filters, for the construction of plate polarizers has also been proposed.<sup>339</sup> The wavelength range over which plate polarizers are effective is much smaller than that of polarizers based on a series of coated plates, but this is acceptable for most laser applications.

Other methods for the design of narrowband plate polarizers based on two or three coating materials have been described by Minkov,<sup>340</sup> Mahlein,<sup>207</sup> and Thelen.<sup>341</sup> However, these solutions require many layers and sometimes very oblique angles of incidence.

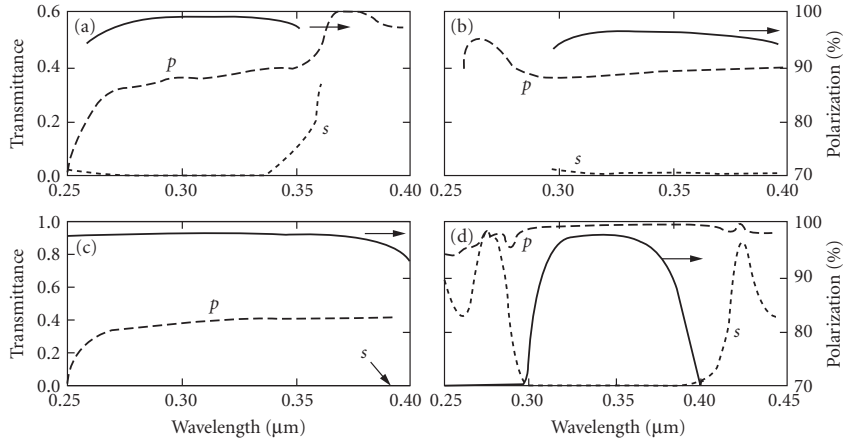
### Embedded Polarizers and Polarizing Beam Splitters Based on Two Coating Materials

Polarizers and polarizing beam splitters effective over a wider spectral region are obtained when multilayer coatings of the type  $[HL]^N H$  or  $[(0.5H)L(0.5H)]^N$  are embedded between media of higher refractive index than air.<sup>342</sup> The higher the refractive index ratio of the two coating materials used, the fewer the number of layers needed to achieve a certain degree of polarization and the wider the spectral region over which the polarizer will be effective. However, a certain relationship between the refractive indexes of the materials and the angle of incidence must be satisfied.<sup>343</sup> The optical thicknesses of the quarterwave layers should be matched for the angle of incidence.

A particularly convenient polarizer with no lateral beam displacement results when the multilayer is embedded between two right-angled prisms, as shown in Fig. 68i.<sup>344,345</sup> MacNeille polarizers operate over



**FIGURE 83** Measured performances (a), (b) of two plate polarizers. (After TechOptics.<sup>86</sup>)



**FIGURE 84** The measured degree of polarization  $P$  and transmittance of parallel and crossed MacNeille interference polarizers for the ultraviolet spectral region. (c) Represents the results obtained when the cemented polarizers shown in (a) and (b) are placed in series (after Sokolova and Krylova<sup>346</sup>); and (d) is the measured performance of an optically contacted polarizer with a high laser damage threshold (after Wimperis<sup>347</sup>).

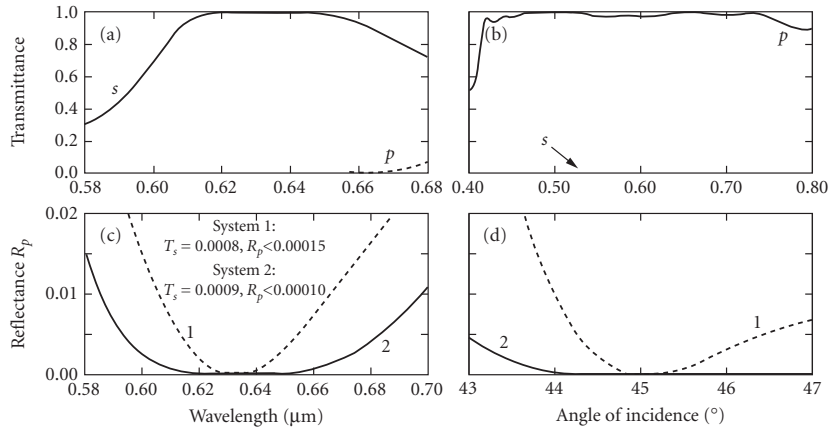
a very broad range of wavelengths (Fig. 84a and b). For best results, the following relationship between the angle of incidence  $\theta_p$  and the refractive indices of the prism and the layers should be satisfied:

$$n_p \sin \theta_p = \frac{n_L n_H}{\sqrt{n_L^2 + n_H^2}} \quad (60)$$

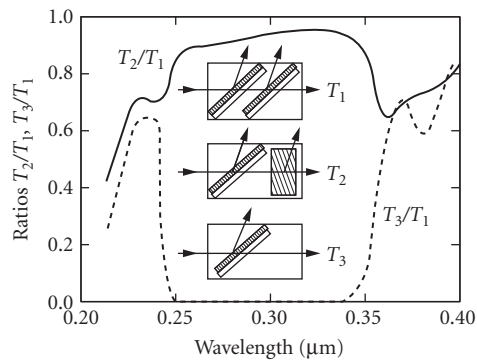
This expression is independent of the thicknesses of the layers and, were it not for the dispersion of the optical constants, the transmission for the  $p$  polarization would be 1.0 across the entire spectral region at the design angle  $\theta_p$ . However, the dispersion of the high-index material as well as the limit of the index ratio  $n_L/n_H$  will tend to decrease the useful spectral range of the polarizer.<sup>348</sup> It is possible to select the  $V$ -number of the substrate material in order to decrease this disturbing effect. The rejection of the unwanted polarization will normally not be the same in both beams, although this can be achieved at the expense of the wavelength range.<sup>349</sup> If polarizers for an even wider spectral region are required, it is possible to extend the range by placing two polarizers in series (Fig. 84c), by using the technique of superposition of stacks with contiguous high-reflection zones (Sec. 7.7, subsection “Rejection Filters”) or of two periodic multilayers with thickness ratios of 1:1 and 1:2.<sup>173</sup> When both beams are used, the useful angular field of the MacNeille polarizer is of the order of  $\pm 2^\circ$ . It is possible to increase it to  $\pm 10^\circ$ , but again at the expense of narrowing the spectral range.<sup>350</sup>

When the MacNeille polarizer is to be used as a polarizing beam splitter, it is possible to design it for normal incidence of the beams onto the prism faces, or for a  $90^\circ$  deflection between the two beams (Fig. 68l).<sup>349,351</sup> However, it is more convenient to embed the multilayers between two  $45^\circ$  prisms. A higher-refractive-index prism material is required if (60) is to be satisfied<sup>350</sup> and the effective wavelength range will once again be reduced (Fig. 85).<sup>352</sup>

MacNeille polarizers and polarizing beam splitter cubes suffer from several disadvantages. The diameter of the light beam that can be used with the polarizer is limited by the size, cost, and availability of the prism material. The attainable degree of polarization is also affected by the residual birefringence in the glass prisms. Cemented polarizers cannot be used with high-power lasers because of the absorption of the glue. To overcome these difficulties a liquid prism polarizer has been proposed consisting of a multilayer on a quartz plate that is immersed in distilled water (Figs. 68j and 86).<sup>353</sup> Another way of avoiding the use of a cement is to optically contact the polarizer prisms (Figs. 68g, and 84d).<sup>354</sup> More frequently the layers are deposited onto the hypotenuse of one of two air-spaced prisms (Fig. 68e).<sup>355</sup> However, this arrangement is similar to a plate polarizer designed for use at  $45^\circ$  and so is its performance.



**FIGURE 85** Measured performance of polarizing beam splitting cubes. (a) and (b) Measured spectral transmittance curves of two commercial devices (after *TechOptics*<sup>86</sup>). (c) and (d) Measured spectral and angular performance of two different systems (after *Netterfield*<sup>352</sup>).



**FIGURE 86** Measured spectral performance of two parallel and crossed coated plates forming a liquid prism McNeille polarizer for the ultraviolet part of the spectrum. The multilayers on both plates were identical and consisted of 13 alternate quarterwave layers of  $\text{HfO}_2$  and  $\text{SiO}_2$ . (After *Dobrowolski*.<sup>353</sup>)

## Embedded Polarizing Beam Splitters Based on More than Two Coating Materials

By using coating materials with more than two refractive indices in the design of embedded polarizing beam splitters, it is possible to obtain devices that match the spectral region of a MacNeille polarizer while increasing its angular field. For example, a polarizing beam splitter has been described with a 72-layer 4-material design that has a  $\pm 6^\circ$  angular field measured in air that is effective across the 0.4 to 0.7  $\mu\text{m}$  wavelength range.<sup>356</sup>

## Li Li Polarizing Beam Splitter

Li Li described the design of a new type of embedded beam splitter for the visible and infrared spectral regions, using a geometry that is depicted in Fig. 68k.<sup>357</sup> What distinguishes this device from the

polarizing beam splitters described in the previous sections is that it operates at angles greater than the critical angle and that it transmits *s*-polarized light and reflects *p*-polarized light, respectively. The calculated performances of these designs in both the transmitted and reflected beams exceed those of any previous devices. For example, one polarizing beam splitter (described in Ref. 357) that consists of 53 layers has a  $\pm 7.4^\circ$  angular field measured in air in the 0.4 to 0.7  $\mu\text{m}$  wavelength region.

However, because the Li Li polarizing beam splitters require the use of prisms of high refractive index for which there are no suitable optical cements, the two prisms must be optically contacted. The measured performance of prototypes produced in this manner was in good agreement with the calculated values.<sup>358</sup> The need for optical contacting, and the rather large size of the prisms, is the reason why the Li Li polarizing beam splitter is not yet widely used.

Metal-dielectric versions of the Li Li polarizer have been described that are simpler and consist of fewer layers, but they absorb some of the incident light.<sup>359</sup>

In Fig. 87*a* to *j* the calculated spectral and angular performances of a number of polarizers and polarizing beam splitters for the near-UV, visible, and near-IR spectral regions are compared. A theoretical comparison of the properties of the MacNeille, cube and plate polarizers for one wavelength has been given by Cojocar.<sup>360</sup>

## Polarizers for the Extreme Ultraviolet and Soft X-Ray Regions

Polarizers based on reflections from two or more single layer coated surfaces have been proposed for the vacuum ultraviolet<sup>366–368</sup> spectral region. The measured performances in the XUV region of two such polarizers that are based on three reflections are depicted in Fig. 88.

Polarizers for the soft x-ray region can also be based on the fact that the reflectance of an x-ray multilayer mirror at oblique angles is very different for radiation polarized parallel and perpendicular to the plane of incidence. Curve 3, Fig. 91 shows the reflectance of such a periodic Mo/B<sub>4</sub>C multilayer with a very high degree of polarization.<sup>370</sup> Because the region of high reflection is very narrow, this type of polarizer essentially operates at one wavelength only.<sup>371</sup> However, if the radiation is reflected from two identical mirrors of this type (Fig. 68*q*), it is possible to construct a device with a reasonable throughput ( $>0.05$ ) that can be tuned over a wide range of wavelengths without changing the direction of the emerging beam (Fig. 89).<sup>372</sup>

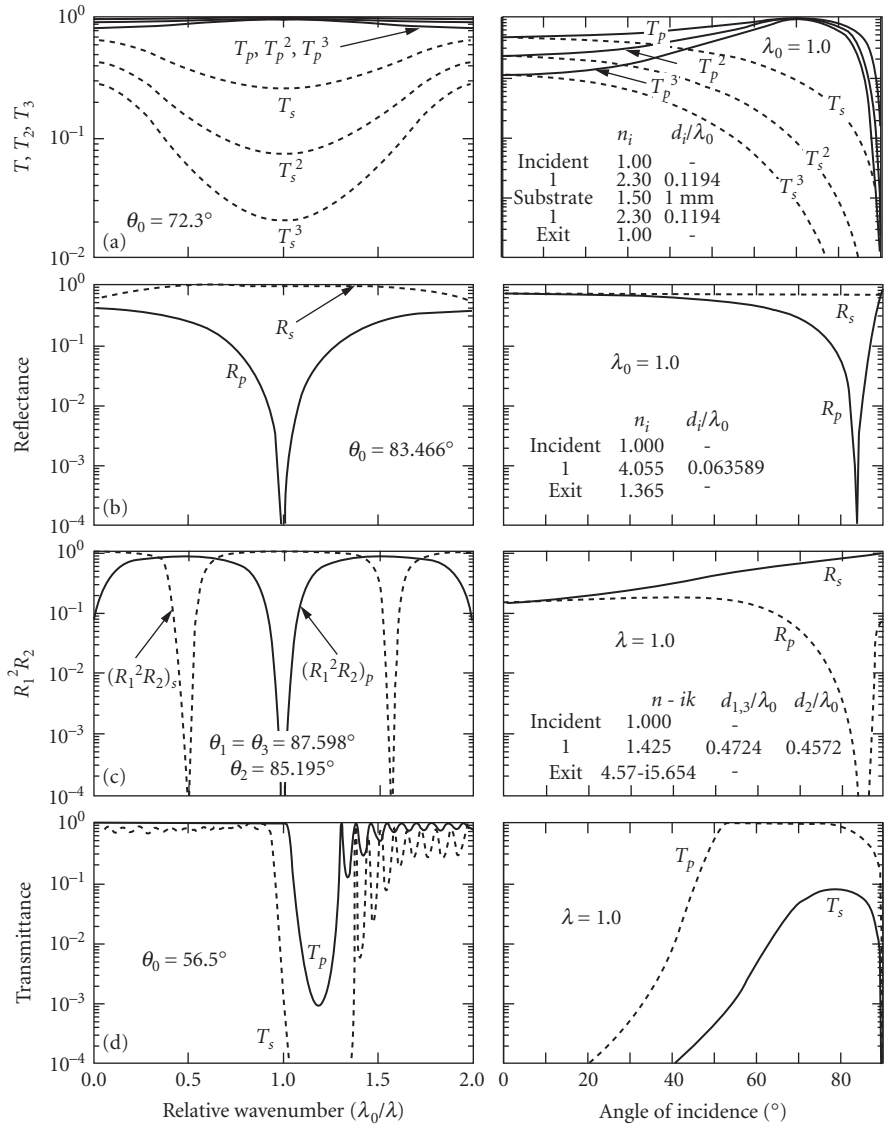
More recently multilayer polarizers effective over a broader range of wavelengths have been constructed. A few examples are shown in Fig. 90.<sup>370,373–375</sup> They are nonperiodic systems made of two suitable materials and they consist of between 60 and 300 layers. The one exception is curve 3 which corresponds to a periodic system and which is shown here for comparison purposes. It will be seen that the effectiveness over a broader range of wavelengths comes at the expense of a lower throughput, but it is also accompanied by a much wider angular field. This is of particular importance when the polarizers are to be used with imaging optics.

## 7.11 BANDPASS FILTERS

An ideal bandpass filter transmits all the incident radiation in one spectral region and rejects all the other radiation. Such a filter is completely described by the width of the transmission region and the wavelength at which it is centered. Practical filters are not perfect and require more parameters to adequately describe their performance. No uniform terminology has yet been developed for this purpose. Care should be taken when reading and writing specifications since often different terms are used to describe different types of filters, and sometimes quantities bearing the same name are defined differently.

The position of the transmission band is variously specified by the wavelength  $\lambda_{\text{max}}$  at which the maximum transmission occurs, the wavelength  $\lambda_0$  about which the filter passband is symmetrical, or the spectral centre of gravity  $\lambda_c$  of the band. When specifying the tolerance on  $\lambda_0$  it should be remembered that the peak of interference filters can be moved only toward shorter wavelengths by tilting (see Sec. 7.2, subsection “Matrix Theory for the Analysis of Multilayer System”).

The peak transmittance  $T_0$  may or may not take into account the absorption within the substrate and/or blocking filters used to remove the unwanted transmission of the interference filter away from the principal passband (Fig. 91).



**FIGURE 87** Calculated spectral and angular performance of several types of polarizers and polarizing beam splitters with an air incident medium (a to d) and embedded between identical prisms (e to j). Calculations assume that all nonmetals are absorption and dispersion free. (a) Multiple plate polarizer; (b) single reflection polarizer (after Azzam<sup>361</sup>); (c) three reflection polarizer (after Thonn<sup>362</sup>); (d) plate polarizer (after Songer<sup>363</sup>); (e) MacNeille polarizing beam splitter (after Mouchart<sup>350</sup>); (f) wide-angle MacNeille polarizing beam splitter (after Mouchart<sup>350</sup>); (g) frustrated total internal reflection polarizing beam splitter (after Lees and Baumeister<sup>364</sup>); (h) penta prism polarizer (after Lotem and Rabinovich<sup>365</sup>); (i) polarizing beam splitter based on more than two materials (after Li Li and Dobrowolski<sup>356</sup>); and (j) Li Li polarizing beam splitter operating at angles greater than the critical angle (after Li Li and Dobrowolski<sup>357</sup>).

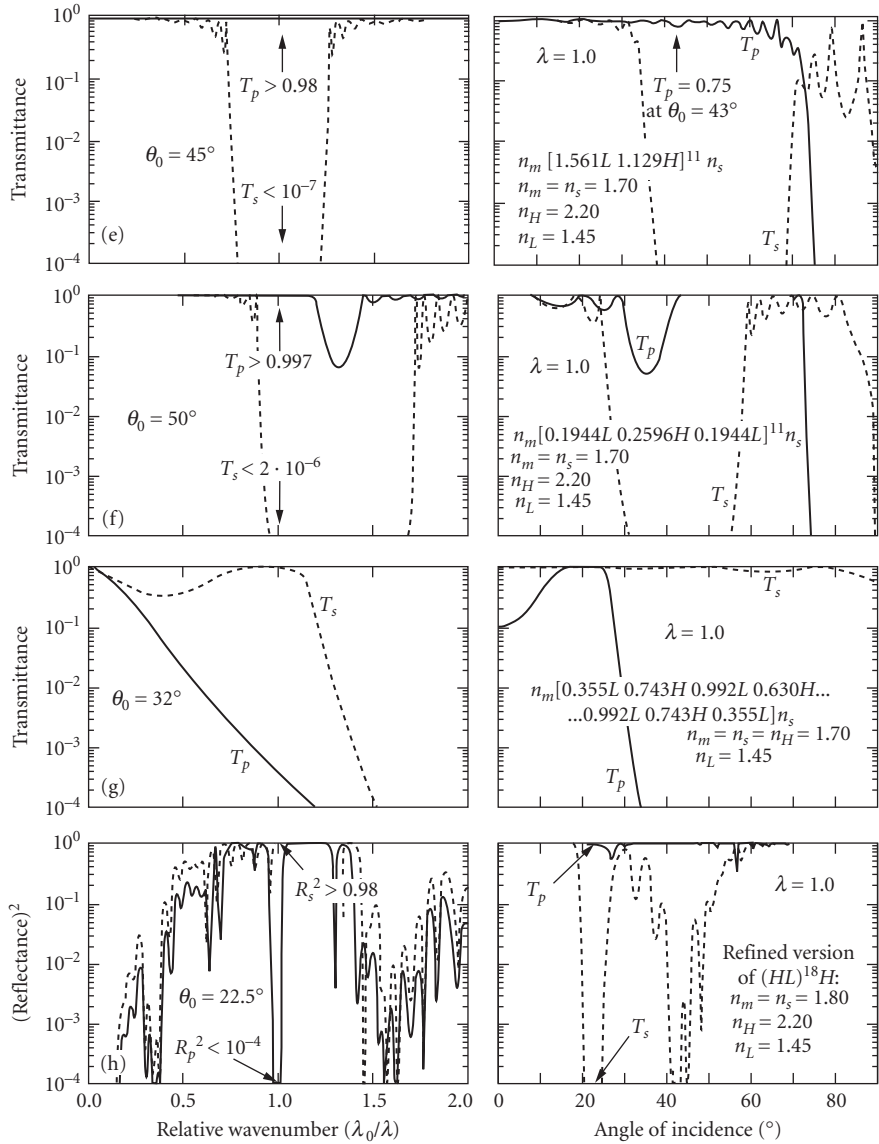


FIGURE 87 (Continued)



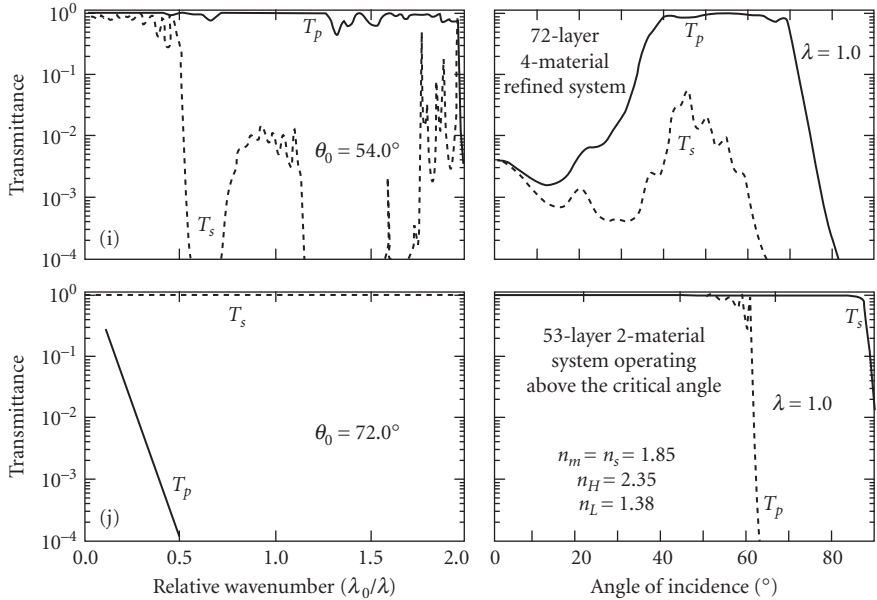


FIGURE 87 (Continued)

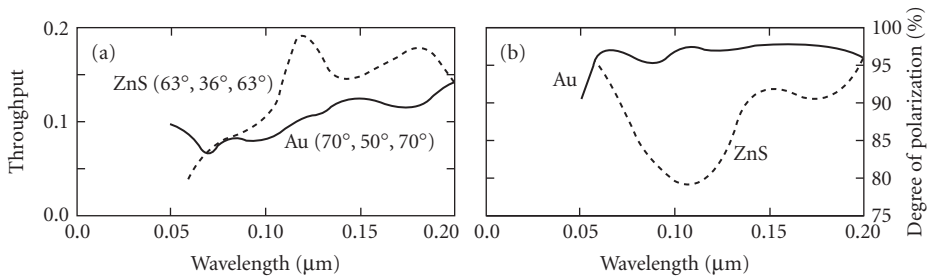


FIGURE 88 Measured throughput (a) and degree of polarization (b) of two extreme ultraviolet polarizers based on three reflections from Au (70°, 50°, 70°) and ZnS (63°, 36°, 63°) surfaces. The angles of incidence on the three mirrors (see Fig. 68r) are given in brackets. (After Remneva et al.<sup>369</sup>)

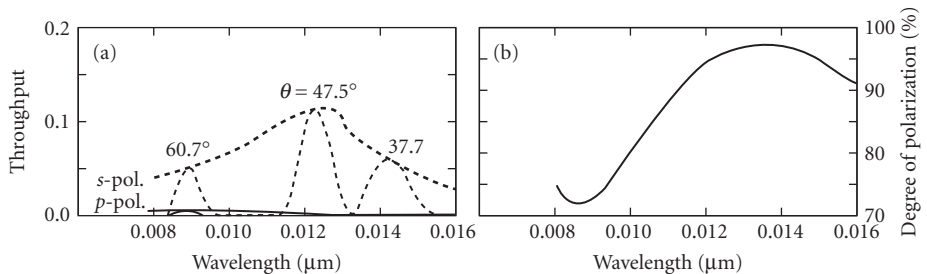
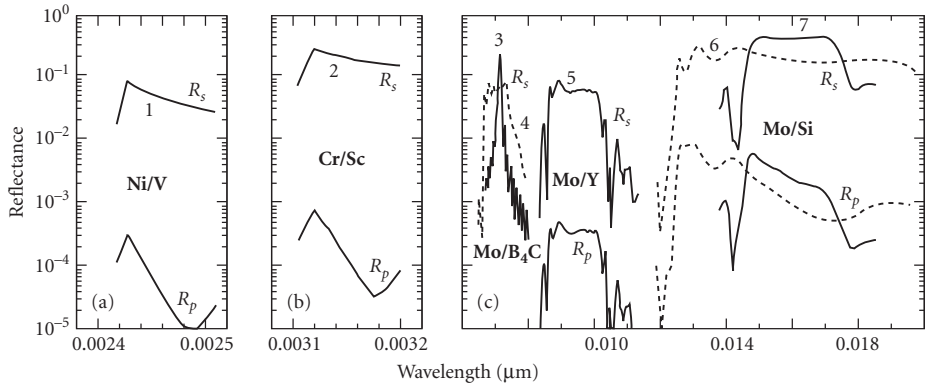
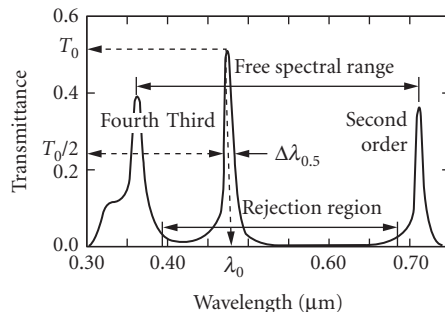


FIGURE 89 Measured throughput (a) and degree of polarization (b) of an x-ray polarizer consisting of two identical 21-layer Ru-C multilayers on Si substrates. The polarizer can be tuned to different wavelengths by changing the angle of incidence  $\theta$  of the radiation on the two mirrors. (After Yanagihara et al.<sup>372</sup>)



**FIGURE 90** Measured spectral performances of two-material multilayer reflection thin-film polarizers for the soft x-ray (a, b) and extreme ultraviolet (c) spectral regions. In the diagrams the reflectances for *s*- and *p*-polarized radiation for each polarizer are plotted with the same line type. The materials of which the multilayers are made are indicated in the figures. The measurements were performed at the Brewster angle which, for all the systems, is close to 45°. (Curves 1 and 2 after Eriksson<sup>256</sup> and curves 3 to 7 after Zhanshan Wang.<sup>370,374,375</sup>)

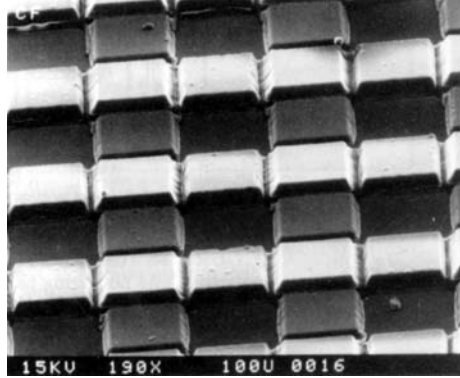


**FIGURE 91** Definition of some of the terms used to describe the properties of narrow-bandpass filters (Sec. 7.11). The curve represents the measured transmittance of an unblocked second-order metal-dielectric interference filter of the Fabry-Perot type (Sec. 7.11, subsection “Filters with metallic reflecting coatings”). (After Bausch & Lomb.<sup>275</sup>)

The half width (HW)  $\Delta\lambda_{0.5}$  of the filter is the difference between the wavelengths at which the transmittance is a half of  $T_0$ . This quantity is also sometimes called the full width half maximum (FWHM). It is often expressed as a percentage of  $\lambda_0$ . The base width (BW)  $\Delta\lambda_{0.01}$  is similarly defined. The ratio  $\Delta\lambda_{0.01}/\Delta\lambda_{0.5}$ , sometimes called the *shape factor*, indicates how “square” the transmission band is. Sometimes widths corresponding to other fractions of the transmittance are used to define it.

The minimum transmittance  $T_{\min}$  of the filter does not take into account the effect of blocking filters. The quantity  $T_{\min}/T_0$  is called the *rejection ratio*.

In all-dielectric transmission-band filters the transmittance rises at some distance on either side of the transmission band. The distance over which the transmittance is low is called the *rejection region*. The distance between the two transmission maxima adjacent to the principal transmission band is called the *free spectral range*. Should either of the above two quantities be inadequate, auxiliary blocking filters might have to be provided.



**FIGURE 92** Four color checkerboard pattern for use with a  $64 \times 64$  element focal plane HgCdTe detector array. The dimensions of each element are  $100 \times 100 \mu\text{m}$ . (Reproduced with permission from Barr Associates.<sup>380</sup>)

The ultimate measure of the suitability of a bandpass filter with a blocked spectral transmittance  $T(\lambda)$  for a particular application is the signal-to-noise ratio SN, defined in terms of the spectral energy distribution  $I(\lambda)$  of the source and the spectral detectivity  $D(\lambda)$  of the detector,

$$\text{SN} = \frac{\int_{\lambda_1}^{\lambda_2} I(\lambda)T(\lambda)D(\lambda)d\lambda}{\int_0^{\lambda_1} I(\lambda)T(\lambda)D(\lambda)d\lambda + \int_{\lambda_2}^{\infty} I(\lambda)T(\lambda)D(\lambda)d\lambda} \quad (61)$$

where  $\lambda_1$ ,  $\lambda_2$  are the lower and upper limits of the transmission region of the filter. The SN ratio is sometimes expressed in terms of optical density.

Useful general reviews of bandpass filters exist.<sup>376,377</sup> Interference filters, and especially bandpass filters, are increasingly deposited in complicated millimeter and sub-millimeter patterns for use with display devices and detectors.<sup>378,379</sup> Very fine masks or photo-lithographic processes are required to produce such structures (Fig. 92).

### Narrow- and Medium-Bandpass Filters (0.1 to 35 percent $hw$ )

Even though the essential components of Fabry-Perot (FP) interference filters, that is, the spacer and the two reflectors that surround it, can take on many different forms (see Fig. 93), the filters are essentially low-order FP interferometers and hence the theory developed for the latter (see, for example, Born and Wolf<sup>9</sup>) applies in full.

The transmittance of a FP type filter, not allowing for absorption and multiple reflections within the substrate, is given by

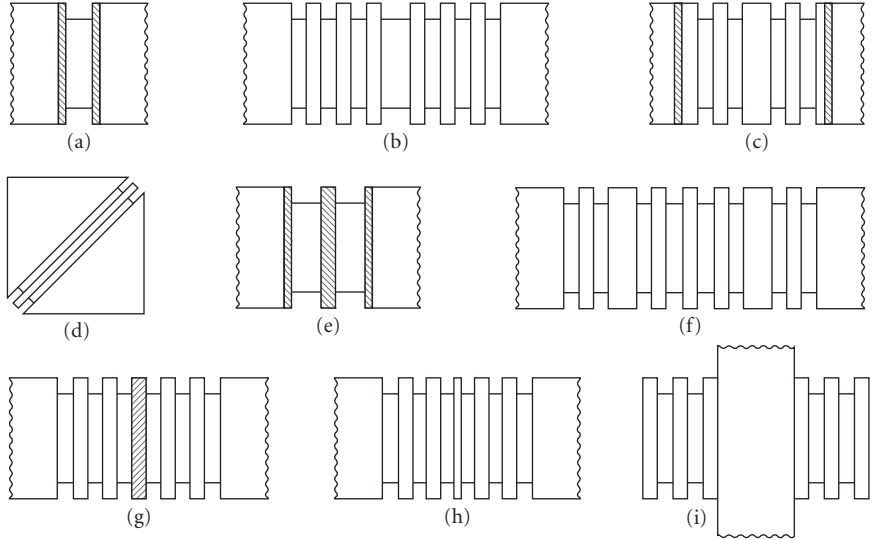
$$T = \frac{T_R^2}{(1-R)^2 + 4R\sin^2 \delta} \quad (62)$$

where

$$T_R = \sqrt{T_1 T_2} \quad R = \sqrt{R_1 R_2} \quad (63)$$

$T_1$ ,  $R_1$  and  $T_2$ ,  $R_2$  are the transmittances and reflectances of the first and second reflectors, respectively, as seen from within the spacer medium, and  $\delta$  is given by

$$\delta = \frac{2\pi}{\lambda} n d \cos \theta + \phi \quad (64)$$



**FIGURE 93** Schematic representations of various types of bandpass interference filters: (a) to (c) Fabry-Perot interference filters with metal, dielectric, and metal-dielectric reflectors; (d) frustrated-total-internal-reflection filter; (e) and (f) square-top multicavity filters with metal and dielectric reflectors; (g) induced-transmission filter; (h) phase-dispersion (spacerless) interference filter; and (i) Fabry-Perot filter with a mica or quartz spacer.

$$\phi = \frac{\phi_1 + \phi_2}{2} \quad (65)$$

$n$ ,  $d$ , and  $\theta$  are the refractive index, thickness, and angle of refraction of the spacer, respectively, and  $\phi_1$  and  $\phi_2$  are the phase changes on reflection from the spacer side of the first and second reflectors at a wavelength  $\lambda$ . Maxima of  $T$  occur at wavelengths

$$\lambda_0 = \frac{2nd\cos\theta}{k - \phi/\pi} \quad k=0,1,2,\dots \quad (66)$$

and are given by

$$T_0 = \left( \frac{T_R}{1-R} \right)^2 = \left( \frac{1}{1+A/T_R} \right)^2 \quad (67)$$

$A (= 1 - T_R - R)$  is the mean absorption of the reflectors. The minimum transmittance

$$T_{\min} = \left( \frac{T_R}{1+R} \right)^2 \quad (68)$$

occurs at

$$\lambda_{\min} = \frac{2nd\cos\theta}{k - \phi/\pi} \quad k = \frac{1}{2}, \frac{3}{2}, \frac{5}{2}, \dots \quad (69)$$

If  $T_R$  and  $R$  are essentially the same at  $\lambda_0$  and  $\lambda_{\min}$ , the rejection ratio is given by

$$\frac{T_{\min}}{T_0} = \left( \frac{1-R}{1+R} \right)^2 \quad (70)$$

For  $R > 0.7$  the half width of the transmission band (expressed as a percentage of  $\lambda_0$ ) is given by

$$\frac{\Delta\lambda_{0.5}}{\lambda_0} \times 100 \approx \frac{1-R}{\sqrt{R}} \frac{100}{\frac{2\pi n d \cos\theta}{\lambda_0} - \lambda_0 \frac{\partial\phi}{\partial\lambda}} \quad (71)$$

For a given order of interference the half width and rejection ratio cannot be varied independently. The formula

$$T \approx \frac{T_0}{1+4[(\lambda-\lambda_0)/\Delta\lambda_{0.5}]^2} \quad (72)$$

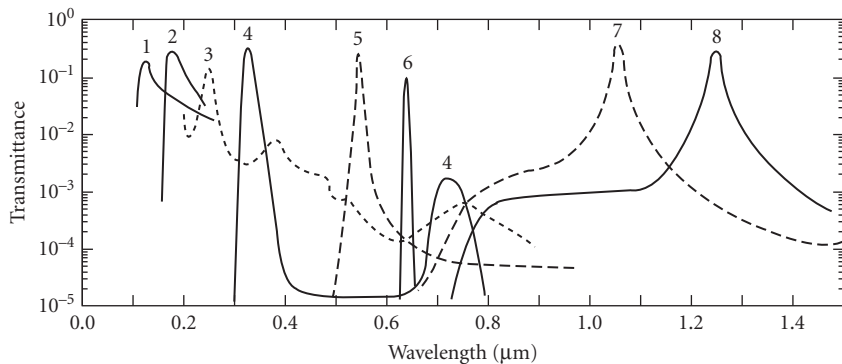
valid for FP filters with small values of  $\partial\phi/\partial\lambda$  in the neighbourhood of  $\lambda_0$ , represents a lorentzian line shape with  $\Delta\lambda_{0.1} = 3\Delta\lambda_{0.5}$  and  $\Delta\lambda_{0.01} = 10\Delta\lambda_{0.5}$ . The shape factor of all FP-type interference filters is therefore of the order of 10.

Southwell has recently shown that a spacer in an interference filter need not consist of a single layer only, and that there are some advantages when it is partitioned into a number of layers.<sup>381</sup>

#### *Fabry-Perot Interference Filters (0.1 to 10 percent hw)*

*Filters with metallic reflecting coatings* This is the first interference bandpass filter ever made, and the simplest.<sup>382</sup> It consists of two partially transmitting, highly reflecting metal layers separated by a dielectric film and is symbolically represented by MDM (Fig. 93a). The best metallic reflectors currently available are aluminium and silver for the 0.125 to 0.34  $\mu\text{m}$  and 0.34 to 3.0  $\mu\text{m}$  spectral ranges, respectively. The measured spectral-transmittance curves of a number of typical filters are shown in Fig. 94.

The phase changes on reflection at the spacer-metal-reflector surface are finite and hence they affect the position of the transmission maxima [Eq. (66)]. But the dispersion of the phase change on reflection can be neglected, and so the half width depends only on the reflectance of the metal layers and the order of the spacer. Filters with half widths of 1 to 8 percent are common. Because the ratio  $A/T$  is not very small for metals, the maximum transmission is limited [Eq. (67)]. Maximum transmittances of 40 percent are relatively common. For filters with the narrower half widths, or for shorter wavelengths, transmittances of the order of 20 percent have to be accepted. This is much less than the transmittances of all-dielectric filters of comparable half widths. Nevertheless, filters of this type are useful because their transmittances remain low except at wavelengths at which the first- and



**FIGURE 94** Measured transmittance of FP filters with metallic reflecting coatings. Curve 6 represents the transmission of two identical filters cemented together. (Curve 1 after Harrison;<sup>383</sup> curve 2 after Bradley et al.;<sup>384</sup> curves 3 and 5 to 7 after Balzers;<sup>385</sup> curves 4 and 8 after Schott & Gen.<sup>386</sup>)

higher-order transmission maxima occur [Eq. (66)]. Blocking is thus easy. In particular, first-order filters usually do not require any blocking on the high-wavelength side—a difficult task at all times. The rejection of the filters is good, though not spectacular. If a better rejection is required and a lower transmittance can be tolerated, two identical filters may be cemented together (curve 6, Fig. 94). This is possible because of the finite absorption in the metal films. Alternatively, metal square-top filters (Sec. 7.11, subsection “Square-Top Multicavity Bandpass Filters”) or filters with even more complicated structures (Sec. XI A 3) can be used.

*Filters with all-dielectric reflectors* Above 0.2  $\mu\text{m}$  the metallic reflectors can be replaced by all-dielectric quarter-wave stacks (Sec. 7.6).<sup>344</sup> The symbolic representation of such a filter (Fig. 93b) is, for example,  $[HL]^N 2mH[LH]^N$  or  $H[LH]^N 2mL[HL]^N H$ ,  $H$  and  $L$  being quarter-wavelength layers of high and low refractive indices, respectively,  $m$  is the order of the spacer and  $N$  the number of full periods in the reflecting stacks. The phase change on reflection at the boundary between the spacer and such a reflector does not affect the position of  $\lambda_0$  [Eq. (66)] but the dispersion of the phase change on reflection is finite, depends on the materials used, and for lower-order spacers, contributes very significantly to the reduction of the half width of the transmission band [Eq. (71)]. Expressions for the half width

$$\begin{aligned} \frac{\Delta\lambda_{0.5}}{\lambda_0} \times 100 &= \frac{4n_0 n_L^{2N} (n_H - n_L) \times 100}{m\pi n_H^{2N+1} (n_H - n_L + n_L/m)} \\ &= \frac{4n_0 n_L^{2N-1} (n_H - n_L) \times 100}{m\pi n_H^{2N} (n_H - n_L + n_L/m)} \end{aligned} \quad (73)$$

for high- and low-refractive-index spacers, respectively have been given by Macleod.<sup>2</sup>

By choosing a suitable combination of the reflectance and order of the spacer almost any half width between 0.1 and 5 percent can be achieved in the visible part of the spectrum while maintaining a useful rejection ratio.

The maximum transmittances of all-dielectric FP filters depart from unity because of the finite absorption, scattering, and errors in the thicknesses and refractive indexes of the films. In the central part of the visible spectrum maximum transmittances of 0.8 are normal for unblocked filters with a half width of 1 percent, although higher transmittances can be achieved. This figure is gradually reduced as  $\lambda_0$  approaches 0.2 or 20  $\mu\text{m}$ , and filters with narrower half widths become impracticable for lack of adequate transmittance.

The transmittance away from the transmission maximum is low only over the extent of the rejection region of the two materials used for the construction of the reflectors (Fig. 34), and additional blocking is often required on both the long- and the short-wavelength sides. This can result in a considerable lowering of the maximum transmittance of the blocked filter, a 30 to 40 percent loss being not uncommon for filters peaked in the ultraviolet or infrared spectral regions.

For those parts of the visible and infrared for which nonabsorbing mechanically robust coating materials abound, square-top interference filters (Sec. 7.11, subsection “Square-Top Multicavity Bandpass Filters”) are often preferred because of their better shape factor and higher rejection ratio. All-dielectric FP filters are still attractive in the ultraviolet, where there is a lack of such materials and where thickness monitoring is difficult, and also in the far-infrared, where very thick layers are required.

The measured transmittance curves of a number of typical all-dielectric FP filters are shown later in Fig. 98. An additional curve on a smaller scale is given, whenever necessary, to show the transmittance away from the passband.

*Filters with metal-dielectric reflectors* In these filters the reflectors consist of metal layers whose reflectance has been enhanced through the addition of several dielectric layers (Sec. 7.14, subsection “Fabry-Perot Filters with Solid Spacers”) (Fig. 93c).<sup>387</sup> The properties of such filters are intermediate to those described in the two previous sections.

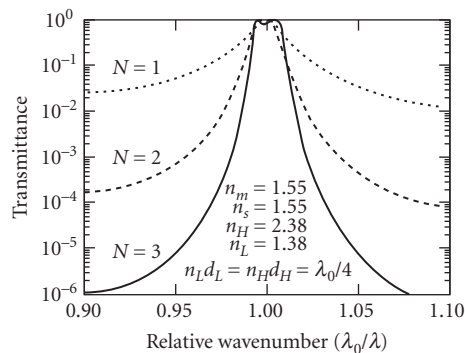
*Frustrated total internal reflection filters* These are essentially FP filters in which the spacer layer is surrounded by two frustrated-total-reflection surfaces (Fig. 93d).<sup>387,388</sup> They have not found wide applications as bandpass filters because the finite absorption and scattering within the layers have prevented the theoretically expected high transmittance and small half widths from being realised and because the angular variation of the wavelength of the transmission peaks is very high.

*Square-Top Multicavity Bandpass Filters (0.1 to 35 percent  $hw$ )* A filter with a “squarer” shape that does not suffer from some of the disadvantages of the FP filters results when the basic FP structure is repeated two or more times.<sup>158,389,390</sup> Such filters may be based on metal<sup>391</sup> or all-dielectric<sup>392,393</sup> reflectors (Fig. 93e and f). Thus, for example,  $[HL]^N 2H [LH]^N C [HL]^N 2H [LH]^N$  represents an all-dielectric square-top filter in which the FP structure  $[HL]^N 2H [LH]^N$  is repeated twice. The quarter-wavelength layer  $C$  is called a *coupling* or *tie layer*, and the half-wavelength-thick spacer layers  $2H$  are often called *cavities*. Small departures from the above model are made at times to improve the transmittance in the pass band or the angular properties of the filter.

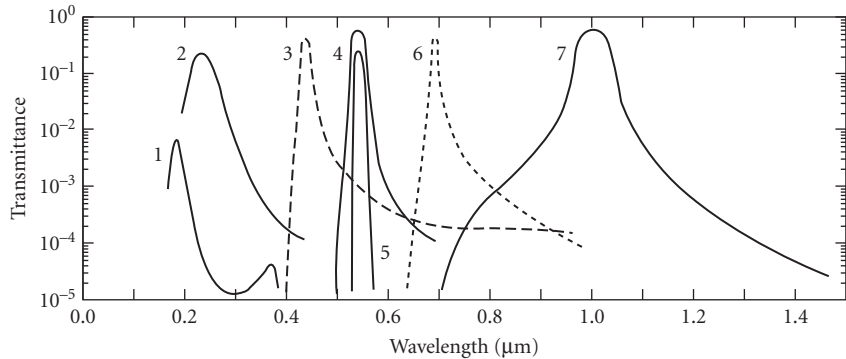
The half widths of the narrower multicavity filters of the above type do not differ very significantly from those of the basic FP structure [Eq. (71)]. The shape factors decrease with an increase in the number of the cavities and do not seem to depend on the materials.<sup>389</sup> They are approximately 11, 3.5, 2.0, and 1.5 for one, two, three, and four cavities, respectively. The minimum transmittance in the rejection region is roughly that which could be obtained if the filter were composed entirely of  $\lambda/4$  layers [Eq. (44)]. Unlike in the FP filter, the half width and rejection ratio can therefore be varied independently. These various points are illustrated in Fig. 95. The peak transmittance of multicavity square-top filters is less affected by the residual absorption in the layers than that of FP type filters. As in the case of their FP counterparts, metal-dielectric square-top filters can be cemented together to enhance the rejection (curve 5, Fig. 96).

The improvement in the performance of square-top bandpass filters over that of the FP type is such that despite their more critical and expensive production, most manufacturers regard them as their standard line of filters. The spectral-transmittance characteristics of typical commercially produced metal-dielectric and all-dielectric bandpass interference filters of different half widths are shown in Figs. 96 and Figs. 97 to 102, respectively. Filters with intermediate half widths and peak wavelengths can readily be obtained.

For very critical or special applications multicavity filters are designed and constructed with properties that exceed those shown in the above figures. For example, for the use in fiber-optic communications systems, multicavity filters are required in which the peak transmittance closely approaches unity. Various procedures for the design of such filters, including some that are based on the use of Chebyshev polynomials, have been described.<sup>407,408</sup> Special care has to be taken during the manufacture of the coatings to meet this requirement. Typical measured spectral transmittance



**FIGURE 95** Calculated transmittance on a logarithmic scale of the bandpass filters: *air*- $[(0.5H)L(0.5H)]^3 H [(0.5H)L(0.5H)]^3 ]^N$ -*glass*,  $N = 1, 2$ , and  $3$ .



**FIGURE 96** Measured transmittance of square-top bandpass filters with metallic reflecting coatings. Curve 5 corresponds to the transmission of two identical filters cemented together. (Curves 1 and 2 after Schröder;<sup>394</sup> curves 3 and 6 after Balzers;<sup>385</sup> and curves 4, 5, and 7 after Schott & Gen.<sup>386</sup>)

curves are shown in Fig. 103. For other applications, such as fluorescence or Raman spectroscopy, the peak transmittance is not important, but signal-to-noise ratios of the order of  $10^{-8}$  are required. This necessitates the use of many cavities (Fig. 104).

**Induced-Transmission Filters** The transmittance of a metal layer can be considerably enhanced by surrounding it with suitable multilayer structures (Fig. 93g). Thus, for example, it is possible to induce a transmittance of 65 percent at  $\lambda = 0.25 \mu\text{m}$  in a  $0.03\text{-}\mu\text{m}$ -thick aluminum film which, when deposited directly onto a quartz substrate, would transmit only 2.5 percent of the same radiation.<sup>410</sup> The induced transmittance is highly wavelength-sensitive and can be used to construct bandpass filters containing one or more metal layers.<sup>411-417</sup> Induced-transmission filters combine the good long-wavelength attenuation properties of the more common types of metal/dielectric filters (Secs. 7.11, subsection "Filters with metallic reflecting coatings" and "Filters with all-dielectric reflectors") with peak transmittances that are closer to those of all-dielectric filters. The performances of some experimentally produced induced-transmission filters are shown in Fig. 105.

### Very Narrow Bandpass Filters (hw - 0.1 percent)

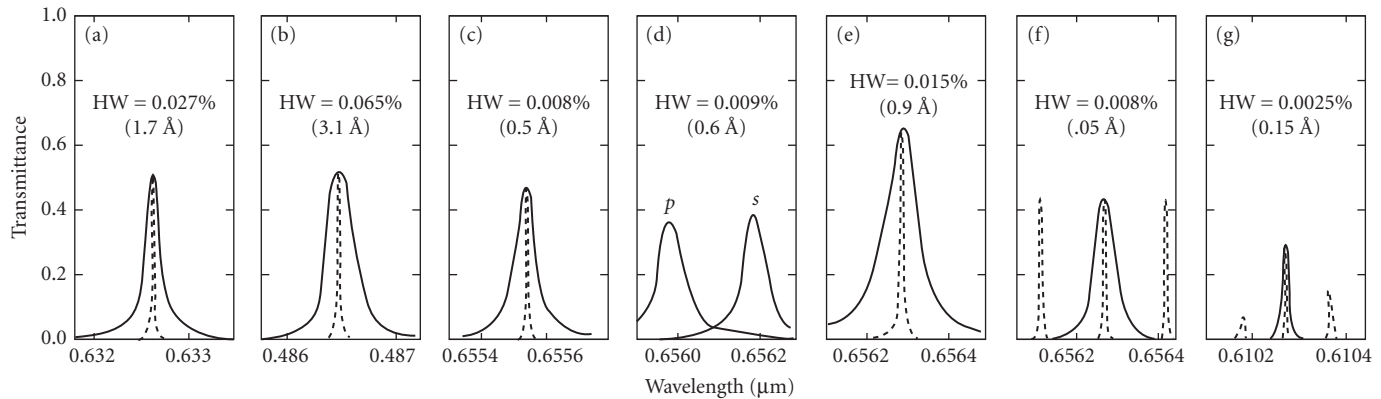
It follows from (71) that the half widths of interference filters can be reduced by increasing the reflectance of the reflectors, the order of interference of the spacer, or the dispersion of the phase change on reflection. All these approaches have been tried in the past.

**Filters with Evaporated Spacers (hw > 0.03 percent)** In narrowband filters of conventional construction both high reflectance and higher-order spacers are used. The manufacturing process is quite critical, and attention must be paid to details. The films have to be very uniform over the filter area, and they must not absorb or scatter. They must not age, or, alternatively, their aging must be capable of being accelerated or arrested. Monitoring must be precise, so that the peak occurs at or close to the desired wavelength.

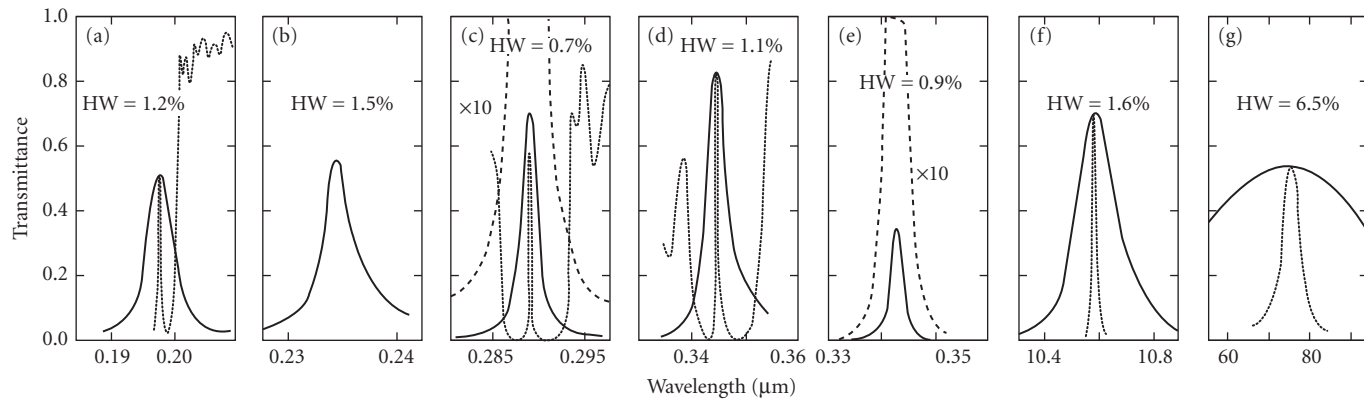
Both FP and square-top filters of very narrow bandwidths can be made, the latter being preferable for most applications. The present limit on the half widths of this type of filter seems to be of the order of 0.03 percent.<sup>419</sup> The performance of two commercially produced filters of this type are shown in Fig. 97a and b.

**Fabry-Perot Filters with Solid Spacers** In practice the half width of interference filters cannot be reduced indefinitely by increasing the optical thickness of an evaporated spacer [Eq. (71)] because

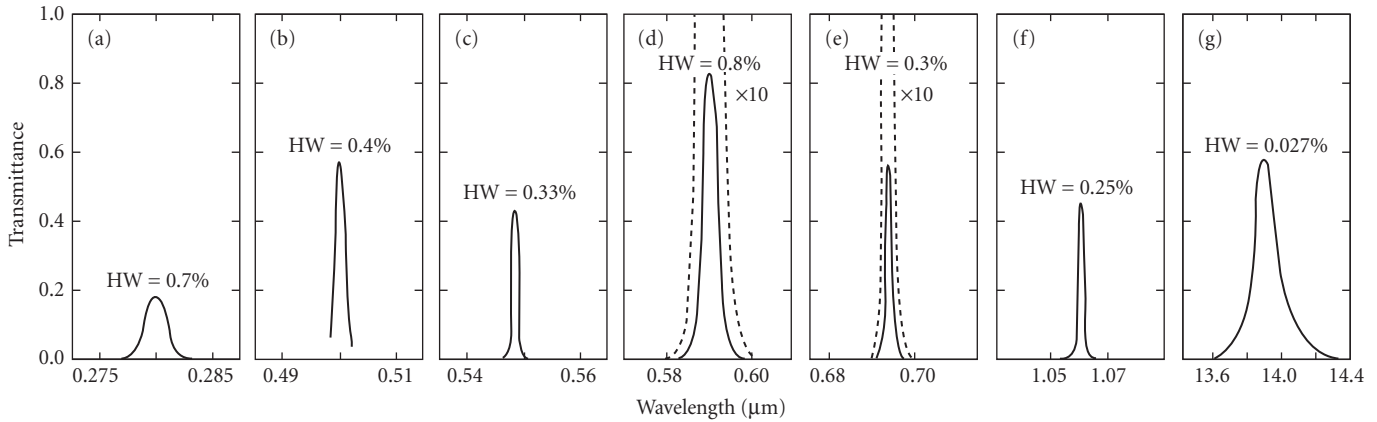




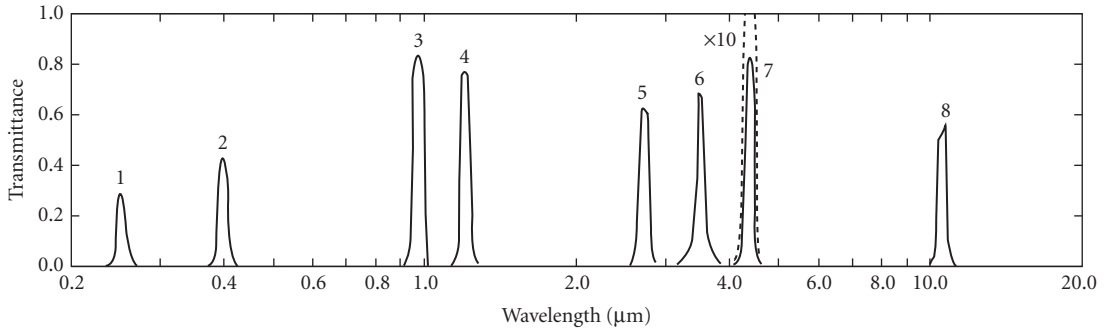
**FIGURE 97** Measured transmittance of very narrow bandpass interference filters with half widths less than 0.1 percent. Evaporated spacers: (a) (after Meltzer<sup>395</sup>); (b) (after Eather and Reasoner<sup>396</sup>); (c) mica interference filter for  $H_{\alpha}$ ; (d) mica interference filter with transmission bands polarized at right angles to one another (Heliotek<sup>281</sup>); (e) single and (f) and (g) double quartz-spacer interference filters (after Austin<sup>397</sup>). The dotted curves in Figs. 97 and 98 represent the transmittances of the filters plotted over a ten-times-wider spectral region.



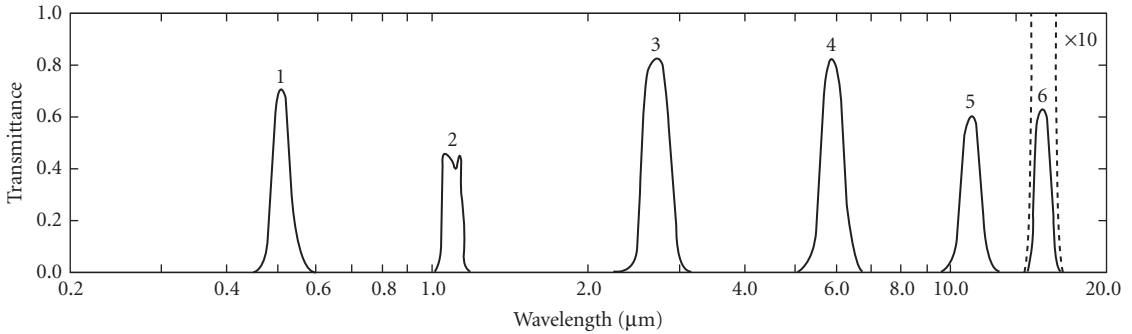
**FIGURE 98** Measured transmittance of FP all-dielectric interference filters with narrow half widths. Evaporated spacers: (a) (after Cohendet and Saudreau<sup>398</sup>); (b) and (d) (after Motovilov<sup>399</sup>); (c) and (e) (after Neilson and Ring<sup>400</sup>); (f) (after Turner and Walsh<sup>401</sup>); and (g) (after Smith and Seeley<sup>402</sup>). The dashed curves in Figs. 98 and 99 correspond to a transmittance range of 0.0 to 0.1.



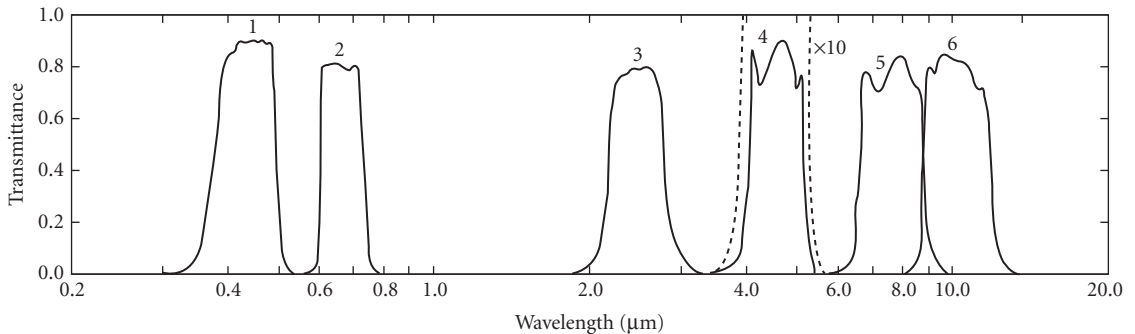
**FIGURE 99** Measured transmittances of fully blocked square-top interference filters with half widths between 0.25 and 1.4 percent. (a), (c) and (f) (after Corion<sup>331</sup>); (b) (after Blifford<sup>403</sup>); (d) (after Heliotek<sup>281</sup>); (e) (after Baird Atomic<sup>404</sup>); and (g) is the only filter in the series that is not blocked (after Smith and Seeley<sup>402</sup>).



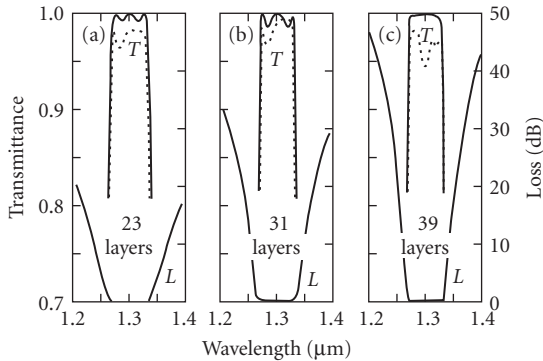
**FIGURE 100** Measured transmittances of fully blocked square-top interference filters with half widths of the order of 5 percent. (Curves 1 and 2 after Corion;<sup>331</sup> curve 3 after Spectrum Systems;<sup>405</sup> curves 4 and 6 after Turner;<sup>83</sup> curve 5 after Eastman Kodak;<sup>276</sup> and curves 7 and 8 after Optical Coating Laboratory.<sup>237,274</sup>)



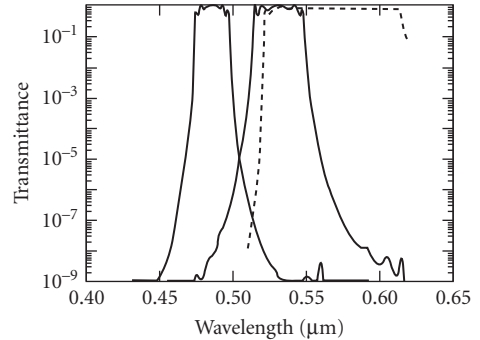
**FIGURE 101** Measured transmittances of fully blocked square-top interference filters with half widths of the order of 10 percent. (Curve 1 after Bausch and Lomb;<sup>275</sup> curve 2 after Baird Atomic;<sup>404</sup> curve 3 Infrared Industries;<sup>406</sup> curve 4 after Turner;<sup>83</sup> curve 5 after Eastman Kodak;<sup>276</sup> and curve 6 after Optical Coating Laboratory.<sup>274</sup>)



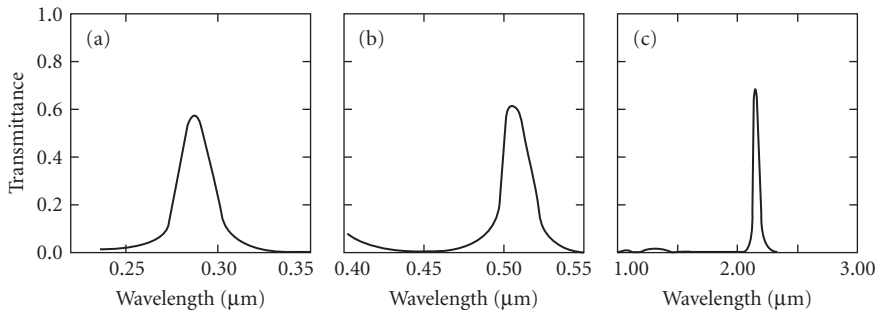
**FIGURE 102** Measured transmittances of blocked square-top interference filters with half widths of the order of 25 percent. (Curve 1 after Heliotek;<sup>281</sup> curves 2 and 4 after Optical Coating Laboratory;<sup>237</sup> curves 3 and 6 after Turner and Walsh<sup>401</sup> and Turner;<sup>83</sup> and curve 5 after Infrared Industries.<sup>406</sup>)



**FIGURE 103** Calculated and experimental spectral transmittance and measured attenuation curves of (a) 3-, (b) 4- and (c) 5 cavity bandpass filters. (After Minowa.<sup>409</sup>)



**FIGURE 104** Measured spectral transmission characteristics of two bandpass filters for fluorescence applications and of a cutoff filter for Raman spectroscopy. (After Omega Optical Inc.<sup>239</sup>)



**FIGURE 105** Measured transmittance of induced transmission filters for the ultraviolet, visible and infrared spectral regions (a) after Tsypin,<sup>418</sup> (b) after Berning and Turner,<sup>411</sup> and (c) after Holloway and Lissberger<sup>414</sup>.

when the latter exceeds about two wavelengths, it may become too rough to be useful.<sup>396</sup> A high-order filter can, however, be constructed by evaporating reflecting coatings on either side of a thin prefabricated spacer (Fig. 93i).

**Mica Spacers ( $hw > 0.01$  percent)** Transmission bands in silvered mica were probably first observed by Wood<sup>420</sup>, but the deliberate use of mica to construct filters came much later.<sup>421-424</sup> The construction of mica interference filters with transmittances of 30 to 80 percent per polarization for half widths of the order of 0.01 to 0.1 percent in the 0.45- to 2.0- $\mu\text{m}$  wavelength region is relatively straightforward.<sup>423</sup> The position of the transmission peak can be located within a fraction of an angstrom, does not change with time, and can be sufficiently uniform over areas of 2 to 5 cm diameter. Because of the very high order of interference (70 to 700 orders) the spectral-free range is quite small, and auxiliary filtering is necessary for most applications. Unless the thickness of the mica is specially selected, the birefringence of mica will result in two mutually perpendicularly polarized sets of transmission bands, a fact that can be used to advantage in some applications. The spectral-transmittance curve of a fully blocked mica interference filter for  $H_\alpha$  is shown in Fig. 97c.

**Optically polished solid spacers ( $hw > 0.002$  percent)** It is possible to construct very narrow bandpass filters having thin fused-quartz spacers.<sup>425-429</sup> A good fused-quartz flat is coated with an all-dielectric reflector, and this coated surface is optically contacted to another flat.<sup>397,430</sup> The flat is then ground down and polished to form a spacer layer of the required thickness, and the second

reflector layers are applied to complete the filter. As in the mica filters, the position of the transmission band is very stable, and auxiliary blocking filters are needed because of the small spectral-free range. The transmittance of filters with silica spacers is higher than that of corresponding mica filters because fused quartz is highly transparent and is not birefringent. A typical unblocked filter with a clear aperture of 3.5 cm and a half width of 0.007 percent had a transmittance of 45 percent for nonpolarized light. An important advantage of filters with fused-silica spacers is that it has been found possible, by repeating the process described above, to construct square-top filters with rejection ratios of the order of  $5 \times 10^{-4}$  (Fig. 97f) and filters with half widths as low as 0.002 percent (Fig. 97g). However, such filters are very expensive.

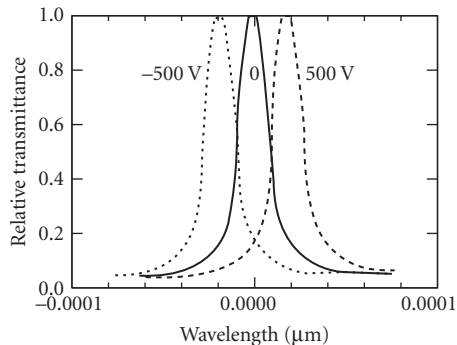
Other materials can also be used to produce solid spacers by optical polishing. Germanium was used by Smith and Pidgeon<sup>431</sup> and by Costich<sup>252</sup> to produce very narrow bandpass filters for the infrared. Roche and Title used a substrate made of a combination of yttrium and thorium oxides to produce a filter with a  $hw = 0.004$  percent at  $3.3 \mu\text{m}$ .<sup>432</sup>

*Plastic spacers ( $hw > 0.15$  percent)* Mylar has very smooth surfaces and areas can be selected that have a sufficiently uniform thickness to permit the use of this material as a solid spacer. Candille and Saurelle have used this material to produce narrow bandpass filters and obtained half widths of the order of  $0.0008 \mu\text{m}$ .<sup>433,434</sup> In some of their designs a second, evaporated narrowband filter deposited onto one side of the solid spacer served to remove unwanted adjacent orders.

*Phase-Dispersion Filters ( $hw > 0.1$  percent)* The dispersion of the phase change on reflection enters into (71) for the half width of FP filters. Typical values of this quantity at  $\lambda = 0.5 \mu\text{m}$  for a silver reflector, a nine-layer quarter-wave stack with  $n_H/n_L = 1.75$ , and for a broadband reflector are  $-0.5$ ,  $-6.8$ , and  $-112.0$ , respectively.<sup>224</sup> As a result, the half widths of FP filters constructed with such reflectors should be reduced by factors of about 1.05, 2, and 20. In the last case the contribution of the spacer to the half width is negligible, and a spacerless design is possible (Fig. 93h).<sup>435,436</sup> Unfortunately, the expected reduction in half width has so far not been fully realised in practice, probably because of errors in the monitoring and lack of uniformity of the layers.<sup>437</sup>

*Tunable filters ( $hw > 0.001$  percent)* These are usually air-spaced FP interferometers, often provided with elaborate automatic plate-parallelism and spacing control, which are more akin to spectrometers than to filters.<sup>438,439</sup> The position of the pass band can be tuned quite significantly by changing the separation between the reflector plates. This type of tuning, unlike the tuning of filters by tilting, does not affect the angular field or shape of the transmission band. Ramsey reviews the various problems associated with the construction and use of such instruments.<sup>440,441</sup>

An electrically tunable 0.005 percent half width interference filter with a lithium niobate spacer sandwiched between two conducting reflecting coatings has also been described (Fig. 106).



**FIGURE 106** Performance of an electrically tunable narrow band filter with a lithium niobate spacer. (After Burton.<sup>442</sup>)

## Wide-Bandpass Filters

Filters with half widths ranging from 10 to 40 percent can be constructed using techniques described in Sec. 7.11, subsection “Square-Top Multicavity Bandpass Filters” (Figs. 101 and 102). Filters with wider transmission bands are usually obtained by combining short- and long-pass filters with cutoffs at the desired wavelengths. The cutoff filters may be all-dielectric (Figs. 61 and 62), glass or gelatine cutoff filters or antireflection-coated infrared materials. Some of the short- or long-pass filters may be regarded as being wide-bandpass filters in their own right. The cutoff filters may be combined into a single filter. Alternatively, it is possible to assemble a number of short- and long-wavelength cutoff filters into sets that make it possible to assemble wide-passband filters of different half widths and peak wavelengths. In this latter arrangement the cutoff positions of all-dielectric short- and long-pass filters can be tuned individually by tilting to coincide with the desired wavelengths. Another way of tuning the edges of the transmission band is to pass the radiation through a pair of circular wedge short- and long-wavelength cutoff filters placed in series.

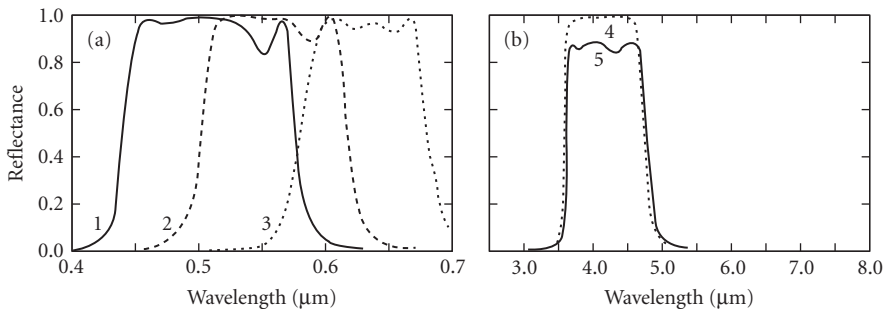
Filters with very broad transmission bands are also obtained when a multilayer is formed from two suitably displaced long-wavelength cutoff filters separated by an appropriate matching layer (Fig. 107a).<sup>443</sup> Automatic computer programs can be used to design high-transmission broadband filters with a high rejection and a shape factor close to unity (Fig. 107b).<sup>444</sup>

## Interference Filters with Multiple Peaks

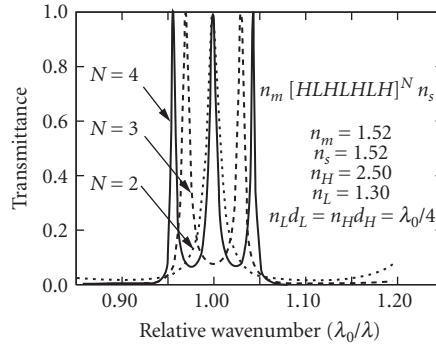
For some applications filters with multiple peaks in one particular spectral region are required. The design of such filters has been considered by Pelletier et al.<sup>447</sup> Typical results are shown in Fig. 108. Filters with different peak separations, rejections and half widths are possible.

## Linear and Circular Wedge Filters

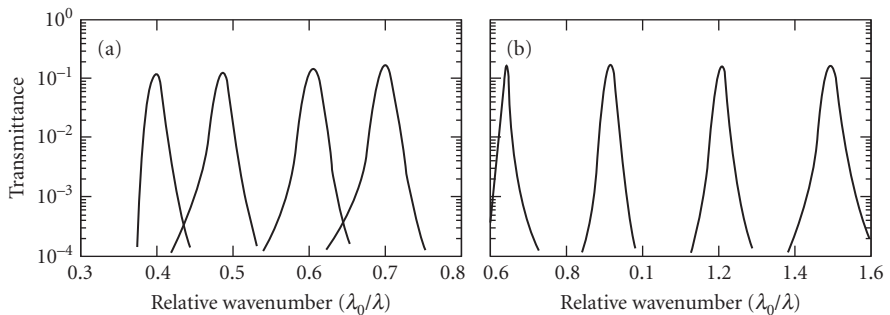
If the thicknesses of all the layers of a bandpass filter vary in proportion across the surface of a substrate, the position of the transmission peak will vary in the same way (Sec. 7.2, subsection “Matrix Theory for the Analysis of Multilayers Systems”). Such wedge filters are as old as the interference filter itself and are available in versions in which the wavelength variation occurs along a straight line or a circle. The latter arrangement is particularly useful because it lends itself well to the construction of low cost, small and light weight rapid-scan monochromators of moderate resolution that are robust and environmentally stable.<sup>448</sup> Methods for the production of circular variable filters with a linear dependence of wavelength on angle and references to some of the previous work on wedge



**FIGURE 107** Broadband transmission filters: (a) calculated transmittance of three filters consisting essentially of two superimposed suitably tuned long-wavelength cutoff filter structures (after McKenney and Turner<sup>445</sup>) and (b) calculated (curve 4) and measured (curve 5) transmittances of a filter designed with an automatic synthesis program (after Michael<sup>446</sup>).



**FIGURE 108** Calculated performance of interference filters with two and three closely spaced peaks of the type glass  $[HLHLHLH]^N$  glass for values of  $N = 3, 4$ . The refractive indices of the surrounding media  $n_m$  and of the layers  $n_H, n_L$  are 1.52 and 2.52, 1.30, respectively. (After Pelletier and Macleod.<sup>447</sup>)



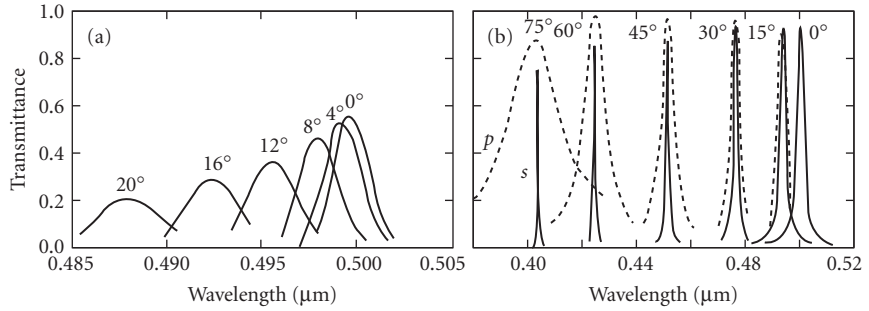
**FIGURE 109** The transmission at different angular positions of two circular variable square-top filters for the (a) visible and (b) near-infrared spectral regions. (After Mussett.<sup>456</sup>)

filters are given in several papers.<sup>449–453</sup> Circular variable square-top filters for the 0.24- to 0.4- and for the 0.4- to 25- $\mu\text{m}$  spectral regions are described by Avilov and by Yen.<sup>454,455</sup> The maximum transmittances for fully blocked filters vary between 15 and 75 percent, depending on the spectral region and the half width of the filter. Rejection levels of 0.1 or 0.01 percent are possible. Typical transmission curves for several angular positions on two circular variable square-top filters are shown in Fig. 109. The ratio of the maximum to minimum wavelength available in one wheel varies between 1.11 and 16.<sup>454</sup> The angular width of the slit used in conjunction with a circular variable filter, expressed as a percentage of the angular size of the filter wedge, should not exceed the nominal half width of the filter (expressed in percent) if it is not to cause a marked reduction in the resolution.

## Angular Properties of Bandpass Interference Filters

With the gradual increase of the angle of incidence the transmittance maximum of a typical bandpass filter moves toward shorter wavelengths (Fig. 110a). On further increase in the angle of incidence the maximum transmittance and the half width deteriorate; the transmission band becomes asymmetric and eventually splits up into  $p$ - and  $s$ -polarized components (Fig. 110b). The deterioration is more rapid for nonparallel radiation.





**FIGURE 110** Angular properties of all-dielectric interference filters. (a) Measured variation with angle of incidence of the spectral transmittance of a typical commercial interference filter (after Bifford<sup>403</sup>) and (b) calculated transmittance of a filter in which the peaks of the two polarized transmission bands at nonnormal incidence coincide. The filter is of the type air-[HL]<sup>4</sup>(2A)[LH]<sup>4</sup>-glass, where  $n_H t_H = n_L t_L = n_A t_A = \lambda/4$  and  $n_s = 1.52$ ,  $n_M = 1.00$ ,  $n_H = 2.30$ ,  $n_L = 1.38$ , and  $n_A = 1.825$ .

**Properties of Bandpass Filters for Angles of Incidence Less than 20°** The behavior of bandpass filters for angles of incidence  $\theta_0 \leq 20^\circ$  can be described quantitatively using the concept of an *effective index*  $\mu^*$  of the filter. In terms of  $\mu^*$  the transmittance  $T$  in the neighborhood of the transmission peak of any FP filter is given by Lissberger:<sup>457</sup>

$$T \approx \frac{T_0}{1 + \left[ \frac{2(\lambda - \lambda_0)}{\Delta\lambda_{0.5}} + \frac{\lambda_0}{\Delta\lambda_{0.5}} \frac{\theta_0^2}{\mu^{*2}} \right]^2} \quad (74)$$

$\Delta\lambda_{0.5}$  and  $T_0$  are the half widths and the maximum transmittance (at  $\lambda_0$ ) for normal incidence of the radiation. Formulas for  $\mu^*$  in terms of the construction parameters have been found for the all-dielectric FP filter and the double-spacer filter<sup>458,459</sup> and for the metal-dielectric FP and induced-transmission filters.<sup>460</sup> The change in position of the transmission peak ( $\delta\lambda$ ) <sub>$\theta$</sub>  and the half width ( $\Delta\lambda_{0.5}$ ) <sub>$\theta$</sub>  at angle  $\theta$  are

$$\left( \frac{\delta\lambda}{\lambda_0} \right)_\theta = -\frac{\theta_0^2}{2\mu^{*2}} \quad (75)$$

and

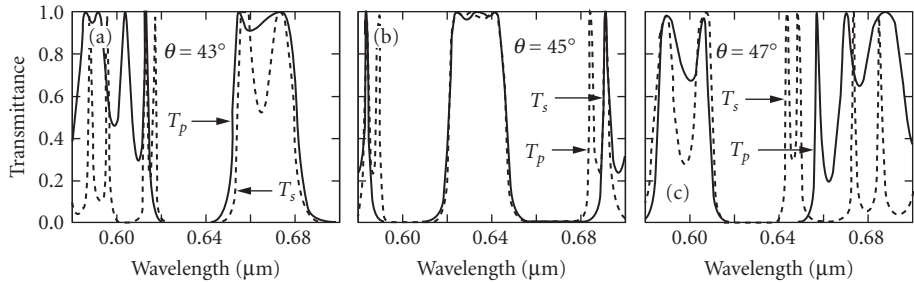
$$\frac{(\Delta\lambda_{0.5})_\theta}{\Delta\lambda_{0.5}} = \left[ 1 + \left( \frac{\theta_0^2 \lambda_0}{\mu^{*2} \Delta\lambda_{0.5}} \right)^2 \right]^{1/2} \quad (76)$$

For convergent radiation of semiangle  $\alpha$  the corresponding expressions are

$$\left( \frac{\delta\lambda}{\lambda_0} \right)_\alpha = -\frac{\alpha^2}{4\mu^{*2}} \quad (77)$$

$$\frac{(\Delta\lambda_{0.5})_\alpha}{\Delta\lambda_{0.5}} = \left[ 1 + \left( \frac{\alpha^2 \lambda_0}{2\mu^{*2} \Delta\lambda_{0.5}} \right)^2 \right]^{1/2} \quad (78)$$

Linder and Lissberger discuss the requirements and design of filters for this case.<sup>457,461</sup>

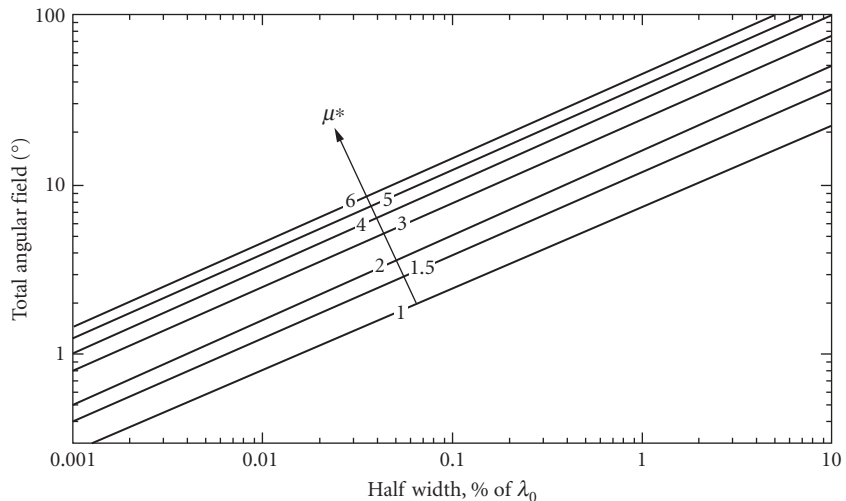


**FIGURE 111** Performance at 43° (a), 45° (b), and 47° (c) of a multicavity bandpass filter designed to show no polarization splitting for light incident at 45°. (After Baumeister.<sup>464</sup>)

Small tilts are commonly used to tune the peak of a filter to the desired wavelength even though they have an adverse effect on the angular field of the filter.

**Bandpass Filters with Little or No Polarization Splitting** It has been shown numerically for the phase-dispersion filter,<sup>435</sup> for the frustrated-total-reflection filter,<sup>462</sup> and for the metal-dielectric<sup>24</sup> and all-dielectric<sup>463</sup> FP filters that it is possible to arrange for the two polarized transmission bands, which may have different widths, to coincide at high angles of incidence (Fig. 110b). The narrow, symmetrical high-transmittance bands that result may be useful for some applications even though the position of the maximum is still displaced with angle. Baumeister has shown how to design multicavity filters with no polarization splitting at one angle of incidence (Fig. 111).<sup>464</sup>

**Wide-Angle Bandpass Filters** Figure 112 shows the variation with effective index  $\mu^*$  of the angular field of FP filters, defined as being twice the angle of tilt necessary to reduce to  $0.8T_0$  the transmittance of the filter for radiation of wavelength  $\lambda_0$ . To increase the angular field  $\mu^*$  must be increased. Thus, for example, in an all-dielectric FP filter the expression for  $\mu^*$  shows that  $n_L < \mu^* < n_H$  and that with increasing spacer order  $\mu^*$  approaches the refractive index of the spacer. The upper limits for  $\mu^*$  for an all-dielectric FP filter in the ultraviolet, visible, and infrared parts of the spectrum are



**FIGURE 112** Angular field of FP filters as a function of the half width for different effective indexes  $\mu^*$ .

of the order of 2.0, 2.35, and 5.0, respectively. Little can be done about the angular field of solid spacer filters (Sec. 7.11, subsection "Fabry-Perot Filters with Solid Spacers").

For metal-dielectric FP and for induced-transmission filters effective indexes  $\mu^*$  of up to 3.2 and 2.0 have been reported.<sup>460</sup>

Wilmot and Schineller<sup>465</sup> and Schineller and Flam<sup>466</sup> have announced a filter consisting of a thin, plane-parallel fiber-optic face plate coated on both sides with all-dielectric mirrors. Since in such a filter the half width is determined only by the thickness of the plate and the reflectivity of the coatings, and since the field of view depends on the ratio of the wavelength to the fiber diameter, the two quantities are independent. The measured transmittance of a 15-Å-half-width, 6-mm-diameter filter composed of 1.5- $\mu\text{m}$ -diameter fibers was 30 percent, and the shift in wavelength with angle of incidence was one-eighth that of a conventional filter.

## Stability and Temperature Dependence of Bandpass Filters

The stability of the position of the transmission peak has been studied by many workers.<sup>389,396,467-475</sup> The observed changes (up to 1 percent of  $\lambda_0$ ) seem to depend greatly on the materials and manufacturing conditions. In filters with evaporated spacers both irreversible changes, probably due to changes in the structure of the films, and reversible changes due to the absorption of water vapor, have been observed. Many manufacturers are now able to minimize these effects through the use of more stable materials, improved high energy deposition methods (see Sec. 7.3), or accelerated artificial ageing processes. No changes were observed in solid spacer filters (Sec. 7.11, subsection "Fabry-Perot filters with Solid Spacers").

Changes in the operating temperature normally do not significantly affect the half widths and peak transmittances of medium and wide bandpass interference filters (see, for example, Refs. 476 to 479). An exception are filters that contain semiconductors that start to absorb significantly on heating (e.g., germanium) or on cooling (PbTe).<sup>480,481</sup>

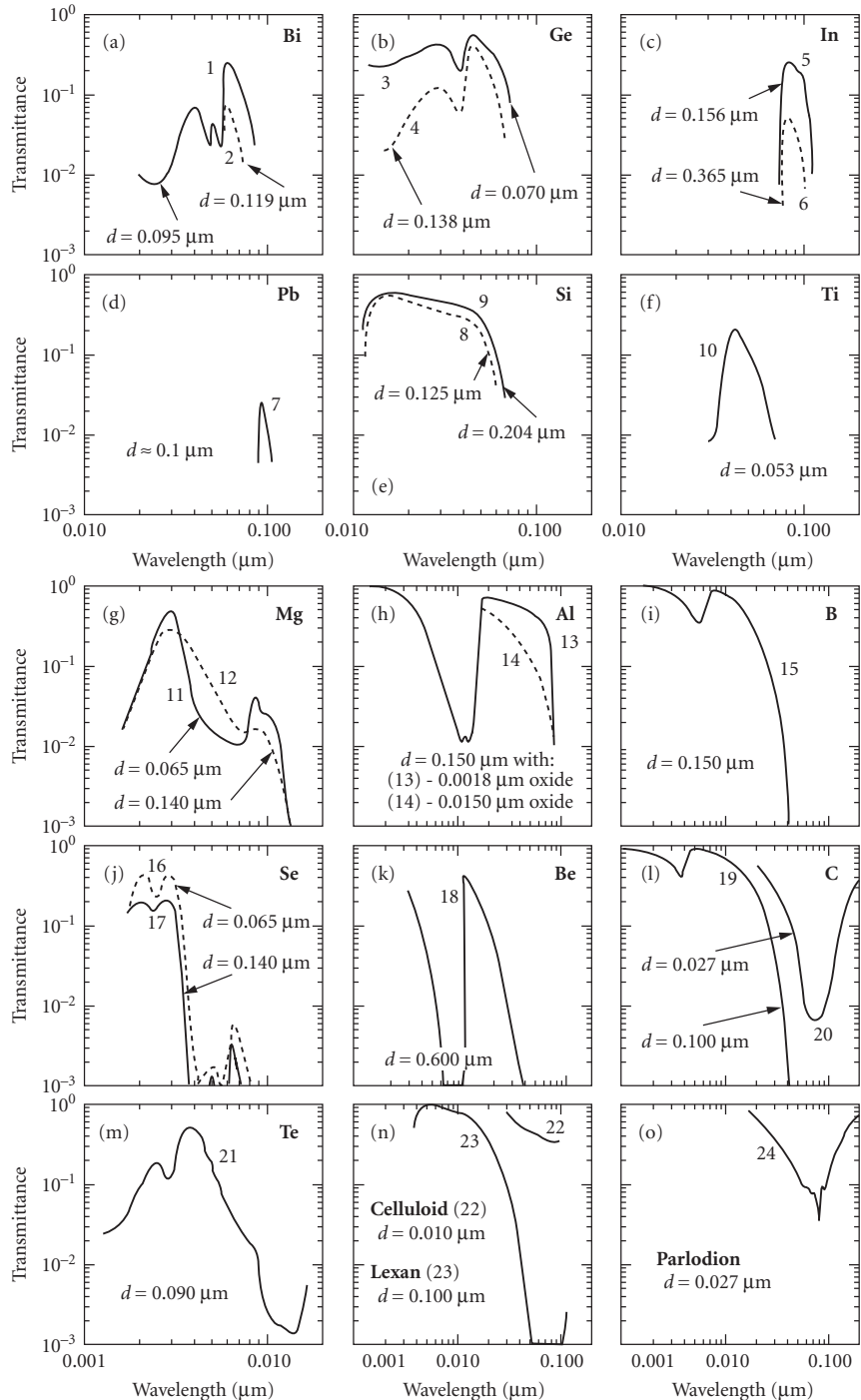
The position of the transmission peaks shift linearly toward longer wavelengths with an increase in temperature, the magnitude of the shift depending largely on the spacer material. The temperature coefficient, expressed as a percentage change in  $\lambda_0$  per degree Celsius change in temperature, lies between  $2 \times 10^{-4}$  and  $3 \times 10^{-3}$  for filters with evaporated spacers for the 0.3- to 1.0- $\mu\text{m}$  spectral region<sup>403</sup> and between  $2 \times 10^{-3}$  and  $2 \times 10^{-2}$  for the infrared spectral region.<sup>389,237</sup> It is of the order of  $1 \times 10^{-3}$  for filters with mica<sup>423</sup> and quartz<sup>397</sup> spacers. Unless temperature control is provided, under adverse conditions all the above temperature coefficients could lead to serious shifts of the transmission peaks of very narrow band filters (Sec. 7.11 subsection "Very Narrow Bandpass Filters"). The temperature control can take the form of an external constant-temperature enclosure, or it might be built in right into the filter. Eather and Reasoner<sup>396</sup> and Mark et al.<sup>482</sup> describe arrangements of the latter type in which two sensors embedded in the filters are used to control the current flowing through two transparent conducting coatings that surround the filter.

Deliberate changes in the temperature can be used for a fine tuning of the transmission wavelength without having an adverse effect on the angular field of the filter.

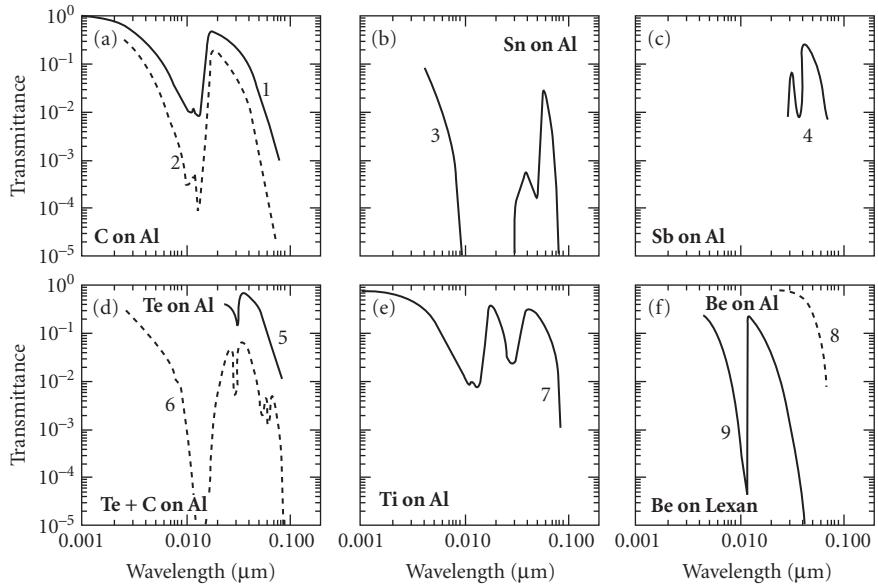
## Bandpass Filters for the XUV and X-Ray Regions

The construction of good bandpass filters for the extreme ultraviolet is hampered by the lack of coating materials with suitable optical constants. However, certain metals in thin-film form can be used as rudimentary bandpass filters in the extreme ultraviolet. The primary process in these filters is absorption, although at times interference within the film may have to be considered to explain the spectral transmission characteristics fully.

The measured spectral transmittance of some of these materials are shown in Figs. 113 and 114. By increasing the thicknesses of the films higher rejection ratios could be obtained at the expense of peak transmissions, and vice versa. The transmittance of the most promising material, aluminum, would be higher if it were not for the formation of absorbing oxide layers.



**FIGURE 113** Measured extreme-ultraviolet and soft x-ray transmittances (a) to (o) of several self-supporting metal films of indicated thicknesses.



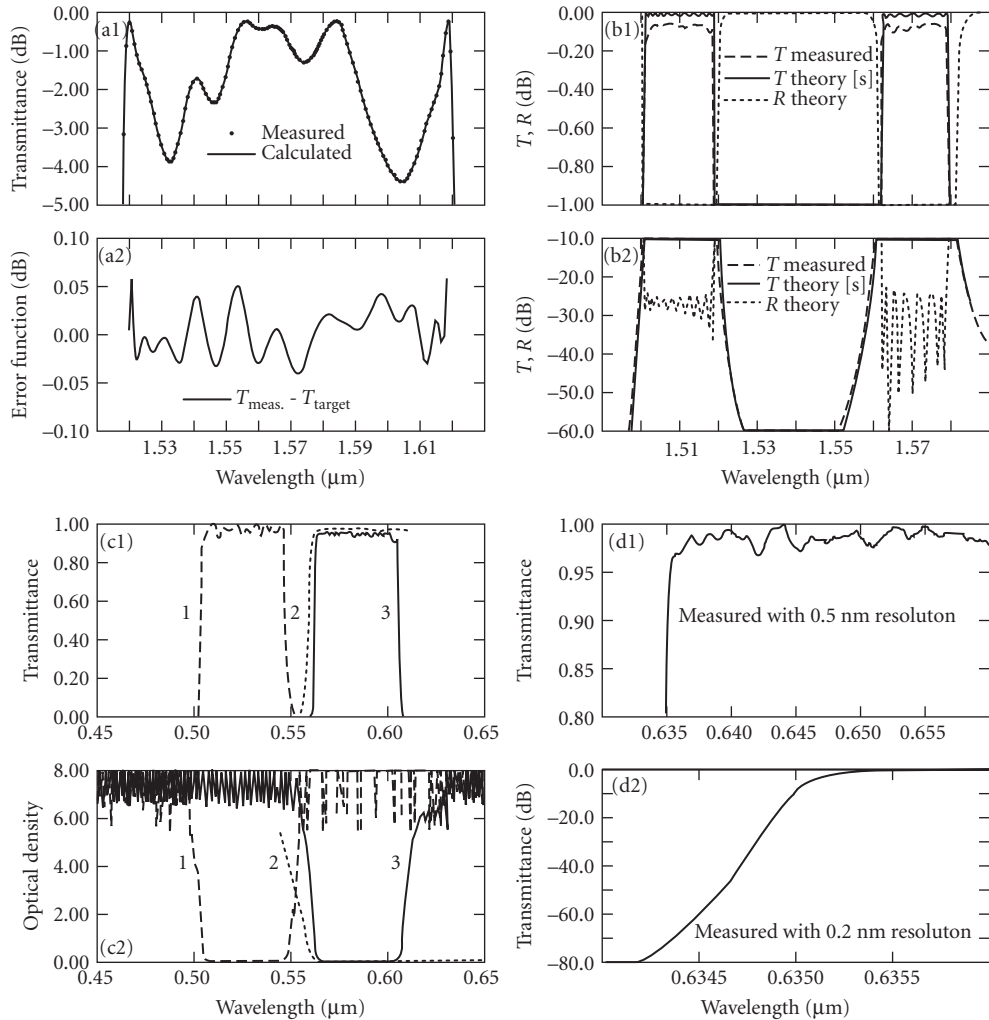
**FIGURE 114** Measured extreme-ultraviolet and soft x-ray transmittances (a) to (f) of six metal films of indicated thicknesses deposited onto thin aluminum or plastic films.

Many of the layers are self-supporting (Fig. 113). Others must be deposited onto a suitable transparent substrate (Fig. 114). Thin aluminum films are sometimes used for this purpose. Other materials used in the past are Zapon (cellulose acetate); collodion, Parlodion, and Celluloid (cellulose nitrates); Mylar (polyethylene terephthalate); and Formvar (polyvinyl formal) (Fig. 113*n* and *o*). Any residual absorption in the substrate contributes, of course, to the overall-transmission curve. The preparation of self-supporting thin films is described by Novikov and by Sorokin and Blank.<sup>483,484</sup> Because of their fragility such films are usually mounted on a very fine mesh screen.

Multilayer Fabry-Perot interference filters for the soft x-ray region have also been constructed.<sup>485-487</sup> However, thus far the only spectral measurements reported are nonnormal incidence reflection.<sup>488</sup> The finesse of the filters is low and the modulation of the reflectance curve depends on the thickness of the spacer. The devices are useful for measurement purposes.

## 7.12 HIGH PERFORMANCE OPTICAL MULTILAYER COATINGS

Advances in the design and the automation of the manufacture of optical multilayer coatings have made possible the routine production of filters with a performance that would have seemed impossible to achieve even fifteen years ago. For the visible and near-infrared parts of the spectrum materials and processes have been developed at a number of commercial and research facilities which permit them to deposit with high accuracy layer systems that consist of more than 4000 layers and with total metric thicknesses exceeding 100  $\mu\text{m}$ . Currently the most common application areas for such coatings are in telecom systems (with filter sizes typically of the order of 1 mm) and in fluorescence and Raman spectroscopy (diameters between 10 and 25 mm). The filter specifications for these filters, as a rule, span such a range of transmittances, or have such sharp gradients, that to depict the results properly, it is usually necessary to present the data in at least two graphs. In this section representative examples will be given to illustrate the type of performance that can be currently achieved.



**FIGURE 115** Measured data for some high performance optical filters. (a) A precise telecom gain flattening filter with an attenuation that is defined over four decades; (b) dual band filters with very high transmission and reflection regions, for adding or removing signals of certain wavelengths in fiber networks; (c) a set of three filters for fluorescence probe microscopy, having very high transmittances and sharp drop-offs; curves 1, 2, and 3 correspond to the transmittance curves of the excitation, beam splitting and emission filters; (d) Raman edge pass filter with an edge steepness of approx. 86 dB/nm. (After Iridian Spectral Technologies.<sup>202</sup>)

In Fig. 115a1 is shown the calculated and measured performance of a 50- $\mu\text{m}$ -thick gain-flattening filter for telecom applications in which the specified transmittance varies in the 1.530- to 1.625- $\mu\text{m}$  spectral region between 0.0 and  $-4.0$  dB. The difference between the target and measured transmittances is shown in Fig. 115a2 and the peak-to-peak variation is  $<0.1$  dB.

Figure 115b1 presents the measured transmittance of a dual band filter of the type that is used for adding or dropping signals of certain wavelengths from a fiber network. Also shown are the theoretical transmittance and reflectance. The main requirements for this application are that the transmittance be as high as possible with low ripple in the transmission bands and have low transmittance

between these bands. The filter shown consisted of more than 300 layers and had a total thickness of 65  $\mu\text{m}$ . Figure 115.b2 shows that the rejection between the two transmission peaks is indeed very high.

In Fig. 115c are shown the measured transmittance curves of the excitation and emission filters and the beam splitter required for fluorescence probe microscopy. For this application the filters must have very high transmittances and sharp drop-offs in order to maximize the signal-to-noise ratio. The emission and excitation filters were about 35  $\mu\text{m}$  thick and consisted of more than 300 layers. The optical density outside the transmission regions are shown in Fig. 115c2. Some of these measurements are noise limited above an optical density 6.

In Fig. 115d is shown the measured transmittance of a steep cutoff filter for Raman spectroscopy. The filter consisted of about 500 layers and had a total thickness of about 40  $\mu\text{m}$ . The ripple in the transmission region is only 4 percent. To appreciate the steepness of the cutoff (about 86 dB/nm) the region around the cutoff is plotted in Fig. 115c2 on an expanded wavelength scale.

Very advanced spectroscopic notch filters are shown in Fig. 42, one of these consisting of as many as 4410 layers. Of course, the processes used to produce the advance coatings described above are used today to produce better coatings with the simpler properties described in the earlier diagrams.

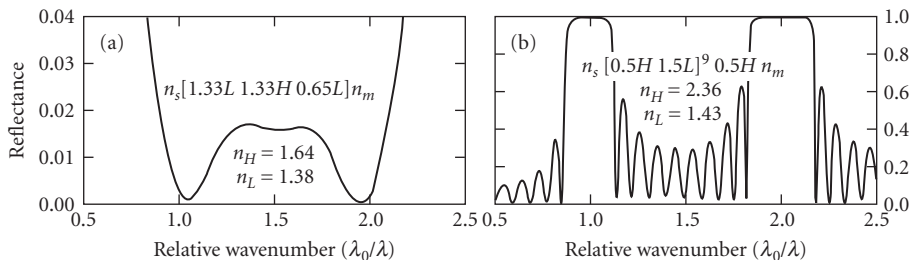
### 7.13 MULTILAYERS FOR TWO OR THREE SPECTRAL REGIONS

Increasingly there are applications, especially in laser science, in which the spectral transmission and/or reflection has to be controlled at two or more wavelengths.<sup>34</sup> The design and construction of such coatings is more difficult than that of systems for one wavelength region only, especially when the ratio of the wavelengths of interest is very large.

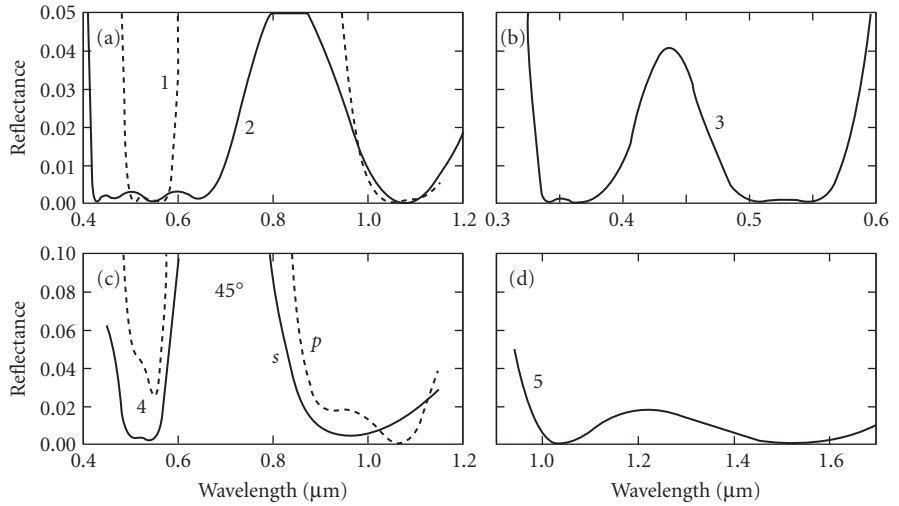
#### Multilayers for Two Spectral Regions

Costich was the first to specify the construction parameters of coatings having all possible combinations of low and high reflection behavior at wavelength ratios of 1.5-, 2.0-, and 3.0: 1.0.<sup>489</sup> His solutions were based on systems composed of quarter-wave layers or layers with other simple thickness relationships. Experimental results are in good agreement with the calculated values. The calculated performance of two coatings not shown before are given in Figs. 116 and 117 presents the performance of a number of commercially produced coatings of this type. Systems for other wavelength ratios and for combinations of other reflection values are possible.

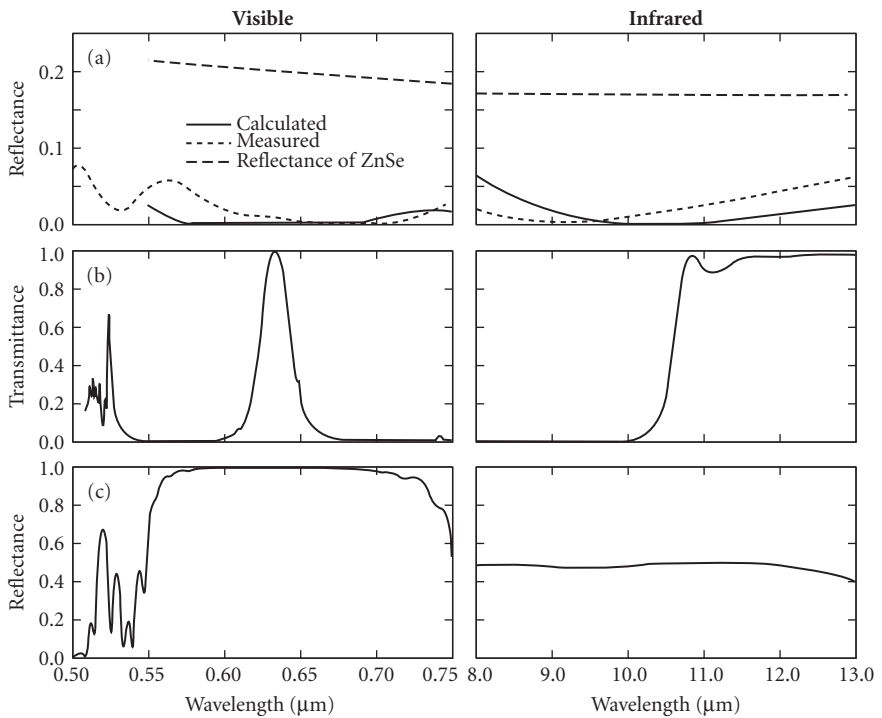
Sometimes coatings are required in which the reflectance is controlled for wavelength ratios of 10:1 or more.<sup>490,491</sup> A systematic method for the design of such multilayers with different reflectance characteristics at the two wavelengths has been described.<sup>492,493</sup> The calculated performance of such coatings for the wavelengths of 0.6328 and 10.6  $\mu\text{m}$  are shown in Fig. 118.



**FIGURE 116** Calculated performance of a commercial antireflection coating (a) and a high reflectance coating (b) for wavenumbers 1.0 and 2.0  $\mu\text{m}^{-1}$ . (After Costich.<sup>34</sup>)



**FIGURE 117** Measured reflectances (a) to (d) of some commercial two-wavelength antireflection coatings. (Curves 1, 3, and 4 after TechOptics<sup>86</sup> and curves 2 and 5 after Thin Film Lab.<sup>85</sup>)



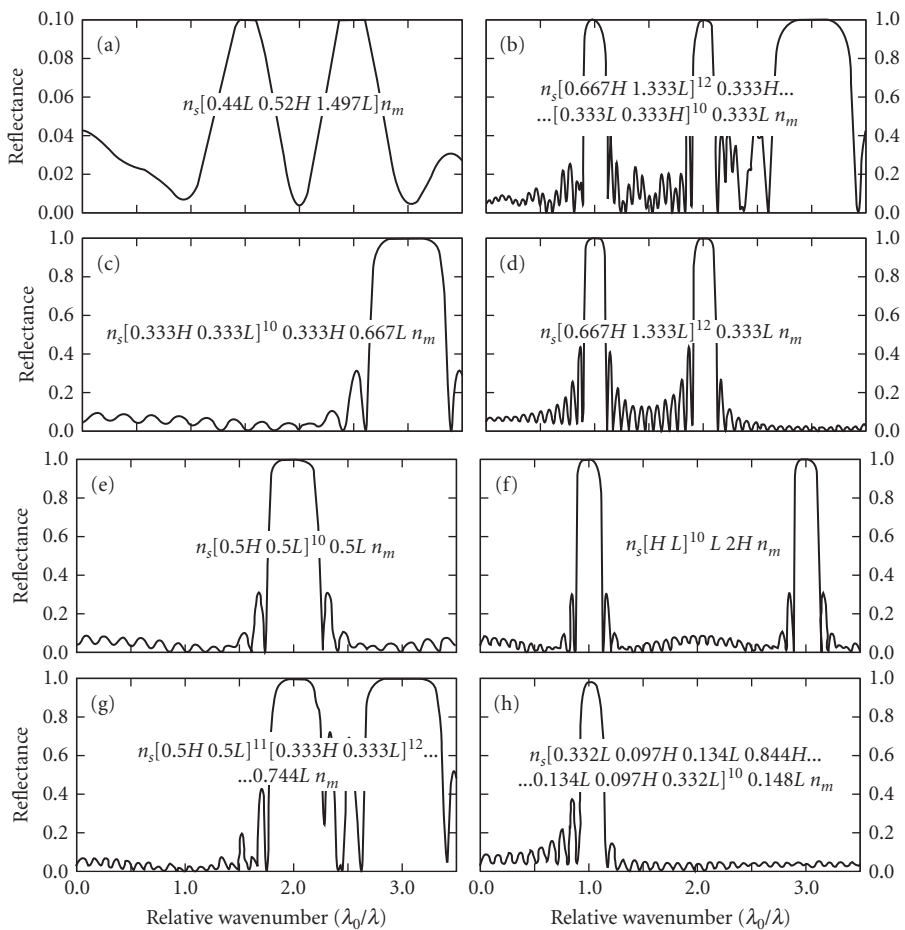
**FIGURE 118** Calculated performance of three multilayer coatings (a), (b), and (c) designed for two widely separated spectral regions. Columns 1 and 2 represent the performance of the multilayers in the visible and in the infrared spectral regions, respectively. The experimental measurements for one coating are also shown. (After Li.<sup>492,493</sup>)



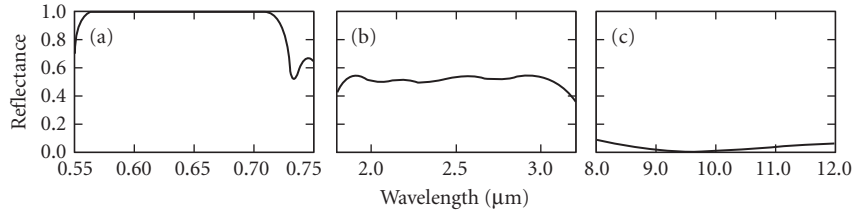
## Multilayers for Three Spectral Regions

For some laser applications the reflectance or transmittance has to be controlled at three or more wavelengths. Solutions to such problems can also be found. Costich has given designs for all possible combinations of low and high reflection for the important special case of a set of wavenumbers  $\sigma_0$ ,  $2\sigma_0$ , and  $3\sigma_0$ .<sup>489</sup> The designs and performances of his solutions to this problem are shown in Fig. 119.

In principle, the method for the design of coatings for two widely separated spectral regions mentioned above can be extended to the design of coatings for three or more wavelengths. However, the number of layers required increases dramatically as the number of layers required for the longest wavelength region increases. Figure 120 shows the calculated performance of a coating that behaves like a high reflection coating, a beam splitter and an antireflection coating at 0.63, 2.52, and 10.6  $\mu\text{m}$ , respectively.



**FIGURE 119** Calculated spectral reflectances of multilayer coatings on glass with various combinations of high and low reflectance at relative wavenumbers  $\lambda_0/\lambda$  1.0, 2.0, and 3.0. In the designs  $H$ ,  $L$  correspond to quarterwave layers at  $\lambda_0 = 1.0 \mu\text{m}$ .  $n_m$ ,  $n_s$ ,  $n_H$ , and  $n_L$  were assumed to be 1.00, 1.52, 1.95, and 1.43, except in (a) where  $n_H$ ,  $n_L$  were 1.64, 1.38, respectively. (After Costich.<sup>34</sup>)



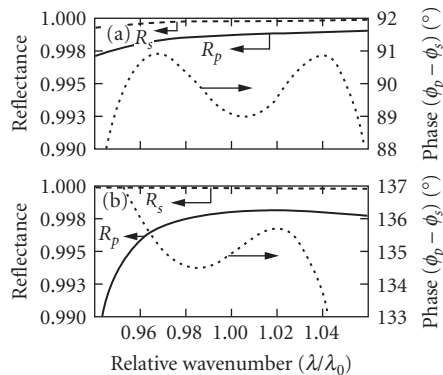
**FIGURE 120** Calculated performance of a multilayer with different properties in three spectral regions. (After Dobrowolski.<sup>494</sup>)

## 7.14 PHASE COATINGS

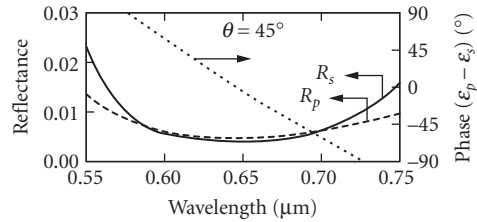
In some applications, in addition to transmittance or reflectance requirements, special phase relationships have to be satisfied. These may be specific phase changes on reflection  $\phi_R$  or transmission  $\phi_T$  for radiation incident at  $0^\circ$ . At other times it is required to displace or to deflect a beam without affecting its state of polarization. However, most frequently it is necessary to introduce a certain phase difference ( $\phi_p - \phi_s$ ) between  $p$ - and  $s$ -polarized light. Quarter-wave plates made of birefringent crystals are normally used to provide this phase difference.

Solutions to these and similar problems based on optical interference coatings can also be found. Porous films with an inclined columnar structure, formed in physical vapor deposition processes when the vapor is incident onto the substrate at an oblique angle, can also be birefringent.<sup>495</sup> Such films have been proposed for the construction of phase retardation plates for use with normal incidence of the radiation.<sup>496</sup> However, more frequently solutions are based on the difference between the effective indices  $\eta_p, \eta_s$  of thin films for obliquely incident radiation [Eq. (19)]. Azzam has shown that, when performance at one wavelength only is specified and when oblique angles of incidence are acceptable, elegant solutions to many of the problems can be found that are based on a single layer only.<sup>335</sup>

Phase retarding reflectors are commonly designed for use at  $45^\circ$ . Many layers are required when the radiation is incident from the air side. The performances of two multilayers of this type with different phase differences are shown in Fig. 121. The multilayers are optimized to maintain a constant phase difference in the vicinity of the design wavelength. Coatings with other phase differences and



**FIGURE 121** Calculated performance of two front surface  $45^\circ$  reflectors with different phase retardations. (a) 20 layers on a Ag substrate (after Southwell<sup>499</sup>) and (b) 22 layers on an Al substrate (after Grishina<sup>500</sup>).



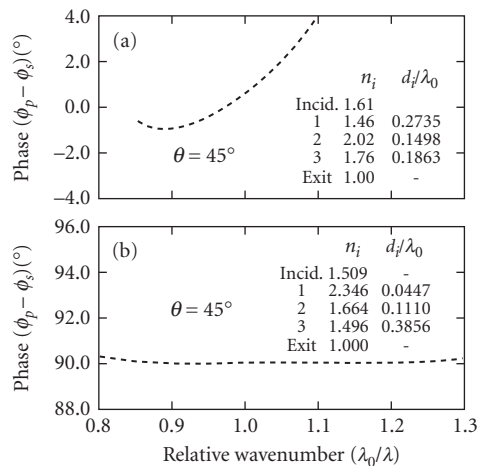
**FIGURE 122** Antireflection coating on glass for use at  $45^\circ$  with zero phase retardation at  $\lambda = 0.6471 \mu\text{m}$ . (After *Thin Film Lab.*<sup>85</sup>)

reflectances can also be constructed.<sup>497,498</sup> For example, an antireflection coating for  $45^\circ$  incidence in which the phase change is  $180^\circ$  is shown in Fig. 122.

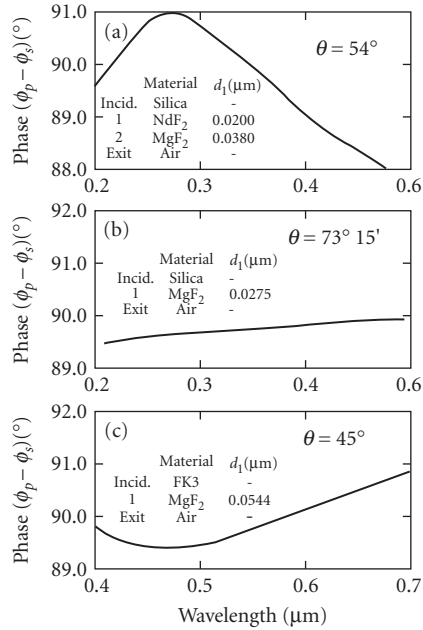
When the radiation is incident on the layers from the substrate side, total internal reflection takes place.<sup>501</sup> The design of thin-film phase retarders based on this approach has also been examined by Apfel<sup>502</sup> and Azzam.<sup>503</sup> Total internal reflection phase retarders operate over broader spectral regions (Fig. 123) but their size is limited by the weight and homogeneity of the prism materials.

More complex phase retardation devices have been constructed in which the radiation is allowed to undergo 2, 3, or even 4 internal reflections.<sup>342,506,507</sup> The performance of some typical total internal reflection devices that are based on the configurations of Fig. 68*u, v, w* is shown in Fig. 124. For high-power laser beam delivery systems front surface reflectors are usually employed (Fig. 125).

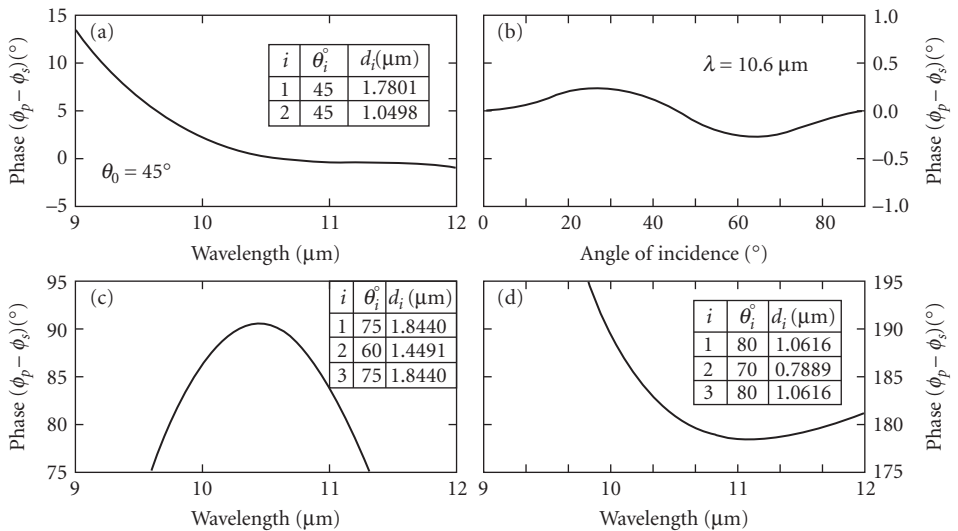
In Fig. 126 are shown the phase changes on reflection of a set of four metal/dielectric interferometer mirrors, all with  $R > 0.97$ , for which the differences in the phase changes on reflection for adjacent members in the set were approximately  $90^\circ$  over an extended spectral region. Other requirements for phase changes or phase change differences can also be satisfied with thin films.



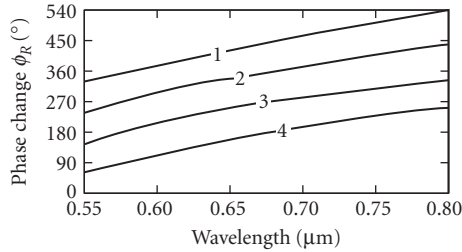
**FIGURE 123** Phase retarders based on total internal reflection, consisting of 3 layers on glass and operating at an angle of incidence of  $45^\circ$ . (a)  $0^\circ$  phase retardation (after Cojocar<sup>504</sup>) and (b)  $90^\circ$  phase retardation (after Spiller<sup>505</sup>).



**FIGURE 124** 90° phase retardation devices based on 2 (a), 3 (b) and 4 (c) total internal reflections (after King,<sup>508</sup> Clapham,<sup>304</sup> and Filinski<sup>507</sup>). The angle of incidence on the first reflecting surface is indicated in the diagrams.



**FIGURE 125** Phase retardation devices for  $\lambda = 10.6 \mu\text{m}$  based on multiple reflections from surfaces coated with opaque silver films and single layers of ZnS layers having specified thicknesses. (a), (b) 0° phase retardation for all angles of incidence (after Azzam<sup>509</sup>); (c), (d) 90°, 180° phase retardations (after Thonn<sup>510</sup>).



**FIGURE 126** Normal incidence phase changes on reflection of a set of four highly reflecting mirrors for Michelson interferometers. (After Piotrowski et al.<sup>22</sup>)

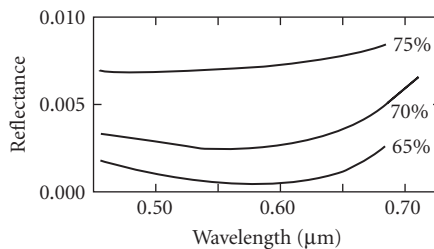
## 7.15 INTERFERENCE FILTERS WITH LOW REFLECTION

### Reducing Reflection with a Thin Metal Film

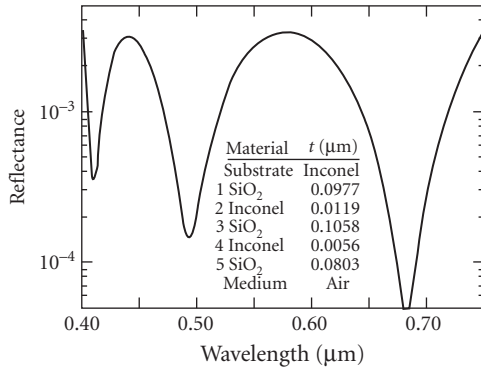
A suitable thin metal film deposited onto a glass surface can act as a very efficient achromatic anti-reflection coating for light incident from the glass side (Fig. 127). The reflectance for light incident from the air side is not reduced and the transmittance suffers as a result of the absorption within the film.<sup>511</sup> By combining such films with additional layers, attractive coloured sun glasses or architectural coatings are obtained.

### Black Absorbers

Black absorbers efficiently absorb the radiation incident upon them in a specified spectral region. They are used, for example, to control radiant energy,<sup>512</sup> to remove stray light in optical systems, to enhance contrast in display devices<sup>513</sup> and to increase the signal-to-noise ratio in multiplexers.<sup>514</sup> Black absorber coatings are based on interference in thin film and generally consist of an opaque metal layer and one or more dielectric layers interspersed with partially transparent metal layers (Figs. 21 and 66a). They can be designed for first- and second-surface application (Fig. 128). Coatings of this type can also be designed for the ultraviolet and infrared spectral regions.<sup>515</sup>



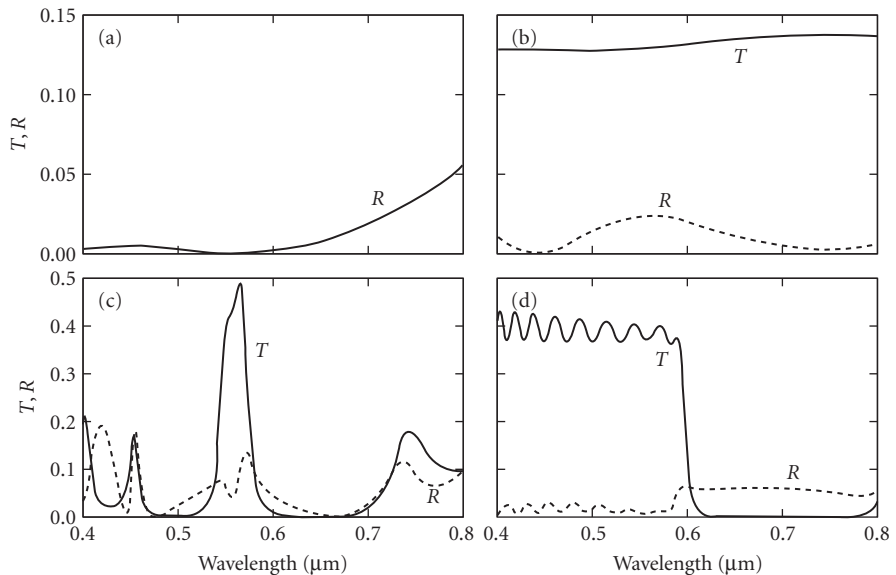
**FIGURE 127** Spectral reflectance of thin chromium films on glass for light incident from the substrate side. The transmittance of the layers at  $\lambda = 0.565 \mu\text{m}$  is indicated. (After Pohlack.<sup>511</sup>)



**FIGURE 128** Calculated performance of a five layer metal/dielectric black absorber. (After Dobrowolski.<sup>516</sup>)

## Neutral Attenuators

Conventional metallic film attenuators described in Sec. 7.9, subsection “Neutral Filters” cannot readily be placed in series because multiple reflections between the components may result in unpredictable density values. However, by using metal and dielectric layer combinations of appropriate optical constants and thicknesses, it is possible to reduce the reflection of the metallic film from one or both sides of the substrate.<sup>82,513–515,517,518</sup> The experimental results for one such attenuator are given in Fig. 129*b*.



**FIGURE 129** Measured performance of interference filters with reduced reflection: (a) black absorber; (b) neutral attenuator; (c) narrow bandpass filter; and (d) long-wavelength cutoff filter. (After Dobrowolski<sup>519</sup> and Sullivan.<sup>520</sup>)

## Other Interference Filters

It is possible, using a similar approach, to reduce the reflection of narrow bandpass filters, cutoff filters, and other filter types. In particular, low reflection narrowband interference filters for welding applications have been described by Jacobsson.<sup>521</sup> The experimental performance of a bandpass filter and of a long-wavelength cutoff filter are given in Fig. 129*c* and *d*. In both cases the luminous reflectance has been reduced by an order of magnitude over that of a conventional design. However, this is at the expense of the transmittance.

## 7.16 REFLECTION FILTERS AND COATINGS

### Metallic Reflectors

The Fresnel reflection coefficient of an interface between two semi-infinite media of complex refractive indices  $\bar{n}_m, \bar{n}_s$  for polarized radiation incident at nonnormal angle is given by

$$R = \frac{|\eta_s - \eta_m|^2}{|\eta_s + \eta_m|^2} \quad (79)$$

where  $\eta_s, \eta_m$  are given by (19). When  $\bar{n}_m, \bar{n}_s$  correspond to air, and the metal, respectively, and when the angle of incidence is zero, the above expression reduces to

$$R = \frac{(n_s - 1)^2 + k_s^2}{(n_s + 1)^2 + k_s^2} \quad (80)$$

If the substrate is opaque, the above represents the total energy reflected, the remaining energy being absorbed within the material.

Metal reflectors are most commonly made by vacuum deposition of the material onto a suitable glass or quartz substrate. Before deposition aluminum or beryllium mirror surfaces are sometimes first chemically plated with a nickel-phosphorus alloy (Kanigen process). Such deposits have excellent adhesion to the substrate and have a very hard surface that can be optically polished before coating.<sup>522</sup>

Visible, infrared, and ultraviolet spectral reflectances of some of the more commonly used metals are shown in Figs. 130 and 131. Using Eq. (80) and the optical constants in Palik's handbook,<sup>58,59</sup> the

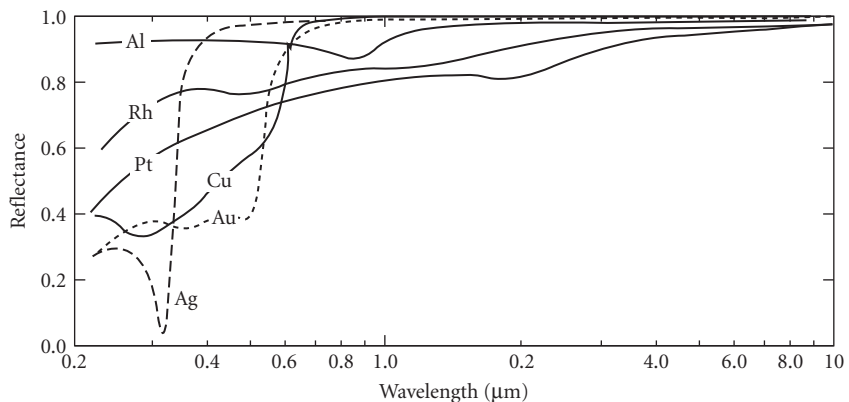
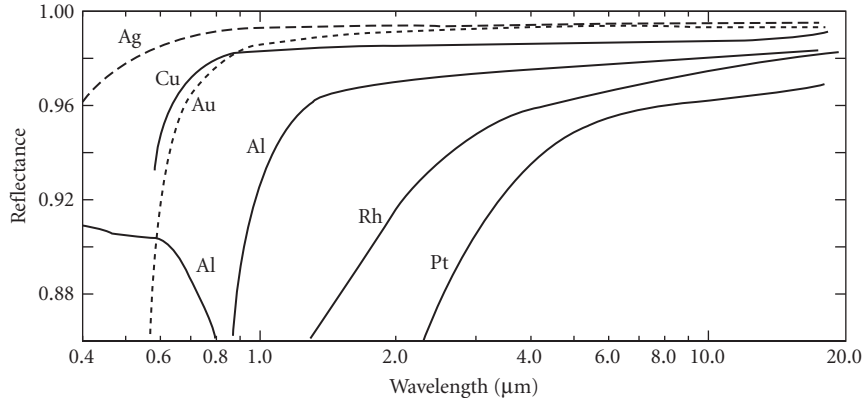


FIGURE 130 Reflectances of some metals. (After Drummer and Hass.<sup>138</sup>)

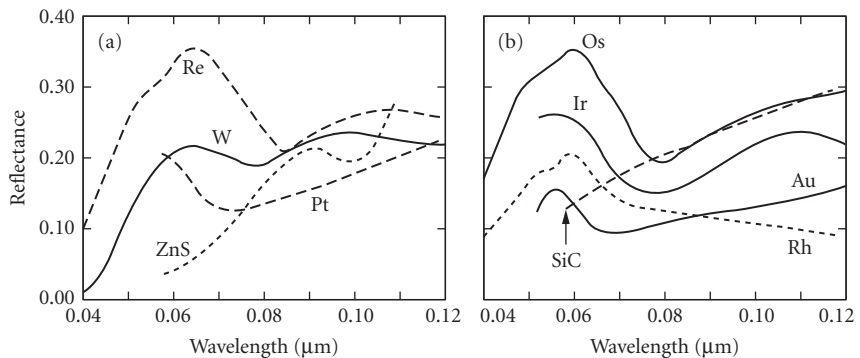


**FIGURE 131** Visible and infrared reflectance of certain metals. (Al after Bennett *et al.*,<sup>525</sup> Ag and Au after Bennett and Ashley,<sup>526</sup> Cu after Hass and Hadley,<sup>527</sup> Rh and Pt after Hass and Fowler.) (See Drummer and Hass.<sup>138</sup>)

spectral reflectances for many additional metals can be calculated. Silver has the highest visible and infrared reflectance, and hence is used for interferometer mirrors and interference filters. Exposed silver films tarnish readily but they can be protected. Aluminum has the broadest high reflectance region of all metals and is commonly used in front-surface mirrors. It would reflect highly down to 0.1  $\mu\text{m}$  were it not for the absorption below 0.18  $\mu\text{m}$  of the thin oxide layer that starts to form seconds after deposition.<sup>523,524</sup> Some of the highest known reflectances in the ultraviolet are shown in Fig. 132.

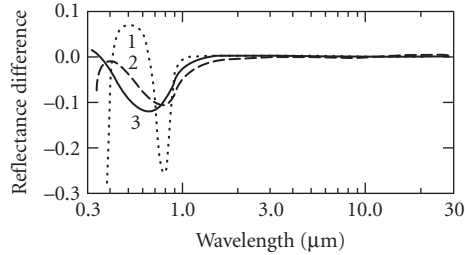
**Protective Coatings** For many applications the thin aluminum oxide layer on an aluminum surface does not offer sufficient protection against abrasion and chemical attack, and therefore aluminum mirrors are often overcoated with single  $\text{SiO}_2$  or of  $\text{MgF}_2$  protective layers. Such mirrors can be repeatedly cleaned with water and even withstand boiling in saltwater.<sup>534</sup> Single protective layers reduce the reflectance (Fig. 133). If necessary this problem can be overcome by using protective coatings consisting of two or more layers (Fig. 134).

The deterioration of the ultraviolet reflectance of aluminum mirrors due to oxidation can be partially avoided by covering the freshly deposited aluminum layer immediately with a suitable

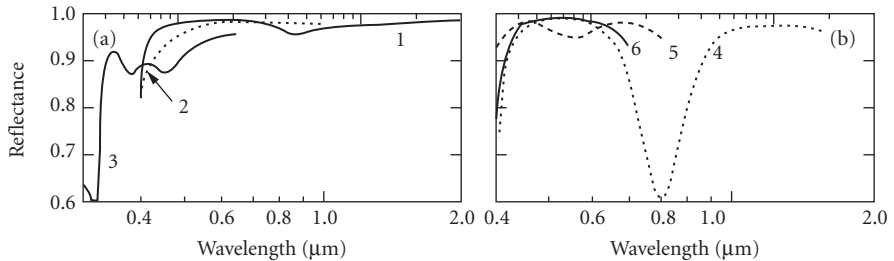


**FIGURE 132** Measured ultraviolet reflectance of certain materials (a) and (b). (Pt, Au, and ZnS after Hunter;<sup>528</sup> Ir after Hass *et al.*;<sup>529</sup> Rh after Cox *et al.*;<sup>530</sup> Re, and W after Cox *et al.*;<sup>531</sup> Os after Cox *et al.*;<sup>532</sup> and SiC after Seely.<sup>533</sup>)





**FIGURE 133** Measured difference between the reflectances of protected and unprotected aluminum mirrors. Curve 1: coating 4 of Fig. 134b; curves 2 and 3:  $0.1122 \pm 0.002$  and  $0.0752 \pm 0.001$   $\mu\text{m}$  thick films of  $\text{MgF}_2$  and  $\text{SiO}_2$ , respectively, on aluminum. (After Bennett.<sup>525</sup>)



**FIGURE 134** Reflectance of very durable overcoated metal mirrors. (a) Silver mirrors: curve 1: protected front-surface mirror (after Denton<sup>535</sup>); curve 2: enhanced reflection (after Vvedenski<sup>536</sup>); curve 3: extended reflection (after Song *et al.*<sup>537</sup>). (b) Aluminum mirrors: curve 4: with four layers of  $\text{MgF}_2$  and  $\text{CeO}_2$  (after Hass<sup>534</sup>); curve 5: with four layers of  $\text{SiO}_2$  and  $\text{TiO}_2$  (after AIRCO<sup>538</sup>); and curve 6: with four layers  $\text{MgF}_2$  and  $\text{ZnS}$  (after Furman and Stolov<sup>539</sup>).

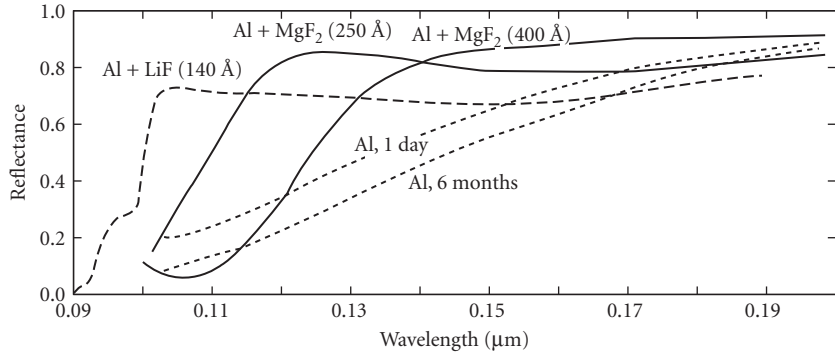
coating of  $\text{MgF}_2$ <sup>540–542</sup> or  $\text{LiF}$ .<sup>540,543,544</sup> The reflectances of such overcoated aluminum reflectors are shown in Fig. 135. Their variation with angle of incidence in the  $0.03$  to  $0.16$   $\mu\text{m}$  spectral region is discussed by Hunter.<sup>56</sup>

The reflectance of unprotected and protected silver mirrors has been investigated by Burge *et al.*<sup>545</sup> Highly adherent and chemically stable mirrors with a reflectance in excess of  $0.95$  for wavelengths greater than  $0.5$   $\mu\text{m}$  have been reported.<sup>546,547</sup>

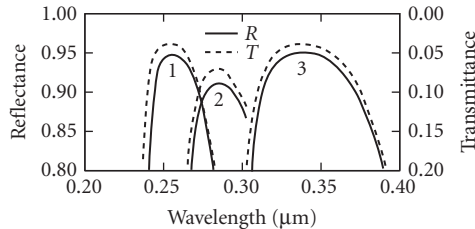
The reflectance of protected metal mirrors at oblique angles of incidence in the infrared part of the spectrum can be seriously reduced at the short-wavelength side of the Reststrahlen peak of the material used for its protection.<sup>548–551</sup>

## Enhancement of Reflection

By depositing a quarter-wave stack (Sec.7.6 subsections “Nonabsorbing  $[AB]^N$  and  $[AB]^N A$  Multilayer Types” and “Periodic Multilayers of the  $[(0.5A) B (0.5A)]^N$  Type”) onto the metal mirror its reflectance can be enhanced considerably.<sup>387</sup> The thickness of the first layer should be adjusted to compensate for the phase change on reflection at the metal surface.<sup>552</sup> The spectral-reflectance curve dips on either side of the high-reflection region whose width is governed by the considerations of Sec. 7.6, subsection “Width of the High-Reflectance Zone” and which can be somewhat enhanced by the use of a half-wave outermost layer (Fig. 134). The measured spectral characteristics of three metal-dielectric reflectors for the ultraviolet region are shown in Fig. 136.



**FIGURE 135** Measured spectral-reflectance curves of unprotected aluminum and aluminum overcoated with  $\text{MgF}_2$  and  $\text{LiF}$  films of indicated thicknesses. (*Al + LiF coating after Cox et al.*<sup>544</sup> and all other curves after Canfield et al.<sup>541</sup>)

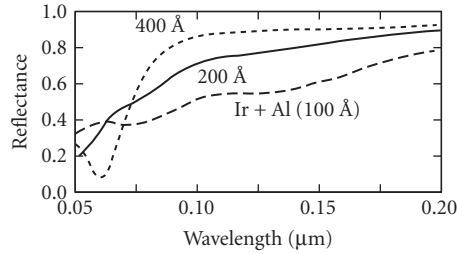


**FIGURE 136** Enhanced ultraviolet reflectances of semitransparent aluminum films obtained through the addition of quarter-wave stacks. Curves 1 and 2: eleven layers of  $\text{PbF}_2$  and  $\text{MgF}_2$  (after Leš et al.<sup>553</sup>); curve 3: nine layers of  $\text{Sb}_2\text{O}_3$  and  $\text{MgF}_2$  (after Leš and Leš<sup>554</sup>).

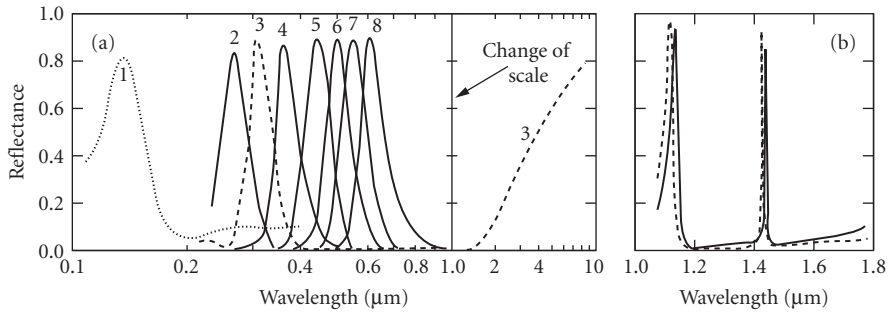
The reflectance of silver, although very high in the visible, falls off rapidly in the near-ultraviolet. Attempts to enhance the reflectance in that part of the spectrum and, at the same time, to protect the silver from tarnish, have been successful (Fig. 134a).<sup>537</sup>

A different kind of reflection enhancement has been reported for the extreme ultraviolet. By depositing semi-transparent platinum films onto different substrates the opaque-film reflectances of 19.3 and 12.8 percent at 0.0584 and 0.0736  $\mu\text{m}$  were increased by up to 2.8 and 3.8 percent, respectively.<sup>555</sup> For space applications suitably thick aluminum films on iridium are expected to yield reflectances as high as 40 and 52 percent at the same wavelengths (Fig. 137). Other proposed reflectance-increasing combinations can be found in Madden et al.<sup>556</sup>

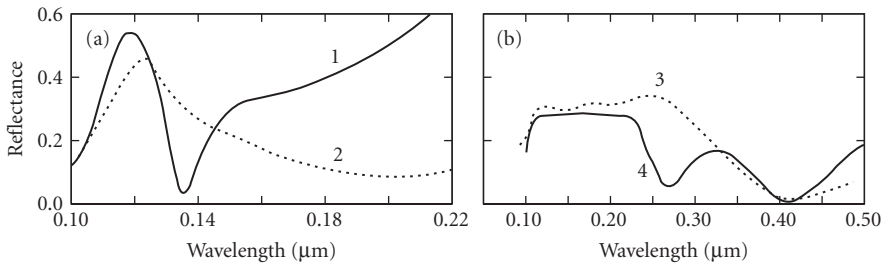
**Selective Metal-Dielectric Reflectors** Several types of coatings that reflect highly in one spectral region, but not in another have been developed in the past for different applications. Hadley and Dennison presented the theory and experimental results of reflection interference filters for the isolation of narrow spectral regions (Fig. 138a).<sup>558,559</sup> Very narrow reflection filters have been described by Zheng (Fig. 138b).<sup>560</sup> High-infrared and low-visible reflectance coatings (Fig. 66) are used to control the temperature of satellites.<sup>138</sup> These coatings could also be used to remove visible light from infrared optical systems. Several reflectors designed to reduce stray visible light in ultraviolet systems are shown in Fig. 139.



**FIGURE 137** Calculated spectral reflectance curves of iridium overcoated with different thicknesses of unoxidized films of aluminum. (After Hass and Hunter.<sup>557</sup>)



**FIGURE 138** Measured performance of selective reflection filters. (a) Reflecting filters for the ultraviolet and visible spectral regions (curve 1 after Stelmack<sup>561</sup>). Curves 2 to 8 represent the performance of filters that consist of three half-wave cryolite or MgF<sub>2</sub> spacer layers separated by Inconel films of suitable transmission deposited on an opaque aluminum film (after Turner and Hopkinson<sup>562</sup>). (b) Calculated and experimental performance of a very narrow band near-infrared reflecting filter (after Gamble<sup>563</sup>).



**FIGURE 139** Measured performance of four multilayer selective ultraviolet reflectors for the control of stray radiation in the intermediate ultraviolet and visible spectral regions (a) and (b). (Curve 1 after Hunter,<sup>528</sup> curve 2 after Berning et al.,<sup>564</sup> and curves 3 and 4 after Hass and Tousey.<sup>542</sup>)

## Reflection at Angles Close to Grazing Incidence

At wavelengths much shorter than the ultraviolet, all materials have refractive indices that are close to unity and extinction coefficients that are rather small. It follows from Eq. (80) that normal incidence reflectances in that part of the spectrum are small. However, for angles of incidence greater than the critical angle  $\theta_c$ ,

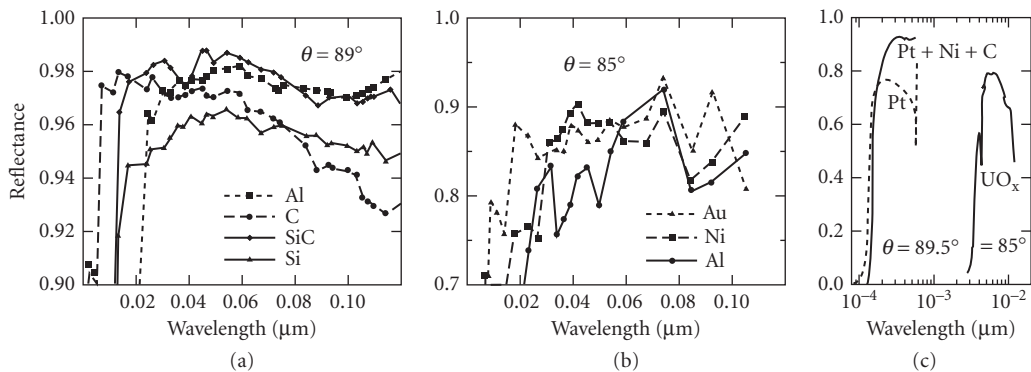
$$\theta_c = \cos^{-1}[\sqrt{2(1-n_s)}] \quad (81)$$

total external reflection occurs resulting in high reflectances. Measured values of oblique angle reflection coefficients in the 0.0023 to 0.019  $\mu\text{m}$  spectral region for a number of materials are given by Lukirskii et al.<sup>565,566</sup> and also on Henke's website.<sup>254</sup> Typical spectral reflectance curves of some elements are shown in Fig. 140a and b. An Al reflectance of 0.987 for an angle of incidence of  $80^\circ$  at 0.0584  $\mu\text{m}$  has been reported by Newnam.<sup>567</sup> It has also been shown that two or three thin films on a suitable substrate can have a better performance than a single metal layer (Fig. 140c).<sup>568</sup> Higher reflectances can be achieved with periodic and nonperiodic multilayers designed for use at grazing incidence. For use in near-grazing incidence telescope optics for the soft x-ray region it may also be a requirement that, for a given wavelength, the reflectance stays constant over a small range of angles. Nonperiodic systems with such properties are sometimes called "supermirrors" and they can be composed of hundreds of layers. The performances of several such coatings are shown in Fig. 141.

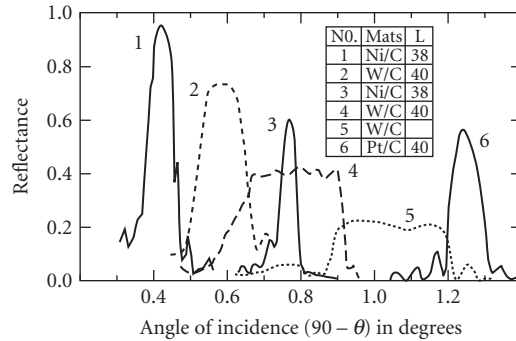
## Multiple-Reflection Filters

**Metal and Metal-Dielectric Multiple-Reflection Filters** Metals such as silver, copper, gold, and metal-dielectric coatings of the type shown in Fig. 64a used in a multiple-reflection arrangement should make low-wavelength cutoff filters with excellent rejection, sharp transition, and a long, unattenuated pass region far superior to those available with transmission filters.

**Multiple-Reflection Filters Made of Thin-Film Interference Coatings** Interference coatings for use in a multiple-reflection filter need not be deposited onto substrates that transmit well in the spectral region of interest, but they should be used at small angles of incidence if disturbing effects due to polarization are not to occur.<sup>578</sup> The following are examples of some of the difficult filtering problems that can be easily solved with multiple reflection filters composed of interference coatings, providing that there is space to use a multiple reflection arrangement.



**FIGURE 140** Measured XUV and x-ray reflectances of (a) Al, Si, C, and CVD SiC films (after Windt et al.<sup>569</sup>); (b) Ni, Au, and Al films (after Malina and Cash<sup>570</sup>); and (c) uranium oxide (after Sandberg et al.<sup>571</sup>) and a single Pt layer and a triple layer of Pt, Ni, and C (after Tamura et al.<sup>568</sup>). The angles of incidence are indicated in the diagrams.



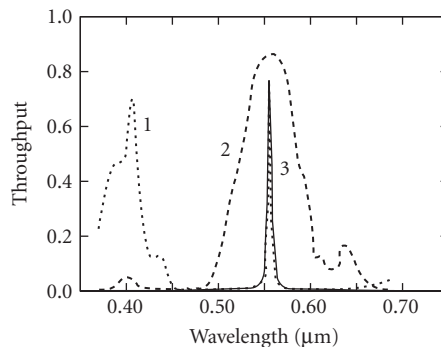
**FIGURE 141** Measured reflectances of some mirrors operating at near-grazing angles of incidence for 8 keV ( $\lambda = 0.0001543 \mu\text{m}$ ) radiation. The total number of layers and the materials used in their construction are indicated in the table. (Curve 1 after Spiga;<sup>572</sup> curve 2 after Protopopov;<sup>573</sup> curve 3 after Citterio;<sup>574</sup> curve 4 after Protopopov;<sup>575</sup> curve 5 after Wang;<sup>576</sup> and curve 6 after Yamashita.<sup>577</sup>)

It is difficult to provide adequate blocking with transmission filters for narrow-bandpass filters of the type shown in Figs. 97 to 102 without considerably reducing the peak transmittance. This is done readily with a multiple-reflection filter composed of quarter-wave stacks of the same materials used for the construction of the bandpass filter and centered at the same wavelength (Fig. 142).

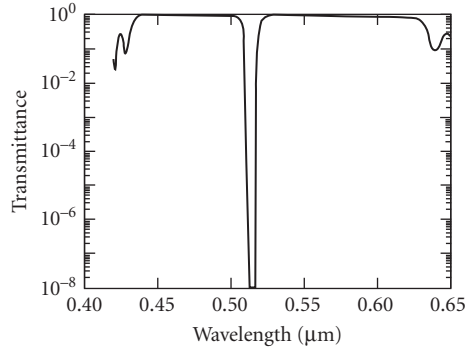
It should be possible to construct highly efficient short-pass filters with a very long and low rejection region by using broadband reflectors consisting of several contiguous stacks (Sec. 7.7, subsection "Rejection Filters").

The use of a narrowband transmission filter in a multiple reflection arrangement of the type shown in Fig. 3 results in a high attenuation narrowband rejection filter surrounded by regions of high transmission (Fig. 143). However, such devices must be used with well-collimated light.

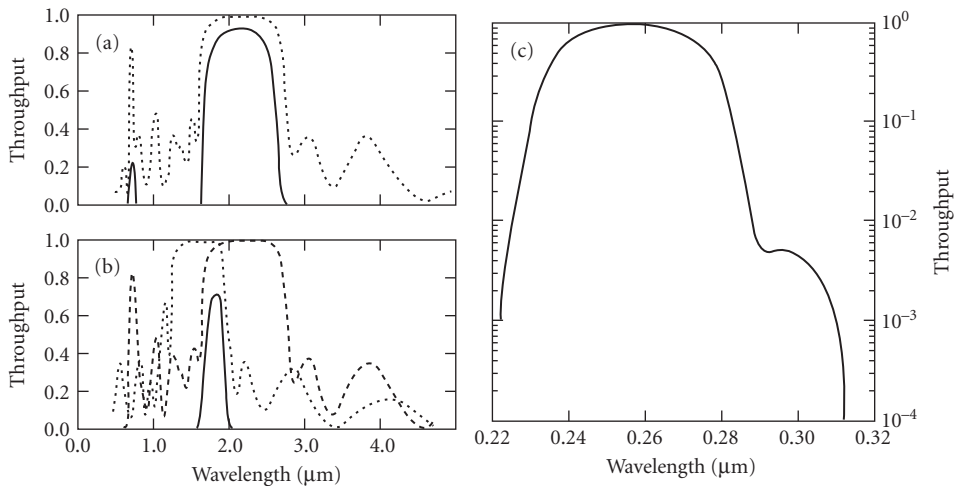
The transmittance curves of three multiple-reflection bandpass filters are shown in Fig. 144a to c. By using a number of multiple reflection filters with sharp features it is possible to separate signals



**FIGURE 142** Blocking an all-dielectric narrowband interference filter with a multiple-reflection filter. Curve 1: transmittance of interference filter alone; curve 2: spectral reflectance of a quarter-wave stack after fourfold reflection; curve 3: transmission of blocked filter. (After Cohendet and Saudreau.<sup>398</sup>)



**FIGURE 143** Measured transmission after four reflections from identical narrowband interference filters. (After Omega Optical Inc.<sup>239</sup>)



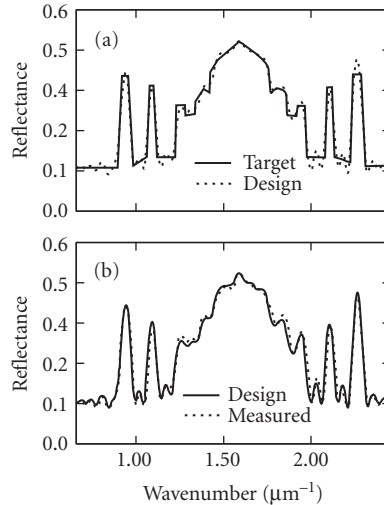
**FIGURE 144** Measured spectral characteristics of broad- and narrowband multiple-reflection filters for the infrared and ultraviolet spectral regions. (a) Eight reflections (solid curves) from identical quarter-wave stacks (dotted); (b) six reflections (solid) from each of two quarter-wave stacks (dotted, dashed) tuned to different wavelengths (after Valejev<sup>579</sup>); and (c) commercial multiple-reflection interference filter (Schott & Gen.<sup>580</sup>).

transmitted by radiation of different, closely spaced wavelengths with a very low cross-talk and small insertion loss.<sup>514</sup>

Additional information on reflection coatings and filters will be found in the reviews by Hass et al. and by Lynch.<sup>581,582</sup>

## 7.17 SPECIAL PURPOSE COATINGS

Space considerations limit the detailed description of coatings and filters for specific applications. Absorbing multilayer coatings on glass for enhancing the visual appearance, thermal and illumination control, and as “one-way-mirrors” find applications in architecture and in the automotive



**FIGURE 145** Calculated and experimentally measured reflectance of a filter that approximates the silhouette of the Taj Mahal. (After Sullivan and Dobrowolski.<sup>583</sup>)

industry. They are also used in solar energy conversion and have been proposed for radiative cooling. Thin-film coatings are used in optical recording media and in optical multiplexers/demultiplexers. Bistable Fabry-Perot structures are proposed for use as light switches in optical computers. Special filters and coatings are used in colorimetry, radiometry, detectors, and in high contrast display devices. Consumer-oriented products include various kinds of decorative coatings, as well as coatings for the protection of documents and products from counterfeiting. There is no doubt that in the future even more applications will appear for optical multilayer coatings. Some of these will require very complex spectral characteristics. At the time of writing of the second edition of this *Handbook*, methods for the design and manufacture of such coatings have just been demonstrated (Fig. 145). Now much more complicated correction and gain flattening filters (Fig. 115a) are important components for the telecommunications industry and they are routinely produced by many companies and laboratories.

The author would like to acknowledge the help and encouragement of his colleagues, Brian T. Sullivan, Li Li, Claude Montcalm, Pierre Verly, Daniel Poitras, Jeffrey Wong, and Allan Waldorf.

## 7.18 REFERENCES

1. J. A. Dobrowolski, "Coatings and Filters," in *Handbook of Optics* (eds. W. G. Driscoll and W. Vaughan), McGraw-Hill, New York, 1978, pp. 8.1–8.124.
2. H. A. Macleod, *Thin Film Optical Filters*, Institute of Physics Publishing, Bristol, 2001.
3. J. D. Rancourt, *Optical Thin Films Users' Handbook*, Macmillan, New York, 1987.
4. P. Baumeister, *Optical Coating Technology*, SPIE—The International Society for Optical Engineering, Bellingham, Washington, 2004.
5. L. B. Tuckerman, "On the Intensity of the Light Reflected from or Transmitted through a Pile of Plates," *Journal of the Optical Society of America* **37**:818–825 (1947).
6. A. M. Dioffo, "Treatment of General Case of  $n$  Dielectric Films with Different Optical Properties," *Revue d'Optique, Theorique et Instrumentale* **47**:117–129 (1968).

7. A. Dresler, "Über eine neuartige Filterkombination zur genauen Angleichung der spektralen Empfindlichkeit von Photozellen an die Augenempfindlichkeitskurve," *Das Licht* 3:41–43 (1933).
8. M. R. Nagel, "A Mosaic Filter Daylight Source for Aerophotographic Sensitometry in the Visible and Infrared Region," *Journal of the Optical Society of America* 44:621–624 (1954).
9. J. A. Dobrowolski, F. C. Ho, A. Belkind, and V. A. Koss, "Merit Functions for More Effective Thin Film Calculations," *Applied Optics* 28:2824–2831 (1989).
10. Z. Knittl, *Optics of Thin Films*, Wiley & Sons, London, 1976.
11. S. A. Furman and A. V. Tikhonravov, *Optics of Multilayer Systems*, Editions Frontieres, Gif-sur-Yvette, 1992.
12. P. H. Berning, "Theory and Calculations of Optical Thin Films," in *Physics of Thin Films* 1, (ed. G. Hass), Academic Press, New York, 1963, pp. 69–121.
13. A. Thelen, *Design of Optical Interference Coatings*, McGraw-Hill Book Company, New York, 1988.
14. P. G. Kard, *Analysis and Synthesis of Multilayer Interference Coatings*, (in Russian) Valrus, Tallin, 1971, pp. 1–236.
15. E. Delano and R. J. Pegis, "Methods of Synthesis for Dielectric Multilayer Filters," in *Progress in Optics* 7, (ed. E. Wolf), North-Holland Publishing Company, Amsterdam, 1969, pp. 68–137.
16. J. A. Dobrowolski and R. A. Kemp, "Refinement of Optical Multilayer Systems with Different Optimization Procedures," *Applied Optics* 29:2876–2893 (1990).
17. L. Li and J. A. Dobrowolski, "Computation Speeds of Different Optical Thin Film Synthesis Methods," *Applied Optics* 31:3790–3799 (1992).
18. H. A. Macleod, "Thin-Film Optical Coatings," in *Applied Optics and Optical Engineering* 10, (eds. R. Kingslake, R. R. Shannon, and J. C. Wyant), Academic Press, 1987, pp. 1–69.
19. M. Born and E. Wolf, *Principles of Optics*, Pergamon Press, New York, 1970.
20. A. Herpin, "Calculation of the Reflecting Power of Any Stratified System," *Comptes Rendus* 225:182–183 (1947).
21. W. Weinstein, "Computations in Thin Film Optics.," in *Vacuum* IV, E. T., Heron & Co. Ltd., London, 1954, pp. 3–19.
22. S. H. C. Piotrowski-McCall, J. A. Dobrowolski, and G. G. Shepherd, "Phase Shifting Thin Film Multilayers for Michelson Interferometers," *Applied Optics* 28:2854–2859 (1989).
23. J. A. Dobrowolski and D. Lowe, "Optical Thin Film Synthesis Program Based on the Use of Fourier Transforms," *Applied Optics* 17:3039–3050 (1978).
24. P. Baumeister, "The Transmission and Degree of Polarization of Quarter-Wave Stacks at Non-normal Incidence," *Optica Acta* 8:105–119 (1961).
25. V. R. Costich, "Reduction of Polarization Effects in Interference Coatings," *Applied Optics* 9:866–870 (1970).
26. K. Rabinovitch and A. Pagis, "Polarization Effects in Multilayer dielectric Thin Films," *Optica Acta* 21:963–980 (1974).
27. Z. Knittl, "Control of Polarization Effects by Internal Antireflection," *Applied Optics* 20:105–110 (1981).
28. Liberty Mirror—a Division of Libbey-Owens Ford Glass Co., "Coatings," 851 Third Avenue, Brackensridge, PA 15014, USA, 1966.
29. O. Arnon and P. Baumeister, "Electric Field Distribution and the Reduction of Laser Damage in the Multilayers," *Applied Optics* 19:1853–1855 (1980).
30. J. L. Vossen and W. Kern, *Thin Film Processes*, Academic Press, New York, 1978.
31. J. L. Vossen and W. Kern, *Thin Film Processes II*, Academic Press, Boston, 1991.
32. M. R. Jacobson (ed.), *Selected Papers on Deposition of Optical Coatings*, SPIE Milestone Series vol. MS 63, SPIE Optical Engineering Press, Bellingham, Washington, 1990.
33. J. M. Bennett, E. Pelletier, G. Albrand, J. P. Borgogno, B. Lazarides, C. K. Carniglia, T. H. Allen, T. Tuttle-Hart, K. H. Guenther, and A. Saxer, "Comparison of the Properties of Titanium Dioxide Films Prepared by Various Techniques," *Applied Optics* 28:3303–3317 (1989).
34. V. R. Costich, "Multilayer Dielectric Coatings," in *Handbook of Laser Science and Technology. Optical Materials: Part 3 V*, (ed. M. J. Weber), CRC Press, Inc., Boca Raton, Florida, 1987, pp. 389–430.
35. P. J. Martin, H. A. Maclean, R. P. Netterfield, C. G. Pacey, and W. G. Sainty, "Ion-Assisted Deposition of Thin Films," *Applied Optics* 22:178–184 (1983).



36. J. K. Hirvonen, "Ion Beam Assisted Thin Film Deposition," *Material Science Reports* **6**:215–274 (1991).
37. F. A. Smidt, "Ion-Beam-Assisted Deposition Provides Control over Thin Film Properties," NRL Publication 215-4670, issued May 1992, 1992.
38. H. Pulker, J. Edlinger, and M. Buehler, "Ion Plating Optical Films," in *Proceedings, 6th International Conference on Ion and Plasma Assisted Techniques*, CEP Consultants, Brighton, England, 1987, pp. 371–381.
39. K. H. Guenther, B. Loo, D. Burns, J. Edgell, D. Windham, and K. -H. Muller, "Microstructure Analysis of Thin Films Deposited by Reactive Evaporation and by Reactive Ion Plating," *Journal of Vacuum Science and Technology* **A7**:1435–1445 (1989).
40. A. J. Waldorf, J. A. Dobrowolski, B. T. Sullivan, and L. M. Plante, "Optical Coatings by Reactive Ion Plating," *Applied Optics* **32**:5583–5593 (1993).
41. A. Zöller, B. Beisswenger, R. Götzelmann, and K. Matl, "Plasma Ion-Assisted Deposition: A Novel Technique for the Production of Optical Coatings," *Proc. SPIE* **2253**:394 (1994).
42. A. Zöller, R. Götzelmann, K. Matl, and D. Cushing, "Temperature-Stable Bandpass Filters Deposited with Plasma Ion-Assisted Deposition," *Applied Optics* **35**:5609–5612 (1996).
43. U. Schulz, U. B. Schallenberg, and N. Kaiser, "Antireflection Coating Design for Plastic Optics," *Applied Optics* **41**:3107–3110 (2002).
44. W. D. Westwood, *Sputter Deposition 2*, American Vacuum Society, 2003.
45. L. Martinu and D. Poitras, "Plasma Deposition of Optical Films and Coatings: A Review," *Journal Vacuum Science Technology A* **18**:2619–2645 (2000).
46. S. Sneek, "Atomic Layer Deposition in Mass Production of Optical Coatings," in *Proceedings, 51 Annual Technical Conference, Society of Vacuum Coaters*, Chicago, IL, April 19–24, 2008, pp. 413–416.
47. B. T. Sullivan and J. A. Dobrowolski, "Deposition Error Compensation for Optical Multilayer Coatings: I. Theoretical Description," *Applied Optics* **31**:3821–3835 (1992).
48. D. Poitras, J. A. Dobrowolski, T. Cassidy, and S. Moisa, "Ion-Beam Etching for the Precise Manufacture of Optical Coatings," *Applied Optics* **42**:4037–4044 (2003).
49. P. A. Temple, "Thin-Film Absorptance Measurements Using Laser Calorimetry," in *Handbook of Optical Constants of Solids* (eds. E. D. Palik), Academic Press, Orlando, 1985, pp. 135–153.
50. D. Z. Anderson, J. C. Friesch, and C. S. Masser, "Mirror Reflectometer Based on Optical Cavity Decay Time," *Applied Optics* **23**:1238–1245 (1984).
51. C. Amra, P. Roche, and E. Pelletier, "Interface Roughness Cross-Correlation Laws Deduced from Scattering Diagram Measurements on Optical Multilayers: Effect of the Material Grain Size," *Journal of the Optical Society of America B* **4**:1087–1093 (1987).
52. J. M. Bennett and L. Mattsson, *Introduction to Surface Roughness and Scattering*, Optical Society of America, Washington, DC, 1989.
53. J. M. Bennett, "Recent Developments in Surface Roughness Characterization," *Measurement Science Technology* **3**:1119–1127 (1992).
54. A. Duparré, "Scattering from Surfaces and Thin Films," in *Encyclopedia of Modern Optics* **4**, (eds. R. D. Guenther, D. G. Steel and L. Bayvel), Elsevier Academic Press, Amsterdam, 2004, pp. 314–321.
55. G. Hass and W. R. Hunter, "Laboratory Experiments to Study Surface Contamination and Degradation of Optical Coatings and Materials in Simulated Space Environments," *Applied Optics* **9**:2101–2110 (1970).
56. W. R. Hunter, "Optical Contamination: Its Prevention in the XUV Spectrographs Flown by the U. S. Naval Research Laboratory in the Apollo Telescope Mount," *Applied Optics* **16**:909–916 (1977).
57. L. Ward, *The Optical Constants of Bulk Materials and Films*, Adam Hilger, Bristol, 1988.
58. E. D. Palik, *Handbook of Optical Constants of Solids*, Academic Press Inc., Orlando, 1985.
59. E. D. Palik, *Handbook of Optical Constants of Solids II*, Academic Press Inc., Boston, 1991.
60. D. P. Arndt, R. M. A. Azzam, J. M. Bennett, J. P. Borgogno, C. K. Carniglia, W. E. Case, J. A. Dobrowolski, "Multiple Determination of the Optical Constants of Thin-Film Coating Materials," *Applied Optics* **23**:3571–3596 (1984).
61. Boulder Symposium, "Laser-Induced Damage in Optical Materials: Collected Papers, 1969–1998 (CD-ROM)," in *Proceedings, Boulder Laser Damage Symposium*, SPIE, 1999.

62. D. Ristau, "Laser Damage in Thin Film Coatings," in *Encyclopedia of Modern Optics* 3, (eds. R. D. Guenther, D. G. Steel, and L. Bayvel), Elsevier Academic Press, Amsterdam, 2004, pp. 339–349.
63. S. P. Baker and W. D. Nix, "Mechanical Properties of Thin Films on Substrates," *Proceedings of the Society of Photo-Optical Instrumentation Engineers* 1323:263–276 (1990).
64. J. E. Klemberg-Sapieha, J. Oberste-Berghaus, L. Martinu, R. Blacker, I. Stevenson, G. Sadkhin, D. Morton, et al. "Mechanical Characteristics of Optical Coatings Prepared by Various Techniques: A Comparative Study," *Applied Optics* 43:2670–2679 (2004).
65. A. W. Czanderna, *Methods of Surface Analysis* 1, Elsevier Scientific Publishing Company, Amsterdam, 1975.
66. J. Bartella, P. H. Berning, B. Bovard, C. K. Carniglia, E. Casparis, V. R. Costich, J. A. Dobrowolski, et al., "Multiple Analysis of an Unknown Optical Multilayer Coating," *Applied Optics* 24:2625–2646 (1985).
67. A. Mussett and A. Thelen, "Multilayer Antireflection Coatings," in *Progress in Optics* 8, (ed. E. Wolf), 1970, pp. 203–237.
68. W. A. Faber, P. W. Kruse and W. D. Saur, "Improvement in Infrared Detector Performance through Use of Antireflection Film," *Journal of the Optical Society of America* 51:115 (1961).
69. I. V. Grebenschchikov, *Prosvetlenie Optiki (Antireflection Coating of Optical Surfaces)* State Publishers of Technical and Theoretical Literature, Moscow-Leningrad, (1946).
70. T. Sawaki, "Studies on Anti-Reflection Films," Research Report No. 315, Osaka Industrial Research Institute, issued September, 1960.
71. J. T. Cox and G. Hass, "Antireflection Coatings for Optical and Infrared Optical Materials," in *Physics of Thin Films* 2, (eds. G. Hass and R. E. Thun), Academic Press, New York, 1964, pp. 239–304.
72. J. G. Wilder, "Porous Silica AR Coating for Use at 248nm or 266nm," *Applied Optics* 23:1448–1449 (1984).
73. F. O'Neill, I. N. Ross, D. Evans, J. U. D. Langridge, B. S. Bilan and S. Bond, "Colloidal Silica Coatings for KrF and Nd: Glass Laser Applications," *Applied Optics* 26:828–832 (1987).
74. I. M. Thomas, "Porous Fluoride Antireflective Coatings," *Applied Optics* 27:3356–3358 (1988).
75. I. M. Thomas, "Method for the Preparation of Porous Silica Antireflection Coatings Varying in Refractive Index from 1.22 to 1.44," *Applied Optics* 31:6145–6149 (1992).
76. Balzers Aktiengesellschaft fur Hochvakuumtechnik und Dünne Schichten, "Kurvenblätter und ihre Bezeichnungen," FL-9496 Balzers, 1962.
77. M. E. Motamedi, W. H. Southwell, and W. J. Gunning, "Antireflection Surfaces in Silicon Using Binary Optics Technology," *Applied Optics* 31:4371–4376 (1993).
78. P. Baumeister, "Antireflection coatings with Chebyshev or Butterworth Response: Design," *Applied Optics* 25:4568–4570 (1986).
79. J. Krepelka, "Maximally Flat Antireflection Coatings," *Jemna Mechanika a Optika* 53–56 (1992).
80. P. Kard, "Optical Theory of Anti-Reflection Coatings," *Loodus ja matemaatika* I 67–85 (1959).
81. A. Thetford, "A Method of Designing Three-Layer Anti-Reflection Coatings," *Optica Acta* 16:37–43 (1969).
82. J. H. Apfel and R. M. Gelber, "Filter with Neutral Transmitting Multilayer Coating Having Asymmetric Reflectance," U. S. patent 3649359, issued 25 July, 1972.
83. A. F. Turner, Bausch & Lomb, Private communication, 1970.
84. Optical Coating Laboratory Inc., "Multilayer Antireflection Coatings," 2789 North Point Parkway, Santa Rosa, CA 9 5407-7397, USA, 1965.
85. Thin Film Lab, Product information, 501B Basin Rd., West Hurley, NY 12491, USA, 1992.
86. TechOptics Ltd., "Laser Optics and Instrumentation," Second Avenue, Onchan, Isle of Man, British Isles, 1992.
87. Reynard Corporation, "Optical Components; Thin Film Coatings; Optical Instruments," 1020 Calle Sombra, San Clemente, CA 92673-6227, USA, 1992.
88. Spindler & Hoyer Inc., "Precision Optics," 459 Fortune Boulevard, Milford, MA 01757-1757, USA, 1990.
89. S. A. Furman, "Broad-Band Antireflection Coatings," *Soviet Journal of Optical Technology* 33:559–564 (1966).
90. E. G. Stolov, "New Constructions of Interference Optical Antireflection Coatings," *Soviet Journal of Optical Technology* 58:175–178 (1991).

91. R. R. Willey, "Broadband Antireflection Coating Design Performance Estimation," in *Proceedings, 34th Annual Technical Conference of the Society of Vacuum Coaters*, Society of Vacuum Coaters, March 17–22, 1991, Philadelphia, pp. 205–209.
92. A. V. Tikhonravov and J. A. Dobrowolski, "A New, Quasi-Optimal Synthesis Method for Antireflection Coatings," *Applied Optics* **32**:4265–4275 (1993).
93. P. T. Scharf, "Transmission Colour in Camera Lenses," *Journal of the SMPTE* **59**:191–194 (1952).
94. A. E. Murray, "Effect of Antireflection Films on Colour in Optical Instruments," *Journal of the Optical Society of America* **46**:790–796 (1956).
95. H. Kubota, "Interference Color," in *Progress in Optics* 1, Elsevier, Amsterdam, 1961, pp. 211–251.
96. V. V. Obodovskiy, V. N. Rozhdestvenskiy, and I. Chernyy, "Amber Coating and Colour Photographic Objectives," *Soviet Journal of Optical Technology* **34**:324–330 (1967).
97. J. A. Dobrowolski and W. Mandler, "Color Correcting Coatings for Photographic Objectives," *Applied Optics* **18**:1879–1880 (1979).
98. T. I. Oh, "Broadband AR Coatings on Germanium Substrates Using Ion-Assisted Deposition," *Applied Optics* **27**:4255–4259 (1988).
99. S. P. Fisher, J. F. Leonard, I. T. Muirhead, G. Buller, and P. Meredith, "The Fabrication of Optical Devices by Molecular Beam Deposition Technology," in *Proceedings, Optical Interference Coatings, Technical Digest Series*, Tucson, AZ, Optical Society of America, Washington, D.C., 1992, pp. 131–133.
100. R. Jacobsson, "Light Reflection from Films of Continuously Varying Refractive Index," in *Progress in Optics* 5, (eds. E. Wolf), North-Holland, Amsterdam, 1966, pp. 247–286.
101. E. Spiller, I. Haller, R. Feder, J. E. E. Baglin, and W. N. Hammer, "Graded-Index AR Surfaces Produced by Ion Implantation on Plastic Materials," *Applied Optics* **19**:3022–3026 (1980).
102. W. H. Southwell, "Gradient-Index Antireflection Coatings," *Optics Letters* **8**:584–586 (1983).
103. B. Sheldon, J. S. Haggerty, and A. G. Emslie, "Exact Computation of the Reflectance of a Surface Layer of Arbitrary Refractive Index Profile and an Approximate Solution of the Inverse Problem," *Journal of the Optical Society of America* **72**:1049–1055 (1982).
104. M. J. Minot, "The Angular Reflectance of Single-Layer Gradient Refractive-Index Films," *Journal of the Optical Society of America* **67**:046–1050 (1977).
105. L. M. Cook and K. -H. Mader, "Integral Antireflective Surfaces on Optical Glass," *Optical Engineering* **21**:SR-008–SR-012 (1982).
106. W. H. Lowdermilk, "Graded-Index Surfaces and Films," in *Handbook of Laser Science and Technology. Optical Materials: Part 3 V*, (ed. M. J. Weber), CRC Press, Inc., Boca Raton, Florida, 1987, pp. 431–458.
107. H. Anders and R. Eichinger, "Die Optische Wirkung und Praktische Bedeutung Inhomogener Schichten," *Applied Optics* **4**:899–905 (1965).
108. G. Lessman, "Optical Properties of Inhomogeneous Thin Films of Varying Modes of Gradation," *Journal of the Optical Society of America* **56**:554 (1966).
109. R. Bertram, M. F. Ouellette, and P. Y. Tse, "Inhomogeneous optical Coatings: An Experimental Study of a New Approach," *Applied Optics* **28**:2935–2939 (1989).
110. R. Jacobsson, "Calculation and Deposition of Inhomogeneous Thin Films," *Journal of the Optical Society of America* **56**:1435 (1966).
111. R. J. Scheurman, Perkin-Elmer Corporation, Private communication, 1968.
112. A. Y. Kuznetsov and A. F. Perveyev, "Multifilm Anti-Reflection Coatings for Materials with High Refractive Index," *Soviet Journal of Optical Technology* **34**:593–595 (1967).
113. P. H. Berning, "Use of Equivalent Films in the Design of Infrared Multilayer Antireflection Coatings," *Journal of the Optical Society of America* **52**:431–436 (1962).
114. J. A. Dobrowolski and F. C. Ho, "High Performance Step-Down AR Coatings for High Refractive-Index IR Materials," *Applied Optics* **21**:288–292 (1982).
115. L. I. Epstein, "The Design of Optical Filters," *Journal of the Optical Society of America* **42**:806–810 (1952).
116. W. H. Southwell, "Coating Design Using Very Thin High- and Low-Index Layers," *Applied Optics* **24**:457–460 (1985).
117. H. M. Moulton, "Method of Forming a Reflection Reducing Coating," U. S. patent 2536764, issued 2 January, 1951.
118. S. M. Thomsen, "Skeletonizing Glass," U. S. patent 2490662, issued 6 December, 1949.

119. M. J. Minot, "Single Layer, Gradient Refractive Index Antireflection Films-Effective 0.35 to 2.5  $\mu\text{m}$ ," *Journal of the Optical Society of America* **66**:515–519 (1976).
120. Y. Asahara and T. Izumitani, "The Properties of Gradient Index Antireflection Layer on the Phase Separable Glass," *Journal of Non-Crystalline Solids* **42**:269–280 (1980).
121. W. H. Lowdermilk and D. Milam, "Graded-Index Antireflection Surfaces for High-Power Laser Applications," *Applied Physics Letters* **36**:891–893 (1980).
122. S. Fujikawa, Y. Oguri, and E. Arai, "Antireflection Surface Modification of Plastic CR-39 by Means of  $^{16}\text{O}$ - and  $^{35}\text{Cl}$ -ion Bombardment," *Optik (Stuttgart)* **84**:1–5 (1990).
123. B. E. Yoldas and D. P. Partlow, "Wide Spectrum Antireflective Coating for Fused Silica and Other Glasses," *Applied Optics* **23**:1418–1424 (1984).
124. K. N. Maffitt, H. U. Bruechner, and D. R. Lowrey, "Polymeric Optical Element Having Antireflecting Surface," U. S. patent 4114983, issued 19 September, 1978.
125. S. J. Wilson and M. C. Hutley, "The Optical Properties of 'Moth Eye' Antireflection Surfaces," *Optica Acta* **29**:993–1009 (1982).
126. S. P. Mukherjee, "Gel-Derived Single-Layer Antireflection Films with a Refractive Index Gradient," *Thin Solid Films* **81**:L89–L90 (1981).
127. S. P. Mukherjee and W. H. Lowdermilk, "Gel-Derived Single Layer Antireflection Films," *Journal of Non-Crystalline Solids* **48**:177–184 (1982).
128. P. B. Clapham and M. C. Hutley, "Reduction of Lens Reflexion by the 'Moth Eye' Principle," *Nature* **244**:281–282 (1973).
129. W. H. Southwell, "Pyramid-Array Surface-Relief Structures Producing Antireflection Index Matching on Optical Surfaces," *Journal of the Optical Society of America* **A8**:549–553 (1991).
130. D. H. Raguin and G. M. Morris, "Antireflection Structured Surfaces for the Infrared Spectral Region," *Applied Optics* **32**:1154–1167 (1993).
131. S. R. Kennedy and M. J. Brett, "Porous Broadband Antireflection Coating by Glancing Angle Deposition," *Applied Optics* **42**:4573–4579 (2003).
132. V. D. Vvedenskii, A. A. Metel'nikov and S. A. Furman, "Achromatic Antireflection Coatings for Materials with Refractive Indices of 1.46–1.8," *Soviet Journal of Optical Technology* **47**:157–159 (1980).
133. J. A. Dobrowolski and B. T. Sullivan, "Universal Antireflection Coatings for the Visible Spectral Region," *Applied Optics* **35**:4993–4997 (1996).
134. L. Yeuh Yeong, "Universal Broad-Band Antireflection Coating Designs for Substrates in the Visible Spectral Region," *Japanese Journal of Applied Physics, Part 1 Regular Papers, Short Notes & Review Papers* **41**:6409–6410 (2002).
135. V. N. Smiley, "Conditions for Zero Reflectance of Thin Dielectric Films on Laser Materials," *Journal of the Optical Society of America* **58**:1469–1475 (1968).
136. E. A. Lupashko and I. N. Shkyarevskii, "Multilayer Dielectric Antireflection Coatings," *Optics and Spectroscopy (USSR)* **16**:279–281 (1964).
137. K. C. Park, "The Extreme Values of the Reflectivity and the Conditions for Zero Reflection from Thin Dielectric Films on Metal," *Applied Optics* **3**:877–881 (1964).
138. L. F. Drummeter and G. Hass, "Solar Absorptance and Thermal Emittance of Evaporated Coatings," in *Physics of Thin Films 2*, (eds. G. Hass and R. E. Thun), Academic Press, New York, 1964, pp. 305–361.
139. R. N. Schmidt and K. C. Park, "High-Temperature Space-Stable Selective Solar Absorber Coatings," *Applied Optics* **4**:917–925 (1965).
140. S. Katsube, Y. Katsube, K. Mitome, and S. Furuta, "Non-Metallic Absorbing Films and the Anti-Reflection Coating," *Japanese Journal of Applied Physics* **37**:225–230 (1968).
141. H. Anders, "Inhomogeneous, Absorbing Layers for Sunglasses," *Vakuum-Technik* **15**:123–126 (1966).
142. V. V. Veremey and T. A. Gorbunova, "Achromatic Coating of Glasses Covered by Conducting Films," *Soviet Journal of Optical Technology* **35**:519–521 (1968).
143. T. Turbadar, "Complete Absorption of Plane Polarized Light by Thin Metallic Films," *Optica Acta* **11**:207–210 (1964).
144. T. Turbadar, "Equi-Reflectance Contours of Double-Layer Anti-Reflection Coatings," *Optica Acta* **11**:159–205 (1964).

145. H. Pohlack, "Zum Problem der Reflexionsminderung Optischer Gläser bei nichtsenkrechtem Lichteinfall," in *Jenaer Jahrbuch 1952* (ed. P. Görlich), Fischer, Jena, 1952, pp. 103–118.
146. J. A. Dobrowolski and S. H. C. Piotrowski, "Refractive Index as a Variable in the Numerical Design of Optical Thin Film Systems," *Applied Optics* **21**:1502–1510 (1982).
147. J. A. Dobrowolski, "The Impact of Computers on the Design and Manufacture of Optical Multilayer Coatings During the Past 50 Years," in *Proceedings, 50th Annual Technical Conference*, Society of Vacuum Coaters, Louisville, KY, 2007, pp. 289–301.
148. J. A. Dobrowolski, Y. Guo, T. Tiwald, P. Ma, and D. Poitras, "Toward Perfect Antireflection Coatings. 3. Experimental Results Obtained with the Use of Reststrahlen Materials," *Applied Optics* **45**:1555–1562 (2006).
149. P. Ma, J. A. Dobrowolski, D. Poitras, T. Cassidy, and F. Lin, "Toward the Manufacture of 'Perfect' Antireflection Coatings," in *Proceedings, Proceedings of the 45 Annual Technical Conference*, Society of Vacuum Coaters, Lake Buena Vista, Florida, 2002, pp. 216–218.
150. U. Schulz and N. Kaiser, "Designing Optical Coatings by Using Low-Index Equivalent Layers and Low-Index Effective Media," in *Proceedings, Annual Technical Conference*, Society of Vacuum Coaters, Santa Clara, CA, 2009.
151. J. A. Dobrowolski, D. Poitras, M. Penghui, V. Himanshu, and M. Acree, "Toward Perfect Antireflection Coatings: Numerical Investigation," *Applied Optics* **41**:3075–3083 (2002).
152. D. Poitras and J. A. Dobrowolski, "Toward Perfect Antireflection Coatings. 2. Theory," *Applied Optics* **43**:1286–1295 (2004).
153. J. C. Monga, "Anti-Reflection Coatings for Grazing Incidence Angles," *Journal of Modern Optics* **36**:381–387 (1989).
154. J. C. Monga, "Double-Layer Broadband Antireflection Coatings for Grazing Incidence Angles," *Applied Optics* **31**:546–553 (1992).
155. S. Bruynooghe, S. Spinzig, M. Fliedner, and G. H. Hsu, "Characterization of the Optical Properties of Hydrophobic Coatings and Realization of High Performance AR-Coatings with Dust- and Water-Repellent Properties," *Proc. SPIE* **7101**:71010Q (2008).
156. P. Giacomo, "Les couches Réfléchissantes Multidiélectriques Appliquées à l'interféromètre de Fabry-Perot etude Théorique et Expérimentale Des Couches Réelles," *Revue d'Optique, Théorique et Instrumentale* **35**:318–354 (1956).
157. J. Arndt and P. Baumeister, "Reflectance and Phase Envelopes of an Iterated Multilayer," *Journal of the Optical Society of America* **56**:1760–1762 (1966).
158. J. S. Seeley, "Resolving Power of Multilayer Filters," *Journal of the Optical Society of America* **54**:342–346 (1964).
159. H. Böhme, "Dielektrische Mehrfachschichtsysteme ohne Dispersion des Phasensprungs," *Optik* **69**:1–7 (1984).
160. P. Kard, E. Nesmelov, and G. Konyukhov, "Theory of a Quarterwave Reflecting Filters," *Eesti NSV Tead. Akad. Toim., Fuus. - Mat.* **17**:314–323 (1968).
161. A. P. Ovcharenko and E. A. Lupashko, "Multilayer Dielectric Coatings of Unequal Thickness," *Optics and Spectroscopy (USSR)* **55**:316–318 (1983).
162. V. A. Smirnova and G. D. Pridatko, "Two-Component Interference Coatings. Optical Properties and Applications," *Optics and Spectroscopy (USSR)* **55**:442–445 (1983).
163. M. Zukic and D. G. Toerr, "Multiple Reflectors as Narrow-Band and Broadband Vacuum Ultraviolet Filters," *Applied Optics* **31**:1588–1596 (1992).
164. J. Shao and J. A. Dobrowolski, "Multilayer Interference Filters for the Far-Infrared and Submillimeter Regions," *Applied Optics* **32**:2361–2370 (1993).
165. T. W. Barbee, "Multilayers for X-Ray Optics," *Optical Engineering* **25**, 898–915 (1986).
166. E. Spiller, *Soft X-Ray Optics* SPIE Optical Engineering Press, 1994.
167. B. L. Henke, "X-Ray Interaction with Matter," [http://henke.lbl.gov/optical\\_constants/](http://henke.lbl.gov/optical_constants/) (2008).
168. A. Attwood, *Soft X-Rays and Extreme Ultraviolet Radiation*, Cambridge University Press, New York, 1999.
169. A. V. Vinogradov and B. Y. Zeldovich, "X-Ray and Far UV Multilayer Mirrors: Principles and Possibilities," *Applied Optics* **16**:89–93 (1977).

170. J. H. Apfel, "Multilayer Interference Coatings for the Ultraviolet," *Journal of the Optical Society of America* **59**:553 (1966).
171. K. Hefft, R. Kern, G. Nöldeke, and A. Steudel, "Über Fabry-Perot-Verspiegelungen aus dielektrischen Vielfachschichten für den Spektralbereich von 2350 bis 20000 Å," *Zeitschrift für Physik* **175**:391–404 (1963).
172. V. R. Costich, Spectra-Physics, Private communication, 1968.
173. A. F. Turner and P. W. Baumeister, "Multilayer Mirrors with High Reflectance over an Extended Spectral Region," *Applied Optics* **5**:69–76 (1966).
174. O. S. Heavens, "All-dielectric High-Reflecting Layers," *Journal of the Optical Society of America* **44**:371–373 (1954).
175. D. H. Rank and H. E. Bennett, "Problem of Phase Variation with Wavelength in Dielectric Films. Extension of Interferometric Standards into the Infrared," *Journal of the Optical Society of America* **45**:69–73 (1955).
176. P. Giacomo, "Propriétés Chromatiques Des Couches Réfléchissantes Multi-diélectriques," *Journal de Physique et le Radium* **19**:307–311 (1958).
177. G. Bouwhuis, "A Dispersion Phenomenon Observable on Dielectric Multilayer Mirrors," *Philips Research Reports* **17**:130–132 (1962).
178. J. V. Ramsay and P. E. Ciddor, "Apparent Shape of Broad Band, Multilayer Reflecting Surfaces," *Applied Optics* **6**:2003–2004 (1967).
179. G. Koppelman, "Zur Theorie der Wechselschichten aus schwachabsorbierenden Substanzen und ihre Verwendung als Interferometerspiegel," *Annalen der Physik* **7**:387–396 (1960).
180. D. J. Hemingway and P. H. Lissberger, "Properties of Weakly Absorbing Multilayer Systems in Terms of the Concept of Potential Transmittance," *Optica Acta* **20**:85–96 (1973).
181. G. Honcia and K. Krebs, "Highly Reflecting Substances for Dielectric Mirror Systems," *Zeitschrift für Physik* **165**:202–212 (1961).
182. K. H. Behrndt and D. W. Doughty, "High-Reflectance Multilayer Dielectric Mirrors," *Journal of Vacuum Science and Technology* **4**:199–202 (1967).
183. D. Gloge, E. L. Chinnock, and H. E. Earl, "Scattering from Dielectric Mirrors," *Bell System Technical Journal* **48**:511–526 (1969).
184. R. Blazey, "Light Scattering by Laser Mirrors," *Applied Optics* **6**:831–836 (1967).
185. G. Rempe, R. J. Thompson, H. J. Kimble, and R. Lalezari, "Measurement of Ultralow Losses in an Optical Interferometer," *Optics Letters* **17**:363–365 (1993).
186. R. Lalezari, PMS Electro-Optics, 1855 South 57th Court, Boulder, CO80301, USA, Private communication, 1993.
187. G. M. Harry, H. Armandula, E. Black, D. R. M. Crooks, G. Cagnoli, J. Hough, P. Murray, et al., "Thermal Noise from Optical Coatings in Gravitational Wave Detectors," *Applied Optics* **45**:1569–1574 (2006).
188. B. Vidal and P. Vincent, "Metallic Multilayers for X-Rays Using Classical Thin-Film Theory," *Applied Optics* **23**:1794–1801 (1984).
189. D. G. Stearns, "X-Ray Scattering from Interfacial Roughness in Multilayer Structures," *Journal of Applied Physics* **71**:4286–4298 (1992).
190. D. G. Stearns, "The Scattering of X-Rays from Nonideal Multilayer Structures," *Journal of Applied Physics* **65**:491–506 (1989).
191. E. Spiller, "Multilayer Optics for X-Rays," in *Physics, Fabrication, and Applications of Multilayered Structures* (eds. P. D. a. C. Weisbuch), Plenum Publishing Corporation, 1988, pp. 271–309.
192. S. Braun, H. Mai, M. Moss, and R. Scholz, "Microstructure of Mo/Si Multilayers with Barrier Layers," *Proc. SPIE* **4782**:185–195 (2002).
193. L. Young, "Multilayer Interference Filters with Narrow Stop Bands," *Applied Optics* **6**:297–315 (1967).
194. Lord Rayleigh, "On the Remarkable Phenomenon of Crystalline Reflexion Described by Prof. Stokes," *Philosophical Magazine* **26**, **Fifth Series**, 256–265 (1888).
195. R. W. Wood, *Physical Optics* Macmillan, New York, 1940.
196. H. Schröder, "The Light Distribution Functions of Multiple-Layers and Their Applications," *Zeitschrift für Angewandte Physik* **2**:53–66 (1951).
197. J. Strong, "Iridescent KClO<sub>3</sub> Crystals and Infrared Reflection Filters," *Journal of the Optical Society of America* **51**:853–855 (1961).

198. T. J. Alfrey, E. F. Gurnee, and W. J. Schrenk, "Physical Optics of Iridescent Multilayered Plastic Films," *Polymer Engineering and Science* **9**:400–404 (1969).
199. T. J. Alfrey, "Multilayer Thermoplastic Sheets and Films," in *Proceedings, 19th Sagamore Army Materials Research Conference*, (eds. J. J. Burke and V. Weiss), Syracuse University Press, 1973, pp. 195–200.
200. O. S. Heavens, J. Ring, and S. D. Smith, "Interference Filters for the Infra-Red," *Spectrochimica Acta* **10**:179–194 (1957).
201. L. Edmonds, P. Baumeister, M. E. Krisl, and N. Boling, "Spectral Characteristics of a Narrowband Rejection Filter," *Applied Optics* **29**:3203–3204 (1990).
202. A. Badeen, M. Briere, P. Hook, C. Montcalm, R. Rinfret, J. Schneider, and B. T. Sullivan, "Advanced Coatings for Telecom and Spectroscopic Applications," *Proc. SPIE* **7101**:71010H1–H16 (2008).
203. K. D. Hendrix, C. A. Hulse, G. J. Ockenfuss, and R. B. Sarget, "Demonstration of Narrowband Notch and Multi-Notch Filters," *Proc. SPIE* **7067**:7067–7102 (2008).
204. M. Hercher, "Single-Mode Operation of a Q-Switched Ruby Laser," *Applied Physics Letters* **7**:39–41 (1965).
205. G. Magyar, "Simple Giant Pulse Ruby Laser of High Spectral Brightness," *Review of Scientific Instruments* **38**:517–519 (1967).
206. J. K. Watts, "Theory of Multiplate Resonant Reflectors," *Applied Optics* **7**:621–1623 (1968).
207. H. F. Mahlein and G. Schollmeier, "Analysis and Synthesis of Periodic Optical Resonant Reflectors," *Applied Optics* **8**:1197–1202 (1966).
208. Anon, "Quartz Etalon Outperforms Sapphire," *Microwaves* September 1969.
209. K. M. Yoo and R. R. Alfano, "Broad Bandwidth Mirror with Random Layer Thicknesses," *Applied Optics* **28**:2456–2458 (1989).
210. D. L. Perry, "Low-Loss Multilayer Dielectric Mirrors," *Applied Optics* **4**:987–991 (1965).
211. O. S. Heavens and H. M. Liddell, "Staggered Broad-Band Reflecting Multilayers," *Applied Optics* **5**:373–376 (1966).
212. Z. N. Elsner, "On the Calculation of Multilayer Interference Coatings with Given Spectral Characteristics," *Optics and Spectroscopy (USSR)* **17**:238–240 (1964).
213. F. A. Korolev, A. Y. Klementeva, T. F. Meshcheryakova, and I. A. Ramazina, "Wide-Band Reflectors with Multilayer Dielectric Coatings," *Optics and Spectroscopy (USSR)* **28**:416–419 (1970).
214. R. S. Sokolova, "Wide-Band Reflectors for Ultraviolet Radiation," *Soviet Journal of Optical Technology* **38**:295–297 (1971).
215. E. G. Stolov, "Constructions of Neutral Lightsplitters and Wide-Band Mirrors," *Soviet Journal of Optical Technology* **57**:632–634 (1990).
216. S. Penselin and A. Steudel, "Fabry-Perot-Interferometerspiegelungen aus dielektrischen Vielfachschechten," *Zeitschrift für Physik* **142**:21–41 (1955).
217. P. W. Baumeister and J. M. Stone, "Broad-Band Multilayer Film for Fabry-Perot Interferometers," *Journal of the Optical Society of America* **46**:228–229 (1956).
218. P. E. Ciddor, "Minimization of the Apparent Curvature of Multilayer Reflecting Surfaces," *Applied Optics* **7**:2328–2329 (1968).
219. A. F. Turner, "Design Principles for Interference Film Combinations," *Journal of the Optical Society of America* **44**:352 (1954).
220. K. V. Popov, J. A. Dobrowolski, A. V. Tikhonravov, and B. T. Sullivan, "Wide-Band High Reflection Multilayer Coatings at Oblique Angles of Incidence," *Applied Optics* **36**:2139–2151 (1997).
221. J. N. Winn, Y. Fink, S. Fan, and J. D. Joannopoulos, "Omnidirectional Reflection from a One-Dimensional Photonic Crystal," *Optics Letters* **23**:1573–1575 (1998).
222. Y. Fink, J. N. Winn, S. Fan, S. Chen, J. Michel, J. D. Joannopoulos, and E. L. Thomas, "A Dielectric Omnidirectional Reflector," *Science* **282**:1679–1682 (1998).
223. R. Gaughan, "New Coatings Break Reflectivity Barriers," *Photonics Spectra* **33**:29–30 (1999).
224. P. W. Baumeister and F. A. Jenkins, "Dispersion of the Phase Change for Dielectric Multilayers. Application to the Interference Filter," *Journal of the Optical Society of America* **47**:57–61 (1957).
225. P. E. Ciddor, "Phase-Dispersion in Interferometry. Interferometers with Solid Spacers and with Broadband-Reflecting Surfaces," *Optica Acta* **12**:177–183 (1965).
226. G. Tempea, V. Yakovlev, and F. Krausz, "Interference Coatings for Ultrafast Optics," in *Optical Interference Coatings* (eds. N. Kaiser and H. K. Pulker), Springer, Berlin, pp. 393–422, 2003.

227. M. Trubetskov, A. Tikhonravov, and V. Pervak, "Time-Domain Approach for Designing Dispersive Mirrors Based on the Needle Optimization Technique. Theory," *Optics Express* **16**:20637–20647 (2008).
228. N. Matuschek, F. X. Kärtner, and U. Keller, "Theory of Double-Chirped Mirrors," *IEEE Journal Selected Topics in Quantum Electronics* **4**:197–208 (1998).
229. V. Pervak, D. Grupe, M. Trubetskov, A. Tikhonravov, A. Apolonski, and F. Krausz, "1.5-Octave Chirped Dielectric Multilayers for Pulse Compression," *Proc. SPIE* **7101**:71016-1-7 (2008).
230. V. Pervak, I. Ahmad, J. Fulop, M. K. Trubetskov, and A. V. Tikhonravov, "Comparison of Dispersive Mirrors Based on the Time-Domain and Conventional Approaches, for Sub-5-fs Pulses," *Optics Express* **17**:2207–2217 (2009).
231. D. Yang, C. Lin, W. Chen, and G. Barbarossa, "Fiber Dispersion and Dispersion Slope Compensation in a 40-channel 10-Gb/s 3200-km Transmission Experiment Using Cascaded Single-Cavity Gire-Tournois Etalons," *IEEE Photonics Technology Letters* **16**:299–301 (2004).
232. Avanex Corp, "www.avanex.com," 2008.
233. V. Pervak, C. Teisset, A. Sugita, S. Naumov, F. Krausz, and A. Apolonski, "High-Dispersive Mirrors for Femtosecond Lasers," *Optics Express* **16**:10220–10230 (2008).
234. J. Kim, J. R. Birge, V. Sharma, J. G. Fujimoto, F. X. Kärtner, V. Scheuer, and G. Angelow, "Ultrabroadband Beam Splitter with Matched Group-Delay Dispersion," *Optics Letters* **30**:1569–1571 (2005).
235. E. Cojocaru, "Second and Third Order Dispersion of Broadband Thin-Film Antireflection Coatings for Ultrafast Lasers," *Optica Applicata* **34**:25–29 (2004).
236. J. A. Dobrowolski, "Optical Interference Filters for the Adjustment of Spectral Response and Spectral Power Distributions," *Applied Optics* **9**:1396–1402 (1970).
237. Optical Coating Laboratory, "Catalog," 2789 Northpoint Parkway, Santa Rosa, CA 95407-7397, USA, 1964.
238. A. Thelen, "Design of Optical Minus Filters," *Journal of the Optical Society of America* **61**:365–369 (1971).
239. Omega Optical Inc., "Bandpass filters," 3 Grove Street, P. O. Box 573, Brattleboro, VT 05302-0573, USA, 1992.
240. R. Jacobsson, "Inhomogeneous and Coevaporated Homogeneous Films for Optical Applications," in *Physics of Thin Films* 8, (eds. G. Hass, M. H. Francombe and R. W. Hoffman), Academic Press, New York, 1975, pp. 51–98.
241. J. A. Dobrowolski and P. G. Verly (eds.), *Inhomogeneous and Quasi-inhomogeneous Optical Coatings*, Proceedings of the Society of Photo-Optical Instrumentation Engineers vol. 2046, SPIE—The International Society for Optical Engineering, Bellingham, Washington, 1993.
242. W. J. Cunniff, R. L. Hall, F. J. Woodberry, W. H. Southwell, and N. S. Gluck, "Codeposition of Continuous Composition Rugate Filters," *Applied Optics* **28**:2945–2948 (1989).
243. P. G. Verly, National Research Council of Canada, Private communication, 1993.
244. Physical Optics Corp., "Holographic Filters Aid Spectroscopy," *Photonics Spectra* **26**:113–114 (1992).
245. Kaiser Optical Systems Inc., "Holographic Notch Filters," 371 Parkland Plaza, P. O. Box 983, Ann Arbor, MI 48106, USA, 1993.
246. S. N. Vlasov and V. I. Talanov, "Selection of Axial Modes in Open Resonators," *Radio Engineering and Electronic Physics* **10**:469–470 (1965).
247. N. G. Vahitov, "Open Resonators with Mirrors Having Variable Reflection Coefficients," *Radio Engineering and Electronic Physics* **10**:1439–1446 (1965).
248. G. Duplain, P. G. Verly, J. A. Dobrowolski, A. Waldorf, and S. Bussière, "Graded Reflectance Mirrors for Beam Quality Control in Laser Resonators," *Applied Optics* **32**:1145–1153 (1993).
249. A. Piegari, "Graded Optical Coatings for Laser Applications," *Proceedings of the Society of Photo-Optical Instrumentation Engineers* **2461**:558–565 (1995).
250. A. Piegari, A. Tirabassi, and G. Emiliani, "Thin Films for Special Laser Mirrors with Radially Variable Reflectance: Production Techniques and Laser Testing," *Proceedings of the Society of Photo-Optical Instrumentation Engineers* **1125**:68–73 (1989).
251. V. G. Vereshchagin and A. D. Zamkovets, "Polymer-Crystalline Multilayer Systems for the Far IR Spectral Region," *Zhurnal Prikladnoi Spektroskopii* **47**:132–135 (1987).
252. V. R. Costich, "Study to Demonstrate a New Process to Produce Infrared Filters," NASA Ames NAS2-12639, issued 1 March 1990.



253. D. L. Windt, S. Donguy, J. Seely, B. Kjornrattanawanich, E. M. Gullikson, L. Golub, and E. DeLuca, "EUV Multilayers for Solar Physics," *Proc. SPIE* **5168**:1–11 (2004).
254. B. L. Henke, "X-Ray Multilayer Results," <http://henke.lbl.gov/multilayer/survey.html> (2008).
255. S. Bajt, J. B. Alameda, T. W. Barbee, W. M. Clift, J. A. Folta, B. Kaufmann, and E. A. Spiller, "Improved Reflectance and Stability of Mo-Si Multilayers," *Optical Engineering* **41**:1797–1804 (2002).
256. F. Eriksson, N. Ghafoor, F. Schäfers, E. M. Gullikson, S. Aouadi, S. Rohde, L. Hultman, and J. Birch, "Atomic Scale Interface Engineering by Modulated Ion-Assisted Deposition Applied to Soft X-Ray Multilayer Optics," *Applied Optics* **47**:4196–4204 (2008).
257. E. M. Gullikson, F. Salmassi, A. L. Aquila, and F. Dollar, "Progress in Short Period Multilayer Coatings for Water Window Applications," in *Proceedings, The 8th International Conference on The Physics of X-Ray Multilayer Structures*, Sapporo, Japan, March 12–16, 2006, abstract S8 O4.
258. E. Spiller and L. Golub, "Fabrication and Testing of Large Area Multilayer Coated X-Ray Optics," *Applied Optics* **28**:2969–2974 (1989).
259. C. Montcalm, B. T. Sullivan, M. Ranger, and H. Pepin, "Ultrahigh Vacuum Deposition Reflectometer System for the In Situ Investigation of Y/Mo Extreme-Ultraviolet Multilayer Mirrors," *Journal of Vacuum Science and Technology a Vacuum Surfaces and Films* **15**:3069–3081 (1997).
260. K. M. Skulina, C. S. Alford, R. M. Bionta, D. M. Makowiecki, E. M. Gullikson, R. Soufli, J. B. Kortright, and J. H. Underwood, "Molybdenum/Beryllium Multilayer Mirrors for Normal Incidence in the Extreme Ultraviolet," *Applied Optics* **34**:3727–3730 (1995).
261. N. Kaiser, S. Yulin, T. Feigl, H. Bernitzki, and H. Lauth, "EUV and Soft X-Ray Multilayer Optics," *Proc. SPIE* **5250**:109–118 (2004).
262. M. F. Ravet, X. Zhang-Song, As. Jerome, F. Delmotte, R. Mercier, M. Bougnet, P. Bouyries, and J. P. Delaboudiniere, "Ion Beam Deposited Mo/Si Multilayers for EUV Imaging Applications in Astrophysics," *Proc. SPIE* **5250**:99–108 (2004).
263. N. M. Ceglio, "Revolution in X-Ray Optics," *Journal of X-Ray Science and Technology* **1**:7–78 (1989).
264. J. Gautier, F. Delmotte, M. Roulliay, F. Bridou, M.-F. Ravet, and A. Jérôme, "Study of Normal Incidence of Three-Component Multilayer Mirrors in the Range 20–40 nm," *Applied Optics* **44**:384–390 (2005).
265. B. Kjornrattanawanich, D. L. Windt, J. F. Seely, and Y. A. Uspenskii, "SiC/Tb and Si/Tb Multilayer Coatings for Extreme Ultraviolet Solar Imaging," *Applied Optics* **45**:1765–1772 (2006).
266. S. Yulin, "Multilayer Coatings for EUV / Soft X-Ray Mirrors," in *Optical Interference Coatings* (eds. N. Kaiser and H. Pulker), Springer, Berlin, 2003, pp. 281–307.
267. P. Baumeister, "Design of Multilayer Filters by Successive Approximations," *Journal of the Optical Society of America* **48**:955–958 (1958).
268. M. A. Gisin, "Cutoff Interference Filters, Transparent to 25  $\mu\text{m}$ ," *Soviet Journal of Optical Technology* **36**:191–194 (1969).
269. R. Jacobsson, "Matching a Multilayer Stack to a High Refractive Index Substrate by Means of an Inhomogeneous Layer," *Journal of the Optical Society of America* **54**:422–423 (1964).
270. E. A. Nesmelov and G. P. Konyukhov, "Theory of a Cutoff Interference Filter," *Optics and Spectroscopy (USSR)* **31**:68–70 (1971).
271. A. Thelen, "Multilayer Filters with Wide Transmittance Bands," *Journal of the Optical Society of America* **53**:1266–1270 (1963).
272. M. Ploke, "Berechnung und Anwendung periodischer Mehrfachinterferenzschichten für ein Wärmereflexionsfilter mit breiter Reflexionsbande," *Zeiss-Mitteilungen* **4**:279–294 (1967).
273. Optical Coating Laboratory Inc., "Effect of the Variation of Angle of Incidence and Temperature on Infrared Filter Characteristics," 2789 Northpoint Parkway, Santa Rosa, CA 95407–7397, USA, 1967.
274. Optical Coating Laboratory Inc., *Infrared Handbook*, Santa Rosa, CA, 1970.
275. Bausch & Lomb, "Bausch and Lomb Multi-Films," 1400 North Goodman Street, P. O. Box 540, Rochester, NY 14692–0450, USA, 1968.
276. Eastman Kodak Company, "Special Filters from Kodak for Technical Applications," 343 State Street, Bldg. 701, Rochester, NY 14650–3512, USA, 1968.
277. Infrared Industries Inc., "Infratron Interference Filters," Thin Film Products Division, 62 Fourth Avenue, Waltham, MA 02154, USA, 1966.

278. H. H. Schroeder and A. F. Turner, "A Commercial Cold Reflector," *Journal of the SMPTE* **69**:351–354 (1960).
279. F. E. Carlson, G. T. Howard, A. F. Turner, and H. H. Schroeder, "Temperature Reduction in Motion-Picture and Television Studios Using Heat-Control Coatings," *Journal of the SMPTE* **65**:136–139 (1956).
280. Corion Corporation, "Optical Filters and Coatings," (1992).
281. Heliotek—a Division of Textron Inc., "Data Sheets," 12500 Gladstane Avenue, Sylmar, CA 91342, USA, 1969.
282. A. F. Turner, "Heat Reflecting Coatings," in *Radiative Heat Transfer from Solid Materials* (eds. H. H. Blau and H. Fischer), Macmillan, New York, 1962.
283. A. Thelen, "The Use of Vacuum Deposited Coatings to Improve the Conversion Efficiency of Silicon Solar Cells in Space," *Progress in Astronautics and Rocketry* **3**:373–383 (1961).
284. D. L. Reynard and A. Andrew, "Improvement of Silicon Solar Cell Performance Through the Use of Thin Film Coatings," *Applied Optics* **5**:23–28 (1966).
285. A. J. Waldorf, National Research Council of Canada, Private communication, 1993.
286. F. Weiting and Z. Pengfei, "Determination of the performance of Edge Filters Containing PbTe on Cooling," *Infrared Physics* **33**:1–7 (1992).
287. B. Hoppert, "Heat Reducing Metal Mirrors," in *Proceedings, Annual Technical Conference*, Society of Vacuum Coaters, 1983, pp. 131–143.
288. A. Piegari and P. Polato, "Wideband Optical Coatings for Artwork Protection from Ultraviolet and Infrared Radiation Damage," *Proc. SPIE* **4829**:64–65 (2003).
289. L. Chang, "Infrared Dispersion of ZnS-Metal Films," Ph. D. thesis, Colorado State University (1964).
290. H. Schröder, "Oxide Layers Deposited from Organic Solutions," in *Physics of Thin Films* **5**, (eds. G. Hass and R. E. Thun), Academic, New York, 1969, pp. 87–141.
291. L. J. Vande Kleff, E. A. Murray, W. M. Frey, and P. W. Yunker, "Construction and Evaluation of Thin Film Beam Dividers," U.S. Army Aberdeen Res. Dev. Cent. Technical Note AD 698025, issued October 1969.
292. K. Hancock, "Membrane Optics," in *Proceedings, Electro-opt. Syst. Des. Conf.*, (editor K. A. Kopetzky), New York, Sept. 16–18, 1969, 1970, Industrial and Scientific Conference Management, Chicago, pp. 231–237.
293. P. L. Heinrich, R. C. Bastien, A. D. Santos, and M. Ostrelch, "Development of an all Dielectric Infrared Beamsplitter Operating in the 5 to 30 Micron Region," Perkin Elmer Technical Report CR-703 to NASA, issued February, 1967.
294. M. L. Lipshutz, "Optomechanical Considerations for Optical Beam Splitters," *Applied Optics* **7**:2326–2328 (1968).
295. H. P. Larson, "Evaluation of Dielectric Film Beamsplitters at Cryogenic Temperature," *Applied Optics* **25**:1917–1921 (1986).
296. F. C. Ho and J. A. Dobrowolski, "Neutral and Color-Selective Beam Splitting Assemblies with Polarization-Independent Intensities," *Applied Optics* **31**: 3813–3820 (1992).
297. H. Anders, *Thin Films in Optics* Focal Press, New York, 1967.
298. W. R. C. Rowley, "Some Aspects of Fringe Counting in Laser Interferometers," *IEEE Transaction Instrumentation Measures* **IM-15**:146–148 (1966).
299. H. Pohlack, "Zur Theorie der absorptionsfreien achromatischen Lichtteilungsspiegel," in *Jenaer Jahrbuch 1956* (eds. P. Görlich), Fischer, Jena, 1956, pp. 79–86.
300. L. A. Catalan and T. Putner, "Study of the Performance of Dielectric Thin Film Beam Dividing Systems," *British Journal of Applied Physics* **12**:499–502 (1961).
301. K. P. Miyake, "Computation of Optical Characteristics of Dielectric Multilayers," *Journal de Physique* **25**:255–257 (1964).
302. R. S. Sokolova, "Beam-Splitter Prisms with Dielectric Layers," *Soviet Journal of Optical Technology* **37**: 318–320 (1970).
303. A. L. Sergeyeva, "Achromatic Nonabsorbing Beam Splitters," *Soviet Journal of Optical Technology* **38**:187–188 (1970).
304. P. B. Clapham, "The Design and Preparation of Achromatic Cemented Cube Beam-Splitters," *Optica Acta* **18**:563–575 (1971).
305. Z. Knittl, "Synthesis of Amplitude and Phase Achromatized Dielectric Mirrors," *Le Journal de Physique* **25**:245–249 (1964).

306. Oriel Optics Corporation, "Catalog Section C: Optical Filters," 2789 Northpoint Parkway, Santa Rosa, CA 95407-7397, USA, 1968.
307. S. F. Pellicori, "Beam Splitter and Reflection Reducing Coatings on ZnSe for 3-14  $\mu\text{m}$ ," *Applied Optics* **18**:1966-1968 (1979).
308. C. K. Malek, J. Susini, A. Madouri, M. Ouahabi, R. Rivoira, F. R. Ladan, Y. Lepêtre, and R. Barchewitz, "Semitransparent Soft X-Ray Multilayer Mirrors," *Optical Engineering* **29**:597-602 (1990).
309. R. M. A. Azzam, "Variable-Reflectance Thin-Film Polarization-Independent Beam Splitters for 0.6328- and 10.6- $\mu\text{m}$  Laser Light," *Optics Letters* **10**:110-112 (1985).
310. V. V. Veremei, V. N. Rozhdestvenskii, and A. B. Khazanov, "Radiation Dividers for the Infrared," *Soviet Journal of Optical Technology* **48**:618-619 (1981).
311. H. A. Macleod and Z. Milanovic, "Immersed Beam Splitters—an Old Problem," in *Proceedings, Optical Interference Coatings*, Optical Society of America, Tucson, AZ, 1992, pp. 28-30.
312. J. A. Dobrowolski, F. C. Ho, and A. Waldorf, "Beam Splitter for a Wide Angle Michelson Doppler Imaging Interferometer," *Applied Optics* **24**:1585-1588 (1985).
313. S. J. Refermat and A. F. Turner, "Polarization Free Beam Divider," U. S. patent 3559090, issued 26 January, 1971.
314. S. Itoh and M. Sawamura, "Achromatized Beam Splitter of Low Polarization," U. S. patent 4415233, issued 15 November, 1983.
315. A. A. M. Saleh, "Polarization-Independent, Multilayer Dielectrics at Oblique Incidence," *The Bell System Technical Journal* **54**:1027-1049 (1975).
316. A. Thelen, "Nonpolarizing Interference Films Inside a Glass Cube," *Applied Optics* **15**:2983-2985 (1976).
317. A. R. Henderson, "The Design of Non-Polarizing Beam Splitters," *Thin Solid Films* **51**:339-347 (1978).
318. Z. Knittl and H. Houserova, "Equivalent Layers in Oblique Incidence: the Problem of Unsplit Admittances and Depolarization of Partial Reflectors," *Applied Optics* **21**:2055-2068 (1982).
319. C. M. d. Sterke, C. J. v. d. Laan, and H. J. Frakena, "Nonpolarizing Beam Splitter Design," *Applied Optics* **22**:595-601 (1983).
320. M. Zukic and K. H. Guenther, "Design of Nonpolarizing Achromatic Beamsplitters with Dielectric Multilayer Coatings," *Optical Engineering* **28**:165-171 (1989).
321. M. Gilo, "Design of a Nonpolarizing Beam Splitter Inside a Glass Cube," *Applied Optics* **31**:5345-5349 (1992).
322. L. Y. Chang and S. H. Mo, "Design of Non-Polarizing Prism Beam Splitter," in *Proceedings, Topical Meeting on Optical Interference Coatings*, Optical Society of America, Tucson, AZ, 1988, pp. 381-384.
323. Y. N. Konoplev, Y. A. Mamaev, V. N. Starostin, and A. A. Turkin, "Nonpolarizing 50% Beam Splitters," *Optics and Spectroscopy (USSR)* **71**:303-305 (1991).
324. H. Pohlack, "Zur theorie der absorptionsfreien achromatischen Lichtteilungs Spiegel," in *Jenaer Jahrbuch* (eds. C. Zeiss), Gustav Fischer Verlag, 1957, pp. 79-86.
325. J. S. Seeley, "Simple Nonpolarizing High-Pass Filter," *Applied Optics* **24**:742-744 (1985).
326. L. N. Kurochkina and N. M. Tulyakova, "Achromatic Lightsplitters for the Ultraviolet Spectrum," *Soviet Journal of Optical Technology* **52**:101-102 (1985).
327. I. J. Hodgkinson and R. G. Stuart, "Achromatic Reflector and Antireflection Coating Designs for Mixed Two-Component Deposition," *Thin Solid Films* **87**:151-158 (1982).
328. J. Mouchart, J. Begel, and S. Chalot, "Dépôts Achromatiques Partiellement Réfléchissants," *Journal of Modern Optics* **37**:875-888 (1990).
329. M. Banning, "Neutral Density Filters of Chromel," *Journal of the Optical Society of America* **37**:686-689 (1947).
330. Eastman Kodak Company, "Kodak Neutral Density Attenuators," 343 State Street, Bldg. 701, Rochester, NY 14650-3512, USA, 1969.
331. Corion Instrument Corporation, "Thin Film Optical Filters," 73 Jeffrey Avenue, Halliston, MA 01746-2082, USA, 1969.
332. Acton Research Corporation, "Optical Filters," P. O. Box 2215, 525 Main Street, Acton, MA 01720, USA, 1992.
333. H. Schröder, "Die Erzeugung von linearpolarisiertem Licht durch dünne dielektrische Schichten," *Optik* **3**:499-503 (1948).

334. R. Messner, "Die theoretischen Grundlagen optischer Interferenzpolarisatoren," *Feinwerktechnik* **57**: 142–147 (1953).
335. R. M. A. Azzam, "Single-Layer-Coated Optical Devices for Polarized Light," *Thin Solid Films* **163**:33–41 (1988).
336. M. Ruiz-Urbieto and E. M. Sparrow, "Reflection Polarization by a Transparent-Film-Absorbing-Substrate System," *Journal of the Optical Society of America* **62**:1188–1094 (1972).
337. J. T. Cox and G. Hass, "Highly Efficient Reflection-Type Polarizers for 10.6- $\mu\text{m}$  CO<sub>2</sub> Laser Radiation Using Aluminum Oxide Coated Aluminum Mirrors," *Applied Optics* **17**:1657–1658 (1978).
338. W. W. Buchman, S. J. Holmes, and F. J. Woodberry, "Single-Wavelength Thin-Film Polarizers," *Journal of the Optical Society of America* **61**:1604–1606 (1971).
339. D. Blanc, P. H. Lissberger, and A. Roy, "The Design, Preparation and Optical Measurement of Thin Film Polarizers," *Thin Solid Films* **57**:191–198 (1979).
340. I. M. Minkov, "Theory of Dielectric Mirrors in Obliquely Incident Light," *Optics and Spectroscopy (USSR)* **33**:175–178 (1973).
341. A. Thelen, "Avoidance or Enhancement of Polarization in Multilayers," *Journal of the Optical Society of America* **70**:118–121 (1980).
342. P. B. Clapham, M. J. Downs, and R. J. King, "Some Applications of Thin Films to Polarization Devices," *Applied Optics* **8**:1965–1974 (1969).
343. P. Kard, "Theory of Achromatic Multilayer Interference Polarizers," *Eesti NSV Tead. Akad. Toim., Fuus. - Mat.* **9**:26–32 (1960).
344. W. Geffcken, "Interference light filter," DB patent 913005, issued June 8, 1954/44.
345. S. M. MacNeille, "Beam splitter," U. S. patent 2403731, issued 6 July, 1946.
346. R. S. Sokolova and T. N. Krylova, "Interference Polarizers for the Ultraviolet Spectral Region," *Optics and Spectroscopy (USSR)* **14**:213–215 (1963).
347. J. Wimperis, Interoptics, A Division of Lumonics, Inc., 14 Capella Court, Nepean (Ottawa) Ontario, Canada K2E 7V6, Private communication, 1993.
348. M. Banning, "Practical Methods of Making and Using Multilayer Filters," *Journal of the Optical Society of America* **37**:792–297 (1947).
349. W. B. Wetherell, "Polarization Matching Mixer in Coherent Optical Communications Systems," *Optical Engineering* **28**:148–156 (1989).
350. J. Mouchart, J. Begel, and E. Duda, "Modified MacNeille Cube Polarizer for a Wide Angular Field," *Applied Optics* **28**:2847–2853 (1989).
351. R. Austin, "Thin Film Polarizing Devices," *Electro-Optical Systems Design* February issue, pp. 30–35, 1974.
352. R. P. Netterfield, "Practical Thin-Film Polarizing Beam-Splitters," *Optica Acta* **24**:69–79 (1977).
353. J. A. Dobrowolski and A. J. Waldorf, "High-Performance Thin Film Polarizer for the UV and Visible Spectral Regions," *Applied Optics* **20**:111–116 (1981).
354. V. P. Sobol', R. A. Petrenko, and A. S. Dimitreev, "Interference Polarizer Employing Optical Contact," *Soviet Journal of Optical Technology* **53**:692 (1986).
355. M. Gilo and K. Rabinovitch, "Design Parameters of Thin-Film Cubic-Type Polarizers for High Power Lasers," *Applied Optics* **26**:2518–2521 (1987).
356. L. Li and J. A. Dobrowolski, "Visible Broadband, Wide-Angle, Thin-Film Multilayer Polarizing Beam Splitter," *Applied Optics* **35**:2221–2225 (1996).
357. L. Li and J. A. Dobrowolski, "High-Performance Thin-Film Polarizing Beam Splitter Operating at Angles Greater Than the Critical Angle," *Applied Optics* **39**:2754–2771 (2000).
358. P. Ma, L. Li, F. Lin, and J. A. Dobrowolski, "Manufacture of High Performance Polarizing Beam Splitter for Projection Display Applications," in *Proceedings, Optical Interference Coatings on CD-ROM*, The Optical Society of America, Washington D. C., 2007, pp. TuC1.
359. L. Li and Z. Pang, "Thin Film Polarizing Device Having Metal-Dielectric Films," US patent 6,317,264, issued November 13, 2001.
360. E. Cojocar, "Comparison of Theoretical Performances for Different Single-Wavelength Thin-Film Polarizers," *Applied Optics* **31**:4501–4504 (1992).

361. R. M. A. Azzam, "Efficient Infrared Reflection Polarizers Using Transparent High-Index Films on Transparent Low-Index Substrates," *Proc. SPIE* **652**:326–332 (1986).
362. T. F. Thonn and R. M. A. Azzam, "Multiple-Reflection Polarizers Using Dielectric-Coated Metallic Mirrors," *Optical Engineering* **24**:202–206 (1985).
363. L. Songer, "The Design and Fabrication of a Thin Film Polarizer," *Optical Spectra*, October issue, pp. 49–50, 1978.
364. D. Lees and P. Bauemeister, "Versatile Frustrated-Total-Reflection Polarizer for the Infrared," *Optics Letters* **4**:66–67 (1979).
365. H. Lotem and K. Rabinovitch, "Penta Prism Laser Polarizer," *Applied Optics* **32**:2017–2020 (1993).
366. H. Winter, H. H. Bukow, and P. H. Heckmann, "A High Transmission Triple-Reflection Polarizer for Lyman- $\alpha$  Radiation," *Optics Communications* **11**:299 (1974).
367. G. Hass and W. R. Hunter, "Reflection Polarizers for the vacuum Ultraviolet Using Al + MgF<sub>2</sub> Mirrors and MgF<sub>2</sub> Plate," *Applied Optics* **17**:76–82 (1978).
368. W. R. Hunter, "Design Criteria for Reflection Polarizers and Analyzers in the Vacuum Ultraviolet," *Applied Optics* **17**:1259–1270 (1978).
369. T. A. Remneva, A. V. Kozhevnikov, and M. M. Nikitin, "Polarizer of Radiation in the Vacuum Ultraviolet," *Journal of Applied Spectroscopy (USSR)* **25**:1587–1590 (1967).
370. Z. Wang, "Non-Periodic Multilayer Coatings in EUV, Soft X-Ray and X-Ray Range," *Proc. SPIE* **7101**:10-1-15 (2008).
371. P. Dhez, "Polarizers and Polarimeters for the X-UV Range," *Nuclear Instrumentation Methods Physics Research* **A261**:66–71 (1987).
372. M. Yanagihara, T. Maehara, H. Normura, M. Yamamoto, T. Namioka, and H. Kimura, "Performance of a wide Bandband Multilayer Polarizer for Soft X-Rays," *Review of Scientific Instruments* **63**:1516–1518 (1992).
373. F. Eriksson, N. Ghafoor, F. Schäfers, E. M. Gullikson, S. Aouadi, S. Rohde, L. Hultman, and J. Birch, "Atomic Scale Interface Engineering by Modulated Ion-Assisted Deposition Applied to Soft X-Ray Multilayer Optics," *Applied Optics* **47**:4196–4204 (2008).
374. Z. Wang, H. Wang, J. Zhu, F. Wang, Z. Gu, L. Chen, A. G. Michette, A. K. Powell, S. J. Pfauntsch, and F. Schäfers, "Broadband Multilayer Polarizers for the Extreme Ultraviolet," *Journal of Applied Physics* **99**:056108 1-3 (2006).
375. Z. Wang, H. Wang, J. Zhu, Y. Xu, S. Zhang, C. Li, and F. Wang, "Extreme Ultraviolet Broadband Mo/Y Multilayer Analyzers," *Applied Physics Letters* **89**:241120-1-3 (2006).
376. Anon, "Metal-Dielectric Interference Filters," in *Physics of Thin Films* 9, (eds. G. Hass, M. H. Francombe, and R. W. Hoffman), Academic Press, New York, (1977), pp. 73–144.
377. E. E. Barr, "The Design and Construction of Evaporated Multilayer Filters for Use in Solar Radiation Technology," in *Advances in Geophysics* 14, (eds. A. J. Drummond), Academic Press, (1970), pp. 391–412.
378. R. Morf and R. E. Kunz, "Dielectric Filter Optimization by Simulated Thermal Annealing," *SPIE—Thin Film Technologies III* **1019**:211 (1988).
379. N. S. Gluck and W. J. Gunning, "Patterned Infrared Spectral Filter Directly Deposited onto Cooled Substrates," *Applied Optics* **28**:5110–5114 (1989).
380. T. A. Mooney, 2 Lyberty Way, Westford, MA 01886, U. S. A. Personal communication, 1993.
381. W. H. Southwell, W. J. Gunning, and R. L. Hall, "Narrow-Bandpass Filter Using Partitioned Cavities," *SPIE - Optical Thin Films II. New Developments* **678**:177–184 (1986).
382. W. Geffcken, "Interference Light Filter," DB patent 716153, issued December 8, 1939.
383. D. H. Harrison, "MDM Bandpass Filters for the Vacuum Ultraviolet," *Applied Optics* **7**:210 (1968).
384. D. J. Bradley, B. Bates, C. O. L. Juulman, and T. Kohno, "Recent Developments in the Application of the Fabry-Perot Interferometer to Space Research," *Journal de Physique* **28**:C2-280–C2-283 (1967).
385. Balzers Aktiengesellschaft für Hochvakuumtechnik und Dünne Schichten, "Interference Filters," FL-9496 Balzers, Principality of Liechtenstein, 1968.
386. Schott Glaswerke, "Monochromatic Interference Filters," Geschäftsbereich Optik, Hattenbergstrasse 10, D-6500 Mainz, Germany, 1965.
387. A. F. Turner, "Some Current Developments in Multilayer Optical Films," *Le Journal de Physique et le Radium* **11**:444–460 (1950).

388. P. W. Baumeister, "Optical Tunneling and Its Applications to Optical Filters," *Applied Optics* **6**:897–905 (1967).
389. S. W. Warren, "Properties and Performance of Basic Designs of Infrared Interference Filters," *Infrared Physics* **8**:65–78 (1968).
390. A. Thelen, "Design of Multilayer Interference Filters," in *Physics of Thin Films* 5, (eds. G. Hass and R. E. Thun), Academic Press, New York & London, 1969, pp. 47–86.
391. W. Geffcken, "The Wave-Band Filter, an Interference Filter of Very High Efficiency," *Zeitschrift für Angewandte Physik* **6**:249–250 (1954).
392. A. F. Turner, "Wide Passband Multilayer Filters," *Journal of the Optical Society of America* **42**:878 (1952).
393. S. D. Smith, "Design of Multilayer Filters by Considering Two Effective Interfaces," *Journal of the Optical Society of America* **48**:43–50 (1958).
394. H. Schröder, "Properties and Applications of Oxide Layers Deposited on Glass from Organic Solutions," *Optica Acta* **9**:249–254 (1962).
395. R. S. Meltzer, Industrial Optics Division, Yardney Razdow Laboratories, Private communications, 1968.
396. R. H. Eather and D. L. Reasoner, "Spectrophotometry of Faint Light Sources with a Tilting-Filter Photometer," *Applied Optics* **8**:227–242 (1969).
397. R. R. Austin, Perkin-Elmer Corporation, Private communication, November 11, 1968.
398. M. A. Cohendet and B. Saudreau, DRME-66-34-443, 1967.
399. O. A. Motovilov, "Narrow-Band Interference Filters for the Ultraviolet Region of the Spectrum," *Optics and Spectroscopy (USSR)* **22**:537–538 (1967).
400. R. G. T. Neilson and J. Ring, "Interference Filters for the Near Ultra-Violet," *Journal de Physique* **28**:C2-270–C2-275 (1967).
401. A. F. Turner and R. Walsh, "Interference Filters for the 8–13 Micron Atmospheric Window," *Bausch & Lomb Technical Report no. 2*, issued 1961.
402. S. D. Smith and J. S. Seely, "Multilayer Filters for the Region 0.8 to 100 Microns," AF61(052)-833, issued May 7, 1968.
403. I. H. Blifford, Jr., "Factors Affecting the Performance of Commercial Interference Filters," *Applied Optics* **5**:105–111 (1966).
404. Baird Atomic, Inc. "Optical Components," 125 Middlesex Turnpike, Bedford, MA 01730–1468, 1968.
405. Spectrum Systems Division—Barnes Engineering Co., "Visible and Near Infrared Filters, Bull. SS-14," 211 Second Avenue, Waltham, MA 02154, USA, 1967.
406. Infrared Industries Inc., "Thin Film Products at Infrared Industries, Inc.," Thin Film Products Division, 62 Fourth Avenue, Waltham, MA 02154, USA, 1967.
407. P. Baumeister, "Use of Microwave Prototype Filters to Design Multilayer Dielectric Bandpass Filters," *Applied Optics* **21**:2965–2967 (1982).
408. A. Zheng, J. S. Seeley, R. Hunneman, and G. J. Hawkins, "Design of Narrowband Filters in the Infrared Region," *Infrared Physics* **31**:237–244 (1991).
409. J. Minowa and Y. Fujii, "High Performance Bandpass Filters for WDM Transmission," *Applied Optics* **23**:193–194 (1984).
410. P. W. Baumeister, V. R. Costich, and S. C. Pieper, "Bandpass Filters for the Ultraviolet," *Applied Optics* **4**:911–914 (1965).
411. P. H. Berning and A. F. Turner, "Induced Transmission in Absorbing Films Applied to Band Pass Filter Design," *Journal of the Optical Society of America* **47**:230–239 (1957).
412. R. L. Maier, "2M Interference Filters for the Ultraviolet," *Thin Solid Films* **1**:31–37 (1967).
413. P. W. Baumeister, "Radiant Power Flow and Absorptance in Thin Films," *Applied Optics* **8**:423–436 (1969).
414. R. J. Holloway and P. H. Lissberger, "The Design and Preparation of Induced Transmission Filters," *Applied Optics* **8**:653–660 (1969).
415. B. V. Landau and P. H. Lissberger, "Theory of Induced-Transmission Filters in Terms of the Concept of Equivalent Layers," *Journal of the Optical Society of America* **62**:1258–1264 (1972).
416. N. P. Matshina, E. A. Nesselov, I. K. Nagimov, R. M. Validov, and N. N. Soboleva, "Theory of Narrow-Band Filters with Induced Transparency," *Journal of Applied Spectroscopy (USSR)* **55**:1273–1278 (1991).

417. D. Gershenzon and L. Sossi, "Conditions for Maximum Transmission of Metal-Dielectric Interference Filters," *Esti NSV Tead Akad Toim, Fuus. Mat.* **41**:142–149 (1992).
418. V. I. Tsyipin and E. A. Sukhanov, "Metal-Dielectric Filters for the 200-350 nm Spectral Regions," *Soviet Journal of Optical Technology* **59**: 438–439 (1992).
419. F. A. Korolev, A. Y. Klement'eva, and T. F. Meshcheryakova, "Interference Filters with a Transmission Band of 1.5 a Half-Width," *Optics and Spectroscopy (USSR)* **9**:341–343 (1960).
420. R. W. Wood, "Some New Cases of Interference and Diffraction," in *The London, Edinburgh, and Dublin Philosophical Magazine and Journal of Science* **7**, Taylor and Francis, London, 1904, pp. 376–388.
421. A. I. Kartashev and N. M. Syromyatnikova, "Mica Interference Filters," in *Wavelength of Light as a Standard of Length, Proc. Mendeleev State Sci. Res. Inst.*, **7**, Leningrad, 1947, pp. 86–93.
422. J. Ring, R. Beer, and V. Hewison, "Reflectance Multilayers," *J. Phys. Radium* **19**:321–323 (1958).
423. J. A. Dobrowolski, "Mica Interference Filters with Transmission Bands of Very Narrow Half-Widths," *Journal of the Optical Society of America* **49**:794–806 (1959).
424. G. S. Chermukhin, V. P. Rozhnov, and G. I. Golubeva, "Narrow-Band Interference Filters Made from Mica," *Soviet Journal of Optical Technology* **43**:312–315 (1976).
425. D. R. Herriott, J. R. Wimperis, and D. L. Perry, "Filters, Wave Plates and Protected Mirrors Made of Thin Polished Supported Layers," *Journal of the Optical Society of America* **4**:546 (abstract) (1965).
426. J. D. Rehnberg, "Design Considerations for an Orbiting Solar Telescope," in *Proceedings, Electro-Opt. Syst. Des. Conf.*, (editor K. A. Kopetzky), New York, Sept 16–18, 1969, 1970, Industrial and Scientific Conference Management, Inc., Chicago, pp. 69–73.
427. A. Title, "Fabry-Perot Interferometers as Narrow-Band Optical Filters: Part one—Theoretical considerations," Harvard College Observatory Technical Report TR-18, issued June, 1970.
428. R. Fisher, "On the Use of a Solid Fabry-Perot Interferometer for Coronal Photography," *Solar Physics* **18**:253–257 (1971).
429. J. F. Markey and R. R. Austin, "High Resolution Solar Observations: The Hydrogen-Alpha Telescopes on Skylab," *Applied Optics* **16**:917–921 (1977).
430. R. R. Austin, "The Use of Solid Etalon Devices as Narrow Band Interference Filters," *Optical Engineering* **11**:65–69 (1972).
431. S. D. Smith and C. R. Pidgeon, "Application of Multiple Beam Interferometric Methods to the Study of CO<sub>2</sub> Emissions at 15  $\mu\text{m}$ ," *Mem. Soc. R. Liege Sieme serie* **9**:336–349 (1963).
432. A. E. Roche and A. M. Title, "Tilt Tunable Ultra Narrow-Band Filters for High Resolution Infrared Photometry," *Applied Optics* **14**:765–770 (1975).
433. J. -M. Saurel and M. Candille, "Réalisation de filtres multidielectriques sur un substrat biréfringent, déformable et de faible épaisseur (mylar)," *Thin Solid Films* **16**:313–324 (1973).
434. M. Candille and J. M. Saurel, "Réalisation de filtres 'souple onde' à bandes passantes très étroites sur supports en matière plastique (mylar)," *Optica Acta* **21**:947–962 (1974).
435. P. W. Baumeister, F. A. Jenkins, and M. A. Jeppesen, "Characteristics of the Phase-Dispersion Interference Filter," *Journal of the Optical Society of America* **49**:1188–1190 (1959).
436. R. R. Austin, "Narrow Band Interference Light Filter," US patent 3528726 issued 15 September, 1970.
437. P. Giacomo, P. W. Baumeister, and F. A. Jenkins, "On the Limiting Bandwidth of Interference Filters," *Proc. Phys. Soc.* **73**:480–489 (1959).
438. S. D. Smith and O. S. Heavens, "A Tunable Infra-Red Interference Filter," *Journal of Scientific Instruments* **34**:492–496 (1957).
439. P. D. Atherton, N. K. Reay, J. Ring, and T. R. Hicks, "Tunable Fabry-Perot Filters," *Optical Engineering* **20**:806–814 (1981).
440. J. V. Ramsay, "Control of Fabry-Perot Interferometers and Some Unusual Applications," *The Australian Physicist* **5**:87–89 (1968).
441. J. V. Ramsay, H. Kobler, and E. G. V. Mugridge, "A New Tunable Filter with a Very Narrow Pass-Band," *Solar Physics* **12**:492–501 (1970).
442. C. H. Burton, A. J. Leistner, and D. M. Rust, "Electrooptic Fabry-Perot Filter Development for the Study of Solar Oscillations," *Applied Optics* **26**:2637–2642 (1987).

443. D. B. McKenney and P. N. Slater, "Design and Use of Interference Passband Filters with Wide-Angle Lenses for Multispectral Photography," *Applied Optics* **9**:2435–2440 (1970).
444. J. A. Dobrowolski and R. C. Bastien, "Square-Top Transmission Band Interference Filters for the Infra-Red," *Journal of the Optical Society of America* **53**:1332 (1963).
445. D. McKenney and A. F. Turner, "Ultra-Wide Bandpass Filters Developed for Spectral Photography," *Univ. Ariz. Opt. Cent. Newsl.* **1**, (1967).
446. J. Michael and Perkin-Elmer Corporation, Private communication, 1968.
447. E. Pelletier and H. A. Macleod, "Interference Filters with Multiple Peaks," *Journal of the Optical Society of America* **72**:683–687 (1982).
448. W. A. Hovis, Jr., W. A. Kley, and M. G. Strange, "Filter Wedge Spectrometer for Field Use," *Applied Optics* **6**:1057 (1967).
449. A. Thelen, "Circularly Wedged Optical Coatings. I. Theory," *Applied Optics* **4**:977–981 (1965).
450. J. H. Apfel, "Circularly Wedged Optical Coatings. II. Experimental," *Applied Optics* **4**:983–985 (1965).
451. V. A. Martsinovskii and F. K. Safullin, "Determination of the Conditions of Formation of Annular Coatings with Linear Dependence of Thickness on Rotation Angle," *Journal of Applied Spectroscopy (USSR)* **39**:976–980 (1983).
452. V. P. Avilov and A. Khosilov, "Apparatus for Producing Annular Variable Interference Filters," *Soviet Journal of Optical Technology* **55**:613–615 (1988).
453. I. M. Minkov, "Calculation of Narrow-Band Circular Wedge Filter for 4–12  $\mu\text{m}$  Spectral Region," *Soviet Journal of Optical Technology* **58**:491–492 (1991).
454. V. L. Yen, "Circular Variable Filters," *Optical Spectra* **3**:78–84 (1969).
455. V. P. Avilov, V. I. Tsy-pin, and E. M. Shipulin, "Circular-Wedge Filter for the 0.24–0.40  $\mu\text{m}$  Region," *Soviet Journal of Optical Technology* **54**:515 (1987).
456. A. Mussett, Optical Coating Laboratory, Private communication, 1969.
457. P. H. Lissberger, "Effective Refractive Index as a Criterion of Performance of Interference Filters," *Journal of the Optical Society of America* **58**:1586–1590 (1968).
458. P. H. Lissberger, "Properties of All-Dielectric Interference Filters. I. A New Method of Calculation," *Journal of the Optical Society of America* **49**:121–125 (1959).
459. C. R. Pidgeon and S. D. Smith, "Resolving Power of Multilayer Filters in Nonparallel Light," *Journal of the Optical Society of America* **54**:1439–1466 (1964).
460. D. J. Hemingway and P. H. Lissberger, "Effective Refractive Indices of Metal-Dielectric Interference Filters," *Applied Optics* **6**:471–476 (1967).
461. S. L. Linder, "Optimization of Narrow Optical Spectral Filters for Nonparallel Monochromatic Radiation," *Applied Optics* **6**:1201–1204 (1967).
462. P. G. Kard, "On Elimination of the Doublet Structure of the Transmission Band in a Total-Reflection Light-Filter," *Optics and Spectroscopy (USSR)* **6**:244–246 (1959).
463. G. P. Konyukhov and E. A. Nesmelov, "On the Theory of Dielectric Narrow-Based Light Filters," *Zhurnal Prikladnoi Spektroskopii* **11**:468- (1969).
464. P. Baumeister, "Bandpass Design—Application to Nonnormal Incidence," *Applied Optics* **31**:504–512 (1992).
465. W. Wilmot and E. R. Schinneler, "A Wide-Angle Narrow-Band Optical Filter," *Journal of the Optical Society of America* **56**:549 (1966).
466. E. R. Schinneler and R. P. Flam, "Development of a Wide-Angle Narrow-Band Optical Filter," in *Proceedings, Spring Meeting Program—Optical Society of America*, 1968, pp. FF11-1–FF11-4.
467. J. Meaburn, "The Stability of Interference Filters," *Applied Optics* **5**:1757–1759 (1966).
468. J. Schild, A. Steudel, and H. Walter, "The Variation of the Transmission Wavelength of Interference Filters by the Influence of Water Vapor," *Journal de Physique* **28**:C2-276–C2-279 (1967).
469. L. D. Lazareva, "The Effect of Temperature on the Position of the Passband Maximum in Interference Filters," *Optical Technology* **36**:801–802 (1970).
470. S. A. Furman and M. D. Levina, "Effect of Moisture on the Optical Characteristics of Narrow Band Interference Filters," *Optics and Spectroscopy (USSR)* **30**:404–408 (1971).



471. S. A. Furman and M. D. Levina, "Strict Stabilization of the Optical Characteristics of Narrow-Band Interference Filters," *Optical Technology* **38**:374–375 (1971).
472. S. A. Furman and M. D. Levina, "Stabilization of the Location of the Transmission Band of a Narrow-Band Dielectric Interference Filter," *Optical Technology* **38**:272–275 (1971).
473. M. D. Levina and S. A. Furman, "Improving the Stability of the Optical Characteristics of Metal-Dielectric Filters," *Soviet Journal of Optical Technology* **49**:128–129 (1982).
474. D. R. Gibson and P. H. Lissberger, "Optical Properties of Narrowband Spectral Filter Coatings Related to Layer Structure and Preparation," *Applied Optics* **22**:269–281 (1983).
475. A. Brunsting, M. A. Kheiri, D. F. Simonaitis, and A. J. Dosmann, "Environmental Effects on All-Dielectric Bandpass Filters," *Applied Optics* **25**:3235–3241 (1986).
476. S. A. Furman and M. D. Levina, "Investigations of Temperature Dependence of Optical Properties of Dielectric Narrow-Band Filters," *Optics and Spectroscopy (USSR)* **28**:412–416 (1970).
477. S. A. Furman, "Effect of Temperature, Angle of Incidence, and Dispersion of Index of Refraction of Layers on the Position of the Pass Bands of a Dielectric Narrow-Band Filters," *Optics and Spectroscopy (USSR)* **28**:218–222 (1970).
478. A. S. Chaikin and V. V. Pukhonin, "An Investigation of the Temperature and Time Dependence of the Parameters of Narrow-Band Interference Filters," *Journal of Applied Spectroscopy (USSR)* **13**:1513–1515 (1970).
479. G. I. Golubeva, M. S. Abakumova, and A. M. Klochkov, "Results of Industrial Studies," *Optical Technology* **38**:228–229 (1971).
480. A. M. Zheng, J. S. Seeley, R. Hunneman, and G. J. Hawkins, "Ultrannarrow Filters with Good Performance when Tilted and Cooled," *Applied Optics* **31**:4336–4338 (1992).
481. W. Feng and Y. Yan, "Shift in Infrared Interference Filters at Cryogenic Temperature," *Applied Optics* **31**:6591–6592 (1992).
482. R. Mark, D. Morand, and S. Waldstein, "Temperature Control of the Bandpass of an Interference Filter," *Applied Optics* **9**:2305–2310 (1970).
483. V. M. Novikov, "Vacuum Installation with a Manipulator," *Soviet Journal of Optical Technology* **35**:121–122 (1968).
484. O. M. Sorokin and V. A. Blank, "Thin-Film Metal and Semiconductor Filters for the Vacuum Ultraviolet," *Optical Technology* **37**:343–346 (1970).
485. T. Barbee and J. H. Underwood, "Solid Fabry-Perot Etalons for X-Rays," *Optics Communications* **48**:161–166 (1983).
486. Y. Lepetre, R. Rivoira, R. Philip, and G. Rasigni, "Fabry-Perot Etalons for X-Rays: Construction and Characterization," *Optics Communications* **51**:127–130 (1984).
487. Y. Lepetre, I. K. Schuller, G. Rasigni, R. Rivoira, and R. Philip, "Novel Characterization of Thin Film Multilayered Structures: Microcleavage Transmission Electron Spectroscopy," *Proceedings of the Society of Photo-Optical Instrumentation Engineers* **563**:258–263 (1985).
488. R. J. Bartlett, W. J. Trela, D. R. Kania, M. P. Hockaday, T. W. Barbee, and P. Lee, "Soft X-Ray Measurements of Solid Fabry-Perot Etalons," *Optics Communications* **55**:229–235 (1985).
489. V. R. Costich, "Coatings for 1, 2, Even 3 Wavelengths," *Laser Focus Magazine* **41**–45 (1969).
490. J. D. Rancourt and W. T. Beauchamp, "Articles Having Improved Reflectance Suppression," U. S. patent 4578527, issued 25 March, 1986.
491. W. C. Herrmann and D. E. Morton, "A Design Technique for Multiband AR Coatings," in *Proceedings, 33rd Annual Technical Conference, Society of Vacuum Coaters, New Orleans, Louisiana, 1990*, pp. 246–249.
492. L. Li, J. A. Dobrowolski, J. D. Sankey, and J. R. Wimperis, "Antireflection Coatings for Both Visible and Far Infrared Spectral Regions," *Applied Optics* **31**:6150–6156 (1992).
493. L. Li and J. A. Dobrowolski, "Design of Optical Coatings for Two Widely Separated Spectral Regions," *Applied Optics* **32**:2969–2975 (1993).
494. J. A. Dobrowolski and L. Li, "Design of Optical Coatings for Three or More Separated Spectral Regions," *Applied Optics* **34**:2934–2940 (1995).
495. H. A. Macleod, "Structure-Related Optical Properties of Thin Films," *Journal of Vacuum Science and Technology* **A4**:418–422 (1986).

496. T. Motohiro and Y. Taga, "Thin Film Retardation Plate by Oblique Deposition," *Applied Optics* **28**:2466–2482 (1989).
497. J. H. Apfel, "Graphical Method to Design Multilayer Phase Retarders," *Applied Optics* **20**:1024–1029 (1981).
498. J. H. Apfel, "Phase Retardance of Periodic Multilayer Mirrors," *Applied Optics* **21**:733–738 (1982).
499. W. H. Southwell, "Multilayer Coating Design Achieving a Broadband 90° Phase Shift," *Applied Optics* **19**:2688–2692 (1980).
500. N. V. Grishina, "Synthesis of Mirrors with Constant Phase Difference Under Oblique Incidence of Light," *Optics and Spectroscopy (USSR)* **69**:262–265 (1990).
501. P. Lostis, "Étude, réalisation et contrôle de lames minces introduisant une différence de marche déterminée entre deux vibrations rectangulaires," *Revue d'Optique, Théorique et Instrumentale* **38**:1–28 (1959).
502. J. H. Apfel, "Graphical Method to Design Internal Reflection Phase Retarders," *Applied Optics* **23**:1178–1183 (1984).
503. R. M. A. Azzam and M. E. R. Khan, "Polarization-Preserving Single-Layer-Coated Beam Displacers and Axicons," *Applied Optics* **21**:3314–3322 (1982).
504. E. Cojocar, "Polarization-Preserving Totally Reflecting Prisms," *Applied Optics* **31**:4340–4342 (1992).
505. E. Spiller, "Totally Reflecting Thin-Film Phase Retarders," *Applied Optics* **23**:3544–3549 (1984).
506. J. M. Bennett, "A Critical Evaluation of Rhomb-Type Quarterwave Retarders," *Applied Optics* **9**:2123–2129 (1970).
507. I. Filinski and T. Skettrup, "Achromatic Phase Retarders Constructed from Right-Angle Prisms: Design," *Applied Optics* **23**:2747–2751 (1984).
508. R. J. King, "Quarter-Wave Retardation Systems Based on the Fresnel Rhomb Principle," *Journal of Scientific Instruments* **43**:627–622 (1966).
509. R. M. A. Azzam, "ZnS-Ag Film-Substrate Parallel-Mirror Beam Displacers that Maintain Polarization of 10.6  $\mu\text{m}$  Radiation Over a Wide Range of Incidence Angles," *Infrared Physics* **23**:195–197 (1983).
510. T. F. Thonn and R. M. A. Azzam, "Three-Reflection Halfwave and Quarterwave Retarder Using Dielectric-Coated Metallic Mirrors," *Applied Optics* **23**:2752–2759 (1985).
511. H. Pohlack, "Über die reflexionsvermindernde Wirkung dünner Metallschichten auf Glas," in *Jenaer Jahrbuch 1956* (eds. P. Görlich), Fischer, Jena, 1956, pp. 87–93.
512. G. Hass, H. H. Schroeder, and A. F. Turner, "Mirror Coatings for Low Visible and High Infrared Reflectance," *Journal of the Optical Society of America* **46**:31–35 (1956).
513. J. A. Dobrowolski, B. T. Sullivan, and R. C. Bajcar, "Optical Interference, Contrast-Enhanced Electroluminescent Device," *Applied Optics* **31**:5988–5996 (1992).
514. J. A. Dobrowolski, E. H. Hara, B. T. Sullivan, and A. J. Waldorf, "High Performance Optical Wavelength Multiplexer-Demultiplexer," *Applied Optics* **31**:3800–3806 (1992).
515. J. A. Dobrowolski and R. A. Kemp, "Flip-Flop Thin-Film Design Program with Enhanced Capabilities," *Applied Optics* **31**:3807–3812 (1992).
516. J. A. Dobrowolski, "Versatile Computer Program for Absorbing Optical Thin-Film Systems," *Applied Optics* **20**:74–81 (1981).
517. J. H. Apfel and R. M. Gelber, "Multilayer Filter with Metal Dielectric Period," U. S. patent 3679291, issued 14 March, 1972.
518. R. J. Fay and J. R. Cicotta, "Neutral density Filter Element with Reduced Surface Reflection," U. S. patent 3781089, issued December 25, 1973.
519. J. A. Dobrowolski, L. Li, and R. A. Kemp, "Metal/Dielectric Transmission Interference Coatings with Low Reflectance 1. Design," *Applied Optics* **34**: 5673–5683 (1995).
520. B. T. Sullivan and K. L. Byrt, "Metal/Dielectric Transmission Interference Coatings with Low Reflectance 2. Experimental Results," *Applied Optics* **34**: 5684–5694 (1995).
521. J. R. Jacobsson, "Protective Device for Protection Against Radiation During Welding," U. S. patent 4169655, issued October 2, 1979.
522. ASTM, "Symposium on Electroless Nickel Plating," *Spec. Tech. Publ.* **265**, (1959).
523. R. P. Madden, "Preparation and Measurement of Reflecting Coatings for the Vacuum Ultraviolet," in *Physics of Thin Films* 1, (ed. G. Hass), Academic Press, New York, 1963, pp. 123–186.

524. M. L. Scott, P. N. Arendt, B. J. Cameron, J. M. Saber, and B. E. Newnam, "Extreme Ultraviolet Reflectance Degradation of Aluminum and Silicon from Surface Oxidation," *Applied Optics* **27**:1503–1507 (1988).
525. H. E. Bennett, M. Silver, and E. J. Ashley, "Infrared Reflectance of Aluminum Evaporated in Ultra-High Vacuum," *Journal of the Optical Society of America* **53**:1089–1095 (1963).
526. J. M. Bennett and E. J. Ashley, "Infrared Reflectance and Emittance of Silver and Gold Evaporated in Ultrahigh Vacuum," *Applied Optics* **4**:221–224 (1965).
527. G. Hass and L. Hadley, in *American Institute of Physics Handbook* (ed. O. F. Gray), McGraw-Hill, New York, 1972, pp. 6–118.
528. W. R. Hunter, "High Reflectance Coatings for the Extreme Ultra-Violet," *Optica Acta* **9**:255–268 (1962).
529. G. Hass and G. F. Jacobus, "Optical Properties of Evaporated Iridium in the Vacuum Ultraviolet from 500 to 2000 Å," *Journal of the Optical Society of America* **57**:758–762 (1967).
530. J. T. Cox, G. Hass, and W. R. Hunter, "Optical Properties of Evaporated Rhodium Films Deposited at Various Substrate Temperatures in the Vacuum Ultraviolet from 150 to 2000 Å," *Journal of the Optical Society of America* **61**:360–364 (1971).
531. J. T. Cox, G. Hass, and J. B. Ramsey, "Reflectance of Evaporated Rhenium and Tungsten Films in the Vacuum Ultraviolet from 300 to 2000 Å," *Journal of the Optical Society of America* **62**:781–785 (1972).
532. J. T. Cox, G. Hass, and J. B. Ramsey, "Reflectance and Optical Constants of Evaporated Osmium in the Vacuum Ultraviolet from 300 to 2000 Å," *Journal of the Optical Society of America* **63**:435–438 (1973).
533. J. F. Seely, G. E. Holland, W. R. Hunter, R. P. McCoy, K. F. Dymond, and M. Corson, "Effect of Oxygen Atom Bombardment on the Reflectance of Silicon Carbide Mirrors in the Extreme Ultraviolet Region," *Applied Optics* **1805**:1805–1810 (1993).
534. G. Hass, "Filmed Surfaces for Reflecting Objects," *Journal of the Optical Society of America* **45**:945–952 (1955).
535. R. Denton and Denton Vacuum Inc., Private communication, 1970.
536. V. D. Vvedenskii, R. Y. Pinskaya, S. A. Furman, and T. V. Shestakova, "Wide-Band Reflectors Based on Silver Films," *Soviet Journal of Optical Technology* **50**:781–782 (1983).
537. D. -Y. Song, R. W. Sprague, H. A. Macleod, and M. R. Jacobson, "Progress in the Development of a Durable Silver-Based High-Reflectance Coating for Astronomical Telescopes," *Applied Optics* **24**:1164–1170 (1985).
538. AIRCO Coating Technology, "Enhanced Front-Surface Aluminum Mirrors," 2700 Maxwell Way, P. O. Box 2529, Fairfield, CA 94533-252, USA, 1990.
539. S. A. Furman and E. G. Stolov, "Synthesis of Achromatic Metal-Dielectric Mirrors," *Soviet Journal of Optical Technology* **44**:359–361 (1977).
540. M. R. Adraens and B. Feuerbacher, "Improved LiF and MgF<sub>2</sub>-Overcoated Aluminum Mirrors for Vacuum Ultraviolet Astronomy," *Applied Optics* **10**:958–959 (1971).
541. L. R. Canfield, G. Hass, and J. E. Waylonis, "Further Studies on MgF<sub>2</sub>-Overcoated Aluminum Mirrors with Highest Reflectance in the Vacuum Ultraviolet," *Applied Optics* **5**:45–50 (1966).
542. G. Hass and R. Tousey, "Reflecting Coatings for the Extreme Ultraviolet," *Journal of the Optical Society of America* **49**:593–602 (1959).
543. D. W. Angel, W. R. Hunter, and R. Tousey, "Extreme Ultraviolet Reflectance of LiF-Coated Aluminum Mirrors," *Journal of the Optical Society of America* **51**:913–914 (1961).
544. J. T. Cox, G. Hass, and J. E. Waylonis, "Further Studies on LiF-Overcoated Aluminum Mirrors with Highest Reflectance in the Vacuum Ultraviolet," *Applied Optics* **7**:1535–1539 (1968).
545. D. K. Burge, H. E. Bennett, and E. J. Ashley, "Effect of Atmospheric Exposure on the Infrared Reflectance of Silvered Mirrors with and without Protective Coatings," *Applied Optics* **12**:42–47 (1973).
546. G. Hass, J. B. Heaney, J. F. Osantowski, and J. J. Triolo, "Reflectance and Durability of Ag Mirrors Coated with Thin Layers of Al<sub>2</sub>O<sub>3</sub> Plus Reactively Deposited Silicon Oxide," *Applied Optics* **14**:2639–2644 (1975).
547. E. A. Volgunova, G. I. Golubeva, and A. M. Klochkov, "Highly Stable Silver Mirrors," *Soviet Journal of Optical Technology* **50**:128–129 (1983).
548. J. T. Cox, G. Hass, and W. R. Hunter, "Infrared Reflectance of Silicon Oxide and Magnesium Fluoride Protected Aluminum Mirrors at Various Angles of Incidence from 8 μm to 12 μm," *Applied Optics* **14**:1247–1250 (1975).
549. J. T. Cox and G. Hass, "Aluminum Mirrors Al<sub>2</sub>O<sub>3</sub>-Protected with High Reflectance at Normal but Greatly Decreased Reflectance at Higher Angles of Incidence in the 8-12-μm Region," *Applied Optics* **17**:333–334 (1978).

550. W. R. Hunter, J. F. Osantowski, and G. Hass, "Reflectance of Aluminum Overcoated with  $MgF_2$  and LiF in the Wavelength Region from 1600 Å to 300 Å at Various Angles of Incidence," *Applied Optics* **10**:540–544 (1971).
551. S. F. Pellicori, "Infrared Reflectance of a Variety of Mirrors at 45° Incidence," *Applied Optics* **17**:3335–3336 (1978).
552. L. Young, "Multilayer Reflection Coatings on a Metal Mirror," *Applied Optics* **2**:445–447 (1963).
553. M. Z. Leś, F. Leś, and L. Gabla, "Semitransparent Metallic-Dielectric Mirrors with Low Absorption Coefficient in the Ultra-Violet Region of the Spectrum," *Acta Physica Polonica* **23**:211–214 (1963).
554. F. Leś and M. Z. Leś, "Metallic-Dielectric Mirrors with High Reflectivity in the Near Ultra-Violet for the Fabry-Perot Interferometer," *Acta Physica Polonica* **21**:523–528 (1962).
555. G. Hass, J. B. Ramsey, and W. R. Hunter, "Reflectance of Semitransparent Platinum Films on Various Substrates in the Vacuum Ultraviolet," *Applied Optics* **8**:2255–2259 (1969).
556. R. P. Madden, L. R. Canfield, and G. Hass, "On the Vacuum-Ultraviolet Reflectance of Evaporated Aluminum Before and During Oxidation," *Journal of the Optical Society of America* **53**:620–625 (1969).
557. G. Hass and W. R. Hunter, "Calculated Reflectance of Aluminum-Overcoated Iridium in the Vacuum Ultraviolet from 500 Å to 2000 Å," *Applied Optics* **6**:2097–2100 (1967).
558. L. N. Hadley and D. M. Dennison, "Reflection and Transmission Interference Filters. Part I. Theory," *Journal of the Optical Society of America* **37**:451–465 (1947).
559. L. N. Hadley and D. M. Dennison, "Reflection and Transmission Interference Filters. Part II. Experimental, Comparison with Theory, Results," *Journal of the Optical Society of America* **38**:483–496 (1948).
560. S. -y. Zheng and J. W. Y. Lit, "Design of a Narrow-Band Reflection IR Multilayer," *Canadian Journal of Physics* **61**:361–368 (1983).
561. L. A. Stelmack, "Vacuum Ultraviolet Reflectance Filter," U. S. patent 4408825, issued 11 October, 1983.
562. A. F. Turner and H. R. Hopkinson, "Reflection filters for the Visible and Ultraviolet," *Journal of the Optical Society of America* **43**:819 (1953).
563. R. Gamble and P. H. Lissberger, "Reflection Filter Multilayers of Metallic and Dielectric Thin Films," *Applied Optics* **28**:2838–2846 (1989).
564. P. H. Berning, G. Hass, and R. P. Maden, "Reflectance-Increasing Coatings for the Vacuum Ultraviolet and their Applications," *Journal of the Optical Society of America* **50**:586–597 (1960).
565. A. P. Lukirskii, E. P. Savinov, O. A. Ershov, and Y. F. Shepelev, "Reflection Coefficients of Radiation on the Wavelength Range from 23.6 to 113 Å for a Number of Elements and Substances and the Determination of the Refractive index and Absorption Coefficient," *Optics and Spectroscopy (USSR)* **16**:168–172 (1964).
566. A. P. Lukirskii, E. P. Savinov, O. A. Ershov, I. I. Zhukova, and V. A. Forichev, "Reflection of X-Rays with Wavelengths from 23.6 to 190.3 Å. Some Remarks on the Performance of Diffraction Gratings," *Optics and Spectroscopy (USSR)* **19**:237–241 (1965).
567. J. Hecht, "A Novel approach to High XUV Reflectivity," *Lasers and Optronics* **April**:14 (1989).
568. K. Tamura, C. Sakai, N. Yamada, Y. Ogasaka, and R. Shibata, "Development of X-Ray Mirrors for X-Ray Telescopes," *Proc. SPIE* **5900**:051–059 (2005).
569. D. L. Windt, W. C. Cash, Jr., M. Scott, P. Arendt, B. Newnam, R. F. Fisher, A. B. Swartzlander, P. Z. Takacs, and J. M. Pinneo, "Optical Constants for Thin Films of C. Diamond, Al, Si and CVD SiC from 24 Å to 1216 Å," *Applied Optics* **27**:279–295 (1988).
570. R. F. Malina and W. Cash, "Extreme Ultraviolet Reflection Efficiencies of Diamond-Turned Aluminum, Polished Nickel, and Evaporated Gold Surfaces," *Applied Optics* **17**:3309–3313 (1978).
571. R. L. Sandberg, D. D. Allred, J. E. Johnson, and R. S. Turley, "A Comparison of Uranium Oxide and Nickel as Single-layer Reflectors from 2. 7 to 11. 6 Nanometers," *Proc. SPIE* **5193**:191–203 (2004).
572. D. Spiga, G. Pareschi, O. Citterio, R. Banham, S. Basso, M. Cassanelli, V. Cotroneo, et al., "Development of Multilayer Coatings (Ni/C-Pt/C) for Hard X-Ray Telescopes by E-Beam Evaporation with Ion Assistance," *Proc. SPIE* **5488**: 813–819 (2004).
573. V. V. Protopopov and V. A. Kalnov, "X-Ray Multilayer Mirrors with an Extended Angular Range," *Optics Communications* **158**:1–6 (1998).
574. O. Citterio, P. Cerutti, F. Mazzoleni, G. Pareschi, E. Poretti, P. Lagana, A. Mengali, C. Misiano, F. Pozzilli, and E. Simonetti, "Multilayer Optics for Hard X-Ray Astronomy by Means of Replication Techniques," *Proc. SPIE* **3766**:310–319 (1999).

575. V. V. Protopopov, A. V. Tikhonravov, A. V. Voronov, M. K. Trubetskov, and G. W. DeBell, "Optimal Design of Graded X-Ray Multilayer Mirrors in the Angular and Spectral Domains," *Proc. SPIE* **3766**:320–326 (1999).
576. Z. Wang, "Multilayers for the EUV and Soft X-Ray Region," *Proc. SPIE* **5963**:0S 1–12 (2005).
577. K. Yamashita, H. Kunieda, Y. Tawara, K. Tamura, Y. Ogasaka, K. Haga, T. Okajima, et al. "New Design Concept of Multilayer Supermirrors for Hard X-Ray Optics," *Proc. SPIE* **3766**:327–335 (1999).
578. E. van Rooyen and E. Theron, "A Multiple Reflection Multilayer Reflection Filter," *Applied Optics* **8**:832–833 (1969).
579. A. S. Valeyev, "Multilayer Reflection-Type Interference Filters," *Soviet Journal of Optical Technology* **34**:317–319 (1967).
580. Schott and Gen., "Interference Reflection Filter UV-R-250," Geschäftsbereich Optik, Hattenbergstrasse 10, D-6500 Mainz, Germany, 1967.
581. G. Hass, J. B. Heaney, and W. R. Hunter, "Reflectance and Preparation of Front Surface Mirrors for Use at Various Angles of Incidence from the Ultraviolet to the Far Infrared," in *Physics of Thin Films* 12, Academic Press, 1982, pp. 1–51.
582. D. W. Lynch, "Mirror and Reflector Materials," in *Handbook of Laser Science and Technology. Optical Materials: Part 2 IV*, (ed. M. J. Weber), CRC Press, Inc., Boca Raton, Florida, 1986, pp. 185–219.
583. B. T. Sullivan and J. A. Dobrowolski, "Deposition of Optical Multilayer Coatings with Automatic Error Compensation: II. Magnetron Sputtering," *Applied Optics* **32**:2351–2360 (1993).

---

# FUNDAMENTAL OPTICAL PROPERTIES OF SOLIDS

---

Alan Miller

*Scottish Universities Physics Alliance  
School of Engineering and Physical Sciences  
Heriot-Watt University  
Edinburgh, Scotland*

---

## 8.1 GLOSSARY

---

$\underline{A}$	vector field
$\underline{B}$	magnetic induction
$c$	speed of light
$\underline{D}$	displacement field
$d_M$	penetration depth of material
$d_{\text{TIR}}$	evanescent field depth for total internal reflection
$\underline{E}$	electric field
$\mathcal{E}_g$	band gap energy
$\underline{E}_{\text{loc}}$	local electric field
$-e$	electronic charge
$e_i^p$	components of unit vectors of incident polarization
$e_s^p$	components of unit vectors of scattered polarization
$f_j$	oscillator strength
$\underline{G}$	reciprocal lattice vector
$\underline{H}$	hamiltonian
$\underline{H}$	magnetic field
$I$	irradiance
$\underline{I}$	unit tensor
$\underline{J}_c$	conduction current density
$\underline{K}$	dielectric constant or relative permittivity
$\underline{k}$	electron wavevector
$\underline{M}$	induced magnetization
$m$	electron mass
$m^*$	effective electron mass

$\mathbf{N}$	charge density
$N_L$	refractive index for left circularly polarized light
$N_R$	refractive index for right circularly polarized light
$n$	real part of refractive index
$P$	Kane momentum matrix element
$\underline{\mathbf{P}}$	induced dipole moment per unit volume
$P_D$	dielectric amplitude reflection polarization ratio
$\mathbf{p}_{jj}$	momentum matrix element
$P_M$	metallic amplitude reflection polarization ratio
$P_{p\sigma,ij}$	elasto-optic coefficients
$\mathbf{p}$	electron momentum
$\hat{\mathbf{q}}$	complex photon wavevector
$\hat{\mathbf{q}}$	unit photon wavevector
$R$	reflectance
$R_{ex}$	exciton Rydberg
$\mathbf{P}_{\sigma,p}$	Raman scattering coefficient
$r_p$	field reflection amplitude for p-polarization
$r_s$	field reflection amplitude for s-polarization
$\underline{\mathbf{S}}$	Poynting vector
$s_{ij}$	components of lattice strain
$S_R$	Raman scattering efficiency
$S_j$	phonon oscillator strength
$T$	transmittance
$t_p$	field transmission amplitude for p-polarization
$t_s$	field transmission amplitude for s-polarization
$V$	volume of unit cell
$\mathbf{P}(\mathbf{r})$	periodic lattice potential
$v$	phase velocity
$W(\omega)$	transition rate
$Z$	number of electrons per atom
$\alpha$	absorption coefficient
$\beta$	two-photon absorption coefficient
$\Gamma$	damping constant
$\Delta_D$	dielectric reflection polarization phase difference
$\Delta_M$	metallic reflection polarization phase difference
$\Delta_S$	specific rotary power
$\Delta_{SO}$	spin-orbit splitting
$\delta$	energy walk-off angle
$\underline{\underline{\epsilon}}$	electrical permittivity
$\underline{\epsilon}$	complex permittivity
$\epsilon(\infty)$	high frequency permittivity
$\epsilon(0)$	static permittivity
$\epsilon_1$	real part of permittivity
$\epsilon_2$	imaginary part of permittivity
$\epsilon_o$	electrical permittivity of vacuum

$\tilde{\eta}$	complex refractive index
$\bar{\theta}$	principal angle for metallic reflection
$\theta_{\text{OA}}$	angle between optic axis and principal axis
$\theta_B$	Brewster's angle
$\theta_C$	total internal reflection critical angle
$\theta_{\text{TIR}}$	phase change for total internal reflection
$\kappa$	imaginary part of refractive index
$\underline{\underline{\mu}}$	magnetic permeability
$\mu_o$	magnetic permeability of vacuum
$\xi$	Hooke's law constant
$\hat{\xi}$	unit polarization vector
$\rho_f$	free charge density
$\rho_p$	band or polarization charge density
$\rho_p$	real field amplitude for p-polarization
$\rho_s$	real field amplitude for s-polarization
$\rho_t$	total charge density
$\tilde{\sigma}$	complex conductivity
$\underline{\underline{\sigma}}$	electrical conductivity
$\sigma_1$	real part of conductivity
$\sigma_2$	imaginary part of conductivity
$\tau$	scattering or relaxation time
$\phi$	scalar field
$\phi_f$	ground state wavefunction
$\tilde{\chi}$	complex susceptibility
$\chi'$	real part of susceptibility
$\chi''$	imaginary part of susceptibility
$\underline{\underline{\chi}}_e$	electrical susceptibility
$\underline{\underline{\chi}}_m$	magnetic susceptibility
$\Psi_{\mathbf{k}}$	Bloch solution wavefunction
$\omega$	photon frequency
$\omega_j$	resonant oscillation frequency
$\omega_{\text{LO}}$	longitudinal optical phonon frequency
$\omega_p$	plasma frequency
$\omega_s$	surface frequency
$\omega_{\text{TO}}$	transverse optical phonon frequency

## 8.2 INTRODUCTION

This chapter describes the fundamental interactions of light with solids. The discussion is restricted to *intrinsic* optical properties. *Extrinsic* optical properties of solids are described in Chap. 10, "Optical Spectroscopy and Spectroscopic Lineshapes," by Brian Henderson in Vol. I. Basic formulas, definitions, and concepts are listed for reference and as a foundation for subsequent chapters of this *Handbook*. More detailed accounts of specific optical properties and particular types of solids are given in later chapters, that is, Chap. 7, "Optical Properties of Films and Coatings,"



by Jerzy A. Dobrowolski in this volume and Chap. 7, “Electro-Optic Modulators” by Georgetanne M. Purvinis and Theresa A. Maldonado in Vol. V. The reader is referred to the many texts which provide more elaborate discussions of the optical properties of solids.<sup>1-13</sup>

Electrical measurements distinguish three general types of solid by their conductivities, i.e., dielectrics, semiconductors, and metals. Optically, these three groups are characterized by different fundamental bandgap energies,  $\mathcal{E}_g$ . Although the boundaries are not sharply defined, an approximate distinction is given by metals,  $\mathcal{E}_g \leq 0$ , semiconductors,  $0 < \mathcal{E}_g < 3$  eV, and dielectrics,  $\mathcal{E}_g > 3$  eV. Solids may be found in single crystal, polycrystalline, and amorphous forms. Rudimentary theories of the optical properties of condensed matter are based on light interactions with perfect crystal lattices characterized by extended (nonlocal) electronic and vibrational energy states. These eigenstates are determined by the periodicity and symmetry of the lattice and the form of the Coulomb potential which arises from the interatomic bonding.

The principal absorption bands in condensed matter occur at photon energies corresponding to the frequencies of the lattice vibrations (phonons) in the infrared, and electronic transitions in the near infrared, visible, or ultraviolet. A quantum mechanical approach is generally required to describe electronic interactions but classical models often suffice for lattice vibrations. Although the mechanical properties of solids can vary enormously between single crystal and polycrystalline forms, the *fundamental* optical properties are similar, even if the crystallite size is smaller than a wavelength, since the optical interaction is microscopic. However, electronic energy levels and hence optical properties are fundamentally altered when one or more dimensions of a solid are reduced to the scale of the de-Broglie wavelength of the electrons. Modern crystal growth techniques allow fabrication of atomic precision epitaxial layers of different solid materials. Ultrathin layers with dimensions comparable with or smaller than the de-Broglie wavelength of an electron may form quantum wells, quantum wires, and quantum dots in which electronic energy levels are quantized. Amorphous solids have random atomic or molecular orientation on the distance scale of several nearest neighbors, but generally have well-defined bonding and local atomic order which determine the overall optical response.

### 8.3 PROPAGATION OF LIGHT IN SOLIDS

Dielectrics and semiconductors provide transparent spectral regions at radiation frequencies between the phonon vibration bands and the fundamental (electronic) absorption edge. Maxwell’s equations successfully describe the propagation, reflection, refraction, and scattering of harmonic electromagnetic waves.

#### Maxwell’s Equations

Four equations relate the macroscopically averaged electric field  $\mathbf{E}$  and magnetic induction  $\mathbf{B}$ , to the total charge density,  $\rho_t$ , (sum of the bound or polarization charge,  $\rho_p$  and the free charge,  $\rho_f$ ), the conduction current density,  $\mathbf{J}_c$ , the induced dipole moment per unit volume,  $\mathbf{P}$ , and the induced magnetization of the medium,  $\mathbf{M}$ , (expressed in SI units),

$$\nabla \cdot \mathbf{E} = \frac{\rho_t}{\epsilon_0} \quad (1)$$

$$\nabla \times \mathbf{E} = -\frac{\partial \mathbf{B}}{\partial t} \quad (2)$$

$$\nabla \cdot \mathbf{B} = 0 \quad (3)$$

$$\nabla \times \mathbf{B} = \mu_0 \left( \epsilon_0 \frac{\partial \mathbf{E}}{\partial t} + \frac{\partial \mathbf{P}}{\partial t} + \mathbf{J}_c + \nabla \times \mathbf{M} \right) \quad (4)$$

where  $\epsilon_0 = 8.854 \times 10^{-12}$  F/m is the permittivity of vacuum,  $\mu_0 = 4\pi \times 10^{-7}$  H/m is the permeability of vacuum and  $c$  the speed of light in vacuum,  $c = (\epsilon_0 \mu_0)^{-1/2}$ . By defining a displacement field,  $\mathbf{D}$ , and magnetic field,  $\mathbf{H}$ , to account for the response of a medium

$$\mathbf{D} = \mathbf{P} + \epsilon_0 \mathbf{E} \quad (5)$$

$$\mathbf{H} = \frac{\mathbf{B}}{\mu_0} - \mathbf{M} \quad (6)$$

and using the relation between polarization and bound charge density,

$$-\nabla \cdot \mathbf{P} = \rho_p \quad (7)$$

Equations (1) and (4) may also be written in the form

$$\nabla \cdot \mathbf{D} = \rho_f \quad (8)$$

and

$$\nabla \times \mathbf{H} = \frac{\partial \mathbf{D}}{\partial t} + \mathbf{J}_c \quad (9)$$

Vector  $\mathbf{A}$  and scalar  $\phi$  fields may be defined by

$$\mathbf{B} = \nabla \times \mathbf{A} \quad (10)$$

$$\mathbf{E} = -\nabla \phi - \frac{\partial \mathbf{A}}{\partial t} \quad (11)$$

A convenient choice of gauge for the optical properties of solids is the Coulomb (or transverse) gauge

$$\nabla \cdot \mathbf{A} = 0 \quad (12)$$

which ensures that the vector potential  $\mathbf{A}$  is transverse for plane electromagnetic waves, while the scalar potential represents any longitudinal current and satisfies Poisson's equation

$$\nabla^2 \phi = -\frac{\rho_f}{\epsilon_0} \quad (13)$$

Three constitutive relations describe the response of conduction and bound electrons to the electric and magnetic fields

$$\mathbf{J}_c = \underline{\underline{\sigma}} \mathbf{E} \quad (14)$$

$$\mathbf{D} = \mathbf{P} + \epsilon_0 \mathbf{E} = \underline{\underline{\epsilon}} \mathbf{E} \quad (15)$$

$$\mathbf{B} = \mu_0 (\mathbf{H} + \mathbf{M}) = \underline{\underline{\mu}} \mathbf{H} \quad (16)$$

where  $\underline{\underline{\sigma}}$  is the electrical conductivity,  $\underline{\underline{\epsilon}}$  is the electrical permittivity, and  $\underline{\underline{\mu}}$  is the magnetic permeability of the medium and are in general tensor quantities which may depend on field strengths. An alternative relation often used to define a dielectric constant (or relative permittivity),  $\underline{\underline{K}}$  is given by,  $\mathbf{D} = \epsilon_0 \underline{\underline{K}} \mathbf{E}$ . In isotropic media using the approximation of linear responses to electric and magnetic fields,  $\sigma$ ,  $\epsilon$ , and  $\mu$  are constant scalar quantities.

Electric,  $\underline{\chi}_e$ , and magnetic,  $\underline{\chi}_m$ , susceptibilities may be defined to relate the induced dipole moment,  $\mathbf{P}$ , and magnetism,  $\mathbf{M}$  to the field strengths  $\mathbf{E}$  and  $\mathbf{H}$ ,

$$\mathbf{P} = \varepsilon_o \underline{\chi}_e \mathbf{E} \quad (17)$$

$$\mathbf{M} = \varepsilon_o \underline{\chi}_m \mathbf{H} \quad (18)$$

Thus,

$$\underline{\underline{\varepsilon}} = \underline{\underline{\varepsilon}}_o (\mathbf{I} + \underline{\underline{\chi}}_e) \quad (19)$$

and

$$\underline{\underline{\mu}} = \underline{\underline{\mu}}_o (\mathbf{I} + \underline{\underline{\chi}}_m) \quad (20)$$

where  $\mathbf{I}$  is the unit tensor.

## Wave Equations and Optical Constants

The general wave equation derived from Maxwell's equations is

$$\nabla^2 \mathbf{E} - \nabla(\nabla \cdot \mathbf{E}) - \varepsilon_o \mu_o \frac{\partial^2 \mathbf{E}}{\partial t^2} = \mu_o \left( \frac{\partial^2 \mathbf{P}}{\partial t^2} + \frac{\partial \mathbf{J}_c}{\partial t} + \nabla \times \frac{\partial \mathbf{M}}{\partial t} \right) \quad (21)$$

For dielectric, (nonconducting) solids

$$\nabla^2 \mathbf{E} = \mu \varepsilon \frac{\partial^2 \mathbf{E}}{\partial t^2} \quad (22)$$

The harmonic plane wave solution of the wave equation for monochromatic light at frequency,  $\omega$ ,

$$\mathbf{E} = \frac{1}{2} \mathbf{E}_o \exp(i(\mathbf{q} \cdot \mathbf{r} - \omega t)) + c.c. \quad (23)$$

in homogeneous ( $\nabla \varepsilon = 0$ ), isotropic ( $\nabla \cdot \mathbf{E} = 0$ ,  $\mathbf{q} \cdot \mathbf{E} = 0$ ), nonmagnetic ( $\mathbf{M} = 0$ ) solids results in a complex wavevector,  $\tilde{\mathbf{q}}$ ,

$$\tilde{\mathbf{q}} = \frac{\omega}{c} \sqrt{\frac{\varepsilon}{\varepsilon_o} + i \frac{\sigma}{\varepsilon_o \omega}} \quad (24)$$

A complex refractive index,  $\tilde{\eta}$ , may be defined by

$$\tilde{\mathbf{q}} = \frac{\omega}{c} \tilde{\eta} \hat{\mathbf{q}} \quad (25)$$

where  $\hat{\mathbf{q}}$  is a unit vector and

$$\tilde{\eta} = n + i\kappa \quad (26)$$

Introducing complex notation for the permittivity,  $\tilde{\varepsilon} = \varepsilon_1 + i\varepsilon_2$ , conductivity,  $\tilde{\sigma} = \sigma_1 + i\sigma_2$ , and susceptibility,  $\tilde{\chi}_e = \chi'_e + i\chi''_e$ , we may relate

$$\varepsilon_1 = \varepsilon = \varepsilon_o (1 + \chi'_e) = \varepsilon_o (n^2 - \kappa^2) = -\frac{\sigma_2}{\omega} \quad (27)$$

and

$$\varepsilon_2 = \varepsilon_o \chi_e'' = 2\varepsilon_o n \kappa = \frac{\sigma}{\omega} = \frac{\sigma_1}{\omega} \quad (28)$$

Alternatively,

$$n = \left[ \frac{1}{2\varepsilon_o} (\sqrt{\varepsilon_1^2 + \varepsilon_2^2} + \varepsilon_1) \right]^{1/2} \quad (29)$$

$$\kappa = \left[ \frac{1}{2\varepsilon_o} (\sqrt{\varepsilon_1^2 + \varepsilon_2^2} - \varepsilon_1) \right]^{1/2} \quad (30)$$

The field will be modified locally by the induced dipoles. If there is no free charge,  $\rho_f$ , the local field,  $\mathbf{E}_{\text{loc}}$ , may be related to the external field  $\mathbf{E}_i$  in isotropic solids using the Clausius-Mossotti equation which leads to the relation

$$\mathbf{E}_{\text{loc}} = \frac{n^2 + 2}{3} \mathbf{E}_i \quad (31)$$

## Energy Flow

The direction and rate of flow of electromagnetic energy is described by the Poynting vector

$$\mathbf{S} = \frac{1}{\mu_o} \mathbf{E} \times \mathbf{H} \quad (32)$$

The average power per unit area, (irradiance,  $I$ ),  $\text{W}/\text{m}^2$ , carried by a uniform plane wave is given by the time averaged magnitude of the Poynting vector

$$I = \langle \mathbf{S} \rangle = \frac{cn |\mathbf{E}_o|^2}{2} \quad (33)$$

The plane wave field in Eq. (23) may be rewritten for absorbing media using Eqs. (25) and (26)

$$\mathbf{E}(\mathbf{r}, t) = \frac{1}{2} \mathbf{E}_o(\mathbf{q}, \omega) \exp\left(-\frac{\omega}{c} \kappa \hat{\mathbf{q}} \cdot \mathbf{r}\right) \exp\left[i\left(\frac{\omega}{c} \mathbf{n} \hat{\mathbf{q}} \cdot \mathbf{r} - \omega t\right)\right] + c.c. \quad (34)$$

The decay of the propagating wave is characterized by the extinction coefficient  $\kappa$ . The attenuation of the wave may also be described by Beer's law

$$I = I_o \exp(-\alpha z) \quad (35)$$

where  $\alpha$  is the absorption coefficient describing the attenuation of the irradiance,  $I$ , with distance,  $z$ . Thus,

$$\alpha = \frac{2\omega\kappa}{c} = \frac{4\pi\kappa}{\lambda} = \frac{\sigma_1}{\varepsilon_o cn} = \frac{\varepsilon_2 \omega}{\varepsilon_o cn} = \frac{\chi_e'' \omega}{cn} \quad (36)$$

The power absorbed per unit volume is given by

$$P_{\text{abs}} = \alpha I = \frac{\omega \chi''_e}{2} |\mathbf{E}_0|^2 \quad (37)$$

The second exponential in Eq. (34) is oscillatory and represents the phase velocity of the wave,  $v = c/n$ .

## Anisotropic Crystals

Only amorphous solids and crystals possessing cubic symmetry are optically isotropic. In general, the speed of propagation of an electromagnetic wave in a crystal depends both on the direction of propagation and on the polarization of the light wave. The linear electric susceptibility and dielectric constant may be represented by tensors with components of  $\underline{\chi}_e$  given by

$$P_i = \epsilon_0 \chi_{ij} E_j \quad (38)$$

where  $i$  and  $j$  refer to coordinate axes. In an anisotropic crystal,  $\mathbf{D} \perp \mathbf{B} \perp \mathbf{q}$  and  $\mathbf{E} \perp \mathbf{H} \perp \mathbf{S}$ , but  $\mathbf{E}$  is not necessarily parallel to  $\mathbf{D}$  and the direction of energy flow  $\mathbf{S}$  is not necessarily in the same direction as the propagation direction  $\mathbf{q}$ .

From energy arguments it can be shown that the susceptibility tensor is symmetric and it therefore follows that there always exists a set of coordinate axes which diagonalize the tensor. This coordinate system defines the principal axes. The number of nonzero elements for the susceptibility (or dielectric constant) is thus reduced to a maximum of three (for any crystal system at a given wavelength). Thus, the dielectric tensor defined by the direction of the electric field vector with respect to the principal axes has the form

$$\begin{bmatrix} \epsilon_1 & 0 & 0 \\ 0 & \epsilon_2 & 0 \\ 0 & 0 & \epsilon_3 \end{bmatrix}$$

The principal indices of refraction are

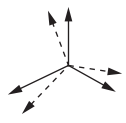
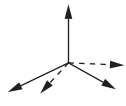
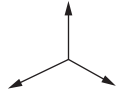
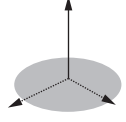
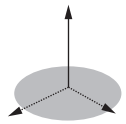
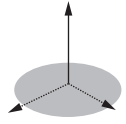
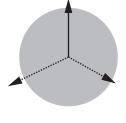
$$n_i = \sqrt{1 + \chi_{ii}} = \sqrt{\epsilon_i} \quad (39)$$

with the  $\mathbf{E}$ -vector polarized along any principal axis, i.e.,  $\mathbf{E} \parallel \mathbf{D}$ . This case is designated as an ordinary or  $\mathbf{o}$ -ray in which the phase velocity is independent of propagation direction. An extraordinary or  $\mathbf{e}$ -ray occurs when both  $\mathbf{E}$  and  $\mathbf{q}$  lie in a plane containing two principal axes with different  $n$ . An *optic axis* is defined by any propagation direction in which the phase velocity of the wave is independent of polarization.

Crystalline solids fall into three classes: (a) optically isotropic, (b) uniaxial, or (c) biaxial (see Table 1). All choices of orthogonal axes are principal axes and  $\epsilon_1 = \epsilon_2 = \epsilon_3$  in *isotropic* solids. For a *uniaxial* crystal,  $\epsilon_1 = \epsilon_2 \neq \epsilon_3$ , a single optic axis exists for propagation in direction  $\mathbf{3}$ . In this case, the ordinary refractive index,  $n_o = n_1 = n_2$ , is independent of the direction of polarization in the 1-2 plane. Any two orthogonal directions in this plane can be chosen as principal axes. For any other propagation direction, the polarization can be divided into an  $\mathbf{o}$ -ray component in the 1-2 plane and a perpendicular  $\mathbf{e}$ -ray component (see Fig. 1). The dependence of the  $\mathbf{e}$ -ray refractive index with propagation direction is given by the ellipsoid,

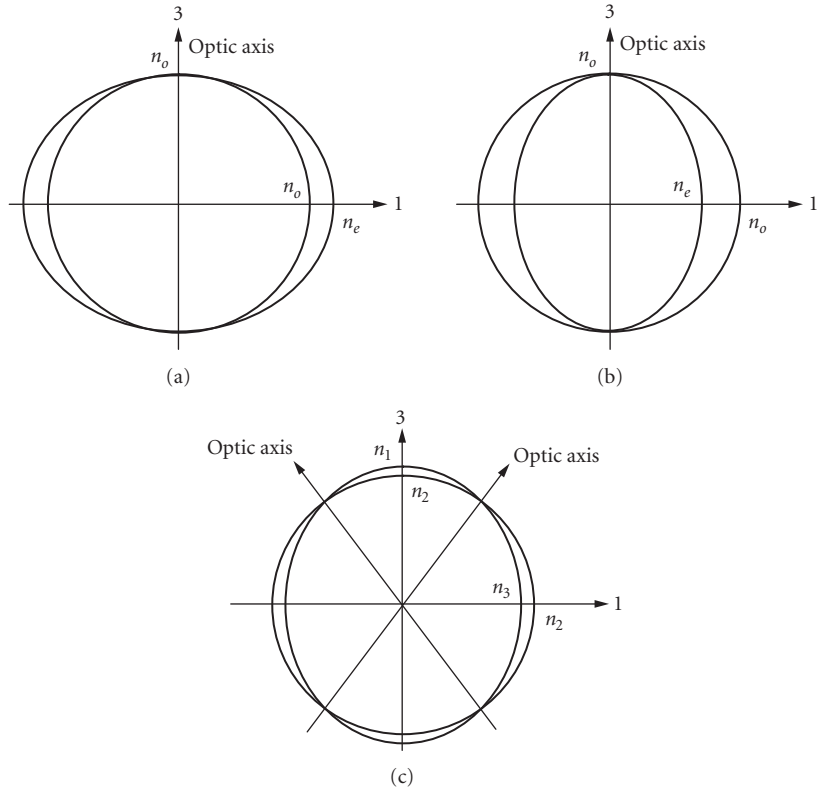
$$n_j(\theta_i) = \frac{n_i n_j}{(n_i^2 \cos^2 \theta_i + n_j^2 \sin^2 \theta_i)^{1/2}} \quad (40)$$

**TABLE 1** Crystallographic Point Groups and Optical Properties

System		Point Group	Symbols	Optical Activity	
		International	Schönflies		
Triclinic	biaxial	$\bar{1}$	$C_1$	A	
		$\bar{1}$	$S_2$	-	
Monoclinic	biaxial	2	$C_2$	A	
		m	$C_v$	-	
		2/m	$C_{2h}$	-	
Orthorhombic	biaxial	mm	$C_{2v}$	-	
		222	$D_2$	A	
		mmm	$D_{2h}$	-	
Trigonal	uniaxial	$\frac{3}{2}$	$C_3$	A	
		$\frac{3}{2}$	$S_6$	-	
		3m	$C_{3v}$	-	
		32	$D_3$	A	
		$\bar{3}m$	$D_{3d}$	-	
Tetragonal	uniaxial	$\frac{4}{2}$	$C_4$	A	
		$\frac{4}{2}$	$S_4$	-	
		4/m	$C_{4h}$	-	
		4mm	$C_{4v}$	-	
		$\bar{4}2m$	$D_{2d}$	A	
		42	$D_4$	A	
		4/mmm	$D_{4h}$	-	
Hexagonal	uniaxial	$\frac{6}{2}$	$C_6$	A	
		$\frac{6}{2}$	$C_{3h}$	-	
		6/m	$C_{6h}$	-	
		6mm	$C_{6v}$	-	
		$\bar{6}m2$	$D_{3h}$	-	
		62	$D_6$	A	
Cubic	isotropic	23	T	A	
		m3	$T_h$	-	
		$\bar{4}3m$	$T_d$	-	
		432	O	A	
		m3m	$O_h$	-	

where  $\theta_i$  is defined with respect to optic axis,  $i = 3$ , and  $j = 1$  or  $2$ .  $\theta_i = 90^\circ$  gives the refractive index  $n_e = n_3$  when the light is polarized along axis 3. The difference between  $n_o$  and  $n_e$  is the birefringence. Figure 1a illustrates the case of positive birefringence,  $n_e > n_o$  and Fig. 1b negative birefringence,  $n_e < n_o$ . The energy walk-off angle,  $\delta$ , (the angle between **S** and **q** or **D** and **E**) is given by

$$\tan \delta = \frac{n^2(\theta)}{2} \left[ \frac{1}{n_3^2} - \frac{1}{n_1^2} \right] \sin 2\theta \quad (41)$$



**FIGURE 1** Illustration of directional dependence of refractive indices and optic axes in (a) a uniaxial, positive birefringent crystal, (b) a uniaxial, negative birefringent crystal, and (c) biaxial crystal.

In *biaxial* crystals, diagonalization of the dielectric tensor results in three independent coefficients,  $\epsilon_1 \neq \epsilon_2 \neq \epsilon_3 \neq \epsilon_1$ . For orthorhombic crystals, a single set of orthogonal principal axes is fixed for all wavelengths. However, in monoclinic structures only one principal axis is fixed. The direction of the other two axes rotates in the plane perpendicular to the fixed axis as the wavelength changes (retaining orthogonality). In triclinic crystals there are no fixed axes and orientation of the set of three principal axes varies with wavelength. Equation (40) provides the e-ray refractive index within planes containing two principal axes. Biaxial crystals possess two optic axes. Defining principal axes such that  $n_1 > n_2 > n_3$ , both optic axes lie in the 1-3 plane, at an angle  $\theta_{OA}$  from axis 1, as illustrated in Fig. 1c, where

$$\sin\theta_{OA} = \pm \frac{n_1}{n_2} \sqrt{\frac{n_2^2 - n_3^2}{n_1^2 - n_3^2}} \quad (42)$$

Crystals with certain point group symmetries (see Table 1) also exhibit optical activity, i.e., the ability to rotate the plane of linearly polarized light. An origin for this phenomenon, is the weak magnetic interaction  $\nabla \times \mathbf{M}$  [see Eq. (21)], when it applies in a direction perpendicular to  $\mathbf{P}$  (i.e.  $\mathbf{M} \parallel \mathbf{P}$ ). The specific rotary power  $\Delta_S$ , (angle of rotation of linearly polarized light per unit length) is given by

$$\Delta_S = \frac{\pi}{\lambda} (n_L - n_R) \quad (43)$$

where  $n_L$  and  $n_R$  are refractive indices for left and right circular polarization. Optical activity is often masked by birefringence; however, polarization rotation can be observed in optically active materials when the propagation is along the optic axis or when the birefringence is coincidentally zero in other directions. In the case of propagation along the optic axis of an optically active uniaxial crystal such as quartz, the susceptibility tensor may be written

$$\begin{bmatrix} \chi_{11} & i\chi_{12} & 0 \\ -i\chi_{12} & \chi_{11} & 0 \\ 0 & 0 & \chi_{33} \end{bmatrix}$$

and the rotary power is proportional to the imaginary part of the magnetic susceptibility,  $\chi_m' = \chi_{12}$ ,

$$\Delta_s = \frac{\pi\chi_{12}}{n\lambda} \quad (44)$$

Crystals can exist in left- or right-handed versions. Other crystal symmetries, e.g.,  $\bar{4}2m$ , can be optically active for propagation along the 2 and 3 axes, but rotation of the polarization is normally masked by the typically larger birefringence except at accidental degeneracies.

## Interfaces

Applying boundary conditions at a plane interface between two media with different indices of refraction leads to the laws of reflection and refraction. Snell's law applies to all o-rays and relates the angle of incidence,  $\theta_A$  in medium A and the angle of refraction,  $\theta_B$  in medium B to the respective ordinary refractive indices  $n_A$  and  $n_B$ ,

$$n_A \sin\theta_A = n_B \sin\theta_B \quad (45)$$

Extraordinary rays do not satisfy Snell's law. The propagation direction for the e-ray can be found graphically by equating the projections of the propagation vectors in the two media along the boundary plane. Double refraction of unpolarized light occurs in anisotropic crystals.

The field amplitude ratios of reflected and transmitted rays to the incident ray ( $r$  and  $t$ ) in isotropic solids (and o-rays in anisotropic crystals) are given by the Fresnel relations. For s- ( $\sigma$  or TE) polarization ( $\mathbf{E}$ -vector perpendicular to the plane of incidence) (see Fig. 2a) and p- ( $\pi$  or TM) polarization ( $\mathbf{E}$ -vector parallel to the plane of incidence) (see Fig. 2b):

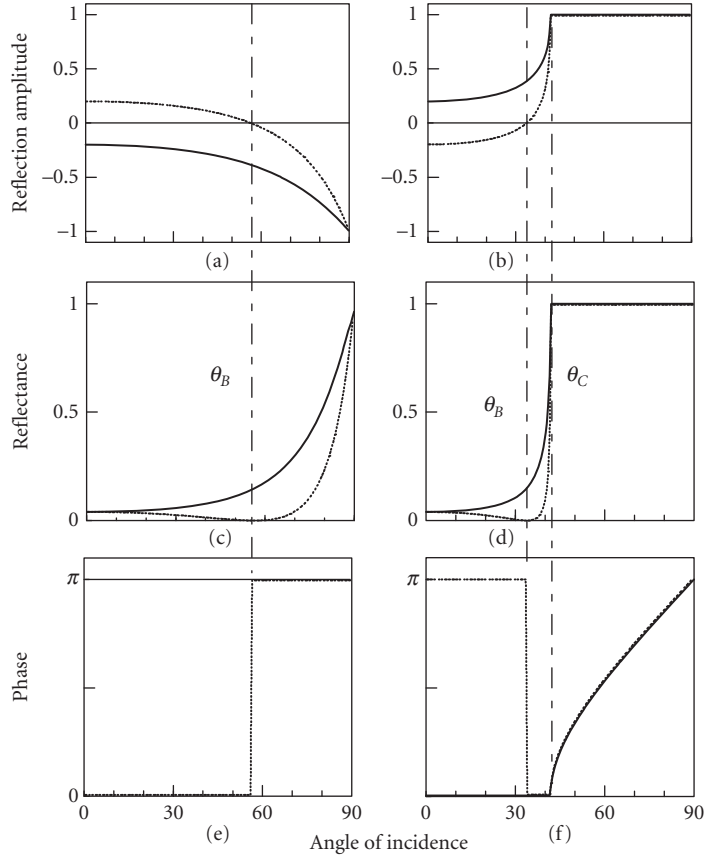
$$r_s = \frac{E_{rs}}{E_{is}} = \frac{n_A \cos\theta_A - \sqrt{n_B^2 - n_A^2 \sin^2\theta_A}}{n_A \cos\theta_A + \sqrt{n_B^2 - n_A^2 \sin^2\theta_A}} \quad (46)$$

$$r_p = \frac{E_{rp}}{E_{ip}} = \frac{\frac{n_B^2 \cos\theta_A - n_A \sqrt{n_B^2 - n_A^2 \sin^2\theta_A}}{n_B^2 \cos\theta_A + n_A \sqrt{n_B^2 - n_A^2 \sin^2\theta_A}}}{n_B^2 \cos\theta_A + n_A \sqrt{n_B^2 - n_A^2 \sin^2\theta_A}} \quad (47)$$

$$t_s = \frac{E_{ts}}{E_{is}} = \frac{2n_A \cos\theta_A}{n_A \cos\theta_A + \sqrt{n_B^2 - n_A^2 \sin^2\theta_A}} \quad (48)$$

$$t_p = \frac{E_{tp}}{E_{ip}} = \frac{2n_A n_B \cos\theta_A}{n_B^2 \cos\theta_A + n_A \sqrt{n_B^2 - n_A^2 \sin^2\theta_A}} \quad (49)$$





**FIGURE 2** The electric field reflection amplitudes (a, b), energy reflectance (c, d), and phase change (e, f) for s- (solid lines) and p- (dashed lines) polarized light for external (a, c, e) and internal (b, d, f) reflection in the case  $n_A = 1$ ,  $n_B = 1.5$ .  $\theta_B$  is the polarizing or Brewster's angle and  $\theta_C$  is the critical angle for total internal reflection.<sup>2</sup>

At normal incidence, the energy reflectance,  $R$ , (see Figs. 2c and d), and transmittance,  $T$ , are

$$R = \frac{|E_r|^2}{|E_i|^2} = \left| \frac{n_B - n_A}{n_B + n_A} \right|^2 \quad (50)$$

$$T = \frac{|E_t|^2}{|E_i|^2} = \frac{4n_A^2}{|n_A + n_B|^2} \quad (51)$$

The p-polarized reflectivity, Eq. (47), goes to zero at Brewster's angle under the condition

$$\theta_B = \tan^{-1} \left( \frac{n_A}{n_B} \right) \quad (52)$$

If  $n_A > n_B$ , total internal reflection (TIR) occurs when the angle of incidence exceeds a critical angle,

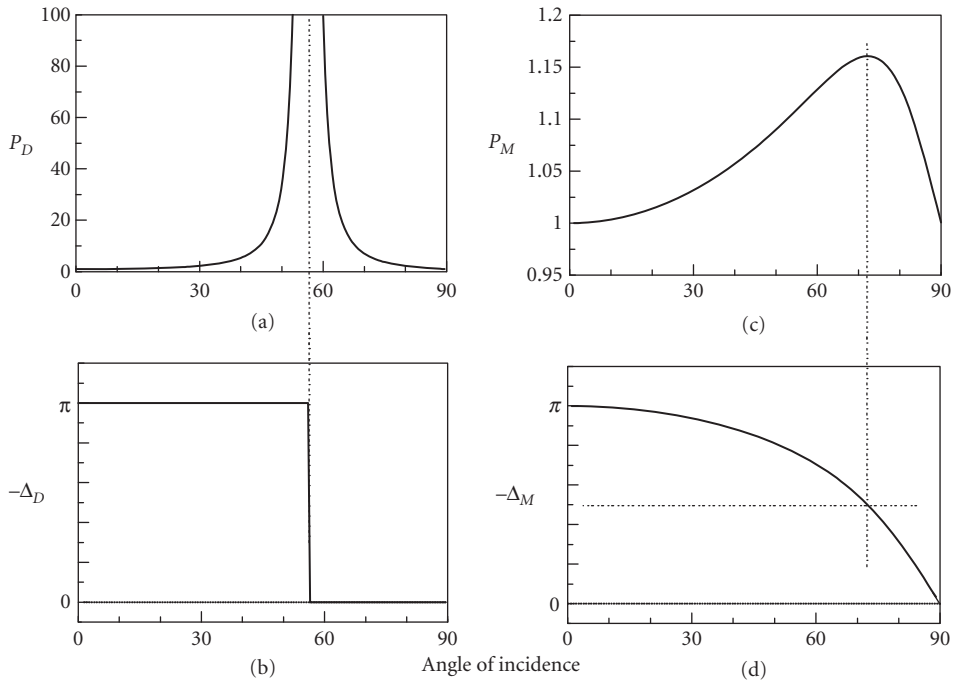
$$\theta_C = \sin^{-1}\left(\frac{n_B}{n_A}\right) \quad (53)$$

This critical angle may be different for s- and p-polarizations in anisotropic crystals. Under conditions of TIR, the evanescent wave amplitude drops to  $e^{-1}$  in a distance

$$d_{\text{TIR}} = \frac{c}{\omega} (n_A^2 \sin^2 \theta_A - n_B^2)^{-1/2} \quad (54)$$

$n_A = 1.5$ ,  $n_B = 1$  are plotted in Fig. 2e and f. Except under TIR conditions, the phase change is either 0 or  $\pi$ . The complex values predicted by Eqs. (46) and (47) for angles of incidence greater than the critical angle for TIR imply phase changes in the reflected light which are neither 0 nor  $\pi$ . The phase of the reflected light changes by  $\pi$  at Brewster's angle in p-polarization. The ratio of s to p reflectance,  $P_D$ , is shown in Fig. 3a and the phase difference,  $\Delta_D = \phi_p - \phi_s$  in Fig. 3b. Under conditions of TIR, the phase change on reflection,  $\phi_{\text{TIR}}$ , is given by

$$\tan \frac{\phi_{\text{TIR}}}{2} = \frac{\sqrt{\sin^2 \theta_A - \sin^2 \theta_C}}{\cos \theta_A} \quad (55)$$



**FIGURE 3** Typical polarization ratios,  $P$ , (a, c) and phase differences  $\Delta$ , (b, d) for s- and p-polarizations at dielectric, D, and metallic, M, surfaces.<sup>1</sup>

## 8.4 DISPERSION RELATIONS

For most purposes, a classical approach is found to provide a sufficient description of dispersion of the refractive index within the transmission window of insulators, and for optical interactions with lattice vibrations and free electrons. However, the details of interband transitions in semiconductors and insulators and the effect of d-levels in transition metals requires a quantum model of dispersion close to these resonances.

### Classical Model

The Lorentz model for dispersion of the optical constants of solids assumes an optical interaction via the polarization produced by a set of damped harmonic oscillators. The polarization  $\mathbf{P}$  induced by a displacement  $\mathbf{r}$  of bound electrons of density  $N$  and charge  $-e$  is

$$\mathbf{P} = -Ne\mathbf{r} \quad (56)$$

Assuming the electrons to be elastically bound (Hooke's law) with a force constant,  $\xi$ ,

$$-e\mathbf{E}_{\text{loc}} = \xi\mathbf{r} \quad (57)$$

the differential equation of motion is

$$m\frac{d^2\mathbf{r}}{dt^2} + m\Gamma\frac{d\mathbf{r}}{dt} + \xi\mathbf{r} = -e\mathbf{E}_{\text{loc}} \quad (58)$$

where  $m$  is the electron mass and  $\Gamma$  is a damping constant. Here the lattice is assumed to have infinite mass and the magnetic interaction has been neglected. Solving the equation of motion for fields of frequency  $\omega$  gives a relation for the complex refractive index and dielectric constant

$$\tilde{n}^2 = \frac{\tilde{\epsilon}}{\epsilon_0} = 1 + \frac{Ne^2}{m\epsilon_0} \sum_j \frac{f_j}{(\omega_j^2 - \omega^2 - i\Gamma_j\omega)} \quad (59)$$

We have given the more general result for a number of resonant frequencies

$$\omega_j = \sqrt{\frac{\xi_j}{m}} \quad (60)$$

where the  $f_j$  represents the fraction of electrons which contributes to each oscillator with force constant  $\xi_j$ .  $f_j$  represents oscillator strengths.

A useful semi-empirical relation for refractive index in the transparency region of a crystal known as the Sellmeier formula follows directly from Eq. (59) under the assumption that, far from resonances, the damping constant terms  $\Gamma_j\omega$  are negligible compared to  $(\omega_j^2 - \omega^2)$

$$n^2 = 1 + \sum_j \frac{A_j\lambda^2}{\lambda^2 - \lambda_j^2} \quad (61)$$

### Sum Rules

The definition of oscillator strength results in the sum rule for electronic interactions

$$\sum_j f_j = Z \quad (62)$$

where  $Z$  is the number of electrons per atom. The periodicity of the lattice in solids (see “Energy Band Structures” in Sec. 8.7) leads to the modification of this sum rule to

$$\sum_m f_{mn} = \frac{m}{\hbar^2} \frac{\partial^2 \mathcal{E}_n}{\partial k^2} - 1 = \frac{m}{m_n^*} - 1 \quad (63)$$

where  $m_n^*$  is an effective mass (see “Energy Band Structures” in Sec. 8.7).

Another sum rule for solids equivalent to Eq. (62) relates the imaginary part of the permittivity or dielectric constant and the plasma frequency,  $\omega_p$ ,

$$\int_0^\infty \omega \varepsilon_2(\omega) d\omega = \frac{1}{2} \pi \omega_p^2 \quad (64)$$

where  $\omega_p^2 = Ne^2 / \varepsilon_0 m$  (see “Drude Model” in Sec. 8.6).

Dispersion relations are integral formulas which relate refractive properties to absorptive process. Kramers-Kronig relations are commonly used dispersion integrals based on the condition of causality which may be related to sum rules. These relations can be expressed in alternative forms. For instance, the reflectivity of a solid is often measured at normal incidence and dispersion relations used to determine the optical properties. Writing the complex reflectivity amplitude as

$$\tilde{r}(\omega) = r_r(\omega) e^{i\theta(\omega)} \quad (65)$$

the phase shift,  $\theta$ , can be determined by integrating the experimental measurement of the real amplitude  $r_r$

$$\theta(\omega) = -\frac{2\omega}{\pi} \mathcal{P} \int_0^\infty \frac{\ln r_r(\omega')}{\omega'^2 - \omega^2} d\omega' \quad (66)$$

and the optical constants determined from the complex Fresnel relation

$$r_r(\omega) e^{i\theta} = \frac{(n-1+i\kappa)}{(n+1+i\kappa)} \quad (67)$$

Sum rules following from the Kramers-Kronig relations relate the refractive index  $n(\omega)$  at a given frequency,  $\omega$ , to the absorption coefficient,  $\alpha(\omega')$ , integrated over all frequencies,  $\omega'$ , according to

$$n(\omega) - 1 = \frac{c}{\omega} \mathcal{P} \int_0^\infty \frac{\alpha(\omega') d\omega'}{\omega'^2 - \omega^2} \quad (68)$$

Similarly, the real and imaginary parts of the dielectric constant,  $\varepsilon_1$  and  $\varepsilon_2$ , may be related via the integral relations

$$\varepsilon_1(\omega) - 1 = \frac{2}{\pi} \mathcal{P} \int_0^\infty \frac{\omega' \varepsilon_2(\omega')}{\omega'^2 - \omega^2} d\omega' \quad (69)$$

$$\varepsilon_2(\omega) = -\frac{2\omega}{\pi} \mathcal{P} \int_0^\infty \frac{\varepsilon_1(\omega') - 1}{\omega'^2 - \omega^2} d\omega' \quad (70)$$

## 8.5 LATTICE INTERACTIONS

The adiabatic approximation is the normal starting point for a consideration of the coupling of light with lattice vibrations, i.e., it is assumed that the response of the outer shell electrons of the atoms to an electric field is much faster than the response of the core together with its inner electron shells. Further, the harmonic approximation assumes that for small displacements, the restoring force on the ions will be proportional to the displacement. The solution of the equations of motion for the atoms within a solid under these conditions gives normal modes of vibration whose frequency eigenvalues and displacement eigenvectors depend on the crystal symmetry, atomic separation, and the detailed form of the interatomic forces. The frequency of lattice vibrations in solids is typically in the 100 to 1000  $\text{cm}^{-1}$  range (wavelengths between 10 and 100  $\mu\text{m}$ ). Longitudinal and doubly degenerate transverse vibrational modes have different natural frequencies due to long range Coulomb interactions. Infrared or Raman activity can be determined for a given crystal symmetry by representing the modes of vibration as irreducible representations of the space group of the crystal lattice.

### Infrared Dipole Active Modes

If the displacement of atoms in a normal mode of vibration produces an oscillating dipole moment, then the motion is dipole active. Thus, harmonic vibrations in ionic crystals contribute directly to the dielectric function, whereas higher order contributions are needed in nonpolar crystals. Since photons have small wavevectors compared to the size of the Brillouin zone in solids, only zone center lattice vibrations, (i.e. long wavelength phonons), can couple to the radiation. This conservation of wavevector (or momentum) also implies that only optical phonons interact. In a dipole active, long wavelength optical mode, oppositely charged ions within each primitive cell undergo oppositely directed displacements giving rise to a nonvanishing polarization. Group theory shows that, within the harmonic approximation, the infrared active modes have irreducible representations with the same transformation properties as  $x$ ,  $y$ , or  $z$ . The strength of the light-dipole coupling will depend on the degree of charge redistribution between the ions, i.e., the relative ionicity of the solid.

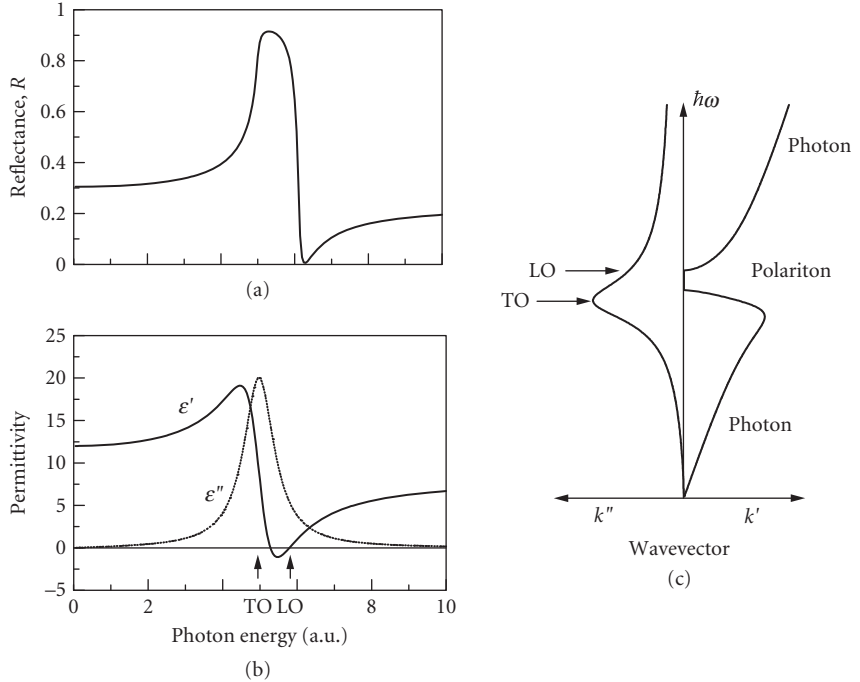
Classical dispersion theory leads to a phenomenological model for the optical interaction with dipole active lattice modes. Because of the transverse nature of electromagnetic radiation, the electric field vector couples with the transverse optical (TO) phonons and the maximum absorption therefore occurs at this resonance. The resonance frequency,  $\omega_{\text{TO}}$ , is inserted into the solution of the equation of motion, Eq. (59). Since electronic transitions typically occur at frequencies  $10^2$  to  $10^3$  higher than the frequency of vibration of the ions, the atomic polarizability can be represented by a single high frequency permittivity,  $\epsilon(\infty)$ . The dispersion relation for a crystal with several zone center TO phonons may be written

$$\tilde{\epsilon}(\omega) = \epsilon(\infty) + \sum_j \frac{S_j}{(\omega_{\text{TO}j}^2 - \omega^2 - i\Gamma_j\omega)} \quad (71)$$

By defining a low frequency permittivity,  $\epsilon(0)$ , the oscillator strength for a crystal possessing two atoms with opposite charge,  $Ze$ , per unit cell of volume,  $V$ , is

$$S = \frac{(\epsilon(\infty)/\epsilon_0 + 2)(Ze)^2}{9m_r V} = \omega_{\text{TO}}^2 (\epsilon(0) - \epsilon(\infty)) \quad (72)$$

where  $Ze$  represents the "effective charge" of the ions,  $m_r$  is the reduced mass of the ions and the local field has been included based on Eq. (31). Figure 4 shows the form of the real and imaginary parts of the dielectric constant, the reflectivity and the polariton dispersion curve. Observing that the real part of the dielectric constant is zero at longitudinal phonon frequencies,  $\omega_{\text{LO}}$ , the



**FIGURE 4** (a) Reflectance and (b) real and imaginary parts of the permittivity of a solid with a single infrared active mode. (c) Polariton dispersion curves (real and imaginary parts) showing the frequencies of the longitudinal and transverse optical modes.

Lyddane-Sachs-Teller relation may be derived, which in its general form for a number of dipole active phonons, is given by

$$\frac{\epsilon(0)}{\epsilon(\infty)} = \prod_j \left( \frac{\omega_{Lj}}{\omega_{Tj}} \right)^2 \quad (73)$$

These relations [see Eqs. (71) to (73)] give good fits to measured reflectivities in a wide range of ionically (or partially ionically) bonded solids. The LO-TO splitting and effective charge,  $Ze$ , depends on the ionicity of the solid; however, the magnitude of  $Ze$  determined from experiments does not necessarily quantify the ionicity since this “rigid ion” model does not account for the change of polarizability due to the distortion of the electron shells during the vibration.

In uniaxial and biaxial crystals, the restoring forces on the ions are anisotropic resulting in different natural frequencies depending on the direction of light propagation as well as the transverse or longitudinal nature of the vibration. Similar to the propagation of light, “ordinary” and “extraordinary” transverse phonons may be defined with respect to the principal axes. For instance, in a uniaxial crystal under the condition that the anisotropy in phonon frequency is smaller than the LO-TO frequency splitting, infrared radiation of frequency  $\omega$  propagating at an angle  $\theta$  to the optic axis will couple to TO phonons according to the relation

$$\omega_T^2 = \omega_{T\parallel}^2 \sin^2 \theta + \omega_{T\perp}^2 \cos^2 \theta \quad (74)$$

where  $\omega_{T\parallel}$  is a TO phonon propagating with atomic displacements parallel to the optic axis, and  $\omega_{T\perp}$  is a TO phonon propagating with atomic displacements perpendicular to the optic axis. The corresponding expression for LO modes is

$$\omega_L^2 = \omega_{L\parallel}^2 \cos^2 \theta + \omega_{L\perp}^2 \sin^2 \theta \quad (75)$$

In Table 2, the irreducible representations of the infrared active normal modes for the different crystal symmetries are labeled  $x$ ,  $y$ , or  $z$ .

## Brillouin and Raman Scattering

Inelastic scattering of radiation by acoustic phonons is known as Brillouin scattering, while the term Raman scattering is normally reserved for inelastic scattering from optic phonons in solids. In the case of Brillouin scattering, long wavelength acoustic modes produce strain and thereby modulate the dielectric constant of the medium thus producing a frequency shift in scattered light. In a Raman active mode, an incident electric field produces a dipole by polarizing the electron cloud of each atom. If this induced dipole is modulated by a lattice vibrational mode, coupling occurs between the light and the phonon and inelastic scattering results. Each Raman or Brillouin scattering event involves the destruction of an incident photon of frequency,  $\omega_i$ , the creation of a scattered photon,  $\omega_s$ , and the creation or destruction of a phonon of frequency,  $\omega_p$ . The frequency shift,  $\omega_i \pm \omega_s = \omega_p$ , is typically 100 to 1000  $\text{cm}^{-1}$  for Raman scattering but only a few wavenumbers for Brillouin scattering.

Atomic polarizability components have exactly the same transformation properties as the quadratic functions  $x^2$ ,  $xy$ ,  $\dots$ ,  $z^2$ . The Raman activity of the modes of vibration of a crystal with a given point group symmetry can thus be deduced from its group theoretical character table. Polarization selection rules may be deduced from the Raman tensors given in Table 2. The scattering efficiency,  $S_R$ , for a mode corresponding to one of the irreducible representations listed is given by

$$S_R = A \left[ \sum_{\rho, \sigma} e_i^\sigma R_{\sigma, \rho} e_s^\rho \right]^2 \quad (76)$$

where  $A$  is a constant of proportionality,  $R_{\sigma, \rho}$  is the Raman coefficient of the representation, and  $e_i^\sigma$  and  $e_s^\rho$  are components of the unit vectors of polarization of the incident,  $i$ , and scattered,  $s$ , radiation along the principal axes, where  $\sigma$  and  $\rho = x, y$ , and  $z$ .

Not all optic modes of zero wavevector are Raman active. Raman activity is often complementary to infrared activity. For instance, since the optic mode in the diamond lattice has even parity, it is Raman active but not infrared active, whereas the zone center mode in sodium chloride is infrared active but not Raman active because the inversion center is on the atom site and so the phonon has odd parity. In piezoelectric crystals, which lack a center of inversion, some modes can be both Raman and infrared active. In this case the Raman scattering can be anomalous due to the long-range electrostatic forces associated with the polar lattice vibrations.

The theory of Brillouin scattering is based on the elastic deformation produced in a crystal by a long wavelength acoustic phonon. The intensity of the scattering depends on the change in refractive index with the strain induced by the vibrational mode. A strain,  $s_{ij}$  in the lattice produces a change in the component of permittivity,  $\epsilon_{\mu\nu}$ , given by

$$\delta \epsilon_{\mu\nu} = - \sum_{\rho, \sigma} \epsilon_{\mu\rho} p_{\rho\sigma, ij} \epsilon_{\sigma\nu} s_{ij} \quad (77)$$

where  $p_{\rho\sigma, ij}$  is an elasto-optical coefficient.<sup>3</sup> The velocity of the acoustic phonons and their anisotropy can be determined from Brillouin scattering measurements.

**TABLE 2** Infrared and Raman-Active Vibrational Symmetries and Raman Tensors<sup>14</sup>

Monoclinic			$\begin{bmatrix} a & d \\ d & c \end{bmatrix}$	$\begin{bmatrix} e & e \\ e & f \end{bmatrix}$			
2	$C_2$		$A(y)$	$B(x,z)$			
m	$C_v$		$A'(x,z)$	$A''(y)$			
2/m	$C_{2h}$		$A_g$	$B_g$			
Orthorhombic			$\begin{bmatrix} a & & \\ & b & \\ & & c \end{bmatrix}$	$\begin{bmatrix} & & d \\ & & d \\ & & e \end{bmatrix}$	$\begin{bmatrix} & & & e \\ & & & f \end{bmatrix}$		
mm	$C_{2v}$		$A_1(z)$	$A_2$	$B_1(x)$	$B_2(y)$	
222	$D_2$		$A$	$B_1(z)$	$B_2(y)$	$B_3(x)$	
mmm	$D_{2h}$		$A_g$	$B_{1g}$	$B_{2g}$	$B_{3g}$	
Trigonal			$\begin{bmatrix} a & & \\ & a & \\ & & b \end{bmatrix}$	$\begin{bmatrix} c & d & e \\ d & -c & f \\ e & f & \end{bmatrix}$	$\begin{bmatrix} d & -c & -f \\ -c & -d & e \\ -f & e & \end{bmatrix}$		
3	$C_3$		$A(z)$	$E(x)$	$E(y)$		
$\bar{3}$	$S_6$		$A_g$	$E_g$	$E_g$		
			$\begin{bmatrix} a & & \\ & a & \\ & & b \end{bmatrix}$	$\begin{bmatrix} c & & d \\ & -c & \\ & d & \end{bmatrix}$	$\begin{bmatrix} & -c & -d \\ -c & & \\ -d & & \end{bmatrix}$		
3m	$C_{3v}$		$A_1(z)$	$E(y)$	$E(-x)$		
32	$D_3$		$A_1$	$E(x)$	$E(y)$		
$\bar{3}m$	$D_{3d}$		$A_{1g}$	$E_g$	$E_g$		
Tetragonal			$\begin{bmatrix} a & & \\ & a & \\ & & b \end{bmatrix}$	$\begin{bmatrix} c & d \\ d & -c \end{bmatrix}$	$\begin{bmatrix} & e & \\ & f & \\ e & f & \end{bmatrix}$	$\begin{bmatrix} & & -f \\ -f & e & e \end{bmatrix}$	
4	$C_4$		$A(z)$	$B$	$E(x)$	$E(y)$	
$\bar{4}$	$S_4$		$A$	$B(z)$	$E(x)$	$E(-y)$	
4/m	$C_{4h}$		$A_g$	$B_g$	$E_g$	$E_g$	
			$\begin{bmatrix} a & & \\ & a & \\ & & b \end{bmatrix}$	$\begin{bmatrix} c & \\ & -c \end{bmatrix}$	$\begin{bmatrix} & d \\ & d \end{bmatrix}$	$\begin{bmatrix} & & e \\ e & & \end{bmatrix}$	$\begin{bmatrix} & & & e \\ & & & e \end{bmatrix}$
4mm	$C_{4v}$		$A_1(z)$	$B_1$	$B_2$	$E(x)$	$E(y)$
$\bar{4}2m$	$D_{2d}$		$A_1$	$B_1$	$B_2(z)$	$E(y)$	$E(x)$
42	$D_4$		$A_1$	$B_1$	$B_2$	$E(-y)$	$E(x)$
4/mmm	$D_{4h}$		$A_{1g}$	$B_{1g}$	$B_{2g}$	$E_g$	$E_g$



**TABLE 2** Infrared and Raman-Active Vibrational Symmetries and Raman Tensors<sup>14</sup>(Continued)

Hexagonal			$\begin{bmatrix} a & & \\ & a & \\ & & b \end{bmatrix}$	$\begin{bmatrix} & c & \\ c & d & \\ & & d \end{bmatrix}$	$\begin{bmatrix} & & -d \\ -d & & c \end{bmatrix}$	$\begin{bmatrix} e & f \\ f & -e \end{bmatrix}$	$\begin{bmatrix} f & -e \\ -e & -f \end{bmatrix}$
6	$C_6$	$A(z)$	$E_1(x)$	$E_1(y)$	$E_2$	$E_2$	
$\bar{6}$	$C_{3h}$	$A'$	$E''$	$E''$	$E'(x)$	$E'(y)$	
6/m	$C_{6h}$	$A_g$	$E_{1g}$	$E_{1g}$	$E_{2g}$	$E_{2g}$	
			$\begin{bmatrix} a & & \\ & a & \\ & & b \end{bmatrix}$	$\begin{bmatrix} & c \\ c & \end{bmatrix}$	$\begin{bmatrix} & -c \\ -c & \end{bmatrix}$	$\begin{bmatrix} d & \\ & d \end{bmatrix}$	$\begin{bmatrix} d & \\ & -d \end{bmatrix}$
6mm	$C_{6v}$	$A_1(z)$	$E_1(y)$	$E_1(-x)$	$E_2$	$E_2$	
$\bar{6}m2$	$D_{3h}$	$A_1$	$E''$	$E''$	$E'(x)$	$E'(y)$	
62	$D_6$	$A_1$	$E_1(x)$	$E_1(y)$	$E_2$	$E_2$	
6/mmm	$D_{6h}$	$A_{1g}$	$E_{1g}$	$E_{1g}$	$E_{2g}$	$E_{2g}$	
Cubic			$\begin{bmatrix} a & & \\ & a & \\ & & a \end{bmatrix}$	$\begin{bmatrix} b & & \\ & b & \\ & & -2b \end{bmatrix}$	$\begin{bmatrix} -3\frac{1}{2}b & & \\ & -3\frac{1}{2}b & \\ & & \end{bmatrix}$	$\begin{bmatrix} & d \\ d & \end{bmatrix}$	$\begin{bmatrix} & & d \\ & d & \\ d & & \end{bmatrix}$
23	$T$	$A$	$E$	$E$	$F(x)$	$F(y)$	$F(z)$
m3	$T_h$	$A_g$	$E_g$	$E_g$	$F_g$	$F_g$	$F_g$
$\bar{4}3m$	$T_d$	$A_1$	$E$	$E$	$F_2(x)$	$F_2(y)$	$F_2(z)$
432	$O$	$A_1$	$E$	$E$	$F_2$	$F_2$	$F_2$
m3m	$O_h$	$A_{1g}$	$E_g$	$E_g$	$F_{2g}$	$F_{2g}$	$F_{2g}$

## 8.6 FREE ELECTRON PROPERTIES

Fundamental optical properties of metals and semiconductors with high densities of free carriers are well described using a classical model. Reflectivity is the primary property of interest because of the high absorption.

### Drude Model

The Drude model for free electrons is a special condition of the classical Lorentz model (Sec. 8.4) with the Hooke's law force constant,  $\xi = 0$ , so that the resonant frequency is zero. In this case,

$$\frac{\epsilon_1}{\epsilon_0} = n^2 - \kappa^2 = 1 - \frac{\omega_p^2}{\omega^2 + \tau^{-2}} \quad (78)$$

and

$$\frac{\epsilon_2}{\epsilon_0} = 2n\kappa = \frac{\omega_p^2}{\omega^2 + \tau^{-2}} \left( \frac{1}{\omega\tau} \right) \quad (79)$$

where  $\omega_p$  is the plasma frequency

$$\omega_p = \sqrt{\frac{Ne^2}{\epsilon_0 m}} = \sqrt{\frac{\mu_0 \sigma c^2}{\tau}} \quad (80)$$

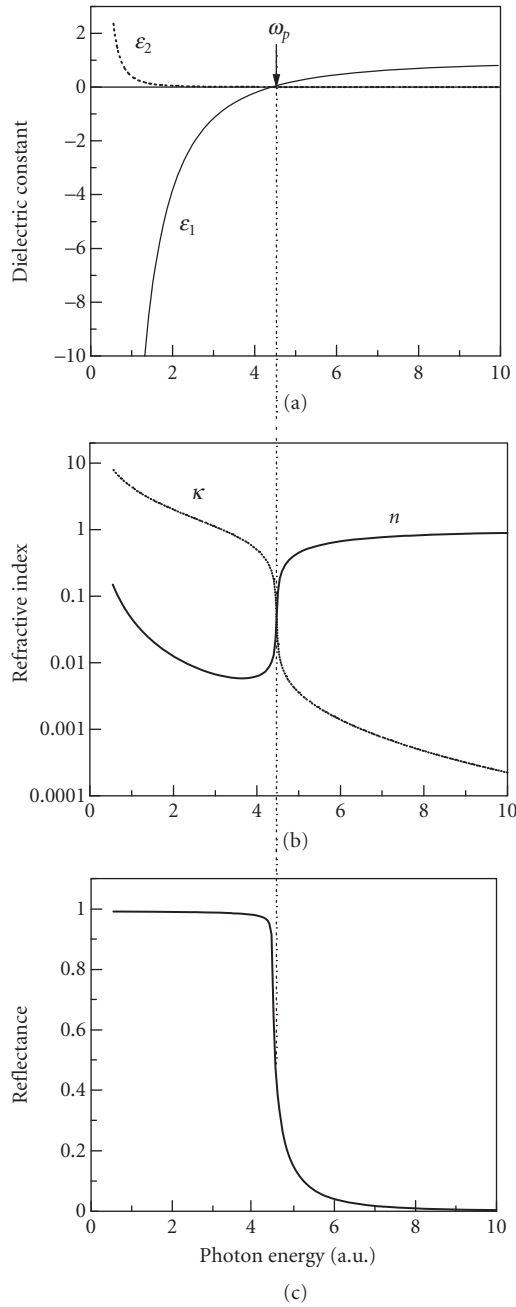
and  $\tau (= 1/\Gamma)$  is the scattering or relaxation time for the electrons. In ideal metals ( $\sigma \rightarrow \infty$ ),  $n = \kappa$ . Figure 5a shows the form of the dispersion in the real and imaginary parts of the dielectric constant for free electrons, while the real and imaginary parts of the refractive index are illustrated in Fig. 5b. The plasma frequency is defined by the point at which the real part changes sign. The reflectivity is plotted in Fig. 5c and shows a magnitude close to 100 percent below the plasma frequency but falls rapidly to a small value above  $\omega_p$ . The plasma frequency determined solely by the free electron term is typically on the order of 10 eV in metals accounting for their high reflectivity in the visible.

### Interband Transitions in Metals

Not all metals are highly reflective below the plasma frequency. The noble metals possess optical properties which combine free electron intraband (Drude) and interband contributions. A typical metal has d-levels at energies a few electron volts below the electron Fermi level. Transitions can be optically induced from these d-states to empty states above the Fermi level. These transitions normally occur in the ultraviolet spectral region but can have a significant influence on the optical properties of metals in the visible spectral region via the real part of the dielectric constant. Describing the interband effects  $\delta\epsilon_b$  within a classical (Lorentz) model the combined effects on the dielectric constant may be added.

$$\tilde{\epsilon} = 1 + \delta\tilde{\epsilon}_b + \delta\tilde{\epsilon}_f \quad (81)$$

The interband contribution to the real part of the dielectric constant is positive and shows a resonance near the transition frequency. On the other hand, the free electron contribution is negative below the plasma frequency. The interband contribution can cause a shift to shorter wavelengths of the zero cross-over in  $\epsilon_1$ , thus causing a reduction of the reflectivity in the blue. For instance d-states in copper lie only 2 eV below the Fermi level, which results in its characteristic color.



**FIGURE 5** Dispersion of: (a) the real and imaginary parts of the dielectric constant; (b) real and imaginary parts of the refractive index; and (c) the reflectance according to the Drude model where  $\omega_p$  is the plasma frequency.

## Reflectivity

Absorption in metals is described by complex optical constants. The reflectivity is accompanied by a phase change and the penetration depth is

$$d_M = \frac{c}{2\omega\kappa} = \frac{\lambda}{4\pi\kappa} \quad (82)$$

At normal incidence at an air-metal interface, the reflectance is given by

$$R = \frac{(n-1)^2 + \kappa^2}{(n+1)^2 + \kappa^2} = 1 - \frac{2}{\kappa} = 1 - 2\sqrt{\frac{2\epsilon_o}{\epsilon_2}} \quad (83)$$

By analogy with the law of refraction (Snell's Law) a complex refractive index can be defined by the refraction equation

$$\sin\theta_t = \frac{1}{\tilde{\eta}} \sin\theta_i \quad (84)$$

Since  $\tilde{\eta}$  is complex,  $\theta_t$  is also complex and the phase change on reflection can take values other than 0 and  $\pi$ . For nonnormal incidence, it can be shown that the surfaces of constant amplitude inside the metal are parallel to the surface, while surfaces of constant phase are at an angle to the surface. The electromagnetic wave in a metal is thus inhomogeneous. The real and imaginary parts of the refractive index can be determined by measuring the amplitude and phase of the reflected light. Writing the s and p components of the complex reflected fields in the form

$$E_{rp} = \rho_p e^{i\phi_p}; \quad E_{rs} = \rho_s e^{i\phi_s} \quad (85)$$

and defining the real amplitude ratio and phase differences as

$$P_M = \tan\psi = \frac{\rho_s}{\rho_p}; \quad \Delta_M = \phi_p - \phi_s \quad (86)$$

then the real and imaginary parts of the refractive index are given by

$$n \approx -\frac{\sin\theta_i \tan\theta_i \cos 2\psi}{1 + \sin 2\psi \cos \Delta_M} = -\sin\bar{\theta}_i \tan\bar{\theta}_i \cos 2\bar{\psi} \quad (87)$$

$$\kappa \approx \tan 2\psi \sin \Delta_M = -\tan 2\bar{\psi} \quad (88)$$

$\bar{\theta}_i$  is the principal angle which occurs at the maximum in  $P_M$  at the condition  $\Delta_M = \pi/2$ , (see Fig. 3c and 3d), which is equivalent to Brewster's angle at an interface between two nonabsorbing dielectrics, (see Fig. 3a and 3b).

## Plasmons

Plasmons are oscillations of fluctuations in charge density. The condition for these oscillations to occur is the same as the condition for the onset of electromagnetic propagation at the plasma frequency. Volume plasmons are not excited by light at normal incidence since they are purely longitudinal. Oscillations cannot be produced by transverse electromagnetic radiation with zero divergence. However at the surface of a solid, an oscillation in surface charge density is possible. At an interface

between a metal with permittivity,  $\epsilon_m$  and a dielectric with permittivity,  $\epsilon_d$ , the condition  $\epsilon_m = -\epsilon_d$  such that (neglecting damping and assuming a free electron metal) a surface plasmon can be created with frequency

$$\omega_s = \frac{\omega_p}{(\epsilon_d/\epsilon_o + 1)^{1/2}} \quad (89)$$

By altering the angle of incidence, the component of the electromagnetic wavevector can be made to match the surface plasmon mode.

## 8.7 BAND STRUCTURES AND INTERBAND TRANSITIONS

Advances in semiconductors for electronic and optoelectronic applications have encouraged the development of highly sophisticated theories of interband absorption in semiconductors. In addition, the development of low dimensional structures (quantum wells, quantum wires, and quantum dots) have provided the means of “engineering” the optical properties of solids. The approach here has been to outline the basic quantum mechanical development for interband transitions in solids.

### Quantum Mechanical Model

The quantum theory of absorption considers the probability of an electron being excited from a lower energy level to a higher level. For instance, an isolated atom has a characteristic set of electron levels with associated wavefunctions and energy eigenvalues. The absorption spectrum of the atom thus consists of a series of lines whose frequencies are given by

$$\hbar \omega_{fi} = \mathcal{E}_f - \mathcal{E}_i \quad (\mathcal{E}_f > \mathcal{E}_i) \quad (90)$$

where  $\mathcal{E}_f$  and  $\mathcal{E}_i$  are a pair of energy eigenvalues. We also know that the spontaneous lifetime,  $\tau$ , for transitions from any excited state to a lower state sets a natural linewidth of order  $\hbar/\tau$  based on the uncertainty principle. The Schrödinger equation for the ground state with wavefunction,  $\varphi_i$ , in the unperturbed system

$$\mathcal{H}_o \varphi_i = \mathcal{E}_i \varphi_i \quad (91)$$

is represented by the time-independent hamiltonian,  $\mathcal{H}_o$ . The optical interaction can be treated by first order perturbation theory. By introducing a perturbation term based on the classical oscillator

$$\mathcal{H}' = e\mathbf{E} \cdot \mathbf{r} \quad (92)$$

this leads to a similar expression to the Lorentz model, Eq. (59)

$$\tilde{\eta}^2 = \frac{\epsilon}{\epsilon_o} = 1 + \frac{Ne^2}{m\epsilon_o} \sum_m \frac{f_{fi}}{(\omega_{fi}^2 - \omega^2 - i\Gamma_{fi}\omega)} \quad (93)$$

where

$$f_{jj} = \frac{2|\mathbf{p}_{jj}|^2}{m\hbar\omega_{jj}} \quad (94)$$

and  $\mathbf{p}_{jj}$  are momentum matrix elements defined by

$$\mathbf{p}_{jj} = \langle \varphi_j | \mathbf{p} | \varphi_j \rangle = \int \varphi_j^* (i\hbar \nabla) \varphi_j d\mathbf{r} \quad (95)$$

Perturbation theory to first order gives the probability per unit time that a perturbation of the form  $\mathcal{H}(t) = \mathcal{H}_p \exp(i\omega t)$  induces a transition from the initial to final state,

$$W_{fi} = \frac{2\pi}{\hbar} \left| \langle \varphi_f | \mathcal{H}_p | \varphi_i \rangle \right|^2 \delta(\mathcal{E}_f - \mathcal{E}_i - \hbar\omega) \quad (96)$$

This is known as Fermi's golden rule.

## Energy Band Structures

If we imagine  $N$  similar atoms brought together to form a crystal, each degenerate energy level of the atoms will spread into a band of  $N$  levels. If  $N$  is large, these levels can be treated as a continuum of energy states. The wavefunctions and electron energies of these energy bands can be calculated by various approximate methods ranging from nearly free electron to tight binding models. The choice of approach depends on the type of bonding between the atoms.

Within the one electron and adiabatic assumptions, each electron moves in the periodic potential,  $V(\mathbf{r})$ , of the lattice leading to the Schrödinger equation for a single particle wavefunction

$$\left[ \frac{p^2}{2m} + V(\mathbf{r}) \right] \psi(\mathbf{r}) = \mathcal{E} \psi(\mathbf{r}) \quad (97)$$

where the momentum operator is given by  $\mathbf{p} = -i\hbar\nabla$ . The simple free electron solution of the Schrödinger equation (i.e., for  $V(\mathbf{r}) = 0$ ), is a parabolic relationship between energy and wavevector. The solution including a periodic potential,  $V(\mathbf{r})$  has the form

$$\psi_{\mathbf{k}}(\mathbf{r}) = \exp(i\mathbf{k} \cdot \mathbf{r}) \cdot u_{\mathbf{k}}(\mathbf{r}) \quad (98)$$

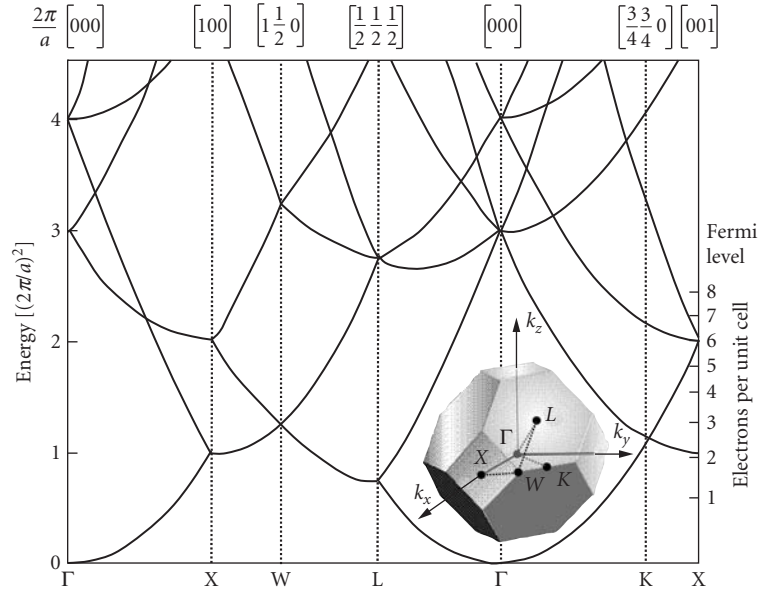
where  $\mathbf{k}$  is the electron wavevector and  $u_{\mathbf{k}}(\mathbf{r})$  has the periodicity of the crystal lattice. This is known as the Bloch solution. The allowed values of  $\mathbf{k}$  are separated by  $2\pi/L$ , where  $L$  is the length of the crystal. The wavevector is not uniquely defined by the wavefunction, but the energy eigenvalues are a periodic function of  $\mathbf{k}$ . For an arbitrarily weak periodic potential

$$\mathcal{E} = \frac{\hbar^2}{2m} |\mathbf{k} + \mathbf{G}|^2 \quad (99)$$

where  $\mathbf{G}$  is a reciprocal lattice vector (in one dimension  $\mathbf{G} = 2\pi n/a$ , where  $a$  is the lattice spacing and  $n$  is an integer. Thus we need only consider solutions which are restricted to a reduced zone, referred to as the first Brillouin zone, in reciprocal space (between  $\mathbf{k} = -\pi/a$  and  $\pi/a$  in one dimension). Higher energy states are folded into the first zone consistent with Eq. (99) to form a series of energy bands. Figure 6 shows the first Brillouin zones for face centered cubic (fcc) crystal lattices and energy levels for a weak lattice potential.

A finite periodic potential,  $V(\mathbf{r})$ , alters the shape of the free electron bands. The curvature of the bands is described by  $m^*$ , an "effective mass," which is defined by the slope of the dispersion curve at a given  $\mathbf{k}$ :

$$\frac{1}{m_{\mathbf{k}}^*} = \frac{1}{\hbar^2 k} \frac{d\mathcal{E}}{dk} \quad (100)$$



**FIGURE 6** Free electron band structure in the reduced Brillouin zone for face-centered-cubic lattices. The insert shows the first Brillouin zone with principal symmetry points labeled. This applies to crystals such as Al, Cu, Ag, Si, Ge, and GaAs.<sup>5</sup>

At the zone center,  $\mathbf{k} = 0$ , this reduces to the parabolic relationship

$$\mathcal{E} = \frac{\hbar^2 k^2}{2m_o^*} \quad (101)$$

Effective masses can be related to interband momentum matrix elements and energy gaps using perturbation theory. Substituting the Bloch function, Eq. (98), into the Schrödinger equation, Eq. (97), and identifying each band by an index,  $j$ , gives

$$\left[ \frac{p^2}{2m} + \frac{\hbar}{m} \mathbf{k} \cdot \mathbf{p} + \frac{\hbar^2 k^2}{2m} + V(\mathbf{r}) \right] u_{j\mathbf{k}}(\mathbf{r}) = \mathcal{E}_{j\mathbf{k}} u_{j\mathbf{k}}(\mathbf{r}) \quad (102)$$

The  $\mathbf{k} \cdot \mathbf{p}$  term can be treated as a perturbation about a specific point in  $\mathbf{k}$ -space. For any  $\mathbf{k}$ , the set of all  $u_{j\mathbf{k}}(\mathbf{r})$  (corresponding to the  $N$  energy levels) forms a complete set, i.e., the wavefunction at any value of  $\mathbf{k}$  can be expressed as a linear combination of all wavefunctions at another  $\mathbf{k}$ . Second order perturbation theory then predicts an effective mass given by

$$\frac{1}{m^*} = \frac{1}{m} + \frac{2}{m} \sum_j \frac{|\mathbf{p}_{jj}|^2}{\mathcal{E}_j(\mathbf{k}) - \mathcal{E}_{j'}} \quad (103)$$

In principle the summation in Eq. (103) is over all bands; however, this can usually be reduced to a few nearest bands because of the resonant denominator. For example, in diamond- and zinc-blended structured semiconductors, the Kane momentum matrix element,  $P$ , defined by

$$P = -\frac{i\hbar}{m} \langle S_{co} | p_x | X_{vo} \rangle \quad (104)$$

successfully characterizes the band structure and optical properties close to zone center. Here  $S_{\text{CO}}$  is a spherically symmetric s-like atomic wavefunction representing the lowest zone center conduction band state and  $X_{\text{VO}}$  is a p-like function with x symmetry from the upper valence bands. In this case, including only the three highest valence bands and the lowest conduction band in the summation of Eq. (91), the conduction band effective mass is given by

$$\frac{1}{m_{\text{co}}^*} = \frac{1}{m} + \frac{2}{3\hbar^2} \left[ \frac{2P^2}{\mathcal{E}_g} + \frac{P^2}{\mathcal{E}_g + \Delta_{\text{SO}}} \right] \quad (105)$$

where  $\mathcal{E}_g$  is the band gap energy and  $\Delta_{\text{SO}}$  is the spin-orbit splitting. By inverting this expression, the momentum matrix element may be determined from measurements of effective mass and the bandgaps.  $P$  is found to have similar magnitudes for a large number of semiconductors. Equation (105) illustrates the general rule that the effective mass of the conduction band is approximately proportional to the band gap energy.

## Direct Interband Absorption

In the case of a solid, the first order perturbation of the single electron hamiltonian by electromagnetic radiation is more appropriately described by

$$\mathcal{H}'(t) = \frac{e}{mc} \mathbf{A} \cdot \mathbf{p} \quad (106)$$

rather than Eq. (92).  $\mathbf{A}$  is the vector potential,

$$\mathbf{A}(\mathbf{r}, t) = A_0 \hat{\xi} \exp[i(\mathbf{q} \cdot \mathbf{r} - \omega t)] + c.c. \quad (107)$$

$\mathbf{q}$  is the wavevector and  $\hat{\xi}$  is the unit polarization vector of the electric field. (Note that this perturbation is of a similar form to the  $\mathbf{k} \cdot \mathbf{p}$  perturbation described earlier.) Using Fermi's golden rule, the transition probability per unit time between a pair of bands is given by

$$W_{fi} = \frac{2\pi}{\hbar} \left( \frac{eA_0}{mc} \right)^2 \left| \langle \psi_f | \hat{\xi} \cdot \mathbf{p} | \psi_i \rangle \right|^2 \delta(\mathcal{E}_f(\mathbf{k}) - \mathcal{E}_i(\mathbf{k}) - \hbar\omega) \quad (108)$$

Conservation of momentum requires a change of electron momentum after the transition; however, the photon momentum is very small, so that vertical transitions in k-space can be assumed in most cases (the electric dipole approximation). The total transition rate per unit volume,  $W_T(\omega)$  is obtained by integrating over all possible vertical transitions in the first Brillouin zone taking account of all contributing bands:

$$W_T(\omega) = \frac{2\pi}{\hbar} \left( \frac{2\pi e^2 I}{ncm^2 \omega^2} \right) \sum_f \int \frac{d\mathbf{k}}{(2\pi)^3} \left| \hat{\xi} \cdot \mathbf{p}_f(\mathbf{k}) \right|^2 \delta(\mathcal{E}_f(\mathbf{k}) - \mathcal{E}_i(\mathbf{k}) - \hbar\omega) \quad (109)$$

Here the vector potential has been replaced with the irradiance,  $I$ , of the radiation through the relation

$$A_0 = \frac{2\pi c}{n\omega^2} I \quad (110)$$



Note that the momentum matrix element as defined in Eq. (95) determines the oscillator strength for the absorption.  $\mathbf{p}_{\bar{n}}$  can often be assumed slowly varying in  $\mathbf{k}$  so that the zone center matrix element can be employed for interband transitions and the frequency dependence of the absorption coefficient is dominated by the density of states.

### Joint Density of States

The delta function in the integration of Eq. (109) represents energy conservation for the transitions between any two bands. If the momentum matrix element can be assumed slowly varying in  $\mathbf{k}$ , then the integral can be rewritten in the form

$$J_{\bar{n}}(\omega) = \frac{1}{(2\pi)^3} \int d\mathbf{k} \delta(\mathcal{E}_f(\mathbf{k}) - \mathcal{E}_i(\mathbf{k}) - \hbar\omega) = \frac{1}{(2\pi)^3} \int \frac{d\mathbf{S}}{|\nabla_{\mathbf{k}} \mathcal{E}_{\bar{n}}(\mathbf{k})|} \quad (111)$$

where  $d\mathbf{S}$  is a surface element on the equal energy surface in  $\mathbf{k}$ -space defined by  $\mathcal{E}_{\bar{n}}(\mathbf{k}) = \mathcal{E}_f(\mathbf{k}) - \mathcal{E}_i(\mathbf{k}) = \hbar\omega$ . Written in this way,  $J(\omega)$  is the joint density of states between the two bands (note the factor of two for spin is excluded in this definition). Points in  $\mathbf{k}$ -space for which the condition

$$\nabla_{\mathbf{k}} \mathcal{E}_{\bar{n}}(\mathbf{k}) = 0 \quad (112)$$

hold form critical points called van Hove singularities which lead to prominent features in the optical constants. In the neighborhood of a critical point at  $\mathbf{k}_c$ , a constant energy surface may be described by the Taylor series

$$\mathcal{E}_{\bar{n}}(\mathbf{k}) = \mathcal{E}_c(\mathbf{k}_c) + \sum_{\mu=1}^3 \beta_{\mu} k_{\mu}^2 \quad (113)$$

where  $\mu$  represents directional coordinates. Minimum, maximum, and saddle points arise depending on the relative signs of the coefficients,  $\beta_{\mu}$ . Table 3 gives the frequency dependence of the joint density of states in three-dimensional (3D), two-dimensional (2D), one-dimensional (1D), and zero-dimensional (0D) solids. The absorption coefficient,  $\alpha$ , defined by Beer's law may now be related to the transition rate by

$$\alpha(\omega) = I^{-1} \frac{dI}{dz} = \frac{\hbar\omega}{I} W_T \quad (114)$$

Thus, the minimum fundamental absorption edge of semiconductors and insulators (in the absence of excitonic effects) has the general form (Fig. 7a)

$$\alpha = A(\hbar\omega - \mathcal{E}_o)^{1/2} \quad (115)$$

### Selection Rules and Forbidden Transitions

Direct interband absorption is allowed when the integral in Eq. (95) is nonzero. This occurs when the wavefunctions of the optically coupled states have opposite parity for single photon transitions. Transitions may be forbidden for other wavefunction symmetries. Although the precise form of the wavefunction may not be known, the selection rules can be determined by group theory from a knowledge of the space group of the crystal and symmetry of the energy band. Commonly, a single photon transition which is not allowed at the zone center because two bands have like parity, will

**TABLE 3** Density of States in 3, 2, 1, and 0 Dimensions

	$\beta_1$	$\beta_2$	$\beta_3$	$E < E_c$	$E > E_c$	
<b>3D</b>						
$M_0$ , min.	+	+	+	0	$C_0(E-E_c)^{1/2}$	
$M_1$ , saddle	+	+	-	$C_1 - C_1'(E_c - E)^{1/2}$	$C_1$	
$M_2$ , saddle	+	-	-	$C_2$	$C_2 - C_2'(E - E_c)^{1/2}$	
$M_3$ , max.	-	-	-	$C_3(E_c - E)^{1/2}$	0	
<b>2D</b>						
$P_0$ , min.	+	+		0	B	
$P_1$ , saddle	+	-		$-\frac{B}{\pi} \ln \left  1 - \frac{E}{E_c} \right $		
$P_2$ , max	-	-		B	0	
<b>1D</b>						
$Q_0$ , min.	+			0	$A(E_c - E)^{-1/2}$	
$Q_1$ , max	-			$A(E - E_c)^{-1/2}$	0	
<b>0D</b>				$\delta(E - E_c)$		

be allowed at finite  $\mathbf{k}$  because wavefunction mixing will give mixed parity states. In this case, the momentum matrix element may have the form

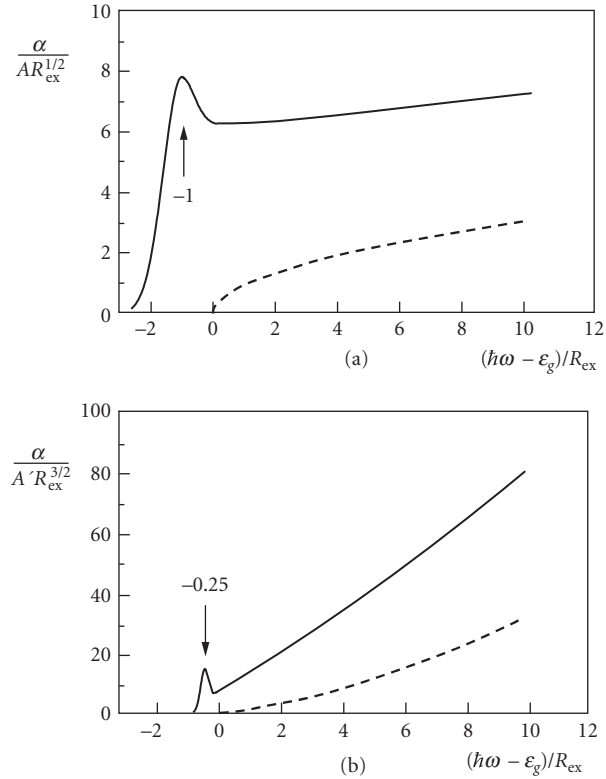
$$p_{\bar{n}}(\mathbf{k}) = (\mathbf{k} - \mathbf{k}_0) \cdot \nabla_{\mathbf{k}} [p_{\bar{n}}(\mathbf{k})]_{\mathbf{k}=\mathbf{k}_0} \quad (116)$$

that is, the matrix element is proportional to  $\mathbf{k}$ . For interband transitions at an  $M_0$  critical point, the frequency dependence of the absorption coefficient can be shown to be (Fig. 7b)

$$\alpha(\omega) = A'(\hbar\omega - \mathcal{E}_c)^{3/2} \quad (117)$$

## Indirect Transitions

Interband transitions may also take place with the assistance of a phonon. The typical situation is a semiconductor or insulator which has a lowest conduction band near a Brillouin zone boundary. The phonon provides the required momentum to move the electron to this location but supplies little energy. The phonon may be treated as an additional perturbation and therefore second order



**FIGURE 7** Illustration of absorption edge of crystals with: (a) direct allowed transitions and (b) direct forbidden transitions, based on density of state (dashed lines) and excitonic enhanced absorption models (solid lines).

perturbation theory is needed in the analysis of this two step processes. Theory predicts a frequency dependence for the absorption of the form

$$\alpha(\omega) \approx (\hbar\omega \pm \hbar\omega_{\text{ph}} - \mathcal{E}_o)^2 \quad (118)$$

where  $\omega_{\text{ph}}$  is the phonon frequency, absorption or emission being possible. For forbidden indirect transitions, this relationship becomes

$$\alpha(\omega) \approx (\hbar\omega \pm \hbar\omega_{\text{ph}} - \mathcal{E}_o)^3 \quad (119)$$

## Multiphoton Absorption

Multiphoton absorption can be treated by higher order perturbation theory. For instance, second order perturbation theory gives a transition rate between two bands

$$W_{\hat{n}}^{(2)} = \frac{2\pi}{\hbar} \left( \frac{eA_o}{mc} \right)^4 \left| \sum_t \frac{\langle \psi_f | \hat{\xi} \cdot \mathbf{P} | \psi_t \rangle \langle \psi_t | \hat{\xi} \cdot \mathbf{P} | \psi_i \rangle}{\mathcal{E}_t - \mathcal{E}_i - \hbar\omega} \right|^2 \delta(\mathcal{E}_f(\mathbf{k}) - \mathcal{E}_i(\mathbf{k}) - 2\hbar\omega) \quad (120)$$

where the summation spans all intermediate states,  $t$ . The interaction can be regarded as two successive steps. An electron first makes a transition from the initial state to an intermediate level of the system,  $t$ , by absorption of one photon. Energy is not conserved at this stage (momentum is) so that the absorption of a second photon must take the electron to its final state in a time determined by the energy mismatch and the uncertainty principle. In multiphoton absorption, one of the transitions may be an intraband self-transition. Since the probability depends on the arrival rate of the second photon, multiphoton absorption is intensity dependent. The total transition rate is given by

$$W_T^{(2)}(\omega) = \frac{2\pi}{\hbar} \left( \frac{4\pi^2 e^4 I^2}{n^2 c^2 m^4 \omega^4} \right) \sum_f \int \frac{d\mathbf{k}}{(2\pi)^3} \left| \sum_t \frac{\hat{\xi}_t \cdot \mathbf{p}_{ft}(\mathbf{k}) \hat{\xi}_t \cdot \mathbf{p}_{ti}(\mathbf{k})}{\mathcal{E}_t - \mathcal{E}_i - \hbar\omega} \right|^2 \delta(\mathcal{E}_f(\mathbf{k}) - \mathcal{E}_i(\mathbf{k}) - 2\hbar\omega) \quad (121)$$

The two photon absorption coefficient is defined by the relation

$$-\frac{dI}{dz} = \alpha I + \beta I^2 \quad (122)$$

so that,

$$\beta(\omega) = \frac{2\hbar\omega}{I^2} W_T^{(2)}(\omega) \quad (123)$$

## Excitons

The interband absorption processes discussed earlier do not take into account Coulomb attraction between the excited electron and hole state left behind. This attraction can lead to the formation of a hydrogen-like bound electron-hole state or exciton. The binding energy of free (Wannier) excitons is typically a few meV. If not thermally washed out, excitons may be observed as a series of discrete absorption lines just below the bandgap energy. The energy of formation of an exciton is

$$\mathcal{E}_{\text{ex}} = \mathcal{E}_g + \frac{\hbar^2 |\mathbf{k}|^2}{2(m_e^* + m_h^*)} - \frac{R_{\text{ex}}}{n^2} \quad (124)$$

where  $R_{\text{ex}}$  is the exciton Rydberg,

$$R_{\text{ex}} = \frac{m_r^* e^4}{2\hbar^2 \epsilon_1^2} \quad (125)$$

$m_r^*$  is the reduced effective mass and  $n$  is a quantum number. Optically created electron-hole pairs have equal and opposite momentum which can only be satisfied if  $\mathbf{K} = 0$  for the bound pair and results in discrete absorption lines. Coulomb attraction also modifies the absorption above the bandgap energy. The theory of exciton absorption developed by Elliot predicts a modification to Eq. (113) for the direct allowed absorption coefficient above the band edge (Fig. 7a)

$$\alpha = \frac{\pi A R_{\text{ex}}^{1/2} e^{\pi\gamma}}{\sinh \pi\gamma} \quad (126)$$

where

$$\gamma = \left( \frac{R_{\text{ex}}}{\hbar\omega - \mathcal{E}_g} \right)^{1/2} \quad (127)$$

Excitons associated with direct forbidden interband transitions do not show absorption to the lowest ( $n = 1$ ) state but transitions to excited levels are allowed. Above the band edge for direct forbidden transitions the absorption has the frequency dependence (Fig. 7b)

$$\alpha = \frac{\pi A' R_{\text{ex}}^{3/2} \left(1 + \frac{1}{\gamma^2}\right) e^{\pi\gamma}}{\sinh \pi\gamma} \quad (128)$$

Figure 7 compares the form of the absorption edge based on the density of states function and a discrete exciton absorption line (dashed lines) with the absorption functions based on the Elliot theory and a typically broadened exciton (solid lines). Figure 7a is an illustration of a direct allowed gap, e.g., GaAs with the  $n = 1$  exciton visible and Fig. 7b shows a forbidden direct absorption edge, e.g.,  $\text{Cu}_2\text{O}$ . In the latter case, optical excitation of the  $n = 1$  exciton is forbidden, but the  $n = 2$  and higher exciton transitions are allowed.

## 8.8 REFERENCES

1. M. Born and E. Wolf, *Principles of Optics*, 6th ed., Pergamon Press, Oxford, 1980.
2. E. A. Wood, *Crystals and Light: An Introduction to Optical Crystallography*, Van Nostrand, Princeton, 1964.
3. J. F. Nye, *Physical Properties of Crystals*, Oxford University Press, Oxford, 1985.
4. J. N. Hodgson, *Optical Absorption and Dispersion in Solids*, Chapman & Hall, London, 1970.
5. F. Wooten, *Optical Properties of Solids*, North Holland, Amsterdam, 1972.
6. F. Abeles (ed.), *Optical Properties of Solids*, North Holland, Amsterdam, 1972.
7. M. Balkanski (ed.), *Optical Properties of Solids*, North Holland, Amsterdam, 1972.
8. G. R. Fowles, *Introduction to Modern Optics*, rev. 2d ed., Dover, Mineola, 1989.
9. B. O. Seraphin, (ed.), *Optical Properties of Solids: New Developments*, North Holland, Amsterdam, 1976.
10. B. E. A. Saleh and M. C. Teich, *Fundamentals of Photonics*, Wiley, New York, 1991.
11. E. Yariv and P. Yey, *Optical Waves in Crystals*, Wiley, New York, 1983.
12. P. Yey, *Optical Waves in Layered Media*, Wiley, New York, 1988.
13. M. Fox, *Optical Properties of Solids*, Oxford University Press, Oxford, 2001.
14. R. Loudon, "The Raman Effect in Crystals," *Adv. Phys.* **13**:423 (1964).

---

# PHOTONIC BANDGAP MATERIALS

---

Pierre R. Villeneuve\*

*Department of Physics  
Massachusetts Institute of Technology  
Cambridge, Massachusetts*

---

## 9.1 GLOSSARY

---

$a$	lattice constant of the periodic structure
$c$	speed of light in vacuum
$E$	energy
$\mathbf{E}$	electric field
$f$	frequency
$f_0$	center frequency of the cavity resonance
$\mathbf{H}$	magnetic field
$\mathbf{k}$	wave vector
$L$	cavity length
$n$	index of refraction
$P$	power
$Q$	quality factor
$\mathbf{r}$	position vector
$V_m$	modal volume
$\Delta f$	frequency width of the cavity resonance
$\epsilon$	macroscopic dielectric function
$\eta$	enhancement factor of the spontaneous emission rate
$\lambda$	wavelength in vacuum
$\omega$	angular frequency
$\Theta$	differential operator

---

\*Current address: MIT Venture Mentoring Service, Massachusetts Institute of Technology, Cambridge, Massachusetts.

## 9.2 INTRODUCTION

---

Electromagnetic waves are known to undergo partial reflection at dielectric interfaces. The magnitude of the reflection is a function of the wave polarization, angle of incidence, and refractive index of the materials at the interface. Inside quarter-wave stacks, electromagnetic waves undergo reflection at multiple interfaces. The multiple reflections can lead to the destructive interference of the waves and the formation of bands of forbidden electromagnetic states. If the frequency of an electromagnetic wave lies inside such a forbidden band, the wave is prevented from propagating inside the stack; instead it is reflected and its amplitude decays exponentially through successive layers.

The operational principle behind fiber Bragg gratings,<sup>1</sup> interference filters,<sup>2</sup> and distributed feedback (DFB) lasers,<sup>3</sup> is also based on multiple reflections that occur inside periodic dielectric materials. The range of frequencies over which waves are reflected (i.e., over which wave propagation is forbidden) defines a stop band, or bandgap, the width of which is proportional to the grating strength (i.e., to the effective index contrast between the different materials). The range is typically less than 1 percent of the midgap frequency, and in some cases much less than 1 percent.

In addition to being forbidden over a small range of frequencies, propagation in dielectric stacks is also forbidden over a small range of angles from normal incidence. This small range of angles defines a cone with its principal axis normal to the surface. Light incident at an angle outside the cone is not reflected, but rather is transmitted through the stack. To increase the angle of the reflection cone, one can increase the index contrast between the different dielectric layers. The cone can be made to extend as far as 90°, allowing light to be reflected off the stack from *any* angle of incidence.<sup>4</sup> Stacks that reflect light from every direction are referred to as *omnidirectional reflectors*.

The existence of omnidirectional reflectors does not necessarily imply the existence of omnidirectional bandgaps. In fact, omnidirectional reflectors do not have complete three-dimensional (3D) bandgaps. Electromagnetic states exist inside the reflectors at every frequency, but incident light cannot couple to them; the wave vector of the incident light cannot be matched to the wave vector of the electromagnetic states inside the reflector. However, if light were to be generated from *within* the reflector, light could propagate along the dielectric planes—hence the absence of a three-dimensional bandgap.

In order to create a complete three-dimensional bandgap and prevent light from propagating anywhere inside the material, periodic structures must possess a three-dimensional periodicity. The principal feature of three-dimensional (3D) bandgap materials is their ability to eliminate the density of electromagnetic states everywhere inside the materials over a given range of frequencies. Since the rate of spontaneous radiative decay of an atom or molecule scales with the density of allowed states at the transition frequency, photonic bandgap (PBG) materials can be used to greatly affect the radiative dynamics of materials and lead to significant changes in the properties of optical devices.

In addition to affecting the radiative properties of atoms, PBG materials can also be used to control the flow of light by allowing certain states to exist within the bandgap. This feature has triggered the imagination of many researchers as it promises to enable the very large-scale integration of photonic components.

Though three-dimensional PBG materials can completely suppress the density of states, some three-dimensional structures possess partial gaps (i.e., gaps that do not extend along every direction). These pseudogaps can lead to small (but nonzero) densities of states and to significant changes in the radiative properties of materials. Moreover, dielectric stacks, in effect one-dimensional periodic structures, can reduce the density of states by suppressing states with wave vectors normal to the layers but they cannot eliminate every state along every direction.

In this chapter, we discuss the radiative properties of emitters and the control of light flow in PBG materials with pseudogaps and complete gaps. An in-depth review of PBG materials can be found in Ref. 5. Early fabrication efforts of 3D PBG materials are described in Ref. 6; a review of PBG materials at near-infrared frequencies is presented in Ref. 7.

## 9.3 MAXWELL'S EQUATIONS

---

Although the word *photon* is used, the appearance of bandgaps arises from a strictly classical treatment of the problem. The properties of PBG materials can be determined from the classical vector wave

equation with a periodic index of refraction. If the fields are expanded in a set of harmonic modes, in the absence of external currents and sources, Maxwell's equations can be written in the following form:

$$\nabla \times \left[ \frac{1}{\varepsilon(\mathbf{r})} \nabla \times \mathbf{H}(\mathbf{r}) \right] = \frac{\omega^2}{c^2} \mathbf{H}(\mathbf{r}) \quad (1)$$

where  $\mathbf{H}(\mathbf{r})$  is the magnetic field,  $\varepsilon(\mathbf{r})$  is the macroscopic dielectric function equal to the square of the index of refraction,  $\mathbf{r}$  is the position vector,  $\omega$  is the angular frequency, and  $c$  is the speed of light in vacuum. The macroscopic dielectric function has a periodic spatial dependence. Equation (1) is an eigenvalue problem; it can be rewritten as

$$\Theta \mathbf{H}_i = \frac{\omega_i^2}{c^2} \mathbf{H}_i \quad (2)$$

where

$$\Theta = \nabla \times \frac{1}{\varepsilon(\mathbf{r})} \nabla \times \quad (3)$$

is a periodic Hermitian differential operator and  $\omega_i^2/c^2$  is the  $i$ th eigenvalue. The solutions  $\mathbf{H}_i$  and  $\omega_i$  are determined entirely from the strength and symmetry properties of  $\varepsilon(\mathbf{r})$ . The solutions are characterized by a wave vector  $\mathbf{k}$  and a band number  $i$ . The region of all allowed wave vectors is called a *Brillouin zone*, and the collection of all solutions is termed a *band structure*.

Equation (2) closely resembles Schrödinger's equation for the problem of an electronic wave function inside a periodic atomic potential. Since the solutions of Schrödinger's equation lead to band diagrams for allowed and forbidden electronic states in crystalline structures, and since PBG materials have similar effects on electromagnetic waves, PBG materials are often referred to as *photonic crystals*. In this chapter, the terms *PBG material* and *photonic crystal* are used interchangeably.

An interesting feature of Eq. (1) is that there is no fundamental constant with dimensions of length, hence no fundamental length scale other than the assumption that the system is macroscopic. The solution at one length scale determines the solutions at all other length scales, assuming a frequency-independent dielectric function. This simple fact is of considerable practical importance as it allows results to be scaled from one wavelength to another, from the ultraviolet to microwaves and beyond, simply by expanding all distances.

The solutions  $\mathbf{H}_i$  and  $\omega_i$  provide information about the frequency of the allowed electromagnetic modes in a PBG structure and their polarization, symmetry, and field distribution. Although Eq. (1) can be applied to any dielectric structure—the only assumptions made were the absence of external currents and sources—early work in this field focused on the search for a complete bandgap, that is, a range of frequencies with no allowed electromagnetic mode for any wave vector  $\mathbf{k}$  inside the Brillouin zone.<sup>6</sup> A review of three-dimensional photonic crystals follows.

Several numerical methods have been used to solve Maxwell's equations in periodic structures, including the use of a variational approach<sup>8</sup> where each eigenvalue in Eq. (2) is computed separately by minimizing the functional  $\langle \mathbf{H}_i | \Theta | \mathbf{H}_i \rangle$ . In this method, fast Fourier transforms are used repeatedly to switch back and forth between real and reciprocal space to avoid storing large matrices.

Other methods include the transfer matrix method<sup>9</sup> and the finite-difference time-domain (FDTD) method,<sup>10</sup> to name but two. In the former, Maxwell's equations are solved at a fixed frequency by stepping the fields forward in space, one plane at a time, satisfying the continuity conditions at every step. The transfer matrix method is well-suited for transmission and reflection computations in photonic crystals. By imposing Bloch conditions, the transfer matrix method can also be used to compute the band structure. In the case of the FDTD method, Maxwell's equations are discretized on a three-dimensional grid, and the derivatives are approximated at each grid point by a corresponding centered difference. Maxwell's equations are solved everywhere in the computational cell at every time step, allowing the temporal response of the fields to be determined inside photonic crystals.



## 9.4 THREE-DIMENSIONAL PHOTONIC CRYSTALS

### Criteria for 3D Bandgaps

The existence of bandgaps in periodic structures is determined entirely from the symmetry and strength of the periodic dielectric function. Since photonic crystals do not occur naturally, somehow one must arrange dielectric material in a 3D periodic structure, and, as with multilayer dielectric stacks, the length of the repeating unit must be on the order of one-half the wavelength in the material. Most structures exhibiting 3D bandgaps satisfy the following three general criteria: the periodic structure has a spherelike Brillouin zone; the refractive index contrast between the different materials is typically larger than 2; and the high- and low-dielectric materials form connected networks.

**Spherelike Brillouin Zone** Waves propagating inside a periodic structure sense a periodicity that leads to the formation of stop bands at the edges of the irreducible Brillouin zone. Since the waves sense a different periodicity along the different directions, the wave vectors at the different points on the surface of the Brillouin zone have different magnitudes. Hence, the gaps are likely to be centered at different frequencies. Spherical Brillouin zones (if they were possible) would guarantee the overlap of all the gaps along every direction, since every point on the surface of a sphere is equidistant from the center—but crystal geometries do not allow for spherical Brillouin zones.

Several hundred years of mineralogy and crystallography have led to the classification of the various three-dimensionally periodic lattice geometries. The Brillouin zone of the face-centered-cubic (fcc) lattice is closer to a sphere than any other common crystal geometry. However, despite having the most spherelike Brillouin zone, the farthest point on the surface of the fcc Brillouin zone (i.e., the point with the largest wave vector, the so-called **W** point) lies 29 percent farther from the origin than the closest point, the **L** point. For a gap to open along every direction, the gaps at **W** and **L** must be large enough to overlap.

**Large Index Contrast** The size of the bandgap at each point on the surface of the Brillouin zone scales with the index contrast between the different materials. For the different gaps to overlap over the entire Brillouin zone the refractive index contrast must be large, typically 2 to 1 or greater. Semiconductor materials such as Si ( $n = 3.5$  at  $\lambda = 1.5 \mu\text{m}$ ) and GaAs ( $n = 3.4$ ) in combination with air or low-index oxides are excellent candidates for the fabrication of photonic crystals at infrared wavelengths.

A large index contrast and a spherelike Brillouin zone, however, are not sufficient to guarantee the formation of a bandgap in 3D structures. It is not sufficient to specify the structure in reciprocal space—there are essentially an infinite number of structures with an fcc lattice, since anything can be put inside the fundamental repeating unit. One must also specify the dielectric structure in real space. An example of a successful 3D photonic crystal is shown in the forthcoming section labeled “Examples of 3D Crystals.”

**Connected Networks** To appreciate the importance of having a connected network, it is useful to consider a one-dimensionally periodic structure such as a multilayer dielectric stack. The energy density of the mode below the stop band is more strongly localized in the high-index layers than the mode above the stop band. The more strongly the energy density of the lower mode is localized in the high-index material and the more strongly the energy density of the upper mode is localized in the low-index material, the larger the bandgap.

In 3D periodic structures, it is generally advantageous for the high-index material to be fully connected to allow the electric field of the mode in the lower band to run through the high-index material as much as possible without having to go through the low-index material. One should be able to connect any point in the high-index material to any other point without having to cross over into the low-index material. The same also holds for the low-index material. Moreover, the low-index material should occupy typically over 50 percent of the total volume. A detailed discussion of the nature of bandgaps in periodic structures is given in Refs. 5 and 11.

The three general criteria just presented should serve only as guidelines. They do not constitute necessary conditions for the creation of 3D bandgaps. For example, though the fcc lattice is the most spherelike, other lattice geometries have been shown to generate 3D bandgaps.

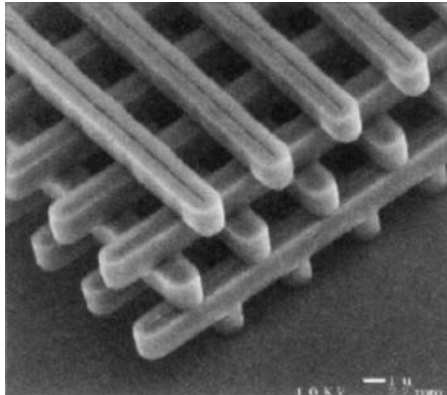
## Examples of 3D Crystals

The earliest antecedent to photonic bandgaps is the observation by Sir Lawrence Bragg of narrow stop bands in crystals from x-ray diffraction. The refractive index contrast, however, was very small, typically less than 1.001 to 1, and produced only narrow rings on the surfaces of the Brillouin zone.

The first structure with a full 3D bandgap was discovered by K. M. Ho et al. in 1990 and consisted of a diamond lattice of air spheres (i.e., an fcc lattice with two air spheres per unit cell) inside a high-index material.<sup>12</sup> Since then, there has been considerable effort to develop a process for the manufacturing of diamond (or diamondlike) structures at micrometer wavelengths. One such approach consists of etching a large number of hole triplets at off-vertical angles in a slab;<sup>13,14</sup> another consists of building an orderly stacking of dielectric rods;<sup>15</sup> yet another consists of etching a series of horizontal grooves into sequentially grown layers and etching vertical holes.<sup>16</sup> These structures are variations of the same diamond lattice grown along either the (1, 1, 1), (0, 0, 1), or (1, 1, 0) directions, respectively.

An example of the structure grown along the (0, 0, 1) direction is shown in Fig. 1. It consists of multiple layers of polycrystalline silicon rods with a stacking sequence that repeats itself every four layers. Within each layer, the rods are parallel to each other; the rods are shifted by half a period every other layer. Only five layers are shown. The structure was fabricated by S. Y. Lin et al. at Sandia National Laboratories in 1998 using a process that involves the repetitive deposition and etching of multiple dielectric films.<sup>17</sup> The width of each rod is roughly 1.2  $\mu\text{m}$ . The bandgap is centered at a wavelength of 10  $\mu\text{m}$ . In addition to fabricating this structure, the researchers also fabricated a structure at shorter wavelengths centered at  $\lambda = 1.5 \mu\text{m}$ .<sup>7</sup>

An overview of the fabrication of 3D PBG materials at micrometer and submicrometer length scales can be found in Ref. 7.



**FIGURE 1** Scanning electron micrograph of a three-dimensional photonic crystal built at Sandia National Laboratories. The crystal consists of five layers of polycrystalline silicon rods. The width of the rods is 1.2  $\mu\text{m}$ . The photonic bandgap is centered around a wavelength of 10  $\mu\text{m}$ .

## 9.5 MICROCAVITIES IN THREE-DIMENSIONAL PHOTONIC CRYSTALS

From Fermi's golden rule, we know that the rate of spontaneous radiative decay of an atom scales with the density of allowed states at the atomic transition frequency. In free space, the density of states scales quadratically with frequency, and the probability of finding an atom in an excited state simply decays exponentially with time.

The introduction of boundaries in the vicinity of the atom has the effect of changing the density of allowed states. For example, in the case of a bounded system with reflecting walls—such as a laser cavity—the density of states is reduced to a spectrally discrete set of peaks, each corresponding to a resonant longitudinal mode of the cavity. When no mode falls within the emission linewidth of the atomic transition, atomic radiative decay is essentially suppressed. However, if the transition frequency overlaps one of the resonant frequencies, the density of available modes for radiative decay becomes very large, which in turn enhances the rate of spontaneous emission. In conventional solid-state lasers, several modes fall within the atomic emission linewidth. The free spectral range of the modes is given by  $c/2nL$ , where  $n$  is the refractive index of the host material and  $L$  is the distance between the reflectors. If  $L$  was made very small, it would be possible to increase the mode spacing such that only one (or even zero) mode would fall within the emission linewidth.

An example of a small laser cavity is the distributed feedback (DFB) laser consisting of a spatially corrugated waveguide with a quarter-wave phase shift. The phase shift defines a cavity, and the grating on either side acts like a mirror. The length  $L$  of the cavity is characterized by the decay length of the evanescent field along the axis of the grating and typically extends over hundreds of wavelengths in the material. The grating creates a stop band along the periodic axis. While the absence of longitudinal modes inside the stop gap reduces the total density of states, the presence of a quarter-wave phase shift generates a resonant mode inside the gap and increases the density of states. The increase is sufficiently large to allow single-mode action of the laser at the resonant frequency. Though DFB lasers have longitudinal stop bands, the total density of states is not zero, since the stop band extends only inside a small cone along one direction. Leaky radiation modes exist along every other direction.

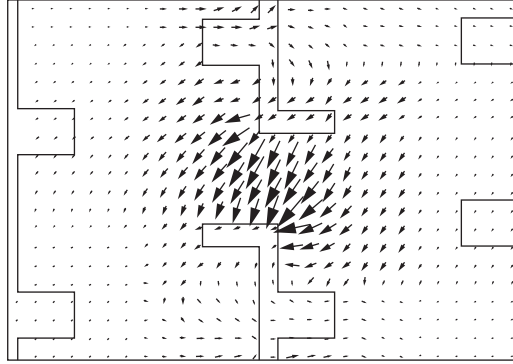
3D PBG materials have the ability to open 3D stop bands that reflect light along every direction in space and that completely eliminate the density of states for a given range of frequencies. In the case where the radiative transition frequency of an atom falls within the frequency gap of the crystal, spontaneous radiative decay is essentially suppressed.

If a small defect (or phase shift) is introduced in the photonic crystal, a mode can be created within the structure at a frequency that lies inside the gap. If the size of the defect is such that it supports a mode, the defect behaves like a microcavity surrounded by reflecting walls. If the radiative transition frequency of the atom matches that of the defect mode, the rate of spontaneous emission can be enhanced.

Figure 2 shows the vector plot of a resonant mode in a 3D photonic crystal similar to the one shown in Fig. 1. The defect is located at the center of the crystal and consists of a broken high-index rib. (The defect could be introduced, for instance, in one of the layers during the growth of the crystal.) The electric field is shown in the vertical plane through the middle of the defect. The mode is strongly localized in all three dimensions, and its amplitude falls off sharply away from the defect. The electric field *jumps* from one edge of the broken rib to the other, while the magnetic field (not shown) has the shape of a torus and runs around the electric field. The frequency of the mode is  $f = 0.59c/a$ , where  $a$  is the lattice constant (i.e., the length of the repeating unit cell) of the crystal. In this particular example, the high-index material has a refractive index of 3.4; the low-dielectric material has an index of 1.0; and the gap extends from  $f = 0.52c/a$  to  $0.66c/a$ .

In contrast to defects in one-dimensional periodic structures (such as DFB lasers), arbitrarily small defects in 3D crystals do not necessarily lead to the creation of localized modes. The volume of the defect must reach a certain threshold to sustain a resonant mode. Furthermore, quarter-wave shifts in DFB lasers lead to resonant modes at the center of the gap. There is no simple equivalent in 3D crystals.

The frequency of the resonant mode changes with the size and shape of the defect. The simple action of adjusting the defect size provides tunability of the resonant mode and affects the localization



**FIGURE 2** Vector plot of the electric field in a 3D PBG with a defect. The overlay indicates the edges of the high-dielectric material. The defect, located at the center of the figure, is fabricated by breaking one of the dielectric ribs. The defect supports a localized resonant mode inside the crystal.

strength. The field attenuation through successive unit cells is stronger for modes lying near the center of the gap than for those lying near the edges.

Although the microcavity in the just-noted example was created by removing part of a high-index rib, a cavity could equally have been created either by adding material between ribs or by changing the shape of one or more ribs. Also, multiple high-order localized modes may appear inside the crystal as the size of the defect is made bigger.

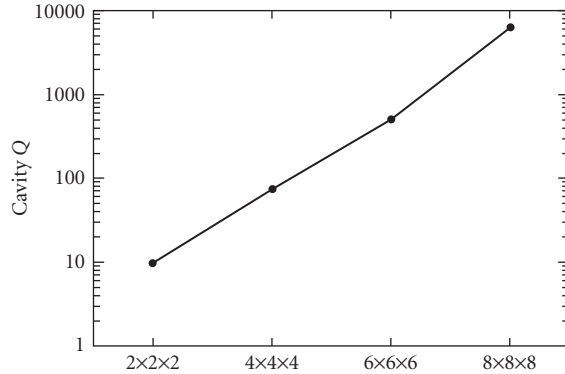
## Quality Factor

One important aspect of microcavities in finite-sized crystals is the quality factor  $Q$  of the resonator defined as:<sup>18</sup>

$$Q = \frac{2\pi f_0 E}{P} = -\frac{2\pi f_0 E}{dE/dt} \quad (4)$$

where  $f_0$  is the resonant frequency,  $E$  is the energy stored inside the resonator, and  $P = -dE/dt$  is the dissipated power. Hence, a resonator can sustain  $Q$  oscillations before its energy decays by a factor of  $e^{-2\pi}$  (i.e., a reduction of 99.8 percent) of its initial value. In the specific case where the line-shape of the resonance is a Lorentzian, Eq. (4) reduces to  $f_0/\Delta f$ , where  $\Delta f$  is the width of the resonance.

Since the quality factor is a measure of the optical energy stored in the microcavity over the cycle-average power radiated out of the cavity,  $Q$  is expected to be largest for modes lying near the center of the gap where the field attenuation is strongest.  $Q$  is also expected to increase with the size of the crystal, since the reflectivity increases with the number of periods (i.e., the leakage from the edges of the crystal becomes progressively smaller). The quality factor of the mode shown in Fig. 2 is plotted in Fig. 3 as a function of the size of the crystal. The quality factor is computed using the finite-difference time-domain method described in Sec. 9.3. First the resonant mode is excited and the total energy is monitored as a function of time. Then the time required for 99.8 percent of the energy to escape is recorded. Results are shown for crystal sizes of dimension  $2N \times 2N \times 2N$ . In each case, the defect is surrounded by  $N$  unit cells along every direction.  $Q$  increases exponentially with the size of the crystal and reaches a value close to  $10^4$  with as little as four unit cells on either side of the defect. The steepness



**FIGURE 3** Quality factor of the resonant cavity shown in Fig. 2 as a function of the size of the 3D photonic crystal, given in units of cubic lattice constants.

of the slope in Fig. 3 follows directly from the field attenuation through each successive lattice of the crystal. Since the only energy loss in the structure occurs from tunneling through the walls of the finite-sized crystal (i.e., intrinsic losses due to material absorption is not considered),  $Q$  does not saturate even for a large number of unit cells. A more detailed description of the properties of resonant modes in photonic crystals can be found in Ref. 19.

### Enhancement of Spontaneous Emission

By coupling an optical transition to the microcavity resonance, the spontaneous emission rate can be enhanced by a factor  $\eta$  over the rate without a cavity. The expression for  $\eta$  is given by:<sup>20</sup>

$$\eta = \frac{2Q}{\pi V_m} \left( \frac{\lambda}{2n} \right)^3 \quad (5)$$

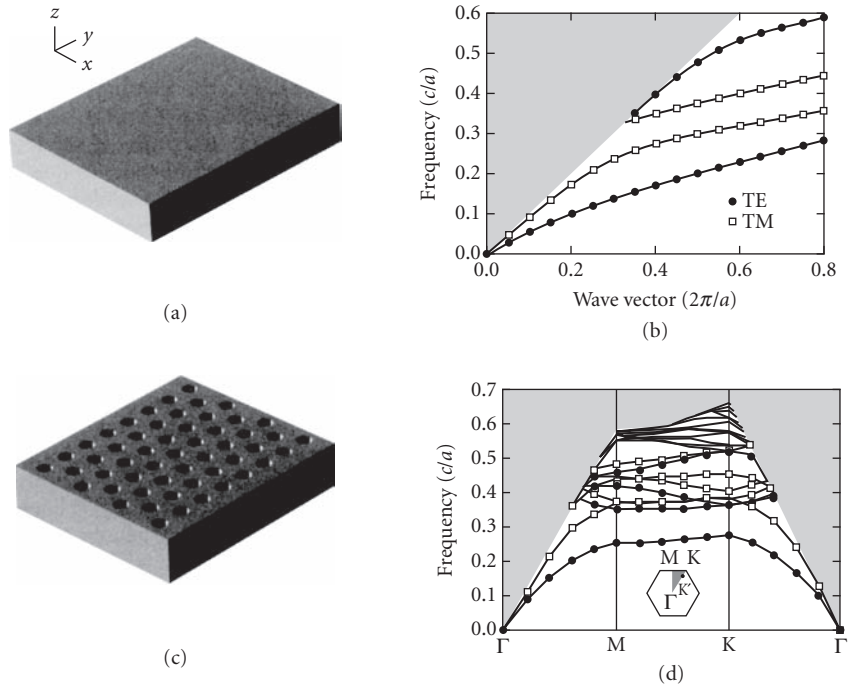
where  $V_m$  is the modal volume,  $n$  is the refractive index of the medium, and  $\lambda$  is the free-space wavelength of the optical transition. Photonic crystals have the ability to enhance the rate of spontaneous emission by enabling microcavities with large quality factors and small modal volumes. In the case where the modal volume is on the order of a cubic half-wavelength in the material [i.e.,  $V_m \sim (\lambda/2n)^3$ ], the enhancement factor is on the order of  $Q$ . A detailed example is provided in the following section.

## 9.6 MICROCAVITIES IN PHOTONIC CRYSTALS WITH TWO-DIMENSIONAL PERIODICITY

Three-dimensional field confinement can be achieved in dielectric structures, in part by the effect of a photonic bandgap and in part by index confinement. An example was given in Sec. 9.5 for the case of a DFB laser (i.e., a structure with a one-dimensional periodicity). One important aspect of structures with dimensional periodicity lower than three is the coupling to radiation modes. By reducing the dimensionality of the periodicity and by resorting to standard index guiding to confine light along the nonperiodic direction(s), one no longer has the ability to contain light completely, and leaves open possible decay pathways through which light can escape.

In this section, we consider a dielectric slab waveguide with a two-dimensional periodic lattice. The periodic lattice is used to confine light in the plane of the waveguide (the  $xy$ -plane, say), and the slab keeps the light from escaping along the transverse direction (the  $z$ -direction). It is useful to begin with a uniform waveguide, and consider the effect of adding a periodic array of holes. The slab is chosen to have a large refractive index ( $n = 3.4$ ) and, for simplicity, is assumed to lie in air. The thickness of the slab is set equal to  $0.5a$ , where  $a$  is a scaling parameter as defined in the text that follows. The use of a high-index waveguide is twofold: first, the high index provides strong field confinement along the  $z$ -direction (i.e., the extent of the guided modes outside the waveguide is small), allowing a large fraction of each mode to interact with the photonic crystal; and second, the high-index contrast between the dielectric material and the holes will increase the likelihood of having a bandgap in the  $xy$ -plane.

The waveguide is shown in Fig. 4a. Its corresponding dispersion relation is shown in Fig. 4b. The solid lines correspond to guided modes, and the shaded region corresponds to the continuum of radiation (i.e., nonguided) modes. The guided modes are labeled transverse electric (TE) and transverse magnetic (TM) with respect to the  $xy$ -plane of symmetry in the middle of the waveguide. TE (TM) modes are characterized by the absence of electric field components in the  $z$  ( $x$  and  $y$ ) direction at the center of the waveguide.



**FIGURE 4** (a) Schematic diagram of a dielectric slab waveguide of thickness  $0.5a$  and refractive index 3.4. (b) Band diagram of the slab waveguide shown in (a). The solid lines correspond to guided modes; the shaded region corresponds to the continuum of radiation modes. The guided modes are labeled TE or TM with respect to the  $xy$ -plane of symmetry in the middle of the slab. (c) Schematic diagram of a slab waveguide with a two-dimensional triangular array of holes with radius  $0.3a$ , where  $a$  is the lattice constant of the periodic array. The parameters of the slab are identical to those in (a). (d) Band diagram for the slab waveguide shown in (c). Only the lowest nine bands are labeled TE and TM. Guided modes do not exist above the cut-off frequency of  $0.66c/a$ . The inset shows the Brillouin zone and symmetry points for a triangular lattice, with the irreducible zone shaded.

The dispersion relation shown in Fig. 4*b* extends to the right of the figure; there is no upper bound on the wave vector. The introduction of a periodic array of holes in the waveguide has the effect of folding the dispersion relation into the first Brillouin zone and splitting the guided-mode bands. Figure 4*c* shows a waveguide with a triangular array of holes. The holes have a radius of  $0.30a$ , where  $a$  is the lattice constant of the array. The associated dispersion relation is shown in Fig. 4*d*. Again, the shaded region above the light line corresponds to the continuum of radiation modes. The solid lines below the light line correspond to guided modes. These modes remain perfectly guided in spite of the holes and propagate in the waveguide with no loss. A bandgap can be seen between the first and second TE bands. An experimental observation of bandgaps in this type of structure is described in Ref. 21.

The introduction of holes in the waveguide also creates a frequency cutoff for guided modes. Every mode above the frequency  $0.66c/a$  is folded into the radiation continuum, and is Bragg-scattered out of the slab. The cutoff frequency is independent of the refractive index of the slab or the size of the holes, and depends only on the lattice geometry of the array of holes.

If a defect is introduced in the PBG structure shown in Fig. 4*c*, localized modes can be formed in the vicinity of the defect. Since each localized mode has a specific polarization, it is possible to create a TE mode between the first and second TE bands, orthogonal to TM modes. If, for example, light were to originate from a quantum well located at the middle of the waveguide, atomic transitions could be made to couple only to TE modes.

Two competing decay mechanisms contribute to the overall decay rate of the localized mode; horizontal in-plane coupling to guided modes at the edges of the crystal in the unperturbed (i.e., holeless) waveguide, and vertical coupling to radiation modes. For some applications (such as photonic integrated circuits) it may be preferable for the localized mode to decay primarily into guided modes, while for other applications (such as off-chip emission) it may be preferable for the mode to decay primarily into the radiation continuum. These two cases are considered separately in the following text.

The total quality factor of the resonant mode,  $Q_{\text{tot}}$ , is given by:<sup>22</sup>

$$\frac{1}{Q_{\text{tot}}} = \frac{1}{Q_{\text{wg}}} + \frac{1}{Q_{\text{rad}}} \quad (6)$$

where  $1/Q_{\text{wg}}$  is a measure of the coupling to waveguide modes and  $1/Q_{\text{rad}}$  is a measure of the coupling to radiation modes. The strength of the two competing coupling mechanisms depends on the size of the crystal (i.e., the total number of holes around the defect), the modal volume, and the choice of substrate.

## In-Plane Coupling

We present the case of an array of 45 holes with a missing hole at the center (i.e., one hole is filled). The structure supports a localized mode inside the TE bandgap. The total quality factor of the mode is computed using the finite-difference time-domain method described in Sec. 9.3 and is found to be 240. The modal volume,  $V_m$ , is defined as:<sup>23</sup>

$$V_m = \frac{\int \epsilon(\mathbf{r}) |\mathbf{E}(\mathbf{r})|^2 d^3\mathbf{r}}{(\epsilon(\mathbf{r}) |\mathbf{E}(\mathbf{r})|^2)_{\text{max}}} \quad (7)$$

where  $\mathbf{E}(\mathbf{r})$  is the electric field distribution of the mode. The computed modal volume is only three cubic half-wavelengths in the material. The spontaneous emission rate enhancement factor, computed from Eq. (5), is equal to 50.

Since the structure does not have a complete three-dimensional bandgap,  $Q_{\text{tot}}$  cannot be made arbitrarily large. While the addition of extra holes would reduce the coupling to the guided modes outside the crystal, light could not be prevented from coupling to radiation modes. Any significant

increase in the number of holes would cause the mode to primarily radiate outside of the waveguide. Moreover, coupling to radiation modes would be enhanced if the waveguide was positioned on a substrate. The substrate would provide a favorable pathway for radiation loss. It has been shown, however, that the adverse effects of a substrate could be minimized with the use of a low-index insulating layer between the waveguide and the substrate.<sup>24,25</sup>

The coupling to radiation modes is also enhanced by reducing the modal volume. The more tightly a mode is confined, the more likely it is to radiate out of the waveguide. Conversely, if the modal volume is made larger, the coupling to radiation modes can be reduced, and, provided the coupling to guided modes remains largely unchanged,  $Q_{\text{tot}}$  can be increased. To increase the modal volume, one could create a different type of defect in the structure. If, instead of removing a single hole from the two-dimensional array, the radius of seven nearest-neighbor holes was reduced from  $0.3a$  to  $0.2a$  while otherwise leaving the structure unchanged, the localized mode would become more extended—the modal volume would increase by 20 percent to  $3.6(\lambda/2n)^3$ —and  $Q_{\text{tot}}$  would increase by more than one order of magnitude to 2500. The frequency of the new localized mode would remain unchanged, and the enhancement factor would exceed 400.

## Out-of-Plane Coupling

While it may be possible to fabricate high- $Q$  cavities that couple predominantly to guided modes, some applications (such as light-emitting diodes) may require a large fraction of the emitted light to be extracted from the high-index guiding layer. As mentioned previously, the emitted radiation can be made to decay primarily into radiation modes by increasing the total number of holes surrounding the defect. In this case,  $Q_{\text{wg}}$  would essentially be infinite, and  $Q_{\text{tot}} \sim Q_{\text{rad}}$ . For simplicity, in this example, we write  $Q_{\text{tot}} = Q_{\text{rad}} = Q$ .

Light-emitting diodes (LEDs) are widely used as incoherent light sources in applications such as lighting, displays, and short-distance fiber communications. Two important performance characteristics of LEDs are the output efficiency (i.e., the amount of light extracted from the structure for a given injection current) and the modulation rate (i.e., the information emission capacity).

Photonic crystals with two-dimensional periodicity can lead to the enhancement of the rate of spontaneous emission and consequently to higher modulation rates. However, photon reabsorption and nonradiative recombination can affect the performance of LEDs by reducing the extraction efficiency and the modulation rate. High- $Q$  cavities, though seemingly favorable for the enhancement of the rate of spontaneous emission, may cause severe reabsorption in certain material systems, since the likelihood of observing photon reabsorption increases with the photon lifetime inside the cavity.

**Display Applications** For display applications, it is usually desired to get as much light as possible out of the high-index material over the entire spontaneous emission bandwidth for a constant applied current. If all emitted frequencies fall inside the guided-mode bandgap, all available optical modes can contribute to the output signal. In the ideal case where there are no nonradiative recombination processes, the extraction efficiency is unity; every photon escapes from the high-index waveguide. Even photons reabsorbed by the atomic system, if given enough time, eventually get reemitted and contribute to the output signal. However, when nonradiative processes are present, reabsorbed photons can be lost. In order to achieve high output efficiency, the effective spontaneous emission rate—the spontaneous emission rate reduced by photon reabsorption—has to dominate over the nonradiative recombination rate. The relative rate of the radiative and nonradiative processes can be controlled by modifying the quality factor of the cavity.

Two limit cases are identified: the case where photon reabsorption is negligible, and the case where it is important. The former arises in certain organic emitters, where the energy levels of the molecules are such that absorption and spontaneous emission are spectrally separated. The latter arises in most semiconductor systems, where both absorption and emission processes occur between the conduction and valence bands.

In the case of low reabsorption, if the cavity linewidth is larger than the emission linewidth, an increase of the cavity  $Q$  can result in an increase of the effective spontaneous emission rate and of



the output efficiency. However, a reduction of the cavity linewidth beyond the material emission linewidth does not further enhance the spontaneous emission rate or output efficiency. In the case of large reabsorption, the rate of spontaneous emission and the output efficiency reach a maximum when the cavity linewidth is comparable to the material linewidth, but fall to zero when the cavity linewidth becomes much smaller than the material linewidth. A more detailed description of these conditions can be found in Ref. 26.

**Communications Applications** For communications applications, it is advantageous to reduce the emission linewidth below the material emission linewidth to improve the temporal coherence of the emitted light. It is also advantageous to increase the modulation speed to improve the information emission capacity. If a time-varying current is applied to the LED, the response time of the electron-photon system will be determined by the slowest of the different relaxation processes.

While electronic recombination lifetimes are typically on the order of a few nanoseconds in both semiconductors and organic dyes, the photon lifetime in a cavity depends on the cavity  $Q$  and, in the case where, say,  $Q = 1000$ , is on the order of several picoseconds. Since the modulation speed is limited by the slower of the two processes, the electronic recombination rate, which is a sum of the effective spontaneous emission rate and the nonradiative recombination rate, constitutes the limiting factor. To achieve high modulation speeds, it is therefore necessary to increase the spontaneous emission rate.

In the case where photon reabsorption is small, such as in organic dyes, the rate of spontaneous emission and the modulation speed increase with the cavity  $Q$ . Conversely, when photon reabsorption is large, such as in semiconductors, the maximum rate of spontaneous emission and the maximum modulation rate are achieved when the cavity linewidth is comparable to the material linewidth. These conclusions are similar to those found for display applications.

**Examples of Low- $Q$  and High- $Q$  Cavities** Low- $Q$  cavities can be fabricated in high-index dielectric waveguides by introducing an array of holes with no defects. The absence of defects ensures that photons inside the waveguide—emitted from a quantum well, say—spend as little time as possible inside the waveguide and minimize the risk of being reabsorbed. The cavity is defined by the waveguide itself, which provides vertical field confinement. To avoid removing active material, the holes can be made to extend only partly into the guiding layer so as to not penetrate into the quantum well. Bandgaps for guided modes can be generated even when the holes do not extend through the entire thickness of the waveguide. The waveguide can also be positioned on a dielectric or metallic mirror to ensure that the output radiation escapes through the top surface.

High- $Q$  cavities can be fabricated in structures similar to those used for low- $Q$  cavities except that, in the case of high- $Q$  cavities, defects are introduced in the periodic array. The introduction of defects creates highly confined modes in the area of the defects, hence only a small fraction of the quantum well overlaps with the resonant modes (i.e., only a fraction of the electron-hole pairs contributes to the emitted signal). To eliminate this problem, high- $Q$  cavities could be generated by placing the dielectric layer between two vertical Bragg mirrors—in analogy to resonant-cavity LEDs—and by getting rid of the defects. The entire active region would then overlap with the resonant cavity mode.

Experimental results of quantum-well emitters and dyes in photonic crystals with two-dimensional periodicity can be found in Refs. 27 through 31. A detailed analysis of the output efficiency and modulation rate of LEDs can be found in Refs. 26 and 32.

---

## 9.7 WAVEGUIDES

While three-dimensional field confinement can be achieved by introducing local-point defects in photonic crystals, two-dimensional field confinement can be achieved by introducing extended line defects. Both point defects and line defects can generate localized modes with

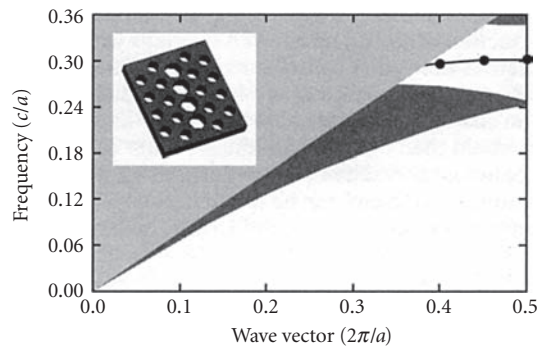
frequencies that lie inside the bandgap. However, unlike point defects, line defects can generate modes that propagate along the lines with nonzero group velocity. Line defects can be made, for example, by *carving* channels in photonic crystals or by creating line dislocations. Electromagnetic waves propagating along the lines are guided not from total internal reflection but from the bandgap effect; they are prevented from leaking into the crystal since their frequencies lie inside the bandgap.

The absence of radiation modes in three-dimensional photonic crystals suggests that it may also be possible to create waveguides with very sharp bends. Since electromagnetic waves are prevented from propagating inside photonic crystals, the waves would only either propagate through the bend or be reflected back. It will be shown in the subsection labeled “Waveguide Bends” that, for certain frequencies, reflection may be eliminated altogether, leading to complete transmission. In three-dimensional crystals, waveguide bends could extend along any direction and could be used for the implementation of interconnected integrated optical circuits on multiple planes. In this chapter, however, we focus only on line defects in photonic crystals with two-dimensional periodicity.

## Waveguides in Photonic Crystals with Two-Dimensional Periodicity

As we saw in Sec. 9.6, photonic crystals with two-dimensional periodicity rely on the existence of bandgaps to control propagation in the plane and on index guiding to confine electromagnetic fields along the third dimension. An example of a photonic crystal with two-dimensional periodicity was shown in Fig. 4c; its corresponding dispersion relation was shown in Fig. 4d. In the bandgap, no *guided* mode existed for TE polarization.

In this section, a line defect is introduced in the photonic crystal shown in Fig. 4c by increasing the radius of a line of nearest-neighbor holes along the  $\Gamma$ -K direction from  $0.30a$  to  $0.45a$ . The resulting dispersion relation is shown in Fig. 5. The dispersion relation is computed using the plane-wave expansion method described in Sec. 9.3. The wave vector along the line defect is plotted on the abscissa.



**FIGURE 5** Projected dispersion relation of the TE modes in the waveguide structure shown in the inset. The dispersion relation is projected along the axis of the waveguide (i.e., along the line defined by the series of larger holes). The light gray region corresponds to the continuum of radiation modes, and the dark gray regions correspond to modes inside the bulk PBG dielectric slab. The thickness of the slab is  $0.5a$ , the refractive index is 3.4, the radius of the small holes is  $0.3a$ , and the radius of the large holes is  $0.45a$ . The figure is to be compared with Fig. 4d along the  $\Gamma$ -K direction.

In this structure, it is necessary to distinguish between the modes which are guided inside the dielectric slab (the so-called bulk crystal modes that correspond to the different bands in Fig. 4d) and the modes which are guided along the line defect. The dispersion relation is obtained from Fig. 4d by projecting the wave vector of every mode along the  $\Gamma$ -K direction; the dark gray regions correspond to the continuum of bulk crystal modes and the light gray region corresponds to the continuum of radiation modes. The bulk crystal modes and radiation modes are depicted with a uniform shading despite the nonuniform density of states in these regions. Since the structure retains an inherent periodicity along the line defect, the wave vector has an upper limit. However, although the line defect extends along the  $\Gamma$ -K direction, K is not the point at the edge of the dispersion relation. The boundary is located at the projected M point along the  $\Gamma$ -K direction, labeled  $K'$  as shown in the inset of Fig. 4d.

Only modes lying outside the shaded regions are truly guided along the line defect. A single guided mode appears inside the bandgap. Since the line defect consists of a series of larger holes, the effective index of the waveguide is lower than that of the surrounding photonic crystal. Hence, the mode is not index-guided in the plane; it is constrained horizontally by the bandgap. The effective index, however, is higher in the waveguide than in the regions above and below the slab, allowing the mode to be guided vertically by index confinement. The electric field of the guided mode is mostly concentrated in the dielectric material. The fraction of electric-field energy inside the high-dielectric material at  $K'$ , for example, is close to 75 percent.

Alternatively, a line defect could have been created by reducing the radius of a series of holes, or by creating lattice dislocations. Also, instead of using a high-index slab with holes, one could have used an array of high-index posts. High-index posts can generate dispersion relations similar to the one shown in Fig. 4c except that the open (solid) circles would now correspond to TE (TM) polarization. A more detailed analysis of these and other similar structures can be found in Refs. 33 and 34.

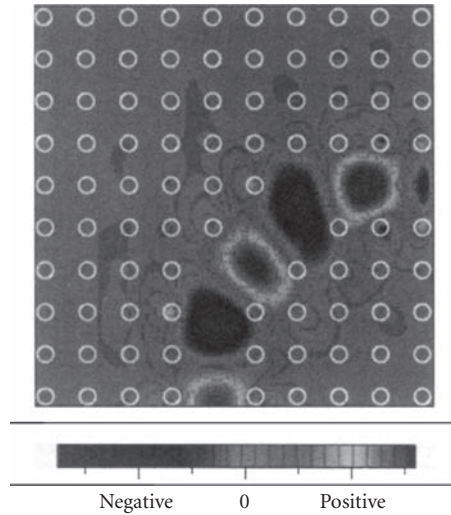
## Waveguide Bends

If a sharp bend is introduced in a PBG waveguide—with a radius of curvature on the order of a few lattice constants—it may be possible to obtain high transmission through the bend for a wide range of frequencies. To obtain high transmission, the waveguide must support a single mode at the frequency of interest, and the radiation losses must be small, since coupling to high-order guided modes and to radiation modes reduces the transmission and increases the reflection.

While it may be possible to obtain 100 percent transmission in photonic crystals with two-dimensional periodicity, we choose to consider waveguide bends in purely two-dimensional crystals. Two-dimensional crystals can be viewed either as flat structures in a two-dimensional Cartesian space or as structures of infinite thickness with no field variation along the vertical direction. Since there is no index confinement along the vertical direction, there are no radiation modes and no light cone. The bandgap in a 2D structure is analogous to a three-dimensional bandgap in that there are truly no modes inside the bandgap.

For simplicity, we consider a 2D photonic crystal of dielectric columns on a square lattice, surrounded by air. The refractive index of the rods is chosen to be 3.4 and the radius  $0.20a$ , where  $a$  is the lattice constant of the array. A large bandgap appears in this structure for TM polarization (electric field parallel to the axis of the columns). A line defect is created inside the crystal by removing a row of rods. The line defect introduces a single guided TM mode inside the gap, similar to the one shown in Fig. 5. The main difference between the dispersion relation for this 2D crystal and the one shown in Fig. 5 is the absence of radiation modes in the 2D crystal. The bandgap extends over the entire range of wave vectors. If a bend is introduced in the waveguide, light will either travel through the bend or be reflected back, since there are no radiation modes to which light can couple. Only back reflection can hinder perfect transmission.

The transmission and reflection can be studied using the finite-difference time-domain method described in Sec. 9.3. In this method, a dipole located at the entrance of the waveguide creates a pulse with a Gaussian envelope in time. The field amplitude is monitored inside the waveguide at two points, one before the bend and one after the bend. The pulses are then Fourier-transformed to



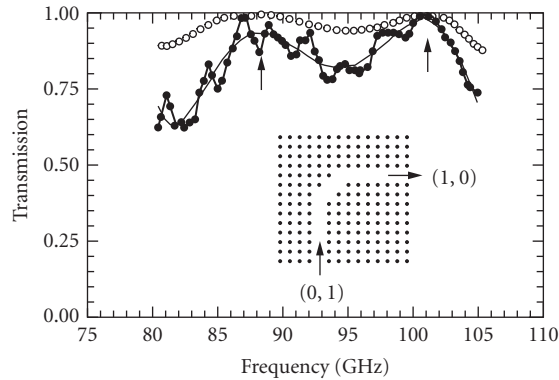
**FIGURE 6** Electric field pattern of a guided mode in a photonic crystal in the vicinity of a bend. The white circles indicate the position of the high-dielectric columns. The electric field is polarized along the axis of the columns. The mode is strongly confined inside the guide and is completely transmitted through the bend. The radius of curvature of the bend is on the order of the wavelength of the guided mode.

obtain the reflection and transmission coefficients for each frequency. A detailed description of this method and computational results are presented in Ref. 35.

The electric field pattern of a mode propagating through the bend is shown in Fig. 6. The mode is strongly guided inside the photonic crystal. One hundred percent of the light travels through the bend despite a radius of curvature on the order of one wavelength.

The transmission through the bend can be modeled as a simple one-dimensional scattering process. The bend can be broken down into three separate waveguide sections: the input waveguide in the (01) direction; the output waveguide in the (10) direction; and a short waveguide section in the (11) direction, connecting the input and output waveguides. Each section supports a single guided mode with wave vector  $\mathbf{k}_1(f)$  for propagation along the (01) or (10) direction, and  $\mathbf{k}_2(f)$  for propagation along (11). These wave vectors are given by dispersion relations similar to the one shown in Fig. 5. The mode propagating along the (01) direction is scattered into the mode propagating along (11), then into the mode propagating along (10). At the interfaces, the fields and their derivatives must be continuous. By complete analogy with the one-dimensional Schrödinger equation for a square potential well, the transmission through the sharp bend can be mapped onto that of a wave propagating in a square *dielectric potential*. This potential consists of three constant pieces corresponding to the (01), (11), and (10) directions, respectively. The model differs from the standard one-dimensional scattering problem in that the depth of the well, determined by the difference  $|\mathbf{k}_1(f)|^2 - |\mathbf{k}_2(f)|^2$ , now depends on the frequency of the traveling wave. The scattering model correctly predicts the general quantitative features of the transmission spectrum obtained from the FDTD method, as well as the frequencies where the reflection coefficient vanishes.<sup>35</sup>

The results have been experimentally confirmed using a structure consisting of a square array of tall circular rods.<sup>36</sup> The rods were made of alumina with a refractive index of 3.0 and a radius of 0.25 mm. The lattice constant was chosen to be 1.27 mm and the rods were close to 10 cm in length. The large aspect ratio between the length and the lattice constant provided a good approximation



**FIGURE 7** Normalized transmission spectrum for the PBG structure shown in the inset. The solid circles correspond to experimental data; the open circles are computed from the one-dimensional scattering model. Near-perfect transmission is observed through the bend near 87 and 101 GHz. The arrows indicate the positions of the reflection nodes from theory. The experimental data is fitted with a polynomial curve.

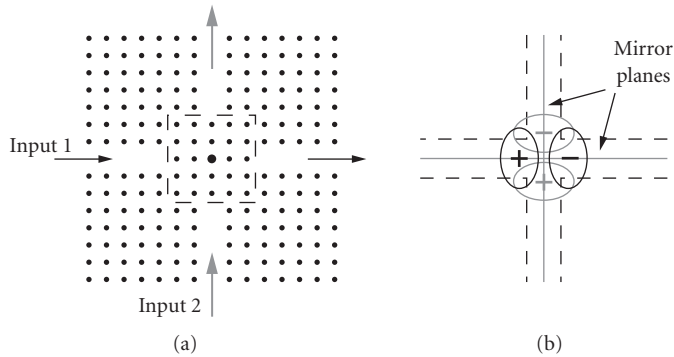
of a two-dimensional system. Because of the absence of vertical confinement, the waveguides were made to extend over less than 100 lattice constants to minimize loss in the vertical direction. The bandgap extended from 76 to 105 GHz. The experiment was carried out at millimeter-wave frequencies to facilitate the fabrication of structures with a large aspect ratio.

To test the PBG structure, millimeter-wave transmitters and receivers were placed next to the entrance and exit of the PBG waveguide. This coupling scheme closely resembled the setup used in the computational simulations. The transmitted signal is shown in Fig. 7. The signal is normalized to the transmitted signal of a straight waveguide. The PBG bend exhibits near-perfect transmission around 87 and 101 GHz. The two arrows indicate the expected positions of the reflection nodes computed from the one-dimensional scattering model. The positions of the nodes confirm a subtle and important point about PBG waveguides: The detection of light at the end of a straight waveguide would not be a sufficient condition, in itself, to confirm PBG guiding. It is the existence of transmission peaks around the sharp bend, along with the specific position of these peaks, that confirms PBG guiding.

## Waveguide Intersections

In addition to sharp bends, photonic crystals can be used to fabricate waveguide intersections with low crosstalk. If two waveguides intersect each other on the same plane, light traveling along one waveguide typically leaks into the second waveguide, causing signal loss and crosstalk. The insertion of a microcavity at the center of the intersection of two PBG waveguides can reduce the crosstalk and increase the throughput. If the resonant mode inside the cavity is such that it can couple only to one waveguide, the crosstalk can be essentially eliminated. In this case, the problem reduces to the well-known phenomenon of resonant tunneling through a cavity.

Figure 8a shows two intersecting waveguides in a two-dimensional photonic crystal identical to the one shown in Fig. 7. At the center of the intersection, a microcavity is created by adding rods inside the waveguides and by increasing the radius of one rod by 60 percent. The cavity is outlined by a dashed box. The cavity supports two degenerate modes with opposite symmetry at a frequency lying inside the bandgap. From symmetry, each resonant mode can couple to only one waveguide, as shown schematically in Fig. 8b. Therefore, under the approximation that the waveguides couple



**FIGURE 8** (a) Diagram of two intersecting waveguides inside a photonic crystal. The two waveguides are aligned along the (10) and (01) directions. A microcavity—outlined by the dashed line—is created at the center of the intersection by adding columns inside the waveguides and by increasing the size of the dielectric column at the center. The microcavity supports two degenerate modes with opposite symmetry. The mode contours are shown schematically in (b). By symmetry, the modes corresponding to the black contour lines cannot couple to even modes in the waveguide along the (01) direction, and the modes corresponding to the gray contour lines cannot couple to even modes in the waveguide along the (10) direction.

to one another only through the resonant cavity, crosstalk is prohibited. The throughput in each waveguide is described by resonant tunneling; the throughput spectrum is a Lorentzian function with 100 percent transmission at resonance. The width of the resonance is given by the inverse of the quality factor of the microcavity.

In general, large throughput and low crosstalk can be achieved if each waveguide has a single guided mode in the frequency range of interest, and if the microcavity supports two resonant modes, each mode having even symmetry with respect to the mirror plane along one waveguide and odd symmetry with respect to the other mirror plane. The presence of radiation loss would reduce the throughput and increase the crosstalk. A detailed description of PBG waveguide intersections can be found in Ref. 37.

## 9.8 CONCLUSION

The routing and interconnection of optical signals through narrow channels and around sharp bends are important for large-scale all-optical circuit applications. In addition to sharp bends and low-crosstalk intersections, photonic bandgap materials can also be used for narrowband filters, add/drop filters, light emitters, low-threshold lasers, modulators, attenuators, and dispersion compensators. PBG materials may enable the high-density integration of optical components on a single chip.

While this chapter focuses mostly on applications for high-density optical circuits, many other applications have been proposed for PBG materials. One such application is the PBG fiber.<sup>38</sup> While photonic crystals can guide light along a periodic plane (as shown in Sec. 9.7), they can also guide light along the direction perpendicular to the plane of periodicity. A PBG fiber is a two-dimensional periodic structure that essentially extends to infinity along the nonperiodic direction. Light is confined inside the fiber by a defect located at the center. PBG fibers may have interesting features such as single-mode operation over a large bandwidth and preferred dispersion compensation properties. Other applications can be found in Ref. 39.

## 9.9 REFERENCES

1. Alan Michette, "Zone and Phase Plates, Bragg-Fresnel Optics," in *Handbook of Optics*, vol. III, McGraw-Hill, New York, 2000.
2. J. A. Dobrowolski, "Optical Properties of Films and Coatings," in *Handbook of Optics*, vol. I, McGraw-Hill, New York, 1978.
3. T. L. Koch, F. J. Leonberger, and P. G. Suchoski, "Integrated Optics," in *Handbook of Optics*, vol. II, McGraw-Hill, New York, 1995.
4. J. N. Winn, Y. Fink, S. Fan, and J. D. Joannopoulos, "Omnidirectional Reflection from a One-Dimensional Photonic Crystal," *Opt. Lett.* **23**:1573–1575 (1998).
5. J. D. Joannopoulos, R. D. Meade, and J. N. Winn, *Photonic Crystals*, Princeton Press, Princeton, New Jersey, 1995.
6. E. Yablonovitch, "Photonic Band-Gap Structures," *J. Opt. Soc. Am. B* **10**:283–295 (1993).
7. B. Goss Levi, "Visible Progress Made in Three-Dimensional Photonic 'Crystals,'" *Phys. Today*, January, 17–19 (1999).
8. R. D. Meade, A. M. Rappe, K. D. Brommer, and J. D. Joannopoulos, "Accurate Theoretical Analysis of Photonic Band-Gap Materials," *Phys. Rev. B* **48**:8434–8437 (1993). Erratum: S. G. Johnson, *Phys. Rev. B* **55**:15942 (1997).
9. J. B. Pendry, "Photonic Band Structures," *J. Mod. Optics* **41**:209–229 (1994).
10. K. S. Kunz and R. J. Luebbers, *The Finite-Difference Time-Domain Method for Electronics*, CRC Press, Boca Raton, Florida, 1993.
11. R. D. Meade, K. D. Brommer, A. M. Rappe, and J. D. Joannopoulos, "Nature of the Photonic Band Gap: Some Insights from a Field Analysis," *J. Opt. Soc. Am. B* **10**:328–332 (1993).
12. K. M. Ho, C. T. Chan, and C. M. Soukoulis, "Existence of a Photonic Gap in Periodic Dielectric Structures," *Phys. Rev. Lett.* **65**:3152–3155 (1990).
13. E. Yablonovitch, T. J. Gmitter, and K. M. Leung, "Photonic Band Structure: The Face-Centered-Cubic Case Employing Nonspherical Atoms," *Phys. Rev. Lett.* **67**:2295–2298 (1991).
14. C. C. Cheng and A. Scherer, "Fabrication of Photonic Band-Gap Crystals," *J. Vac. Sci. Technol. B* **13**:2696–2700 (1995).
15. E. Ozbay, A. Abeyta, G. Tuttle, M. Tringides, R. Biswas, C. T. Chan, C. M. Soukoulis, and K. M. Ho, "Measurement of a Three-Dimensional Photonic Band Gap in a Crystal Structure Made of Dielectric Rods," *Phys. Rev. B* **50**:1945–1948 (1994).
16. S. Fan, P. R. Villeneuve, R. D. Meade, and J. D. Joannopoulos, "Design of Three-Dimensional Photonic Crystals at Submicron Lengthscales," *Appl. Phys. Lett.* **65**:1466–1468 (1994).
17. S. Y. Lin, J. G. Fleming, D. L. Hetherington, B. K. Smith, R. Biswas, K. M. Ho, M. M. Sigalas, W. Zubrzycki, S. R. Kurtz, and J. Bur, "A Three-Dimensional Photonic Crystal Operating at Infrared Wavelengths," *Nature* **394**:251–253 (1998).
18. A. Yariv, *Optical Electronics*, Saunders, Philadelphia, Pennsylvania, 1991.
19. P. R. Villeneuve, S. Fan, and J. D. Joannopoulos, "Microcavities in Photonic Crystals: Mode Symmetry, Tunability, and Coupling Efficiency," *Phys. Rev. B* **54**:7837–7842 (1996).
20. H. Yokoyama and S. D. Brorson, "Rate Equation Analysis of Microcavity Lasers," *J. Appl. Phys.* **66**:4801–4805 (1989).
21. T. F. Krauss, R. M. De La Rue, and S. Band, "Two-Dimensional Photonic Bandgap Structures Operating at Near-Infrared Wavelengths," *Nature* **383**:699–702 (1996).
22. H. A. Haus, *Waves and Fields in Optoelectronics*, Prentice Hall, Englewood Cliffs, New Jersey, 1984.
23. R. Coccioli, M. Boroditsky, K. W. Kim, Y. Rahmat-Samii, and E. Yablonovitch, "Smallest Possible Electromagnetic Mode Volume in a Dielectric Cavity," *IEE Proc.-Optoelectron.* **145**:391–397 (1998).
24. P. R. Villeneuve, S. Fan, S. G. Johnson, and J. D. Joannopoulos, "Three-Dimensional Photon Confinement in Photonic Crystals of Low-Dimensional Periodicity," *IEE Proc.-Optoelectron.* **145**:384–390 (1998).
25. J. S. Foresi, P. R. Villeneuve, J. Ferrera, E. R. Thoen, G. Steinmeyer, S. Fan, J. D. Joannopoulos, L. C. Kimerling, Henry I. Smith, and E. P. Ippen, "Photonic-Bandgap Microcavities in Optical Waveguides," *Nature* **390**:143–145 (1997).

26. S. Fan, P. R. Villeneuve, and J. D. Joannopoulos, "Rate-Equation Analysis of Output Efficiency and Modulation Rate of Photonic-Crystal Light Emitting Diodes," *IEEE J. Quantum Electron* **36**: October (2000).
27. R. K. Lee, O. J. Painter, B. D'Urso, A. Scherer, and A. Yariv, "Measurement of Spontaneous Emission from a Two-Dimensional Photonic Band Gap Defined Microcavity at Near-Infrared Wave lengths," *Appl. Phys. Lett.* **74**:1522–1524 (1999).
28. M. Meier, A. Mekis, A. Dodabalapur, A. Timko, R. E. Slusher, J. D. Joannopoulos, and O. Nalamasu, "Laser Action from Two-Dimensional Feedback in Photonic Crystals," *Appl. Phys. Lett.* **74**:7–9 (1999).
29. K. Inoue, M. Sasada, J. Kawamata, K. Sakoda, and J. Haus, "A Two-Dimensional Photonic Crystal Laser," *Jpn. J. Appl. Phys.* **38**:L157–L159 (1999).
30. T. Baba and T. Matsuzaki, "Fabrication and Photoluminescence Studies of GaInAsP/InP 2-Dimensional Photonic Crystals," *Jpn. J. Appl. Phys.* **35**:1348–1352 (1996).
31. P. L. Gourley, J. R. Wendt, G. A. Vawter, T. M. Brennan, and B. E. Hammons, "Optical Properties of Two-Dimensional Photonic Lattices Fabricated as Honeycomb Nanostructures in Compound Semiconductors," *Appl. Phys. Lett.* **64**:687–689 (1994).
32. M. Boroditsky, R. Vrijen, T. F. Krauss, R. Coccioli, R. Bhat, and E. Yablonovitch, "Spontaneous Emission Extraction and Purcell Enhancement from Thin-Film 2-d Photonic Crystals," *J. Lightwave Technol.* **17**:2096–2112 (1999).
33. S. G. Johnson, S. Fan, P. R. Villeneuve, and J. D. Joannopoulos, "Guided Modes in Photonic Crystal Slabs," *Phys. Rev. B* **60**:5751–5758 (1999).
34. S. G. Johnson, P. R. Villeneuve, S. Fan, and J. D. Joannopoulos, "Linear Waveguides in Photonic-Crystal Slabs," *Phys. Rev. B* **62**: September (2000).
35. A. Mekis, J. C. Chen, I. Kurland, S. Fan, P. R. Villeneuve, and J. D. Joannopoulos, "High Transmission Through Sharp Bends in Photonic Crystal Waveguides," *Phys. Rev. Lett.* **77**:3787–3790 (1996).
36. S. Y. Lin, E. Chow, V. Hietala, P. R. Villeneuve, and J. D. Joannopoulos, "Experimental Demonstration of Guiding and Bending of Electromagnetic Waves in a Photonic Crystal," *Science* **282**:274–276 (1998).
37. S. G. Johnson, C. Manolatu, S. Fan, P. R. Villeneuve, J. D. Joannopoulos, and H. A. Haus, "Elimination of Cross Talk in Waveguide Intersections," *Opt. Lett.* **23**:1855–1857 (1998).
38. J. C. Knight, J. Broeng, T. A. Birks, and P. St. J. Russel, "Photonic Band Gap Guidance in Optical Fibers," *Science* **282**:1476–1478 (1998).
39. C. M. Soukoulis, ed., *Photonic Band Gap Materials*, NATO ASI Series E: Applied Sciences, Kluwer Academic, Dordrecht, 1996.



*This page intentionally left blank*

PART

2

---

NONLINEAR  
OPTICS

---

*This page intentionally left blank*

Chung L. Tang

School of Electrical and Computer Engineering  
Cornell University  
Ithaca, New York

## 10.1 GLOSSARY

$c$	velocity of light in free space
$\mathbf{D}$	displacement vector
$d_{mn}$	Kleinman's $\mathbf{d}$ -coefficient
$\tilde{\mathbf{E}}$	electric field in lightwave
$\tilde{\mathbf{E}}$	complex amplitude of electric field
$e$	electronic charge
$f$	oscillator strength
$\hbar$	Planck's constant
$I$	intensity of lightwave
$\mathbf{k}$	propagation vector
$m$	mass of electron
$N$	number of equivalent harmonic or anharmonic oscillators per volume
$n_{1,2}$	index of refraction at the fundamental and second-harmonic frequencies, respectively
$\mathbf{P}$	macroscopic polarization
$\mathbf{P}^{(n)}$	$n$ th-order macroscopic polarization
$P_{0,2,+,-}$	power of lightwave at the fundamental, second-harmonic, sum-, and difference-frequencies, respectively
$\tilde{\mathbf{P}}$	complex amplitude of macroscopic polarization
$\mathbf{Q}$	amplitude of vibrational wave or optic phonons
$\mathbf{S}$	strain of acoustic wave or acoustic phonons
$T_{mn}$	relaxation time of the density matrix element $\rho_{mn}$
$\Gamma_j$	damping constant of $j$ th optical transition mode
$\delta$	Miller's coefficient
$\epsilon(\mathbf{E})$	field-dependent optical dielectric tensor
$\epsilon_n$	$n$ th-order optic dielectric tensor
$\epsilon_0$	optical dielectric constant of free space
$\eta$	amplitude of plasma wave or plasmons
$\lambda$	wavelength
$\rho_{mn}$	density matrix element

$\chi(\mathbf{E})$	field-dependent optic susceptibility tensor
$\chi_1$ or $\chi(1)$	linear optic susceptibility tensor
$\chi_n$ or $\chi(n)$	$n$ th-order optic susceptibility tensor
$\omega_p$	plasma frequency
$\langle a   \mathbf{p}   b \rangle$	dipole moment between states $a$ and $b$

## 10.2 INTRODUCTION

For linear optical materials, the macroscopic polarization induced by light propagating in the medium is proportional to the electric field:

$$\mathbf{P} = \epsilon_0 \chi_1 \cdot \mathbf{E} \quad (1)$$

where the linear optical susceptibility  $\chi_1$  and the corresponding linear dielectric constant  $\epsilon_1 = \epsilon_0(1 + \chi_1)$  are field-independent constants of the medium.

With the advent of the laser, light intensities orders of magnitude brighter than what could be produced by any conventional sources are now possible. When the corresponding field strength reaches a level on the order of, say, 100 KV/m or more, materials that are normally “linear” at lower light-intensity levels may become “nonlinear” in the sense that the optical “constants” are no longer “constants” independent of the light intensity. As a consequence, when the field is not weak, the optical susceptibility  $\chi$  and the corresponding dielectric constant  $\epsilon$  of the medium can become functions of the electric field  $\chi(\mathbf{E})$  and  $\epsilon(\mathbf{E})$ , respectively. Such a field-dependence in the optical parameters of the material can lead to a wide range of nonlinear optical phenomena and can be made use of for a great variety of new applications.

Since the first experimental observation of optical second-harmonic generation by Franken<sup>1</sup> and the formulation of the basic principles of nonlinear optics by Bloembergen and coworkers<sup>2</sup> shortly afterward, the field of nonlinear optics has blossomed into a wide-ranging and rapidly developing branch of optics. There is now a vast literature on this subject including numerous review articles and books.<sup>3-6</sup> It is not possible to give a full review of such a rich subject in a short introductory chapter in this *Handbook*; only the basic principles underlying the lowest order, the second-order, nonlinear optical processes and some illustrative examples of related applications will be discussed here. The reader is referred to the original literature for a more complete account of the full scope of this field.

If the light intensity is not so weak that the field dependence can be neglected and yet not too strong, the optical susceptibility and the corresponding dielectric constant can be expanded in a Taylor series:

$$\chi(\mathbf{E}) = \chi_1 + \chi_2 \cdot \mathbf{E} + \chi_3 : \mathbf{E}\mathbf{E} + \dots \quad (2)$$

or

$$\epsilon(\mathbf{E}) = \epsilon_1 + \epsilon_2 \cdot \mathbf{E} + \epsilon_3 : \mathbf{E}\mathbf{E} + \dots \quad (3)$$

where

$$\epsilon_1 = \epsilon_0(1 + \chi_1) \quad (4)$$

$$\epsilon_n = \epsilon_0 \chi_n \quad \text{for } n \geq 2 \quad (5)$$

and  $\epsilon_0$  is the dielectric constant of free space. When these field-dependent terms in the optical susceptibility are not negligible, the induced macroscopic polarization in the medium contains terms that are proportional nonlinearly to the field:

$$\begin{aligned}\mathbf{P} &= \epsilon_0 \chi_1 \cdot \mathbf{E} + \epsilon_0 \chi_2 : \mathbf{E}\mathbf{E} + \epsilon_0 \chi_3 \vdots \mathbf{E}\mathbf{E}\mathbf{E} + \dots \\ &= \mathbf{P}^{(1)} + \mathbf{P}^{(2)} + \mathbf{P}^{(3)} + \dots\end{aligned}\quad (6)$$

As the field intensity increases, these nonlinear polarization terms  $\mathbf{P}^{(n>1)}$  become more and more important, and will lead to a large variety of nonlinear optical effects.

The more widely studied of these nonlinear optical effects are, of course, those associated with the lower-order terms in Eq. (6). The second-order nonlinear effects will be discussed in some detail in this chapter. Many of the higher-order nonlinear terms have been observed and are the bases of a variety of useful nonlinear optical devices. Examples of the third-order effects are third-harmonic generation<sup>7,8</sup> associated with  $|\chi^{(3)}(3\omega = \omega + \omega + \omega)|^2$ , two-photon absorption<sup>9</sup> associated with  $\text{Im } \chi^{(3)}(\omega_1 = \omega_1 + \omega_2 - \omega_2)$ , self-focusing<sup>10,11</sup> and light-induced index-of-refraction<sup>12</sup> change associated with  $\text{Re } \chi^{(3)}(\omega = \omega + \omega - \omega)$ , four-wave mixing<sup>13</sup>  $|\chi^{(3)}(\omega_4 = \omega_1 + \omega_2 - \omega_3)|^2$ , degenerate four-wave mixing or phase-conjugation<sup>14,15</sup>  $|\chi^{(3)}(\omega = \omega + \omega - \omega)|^2$ , optical Kerr effect<sup>16</sup>  $\text{Re } \chi^{(3)}(\omega = 0 + 0 + \omega)$ , and many others.

There is also a large variety of dynamic nonlinear optical effects such as photon echo,<sup>17</sup> optical nutation<sup>18</sup> (or optical Rabi effect<sup>19</sup>), self-induced transparency,<sup>20</sup> picosecond<sup>21</sup> and femtosecond<sup>22</sup> quantum beats, and others.

In addition to the nonlinear optical processes involving only photons that are related to the nonlinear dependence on the  $\mathbf{E}$ -field as shown in Eq. (6), the medium can become nonlinear indirectly through other types of excitations as well. For example, the optical susceptibility can be a function of the molecular vibrational amplitude  $Q$  in the medium, or the stress associated with an acoustic wave  $S$  in the medium, or the amplitude  $\eta$  of any space-charge or plasma wave, or even a combination of these excitations as in a polariton, in the medium:

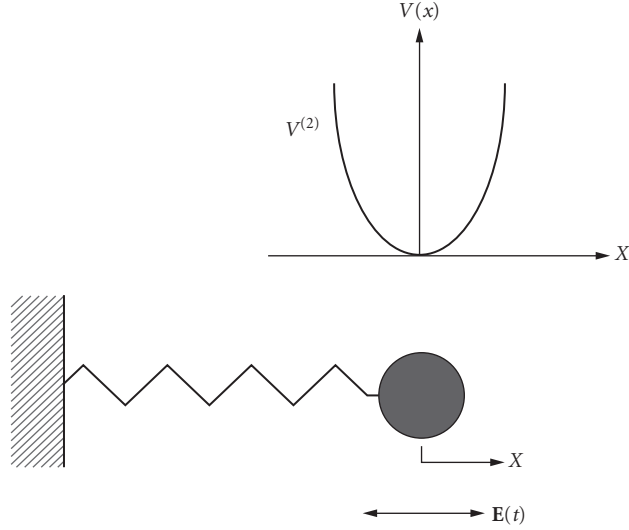
$$\begin{aligned}\mathbf{P} &= \epsilon_0 [\chi_1 + \chi_2 : \mathbf{E} + \chi_3 \vdots \mathbf{E}\mathbf{E} + \dots] \mathbf{E} \\ &\quad + \epsilon_0 [\chi_q : \mathbf{Q} + \chi_s : \mathbf{S} + \chi_\eta : \boldsymbol{\eta} + \dots] \mathbf{E}\end{aligned}\quad (7)$$

giving rise to the interaction of optical and molecular vibrational waves, or optical and acoustic phonons, etc. Nonlinear optical processes involving interaction of laser light and molecular vibrations in gases or liquids or optical phonon in solids can lead to stimulated Raman<sup>23–25</sup> processes. Those involving laser light and acoustic waves or acoustic phonons lead to stimulated Brillouin<sup>26–28</sup> processes. Those involving laser light and mixed excitations of photons and phonons lead to stimulated polariton<sup>29</sup> processes. Again, there is a great variety of such general nonlinear optical processes in which excitations other than photons in the medium may play a role. It is not possible to include all such nonlinear optical processes in the discussions here. Extensive reviews of the subject can be found in the literature.<sup>3–5</sup>

## 10.3 BASIC CONCEPTS

### Microscopic Origin of Optical Nonlinearity

*Classical Harmonic Oscillator Model of Linear Optical Media* The linear optical properties, including dispersion and single-photon absorption, of optical materials can be understood phenomenologically on the basis of the classical harmonic oscillator model (or Drude model). In this simple model, the optical medium is represented by a collection of independent identical harmonic oscillators



**FIGURE 1** Harmonic oscillator model of linear optical media.

embedded in a host medium. The harmonic oscillator is characterized by four parameters: a spring constant  $k$ , a damping constant  $\Gamma$ , a mass  $m$ , and a charge  $-e\sqrt{f}$  as shown schematically in Fig. 1.  $f$  is also known as the oscillator-strength and  $-e$  is the charge of an electron. The resonance frequency  $\omega_0$  of the oscillator is then equal to  $[k/m]^{1/2}$ .

In the presence of, for example, a monochromatic wave:

$$\mathbf{E} = \frac{1}{2} [\tilde{\mathbf{E}} e^{-i\omega t} + \tilde{\mathbf{E}}^* e^{i\omega t}] \quad (8)$$

the response of the medium is determined by the equation of motion of the oscillator in the presence of the field:

$$\frac{\partial^2 X^{(1)}(t)}{\partial t^2} + \Gamma \frac{\partial X^{(1)}(t)}{\partial t} + \omega_0^2 X^{(1)}(t) = \frac{-e\sqrt{f}}{2m} [\tilde{\mathbf{E}} e^{-i\omega t} + \text{c.c.}] \cdot x \quad (9)$$

where  $X^{(1)}(t)$  is the deviation of the harmonic oscillator from its equilibrium position in the absence of the field. The corresponding linear polarization in the steady state and linear complex susceptibility are from Eqs. (8) and (9):

$$\begin{aligned} \mathbf{P}^{(1)} &= -NeX^{(1)}(t)x = \frac{1}{2} [\tilde{\mathbf{P}}^{(1)} e^{-i\omega t} + \tilde{\mathbf{P}}^{(1)*} e^{i\omega t}] \\ &= \frac{Ne^2 f \tilde{\mathbf{E}}}{2mD(\omega)} e^{-i\omega t} + \text{c.c.} \end{aligned} \quad (10)$$

and

$$\epsilon_0 \chi^{(1)} = \frac{|\tilde{\mathbf{P}}|}{|\tilde{\mathbf{E}}|} = \frac{Ne^2 f}{mD(\omega)} \quad (11)$$

where  $N$  is the volume density of the oscillators and  $D(\omega) = \omega_0^2 - \omega^2 - i\omega\Gamma$ . The corresponding real and imaginary parts of the corresponding linear complex dielectric constant of the medium  $\text{Re } \epsilon_1$

and  $\text{Im } \varepsilon_1$ , respectively, describe then the dispersion and absorption properties of the linear optical medium. To represent a real medium, the results must be summed over all the effective oscillators ( $j$ ):

$$\text{Re } \varepsilon_1 = \varepsilon_0 + \sum_j \frac{\omega_{pj}^2 f_j (\omega_{0j}^2 - \omega^2)}{(\omega_{0j}^2 - \omega^2)^2 + \omega^2 \Gamma_j^2} \quad (12)$$

and

$$\text{Im } \varepsilon_1 = \sum_j \frac{\omega_{pj}^2 f_j \omega \Gamma_j}{(\omega_{0j}^2 - \omega^2)^2 + \omega^2 \Gamma_j^2} \rightarrow \frac{\omega_{pj}^2 f_j}{2\omega} \frac{\Gamma_j / 2}{(\omega - \omega_{0j})^2 - (\Gamma_j / 2)^2} \quad \text{for } \omega \approx \omega_{0j} \quad (13)$$

where  $\omega_{pj}^2 = 4\pi N_j e^2 / m$  is the plasma frequency for the  $j$ th specie of oscillators. Each specie of oscillators is characterized by four parameters: the plasma frequency  $\omega_{pj}$ , the oscillator-strength  $f_j$ , the resonance frequency  $\omega_{0j}$ , and the damping constant  $\Gamma_j$ . These results show the well-known anomalous dispersion and lorentzian absorption lineshape near the transition or resonance frequencies.

The difference between the results derived using the classic harmonic oscillator or the Drude model and those derived quantum mechanically from first principles is that, in the latter case, the oscillator strengths and the resonance frequencies can be obtained directly from the transition frequencies and induced dipole moments of the transitions between the relevant quantum states in the medium. For an understanding of the macroscopic linear optical properties of the medium, extended versions of Eqs. (12) and (13), including the tensor nature of the complex linear susceptibility, are quite adequate.

**Anharmonic Oscillator Model of the Second-Order Nonlinear Optical Susceptibility** An extension of the Drude model with the inclusion of suitable anharmonicities in the oscillator serves as a useful starting point in understanding the microscopic origin of the optical nonlinearity classically. Suppose the spring constant of the oscillator representing the optical medium is not quite linear in the sense that the potential energy of the oscillator is not quite a quadratic function of the deviation from the equilibrium position, as shown schematically in Fig. 2. In this case, the response of the oscillator to a harmonic force is asymmetric. The deviation (solid line) from the equilibrium position is larger and smaller on alternate half-cycles than that in the case of the harmonic oscillator. This means that there must be a second-harmonic component (dark shaded curve) in the response of the oscillator as shown schematically in Fig. 3. It is clear, then, that the larger the anharmonicity and the corresponding asymmetry in the oscillator potential, the larger the second-harmonic in the response. Extending this kind of consideration to a three-dimensional model, it implies that to have second-harmonic generation, the material must not have inversion symmetry and, therefore, must be crystalline. It is also clear that for the third and higher odd harmonics, the anharmonicity in the oscillator potential should be symmetric. Even harmonics will always require the absence of inversion symmetry. Beyond that, obviously, the larger the anharmonicities, the larger the nonlinear effects.

Consider first the second-harmonic case. The corresponding anharmonic oscillator equation is:

$$\frac{\partial^2 X(t)}{\partial t^2} + \Gamma \frac{\partial X(t)}{\partial t} + \omega_0^2 X(t) + \nu X(t)^2 = \frac{-e\sqrt{f}}{2m} [\tilde{\mathbf{E}} e^{-i\omega t} + \text{c.c.}] \cdot x \quad (14)$$

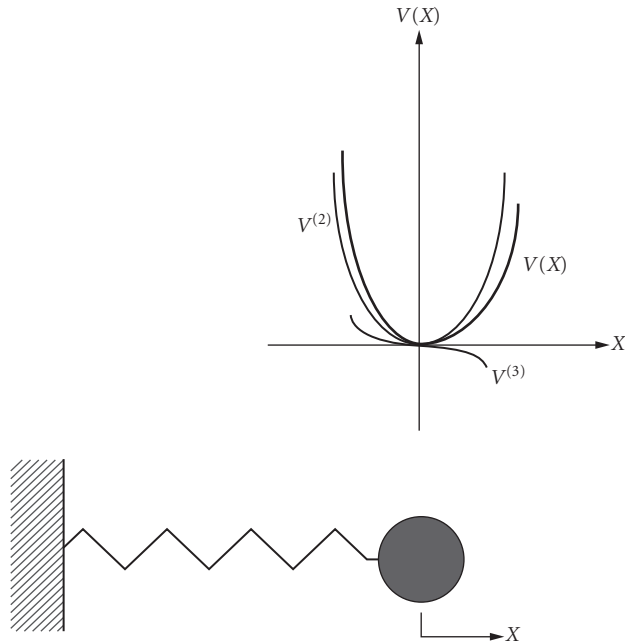
Solving this equation by perturbation expansion in powers of the  $\mathbf{E}$ -field:

$$X(t) = X^{(1)}(t) + X^{(2)}(t) + X^{(3)}(t) + \dots \quad (15)$$

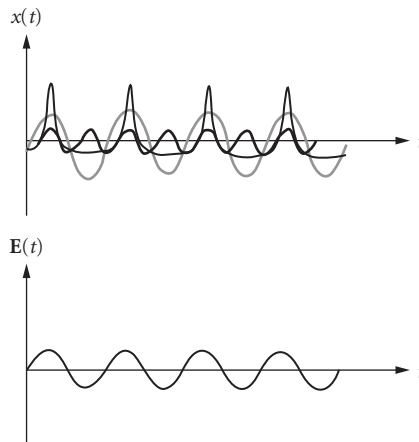
leads to the second-order nonlinear optical susceptibility

$$\varepsilon_0 \chi^{(2)} = \frac{|\tilde{\mathbf{P}}^{(2)}|}{|\tilde{\mathbf{E}}^2|} = \frac{Ne^3 f \nu}{2m^2 D^2(\omega) D(2\omega)} \quad (16)$$





**FIGURE 2** Anharmonic oscillator model of nonlinear optical media.



**FIGURE 3** Response  $[x(t)]$  of anharmonic oscillator to sinusoidal driving field  $[E(t)]$ .

Unlike in the linear case, a more exact expression of the nonlinear susceptibility-derived quantum mechanically will, in general, have a more complicated form and will involve the excitation energies of, and dipole matrix elements between, all the states. Nevertheless, an expression like Eq. (16) obtained on the basis of the classical anharmonic oscillator model is very useful in discussing qualitatively the second-order nonlinear optical properties of materials. Equation (16) is particularly useful in understanding the dispersion properties of the second nonlinearity.

It is also the basis for understanding the so-called Miller's rule<sup>30</sup> which gives a very rough estimate of the order of magnitude of the nonlinear coefficient. We note that the strong frequency dependence in the denominator of the  $\chi^{(2)}$  involves factors that are of the same form as those that appeared in  $\chi^{(1)}$ . Suppose we divide out these factors and define a parameter which is called Miller's coefficient:

$$\delta = \chi^{(2)}(2\omega) / [\chi^{(1)}(\omega)]^2 \chi^{(1)}(2\omega) \epsilon_0^2 = mv / 2e^3 f^{1/2} N^2 \epsilon_0^2 \quad (17)$$

from Eqs. (16) and (11). For many inorganic second-order nonlinear optical crystals, it was first suggested by R. C. Miller that  $\delta$  was approximately a constant for all materials, and its value was found empirically to be on the order of  $2-3 \times 10^{-6}$  esu. If this were true, to find materials with large nonlinear coefficients, one should simply look for materials with large values of  $\chi^{(1)}(\omega)$  and  $\chi^{(1)}(2\omega)$ . This empirical rule was known as Miller's rule. It played an important historical role in the search for new nonlinear optical crystals and in explaining the order of magnitude of nonlinear coefficients for many classes of nonlinear optical materials including such well-known materials as the ADP-isomorphs—for example,  $\text{KH}_2\text{PO}_4$  (KDP),  $\text{NH}_4\text{PO}_4$  (ADP), etc.—and the  $\text{ABO}_3$  type of ferroelectrics—for example,  $\text{LiIO}_3$ ,  $\text{LiNbO}_3$ , etc.—or III-V and II-VI compound semiconductors in the early days of nonlinear optics.

On a very crude basis, a value of  $\delta$  can be estimated from Eq. (17) by assuming that the anharmonic potential term in Eq. (14) becomes comparable to the harmonic term when the deviation  $X$  is on the order of one lattice spacing in a typical solid, or on the order of an Angstrom. Thus, using standard numbers, Eq. (17) predicts that, in a typical solid,  $\delta$  is on the order of  $4 \times 10^{-6}$  esu in the visible. It is now known that there are many classes of materials that do not fit this rule at all. For example, there are organic crystals with Miller's coefficients thousands of times larger than this value.

A more rigorous theory for the nonlinear optical susceptibility will clearly have to come from appropriate calculations based upon the principles of quantum mechanics.

**Quantum Theory of Nonlinear Optical Susceptibility** Quantum mechanically, the nonlinearities in the optical susceptibility originate from the higher-order terms in the perturbation solutions of the appropriate Schrödinger's equation or the density-matrix equation.

According to the density-matrix formalism, the induced macroscopic polarization  $\mathbf{P}$  of the medium is specified completely in terms of the density matrix:

$$\mathbf{P} = N \text{Trace}[\mathbf{p}\rho] \quad (18)$$

where  $\mathbf{p}$  is the dipole moment operator of the essentially noninteracting individual polarizable units, or "atoms" or molecules or unit cells in a solid, as the case may be, and  $N$  is the volume density of such units.

The density-matrix satisfies the quantum mechanical Boltzmann equation or the density-matrix equation:

$$\frac{\partial \rho_{mn}}{\partial t} + i\omega_{mn} \rho_{mn} + \frac{\rho_{mn} - \bar{\rho}_{mn}}{T_{mn}} = \frac{i}{\hbar} \sum_k [\rho_{mk} V_{kn} - V_{mk} \rho_{kn}] \quad (19)$$

where  $\bar{\rho}_{mn}$  is the equilibrium density matrix in the absence of the perturbation  $V$  and  $T_{mn}$  is the relaxation time of the density-matrix element  $\rho_{mn}$ . The  $n$ th-order perturbation solution of Eq. (19) in the steady state is:

$$\rho_{mn}^{(n)}(t) = \frac{i}{\hbar} \sum_k \int_{-\infty}^t [\rho_{mk}^{(n-1)}(t') V_{kn}(t') - V_{mk}(t') \rho_{kn}^{(n-1)}(t')] \exp\left[\left(i\omega_{mn} + \frac{1}{T_{mn}}\right)(t' - t)\right] dt' \quad (20)$$

The zeroth-order solution is clearly that in the absence of any perturbation or:

$$\rho_{mn}^{(0)} = \bar{\rho}_{mn} \quad (21)$$

In principle, once the zeroth-order solution is known, one can generate the solution to any order corresponding to all the nonlinear optical processes. While such solutions are formally complete and correct, they are generally not very useful, because it is difficult to know all the excitation energies and transition moments of all the states needed to calculate  $\chi^{(n)}$ . For numerical evaluations of  $\chi^{(n)}$ , various simplifying approximations must be made.

To gain some qualitative insight into the microscopic origin of the nonlinearity, it can be shown on the basis of a simple two-level system that the second-order solution of Eq. (20) leads to the approximate result:

$$\chi^{(2)\infty}[(\omega_{ge} - \omega)(\omega_{ge} - 2\omega)]^{-1} |\langle g|\mathbf{p}|e\rangle|^2 [\langle e|\mathbf{p}|e\rangle - \langle g|\mathbf{p}|g\rangle] \quad (22)$$

It shows that for such a two-level system at least, there are three important factors: the resonance denominator, the transition-moment squared, and the change in the dipole moment of the molecule going from the ground state to the excited state. Thus, to get a large second-order optical nonlinearity, it is preferable to be near a transition with a large oscillator strength and there should be a large change in the dipole moment in going from the ground state to that particular excited state. It is known, for example, that substituted benzenes with a donor and an acceptor group have strong charge-transfer bands where the transfer of charges from the donor to the acceptor leads to a large change in the dipole moment in going from the ground state to the excited state. The transfer of the charges is mediated by the delocalized  $\pi$  electrons along the benzene ring. Thus, there was a great deal of interest in organic crystals of benzene derivatives. This led to the discovery of many organic nonlinear materials. In fact, it was the analogy between the benzene ring structure and the boroxal ring structure that led to the discovery of some of the best known recently discovered inorganic nonlinear crystals such as  $\beta$ -BaB<sub>2</sub>O<sub>4</sub> (BBO)<sup>31</sup> and LiB<sub>3</sub>O<sub>5</sub> (LBO).<sup>32</sup>

In general, however, there are few rules that can guide the search for new nonlinear optical crystals. It must be emphasized, however, that the usefulness of a material is not determined by its nonlinearity alone. Many other equally important criteria must be satisfied for the nonlinear material to be useful, for example, the transparency, the phase-matching property, the optical damage threshold, the mechanical strength, chemical stability, etc. Most important is that it must be possible to grow single crystals of this material of good optical quality for second-order nonlinear optical applications in bulk crystals. In fact, optical nonlinearity is often the easiest property to come by. It is these other equally important properties that are often harder to predict and control.

## Form of the Second-Order Nonlinear Optical Susceptibility Tensor

The simple anharmonic oscillator model shows that to have second-order optical nonlinearity, there must be asymmetry in the crystal potential in some direction. Thus, the crystal must not have inversion symmetry. This is just a special example of how the spatial symmetry of the crystal affects the form of the optical susceptibility. In this case, if the crystal contains inversion symmetry, all the elements of the susceptibility tensor must be zero. In a more general way, the form of the optical susceptibility tensor is dictated by the spatial symmetry of the crystal structure.<sup>33</sup>

For second-order nonlinear susceptibilities in the cartesian coordinate system:

$$P_i^{(2)} = \sum_{j,k} \epsilon_0 \chi_{ijk}^{(2)} E_j E_k \quad (23)$$

$\chi_{ijk}^{(2)}$  in general has 27 independent coefficients before any symmetry conditions are taken into account. Taking into account the permutation symmetry condition, namely, the order  $E_j$  and  $E_k$  appearing in Eq. (23) is not important, or

$$\chi_{ijk}^{(2)} = \chi_{ikj}^{(2)} \quad (24)$$

the number of independent coefficients reduces down to 18. With 18 coefficients, it is sometimes more convenient to define a two-dimensional  $3 \times 6$  tensor, commonly known as the Kleinman  $\mathbf{d}$ -tensor:<sup>34</sup>

$$\begin{pmatrix} P_x \\ P_y \\ P_z \end{pmatrix} = \epsilon_0 \begin{pmatrix} d_{11} & d_{12} & d_{13} & d_{14} & d_{15} & d_{16} \\ d_{21} & d_{22} & d_{23} & d_{24} & d_{25} & d_{26} \\ d_{31} & d_{32} & d_{33} & d_{34} & d_{35} & d_{36} \end{pmatrix} \begin{pmatrix} E_x^2 \\ E_y^2 \\ E_z^2 \\ 2E_y E_z \\ 2E_x E_z \\ 2E_x E_y \end{pmatrix} \quad (25)$$

rather than the three-dimensional tensor  $\chi_{ijk}^{(2)} = \chi_{ikj}^{(2)}$ . One obvious advantage of the  $\mathbf{d}_{im}$  = tensor form is that the full tensor can be written in the two-dimensional matrix form, whereas it would be difficult to exhibit on paper any three-dimensional matrix.

An additional important point about the  $\mathbf{d}$ -tensor is that it is defined in terms of the complex amplitudes of the  $\mathbf{E}$ -field and the induced polarization with the  $1/2$  factor explicitly separated out in the front as shown in Eq. (8). In contrast, the definition of  $\chi_{ijk}$  may be ambiguous in the literature because not all the authors define the complex amplitude with a  $1/2$  factor in the front. For linear processes, it makes no difference, because the  $1/2$  factors in the induced polarization and the  $\mathbf{E}$ -field cancel out. In nonlinear processes, the  $1/2$  factors do not cancel and the numerical value of the complex susceptibility will depend on how the complex amplitudes of the  $\mathbf{E}$ -field and polarization are defined.

For crystalline materials, the remaining 18 coefficients are, in general, not all independent of each other. Spatial symmetry requires, in addition, that they must satisfy the characteristic equation:

$$\chi_{ijk}^{(2)} = \sum_{\alpha\beta\gamma} \chi_{\alpha\beta\gamma}^{(2)} R_{\alpha i} R_{\beta j} R_{\gamma k} \quad (26)$$

where  $R_{\alpha i}$ , etc., represent the symmetry operations contained in the space group for the particular crystal structure and Eq. (26) must be satisfied for all the  $R$ s in the group. For example, if a crystal has inversion symmetry, or  $R_{\alpha i, \beta j, \gamma k} = (-1)\delta_{\alpha i, \beta j, \gamma k}$ , Eq. (26) implies that  $\chi_{ijk}^{(2)} = (-1)\chi_{ikj}^{(2)} = 0$  as expected. From the known symmetry elements of all 32 crystallographic point groups, the forms of the corresponding second-order nonlinear susceptibility tensors can be worked out and are tabulated. Equation (26) can in fact be generalized<sup>33</sup> to an arbitrarily high order  $n$ :

$$\chi_{ijk\dots}^{(n)} = \sum_{\alpha\beta\gamma\dots} \chi_{\alpha\beta\gamma\dots}^{(n)} R_{\alpha i} R_{\beta j} R_{\gamma k} \dots \quad (27)$$

for all the  $R$ s in the group. Thus, the forms of any nonlinear optical susceptibility tensors can in principle be worked out once the symmetry group of the optical medium is known.

The  $\mathbf{d}$ -tensors for the second-order nonlinear optical process for all 32-point groups derived from Eq. (26) are shown in, for example, Ref. 34. Similar tensors can in principle be derived from Eq. (27) for the nonlinear optical susceptibilities to any order for any point group.

## Phase-Matching Condition (or Conservation of Linear Photon Momentum) in Second-Order Nonlinear Optical Processes

On a microscopic scale, the nonlinear optical effect is usually rather small even at relatively high light-intensity levels. In the case of the second-order effects, the ratio of the second-order term to

the first-order term in Eq. (2), for example, is very roughly the ratio of the applied **E**-field strength to the “atomic **E**-field” in the material or:

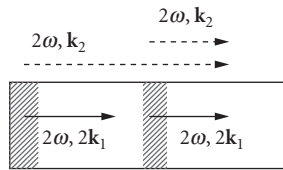
$$\frac{\chi_2 E}{\chi_1} \approx \frac{E}{E_{\text{atomic}}} \tag{28}$$

which is on the order of  $10^{-4}$  even at an intensity level of  $1 \text{ MW/cm}^2$ . The same ratio holds very roughly in each successively higher order. To see such a small effect, it is important that the waves generated through the nonlinear optical process add coherently on a macroscopic scale. That is, the new waves generated over different parts of the optical medium add coherently on a macroscopic scale. This requires that the phase velocities of the generated wave and the incident fundamental wave be “matched.”<sup>35</sup>

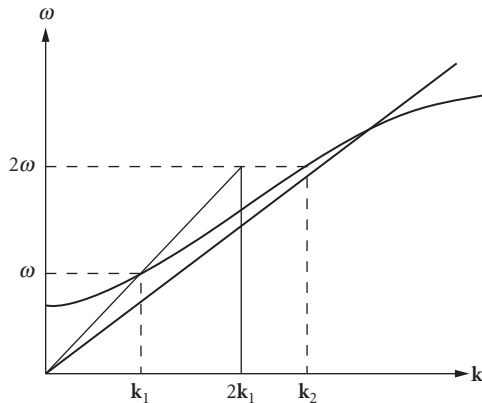
Because of the inevitable material dispersion, in general the phases are not matched because the freely propagating second-harmonic wave will propagate at the phase velocity corresponding to the second-harmonic while the source polarization at the second-harmonic will propagate at the phase velocity of the fundamental. Phase matching requires that the propagation constant of the source polarization  $2\mathbf{k}_1$  be equal to the propagation constant  $\mathbf{k}_2$  of the second-harmonic or:

$$2\mathbf{k}_1 = \mathbf{k}_2 \tag{29}$$

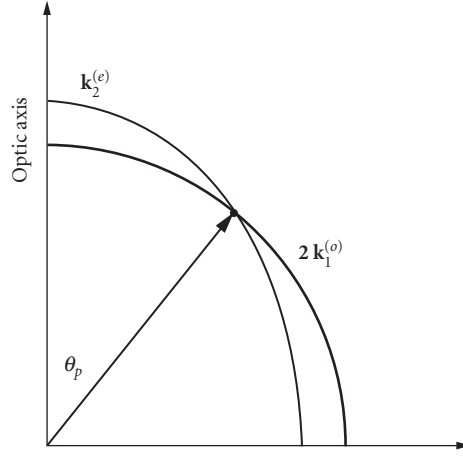
Multiplying Eq. (29) by  $\hbar$  implies that the linear momentum of the photons must be conserved. As shown in the schematic diagram in Fig. 4, in a normally dispersive region of an optical medium,  $\mathbf{k}_2$  is always too long and must be reduced to achieve phase matching.



Phase-matching condition:  $2\mathbf{k}_1 = \mathbf{k}_2$



**FIGURE 4** Phase-matching requirement and the effect of materials dispersion on momentum mismatch in second-harmonic process.



**FIGURE 5** Phase matching using birefringence to compensate material dispersion in second-harmonic generation.

In bulk crystals, the most effective and commonly used method is to use birefringence to compensate for material dispersion, as shown schematically in Fig. 5. In this scheme, the  $\mathbf{k}$ -vector of the extraordinary wave in the anisotropic crystal is used to shorten  $\mathbf{k}_2$  or lengthen  $2\mathbf{k}_1$  as needed. For example, in a negative uniaxial crystal, the fundamental wave is sent into the crystal as an ordinary wave and the second-harmonic wave is generated as an extraordinary wave in a so-called Type I phase-matching condition:

$$2\mathbf{k}_1^{(o)} = \mathbf{k}_2^{(e)} \quad (30)$$

or the fundamental wave is sent in both as an ordinary wave and an extraordinary wave while the second-harmonic is generated as an extraordinary wave in the so-called Type II phase-matching condition:

$$\mathbf{k}_1^{(o)} + \mathbf{k}_1^{(e)} = \mathbf{k}_2^{(e)} \quad (31)$$

In a positive uniaxial crystal,  $\mathbf{k}_2^{(e)}$  in Eqs. (30) and (31) should be replaced by  $\mathbf{k}_2^{(o)}$  and  $\mathbf{k}_1^{(o)}$  in Eq. (30) should be replaced by  $\mathbf{k}_1^{(e)}$ . Crystals with isotropic linear optical properties clearly lack birefringence and cannot use this scheme for phase matching. Semiconductors of zinc-blende structure, such as the III-V and some of the II-VI compounds, have very large second-order optical nonlinearity but are nevertheless not very useful in the bulk crystal form for second-order nonlinear optical processes because they are cubic and lack birefringence and, hence, difficult to phase match. Phase matching can also be achieved by using waveguide dispersion to compensate for material dispersion. This scheme is often used in the case of III-V and II-VI compounds of zinc-blende structure. Other phase-matching schemes include the use of the dispersion of the spatial harmonics of artificial period structures to compensate for material dispersion.

These phase-matching conditions for the second-harmonic processes can clearly be generalized to other second-order nonlinear optical processes such as the sum- and difference-frequency processes in which two photons of different frequencies and momenta  $\mathbf{k}_1$  and  $\mathbf{k}_2$  either add or subtract to create a third photon of momentum  $\mathbf{k}_3$ . The corresponding phase-matching conditions are:

$$\mathbf{k}_1 \pm \mathbf{k}_2 = \mathbf{k}_3 \quad (32)$$

The practical phase-matching schemes for these processes are completely analogous to those for the second-harmonic process. For example, one can use the birefringence in a bulk optical crystal or the waveguide dispersion to compensate for the material dispersion in a sum- or difference-frequency process.

### Conversion Efficiencies for the Second-Harmonic and Sum- and Difference-Frequency Processes

With phase matching, the waves generated through the nonlinear optical process can coherently accumulate spatially. The spatial variation of the complex amplitude of the generated wave follows from the wave equation:

$$\frac{\partial^2}{\partial z^2} E_i(z, t) - \frac{1}{c^2} \frac{\partial^2}{\partial t^2} E_i(z, t) = \frac{1}{c^2 \epsilon_0} \frac{\partial^2}{\partial t^2} P_i(z, t) \quad (33)$$

where

$$E_i(z, t) = \frac{1}{2} [\tilde{E}_{0,i} e^{ik_0 z - i\omega_0 t} + \text{c.c.}] + \frac{1}{2} [\tilde{E}_{2,i}(z) e^{-ik_2 z - i\omega_2 t} + \text{c.c.}] \quad (34)$$

and

$$P_i(z, t) = P_i^{(\omega_0)}(z, t) + [P_{\text{source},i}^{(2\omega_0)}(z, t) + P_i^{(2\omega_0)}(z, t)] \quad (35)$$

$$P_i^{(2\omega_0)}(z, t) = \frac{1}{2} \left[ \sum_j \epsilon_0 \chi_{ij}^{(1)}(2\omega_0) \tilde{E}_{2,j}(z) e^{ik_2 z - i\omega_2 t} + \text{c.c.} \right] \quad (36)$$

$$P_{\text{source},i}^{(2\omega_0)}(z, t) = \frac{1}{2} [\tilde{P}_{s,i}(z) e^{-i2k_0 z - i\omega_2 t} + \text{c.c.}] \quad (37)$$

$$\tilde{P}_{s,i}^{(2\omega_0)}(z, t) = \frac{1}{2} \sum_{jk} \epsilon_0 \chi_{ijk}^{(2)}(2\omega_0) \tilde{E}_{0,j} \tilde{E}_{0,k} \quad (38)$$

The spatial variation in the complex amplitude of the fundamental wave  $\tilde{E}_{0,i}$  in Eq. (34) is assumed negligible and, in fact, we assume it to be that of the incident wave in the absence of any nonlinear conversion in the medium. It is, therefore, implied that the nonlinear conversion efficiency is not so large that the fundamental intensity is appreciably depleted. In other words, the small-signal approximation is implied. Solving Eq. (33) with the boundary conditions that there is no second-harmonic at the input and no reflection at the output end of the crystal, one finds the second-harmonic at the output end of the crystal  $z = L$  to be:

$$I^{2\omega_0}(z = L) = \frac{2d^2 I_0^2}{c \epsilon_0 n_2 (n_1 - n_2)^2} \sin^2 \left( \frac{L \omega_0}{c} \right) (n_1 - n_2) \quad (39)$$

where  $d$  is the appropriate Kleinman  $\mathbf{d}$ -coefficient and the intensities refer to those inside the medium. When the phases of the fundamental and second-harmonic waves are not matched, or  $n_1 \neq n_2$ , it is clear from Eq. (39) that the second-harmonic intensity is an oscillating function of the crystal length. The maximum intensity is reached at a crystal length of:

$$L_{\text{max}} = \frac{\lambda}{4|n_2 - n_1|} \quad (40)$$

which is also known as the coherence length for the second-harmonic process. The maximum intensity that can be reached is:

$$I_{\max}^{2\omega_0}(z = L_{\max}) = \frac{2d^2}{c\epsilon_0 n_2 (n_1 - n_2)^2} I_0^2 \quad (41)$$

regardless of the crystal length as long as it is greater than the coherence length. The coherence length for many nonlinear optical materials could be on the order of a few microns. Therefore, without phase matching, the second-harmonic intensity in such crystals corresponds to what is generated within a few microns of the output surface of the nonlinear crystal. A much more interesting or important case is clearly when there is phase matching or  $n_1 = n_2$ .

The second-harmonic intensity under the phase-matched condition is, from Eq. (39):

$$I_2 = \left( \frac{8\pi^2}{c\epsilon_0 n_1^2 n_2} \right) \left( \frac{L}{\lambda_1} \right)^2 d_{\text{eff}}^2 I_0^2 \quad (42)$$

where  $d_{\text{eff}}$  is the effective  $\mathbf{d}$ -coefficient which takes into account the projections of the  $\mathbf{E}$ -field and the second-harmonic polarization along the crystallographic axes and the form of the proper  $\mathbf{d}$ -tensor for the particular crystal structure. The intensities in this equation refer to the intensities inside the nonlinear medium and the wavelength refers to the free-space wavelength. Equation (42) shows that the second-harmonic intensity under phase-matched conditions is proportional to the square of the length of the crystal measured in the wavelength, as expected for coherent processes. The second-harmonic intensity is also proportional to the effective  $\mathbf{d}$ -coefficient squared and the fundamental intensity squared, as expected.

One might be tempted to think that, to increase the second-harmonic power conversion efficiency indefinitely, all one has to do is to focus the beam very tight since the left-hand side is inversely proportional to the beam cross section while the right-hand side is inversely proportional to the cross section squared. Because of diffraction, however, as the fundamental beam is focused tighter and tighter, the effective focal region becomes shorter and shorter. Optimum focusing is achieved when the Rayleigh range of the focal region becomes the limiting interaction length rather than the crystal length. A rough estimate assumes that a beam of square cross section doubles in width ( $w$ ) due to diffraction in an "optimum focusing length,"  $L_{\text{opt}} \sim w^2/\lambda_2$ , and that this optimum focusing length is equal to the crystal length  $L$ . Under such a nominally optimum focusing condition, the maximum second-harmonic power that can be generated in practice is, therefore, approximately:

$$P_2^{(\text{opt})} = \left( \frac{2\pi^2}{c\epsilon_0 n_1^2 n_2} \right) \left( \frac{L}{\lambda_2^3} \right) d_{\text{eff}}^2 P_0^2 \quad (43)$$

Note that this maximum power is linearly proportional to the crystal length. It must be emphasized, however, that this linear dependence is not an indication of incoherent optical process. It is because the beam spot size (area) under the optimum focusing condition is linearly proportional to the crystal length. Numerically, for example, approximately 3 W of second-harmonic power could be generated under optimum focusing in a 1-cm-long  $\text{LiIO}_3$  crystal with 30 W of incident fundamental power at 1  $\mu\text{m}$ .

Equation (43) can, in fact, be generalized to other three-photon processes such as the sum-frequency and difference-frequency processes:

$$P_+^{(\text{opt})} = \left( \frac{2\pi^2}{c\epsilon_0 n_1 n_2 n_+} \right) \left( \frac{L}{\lambda_+^3} \right) d_{\text{eff}}^2 (\omega_+ = \omega_1 + \omega_2) P_1 P_2 \quad (44)$$



and

$$P_-^{(\text{opt})} = \left( \frac{2\pi^2}{c\mathcal{E}_0 n_1 n_2 n_-} \right) \left( \frac{L}{\lambda_-^3} \right) d_{\text{eff}}^2 (\omega_- = \omega_1 - \omega_2) P_1 P_2 \quad (45)$$

In using Eqs. (44) and (45), one must be especially careful in relating the numerical values of the  $d_{\text{eff}}$  coefficients for the sum- and difference-frequency processes to that measured in the second-harmonic process because the two low-frequency photons degenerate in frequency in the latter process.

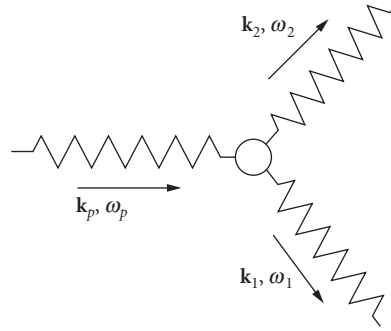
## The Optical Parametric Process

A somewhat different, but rather important, second-order nonlinear optical process is the optical parametric process.<sup>36,37</sup> Optical parametric amplifiers and oscillators powerful solid-state sources of broadly tunable coherent radiation capable of covering the entire spectral range from the near-UV to the mid-IR and can operate down to the femtosecond time domain. The basic principles of optical parametric process were known even before the invention of the laser, dating back to the days of the masers. The practical development of the optical parametric oscillator had been impeded, however, due to the lack of suitable nonlinear optical materials. As a result of recent advances<sup>38</sup> in nonlinear optical materials research, these oscillators are now practical devices with broad potential applications in research and industry. The basic physics of the optical parametric process and recent developments in practical optical parametric oscillators are reviewed in this section as an example of wavelength-shifting nonlinear optical devices.

Studies of the optical parameters of materials clearly have always been a powerful tool to gain access to the atomic and molecular structures of optical materials and have played a key role in the formulation of the basic principles of quantum mechanics and, indeed, modern physics. Much of the information obtained through linear optics and linear optical spectroscopy came basically from just the first term in the expansion of the complex susceptibility, Eq. (2). The possibility of studying the higher-order terms in the complex susceptibility through nonlinear optical techniques greatly expands the power of such studies to gain access to the basic building blocks of materials on the atomic or molecular level. Of equal importance, however, are the numerous practical applications of nonlinear optics. Although there are now thousands of known laser transitions in all kinds of laser media, the practically useful ones are still relatively few compared to the needs. Thus, there is always a need to shift the laser wavelengths from where they are available to where they are needed. Nonlinear optical processes are the way to accomplish this. Until recently, the most commonly used wavelength-shifting processes were harmonic generation, sum-, and difference-frequency generation processes. In all these processes, the generated frequencies are always uniquely related to the frequencies of the incident waves. The parametric process is different. In this process, there is the possibility of generating a continuous range of frequencies from a single-frequency input.

For harmonic, sum-, and difference-frequency generation, the basic devices are nothing more than suitably chosen nonlinear optical crystals that are oriented and cut according to the basic principles already discussed in the previous sections and there is a vast literature on all aspects of such devices. The spontaneous optical parametric process can be viewed as the inverse of the sum-frequency process and the stimulated parametric process, or the parametric amplification process, can be viewed as a repeated difference-frequency process.

**Spontaneous Parametric Process** The spontaneous parametric process, also known as the parametric luminescence or parametric fluorescence process, is described by a simple Feynman diagram as shown in Fig. 6. It describes the process in which an incident photon, called a pump photon, propagating in a nonlinear optical medium breaks down spontaneously into two photons of lower frequencies, called signal and idler photons using a terminology borrowed from earlier microwave



**FIGURE 6** Spontaneous breakdown of a pump photon into a signal and an idler photon.

parametric amplifier work, with the energy and momentum conserved:

$$\omega_p = \omega_s + \omega_i \quad (46)$$

$$\mathbf{k}_p = \mathbf{k}_s + \mathbf{k}_i \quad (47)$$

The important point about this second-order nonlinear optical process is that the frequency condition Eq. (46) does not predict a unique pair of signal and idler frequencies for each fixed pump frequency  $\omega_p$ . Neglecting the dispersion in the optical material, there is a continuous range of frequencies that can satisfy this condition. Taking into account the dispersion in real optical materials, the frequency and momentum matching conditions Eqs. (46) and (47), in general, cannot be satisfied simultaneously. In analogy with the second-harmonic or the sum- or difference-frequency processes, one can use the birefringence in the material to compensate for the material dispersion for a set of photons propagating in the nonlinear crystal. By rotating the crystals, the birefringence in the direction of propagation can be tuned, thereby leading to tuning of the signal and idler frequencies. This tunability gives rise to the possibility of generating photons over a continuous range of frequencies from incident pump photons at one particular frequency, which means the possibility of constructing a continuously tunable amplifier or oscillator by making use of the parametric process.

A complete theory for the spontaneous parametric emission is beyond the scope of this introductory chapter because, as all spontaneous processes, it requires the quantization of the electromagnetic waves. Detailed descriptions of the process can be found in the literature.<sup>4</sup>

**Stimulated Parametric Process, or the Parametric Amplification Process** With only the pump photons present in the initial state, spontaneous emission occurs at the signal and idler frequencies under phase-matched conditions. With signal and pump photons present in the initial state, stimulated parametric emission occurs in the same way as in a laser medium, except here the pump photons are converted directly into the signal and the corresponding idler photons through the second-order nonlinear optical process and no exchange of energy with the medium is involved. The stimulated parametric process can also be viewed as a repeated difference-frequency process in which the signal and idler photons repeatedly mix with the pump photons in the medium, generating more and more signal and idler photons under the phase-matched condition.

The spatial dependencies of the signal and idler waves can be found from the appropriate coupled-wave equations under the condition when the pump depletion can be neglected. The corresponding complex amplitude of the signal wave at the output  $\mathbf{E}_s(L)$  is proportional to that at the input  $\mathbf{E}_s(0)$ , as in any amplification process.<sup>39</sup>

$$\mathbf{E}_s(L) = \mathbf{E}_s(0) \cosh gL \quad (48)$$

where

$$g = \frac{d_{\text{eff}} |E_p| \sqrt{k_s k_i}}{2n_s n_i} \quad (49)$$

is the spatial gain coefficient of the parametric amplification process.  $d_{\text{eff}}$  is the effective Kleinman  $d$ -coefficient for the parametric process.  $k_s$  and  $k_i$  are the phase-matched propagation constants of the signal and idler waves, respectively;  $n_s$  and  $n_i$  are the corresponding indices of refraction.

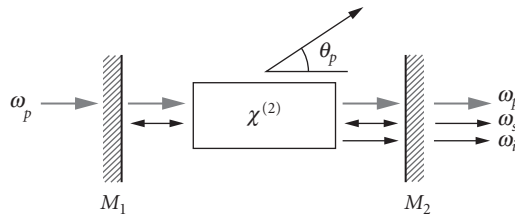
**Optical Parametric Oscillator** Given the parametric amplification process, a parametric oscillator can be constructed by simply adding a pair of Fabry-Perot mirrors, as in a laser, to provide the needed optical feedback of the stimulated emission. The optical parametric oscillator has the unique characteristic of being continuously tunable over a very broad spectral range. This is perhaps one of the most important applications of second-order nonlinear optics.

The basic configuration of an optical parametric oscillator (OPO) is extremely simple. It is shown schematically in Fig. 7. Typically, it consists of a suitable nonlinear optical crystal in a Fabry-Perot cavity with dichroic cavity mirrors which transmit at the pump frequency and reflect at the signal frequency or at the signal and idler frequencies. In the former case, the OPO is a singly resonant OPO (SRO) and, in the latter case, it is a doubly resonant OPO (DRO). The threshold for the SRO is much higher than that for the DRO. The trade-off is that the DRO tends to be highly unstable and, thus, not as useful.

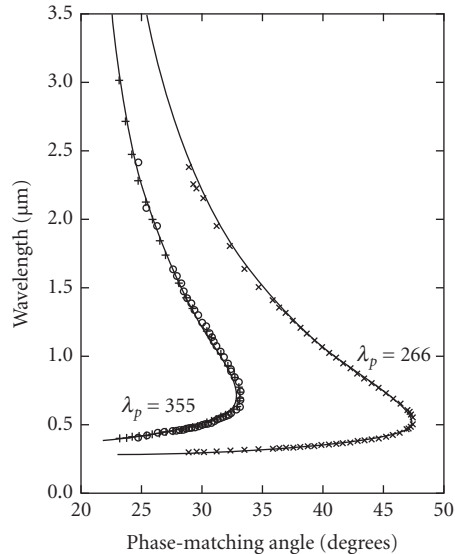
Tuning of the oscillator can be achieved by simply rotating the crystal relative to the direction of propagation of the pump beam or the axis of the Fabry-Perot cavity. As an example of the spectral range that can be covered by the OPO, Fig. 8 shows the tuning curve of a  $\beta$ -barium borate OPO pumped by the third-harmonic output at 355  $\mu\text{m}$  and the fourth-harmonic at 266  $\mu\text{m}$  of a Nd:YAG laser. Also shown are the corresponding spontaneous parametric emissions. The symbols correspond to the experimental data and the solid curves are calculated.<sup>38</sup> With a single set of mirrors to resonate the signal wave in the visible, the entire spectral range from about 400 nm to the IR absorption edge of the  $\beta$ -barium borate crystal can be covered. With  $\text{KTiO}_2\text{PO}_4$  (KTP) or the more recently developed  $\text{KTiO}_2\text{AsO}_4$  (KTA) crystals, the tuning range can be extended well into the mid-IR range to the 3- to 5- $\mu\text{m}$  range. With  $\text{AgGaSe}_2$ , the potential tuning range could be extended to the 18- to 20- $\mu\text{m}$  range.

The efficiency of the SRO that can be achieved in practice is relatively high, typically over 30 percent on a pulsed basis. Since the OPO is scalable, the output energy is only limited by the pump energy available and can be in the multijoule range.

A serious limitation at the early stage of development is the oscillator linewidth that can be achieved. Without rather complicated and special arrangements, the oscillator linewidth is typically a few Angstroms or more, which is not useful for high-resolution spectroscopic applications. The linewidth problem is, however, not a basic limitation inherent in the parametric process. It is primarily due to the finite pulse length of the pump sources, which limits the cavity length that can be used so that the number of passes by the signal through the nonlinear crystal is not too small. As more suitable pump sources are developed, various line-narrowing schemes<sup>40</sup> typically used in tunable lasers can be adapted for use in OPOs as well.



**FIGURE 7** Schematic of singly resonant optical parametric oscillator.



**FIGURE 8** Tuning characteristics of BBO spontaneous parametric emission ( $\times$  and  $+$ ) and OPO (circles) pumped at the third (355 nm) and fourth (266 nm) harmonics of Nd-YAG laser output. Solid curves are calculated.

The OPO holds promise to become a truly continuously tunable powerful solid-state source of coherent radiation with broad applications as a research tool and in industry.

## 10.4 MATERIAL CONSIDERATIONS

The second-order nonlinearity is the lowest-order nonlinearity and the first to be observed as the intensity increases. As the discussion following Eq. (26) indicates, only materials without inversion symmetry can have second-order nonlinearity, which means that these must be crystalline materials. The lowest-order nonlinearity in a centrosymmetric system is the third-order nonlinearity.

To observe and to make use of the second-order nonlinear optical effects in a nonlinear crystal, an effective  $d$ -coefficient on the order of  $10^{-13}$  m/V or larger is typically needed. In the case of the third-order nonlinearity, the effect becomes nonnegligible or useful in most applications when it is on the order of  $10^{-21}$  MKS units or more.

Ever since the first observation of the nonlinear optical effect<sup>1</sup> shortly after the advent of the laser, there has been a constant search for new efficient nonlinear materials. To be useful, a large nonlinearity is, however, hardly enough. Minimum requirements in other properties must also be satisfied, such as transparency window, phase-matching condition, optical damage threshold, mechanical hardness, thermal and chemical stability, etc. Above all, it must be possible to grow large single crystals of good optical quality for second-order effects. The perfection of the growth technology for each crystal can, however, be a time-consuming process. All these difficulties tend to conspire to make good nonlinear optical materials difficult to come by.

The most commonly used second-order nonlinear optical crystals in the bulk form tend to be inorganic crystals such as the ADP-isomorphs  $\text{NH}_4\text{H}_2\text{PO}_4$  (ADP),  $\text{KH}_2\text{PO}_4$  (KDP),  $\text{NH}_4\text{H}_2\text{AsO}_4$  (ADA),  $\text{CsH}_2\text{AsO}_4$  (CDA), etc. and the corresponding deuterated version; the  $\text{ABO}_3$  type of ferroelectrics such as  $\text{LiIO}_3$ ,  $\text{LiNbO}_3$ ,  $\text{KNbO}_3$ , etc.; and the borates such as  $\beta\text{-BaB}_2\text{O}_4$ ,  $\text{LiB}_3\text{O}_5$ , etc.

Although the III-V and II-VI compounds such as GaAs, InSb, GaP, ZrTe, etc. generally have large  $d$ -coefficients, because their structures are cubic, there is no birefringence that can be used to compensate for material dispersion. Therefore, they cannot be phase-matched in the bulk and are useful only in waveguide forms. Organic crystals hold promise because of the large variety of such materials and the potential to synthesize molecules according to some design principles. As a result, there have been extensive efforts at developing such materials for applications in nonlinear optics, but very few useful second-order organic crystals have been identified so far. Nevertheless, organic materials, especially for third-order processes, continue to attract a great deal of interest and remain a promising class of nonlinear materials.

To illustrate the important points in considering materials for nonlinear optical applications, a few examples of second-order nonlinear crystals with their key properties are tabulated in Tables 1 through 3. It must be emphasized, however, that because some of the materials are relatively new, some of the numbers listed are subject to confirmation and possibly revision. Discussions of other inorganic and organic nonlinear optical crystals can be found in the literature.<sup>41</sup>

As nonlinear crystals and devices become more commercialized, the issues of standardization of nomenclature and conventions and quantitative accuracy are becoming increasingly important. Some of these issues are being addressed<sup>42</sup> but much work remains to be done.

**TABLE 1** Properties of Some Nonlinear Optical Crystals<sup>a</sup>

Crystal	LiB <sub>3</sub> O <sub>5</sub>	$\beta$ -BaB <sub>2</sub> O <sub>4</sub> <sup>f</sup>
Point group	mm <sup>2a</sup>	3 m
Birefringence	$n_{x=a} = 1.5656^b$ $n_{y=c} = 1.5905$ $n_{z=b} = 1.6055$	$n_e = 1.54254$ $n_o = 1.65510$
Nonlinearity [pm/V]	$d_{32} = 1.16^b$	$d_{22} = 16$ $d_{31} = 0.08$
Transparency [ $\mu\text{m}$ ]	0.16–2.6 <sup>c</sup>	0.19–2.5
$\Gamma_{\text{max}}$ [GW/cm <sup>2</sup> ]	$\sim 25^b$	$\sim 5^e$
SHG cutoff [nm]	555 <sup>d</sup>	411
$\ell\Delta T$ [ $^\circ\text{C} \cdot \text{cm}$ ]	3.9 <sup>e</sup>	55
$\ell\Delta\Theta$ [mrad $\cdot \text{cm}$ ], CPM	31.3 <sup>e</sup>	0.52
$\ell^{1/2}\Delta\Theta$ [mrad (cm) <sup>1/2</sup> ]	71.9 <sup>e</sup> NCPM @ 148.0 $^\circ\text{C}$	Not available
$\ell\Delta\lambda$ [ $\text{\AA} \cdot \text{cm}$ ]	Not available	21.1
$\Delta v_g^{-1}$ @ 630 nm [fs/mm]	240 <sup>d</sup>	360
OPO tuning range [nm]	$\sim 415\text{--}2500^d$ ( $\lambda_p = 355$ )	$\sim 410\text{--}2500$ ( $\lambda_p = 355$ )
Boule size	$20 \times 20 \times 15 \text{ mm}^{3e}$	$\text{\O} 84 \text{ mm} \times 18 \text{ mm}$
Growth	TSSG <sup>e</sup> @ $\sim 810^\circ\text{C}$	TSSG from Na <sub>2</sub> O @ $\sim 900^\circ\text{C}$
Predominant growth defects	Flux <sup>e</sup> inclusions	Flux and bubble inclusions
Chemical properties	Nonhygroscopic <sup>e</sup> (m.p. $\sim 834^\circ\text{C}$ )	Slightly hygroscopic ( $\beta \rightarrow \alpha \sim 925^\circ\text{C}$ )

<sup>a</sup>Data shown is at 1.064  $\mu\text{m}$  unless otherwise indicated.  $\Gamma_{\text{max}}$ —surface damage threshold;  $\ell\Delta T$ —temperature-tuning bandwidth;  $\ell\Delta\Theta$ , CPM—critical phase-matching acceptance angle;  $\ell^{1/2}\Delta\Theta$ —noncritical phase-matching acceptance angle;  $\ell\Delta\lambda$ —SHG bandwidth;  $\Delta v_g^{-1}$ —group-velocity dispersion for SHG at 630 nm.

<sup>b</sup>Von H. König and A. Hoppe, *Z. Anorg. Allg. Chem.* **439**:71 (1978); M. Ihara, M. Yuge, and J. Krogh-Moe, *Yogyo-Kyokai-Shi* **88**:179 (1980); Z. Shuqing, H. Chaoen, and Z. Hongwu, *J. Cryst. Growth* **99**:805 (1990).

<sup>c</sup>C. Chen, Y. Wu, A. Jiang, B. Wu, G. You, R. Li, and S. Lin, *J. Opt. Soc. Am.* **B6**:616 (1989); S. Liu, Z. Sun, B. Wu, and C. Chen, *J. App. Phys.* **67**:634 (1989). On the basis of  $d_{32} = 2.69 \times d_{36}$  (KDP) and using the value  $d_{36}$  (KDP) = 0.39 pm/V according to R. C. Ekart et al., *J. Quan. Elec.* **26**:922 (May 1990).

<sup>d</sup>0.16–2.6  $\mu\text{m}$ : C. Chen, Y. Wu, A. Jiang, B. Wu, G. You, R. Li, and S. Lin, *J. Opt. Soc. Am.* **B6**:616 (1989). 0.165–3.2  $\mu\text{m}$ ; S. Zhao, C. Huang, and H. Zhang, *J. Cryst. Growth* **99**:805 (1990).

<sup>e</sup>Calculated by using Sellmeier equations reported in reference; B. Wu, N. Chen, C. Chen, D. Deng, and Z. Xu, *Opt. Lett.* **14**:1080 (1989).

<sup>f</sup>T. Ukachi and R. J. Lane, measurements carried out on Cornell LBO crystals grown by self-flux method.

<sup>g</sup>Reference sources given in: "Growth and Characterization of Nonlinear Optical Crystals Suitable for Frequency Conversion," by L. K. Cheng, W. R. Bosenberg, and C. L. Tang, review article in *Progress in Crystal Growth and Characterization* **20**:9–57 (Pergamon Press, 1990), unless indicated otherwise.

<sup>h</sup>Estimated surface damage threshold scaled from detailed bulk damage results reported by H. Nakatani et al., *Appl. Phys. Lett.* **53**:2587 (26 December, 1988).

**TABLE 2** Properties of Several Visible Near-IR Nonlinear Optical Crystals\*

Characteristics	KNbO <sub>3</sub> <sup>†</sup>	LiNbO <sub>3</sub> <sup>‡</sup>	Ba <sub>2</sub> NaNb <sub>5</sub> O <sub>15</sub>
Point group	mm <sup>2</sup>	3 m	mm <sup>2</sup>
Transparency [μm]	0.4–5.5	0.4–5.0	0.37–5.0
Birefringence	negative biaxial $n_{x=c} = 2.2574$ $n_{y=a} = 2.2200$ $n_{z=b} = 2.1196$	negative uniaxial $n^o = 2.2325$ $n^e = 2.1560$	negative biaxial $n_{x=b} = 2.2580$ $n_{y=a} = 2.2567$ $n_{z=c} = 2.1700$
Second-order nonlinearity [pm/V]	$d_{32} = 12.9, d_{31} = -11.3$ $d_{24} = 11.9, d_{15} = -12.4$ $d_{33} = -19.6$ $1.6 \times 10^{-4}$	$d_{33} = -29.7$ $d_{31} = -4.8$ $d_{23} = 2.3$ $-5.9 \times 10^{-5}$	$d_{32} = -12.8, d_{31} = -12.8$ $d_{24} = 12.8, d_{15} = -12.8$ $d_{33} = -17.6$ $1.05 \times 10^{-4}$
$\partial(n^o - n^{2o})/\partial T [^{\circ}\text{C}^{-1}]$	$1.6 \times 10^{-4}$	$-5.9 \times 10^{-5}$	$1.05 \times 10^{-4}$
T <sub>pm</sub> [°C]	181, $d_{32}$	-8, $d_{31}$	89, $d_{32}$ 101, $d_{31}$
$\ell\Delta T$ [°C-cm]	0.3	0.8	0.5
$\lambda_{\text{SHG}}$ (cutoff)[μm] @ 25°C	0.860	~1.08	1.01
$\Gamma_{\text{max}}$ [MW/cm <sup>2</sup> ]	Not available	~120	40
Phase transition temperature (°C)	225 and 435	~1000	300
Growth technique	TSSG from K <sub>2</sub> O @ ~ 1050°C	Czochralski @ ~ 1200°C	Czochralski @ ~ 1440°C
Predominant growth problems	Cracks, blue coloration, multidomains	Temp, induced compositional striations	Striations, microtwinning, multidomains
Postgrowth processing	Poling	Poling	Poling and detwinning
Crystal size	20 × 20 × 20 mm <sup>3</sup> (single domain)	Ø 100 mm × 200 mm (as grown boule)	Ø 20 mm × 50 mm (with striations)

\*Unless otherwise specified, data are for  $\lambda = 1.064 \mu\text{m}$ . (Data taken from:  $a, e-i; a, b-c;$  and  $a, d,$  respectively.)

<sup>†</sup>There is a disagreement on the sign of the nonlinear coefficients of KNbO<sub>3</sub> in the literature. Data used here are taken from Ref.  $\epsilon$  with the appropriate correction for the IRE convention.

<sup>‡</sup>Data are for congruent melting LiNbO<sub>3</sub>. Five-percent MgO doped crystals gives photorefractive damage threshold about 10–100 times higher.<sup>k,l</sup> The phase-matching properties for these crystals may differ due to the resulting changes in the lattice constants.<sup>j</sup>

<sup>a</sup>S. Singh in *CRC Handbook of Laser Science and Technology*, vol. 4, *Optical Materials*, part I, M. J. Weber (ed.), CRC Press, 1986, pp. 3–228.

<sup>b</sup>R. L. Byer, J. F. Young, and R. S. Feigelson, *J. Appl. Phys.* **41**:2320 (1970).

<sup>c</sup>R. L. Byer in *Quantum Electronics: A Treatise*, H. Rabin and C. L. Tang (eds), vol. 1, part A, Academic Press, 1975.

<sup>d</sup>S. Singh, D. A. Draeger, and J. E. Geusic, *Phys. Rev. B* **2**:2709 (1970).

<sup>e</sup>Y. Uematsu, *Jap. J. Appl. Phys.* **13**: 1362 (1974).

<sup>f</sup>P. Gunter, *Appl. Phys. Lett.* **34**:650 (1979).

<sup>g</sup>W. Xing, H. Looser, H. Wuest, and H. Arend, *J. Crystal Growth* **78**:431 (1986).

<sup>h</sup>D. Shen, *Mat. Res. Bull.* **21**: 1375 (1986).

<sup>i</sup>T. Fukuda and Y. Uematsu, *Jap. J. Appl. Phys.* **11**:163 (1972).

<sup>j</sup>B. C. Grabmaier and F. Otto, *J. Crystal Growth* **79**: 682 (1986).

<sup>k</sup>D. A. Bryan, R. Gerson, and H. E. Tomaschke, *Appl. Phys. Lett.* **44**:847 (1984).

<sup>l</sup>G. Zhong, J. Jian, and Z. Wu, *11th International Quantum Electronics Conference*, IEEE Cat. No. 80 CH 1561-0, June 1980, p. 631.

## 10.5 APPENDIX

The results in this article are given in the rationalized MKS systems. Unfortunately, many of the pioneering papers on nonlinear optics were written in the cgs gaussian system. In addition, different conventions and definitions of the nonlinear optical coefficients are used in the literature by different authors. These choices have led to a great deal of confusion. In this Appendix, we give a few key results to facilitate comparison of the results using different definitions and units.

First, in the MKS system, the displacement vector  $\mathbf{D}$  is related to the  $\mathbf{E}$ -field and the induced polarization  $\mathbf{P}$  in the medium as follows:

$$\begin{aligned} \mathbf{D} &= \epsilon_0 \mathbf{E} + \mathbf{P} \\ &= \epsilon_0 \mathbf{E} + \mathbf{P}^{(1)} + \mathbf{P}^{(2)} + \dots \end{aligned} \quad (\text{A-1})$$

**TABLE 3** Properties of Several UV, Visible, and Near-IR Crystals\*

Crystal	KDP	KTP (II) <sup>†</sup>
Point group	42 m	mm <sup>2</sup>
Birefringence	$n_e = 1.4599$ $n_o = 1.4938$	$n_{x=a} = 1.7367$ $n_{y=b} = 1.7395$ $n_{z=c} = 1.8305$
Nonlinearity [pm/V]	$d_{36} = 0.39$	$d_{32} = 5.0, d_{31} = 6.5$ $d_{24} = 7.6, d_{15} = 6.1$ $d_{33} = 13.7$
Transparency [ $\mu\text{m}$ ]	0.2–1.4	0.35–4.4
$\Gamma_{\text{max}}$ [GW/cm <sup>2</sup> ]	~3.5	~15.0
SHG cutoff [nm]	487	~990
$\ell\Delta T$ [ $^{\circ}\text{C}\cdot\text{cm}$ ]	7	22
$\ell\Delta\theta$ [mrad-cm]	1.2	15.7
$\ell\Delta\lambda$ [ $\text{\AA}\cdot\text{cm}$ ]	208 <sup>‡</sup>	4.5
$\Delta\nu^{-1}$ @ 630 nm [fs/mm]	185	Not applicable
OPO tuning range [nm]	~430–700	~610–4200
[nm]	( $\lambda_p = 266$ )	( $\lambda_p = 532$ )
$\Delta T_F$ [ $^{\circ}\text{C}$ ]	12	Not available
Boule size	$40 \times 40 \times 100 \text{ mm}^3$	~ $20 \times 20 \times 20 \text{ mm}^3$
Growth technique	Solution growth from H <sub>2</sub> O	TSSG from 2KPO <sub>3</sub> -K <sub>4</sub> P <sub>2</sub> O <sub>7</sub> @ ~1000 $^{\circ}\text{C}$
Predominant growth defects	Organic impurities	Flux inclusions
Chemical properties	Hygroscopic (m.p. ~253 $^{\circ}\text{C}$ )	Nonhygroscopic (m.p. ~1172 $^{\circ}\text{C}$ )

\*Unless otherwise stated, all data for 1064 nm. (Data taken from  $c, e; a, b, f, m$ ; and  $d, g-i$ , respectively.)

<sup>†</sup>KTP Type I interaction gives  $d_{\text{eff}} \sim d_{36}$  (KDP) or less for most processes.<sup>m</sup> The  $d_{ij}$  values<sup>d</sup> are for crystals grown by the hydrothermal technique.<sup>j-l</sup> Significantly lower damage thresholds were reported for hydrothermally grown crystals.

<sup>‡</sup>The anomalously large spectral bandwidth is a manifestation of the  $\lambda$ -noncritical phase matching.<sup>n</sup> This is equivalent to a very good group-velocity matching ( $\Delta\nu_g^{-1} \sim 8 \text{ fs/mm}$ ) for this interaction in KDP.

<sup>a</sup>D. Eimerl, *J. Quant. Elect.* **QE-23**:575 (1987).

<sup>b</sup>D. Eimerl, L. Davis, S. Velsko, E. K. Graham, and A. Zalkin, *J. Appl. Phys.* **62**:1968 (1987).

<sup>c</sup>D. Eimerl, *Ferroelectrics* **72**:95 (1987).

<sup>d</sup>Y. S. Liu, L. Drafall, D. Dentz, and R. Belt, *G. E. Technical Information Series Report*, 82CRD016, Feb. 1982.

<sup>e</sup>Y. Nishida, A. Yokotani, T. Sasaki, K. Yoshida, T. Yamanaka, and C. Yamanaka, *Appl. Phys. Lett.* **52**:420 (1988).

<sup>f</sup>A. Jiang, F. Cheng, Q. Lin, Z. Cheng, and Y. Zheng, *J. Crystal Growth* **79**:963 (1986).

<sup>g</sup>P. Bordui, in *Crystal Growth of KTiOPO<sub>4</sub> from High Temperature Solution*, Ph.D. thesis, Massachusetts Institute of Technology, 1987.

<sup>h</sup>*Information Sheet on KTiOPO<sub>4</sub>*, Ferroxcube, Division of Ampere Electronic Corp., Saugerties, New York, 1987.

<sup>i</sup>P. Bordui, J. C. Jacco, G. M. Loiacono, R. A. Stolzenberger, and J. J. Zola, *J. Crystal Growth* **84**:403 (1987).

<sup>j</sup>F. C. Zumsteg, J. D. Bierlein, and T. E. Gier, *J. Appl. Phys.* **47**:4980 (1976).

<sup>k</sup>R. A. Laudis, R. J. Cava, and A. J. Caporaso, *J. Crystal Growth* **74**:275 (1986).

<sup>l</sup>S. Jia, P. Jiang, H. Niu, D. Li, and X. Fan, *J. Crystal Growth* **79**:970 (1986).

<sup>m</sup>L. K. Cheng, unpublished.

<sup>n</sup>J. Zyss and D. S. Chemla, in *Nonlinear Optical Properties of Organic Molecules and Crystals*, vol. 1, D. S. Chemla and J. Zyss (eds), Academic Press, 1987, pp. 146–159.

The corresponding wave equation is given in Eq. (33). For the second-order polarization and the corresponding Kleinman  $\mathbf{d}$ -coefficients, two definitions are in use. A more popular definition in the current literature is as follows:

$$\mathbf{P}^{(2)} = \varepsilon_0 \mathbf{d}_2 : \mathbf{E}\mathbf{E} \quad (\text{A-2})$$

In an earlier widely used reference,<sup>34</sup> Yariv defined his  $\mathbf{d}$ -coefficient as follows:

$$\mathbf{P}^{(2)} = \mathbf{d}_2^{(\text{Yariv})} : \mathbf{E}\mathbf{E} \quad (\text{A-3})$$

The numerical values of  $\mathbf{d}_2^{(\text{Yariv})}$  in this reference (e.g., Table 16.2)<sup>34</sup> are given in  $(1/9) \times 10^{-22}$  MKS units. The numerical value of  $\epsilon_0$  in the MKS system is  $10^7 \times (1/4\pi^2)$  in MKS units. Thus, for example, a tabulated value of  $\mathbf{d}_2^{(\text{Yariv})} = 0.5 \times (1/9) \times 10^{-22}$  MKS units in Ref. 34 converts to a numerical value of  $d_2 = 0.628$  pm/V in MKS units.

In the cgs gaussian system, the displacement vector  $\mathbf{D}$  is related to the  $\mathbf{E}$ -field and the induced polarization  $\mathbf{P}$  in the medium as follows:

$$\begin{aligned} \mathbf{D} &= \epsilon_0 \mathbf{E} + 4\pi \mathbf{P} \\ &= \epsilon_0 \mathbf{E} + 4\pi \mathbf{P}^{(1)} + 4\pi \mathbf{P}^{(2)} + \dots \end{aligned} \quad (\text{A-4})$$

The corresponding wave equation is:

$$\frac{\partial^2}{\partial z^2} E_i(z, t) - \frac{1}{c^2} \frac{\partial^2}{\partial t^2} E_i(z, t) = \frac{4\pi \partial^2}{c^2 \partial t^2} P_i(z, t) \quad (\text{A-5})$$

The conventional definition of  $\mathbf{d}_2$  is as follows:

$$\mathbf{P}^{(2)} = \mathbf{d}_2 : \mathbf{E}\mathbf{E} \quad (\text{A-6})$$

The numerical value of  $\mathbf{d}_2$  in cgs gaussian units is, therefore, equal to  $(3 \times 10^4/4\pi)$  times the numerical value of  $\mathbf{d}_2$  in rationalized MKS units. Thus, continuing with the numerical example given in the preceding paragraph,  $\mathbf{d}_2 = 0.628$  pm/V is equal to  $1.5 \times 10^{-9}$  cm/Stat-Volt or  $1.5 \times 10^{-9}$  esu.

As a final check, the expression Eq. (42) for the second-harmonic intensity in the MKS system becomes, in the cgs gaussian system:

$$I_2 = \left( \frac{512\pi^5}{cn_1^2 n_2} \right) \left( \frac{L}{\lambda_1} \right)^2 d_{\text{eff}}^2 I_0^2 \quad (\text{A-7})$$

All the intensities refer to those inside the medium, and the wavelength is the free-space wavelength.

## 10.6 REFERENCES

1. P. A. Franken, A. E. Hill, C. W. Peters, and G. Weinreich, *Phys. Rev. Lett.* **7**:118 (1961).
2. J. A. Armstrong, N. Bloembergen, J. Ducuing, and P. S. Pershan, *Phys. Rev.* **127**:1918 (1962); N. Bloembergen and Y. R. Shen, *Phys. Rev.* **133**:A37 (1964).
3. N. Bloembergen, *Nonlinear Optics*, Benjamin, New York, 1965.
4. See, for example, H. Rabin and C. L. Tang (eds.), *Quantum Electronics: A Treatise*, vol. 1A and B *Nonlinear Optics*, Academic Press, New York, 1975, and the references therein.
5. See, for example, Y. R. Shen, *The Principles of Nonlinear Optics*, J. W. Wiley Interscience, New York, 1984.
6. M. D. Levenson and S. S. Kano, *Introduction to Nonlinear Laser Spectroscopy*, Academic Press, New York, 1988, and the references therein.
7. P. D. Maker and R. W. Terhune, *Phys. Rev. A* **137**:801 (1965).
8. See, for example, secs. 7.3 and 7.4 of Ref. 5.
9. H. Mahr, "Two-Photon Absorption Spectroscopy," in Ref. 4.
10. G. A. Askar'yan, *Sov. Phys. JETP* **15**:1088, 1161 (1962); M. Hercher, *J. Opt. Soc. Am.* **54**:563 (1964); R. Y. Chiao, E. Garmire, and C. H. Townes, *Phys. Rev. Lett.* **13**:479 (1964) [Erratum, **14**:1056 (1965)].
11. See, for example, Y. R. Shen, "Self-Focusing," chap. 17 in Ref. 5.



12. See, for example, R. W. Boyd, *Nonlinear Optics*, chap. 4, Academic Press, 1992.
13. See, for example, chap. 15 in Ref. 5.
14. Y. B. Zeldovich, V. I. Popovichev, V. V. Ragul'skii, and F. S. Faizullof, *JETP Letters* **15**:109 (1972).
15. R. W. Hellwarth, *J. Opt. Soc. Am.* **68**:1050 (1978); A. Yariv, *IEEE J. Quant. Elect.* **QE-14**:650 (1978).
16. See, for example, A. Yariv and P. Yeh, *Optical Waves in Crystals*, Wiley, New York, 1984, p. 221.
17. N. A. Kurnit, I. D. Abella, and S. R. Hartmann, *Phys. Rev. Lett.* **13**:567 (1964); S. Hartmann, in R. Glauber (ed.), *Proc. of the Int. School of Phys. Enrico Fermi Course XLII*, Academic Press, New York, 1969, p. 532.
18. C. L. Tang and B. D. Silverman, "Physics of Quantum Electronics," P. Kelley, B. Lax, and P. E. Tannenwald (eds.), McGraw-Hill, 1966, p. 280. G. B. Hocker and C. L. Tang, *Phys. Rev. Lett.* **21**:591 (1969); *Phys. Rev.* **184**:356 (1969).
19. R. G. Brewer, *Phys. Today*, May 1977.
20. S. L. McCall and E. L. Hahn, *Phys. Rev. Lett.* **18**:908 (1967); *Phys. Rev.* **183**:457 (1969).
21. N. Bloembergen and A. H. Zewail, *J. Phys. Chem.* **88**:5459 (1984).
22. M. J. Rosker, F. W. Wise, and C. L. Tang, *Phys. Rev. Lett.* **57**:321 (1986); *J. Chem. Phys.* **86**:2827 (1987).
23. E. J. Woodbury and W. K. Ng, *Proc. IRE* **50**:2347 (1962); R. W. Hellwarth, *Phys. Rev.* **130**:1850 (1963).
24. E. Garmire, E. Pandarese, and C. H. Townes, *Phys. Rev. Lett.* **11**:160 (1963).
25. C. S. Wang, "The Stimulated Raman Process," chap. 7 in Ref. 4.
26. R. Y. Chiao, C. H. Townes, and B. P. Stoicheff, *Phys. Rev. Lett.* **12**:592 (1964); E. Garmire and C. H. Townes, *App. Phys. Lett.* **5**:84 (1964).
27. C. L. Tang, *J. App. Phys.* **37**:2945 (1966).
28. I. L. Fabellinskii, "Stimulated Mandelstam-Brillouin Process," chap. 5 in Ref. 4.
29. See, for example, sec. 10.7 in Ref. 5.
30. R. C. Miller, *App. Phys. Lett.* **5**:17 (1964).
31. C. Chen, B. Wu, A. Jiang, and G. You, *Sci. Sin. Ser. B* **28**:235 (1985).
32. C. Chen, Y. Wu, A. Jiang, B. Wu, G. You, R. Li, and S. Lin, *J. Opt. Soc. Am.* **B6**:616 (1989).
33. P. A. Franken and J. F. Ward, *Rev. of Mod. Phys.* **35**:23 (1963).
34. A. Yariv, *Quantum Electronics*, John Wiley, New York, 1975, pp. 410–411.
35. J. A. Giordmaine, *Phys. Rev. Lett.* **8**:19 (1962); P. D. Maker, R. W. Terhune, M. Nisenhoff, and C. M. Savage, *Phys. Rev. Lett.* **8**:21 (1962).
36. W. H. Louisell, *Coupled Mode and Parametric Electronics*, John Wiley, New York, 1960.
37. N. Kroll, *Phys. Rev.* **127**:1207 (1962).
38. See, for example, C. L. Tang, *Proc. IEEE* **80**:365 (March 1992).
39. Ref. 4, p. 428.
40. See, for example, L. F. Mollenauer and J. C. White (eds.), *Tunable Lasers*, Springer-Verlag, Berlin, 1987.
41. See, for example, S. K. Kurtz, J. Jerphagnon, and M. M. Choy, in *Landolt-Boerstein Numerical Data and Functional Relationships in Science and Technology*, New Series, K. H. Hellwege (ed.), Group III, vol. 11, Springer-Verlag, Berlin, 1979; *Nonlinear Optical Properties of Organic and Polymeric Materials*, D. Williams (ed.), Am. Chem. Soc, Wash., D.C., 1983; *Nonlinear Optical Properties of Organic Molecules*, D. Chemla and J. Zyss (eds.), Academic Press, New York, 1987.
42. D. A. Roberts, *IEEE J. Quant. Elect.* **28**:2057 (1992).

---

# COHERENT OPTICAL TRANSIENTS

---

Paul R. Berman and Duncan G. Steel

*Physics Department  
University of Michigan  
Ann Arbor, Michigan*

---

## 11.1 GLOSSARY

---

$\mathbf{E}(\mathbf{R}, t)$	electric field vector
$E(t)$	electric field amplitude
$\omega$	field frequency
$\phi(t)$	field phase
$\omega_0$	atomic transition frequency
$\bar{\omega}_0$	average atomic transition frequency
$\delta$	atom-field detuning
$\delta_0$	average atom-field detuning
$\Omega_0(t)$	Rabi frequency
$\mathbf{\Omega}(t)$	pseudofield vector
$\Omega(t)$	generalized Rabi frequency
$\mathbf{U}(t)$	Bloch vector
$\rho_{ij}(Z, t)$	density matrix element in a field interaction representation
$\rho_{ij}^T(\mathbf{R}, t)$	density matrix element in Schrödinger representation
$(u, v, w)$	elements of Bloch vector
$\gamma$	transverse relaxation rate
$\gamma_2$	excited-state decay rate or longitudinal relaxation rate
$\mathbf{P}(\mathbf{R}, t)$	polarization vector
$\mathbf{k}$	field propagation vector
$E_s(Z, t)$	complex signal electric field amplitude
$P(Z, t)$	complex polarization field amplitude
$\mathcal{N}$	atomic density

---

This chapter is dedicated to Richard G. Brewer, a pioneer in coherent optical transients, a mentor and a friend.

$L$	sample length
$\mu$	dipole moment matrix element
$\tau, \tau_{\text{ref}}$	pulse durations
$\theta$	pulse area
$\Delta$	difference between local and average transition frequency in a solid
$W_f(\Delta)$	distribution of frequencies in a solid
$\sigma_w$	width of $W_f(\Delta)$
$\mathbf{v}$	atomic velocity
$u$	most probable atomic speed
$W_0(\mathbf{v})$	atomic velocity distribution
$I(L, t)$	signal intensity exiting the sample
$T_{21}, T$	time interval between pulses
$\Gamma_t$	transit time decay rate
$\Gamma_{2,0}, \Gamma_{2,1}$	branching decay rates of the excited state
$\Omega_i^{(s)} t$	two-photon Rabi frequency
$\omega_k$	recoil frequency
$\mathbf{P}$	center-of-mass momentum
$E_b(t_1, t_2)$	backscattered electric field amplitude
$J_N(x)$	Bessel function
$\xi$	one-half of the frequency chirp rate
$\omega_{\text{RD}}$	frequency offset between reference and data pulses

## 11.2 INTRODUCTION

Optical spectroscopy is a traditional method for determining transition frequencies in atoms and molecules. One can classify optical spectroscopy into two broad categories: *continuous-wave* (CW) or stationary spectroscopy and *time-dependent* or transient spectroscopy. In CW spectroscopy, one measures absorption or emission line shapes as a function of the incident frequency of a probe field. The absorption or emission maximum determines the transition frequency, while the width of the line is a measure of relaxation processes affecting the atoms or molecules. It is necessary to model the atom-field interaction to obtain predictions for the line shapes, but, once this is done, it is possible to extract the relevant transition frequencies and relaxation rates from the line shapes. In transient spectroscopy, one can also determine relaxation rates and transition frequencies, but the methodology is quite different. Atomic state populations or coherences between atomic states are excited by pulsed optical fields. Following the excitation, the time-evolution of the atoms is monitored, from which transition frequencies and relaxation rates can be obtained. In certain cases the transient response is studied as a function of incident field frequency or intensity. Whether or not transient or CW spectroscopy offers distinct advantages depends on a number of factors, such as signal to noise and the reliability of lineshape formulas.<sup>1</sup>

In this chapter, we present basic concepts of coherent optical transient spectroscopy,<sup>2-12</sup> along with applications involving atomic vapors or condensed matter systems. Experimental techniques are discussed in Sec. 11.11. As in the case of CW spectroscopy, it will prove useful to consider both linear and nonlinear interactions of the atoms with the fields. The examples chosen to illustrate the concepts are relatively simple, but it is important to note that sophisticated coherent transient techniques can now be used to probe complex structures, such as liquids and semiconductors. Although we consider ensembles of atoms interacting with the applied fields, current technology allows one to study the transient response of single atoms or molecules.<sup>13</sup>

### 11.3 OPTICAL BLOCH EQUATIONS

Many of the important features of coherent optical transients can be illustrated by considering the interaction of a radiation field with a two-level atom, with lower state  $|1\rangle$  having energy  $-\hbar\omega_0/2$  and upper state  $|2\rangle$  having energy  $\hbar\omega_0/2$ . For the moment, the atom is assumed to be fixed at  $\mathbf{R} = 0$  and all relaxation processes are neglected. The incident electric field is

$$\mathbf{E}(\mathbf{R}=0, t) = \frac{1}{2}\boldsymbol{\epsilon}\{E(t)\exp(-i[\omega t - \phi(t)]) + E(t)\exp(i[\omega t - \phi(t)])\} \quad (1)$$

where  $E(t)$  is the field amplitude,  $\boldsymbol{\epsilon}$  is the field polarization,  $\phi(t)$  is the field phase, and  $\omega$  is the carrier frequency. The time dependence of  $E(t)$  allows one to consider pulses having arbitrary shape while the time dependence of  $\phi(t)$  allows one to consider arbitrary frequency *chirps*. It is convenient to expand the atomic state wave function in a field interaction representation as

$$|\psi(t)\rangle = c_1(t)\exp\left\{\frac{i[\omega t - \phi(t)]}{2}\right\}|1\rangle + c_2(t)\exp\left\{-\frac{i[\omega t - \phi(t)]}{2}\right\}|2\rangle \quad (2)$$

The atom-field interaction potential is

$$V(\mathbf{R}, t) = -\boldsymbol{\mu} \cdot \mathbf{E}(\mathbf{R}, t) \quad (3)$$

where  $\boldsymbol{\mu}$  is a dipole moment operator. Substituting the state vector Eq. (2) into Schrödinger's equation and neglecting rapidly varying terms (rotating-wave approximation), one finds that the state amplitudes evolve according to

$$i\hbar\frac{d\mathbf{c}}{dt} = \tilde{\mathbf{H}}\mathbf{c} \quad \tilde{\mathbf{H}} = \left(\frac{\hbar}{2}\right) \begin{pmatrix} -\delta(t) & \Omega_0(t) \\ \Omega_0(t) & \delta(t) \end{pmatrix} \quad (4)$$

where  $\mathbf{c}$  is a vector having components  $(c_1, c_2)$ ,

$$\delta = \omega_0 - \omega \quad (5)$$

is an atom-field detuning,

$$\Omega_0(t) = -\frac{\mu E(t)}{\hbar} = -\frac{\mu}{\hbar} \sqrt{\frac{2S(t)}{\epsilon_0 c}} \quad (6)$$

is a Rabi frequency,  $\mu = \langle 1|\boldsymbol{\mu} \cdot \boldsymbol{\epsilon}|2\rangle = \langle 2|\boldsymbol{\mu} \cdot \boldsymbol{\epsilon}|1\rangle$  is a dipole moment matrix element,  $\epsilon_0$  is the permittivity of free space,  $S(t)$  is the time-averaged Poynting vector of the field, and

$$\delta(t) = \delta + \frac{d\phi(t)}{dt} \quad (7)$$

is a generalized atom-field detuning. Equation (4) can be solved numerically for arbitrary pulse envelope and phase factors.

Expectation values of physical observables are conveniently expressed in terms of density matrix elements defined by

$$\rho_{ij} = c_i c_j^* \quad (8)$$

which obey equations of motion

$$\begin{aligned}
 \dot{\rho}_{11} &= -\frac{i\Omega_0(t)}{2}(\rho_{21} - \rho_{12}) \\
 \dot{\rho}_{22} &= \frac{i\Omega_0(t)}{2}(\rho_{21} - \rho_{12}) \\
 \dot{\rho}_{12} &= -\frac{i\Omega_0(t)}{2}(\rho_{22} - \rho_{11}) + i\delta(t)\rho_{12} \\
 \dot{\rho}_{21} &= \frac{i\Omega_0(t)}{2}(\rho_{22} - \rho_{11}) - i\delta(t)\rho_{21}
 \end{aligned} \tag{9}$$

An alternative set of equations in terms of real variables can be obtained if one defines new parameters

$$\begin{aligned}
 u &= \rho_{12} + \rho_{21} & \rho_{12} &= \frac{u + iv}{2} \\
 v &= i(\rho_{21} - \rho_{12}) & \rho_{21} &= \frac{u - iv}{2} \\
 w &= \rho_{22} - \rho_{11} & \rho_{22} &= \frac{m + w}{2} \\
 m &= \rho_{11} + \rho_{22} & \rho_{11} &= \frac{m - w}{2}
 \end{aligned} \tag{10}$$

which obey the equations of motion

$$\begin{aligned}
 \dot{u} &= -\delta(t)v \\
 \dot{v} &= \delta(t)u - \Omega_0(t)w \\
 \dot{w} &= \Omega_0(t)v \\
 \dot{m} &= 0
 \end{aligned} \tag{11}$$

The last of these equations reflects the fact that  $\rho_{11} + \rho_{22} = 1$ , while the first three can be rewritten as

$$\dot{\mathbf{U}} = \mathbf{\Omega}(t) \times \mathbf{U} \tag{12}$$

where the *Bloch vector*  $\mathbf{U}$  has components  $(u, v, w)$  and the *pseudofield vector*  $\mathbf{\Omega}(t)$  has components  $[\Omega_0(t), 0, \delta(t)]$ . An important feature of a density matrix description is that relaxation can be incorporated easily into density matrix equations, but *not* into amplitude equations.

Equations (9) or (11) constitute the *optical Bloch equations* without decay.<sup>8-10,14</sup> The vector  $\mathbf{U}$  has unit magnitude and precesses about the pseudofield vector with an instantaneous rate

$$\Omega(t) = \sqrt{[\Omega_0(t)]^2 + [\delta(t)]^2} \tag{13}$$

that is referred to as the *generalized Rabi frequency*. The tip of the Bloch vector traces out a path on the *Bloch sphere*. The component  $w$  is the population difference of the two atomic states, while  $u$  and  $v$  are related to the quadrature components of the atomic polarization (see following discussion).

It is possible to generalize Eqs. (9) and (11) to include relaxation. In the most general situation, each density matrix element can be coupled to all density matrix elements via relaxation. For optical transitions,

however, it is often the case that the energy separation of levels 1 and 2 is sufficiently large to preclude any relaxational transfer of population from level 1 to level 2, although state  $|2\rangle$  can decay to state  $|1\rangle$  via spontaneous emission. For the present, we also assume that  $\rho_{11} + \rho_{22} = 1$ ; there is no relaxation outside the two-level subspace. In this limit, relaxation can be included in Eq. (9) by modifying the equations as

$$\dot{\rho}_{11} = -\frac{i\Omega_0(t)}{2}(\rho_{21} - \rho_{12}) + \gamma_2 \rho_{22} \quad (14a)$$

$$\dot{\rho}_{22} = \frac{i\Omega_0(t)}{2}(\rho_{21} - \rho_{12}) - \gamma_2 \rho_{22} \quad (14b)$$

$$\dot{\rho}_{12} = -i\frac{\Omega_0(t)}{2}(\rho_{22} - \rho_{11}) - [\gamma - i\delta(t)]\rho_{12} \quad (14c)$$

$$\dot{\rho}_{21} = i\frac{\Omega_0(t)}{2}(\rho_{22} - \rho_{11}) - [\gamma + i\delta(t)]\rho_{21} \quad (14d)$$

where  $\gamma_2$  is the spontaneous decay rate of level 2,  $\gamma$  is the real part of the decay rate of the coherence  $\rho_{12}$ , and the detuning

$$\delta(t) = \delta + \frac{d\phi(t)}{dt} - s \quad (15)$$

is modified to include the imaginary part  $s$  of the decay rate of the coherence  $\rho_{12}$ . The corresponding equations for the Bloch vector are

$$\begin{aligned} \dot{u} &= -\delta(t)v - \gamma u \\ \dot{v} &= \delta(t)u - \Omega_0(t)w - \gamma v \\ \dot{w} &= \Omega_0(t)v - \gamma_2(w+1) \\ \dot{m} &= 0 \end{aligned} \quad (16)$$

With the addition of decay, the length of the Bloch vector is no longer conserved.

One can write

$$\gamma = \frac{\gamma_2}{2} + \text{Re}(\Gamma_{12}) \quad s = \text{Im}(\Gamma_{12}) \quad (17)$$

where  $\gamma_2/2$  is a radiative component and  $\Gamma_{12}$  is a complex decay parameter that could arise, for example, as a result of phase-interrupting collisions with a background gas. The quantity  $\gamma_2$  is referred to as the *longitudinal relaxation rate*. Moreover, one usually refers to  $T_1 = \gamma_2^{-1}$  as the *longitudinal relaxation time* and  $T_2 = \gamma^{-1}$  as the *transverse relaxation time*. In the case of purely radiative broadening,  $\gamma_2 = 2\gamma$  and  $T_1 = T_2/2$ .

The optical Bloch equations are easily generalized to include additional levels and additional fields. In particular, for an ensemble of three-level atoms interacting with two radiation fields, new

classes of coherent optical transient effects can appear. Moreover, the sensitivity of the coherent transients to the polarization of the applied fields offers an additional degree of selectivity in the detection of the transient signals. Some examples of coherent transient phenomena in three-level and multilevel systems can be found in the references.<sup>11,15-20</sup> Chapter 14, “Electromagnetically Induced Transparency,” contains some interesting phenomena associated with such multilevel systems.

## 11.4 MAXWELL-BLOCH EQUATIONS

The optical Bloch equations must be coupled to Maxwell’s equations to determine in a self-consistent way the modification of the atoms by the fields and the fields by the atoms. To accomplish this task, we start with Maxwell’s equations, setting  $\mathbf{D} = \epsilon_0 \mathbf{E} + \mathbf{P}$ . The wave equation derived from Maxwell’s equations is

$$\nabla^2 \mathbf{E} - \nabla(\nabla \cdot \mathbf{E}) = \frac{1}{c^2} \frac{\partial^2 \mathbf{E}}{\partial t^2} + \frac{1}{\epsilon_0 c^2} \frac{\partial^2 \mathbf{P}}{\partial t^2} \quad (18)$$

As a result of atom-field interactions, it is assumed that a polarization is created in the medium of the form

$$\mathbf{P}(\mathbf{R}, t) = \frac{1}{2} \mathcal{E} [P(\mathbf{R}, t) \exp i(kZ - \omega t) + P^*(\mathbf{R}, t) \exp -i(kZ - \omega t)] \quad (19)$$

which gives rise to a signal electric field of the form

$$\mathbf{E}_s(\mathbf{R}, t) = \frac{1}{2} \mathcal{E} [E_s(\mathbf{R}, t) \exp i(kZ - \omega t) + E_s^*(\mathbf{R}, t) \exp -i(kZ - \omega t)] \quad (20)$$

The  $Z$  axis has been chosen in the direction of  $\mathbf{k}$ . It is assumed that the complex field amplitudes  $P(\mathbf{R}, t)$  and  $E_s(\mathbf{R}, t)$  vary slowly in space compared with  $\exp(ikZ)$  and slowly in time compared with  $\exp(i\omega t)$ . To simplify matters further, transverse effects such as self-trapping, self-focusing, diffraction, and ring formation<sup>21-25</sup> are neglected. In other words, we take  $P(\mathbf{R}, t)$  and  $E_s(\mathbf{R}, t)$  to be functions of  $Z$  and  $t$  only, choose  $\epsilon \cdot \mathbf{k} = 0$ , and drop the  $\nabla(\nabla \cdot \mathbf{E})$  term in the wave equation. When Eqs. (19) and (20) are substituted into the wave equation and terms of order  $\partial^2 E_s(Z, t)/\partial t^2$ ,  $\partial^2 E_s(Z, t)/\partial Z^2$ ,  $\partial^2 P(Z, t)/\partial t^2$ , and  $\partial P(Z, t)/\partial t$  are neglected, one finds

$$2ik \left( \frac{\partial}{\partial Z} + \frac{\omega}{kc^2} \frac{\partial}{\partial t} \right) E_s(Z, t) - \left( k^2 - \frac{\omega^2}{c^2} \right) E_s(Z, t) = -\frac{\omega^2}{\epsilon_0 c^2} P(Z, t) \quad (21)$$

It is important to note that the polarization field acts as the source of the signal field. Consequently, the signal field does *not* satisfy Maxwell’s equations in vacuum, implying that there can be cases when  $k \neq \omega/c$ . For the moment, however, we assume that this *phase-matching* condition is met. Moreover, it is assumed that a quasi-steady state has been reached in which one can neglect the  $\partial E_s(Z, t)/\partial t$  in Eq. (21). With these assumptions, Eq. (21) reduces to

$$\frac{\partial E_s(Z, t)}{\partial Z} = \frac{ik}{2\epsilon_0} P(Z, t) \quad (22)$$

Additional equations would be needed if the applied fields giving rise to the polarization of the medium are themselves modified to any extent by the signal field.

The polarization  $P(\mathbf{R}, t)$  is the link between Maxwell's equations and the optical Bloch equations. The polarization is defined as the average dipole moment per unit volume, or

$$\begin{aligned} \mathbf{P}(\mathbf{R}, t) &= \text{Tr}(\rho^T \boldsymbol{\mu}) = \frac{1}{V} \text{Tr} \left[ \sum_j \int d\mathbf{R}_j \rho^{T(j)}(\mathbf{R}_j, t) \boldsymbol{\mu} \delta(\mathbf{R} - \mathbf{R}_j) \right] \\ &= \mathcal{N} \boldsymbol{\mu} [\langle \rho_{12}^T(\mathbf{R}, t) \rangle + \langle \rho_{21}^T(\mathbf{R}, t) \rangle] \end{aligned} \quad (23)$$

where  $\rho^{T(j)}(\mathbf{R}, t)$  and  $\rho_{12}^T(\mathbf{R}, t)$  are single-particle density matrix elements,  $V$  is the sample volume, and  $\mathcal{N}$  is the atomic density. The superscript  $T$  indicates that these are "total" density matrix elements written in the Schrödinger representation rather than the field interaction representation. The relationship between the two is

$$\rho_{12}^T(\mathbf{R}, t) = \rho_{12}(Z, t) \exp[-i(kZ - \omega t)] \quad (24)$$

The angle brackets in Eq. (23) indicate that there may be additional averages that must be carried out. For example, in a vapor, there is a distribution of atomic velocities that must be summed over, while in a solid, there may be an inhomogeneous distribution of atomic frequencies owing to local strains in the media. By combining Eqs. (19), (23), and (24), one arrives at

$$\frac{\partial E_s(Z, t)}{\partial Z} = \frac{ik\mathcal{N}\boldsymbol{\mu}}{\epsilon_0} \langle \rho_{21}(Z, t) \rangle = \frac{ik\mathcal{N}\boldsymbol{\mu}}{2\epsilon_0} \langle u(z, t) - iv(Z, t) \rangle \quad (25)$$

which, together with Eqs. (14) or (16), constitute the Maxwell-Bloch equations.

## 11.5 FREE POLARIZATION DECAY

As a first application of the Maxwell-Bloch equations, we consider free polarization decay (FPD),<sup>26–30</sup> which is the analog of free induction decay (FID) in nuclear magnetic resonance (NMR).<sup>31,32</sup> The basic idea behind FPD is very simple. An external field is applied to an ensemble of atoms and then removed. The field creates a phased array of atomic dipoles that radiate coherently in the direction of the incident applied field. The decay of the FPD signal provides information about the transverse relaxation times. We will discuss several possible scenarios for observing FPD. For the present, we assume that there is no inhomogeneous broadening of the sample (all atoms have the same frequency). Moreover, in this and all future examples, it is assumed that one can neglect any changes in the applied fields' amplitudes or phases as the fields propagate in the medium; the Rabi frequencies of the applied fields are functions of  $t$  only.

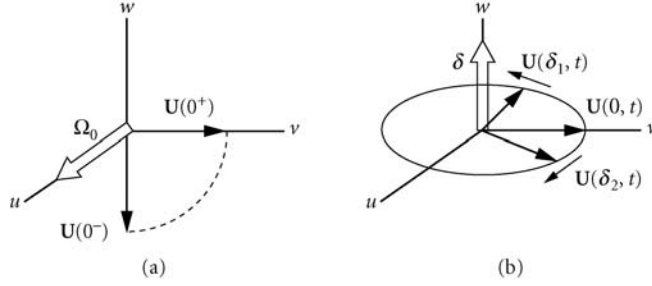
A short pulse is applied at  $t = 0$ , *short* meaning that

$$|\delta(t)|\tau, \gamma\tau, \gamma_2\tau \ll 1 \quad (26)$$

where  $\tau$  is the pulse duration. The inequality Eq. (26) allows one to neglect any effects of detuning or relaxation during the pulse's action. Before the pulse arrives, the atom is in its ground state, implying that the components of the Bloch vector are  $u = v = 0$ ,  $w = -1$ ; that is, the Bloch vector points down (see Fig. 1a). *During* the pulse, the pseudofield vector can be approximated as  $\boldsymbol{\Omega}(t) = [\boldsymbol{\Omega}_0(t), 0, 0]$ , owing to Eq. (26). The Bloch vector precesses in the  $wv$  plane and reaches a final value following the pulse given by

$$u(0^+) = 0 \quad v(0^+) = \sin\theta \quad w(0^+) = -\cos\theta \quad (27)$$





**FIGURE 1** Evolution of the Bloch vector in free polarization decay. (a) A radiation pulse brings the Bloch vector from its initial position along the  $-w$  axis to the  $uv$  plane. (b) With the field off, the Bloch vector precesses in the  $uv$  plane. In an inhomogeneously broadened sample, atoms having different detunings  $\delta$  precess at different rates. The decay of the Bloch vector is not indicated in the figure.

where

$$\theta = \int_{-\infty}^{\infty} \Omega_0(t) dt \quad (28)$$

is a *pulse area* and  $0^+$  is a time just after the pulse. Following the pulse, the pseudofield vector is  $\Omega = (0, 0, \delta)$ , and the Bloch vector precesses about the  $w$  axis as it decays (see Fig. 1b). Explicitly, one finds

$$\begin{aligned} u(t) &= -\sin\theta \sin(\delta t) \exp(-\gamma t) \\ v(t) &= \sin\theta \cos(\delta t) \exp(-\gamma t) \\ w(t) &= -1 + (1 - \cos\theta) \exp(-\gamma_2 t) \end{aligned} \quad (29)$$

From this result, we can draw two conclusions. First, since the applied field is off when the atoms radiate, radiation is emitted at the natural frequency  $\omega_0$ . This conclusion follows formally from Eqs. (29), (10), (23), and (24), which can be used to show that  $P(Z, t)$  varies as  $\exp(-i\delta t)$ , and both  $\mathbf{P}(\mathbf{R}, t)$  and  $\mathbf{E}(\mathbf{R}, t)$  oscillate at frequency  $\omega + \delta = \omega_0$ . Second, one can use Eqs. (29) and (25) to obtain

$$\frac{\partial E_s(Z, t)}{\partial Z} = \frac{kN\mu}{2\epsilon_0} \sin\theta \exp[-(\gamma + i\delta)t] \quad (30)$$

If the sample under consideration is optically thin, the power exiting a sample of length  $L$  in the  $\hat{Z}$  direction is proportional to

$$I(L, t) = |E_s(L, t)|^2 = \left( \frac{kN\mu L}{2\epsilon_0} \sin\theta \right)^2 \exp(-2\gamma t) \quad (31)$$

The signal is maximal for a pulse area of  $\pi/2$ . A measure of the output power as a function of time following the excitation pulse enables one to obtain a value for the transverse relaxation rate. For a pencil-like sample, the neglect of cooperative effects such as superradiance is based on the assumption that  $NL/k^2 \ll 1$ .<sup>25,33-35</sup>

An alternative means for observing an FPD signal is to use an atomic beam that traverses a field interaction zone. The atom “sees” a radiation pulse in the atomic rest frame. If the atoms all have

the same longitudinal velocity  $u_0$ , then the FPD signal measured at a distance  $L$  from the field interaction zone arises from atoms which were excited at time  $t_e = t - L/u_0$ . This implies that the phase factor  $\exp[-(\gamma + i\delta)t]$  in Eq. (30) should be replaced by  $\exp[-(\gamma + i\delta)(t - t_e)] = \exp[-(\gamma + i\delta)L/c]$ . The emitted field is radiated at the incident field frequency  $\omega$  rather than the atomic frequency  $\omega_0$ . If the intensity is monitored as a function of  $L$ , one can obtain the transverse relaxation rate.

Often the atoms or molecules are characterized by an inhomogeneous distribution of frequencies. In a solid, this can occur as a result of different strains in the host medium. In a vapor, the velocity distribution of the atoms is equivalent to a distribution of atomic transition frequencies, when viewed in the laboratory frame. To discuss both solids and vapors in the same context, we define

$$\delta \equiv \delta(\omega_0, \mathbf{v}) = \omega_0 - \omega + \mathbf{k} \cdot \mathbf{v} = \delta_0 + \Delta + \mathbf{k} \cdot \mathbf{v} \quad (32)$$

where

$$\delta_0 = \bar{\omega}_0 - \omega \quad \Delta = \omega_0 - \bar{\omega}_0 \quad (33)$$

and  $\bar{\omega}_0$  is the average transition frequency. In a solid,  $\mathbf{v} = 0$ , but there is an inhomogeneous distribution of frequencies given by

$$W_f(\Delta) = \frac{1}{\sqrt{\pi}\sigma_w} \exp\left(-\frac{\Delta}{\sigma_w}\right)^2 \quad (34)$$

where  $\sigma_w$  characterizes the width of the inhomogeneous distribution. In a vapor,  $\Delta = \sigma_w = 0$ , but there is a Maxwellian velocity distribution

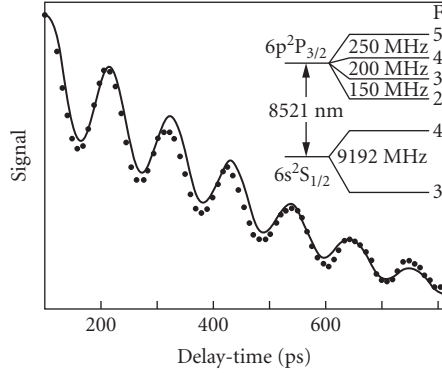
$$W_0(\mathbf{v}) = \frac{1}{(\pi u^2)^{3/2}} \exp[-(v/u)^2] \quad (35)$$

where  $u$  is the most probable atomic speed. The net effect is that Eq. (31) must be replaced by

$$\begin{aligned} I(L, t) &= \left( \frac{kN\mu L}{\epsilon_0} \right)^2 \left| \langle \rho_{21}(t) \rangle \right|^2 \\ &= \left( \frac{kN\mu L}{2\epsilon_0} \sin\theta \right)^2 \left| \int d\mathbf{v} W_0(\mathbf{v}) \int d\Delta W_f(\Delta) \exp(-[\gamma - i(\bar{\omega}_0 + \Delta + \mathbf{k} \cdot \mathbf{v})]t) \right|^2 \\ &= \left( \frac{kN\mu L}{2\epsilon_0} \sin\theta \right)^2 \exp(-2\gamma t) \exp\left[ \frac{-(\sigma_w t)^2}{2} \right] \exp\left[ \frac{-(kut)^2}{2} \right] \end{aligned} \quad (36)$$

If  $\sigma_w \gg \gamma$  (solids) or  $ku \gg \gamma$  (vapors), the signal decays mainly owing to inhomogeneous broadening. Bloch vectors corresponding to different frequencies process about the  $w$  axis at different rates, implying that the optical dipoles created by the pulse lose their relative phase in a time of order  $T_2^* = (2\sigma_w)^{-1}$  or  $(2ku)^{-1}$  (see Fig. 1b). The FPD signal can be used to measure  $T_2^*$ , which can be viewed as an inhomogeneous, transverse relaxation time. At room temperature,  $ku/\gamma$  is typically on the order of 100. In a solid,  $\sigma_w/\gamma$  can be orders of magnitude larger. An experimental FPD signal is shown in Fig. 2.

It is also possible to produce an FPD signal by preparing the atoms with a CW laser field and suddenly turning off the field. This method was used by Brewer and coworkers in a series of experiments on coherent optical transients in which Stark fields were used to tune molecules in a vapor into and out of resonance.<sup>26</sup> The CW field modifies the velocity distribution for the molecules. In



**FIGURE 2** An FPD signal obtained on the  $D_2$  transition in cesium. The excitation pulse has a duration of 20 ps. The decay time of the signal is determined by the inhomogeneous transverse relaxation rate  $T_2^* = 1.4$  ns. Oscillations in the signal originate from the ground state hyperfine splitting. (From Ref. 28. Reprinted with permission.)

the linear field regime, this again leads to an FPD signal that decays on a time scale of order  $(ku)^{-1}$ . It is fairly easy to obtain this result. To first order in the field, the steady-state solution of Eq. (14d), generalized to include the Doppler shift  $\mathbf{k} \cdot \mathbf{v}$  and initial velocity distribution  $W_0(\mathbf{v})$ , is

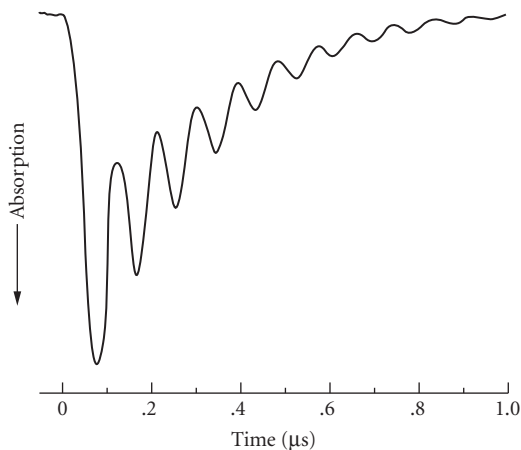
$$\rho_{21}(\mathbf{v}) = -i \left( \frac{\Omega_0}{2} \right) [\gamma - i(\delta_0 + \mathbf{k} \cdot \mathbf{v})]^{-1} W_0(\mathbf{v}) \quad (37)$$

With this initial condition, it follows from Eq. (14d) that, for  $t > 0$ ,

$$\begin{aligned} \langle \rho_{21}(\mathbf{v}, t) \rangle &= \int d\mathbf{v} \frac{-i(\Omega_0/2) \exp[-\gamma t - i(\delta_0 + \mathbf{k} \cdot \mathbf{v})t]}{\gamma + i(\delta_0 + \mathbf{k} \cdot \mathbf{v})} W_0(\mathbf{v}) \\ &= -i \frac{\sqrt{\pi} \Omega_0}{2ku} \exp \left[ \left( \frac{\gamma + i\delta_0}{ku} \right)^2 \right] \left[ 1 - \Phi \left( \frac{\gamma + i\delta_0}{ku} + \frac{kut}{2} \right) \right] \end{aligned} \quad (38)$$

where  $\Phi$  is the error function. For  $kut > 1$  and  $|\gamma + i\delta_0|/ku \ll 1$ ,  $\langle \rho_{21}(\mathbf{v}) \rangle \sim -i[\Omega_0/(k^2 u^2 t)] \exp(-k^2 u^2 t^2/4)$ .

When one considers *nonlinear* interactions with the field, the situation changes. The CW field excites only those atoms having  $\mathbf{k} \cdot \mathbf{v} = -\delta \pm \gamma'$ , where  $\gamma'$  is a power-broadened homogeneous width. These velocity-selected atoms are no longer subject to inhomogeneous broadening and give rise to a contribution to the FPD signal that decays with rate  $T_2^{-1} = (\gamma + \gamma')$ .<sup>26</sup> Thus, by using *nonlinear* atom-field interactions, one can extract *homogeneous* decay rates in situations where there is large inhomogeneous broadening. The price one pays is that only a small percentage of the atoms (those that have velocities for which the applied field is resonant) contribute to the signal. An example of an FPD signal of this type is shown in Fig. 3.

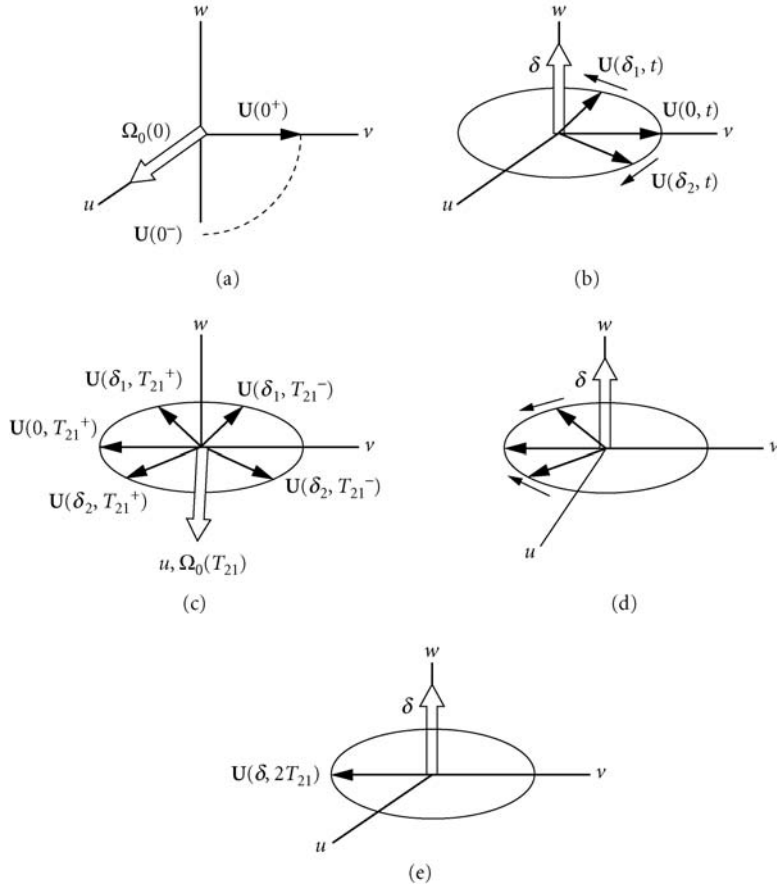


**FIGURE 3** An FPD signal obtained in  $\text{NH}_2\text{D}$  at  $10.6\ \mu\text{m}$  using the method of Stark switching of a molecular transition frequency. Molecules that interact resonantly with a CW field are suddenly tuned out of resonance by the Stark switching. The oscillations result from the heterodyne detection method that is used, while the slowly varying increase in the signal is the result of optical nutation of molecules switched *into* resonance by the Stark pulse. The FPD signal manifests itself as a *reduction of the amplitude of the oscillation* with time. This amplitude decays with the (power-broadened) *homogeneous* decay rate  $T_2$ , owing to the fact that the nonlinear interaction with a CW field results in the excitation of only a small fraction of the Doppler profile of the molecules. (From Ref. 26. Reprinted with permission.)

## 11.6 PHOTON ECHO

We have seen that it is possible to measure the transverse relaxation rate  $T_2$  in an inhomogeneously broadened sample using FPD, but only a relatively small percentage of the atoms participate. The question arises as to whether other techniques would allow for full participation of the atoms. The *photon echo* is one such method.<sup>8-10,36-38</sup> The photon echo has very little to do with either photons or echoes, but the name has a nice ring to it. The photon echo, the optical analog of the spin echo,<sup>39</sup> was first observed in ruby by Kurnit et al.<sup>36</sup> A pulse having propagation vector  $\mathbf{k}_1$  is applied at  $t = 0$ , a second pulse having propagation vector  $\mathbf{k}_2 = \mathbf{k}_1$  is applied at  $t = T_{21}$ , and an echo is radiated at time  $t = 2T_{21}$  in a direction  $\mathbf{k} = \mathbf{k}_1$ . There are many ways to explain echo formation, and some of these are indicated in the following discussion.

In the Bloch vector picture, a  $\pi/2$  pulse excites the optical dipoles at  $t = 0$ , bringing the Bloch vector along the  $v$  axis (Fig. 4a). The Bloch vector then begins to precess in the  $uv$  plane at a rate equal to the atom-field detuning. In an inhomogeneously broadened medium, different atoms have different resonant frequencies. As a consequence, the Bloch vectors associated with different atoms precess at different rates and dephase relative to each other in a time  $T_2^*$  (Fig. 4b). The dipole coherence is not lost, however. If at time  $T_{21}$  a  $\pi$  pulse is applied, the net effect of the pulse is to cause a reflection about the  $uv$  plane (Fig. 4c). As the atoms continue to precess at different rates (Fig. 4d), the rates are such that the Bloch vectors for *all* the atoms will become aligned with the  $-v$  axis at time  $t = 2T_{21}$  and an *echo signal* is emitted (Fig. 4e). From time  $t = 0$  to  $t = 2T_{21}$  the dipoles decay with the homogeneous decay rate  $\gamma$ .

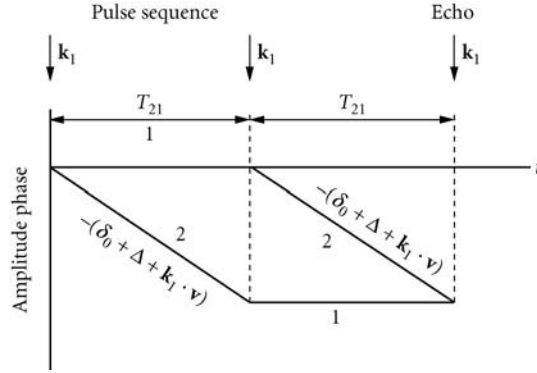


**FIGURE 4** Bloch vector picture of echo formation. (a) An initial  $\pi/2$  pulse brings the Bloch vector to the  $uv$  plane. (b) In a field-free region, the Bloch vector precesses in the  $uv$  plane; atoms with different detunings dephase relative to one another in a time equal to the inhomogeneous, transverse relaxation rate  $T_2^*$ . (c) At time  $T_{21}$ , a second pulse, this time a  $\pi$  pulse, reflects the Bloch vectors with respect to the  $uw$  plane. (d) In a field-free region, the Bloch vectors continue to precess. (e) At time  $t = 2T_{21}$ , all the vectors are aligned along the  $-v$  axis (the optical dipoles have rephased), and an echo signal is emitted. The decay of the Bloch vector is not indicated in the figure.

By measuring the echo signal as a function of delay time  $T_{21}$  between the pulses, one can obtain the transverse relaxation time  $T_2 = \gamma^{-1}$ .

It is not necessary that the pulse areas be equal to  $\pi/2$  and  $\pi$ , although these areas lead to a maximal signal. What is necessary is that the second pulse produce at least a partial reflection about the  $uw$  plane. This reflection takes the Bloch vector components  $u + iv$  into  $u - iv$ , or, equivalently, takes density matrix element  $\rho_{12}$  into  $\rho_{21}$ . Since  $\rho_{12}$  and  $\rho_{21}$  are related to the real and imaginary parts of the average dipole moment operator, the second pulse must couple these real and imaginary parts. Such coupling is impossible for a linear atom-field interaction. Thus, by its very nature, the photon echo can occur only when nonlinear atom-field interactions are present.

An alternative way to picture echo formation is to use double-sided Feynman diagrams<sup>40</sup> that keep track of the relative phase of the different dipoles. Diagrams similar to those indicated in Fig. 5 were



**FIGURE 5** A phase diagram that can be used to analyze coherent transient phenomena. Each line corresponds to a state amplitude, and density matrix elements are obtained by multiplying a top line by the conjugate of a bottom line *at the same time*. The relative phase of a given density matrix element is given by the vertical separation of the two lines. The slopes of various line segments are shown on the graph. Lines corresponding to atoms having different atom-field detunings  $\Delta$  (solid) or different velocities  $\mathbf{v}$  (vapor) would have different slopes. The pulse sequence is shown at the top of the figure along with the temporal position and direction of the echo. This diagram corresponds to the two-pulse photon echo. Regardless of the atom-field detuning or atomic velocity, all lines cross at  $t = 2T_{21}$ , indicating that all the optical dipoles are in phase at this point.

introduced by Hartmann and Friedberg in the context of a billiard ball echo model<sup>41</sup> and have been used extensively in theories of atom interferometry.<sup>42–44</sup> Each line represents a field amplitude. The abscissa is time, and the ordinate is the *phase* associated with the amplitude. In the absence of any interactions, it follows from Eq. (4) that the phase associated with the state  $|1\rangle$  amplitude is  $\delta t/2$  and that associated with the state  $|2\rangle$  amplitude is  $-\delta t/2$ . In these diagrams, the phase of each amplitude is displaced by  $-\delta t/2$  so that the state  $|1\rangle$  amplitude evolves without any phase change and the state  $|2\rangle$  amplitude evolves with a phase equal to  $-\delta t$ .

We start with the atom in state  $|1\rangle$  at  $t = 0$ . The atom-field interaction takes state  $|1\rangle$  to  $|2\rangle$  on absorption with a phase factor  $\exp(i\mathbf{k}_1 \cdot \mathbf{R})$  and  $|2\rangle$  to  $|1\rangle$  on emission with a phase factor  $\exp(-i\mathbf{k}_1 \cdot \mathbf{R})$ . A vertical cut establishes the density matrix element of interest and the vertical distance between the two amplitudes is a measure of the *relative* phase of the amplitudes. For example, between  $t = 0$  and  $t = T_{21}$  in Fig. 5, the density matrix element  $\rho_{12}$  has been created with relative phase  $(\delta_0 + \Delta + \mathbf{k}_1 \cdot \mathbf{v})t$  which grows with increasing  $t$ . One finds significant contributions to the dipole coherence at a given time *only* when the relative phase is the *same* for all the optical dipoles at that time. In a solid  $\mathbf{v} = 0$ , but  $\Delta = \omega_0 - \bar{\omega}_0$  is different for different atoms owing to variations in  $\omega_0$ ; in a vapor  $\Delta = 0$ , but  $\mathbf{k}_1 \cdot \mathbf{v}$  is different for different velocity subclasses of atoms. Thus, the slopes of the lines in Fig. 5 would differ for different atoms in both solids and vapors. On averaging over an inhomogeneous frequency distribution, the average dipole coherence would vanish, except at times near crossings of the state amplitudes, where the relative phase of all the dipoles is nearly equal to zero. Between  $t = 0$  and  $t = T_{21}$ , this occurs only near  $t = 0$ , where an FPD signal is emitted. The application of a second pulse at  $t = T_{21}$ , however, converts  $\rho_{12}$  into  $\rho_{21}$  and begins a rephasing process for the dipoles. The state amplitudes in Fig. 5 intersect and the dipoles are rephased at  $t = 2T_{21}$ , *independent of the value of  $\mathbf{v}$  or  $\Delta$* . The echo signal is radiated for times  $t \approx 2T_{21}$ .

Analytical calculations of the signal intensity can be carried out using Eqs. (14) and (16). One simply pieces together periods in which the pulses act with periods of free evolution. The results are rather complicated, in general. However, if  $\sigma_w T_{21} \gg 1$  (solid) or  $k_i u T_{21} \gg 1$  (vapor), only terms in the density matrix sequence indicated schematically in Fig. 5 survive the average over the inhomogeneous frequency distribution in the vicinity of the echo at  $t \approx 2T_{21}$ . At these times, one finds a total averaged density matrix element

$$\langle \rho_{21}^T(\mathbf{R}, t) \rangle = \langle \rho_{21}(t) \rangle \exp(i[kZ - \omega t])$$

where

$$\mathbf{k} = -\mathbf{k}_1 + 2\mathbf{k}_1 = \mathbf{k}_1$$

$$\begin{aligned} \langle \rho_{21}(t) \rangle &= \frac{1}{2} \sin \theta_1 \sin^2 \left( \frac{\theta_2}{2} \right) \exp(-2\gamma T_{21}) \exp[-i\delta_0(t - 2T_{21})] \\ &\times \exp \left[ \frac{-\sigma_\omega^2(t - 2T_{21})^2}{4} \right] \exp \left[ \frac{-k_1^2 u^2(t - 2T_{21})^2}{4} \right] \end{aligned} \quad (39)$$

and  $\theta_i$  is the pulse area of pulse  $i$ . The corresponding echo intensity is

$$\begin{aligned} I(L, t) &= \left( \frac{kN\mu L}{\epsilon_0} \right)^2 |\langle \rho_{21}(t) \rangle|^2 = \left[ \frac{kN\mu L}{2\epsilon_0} \sin \theta_1 \sin^2 \left( \frac{\theta_2}{2} \right) \right]^2 \\ &\times \exp(-4\gamma T_{21}) \exp \left[ \frac{-\sigma_\omega^2(t - 2T_{21})^2}{2} \right] \exp \left[ \frac{-k_1^2 u^2(t - 2T_{21})^2}{2} \right] \end{aligned} \quad (40)$$

It is interesting to note that the echo intensity near  $t = 2T_{21}$  mirrors the FPD intensity immediately following the first pulse.

For experimental reasons it is often convenient to use a different propagation vector for the second pulse. Let  $\mathbf{k}_1$  and  $\mathbf{k}_2$  be the propagation vectors of the first and second pulses, which have identical carrier frequencies  $\omega$ . In this case, one must modify the definition (24) of the field interaction representation to account for the different  $\mathbf{k}$  vectors. The final result for the total averaged density matrix element in the vicinity of the echo is

$$\langle \rho_{21}^T(\mathbf{R}, t) \rangle = \langle \rho_{21}(t) \rangle \exp(i[kZ - \omega t])$$

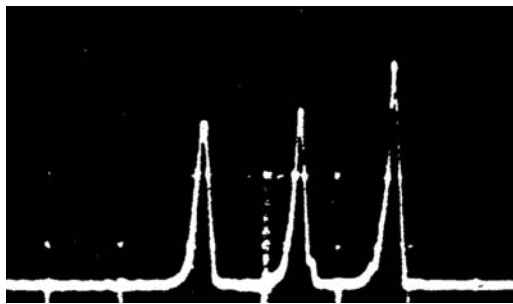
where

$$\mathbf{k} = 2\mathbf{k}_2 - \mathbf{k}_1$$

and

$$\begin{aligned} \langle \rho_{21}(t) \rangle &= \frac{i}{2} \sin \theta_1 \sin^2 \left( \frac{\theta_2}{2} \right) \exp(-2\gamma T_{21}) \exp[-i\delta_0(t - 2T_{21})] \\ &\exp \left[ \frac{-\sigma_\omega^2(t - 2T_{21})^2}{4} \right] \int d\mathbf{v} W_0(\mathbf{v}) \exp\{i\mathbf{k}_1 \cdot \mathbf{v} T_{21} - \mathbf{k}_2 \cdot \mathbf{v}(t - T_{21})\} \end{aligned} \quad (41)$$

Recall that  $\sigma_\omega = 0$  for a vapor and  $W_0(\mathbf{v}) = \delta_D(\mathbf{v})$  for a solid, where  $\delta_D$  is the Dirac delta function. In these equations there are three things to note. First, the signal is emitted in a direction different from that of the applied fields, a desirable feature from an experimental point of view. Second, the phase



**FIGURE 6** A photon echo signal from ruby. Time increases to the right with a scale of 100 ns/division. The pulse on the right is the echo signal, while the first two pulses are the (attenuated) input pulses. The echo appears at  $t = 2T_{21}$  where  $T_{21}$  is the separation of the input pulses. (From Ref. 36. Reprinted with permission.)

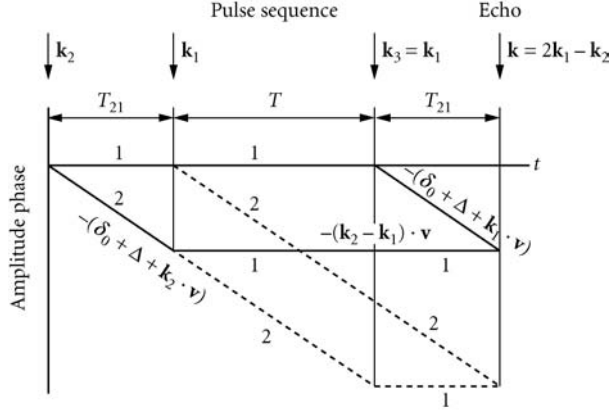
matching condition  $k = \omega/c$  is no longer satisfied since  $k = |2\mathbf{k}_2 - \mathbf{k}_1|$  and  $k_1 = k_2 = \omega/c$ ; however, if the fields are nearly collinear such that  $(k^2 - \omega^2/c^2)L^2 \ll 1$ , the effects of phase mismatch are negligible. Third, there is now a qualitative difference between the solid and vapor case. Owing to the fact that the detuning depends on the propagation vectors for the vapor, it is not possible to exactly rephase all the dipoles in the vapor when  $\mathbf{k}_1 \neq \mathbf{k}_2$ . If  $|\mathbf{k}_2 - \mathbf{k}_1|/k_1 \ll 1$ , however, nearly complete rephasing of the dipoles occurs for  $t \approx 2T_{21}$ . The photon echo signal observed by Kurnit et al.<sup>36</sup> is shown in Fig. 6.

As can be deduced from Fig. 5, the signal is sensitive only to off-diagonal density matrix elements in the entire time interval of interest. Thus, any disturbance of the off-diagonal density matrix elements or optical coherence will be reflected as a decrease in the echo intensity. As such, echo signals can serve as a probe of all contributions to transverse relaxation. Transverse relaxation generally falls into two broad categories which can lead to qualitatively different modifications of the coherent transient signals. First, there are *dephasing processes*, which produce an exponential damping of the coherences and contribute to  $\gamma$ . Second, there are *spectral diffusion* (solid)<sup>45-48</sup> or *velocity-changing collisions* (vapor),<sup>47-49</sup> which change the frequency associated with the optical coherences. Such terms enter the optical Bloch equations as *integral* terms, transforming the equations into differential-integral equations. In a solid the change in frequency can be produced by fluctuating fields acting at each atomic site. Spectral diffusion of coherences in solids is difficult to detect, since phase-interrupting processes often dominate the signals. It has been measured in FPD using impurity ions in a crystalline host.<sup>50</sup> The situation in vapors is a bit more subtle. The phase-changing and velocity-changing aspects of collisions are entangled and cannot be separated, in general.<sup>49</sup> If the collisional interaction is *state independent*, however, as it is for some molecular transitions, then collisions are purely velocity changing in nature, leading to an echo that decays exponentially as  $T_{21}^3$  for early times and  $T_{21}$  for later times.<sup>51</sup> For electronic transitions, collisions are mainly phase changing in nature, but there is a velocity-changing contribution that persists in the forward diffractive-scattering cone. This diffractive scattering has been observed for Na-,<sup>52</sup> Li-,<sup>53</sup> and Yb-rare gas collisions<sup>54</sup> using photon echo techniques.

## 11.7 STIMULATED PHOTON ECHO

Up to this point, we have considered pulse sequences that are useful for measuring transverse relaxation times. Now we examine *stimulated photon echoes*,<sup>8-10</sup> which can be used to *simultaneously* measure both transverse and longitudinal relaxation times. Stimulated photon echoes have become an important diagnostic probe of relaxation in condensed-matter systems. The pulse sequence consists of three pulses, having





**FIGURE 7** A phase diagram for the stimulated photon echo in which field 2 acts first and the echo is emitted in the  $(-\mathbf{k}_2 + \mathbf{k}_1 + \mathbf{k}_3) = (2\mathbf{k}_1 - \mathbf{k}_2)$  direction. The solid lines involve the intermediate state population  $\rho_{11}$  while the dashed lines involve the intermediate state population  $\rho_{22}$ . All dipoles are in phase at  $t = 2T_{21} + T$ .

areas  $\theta_1, \theta_2, \theta_3$  and propagation vectors  $\mathbf{k}_1, \mathbf{k}_2, \mathbf{k}_3$ , with  $k_i = \omega/c$ . In this section we take  $\mathbf{k}_3 = \mathbf{k}_1$ , and in the next section we will set  $\mathbf{k}_3 = -\mathbf{k}_1$ . The time interval between the first two pulses is  $T_{21}$ , and pulse 1 can precede or follow pulse 2. Pulse 3 occurs at time  $t = T_{21} + T$  (Fig. 7). Signals can be generated in many different directions. For the sake of definiteness, we consider only the signal radiated in the  $-\mathbf{k}_2 + \mathbf{k}_1 + \mathbf{k}_3$  direction. The phase diagram giving rise to this signal is shown in Fig. 7. For radiation to be emitted in the  $-\mathbf{k}_2 + \mathbf{k}_1 + \mathbf{k}_3$  direction when  $\mathbf{k}_3 = \mathbf{k}_1$  pulse 2 must precede pulse 1. (Of course, there are diagrams with pulse 1 preceding pulse 2, but these give rise to radiation in the  $-\mathbf{k}_1 + \mathbf{k}_2 + \mathbf{k}_3$  direction.) It is assumed that  $T_{21}$  is greater than the inhomogeneous relaxation time  $T_2^*$ . The signal contains contributions from the optical coherence (off-diagonal density matrix elements) in the time intervals  $(0, T_{21})$ ,  $(T + T_{21}, t)$  and contributions from atomic state populations (diagonal density matrix elements) in the time interval  $T$  between the second and the third pulses. The echo appears when  $t - (T_{21} + T) = T_{21}$ .

The calculation of the echo signal is straightforward. Just before the second pulse, the density matrix  $\rho_{12}(T_{21})$  varies as  $\exp[-(\gamma - i\delta_2)T_{21}]$ , where  $\delta_1 = \omega_0 - \omega + \mathbf{k}_1 \cdot \mathbf{v}$ . In the time interval  $T$ , the population difference  $\omega = \rho_{22} - \rho_{11}$  decays at rate  $\gamma_2$  and oscillates at frequency  $\delta_2 - \delta_1 = (\mathbf{k}_2 - \mathbf{k}_1) \cdot \mathbf{v}$ . In the final time interval,  $\rho_{21}(t)$  varies as  $\exp[-(\gamma + i\delta_3)(t - T - T_{21})]$ , where  $\delta_3 = \delta_1$  since  $\mathbf{k}_3 = \mathbf{k}_1$ . Combining the various field interaction and free propagation zones, one finds that the total averaged density matrix element in the vicinity of the echo  $t \approx T + 2T_{21}$  is

$$\langle \rho_{21}^T(\mathbf{R}, t) \rangle = \langle \rho_{21}(t) \rangle \exp[i(kZ - \omega t)]$$

with

$$\mathbf{k} = -\mathbf{k}_2 + \mathbf{k}_1 + \mathbf{k}_3 = 2\mathbf{k}_1 - \mathbf{k}_2$$

and

$$\begin{aligned} \langle \rho_{21}(t) \rangle = & \left( \frac{i}{8} \right) \sin\theta_1 \sin\theta_2 \sin\theta_3 \sin(-\gamma_2 T) \exp(-2\gamma T_{21}) \exp\{-i\delta_0[t - T_{21} - T] - T_{21}\} \\ & \times \exp\left\{ \frac{-\sigma_\omega^2 [(t - T_{21} - T) - T_{21}]^2}{4} \right\} \int d\mathbf{v} W_0(\mathbf{v}) \\ & \times \exp\{i[\mathbf{k}_2 \cdot \mathbf{v} T_{21} + (\mathbf{k}_2 - \mathbf{k}_1) \cdot \mathbf{v} T - (2\mathbf{k}_1 - \mathbf{k}_2) \cdot \mathbf{v}(t - T_{21} - T)]\} \end{aligned} \quad (42)$$

The optimal pulse sequence consists of three  $\pi/2$  pulses. Phase matching can be achieved only for  $|\mathbf{k}_1 - \mathbf{k}_2|L \ll 1$ . In a solid, the integral in Eq. (42) is equal to unity, and the echo signal is maximal for  $t = T + 2T_{21}$ . In a vapor, the echo signal is degraded if  $\mathbf{k}_1 \neq \mathbf{k}_2$ ; however, if  $\mathbf{k}_1 \approx \mathbf{k}_2$ , then, at  $t = T + 2T_{21}$ , the echo amplitude varies as

$$\exp(-\gamma_2 T) \exp(-2\gamma T_{21}) \exp\left[-\frac{|\mathbf{k}_1 - \mathbf{k}_2|^2 u^2 (T + 2T_{21})^2}{4}\right]$$

By varying the angle between  $\mathbf{k}_1$  and  $\mathbf{k}_2$ , one can determine the Doppler width  $ku$ . By monitoring the echo signal as a function of  $T_{21}(T)$ , one obtains information on the transverse (longitudinal) relaxation.

Relaxation other than spontaneous emission can occur for the populations in the time interval  $T$ . The inhomogeneous phase  $\delta_1 T_{21}$ , acquired in the time interval  $T_{21}$ , is canceled by the phase  $\delta_3 T_{21}$ , acquired in the interval  $T_{21}$  following the third pulse. If, between the second and third pulses, the frequency (solid) or velocity (vapor) has changed owing to spectral diffusion (solid)<sup>45-48</sup> or velocity-changing collisions (vapor),<sup>47-49,55,56</sup> the phase cancellation will not be complete. Thus, the echo signal as a function of  $T$  provides information on these relaxation processes. The rate of spectral diffusion or velocity-changing collisions must be of order or greater than  $\gamma_2$  to be observable. One would have a longer time to observe such effects if it were the ground-state lifetime rather than the excited-state lifetime that was the relevant time scale, but, in a closed two-level system, such is not the case.

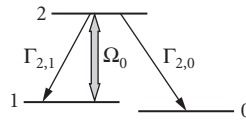
The situation changes if a three-level system, such as the one shown in Fig. 8, is used. The fields drive the 1-2 transition, but level 2 decays to both level 1 and level 0. The total population of the 1-2 state subsystem is no longer conserved, requiring an *additional* decay rate to account for relaxation. Let us suppose that all states decay with rate  $\Gamma_i$  as a result of their finite time in the laser beams. Moreover, let  $\Gamma_{2,1}$  and  $\Gamma_{2,0}$  be the decay rates of level 2 to levels 1 and 0, respectively, such that  $\gamma_1 = \gamma_0 = \Gamma_i$  and  $\gamma_2 = \Gamma_{2,1} + \Gamma_{2,0} + \Gamma_i$ . For simplicity, let us also take  $\mathbf{k}_1 \approx \mathbf{k}_2$ . In the interval  $T$ , the decay dynamics resulting from spontaneous emission and transit time effects is

$$\begin{aligned} \dot{\rho}_{22} &= -\gamma_2 \rho_{22} = -(\Gamma_{2,1} + \Gamma_{2,0} + \Gamma_i) \rho_{22} \\ \dot{\rho}_{11} &= -\Gamma_i \rho_{11} + \Gamma_{2,1} \rho_{22} \end{aligned}$$

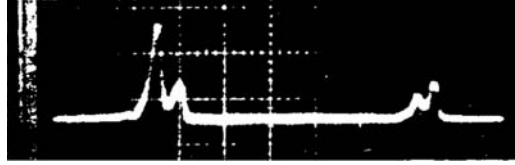
Assuming that  $\gamma_2 T \gg 1$ , one finds that at time  $t = T_{21} + T$ ,  $\rho_{22}(T_{21} + T) \sim 0$ , and

$$\rho_{11}(T_{21} + T) \sim \frac{\Gamma_{2,0}}{\Gamma_{2,1} + \Gamma_{2,0}} \exp(-\Gamma_i T)$$

which then replaces the factor  $\exp(-\gamma_2 T)$  in Eq. (42). If  $\Gamma_{2,0} \neq 0$ , there is a long-lived component in the ground-state population. One can exploit this feature of *open systems* to study spectral diffusion or velocity-changing collisions with very high sensitivity.<sup>57,58</sup> In Fig. 9, stimulated echo data is shown



**FIGURE 8** Open atomic-level scheme that can be used to observe transient signals limited only by some effective ground state lifetime. The field couples only states  $|1\rangle$  and  $|2\rangle$ , but level 2 decays to both levels 1 and 0.



**FIGURE 9** Stimulated photon echo observed on the  $D_1$  transition in sodium. This is an “open” system for which a stimulated echo signal can be produced for separations  $T$  between the second and third pulses much larger than the excited-state lifetime. In this diagram  $T$  is 17 times the 16-ns lifetime of the excited state. The first three pulses are scattered light from the three input pulses and the fourth pulse is the echo. The echo appears at  $t = T + 2T_{21}$ , where  $T_{21}$  is the separation of the first two input pulses. (From Ref. 58. Reprinted with permission.)

that was used to measure a cross section for collisions between ground-state Na and He atoms.<sup>58</sup> The echo occurs for time separations  $T$  much greater than the excited-state lifetime.

Open systems also offer interesting possibilities as storage devices. Since the effective ground-state lifetime can be as long as days in certain solids, one can write interferometric information into the sample by replacing one of the first two pulses by a signal pulse and reading it out at a later time with the third pulse.<sup>59–62</sup> In the case of vapors, it is also possible to replace some of the incident pulses by standing-wave fields.<sup>63–71</sup> In this manner, modulated ground-state populations with associated Doppler phases of order  $kuT$  can be created and rephased, providing sensitivity to velocity-changing collisions as small as a few centimeters per second.<sup>72</sup>

Before leaving this section, it is perhaps useful to make a slight digression on *homogeneously* broadened systems. A diagram similar to that shown in Fig. 10, in which field 1 acts first, also leads to a signal in the  $\mathbf{k} = \mathbf{k}_1 - \mathbf{k}_2 + \mathbf{k}_3 = 2\mathbf{k}_1 - \mathbf{k}_2$ , provided  $\mathbf{k}_3 = \mathbf{k}_1$  (in the figure,  $\mathbf{k}_3 = -\mathbf{k}_1$ ). We have not considered this contribution for inhomogeneously broadened systems since such a diagram leads to an overall phase of  $\phi_d = -2(\delta_0 + \Delta + 2\mathbf{k}_1 \cdot \mathbf{v})T_{21}$  at time  $t = T + 2T_{21}$ . On averaging over either  $\Delta$  or  $\mathbf{v}$  in an inhomogeneously broadened sample, this contribution would vanish. In a homogeneously broadened sample, however,  $\Delta = 0$  and  $\mathbf{v} = 0$ , giving an *identical* relative phase  $\phi_d$  to all the atoms. For  $t > T + T_{21}$ , the corresponding density matrix element associated with this diagram is

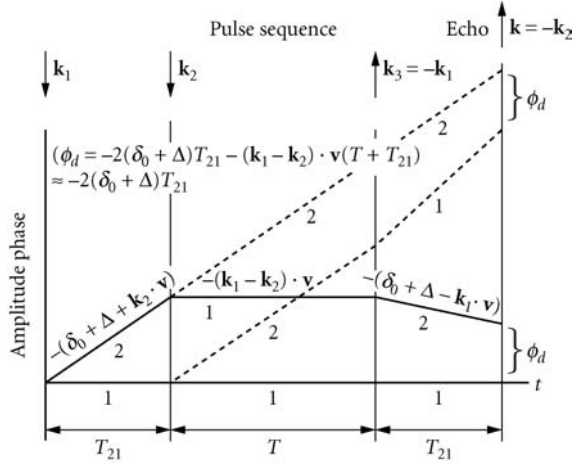
$$\langle \rho_{21}(t) \rangle = \left( \frac{i}{8} \right) \sin\theta_1 \sin\theta_2 \sin\theta_3 \exp(-\gamma_2 T) \exp[-\gamma(t-T)] \exp[-i\delta_0(t-T)] \quad (43)$$

Equation (43) does not constitute an echo in the usual sense, since there is no dephasing-rephasing cycle. The signal appears promptly (it is actually an FPD signal) following the third pulse. If one measures the *time-integrated* intensity in the signal following the third pulse, however (as is often the case with ultrafast pulses in which time resolution of the echo is not possible), it is impossible to tell directly whether an echo has occurred or not. For such measurements, a signal emitted in the  $\mathbf{k} = 2\mathbf{k}_1 - \mathbf{k}_2$  direction when pulse 1 acts first is a clear signature of a homogeneously broadened system, since such a signal vanishes for inhomogeneously broadened samples.

The time-integrated signal is proportional to

$$\int_{T+T_{21}}^{\infty} |\langle \rho_{21}(t) \rangle|^2 dt$$

When field 2 acts first, the time integrated, inhomogeneously broadened signal varies as  $\exp(-4\gamma T_{21})$ , while the homogeneously broadened signal varies as  $\exp(-2\gamma T_{21})$ . When field 1 acts



**FIGURE 10** A phase diagram for the stimulated photon echo in which field 1 acts first. The direction of field 3 is opposite to that of field 1, and the echo is emitted in the  $(\mathbf{k}_1 - \mathbf{k}_2 + \mathbf{k}_3) = -\mathbf{k}_2$  direction. We have taken  $\mathbf{k}_2 \approx \mathbf{k}_1$ . The solid lines involve the intermediate state population  $\rho_{11}$ , while the dashed lines involve the intermediate state population  $\rho_{22}$ . At time  $t = 2T_{21} + T$ , the relative phase is  $\phi_d \approx -2(\delta_0 + \Delta)T_{21}$ . For solids, the average over  $\Delta$  washes out the signal. For vapors,  $\Delta = 0$ , the phase  $\phi_d \approx -2\delta_0 T_{21}$  is the same for all the atoms, and an echo is emitted.

first, the signal is vanishingly small {varying as  $\exp[-(\sigma_w^2 + k^2 u^2)T_{21}^2/2]$ } for inhomogeneously broadened samples, while the homogeneously broadened signal strength is essentially unchanged from that when pulse 2 acts first. This time-ordering asymmetry can be used to distinguish between homogeneously and inhomogeneously broadened samples.<sup>73</sup>

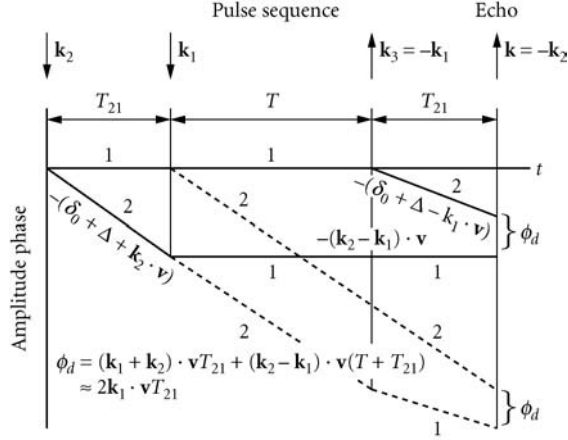
## 11.8 PHASE CONJUGATE GEOMETRY AND OPTICAL RAMSEY FRINGES

A qualitative difference between stimulated photon echo signals arises when  $\mathbf{k}_3$  is in the  $-\mathbf{k}_1$  direction rather than the  $\mathbf{k}_1$  direction.<sup>61,74,75</sup> In this case, it is possible to generate a phase-matched signal in the

$$\mathbf{k} = \mathbf{k}_1 - \mathbf{k}_2 + \mathbf{k}_3 = -\mathbf{k}_2$$

direction for *both* time orderings of fields 1 and 2. Moreover, in weak fields, the amplitude of the signal field is proportional to the conjugate of input field 2. As a consequence, the signal is referred to as a *phase conjugate* signal for this geometry.<sup>76,77</sup> To simplify matters, we will set  $\mathbf{k}_1 \approx \mathbf{k}_2 = -\mathbf{k}$  and neglect terms of order  $|\mathbf{k}_1 - \mathbf{k}_2|u(T + 2T_{21})$ .

The appropriate phase diagrams are shown in Fig. 10 when field 1 acts before field 2 and Fig. 11 when field 2 acts before field 1. There is a qualitative difference between the phase diagrams of Fig. 10 and Fig. 7. At time  $t = 2T_{21} + T$ , the lines representing the state amplitudes *do not* cross in Fig. 10. Rather, they are separated by a phase difference of  $\phi_d = -2(\delta_0 + \Delta)T_{21}$ . The phase shift resulting from *Doppler shifts* cancels at  $t = 2T_{21} + T$ , but *not* the phase shift resulting from the atom-field detuning.



**FIGURE 11** A phase diagram for the stimulated photon echo in which field 2 acts first and  $\mathbf{k}_3 = -\mathbf{k}_1$ . The echo is emitted in the  $(-\mathbf{k}_2 + \mathbf{k}_1 + \mathbf{k}_3) = -\mathbf{k}_2$  direction, and we have taken  $\mathbf{k}_e \approx \mathbf{k}_1$ . The solid lines involve the intermediate state population  $\rho_{11}$ , while the dashed lines involve the intermediate state population  $\rho_{22}$ . At time  $t = 2T_{21} + T$ , the relative phase is  $\phi_d \approx 2\mathbf{k}_1 \cdot \mathbf{v}T_{21}$ . For vapors, the average over the velocity distribution washes out the signal. For solids,  $\mathbf{v} = 0$ , the relative phase is zero for all the atoms, and an echo is emitted.

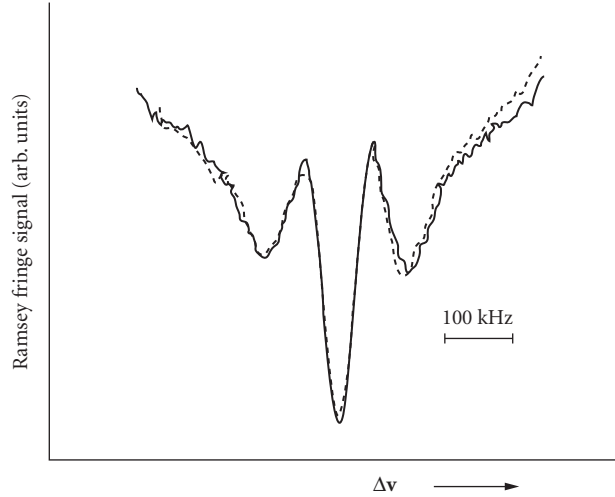
The significance of these results will become apparent immediately. The averaged density matrix element in the vicinity of the echo is

$$\begin{aligned} \langle \rho_{21}(t) \rangle = & \left( \frac{i}{8} \right) \sin\theta_1 \sin\theta_2 \sin\theta_3 \exp(-\gamma_2 T) \exp(-2\gamma T_{21}) \exp\{-i\delta_0(t - T_{21} - T) + T_{21}\} \\ & \times \exp\left[ \frac{-\sigma_\omega^2 [(t - T_{21} - T) + T_{21}]^2}{4} \right] \exp\left[ \frac{-k^2 u^2 [(t - T_{21} - T) - T_{21}]^2}{4} \right] \end{aligned} \quad (44)$$

In a solid, the signal vanishes near  $t = 2T_{21} + T$ , since  $\sigma_\omega T_{21} \gg 1$ .

In a vapor, an echo is formed at time  $t = T + 2T_{21}$ . At this time, the averaged density matrix element varies as  $\exp(-2i\delta_0 T_{21})$ , a factor which was absent for the nearly collinear geometry. This phase factor is the optical analog<sup>78-80</sup> of the phase factor that is responsible for the generation of Ramsey fringes.<sup>81</sup> One can measure the phase factor directly by heterodyning the signal field with a reference field, or by converting the off-diagonal density matrix element into a population by the addition of a *fourth pulse* in the  $\mathbf{k}_3$  direction at time  $t = T + 2T_{21}$ .<sup>\*</sup> In either case, the signal varies as  $\cos(2\delta_0 T_{21})$ . In itself, this dependence is useless for determining the optical frequency since one cannot identify the fringe corresponding to  $\delta_0 = 0$ . To accomplish this identification, there are two possibilities. If the experiment is carried out using an atomic beam rather than atoms in a cell,  $T_{21} = L/u_0$  will be different for atoms having different  $u_0$  ( $L$  = spatial separation of the first two pulses and  $u_0$  is the

<sup>\*</sup>In the case of atoms moving through spatially separated fields with different longitudinal velocities, one must first average Eq. (44) over *longitudinal* velocities before taking the absolute square to calculate the radiated field. As a result of this averaging, the radiated signal intensity is maximum for  $\delta_0 = 0$ . Consequently, for spatially separated fields, heterodyne detection or a fourth field is not necessary since the radiated field intensity as a function of  $\delta_0$  allows one to determine the line center.



**FIGURE 12** An optical Ramsey fringe signal on the 657-nm intercombination line in calcium. Four field zones were used. The most probable value of  $T_{21}$  was about  $10^{-5}$  s for an effusive beam having a most probable longitudinal speed equal to 800 m/s, giving a central fringe width on the order of 60 kHz. The dashed and dotted lines represent runs with the directions of the laser field reversed, to investigate phase errors in the signals. (From Ref. 82. Copyright © 1994; reprinted with permission from Elsevier Science.)

longitudinal velocity of the atoms). When a distribution of  $u_0$  is averaged over, the fringe having  $\delta_0 = 0$  will have the maximum amplitude. Experiments of this type allow one to measure optical frequencies with accuracy of order  $T_{21}^{-1}$  (see Fig. 12). For experiments carried out using temporally separated pulses acting on atoms in a cell, it is necessary to take data as a function of  $\delta_0$  for several values of  $T_{21}$ , and then average the data over  $T_{21}$ ; in this manner the central fringe can be identified. The optical Ramsey fringe geometry has been reinterpreted as an atom interferometer.<sup>42,83</sup> Atom interferometers are discussed in Sec. 11.9.

We now move to Fig. 11, in which field 2 acts before field 1. At time  $t = 2T_{21} + T$ , the lines representing the state amplitudes are separated by a phase difference of  $\phi_d = -2\mathbf{k} \cdot \mathbf{v}T_{21}$ . The phase shift resulting from the atom-field detuning cancels at  $t = 2T_{21} + T$ , but *not* the phase shift resulting from the Doppler effect. The corresponding density matrix element is

$$\begin{aligned} \langle \rho_{21}(t) \rangle &= \frac{i}{8} \sin\theta_1 \sin\theta_2 \sin\theta_3 \exp(-\gamma_2 T) \exp(-2\gamma T_{21}) \exp\{-i\delta_0[(t - T_{21} - T) - T_{21}]\} \\ &\times \exp\left[\frac{-\sigma_\omega^2[(t - T_{21} - T) - T_{21}]^2}{4}\right] \exp\left[\frac{-k^2 u^2[(t - T_{21} - T) + T_{21}]^2}{4}\right] \end{aligned} \quad (45)$$

Near  $t = T + 2T_{21}$ , the signal vanishes for a vapor since  $kuT_{21} \gg 1$ , but gives rise to a phase conjugate signal in solids ( $u = 0$ ). There are no Ramsey fringes in this geometry; optical Ramsey fringes cannot be generated in an inhomogeneously broadened solid.

When the first two fields are *identical*, there is no way to distinguish which field acts first, and Eqs. (44) and (45) must be added before taking the absolute square to determine the radiated electric field. There is no interference between the two terms, however, since one of the terms is approximately equal to zero in the vicinity of the echo for either the solid or the vapor.

## 11.9 TWO-PHOTON TRANSITIONS AND ATOM INTERFEROMETRY

In the previous section, we have already alluded to the fact that optical Ramsey fringes can serve as the basis of an atom interferometer.<sup>44</sup> There is some disagreement in the literature as to exactly what constitutes an atom interferometer. Ramsey fringes and optical Ramsey fringes were developed without any reference to quantization of the atoms' center-of-mass motion. As such, optical Ramsey fringes can be observed in situations where quantization of the center-of-mass motion is irrelevant. The interference observed in these interferometers is based on an *internal state* coherence of the atoms. Matter-wave effects (that is, effects related to quantization of the center-of-mass motion) may play a role under certain circumstances, but they are not critical to the basic operating principle associated with optical Ramsey fringes.

In this section, we consider a time-domain, matter-wave atom interferometer<sup>84</sup> which relies on the wave nature of the center-of-mass motion for its operation. Moreover, the interferometer illustrates some interesting features of coherent optical transients not found in NMR. We return to an ensemble of two-level atoms, which have been cooled in a magneto-optical trap. See Chap. 20, "Laser Cooling and Trapping of Atoms," for a more detailed description of trapping of atoms. The atoms are subjected to two *standing-wave* optical pulses separated in time by  $T$ . The electric field amplitude of pulse  $i$  ( $i = 1, 2$ ) is given by  $E_i(\mathbf{Z}, t) = \epsilon E_i(t) \cos(kZ) \cos(\omega t)$ . Either off-resonant<sup>84,85</sup> or resonant<sup>86</sup> pulses can be used. For resonant pulses, grating echoes can be observed in situations where a classical description of the center-of-mass motion is valid.<sup>66-68</sup> We consider only off-resonant pulses in this discussion, for which echoes can occur only when quantized motion of the atoms is included. For an atom-field detuning  $|\delta| \gg \Omega_0, \gamma, \gamma_2, k u$ , it is possible to adiabatically eliminate the excited state amplitude and arrive at an effective hamiltonian for the ground state atoms given by

$$H = \frac{P^2}{2M} - \sum_{i=1,2} \hbar \Omega_i^{(s)}(t) \cos(2kZ)$$

where  $\mathbf{P}$  is the center-of-mass momentum operator,  $M$  is the atomic mass, and

$$\Omega_i^{(s)}(t) = \frac{\mu^2 E_i^2(t)}{8\hbar^2 \delta}$$

is a two-photon Rabi frequency. A spatially homogeneous term has been dropped from the hamiltonian.

The net effect of the field is to produce a spatially modulated, AC Stark or light shift of the ground state energy. Let us assume that the pulse duration  $\tau$  is sufficiently short to ensure that  $\tau^{-1} \gg \omega_{2k}, \gamma, \gamma_2, k u, \sqrt{\omega_{2k} \Omega_i^{(s)}(t)}$ , where

$$\omega_{2k} = \frac{\hbar(2k)^2}{2M}$$

is a two-photon recoil frequency whose importance will become apparent. In this limit, any motion of the atoms during the pulses can be neglected. The net effect of pulse  $i$  is to produce a ground state amplitude that varies as  $\exp[i\theta_i^{(s)} \cos(2kZ)]$ , where  $\theta_i^{(s)} = \int \Omega_i^{(s)}(t) dt$  is a pulse area. In other words, the standing-wave field acts as a *phase grating* for the atoms. One can think of the two traveling-wave

components of the standing-wave field exchanging momentum via the atoms. All even integral multiples of  $2\hbar k$  can be exchanged by the fields, imparting impulsive momenta of  $2n\hbar k$  ( $n$  is a positive or negative integer) to the atoms. The frequency change associated with this momentum change for an atom having momentum  $\mathbf{P}$  is

$$\frac{E_{\mathbf{P}, \mathbf{P} \pm 2n\hbar k \hat{z}}}{\hbar} = \frac{\left( \frac{p^2}{2M} \frac{|\mathbf{P} \pm 2n\hbar k \hat{z}|^2}{2M} \right)}{\hbar} = \mp \frac{2nP_z k}{M} - \omega_{2nk}$$

and consists of two parts. The first part is independent of  $\hbar$  and represents a classical Doppler shift, while the second part is proportional to  $\hbar$  and represents a quantum matter-wave effect. The quantum contribution will become important for times of order  $\omega_{2nk}^{-1}$ . In other words, following the first pulse, the atomic density will remain approximately constant for times  $t < \omega_{2nk}^{-1}$  (the maximum value of  $n$  is the larger of  $\theta_i^{(s)}$  and unity). For times larger than this, the quantum evolution of the center-of-mass motion can transform the phase grating into an amplitude grating which can be deposited on a substrate or probed with optical fields. In contrast to closed two-level systems, the signals can persist here for arbitrarily long times. The recoil associated with absorption and emission “opens” the system and allows for long-lived transients.<sup>87</sup>

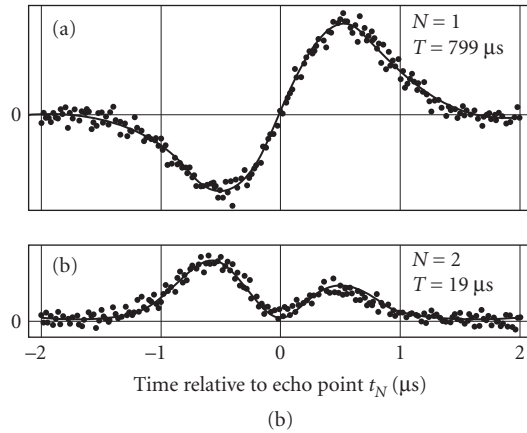
The evolution of the system can be followed using phase diagrams in a manner similar to that used in Secs. 11.6 to 11.8. The situation is more complex, however, since a standing-wave field generates an infinity of different phase shifts  $\mp 2nkvt$ , where  $v = P_z/M$ . Details of the calculation can be found in the article by Cahn et al.<sup>84</sup> Here we sketch the general idea. The first pulse creates all even spatial harmonics of the fields, with weighting functions that are Bessel functions of the pulse area. The atomic density remains constant until a time  $t \sim \omega_{2nk}^{-1}$ . At this time one would expect to find a spatially modulated atomic density; however, if  $ku \gg \omega_{2k}$  as is assumed, by the time the spatial modulation is established, the modulation is totally destroyed as a result of Doppler dephasing. As in the photon echo experiment, the Doppler dephasing can be reversed by the second pulse at time  $t = T$ . Since standing waves are used, there is an infinity of echo positions possible, corresponding to different dephasing-rephasing conditions for the various momentum components created by the fields.

Of the many echoes that can be produced, we consider only those echoes that are formed at times  $t_N = (N+1)T$ ,  $N=1, 2, \dots$ . Moreover, in an expansion of the atomic density in harmonics of the field, we keep only the second harmonic, since it can be probed by sending in a traveling-wave field and observing a *backscattered* signal. Phase matching is automatically guaranteed for the backscattered signal. For times  $t = t_N + t_d$  with  $t_d \approx \frac{1}{2}ku \ll T$ , the backscattered electric field amplitude varies as<sup>84</sup>

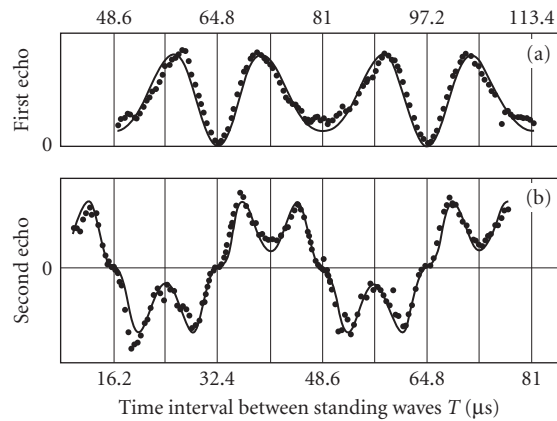
$$E_b(t_d, NT) = \exp\left[\frac{-(2k)^2 u^2 (t_d)^2}{4}\right] J_N[2\theta_1 \sin(\omega_{2k} t_d)] J_{N+1}[2\theta_2 \sin(N\omega_{2k} T + \omega_{2k} t_d)] \quad (46)$$

where the  $J$ s are Bessel functions. The electric field can be measured using a heterodyne technique. The experimental data is shown as a function of  $t_d$  and  $T$  for  $N = 1, 2$  in Figs. 13 and 14. One sees that the signal vanishes identically at the echo times, but not in the immediate vicinity of the echo points. The uniform atomic density at the echo point mirrors the uniform atomic density immediately after excitation by the first pulse. As a function of  $T$ , the signal is periodic with period  $\pi/N\omega_{2k}$  for  $N$  odd and  $2\pi/N\omega_{2k}$  for  $N$  even. By measuring the period, one can obtain values for  $\hbar/M$ . The interferometer can also be used to measure inertial effects such as the acceleration of the atoms owing to gravity. The advantage of this interferometer is that large interaction times are possible—one is limited only by the time it takes for the atoms to leave the atom-field interaction zone.





**FIGURE 13** A time-domain atom interferometer. Two off-resonant, standing-wave optical pulses separated in time by  $T$  are applied to rubidium atoms in a magneto-optical trap and a probe field is applied near (a)  $t = 2T$  or (b)  $t = 3T$ , giving rise to backscattered electric field signals. The electric field amplitude  $E_b(t_p, NT)$  is recorded in the graphs as a function of  $t_p$ , the time from the echo position. The solid line is theory and the dots are experimental points. Note that the time delay between pulses is  $799 \mu\text{s}$  in (a), indicating that these ground-state transients are limited only by some effective ground-state lifetime. (From Ref. 84. Reprinted with permission.)



**FIGURE 14** Same as in Fig. 13, but  $E_b(t_p, NT)$  is now recorded as a function of  $T$ , the time separation of the pulses. The period of the signals is  $\pi\omega_{2k} = 32.39 \mu\text{s}$ . (From Ref. 84. Reprinted with permission.)

## 11.10 CHIRPED PULSE EXCITATION

The discussion in this chapter has focused on transform-limited optical pulses, possessing smooth Fourier transforms centered about the carrier frequency. Alternative pulse shapes offer new and interesting possibilities. If one uses *stochastic* pulse envelope functions,<sup>88–90</sup> the correlation time  $\tau_c$  associated with the pulse is much smaller than the pulse duration. In some sense, *each* pulse can be viewed as a sequence of pulses having duration of order  $\tau_c$ . As a consequence, stimulated photon echoes using stochastic pulses can be used to measure relaxation times as short as  $\tau_c$  rather than the pulse duration.

The idea of using a pulse whose effective coherence time is shorter than the pulse duration has been exploited by others<sup>91–93</sup> in schemes involving chirped pulses. It was shown both theoretically<sup>91</sup> and experimentally<sup>92,93</sup> that, by sweeping the pulse frequency, one can write and read data encoded in solids, using the equivalent of stimulated echoes, a process Mossberg<sup>91</sup> refers to as *swept-carrier time-domain optical memory*. Without going into the mathematical details of the calculations needed to arrive at expressions for the signals, we present the underlying physical concepts pertinent to this excitation scheme.

There are three pulses, as in a traditional stimulated photon echo, but the pulse characteristics differ markedly from those discussed in Sec. 11.7. The first pulse is a reference pulse having electric field

$$\mathbf{E}_1(\mathbf{R}, t) = \epsilon E_1(t) \cos(\mathbf{k}_1 \cdot \mathbf{R} - \bar{\omega}_0 t - \xi t^2)$$

where the amplitude  $E_1(t)$  is a smooth function of  $t$  centered at  $t = 0$  having temporal width  $\tau_{\text{ref}}$  and  $\phi(t) = -\xi t^2$  is the pulse phase. The central frequency of the pulse coincides with the optical frequency, but the frequency is chirped at rate  $2\xi$ , giving an instantaneous frequency  $\omega(t) = \omega - \dot{\phi} = \omega + 2\xi t$  and an atom-field detuning  $\delta(t) = \Delta - 2\xi t$ . The frequency shifts  $\pm \xi \tau_{\text{ref}}$  are assumed to be less than the inhomogeneous width  $\sigma_w$ . As the frequency is scanned, different atoms in the inhomogeneous distribution in the sample come into resonance with the field at different times. If  $\sqrt{\xi} \gg \gamma, \tau_{\text{ref}}^{-1}$ , for atoms having detuning  $\Delta = \omega_0 - \omega$ , the field comes into resonance at time  $t_1 = \Delta/2\xi$  for a duration of order  $\xi^{-1/2} \ll \tau_{\text{ref}}$ . Thus, for each frequency group of atoms, the field acts as a *pulse having temporal width much less than the width of the pulse*. In calculating  $\rho_{12}$  resulting from this pulse one finds a phase factor of the form  $\exp[i(-\mathbf{k}_1 \cdot \mathbf{R} + \Delta t_1 - \xi t_1^2)] = \exp[-i(\mathbf{k}_1 \cdot \mathbf{R} - \Delta^2/4\xi)]$ .

The second or data pulse

$$\mathbf{E}_2(\mathbf{R}, t) = \epsilon E_2(t) \cos[\mathbf{k}_2 \cdot \mathbf{R} - (\bar{\omega}_0 - \omega_{\text{RD}})t - \xi t^2]$$

is similar to the first except that it is offset from the first by frequency  $\omega_{\text{RD}}$ . Moreover, the field amplitude  $E_2(t)$  is now assumed to consist of a sequence of input data, such as a number of individual pulses contained in the overall pulse envelope. If the Fourier spectrum of  $E_2(t)$  contains frequency components  $\omega_f$ , then the second pulse will come into resonance with atoms having detuning  $\Delta$  at time  $t_2 = (\Delta + \omega_{\text{RD}} - \omega_f)/2\xi$ . To have pulse 2 act on the same atoms at a time greater than  $t_1$ , one must restrict the maximum value of  $\omega_f$  to be less than  $\omega_{\text{RD}}$ . We shall neglect  $\omega_f$  in what follows. For each frequency group, the first two pulses act as a *sequence of short pulses*, separated in time by

$$T_{21} = \omega_{\text{RD}}/2\xi$$

As in the normal stimulated photon echo, the second pulse converts the density matrix element  $\rho_{12}$  created by the first pulse into population. One finds a population difference  $(\rho_{22} - \rho_{11})$  that varies as  $\exp[-i(\mathbf{k}_1 \cdot \mathbf{R} - \Delta^2/4\xi)] \exp(-\gamma T_{21}) \exp\{i[\mathbf{k}_2 \cdot \mathbf{R} - (\Delta + \omega_{\text{RD}})^2/4\xi]\} + \text{c.c.}$  Although the pulse durations are of order  $\tau_{\text{ref}}$  homogeneous decay occurs only on a time scale  $T_{21} = \omega_{\text{RD}}/2\xi \ll \tau_{\text{ref}}$  which is

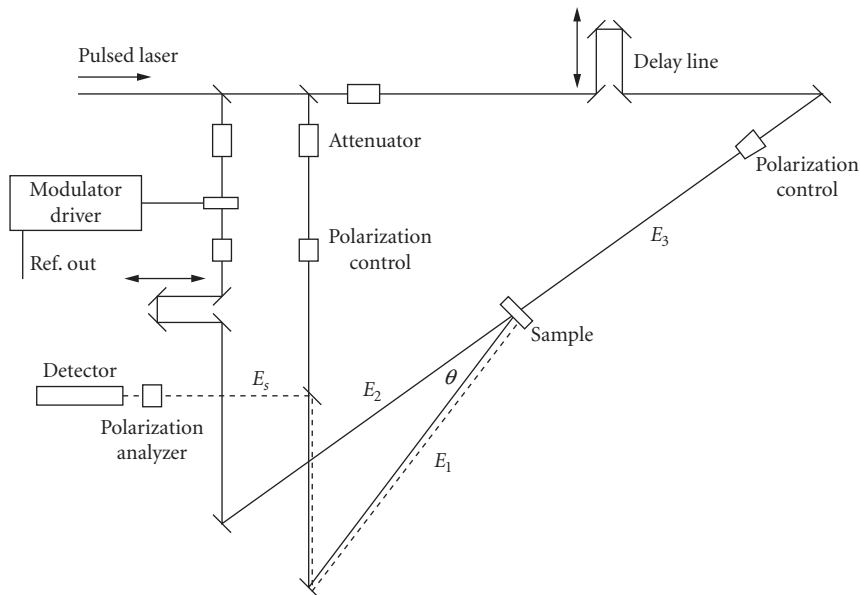
the effective pulse separation for a given frequency group. The phase factor  $\exp\{i[(\mathbf{k}_2 - \mathbf{k}_1) \cdot \mathbf{R} - \Delta T_{21}]\}$  associated with  $(\rho_{22} - \rho_{11})$  is identical in form to that found in the normal stimulated photon echo. It is not surprising then that a third pulse, identical to the first but propagating in the  $\mathbf{k}_3$  direction and displaced in time from the first by  $T > \tau_{\text{ref}}$ , leads to a reconstruction of the data pulse propagating in the  $(-\mathbf{k}_1 + \mathbf{k}_2 + \mathbf{k}_3)$  direction. In other words, on averaging over the inhomogeneous frequency distribution, one finds contributions to the signal only for those times that correspond to the time sequence of pulse 2, displaced by time  $T$ .

## 11.11 EXPERIMENTAL CONSIDERATIONS

Early coherent optical transient experiments were the optical analogs of NMR experiments. These experiments firmly established coherent transient spectroscopy as a viable technique in the optical domain. The relatively simple atomic and molecular vapors or rare earth-doped crystals that were used for these studies were chosen for practical reasons—their transition frequencies coincided with available laser frequencies and relaxation times ( $T_2$  is typically on the order of 10 ns or longer) were longer than the lasers' pulse widths. The methodology is well described in numerous earlier reviews (see, for example, Levenson<sup>9</sup>). These relaxation time scales are relatively long by today's standards. Hence, the technology that was available based on photomultipliers, high-speed diodes, and fast oscilloscopes made it possible to observe the coherent transient phenomena that were created by fast laser-frequency or Stark switching. With high-speed detectors, photon echoes were readily observed with single-shot  $Q$ -switched lasers.

The continued advances in the development of ultrafast lasers have now reduced the pulse widths by nearly 6 orders of magnitude compared to the early  $Q$ -switched lasers. In addition, modern laser systems are characterized by high repetition rates (100 MHz if no amplification is used) compared to the relatively slow repetition rates of older laser systems (1 to 10 Hz). Ultrafast lasers have opened a host of possibilities for studying complex molecules, fluids, and solids, including semiconductors. This new capability was accompanied by new challenges, since standard detectors and electronics were not capable of time-resolving the emitted signals. In some cases, it was not even known whether the materials being investigated were homogeneously or inhomogeneously broadened. For these cases, it is important to check for the asymmetry predicted as a function of time delay in the stimulated photon echo, as described in Sec. 11.7. For the very shortest pulses (typically  $< 100$  fs), even the simplest laboratory operations of reflection from a mirror or transmission through a cryostat window or beam splitter become an issue. The transform-limited pulse bandwidth is so large that the linear dispersion in these systems leads to a chirp in the pulse, which can give rise to artifacts in the data if the chirp is not compensated at the sample by incorporation of grating or prism pairs in the system. High-repetition-rate systems also can give rise to thermal heating of the sample, leading to gratings which give signals that easily dominate the electronic signals of interest. Discrimination against these signals is critical. Sometimes, it is possible to perform the measurements of interest using orthogonally polarized fields, giving rise to a signal that is sensitive to spatially modulated magnetic-state coherence, but not thermal gratings. An alternative approach is to amplitude modulate one of the optical fields at a high frequency and use phase-sensitive detection. If the modulation frequency chosen is sufficiently high, then the modulation of the thermal grating is weak, and the electronic term dominates.

In the case of photon echo spectroscopy, determining the time origin  $t = 0$  is important for accurate analysis of the signals. Although this does not pose any serious technical problems when dealing with nanosecond time-scale resolution, for femtosecond laser pulses, where distance scales can be as small as a few microns, the problem is not trivial. One solution, discussed in a recent review of photon echo spectroscopy,<sup>73</sup> is to measure the time-integrated signal as a function of pulse separation for the ordinary signal (in the  $2\mathbf{k}_2 - \mathbf{k}_1$  direction for self-diffracted four-wave mixing) and the complimentary echo (in the  $2\mathbf{k}_1 - \mathbf{k}_2$  direction). The intersection of the two superimposed mirror images allows one to determine the time origin. In some cases, it may be necessary to time-resolve the emission either to confirm absolutely that the signal is indeed an echo or to determine the



**FIGURE 15** A typical experimental configuration, employing a high-repetition short-pulse laser system, that can be used for stimulated photon echo or transient four-wave mixing studies of an arbitrary sample.

inhomogeneous broadening. The usual approach to achieve this goal is to mix some of the original laser beam with the signal beam in a second harmonic crystal and detect the upconverted signal. The signal is time resolved by measuring the upconverted signal as a function of delay between the signal and reference fields.<sup>94,95</sup>

An experimental configuration incorporating many of these features is shown in Fig. 15. Measurements of the dephasing rate are made by monitoring the signal amplitude as a function of time delay between fields  $E_1$  and  $E_2$ , while measurements of the energy relaxation rate are made as a function of the time delay between fields  $E_2$  and  $E_3$ . In the latter case, measurement of the relaxation rate as a function of the angle between fields  $E_1$  and  $E_2$  allows one to measure the grating (e.g., spatially modulated population) relaxation rate, due, for example, to diffusion.<sup>96</sup> Control of the fields' polarizations is essential in these experiments since the allowed electronic excitation depends critically on the selection rules. The modulator is used to amplitude modulate one of the optical fields to allow phase-sensitive detection. Because of scattering, it may also be necessary in some cases to modulate field  $E_1$  at a different frequency and detect the sum or difference frequency in the lock-in amplifier. The forward three-pulse geometry is most prevalent in the literature; however, the more recently developed phase conjugate geometry shown in the figure is more desirable, owing to reduced incoherent scattering into the detector. In addition, this system is much easier to align, since the signal is exactly counterpropagating with respect to field  $E_2$ . Usually, the feedback into the oscillator for spectroscopy applications is small because of the presence of the attenuators. However, for high-intensity studies it may be necessary to add an optical isolator to eliminate feedback, or, as is more typical, simply arrange for a slight misalignment of fields  $E_1$  and  $E_3$ . This results in a slight deviation of the signal field from the  $-\mathbf{k}_2$  direction, but this poses no problem. It should also be noted that for ultrafast laser systems, the narrow pulses may experience group velocity dispersion (GVD) in propagating through various optical components and in reflection, requiring GVD compensation to avoid artifacts due to frequency chirps. In some cases, additional information can be obtained by time-resolving the optical phase<sup>97</sup> and/or polarization<sup>98</sup> of the signal, both of which may change during the time interval in which the signal is emitted.

Atoms undergoing collisions in a vapor and rare earth-doped solids provided a convenient laboratory environment both to study coherent transients and to examine new physical phenomena associated with reservoir interactions. Moreover, such studies allowed one to gain theoretical and experimental insights upon which the new technology could build. It has now been possible to elevate the utility of these spectroscopic tools for application to more complex systems. In particular, coherent optical transients have yielded important data in both chemical physics<sup>99,100</sup> and condensed-matter physics.<sup>101</sup> In many cases, the theoretical framework described here, with appropriate refinements of the unperturbed hamiltonian and reservoir interactions, can adequately model these systems. For example, local field corrections and excitation-induced scattering can be accounted for by a relatively simple modification of the optical Bloch equations. As a result, additional phase diagrams, with time orderings different from those shown in Figs. 10 and 11, can contribute to echo signals.<sup>102</sup> However, in other cases, a major revision of the theoretical picture is needed to account for more complex many-body interactions.<sup>103–105</sup> An approach based on modified optical Bloch equation may not be appropriate in this limit.

## 11.12 CONCLUSION

Information on level structure and relaxation processes in vapors, solids, and liquids can be extracted from coherent optical transient signals. The most basic coherent optical transients have been reviewed in this chapter. Coherent optical transient spectroscopy is still an evolving field, as new techniques are being added to established ones. It is likely that one will see increased use of both temporal and spatial masks for coherent control of atomic state coherence. Although many of the coherent optical transients are direct analogs of similar effects in NMR, others are unique to the optical domain. The velocity selectivity associated with the Doppler effect offers unique possibilities. Velocity diffusion has been studied extensively using coherent optical transients, and coherent optical transients are being rediscovered as an important probe of cold atoms and Bose condensates.<sup>106,107</sup> Beyond the gas phase, developments in the area of coherent optical transient spectroscopy are moving very rapidly, as the power of this methodology is seen as a key that can help unlock the decay dynamics of complex molecules and semiconductor systems. One is also examining whether coherent optical transient methods similar to those employed in multidimensional NMR<sup>108,109</sup> can be used to probe electronic and molecular structure.

## 11.13 REFERENCES

1. H. Metcalf and W. D. Phillips, "Time-Resolved Subnatural-Width Spectroscopy," *Opt. Lett.* **5**:540 (1980); W. D. Phillips and H. J. Metcalf, "Time Resolved Sub-Natural Width Spectroscopy," in *Precision Measurements and Fundamental Constants II*, B. N. Taylor and W. D. Phillips (eds.), U.S. National Bureau of Standards Special Publication 617 (1984).
2. R. G. Brewer, "Coherent Optical Spectroscopy," in *Frontiers in Laser Spectroscopy* (Les Houches, Session 27), R. Balian, S. Haroche, and S. Liberman (eds.) (North-Holland, Amsterdam, 1977), Vol. 1, pp. 341–396.
3. R. G. Brewer, "Coherent Optical Spectroscopy," in *Nonlinear Spectroscopy* (Proc. Int. School Phys., Enrico Fermi, Course 64), N. Bloembergen (ed.) (North-Holland, Amsterdam, 1977).
4. R. G. Brewer, "Coherent Optical Transients," *Physics Today* **30**(5):50 (1977).
5. R. L. Shoemaker, "Coherent Transient Infrared Spectroscopy," in *Laser and Coherence Spectroscopy*, J. I. Steinfeld (ed.) (Plenum Press, New York, 1978), pp. 197–371.
6. R. G. Brewer and E. L. Hahn, "Optical Memory," *Scientific American* **271**(6):50 (1984).
7. Special issue on coherent optical spectroscopy, *J. Opt. Soc. Amer.* **3**(4) (1986).
8. L. Allen and J. Eberly, *Optical Resonance and Two-Level Atoms* (Wiley, New York, 1975), Chaps. 2, 4, and 9.
9. M. D. Levenson and S. S. Kano, *Introduction to Nonlinear Laser Spectroscopy* (Academic Press, Boston, 1988), Chap. 6.

10. P. Meystre and M. Sargent III, *Elements of Quantum Optics* (Springer-Verlag, Berlin, 1991), Chap. 11.
11. T. W. Mossberg, R. Kachru, S. R. Hartmann, and A. M. Flusberg, "Echoes in Gaseous Media: A Generalized Theory of Rephasing Phenomena," *Phys. Rev. A* **20**:1976 (1979).
12. W. Zinth and W. Kaiser "Ultrafast Coherent Spectroscopy," in *Ultrashort Laser Pulses and Applications*, W. Kaiser (ed.), Vol. 60, Springer Topics in Applied Physics series (Springer-Verlag, Berlin, 1988), pp. 235–277.
13. Special issue on single-molecule spectroscopy, *Science* **283**:1167–1694 (1999).
14. R. P. Feynman, F. L. Vernon, Jr., and R. W. Hellwarth, "Geometrical Representation of the Schrödinger Equation for Solving Maser Problems," *J. Appl. Phys.* **28**:49 (1957).
15. R. G. Brewer and E. L. Hahn, "Coherent Raman Beats," *Phys. Rev. A* **8**:464 (1973).
16. P. Hu, S. Geschwind, and T. M. Jedju, "Spin-Flip Raman Echo in *n*-Type Cds," *Phys. Rev. Lett.* **37**:1357 (1976).
17. T. Mossberg, A. Flusberg, R. Kachru, and S. R. Hartmann, "Tri-Level Echoes," *Phys. Rev. Lett.* **39**:1523 (1977).
18. M. Ducloy, J. R. R. Leite, and M. S. Feld, "Laser Saturation Spectroscopy in the Time-Delayed Mode: Theory of Optical Free Induction Decay in Coupled Doppler-Broadened Systems," *Phys. Rev. A* **17**:623 (1978).
19. N. Lu and P. R. Berman, "Photon Echoes Using Double-Resonance Optical Pulses," *J. Opt. Soc. Amer. B* **2**:1883 (1985).
20. I. V. Yevseyev, V. M. Yermachenko, and V. A. Reshtov, "The Stimulated Photon Echo as a New Method for Measuring Population, Orientation, and Alignment Relaxation Times," *J. Phys. B* **19**:185 (1986).
21. See, for example, R. Boyd, *Nonlinear Optics* (Academic Press, Boston, 1992), Chap. 6, and references therein.
22. See, for example, Y. R. Shen, *The Principles of Nonlinear Optics* (Wiley, New York, 1984), Chap. 17, and references therein.
23. See, for example, J. F. Valley, G. Khitrova, H. M. Gibbs, J. W. Grantham, and X. Jiajin, "CW Conical Emission: First Comparison and Agreement between Theory and Experiment," *Phys. Rev. Lett.* **64**:2362 (1990), and references therein.
24. See, for example, B. D. Paul, M. L. Dowell, A. Gallagher, and J. Cooper, "Observation of Conical Emission from a Single Self-Trapped Beam," *Phys. Rev. A* **59**:4784 (1999), and references therein.
25. A. I. Lvovsky and S. R. Hartmann, "Superradiant Self-Diffraction," *Phys. Rev. A* **59**:4052 (1999).
26. R. G. Brewer and R. L. Shoemaker, "Optical Free Induction Decay," *Phys. Rev. A* **6**:2001 (1972).
27. R. G. Brewer and A. Z. Genack, "Optical Coherent Transients by Laser Frequency Switching," *Phys. Rev. Lett.* **36**:959 (1976).
28. H. Lehmitz and H. Harde, "Measurement of First-Order Free-Induction Decay," in *Methods of Laser Spectroscopy*, Y. Prior, A. Ben-Reuven, and M. Rosenbluh (eds.) (Plenum Press, New York, 1986), pp. 109–112.
29. P. Dubé, M. D. Levenson, and J. L. Hall, "Free-Induction Decay in Molecular Iodine Measured with an Extended-Cavity Diode Laser," *Opt. Lett.* **22**:184 (1997).
30. R. M. Macfarlane and M. Zhu, "Observation of Coherent Transients by Use of Current Switching of a Semiconductor Diode Laser," *Opt. Lett.* **22**:248 (1997).
31. A. Abragam, *The Principles of Nuclear Magnetism* (Oxford University Press, New York, 1961).
32. C. P. Slichter, *Principles of Magnetic Resonance* (Harper & Row, New York, 1963).
33. R. H. Dicke, "Coherence in Spontaneous Radiation Processes," *Phys. Rev.* **93**:99 (1954).
34. See, for example, I. P. Herman, J. C. MacGillivray, N. Skribanowitz, and M. S. Feld, "Self-Induced Emission in Optically Pumped HF Gas: The Rise and Fall of the Superradiant State," in *Laser Spectroscopy*, R. G. Brewer and A. Mooradian (eds.) (Plenum Press, New York, 1974), pp. 379–412.
35. D. Polder, M. F. H. Schuurmans, and Q. H. F. Vreken, "Superfluorescence: Quantum-Mechanical Derivation of Maxwell-Bloch Description with Fluctuating Field Source," *Phys. Rev. A* **19**:1192 (1979).
36. N. A. Kurnit, I. D. Abella, and S. R. Hartmann, "Observation of a Photon Echo," *Phys. Rev. Lett.* **13**:567 (1964).
37. R. G. Brewer and R. L. Shoemaker, "Photon Echo and Optical Nutation in Molecules," *Phys. Rev. Lett.* **27**:631 (1971).
38. L. S. Vasilenko and N. N. Rubtsova, "Photon Echo in Molecular Gases: I. Spatial, Temporal, Polarization, and Spectral Properties, II. Investigation of Collisional Relaxation," *Laser Phys.* **6**:821 (1996); **7**:903 (1997), and references therein.

39. E. L. Hahn, "Spin Echoes," *Phys. Rev.* **80**:580 (1950).
40. P. R. Berman, "Theory of Collision Effects on Line Shapes Using a Quantum-Mechanical Description of the Atomic Center-of-Mass Motion—Application to Lasers. I," *Phys. Rev. A* **2**:2435 (1970).
41. R. Beach, S. R. Hartmann, and R. Friedberg, "Billiard Ball Echo Model," *Phys. Rev. A* **25**:2658 (1982); R. Friedberg and S. R. Hartmann, "Billiard Balls and Matter-Wave Interferometry," *Phys. Rev. A* **48**:1446 (1993); "Echoes and Billiard Balls," *Laser Phys.* **3**:1128 (1993). See also T. W. Mossberg and S. R. Hartmann, "Diagrammatic Representation of Photon Echoes and Other Laser-Induced Ordering Processes in Gases," *Phys. Rev. A* **23**:1271 (1981).
42. C. J. Bordé, "Atomic Interferometry with Internal State Labeling," *Phys. Lett. A* **140**:10 (1989).
43. R. Friedberg and S. R. Hartmann, "Relaxation and Interferometry via Multiple Order Coherent Scattering in Atomic Vapors," *Laser Phys.* **5**:526 (1993).
44. P. R. Berman (ed.), *Atom Interferometry* (Academic Press, San Diego, 1997).
45. P. W. Anderson, B. I. Halperin, and C. M. Varma, "Anomalous Low Temperature Thermal Properties of Glasses and Spin Glasses," *Phil. Mag.* **25**:1 (1972).
46. W. M. Yen and P. M. Silzer (eds.), *Laser Spectroscopy of Solids*, Vol. 49, Springer Topics in Applied Physics series (Springer-Verlag, Berlin, 1986).
47. P. R. Berman, "Validity Conditions for the Optical Bloch Equations," *J. Opt. Soc. Amer. B* **3**:564 (1986), and references therein.
48. P. R. Berman, "Markovian Relaxation Processes for Atoms in Vapors and in Solids: Calculation of Free-Induction Decay in the Weak External-Field Limit," *J. Opt. Soc. Amer. B* **3**:572 (1986), and references therein.
49. P. R. Berman, in *New Trends in Atomic Physics* (Les Houches, Session 38), G. Grynberg and R. Stora (eds.) (North-Holland, Amsterdam, 1984), Vol. 1, pp. 451–514.
50. R. G. Devoe and R. G. Brewer, "Experimental Test of the Optical Bloch Equations for Solids," *Phys. Rev. Lett.* **50**:1269 (1983).
51. P. R. Berman, J. M. Levy, and R. G. Brewer, "Coherent Optical Transient Study of Molecular Collisions: Theory and Observations," *Phys. Rev. A* **11**:1668 (1975).
52. T. W. Mossberg, R. Kachru, and S. R. Hartmann, "Observation of Collisional Velocity Changes Associated with Atoms in a Superposition of Dissimilar Electronic States," *Phys. Rev. Lett.* **44**:73 (1980).
53. R. Kachru, T. J. Chen, S. R. Hartmann, T. W. Mossberg, and P. R. Berman, "Measurement of a Total Atomic-Radiator-Perturber Scattering Cross Section," *Phys. Rev. Lett.* **47**:902 (1981).
54. R. A. Forber, L. Spinelli, J. E. Thomas, and M. S. Feld, "Observation of Quantum Diffractive Velocity-Changing Collisions by Use of Two-Level Heavy Optical Radiators," *Phys. Rev. Lett.* **50**:331 (1982).
55. J. C. Keller and J. L. LeGouët, "Stimulated Photon Echo for Collisional Study in Yb Vapor," *Phys. Rev. Lett.* **52**:2034 (1984).
56. A. G. Yodh, J. Golub, and T. W. Mossberg, "Collisional Relaxation of Excited State Zeeman Coherences in Atomic Ytterbium Vapor," *Phys. Rev. A* **32**:844 (1985).
57. R. Kachru, T. W. Mossberg, and S. R. Hartmann, "Stimulated Photon Echo Study of Na( $3^2S_{1/2}$ )-CO Velocity-Changing Collisions," *Opt. Comm.* **30**:57 (1979).
58. T. Mossberg, A. Flusberg, R. Kachru, and S. R. Hartmann, "Total Scattering Cross Section for Na on He Measured by Stimulated Photon Echoes," *Phys. Rev. Lett.* **42**:1665 (1979).
59. T. W. Mossberg, "Time-Domain Frequency-Selective Optical Storage Data," *Opt. Lett.* **7**:77 (1982).
60. N. W. Carlson, W. R. Babbitt, and T. W. Mossberg, "Storage and Phase Conjugation of Light Pulses Using Stimulated Photon Echoes," *Opt. Lett.* **8**:623 (1983).
61. M. K. Kim and R. Kachru, "Long Term Image Storage and Phase Conjugation by a Backward-Stimulated Echo in Pr<sup>3+</sup>LaF<sub>3</sub>," *J. Opt. Soc. Amer. B* **4**:305 (1987).
62. X. A. Shen and R. Kachru, "High Speed Recognition by Using Stimulated Echoes," *Opt. Lett.* **17**:520 (1992).
63. L. S. Vasilenko, N. M. Dyuba, and M. N. Skvortsov, "Coherent Emission in Time-Separated Fields," *Sov. J. Quant. Electron.* **8**:980 (1978).
64. Y. V. Baklonov, B. Y. Dubetsky, and V. P. Chebotayev, "Non-linear Ramsey Resonance in the Optical Region," *Appl. Phys.* **9**:171 (1976).

65. E. V. Baklonov, B. Y. Dubetsky and V. M. Semibalamut, "Theory of Stimulated Coherent Emission from Atoms in Spatially Separated Optical Fields," *Sov. Phys. JETP* **49**:244 (1979).
66. T. W. Mossberg, R. Kachru, E. Whittaker, and S. R. Hartmann, "Temporally Recurrent Spatial Ordering of Atomic Population in Gases: Grating Echoes," *Phys. Rev. Lett.* **43**:851 (1979).
67. J. L. LeGouët and P. R. Berman, "Photon Echoes in Standing Wave Fields: Time Separation of Spatial Harmonics," *Phys. Rev. A* **20**:1105 (1979).
68. R. Kachru, T. W. Mossberg, E. Whittaker, and S. R. Hartmann, "Optical Echoes Generated by Standing Wave Fields: Observations in Atomic Vapors," *Opt. Comm.* **31**:223 (1979).
69. M. V. Belyayev, V. P. Chebotaev, M. N. Skvortsov, and L. S. Vasilenko, "Resonant Coherent Transients in a Gas in the Standing Wave Field," *Appl. Phys. B* **26**:67 (1981).
70. L. S. Vasilenko, I. D. Matveyenko, and N. N. Rubtsova, "Study of Narrow Resonances of Coherent Radiation in Time Separated Fields in SF<sub>6</sub>," *Opt. Comm.* **53**:371 (1985).
71. B. Dubetsky, P. R. Berman, and T. Sleator, "Grating Stimulated Echo," *Phys. Rev. A* **46**:2213 (1992).
72. P. R. Berman, "Collisional Decay and Revival of the Grating Stimulated Echo," *Phys. Rev. A* **49**:2922 (1994).
73. A. M. Weiner, S. De Silvestri, and E. P. Ippen, "Three-Pulse Scattering for Femtosecond Dephasing Studies: Theory and Experiments," *J. Opt. Soc. Amer. B* **2**:624 (1985).
74. M. Fujita, H. Nakatsuka, H. Nakanishi, and M. Matsuoka, "Backward Echo in Two-Level Systems," *Phys. Rev. Lett.* **42**:974 (1979).
75. A. I. Alekseev and V. N. Beloborodov, "Forward and Backward Photon Echoes in Gases and Solids," *Opt. Spectrosc.* **57**:277 (1984).
76. R. A. Fisher (ed.), *Optical Phase Conjugation* (Academic Press, New York, 1983).
77. M. Gower and D. Proch (eds.), *Optical Phase Conjugation* (Springer-Verlag, Berlin, 1994).
78. J. C. Bergquist, S. A. Lee, and J. L. Hall, "Saturated Absorption with Spatially Separated Laser Fields: Observation of Optical 'Ramsey' Fringes," *Phys. Rev. Lett.* **38**:159 (1977), and references therein.
79. R. L. Barger, "Influence of Second-Order Doppler Effect on Optical Ramsey Fringe Profiles," *Opt. Lett.* **6**:145 (1981).
80. C. J. Bordé, C. Salomon, S. Avrillier, A. Van Lerberghe, C. Bréant, D. Bassi, and G. Scoles, "Optical Ramsey Fringes with Traveling Waves," *Phys. Rev. A* **30**:1836 (1984).
81. N. Ramsey, "A Molecular Beam Resonance Method with Separated Oscillating Fields," *Phys. Rev.* **78**:695 (1950).
82. N. Ito, J. Ishikawa, and A. Morinaga, "Evaluation of the Optical Phase Shift in a Ca Ramsey Fringe Stabilized Optical Frequency Standard by Means of Laser Beam Reversal," *Opt. Comm.* **109**:414 (1994).
83. B. Y. Dubetsky, A. P. Kazantsev, V. P. Chebotaev, and V. P. Yakolev, "Interference of Atoms in Separated Optical Fields," *Sov. Phys. JETP* **62**:685 (1985).
84. S. B. Cahn, A. Kumarakrishnan, U. Shim, T. Sleator, P. R. Berman, and B. Dubetsky, "Time-Domain de Broglie Wave Interferometry," *Phys. Rev. Lett.* **79**:784 (1997).
85. E. M. Rasel, M. K. Oberthaler, H. Batelaan, J. Schmiedmayer, and A. Zeilinger, "Atom Wave Interferometry with Diffraction Gratings of Light," *Phys. Rev. Lett.* **75**:2633 (1995).
86. B. Dubetsky and P. R. Berman, "Matter-Wave Interference Using Two-Level Atoms and Resonant Optical Fields," *Phys. Rev. A* **59**:2269 (1999).
87. J. Guo, P. R. Berman, D. Dubetsky, and G. Grynberg, "Recoil-Induced Resonances in Nonlinear Spectroscopy," *Phys. Rev. A* **46**:1426 (1992).
88. R. Beach and S. R. Hartmann, "Incoherent Photon Echoes," *Phys. Rev. Lett.* **53**:663 (1984).
89. M. Mitsunaga, "CW Photon Echo: Theory and Observations," *Phys. Rev. A* **42**:1617 (1990).
90. See, for example, B. Do, J. Cha, D. S. Elliott, and S. J. Smith, "Phase Conjugate Four Wave Mixing with Partially-Coherent Laser Fields," *Phys. Rev. A* **60**:508 (1999). This paper contains an extensive bibliography citing earlier work in this field.
91. T. W. Mossberg, "Swept-Carrier Time-Domain Optical Memory," *Opt. Lett.* **17**:535 (1992).
92. H. Lin, T. Wang, G. A. Wilson, and T. W. Mossberg, "Experimental Demonstration of Swept-Carrier Time-Domain Optical Memory," *Opt. Lett.* **20**:91 (1995).



93. K. D. Merkel and W. R. Babbitt, "Chirped-Pulse Programming of Optical Coherent Transient True-Time Delay," *Opt. Lett.* **23**:528 (1998).
94. L. Schultheis, M. D. Sturge, and J. Hegarty, "Photon Echoes from Two-Dimensional Excitons in GaAs-AlGaAs Quantum Wells," *Appl. Phys. Lett.* **47**:995 (1985).
95. M. D. Webb, S. T. Cundiff, and D. G. Steel, "Observation of Time-Resolved Picosecond Stimulated Photon Echoes and Free Polarization Decay in GaAs/AlGaAs Multiple Quantum Wells," *Phys. Rev. Lett.* **66**:934 (1991).
96. H. J. Eichler, P. Günter, and D. W. Pohl, *Laser-Induced Dynamic Gratings* (Springer-Verlag, Berlin, 1986).
97. J. Y. Bigot, M. A. Mycek, S. Weiss, R. G. Ulbrich, and D. S. Chemla, "Instantaneous Frequency Dynamics of Coherent Wave Mixing in Semiconductor Quantum-Wells," *Phys. Rev. Lett.* **70**:3307 (1993).
98. A. L. Smirl, "Coherent Exciton Dynamics: Time-Resolved Polarimetry," in *Semiconductor Quantum Optoelectronics: From Quantum Physics to Smart Devices*, A. Miller and D. M. Finlayson (eds.) (Institute of Physics, London, 1999).
99. C. J. Bardeen, W. Wang, and C. V. Shank, "Femtosecond Chirped Pulse Excitation of Vibrational Wave Packets in LD690 and Bacteriorhodopsin," *J. Phys. Chem. A* **102**:2759 (1998).
100. W. P. de Boeij, M. S. Pshenichnikov, and D. A. Wiersma, "Ultrafast Solvation Dynamics Explored by Femtosecond Photon Echo Spectroscopies," *Ann. Rev. Phys. Chem.* **49**:99 (1998).
101. J. Shah, *Ultrafast Processes in Semiconductors and Semiconductor Nanostructures*, Vol. 115 in Springer Solid-State Sciences series (Springer, Berlin, 1996).
102. See, for example, H. Wang, K. B. Ferrio, D. G. Steel, P. R. Berman, Y. Z. Hu, R. Binder, and S. W. Koch, "Transient Four-Wave Mixing Line Shapes: Effects of Excitation Induced Dephasing," *Phys. Rev. A* **49**:1551 (1994).
103. H. Haug and S. W. Koch, *Quantum Theory of the Optical and Electronic Properties of Semiconductors* (World Scientific, Singapore, 1993).
104. C. Sieh, T. Meier, F. Jahnke, A. Knorr, S. W. Koch, P. Brick, M. Hübner, C. Ell, J. Prineas, G. Khitrova, and H. M. Gibbs, "Coulomb Memory Signatures in the Excitonic Optical Stark Effect," *Phys. Rev. Lett.* **82**:3112 (1999).
105. D. S. Chemla, "Ultrafast Transient Nonlinear Optical Processes in Semiconductors," *Semiconductors and Semimetals* **58**:175 (1999).
106. J. Stenger, S. Inouye, A. P. Chikkatur, D. M. Stamper-Kurn, D. E. Pritchard, and W. Ketterle, "Bragg Spectroscopy of a Bose-Einstein Condensate," *Phys. Rev. Lett.* **82**:4569 (1999).
107. Y. B. Ovchinnikov, J. H. Müller, M. R. Doery, E. I. D. Vredenburg, K. Helmerson, S. L. Rolston, and W. D. Phillips, "Diffraction of a Released Bose-Einstein Condensate by a Pulsed Standing Light Wave," *Phys. Rev. Lett.* **83**:284 (1999).
108. S. Mukamel, A. Piryatinski, and V. Chernyak, "Two-Dimensional Raman Echoes: Femtosecond View of Molecular Structure and Vibrational Coherence" *Accts. Chem. Res.* **32**:145 (1999).
109. P. Hamm, M. Lim, W. F. DeGrado, and R. M. Hochstrasser, "The Two-Dimensional IR Nonlinear Spectroscopy of a Cyclic Penta-peptide in Relation to its Three-Dimensional Structure," *Proc. Natl. Acad. Sci. USA* **96**:2036 (1999).

---

# PHOTOREFRACTIVE MATERIALS AND DEVICES

---

Mark Cronin-Golomb

*Department of Biomedical Engineering  
Tufts University  
Medford, Massachusetts*

Marvin Klein

*Intelligent Optical Systems, Inc.  
Torrance, California*

---

## 12.1 INTRODUCTION

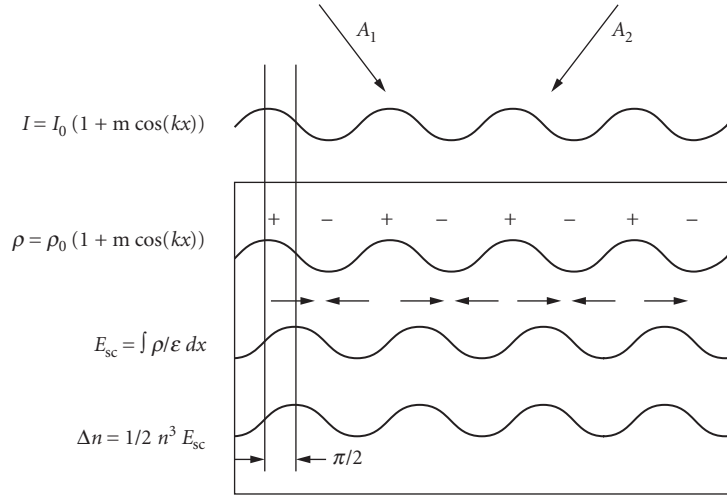
---

The photorefractive effect is a real time holographic optical nonlinearity that is effective for low-power lasers over a wide range of wavelengths. It is relatively easy to use even in modestly equipped laboratories: all that is needed to get started is a sample of photorefractive material, almost any laser operating in the visible or near-infrared, and a few simple optics such as lenses and beam splitters. The diffraction efficiency of photorefractive holograms is roughly independent of the intensity of the writing beams and in many materials, the diffraction efficiency of these holograms can approach 100 percent, so that sophisticated detectors are not required. Its simplicity of use has been largely responsible for its widespread popularity. As is often the case, however, attractive features such as these come only with associated disadvantages. For the photorefractive effect, the main disadvantage is one of speed. The nonlinearities come to steady state at a rate which is approximately inversely proportional to intensity. The fastest high-diffraction efficiency materials have response times of the order of 1 ms at 1 W/cm<sup>2</sup>. Even so, in certain applications, the characteristic slowness is not a disadvantage. In the first part of this chapter, we explain the basic mechanisms of the photorefractive effect. The second part deals with material selection considerations and the third part describes some typical applications. For the reader in need of an extensive overview of the photorefractive effect and its applications, we recommend a two-volume set edited by Gunter and Huignard and the three-volume updated version two.<sup>1</sup>

### Grating Formation

The photorefractive effect is observed in materials which

1. Exhibit a linear electro-optic effect
2. Are photoconductive
3. Have a low dark conductivity



**FIGURE 1** The photorefractive mechanism. Two laser beams intersect, forming an interference pattern  $I(x)$ . Charge is excited where the intensity is large and migrates to regions of low intensity. The electric field  $E_{sc}$  associated with the resultant space charge  $\rho_{sc}$  operates through the linear electro-optic coefficients to produce a refractive index grating  $\Delta n$ .

Two laser beams record a photorefractive hologram when their interference pattern is incident on a photorefractive crystal (Fig. 1). Charge carriers are preferentially excited in the bright fringes and are then free to drift and diffuse until they recombine with traps, most likely in the darker regions of the interference pattern. In this way, a space charge builds up inside the crystal in phase with the interference pattern. The electric field of this space charge acts through the linear electro-optic effect to form a volume holographic refractive index grating in real time. Real time means that the development occurs with a time constant of the order of the response time of the photorefractive crystal. The writing beams then diffract from the hologram into each other. Even though the process depends on the linear electro-optic effect, which is second-order, the whole process acts effectively as a third-order nonlinearity as far as the writing beams are concerned, and third-order coupled-wave equations can be written for their amplitudes. It is important to notice that the electric field is spatially shifted by  $90^\circ$  with respect to the interference pattern because of the Gauss's law integration that links the space charge to the electric field. The refractive index gradient is also shifted by  $\pm 90^\circ$ . This shift is possible because the refractive index perturbation depends on the direction of the electric field, not just on its magnitude. The direction of the grating shift is determined by the sign of the electro-optic coefficient and crystal orientation. This dependence on crystal orientation is due to the lack of inversion symmetry associated with the linear electro-optic coefficient: if the crystal is inverted through its origin, the sign of the phase shift changes. In uniaxial crystals, inversion corresponds simply to reversing the direction of the optic axis. These symmetry effects are intimately related to the origin of photorefractive beam amplification.

The reason that use of the linear electro-optic effect is important is that a Bragg-matched volume hologram should have the same period as the optical interference pattern that wrote it. The refractive index change should be directly proportional to the space charge electric field. This is only possible if the material displays the linear electro-optic effect leading to a refractive index distribution  $\Delta n \propto r_{\text{eff}} E_{sc}$ , where  $r_{\text{eff}}$  is an effective electro-optic coefficient and  $E_{sc}$  is the space charge field. The lack of inversion symmetry needed by the linear electro-optic effect may be found in ferroelectric

materials such as barium titanate, optically active materials such as bismuth silicon oxide and cubic compound semiconductors such as GaAs and InP.

When the charge transport is purely diffusive, the magnitude of the spatial phase shift is  $90^\circ$ . However, in certain circumstances the phase shift can depart from  $90^\circ$ . This occurs if electric fields are applied to the crystal or if the crystal exhibits the photovoltaic effect<sup>2</sup> so that drift mechanisms come into play, or, if the writing beams have different frequencies, so that the interference pattern moves in the crystal with the index grating lagging behind it.

The second requirement implies that the material should contain photoexcitable impurities. Direct band-to-band photoconductivity is usually not useful since it limits the optical interaction distances to rather small absorption depths.

The requirement for low dark conductivity ensures that the space charge can support itself against decay by leakage through background conduction.

## The Standard Rate Equation Model

The simplest model, as formulated by Vinetskii and Kukhtarev,<sup>3</sup> involves optical excitation of charge carriers. For the purposes of this introduction, we will assume that the carriers are electrons which can be excited from a donor species such as  $\text{Fe}^{2+}$  and which can recombine into an acceptor such as  $\text{Fe}^{3+}$ . Let  $n$  be the local number density of mobile excited electrons and  $N_D = N + N^+$  be the number density of the impurities or defects responsible for the photorefractive effect, where  $N^+$  is the number density of acceptor dopants (e.g.,  $\text{Fe}^{3+}$ ) and  $N$  is the number density of donor dopants (e.g.,  $\text{Fe}^{2+}$ ). Let  $N_A$  be the number density of negative ions that compensate the excess positive charge of acceptor dopants when the charge is uniformly distributed in the dark. Neglecting the photovoltaic effect, we may write the following rate equations of generation and recombination, continuity, electric field (Poisson equation), and total drift and diffusion current:

$$\begin{aligned}\frac{\partial N^+}{\partial t} &= (sI + \beta)N - \gamma n N^+ \\ \frac{\partial N^+}{\partial t} &= \frac{\partial n}{\partial t} - \frac{1}{e} \nabla \cdot \mathbf{j} \\ \nabla \cdot \mathbf{E} &= (N^+ - N_A - n)e/\epsilon \\ \mathbf{j} &= \mu n \mathbf{E} + k_B T \mu \nabla n\end{aligned}\tag{1}$$

where  $s$  is proportional to the photoionization cross section ( $s = \sigma/h\nu$ ),  $\beta$  is the dark generation rate,  $\gamma$  is a recombination coefficient,  $\mathbf{j}$  is the electric current density. At steady state, the space charge is determined by a balance between charge diffusion away from bright fringes and electrostatic repulsion from charge concentrations. Extensions of these equations to include the effects of electron-hole competition,<sup>4</sup> multiple dopants,<sup>5,6</sup> photovoltaic effects,<sup>7,8</sup> and short pulse excitation<sup>9</sup> have been developed over the past few years. Nevertheless, the most important features of the photorefractive effect may be well-modeled by the simple equations shown here. Assuming that the number density of charge carriers is much less than the optically induced donor density perturbation ( $N^+ - N_A$ ), a situation that almost always holds, the rate equations can be linearized to give the following solution for the fundamental spatial Fourier component of the space charge field  $E_{sc}$  induced by a sinusoidal optical fringe pattern of wave number  $k_g$  and fringe visibility  $m$  when a dc field  $E_0$  is applied to the crystal:

$$E_{sc} = \frac{m/2}{1 + \beta/sI_0} \frac{E_q(iE_0 - E_d)}{E_0 + i(E_d + E_q)}\tag{2}$$

where  $I_0$  is the total average intensity of the interacting beams,  $E_q$  and  $E_d$  are characteristic fields of maximum space charge and diffusion, respectively  $E_d = k_B T k_g / e$ ,  $E_q = e N_A / e k_g$ . The response time  $\tau$  is given by

$$\tau = \frac{N_A}{SN_D(I_0 + \beta/s)} \frac{E_0 + i(E_d + E_\mu)}{E_0 + i(E_d + E_q)} \quad (3)$$

where  $E_\mu$  is the characteristic mobility field  $E_\mu = \gamma N_A / \mu k_g$ . These results show that the steady-state space charge field is approximately independent of total intensity and that the response time is inversely proportional to total intensity if the intensity exceeds the saturation intensity  $\beta/s$ .

In the absence of a dc applied field, the fundamental Fourier component of the space charge field is purely imaginary, indicating a  $90^\circ$  spatial phase shift between the interference pattern and the index grating. The effect of an applied dc field is to increase the magnitude of the space charge field and to move the spatial phase shift from  $90^\circ$ . The  $90^\circ$  phase shift is optimal for two-beam coupling amplifiers, as will be indicated, and can be restored by inducing a compensating phase difference through detuning the writing beams from each other to cause the grating to lag behind the interference pattern.<sup>10</sup> Alternatively, an ac applied field may be used to enhance the magnitude of the photorefractive grating and maintain the  $90^\circ$  phase shift.<sup>11,12</sup> For externally pumped four-wave mixing, the  $90^\circ$  phase shift is not optimum, so the applied field-induced deviation of the phase shift is advantageous.<sup>13</sup>

## Wave Interactions

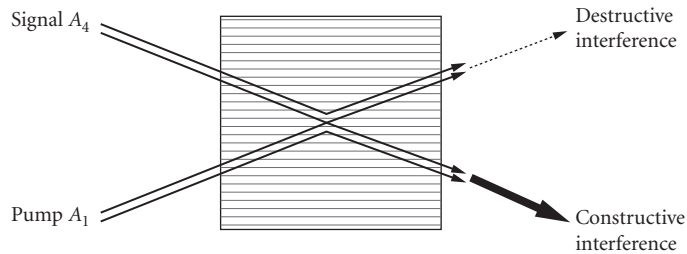
**Two-Beam Coupling** Consider two laser beams writing a grating in a photorefractive medium as depicted in Fig. 2. The effect of the photorefractive nonlinearity on the writing beams can be described quite accurately by conventional coupled-wave theory. Coupled-wave equations for two-beam coupling can be found by taking the slowly varying envelope approximation and substituting the optical electric fields into the scalar wave equation.<sup>14</sup>

$$\nabla^2 E + k^2 E = 0 \quad (4)$$

where

$$k = \frac{\omega n}{c} = \frac{\omega(n_0 + \Delta n)}{c} \quad (5)$$

with  $\Delta n$  being the optically induced refractive index change.



**FIGURE 2** Two-beam coupling amplification. Beams 1 and 4 write a diffraction grating. Beam 1 diffracts from the grating to constructively interfere with and amplify beam 4. Beam 4 diffracts from the grating to destructively interfere with and attenuate beam 1.

The resultant coupled-wave equations read:

$$\begin{aligned}\frac{dA_1}{dz} &= -\gamma \frac{A_1 A_4^*}{I_0} A_4 \\ \frac{dA_4^*}{dz} &= \gamma \frac{A_1 A_4^*}{I_0} A_1^*\end{aligned}\quad (6)$$

where  $I_0$  is sum of the intensities  $I_1$  and  $I_4$  of the interacting beams. The coupling constant  $\gamma$  is related to the space charge field by

$$\gamma = \frac{i\omega}{c \cos\theta} \frac{r_{\text{eff}} n^3 E_{\text{sc}} / m}{2} \quad (7)$$

It is proportional to the effective electro-optic coefficient  $r_{\text{eff}}^{15}$  and is real when the index grating is  $90^\circ$  out of phase with the interference pattern (as in the case without an applied dc electric field, or with high-frequency ac applied fields). In that case, the coupled-wave equations show that beam 4 is amplified at the expense of beam 1 if  $\gamma$  is positive. The amplification effect can be explained in physical terms: the light diffracted by the grating from beam 1 interferes constructively with beam 4, so beam 4 is amplified. The light diffracted by the grating from beam 4 interferes destructively with beam 1, which consequently loses energy. At the same time, the phases of the interacting beams are preserved. If the spatial phase shift departs from  $90^\circ$  then the energy transfer effect becomes less, and phase coupling begins to appear.

The photorefractive beam coupling gain can be substantial in materials with large electro-optic coefficients. The intensity gain coefficient  $\Gamma$  which characterizes the transfer of energy between two beams [ $\Gamma = \gamma + \gamma^*$ ; see Eq. (8)] can exceed  $60 \text{ cm}^{-1}$  in  $\text{BaTiO}_3$ <sup>16</sup> and in SBN.<sup>17</sup> Such high gain makes possible the construction of devices such as photorefractive parametric oscillators and recursive image processors. In the high gain case, signal-to-noise issues become important. Generally, defects in photorefractive crystals act as scattering centers. In a process similar to amplified spontaneous emission, this scattered light can be very strongly amplified into a broad fan of light. This fanning effect<sup>18-20</sup> is a significant source of noise for photorefractive image amplifiers, and considerable effort has been devoted to lessening the effect by growing more uniform crystals and making device design modifications.<sup>21, 22</sup> On the other hand, the fanning effect can be a useful source of seed beams for various oscillators<sup>23, 24</sup> or as the basis for optical limiters.<sup>25</sup>

In the undepleted pump approximation ( $I_1 \gg I_4$ ), theoretical analysis is extremely simple: the gain is exponential, with amplitude gain coefficient simply  $\gamma$ . But even in the pump depletion case, analysis is quite straightforward because, as in the case of second-harmonic generation, the nonlinear coupled-wave equations can be solved exactly.<sup>14</sup>

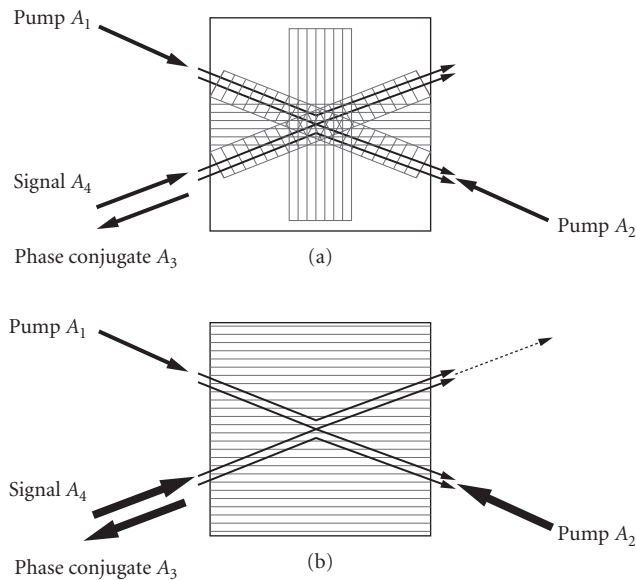
$$\begin{aligned}I_1(z) &= \frac{I_0}{1 + (I_4(0)/I_1(0)) \exp(\Gamma z)} \\ I_4(z) &= \frac{I_0}{1 + (I_1(0)/I_4(0)) \exp(-\Gamma z)} \\ \psi_1(z) &= \psi_1(0) - \Gamma' z + \frac{\Gamma'}{\Gamma} \ln(I_4(z)/I_4(0)) \\ \psi_4(z) &= \psi_4(0) - \Gamma' z - \frac{\Gamma'}{\Gamma} \ln(I_1(z)/I_1(0))\end{aligned}\quad (8)$$

where  $\Gamma = \gamma + \gamma^*$  and  $\Gamma' = (\gamma - \gamma^*)/2i$ . The physical implications of these equations are clear: for  $I_4(0) \exp(\Gamma z) \ll I_1(0)$ , beam 4 is exponentially amplified; for  $I_4(0) \exp(\Gamma z) \gg I_1(0)$ , beam 4

receives all of the intensity of both input beams, and beam 1 is completely depleted. There is phase transfer only if  $\gamma$  has an imaginary component. Linear absorption is accounted for simply by multiplying each of the intensity equations by  $\exp(-\alpha z)$ , where  $\alpha$  is the intensity absorption coefficient.

The plane-wave transfer function of a photorefractive two-beam coupling amplifier may be used to determine thresholds (given in terms of  $\gamma\ell$ , where  $\ell$  is the interaction length), oscillation intensities, and frequency pulling effects in unidirectional ring oscillators based on two-beam coupling.<sup>26–29</sup>

**Four-Wave Mixing** Four-wave mixing and optical phase conjugation may also be modeled by plane-wave coupled-wave theories for four interacting beams<sup>13</sup> (Fig. 3). In general, when all four beams are mutually coherent, they couple through four sets of gratings: (1) the transmission grating driven by the interference term  $(A_1A_4^* + A_2^*A_3)$ , (2) the reflection grating driven by  $(A_2A_4^* + A_1^*A_3)$ , (3) the counterpropagating pump grating  $(A_1A_2^*)$ , and (4) the signal/phase conjugate grating  $(A_3A_4^*)$ . The theories can be considerably simplified by modeling cases in which the transmission grating only or the reflection grating only is important. The transmission grating case may be experimentally realized by making beams 1 and 4 mutually coherent but incoherent with beam 2 (and hence beam 3, which is derived directly from beam 2). The four-wave mixing coupled-wave equations can be solved analytically in several useful cases by taking advantage of conservation relations inherent in the four-wave mixing process,<sup>30,31</sup> and by using group theoretic arguments.<sup>32</sup> Such



**FIGURE 3** Four-wave mixing phase conjugation. (a) Beams 1 and 2 are pump beams, beam 4 is the signal, and beam 3 is the phase conjugate. All four interaction gratings are shown: reflection, transmission, counterpropagating pump, and signal/phase conjugate. Beam 1 interferes with beam 4 and beam 2 interferes with beam 3 to write the transmission grating. Beam 2 interferes with beam 4 and beam 1 interferes with beam 3 to write the reflection grating. Beam 1 interferes with beam 2 to write a counterpropagating beam grating, as do beams 3 and 4. (b) If beams 1 and 4 are mutually incoherent, but incoherent with beam 2, only the transmission grating will be written. This interaction is the basis for many self-pumped phase conjugate mirrors.

analytic solutions are of considerable assistance in the design and understanding of various four-wave mixing devices. But as in other types of four-wave mixing, the coupled-wave equations can be linearized by assuming the undepleted pump approximation. Considerable insight can be obtained from these linearized solutions.<sup>13</sup> For example, they predict phase conjugation with gain and self-oscillation. The minimum threshold for phase conjugation with gain in the transmission grating case is  $\gamma\ell = 2\ln(1 + \sqrt{2}) \approx 1.76$ , whereas the minimum threshold for the usual  $\chi^{(3)}$  nonlinearities is  $\gamma\ell = i\pi/4 \approx 0.79i$ .

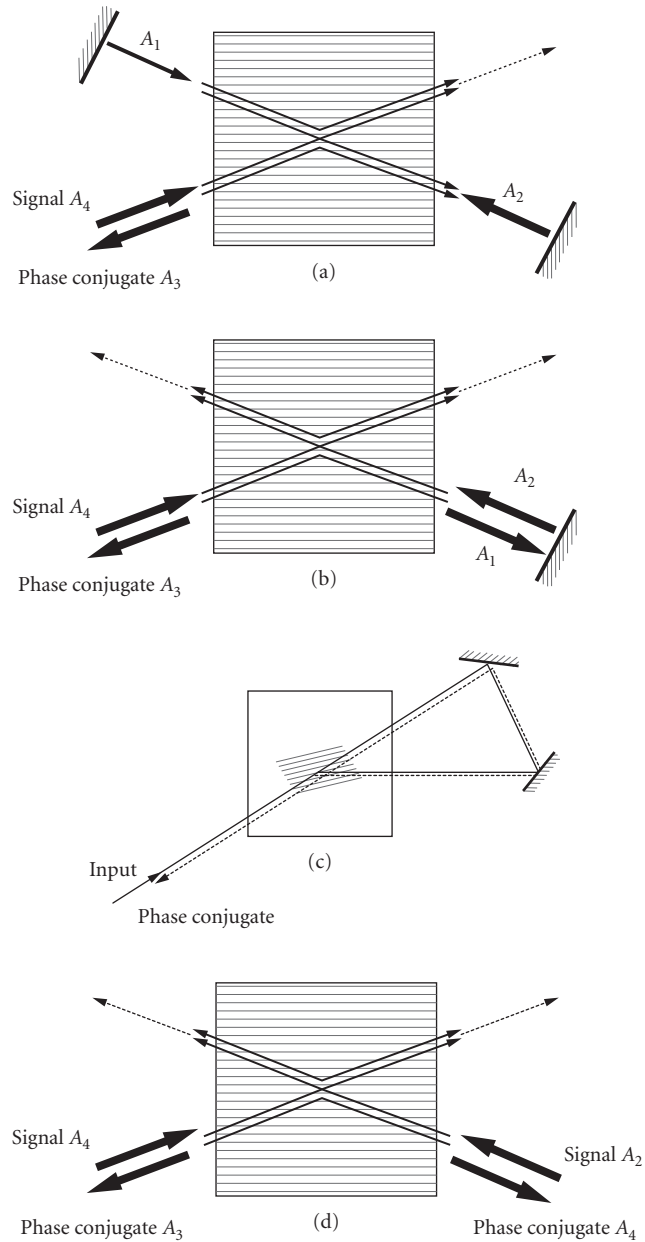
Self-oscillation (when the phase conjugate reflectivity tends to infinity) can only be achieved if the coupling constant is complex. In the  $\chi^{(3)}$  case this is the normal state of affairs, but in the photorefractive case, as mentioned, it requires some additional effect such as provided by applied electric fields, photovoltaic effect, or frequency detuning. Photorefractive four-wave mixing thresholds are usually higher than the corresponding  $\chi^{(3)}$  thresholds because photorefractive symmetry implies that either the signal or the phase conjugate tend to be deamplified in the interaction. In the  $\chi^{(3)}$  case, both signals and phase conjugate can be amplified. This effect results in the fact that while the optimum pump intensity ratio is unity in the  $\chi^{(3)}$  case, the optimum beam intensities are asymmetric in the photorefractive case. A consequence of the interplay between self-oscillation and coupling constant phase is that high-gain photorefractive phase conjugate mirrors tend to be unstable. Even if the crystal used is purely diffusive, running gratings can be induced which cause the coupling constant to become complex, giving rise to self-oscillation instabilities.<sup>33,34</sup>

**Anisotropic Scattering** Because of the tensor nature of the electro-optic effect, it is possible to observe interactions with changing beam polarization. One of the most commonly seen examples is the anisotropic diffraction ring of ordinary polarization that appears on the opposite side of the amplified beam fan when a single incident beam of extraordinary polarization propagates approximately perpendicular to the crystal optic axis.<sup>35–37</sup> Since the refractive indices for ordinary and extraordinary waves differ from each other, phase matching for such an interaction can only be satisfied along specific directions, leading to the appearance of phase-matched rings. There are several other types of anisotropic scattering, such as broad fans of scattered light due to the circular photovoltaic effect,<sup>38</sup> and rings that appear when ordinary and extraordinary polarized beams intersect in a crystal.<sup>39</sup>

## Oscillators with Photorefractive Gain and Self-Pumped Phase Conjugate Mirrors

Photorefractive beam amplification makes possible several four-wave mixing oscillators, including the unidirectional ring resonator and self-pumped phase conjugate mirrors (SPPCMs). The simplest of these is the linear self-pumped phase conjugate mirror.<sup>40</sup> Two-beam coupling photorefractive gains supports oscillation in a linear cavity (Fig. 4a). The counterpropagating oscillation beams pump the crystal as a self-pumped phase conjugate mirror for the incident beam. The phase conjugate reflectivity of such a device can theoretically approach 100 percent, with commonly available crystals. In practice, the reflectivity is limited by parasitic fanning loss. Other types of self-pumped phase conjugate mirrors include the following. The semilinear mirror, consisting of a linear mirror with one of its cavity mirrors removed<sup>40</sup> (Fig. 4b). The ring mirror (transmission grating<sup>41</sup> and reflection grating<sup>42</sup> types). The transmission grating type is shown in Fig. 4c. The double phase conjugate mirror<sup>43</sup> (Fig. 4d). This device is also sometimes known as a mutually pumped phase conjugator (MPPC). Referring to Fig. 4b, it can be seen that the double phase conjugate mirror is part of the semilinear mirror. Several variants involving combinations of the transmission grating ring mirror and double phase conjugate mirror: the cat mirror<sup>23</sup> (Fig. 4e) so named after its first subject, frogs legs<sup>44</sup> (Fig. 4f), bird-wing<sup>45</sup> (Fig. 4g), bridge<sup>46</sup> (Fig. 4h), and mutually incoherent beam coupler<sup>47</sup> (Fig. 4i). The properties of these devices are sometimes influenced by the additional simultaneous presence of reflection gratings and gratings written between the various pairs of counterpropagating beams. The double phase conjugate mirror can be physically understood as being supported by a special sort of photorefractive self-oscillation in which beams 2 and 4 of Fig. 3 are





**FIGURE 4** Self-pumped phase conjugate mirrors: those with external feedback: (a) linear; (b) semilinear; (c) ring; those self-contained in a single crystal with feedback (when needed) provided by total internal reflection; (d) double phase conjugate mirror; (e) cat; (f) frogs' legs; (g) bird-wing; (h) bridge; and (i) mutually incoherent beam coupler.

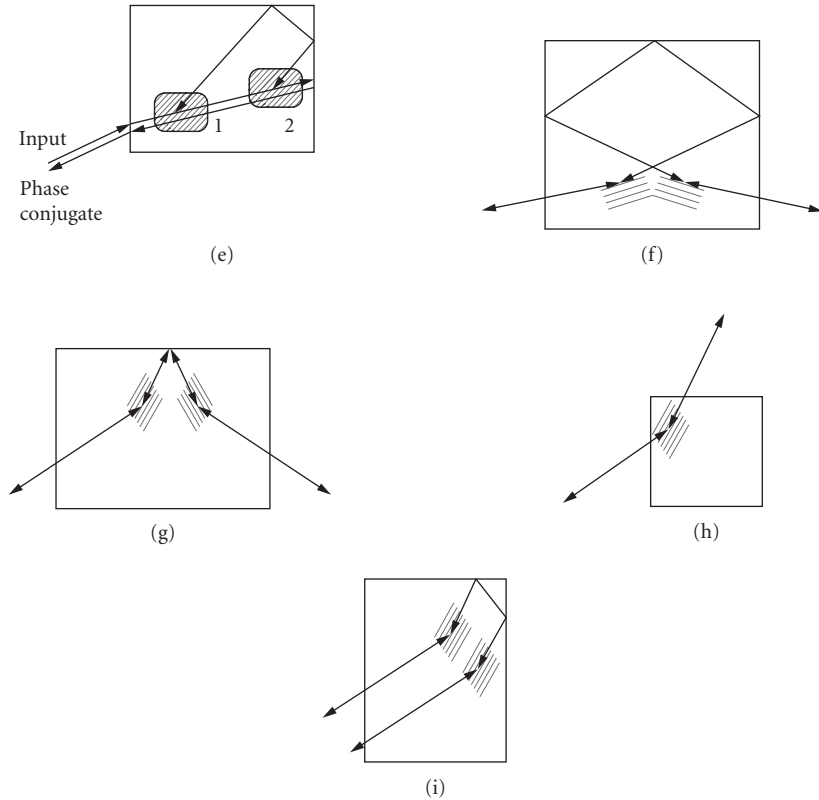


FIGURE 4 (Continued)

taken as strong and depleted. The self-oscillation threshold for the appearance of beams 1 and 3 is  $\gamma\ell = 2.0$  with purely diffusive coupling.<sup>48</sup> It can be shown that a transmission grating ring mirror with coupling constant  $\gamma\ell$  is equivalent in the plane-wave theory to a double phase conjugate mirror with coupling constant  $2\gamma\ell$ .<sup>49</sup>

The matter of whether the various devices represent the results of absolute instabilities or convective instabilities has been the subject of some debate.<sup>50, 51</sup>

## Stimulated Photorefractive Scattering

It is natural to ask whether there is a photorefractive analogue to stimulated Brillouin scattering (SBS, a convective instability). In SBS, an intense laser beam stimulates a sound wave whose phase fronts are the same as those of the incident radiation. The Stokes wave reflected from the sound grating has the same phase fronts as the incident beam, and is traveling in the backward phase conjugate sense. The backward wave experiences gain because the sonic grating is  $90^\circ$  spatially out of phase with the incident beam. In the photorefractive case, the required  $90^\circ$  phase shift is provided automatically, so that stimulated photorefractive scattering (SPS) can be observed without any Stokes frequency shift.<sup>52, 53</sup> However, the fidelity of SPS tends to be worse than that of SBS because the intensity gain discrimination mechanism is not as strong, as can be seen by examining the coupled-wave equations in each case.<sup>54</sup>

## Time-Dependent Effects

Time-dependent coupled-wave theory is important for studying the temporal response and temporal stability of photorefractive devices. Such a theory can be developed by including a differential equation for the temporal evolution of the grating. The spatiotemporal two-beam coupled-wave equations can be written, for example, as

$$\begin{aligned}\frac{\partial A_1}{\partial z} &= -GA_4 \\ \frac{\partial A_4^*}{\partial z} &= GA_1^* \\ \frac{\partial G}{\partial t} + G/\tau &= \frac{\gamma}{\tau} \frac{A_1 A_4^*}{I_0}\end{aligned}\tag{9}$$

where  $\tau$  is an intensity-dependent possibly complex response time determined from photorefractive charge transport models. Models like this can be used to show that the response time for beam amplification and deamplification is increased by a factor of  $\gamma\ell$  over the basic photorefractive response time  $\tau$ .<sup>55</sup> The potential for photorefractive bistability can be studied by examining the stability of the multiple solutions of the steady-state four-wave mixing equations. In general, there is no reversible plane-wave bistability except when other nonlinearities are included in photorefractive oscillator cavities.<sup>56,57</sup> (See the section on “Thresholding.”) Temporal instabilities generate interesting effects such as deterministic chaos, found both experimentally<sup>58</sup> and theoretically<sup>59,60</sup> in high-gain photorefractive devices.

## Influence of the Nonlinearity on Beam Spatial Profiles

In modeling the changes in the transverse cross section of beams as they interact, it is necessary to go beyond simple one-dimensional plane-wave theory. Such extensions are useful for analyzing fidelity of phase conjugation and image amplification, and for treating transverse mode structure in photorefractive oscillators. Several different methods have been used to approach the transverse profile problem.<sup>61</sup> In the quasi-plane-wave method, one assumes that each beam can be described by a single plane wave whose amplitude varies perpendicular to its direction of propagation. The resulting two-dimensional coupled partial differential equations give good results when propagative diffraction effects can be neglected.<sup>62</sup> Generalization of the one-dimensional coupled-wave equations to multi-coupled wave theory also works quite well,<sup>63</sup> as does the further generalization to coupling of continuous distributions of plane waves summed by integration.<sup>20</sup> This latter method has been used quite successfully to model beam fanning.<sup>20</sup> The split-step beam propagation method has also been used to include diffractive beam propagation effects as well as nonlinear models of the optically induced grating formation.<sup>64</sup>

Spatiotemporal instabilities have been studied in phase conjugate resonators.<sup>65,66</sup> These instabilities often involve optical vortices.<sup>67</sup>

## 12.2 MATERIALS

### Introduction

Photorefractive materials have been used in a wide variety of applications, as will be discussed later. These materials have several features which make them particularly attractive.

- The characteristic phase shift between the writing intensity pattern and the induced space charge field leads to energy exchange between the two writing beams, amplified scattered light (beam fanning), and self-pumped oscillators and conjugators.

- Photorefractive materials can be highly efficient at power levels obtained using CW lasers. Image amplification with a gain of 4000<sup>68</sup> and degenerate four-wave mixing with a reflectivity of 2000 percent<sup>69</sup> have been demonstrated.
- In optimized bulk photorefractive materials, the required energy to write a grating can approach that of photographic emulsion (50  $\mu\text{J}/\text{cm}^2$ ), with even lower values of write energy measured in photorefractive multiple quantum wells.
- The response time of most bulk photorefractive materials varies inversely with intensity. Gratings can be written with submillisecond response times at CW power levels and with nanosecond response times using nanosecond pulsed lasers. Most materials have a useful response with picosecond lasers.
- The high dark resistivity of oxide photorefractive materials allows the storage of holograms for time periods up to a year in the dark.

In spite of the great appeal of photorefractive materials, they have specific limitations which have restricted their use in practical devices. For example, oxide ferroelectric materials are very efficient, but are rather insensitive. Conversely, the bulk compound semiconductors are extremely sensitive, but suffer from low efficiency in the absence of an applied field. In this section we will first review the figures of merit used to characterize photorefractive materials, and then discuss the properties of the different classes of materials.

## Figures of Merit

The figures of merit for photorefractive materials can be conveniently divided into those which characterize the steady-state response, and those which characterize the early portion of the transient response<sup>70-72</sup>. Most applications fall into one or the other of these regimes, although some may be useful in either regime. For example, aberration correction, optical limiting, and laser coupling are applications which generally require operation in the steady state. On the other hand, certain optical processing applications require a response only to a given level of index change or efficiency, and are thus better characterized by the initial recording slope of a photorefractive grating.

**Steady-State Performance** The steady-state change in the refractive index is related to the space charge electric field by

$$\Delta n_{ss} = \frac{1}{2} n_b^3 r_{eff} E_{sc} \quad (10)$$

where  $n_b$  is the background refractive index,  $r_{eff}$  is the effective electro-optic coefficient (which accounts for the specific propagation direction and optical polarization in the sample), and  $E_{sc}$  is the space charge electric field. For large grating periods where diffusion limits the space charge field, the magnitude of the field is independent of material parameters and thus  $\Delta n_{ss} \propto n_b^3 r_{eff}$ . In this case (which is typical for many applications), the ferroelectric oxides are favored, because of their large electro-optic coefficients. For short grating periods or for very large applied fields, the space charge field is trap-limited and  $\Delta n_{ss} \propto n_b^3 r_{eff} / \epsilon_r$ , where  $\epsilon_r$  is the relative dielectric constant.

The temporal behavior of the local space charge field in a given material depends on the details of the energy levels which contribute to the photorefractive effect. In many cases, the buildup or decay of the field is exponential. The fundamental parameter which characterizes this transient response is the write or erase energy  $W_{sat}$ . In many materials the response time  $\tau$  at an average intensity  $I_0$  is simply given by

$$\tau = W_{sat} / I_0 \quad (11)$$

This clearly points out the dependence of the response time on the intensity. As long as enough energy is provided, photorefractive gratings can be written with beams ranging in intensity from  $\text{mW}/\text{cm}^2$  to  $\text{MW}/\text{cm}^2$ . The corresponding response time can be calculated simply from Eq. (11).

In the absence of an applied or photovoltaic field (assuming only a single charge carrier), the response time can be written as<sup>70</sup>

$$\tau = \tau_{\text{di}}(1 + 4\pi^2 L_d^2 / \Lambda_g^2) \quad (12)$$

where  $\tau_{\text{di}}$  is the dielectric relaxation time,  $L_d$  is the diffusion length, and  $\Lambda_g$  is the grating period. The diffusion length is given by

$$L_d = (\mu \tau_r k_B T / e)^{1/2} \quad (13)$$

where  $\mu$  is the mobility,  $\tau_r$  is the recombination time,  $k_B$  is Boltzmann's constant,  $T$  is the temperature, and  $e$  is the charge of an electron. The dielectric relaxation time is given by

$$\tau_{\text{di}} = \epsilon_r \epsilon_0 / (\sigma_d + \sigma_p) \quad (14)$$

where  $\sigma_d$  is the dark conductivity and  $\sigma_p$  is the photoconductivity, given by

$$\sigma_p = \alpha e \mu \tau_r I_0 / h\nu \quad (15)$$

where  $\alpha$  is the absorption coefficient.

In as-grown oxide ferroelectric materials, the diffusion length is usually much less than the grating period. In this case, the response time is given by

$$\tau = \tau_{\text{di}} \quad (16)$$

In addition, the contribution from dark conductivity in Eq. (14) can be neglected for intensities greater than  $\sim \text{mW}/\text{cm}^2$ . In this regime, materials with large values of absorption coefficient and photoconductivity ( $\mu \tau_r$ ) are favored.

In bulk semiconductors, the diffusion length is usually much larger than the grating period. In this case, the response time is given by

$$\tau \approx \tau_{\text{di}}(4\pi^2 L_d^2 / \Lambda_g^2) \quad (17)$$

If we again neglect the dark conductivity in Eq. (14), then

$$\tau \approx \pi \epsilon k_B T / e^2 \alpha I_0 \Lambda_g^2 \quad (18)$$

In this regime, materials with small values of dielectric constant and large values of absorption coefficient are favored. For a typical bulk semiconductor with  $\epsilon_r \approx 12$ ,  $\alpha = 1 \text{ cm}^{-1}$ , and  $\Lambda_g = 1 \mu\text{m}$ , we find  $W_{\text{sat}} \approx 100 \mu\text{J}/\text{cm}^2$ . This saturation energy is comparable to that required to expose high resolution photographic emulsion. In photorefractive multiple quantum wells (with  $\alpha \approx 10^{13} \text{ cm}^{-1}$ ), the saturation energy can be much smaller. Note finally that an applied field leads to an increase in the write energy in the bulk semiconductors.<sup>72</sup>

**Transient Performance** In the transient regime, we are typically concerned with the time or energy required to achieve a design value of index change or diffraction efficiency. This generally can be obtained from the initial *recording slope* of a photorefractive grating. One common figure of merit which characterizes the recording slope is the sensitivity,<sup>70-72</sup> defined as the index change per absorbed energy per unit volume:

$$S = \Delta n / \alpha I_0 \tau = \Delta n / \alpha W_{\text{sat}} \quad (19)$$

**TABLE 1** Materials Parameters for BaTiO<sub>3</sub>, BSO, and GaAs

Material Class	Ferroelectric Oxide	Ferroelectric Nonoxide	Sillenite	Compound Semiconductor
Material	BaTiO <sub>3</sub>	Sn <sub>2</sub> P <sub>2</sub> S <sub>6</sub>	BSO	GaAs
Wavelength range (μm)	0.4–1.1	0.65–1.3	0.45–0.65	0.9–1.3
Electro-optic coefficient $r_{\text{eff}}$ (pm/V)	<b>100</b> ( $r_{33}$ ) <b>1640</b> ( $r_{42}$ )	174( $r_{11}$ ) 92( $r_{21}$ ) 140( $r_{31}$ ) –25( $r_{51}$ )	4( $r_{41}$ )	1.4( $r_{41}$ )
Dielectric constant	135( $\epsilon_{33}$ ) 3700( $\epsilon_{11}$ )	230–300 ( $\epsilon_{11}$ )	56	13.2
$n_b^3 r_{\text{eff}} / \epsilon$ (pm/V)	10( $r_{33}$ ) 6( $r_{42}$ )	18( $r_{11}$ )	1.4	3.3
Mobility $\mu$ (cm <sup>2</sup> /V-s)	0.01		0.1	<b>6000</b>
Recombination time $\tau_r$ (s)	10 <sup>–8</sup>		<b>10<sup>–6</sup></b>	3 × 10 <sup>–8</sup>
Diffusion length $L_d$ (μm)	0.01	0.55	0.5	20
Photoconductivity $\mu\tau_r$ (cm <sup>2</sup> /V)	10 <sup>–10</sup>	1.6 × 10 <sup>–7</sup>	10 <sup>–7</sup>	1.8 × 10 <sup>–4</sup>

(The parameters in bold type are particularly distinctive for that material.)

In the absence of an applied field and for large diffusion lengths, we find the limiting value of the sensitivity:

$$S \approx 1/4\pi(n_b^3 r_{\text{eff}} / hv\epsilon)(me/\epsilon_0)\Lambda_g \quad (20)$$

where  $m$  is the modulation index.

We will see that the only material dependence in the limiting sensitivity is through the figure of merit  $n_b^3 r_{\text{eff}} / \epsilon$ . This quantity varies little from material to material. Using typical values of the materials parameters and assuming  $\Lambda_g = 1 \mu\text{m}$ , we find the limiting value  $S = 400 \text{ cm}^3/\text{kJ}$ . Values in this range are routinely observed in the bulk semiconductors. In the as-grown ferroelectric oxides, in which the diffusion length is generally less than the grating period, the sensitivity values are typically two to three orders of magnitude smaller.

**Comparison of Materials** In the following sections, we will briefly review the specific properties of photorefractive materials, organized by crystalline structure. To introduce this discussion, we have listed relevant materials parameters in Table 1. This table allows the direct comparison among BaTiO<sub>3</sub>, Sn<sub>2</sub>P<sub>2</sub>S<sub>6</sub> (SPS), Bi<sub>12</sub>SiO<sub>20</sub> (BSO), and GaAs, which are representative of the four most common classes of photorefractive materials.

The distinguishing feature of BaTiO<sub>3</sub> is the magnitude of its electro-optic coefficients, leading to large values of steady-state index change. The sillenites are distinguished by their large value of recombination time, leading to a larger photoconductivity and diffusion length. The compound semiconductors are distinguished by their large values of mobility, leading to very large values of photoconductivity and diffusion length. Note also the different spectral regions covered by these four materials.

## Ferroelectric Materials

The photorefractive effect was first observed in ferroelectric oxides that were of interest for electro-optic modulators and second-harmonic generation.<sup>73</sup> Initially, the effect was regarded as “optical

damage” that degraded device performance.<sup>74</sup> Soon, however, it became apparent that refractive index gratings could be written and stored in these materials.<sup>75</sup> Since that time, extensive research on material properties and device applications has been undertaken.

The photorefractive ferroelectric oxides can be divided into three structural classes: ilmenites ( $\text{LiNbO}_3$ ,  $\text{LiTaO}_3$ ), perovskites [ $\text{BaTiO}_3$ ,  $\text{KNbO}_3$ ,  $\text{KTa}_{1-x}\text{Nb}_x\text{O}_3$  (KTN)], and tungsten bronzes [ $\text{Sr}_{1-x}\text{Ba}_x\text{Nb}_2\text{O}_6$  (SBN),  $\text{Ba}_2\text{NaNb}_5\text{O}_{15}$  (BNN) and related compounds]. In spite of their varying crystal structure, these materials have several features in common. They are transparent from the bandgap ( $\sim 350$  nm) to the intrinsic IR absorption edge near 4  $\mu\text{m}$ . Their wavelength range of sensitivity is also much broader than that of other photorefractive materials. For example, useful photorefractive properties have been measured in  $\text{BaTiO}_3$  from 442 nm<sup>76</sup> to 1.09  $\mu\text{m}$ ,<sup>77</sup> a range of a factor of  $2\frac{1}{2}$ . Ferroelectric oxides are hard, nonhygroscopic materials—properties which are advantageous for the preparation of high-quality surfaces. Their linear and nonlinear dielectric properties are inherently temperature-dependent, because of their ferroelectric nature. As these materials are cooled below their melting point, they undergo a structural phase transition to a ferroelectric phase. Additional transitions may occur in the ferroelectric phase on further lowering of the temperature. In general, samples in the ferroelectric phase contain regions of differing polarization orientation called domains, leading to a reduction in the net polar properties of the sample. To make use of the electro-optic and nonlinear optic properties of the ferroelectric oxides, these domains must be aligned to a single domain state. This process, called poling, can take place during the growth process, or more commonly, after polydomain samples have been cut from an as-grown boule.

Growth of large single crystals of ferroelectric oxides has been greatly stimulated by the intense interest in photorefractive and nonlinear optic applications. Currently, most materials of interest are commercially available. However, considerably more materials development is required before optimized samples for specific applications can be purchased.

**Lithium Niobate and Lithium Tantalate**  $\text{LiNbO}_3$  was the first material in which photorefractive “damage” was observed.<sup>73</sup> This material has been developed extensively for frequency conversion and integrated optics applications. It is available in large samples with high optical quality. For photorefractive applications, iron-doped samples are generally used. The commonly observed valence states are  $\text{Fe}^{2+}$  and  $\text{Fe}^{3+}$ . The relative populations of these valence states can be controlled by annealing in an atmosphere with a controlled oxygen partial pressure. In a reducing atmosphere (low oxygen partial pressure),  $\text{Fe}^{2+}$  is favored, while  $\text{Fe}^{3+}$  is favored in an oxidizing atmosphere. The relative  $\text{Fe}^{2+}/\text{Fe}^{3+}$  population ratio will determine the relative contributions of electrons and holes to the photoconductivity.<sup>78</sup> When  $\text{Fe}^{2+}$  is favored, the dominant photocarriers are electrons; when  $\text{Fe}^{3+}$  is favored, the dominant photocarriers are holes. In most oxides, electrons have higher mobilities, so that electron-dominated samples yield faster photorefractive response times. Even in heavily reduced  $\text{LiNbO}_3$ , the write energy is rarely lower than 10 J/cm<sup>2</sup>, so this material has not found use for real-time applications. The properties of  $\text{LiTaO}_3$  are essentially the same as those of  $\text{LiNbO}_3$ .

Currently, the most promising application of  $\text{LiNbO}_3$  is for holographic storage.  $\text{LiNbO}_3$  is notable for its very large value of dark resistivity, leading to very long storage times in the dark. In addition, the relatively large write or erase energy of  $\text{LiNbO}_3$  makes this material relatively unsusceptible to erasure during readout of stored holograms.

Improved retention of stored holograms can be obtained by fixing techniques. The most common fixing approach makes use of complementary gratings produced in an ionic species which is not photoactive.<sup>79, 80</sup> Typically, one or more holograms are written into the sample by conventional means. The sample is then heated to 150°C, where it is annealed for a few hours. At this temperature, a separate optically inactive ionic species is thermally activated and drifts in the presence of the photorefractive space charge field until it compensates this field. The sample is then cooled to room temperature to “freeze” the compensating ion grating. Finally, uniform illumination washes out the photorefractive grating and “reveals” the permanent ion grating.

Another important feature of  $\text{LiNbO}_3$  for storage applications is the large values of diffraction efficiency (approaching 100 percent for a single grating) which can be obtained. These large efficiencies arise primarily from the large values of space charge field, which, in turn, result from the very large value of photovoltaic field.

**Barium Titanate** BaTiO<sub>3</sub> was one of the first ferroelectric materials to be discovered, and also one of the first to be recognized as photorefractive.<sup>81</sup> The particular advantage of BaTiO<sub>3</sub> for photorefractive applications is the very large value of the electro-optic coefficient  $r_{42}$  (see Table 1), which, in turn, leads to large values of grating efficiency, beam-coupling gain, and conjugate reflectivity. For example, four-wave mixing reflectivities as large as 20 have been observed,<sup>69</sup> as well as an image intensity gain of 4000.<sup>68</sup>

After the first observation of the photorefractive effect in BaTiO<sub>3</sub> in 1970, little further research was performed until 1980 when Feinberg et al.<sup>82</sup> and Krätzig et al.<sup>83</sup> pointed out the favorable features of this material for real-time applications. Since that time, BaTiO<sub>3</sub> has been widely used in a large number of experiments in the areas of optical processing, laser power combining, spatial light modulation, optical limiting, and neural networks.

The photorefractive properties of BaTiO<sub>3</sub> have been reviewed in Ref. 84. Crystals of this material are grown by top-seeded solution growth in a solution containing excess TiO<sub>2</sub>.<sup>85</sup> Crystal growth occurs while cooling the melt from 1400 to 1330°C. At the growth temperature, BaTiO<sub>3</sub> has the cubic perovskite structure, but on cooling through  $T_c = 132^\circ\text{C}$ , the crystal undergoes a transition to the tetragonal ferroelectric phase. Several approaches to poling have been successfully demonstrated. In general, the simplest approach is to heat the sample to just below or just above the Curie temperature, apply an electric field, and cool the sample with the field present.

Considerable efforts have been expended to identify the photorefractive species in as-grown BaTiO<sub>3</sub>. Early efforts suggested that transition metal impurities (most likely iron) were responsible.<sup>86</sup> In later experiments, samples grown from ultrapure starting materials were still observed to be photorefractive.<sup>87</sup> In this case, barium vacancies have been proposed as the dominant species.<sup>88</sup> Since that time, samples have been grown with a variety of transition metal dopants. All dopants produce useful photorefractive properties, but cobalt-doped samples<sup>89</sup> and rhodium-doped samples<sup>90</sup> appear particularly promising, because of their reproducible high gain in the visible and enhanced sensitivity in the infrared.<sup>90</sup>

One particular complication in developing a full understanding of the photorefractive properties of BaTiO<sub>3</sub> is the presence of shallow levels in the bandgap, in addition to the deeper levels typically associated with transition-metal impurities or dopants. The shallow levels are manifested in several ways. Perhaps the most prominent of these is the observation that the response time (and photoconductivity) of as-grown samples does not scale inversely with intensity [see Eq. (11)], but rather has a dependence of the type  $\tau \sim (I_0)^{-x}$  is observed, where  $x = 0.6-1.0$ .<sup>81-84,91</sup> Several models relating to the sublinear behavior of the response time and photoconductivity to shallow levels have been reported.<sup>92-95</sup>

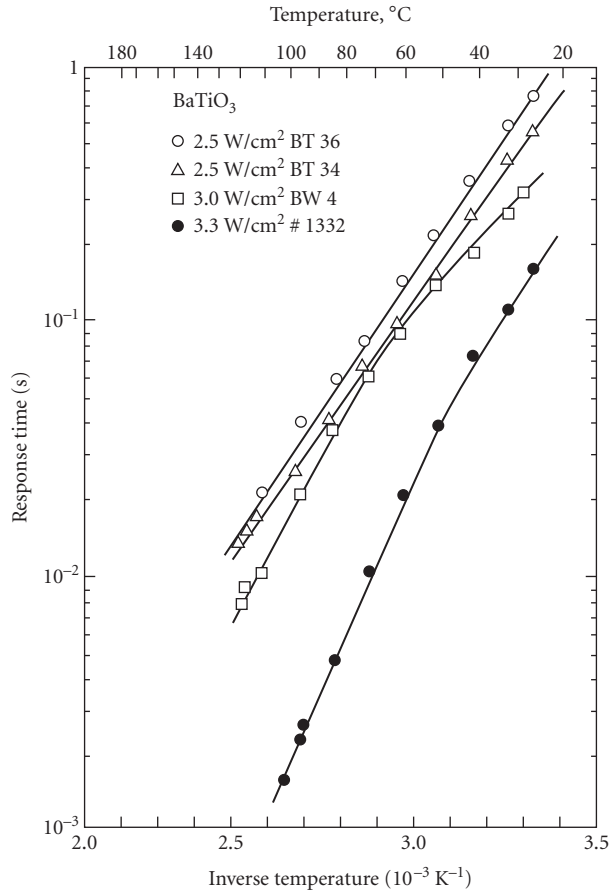
The characteristic sublinear variation of response time with intensity implies that the write or erase energy  $W_{\text{sat}}$  increases with intensity, which is a clear disadvantage for high-power, short-pulse operation. Nevertheless, useful gratings have been written in BaTiO<sub>3</sub> using nanosecond pulses<sup>96,97</sup> and picosecond pulses.<sup>98</sup> Another manifestation of the presence of shallow levels is intensity-dependent absorption.<sup>99</sup> The shallow levels have been attributed to oxygen vacancies or barium vacancies, but no unambiguous identification has been made to date.

The major limitation of BaTiO<sub>3</sub> for many applications is the relatively slow response time of this material at typical CW intensity levels. In as-grown crystals, typical values of response time are 0.1 to 1 s at 1 W/cm<sup>2</sup>. These values are approximately three orders of magnitude longer than theoretical values determined from the band transport model (see "Steady-State Performance"), or from more fundamental arguments.<sup>100,101</sup>

Two different approaches have been studied to improve the response time of BaTiO<sub>3</sub>. In the first, as-grown samples can be operated at an elevated temperature (but below the Curie temperature). In a typical experiment (see Fig. 5), an improvement in response time by two orders of magnitude was observed<sup>102</sup> when different samples were operated at 120°C. In some of these samples, the magnitude of the peak beam-coupling gain did not vary significantly with temperature. In these cases, the improvement in response time translates directly to an equivalent improvement in sensitivity.

While operation at an elevated temperature may not be practical for many experiments, the importance of the preceding experiment is that it demonstrates the *capability for improvement in response time*, based on continuing materials research.





**FIGURE 5** Measured response time as a function of temperature for four samples of BaTiO<sub>3</sub>. The measurement wavelength was 515 nm and the grating period was 0.79 μm.

Other materials research efforts concentrated on studies of new dopants, as well as heat treatments in reducing atmospheres.<sup>88,89,103,104</sup> The purpose of the reducing treatments is to control the valence states of the dopants to produce beneficial changes of the trap density and the sign of the dominant photocarrier. While some success has been achieved,<sup>89,104</sup> a considerably better understanding of the energy levels in the BaTiO<sub>3</sub> bandgap is required before substantial further progress can be made.

**Potassium Niobate** KNbO<sub>3</sub> is another important photorefractive material with the perovskite structure. It undergoes the same sequence of phase transitions as BaTiO<sub>3</sub>, but at higher transition temperatures. At room temperature it is orthorhombic, with large values of the electro-optic coefficients  $r_{42}$  and  $r_{51}$ .

KNbO<sub>3</sub> has been under active development for frequency conversion and photorefractive experiments since 1977 (Ref. 70). Unlike BaTiO<sub>3</sub>, undoped samples of KNbO<sub>3</sub> have weak photorefractive properties. Iron doping has been widely used for photorefractive applications,<sup>70</sup> but other transition metals have also been studied.

Response times in as-grown KNbO<sub>3</sub> at 1 W/cm<sup>2</sup> are somewhat faster than those of BaTiO<sub>3</sub>, but are still several orders of magnitude longer than the limiting value. The most common approach

to improving the response time of  $\text{KNbO}_3$  is electrochemical reduction. In one experiment at 488 nm,<sup>101</sup> a photorefractive response time of 100  $\mu\text{s}$  at 1  $\text{W}/\text{cm}^2$  was measured in a reduced sample. This response time is very close to the limiting value, which indicates again the promise for faster performance in all the ferroelectric oxides.

**Strontium Barium Niobate and Related Compounds**  $\text{Sr}_{1-x}\text{Ba}_x\text{Nb}_2\text{O}_6$  (SBN) is a member of the tungsten bronze family,<sup>105</sup> which includes materials such as  $\text{Ba}_2\text{NaNb}_5\text{O}_{15}$  (BNN) and  $\text{Ba}_{1-x}\text{Sr}_x\text{K}_{1-y}\text{Na}_y\text{Nb}_5\text{O}_{15}$  (BSKNN). SBN is a mixed composition material with a phase transition temperature which varies from 60 to 200°C as  $x$  varies from 0.75 to 0.25. Of particular interest is the composition SBN-60, which melts congruently,<sup>106</sup> and is thus easier to grow with high quality. SBN is notable for the very large values of the electro-optic tensor component  $r_{33}$ . In other materials such as BSKNN, the largest tensor component is  $r_{42}$ . In this sense it resembles  $\text{BaTiO}_3$ .

In general, the tungsten bronze system contains a large number of mixed composition materials, thus offering a rich variety of choices for photorefractive applications. In general, the crystalline structure is quite open, with only partial occupancy of all lattice sites. This offers greater possibilities for doping, but also leads to unusual properties at the phase transition, due to its diffuse nature.<sup>105</sup>

The photorefractive properties of SBN were first reported in 1969,<sup>107</sup> very soon after gratings were first recorded in  $\text{LiNbO}_3$ . Since that time, there has been considerable interest in determining the optimum dopant for this material. The most common dopant has been cerium.<sup>108–110</sup> Cerium-doped samples can be grown with high optical quality and large values of photorefractive gain.<sup>111,112</sup> Another promising dopant is rhodium, which also yields high values of gain coefficient.<sup>113</sup>

As with  $\text{BaTiO}_3$  and  $\text{KNbO}_3$ , as-grown samples of SBN and other tungsten bronzes are relatively slow at an intensity of 1  $\text{W}/\text{cm}^2$ .<sup>114</sup> Doping and codoping has produced some improvement. In addition, the use of an applied dc electric field has led to improvement in the response time.<sup>115</sup>

The photorefractive effect has also been observed in fibers of SBN.<sup>116</sup> The fiber geometry has promise in holographic storage architectures.

**Tin Hypothiodiphosphate**  $\text{Sn}_2\text{P}_2\text{S}_6$  has been known as a ferroelectric since 1974,<sup>117</sup> but has been investigated as a photorefractive material only since 1991.<sup>118</sup> Its Curie point is 337 K, only a few tens of degrees above room temperature, so its electro-optic coefficients are expected to be high (Table 1). It is distinguished from the ferroelectric oxide photorefractives by its useful wavelength range and speed of response. Its bandgap is narrower than that of typical photorefractive oxides, so its wavelength range is pushed deeper into the infrared, and will operate with high gain from 0.65 to 1.3  $\mu\text{m}$ <sup>119,120</sup> and at least as far as 1.55  $\mu\text{m}$  for tellurium doped crystals.<sup>121</sup> There are several variants of nominally undoped material, known by their color (type I yellow, type II yellow, and modified brown), as well as doped crystals, each with their different characteristics. The properties of type I yellow crystals depend on their history of illumination, and are characterized by the existence of a photoinduced fast grating mediated by positive charge carriers and a thermally induced slow grating mediated by electrons. By virtue of the fact that these are due to oppositely charged carriers, they are 180° out of phase with each other, and tend to cancel each other out. In type II yellow crystals, the slow grating is suppressed, thus improving the steady-state gain.<sup>122</sup> The response time of the fast grating at 1.06  $\mu\text{m}$  is 300 ms at 1  $\text{W}/\text{cm}^2$  and is inversely proportional to intensity while the response time of the slow grating is of the order of 100 s, and is approximately independent of intensity. Brown crystals are produced by modifying the vapor transport crystal growth method in such a way as to increase the concentration of intrinsic defects. Typical photorefractive properties for type II, brown, and Te-doped crystals are shown in Table 2.

## Cubic Oxides (Sillenites)

The cubic oxides are notable for their high photoconductivity, leading to early applications for spatial light modulation<sup>123</sup> and real-time holography using the photorefractive effect.<sup>124</sup> The commonly used sillenites are  $\text{Bi}_{12}\text{SiO}_{20}$  (BSO),  $\text{Bi}_{12}\text{GeO}_{20}$  (BGO), and  $\text{Bi}_{12}\text{TiO}_{20}$  (BTO). Some relevant properties of these materials are listed in Table 3.

The sillenites are cubic and noncentrosymmetric, with one nonzero electro-optic tensor component  $r_{41}$ . The magnitude of  $r_{41}$  in the sillenites is small, ranging from approximately 4 to 6 pm/V in the

**TABLE 2** Typical Photorefractive Parameters of Various  $\text{Sn}_2\text{P}_2\text{S}_6$  Crystals at Two Light Wavelengths

$\text{Sn}_2\text{P}_2\text{S}_6$ Sample	$\lambda$ (nm)	$\alpha_x$ ( $\text{cm}^{-1}$ )	$\Gamma_{\text{max}}$ ( $\text{cm}^{-1}$ )	$\tau$ (ms)	$N_{\text{eff}} 10^{16} \text{ cm}^{-1}$
Yellow type II	633	0.5	4–7	10–50	0.7
	780	0.2	2–5	100	0.2
Brown	633	5.7	38	4	2.5
	780	1.0	18	10	0.7
Te-doped (1%)	633	1.0	10	2.5	0.9
	780	0.4	6	7	1.0

$\lambda$ , without pre-illumination;  $\alpha_x$ , absorption coefficient for  $x$ -polarized light;  $\Gamma_{\text{max}}$ , maximal two-wave mixing gain;  $\tau$ , faster response time at a grating spacing of 1  $\mu\text{m}$  and scaled to a light intensity of 1  $\text{W}/\text{cm}^2$ ;  $N_{\text{eff}}$ , effective trap density. (After Grabar *et al.*<sup>117</sup>)

**TABLE 3** Material Properties of BSO, BGO, and BTO

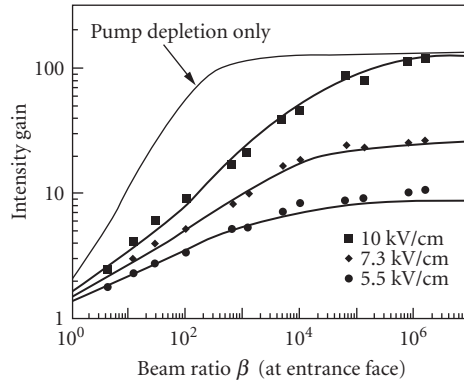
Material	BSO	BGO	BTO
Wavelength range ( $\mu\text{m}$ )	0.5–0.65	0.5–0.65	0.6–0.75
Electro-optic coefficient $r_{41}$ (pm/V)	4.5	3.4	5.7
$n_o^3 r_{41}$ (pm/V)	81	56	89
Dielectric constant	56	47	48
$n_o^3 r_{41} / \epsilon$ (pm/V)	1.4	1.2	1.9
Optical activity at 633 nm (degrees/mm)	21	21	6

visible. In addition, the sillenites are optically active, with a rotatory power (at 633 nm) of  $21^\circ/\text{mm}$  in BSO and BGO, and  $6^\circ/\text{mm}$  in BTO. These values increase sharply at shorter wavelengths. The optical activity of the sillenites tends to reduce the effective gain or diffraction efficiency of samples with normal thickness, but in certain experiments it also allows the use of an output analyzer to reduce noise.

The energy levels due to defects and impurities tend to be similar in each of the sillenites. In spite of many years of research, the identity of the photorefractive species is still not known. It is likely that intrinsic defects such as metal ion vacancies play an important role. With only one metal ion for each 12 bismuth ions and 20 oxygen ions, small deviations in metal ion stoichiometry can lead to large populations of intrinsic defects. In each of the sillenites, the effect of the energy levels in the bandgap is to shift the fundamental absorption edge approximately 100 nm to the red.

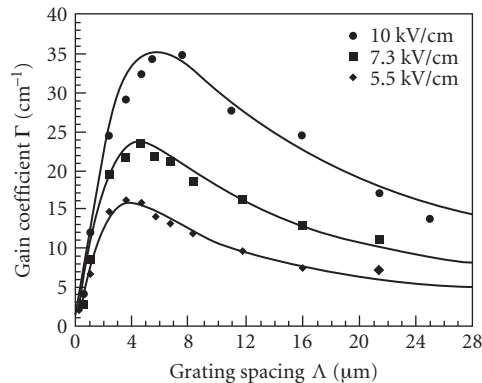
BSO and BGO melt congruently and can be grown from stoichiometric melts by the Czochralski technique. On the other hand, BTO melts incongruently and is commonly grown by the top-seeded solution growth technique, using excess  $\text{Bi}_2\text{O}_3$ . BTO is particularly interesting for photorefractive applications (compared with BSO and BGO), because of its lower optical activity at 633 nm and its slightly larger electro-optic coefficient (5.7 pm/V).<sup>125</sup> It has been studied extensively at the Ioffe Institute in Russia, where both material properties and device applications have been examined.<sup>126–128</sup>

In the sillenites it is very common to apply large dc or ac electric fields to enhance the photorefractive space charge field, and thus provide useful values of gain or diffraction efficiency. A dc field will increase the amplitude of the space charge field, but the spatial phase will decrease from the value of  $90^\circ$  which optimizes the gain. In order to restore the ideal  $90^\circ$  phase shift, moving grating techniques are typically used.<sup>129,130</sup> By contrast, an ac field can enhance the amplitude of the space charge field, while maintaining the spatial phase at the optimum value of  $90^\circ$ .<sup>12</sup> In this case, the best performance is obtained when a square waveform is used, and when the period is long compared with the recombination time, and short compared with the grating formation time. Both dc and ac field techniques have produced large gain enhancements in sillenites and semiconductors, but only when the signal beam is very weak, i.e., when the pump/signal intensity ratio is large. As the amplitude of the signal beam increases, the gain decreases sharply, by an amount which cannot be explained by pump depletion. This effect is significant for applications such as self-pumped phase conjugation, in which the buildup of the signal wave will reduce the effective gain and limit the device performance.



**FIGURE 6** Measured two-wave mixing gain as a function of input pump-to-signal beam ratio in BTO. The measurement wavelength was 633 nm, the applied field was a 60-Hz ac square wave, and the grating period was 5.5  $\mu\text{m}$ . The individual points are experimental data; the bold curves are fits using a large signal model. The thin curve is the standard pump depletion theory for the 10-kV/cm case.

A typical plot of intensity gain in BTO as a function of beam ratio for several values of ac square-wave voltage amplitude is given in Fig. 6.<sup>127</sup> Note that the highest gain is observed only for a beam ratio on the order of  $10^5$  (small signal limit). The simplest physical description of this nonlinearity is that the internal space charge field is clamped to the magnitude of the applied field; this condition only impacts performance for decreasing beam ratios (large signal limit). In a carefully established experiment using a very large beam ratio ( $10^5$ ), gain coefficients approaching  $35\text{ cm}^{-1}$  have been measured using an ac square wave field with an amplitude of 10 kV/cm (see Fig. 7).<sup>131</sup>



**FIGURE 7** Measured gain coefficient as a function of grating spacing in BTO. The measurement wavelength was 633 nm, the applied field was a 60-Hz ac square wave, and the beam ratio was  $10^5$ . The individual points are experimental data; the solid curves are fits using the basic band transport model.

## Bulk Compound Semiconductors

The third class of commonly used photorefractive materials consists of the compound semiconductors (Si and Ge are cubic centrosymmetric materials, and thus have no linear electro-optic effect). Gratings have been written in CdS,<sup>132</sup> GaAs:Cr,<sup>133</sup> GaAs:EL2,<sup>134</sup> InP:Fe,<sup>133</sup> CdTe,<sup>135</sup> GaP,<sup>136</sup> and ZnTe.<sup>137</sup> These materials have several attractive features for photorefractive applications (see Table 4). First, many of these semiconductors are readily available in large sizes and high optical quality, for use as electronic device substrates. These substrates are generally required to be semi-insulating; the deep levels provided for this purpose are generally photoactive, with favorable photorefractive properties. Second, the semiconductors have peak sensitivity for wavelengths in the red and near-infrared. The range of wavelengths extends from 633 nm in GaP,<sup>136</sup> CdS,<sup>139</sup> and ZnTe<sup>137</sup> to 1.52  $\mu\text{m}$  in CdTe:V.<sup>135</sup> Third, the mobilities of the semiconductors are several orders of magnitude larger than those in the oxides. There are several important consequences of these large mobilities. Most importantly, the resulting large diffusion lengths lead to fast response times [see Eqs. (12) and (18)]. The corresponding values of write/erase energies (10 to 100  $\mu\text{J}/\text{cm}^2$ ) are very near the limiting values. These low values of write/erase energy have been observed not only at the infrared wavelengths used for experiments in InP and GaAs, but also at 633 nm in ZnTe.<sup>137</sup>

The large mobilities of the compound semiconductors also yield large values of dark conductivity (compared with the oxides), so the storage times in the dark are normally less than 1 s. Thus, these materials are not suited for long-term storage, but may still be useful for short-term memory applications. Finally, the short diffusion times in the semiconductors yield useful photorefractive performance with picosecond pulses.<sup>96</sup>

The electro-optic coefficients for the compound semiconductors are quite small (see Table 4), leading to low values of beam-coupling gain and diffraction efficiency in the absence of an applied electric field. As in the sillenites, both dc and ac field techniques have been used to enhance the space charge field. Early experiments with applied fields produced enhancements in the gain or diffraction efficiency which were considerably below the calculated values.<sup>140–142</sup> The causes of these discrepancies are now fairly well understood. First, space charge screening can significantly reduce the magnitude of the applied field inside the sample. This effect is reduced by using an ac field, but even in this case the required frequencies to overcome all screening effects are quite high.<sup>142</sup> Second, the mobility-lifetime product is known to reduce at high values of electric field due to scattering of electrons into other conduction bands and cascade recombination. This effect is particularly prominent in GaAs.<sup>143</sup> Third, large signal effects act to reduce the gain when large fields are used.<sup>144</sup> As in the sillenites, the highest gains are only measured when weak signal beams (large pump/signal beam ratios) are used. Finally, when ac square-wave fields are used, the theoretical gain value is only obtained for sharp transitions in the waveform.<sup>145,146</sup>

Another form of electric field enhancement has been demonstrated in iron-doped InP.<sup>147,148</sup> This material is unique among the semiconductors in that the operating temperature and incident intensity can be chosen so that the photoconductivity (dominated by holes) exactly equals the dark conductivity (dominated by electrons). In this case, an applied field will enhance the amplitude of the space charge field, while maintaining the ideal spatial phase of 90°. Gain coefficients as high as 11  $\text{cm}^{-1}$  have been reported in InP:Fe at 1.06  $\mu\text{m}$  using this technique.<sup>148</sup>

**TABLE 4** Relevant Materials Properties of Photorefractive Compound Semiconductors

Material	GaAs	InP	GaP	CdTe	ZnTe
Wavelength range ( $\mu\text{m}$ )	0.92–1.3	0.96–1.3	0.63	1.06–1.5	0.63–1.3
EO coeff. $r_{41}$ (pm/V)	1.2	1.45	1.1	6.8	4.5
$n_o^3 r_{41}$ (pm/V)	43	52	44	152	133
$n_o^3 r_{41} / \mathcal{E}$	3.3	4.1	3.7	16	13
Dielectric constant	13.2	12.6	12	9.4	10.1

(Most of the values are taken from Ref. 138.)

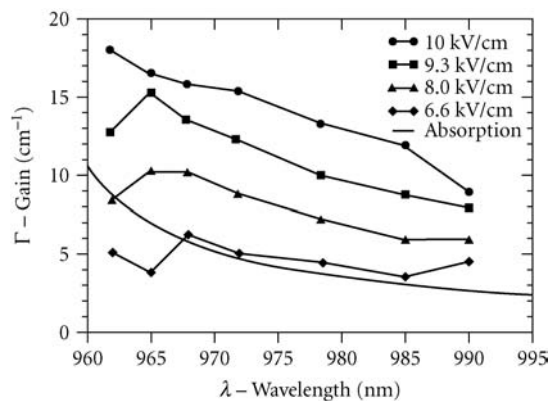
In early research on the photorefractive semiconductors, the wavelengths of operation were determined by available laser sources. Thus, all early experiments were performed at 1.06  $\mu\text{m}$  (Nd:YAG),  $\sim 1.3 \mu\text{m}$  (Nd:YAG or laser diode), and  $\sim 1.5 \mu\text{m}$  (laser diode). Later, the He-Ne laser (633 nm) was used to study wider bandgap materials. As the Ti:sapphire laser became available, interest turned to investigating the wavelength variation of photorefractive properties, especially near the band edge. Near the band edge, a new nonlinear mechanism contributes to the refractive index change: the Franz-Keldysh effect.<sup>149</sup> In this case, the internal space charge field develops as before. This field slightly shifts the band edge, leading to characteristic electroabsorption and electrorefraction. These effects can be quite large at wavelengths near the band edge, where the background absorption is also high. However, the peak of the electrorefraction spectrum is shifted slightly to longer wavelengths, where the background absorption is smaller. This is generally the wavelength region where these effects are studied.

The electrorefractive photorefractive (ERPR) effect has different symmetry properties than the conventional electro-optic photorefractive effect. It is thus possible to arrange an experiment so that only the ERPR effect contributes, or both effects contribute to the gain. In addition, the ERPR effect is quadratic in applied electric field. Thus, energy transfer between two writing beams only occurs when a dc field is present. The direction of energy transfer is determined by the sign of the electric field; this allows switching energy between two output beams via switching of the sign of the applied field.

In the first report of the band-edge photorefractive effect,<sup>149</sup> a gain coefficient of  $7.6 \text{ cm}^{-1}$  was measured in GaAs:EL2 at 922 nm, for a field of 10 kV/cm. In this case, both nonlinear mechanisms contributed to the gain. When a moving grating was used to optimize the spatial phase of the grating, the gain coefficient increased to  $16.3 \text{ cm}^{-1}$ .

In InP the temperature/intensity resonance can be used to optimize the spatial phase, thus eliminating the need for a moving grating. In the first experiment using band-edge resonance and temperature stabilization, gain coefficients approaching  $20 \text{ cm}^{-1}$  were measured in InP:Fe (see Fig. 8).<sup>150</sup> Later experiments on a thin sample using a beam ratio of  $10^6$  resulted in a measured gain coefficient of  $31 \text{ cm}^{-1}$ .<sup>151</sup>

The photorefractive effect can also be used to measure basic materials properties of electro-optic semiconductors, without the need for electrical contacts.<sup>152–154</sup> Quantities which can be measured include the populations of filled and empty traps and the mobility-recombination time product. One particular feature of the photorefractive technique is the ability to map properties across a wafer.<sup>154</sup>



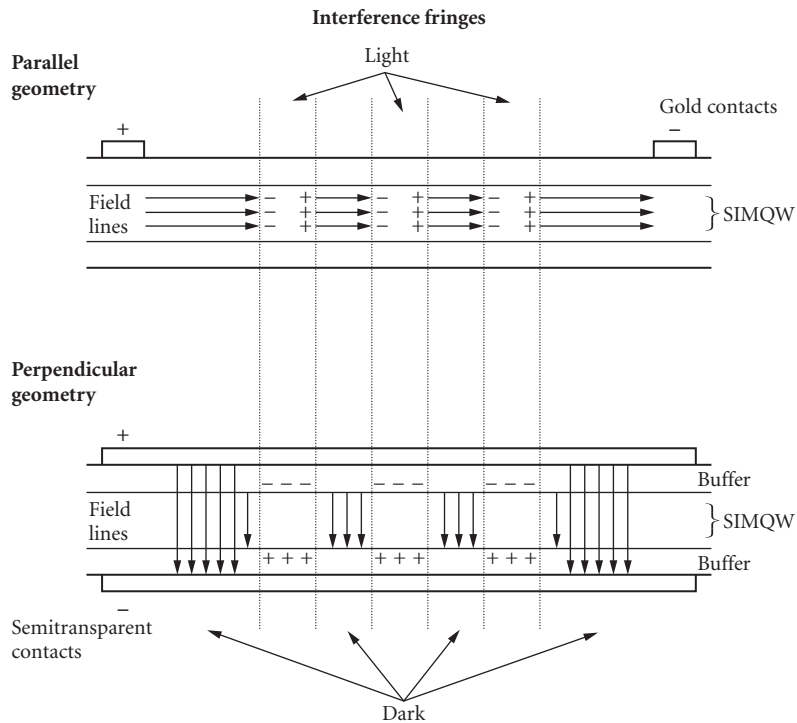
**FIGURE 8** Measured gain coefficient as a function of wavelength in InP:Fe, for a grating period of  $5 \mu\text{m}$  and four values of applied dc field. The beam ratio was 1000, and the intensity was adjusted at each point to produce the maximum gain. The background absorption coefficient is also plotted.

## Multiple Quantum Wells

While the enhancement of the electro-optic effect near the band edge of bulk semiconductors is significant, much larger nonlinearities are obtained at wavelengths near prominent band-edge exciton features in multiple quantum wells (MQWs). In addition, the large absorption in these structures yields much faster response times than those in bulk semiconductors. Finally, the small device thickness of typical MQW structures (typically 1 to 2  $\mu\text{m}$ ) provides improved performance of Fourier plane processors such as optical correlators.<sup>155,156</sup> One disadvantage of the small device thickness is that diffraction from gratings in these devices is in the Raman-Nath regime, yielding multiple diffraction orders.

In their early stages of development, MQWs were not optimized for photorefractive applications because of the absence of deep traps and the large background conductivity within the plane of the structure. It was later recognized that defects resulting from ion implantation can provide the required traps and increase the resistivity of the structure.

The first photorefractive MQWs were GaAs/AlGaAs structures which were proton-implanted for high resistivity ( $\rho = 10^9/\text{ohm-cm}$ ).<sup>157,158</sup> Two device geometries were considered (see Fig. 9), but only devices with applied fields parallel to the layers were studied. The principles of operation are initially the same for both device geometries. When two incident waves interfere in the sample, the spatially modulated intensity screens the applied field in direct proportion to the intensity, leading to a spatially modulated internal field. This spatially modulated field induces changes in both the refractive index and the absorption coefficient. The mechanism for these changes<sup>158</sup> is field ionization of excitons (Franz-Keldysh effect) in the parallel geometry and the quantum-confined Stark effect in the perpendicular geometry.



**FIGURE 9** Device geometries for photorefractive MQWs.

The magnitudes of the change in refractive index and absorption coefficient are strongly dependent on wavelength near the characteristic exciton peak. Both the index and the absorption grating contribute to the diffraction efficiency through the relationship

$$\eta = (2\pi \Delta n L / \lambda)^2 + (\Delta \alpha L / 2)^2 \quad (21)$$

where  $\Delta n$  and  $\Delta \alpha$  are the amplitudes of the index and absorption gratings, respectively, and  $L$  is the device thickness. Although the device thickness of typical MQWs is much less than the thickness of a typical bulk sample (by 3 to 4 orders of magnitude), the values of  $\Delta n$  can be made larger, leading to practical values of diffraction efficiency (see following).

The first III-V MQWs using the parallel geometry<sup>157,158</sup> had rather small values of diffraction efficiency ( $10^{-5}$ ). In later experiments, a diffraction efficiency of  $3 \times 10^{-4}$  and a gain coefficient of  $1000 \text{ cm}^{-1}$  were observed.<sup>159</sup> Still higher values of diffraction efficiency (on the order of 1.3 percent) were obtained using the perpendicular geometry in CdZnTe/ZnTe MQWs.<sup>160</sup> These II-VI MQWs have the added feature of allowing operation at wavelengths in the visible spectral region, in this case 596 nm.

In recent work on GaAs/AlGaAs MQWs in the perpendicular geometry, several device improvements were introduced.<sup>161</sup> First, Cr-doping was used to make the structure semi-insulating, thus eliminating the added implantation procedure and allowing separate control of each layer. Second, the barrier thickness and Al ratio were adjusted to give a reduced carrier escape time, leading to a larger diffraction efficiency. In these samples, a diffraction efficiency of 3 percent was observed at 850 nm for an applied voltage of 20 V across a 2- $\mu\text{m}$ -thick device. The response time was 2  $\mu\text{s}$  at an intensity of  $0.28 \text{ W/cm}^2$ , corresponding to a very low write energy of  $0.56 \text{ }\mu\text{J/cm}^2$ . The diffraction efficiency cited here was obtained at a grating period of 30  $\mu\text{m}$ . For smaller values of grating period, the diffraction efficiency was smaller, due to charge smearing effects. The fast response time and small thickness of these structures make them ideal candidates for Fourier plane processors such as optical correlators. Competing bulk semiconductors or spatial light modulators have frame rates which are 2 to 3 orders of magnitude below the potential frame rate of  $\sim 10^6 \text{ s}^{-1}$  which is available from photorefractive MQWs.

Future work on photorefractive MQWs would include efforts to grow thicker devices (so as to reduce the diffraction into higher grating orders) and to improve the diffraction efficiency at high spatial frequencies.

## Organic Crystals and Polymer Films

Organic materials are increasingly providing a viable alternative to their inorganic counterparts. Examples include organic crystals for frequency conversion applications and polymer films for electro-optic waveguide devices. These materials are, in general, simpler to produce than their inorganic counterparts. In addition, the second-order nonlinear coefficients in these materials can be quite large, with values comparable to those of the well-known inorganic material  $\text{LiNbO}_3$ . In most organic materials the electronic nonlinearity results from an extended system of  $\pi$  electrons produced by electron donor and acceptor groups. For a purely electronic nonlinearity, the dielectric constant  $\epsilon$  is just the square of the refractive index, leading to much smaller values of  $\epsilon$  than those in inorganic crystals. Thus, the electro-optic figure of merit  $n_b^3/\epsilon$  is enhanced in organic materials. This enhancement makes organic materials very appealing for photorefractive applications.

The first experiments reported on the photorefractive effect in organic crystals were those of Sutter et al.<sup>162,163</sup> on 2-cyclooctylamino-5-nitropyridine (COANP) doped with the electron acceptor 7,7,8,8-tetracyanoquinodimethane (TCNQ). Pure COANP crystals (used for frequency doubling) are yellow, whereas the TCNQ-doped samples are green, due to a prominent extrinsic absorption band between 600 and 700 nm. In experiments at 676 nm with a grating period of 1.2  $\mu\text{m}$ , both absorption and refractive index gratings were observed. Typical diffraction efficiencies were 0.1 percent, with a corresponding refractive index grating amplitude of  $10^{-6}$ . The recorded buildup times of the index gratings were on the order of 30 to 50 min at  $3.2 \text{ W/cm}^2$ . Following this initial demonstration of the photorefractive effect in organic crystals there has been very little progress since most attempts at doping these



crystals for photoexcitation and charge transport have simply resulted in expulsion of the dopants from the crystal structure. Only one additional crystal has been reported.<sup>164</sup>

The situation is much more promising for the photorefractive effect in composite polymer films. These materials were first reported in 1991<sup>165,166</sup> and from a materials science point of view, they are much easier to prepare than organic single crystals. In addition, there is greater flexibility in modifying the films to optimize photorefractive performance. In this respect, there are four requirements for an efficient photorefractive material:

1. A linear electro-optic effect, or a quadratic electrooptic effect with a linear component induced by a dc bias electric field
2. A source of photoionizable charges
3. A means of transporting these charges
4. A means of trapping the charges

In an organic polymer composite, each of these functions can be separately optimized. The space charge field due to the holographic interference pattern not only perturbs the refractive index via the electro-optic effect, but can also reorient molecules in the medium giving rise to a refractive index variation via polarizability anisotropy, an effect known as orientational enhancement.<sup>167</sup>

In spite of the large EO coefficients and the great flexibility in the materials engineering of organic polymers, there are also some practical problems which need to be addressed. First, polymers are most easily prepared as thin films. If propagation in the plane of the films is desired, then extremely high optical quality and low absorption are required. If propagation through the film is desired, then the grating diffraction efficiency is reduced. As the film thickness is made larger to enhance efficiency, the quality of the films is harder to maintain.

One important requirement of polymer films is that they must be poled to induce a linear electro-optic effect. If the poling voltage is applied normal to the film plane, then there is no electro-optic effect for light diffracted from gratings written with their wave-vectors in the plane of the film. In a practical sense, this means that the writing beams must enter the film at large angles to its normal. In addition, it becomes more difficult to provide large poling fields as the film thickness increases.

The first polymeric photorefractive material<sup>165,166</sup> was composed of the epoxy polymer bisphenol-A-diglycidylether 4-nitro-1,2-phenylenediamine (bisA-NPDA) made photoconductive by doping with the hole transport agent diethylamino-benzaldehyde diphenyl hydrazone (DEH). In this case, the polymer provided the nonlinearity leading to the electro-optic effect, as well as a mechanism for charge generation. The dopant provided a means for charge transport, while trapping was provided by intrinsic defects.

Films of this material with thicknesses between 200 and 500  $\mu\text{m}$  were prepared. The material was not cross-linked, so a large field was required at room temperature to maintain the polarization of the sample. For an applied field of 120 kV/cm, the measured value of the electro-optic figure of merit  $n_o^3 \gamma / \epsilon$  was 1.4 pm/V. Using interference fringes with a spacing of 1.6  $\mu\text{m}$  oriented 25° from the film plane, the measured grating efficiency at 647 nm was  $2 \times 10^{-5}$ . The grating buildup time was on the order of 100 s at an intensity of 25 W/cm<sup>2</sup>. Analysis of the data showed that the photorefractive trap density had the relatively small value of  $2 \times 10^{15}$  cm<sup>-3</sup>. In spite of the low value of trap density, relatively large values of space charge electric field were obtained, due to the low value of dielectric constant.

Subsequent research has led to general design principles for photorefractive polymer composites. Photoexcitation of charge is often accomplished by using donor-acceptor charge transfer complexes. In this way, the absorption spectrum can be tailored to the wavelengths of interest. Carbazole is often used as an electron donor entity, coupled with electron acceptors 2,4,7-trinitro-9-fluorenone (TNF),<sup>168</sup> (2,4,7-trinitro-9-fluorenylidene) malononitrile (TNFM),<sup>168,169</sup> or C<sub>60</sub>.<sup>170,171</sup> As in the case of the formation of inorganic photorefractive gratings in response to illumination by the optical interference pattern of two intersecting laser beams, the photoexcited charges should be free to move away from the site of excitation and be preferentially retrapped in the darker regions of the interference pattern to form a spatially varying charge distribution following the interference pattern. However, in contrast to the case of inorganic crystals, diffusion is not effective in driving charge separation, so electric fields

have to be applied to force charge separation by drift. These fields are applied by sandwiching a several micrometer thick layer of the polymer system between transparent electrodes. The electrodes have to be tilted with respect to the grating wave vector so as to provide a component of the bias field parallel to the grating vector. Another way in which organics differ from inorganics is that both the photogeneration rate and mobility depend on the electric fields in the material. Hole mobility is usually much greater than electron mobility. This has the effect of allowing the hole grating to dominate the electron grating. If the hole and electron gratings were of similar magnitude, their electric fields would tend to cancel each other out and weaken the photorefractive grating.

The holes migrate via hopping along a network of oxidizable charge transport agents. This network can be provided by the donor entity carbazole itself, or by hydrazones such as DEH or arylamines such as tri-tolylamine (TTA) or *N,N*-bis(4-methylphenyl)-*N,N*-bis-(phenyl)-benzidine (TPD). These can be added as dopants, or attached to the polymer backbone of the host polymer, as is the case in PVK. As in the case of inorganic photorefractives, a population of empty shallow traps is required to enable the nonuniform space charge distribution of the photorefractive grating. This is often achieved by providing a population of deep traps for some of the shallow traps to empty into, and it has been shown that the nonlinear optical chromophores can serve this purpose in PVK-based materials. These chromophores serve double duty as the moieties providing the optical nonlinearity. They should have large hyperpolarizability  $\beta$  for electro-optic susceptibility and/or large polarizability anisotropy  $\Delta\alpha = \alpha_{\parallel} - \alpha_{\perp}$ , where parallel and perpendicular refer to the molecular axis. They should also have a large ground state dipole moment  $\mu_g$  to enable the molecular orientation effect. These parameters can be combined into a single figure of merit (FOM) defined as

$$\text{FOM} = \frac{1}{M} \left[ 9\mu_g \beta + \frac{2\mu_g^2 \Delta\alpha}{k_B T} \right] \quad (22)$$

where  $M$  is the molar mass,  $k_B$  is Boltzmann's constant, and  $T$  is the temperature.

The final component in the composite is a plasticizer to lower the glass transition temperature  $T_g$  so as to better enable the orientational orientation effect.

An example of a complete composite comprising hole transporter-electron donor/nonlinear chromophore-deep trap/plasticizer/sensitizer-electron acceptor is PVK/AODCST/BBP/ $C_{60}$  in the ratio 49.5:35:15:0.5 percent, where AODCST 2-[[4-[bis(2-methoxyethyl)amino]phenyl]methylene]-malononitrile and BBP is butyl benzyl phthalate. It showed a gain coefficient of  $235 \text{ cm}^{-1}$  with a response time of 5 ms at  $1 \text{ Wcm}^{-2}$  for 647-nm light.<sup>170,172</sup> There are many variations on this theme for the design of photorefractive polymer systems, including the use of sol-gel processing,<sup>171</sup> and the use of alternative sensitizers such as gold nanoparticles,<sup>173</sup> transition metal complexes,<sup>174–177</sup> and quantum dots. Quantum dots have been investigated as sensitizers;<sup>178</sup> this is attractive since the spectral sensitivity of the system could be tuned through selection of the size of the quantum dots. It is tempting to try to increase the nonlinearity by increasing the proportion of nonlinear chromophore; however, this can lead to phase separation in a composite polymer. This drawback can be overcome by using an organic amorphous glass as photoconductor and NLO molecule simultaneously, or by using fully functionalized polymers in which the charge generator, charge transporter, and NLO components are incorporated as side chains. Liquid crystals have large orientational nonlinearity, and they have been successfully made photorefractive via the addition of small amounts of sensitizer.<sup>179</sup> They have also been combined with photoconductive polymers as polymer-dispersed or polymer-dissolved liquid crystals.<sup>180,181</sup> Another approach is to replace the transparent electrodes that bias the liquid crystal with thin plates of inorganic photorefractive material such as cerium-doped strontium barium niobate.<sup>182</sup> In this way, the large photorefractive space charge generated in the inorganic plates can extend into the liquid crystal layer and generate a large orientational nonlinearity. This removes the need to tilt the liquid crystal cell and resulted in gain coefficients as large as  $1600 \text{ cm}^{-1}$  and grating periods as small as 300 nm.

Table 5, reprinted from a review article by Ostroverkhova and Moerner,<sup>183</sup> shows the characteristics of several organic photorefractive systems. That review provides many further details on modeling, design, and characterization of organic photorefractive materials.

**TABLE 5** PR Properties of High Performance Organic Materials in the Visible Part of the Spectrum<sup>a</sup>

Composite (conc of Constituents, wt %)	$T_g$ , °C	$\alpha$ , cm <sup>-1</sup>	$d$ , $\mu\text{m}$	$\lambda$ , nm	$\Gamma$ , cm <sup>-1</sup> (E, V/ $\mu\text{m}$ )	$\tau_g^{-1}$ , s <sup>-1</sup> (I, W/cm <sup>2</sup> )	$\eta_{\text{max}}^{\%}$ (E, V/ $\mu\text{m}$ )	$\tau_{\text{FWM}}^{-1}$ , s <sup>-1</sup> (I, W/cm <sup>2</sup> )	$\Delta n$ , 10 <sup>-3</sup> (E, V/ $\mu\text{m}$ )	Refs.
Polymer composites										
PVK/AODCST/BBP/C <sub>60</sub> (49.5/35/15/0.5)		9	80	647	235 (100)	200 (1) 6 (0.1)				170, 172
PVK/DCDHF-6/BBP/C <sub>60</sub> (49.5/30/20/0.5)		15	80	647	400 (100)	4 (0.1)				172
PVK/BDMNPAB/TNF (55/44/1)	43		100	633	195 (85)	~1 (0.004)	40 <sup>int</sup> (70)		4.2 (92)	184
PVK/6OCB/C <sub>60</sub> (49.8/50/0.2)	47.1		70		210 (65)					185
PSX/DB-IP-DC/TNF (69/30/1)	27.5	60	100	633	390 (100)	30 (0.04)	92 <sup>int</sup> (30)		3 (30)	186, 187
PSX/DMNPAA/TNF (53/46/1)	25			670	221 (80)			0.2(1.2)	5.8 (80)	188
PSX/stilbene A/TNF (51/48/1)	25		40	670	53 (100)		100 <sup>int</sup> , 60 <sup>ext</sup> (70)	0.017 (1.2)	10.5 (100)	188
DBOP-PPV/DMNPAA/ MNPAA/DPP/PCBM (52/20/20/5/3)	14.4	34	105	633			90 <sup>int</sup> (62)	1.7 (0.305)	2.6 (62)	189
<i>p</i> -PMEH-PPV/DO3/DPP/C <sub>60</sub> (74/5/20/1)	45			633	403 (0 <sup>b</sup> )	0.003 (0.28)				190
PPT-Cz/DDCST/C <sub>60</sub> (64.5/35/0.5)	-7	36.6	100	633	250 (60)		93 <sup>int</sup> (100)	0.37 (0.034)	1 (50)	191
PTCB/DHADC-MPN/ DIP/ TNFM (49.7/37.6/12.5/0.18)		22.6	105	633	225 (50)		71 <sup>ext</sup> (28)	0.07 (0.78)	8.5 (50)	192
Amorphous glasses										
2BNCM/PMMA/TNF (90/9.7/0.3)	22	4	150	676	69 (40)		80 (40)	0.012 (1)	10 (40)	193
DCDHF-6/C <sub>60</sub> (99.5/0.5)	19	12.7	70	676	240 (30)	0.6 (0.1)		0.41 (0.8)		194
DCDHF-6-CF3/C <sub>60</sub> (99.5/0.5)	17	19.9	70	676	255 (40)	0.116 (0.1)		0.21 (0.8)		194
EHCN/TNF (99/1)	25	41	100	633	84 (40)		90 <sup>int</sup> (30)	0.67 (0.121)	1.3 (30)	195
Cz-C6-THDC/ECZ/TNF (89/10/1) <sup>c</sup>	33		50				65 (70)		4.5 (70)	196
Methine A	6	1.64	130	633	118 (89)		74 <sup>int</sup> (53)		5.6 (53)	197

Fully functional polymers								
Ru-FFP	130	102	690	380 (0 <sup>b</sup> )	0.0014			174
Polymer-dispersed liquid crystals and liquid crystals								
PMMA/TL202/ECZ/TNFM (42/40/17/1)		99 <sup>d</sup>	105 53	633	136 (10)		100 <sup>int</sup> (8) 56 <sup>ext</sup> (22)	3.2 (22) 180
PMMA/TL202/ECZ/CdS (42/40/16/2)		7.5	129	514.5	30 (31)		72 <sup>ext</sup> , 90 <sup>int</sup> (50)	~0.1 (3) 178
SCLP/E7/C <sub>60</sub> E7 on PVK/TNF (83/17) <sup>e</sup>		<20 20	50 10	633 514.5	640 (0.7) 3700 <sup>e</sup> (0.9)	0.29 (8)		198 199
							44 <sup>ext</sup> , <i>f</i> (0.9)	~100
Hybrid organic-inorganic composites, glasses, and sol-gels								
PIBM/AZPON (40/60)		113	55	633	350 (35)		80 <sup>int</sup> (13)	9 (25) 177
BEPON	24	49	40	633	750 (100)		40 <sup>int</sup> (28) <sup>c</sup>	11 (33) 177
PVK/DCVDEA/TNF/Au (70/28.6/1.4/<1)	40		70	633	240 (130)		43 (90)	173
Sol-gel DMHNAB-urethane- SiO1.5/ SiO1.5OH/ECZ/TNF (1:1.1:0.2:0.002) <sup>g</sup>		29	30	633	444 (0 <sup>b</sup> )		25.6 <sup>int, h</sup> (0 <sup>b</sup> )	0.0056 3.5h (0 <sup>b</sup> ) 200
Sol-gel SG-Cz/SG-MN/PEG/ TNF (45/45/9/1)	2		75	633	55 (94)		82.4 <sup>ext</sup> (94)	0.59 (0.14) 201

<sup>a</sup>Columns represent: (1) composition (concentration of the constituents in wt %, unless stated otherwise); (2) glass transition temperature  $T_g$ ; (3) absorption coefficient  $\alpha$ ; (4) sample thickness  $d$ ; (5) wavelength of the PR experiments  $\lambda$ ; (6) 2BC gain coefficient, measured with  $p$ -polarized writing beams,  $\Gamma$  (electric field  $\mathbf{E}$ , at which the indicated  $\Gamma$  was obtained); (7) PR response time  $\tau_g^{-1}$  obtained from fits to 2BC dynamics (total light intensity of writing beams, at which the indicated value of  $\tau_g^{-1}$  was obtained); (8) maximal diffraction efficiency  $\eta_{\max}$ , measured with  $p$ -polarized probe and  $s$ -polarized writing beams. External ( $\eta_{\text{ext}}$ ) or internal ( $\eta_{\text{int}}$ ) diffraction efficiency is indicated, where applicable (electric field  $\mathbf{E}$ , at which the indicated  $\eta$  was obtained); (9) PR speed  $\tau_{\text{FWM}}^{-1}$  obtained from fits to either formation or erasure of the PR grating measured in the FWM experiment (total light intensity of either writing beams or erasing beam); (10) refractive index modulation  $\Delta n$ , calculated from the diffraction efficiency (electric field  $\mathbf{E}$ , at which the indicated refractive index modulation was obtained); (11) reference to work from which the data was taken. All data reported were obtained in Bragg regime (volume grating) at room temperature, unless stated otherwise. <sup>b</sup>Prepoled material. <sup>c</sup>Temperature of the measurements  $T_m$ ) 30°C. <sup>d</sup>Includes scattering losses. <sup>e</sup>All the measurements were done in the Raman-Nath regime. See discussion about the relevance of the gain coefficient in the text. <sup>f</sup>Maximal diffraction efficiency possible in the Raman-Nath regime is ~34 percent. The authors attributed their high diffraction efficiency by nonsinusoidal space-charge field. <sup>g</sup>Molar concentrations. <sup>h</sup>This value was obtained with  $p$ -polarized writing beams and  $p$ -polarized readout.

## 12.3 DEVICES

### Real-Time Holography

The real-time phase holograms produced by the photorefractive effect can be used to perform any of the functions of regular holograms. In fact, many of the first applications of photorefractive nonlinear optics were replications of experiments and ideas first introduced in the 1960s in terms of the then new static holography. These include distortion correction by phase conjugation and one-way imaging through distortions, holographic interferometry for nondestructive testing, vibration mode visualization, and pattern recognition by matched filtering. A concise overview of these applications may be found in Goodman's classic text.<sup>202</sup> Their photorefractive realizations are well described in Huignard and Gunter.<sup>1</sup> Some of the advantages of photorefractive holography over conventional holography are

- Photorefractive holograms are volume phase holograms. This results in high diffraction efficiencies.
- Photorefractive holograms are self-developing.
- Photorefractive holograms diffract light from the writing beams into each other during the writing process. This gives rise to a dynamic feedback process in which the grating and writing beams influence each other.
- Photorefractive holograms adapt to changing optical fields.

It is the last two features that most strongly differentiate the photorefractive effect from regular holography.

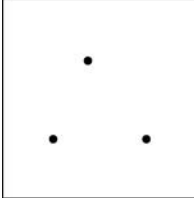

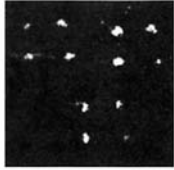
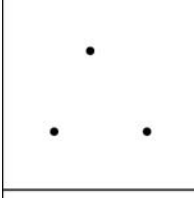

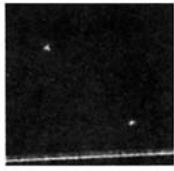
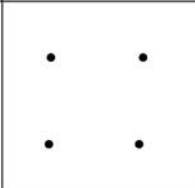
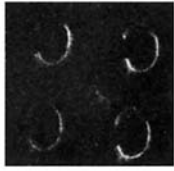
**Pattern Recognition** As an example of the transfer of applications of conventional holography to photorefractive nonlinear optics we consider the case of pattern recognition by matched filtering.

A matched filter for pattern recognition is simply a Fourier transform hologram of the desired impulse response. It can be made in real time in a photorefractive crystal, a lens being used to produce the Fourier transform. The best-known system is a nonlinear optical triple processor based on four-wave mixing<sup>203</sup> (Fig. 10). For a phase conjugate mirror, the coupled-wave equation for beam 3 which is the phase conjugate of beam 4 pumped by beams 1 and 2 is

$$\begin{aligned} \frac{dA_3}{dz} &= \gamma \frac{(A_1 A_4^* + A_2^* A_3)}{I_0} A_2 \\ &= \frac{\gamma}{I_0} I_2 A_3 + \frac{\gamma}{I_0} A_1 A_2 A_4^* \end{aligned} \quad (23)$$

where the  $A_j$  and  $I_j$  are the amplitudes and intensities of beams  $j$ , respectively, and  $I_0$  is the total intensity of the interacting beams. The first term on the right-hand side simply corresponds to amplification of beam 3. The second term is the source for beam 3. Thus, the amplitude of beam 3 is proportional to the product  $A_1 A_2 A_4^*/I_0$ . As depicted in Fig. 10,  $A_1$ ,  $A_2$ , and  $A_4$  are the Fourier transforms of the spatially varying input fields  $a_1$ ,  $a_2$ , and  $a_4$ . The output  $a_3$  is proportional to the inverse Fourier transform of the product of the three Fourier transforms  $A_1 A_2 A_4^*/I_0$ . If  $I_0$  is spatially constant the output is beam 1 convolved with beam 2 correlated with beam 4 ( $a_3 \propto a_1 \otimes a_2 * a_4$ ) where  $*$  represents the spatial correlation operation and  $\otimes$  represents the convolution operation, all produced in real time. Modified filters such as phase-only filters can be produced by taking advantage of energy transfer during the filter writing process,<sup>204–206</sup> or by saturation induced by the presence of the possibly spatially varying intensity denominator  $I_0$ .<sup>207–209</sup>

Sometimes, applications directly transferred from static holography inspire further developments made possible by exploitation of the physical mechanisms involved in the photorefractive effect. For example, acoustic signals can be temporally correlated with optical signals. An acoustic

$U_1$	$U_2$	$U_4$	$U_3$
	DELTA FUNCTION		
	DELTA FUNCTION	E	
C	DELTA FUNCTION	CAL TECH	
C		DELTA FUNCTION	

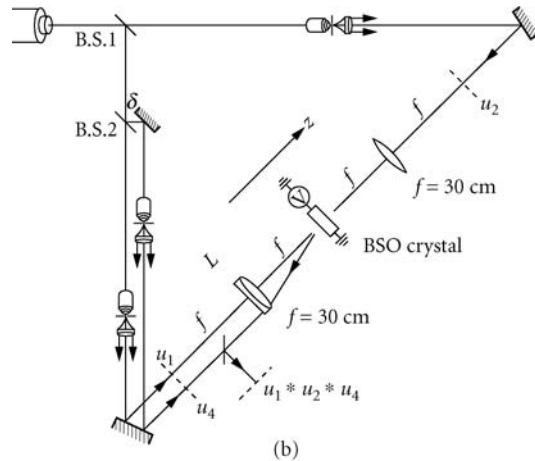
(a)

**FIGURE 10** (a) Results demonstrating real-time spatial convolution and correlation of two-dimensional images. The input fields are labeled  $E_1$ ,  $E_2$ , and  $E_p$ ; the output is labeled  $E_c$ . (After White and Yariv.<sup>203</sup>)

signal applied to a photorefractive crystal induces piezoelectric fields. If the crystal is illuminated by a temporally varying optical signal, then the photorefractive space charge generated by the photocurrent will be proportional to the product of the time-varying photoconductivity and the time-varying piezoelectric fields. Such correlators can be used to make photorefractive tapped delay lines with tap weights proportional to correlation values.<sup>210–212</sup> It is also possible to make acoustic filters which detect Bragg-matched retroreflection of acoustic waves from a photorefractive grating in a crystal such as lithium niobate that has low acoustic loss.<sup>213</sup>

## Applications of Photorefractive Gain in Two-Beam Coupling

**Coherent Image Amplification** Coherent image amplification is especially important for coherent optical processors. Without it, the losses introduced by successive filtering operations would soon become intolerable. Practical considerations include maintenance of signal-to-noise ratio and

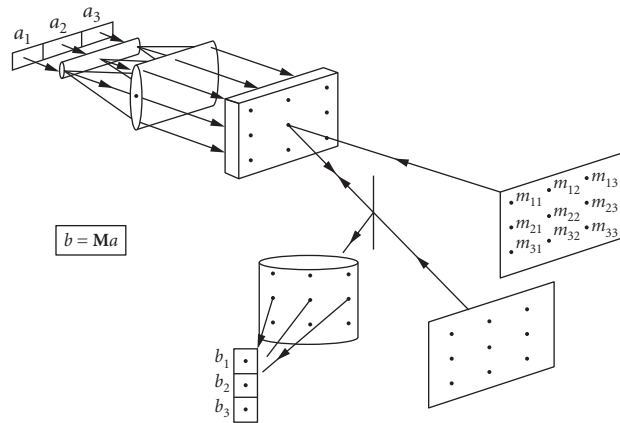


**FIGURE 10** (b) Experimental apparatus for performing spatial convolution and correlation using four-wave mixing in photorefractive bismuth silicon oxide. Input and output planes are shown by dashed lines. (After White and Yariv.<sup>203</sup>)

amplification fidelity. The main contribution to noise introduced by photorefractive amplifiers is from the fanning effect. Although it can be reduced in a given crystal in a variety of different ways, such as by crystal rotation<sup>21</sup> and multiwavelength recording,<sup>22</sup> by far the best approach to this problem would be to undertake research to grow cleaner crystals. Amplification fidelity is determined by gain uniformity. In the spatial frequency domain, it is limited because photorefractive gain depends on the grating period. Images with a high spatial bandwidth write holograms with a wide range of spatial frequencies and grating periods. Optimal uniformity is obtained for reflection gratings, in which the image beam counterpropagates with respect to the pump. In that case, the change in grating period depends only to second order on the image spatial frequency. Any remaining first-order nonuniformity is due to the angular dependence of the effective electro-optic coefficient. In the space domain, gain uniformity is limited by pump depletion so that the most accurate results will be obtained if the pump beam is strong enough that it is not significantly depleted in the interaction.

Two-beam coupling amplification can also be used for beam cleanup:<sup>214</sup> a badly distorted beam, say from a laser diode, can be converted to a gaussian beam. A small sample of the beam is split off, spatially filtered and amplified in two-beam coupling by the remaining bulk of the distorted beam. The efficiency of the method can be quite high: fidelity limitations due to spatial variations in gain are usually quite small and can be removed by a second round of spatial filtering. A unidirectional ring resonator with an intracavity spatial filter can also be used for beam cleanup.<sup>215</sup>

**Laser Power Combining** An application related to two-beam coupling image amplification is coherent power combining, which would be especially useful for semiconductor lasers. The output of a single laser gain stripe is limited to values of the order of a few hundred milliwatts. Some applications require diffraction-limited beams containing many watts produced at high efficiency. Such a source can in principle be made by using two-beam coupling amplification of a diffraction-limited seed by the mutually injection locked outputs of many diode stripes. The injection locking can be achieved by evanescent coupling between laser gain stripes<sup>216,217</sup> or by retroreflecting a portion of the amplified beam with a partially transmitting mirror.<sup>218</sup> Another possibility involves forming a double phase conjugate mirror<sup>219,220</sup> or ring self-pumped phase conjugate mirror with a master laser providing one input, and the light from the gain elements loosely focused into the crystal providing the other inputs. Such a system will be self-aligning and will correct intracavity distortions by phase conjugation.



**FIGURE 11** Schematic drawing of the basic principle of optical matrix vector multiplication through four-wave mixing in nonlinear media. Light from a linear source array  $a$  is fanned out by a cylindrical lens, where it diffracts from an image plane hologram of the matrix  $M$  to produce a set of beams bearing the required products  $M_{ij}a_j$ . A second cylindrical lens sums the diffracted beams to form  $b = Ma$ . (After Yeh and Chiou.<sup>229</sup>)

Phase conjugate master oscillator/power amplifiers have also been used with some success.<sup>221</sup> Practical problems include the need to control the spectral effects of the associated multiple coupled cavities. Reference<sup>222</sup> gives an excellent exposition of these problems. Also, while self-pumped phase conjugate reflectivities and two-beam coupling efficiencies can theoretically approach 100 percent, in practice these efficiencies rarely exceed 80 percent. Among oxide ferroelectrics, barium titanate exhibits high gain at GaAs laser wavelengths. However, while some bulk semiconductors such as InP:Fe and CdTe:V are sensitive in the 1.3- to 1.5- $\mu\text{m}$  wavelength range of interest for optical fiber communications, high gain requires the application of high electric fields.

**Optical Interconnects** Use of the double phase conjugate mirror for laser locking suggests another application. The beam-coupling crystal can be viewed as a device that provides optical interconnection of the laser gain elements to each other.<sup>223</sup> The basic idea exists in the realm of static holography in terms of computer interconnection by holographic optical elements<sup>224,225</sup> (HOEs). The use of photorefractive crystals should enable the construction of reprogrammable interconnects that would be self-aligning if phase conjugation were used:<sup>226</sup> the laser gain elements in the power combining case can be imagined as the input/output ports of an electronic chip.<sup>227</sup> Another way to go about the interconnection problem is to design in terms of an optical crossbar switch, or matrix vector multiplier.<sup>228,229</sup> The vector is an array of laser diode sources and the matrix describes connection patterns of the sources to a vector array of detectors (Fig. 11). The interconnection matrix is realized as a photorefractive hologram.

## Applications of Photorefractive Loss in Two-Beam Coupling

If the sign of the coupling constant is reversed (for example, by rotation of the uniaxial crystal by  $180^\circ$  so that the direction of the optic axis is reversed) the pump interferes destructively with the signal so that the output is reduced to a very low level. This resulting photorefractive loss can be used in a number of applications such as for optical limiters, optical bistability,<sup>230</sup> and novelty filters and achieved using a variety of different devices such as ring resonators and phenomena such as beam fanning.



**Optical Limiters** The process of beam depletion in photorefractive materials forms the basis of their use as optical limiters. For this application, another important property of photorefractive materials is their ability to respond selectively to coherent optical inputs. Any portion of the input which is temporally incoherent is transmitted through a photorefractive material in a linear manner. Thus, photorefractive limiters will also selectively attenuate (or *excise*) a coherent beam while transmitting an incoherent beam; these devices have thus also been referred to as excisors.

The first studies of photorefractive limiters were published in 1985.<sup>25</sup> A number of device architectures involving resonators and self-pumped phase conjugate mirrors were discussed, but the primary emphasis was on beam fanning. Several features of limiters or excisors using beam fanning were pointed out: (1) the device design is very simple, with a single input beam and no separate external paths required; (2) the limiting mechanism is due to scattering (and not absorption), so that added heating is not present; (3) the device will operate at one or more wavelengths within the bandwidth of its photorefractive response, which (for ferroelectric oxides) extends over the entire visible band; and (4) the device will respond to sources with a relatively small coherence length, including mode-locked lasers producing picosecond pulses.

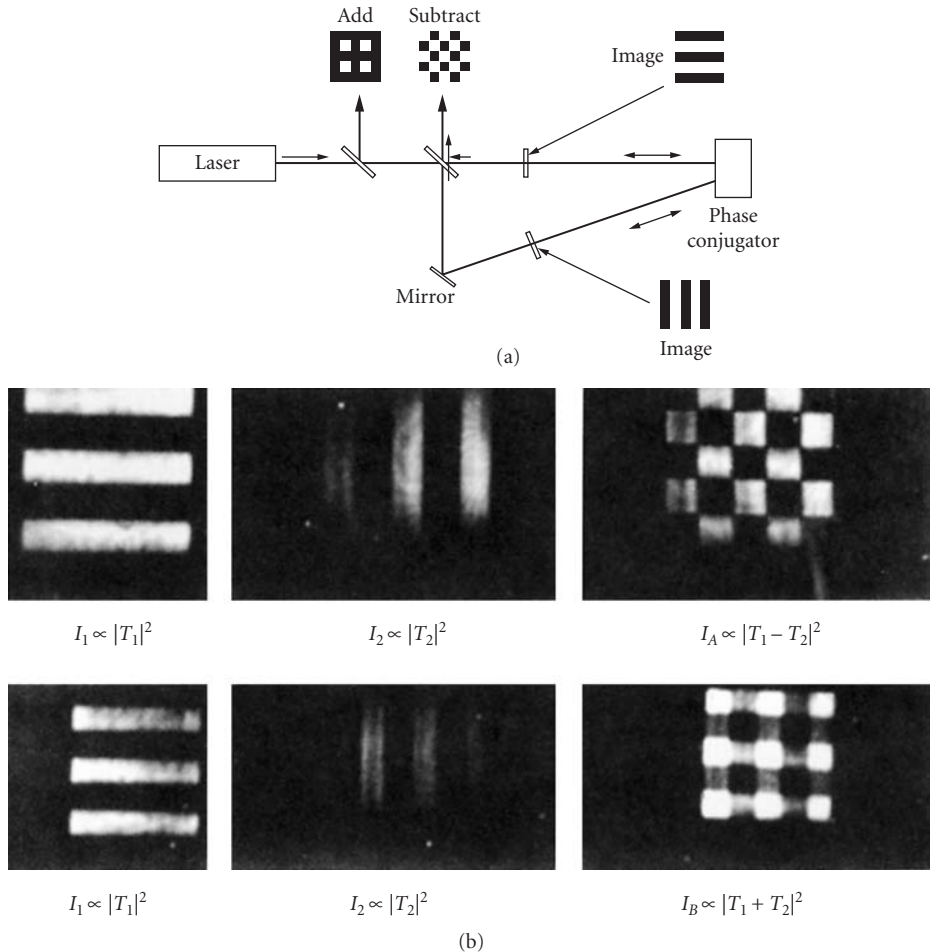
Experiments at 488 nm using BaTiO<sub>3</sub> in the beam fanning geometry<sup>25</sup> produced a steady-state device transmission of 2.5 percent, and a response time of 1.1 s at 1 W/cm<sup>2</sup>. Using the measured response time and intensity, we note that 1.1 J/cm<sup>2</sup> will pass through the device before it fully activates. In later measurements in the beam fanning geometry, attenuation values exceeding 30 dB and device activation energies as low as 1 to 10 mJ/cm<sup>2</sup> have been measured.

Two-beam coupling amplification of a second beam produced by beam splitters<sup>231,232</sup> or gratings in contact with the crystal<sup>233,234</sup> has also been studied as a mechanism for optical limiting. This mechanism is closely related to fanning, with the only difference that the second beam in a fanning device is produced internally by scattering.

**Novelty Filters** Novelty filters are devices whose output consists of only the changing part of the input. The photorefractive effect can be used to realize the novelty filter operation in several different ways. The simplest way is to use two-beam coupling for image deamplification as was used in the fanning and two-beam coupling optical limiters. In that case, the pump interferes destructively with the signal so that the output is reduced to a very low level. Now if the signal suddenly changes, the output will be the difference between the new input signal and the reconstruction of the old signal by diffraction of the pump from the old grating. Thus, the output will show the changed parts of the scene until the grating adapts during the photorefractive response time to the new scene.<sup>235,236</sup> Such interferometers have been used, for example, to map turbulent flow,<sup>237,238</sup> to make photothermal measurements,<sup>239</sup> and to build acoustic spectrum analyzers.<sup>240</sup>

## Phase Conjugate Interferometry

Another way to produce a novelty filter is to use a phase conjugate interferometer.<sup>241,242</sup> This is an interferometer in which some or all of the conventional mirrors are replaced by phase conjugate mirrors, thus achieving the benefit of self-alignment. The effects of phase objects inserted in the interferometer are canceled out by phase conjugation. One of the most common realizations is a phase conjugate Michelson interferometer (Figs. 12 and 13). If the phase conjugate mirrors have common pumping beams (this can be achieved by illuminating the same self-pumped phase conjugator with the beams in both arms), the phase of reflection for both beams will be the same and there will be a null at the output from the second port of the device. If a phase object inserted in one of the arms suddenly changes, the null will be disturbed, and the nonzero output will represent the changing parts of the phase object. The nonzero output persists until the gratings in the phase conjugate mirror adapt to the new input fields.<sup>243</sup> If two amplitude objects are inserted in the interferometer, one in each arm, the intensity of the output at the nulling port is the square of the difference between the squared moduli of the objects. This architecture thus gives rise to image subtraction.<sup>244,245</sup> A slightly modified version can be used to measure thin-film properties (refractive index, absorption coefficient, and thickness): the film under test on its substrate is used as the interferometer beam splitter.<sup>246</sup>

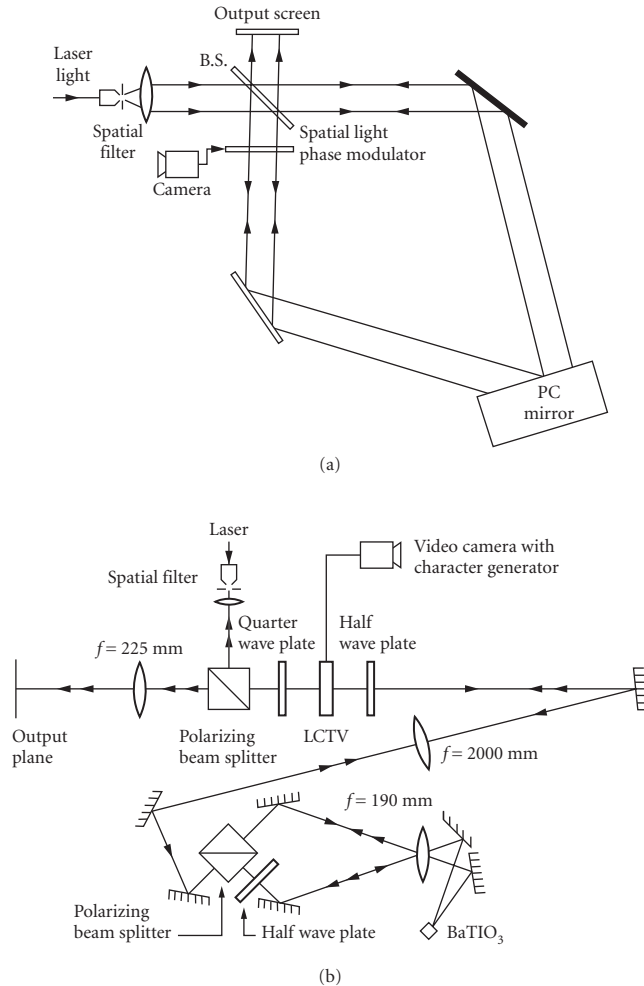


**FIGURE 12** Phase conjugate interferometer for image subtraction: (a) amplitude images are placed in the interferometer arms. Their difference appears at the nulling output, the sum appears at the retroreflection output. (b) Real-time image subtraction and addition of images using above apparatus. (After Chiu and Yeh.<sup>245</sup>)

## Associative Memories and Neural Networks

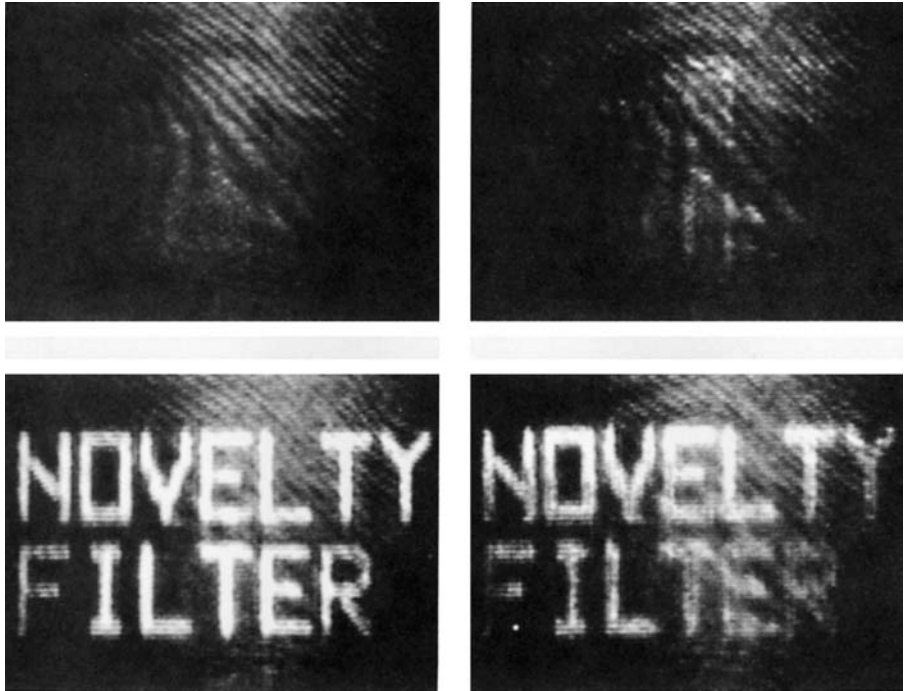
There are a number of adaptive processors that can be designed using photorefractive beam coupling. In addition to novelty filters, these include associative memories, neural network models, and other recursive image processors.

Photorefractive phase conjugate mirrors provide an elegant way to realize linear associative memories in which a fragment of an image can be used to recall the entire image from a bank of multiplexed holograms stored in a long-term storage photorefractive crystal such as lithium niobate.<sup>247,248</sup> Neural networks, on the other hand, are nets of interconnected signals with nonlinear feedback. They have been extensively investigated in the artificial intelligence community.<sup>249</sup> Typical applications are modeling of neural and cognitive systems and the construction of classification machines. As we have seen, there are a number of different ways to realize optical interconnections



**FIGURE 13** Phase conjugate interferometer as a novelty filter: any phase change in the object arm disturbs the null at the output until the phase conjugate mirror adjusts to the change. (a) Optical tracking novelty filter incorporating a spatial phase modulator. BS, beam splitter; PC, phase conjugate mirror. (b) Modification of preceding device to enable the use of a polarization modulating liquid crystal television (LCTV).

using the photorefractive effect, and nonlinear feedback can be introduced by using the nonlinear transfer properties of pumped photorefractive crystals. A pattern classifier can be built by recording a hologram for each image class (e.g., represented by a clear fingerprint) in a photorefractive crystal with a long time constant. Many holograms can be superposed if they are recorded with spatially orthogonal reference beams. As in the case of the linear associative memory, a smudged fingerprint introduced to the system will partially reconstruct each of the reference beams. The brightest reconstruction will be the reference associated with the fingerprint most like the smudged input. An oscillator with internal saturable absorption is built to provide competitive feedback of the reference reconstructions to themselves. The oscillator mode should be the mode associated with the proper fingerprint. That



(c)

**FIGURE 13** (c) Photograph of the output of the tracking novelty filter shown in (b). Input to the LCTV is taken from a character generator driving a video camera: (1) the character generator is off; the interferometer is essentially dark; (2) the character-generator display, showing the phrase NOVELTY FILTER is activated; (3) the filter adapts to the new scene and becomes nearly blank, as in (1). Some letters are visible; (4) the character-generator display is deactivated. The previous phrase appears at the output of the interferometer. Shortly thereafter it fades to (1). (After Anderson *et al.*<sup>243</sup>)

mode then reconstructs the clear fingerprint. The output of the device is the stored fingerprint which is most like the smudged input. We have described just one optical neural network model, but just as there are many theoretical neural network models, there are also many optical neural network models.<sup>250–254</sup> Each of them has its own practical difficulties, including those of reliability, suitability of available threshold functions, and stability.

In addition, the optical gain of photorefractive oscillators makes possible the design of other recursive image processors, for example, to realize Gerschberg-Saxton-type algorithms in phase conjugate resonators.<sup>255</sup>

## Thresholding

In optical data processing it is often necessary to determine if one or more elements of an optical pattern has an intensity above (or below) a set threshold value. For example, in optical associative memory applications, it is necessary to select the stronger modes among many in an optical resonator. In optical correlator applications, the output information plane may be thresholded to determine whether a correlation has been obtained, and to determine the location of the correlation peak(s). A closely related operation which is also useful for these applications is the Max or winner-take-all operation.

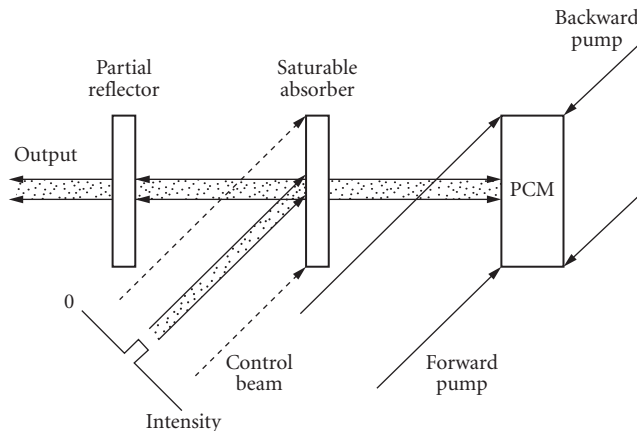
The ideal thresholding device should have the following properties: (1) the capability to process complex images with high resolution, (2) high sensitivity, (3) low crosstalk between pixels, (4) a sharp threshold, with constant output for intensities above the threshold value, (5) large signal-to-noise, and (6) the ability to control the threshold level by external means.

A large number of thresholding schemes using the photorefractive effect have been proposed or demonstrated, although only a few experimental demonstrations of thresholding of spatial patterns or images have been reported. Techniques used in early investigations include (1) uniform incoherent erasure of self-pumped phase conjugate mirrors<sup>256</sup> and of photorefractive end mirrors in phase conjugate resonators<sup>257,258</sup> and (2) pump depletion in externally pumped phase conjugate mirrors and double phase conjugate mirrors.<sup>55</sup> A number of thresholding devices using ring resonators have also been demonstrated.<sup>55,259</sup> One way of increasing the sharpness of the threshold is to insert additional nonlinear media in the photorefractive resonator cavities.

Ingold et al.<sup>260</sup> demonstrated winner-take-all behavior in a nonresonant cavity containing a nematic liquid crystal and a photorefractive crystal. In later experiments,<sup>261</sup> a thresholding phase conjugate resonator containing a saturable absorber consisting of a thin film of fluorescein-doped boric acid glass demonstrated several performance improvements. In this architecture (shown schematically in Fig. 14) the input image was amplitude-encoded as a two-dimensional array of pixels on an incoherent control beam that was incident on the saturable absorber (a single pixel is shown in Fig. 14). If the intensity at a given pixel was above a threshold intensity, the saturable absorber bleached locally by an amount sufficient to switch on the phase conjugate resonator. The phase conjugate resonator continued to oscillate at these pixel locations even when the control beam was removed. The output was thus bistable and latching.

## Photorefractive Holographic Storage

The neural networks described above rely on optical information storage in a material whose gratings are long-lived. One of the earliest potential applications for the photorefractive effect was for



**FIGURE 14** Schematic diagram of linear phase conjugate resonator containing an intracavity saturable absorber. Information is read into the resonator by means of a separate control beam incident on the saturable absorber. The control beam can be brought in through a beam splitter, or at an angle to the optic axis (as shown). The fluorescein-doped boric acid glass saturable absorber had a saturation intensity ( $I_s = 20 \text{ mW/cm}^2$ ) at its absorption peak (450 nm). The  $\text{BaTiO}_3$  phase conjugate mirror was pumped at the neighboring Ar laser wavelength of 458 nm. The control beam was generated from the same laser, and cross-polarized to a void feedback into the resonator. (After McCahon et al.<sup>261</sup>)

holographic information storage. One of the best materials for the purpose was and still is lithium niobate; it has storage times which can be as long as years. The principal concerns for holographic storage are information density, crosstalk minimization, fixing efficiency, signal-to-noise ratio, and development of practical readout/writing architectures. There has been a recent renewed interest in optical memory design, now that materials and computer technology have improved and schemes for rapid addressing have matured. The two main classes of addressing scheme use spatially orthogonal reference beams<sup>262–264</sup> and temporally orthogonal reference beams<sup>265</sup> (spatial multiplexing vs. frequency multiplexing). Spatial multiplexing has the advantage that relatively simple optical sources can be used. Frequency multiplexing has the advantage that spatial crosstalk is reduced compared to that associated with spatial multiplexing. However, it has the drawback of requiring frequency-tunable laser sources. An important consideration is the need to pack as much information as possible into each individual hologram. Here the frequency multiplexing approach is superior, because the information density can reach much higher values before crosstalk sets in. Crosstalk can also be reduced by storing information in photorefractive fiber bundles instead of bulk, so that the information is more localized.<sup>266,267</sup>

## Holographic Data Storage

A photorefractive holographic digital storage system demonstrated in 1994 had a storage capacity of 163 kB using lithium niobate as the storage medium.<sup>268</sup> It used angular multiplexing to record data pages as separate holograms and distributed consecutive bits over multiple pages to reduce the probability of burst errors. The raw bit error rate was between  $10^{-3}$  and  $10^{-4}$  but was improved to  $10^{-6}$  by use of a Hamming error correcting code. Shortly after that, the capacity was increased to 5 MB using Reed-Solomon error correcting codes,<sup>269</sup> and in 2000 a 1-GB lithium niobate system was demonstrated with 50  $\mu$ s seek time.<sup>270</sup> Lithium niobate suffers from a low recording sensitivity, of the order of 0.1 cm/J and it has been largely replaced as a holographic recording medium by photopolymers, whose sensitivity can be several orders of magnitude larger (1000 cm/J).<sup>269</sup>

## Photorefractive Waveguides

There are three essentially different ways to prepare electro-optic (possibly photorefractive) waveguides. One is to produce local alterations in the chemistry of an electro-optic substrate, for example, by titanium in-diffusion into LiNbO<sub>3</sub> or ion implantation in BaTiO<sub>3</sub>.<sup>271</sup> Another way is to grow waveguides in layers by techniques such as RF sputtering, liquid phase epitaxy, laser ablation,<sup>272</sup> and metalorganic chemical vapor deposition (MOCVD).<sup>273</sup> A third way is to polish bulk material down to a thin wafer.<sup>274</sup>

The performance of electro-optic waveguide devices such as couplers and switches can be seriously compromised by the refractive index changes induced by the photorefractive effect in the host electro-optic materials such as lithium niobate. Therefore, one of the main motivations for understanding the photorefractive effect in waveguides is to develop ways to minimize its effects. MgO doping of lithium niobate is commonly used in attempts to reduce the photorefractive effect.<sup>275</sup>

Some researchers have taken advantage of waveguide photorefractivity. Optical confinement in waveguides enhances the effectiveness of optical nonlinearities. With conventional  $\chi^{(3)}$  materials, waveguiding confinement increases the coupling constant-length product by maintaining high intensity over longer distances than would be possible in bulk interactions. In the photorefractive case, optical confinement reduces the response time.

An excellent review of earlier work on photorefractivity in waveguides may be found in Ref. 276. More recently Eason and coworkers have measured a response time improvement by a factor of 100 in an ion-implanted BaTiO<sub>3</sub> waveguide.<sup>271</sup> A bridge mutually pumped phase conjugator was also demonstrated.<sup>277</sup>

## Photorefractive Solitons

In 1992, the possibility that photorefractive crystal might be able to support spatial solitons was proposed,<sup>278</sup> and subsequently demonstrated, first as a transient effect,<sup>279</sup> and then in the steady state.<sup>280</sup> Optical spatial solitons are beams of light in which the normal tendency toward diffractive spreading is counterbalanced by a nonlinear optical self-focusing effect. Solitons that are stable in 2 transverse directions and the 1 propagation direction (2 + 1 solitons) are made possible by the fact that the photorefractive nonlinearity is saturable, in contrast to the situation with Kerr nonlinearities where self-focusing leads to catastrophic collapse.<sup>281</sup> Solitons can form in photorefractive crystals, where drift is made to dominate diffusion through the application of a DC electric field (screening solitons) or by use of the photovoltaic effect (photovoltaic solitons) and where the degree of saturation of the nonlinearity is controlled through provision of background illumination.<sup>282</sup> These solitons can be described by the nonlinear Schrodinger equation with saturable nonlinearity:<sup>283</sup>

$$i \frac{\partial u}{\partial z} + \frac{1}{2} \frac{\partial^2 u}{\partial x^2} - \frac{u}{|u|^2 + 1} = 0 \quad (24)$$

where  $u$  is the amplitude of the soliton normalized by the square root of the sum of the background and dark intensities,  $x$  is the transverse coordinate, and  $z$  is the propagation direction. More exact versions of this equation have been used, for example, including the diffusion component of the photorefractive effect,<sup>284</sup> but Eq. (24) does describe the basic features.

Since the initial demonstration of basic screening solitons, many different types of solitons have been found, providing a very active research area both in fundamental physics and potential applications. These include bright and dark solitons,<sup>285</sup> vortex solitons,<sup>286</sup> vector solitons,<sup>287</sup> incoherent,<sup>288</sup> and white light solitons.<sup>289</sup> One of the main research interests has been in the study of soliton collisions and interactions.<sup>290</sup> Applications have included optically induced waveguides for optical routing,<sup>291</sup> and for beam confinement for nonlinear frequency conversion.<sup>292</sup>

## 12.4 REFERENCES

1. Gunter, P. and J.-P. Huignard (eds), *Photorefractive Materials and Their Applications 1, 2, and 3*. Springer-Verlag, New York, 2005, 2006, 2007.
2. A. M. Glass, D. von der Linde, and T. J. Negran, *Appl. Phys. Lett.* **25**:233 (1974).
3. V. L. Vinetskii and N. V. Khukhtarev, *Sov. Phys. Solid State* **16**:2414 (1975).
4. F. P. Strohkendl, J. M. C. Jonathan, and R. W. Hellwarth, *Opt. Lett.* **11**:312 (1986).
5. N. V. Kukhtarev, G. E. Dovgalenko, and V. N. Starkov, *Appl. Phys. A* **33**:227 (1984).
6. G. C. Valley, *Appl. Opt.* **22**:3160 (1983).
7. N. V. Khukhtarev, V. B. Markov, S. G. Odoulov, M. S. Soskin, and V. L. Vinetskii, *Ferroelectrics* **22**:949, 961 (1979).
8. B. Belinicher and B. Sturman, *Usp. Fiz. Nauk.* **130**:415 (1980).
9. G. C. Valley, *IEEE J. Quantum Electron.* **QE19**:1637 (1983).
10. J. P. Huignard and J. P. Herriau, *Appl. Opt.* **24**:4285 (1985).
11. S. I. Stepanov and M. P. Petrov, *Sov. Tech. Phys. Lett.* **10**:572 (1984).
12. M. Ziari, W. H. Steier, P. M. Ranon, M. B. Klein, and S. Trivedi, *J. Opt. Soc. Am. B* **9**:1461 (1992).
13. B. Fischer, M. Cronin-Golomb, J. O. White, and A. Yariv, *Opt. Lett.* **6**:519 (1981).
14. D. W. Vahey, *J. Appl. Phys.* **46**:3510 (1975).
15. J. Feinberg and K. R. MacDonald, "Phase Conjugate Mirrors and Resonators with Photorefractive Materials," in P. Gunter and J. P. Huignard (eds.), *Photorefractive Materials and Their Applications II, Survey of Applications*, Springer Verlag, Berlin, 1989.

16. M. D. Ewbank, R. A. Vasquez, R. S. Cudney, G. D. Bacher, and J. Feinberg, Paper FS1, *Technical Digest, 1990 OSA Annual Meeting*, Boston, MA, Nov. 4–9 (1990).
17. R. A. Vasquez, R. R. Neurgaonkar, and M. D. Ewbank, *J. Opt. Soc. Am. B* **8**:1416 (1992).
18. V. V. Voronov, I. R. Dorosh, Yu. S. Kuz'minov, and N. V. Tkachenko, *Sov. J. Quantum Electron.* **10**:1346 (1980).
19. J. Feinberg, *J. Opt. Soc. Am.* **72**:46 (1982).
20. M. Segev, Y. Ophir, and B. Fischer, *Opt. Commun.* **77**:265 (1990).
21. H. Rajbenbach, A. Delboulbe, and J. P. Huignard, *Opt. Lett.* **14**:1275 (1989).
22. W. S. Rabinovich, B. J. Feldman, and G. C. Gilbreath, *Opt. Lett.* **16**:1147 (1991).
23. J. Feinberg, *Opt. Lett.* **7**:486 (1982).
24. A. Zozulya, *Sov. J. Quantum Electron.* **22**:677 (1992).
25. M. Cronin-Golomb and A. Yariv, *J. Appl. Phys.* **57**:4906 (1985).
26. J. O. White, M. Cronin-Golomb, B. Fischer, and A. Yariv, *Appl. Phys. Lett.* **40**:450 (1982).
27. S. K. Kwong, A. Yariv, M. Cronin-Golomb, and I. Ury, *Appl. Phys. Lett.* **47**:460 (1985).
28. M. D. Ewbank and P. Yeh, *Opt. Lett.* **10**:496 (1985).
29. D. Anderson and R. Saxena, *J. Opt. Soc. Am. B* **4**:164 (1987).
30. M. Cronin-Golomb, B. Fischer, J. O. White, and A. Yariv, *IEEE J. Quantum Electron.* **QE20**:12 (1984).
31. A. A. Zozulya and V. T. Tikonchuk, *Sov. J. Quantum Electron.* **18**:981 (1988).
32. D. A. Fish, A. K. Powell, and T. J. Hall, *Opt. Commun.* **88**:281 (1992).
33. W. Krolikowski, K. D. Shaw, and M. Cronin-Golomb, *J. Opt. Soc. Am. B* **6**:1828 (1989).
34. W. Krolikowski, M. Belic, M. Cronin-Golomb, and A. Bledowski, *J. Opt. Soc. Am. B* **7**:1204 (1990).
35. R. A. Rupp and F. W. Drees, *Appl. Phys. B* **39**:223 (1986).
36. D. A. Temple and C. Warde, *J. Opt. Soc. Am. B* **3**:337 (1986).
37. M. D. Ewbank, P. Yeh, and J. Feinberg, *Opt. Commun.* **59**:423 (1986).
38. E. M. Avakyan, K. G. Belabaev, V. Kh. Sarkisov, and K. M. Tumanyan, *Sov. Phys. Solid State* **25**:1887 (1983).
39. L. Holtmann, E. Kratzig, and S. Odoulov, *Appl. Phys. B* **53**:1 (1991).
40. M. Cronin-Golomb, B. Fischer, J. O. White, and A. Yariv, *Appl. Phys. Lett.* **41**:689 (1982).
41. M. Cronin-Golomb, B. Fischer, J. O. White, and A. Yariv, *Appl. Phys. Lett.* **42**:919 (1983).
42. V. A. D'yakov, S. A. Korol'kov, A. Mamaev, V. V. Shkunov, and A. A. Zozulya, *Opt. Lett.* **16**:1614 (1991).
43. S. Weiss, S. Sternklar, and B. Fischer, *Opt. Lett.* **12**:114 (1987).
44. M. D. Ewbank, R. A. Vasquez, R. R. Neurgaonkar, and J. Feinberg, *J. Opt. Soc. Am. B* **7**:2306 (1990).
45. M. D. Ewbank, *Opt. Lett.* **13**:47 (1988).
46. D. Wang, Z. Zhang, Y. Zhu, S. Zhang, and P. Ye, *Opt. Commun.* **73**:495 (1989).
47. A. M. C. Smout and R. W. Eason, *Opt. Lett.* **12**:498 (1987).
48. B. Fischer, S. Sternklar, and S. Weiss, *IEEE J. Quantum Electron.* **QE25**:550 (1989).
49. M. Cronin-Golomb, *Opt. Lett.* **15**:897 (1990).
50. A. A. Zozulya, *Opt. Lett.* **16**:2042 (1991).
51. K. D. Shaw, *Opt. Commun.* **94**:458 (1992).
52. T. Y. Chang and R. W. Hellwarth, *Opt. Lett.* **10**:408 (1985).
53. R. A. Mullen, D. J. Vickers, L. West, and D. M. Pepper, *J. Opt. Soc. Am. B* **9**:1726 (1992).
54. G. C. Valley, *J. Opt. Soc. Am. B* **9**:1440 (1992).
55. M. Horowitz, D. Kliger, and B. Fischer, *J. Opt. Soc. Am. B* **8**:2204 (1991).
56. W. Krolikowski, K. D. Shaw, M. Cronin-Golomb, and A. Bledowski, *J. Opt. Soc. Am. B* **6**:1828 (1989).
57. W. Krolikowski and M. Cronin-Golomb, *Appl. Phys. B* **52**:150 (1991).
58. K. D. Shaw, *Opt. Commun.* **97**:148 (1993).
59. D. J. Gauthier, P. Narum, and R. W. Boyd, *Phys. Rev. Lett.* **58**:1640 (1987).
60. W. Krolikowski, M. Belic, M. Cronin-Golomb, and A. Bledowski, *J. Opt. Soc. Am. B* **7**:1204 (1990).



61. F. Vacchs and P. Yeh, *J. Opt. Soc. Am. B* **6**:1834 (1989).
62. W. Krolikowski and M. Cronin-Golomb, *Opt. Commun.* **89**:88 (1992).
63. J. Hong, A. E. Chiou, and P. Yeh, *Appl. Opt.* **29**:3027 (1990).
64. M. Cronin-Golomb, *Opt. Commun.* **89**:276 (1992).
65. G. C. Valley and G. J. Dunning, *Opt. Lett.* **9**:513 (1984).
66. R. Blumrich, T. Kobialka, and T. Tschudi, *J. Opt. Soc. Am. B* **7**:2299 (1990).
67. S. R. Liu and G. Indebetouw, *J. Opt. Soc. Am. B* **9**:1507 (1992).
68. F. Laeri, T. Tschudi, and J. Libers, *Opt. Commun.* **47**:387 (1983).
69. J. Feinberg and R. W. Hellwarth, *Opt. Lett.* **5**:519 (1980).
70. P. Gunter, *Phys. Reports* **93**:200 (1983).
71. D. von der Linde and A. M. Glass, *Appl. Phys.* **8**:85 (1975).
72. G. C. Valley and M. B. Klein, *Opt. Eng.* **22**:704 (1983).
73. A. Ashkin, G. D. Boyd, J. M. Dziedzic, R. G. Smith, A. A. Ballman, J. J. Levinstein, and K. Nassau, *Appl. Phys. Lett.* **9**:72 (1966).
74. F. S. Chen, *J. Appl. Phys.* **38**:3418 (1967).
75. F. S. Chen, J. T. LaMacchia, and D. B. Fraser, *Appl. Phys. Lett.* **3**:213 (1968).
76. M. B. Klein and G. C. Valley, *J. Appl. Phys.* **57**:4901 (1985).
77. M. Cronin-Golomb, K. Y. Lau, and A. Yariv, *Appl. Phys. Lett.* **47**:567 (1985).
78. R. Orlowski and E. Kratzig, *Solid St. Comm.* **27**:1351 (1978).
79. J. J. Amodei and D. L. Staebler, *Appl. Phys. Lett.* **18**:540 (1971).
80. R. L. Townsend and J. T. LaMacchia, *J. Appl. Phys.* **41**:5188 (1970).
81. R. L. Townsend and J. T. LaMacchia, *J. Appl. Phys.* **41**:5188 (1970).
82. J. Feinberg, D. Heiman, A. R. Tanguay, Jr., and R. W. Hellwarth, *J. Appl. Phys.* **51**:1297 (1980).
83. E. Kratzig, F. Welz, R. Orlowski, V. Doorman, and M. Rosenkranz, *Solid St. Comm.* **34**:817 (1980).
84. M. B. Klein, "Photorefractive Properties of BaTiO<sub>3</sub>," in P. Gunter and J.-P. Huignard (eds.), *Photorefractive Materials and Their Applications*, Springer-Verlag, Berlin, 1988.
85. V. Belruss, J. Kalnajs, A. Linz, and R. C. Folweiler, *Mater. Res. Bull.* **6**:899 (1971).
86. M. B. Klein and R. N. Schwartz, *J. Opt. Soc. Am. B* **3**:293 (1986).
87. P. G. Schunemann, T. M. Pollak, Y. Yang, Y. Y. Teng, and C. Wong, *J. Opt. Soc. Am. B* **5**:1702 (1988).
88. B. A. Wechsler and M. B. Klein, *J. Opt. Soc. Am. B* **5**:1713 (1988).
89. D. Rytz, R. R. Stephens, B. A. Wechsler, M. S. Keirstad, and T. M. Baer, *Opt. Lett.* **15**:1279 (1990).
90. G. W. Ross, P. Hribek, R. W. Eason, M. H. Garrett, and D. Rytz, *Opt. Commun.* **101**:60 (1993); B. A. Wechsler, M. B. Klein, C. C. Nelson, and R. N. Schwartz, *Opt. Lett.* **19**, April 15 (1994).
91. S. Ducharme and J. Feinberg, *J. Appl. Phys.* **56**:839 (1984).
92. R. A. Rupp, A. Maillard, and J. Walter, *Appl. Phys.* **A49**:259 (1989).
93. L. Holtmann, *Phys. Status Solidi* **A113**:K89 (1989).
94. D. Mahgerefteh and J. Feinberg, *Phys. Rev. Lett.* **64**:2195 (1990).
95. G. A. Brost and R. A. Motes, *Opt. Lett.* **15**:1194 (1990).
96. L. K. Lam, T. Y. Chang, J. Feinberg, and R. W. Hellwarth, *Opt. Lett.* **6**:475 (1981).
97. N. Barry and M. J. Damzen, *J. Opt. Soc. B* **9**:1488 (1992).
98. A. L. Smirl, G. C. Valley, R. A. Mullen, K. Bohnert, C. D. Mire, and T. F. Boggess, *Opt. Lett.* **12**:501 (1987).
99. G. A. Brost, R. A. Motes, and J. R. Rotge, *J. Opt. Soc. Am. B* **5**:1879 (1988).
100. P. Yeh, *Appl. Opt.* **26**:602 (1987); A. M. Glass, M. B. Klein, and G. C. Valley, *Appl. Opt.* **26**:3189 (1987).
101. E. Voit, M. Z. Zha, P. Amrein, and P. Gunter, *Appl. Phys. Lett.* **51**:2079 (1987).
102. D. Rytz, M. B. Klein, R. A. Mullen, R. N. Schwartz, G. C. Valley, and B. A. Wechsler, *Appl. Phys. Lett.* **52**:1759 (1988).

103. S. Ducharme and J. Feinberg, *J. Opt. Soc. Am. B* **3**:283 (1986).
104. M. H. Garrett, J. Y. Chang, H. P. Jenssen, and C. Warde, *Opt. Lett.* **17**:103 (1992).
105. M. E. Lines and A. M. Glass, *Principles And Applications of Ferroelectrics And Related Materials*, Clarendon Press, Oxford, 1977, pp. 280–292.
106. K. Megumi, N. Nagatshuma, Y. Kashiwada, and Y. Furuhashi, *J. Matls. Sci.* **11**:1583 (1976).
107. J. B. Thaxter, *Appl. Phys. Lett.* **15**:210 (1969).
108. K. Megumi, H. Kozuka, M. Kobayashi, and Y. Furuhashi, *Appl. Phys. Lett.* **30**:631 (1977).
109. V. V. Voronov, I. R. Dorosh, Y. S. Kuzminov, and N. V. Tkachenko, *Sov. J. Quantum Electron.* **10**:1346 (1980).
110. R. R. Neurgaonkar, W. K. Cory, J. R. Oliver, M. D. Ewbank, and W. F. Hall, *Opt. Eng.* **26**:392 (1987).
111. G. L. Wood and R. R. Neurgaonkar, *Opt. Lett.* **17**:94 (1992).
112. R. A. Vasquez, F. R. Vachss, R. R. Neurgaonkar, and M. D. Ewbank, *J. Opt. Soc. Am. B* **8**:1932 (1991).
113. R. A. Vasquez, R. R. Neurgaonkar, and M. D. Ewbank, *J. Opt. Soc. Am. B* **9**:1416 (1992).
114. M. D. Ewbank, R. R. Neurgaonkar, W. K. Cory, and J. Feinberg, *J. Appl. Phys.* **62**:374 (1987).
115. K. Sayano, A. Yariv, and R. R. Neurgaonkar, *Opt. Lett.* **15**:9 (1990).
116. L. Hesselink and S. Redfield, *Opt. Lett.* **13**:877 (1988).
117. A. A. Grabar, M. Jazbinsek, A. N. Shumelyuk, Y. M. Vysochanskii, G. Montemezzani, and P. Gunter, in *Photorefractive Materials and Their Applications 2: Materials*, P. Gunter and J.-P. Huignard, (eds.) Springer, New York, 2006, Chap. 10, pp. 327–362.
118. A. A. Grabar, R. I. Muzhikash, A. D. Kostyuk, and Y. M. Vysochanskii, *Fizika Tverdogo Tela* **33**:2335 (1991).
119. M. Jazbinsek, D. Haertle, G. Montemezzani, P. Gunter, A. A. Grabar, I. M. Stoika, and Y. M. Vysochanskii, *J. Opt. Soc. Am. B Opt. Phys.* **22**:2459 (2005).
120. A. Shumelyuk, S. Odoulov, O. Oleynik, G. Brost, and A. Grabar, *Appl. Phys. B-Lasers and Optics* **88**:79 (2007).
121. R. Mosimann, P. Marty, T. Bach, F. Juvalta, M. Jazbinsek, P. Gunter, and A. A. Grabar, *Opt. Lett.* **32**:3230 (2007).
122. M. Jazbinsek, D. Haertle, G. Montemezzani, P. Gunter, A. A. Grabar, I. M. Stoika, and Y. M. Vysochanskii, *J. Opt. Soc. Am. B-Opt. Phys.* **22**:2459 (2005).
123. B. A. Horowitz and F. J. Corbitt, *Opt. Eng.* **17**:353 (1978).
124. J. P. Huignard and F. Micheron, *Appl. Phys. Lett.* **29**:591 (1976).
125. J. P. Wilde, L. Hesselink, S. W. McCahon, M. B. Klein, D. Rytz, and B. A. Wechsler, *J. Appl. Phys.* **67**:2245 (1990).
126. S. I. Stepanov and M. P. Petrov, *Opt. Commun.* **52**:292 (1985).
127. S. L. Sochava, S. I. Stepanov, and M. P. Petrov, *Sov. Tech. Phys. Lett.* **13**:274 (1987).
128. M. P. Petrov, S. L. Sochava, and M. P. Petrov, *Opt. Lett.* **14**:284 (1989).
129. S. I. Stepanov, V. V. Kulikov, and M. P. Petrov, *Opt. Commun.* **44**:19 (1982).
130. B. Imbert, H. Rajbenbach, S. Mallick, J. P. Herriau, and J.-P. Huignard, *Opt. Lett.* **13**:327 (1988).
131. J. E. Millerd, E. M. Garmire, M. B. Klein, B. A. Wechsler, F. P. Strohkendl, and G. A. Brost, *J. Opt. Soc. Am. B* **9**:1449 (1992).
132. R. Baltrameyunas, Yu. Vaitkus, D. Veletskas, and I. Kapturauskas, *Sov. Tech. Phys. Lett.* **7**:155 (1981).
133. A. M. Glass, A. M. Johnson, D. H. Olson, W. Simpson, and A. A. Ballman, *Appl. Phys. Lett.* **44**:948 (1984).
134. M. B. Klein, *Opt. Lett.* **9**:350 (1984).
135. A. Partovi, J. Millerd, E. M. Garmire, M. Ziari, W. H. Steier, S. B. Trivedi, and M. B. Klein, *Appl. Phys. Lett.* **57**:846 (1990).
136. K. Kuroda, Y. Okazaki, T. Shimura, H. Okimura, M. Chihara, M. Itoh, and I. Ogura, *Opt. Lett.* **15**:1197 (1990).
137. M. Ziari, W. H. Steier, P. M. Ranon, S. Trivedi, and M. B. Klein, *Appl. Phys. Lett.* **60**:1052 (1992).
138. A. M. Glass and J. Strait, “The Photorefractive Effect in Semiconductors,” in P. Gunter and J.-P. Huignard (eds.), *Photorefractive Materials and Their Applications I*, Springer-Verlag, Berlin, 1989, vol. 61, pp. 237–262.
139. P. Tayebati, J. Kumar, and S. Scott, *Appl. Phys. Lett.* **59**:3366 (1991).
140. J. Kumar, G. Albanese, and W. H. Steier, *J. Opt. Soc. Am. B* **4**:1079 (1987).
141. B. Imbert, H. Rajbenbach, S. Mallick, J. P. Herriau, and J.-P. Huignard, *Opt. Lett.* **13**:327 (1988).

142. M. B. Klein, S. W. McCahon, T. F. Boggess, and G. C. Valley, *J. Opt. Soc. Am. B* **5**:2467 (1988).
143. G. C. Valley, H. Rajbenbach, and H. J. von Bardeleben, *Appl. Phys. Lett.* **56**:364 (1990).
144. Ph. Refregier, L. Solymar, H. Rajbenbach, and J.-P. Huignard, *J. Appl. Phys.* **58**:45 (1985).
145. K. Walsh, A. K. Powell, C. Stace, and T. J. Hall, *J. Opt. Soc. Am. B* **7**:288 (1990).
146. M. Ziari, W. H. Steier, P. M. Ranon, M. B. Klein, and S. Trivedi, *J. Opt. Soc. Am. B* **9**:1461 (1992).
147. P. Gravey, G. Picoli, and J. Y. Labandibar, *Opt. Commun.* **70**:190 (1989).
148. G. Picoli, P. Gravey, C. Ozkul, and V. Vieux, *J. Appl. Phys.* **66**:3798 (1989).
149. A. Partovi, A. Kost, E. M. Garmire, G. C. Valley, and M. B. Klein, *Appl. Phys. Lett.* **56**:1089 (1990).
150. J. E. Millerd, S. D. Koehler, E. M. Garmire, A. Partovi, A. M. Glass, and M. B. Klein, *Appl. Phys. Lett.* **57**:2776 (1990).
151. J. E. Millerd, E. M. Garmire, and M. B. Klein, *Opt. Lett.* **17**:100 (1992).
152. G. C. Valley, S. W. McCahon, and M. B. Klein, *J. Appl. Phys.* **64**:6684 (1988).
153. A. Partovi, E. M. Garmire, G. C. Valley, and M. B. Klein, *Appl. Phys. Lett.* **55**:2701 (1989).
154. R. B. Bylsma, D. H. Olson, and A. M. Glass, *Appl. Phys. Lett.* **52**:1083 (1988).
155. D. M. Pepper, J. AuYeung, D. Fekete, and A. Yariv, *Opt. Lett.* **3**:7 (1978).
156. L. Pichon and J.-P. Huignard, *Opt. Commun.* **36**:277 (1981).
157. A. M. Glass, D. D. Nolte, D. H. Olson, G. E. Doran, D. S. Chemla, and W. H. Knox, *Opt. Lett.* **15**:264 (1990).
158. D. D. Nolte, D. H. Olson, G. E. Doran, W. H. Knox, and A. M. Glass, *J. Opt. Soc. Am. B* **7**:2217 (1990).
159. Q. N. Wang, R. M. Brubaker, D. D. Nolte, and M. R. Melloch, *J. Opt. Soc. Am. B* **9**:1626 (1992).
160. A. Partovi, A. M. Glass, D. H. Olson, G. J. Zyzdik, K. T. Short, R. D. Feldman, and R. F. Austin, *Opt. Lett.* **17**:655 (1992).
161. A. Partovi, A. M. Glass, D. H. Olson, G. J. Zyzdik, H. M. O'Bryan, T. H. Chiu, and W. H. Knox, *Appl. Phys. Lett.* **62**:464 (1993).
162. K. Sutter and P. Gunter, *J. Opt. Soc. Am. B-Opt. Phys.* **7**:2274 (1990).
163. K. Sutter, J. Hulliger, and P. Gunter, *Solid St. Comm.* **74**:867 (1990).
164. K. Sutter, J. Hulliger, R. Schlessler, and P. Gunter, *Opt. Lett.* **18**:778 (1993).
165. S. Ducharme, J. C. Scott, R. J. Twieg, and W. E. Moerner, *Phys. Rev. Lett.* **66**:1846 (1991).
166. W. E. Moerner, C. Walsh, J. C. Scott, S. Ducharme, D. M. Burland, G. C. Bjorklund, and R. J. Twieg, *Nonlinear Optical Properties of Organic Materials IV* **1560**:278 (1991).
167. W. E. Moerner, S. M. Silence, F. Hache, and G. C. Bjorklund, *J. Opt. Soc. Am. B-Opt. Phys.* **11**:320 (1994).
168. B. Kippelen, S. R. Marder, E. Hendrickx, J. L. Maldonado, G. Guillemet, B. L. Volodin, D. D. Steele, et al., *Science* **279**, 54 (1998).
169. F. Wurthner, S. Yao, J. Schilling, R. Wortmann, M. Redi-Abshiro, E. Mecher, F. Gallego-Gomez, and K. Meerholz, *J. Am. Chem. Soc.* **123**:2810 (2001).
170. D. Wright, M. A. Diaz-Garcia, J. D. Casperson, M. DeClue, W. E. Moerner, and R. J. Twieg, *Appl. Phys. Lett.* **73**:1490 (1998).
171. J. D. Wright and N. A. J. M. Sommerdijk, *Sol-Gel Materials: Chemistry and Applications*, Gordon and Breach, Amsterdam, 2001.
172. D. Wright, U. Gubler, Y. Roh, W. E. Moerner, M. He, and R. J. Twieg, *Appl. Phys. Lett.* **79**:4274 (2001).
173. F. Wang, Z. J. Chen, B. Zhang, Q. H. Gong, K. W. Wu, X. S. Wang, B. W. Zhang, and F. Q. Tang, *Appl. Phys. Lett.* **75**:3243 (1999).
174. Z. H. Peng, A. R. Gharavi, and L. P. Yu, *J. Am. Chem. Soc.* **119**:4622 (1997).
175. Q. Wang, L. M. Wang, J. J. Yu, and L. P. Yu, *Adv. Mater.* **12**:974 (2000).
176. W. You, L. M. Wang, Q. Wang, and L. P. Yu, *Macromolecules* **35**:4636 (2002).
177. I. Aiello, D. Dattilo, M. Ghedini, A. Bruno, R. Termine, and A. Golemme, *Adv. Mater.* **14**:1233 (2002).
178. J. G. Winiarz and P. N. Prasad, *Opt. Lett.* **27**:1330 (2002).
179. G. P. Wiederrecht, B. A. Yoon, and M. R. Wasielewski, *Science* **270**:1794 (1995).
180. A. Golemme, B. Kippelen, and N. Peyghambarian, *Appl. Phys. Lett.* **73**:2408 (1998).

181. R. Termine and A. Golemme, *Opt. Lett.* **26**:1001 (2001).
182. G. Cook, C. A. Wyres, M. J. Deer, and D. C. Jones, *Proc. SPIE* **5213**:63 (2003).
183. O. Ostroverkhova and W. E. Moerner, *Chem. Rev.* **104**:3267 (2004).
184. Z. J. Chen, F. Wang, Z. W. Huang, Q. H. Gong, Y. W. Chen, Z. J. Zhang, and H. Y. Chen, *J. Phys. D-Appl. Phys.* **31**:2245 (1998).
185. Y. W. Bai, X. F. Chen, X. H. Wan, Q. F. Zhou, H. Liu, B. Zhang, and Q. H. Gong, *Appl. Phys. Lett.* **80**:10 (2002).
186. H. Chun, I. K. Moon, D. H. Shin, S. Song, and N. Kim, *J. Mater. Chem.* **12**:858 (2002).
187. W. J. Joo, N. J. Kim, H. Chun, I. K. Moon, and N. Kim, *Polymer* **42**:9863 (2001).
188. S. Schlöter, U. Hofmann, P. Strohrriegel, H. W. Schmidt, and D. Haarer, *J. Opt. Soc. Am. B-Opt. Phys.* **15**:2473 (1998).
189. E. H. Mecher, C. Brauchle, H. H. Horhold, J. C. Hummelen, and K. Meerholz, *Phys. Chem. Chem. Phys.* **1**:1749 (1999).
190. D. J. Suh, O. O. Park, T. Ahn, and H. K. Shim, *Jpn. J. Appl. Phys. Part 2-Letters* **41**:L428 (2002).
191. O. P. Kwon, S. H. Lee, G. Montemezzani, and P. Gunter, *Adv. Function. Mater.* **13**:434 (2003).
192. E. Hendrickx, J. Herlocker, J. L. Maldonado, S. R. Marder, B. Kippelen, A. Persoons, and N. Peyghambarian, *Appl. Phys. Lett.* **72**:1679 (1998).
193. P. M. Lundquist, R. Wortmann, C. Geletneky, R. J. Twieg, M. Jurich, V. Y. Lee, C. R. Moylan, and D. M. Burland, *Science* **274**:1182 (1996).
194. O. Ostroverkhova, D. Wright, U. Gubler, W. E. Moerner, M. He, A. Sastre-Santos, and R. J. Twieg, *Adv. Function. Mater.* **12**:621 (2002).
195. J. Sohn, J. Hwang, S. Y. Park, and G. J. Lee, *Jpn. J. Appl. Phys. Part 1-Regular Papers Short Notes & Review Papers* **40**:3301 (2001).
196. H. Chun, N. J. Kim, W. J. Joo, J. W. Han, C. H. Oh, and N. Kim, *Synth. Met.* **129**:281 (2002).
197. L. M. Wang, M. K. Ng, and L. P. Yu, *Appl. Phys. Lett.* **78**:700 (2001).
198. H. Ono and N. Kawatsuki, *J. Appl. Phys.* **85**:2482 (1999).
199. S. Bartkiewicz, K. Matczyszyn, A. Miniewicz, and F. Kajzar, *Opt. Commun.* **187**:257 (2001).
200. P. Cheben, F. del Monte, D. J. Worsfold, D. J. Carlsson, C. P. Grover, and J. D. Mackenzie, *Nature* **408**:64 (2000).
201. D. H. Choi, H. T. Hong, W. G. Jun, and K. Y. Oh, *Opt. Mater.* **21**:373 (2003).
202. J. W. Goodman, *Introduction to Fourier Optics*, 3rd ed, Roberts, Greenwood Village, CO.
203. J. O. White and A. Yariv, *Appl. Phys. Lett.* **37**:5 (1980).
204. J. Joseph, K. Singh, and P. K. C. Pillai, *Opt. Commun.* **85**:389 (1991).
205. T. Y. Chang, J. H. Hong, S. Campbell, and P. Yeh, *Opt. Lett.* **17**:1694 (1992).
206. J. Khoury, T. C. Fu, M. Cronin-Golomb, and C. Woods, *J. Opt. Soc. Am. B* **11**:1960 (1994).
207. J. P. Huignard and J. P. Herriau, *Appl. Opt.* **17**:2671 (1978).
208. J. Feinberg, *Opt. Lett.* **5**:330 (1980).
209. E. Ochoa, J. W. Goodman, and L. Hesselink, *Opt. Lett.* **10**:430 (1985).
210. J. J. Berg, J. N. Lee, M. W. Casseday, and B. J. Udelson, *Opt. Eng.* **19**:359 (1980).
211. H. Lee and D. Psaltis, *Opt. Lett.* **12**:459 (1987).
212. R. M. Montgomery and M. R. Lange, *Appl. Opt.* **30**:2844 (1991).
213. D. E. Oates, P. G. Gottschalk, and P. B. Wright, *Appl. Phys. Lett.* **46**:1125 (1985).
214. A. E. T. Chiou and P. Yeh, *Opt. Lett.* **10**:621 (1985).
215. S. K. Kwong and A. Yariv, *Appl. Phys. Lett.* **48**:564 (1986).
216. S. MacCormack and R. W. Eason, *Opt. Lett.* **15**:1212 (1990).
217. S. MacCormack and R. W. Eason, *J. Appl. Phys.* **67**:7160 (1990).
218. W. R. Christian, P. H. Beckwith, and I. McMichael, *Opt. Lett.* **14**:81 (1989).

219. M. Segev, S. Weiss, and B. Fischer, *Appl. Phys. Lett.* **50**:1397 (1987).
220. S. Weiss, M. Segev, and B. Fischer, *IEEE J. Quantum Electron.* **QE24**:706 (1988).
221. R. R. Stephens, R. C. Lind, and C. R. Guiliano, *Appl. Phys. Lett.* **50**:647 (1987).
222. P. D. Hillman and M. Marciniak, *J. Appl. Phys.* **66**:5731 (1989).
223. S. Weiss, M. Segev, S. Sternklar, and B. Fischer, *Appl. Opt.* **27**:3422 (1988).
224. J. W. Goodman, F. I. Leonberger, S. Y. Kung, and R. A. Athale, *Proc. IEEE* **72**:850 (1984).
225. J. W. Goodman, in *Optical Processing and Computing*, H. H. Arsenault, T. Szoplik, and B. Macukow (eds.), Academic Press, San Diego, 1989, chap. 1.
226. K. Wagner and D. Psaltis, *Appl. Opt.* **26**:5061 (1987).
227. M. Cronin-Golomb, *Appl. Phys. Lett.* **23**:2189 (1989).
228. A. E. T. Chiou and P. Yeh, *Appl. Opt.* **31**:5536 (1992).
229. P. Yeh and A. E. T. Chiou, *Opt. Lett.* **12**:138 (1987).
230. D. M. Lininger, P. J. Martin, and D. Z. Anderson, *Opt. Lett.* **14**:697 (1989).
231. S. W. McCahon and M. B. Klein, *Proc. SPIE* **1105**:119 (1989).
232. G. L. Wood, W. W. Clark III, G. J. Salamo, A. Mott, and E. J. Sharp, *J. Appl. Phys.* **71**:37 (1992).
233. M. B. Klein and G. J. Dunning, *Proc. SPIE* **1692**:73 (1992).
234. J. L. Schultz, G. J. Salamo, E. J. Sharp, G. L. Wood, R. J. Anderson, and R. R. Neurgaonkar, *Proc. SPIE* **1692**:78 (1992).
235. J. E. Ford, Y. Fainman, and S. H. Lee, *Opt. Lett.* **13**:856 (1988).
236. M. Cronin-Golomb, A. M. Biernacki, C. Lin, and H. Kong, *Opt. Lett.* **12**:1029 (1987).
237. G. F. Albrecht, H. F. Robey, and T. R. Moore, *Appl. Phys. Lett.* **57**:864 (1990).
238. H. F. Robey, *Phys. Rev. Lett.* **65**:1360 (1990).
239. S. D. Kalaskar and S. E. Bialkowski, *Anal. Chem.* **64**:1824 (1992).
240. G. Zhou, L. Bintz, and D. Z. Anderson, *Appl. Opt.* **31**:1740 (1992).
241. J. Feinberg, *Opt. Lett.* **8**:569 (1983).
242. M. D. Ewbank, P. Yeh, M. Khoshnevisan, and J. Feinberg, *Opt. Lett.* **10**:282 (1985).
243. D. Z. Anderson, D. M. Lininger, and J. Feinberg, *Opt. Lett.* **12**:123 (1987).
244. S. K. Kwong, G. A. Rakuljic, and A. Yariv, *Appl. Phys. Lett.* **48**:201 (1986).
245. A. E. Chiou and P. Yeh, *Opt. Lett.* **11**:306 (1986); J. Feinberg and K. R. MacDonald, in *Photorefractive Materials and their Applications II*, Springer Verlag, Berlin (1989).
246. E. Parshall and M. Cronin-Golomb, *Appl. Opt.* **30**:5090 (1991).
247. G. J. Dunning, E. Marom, Y. Owechko, and B. H. Softer, *Opt. Lett.* **12**:346 (1987).
248. Y. Owechko, *IEEE J. Quantum Electron.* **QE25**:619 (1989).
249. T. Kohonen, *Self-Organization and Associative Memory*, Springer-Verlag, New York, 1984.
250. D. Z. Anderson, *Opt. Lett.* **11**:56 (1986).
251. J. Hong, S. Campbell, and P. Yeh, *Appl. Opt.* **29**:3019 (1990).
252. D. Psaltis, D. Brady, and K. Wagner, *Appl. Opt.* **27**:1752 (1988).
253. A. V. Huynh, J. F. Walkup, and T. F. Krile, *Opt. Eng.* **31**:979 (1992).
254. E. G. Paek, P. F. Liao, and H. Gharavi, *Opt. Eng.* **31**:986 (1992).
255. K. P. Lo and G. Indebetouw, *Appl. Opt.* **31**:1745 (1992).
256. M. Cronin-Golomb and A. Yariv, *Proc. SPIE* **700**:301 (1986).
257. M. B. Klein, G. J. Dunning, G. C. Valley, R. C. Lind, and T. R. O'Meara, *Opt. Lett.* **11**:575 (1986).
258. S. W. McCahon, G. J. Dunning, K. W. Kirby, G. C. Valley, and M. B. Klein, *Opt. Lett.* **17**:517 (1992).
259. D. M. Lininger, P. J. Martin, and D. Z. Anderson, *Opt. Lett.* **14**:697 (1989).
260. M. Ingold, P. Gunter, and M. Schadt, *J. Opt. Soc. Am. B* **7**:2380 (1990).
261. S. W. McCahon, G. J. Dunning, K. W. Kirby, G. C. Valley, and M. B. Klein, *Opt. Lett.* **17**:517 (1992).

262. C. Denz, G. Paulilat, G. Roosen, and T. Tschudi, *Opt. Commun.* **85**:171 (1991).
263. F. Mok, M. C. Tackitt, and H. M. Stoll, *Opt. Lett.* **16**:605 (1991).
264. Y. Taketomi, J. E. Ford, H. Sasaki, J. Ma, Y. Fainman, and S. H. Lee, *Opt. Lett.* **16**:1774 (1991).
265. G. A. Rakuljic, V. Levya, and A. Yariv, *Opt. Lett.* **17**:1471 (1992).
266. L. Hesselink and S. Redfield, *Opt. Lett.* **13**:877 (1988).
267. F. Ito, K. Kitayama, and H. Oguri, *J. Opt. Soc. Am. B* **9**:1432 (1992).
268. J. F. Heanue, M. C. Bashaw, and L. Hesselink, *Science* **265**:749 (1994).
269. L. Hesselink, S. S. Orlov, and M. C. Bashaw, *Proc IEEE* **92**:1231 (2004).
270. J. A. Ma, T. Chang, S. Choi, and J. Hong, *Opt. Quant. Electron.* **32**:383 (2000).
271. K. E. Youden, S. W. James, R. W. Eason, P. J. Chandler, L. Zhang, and P. D. Townsend, *Opt. Lett.* **17**:1509 (1992).
272. K. E. Youden, R. W. Eason, M. C. Gower, and N. A. Vainos, *Appl. Phys. Lett.* **59**:1929 (1991).
273. Y. Nagao, H. Sakata, and Y. Mimura, *Appl. Opt.* **31**:3966 (1992).
274. B. Fischer and M. Segev, *Appl. Phys. Lett.* **54**:684 (1989).
275. J. L. Jackel, *Electron. Lett.* **21**:509 (1985).
276. V. E. Wood, P. J. Cressman, R. J. Holman, and C. M. Verber, in P. Gunter and J. P. Huignard (eds), *Photorefractive Materials and their Applications*, Springer-Verlag, Berlin, 1989.
277. S. W. James, K. E. Youden, P. M. Jeffrey, R. W. Eason, P. J. Chandler, L. Zhang, and P. D. Townsend, *Appl. Opt.* **32**:5299 (1993).
278. M. Segev, B. Crosignani, A. Yariv, and B. Fischer, *Phys. Rev. Lett.* **68**:923 (1992).
279. G. C. Duree, J. L. Shultz, G. J. Salamo, M. Segev, A. Yariv, B. Crosignani, P. Diporto, E. J. Sharp, and R. R. Neurgaonkar, *Phys. Rev. Lett.* **71**:533 (1993).
280. M. D. I. Castillo, P. A. M. Aguilar, J. J. Sanchezmondragon, S. Stepanov, and V. Vysloukh, *Appl. Phys. Lett.* **64**:408 (1994).
281. P. L. Kelley, *Phys. Rev. Lett.* **15**:1005 (1965).
282. K. Kos, H. X. Meng, G. Salamo, M. F. Shih, M. Segev, and G. C. Valley, *Phys. Rev. E* **53**:R4330 (1996).
283. W. Krolikowski, B. Luther-Davies, and C. Denz., *IEEE J. Quant. Electron.* **39**:3 (2003).
284. A. A. Zozulya and D. Z. Anderson, *Phys. Rev. A* **51**:1520 (1995).
285. Z. G. Chen, M. Mitchell, M. F. Shih, M. Segev, M. H. Garrett, and G. C. Valley, *Opt. Lett.* **21**:629 (1996).
286. Z. G. Che, M. Segev, D. W. Wilson, R. E. Muller, and P. D. Maker, *Phys. Rev. Lett.* **78**:2948 (1997).
287. M. I. Carvalho, S. R. Singh, D. N. Christodoulides, and R. I. Joseph, *Phys. Rev. E* **53**:R53 (1996).
288. M. Mitchell, M. Segev, T. H. Coskun, and D. N. Christodoulides, *Phys. Rev. Lett.* **79**:4990 (1997).
289. M. Mitchell and M. Segev, *Nature* **387**:880 (1997).
290. G. I. Stegeman and M. Segev, *Science* **286**:1518 (1999).
291. M. Tiemann, J. Schmidt, V. M. Petrov, J. Petter, and T. Tschudi, *Appl. Opt.* **46**:2683 (2007).
292. S. Lan, M. F. Shih, G. Mizell, J. A. Giordmaine, Z. G. Chen, C. Anastassiou, J. Martin, and M. Segev, *Opt. Lett.* **24**:1145 (1999).

## 12.5 FURTHER READING

### Books and Review Articles on Photorefractive Materials, Effects, and Devices

- Gunter, P., "Holography, Coherent Light Amplification and Phase Conjugation in Photorefractive Materials," *Phys. Rep.* **93**:199 (1982).
- Gunter, P., "Photorefractive Materials," in *CRC Handbook of Laser Science and Technology*, vol. IV, part 2, CRC Press Boca Raton, 1986.

- Gunter, P. and J.-P. Huignard (eds.), *Photorefractive Materials and Their Applications I and II*, Springer Science, Berlin, 1988, 1989.
- Gunter, P. and J.-P. Huignard (eds.), *Photorefractive Materials and Their Applications 1, 2, and 3*. Springer-Verlag, New York, 2005, 2006, 2007.
- Klein, M. B. and G. C. Valley, "Optimal Properties of Photorefractive Materials for Optical Data Processing," *Opt. Engin.* **22**:704 (1983).
- Odoulov, S., M. Soskin, and A. Khizniak, *Optical Oscillators with Degenerate Four-Wave Mixing (Dynamic Grating Lasers)*, Harwood Academic Publishers, London, 1989.
- Petrov, M. P., S. I. Stepanov, and A. V. Khomenko, *Photorefractive Crystals in Coherent Optical Systems*, Springer-Verlag, Berlin, 1991.
- Solymar, L., D. J. Webb, and A. Grunnet-Jepsen, *The Physics and Applications of Photorefractive Materials* (Oxford Series in Optical and Imaging Sciences) 1996.
- Yeh, P., *Introduction to Photorefractive Nonlinear Optics*, Wiley, New York, 1993.
- Yu, F. and S. Yin (eds), *Photorefractive Optics*, Academic Press, San Diego, 2000.

---

# OPTICAL LIMITING

---

David J. Hagan

*CREOL, The College of Optics and Photonics  
University of Central Florida  
Orlando, Florida*

---

## 13.1 INTRODUCTION

---

As the name implies, an optical limiter is a device designed to keep the power, irradiance, energy, or fluence transmitted by an optical system below some specified maximum value, regardless of the magnitude of the input. It must do this while maintaining high transmittance at low input powers. The most important application of such a device is the protection of sensitive optical sensors and components from laser damage. There are many other potential applications for such devices, including laser power regulation or stabilization, or restoration of signal levels in optical data transmission or logic systems, but this chapter will primarily concentrate on devices for sensor protection.

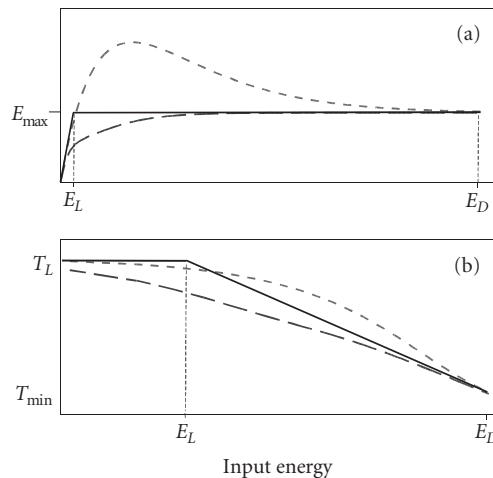
Perhaps the most obvious way of achieving optical limiting is by active control, where input light levels are monitored by a sensor, which through some processor activates a modulator or shutter that in turn limits the transmitted light. The best-known examples of these are the iris and blink response of the eye. However, these are limited in speed to about 0.1 second, so that any intense pulse of light shorter than this can get past these defense mechanisms and damage the retina before they can respond. Speed is an issue with most active control systems for optical limiting. To protect sensors, the transmittance must be reduced in a time much shorter than the width of the potentially damaging pulse. Even very fast electro-optic shutters are limited to rise times on the order of 1 ns, which may be insufficient to adequately block Q-switched pulses shorter than 50 ns or so in duration. Even for protection against longer pulses, cost and complexity are disadvantages of active optical limiting systems. Another direct way to protect sensors against high-power lasers is to use narrow-line spectral filters. These can work well when the laser wavelength is known, such as in laboratory laser safety goggles, but would be largely ineffective against tunable lasers.

Passive systems, on the other hand, use a nonlinear optical material that functions as a combined sensor, processor, and modulator. This offers the potential for high speed, simplicity, compactness, and low cost. However, passive systems place severe requirements on the nonlinear medium.<sup>1-3</sup> While many materials exhibit the type of effects that produce optical limiting, usually these effects prove not to be large enough. Because of this, all prototype passive systems demonstrated to date place the nonlinear optical component in or near a focal plane. In a focal plane, the energy density of a beam from a distant laser source is  $10^5 \sim 10^8$  times greater than in a pupil plane. Even in this focused geometry, material nonlinearities are barely large enough, and systems that adequately protect eyes and other common sensors over a broad wavelength band have yet to be demonstrated, at least in the



visible and near-infrared. The idea of using a nonlinear material in a pupil plane (e.g., a coating on the surface of goggles) is therefore far from reality. For mid-infrared (3 to 12  $\mu\text{m}$  wavelength range), optical nonlinearities are typically much larger than in the visible and results have been more promising than in the visible.<sup>4-6</sup> Still, however, limiting elements must be placed near a focal plane. Hence, research to date on optical limiting has predominantly focused on the search for new or modified materials with stronger nonlinearities, and on how to optimally use the best available nonlinear materials. This chapter will concentrate on passive devices.

The response of an *ideal* optical limiter is shown in Fig. 1, along with some typical responses of passive limiters. Clearly, an optical sensor requires high linear transmittance,  $T_L$ , at low input light levels for the transmission of images. Meanwhile, for higher inputs the limiter must clamp the transmitted energy below some maximum value,  $E_{\text{max}}$ , up to the maximum energy the limiter can withstand,  $E_D$ . This is usually the energy damage threshold for the limiting material itself. Usually the minimum transmittance of the device,  $T_{\text{min}}$ , occurs at this energy. Often, the performance of a limiting system or device is characterized by some type of figure of merit (FOM).<sup>7,8</sup> One of the most commonly used is  $\text{FOM} = T_L/T_{\text{min}}$ , which states that a large linear transmittance combined with a low minimum transmittance is desirable.<sup>8</sup> A slightly different way of expressing this is in terms of the optical density (OD), defined as  $\text{OD} = -\log_{10}(T)$ , so that the FOM may be reexpressed as the change in OD, or  $\Delta\text{OD} = \log_{10}(T_L/T_{\text{min}})$ . For the ideal limiter shown in Fig. 1, the FOM is equivalent to the *dynamic range*, which is defined as  $\text{D.R.} = E_D/E_L$ .<sup>7</sup> However, although such merit figures are of some use, it is usually necessary to separately specify parameters such as linear transmittance, maximum transmitted energy, and damage energy. For example, in some applications, a linear transmittance of  $>50$  percent could be an absolute requirement that cannot be offset by an improvement in

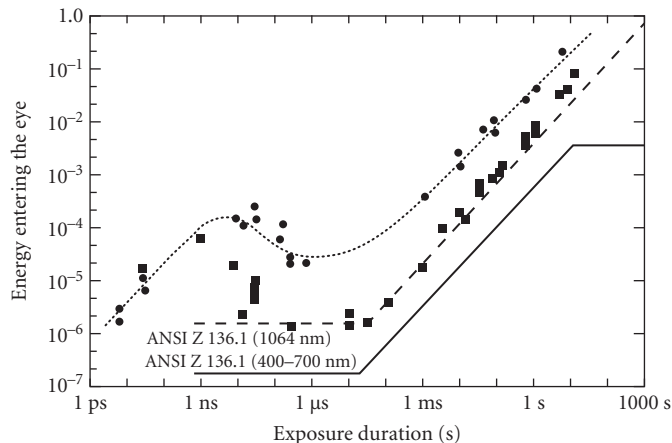


**FIGURE 1** Typical limiting curves, drawn as (a) transmitted energy versus input energy, and (b) transmittance versus input energy, on a log-log scale. The solid line is the *ideal* optical limiter response, while the short- and long-dashed lines are typical of real systems.  $E_D$  is the energy at which the limiter undergoes irreversible laser damage.  $E_{\text{max}}$  is the maximum transmitted energy, here measured at the maximum input energy  $E_D$ .  $E_L$  is the limiting threshold for the ideal limiter,  $T_L$  is the linear transmittance, and  $T_{\text{min}}$  is the minimum transmittance, usually obtained for the maximum input energy,  $E_D$ .

protection. In addition, for nonideal limiting responses, the FOM may not give a clear indication of whether a device provides adequate protection at all input energies. For example, the dashed curves in Fig. 1*b* look very similar when plotted as transmittance versus input energy. Although they have the same FOM, when plotted as transmitted versus input energy, it is clear that the long-dashed curve provides considerably better protection than the short-dashed curve.

The maximum permissible transmitted energy is highly dependent on the threat laser wavelength and pulse width, on the sensor to be protected, and on the  $f$ -number (defined as the ratio of focal length to lens diameter) of the imaging system. Most practical imaging systems use an  $f$ -number of 5 or less. However, one very common sensor for which we can specify maximum safe exposure levels is the human eye.<sup>9</sup> Mostly, we are concerned with retinal damage. Visible or near-infrared radiation is not absorbed in the cornea or lens of the eye, and the focusing of light onto the retina produces an optical gain on the order of  $10^4$  [i.e., the fluence (incident energy/unit area) at the retina is  $\sim 10^4$  times that incident on the cornea]. Hence for visible or near-infrared radiation, damage will always occur first at the retina. For wavelengths in the UV and further into the infrared, light does not reach the retina, as it is absorbed in the lens or cornea where the fluence is much lower. If necessary, damage may be avoided by use of optical elements that simply block those wavelengths by reflection or absorption, as the eye cannot detect those wavelengths anyway. As shown in Fig. 2, the ANSI standard for the maximum safe energy entering the eye for pulse lengths less than  $17 \mu\text{s}$  is  $0.2 \mu\text{J}$ .<sup>10</sup> However, larger energies may be tolerated where there is a finite probability of a retinal lesion but little chance of retinal hemorrhaging. For example, the ED-50 exposure level, for which there is a 50 percent chance of a retinal lesion but little chance of permanent damage, corresponds to  $\sim 1 \mu\text{J}$  in the visible. Therefore, ideally one would desire  $E_{\text{max}} \ll 1 \mu\text{J}$  for an eye-protection limiter. However, since no practical prototype limiter so far has come close to this value, a more common target value for  $E_{\text{max}}$  in recent literature has been  $\sim 1 \mu\text{J}$ .<sup>11,12</sup> As will be subsequently described, the total energy entering the eye is not a complete measure of performance, as many nonlinear optical mechanisms that give rise to limiting strongly distort a laser beam as well as controlling its total transmitted energy. Therefore, a better measure of limiting performance is the focusable component of the energy entering the eye,  $E_{\text{foc}}$ .  $E_{\text{foc}}$  is defined as the energy falling within a 1.5-mrad-diameter circle in the retinal plane.<sup>13</sup> The accepted value for the minimum resolution of the eye is 1.5 mrad. Should the limiter defocus the beam enough that the focused beam significantly exceeds 1.5 mrad, an  $E_{\text{max}}$  of  $> 1 \mu\text{J}$  may be tolerable as long as  $E_{\text{foc}} < 1 \mu\text{J}$ .

In the remainder of this chapter, we describe some of the fundamental principles of passive optical limiting, including nonlinear mechanisms and optimization of geometry. We also present a few examples of experimental demonstrations of some types of optical limiters, although this is by no means intended



**FIGURE 2** Damage thresholds for the eye. (After Ref. 10.)

to be a comprehensive review. Rather, this chapter is intended as a starting point for newcomers to the field of optical limiting. For more detailed surveys of published research in this field, the reader is referred to the review papers,<sup>1,3,12</sup> journal special issues,<sup>14</sup> and conference proceedings<sup>15–22</sup> on the subject.

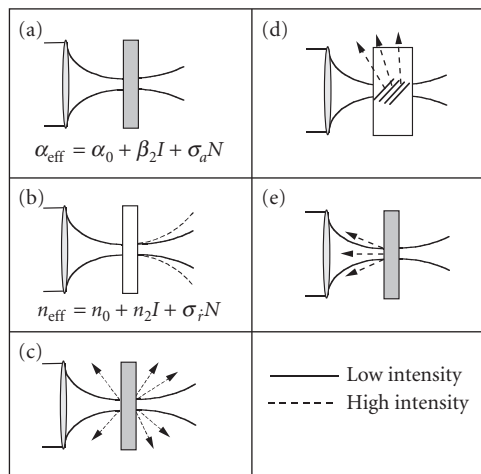
## 13.2 BASIC PRINCIPLES OF PASSIVE OPTICAL LIMITING

By way of an introduction to passive optical limiting, we briefly describe five of the most common nonlinear mechanisms used. As summarized in Fig. 3, these are (a) nonlinear absorption, (b) nonlinear refraction, (c) nonlinear scattering, (d) photorefraction, and (e) optically induced phase transitions. There have been many other schemes proposed for passive optical limiting, but those mentioned here form the basis for the vast majority of practical limiting devices that have appeared in the literature. A common theme to all schemes is that they each require the nonlinear optical material to be placed in or near a focal plane. Here we concentrate on how each nonlinear optical property results in limiting and we avoid detailed descriptions of the nonlinear mechanisms. For a more complete description of nonlinear optical phenomena and mechanisms, the reader is referred to Chap. 16, “Third-Order Optical Nonlinearities,” of this volume.

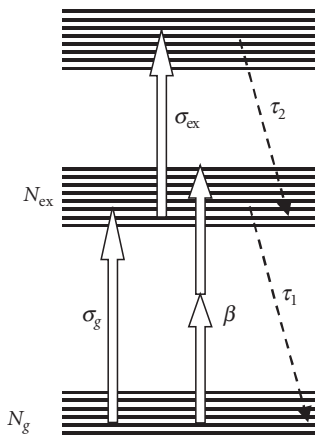
### Limiting via Nonlinear Absorption

Perhaps the most obvious and direct way to produce passive optical limiting is via nonlinear absorption (NLA), where we require the absorption to increase with increasing incident pulse fluence or irradiance. This can occur in a number of ways, as illustrated in Fig. 4, which shows some of the possible optical transitions for a generic material system. These could represent electronic transitions in many different material types (for example, an organic molecule or a semiconductor crystal).

Two-photon absorption (2PA) is a third-order nonlinear optical process that involves the simultaneous absorption of two photons.<sup>23</sup> For 2PA, the absorption increases in proportion to the incident irradiance,  $I$ . Another possibility is a two-step absorption process, where linear absorption populates excited states, from which a second absorption to a higher-lying energy state is possible.<sup>24,25</sup> If the



**FIGURE 3** Fundamental mechanisms for passive optical limiting: (a) nonlinear absorption; (b) nonlinear refraction; (c) nonlinear scattering; (d) photorefraction; and (e) optically induced phase transitions.



**FIGURE 4** Nonlinear absorption processes.

excited state cross section,  $\sigma_{\text{ex}}$ , exceeds the ground state cross section,  $\sigma_g$ , then the absorption will increase with increasing excited state population density,  $N_{\text{ex}}$ , and hence with increasing incident fluence. This is usually referred to as *excited state absorption* (ESA) or *reverse-saturable absorption* (RSA). The latter nomenclature grew out of the more commonly observed *saturable absorption*, where  $\sigma_{\text{ex}} < \sigma_g$  and the absorption decreases with increasing fluence. In materials with suitable energy levels, it is also possible to populate the excited state by two-photon absorption, and still produce excited state absorption at the excitation wavelength.<sup>23,26</sup> For any of these cases, we may write an approximate effective absorption coefficient,  $\alpha_{\text{eff}}$

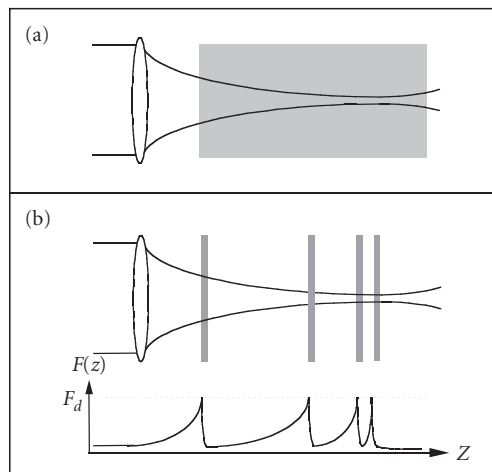
$$\alpha_{\text{eff}} = \alpha + \beta I + \sigma_{\text{ex}} N_{\text{ex}} = \sigma_g N_g + \beta I + \sigma_{\text{ex}} N_{\text{ex}} \quad (1)$$

where  $\beta$  is the 2PA coefficient and  $N_g$  and  $N_{\text{ex}}$  are the ground state and excited state absorption cross sections, respectively. For a laser pulse shorter than the excited state lifetime,  $\tau_1$ , and for low excitation levels,  $N_{\text{ex}}$  is directly proportional to the incident fluence. However, an optical limiter is required to work under high levels of excitation, so usually rate equations must be solved to determine the overall transmittance. Nevertheless, it is clear that a large ratio of  $\sigma_{\text{ex}}/\sigma_g$  is desirable, as we want large ESA, but small linear absorption. However,  $\sigma_g$  cannot be too small, as  $N_{\text{ex}}$  must become large enough to produce a strong limiting effect. The minimum achievable transmittance should occur when all molecules have been promoted to the first excited state, so that the transmittance is  $T_{\text{min}} = \exp(-\sigma_{\text{ex}}NL)$ , where  $N$  is the total molecular density and  $L$  is the material thickness. Hence the maximum achievable FOM is  $T_{\text{min}}/T_L = \exp[-(\sigma_{\text{ex}} - \sigma_g)NL]$ .<sup>27</sup> However, it is not practical to expect such a physical situation. Before such a high excitation is reached, other effects, including ionization, heating, and so forth will occur.<sup>11</sup>

In theory, 2PA is ideal for optical limiting, as the linear absorption is zero. Moreover, it can be shown that there is an absolute upper limit to the irradiance that can propagate through a two-photon absorber, given by  $I_{\text{max}} = (\beta L)^{-1}$ . 2PA also may populate excited states without the inconvenience of linear absorption, so that one can obtain limiting due to both 2PA and ESA. However, it is difficult to find materials with sufficiently large and broadband 2PA coefficients to work well with nanosecond or longer pulses.<sup>26,28,29</sup>

Regardless of the excitation mechanism, it is desirable to have an excited state lifetime,  $\tau_1$ , longer than the laser pulse width, so that each electron or molecule need only be excited one time per pulse. A short upper excited state lifetime,  $\tau_2$ , is required to reduce saturation of the excited state absorption, which detracts from limiting performance.

**Optimization of NLA Limiters** While NLA gives the best optical limiting by placing the nonlinear material in a focal plane, this is also where the damage energy threshold of the nonlinear material is lowest. Very often, this gives an unacceptably low FOM. The damage threshold may be greatly increased by placing another nonlinear absorber in front of the one at focus, hence protecting it from damage. In the case of 2PA, this can be achieved by using a *thick* 2PA material, as illustrated in Fig. 5a.<sup>7,28,30</sup> Here, the term *thick* means that the material thickness is much greater than the depth of focus of the beam. The front surface is far from focus, and the 2PA away from focus protects the material near focus. Theoretically, this can be done with no reduction in  $T_L$ , as there need be no linear absorption. In reality, parasitic linear transmittance and scatter may reduce  $T_L$ . For RSA materials, the intrinsic linear absorption does not permit us to use an arbitrarily thick medium. Instead, discrete elements can be used. This geometry is usually referred to a *cascaded* or *tandem* limiter.<sup>31</sup> In the simplest case, this can consist of two or more elements in tandem, as illustrated in Fig. 5b. The elements can be positioned so that the damage fluence,  $F_d$ , is reached simultaneously by all elements. This gives the maximum damage energy.<sup>8,11,27</sup> It has been shown that the total FOM of the limiter is given by the product of the FOMs of each individual element. However, because of beam distortion due to NLA or to any NLR that may be present in the material, the FOM of an individual element in a cascaded geometry does not usually approach the FOM of the same element when used alone. Miles<sup>11</sup> pointed out that this geometry helps keep the fluence high through the length of the limiter, by balancing the decrease in fluence due to absorption with the increase in fluence due to focusing. This is illustrated in Fig. 5b, which shows a sketch of on-axis fluence versus distance for a four-element tandem limiter. This can be understood by considering the example of a limiter with  $T_{\min} = 10^{-4}$ . If such a limiter were to have only a single element, the fluence on the front surface of the cell would have to exceed that on the rear surface by  $10^4$ . If damage to the front of the cell were to be avoided, the fluence on the rear surface would be so low that the molecules near the rear surface could not contribute significantly to the limiting. Therefore, these molecules only serve to reduce the linear transmittance. However, for a 4-cell tandem limiter,  $T_{\min} = 0.1$  for each element, and the net value of  $T_{\min}$  for the tandem limiter is  $10^{-4}$ . This is much easier to achieve. The greater the number of cells, the larger the average fluence in each cell, and the separation of the cells is proportional to the square of the distance from focus,  $Z$ .<sup>8</sup> This can be extended to the limiting case of a single element with a graded molecular density,  $N(z) \approx 1/\sigma_{\text{ex}}|Z|$ .<sup>11,32</sup> In this case, the on-axis fluence



**FIGURE 5** Optimization of limiter geometry: (a) for a 2PA limiter and (b) for an RSA limiter. The graph in (b) is a sketch of the on-axis fluence through the limiter near the maximum operating energy.

would remain constant through the RSA material at some designed value of the input energy, usually just below the damage threshold. To avoid problems of generating the exact molecular density distribution, approximating the distribution with a steplike series of adjacent cells of different thickness and density has also been proposed. Like the tandem devices, these designs must be modified to account for beam distortion.<sup>27</sup>

## Limiting via Nonlinear Refraction

From Kramers-Krönig relations, we know that all materials exhibiting nonlinear absorption must also exhibit nonlinear refraction.<sup>33</sup> A consequence of this is that each process that gives rise to optically induced changes in absorption must also result in changes to the refractive index. This can usually be expressed as

$$n_{\text{eff}} = n_0 + n_2 I + \sigma_r N_{\text{ex}} \quad (2)$$

where  $n_2$  describes instantaneous index changes proportional to incident irradiance and  $\sigma_r$  describes the change in index due to population of excited states. As described in Chap. 16, “Third-Order Optical Nonlinearities,” of this volume and in Refs. 33 and 34,  $n_2$  is related to the 2PA coefficient,  $\beta$ , by Kramers-Krönig relations.  $\sigma_r$  and  $\sigma_{\text{ex}}$  are related in a similar manner. Such index changes can occur even at wavelengths where there is no change in absorption.

As a focused beam has a spatially varying irradiance, then the induced index change varies across the beam profile, causing the beam to be strongly distorted upon propagation. Near focus, the beam is usually brightest in the center, so for a negative index change (where the index decreases with increasing irradiance or fluence), the nonlinear material will behave like a lens with negative focal length, and the beam is defocused. This process is referred to as *self defocusing*. If the sign of the index change is positive, *self-focusing* results. Both of these effects can cause the beam to spread in the far field and hence limit the energy density in the far field, although the geometrical alignment may be different for optimal limiting in each case.<sup>35</sup> This means that  $E_{\text{foc}}$  may be strongly limited without necessarily limiting  $E_{\text{max}}$ . The presence of pupil-plane apertures in the imaging system combined with the beam distortion may also result in limiting of  $E_{\text{max}}$ . An advantage of this method over nonlinear absorption devices is that there is no need to absorb large amounts of energy in the nonlinear material, which could cause thermal damage problems. A potential problem is that inadvertent refocusing of the eye could reduce the defocusing effect of the limiter. However, the nonlinear refraction usually aberrates the beam sufficiently that this is not a concern.

In terms of NLR, a *thick* limiter is defined as one where the propagation path in the nonlinear material is long enough that the index changes cause the beam to change its size inside the material. This process is sometimes refers to as *internal self-action*.<sup>36</sup> In this situation, the limiting behavior differs considerably between positive and negative index changes. Self-focusing causes the irradiance to be increased, causing more self-focusing, which becomes a catastrophic effect once a critical input power is reached.<sup>37</sup> This results in breakdown of the medium, which can strongly scatter the light and hence effectively limit the transmitted energy. It also causes damage to the material, but this is not a problem if the nonlinear medium is a liquid. Self-defocusing, on the other hand, reduces the irradiance, so that the limiting occurs more gradually as the input energy is increased.

Thermally induced index changes are also important in optical limiters. In liquids, where the thermal expansion is large, the index change results from the change in density upon heating due to laser absorption.<sup>38</sup> Hence the index decreases with temperature, giving a selfdefocusing effect. The turn-on time for defocusing is dictated by the time taken for the liquid to expand across the width of the laser beam, which is roughly given by the beam radius divided by the speed of sound.<sup>39</sup> The turn-off time is dictated by thermal diffusion. In solids, thermal expansion is much smaller, but other effects, such as temperature dependence of the absorption edge, can cause thermally induced index changes. These usually result in an increase in index with temperature. As this is a local effect, the turn-on time is usually very fast, but turn-off times depend again on thermal diffusion. Thermal

self-focusing in solid-state limiters can be a problem, leading to optical damage. Although thermal defocusing in liquids can be used to produce limiting, and some of the first passive optical limiters were based on this effect,<sup>38</sup> it usually degrades the performance of limiters based on NLA. This is one reason to use solid polymer host matrices for RSA dyes.<sup>40</sup>

## Limiting via Nonlinear Scattering

Like absorption, scattering is also capable of strongly attenuating a transmitted beam. Nonlinear scattering is possible by laser-induced creation of new scatter centers or by laser-induced changes in the refractive index difference between existing scatter centers and their surroundings. In the latter case, glass scatterers (such as small particles, a rough surface, highly porous glass, or a regular array of holes in glass) are index-matched by immersion in a liquid.<sup>41–43</sup> In this state, the composite material is clear and highly transparent. A small amount of absorber dye is dissolved in the liquid, so that when illuminated by a strong laser pulse, the solvent is heated and the index matching is lost, resulting in strong scattering.

In the former case, new scatter centers can be created when small particles, such as carbon black, molecular clusters, or other absorbing particles, are exposed to intense laser radiation.<sup>44,45</sup> In their normal state, such particles are very small, and although they may have a very strong optical absorption coefficient, due to their small size they neither absorb nor scatter much radiation. Upon absorption of radiation, the particles rapidly heat and ionize. This can cause the formation of microplasmas, which grow rapidly and strongly scatter the laser radiation. If the particles are suspended in a liquid, the heating can cause subsequent formation of microbubbles, which also strongly scatter light.<sup>46,47</sup> In either event, the scattering produces strong optical limiting. As the size of the scattering particles approaches the wavelength, the scattering is predominantly in the forward direction, which could reduce performance for low  $f$ -number imaging systems. Another problem is that the limiting process destroys the particles, making this mechanism unsuited to protection against high repetition-rate lasers. This might be overcome by flowing the suspensions. It has been shown that nonlinear scattering may also be an important yet unintentional mechanism in the operation of RSA limiters based on organic molecules.<sup>47</sup> It is likely that this is due to incomplete dissolution of the organic material, which leaves small clusters of undissolved material in suspension in the solvent.

## Other Mechanisms

While the majority of the results reported on passive limiting employ one of the three previously noted mechanisms, many other schemes have been proposed and demonstrated. Most of these may involve some sort of change in refractive index or absorption, but they may use the change in a manner different from those just described. Although such schemes are too numerous to fully document here, the two following examples are worthy of mention.

**Photorefraction** Photorefractives change their index when exposed to light, and they do so in such a way that the index change is in proportion to the gradient of light intensity. This is achieved by a complex process involving photoexcitation of charge carriers and diffusion of those carriers that results in a space charge field.<sup>48</sup> This field in turn causes an index change via the electro-optic effect. Due to the dependence on the gradient of intensity, the photo-refractive effect is usually employed in situations where a periodic modulation of the irradiance induces a phase grating (a periodic modulation of the index). For optical-limiting applications, the interference is obtained by picking off a portion of the input laser beam with a beam splitter and overlapping it with the original beam in a photorefractive crystal.<sup>49</sup> Alternatively, a reflection from the rear surface of the crystal is used to interfere with the forward-going beam.<sup>50</sup> In both cases, a grating is produced that, via *two-beam coupling*, strongly scatters the incoming laser beam, limiting the transmitted energy.<sup>51</sup> An interesting side effect of this mechanism is that the limiting is coherence-dependent as well as

intensity-dependent. Due to the requirement for charge diffusion, the turn on time is relatively slow, so that this type of limiter is usually only suitable for pulses of millisecond or longer duration.

**Optically Induced Phase Change** A number of materials show a reversible, thermally induced semiconductor-metal phase transition upon illumination with strong laser radiation.<sup>52</sup> These materials are transparent to infrared radiation in their semiconducting state but highly reflective in their metallic state. Hence, in the infrared these materials may be transparent for low powers, while at high powers, weak optical absorption and subsequent heating may induce the strongly reflecting metallic phase, blocking the transmitted light. Some examples of materials of this type are  $\text{Ag}_2\text{S}$ ,  $\text{TmSe}_x\text{Te}_{1-x}$ , and vanadium oxides,  $\text{V}_x\text{O}_{2x-1}$ . To be effective, such a material must be stable in its transparent state, have a small latent heat associated with the phase transition, and require a reasonably small temperature change ( $\sim 100$  K) to induce the phase transition. Vanadium oxides with compositions close to  $\text{VO}_2$  or  $\text{V}_2\text{O}_3$  comprise the most-studied class of these materials for optical limiting, having a phase transition temperature at around  $70^\circ\text{C}$ . In thin-film form and with appropriate antireflection coatings, these materials have high broadband transmission through the infrared (3 to 12  $\mu\text{m}$ ) which drops to around 1 percent in the metallic phase.<sup>52</sup>

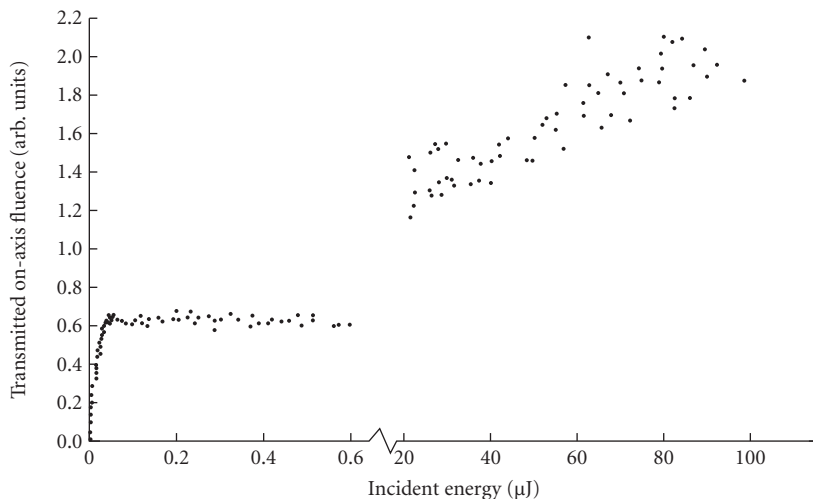
### 13.3 EXAMPLES OF PASSIVE OPTICAL LIMITING IN SPECIFIC MATERIALS

Unavoidably, most of the materials used for passive optical limiting exhibit a combination of the nonlinear properties previously described. This usually complicates matters, but in some cases the different nonlinearities may be used to complement each other. In this section, we briefly present a few specific examples of limiting devices that illustrate how some of the principles just described may be applied in practice.

#### Semiconductors

Semiconductors exhibit a variety of strong nonlinear absorption and refraction effects.<sup>53</sup> Due to their broad absorption bands, they are capable of producing 2PA over a broad wavelength range where the linear absorption is low. Moreover, the carriers excited by 2PA produce very strong absorption and negative nonlinear refraction. The wavelength range of operation for 2PA, avoiding linear interband absorption, is  $E_g/2 < h\nu < E_g$ .  $E_g$  is the bandgap of the semiconductor and  $h\nu$  is the photon energy. For example, in ZnSe, this corresponds to an operating wavelength range of about 480 to 900 nm, while in InSb the range is 7 to 14  $\mu\text{m}$  at room temperature. Over this range, the combined effects of 2PA and free carrier absorption and refraction are more or less constant for a given semiconductor. However, the nonlinearities scale very strongly with bandgap. If we keep the ratio of photon energy to bandgap energy fixed, 2PA scales as  $E_g^{-3}$  and free carrier absorption and refraction scale approximately as  $E_g^{-2}$ .<sup>6,23</sup> Hence, semiconductors work significantly better for the infrared than for the visible. A problem with semiconductors is that they tend to have low damage thresholds. It was shown by Van Stryland et al.<sup>28</sup> that this can be overcome by the use of the thick-limiter geometry. In this case, a thick sample of the large-gap semiconductor ZnSe was used to demonstrate limiting of 30-ps pulses at a wavelength of 532 nm, as shown in Fig. 6. Due to a combination of 2PA and free-carrier absorption and refraction that occurs prior to focus, it was not possible to damage the ZnSe in the bulk. Hence, these devices were labeled *self-protecting* limiters. The FOM was measured as  $2 \times 10^4$ . The linear transmittance was 40 percent, probably due to a combination of scatter and parasitic absorption. Despite this good performance with ps pulses, the self-protection does not prevail for nanosecond pulses. This is thought to be due to the effects of carrier recombination and diffusion, which reduce the carrier defocusing effect, allowing positive thermal index changes to dominate.





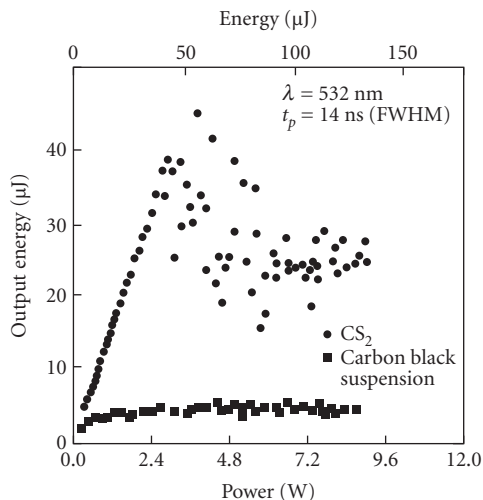
**FIGURE 6** Limiting curve for ZnSe thick limiter for 30 ps, 532 nm. (After Ref. 28.)

## Organics

Organic molecules have attracted interest for optical limiting for their attractive NLA properties in the visible and near-infrared. While some materials have shown promise for their combined 2PA and excited-state absorption properties,<sup>26,29</sup> so far these effects have not proven large enough over a sufficiently broad wavelength band to be practical. By far the most attention has been paid to organics for their RSA properties.<sup>25,54</sup> Generally, the mechanism is as shown in Fig. 4, but often the excited states may also relax into long-lived triplet states. This effectively increases the lifetime of the highly absorbing excited state. The transfer to triplet states may be enhanced by the addition of heavy atoms or paramagnetic groups to the molecule or solvent.<sup>55</sup> Several groups have demonstrated promising results with optimized limiting devices using phthalocyanines or other similar RSA molecules.<sup>40,56</sup> One example of an optimized limiter based on this type of material is that of Perry et al.<sup>40</sup> Here an indium phthalocyanine chloride (InClPc) was incorporated into a PMMA polymer host to make a solid-state limiting material. Slices of this material were used to make a three-element tandem limiter. The device, which had a linear transmittance of about 55 percent (70 percent internal transmittance), was designed to operate with a maximum fluence of  $3 \text{ J/cm}^2$  in an  $f/5$  focusing geometry. The combination of solid-state host and low design fluence helps minimize the detrimental effects of thermally induced refractive index changes. The device had a minimum transmittance of 0.185 percent at the maximum input energy of 6.5 mJ, corresponding to a maximum output energy of 12  $\mu\text{J}$ . This was a factor of four greater than predicted by simple design models, which assume a constant beam shape. This discrepancy is small compared with similar liquid-based limiters, which suffer from much greater thermal refraction. To properly design limiters of this type, propagation codes have been developed that account for all NLA and NLR mechanisms, including thermal refraction, and that are capable of modeling internal self-action.<sup>57</sup>

## Carbon-Black Suspensions

It was shown by Mansour et al.<sup>44</sup> that dilute ink exhibits very strong, broadband optical limiting properties for nanosecond pulses. Ink is a liquid suspension of amorphous carbon particles. Figure 7 shows an example of limiting of 14-ns, 532-nm pulses using a carbon-black suspension (CBS) in a 50:50 water/ethanol mixture with  $T_L = 70$  percent. Similar results are obtained with a

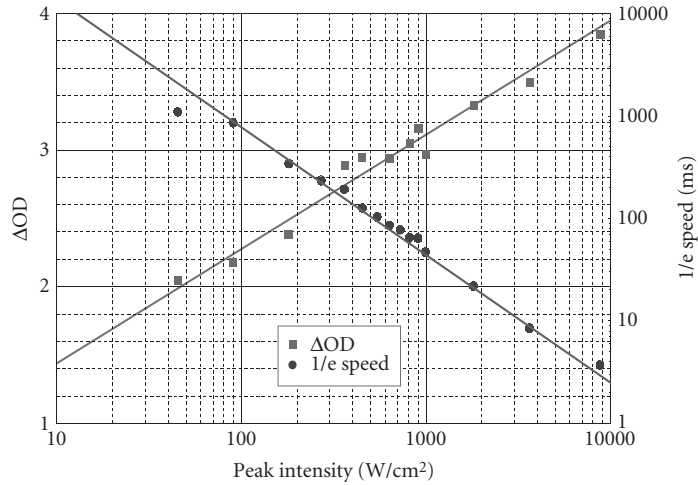


**FIGURE 7** Optical limiting of 14-ns pulses at 532-nm wavelength in 1-cm thick, 70 percent linear transmittance CBS. Also shown are results of limiting in  $\text{CS}_2$ , for comparison. (After Ref. 44.)

1064-nm laser wavelength, indicating an extremely broadband limiting response. By observing scattered light intensity as a function of input irradiance, it was clearly shown that the incident light becomes very strongly scattered as the incident energy increases. Measurements of the angular distribution of scattered light show a Mie scattering pattern typical of scattering particles a factor of  $\approx 3$  larger than the original carbon-black particles. Similar results were found for a layer of small carbon particles deposited on a glass surface. It was concluded from this that the limiting is a result of scattering and absorption by microplasmas formed after thermionic emission from the laser-heated carbon particles. Later studies have indicated that the nonlinear scattering may result from microbubbles formed in the solvent by heating of the carbon. There is clear evidence that for longer pulses, the limiting is dependent on the volatility of the solvent,<sup>46</sup> and imaging techniques have shown that bubbles may persist in the focal volume 100 ns after the pulse.<sup>47</sup> It is quite feasible that microplasmas may be responsible for limiting on shorter ( $< 10$  ns) time scales, while bubbles play a more important role for longer ( $\sim 100$  ns) pulses.

## Photorefractives

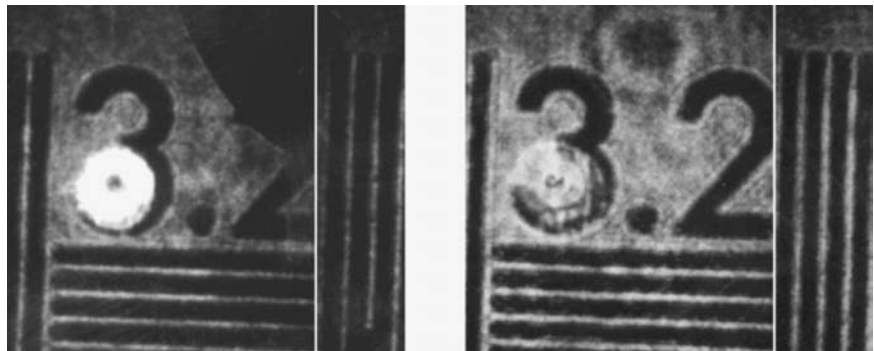
Although it has been shown that the photorefractive effect can occur over a vast range of time scales, effects large enough for practical devices typically have millisecond and longer response times. Cook et al.<sup>50</sup> exploited the large photorefractive two-beam coupling gain in  $\text{Fe}:\text{LiNbO}_3$  to demonstrate strong optical limiting for millisecond pulses or c.w. lasers. A weak reflection of the input beam from the rear surface of the lithium niobate crystal was sufficient to initiate the two-beam coupling. As shown in Fig. 8, this produced a change in OD of up to 4 with a response time of about 2 ms. The linear transmittance for these samples is typically in the range of 30 to 60 percent. The limiting effect is not strongly sensitive to wavelength, operating between 420 and 670 nm. It is found that the optimum  $f$ -number for limiting was about  $f/20$ , and limiting performance drops off rapidly as the  $f$ -number is decreased. This results from the trade-off between the high irradiance produced by small focused spot sizes and the long interaction length produced by large spot sizes.



**FIGURE 8** Far-field optical limiting and response time in a 3.4-mm path crystal of 0.03 percent Fe + 0.05 percent Tb:LiNbO<sub>3</sub> at 523.5 nm. (After Ref. 50.)

## Liquid Crystals

Liquid crystals are composed of highly anisotropic molecules. By illuminating a nematic liquid crystal with a linearly polarized laser beam, the molecules can align with the electric field in the beam, inducing an irradiance-dependent birefringence in the bulk liquid. These effects are large, but typically take milliseconds to seconds for the realignment process. Recently, it has been shown that doping a liquid crystal with certain dyes can induce molecular reorientation at extremely low powers.<sup>58</sup> Khoo et al.<sup>59</sup> have shown that this effect may be used to achieve extremely low-power c.w. limiting. Using a twisted nematic 5CB film with 1 percent methyl red doping, between crossed polarizers, the maximum transmitted energy of a c.w. argon ion laser beam was kept below 13  $\mu$ W for inputs up to 140 mW, with  $T_L = 10$  percent, including Fresnel reflections and losses at the polarizers. Figure 9 shows a photograph of the transmitted beam for low and high powers, with an image that was simultaneously transmitted by the system. An advantage of liquid crystals is that they can be highly transparent across the entire visible spectrum.



**FIGURE 9** Suppression of a c.w. visible laser beam while transmitting the image of a resolution test chart, using a dye-doped nematic liquid crystal passive limiter. (a) Low laser intensity, showing no limiting effect and (b) above the limiting threshold. (After Ref. 59.)

## 13.4 REFERENCES

1. L. W. Tutt and T. F. Boggess, "A Review of Optical Limiting Mechanisms and Devices Using Organics, Fullerenes, Semiconductors and Other Materials," *Prog. Quantum. Electron.* **17**:299–338 (1993).
2. G. L. Wood, W. W. Clark, M. J. Miller, G. J. Salamo, and E. J. Sharp, "Evaluation of Passive Optical Limiters and Switches," *Proceedings of SPIE Conference on Materials for Optical Switches, Isolators and Limiters*, **1105**:154–181 (1989).
3. E. W. Van Stryland, M. J. Soileau, S. Ross, and D. J. Hagan, "Passive Optical Limiting: Where Are We?" *Nonlinear Optics* **21**:29–38 (1998).
4. M. Sheik-Bahae, D. C. Hutchings, D. J. Hagan, and E. W. Van Stryland, "Dispersion of Bound Electronic Nonlinear Refraction in Solids," *IEEE J. Quantum Electron.* **27**:1296–1309 (1991).
5. A. A. Said, M. Sheik-Bahae, D. J. Hagan, T. H. Wei, J. Wang, J. Young, and E. W. V. Stryland, "Determination of Bound and Free-Carrier Nonlinearities in ZnSe, GaAs, CdTe and ZnTe," *J. Opt. Soc. Am. B* **9**:409 (1991).
6. B. S. Wherrett, "Scaling Rules for Multiphoton Interband Absorption in Semiconductors," *J. Opt. Soc. Am. B-Optical Physics* **1**:67–72 (1984).
7. D. J. Hagan, E. W. Van Stryland, M. J. Soileau, Y. Y. Wu, and S. Guha, "Self-Protecting Semiconductor Optical Limiters," *Opt. Lett.* **13**:315–317 (1988).
8. D. J. Hagan, T. Xia, A. A. Said, T. H. Wei, and E. W. V. Stryland, "High Dynamic Range Passive Optical Limiters," *Int. J. Nonlin. Opt. Phys.* **2**:483–501 (1993).
9. D. H. Sliney and M. L. Wolbarsht, *Safety with Lasers and Other Optical Sources*, Plenum, New York, 1980.
10. D. H. Sliney, "Retinal Damage from Laser Radiation," *Nonlinear Optics* **21**:1–18 (1998).
11. P. A. Miles, "Bottleneck Optical Limiters: The Optimal Use of Excited-State Absorbers," *Appl. Opt.* **33**:6965 (1994).
12. R. C. Hollins, "Optical Limiters, Spatial, Temporal and Spectral Effects," *Nonlinear Optics* **21**:39–48 (1998).
13. J. A. Zuclich, D. J. Lund, P. R. Edsall, R. C. Hollins, P. A. Smith, B. E. Stuck, and L. N. McLin, "Experimental Study of the Variation of Laser-Induced Retinal Damage Threshold with Retinal Image Size," *Nonlinear Optics* **21**:19–28 (1998).
14. J. A. Hermann and J. Staromlynska, "Special Issue on Optical Limiters, Switches and Discriminators," *J. Nonlinear Optical Phys. and Materials* **2**:271–337(1993).
15. F. Kajzar, "Proceedings of First International Workshop on Optical Power Limiting, Cannes, France," in *Nonlinear Optics, Principles, Materials, Phenomena, Devices*, Gordon & Breach, 1998.
16. C. M. Lawson, "Nonlinear Optical Liquids," *Proceedings of SPIE*, SPIE, **2853**, Denver, 1996.
17. C. M. Lawson, "Nonlinear Optical Liquids for Power Limiting and Imaging," *Proceedings of SPIE*, SPIE, **3472**, San Diego, 1998.
18. C. M. Lawson, "Power Limiting Materials and Devices," *Proceedings of SPIE*, SPIE, **3798**, Denver, 1999.
19. M. J. Soileau, "Materials for Optical Switches, Isolators and Limiters," *Proceedings of SPIE*, SPIE, **1105**, Orlando, 1989.
20. M. J. Soileau, *Electro-Optical Materials for Switches, Coatings, Sensor Optics and Detectors*, SPIE, **1307**, Orlando, 1990.
21. Crane, K. Lewis, E. W. Van Stryland, and M. Khoshnevisan, *Materials for Optical Limiting*, **374**, MRS, Boston, 1994.
22. R. Sutherland, R. Pachter, P. Hood, D. J. Hagan, K. Lewis, and J. Perry, *Materials for Optical Limiting II*, **479**, MRS, San Francisco, 1997.
23. E. W. Van Stryland, H. Vanherzeele, M. A. Woodall, M. J. Soileau, A. L. Smirl, S. Guha, and T. F. Boggess, "2 Photon-Absorption; Nonlinear Refraction; and Optical Limiting in Semiconductors," *Opt. Eng.*, **24**:613–623 (1985).
24. C. R. Gulliano and L. D. Hess, "Nonlinear Absorption of Light: Optical Saturation of Electronic Transitions in Organic Molecules with High Intensity Laser Radiation," *IEEE J. Quantum Electron.* **QE3**:358–367 (1967).
25. T. H. Wei, D. J. Hagan, M. J. Sence, E. W. V. Stryland, J. W. Perry, and D. R. Coulter, "Direct Measurements of Nonlinear Absorption and Refraction in Solutions of Phthalocyanines," *Appl. Phys.* **B54**:46 (1992).
26. A. A. Said, C. Wamsley, D. J. Hagan, E. W. V. Stryland, B. A. Reinhardt, P. Roderer, and A. G. Dillard, "Third and Fifth Order Optical Nonlinearities in Organic Materials," *Chem. Phys. Lett.* **228**:646–650 (1994).

27. T. Xia, D. J. Hagan, A. Dogariu, A. A. Said, and E. W. V. Stryland, "Optimization of Optical Limiting Devices Based on Excited-State Absorption," *Appl. Opt.* **36**:4110–4122 (1997).
28. E. W. Van Stryland, Y. Y. Wu, D. J. Hagan, M. J. Soileau, and K. Mansour, "Optical Limiting with Semiconductors," *J. Opt. Soc. Am. B* **5**:1980–1989 (1988).
29. M. Albota, D. Beljonne, J. L. Brédas, J. Ehrlich, J. Fu, A. Heikal, T. Kogej, M. Levin, S. R. Marder, D. McCord-Maughon, J. W. Perry, H. Röckel, M. Rumi, G. Subramaniam, W. W. Webb, X. L. Wu, and C. Xu, "Design of Organic Molecules with Large Two-Photon Absorption Cross Sections," *Science* **281**:1653–1656 (1998).
30. M. Sheik-Bahae, A. A. Said, D. J. Hagan, M. J. Soileau, and E. W. Van Stryland, "Nonlinear Refraction and Optical Limiting in Thick Media," *Opt. Eng.* **30**:1228–1235 (1991).
31. A. A. Said, R. DeSalvo, M. Sheik-Bahae, D. J. Hagan, and E. W. V. Stryland, "Self Protecting Optical Limiters Using Cascading Geometries," *Proceedings of SPIE*, SPIE, Orlando, Florida, 1992.
32. S. W. McCahon and L. W. Tutt, "Optical Limiter Including Optical Congruence and Absorbing Body with Inhomogeneous Distribution of Reverse Saturable Absorption," U.S. Patent 5,080,469, 1992.
33. D. C. Hutchings, M. Sheik-Bahae, D. J. Hagan, and E. W. Van Stryland, "Kramers-Kronig Relations in Nonlinear Optics," *Opt. and Quantum Electron.* **24**:1–30 (1992).
34. M. Sheik-Bahae, D. J. Hagan, and E. W. V. Stryland, "Dispersion of Bound Electronic Nonlinear Refraction in Solids," *Phys. Rev. Lett.* **65**:96–99 (1990).
35. M. Sheik-Bahae, A. A. Said, and E. W. V. Stryland, "High-Sensitivity, Single-Beam  $n_2$  Measurements," *Opt. Lett.* **14**:955–957 (1989).
36. A. E. Kaplan, "External Self-Focusing of Light by a Nonlinear Layer," *Radiophys. Quantum Electron.* **12**:692–696 (1969).
37. M. J. Soileau, W. E. Williams, and E. W. Van Stryland, "Optical Power Limiter with Picosecond Response Time," *IEEE J. Quantum Electron.* **QE-19**:731–735 (1983).
38. R. C. Leite, S. P. S. Porto, and T. C. Damen, *Appl. Phys. Lett.* **10**:100 (1967).
39. D. I. Kovsh, D. J. Hagan, and E. W. V. Stryland, "Numerical Modeling of Thermal Refraction in Liquids in the Transient Regime," *Opt. Exp.* **4** (1999).
40. J. W. Perry, K. Mansour, I.-Y. S. Lee, X.-L. Wu, P. V. Bedworth, C.-T. Chen, D. Ng, S. R. Marder, P. Miles, T. Wada, M. Tian, and H. Sasabe, "Organic Optical Limiter with a Strong Nonlinear Absorptive Response," *Science* **273**:1533 (1996).
41. B. L. Justus, A. J. Campillo, and A. L. Huston, "Thermal-Defocusing/Scattering Optical Limiter," *Opt. Lett.* **19**:673 (1994).
42. H.-B. Lin, R. J. Tonucci, and A. J. Campillo, "Two-Dimensional Photonic Bandgap Optical Limiter in the Visible," *Opt. Lett.* **23**:94–96 (1998).
43. D. J. Hagan, S. S. Yang, C. Basanez, E. W. Van Stryland, W. Moreshead, and J. L. Nogues, "Optical Limiting via Nonlinear Scattering with Solgel Hosts," *Proceedings of SPIE Conf. on Power Limiting Materials and Devices*, SPIE, **3798**, Denver, Colorado, 1999.
44. K. Mansour, E. W. V. Stryland, and M. J. Soileau, "Nonlinear Properties of Carbon Black Suspensions," *J. Opt. Soc. Am. B* **9**:1100 (1992).
45. T. Xia, A. Dogariu, K. Mansour, D. J. Hagan, A. A. Said, E. W. V. Stryland, and S. Shi, "Nonlinear Optical Properties of Inorganic Metallic Clusters," *J. Opt. Soc. Am. B* **15**:1497 (1998).
46. K. J. McEwan, P. K. Milsom, and D. B. James, "Nonlinear Optical Effects in Carbon Suspensions," *Proceedings of Nonlinear Optical Liquids for Power Limiting and Imaging*, SPIE, **3472**, San Diego, California, 1998.
47. R. V. Goedert, R. J. Becker, A. Clements, and T. A. Whitaker III, "Overview of the Shadowgraphic Imaging Technique and Results for Various Materials," *Proceedings of Nonlinear Optical Liquids for Power Limiting and Imaging*, SPIE, **3472**, San Diego, California, 1998.
48. M. Cronin-Golumb and A. Yariv, "Optical Limiters Using Photorefractive Limiters," *J. Appl. Phys.* **57**:4906 (1985).
49. S. W. McCahon and M. V. Klein, "Coherent Beam Excisors Using the Photorefractive Effect in BaTiO<sub>3</sub>," *Proceedings of SPIE Conference on Materials for Optical Switches, Isolators and Limiters*, SPIE, **1105**, Orlando, Florida, 1989.
50. G. Cook, D. C. Jones, C. J. Finnan, L. L. Taylor, and T. W. Vere, "Optical Limiting with Lithium Niobate," *Proceedings of Power-Limiting Materials and Devices*, SPIE, **3798**, Denver, Colorado, 1999.

51. R. W. Boyd, *Nonlinear Optics*, Academic Press, Boston, 1992.
52. K. L. Lewis, A. M. Pitt, T. Wyatt-Davies, and J. R. Milward, "Thin Film Thermochromic Devices for Non-Linear Optical Devices," *Proceedings of MRS Symposium on Materials for Optical Limiting*, MRS, Boston, 1994.
53. N. Peyghambarian, S. W. Koch, and A. Mysyrowicz, *Introduction to Semiconductor Optics*, Prentice Hall, Englewood Cliffs, New Jersey, 1993.
54. J. S. Shirk, R. G. S. Pong, F. J. Bartoli, and A. W. Snow, "Optical Limiter Using a Lead Phthalocyanine," *Appl. Phys. Lett.* **63**:1880 (1993).
55. J. W. Perry, "Organic and Metal-Containing Reverse Saturable Absorbers for Optical Limiters," in *NonLinear Optics of Organic Molecules and Polymers*, H. S. Nalwa and S. Miyata, (ed.), CRC Press, New York, 1997.
56. A. A. Said, T. Xia, D. J. Hagan, A. Wajsgros, S. Yang, D. Kovsh, and E. W. V. Stryland, "Liquid-Based Multicell Optical Limiter," *Proceedings of SPIE Conference on Nonlinear Optical Liquids*, SPIE, **2853**, Denver, Colorado, 1996.
57. D. Kovsh, S. Yang, D. J. Hagan, and E. W. Van Stryland, "Nonlinear Optical Beam Propagation for Optical Limiting," *App. Opt.* **38**:5168–5180 (1999).
58. L. Marrucci, D. Paparo, G. Abbate, E. Santamo, M. Kreuzer, P. Lehnert, and T. Vogeler, "Enhanced Optical Nonlinearity by Photoinduced Molecular Orientation in Absorbing Liquids," *Phys. Rev. A* **58**:4926 (1998).
59. I. C. Khoo, M. V. Wood, M. Y. Shih, and P. H. Chen, "Extremely Nonlinear Photosensitive Liquid Crystals for Image Sensing and Sensor Protection," *Opt. Exp.* **4**:432–442 (1999).

*This page intentionally left blank*

---

# ELECTROMAGNETICALLY INDUCED TRANSPARENCY

---

Jonathan P. Marangos

*Quantum Optics and Laser Science Group  
Blackett Laboratory, Imperial College  
London, United Kingdom*

Thomas Halfmann

*Institute of Applied Physics  
Technical University of Darmstadt  
Darmstadt, Germany*

## 14.1 GLOSSARY

---

### Terms and Acronyms

EIT	electromagnetically induced transparency
CPT	coherent population trapping
STIRAP	stimulated Raman adiabatic passage
RAP	rapid adiabatic passage
SCRAP	Stark chirped rapid adiabatic passage
CPR	coherent population return
LWI	lasing without inversion
lambda ( $\Lambda$ ) scheme	three coupled atomic levels with the initial and final states at lower energy than the intermediate state
ladder scheme	three coupled atomic levels with the energy of the initial state below the intermediate state, and the energy of the intermediate state below the final state
vee ( $V$ ) scheme	three coupled atomic levels with the initial and final states at higher energy than the intermediate state
cw	continuous wave

### Symbols

$ a\rangle$	quantum state of atom
$E_a$	energy of quantum state $ a\rangle$
$\omega_{ab}$	angular transition frequency between states $ a\rangle$ and $ b\rangle$ ( $\text{rad s}^{-1}$ )
$\Delta_{ab}$	detuning of a light field from an atomic transition at $\omega_{ab}$ ( $\text{rad s}^{-1}$ )
$\mu_{ab}$	transition dipole moment between two states $ a\rangle$ and $ b\rangle$ (Cm)



$\text{Re } \chi^{(1)}$	real part of linear susceptibility (dispersion)
$\text{Im } \chi^{(1)}$	imaginary part of linear susceptibility (absorption)
$\chi^{(3)}$	nonlinear susceptibility of third order ( $\text{m}^2 \text{V}^{-2}$ )
$N_A$	number of atoms
$n_A$	atomic density ( $\text{cm}^{-3}$ )
$E$	electric field strength ( $\text{Vm}^{-1}$ )
$\omega$	angular frequency of a radiation field ( $\text{rad s}^{-1}$ )
$\lambda$	wavelength of a radiation field (nm)
$P$	macroscopic polarization ( $\text{Cm}^{-2}$ )
$\Omega$	Rabi frequency ( $\text{rad s}^{-1}$ )
$\rho_{ab}$	density matrix element
$\Gamma_a$	decay rate of state $ a\rangle$ ( $\text{rad s}^{-1}$ )
$\gamma_{ab}$	dephasing rate of the coherence $\rho_{ab}$ ( $\text{rad s}^{-1}$ )
$\gamma_{\text{Doppler}}$	Doppler (inhomogeneous) linewidth ( $\text{rad s}^{-1}$ )
$\gamma_{\text{laser}}$	laser bandwidth ( $\text{rad s}^{-1}$ )

## 14.2 INTRODUCTION

Electromagnetically induced transparency (EIT) is a quantum interference phenomenon that arises when coherent optical fields couple to the states of a material quantum system. In EIT the interference occurs between alternative transition pathways, driven by radiation fields within the internal states of the quantum system. Interference effects arise, because in quantum mechanics the probability amplitudes (which may be positive or negative in sign), rather than probabilities, must be summed and squared to obtain the total transition probability between the relevant quantum states. Interference between the amplitudes may lead to either an enhancement (constructive interference) or a complete cancellation (destructive interference) in the total transition probability. As a consequence, interference effects can lead to profound modification of the optical and nonlinear optical properties of a medium. Thus, control of optical or nonlinear optical properties and processes becomes possible.

Interference effects of this kind are well known in physics. These occur naturally if there are two transition pathways available to the same final state. Fano interferences exhibit an example of interference between two transition pathways. In this case the two pathways are direct photoionization from a quantum state to the ionization continuum and photoionization from the quantum state via an intermediate autoionizing state.<sup>1,2</sup> The interference between these two pathways leads to asymmetric resonances in the photoionization spectrum. The photoionization cross section vanishes at certain excitation frequencies, that is, complete destructive interference occurs. This process is well known for radiative transitions to autoionizing states in atoms or to predissociating states in molecules. It was also predicted to occur in semiconductor quantum wells.<sup>3</sup>

Interfering transition pathways can also be deliberately induced by application of resonant laser fields to multilevel atomic systems. Perhaps the most striking example for this type of interference is the cancellation of absorption for a probe radiation field, tuned in resonance to an atomic transition. Usually the resonant excitation would lead to strong absorption of the probe field. However, if the atoms are prepared by EIT,<sup>4-6</sup> the absorption is essentially switched off. EIT exhibits a laser-induced interference effect between the quantum coherences in the atom, which renders an initially highly opaque medium into an almost transparent medium. Similarly the refractive properties of the medium may be greatly modified.<sup>5,7,8</sup> For instance the usual correlation of high refractive index with high absorption can be broken, leading to the creation of media with unique optical properties.

There has been a considerable research effort devoted to EIT and related topics over the last few years. This has been motivated by the recognition of a number of new potential applications, for example, lasers without inversion, highly efficient nonlinear optical processes, storage of light pulses

and quantum information, lossless propagation of laser beams through optically thick media, and highly efficient and selective population transfer via coherent adiabatic processes. EIT is one of an interrelated group of processes, for example, including coherent population trapping (CPT) and coherent adiabatic population transfer, that result from externally induced quantum mechanical coherence and interference. In contrast, the earlier ideas associated with CPT (first observed in 1976)<sup>9</sup> had found application mostly as a tool of high-resolution spectroscopy, rather than as a new direction in nonlinear optics. Therefore, the concept of EIT has contributed a distinctive new thrust to work on atomic coherence and its applications—a thrust, which is of direct interest to optical scientists and engineers.

To explain the basic idea and applications of EIT, an equivalent picture to interfering transition pathways is provided by the concept of laser-dressed states. In terms of quantum mechanics, the *dressed states* are the eigenstates of the quantum system, including strong interaction with driving radiation fields. The dressed states are coherent superpositions of the *bare states*, that is, the eigenstates of the quantum system without external interaction. The coherent superpositions have well-defined amplitudes and phases that describe the relationship between the atomic states in the superposition. The reader is referred to *The Theory of Coherent Atomic Excitation* by Shore<sup>10</sup> for a complete account of these ideas. An important feature of EIT is the preparation of large populations of these coherently driven, uniformly phased atoms. Such media are termed *phasesonium* by Scully,<sup>7</sup> to convey the basic idea. The (both linear and nonlinear) optical properties of the coherent medium are very different from those of a normal, incoherently driven medium. In the dressed medium the terms of linear and nonlinear susceptibilities can be retained only to the extent that it is recognized that all these resonant processes are highly nonperturbative. As we will discuss later, even the so-called “linear” processes now involve the coupling of atoms with many photons. An important consequence of this is that the magnitudes of linear and nonlinear susceptibilities can reach equality in a phase-coherent medium. This is in marked contrast to the normal situation. Usually the nonlinear susceptibility would give rise to nonlinear optical processes, which are many orders of magnitude weaker than those arising from the linear susceptibility.

The exceptionally high efficiencies of nonlinear optical processes in gas phase media, prepared by EIT, therefore constitute an important feature of EIT. The large conversion efficiencies in gas phase media, driven to EIT, become comparable to nonlinear optical processes in optical crystals. Thus a renewed interest in gas phase nonlinear optical devices possessing unique capabilities [e.g., high conversion efficiencies into the spectral regions of vacuum-ultraviolet (VUV) and far-infrared (IR) radiation] has occurred. There have been a number of notable recent demonstrations of EIT, applied to frequency conversion. A near-unity frequency conversion into the far-ultraviolet spectral region was reported for a four-wave mixing scheme in lead vapor. The lead atoms were prepared in the state of *maximal coherence*, that is, maximal polarization, by EIT. The uniquely high conversion efficiency arises since the nonlinear terms become equal in magnitude to the linear terms. Besides applications in dense gas phase media with thermal velocity distribution, large optical nonlinearities, induced by EIT were also studied in laser-cooled atoms. In such media, a successful implementation of EIT requires only quite weak laser couplings. Thus, at maximum transparency there is an extremely steep dispersion as a function of the driving laser frequency, that is, the detuning from the atomic resonance. The consequence of this steep slope is a very slow group velocity for optical pulses propagating through the medium.<sup>11</sup> Massive optical nonlinearities accompany the steep dispersion. These are manifested as very large nonlinear refractive indices that are many orders of magnitude larger than any previously observed. These huge nonlinearities are the subject of current research activity. They offer the likelihood of efficient nonlinear optical processes at the few photon level.

In addition to the applications, described above, the coherence and interference effects related to EIT may also permit new possibilities to build short wavelength lasers, that is, lasers in the x-ray spectral range. As the Einstein coefficient for spontaneous emission scales with the cube of the transition frequency  $\omega$ ,<sup>3</sup> it is usually hard to achieve population inversion by optical pumping in an x-ray laser. In contrast, the laser concept based on EIT does not rely on population inversion in the atomic laser medium anymore.<sup>12,13</sup> Lasing without inversion (LWI) has been demonstrated in sodium atoms and rubidium atoms in the visible range.<sup>14,15</sup> The prospects that this might lead to the construction of lasers which are able to circumvent the usual constraints of achieving inversion in short wavelength

lasers has been much discussed.<sup>16,17</sup> Related effects on LWI and EIT in semiconductor quantum wells have also been theoretically explored using laser-induced processes<sup>18</sup> or bandgap engineering<sup>19</sup> to create the necessary coherences. Moreover, atomic and molecular coherences, driven by EIT, were also exploited for efficient frequency conversion and the generation of ultrashort laser pulses.<sup>20–27,28–39</sup>

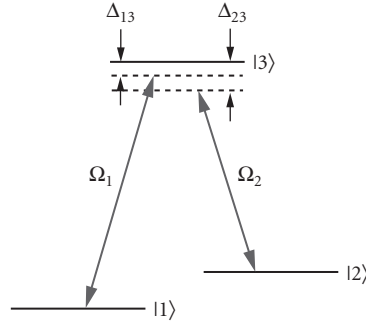
It is the aim of this chapter to provide an accessible summary of EIT and to present some of the main results obtained in recent research. It is not possible in the space available to cover all work in this field, and we apologize to authors whose important contributions are not directly mentioned. An extensive review of all theoretical and experimental work on related atomic coherence phenomena is also beyond the scope of the present article. The reader is advised to look at a number of reviews on LWI,<sup>16,17</sup> coherent population trapping,<sup>10,40–43</sup> coherent adiabatic population transfer,<sup>44</sup> efficient frequency conversion in coherently prepared media<sup>45</sup> and laser-induced continuum structure<sup>46–50</sup> to find these topics presented in detail. The theory pertinent to EIT is sketched in the text, but again the reader is referred to the more detailed treatments published in the literature.<sup>5</sup> References to relevant literature will be given as they arise. The purpose of the chapter is (1) to communicate the underlying physical principles of EIT and related effects, (2) to describe the manifestations of EIT and to summarize the conditions required to create EIT, and (3) to introduce some potential applications in optical technology.

### 14.3 COHERENCE IN TWO- AND THREE-LEVEL ATOMIC SYSTEMS

The first experimental work on laser-induced atomic coherence was carried out in the 1970s. Earlier relevant work includes the investigation of dressing two-level systems by strong microwave fields. This led to the observation of splittings between dressed states, that is, Autler-Townes splittings,<sup>51</sup> and photon echoes in two-level systems.<sup>52</sup> Mollow<sup>53,54</sup> reported novel features, subsequently termed the Mollow triplet, of resonance fluorescence in a two-level system driven by a strong resonant laser. Much work on two-level systems has been carried out since.<sup>10,44,55,56</sup> Although two-level systems remain a subject of considerable interest, our concern here is primarily with three-level systems (and in some cases four-level systems).

Atomic coherence and interference in three-level systems was first observed experimentally by Alzetta, Arimondo et al.,<sup>9,57</sup> and by Gray et al.<sup>58</sup> The first group of authors performed experiments that established coherence between the Zeeman split lower levels of a sodium atom using a multimode laser. By employing a spatially varying magnetic field Alzetta, Arimondo et al. observed a series of spatially separated dark lines. These resonances correspond to the locations in the magnetic field where the Zeeman splitting matched the frequency difference between modes of the coupling laser. This situation corresponds to a two-photon resonant lambda-type level scheme. Thus, this was the first experimental observation of CPT. The experiments of Gray et al.<sup>58</sup> involved the preparation of coherence between the hyperfine lower levels of sodium atoms. In these experiments two coincident laser fields are coupled to a three-level lambda scheme of states to create superpositions of the two lower states  $|1\rangle$  and  $|2\rangle$  (see Fig. 1). One of the superpositions, that is, the coupled state or *bright state*  $|C\rangle$  interacts with the fields [see Eq. (1)]. For the other superposition, that is, the noncoupled or *dark state*  $|NC\rangle$ , interference causes cancellation of the two driven dipoles. Once the coherent states are formed, the population in the system will all be “optically pumped” into the dark state through spontaneous emission from the intermediate state. The optical pumping process occurs on the timescale of a few times the radiative decay time. Once in the dark state there is no process to remove the population. Thus the population is trapped in the dark state.

The basic idea of CPT has been extended to systems, driven by time-varying optical fields to yield very efficient excitation of atomic and molecular states.<sup>44,59–61</sup> In stimulated Raman adiabatic passage (STIRAP), the noncoupled state  $|NC\rangle$  exhibits a specific evolution in time. Initially  $|NC\rangle$  is prepared such that it is composed purely of the lowest state  $|1\rangle$ . For intermediate times  $|NC\rangle$  evolves as a superposition of the two lower states  $|1\rangle$  and  $|2\rangle$ , with no contribution from the intermediate state  $|3\rangle$ . Finally  $|NC\rangle$  is composed purely of state  $|2\rangle$ . Thus, population is transferred completely



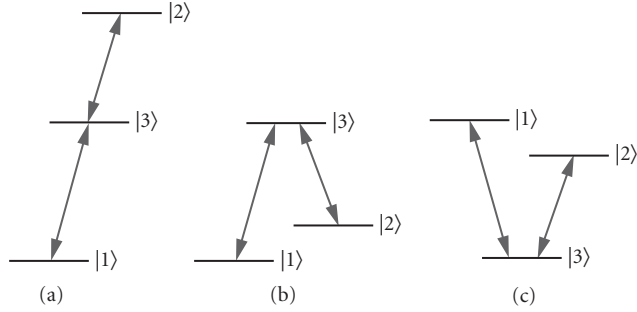
**FIGURE 1** CPT in a three-level lambda configuration. Two radiation fields, that is, couplings  $\Omega_1$  and  $\Omega_2$ , are applied with frequencies close to the single-photon resonances at  $\omega_{13}$  and  $\omega_{23}$ .

between the lower states  $|1\rangle$  and  $|2\rangle$ , with no intermediate storage in state  $|3\rangle$ . The bright state is not populated during the process. This specific preparation of a dark state in STIRAP is achieved by employing counterintuitive pulse sequences, that is, the couplings (or the laser pulses)  $\Omega_1$  and  $\Omega_2$  still partly overlap in time, but  $\Omega_2$  reaches its peak value *prior* to the peak of  $\Omega_1$ . The timescale for STIRAP is determined by the evolution of the laser pulses. This contrasts to conventional CPT, that is, driven with coincident radiation fields, when the time evolution is determined by spontaneous emission. We also note that recently extended work has been performed to utilize CPT also in laser cooling and manipulation of trapped atoms. The technique, used in these experiments was termed *velocity-selective coherent population trapping* (VSCPT).<sup>62–64</sup>

In experiments, dedicated to CPT the primary concern is focused on the manipulation of state populations, essentially of individual atoms. In contrast, for EIT the main interest is the optical response, rather than simply the populations, of the entire medium. The optical response is determined by the coherences rather than the populations. In terms of density matrix elements, in CPT the pertinent quantities are the on-diagonal density matrix elements, that is, the populations; while in EIT they are the off-diagonal density matrix elements, that is, the coherences. Most important, in the limit of a strong coupling field  $\Omega_2$  and population initially in the ground state, the coherences, driven by EIT are almost instantaneously established. The timescale of the evolution in EIT is determined by  $1/\Omega_2$ . For strong excitation, even driven by quite long nanosecond (ns) pulses, the timescale of  $1/\Omega_2$  easily reaches the regime of picoseconds, that is, well below the pulse duration. For a successful implementation of population trapping a timescale of several radiative lifetimes is required, that is, typically in the regime of many nanoseconds. From these considerations we see, that though EIT and CPT are closely related, some of their important features as well as their aim are very different.

## 14.4 THE BASIC PHYSICAL CONCEPT OF ELECTROMAGNETICALLY INDUCED TRANSPARENCY

As discussed in the preceding section, there is a close link between EIT and other phenomena, relying on atomic coherence, that is, adiabatic population transfer processes.<sup>9,43,44,57–61,65–67</sup> In all these processes, three-level atomic systems are involved—that is, systems that can be adequately reduced to three levels when interaction with the pertinent electromagnetic fields are considered. The atomic dipole selection rules require that two pairs of levels are dipole-coupled, while the transition between the third pair is dipole-forbidden. In Fig. 2, we show the basic three-level schemes. All of the level schemes, discussed in this paper can be reduced to one or other of these schemes. Following



**FIGURE 2** Basic three-level schemes: (a) ladder (or cascade) scheme with  $E_1 < E_3 < E_2$ ; (b) lambda ( $\Lambda$ ) scheme with  $E_1 < E_2 < E_3$ ; and (c) vee scheme with  $E_3 < E_1$  and  $E_3 < E_2$ .

the nomenclature of Harris et al.,<sup>6</sup> we label the levels  $|1\rangle$ ,  $|2\rangle$ , and  $|3\rangle$ . The dipole-allowed transitions are between states  $|1\rangle$  and  $|3\rangle$  and between states  $|2\rangle$  and  $|3\rangle$ . Classification of the schemes then depends upon the relative energies of the three states: (1) ladder (or cascade) scheme with  $E_1 < E_3 < E_2$  (2) lambda ( $\Lambda$ ) scheme with  $E_1 < E_2 < E_3$ , and (3) vee (V) scheme with  $E_3 < E_1$  and  $E_3 < E_2$ . EIT has been extensively studied in all three of these configurations. In a lambda or ladder scheme state  $|1\rangle$  is normally the ground state of the atom. This is, where initially the majority of the population resides. In EIT there is no need for significant population transfer. Thus states  $|2\rangle$  and  $|3\rangle$  remain essentially unpopulated throughout the process. It should be noted that the lambda scheme has a special importance due to the metastability of state  $|2\rangle$ . As a consequence, very long-lived coherences can be established between states  $|1\rangle$  and  $|2\rangle$ . This leads to near-perfect conditions for EIT.

To understand in more detail, how laser fields interact with a three-level atom to create coherent superpositions of the atomic bare states, we will consider now CPT in a lambda scheme. A three-level lambda system (see Fig. 1) is coupled by two near-resonant laser fields. The interaction strength is defined by the Rabi frequencies  $\Omega_1 = \mu_{13} E_1 / \hbar V$  at frequency  $\omega_1$  and  $\Omega_2 = \mu_{23} E_2 / \hbar V$  at frequency  $\omega_2$  with the dipole transition moments  $\mu_{13}$  and  $\mu_{23}$ , and the electric fields  $E_1$  and  $E_2$ . The transition frequencies are defined as  $\omega_{12}$  and  $\omega_{23}$ . The one-photon detunings of the radiation fields from the atomic resonances are  $\Delta_{13} = \omega_{13} - \omega_1$ ,  $\Delta_{23} = \omega_{23} - \omega_2$ . The two-photon (Raman) detuning is  $\Delta = [(\omega_{13} - \omega_{23}) - (\omega_1 - \omega_2)]$ . The Hamiltonian of the bare atom  $H_0$  must be modified to include the interactions due to the two couplings. Thus  $H = H_0 + V_1 + V_2$ , with the interactions  $V_j = \hbar \Omega_j$ . The eigenstates of this new Hamiltonian will be linear superpositions of the bare atomic states  $|1\rangle$ ,  $|2\rangle$ , and  $|3\rangle$  (see Refs. 10, 42, 68). For exact two-photon resonance and, that is,  $\Delta = 0$ , two of the three eigenstates of the total Hamiltonian  $H$  turn out to be symmetric and antisymmetric coherent superpositions of the two lower bare states. These superpositions read

$$|C\rangle = \frac{1}{\Omega'} (\Omega_1 |1\rangle + \Omega_2 |2\rangle) \quad (1a)$$

$$|NC\rangle = \frac{1}{\Omega'} (\Omega_2 |1\rangle - \Omega_1 |2\rangle) \quad (1b)$$

where  $\Omega' = [\Omega_1^2 + \Omega_2^2]^{1/2}$ . It is important to note that no component of the bare state  $|3\rangle$  appears in these superpositions. The superposition state  $|C\rangle$  is coupled to the intermediate state  $|3\rangle$  via electric dipole interaction, that is,  $|C\rangle$  is a bright state. In contrast, the other state  $|NC\rangle$  is not coupled to state  $|3\rangle$ , that is,  $|NC\rangle$  is a *dark state* or *trapped state*. This is obvious from the total dipole moment for a transition from state  $|NC\rangle$  to the bare state  $|3\rangle$ . If the magnitudes of the coupling fields  $\Omega_1$  and  $\Omega_2$  are appropriately balanced, the negative sign in the superposition of  $|1\rangle$  and  $|2\rangle$ , which forms the state  $|NC\rangle$ , causes the transition moment  $\langle NC | \mu | 3 \rangle$  to vanish. In effect, the two terms

that are summed to give the transition amplitude between  $|NC\rangle$  and  $|3\rangle$  are of equal and opposite magnitude, and hence the total amplitude will vanish. In a classical picture, this corresponds to the electron driven by two fields, both of which may be strong, but which exert forces of exactly equal magnitude and opposite directions. This interaction leads to a zero net force and hence the electron stays at rest. In conventional CPT and assuming steady-state conditions, the superposition state  $|NC\rangle$  will acquire all of the population of the system through optical pumping. Thus spontaneous emission from state  $|3\rangle$  populates state  $|NC\rangle$ , but absorption losses from state  $|NC\rangle$  back to state  $|3\rangle$  are not possible.

The noncoupled state  $|NC\rangle$  also serves as the key component for coherent population transfer by STIRAP,<sup>44</sup> which was already briefly discussed above. We assume, that initially all population is in state  $|1\rangle$ . State  $|2\rangle$  is assumed to be metastable, for example, if the level scheme is of lambda-type configuration. If at early times the Rabi frequencies (i.e., the corresponding radiation fields) are applied such that  $\Omega_2 \gg \Omega_1$ , state  $|NC\rangle$  is equal to state  $|1\rangle$  [see Eq. (1)]. All population of the system is prepared in the dark state  $|NC\rangle$ . No population is in the bright state  $|C\rangle$ . If at the end of the interaction  $\Omega_1 \gg \Omega_2$ , state  $|NC\rangle$  aligns now parallel to the target state  $|2\rangle$ . As  $\Omega_1 \gg \Omega_2$ , the contribution of state  $|1\rangle$  is negligible, that is, all population is transferred to the target state  $|2\rangle$ . The sequence of an initially strong coupling between the states  $|2\rangle$  and  $|3\rangle$  and a finally strong coupling between the states  $|1\rangle$  and  $|2\rangle$  exhibits a counterintuitive laser pulse order, which is the typical feature of STIRAP.

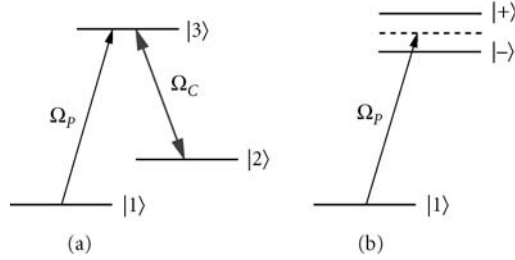
We note that in the previous description we ignored a fast time oscillation of the bare states  $|1\rangle$  and  $|2\rangle$  in the superpositions in Eq. (1). The oscillation occurs at frequencies  $\epsilon_1/\hbar$  and  $\epsilon_3/\hbar$ , with the energy of the bare states  $\epsilon_i$ . In fact these terms disappear when the dipole moments are formed. In typical implementations of CPT, for example, STIRAP, the couplings are of comparable strength, that is,  $\Omega_1 \approx \Omega_2$ , and the two-photon transition is strongly driven. The transition is “saturated” if the terminology of incoherent excitation is used. We note an interesting feature of CPT with respect to the coherences for the case of the laser frequencies tuned to exact two-photon resonance, but with large single-photon detunings. In this case, state  $|3\rangle$  can be adiabatically eliminated from the level scheme.<sup>10</sup> Thus state  $|3\rangle$  does not enter into the consideration of the coupling between atoms and fields any more. However, also in this case, that is, even far detuned from the single-photon resonances, the two-photon resonance condition alone is sufficient to drive large coherences between states  $|1\rangle$  and  $|2\rangle$ . We also stress the point that in general in CPT the initial population may be distributed between the lower states  $|1\rangle$  and  $|2\rangle$ . This is usually the case if the lower states are provided by sublevels of an atomic ground state, for example, for Zeeman or hyperfine split states. As the energy difference of the lower states  $|1\rangle$  and  $|2\rangle$  is very small in this case, the initial thermal populations will be almost the same. In this case, a careful analysis of states  $|NC\rangle$  and dark state  $|C\rangle$  is required to determine the population dynamics for the specific CPT process under consideration, for example, STIRAP. However, also in the case of an initial population in both lower states, the state  $|NC\rangle$  is still a dark state. In contrast, in implementations of EIT, the population is initially and for all times completely stored in state  $|1\rangle$ .

In CPT, interference effects arise from both coupling fields, since they are of comparable strength. If only one of the fields is strong, that is,  $\Omega_1 \ll \Omega_2$ , only interference effects due to processes driven by  $\Omega_2$  will be important. This is the situation in many implementations of EIT and is discussed by a number of authors (see, e.g., Ref. 5 and references therein). In such EIT experiments,  $\Omega_2$  is usually called the coupling field and labeled  $\Omega_C$  and  $\Omega_1$  is a weaker probe field, labeled  $\Omega_p$ . In the following we will use the notations  $\Omega_C$  and  $\Omega_p$ , whenever appropriate. Based on the considerations, presented above, we will now discuss some simple and straightforward approaches alternative approaches to understand the basic concept of EIT.

First, let us consider the basis, formed by the coupled state  $|C\rangle$  and the noncoupled state  $|NC\rangle$  [see Eq. (1)]. We can write the bare state  $|1\rangle$  in this basis:

$$|1\rangle = \frac{1}{\Omega} (\Omega_C |NC\rangle + \Omega_p |C\rangle) \quad (2)$$

Very obviously, for the case  $\Omega_p \ll \Omega_C$  state  $|1\rangle$  is almost equivalent to  $|NC\rangle$ , that is, the dark state. Thus absorption to state  $|3\rangle$  vanishes. The population remains in the ground state  $|1\rangle$  throughout



**FIGURE 3** EIT in a lambda scheme (compare Fig. 4) viewed in terms of (a) bare atomic states, driven by a weak probe field  $\Omega_p$  and a strong coupling field  $\Omega_C$  and (b) dressed states, generated by the strong coupling  $\Omega_C$ . The probe field is still at the bare state resonance frequency  $\omega_{13}$ .

the interaction with the two radiation fields. The probe laser propagates through the medium without any absorption losses, that is, the medium is driven to EIT.

Alternatively, as  $\Omega_p \ll \Omega_C$ , we can treat the three-level system of states  $|1\rangle$ ,  $|2\rangle$ , and  $|3\rangle$  as a composition of a strongly coupled two-level subsystem of states  $|2\rangle$  and  $|3\rangle$ , with the weakly coupled state  $|1\rangle$  attached to the subsystem. Thus it is straightforward to describe the subsystem in terms of the dressed states, which arise due to the strong interaction<sup>5</sup> (see Fig. 3). For a strong resonant coupling at the single-photon resonance  $\Delta_{23} = 0$  the dressed states of the subsystem are

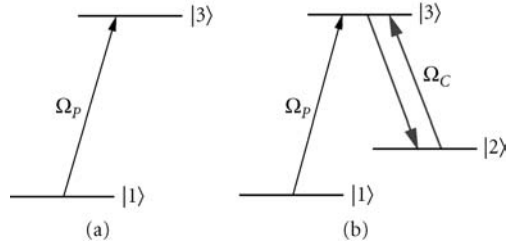
$$|+\rangle = \frac{1}{\sqrt{2}}(|2\rangle + |3\rangle) \quad (3a)$$

$$|-\rangle = \frac{1}{\sqrt{2}}(|2\rangle - |3\rangle) \quad (3b)$$

The transition amplitude at the (undressed) resonant frequency  $\omega_{13}$  from the ground state  $|1\rangle$  to the dressed states will be the sum of the contributions to the dressed states  $|+\rangle$  and  $|-\rangle$ , that is,  $[\langle 1|\mu|+\rangle + \langle 1|\mu|-\rangle] = [\langle 1|\mu|2\rangle + \langle 1|\mu|3\rangle + \langle 1|\mu|2\rangle - \langle 1|\mu|3\rangle] = \mu_{12} + \mu_{13} + \mu_{12} - \mu_{13}$ , with the transition moments  $\mu_{ij}$ . As we assumed in the definition of our three-level system, the transition between states  $|1\rangle$  and  $|2\rangle$  is forbidden, that is,  $\mu_{12} = 0$ . The transition moments  $\mu_{13}$  enter the sum with opposite signs. Thus the transition amplitude, that is, the absorption, reduces exactly to zero. The system is driven now to EIT.

Finally, another approach to an understanding of EIT is based on the concept of quantum interferences.<sup>13,69-71</sup> Interference, associated with EIT, arises because the transition amplitude between states  $|1\rangle$  and  $|3\rangle$  includes different pathways from the ground state  $|1\rangle$  to the excited state  $|3\rangle$ : One term, which is due to excitation by the resonant field  $\Omega_p$  only, that is, a direct path from state  $|1\rangle$  to state  $|3\rangle$ ; an additional term, which is due to the presence of the second field  $\Omega_C$  (see Fig. 4), that is, an indirect path from state  $|1\rangle$  to  $|3\rangle$  further on to state  $|2\rangle$  and back to  $|3\rangle$ . The additional term and similar higher-order terms have a negative sign with respect to the direct path. Hence the higher-order terms cancel completely the direct path. This situation is closely related to interferences, mediated at Fano-type resonances,<sup>1</sup> for example, via autoionizing states, or to laser-induced continuum structure.<sup>46-50</sup>

Equivalently within the picture of EIT in terms of the interfering pathways between the bare atomic states, the coherences are the quantities pertinent to the interference. Coherences can be thought of, in a semiclassical picture, as associated with the oscillating electric dipoles driven by the coupling fields applied between pairs of quantum states of the system, for example, between states  $|i\rangle$  and  $|j\rangle$ . Strong excitation of these dipoles occurs whenever electromagnetic fields are applied close to resonance with an electric dipole transition between two states. If there are several pathways



**FIGURE 4** EIT in a lambda scheme, viewed in terms of Fano-type interference (compare Fig. 3), (a) shows the direct channel for the excitation  $|1\rangle \rightarrow |3\rangle$  by the probe field  $\Omega_p$ , (b) shows the lowest-order multiphoton channel induced by the coupling field  $\Omega_C$ , that is, the sequence  $|1\rangle \rightarrow |3\rangle \rightarrow |2\rangle \rightarrow |3\rangle$ . Interference between pathway (a) and (b) (also including higher-order terms) occurs.

to excite the oscillating dipole at frequency  $\omega_{ij}$ , then interference arises between the various contributions to this dipole. These contributions must be summed to give the total amplitude to the electric dipole oscillation (see Fig. 4).

Mathematically, coherences are identified with the off-diagonal density matrix elements  $\rho_{ij}$ . These are formed by taking bilinear combinations of probability amplitudes of two quantum states, that is, by the weighting factors associated with the outer products such as  $|i\rangle\langle j|$ .<sup>72</sup> Off-diagonal elements in the density matrix play a critical role in the evolution of an atom coupled to electro-magnetic fields.<sup>73</sup> Many calculations of atomic coherence effects and of EIT, as well as general nonlinear optics and laser action, in three-level systems are therefore developed in terms of the density matrix. The magnitudes of the relevant density matrix elements are computed from the basic coupled evolution equations, that is, the Liouville equation,<sup>10,72</sup> and are found to depend upon experimental parameters (e.g., detunings and laser intensities). This approach also naturally lends itself to the inclusion of dampings that cause the decay of populations and coherences (e.g., radiative decay and collisions).<sup>67</sup>

EIT serves to control the absorption of a probe laser on the transition between the states  $|1\rangle$  and  $|3\rangle$  in the three-level systems, defined and discussed above. Thus EIT will manifest itself in the density matrix element  $\rho_{13}$ . The real and imaginary parts of  $\rho_{13}$  both vanish at zero detuning, that is, the coherence is cancelled by interference of the excitation pathways. A set of coupled equations connecting the density matrix elements (e.g.,  $\rho_{12}$ ,  $\rho_{23}$ , and  $\rho_{13}$ ) and their temporal derivatives is deduced from the Liouville equation. These coupled equations are then solved for various sets of conditions by either analytical or numerical means. Interference that leads to EIT arises from the coherences  $\rho_{23}$  and  $\rho_{12}$ , which are coupled to  $\rho_{13}$ . The coherence  $\rho_{12}$  between the ground state  $|1\rangle$  and state  $|2\rangle$  is present only due to the additional laser coupling. The contribution to the coherence  $\rho_{13}$  from the coherences  $\rho_{23}$  and  $\rho_{12}$  (driven by both laser fields) cancels with the direct contribution (driven by the probe laser field alone).

Although this use of density matrix elements is convenient, it is by no means essential, and many theoretical treatments that give clear physical insight have been performed in terms of probability amplitudes. Additional physical insights have been obtained by adopting alternative approaches, for instance by a careful consideration of the Feynman diagrams representing the various processes involved that lead to interference,<sup>69-71</sup> or by applying a quantum jump approach.<sup>74</sup> In all cases the predictions are essentially identical.

Analytical solutions are generally only possible for steady-state conditions [corresponding to continuous wave (cw) laser fields]. A time-dependent calculation of the density matrix is appropriate, if laser pulses rather than cw radiation drives the atom. A time-dependent calculation is also vital to account for transient effects or pulse propagation. Some analytical solutions also for time-dependent calculations of the density matrix have been obtained, but unless restrictive simplifying assumptions are applied,<sup>75</sup> time-dependent calculations must be performed numerically. In many



cases the results of a full time-dependent treatment will be comparable to the results, obtained in a steady-state approach. This holds true at least in so far, as qualitative trends are concerned. To calculate the propagation of laser pulses through an extended medium the time-dependent equations for the density matrix elements must be coupled to Maxwell's equations.<sup>10</sup> This is necessary, for example, to compute the propagation of matched pulses,<sup>76–78</sup> the efficiency of frequency conversion processes in coherently prepared media,<sup>20–27,28–39</sup> to account for losses in the driving laser fields or to model pulse shape modifications.<sup>79</sup>

## 14.5 MANIPULATION OF OPTICAL PROPERTIES BY ELECTROMAGNETICALLY INDUCED TRANSPARENCY

Any optical process in a medium, driven by radiation pulses, is determined by the polarization, that is induced by the light fields. The macroscopic polarization  $P$  at the transition frequency  $\omega_{13}$  can be related to the microscopic coherence  $\rho_{13}$  via the expression

$$P_{13} = n_A \mu_{13} \rho_{13} \quad (4)$$

where  $n_A$  is the number of atoms per unit volume in the ground state within the medium, and  $\mu_{13}$  is the dipole matrix element associated with the (undressed) transition.<sup>73</sup> In this way imaginary and real parts of the linear susceptibility at frequency  $\omega$  can be directly related to  $\rho_{13}$  via the macroscopic polarization.<sup>55</sup> The latter is defined as

$$P_{13}(\omega) = \epsilon_0 \chi(\omega) E \quad (5)$$

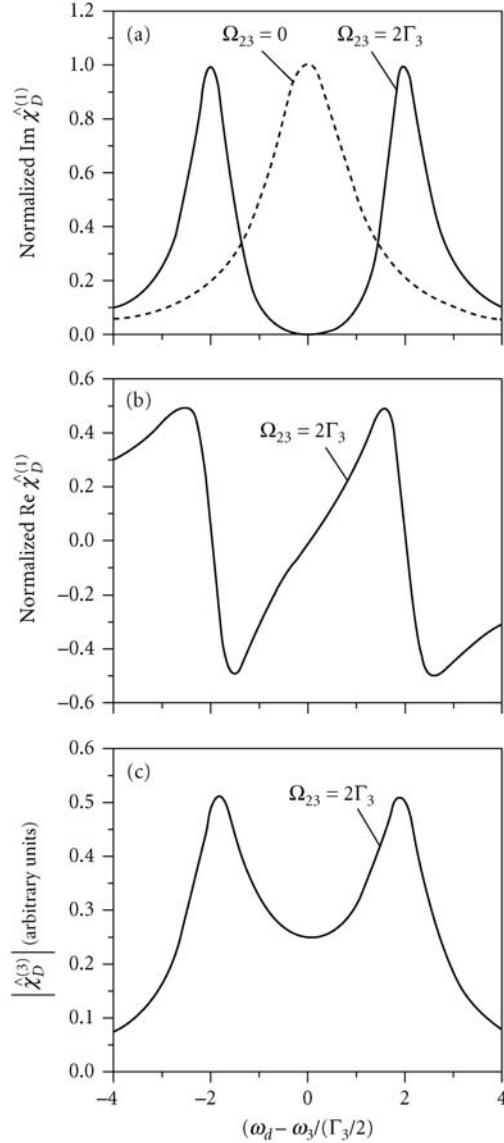
introducing the susceptibility  $\chi(\omega)$ . In this paper, the microscopic coherences are treated quantum mechanically, while the electromagnetic fields are treated classically (i.e., using Maxwell's equations and the susceptibilities). This semiclassical approach is not essential, and fully quantum mechanical treatments for CPT (see, Ref. 41) and EIT<sup>78–80</sup> have been developed. These fully quantum approaches are appropriate for cases such as the coupling of atoms to modes in cavities,<sup>80,81</sup> or when the statistical properties of the light fields are of interest. The latter is the case, for example, in proposals to generate squeezed light using EIT.<sup>79</sup> For relatively strong light fields, present in most laser experiments, a semiclassical treatment, with spontaneous decay added as a phenomenological damping process, proves adequate.

The real and imaginary parts of the (dressed) linear susceptibility, associated with the dispersion and absorption of the medium respectively, are given by<sup>5,6</sup>

$$\text{Re } \chi_D^{(1)}(-\omega_p, \omega_p) = \frac{|\mu_{13}|^2 n_A}{\epsilon_0 \hbar} \left[ \frac{-4\Delta_{21}(|\Omega_C|^2 - 4\Delta_{21}\Delta_{32}) + 4\Delta_{31}\Gamma_2^2}{(4\Delta_{31}\Delta_{21} - \Gamma_3\Gamma_2 - |\Omega_C|^2)^2 + 4(\Gamma_3\Delta_{21} + \Gamma_2\Delta_{31})^2} \right] \quad (6a)$$

$$\text{Im } \chi_D^{(1)}(-\omega_p, \omega_p) = \frac{|\mu_{13}|^2 n_A}{\epsilon_0 \hbar} \left[ \frac{8\Delta_{21}^2\Gamma_3 + 2\Gamma_2(|\Omega_C|^2 + \Gamma_3\Gamma_2)}{(4\Delta_{31}\Delta_{21} - \Gamma_3\Gamma_2 - |\Omega_C|^2)^2 + 4(\Gamma_3\Delta_{21} + \Gamma_2\Delta_{31})^2} \right] \quad (6b)$$

To deduce the linear susceptibility, monochromatic fields and negligible collisional or Doppler broadening were assumed. The real and imaginary parts of the linear susceptibility, along with the nonlinear susceptibility, are plotted in Fig. 5 (see figure caption for explanation of the labeling) as a function of the detuning  $\Delta_{13}$ , at  $\Delta_{23} = 0$ , that is, for resonant excitation by the coupling field  $\Omega_C$ . A striking result, the absorption for the probe field vanishes at exact resonance, if the coupling field  $\Omega_C$  is switched on and state |2> is perfectly metastable (i.e.,  $\Gamma_2 = 0$ ). Simultaneously the dispersion is significantly modified. The dispersion is still zero at line center, that is, the same value as in the case of the coupling field  $\Omega_C$  switched off. However, the group velocity (dependent upon the slope of  $[\text{Re } \chi^{(1)}]$ ) becomes anomalously low<sup>5,82</sup> when absorption has vanished. This offers the possibility of



**FIGURE 5** The dressed susceptibilities in terms of the normalized detuning  $(\omega_d - \omega_3)/(\Gamma_3/2)$  [in our notation this corresponds to the detuning of the probe laser, scaled to the decay rate, i.e.,  $\Delta_{13}/(\Gamma_3/2)$ ] for a value of the coupling Rabi field  $\Omega_{23} = 2\Gamma_3$  [in our notation  $\Omega_C = 2\Gamma_3$ ]. (a)  $[\text{Im } \hat{\chi}^{(1)}]$ , i.e. absorption; (b)  $[\text{Re } \hat{\chi}^{(1)}]$ , i.e. dispersion; and (c)  $|\hat{\chi}^{(3)}|$ , i.e. nonlinear response. [Reprinted figure with permission from Ref 6. Copyright (1990) by the American Physical Society.]

slowing down the speed of light by EIT, that is, a most prominent example for the striking features of EIT, which is discussed elsewhere in this book. Inclusion of finite laser linewidths, collisional and Doppler broadening in these deductions is straightforward.<sup>6</sup> Including these effect, the dressed susceptibilities still retain the key features, provided some limits for the experimental parameters are kept in view.

The medium that would in the absence of the coupling field be optically thick is now rendered transparent. The reduction in absorption is not merely that caused by the effective detuning induced by the Autler-Townes splitting of the dressed state absorption peaks (see Fig. 3), that is, the absorption that would be measured if the probe field were interrogating the absorption coefficient of the medium in the wing of the absorption lines of the dressed states. Additionally, there is destructive interference at the transition frequency  $\omega_{13}$  that leads to *complete* cancellation of all absorption, provided there are no additional dephasing processes in the system. Even if the transition dipole moment  $\mu_{12}$  is not zero (i.e., if the spontaneous decay rate is  $\Gamma_2 \neq 0$ ), the absorption due to EIT will be reduced compared to the weak field absorption by a factor of  $\Gamma_2/\Gamma_3$ .<sup>6</sup>

In the preceding considerations it was implicitly assumed that the probability amplitudes of state  $|3\rangle$  remain close to zero (i.e., the probe field is very weak). If there is an incoherent population pump process into the upper states  $|2\rangle$  or  $|3\rangle$ , such that these populations no longer remain negligible, then gain on the transition between the states  $|3\rangle$  and  $|1\rangle$  can result (see Sec. 14.8). The remarkable feature of this gain is that under the circumstances in which EIT occurs, that is, when absorption is cancelled, the gain can be present without the requirement of population inversion in the bare atomic states. This is an example of amplification without inversion. The process has successfully been implemented in a vee-type scheme in Rubidium atoms<sup>15</sup> and a lambda scheme in sodium atoms.<sup>83</sup> Much theoretical work<sup>12-14, 84-86</sup> has been reported on LWI. In early work, LWI was predicted by Arkhipkin and Heller,<sup>85</sup> and then further elucidated by Harris,<sup>86</sup> Kocharovskaya and Khanin,<sup>12</sup> and Scully et al.<sup>84</sup> A long-term objective in this work is the prospect of overcoming the familiar difficulties of constructing short wavelength lasers, that is, the requirement of very high energy pump fields in order to compensate for the small transition moment at far-infrared wavelengths.

In addition to gain without population inversion, any incoherent pumping of population into the upper states also modifies the dispersion in the medium. In particular, it is then possible to obtain a very large refractive index for specific wavelength regimes. The refractive index can reach values comparable to those normally encountered very close to an absorption line, while here the absorption now vanishes.<sup>8</sup> The prospects for engineering the refractive properties of media to give novel combinations of absorption, gain, and dispersion have been explored in a number of theoretical<sup>87-93</sup> and experimental studies (see Sec. 14.9).

The successful implementation of EIT depends upon a number of critical parameters, both inherent to the quantum system and the experimental setup, for example, the driving laser pulses. A correct choice of the atomic energy level configuration is essential. The configuration must satisfy the conditions, already discussed above, that is, dipole allowed transitions  $|1\rangle \rightarrow |3\rangle$  and  $|2\rangle \rightarrow |3\rangle$ , while the transition  $|1\rangle \rightarrow |2\rangle$  is dipole forbidden. Radiative couplings to other energy levels outside of these states, that lead to an open three-level system, and additional level substructure must also be considered. Collisions with other species in the medium or photoionization must be minimized in order to prohibit perturbing decay or dephasing of the coherence  $\rho_{12}$ , which is essential to EIT. The couplings may be either driven by cw or pulsed lasers. In both cases the couplings must be sufficiently strong to overcome the inhomogeneous broadening. Moreover, sufficiently monochromatic or radiation with transform-limited bandwidth in the pulsed case is required, in order not to dephase the coherence  $\rho_{12}$ . These critical parameters are summarized in Table 1. In the following section we discuss in more detail the most crucial parameters for a successful implementation of EIT.

## Intrinsic Dephasing of Atomic Coherence in Gas Phase Media

For processes of laser-induced atomic coherence in a realistic medium the maintenance of the phase of the coherence during the interaction is essential for effective quantum interference. Any dephasing of the coherence will wash out and eventually nullify the interference effects. Dephasing can

**TABLE 1** Summary of Critical Experimental Parameters for a Successful Implementation of EIT

Physical Parameter	Constraint	Typical Values
Radiative decay rate $\Gamma_3$ of state $ 3\rangle$	–	1–100 MHz
Radiative decay rate $\Gamma_2$ of state $ 2\rangle$	$\Gamma_2 \ll \Gamma_3$	<1 MHz
Photoionization rate $\Gamma_{\text{ion}}$	$\Gamma_{\text{ion}} \gg \Gamma_3$	Depends upon the laser intensity
Coherence dephasing $\gamma_{ij}$	$\gamma_{12} < \gamma_{13}, \gamma_{23}$	0–1 MHz (gases), 0–100 GHz (solids)
Laser linewidth $\gamma_{\text{laser}}$	Transform-limited	<1 MHz (cw) or $1/\tau_{\text{pulse}}$ (pulsed)
Doppler linewidth $\gamma_{\text{Doppler}}$	$\gamma_{\text{Doppler}} < \Omega_C$	1 GHz
Rabi frequency $\Omega_C$	$\Omega_C > \gamma_{12}$	$\Omega_C = \mu_{23} E_C / \hbar$
Laser pulse energy $E_C$ [see Eq. (8)]	$E_C > f_{13}/f_{23} \hbar \omega N_A$	

arise from a variety of different sources, for example, the excitation of a multitude of closely spaced hyperfine or Zeeman components (see, e.g., Refs. 10,15,94), radiative decay of state  $|2\rangle$ , photoionization channels,<sup>95</sup> and collisions.<sup>6,96</sup> Following these arguments, it is obvious, that in a ladder scheme perfect EIT is usually not possible, because state  $|2\rangle$  is not metastable, but undergoes spontaneous emission to state  $|3\rangle$ —as well as to other states outside the three-state system. Collisional broadening with atoms of the same and other species is also critical and places strict limits on sample purity, otherwise leading to foreign gas broadening. Possibly also limits are imposed on the sample density. Moreover, at large atomic density the local field effects due to dipole-dipole couplings between the atoms may be important.<sup>96,97</sup> In this case the simple relationship between macroscopic polarization and the coherences in Eq. (5) may break down.

## Dephasing due to Phase Fluctuations in the Laser Fields

If cw lasers with narrow bandwidth  $\Delta\nu < 1$  MHz (i.e., negligible phase fluctuations) are used, the quality of an implementation of EIT usually approaches the expectations, based on steady-state conditions and strictly monochromatic excitation. Due to phase-diffusion processes<sup>92–102</sup> laser line broadening gives rise to linewidths above the limit of the allowed radiative decay rate. This will destroy EIT. EIT may also be implemented with pulsed laser, provided the laser pulses exhibits transform limited bandwidth. Though these transform-limited bandwidth is inevitably larger than those of cw lasers, EIT is not reduced at all. A single-mode transform-limited laser pulse (i.e., without excess phase fluctuation) will introduce insufficient dephasing during the interaction time (i.e., the pulse duration  $\tau_{\text{pulse}}$ ) to disturb the phases of the atomic coherences. It should also be appreciated that hyperfine sublevels will in general cause dephasing of coherences on a timescale, which is given by the inverse of their frequency separation  $\Delta\omega_{\text{HFS}}$ .<sup>10</sup> In a pulsed excitation the dephasing due to hyperfine splitting within the laser bandwidth will therefore be negligible, provided  $\tau_{\text{pulse}} < 1/\Delta\omega_{\text{HFS}}$  (i.e., if the hyperfine splittings are sufficiently small).

## Dephasing Processes in Solids

A few experiments on EIT have also been performed in solid-state media.<sup>103–115</sup> In contrast to implementations of EIT in gaseous media, coherent interactions in solids suffer from additional dephasings. These dephasings are induced by quantum processes in the crystal lattice (e.g., by photon-phonon interactions). The dephasings lead to significant additional homogeneous broadening in spectral lines of optical transitions. At room temperature the broadening may reach the regime of many gigahertz. In the gas phase, homogeneous broadening (e.g., as observed in the natural linewidth of a transitions) is usually much smaller than inhomogeneous broadening [e.g., induced by Doppler shifts (see below)]. In contrast, in solids it is usually the homogeneous broadening which dominates. This homogeneous broadening (i.e., the dephasing) will wash out any quantum interferences. In principle, there are two ways to deal with the fast dephasing processes in solids: (1) to “freeze” phonon processes, that is, to cool

the medium to cryogenic temperatures such that phonon interactions may be neglected; (2) to drive the medium with ultrafast laser pulses, that is, pulse durations below the timescale of the dephasing processes. However, ultrashort laser pulses usually do not provide sufficient pulse energy to saturate the transitions in EIT. Thus, in most experiments on EIT in solids, cryogenic cooling of the medium is a necessary requirement.

## Inhomogeneous Broadening

In many experiments (inhomogeneous) Doppler broadening presents a serious limit since it introduces a randomization in the effective laser detunings over the ensemble of atoms in the sample.<sup>6,116,117</sup> Various methods have been employed to eliminate this effect, for example, Doppler-free excitation<sup>118,119</sup> or using cooled atoms in a magneto-optical trap.<sup>120,121</sup> Alternatively, at coupling Rabi frequencies larger than the Doppler width the influence of inhomogeneous broadening can be overcome.<sup>6</sup> In spectroscopic terms, the laser-induced power broadening beats the Doppler broadening in this case. This concept requires Rabi frequencies exceeding the Doppler width, that is, typically in the regime of 1 GHz. Such Rabi frequencies can be provided by a cw laser, with a typical power of 1 W or less, only under conditions of tight focusing. This may lead to undesirable effects such as defocusing due to the interplay between the dressed refractive index and the transverse intensity variation across the beam waist in the region of the focus.<sup>119</sup> For pulsed lasers, with intrinsically high peak power, it is usually not necessary to focus the laser to reach the required intensity. Thus defocusing effects are negligible and the interaction volume (i.e., the atom number) will be much larger than under conditions of focusing. Moreover, for short- or ultrashort laser pulses the laser bandwidth already exceeds the Doppler width. However, short- or ultrashort laser pulses are usually no good choice to drive EIT (see below).

Inhomogeneous broadening also plays a major role for applications of EIT in solid-state systems. Such inhomogeneous broadenings are induced, for example, when doped atoms in a crystal experience different electric fields in the background of the host crystal. This leads to an inhomogeneous distribution of transition frequencies. In general, the implementation of EIT in inhomogeneously broadened solids requires large laser intensities. This increases the risk of optical damage to the sample. An exception to this is the work on solids under conditions of cryogenic cooling. In such media, exceptionally small inhomogeneous widths are encountered.<sup>122</sup> Moreover, inhomogeneous broadening in doped solids can be overcome by appropriate optical preparation (e.g., spectral hole burning). In this case, a specific ensemble of atoms in the inhomogeneously broadened medium is prepared to exhibit spectrally narrow transitions.

## Coupling Laser Power

In addition to the conditions, described above, there are some more constraints for the coupling laser Rabi frequency: (1) The coupling laser Rabi frequency must be sufficiently large to induce a transparency with a spectral width exceeding the linewidth of the Raman (two-photon) transition. For Raman transitions involving large detunings from the single-photon resonances, this may require large laser powers. (2) Harris and Luo<sup>79</sup> derived a condition for the laser pulse energy, which demands a sufficient number of photons in the laser pulse to match the number of atoms, weighted by the transition oscillator strength, in the laser path [see Eq. (8)]. Essentially, the number of photons in the coupling laser pulse must exceed the number of atoms in the medium. (3) In the adiabatic limit, the pulse durations must exceed the time evolution of the transparency, which is in the order of  $1/\Omega_C$ . Thus, the product  $\Omega \cdot \tau_{\text{pulse}}$  must be large, that is,  $\Omega \cdot \tau_{\text{pulse}} \gg 1$ . In terms of incoherent excitation, the laser must “saturate” the transition. This adiabaticity criterion can be derived in a very similar form also for other adiabatic processes.<sup>44</sup> As  $\Omega \cdot \tau_{\text{pulse}}$  is a combination of the electric field and the pulse duration, laser pulses with large intensity and/or large interaction time are a good choice to fulfill the adiabaticity criterion. An analysis of typical laser systems with specific pulse duration reveals that laser pulses with medium pulse duration [i.e., in the regime of short nanosecond (ns)

or long picosecond (ps) pulses] yield the largest product  $\Omega \cdot \tau_{\text{pulse}}$ , if one-photon transitions are driven. Shorter laser pulses usually cannot compensate for the reduced pulse duration by a sufficient increase in the electric field. On the other hand, long pulses or cw radiation permits for long interaction time, but the electric field is weak. Thus, laser pulses with intermediate pulse duration and pulse energies in the regime of mJ are the best choice. However, if multiphoton excitations or specific atomic systems with large transition moments are considered, also ultrashort laser pulses may drive adiabatic interactions.

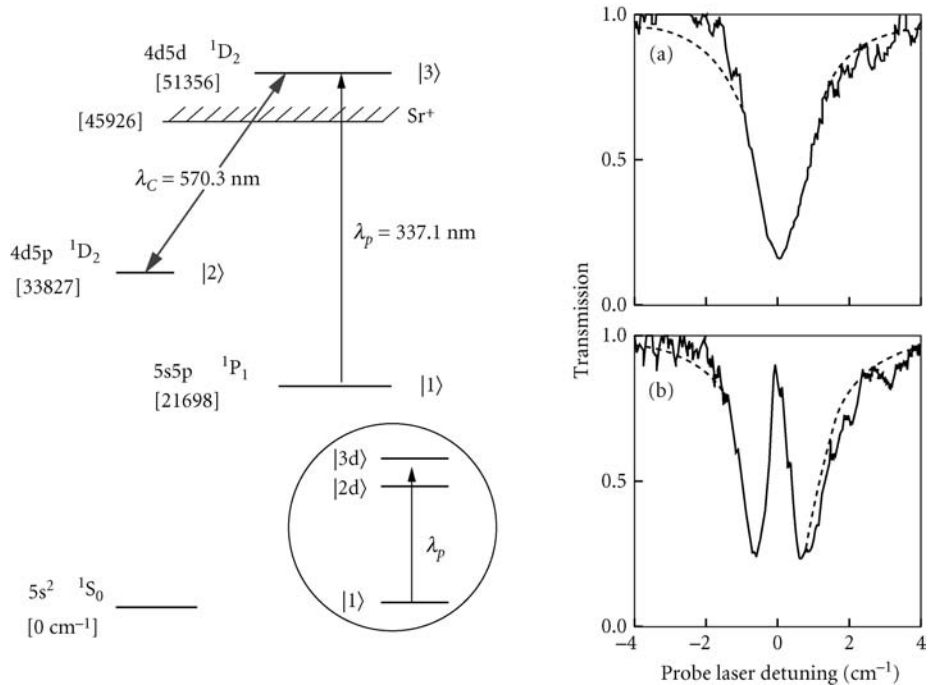
## 14.6 ELECTROMAGNETICALLY INDUCED TRANSPARENCY, DRIVEN BY PULSED LASERS

In the earliest work on EIT, driven by pulsed lasers, the *linear* optical response of an extended ensemble of atoms in the gas phase was investigated. In these experiments the transmission of a weak probe laser pulse, propagating through an otherwise optically dense medium, was measured. The medium was rendered transparent in the presence of a strong coupling laser pulse. In pulsed laser experiments there is usually no difficulty to induce Rabi frequencies, which exceed the inhomogeneous bandwidth of the medium (i.e., to drive the complete medium in EIT). It is essential, however, that the laser pulse exhibits transform-limited bandwidth. Thus, for example, single-mode transform-limited nanosecond lasers are an appropriate choice (see Sec. 14.5). Such laser pulses are, for example, provided by injection seeding an amplifier or optical parametric oscillator (OPO) with narrow-bandwidth cw radiation of appropriate frequency.

The first demonstration of EIT, driven with pulsed lasers, was performed by Harris et al. in strontium vapor<sup>123</sup> and lead vapor.<sup>124</sup> In both experiments laser pulses with transform-limited radiation were used. In the experiment on strontium (see Fig. 6) the atoms are initially optically pumped into the excited state  $5s\ 5p\ ^1P_1$ . The transition between state  $|1\rangle = 5s\ 5p\ ^1P_1$  and the autoionizing state  $|3\rangle = 4d\ 5d\ ^1D_2$  at a wavelength of  $\lambda_p = 337.1\ \text{nm}$  is rendered transparent. A coupling laser, derived from a single-mode Littman dye laser, at wavelength  $\lambda_c = 570.3\ \text{nm}$  drove the transition between the metastable state  $|2\rangle = 4d\ 5p\ ^1D_2$  and  $|3\rangle = 4d\ 5d\ ^1D_2$ . As in the prototypical scheme, the probe field excited the system to a state  $|3\rangle$  with a large decay rate. In the absence of the coupling laser the probe laser experienced strong absorption. Thus the strontium vapor was completely opaque at resonance, with an inferred transmission of  $\exp(-20 \pm 1)$ . When the coupling laser was applied, the transmission at line center increased dramatically to  $\exp(-1 \pm 0.1)$ . It was pointed out by the authors that for this large transparency the interference effect is essential. The detuning from the (dressed) absorption lines, separated by the Autler-Townes splitting alone would only account for an increase in transmission to a value of  $\exp(-7.0)$ .

The experiment in lead vapor<sup>124</sup> demonstrated EIT within the bound states of a medium, experiencing significant collisional broadening. Here EIT was implemented in a ladder configuration with the probe laser, driving the transition between the ground state  $|1\rangle = 6s^2\ 6p^2\ ^3P_0$  and the excited state  $|3\rangle = 6s^2\ 6p\ 7s\ ^3P_1^0$ . The coupling laser drove the transition between states  $|2\rangle = 6s^2\ 6p\ 7p\ ^3D_1$  and  $|3\rangle = 6s^2\ 6p\ 7s\ ^3P_1^0$ . The reduction in opacity, driven by the transform-limited coupling laser, reached a factor of  $\exp(-10)$ . The particular coupling scheme in lead was chosen because of approximate coincidence between the frequency of an injection seeded Nd:YAG laser at  $\lambda_c = 1064\ \text{nm}$  and the transition frequency  $\omega_{23}$ . The detuning was  $\Delta_{23} = 6\ \text{cm}^{-1}$ . An important feature of this experiment was the role of resonance broadening, which was the dominant broadening channel for state  $|3\rangle$ , that is, about 40 times larger than the natural linewidth. Due to the destructive interference between the contributions to state  $|3\rangle$  in the two dressed states (see Sec. 14.4), these collisions have no effect on transparency. In contrast, the collisions, which dephase state  $|2\rangle$ , also affect the degree of EIT. As these are no resonance collisions, their strength is small.

Both experiments served to demonstrate the principle of EIT in a three-level system. They show, that EIT also works in systems including autoionization or collisional broadening. In both cases the coupling laser exhibited near transform-limited bandwidth. No special requirements were imposed on the probe laser, although the probe laser bandwidth must be less than the spectral width of the EIT.

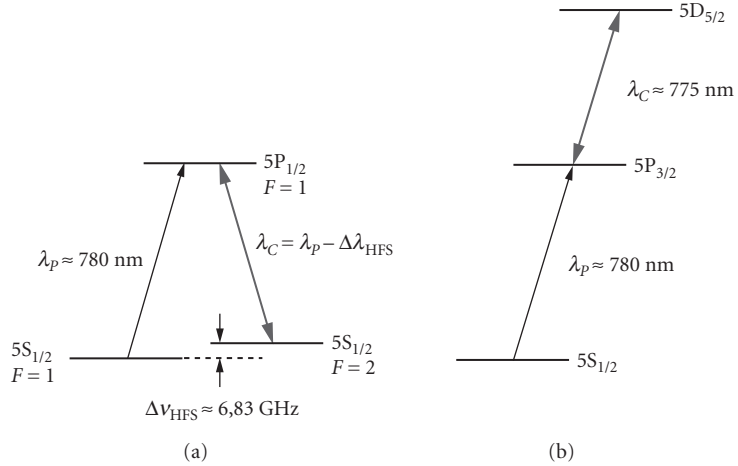


**FIGURE 6** Coupling scheme for EIT in strontium atoms and transmission of a probe laser pulse versus the probe laser detuning. Inset in the coupling scheme: dressed states [in our notation state  $|-\rangle$  corresponds to  $|2d\rangle$  and state  $|+\rangle$  corresponds to  $|3d\rangle$ ; compare Fig. 3]. (a) When the coupling laser is switched off, the probe laser experiences absorption in the line center. (b) When the coupling laser is switched on, the probe laser absorption is dramatically reduced in the line center. [Reprinted figure with permission from Ref. 123. Copyright (1991) by the American Physical Society.]

Experiments using pulsed lasers continue to be important, most especially in the context of nonlinear optics and matched pulse propagation. A related resonant EIT scheme in lead has been explored by Kasapi as a technique for enhanced isotope discrimination.<sup>125</sup> This method utilized the resonant opacity of a low abundance lead isotope  $^{207}\text{Pb}$  at EIT for the most common lead isotope  $^{208}\text{Pb}$  in their sample. Additional work has also recently illustrated how EIT can be established in the lead isotope  $^{207}\text{Pb}$  despite the presence of hyperfine structure. This was done by adjusting the laser frequencies to coincide with the center of gravity of the hyperfine split transitions.<sup>126,127</sup> Under this condition, interference of the manifold of hyperfine states yields EIT.

## 14.7 STEADY STATE ELECTROMAGNETICALLY INDUCED TRANSPARENCY, DRIVEN BY CW LASERS

Continuous wave (cw) lasers permit the implementation of EIT under steady-state conditions. Such experiments provide an excellent case to test the theoretical concept of EIT against experimental data from excitations under near-ideal conditions. Investigations of new effects in the cw regime permit straightforward comparison with theoretical predictions. A monochromatic laser is required, with a linewidth significantly less than the radiative decay rate  $\Gamma_3$  (i.e., in the range of 10 kHz to 10 MHz). Such radiation is typically provided by either dye or titanium sapphire ring lasers or more cheaply,



**FIGURE 7** Coupling schemes for EIT in rubidium atoms. (a) A lambda scheme involving the hyperfine sublevels of the ground state [which correspond to states |1> and |2> in our notation] of  $^{87}\text{Rb}$  (or  $^{85}\text{Rb}$ ) and the excited states  $5P_{1/2}$  or  $5P_{3/2}$  [which correspond to state |3> in our notation] and (b) a ladder-type scheme involving the ground state  $5S_{1/2}$  [i.e., state |1> in our notation], and the excited states  $5P_{3/2}$  [i.e., state |3> in our notation] and  $5D_{5/2}$  [i.e., state |2> in our notation].

but also with limited tunability and power, by external cavity stabilized laser diodes. However, in contrast to pulsed laser experiments, in cw EIT experiments it is more difficult to reach sufficient coupling strengths  $\Omega_C$  in order to exceed the inhomogeneous broadening. This has required the employment of both Doppler-free techniques and the reduction of the Doppler width by atom cooling methods.

Much work has been carried out in rubidium vapor. This is due to suitability of the rubidium atom's energy level configuration for EIT (see Fig. 7), the possibility of near-complete elimination of Doppler shifts in certain configurations, and the ease of handling the vapor. Xiao et al. as well as Moseley et al. performed important demonstrations of steady state EIT in rubidium atoms. A near-ideal lambda scheme is formed in rubidium (see Fig. 7a) between the ground states  $5S_{1/2}$  ( $F=1$ ) and ( $F=2$ ) and the excited state  $5P_{1/2}$  ( $F=1$ ) state. The transitions in this case are around 780 nm, separated by the ground state hyperfine splitting of  $\Delta v_{\text{HFS}} \approx 6.83$  GHz. In a detailed theoretical treatment of this system it is necessary to include all hyperfine sublevels of the three states. However, in essence the behavior is that of a simple three-level system. Likewise, also a ladder scheme is formed in this atom between the states  $5S_{1/2}$ ,  $5P_{3/2}$ , and  $5D_{5/2}$  (see Fig. 7b), with the transition wavelengths at  $\lambda_p = 780$  nm and  $\lambda_C = 775$  nm. Excitation of the transition at these wavelengths is easily possible using either cw titanium sapphire ring lasers or grating stabilized laser diodes. These schemes in rubidium also exhibit the additional advantage of Doppler-free excitation with the two closely spaced wavelengths. In such experimental configuration, Xiao et al. and Moseley et al. studied transparency,<sup>116,128,129</sup> refractive index modification,<sup>118</sup> and propagation effects.<sup>119,130</sup>

Observation of EIT in the rubidium ladder scheme showed good agreement with a steady-state calculation, involving residual effects of inhomogeneous (Doppler) broadening.<sup>116</sup> Due to the near-frequency coincidence between the transitions at 780 and 775 nm in this scheme, the effect of inhomogeneous broadening on the experiment was almost eliminated by using counterpropagating beams. This elimination of inhomogeneous broadening permitted the application of grating-stabilized laser diodes, operating with relatively low power ( $P < 10$  mW), to provide both probe and coupling fields in these experiments.

Results of experiments on the rubidium lambda scheme also proved to be consistent with theory. EIT was observed at the probe transition line center with a linewidth and depth in reasonable



agreement with the steady-state calculation.<sup>128</sup> In the case of the lambda scheme, copropagating beams lead to a Doppler-free excitation. Again this was possible due to the closely spaced probe and coupling laser wavelengths. As mentioned before, also here only low laser powers were required for EIT. This elimination of Doppler broadening was exploited by the same authors to perform an experiment that stresses the quantum interference nature of the EIT effect. By employing a coupling laser strength  $\Omega_C < \Gamma_3$  (i.e., the Rabi splitting is too small to give rise, on its own, to any significant absorption reduction) a well-developed transparency, with a depth limited only by the laser linewidths, was reported.<sup>129</sup> This experiment illustrates clearly how the additional coherence due to the coupling laser causes interference that cancels the effect of probe absorption.

The limits for a successful implementation of steady-state EIT with respect to the probe laser power has also been examined in the rubidium ladder scheme, as discussed above.<sup>131</sup> When the coupling laser was strong, but the probe relatively weak, EIT was induced as usual. In the case of a strong probe with a power comparable to the coupling laser ( $\Omega_p \sim \Omega_C$ ), the EIT was destroyed and replaced by enhanced absorption (i.e., electromagnetically induced absorption). This is explained by the opening of additional pathways in the absorption process (due to higher-order interactions with the probe field) leading to constructive interference in absorption. This result has implications in certain nonlinear frequency mixing schemes where a strong field should be generated at the probe frequency. The results suggest that there may be a limitation to the strength of the generated fields (see Sec. 14.12).

Besides operation in Doppler-free excitation schemes, also laser cooling of the atoms can be used to fully eliminate Doppler broadening. This also enables steady-state EIT in systems where the laser frequencies  $\omega_C$  and  $\omega_p$  differ significantly. Recently work has been reported on EIT (and CPT) in lambda systems in cold rubidium and cesium atoms, confined in a magneto-optical trap (MOT).<sup>120,121</sup> In rubidium a coupling scheme involving Zeeman splittings has also been studied.<sup>129</sup> These systems are close to ideal as the trapped atoms are very cool, that is, Doppler broadening is almost absent. Moreover the system exhibits very low density and hence may be considered as collisionless. If required, larger densities of trapped atoms can be provided by using dark-spot trap techniques.<sup>132</sup> Work has been carried out that exploits the characteristics of cold, confined rubidium atoms to study nonlinear absorption and dispersion.<sup>133</sup> Also temporal evolution of EIT in the transient regime has been investigated in a MOT with rubidium atoms.<sup>134</sup> In cold cesium atoms in a MOT the nonlinear sum rule<sup>135</sup> for EIT-type situations has been experimentally verified.<sup>136</sup>

## 14.8 GAIN WITHOUT INVERSION AND LASING WITHOUT INVERSION

We consider now the case of population, transferred via an incoherent pump process into the excited states of a three-level system, driven in EIT. Thus a small population in the upper state of the probe transition results in inversionless gain of the probe field. The reader is referred to the extensive literature on this subject for further discussion (see, Ref. 16). In studying gain without inversion, precautions should be taken to confirm that the system is indeed noninverted. This is in practice rather difficult to confirm. Experimenters must verify that there is clear evidence for gain on the probe transition and truly no population inversion on this transition.

Gao et al.<sup>137</sup> performed an early experiment that stimulated discussion and subsequent work. A four-level system of the hyperfine ground states  $3S_{1/2}$  ( $F = 0, 1$ ) and the excited states  $3P_{3/2}$  and  $3P_{1/2}$  in sodium atoms, driven in a Raman process, was investigated. A laser pulse excited the transition between the ground states  $3S_{1/2}$  ( $F = 0, 1$ ) and state  $3P_{1/2}$ . This created a coherence between the two hyperfine ground states. A cw probe laser was tuned close to the transition between the ground states  $3S_{1/2}$  ( $F = 0, 1$ ) and state  $3P_{3/2}$ . The probe laser experienced amplification, when the probe laser frequency was appropriately tuned—and provided a small amount of population was pumped into the  $3P_{3/2}$  state. The incoherent pumping process was driven by a DC gas discharge in the sodium vapor. The authors claimed, that the amplification process was inversionless. Initial criticism arose, as there was no independent monitoring of the excited state populations in this experiment.

Subsequent work on this issue, involving measurements of absorption, provided firmer evidence for inversionless conditions.<sup>138</sup> A similar excitation and amplification scheme in potassium vapor was reported by Kleinfeld et al.<sup>139</sup> The authors performed a careful numerical analysis that supports their claims for amplification without inversion. Further evidence for amplification without inversion has been found in several systems. In a lambda scheme in sodium atoms, with additional incoherent pumping into the upper state, Fry et al.<sup>140</sup> observed effects, based on atomic coherence, leading to amplification without inversion. The role of atomic coherence was confirmed by switching the coupling field on or off. Amplification was only observed when the field was present, and when it was absent the large population always present in the lowest state led to absorption of the probe. In another demonstration, picosecond pulses were used to excite atomic coherence among the Zeeman sublevels of the ground state in sodium atoms. Amplification without inversion was monitored and unambiguously confirmed by Nottelman et al.<sup>141</sup> Amplification without inversion was also demonstrated in a transient scheme in cadmium vapor through the formation of a linear superposition of coherently populated Zeeman sublevels by van de Veer et al.<sup>142</sup> In this experiment nanosecond laser pulses were used. The coherent nature of the process was proven (1) by the dependence of the gain on the time delay between the coherence preparation and probe pulse; and (2) by the dependence of the gain on the magnitude of the Zeeman splitting, which controlled the period for coherent transfer of population in the atom. Recently a double lambda scheme in helium atoms, driven by infrared radiation at 877.9 nm radiation in a helium-neon gas discharge, was used to observe amplification at both wavelengths 1079.8 and 611 nm (i.e., the latter in an up-conversion process). Here the evidence for amplification without inversion rests on comparison to calculation.<sup>143</sup>

To demonstrate LWI, the gain medium must be placed within an optical cavity. In two experiments<sup>15,83</sup> on this subject, amplification of a probe laser in the inversionless medium was demonstrated. Then the cavity was set up and lasing was observed even under conditions where no inversion was possible at all. The first of these experiments by Zibrov et al.<sup>15</sup> was implemented in a vee-type scheme, formed on the D1 and D2 lines of rubidium, with incoherent pumping from the  $F = 2$  hyperfine level into the upper state of the D1 transition. The latter provided the lasing transition. Laser diodes were used to derive all driving fields. The incoherent pump was generated by injecting white noise into an acousto-optic modulator (AOM). The AOM modulated one of the diodes. This work was also the first experiment to demonstrate amplification without inversion using laser diodes. An important conceptual advantage of the vee scheme is that there is no possibility for “hidden” inversion in a dressed basis at all. Thus the vee scheme serves as a very appropriate basis to demonstrate inversionless gain. The coupling scheme in the experiment could be considered in a simplified form as a four-level system, that is, three levels coherently coupled and a fourth coupled via the incoherent field. There are, however, 32 hyperfine sublevels in the particular experiment in rubidium, which must be considered in a detailed analysis. This complete analysis was carried out by the authors to yield predictions in good agreement with their experiment. Subsequently work was reported by Padmabandu et al.<sup>83</sup> demonstrating LWI in the same lambda scheme in sodium atoms, as also considered by the authors of Ref. 140.

## 14.9 MANIPULATION OF THE INDEX OF REFRACTION IN DRESSED ATOMS

Besides the manipulation of absorption or transmission, EIT also permits control of the refractive index of a laser-driven medium. Figure 5 shows the dependence of the real part of the linear susceptibility  $[\text{Re } \chi^{(1)}]$ , which determines the refractive index, on the probe laser detuning. The dispersion is most significantly modified between the absorption peaks, that is, for probe laser detunings in the range  $\Delta_{13} = \pm\Omega_c/2$ . In the absence of a coupling field the usual form of  $[\text{Re } \chi^{(1)}]$ , for an atom leads to anomalous dispersion, that is, a negative slope in  $[\text{Re } \chi^{(1)}]$ , in the vicinity of the resonance (i.e., for detunings  $\Delta_{13} = \pm\Gamma_3$ ). The dispersion  $[\text{Re } \chi^{(1)}]$  vanishes at exact resonance. This usual behavior of  $[\text{Re } \chi^{(1)}]$  is not significant, since the medium is highly opaque in the frequency range close to the resonance. However, in EIT the absorption is nearly zero close to resonance. Thus the modified dispersion can have a large effect on the refractive properties of the medium.

In a medium, driven to EIT, the dispersion  $[\text{Re } \chi^{(1)}] = 0$  at resonance. Thus the refractive index will attain the vacuum value ( $n = 1$ ), while the medium is fully transparent. As the assumption of a (closed) three-level atomic system is only an approximation, there will always be contributions to the total refractive index due to all other states of the atom. These other levels, however, are typically far from resonant with the driving laser fields. Thus they lead to relatively small contributions to the dispersion. In nonlinear frequency mixing the vanishing dispersion results in near-perfect phase-matching, which is essential for efficient frequency up-conversion (see Sec. 14.12). A second important modification to the dispersion in the frequency range  $\Delta_{13} = \pm\Omega_C/2$  is that the medium shows *normal* dispersion, that is, a positive slope in  $[\text{Re } \chi^{(1)}]$ . The value of the dispersion in this frequency range will depend on the shape of the curve and hence on the coupling laser intensity, which determines  $\Omega_C$ . In Sec. 14.11, we will examine the situation, when  $\Omega_C$  is small. In this case the dispersion profile can be very steep, and consequently very low group velocities result. The intensity dependence of  $[\text{Re } \chi^{(1)}]$  leads also to the strong spatial dependence of the refractive index across the intensity profile of a focused laser beam.

Investigations of the modification of dispersion (i.e., the refractive index) as induced by EIT have been carried out for steady-state excitation with cw lasers.<sup>118,119,130</sup> Direct measurements of the modified refractive index confirm the theoretical predictions. The dispersive properties of rubidium atoms, driven by EIT, was investigated using a Mach-Zehnder interferometer.<sup>118</sup> The dispersion measured at the center frequency was inferred to be equivalent to a small group velocity of  $v_g = c/13.2$ . In the last years, many experiments have been implemented in order to slow down the speed of light in media, driven to EIT. In this article we will only briefly mention some of the experiments, while a detailed discussion of slow light and storage of photons is subject to another article in this book.

A number of observations on electromagnetically induced focusing and defocusing, based on spatial variations in the index of refraction, have also been performed. A wavelength-dependent-induced focusing or defocusing was reported by Moseley et al.<sup>119,130</sup> employing a coupling scheme in rubidium. Constraints are introduced to the tightness of focusing in strongly driven media. However, these experiments also indicate possibilities to control the spatial properties of a beam at frequency  $\omega_p$  by a beam at another (i.e., perhaps very different, frequency  $\omega_C$ ).

In a scheme where a small amount of population is incoherently pumped into the excited state, gain was predicted<sup>8</sup> at exact resonance (i.e.,  $\Delta_{13} = 0$ ). Thus, the imaginary part of the linear susceptibility  $[\text{Im } \chi^{(1)}]$  becomes negative at resonance. When absorption vanishes at nearby frequencies, that is,  $[\text{Im } \chi^{(1)}] = 0$ , the value of  $[\text{Re } \chi^{(1)}]$  can be very large. This situation is termed *enhanced refraction*. Enhanced refraction has been observed in a lambda scheme in rubidium, provided there is an additional pumping field to result in a small (noninverted) population in the upper state of the system.<sup>144</sup> In this experiment an enhanced index of refraction was found at frequencies where the absorption was zero. A proposed application for refractive index modifications of this kind is high-sensitivity magnetometry.<sup>145</sup> The large dispersion at the point of vanishing absorption could be used to detect magnetic level shifts via optical phase measurements in a Mach-Zehnder interferometer with high accuracy.

## 14.10 PULSE PROPAGATION EFFECTS

Propagation of pulses is significantly modified in the presence of EIT. Figure 5b shows the changes to  $[\text{Re } \chi^{(1)}]$  in media, driven in EIT. An analysis of the refractive changes has been provided by Harris et al.<sup>82</sup> who expanded the susceptibilities (both real and imaginary parts) of the dressed atom in a series around the resonance frequency to determine various terms in  $[\text{Re } \chi^{(1)}]$ . The first term of the series (zero order)  $[\text{Re } \chi^{(1)}(\omega_{13})] = 0$  corresponds to the vanishing dispersion at resonance. The next term  $\partial/\partial\omega [\text{Re } \chi^{(1)}]$  gives the slope of the dispersion curve. At the transition frequency  $\omega_{13}$  this slope yields

$$\frac{\partial}{\partial\omega}[\text{Re } \chi^{(1)}] = \mu_{13}^2 \frac{4n_A}{\hbar\epsilon_0} \frac{(\Omega_C^2 - \Gamma_2^2)}{(\Omega_C^2 + \Gamma_2\Gamma_3)^2} \quad (7)$$

This expression shows the dependence of the slope of  $[\text{Re } \chi^{(1)}]$  on  $\Omega_C$ . The latter parameter permits controls of the group velocity of a laser pulse at frequency  $\omega_{13}$  propagating through the medium. Higher-order terms in the expansion lead to pulse distortions (group velocity dispersion), but at resonance the lowest nonvanishing term is of third order.

The first experimental studies of pulse propagation in media, driven to EIT system, were conducted by Kasapi et al.<sup>146</sup> In a lambda scheme in lead vapor, Kasapi et al. measured the delay of a probe pulse for various coupling laser strengths. Whilst the transmission through the medium was still large (i.e., 55%), pulses were found to propagate with velocities as low as  $v_g = c/165$ . The authors showed that the delay time  $\tau_{\text{delay}}$  for the pulse in the medium compared to a propagation through the vacuum was correlated to the attenuation of the transmitted pulse and the residual decay rate  $\gamma_{12}$  of the (dipole forbidden) transition  $|1\rangle \rightarrow |2\rangle$ —transition via the relation  $\ln\{E_{\text{out}}/E_{\text{in}}\} = -\gamma_{12} \cdot \tau_{\text{delay}}$ , with  $E_{\text{out}}$  and  $E_{\text{in}}$  as the energies of the probe pulse leaving and entering the medium. This idea was subsequently demonstrated as a method for measuring Lorentzian linewidths.<sup>147</sup> It was also demonstrated<sup>146</sup> that the presence of the coupling pulse leads to a near-diffraction-limited transmitted beam quality for a strong probe field under conditions where severe spatial distortion was present in the absence of the coupling laser. The situation where probe and coupling pulses were both strong was studied in a subsequent experiment that investigated further the elimination of optical self-focusing and filamentation, which afflict a strong probe field.<sup>148</sup>

The prospects of controlling the refractive index using strong off-resonant pulses was examined theoretically for a lambda scheme.<sup>93</sup> In this treatment it was shown that the off-resonant bound and continuum states lead to Stark shifts of states  $|1\rangle$  and  $|2\rangle$ , which can be compensated by detuning the lasers from the exact Raman resonance between the bare states. If this is done correctly, the additional coherence  $\rho_{12}$  will lead to EIT-like modification of the refractive index experienced by both pulses. This extends to the situation for which the probe pulse is also strong. With both strong laser pulses, off-resonant CPT is possible. Formation of an off-resonance trapped state is an important aspect of an experiment investigating the elimination of optical-self focusing,<sup>148</sup> in which a nonlinear refractive index would otherwise lead to self-focusing, filamentation, and beam breakup of the strong probe field. Off-resonant CPT is also important in nonlinear frequency mixing, as demonstrated in experiments in lead vapor<sup>149</sup> and solid hydrogen.<sup>126</sup> In this case the condition  $\Omega' > [\Delta \cdot \gamma_{12}]$  must be met, where  $\Delta$  is the detuning of the fields from the intermediate resonances. This leads to the requirement of high peak powers, if the detunings  $\Delta$  are large.

Propagation of two coupled strong pulses in a lambda-type system was discussed by Harris<sup>76,77</sup> and Eberly et al.<sup>42,78</sup> The discussed excitations scheme was equivalent to EIT. However, if both fields  $\Omega_p$  and  $\Omega_C$  are strong, the dressed atomic system reacts back on the field modes. This results in lossless propagation through the medium for both fields. For laser pulses with matched intensity envelopes (i.e., an identical form of temporal variation) any losses are minimal. If two initially matched pulses are simultaneously launched into a medium comprising atoms in the ground state, the system will self-organize so as to preserve the matched pulses and generate states, showing CPT. As the atoms are initially in the ground state  $|1\rangle$ , the probe pulse will initially experience loss and will have a lower group velocity than the coupling pulse. It will then start to lag the coupling pulse and so the pulse pair will automatically satisfy the condition for adiabatic preparation of trapped states (i.e., a counterintuitive pulse sequence). So, following the initial loss of probe pulse energy, the medium is set up for lossless transmission.

A proper insight into this process is best obtained in terms of CPT. The laser fields cause the formation of the superposition states  $|C\rangle$  and  $|NC\rangle$  [see Eq. (1)]. However, the atoms in the phase-coherent medium that is formed are also responsible for driving the two fields, and this means that even intensity envelopes which are initially different will evolve into matched pulses. This process results in the self-consistent formation of stable normal modes of the driving fields, one of which is uncoupled from the “uncoupled” atomic state and the other of which is “uncoupled” from the coupled atomic state. These new field modes result in the lossless propagation of pulses through a normally lossy medium, once a certain preparation energy has been extracted from the laser fields.

In the adiabatic limit the pulses are sufficiently intense, such that the timescale to establish EIT (i.e.,  $1/\Omega_C$ ) in the whole medium is fast with respect to the envelope evolution. Indeed, EIT can be much faster than the timescale required to establish population-trapped states in an individual

atom. This is due to the fact, that the latter process requires transfer of population, that is, irreversible exchange of energy between the field and the medium. In fact, the preparation time for EIT corresponds to a certain necessary pulse energy. The minimum energy  $E_C^{(\min)}$  required to prepare the medium in EIT is essentially given by the photon energy of the coupling laser multiplied by the oscillator strength-weighted number of atoms:<sup>79</sup>

$$E_C^{(\min)} = \frac{f_{13}}{f_{23}} \hbar \omega N_A \quad (8)$$

with the number of atoms  $N_A$  in the interaction volume and the oscillator strengths of the transitions at  $\omega_{13}$  and  $\omega_{23}$ . If the oscillator strength (or dipole moments) of the two transitions are comparable, Eq. (8) simply demands photon numbers, which exceed the number of atoms. Once the coupling laser pulse fulfills this condition (e.g., is long enough to provide a sufficient number of photons), the medium will be rendered transparent for all subsequent times. Application of this effect to the propagation of strong picosecond (ps) and femtosecond (fs) pulses a straightforward consideration. The preparation energy is not transferred irreversibly to the medium but is stored reversibly in the coherent excitation of state |2).

## 14.11 ULTRASLOW LIGHT PULSES

As already briefly discussed above (see Sec. 14.9), the steep, positive slope of the dispersion  $[\text{Re } \chi^{(1)}(\omega)]$  leads to a reduced group velocity  $v_g$ . The group velocity depends upon the slope, that is, the derivative of  $\chi^{(1)}(\omega)$ , as follows:

$$\frac{1}{v_g} = \frac{1}{c} + \frac{\pi}{\lambda} \left( \frac{\partial}{\partial \omega} [\text{Re } \chi^{(1)}] \right) \quad (9)$$

From the expression for the derivative  $\partial \chi^{(1)}/\partial \omega$  [Eq. (7)], we see that this slope is steepest (i.e.,  $v_g$  reaches a minimum) for  $\Omega_C \gg \Gamma_2$  and  $\Omega_C^2 \gg \Gamma_2 \Gamma_3$ , but when  $\Omega_C$  is still small compared to  $\Gamma_3$ . Hence  $\partial \chi^{(1)}/\partial \omega \sim 1/\Omega_C^2$ . In the limit of small coupling Rabi frequency  $\Omega_C$  the group velocity  $v_g$  therefore yields

$$v_g = \frac{\hbar c \epsilon_0 \Omega_C^2}{2 n_A \omega_p \mu_{13}^2} \quad (10)$$

In an inhomogeneously broadened system the requirement for EIT is  $\Omega_C > \gamma_{\text{Doppler}}$  (see Sec. 14.5). For typical atomic systems this usually also means  $\Omega_C > \Gamma_3$ . This condition constrains the group velocity reduction to relatively modest values. Thus in experiments in lead vapor<sup>146</sup> (see also Sec. 14.13), a group velocity reduction was clearly demonstrated, but the absolute reduction was only  $v_g = c/165$ . Further reductions in  $v_g$  are possible in media with small Doppler broadening  $\gamma_{\text{Doppler}}$ . In these media lower values for  $\Omega_C$  (i.e.,  $\Omega_C \ll \Gamma_3$ ) still permit implementation of EIT. An elimination of Doppler broadening of spectral transitions is, for example, possible in a coupling scheme with transition frequencies  $\omega_{13} \approx \omega_{23}$  and employing a Doppler-free geometry for the laser beams, that is, copropagating beams in a vee or lambda scheme and counterpropagating beam in a ladder scheme. Alternatively, laser-cooled and -trapped atomic samples can be used to reduce the Doppler width such that  $\gamma_{\text{Doppler}} \ll \Gamma_3$ . Cooled atoms also permit an excitation at frequencies  $\omega_{13} \neq \omega_{23}$  and no restrictions are set on the beam geometry.

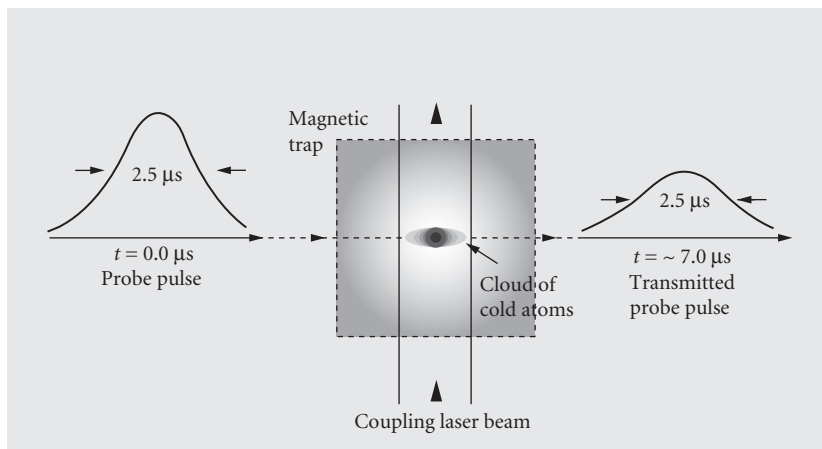
The spectral bandwidth of a light pulse determines a limitation for the possible reduction in the group velocity in a medium, or vice versa. The limit is set by the spectral linewidth of the EIT and by increased group velocity dispersion at frequencies detuned from exact resonance  $\omega_p = \omega_{13}$ . These effects

limit the permitted bandwidth of a light pulse with reduced group velocity to values significantly less than  $\Omega_c$ . Thus only light pulses with sufficiently long duration (i.e., small spectral bandwidth without significant contribution from frequency components outside the bandwidth of EIT) are subject to an efficient reduction of the group velocity.

A number of experimental observations of ultraslow group velocity have been reported. In a Doppler-free excitation scheme, closely related to CPT, in cesium vapor the dispersion profile near resonance was determined using a Mach-Zehnder interferometer.<sup>150</sup> From the measured steep dispersion, a group velocity of  $v_g = c/3000$  was inferred. A Doppler-free experiment in rubidium vapor was carried out, which directly measured a very large group velocity reduction. A probe beam with fast modulated amplitude was passed through the sample. The phase lag of the modulation with reference to the input signal was used to measure the group velocity. Very low values of  $v_g = 90 \text{ ms}^{-1}$  were determined, even though the temperature of the sample was as high as 360 K.<sup>151</sup> A lambda-type coupling scheme with Zeeman sublevels in rubidium was recently investigated and a magnetic field dependent group velocity as low as  $v_g = 8 \text{ ms}^{-1}$  was measured.<sup>152</sup>

A very dramatic demonstration of ultraslow light propagation was provided by Hau et al.<sup>11</sup> They employed a laser-cooled sodium sample trapped in a novel magnetic trap. Evaporative cooling of this sample was used to prepare a Bose-Einstein condensed (BEC) state. Experiments were performed (see Fig. 8) to investigate the delay in propagation of a probe pulse with pulse duration  $\tau_p = 2.5 \mu\text{s}$ , when a coupling laser was applied to the sample in the perpendicular direction. The reduced group velocity was studied both above and below the BEC transition temperature  $T_C$ . The lower group velocities found below  $T_C$  were due to the increased density of the sample when in this state. The lowest value of  $v_g$  that was measured was  $v_g = 17 \text{ ms}^{-1}$ . Other experiments on EIT also permitted the reduction of the speed of light in solids.<sup>g</sup> We will discuss these experiments below (see Sec. 14.15).

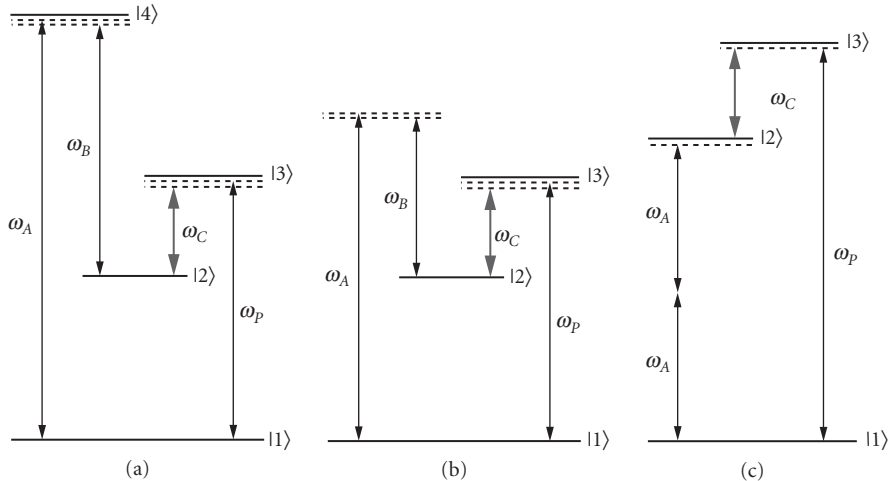
In this section we gave only a very short introduction to the field of ultraslow light in coherently prepared media. The subject of ultraslow light as well as the related topic of storing light in media, prepared by EIT, attracted a huge attention in the last years. For a detailed review on ultraslow light and storage of light pulses, we like to draw the attention of the reader to a related article on this subject elsewhere in this book.



**FIGURE 8** Schematic experimental setup for the observation of ultraslow light in a cloud of cold atoms, as reported by Hau et al.<sup>11</sup> A circularly polarized probe pulse passes through a cloud of cold atoms (length  $L = 0.2 \text{ mm}$ ) with a transit time of  $T = 7 \mu\text{s}$ . This corresponds to a group velocity of 1/10 millionth of the speed of light in vacuum. [Reprinted by permission from Ref. 153. Copyright (1999).]

## 14.12 NONLINEAR OPTICAL FREQUENCY CONVERSION

In the previous sections, we discussed the manipulation of linear optical properties (i.e., absorption and dispersion) by EIT. In addition to these effects, also the nonlinear optical response of a medium is significantly modified by EIT. This has been shown to lead to frequency mixing with greatly enhanced efficiencies and to large Kerr-type nonlinearities. In addition to the dressed linear susceptibility [see Eq. (6)], there is also a dressed nonlinear susceptibility. This nonlinear susceptibility describes the coupling of the atom to fields at frequencies other than the frequencies of the probe laser and the coupling laser, that is, to frequencies which are generated by nonlinear interaction between the driving radiation fields. Consider, for example, a four-wave mixing process. Three fields at frequencies  $\omega_A$ ,  $\omega_B$ , and  $\omega_C$  couple via the nonlinear response of the medium to generate a new field at frequency  $\omega_p$  with  $\omega_p = \omega_A \pm \omega_B \pm \omega_C$ . In general, the nonlinear susceptibility reaches maxima close to atomic resonances. Thus laser fields with frequencies tuned close to atomic resonances will yield enhanced frequency conversion. Figure 9 shows some basic coupling schemes for resonantly enhanced frequency conversion. Figure 9a depicts a situation, which we are already familiar with: Two radiation fields at frequencies  $\omega_A$  and  $\omega_B$  are tuned close to single-photon resonances at transitions  $|1\rangle \rightarrow |4\rangle$  and  $|2\rangle \rightarrow |4\rangle$  in a lambda-type level scheme. A third radiation field at frequency  $\omega_C$  (i.e., tuned to resonance at the transition  $|2\rangle \rightarrow |3\rangle$ ) mixes with the radiation fields at  $\omega_A$  and  $\omega_B$  to produce a wave at  $\omega_p = \omega_A - \omega_B + \omega_C$ . It is obvious from the coupling scheme, that the radiation fields  $\omega_A$  and  $\omega_B$  as well as the fields  $\omega_C$  and  $\omega_p$  will be automatically tuned close to two-photon resonance between the two lower states  $|1\rangle$  and  $|2\rangle$ . The same holds true for the slightly modified coupling scheme in Fig. 9b. Here the lasers at  $\omega_A$  and  $\omega_B$  are far detuned from any single-photon resonance. Still, the two-photon resonance between the lower states  $|1\rangle$  and  $|2\rangle$  is maintained. If the laser frequencies  $\omega_A$  and  $\omega_B$  are degenerate (i.e.,  $\omega_A = \omega_B$ ) and the lambda system is modified to a ladder-type system, as depicted in Fig. 9c, the probe field is generated at frequency  $\omega_p = 2\omega_A + \omega_C$ . The latter is a typical scheme for frequency conversion to the regime of short-wavelength radiation [e.g., to the regime of vacuum-ultraviolet (VUV) or extreme-ultraviolet (XUV) radiation].



**FIGURE 9** Three basic coupling schemes for four-wave mixing in coherently driven media. (a) Double-lambda system, driven on single-photon transitions by four radiation fields  $\omega_A$ ,  $\omega_B$ , and  $\omega_C$  generating a probe radiation field at frequency  $\omega_p = \omega_A - \omega_B + \omega_C$ . (b) Modified lambda system with the fields at  $\omega_A$  and  $\omega_B$  still tuned close to two-photon, but far detuned from any single-photon resonance. (c) Ladder system with degenerated fields at  $\omega_A = \omega_B$  driving a four-wave mixing process to generate the probe field at  $\omega_p = 2\omega_A + \omega_C$ .

In conventional “incoherent” frequency mixing, the laser-driven resonances will enhance the efficiency of the frequency conversion process. There is also a significant drawback of this resonant excitation scheme: As also the generated wave at  $\omega_p$  is resonant with the transition  $|1\rangle \rightarrow |3\rangle$ , it will be reabsorbed in the medium. However, if coherent interaction by EIT is considered, reabsorption is suppressed. To understand this feature of four-wave mixing, supported by EIT, let us consider the excitation processes in Fig. 9a in a slightly different way. The excitation scheme is equivalent to two coupled lambda systems. One lambda system is defined by the states  $|1\rangle$ ,  $|2\rangle$ , and  $|4\rangle$ . The other lambda system is defined by the states  $|1\rangle$ ,  $|2\rangle$ , and  $|3\rangle$ . If the laser at frequency  $\omega_C$  is strong, it will drive EIT in the second lambda system of states  $|1\rangle$ ,  $|2\rangle$ , and  $|3\rangle$ . In our previous notation, the generated wave at  $\omega_p$  corresponds to the probe laser, and the laser at  $\omega_C$  corresponds to the coupling laser. As the medium is prepared in EIT now for the probe laser, the generated field at frequency  $\omega_p$  will experience no reabsorption any more, that is, the dressed linear susceptibility at the transition  $|1\rangle \rightarrow |3\rangle$  is zero. In contrast, the dressed nonlinear susceptibility is not reduced to zero (see below and Fig. 5c). Thus the susceptibility provides a nonlinear coupling between the radiation fields, while absorption is suppressed.

The nonlinear susceptibility is calculated from Eqs. (4) and (5) in the same way as the linear susceptibilities in Eq. (6), however, now terms in  $\rho_{13}$  involving the fields at frequencies  $\omega_A$  and  $\omega_B$  are also included. The nonlinear susceptibility for the four-wave mixing process reads<sup>5</sup>

$$\chi_D^{(3)}(-\omega_p, \omega_A, \omega_B, \omega_C) = \frac{2\mu_{23}\mu_{31}n_A}{3\epsilon_0\hbar^3} \frac{1}{\Omega_C^2 + (\Gamma_3 + 2i\Delta_{13})(\Gamma_2 + 2i[\Delta_{13} - \Delta_{23}])} \times \sum_j \mu_{1j}\mu_{j2} \left( \frac{1}{\omega_{j1} - \omega_A} + \frac{1}{\omega_{j1} - \omega_B} \right) \quad (11)$$

where the sum on the right-hand side of Eq. (11) represents the contributions to the nonlinear susceptibility by all the states  $|j\rangle$  of the atom, the fields at frequencies  $\omega_A$  and  $\omega_B$  are close to the two-photon resonance between the states  $|1\rangle$  and  $|2\rangle$ . The modulus of this nonlinear susceptibility is plotted in Fig. 5c, although superficially similar to  $[\text{Im } \chi_D^{(1)}]$  (see Fig. 5a) in the sense that both display the familiar Autler-Townes splitting. However, there is a fundamental difference. Paying attention to the center of the profile at detuning  $\Delta_{13} = 0$ , we see that, instead of destructive interference, there is constructive interference at this point. The value of the nonlinear susceptibility is indeed larger than the incoherent sum of the contributions from the dressed states.

Constructive interference in the nonlinear optical response of the atom is one of the most significant consequences of EIT. It accompanies the destructive interference which causes transparency at the same frequency. Already in 1990 Harris et al. recognized how this could be used to greatly improve four-wave mixing efficiencies.<sup>6</sup> Enhancement of frequency mixing by atomic coherence and interference has been examined theoretically by a number of authors (see, e.g., Refs. 5, 6, 154, 155). The interference effects lead to improved frequency mixing in resonant systems because of three connected effects: (1) The resonant reabsorption in the medium is reduced due to the creation of transparency. (2) Phase matching is optimized due to vanishing dispersion near resonance. (3) Although the coupling field causes some reduction in the absolute value of the nonlinear susceptibility at resonance, the susceptibility is subject to constructive rather than destructive interference. For a medium with a large product of density and length ( $n_A L$ ) (i.e., the uncoupled system is optically thick) there will be a large enhancement in the four-wave mixing conversion efficiency. This persists in a Doppler-broadened medium, providing the Rabi frequency  $\Omega_C$  exceeds the Doppler width.

In a finite medium a calculation including absorption and phase-matching must be performed to predict the enhancement and the frequency dependence of the nonlinear response.<sup>5,6,101,102</sup> In the limit of an optically deep medium and considering plane wave fields, the figure of merit for the conversion efficiency is given by the ratio  $|\chi_D^{(3)}/\chi_D^{(1)}|$ . This is physically reasonable, since  $\chi_D^{(1)}$  characterizes the reabsorption and wave-vector mismatch in the medium, while  $\chi_D^{(3)}$  determines the strength of the nonlinear coupling, which generates the new field. Thus we can see the importance of the destructive interference in the value of  $\chi_D^{(1)}$  in the same frequency range, where  $\chi_D^{(3)}$  experiences constructive interference. This enhances the generation efficiency in a Doppler-broadened



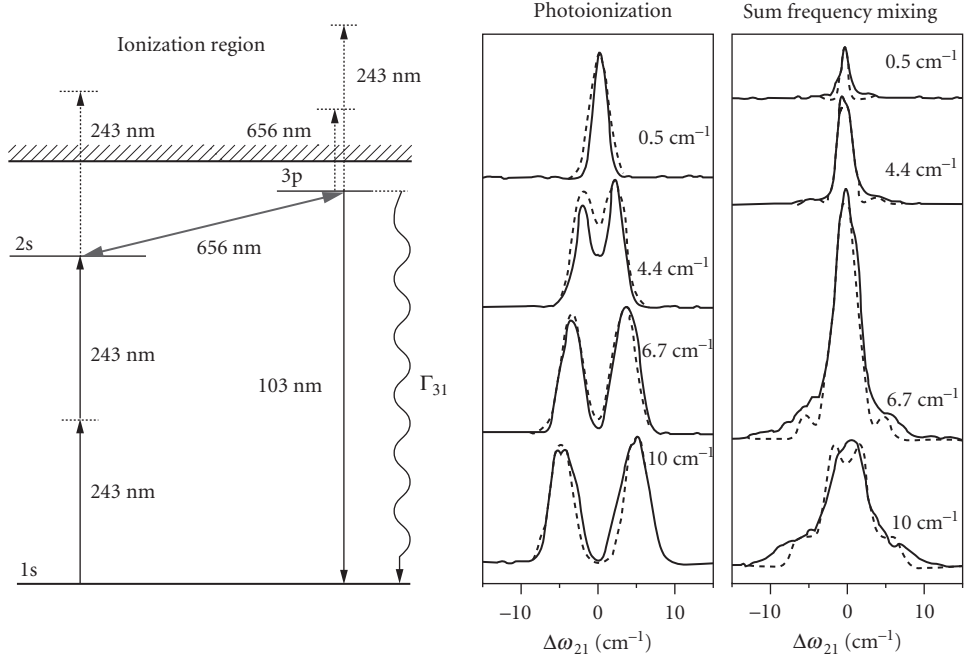
medium by many orders of magnitude, provided the Rabi frequency  $\Omega_C$  exceeds the Doppler width. Modifications of  $\chi_D^{(1)}$  result in reduced absorption and the essentially perfect phase matching for all resonant fields. Residual phase mismatch then appears only because of the dispersion caused by the remaining off-resonant states.

Electromagnetically induced phase matching was observed in an off-resonance four-wave mixing scheme in lead vapor.<sup>156</sup> In this experiment, the small detuning from resonance  $\Delta = 6 \text{ cm}^{-1}$  indicated that transparency played little role in the enhancement (since the sample was optically thin). However, once the coupling laser strength exceeded a critical value, that is,  $\Omega_C > [\gamma_{\text{doppler}}^2 + \Delta^2]^{1/2}$ , the dispersion became effectively zero. This led to perfect phase matching and enhanced conversion efficiency.

In the first experiment to demonstrate enhancement by EIT, Hakuta, Stoicheff et al. investigated three-wave mixing (normally forbidden) in hydrogen when a DC electric field was applied to the sample.<sup>157,158</sup> This experiment can also be viewed in the context of EIT. The DC field may be considered as an electromagnetic field at zero frequency. This field dresses the atom, creating two Stark states between which absorption cancellation occurs through interference. Second harmonic generation of a field at wavelength 243 nm is then resonantly enhanced at the two-photon transition between the states 1s and 2s. Due to EIT, the generated radiation at the Lyman- $\alpha$  wavelength 121.6 nm is no more reabsorbed. Further experiments by the same group then demonstrated EIT enhancement of a resonant four-wave mixing scheme in hydrogen atoms.<sup>159</sup> This was achieved in a scheme involving the states 1s, 2s, and 3p (corresponding to states |1>, |2> and |3> in our notation). The coupling laser at  $\lambda_C = 656 \text{ nm}$  drove the transition between states 2s and 3p. The coupling laser mixed with a field at  $\lambda_A = 243 \text{ nm}$ , driving the two-photon transition between states 1s and 2s. This nonlinear interaction generated a field at  $\lambda_p = 103 \text{ nm}$  (see Fig. 10, compare also Fig. 9c). Both lasers at  $\lambda_C$  and  $\lambda_A$  were derived from single-mode pulsed dye lasers. In this scheme photoionization of state 2s was an order of magnitude smaller than the ionization loss from state 3p. This is an important feature, since the coherence between the states 1s and 2s is essential for EIT effect to survive. Thus decay due to photoionization is a critical effect. However, so long as the decay rate of state 2s is significantly smaller than the rate of state 3p, the destructive interference in the absorption will persist and still lead to enhancement of the frequency mixing efficiency.

High conversion efficiencies require that the product of density and path length ( $n_A L$ ) is large enough to ensure that the medium is initially strongly opaque. An atomic hydrogen beam was specially designed in the experiments, discussed above, in order to increase the beam density and path length. Thus EIT could be studied for the regime of an optically thin up to an optically thick medium.<sup>95,160</sup> Working with products ( $n_A L$ ) up to  $10^{16} \text{ cm}^{-2}$ , conversion efficiencies of  $>10^{-3}$  were found. This is an extraordinarily large value for frequency conversion in a gaseous medium. There was, however, a limit to the obtainable conversion efficiency in this scheme, due to the large Doppler width in hydrogen. This a consequence of the low mass of hydrogen and the elevated temperatures in the discharge used to produce the atoms. The coupling Rabi frequency  $\Omega_C$  had to exceed the large Doppler width, leading to large Autler-Townes splittings and reduction in the magnitude of  $\chi^{(3)}$  available for mixing. To overcome this, four-wave mixing schemes in atoms with smaller Doppler widths (e.g., krypton) have been studied. Experiments with a four-wave mixing scheme at a large product ( $n_A L$ )  $\approx 5 \times 10^{16} \text{ cm}^{-2}$  in krypton at room temperature have recently demonstrated a conversion efficiency of  $10^{-2}$  for generation of a field at 123.6 nm.<sup>161</sup> Quantum interference effects arising from the generated field itself have been reported to a limit in the optimum density for resonantly enhanced four-wave mixing. In a conversion scheme in rubidium<sup>162</sup> at higher density the generated field itself became strong enough to cause a significant perturbation to the coherences in the system. This latter work, however, did not employ a single-mode coupling laser. Thus, the low limit in the rubidium density ( $n_A < 10^{15} \text{ cm}^{-3}$ ), measured in these experiments, may not be reflected in situations where EIT is present.

Finally, we mention some alternative frequency conversion processes in lambda-type coupling schemes. In such schemes, the metastable state |2> often exhibits very long lifetimes. This leads to intrinsically low decay rates for the coherence  $\rho_{12}$  and near-perfect transparency is possible. Also in some selected systems (e.g., rubidium or sodium atoms) where the two lower states are hyperfine sublevels, Doppler-free configurations can be employed. These features make lambda systems a



**FIGURE 10** Four-wave mixing scheme in hydrogen atoms (compare also Fig. 9c). EIT is driven by the coupling laser at wavelength  $\lambda_C = 656$  nm, tuned to the single-photon transition between states 2s and 3p [corresponding to states |2⟩ and |3⟩ in our notation]. A laser at  $\lambda_A = 243$  nm drove the two-photon transition between states 1s and 2s [corresponding to states |1⟩ and |2⟩ in our notation]. A probe field with wavelength  $\lambda_p = 103$  nm, i.e., on the transition between the states 1s and 3p [corresponding to states |1⟩ and |3⟩ in our notation]. The photoionization yield and the sum-frequency mixing efficiency were measured versus the detuning  $\Delta\omega_{21}$  [in our notation  $\Delta_{21}$ ] for different values of the coupling Rabi frequency  $\Omega_C$  (given in wavenumbers). The photoionization spectra show that the Autler-Townes splitting increases with the Rabi frequency  $\Omega_C$ . The conversion efficiency increases faster than the Autler-Townes splitting. A maximum is reached for a Rabi frequency of  $\Omega_C = 6.7$  cm<sup>-1</sup>. The medium is driven in EIT. For larger Rabi frequency there is no further enhancement in the conversion efficiency, as the re-absorption is already completely cancelled. However, the Autler-Townes splitting still increases with  $\Omega_C = 6.7$  cm<sup>-1</sup>. Thus the nonlinear coupling (i.e., the value of the nonlinear susceptibility) is reduced for further increasing Rabi frequency (compare the separation of the dressed states in Fig. 5c). [Reprinted figure with permission Ref 159. Copyright (1993) by the American Physical Society.]

very favorable choice for frequency conversion processes. Let us consider again the lambda scheme in Fig. 9a. In contrast to the above discussion, we will permit now for alternative combinations of the applied laser frequencies. For example, consider the coupling field at  $\omega_C$  applied so as to create EIT. With two additional fields, a large number of different frequency mixing processes may arise. Radiation at frequencies  $\omega_p$  and  $\omega_A$  (or  $\omega_B$ ) in combination with the coupling field at  $\omega_C$  drive the generation of new fields via four-wave mixing. The sign of the detuning from resonance for the applied or generated fields  $\omega_A$  or  $\omega_B$  may be positive or negative. The additional state |4⟩ may be present at small detuning (i.e., a double-lambda scheme is prepared) or the detuning may be very large (i.e., the lasers drive essentially a three-level system) (compare Fig. 9b). Also if only two fields (e.g.,  $\omega_C$  and  $\omega_p$ ) are applied, they will drive a coherence  $\rho_{12}$  that can give rise to four-wave mixing processes. The coherence  $\rho_{12}$  can mix again with either of the fields  $\omega_C$  and  $\omega_p$  to generate, via a stimulated Raman process, Stokes and anti-Stokes fields. Moreover, if strong fields at  $\omega_C$  and  $\omega_A$  and a weak field at  $\omega_B$  are applied, four-wave mixing yields a field at frequency  $\omega_p$ , which is phase-conjugated to  $\omega_B$ .

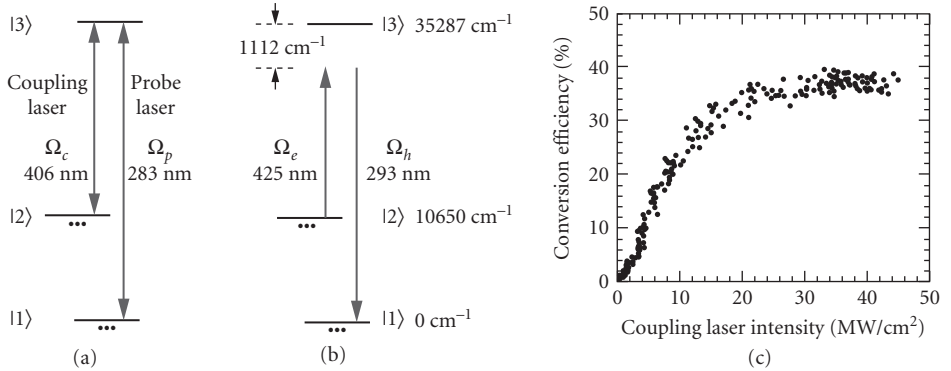
Nondegenerate four-wave mixing (NDFWM) based on EIT in a lambda scheme has been experimentally studied. In rubidium<sup>163</sup> a coupling field  $\omega_c$  was applied resonantly, while a second field  $\omega_A$  and a weak probe at  $\omega_B$  were both applied with a detuning of 450 MHz from the resonance to state  $|3\rangle$ . A phase-conjugate field was generated at frequency  $\omega_B$ . Due to EIT, absorption of this generated field vanished, but the nonlinearity remained resonantly enhanced. The susceptibilities [ $\text{Im } \chi^{(1)}$ ] and  $\chi^{(3)}$  were measured independently under conditions of an optically thin medium. The data confirmed that  $\chi^{(3)}$  was indeed enhanced by constructive interference. If an optically dense medium was used, a significant enhancement in NDFWM was observed. High phase-conjugate gain was also recently observed, applying very low laser powers. The effect arose from the presence of population trapping in a double-lambda scheme in sodium atoms.<sup>105,164</sup> Resonant four-wave mixing,<sup>165</sup> driven by cw lasers, and frequency up-conversion<sup>166</sup> have also been observed in an experiment investigating a double-lambda scheme in sodium dimers.

## 14.13 NONLINEAR OPTICS AT MAXIMAL ATOMIC COHERENCE

When two laser pulses (i.e., a probe and a coupling laser pulse) propagate as matched pulses through a medium (see Sec. 14.10), large amounts of populations are prepared in trapped states. This is possible under conditions of strong excitation, that is, when the laser electric field strengths are large enough to drive adiabatic evolution for all atoms in the beam path. In this case the coherence  $\rho_{12}$  will reach a maximum magnitude (i.e.  $|\rho_{12}| = |c_1^* c_2| = 1/2$ ). Thus, all the atoms are prepared in the trapped state  $|NC\rangle$ , that is, in a coherent superposition of the ground and the excited state with equal amplitudes  $|c_1| = |c_2| = \sqrt{1/2}$ . As the polarization of an atom is directly proportional to the coherence [compare Eq. (4)], also the polarization reaches a maximum at maximal atomic coherence. Under these circumstances, mixing of additional fields with the atom will become extremely efficient. We must not fail to mention, that the preparation of maximal coherences is also possible by adiabatic passage processes, other than EIT. Thus, STIRAP (see Sec. 14.3), coherent population return (CPR), rapid adiabatic passage (RAP), or Stark chirped rapid adiabatic passage (SCRAP) serve as alternative tools.<sup>45</sup>

We consider now again a frequency conversion process under conditions of EIT in the coupling scheme, depicted in Fig. 9a and b. If the lasers at frequencies  $\omega_p$  and  $\omega_c$  induce a maximal coherence, any frequency conversion process, driven by the fields  $\omega_A$  or  $\omega_B$  occurs with high efficiency. This is due to the fact that the linear susceptibility, which governs the amount of absorption and dispersion, and the nonlinear susceptibility, which govern the frequency conversion efficiency, both have only a single nonresonant denominator with respect to the detuning. Thus the strengths for the nonlinear and the linear susceptibility for the fields at frequencies  $\omega_A$  or  $\omega_B$  are of the same order of magnitude. As a consequence, efficient energy exchange between the electric fields can occur in a distance of the order of the optical coherence length. The latter is determined by the real part of the susceptibility. This is equivalent to near-vacuum conditions for the dispersion and absorption of the medium while the nonlinearity is large.

The preparation of trapped states leading to the formation of a large atomic coherence has been applied by the Harris et al. to drive very efficient nonlinear frequency conversion.<sup>149</sup> The adiabatic frequency conversion process was implemented in a lambda-type scheme in lead vapor, driven by two strong lasers, that is, the coupling laser at  $\lambda_c = 406$  nm and the probe laser at  $\lambda_p = 283$  nm. A large, near-maximal coherence was created between the states  $|1\rangle$  and  $|2\rangle$  (see Fig. 11). The phase-coherent atoms acted as a local oscillator that mixed with a third laser field at 425 nm, detuned by  $1112 \text{ cm}^{-1}$  from the resonance frequency  $\omega_{13}$ . By a four-wave mixing process, involving the three fields, a new field at 293 nm was generated. The conversion efficiency was exceptionally large, reaching ~40 percent. The high conversion efficiency occurs since in this system the preparation of the optimal coherence  $\rho_{12}$  yielded a large nonlinear susceptibility, which was of the same size as the linear susceptibility. The same scheme was used, this time mixing a field at 233 nm to generate a field in the far-ultraviolet spectral region at 186 nm. In this case, the nonresonant detuning from the



**FIGURE 11** Efficient frequency conversion at maximal atomic coherence in lead vapor. (a) A large atomic coherence  $\rho_{12}$  was prepared by the probe and the coupling laser at wavelength  $\lambda_p = 283$  nm and  $\lambda_c = 406$  nm. (b) A laser at  $\lambda_e = 425$  nm [in our notation  $\lambda_A$ ] mixes with this coherence to generate a strong sum frequency mixing signal at  $\lambda_h = 293$  nm [in our notation  $\lambda_B$ ]. (c) Conversion efficiency versus coupling laser intensity. The efficiency increases linearly, till it reaches a plateau of 40 percent. This exhibits an extraordinary large value for a conversion process in a gaseous medium. [Reprinted figure with permission from Ref. 149. Copyright (1996) by the American Physical Society.]

third state in lead vapor was only  $\sim 40$  cm $^{-1}$ . A near-unity conversion efficiency was demonstrated in this case.<sup>20</sup>

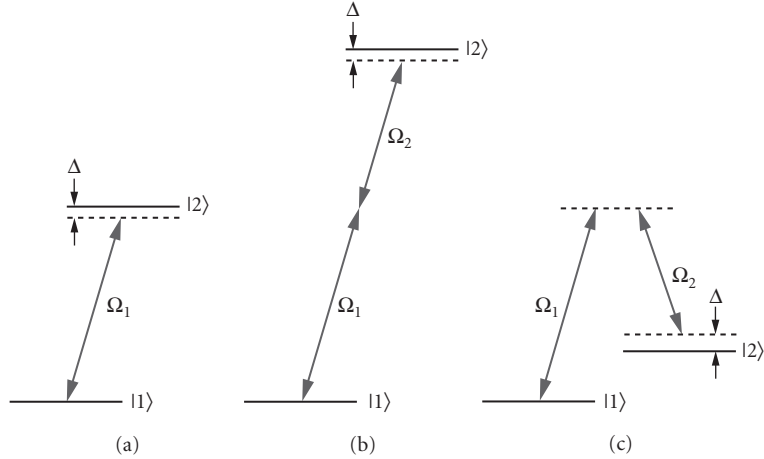
The coupling scheme in lead vapor, as discussed above, was recently the subject of a proposal for a broadband, high-efficiency, optical parametric oscillator (OPO).<sup>21,22</sup> In this case, a maximal coherence  $\rho_{12}$  between the states  $|1\rangle$  and  $|2\rangle$  was created in the same fashion as discussed above. The coherence  $\rho_{12}$  then acts as a local oscillator in an optical parametric down-conversion process generating signal and idler waves in the infrared and far-infrared spectral region. In this system the nonlinear and linear responses of the medium were calculated to be of the same order and high conversion efficiencies up to 10 percent were predicted for the center of the OPO tuning range. Furthermore the device was predicted to cover the entire spectrum from the infrared to very long wavelength (i.e., essentially almost to the regime of DC fields).

The concept of maximal atomic coherence has been proposed to eliminate phase-mismatch in Raman scattering (i.e., the generation of Stokes and anti-Stokes radiation).<sup>122</sup> In this scheme, the vibrational states  $v = 0$  and  $v = 1$  in the electronic ground state of a molecule form the lower states  $|1\rangle$  and  $|2\rangle$  of a Raman-type excitation scheme. The Raman scheme is equivalent to a lambda-type excitation scheme with large single-photon detunings  $\Delta_{12}$  and  $\Delta_{13}$ , while still the laser frequencies are tuned close to two-photon resonance ( $\Delta_{12} - \Delta_{13}$ ). In such an excitation scheme, the dephasing rate  $\gamma_{12}$  is very small. Thus interference can occur and cause the dispersion to become negligible. Because of the removal of the usual phase mismatch, efficient operation of Raman scattering over a broad range of frequencies, that is, from the infrared to the vacuum-ultraviolet is possible. Another important prediction concerned efficient generation of broadband coherent spectra, associated with strong-field refractive index control under conditions of maximal coherence.<sup>23</sup> In this case a pair of laser pulses are slightly detuned from exact two-photon (Raman) resonance. Also in this case, which is closely related to EIT, a maximal coherence is generated.

To understand this feature of adiabatic excitation, we consider a two-level system of states  $|1\rangle$  and  $|2\rangle$ , driven by a single laser pulse (see Fig. 12a). The dressed (adiabatic) eigenstates of the system read

$$|+\rangle = \sin\vartheta(t)|1\rangle + \cos\vartheta(t)|2\rangle \quad (12a)$$

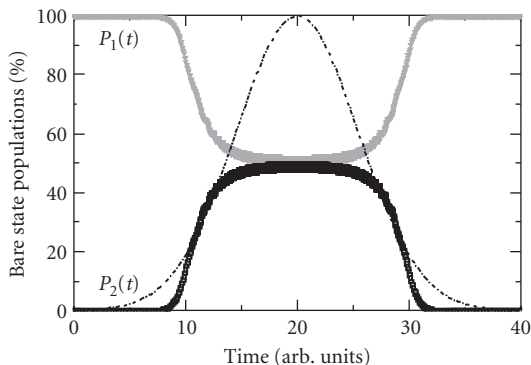
$$|-\rangle = \cos\vartheta(t)|1\rangle - \sin\vartheta(t)|2\rangle \quad (12b)$$



**FIGURE 12** Coupling schemes for preparation of a maximal coherence by CPR. (a) Two-level system, driven by a single laser pulse on a single-photon transition. (b) Effective two-level system, driven by two laser pulses on a one-photon transition. (c) Effective two-level system, driven by two laser pulses on a Raman-type transition.

with the mixing angle  $\vartheta(t)$ , defined by  $\vartheta(t) = 1/2 \arctan [\Omega_1(t)/\Delta]$ . As we will consider now two strong laser pulses, we return to our previous designation of  $\Omega_1$  and  $\Omega_2$  (rather than  $\Omega_p$  and  $\Omega_c$ ). We note that for resonant excitation at  $\Delta = 0$  Eq. (12) yields the resonant form of the dressed states, as already introduced in Eq. (3). Let us assume now the Rabi frequency  $\Omega_1(t)$  to be negligibly small outside a finite time interval  $t_0 < t < t_1$ , that is, outside the pulse duration  $\tau_{\text{pulse}} = t_1 - t_0$ . Consider now the case of the laser frequency detuned from exact resonance (i.e.,  $|\Delta| > 1/\tau_{\text{pulse}}$ ). If at the beginning of the interaction all the population is in the ground state, the state vector  $\Psi(t)$  of the system at time  $t = -\infty$  is aligned parallel to the adiabatic state  $|-\rangle$ . If the evolution of the system is adiabatic, the state vector  $\Psi(t)$  remains always aligned with the adiabatic state  $|-\rangle$  [see Eq. (12b) and the definition of the mixing angle  $\vartheta$ ]. Thus, during the excitation process (i.e., at intermediate times  $t_0 < t < t_1$ ) the state vector  $\Psi(t)$  is a coherent superposition of the bare states  $|1\rangle$  and  $|2\rangle$ . Therefore, population is transiently excited to the upper state. However, at the end of the interaction at  $t = +\infty$ , the state vector  $\Psi(t)$  becomes once again aligned with the initial state  $|1\rangle$  [see Eq. (12b) and the definition of the mixing angle  $\vartheta$ ]. The population transferred during the process from the ground state  $|1\rangle$  to the excited state  $|2\rangle$  returns completely to the ground state after the excitation process. No population resides permanently in the excited state, no matter how large the transient intensity of the laser pulse may be. This phenomenon is called coherent population return (CPR), and is also known from coherent spectroscopy.<sup>167–169</sup> Figure 13 shows the bare state population dynamics in CPR. As expected from the analytical considerations, population flows from the ground state to the excited state during the excitation and returns back to the ground state after the excitation process. If the peak Rabi frequency  $\Omega_1^{(\text{max})}$  is sufficiently large (i.e.,  $\Omega_1^{(\text{max})} \gg \Delta$ ), the mixing angle during the process becomes  $\vartheta = \pi/4$ . Thus the coherence is  $|\rho_{12}| = |c_1^* c_2| = \sin \vartheta \cos \vartheta = 1/2$  (i.e., a maximal coherence is prepared during the process).

The dynamics, discussed above, are not restricted to excitations of single-photon transitions, as depicted in Fig. 12a. Also multiphoton transitions [e.g., a two-photon transition (see Fig. 12b)], are driven in CPR, provided the laser frequencies are slightly detuned from the multiphoton transition frequency. This holds true also for Raman-type excitation schemes (see Fig. 12c), when the laser frequencies are tuned such that large detunings from any single-photon resonance as well as a small detuning from exact two-photon resonance occur. Thus, also in the case of Raman transitions between molecular vibrational states, a maximal coherence can be established and used for efficient frequency conversion processes. Moreover, a detailed theoretical analysis shows, that the adiabatic



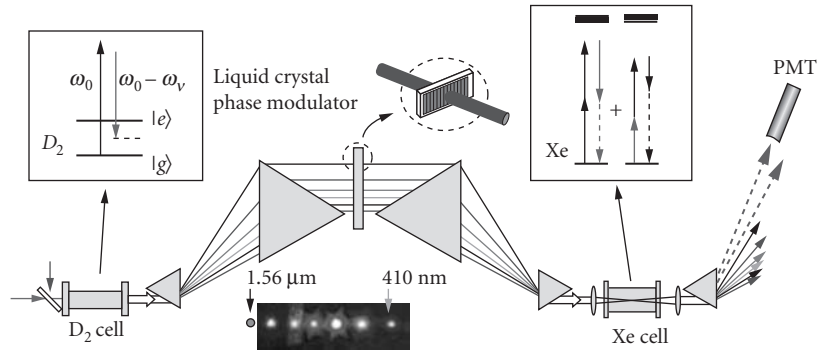
**FIGURE 13** Numerical simulation of CPR.<sup>167</sup> When a transition in a two-level system is coherently driven, slightly detuned from the exact transition frequency (compare Fig. 12), population flows from the ground state |1⟩ to the excited state |2⟩ and back again [the probabilities  $P_i(t)$  are indicated by the solid data points]. A transient maximal coherence is established during the process. The dashed line shows the temporal profile of the driving laser pulse.

excitation also permits control of the refractive index, that is, phase matching or phase mismatch plays only a minor role in the conversion process.

Harris et al. proposed, demonstrated, and applied the efficient generation of Raman sidebands in gaseous media under the conditions of maximal coherence.<sup>22–24,26–28,33,35</sup> The experiment was performed in deuterium molecules in the gas phase. The deuterium molecules were cooled to 77 K in order to increase the population in the lowest rotational state and to reduce dephasing by collisions. Two nanosecond radiation pulses at frequencies  $\omega_1$  (pump) and  $\omega_2$  (Stokes) excited a Raman transition between the vibrational ground state  $v = 0$  and the first excited state  $v = 1$  (compare Fig. 12c). If the laser frequencies are slightly detuned from the Raman resonance, a maximum coherence is established. The medium acts now like a molecular modulator, oscillating at the frequency  $\Delta\omega$  (i.e., the difference frequency between the vibrational states  $v = 0$  and  $v = 1$ ). The generation of Raman sidebands can be viewed as subsequent mixing process of the molecular modulator and the laser fields: Interaction of the field at  $\omega_2$  with the coherence at  $\Delta\omega$  produces the first anti-Stokes sideband at  $\omega_2 + \Delta\omega$  with large efficiency. Interaction of the first sideband with the coherence generates the second anti-Stokes sideband at  $\omega_2 + 2\Delta\omega$ . The process proceeds to higher-order sidebands. In their experiment, Harris et al. demonstrated conversion of the two driving radiation fields into Raman sidebands, covering a spectral region from 2.94  $\mu\text{m}$  to 195 nm (i.e., from the far-infrared to the far-ultraviolet).<sup>24</sup> The largest conversion efficiency occurs, when the two radiation fields are slightly detuned from exact two-photon resonance. This, on the first glance surprising feature, confirms the theoretical expectations, as discussed above: Adiabaticity is maintained and a maximal coherence is prepared for detunings  $|\Delta| > 1/\tau_{\text{pulse}}$ .

Harris, Sokolov et al. applied the scheme for efficient generation of Raman sideband, as discussed above, to generate intense ultrashort radiation pulses.<sup>27,28,33</sup> In an impressive experiment, Raman sidebands, with pulse durations in the nanosecond regime, were overlapped and combined. When their relative phases were appropriately adjusted, the combination of the phase-locked frequency components yielded a train of ultrashort radiation pulses with pulse duration in the regime of down to 1.6 fs (see Fig. 14).<sup>33</sup>

We must not fail to mention that Hakuta et al. performed some of the early investigations on Raman sideband generation in coherently prepared media.<sup>25,31,32,34</sup> These experiments were conducted in solid hydrogen. Other experiments on Raman sideband generation in media, coherently driven by nanosecond radiation pulses, were also performed by Marangos et al.<sup>29,30</sup> In these experiments



**FIGURE 14** Experimental setup for temporal synthesis and characterization of single cycle optical pulses, generated by combination of Raman sidebands. The sidebands are generated in a cell with deuterium molecules, dispersed and their phases are independently varied by a liquid crystal modulator. The sidebands are recombined and focused into a target cell with xenon gas. The figure also shows the spectrum of the seven sidebands in the wavelength regime from 1.56  $\mu\text{m}$  to 410 nm, used for generation of the ultrashort pulse. The duration of the ultrashort single-cycle pulses was 1.6 fs with a peak power of 1 MW. [Reprinted figure with permission from Ref. 33. Copyright (2005) by the American Physical Society.]

the coherence was probed by long (nanosecond) as well as ultrashort (femtosecond) radiation pulses.

Other work extended the concept of maximal coherence to the regime of excitations by ultrashort radiation pulses.<sup>170,171</sup> As discussed above (see Sec. 14.5), ultrashort pulses are usually not favourable choice to drive adiabatic excitations on single-photon transitions. Thus, usually a maximal coherence cannot be prepared by ultrashort radiation pulses. However, in selected molecular media and with sufficient pulse energies, already a significantly enhanced molecular coherence (though not maximal) may enable efficient frequency conversion. Thus the efficient generation of Raman sidebands with pulse durations in the femtosecond time domain was demonstrated in hydrogen and methane molecules.<sup>170,171</sup> The total conversion efficiency approached 10 percent.

Other extensions of the concepts, discussed above, utilize the excitation of Raman transitions by lasers of ultrabroad bandwidth.<sup>36–39</sup> If the bandwidth  $\gamma_{\text{laser}}$  of a single ultrashort laser pulse covers the spacing  $\Delta\omega$  between the vibrational ground state and the first excited state, the Raman transition is driven with frequency components, deduced from the single radiation pulse. Using  $\text{SF}_6$  molecules as the Raman-active medium, an ultrashort pump pulse with wavelength  $\lambda_p = 800$  nm and an additional ultrashort probe pulse with wavelength  $\lambda_{\text{pr}} = 400$  nm, the molecular modulation technique has led to the generation of pulse trains and isolated pulses with a duration of a few femtoseconds.<sup>37–39</sup>

## 14.14 NONLINEAR OPTICS AT THE FEW PHOTON LEVEL

As we have noted, one of the most remarkable features of EIT is that the nonlinear susceptibility undergoes constructive interference, while the linear susceptibility undergoes destructive interference. In a system without inhomogeneous broadening, perfect transparency can be induced for a coupling Rabi frequency  $\Omega_C \ll \Gamma_3$ . In this case the medium becomes transparent. Due to the small size of  $\Omega_C$  with respect to the decay rate  $\Gamma_3$  the nonlinear susceptibility will reach a value essentially identical to the value in the bare atomic system. Since atomic resonances are generally much narrower than those of a solid-state system, the magnitudes of the nonlinearity in this case can be many orders of magnitude larger than that of any solid. For instance, a very large nonlinear refractive

index was reported by Hau et al.<sup>11</sup> for EIT in an ultracold sodium vapor. They measured a value for the nonlinear refractive index that was  $0.18 \text{ cm}^2 \text{ W}^{-1}$ . This was  $10^6$  times larger than the nonlinear refractive index measured for cold cesium atoms in a system, which was not driven to EIT.<sup>172</sup> In fact, the refractive index in cesium was itself much larger than the refractive index in a solid. For comparison, the largest nonlinear refractive indices of solid-state materials are on the order of less than  $10^{-12} \text{ cm}^2 \text{ W}^{-1}$ .<sup>173</sup>

An important feature in the regime, discussed above, is the Kerr-type nonlinearity. This can be understood from examination of Fig. 9a. If fields at frequencies  $\omega_p$ ,  $\omega_C$ , and  $\omega_B$  are considered, the Kerr-type nonlinearity describes the coupling between the fields at  $\omega_p$  and  $\omega_B$ . The detuning between of field  $\omega_A$  from state |4) is usually smaller than the detuning from state |3). Via the susceptibility  $[\text{Re } \chi^{(3)}]$ , the field at  $\omega_A$  causes a cross-modulation with the field at  $\omega_p$ . This effect was recently predicted to lead to a giant Kerr nonlinearity if the field at  $\omega_C$  is of moderate strength. This is viable even when extremely low-power laser fields at  $\omega_p$  and  $\omega_B$  are applied. In a theoretical analysis,<sup>174</sup> values of  $[\text{Re } \chi^{(3)}] \approx 3 \times 10^{-6} \text{ m}^2 \text{ V}^{-2}$  are found. These are large enough to permit measurable cross-phase modulations between fields containing only a few photons.

In the experiments of Hau et al.<sup>11</sup> under the same conditions where ultraslow light pulse propagation was measured, a large nonlinearity was deduced. This was extrapolated from the measurement of the AC Stark shift of the transparency minimum due to the interaction between the field at  $\omega_C$  and state |4). This interaction is equivalent to the Kerr nonlinearity discussed in Ref. 174, when the field at  $\omega_C$  also plays the role of the additional field (previously  $\omega_B$ ). The connection between the large nonlinearity and the ultraslow light propagation has been studied by several authors.<sup>151,175</sup> In the case of the experiments discussed here, the connection is seen clearly to arise through the AC Stark shift of the steep dispersion curve responsible for ultralow group velocities. For even very modest fields at  $\omega_C$ , large changes in the absolute value of the dispersion are obtained, which result in significant phaseshifts. The latter are imparted on the probe field by itself. Similarly, in an experiment on ultraslow light, driven in a Doppler-free excitation scheme in rubidium,<sup>151</sup> very large nonlinearities are evidenced by the highly efficient four-wave mixing process that was observed. Therefore, the authors highlight the strong connection between ultraslow group velocities and ultralarge nonlinearity.

A number of investigations showed, that the huge nonlinearities available in the excitation schemes, discussed above, are large enough to mediate significant interaction between pairs of photons. There are important implications if a single photon can cause a measurable modification to another single photon (e.g., by a strong cross-phase modulation). For instance, applications are proposed for quantum nondemolition measurements and for quantum information processing. In the latter case strong mutual interactions can be utilized to generate entangled pairs of photons that form the basis of quantum logic gates. Discussions of this topic include an analysis of frequency mixing and nonlinear phase shifts at the few photon level,<sup>175</sup> techniques for generating squeezed light at very low input powers,<sup>176</sup> photon switching,<sup>177</sup> and photon blockade within an atom-cavity system.<sup>178</sup>

## 14.15 ELECTROMAGNETICALLY INDUCED TRANSPARENCY IN SOLIDS

While adiabatic processes (e.g., EIT) have been very extensively studied in the gas phase, only a few experiments were performed in solids.<sup>105–107,108–115</sup> In contrast to gaseous media, solids offer large density, scalability, compactness, and convenience in their preparation and usage. Moreover, atomic diffusion is absent in solids. All of these features are of significant interest for applications in optical data storage and quantum information processing. However, large homogeneous and inhomogeneous broadenings exhibit an obstacle for the implementation of EIT in solids (see Sec. 14.5). Thus, only very specific systems in the solid phase permit appropriate conditions for EIT.

Some larger classes of solids, which are appropriate candidates for the implementation of adiabatic processes, combine the advantages of gaseous media and solids. Such media are (e.g., quantum

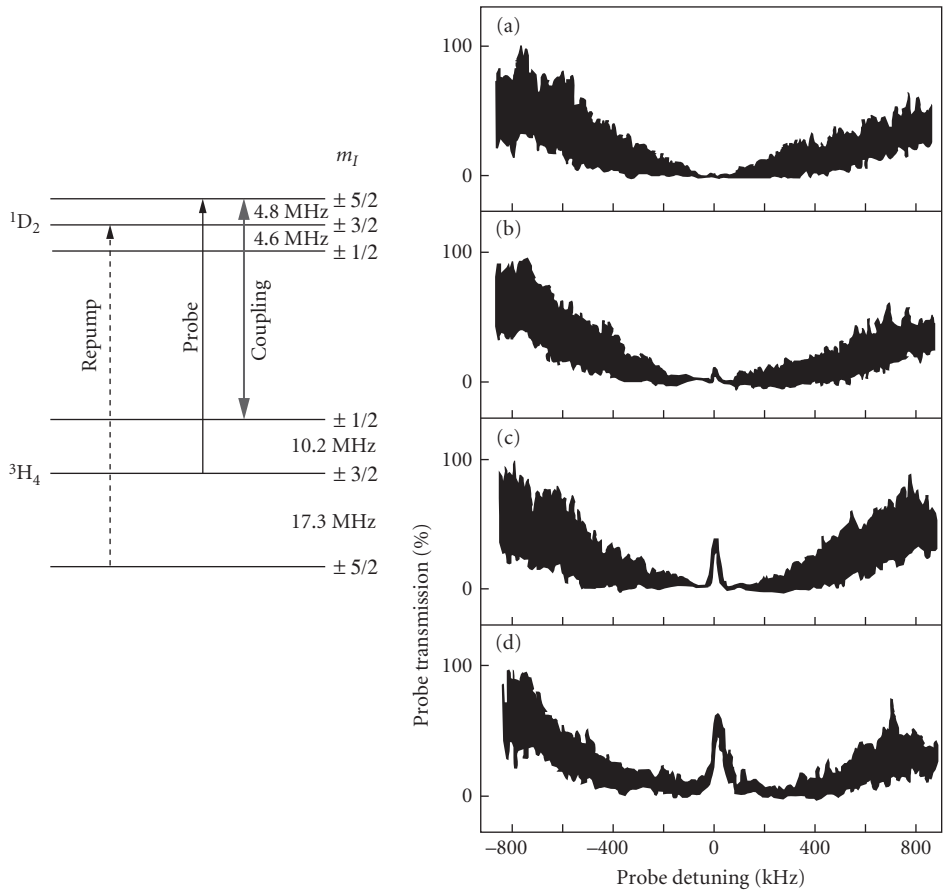


wells) electron-hole pairs (excitons), doped solids, and specific color centers. Quantum wells show a quite defined level structure, which is very similar to atoms in the gas phase. However, quantum wells are also subject to tremendous inhomogeneous broadening, because it is very hard to control the size, shape, and depths of a larger ensemble during the manufacturing process. Thus, usually only coherent excitation of a very small ensemble (or even single) quantum wells is possible—which is a significant drawback for applications, as one major advantage of a solid state medium (i.e., a large density) is lost. Electron-hole pairs have also been discussed in the scientific community as appropriate quantum systems for the implementation of adiabatic interactions. Like quantum dots, the electron-hole pairs also exhibit relatively well-defined level structure. As the dephasing times in quantum wells and electron-hole pairs are in the order of picoseconds or below, experimental implementations require ultrashort laser pulses. On the other hand, ultrashort laser pulses are usually not a good choice for driving adiabatic excitation of single-photon transitions (see Sec. 14.5). However, if the transition moments and the laser pulse energies are large enough, quantum wells and electron-hole pairs may serve as appropriate media for the implementation of EIT. Thus, coherent excitations in quantum wells or related nanostructures attracted significant attention in the recent years and already lead to first successful implementations of EIT in quantum wells.<sup>108–111</sup>

A class of solid media, which combines the properties of the gas phase and the solid phase in a very advantageous way, are doped solids. In such media, atoms or ions are doped in a host crystal. The dopants in the host crystal still exhibit the level structure of the free atom. At room temperature, interaction with the host lattice leads to large homogeneous broadening. Moreover, as the dopants experience spatially varying electric fields from the host lattice, the atomic transitions are subject to substantial inhomogeneous broadening. At cryogenic temperatures, the homogeneous linewidth can be reduced well below the width of the inhomogeneous broadening, that is, selective optical excitation at zero-phonon transitions becomes possible. The still remaining inhomogeneous broadening might be considered as an advantage, as it permits the selective excitation of different ensembles of dopants. This was already utilized two decades ago, when spectral hole burning<sup>179</sup> was discovered as an appropriate way to address specific ensembles in an inhomogeneously broadened medium (e.g., for applications in frequency-selective, multichannel storage of information). Thus, when the dopants in a cryogenically cooled host crystal are appropriately prepared by spectral hole burning or related techniques, a specific subset of the atoms exhibits a quantum system with very narrow spectral linewidth.

Some basic adiabatic interactions have been demonstrated in the recent years in rare-earth doped solids. Thus, EIT,<sup>105–107,112,113</sup> RAP,<sup>180,183</sup> and recently STIRAP<sup>182,183</sup> were successfully implemented in praseodymium ions  $\text{Pr}^{3+}$ , doped in a cryogenically cooled  $\text{Y}_2\text{SiO}_5$  host crystal.  $\text{Pr}^{3+}:\text{Y}_2\text{SiO}_5$  is a well-established and commercially available material for optical data storage (e.g., by spectral hole burning). The spin coherence, that is, the dephasing time in the medium is pretty large (i.e., exceeding the timescale of 100  $\mu\text{s}$ ).<sup>114,179</sup> This enables the implementation and observation of EIT with long interaction times, driven, for example, by modulated radiation, derived from cw lasers.

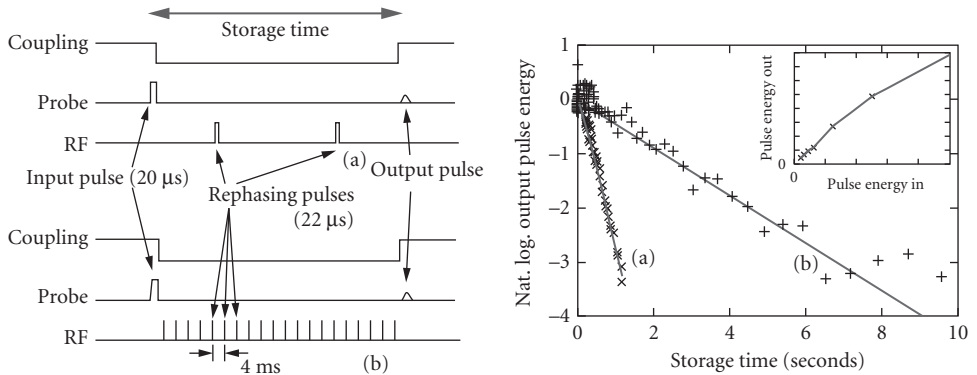
In the first successful implementation of EIT in a doped solid, Hemmer et al.<sup>105</sup> used a cw laser, operating at 606 nm, split in three beams, which are frequency modulated in acousto-optical modulators. Two of the three beams form the probe and the coupling laser. A third beam (i.e., the repump laser) is necessary to refill the spectral holes, burned by the probe and coupling laser. The  $\text{Pr}^{3+}:\text{Y}_2\text{SiO}_5$  crystal was cooled to a temperature of approximately 2 K to reduce the otherwise huge homogeneous broadening. Figure 15 shows the coupling scheme and the transmission of a probe laser in the medium. The praseodymium ions show a quite complicated level structure, as the ground state  $^3\text{H}_4$  and the excited state  $^1\text{D}_2$  interact with the electric field in the background of the host crystal and split in Stark components. The local variations in the electric field cause substantial inhomogeneous broadening in the crystal. However, by appropriate tuning and matching of the laser frequencies, a specific ensemble of ions is selected and driven in EIT. When the intensity of the coupling laser is large enough, the transmission of the probe laser is significantly enhanced in the center of the bare state resonance (see Fig. 15). Similar experiments on EIT in  $\text{Pr}^{3+}:\text{Y}_2\text{SiO}_5$  were also conducted by Ichimura et al.<sup>183</sup>



**FIGURE 15** EIT in  $\text{Pr}^{3+}:\text{Y}_2\text{SiO}_5$ . Coupling scheme and transmission of the probe laser versus detuning. The intensity of the coupling laser increases from graph (a) to (d). When the coupling laser is strong, the medium is driven to EIT and the probe laser, tuned to the bare state resonance, passes the medium with largely reduced losses. [The figure was published from Ref. 105. Copyright Elsevier (1997).]

In projects, dealing with the manipulation of optical processes by EIT, Hemmer et al. also reported efficient phase conjugation as well as ultraslow propagation of light pulses in  $\text{Pr}^{3+}:\text{Y}_2\text{SiO}_5$ .<sup>113</sup> The speed of light was reduced down to values of  $v_g = 45$  m/s. Moreover, in these experiments also stopping of a light pulse in the crystal was observed. Recently, Longdell et al. reported stopping of light with storage times larger than 1 second in  $\text{Pr}^{3+}:\text{Y}_2\text{SiO}_5$ , prepared by EIT (see Fig. 16).<sup>115</sup>

In addition to rare-earth doped solids, also special color centers are appropriate media for adiabatic interactions. Thus, Hemmer et al. also demonstrated EIT in nitrogen vacancy (N-V) color centers in diamond.<sup>184</sup> The transition moments in these color centers are much larger than in  $\text{Pr}^{3+}:\text{Y}_2\text{SiO}_5$ . Therefore lower laser intensities are required to drive the medium. N-V color centers are interesting candidates for applications in quantum computation.<sup>185</sup> Thus the experimental investigations in  $\text{Pr}^{3+}:\text{Y}_2\text{SiO}_5$  and N-V diamonds, as well as theoretical proposals for EIT and other adiabatic interactions in nanostructures (see, e.g. Refs. 186 to 188 and references therein), may pave the way toward the implementation of solid state quantum information processors.



**FIGURE 16** Demonstration of storage of light in  $\text{Pr}^{3+}:\text{Y}_2\text{SiO}_5$ , prepared by EIT. Pulse sequences and output pulse energy storage time, for two different techniques (a, b) to control decoherence by an additional radio frequency (RF) field. The coupling laser pulse prepares the medium in EIT for the probe laser pulse. When the coupling pulse is switched off, the probe pulse is stored in the medium and recovered, when the coupling pulse is switched on again. The storage time exceeds several seconds. [Reprinted figure with permission from Ref. 115. Copyright by the American Physical Society (2005).]

## 14.16 CONCLUSION

In this chapter, we reviewed the basic concepts, implementations, and applications of EIT. We discussed the principles of EIT in terms of quantum interferences, atomic coherences, and dressed atomic states in a system of three quantum states, coherently driven by two radiation fields, that is, the probe laser field and the coupling laser field. The concept of EIT is closely related to other coherent, adiabatic interactions, for example, RAP, SCRAP, STIRAP, CPT, and CPR. However, while the latter techniques are focused to a large extent on the manipulation of population distributions, the ideas of EIT are mainly connected with atomic coherences and the manipulation of optical properties.

From some very basic considerations, we derived the main features of EIT, that is, vanishing absorption and dispersion at atomic resonances (due to destructive quantum interference), a steep slope of the dispersion at the atomic resonance, and enhanced nonlinear optical response of the medium (by constructive quantum interference). Thus the optical properties of quantum systems, manipulated by EIT, are very different from the properties of common optical media. These features lead to a rich variety of applications in the field of optical physics, for example, transmission through otherwise optically dense media, gain in quantum systems without population inversion, propagation of light with ultraslow velocity, storage of light pulses, and the significant enhancement of nonlinear optical processes. In the latter field, EIT permits frequency conversion in gaseous media with extraordinary large efficiencies.

We reviewed convincing experiments and striking applications of EIT. The majority of these experiments were implemented in atoms or molecules in the gas phase, but some also in selected solids. The investigations, as conducted so far, already lead to tremendous impact in the fields of optical information processing and quantum computation, applied optics, laser physics and physics on ultrashort timescales. However, we believe, there is a huge potential of EIT and related concepts, which is still to be explored in the future.

## 14.17 FURTHER READING

- Arimondo, E., "Coherent Population Trapping in Laser Spectroscopy," *Progr. Opt.* **35**:259 (1996).  
 Fleischhauer, M., Imamoglu, A., and Marangos, J. P., "Electromagnetically Induced Transparency: Optics in Coherent Media," *Rev. Mod. Phys.* **77**:633 (2005).

- Harris, S. E., "Electromagnetically Induced Transparency," *Phys. Today* **50**:36 (1997).
- Kocharovskaya, O., "Amplification and Lasing without Inversion," *Phys. Rep.* **219**:175 (1992).
- Marangos, J. P., "Electromagnetically Induced Transparency," *J. Mod. Opt.* **45**:471 (1998).
- Sargent III, M., Scully, M. O., and Lamb, W. E., Jr., *Laser Physics*, Addison-Wesley, Reading (1974).
- Scully, M. O., "From Lasers and Masers to Phaseonium and Phasers," *Phys. Rep.* **219**:191 (1992).
- Scully, M. O., and Zubairy, M. S., *Quantum Optics*, Cambridge University Press, Cambridge (1997).
- Shore, B. W., "The Theory of Coherent Atomic Excitation," John Wiley & Sons, New York (1990).
- Shore, B. W., "Counter Intuitive Physics," *Contemp. Phys.* **36**:15 (1995).
- Vitanov, N. V., Halfmann, T., Shore, B. W., and Bergmann, K., "Laser-Induced Population Transfer by Adiabatic Passage Techniques," *Annu. Rev. Phys. Chem.* **52**:763 (2001).

## 14.18 REFERENCES

1. U. Fano, "Effects of Configuration Interaction on Intensities and Phase-Shifts," *Phys. Rev.* **124**:1866 (1961).
2. R. B. Madden and K. Codling, "Two-Electron Excitation States in Helium," *Astrophys. J.* **141**:364 (1965).
3. K. Maschke, P. Thomas, and E. O. Gobel, "Fano Interference in Type-II Semiconductor Quantum-Well Structures," *Phys. Rev. Lett.* **67**:2646 (1991).
4. S. E. Harris, "Electromagnetically Induced Transparency," *Phys. Today* **50**:36 (1997).
5. M. Fleischhauer, A. Imamoglu, and J. P. Marangos, "Electromagnetically Induced Transparency: Optics in Coherent Media," *Rev. Mod. Phys.* **77**:633 (2005).
6. S. E. Harris, J. E. Field, and A. Imamoglu, "Non-Linear Optical Processes Using Electromagnetically Induced Transparency," *Phys. Rev. Lett.* **64**:1107 (1990).
7. M. O. Scully, "From Lasers and Masers to Phaseonium and Phasers," *Phys. Rep.* **219**:191 (1992).
8. M. O. Scully, "Enhancement of the Index of Refraction via Quantum Coherence," *Phys. Rev. Lett.* **67**:1855 (1991).
9. E. Arimondo and G. Orriols, "Nonabsorbing Atomic Coherences by Coherent Two-Photon Transitions in a Three-Level Optical Pumping," *Lett. Nuovo Cimento* **17**:333 (1976).
10. B. W. Shore, "*The Theory of Coherent Atomic Excitation*," John Wiley & Sons, New York (1990).
11. L. V. Hau, S. E. Harris, Z. Dunon, and C. H. Behroozi, "Light Speed Reduction to 17 Metres per Second in an Ultracold Atomic Gas," *Nature* **397**:594 (1999).
12. O. Kocharovskaya and Ya. I. Khanin, "Coherent Amplification of an Ultrashort Pulse in a Three Level Medium without Population Inversion," *JETP Lett.* **48**:630 (1988).
13. A. Imamoglu and S. E. Harris, "Lasers without Inversion: Interference of Dressed Lifetime Broadened States," *Opt. Lett.* **14**:1344 (1989).
14. E. E. Fill, M. O. Scully, and S.-Y. Zhu, "Lasing without Inversion via the Lambda Quantum-Beat Laser in the Collision Dominated Regime," *Opt. Comm.* **77**:36 (1990).
15. A. S. Zibrov, M. D. Lukin, D. E. Nikonov, L. Hollberg, M. O. Scully, V. L. Velichansky, and H. G. Robinson, "Experimental Observation of Laser Oscillation without Population Inversion via Quantum Interference in Rb," *Phys. Rev. Lett.* **75**:1499 (1995).
16. O. Kocharovskaya, "Amplification and Lasing without Inversion," *Phys. Rep.* **219**:175 (1992).
17. P. Mandel, "Lasing without Inversion: A Useful Concept?," *Contemp. Phys.* **34**:235 (1993).
18. D. S. Lee and K. J. Malloy, "Analysis of Reduced Interband Absorption Mechanisms in Semiconductor Quantum Wells," *IEEE J. Quant. Electr.* **30**:85 (1994).
19. A. Imamoglu and R. J. Ram, "Semiconductor Lasers without Population Inversion," *Opt. Lett.* **19**:1744 (1994).
20. A. J. Merriam, S. J. Sharpe, H. Xia, D. Manuszak, G. Y. Yin, and S. E. Harris, "Efficient Gas-Phase Generation of Coherent Vacuum Ultra-Violet Radiation," *Opt. Lett.* **24**:625 (1999).
21. S. E. Harris and M. Jain, "Optical Parametric Oscillators Pumped by Population-Trapped Atoms," *Opt. Lett.* **22**:636 (1997).

22. S. E. Harris, G. Y. Yin, M. Jain, H. Xia, and A. J. Merriam, "Nonlinear Optics at Maximum Coherence," *Phil. Trans. Roy. Soc. London* (Ser A. Mathematical, Physical and Engineering Sciences) **355**:2291 (1997).
23. S. E. Harris and A. V. Sokolov, "Broadband Spectral Generation with Refractive Index Control," *Phys. Rev. A* **55**:R4019 (1997).
24. S. E. Harris and A. V. Sokolov, "Raman Generation by Phased and Antiphased Molecular States," *Phys. Rev. Lett.* **85**:562 (2000).
25. F. E. Kien, J. Q. Liang, M. Katsuragawa, K. Ohtsuki, K. Hakuta, and A. V. Sokolov, "Sub-Femtosecond Pulse Generation with Molecular Coherence Control in Stimulated Raman Scattering," *Phys. Rev. A* **60**:1562 (1999).
26. D. D. Yavuz, A. V. Sokolov, and S. E. Harris, "Eigenvectors of a Raman Medium," *Phys. Rev. Lett.* **84**:000075 (2000).
27. S. E. Harris and A. V. Sokolov, "Subfemtosecond Pulse Generation by Molecular Modulation," *Phys. Rev. Lett.* **81**:002894 (1998).
28. A. V. Sokolov, D. R. Walker, D. D. Yavuz, G. Y. Yin, and S. E. Harris, "Femtosecond Light Source for Phase-Controlled Multiphoton Ionization," *Phys. Rev. Lett.* **87**:033402 (2001).
29. S. Gundry, M. P. Anscombe, A. M. Abdulla, S. D. Hogan, E. Sali, J. W. G. Tisch, and J. P. Marangos, "Off-Resonant Preparation of a Vibrational Coherence for Enhanced Stimulated Raman Scattering," *Phys. Rev. A* **72**:033824 (2005).
30. S. Gundry, M. P. Anscombe, A. M. Abdulla, E. Sali, J. W. G. Tisch, P. Kinsler, G. H. C. New, and J. P. Marangos, "Ultrashort-Pulse Modulation in Adiabatically Prepared Raman Media," *Opt. Lett.* **30**:180 (2005).
31. Fam Le Kien, Nguyen Hong Shon, and K. Hakuta, "Generation of Subfemtosecond Pulses by Beating a Femtosecond Pulse with a Raman Coherence Adiabatically Prepared in Solid Hydrogen," *Phys. Rev. A* **64**:051803(R) (2001).
32. Fam Le Kien, J. Q. Liang, M. Katsuragawa, K. Ohtsuki, and K. Hakuta, "Subfemtosecond Pulse Generation with Molecular Coherence Control in Stimulated Raman Scattering," *Phys. Rev. A* **60**:1562 (1999).
33. M. Y. Shverdin, D. R. Walker, D. D. Yavuz, G. Y. Yin, and S. E. Harris, "Generation of a Single-Cycle Optical Pulse," *Phys. Rev. Lett.* **94**:033904 (2005).
34. J. Q. Liang, M. Katsuragawa, Fam Le Kien, and K. Hakuta, "Sideband Generation Using Strongly Driven Raman Coherence in Solid Hydrogen," *Phys. Rev. Lett.* **85**:2474 (2000).
35. Fam Le Kein, K. Hakuta, and A. V. Sokolov, "Pulse Compression by Parametric Beating with a Prepared Raman Coherence," *Phys. Rev. A* **66**:023813 (2002).
36. B. R. Washburn, S. R. Ralph, R. S. Windeler, "Ultrashort Pulse Propagation in Air-Silica Microstructure Fiber," *Opt. Expr.* **10**:575 (2002).
37. M. Wittmann, A. Nazarkin, and G. Korn, "Fs-Pulse Synthesis Using Phase Modulation by Impulsively Excited Molecular Vibrations," *Phys. Rev. Lett.* **84**:5508 (2000).
38. M. Wittmann, A. Nazarkin, and G. Korn, "Synthesis of Periodic Femtosecond Pulse Trains in the Ultraviolet by Phase-Locked Raman Sideband Generation," *Opt. Lett.* **26**:298 (2001).
39. N. Zhavoronkov and G. Korn, "Generation of Single Intense Short Optical Pulses by Ultrafast Molecular Phase Modulation," *Phys. Rev. Lett.* **88**:203901 (2002).
40. B. J. Dalton and P. L. Knight, *Laser Physics, Lecture Notes in Physics*, Vol. 182, I. D. Harvey and D. F. Walls (eds.), Springer-Verlag, Berlin (1983).
41. H. I. Yoo and J. H. Eberly, "Dynamical Theory of an Atom with Two or Three Levels Interacting with Quantized Cavity Fields," *Phys. Rep.* **118**:239 (1985).
42. J. H. Eberly, "Transmission of Dressed Fields in Three-Level Media," *Quant. Semiclass. Opt.* **7**:373 (1995).
43. E. Arimondo, "Coherent Population Trapping in Laser Spectroscopy," *Progr. Opt.* **35**:259 (1996).
44. N. V. Vitanov, T. Halfmann, B. W. Shore, and K. Bergmann, "Laser-Induced Population Transfer by Adiabatic Passage Techniques," *Annu. Rev. Phys. Chem.* **52**:763 (2001).
45. T. Halfmann, "Enhanced Frequency Conversion in Coherently Prepared Media," in *Recent Research Activities in Chemical Physics: From Atomic Scale to Macroscale*, edited by A. F. Terzis and E. Paspalakis, Research Signpost, India (2007).
46. P. L. Knight, "Laser Induced Continuum Structure," *Comm. Ac. Mol. Phys.* **15**:193 (1984).
47. P. L. Knight, M. A. Lauder, and B. J. Dalton, "Laser Induced Continuum Structure," *Phys. Rep.* **190**:1 (1990).

48. K. Böhmer, T. Halfmann, L. P. Yatsenko, D. Charalambidis, A. Horsmans, and K. Bergmann, "Laser-Induced Continuum Structure in the Two Ionization Continua of Xenon," *Phys. Rev. A* **66**:013406 (2002).
49. T. Halfmann, L. P. Yatsenko, M. Shapiro, B. W. Shore, and K. Bergmann, "Population Trapping and Laser-Induced Continuum Structure in Helium: Experiment and Theory," *Phys. Rev. A* **58**:R46 (1998).
50. L. P. Yatsenko, T. Halfmann, B. W. Shore, and K. Bergmann, "Photoionization Suppression by Continuum Coherence: Experiment and Theory," *Phys. Rev.* **59**:2926 (1999).
51. S. H. Autler and C. H. Townes, "Stark Effect in Rapidly Varying Fields," *Phys. Rev.* **100**:703 (1955).
52. I. D. Abella, N. A. Kunitz, and S. R. Hanmann, "Photon Echoes," *Phys. Rev.* **141**:391 (1966).
53. B. R. Mollow, "Power Spectrum of Light Scattered by 2-Level Systems," *Phys. Rev.* **188**:1969 (1969).
54. B. R. Mollow, "Stimulated Emission and Absorption near Resonance for Driven Systems," *Phys. Rev. A* **5**:2217 (1972).
55. P. L. Knight and P. W. Miloni, "The Rabi Frequency in Optical Spectra," *Phys. Rep.* **66**:21 (1980).
56. L. Alien and J. H. Eberly, *Optical Resonance and 2-Level Atoms*, Dover, New York (1987).
57. G. Alzetta, L. Moi, and G. Orriols, "Nonabsorption Hyperfine Resonances in a Sodium Vapour Irradiated with a Multimode Dye Laser," *Nuovo Cimento B* **52**:209 (1979).
58. H. R. Gray, R. M. Whitley, and C. R. Stroud, "Coherent Trapping of Atomic Populations," *Opt. Lett.* **3**:218 (1978).
59. J. Oreg, F. T. Hioe, and J. H. Eberly, "Adiabatic Following in Multilevel Systems," *Phys. Rev. A* **29**:690 (1984).
60. U. Gaubatz, P. Rudecki, S. Schiemann, and K. Bergmann, "Population Transfer between Molecular Vibrational Levels by Stimulated Raman-Scattering with Partially Overlapping Laser Fields: A New Concept and Experimental Results," *J. Chem. Phys.* **92**:5363 (1990).
61. N. Dam, L. Oudejans, and J. Reuss, "Relaxation Rates of Ethylene Obtained from Their Effect on Coherent Transients," *Chem. Phys.* **140**:217 (1990).
62. A. Aspect, E. Arimondo, R. Kaiser, N. Vansteenkiste, and C. Cohen-Tannoudji, "Laser Cooling below the One-Photon Recoil Energy by Velocity-Selective Coherent Population Trapping," *Phys. Rev. Lett.* **61**:826 (1988).
63. F. Bardou, B. Saubamea, J. Lawall, K. Shimizu, O. Emile, C. Westbrook, A. Aspect, and C. Cohen-Tannoudji, "Sub-Recoil Laser Cooling with Pre-Cooled Atoms," *Comptes Rendus de Acad. Sci. Paris, Ser. II*, **318**:877 (1994).
64. M. R. Doery, M. T. Widmer, M. J. Bellanca, W. F. Buell, T. H. Bergemann, H. Metcalf, and E. J. D. Vrenbregt, "Population Accumulation in Dark States and Sub-Recoil Laser Cooling," *Phys. Rev. A* **52**:2295 (1995).
65. R. M. Whitley and C. R. Stroud, Jr, "Double Optical Resonance," *Phys. Rev. A* **14**:1498 (1976).
66. P. M. Radmore and P. L. Knight, "Population Trapping and Dispersion in a Three-Level System," *J. Phys. B* **15**:561 (1982).
67. B. W. Shore, "Counter Intuitive Physics," *Contemp. Phys.* **36**:15 (1995).
68. M. O. Scully and M. Suhail Zubairy, *Quantum Optics*, Cambridge University Press, Cambridge (1997).
69. B. Lounis and C. Cohen-Tannoudji, "Coherent Population Trapping and Fano Profiles," *J. Phys.* **11**(2):579 (1992).
70. S. E. Harris and J. J. Macklin, "Lasers without Inversion: Single-Atom Transient Response," *Phys. Rev. A* **40**:4135 (1989).
71. J. L. Cohen and P. R. Berman, "Amplification without Inversion: Understanding Probability Amplitudes, Quantum Interferences and Feynman Rules in a Strongly Driven System," *Phys. Rev. A* **55**:3900 (1997).
72. D. ter Haar, "Theory and Application of the Density Matrix," *Rep. Prog. Phys.* **24**:304 (1961).
73. M. Sargent III, M. O. Scully, and W. E. Lamb, Jr., *Laser Physics*, Addison-Wesley, Reading (1974).
74. C. Cohen-Tannoudji, B. Zambon, and E. Arimondo, "Quantum-Jump Approach to Dissipative Processes: Application to Amplification without Inversion," *J. Opt. Soc. Am. B* **10**:2107 (1993).
75. Y.-Q. Li and M. Xiao, "Transient Properties of an Electromagnetically Induced Transparency in Three-Level Atoms," *Opt. Lett.* **20**:1489 (1995).
76. S. E. Harris, "Electromagnetically Induced Transparency with Matched Pulses," *Phys. Rev. Lett.* **72**:552 (1993).
77. S. E. Harris, "Normal-Modes for Electromagnetically Induced Transparency," *Phys. Rev. Lett.* **72**:52 (1994).
78. J. H. Eberly, M. L. Pons, and H. R. Haq, "Dressed-Field Pulses in an Absorbing Medium," *Phys. Rev. Lett.* **72**:56 (1994).

79. S. E. Harris and Z.-F. Luo, "Preparation Energy for Electromagnetically Induced Transparency," *Phys. Rev. A* **52**:928 (1995).
80. J. E. Field, "Vacuum-Rabi-Splitting-Induced Transparency," *Phys. Rev. A* **47**:5064 (1993).
81. J. E. Field and A. Imamoglu, "Spontaneous Emission into an Electromagnetically Induced Transparency," *Phys. Rev. A* **48**:2486 (1993).
82. S. E. Harris, J. E. Field, and A. Kasapi, "Dispersive Properties of Electromagnetically Induced Transparency," *Phys. Rev. A* **46**:R29 (1992).
83. G. G. Padmabandu, G. R. Welch, I. N. Shubin, E. S. Fry, D. E. Nikonov, M. D. Lukin, and M. O. Scully, "Laser Oscillation without Population Inversion in a Sodium Atomic Beam," *Phys. Rev. Lett.* **76**:2053 (1996).
84. M. O. Scully, S.-Y. Zhu, and A. Gavrielides, "Degenerate Quantum-Beat Laser: Lasing without Inversion and Inversion without Lasing," *Phys. Rev. Lett.* **62**:2813 (1989).
85. V. G. Arkhipkin and Yu. I. Heller, "Radiation Amplification without Population Inversion at Transitions to Autoionising States," *Phys. Lett. A* **98**:12 (1983).
86. S. E. Harris, "Lasers without Inversion: Interference of a Lifetime Broadened Resonance," *Phys. Rev. Lett.* **62**:1033 (1989).
87. M. O. Scully and S.-Y. Zhu, "Ultra-Large Index of Refraction via Quantum Interference," *Opt. Comm.* **87**, 134 (1992).
88. M. Fleischhauer, C. H. Keitel, M. O. Scully, and C. Su, "Lasing without Inversion and Enhancement of the Index of Refraction via Interference of Incoherent Pump Processes," *Opt. Comm.* **87**:109 (1992).
89. A. D. Wilson-Gordon and H. Friedman, "Enhanced Index of Refraction: A Comparison between Two- and Three-Level Systems," *Opt. Comm.* **94**:238 (1992).
90. M. Fleischhauer, C. H. Keitel, M. O. Scully, C. Su, B. T. Ulrich, and S.-Y. Zhu, "Resonantly Enhanced Refractive Index without Absorption via Atomic Coherence," *Phys. Rev. A* **46**:1468 (1992).
91. U. Rathe, M. Fleischhauer, S.-Y. Zhu, T. W. Hänsch, and M. O. Scully, "Non-Linear Theory of Index Enhancement via Quantum Coherence and Interference," *Phys. Rev. A* **47**:4994 (1993).
92. A. S. Manka, J. P. Dowling, C. M. Bowden, and M. Fleischhauer, "Piezophotonic Switching due to Local-Field Effects in a Coherently Prepared Medium of 3-Level Atoms," *Phys. Rev. Lett.* **73**:1789 (1994).
93. S. E. Harris, "Refractive-Index Control with Strong Fields," *Opt. Lett.* **19**:2018 (1994).
94. D. J. Fulton, R. R. Moseley, S. Shepherd, B. D. Sinclair, and M. H. Dunn, "Effects of Zeeman Splitting on Electromagnetically Induced Transparency," *Opt. Comm.* **116**:231 (1995).
95. G. Z. Zhang, M. Kasuragawa, K. Hakuta, R. I. Thompson, and B. P. Stoicheff, "Sum-Frequency Generation Using Strong-Field Coupling and Induced Transparency in Atomic Hydrogen," *Phys. Rev. A* **52**:1584 (1995).
96. R. R. Moseley, B. D. Sinclair, and M. H. Dunn, "Local Field Effects in the Three-Level Atom," *Opt. Comm.* **108**:247 (1994).
97. J. P. Dowling and C. M. Bowden, "Near Dipole-Dipole Effects in Lasing without Inversion: An Enhancement of Gain and Absorptionless Index of Refraction," *Phys. Rev. Lett.* **70**:1421 (1993).
98. G. S. Agarwal, "Exact Solution for the Influence of Laser Temporal Fluctuations on Resonance Fluorescence," *Phys. Rev. Lett.* **37**:1383 (1976).
99. S. Swain, "Theory of Atomic Processes in Strong Resonant Electromagnetic Fields," *Adv. At. Mol. Phys.* **16**:159 (1980).
100. B. J. Dalton and P. L. Knight, "The Effect of Laser Field Fluctuations on Coherent Population Trapping," *J. Phys. B* **15**:3997 (1982).
101. P. A. Lakshmi and S. Swain, "Effects of Laser Linewidths on Nonlinear Optical Processes Exploiting Electromagnetically Induced Transparency," *J. Mod. Opt.* **38**:2031 (1991).
102. J. C. Petch, C. H. Keitel, P. L. Knight, and J. P. Marangos, "Role of Electromagnetically Induced Transparency in Resonant Four-Wave Mixing Schemes," *Phys. Rev. A* **53**:543 (1996).
103. Y. Zhao, C. Wu, B. S. Ham, M. K. Kirn, and E. Awad, "Microwave Induced Transparency in Ruby," *Phys. Rev. Lett.* **79**:64 (1997).
104. G. B. Serapiglia, E. Paspalakis, C. Sirtori, K. L. Vodopyanov, and C. C. Phillips, "Laser-Induced Quantum Coherence in a Semiconductor Quantum Well," *Phys. Rev. Lett.* **84**:1019 (2000).
105. B. S. Ham, P. R. Hemmer, and M. S. Shahar, "Efficient Electromagnetically Induced Transparency in Rare-Earth Doped Crystals," *Opt. Comm.* **144**:227 (1997).

106. B. S. Ham, S. M. Shahriar, and P. R. Hemmer, "Electromagnetically Induced Transparency over Spectral Hole-Burning Temperature in a Rare-Earth-Doped Solid," *J. Opt. Soc. Am. B* **16**:801 (1999).
107. P. R. Hemmer, D. P. Katz, J. Donoghue, M. Cronin-GoIomb, M. S. Shahriar, and P. Kumar, "Efficient Low-Intensity Optical Phase Conjugation Based on Coherent Population Trapping in Sodium," *Opt. Lett.* **20**:982 (1995).
108. M. Philipps and H. Wang, "Spin Coherence and Electromagnetically Induced Transparency via Exciton Correlations," *Phys. Rev. Lett.* **84**:186401 (2002).
109. M. Philipps and H. Wang, "Electromagnetically Induced Transparency due to Intervalence Band Coherence in a GaAs Quantum Well," *Opt. Lett.* **28**:831 (2002).
110. M. C. Phillips, H. Wang, I. Romyantsev, N. H. Kwong, R. Takayama, and R. Binder, "Electromagnetically Induced Transparency in Semiconductors via Biexciton Coherence," *Phys. Rev. Lett.* **91**:183602 (2003).
111. W. W. Chow, H. C. Schneider, and M. C. Phillips, "Theory of Quantum-Coherence Phenomena in Semiconductor Quantum Dots," *Phys. Rev. A* **68**:053802 (2003).
112. K. Ichimura, K. Yamamoto, and N. Gemma, "Evidence for Electromagnetically Induced Transparency in a Solid Medium," *Phys. Rev. A* **58**:4116 (1998).
113. A. V. Turukhin, V. S. Sudarshanam, M. S. Shahriar, J. A. Musser, B. S. Ham, and P. R. Hemmer, "Observation of Ultraslow and Stored Light Pulses in a Solid," *Phys. Rev. Lett.* **88**:023602 (2002).
114. E. Kuznetsova, O. Kocharovskaya, P. Hemmer, and M. O. Scully, "Atomic Interference Phenomena in Solids with a Long-Lived Spin Coherence," *Phys. Rev. A* **66**:063802 (2002).
115. J. J. Longdell, E. Fraval, M. J. Sellars, and N. B. Manson, "Stopped Light with Storage Times Greater than One Second Using Electromagnetically Induced Transparency in a Solid," *Phys. Rev. Lett.* **95**:063601 (2005).
116. J. Y. Gea-Banacloche, Y.-Q. Li, S.-Z. Jin, and M. Xiao, "Electromagnetically Induced Transparency in Ladder-Type Inhomogeneously Broadened Media: Theory and Experiment," *Phys. Rev. A* **51**:576 (1995).
117. S. Shepherd, D. J. Fulton, and M. H. Dunn, "Wavelength Dependence of Coherently Induced Transparency in a Doppler-Broadened Cascade Medium," *Phys. Rev. A* **54**:5394 (1996).
118. M. Xiao, Y.-Q. Li, and J. Gea-Banacloche, "Measurements of Dispersive Properties of Electromagnetically Induced Transparency in Rubidium Atoms," *Phys. Rev. Lett.* **74**:666 (1995).
119. R. R. Moseley, S. Shepherd, D. J. Fulton, B. D. Sinclair, and M. H. Dunn, "Spatial Consequences of Electromagnetically Induced Transparency: Observation of Electromagnetically Induced Focusing," *Phys. Rev. Lett.* **74**:670 (1995).
120. M. Misunga, T. Mukai, K. Watanabe, and T. Mukai, "Dressed-Atom Spectroscopy of Cold Cs Atoms," *J. Opt. Soc. B* **13**:2696 (1996).
121. S. A. Hopkins, E. Usadi, H. X. Chen, and A. V. Durrant, "Electromagnetically Induced Transparency of Laser-Cooled Rubidium Atoms in Three-Level  $\Lambda$  Type Systems," *Opt. Comm.* **134**:185 (1997).
122. K. Hakuta, M. Suzuki, M. Katsuragawa, and J. Z. Li, "Self-Induced Phase Matching in Parametric Anti-Stokes Stimulated Raman Scattering," *Phys. Rev. Lett.* **79**:209 (1997).
123. K. J. Boller, A. Imamoglu, and S. E. Harris, "Observation of Electromagnetically Induced Transparency," *Phys. Rev. Lett.* **66**:2593 (1991).
124. J. E. Field, K. H. Hahn, and S. E. Harris, "Observation of Electromagnetically Induced Transparency in Collisionally Broadened Lead Vapor," *Phys. Rev. Lett.* **67**:3062 (1991).
125. A. Kasapi, "Enhanced Isotope Discrimination Using Electromagnetically Induced Transparency," *Phys. Rev. Lett.* **77**:1035 (1996).
126. Hui Xia, A. J. Merriam, S. J. Sharpe, G. Y. Yin, and S. E. Harris, "Electromagnetically Induced Transparency with Spectator Momenta," *Phys. Rev. A* **59**:R3190 (1999).
127. Hui Xia, S. J. Sharpe, A. J. Merriam, and S. E. Harris, "Electromagnetically Induced Transparency in Atoms with Hyperfine Structure," *Phys. Rev. A* **56**:R3362 (1998).
128. Y.-Q. Li and M. Xiao, "Electromagnetically Induced Transparency in a Three-Level System in Rubidium Atoms," *Phys. Rev. A* **51**:R2703 (1995).
129. Y.-Q. Li and M. Xiao, "Observation of Quantum Interference between the Dressed States in an Electromagnetically Induced Transparency," *Phys. Rev. A* **51**:4959 (1995).
130. R. R. Moseley, S. Shepherd, D. J. Fulton, B. D. Sinclair, and M. H. Dunn, "Electromagnetically Induced Focusing," *Phys. Rev. A* **53**:408 (1996).



131. S. Wielandy and Alexander L. Gaeta, "Investigation of Electromagnetically Induced Transparency in the Strong Probe Regime," *Phys. Rev. A* **58**:2500 (1998).
132. W. Ketterle, K. B. Davis, M. A. Joffe, A. Martin, and D. E. Pritchard, "High Densities of Cold Atoms in a Dark Spontaneous-Force Optical Trap," *Phys. Rev. Lett.* **77**:2253 (1993).
133. T. van der Veldt, J.-F. Roch, P. Grelu, and P. Grangier, "Nonlinear Absorption and Dispersion of Cold Rb-87 Atoms," *Opt. Comm.* **137**:420 (1997).
134. H. X. Chen, A. V. Durran, J. P. Marangos, and J. A. Vaccaro, "Observation of Transient Electromagnetically Induced Transparency in a Rubidium Lambda System," *Phys. Rev. A* **58**:1545 (1998).
135. S. Scandolo and F. Bassani, "Non-Linear Sum Rules: The Three-Level and Anharmonic-Oscillator Modes," *Phys. Rev. B* **45**:13257 (1992).
136. F. S. Cataliotti, C. Fort, T. W. Hansch, M. Inguscio, and M. Prevedelli, "Electromagnetically Induced Transparency in Cold Free Atoms: Test of a Sum Rule for Non-Linear Optics," *Phys. Rev. A* **56**:2221 (1997).
137. J. Gao, C. Guo, X. Guo, G. Jin, P. Wang, J. Zhao, H. Zhang, Y. Jiang, D. Wang, and D. Jiang, "Observation of Light Amplification without Population Inversion," *Opt. Comm.* **93**:323 (1992).
138. J. Gao, H. Z. Zhang, H. F. Cui, X. Z. Guo, Y. Jiang, Q. W. Wang, G. X. Jin, and J. S. Li, "Inversionless Amplification in Sodium," *Opt. Comm.* **110**:590 (1994).
139. J. A. Kleinfeld and A. D. Streater, "Observation of Gain due to Coherence Effects in Potassium-Helium Mixture," *Phys. Rev. A* **49**:R4301 (1994).
140. E. S. Fry, X. Li, D. Nikonov, G. G. Padmabandu, M. O. Scully, A. V. Smith, F. K. Tittel, C. Wang, S. R. Wilkinson, and S.-Y. Zhu, "Atomic Coherence Effects within the Sodium D1 Line: Lasing without Inversion via Population Trapping," *Phys. Rev. Lett.* **70**:3235 (1993).
141. A. Nottelman, C. Peters, and W. Lange, "Inversionless Amplification of Picosecond Pulses due to Zeeman Coherence," *Phys. Rev. Lett.* **70**:1783 (1993).
142. W. E. van der Veer, R. J. J. van Dienst, A. Donselmann, and H. B. van Linden van den Huevcll, "Experimental Demonstration of Light Amplification without Population Inversion," *Phys. Rev. Lett.* **70**:3243 (1993).
143. C. Peters and W. Lang, "Laser Action Below Threshold Inversion due to Coherent Population Trapping," *Appl. Phys. B* **62**:221 (1996).
144. A. S. Zibrov, M. D. Lukin, L. Hollberg, D. E. Nikonov, M. O. Scully, H. G. Robinson, and V. L. Velichansky, "Experimental Demonstration of Enhanced Index of Refraction via Quantum Coherence in Rb," *Phys. Rev. Lett.* **76**:3935 (1996).
145. M. Fleischhauer and M. O. Scully, "Quantum Sensitivity Limits of an Optical Magnetometer Based on Phase Coherence," *Phys. Rev. A* **49**:1973 (1994).
146. A. Kasapi, M. Jain, G. Y. Yin, and S. E. Harris, "Electromagnetically Induced Transparency: Propagation Dynamics," *Phys. Rev. Lett.* **74**:2447 (1995).
147. A. Kasapi, G. Y. Yin, M. Jain, and S. E. Harris, "Measurement of Lorentzian Linewidth by Pulse-Propagation Delay," *Phys. Rev. A* **53**:4547 (1996).
148. M. Jain, A. J. Merriam, A. Kasapi, G. Y. Yin, and S. E. Harris, "Elimination of Optical Self-Focusing by Population Trapping," *Phys. Rev. Lett.* **75**:4385 (1995).
149. M. Jain, H. Xia, G. Y. Yin, A. J. Merriam, and S. E. Harris, "Efficient Non-Linear Frequency Conversion with Maximal Atomic Coherence," *Phys. Rev. Lett.* **77**:4326 (1996).
150. O. Schmidt, R. Wynands, Z. Hussein, and D. Meschede, "Steep Dispersion and Group Velocity Dispersion below  $c/3000$  in Coherent Population Trapping," *Phys. Rev. A* **53**:R27 (1996).
151. M. M. Kash, V. A. Sautenkov, A. S. Zibrov, L. Hollberg, G. R. Welch, M. D. Lukin, Y. Roslovtssev, E. S. Fry, and M. O. Scully, "Ultraslow Group Velocity and Enhanced Non-Linear Optical Effects in a Coherently Driven Hot Atomic Gas," *Phys. Rev. Lett.* **82**:5229 (1999).
152. D. Budker, D. F. Kimball, S. M. Rochester, and V. V. Yaschuk, "Nonlinear Magneto-Optics and Reduced Velocity of Light in Atomic Vapour with Slow Ground State Relaxation," *Phys. Rev. Lett.* **83**:1767 (1999).
153. J. P. Marangos, "Slow Light in Cool Atoms," *Nature* **397**:559 (1999).
154. S. P. Tewari and G. S. Agarwal, "Control of Phase-Matching and Nonlinear Generation in Dense Media by Resonant Fields," *Phys. Rev. Lett.* **56**:1811 (1986).
155. G. S. Agarwal and S. P. Tewari, "Large Enhancements in Non-Linear Generation by External Electromagnetic Fields," *Phys. Rev. Lett.* **70**:1417 (1993).

156. M. Jain, G. Y. Yin, J. E. Field, and S. E. Harris, "Observation of Electromagnetically Induced Phase Matching," *Opt. Lett.* **18**:998 (1993).
157. K. Hakuta, L. Marmet, and B. P. Stoicheff, "Electric-Field-Induced Second-Harmonic Generation with Reduced Absorption," *Phys. Rev. Lett.* **66**:596 (1991).
158. K. Hakuta, L. Marmet, and B. P. Stoicheff, "Nonlinear Optical Generation with Reduced Absorption Using Electric-Field Coupling in Atomic Hydrogen," *Phys. Rev. A* **45**:5152 (1992).
159. G. Z. Zhang, K. Hakuta, and B. P. Stoicheff, "Nonlinear Optical Generation Using Electromagnetically Induced Transparency in Hydrogen," *Phys. Rev. Lett.* **71**:3099 (1993).
160. R. S. D. Sihombing, M. Katsuragawa, G. Z. Zhang, and K. Hakuta, "Quantum Interference in Resonant Multi-Photon Ionisation Processes for Strongly Coupled Atomic Systems," *Phys. Rev. A* **54**:1551 (1996).
161. C. Dorman, I. Kucukkara, and J. P. Marangos, "Measurement of High Conversion Efficiency to 123.6 nm Radiation in a Four-Wave Mixing Scheme Enhanced by Electromagnetically Induced Transparency," *Phys. Rev. A* **61**:013802-1 (2000).
162. L. Deng, W. R. Garret, M. G. Payne, and D. Z. Lee, "Observation of a Critical Concentration in Laser-Induced Transparency and Multi-Photon Excitation and Ionisation in Rubidium," *Opt. Lett.* **21**:928 (1996).
163. Y.-Q. Li and M. Xiao, "Enhancement of Non-Degenerate Four-Wave-Mixing Based on Electromagnetically Induced Transparency in Rubidium Atoms," *Opt. Lett.* **21**:1064 (1996).
164. T. T. Grove, M. S. Shahriar, P. R. Hemmer, P. Kumar, V. S. Sudarshanam, and M. Cronin-GoIomb, "Distortion-Free Gain and Noise Correlation in Sodium Vapor with Four-Wave Mixing and Coherent Population Trapping," *Opt. Lett.* **22**:769 (1997).
165. S. Babin, U. Hinze, E. Tiemann, and B. Wellegehausen, "Continuous Resonant Four-Wave-Mixing in Double-A Level Configurations of Na," *Opt. Lett.* **21**:1186 (1996).
166. A. Apolonskii, S. Balischev, U. Hinze, E. Tiemann, and B. Wellegehausen, "Continuous Frequency Up-Conversion in a Double-A Scheme in Na," *Appl. Phys. B* **64**:435 (1997).
167. A. Peralta Conde, L. Brandt, and T. Halfmann, "Trace Isotope Detection Enhanced by Coherent Elimination of Power Broadening," *Phys. Rev. Lett.* **97**:243004 (2006).
168. T. Halfmann, T. Ricketts, N. Vitanov, and K. Bergmann, "Lineshapes in Coherent Two-Photon Excitation," *Opt. Comm.* **220**:353 (2003).
169. N. V. Vitanov, B. W. Shore, L. P. Yatsenko, T. Halfmann, T. Ricketts, K. Böhmer, and K. Bergmann, "Power Broadening Revisited: Theory and Experiment," *Opt. Comm.* **199**:117 (2001).
170. E. Sali, P. Kinsler, G. H. New, K. J. Mendham, T. Halfmann, J. W. G. Tisch, and J. P. Marangos, "Behavior of High-Order Stimulated Raman Scattering in a Highly Transient Regime," *Phys. Rev. A* **72**:013813 (2005).
171. E. Sali, K. J. Mendham, J. W. G. Tisch, T. Halfmann, and J. P. Marangos, "High-Order Stimulated Raman Scattering in a Highly Transient Regime Driven by a Pair of Ultrashort Pulses," *Opt. Lett.* **29**:495 (2004).
172. A. Lambrecht, J. M. Courty, S. Reynaud, and E. Giacobino, "Cold Atoms: A New Medium for Quantum Optics," *Appl. Phys. B* **60**:129 (1995).
173. D. N. Nikogosyan, *Properties of Optical and Laser-Related Materials: A Handbook*, John Wiley & Sons, New York (1997).
174. H. Schmidt and A. Imamoglu, "Giant Kerr Nonlinearities Obtained by Electromagnetically Induced Transparency," *Opt. Lett.* **21**:1936 (1996).
175. S. E. Harris and L. V. Hau, "Non-Linear Optics at Low Light Levels," *Phys. Rev. Lett.* **82**:4611 (1999).
176. M. D. Lukin, A. B. Matsko, M. Fleischhauer, and M. O. Scully, "Quantum Noise and Correlations in Resonantly Enhanced Wave-Mixing Based on Atomic Coherence," *Phys. Rev. Lett.* **82**:1847 (1999).
177. S. E. Harris and Y. Yamamoto, "Photon Switching by Quantum Interference," *Phys. Rev. Lett.* **81**:3611 (1998).
178. A. Imamoglu, H. Schmidt, G. Woods, and M. Deutsch, "Strongly Interacting Photons in a Non-Linear Cavity," *Phys. Rev. Lett.* **79**:1467 (1997).
179. W. E. Moerner (ed.), *Persistent Spectral Hole Burning: Science and Applications*, Springer, Berlin (1988).
180. J. Klein, F. Beil, and T. Halfmann, "Rapid Adiabatic Passage in a  $\text{Pr}^{3+}:\text{Y}_2\text{SiO}_5$  Crystal," *J. Phys. B*, in press (2007).
181. L. Rippe, M. Nilsson, and S. Kröll, "Experimental Demonstration of Efficient and Selective Population Transfer and Qubit Distillation in a Rare-Earth-Metal-Ion-Doped Crystal," *Phys. Rev. A* **71**:062328 (2005).

182. J. Klein, F. Beil, and T. Halfmann, "Stimulated Raman Adiabatic Passage in a  $\text{Pr}^{3+}:\text{Y}_2\text{SiO}_5$  Crystal," submitted (2007).
183. H. Goto and K. Ichimura, "Population Transfer via Stimulated Raman Adiabatic Passage in a Solid," *Phys. Rev. A* **74**:049902 (2006).
184. P. R. Hemmer, A. V. Turukhin, M. S. Shahriar, and J. A. Musser, "Raman-Excited Spin Coherences in Nitrogen-Vacancy Color Centers in Diamond," *Opt. Lett.* **26**:361 (2001).
185. L. Childress, M. V. Gurudev-Dutt, J. M. Taylor, A. S. Zibrov, F. Jelezko, J. Wrachtrup, P. R. Hemmer, and M. D. Lukin, "Coherent Dynamics of Coupled Electron and Nuclear Spin Qubits in Diamond," *Science* **314**:281 (2006).
186. U. Hohenester, J. Fabian, and F. Troiani, "Adiabatic Passage Schemes in Coupled Semiconductor Nanostructures," *Opt. Comm.* **264**:426 (2006).
187. J. Siewert, T. Brandes, and G. Falci, "Adiabatic Passage with Superconducting Nanocircuits," *Opt. Comm.* **264**:435 (2006).
188. W. W. Chow, H. C. Schneider, and M. C. Philipps, "Theory of Quantum Coherence Phenomena in Semiconductor Quantum Dots," *Phys. Rev. A* **68**:053802 (2003).

---

# STIMULATED RAMAN AND BRILLOUIN SCATTERING

---

John Reintjes and Mark Bashkansky

*Optical Sciences Division  
Naval Research Laboratory  
Washington, D.C.*

---

## 15.1 INTRODUCTION

---

Raman and Brillouin scattering are inelastic scattering processes in which the wavelength of the scattered radiation is different from that of the incident light and a change in the internal energy of the scattering medium occurs. The main distinction between Raman and Brillouin scattering is the type of internal mode involved. Raman scattering involves nonpropagating collective modes in the material. Examples include electronic excitations and molecular vibrations and rotations in liquids and gases, electronic excitations and optical phonons in solids, and electron-plasma oscillations in plasmas. Brillouin scattering involves low-frequency propagating waves, for example acoustic waves in solids, liquids, and gases and ion-acoustic waves in plasmas. The two processes exhibit a range of similarities and differences in the properties of the scattering process as well as in the materials that are involved. General descriptions of Raman and Brillouin scattering are given in Refs. 1–8. Collections of papers on specific aspects of Raman and Brillouin scattering are contained in Refs. 9–11. Review articles are given in Refs. 12 and 13.

---

## 15.2 RAMAN SCATTERING

---

Raman scattering occurs in a wide variety of solids, liquids, gases, and plasmas. The most common form of Raman scattering is one in which the incident light, termed the *pump*, is scattered into light at a longer wavelength, termed the *Stokes wave*, with the energy difference between the incident and scattered photons being taken up in excitation of the appropriate mode of the material. The difference between the incident and scattered photon energy is termed the *Stokes shift*. The identification of the scattered wave as the Stokes wave is made in analogy with the Stokes shift to longer wavelengths in fluorescence, but the dynamics of the two processes are different except for interactions that are resonant with an allowed single-photon resonant transition. Raman scattering in which the incident light is scattered to a light wave at a shorter wavelength, accompanied by a deexcitation of an internal mode of the medium, is termed *anti-Stokes scattering*, and the scattered wave is termed the *anti-Stokes wave*. The difference between the anti-Stokes and pump photon energies is termed the

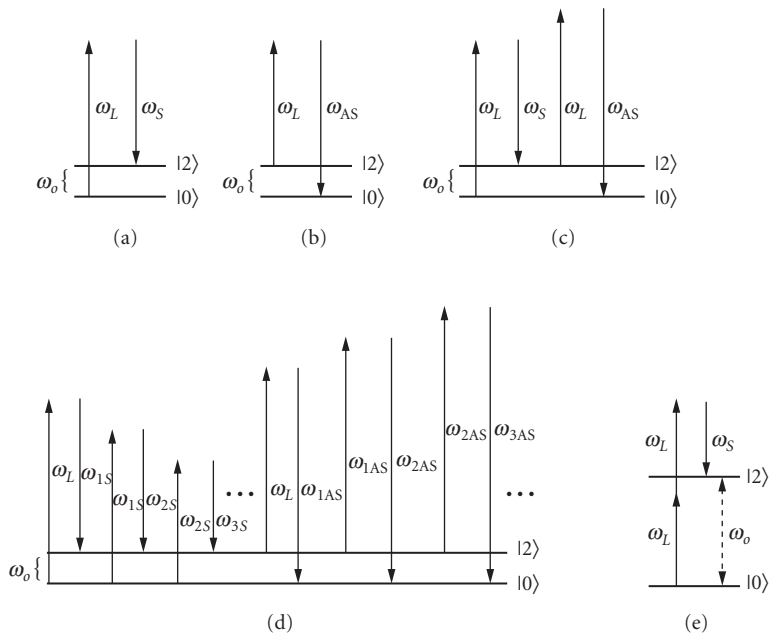
*anti-Stokes shift.* Again, the analogy is with the corresponding process in fluorescence. Raman shifts can range from tens to tens of thousands of wavenumbers, and are determined entirely by the material and the mode involved.

## Raman Interactions

Raman scattering can be viewed in the semiclassical model as a two-photon interaction in which the material makes a real transition from an initial to a final state and a pump photon is destroyed while a Stokes or anti-Stokes photon is created. Several types of Raman interactions are possible. These are illustrated in the level diagrams of Fig. 1, which show Stokes scattering, anti-Stokes scattering, anti-Stokes scattering with four-wave mixing, multiple Stokes scattering, and hyper-Raman scattering. Of these, the most common is Stokes scattering (Fig. 1a), in which the pump photon at frequency  $\omega_L$  is scattered into a longer-wavelength Stokes photon  $\omega_S$ , accompanied by the excitation of an internal mode of the medium at frequency  $\omega_o$ .

Anti-Stokes scattering (Fig. 1b), in which the pump photon is scattered into a shorter-wavelength anti-Stokes photon  $\omega_{AS}$  accompanied by the deexcitation of an internal mode of the medium, requires initial excitation into upper levels of the medium. The anti-Stokes interaction illustrated in Fig. 1b is less common than the Stokes interaction, occurring most often in spontaneous Raman scattering when the levels are excited thermally. In stimulated processes, this interaction incurs exponential loss unless a population inversion is created between the initial and final states.

Anti-Stokes Raman scattering involving a four-wave mixing interaction, as illustrated in Fig. 1c, is much more common in Raman scattering. In this interaction, two pump photons are scattered into a Stokes and anti-Stokes interaction with no net excitation or deexcitation of the medium. This interaction requires perfect or approximate phase matching, depending on the conditions of the scattering interaction. Multiple Raman scattering (Fig. 1d) occurs when the Stokes wave becomes



**FIGURE 1** Level diagrams showing (a) stimulated Raman Stokes scattering; (b) stimulated Raman anti-Stokes scattering; (c) coherent anti-Stokes four-wave mixing; (d) multiple Stokes and anti-Stokes scattering; and (e) hyper-Raman scattering.

**TABLE 1** Frequency and  $k$ -Vector Relationships in Various Raman Interactions

Stokes scattering	$\omega_s = \omega_L - \omega_o$ $k_o = k_L - k_s$
Anti-Stokes scattering	$\omega_{AS} = \omega_L + \omega_o$ $k_o = k_{AS} - k_L$
Coherent anti-Stokes scattering	$\omega_s + \omega_{AS} = 2\omega_L$ $k_{AS} = 2k_L - k_s$
Multiple Stokes scattering	$\omega_{ns} = \omega_{(n-1)s} - \omega_o = \omega_L - n\omega_o$ $k_o = k_{(n-1)s} - k_{ns}$
Hyper-Raman scattering	$\omega_s = 2\omega_L - \omega_o$ $k_o = 2k_L - k_s$

powerful enough to drive its own Raman interaction. This generally occurs when the pump wave is significantly above the stimulated Raman threshold. Under these conditions, multiple Stokes waves are generated, each one shifted from its effective pump wave by the frequency of the internal mode of the medium. Multiple Stokes and anti-Stokes waves can also be created through four-wave mixing processes involving one or more of the pump- or frequency-shifted waves. Hyper-Raman scattering (Fig. 1e) involves multiphoton interactions in which two or more pump photons are scattered into a single Stokes photon with excitation of an appropriate mode of the material.

In all of these interactions, energy is conserved among the incident and scattered photons and internal energy of the medium. The appropriate relations are summarized in Table 1.

Not all levels in a material can be involved in Raman scattering. In general, Raman scattering follows the rules for two-photon dipole transitions. In materials with inversion symmetry, the initial and final states must have the same parity, and therefore are mutually exclusive with absorptive transitions. In materials without inversion symmetry, internal levels can be both Raman and optically active.

## Regimes of Raman Scattering

Raman scattering can occur in the spontaneous and stimulated regimes. In the spontaneous regime, the power of the Stokes and anti-Stokes waves is proportional to the power of the pump wave. The entire manifold of Raman-active internal modes is present in the scattered spectrum, with relative intensities of the Stokes components being determined by the relative Raman scattering cross sections for the various modes. Anti-Stokes scattering arises in spontaneous Raman scattering through thermal excitation of the internal modes. Therefore, the intensity of anti-Stokes modes is reduced from that of the Stokes modes for the same internal level by the thermal excitation factor  $e^{-h\omega_o/kT}$ . Anti-Stokes scattering in the spontaneous regime is generally less common than Stokes scattering, except when low-lying rotational levels of molecules or low-frequency phonons in solids are involved, because thermal excitation of the internal mode is required. Anti-Stokes scattering can be more prominent in stimulated or coherent scattering processes, as will be described in later sections. Spontaneous Raman scattering is used primarily for spectroscopic studies, especially for modes that are forbidden in single-photon absorption or emission measurements.

Stimulated Raman Scattering (SRS) occurs when the intensity of the incident pump wave is strong enough to initiate a positive feedback effect in the medium, resulting in exponential growth of the scattered wave. Stimulated Raman scattering is used for wavelength shifting of coherent light, amplification, improved optical beam properties, pulse compression, phase conjugation, and beam combining. Coherent Raman interactions are used for spectroscopy.

## Stimulated Raman Scattering

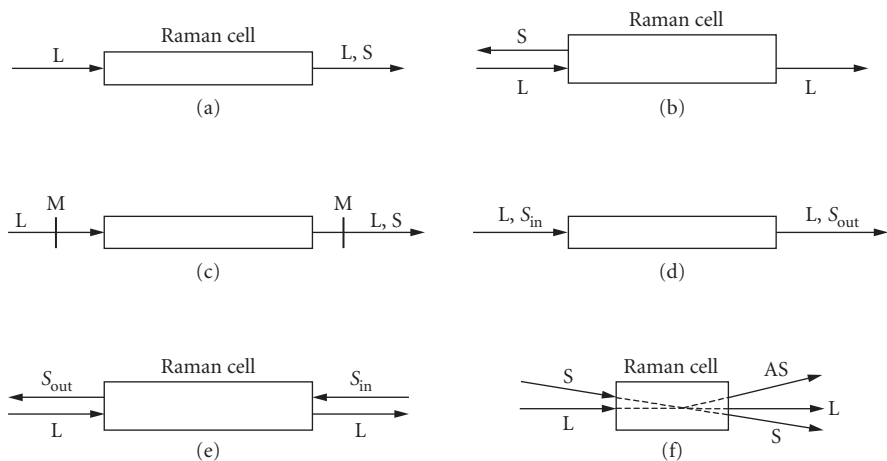
In stimulated Raman scattering, the internal mode of the medium is driven by the interference of the pump and Stokes waves while the Stokes wave is driven by the modulation of the pump wave

by the material oscillation. Thus, the growth rate of the Stokes wave, which is determined by the strength of the internal excitation, increases as the Stokes intensity increases. This is exactly the condition needed for exponential growth of the Stokes wave. Stimulated Raman scattering was observed soon after the development of Q-switched lasers.<sup>14</sup>

**Stimulated Raman Geometries** Stimulated Raman scattering can occur in several geometries, each with its own applications. Stimulated Raman generators are illustrated in Fig. 2*a* and *b*. In this arrangement, only a pump wave is incident on the medium, and the Stokes wave grows from quantum noise. Forward scattering is the most common form of Raman generator (Fig. 2*a*), but backward wave generation can occur under some conditions (Fig. 2*b*). Single-pass Raman generators involve amplified spontaneous emission (ASE), and the coherence and divergence properties are characteristic of ASE devices. If the interaction is strong enough to involve pump depletion, the coherence of the Stokes wave can approach that of the pump wave. Raman generators are typically used for frequency conversion from the pump to the Stokes wavelength or for creation of a Stokes wave for other applications. Conversion to multiple Stokes or anti-Stokes waves can also be done with Raman generators. Mirrors can be used with the Raman generator to create a Raman oscillator as in Fig. 2*c*. This arrangement is used with low-intensity continuous-wave (cw) or pulsed pump lasers to reduce the Raman threshold.<sup>13</sup>

Raman amplification can be achieved with the arrangements shown in Fig. 2*d* and *e*, in which a Stokes wave is supplied along with the pump wave. The Stokes wave is amplified at the expense of the pump wave. The Stokes wave is usually created in a separate low-power Raman generator and may be spatially filtered for control of the spatial divergence. Raman amplification is used when a high-quality Stokes beam is desired or when highly efficient conversion of the pump energy is desired without creation of multiple Stokes components. Backward amplification (Fig. 2*e*) is used for Stokes amplification or for pulse compression. In Raman generators, usually only a single Stokes frequency is generated corresponding to the material mode with the highest gain. Amplification of any of the Raman modes is possible if a suitable input Stokes signal is provided.

Coherent anti-Stokes Raman scattering (CARS) is illustrated in Fig. 2*f*. Here the pump and Stokes waves are supplied, often having comparable intensities and propagating at the appropriate phase-matching angle. The anti-Stokes wave is created at the appropriate angle for phase matching. CARS is used for spectroscopy and other diagnostic applications.



**FIGURE 2** Schematic diagrams of various Raman interaction geometries. (a) Forward Raman generator. (b) Backward Raman generator. (c) Raman oscillator. (d) Forward Raman amplifier. (e) Backward Raman amplifier. (f) Coherent anti-Stokes four-wave mixing. AS, generated anti-Stokes mixing; L, pump laser; M, mirrors; S, Stokes wave;  $S_{in}$ , Stokes wave from Raman generator;  $S_{out}$ , amplified Stokes wave.

**Raman Susceptibilities** Classically, the Raman effect occurs because of modulation of the polarization in the medium induced by the pump at the difference frequency between the pump and material mode. This arises from the hyperpolarizability of the medium. The polarization of the medium is given by<sup>6,7</sup>

$$P = \epsilon_0 \left( \mu_o + \mu E + \frac{\partial \alpha}{\partial Q} QE + \dots \right) \quad (1)$$

where  $\mu_o$  is the permanent dipole moment of the material,  $\mu$  is the first-order dipole moment,  $(\partial \alpha / \partial Q)$  is the hyperpolarizability, and  $Q$  is the normal mode coordinate of the material oscillation. Spontaneous Raman scattering is given classically by the relation

$$P_s = NA \frac{\partial \sigma}{\partial \Omega} d\Omega P_L L \quad (2a)$$

where  $d\sigma/d\Omega$  is the differential cross section of the Raman transition,  $L$  is the length of the scattering medium,  $A$  is the cross-sectional area, and  $d\Omega$  is its solid angle. The Raman cross section is related to the hyperpolarizability by

$$\frac{\partial \sigma}{\partial \Omega} = \frac{\pi \hbar n_s v_s^4}{4n_L m \omega_o c^2} \left( \frac{\partial \alpha}{\partial Q} \right)^2 \quad (2b)$$

The Raman effect can also be analyzed quantum-mechanically through the use of the density matrix<sup>15</sup> using the third-order elements  $\rho_{0i}$  and  $\rho_{i2}$  and the second-order element  $\rho_{02}$ , where the subscripts 0 and 2 designate the initial and final Raman levels and the subscript  $i$  designates intermediate levels. The classical parameter  $Q$  is related to the off-diagonal density matrix element  $\rho_{02}$ , while the population density is related to the element  $\rho_{22}$ . Thus the normal mode coordinate of the material oscillation is associated with quantum mechanical transition probabilities and not directly with the population of the excited state of the material.

The Raman cross section can be related to the susceptibilities of nonlinear optics<sup>15</sup> through density matrix calculations involving the third-order elements  $\rho_{0i}$  and  $\rho_{i2}$  and the second-order element  $\rho_{02}$ . The nonlinear Raman polarization amplitude is

$$P(\omega_s) = \frac{3}{2} \epsilon_0 \chi^{(3)}(-\omega_s, \omega_L, -\omega_L, \omega_s) |A_L|^2 A_s \quad (3a)$$

and the Raman susceptibility per atom or molecule is

$$\chi_{\text{Raman}}^{(3)} = \frac{1}{6\hbar^3 \epsilon_o} \frac{1}{\omega_{20} - (\omega_L - \omega_s) + i/T_2} \left| \sum_i \mu_{0i} \mu_{i2} \left( \frac{1}{\omega_{i0} - \omega_L} + \frac{1}{\omega_{i0} + \omega_s} \right) \right|^2 \quad (3b)$$

where  $T_2$  is the homogeneous Raman dephasing time and  $M_{ij}$  is the transition dipole moment between states  $i$  and  $j$ .

The Raman susceptibility has real and imaginary parts. The imaginary part, which is negative and proportional to  $T_2$ , is responsible for spontaneous and stimulated Raman scattering. The real part contributes to the nonlinear refractive index through Raman-type interactions. The Raman susceptibility is related to the hyperpolarizability as

$$\chi^r = -\frac{1}{12\Gamma m \omega_o} \left( \frac{\partial \alpha}{\partial Q} \right)^2 \quad (4)$$



where  $\chi''$  is the imaginary part of the Raman susceptibility,  $\Gamma$  is the inverse of the dephasing time,  $m$  is the effective mass of the material oscillator, and  $\omega_0$  is the frequency of the material transition. The Raman susceptibility is defined only for steady-state interactions. In transient interactions, the Raman polarization must be solved for as a dynamic variable along with the optical fields.

**SRS Equations** Stimulated Raman scattering is described in the most general form by the equations:<sup>2</sup>

$$\nabla_{\perp}^2 A_S + 2ik_S \left( \frac{\partial A_S}{\partial z} + \frac{1}{v_{gS}} \frac{\partial A_S}{\partial t} \right) = -\frac{\Delta N}{2} \frac{\omega_S^2}{c^2} \left( \frac{\partial \alpha}{\partial Q} \right)_S Q^* A_L \quad (5a)$$

$$\nabla_{\perp}^2 A_L + 2ik_L \left( \frac{\partial A_L}{\partial z} + \frac{1}{v_{gL}} \frac{\partial A_L}{\partial t} \right) = -\frac{\Delta N}{2} \frac{\omega_L^2}{c^2} \left[ \left( \frac{\partial \alpha}{\partial Q} \right)_S Q A_S + \left( \frac{\partial \alpha}{\partial Q} \right)_{AS} Q^* A_{AS} e^{i\Delta kz} \right] \quad (5b)$$

$$\nabla_{\perp}^2 A_{AS} + 2ik_{AS} \left( \frac{\partial A_{AS}}{\partial z} + \frac{1}{v_{gAS}} \frac{\partial A_{AS}}{\partial t} \right) = -\frac{\Delta N}{2} \frac{\omega_{AS}^2}{c^2} \left( \frac{\partial \alpha}{\partial Q} \right)_{AS} Q A_L e^{-i\Delta kz} \quad (5c)$$

$$\frac{\partial Q^*}{\partial t} + \left[ i \left( \frac{\omega_o^2 - \Omega^2}{2\Omega} \right) + \Gamma \right] Q^* = -\frac{i}{4\omega_o m} \left[ \left( \frac{\partial \alpha}{\partial Q} \right)_S A_L A_S + \left( \frac{\partial \alpha}{\partial Q} \right)_{AS} A_{AS}^* A_L e^{-i\Delta kz} \right] \quad (5d)$$

$$\frac{\partial \Delta N}{\partial \tau} + \frac{1}{T_1} (\Delta N - N) = -i \frac{\Delta N \epsilon_o}{4\hbar} \left[ \left( \frac{\partial \alpha}{\partial Q} \right)_S (Q^* A_L A_S^* - Q A_L^* A_S) + \left( \frac{\partial \alpha}{\partial Q} \right)_{AS} (Q^* A_L^* A_{AS} e^{i\Delta kz} - Q A_L A_{AS}^* e^{-i\Delta kz}) \right] \quad (5e)$$

where  $A_S$ ,  $A_L$ , and  $A_{AS}$  are the slowly varying optical field amplitudes of the Stokes, laser (pump), and anti-Stokes waves given by

$$E_{S,L,AS}(x, y, z, t) = \frac{1}{2} \left[ A_{S,L,AS}(x, y, z, t) e^{-i(\omega_{S,L,AS} t - k_{S,L,AS} z)} + c.c. \right] \quad (6)$$

where  $\omega_{S,L,AS}$  are the optical frequencies,  $k_{S,L,AS}$  are the  $k$  vectors,  $v_{S,L,AS}$  are the group velocities,  $\Delta N$  is the difference in the population between the lower and the upper Raman transition levels,  $\Delta N = N_0 - N_2$ ,  $N$  is the total population density, and  $Q$  is the amplitude of the normal mode coordinate of the material excitation defined by

$$Q(x, y, z, t) = \frac{1}{2} \left[ Q(x, y, z, t) e^{-i(\Omega t - k_o z)} + c.c. \right] \quad (7)$$

$(\partial \alpha / \partial Q)_S$  and  $(\partial \alpha / \partial Q)_{AS}$  are the hyperpolarizabilities for the Stokes and anti-Stokes waves, respectively,  $\omega_o$  is the Raman transition frequency, and  $k_o$  is the nonpropagating  $k$  vector of the material excitation.  $\Gamma$  is the half-width at half-maximum of the Raman linewidth given by  $\Gamma = 1/T_2$ ,  $\Delta k$  is the phase mismatch of the anti-Stokes scattering,  $m$  is the effective reduced mass of the material oscillation, and  $\epsilon_o$  is the permittivity of the free space.

The relation between various frequencies and  $k$  vectors is

$$\omega_s = \omega_L - \Omega \quad (8a)$$

$$\omega_{AS} = \omega_L + \Omega \quad (8b)$$

$$k_o = k_L - k_s \quad (8c)$$

$$\Delta k = k_s + k_{AS} - 2k_L \quad (8d)$$

The intensity of the various light waves is given by

$$I_{S,L,AS} = \frac{1}{2} (cn\epsilon_o) |A_{S,L,AS}|^2 \quad (9)$$

Phase matching, which is of central importance in many nonlinear interactions, is automatically satisfied in stimulated Raman scattering because  $k_o$  automatically adjusts to satisfy Eq. (8c). Phase matching in anti-Stokes scattering through four-wave mixing is not automatic, and phase-matching conditions determine many of the properties of the four-wave mixing anti-Stokes scattering interaction.

These equations describe most of the effects that are commonly encountered in Raman scattering, including amplification, diffraction, growth from noise, multiple Stokes generation, forward and backward interactions, coherent anti-Stokes interactions, and transient and steady-state interactions. Each of these will be discussed individually in subsequent parts of this chapter. In most of these effects the population of the ground state is undisturbed and the approximation  $\Delta N = N$  is valid. In some situations involving high-power lasers or resonant interactions,  $\Delta N$  will vary and Eq. (5e) must be used.

**Steady-State Stokes Scattering** Many of the effects associated with stimulated Raman scattering can be illustrated by considering plane-wave steady-state forward Raman amplification. In this interaction, an incident Stokes wave at frequency  $\omega_s$  is amplified by a pump wave at frequency  $\omega_L$  in the geometry of Fig. 2d. The plane-wave steady-state Raman amplification equations are obtained from Eq. (5a and b) by assuming that the time variation of the wave envelopes is slow compared to the dephasing time  $T_2$ , allowing the time derivatives to be neglected; by neglecting the transverse spatial derivative; and by assuming that the ground state population is unchanged, allowing Eq. (5e) to be neglected and the ground state population  $N_o = N$  to be treated as a constant. The resulting equations are

$$\frac{dA_s}{dz} = i\kappa_2 Q^* A_L \quad (10a)$$

$$\frac{dA_L}{dz} = i \frac{\omega_L n_s}{\omega_s n_L} \kappa_2 A_s Q \quad (10b)$$

$$Q^* = -i \frac{1}{4\omega_o m} \left( \frac{\partial \alpha}{\partial Q} \right) \frac{1}{\Gamma + i(\omega_o - \Omega)} A_L^* A_s \quad (10c)$$

where

$$\kappa_2 = \frac{N\omega_s}{4n_s c} \left( \frac{\partial \alpha}{\partial Q} \right) \quad (11)$$

Equation (10c) results from solution of Eq. (5d) neglecting the time derivative and the anti-Stokes term.

*Steady-state gain* If the pump wave intensity is taken as a constant, then Eq. (10a) can be solved for the Stokes intensity:

$$I_S(L) = I_S(0)e^{g_{ss}I_L L} \quad (12)$$

where  $L$  is the length of the interaction region and  $g_{ss}$  is the steady-state Raman gain coefficient, given by

$$g_{ss} = \frac{N\omega_s}{4\Gamma n_s n_L m \omega_o c^2 \epsilon_o} \left( \frac{\partial \alpha}{\partial Q} \right)^2 \quad (13)$$

This result is also written in the literature in the forms

$$I_S(L) = I_S(0)e^{G_{ss}} \quad (14a)$$

$$I_S(L) = I_S(0)e^{N\sigma_R I_L L} \quad (14b)$$

where

$$G_{ss} = g_{ss} I_L L \quad (15a)$$

is the total steady-state Raman gain and

$$\sigma_R = \frac{\omega_s}{4\Gamma n_s n_L m \omega_o c^2 \epsilon_o} \left( \frac{\partial \alpha}{\partial Q} \right)^2 \quad (15b)$$

is the stimulated Raman cross section. The gain coefficient is given in terms of the Raman susceptibility as

$$g_{ss} = -\frac{3N\omega_s}{c^2 n_s n_L \epsilon_o} \chi'' \quad (16)$$

The classical Raman scattering cross section is related to the Raman gain, given in Eq. (13), by

$$g_{ss} = \frac{2Nc^2}{\pi n_s^2 h \nu_s^3 \Delta \nu_R} \frac{\partial \sigma}{\partial \Omega} \quad (17)$$

where  $\Delta \nu_R$  is the Raman linewidth [full width at half-maximum (FWHM)] related to the dephasing time as

$$\Delta \nu_R = \frac{1}{\pi T_2} \quad (18)$$

In transparent regions of the spectrum, the Raman cross section scales as  $\nu_s^4$  and the Raman gain coefficient scales as  $\nu_s$ . In dispersive regions of the spectrum, as for example when the pump wavelength is in the ultraviolet, additional frequency variation in the Raman gain arises from the resonant term  $1/(\omega_o - \omega_L)$  in the susceptibility.

Initially, stimulated Raman gain coefficients were calculated from measurements of the spontaneous Raman scattering cross section or estimated from measurements of the Raman threshold. The most accurate determinations of Raman gain coefficients are now made with steady-state amplification measurements in the low-gain regime.

The conditions for steady-state Raman amplification are encountered when both the pump and incident Stokes radiation are either cw or narrowband pulses with pulse duration longer than a steady-state time given by<sup>16-19</sup>

$$t_{ss} = G_{ss} T_2 \quad (19)$$

and contain no rapid internal temporal variation, requiring that the linewidths  $\Delta\nu_L$  and  $\Delta\nu_S$  satisfy the condition

$$\Delta\nu_{L(S)} \ll \Delta\nu_R \quad (20)$$

*Raman linewidths* The steady-state Raman gain scales as the medium density and inversely with the Stokes wavelength and the material linewidth. In materials such as some molecular gases, the linewidth is pressure dependent due to pressure broadening with a variation of the form:<sup>20</sup>

$$\Delta\nu_R = \Delta\nu_0 + \beta\rho \quad (21)$$

where  $\rho$  is the density of the material and  $\Delta\nu_0$  is the Raman linewidth at low pressures. In materials that exhibit this behavior, the gain increases at low pressures but levels off at higher pressures, becoming independent of pressure in the limit of high pressures. In hydrogen, for example, the steady-state gain for the Q(1) vibrational mode is effectively independent of pressure for pressures above about 10 atmospheres. The rotational lines in some gases such as hydrogen reach their pressure-broadened limit at lower pressures than do the vibrational lines. As a result, rotational Raman scattering in these materials is more prominent at low pressures, while the vibrational scattering is dominant at higher pressures.

The linewidth for forward scattering in some gases such as hydrogen exhibits Dicke narrowing,<sup>21</sup> in which inelastic collisions cause a narrowing of the linewidth at small but nonzero pressures before the material enters a pressure-broadened regime. The linewidth exhibits a variation in a region above some cutoff pressure of the form:<sup>22</sup>

$$\Delta\nu_R = \frac{A}{\rho} + B\delta\rho \quad (22)$$

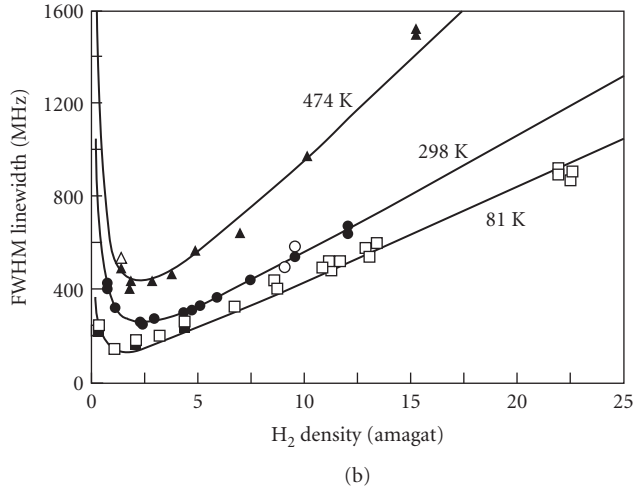
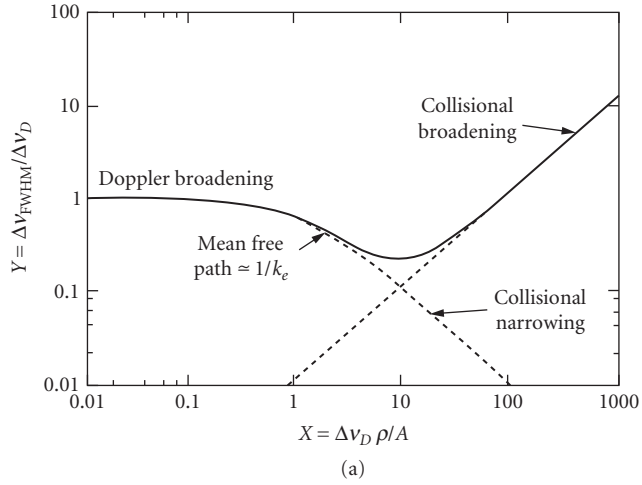
This behavior is shown for hydrogen in Fig. 3. Raman frequency shifts for a number of materials are shown in Table 2. Linewidths and gain coefficients for selected materials are given in Table 3. The temperature dependence of the frequency shift parameters for hydrogen is given in Table 4. Temperature dependence of line-broadening parameters for hydrogen and nitrogen is given in Table 5. Formulas for quantities appropriate for Raman scattering in molecular gases are given in Table 6.

*Pump depletion* If the Stokes intensity becomes large enough, the depletion of the pump wave must be taken into account and Eq. (10a and b) must be solved together.

The solutions are

$$I_S(z) = \frac{\left[ I_S(0) + \frac{\omega_S}{\omega_L} I_L(0) \right] \frac{\omega_L}{\omega_S} \frac{I_S(0)}{I_L(0)} e^{\left[ I_L(0) + \frac{\omega_L}{\omega_S} I_S(0) \right] gz}}{1 + \frac{\omega_L}{\omega_S} \frac{I_S(0)}{I_L(0)} e^{\left[ I_L(0) + \frac{\omega_L}{\omega_S} I_S(0) \right] gz}} \quad (23a)$$

$$I_L(z) = \frac{\left[ 1 + \frac{\omega_S}{\omega_L} \frac{I_L(0)}{I_S(0)} \right] I_L(0) e^{-\left[ I_L(0) + \frac{\omega_L}{\omega_S} I_S(0) \right] gz}}{1 + \frac{\omega_S}{\omega_L} \frac{I_L(0)}{I_S(0)} e^{-\left[ I_L(0) + \frac{\omega_L}{\omega_S} I_S(0) \right] gz}} \quad (23b)$$



**FIGURE 3** Calculated (a) and experimental (b) variation with pressure of the linewidth of the Q(1) transition in hydrogen gas showing Dicke narrowing and pressure broadening. (From Ref. 22; copyright 1986 by the American Physical Society.)

When  $I_S(0) \ll I_L(0)$ , the pump depletion solutions simplify to

$$I_S(z) = \frac{I_S(0)e^{I_L(0)gz}}{1 + \frac{\omega_L}{\omega_S} \frac{I_S(0)}{I_L(0)} e^{I_L(0)gz}} \quad (24a)$$

$$I_L(z) = \frac{\left[1 + \frac{\omega_S}{\omega_L} \frac{I_L(0)}{I_S(0)}\right] I_L(0) e^{-I_L(0)gz}}{1 + \frac{\omega_S}{\omega_L} \frac{I_L(0)}{I_S(0)} e^{-I_L(0)gz}} \quad (24b)$$

**TABLE 2** Raman Transition Frequencies of Selected Materials

Liquids		
Substance	$\nu_R$ (cm <sup>-1</sup> )	Reference
Bromoform	222	23
Tetrachloroethylene	448	24
Carbon tetrachloride <sup>a</sup>	460	25
Ethyl iodide	497	26
Hexafluorobenzene <sup>a</sup>	515	25
Bromoform	539	23
Chlorine	552	2
Methylene bromide	580	25
Trichloroethylene	640	23
Carbon disulfide	655	27
Ethylene bromide	660	28
Chloroform	667	23
<i>o</i> -Xylene	730	29
FC104 <sup>b</sup>	757	30
Sulfur hexafluoride	775	31
$\alpha$ -Dimethylphenethylamine	836	32
Dioxane	836	23
Morpholine <sup>a</sup>	841	25
Thiophenol <sup>a</sup>	916	25
Nitromethane <sup>a</sup>	927	25
Deuterated benzene	944	14
Potassium dihydrogen phosphate	980	33
Cumene <sup>a</sup>	990	25
Pyridine	991	14
1,3-Dibromobenzene	992	24
Benzene	992	14
Aniline	997	34
Styrene	998	35
<i>m</i> -Toluidine <sup>a</sup>	999	25
Acetophenone	999	36
Bromobenzene	1000	34
Chlorobenzene <sup>a</sup>	1001	25
<i>tert</i> -Butylbenzene	1000	24
Benz aldehyde <sup>c</sup>	1001	24
Ethylbenzoate	1001	36
Benzonitrile	1002	34
Ethylbenzene	1002	29
Toluene	1004	14
Fluorobenzene	1012	37
$\gamma$ -Picoline	1016	25
<i>m</i> -Cresol <sup>a</sup>	1029	25
<i>m</i> -Dichlorobenzene <sup>a</sup>	1034	25
1-Fluoro-2-chlorobenzene <sup>d</sup>	1034	24
Iodo-Benzene <sup>a</sup>	1070	25
Benzoyl chloride <sup>a</sup>	1086	25
Benzaldehyde <sup>a</sup>	1086	25
Anisole <sup>a</sup>	1097	25
Pyrrole <sup>a</sup>	1178	25
Furan <sup>a</sup>	1180	25
Nitrous oxide	1289	31
Styrene	1315	35

(Continued)

**TABLE 2** Raman Transition Frequencies of Selected Materials (*Continued*)

Liquids		
Substance	$\nu_R$ (cm <sup>-1</sup> )	Reference
Nitrobenzene	1344	14
1-Bromonaphthalene	1363	14
1-Chloronaphthalene	1374	38
2-Ethyl-naphthalene	1382	24
<i>m</i> -Nitrotoluene <sup>a</sup>	1389	25
Carbon dioxide	1392	31
Quinoline <sup>a</sup>	1427	25
Bromocyclohexane	1438	26
Furan <sup>a</sup>	1522	25
Methyl salicylate <sup>a</sup>	1612	25
Cinnamaldehyde	1624	38
Styrene	1631	35
3-Methylbutadiene	1638	39
Pentadiene	1655	39
Isoprene	1792	32
1-Hexyne	2116	24
Dimethyl sulfoxide <sup>c</sup>	2128	40
<i>o</i> -Dichlorobenzene <sup>a</sup>	2202	25
Benzonitrile	2229	38
Acetonitrile	2250	26
1,2-Dimethylaniline <sup>a</sup>	2292	25
Nitrogen	2327	41
Hydrobromic acid	2493	30
Hydrochloric acid	2814	42
Methylcyclohexane <sup>a</sup>	2817	25
Methanol	2831	23
<i>cis,trans</i> -1,3-Dimethylcyclohexane	2844	24
Tetrahydrofuran	2849	38
Cyclohexane	2852	14
<i>cis</i> -1,2-Dimethylcyclohexane	2853	24
$\alpha$ -Dimethylphenethylamine	2856	32
Dioxane	2856	23
Decahydronaphthalene	2860	30
Cyclohexane	2863	23
Cyclohexanone	2863	29
<i>cis,trans</i> -1,3-Dimethylcyclohexane	2866	24
<i>cis</i> ,1,4-Dimethylcyclohexane	2866	24
Cyclohexane	2884	23
Dichloromethane <sup>a</sup>	2902	25
Dimethyl sulfoxide	2916	40
Morpholine <sup>a</sup>	2902	25
Cargille 5610 <sup>f</sup>	2908	30
2,3-Dimethyl-1,5-hexadiene	2910	24
Limonene	2910	32
<i>o</i> -Xylene	2913	29
1-Hexyne	2916	24
<i>cis</i> -2-Heptene	2916	24
2-Octene	2918	24
Acetonitrile	2920	30
Mesitylene	2920	32
2-Bromopropane	2920	24

**TABLE 2** Raman Transition Frequencies of Selected Materials (*Continued*)

Substance	Liquids	
	$\nu_R$ (cm <sup>-1</sup> )	Reference
Acetone	2921	29
Ethanol	2921	23
<i>cis</i> -1,2-Dimethylcyclohexane	2921	24
Carvone	2922	32
2-Chloro-2-methylbutane	2927	24
Dimethylformamide	2930	23
<i>Cis,trans</i> -1,3-Dimethylcyclohexane	2926	24
<i>m</i> -Xylene	2933	29
1,2-Diethyl tartrate	2933	32
<i>o</i> -Xylene	2933	29
Piperidine	2933	29
1,2-Diethylbenzene	2934	24
1-Bromopropane	2935	24
Piperidine	2936	29
Tetrahydrofuran	2939	38
Decahydronaphthalene	2940	30
Piperidine	2940	29
Cyclohexanone	2945	29
2-Nitropropane	2945	24
1,2 Diethyl carbonate <sup>a</sup>	2955	25
1,2 Dichloroethane <sup>a</sup>	2956	25
<i>trans</i> -Dichloroethylene	2956	23
Methyl fluoride	2960	31
1-Bromopropane	2962	24
2-Chloro-2-methylbutane	2962	24
$\alpha$ -Dimethylphenethylamine	2967	32
Dioxane	2967	23
Methyl chloride	2970	31
Cyclohexanol <sup>a</sup>	2982	25
Cyclopentane <sup>a</sup>	2982	25
Cyclopentanol <sup>a</sup>	2982	25
Bromocyclopentane <sup>a</sup>	2982	25
<i>o</i> -Dichlorobenzene <sup>a</sup>	2982	25
<i>p</i> -Chloro toluene <sup>a</sup>	2982	25
$\alpha$ -Picoline <sup>a</sup>	2982	25
<i>p</i> -Xylene	2988	29
<i>o</i> -Xylene	2992	29
Dibutyl-phthalate <sup>a</sup>	2992	25
1,1,1-Trichloroethane	3018	23
Ethylene chlorohydrin <sup>a</sup>	3022	25
Isophorone <sup>a</sup>	3022	25
Nitrosodimethylamine <sup>a</sup>	3022	25
Propylene glycol <sup>a</sup>	3022	25
Cyclohexane <sup>a</sup>	3038	25
Styrene	3056	35
Pyridine	3058	24
Benzene	3064	14
<i>tert</i> -Butylbenzene	3065	24
1-Fluoro-2-chlorobenzene	3082	24
Turpentine <sup>a</sup>	3090	25
Pseudocumene <sup>a</sup>	3093	25

*(Continued)*



**TABLE 2** Raman Transition Frequencies of Selected Materials (*Continued*)

Liquids		
Substance	$\nu_R$ (cm <sup>-1</sup> )	Reference
Acetic acid <sup>a</sup>	3162	25
Acetylacetone <sup>a</sup>	3162	25
Methyl methacrylate <sup>a</sup>	3162	25
$\gamma$ -Picoline <sup>a</sup>	3182	25
Aniline	3300	34
Water <sup>a</sup>	3651	25
Solids		
Substance	$\nu_R$ (cm <sup>-1</sup> )	Reference
Quartz	128	43
Lithium niobate	152	44
$\alpha$ -Sulfur	216	45
Lithium niobate	248	44
Bromine	295	45
Bromine	303	45
Quartz	466	43
$\alpha$ -Sulfur	470	45
Chlorine	543	46
Lithium niobate	628	44
Carbon disulfide	656	46
Potassium iodate	746	47
Potassium bromate <sup>a</sup>	780	47
Potassium periodate	790	47
Potassium bromate	798	47
Potassium chromate	844	47
Sodium molybdate <sup>a</sup>	884	47
Potassium dichromate	906	47
Calcium tungstate	911	38
Potassium dihydrogen phosphate	915	33
Ammonium vanadate	915	47
Sodium tungstate	915	47
Potassium perchlorate <sup>a</sup>	936	47
Potassium chlorate <sup>a</sup>	938	47
Ammonium sulfate <sup>a</sup>	975	47
Potassium sulfate <sup>a</sup>	985	47
Stilbene	997	48
Polystyrene	1001	23
Calcium nitrate	1050	47
Calcium nitrate tetrahydrate <sup>a</sup>	1052	47
Potassium nitrate	1060	47
Magnesium nitrate dehydrate <sup>a</sup>	1060	47
Ammonium nitrate <sup>a</sup>	1062	47
Magnesium nitrate hexahydrate <sup>a</sup>	1063	47
Sodium nitrate	1075	47
77 K (not observed at 293 K) <sup>a</sup>		
Calcite	1086	45
Diamond	1332	45
Naphthalene	1380	38
Anthracene	1403	49
Stilbene	1591	48
Potassium thiocyanate	1040	47

**TABLE 2** Raman Transition Frequencies of Selected Materials (*Continued*)

Solids		
Substance	$\nu_R$ (cm <sup>-1</sup> )	Reference
Potassium ferricyanide <sup>a</sup>	2100	47
Triglycine sulfate	2422	25
Triglycine sulfate	2702	25
Triglycine sulfate	3022	25
Polystyrene	3054	23
Gases		
Substance	$\nu_R$ (cm <sup>-1</sup> )	Reference
Barium vapor <sup>g</sup>	IR <sup>h</sup>	50
Cesium vapor <sup>g</sup>	IR <sup>h</sup>	51,52
Hydrogen fluoride	FIR <sup>h</sup>	53
Potassium vapor <sup>g</sup>	IR <sup>h</sup>	51,52
Rubidium vapor <sup>g</sup>	IR <sup>h</sup>	54
$\rho$ -H <sub>2</sub>	354	55,56
Carbon tetrafluoride	980	57
Oxygen	1552	29
Nitrogen	2331	58
Potassium vapor	2721	59
Methane	2916	60
Deuterium	2991	60
Hydrogen deuteride	3628	61
Hydrogen	4155	60

<sup>a</sup>Observed at low resolution.

<sup>b</sup>Product of 3M Co., St. Paul, Minnesota.

<sup>c</sup>1:1 mixture with tetrachloroethylene.

<sup>d</sup>Very weak and diffuse.

<sup>e</sup>Deuterated.

<sup>f</sup>Product of Cargille Laboratories, Cedar Falls, N.J.

<sup>g</sup>Stimulated electronic Raman scattering (SERS).

<sup>h</sup>Generally tunable transitions in the infrared (IR) and far infrared (FIR).

Reprinted with permission from M. J. Weber (ed.), *CRC Handbook of Laser Science and Technology: Optical Materials*, part 1, vol. III. Copyright CRC Press, Boca Raton, FL, 1988.

The conditions for exponential Raman amplification can now be identified. In order for the approximate solution of Eq. (12) to be valid, it is necessary for the condition

$$I_S(0)e^{g_{SS}I_L z} \ll I_L(0) \quad (25)$$

to be satisfied. When the condition in Eq. (25) is not satisfied, the full solution of Eq. (23) [or Eq. (24), if  $I_S(0) \ll I_L(0)$ ] must be used. The calculated behavior of the pump and Stokes waves in the depletion regime is shown in Fig. 4.

In the limit of large pump depletion, the Stokes intensity becomes

$$I_S(z) = I_S(0) + \frac{\omega_S}{\omega_L} I_L(0) \quad (26)$$

Equation (26) indicates that the maximum energy that can be added to the Stokes wave is reduced from the energy of the pump wave by the fraction  $(\omega_S/\omega_L)$ . This ratio is termed the *Manly Rowe fraction*. The difference between the energy given up by the pump wave and that gained by the Stokes wave is taken up by energy deposited in the material excitation. Although complete energy

**TABLE 3** Linewidths and Gain Coefficients for Selected Materials

Raman transition frequencies, linewidths, and gains of selected materials at room temperature <sup>a</sup>						
Material	Mode	$\nu_0$ (cm <sup>-1</sup> )	$\Delta\nu$ (MHz)	$\lambda_L$ (nm)	$g$ (cm/GW)	Reference
H <sub>2</sub> gas (20 atm)	Q(1)	4155	$309/\rho + 5.22\rho$	532	2.5	22, 62, 63
H <sub>2</sub> gas (high)	S(1)	587	$119\rho$	350	1.2	64
D <sub>2</sub> gas (60 atm)	Q(2)	2987	$101/\rho + 120\rho$	532	0.45	63, 65, 66, 67
D <sub>2</sub> gas	S(2)	414	$124\rho$	350		64
HD	Q(1)	3628	$693\rho$	532		68
HD	S(1)	443	$760\rho$	350	0.098	64
CH <sub>4</sub> (115 atm)	$\nu_1$	2913	$8220 + 384\rho$	532	1.26	63, 65
N <sub>2</sub>	Q	2327	$4500$ ( $\rho < 10$ )	248	$0.003\rho$	69
N <sub>2</sub>	S(6)	60	$3570\rho$	566	0.0063	70
O <sub>2</sub>	Q	1552	54000	248	$0.012\rho$	69
SiH <sub>4</sub>	Q	2186	15000 (est.)	248	$0.19\rho$	69
GeH <sub>4</sub>	$\nu_1$	2111	15000 (est.)	248	$0.27\rho$	69
CF <sub>4</sub>	$\nu_1$	908	21000 (est.)	248	$0.008\rho$	69
SF <sub>6</sub>	$\nu_1$	775	30000 (est.)	248	$0.014\rho$	69
Liquid N <sub>2</sub>		2326.5	0.067	694	$16 \pm 5$	2
Liquid O <sub>2</sub>		1552	0.117	694	$14.5 \pm 4$	2
H <sub>2</sub> O		3290	200	694	0.14	1, 2, 71
Benzene		992	2.15		2.8	2
CS <sub>2</sub>		655.6	0.50	694	24	2
Nitrobenzene		1345	6.6		2.1	2
Bromobenzene		1000	1.9		1.5	2
Chlorobenzene		1002	1.6		1.2	2
Toluene		1003	1.94		1.2	2
LiNbO <sub>3</sub>		637	20	694	9.4	2
Ba <sub>2</sub> NaNb <sub>5</sub> O <sub>15</sub>		650		694	6.7	2
LiTaO <sub>3</sub>		201	22	694	4.4	2
SiO <sub>2</sub>		467		694	0.8	2
Ba(NO <sub>3</sub> ) <sub>2</sub>		1047	$1.5 \text{ cm}^{-1}$	532	47	72–76

Calculated<sup>b</sup> and measured gain ( $g_s$ ) factor for stimulated Raman transitions in liquids ( $\ell$ ), gases ( $g$ ), and solids ( $s$ )

Substance	Pump		Linewidth $\Delta\nu_R$ ( $\text{cm}^{-1}$ )	Gain ( $g_s$ ) $\times 10^9$ ( $\text{cm}/\text{W}$ )	$g_s$ calc. $\times 10^9$ ( $\text{cm}/\text{W}$ )	$g_s$ at 532 nm <sup>c</sup>	$g_s$ Relative to $\text{C}_6\text{H}_6(\ell)$ <sup>d</sup>	Reference
	Wavelength (nm)	Frequency ( $\text{cm}^{-1}$ )						
Benzene ( $\ell$ )	532	992	2.15	5.5 <sup>e</sup>		5.5	1.0	132
	532	992	2.15	5.5 <sup>f</sup>		5.5		133
	532	992	2.15	4.3 $\pm$ 0.9 <sup>g</sup>		4.3 $\pm$ 0.9		134
	694.3	992	2.15		2.8	5.9 <sup>h,i</sup>		135
Oxygen ( $\ell$ )	694.3	1552	0.117	16.0 $\pm$ 0.5	14.5 $\pm$ 0.4	21.5	3.9	135
Nitrogen ( $\ell$ )	532	2327	0.067	30.0	24.0 $\pm$ 7.0	30.0	5.4	136
	694.3	2327	0.067	16.0 $\pm$ 0.55	17.0 $\pm$ 0.5	21.5	3.9	135
	1060	2327	0.067	10.0	9.0 $\pm$ 3.0	23.2	4.2	137
	1315	2327	0.067	5.0 $\pm$ 2.0	6.0 $\pm$ 2.0	15.6 $\pm$ 6.2	2.9	138
Carbon disulfide ( $\ell$ )	694.3	655.6	0.50	24.0		32.2	5.9	135
Methanol ( $\ell$ )	694.3	2837	18	0.4		0.53	0.10	139
Carbon tetrachloride ( $\ell$ )	597.6	458		1.3		1.5	0.27	140
	532						0.12 <sup>j</sup>	141
Acetone ( $\ell$ )	532						0.20 <sup>j</sup>	141
Cyclohexane ( $\ell$ )	532						0.25 <sup>j</sup>	141
Hydrogen <sup>k</sup> ( $g$ )	694.3	4155			1.5 <sup>l</sup>	2.14		142
	694.3	4155		1.9 $\pm$ 0.3 <sup>l</sup>	1.5 <sup>l</sup>	2.7		142
	694.3	4155		1.5 <sup>l</sup>		2.1		143
	353	4155		5.0 <sup>l</sup>	5.7 <sup>l</sup>			131
	308	4155			6.7 <sup>l</sup>			131
	10600	354			0.07	0.09		144
Hydrogen deuteride ( $g$ )	353	3628		0.2				131
Nitrogen ( $g$ , 1 atm)	694.3	2330.7		0.0022		0.0030		128
	694.3	2330.7	0.075		0.0027 <sup>m</sup>	0.0038		145
Carbon tetrafluoride ( $g$ , 500 atm)	532	980	0.17	24.6 $\pm$ 2 <sup>n</sup>		2.46 $\pm$ 2 <sup>n</sup>		127
Calcite ( $s$ )	532	1086	1.2	5.5		5.5		146

(Continued)

**TABLE 3** Linewidths and Gain Coefficients for Selected Materials (*Continued*)

Calculated <sup>b</sup> and measured gain ( $g_s$ ) factor for stimulated Raman transitions in liquids ( $\ell$ ), gases ( $g$ ), and solids ( $s$ )								
Substance	Pump Wavelength (nm)	Frequency (cm <sup>-1</sup> )	Linewidth $\Delta\nu_R$ (cm <sup>-1</sup> )	Gain ( $g_s$ ) $\times 10^9$ (cm/W)	$g_s$ calc. $\times 10^9$ (cm/W)	$g_s$ at 532 nm <sup>c</sup>	$g_s$ Relative to C <sub>6</sub> H <sub>6</sub> ( $\ell$ ) <sup>d</sup>	Reference
Fused quartz ( $s$ )	495.4	420		0.017		0.016		147
Potassium dihydrogen phosphate ( $s$ )	532	918	18	0.21 $\pm$ 0.05 <sup>g</sup>		0.21 $\pm$ 0.05		134

<sup>a</sup> $\rho$  is measured in amagats (1 amagat =  $2.68 \times 10^{-19}$  cm<sup>-3</sup>).

<sup>b</sup>Only those supporting measured values of special interest are given.

<sup>c</sup>Except where noted,  $g_s/532 = (\omega_s/532)/((\omega_s/\text{meas}) g_s/\text{meas})$ .

<sup>d</sup>For qualitative use only; see previous text.

<sup>e</sup>Estimated from stimulated threshold.

<sup>f</sup>Estimated from stimulated conversion.

<sup>g</sup>Direct measurements with single-frequency lasers.

<sup>h</sup>Extrapolated using  $1\alpha \omega_s^4 (\omega_a - \omega_s)^{-2}$ ;  $\omega_a = 39,000$  cm<sup>-1</sup>.

<sup>i</sup>See Ref. 77 for discussion of peak cross section measurements.

<sup>j</sup>Relative threshold measurement.

<sup>k</sup>For detailed analysis of H<sub>2</sub> cross-section pump frequency dependence, see Ref. 63.

<sup>l</sup>Pressure independent gain; Q(1) transition.

<sup>m</sup>Corrected using linewidth of Ref. 58; Q(6) transition.

<sup>n</sup>Transient gain.

Reprinted with permission from M. J. Weber (ed.), *CRC Handbook of Laser Science and Technology: Optical Materials*, suppl. 2, copyright CRC Press, Boca Raton, FL, 1988; R. W. Boyd, *Nonlinear Optics*, Academic Press, New York, 1992; M. J. Weber (ed.), *CRC Handbook of Laser Science and Technology: Optical Materials*, part 1, vol. III, copyright CRC Press, Boca Raton, FL, 1988.

**TABLE 4** Temperature Dependence of Line Shift Parameters for H<sub>2</sub>

T (K)	Transition	$\nu_R(0)$ (cm <sup>-1</sup> )	C (MHz/amagat)	D (MHz/amagat <sup>2</sup> )	Reference
474	Q(l)	4155	9.5 ± 0.9	0.51 ± 0.07	22
298	Q(l)		-96 ± 1		22
298	Q(0)		-64 ± 5		22
81	Q(l)		-305 ± 10		22
81	Q(0)		-250 ± 10		22
81	Q(0)		-336 ± 10		22
<i>p</i> -H <sub>2</sub>					
295	S(0)		6.5 ± 3		78
	S(l)		5.9 ± 1		78
80	S(0)		-22.3 ± 0.6		78
	S(l)		-23 ± 0.6		78

Line shift parameters:  $\nu_R = \nu_R(0) + C\rho + D\rho^2$   
 Reprinted with permission from M. J. Weber (ed.), *CRC Handbook of Laser Science and Technology: Optical Materials*, suppl. 2. Copyright CRC Press, Boca Raton, FL, 1988.

**TABLE 5** Temperature Dependence of Line Broadening Parameters for H<sub>2</sub> and N<sub>2</sub>

		H <sub>2</sub>						
T (K)	Transition	A (MHz – amagat)	B (MHz/amagat)	$\rho_c$ (amagat)	Reference			
474	Q(1)	508 ± 29	94.0 ± 2.0	1.23	22			
298	Q(l)	309 ± 11	52.2 ± 0.5	0.92	22			
298	Q(0)	257 ± 12	76.6 ± 0.8	0.79	22			
81	Q(1)	107 ± 20	41.5 ± 0.6	0.63	22			
81	Q(0)	189 ± 40	29 ± 1	1.1	22			
81	Q(0)	76 ± 6	45.4 ± 0.8	0.45	22			
<i>p</i> -H <sub>2</sub>								
295	S(l)	6.15	114 ± 5	0.134	78			
	S(0)	1.87	77 ± 2	0.068	78			
80	S(l)	2.1	110 ± 3	0.088	78			
	S(0)	1.37	67 ± 2	0.095	78			
		N <sub>2</sub>						
T (K)	Transition	$\nu_R$ (cm <sup>-1</sup> )	$\lambda_s$ (nm)	$B_0$ (MHz/amagat)	$\gamma$	$\Delta N/N$	$g$ (cm/GW)	Reference
298	S(6)	60	568	3560	0.26 ± .04	0.0282	0.0036	70, 78
	S(8)	76	568	3270	0.33 ± .004	0.0337	0.0046	70, 78
	S(10)	92	568	3060	0.35 ± .002	0.0335	0.0048	70, 78
	S(12)	108	568	2870	0.39 ± .03	0.0289	0.0043	70, 78
195	S(6)		568	3070		0.0485	0.0072	70, 78
	S(8)		568	2860		0.0491	0.0076	70, 78
	S(10)		568	2660		0.0399	0.0065	70, 78
	S(12)		568	2340		0.0271	0.0049	70, 78
80	S(6)		568	2520		0.0897	0.0161	70, 78
	S(8)		568	2120		0.0452	0.0093	70, 78
	S(10)		568	1940		0.0156	0.0034	70, 78
	S(12)		568	1690		0.00378	0.00091	70, 78

Broadening coefficients for H<sub>2</sub>:  $\Delta\nu_R = A/\rho + B\rho$   
 $A = 309/\rho(T/298)^{0.92}$   $B = [51.8 + 0.152(T - 298) + 4.85 \times 10^{-4}(T - 298)^2] \rho$

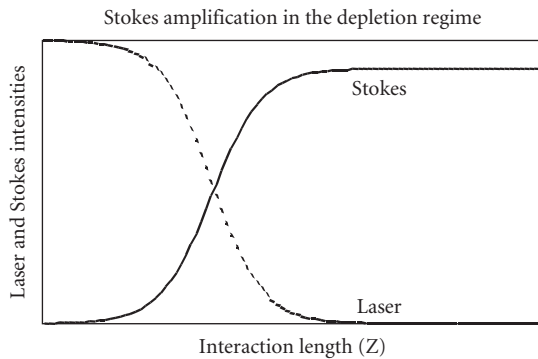
Broadening coefficients for N<sub>2</sub>:  $\Delta\nu_R = B_0 \rho(T/295)^7$

Reprinted with permission from M. J. Weber (ed), *CRC Handbook of Laser Science and Technology: Optical Materials*, suppl. 2. Copyright CRC Press, Boca Raton, FL, 1988.

**TABLE 6** Formula Summary for SRS in Molecules 1

Quantity	Formula	Reference
$\partial\sigma/\partial\Omega$ (vibrational, averaged over rotational levels)	$(2\pi\nu_s)^4(\alpha_{01}^2 + 7/45\sum_j f_j b_{jj} \gamma_{01}^2)$	62
$\partial\sigma/\partial\Omega$ (vibrational, single rotational levels)	$(2\pi\nu_s)^4(\alpha_{01}^2 + 4/45 b_{jj} \gamma_{01}^2)$	62
	$b_{jj} = J(J+1)(2J-1)(2J+1)$ $f_j$ -relative population of level $J$ For hydrogen: $\gamma_{01} = 1.11 \times 10^{-25} \text{ cm}^{-3}$ $\gamma_{01} = 0.951 \times 10^{-25}$ for $\lambda_L = 500 \text{ nm}$	
$\partial\sigma/\partial\Omega$ (vibrational, wavelength dependence for hydrogen)	$A \nu_s^4 / (\nu_i^2 - \nu_L^2)^2$	62
$\nu_R$ (Raman shift in H2, pressure dependence)	$\nu_R(0) + C\rho + \Delta\rho^2$ ( $\rho$ in amagats)	62
$\Delta\nu_R$ (linewidth of H2, pressure and temperature dependence)	$(309/\rho)(T/298)^{0.92} + [51.8 + 0.152(T - 298) + 4.85 \times 10^{-4}(T - 298)^2] \rho$ ( $\rho$ in amagats)	62
$\partial\sigma/\partial\Omega$ (rotational scattering in linear molecules)	$(2/15)(2\pi\nu_s/c)^4 \gamma^2 [(J+1)(J+2)] / [(2J+1)(2J+3)]$	70
	$J$ is lower-state rotational number $\gamma(\nu) = \alpha_{s\parallel} [v_{s\parallel}^2 / (v_{s\parallel}^2 - \nu^2)] - \alpha_{s\perp} [v_{s\perp}^2 / (v_{s\perp}^2 - \nu^2)]$ For nitrogen: $v_{s\parallel} = 1.26 \times 10^5 \text{ cm}^{-1}$ $v_{s\perp} = 1.323 \times 10^5 \text{ cm}^{-1}$ $\alpha_{s\parallel} = 2.2 \times 10^{-24} \text{ cm}^{-3}$ $\alpha_{s\perp} = 1.507 \times 10^{-24} \text{ cm}^{-3}$	

Reprinted with permission from M. J. Weber (ed.), *CRC Handbook of Laser Science and Technology, Optical Materials*, suppl. 2. Copyright CRC Press, Boca Raton, FL, 1988.



**FIGURE 4** Calculated pump and Stokes dependence on interaction length in pump depletion regime.

conversion is not possible with Raman scattering, in principle 100 percent of the pump photons can be converted to the Stokes wave. In practice, high photon conversion efficiency to a single Stokes wave is limited in Raman generators by multiple Stokes or anti-Stokes scattering. High conversion efficiencies are generally obtained in practice in Raman amplifiers or in Raman generators where multiple Stokes generation is unfavorable because of energy level structure. Photon conversion efficiencies in excess of 90 percent have been reported with pulsed lasers.

*Gain narrowing* Gain narrowing can occur when the Raman gain varies in one of the parameters of the interaction—for example, time, because of pulsed radiation; space, because of a special mode profile; or spectrum, because of use of broadband light; or when a Raman generator is used.

*Spectral gain narrowing* Spectral gain narrowing is commonly encountered in Raman generators. The spontaneous Stokes emission has the spectral variation of the appropriate Raman transition. For a lorentzian line shape, this variation is given by

$$P_s(\Delta\omega) = P_s(0) \frac{1}{\Delta\omega^2 T^2 + 1} \quad (27)$$

where  $\Delta\omega = \omega_o - (\omega_L - \omega_s)$ .

This variation with detuning also appears in the Raman gain of Eq. (13) or (15). The Stokes light generated from such a signal can be represented approximately as

$$I(\Delta\omega, L) = I(0) \frac{1}{\Delta\omega^2 T^2 + 1} \exp\left[\frac{G(0)}{\Delta\omega^2 T^2 + 1}\right] \quad (28)$$

The reduced gain at nonzero detunings from the Raman resonance leads to narrowing of the amplified Stokes spectrum relative to the spontaneous spectrum.<sup>22</sup> If we use the quantity  $\Delta\omega(G)$  to describe the spectral width (FWHM) of the generated or amplified Stokes light, then the spectral width of the amplified Stokes light is

$$\Delta\omega(G) = \Delta\omega(0) \sqrt{\frac{\ln 2/G(0)}{1 - \ln 2/G(0)}} \quad (29)$$

where  $G(0)$  is the gain at the center of the line. If we consider the range of values of  $G$  that can be achieved without driving the interaction into saturation to be  $23 < G_{\max} < 40$ , then the maximum gain narrowing that can be experienced without driving the interaction into saturation is on the order of 5.5 to 7.5.

*Photon description* The steady-state Raman gain can be recast in the formulation of photon interactions. In this situation, the pump and Stokes intensities are given by

$$I_s = h\nu_s n_s \quad (30a)$$

$$I_L = h\nu_L n_L \quad (30b)$$

where  $n_s$  and  $n_L$  are the photon flux densities (photons per square centimeter per second), which are related to the corresponding photon densities (photons per cubic centimeter) without dispersion as

$$n_s = N_s c \quad (31a)$$

$$n_L = N_L c \quad (31b)$$

Equations for the growth of pump and Stokes photon densities can be derived from quantum mechanical rate equations as<sup>7</sup>

$$\frac{dN_s}{dt} = K(N_s + 1)N_L \quad (32a)$$

$$\frac{dN_L}{dt} = -K(N_L + 1)N_s \quad (32b)$$

where  $K$  is the appropriate transition rate for the Raman interaction.



These can be converted to the spatial gain equations for the photon flux density through the relations

$$\frac{dN_s}{dt} = \frac{dn_s}{dz} \quad (33a)$$

$$\frac{dN_L}{dt} = \frac{dn_L}{dz} \quad (33b)$$

giving

$$\frac{dn_s}{dz} = K(n_s + 1)n_L \quad (34a)$$

$$\frac{dn_L}{dt} = -K(n_L + 1)n_s \quad (34b)$$

The 1 in Eq. (34a and b) arises from quantum mechanical commutators and represents spontaneous Raman scattering. When the number of Stokes photons per mode is small compared to unity, the spontaneous Raman emission result is obtained:

$$n_s = Kn_L L \quad (35)$$

where  $L$  is the length of the scattering medium. When  $n_s \gg 1$ , the exponential gain of stimulated Raman scattering is obtained:

$$n_s(L) = n_s(0)e^{Kn_L z} \quad (36)$$

where  $K = hv_{g_{SS}}$ . The relation of spontaneous and stimulated Raman scattering will be discussed again later in the chapter.

**Transient Effects** When the temporal structure of the pump or Stokes wave varies on a time scale comparable to or shorter than the steady-state time given in Eq. (19), transient effects must be taken into account. In this situation, the integrating effects of the material excitation affect the properties of the Raman interaction. Depending on the situation, this can result in reduced Raman gain for pulses of a given intensity or alteration of the coherence properties of the Stokes radiation. Transient effects can occur for short pump pulses or broadband pump and/or Stokes waves.

**Pulsed transient effects** Transient Raman scattering with pulsed Raman radiation is described by the equations

$$\frac{\partial A_s(z, t)}{\partial z} + \frac{n_s}{c} \frac{\partial A_s(z, t)}{\partial t} = i\kappa_2 Q^*(z, t) A_L(z, t) \quad (37a)$$

$$\frac{\partial A_L(z, t)}{\partial z} + \frac{n_L}{c} \frac{\partial A_L(z, t)}{\partial t} = i \frac{\omega_L n_s}{\omega_s n_L} \kappa_2 Q(z, t) A_s(z, t) \quad (37b)$$

$$\frac{\partial Q^*(z, t)}{\partial t} + \Gamma Q^* = -i\kappa_1 A_s(z, t) A_L^*(z, t) \quad (37c)$$

where

$$\kappa_1 = \frac{1}{4\omega_0 m} \left( \frac{\partial \alpha}{\partial Q} \right) \quad (38)$$

and  $\kappa_2$  is given in Eq. (11).

In the most general form, when pump depletion is involved, these equations must be solved numerically. When pump depletion and dispersion can be neglected, the pump field can be taken as a prescribed function of  $z$  and  $t$ , and the equations take on the form

$$\frac{\partial A_s(z', \tau)}{\partial z'} = i\kappa_2 Q^*(z', \tau) A_L(\tau) \quad (39a)$$

$$\frac{\partial Q^*(z', \tau)}{\partial \tau} + \Gamma Q^*(z', \tau) = -i\kappa_1 A_s(z', \tau) A_L^*(\tau) \quad (39b)$$

where  $z'$  and  $\tau$  are coordinates moving with the common velocity of the pump and Stokes pulses:

$$z' = z \quad (40a)$$

$$\tau = t - z/c \quad (40b)$$

An integral solution for these equations can be written as<sup>16-19</sup>

$$A_s(z, \tau) = A_s(0, \tau) + \sqrt{\kappa_1 \kappa_2 z} A_L(\tau) \int_{-\infty}^{\tau} \frac{e^{-\Gamma(\tau-\tau')} A_L^*(\tau') A_s(0, \tau') I_1(\sqrt{4\kappa_1 \kappa_2 z [p(\tau) - p(\tau')])}}{\sqrt{p(\tau) - p(\tau')}} d\tau' \quad (41a)$$

where  $I_0$  and  $I_1$  are modified Bessel functions and

$$p(\tau) = \int_{-\infty}^{\tau} |A_L(\tau')|^2 d\tau' \quad (42)$$

is proportional to the total pump energy integrated to time  $\tau$ .

In the extreme transient regime, when  $t_p \ll T_2$ , and when the incident Stokes pulse has the same functional form as the pump, an analytic solution for the Stokes intensity can be found:

$$I_s(z, \tau) = I_s(0, \tau) I_0^2(u(z, \tau)) \quad (43)$$

where

$$u(z, \tau) = \sqrt{4\kappa_1 \kappa_2 z p(\tau)} = \sqrt{2g_{ss}\Gamma z} \int_{-\infty}^{\tau} I_L(\tau') d\tau' \quad (44)$$

and  $g_{ss}$  is the steady-state gain coefficient as given in Eq. (13).

When the conditions for Eq. (43) are valid, the solution can be approximated for values of  $u$  greater than about 3, corresponding to intensity amplifications of about 24, with the first term in the asymptotic expansion:

$$I_s(z, \tau) = I_s(0, \tau) \frac{e^{2u}}{2\pi u} \quad (45)$$

Quantities other than the instantaneous intensity, such as power density, energy density, or total pulse energy, are useful for characterizing transient Raman measurements done with short pulses. Expressions corresponding to Eq. (45) and for the first and second terms of the expansion of Eq. (43) in  $u$  are given in Table 7. The variation of these quantities with the transient gain parameter

**TABLE 7** Analytic Expressions and High-Gain Limiting Forms for Small-Signal Transient Raman Amplification of Various Quantities<sup>19,a</sup>

	Intensity, $I_S^b$	Energy Density, $\mathcal{W}_S^c$	Power, $\mathcal{P}_S^d$	Energy, $\mathcal{E}_S^e$
Approximation	$I_S(r, z, t) = \frac{I_S(r, z, t)}{I_S(r, 0, t)}$	$\mathcal{W}_S(r, z) = \frac{\int_{-\infty}^{\infty} I_S(r, z, t') dt'}{\int_{-\infty}^{\infty} I_S(r, 0, t') dt'}$	$\mathcal{P}_S(r, z) = \frac{\int_0^{\infty} I_S(r, z, t) dr^2}{\int_0^{\infty} I_S(r, 0, t) dr^2}$	$\mathcal{E}_S(r, z) = \frac{\int_0^{\infty} \int_{-\infty}^{\infty} I_S(r, z, t') dt' dr^2}{\int_0^{\infty} \int_{-\infty}^{\infty} I_S(r, 0, t') dt' dr^2}$
Exact	$I_0^2(u)$	$I_0^2(u) - I_1^2(u)$	$I_0^2(u) - I_1^2(u)$	$I_0^2(u) - 2I_1^2(u) + I_0(u)I_2(u)$
High-gain limit (1st term)	$e^{2u}/2\pi u$	$e^{2u}/2\pi u^2$	$e^{2u}/2\pi u^2$	$e^{2u}/2\pi u^3$
High-gain limit (1st 2 terms)	$(e^{2u}/2\pi u)(1 + 1/4u)$	$(e^{2u}/2\pi u^2)(1 + 1/4u)$	$(e^{2u}/2\pi u^2)(1 + 1/4u)$	$(e^{2u}/2\pi u^3)(1 + 3/4u)$

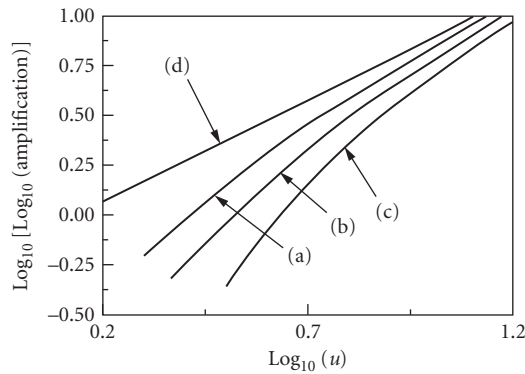
$$^a u = u_m(r, z, t) = 2[\kappa_1 \kappa_2 \int_{-\infty}^t |A_L(r, t')|^2 dt']^{1/2}$$

$$^b u = u_m(r, z, t)$$

$$^c u = u_m(r, z, \infty)$$

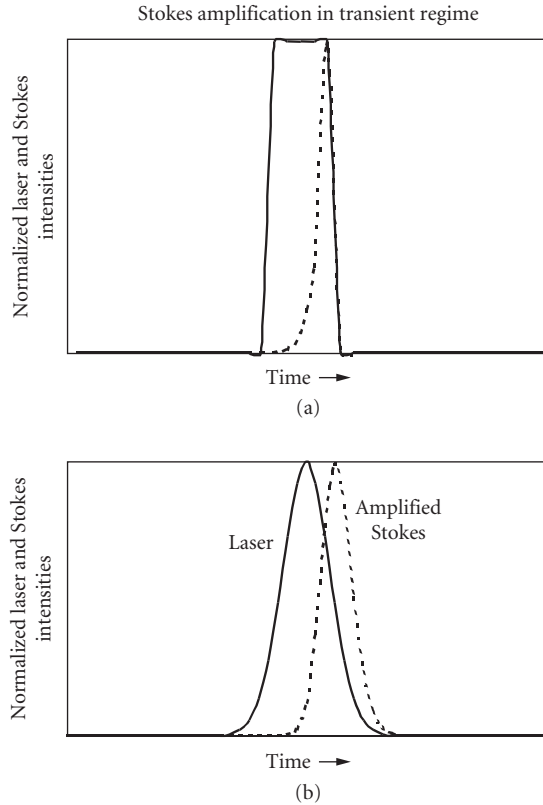
$$^d u = u_m(0, z, t)$$

$$^e u = u_m(0, z, \infty)$$


**FIGURE 5** Theoretical dependence of the small-signal amplification on the transient gain parameter  $u$  for (a) the intensity, (b) the energy density or power, and (c) the energy as predicted by the exact Bessel function solution. The exponential form  $\exp(2u)$  is shown for comparison in (d). (From Ref. 19.)

$u$  is shown in Fig. 5. These solutions are useful for modeling the approximate properties of transient interactions. However, in most practical situations the incident pump and Stokes pulses do not have the same functional form, and the more general integral solution of Eq. (41a) must be used for accurate results, taking into account the specific variation of the Stokes amplitude and phase and the relative timing between the incident Stokes and pump pulses. An approximate analytic expression has been given in the limit of high conversion in which the Stokes pulse evolves to an approximate constant form and the pump pulse is described by regular Bessel functions.<sup>79</sup>

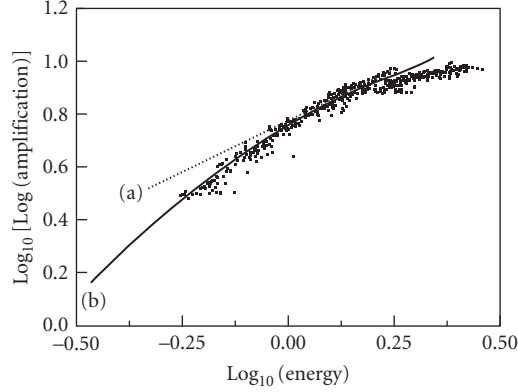
In the extreme transient regime  $t_p \ll T_s$ , growth of the Stokes pulse in the leading part of the pulse is dominated by the Bessel function and the Stokes pulse rises more slowly than the pump. In the trailing part of the pulse, the integral contribution remains fairly constant and the Stokes amplitude



**FIGURE 6** Calculated Stokes intensity (dotted line) and pump (solid line) for square pump pulses (a) and gaussian pump pulses (b). The input Stokes signal was assumed to be constant in both cases.

follows the pump amplitude.<sup>17</sup> The result is that the Stokes pulse is delayed relative to the pump and is shorter than the pump. Ideal square pulses can be shortened by an arbitrarily large factor, while more realistic gaussian pulses can be shortened by about a factor of 2.<sup>17,80</sup> The transient response for square and gaussian pulses is illustrated in Fig. 6. Optimal amplification of the Stokes pulse has been shown to require that the incident Stokes pulse arrive earlier than the pump by about half the pulse duration.<sup>19</sup> An example of experimentally measured transient Raman amplification is given in Fig. 7 along with a theoretical comparison. The theoretical curve was obtained by integrating the square magnitude of Eq. (41a) over space and time using the experimentally measured amplitude and phase variations of the incident Stokes pulse. Agreement between experiment and theory was obtained over approximately eight orders of magnitude using one adjustable parameter in the region below pump depletion.

The peak intensity amplification in the extreme transient limit is reduced from the steady-state amplification for pump pulses with the same peak intensity. The intensity amplification grows as the pulse length increases, approaching the steady-state value when  $t_p \gg G_s T_2$ . For pulses of a given energy, the total integrated energy amplification increases steadily as the pulse duration decreases, reaching a maximum in the extreme transient regime.



**FIGURE 7** Experimental measurement of transient Stokes amplification in hydrogen gas. Solid line includes measured phase and amplitude structure of incident Stokes pulse. Dotted line was calculated for the same conditions, neglecting the phase structure of the incident Stokes pulse. The deviation of the solid curve from the measurements at the high end is due to pump depletion. (From Ref. 19.)

*Phase pulling* There is a tendency for the Stokes phase to become locked to the pump phase in the transient regime. This can be seen from the equations for the phases of the pump and Stokes pulses:<sup>19</sup>

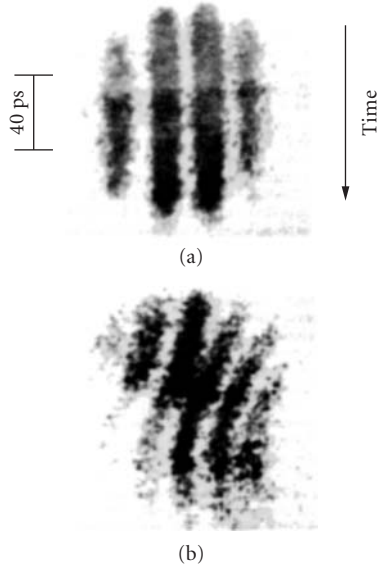
$$\frac{\partial \phi_s}{\partial z} = -\kappa_2 \frac{A_L}{A_S} Q \sin \Phi \quad (46a)$$

$$\frac{\partial \phi_L}{\partial z} = -\kappa_2 \frac{n_s \omega_L}{n_l \omega_s} \frac{A_S}{A_L} Q \sin \Phi \quad (46b)$$

$$\frac{\partial \phi_Q}{\partial z} = -\kappa_1 \frac{A_L A_S}{Q} \sin \Phi \quad (46c)$$

where  $\Phi = \phi_s + \phi_Q - \phi_L$ .

The phase driving terms vanish for the condition  $\Phi = 0$  or  $\pi$ , which are the conditions for optimum power transfer from the pump beam and to the pump beam, respectively. Phase pulling occurs only when  $\Phi \neq 0$  or  $\pi$  and when the time derivatives are important. When the time derivatives are not important,  $\phi_Q$  automatically adjusts itself so that the condition  $\Phi = 0$  is satisfied. When the transient response is important, phase pulling occurs whenever  $\phi_s$  and  $\phi_L$  have different time dependencies. If the amplitude of the initial Stokes wave is small compared to that of the pump, the phase of the material excitation will be established at some constant value early in the pulse after the material excitation has been amplified above the noise level. At later times the phase of the Stokes wave will be driven according to Eq. (46a) so as to establish the condition  $\Phi = 0$ . In the early stages of the amplification, the corresponding driving term for the pump phase is much smaller, so that the Stokes phase becomes effectively locked to that of the incident pump, with a possible constant offset due to the phase of the material excitation. If the amplitude of the incident Stokes wave is comparable to that of the pump, the phases of all of the waves can evolve during the interaction, and the



**FIGURE 8** Experimental demonstration of phase pulling in transient Raman amplification. The pump beam and incident Stokes beam both carry phase modulation due to the nonlinear index in the laser. The measurement shows time-dependent interference between the incident and amplified Stokes waves. When the incident Stokes phase structure is aligned with the pump phase structure, no phase pulling is observed (a). When the incident Stokes pulse is advanced to misalign the pump and Stokes phase structure, phase pulling is observed (b). (From Ref. 19.)

transfer of power from the pump to the Stokes wave can be affected or greatly reduced. An example of phase pulling in short-pulse Raman interactions is shown in Fig. 8.

*Solitons* Soliton and other self-similar solutions to the transient Raman equations can also be derived. Using Eq. (37) in the form

$$\frac{\partial A_s}{\partial \xi} = i\kappa_2 A_L Q^* \quad (47a)$$

$$\frac{\partial A_L}{\partial \xi} = i \frac{\omega_L}{\omega_s} \kappa_2 A_s Q \quad (47b)$$

$$\frac{\partial Q}{\partial \tau} + \Gamma Q = i\kappa_1 A_L A_s^* \quad (47c)$$

where  $\kappa_1$  and  $\kappa_2$  are given in Eqs. (38) and (11), respectively, and  $\xi$  and  $\tau$  are moving coordinates related to the laboratory coordinates by

$$\xi = z \quad (48a)$$

$$\tau = t - zn/c \quad (48b)$$

In the extreme transient limit, the term with  $\Gamma$  in Eq. (47c) can be neglected and the equations can be expressed in normalized quantities as

$$\frac{\partial A_1}{\partial \chi} = -A_2 X \quad (49a)$$

$$\frac{\partial A_2}{\partial \chi} = A_1 X^* \quad (49b)$$

$$\frac{\partial X}{\partial \tau'} = A_1 A_2^* \quad (49c)$$

where  $A_1 = \sqrt{\omega_s n_L \kappa_1 / \omega_L n_S \kappa_2} A_L$ ,  $A_2 = \sqrt{\kappa_1 / \kappa_2} A_S$ , and  $X = -i \sqrt{\omega_L n_S / \omega_s n_L} Q$ ,  $\chi = \kappa_2 \xi$ ,  $\tau' = (\omega_L n_S / \omega_s n_L) \kappa_2 \tau$ .

The soliton solutions are:<sup>81</sup>

$$A_1(\chi, \tau) = K(\tau) \left(1 - \frac{a^2}{4\alpha^2}\right)^{1/2} \exp(i\alpha\chi/2) \operatorname{sech} \left\{ \left(\alpha^2 - \frac{a^2}{4}\right)^{1/2} \left[\chi - \frac{I(\tau)}{\alpha^2}\right] \right\} \quad (50a)$$

$$A_2(\chi, \tau) = K(\tau) \left(1 - \frac{a^2}{4\alpha^2}\right)^{1/2} \tanh \left\{ \left(\alpha^2 - \frac{a^2}{4}\right)^{1/2} \left[\chi - \frac{I(\tau)}{\alpha^2}\right] \right\} \quad (50b)$$

$$X(\chi, \tau) = \left(\alpha^2 - \frac{a^2}{4}\right)^{1/2} \exp(i\alpha\chi/2) \operatorname{sech} \left\{ \left(\alpha^2 - \frac{a^2}{4}\right)^{1/2} \left[\chi - \frac{I(\tau)}{\alpha^2}\right] \right\} \quad (50c)$$

where  $K^2(\tau) = |A_1(\chi, \tau)|^2 + |A_2(\chi, \tau)|^2$ ,  $I(\tau) = \int_{-\infty}^{\tau} K^2(\tau') d\tau'$  and  $a$  and  $\alpha$  are arbitrary parameters such that  $a > \alpha/2$ .

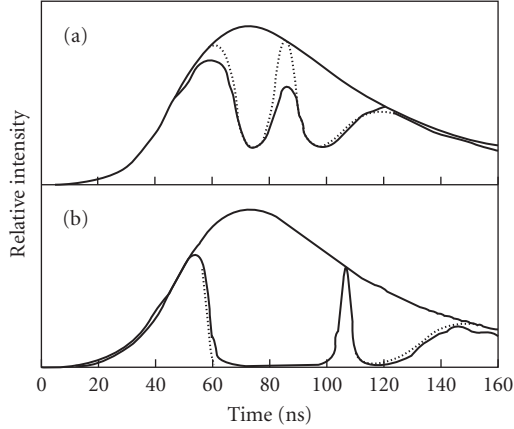
These are transient solutions in which the Stokes pulse is large everywhere except for a dip centered on the position  $\chi = I(\tau)/\alpha^2$ . The Stokes pulse also has a phase shift at its center. When  $a = 0$ , the phase shift is  $\pi$ , and when  $a \neq 0$ , it is smaller. The pump intensity is small except for a narrow region centered about  $\chi = I(\tau)/\alpha^2$ , and the behavior of the material excitation is similar to that of the pump.

The form of these solutions is opposite to those normally encountered in Raman interactions. Once they are established, they propagate in self-similar form at a speed that is slower than that of the optical pulses, gradually "walking" backward in the optical pulse and eventually disappearing. However, the pulse shapes necessary for soliton formation do not occur in all experimental situations. In normal transient experiments, with the incident Stokes wave weak and the pump strong, the Stokes phase will lock to the pump phase, and solitons cannot develop. They have been produced with a phase shift introduced onto the Stokes pulse externally.<sup>82</sup> In this situation, the soliton pulse of Eq. (50a), which is significantly shorter than  $T_2$ , evolves from longer pulses and damping plays a central role in its formation. An experimental demonstration of this behavior has been done by Druhl et al.<sup>82</sup> and their results are reproduced in Fig. 9. Conditions for soliton formation can also be encountered in growth from noise using narrowband pump pulses due to phase fluctuations in the zero point starting signal of the Stokes field. Other self-similar solutions are possible as well. Forms with damped oscillations, termed *accordion solutions*, have been described by Menyuk.<sup>83</sup>

**Broadband effects** Transient effects also appear in the conversion of broadband radiation, which is produced, for example, in many types of pulsed lasers, when the overall pulse duration is longer than  $T_2$  but the pump linewidth is wider than the Raman linewidth:<sup>84-99</sup>

$$t_p \gg T_2 \quad (51a)$$

$$\Delta\nu_L > \frac{1}{\pi T_2} \quad (51b)$$



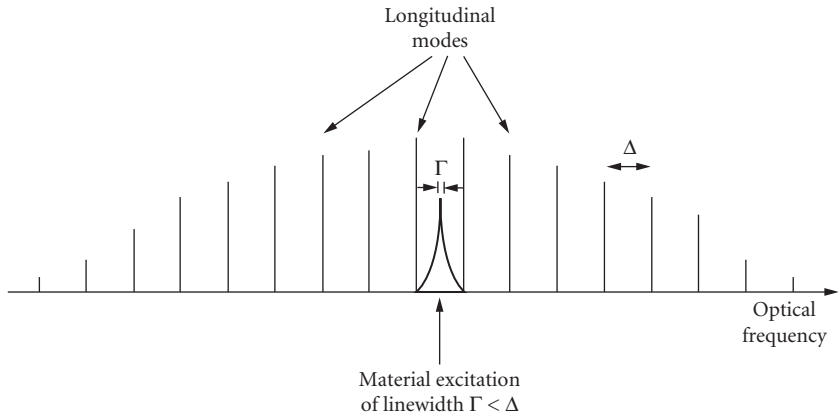
**FIGURE 9** Experimental (solid curves) and theoretical (dashed curves) behavior of Raman soliton formation in hydrogen gas showing the input (upper curves) and output (lower curves) pump pulses. The soliton was initiated by introducing a phase shift on the incident Stokes pulse. The overall pulse duration was about 70 ns. The curves in (b) were obtained with higher pump power than the curves in (a). (From Ref. 82; copyright 1983 by American Physical Society.)

The equations for the Stokes and material excitation are as given in Eq. (37). The interaction can be modeled in the time domain, or in the frequency domain using a mode model for the laser radiation.

In the mode picture, the pump and Stokes radiation is modeled as being made up of a combination of randomly phased modes separated by an amount  $\Delta$ , shown in Fig. 10:

$$E_S = \frac{1}{2} \sum_m A_{S,m} e^{-i(m\Delta t + \phi_{S,m})} e^{-i(\omega_S t - k_S z)} \quad (52a)$$

$$E_L = \frac{1}{2} \sum_m A_{L,m} e^{-i(m\Delta t + \phi_{L,m})} e^{-i(\omega_L t - k_L z)} \quad (52b)$$



**FIGURE 10** Mode structure used to model the broadband Raman scattering. The laser and Stokes modes are spaced by frequency  $\Delta$ , and, for approximations of Eq. (56), the Raman linewidth is narrower than the mode spacing.



In the absence of dispersion, Eq. (37c) can be solved in the frequency domain:

$$Q_k^* = i\kappa_2 \sum_m \frac{A_{L,m+k}^* A_{S,m}}{\Gamma - im\Delta} \quad (53)$$

The average Stokes intensity is given by<sup>93</sup>

$$\bar{I}_S(z) = \bar{I}_S(0) + \bar{I}_S(0) \sum_k \left[ \frac{\left| \sum_m A_{L,m+k} A_{S,m}^*(0) \right|^2}{\sum_m A_{L,m} A_{L,m}^* \sum_m A_{S,m}(0) A_{S,m}^*(0)} \right] \left\{ \exp \left[ \frac{\bar{I}_L g z}{1 + (k\Delta/\Gamma)^2} \right] - 1 \right\} \quad (54)$$

where the bar symbol denotes the average intensity given by

$$\bar{I}_S = \frac{1}{2} c n_s \epsilon_o \sum_m A_{S,m}^* A_{S,m} \quad (55)$$

If the longitudinal mode spacing is much wider than the Raman linewidth and the pump linewidth is broad enough, the material excitation  $Q$  will not be able to follow the temporal variations of the light due to the mode structure. This is equivalent to the steady-state approximation. Only the  $k = 0$  term survives in Eq. (54), and the average intensity is given by

$$\bar{I}_S(z) = \bar{I}_S(0) [1 + R(e^{g\bar{I}_L z} - 1)] \quad (56)$$

where  $R$  is the field cross-correlation function given by

$$R = \frac{\left| \sum_n A_{S,n}(0) A_{P,n}^*(0) \right|^2}{\sum_n |A_{S,n}|^2 \sum_n |A_{L,n}|^2} \quad (57)$$

In this approximation the double summation in the product of the Stokes and pump waves has collapsed to a single sum. Each Stokes mode  $m$  interacts only with the corresponding pump mode  $m$ .

When the Stokes field is correlated with the pump, the correlation function is unity and the broadband Stokes light has the same exponential gain as in a narrowband interaction with the same average pump intensity. When the incident Stokes wave is not fully correlated with the pump, the component of the Stokes wave that is correlated with the pump has the largest gain, while Stokes components that are not correlated with the pump ( $R = 0$ ) do not receive amplification.<sup>86-88</sup> The Stokes wave thus becomes more correlated with the pump wave as it is amplified. This behavior is equivalent to the phase-pulling effects discussed earlier. The effective Stokes input signal to the amplifier is reduced by the factor  $1/M$ , where  $M$  is the number of spectral modes of the Stokes wave. However, when growth from noise is considered, the total input Stokes signal increases in proportion to the Stokes bandwidth and the effective Stokes input is one photon per mode independent of the Stokes bandwidth. The threshold for growth from noise is therefore the same for broadband and narrowband interactions.

When dispersion is taken into account,<sup>84,88,96</sup> the exponential gain becomes:

$$G = G_0 - \frac{4\tau_w^2}{G_0\tau_c^2} \quad (58)$$

where  $G_0$  is the gain without dispersion,  $\tau_c$  is the correlation time of the laser radiation, defined by  $\tau_c = [1/\delta\omega_L^2]^{1/2}$  where  $\delta\omega_L^2$  is the variance of the laser spectrum, and  $\tau_w$  is the beam walkoff time, given by

$$\tau_w = z\Delta(1/\nu) \quad (59)$$

where  $\Delta(1/\nu) = 1/\nu_{gl} - 1/\nu_{gs}$ .

Solutions also exist for pump depletion when the mode spacing is large and the dispersion can be neglected:<sup>98</sup>

$$I_S(z) = I_S(0) \frac{1 + \alpha(1 + \beta)\gamma + (1 - \beta)e^{-\beta \left[ I_L(0) + \frac{\omega_L}{\omega_S} I_S(0) \right] gz}}{2 \gamma + e^{-\beta \left[ I_L(0) + \frac{\omega_L}{\omega_S} I_S(0) \right] gz}} \quad (60)$$

where

$$\alpha = \frac{\omega_S I_L(0)}{\omega_L I_S(0)} \quad (61)$$

$$\beta = \left[ \left( I_S(0) - \frac{\omega_S}{\omega_L} I_L(0) \right)^2 + 4 \frac{\omega_S}{\omega_L} I_L(0) I_S(0) R \right]^{1/2} \left/ \left[ I_S(0) - \frac{\omega_S}{\omega_L} I_L(0) \right] \right. \quad (62)$$

$$\gamma = \frac{(1 + \beta) - \alpha(1 - \beta)}{\alpha(1 + \beta) - (1 - \beta)} \quad (63)$$

Broadband Raman scattering has also been analyzed within the time domain.<sup>99</sup> Here the starting point is Eq. (39a and b). The average of quantities is calculated as

$$\langle f(t) \rangle = \frac{1}{T} \int_t^{t+T} f(t') dt' \quad (64)$$

where the interval  $T$  is chosen to be large enough to provide a stationary average of the temporal structure in the signal. Generally speaking,

$$T \gg \frac{1}{\Delta\nu_L} \quad (65)$$

If  $\Delta\nu_L \gg \Delta\nu_R$ , again the material excitation cannot follow the time variations of the optical signals and Eq. (39b) can be solved as

$$\langle Q^*(t) \rangle = -\frac{i\kappa}{\Gamma} \langle A_S(t) A_L^*(t) \rangle \quad (66)$$

$\langle Q^*(t) \rangle$  is a slowly varying quantity even though  $A_S(t)$  and  $A_L(t)$  individually have rapid time variations. The equation for the average Stokes intensity is

$$\frac{\partial}{\partial z} \langle A_S(t) A_S^*(t) \rangle = i\kappa_2 \langle A_S^*(t) A_L(t) Q^*(t) - A_S(t) A_L^*(t) Q(t) \rangle \quad (67)$$

Making use of the fact that  $Q$  is not correlated with  $A_L$  or  $A_S$  and using Eq. (66) gives

$$\frac{\partial}{\partial z} \langle A_S(t) A_S^*(t) \rangle = i\kappa_2 [\langle A_S^*(t) A_L(t) \rangle \langle Q^*(t) \rangle - \langle A_S(t) A_L^*(t) \rangle \langle Q(t) \rangle] \quad (68)$$

$$\frac{\partial}{\partial z} \langle A_S(t) A_S^*(t) \rangle = \frac{\kappa_1 \kappa_2}{\Gamma} [\langle A_S^*(t) A_L(t) \rangle \langle A_S(t) A_L^*(t) \rangle] \quad (69)$$

The Stokes intensity is given by

$$\langle I_S(z, t) \rangle = \langle I_S(0, t) \rangle [1 + R(e^{g I_L} - 1)] \quad (70a)$$

where  $R$  is the normalized Stokes pump cross-correlation function at the input:

$$R = \frac{\langle A_S(0, t) A_L^*(0, t) \rangle \langle A_S^*(0, t) A_L(0, t) \rangle}{\langle |A_S(0, t)|^2 \rangle \langle |A_L(0, t)|^2 \rangle} \quad (70b)$$

The result of Eq. (70a) has the same form as that of Eq. (56). Akhmanov et al.<sup>99</sup> have discussed the statistical properties of stimulated Raman scattering with broadband radiation under a number of other conditions.

*Spectral properties* As described, the Stokes radiation produced in a Raman generator in the steady-state regime is expected to be a gain-narrowed version of the spontaneous Stokes emission. Druhl et al.<sup>82</sup> have shown that when narrowband pump radiation is used, the linewidth of the generated Stokes radiation with single pulses varies randomly from the same width as the pump radiation to a value several times greater than the spontaneous Raman linewidth. Only in the ensemble average does the linewidth of the generated Stokes radiation coincide with the gain-narrowed spontaneous line. Individual pulses exhibit considerable spectral structure. This behavior is traceable to the stochastic nature of the damping process, by which the Raman coherence has decreased to  $1/e$  of its initial value on a statistical basis.

When broadband radiation is used, the Stokes wave has a tendency to be pulled into correlation with the pump and the Stokes spectral variation matches that of the pump. Duncan et al.<sup>100</sup> have shown that the spectrum of transient spontaneous Raman scattering matches that of the pump.

*Anti-Stokes Raman Scattering* Anti-Stokes scattering produces a scattered wave at a shorter wavelength than the pump with frequency

$$\omega_{AS} = \omega_L + \omega_o \quad (71)$$

Anti-Stokes scattering can occur either as a two-photon transition between an upper and lower state, as illustrated in Fig. 1b, or as a resonant four-wave mixing process, as illustrated in Fig. 1c. The first interaction is directly analogous with the transitions involved in stimulated Stokes Raman scattering that have been discussed in previous sections. For a normal thermal distribution of population, the stimulated version of the anti-Stokes interaction incurs exponential loss. Anti-Stokes components are produced in the spontaneous Raman spectrum. When a population inversion is created between the upper and lower states, the anti-Stokes process has exponential gain, with properties similar to those of normal stimulated Stokes Raman scattering. This interaction, termed as *anti-Stokes Raman laser*, has been described by several authors.<sup>101–104</sup>

Anti-Stokes radiation can also be produced through a four-wave mixing process, illustrated in Fig. 1c (Refs. 1, 71, 105–107, 107a, 107b). In this interaction, two pump wave photons are converted to one Stokes and one anti-Stokes photon with the relation

$$2\omega_L = \omega_S + \omega_{AS} \quad (72a)$$

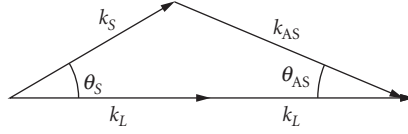
The process is sensitive to the phase mismatch given by

$$\Delta k = k_{AS} - 2k_L + k_S \quad (72b)$$

Usually, four-wave mixing processes are optimized when the phase mismatch is zero. For materials with normal dispersion, this occurs when the Stokes and anti-Stokes waves propagate at angles to the pump light, as shown in Fig. 11. The angles  $\theta_S$  and  $\theta_{AS}$  are given in the small angle and small  $\Delta k$  approximation by

$$\theta_S = \sqrt{\frac{2(k_S + k_{AS} - 2k_L)}{k_S(1 + k_S/k_{AS})}} \quad (73a)$$

$$\theta_{AS} = \sqrt{\frac{2(k_S + k_{AS} - 2k_L)}{k_{AS}(1 + k_{AS}/k_S)}} \quad (73b)$$



**FIGURE 11**  $k$  vector diagram for coherent anti-Stokes Raman scattering showing laser and Stokes and anti-Stokes propagation directions for a medium with positive dispersion.

When the dispersion of the material is small, so that the refractive indexes at the various wavelengths can be approximated as  $n_s = n_L - \delta$  and  $n_{AS} = n_L + \delta$ , the phase-matching angles are given by

$$\theta_S = \sqrt{\frac{2(\lambda_S - \lambda_{AS})\delta}{n_L \lambda_{AS} (1 + \lambda_{AS} / \lambda_S)}} \quad (74a)$$

$$\theta_{AS} = \sqrt{\frac{2(\lambda_S - \lambda_{AS})\delta}{n_L \lambda_S (1 + \lambda_S / \lambda_{AS})}} \quad (74b)$$

The plane-wave steady-state equations describing anti-Stokes generation with four-wave mixing are

$$\frac{dA_S^*}{dz} = K_3 |A_L|^2 A_S^* + K_2 \left( \frac{\omega_S n_{AS}}{\omega_{AS} n_S} \right) A_L^{*2} A_{AS} e^{i\Delta k z} \quad (75a)$$

$$\frac{dA_{AS}}{dz} = -K_1 |A_L|^2 A_{AS} - K_2 A_L^2 A_S^* e^{-i\Delta k z} \quad (75b)$$

where  $K_1 = -iK_{AS}\chi_{AS}$ ;  $K_2 = -iK_{AS}\sqrt{\chi_{AS}\chi_S^*}$ ;  $K_3 = -iK_S\chi_S^*$ ;  $\chi_S$ , and  $\chi_{AS}$  are nonlinear susceptibilities for stimulated growth of the Stokes and anti-Stokes waves, respectively;  $K_{S(AS)} = N\omega_{S(AS)}/n_{S(AS)}c$ ;  $N$  is the number density, and  $\Delta k = k_S + k_{AS} - 2k_L$  is the phase mismatch.

General solutions have been discussed by Bloembergen and Shen.<sup>105</sup> These have shown that the Stokes and anti-Stokes waves grow as part of a mixed mode with amplitudes

$$A_{\text{Raman}} = \begin{pmatrix} A_S \\ A_{AS} \end{pmatrix} \quad (76)$$

One mode is primarily anti-Stokes in character and has exponential loss. The other mode is primarily Stokes in character and has exponential gain given by

$$A_{\text{Raman}} = \begin{pmatrix} A_S \\ A_{AS} \end{pmatrix} e^{g z} \quad (77)$$

where  $g$  is given by

$$g = \text{Re}\{(1/2)(K_3 - K_1)|A_L|^2 - (i/2)[\Delta k^2 + 2i\Delta k(K_3 + K_1)|A_L|^2 - (K_1 - K_3)^2|A_L|^4]^{1/2}\} \quad (78)$$

The exponential gain for the coupled mode is zero for exact phase matching,  $\Delta k = 0$ , and increases for nonzero  $\Delta k$  until it reaches its full decoupled value for  $\Delta k > 2g_{SS}$ , where  $g_{SS}$  is the steady-state gain

coefficient. For nonzero  $\Delta k$ , the maximum gain occurs at small detunings from exact resonance. The ratio of anti-Stokes to Stokes intensities is given by

$$\frac{|A_{AS}|^2}{|A_S|^2} = \left( \frac{\omega_S^2}{c^2 k_{sz}} \right)^2 |\chi_S|^2 |A_L|^4 \Delta k^{-2} \quad (79)$$

Solutions for phase-matched conditions have been discussed by Duncan et al.<sup>106</sup> They have the form

$$A_S(z) = A_S(0) \left\{ \frac{K_1}{K_1 - K_3} - \left( \frac{K_3}{K_1 - K_3} \right) \exp[-(K_1 - K_3)|A_L|^2 z] \right\} + \left( \frac{\omega_S n_{AS}}{\omega_{AS} n_S} \right) \left( \frac{K_2}{K_1 - K_3} \right) A_{AS}(0) \{1 - \exp[-(K_1 - K_3)|A_L|^2 z]\} \quad (80)$$

$$A_{AS}(z) = A_{AS}(0) \left\{ \left( \frac{K_1}{K_1 - K_3} \right) \exp[-(K_1 - K_3)|A_L|^2 z] - \left( \frac{K_3}{K_1 - K_3} \right) \right\} - \left( \frac{K_2}{K_1 - K_3} \right) A_S(0) \{1 - \exp[-(K_1 - K_3)|A_L|^2 z]\} \quad (81)$$

Initially the Stokes and anti-Stokes amplitudes grow linearly in  $z$  with opposite phases. The growth slows down as  $z$  increases and the condition

$$\frac{A_{AS}(z)}{A_S(z)} = -\frac{K_2}{K_1} = \sqrt{\frac{\chi_S^*}{\chi_{AS}}} \quad (82)$$

is approached asymptotically in the limit of large  $z$ . This ratio is approximately equal to unity except when there is strong resonant enhancement of the anti-Stokes susceptibility. The maximum value of the anti-Stokes amplitude is

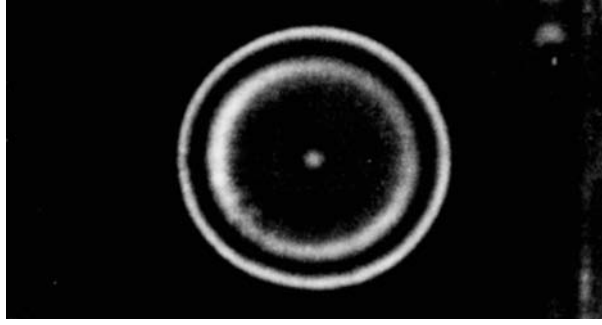
$$A_{AS, \max}(z) = -A_{AS}(0) \frac{K_3}{K_1 - K_3} - A_S(0) \frac{K_2}{K_1 - K_3} \quad (83a)$$

$$\approx -A_{AS}(0) \frac{\omega_S}{\omega_{AS} - \omega_S} - A_S(0) \frac{\omega_{AS}}{\omega_{AS} - \omega_S} \quad (83b)$$

where the second of these relations is approximately valid when  $\chi_S^* \approx \chi_{AS}$  and  $n_{AS} \approx n_S$ .

If the initial Stokes amplitude is small, as for example in a Raman generator, the limiting value of the anti-Stokes amplitude will be small and the predominant anti-Stokes generation will occur at small but finite phase mismatches. For Raman generators, the anti-Stokes radiation is produced in a cone about the phase-matching angle with a dark ring at exact phase matching. Experimental limitations can make the phase-matching minimum difficult to observe, but measurements of the dark ring in the phase-matching cone have been reported, as shown in Fig. 12. If the incident Stokes intensity is comparable to the pump intensity, considerable conversion can be made to the anti-Stokes wave at exact phase matching.<sup>107</sup>

In spectroscopic applications of CARS,<sup>108</sup> the usual input condition is for approximately equal pump and Stokes amplitudes with no anti-Stokes input. These experiments are usually performed under conditions of low exponential gain well below the limiting conditions of Eq. (82). Under these conditions, the anti-Stokes generation is maximized at the phase-matching conditions.



**FIGURE 12** Photograph of the far field of the anti-Stokes emission pattern in hydrogen gas at a pressure of 14 atm. The anti-Stokes radiation is emitted in a cone about the phase-matching angle. The dark ring in the center of the cone is due to parametric gain suppression. (From Ref. 106.)

**Growth from Noise** The most common configuration for Stokes Raman interactions is a Raman generator in which only a pump signal is provided at the input, as shown in Fig. 1a. The Stokes wave is generated in the interaction. The Stokes generation process can be viewed as one in which the effective Stokes noise at the beginning of the cell is amplified in the stimulated Raman interaction as described in the previous sections.

Classically, the Stokes noise is considered as arising from the spontaneous Raman scattering that is produced at the beginning of the cell. If we consider the effective spontaneous Stokes radiation that serves as a source for amplification to be that generated in the first  $e$ -folding length of the Raman generator, the Stokes intensity at the output is

$$I_s = \frac{\partial \sigma}{\partial \Omega} d\Omega NA (e^{N\sigma L} - 1) \quad (84)$$

where  $N$  is the number density of the medium,  $A$  is the cross-sectional area, and  $d\Omega$ , is the solid angle of the gain column.

The growth from noise has been modeled more rigorously in terms of quantum fluctuations of the Stokes field amplitude and material excitation.<sup>97,100,109-112</sup> In this treatment, the Stokes and material oscillators are described by quantum mechanical creation and annihilation operators while the pump field is treated classically. The equations for the Stokes and material oscillators are:<sup>97</sup>

$$\frac{\partial}{\partial z} \hat{A}_s^{(-)}(z, \tau) = i\kappa_2 A_L(t) \hat{Q}^{(+)}(z, \tau) \quad (85a)$$

$$\frac{\partial}{\partial \tau} \hat{Q}^{(+)}(\tau) + \Gamma \hat{Q}^{(+)}(\tau) = -i\kappa_1 A_L^*(\tau) \hat{A}_s^{(-)}(z, \tau) + \hat{F}^{(+)}(z, \tau) \quad (85b)$$

where the symbol  $\hat{\phantom{A}}$  indicates a quantum mechanical operator, the symbols  $(-)$  and  $(+)$  indicate creation and annihilation operators, respectively, and  $\hat{F}$  is a Langevin operator that ensures the correct longtime behavior of  $Q$ .

The initial fluctuations of the Stokes and material oscillators satisfy the conditions:

$$\langle \hat{A}_s^{(+)}(0, t) \hat{A}_s^{(-)}(0, t') \rangle = \frac{2\hbar\omega_s}{cn_s \epsilon_0 a} \delta(t - t') \quad (86a)$$

$$\langle \hat{A}_s^{(-)}(0, t) \hat{A}_s^{(+)}(0, t') \rangle = 0 \quad (86b)$$

$$\langle \hat{Q}^{(+)}(z, 0) \hat{Q}^{(-)}(z', 0) \rangle = \frac{1}{\rho} \delta(z - z') \quad (86c)$$

$$\langle \hat{Q}^{(-)}(z, 0) \hat{Q}^{(+)}(z', 0) \rangle = 0 \quad (86d)$$

$$\langle \hat{F}^{(+)}(z, t) \hat{F}^{(-)}(z', t') \rangle = \frac{2\Gamma}{\rho} \delta(z - z') \delta(t - t') \quad (86e)$$

$$\langle \hat{F}^{(-)}(z, t) \hat{F}^{(+)}(z', t') \rangle = 0 \quad (86f)$$

where  $a$  is the cross-sectional area of the beam. The average Stokes intensity is given by the expectation of the normally ordered number operator:

$$I_S(z, \tau) = \frac{1}{2} c n_s \epsilon_o \langle A_S^{(-)}(z, \tau) A_S^{(+)}(z, \tau) \rangle \quad (87)$$

The formal solution is<sup>97</sup>

$$\begin{aligned} \hat{A}_S^{(-)}(z, \tau) = & \hat{A}_S^{(-)}(0, \tau) \\ & + (\kappa_1 \kappa_2 z)^{1/2} A_L(\tau) \int_{-\infty}^{\tau} d\tau' \hat{A}_S^{(-)}(0, \tau') A_L^*(\tau') e^{-\Gamma(\tau - \tau')} \frac{I_1(\{4\kappa_1 \kappa_2 z [p(\tau) - p(\tau')] \}^{1/2})}{[p(\tau) - p(\tau')]^{1/2}} \\ & - i \kappa_2 A_L(\tau) e^{-\Gamma\tau} \int_0^z dz' \hat{Q}^+(z', 0) I_0(\{4\kappa_1 \kappa_2 (z - z') p(\tau) \}^{1/2}) \\ & - i \kappa_2 A_L(\tau) \int_{-\infty}^{\tau} d\tau' \int_0^z dz' \hat{F}(z', \tau') e^{-\Gamma(\tau - \tau')} I_0(\{4\kappa_1 \kappa_2 (z - z') [p(\tau) - p(\tau')] \}^{1/2}) \end{aligned} \quad (88)$$

The Stokes intensity obtained from use of Eq. (87) is

$$\begin{aligned} I_S(z, \tau) = & \frac{1}{2} c n_s \epsilon_o |\kappa_2 A_L(\tau)|^2 z \{ e^{-2\Gamma\tau} (I_0^2[4\kappa_1 \kappa_2 z p(\tau)]^{1/2}) - I_1^2([4\kappa_1 \kappa_2 z p(\tau)]^{1/2}) \\ & + 2\Gamma \int_{-\infty}^{\tau} e^{-2\Gamma(\tau - \tau')} (I_0^2(4\kappa_1 \kappa_2 z [p(\tau) - p(\tau')]^{1/2}) - I_1^2(\{4\kappa_1 \kappa_2 z [p(\tau) - p(\tau')] \}^{1/2})) d\tau' \} \end{aligned} \quad (89)$$

In this formulation, only the third and fourth terms of Eq. (88) survive because the expectation values on the right side are taken over the initial state, which contains no quanta in either the Stokes or molecular fields. The first and second terms involve a Stokes annihilation operator acting on the Stokes ground state and return zero. The third term returns a nonzero result because it involves a creation operator acting on the molecular ground state, as discussed by Raymer.<sup>97</sup> In this treatment the Stokes light is generated entirely from fluctuations in the material oscillators, while the material excitation is generated from zero-point fluctuations in the material oscillators.

In the extreme transient regime, this result reduces to

$$I_S(z, \tau) = \frac{1}{2} \Gamma g_{ss} I_L(\tau) z \{ I_0^2((2g_{ss} z I_L \Gamma \tau)^{1/2}) - I_1^2((2g_{ss} z I_L \Gamma \tau)^{1/2}) \} \quad (90)$$

Comparison of this result with that of Eq. (43) shows a different functional dependence on the modified Bessel functions, which reflects the effects of buildup of the signal from the distributed noise source.

In the steady state, Eq. (89) reduces to

$$I_S(z, \tau = \infty) = \frac{1}{2} \Gamma g_{ss} I_L z [I_0(g_{ss} I_L z / 2) - I_1(g_{ss} I_L z / 2)] e^{g_{ss} I_L z / 2} \quad (91)$$

An alternative analysis for transient scattering has been presented using antinormal ordering of the creation and annihilation operators for the intensity.<sup>109</sup> In this formalism, the zero-point term must be subtracted explicitly. The intensity is given by

$$I_S(z, \tau) = \frac{1}{2} c n_s \epsilon_o \left\{ \langle \hat{A}_S^{(+)}(z, \tau) \hat{A}_S^{(-)}(z, \tau) \rangle - \langle \hat{A}_S^{(-)}(0, \tau) \hat{A}_S^{(+)}(0, \tau) \rangle \right\} \quad (92)$$

The Stokes intensity is given by

$$\begin{aligned} I_S(z, \tau) = & \frac{1}{2} c n_s \epsilon_o \left\{ \kappa_2^2 |A_L(\tau)|^2 \iint dz' dz'' I_o(\sqrt{4\kappa_1 \kappa_2 (z-z') p(\tau)}) I_o(\sqrt{4\kappa_1 \kappa_2 (z-z'') p(\tau)}) \right. \\ & \times \langle \hat{Q}^{(-)}(z', 0) \hat{Q}^{(+)}(z'', 0) \rangle + \kappa_1 \kappa_2 z |A_L(\tau)|^2 \iint I_1(\sqrt{4\kappa_1 \kappa_2 z [p(\tau) - p(\tau')]})) \\ & \times I_1(\sqrt{4\kappa_1 \kappa_2 z [p(\tau) - p(\tau'')]})) / \sqrt{[p(\tau) - p(\tau')] [p(\tau) - p(\tau'')]} \\ & \times A_L(\tau') A_L^*(\tau'') \langle \hat{A}_S^{(+)}(0, \tau') \hat{A}_S^{(-)}(0, \tau'') \rangle d\tau' d\tau'' + \sqrt{\kappa_1 \kappa_2 z} \left\{ (A_L^*(\tau) - \int_{-\infty}^{\tau} A_L(\tau') \langle \hat{A}_S^{(+)}(0, \tau') \hat{A}_S^{(-)}(0, \tau) \rangle \right. \\ & \times I_1(\sqrt{4\kappa_1 \kappa_2 z [p(\tau) - p(\tau')]})) / \sqrt{p(\tau) - p(\tau')} d\tau' + A_L(\tau) \int_{-\infty}^{\tau} A_L^*(\tau') \\ & \left. \times \langle \hat{A}_S^{(+)}(0, \tau) \hat{A}_S^{(-)}(0, \tau') \rangle I_1(\sqrt{4\kappa_1 \kappa_2 z [p(\tau) - p(\tau')]})) / \sqrt{p(\tau) - p(\tau')} d\tau' \right\} \end{aligned} \quad (93)$$

Here the first term in  $Q$  is 0 because it represents an annihilation operator operating on the ground state. Further analysis shows that this result is identical to the one in Eq. (90). The second term gives the transient stimulated Raman signal, and the last two terms in brackets describe spontaneous Raman scattering. In this formalism, the Stokes wave is started by its own zero-point motion and does not involve the zero-point motion of the molecular oscillators. The zero-point motion of the molecular oscillators is responsible for the initiation of the molecular excitation. Further analysis has shown that the Stokes signal can be viewed as arising from quantum fluctuations of the Stokes radiation,<sup>97</sup> the material oscillator,<sup>109</sup> or a combination of both.<sup>100</sup>

The effective Stokes noise amplitude corresponds to one Stokes photon at the input of the generator. This result is expected for this model, which assumes plane wave propagation, effectively assuming a single mode in the amplifier. In a more general case, the effective Stokes noise level will be one Stokes photon for each temporal and spatial mode of the amplifier. The number of spatial modes is given by the square of the effective Fresnel number of the amplifier:<sup>113</sup>

$$N_{\text{spatial modes}} = F^2 \quad (94)$$

where

$$F = \frac{A}{\lambda L} \quad (95)$$

where  $A$  is the effective area of the gain region and  $L$  is the interaction length. Because of spatial gain narrowing, the effective area of the generator can be significantly less than the nominal diameter of the pump beam and can depend on the gain level. The number of temporal modes depends on the relation of the pump pulse duration to the dephasing time  $T_2$ . A single temporal mode will be present when  $t_p \ll T_2$ . For longer pulses, the number of temporal modes has been modeled as<sup>110</sup>

$$N_{\text{temporal modes}} = 1, \quad t_p < t_{ss} \quad (96a)$$

$$N_{\text{temporal modes}} = \frac{t_p}{G_{ss} T_2}, \quad t_p > t_{ss} \quad (96b)$$



or alternatively as<sup>114</sup>

$$N_{\text{temporal modes}} = \sqrt{\frac{\ln 2/G_{ss}}{1 - \ln 2/G_{ss}}} \frac{t_p}{\pi T_2} \quad (97)$$

The first of these derives the number of temporal modes from the steady-state time of Eq. (19) and the second from the gain-narrowing formula of Eq. (29).

**Raman threshold** Generation of first Stokes radiation from noise in a single-pass generator passes smoothly from exponential amplification of noise to depletion of the pump radiation without a true threshold. Thresholdlike behavior has been reported in some situations but has been due to multimode structure of the radiation or secondary reflections. A Raman threshold is, however, commonly associated with a single-pass gain. This is done by assigning the threshold to a pump value (intensity or energy) at which the Stokes signal from a Raman generator is an arbitrary fraction of the incident pump (typically of the order of 1 percent). At this level, pump saturation is generally not important, but for higher pump powers the process rapidly transitions to saturation. Thus, the concept of Raman threshold in Raman generators is reasonably practical, if not technically precise. The gain that is required to reach threshold depends on the number of noise modes present in the generator. For typical geometries of long, narrow interaction lengths, the Raman gain at threshold is of the order of  $e^{23}$  to  $e^{40}$ . Raman amplifiers are typically operated at gain levels below threshold. Stable amplifier gains of the order of  $e^{19}$  are achievable.

**Quantum fluctuations** Macroscopic manifestations of the stochastic nature of the Raman initiating fluctuations have been reported in spatial fluctuations of the output Stokes intensity profile, in the pointing of the Stokes beam, and in the spectral and temporal structure of the Stokes signal generated by narrowband radiation.<sup>110,111,115–120</sup> The stochastic nature of the starting signal is manifest in the pulse energy statistics of Raman generators operated below threshold. In this regime, the statistical distribution of the Stokes pulse energy is of the form  $p(W_s) = \exp\{-W_s/\langle W_s \rangle\}$ , where  $W_s$  is the energy of a Stokes pulse and  $\langle W_s \rangle$  is the average energy over an ensemble. When the Raman generator is operated below threshold, energy of the output pulses fluctuates in accordance with this distribution. As the generator approaches pump depletion, the Stokes pulse energy distribution approaches one that is peaked about the average value. Statistical distributions of pulse radiation in short pulse experiments show exponential behavior characteristic of stochastic input for gains below threshold, and a gradual evolution to coherent behavior as saturation is approached.

Competition of the quantum noise with real Stokes signals in Raman amplifiers at the quantum level has been reported by Duncan et al.<sup>113</sup> Their results show experimentally that the effective initiating signal is consistent with a noise level of one photon per mode of the amplifier. When the incident Stokes signal exceeds the noise level of one photon per mode by a sufficient amount, the fluctuations are effectively suppressed in both the spatial profile and the pulse energy statistics. An example of the evolution of the amplified Stokes signal from one dominated by quantum noise to one dominated by the coherent Stokes input signal in the image of bars in a resolution chart is shown in Fig. 13.

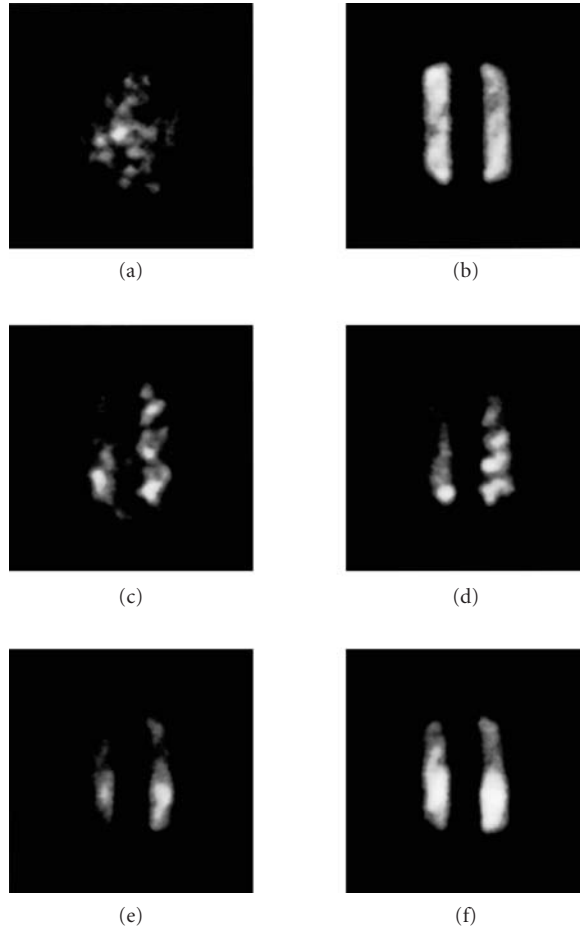
**Multiple Stokes Generation** Once a significant signal is produced in the first Stokes wave, it can serve as a pump wave for a second Raman process, generating a second Stokes wave at

$$\omega_{2s} = \omega_s - \omega_o = \omega_L - 2\omega_o \quad (98)$$

This usually occurs at a pump power such that significant Stokes conversion occurs within the first half of the Raman cell, allowing generation of the second Stokes wave in the last part of the cell. Once the first Stokes wave is generated, the second Stokes radiation can also arise from a four-wave mixing interaction of the form

$$\omega_{2s} = 2\omega_s - \omega_L \quad (99a)$$

which has properties similar to the anti-Stokes four-wave mixing interaction.



**FIGURE 13** Images of bars in a resolution chart from a Stokes amplifier with amplification of  $1.4 \times 10^4$  for different levels of incident Stokes energy, showing effects of competition between incident Stokes energy and quantum noise, (a) Incident Stokes wave blocked. (b) Incident Stokes wave. (c) 210 seed Stokes photons, camera sensitivity 1. (d) 800 seed Stokes photons, camera sensitivity 0.3. (e)  $3.2 \times 10^4$  seed Stokes photons, camera sensitivity  $7.4 \times 10^{-3}$ . (f)  $1.5 \times 10^{10}$  seed Stokes photons, camera sensitivity  $3.2 \times 10^{-8}$ . (From Ref. 121.)

The four-wave mixing interaction is a coherent one and will produce second Stokes radiation with coherent statistics when the first Stokes radiation has saturated the pump. The second Stokes radiation generated from stimulated scattering will exhibit the stochastic behavior characteristic of growth from quantum noise. The relative importance of the two sources of second Stokes radiation is affected by the phase mismatch for the four-wave mixing interaction and depends on the density of the material.

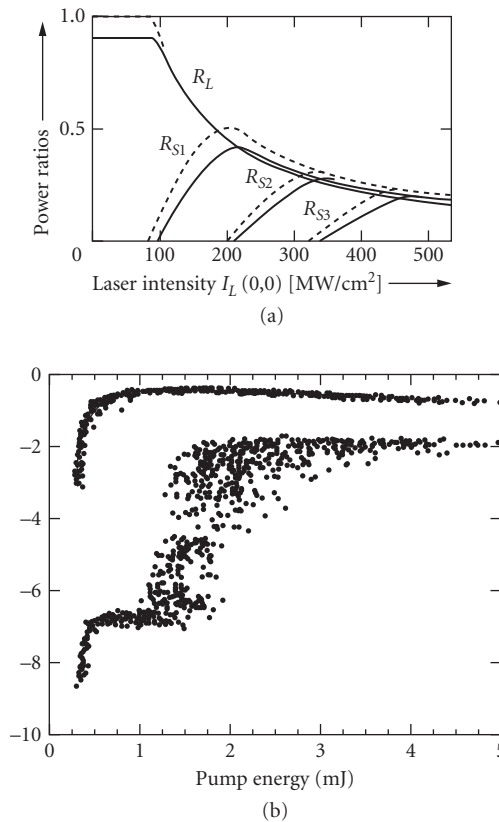
Still higher pump powers can result in conversion to third or higher Stokes orders. Each of the orders involves a frequency shift due to the same material transition, rather than higher excitation of the material system. In most materials, conditions for multiple Stokes generation are sufficient

to produce significant amounts of anti-Stokes energy through the four-wave mixing interaction. Multiple-order anti-Stokes energy can also be generated using various combinations of Stokes and anti-Stokes orders of the form

$$\omega_{nAS} = \omega_{mS} - \omega_{(m+1)S} + \omega_{(n-1)AS} \quad (99b)$$

where  $n$  and  $m$  are orders of Stokes and anti-Stokes radiation and  $\omega_{0S} = \omega_{0AS} = \omega_L$ . Multiple-order Stokes radiation can also be produced through four-wave mixing involving similar terms.

An ideal progression of Raman scattering through multiple Stokes modes is shown in Fig. 14a. Such a progression is seldom seen in practice because of the onset of anti-Stokes and four-wave mixing interactions. Higher-order Stokes energy can be suppressed through choice of resonant structure in the material or through use of high pressures that suppress four-wave mixing through disruption of phase matching. An example of second Stokes generation in hydrogen is shown in Fig. 14b, in which initiation through four-wave mixing occurs at low powers and initiation through a stimulated process, evidenced by the wide scatter of points, occurs at higher powers.<sup>122</sup>



**FIGURE 14** (a) Theoretical calculation of multiple Stokes generation for gaussian pulses. (From Ref. 2.) (b) Second Stokes generation (lower curve) in hydrogen at 1600 psi showing growth from four-wave mixing at low pump energies and the transition to stimulated emission from quantum fluctuations at higher pump energies. The first Stokes wave is shown in the upper curve. (From Ref. 122.)

**Focused Beams** The effects of focusing are described by the spatial derivative in Eq. (5a and b). When the pump intensity varies with  $z$ , the gain must be integrated over the interaction length. For steady-state interactions, the Stokes intensity takes the form

$$I_S(r, z) = I_S(r, 0) \exp \left[ g \int_0^L I_L dz \right] \quad (100)$$

The profile of a gaussian beam is described by a  $1/e$  field radius  $w$ , given by

$$w(z) = w_0 \sqrt{1 + \xi^2} \quad (101)$$

where  $w_0$  is the radius of the beam waist,  $\xi = 2z/b$ , and  $b = 2\pi w_0^2/\lambda$  is the confocal parameter. When  $b \gg L$ , the pump beam is collimated over the interaction length and the primary effect of the gaussian profile is to produce gain narrowing, effectively confining the Stokes intensity near the beam axis. When the beam is tightly focused, so that  $b \ll L$ , the integrated gain is independent of the interaction length and depends only on the total pump power:

$$G = g \int I_L dz = g4P/b\lambda \quad (102)$$

where  $P$  is the total pump power. Amplification or generation with focused beams can result in changes of the Stokes beam divergence and displacements of the apparent source point for divergence of the Stokes beam.

**Backward Raman Scattering** Stimulated Raman scattering also occurs in the backward direction, for which the Stokes and pump waves travel in opposite directions.<sup>2,69</sup> This type of interaction is much more dependent on the geometry and the laser linewidth than the forward interaction. Backward interaction can involve growth from noise (Fig. 2b) or amplification (Fig. 2d). Generally, it occurs for sufficiently narrow line widths that the coherence length of the radiation is longer than the interaction length. One of the characteristic differences of the backward interaction is that the growing Stokes wave continually interacts with undepleted pump as it propagates. Thus, for conditions in which the Stokes wave can grow to saturate the Raman interaction, the Stokes wave continually experiences the full pump intensity rather than a continually decreasing intensity as in the forward direction. One consequence of this property is that the intensity of the backward Stokes pulse can grow to be much higher than the initial pump intensity, while the pulse duration decreases, producing pulse compression, one of the common applications for backward Raman scattering.<sup>69</sup> For this application, the optimal duration for the pump pulse is twice the length of the Raman cell. The Stokes wave grows to depletion level in the first half of the pump pulse and depletes the pump in the second half. Factors affecting pulse compression have been discussed in Ref. 69, where designs of systems to give a factor-of-10 shortening were described.

Backward scattering also results in Stokes pulses of higher spatial quality than are obtained in the forward direction. If the backward Stokes wave depletes the pump pulse too much before it travels an entire cell length, the initiating signal for Stokes radiation in subsequent parts of the pulse can be suppressed and oscillations can result.<sup>123</sup>

**Polarization Dependence** The Raman gain for various polarizations depends on the symmetry of the Raman transition and is governed by the depolarization ratio. For many materials and transitions, the maximum gain occurs for pump and Stokes polarizations that are linear and parallel. For other types of transitions—for example, rotational transitions in diatomic molecules—circular polarization is preferred with the pump and Stokes waves polarized in the opposite sense. The relative gains for various polarization combinations are shown in Table 8.<sup>124</sup>

The earliest and most common application of stimulated Raman scattering is the production of coherent sources at wavelengths different from those of the pump laser. Prior to the introduction of tunable lasers, this was one of the few methods available for obtaining coherent radiation at any but a small number of wavelengths at which fixed-frequency lasers existed. This application remains an important one today for extending the versatility of tunable lasers, and for generation of radiation

**TABLE 8** Polarization Dependence of Relative Gain for SRS

	Laser Polarization	Stokes Polarization	Relative Gain
Rotational scattering,	Linear	Linear, parallel	1
linear molecules	Linear	Linear, perpendicular	0.75
	Circular	Circular, same sense	0.25
	Circular	Circular, opposite sense	1.5

at wavelengths required for specific applications such as the eye-safe region around 1.5  $\mu\text{m}$ . Other applications of Raman scattering include Raman beam cleanup, pulse compression, time-gated imaging, and coherent spectroscopy. Two of these are described in the following text.

**Coherent Spectroscopy** Several Raman interactions are used for coherent spectroscopy.<sup>108,125</sup> These interactions have the advantage of producing a stronger signal than incoherent spectroscopy under some conditions. These advantages occur primarily when prominent Raman modes are studied in pure materials or the dominant constituent of a mixture. A summary of interactions used in coherent spectroscopy along with names given to them is given in Table 9. The most common of these is coherent anti-Stokes Raman scattering (CARS). A typical CARS spectroscopic interaction is shown in Fig. 11. Incident light at both the pump and Stokes wavelengths is supplied. The anti-Stokes signal is measured as the wavelength of the Stokes light is varied. The spectral structure is recorded as the frequency difference  $\omega_L - \omega_S$  is tuned through Raman resonances of the material.

The anti-Stokes intensity is given in a steady-state plane-wave approximation as

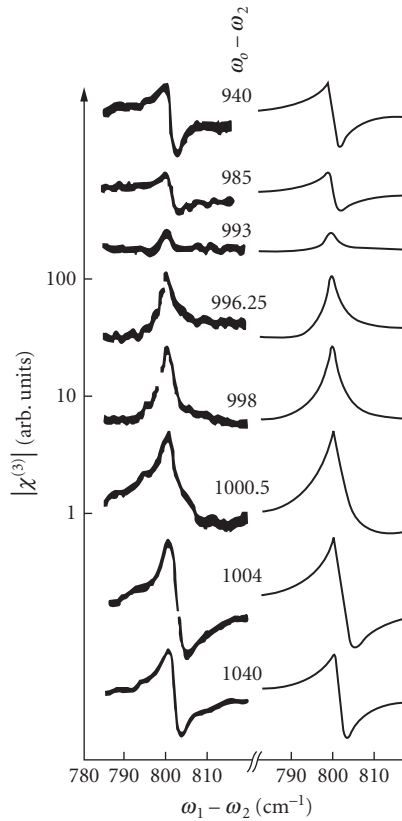
$$I_{AS} = |\chi_R + \chi_{NR}|^2 I_L^2 I_S \quad (103)$$

where  $\chi_R$  is the Raman susceptibility that carries the resonance and  $\chi_{NR}$  is the nonresonant nonlinear susceptibility due to electronic or other transitions in the medium. The Raman susceptibility exhibits resonant behavior as  $\omega_L - \omega_S$  is tuned through the Raman resonance  $\omega_o$ , while the nonresonant susceptibility is generally constant through the resonance region. The wavelength variation of the anti-Stokes intensity reflects the influence of the interference between the resonant and nonresonant susceptibilities. In particular, the anti-Stokes intensity goes through zero when  $\chi_R = -\chi_{NR}$ , which always occurs on the high-frequency side of the resonance. Depending on the situation, the anti-Stokes intensity can exhibit a resonant-like peak if  $\chi_{NR}$  is small compared to  $\chi_R$  at the resonance or a dispersive-like behavior if  $\chi_{NR}$  is larger than  $\chi_R$ . Intermediate behavior between these two extremes is also possible depending on the relative magnitudes of  $\chi_R$  and  $\chi_{NR}$ . Dispersive-like behavior can occur for relatively weak Raman transitions, or for Raman transitions in materials that are minor constituents in mixtures. An example of CARS spectral behavior for various conditions is shown in Fig. 15.

**Time-Gated Imaging** Raman amplification has also been applied to time-gated imaging to suppress background light in highly scattering materials, for example biological tissue or materials such as ceramics.<sup>127–129</sup> Time gating with Raman scattering can be done with either short pulses, in which case the gate time is comparable to the pulse duration, or with broadband radiation, in which case the time gate is determined by the coherence time of the pulse. In pulsed gating, only that part of the signal that overlaps with the pump pulse in time is amplified, and light that is delayed through multiple scattering is suppressed. In coherence gating, only the Stokes components that are coherent with the pump are amplified, and components that

**TABLE 9** Raman Interactions Used for Coherent Spectroscopy

Interaction	Frequency Relations	Measured Quantity
Coherent anti-Stokes Raman scattering (CARS)	$\omega_{AS} = 2\omega_L - \omega_S$	Anti-Stokes power
Coherent Stokes Raman spectroscopy (CSRS)	$\omega_S = \omega_L - \omega_o$	Amplified Stokes power
Raman-induced Kerr effect spectroscopy (RIKES)	$\omega_S = \omega_L - \omega_o$	Stokes power in orthogonal polarization component

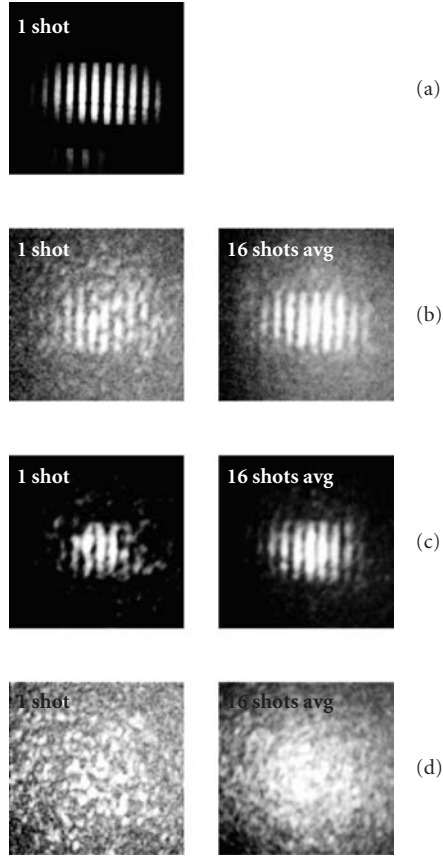


**FIGURE 15** Signal from coherent anti-Stokes Raman scattering showing variation of line shape due to interference of Raman and nonresonant susceptibilities. (From Ref. 126; copyright 1976 by American Physical Society.)

are decorrelated because of multiple-path scattering are suppressed. Gate contrasts of the order of  $10^9$  are possible with pulse gating, while contrasts of the order of  $10^6$  can be obtained with correlation gating. An example of the use of pulsed gating for imaging in a scattering solution is shown in Fig. 16.

### 15.3 STIMULATED BRILLOUIN SCATTERING

Brillouin scattering involves low-frequency propagating waves—for example, acoustic waves in solids, liquids, and gases and ion-acoustic waves in plasmas. Again, scattering can be to a longer or shorter wavelength than the incident radiation, with the long-wavelength scattered wave being termed the *Stokes wave* and the short-wavelength scattered wave termed the *anti-Stokes wave*. The difference between the incident and scattered frequencies is again termed the *Stokes shift* or *anti-Stokes shift* as appropriate. For Brillouin scattering, the energies of the modes are much lower than for Raman scattering, and anti-Stokes radiation is much more common. Common Brillouin shifts are typically on the order of 0.1 to 100 GHz, and depend on the excitation wavelength and interaction geometry as well as on material properties. Brillouin scattering is used most commonly for phase conjugation and pulse compression. It is also prominent as a limiting process for intensity in fiber-optic systems.



**FIGURE 16** Use of Raman amplification with short pulses for time gating to photograph objects through scattering materials. (a) Image of bar chart, no scatterer. The relative timing of the pump and Stokes pulses were (b)  $-16$  ps, (c)  $0$  ps, and (d)  $+24$  ps. (From Ref. 128.)

The equations for Stokes Brillouin scattering for forward ( $+v_g$ ) and backward ( $-v_g$ ) waves are<sup>2,6,7</sup>

$$\frac{\partial A_S}{\partial z} \pm \frac{1}{v_g} \frac{\partial A_S}{\partial t} = i \frac{\omega_s}{4n_s c} \gamma \frac{\Delta \rho^*}{\rho_o} A_L \quad (104a)$$

$$\begin{aligned} -2i\Omega \frac{\partial \Delta \rho^*}{\partial t} + (v^2 q^2 - \Omega^2 + iq^2 \Gamma' \Omega) \Delta \rho^* + 2iqv^2 \frac{\partial \Delta \rho^*}{\partial z} - \frac{v^2 s q^2 \beta_p \rho_o}{\gamma} \Delta T^* \\ + 2iq \frac{v_s^2 \beta_p \rho_o}{\gamma} \frac{\partial \Delta T^*}{\partial z} = q^2 \gamma A_L^* A_S \end{aligned} \quad (104b)$$

$$\rho_o C_v \frac{\partial \Delta T^*}{\partial t} - i\Omega \rho_o C_v \Delta T^* - \frac{C_v (\gamma - 1)}{\beta_p} \frac{\partial \Delta \rho}{\partial t} + i\Omega \frac{C_v (\gamma - 1)}{\beta_p} \Delta \rho + \kappa q^2 (\Delta T) = c n \epsilon_o \alpha A_L^* A_S \quad (104c)$$

where  $v_s$  is the sound velocity and

$$\Gamma' = \frac{1}{\rho} \left[ \frac{4}{3} \eta_s + \eta_b + \frac{\kappa}{C_p} \left( \frac{C_p}{C_v} - 1 \right) \right] \quad (105)$$

and  $\eta_s$  is the coefficient of shear viscosity,  $\eta_b$  is the coefficient of bulk viscosity,  $\kappa$  is the thermal conductivity,  $C_p$  is the specific heat at constant pressure, and  $C_v$  is the specific heat at constant volume.

The fields are described by the equations

$$E_L(z, t) = \frac{1}{2} [A_L(z, t) e^{-i(\omega_L t - k_L z)} + \text{c.c.}] \quad (106a)$$

$$E_S(\zeta, t) = \frac{1}{2} [A_S(z, t) e^{-i(\omega_S t - k_S \zeta)} + \text{c.c.}] \quad (106b)$$

$$\rho(\zeta, t) = \rho_o + \frac{1}{2} [\Delta \rho e^{-i(\Omega t - q \zeta)} + \text{c.c.}] \quad (106c)$$

where  $A_L$ ,  $A_S$ , and  $\rho$  are the amplitudes of the laser, scattered optical wave, and sound wave density, respectively, and  $\omega_L$ ,  $\omega_S$ ,  $\Omega$ , and  $k_L$ ,  $k_S$ , and  $q$  are the frequencies and  $k$  vectors of the various waves. The scattered optical wave propagates along the direction  $\zeta$  and the sound wave propagates along direction  $\xi$ , neither of which is required to coincide with  $z$ . The frequencies and  $k$  vectors obey the following relations:

$$\omega_L - \omega_S = \Omega \quad (107a)$$

$$\vec{k}_L - \vec{k}_S = \vec{q} \quad (107b)$$

$$q = \frac{2\pi}{\Lambda_s} \quad (107c)$$

where  $\Lambda_s$  is the sound wavelength. The  $k$  vectors of the various waves are arranged according to the diagram in Fig. 17.

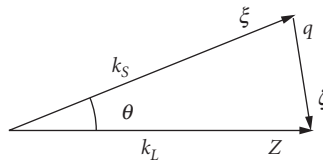
Because the sound frequency is much less than the optical frequency,  $|k_L| \approx |k_S|$  and

$$q \approx 2k_L \sin(\theta/2) \quad (108)$$

The Brillouin frequency shift can then be written as

$$\Omega_B = 2n_L \omega_L \frac{v_s}{c} \sin(\theta/2) \quad (109)$$

Unlike the Raman frequency shift, the Brillouin frequency shift depends on the laser frequency and the interaction geometry. It has its maximum value for backward scattering ( $\theta = 180^\circ$ ).



**FIGURE 17**  $k$  vector diagram for stimulated Brillouin scattering showing  $k$  vectors for laser  $k_L$  Stokes  $k_S$  and sound wave  $q$ .



The Brillouin interaction involves both electrostrictive and thermal effects. Equation (104c) was obtained from the equation for the low-frequency acoustic and thermal response of liquids and gases to optical radiation:<sup>2,6,7</sup>

$$-\frac{\partial^2 \Delta \rho}{\partial t^2} + \frac{v_s^2}{\gamma} \nabla^2 (\Delta \rho) + \frac{2\eta_s + \eta_b}{\rho_o} \nabla^2 \frac{\partial \Delta \rho}{\partial t} + \frac{v_s^2 \beta_p \rho_o}{\gamma} \nabla^2 (\Delta T) = \frac{1}{2} c n \epsilon_o \gamma_e \nabla^2 \langle E_{\text{tot}} \rangle^2 \quad (110a)$$

$$\rho_o C_v \frac{\partial \Delta T}{\partial t} - \frac{C_v (\gamma - 1)}{\beta_p} \frac{\partial \Delta \rho}{\partial t} - \kappa \nabla^2 (\Delta T) = c n \epsilon_o \alpha \langle E_{\text{tot}} \rangle^2 \quad (110b)$$

where  $\gamma = C_p/C_v$  is the ratio of specific heats at constant pressure and volume,  $\eta_s$  is the coefficient of shear viscosity,  $\eta_b$  is the coefficient of bulk viscosity,  $\beta_p$  is the thermal expansion coefficient at constant pressure,  $\gamma_e = \rho(\partial \epsilon / \partial \rho)$  is the electrostrictive constant,  $\alpha$  is the absorption coefficient,  $\kappa$  is the thermal conductivity,  $E_{\text{tot}} = E_L + E_S$  is the total optical field, and  $\Delta T$  is the change in temperature. The following form for the temperature

$$T = T_o + \frac{1}{2} [\Delta T e^{-i(\Omega t - qz)} + \text{c.c.}] \quad (111)$$

can be used to reduce Eq. (110a and b) to first order, giving Eq. (104b and c).

The Brillouin equations can be solved under various approximations. The propagating terms in  $\partial \Delta \rho / \partial z$  and  $\partial \Delta T / \partial z$  are usually neglected because the sound waves are strongly damped. The steady-state solution for the Stokes intensity is

$$I_S(L) = I_S(0) e^{gLL} \quad (112)$$

where the gain coefficient  $g$  is given by  $g = g^e + g^a$ , where  $g^e$  is the electrostrictive gain coefficient given by

$$g^e = \frac{\omega_s \gamma_e^2 \Omega_B}{n_s n_L c^2 \epsilon_o \rho_o \Gamma_B v_s^2} \frac{1}{1 + \left( \frac{2\delta\Omega}{\Gamma_B} \right)^2} \quad (113a)$$

and  $g^a$  is the absorptive Brillouin gain coefficient given by

$$g^a = \frac{\omega_s \gamma_e \gamma_a \Omega_B}{2 n_s n_L c^2 \epsilon_o \rho_o \Gamma_B v_s^2} \frac{4\delta\Omega / \Gamma_B}{1 + \left( \frac{2\delta\Omega}{\Gamma_B} \right)^2} \quad (113b)$$

where  $\gamma_a = 2\alpha n v^2 \beta_p / C_p \Omega_B$ ,

$$\Omega_B = v_s q \quad (114)$$

is the Brillouin frequency shift,  $\delta\Omega = \Omega - \Omega_B$ , and

$$\Gamma_B = q^2 \left[ \frac{1}{\rho} (2\eta_s + \eta_b) + \frac{\kappa}{C_p} \left( \frac{C_p}{C_v} - 1 \right) \right] \quad (115a)$$

$$= q^2 \Gamma'' \quad (115b)$$

is the Brillouin damping constant.

The gain due to the electrostrictive interaction is peaked about the Brillouin frequency shift  $\Omega = \Omega_B$  with a linewidth (FWHM) of  $\Delta\nu_B = \Gamma_B/2\pi$ . The acoustic energy damping time is given by

$$\tau_B = 1/2\pi\Delta\nu_B \quad (116)$$

The electrostrictive gain coefficient  $g$  can also be written as

$$g^e = \frac{2\omega_s \gamma_e^2 \omega_L}{n_s c^3 \epsilon_o \rho_o \Gamma_B \nu_s} \sin(\theta/2) \frac{1}{1 + \left( \frac{\delta\Omega}{\Gamma_B/2} \right)^2} \quad (117a)$$

$$= \frac{\omega_s \gamma_e^2}{2\omega_L n_s n_L^2 c \epsilon_o \rho_o \Gamma^* \nu_s} \frac{1}{\sin(\theta/2)} \frac{1}{1 + \left( \frac{\delta\Omega}{\Gamma_B/2} \right)^2} \quad (117b)$$

The maximum steady-state gain is

$$g_{B,\max}^e = \frac{\omega_s \omega_L \gamma_e^2}{\pi n_s c^3 \epsilon_o \rho_o \nu_s \Delta\nu_B} \quad (118)$$

and occurs for backward scattering ( $\theta = 180^\circ$ ). The frequency shift for backward scattering is

$$\Omega_B(180^\circ) = 2n\omega_L \frac{\nu_s}{c} \quad (119)$$

Since the Brillouin frequency shift is small,  $\omega_s \approx \omega_L$  and the maximum Brillouin gain apparently scales as  $\omega_L^2$ . However, the linewidth also scales as  $\omega_L^2$  [see Eq. (115b)], leaving the maximum Brillouin gain independent of wavelength as indicated in Eq. (117b).

The dependence of the linewidth on  $q^2$  causes the steady-state gain in the forward direction to go to infinity [Eq. (117b)] rather than to zero [Eq. (117a)]. However, the forward interaction is always transient because the steady-state time for forward scattering also goes to infinity. As a result, the forward gain is zero. Brillouin scattering at  $90^\circ$  is important in propagation of high-power laser radiation through large-diameter optics.

Transient Brillouin scattering has been described by Kroll<sup>16</sup> and Faris et al.<sup>130</sup> The transient solutions to the stimulated Brillouin scattering are formally similar to those for Raman scattering and can be written as

$$A_s(z, \tau) = A_s(0, \tau) + \sqrt{\Gamma_B g_B z / cn_L \epsilon_o} A_L(\tau) \int_{-\infty}^{\tau} \frac{e^{-(\tau-\tau')/T_2} A_L^*(\tau') A_s(0, \tau') I_1(\sqrt{\Gamma_B g_B z [p(\tau) - p(\tau')] / cv_L \epsilon_o})}{\sqrt{p(\tau) - p(\tau')}} d\tau \quad (120)$$

Again, the transient gain depends on the time integral of the laser intensity, and the scattered intensity grows as a Bessel function. The steady-state solution of Eq. (112) applies when the pulse duration is greater than the steady-state time given by

$$t_{ss} = \frac{G_{ss}}{\Gamma_B} \quad (121)$$

where  $G_{ss} = GI_L L$ .

Brillouin scattering in solids has been discussed in Refs. 131 to 134. The formal equations for electrostrictive Brillouin scattering are similar to those for liquids and gases. However, the gain coefficient depends on the polarization of the laser and scattered light, and Brillouin resonances exist for both longitudinal and shear acoustic waves. The Brillouin gain is given by

$$g^e = \frac{\omega_s \Omega_B n_s^3 n_L^4 p'^2}{n_s n_L c^2 \epsilon_0 \rho_o \Gamma_B v_s^2} \frac{1}{1 + \left( \frac{2\delta\Omega}{\Gamma_B} \right)} \quad (122)$$

where  $p'$  is the photoelastic constant appropriate for the specific combination of polarizations for the optical and acoustic waves. For longitudinal acoustic waves in isotropic materials<sup>134</sup>

$$p' = p_{12}(\hat{\epsilon}_L \cdot \hat{\epsilon}_S) + p_{44}[(\hat{\epsilon}_L \cdot \hat{\kappa}_a)(\hat{\epsilon}_L \cdot \hat{\epsilon}_S) + (\hat{\epsilon}_L \cdot \hat{\epsilon}_a)(\hat{\epsilon}_S \cdot \hat{\kappa}_a)] \quad (123a)$$

while for shear acoustic waves

$$p' = p_{44}[(\hat{\epsilon}_L \cdot \hat{\kappa}_a)(\hat{\epsilon}_S \cdot \hat{\epsilon}_a) + (\hat{\epsilon}_L \cdot \hat{\epsilon}_a)(\hat{\epsilon}_S \cdot \hat{\kappa}_a)] \quad (123b)$$

where  $\hat{\epsilon}_{L(S)(a)}$  is the unit polarization vector of the pump (Stokes) (acoustic) wave and  $\kappa_a$  is the unit propagation vector of the acoustic wave.

Buildup of noise in a generator with Brillouin scattering is similar in principle to buildup with Raman scattering. However, the primary noise source for Brillouin scattering is the thermally excited acoustic phonons. As a result, the equivalent noise level for Brillouin scattering can be several orders of magnitude larger than the Raman noise level.<sup>135–137</sup> The noise power into a given solid angle  $d\Omega = \pi\theta^2/4$  is given by<sup>135</sup>

$$P_{\text{noise}} = \frac{\omega_s}{\Omega} k_B T \Delta v_B \left( \frac{\theta}{2\theta_D} \right)^2 \quad (124)$$

where  $\theta_D = \lambda/2\pi D$  is the diffraction angle that can be resolved by a gain column of diameter  $D$ . Brillouin scattering with broadband radiation is discussed in Refs. 138 and 139. Multiline Brillouin scattering is treated in Ref. 140. As with backward Raman scattering, the gain decreases when the coherence length becomes comparable to or shorter than the interaction length.

Thermal Brillouin scattering is driven by nonuniform heating due to absorption and is described by  $g^a$  in Eq. (113b). The gain shows a dispersive behavior with frequency, with zero gain at the Brillouin frequency, gain for frequencies less than  $\Omega_B$ , and loss for frequencies greater than  $\Omega_B$ . Brillouin scattering parameters for various materials are listed in Table 10.

## Brillouin Phase Conjugation

One of the major uses of stimulated Brillouin scattering (SBS) is phase conjugation.<sup>140a</sup> Phase conjugation is also possible with stimulated Raman scattering, but SRS is not used for this purpose as much as SBS. Phase conjugation is used to correct distortions on optical beams that arise from propagation through nonideal optical media, such as the atmosphere or low-quality optical components. It can also be used for correcting or stabilizing aiming errors that arise from motion of components in an optical train, for improving the beam quality of laser oscillators and oscillator amplifier systems, and for beam combining.

A typical arrangement for phase conjugation is shown in Fig. 18. The distorting medium impresses a transverse phase variation on the optical beam propagating from left to right that can result in increased divergence, intensity structure, or reduced focal plane intensity if focused by a subsequent lens or mirror. If the beam entering the distorting material carried an initial distortion that would be undone by the material, then the beam would emerge from the medium undistorted.

**TABLE 10** Brillouin Parameters for Various Materials

	Liquids							Reference
	Laser Wavelength (nm)	Frequency Shift (GHz)	$\Delta\nu$ (MHz)	$\tau_B$ (ns)	$g_B$ (cm/GW)	$n$	Density (g/cm <sup>3</sup> )	
Acetone	1059	2.987	119 ± 5	1.34	15.8	1.355	0.791	141
	532	5.93	361	0.44	12.9	1.359(Na-D)		142
	532	6.0	320	0.497	20			138
Benzene	1059	4.124	228	0.7	9.6	1.4837	0.879	141
	532	8.33	515	0.31	12.3	1.501(Na-D)	0.874	142
Benzyl alcohol	532	9.38	2120	0.08	5.75	1.54(Na-D)	1.045	142
Butyl acetate	532	6.23	575	0.28	9.13	1.394(Na-D)	0.882	142
CS <sub>2</sub>	1060	3.761	50	3.2	68	1.595	1.262	141
	532	7.7	120	1.9	130			138
CCl <sub>4</sub>	1060	2.772	528	0.3	3.8	1.452	1.595	141
	532	5.72	890	0.18	8.77	1.4595	1.594	142
Chloroform	532	5.75	635	0.25	11.7	1.446(Na-D)	1.492	142
Cyclohexane	532	7.19	1440	0.11	5.8	1.426(Na-D)	0.779	142
N,N-Dimethyl formamide	532	7.93	615	0.26	7.8	1.431(Na-D)	0.944	142
Dichloromethane	532	5.92	255	0.62	16.8	1.424	1.325	142
<i>o</i> -Dichlorobenzene	532	8.03	1340	0.12	4.7	1.551	1.306	142
Ethanol	532	5.91	546	0.29		1.36	0.785	142
Ethylene glycol	532	10.2	3630	0.04	0.85	1.431	1.113	142
Freon 113	532	3.72	865	0.18	5.5	1.3578	1.575	142
<i>n</i> -Hexane	532	5.64	580	0.27	8.8	1.379	0.67	142
Nitrobenzene	1060	4.255	396	0.4	7.2	1.5297	1.206	141
Methanol	532	5.47	325	0.49	10.6	1.329	0.791	142
	530	5.6	210	0.334	13			138
Pyridine	532	8.92	746	0.21	14	1.51	0.978	142
Tin tetrachloride	1064	2.21 ± 0.02	182 ± 12	0.874	11.2 ± 0.5	1.36	2.226	143
	532	4.71	357	0.45				
Titanium tetrachloride	1060	3.070	216	0.735	14.2	1.577	1.73	141
Toluene	532	7.72	1314	0.12	8.4	1.496	0.867	142
Trichloroethylene	532	5.94	765	0.21	12	1.4755	1.464	142
Water	1060	3.703	170	0.935	3.8	1.324	1	141
	532	7.4	607	0.26	2.94	1.333	1	142
Xylenes	532	7.74	1211	0.13	9.3	1.497	0.86	142

(Continued)

**TABLE 10** Brillouin Parameters for Various Materials (*Continued*)

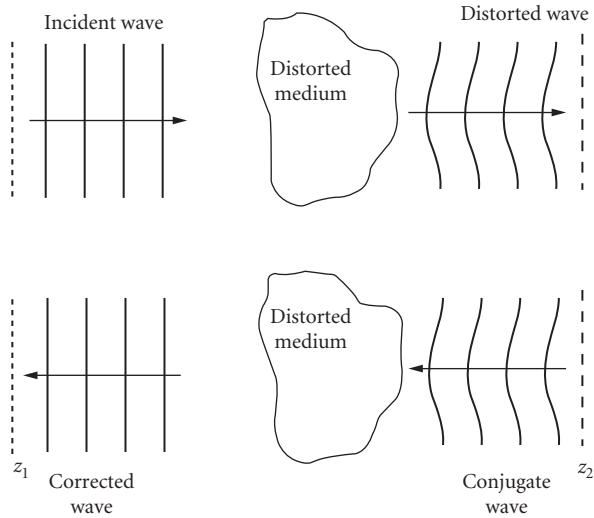
Gases										
	Laser Wavelength (nm)	Frequency Shift (GHz)	$\Delta\nu$ (MHz)	$\tau_B$ (ns)	$g_B$ (cm/GW)	$n$	Density (g/cm <sup>3</sup> )	Reference		
Xenon										
7599 Torr	532	0.654 ± 0.024	98.1 ± 8.9			1.0069	0.05767	134		
6840 Torr	532	0.627 ± 0.030	107.4 ± 16.9			1.0062	0.05159	134		
				0.65	$\lambda_p^2 P$			144		
CClF <sub>3</sub>										
3310 kPa (liquid)	1060		305					145		
3860	1060		155					145		
3950	1060		200					145		
32 atm (liquid)				6.2 ± 0.4				146		
Gas										
SF <sub>6</sub>				$(4.78 \times 10^9 / \rho \lambda_L^2 + 3.25 \times 10^5)^{-1}$				144		
				$(5.9 \times 10^9 / \rho \lambda_L^2 + 1.6 \times 10^5)^{-1}$				144		
<i>P</i> in atmospheres, $\rho$ in bg/m <sup>3</sup>										
Solids										
Substance	Polarization		Laser Wavelength (nm)	Frequency Shift (GHz)	$\Delta\nu$ (MHz)	$\tau_B$ (ns)	$g_B$ (cm/GW)	$n$	Density (g/cm <sup>3</sup> )	Reference
	<i>P</i>	<i>k</i>								
d-LAP			1053		28.9 ( $\theta = 180^\circ$ )	5.5 ( $\theta = 180^\circ$ )	18 ( $\theta = 180^\circ$ )			147
					14.4 ( $\theta = 90^\circ$ )	11 ( $\theta = 90^\circ$ )	26 ( $\theta = 90^\circ$ )			147
	<i>x</i>	<i>y = b = Y</i>	532	25.374 ± 0.051	84.1 ± 3.5		20.7 ± 2.99	1.5090	1.600	134
	<i>x</i>	<i>z</i>	532	25.207 ± 0.042	100.4 ± 7.5		10.99 ± 1.88	1.5090	1.600	134
	<i>y</i>	<i>x</i>	532	19.590 ± 0.087	79.8 ± 6.3		27.96 ± 2.85	1.5764	1.600	134
	<i>y</i>	<i>z</i>	532	26.415 ± 0.009	104.1 ± 5.2		12.25 ± 0.93	1.5764	1.600	134
	<i>z</i>	<i>x</i>	532	19.644 ± 0.048	82.3 ± 6.2		29.85 ± 2.4	1.5847	1.600	134
	<i>z</i>	<i>y</i>	532	26.709 ± 0.039	91.9 ± 5.1		24.33 ± 3.26	1.5847	1.600	134
	THG		532	25.149 ± 0.072	94.8 ± 8.4		17.45 ± 3.41			134
			351		261 ( $\theta = 180^\circ$ )	0.61 ( $\theta = 180^\circ$ )	22 ( $\theta = 180^\circ$ )			147
				132 ( $\theta = 90^\circ$ )	1.2 ( $\theta = 90^\circ$ )	31 ( $\theta = 90^\circ$ )			147	
Fused silica			1053		40.8 ( $\theta = 180^\circ$ )	3.9 ( $\theta = 180^\circ$ )	4.8 ( $\theta = 180^\circ$ )		2.202	147
			1053		20.4 ( $\theta = 90^\circ$ )	7.8 ( $\theta = 90^\circ$ )	6.8 ( $\theta = 90^\circ$ )			147
			532	32.65 ± 0.054	163 ± 7.6		2.9 ± 0.015	1.4607		134
			532	32.62	167.6 ± 13.5		2.69 ± 0.22			134
			351		370 ( $\theta = 180^\circ$ )	0.43 ( $\theta = 180^\circ$ )	5.4 ( $\theta = 180^\circ$ )			147
			351		185 ( $\theta = 90^\circ$ )	0.86 ( $\theta = 90^\circ$ )	7.6 ( $\theta = 90^\circ$ )			147
KD*P	<i>x = c = Z</i>	<i>z = Y</i>	532	29.763 ± 0.06	101.5 ± 7.5		3.53 ± 0.31	1.4683	2.355	134
	<i>z</i>	<i>x</i>	532	27.627 ± 0.087	120.0 ± 6.9		4.57 ± 0.38	1.5073	2.355	134
	<i>z</i>	<i>Z</i>	532	30.525 ± 0.156	107.4 ± 7.2		5.09 ± 0.40	1.5073	2.355	134

KDP, THG		532	$28.554 \pm 0.036$	$72.9 \pm 5.7$		$6.5 \pm 0.95$	1.5073	2.355	134
LAA	y	532	$20.892 \pm 0.009$	$100.4 \pm 7.6$		$24.9 \pm 3.75$			134
BK3		532	$31.383 \pm 0.036$	$198.6 \pm 6.6$		$1.78 \pm 0.13$	1.5008	2.37	134
LHG-8		532	$27.786 \pm 0.024$	$219.0 \pm 6.2$		$2.74 \pm 0.23$	1.5316	2.83	134
BK7		532	$34.65 \pm 0.039$	$165.0 \pm 8.6$		$2.15 \pm 0.21$	1.5195	2.51	134
CaF2		532	$37.164 \pm 1.185$	$45.6 \pm 8.8$		$4.11 \pm 0.65$	1.4354	3.179	134
Plexiglas		532	$15.687 \pm 0.036$	$253.7 \pm 12.6$			1.4938	1.19	134
GGG		532	$26.283 \pm 0.005$	$12.5 \pm 6.9$		$1.02 \pm 0.5$	1.9788	7.09	134

Glasses

	Laser Wavelength (nm)	Frequency Shift (GHz)	$\Delta\nu$ (MHz)	$v_s$ (m/s)	$g_B$ (cm/GW)	$n$	Density (g/cm <sup>3</sup> )	Reference
SiO <sub>2</sub>	488	35.6	156	5944.2	4.482	1.462	2.203	132
ZBL	488	25.0	213.6	3979.0	2.832	1.530	4.672	132
ZBLA	488	25.2	98.7	3968.4	1.713	1.548	4.579	132
ZBLAN	488	26.6	96.0	4270	3.608	1.521	4.301	132
HBL	488	22.4	151.4	3608.9	1.127	1.514	5.78	132
HBLA	488	22.1	162.3	3470	0.96	1.554	5.83	132
HBLAPC	488	25.2	179.5	4035	1.023	1.524	5.1	132
BeF <sub>2</sub>	488	24.3	52.5	4634.1	16.06	1.28	2.01	132
95BeF <sub>2</sub> -5THF <sub>4</sub>	488	24.9	74.8	4638.5	11.54	1.31	2.1	132
4.97 Li <sub>2</sub> O 94.27 B <sub>2</sub> O <sub>3</sub> 0.13 Al <sub>2</sub> O <sub>3</sub>	488	26.9	100	4364	12.88	1.5056	1.9434	132
4.97 Li <sub>2</sub> O 94.27 B <sub>2</sub> O <sub>3</sub> 0.13 Al <sub>2</sub> O <sub>3</sub>	488	26.8	116	4351	14.29	1.5053	1.9439	132
4.97 Li <sub>2</sub> O 94.27 B <sub>2</sub> O <sub>3</sub> 0.13 Al <sub>2</sub> O <sub>3</sub>	488	24.8	113	4050	11.74	1.4946	1.9025	132
4.97 Li <sub>2</sub> O 94.27 B <sub>2</sub> O <sub>3</sub> 0.13 Al <sub>2</sub> O <sub>3</sub>	488	32.1	124	5109	10.93	1.5324	2.0753	132
4.97 Li <sub>2</sub> O 94.27 B <sub>2</sub> O <sub>3</sub> 0.13 Al <sub>2</sub> O <sub>3</sub>	488	29.0	138	4662	12.66	1.5189	1.9823	132
4.97 Li <sub>2</sub> O 94.27 B <sub>2</sub> O <sub>3</sub> 0.13 Al <sub>2</sub> O <sub>3</sub>	488	33.0	104	5205	3.441	1.5455	2.0541	132
6 K <sub>2</sub> O-94SiO <sub>2</sub> 673°C 78.56 h	488	33.1	184	5458	3.905	1.4781	2.2416	132
6 K <sub>2</sub> O-94SiO <sub>2</sub> 604.8°C 231.8 h	488	33.1	186	5465	2.783	1.4781	2.2519	132
8 K <sub>2</sub> O-92SiO <sub>2</sub> 547°C	488	32.4	175	5330	3.354	1.4845	2.2703	132
8 K <sub>2</sub> O-92SiO <sub>2</sub> 603.5°C 103.42 h	488	32.5	190	5335	3.587	1.4844	2.2725	132
8 K <sub>2</sub> O-92SiO <sub>2</sub> 589.5°C 141.79 h	488	32.4	177	5332	5.181	1.4846	2.2716	132
8 K <sub>2</sub> O-92SiO <sub>2</sub> 574.3°C 345.68 h	488	32.4	170	5321	3.704	1.4844	2.2696	132
8 K <sub>2</sub> O-92SiO <sub>2</sub> 573.4°C 84.66 h	488	32.5	187	5339	4.038	1.4846	2.2702	132
10 K <sub>2</sub> O-90SiO <sub>2</sub>	488	30.8	208	5039	3.122	1.4923	2.2991	132
10 K <sub>2</sub> O-90SiO <sub>2</sub>	488	25.8	104	4190	8.169	1.5037	2.0281	132
30 K <sub>2</sub> O-70SiO <sub>2</sub>	488	30.2	134	4839	4.675	1.5231	2.2699	132

Reprinted with permission from M. X Weber (ed), *CRC Handbook of Laser Science and Technology: Optical Materials*, suppl. 2. Copyright CRC Press, Boca Raton, FL, 1988.

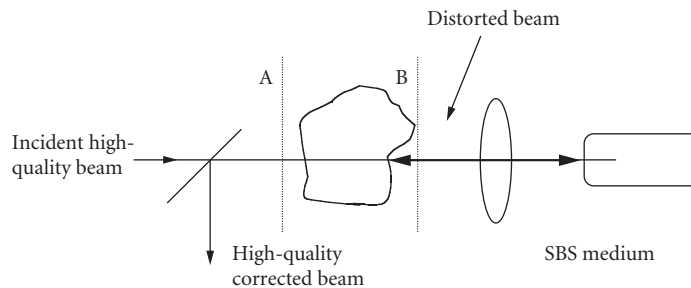


**FIGURE 18** Schematic diagram for correction of phase distortions caused by distorting medium with double-pass propagation.

The general concept is that the initial distortion required for this compensation is the inverse of the distortion imposed by the medium. However, determining precisely what that distortion is and imposing it on the initial beam is the heart of the matter in phase compensation.

The arrangement shown in Fig. 19 illustrates how this is done with nonlinear optical phase conjugation. The beam propagating from left to right is initially undistorted. It emerges from the medium at point B with a complete record of the distortion imposed by the medium. In the nonlinear medium, the beam undergoes a backward nonlinear optical interaction in which a second beam is generated that travels in the opposite direction and has phase variations that are reversed from the original distorted beam. When this beam propagates through the distorting medium again from right to left, the medium again impresses a phase variation on it, but this time the process simply undoes the initial phase distortion instead of creating one. The beam emerging from the distorting medium at point A is undistorted.

Several types of nonlinear interactions have been used for phase conjugation, including degenerate and nondegenerate four-wave mixing, stimulated Brillouin scattering, Brillouin-enhanced four-wave mixing, and stimulated Raman scattering. Of these, degenerate four-wave mixing is used most often for low-power interactions and stimulated Brillouin scattering is used for high-power applications. Brillouin-enhanced four-wave mixing provides a high-gain Brillouin system.

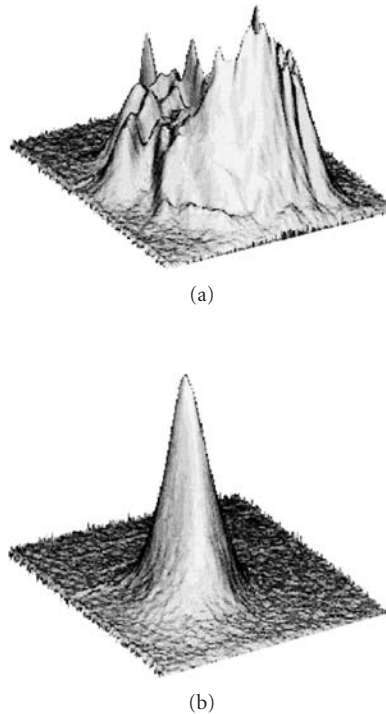


**FIGURE 19** Schematic diagram of use of stimulated Brillouin scattering for phase distortion correction with phase conjugation.

Phase conjugation with SBS is the result of mode competition in which the mode that corresponds to the conjugate of the pump has higher gain than other possible modes. The gain for the backward-generated beam involves a sum over all possible spatial modes of the backward Stokes wave. The mode that matches the pump wave has the highest gain because the high- and low-intensity points coincide, providing reinforcement of that mode over the entire interaction length. The exponential gain for this mode is twice that for the noncorrelated modes when the pump beam carries a large number of spatial modes.

In order for the conjugate mode to dominate over the other modes, it is necessary that it experiences preferential gain over an extended region. Essentially, it is required that the Stokes beam diffract across the entire pump beam in the interaction region before it grows to a saturation level. This has been accomplished by using a light guide to confine the beams. In free-focused interactions, it requires that the divergence of the pump beam be sufficient to provide a wide focal area relative to its depth. An example of phase conjugate correction in a two-pass Q-switched Nd:YAG amplifier system is shown in Fig. 20 using liquid Freon-113 as the conjugating medium.<sup>148</sup> Properties of phase-conjugated beams, quality of correction, and efficiency of conversion are given in Ref. 10.

**Brillouin-Enhanced Four-Wave Mixing** Brillouin-enhanced four-wave mixing (BEFWM) is a nearly degenerate four-wave mixing process where the four waves are coupled by the Brillouin nonlinearity as shown schematically in the Fig. 21. BEFWM was first observed and explained by Basov et al.<sup>149</sup> In addition to the beam to be conjugated, two oppositely propagating pump beams are



**FIGURE 20** Spatial beam profiles of a Q-switched Nd:YAG oscillator-amplifier system using a two-pass amplifier configuration with a conventional mirror in the two-pass amplifier (a) and an SBS mirror (b). The Brillouin mirror was a cell of liquid Freon-113. (From Ref. 148.)





**FIGURE 21**  $k$  vector diagram for Brillouin-enhanced four-wave mixing.

provided at frequency  $\omega_L$ . In general, the two pump beams do not need to be at the same frequency, but in practice they usually are. The signal beam  $k_s$  at a frequency  $\omega_s = \omega_p - \Delta\omega_B$  interacts with the laser beam  $k_1$  at a frequency  $\omega_p$  to produce an acoustic wave that moves in the direction of the laser beam. The second laser beam  $k_2$  scatters from the moving grating to generate the conjugated anti-Stokes beam  $k_{AS}$  at a frequency  $\omega_{AS} = \omega_p + \Delta\omega_B$ . The phase-conjugated beam, traveling in the opposite direction of the signal beam, can be amplified when the pump beams do not interact with each other. Therefore, BEFWM represents a mirror with reflectivity greater than 1. The pump beams are usually decoupled by frequency or polarization control. A reflectivity as high as  $\sim 7 \times 10^5$  has been observed.<sup>150</sup> The process can also be done with the anti-Stokes wave as the signal beam. The signal Stokes beam is usually generated externally via a separate SBS process. The angles between the beams can be adjusted to make the phase matching possible. Various aspects of BEFWM are described in detail in Ref. 151.

## 15.4 REFERENCES

1. N. Bloembergen, *Nonlinear Optics*, Benjamin, New York, 1965.
2. W. Kaiser and M. Maier, "Stimulated Rayleigh, Brillouin and Raman Spectroscopy," in F. T. Arecchi and E. O. Schulz-DuBois (eds.), *Laser Handbook*, vol. 2, North-Holland, Amsterdam, New York, 1972, pp. 1077–1150.
3. C. S. Wang, "The Stimulated Raman Process," in Herbert Rabin and C. L. Tang (eds.), *Quantum Electronics: A Treatise*, vol. 1, part A, Academic Press, New York, 1975.
4. A. Penzkofer, A. Laubereau, and W. Kaiser, "High Intensity Raman Interactions," *Prog. Quant. Electron.* **6**:55–140 (1979).
5. F. Milanovich, "Stimulated Raman Scattering," in M. J. Weber (ed.), *Handbook of Laser Science and Technology: Optical Materials*, vol. III, CRC, Boca Raton, FL, 1986.
6. Y. R. Shen, *Principles of Nonlinear Optics*, Wiley, New York, 1984.
7. R. W. Boyd, *Nonlinear Optics*, Academic, New York, 1992.
8. J. F. Reintjes, "Stimulated Raman and Brillouin Scattering," in M. J. Weber (ed.), *Handbook of Laser Science and Technology: Optical Materials*, suppl. 2, CRC, Boca Raton, FL, 1995, pp. 334–364.
9. "Stimulated Raman and Brillouin Scattering for Laser Beam Control," special issue of *JOSA B* **3** (October 1986).
10. J. Reintjes (ed.), "Laser Wavefront Control," *SPIE* **1000** (1988).
11. D. Levi, C. R. Menyuk, and P. Winternitz (eds.), *Self-Similarity in Stimulated Raman Scattering*, Les Publications CRM, Montreal, Canada, 1994.
12. N. Bloembergen, "The Stimulated Raman Effect," *Am. J. Phys.* **35**:989 (1967).
13. A. Z. Grasyuk, "Raman Lasers (Review)," *Sov. J. Quant. Electron.* **4**:269 (1974).
14. G. Eckardt, R. W. Hellwarth, F. J. McClung, S. E. Schwarz, and D. Weiner, "Stimulated Raman Scattering from Organic Liquids," *Phys. Rev. Lett.* **9**:455 (1962).
15. Y. R. Shen and N. Bloembergen, "Theory of Stimulated Raman and Brillouin Scattering," *Phys. Rev.* **137**:A1787 (1965).

16. N. M. Kroll, "Excitation of Hypersonic Vibrations by Means of Photoelastic Coupling of High Intensity Light Waves to Elastic Waves," *J. Appl. Phys.* **36**:34 (1965).
17. R. L. Carman, F. Shimizu, C. S. Wang, and N. Bloembergen, "Theory of Stokes Pulse Shapes in Transient Stimulated Raman Scattering," *Phys. Rev. A* **2**:60 (1970).
18. C. S. Wang, "Theory of Stimulated Raman Scattering," *Phys. Rev.* **182**:482 (1969).
19. M. D. Duncan, R. Mahon, L. L. Tankersley, and J. Reintjes, "Transient Stimulated Raman Amplification in Hydrogen," *JOSA B* **5**:37 (1988).
20. J. R. Murray and A. Javan, "Effects of Collisions on Raman Line Profiles of Hydrogen and Deuterium Gas," *J. Mol. Spectrosc.* **42**:1-26 (1972).
21. R. H. Dicke, *Phys. Rev.* **89**:472 (1953).
22. W. K. Bischel and M. J. Dyer, "Temperature Dependence of the Raman Linewidth and Lineshift for the Q(1) and Q(0) Transitions in Normal and Para H<sub>2</sub>," *Phys. Rev. A* **33**:3113 (1986).
23. S. Kern and B. Feldman, *Stimulated Raman Emission*, vol. 3, Massachusetts Institute of Technology, Lincoln Laboratory, Bedford, MA, 1974, p. 18.
24. J. J. Barrett and M. C. Tobin, "Stimulated Raman Emission Frequencies in 21 Organic Liquids," *J. Opt. Soc. Am.* **56**:129 (1966).
25. M. D. Martin and E. L. Thomas, "Infrared Difference Frequency Generation," *IEEE J. Quant. Electron.* **QE-2**:196 (1966).
26. M. A. El-Sayed, F. M. Johnson, and J. Duardo, "A Comparative Study of the Coherent Raman Processes Using the Ruby and the Second Harmonic Neodymium Giant-Pulsed Lasers," *J. Chem. Phys.* **1**:227 (1967).
27. J. A. Giordmaine and J. A. Howe, "Intensity-Induced Optical Absorption Cross Section in CS<sub>2</sub>," *Phys. Rev. Lett.* **11**:207 (1963).
28. T. A. Prasada Rao and N. Seetharaman, "Amplification of Stimulated Raman Scattering by a Dye," *Ind. J. Pure Appl. Phys.* **13**:207 (1975).
29. M. Geller, D. P. Bortfeld, and W. R. Sooy, "New Woodbury-Raman Laser Materials," *Appl. Phys. Lett.* **3**:36 (1963).
30. W. L. Smith and F. P. Milanovich, Lawrence Livermore National Laboratory, Livermore, CA, Private Communication, 1983.
31. J. R. Maple and J. T. Knudtson, "Transient Stimulated Vibrational Raman Scattering in Small Molecule Liquids," *Chem. Phys. Lett.* **56**:241 (1978).
32. J. K. Wright, C. H. H. Carmichael, and B. J. Brown, "Narrow Linewidth Output from a Q-switched Nd 3-/Glass Laser," *Phys. Lett.* **16**:264 (1965).
33. M. K. Srivastava and R. W. Crow, "Raman Susceptibility Measurements and Stimulated Raman Effect in KDP," *Opt. Commun.* **8**:82 (1973).
34. P. D. Maker and R. W. Terhune, "Study of Optical Effects due to an Induced Polarization Third Order in the Electric Field Strength," *Phys. Rev.* **137**:A801 (1965).
35. D. P. Bortfeld, M. Geiller, and G. Eckhardt, "Combination Lines in the Stimulated Raman Spectrum of Styrene," *J. Chem. Phys.* **40**:1770 (1964).
36. V. A. Orlovich, "Measurement of the Coefficient of Stimulated Raman Scattering in Organic Liquids with the Aid of an Amplifier with Transverse Pumping," *Zh. Prikl. Spektrosk.* **23**:224 (1975).
37. J. A. Calvieleo and Z. H. Heller, "Raman Laser Action in Mixed Liquids," *Appl. Phys. Lett.* **5**:112 (1964).
38. G. Eckhardt, "Selection of Raman Laser Materials," *IEEE J. Quant. Electron.* **QE-2**:1 (1966).
39. V. A. Subov, M. M. Sushchinskii, and I. K. Shuvalov, "Investigation of the Excitation Threshold of Induced Raman Scattering," *J. Exp. Theor. Phys. USSR* **47**:784 (1964).
40. C. D. Decker, "High-Efficiency Stimulated Raman Scattering/Dye Radiation Source," *Appl. Phys. Lett.* **33**:323 (1978).
41. B. P. Stoicheff, "Characteristics of Stimulated Raman Radiation Generated by Coherent Light," *Phys. Lett.* **7**:186 (1963).
42. D. Cotter, D. C. Hanna, and R. Wyatt, "A High Power, Widely Tunable Infrared Source Based on Stimulated Electronic Raman Scattering in Caesium Vapour," *Opt. Commun.* **16**:256 (1976).
43. P. E. Tannenwaid and J. B. Thaxter, "Stimulated Brillouin and Raman Scattering in Quartz at 2.1 to 293 Kelvin," *Science* **134**:1319 (1966).

44. J. Gelbwachs, R. H. Pantell, H. E. Puthoff, and J. M. Yarborough, "A Tunable Stimulated Raman Oscillator," *Appl. Phys. Lett.* **14** (1969).
45. G. Eckhardt, D. P. Bortfeld, and M. Geller, "Stimulated Emission of Stokes and Anti-Stokes Raman Lines from Diamond, Calcite and  $\alpha$ -Sulfur Single Crystals," *Appl. Phys. Lett.* **3**:137 (1963).
46. I. V. Aleksandrov, Y. S. Bobovitch, A. V. Bortkevich, and M. Y. Tsenter, "Raman Scattering in Crystalline Chlorine and Bromine," *Opt. Spektrosk.* **36**:150 (1974).
47. I. I. Kondilenko, P. A. Korotkov, and V. I. Maly, "Temperature Dependence of SRS Thresholds for Some Salts of Inorganic Acids in the Crystalline Phase," *Opt. Commun.* **10**:50 (1974).
48. D. L. Weinberg, "Stimulated Raman Emission in Crystals and Organic Liquids," *Mass. Inst. Technol. Lincoln Lab. Solid-State Res. Rep.* **3**:31 (1965).
49. O. S. Avanesyan, V. A. Benderskii, V. K. H. Brikenshtein, V. L. Broude, A. G. Lavrushko, I. I. Tartakovskii, and P. V. Filippov, "Characteristics of Stimulated Light Generation and Stimulated Raman Scattering in Anthracene Crystals," *Sov. J. Quant. Electron.* **7**:403 (1977).
50. J. L. Carlsten and P. C. Dunn, "Stimulated Stokes Emission with a Dye Laser: Intense Tunable Radiation in the Infrared," *Opt. Commun.* **14**:8 (1975).
51. D. Cotter, D. C. Hanna, P. A. Kärkkäinen, and R. Wyatt, "Stimulated Electronic Raman Scattering as a Tunable Infrared Source," *Opt. Commun.* **15**:143 (1975).
52. P. P. Sorokin, J. J. Wynne, and J. R. Landkard, "Tunable Coherent IR Source Based upon Four-Wave Parametric Conversion in Alkali Metal Vapors," *Appl. Phys. Lett.* **22**:342 (1973).
53. A. DeMartino, R. Frey, and F. Pradere, "Tunable Far Infrared Generation in Hydrogen Fluoride," *Opt. Commun.* **27**:262 (1978).
54. P. May, P. Bernage, and H. Boequet, "Stimulated Electronic Raman Scattering in Rubidium Vapour," *Opt. Commun.* **29**:369 (1979).
55. R. L. Byer and W. R. Trutna, "16- $\mu$ m Generation by CO<sub>2</sub>-Pumped Rotational Raman Scattering in H<sub>2</sub>," *Opt. Lett.* **3**:144 (1978).
56. P. Rabinowitz, A. Stein, R. Brickman, and A. Kaldor, "Efficient Tunable H<sub>2</sub> Raman Laser," *Appl. Phys. Lett.* **35**:739 (1979).
57. E. Pochon, "Determination of the Spontaneous Raman Linewidth of CF<sub>4</sub> by Measurements of Stimulated Raman Scattering in Both Transient and Steady States," *Chem. Phys. Lett.* **77**:500 (1981).
58. B. E. Kinkaid and J. R. Fontana, "Raman Cross-Section Determination by Direction Stimulated Raman Gain Measurements," *Appl. Phys. Lett.* **28**:12 (1975).
59. M. Rokni and S. Yatsiv, "Resonance Raman Effects in Free Atoms of Potassium," *Phys. Lett.* **24**:277 (1967).
60. R. W. Minek, R. W. Terhune, and W. G. Rado, "Laser-Stimulated Raman Effect and Resonant Four-Photon Interactions in Gases H<sub>2</sub>, D<sub>2</sub>, and CH<sub>4</sub>," *Appl. Phys. Lett.* **3**:181 (1963).
61. H. Komine, Northrop Corp., Palos Verdes, Calif., Private Communication, 1983.
62. W. K. Bischel and M. J. Dyer, "Wavelength Dependence of the Absolute Raman Gain Coefficient for the Q(1) Transition in H<sub>2</sub>," *JOSA B* **5**:677 (1986).
63. W. K. Bischel and G. Black, "Wavelength Dependence of Raman Scattering Cross Sections from 200–600 nm," in C. K. Rhodes, H. Egger, and H. Pummer (eds.), *Excimer Lasers—1983*, AIP, New York, 1983.
64. W. K. Bischel, "Stimulated Raman Gain Processes in H<sub>2</sub>, HD and D<sub>2</sub>," unpublished data.
65. J. J. Ottusch and D. A. Rockwell, "Measurement of Raman Gain Coefficients of Hydrogen, Deuterium and Methane," *IEEE J. Quant. Electron.* **QE-24**:2076 (1988).
66. D. A. Russel and W. B. Roh, "High Resolution CARS Measurements of Raman Linewidths of Deuterium," *J. Mol. Spect.* **24**:240 (1987).
67. K. C. Smyth, G. J. Rosasco, and W. S. Hurst, "Measurements and Rate Law Analysis of D2 Q-Branch Line Broadening Coefficients for Collisions with D<sub>2</sub>, He, Ar, H<sub>2</sub> and CH<sub>4</sub>," *J. Chem. Phys.* **87**:1001 (1987).
68. D. Haner and I. S. McDermid, "Stimulated Raman Shifting of the Nd:YAG Fourth Harmonic (266 nm) in H<sub>2</sub>, HD and D<sub>2</sub>," *IEEE J. Quant. Electron.* **QE-26**:1292 (1990).
69. J. R. Murray, J. Goldhar, D. Eimerl, and A. Szoke, "Raman Pulse Compression of Excimer Lasers for Application to Laser Fusion," *IEEE J. Quant. Electron.* **QE-15**:342 (1979).
70. G. C. Herring, M. X Dyer, and W. K. Bischel, "Temperature and Wavelength Dependence of the Rotational Raman Gain Coefficient in N<sub>2</sub>," *Opt. Lett.* **11**:348 (1986).

71. A. P. Hickman, J. A. Paisner, and W. K. Bischel, *Phys. Rev. A* **33**:1788 (1986).
72. H. Chuan and T. H. Chyba, "Solid-State Barium Nitrate Raman Laser in the Visible Region," *Opt. Commun.* **135**:273 (1997).
73. P. G. Zverev, T. T. Basiev, V. V. Osiko, A. M. Kulkov, V. N. Voitsekhovskii, and V. E. Yakobson, "Physical, Chemical and Optical Properties of Barium Nitrate Raman Crystal," *Opt. Mat.* **11**:315 (1999).
74. P. G. Zverev and T. T. Basiev, "Investigation of the Line Broadening of an SRS-Active Vibration in a Barium Nitrate Crystal by Two-Photon Raman Amplification Spectroscopy," *Quant. Electron.* **25**:1204 (1995).
75. V. N. Voitsekhovskii, S. N. Karpukhin, and V. E. Yakobson, "Single-Crystal Barium Nitrate and Sodium Nitrate as Efficient Materials for Laser-Radiation Frequency Conversion Based on Stimulated Raman Scattering," *J. Opt. Tech.* **62**:770 (1995).
76. P. G. Zverev, J. T. Murray, R. C. Powell, R. J. Reeves, and T. T. Basiev, "Stimulated Raman Scattering of Picosecond Pulses in Barium Nitrate Crystals," *Opt. Commun.* **97**:59 (1993).
77. A. Owyong and P. S. Percy, "Precise Characterization of the Raman Nonlinearity in Benzene Using Nonlinear Interferometry," *J. Appl. Phys.* **48**:674 (1977).
78. G. C. Herring, M. J. Dyer, and W. K. Bischel, "Temperature and Density Dependence of the Linewidths and Lineshifts of the Rotational Raman Lines in  $N_2$  and  $H_2$ ," *Phys. Rev. A* **34**:1944 (1986).
79. G. Hilfer and C. R. Menyuk, "Stimulated Raman Scattering in the Transient Limit," *J. Opt. Soc. Am. B* **7**:739-749 (1990).
80. M. J. Colles, *Appl Phys. Lett.* **19**:23 (1971).
81. C. R. Menyuk, in D. Levi, C. R. Menyuk, and P. Winternitz (eds.), *Self-Similarity in Stimulated Raman Scattering*, Les Publications CRM, Montreal, Canada, 1994.
82. K. J. Druhl, R. G. Wenzel, and J. L. Carlsten, *Phys. Rev. Lett.* **51**:1171 (1983).
83. C. R. Menyuk, *Phys. Rev. A* **47**:2235 (1993).
84. W. R. Trutna, Y. K. Park, and R. L. Byer, *IEEE J. Quant. Electron.* **QE-15**:648 (1979).
85. M. G. Raymer, J. Mostowski, and J. L. Carlsten, "Theory of Stimulated Raman Scattering with Broadband Lasers," *Phys. Rev. A* **19**:2304 (1979).
86. J. Eggleston and R. L. Byer, *IEEE J. Quant. Electron.* **QE-16**:850 (1980).
87. E. A. Stappaerts, W. H. Long Jr., and H. Komine, *Opt. Lett.* **5**:4 (1980).
88. A. Flusberg, D. Korff, and C. Duzy, "The Effect of Weak Dispersion on Stimulated Raman Scattering," *IEEE J. Quant. Electron.* **QE-21**:232 (1985).
89. K. A. Druhl, "Coherence Properties of Stokes Beams for Incoherent Broadband Pumps," *JOSA B* **3**:1363 (1986).
90. D. Korff, E. Mazur, C. Duzy, and A. Flusberg, "Raman Conversion Using Crossed Broadband Pump Beams and Bisecting Stokes," *JOSA B* **3**:1333 (1986).
91. G. C. Lombardi and H. Injeyan, "Phase Correlation Effects in a Raman Amplifier," *JOSA B* **3**:1461 (1986).
92. M. Bashkansky and J. Reintjes, "Correlation Effects in Pump-Depleted Broad-Band Stimulated Raman Amplification," *Opt. Commun.* **83**:103 (1991).
93. M. Bashkansky and J. Reintjes, "Incoherent Multimode Raman Amplification Theory," *JOSA B* **8**: 1843 (1991).
94. M. D. Skeldon and R. Bahr, "Stimulated Rotational Raman Scattering in Air with a High Power Broadband Laser," *Opt. Lett.* **16**:366 (1991).
95. M. Trippenbach, K. Rzazewski, and M. G. Raymer, "Stimulated Raman Scattering of Colored Light," *JOSA B* **1**:671 (1984).
96. B. W. Shore, S. Lowder, and M. A. Johnson, "Some General Properties of Stimulated Raman Propagation with Pump Depletion, Transiency and Dispersion," LLNL Report No. UCRL-ID-1-7967 R1, 1991.
97. M. G. Raymer and J. Mostowski, "Stimulated Raman Scattering: Unified Treatment of Spontaneous Initiation and Spatial Propagation," *Phys. Rev. A* **24**:1980 (1981).
98. G. P. Dzhotyan, Y. E. D'yakov, I. G. Zubarev, A. B. Mironov, and S. I. Mikhailov, "Amplification during Stimulated Raman Scattering in a Nonmonochromatic Pump Field," *Sov. Phys. JETP* **46**:431 (1978).
99. S. A. Akhmanov, Y. E. D'yakov, and L. I. Pavlov, "Statistical Phenomena in Raman Scattering Stimulated by a Broad-Band Pump," *Sov. Phys. JETP* **39**:249 (1975).

100. M. D. Duncan, R. Mahon, L. L. Tankersley, and J. Reintjes, "Spectral and Temporal Characteristics of Spontaneous Raman Scattering in the Transient Regime," *JOSA B* **8**:300 (1991).
101. J. C. White and D. Henderson, "Anti-Stokes Raman Lasers," *AIP Conf. Proc.* **90**:117–127 (1982).
102. J. C. White and D. Henderson, "TI: Threshold and Dispersion Effects in the Anti-Stokes Raman Laser," *Opt. Lett.* **7**:517 (1982).
103. K. Ludewigt, R. Dierking, W. Pfungsten, and B. Wellegehausen, "Vacuum Ultraviolet Anti-Stokes Raman Lasers," *IEEE J. Quant. Electron.* **QE 22**:1967–1974 (1986).
104. A. Z. Grasyuk, L. L. Losev, A. P. Lutsenko, and S. N. Sazonov, "Parametric Raman Anti-Stokes Laser," *Sov. J. Quant. Electron.* **20**:1153–1155 (1990).
105. N. Bloembergen and Y. R. Shen, "Coupling between Vibrations and Light Waves in Raman Laser Media," *Phys. Rev. Lett.* **12**:504 (1964).
106. M. D. Duncan, R. Mahon, L. L. Tankersley, and J. Reintjes, "Parametric Raman Gain Suppression in D<sub>2</sub> and H<sub>2</sub>," *Opt. Lett.* **11**:803 (1986).
107. C. Reiser, T. D. Raymond, R. B. Michie, and A. P. Hickman, "Efficient Anti-Stokes Raman Conversion in Collimated Beams," *JOSA B* **6**:1859 (1989).
- 107a. K. Leung, M. Oron, D. Klimek, R. Holmes, and A. Flusberg, "Observation of Parametric Gain Suppression in Rotational Raman Transitions in N<sub>2</sub> and H<sub>2</sub>," *Opt. Lett.* **13**:33 (1988).
- 107b. B. N. Perry, P. Raninowitz, and O. S. Bomse, *Opt. Lett.* **10**:146 (1985).
108. M. D. Levenson, "Coherent Raman Spectroscopy," (see also included references), *Phys. Today* (May 1977).
109. C. M. Bowden and J. C. Englund, "Macroscopic Manifestation of Quantum Noise," *Opt. Commun.* **67**:71 (1988).
110. M. G. Raymer, I. A. Walmsley, X. Mostowski, and B. Sobolewska, "Quantum Theory of Spatial and Temporal Coherence Properties of Stimulated Raman Scattering," *Phys. Rev. A* **32**:332 (1985).
111. M. G. Raymer, Z. W. Li, and I. A. Walmsley, "Temporal Quantum Fluctuations in Stimulated Raman Scattering," *Phys. Rev. Lett.* **63**:1586 (1989).
112. M. G. Raymer and L. A. Westling, "Quantum Theory of Stokes Generation with a Multimode Laser," *JOSA B* **2**:1417 (1985).
113. M. D. Duncan, R. Mahon, L. L. Tankersley, and J. Reintjes, "Low-Light Level, Quantum-Noise-Limited Amplification in a Stimulated Raman Amplifier," *JOSA B* **9**:2107 (1992).
114. R. C. Swanson, P. R. Battle, and J. Carlsten, "Interferometric Measurement of Quantum Noise in a Raman Amplifier," *Phys. Rev. Lett.* **67**:38 (1991).
115. N. Fabriucius, K. Nattermann, and D. von der Linde, "Macroscopic Manifestation of Quantum Fluctuations in Transient Stimulated Raman Scattering," *Phys. Rev. Lett.* **52**:1113 (1984).
116. K. Nattermann, N. Fabricius, and D. von der Linde, "Observation of Transverse Effects on Quantum Fluctuations in Stimulated Raman Scattering," *Opt. Commun.* **57**:212 (1986).
117. M. G. Raymer, K. Rzazewski, and J. Mostowski, "Pulse Energy Statistics in Stimulated Raman Scattering," *Opt. Lett.* **7**:71 (1982).
118. K. Rzazewski, M. Lewenstein, and M. G. Raymer, "Statistics of Stimulated Stokes Pulse Energies in the Steady State Regime," *Opt. Commun.* **43**:451 (1982).
119. D. C. MacPherson, R. C. Swanson, and J. L. Carlsten, "Quantum Fluctuations in the Stimulated Scattering Linewidth," *Phys. Rev. Lett.* **61**:66 (1988).
120. M. G. Raymer and I. A. Walmsley, "Quantum Statistics of Stimulated Raman Scattering," in L. Mandel (ed.), *Coherence and Quantum Optics*, vol. V, Plenum, New York, 1983, p. 63.
121. M. D. Duncan, R. Mahon, L. L. Tankersley, and J. Reintjes, "Imaging through a Low Light Level Amplifier," *SPIE* **1409**:127–134 (1991).
122. M. D. Duncan, R. Mahon, L. L. Tankersley, and J. Reintjes, "Second Stokes Generation in Deuterium and Hydrogen," *Opt. Commun.* **86**:538–546 (1991).
123. G. I. Kachen and W. H. Lowdermilk, "Subnanosecond Pulsations in Forward and Backward Stimulated Raman Scattering," *Opt. Commun.* **18**:112 (1976).
124. M. Rokni and A. Flusberg, "Stimulated Rotational Raman Scattering in the Atmosphere," *IEEE J. Quant. Electron.* **QE-22**:1102 (1986).

125. M. D. Levenson, *Introduction to Nonlinear Laser Spectroscopy*, Academic Press, New York, 1982.
126. H. Lotem and R. T. Lynch Jr., *Phys. Rev. Lett.* **37**:334 (1976).
127. M. D. Duncan, R. Mahon, L. L. Tankersley, and J. Reintjes, "Time-Gated Imaging through Scattering Media Using Stimulated Raman Amplification," *Opt. Lett.* **16**:1868–1870 (1991).
128. R. Mahon, M. D. Duncan, L. L. Tankersley, and J. Reintjes, "Time-Gated Imaging through Dense Scatterers with a Raman Amplifier," *Appl. Opt.* **32**:7425–7433 (1993).
129. M. Bashkansky, P. R. Battle, R. Mahon, and J. Reintjes, "Subsurface Defect Detection in Ceramic Materials Using Ultrafast Optical Techniques," *22nd Ann. Rev. of Prog. in Quantitative Nondestructive Evaluation*, Seattle, WA, 1995.
130. G. W. Faris, M. J. Dyer, and A. Peet Hickman, "Transient Effects on Stimulated Brillouin Scattering," *Opt. Lett.* **17**:1049 (1992).
131. L. G. Hwa, J. Schroeder, and X.-S. Zhao, "Intrinsic Brillouin Linewidths and Stimulated Brillouin Coefficients in Glasses Studied by Inelastic Light Scattering," *JOSA B* **6**:833 (1989).
132. J. Schroeder, L. G. Hwa, G. Kendall, C. S. Dumais, M. C. Shyong, and D. A. Thompson, "Inelastic Light Scattering in Halide and Oxide Glasses: Intrinsic Brillouin Linewidths and Stimulated Brillouin Gain," *J. Noncryst. Solids* **102**:240 (1988).
133. G. W. Faris, L. E. Jusinski, M. J. Dyer, W. K. Bischel, and A. Peet Hickman, "High Resolution Brillouin Gain Spectroscopy in Fused Silica," *Opt. Lett.* **15**:703 (1990).
134. G. W. Faris, L. E. Jusinski, and A. Peet Hickman, "High Resolution Stimulated Brillouin Gain Spectroscopy in Glasses and Crystals," *JOSA B* **10**:587 (1990).
135. A. M. Scott, D. E. Watkins, and P. Tapster, "Gain and Noise Characteristics of Brillouin Amplifier and Their Dependence on the Spatial Structure of the Pump Beam," *JOSA B* **7**:929 (1990).
136. R. W. F. Gross, S. T. Amimoto, and L. Garman-DuVall, "Gain and Phase Conjugation Fidelity of a Four Wave Brillouin Mirror Based on Methane," *Opt. Lett.* **16**:94 (1991).
137. V. I. Bespalov, O. V. Kulagin, A. I. Makarov, G. A. Pasmanik, A. K. Potjomkin, P. B. Potlov, and A. A. Shilov, "High-Sensitivity Optical System with Laser Amplifiers and Phase Conjugating Mirrors," *Opt. Acoust. Rev.* **1**:71 (1989).
138. P. Narum, M. D. Skeldon, and R. W. Boyd, "Effect of Laser Mode Structure on Stimulated Brillouin Scattering," *IEEE J. Quant. Electron.* **QE-22**:2161 (1986).
139. G. C. Valley, "A Review of Stimulated Brillouin Scattering Excited with a Broad Pump Laser," *IEEE J. Quant. Electron.* **QE-22**:704 (1986).
140. W. T. Whitney, M. T. Duignan, and B. J. Feldman, "Stimulated Brillouin Scattering and Phase Conjugation of Multiline Hydrogen Fluoride Laser Radiation," *JOSA B* **7**:2160 (1990).
- 140a. Robert A. Fisher (ed.), *Optical Phase Conjugation*, Academic Press, New York, 1983.
141. A. I. Erohkin, V. I. Kovalev, and F. S. Faizullov, "Determination of the Parameters of a Nonlinear Response of Liquids in an Acoustic Resonance Region by the Method of Nondegenerate Four Wave Interaction," *Sov. J. Quant. Electron.* **16**:872 (1986).
142. M. J. Dyer and W. K. Bischel, unpublished data.
143. S. T. Amimoto, R. W. F. Gross, L. Garman-DuVall, T. W. Good, and J. D. Piranian, "Stimulated Brillouin-Scattering Properties of SnCl<sub>4</sub>," *Opt. Lett.* **16**:1382 (1991).
144. M. J. Damzen, M. H. R. Hutchinson, and W. A. Schroeder, "Direct Measurement of the Acoustic Decay Times of Hypersonic Waves Generated by SBS," *IEEE I. Quant. Electron.* **QE-23**:328 (1987).
145. F. E. Hovis and J. D. Kelley, "Phase Conjugation by Stimulated Brillouin Scattering in CCl<sub>4</sub> near the Gas-Liquid Critical Temperature," *JOSA B* **6**:840 (1989).
146. S. Y. Tang, C. Y. She, and S. A. Lee, "Continuous Wave Rayleigh-Brillouin Gain Spectroscopy in SF<sub>6</sub>," *Opt. Lett.* **12** (1987).
147. D. Milam, LLNL Report No. 90-011/6330K.
148. P. Klovekom and J. Munch, "Variable Stimulated Brillouin Scattering Pulse Compressor for Nonlinear Optical Measurements," *Appl. Opt.* **36**:5913 (1997).
149. N. G. Basov, I. G. Zubarev, A. V. Kotov, S. I. Mikhailov, and M. G. Smirnov, "Small-Signal Wavefront Reversal in Non-Threshold Reflection from a Brillouin Mirror," *Sov. J. Quant. Electron.* **9**:237–239 (1979).

150. N. F. Andreev, V. I. Bespalov, A. M. Kiselev, A. Z. Matreev, G. A. Pasmanik, and A. A. Shilov, "Wavefront Inversion of Weak Optical Signals with a Large Reflection Coefficient," *JETP Lett.* **32**:625–629 (1980).
151. A. M. Scott and K. D. Ridley, "A Review of Brillouin-Enhanced Four-Wave Mixing," *IEEE J. Quant. Electron.* **25**:438–459 (1989).

---

## 15.5 ADDITIONAL REFERENCES

---

- S. A. Akmanov, B. V. Zhdanov, A. I. Kovrigin, and S. A. Pershin, "Effective Stimulated Scattering in the Ultraviolet and Dispersion of Gain in the 1.06–0.26  $\mu$  Band," *JETP Lett.* **15**:185 (1972).
- F. Aussenegg and V. Deserno, "Stimulated Raman Scattering Excited by Light of 5300 Å," *Opt. Commun.* **2**:295 (1970).
- G. Bisson and G. Mayer, "Effets Raman stimulés dans la calcite," *Crit. Acad. Set Paris* **265**:397 (1967).
- N. Bloembergen, B. P. Lallemand, A. Pine, and P. Simova, "Controlled Stimulated Raman Amplification and Oscillation in Hydrogen Gas," *IEEE J. Quant. Electron.* **QE-3**:197 (1967).
- R. L. Byer, "A 16- $\mu$ m Source for Laser Isotope Enrichment," *IEEE J. Quant. Electron.* **QE-12**:732 (1976).
- M. J. Colles, "Efficient Stimulated Raman Scattering from Picosecond Pulses," *Opt. Commun.* **1**:169 (1969).
- J. Gazengel, N. P. Xuan, and G. Rivoire, "Stimulated Raman Scattering Thresholds for Ultra-Short Excitation," *Opt. Acta* **26**:1245 (1979).
- H. Gorner, M. Maier, and W. Kaiser, "Raman Gain in Liquid Core Fibers," *J. Raman Spectrosc.* **2**:363 (1974).
- A. Z. Grasyuk, V. F. Erinkov, I. G. Zubarev, V. I. Mishin, and V. G. Smirnov, "Laser Based on Raman Scattering in Liquid Nitrogen," *JETP Lett.* **8**:291 (1968).
- J. B. Grun, A. K. McQuillan, and B. P. Stoicheff, "Intensity and Gain Measurements on the Stimulated Raman Emission in Liquid O<sub>2</sub> and N<sub>2</sub>," *Phys. Rev.* **181**:61 (1969).
- E. E. Hagenlocker, R. W. Minck, and W. G. Rado, "Effects of Phonon Lifetime on Stimulated Optical Scattering in Gases," *Phys. Rev.* **154**:226 (1967).
- E. P. Ippen, "Low-Power Quasi-cw Raman Oscillator," *Appl. Phys. Lett.* **16**:303 (1970).
- R. W. Minck, E. E. Hagenlocker, and W. G. Rado, "Consideration and Evaluation of Factors Influencing the Stimulated Optical Scattering in Gases," Scientific Laboratory, Ford Motor Company, Dearborn, MI, SC66-24, 1966.
- I. Reinhold and M. Maier, "Gain Measurements of Stimulated Raman Scattering Using a Tunable Dye Laser," *Opt. Commun.* **5**:31 (1972).
- W. L. Smith, F. P. Milanovich, and M. Hennesian, Lawrence Livermore National Laboratory, Private Communication, 1983.
- M. B. Vakhonev, V. N. Volkov, A. Z. Grasyuk, and A. N. Kirkin, "Determination of the Gain in Stimulated Raman Scattering under Spatially Inhomogeneous Pumping Conditions," *Sov. J. Quant. Electron.* **6**:1369 (1976).

# THIRD-ORDER OPTICAL NONLINEARITIES

Mansoor Sheik-Bahae and Michael P. Hasselbeck

*Department of Physics and Astronomy  
University of New Mexico  
Albuquerque, New Mexico*

## 16.1 INTRODUCTION

The subject of this chapter could well fill a textbook, and indeed the topic comprises a significant portion of the many books on nonlinear optics. A large (but by no means exhaustive or complete) list of texts that provide extensive discussion of high-order nonlinearities appears in Refs. 1 through 30. We have not attempted to write a review chapter nor mentioned or even listed every known third-order nonlinear optical phenomenon. Our aim is to illustrate important and representative third-order effects, emphasizing qualitative descriptions. Details can be found in the references. An exception is our discussion of the Kramers-Kronig relations in nonlinear optics. A fundamental premise of this transformation is the causal link between nonlinear refraction and nonlinear absorption, which is a key aspect of the third-order susceptibility. It has not been treated in most texts; some of the important mathematical steps are given here. Our treatment of third-order nonlinear optics assumes that the reader is familiar with electromagnetic theory, physical optics, and quantum mechanical energy level diagrams.

Any real, physical oscillating system will exhibit a nonlinear response when it is overdriven. In an optical system, a nonlinear response can occur when there is sufficiently intense illumination. The nonlinearity is exhibited in the polarization ( $\vec{\mathcal{P}}$ ) of the material, which is often represented by a power series expansion of the total applied optical field ( $\vec{\mathcal{E}}$ ):

$$(\vec{\mathcal{P}}) = \epsilon_0 \chi^{(1)} \vec{\mathcal{E}} + \epsilon_0 \chi^{(2)} \vec{\mathcal{E}}^2 + \epsilon_0 \chi^{(3)} \vec{\mathcal{E}}^3 + \dots \quad (1)$$

Here  $\chi^{(1)}$  is the linear susceptibility representing the linear response (i.e., linear absorption and the refractive index) of the material. The two lowest-order nonlinear responses are accounted for by the second- and third-order nonlinear susceptibilities  $\chi^{(2)}$  and  $\chi^{(3)}$ . The subject of this chapter is third-order effects. Processes arising from the second-order response (including second-harmonic generation and optical parametric processes) are discussed elsewhere (see Chap. 10, “Nonlinear Optics” and Chap. 17, “Continuous-Wave Optical Parametric Oscillators”). We will, however, briefly consider the cascading of second-order nonlinearities that appear as an *effective* third-order process in Sec. 16.10.



Third-order optical nonlinearities cover a vast and diverse area in nonlinear optics. A simple illustration of this point is the reported range of magnitudes and response times for  $\chi^{(3)}$  in various materials, which span 15 orders of magnitude! This has led to unavoidable inconsistency and confusion in the definition and interpretation of the nonlinear susceptibility. We will not be immune from such inconsistencies and errors. In that spirit, we note that the simple power series representation of the nonlinear optical response described by Eq. (1) is not rigorously correct because it assumes the response is instantaneous. In the case of the bound electronic nonlinearity, for example, this assumption is excellent because the response is exceedingly fast. The response is not *infinitely* fast, however. Response times can vary by orders of magnitude depending on the physical mechanism and resonance conditions involved. Furthermore, Eq. (1) assumes locality, which implies that the nonlinear polarization at a given point in space depends on the magnitude of the electric field only at that point. This condition is not always satisfied. The electrostrictive nonlinearity, for example, is the result of physical displacement of charged particles in a material subject to the ponder-motive force due to the gradient of light irradiance. It is therefore nonlocal. It is nevertheless instructive to apply Eq. (1) to describe various third-order effects that are local and (single photon) nonresonant.

The nonlinear polarization represented in Eq. (1) excludes *effective* third-order nonlinear processes involving linear absorption ( $\chi^{(1)}$  process) of one of the excitation beams. An example is the thermal nonlinearity resulting from linear absorption and heating that causes a change of refractive index. Although this is effectively a third-order nonlinear response, we group this and similar phenomena in Sec. 16.9 on cascaded  $\chi^{(1)}$ : $\chi^{(1)}$  effects.

The term involving  $\bar{\mathcal{E}}^3$  in Eq. (1) implies that three optical fields interact to produce a fourth field. The  $\chi^{(3)}$  interaction is thus a four-photon process. This is a consequence of the quantum mechanical picture of the nonlinear susceptibility. Conservation of photon energy is always required to complete the interaction process. Assuming the applied optical fields are monochromatic plane waves, we write the total input electric field  $\bar{\mathcal{E}}$  as

$$\bar{\mathcal{E}}(r, t) = \bar{\mathcal{E}}_1(r, t) + \bar{\mathcal{E}}_2(r, t) + \bar{\mathcal{E}}_3(r, t) \quad (2)$$

In general, each beam has a different frequency ( $\omega$ ) and wave vector ( $\vec{k}$ ), represented in complex notation:

$$\bar{\mathcal{E}}_j(r, t) = \frac{\bar{E}_j}{2} \exp(i\omega_j t - i\vec{k}_j \cdot r) + \text{c.c.} \quad \text{for } j=1, 2, 3 \quad (3)$$

where c.c. stands for complex conjugate and  $\bar{E}_j$  is a complex vector describing the amplitude, phase, and polarization of each beam. It is important to realize that there can be up to three different input laser frequencies, but there can also be as few as one. Ignoring the  $\chi^{(1)}$  and  $\chi^{(2)}$  components in Eq. (1), the nonlinear polarization resulting from the  $\bar{\mathcal{E}}^3$  interaction leads to a total of 108 terms involving all possible permutations of the fields at three frequencies. The nonlinear polarization occurs at frequencies given by

$$\omega_4 = \pm\omega_i \pm \omega_j \pm \omega_k \quad \text{for } i, j, k=1, 2, 3 \quad (4)$$

The existence of 108 terms does not mean there are as many distinct mechanisms involved. For instance, three terms give  $\omega_4 = 3\omega_j$  for  $j = 1, 2, 3$ , describing exactly the same process of third-harmonic generation (THG). Furthermore, THG is a special case of sum frequency generation (SFG) involving one, two, or three different frequencies giving  $\omega_4 = \omega_i + \omega_j + \omega_k$ ,  $i, j, k = 1, 2, 3$  accounting for 27 terms.

One realizes 108 permutations with different time ordering of three different laser beams distinguished by frequency, and/or wave vector, and/or polarization. If only two distinguishable laser beams are available, the number of permutations decreases to 48. When the system is driven by a single beam, the third-order response involves only four terms in three fields. In general, the  $\chi^{(3)}$  coefficients associated with each term will be different due to the ever-present dispersion (i.e., frequency dependence) of the susceptibilities. The frequency dependence is a direct consequence of the finite response time of the interaction. We will expand on this subject in the discussion of the Kramers-Kronig dispersion relations in Sec. 16.4.

Another important property of nonlinear susceptibilities is their tensor nature. Because of the molecular or lattice structure of materials, the nonlinear response will depend on the state of

polarization of the optical fields. For the sake of brevity, we neglect the tensor properties of  $\chi^{(3)}$  and treat all the susceptibilities and electric fields as scalar quantities. The reader may consult textbooks on nonlinear optics for detailed discussions of this subject.

Propagation of interacting beams is also an important consideration, and one must account for wave vector summation (i.e., conservation of momentum) that results from the  $\bar{\epsilon}^3$  operation. It is useful to invoke the four photon picture, recalling that the momentum of each photon is given by  $\hbar k_j$ . Taking the resultant nonlinear polarization to be a plane wave with a wave vector  $k_4$ , momentum conservation requires that:

$$\bar{k}_4 = \pm \bar{k}_i \pm \bar{k}_j \pm \bar{k}_k \quad (5)$$

where  $|\bar{k}_j| = n(\omega_j)\omega_j/c$ . This phase-matching requirement is not necessarily satisfied in every interaction due to dispersion of the linear refractive index in the material. Phase matching can be a serious obstacle in interactions leading to new-frequency generation, that is, when  $\omega_4 \neq \omega_1, \omega_2$  and  $\omega_3$  (e.g., Sec. 16.6 on THG). When the nonlinear polarization is at one of the driving frequencies,  $\omega_4 = \omega_i$  for example, conservation of energy [Eq. (4)] implies that  $\omega_j = -\omega_k$ . In this case, Eq. (5) reduces to a vector-matching condition that depends only on the geometry (i.e., direction) of the beams (Secs. 16.11 and 16.12).

The frequency terms arising from the third-order nonlinear polarization described by Eq. (1) are collected in Table 1. In the following section, we discuss the physical mechanisms and important features of these processes.

**TABLE 1** Frequency Terms Arising from Third-Order Nonlinear Polarization

Nonlinear Process	$8P(\omega_4)/\epsilon_0\chi^{(3)}$	$\omega_4$
• Third-harmonic generation (THG)	$E_j^3, j=1, \dots, 3$	$3\omega_1, 3\omega_2, 3\omega_3$
• Sum frequency generation (SFG)	$3E_iE_j^2, i, j=1, 2, 3, i \neq j$	$2\omega_1 + \omega_2, 2\omega_1 + \omega_3,$ $2\omega_2 + \omega_3, 2\omega_2 + \omega_1,$ $2\omega_3 + \omega_1, 2\omega_3 + \omega_2,$
	$6E_1E_2E_3$	$\omega_1 + \omega_2 + \omega_3$
• Frequency mixing	$3E_i^*E_j^2, i, j=1, 2, 3, i \neq j$	$2\omega_1 - \omega_2, 2\omega_1 - \omega_3,$
• Parametric amplification		$2\omega_2 - \omega_3, 2\omega_2 - \omega_1,$ $2\omega_3 - \omega_1, 2\omega_3 - \omega_2,$
• Coherent Stokes and anti-Stokes Raman scattering (CSRS and CARS)	$6E_i^*E_jE_k, i, j, k=1, 2, 3, i \neq j \neq k$	$\omega_1 + \omega_2 - \omega_3,$ $\omega_1 - \omega_2 + \omega_3,$ $-\omega_1 + \omega_2 + \omega_3$
	$6E_i^*E_j^*E_k, i, j, k=1, 2, 3, i \neq j \neq k$	$\omega_1 - \omega_2 - \omega_3,$ $-\omega_1 - \omega_2 + \omega_3,$ $-\omega_1 + \omega_2 - \omega_3$
• Bound electronic optical Kerr effect	$3E_i^2E_i^*, i=1, 2, 3$	$\omega_1, \omega_2, \omega_3$
• Raman-induced Kerr effect (RIKE)		
• Molecular orientational Kerr effect	$6E_iE_jE_j^*, i, j=1, 2, 3, i \neq j$	
• Two-photon absorption (2PA)		
• ac Stark effect		
• Stimulated Raman scattering (SRS)		
• Stimulated Rayleigh-Wing Scattering		

## 16.2 QUANTUM MECHANICAL PICTURE

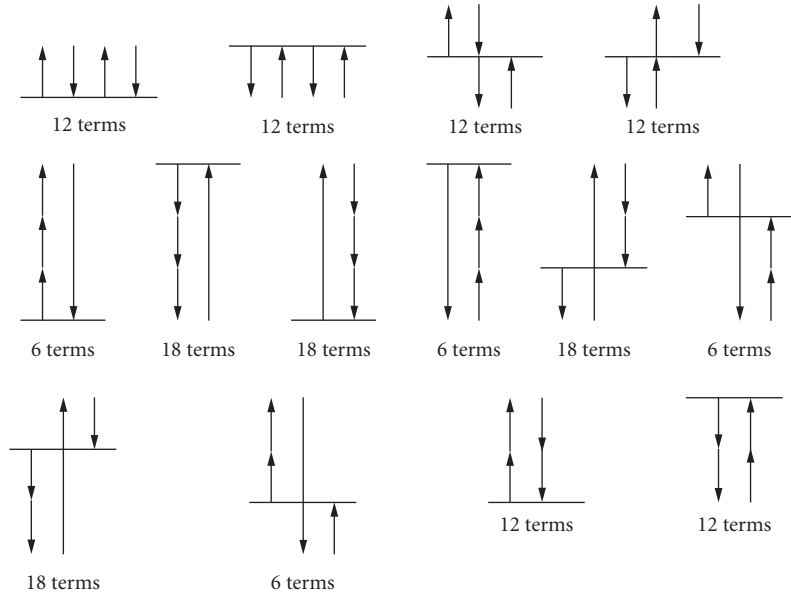
The conservation of energy shown in the frequency summation of Eq. (4) contains both positive and negative signs from each of the input beams. A positive sign represents the annihilation (absorption) of a photon, while the negative sign is interpreted as the generation (gain) of a photon. Both annihilation and generation of photons involve atomic and/or molecular transitions from one state to another. It is instructive to use diagrams to keep track of transitions participating in the nonlinear interactions. Let us take the most general case, where four distinguishable beams (i.e., three input photons at  $\omega_1, \omega_2, \omega_3$ , and the final photon at  $\omega_4$ ) are involved. The third-order nonlinear interaction follows a path corresponding to one of 14 sign-ordering possibilities, assuming emission at the photon frequency  $\omega_4$ . All possible time-ordering sequences are illustrated in Fig. 1. In addition, the interacting photons are in general distinguishable; to preserve the clarity of presentation we have not shown this in Fig. 1. Because the photons are (in general) distinct, we must allow for permutation of frequencies in the diagrams. Assuming emission at  $\omega_4$  (i.e., we can only assign  $\omega_4$  to a downward-pointing arrow), we count up the various time-ordering permutations for each interaction path shown in Fig. 1. This gives a total of 168 terms! Little would be gained by a tedious analysis of all these terms, and such a task is far beyond the scope of this chapter. Instead, we illustrate some important third-order mechanisms and the role of resonances in Fig. 2, where we have labeled the three most important diagrams in Fig. 1. The energy level  $|g\rangle$  is the ground state, while  $|a\rangle, |u\rangle$ , and  $|b\rangle$  are intermediate states of the system in a sequence of transitions involving photons with frequencies  $\omega_p, \omega_j, \omega_k$ , and  $\omega_l$  ( $i, j, k, l = 1, 2, 3, 4$ ) such that  $\pm\omega_i \pm \omega_j \pm \omega_k \pm \omega_l = 0$ . The three time-ordering processes shown in the figure are:

Figure 2a. Consecutive absorption of three photons followed by the generation of the final photon, partly describing sum frequency generation and third-harmonic generation. The reverse process is third-order parametric amplification, which is the absorption of a photon together with emission of three photons.

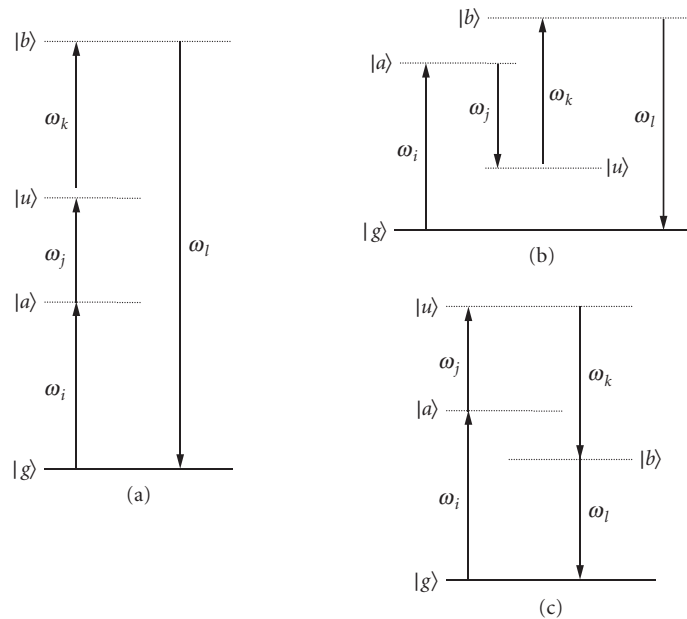
Figure 2b. An absorption-emission-absorption-emission sequence. Difference frequency generation and frequency mixing are examples of this type of interaction. Coherent anti-Stokes Raman spectroscopy (CARS) is also represented by this transition sequence.

Figure 2c. Absorption of two photons followed by emission of the two photons. As can be seen in the third section of Table 1, a variety of physical mechanisms fall under this general description. Note that the essential difference between (b) and (c) is the time ordering of the transitions. This is extremely important in resonant cases: a Raman-type resonance occurs in (b), and a two-photon resonance exists in (c).

Energy conservation is strictly obeyed upon the completion of the interaction [as dictated by Eq. (4)] but may be violated in the time frame of intermediate state transitions. This is allowed by Heisenberg's Uncertainty Principle. In many cases, an intermediate state is a virtual state, which is a convenient way of stating that a real, intermediate state of the system does not exist to support the transition of a photon at the selected wavelength. The virtual, intermediate state allows for energy bookkeeping in transition diagrams, but a physical description of the optical interaction using quantum mechanics involves only real eigenstates of the system. In particular, there must be a dipole-allowed transition between the initial state  $|g\rangle$  and a real state *associated* with the virtual state. The time scale and strength of the interaction is partly determined by the energy mismatch between the virtual, intermediate state and an associated real, electronic state. This means a system can absorb a photon of energy  $\hbar\omega_i$  and make a transition from the ground state  $|g\rangle$  to a real intermediate state  $|a\rangle$  even though there is insufficient photon energy to bridge the gap (i.e., there is an energy mismatch  $\Delta E = |\hbar\omega_i - E_a + E_g| > 0$ ). This is possible, provided the interaction occurs in a time faster than the observation time  $\Delta t \sim \hbar/\Delta E$  permitted by the Uncertainty Principle. Transitions of this type are called *virtual* transitions, as opposed to *real* transitions, where energy is conserved. In the former case,  $\Delta t$  is known as the virtual lifetime of the transition.



**FIGURE 1** Time-ordering sequence illustrating all possible third-order paths. Arrows depict photons. Note that in general, the size of the arrows can be different provided their vector sum is zero. The number of terms is obtained assuming emission of a photon at  $\omega_4$ . For clarity, arrows are not marked.



**FIGURE 2** Energy level diagrams for some important third-order nonlinear optical processes: (a) third-harmonic generation (THG); (b) coherent anti-Stokes Raman scattering (CARS); and (c) two-photon absorption (2PA).

If the entire sequence of transitions comprising the third-order interaction is not completed within the virtual lifetime, the intermediate state collapses back to the ground state, and no nonlinear interaction occurs. In other words, all the required particles must be present in the system during the virtual lifetime. The longer the virtual lifetime, the greater the probability that the required photons will appear, allowing the multiparticle interaction to run to completion. A longer virtual lifetime translates to a larger third-order nonlinear susceptibility  $\chi^{(3)}$ . The closer an input photon moves to a dipole-allowed system resonance, the longer the virtual lifetime and the stronger the resulting  $\chi^{(3)}$  will be.

These quantum mechanical issues are manifest in the mathematical formulation of  $\chi^{(3)}$  derived from perturbation theory:<sup>1,3,17</sup>

$$\chi^{(3)}(\pm\omega_1, \pm\omega_2, \pm\omega_3) = \frac{N}{\hbar^3} \sum_{i,j,k,l} \sum_{a,u,b} \mu_{ga} \frac{\mu_{au}}{(\omega_{ag} \mp \omega_i)} \frac{\mu_{ub}}{(\omega_{ug} \mp \omega_i \mp \omega_j)} \frac{\mu_{bg}}{(\omega_{bg} \mp \omega_i \mp \omega_j \mp \omega_k)} \quad (6)$$

In Eq. (6),  $N$  is the total population in the ground state  $|g\rangle$ , and  $\mu$ 's are dipole-moment matrix elements associated with each of the transitions. The first sum describes the frequency permutations:  $i, j, k$ , and  $l$  can take any integer value 1, 2, 3, 4, provided energy conservation ( $\pm\omega_i \pm \omega_j \pm \omega_k \pm \omega_l = 0$ ) is obeyed. The second sum is over all possible real, intermediate quantum eigenstates of the system. This complicated-looking equation is nothing more than the sequence of optical transitions weighted by the appropriate virtual lifetime. The first coefficient represents the virtual transition initiated by a photon of energy  $\hbar\omega_i$  from the ground state to the intermediate state  $|a\rangle$  with strength given by the matrix element  $\mu_{ga}$ . The next three matrix elements are weighted by the virtual lifetimes of their initial state. The virtual lifetimes are represented by energy (i.e., frequency) denominators; as the photon frequency approaches a system resonance, the virtual lifetime and magnitude of  $\chi^{(3)}$  grow accordingly.

The  $\pm$  signs in front of the frequency arguments in Eq. (6) indicate there is a physical significance to the time ordering of the participating photons. This representation distinguishes the various components of the third-order susceptibility. In many textbooks, a permutation of all the frequencies (including the signs) is already incorporated in the final calculation of  $\chi^{(3)}$ .<sup>3,4</sup> In that case, for a given  $\omega_4$ , one obtains the total contribution to  $\chi^{(3)}$  with the order of frequency arguments having no particular physical relevance.

We also point out that the nonlinear susceptibility described by Eq. (6) and shown in our example is *real*. A resonance condition occurs when any one of the energy/frequency denominators approaches zero. This not only enhances  $\chi^{(3)}$  but also makes it a complex quantity (i.e., a resonance condition introduces an imaginary component to  $\chi^{(3)}$ ). This is better understood by making the following substitution:

$$\frac{1}{\Delta\omega} \rightarrow \frac{1}{\Delta\omega + i\Gamma} \quad (7)$$

where  $\Gamma$  represents a phenomenological broadening of the particular transition. This complex damping term accounts for the physical impossibility of the nonlinear susceptibility becoming infinite in a resonance condition. Even in the case of vanishing damping, a basic theorem of complex variables can be applied to Eq. (7):

$$\lim_{\Gamma \rightarrow 0} \frac{1}{\Delta\omega + i\Gamma} = \mathcal{P} \left( \frac{1}{\Delta\omega} \right) + i\pi\delta(\Delta\omega) \quad (8)$$

where  $\mathcal{P}$  stands for the principle value and  $\delta$  is the Dirac delta function. The important message is that in general, the nonlinear susceptibility  $\chi^{(3)}$  is a complex quantity that will be dominated by its imaginary component when photon frequencies move into resonance with real eigenstates of the system.

The resonance conditions leading to a strong imaginary  $\chi^{(3)}$  are associated with one or more of the following processes: three-photon ( $\omega_i + \omega_j + \omega_k = -\omega_l \approx \omega_{bg}$ ), two-photon ( $\omega_i + \omega_j = -\omega_k - \omega_l \approx \omega_{ug}$ ), Raman-type ( $\omega_i - \omega_j = \omega_l - \omega_k \approx \omega_{ug}$ ), and/or single-photon ( $\omega_i \approx \omega_{ug}$ ) resonances. The latter cases (i.e., those having linear resonance) will be discussed in Sec. 16.9, which deals with cascaded  $\chi^{(1)} \cdot \chi^{(1)}$  nonlinearities. A special case of linear resonance can occur in Raman-type transitions, where  $\omega_{ug} = 0$  (i.e., when the second intermediate state is degenerate with the ground state). This corresponds to the optical Stark effect (ac Stark effect). The three-photon resonance that gives rise to an imaginary  $\chi^{(3)}$  in third-harmonic generation does not have a significant physical implication. It only influences the phase of the interacting fields, similar to the case of second-order effects (e.g., second-harmonic generation).<sup>1</sup> The remaining two processes involving two-photon and Raman resonances are of significant interest and will be discussed in detail.

### 16.3 NONLINEAR ABSORPTION AND NONLINEAR REFRACTION

Just as the real and imaginary components of the linear susceptibility  $\chi^{(1)}$  are associated with refraction and absorption, the real and imaginary parts of  $\chi^{(3)}$  describe nonlinear refraction (NLR) and nonlinear absorption (NLA) or gain. This can be understood by considering situations in which the nonlinear polarization is at one of the driving frequencies. These are particular cases of Fig. 2b and c, with corresponding polarization terms given in the third section of Table 1. Taking the interacting photons to have frequencies  $\omega_a$  and  $\omega_b$ , the total polarization (linear and third order) at  $\omega_a$  can be written as

$$P(\omega_a) = \varepsilon_0 \left[ \frac{1}{2} \chi^{(1)}(\omega_a) E_a + \frac{3}{8} \chi^{(3)}(\omega_a, \omega_a, -\omega_a) E_a^2 E_a \right] \quad (9)$$

For the sake of brevity, we ignore time ordering in the frequency arguments of  $\chi^{(3)}$ . This means that the  $\chi^{(3)}$  component in Eq. (9) is assumed to contain the various permutations of frequencies including, for example, two-photon as well as Raman transitions shown in Fig. 2b and c. From Eq. (9), we introduce an effective susceptibility  $\chi_{\text{eff}}$ :

$$\chi_{\text{eff}}(\omega_a) = \chi^{(1)}(\omega_a) + \frac{3}{4} \chi^{(3)}(\omega_a, \omega_a, -\omega_a) |E_a|^2 + \frac{6}{4} \chi^{(3)}(\omega_a, \omega_b, -\omega_b) |E_b|^2 \quad (10)$$

Deriving the coefficients of nonlinear absorption and refraction from Eq. (10) is now straightforward. The complex refractive index is defined as

$$n + i\kappa = (1 + \chi_{\text{eff}})^{1/2} \quad (11)$$

Making the very realistic assumption that the nonlinear terms in Eq. (10) are small compared to the linear terms, we use the binomial expansion to simplify Eq. (11):

$$n + i\kappa \cong n_0 + i \frac{c}{2\omega_a} \alpha_0 + \Delta n + i \frac{c}{2\omega_a} \Delta \alpha \quad (12)$$

where  $n_0 = (1 + \Re\{\chi^{(1)}\})^{1/2}$ . We also assume the background linear absorption coefficient is small, that is,  $\alpha_0 \approx \Im\{\chi^{(1)}\} \ll \Re\{\chi^{(1)}\}$ . We define the irradiance as  $I_i = (1/2)c\epsilon_0 n_0(\omega_i) |E_i|^2$  ( $i = a, b$ ) and the nonlinear refraction coefficient  $n_2$  and the nonlinear absorption coefficient  $\alpha_2$  as follows:

$$n_2(\omega_a; \omega_b) = \frac{3}{4\epsilon_0 n_0(\omega_a) n_0(\omega_b) c} \Re\{\chi^{(3)}(\omega_a, -\omega_b, \omega_b)\} \quad (13)$$

$$\alpha_2(\omega_a; \omega_b) = \frac{3\omega_a}{4\epsilon_0 n_0(\omega_a) n_0(\omega_b) c^2} \Im\{\chi^{(3)}(\omega_a, -\omega_b, \omega_b)\} \quad (14)$$

The change of refractive index due to the presence of fields  $E_a$  and  $E_b$  is

$$\Delta n(\omega_a) = n_2(\omega_a; \omega_a) I_a + 2n_2(\omega_a; \omega_b) I_b \quad (15)$$

and the change of absorption is

$$\Delta\alpha(\omega_a) = \alpha_2(\omega_a; \omega_a) I_a + 2\alpha_2(\omega_a; \omega_b) I_b \quad (16)$$

where  $I_a$  and  $I_b$  are the irradiances of the two beams. Note that without loss of generality we assume the measurement is performed on the laser beam corresponding to field  $E_a$ , while the field  $E_b$  acts as an excitation source only. The first terms on the right-hand side of the just-noted equations correspond to self-action (i.e., commonly performed single-beam experiments). The second terms correspond to the case of an excite-probe experiment where the two beams are distinguishable either by frequency and/or wave vector. The factor of 2 in front of the second terms in Eqs. (15) and (16) arises from the larger number of permutations in this component of the nonlinear susceptibility.<sup>3,4,31</sup> The stronger nondegenerate response (i.e., distinguishable beams) is sometimes referred to as *weak-wave retardation*.<sup>32</sup> While most reported measurements and applications involve degenerate self-action processes (i.e., a single laser beam), the theoretical treatment presented in this chapter considers the more general nondegenerate case. One must keep in mind that degenerate third-order coefficients are only the limit of the nondegenerate case, where  $\omega_a = \omega_b$ . The need for generality in the theoretical approach is very important for correct implementation of the Kramers-Kronig dispersion relations in nonlinear optics. This allows us to establish a rigorous mathematical relation between NLR and NLA, discussed in the next section.

Another commonly used coefficient for describing the nonlinear index is  $\tilde{n}_2$  defined as

$$n = n_0 + \tilde{n}_2(\omega_a; \omega_a) \frac{|E_a|^2}{2} + 2\tilde{n}_2(\omega_a; \omega_b) \frac{|E_b|^2}{2} \quad (17)$$

where  $\tilde{n}_2$  is usually given in Gaussian units (esu).  $\tilde{n}_2$  is related to  $n_2$  by

$$\tilde{n}_2(\text{esu}) = \frac{cn}{40\pi} n_2(\text{SI}) \quad (18)$$

where the right-hand side is in SI/MKS units. The reader is cautioned that in the literature various symbols and definitions different from those given here are often used to describe the nonlinear refractive index. The symbol  $\beta$  is commonly used in place of  $\alpha_2$  to denote two-photon absorption (2PA).

The propagation of electromagnetic waves  $E_a$  and  $E_b$  through a nonlinear medium, ignoring the effect of diffraction and dispersion (i.e., pulse distortion), is governed by the following equations for the irradiance and phase of the probe beam ( $E_a$ ):

$$\frac{dI_a}{dz} = -\alpha_0(\omega_a)I_a - \alpha_2(\omega_a; \omega_a)I_a^2 - 2\alpha_2(\omega_a; \omega_b)I_a I_b \quad (19)$$

and

$$\frac{d\phi_a}{dz} = \frac{\omega_a}{c} [n_0(\omega_a) + n_2(\omega_a; \omega_a)I_a + 2n_2(\omega_a; \omega_b)I_b] \quad (20)$$

The coefficient  $n_2$  is often used to describe the nonlinear index change due to mechanisms such as thermally induced material changes, molecular orientation effects, saturation of absorption, and ultrafast  $\chi^{(3)}$  processes. Here, consistent with our definition of  $\chi^{(3)}$ , we designate the  $n_2$  notation for local and linearly nonresonant nonlinearities only. Processes that appear as an *effective*  $n_2$  are treated separately as cascaded  $\chi^{(1)}; \chi^{(1)}$  or  $\chi^{(2)}; \chi^{(2)}$  phenomena.

As a consequence of the principle of causality, the real and imaginary parts of the linear susceptibility are connected through the Kramers-Kronig relations of linear optics. Equations (19) and (20) suggest a similar relation in nonlinear optics. We discuss the Kramers-Kronig relations of nonlinear optics and their underlying physics next.

## 16.4 KRAMERS-KRONIG DISPERSION RELATIONS

The complex response function of any linear, causal system obeys a dispersion relation linking its real and imaginary parts as Hilbert transform pairs. In linear optics, causality is manifest in the Kramers-Kronig (K-K) dispersion relations (see Chap. 5, “Optical Properties of Semiconductors”) that tie the frequency-dependent refractive index,  $n(\omega)$ , to the absorption coefficient  $\alpha(\omega)$  and vice versa:

$$n(\omega) - 1 = \frac{c}{\pi} \mathcal{P} \int_0^\infty \frac{\alpha(\omega')}{\omega'^2 - \omega^2} d\omega' \quad (21)$$

where  $\mathcal{P}$  denotes the Cauchy principal value. The principal value is really just a warning to be careful when integrating near the singularity in the denominator of the integrand. We drop the  $\mathcal{P}$  notation for simplicity, although it is always implied. There is an equivalent relation for the real and imaginary parts of the linear susceptibility:

$$\Re\{\chi^{(1)}(\omega)\} = \frac{1}{\pi} \int_{-\infty}^\infty \frac{\Im\{\chi^{(1)}(\omega')\}}{\omega' - \omega} d\omega' \quad (22)$$

The K-K relation is the mathematical expression of causality, and a simple, intuitive derivation of these relations can be made.<sup>33,34</sup>

Causality clearly holds for any real, linear system. Real, nonlinear systems must also be causal—does that imply there are dispersion relations as well? If so, what form do they take? The Kramers-Kronig relations of linear optics are derived from linear dispersion theory, suggesting this procedure is completely inappropriate for a nonlinear system. Fortunately, this is not the case, and since the early days of nonlinear optics, many authors have addressed the K-K relations in the nonlinear regime.<sup>35–39</sup>



The usefulness of these relations was not fully appreciated until recently, however.<sup>31,39,40</sup> The key insight is that one can linearize the system; we view it as the material *plus* a strong perturbing light beam. This new linear system, which is different from the system in the presence of weak light, has a modified absorption spectrum. The linear Kramers-Kronig relation is applied in the presence of and in the absence of a high field perturbation, and we study the difference between these two regimes. It is important to appreciate the fact that our new system is causal even in the presence of an external perturbation. This allows us to write down a modified form of the Kramers-Kronig relation linking the index of refraction to the absorption<sup>31,39</sup>:

$$[n(\omega) + \Delta n(\omega; \zeta)] - 1 = \frac{c}{\pi} \int_{-\infty}^{\infty} \frac{\alpha(\omega') + \Delta\alpha(\omega'; \zeta)}{\omega'^2 - \omega^2} d\omega' \quad (23)$$

After subtracting the linear terms  $n$  and  $\alpha$ , we are left with a relationship between the changes in refractive index and change of absorption:

$$\Delta n(\omega; \zeta) = \frac{c}{\pi} \int_0^{\infty} \frac{\Delta\alpha(\omega'; \zeta)}{\omega'^2 - \omega^2} d\omega' \quad (24)$$

where  $\zeta$  denotes the perturbation. An equivalent relation also exists that allows calculation of the change in absorption coefficient, given the change in the refractive index. This relation is rarely used in practice for reasons described momentarily. In evaluating Eq. (24), it is essential that the perturbation be independent of the frequency of observation ( $\omega'$ ). In other words, the excitation  $\zeta$  must remain constant as  $\omega'$  is varied.

It is an interesting fact that calculation of the refractive index change from data obtained in nonlinear optics experiments is often easier than extracting the absolute refractive index from the K-K transform in linear optics! The reason is that absorption changes in nonlinear optics are usually strong only in a very limited frequency range; the integration range in Eq. (24) need only consider this spectrum. In contrast, evaluation of the linear index based on the linear absorption spectrum normally involves a much larger amount of data. One must take full account of the entire linear absorption data to obtain quantitative agreement with experiments that measure the refractive index. In the same way, the reverse transformation in nonlinear optics (obtaining  $\Delta\alpha$  from  $\Delta n$ ) is not as accommodating as the transformation of Eq. (24). Experiments show that irradiance-dependent changes of the refractive index occur over a relatively broad frequency spectrum. A large and impractical amount of nonlinear dispersion data must be collected and incorporated into a K-K calculation of nonlinear absorption. The reverse transformation is thus difficult to accomplish in practice.

Equation (24) has been used to determine refractive changes due to *real* excitations (i.e.,  $\chi^{(1)}; \chi^{(1)}$  cascaded processes) such as thermal and free-carrier nonlinearities in semiconductors.<sup>41,42</sup> In these examples,  $\zeta$  denotes either change of temperature or change of free-carrier density, respectively. This K-K methodology has also been applied with great success to the situation where the perturbation is *virtual* or nonresonant. This work unified the bound electronic Kerr effect in bulk semiconductors (i.e., the dispersive nonlinearity resulting from anharmonic motion of bound, valence electrons) to its absorptive counterparts: two-photon absorption, the electronic Raman effect, and the ac Stark effect.<sup>31,39,43-45</sup> The dispersion relation between  $\alpha_2$  and  $n_2$  is given by

$$n_2(\omega_a; \omega_b) = \frac{c}{\pi} \int_0^{\infty} \frac{\alpha_2(\omega'; \omega_b)}{\omega'^2 - \omega_a^2} d\omega' \quad (25)$$

Note that in the general case we are dealing with two frequencies:  $\omega_a$  and  $\omega_b$ . Even in the degenerate situation (i.e.,  $n_2 = n_2(\omega_a; \omega_a)$ ) where we desire the nonlinear index coefficient at a single frequency  $\omega_a$ , we are still required to provide the nondegenerate absorption spectrum  $\alpha_2(\omega'; \omega_b)$  at

all frequencies  $\omega'$  as input to the calculation. We also point out that Eq. (25) can be used to derive relations linking the real and imaginary parts of the nonlinear susceptibility via Eq. (13) [the inverse transformation is obtained with Eq. (14)]:

$$\Re\{\chi^{(3)}(\omega_a, \omega_b, -\omega_b)\} = \frac{2}{\pi} \int_0^{\infty} \frac{\omega' \Im\{\chi^{(3)}(\omega', \omega_b, \omega_b)\}}{\omega'^2 - \omega_a^2} d\omega' \quad (26)$$

Using the symmetry properties of  $\chi^{(3)}$ , an equivalent representation is

$$\Re\{\chi^{(3)}(\omega_a, \omega_b, -\omega_b)\} = \frac{1}{\pi} \int_{-\infty}^{\infty} \frac{\Im\{\chi^{(3)}(\omega', \omega_b, \omega_b)\}}{\omega' - \omega_b} d\omega' \quad (27)$$

Equation (27) can also be derived in a very general way from a first-principles approach that applies the causality condition directly in the temporal nonlinear response. In this way, one can obtain the dispersion relations for the  $n$ th order optical susceptibility:<sup>39</sup>

$$\chi^{(n)}(\omega_1, \omega_2, \dots, \omega_j, \dots, \omega_n) = \frac{-i}{\pi} \int_{-\infty}^{\infty} \frac{\chi^{(n)}(\omega_1, \omega_2, \dots, \omega', \dots, \omega_n)}{\omega_j - \omega'} d\omega' \quad (28)$$

where  $\chi^{(n)}$  is a complex quantity. By separating the real and imaginary parts of this equation, we get the generalized Kramers-Kronig relation for a nondegenerate,  $n$ th order nonlinear susceptibility:

$$\Re\chi^{(n)}(\omega_1, \omega_2, \dots, \omega_j, \dots, \omega_n) = \frac{1}{\pi} \int_{-\infty}^{\infty} \frac{\Im\chi^{(n)}(\omega_1, \omega_2, \dots, \omega', \dots, \omega_n)}{\omega' - \omega_j} d\omega' \quad (29)$$

Note that for  $n = 3$  with the substitutions  $\omega_1 = \omega_a$ ,  $\omega_2 = \omega_b$ , and  $\omega_3 = -\omega_b$ , Eq. (29) becomes identical to Eq. (27). When the susceptibilities for generating frequency harmonics are included, Eq. (29) can be further generalized.<sup>39</sup> If we consider the  $\chi^{(3)}$  associated with third-harmonic generation, it can be shown that:

$$\Re\{\chi^{(3)}(+\omega, +\omega, +\omega)\} = \frac{1}{\pi} \int_{-\infty}^{\infty} \frac{\Im\{\chi^{(3)}(+\omega', +\omega', +\omega')\}}{\omega' - \omega} d\omega' \quad (30)$$

Such relationships have been utilized in calculations of the total  $\chi^{(3)}$  (THG) in semiconductors. It is computationally more convenient to first calculate the imaginary part because of the presence of  $\delta$  functions in its frequency domain. The real part is then calculated using the K-K dispersion relations.<sup>46</sup>

## 16.5 OPTICAL KERR EFFECT

The  $\chi^{(3)}$  process leading to an intensity-dependent refractive index is known as the *optical Kerr effect* (OKE). Experimental observation is relatively straightforward, usually requiring just a single laser beam. The OKE is described by Eq. (15) where, for the sake of brevity, we ignore cross-modulation terms and drop the frequency terms to write

$$n = n_0 + n_2 I \quad (31)$$

There are a variety of physical mechanisms that submit to this mathematical representation, many different ways to observe the effect experimentally, and an assortment of practical devices that can be built.

Optical transitions giving rise to a nonlinear susceptibility  $\chi^{(3)}$  (see Figs. 1 and 2, for example) are intimately related to the energy eigenstates of the system. These eigenstates can be associated with bound electronic motion, molecular vibrations, or molecular rotations of the system. Electronic transitions involve the largest energy separation and rotational transitions the smallest. In a given material (gas, liquid, or solid), one or more of these excitations may contribute to the optical Kerr effect. In general, the various contributions differ in their response time, magnitude, and frequency dependence. Referring to our earlier discussion of Eq. (6), the time response of an optical nonlinearity is governed by the virtual lifetime of the relevant transitions. This implies that the nonlinearities associated with the electronic transitions give the fastest response time because they possess large energy denominators. Experiments have shown that electronic nonlinearities are usually faster than the time resolution provided by the shortest optical pulses available at the time of this writing ( $<10$  fs). For practical purposes, then, the nonlinearity associated with the motion of bound electrons can be regarded as instantaneous. At the other extreme, the nonlinearity associated with rotational motion of molecules is relatively sluggish—response times in the picosecond regime have been measured. In the middle range are nonlinearities arising from molecular vibrations. For a Raman-type transition as shown in Fig. 2*b* this effect is manifest as the Raman-induced Kerr effect (RIKE). We discuss two important cases of NLR: the bound electronic Kerr effect in solids ( $n_2$ ), and the rotational (or orientational) Kerr effect in liquids.

### Bound Electronic Optical Kerr Effect in Solids

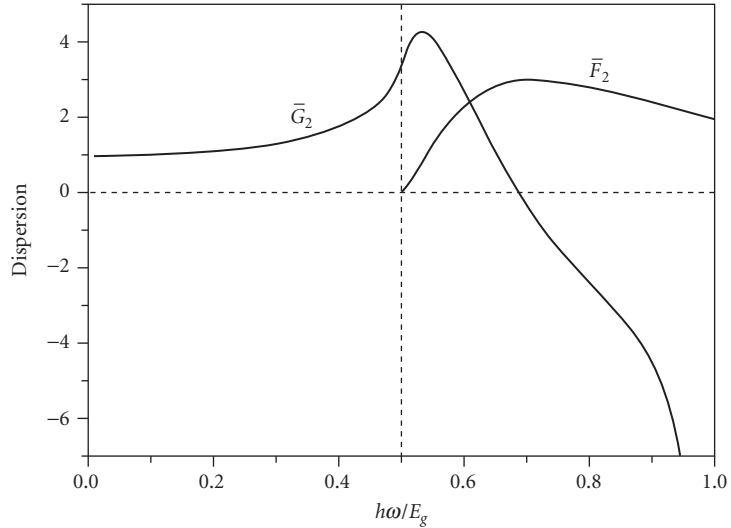
The optical Kerr effect in solids has been extensively studied in materials ranging from large-gap dielectrics and glasses to narrow-gap semiconductors.<sup>31,44,47–50</sup> The fundamental energy gap  $E_g$  turns out to be a parameter of critical importance. Because of direct, linear absorption of the incident laser light, we are interested in the transparency regime where the photon frequency is less than the bandgap energy (i.e.,  $\omega < \omega_g = E_g / \hbar$ ). We estimate the response time ( $\tau_r$ ) of the nonlinearity using the virtual lifetime of the transition:  $\tau_r \approx 1/|\omega - \omega_g|$ . Far below the bandgap, where  $\omega \ll \omega_g$ , the response time can be very fast ( $\ll 10$  fs) and for most applications can be assumed as instantaneous. This ultrafast response has been exploited in soliton propagation in glass fibers<sup>5,51</sup> (Sec. 16.11) and in the generation of femtosecond pulses in solid-state lasers.<sup>52</sup> The optical Kerr effect also causes self-focusing, sometimes resulting in beam distortion and damage in transparent media (Sec. 16.11). Another significant application is the development of ultrafast all-optical-switching devices.<sup>53,54</sup> Although much progress has been made in this area of research, development of a practical switch has been hindered by the relatively small magnitude of bound electronic nonlinearities.

The bound electronic optical Kerr effect in optical solids has been analyzed using semiempirical methods<sup>55</sup> and, more recently, by simple two-band models appropriate for semiconductors.<sup>31,44</sup> The latter treatment provides information about the dispersion, bandgap scaling, and the relationship between the NLA (e.g., two-photon absorption) and NLR through Kramers-Kronig transformation. The resulting simple formula allows one to predict the nonlinear refraction coefficient  $n_2$  knowing only the photon frequency ( $\omega$ ), energy bandgap ( $E_g$ ), and linear index ( $n_0$ ):

$$n_2(m^2/W) = \frac{A}{n_0^2 E_g^4} \bar{G}_2 \left( \frac{\hbar \omega}{E_g} \right) \quad (32)$$

where  $A \approx 3 \times 10^{-35}$  (MKS);  $E_g$  is in joules. The function  $\bar{G}_2$  describes the normalized dispersion of the coefficient  $n_2$  and is depicted in Fig. 3, along with the normalized two-photon absorption spectrum for bulk semiconductors (Sec. 16.8).

Recall that NLA and NLR correspond to the imaginary and real parts of the third-order susceptibility, respectively. The derivation of Eq. (32) by a Kramers-Kronig transformation required knowledge of the NLA spectrum. Three different mechanisms of NLA were employed in the analysis, corresponding to the three relevant time-ordering sequences depicted in Fig. 2: two-photon absorption, electronic



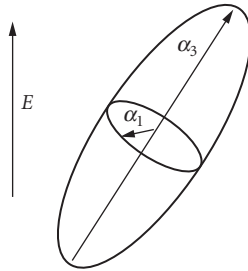
**FIGURE 3** Calculated dispersion of nonlinear absorption. Also shown is the two-photon absorption spectrum.

Raman scattering, and the optical (ac) Stark shift of electronic states. The optical Stark effect is a change of the fundamental energy gap that occurs when the oscillating laser field becomes comparable to the electric field binding valence electrons to the positively charge nuclei. In experiments where only a single beam is used (i.e., all the input frequencies are the same), the only observable NLA effect is two-photon absorption, which is discussed in Sec. 16.8.

The plot of the dispersion function  $\bar{G}_2$  (Fig. 3) is consistent with our intuitive arguments about resonance enhancement presented in Sec. 16.2. At long wavelengths (i.e., for  $\hbar\omega \ll E_g$ ), we are far from resonance so  $\bar{G}_2 \approx 1$  and is nearly frequency independent (i.e., there is very weak dispersion). Approaching the two-photon resonance (i.e., as  $2\hbar\omega$  gets close to  $E_g$ ), there is an approximately fivefold enhancement of  $n_2$ . With increasing photon energy, the sign of  $n_2$  reverses; this is a direct consequence of the sign change in the energy denominator associated with two-photon absorption. With further photon energy increase, there is enhancement due to resonances ascribed to two-photon absorption and the optical Stark effect. The inverse fourth-power bandgap scaling (i.e.,  $E_g^{-4}$ ) and the dispersion predicted by this simple expression display remarkable agreement with data obtained with many different semiconductors and dielectrics.<sup>44</sup>

## Reorientational Kerr Effect in Liquids

The reorientational Kerr effect involves transitions between rotational energy levels of a molecule. It is nonresonant and therefore associated with the real part of  $\chi^{(3)}$ . The absorptive nonlinearity associated with these rotational levels gives an imaginary component to  $\chi^{(3)}$ ; this is a Raman-type transition known as *Rayleigh-wing scattering*.<sup>3,17</sup> For simplicity, we make a classical description of this phenomenon. Consider a carbon disulfide ( $\text{CS}_2$ ) molecule as shown in Fig. 4. This is a cigar-shaped molecule with different polarizabilities along its principal axes (here we show  $\alpha_3 > \alpha_1$ ). As discussed in Sec. 16.7, the polarizability describes the propensity for an external field to produce a dipole in a molecule. In the first step of the interaction, the optical field polarizes this molecule (i.e., induces a dipole moment). The induced dipole interacts with the applied field and aligns itself along the direction of polarization. This molecular reorientation (rotation) causes a birefringence in an isotropic



**FIGURE 4** Simple picture of  $\text{CS}_2$  molecule.

solution; initially, the molecules were randomly oriented and there was no birefringence. The response time of the molecule depends on its mass: the heavier molecule, the slower the response. As an example,  $\text{CS}_2$  has a reorientational  $n_2 \approx 3.4 \times 10^{-18} \text{ m}^2/\text{W}$  with a relaxation time  $\tau \approx 1$  to 2 ps.<sup>56</sup>

## 16.6 THIRD-HARMONIC GENERATION

In crystals where there is no inversion symmetry,  $\chi^{(2)}$  vanishes, making sum and difference frequency mixing impossible. The possibility of third-harmonic generation always exists in principle, although it usually suffers from practical drawbacks. Typical values of  $\chi^{(3)}$  are orders of magnitude smaller than  $\chi^{(2)}$  coefficients found in popular frequency conversion crystals. This means the laser irradiance must be increased to compensate, often leading to material damage. Moreover, third-harmonic generation in crystals is usually difficult to phase match. Because of these obstacles, cascading of two second-order effects (second-harmonic generation, followed by sum-frequency generation) in two separate crystals is usually the preferred method of obtaining high multiples of the pump laser frequency (see Sec. 16.10).

Gases do not have the damage limitations of crystals. Third-harmonic generation was extensively studied in many different gases around the time that high-power, Q-switched lasers became widely available, and conversion efficiencies as high as several percent were obtained. Studies of sodium vapor have been helpful in elucidating the resonant enhancement that occurs near  $\omega$ ,  $2\omega$ , and  $3\omega$ .

## 16.7 STIMULATED SCATTERING

Useful spectroscopic information can be obtained when light is scattered from material, often at frequencies far removed from absorption and emission resonances. Spontaneous scattering is a linear process, in which the material is unmodified by the probing light beam. The various forms of spontaneous scattering (Raman, Brillouin, and Rayleigh) have been known for the better part of a century. In the presence of a sufficiently intense laser beam, however, these scattering processes can be strongly amplified by a nonlinear interaction of the excitation beam with the material, resulting in stimulated scattering.

Raman scattering is most commonly described as the interaction of light with vibrational waves in a material. (Electronic and magnetic excitations can also be measured in Raman experiments.) These vibrational frequencies are typically in the infrared, meaning that Raman-scattered light can have a substantial spectral shift with respect to near-infrared or visible excitation light. Brillouin scattering involves the interaction of light with acoustic waves—waves associated with the propagation of pressure in the medium, leading to periodic density fluctuations. Acoustic waves occur at frequencies that are orders of magnitude smaller than material vibrations; Brillouin scattered light is therefore frequency-shifted from the incident light by a much smaller amount. Rayleigh scattering

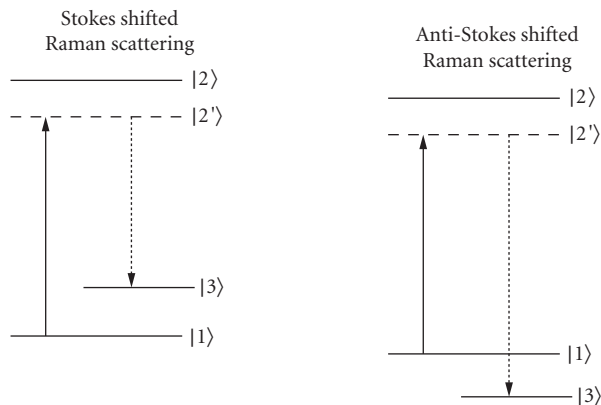
results from the interaction of light with stationary density variations—variations much smaller than the wavelength of the incident light. Scattering takes place without any frequency shift relative to the incident light. Rayleigh scattering is of interest because of its strong wavelength dependence and polarization properties. Spontaneous scattering processes scale linearly with input irradiance.

## Stimulated Raman Scattering

In Raman scattering (Fig. 5), a photon is absorbed by a material that makes a quantum-mechanical transition from a low energy state  $|1\rangle$  to a high energy state  $|2\rangle$ . At some short time later (i.e., not instantaneously), the material relaxes to a lower energy state  $|3\rangle$  different from the original state, giving up its energy in the form of a photon of different energy than the excitation photon. If the lower state  $|3\rangle$  is at a higher energy than state  $|1\rangle$ , the emitted photon will be at a longer wavelength than the excitation light. This is called *Stokes shifted Raman scattering*. If the terminal state  $|3\rangle$  is at a lower energy than state  $|1\rangle$ , the emitted photon will be shorter in wavelength than the incident light, leading to *anti-Stokes shifted Raman scattering*. The difference between the incident and emitted light thus provides information about the relative positions of the different energy levels. Maintaining the same nomenclature, there is also Stokes and anti-Stokes shifted Brillouin scattering. Note that when state  $|1\rangle$  and  $|3\rangle$  are the same, there is no frequency shift and we have Rayleigh scattering.

The intermediate state can be a real state corresponding to a quantum mechanical energy level of the system; this is known as *resonant Raman scattering*. In the theme of this chapter, resonant Raman scattering is an example of a cascaded linear process leading to an effective  $\chi^{(3)}$ . More often, the intermediate level is not resonant with the photon, and the transition from  $|1\rangle$  to  $|2\rangle$  is virtual (illustrated by a horizontal dotted line in Fig. 5). The distinction between the resonant and nonresonant processes can be confusing because both are referred to as Raman scattering. To maintain consistency with standard nomenclature, we briefly depart from the logical organization of this chapter and discuss both resonant and nonresonant Raman scattering in this section.

The essential physics of Raman scattering can be understood from the classical picture of a diatomic molecule of identical atoms vibrating back and forth at frequency  $\omega_l$ . The diatomic molecule is an illustrative example; in principle all Raman-active and some normal modes of vibration of a solid, liquid, or gas can be probed with Raman techniques.<sup>57</sup> We assume that the electronic charge distribution on the molecule is perfectly symmetric, hence there is no permanent dipole or a dipole moment modulated by the vibration. This normal mode is therefore not dipole active, that is, it cannot absorb electromagnetic radiation (see Chap. 8, “Fundamental Optical Properties of Solids”).



**FIGURE 5** Raman scattering.

When an external electric field is applied, the situation changes. The field in an electromagnetic wave polarizes the charge distribution on the molecule and it acquires a dipole. If the induced dipole is also modulated by a normal mode of vibration, the mode is said to be Raman active. The extent to which an external field can polarize the molecule is quantified by the following equation:

$$\mathbf{p}(r, t) = \alpha \mathbf{E}(r, t) \quad (33)$$

where  $\mathbf{p}(r, t)$  is the induced dipole moment,  $\alpha$  is the polarizability,  $\mathbf{E}(r, t)$  is the time- and spatially-varying electric field, and bold type denotes vector quantities. The polarizability is not constant, however, but rather is a function of the molecular separation distance  $q$ . Writing the first two terms of a Taylor series expansion of  $\alpha(q)$  we have:

$$\alpha(q) = \alpha_o + \left( \frac{\partial \alpha}{\partial q} \right)_{q_o} q \quad (34)$$

where  $\alpha_o$  is a constant representing the polarizability at the equilibrium position of the molecule ( $q_o$ ). The molecule vibrates at a frequency  $\pm \omega_L$ , which is the energy difference between the states  $|1\rangle$  and  $|3\rangle$  in Fig. 5, hence:

$$q = q_o \exp(\pm i \omega_L t) \quad (35)$$

Inserting Eqs. (34) and (35) into Eq. (33), and realizing that the electromagnetic field varies sinusoidally at the optical frequency  $\omega$ , we find that the second term in the polarizability expansion is responsible for the appearance of induced dipoles oscillating at a frequency offset from the incident electromagnetic wave by  $\pm \omega_L$ :

$$p(r, t)_{\text{Raman}} = E_o(r) \left( \frac{\partial \alpha}{\partial q} \right)_{q_o} q_o \exp(i \omega t \pm i \omega_L t) \quad (36)$$

These dipoles can radiate and are the origin of spontaneous Raman scattering. There is also an oscillating dipole unaffected by the vibration corresponding to the term  $\alpha_o$ . This dipole oscillation is exactly at the frequency of the incident light and corresponds to spontaneous Rayleigh scattering:

$$p(r, t)_{\text{Rayleigh}} = E_o(r) \alpha_o \exp(i \omega t) \quad (37)$$

In stimulated scattering, we have to consider the force exerted on the vibrating molecule by the external field as a consequence of its polarizability. This force involves only the second term in Eq. (34):

$$F = \frac{1}{2} \left( \frac{\partial \alpha}{\partial q} \right)_{q_o} \langle E^2(r, t) \rangle \quad (38)$$

where the angular brackets represent a time average over an optical period. In a dipole-active interaction, the lowest order forcing term is proportional to  $E$ , resulting in linear absorption of light. In the case of a Raman-active mode, Eq. (38) shows the force scales as  $E^2$ ; therefore, the force is nonlinear in the field. The forcing term is negligible at low light intensities, but becomes important when large electromagnetic field levels generated by lasers are encountered.

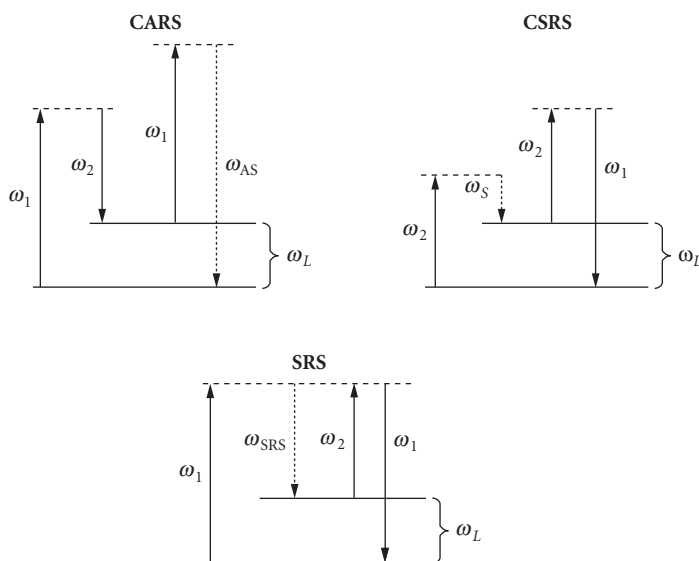
Because the Raman active mode of the molecule is subject to a force proportional to  $E^2$ , there must be two input photons driving the interaction. If the two photons are at different frequencies,

the molecule will experience a force at the beat frequency of the two photons. If the wavelengths of the two photons are chosen so that their beat frequency equals that of the molecular vibration  $\omega_L$ , strong amplification of all three waves (two input electromagnetic waves and the molecular vibration) can occur, resulting in stimulated scattering. The molecular polarizability thus acts as a nonlinear mixing term to reinforce and amplify the interacting waves. It is important to realize this is of practical consequence only when the input electromagnetic fields are sufficiently high.

The nonlinear polarizability impresses sidebands on the pump light, resulting in three distinct electromagnetic waves (laser beam, Stokes shifted Raman, and anti-Stokes shifted Raman) propagating in the medium. The same nonlinear mixing process that led to the generation of the Raman sidebands in the first place can cause coherent excitation of additional molecules due to their polarizability. In this way, a coherent vibrational wave builds up, which in turn feeds more energy into the Raman-shifted components, thus amplifying them. In stimulated scattering, the fluctuations of the optical medium (vibrations, density variations, etc.) are *induced* and *amplified* by the external electromagnetic radiation. In contrast, spontaneous scattering originates from the naturally occurring (thermally driven, for example) fluctuations of the material. Because the linear optical properties of the medium are modified by the presence of an exciting laser beam (specifically its irradiance), the various stimulated scattering mechanisms are classified as third-order nonlinear optical processes.

In stimulated Raman scattering (SRS), one is most often looking for a new frequency generation at the wavelength corresponding to the energy difference of levels  $|2' \rangle$  (or  $|2 \rangle$ ) and  $|3 \rangle$  shown in Fig. 5. Stimulated Raman gain and loss applied to an input beam at this frequency can be obtained as well. Polarization effects occurring in the nonlinear wave mixing process can also be studied in what is known as *Raman-induced Kerr effect spectroscopy* (RIKES, see Chap. 5, "Optical Properties of Semiconductors"). We also mention two other classes of third-order nonlinear spectroscopy: coherent anti-Stokes Raman spectroscopy (CARS) and coherent Stokes Raman spectroscopy (CSRS). In these interactions, illustrated in Fig. 6, two external laser fields at frequencies  $\omega_1$  and  $\omega_2$  are supplied. There must be a third-order nonlinear polarization present as in SRS, leading to frequency mixing and new wavelengths.

The somewhat subtle differences distinguishing SRS, CARS, and CSRS are the number and location of intermediate levels (designated by dashed lines in Fig. 6). Consider two excitation frequencies



**FIGURE 6** Stimulated Raman processes.



with  $\omega_1 > \omega_2$  probing a given material system with real energy levels separated by frequency  $\omega_L$  in Fig. 6. In CARS, short-wavelength photons are detected at  $\omega_{as} = 2\omega_1 - \omega_2$ . For the CSRS arrangement, the excited intermediate states are at lower energy and a longer-wavelength photon at frequency  $\omega_s = 2\omega_2 - \omega_1$  is detected. Note that SRS is obtained when the intermediate levels are degenerate; SRS is thus a special case of the nonlinear interaction. In linear, spontaneous Raman scattering, a single exciting electromagnetic wave is required. In SRS, two input fields are involved; they just happen to be at the same frequency and invariably are supplied by a single laser source. Unlike spontaneous Raman scattering, however, SRS is a function of the third-order nonlinear susceptibility and hence depends nonlinearly on the irradiance of the excitation laser.

It is important to emphasize that all three of these stimulated Raman processes (SRS, CARS, and CSRS) are essentially a mixing of three waves to produce a fourth wave via the third-order nonlinear polarization. Analysis of the problem is made using second-order perturbation theory in quantum mechanics. The tensor nature of the third-order susceptibility and the multitude of ways the interacting waves of various polarization states can mix lead to complicated expressions. One finds resonance denominators quantifying the efficiency of the wave mixing process. The scattering efficiency is governed by the proximity of photon energies to real energy eigen states in the system. In principle, SRS, CSRS, and CARS can all take place in an experiment; the various generated beams can be distinguished by substantially different angles of propagation when leaving the irradiated sample. These angles are readily determined by phase-matching conditions for the nonlinear interaction. The wave vectors of the interacting photons can be arranged for maximum output signal of the desired Raman process. The phase-matching condition is obtained automatically in SRS, but careful orientation of the interacting beams can lead to very narrow linewidths and extremely accurate spectroscopic measurements. Some applications of stimulated Raman scattering include high-resolution spectroscopy of gases,<sup>11,17,58,59</sup> spin-flip Raman scattering, stimulated polariton (the quanta of photon-phonon coupling) scattering, and ultrafast time-resolved measurements.<sup>60,61</sup> The reader should also be aware that Raman spectroscopy beyond the third-order nonlinear susceptibility has been demonstrated. Further information can be obtained in texts on nonlinear laser spectroscopy.<sup>3,6,10,16,62-65</sup>

## Stimulated Brillouin Scattering

Stimulated Brillouin scattering (SBS) is an important third-order nonlinear optical effect that has been widely used for efficient phase conjugate reflection of high-power lasers.<sup>26</sup> An incident laser beam can scatter with the periodic refractive index variations associated with a propagating acoustic wave. The scattered light, depending on the propagation direction of the acoustic wave, will be Stokes or anti-Stokes shifted by the frequency of the acoustic wave. The process is stimulated because the interference of the incident and scattered wave can lead to an amplification of the acoustic wave, which then tends to pump more energy into the scattered wave. This positive feedback process can cause an exponential growth of the SBS beam and very high efficiencies in the right circumstances. Optical feedback to the medium is accomplished in one of two ways: (1) *electrostriction* is local compression of the material in response to the strength of the electromagnetic field with a commensurate refractive index change; and (2) *linear optical absorption* by the laser field leads to local heating, expansion, density fluctuations, and thus periodic modulation of the refractive index. The latter effect is an example of a cascaded  $\chi^{(1)}:\chi^{(1)}$  process, which is the subject of Sec. 16.9. Electrostriction is usually associated with SBS, and we discuss it here.

Consider again the diatomic molecule that was used to illustrate the Raman effect. In the presence of an external electric field, it acquires a polarizability described by Eq. (34). As we have seen, the induced dipole can interact with the field. Electrostriction accounts for the ability of the electric field to do work on the polarized molecule—pulling and pushing it by electrostatic forces. The molecules will move and tend to pile up in regions of high field, increasing the local density. Associated with these density changes will be a change of refractive index. Density fluctuations can also be generated by the change in pressure that accompanies a propagating acoustic wave: Pressure nodes will exist in the peaks and valleys of the acoustic wave. Electrostriction therefore provides a coupling mechanism between acoustic waves and electromagnetic waves.

It is important to emphasize that the periodic modulations in an electrostrictive medium are propagating spatial fluctuations modulated at the frequency of traveling acoustic waves. When the density fluctuations are stationary, we can have stimulated Rayleigh scattering. A thorough, detailed discussion of the many (often intricate) issues in stimulated Brillouin and Rayleigh scattering can be found in textbooks on nonlinear optics.<sup>3,11,16,17,28</sup>

## 16.8 TWO-PHOTON ABSORPTION

Two-photon absorption (2PA) is the process by which the energy gap between two real states is bridged by the simultaneous (in the context of the Uncertainty Principle discussed in Sec. 16.2) absorption of two photons, not necessarily at the same frequency. Both photons have insufficient energy to complete the transition alone; 2PA is thus observed in the spectral range where the material is normally transparent. When the two photons are present together for a fleeting instant of time determined by the Uncertainty Principle, an optical transition can take place.

Quantum mechanically, we can think of the first photon making a virtual transition to a non-existent state between the upper and lower levels (Fig. 2c). If the second photon appears within the virtual lifetime of that state, the absorption sequence to the upper state can be completed. If not, the virtual transition collapses back to the ground state, and no absorption takes place. To have an appreciable rate of 2PA, photons must be supplied at a rate high enough that there is a reasonable probability two photons will both be present during the virtual lifetime. Because the virtual lifetime is so short, photon fluxes must be high, and therefore power levels from laser beams are required.

The efficiency of 2PA is affected by the proximity of the input photons to a real state of the system. It is important to note that there must be an allowed optical transition linking the initial state and this real state. The closer one of the input photons coincides with a real state, the stronger the 2PA. When the intermediate state of 2PA is also a system resonance, the situation is commonly referred to as *excited state absorption* (ESA)—a sequence of two linear absorption processes that leads to an effective third-order nonlinearity. Excited state absorption is thus a cascaded  $\chi^{(1)}:\chi^{(1)}$  effect, giving rise to an effective third-order nonlinearity (Sec. 16.9). It has implications for optical power limiting and is discussed in Chap. 13, “Optical Limiting.”

In stimulated scattering, the *difference* frequency of two input electromagnetic fields  $\hbar\omega_i - \hbar\omega_j$  equals a characteristic energy resonance of the material system. In 2PA, an energy resonance exists at the *sum* of the two input fields:  $\hbar\omega_i + \hbar\omega_j$ . In Secs. 16.2 and 16.3, 2PA was shown to be associated with the imaginary part of  $\chi^{(3)}$ . This is because it is an absorption process (i.e., it is exactly resonant with two eigenstates of the system). It is the only NLA process (i.e., a process associated with the imaginary part of  $\chi^{(3)}$ ) that can be simply studied with a single photon frequency.

Two-photon absorption in semiconductors is one of the most thoroughly studied subjects in the entire field of nonlinear optics.<sup>66</sup> The 2PA coefficient (often written  $\beta$  or  $\alpha_2^{2PA}$ ) of bulk semiconductors has been calculated using models involving only two parabolic bands and also with more complex band structure.<sup>67</sup> It is defined by the rate of electron-hole pair excitation:  $dN/dt = \beta I^2 / (2\hbar\omega)$ . The two-parabolic band model gives a comparatively simple yet general and accurate description of 2PA for a large class of semiconductors. The theoretical result for single frequency excitation can be expressed as

$$\beta(m/W) = \frac{B}{n_0^2 E_g^3} \bar{F}_2^2 \left( \frac{\hbar\omega}{E_g} \right) \quad (39)$$

where  $\bar{F}_2(x) = 2(2x-1)^{3/2}/x^5$  and  $B = 5.67 \times 10^{-66}$  ( $x = \hbar\omega/E_g$  and the energy bandgap  $E_g$  is in joules). The best empirical fit to experimental data is obtained with  $B$  adjusted to a slightly higher value of  $9.06 \times 10^{-66}$ . The function  $\bar{F}_2^2$  describes the dispersion of 2PA and is plotted in Fig. 3. The intimate relation between NLA and NLR and the role of 2PA in semiconductors is explored in Sec. 16.4 and in Refs. 31 and 67 to 69. There are important practical implications for 2PA in

semiconductors and dielectrics. It can enhance or degrade optical switching performance in semiconductor devices and lead to optical damage in laser window materials. 2PA is also the basis of Doppler-free spectroscopy of gases.<sup>57,59</sup>

## 16.9 EFFECTIVE THIRD-ORDER NONLINEARITIES; CASCADED $\chi^{(1)}:\chi^{(1)}$ PROCESSES

Effective third-order nonlinearities occur when one of the transitions in our four-photon interaction picture is resonant, providing a path of linear absorption. Linear absorption is a mechanism to directly couple laser light into the system—with sufficiently intense laser light, the linear optical properties of a material can be modified. An effective third-order nonlinearity occurs when linear absorption affects the refractive index. We give some examples here.

### Optically Generated Plasmas

Optical generation of stable plasmas is readily obtained in semiconductors and most studies of this subject have been made with these materials (see Chap. 8, “Fundamental Optical Properties of Solids” and Chap. 5, “Optical Properties of Semiconductors”). For cascaded linear processes that we discuss here, the formation of a free electron-hole pair occurs by direct bandgap excitation by an incident photon. The optically produced carriers augment the background electron-hole density, and the plasma remains electrostatically neutral. If the generation of an excess amount of plasma exceeds the rate of loss (by recombination or diffusion) on the time scale of interest, the plasma will modify the linear optical properties of the semiconducting material. The simplest way to see this is via the classical Drude model, where the refractive index of a metal or semiconductor is<sup>70,71</sup>

$$n = n_0 \sqrt{1 - \frac{\omega_p^2}{\omega^2}} \quad (40)$$

In this equation,  $\omega$  is the angular frequency of the light,  $n_0$  is the linear index in the absence of significant free carrier density, and  $\omega_p$  is the density-dependent plasma frequency:

$$\omega_p = \sqrt{\frac{Ne^2}{m\epsilon}} \quad (41)$$

where  $N$  is the electron-hole pair density,  $e$  is the electronic charge,  $m$  is the reduced mass of the positive and negative charge carriers (electrons, holes, or ions), and  $\epsilon$  is an appropriate background dielectric constant. Note that as the carrier density increases, the refractive index decreases. The material is usually excited by a laser beam with a nonuniform spatial profile such as a Gaussian, giving rise to negative-lensing and self-defocusing, assuming  $\omega < \omega_p$ .

The situation becomes complicated at densities where many-body effects become important or when the Drude model ceases to be valid. We also note that optical generation of plasmas can also occur as the result of nonlinear mechanisms in the presence of high laser fields, and we aren't, of course, restricted only to solid-state plasmas. Examples of nonlinear plasma production are multiphoton absorption, laser-induced impact ionization, and tunneling. Because plasma generation and the concomitant refractive index modification are caused by a nonlinear optical process, the order of the nonlinearity is higher than three. Although high-order nonlinearities are a rich subset of the field, they are not dealt with in this chapter. A number of review articles and textbooks on laser-induced change to the refractive index due to plasma generation via linear absorption are available.<sup>31,42,72-74</sup>

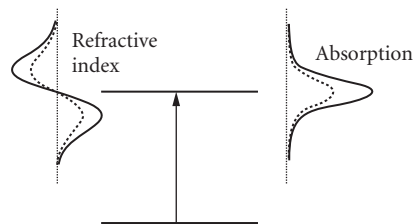
## Absorption Saturation

Absorption saturation is a well-known example of a cascaded linear process. Consider a homogeneously broadened system of two-level atoms (i.e., a system of identical two-level atoms) with the energy diagram shown in Fig. 7. The lower and upper states are resonant with a photon depicted by the vertical arrow, and there is linear absorption of incident light. Associated with the absorption is a spectral linewidth (with a Lorentzian shape for a homogeneous system), illustrated on the right side of the diagram in Fig. 7. An induced dipole or polarization is set up between the two states upon excitation by a photon. The states are coherently coupled, and this coherence is in phase with the exciting electromagnetic field. In a real system, this coherence will be quickly destroyed by collisions with other atoms. The rate at which the coherence is washed out determines the spectral width of the absorption profile and hence the frequency response of the imaginary component of the linear susceptibility. The real part of the linear susceptibility is obtained by the Kramers-Kronig transformation, giving rise to what is traditionally known as anomalous dispersion of the refractive index shown on the left side of Fig. 7. Note that the refractive index is positive for frequencies below resonance and negative at frequencies above it.

We have assumed that the rate at which photons are supplied to the system produces a negligible change of population in the upper and lower states. This means that the rate of population relaxation (recombination and diffusion, for example) is much faster than excitation. When the incident irradiance is sufficiently high, however, this may no longer be the case. The upper level can become appreciably occupied, reducing the availability of terminal states for optical transitions. The absorption thus decreases or bleaches, indicated by the dashed lines in Fig. 7. Associated with the change of absorption is a change of refractive index. The relationship between absorption and refraction can again be handled with the Kramers-Kronig transformation *provided* we consider the system as being composed of both the atoms *and* the input light beam, specifically the nonequilibrium change of population created by the input light. This is exactly the same mathematical formulation used in the description of nonresonant third-order nonlinearities introduced in Sec. 16.4. The difference here is that the absorption of photons is a resonant, linear process. The linear absorption of light then affects the linear optical properties of absorption and dispersion. Because the reduction of absorption depends directly on laser irradiance, it behaves like a third-order nonlinearity. We point out that the resonant nature of absorption saturation (and the associated nonlinear refraction) can lead to an unacceptable deviation from a third-order susceptibility description when the input irradiance goes even higher. In the high-power regime, a nonperturbative approach (i.e., not represented by a power series expansion) must be used.<sup>75</sup>

Absorption saturation spectroscopy (with emphasis on gases) is discussed at length in Ref. 59. It is also a principle nonlinear effect in bulk and quantum-confined semiconductors (where the simple two-level picture previously outlined must be substantially modified), having implications for optical switching and bistability.<sup>42,53,72,76</sup>

We briefly mention the density matrix (see Chap. 10,<sup>76</sup> “Nonlinear Optics”). This is a powerful method of analysis for the resonant interaction of light with a two-level system. In addition to absorption saturation, the nonlinear optical effects described by the density matrix include Rabi oscillations, photon echoes, optical nutation, superradiance, self-induced transparency, and optical-free induction



**FIGURE 7** Absorption saturation and refraction of a two-level atomic system.

decay, which are not immediately associated with a third-order nonlinearity derived from a perturbation expansion of the polarization. Experimental manifestations of these phenomena, however, can often be represented by an effective third-order nonlinearity. The nonlinear optics of the two-level system and the associated optical Bloch equations derived from the density matrix formulation of the problem are discussed in Chap. 11, “Coherent Optical Transients.” The reader is also referred to many excellent textbooks and monographs.<sup>3,11,24,77,78</sup>

## Thermal Effects

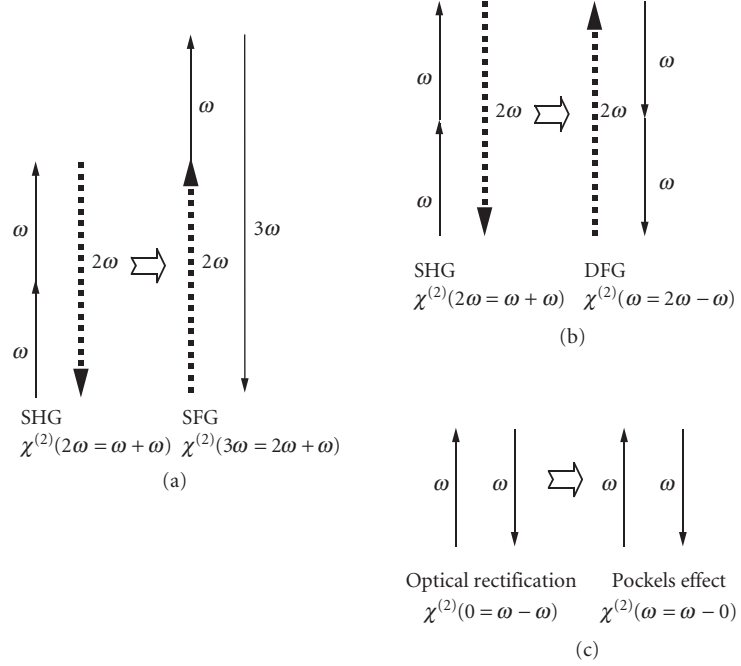
Linear absorption of light must result in energy deposition in the irradiated material. If the rate of energy deposition significantly exceeds its rate of removal, heating can take place. As the energy of a collection of atoms and molecules increases, it's easy to understand that their macroscopic optical properties will be altered. When there is a linear relationship between laser irradiance and the refractive index, an effective third-order nonlinearity will result. The thermo-optic effect has a relatively straightforward physical interpretation and is arguably one of the most important optical nonlinearities. It is often the power-limiting mechanism of a high-power solid-state laser—where excessive circulating optical flux can cause *thermal blooming* in the laser crystal. This heat-induced lensing effect can destroy the beam quality. Thermal-index coefficients have been extensively tabulated, and the reader is referred to Refs. 18 and 42.

## Photorefraction

Photorefraction results from the spatial redistribution of electrons and/or holes in a solid (see Chap. 12, “Photorefractive Materials and Devices”). Electron-hole pairs are generated by linear absorption of laser light. If the excitation geometry produces a spatial modulation of irradiance such as a two-beam interference pattern, the electrons and holes will arrange themselves in accordance with the spatial irradiance profile. Often the linear absorption involves impurity levels. Mobile carriers tend to diffuse from the bright regions, leaving fixed charges behind. If a sinusoidally modulated, two-beam interference fringe pattern is written in a doped photorefractive crystal, for example, fixed charges of ionized states will be prevalent in the high irradiance regions while mobile charge carriers will tend to accumulate in regions with low light levels. A modulated space charge must exist, and therefore a modulated electric field pattern must be present as well. This field alters the refractive index via the linear electro-optic effect (i.e., Pockel's effect). The photorefractive nonlinearity is clearly nonlocal, as it requires a spatial modulation of charge density. Manipulation of the carriers can also be obtained with static electric fields, and the response time tends to be of the order of seconds.<sup>3,18,79,80</sup>

## 16.10 EFFECTIVE THIRD-ORDER NONLINEARITIES; CASCADED $\chi^{(2)}:\chi^{(2)}$ PROCESSES

Materials lacking a center of inversion symmetry have nonzero  $\chi^{(2)}$  and exhibit a second-order nonlinear polarization. This is the second term in the polarization power series expansion of Eq. (1) that is responsible for the most well-known effects in nonlinear optics, including second-harmonic generation (sum and difference frequency generation, optical rectification), and optical parametric processes (see Chap. 17, “Continuous-Wave Optical Parametric Oscillators”). It is also possible to cascade two  $\chi^{(2)}$  processes to produce an effect that mimics a  $\chi^{(3)}$  process. The most common and efficient way of producing THG, for example, is by a  $\chi^{(2)}$  cascade process. In this interaction, an input source at  $\omega$  generates SHG via the second-order susceptibility  $\chi^{(2)}$  ( $2\omega = \omega + \omega$ ); the second harmonic and fundamental then mix in a second (or the same) nonlinear crystal to produce the third harmonic by sum frequency generation  $\chi^{(2)}$  ( $3\omega = 2\omega + \omega$ ). This type of nonlinearity is nonlocal because the two processes (SHG and SFG) take place in spatially separate regions.



**FIGURE 8** Cascaded  $\chi^{(2)}:\chi^{(2)}$  effective third-order nonlinearities.

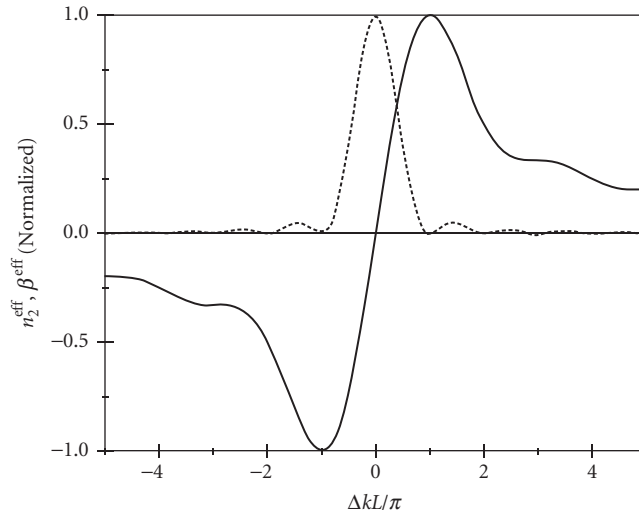
In addition to THG, all other  $\chi^{(3)}$  effects have an analogous process in  $\chi^{(2)}:\chi^{(2)}$  cascading. Consider the case where we have one frequency  $\omega$ . The corresponding cascaded  $\chi^{(2)}$  effects are depicted in Fig. 8. Recall that the intrinsic  $\chi^{(3)}$  is manifest as: (1) THG, (2) 2PA, and (3) the ac Stark effect. The horizontal block arrows indicate the point of cascade (i.e., the propagation of the beams between the two  $\chi^{(2)}$  interactions). There are always two distinguishable  $\chi^{(2)}$  interaction regions; hence  $\chi^{(2)}:\chi^{(2)}$  is clearly nonlocal. We also point out that in general the photon frequencies can be different.

Although the analogy is limited, cascaded  $\chi^{(2)}$  effects exhibit NLA and NLR mimicking  $\chi^{(3)}$ . In the case of SHG, for example, the manifestation of  $\chi^{(3)}$  NLA is depletion of the pump beam. The utility of cascaded  $\chi^{(2)}:\chi^{(2)}$  for producing large nonlinear phase shifts has been realized only recently.<sup>81–83</sup> The analysis of  $\chi^{(2)}$  is relatively straightforward, involving the coupled amplitude equations governing the propagation of the interacting beams. For example, the nonlinear phase shift imposed on a fundamental beam ( $\omega$ ) as it propagates through an SHG crystal of length  $L$  with a phase mismatch  $\Delta k = k(2\omega) - 2k(\omega)$  and assuming small depletion is<sup>82</sup>

$$\Delta\phi \approx \tan^{-1}\left(\frac{\Delta k L \tan(\beta L)}{2} \frac{\Delta k L}{\beta L}\right) - \frac{\Delta k L}{2} \quad (42)$$

where  $\beta = \sqrt{(\Delta k L / 2)^2 + \Gamma^2}$ ,  $\Gamma = \omega \chi^{(2)} |E_0| / 2c \sqrt{n(2\omega)n(\omega)}$ , and  $E_0$  denotes the electric field of the fundamental beam. An effective  $\chi^{(3)}$  can be obtained if we expand  $\Delta\phi$  to lowest order in  $\Gamma$  and use  $\Delta\phi = \omega L n_2^{\text{eff}} I / c$  to give<sup>84</sup>

$$n_2^{\text{eff}} = \frac{9}{c^2 4\pi\epsilon_0} \frac{\omega d_{\text{eff}}^2 L}{n^2(\omega)n(2\omega)} \left[ \frac{\pi}{\Delta k L} \left( 1 - \frac{\sin(\Delta k L)}{\Delta k L} \right) \right] \quad (43)$$



**FIGURE 9** Calculated phase shifts in cascaded  $\chi^{(2)}:\chi^{(2)}$ .

Here  $d_{\text{eff}} = \chi^{(2)}(2\omega = \omega + \omega)/2$  is the effective tensor component of the second-order nonlinear susceptibility for a given experimental geometry.

Phase mismatch is represented by the bracketed term in Eq. (43), plotted in Fig. 9. Also shown in Fig. 9 is the depletion of the fundamental beam which, on the same level of approximation, can be regarded as an effective two-photon absorption coefficient that scales as  $\beta^{\text{eff}} \sim \text{sinc}^2(\Delta kL)$ . Cascaded  $\chi^{(2)}$  leads to an effective refractive index modulation ( $n_2^{\text{eff}}$ ) and two-photon absorption ( $\beta^{\text{eff}}$ ), but one should not conclude that the material's index of refraction is altered or energy is deposited in the material. These coefficients describe only nonlinear phase shifts and the conversion of the fundamental beam to second-harmonic beams. The nonlinear phase shift from the  $\chi^{(2)}:\chi^{(2)}$  process has been used to demonstrate nonlinear effects analogous to those observed previously with the intrinsic optical Kerr effect. These include self-focusing and self-defocusing,<sup>81</sup> all-optical switching,<sup>85,86</sup> soliton propagation,<sup>87,88</sup> and laser mode-locking.<sup>89</sup>

## 16.11 PROPAGATION EFFECTS

When the nonlinear optical polarization  $P^{\text{NL}}(t)$  is known, the propagation of optical fields in a nonlinear medium can be analyzed with the aid of Maxwell's equations:

$$\nabla \times \nabla \times E + \frac{1}{c^2} \frac{\partial^2 E}{\partial t^2} = -\mu \frac{\partial^2 P}{\partial t^2} \quad (44)$$

where  $P(t)$  is the total polarization including the linear and nonlinear terms. The slowly varying envelope approximation is then usually made to reduce the above equation to a system of four coupled nonlinear differential equations for the four interacting fields. For *thin* nonlinear media, where there is no significant distortion of the spatial beam and temporal shape upon propagation, the problem simplifies greatly. Equations (19) and (20) were obtained with this approximation. For *thick* nonlinear media, however, linear and nonlinear diffraction as well as dispersion cannot be ignored. In this section, we discuss two important propagation phenomena: *self-focusing* and *soliton formation*.

## Self-Focusing

Self-focusing occurs in materials with a positive intensity-dependent refractive index coefficient ( $n_2 > 0$ ). Self-focusing (or *Kerr-lensing*) causes spatial collapse of the laser beam when it propagates through transparent optical materials, often leading to optical damage. It is a consequence of the nonuniform spatial profile of the laser beam.<sup>2,3,17,18</sup> For a *thin* nonlinear material, one makes the so-called parabolic approximation for the nonlinear phase shift to obtain an approximate Kerr-lens focal length, assuming a Gaussian beam of radius  $w$  ( $1/e$  of the electric field profile):<sup>90</sup>

$$f_{\text{NL}} \approx \frac{aw^2}{4Ln_2I} \quad (45)$$

where  $L$  is the thickness of the medium,  $I$  is the irradiance, and  $6 > a > 4$  is a correction term. Note that when  $n_2$  is negative, Eq. (45) shows there will be a negative focal length and thus self-defocusing of the incident beam.

Equation (45) is valid for  $f_{\text{NL}} \gg L$  and  $Z_0 \gg L$ , where  $Z_0$  is the diffraction length (Rayleigh range) of the incident beam. This is the so-called *external self-action* regime.<sup>91</sup> This approximation fails for thick nonlinear media and/or at high irradiance (i.e., *internal self-action*). Equation (44) must then be solved numerically. Analysis shows that self-lensing of a Gaussian beam overcomes diffraction at a distinct threshold power (i.e., the self-focusing threshold), given by the approximate formula:<sup>90,92</sup>

$$P_{\text{cr}} \approx \frac{a\lambda^2}{8\pi n_2 n_0} \quad (46)$$

Note that for sufficiently thick media, the self-focusing threshold occurs at a critical power, not at a threshold irradiance (i.e., the power at which the self-focusing overcomes diffraction). Self-focusing and diffraction both scale with beam area, thus canceling out the spot size dependence in Eq. (46). Self-focusing and self-defocusing (collectively called *self-action effects*) are often employed in optical limiting applications. Self-action is also the essential mechanism for mode-locking cw solid-state lasers, commonly known as *Kerr-lens mode-locking*.<sup>93</sup>

## Solitons

Soliton waves are realized in many different physical circumstances, ranging from mechanical motion to light propagation. In general, they are robust disturbances that can propagate distortion-free for relatively long distances. The robustness of optical solitons can be manifest in the time domain (temporal solitons), transverse space (spatial solitons), or both (light bullets). Temporal solitons have been extensively studied in optical fibers because of their tremendous utility in long-distance optical communication. They exist as a consequence of a balance between the competing effects of linear refractive index dispersion and nonlinear phase modulation.

Assume a single beam propagating in a long nonlinear waveguide characterized by an instantaneous nonlinear index coefficient  $n_2$  and a linear refractive index  $n(\omega)$ . Ignoring spatial effects (i.e., diffraction), we write the electric field as  $\mathcal{E}(z, t) = A_0 u(z, t - z/v_g) \exp(i\omega_0 t - ik_0 z) + \text{c.c.}$  From Eq. (44), one derives a differential equation describing the evolution of the soliton field envelope  $u(z, t)$ :<sup>3,51,94</sup>

$$-i \frac{\partial u}{\partial z} + \frac{k_2}{2} \frac{\partial^2 u}{\partial \tau^2} = \Delta k_{\text{NL}} |u|^2 u \quad (47)$$

Here  $v_g = d\omega/dk|_{\omega=\omega_0}$  is the soliton pulse group velocity,  $\tau$  is a retarded time  $\tau = t - z/v_g$ ,  $k_2 = d^2k/d\omega^2|_{\omega=\omega_0}$  gives the group velocity dispersion (GVD), and  $\Delta k_{\text{NL}} = n_2 I_0 \omega_0 / c$  is the irradiance-dependent change of the propagation wave vector. In MKS units, the peak intensity of the soliton pulse is  $I_0 = n_0 \epsilon_0 c |A_0|^2 / 2$ . Equation (47) is called the *nonlinear Schrödinger equation* (NLSE) and can be solved exactly. One solution gives the fundamental soliton pulse:

$$u(z, \tau) = \text{sech}(\tau/\tau_0) e^{ikx} \quad (48)$$



where  $\tau_0^2 = -k_2 / \Delta k_{\text{NL}}$  is the soliton pulsewidth and  $\kappa = -k_2 / 2\tau_0^2$ . Note that the modulus of the soliton pulse envelope  $|u|$  remains unperturbed upon propagation. For this solution to exist, the GVD ( $k_2$ ) and the nonlinear refraction ( $\Delta k_{\text{NL}}$ ) must have opposite signs. For transparent optical solids, including silica glass optical fibers, the nonlinear index coefficient  $n_2$  is almost always positive, which means that a negative GVD is required. In fused silica fibers, the point of balance is attained at a wavelength of  $\lambda \approx 1.55 \mu\text{m}$ . This is also a spectral region with very low absorption loss. This wavelength has become the standard for the telecommunications industry. Optical solitons in fibers were first reported by Mollenauer et al.<sup>51</sup>

Spatial solitons refer to the propagation of an optical beam without any change or distortion to its spatial irradiance distribution. In this type of soliton, a point of stability is achieved between linear diffraction (causing the beam to diverge) and nonlinear self-focusing. In the presence of a  $\chi^{(3)}$  nonlinearity, a stable solution to the NLSE can be found in one spatial dimension only.<sup>95,96</sup> Using a cascaded  $\chi^{(2)}:\chi^{(2)}$  nonlinearity, however, two-dimensional spatial solitons (or solitary waves) have been demonstrated.<sup>87,88</sup> Two-dimensional spatial solitons can be realized for a cascaded  $\chi^{(2)}:\chi^{(2)}$  process because of its different behavior compared to  $\chi^{(3)}$  at large nonlinear phase shifts. Specifically, cascaded  $\chi^{(2)}:\chi^{(2)}$  exhibits a saturation of the nonlinear phase-shift that is a direct consequence of depletion of the fundamental beam.

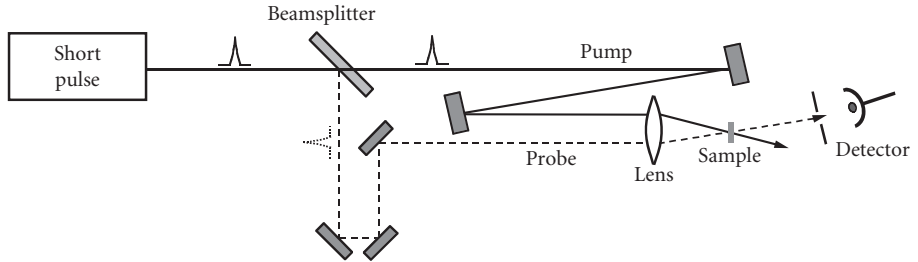
## 16.12 COMMON EXPERIMENTAL TECHNIQUES AND APPLICATIONS

There are a variety of experimental methods for determining the characteristics (magnitude, response time, spectrum, etc.) of  $\chi^{(3)}$  (or  $\chi_{\text{eff}}^{(3)}$ ). The merit of a technique depends on the nature of the nonlinearity and/or the specific property that we wish to measure. An example is obtaining short-time resolution at the expense of sensitivity. Nonlinear optical coefficients can be determined absolutely or relative to a reference material. In the former case, accuracy is determined by the ability to precisely characterize the incident beams. There are many potential sources of error and misinterpretation in nonlinear optical measurements. In *thick* samples, for example, the phase shift that occurs during beam propagation can lead to varying irradiance at different points within the sample. This can be quite difficult to account for and properly model. It is usually best to work in the *external self-action* regime (i.e., thin-sample limit so that beam propagation effects can be ignored)<sup>91</sup> (see also Sec. 16.3). This greatly simplifies data analysis, since the equation describing nonlinear absorption can be separated from nonlinear refraction. Even if the thin-sample approximation is satisfied, nonlinear refraction can deflect light so strongly *after* the sample that the detector does not collect all the transmitted energy. This will lead to an overestimation of the nonlinear loss. Particular care must be exercised when using ultrashort pulses. Pulse broadening effects due to group velocity dispersion, for example, may cast ambiguity on the magnitude as well as response time associated with a nonlinearity.

We briefly discuss a few of the commonly used experimental methods: four-wave mixing, excite-probe techniques, interferometry, and Z-scan. It is practically impossible for any single technique to unambiguously separate the different nonlinear responses. Experiments are generally sensitive to several different nonlinearities at once. Different measurements are usually required to unravel the underlying physics, by varying parameters such as irradiance and pulse width. Near-instantaneous nonlinearities such as two-photon absorption and the optical Kerr effect should be independent of pulse width. Slower nonlinear responses will change as the pulse width approaches the response time. Ultrafast and cumulative nonlinearities are often present simultaneously in experiments (e.g., semiconductors), thus hindering their experimental isolation.

### Time-Resolved Excite-Probe Techniques

Pump-probe (excite-probe) measurements allow the study of temporal dynamics in nonlinear absorption.<sup>27,60</sup> In the usual implementation, a relatively strong pump pulse excites the sample and



**FIGURE 10** Pump-probe experiment.

changes its optical properties (see Fig. 10). A weaker probe pulse interrogates the excitation region and detects changes. By varying the relative time separation of the two pulses (i.e., by appropriately advancing and delaying the probe pulse), the temporal response can be mapped out. Specifically, relatively slow and fast nonlinear responses can be identified. Often, but not always, the probe is derived from the excitation beam. In degenerate pump-probe (identical frequencies), the probe beam is isolated from the pump beam in a noncollinear geometry (i.e., spatial separation as in Fig. 10) or by orienting the probe with a different polarization.

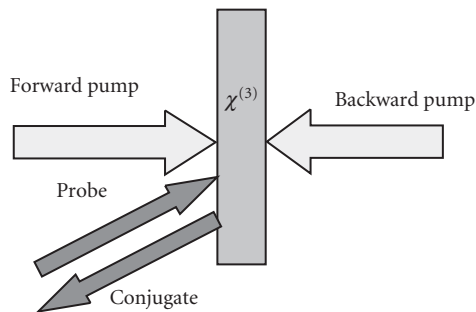
Nondegenerate nonlinear absorption spectra can also be measured; one approach is to use a fixed-frequency laser pump and continuum (white light) probe such as the output of a flash-lamp.<sup>97</sup> The temporal width of a flashlamp source is usually much longer than the laser pulse, which causes a convolution of the fast two-photon response with much longer-lived cumulative nonlinearities in the probe spectrum. The availability of femtosecond white-light continuum sources has allowed nondegenerate spectra to be obtained on short time scales where the ultrafast response dominates.<sup>27,98</sup>

Interpretation of the nonlinear response is complicated by the fact that pump-probe experimental methods are sensitive to any and all induced changes in transmission (or reflection); pump-induced phase shifts on the probe are not readily detected. A time-resolved technique that is very sensitive to index changes is the optical Kerr-gate. This is a form of the pump-probe experiment where induced anisotropy in a time-gated crystal leads to polarization changes.<sup>99</sup> Beyond the two-beam pump probe, three-beam interactions can produce a fourth beam through NLA and/or NLR. This is known as *four-wave mixing* and is discussed in the next section. The development of high-irradiance, femtosecond-pulsed laser systems has led to the evolution of pump-probe measurements that automatically yield the nondegenerate nonlinear absorption spectrum. The femtosecond pulse is split into two beams: one beam is used for sample excitation while the other beam is focused into an appropriate material to produce a white-light continuum for probing. This white-light continuum is used to measure the response over a range of frequencies  $\omega$ ; this data is suitable for numerical evaluation via the K-K integral in Eq. (24). For a sufficiently broad spectrum of data, the K-K integration yields the nondegenerate  $n_2$  coefficient.<sup>100</sup>

## Four-Wave Mixing

The most general case of third-order interaction has all four interacting waves (three input and one scattered) at different frequencies. Generating and phase-matching three different laser wavelengths in an experiment is a formidable task; the benefit is often an improved signal-to-noise ratio.

The other extreme is when all four waves have identical frequency, a situation known as *degenerate four-wave mixing* (DFWM), although it is commonly (and less precisely) referred to as *four-wave mixing* (see Chap. 12, “Photorefractive Materials and Devices” and Chap. 5, “Optical Properties of Semiconductors”). DFWM is readily implemented in the laboratory, since only a single laser source is needed. There are two general cases: *nonresonant* and *resonant* DFWM. In transparent media (i.e., nonresonant) the index of refraction is usually a linear function of laser irradiance, and nonresonant DFWM (wavelength far from an absorption resonance) leads to optical phase conjugation. Phase



**FIGURE 11** Schematic diagram of a four-wave mixing experiment.

conjugation by the optical Kerr effect (Sec. 16.5) is one of the most important applications involving third-order nonlinearities.<sup>26</sup> Nonresonant DFWM leads to the formation of a phase grating due to the spatial modulation of the refractive index. Two of the beams write the phase grating while a third reads or probes the grating by diffracting from it, thereby generating a fourth beam (see Fig. 11). The diffracted beam can either be transmitted or reflected (i.e., a phase-conjugate beam) from the material in a direction determined by the wave vectors of the interacting photons. In some experiments, the writing beams also serve to read the grating. One of the difficulties in interpreting DFWM data for third-order nonlinearities is that the signal is proportional to  $|\chi^{(3)}|^2 = \Re\{\chi^{(3)}\} + \Im\{m\chi^{(3)}\}$  (i.e., NLA and NLR both contribute). Separating the effects is difficult without performing additional experiments. Techniques that study different polarizations can provide information on the symmetry properties of  $\chi^{(3)}$ .

In resonant DFWM, there is the added complication of optical absorption at the frequency of the interacting light beams.<sup>101</sup> This is an example of a cascaded  $\chi^{(1)};\chi^{(1)}$  effective third-order nonlinearity discussed in Sec. 16.9, where absorption causes population in excited states, resulting in a spatial grating due to the spatial modulation of population. In principle, both phase and absorption gratings are present in resonant DFWM. In practice, it is usually the intensity-dependent changes of population (i.e., effective  $\chi^{(3)}$ ) that dominate the nonlinear polarization, although this is not always the case.<sup>76</sup> For example, photocarrier generation in a semiconductor can alter the bulk plasma frequency and thus modulate the refractive index, leading to a strong phase grating (see Sec. 16.9).

The diffracted beam contains a wealth of information about the system under study. In nonresonant DFWM, the absolute magnitude and spectral width of the Kerr-effect nonlinearity ( $n_2$ ) can be obtained. Even more can be deduced from time-resolved DFWM, where the interacting beams are short laser pulses. If the pulses (two and sometimes three separate pulses) are delayed with respect to each other, the dynamic response of the nonlinear polarization can be measured. In resonant DFWM, the diffracted beam measures the coherent response of the optically coupled eigenstates of the system. The linewidth of the diffracted beam indicates the rate at which various physical processes broaden the transition. The nonlinear polarization can be washed out by mechanisms such as population relaxation and diffusion and scattering events associated with optically coupled states. Because of selection rules linking resonant states, various polarization geometries can be employed to study specific transitions. This can be very useful in studies of a complex system such as a semiconductor. Time-resolved experiments with short pulses provide information that complements and elucidates spectral linewidth data obtained from measurements with long duration or continuous laser beams.<sup>26,60,102</sup>

## Interferometry

Interferometric methods can be used to measure nonlinearly induced phase distortion.<sup>103,104</sup> One implementation of this approach places a sample in one path (e.g., arm) of an interferometer,

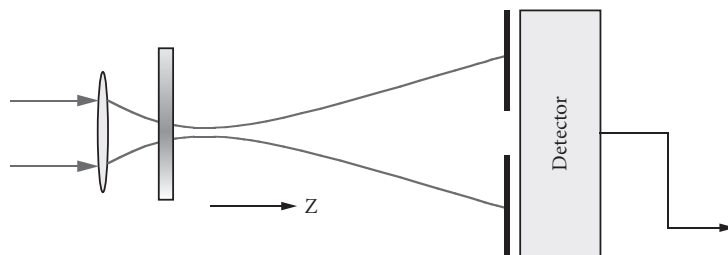
and the interference fringes are monitored as a function of irradiance. If the interferometer is set up to give a series of straight-line interference fringes for low-input irradiance (linear regime), the fringes become curved near the region of high irradiance, such as the center of a Gaussian beam. The addition of a streak camera can add time resolution.<sup>27</sup> Alternatively, a third beam can be added to the experiment. The sample is in the path of one weak beam and the strong third beam. The fringe pattern of the two weak beams is monitored as a function of sample irradiance provided by the strong beam. The relative fringe shift observed when the strong beam is present and blocked gives the optical path length change. The nonlinear phase shift can thus be determined. Interferometric experiments require excellent stability and precise alignment. When these conditions are met, sensitivities of better than  $\lambda/10^4$  induced optical path length change can be measured.

## Z-Scan

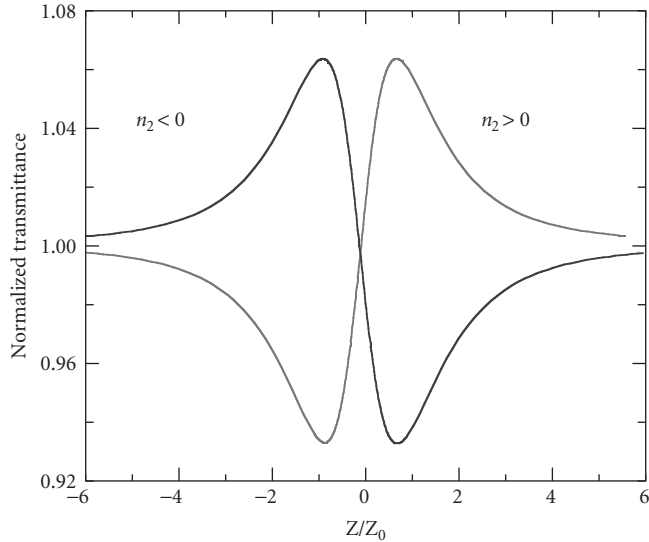
The Z-scan was developed to measure the magnitude and sign of nonlinear refraction (NLR). It is also useful for characterizing nonlinear absorption (NLA) and for separating the effects of NLR from NLA.<sup>105,106</sup> The essential geometry is shown in Fig. 12. Using a single, focused laser beam, one measures the transmittance of a sample through a partially obscuring circular aperture (Z-scan) or around a partially obscuring disk (EZ-scan<sup>107</sup>) placed in the far field. The transmittance is determined as a function of the sample position (Z) measured with respect to the focal plane. Employing a Gaussian spatial profile beam simplifies the analysis.

We illustrate how Z-scan (or EZ-scan) data is related to the NLR of a sample. Assume, for example, a material with a positive nonlinear refractive index. We start the Z-scan far from the focus at a large value of negative Z (i.e., close to the lens). The beam irradiance is low and negligible NLR occurs; the transmittance remains relatively constant near this sample position. The transmittance is normalized to unity in this linear regime as depicted in Fig. 13. As the sample is brought closer to focus, the beam irradiance increases, leading to self-focusing. This positive NLR moves the focal point closer to the lens, causing greater beam divergence in the far field. Transmittance through the aperture is reduced. As the sample is moved past the focus, self-focusing increasingly collimates the beam, resulting in enhanced transmittance through the aperture. Translating the sample farther toward the detector reduces the irradiance to the linear regime and returns the normalized transmittance to unity. Reading the data right to left, a valley followed by peak is indicative of positive NLR. In negative NLR, one finds exactly the opposite: a peak followed by a valley. This is due to laser-induced self-defocusing. Characteristic curves for both types of NLR are shown in Fig. 12. The EZ-scan reverses the peak and valley in both cases. In the far field, the largest fractional changes in irradiance occur in the wings of a Gaussian beam. For this reason, the EZ-scan can be more than an order of magnitude more sensitive than the Z-scan.

We define an easily measurable quantity  $\Delta T_{pv}$  as the difference between the normalized peak and valley transmittance:  $T_p - T_v$ . Analysis shows that variation of  $\Delta T_{pv}$  is linearly dependent on the



**FIGURE 12** Z-scan experimental arrangement.



**FIGURE 13** Representative curves depicting nonlinear refraction (both positive and negative) as measured by the Z-scan.

temporally averaged induced phase distortion, defined here as  $\Delta\Phi_0$ . If the Z-scan aperture is closed to allow linear transmission of less than 10 percent, and  $\Delta T_{pv} < 1$ :<sup>103,108</sup>

$$\Delta T_{pv} \cong 0.41 |\Delta\Phi_0| \quad (49)$$

assuming cw illumination. If the experiment is capable of resolving transmission changes  $\Delta T_{pv} \cong 1\%$ , the Z-scan will be sensitive to wavefront distortion of less than  $\lambda/250$  (i.e.,  $\Delta\Phi_0 = 2\pi/250$ ). The Z-scan has demonstrated sensitivity to a nonlinearly induced optical path length change of nearly  $\lambda/10^3$ , while the EZ-scan has shown a sensitivity of  $\lambda/10^4$ , including temporal averaging over the pulsewidth.

To this point in the discussion, we have assumed a purely refractive nonlinearity with no NLA. It has been shown that two-photon absorption will suppress the peak and enhance the valley. If NLA and NLR are present simultaneously, a numerical fitting procedure can extract both the nonlinear refractive and absorptive coefficients. Alternatively, a second Z-scan with the aperture removed (all the transmitted light collected) can independently determine the NLA. Considering 2PA only and a Gaussian input beam, the Z-scan traces out a symmetric Lorentzian shape. The so-called *open aperture* Z-scan is sensitive *only* to NLA. One can then divide the partially obscuring Z-scan data by the open aperture data to give a curve that shows only nonlinear refraction. By performing these two types of Z-scans, we can isolate NLR and NLA without the need for a complicated numerical analysis of a single data set obtained with an aperture.

## All-Optical Switching and Optical Bistability

Since the early 1980s, there has been substantial interest in third-order nonlinear optical behavior in materials because of the potential for performing high-speed switching operations—gate speeds many orders of magnitude faster than conventional electronics have been demonstrated. The possibility of increasing data rates on information networks provides the obvious motivation for this

research. A bistable optical switch has two stable output states for a given input (i.e., a specific optical power level). This has implications for applications such as optical data storage and power limiting. Both nonresonant  $\chi^{(3)}$  and resonant effective  $\chi^{(3)}$  processes have been extensively studied, primarily in semiconductors. The early work looked at bulk semiconductor behavior, but as the technology matured the emphasis shifted to specially designed optical waveguides made from suitable material. At the time of this writing, both resonant and nonresonant approaches have encountered problems that have limited practical use. The bound electronic nonlinearity responds on a femtosecond time-scale but is inherently weak. The laser irradiance must be increased to compensate, but this leads to the unwelcome presence of 2PA and associated losses. Resonant nonlinearities must involve the generation of carriers (electrons and holes). While such nonlinearities can be exceptionally strong, the speed of an optical switch depends crucially on the ability to manipulate the carriers. Generation of electron-hole pairs, for example, may dramatically affect the refractive index of a semiconductor and its ability to modulate light, but if the carriers have a long recombination lifetime the switch recovery time will be relatively slow. Other significant issues that must be weighed when comparing optical switching schemes to the all-electronic approach (i.e., transistors and integrated circuits) include device packaging density and heat removal.<sup>18,42,53,72,109,110</sup>

## 16.13 REFERENCES

1. N. Bloembergen, *Nonlinear Optics*, Addison-Wesley, Redwood City, California, 1992.
2. S. A. Akhmanov and R. V. Khokhlov, *Problems of Nonlinear Optics: Electromagnetic Waves in Nonlinear Dispersive Media*, Gordon and Breach Science Publishers, New York, 1972.
3. R. W. Boyd, *Nonlinear Optics*, Academic Press, Boston, 1992.
4. P. N. Butcher and D. Cotter, *The Elements of Nonlinear Optics*, Cambridge University Press, Cambridge and New York, 1990.
5. G. P. Agrawal, *Nonlinear Fiber Optics*, 2nd ed., Academic Press, San Diego, California, 1995.
6. W. Demtröder, M. Inguscio, and North Atlantic Treaty Organization, Scientific Affairs Division, *Applied Laser Spectroscopy*, Plenum Press, New York, 1990.
7. D. C. Hanna, M. A. Yuratich, and D. Cotter, *Nonlinear Optics of Free Atoms and Molecules*, Springer-Verlag, Berlin and New York, 1979.
8. F. A. Hopf and G. I. Stegeman, *Applied Classical Electrodynamics*, Reprint ed., Krieger Pub. Co., Malabar, Florida, 1992.
9. I.-C. Khoo, J.-F. Lam, and F. Simoni, *Nonlinear Optics and Optical Physics*, World Scientific, Singapore and River Edge, New Jersey, 1994.
10. V. S. Letokhov and V. P. Chebotava, *Nonlinear Laser Spectroscopy*, Springer-Verlag, Berlin and New York, 1977.
11. M. D. Levenson and S. Kano, *Introduction to Nonlinear Laser Spectroscopy*, Rev. ed., Academic Press, Boston, 1988.
12. S. R. Marder, J. E. Sohn, G. D. Stucky, American Chemical Society, Division of Organic Chemistry, American Chemical Society, Division of Inorganic Chemistry, and American Chemical Society, Meeting, *Materials for Nonlinear Optics: Chemical Perspectives*, American Chemical Society, Washington, D.C., 1991.
13. D. L. Mills, *Nonlinear Optics: Basic Concepts*, 2nd enl. ed., Springer, New York, 1998.
14. A. C. Newell and J. V. Moloney, *Nonlinear Optics*, Addison-Wesley, Redwood City, California, 1992.
15. E. G. Sauter, *Nonlinear Optics*, John Wiley & Sons, New York, 1996.
16. M. Schubert and B. Wilhelmi, *Nonlinear Optics and Quantum Electronics*, John Wiley & Sons, New York, 1986.
17. Y. R. Shen, *The Principles of Nonlinear Optics*, John Wiley & Sons, New York, 1984.
18. R. L. Sutherland, *Handbook of Nonlinear Optics*, Marcel Dekker, New York, 1996.
19. P. Yeh, *Nonlinear Optics and Applications*, vol. 613, Society of Photo-Optical Instrumentation Engineers, Bellingham, Washington, 1986.
20. P. Yeh, *Introduction to Photorefractive Nonlinear Optics*, John Wiley & Sons, New York, 1993.

21. F. Zernike and J. E. Midwinter, *Applied Nonlinear Optics*, John Wiley & Sons, New York, 1973.
22. B. E. A. Saleh and M. C. Teich, *Fundamentals of Photonics*, John Wiley & Sons, New York, 1991.
23. A. Yariv, *Optical Electronics in Modern Communications*, 5th ed., Oxford University Press, New York, 1997.
24. A. Yariv, *Quantum Electronics*, 3rd ed., John Wiley & Sons, New York, 1989.
25. A. Yariv and P. Yeh, *Optical Waves in Crystals: Propagation and Control of Laser Radiation*, John Wiley & Sons, New York, 1984.
26. R. A. Fisher, *Optical Phase Conjugation*, Academic Press, New York, 1983.
27. J.-C. Diels and W. Rudolph, *Ultrashort Laser Pulse Phenomena: Fundamentals, Techniques, and Applications on a Femtosecond Time Scale*, Academic Press, San Diego, 1996.
28. B. I. A. Zel'dovich, N. F. Pilipetskii, and V. V. Shkunov, *Principles of Phase Conjugation*, Springer-Verlag, Berlin and New York, 1985.
29. B. S. Wherrett and P. G. Harper, *Nonlinear Optics*, Academic Press, London, 1977.
30. E. Garmire and A. Kost, "Nonlinear Optics in Semiconductors I & II," in *Semiconductors and Semimetals*, R. K. Wilardson and E. R. Webber, eds., Academic Press, 1999.
31. M. Sheik-Bahae and E. W. Van Stryland, "Optical Nonlinearities in the Transparency Region of Bulk Semiconductors," in *Nonlinear Optics in Semiconductors I*, vol. 58, *Semiconductors and Semimetals*, E. Garmire and A. Kost, eds., Academic Press, 1999.
32. E. W. Van Stryland, A. L. Smirl, T. F. Boggess, M. J. Soileau, B. S. Wherrett, and F. Hopf, "Weak-Wave Retardation and Phase-Conjugate Self-Defocusing in Si," in *Picosecond Phenomena III*, R. M. H. K. B. Eisenthal, W. Kaiser, and A. Laubereau, eds., Springer-Verlag, Berlin, 1982.
33. J. S. Toll, "Casuality and Dispersion Relation: Logical Foundation," *Phys. Rev.* **104**:1760–1770 (1956).
34. H. M. Nussenzveig, *Causality and Dispersion Relations*, Academic Press, New York, 1972.
35. P. J. Caspers, "Dispersion Relations for Nonlinear Response," *Phys. Rev. A.* **133**:1249 (1964).
36. S. M. Kogan, "On the Electromagnetics of Weakly Nonlinear Media," *Sov. Phys. JETP* **16**:217 (1963).
37. P. J. Price, "Theory of Quadratic Response Functions," *Phys. Rev.* **130**:1792 (1964).
38. F. L. J. Ridener and R. H. J. Good, "Dispersion Relations for Nonlinear Systems or Arbitrary Degree," *Phys. Rev. B* **11**:2768 (1975).
39. D. C. Hutchings, M. Sheik-Bahae, D. J. Hagan, and E. W. Van Stryland, "Kramers-Kronig Relations in Nonlinear Optics," *Optical and Quantum Electronics* **24**:1–30 (1992).
40. F. Bassani and S. Scandolo, "Dispersion-Relations and Sum-Rules in Nonlinear Optics," *Phys. Rev. B-Condensed Matter* **44**:8446–8453 (1991).
41. D. A. B. Miller, C. T. Seaton, M. E. Prise, and S. D. Smith, "Band-Gap-Resonant Non-Linear Refraction in Iii-V Semiconductors," *Phys. Rev. Lett.* **47**:197–200 (1981).
42. B. S. Wherrett, A. C. Walker, and F. A. P. Tooley, "Nonlinear Refraction for CW Optical Bistability," in *Optical Nonlinearities and Instabilities in Semiconductors*, H. Haug, ed., Academic Press, Boston, 1988.
43. M. Sheik-Bahae, D. J. Hagan, and E. W. Van Stryland, "Dispersion and Band-Gap Scaling of the Electronic Kerr Effect in Solids Associated with 2-Photon Absorption," *Phys. Rev. Lett.* **65**:96–99 (1990).
44. M. Sheik-Bahae, D. C. Hutchings, D. J. Hagan, and E. W. Van Stryland, "Dispersion of Bound Electronic Nonlinear Refraction in Solids," *IEEE J. Quantum Electron.* **27**:1296–1309 (1991).
45. M. Sheik-Bahae, "Nonlinear Optics of Bound Electrons in Solids," in *Nonlinear Optical Materials*, J. V. Moloney, ed., Springer, New York, 1998.
46. D. J. Moss, E. Ghahramani, J. E. Sipe, and H. M. Van Driel, "Band-Structure Calculation of Dispersion and Anisotropy in  $\chi^{(3)}$  For 3rd-Harmonic Generation in Si, Ge, and GaAs," *Phys. Rev. B* **41**:1542–1560 (1990).
47. R. Adair, L. L. Chase, and S. A. Payne, "Nonlinear Refractive-Index Measurements of Glasses Using 3-Wave Frequency Mixing," *Journal of the Optical Society of America B-Optical Physics* **4**:875–881 (1987).
48. R. Adair, L. L. Chase, and S. A. Payne, "Nonlinear Refractive-Index of Optical-Crystals," *Phys. Rev. B-Condensed Matter* **39**:3337–3350 (1989).
49. S. R. Friberg, A. M. Weiner, Y. Silberberg, B. G. Sfez, and P. S. Smith, "Femtosecond Switching in a Dual-Core-Fiber Nonlinear Coupler," *Opt. Lett.* **13**:904–906 (1988).
50. M. J. Weber, D. Milam, and W. L. Smith, "Non-Linear Refractive-Index of Glasses and Crystals," *Optical Engineering* **17**:463–469 (1978).

51. L. F. Mollenauer, R. H. Stolen, and J. P. Gordon, *Phys. Rev. Lett.* **45**:1095 (1980).
52. D. E. Spence, P. N. Kean, and W. Sibbett, "60-Fsec Pulse Generation from a Self-Mode-Locked Ti-Sapphire Laser," *Opt. Lett.* **16**:42–44 (1991).
53. H. M. Gibbs, *Optical Bistability: Controlling Light with Light*, Academic Press, Orlando, Florida, 1985.
54. M. N. Islam, *Ultrafast Fiber Switching Devices and Systems*, Cambridge University Press, Cambridge and New York, 1992.
55. N. L. Boling, A. J. Glass, and A. Owyong, "Empirical Relationships for Predicting Nonlinear Refractive Index Changes in Optical Solids," *IEEE J. Quantum Electron.* **QE-14**:601 (1978).
56. P. P. Ho and R. R. Alfano, "Optical Kerr Effect in Liquids," *Phys. Rev. A* **20**:2170 (1979).
57. F. A. Hopf and G. I. Stegeman, *Applied Classical Electrodynamics*, John Wiley & Sons, New York, 1985.
58. J. F. Reintjes, *Nonlinear Optical Parametric Processes in Liquids and Gases*, Academic Press, New York, 1984.
59. M. D. Levenson, *Introduction to Nonlinear Laser Spectroscopy*, Academic Press, New York, 1982.
60. W. Kaiser and D. H. Auston, *Ultrashort Laser Pulses: Generation and Applications*, 2nd ed., Springer, Berlin and New York, 1993.
61. M. Cardona and G. Güntherodt, *Light Scattering in Solids VI: Recent Results, Including High-Tc Superconductivity*, Springer-Verlag, Berlin and New York, 1991.
62. J. J. Valentini, "Laser Raman Techniques," in *Optical Engineering: Laser Spectroscopy and Its Applications*, vol. 11, L. J. Radziemski, R. W. Solarz, and J. A. Paisner, eds., Dekker, New York, 1987.
63. D. A. Long, *Raman Spectroscopy*, McGraw-Hill, New York, 1977.
64. G. L. Easley, *Cohernet Raman Spectroscopy*, Pergamon, Oxford, 1981.
65. L. A. Woodward, *Raman Spectroscopy: Theory and Practice*, H. A. Szymanski, ed., Plenum, New York, 1987.
66. E. W. Van Stryland and L. Chase, "Two-Photon Absorption: Inorganic Materials," in *Handbook of Laser Science and Technology, Supplement 2, Optical Materials*, M. Weber, ed., CRC Press, 1994.
67. E. W. Van Stryland, H. Vanherzeele, M. A. Woodall, M. J. Soileau, A. L. Smirl, S. Guha, and T. F. Boggess, "2 Photon-Absorption; Nonlinear Refraction; and Optical Limiting in Semiconductors," *Optical Engineering*, **24**:613–623 (1985).
68. E. W. Van Stryland, M. A. Woodall, H. Vanherzeele, and M. J. Soileau, "Energy Band-Gap Dependence of 2-Photon Absorption," *Opt. Lett.* **10**:490–492 (1985).
69. B. S. Wherrett, "Scaling Rules for Multiphoton Interband Absorption in Semiconductors," *Journal of the Optical Society of America B-Optical Physics* **1**:67–72 (1984).
70. J. I. Pankove, *Optical Processes in Semiconductors*, Dover, New York, 1971.
71. C. Kittel, *Introduction to Solid State Physics*, 7th ed., John Wiley & Sons, New York, 1996.
72. A. Miller, D. A. B. Miller, and S. D. Smith, "Dynamic Non-Linear Optical Processes in Semiconductors," *Advances in Physics* **30**:697–800 (1981).
73. H. Haug and S. W. Koch, *Quantum Theory of the Optical and Electronic Properties of Semiconductors*, 3rd ed., World Scientific, Singapore, 1994.
74. W. W. Chow, S. W. Koch, and M. Sargent, *Semiconductor-Laser Physics*, corrected printing ed., Springer-Verlag, Berlin and New York, 1997.
75. L. Banyai and S. W. Koch, "A Simple Theory for the Effects of Plasma Screening on the Optical Spectra of Highly Excited Semiconductors," *Zeitschrift Fur Physik B-Condensed Matter* **63**:283–291 (1986).
76. R. K. Jain and M. B. Klein, "Degenerate Four-Wave Mixing in Semiconductors," in *Optical Phase Conjugation*, R. A. Fisher, ed., Academic Press, New York, 1983.
77. J. I. Steinfeld, *Laser and Coherence Spectroscopy*, Plenum Press, New York, 1978.
78. M. Sargent, M. O. Scully, and W. E. Lamb, *Laser Physics*, Addison-Wesley, Reading, Massachusetts and London, 1977.
79. J. Feinberg, "Optical Phase Conjugation in Photorefractive Materials," in *Optical Phase Conjugation*, R. A. Fisher, ed., Academic Press, New York, 1983.
80. J. E. Millard, M. Ziari, and A. Partovi, "Photorefractivity in Semiconductors," in *Nonlinear Optics in Semiconductors I*, vol. 58, *Semiconductors and Semimetals*, E. Garmire and A. Kost, eds., Academic Press, 1999.



81. R. DeSalvo, D. J. Hagan, M. Sheik-Bahae, G. Stegeman, E. W. Van Stryland, and H. Vanherzeele, "Self-Focusing and Self-Defocusing by Cascaded 2nd-Order Effects in Ktp," *Opt. Lett.* **17**:28–30 (1992).
82. N. R. Belashenkov, S. V. Gagarinskii, and M. V. Inochkin, "Nonlinear Refraction of Light on Second-Harmonic Generation," *Opt. Spektrosk.* **66**:1383–1386 (1989).
83. G. I. Stegeman, M. Sheik-Bahae, E. Van Stryland, and G. Assanto, "Large Nonlinear Phase-Shifts in 2nd-Order Nonlinear-Optical Processes," *Opt. Lett.* **18**:13–15 (1993).
84. E. W. Van Stryland, "Third-Order and Cascaded Nonlinearities," presented at Laser Sources and Applications, 1996.
85. G. Assanto, G. Stegeman, M. Sheik-Bahae, and E. Van Stryland, "All-Optical Switching Devices Based on Large Nonlinear Phase-Shifts from 2nd Harmonic-Generation," *Appl. Phys. Lett.* **62**:1323–1325 (1993).
86. G. Assanto, G. I. Stegeman, M. Sheik-Bahae, and E. Van Stryland, "Coherent Interactions for All-Optical Signal-Processing via Quadratic Nonlinearities," *IEEE J. Quantum Electron.* **31**:673–681 (1995).
87. W. Torruellas, B. Lawrence, and G. I. Stegeman, "Self-Focusing and 2d Spatial Solutions in Pts," *Electronics Letters* **32**:2092–2094 (1996).
88. W. E. Torruellas, Z. Wang, D. J. Hagan, E. W. Vanstryland, G. I. Stegeman, L. Torner, and C. R. Menyuk, "Observation of 2-Dimensional Spatial Solitary Waves in a Quadratic Medium," *Phys. Rev. Lett.* **74**:5036–5039, 1995.
89. L. J. Qian, X. Liu, and F. W. Wise, "Femtosecond Kerr-Lens Mode Locking with Negative Nonlinear Phase Shifts," *Opt. Lett.* **24**:166–168, 1999.
90. M. Sheik-Bahae, A. A. Said, D. J. Hagan, M. J. Soileau, and E. W. Van Stryland, "Nonlinear Refraction and Optical Limiting in Thick Media," *Optical Engineering* **30**:1228–1235 (1991).
91. A. E. Kaplan, "External Self-Focusing of Light by a Nonlinear Layer," *Radiophys. Quantum Electron.* **12**:692–696 (1969).
92. J. H. Marburger, in *Progress in Quantum Electronics*, J. H. Sanders and S. Stenholm, eds., Pergamon Press, New York, 1977.
93. H. A. Haus, J. G. Fujimoto, and E. P. Ippen, "Analytic Theory of Additive Pulse and Kerr Lens Mode-Locking," *IEEE J. Quantum Electron.* **28**:2086–2096 (1992).
94. G. P. Agrawal, *Nonlinear Fiber Optics*. Academic Press, Boston, 1989.
95. A. Barthelemy, S. Maneuf, and C. Froehly, "Soliton Propagation and Self-Confinement of Laser-Beams by Kerr Optical Non-Linearity," *Optics Communications* **55**:201–206 (1985).
96. S. Maneuf, A. Barthelemy, and C. Froehly, "Soliton Beam Propagation: Space-Time Behavior and Spectral Features," *Journal of Optics* **17**:139–145 (1986).
97. J. J. Hopfield, J. M. Worlock, and K. Park, "Two-Quantum Absorption Spectrum of KI," *Phys. Rev. Lett.* **11**:414 (1963).
98. J. A. Bolger, A. K. Kar, B. S. Wherrett, R. Desalvo, D. C. Hutchings, and D. J. Hagan, "Nondegenerate 2-Photon Absorption-Spectra of Znse; Zns and Zno," *Optics Communications* **97**:203–209 (1993).
99. P. Maker, R. Terhune, and C. Savage, "Intensity-Dependent Changes in the Refractive Index of Liquids," *Phys. Rev. Lett.* **12**:507 (1964).
100. D. J. Hagan, E. Miesak, R. Negres, S. Ross, J. Lim, and E. W. Van Stryland, "Nonlinear Spectrometry of Chromophores for Optical Limiting," *SPIE Proceedings* **3472**:80–90 (1998).
101. R. L. Abrams, J. F. Lam, R. C. Lind, D. G. Steel, and P. F. Liao, "Phase Conjugation and High Resolution Spectroscopy by Resonant Degenerate Four-Wave Mixing," in *Optical Phase Conjugation*, R. A. Fisher, ed., Academic Press, New York, 1983.
102. J. Shah, *Ultrafast Spectroscopy of Semiconductors and Semiconductor Nanostructures*, Springer, Berlin and New York, 1996.
103. M. J. Weber, D. Milam, and W. L. Smith, "Nonlinear Refractive Index of Glasses and Crystals," *Opt. Eng.* **463** (1978).
104. M. J. Moran, C. Y. She, and R. L. Carmen, "Interferometric Measurements of the Nonlinear Refractive Index Coefficient Relative to CS<sub>2</sub> in the Laser System Related Materials," *IEEE J. Quantum Electron.* **11**:259 (1975).
105. M. Sheik-Bahae, A. A. Said, T. H. Wei, D. J. Hagan, and E. W. Van Stryland, "Sensitive Measurement of Optical Nonlinearities Using a Single Beam," *IEEE J. Quantum Electron.* **26**:760–769 (1990).

106. E. W. Van Stryland and M. Sheik-Bahae, "Z-Scan," in *Characterization Techniques and Tabulations for Organic Nonlinear Optical Materials*, M. G. Kuzyk and C. W. Dirk, eds., Marcel Dekker, New York, 1998.
107. T. Xia, D. J. Hagan, M. Sheik-Bahae, and E. W. Van Stryland, "Eclipsing Z-Scan Measurement of  $\Lambda/10(4)$  Wave-Front Distortion," *Opt. Lett.* **19**:317–319 (1994).
108. M. Sheik-Bahae, A. A. Said, and E. W. Van Stryland, "High-Sensitivity; Single-Beam N2 Measurements," *Opt. Lett.* **14**:955–957 (1989).
109. G. Stegeman and E. Wright, "All-Optical Waveguide Switching," *Opt. and Quantum Electron.* **22**:95 (1990).
110. G. I. Stegeman, A. Villeneuve, J. Kang, J. S. Aitchison, C. N. Ironside, K. Alhemyari, C. C. Yang, C. H. Lin, H. H. Lin, G. T. Kennedy, R. S. Grant, and W. Sibbett, "AlGaAs Below Half Bandgap: The Silicon of Nonlinear-Optical Materials," *International Journal of Nonlinear Optical Physics* **3**:347–371 (1994).

*This page intentionally left blank*

---

# CONTINUOUS-WAVE OPTICAL PARAMETRIC OSCILLATORS

---

Majid Ebrahim-Zadeh

*ICFO—Institut de Ciències Fòniques  
Mediterranean Technology Park  
Barcelona, Spain, and  
Institució Catalana de Recerca i Estudis Avançats (ICREA)  
Passeig Lluís Companys  
Barcelona, Spain*

---

## 17.1 INTRODUCTION

---

Since the publication of an earlier review on optical parametric oscillators (OPOs) in 2000,<sup>1</sup> there has been remarkable progress in the technological development and applications of OPO devices. Once considered an impractical approach for the generation of coherent radiation, OPOs have now been finally transformed into truly viable, state-of-the-art light sources capable of accessing difficult spectral regions and addressing real applications beyond the reach of conventional lasers. While the first experimental demonstration of an OPO was reported in 1965,<sup>2</sup> for nearly two decades thereafter there was little or no progress in the practical development of OPO devices, owing to the absence of suitable nonlinear materials and laser pump sources. With the advent of a new generation of birefringent nonlinear crystals, most notably  $\beta$ -BaB<sub>2</sub>O<sub>4</sub> (BBO), LiB<sub>3</sub>O<sub>5</sub> (LBO), and KTiOPO<sub>4</sub> (KTP), but also KTiOAsO<sub>4</sub> (KTA) and RbTiOAsO<sub>4</sub> (RTA) in the mid-1980s, and advances in solid-state laser technology, there began a resurgence of interest in OPOs as potential alternatives to conventional lasers for the generation of coherent radiation in new spectral regions. The high optical damage threshold, moderate optical nonlinearity, and favorable phase-matching properties of the newfound materials led to important breakthroughs in OPO technology. In the years to follow, tremendous progress was achieved in the development of OPO devices, particularly in the pulsed regime, and a variety of OPO systems from the nanosecond to the ultrafast picosecond and femtosecond timescales, and operating from the near-ultraviolet (near-UV) to the infrared (IR) were rapidly developed. These developments led to the availability of a wide range of practical OPO devices and their deployment in new applications, with some systems finding their way to the commercial market. A decade later, in the mid-1990s, the emergence of quasi-phase-matched (QPM) ferroelectric nonlinear crystals, particularly periodically poled LiNbO<sub>3</sub> (PPLN) stimulated new impetus for the advancement of continuous-wave (cw) OPO devices, traditionally the most challenging regime for OPO operation due to almost negligible nonlinear gains available under cw pumping. The flexibility offered by grating-engineered QPM materials, allowing access to the highest nonlinear tensor coefficients, combined with noncritical phase matching (NCPM) and long interaction lengths (>50 mm in PPLN), enabled the low available nonlinear gains to be overcome, hence permitting the development of practical cw OPOs in a variety of resonance configurations. As such, the advent of QPM

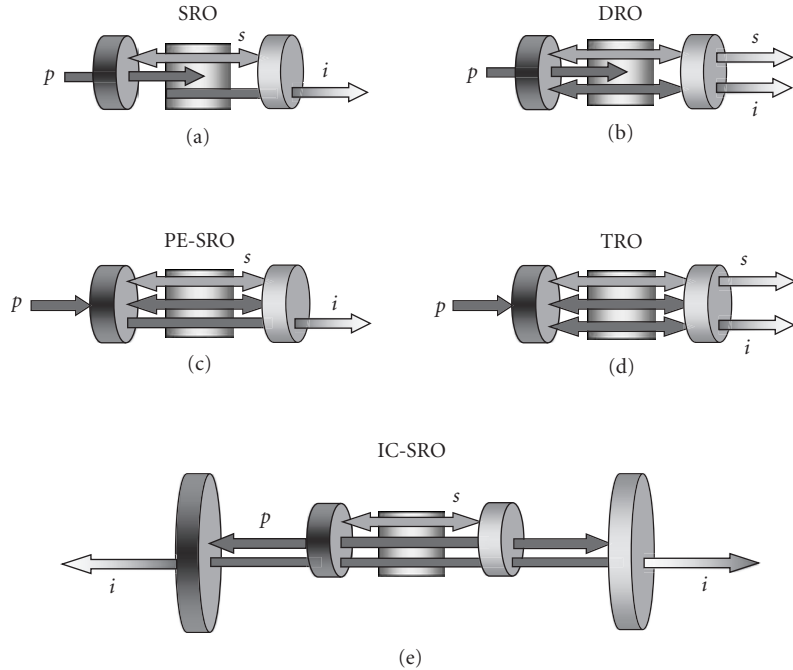
materials, most notably PPLN, but also periodically poled KTP (PPKTP), RbTiOAsO<sub>4</sub> (PPRTA), and LiTaO<sub>3</sub> (PPLT), has had an unparalleled impact on cw OPO technology. Combined with advances in novel high-power solid-state crystalline, semiconductor, and fiber pump sources over the past decade, these developments have led to the practical realization of a new class of cw OPOs with previously unattainable performance capabilities with regard to wavelength coverage, output power and efficiency, frequency and power stability, spectral and spatial coherence, and fine frequency tuning.

With their exceptional spectral coverage and tuning versatility, temporal flexibility from the cw to femtosecond timescales, practical performance parameters, and compact solid-state design, OPO devices have now been firmly established as truly competitive alternatives to conventional lasers and other technologies for the generation of widely tunable coherent radiation in difficult spectral and temporal domains. In the current state of technology, OPO devices can provide spectral access from ~400 nm in the ultraviolet (UV) to ~12 μm in the mid-infrared (mid-IR), as well as the terahertz (THz) spectral region. They can also provide temporal output from the cw and long-pulse microsecond regime to nanosecond, picosecond, and ultrafast sub-20 fs timescales. Many of the developed OPO systems are now routinely deployed in a variety of applications including spectroscopy, optical microscopy, environmental trace gas detection and monitoring, life sciences, biomedicine, optical frequency metrology and synthesis, and imaging.

The aim of this chapter is to provide an overview of the advances in OPO device technology and applications since the publication of the earlier review in 2000.<sup>1</sup> The chapter is concerned only with the developments after 2000, since many of the important advances in this area prior to that date can already be found in the previous treatment<sup>1</sup> as well as other reviews on the subject.<sup>3–10</sup> Because of limited scope, and given that most of the important advances over the last decade have been in the CW operating regime, the chapter is focused only on a discussion of cw OPOs. Reviews on pulsed and ultrafast OPOs can be found elsewhere.<sup>3,4,6–10</sup> This chapter also does not include a description of the fundamental concepts in nonlinear and crystal optics, parametric generation, amplification and gain, or a comprehensive description of the design criteria and operating principles of OPO devices, which have been the subject of several earlier treatments.<sup>11–16</sup>

## 17.2 CONTINUOUS-WAVE OPTICAL PARAMETRIC OSCILLATORS

Of the different types of OPO devices developed to date, advancement of practical OPOs in the cw operating regime has been traditionally most difficult, since the substantially lower nonlinear gains available under cw pumping necessitate the use of high-power cw pump laser or the deployment of multiple-resonant cavities to reach operation threshold. As in a conventional laser oscillator, the OPO is characterised by a threshold condition, defined by the pumping intensity at which the growth of the parametric waves in one round-trip of the optical cavity just balances the total loss in that round-trip. Once threshold has been surpassed, coherent light at macroscopic levels can be extracted from the oscillator. In order to provide feedback in an OPO, a variety of resonance schemes may be deployed by suitable choice of mirrors forming the optical cavity, as illustrated in Fig. 1a to e. The mirrors may be highly reflecting at only one of the parametric waves (*signal* or *idler*, but not both), as in Fig. 1a, in which case the device is known as a *singly resonant oscillator* (SRO). This configuration is characterised by the highest cw operation threshold. In order to reduce threshold, alternative resonator schemes may be employed where additional optical waves are resonated in the optical cavity. These include the *doubly resonant oscillator* (DRO), Fig. 1b, in which both the signal and idler waves are resonant in the optical cavity, and the *pump-resonant* or *pump-enhanced* SRO, Fig. 1c, where the *pump* as well as one of the generated waves (signal or idler) is resonated. In an alternative scheme, Fig. 1d, the pump may be resonated together with both parametric waves, in which case the device is known as a *triply resonant oscillator* (TRO). Such schemes can bring about substantial reductions in threshold from the cw SRO configuration, with the TRO offering the lowest operation threshold. In an alternative scheme, the external pump power threshold for a cw SRO may also be substantially reduced by deploying internal pumping, where the OPO is placed inside

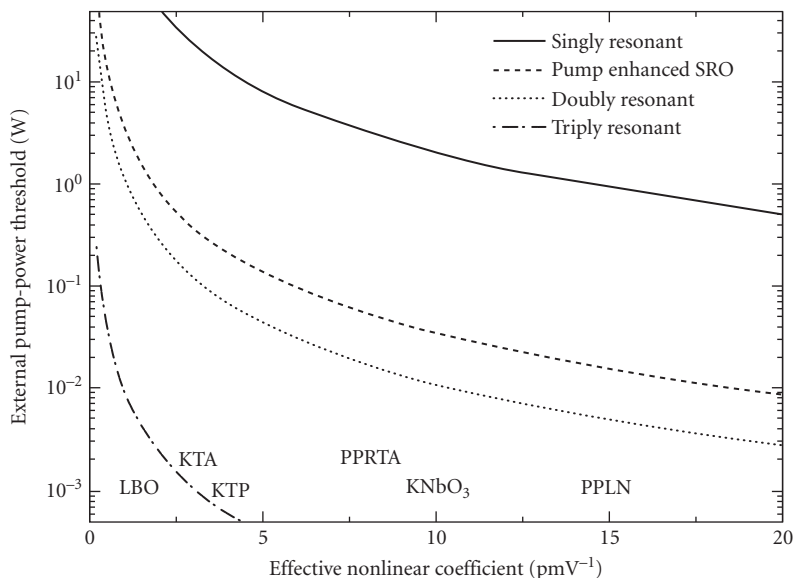


**FIGURE 1** Cavity resonance configurations for cw OPOs. The symbols  $p$ ,  $s$ , and  $i$  denote pump, signal, and idler, respectively.

a minimally output-coupled pump laser. A schematic of such an *intracavity SRO (IC-SRO)* is illustrated in Fig. 1e.

The comparison of steady-state threshold for conventional externally pumped cw OPOs under different resonance schemes is shown in Fig. 2, where the calculated external pump power threshold is plotted as a function of the effective nonlinear coefficient of several materials including LBO, KTA, KTP, KNbO<sub>3</sub>, PPLN, and PPRTA. From the plot, it is clear that for the majority of birefringent materials the attainment of cw SRO threshold requires pump powers on the order of tens of watts, well outside the range of the most widely available cw laser sources. However, in the case of PPLN, the cw SRO threshold is substantially reduced to acceptable levels below ~1 W, bringing operation of cw SROs within the convenient range of widespread cw solid-state pump lasers. With the cw PE-SRO, considerably lower thresholds can be achieved, from a few hundred milliwatts to ~1 W for birefringent materials and below ~100 mW for PPLN. In the case of cw DRO, still lower thresholds of the order of 100 mW are attainable with birefringent materials, with only a few milliwatts for PPLN, whereas with the cw TRO, thresholds from below 1 mW to a few milliwatts can be obtained in birefringent materials.

It is thus clear that practical operation of cw OPOs in SRO configurations is generally beyond the reach of birefringent materials, but requires DRO, TRO, and PE-SRO cavities. On the other hand, implementation of cw SROs necessitates the use of PPLN or similar QPM materials, offering enhanced optical nonlinearities, and long interaction lengths under NCPM. However, the threshold reduction from SRO to PE-SRO, DRO, and TRO cavity configurations is often achieved at the expense of increased spectral and power instability in the OPO output arising from the difficulty in maintaining resonance for more than one optical wave in a single optical cavity. For this reason, the cw SRO offers the most direct route to the attainment of high output stability and spectral control without stringent demands on the frequency stability of the laser pump source. On the other hand,



**FIGURE 2** Calculated minimum thresholds for different OPO resonance configurations versus the effective nonlinear coefficients in various nonlinear materials. The calculation assumes confocal focusing and loss values that are typically encountered in experimental cw OPOs, the finesse representing round-trip power losses of approximately 2.0 percent. The plots correspond to a pump wavelength of 800 nm, degenerate operation, a pump refractive index of  $\sim 1.7$ , a crystal length of 20 mm, signal and idler cavity finesse of  $\sim 300$ , and a pump enhancement factor of  $\sim 30$ . In the case of PE-SRO and TRO, the enhancement factor of 30 represents the maximum enhancement attainable with parasitic losses of  $\sim 3$  percent at the pump.<sup>17</sup>

practical implementation of cw PE-SRO, DRO, and TRO requires active stabilization techniques to control output power and frequency stability, with the PE-SRO offering the most robust configuration for active stabilization and TRO representing the most difficult in practice. In addition, practical operation of OPOs in multiple resonant cavities can only be achieved using stable, single-frequency pump lasers and such devices also require more complex protocols for frequency tuning and control than the cw SRO. More detailed description of the different resonance and pumping schemes for OPOs and analytical treatment of tuning mechanisms, spectral behavior, frequency control, and stabilisation can be found in an earlier review.<sup>1</sup>

## Singly Resonant Oscillators

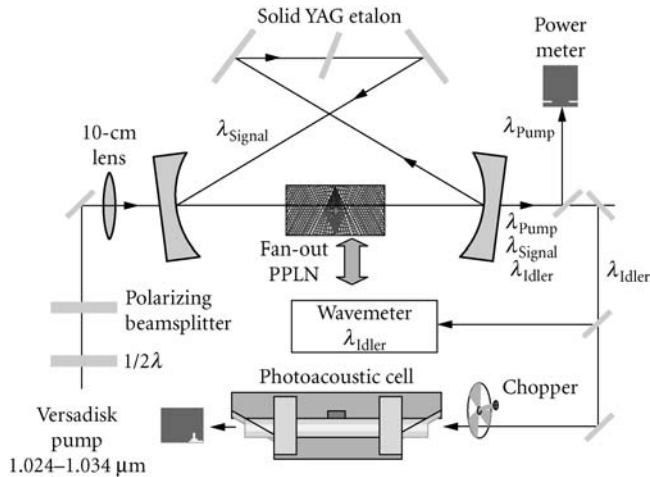
By deploying the intracavity pumping scheme using a Ti:sapphire laser in combination with a 20-mm PPKTP crystal, Edwards et al.<sup>18</sup> reported a cw IC-SRO capable of providing up to 455 mW of non-resonant infrared idler power at a down-conversion efficiency of 87 percent. Using a combination of pump tuning at room temperature and crystal temperature tuning, idler (signal) coverage in the 2.23 to 2.73  $\mu\text{m}$  (1.14 to 1.27  $\mu\text{m}$ ) spectral ranges was demonstrated. By configuring the Ti:sapphire pump laser and the SRO in ring cavity geometries and using intracavity etalons, 115 mW of unidirectional, single-frequency idler power was generated at 2.35  $\mu\text{m}$  with mode-hop-free operating time intervals of about 10 s under free-running conditions. The resonant signal was measured to have a linewidth  $< 15$  MHz for a pump linewidth  $< 25$  MHz.

The advent of PPLN with large effective nonlinearity ( $d_{\text{eff}} \sim 15$  pm/V) and long interaction lengths (currently up to 80 mm) under NCPM has enabled the development of cw SROs in conventional

external pumping configurations using more commonly available, moderate- to high-power solid-state pump sources. By deploying a fixed-frequency, cw, single-mode Nd:YVO<sub>4</sub> pump laser at 1.064  $\mu\text{m}$ , Bisson et al.<sup>19</sup> developed a portable source for mid-IR photoacoustic spectroscopy based on a PPLN cw SRO by using discrete mode-hop tuning of the idler. The SRO, based on a 50-mm PPLN crystal with fanned grating ( $\Lambda = 29.3$  to  $30.1 \mu\text{m}$ ), was configured in a ring cavity, and frequency selection and fine tuning was implemented using solid or air-spaced intracavity etalons. With an uncoated, 400- $\mu\text{m}$ -thick, solid Nd:YAG etalon, a total mode-hop-tuning range of  $\sim 4 \text{ cm}^{-1}$  for the idler in discrete steps of  $0.02$  to  $0.1 \text{ cm}^{-1}$  was achieved by rotation of the etalon. The SRO could deliver a maximum idler power of  $\sim 120 \text{ mW}$  at a pump depletion of 40 to 50 percent for 6 W of pump power. Using the mode-hop-tuned idler output near 3.3  $\mu\text{m}$ , photoacoustic spectroscopy of the methane Q branch was performed at atmospheric pressure by simultaneous tuning of the PPLN crystal combined with etalon rotation. A total of four etalon scans covering  $\sim 10 \text{ cm}^{-1}$  was necessary to trace the Q branch spectrum. In an effort to achieve a constant tuning rate as well as minimize insertion loss due to etalon rotation, which in turn leads to mode hops arising from variable heating of the PPLN crystal due to the changes in intracavity power, an alternative air-spaced fused silica etalon with  $\sim 0.5$  to  $1.5 \text{ mm}$  spacing and  $\sim 5$  percent reflectivity at the signal ( $\sim 1.57 \mu\text{m}$ ) was also employed in the present device. While resulting in a higher oscillation threshold ( $\sim 4 \text{ W}$ ) and lower idler output ( $\sim 80 \text{ mW}$ ), the combination of PPLN tuning and piezoelectric scan of the etalon over a distance of 3  $\mu\text{m}$  (at 1.5 mm separation) yielded a total mode-hop tuning range of  $\sim 14 \text{ cm}^{-1}$  for the idler at a constant tuning rate and in discrete steps of  $0.1 \text{ cm}^{-1}$ , providing sufficient resolution for atmospheric sensing and pressure-broadened spectroscopy. The measured linewidth of the idler was  $< 10 \text{ MHz}$  with a passive stability of  $\sim 50 \text{ MHz}$  over 30 s.

By using a 10-W cw single-frequency diode-pumped Nd:YAG laser at 1.064  $\mu\text{m}$ , Van Herpen et al.<sup>20</sup> demonstrated a cw SRO based on PPLN with a mid-IR idler tuning range of 3.0 to 3.8  $\mu\text{m}$ . The SRO, configured in a ring cavity and using a crystal with fanned grating ( $L = 50 \text{ mm}$ ,  $\Lambda = 29.3$  to  $30.1 \mu\text{m}$ ) exhibited a pump power threshold of  $\sim 3 \text{ W}$  and could provide a maximum idler output power of 1.5 W at 3.3  $\mu\text{m}$  for 9 W of pump power. The combination of the single-mode pump laser, a ring cavity for the SRO, and the inclusion of an intracavity air-spaced etalon enabled mode-hop-free tuning of the idler over 12 GHz by tuning the pump frequency over 24 GHz, with the idler mode-hop tuning range limited by mode hopping in the pump laser. Under this condition, 700 mW of single-frequency, smoothly tunable idler power could be provided by the SRO. In a later experiment,<sup>21</sup> using the same PPLN crystal and identical cavity design for the SRO, the authors were able to improve the idler output power in the 3.0 to 3.8  $\mu\text{m}$  range by increasing the available Nd:YAG pump power to 15 W and by optimizing pump focusing and the SRO cavity length. The SRO similarly exhibited a cw power threshold of  $\sim 3 \text{ W}$ , but could provide 2.2 W of idler power for 10.5 W of input pump power. The coarse and fine tuning properties of this SRO were similar to the earlier device. For fine tuning, an intracavity air-spaced etalon with variable spacing of 0.2 to 3 mm (FSR = 50 to 750 GHz) was used. Continuous scanning of etalon spacing resulted in discrete mode-hop tuning of the idler over 100 GHz. With a 400- $\mu\text{m}$  uncoated solid YAG etalon (FSR = 207 GHz), an idler mode-hop tuning range of  $10 \text{ cm}^{-1}$  in steps of  $0.02$  to  $0.1 \text{ cm}^{-1}$  (0.6 to 3 GHz) could be obtained by rotation of the etalon. Subsequently, using the same pump laser, the authors reported a cw SRO based on a multigrating PPLN crystal ( $\Lambda = 25.9$  to  $28.7 \mu\text{m}$ ) and providing extended idler coverage into the 3.7 to 4.7  $\mu\text{m}$  spectral range in the mid-IR.<sup>22</sup> The ring-cavity SRO exhibited an oscillation threshold of between 5 and 7.5 W over this spectral range and for an input pump power of 11 W could provide a maximum idler output of 1.2 W at 3.9  $\mu\text{m}$ , decreasing to 120 mW at 4.7  $\mu\text{m}$ . The increase in SRO threshold and corresponding decrease in output power were attributed to the increasing idler absorption in PPLN at longer wavelengths toward 5  $\mu\text{m}$ . With the inclusion of the same 400- $\mu\text{m}$  uncoated YAG etalon to stabilize the resonant signal frequency, continuous mode-hop free tuning of the idler was achieved by tuning the pump frequency over 24 GHz, but with a reduction in idler power by as much as 50 percent. Discontinuous mode-hop tuning of the idler output could also be obtained through rotation of the intracavity etalon. In a later report, the use of a tunable high-power ( $> 20 \text{ W}$ ) diode-pumped Yb:YAG laser in combination with two PPLN crystals with fanned gratings ( $\Lambda = 28.5$  to  $29.9 \mu\text{m}$ ) and two sets of OPO mirrors enabled the generation of widely tunable idler radiation with a total tuning range of 2.6 to 4.66  $\mu\text{m}$ , and at increased

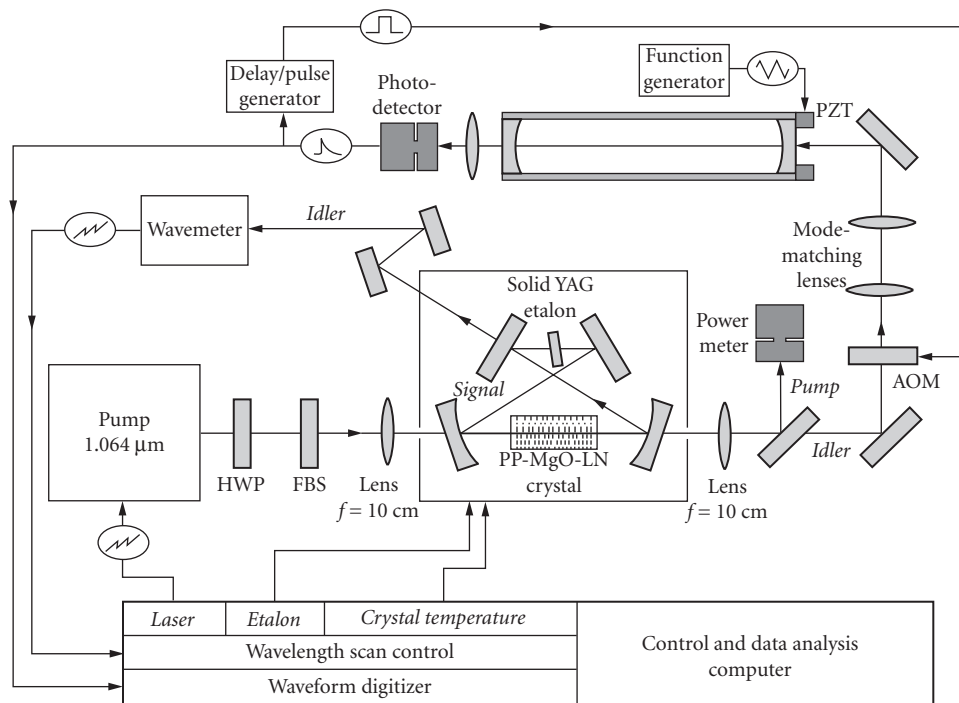




**FIGURE 3** Experimental setup of the cw SRO. The pump wavelength varies from 1024 to 1034 nm and the idler wavelength from 2.6 to 4.7  $\mu\text{m}$ . A pump rejecter mirror separates the pump light from the idler and signal beams, after which the idler beam is reflected toward the wavemeter and photoacoustic cell. The signal wavelength can be measured with the same wavemeter by replacing the idler reflector with a signal reflector.<sup>23</sup>

cw power levels up to 3 W.<sup>23</sup> For frequency stability, a 400- $\mu\text{m}$  uncoated YAG etalon (FSR = 207 GHz) was similarly used internal to the SRO cavity (Fig. 3). The SRO had a threshold of 8 W and, with nonoptimized mirror and crystal coatings, could provide 3.0 W of mid-IR idler output at 2.954  $\mu\text{m}$  for 18 W of pump power. The SRO could provide an idler mode-hop tuning range of 25 GHz in steps of 100 MHz (FSR of the pump laser cavity) by tuning the intracavity pump etalon. Combined with the tuning of the Lyot filter within the pump laser, a total mode-hop tuning range of 190 GHz could be scanned, limited by a mode hop in signal frequency of 207 GHz corresponding to the FSR of the YAG etalon within the SRO cavity. By recording the photoacoustic signal in ethane, the authors characterized the frequency stability of the SRO. Due to unoptimized coatings, the idler exhibited frequency instabilities of 90 MHz/s, while temperature fluctuations in the PPLN crystal resulted in an idler frequency drift of 250 MHz over 200 s. In the same report, the authors demonstrated extension of the idler wavelength to 3.3 to 4.66  $\mu\text{m}$  using the broad tuning of the pump laser (1.024 to 1.034  $\mu\text{m}$ ) in combination with grating tuning of the PPLN crystal, providing 200 mW of idler power at 4.235  $\mu\text{m}$ , corresponding to the strongest  $\text{CO}_2$  absorption line.

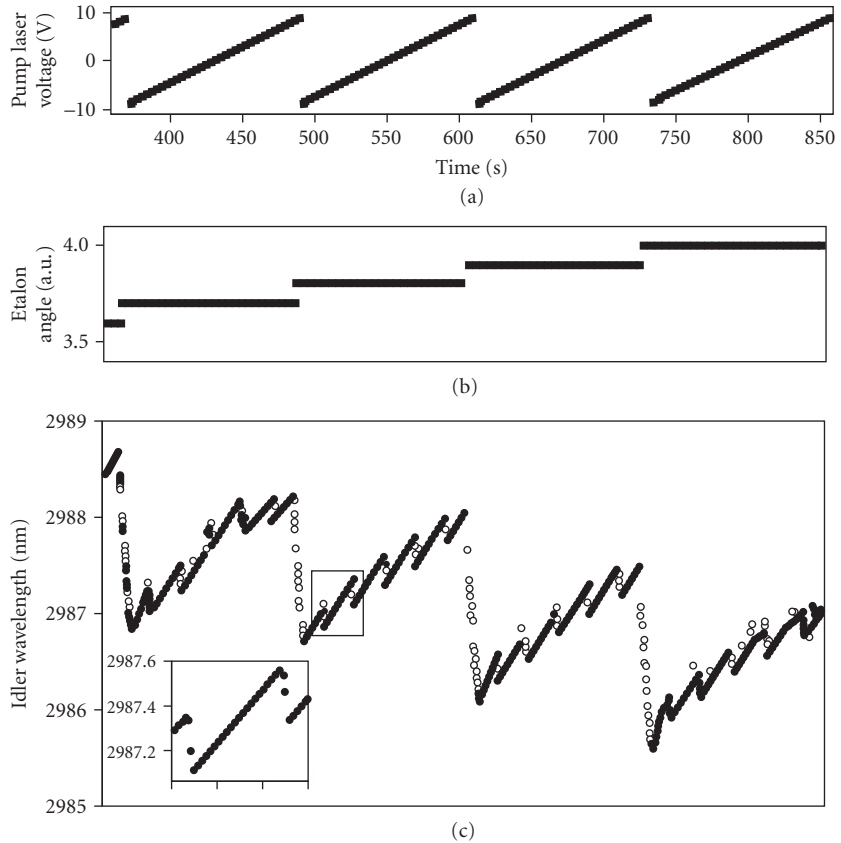
Subsequently, Ngai et al.<sup>24</sup> reported a cw SRO with automatic tuning control based on a multigrating  $\text{MgO}:\text{PPLN}$  ( $L = 50$  mm,  $\Lambda = 29.0$  to 31.5  $\mu\text{m}$ ). A schematic of the experimental setup is shown in Fig. 4. The SRO was pumped by a master oscillator-power amplifier (MOPA) laser at 1064 nm, providing 11.5 W of single-frequency output with a linewidth of 5 kHz (over 1 ms), frequency stability of 50 MHz/h, and continuous tuning over 48 GHz. The combination of temperature and grating tuning in the  $\text{MgO}:\text{PPLN}$  crystal provided coarse coverage over 2.75 to 3.83  $\mu\text{m}$  in the idler and 1.47 to 1.73  $\mu\text{m}$  in the signal, with a maximum idler power of 2.75 W. By using a ring SRO cavity containing a 400- $\mu\text{m}$ -thick uncoated solid YAG etalon (FSR = 207 GHz), a short-term frequency stability of 4.5 MHz over 1 s was attainable in the absence of active stabilization. Fine wavelength scanning of the idler output was achieved through a combination of pump tuning, etalon rotation, and temperature tuning using an automated process with computer control. First, by continuous tuning of the pump frequency over 48 GHz at a fixed etalon angle, the idler could be tuned over 12 GHz before the occurrence of a mode hop in the pump laser (Fig. 5). The total idler tuning range attainable in this way was 207 GHz, limited by an etalon mode hop. Then, by rotation of the



**FIGURE 4** Experimental setup of automatically tunable cw SRO combined with continuous-wave cavity leak-out spectroscopy. The OPO cavity is resonant for the signal wavelength. The idler beam is sent to a cw leak-out cavity and to a wavemeter.<sup>24</sup>

etalon to a new angle, the pump was again scanned until a new total tuning range of 207 GHz was covered, and process was repeated. Finally, changing the crystal temperature by 2 to 5°C, and repeating the entire process, wavelength scans of up to 450  $\text{cm}^{-1}$  with a resolution of  $<5 \times 10^{-4} \text{ cm}^{-1}$  could be obtained with a single grating period. Using this automated tuning process, the utility of the cw SRO for sensitive detection of  $\text{CO}_2$ , methane, and ethane was demonstrated with photoacoustic and cavity leak-out spectroscopy, and analysis of human breath was performed by recording the absorption spectra of methane, ethane, and water in two test persons using photoacoustic spectroscopy.

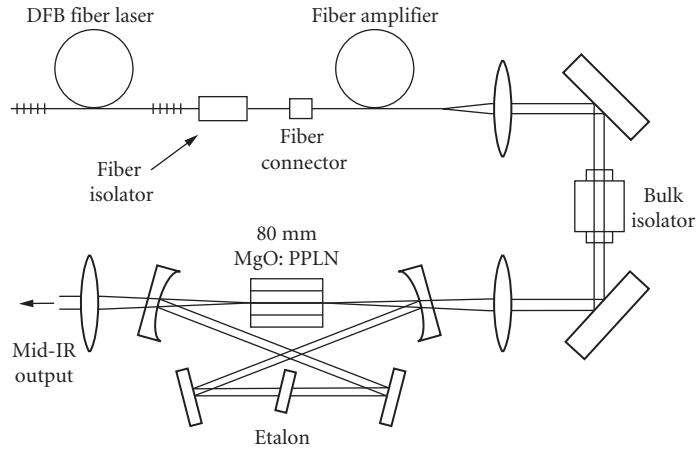
With the continued advances in pump laser technology, the development of cw SROs based on high-power diode-pumped fiber lasers and amplifiers has also become a reality. Fiber lasers are attractive alternatives as pump sources for cw SROs, because they combine the high-power properties of crystalline solid-state laser materials with significant wavelength tuning and excellent spatial beam quality in compact and portable design. The pump tuning capability allows rapid and wide tuning of the SRO output without recourse to temperature or grating period variation, while the high available powers and excellent beam quality allow access to SRO threshold and enable the generation of practical output powers. The use of fiber pump lasers can thus provide a versatile class of cw SROs for the mid-IR that offer the advantages of simplicity, compact all-solid-state design, portability, reduced cost, improved functionality, and high output power and efficiency. Operation of a cw SRO pumped by a fiber laser was first reported by Gross et al.<sup>25</sup> using a tunable Yb-doped fiber laser. The laser delivered more than 8 W of cw output power in excellent spatial beam quality and was tunable over the wavelength range of 1031 to 1100 nm. With the use of a 40-mm-long multi-grating PPLN crystal and a ring cavity for the SRO, a cw idler output power of 1.9 W was generated at a wavelength of 3.2 μm in the mid-IR for 8.3 W of fiber pump power, with a corresponding SRO power threshold of 3.5 W. Idler wavelength tuning over 3.057 to 3.574 μm could be accomplished



**FIGURE 5** Combined pump-etalon scan. By scanning the pump laser (a) and stepping the etalon angle after each pump laser scan (b), a continuous wavelength coverage over 207 GHz can be realized (c). The resolution of the idler frequency is limited by the resolution of the wavemeter [inset in (c)].<sup>24</sup>

by varying the crystal temperature or changing the grating period. However, wider and more convenient wavelength tuning was also available by exploiting the tuning capability of the fiber pump laser, where an idler tuning range of more than 700 nm over 2.980 to 3.700  $\mu\text{m}$  was obtained by varying the pump wavelength between 1.032 and 1.095  $\mu\text{m}$ . In a subsequent experiment, Klein et al.<sup>26</sup> demonstrated rapid wavelength tuning of a similar cw SRO by using electronic wavelength control of the Yb-doped fiber pump laser with an acousto-optic tunable filter. The SRO, based on a 40-mm-long single-grating PPLN crystal, was arranged in a similar ring cavity and, at a fixed crystal temperature and grating period, could be rapidly tuned over 3.160 to 3.500  $\mu\text{m}$  in the idler wavelength by electronically tuning the fiber pump laser from 1060 to 1094 nm. The 340-nm idler tuning could be achieved within a time interval of 330  $\mu\text{s}$ , representing a frequency tuning rate of 28 THz/ms. The overall electronic tuning range of the fiber pump laser over 1.057 to 1.100  $\mu\text{m}$  resulted in an SRO idler tuning range of 437 nm in the mid-IR, from 3.132 to 3.569  $\mu\text{m}$ . For the maximum fiber pump power of 6.6 W at 1.074  $\mu\text{m}$ , the SRO generated an idler output power of 1.13 W at 3.200  $\mu\text{m}$ .

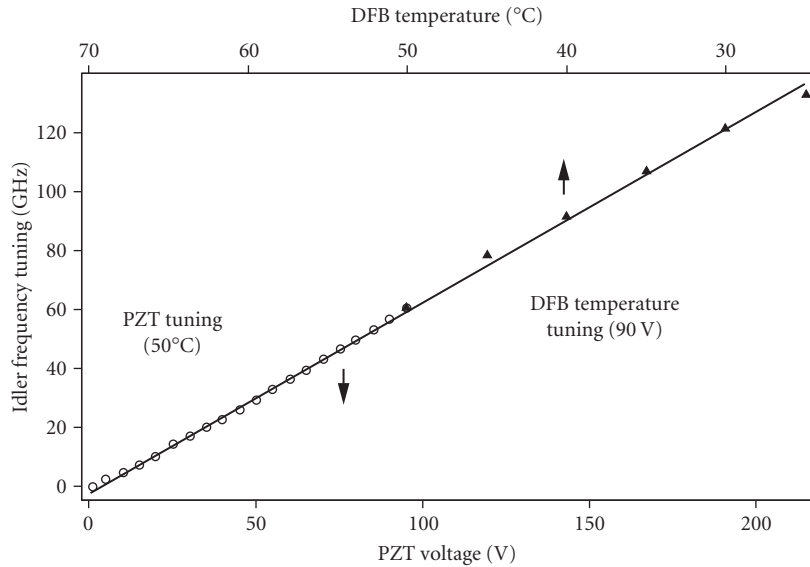
More recently, operation of a low-threshold mid-IR cw SRO was reported by Henderson and Stafford<sup>27</sup> using MgO:PPLN and an all-fiber laser pump source. A schematic of the experimental setup is shown in Fig. 6. The cw single-frequency pump at 1083 nm was configured in a MOPA



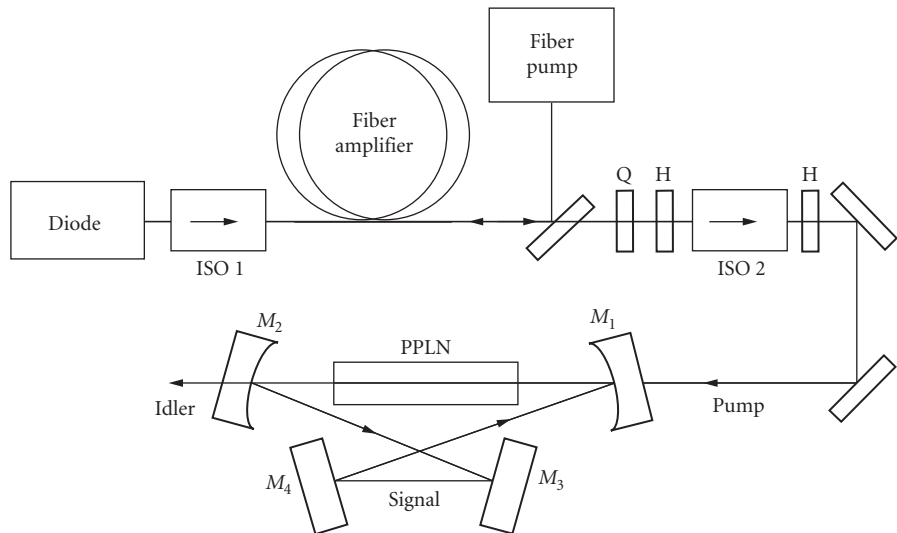
**FIGURE 6** Schematic of experimental configuration for the fiber-pumped cw SRO.<sup>27</sup>

arrangement using a 20-mW distributed feedback (DFB) fiber laser with 50-kHz linewidth as the seed and a polarization-maintaining fiber as the amplifier. The use of fiber connection between the two stages ensured an all-fiber configuration with no free-space components, alignment-free injection, and minimum long-term cavity misalignment. The MOPA could provide up to 3.5 W of amplified single-mode pump power for 20 mW of input seed power. Using multigrating and fanned crystals ( $\Lambda = 31.3$  to  $32.5 \mu\text{m}$ ) of 80-mm interaction length and operating the SRO just above room temperature ( $30^\circ\text{C}$ ), oscillation thresholds as low as 780 mW were obtained, with up to 750 mW of idler power generated for 2.8 W of fiber pump power. The idler output was tunable over 2650 to 3200 nm with a near-diffraction-limited spatial mode up to 500 mW and beam quality factor  $M^2 = 1.04$ . By exploiting the tunability of the pump laser through application of a voltage to the piezoelectric transducer attached to the fiber (rapid) and temperature variation of the seed source (slow), continuous mode-hop-free tuning of the idler over more than 120 GHz was demonstrated (Fig. 7). Using a Fabry-Perot interferometer, the idler linewidth was measured to be 1.1 MHz at  $3.17 \mu\text{m}$ . The narrow linewidth, broad coarse wavelength coverage, and rapid mode-hop-free tuning of the idler through piezoelectric tuning of the pump enabled high-resolution spectroscopy in a variety of mid-IR gases including water vapor,  $\text{CO}_2$ , and methane.

The development of PPLN has also led to substantial reductions in cw SRO power threshold, compatible with the direct use of semiconductor diode lasers as pumps for cw SROs. In addition to a compact design, an important advantage of this approach is the tunability of diode laser, which allows rapid and continuous tuning of SRO output at a fixed temperature and grating period through pump tuning. However, to provide the sufficiently high cw pump powers (typically  $>1 \text{ W}$ ) and the highest beam quality to attain SRO threshold, it has been necessary to boost the available power from single-mode diode lasers using amplification schemes. By employing a grating stabilized, extended-cavity single-stripe InGaAs semiconductor diode laser at 924 nm as a master oscillator and a single-pass tapered amplifier, Klein et al.<sup>28</sup> demonstrated operation of a cw SRO based on a 38-mm-long PPLN crystal with a pump power threshold of 1.9 W. For 2.25 W of diode pump power, 200 mW of single-frequency idler radiation was generated at  $2.11 \mu\text{m}$ . Wavelength tuning was achieved by electronic control of the master oscillator cavity, providing continuous mode-hop-free tuning of the diode pump radiation over 60 GHz from the power amplifier with a corresponding linewidth of  $<4 \text{ MHz}$ . By using an intracavity etalon to fix the resonant signal frequency, a continuous mode-hop-free idler tuning of 56 GHz was obtained at  $2.11 \mu\text{m}$  by tuning the pump wavelength. In an alternative scheme, using a distributed Bragg reflector (DBR) diode laser at 1082 nm, which was amplified in an Yb-doped fiber, Lindsay et al.<sup>29</sup> achieved rapid mode-hop-free tuning of a mid-IR cw SRO. A schematic of the experimental configuration is shown in Fig. 8, and the SRO idler

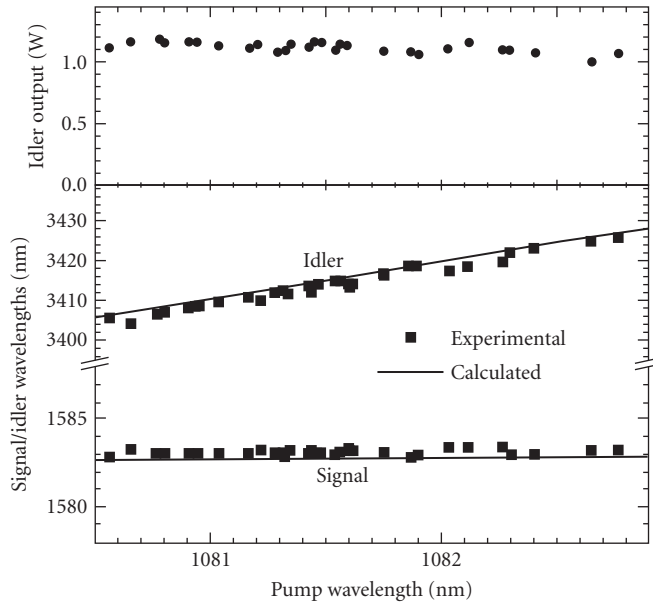


**FIGURE 7** Fine tuning of the OPO idler frequency measured as a function of pump tuning parameter, performed by PZT voltage and fiber temperature variation.<sup>27</sup>



**FIGURE 8** Schematic of experimental arrangement for the cw SRO pumped by a fiber-amplified DBR diode laser.<sup>29</sup>

output power and tuning range are shown in Fig. 9. The SRO was based on a 40-mm PPLN crystal and could provide rapid continuous tuning over 110 GHz in 29 ms. Coarse and discontinuous wavelength tuning of the idler wave was also obtained over 20 nm by tuning the DBR diode laser, and more than 1 W of idler output power was generated across the 3.405 to 3425  $\mu\text{m}$  range for 6.9 W of input pump power. An overall idler tuning range of 300 nm in the 3 to 3.5  $\mu\text{m}$  band in the mid-IR was also available by varying the temperature of the PPLN crystal.



**FIGURE 9** Variation of OPO output wavelengths (lower plot), and corresponding idler output power (upper plot), during pump tuning by seed laser DBR section alone. PPLN grating period was  $29.75 \mu\text{m}$  and temperature was  $180.5^\circ\text{C}$ . Solid lines are calculated tuning range.<sup>29</sup>

The availability of increasingly powerful pump sources such as cw fiber lasers, together with the high nonlinear coefficient ( $d_{\text{eff}} \sim 17 \text{ pm/V}$ ) and long interaction lengths (50 to 80 mm) in PPLN, can now readily permit practical operation of cw SROs many times above operation threshold, providing multiwatt idler output powers. At the same time, the presence of high optical powers can lead to additional linear and nonlinear optical effects which can modify SRO output characteristics. These include thermal loading of the crystal due to linear absorption, which can result in thermal lensing, thermal phase mismatching and output beam quality degradation, or spectral generation and broadening due to higher-order nonlinear optical effects. As such, optimum performance of cw SROs at high pump powers requires strategies to combat such effects in order to achieve maximum conversion efficiency and output extraction at full pump power, while maintaining the highest spectral and spatial beam quality, power, and frequency stability. The performance characteristics of cw SROs at high pump powers many times threshold have been studied by Henderson and Stafford.<sup>30</sup> By deploying a 15-W cw single-frequency Yb fiber laser at 1064 nm as the pump and 50-mm MgO:PPLN crystals with multiple ( $\Lambda = 31.5$  to  $32.1 \mu\text{m}$ ) and fanned ( $\Lambda = 30.8$  to  $31.65 \mu\text{m}$ ) gratings, they investigated the effects of pump power on crystal heating, wavelength tuning, beam quality, and optimum output power and extraction efficiency. With the high beam quality of the fiber laser ( $M^2 \sim 1.06$ ), and using a ring cavity with mirrors of highest reflectivity at the signal ( $R \sim 99.9$  percent) and optimum mode-matching, they achieved a threshold as low as 1.0 W, enabling SRO operation at up to 15 times threshold. With the multi-grating crystal, the SRO reached a pump depletion of 91 percent at 2.5 times threshold, remaining constant to within  $\sim 10$  percent up to the maximum pump power at 15 times above threshold. The idler output, measured at 2610 nm, exhibited a linear increase with input pump power, reaching 4.5 W at 15 W of pump, with a corresponding external photon conversion efficiency of  $\sim 74$  percent. However, operation of SRO at increasing levels of pump power was found to result in a passive increase in crystal temperature and thus a shift in the output wavelength. At the highest pump power the rise in crystal temperature was as much as  $23^\circ\text{C}$ , leading to a significant shift in

signal (26 nm) and idler (57 nm) wavelengths compared to operation at low pump power. Given the minimal absorption of the MgO:PPLN crystal at idler wavelengths of 2 to 3  $\mu\text{m}$  in this SRO, the self-heating effect was attributed to the finite absorption of the intracavity signal power. To confirm this, the authors deployed output coupling of the signal by replacing one of the high reflectors with a 4.2 percent output coupler. By operating the SRO at an ambient temperature of 26°C, they observed a 22°C rise in crystal temperature to 47°C under minimum output coupling at the maximum pump power. However, when using the 4.2 percent output coupler, the corresponding temperature rise was only 2.5°C, from 26°C to 28.5°C. Using measurements of signal output power, they estimated the circulating signal power to be as high as  $\sim 1.4$  kW at the maximum pump power under minimum output coupling, decreasing to  $\sim 100$  W with the 4.2 percent output coupler. By estimating the total absorption in the 50-mm crystal as 0.4 percent (0.08 percent/cm), they were able to conclude that an absorbed signal power of 5 W was responsible for the 22°C rise in crystal temperature. These measurements clearly confirmed the role of the intracavity signal power in heating of the MgO:PPLN crystal and its influence on spectral shifting of SRO output. The rise in crystal temperature was also observed to have a significant influence on the degradation of spatial quality of the idler beam by inducing thermal lensing effects within the crystal. From measurement of idler beam quality at the same output power level of 3.2 W, they were able to deduce a quality factor of  $M^2 \sim 1.35$  under minimum output coupling compared to  $M^2 \sim 1.0$  when using the 4.2 percent output coupler, hence confirming the deleterious effects of high circulating signal power on SRO beam quality and thus the need for optimization of output coupling at a given pump power to achieve the highest beam quality while maintaining maximum extraction efficiency. To this end, the authors also investigated the optimization of SRO output power and extraction efficiency at the maximum pump power by using variable output coupling (0 to 5 percent) for the signal across a limited tuning range. Using the fanned crystal, they found the optimum output coupling value to be 3.0 percent, resulting in the simultaneous extraction of 3.0 W of idler and 4.2 W of signal at an overall extraction efficiency of 48 percent. Under this condition, the pump depletion was 78 percent and SRO threshold was 5.8 W, corresponding to the optimum pumping ratio of  $\sim 2.5$  for maximum power extraction. The effect of use of signal output coupling as a means of optimizing the performance of cw SROs was also later investigated in a separate experiment by Samanta and Ebrahim-Zadeh.<sup>31</sup> Using a cw SRO based on MgO:sPPLT pumped at 532 nm, the authors demonstrated improvements of 1.08 W in total output power, 10 percent in total extraction efficiency, and a 130-nm extension in the useful tuning range, while maintaining pump depletions of 70 percent, idler output powers of 2.59 W, and a minimal increase in oscillation threshold of 24 percent. The output-coupled cw SRO could deliver a total power of up to 3.6 W at 40 percent extraction efficiency across 848 to 1427 nm. The single-frequency resonant signal also exhibited a higher spectral purity than the nonresonant idler output.

The high nonlinear gain coefficient of PPLN combined with the large optical powers present in cw SROs has also been observed to give rise to higher-order nonlinear effects in addition to the second-order parametric process. In a recent example of such an effect,<sup>32</sup> operation of a cw SRO based on MgO:PPLN was reported together with simultaneous Raman action driven by the high intracavity signal intensity. The SRO, based on a multigrating MgO:PPLN crystal ( $L = 50$  mm,  $\Lambda = 28.5$  to 31.5  $\mu\text{m}$ ), was configured in a linear standing-wave cavity and pumped by a 10-W Yb fiber laser at 1070 nm. Two sets of cavity mirrors were used for the SRO, providing different reflectivities for the signal over 1500 to 1700 nm. With the low-Q cavity ( $R = 98.2$  to 99 percent;  $Q \sim 10^8$ ), normal cw SRO operation with the expected signal and idler spectra was achieved with a 3.3-W threshold, and 1.6 W of idler power was generated at 3620 nm for 8 W of pump at an optical efficiency of 20 percent and slope efficiency of 35 percent. With the high-Q SRO cavity ( $R = 99.4$  to 99.8 percent;  $Q \sim 10^9$ ), stimulated Raman action with characteristic spectra was simultaneously observed in the vicinity of signal spectrum, driven by the tenfold increase in intracavity signal power to  $\sim 100$  W. The cw SRO threshold in this case was reduced to 0.5 W, with a corresponding reduction in optical efficiency to 16 percent and slope efficiency to 15 percent. The pump power threshold for Raman conversion was 1.9 W. While stimulated by intracavity signal power, Raman action was present only for grating periods and mirror reflectivities with lowest loss at the corresponding wavelengths, confirming the resonant nature of the observed effect. It was also observed that the presence of Raman oscillation with the high-Q SRO cavity resulted in improved idler RMS power stability of 1.46 percent compared to a 4.1 percent variation with the low-Q cavity, suggesting power limiting of intracavity signal by the Raman conversion.

In a subsequent experiment, Henderson and Stafford<sup>33</sup> also observed stimulated Raman oscillation in a high-power cw SRO based on MgO:PPLN. Using a 14.5-W cw single-frequency Yb fiber laser at 1064 nm and the same SRO arrangement as in Ref. 30, they observed Raman conversion of the intracavity signal under minimum output coupling and at pump powers more than 2 times above threshold, corresponding to circulating signal powers in excess of 230 W. Because of the increasing loss of SRO cavity across an extended tuning range, only two components of the Raman spectrum could be observed. However, under conditions of output coupling no Raman generation was observed up to the maximum available pump corresponding to 170 W of intracavity signal power. In the same cw SRO, the authors also observed spectral broadening of the resonant signal wave at high pump powers. Using highly reflecting mirrors to minimize threshold to 1.5 W, they were able to investigate the evolution of signal spectrum with pump power above threshold. It was observed that while at pump powers up to 3 times above threshold, the signal spectrum remained single-frequency, at pumping ratios between 3 to 4.7 the spectrum exhibited broadening with a symmetric pattern of side modes. The side modes were separated by between 0.2 and 0.5 nm, with their number and intensity increasing with pump power. Above a pumping ratio of 4.7, the signal spectrum was observed to become continuous with a FWHM bandwidth of  $\sim 2$  nm. These observations, which were found to be in qualitative agreement with predicted theory, confirm that the operation of cw SROs at high pump powers and under the conditions of minimum signal coupling must be limited below a critical pumping ratio of  $\sim 4.5$ , if single-frequency oscillation is to be maintained. Since the maximum conversion in the same experiments was found to be attainable at a pumping ratio of 2.5, by choosing an optimum output coupling of 3.0 percent, the authors increased the SRO threshold to 5.1 W and so were able to maintain single-frequency operation up to the full available pump power of 14.5 W by remaining above the optimum pumping ratio ( $\sim 2.5$ ) for optimum conversion, but below the critical ratio ( $\sim 4.5$ ) for spectral broadening and multimode operation. Under this condition, 5.1 W of single-mode signal and 3.5 W of single-mode idler were simultaneously generated for 14.5 W of pump at an overall extraction efficiency of nearly 60 percent, with a measured idler bandwidth of 30 kHz over 500  $\mu$ s.

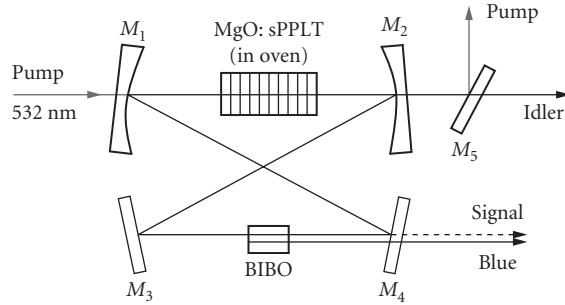
The advent of QPM nonlinear materials has had a profound impact on cw SROs, with the vast majority of devices developed to date based on PPLN as the nonlinear material. When pumped near  $\sim 1$   $\mu$ m by solid-state, amplified semiconductor, or fiber lasers, they can provide potential coverage from above  $\sim 1.3$   $\mu$ m up to the absorption edge of the material near  $\sim 5$   $\mu$ m. For wavelength generation below  $\sim 1.3$   $\mu$ m, the use of PPLN is generally precluded by photorefractive damage induced by visible pump or signal radiation. As such, the development of practical cw OPOs for visible and near-IR at wavelength below  $\sim 1.3$   $\mu$ m has remained difficult, particularly in high-power SRO configuration where strong visible pump and signal radiation are present. This has thus necessitated the use of additional frequency conversion schemes or deployment of alternative QPM materials such as PPKTP and, more recently, MgO-doped periodically poled stoichiometric LiTaO<sub>3</sub> (MgO:sPPLT). To extend the tunable range of cw SROs to the visible range, Strossner et al.<sup>34</sup> used an approach based on second harmonic generation (SHG) of the idler output from a cw SRO in an external enhancement cavity. By deploying a 10-W, single-frequency, cw pump laser at 532 nm in combination with multigrating PPKTP ( $L = 24$  mm,  $\Lambda = 8.96$  to 12.194  $\mu$ m) and PPLN ( $L = 25$  mm,  $\Lambda = 6.51$  to 9.59  $\mu$ m) crystals as the OPO gain medium, and PPLN ( $L = 43$  mm,  $\Lambda = 6.51$  to 20.93  $\mu$ m) for SHG, a visible green-to-red tuning range of 550 to 770 nm in the frequency-doubled idler was demonstrated. Together with direct signal (656 to 1035 nm) and idler (1096 to 2830 nm) tuning, this resulted in a total system tuning range of 550 to 2830 nm, with a tuning gap of  $\sim 60$  nm over 1035 to 1096 nm. The output power, limited by photorefractive damage to the PPLN crystal, and optical damage to the PPKTP crystal and coatings induced by input pump, was 60 mW (signal), 800 mW (idler), and 70 mW (visible frequency-doubled idler) for up to 3.3 W of pump. The output signal from the free-running SRO exhibited a short-term linewidth of 20 kHz over 50  $\mu$ s, with a jitter of 300 kHz over 5 ms, and 5 MHz over 1 s. By frequency locking the SRO to a monolithic Nd:YAG laser, a jitter-free linewidth of 20 kHz was measured at a signal wavelength of 946 nm. In the absence of pump tuning, mode-hop-free tuning of SRO output was obtained by adjustment of the cavity length using piezo control and synchronous rotation of the etalon using a feedback loop, resulting in 38 GHz of fine tuning in the signal for PPKTP and 5 to 16 GHz for PPLN, limited by photorefractive effects. The



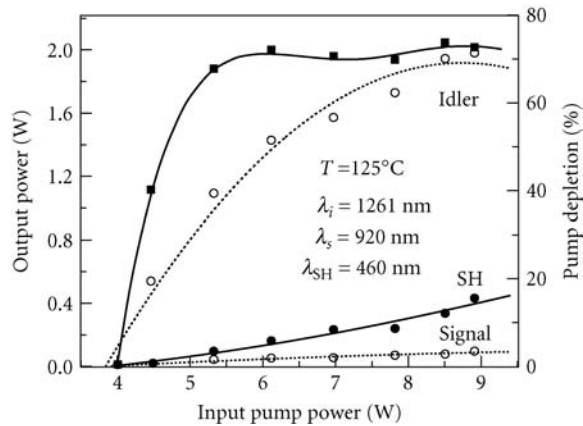
free-running SRO exhibited a mode hop over a free-spectral range (680 MHz) every 10 min, but locking the SRO cavity to the 532-nm pump ensured a long-term frequency drift of <50 MHz/h in the signal and idler, accompanied by a reduction in output power by ~10 percent.

More recently, the development of MgO:sPPLT has brought about new opportunities for the advancement of practical cw SROs for the visible and near-IR at wavelength below ~1.3  $\mu\text{m}$  with the direct use of high-power solid-state laser sources in the green. By deploying a 10-W, single-frequency, cw, frequency-doubled Nd:YVO<sub>4</sub> pump laser at 532 nm, MgO:sPPLT ( $L = 30.14$  mm,  $\Lambda = 7.97$   $\mu\text{m}$ ) as the nonlinear crystal and temperature tuning, Samanta et al.<sup>35</sup> demonstrated a cw SRO with a tunable range of 848 to 1430 nm. Using a linear standing-wave cavity and double-pass pumping, the cw SRO had an oscillation threshold of 2.88 W, and could provide >1.51 W of single-pass idler power for 6 W of pump at an extraction efficiency of >25 percent and photon conversion efficiency of >56 percent. The maximum idler power and conversion efficiency in this SRO was limited by thermal lensing effects, attributed to the finite liner absorption of the green pump light in the MgO:sPPLT crystal. Despite this, the SRO could deliver >500 mW of single-pass power across the entire idler tuning range of 1104 to 1430 nm, and in a Gaussian profile, confirming the absence of photorefractive damage as is present in PPLN. With a standing-wave SRO cavity and in the absence of intracavity frequency selection, the output frequency in both signal and idler was characterized by mode hops. Soon after, by deploying a compact ring cavity with a 500- $\mu\text{m}$  intracavity etalon, the authors demonstrated single-frequency operation of the cw SRO.<sup>36</sup> Using the same pump laser and MgO:sPPLT crystal in a single-pass pumping arrangement, the SRO had a pump power threshold of 2.84 W and could deliver 1.59 W of single-mode idler power over 1140 to 1417 nm for 7.8 W of pump at >20 percent extraction efficiency. The total SRO tuning range was 852 to 1417 nm, obtained for a variation in crystal temperature from 61 to 236°C. Under free-running conditions, the idler had an instantaneous linewidth of ~7 MHz and exhibited a peak-to-peak power stability of 16 percent over 5 hours. Measurements of idler power at different crystal temperatures revealed stronger thermal lensing at higher temperatures. In a separate experiment, operation of a similar cw SRO based on MgO:sPPLT and pumped by a Nd:YVO<sub>4</sub> laser at 532 nm was reported by Melkonian et al.,<sup>37</sup> providing tunable signal over 619 to 640 nm in the red. Using a ring cavity for the SRO containing a 30-mm multigrating crystal ( $\Lambda = 11.55$  to 12.95  $\mu\text{m}$ ) and a 2-mm-thick intracavity silica etalon, the SRO could provide ~100 mW of nonresonant idler power. The resonant signal was extracted using a 1.7 percent output coupler, providing 100 mW of single-frequency red radiation for 10 W of input pump power. The cw SRO threshold varied from 3.6 W in the absence of the intracavity etalon up to 6.6 W with signal output coupling, and rising to 6.8 W depending on the exact signal wavelength. The maximum pump depletion was 15 percent, limited by thermal effects attributed to pump and signal absorption. The output signal frequency could be mode-hop-tuned over a total range of 27 GHz by rotation of the intracavity etalon, in steps of 255 MHz corresponding to free-spectral-range of the SRO cavity. With active stabilization of SRO cavity length, a frequency stability of 20 MHz over 3 min was obtained for the signal.

The development of practical, high-power, single-frequency cw SROs based on MgO:sPPLT pumped in the green and operating below 1  $\mu\text{m}$ <sup>35–37</sup> has also provided new motivation for spectral extension to shorter wavelengths. By using internal SHG of the resonant near-IR signal in a cw SRO based on MgO:sPPLT, Samanta and Ebrahim-Zadeh<sup>38</sup> demonstrated the first cw SRO tunable in the blue. A schematic of the SRO configuration is shown in Fig. 10. The device was based on similar experimental design as in Ref. 36, except for the exclusion of the intracavity etalon and inclusion of a 5-mm BiB<sub>3</sub>O<sub>6</sub> (BIBO) crystal at the secondary waist of the bow-tie SRO ring resonator to frequency double the circulating signal radiation in a single direction. By varying the temperature of the MgO:sPPLT crystal to tune the signal over 850 to 978 nm, and simultaneous rotation of the BIBO phase-matching angle, a wavelength range of 425 to 489 nm in the blue was accessed. The generated blue power varied from 45 to 448 mW across the tuning range, with the variation arising from the non-optimum reflectivity of the blue coupling mirror over the signal wavelength range. The output power behavior and pump depletion of the SRO with pump power is shown in Fig. 11. The frequency-doubled SRO had a threshold of 4 W (2.4 W without the BIBO crystal), and exhibited a pump depletion of up to ~73 percent under blue generation. In addition to the blue, the device could provide in excess of 100 mW of signal and as much as 2.6 W of idler output power. Without an intracavity etalon, the



**FIGURE 10** Schematic of the intracavity frequency-doubled MgO:sPPLT cw SRO for blue generation.<sup>38</sup>



**FIGURE 11** Single-frequency blue power, signal power, idler power, and pump depletion as functions of input pump power to the frequency-doubled cw SRO. Solid and dotted lines are guide for the eye.<sup>38</sup>

single-mode nature of the pump and resonant signal resulted in single-frequency blue generation and a measured instantaneous linewidth of  $\sim 8.5$  MHz in the absence of active stabilization. The blue output beam also exhibited a gaussian spatial profile. In the meantime, operation of an intracavity frequency-doubled cw SRO based on MgO:sPPLT was also reported by My et al.,<sup>39</sup> providing tunable output in the orange-red. By resonating the idler wave in the 1170 to 1355 nm range in a ring resonator and employing a 10-mm intracavity  $\beta$ -BaB<sub>2</sub>O<sub>4</sub> (BBO) crystal for doubling, tuning output over 585 to 678 nm was generated. With a 30-mm MgO:sPPLT crystal ( $\Lambda = 7.97 \mu\text{m}$ ), up to 485 mW of visible radiation was internally generated for 7.6 W of pump, with 170 mW extracted as useful output. The device could also provide up to 3 W of nonresonant infrared signal power. The power threshold for the cw SRO was 4.5 W (4 W without the BBO crystal) and pump depletions of  $\sim 80$  percent were measured for input powers  $> 6$  W. Without active stabilization, the visible SHG output was single mode with a frequency stability of 12 MHz over 12 min, and mode-hop-free operation could be maintained over several minutes.

In a departure from conventional cw OPOs based on bulk materials, the use of guided-wave nonlinear structures can also in principle offer an attractive approach to the realization of OPO sources in miniature integrated formats. The tight confinement of optical waves in a waveguide can

provide substantial enhancement in nonlinear gain per input pump power compared with the bulk materials, but a major drawback of the approach is the unacceptably high input and output coupling losses in the waveguide, hindering OPO operation. The problem is further exacerbated in the cw regime, and in the SRO configuration, which is characterized by the highest oscillation threshold. In an effort to overcome this difficulty, Langrock et al.<sup>40</sup> deployed the technique of fiber-feedback to achieve operation of a cw SRO based on a reverse-proton-exchanged (RPE) PPLN waveguide. In this approach, the SRO cavity was formed in a ring using a single-mode optical fiber pigtailed to both ends of the waveguide, providing feedback at the resonant signal wave. The pump was similarly coupled into the PPLN waveguide using a separate fiber and, together with the nonresonant idler, exited the waveguide in a single pass. The configuration resulted in minimum coupling losses of 0.7 dB (signal input) and 0.6 dB (signal output), and alignment-free operation. Using a 67-mm RPE PPLN waveguide containing a 49-mm grating ( $\Lambda = 16.1 \mu\text{m}$ ), and a tunable external cavity diode laser at 779 nm as the pump, cw SRO threshold was reached at  $\sim 200$  mW of coupled pump power. The waveguide cw SRO exhibited gain bandwidths in excess of 60 nm. Ultimately, however, practical realization of such waveguide cw SROs offering significant output will require further optimization of waveguide fabrication process to minimize propagation losses ( $\alpha = 0.2$  dB/cm) and loop losses (1.5 dB) in the present device, as well as further reductions in the waveguide-to-fiber coupling losses.

## Multiple-Resonant Oscillators

Because the high pump power requirement for cw SROs can be prohibitive for many practical applications, extensive efforts have been directed to the development of cw OPOs in alternative resonance configurations, from the traditional DRO to the more recently devised PE-SRO and TRO, with the goal minimizing the pump power thresholds. These efforts have brought the operation of cw OPOs within the reach of more commonly available low- to moderate-power cw laser sources, albeit at the expense of added system complexity arising from the need for more elaborate cavity designs, more complex tuning protocols and the imperative requirement for active stabilization and control. In particular, the use of DRO and PE-SRO resonance schemes in combination with novel cavity designs have led to the practical generation of cw mid-IR radiation with the highest degree of frequency stability, and continuous mode-hop-free tuning capability over extended frequency spans at practical powers. These efforts have led to the realization of novel cw OPO systems in PE-SRO, DRO, and TRO configurations pumped by a variety of laser sources. These sources offer practical cw output powers in the mW to 100s mW range, high frequency stability, significant mode-hop-free tuning capability and extended wavelength coverage in the 1 to  $5 \mu\text{m}$  spectral range.

**Doubly Resonant Oscillators** The use of DRO configurations in combination with PPLN has permitted substantial reductions in cw pump power threshold in cw OPOs, to levels compatible with the direct use single-mode semiconductor diode lasers, without the need for power amplification. The smooth wavelength tuning capability of the diode laser pump can then be similarly exploited to achieve continuous mode-hop-free tuning of the DRO output. In an example of such an approach, Henderson et al.<sup>41</sup> demonstrated a PPLN cw DRO pumped directly with a 150-mW, single-mode, single-stripe, DBR diode laser at 852 nm. Configured in a single, linear, standing-wave resonator and using a 19-mm-long multigrating crystal ( $\Lambda = 23.0$  to  $23.45 \mu\text{m}$ ), the DRO exhibited a pump power threshold of  $\sim 17$  mW, with thresholds as low as 5 mW under optimum alignment and minimum output coupling. Using three DRO mirror sets, a signal (idler) wavelength range of 1.1 to  $1.4 \mu\text{m}$  ( $2.2$  to  $3.7 \mu\text{m}$ ) was accessed by temperature tuning the PPLN crystal. The DRO generated a total signal and idler power of 18 mW at 1.3 and  $2.3 \mu\text{m}$ , respectively, for 89 mW of input diode pump power, with 4 mW of output in the idler beam. Continuous mode-hop-free tuning of the signal (idler) at  $1.3 \mu\text{m}$  ( $2.3 \mu\text{m}$ ) could be obtained over 12 GHz (7 GHz) by smooth tuning the frequency diode laser using temperature variation and over 17 GHz (10 GHz) using current control in combination with active servo control of the DRO cavity length to follow the pump frequency scan. The continuous mode-hop-free tuning ranges were limited by the restrictions on DRO cavity length variation imposed by the piezoelectric transducer. With a pump linewidth of  $<3$  MHz, the signal wave was measured to have

a linewidth of  $<7$  MHz and a free-running frequency stability of  $\sim 20$  MHz over 10 s without active stabilization. To demonstrate the utility of the diode-pumped cw DRO, continuous tuning of the idler was used in single-pass absorption spectroscopy of R6 line in CO gas at  $2.3 \mu\text{m}$ .

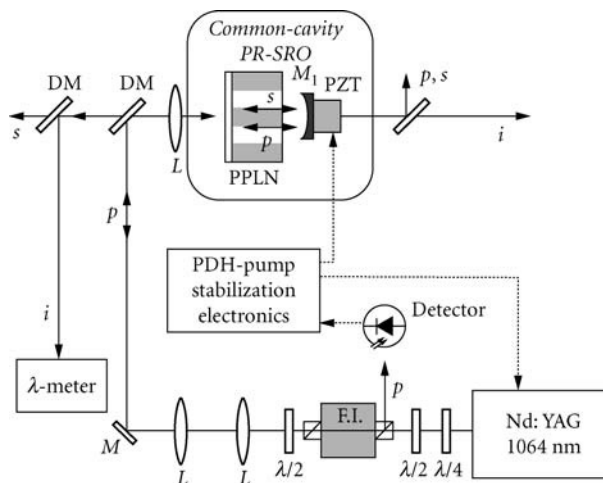
In an effort to extend the wavelength coverage of cw OPOs to the visible spectrum, Petelski et al.<sup>42</sup> demonstrated a DRO tunable in the yellow, using a cascaded frequency scheme comprising three resonators including two external enhancement cavities, and a cw single-frequency monolithic ring Nd:YAG laser as the primary pump source. The pump light at  $1.064 \mu\text{m}$  was frequency doubled in an external enhancement cavity using MgO:LiNbO<sub>3</sub> as the nonlinear crystal, to provide the input radiation for the cw DRO based on an identical crystal. With a threshold of 15 mW, the DRO delivered 95 mW of idler power for 450 mW of input at 532 nm, with the idler tunable over  $1.130$  to  $1.190 \mu\text{m}$  by changing the temperature of the MgO:LiNbO<sub>3</sub> crystal. The generated idler output was then frequency doubled in an external enhancement cavity based on a 16-mm PPLN crystal ( $\Lambda = 8.0$  to  $8.6 \mu\text{m}$ ) to provide tunable radiation across the 565 to 590 nm range. For 1.05 W of primary pump power at  $1.064 \mu\text{m}$ , an output power of 3.8 mW was obtained at 580 nm, with active stabilization of the DRO and enhancement cavities providing single-mode output with a 3 percent intensity noise and stable operation over 10 hours. Fine tuning of the yellow output was obtained by smooth tuning of the Nd:YAG pump source, as well as mode-hop tuning of the DRO by scanning the cavity length. By tuning the pump frequency over 10 GHz, the yellow output at 580 nm was tuned continuously over 18 GHz, while mode-hop tuning could provide 160 GHz of step tuning across 20 mode pairs.

**Pump-Enhanced Singly Resonant Oscillators** In separate experiments, using a single-mode, single-stripe, grating-stabilized AlGaAs diode lasers at  $\sim 810$  nm in both solitary and external-cavity configurations, Lindsay et al.<sup>43</sup> demonstrated a PPLN cw OPO in pump-enhanced configuration. Using a single, linear, standing-wave cavity for the OPO and a 50-mm, multigrating ( $\Lambda = 21.0$  to  $22.4 \mu\text{m}$ ) crystal, a typical pump power threshold of 25 to 30 mW over a signal (idler) tuning range of  $1.06$  to  $1.19 \mu\text{m}$  ( $2.58$  to  $3.44 \mu\text{m}$ ) was demonstrated, with  $\sim 4$  mW of single-mode idler power available for 62 mW of pump. Wavelength tuning could be achieved by the variation of pump wavelength, PPLN crystal temperature, or grating period. In the external cavity configuration, locking of the OPO cavity length to the pump laser frequency using the Pound-Drever technique enabled stabilized single-mode operation with a signal (idler) intensity fluctuation of  $\pm 3.5$  percent (2.6 percent) at 0.5 mW (4 mW) power level over 1 hour. Over this period, pump frequency fluctuations of  $\pm 125$  MHz resulted in  $\pm 100$  MHz variation in signal frequency. However, mode-hop-free operation was maintained throughout the entire period. By continuous tuning of the external cavity diode laser over 510 MHz, a mode-hop-free tuning range of 377 MHz for the signal and 133 MHz for the idler was obtained, limited by the relative tuning rate of parametric gain curve and resonant signal modes with frequency tuning of the pump in the common-cavity PE-SRO, and so could be extended using a dual-cavity arrangement for the OPO.

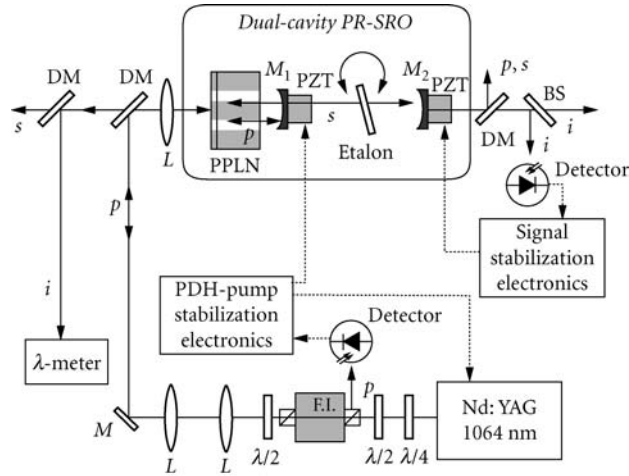
By deploying a single-frequency cw Ti:sapphire pump laser, Turnbull et al.<sup>44</sup> demonstrated a cw PE-SRO based on a multigrating PPLN crystal ( $L = 19$  mm,  $\Lambda = 21.0$  to  $22.4 \mu\text{m}$ ) with an extended mid-IR idler coverage to  $5.26 \mu\text{m}$ , well into the strong absorption region of the material beyond  $\sim 4.5 \mu\text{m}$ . The PE-SRO could provide idler tuning in two regions from  $2.71$  to  $3.26 \mu\text{m}$  and from  $4.07$  to  $5.26 \mu\text{m}$ , using a combination of temperature tuning and grating period variation. The oscillator exhibited a typical cw pump power threshold of 100 mW, increasing to more than 500 mW near  $5 \mu\text{m}$ . For 750 mW of input pump power, the PE-SRO could typically provide a maximum one-way cw idler power of 16 mW. By employing a dual-cavity arrangement for the PE-SRO and a solid etalon in one arm of the resonant signal cavity, the authors were able to demonstrate mode-hop-free tuning of the idler over 10.8 GHz by smoothly tuning the pump laser over 12.3 GHz. In a further experiment, Stothard et al.<sup>45</sup> extended operation of the same PE-SRO to a single-cavity, traveling-wave ring geometry with the aim of extending the total fine-tuning performance of the oscillator and improving the idler output power. By using a low-finesse intracavity etalon to control the resonant signal frequency, the authors were able to achieve discontinuous mode-hop tuning of the idler frequency across the entire free spectral range of the etalon, corresponding to 83 GHz. The PE-SRO exhibited an oscillation threshold of 250 mW and could generate 35 mW of cw single-frequency mid-IR

idler radiation in the 2.8 to 3- $\mu\text{m}$  spectral range for 600 mW of input Ti:sapphire pump power. In a separate experiment, Lindsay et al.<sup>46</sup> reported the operation of a cw PE-SRO based on PPRTA ( $L = 20$  mm,  $\Lambda = 39.6$   $\mu\text{m}$ ) as the nonlinear crystal. The PE-SRO was pumped by a diode-pumped cw single-frequency Nd:YVO<sub>4</sub> laser at 1.064  $\mu\text{m}$  and was configured in a linear standing-wave resonator with the nonresonant idler double-passed through the cavity. With the 20-mm crystal length, the oscillator had an external pump power threshold of 250 mW and could deliver 87 mW of cw mid-IR idler output for 900 mW of input pump power. Coarse tuning of the idler over the wavelength range of 3.245 to 3.520  $\mu\text{m}$  was achieved by temperature tuning the single-grating PPRTA crystal. Continuous mode-hop-free tuning of the PE-SRO over 0.7 GHz was also demonstrated by fine tuning the Nd:YVO<sub>4</sub> pump laser frequency.

In subsequent experiments, Muller et al.<sup>47</sup> investigated long-term frequency stability and linewidth properties of cw PE-SROs in common-cavity and dual-cavity configurations. Using multi-grating PPLN crystals ( $L = 50$  mm,  $\Lambda = 28.64$  to 30.16  $\mu\text{m}$ ), a 2.5 W cw Nd:YAG pump laser (linewidth  $\sim 1$  kHz/100 ms, frequency drift  $\sim 1$  MHz/min) at 1064 nm, and linear standing-wave cavity arrangements for both configurations, they studied frequency stability and linewidth of the idler output tunable in the 3.1 to 3.9  $\mu\text{m}$  spectral range. Schematics of the experimental setups for both cavity configurations are shown in Figs. 12 and 13. In the common-cavity PE-SRO (Fig. 12) with the pump and signal resonant in the same cavity, the OPO was locked to the pump laser using the Pound-Drever-Hall (PDH) technique, and the oscillator exhibited a threshold of 280 mW. In dual-cavity arrangement (Fig. 13), the pump and signal were resonated in separate linear cavities, with an intracavity 500- $\mu\text{m}$ -thick Nd:YAG etalon inserted into the signal cavity for improved frequency control. The pump cavity was locked to the pump laser using the PDH method, while the signal cavity was locked to the point of maximum idler power using an intensity lock without an external reference. The use of dual-cavity configuration increased the threshold to 380 mW, but resulted in stable, mode-hop-free operation over 30 min. While an intrinsic advantage of the common-cavity PE-SRO is direct stabilization of the signal frequency to pump, it is more sensitive to mechanical perturbations, leading to mode hops. Moreover, reliable mode-hop-free operation and continuous frequency tuning by tuning the pump laser are more difficult due to the simultaneous resonance of two different wavelengths within a single cavity. On the other hand, the dual-cavity approach can overcome spontaneous mode hops and continuous tuning limitations of common-cavity PE-SROs, and can also offer several tuning methods combining etalon, signal cavity and pump frequency tuning. The

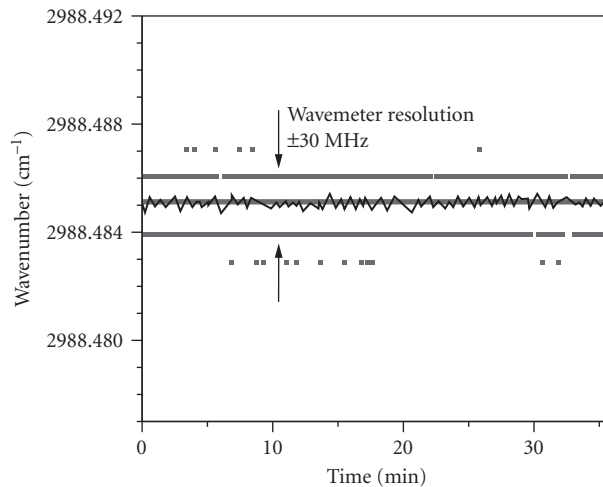


**FIGURE 12** Common-cavity cw PE-SRO setup;  $M$  = mirror, DM = dichroic mirror, FI = Faraday isolator,  $L$  = lens,  $p$  = pump,  $s$  = signal,  $i$  = idler.<sup>47</sup>

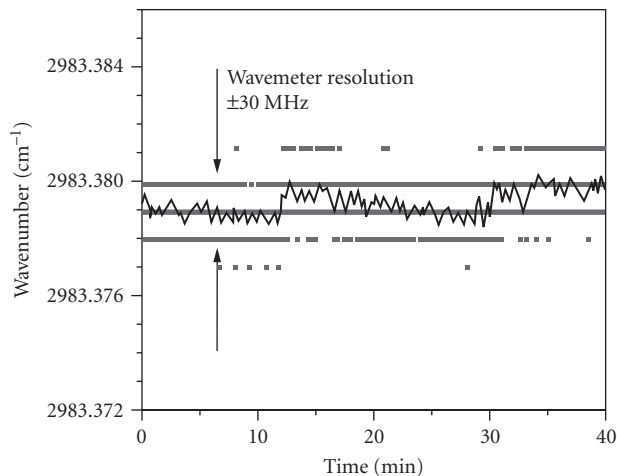


**FIGURE 13** Dual-cavity cw PE-SRO setup;  $M$  = mirror,  $DM$  = dichroic mirror,  $FI$  = Faraday isolator,  $L$  = lens,  $p$  = pump,  $s$  = signal,  $i$  = idler.<sup>47</sup>

results of the investigations revealed long-term frequency stability better than  $\pm 30$  MHz over more than 30 min for both configurations (Figs. 14 and 15), limited by the resolution of the wavemeter. The short-term frequency jitter was 56 kHz over 1.8 s for the common-cavity PE-SRO and 13.5 MHz over 1.5 s for the dual-cavity PE-SRO. The short-term linewidths, measured using the cavity leak-out technique in external high-finesse cavities, were  $(9 \pm 2)$  kHz for the common-cavity and  $(6 \pm 1)$  kHz for the dual-cavity over 20  $\mu$ s. The difference in frequency stability and linewidth of the two configurations is a result of the stabilization methods used. In the common-cavity PE-SRO, direct locking of the cavity to the pump laser provides a strong stabilization of the signal to pump frequency. In the



**FIGURE 14** Long-term frequency stability (digital wavemeter read-out in 30 MHz steps and running average over 20 points) of the common-cavity cw PE-SRO.<sup>47</sup>

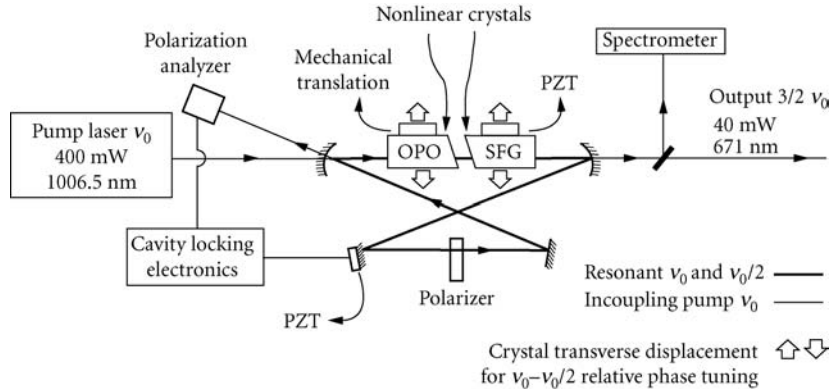


**FIGURE 15** Long-term frequency stability (digital wavemeter read-out in 30 MHz steps and running average over 20 points) of the dual-cavity cw PE-SRO.<sup>47</sup>

dual-cavity PE-SRO, the signal cavity is locked to the maximum idler output power and so the idler frequency is coupled to the maximum of the phase-matching gain curve. Any shifts in the gain curve in time will also result in corresponding variations in the signal and idler frequencies. However, the reported results confirm that despite this limitation, the dual-cavity PE-SRO provides the required frequency stability and linewidths as well as continuous mode-hop-free tuning necessary for high-resolution spectroscopy.

**Triply Resonant Oscillators** Characterized by the lowest oscillation threshold, the TRO represents the least demanding configuration for cw OPOs with regard to pump power. However, practical operation of such oscillators requires active cavity length control to maintain simultaneous resonance of the pump, signal and idler within the OPO resonator. In an example of such a device, Gross et al.<sup>48</sup> reported a TRO based on a 58-mm PPLN crystal using only 14 mW of pump power from a grating-stabilized, single-frequency, extended-cavity diode laser at 805 nm. By deploying a linear two-mirror cavity, highly reflecting mirrors, optimum mode-matching and active stabilization, they achieved a threshold pump power as low as 600  $\mu$ W at resonance, with a maximum total (signal and idler) output power of 47  $\mu$ W generated for 13.5 mW of pump. With mirrors of higher transmission (4 percent) at the signal and idler, a total output power of 2.1 mW was generated for 13.8 mW of pump, but at the expense of an increase in pump power threshold to 4.5 mW. Using a segmented design for the PPLN crystal consisting of two 19-mm outer sections poled with multiple grating of identical periods ( $\Lambda = 20.2$  to 20.8  $\mu$ m) at 50 percent duty cycle and a single-domain section of length 20 mm at the centre, they demonstrated electro-optic tuning of the TRO output wavelengths at a fixed temperature, grating period, and pump wavelength. By applying an electric voltage of up to +1230 V across the single-domain section, wavelength tuning of the signal and idler over 1560 to 1660 nm could be obtained through modification of the phase-matching gain spectrum induced by the electro-optic effect. By applying a voltage modulation of amplitude 513 V at 0.11 Hz, signal (idler) tuning over 9.7 nm (10.8 nm) was demonstrated over 4.6 s, limited by the bandwidth of servo electronics.

Because of their phase coherent properties and the ability to generate exactly correlated frequencies, cw OPOs are also uniquely versatile sources for applications in optical frequency synthesis and metrology. Combined with compact solid-state semiconductor, or fiber pump lasers, they can offer practical tools for precision frequency generation, measurement, and control across extended regions spanning



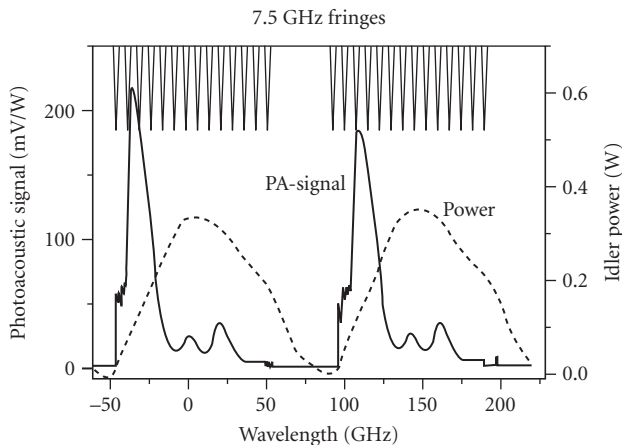
**FIGURE 16** Schematic of the cw TRO for 3/2 frequency multiplier, converting a cw single-frequency radiation at 1006.5 nm into 671 nm. The wedged surfaces of the crystals are cut at an angle of 100 mrad with respect to the crystal axis. The input (output) facet of the OPO (SFG) crystal is at normal incidence. The two inclined surfaces facing each other are parallel. The transverse displacement of the nonlinear crystals provides an independent control over the cavity dispersion, ensuring simultaneous resonance of the two infrared fields.<sup>49</sup>

the optical spectrum. In a report, Ferrari<sup>49</sup> demonstrated a particular architecture for optical frequency synthesis based on a cw OPO in TRO configuration. By taking advantage of the lowest oscillation threshold offered by the TRO, the author developed a 3/2 pump frequency multiplier from the near-IR to visible using a 400-mW, single-mode semiconductor MOPA device at 1006.5 nm as the pump source (Fig. 16). The TRO, based on PPKTP as the nonlinear crystal ( $L = 20$  mm,  $\Lambda = 38$   $\mu\text{m}$ ), was operated at degeneracy to provide identical signal and idler frequencies at half the pump frequency. A second intra-cavity PPKTP crystal ( $L = 20$  mm,  $\Lambda = 19.8$   $\mu\text{m}$ ) was then used to sum the pump with the degenerate frequency, resulting in 3/2 frequency multiplication of the pump, corresponding to a wavelength of 671 nm in the red. To provide stable operation, the TRO cavity length was locked using the pump resonance, and independent control of the degenerate signal and idler oscillating modes was obtained by using wedged crystals. Fine tuning of the TRO cavity modes could be obtained while maintaining pump resonance by lateral translation of the wedged crystals to alter in the optical path lengths within the crystals, thus enabling single-frequency operation to be achieved at degeneracy. The TRO had a threshold of  $<50$  mW and could provide 40 mW of single-mode output at degeneracy in a near-gaussian spatial mode with an RMS amplitude noise of 1.4 percent (50 kHz bandwidth) over 3 min at full power.

## 17.3 APPLICATIONS

The important advances in cw OPOs over the last decade have led to the realization of a new generation of practical coherent light sources in new spectral regions from the visible to the near- and mid-IR offering unprecedented optical powers, high frequency stability and narrow linewidth, excellent beam quality, and extended fine and coarse tuning. These capabilities have paved the way for the deployment of cw OPOs in new application areas, in particular spectroscopy. Most notably, cw OPOs based on PPLN have found important applications in sensitive detection and analysis of trace gases in mid-IR, where a variety of important molecular finger prints exist. A wide range of experiments, from simple single-pass absorption to high-resolution Doppler-free and cavity leak-out spectroscopy have been successfully performed by deploying cw OPOs based mainly on PPLN and operating in different resonance configurations of SRO, PE-SRO, or DRO. The higher cw output powers available to SROs and PE-SROs have also enabled detection of trace gases in the mid-IR with unprecedented sensitivity using photoacoustic spectroscopy.

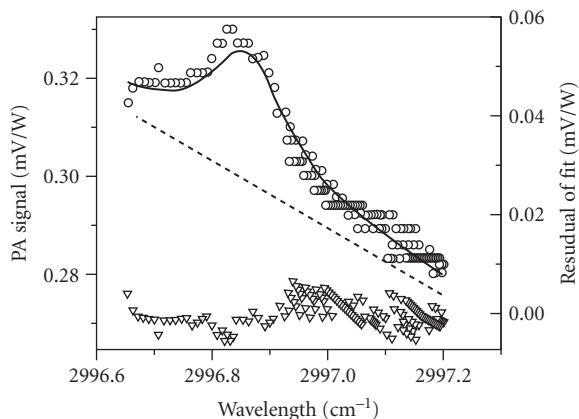




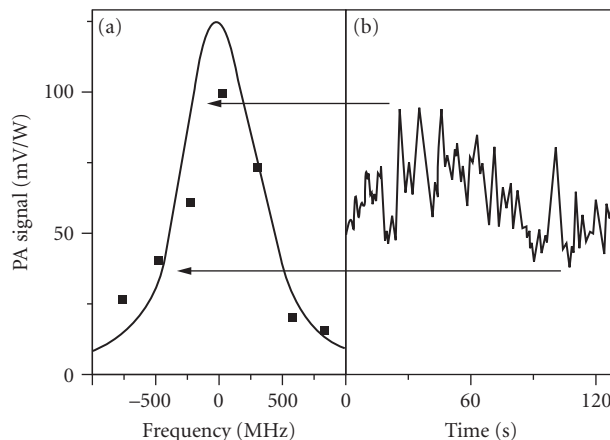
**FIGURE 17** 100-GHz-wide mode-hop scan of 10 ppm ethane in nitrogen was made around  $2996.9 \text{ cm}^{-1}$ . The solid line at the bottom shows the photoacoustic signal, the dashed line the idler power and the solid line at the top the fringes from a 7.5-GHz external Fabry-Perot etalon.<sup>21</sup>

By exploiting fine frequency tuning in a diode-pumped PPLN cw SRO, Klein et al.<sup>28</sup> performed single-pass absorption spectroscopy of rovibrational transitions in  $\text{N}_2\text{O}$  gas near  $2.1 \mu\text{m}$ . The wide and continuous mode-hop-free tuning of the idler over 56 GHz enabled monitoring of three molecular lines separated by  $\sim 20 \text{ GHz}$  within a single frequency scan.

Using a cw SRO based on PPLN, providing 700 mW of idler power and a total single-frequency fine tuning range of 24 GHz, Van Herpen et al.<sup>20</sup> recorded absorption line of ethane in nitrogen using the photoacoustic spectroscopy technique. In a later experiment,<sup>21</sup> by deploying a more powerful pump laser and a similar SRO configuration, photoacoustic spectroscopy of ethane in nitrogen was demonstrated with a detection sensitivity of 10 parts per trillion (ppt) (Figs. 17 and 18). The

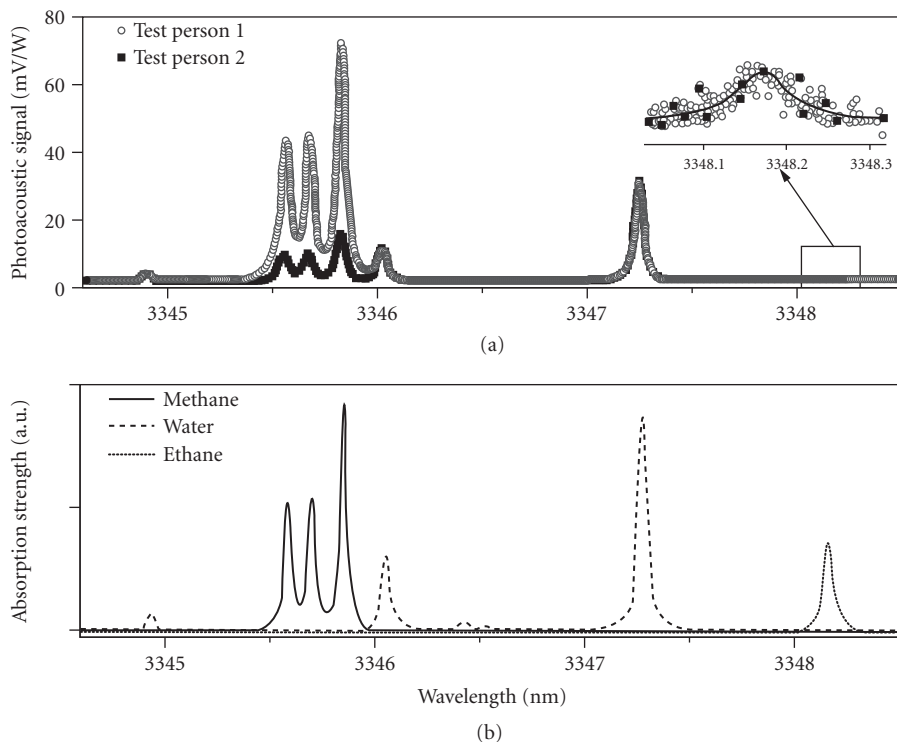


**FIGURE 18** Pump-scan around  $2996.9 \text{ cm}^{-1}$  of 0.4-ppb ethane in nitrogen at atmospheric pressure. A Lorentzian fit with linearly decreasing background has been plotted through the data (dashed line). The linearly decreasing background is also shown separately with a dotted line. The bottom of the picture shows the residual if the fit is subtracted from the data.<sup>21</sup>



**FIGURE 19** The high resolution performance and the wavelength stability of the SRO are demonstrated by recording the photoacoustic signal from the half maximum of a 77 mbar pressure broadened absorption line of 20 ppm of ethane in nitrogen at 2996.9  $\text{cm}^{-1}$ . When not tuning the pump frequency, the photoacoustic signal shows random oscillations at a rather high frequency (90 MHz/s), combined with an oscillation at a lower frequency (250 MHz in 200 s).<sup>23</sup>

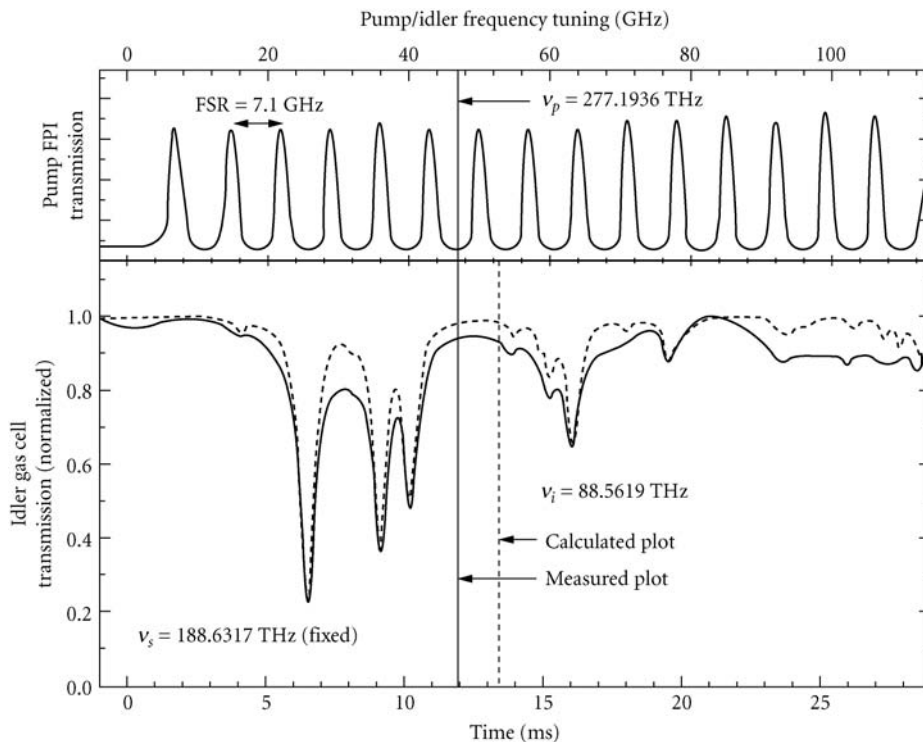
extension of operation of the SRO to the 3.7 to 4.7- $\mu\text{m}$  spectral range enabled photoacoustic detection of the  $\text{CO}_2$  absorption line in nitrogen near 4.235  $\mu\text{m}$  using 24-GHz continuous scan of the idler frequency.<sup>22</sup> By using a high-power cw SRO based on PPLN operating in the 2.6 to 4.7  $\mu\text{m}$  in the mid-IR, photoacoustic spectroscopy of a mixture of 20-ppm ethane in nitrogen was performed near 3.33  $\mu\text{m}$ .<sup>23</sup> The SRO was pumped by a 20-W, cw single-frequency Yb:YAG laser (tunable over 1.024 to 1.034  $\mu\text{m}$ ) and could deliver 3 W of idler power at 2.954  $\mu\text{m}$  (Fig. 3). By step-tuning the pump frequency using a combination of intracavity etalon and a Lyot filter, mode-hop-tuning of the idler over 190 GHz could be achieved, enabling coverage of several absorption lines of ethane. With 2.15 W of idler power available at 3.33  $\mu\text{m}$ , a photoacoustic detection sensitivity of 0.005 ppb was deduced. By monitoring the photoacoustic signal corresponding to the strongest absorption peak in the same 20-ppm mixture of ethane in nitrogen at low pressure (77 mbar) as a function of time (Fig. 19), a slow idler frequency drift of 250 MHz over 200 s was measured, which was attributed to the fluctuations in the PPLN crystal temperature and lack of thermal isolation of the SRO from the environment. The idler frequency also exhibited fast frequency fluctuations of 90 MHz/s, attributed to the nonoptimized coatings of the PPLN crystal and cavity mirrors, which resulted in unwanted etalon and resonance effects in the SRO cavity. In a later report, Ngai et al.<sup>24</sup> performed photoacoustic and cavity leak-out spectroscopy of several trace gases including  $\text{CO}_2$  and multicomponent gas mixtures of methane, ethane, and water in human breath using an automatically tunable cw SRO based on a multigrating MgO:PPLN crystal (Figs. 4 and 5). By deploying a ring SRO cavity with an uncoated intracavity YAG etalon and using a combination of pump tuning and etalon rotation, step-tuning of the idler over 207 GHz could be achieved. Adjustment of the crystal temperature could further be used to repeat this process, to provide wavelength scans of up to 450  $\text{cm}^{-1}$  with a single grating period at high resolution ( $<5 \times 10^{-4} \text{ cm}^{-1}$ ). By translating the crystal to other grating periods, an extended idler wavelength range of 2.75 to 3.83  $\mu\text{m}$  could be accessed. Using the wide wavelength scanning capability, extended wavelength coverage, and automatic tuning capability of this source, photoacoustic spectroscopy of strong  $\text{CO}_2$  combination bands in laboratory air (460 ppmv) extending over 14 nm (from 2788 to 2802 nm) was recorded by a combination of pump tuning, etalon rotation and crystal temperature tuning with a spectral resolution of 0.01 nm and a recording time of 1 hour. The recorded spectra were corrected for the water-vapor contribution to reveal the true



**FIGURE 20** (a) Photoacoustic spectra measured from the breath of two different test persons. The recorded spectra reveal a higher methane concentration in the breath of person 1, indicating the presence of methanogenic flora. (b) Calculated absorption spectra based on the HITRAN database for methane, ethane, and water.<sup>24</sup>

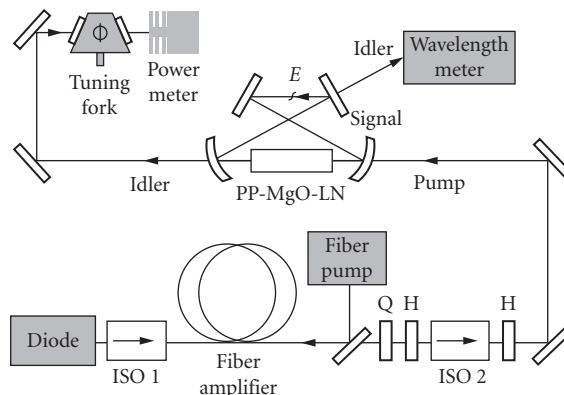
CO<sub>2</sub> spectra, with the results in excellent agreement with calculations. Similarly, using the same automatic tuning protocol, photoacoustic spectroscopy of methane, ethane, and water vapor in human breath were simultaneously recorded by scanning the idler wavelength in the 3344 to 3349 spectral range (Fig. 20). Concentrations of 21 ppmv and 13 ppbv were calculated for methane and ethane, respectively, in the first sample, and 4.5 ppmv and 13 ppbv in the second sample. Using the same cw SRO, cavity leak-out spectroscopy was performed for gas mixtures containing methane (at 3.221  $\mu\text{m}$ ) and ethane (at 3.337  $\mu\text{m}$ ) in N<sub>2</sub> at 100 mbar pressure. In the case of methane, the absorption peak was scanned over 200 s with a spectral resolution of 0.001 cm<sup>-1</sup>, resulting in a background methane concentration of 31 ppbv in N<sub>2</sub>, a noise-equivalent detection limit of 0.16 ppbv, and a minimum detectable absorption coefficient of  $2.0 \times 10^{-9}$  cm<sup>-1</sup>. For ethane, the idler was scanned over 60 s with a lower resolution of 0.01 cm<sup>-1</sup>, resulting in concentrations from 5 to 100 ppbv, a noise-equivalent detection limit of 0.07 ppbv, and a minimum detectable absorption coefficient of  $1.4 \times 10^{-9}$  cm<sup>-1</sup>. The cw SRO was also used to record the spectrum of <sup>12</sup>CH<sub>4</sub> and <sup>13</sup>CH<sub>4</sub> isotopes of methane in laboratory air with cavity leak-out spectroscopy. Scanning the idler wavelength from 3210 to 3211.5 nm revealed the absorption features corresponding to the two isotopes as well as water vapor, with the measured data in good agreement with calculated spectra.

The rapid and continuous mode-hop-free idler tuning over 110 GHz in a PPLN cw SRO pumped by a fiber-amplified DBR diode laser<sup>29</sup> has been used to perform real-time single-pass absorption spectroscopy of methane near 3.39  $\mu\text{m}$  with a refresh period of 29 ms and a corresponding refresh rate of 34 Hz, demonstrating the suitability of the system for rapid spectroscopic measurements (Fig. 21). In a subsequent experiment,<sup>50</sup> by taking advantage of frequency modulation capabilities

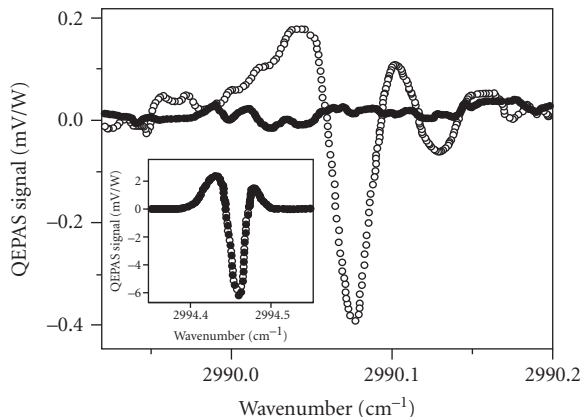


**FIGURE 21** Rapid mode-hop-free tuning of a cw SRO pumped by a fiber-amplified DBR diode laser, and application absorption spectroscopy of  $\text{CH}_4$ .<sup>29</sup>

of the idler output from a similar fiber-amplified DBR diode-pumped cw SRO, sensitive detection of multicomponent trace gas mixtures was performed using quartz-enhanced photoacoustic spectroscopy (QEPAS). The SRO, based on a multigrating  $\text{MgO}:\text{PPLN}$  crystal ( $L = 50$  mm,  $\Lambda = 28.5$  to  $31.5$   $\mu\text{m}$ ), was similarly configured in a ring cavity with a  $400$ - $\mu\text{m}$ -thick uncoated intracavity YAG etalon to provide enhanced frequency selection and stability (Fig. 22). The pump laser delivered  $7.9$  W of single-frequency power at  $1082$  nm with a linewidth of  $\sim 100$  MHz. The idler wavelength was tuned coarsely over  $3$  to  $4$   $\mu\text{m}$  by a combination of grating and temperature tuning, in discrete steps of  $1$  to  $4$   $\text{cm}^{-1}$  due to the combination of SRO cavity modes, etalon mode selection and phase-matching bandwidth of the crystal. Pump tuning was then used to provide fine wavelength control and mode-hop-free tuning of the idler over  $5.2$   $\text{cm}^{-1}$ , which could be shifted within a total range of  $16.5$   $\text{cm}^{-1}$  by current control of the DBR diode laser. By monitoring the idler wavelength with a wavemeter, and using a computer-controlled feedback loop to adjust the phase and current to the DBR, locking of idler frequency at  $2990.076$   $\text{cm}^{-1}$  could be achieved with a stability of  $1.7 \times 10^{-3}$   $\text{cm}^{-1}$  over  $30$  min. With the programmed tuning, idler wavenumbers from  $2987$  to  $2994$   $\text{cm}^{-1}$  could be accessed in  $1$ - $\text{cm}^{-1}$  steps within the pump tuning range, with any desired wavelength reached within  $\sim 20$  s of tuning the pump. Using this source, QEPAS spectral data of  $2$ -ppmv ethane in nitrogen were successfully recorded at  $2990.1$   $\text{cm}^{-1}$ , as well as isolated  $1.2$  percent water vapor at  $2994.4$   $\text{cm}^{-1}$  (Fig. 23). By locking the pump laser frequency to the maximum ethane absorption peak at  $2990.08$   $\text{cm}^{-1}$  and measuring concentrations from  $20$  ppmv down to  $100$  ppbv, a QEPAS detection limit of  $25$  ppbv was deduced. By keeping the idler wavelength fixed at the same absorption peak with a  $2$  ppmv methane concentration, a linear dependence of QEPAS signal on input power was verified, confirming the advantage of higher powers for improved detection sensitivity. To further demonstrate the



**FIGURE 22** Schematic of the cw SRO experimental setup for quartz-enhanced photoacoustic spectroscopy.<sup>50</sup>



**FIGURE 23** Example of a QEPAS scan over a 2 ppmv ethane peak at  $2990.08 \text{ cm}^{-1}$  (open circles) in 200 mbar nitrogen gas. QEPAS signal detected from pure nitrogen in the same spectral range is also shown, revealing a flat background signal (filled circles). Another example of a QEPAS scan is given in the inset for 1.2 percent water at  $2994.4 \text{ cm}^{-1}$ .<sup>50</sup>

unique advantages offered by the wide tuning coverage of the cw SRO, QEPAS data corresponding to a multiple gas mixture containing 2.2 ppmv ethane, 1.1 percent water, and 1.5 ppmv methane were successfully recorded by pump-tuning the idler from  $2979.4$  to  $2994.6 \text{ cm}^{-1}$ , with the obtained spectra in good agreement with calculations. From the obtained data, it was also possible to deduce an improved QEPAS detection limit of 13 ppbv for the stronger methane absorption line at  $2983.3 \text{ cm}^{-1}$  and 6.8 ppmv for water at  $2994.4 \text{ cm}^{-1}$ .

By deploying an all-fiber-pumped PPLN cw SRO,<sup>27</sup> single-pass absorption spectroscopy of several gases over the wavelength range of 2700 to 3200 nm was performed by continuous scanning of the idler frequency with a linewidth of  $\sim 1$  MHz. Using piezoelectric tuning of the fiber pump laser allowed mode-hop-free tuning of the idler frequency up to 60 GHz, enabling high-resolution spectroscopy of various absorption features in water vapor (2709 nm), carbon dioxide (2810 nm), nitrous oxide (2879 nm), ammonia (2897 nm), and methane (3167 nm).

In a separate experiment, using a PPLN cw DRO pumped directly by a 150-mW DBR diode laser and delivering 4 mW of idler output with a mode-hop-free tuning range of 10 GHz, simple single-pass absorption spectroscopy of CO molecule at 2.3  $\mu\text{m}$  was demonstrated.<sup>41</sup> Spectroscopic applications of cw OPOs in the visible spectral range has also been performed by external frequency doubling of the idler output from a cw DRO in an external enhancement cavity to generate yellow radiation in the 565 to 590 nm region.<sup>42</sup> The DRO was pumped by a cw, monolithic ring Nd:YAG laser at 1064 nm and by tuning the pump frequency over 10 GHz, the yellow output at 580 nm could be tuned smoothly over 18 GHz, while mode-hop tuning could provide 160 GHz of step-tuning across 20 mode pairs. This tuning capability enabled spectroscopy of the  ${}^5D_0 \rightarrow {}^7F_0$  transition in  $\text{Eu}^{3+}:\text{Y}_2\text{SiO}_5$  at 4 K, which is of interest because it exhibits the lowest known homogeneous linewidth for an optical transition in a solid. The step-tuning capability enabled the full spectrum of the transition containing two absorption peaks at 580.070 and 580.224 nm to be scanned, while the fine mode-hop-free tuning enabled continuous scan of each inhomogeneously broadened absorption peak, resulting in linewidths of  $\Delta\nu = 3$  GHz and  $\Delta\nu = 2.5$  GHz, respectively. Persistent spectral hole-burning was also observed by continuous tuning of the pump, and linewidths  $<1$  MHz were recorded after 40 min of burning. By monitoring the hole spectrum every few hours, it was possible to follow the hole decay as long as 15 hours, demonstrating the repeatability of frequency tuning and stability of the cw DRO over many hours.

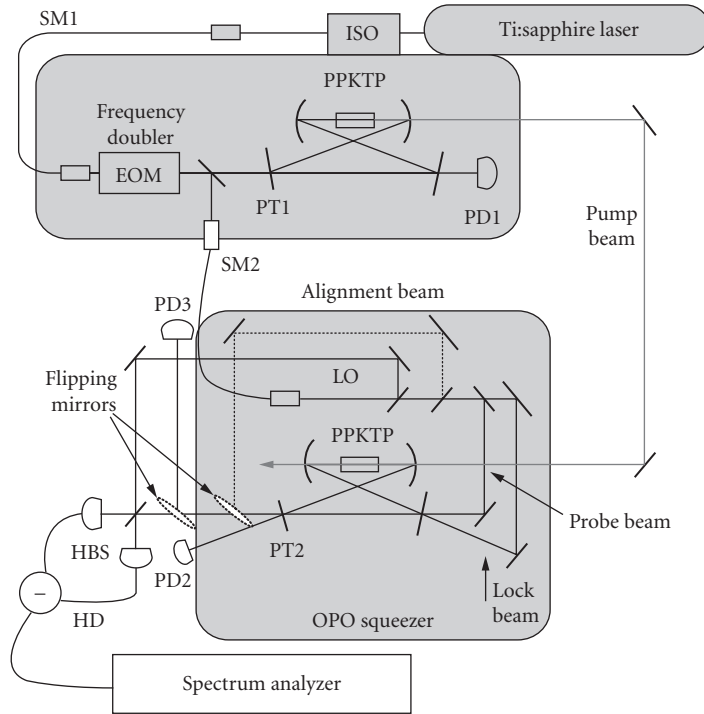
By deploying a cw PE-SRO based on a 19-mm-long PPLN crystal, Kovalchuk et al.<sup>51</sup> performed high-resolution Doppler-free spectroscopy of rovibrational transition of methane molecule at 3.39  $\mu\text{m}$ . The PE-SRO, configured in semi-monolithic cavity design and containing an intracavity etalon, was pumped by a cw single-mode Nd:YAG ring laser with a linewidth of  $\sim 5$  kHz. It could provide single-frequency idler output with a linewidth of  $\sim 100$  kHz and a mode-hop-free tuning range of 1 GHz, obtained by smooth tuning of the pump laser. The PE-SRO had a minimum oscillation threshold of 305 mW and generated a total two-way idler power of 58 mW at 3.39  $\mu\text{m}$  for 808 mW of input pump power. With this set-up, Doppler-free resonances with a resolution of  $\sim 500$  kHz were recorded in methane, limited by the frequency jitter of the PE-SRO idler output and pressure broadening. Subsequently, Muller et al.<sup>52</sup> reported a transportable, all-solid-state photoacoustic spectrometer based on a cw PE-SRO using an alternative dual-cavity semi-monolithic cavity design. The PE-SRO used a 19-mm-long multigrating PPLN crystal and was pumped by a 2.5-W cw single-frequency Nd:YAG laser at 1.064  $\mu\text{m}$ . The oscillator was characterized by a pump power threshold of 380 mW and could generate a total two-way idler power of 200 mW. Using active signal cavity length stabilization, an idler frequency stability better than  $\pm 30$  MHz was obtained. Coarse tuning of the idler wavelength over 3.1 to 3.9  $\mu\text{m}$  was performed by a combination of temperature and grating period variation, while the use of an etalon inside the signal cavity enabled continuous mode-hop-free tuning of the idler over 1.5 GHz by tuning the pump laser. Mode-hop tuning of the idler frequency in steps of 450 MHz could also be achieved over 52 GHz by rotation of the intracavity etalon. Using this mode-hop tuning method and with 70 mW of available idler power, photoacoustic spectroscopy of ethane was performed with a detection sensitivity of 110 ppt. By deploying the same dual-cavity cw PE-SRO in combination with cavity leak-out spectroscopy, substantial improvement in detection sensitivity of ethane down to 0.5 ppt was demonstrated near 3  $\mu\text{m}$ ,<sup>53</sup> and by exploiting the frequency tuning capability of the PE-SRO, simultaneous monitoring of ethane, methane, and water vapor in human breath could be performed, without significant interference from other gases.

In a further application, Stothard et al.<sup>54</sup> demonstrated the use of a cw PE-SRO for hyperspectral imaging of gases in the mid-IR. Based on a 20-mm-long, single-grating crystal of PPRTA and pumped by a 1-W diode-pumped Nd:YVO<sub>4</sub> laser, the PE-SRO could provide  $\sim 50$  mW of idler output power and coverage in the 3.18 to 3.50- $\mu\text{m}$  spectral range by temperature tuning the crystal. The use of a three-mirror standing-wave PE-SRO cavity and an intracavity etalon at the signal wavelength-enabled mode-hop tuning of the idler frequency over  $\sim 30$  GHz, in steps of 1.4 to 2 GHz, by rotation of the etalon. This frequency resolution was sufficient compared to the typical linewidth of  $\sim 5$  GHz for pressure-broadened transitions in gases under atmospheric pressure, thus enabling the deployment of the cw PE-SRO for imaging of methane gas in the atmosphere. By tuning the cw PE-SRO idler frequency to the strong methane absorption lines near 3.27 and 3.35  $\mu\text{m}$ , gas concentrations of

the order of 30 ppm-m could be detected and significant target areas ( $\sim 4 \text{ m}^2$  at 3 m) could be effectively imaged with the subsecond acquisition times.

As well as versatile spectroscopic tools, cw OPOs offer unique sources of correlated twin beams and nonclassical states of light for applications in quantum optics and quantum information processing. When pumped by cw all-solid-state lasers, they can provide compact twin-beam optical sources for quantum cryptography and sub-shot-noise measurement. In one configuration of such a device, a cw TRO based on a 10-mm KTP crystal and using a linear semi-monolithic resonator to separate the pump and parametric wave cavities, was reported by Hayasaka et al.<sup>55</sup> The TRO was pumped at 540 nm by the second harmonic of an extended-cavity single-stripe cw diode laser and was operated close to degeneracy. The use of this pump wavelength permitted type II NCPM in KTP, resulting in a TRO pump power threshold as low as 2.5 mW near degeneracy and providing 5.1 mW of cw output power for 16 mW of pump power. By recording the noise spectrum of the twin-beam intensities, 4.3 dB of intensity-difference squeezing was observed at  $\sim 3$  MHz. In a subsequent experiment, Su et al.<sup>56</sup> demonstrated quantum entanglement between the signal and idler twin beams in a nondegenerate cw DRO above threshold. The DRO, based on a 10-mm PPKTP crystal cut for type II nondegenerate phase matching, was configured in a linear semi-monolithic cavity and was pumped by the stabilized cw single-mode output of a frequency-doubled Nd:YAP laser at 540 nm. Using a pair of unbalanced Mach-Zender interferometers with unequal arm lengths, the amplitude and phase noise of the signal and idler beams above threshold were recorded at 20 MHz, enabling quantum correlations to be deduced from the noise levels of the intensity difference and phase sum of the photocurrents measured by the unbalanced interferometers. Using this method, the authors were able to deduce correlations of amplitude and phase quadratures of signal and idler below the shot-noise-limit, amounting to  $\sim 2.58$  and  $\sim 1.05$  dB, respectively, and from the sum of the amplitude and phase correlation variances, demonstrate quantum entanglement of the twin beams below the shot-noise-limit. For 230 mW of input pump power, nearly twice the 120-mW DRO threshold, the output power in the correlated twin beams was 22 mW. The nondegenerate signal and idler twin beams were at wavelengths of 1079.130 and 1080.215 nm, respectively, separated by 1.085 nm. In another experiment, Tanimura et al.<sup>57</sup> deployed a cw DRO below threshold to generate squeezed vacuum on resonance with the rubidium *D* line at 795 nm. The DRO, based on a 10-mm crystal of PPKTP, was configured in a ring cavity and pumped at 397.5 nm by the second harmonic of a cw single-frequency Ti:sapphire laser to provide near-degenerate signal and idler frequencies at 795 nm (Fig. 24). Operating the cw DRO below threshold and using homodyne detection, the authors were able to measure strongly squeezed vacuum at the OPO output. With the DRO operated at 61 mW of input pump power, below a calculated threshold of 150 mW, a squeezing level of  $-2.75$  dB below the shot-noise-limit and anti-squeezing level of  $+7.00$  dB above the shot-noise-limit was observed (Fig. 25). Such a system could find useful applications for ultraprecise measurements of atomic spins as well as quantum information processing by mapping squeezed vacuum onto an atomic ensemble.

Because of their phase coherent properties and the ability to lock correlated frequencies to stable optical references, cw OPOs also represent highly promising light sources for applications in optical frequency synthesis and metrology. In an example of such application, a novel approach based on the combination of a cw OPO with a femtosecond Ti:sapphire frequency comb was used to provide a phase-coherent bridge from the visible to mid-IR spectral regions.<sup>58</sup> The cw PE-SRO, based on a 19-mm PPLN crystal and deploying a similar configuration to that in Ref. 51 was pumped by a cw single-frequency Nd:YAG laser. The oscillator provided idler emission in the 2.4 to 3.7- $\mu\text{m}$  spectral range, with 50 mW of idler power and an instantaneous linewidth of  $\sim 10$  kHz at 3.39  $\mu\text{m}$ . The technique takes advantage of the fact that in a PPLN cw PE-SRO, in addition to the phase-matched signal and idler, there are also non-phase-matched frequencies generated by mixing of the resonant pump and signal waves. This process provides a range of visible frequencies within the emission bandwidth of a femtosecond Ti:sapphire laser, which can be used for frequency comparison with the nearest comb lines. By forming suitable differences of the heterodyne beat frequencies between the visible frequency components from the cw OPO and adjacent comb lines in the femtosecond laser, mutual phase locking of OPO optical frequencies, Ti:sapphire repetition frequency and carrier-envelope offset frequency could be obtained. Using this method, the authors performed direct frequency comparison between an iodine-stabilized Nd:YAG laser at 1.064  $\mu\text{m}$  and a mid-IR methane



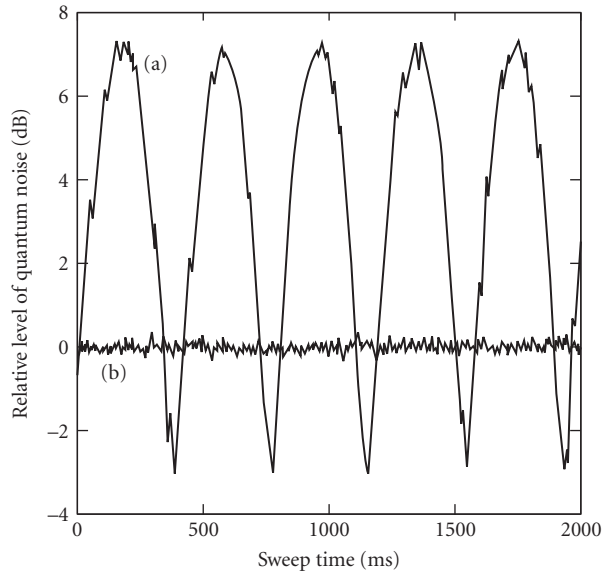
**FIGURE 24** Experimental setup for PPKTP cw DRO for the generation of squeezed vacuum. ISO, optical isolator; EOM, electro-optic modulator; OPO, subthreshold degenerate optical parametric oscillator; HBS, half-beam splitter; PT, partial transmittance mirror; HD, balanced homodyne detector; PD, photodiode; SM, single-mode fiber.<sup>57</sup>

optical frequency standard at  $3.39\ \mu\text{m}$ . Subsequent demonstrations, taking advantage of the unique coherence properties of cw OPOs for frequency synthesis, include the development of a precise  $3/2$  frequency multiplier from a near-IR pump to the visible using a cw TRO.<sup>49</sup>

## 17.4 SUMMARY

This chapter has provided an overview of the latest advances in cw OPOs and their applications over the past decade. The advent of QPM nonlinear materials has had an unprecedented impact on cw OPO technology which, combined with major advances in solid-state laser technology and innovative design architectures, has led to the realization of a new generation of truly practical cw OPOs with performance capabilities surpassing conventional lasers. The mature technology and ready availability of PPLN has enabled the development of near- and mid-IR cw OPOs for the 1 to  $5\ \mu\text{m}$  spectral range in various resonance configurations, from TROs offering minimal oscillation threshold and lowest output power to cw SROs with highest threshold and watt-level output power, previously unattainable with birefringent nonlinear materials, and using a variety of pump sources from miniature semiconductor diode lasers to high-power solid-state and fiber lasers. The application of novel cavity designs and resonance schemes including pump enhancement, dual cavities and





**FIGURE 25** Measured quantum noise levels in cw DRO base on PPKTP. (a) Local oscillator beam phase was scanned. (b) Shot-noise level. Noise levels are displayed as the relative power compared to the shotnoise level (0 dB). The settings of the spectrum analyzer were zero-span mode at 1 MHz, resolution bandwidth = 100 kHz, and video bandwidth = 30 Hz.<sup>57</sup>

intracavity pumping, together with innovative tuning and stabilization techniques have enabled the generation of coherent output with excellent power and frequency stability and short-term linewidths down to a few kHz, long-term stability of a few MHz, and smooth mode-hop-free tuning of more than 100 GHz from cw OPOs. With the continuing advances in QPM material technology, reliable fabrication of MgO-doped PPLN has led to significant reductions in photorefractive damage, enabling its use at lower temperatures and higher powers with reduced output beam degradation. By deploying high-power fiber pump lasers in combination with MgO:PPLN, output powers in excess of 10 W have now been realized in cw SROs and power scaling to several tens of watts appears a clear possibility.

While photorefractive damage has placed limitations on the use of (MgO:)PPLN under visible pumping and confined operation of cw OPOs to near- and mid-IR above  $\sim 1 \mu\text{m}$ , advances in QPM material technology have enabled reliable fabrication of alternative QPM crystals with short grating periods, long interaction lengths, and immunity to photorefractive. This has paved the way for spectral extension of cw OPOs to the wavelengths below  $1 \mu\text{m}$  by exploiting QPM materials including MgO:sPPLT and PPKTP and using direct pumping in the visible followed by additional frequency upconversion steps internal or external to the OPO cavity. By exploiting such techniques, spectral regions in orange and red have been successfully accessed and wavelengths down to 425 nm in the blue have been generated at several hundred milliwatts of output power in single-frequency spectrum and high beam quality. These developments have opened up new opportunities for the realization of practical solid-state sources with wide tunability across the visible and into the UV, where there is a severe shortage of conventional laser sources or other solid-state technologies.

The rapid advances in cw OPOs over the past decade have paved the way for the routine deployment of practical devices in a wide range of applications, from spectroscopy and imaging to frequency metrology and quantum optics. The unique capabilities of cw OPOs with regard to spectral versatility, output power, frequency and power stability, and compact solid-state design

open up new avenues for the ultimate development of these devices in real applications including portable gas detectors, mobile breath analyzers, handheld imaging systems or transportable optical frequency meters. At the same time, significant challenges and opportunities remain for further advancement of cw OPOs. In particular, wavelength extension of these devices into the mid-IR wavelength regions beyond 5  $\mu\text{m}$  remains difficult because of the absorption of oxide-based QPM nonlinear materials, the key building blocks for the successful development of cw OPOs. The 5 to 12- $\mu\text{m}$  spectral range is a particularly important and interesting region because of the presence of several atmospheric windows as well as many molecular absorption finger prints, including volatile substances in exhaled breath. The development of cw OPOs for this wavelength range will thus be of significant interest for spectroscopy, gas sensing, biomedicine, and atmospheric transmission. Progress toward the development of cw OPOs in this spectral range will require the deployment of alternative mid-IR birefringent nonlinear materials such as  $\text{ZnGeP}_2$ , or the more recently developed nonlinear crystals such as  $\text{CdSiP}_2$  and orientation-patterned GaAs, together with suitable near- to mid-IR laser pump sources and cascaded two-step pumping schemes. On the other hand, advancement of cw OPOs toward shorter UV wavelengths below the current 425-nm limit will be feasible with the use of recently demonstrated frequency upconversion techniques internal to cw SROs by exploiting existing birefringent crystals such as BBO, BIBO, and LBO. With the rapid advances in cw fiber laser technology and the potential for wavelength extension toward the extremes of the optical spectrum, the realization of compact, high-power and practical coherent solid-state light sources across the entire 300 to 12000 nm range based on cw OPOs appears a clear possibility in not too distant a future.

## 17.5 REFERENCES

1. M. Ebrahim-Zadeh and M. H. Dunn, "Optical Parametric Oscillators," in *OSA Handbook of Optics*, Vol. 4, (McGraw-Hill, New York, 2000) pp. 22.1–22.72.
2. J. A. Giordmaine and R. C. Miller, "Tunable Coherent Parametric Oscillation in  $\text{LiNbO}_3$  at Optical Frequencies," *Phys. Rev. Lett.* **14**:973–976 (1965).
3. R. L. Byer and A. Piskarskas, "Optical Parametric Oscillation and Amplification," Special Issue, *J. Opt. Soc. Am. B* **10**:1656–1791; 2148–2243 (1993).
4. W. R. Bosenberg and R. C. Eckardt, "Optical Parametric Devices," Special issue, *J. Opt. Soc. Am. B* **12**: 2084–2322 (1995).
5. S. Schiller and J. Mlynek, "Continuous-Wave Optical Parametric Oscillators," Special Issue, *Appl. Phys. B* **66**: 661–764 (1998).
6. M. Ebrahim-Zadeh, R. C. Eckardt, and M. H. Dunn, "Optical Parametric Devices and Processes," Special Issue, *J. Opt. Soc. Am. B* **16**:1477–1602 (1999).
7. M. Ebrahim-Zadeh, "Mid-Infrared Ultrafast and Continuous-Wave Optical Parametric Oscillators," in *Solid-State Mid-Infrared Laser Sources* (Springer, Berlin, Heidelberg, 2003) pp. 179–218.
8. M. Ebrahim-Zadeh, "Optical Parametric Devices," in *Handbook of Laser Technology and Applications* (Institute of Physics Publishing, London, 2003) pp. 1347–1392.
9. K. L. Vodopyanov, "Pulsed Mid-Infrared Optical Parametric Oscillators," in *Solid-State Mid-Infrared Laser Sources*, I. T. Sorokina and K. L. Vodopyanov, eds. (Springer, Berlin, Heidelberg, 2003) pp. 141–178.
10. M. Ebrahim-Zadeh, "Mid-Infrared Optical Parametric Oscillators and Applications," in *Mid-Infrared Coherent Sources and Applications*, M. Ebrahim-Zadeh and I. T. Sorokins, eds. (Springer, Berlin, Heidelberg, 2007) pp. 347–375.
11. R. L. Sutherland, *Handbook of Nonlinear Optics* (Marcel Dekker, New York, 1996).
12. M. H. Dunn and M. Ebrahim-Zadeh, "Parametric Generation of Tunable Light from Continuous-Wave to Femtosecond Pulses," *Science* **286**:1513–1517 (1999).
13. M. Ebrahim-Zadeh, "Parametric Light Generation," *Phil. Trans. Roy. Soc. London A* **263**:2731–2750 (2003).
14. S. E. Harris, "Tunable Optical Parametric Oscillators," *Proc. IEEE* **57**:2096–2113 (1969).

15. R. L. Byer, "Optical Parametric Oscillators," in *Treatise in Quantum Electronics* (Academic Press, New York, 1973) pp. 587–702.
16. R. G. Smith, "Optical Parametric Oscillators," in *Lasers* (Marcel Dekker, New York, 1976) pp. 189–307.
17. I. D. Lindsay, "High Spatial and Spectral Quality Diode-Laser-Based Pump Sources for Solid-State Lasers and Optical Parametric Oscillators," PhD. Thesis, University of St Andrews (1999).
18. T. J. Edwards, G. A. Turnbull, M. H. Dunn, and M. Ebrahim-Zadeh, "Continuous-Wave, Singly-Resonant, Optical Parametric Oscillator Based on Periodically Poled KTiOPO<sub>4</sub>," *Opt. Exp.* **16**:58–63 (2000).
19. S. E. Bisson, K. M. Armstrong, T. J. Kulp, and M. Hartings, "Broadly Tunable, Mode-Hop-Tuned CW Optical Parametric Oscillator Based on Periodically Poled Lithium Niobate," *Appl. Phys. B* **40**:6049–6055 (2001).
20. M. Van Herpen, S. te Lintel Hekkert, S. E. Bisson, and F. J. M. Harren, "Wide Single-Mode Tuning of a 3.0–3.8- $\mu\text{m}$ , 700-mW, Continuous-Wave Nd:YAG-Pumped Optical Parametric Oscillator Based on Periodically-Poled Lithium Niobate," *Opt. Lett.* **27**:640–642 (2002).
21. M. M. J. W. Van Herpen, S. Li, S. E. Bisson, S. te Lintel Hekkert, and F. J. M. Harren, "Tuning and Stability of Continuous-Wave Mid-Infrared High-Power Single Resonant Optical Parametric Oscillator," *Appl. Phys. B* **75**:329–333 (2002).
22. M. M. J. W. Van Herpen, S. E. Bisson, and F. J. M. Harren, "Continuous-Wave Operation of a Single-Frequency Optical Parametric Oscillator at 4–5  $\mu\text{m}$  Based on Periodically Poled LiNbO<sub>3</sub>," *Opt. Lett.* **28**:2497–2499 (2003).
23. M. M. J. W. Van Herpen, S. E. Bisson, A. K. Y. Ngai, and F. J. M. Harren, "Combined Wide Pump Tuning and High Power of a Continuous-Wave, Singly Resonant Optical Parametric Oscillator," *Appl. Phys. B* **78**:281–286 (2004).
24. A. K. Y. Ngai, S. T. Persijn, G. Von Basum, and F. J. M. Harren, "Automatically Tunable Continuous-Wave Optical Parametric Oscillator for High-Resolution Spectroscopy and Sensitive Trace-Gas Detection," *Appl. Phys. B* **85**:173–180 (2006).
25. P. Gross, M. E. Klein, T. Walde, K.-J. Boller, M. Auerbach, P. Wessels, and C. Fallnich, "Fiber-Laser-Pumped Continuous-Wave Singly Resonant Optical Parametric Oscillator," *Opt. Lett.* **27**:418–420 (2002).
26. M. E. Klein, P. Gross, K.-J. Boller, M. Auerbach, P. Wessels, and C. Fallnich, "Rapidly Tunable Continuous-Wave Optical Parametric Oscillator Pumped by a Fiber Laser," *Opt. Lett.* **28**:920–922 (2003).
27. A. Henderson and R. Stafford, "Low Threshold, Singly Resonant CW OPO Pumped by an All-Fiber Pump Source," *Opt. Exp.* **14**:767–772 (2006).
28. M. E. Klein, C. K. Laue, D.-H. Lee, K.-J. Boller, and R. Wallenstein, "Diode-Pumped Singly Resonant Continuous-Wave Optical Parametric Oscillator with Wide Continuous Tuning of the Near-Infrared Idler Wave," *Opt. Lett.* **25**:490–492 (2000).
29. I. D. Lindsay, B. Adhimoolam, P. Gross, M. E. Klein, and K.-J. Boller, "110 GHz Rapid, Continuous Tuning from an Optical Parametric Oscillator Pumped by a Fiber-Amplified DBR Diode Laser," *Opt. Exp.* **13**:1234–1239 (2005).
30. A. Henderson and R. Stafford, "Intracavity Power Effects in Singly Resonant CW OPOs," *Appl. Phys. B* **85**:181–184 (2006).
31. G. K. Samanta and M. Ebrahim-Zadeh, "Continuous-Wave Singly Resonant Optical Parametric Oscillator with Resonant Wave Coupling," *Opt. Exp.* **16**:6883–6888 (2008).
32. A. V. Okishev and J. D. Zuegel, "Intracavity-Pumped Raman Laser Action in a Mid-IR, Continuous-Wave (CW) MgO:PPLN Optical Parametric Oscillator," *Opt. Exp.* **14**:12169–12173 (2006).
33. A. Henderson and R. Stafford, "Spectral Broadening and Stimulated Raman Conversion in a Continuous-Wave Optical Parametric Oscillator," *Opt. Lett.* **32**:1281–1283 (2007).
34. U. Strossner, J. P. Meyn, R. Wallenstein, P. Urenski, A. Arie, G. Rosenman, J. Mlynek, S. Schiller, and A. Peters, "Single-Frequency Continuous-Wave Optical Parametric Oscillator System with an Ultrawide Tuning Range of 550–2830 nm," *J. Opt. Soc. Am. B* **19**:1419–1424 (2002).
35. G. K. Samanta, G. R. Fayaz, Z. Sun, and M. Ebrahim-Zadeh, "High-Power, Continuous-Wave, Singly Resonant Optical Parametric Oscillator Based on MgO:sPPLT," *Opt. Lett.* **32**:400–402 (2007).
36. G. K. Samanta, G. R. Fayaz, and M. Ebrahim-Zadeh, "1.59-W, Single-Frequency, Continuous-Wave Optical Parametric Oscillator Based on MgO:sPPLT," *Opt. Lett.* **32**:2623–2625 (2007).
37. J.-M. Melkonian, T.-H. My, F. Bretenaker, and C. Drag, "High Spectral Purity and Tunable Operation of a Continuous Singly Resonant Optical Parametric Oscillator Emitting in the Red," *Opt. Lett.* **32**:518–520 (2007).

38. G. K. Samanta and M. Ebrahim-Zadeh, "Continuous-Wave, Single-Frequency, Solid-State Blue Source for the 425-489 nm Spectral Range," *Opt. Lett.* **33**:1228–1230 (2008).
39. T.-H. My, C. Drag, and F. Bretenaker, "Single-Frequency and Tunable Operation of a Continuous Intracavity Frequency Doubled Singly Resonant Optical Parametric Oscillator," *Opt. Lett.* **33**:1455–1457 (2008).
40. C. Langrock and M. M. Fejer, "Fiber-Feedback Continuous-Wave and Synchronously Pumped Singly Resonant Ring Optical Parametric Oscillators Using Reverse-Proton-Exchanged Periodically Poled Lithium Niobate Waveguides," *Opt. Lett.* **32**:2263–2265 (2007).
41. A. J. Henderson, P. M. Roper, L. A. Borschowa, and R. D. Mead, "Stable, Continuously Tunable Operation of a Diode-Pumped Doubly Resonant Optical Parametric Oscillator," *Opt. Lett.* **25**:1264–1266 (2000).
42. T. Petelski, R. S. Conroy, K. Benecheikh, J. Mlynek, and S. Schiller, "All-Solid-State, Tunable, Single-Frequency Source of Yellow Light for High-Resolution Spectroscopy," *Opt. Lett.* **26**:1013–1015 (2001).
43. I. D. Lindsay, C. Petridis, M. H. Dunn, and M. Ebrahim-Zadeh, "Continuous-Wave Pump-Enhanced Singly Resonant Optical Parametric Oscillator Pumped by an Extended-Cavity Diode Laser," *Appl. Phys. Lett.* **78**:871–873 (2001).
44. G. A. Turnbull, D. McGloin, I. D. Lindsay, M. Ebrahim-Zadeh, and M. H. Dunn, "Extended Mode-Hop-Free Tuning by Use of Dual-Cavity, Pump-Enhanced Optical Parametric Oscillator," *Opt. Lett.* **25**:341–343 (2000).
45. D. J. M. Stothard, I. D. Lindsay, M. H. Dunn, "Continuous-Wave Pump-Enhanced Optical Parametric Oscillator with Ring Resonator for Wide and Continuous Tuning of Single-Frequency Radiation," *Opt. Exp.* **12**:502–511 (2004).
46. I. D. Lindsay, D. J. M. Stothard, C. F. Rae, and M. H. Dunn, "Continuous-Wave Pump-Enhanced Optical Parametric Oscillator Based on Periodically Poled RbTiOAsO<sub>4</sub>," *Opt. Exp.* **11**:134–140 (2003).
47. F. Muller, G. Von Basum, A. Pop, D. Halmer, P. Hering, M. Murtz, F. Kunnermann, and S. Schiller, "Long-Term Frequency Stability and Linewidth Properties of Continuous-Wave Pump-Resonant Optical Parametric Oscillators," *Appl. Phys. B* **80**:307–313 (2005).
48. P. Gross, M. E. Klein, H. Ridderbusch, D.-H. Lee, J.-P. Meyn, R. Wallenstein, and K.-J. Boller, "Wide Wavelength Tuning of an Optical Parametric Oscillator Through Electro-Optic Shaping of the Gain Spectrum," *Opt. Lett.* **27**:1433–1435 (2002).
49. G. Ferrari, "Generating Green to Red Light with Semiconductor Lasers," *Opt. Exp.* **15**:1672–1678 (2007).
50. A. K. Y. Ngai, S. T. Persijn, I. D. Lindsay, A. A. Kosterev, P. Gross, C. J. Lee, S. M. Cristescu, F. K. Tittel, K.-J. Boller, and F. J. M. Harren, "Continuous Wave Optical Parametric Oscillator for Quartz-Enhanced Photoacoustic Trace Gas Sensing," *Appl. Phys. B* **89**:123–128 (2007).
51. E. V. Kovalchuk, D. Dekorsy, A. I. Lvovsky, C. Braxmaier, J. Mlynek, A. Peters, and S. Schiller, "High-Resolution Doppler-Free Molecular Spectroscopy with a Continuous-Wave Optical Parametric Oscillator," *Opt. Lett.* **26**:1430–1432 (2001).
52. F. Muller, A. Popp, F. Kuhnemann, and S. Schiller, "Transportable, Highly Sensitive Photoacoustic Spectrometer Based on Continuous-Wave Dual-Cavity Optical Parametric Oscillator," *Opt. Exp.* **11**:2820–2825 (2003).
53. G. von Basum, D. Halmer, P. Hering, M. Murtz, S. Schiller, F. Muller, A. Popp, and F. Kuhnemann, "Parts per Trillion Sensitivity for Ethane in Air with an Optical Parametric Oscillator Cavity Leak-Out Spectrometer," *Opt. Lett.* **29**:797–799 (2004).
54. D. J. M. Stothard, M. H. Dunn, and C. F. Rae, "Hyperspectral Imaging of Gases with a Continuous-Wave Pump-Enhanced Optical Parametric Oscillator," *Opt. Exp.* **12**:947–955 (2004).
55. K. Hayasaka, Y. Zhang, and K. Kasai, "Generation of Twin Beams from an Optical Parametric Oscillator Pumped by a Frequency-Doubled Diode Laser," *Opt. Lett.* **29**:1665–1667 (2004).
56. X. Su, A. Tan, X. Jia, Q. Pan, C. Xie, and K. Peng, "Experimental Demonstration of Quantum Entanglement Between Frequency Non-Degenerate Optical Twin Beams," *Opt. Lett.* **31**:1133–1135 (2006).
57. T. Tanimura, D. Akamatsu, Y. Yokoi, A. Furusawa, and M. Kozuma, "Generation of a Squeezed Vacuum Resonant on a Rubidium  $D_1$  Line with Periodically Poled KTiOPO<sub>4</sub>," *Opt. Lett.* **31**:2344–2364 (2006).
58. E. V. Kovalchuk, T. Schuldt, and A. Peters, "Combination of a Continuous-Wave Optical Parametric Oscillator and a Femtosecond Frequency Comb for Optical Frequency Metrology," *Opt. Lett.* **30**:3141–3143 (2005).

*This page intentionally left blank*

# NONLINEAR OPTICAL PROCESSES FOR ULTRASHORT PULSE GENERATION

Uwe Siegner and Ursula Keller

*Institute of Quantum Electronics  
Physics Department  
Swiss Federal Institute of Technology (ETH)  
Zurich, Switzerland*

## 18.1 GLOSSARY

- $A_A$  laser beam cross section on the absorber  
 $A_L$  laser beam cross section in the laser gain material. If the cavity mode is not constant inside the gain medium, this area corresponds to an effective averaged value.  
 $c$  light velocity in vacuum  
 $D_2$  total group delay dispersion inside the laser cavity per cavity round-trip (i.e., second-order dispersion)  
 $d$  sample thickness  
DR differential reflectivity  
DT differential transmission  
 $E_p$  intracavity pulse energy  
 $E_{\text{sat},A}$  saturation energy of the saturable absorber  
 $E_{\text{sat},L}$  saturation energy of laser material  
 $F_{p,A}$  pulse fluence on the absorber

$$F_{p,A} = \frac{E_p}{A_A} = \int I_A(t) dt$$

- $F_{\text{sat},A}$  saturation fluence of the absorber

$$F_{\text{sat},A} = \frac{E_{\text{sat},A}}{A_A}$$

- $F_{\text{sat},L}$  saturation fluence of laser material

$$F_{\text{sat},L} = \frac{h\nu}{2\sigma_L} = \frac{E_{\text{sat},L}}{A_L}$$

The factor of 2 is used in case of a linear resonator with a standing wave.

$g$	saturated amplitude gain cross section
$g_0$	small signal amplitude gain coefficient
$I(t)$	time-dependent intensity
$I_A(t)$	time-dependent intensity on absorber
$I_L(t)$	time-dependent intensity inside the laser gain material
$I_{\text{sat},A}$	saturation intensity of the absorber

$$I_{\text{sat},A} = \frac{F_{\text{sat},A}}{\tau_A}$$

$I_{\text{sat},L}$  saturation intensity of laser material

$$I_{\text{sat},L} = \frac{F_{\text{sat},L}}{\tau_L}$$

$k$	wave number in vacuum $k = \omega/c = 2\pi/\lambda$
$k_n$	wave number in a dielectric with refractive index $n$ : $k_n = kn$
$\mathbf{k}_1$	wave vector of the pump pulse in a pump-probe experiment or of the first pulse applied in an FWM experiment for positive time delay $\Delta t$
$\mathbf{k}_2$	wave vector of the probe pulse in a pump-probe experiment or of the second pulse applied in an FWM experiment for positive time delay $\Delta t$
$L_L$	length of the laser gain medium
$n_2$	nonlinear refractive index
$P(t)$	time-dependent power: $E_p = \int P(t)dt$
$q(t)$	saturable amplitude loss coefficient (does not include any nonsaturable losses)
$q_0$	unsaturated amplitude loss coefficient, also corresponds to the maximal loss coefficient
$\alpha$	intensity absorption constant
$\Delta\alpha$	nonlinear change of the intensity absorption constant
$\Delta R$	maximum modulation depth of a saturable absorber integrated within a mirror structure (i.e., the maximum nonlinear intensity reflectivity change)
$\Delta R_{\text{ns}}$	nonsaturable loss of a saturable absorber integrated within a mirror structure
$\Delta t$	time delay between the excitation pulses in a pump-probe or FWM experiment
$\nu$	frequency
$\nu_0$	center frequency
$\Delta\nu_g$	FWHM (full width half maximum) gain bandwidth
$\lambda$	wavelength in vacuum
$\lambda_n$	wavelength in a dielectric medium with a refractive index $n$
$\lambda_0$	center wavelength
$\sigma_L$	gain cross section: $F_{\text{sat},L} = h\nu/\sigma_L$ , where $h$ is the Planck's constant
$\sigma_A$	absorber cross section: $F_{\text{sat},A} = h\nu/\sigma_A$
$\tau_p$	FWHM (full width half maximum) of pulse intensity
$\tau_A$	recovery time of the saturable absorber
$\tau_L$	upper state lifetime of laser medium

## 18.2 ABBREVIATIONS

A-FPSA	antiresonant Fabry-Perot saturable absorber
APM	additive pulse modelocking
$\text{As}_{\text{Ga}}$	arsenic antisite
$\text{As}_{\text{Ga}}^0$	neutral arsenic antisite
$\text{As}_{\text{Ga}}^+$	ionized arsenic antisite
CB	conduction band
CPM	colliding pulse modelocking
FWHM	full width half maximum
FWM	four-wave mixing
KLM	Kerr lens modelocking
LT	low temperature
MBE	molecular beam epitaxy
MOCVD	metal-organic chemical vapor deposition
SAM	self-amplitude modulation
SBR	saturable Bragg reflector
SESAM	semiconductor saturable absorber mirror
SPM	self-phase modulation
$V_{\text{Ga}}$	Ga vacancy
VB	valence band

## 18.3 INTRODUCTION

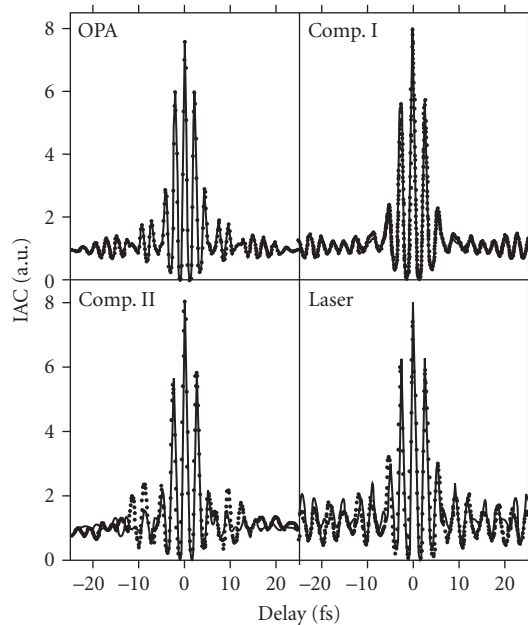
Since 1990 we have observed tremendous progress in ultrafast laser sources—a development that was triggered by the invention of the Ti:sapphire laser.<sup>1</sup> The strong interest in all-solid-state ultrafast laser technology was the driving force and formed the basis for many new inventions and discoveries. Solid-state lasers provide some of the best laser qualities in terms of high-quality spatial modes, high output power, energy storage and large pulse energy when Q-switched, and large optical bandwidth necessary for ultrashort pulse generation. Today, the most important nonlinear optical processes that support short and ultrashort passive pulse generation are based on Kerr and/or semiconductor nonlinearities. Saturable absorbers based on either the Kerr effect or on semiconductors play a major role in ultrashort pulse generation. However, independent of the specific saturable absorber material or mechanism, we can define a few macroscopic saturable absorber parameters that will determine the pulse formation process. These parameters are defined in Sec. 18.4 and discussed in more detail for the specific cases of a slow and a fast saturable absorber. The material properties then can be modified over an even larger range if the absorber is integrated within a device structure. This will be discussed at the end of Sec. 18.4. Stable pulse generation can then be obtained when these macroscopic saturable absorber parameters are designed correctly. The crucial role of the optical Kerr effect in ultrashort pulse generation will be discussed in Sec. 18.5. Optimization of semiconductor saturable absorber parameters normally requires a better understanding of the underlying physics, that is, the microscopic properties (Sec. 18.6). Ultrafast nonlinear optical processes can be analyzed in various ways to extract the information about the material system involved in the process. Numerous studies with ultrafast laser pulses have been performed in atomic, molecular, and condensed matter systems. Thus, some of the most common experimental techniques in ultrafast spectroscopy will also be reviewed in Sec. 18.6. The results of such ultrafast spectroscopy measurements are then summarized for semiconductor materials because of their importance in ultrashort pulse generation.



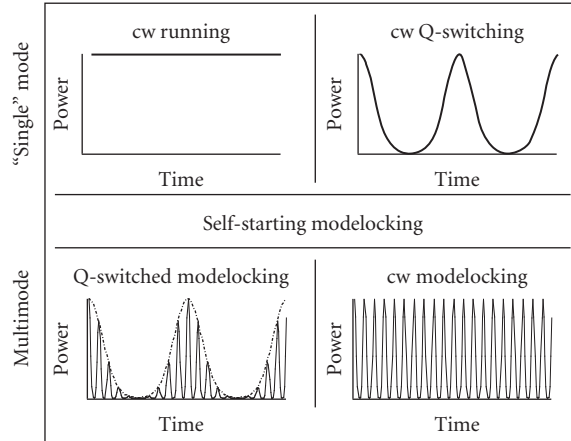
Today ultrafast lasers demonstrate unsurpassed performances: pulse duration in the two-cycle regime,<sup>2,3</sup> compact and reliable picosecond and femtosecond all-solid-state lasers,<sup>4,5</sup> pulse repetition rates in the 100-GHz regime,<sup>6,7</sup> average powers well above 10 W,<sup>8</sup> and novel Q-switching performances that bridge the gap between modelocking and Q-switching both in terms of pulse durations and pulse repetition rates.<sup>9</sup> A more recent review is given in Ref. 10 with detailed tables summarizing the different modelocking results for many solid-state lasers. Further average power scaling towards the 1-kW regime looks very promising with SESAM modelocked Yb-doped thin disk lasers<sup>11</sup> and this concept could be transferred to optically pumped semiconductor lasers.<sup>12,13</sup>

Optical pulses in the two-cycle regime have been produced by a variety of methods: direct generation in a modelocked laser oscillator,<sup>2,3</sup> continuum generation together with parametric optical amplification,<sup>14</sup> and external pulse compression.<sup>15,16</sup> In Fig. 1, interferometric autocorrelation measurements of the two-cycle pulses are shown. Although this is a relatively crude characterization technique, it is the only common measurement that has been performed on these sources; thus it allows for a direct comparison. These pulse generation techniques rely essentially on three identical ingredients:<sup>17</sup> (1) an ultrabroadband amplifying process, (2) precise control of dispersion, and (3) the nonlinear optical Kerr effect.

Ultrafast all-solid-state lasers are based on diode-pumped solid-state lasers. Semiconductor saturable absorbers were the first intracavity saturable absorbers that reliably started and sustained passive modelocked diode-pumped solid-state lasers.<sup>18,19</sup> Any previous attempts to passively modelock such lasers with intracavity saturable absorbers resulted in Q-switching instabilities or Q-switched modelocking (see Fig. 2). The precise control of optical nonlinearities was necessary to resolve



**FIGURE 1** Interferometric autocorrelation measurements of different sources in the 5-fs range: OPA: optical parametric amplification.<sup>14</sup> Comp. I: compression of Ti:sapphire cavity-dumped pulses in silica fiber.<sup>15</sup> Comp. II: compression of amplified  $\mu\text{J}$  pulses in a hollow fiber filled with Krypton.<sup>16</sup> Laser: pulses directly obtained from a Ti:sapphire laser without any external pulse compression.<sup>2</sup> Dots are measured data and lines correspond to fits that were used to estimate pulse duration from autocorrelation.



**FIGURE 2** Different modes of operation of a laser with a saturable absorber. Continuous wave (cw) Q-switching typically occurs with much longer pulses and lower pulse repetition rates than cw mode-locking.

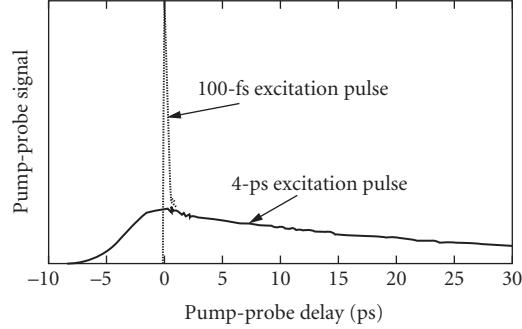
the Q-switching problem. Such a control can be achieved with epitaxially grown semiconductor saturable absorbers, which makes them very attractive for use as saturable absorbers in solid-state lasers. Semiconductor saturable absorbers provide a variety of bandgaps, ranging from the visible to the infrared, and can be easily integrated into different device structures (such as a mirror, for example), which allows for the control of the absorber parameters over an even larger range. This is actually required to obtain stable pulse generation with many solid-state lasers. The specific saturable absorber nonlinearities required for stable cw modelocking or Q-switching have recently been discussed in much more detail in Ref. 4 and will be briefly summarized in Sec. 18.4.

In this section we will put the emphasis on the nonlinearities used for ultrashort pulse generation. It is not our goal to provide a tutorial for pulse generation techniques such as passive modelocking or Q-switching. A more tutorial-type overview of the physics of ultrashort pulse generation was given in Refs. 5, 10, 20, and 21. We would like to refer the interested readers to those chapters and the extensive references therein.

## 18.4 SATURABLE ABSORBERS: MACROSCOPIC DESCRIPTION

### Saturable Absorber: Self-Amplitude Modulation

Saturable absorbers have been used to passively Q-switch and modelock many different lasers. Different saturable absorbers, such as organic dyes, colored filter glasses, dye-doped crystals, and semiconductors have been used. Independent of the specific saturable absorber material, we can define a few macroscopic absorber parameters that will determine the pulse generation process. The macroscopic properties of a saturable absorber are the modulation depth, the nonsaturable loss, the saturation fluence, the saturation intensity, and the impulse response or recovery times. These parameters determine the operation of a passively mode locked or Q-switched laser. In our notation we assume that the saturable absorber is integrated within a mirror structure. Thus we are interested in the nonlinear reflectivity change or the *differential reflectivity*  $DR(t)$  as a function of time or in the reflectivity  $R(F_{p,A})$  as a function of the incident pulse energy fluence on the saturable absorber. If the saturable absorber is used in transmission, we simply characterize the absorber by nonlinear transmission measurements. Both the saturation fluence  $F_{\text{sat},A}$  and the absorber recovery time  $\tau_A$  are determined



**FIGURE 3** Standard pump-probe techniques determine the impulse response  $DR(t)$ . (Here we assume that the saturable absorber is integrated within a mirror structure.)  $DR(t)$  for the same saturable absorber is different for different excitation pulse durations. For excitation with a picosecond pulse, the pump-probe trace clearly shows no significant modulation depth with a fast time constant.

experimentally without any need to determine the microscopic properties of the nonlinearities. Thus, the saturation fluence of the absorber is not only dependent on material properties but also on the specific device structure the absorber is integrated in.

Standard pump-probe techniques determine the impulse response  $DR(t)$  and therefore  $\tau_A$  (see Fig. 3). In the picosecond regime we normally only have to consider one recovery time, because much faster femtosecond nonlinearities in the saturable absorber result in a negligible modulation depth. This is shown in Fig. 3, where the impulse response  $DR(t)$  was measured for two different excitation pulse durations. For excitation with a picosecond pulse, the pump-probe trace clearly shows no significant modulation depth with a fast time constant. In the femtosecond pulse regime we normally have to consider more than one absorber recovery time. In this case the slow component normally helps to start the initial pulse formation process. The modulation depth of the fast component then determines the pulse duration at steady state. Further improvements of the saturable absorber normally require some better understanding of the underlying physics, which will be discussed in more detail in Sec. 18.6.

The saturation fluence  $F_{\text{sat}, A}$  is determined and defined by the measurement of the nonlinear change in reflectivity  $R(F_{p, A})$  as a function of increased incident pulse fluence (see Fig. 4). The common traveling wave rate equations<sup>22</sup> in the slow absorber approximation normally give a very good fit and determine the saturation fluence  $F_{\text{sat}, A}$ , modulation depth  $\Delta R$ , and nonsaturable losses  $\Delta R^{\text{ns}}$  of the absorber. The modulation depth is typically small to prevent Q-switching instabilities in passively modelocked solid-state lasers.<sup>23</sup> Thus it is reasonable to make the following approximation:

$$\Delta R = 1 - e^{-2q_0} \approx 2q_0, q_0 \ll 1 \quad (1)$$

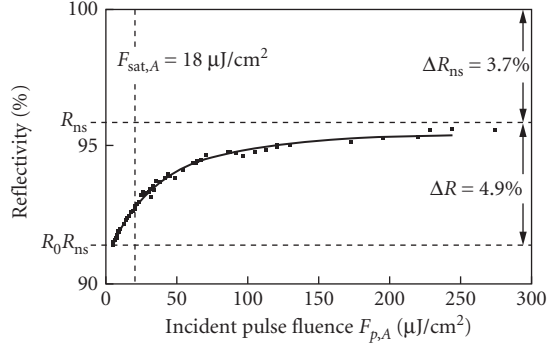
where  $q_0$  is the unsaturated amplitude loss coefficient. Here, it is assumed that the nonsaturable losses are negligible.

The saturation of an absorber can be described with the following differential equation:<sup>22</sup>

$$\frac{dq(t)}{dt} = -\frac{q(t) - q_0}{\tau_A} - \frac{q(t)P(t)}{E_{\text{sat}, A}} \quad (2)$$

where  $q(t)$  is the saturable amplitude loss coefficient that does not include any nonsaturable losses. At any time  $t$  the reflected (or transmitted) intensity  $I_{\text{out}}(t)$  from the saturable absorber is given by

$$I_{\text{out}}(t) = R(t)I_{\text{in}}(t) = e^{-2q(t)}I_{\text{in}}(t) \quad (3)$$



**FIGURE 4** Nonlinear Reflectivity as function of the incident pulse fluence  $R(F_{p,A})$ . The measurement was made with a SESAM supporting 34-fs pulses in a Ti:sapphire laser. The measurements are fitted with common traveling wave rate equations<sup>22</sup> in the slow absorber approximation which normally give a very good fit and determine the saturation fluence  $F_{\text{sat},A}$ , modulation depth  $\Delta R$ , and nonsaturable losses  $\Delta R_{\text{ns}}$  of the absorber. Detailed guidelines how to measure the macroscopic SESAM parameters are given in Refs. 24 and 25.

Then the total net reflectivity is given by

$$R_{\text{tot}} = \frac{\int I_{\text{out}}(t) dt}{\int I_{\text{in}}(t) dt} = \frac{F_{\text{out}}}{F_{\text{in}}} = 1 - \frac{2}{F_{\text{in}}} \int q(t) I_{\text{in}}(t) dt \quad (4)$$

This determines the total absorber loss coefficient  $q_p$ , which results from the fact that part of the excitation pulse needs to be absorbed to saturate the absorber:

$$R_{\text{tot}} = e^{-2q_p} \approx 1 - 2q_p \quad (5)$$

From Eqs. (4) and (5) it then follows that for  $q_p \ll 1$

$$q_p = \frac{1}{F_{\text{in}}} \int q(t) I_{\text{in}}(t) dt = \int q(t) f(t) dt \quad (6)$$

where

$$f(t) \equiv \frac{I_{\text{in}}(t)}{F_{\text{in}}} = \frac{P_{\text{in}}(t)}{E_{p,\text{in}}}, \quad \text{with} \quad \int f(t) dt = \frac{1}{F_{\text{in}}} \int I_{\text{in}}(t) dt = 1 \quad (7)$$

We then distinguish between two typical cases: a slow and a fast saturable absorber.

### Slow Saturable Absorber

In the case of a slow saturable absorber, we assume that the excitation pulse duration is much shorter than the recovery time of the absorber (i.e.,  $\tau_p \ll \tau_A$ ). Thus, we can neglect the recovery of the absorber during pulse excitation, and Eq. (2) reduces to:

$$\frac{dq(t)}{dt} \approx -\frac{q(t)P(t)}{E_{\text{sat},A}} \quad (8)$$

This differential equation can be solved, and we obtain for the self-amplitude modulation (SAM):

$$q(t) = q_0 \exp \left[ -\frac{E_p}{E_{\text{sat},A}} \int_0^t f(t') dt' \right] \quad (9)$$

Equation (6) then determines the total absorber loss coefficient for a given incident pulse fluence  $F_{p,A}$ :

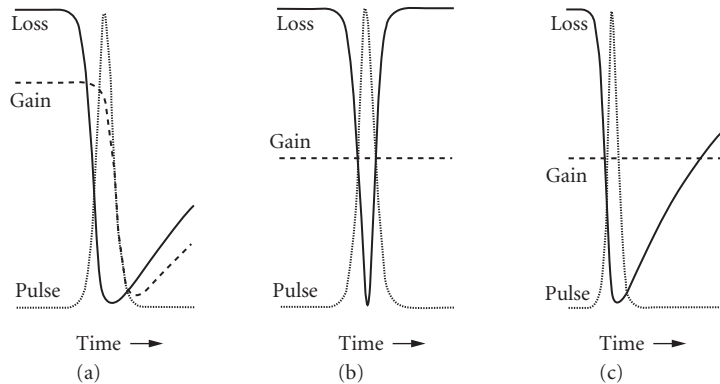
$$q_p(F_{p,A}) = \int q(t) f(t) dt = q_0 \frac{F_{\text{sat},A}}{F_{p,A}} (1 - e^{-F_{p,A}/F_{\text{sat},A}}) \quad (10)$$

It is not surprising that  $q_p$  does not depend on any specific pulse form, because  $\tau_p \ll \tau_A$ .

A slow saturable absorber has been successfully used to passively modelock dye and semiconductor lasers. In this case, dynamic gain saturation was supporting the pulse formation process (Fig. 5a), and much shorter pulses than the recovery time of the saturable absorber were obtained.<sup>26,27</sup> Dynamic gain saturation means that the gain experiences a fast pulse-induced saturation that then recovers again between consecutive pulses. Therefore, an ultrashort net-gain window can be formed by the combined saturation of absorber and gain for which the absorber has to saturate and recover faster than the gain, while the recovery time of the saturable absorber can be much longer than the pulse duration. Haus's master equation formalism can describe this passive modelocking technique very well.<sup>28</sup> This formalism is based on linearized differential operators that describe the temporal evolution of a pulse envelope inside the laser cavity. Generally, the linearized master equations of Haus describe modelocking very well, as long as they only have to deal with small nonlinearities and loss modulation. This is true for most lasers; otherwise a strong tendency for instabilities is observed. A review of Haus's modelocking formalism is presented in more recent articles and book chapters.<sup>5,10,21,29</sup> Assuming passive modelocking according to Fig. 5a, Haus predicts a mode locked pulse duration for a fully saturated absorber

$$\tau \approx \frac{4}{\pi} \frac{1}{\Delta \nu_g} \quad (11)$$

$$\tau_p \approx 1.76 \times \frac{4}{\pi} \frac{1}{\Delta \nu_g}$$



**FIGURE 5** Passive modelocking mechanisms explained by three fundamental models: (a) slow saturable absorber modelocking with dynamic gain saturation, (b) fast saturable absorber modelocking, and (c) soliton modelocking.

with a predicted pulse form of

$$I(t) = I_0 \operatorname{sech}^2(t/\tau), \quad \tau_p = 1.76 \cdot \tau \quad (12)$$

where  $\tau_p$  is the FWHM pulse width of the pulse intensity. For dye lasers using Rhodamin 6G with a gain bandwidth  $\Delta\nu \approx 4 \cdot 10^{13}$  Hz and DODCI as the saturable absorber with an absorber cross section  $\sigma_A = 0.52 \cdot 10^{-16} \text{ cm}^2$ , we would then predict a pulse duration  $\tau_p$  of 56 fs at a center wavelength of 620 nm [Eqs. (11) and (12)]. Slightly shorter pulses of 27 fs duration were demonstrated.<sup>30,31</sup> The interplay of self-phase modulation and negative group velocity dispersion can result in pulses that are shorter than would be predicted by the SAM alone [Eq. (10)]. Martinez estimated the additional pulse shortening to be about a factor of 2.<sup>32,33</sup> This will be discussed in Sec. 18.5.

For solid-state lasers we cannot apply slow saturable absorber modelocking as shown in Fig. 5a, because no significant dynamic gain saturation is taking place, due to the small gain cross section and the long upper state lifetime of the laser. The gain cross section of ion-doped solid-state lasers is typically  $10^{-19} \text{ cm}^2$  and smaller. This is at least 1000 times smaller than dye, semiconductor, or color center lasers. In addition, the upper-state lifetime of ion-doped solid-state lasers is typically in the  $\mu\text{s}$  to ms regime—much longer than the pulse repetition period that is typically in the ns regime. We therefore do not observe any significant dynamic gain saturation, and the gain is only saturated to a constant level by the average intracavity intensity (Fig. 5b and c).

## Fast Saturable Absorber

In the case of a fast saturable absorber, the absorber recovery time is much faster than the pulse duration (i.e.,  $\tau_p \gg \tau_A$ ). Thus, we can assume that the absorption instantaneously follows the absorption of a certain power  $P(t)$ , and Eq. (2) reduces to

$$0 = -\frac{q(t) - q_0}{\tau_A} - \frac{q(t)P(t)}{E_{\text{sat},A}} \quad (13)$$

The saturation of the fast absorber then follows directly from Eq. (13):

$$q(t) = \frac{q_0}{1 + \frac{I_A(t)}{I_{\text{sat},A}}} \quad (14)$$

where we used the fact that  $P_{\text{sat},A} = E_{\text{sat},A}/\tau_A$  and  $P(t)/P_{\text{sat},A} = I_A(t)/I_{\text{sat},A}$ . In the linear regime we can make the following approximation in Eq. (14):

$$q(t) \approx q_0 - \gamma I_A(t), \quad \text{with} \quad \gamma \equiv \frac{q_0}{I_{\text{sat},A}} \quad (15)$$

The total absorber loss coefficient  $q_p$  [Eqs. (10) to (12)] now depends on the pulse form, and for a  $\operatorname{sech}^2$ -pulse shape we obtain for an incident pulse fluence  $F_{p,A}$  and the linear approximation of  $q(t)$  [Eq. (15)]:

$$q_p(F_{p,A}) = \frac{1}{F_{p,A}} \int q(t) I_A(t) dt = q_0 \left( 1 - \frac{1}{3} \frac{F_{p,A}}{\tau I_{\text{sat},A}} \right) \quad (16)$$

We only obtain an analytic solution for fast saturable absorber modelocking if we assume an ideal fast absorber that saturates linearly with pulse intensity over the full modulation depth [Eq. (15)].

For a maximum modulation depth, we then can assume that  $q_0 = \mathcal{I}_{0,A}$ , where  $I_{0,A}$  is the peak intensity on the saturable absorber. We then obtain with Eq. (16) a residual saturable absorber loss of  $q_0/3$ , which the pulse experiences to fully saturate the ideal fast saturable absorber.

A fast saturable absorber has been successfully used to passively modelock solid-state lasers (Fig. 5b). An analytical solution with Haus's master formalism<sup>34</sup> is only obtained if we assume an ideal fast saturable absorber that produces a decreased loss directly proportional to intensity of the incident laser pulse [Eq. (15)]. Then again a sech<sup>2</sup>-pulse shape [Eq. (12)] with the following pulse duration is predicted:

$$\tau_p = 1.76 \frac{4D_g}{\gamma_{F_{p,A}}^F}, \quad \text{with} \quad D_g = -\frac{g}{\pi^2(\Delta v_g)^2} \quad (17)$$

where  $D_g$  is the gain dispersion. Unfortunately, fast saturable absorbers with femtosecond recovery times are often not sufficient for reliable self-starting of the modelocking process. In passive modelocking, pulse formation should start from normal noise fluctuations in a laser. One noise spike is strong enough to start saturating the absorber and thereby lowers the loss. This noise spike begins to grow in amplitude and becomes shorter until a stable pulse duration is obtained. Initially, these noise spike durations are on the order of the cavity round-trip time, introducing only very small loss modulations in a fast saturable absorber (see Fig. 3). A combination of a fast and a slow saturable absorber can help to solve this problem. Thus, semiconductor saturable absorbers are very interesting because they typically have a bitemporal impulse response which even can be modified.

For picosecond solid-state lasers, the self-amplitude modulation of a fast saturable absorber with a picosecond recovery time is sufficient for stable pulse generation. A picosecond recovery time can be achieved with low-temperature-grown semiconductor saturable absorbers where midgap defect states form very efficient traps for the photoexcited electrons in the conduction band. A more detailed description of the microscopic nonlinearities is given in Sec. 18.6. In the picosecond regime, we developed a very simple stability criteria for stable passive modelocking without Q-switching instabilities.<sup>23</sup>

$$E_p^2 > E_{p,c}^2 = E_{\text{sat},L} E_{\text{sat},A} \Delta R \quad (18)$$

The critical intracavity pulse energy  $E_{p,c}$  is the minimum intracavity pulse energy that is required to obtain stable cw modelocking; that is, for  $E_p > E_{p,c}$  we obtain stable cw modelocking and for  $E_p < E_{p,c}$  we obtain Q-switched modelocking (see Fig. 2). For good stability of a mode locked laser against unwanted fluctuations of pulse energy, operation close to the stability limit is not recommended. Thus, a large modulation depth supports shorter pulses [Eqs. (1), (15), and (17)], but an upper limit is given by the onset of self-Q-switching instabilities [Eq. (18)].

## Semiconductor Saturable Absorber Mirrors

Semiconductor saturable absorbers were used as early as 1974 in CO<sub>2</sub> lasers and as early as 1980 for semiconductor diode lasers. A color center laser was the first solid-state laser that was cw modelocked with an intracavity semiconductor saturable absorber.<sup>35</sup> However, for both the diode and color center laser, dynamic gain saturation supported pulse formation, and a slow saturable absorber was sufficient for pulse generation (Fig. 5a). In addition, because of the much larger gain cross section and therefore smaller saturation energy  $E_{\text{sat},L}$  [Eq. (18)] (i.e., typically 1000 to 10,000 times smaller than ion-doped solid-state lasers), Q-switching instabilities were not a problem. Thus, semiconductor saturable absorber parameters (see Figs. 3 and 4) have to be chosen much more carefully for stable cw modelocking.

We typically integrate the semiconductor saturable absorber into a mirror structure that results in a device whose reflectivity increases as the incident optical intensity increases. This general class of device is called a *semiconductor saturable absorber mirror* (SESAM).<sup>18,36</sup> A detailed description and guidelines on how to design a SESAM for either passive modelocking or Q-switching for different laser parameters is

given in Ref. 4. Such a SESAM device structure can be a simple Bragg mirror, where at least one quarter-wave-layer contains an absorber layer (saturable Bragg reflector -SBR).<sup>37–39</sup> A larger parameter range for the saturation fluence and modulation depth can be achieved if the saturable absorber is integrated inside a Fabry-Perot structure that is operated at antiresonance (A-FPSA).<sup>18,40</sup> The antiresonant Fabry-Perot structure is broadband and can be designed to have no significant bandwidth limitations even in the sub-10-fs pulse-width regime.<sup>41</sup> The top reflector of the A-FPSA provides an adjustable parameter that determines the intensity entering the semiconductor saturable absorber and therefore the saturation fluence of the saturable absorber device. A  $\text{SiO}_2/\text{TiO}_2$  dielectric top reflector has an additional advantage in that the damage threshold for this SESAM design is significantly higher compared to a SESAM design with the same saturation fluence but based on semiconductor materials alone. We also distinguish between resonant and antiresonant SESAM designs. There are different trade-offs between these design regimes, but a compromise can be found to obtain both low saturation fluence and sufficiently small group delay dispersion.<sup>42</sup>

More recently, semiconductor-doped dielectric films have been demonstrated for saturable absorber applications.<sup>43</sup> Semiconductor-doped glasses have been used to modelock lasers as early as 1990.<sup>44</sup> However, the recently developed InAs-doped thin-film rf-sputtering technology offers similar advantages as SESAMs, which allows for the integration of the absorber into a device structure. At this point, however, the saturation fluence of  $\approx 10 \text{ mJ}/\text{cm}^2$  is still rather high for stable solid-state laser modelocking [Eq. (18)]. In comparison, MBE or MOCVD-grown SESAMs have typically a saturation fluence of  $\approx 10 \mu\text{J}/\text{cm}^2$ , even though they can be modified from the  $\mu\text{J}/\text{cm}^2$  to the  $\text{mJ}/\text{cm}^2$ -range depending on the specific device structure.<sup>4,36</sup>

A more detailed discussion of microscopic semiconductor nonlinearities will be presented in Sec. 18.6. In principle, knowledge of the macroscopic absorber parameters is sufficient to understand pulse generation. However, further improvements of saturable absorbers will require a more detailed understanding of microscopic optical nonlinearities.

## 18.5 KERR EFFECT

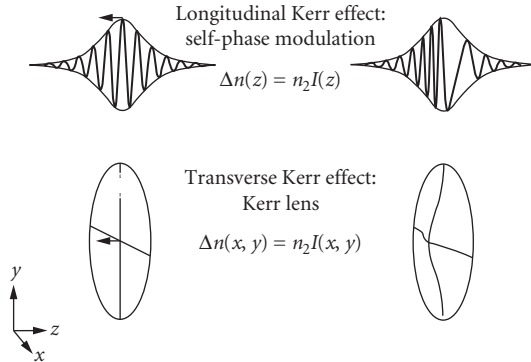
### Longitudinal and Transverse Kerr Effect

The extremely rapid response and broad bandwidth of the Kerr nonlinearity are very attractive for a modelocking process. For high intensities, polarization inside a dielectric medium does not proportionally follow the electric field anymore. This gives rise to an index change that is proportional to intensity. Off-resonance, this nonlinear optical effect is extremely fast, with estimated response times in the few-femtosecond range. The transverse and longitudinal effects resulting from the intensity dependence are shown schematically in Fig. 6. The transverse Kerr effect retards the central and most intense part of a plane wavefront, thus acting as a focusing lens, referred to as the Kerr lens. Later we will indicate concepts that make use of the Kerr lens to produce short pulses. Along the axis of propagation, the longitudinal Kerr effect retards the center of an optical pulse, producing a red shift of the leading part of the pulse and a blue shift in the trailing part. Consequently, the longitudinal Kerr effect has been named *self-phase modulation* (SPM).

### Longitudinal Kerr Effect for External Pulse Compression

SPM generates extra bandwidth; in other words, it spectrally broadens the pulse. SPM alone does not modify the pulse width—but a much shorter pulse can be generated with the extra bandwidth and proper dispersion compensation.<sup>45</sup> To create a short pulse, the blue spectral components have to be advanced relative to the red ones, exactly counteracting the phase delays induced by the SPM (assuming  $n_2 > 0$ ). To do so an effect opposite to the normal material dispersion is needed. This type of dispersion is called *anomalous* or *negative* dispersion. A careful balance between a nonlinear spectral broadening process and negative dispersion is needed for efficient compression of a pulse.





**FIGURE 6** The Kerr effect produces a nonlinear intensity-dependent refractive index change. The longitudinal Kerr effect (top) causes self-phase modulation (SPM). The transverse Kerr effect (bottom) causes a nonlinear focusing lens (Kerr lens).

Typically, self-phase modulation in a single-mode fiber is used to chirp the pulse, which is then compressed with a grating pair compressor.<sup>46</sup>

Ultimately, compression schemes are limited by uncompensated higher-order dispersion and higher-order nonlinearities. For pulses shorter than 100 fs, compression is typically limited to factors of less than 10. Compression of amplified CPM dye laser pulses with 50 fs duration produced the long-standing world record of 6 fs for short pulses.<sup>47</sup> Similar concepts have been recently used for external pulse compression of 13-fs pulses from a cavity dumped Ti:sapphire laser<sup>15</sup> and of 20-fs pulses from a Ti:sapphire laser amplifier<sup>16</sup> resulting, in both cases, in approximately 4.5-fs pulses (see Fig. 1). In the latter case, the use of a noble-gas-filled hollow fiber resulted in unsurpassed pulse energies of about 0.5 mJ, with 5.2-fs pulses and a peak power of 0.1 TW.<sup>48</sup>

### Longitudinal Kerr Effect for Broadband Parametric Amplification

The extra bandwidth obtained with SPM can be extremely large, producing a white-light continuum<sup>49</sup> that can be used as a seed for broadband parametric amplification. Parametric processes can provide amplification with even broader bandwidth than can typically be achieved in laser amplifiers. Noncollinear phase-matching at a crossing angle of  $3.8^\circ$  in Barium beta borate (BBO) provides more than 150 THz amplification bandwidth.<sup>50</sup> With this type of setup, parametric amplification has been successfully demonstrated with pulse durations of less than 5 fs.<sup>14</sup>

### Longitudinal Kerr Effect for Passive Modelocking: Soliton Modelocking

It was recognized early on that the longitudinal Kerr effect or SPM together with negative dispersion results in soliton formation and further reduces pulse duration by about a factor of 2 in dye lasers.<sup>32,33</sup> However, at that time an analytic solution for the pulse-shortening effect was not presented. Using soliton perturbation theory, an analytic solution has been derived that describes how to make use of much more significant soliton pulse shortening in solid-state lasers.<sup>51,52</sup> This modelocking model, referred to as *soliton* modelocking, is fundamentally different from any previous models, because it treats soliton pulse shaping as the dominant pulse formation process and the saturable absorber as a perturbation to the soliton. This strongly relaxes the requirements of the saturable absorber as compared to pure saturable absorber modelocking. However, the saturable

absorber is still required to start the modelocking process and to stabilize the soliton pulses against continuous wave breakthrough.

The soliton modelocking model was experimentally confirmed by the production of 300-fs-long soliton pulses with a saturable absorber response time of only 10 ps.<sup>53</sup> Pulses of 13 fs were achieved with a saturable absorber response time of about 60 fs.<sup>52</sup> Further improvements of extremely broadband saturable absorbers<sup>41</sup> with a higher modulation depth would be necessary to obtain even shorter pulses based on this modelocking mechanism.

In soliton modelocking the pulse duration is given by the soliton condition:

$$\tau_p = 1.76 \frac{|D_2|}{kn_2 L_L F_{p,L}} \quad (19)$$

where  $D_2$  is the total group delay dispersion inside the laser cavity per cavity round-trip. Here we assume that the dominant SPM is produced in the laser material (i.e.,  $n_2$  is the nonlinear refractive index of the laser material,  $L_L$  is the length of the laser material, and  $F_{p,L}$  the pulse fluence inside the laser material). In other cases we have to add all other contributions as well. The pulse duration scales linearly with the negative intracavity dispersion. Reducing the intracavity dispersion results in shorter transform-limited pulses.<sup>53</sup> However, there is a limit. The soliton loses energy due to gain dispersion and losses in the cavity. This lost energy, called *continuum* in soliton perturbation theory,<sup>54</sup> is initially contained in a low-intensity background pulse, which experiences negligible SPM, but spreads in time due to group velocity dispersion. This continuum experiences a higher gain compared to the soliton pulse, because it only sees the gain at line center (while the soliton sees an effectively lower average gain due to its larger bandwidth). After a sufficient build-up time, the continuum would actually grow until it reaches lasing threshold, destabilizing the soliton. However, we can stabilize the soliton by introducing a “slow” saturable absorber into the cavity. This “slow” absorber has to be fast enough to add sufficient additional loss for the growing continuum that spreads in time so that it no longer reaches lasing threshold. For a given recovery time of the saturable absorber, the continuum pulse will not broaden fast enough when the negative dispersion becomes too small. Therefore there is a minimum pulse duration that can be achieved for a given set of absorber and laser parameters:

$$\tau_{p,\min} = 1.7627 \left( \frac{1}{\sqrt{6\pi\Delta\nu_g}} \right)^{3/4} \phi_s^{-1/8} \left( \frac{\tau_A \delta^{3/2}}{q_0} \right)^{1/4} \quad (20)$$

where  $\phi_s$  is the phase shift of the soliton per cavity round trip (assuming that the dominant SPM occurs in the laser gain medium) and is given by

$$\phi_s = \phi_s(z=2L_L) = kn_2 L_L I_{0,L} \quad (21)$$

Here we assume a fully saturated slow absorber with a linear approximation for the exponential decay of the slow saturable absorber, and a slow saturable absorber.

In the femtosecond regime, we observe a significant reduction of the tendency of Q-switching instabilities compared to pure saturable absorber modelocked picosecond lasers [Eq. (18)]. This can be explained as follows: If the energy of an ultrashort pulse rises slightly due to relaxation oscillations, SPM and/or SAM broadens the pulse spectrum. A broader spectrum, however, reduces the effective gain due to the finite gain bandwidth, which provides some negative feedback, thus decreasing the critical pulse energy which is necessary for stable cw modelocking. The simple stability requirement of Eq. (18) then has to be modified as follows:<sup>23</sup>

$$E_{\text{sat},L} \delta K^2 E_p^2 + E_p^2 > E_{\text{sat},L} E_{\text{sat},A} \Delta R \quad (22)$$

where  $K$  is given by

$$K \equiv \frac{0.315}{1.76} \frac{4\pi n_2 L_L}{D_2 A_L \lambda_0 \Delta v_g} \quad (23)$$

Here we assume that the dominant SPM is produced in the laser medium. In other cases we have to add all other contributions as well.

### Longitudinal Kerr Effect for Passive Modelocking with a Coupled Cavity: Soliton Laser, Additive Pulse Modelocking

The longitudinal Kerr effect can also be used to produce the same effect as a fast saturable absorber. To do this, the phase nonlinearity provided by the longitudinal Kerr effect has to be converted into an effective amplitude nonlinearity. The earliest modelocking schemes (based only on SPM) used a coupled cavity to convert SPM into SAM. In the soliton laser,<sup>55</sup> pulses compressed by SPM and anomalous dispersion in the coupled cavity are directly coupled back into the main laser cavity. This provides more gain for the center of the pulse. Pulses as short as 19 fs have been demonstrated with color center lasers.<sup>56</sup> Later, the SPM-to-SAM conversion with a coupled cavity was demonstrated for a case when the pulses inside the coupled cavity were broadened due to positive group velocity dispersion.<sup>57</sup> In this case, no compressed pulse was fed back into the main cavity. An effective SAM was obtained because SPM inside the coupled cavity generates a phase modulation on the pulse that adds constructively at the peak of the pulse in the main cavity and destructively in the wings, thus shortening the pulse duration inside the main cavity. This was also referred to as additive pulse modelocking (APM).<sup>58</sup> Although very powerful in principle, these coupled-cavity schemes have the severe disadvantage that the auxiliary cavity has to be stabilized interferometrically. An alternative method for converting the reactive Kerr nonlinearity into an effective saturable absorber has been developed: Kerr-lens modelocking (KLM).<sup>59</sup>

### Transverse Kerr Effect for Passive Modelocking: Kerr Lens Modelocking

The discovery of Kerr lens modelocking has been a breakthrough in ultrashort pulse generation.<sup>59</sup> Initially the modelocking mechanism was not understood and was somewhat of a mystery. But within a short time after the initial discovery it became clear that the transverse Kerr effect provides a fast saturable absorber. In KLM, the transverse Kerr effect produces a Kerr lens (see Fig. 6) that focuses the high intensity part of the beam more strongly than the low intensity part. Thus, combined with an intracavity aperture the Kerr lens produces less loss for high intensity and forms an effective fast saturable absorber.<sup>60-62</sup> A similar modelocking effect can be obtained without a hard aperture when the Kerr lens produces an increased overlap of the laser mode with the pump profile in the gain medium.<sup>63</sup> The Kerr lens provides the strongest advantage for the pulsed operation when the cavity is operated close to the stability limit. Optimization guidelines for SAM produced by the Kerr lens in different cavities can be found in Ref. 64. Unfortunately, the transverse Kerr effect couples the modelocking process with the laser cavity mode. In contrast, the use of only the longitudinal Kerr effect in modelocking decouples the modelocking process from the laser mode. This allows optimum cavity design for scaling the laser to higher powers and to higher pulse repetition rates without being constrained by the Kerr lens.

KLM is well described by the fast absorber modelocking model discussed above<sup>65</sup> even though it is not so easy to determine the exact saturable absorber parameters such as the effective saturation fluence. However, the linearized model does not describe the pulse generation with Ti:sapphire lasers in the sub-10-fs regime very well. Pulse-shaping processes in these lasers are more complex.<sup>66,67</sup> Under the influence of the different linear and nonlinear pulse shaping mechanism, the pulse is significantly broadened and recompressed, giving rise to a “breathing” of the pulse width. The order of

the pulse shaping elements in the laser cavity becomes relevant and the spectrum of the modelocked pulses becomes more complex. In this case, an analytical solution can no longer be obtained. As a rough approximation, the pulses still behave like solitons and consequently these lasers are also called solitary lasers.<sup>66</sup>

### Longitudinal Kerr Effect for Passive Modelocking with Nonlinear Polarization Rotation

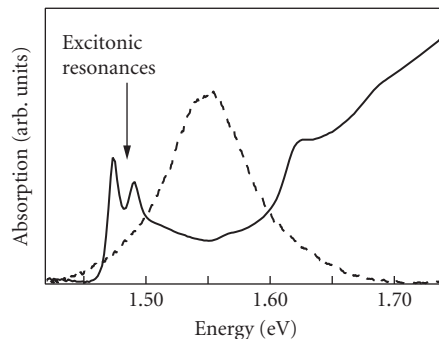
A Kerr effect-induced nonlinear polarization rotation in a weakly birefringent fiber has been used as a “pulse cleaner” to reduce the low-intensity pulse pedestals.<sup>68,69</sup> The same effect can also be used to form an effective fast saturable absorber.<sup>70</sup> Pulses as short as 38 fs have been generated with Nd-doped fiber lasers.

## 18.6 SEMICONDUCTOR ULTRAFAST NONLINEARITIES: MICROSCOPIC PROCESSES

The discussion of saturable absorbers in Sec. 18.4 has shown that semiconductors are well-suited absorber materials for ultrashort pulse generation. In contrast to saturable absorber mechanisms based on the Kerr effect (Sec. 18.5), ultrafast semiconductor nonlinearities can be studied outside the laser. Such studies give insight into the microscopic processes that determine the nonlinear optical properties of semiconductors on ultrashort time scales. This insight has substantially contributed to our understanding of the physics of semiconductors. Moreover, the information obtained from ultrafast semiconductor spectroscopy provides the basis for further improvement of ultrashort pulse generation with semiconductor saturable absorbers.

In this section, we will first give an overview of ultrafast semiconductor dynamics, which will be followed by a description of the most important experimental techniques for the study of ultrafast processes and nonlinearities. Then we summarize some of the results that have been obtained with these experimental techniques. This summary emphasizes aspects that are particularly relevant for saturable absorber applications, but goes beyond the saturable absorber issue if this is helpful to illustrate general concepts.

In ultrafast semiconductor spectroscopy, it is often convenient to distinguish between excitonic excitations (i.e., Coulomb-bound electron-hole pairs at the band edge<sup>71</sup>) and unbound electron-hole pairs in the continuum of the spectrum. Laser pulses with a temporal width well below 100 fs have a spectral bandwidth that is much larger than the spectral width of the exciton resonance and the exciton binding energy in most semiconductors. This is illustrated in Fig. 7 for the example of



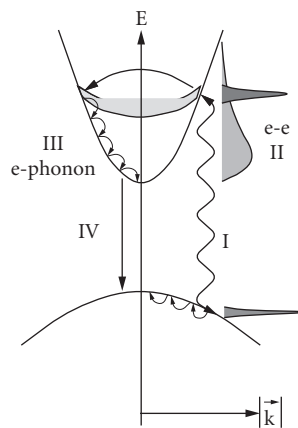
**FIGURE 7** Room temperature linear absorption spectrum (solid) of a GaAs/AlGaAs semiconductor quantum well and power spectrum of a 16-fs laser pulse (dashed).

a 16-fs pulse and the absorption spectrum of a GaAs/AlGaAs quantum well<sup>72</sup> at room temperature. Therefore, saturable absorber applications with sub-100-fs pulses very often involve broadband continuum excitations. For this reason, we will focus on ultrafast continuum nonlinearities and dynamics. Exciton dynamics will be discussed only to outline some general concepts of ultrafast semiconductor spectroscopy. For a comprehensive, in-depth review of ultrafast semiconductor spectroscopy the interested reader is referred to Ref. 73.

## Overview

Semiconductors are characterized by closely spaced electronic eigenstates in energy space. This electronic structure gives rise to strong interaction among optical excitations on ultrafast time scales and very complex dynamics. Despite the complexity of the dynamics, different time regimes can be distinguished in the evolution of optical excitations in semiconductors.<sup>73,74</sup> These different time regimes are schematically illustrated in Fig. 8, which shows the energy dispersion diagram of a 2-band bulk semiconductor. Optical excitation with an ultrafast laser pulse prepares the semiconductor in the coherent regime (time regime I in Fig. 8). In this regime, a well-defined phase relation exists between the optical excitations and the electric field of the laser pulse and among the optical excitations themselves. The coherence among the excitations in the semiconductor gives rise to a macroscopic polarization (dipole moment density). Since the macroscopic polarization enters as a source term in Maxwell's equations, it leads to an electric field which is experimentally accessible. The magnitude and decay of the polarization provide information on the properties of the semiconductor in the coherent regime. The irreversible decay of the polarization is due to scattering processes and is usually described by the so-called dephasing or transversal relaxation time. For a mathematical definition of this time constant the reader is referred to Refs. 73, 75, 76, and 77. Some more details about dephasing and coherent dynamics in semiconductors will be given later.

After the loss of coherence, ultrafast spectroscopy of semiconductors is solely concerned with the dynamics of the population (i.e., electron and hole distributions). In this incoherent regime, the time regimes II–IV can be distinguished, as described in the text that follows. The initial electron and hole distributions are nonthermal in most cases (i.e., they cannot be described by Fermi-Dirac statistics with a well-defined temperature). Scattering among charge carriers is mainly responsible for the redistribution of energy within the carrier distributions and for the formation of thermal



**FIGURE 8** Schematic dispersion diagram of a two-band bulk semiconductor showing the time regimes I–IV after optical excitation; see text for more details. e–e: electron-electron scattering, e-phonon: electron-phonon scattering.

distributions. This thermalization is shown as time regime II in Fig. 8, for the example of a thermalizing electron distribution where thermalization occurs through scattering among the electrons. For excitation of the continuum, thermalization usually occurs on a time scale of 100 fs under most experimental conditions. More details about the dynamics in the thermalization regime will be presented later.

In general, the carriers have a temperature different from the lattice temperature after thermalization has been completed. In Fig. 8 it is assumed that the carriers have a higher temperature than the lattice. For this case, Fig. 8 schematically shows the cooling of carriers by the emission of phonons (i.e., energy transfer to the lattice). Cooling defines the time regime III. Typical time constants are in the picosecond and tens of picosecond range.

Finally, the optically excited semiconductor returns to thermodynamic equilibrium by the recombination of electron-hole pairs. Recombination is shown as time regime IV in Fig. 8. In a perfect semiconductor crystal, recombination proceeds via the emission of photons or Auger processes at high carrier densities. These recombination processes take place on time scales of tens of picoseconds and longer. These slow recombination processes as well as the relatively slow carrier cooling will not be discussed in more detail in this chapter. An excellent review can be found in Ref. 73.

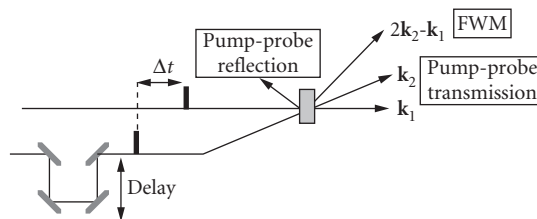
Another ultrafast process is encountered if large densities of deep-level traps are incorporated in a semiconductor. Trapping of carriers into deep levels can proceed on subpicosecond time scales (not shown in Fig. 8). Since carrier trapping is important in many saturable absorber applications, it is discussed at the end of this section.

We note that the different time regimes temporally overlap. For example, a scattering process may destroy the coherence and contribute to thermalization. Nevertheless, it is very useful to distinguish between the different time regimes because they are a convenient means for the description of the complex semiconductor dynamics. The schematic picture of the different time regimes also demonstrates that two or more time constants are usually required to describe the temporal response of a semiconductor absorber. For example, we recall that thermalization typically takes place on the 100-fs time scale, while carrier trapping proceeds on times scales from a few hundreds of femtoseconds to picoseconds.

## Experimental Techniques

In the following, we describe two very common experimental techniques for the study of ultrafast processes and nonlinearities. The discussion focuses on semiconductors. However, the experimental techniques have also been intensively used for the study of other condensed matter systems or molecules.

**Transient Four-Wave Mixing** Transient four-wave mixing (FWM) is an experimental technique for the study of the coherent regime. A schematic diagram of a transient FWM experiment is shown in Fig. 9. Two excitation pulses with wave vectors  $\mathbf{k}_1$  and  $\mathbf{k}_2$  excite the sample. In most FWM experiments the two pulses have the same spectrum (degenerate FWM). We assume here that the case of degenerate FWM is realized. An optical delay line is used to introduce a time delay  $\Delta t$  between the pulses where positive  $\Delta t$  refers to pulse  $\mathbf{k}_1$  arriving before pulse  $\mathbf{k}_2$  at the sample.



**FIGURE 9** Schematic experimental setup for four-wave-mixing (FWM) and pump-probe spectroscopy.

Pulse  $\mathbf{k}_1$  generates a coherent polarization in direction  $\mathbf{k}_1$  in the sample. If the time delay  $\Delta t$  is smaller than the dephasing time of the coherent polarization, in a second step, this polarization interacts with the electric field of pulse  $\mathbf{k}_2$  to set up an interference grating. In a third step, pulse  $\mathbf{k}_2$  is self-diffracted from this grating and an electric field is emitted in the phase-matching direction  $2\mathbf{k}_2 - \mathbf{k}_1$ . The diffracted field constitutes the FWM signal. A more detailed analysis shows that the FWM signal is due to a nonlinear polarization in direction  $2\mathbf{k}_2 - \mathbf{k}_1$ .<sup>73,78</sup>

The FWM emission can be analyzed in different ways. First, the time integral over the FWM intensity can be measured versus the time delay. Such measurements usually provide information about the dephasing time since the strength of the FWM emission is determined by the coherent polarization in direction  $\mathbf{k}_1$  that is left when pulse  $\mathbf{k}_2$  is applied.<sup>73,78</sup> Spectral information is obtained if the FWM emission is analyzed with a spectrometer at fixed time delays. If more than one resonance is excited, the FWM spectrum shows the magnitude of the optical nonlinearity of the different resonances. Moreover, for homogeneously broadened transitions, the dephasing time can be obtained from the spectral width of the FWM emission. For a fixed time delay, the decay of the FWM signal can be measured in real time by optical gating with a reference pulse. Usually, sum frequency generation in a nonlinear crystal is used for this purpose. This is essentially a cross correlation measurement between the FWM signal pulse and the reference pulse, in which the time resolution is determined by the duration of the reference pulse. In such a correlation measurement, a slow photodetector can be used to detect the sum frequency signal. Real-time detection of FWM signals shows whether the excited optical transitions are homogeneously or inhomogeneously broadened. For homogeneous broadening, the FWM signal in direction  $2\mathbf{k}_2 - \mathbf{k}_1$  immediately sets in when pulse  $\mathbf{k}_2$  is applied (for positive time delays). For inhomogeneous broadening, the FWM signal is emitted time-delayed with respect to pulse  $\mathbf{k}_2$  as a so-called photon echo.<sup>75</sup> More details as well as a mathematical analysis of degenerate two-pulse FWM can be found in Refs. 73 and 78. Transient FWM with three pulses is treated in Ref. 79.

For excitation of interband transitions in semiconductors, occupation of valence and conduction band states contributes to the optical nonlinearity exploited in the FWM process. Occupation effects are a source of nonlinearity in many electronic systems, as shown by the analysis of simple two-level systems.<sup>73,78</sup> Other sources of nonlinearity will be briefly mentioned when we present some results of coherent semiconductor spectroscopy.

**Pump-Probe Spectroscopy** Pump-probe spectroscopy is the most widely used technique for the study of ultrafast optical nonlinearities. As shown in Fig. 9, the sample is excited by the pump pulse  $\mathbf{k}_1$ . The nonlinear changes of the transmission or reflectivity of the sample are detected by the time-delayed probe pulse  $\mathbf{k}_2$ . The time delay is defined as positive if the pump pulse precedes the probe. Often, the pump pulse train is amplitude-modulated and a lock-in amplifier is used for detection of the nonlinear transmission or reflectivity changes at the modulation frequency. It is important to note that the pump-probe experiment is a correlation experiment, in which a slow photodetector can be used.

With this technique, nonlinear reflectivity changes are measured in saturable absorbers which are integrated within a mirror structure, as mentioned in Sec. 18.4. In studies of microscopic processes, very often the nonlinear changes of the probe transmission are measured, which is referred to as *differential transmission* (DT) spectroscopy. In the simplest arrangement, the DT signal is spectrally integrated over the spectrum of the probe pulse. If the probe pulse has a large bandwidth, the DT signal at various photon energies can be obtained from measurements of the spectrum of the transmitted probe pulse in the presence and absence of the pump. The difference between those spectra represents the DT spectrum. Spectral information can also be obtained if a tunable narrowband probe pulse is scanned over a spectral window.

The differential transmission signal contains information on the coherent and the incoherent regime. In the coherent regime, the DT signal is determined by the nonlinear polarization in the direction of the probe pulse. The DT signal in the coherent regime is analyzed in more detail in Refs. 80, 81, 82, and 83.

Coherent effects can be neglected on time scales much longer than the dephasing time of the polarization. The DT signal is then determined by the population (i.e., the electron and hole distributions) generated by the pump pulse. In the incoherent regime, one can roughly distinguish between

two different sorts of effects that determine the DT signal of semiconductors: (1) occupation effects and (2) many-body Coulomb effects. Occupation effects are based on the fermionic nature of optical excitations and can be understood in the following way. A nonequilibrium carrier population in excited states reduces the optical transition rate into these states due to the reduced density of empty final states. This manifests itself by the reduction of the absorption at certain photon energies. Occupation effects are important in many electronic systems. Many-body effects are particularly important in semiconductors. They include the renormalization of the bandgap and screening of the Coulomb interaction. Details can be found in Refs. 84 through 87. Of course, the many-body effects are related to the occupation effects since they depend on the distribution of carriers.

If many-body effects can be neglected and if the optical matrix elements do not depend on the pump excitation, the nonlinear change  $\Delta\alpha$  of the absorption constant  $\alpha$  is directly proportional to the magnitude of the population (i.e., the electron and hole densities). In general, both refractive index changes and absorption changes  $\Delta\alpha$  contribute to the differential transmission signal.<sup>88</sup> A considerable simplification is obtained if refractive index changes can be neglected and if the relation  $\Delta\alpha d \ll 1$  holds ( $d$  sample thickness). Then the DT signal is proportional to  $\Delta\alpha$ , and the decay of the DT signal can be identified with the decay of the electron and hole densities. We note that in studies of carrier trapping, pump-probe data are very often analyzed under the just-described assumptions.

## Results

In this subsection, examples are given that show how ultrafast spectroscopy has contributed to the understanding of ultrafast processes and nonlinearities in semiconductors. We will highlight those aspects that are particularly relevant for broadband saturable absorbers. The material is organized according to the different time regimes which have been identified at the beginning of Sec. 18.6.

*Coherent Regime: Excitonic Excitations* Studies of excitons in the coherent regime are an illustrative example for the issues addressed in coherent ultrafast spectroscopy of semiconductors. Therefore, we briefly discuss some aspects of coherent exciton dynamics even though excitonic excitations are less important for many ultrafast saturable absorber applications. This discussion will illustrate the main issues addressed in ultrafast semiconductor spectroscopy in the coherent regime: (1) dephasing times and underlying scattering mechanisms, (2) coupling and interference between optical excitations, and (3) the nature of the optical nonlinearity.

Four-wave mixing has been intensively used to study the dephasing of excitons and the underlying scattering mechanisms. Varying the excitation intensity, the effects of exciton-exciton and exciton-electron scattering on the dephasing of excitons have been investigated in bulk semiconductors<sup>89</sup> and quantum wells.<sup>90</sup> Varying the temperature, dephasing of excitons due to interaction with lattice vibrations (phonons) has been studied in Ref. 91. Summarizing these results, exciton dephasing times can be in the picosecond range at moderate exciton and free-carrier densities and Helium temperatures. Increasing the temperature decreases the dephasing time due to enhanced phonon scattering. Likewise, enhanced carrier or exciton densities cause faster dephasing. A detailed analysis of exciton dephasing in three- and two-dimensional semiconductors is presented in Ref. 92. We note that exciton dephasing can also give insight into the structural properties of a semiconductor, such as interface roughness in quantum wells and alloy disorder in mixed crystals.<sup>93,94</sup>

More recent four-wave mixing investigations of coherent exciton dynamics focus on quantum-mechanical coupling and interference between different exciton transitions. Beating phenomena between two exciton transitions have been observed in various systems<sup>95–98</sup> as well as beats involving the whole excitonic Rydberg series.<sup>99</sup> The study of beating phenomena allows for the extraction of level splittings and yields information on the quantum-mechanical coupling in multilevel systems (i.e., their internal structure<sup>100,101</sup>).

The nature of the optical nonlinearity in the coherent regime is another subject that has been intensively studied in four-wave-mixing experiments on excitons.<sup>87,102–110</sup> It has been shown that many-body Coulomb interaction substantially contributes to the coherent optical nonlinearity. With respect to the essence of this result we note that the polarization of a certain interband excitation



gives rise to an electric field which has to be added to the external laser field in order to determine the coherent dynamics of other excitations. A rigorous theoretical treatment can be found in Refs. 85 and 87.

**Coherent Regime: Continuum Excitations** Four-wave-mixing studies of continuum dephasing have been performed with broadband sub-10-fs pulses in three-dimensional bulk semiconductors<sup>111</sup> and quasi two-dimensional quantum wells.<sup>112</sup> These studies have shown that the decay of the coherent polarization of the semiconductor continuum is extremely fast. Decay times are only about 10 fs at high carrier densities, which are likely to be obtained in a saturable absorber in a laser cavity. The ultrafast dephasing is mainly due to carrier-carrier scattering with a density dependence that reflects the dimensionality of the semiconductor.<sup>112</sup> More recent work<sup>113</sup> shows that at reduced carrier densities interaction with the lattice also needs to be considered in continuum dephasing experiments. The interaction with the lattice has been identified as electron-LO-phonon scattering,<sup>113</sup> which has a time constant of about 200 fs.<sup>114–116</sup>

The internal structure of the continuum has been experimentally investigated in Ref. 117. The observation of a photon echo has demonstrated that the semiconductor continuum can be treated as an ensemble of uncoupled excitations at higher carrier densities.<sup>117</sup> Interaction between continuum and exciton transitions in coherent nonlinear optics has been studied both for degenerate<sup>118–120</sup> and nondegenerate excitons and continua.<sup>121–124</sup> This work has demonstrated the importance of many-body coupling effects between different interband transitions at lower carrier densities.

We note that it is not yet clear how coherence in a semiconductor saturable absorber affects the formation of broadband ultrashort pulses in a laser cavity. Some theoretical predictions can be found in Refs. 125 and 126. Experimental results about this issue are missing so far. Given the ultrafast dephasing times in semiconductors under the conditions in a laser cavity, coherence effects are most likely to be important for the generation of sub-10-fs pulses.

**Thermalization Regime** Here we will focus on the excitation of semiconductor continuum states. Studies of the thermalization of free electron and hole distributions are an instructive example for the usefulness of the differential transmission (DT) technique. In particular, measurements of differential transmission spectra have yielded considerable insight into the complex processes that determine the dynamics in the thermalization regime. For excitation well above the bandgap, nonthermal carrier distributions can be observed in bulk semiconductors, such as GaAs<sup>127</sup> and quantum wells.<sup>128</sup> These nonthermal distributions manifest themselves as positive signal in the DT spectrum with a shape that is approximately given by the spectrum of the pump pulse. Often, this signature in the DT spectrum is referred to as a *spectral hole*. The decay of the spectral hole and the thermalization of the carrier distributions lead to a substantial change of the shape of the DT spectrum. Thermalization occurs on the 100-fs time scale in undoped semiconductors and is determined by carrier-carrier scattering in many experiments. The exact thermalization time strongly depends on the carrier density, the excess photon energy with respect to the band edge, and the type of carrier.<sup>73,127–129</sup> Thermalization of optically excited carriers in the presence of cold electron or hole plasmas has also been investigated by the differential transmission technique.<sup>73,130</sup> These experiments have been performed in modulation-doped quantum wells<sup>72</sup> and show that thermalization can occur in less than 10 fs.

Besides carrier-carrier scattering, intervalley scattering is another process which can affect carrier dynamics in the thermalization regime. Semiconductors such as GaAs possess several conduction band minima at different points of the Brillouin zone. If electrons are created near the center of the Brillouin zone with large enough excess energy, they can scatter to the side valleys. This process has been investigated in DT experiments, and intervalley scattering times in the sub-100-fs range have been deduced.<sup>131,132</sup>

Spectrally resolved DT measurements have also revealed interesting many-body effects. A closer inspection of DT spectra has shown that the spectral hole is redshifted with respect to the pump spectrum.<sup>133</sup> Moreover, at the high-energy edge of the pump spectrum a negative DT signal is observed. These signatures have been interpreted in terms of Fermi edge singularities at the upper and lower edge of the nonthermal electron distribution generated by the pump pulse.<sup>133,134</sup> The

work on Fermi edge singularities is an instructive example for the interplay between occupation and many-body effects in differential transmission experiments in semiconductors.

Thermalization of carrier distributions and many-body effects also change the spectrally integrated DT signal or the impulse response of a semiconductor saturable absorber. In particular, thermalization contributes to the fast decay seen in the impulse response at early times (cp. Fig. 3). It is important to note that this fast decay is the result of the complex redistribution of nonlinear transmission or reflectivity changes in frequency space. As a consequence, no general concept has evolved so far for the engineering of this fast decay.

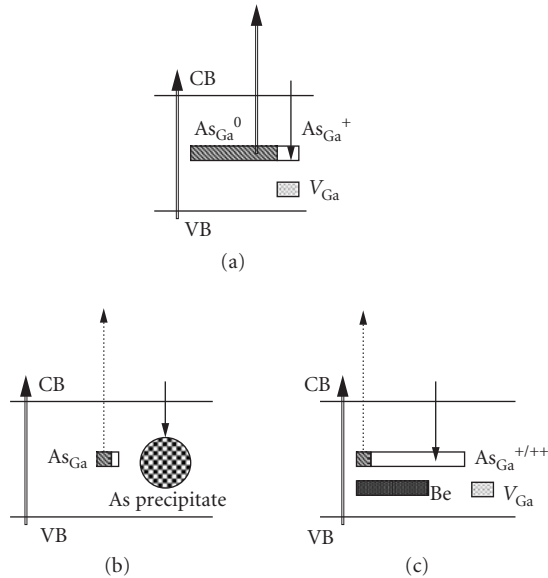
The fast decay of a spectrally integrated DT curve in the thermalization regime also depends on the temporal structure of the pump and probe pulses themselves.<sup>135,136</sup> This point has been recently demonstrated in experiments in which a so-called frequency chirp was imposed on 20-fs pulses. In a frequency-chirped laser pulse the frequency varies over the temporal profile of the pulse. Such chirped pulses have been used in DT experiments on continuum transitions in bulk semiconductors. The results show that the fast decay of spectrally integrated DT curves can be enhanced by an appropriate frequency chirp.<sup>135,136</sup> The manipulation of ultrafast nonlinearities by the chirp of the pulses can be viewed as an example of a much more general concept known as *coherent control*.<sup>137</sup> In coherent control experiments, the temporal shape or spectral content of ultrafast laser pulses are adjusted<sup>138</sup> to reach preset goals. The chirp control experiments in Refs. 135 and 136 demonstrate that the detailed temporal and spectral structure of the laser pulses should be included in the optimization of semiconductor saturable absorbers. That probably also means that the position of the SESAM within the laser cavity may play a role in sub-10-fs pulse generation.

**Carrier Trapping** Processes that remove electrons and holes from the bands of a semiconductor lead to a decay of the nonlinear transmission or to reflectivity changes resulting from the interband transitions. As discussed in Sec. 18.4, semiconductor saturable absorber applications in ultrashort pulse generation often require picosecond or subpicosecond absorber recovery times. The simplest way to obtain such short absorber recovery times would be to remove the optically excited carriers from the bands a few hundreds of femtoseconds after they have been created. Ultrafast depletion of the semiconductor band states is also important in all-optical switching devices<sup>139,140</sup> and optoelectronics.<sup>141</sup> However, intrinsic recombination processes are usually too slow to deplete the band states of a semiconductor on picosecond or subpicosecond time scales. Therefore, one generates defect states in the bandgap which give rise to fast carrier trapping, thereby depleting the bands. The trapping time is determined by the density and the type of the traps. Higher trap densities give rise to faster trapping.

Standard methods for the controlled incorporation of defect and trap states are ion implantation<sup>142</sup> and low-temperature (LT) molecular beam epitaxy.<sup>143</sup> In ion-implanted semiconductors, the trap density and the type of defect are determined by the implantation dose. The growth temperature controls the defect density in LT semiconductors, where larger defect densities are incorporated at lower temperatures.<sup>144</sup> GaAs is the best understood LT-grown III-V semiconductor. Low-temperature growth of GaAs is performed at temperatures of 200 to 300°C, as compared to about 600°C in standard molecular beam epitaxy. During LT growth of GaAs, excess arsenic is incorporated in the form of arsenic antisites (As on Ga lattice site:  $\text{As}_{\text{Ga}}$ ) at densities as large as  $10^{20} \text{ cm}^{-3}$ .<sup>144,145</sup> In undoped LT GaAs, more than 90 percent of the antisites are neutral, while the rest is singly ionized due to presence of Ga vacancies ( $V_{\text{Ga}}$ ) which are the native acceptors in the material (see Fig. 10a).<sup>144,146</sup> The ionized arsenic antisites have been identified as electron traps.<sup>147</sup> Annealing at higher temperatures (typically 600°C and higher) converts the arsenic antisite point defects into arsenic clusters, so-called As precipitates (see Fig. 10b).<sup>148</sup> A detailed review of the properties of LT GaAs can be found in Refs. 149 and 150.

The carrier trapping times in as-grown LT GaAs can be in the subpicosecond regime and show the expected decrease with decreasing growth temperature.<sup>151,152</sup> Subpicosecond recovery times of nonlinear transmission or reflectivity changes are also found in annealed LT GaAs, indicating that arsenic precipitates efficiently deplete the band states.<sup>153,154</sup> For more details about carrier trapping in LT semiconductors the reader is referred to Refs. 155 through 162.

Picosecond and subpicosecond carrier trapping times have also been found in semiconductors implanted with various ion species.<sup>163–168</sup> A decrease of the trapping time with increasing ion dose



**FIGURE 10** Electronic structure of undoped as-grown (a), undoped annealed (b), and Beryllium doped as-grown LT GaAs (c). The double arrows mark strong optical absorption transitions. Weak optical absorption transitions are indicated by dotted arrows. Trapping processes are shown by arrows that point downward.

was observed at lower doses.<sup>163,164,167</sup> At higher ion doses, the trapping time can increase with the dose.<sup>168</sup> The correlation of trapping times with structural properties of ion implanted semiconductors has given more insight into this unexpected dose dependence of the trapping time.<sup>169</sup> This work indicates that not only the defect density but also the type of defect depends on the ion dose.<sup>169</sup> Both the density and the type of defect affect carrier trapping, leading to longer trapping times if less effective traps are generated at higher ion doses.<sup>169</sup>

Besides an ultrafast carrier trapping and absorber recovery time, other important saturable absorber parameters are the modulation depth and the nonsaturable losses which remain even at the highest pump energy fluences (see Sec. 18.4). Optimized materials combine an ultrafast recovery time with high modulation and small nonsaturable losses. This material optimization issue has been addressed in recent publications.<sup>154,168,170</sup> In these studies, the nonlinearity of continuum transitions was investigated in different modifications of GaAs. The preparation of the semiconductor layers ensured that the modulation depth and the nonsaturable losses were determined by nonlinear absorption changes.

It has been shown that standard as-grown LT GaAs with an ultrafast carrier trapping time suffers from a small absorption modulation and high nonsaturable absorption losses.<sup>154,170</sup> Note that large nonsaturable absorption decreases the modulation depth and causes large nonsaturable losses when the semiconductor absorber is integrated within a mirror structure. The high nonsaturable absorption mainly results from the strong defect absorption from the neutral As antisites to the conduction band (see Fig. 10a) whose saturation fluence has been shown to be extremely high.<sup>154</sup> Therefore, the goals of material optimization are (1) to reduce the nonsaturable absorption by the reduction of the density of neutral As antisites and (2) to maintain a fast trapping and absorber recovery time.

We have demonstrated two different ways to reach those goals. Annealing of LT GaAs strongly reduces the density of neutral As antisites and the nonsaturable absorption.<sup>154</sup> The simultaneous reduction of the density of useful ionized As antisite electron traps does not substantially increase the

absorber recovery time due to the presence of the As precipitates (see Fig. 10b). Alternatively, doping with acceptors, such as Beryllium, can be used to reduce the density of neutral As antisites.<sup>171</sup> The simultaneous increase of the ionized As antisite density results in ultrafast carrier trapping and absorber recovery times (see Fig. 10c).<sup>170</sup> Annealed LT GaAs and Be doped LT GaAs combine ultrafast recovery times with high modulation depth and small nonsaturable losses. These materials are well suited for saturable absorber devices in laser physics and for all-optical switching applications.

Studies of the modulation depth  $\Delta R$ , the nonsaturable losses  $\Delta R_{ns}$ , and the recovery time  $\tau_A$  in ion implanted GaAs have shown that  $\Delta R$  decreases and  $\Delta R_{ns}$  increases with decreasing recovery time.<sup>168</sup> Nevertheless, if the ion species, ion dose, and annealing conditions are properly chosen, combinations of  $\Delta R$ ,  $\Delta R_{ns}$ , and  $\tau_A$  can be obtained which are appropriate for saturable absorber applications. Ion-implanted GaAs is an alternative to annealed or Be doped LT GaAs as a material for saturable absorber devices.<sup>168</sup>

## 18.7 REFERENCES

1. P. F. Moulton, "Spectroscopic and Laser Characteristics of  $Ti:Al_2O_3$ ," *J. Opt. Soc. Am. B.* **3**:125–132 (1986).
2. D. H. Sutter, G. Steinmeyer, L. Gallmann, N. Matuschek, F. Morier-Genoud, U. Keller, V. Scheuer, G. Angelow, and T. Tschudi, "Semiconductor Saturable-Absorber Mirror-assisted Kerr-Lens Mode-Locked  $Ti:Sapphire$  Laser Producing Pulses in the Two-Cycle Regime," *Optics Lett.* **24**:631–633 (1999).
3. U. Morgner, F. X. Kärtner, S. H. Cho, Y. Chen, H. A. Haus, J. G. Fujimoto, E. P. Ippen, V. Scheuer, G. Angelow, and T. Tschudi, "Sub-Two-Cycle Pulses from a Kerr-Lens Mode-Locked  $Ti:Sapphire$  Laser: Addenda," *Optics Lett.* **24**:920 (1999).
4. U. Keller, "Semiconductor Nonlinearities for Solid-State Laser Modelocking and Q-Switching," in Chapter 4 in *Nonlinear Optics in Semiconductors*, E. Garmire and A. Kost, (eds.), Academic Press, Inc., Boston, 1999, vol. 59, pp. 211–286.
5. U. Keller, "Ultrafast Solid-State Lasers," *Progress in Optics*, Elsevier, 2004, vol. 46, pp. 1–115.
6. L. Kraimer, R. Paschotta, S. Lecomte, M. Moser, K. J. Weingarten, and U. Keller, "Compact  $Nd:YVO_4$  Lasers with Pulse Repetition Rates up to 160 GHz," *IEEE J. Quantum Electron.* **38**:1331–1338 (2002).
7. A. E. H. Oehler, T. Südmeyer, K. J. Weingarten, and U. Keller, "100-GHz Passively Modelocked  $Er:Yb:Glass$  Laser at 1.5  $\mu m$  with 1.6-ps Pulses" *Optics Express* **16**(26): 21930–21935 (2008).
8. R. Paschotta, J. Aus der Au, G. J. Spühler, F. Morier-Genoud, R. Hövel, M. Moser, S. Erhard, M. Karszewski, A. Giesen, and U. Keller, "Diode-Pumped Passively Modelocked Lasers with High Average Power," *Appl. Phys. B.* **70**:S25–S32 (2000).
9. G. J. Spühler, R. Paschotta, R. Fluck, B. Braun, M. Moser, G. Zhang, E. Gini, and U. Keller, "Experimentally Confirmed Design Guidelines for Passively Q-Switched Microchip Lasers Using Semiconductor Saturable Absorbers," *J. Opt. Soc. Am. B.* **16**:376–388 (1999).
10. U. Keller, *Ultrafast Solid-State Lasers*, Landolt-Börnstein, Group VIII/1B1, Laser Physics and Applications. Subvolume B: Laser Systems. Part 1. G. Herziger, H. Weber, R. Proprawe (eds.), Springer-Verlag, Berlin, Heidelberg, New York, pp. 33–167, October, 2007.
11. T. Südmeyer, S. V. Marchese, S. Hashimoto, C. R. E. Baer, G. Gingras, B. Witzel, and U. Keller, "Femtosecond Laser Oscillators for High-Field Science," *Nature Photonics* **2**:599–604 (2008).
12. U. Keller and A. C. Tropper, "Passively Modelocked Surface-Emitting Semiconductor Lasers," *Physics Reports* **429**(2):67–120 (2006).
13. A. R. Bellancourt, D. J. H. C. Maas, B. Rudin, M. Golling, T. Südmeyer, and U. Keller, "Modelocked Integrated External-Cavity Surface Emitting Laser (MIXSEL)," *IET Optoelectronics* **3**:61–72 (2009).
14. A. Shirakawa, I. Sakane, M. Takasaka, and T. Kobayashi, "Sub-5-fs Visible Pulse Generation by Pulse-Front-Matched Noncollinear Optical Parametric Amplification," *Appl. Phys. Lett.* **74**:2268–2270 (1999).
15. A. Baltuska, Z. Wei, M. S. Pshenichnikov, D. A. Wiersma, and R. Szipöcs, "All-Solid-State Cavity Dumped Sub-5-fs laser," *Appl. Phys. B.* **65**:175–188 (1997).
16. M. Nisoli, S. Stagira, S. D. Silvestri, O. Svelto, S. Sartania, Z. Cheng, M. Lenzner, C. Spielmann, and F. Krausz, "A Novel High-Energy Pulse Compression System: Generation of Multigigawatt Sub-5-fs Pulses," *Appl. Phys. B.* **65**:189–196 (1997).

17. G. Steinmeyer, D. H. Sutter, L. Gallmann, N. Matuschek, and U. Keller, "New Frontiers in Ultra-short Pulse Generation: Pushing the Limits in Linear and Nonlinear Optics," *Science* **286**:1507–1512 (1999).
18. U. Keller, D. A. B. Miller, G. D. Boyd, T. H. Chiu, I. F. Ferguson, and M. T. Asom, "Solid-State Low-Loss Intracavity Saturable Absorber for Nd:YLF Lasers: An Antiresonant Semiconductor Fabry-Perot Saturable Absorber," *Optics Lett.* **17**:505–507 (1992).
19. K. J. Weingarten, U. Keller, T. H. Chiu, and J. F. Ferguson, "Passively Mode-Locked Diode-Pumped Solid-State Lasers Using an Antiresonant Fabry-Perot Saturable Absorber," *Optics Lett.* **18**:640–642 (1993).
20. X. M. Zhao and J.-C. Diels, "Ultrashort Laser Sources," in *Handbook of Optics*, M. Bass, E. W. Stryland, D. R. Williams, and W. L. Wolfe, (eds.) McGraw-Hill, Inc., New York, 1995, vol. 1, pp. 14.1–14.29.
21. H. A. Haus, "Short Pulse Generation," in *Compact Sources of Ultrashort Pulses I*, I. N. Duling (ed.) Cambridge University Press, New York, 1995, pp. 1–56.
22. G. P. Agrawal and N. A. Olsson, "Self-Phase Modulation and Spectral Broadening of Optical Pulses in Semiconductor Laser Amplifiers," *IEEE J. Quantum Electron.* **25**:2297–2306 (1989).
23. C. Hönninger, R. Paschotta, F. Morier-Genoud, M. Moser, and U. Keller, "Q-Switching Stability Limits of Continuous-Wave Passive Mode Locking," *J. Opt. Soc. Am. B.* **16**:46–56 (1999).
24. M. Haiml, R. Grange, and U. Keller "Optical Characterization of Semiconductor Saturable Absorbers," *Appl. Phys. B.* **79**:331–339 (2004).
25. D. J. H. Maas, B. Rudin, A.-R. Bellancourt, D. Iwaniuk, S. V. Marchese, T. Südmeyer, and U. Keller, "High Precision Optical Characterization of Semiconductor Saturable Absorber Mirrors," *Optics Express* **16**:7571–7579 (2008).
26. G. H. C. New, "Modelocking of Quasi-Continuous Lasers," *Opt. Commun.* **6**:188–192 (1972).
27. G. H. C. New, "Pulse Evolution in Mode-Locked Quasi-Continuous Lasers," *IEEE J. Quantum Electron.* **10**:115–124 (1974).
28. H. A. Haus, "Theory of Mode Locking with a Slow Saturable Absorber," *IEEE J. Quantum Electron.* **11**:736–746 (1975).
29. U. Keller, "Recent Developments in Compact Ultrafast Lasers," *Nature* **424**:831–838 (2003).
30. J. A. Valdmanis, R. L. Fork, and J. P. Gordon, "Generation of Optical Pulses as Short as 27 fs Directly from a Laser Balancing Self-Phase Modulation, Group-Velocity Dispersion, Saturable Absorption, and Saturable Gain," *Optics Lett.* **10**:131–133 (1985).
31. J. A. Valdmanis and R. L. Fork, "Design Considerations for a Femtosecond Pulse Laser Balancing Self-Phase Modulation, Group Velocity Dispersion, Saturable Absorption, and Saturable Gain," *IEEE J. Quantum Electron.* **22**:112–118 (1986).
32. O. E. Martinez, R. L. Fork, and J. P. Gordon, "Theory of Passively Modelocked Lasers Including Self-Phase Modulation and Group-Velocity Dispersion," *Optics Lett.* **9**:156–158 (1984).
33. O. E. Martinez, R. L. Fork, and J. P. Gordon, "Theory of Passively Modelocked Lasers for the Case of a Nonlinear Complex Propagation Coefficient," *J. Opt. Soc. Am. B.* **2**:753 (1985).
34. H. A. Haus, "Theory of Modelocking with a Fast Saturable Absorber," *J. Appl. Phys.* **46**:3049–3058 (1975).
35. K. N. Islam, E. R. Sunderman, C. E. Soccolich, I. Bar-Joseph, N. Sauer, T. Y. Chang, and B. I. Miller, "Color Center Lasers Passively Mode Locked by Quantum Wells," *IEEE J. Quantum Electron.* **25**:2454–2463 (1989).
36. U. Keller, K. J. Weingarten, F. X. Kärtner, D. Kopf, B. Braun, I. D. Jung, R. Fluck, C. Hönninger, N. Matuschek, and J. Aus der Au, "Semiconductor Saturable Absorber Mirrors (SESAMs) for Femtosecond to Nanosecond Pulse Generation in Solid-State Lasers," *IEEE J. Sel. Top. Quantum Electron.* **2**:435–453 (1996).
37. B. G. Kim, E. Garmire, S. G. Hummel, and P. D. Dapkus, "Nonlinear Bragg Reflector Based on Saturable Absorption," *Appl. Phys. Lett.* **54**:1095–1097 (1989).
38. L. R. Brovelli, I. D. Jung, D. Kopf, M. Kamp, M. Moser, F. X. Kärtner, and U. Keller, "Self-Starting Soliton Modelocked Ti:sapphire Laser Using a Thin Semiconductor Saturable Absorber," *Electronics Lett.* **31**:287–289 (1995).
39. S. Tsuda, W. H. Knox, E. A. D. Souza, W. Y. Jan, and J. E. Cunningham, "Low-Loss Intracavity AlAs/AlGaAs Saturable Bragg Reflector for Femtosecond Mode Locking in Solid-State Lasers," *Optics Lett.* **20**:1406–1408 (1995).
40. L. R. Brovelli, U. Keller, and T. H. Chiu, "Design and Operation of Antiresonant Fabry-Perot Saturable Semiconductor Absorbers for Mode-Locked Solid-State Lasers," *J. Opt. Soc. Am. B.* **12**:311–322 (1995).

41. I. D. Jung, F. X. Kärtner, N. Matuschek, D. H. Sutter, F. Morier-Genoud, Z. Shi, V. Scheuer, M. Tilsch, T. Tschudi, and U. Keller, "Semiconductor Saturable Absorber Mirrors Supporting Sub-10 fs Pulses," *Applied Physics B: Special Issue on Ultrashort Pulse Generation* **65**:137–150 (1997).
42. G. J. Spühler, K. J. Weingarten, R. Grange, L. Kraimer, M. Haiml, V. Liverini, M. Golling, S. Schön, and U. Keller, "Semiconductor Saturable Absorber Mirror Structure with Low Saturation Fluence," *Appl. Phys. B* **81**(1): 27–32 (2005).
43. I. P. Bilinsky, J. G. Fujimoto, J. N. Walpole, and L. J. Missaggia, "InAs-Doped Silica Films for Saturable Absorber Applications," *Appl. Phys. Lett.* **74**:2411–2413 (1999).
44. N. Sarukura, Y. Ishida, T. Yanagawa, and H. Nakano, "All Solid-State cw Passively Modelocked Ti:Sapphire Laser Using a Colored Glass Filter," *Appl. Phys. Lett.* **57**:229–230 (1990).
45. L. F. Mollenauer, R. H. Stolen, and J. P. Gordon, "Experimental Observation of Picosecond Pulse Narrowing and Solitons in Optical Fibers," *Phys. Rev. Lett.* **45**:1095–1098 (1980).
46. W. J. Tomlinson, R. H. Stolen, and C. V. Shank, "Compression of Optical Pulses Chirped by Self-Phase Modulation in Fibers," *J. Opt. Soc. Am. B* **1**:139–149 (1984).
47. R. L. Fork, C. H. B. Cruz, P. C. Becker, and C. V. Shank, "Compression of Optical Pulses to Six Femtoseconds by Using Cubic Phase Compensation," *Optics Lett.* **12**:483–485 (1987).
48. S. Sartania, Z. Cheng, M. Lenzner, G. Tempea, C. Spielmann, F. Krausz, and K. Ferencz, "Generation of 0.1-TW 5-fs Optical Pulses at a 1-kHz Repetition Rate," *Optics Lett.* **22**:1562–1564 (1997).
49. R. L. Fork, C. V. Shank, C. Hirlimann, R. Yen, and W. J. Tomlinson, "Femtosecond White-Light Continuum Pulses," *Optics Lett.* **8**:1–3 (1983).
50. G. M. Gale, M. Cavallari, T. J. Driscoll, and F. Hache, "Sub-20 fs Tunable Pulses in the Visible from an 82 MHz Optical Parametric Oscillator," *Optics Lett.* **20**:1562–1564 (1995).
51. F. X. Kärtner and U. Keller, "Stabilization of Soliton-Like Pulses with a Slow Saturable Absorber," *Optics Lett.* **20**:16–18 (1995).
52. F. X. Kärtner, I. D. Jung, and U. Keller, "Soliton Modelocking with Saturable Absorbers," Special Issue on Ultrafast Electronics, Photonics and Optoelectronics, *IEEE J. Sel. Topics in Quantum Electronics (JSTQE)* **2**:540–556 (1996).
53. I. D. Jung, F. X. Kärtner, L. R. Brovelli, M. Kamp, and U. Keller, "Experimental Verification of Soliton Modelocking Using Only a Slow Saturable Absorber," *Optics Lett.* **20**:1892–1894 (1995).
54. D. J. Kaup, "Perturbation Theory for Solitons in Optical Fibers," *Phys. Rev. A* **42**:5689–5694 (1990).
55. L. F. Mollenauer and R. H. Stolen, "The Soliton Laser," *Optics Lett.* **9**:13–15 (1984).
56. F. M. Mitschke and L. F. Mollenauer, "Ultrashort Pulses from the Soliton Laser," *Optics Lett.* **12**:407–409 (1987).
57. P. N. Kean, X. Zhu, D. W. Crust, R. S. Grant, N. Landford, and W. Sibbett, "Enhanced Modelocking of Color Center Lasers," *Optics Lett.* **14**:39–11 (1989).
58. E. P. Ippen, H. A. Haus, and L. Y. Liu, "Additive Pulse Modelocking," *J. Opt. Soc. Am. B* **6**:1736–1745 (1989).
59. D. E. Spence, P. N. Kean, and W. Sibbett, "60-fsec Pulse Generation from a Self-Mode-Locked Ti:Sapphire Laser," *Optics Lett.* **16**:42–44 (1991).
60. U. Keller, G. W. 'tHooft, W. H. Knox, and J. E. Cunningham, "Femtosecond Pulses from a Continuously Self-Starting Passively Mode-Locked Ti:Sapphire Laser," *Optics Lett.* **16**:1022–1024 (1991).
61. F. Salin, J. Squier, and M. Piché, "Modelocking of Ti:Sapphire Lasers and Self-Focusing: A Gaussian Approximation," *Optics Lett.* **16**:1674–1676 (1991).
62. D. K. Negus, L. Spinelli, N. Goldblatt, and G. Feugnet, "Sub-100 Femtosecond Pulse Generation by Kerr Lens Modelocking in Ti:Sapphire," in *Advanced Solid-State Lasers*, G. Dubé and L. Chase (eds.) Optical Society of America, Washington, D.C., 1991, vol. 10, pp. 120–124.
63. M. Piche and F. Salin, "Self-Mode Locking of Solid-State Lasers without Apertures," *Optics Lett.* **18**:1041–1043 (1993).
64. V. Magni, G. Cerullo, S. D. Silvestri, and A. Monguzzi, "Astigmatism in Gaussian-Beam Self-Focussing and in Resonators for Kerr-Lens Mode-Locking," *JOSA B* **12**:476–485 (1995).
65. H. A. Haus, J. G. Fujimoto, and E. P. Ippen, "Analytic Theory of Additive Pulse and Kerr Lens Mode Locking," *IEEE J. Quantum Electron.* **28**:2086–2096 (1992).
66. T. Brabec, C. Spielmann, and F. Krausz, "Mode Locking in Solitary Lasers," *Optics Lett.* **16**:1961–1963 (1991).

67. F. Krausz, M. E. Fermann, T. Brabec, P. F. Curley, M. Hofer, M. H. Ober, C. Spielmann, E. Wintner, and A. J. Schmidt, "Femtosecond Solid-State Lasers," *IEEE J. Quantum Electron.* **28**:2097–2122 (1992).
68. J.-L. Tapié, and G. Mourou, "Shaping of Clean, Femtosecond Pulses at 1.053  $\mu\text{m}$  for Chirped-Pulse Amplification," *Optics Lett.* **17**:136–138 (1992).
69. Y. Beaudoin, C. Y. Chien, J. S. Coe, J. L. Tapié, and G. Mourou, "Ultra-high-Contrast Ti:Sapphire/Nd:Glass Terawatt Laser System," *Optics Lett.* **17**:865–867 (1992).
70. M. Hofer, M. H. Ober, F. Haberl, and M. E. Fermann, "Characterization of Ultrashort Pulse Formation in Passively Mode-Locked Fiber Lasers," *IEEE J. Quantum Electron.* **28**:720–728 (1992).
71. R. J. Elliot, in *Polarons and Excitons*, C. G. Kuper and G. D. Whitefield (eds.), Plenum, New York, 1963.
72. C. Weisbuch and B. Vinter, *Quantum Semiconductor Structures: Fundamentals and Applications*, Academic, San Diego, 1991.
73. J. Shah, *Ultrafast Spectroscopy of Semiconductors and Semiconductor Nanostructures*, Springer-Verlag, Berlin, 1996.
74. E. O. Göbel, "Ultrafast Spectroscopy of Semiconductors," in *Advances in Solid State Physics*, U. Rössler (ed.) Friedrich Vieweg & Sohn, Braunschweig/Wiesbaden, 1990, vol. 30, pp. 269–294.
75. L. Allen and J. H. Eberly, *Optical Resonance and Two-Level Atoms*, Dover, New York, 1975.
76. Y. R. Shen, *The Principles of Nonlinear Optics*, John Wiley & Sons, New York, 1984.
77. K. Shimoda, *Introduction to Laser Physics* (Springer Series in Optical Science) Springer, Heidelberg, 1984.
78. T. Yajima, and Y. Taira, "Spatial Optical Parametric Coupling of Picosecond Light Pulses and Transverse Relaxation Effects in Resonant Media," *Journal of the Physical Society of Japan* **47**:1620–1626 (1979).
79. A. M. Weiner, S. De Silvestri, and E. P. Ippen, "Three-Pulse Scattering for Femtosecond Dephasing Studies: Theory and Experiment," *J. Opt. Soc. Am. B.* **2**:654–661 (1985).
80. C. H. Brito Cruz, J. P. Gordon, P. C. Becker, R. L. Fork, and C. V. Shank, "Dynamics of Spectral Hole Burning," *IEEE J. Quantum Electron.* **24**:261–266 (1988).
81. B. Fluegel, N. Peyghambarian, G. Olbright, M. Lindberg, S. W. Koch, M. Joffe, D. Hulin, A. Migus, and A. Antonetti, "Femtosecond Studies of Coherent Transients in Semiconductors," *Phys. Rev. Lett.* **59**:2588–2591 (1987).
82. M. Lindberg and S. W. Koch, "Transient Oscillations and Dynamics Stark Effect in Semiconductors," *Phys. Rev. B.* **38**:7607–7614 (1988).
83. J. P. Sokoloff, M. Joffe, B. Fluegel, D. J. Hulin, M. Lindberg, S. W. Koch, A. Migus, A. Antonetti, and N. Peyghambarian, "Transient Oscillations in the Vicinity of Excitons and in the Band of Semiconductors," *Phys. Rev. B.* **38**:7615–7621 (1988).
84. H. Haug and S. Schmitt-Rink, "Basic Mechanisms of the Optical Nonlinearities of Semiconductors near the Band Edge," *J. Opt. Soc. Am. B.* **2**:1135–1142 (1985).
85. H. Haug and S. W. Koch, *Quantum Theory of the Optical and Electronic Properties of Semiconductors*, World Scientific, Singapore, 1993.
86. S. Schmitt-Rink, D. S. Chemla, and D. A. B. Miller, "Linear and Nonlinear Optical Properties of Semiconductor Quantum Wells," *Advances in Physics*, **38**:89–188 (1989).
87. D. S. Chemla, "Ultrafast Transient Nonlinear Optical Processes in Semiconductors," in *Semiconductors and Semimetals*, Academic Press, Boston, 1999, vol. 58, pp. 175–256.
88. S. Hunsche, H. Heesel, A. Ewertz, H. Kurz, and J. H. Collet, "Spectral-Hole Burning and Carrier Thermalization in GaAs at Room Temperature," *Phys. Rev. B.* **48**:17818–17826 (1993).
89. L. Schultheis, J. Kuhl, A. Honold, and C. W. Tu, "Ultrafast Phase Relaxation of Excitons via Exciton-Exciton and Exciton-Electron Collisions," *Phys. Rev. Lett.* **57**:1635–1638 (1986).
90. A. Honold, L. Schultheis, J. Kuhl, and C. W. Tu, "Collision Broadening of Two-Dimensional Excitons in a GaAs Single Quantum Well," *Phys. Rev. B.* **40**:6442–6445 (1989).
91. L. Schultheis, A. Honold, J. Kuhl, K. Kohler, and C. W. Tu, "Optical Dephasing of Homogeneously Broadened Two-Dimensional Exciton Transitions in GaAs Quantum Wells," *Phys. Rev. B.* **34**:9027–9030 (1986).
92. J. Kuhl, A. Honold, L. Schultheis, and C. W. Tu, "Optical Dephasing and Orientational Relaxation of Wannier Excitons and Free Carriers in GaAs and GaAs/AlGaAs Quantum Wells," in *Advances in Solid State Physics*, U. Rössler (ed.) Friedrich Vieweg & Sohn, Braunschweig/Wiesbaden, 1989, vol. 29, pp. 157–181.

93. U. Siegner, D. Weber, E. O. Göbel, D. Bennhardt, V. Heuckeroth, R. Saleh, S. D. Baranovskii, P. Thomas, H. Schwab, C. Klingshirn, J. M. Hvam, and V. G. Lyssenko, "Optical Dephasing in Semiconductor Mixed Crystals," *Phys. Rev. B* **46**:4564–4581 (1992).
94. S. T. Cundiff and D. G. Steel, "Coherent Transient Spectroscopy of Excitons in GaAs-AlGaAs Quantum Wells," *IEEE J. Quantum Electron.* **28**:2423 (1992).
95. E. O. Göbel, K. Leo, T. C. Damen, J. Shah, S. Schmitt-Rink, W. Schäfer, J. F. Müller, and K. Köhler, "Quantum Beats of Excitons in Quantum Wells," *Phys. Rev. Lett.* **64**:1801–1804 (1990).
96. K. Leo, T. C. Damen, J. Shah, E. O. Göbel, and K. Köhler, "Quantum Beats of Light and Heavy Hole Excitons in Quantum Wells," *Appl. Phys. Lett.* **57**:19–21 (1990).
97. B. F. Feuerbacher, J. Kuhl, R. Eccleston, and K. Ploog, "Quantum Beats Between the Light and Heavy Hole Excitons in a Quantum Well," *Solid State Communications* **74**:1279–1283 (1990).
98. K. Leo, T. C. Damen, J. Shah, and K. Köhler, "Quantum Beats of Free and Bound Excitons in GaAs/Al<sub>x</sub>Ga<sub>1-x</sub>As Quantum Wells," *Phys. Rev. B* **42**:11359 (1990).
99. J. Feldmann, T. Meier, G. V. Plessen, M. Koch, E. O. Göbel, P. Thomas, G. Bacher, C. Hartmann, H. Schweizer, W. Schäfer, and N. Nickel, "Coherent Dynamics of Excitonic Wave Packets," *Phys. Rev. Lett.* **70**:3027–3030 (1993).
100. M. Koch, J. Feldmann, G. V. Plessen, E. O. Göbel, P. Thomas, and K. Köhler, "Quantum Beats versus Polarization Interference: An Experimental Distinction," *Phys. Rev. Lett.* **69**:3631–3634 (1992).
101. V. G. Lyssenko, J. Erland, I. Balslev, K.-H. Pantke, B. S. Razbirin, and J. M. Hvam, "Nature of Nonlinear Four-Wave-Mixing Beats in Semiconductors," *Phys. Rev. B* **48**:5720–5723 (1993).
102. K. Leo, M. Wegener, J. Shah, D. S. Chemla, E. O. Göbel, T. C. Damen, S. Schmitt-Rink, and W. Schäfer, "Effects of Coherent Polarization Interaction on Time-Resolved Degenerate Four-Wave Mixing," *Phys. Rev. Lett.* **65**:1340–1343 (1990).
103. M. Wegener, D. S. Chemla, S. Schmitt-Rink, and W. Schäfer, "Line Shape of Time-Resolved Four-Wave Mixing," *Phys. Rev. A* **42**:5675–5683 (1990).
104. D. S. Kim, J. Shah, T. C. Damen, W. Schäfer, F. Jahnke, S. Schmitt-Rink, and K. Köhler, "Unusual Slow Temporal Evolution of Femtosecond Four-Wave-Mixing Signals in Intrinsic GaAs Quantum Wells: Direct Evidence for the Dominance of Interaction Effects," *Phys. Rev. Lett.* **69**:2725 (1992).
105. S. Weiss, M.-A. Mycek, J.-Y. Bigot, S. Schmitt-Rink, and D. S. Chemla, "Collective Effects in Excitonic Free Induction Decay: Do Semiconductors and Atoms Emit Coherent Light in Different Ways?" *Phys. Rev. Lett.* **69**:2685–2688 (1992).
106. H. Wang, K. Ferrio, D. G. Steel, Y. Z. Hu, R. Binder, and S. W. Koch, "Transient Nonlinear Optical Response from Excitation Induced Dephasing in GaAs," *Phys. Rev. Lett.* **71**:1261–1264 (1993).
107. P. Kner, S. Bar-Ad, M. V. Marquezini, D. S. Chemla, and W. Schäfer, "Magnetically Enhanced Exciton-Exciton Correlations in Semiconductors," *Phys. Rev. Lett.* **78**:1319–1322 (1997).
108. P. Kner, W. Schäfer, R. Lövenich, and D. S. Chemla, "Coherence of Four-Particle Correlations in Semiconductors," *Phys. Rev. Lett.* **81**:5386–5389 (1998).
109. G. Bartels, A. Stahl, V. M. Axt, B. Haase, U. Neukirch, and J. Gutowski, "Identification of Higher-Order Electronic Coherences in Semiconductors by their Signature in Four-Wave-Mixing Signals," *Phys. Rev. Lett.* **81**:5880–5883 (1998).
110. P. Kner, S. Bar-Ad, M. V. Marquezini, D. S. Chemla, R. Lövenich, and W. Schäfer, "Effect of Magnetoexciton Correlations on the Coherent Emission of Semiconductors," *Phys. Rev. B* **60**:4731 (1999).
111. P. C. Becker, H. L. Fragnito, C. H. Brito Cruz, R. L. Fork, J. E. Cunningham, J. E. Henry, and C. V. Shank, "Femtosecond Photon Echoes from Band-to-Band Transitions in GaAs," *Phys. Rev. Lett.* **61**:1647–1649 (1988).
112. J.-Y. Bigot, M. T. Portella, R. W. Schoenlein, J. E. Cunningham, and C. V. Shank, "Two-Dimensional Carrier-Carrier Screening in a Quantum Well," *Phys. Rev. Lett.* **67**:636–639 (1991).
113. S. Arlt, U. Siegner, J. Kunde, F. Morier-Genoud, and U. Keller, "Ultrafast Dephasing of Continuum Transitions in Bulk Semiconductors," *Phys. Rev. B* **59**:14860–14863 (1999).
114. J. A. Kash, J. C. Tsang, and J. M. Hvam, "Subpicosecond Time-Resolved Raman Spectroscopy of LO Phonons in GaAs," *Phys. Rev. Lett.* **54**:2151–2154 (1985).
115. G. Fasol, W. Hackenburger, H. P. Hughes, K. Ploog, E. Bauser, and H. Kano, "Continuous-Wave Spectroscopy of Femtosecond Carrier Scattering in GaAs," *Phys. Rev. B* **41**:1461–1478 (1990).



116. J. H. Collet, "Screening and Exchange in the Theory of the Femtosecond Kinetics of the Electron-Hole Plasma," *Phys. Rev. B* **47**:10279–10291 (1993).
117. A. Lohner, K. Rick, P. Leisching, A. Leitenstorfer, T. Elsaesser, T. Kuhn, F. Rossi, and W. Stolz, "Coherent Optical Polarization of Bulk GaAs Studied by Femtosecond Photon-Echo Spectroscopy," *Phys. Rev. Lett.* **71**:77–80 (1993).
118. U. Siegner, M.-A. Mycek, S. Glutsch, and D. S. Chemla, "Ultrafast Coherent Dynamics of Fano Resonances in Semiconductors," *Phys. Rev. Lett.* **74**:470–473 (1995).
119. U. Siegner, M.-A. Mycek, S. Glutsch, and D. S. Chemla, "Quantum Interference in the System of Lorentzian and Fano Magnetoexciton Resonances in GaAs," *Phys. Rev. B* **51**:4953–4961 (1995).
120. S. Arlt, U. Siegner, F. Morier-Genoud, and U. Keller, "Ultrafast Coherent Dynamics in Semiconductor Quantum Wells for Multi-Subband Excitation in Different Density Regimes," *Phys. Rev. B* **58**:13073–13080 (1998).
121. T. Rappen, U. Peter, M. Wegener, and W. Schäfer, "Coherent Dynamics of Continuum and Exciton States Studied by Spectrally Resolved fs Four-Wave Mixing," *Phys. Rev. B* **48**:4879–4882 (1993).
122. M. U. Wehner, D. Steinbach, and M. Wegener, "Ultrafast Coherent Transients due to Exciton-Continuum Scattering in Bulk GaAs," *Phys. Rev. B* **54**:R5211–R5214 (1996).
123. D. Birkedal, V. G. Lyssenko, J. M. Hvam, and K. ElSayed, "Continuum Contribution to Excitonic Four-Wave Mixing Due to Interaction-Induced Nonlinearities," *Phys. Rev. B* **54**:R14250–R14253 (1996).
124. S. T. Cundiff, M. Koch, W. H. Knox, J. Shah, and W. Stolz, "Optical Coherence in Semiconductors: Strong Emission Mediated by Nondegenerate Interactions," *Phys. Rev. Lett.* **77**:1107–1110 (1996).
125. V. P. Kalosha, M. Müller, and J. Herrmann, "Coherent-Absorber Mode Locking of Solid-State Lasers," *Optics Lett.* **23**:117–119 (1998).
126. V. P. Kalosha, M. Müller, and J. Herrmann, "Theory of Solid-State Laser Mode Locking by Coherent Semiconductor Quantum-Well Absorbers," *J. Opt. Soc. Am. B* **16**:323 (1999).
127. J. L. Oudar, D. Hulin, A. Migus, A. Antonetti, and F. Alexandre, "Subpicosecond Spectral Hole Burning due to Nonthermalized Photoexcited Carriers in GaAs," *Phys. Rev. Lett.* **55**:2074–2077 (1985).
128. W. H. Knox, C. Hirlimann, D. A. B. Miller, J. Shah, D. S. Chemla, and C. V. Shank, "Femtosecond Excitation of Nonthermal Carrier Populations in GaAs Quantum Wells," *Phys. Rev. Lett.* **56**:1191–1193 (1986).
129. R. W. Schoenlein, W. Z. Lin, E. P. Ippen, and J. G. Fujimoto, "Femtosecond Hot-Carrier Energy Relaxation in GaAs," *Appl. Phys. Lett.* **51**:1442–1444 (1987).
130. W. H. Knox, D. S. Chemla, G. Livescu, J. E. Cunningham, and J. E. Henry, "Femtosecond Carrier Thermalization in Dense Fermi Seas," *Phys. Rev. Lett.* **61**:1290–1293 (1988).
131. J.-Y. Bigot, M. T. Portella, R. W. Schoenlein, J. E. Cunningham, and C. V. Shank, "Resonant Intervalley Scattering in GaAs," *Phys. Rev. Lett.* **65**:3429–3432 (1990).
132. P. C. Becker, H. L. Fragnito, C. H. Brito Cruz, J. Shah, R. L. Fork, J. E. Cunningham, J. E. Henry, and C. V. Shank, "Femtosecond Intervalley Scattering in GaAs," *Appl. Phys. Lett.* **53**:2089 (1988).
133. J.-P. Foing, D. Hulin, M. Joffre, M. K. Jackson, J. L. Oudar, C. Tanguy, and M. Combescot, "Absorption Edge Singularities in Highly Excited Semiconductors," *Phys. Rev. Lett.* **68**:110–113 (1992).
134. C. Tanguy and M. Combescot, "X-Ray-Like Singularities for Nonequilibrium Fermi Sea," *Phys. Rev. Lett.* **68**:1935–1938 (1992).
135. J. Kunde, U. Siegner, S. Arlt, F. Morier-Genoud, and U. Keller, "Chirp-Controlled Ultrafast Optical Nonlinearities in Semiconductors," *Appl. Phys. Lett.* **73**:3025–3027 (1998).
136. J. Kunde, U. Siegner, S. Arlt, G. Steinmeyer, F. Morier-Genoud, and U. Keller, "Potential of Femtosecond Chirp Control of Ultrabroadband Semiconductor Continuum Nonlinearities," *J. Opt. Soc. Am. B* **16**:2285–2294 (1999).
137. W. S. Warren, H. Rabitz and M. Dahleh, "Coherent Control of Quantum Dynamics: The Dream Is Alive," *Science* **259**:1581–1589 (1993).
138. A. M. Weiner, "Femtosecond Pulse Shaping Using Spatial Light Modulators," *Rev. Sci. Instruments* **71**:1929–1960 (2000).
139. R. Takahashi, Y. Kawamura, and H. Iwamura, "Ultrafast 1.55  $\mu\text{m}$  All-Optical Switching Using Low-Temperature-Grown Multiple Quantum Wells," *Appl. Phys. Lett.* **68**:153–155 (1996).
140. H. S. Loka and P. W. E. Smith, "Ultrafast All-Optical Switching in an Asymmetric Fabry-Perot Device Using Low-Temperature-Grown GaAs," *IEEE Phot. Tech. Lett.* **10**:1733–1735 (1998).

141. J. F. Whitaker, "Optoelectronic Applications of LTMBE III-V Materials," *Mater. Sci. Eng.* **B22**:61–67 (1993).
142. J. F. Ziegler, J. P. Biersack, and U. Littmark, *The Stopping and Range of Ions in Solids*, Pergamon, New York, 1989.
143. F. W. Smith, A. R. Calawa, C.-L. Chen, M. J. Manfra, and L. J. Mahoney, "New MBE Buffer Used to Eliminate Backgating in GaAs MESFETs," *IEEE Electron. Device Lett.* **9**:77–80 (1988).
144. X. Liu, A. Prasad, W. M. Chen, A. Kurpiewski, A. Stoschek, Z. Liliental-Weber, and E. R. Weber, "Mechanism Responsible for the Semi-Insulating Properties of Low-Temperature-Grown GaAs," *Appl. Phys. Lett.* **65**:3002–3004 (1994).
145. X. Liu, A. Prasad, J. Nishio, E. R. Weber, Z. Liliental-Weber, and W. Walukiewicz, "Native Point Defects in Low-Temperature Grown GaAs," *Appl. Phys. Lett.* **67**:279 (1995).
146. M. Luysberg, H. Sohn, A. Prasad, P. Specht, Z. Liliental-Weber, E. R. Weber, J. Gebauer, and R. Krause-Rehberg, "Effects of the Growth Temperature and As/Ga Flux Ratio on the Incorporation of Excess As into Low Temperature Grown GaAs," *J. Appl. Phys.* **83**:561–6,1998.
147. Z. Liliental-Weber, J. Ager, D. Look, X. W. Lin, X. Liu, J. Nishio, K. Nichols, W. Schaff, W. Swider, K. Wang, J. Wasburn, E. R. Weber, and J. Whitaker, in *Proceedings of the Eighth Conference on Semi-insulating III-V Materials*, edited by M. Godlewski (World Scientific, Singapore, 1994), p. 305.
148. M. R. Melloch, N. Otsuka, J. M. Woodall, A. C. Warren, and J. L. Freeouf, "Formation of Arsenic Precipitates in GaAs Buffer Layers Grown by Molecular Beam Epitaxy at Low Substrate Temperatures," *Appl. Phys. Lett.* **57**:1531 (1990).
149. G. L. Witt, R. Calawa, U. Mishra, E. Weber (eds.), *Low Temperature (LT) GaAs and Related Materials*, Mat. Res. Soc. Symp. Proceedings, vol. 241 Pittsburgh, 1992.
150. G. L. Witt, "LTMBE GaAs: Present Status and Perspectives," *Mater. Sci. Eng.* **B22**:9 (1993).
151. S. Gupta, M. Y. Frankel, J. A. Valdmanis, J. F. Whitaker, G. A. Mourou, F. W. Smith, and A. R. Calawa, "Subpicosecond Carrier Lifetime in GaAs Grown by Molecular Beam Epitaxy at Low Temperatures," *Appl. Phys. Lett.* **59**:3276–3278 (1991).
152. S. Gupta, J. F. Whitaker, and G. A. Mourou, "Ultrafast Carrier Dynamics in III-V Semiconductors Grown by Molecular-Beam Epitaxy at Very Low Substrate Temperatures," *IEEE J. Quantum Electron.* **28**:2464–2472 (1992).
153. K. A. McIntosh, K. B. Nichols, S. Verghese, and E. R. Brown, "Investigation of Ultrashort Photo-carrier Relaxation Times in Low-Temperature-Grown GaAs," *Appl. Phys. Lett.* **70**:354–356 (1997).
154. M. Haiml, U. Siegner, F. Morier-Genoud, U. Keller, M. Luysberg, R. C. Lutz, P. Specht, and E. R. Weber, "Optical Nonlinearity in Low-Temperature Grown GaAs: Microscopic Limitations and Optimization Strategies," *Appl. Phys. Lett.* **74**:3134 (1999).
155. E. S. Harmon, M. R. Melloch, J. M. Woodall, D. D. Nolte, N. Otsuka, and C. L. Chang, "Carrier Life time versus Anneal in Low Temperature Growth GaAs," *Appl. Phys. Lett.* **63**:2248–2250 (1993).
156. Y. Kostoulas, L. J. Waxer, I. A. Walmsley, G. W. Wicks, and P. M. Fauchet, "Femtosecond Carrier Dynamics in Low-Temperature-Grown Indium Phosphide," *Appl. Phys. Lett.* **66**:1821–1823 (1995).
157. Y. Kostoulas, K. B. Ucer, G. W. Wicks, and P. M. Fauchet, "Femtosecond Carrier Dynamics in Low-Temperature Grown  $\text{Ga}_{0.51}\text{In}_{0.49}\text{P}$ ," *Appl. Phys. Lett.* **67**:3756–3758 (1995).
158. U. Siegner, R. Fluck, G. Zhang, and U. Keller, "Ultrafast High-Intensity Nonlinear Absorption Dynamics in Low-Temperature Grown Gallium Arsenide," *Appl. Phys. Lett.* **69**:2566–2568 (1996).
159. A. J. Lochtefeld, M. R. Melloch, J. C. P. Chang, and E. S. Harmon, "The Role of Point Defects and Arsenic Precipitates in Carrier Trapping and Recombination in Low-Temperature Grown GaAs," *Appl. Phys. Lett.* **69**:1465–1467 (1996).
160. G. Segsneider, T. Dekorsky, H. Kurz, R. Hey, and K. Ploog, "Energy Resolved Ultrafast Relaxation Dynamics Close to the Band Edge of Low-Temperature Grown GaAs," *Appl. Phys. Lett.* **71**:2779–2781 (1997).
161. T. S. Sosnowski, T. B. Norris, H. H. Wang, P. Grenier, and J. F. Whitaker, "High-Carrier-Density Electron Dynamics in Low-Temperature-Grown GaAs," *Appl. Phys. Lett.* **70**:3245–3247 (1997).
162. H. S. Loka, S. D. Benjamin, and P. W. E. Smith, "Optical Characterization of Low-Temperature-Grown GaAs for Ultrafast All-Optical Switching Devices," *IEEE J. Quantum Electron.* **34**:1426–1437 (1998).
163. M. B. Johnson, T. C. McGill, and N. G. Paulter, "Carrier Lifetimes in Ion-Damaged GaAs," *Appl. Phys. Lett.* **54**:2424–2426 (1989).

164. M. Lambsdorff, J. Kuhl, J. Rosenzweig, A. Axmann, and J. Schneider, "Subpicosecond Carrier Lifetimes in Radiation-Damaged GaAs," *Appl. Phys. Lett.* **58**:1881–1883 (1991).
165. A. Krotkus, S. Marcinkevicius, J. Jasinski, M. Kaminska, H. H. Tan, and C. Jagadish, "Picosecond Carrier Lifetime in GaAs Implanted with High Doses of As Ions: An Alternative Material to Low-Temperature GaAs for Optoelectronic Applications," *Appl. Phys. Lett.* **66**:3304–3306 (1995).
166. F. Ganikhanov, G.-R. Lin, W.-C. Chen, C.-S. Chang, and C.-L. Pan, "Subpicosecond Carrier Lifetimes in Arsenic-Implanted GaAs," *Appl. Phys. Lett.* **67**:3465–3467 (1995).
167. C. Jagadish, H. H. Tan, A. Krotkus, S. Marcinkevicius, K. P. Korona, and M. Kaminska, "Ultrafast Carrier Trapping in High Energy Ion Implanted Gallium Arsenide," *Appl. Phys. Lett.* **68**:2225–2227 (1996).
168. M. J. Lederer, B. Luther-Davies, H. H. Tan, C. Jagadish, M. Haiml, U. Siegner, and U. Keller, "Non linear Optical Absorption and Temporal Response of Arsenic- and Oxygen-Implanted GaAs," *Appl. Phys. Lett.* **74**:1993–1995 (1999).
169. H. H. Tan, C. Jagadish, M. J. Lederer, B. Luther-Davies, J. Zou, D. J. H. Cockayne, M. Haiml, U. Siegner, and U. Keller, "Role of Implantation-Induced Defects on the Response Time of Semiconductor Saturable Absorbers," *Appl. Phys. Lett.* **75**:1437–1439 (1999).
170. M. Haiml, U. Siegner, F. Morier-Genoud, U. Keller, M. Luysberg, P. Specht, and E. R. Weber, "Femtosecond Response Times and High Optical Nonlinearity in Beryllium Doped Low-Temperature Grown GaAs," *Appl. Phys. Lett.* **74**:1269–1271 (1999).
171. P. Specht, S. Jeong, H. Sohn, M. Luysberg, A. Prasad, J. Gebauer, R. Krause-Rehberg, and E. R. Weber, "Defect Control in As-rich GaAs," *Mater. Sci. Forum* **951**:258–263 (1997).

---

# LASER-INDUCED DAMAGE TO OPTICAL MATERIALS

---

Marion J. Soileau

*CREOL, The College of Optics and Photonics  
University of Central Florida  
Orlando, Florida*

---

## 19.1 INTRODUCTION

---

For the general public the word “laser” brings to mind images of space ships zapping evil invaders, or perhaps earthbound military planners engineering speed-of-light weapons for destroying incoming ICBMs. However, the reality is that the things most often “zapped” or damaged by lasers are the various optical components used to make or direct laser beams.

This chapter deals with laser-induced damage (LID) in optical materials. LID refers to permanent damage produced by melting, ablation, cracking, plasma formation (spark), and so on in or on an optical material as a result of exposure to laser radiation. The LID threshold refers to the fluence or irradiance which causes such damage. In early literature on this topic LID thresholds were defined to be the average between the highest fluence or irradiance levels for which no damage was observed and the lowest levels for which damage was observed. Most recent literature defines the LID threshold as the fluence or irradiance level for which probability for damage goes to zero (a much more useful definition for use in designing laser systems). For more defect-free samples these two definitions give approximately the same values for LID thresholds.

The problem of LID is as old as the first pulsed laser. The reason for this is that the power density, or fluence, is most often largest inside the laser resonator itself. The problem can, in principle, be avoided by lowering the power density or fluence inside the laser system by appropriate expansion of the beam. However, such expansions can greatly increase the cost, weight, and volume of laser systems. In many cases, larger size components are simply not available.

The net result is that systems are constrained by cost, weight, and volume to be as compact as possible. In practical terms, this means that the LID thresholds of critical components form the limit of laser output power, or energy, for many pulsed laser systems.

Thus, the critical nature of LID has led to many efforts to understand the mechanisms of LID and to improve the damage resistance of optical components. As will be shown later, the LID processes are often highly nonlinear as well as complex. The range of operating wavelengths of lasers (infrared to the ultraviolet), pulse widths (continuous output to tens of femtoseconds), and variable repetition rates further complicate the situation.

There is vast literature on the subject of LID. A good start for data on LID of optical materials can be found in the proceedings of the annual Conference on Laser-Induced Optical Materials, also known as Boulder Damage Symposium, held in Boulder, Colorado, since 1969.<sup>1</sup> These proceedings

are available from the SPIE in hardcopy, online, or a set of CD-ROMs. The CDs and online versions are searchable by topics, key words, and authorship. The proceedings<sup>7</sup> of the 2008 meeting contain review articles on LID to surfaces and mirrors,<sup>2</sup> materials and measurements,<sup>3</sup> thin films,<sup>4</sup> and fundamental mechanisms,<sup>5</sup> for the previous 40 years of research on these topics. Much of the material in this chapter on fundamental mechanism is taken from Ref. 5.

## 19.2 PRACTICAL ESTIMATES

With few exceptions LID practical limits are determined at the surfaces and interfaces of optical materials. The reason for this is that these are the locations with the most defects and impurities. LID at such locations can occur at fluences that are orders of magnitude smaller than that in the bulk of materials, and below that expected from measurements of average absorption of light, or required for failure through operation of some fundamental mechanisms such as multiphoton absorption.

Given the large parameter space of laser operations many authors have tried to develop scaling rules for LID to aid the design of laser systems.<sup>6</sup> These models try to incorporate parametric dependence in various mechanisms but the parameter space can be huge. For example, in one of the earlier papers on LID<sup>7</sup> E.L. Bliss noted that LID depends on laser frequency, pulse duration, beam diameter, temperature, beam focusing, and the details of the materials growth and preparation. Even after more than 40 years of study, the parametric dependence of the various mechanisms of LID are not understood well enough to allow accurate scaling models that can ensure adequate design of laser systems.

However, there is a “rule of thumb,” which gives a good starting point in estimating limits imposed by LID:<sup>5</sup>

$$E_d = (10 \text{ J/cm}^2)(t_p/1 \text{ ns})^{1/2} \quad (1)$$

where  $E_d$  = damage threshold fluence,  $\text{J/cm}^2$   
 $t_p$  = laser pulse width, ns

Equation (1) gives an *approximation* of the threshold fluence to within plus or minus an order of magnitude for optical materials (transparent dielectrics) over the wavelength range from the UV to the infrared. This is admittedly a gross over simplification. The proper use of this equation is simply to get an idea as to whether or not one should be concerned about the possibility of LID. Laser systems designs that anticipate fluences on the high side of this equation will likely be dominated by LID considerations. For fluences below this range, one can reasonably assume that LID will not be a major factor limiting system performance.

Note that Eq. (1) has little theoretical basis except for the case where damage is caused by a thin absorbing film on a surface or interface. For that case, damage fluence should be scaled as the square root of the pulse width due to one-dimensional heat dissipation into the surface.

If one must know the damage threshold to better than the approximation in Eq. (1), then one should make a careful measurement of the threshold for conditions ( $t_p$ , wavelength, etc.) similar to those expected in use.

## 19.3 SURFACE DAMAGE

A good optical surface can be polished and cleaned to have optical absorption of order  $10^{-4}$  of the incident radiation,<sup>8</sup> which by itself should not result in optical damage. However, surfaces are subject to contamination and will have some amount of subsurface defects and imbedded impurities<sup>9</sup> (such as polishing particles). While minor surface contamination and point defects may not substantially contribute to the average linear absorption of light by a surface such factors can, and usually do, dominate LID of optical surfaces. Examination of surface damage sites indicates a morphology consistent with defect-initiated damage.

Surface damage thresholds can be raised by

- Using grinding and polishing techniques that produce minimum subsurface damage<sup>10</sup>
- Postpolishing etching or annealing<sup>11</sup>
- Proper surface cleaning<sup>12</sup>

A note of caution: Care must be used in cleaning optical surfaces as to not scratch the surface and not leave behind residue from the cleaning process. It is best not to get surfaces dirty! Holding a laser component on its edge by an ungloved hand will result in the diffusion of body oils across the surface sufficient to cause LID at low fluences. The references cited above are just a sampling. The Boulder proceedings<sup>1</sup> contain over 100 papers that relate to this one topic.

Standard optical polishing techniques can lead to substantial subsurface damage and contamination that in turn leads to LID. Typical procedures for preparing optical surfaces consist of a series of polishing or grinding steps with each subsequent step using finer grinding or polishing agents. A process sometimes referred to as “controlled grinding”<sup>8</sup> can raise LID thresholds. In such processes, each step first removes damaged layer (approximately 3 times the size of the previous grinding or polishing grit), then proceeds with the next step in surface finishing.

An effective method of surface annealing is pre-irradiation of surfaces with fluence levels below the single shot LID threshold of a surface. Two methods are used: the so-called N on 1 method, where multiple subthreshold irradiations are undertaken,<sup>13</sup> and the S on 1 process,<sup>14</sup> in which the surface is irradiated at levels substantially below the single-shot damage threshold and then ramped up to the expected operational level. Substantial increases in LID fluences have been observed by using these techniques.

## Entrance versus Exit Surface Damage

Consider an optical component illuminated by laser radiation at normal incidence. An interesting damage phenomenon is that for a given power or fluence incident upon an optical component, the exit (or rear) surface will damage before the entrance (or front) surface. This is at first counterintuitive, since Fresnel reflection loss at the entrance surfaces results in less energy reaching the rear surface.

The puzzling fact that the exit surface damages first provided an important clue as to the more fundamental aspects of LID. Several exotic explanations were proposed, but the explanation from linear optics is simply that the electric field associated with the laser is larger at the exit surface than at the entrance (even though the beam is partially depleted by Fresnel reflection at the front surface).<sup>15</sup>

This is understood by considering that the reflected wave at the entrance surface is 180° out of phase with the incident field (Fresnel reflection for propagating from a low-index medium to a high-index medium). At the exit surface, propagation is from the high-index medium (say, glass) to the low (say, air). In that case, the reflected field is in phase with the incident field. Therefore, the exit surface damages first simply because the electric field is higher at the rear surface. The fluence and irradiance are proportional to the electric field squared thus for even linear damage mechanisms, for example, simple absorption, the LID thresholds (expressed in terms of incident energy or power) for the exit surface will be lower than that of the entrance surface.

This field dependence of LID has played an important role in the design of thin film coatings (“move” the E-field away from coating interfaces), understanding the effects of cracks, voids, and other surface defects, and in formulation of various models for fundamental mechanisms of LID.

## LID in Optical Coatings

Section 19.3 emphasizes the dominance of surface damage in most damage-limited laser systems. In fact, most optical surfaces in high-performance laser systems are coated with thin films (usually multiple layers) to control or manage reflectivity. Examples include high-reflection mirrors, antireflection coatings on transmitting optics, partial reflecting beam splitters, and wavelength selectivity elements.

LID to thin films is the most likely factor limiting the performance of high-power laser systems. (See Ref. 4 and references contained therein.) Multilayer (ML) coatings are affected by the defects, contamination, and subsurface damage of the surfaces upon which they are applied. In addition, each coating interface contributes an additional surface to the system and thus additional opportunities for surface defects to effect damage. Among other thin-film problems affecting LID are: adhesion; differential expansion; defects in the films themselves; porosity, which allows diffusion of defects; and enhancement of E-fields within the thin film stack.

A few general statements and guidelines to minimize thin-film damage are

1. Proper surface preparation and surface cleaning is essential to maximize LID thresholds in thin films.
2. The problem is more severe for transmitting thin films. Among the issues is the simple fact that the film-substrate interface cannot be avoided and this is a common initiator of LID. In general, antireflection (AR) coatings exhibit lower thresholds than high-reflection (HR) coatings.
3. Stress in thin films can reduce LID thresholds so that coating materials choices and deposition conditions should be selected to minimize internal stress in the thin-film stack.
4. In general, lower index coatings will have higher damage thresholds than higher index films. However, multilayer systems must have both high- and low-index components and the smaller the index difference, the more layers are needed to achieve the same desired reflectivity or antireflectivity.
5. Amorphous coatings have less problems with impurity diffusion than do single or multicrystalline materials and so are better choices when available.
6. Inherent in thin-film design is arranging thicknesses and indices so that multiple reflections either enhance the E-field or reduce the E-field. One important design consideration is to ensure that regions of enhanced E-field are moved away from surfaces and interfaces. The simple addition of a half-wave layer can move the high-field region away from coatings interfaces.<sup>16</sup>
7. Modern thin-film design codes allow easy design of extremely complex multilayer systems for managing reflection and transmission of multiple laser systems and wavelengths. However, designers should be mindful that larger multilayer stacks and more complex designs are likely to significantly lower the LID thresholds of these optical elements and thus limit system performance. The general design rule is “keep it simple!”

## Multishot LID

LID for sites experiencing multiple irradiations are different than those of sites irradiated once. Several multishot effects have been observed. Irradiation below the single-shot damage threshold can produce LID thresholds substantially larger than the single-shot values for surfaces, thin films, and even in the bulk of a material. This is sometimes referred to as laser conditioning or laser annealing. The N on 1<sup>13</sup> and S on 1<sup>14</sup> previously discussed are examples of this phenomena.

N on 1 or S on 1 conditioning are typically used in very large, high-power laser systems such as those used in laser fusion experiments. Such systems are typically dominated by LID limits so extra efforts in laser conditioning are essential for reliably achieving maximum output power. In some cases the LID threshold seems to be reduced by repetitive pulses. In such cases, small damage sites, which initially go undetected, grow in size until the damage reaches catastrophic portions. There has been much work done on this critical question. In some cases, damaged sites can be effectively annealed by multiple shots below the damage threshold, thus extending the useful life of a component.

---

## 19.4 PACKAGE-INDUCED DAMAGE

The cliché “cleanliness is next to godliness” is usually associated with LID. Care must be taken to avoid dust or other particulates on optical surfaces and samples should be handled with gloved hands to avoid diffusion of body oils onto surfaces. Exposure to water and other solvents can

substantially lower LID thresholds, and indeed many procedures meant to clean surfaces can leave behind residue that can substantially reduce the LID threshold.

The problem of contamination of optics has led to construction of laser systems, in which the laser cavity is backfilled with clean, inert gas (such as nitrogen). This approach is particularly attractive for laser systems that are expected to operate for extended periods without possibility of access or repair, for example, a laser rangefinder in orbit around Mars to map the planet's surface.

A nonintuitive consequence of such packaging is a substantial reduction in system's lifetime due to LID, even for systems conservatively designed with fluence levels safely below the expected LID thresholds. What is observed in repetitively pulsed laser systems is that any residual hydrocarbons inside the sealed system can be dissociated due to complex interactions with the packaging gas (which acts like a buffer), the residual hydrocarbons, and the laser pulses. The "freed" carbon in the system can then be deposited, with the assistance of the laser light, on the various optical surfaces. The carbon is deposited on the surfaces in the beam path. LID will be initiated at such sites if these carbon deposits become sufficiently dense.<sup>17</sup>

The problem of package-induced LID can be avoided by back filling the laser system with oxygen (or just air.) In this case any free carbon from laser-assisted decomposition of hydrocarbons forms carbon dioxide gas, which is transparent for lasers operated from the UV to the infrared. Since any free carbon is combined with oxygen, laser-assisted carbon deposition is avoided.

## 19.5 NONLINEAR OPTICAL EFFECTS

---

Since the time of James Clark Maxwell, it has been known that light is an electromagnetic wave. However, for "natural," incoherent light there are no easily observed effects of the E-field (other than that of the "carrier" of the light energy in the Poynting vector). The field strength in some cases results in substantial nonlinear optical (NLO) effects, some of which can cause LID. Examples include electrostriction (density changes due to an impressed electric field) and E-field-dependent electronic polarizability of optical materials.<sup>18</sup> These effects result in an increase in the index of refraction in regions of high fields. This in turn produces lensing within a material, which further increases the E-field, resulting in further increases in self-lensing until the threshold for damage is reached. This process, called self-focusing and is reviewed in the classic paper by Marburger.<sup>18</sup>

An important feature of self-focusing is that one can calculate a critical *power* at which it takes place. This is the beam power at which nonlinear refractive effects (self-focusing) overcome linear refractive effects (diffraction) leading to beam collapse. For a beam focused into the bulk of the sample this collapse can result in LID.<sup>19</sup>

Among the many effects of self-focusing is to confuse efforts to identify fundamental mechanisms of LID and the dependence of LID thresholds on various parameters, for example, pulse width, spot size, and wavelength dependence. Since self-focusing depends on the state of polarization of the light, linear or circular, a simple test for its contribution to LID in isotropic media is to measure the polarization dependence of the damage threshold.<sup>20,21</sup> If a polarization dependence is found the measured threshold is due to self-focusing and not the mechanism of LID.

## 19.6 AVOIDANCE OF DAMAGE

---

Given the NLO effects that influence damage, it is essential to avoid situation where field enhancement occurs. A simple example is diffraction associated with an aperture or edge. This diffraction produces regions of enhanced (coherent sum of fields) electric fields. This enhancement of fields can also cause regions of self-focusing along the beam, which in turn cause damage.

Such effects are minimized through the use of single-mode beams, avoidance of linear diffraction by apertures or other hard edges, and special filters to remove high spatial frequencies within the beam. These techniques are particularly useful in oscillator-amplifier systems. The amplifier(s)



will further enhance the interference patterns produced by diffraction, and thus increase the likelihood of self-focusing causing damage.

## 19.7 FUNDAMENTAL MECHANISMS

---

A subset of LID is laser-induced breakdown (LIB). LIB is the damage observed with pulsed lasers for highly transparent materials. Early observations of LIB include the following:

1. Abrupt truncation of the beam transmitted through the sample, that is, threshold like behavior. (See e.g., the work of Anthes and Bass<sup>22</sup> that showed that when damage occurs in a highly transparent material it goes from transparent to highly absorbing within less than 2 ps.)<sup>22</sup>
2. Bright, hot plasma accompanying damage.
3. Damage occurs at the peak of the pulse when at the threshold irradiance.
4. LIB in transparent dielectrics is the most complicated since it depends on materials, properties (most of which are not properly understood), laser parameters (wavelength and pulse width), beam spatial modes, and focusing conditions.

These observations plus the lack of any reasonable alternative for energy coupling in otherwise transparent materials with bandgaps 5 to 20 times the photon energy of the laser that produced damage led early investigators to conclude that LID was due to electron avalanche breakdown.

As early as in 1965 Yasojima showed<sup>23</sup> that

1. Laser damage in NaCl at 10.6  $\mu\text{m}$  showed LIB, that is, avalanche like behavior.
2. LIB could be substantially reduced by “seeding” the damage with a flash of blue light, thus producing “starter” electrons for the LIB.
3. The author speculated that this avalanche was seeded by nonlinear processes.

This was a remarkable bit of work and went unnoticed in work reported in Western and Soviet literature on this subject.

Based upon his seeding experiments, Yasojima speculated that LIB was initiated by either multiphoton absorption or tunneling to produce free carrier that could be rapidly accelerated by the several megavolt E-fields associated with focused pulsed laser beams.

In the 43 years, since Yasojima’s work, most work done by others has produced further evidence supporting the ideas of this unrecognized scholar!

Great progress in understanding multiphonon absorption—new materials, new methods, and design considerations—has been made over the past 40 years.<sup>1</sup> Among the many important fundamental results reported are multiphonon limits of linear absorption, very good models for LID to metals, the role of stress in high-power CW applications and the effects of absorption on beam quality. Many of these advances were made possible by progress in precision measurement of small levels of absorption, surface roughness, and scattering.

Linear absorption by defects, inclusions, and contamination remains practical concern, but the fundamentals of damage due to defects are reasonably well understood. LIB, the catastrophic, threshold like process in highly transparent materials has been the subject of much controversy and is where understanding still lags. The quest for understanding fundamental limits runs head on with the many varied and complex nonlinear processes involved. However, there is general agreement that for damage to occur there must be absorption of laser radiation by the material.

Beyond that there is little agreement, or perhaps more properly stated, no detailed understanding as to how a material goes from highly transparent to totally absorbing within just a few picoseconds.<sup>22</sup> The discussion of LIB mechanism is a discussion of the process(s) by which this sort of “change of phase” occurs.

One reason to seek understanding of fundamental mechanisms is to be able to do reasonable scaling with respect to various parameters such as pulse width, wavelength, beam properties, and

materials' properties. Another reason to seek this understanding is that if the fundamental mechanisms of failure are understood, ways to improve materials could be found.

Self-focusing complicates efforts to understand LIB. Self-focusing is not in itself a mechanism for LIB. Rather, it is a mechanism for concentrating the beam so that local intensities reach critical values at which other nonlinear processes occur.

Among the major advances in improving LID limits was understanding of how to pick and sometimes design materials to minimize the nonlinear refractive index,  $n_2$ , that governs self-focusing in a medium. Probably the most practical advance was the understanding that this problem could be managed by careful control of the mode of laser oscillators and properly accounting for self-focusing in the propagation of beams in large oscillator-amplifier systems. The key is to avoid and remove high spatial frequencies. In practical terms, this means oversizing the optics so that the beam is not clipped and using spatial filters to remove any high spatial frequencies that may occur during beam propagation. As a result, self-focusing in gain media in large laser systems such as those used in laser fusion experiments can be effectively managed. However, the problem often reappears as laser makers try to maximize energy output from gain media of limited size by multimode operation, a problem made worse by trying to compact multimode systems in limited space. This prevents the loss of high spatial frequencies and in turn results in catastrophic damage due to small-scale self-focusing.

The influence of self-focusing in damage experiments is a bit more problematic and has been a major issue in understanding the parametric dependence of LIB in transparent solids. Examples include the fact that the critical power for self-focusing scales as the square of the wavelength and as the inverse of the pulse width. Multiple mechanisms exist for self-focusing and these can scale as the spot size and pulse width together (electrostriction) and self-focusing can exhibit large dispersion. Thus self-focusing can be confused with the wavelength, pulse width, and spot size dependences of LIB.

The problem is trying to describe such a nonlinear process in enough detail such that materials may be improved, and predictions of the dependence on pulse width, wavelength, and spot size may be made with confidence. This situation was made more complex by the simple fact that no precursor to LIB has been found and experiments are hard to replicate since the sample(s) studied are consumed in the experiment and new samples often produced different results.

Early work concluded<sup>24</sup> that LIB was an intrinsic property of materials. This claim was based on the following factors:

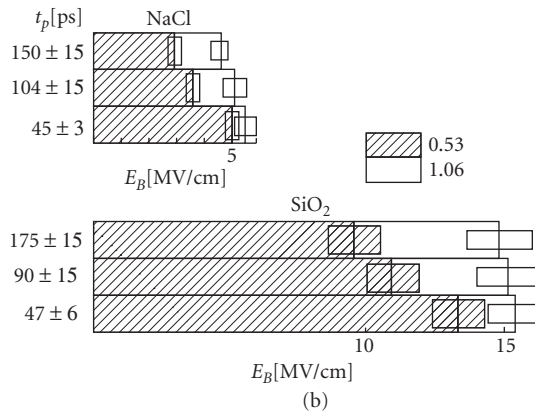
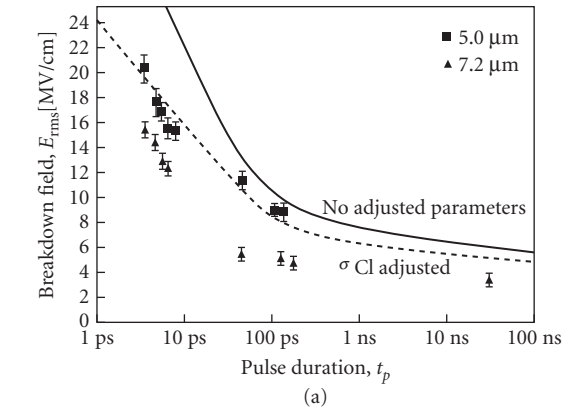
- The observations of breakdown-like behavior previously mentioned
- The observed frequency dependence (really very little frequency dependence) of LIB in NaCl from 0.35 to 10.6  $\mu\text{m}$

This work assumed that the breakdown irradiance was an intrinsic property of a material, thus any sample-to-sample variations measured by others were due to poor quality samples and any spot-size dependence was purely due to self-focusing.

Other work produced different results<sup>25–28</sup> such as

- There are just not enough free carriers present in good insulators (highly transparent materials) to initiate damage for very small spot sizes, that is, it takes at least a few free electrons to be present to initiate the avalanche.
- Better materials with higher thresholds than the so-called “intrinsic” thresholds became available, some with a factor of 20 higher threshold than the previously reported “intrinsic” results.
- Subsequent frequency dependence measurements showed a decrease in threshold at 0.5  $\mu\text{m}$ , inconsistent with a pure avalanche model.
- Evidence was produced that indicated that not all spot-size dependence was due to self-focusing. Feldman's<sup>21</sup> work on the polarization dependence of self-focusing was used to rule out self-focusing in some spot-size dependence measurements.

Where does this leave us? Figure 1 is an illustration of the problem. Here the spot size is constant and the pulse width and wavelength dependence is given for NaCl and SiO<sub>2</sub>. Note that in this case



**FIGURE 1** (a) The RMS breakdown field data for NaCl (78-NC-6) at  $1.06 \mu\text{m}$  are plotted as a function of pulse duration,  $t_p$ . The solid line and dotted line were obtained from the theory developed by Sparks *et al.*<sup>30</sup> for NaCl at room temperature. The dotted line uses a different value for the absorption cross section for Cl ions in the theory than the solid line. (b) Wavelength dependence of the breakdown field  $E_B$  for NaCl and  $\text{SiO}_2$  for a variety of laser pulse widths. All the above data was taken on the same sample of NaCl and the same sample of  $\text{SiO}_2$ . The  $1.06 \mu\text{m}$  thresholds are taken from Ref. 2 and are interpolated from measurements made at spot size  $6.1$  and  $10.3 \mu\text{m}$ . (From Ref. 29.)

the spot size was the same at both wavelengths, and lack of self-focusing was confirmed from measurement of lack of polarization dependence in the LIB thresholds.

The decrease in LIB field with pulse width in Fig. 1 is consistent with an avalanche process for these pulses in the picosecond regime. However, the wavelength dependence is not consistent with a purely avalanche model, and not strong enough to suggest a multiphoton model for LIB.

The pulse width dependence shown in Fig. 1 is consistent with the avalanche ionization model. Note that this model is very much dependent on the very nonlinear ionization rates, which in fact

are estimated from DC measurements! These results are *not inconsistent* with a model that assumes an avalanche initiated by multiphoton or by tunneling.

After more than 40 years of “*not inconsistent*” is the best one can do. We do not have quantitative information about avalanche ionization dependence of laser fields in solids. We have no accurate parameters for  $n$  photon absorption ( $n$ PA) (for  $n > 3$ ) or tunneling models and we do not have definitive information that confirms that all the critical parameters have been considered.

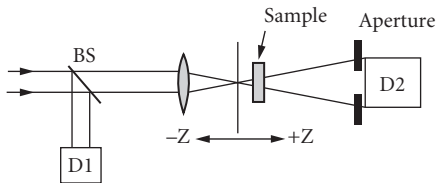
## 19.8 PROGRESS IN MEASUREMENTS OF CRITICAL NLO PARAMETERS

A difficulty in the past has been lack of accurate measurements of NLO parameters. A great breakthrough was the invention of the so-called Z-scan<sup>31,32</sup> technique for measuring the sign and magnitude of the nonlinear of refractive index as a function of wavelength and pulse width. This technique also allows one to measure the  $n$ PA coefficients and free carrier cross section. Shown in Fig. 2<sup>31,32</sup> is the Z-scan technique for measuring nonlinear refraction (with sign as well as magnitude) and nonlinear absorption.

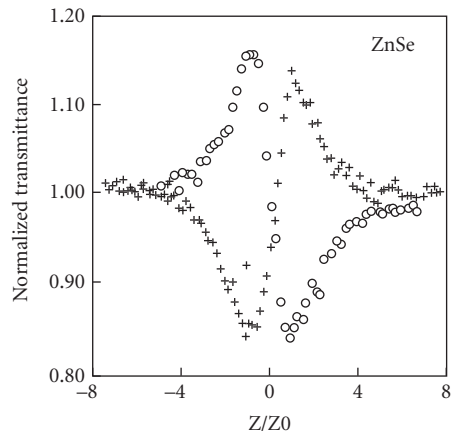
Note, in Fig. 3 the difference in signal for negative nonlinear refraction compared to positive nonlinear refraction. The sign of nonlinear refraction changes from 1 to 0.5  $\mu\text{m}$ ! By fully opening the aperture in front of the detector one can measure nonlinear absorption as is shown in Fig. 4.

The bottom curve shows the results of increasing the irradiance by about a factor of 5, and the fit is excellent, with no additional adjustment of parameters, indicating that the essential physics [linear and nonlinear absorption, positive and negative nonlinear refraction, and two photon absorption (2PA) and excited state absorption] is accounted for in this measurement. ZnSe is a 2PA material at 0.5  $\mu\text{m}$  and a 4PA material at 1  $\mu\text{m}$ . The nonlinearity shown is for picosecond pulses and is due to electronic effects. For nanosecond pulses electrostriction can also play a role for small spot sizes. An in-depth understanding of fundamental mechanisms LIB awaits such detailed, reproducible, nondestructive measurements of processes leading to damage.

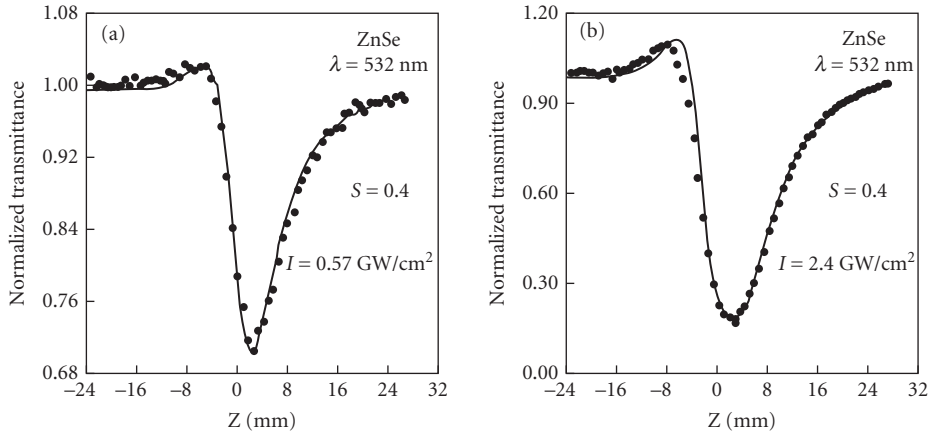
What about many or  $n$  photon absorption ( $n$ PA)? Can this process be the mechanism leading to LIB? Figure 5<sup>32</sup> shows results for 2, 3, and 4PA materials at 1  $\mu\text{m}$  for 49 ps pulses. The net result is that for 2 or 3PA the generated carriers prevent damage by defocusing the beam. Self-defocusing



**FIGURE 2** Note that the sample is scanned through the beam focus. The ratio of the readings of D1 and D2 is measured. The fit to the plot of this ratio versus  $Z$  (position relative to the focus) gives the nonlinear index of refraction. If the aperture D2 is fully open and captures all the transmitted beam then the nonlinear absorption is measured. (From Ref. 31.)

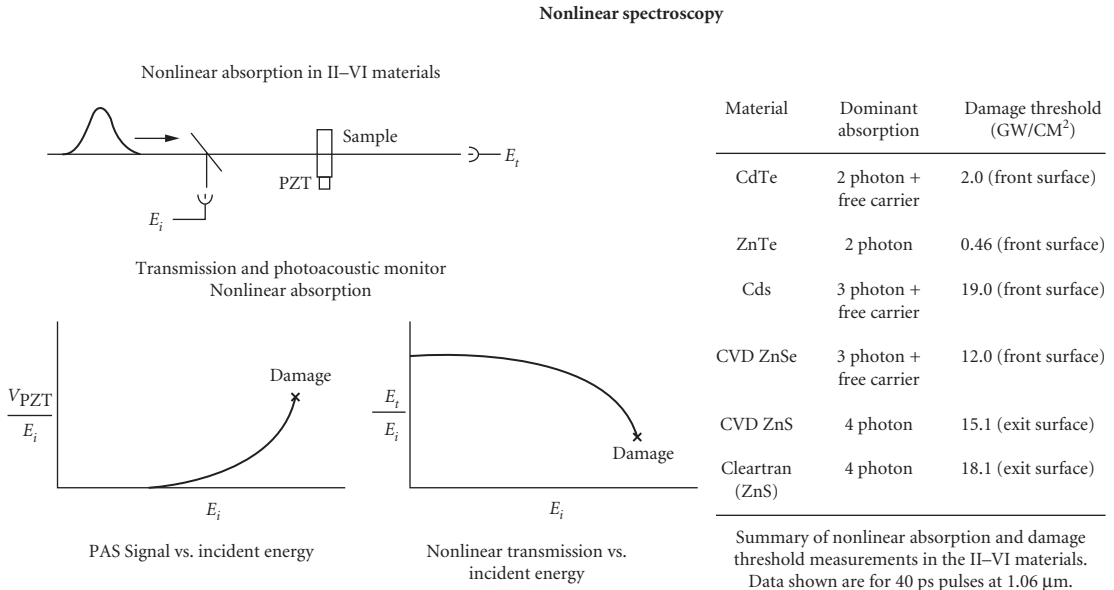


**FIGURE 3** Measurement of  $n_2$  (circles) at 1.06 and 0.53  $\mu\text{m}$  (crosses) showing the sign change for ZnSe (positive  $n_2$  and negative  $n_2$ , respectively). (From Ref. 32.)



**FIGURE 4** This figure shows the power of the Z-scan technique to help understand relevant nonlinear interactions, including two photon absorption, excited state absorption (free carrier absorption), and nonlinear refraction for ZnSe at 0.53  $\mu\text{m}$  and 30 ps pulses. (From Ref. 31.)

of the 2 to 3PA-generated carriers prevents bulk and rear surface damage. What happens when the process is 4PA? The carrier generation rate by 4PA is not sufficient to cause defocusing and thus allows the irradiance at the exit surface to increase to the LID threshold. Recent measurements using femtosecond pulses and interferometric techniques for measuring carrier generation at focus, and so on offer hope of helping understand LIB in highly transparent materials.<sup>33</sup> One must be able to



**FIGURE 5** These data demonstrate different responses for  $n$ PA. The dynamics of 2 and 3PA are such that the rate of generation of free carriers is such that self-defocusing dominates propagation, preventing damage in the bulk of the material or the rear surface. For bandgaps beyond 3PA the LID of the rear surface occurs prior to field strengths that would cause significant 4PA. (From Ref. 32.)

measure the dynamical parameters with sufficient accuracy and time resolution to sort out different nonlinear parameters critical to the damage process. Only then will a more complete description and rigorous models for LID be possible.

## 19.9 REFERENCES

1. Proceedings of Laser-Induced Damage to Optical Materials, available from the SPIE, The International Society for Optical Engineering, Bellingham, WA, in hard-copy, via the web (<http://www.spiedigitallibrary.org>) or in searchable CD-ROM format.
2. S. Papernov and A. W. Schmid, "Laser-Induced Surface Damage of Optical Materials: Absorption Sources, Initiation, Growth, and Mitigation," in G. J. Exarhos, D. Ristau, M. J. Soileau, and C. J. Stolz (eds.), *Proceedings of the SPIE*, Vol. 7132 (2008).
3. M. Commandre, "The Transparent-Media Characterization Dedicated to Laser Damage Studies: A Key Task, Multi-Faceted and Always Renewed," in G. J. Exarhos, D. Ristau, M. J. Soileau, and C. J. Stolz (eds.), *Proceedings of the SPIE*, Vol. 7132 (2008).
4. B. E. Newnam, "Laser-Induced Damage in Thin-Film Optical Materials: 1970–2008," in G. J. Exarhos, D. Ristau, M. J. Soileau, and C. J. Stolz (eds.), to be published in the *Proceedings of the Symposium on Laser-Induced Damage to Optical Materials*, Sept. 2008, SPIE.
5. M. J. Soileau, "40 Year Retrospective of Fundamental Mechanisms" in G. J. Exarhos, D. Ristau, M. J. Soileau, and C. J. Stolz (eds.), *Proceedings of the SPIE*, Vol. 7132 (2008).
6. J. R. Bettis, R. A. House II, "Damage in Laser Materials: 1976," in A. J. Glass and A. H. Guenther (eds.), *Nat. Bur. Stand. (U.S.) Spec. Publ.* 462 (1976), p. 338., available from the SPIE, see Ref. 1.
7. E. L. Bliss, "Damage in Laser Glass, ASTM," in A. J. Glass and A. H. Guenther (eds.), *Spec. Tech. Publ.* 469 (1969), ASTM, Philadelphia, PA, available from the SPIE, see Ref. 1.
8. M. J. Soileau, H. E. Bennett, J. M. Bethke, and J. Shaffer, "Damage in Laser Materials: 1975," in A. J. Glass and A. H. Guenther (eds.), *Nat. Bur. Stand. (U.S.) Spec. Publ.* 435 (1975), available from the SPIE, see Ref. 1.
9. F. Cooke, N. Brown, and E. Prochnow, "Annular Lapping of Precision Optical Flatware," *Opt. Eng.* 15:407 (1976).
10. M. R. Kozlowski, J. Carr, I. Hutcheon, R. Torres, L. Sheehan, D. Camp, M. Yan, "Laser-Induced Damage in Optical Materials: 1997," in G. J. Exarhos, A. H. Guenther, M. R. Kozlowski, and M. J. Soileau (eds.), *Proceedings of SPIE*, Vol. 3244 (1998), p. 365.
11. V. Wang, J. E. Rudisill, C. R. Giuliano, M. Braunstein, and A. Braunstein, "Damage in Laser Materials: 1975," in A. J. Glass and A. H. Guenther (eds.), *Nat. Bur. Stand. (U.S.) Spec. Publ.* 435 (1975), available from the SPIE, see Ref. 1.
12. J. O. Porteus, P. C. Archibald, J. W. Bethke, J. H. Dancy, W. N. Faith, J. B. Franck, and P. A. Tmeple, "Influence of Cleaning Solvents, Sunlight, Humidity, and HF Gas on Pulsed Damage and Optical Characteristics of 3.8- $\mu\text{m}$  Multilayer Coatings," in H. E. Bennett, A. H. Guenther, D. Milam, and B. E. Newnam (eds.), *NBS Special Publication #638, 397* (1983), available from the SPIE, see Ref. 1.
13. See for example, K. Yoshida, H. Yoshida, and S. Nakai, "Laser-Induced Damage in Optical Materials: 1991," in H. E. Bennett, L. L. Chase, A. H. Guenther, B. E. Newnam, and M. J. Soileau (eds.), *Proceedings of SPIE*, Vol. 1624 (1992).
14. For examples of S-on-I damage see: F. Y. Ganin, K. Michlitsch, J. FLU-I, M. R. Korlouski, and P. Krulevitch, "Laser-Induced Damage in Optical Materials: 1996," in H. E. Bennett, A. H. Guenther, M. R. Kozlowski, B. E. Newman, and M. J. Soileau (eds.), *Proceedings of SPIE*, Vol. 2966 (1997).
15. M. D. Crisp, "Damage in Laser Materials: 1973," in A. J. Glass and A. H. Guenther (eds.), *Nat. Bur. Stand. (U.S.) Spec. Publ.* 387 (1973), available from the SPIE, see Ref. 1.
16. B. E. Newnam, D. H. Gill, and G. Faulkner, "Damage in Laser Materials: 1975," in A. J. Glass and A. H. Guenther (eds.), *Nat. Bur. Stand. (U.S.) Spec. Publ.* 435 (1975). Also see Ref. 4 of this chapter and references contained therein.
17. J. A. Sharps, "Laser-Induced Damage in Optical Materials: 1995," in H. E. Bennett, A. H. Guenther, M. R. Kozlowski, B. E. Newnam, and M. J. Soileau (eds.), *Proceedings of SPIE*, Vol. 2714 (1996), and the results of a Mini-Symposium on semiconductor laser lifetimes which is related to this topic is published in "Laser-Induced Damage to Optical Materials: 1997," *Proceedings of the SPIE*, Vol. 3244.

18. J. Marburger, "Theory of Self-Focusing for Fast Nonlinear Response," *NBS Special Publication #356*, SPIE, 1971, p. 51.
19. J. Marburger, "Self-Focusing: Theory," *Prog. Quant. Electr.*, No. 4, Pergamon Press, 1975, pp. 35–110, and references contained therein.
20. M. J. Soileau, M. Bass, and E. W. Van Stryland, "Frequency Dependence of Breakdown Fields in Single-Crystal NaCl and KCl," in A. J. Glass and A. H. Guenther (eds.), *NBS Special Publication #541*, SPIE, 1978, p. 309.
21. A. Feldman, D. Horowitz, and R. M. Waxler, "Mechanisms for Self-Focusing in Optical Glasses," *IEEE J. Quant. Elec.* **QE-9**:1054 (1973).
22. J. Anthes and M. Bass, "Direct Observation of the Dynamics of Picosecond-Pulse Optical Breakdown," *Appl. Phys. Lett.* **31**:412 (1977).
23. Y. Yasojima, M. Takeda, and Y. Inuishi, "Laser-Induced Breakdown in Ionic Crystals and a Polymer," *Jpn. J. Appl. Phys.* **7**(5):552 (1968).
24. N. Bloembergen, "Laser-Induced Electric Breakdown in Solids," *IEEE J. Quant. Elec.* **10**(3):375 (1974). M. J. Weber, D. Milam, and W. L. Smith, "Non-linear Refractive Index of Glasses and Crystals," *Opt. Engineering* **17**(5):489 (1978).
25. M. Sparks, "Current Status of Electron-Avalanche-Breakdown Theories," in A. J. Glass and A. H. Guenther (eds.), *NBS Special Publication #435*, SPIE, 1975, p. 331.
26. A. A. Manenkov, "New Results on Avalanche Ionization as a Laser Damage Mechanism in Transparent Solids," in A. J. Glass and A. H. Guenther (eds.), *NBS Special Publication #509*, SPIE, 1977, p. 455.
27. M. J. Soileau, M. Bass, and E. W. Van Stryland, "Frequency Dependence of Breakdown Fields in Single-Crystal NaCl and KCl," in A. J. Glass and A. H. Guenther (eds.), *NBS Special Publication #541*, SPIE, 1978, p. 309.
28. M. Soileau and M. Bass, "Optical Breakdown in NaCl and KCl from 0.53 to 10.6 Microns," *Appl. Phys. Lett.* **35**:370 (1979).
29. M. J. Soileau, W. E. Williams, E. W. Van Stryland, T. F. Boggess, and A. L. Smirl, "Temporal Dependence of Laser-Induced Breakdown in NaCl and SiO<sub>2</sub>," in H. E. Bennett, A. H. Guenther, D. Milam, and B. E. Newnam (eds.), *NBS Special Publication #669*, SPIE, 1982, p. 387.
30. M. Sparks, T. Holstein, R. Warren, D. L. Mills, A. A. Maradudin, L. J. Sham, E. Loh, Jr., and F. King, "Theory of Electron-Avalanche Breakdown in Solids," in H. E. Bennett, A. J. Glass, A. H. Guenther, and B. E. Newnam (ed.), *NBS Special Publication #568*, SPIE, 1979, p. 467.
31. E. W. Van Stryland, M. Sheik Bahae, A. A. Said, D. J. Hagan, and M. J. Soileau, "Laser-Induced Damage in Optical Materials: 1993," in H. E. Bennett, L. L. Chase, A. H. Guenther, B. E. Newnam, and M. J. Soileau (eds.), *Proceedings of SPIE*, Vol. 2114 (1994); available from the SPIE, see Ref. 1.
32. E. W. Van Stryland, M. A. Woodall, W. E. Williams, and M. J. Soileau, "Damage in Laser Materials: 1981," in H. E. Bennett, A. H. Guenther, D. Milam, and B. E. Newnam (eds.), *Nat. Bur. Stand. (U.S.) Spec. Publ.* 638 (1983), available from the SPIE, see Ref. 1.
33. S. Garnov, G. J. Exarhos, A. H. Guenther, K. L. Lewis, D. Ristau, M. J. Soileau, C. J. Stolz (eds.), *Proceedings of the 40 Anniversary Boulder Damage Symposium*, 2008. Available from the SPIE, see Ref. 1.

PART

3

---

QUANTUM AND  
MOLECULAR  
OPTICS

---



*This page intentionally left blank*

---

# LASER COOLING AND TRAPPING OF ATOMS

---

Harold J. Metcalf

*Department of Physics  
State University of New York  
Stony Brook, New York*

Peter van der Straten

*Debye Institute  
Department of Atomic and Interface Physics  
Utrecht University  
Utrecht, The Netherlands*

---

## 20.1 INTRODUCTION

---

This chapter begins with some of the general ideas about laser cooling. One of the characteristics of optical control of atomic motion is that the speed of atoms can be considerably reduced. Since the spread of velocities of a sample of atoms is directly related to its temperature, the field has been dubbed *laser cooling*, and this name has persisted throughout the years.

In Sec. 20.2 we introduce the general idea of optical forces and how they can act on atoms. We show how such forces can be velocity dependent, and thus nonconservative, which makes it possible to use optical forces for cooling. The section concludes with the discussion of a few special temperatures. Section 20.3 presents a quantum mechanical description of the origin of the force resulting from the atomic response to both stimulated and spontaneous emission processes. This is quite different from the familiar quantum mechanical calculations using state vectors to describe the state of the system, since spontaneous emission causes the state of the system to evolve from a pure state into a mixed state. Since spontaneous emission is an essential ingredient for the dissipative nature of the optical forces, the density matrix is introduced to describe it. The evolution of the density matrix is given by the optical Bloch equations (OBE), and the optical force is calculated from them. It is through the OBE that the dissipative aspects of laser cooling are introduced to the otherwise conservative quantum mechanics. The velocity dependence is treated as an extension of the force on an atom at rest.

In Sec. 20.4 the first modern laser cooling experiments are described. Atoms in beams were slowed down from thermal velocity to a few m/s, and the dominant problem was the change in Doppler shift arising from such a large change in velocity. Some typical values of parameters are discussed and tabulated. Section 20.5 introduces true cooling by optical forces to the  $\mu\text{K}$  regime. Such experiments require at least two laser beams, and are called *optical molasses* because the resulting viscous force can slow atoms to extremely slow velocities, and hence compress the width of the velocity distribution. The limits of such laser cooling are discussed, as well as the extension from experiments in 1D to 3D. Here the velocity dependence of the force is built into the description via the Doppler shift instead of being added in as an extension of the treatment. In 1988 some experiments reported temperatures below the limit calculated for optical molasses, and Sec. 20.6 presents the new description of laser cooling that emerged from this surprise. For the first time, the force

resulting from spontaneous emission in combination with the multiple level structure of real atoms were embodied in the discussion. Here the new limits of laser cooling are presented.

The discussion up to this point has been on atomic velocities, and thus can be described in terms of a velocity space. Laser cooling thus collects atoms near the origin of velocity space. It is also possible to collect atoms into a small region of ordinary configuration space, and such trapping is discussed in Sec. 20.7. Neutral atom traps can employ magnetic fields, optical fields, and both working together. However, such traps are always very shallow, and so only atoms that have been cooled to the few mK domain can be captured. The combination of laser cooling and atom trapping has produced astounding new tools for atomic physicists, and Sec. 20.8 describes some of the applications and uses of these wonderful new capabilities.

## 20.2 GENERAL PROPERTIES CONCERNING LASER COOLING

These experiments almost always involve atomic absorption of nearly resonant light. The energy of the light  $\hbar\omega$  raises the internal energy of the atom, and the angular momentum  $\hbar$  changes the internal angular momentum  $\ell$  of the electron, as described by the well-known selection rule  $\Delta\ell = \pm 1$ . By contrast, the linear momentum of the light  $p = E/c = \hbar/\lambda(\vec{p} = \hbar\vec{k})$  cannot be absorbed by internal atomic degrees of freedom, and therefore must change the motion of the atoms in the laboratory frame. The force resulting from this momentum exchange between the light field and the atoms can be used in many ways to control atomic motion, and is the subject of this chapter.

Absorption of light populates the atomic excited state, and the return to the ground state can be either by spontaneous or by stimulated emission. The nature of the optical force that arises from these two different processes is quite different, and will be described separately. Such atomic transitions (i.e., the motion of the atomic electrons) must be described quantum mechanically in the well-known form of the Schrödinger equation. By contrast, the center-of-mass motion of the atoms can usually be described classically, but there are many cases where even this is not possible so it must also involve quantum mechanics.

In the simplest possible case, the absorption of well-directed light from a laser beam, the momentum exchange between the light field and the atoms results in a force

$$\vec{F} = d\vec{p}/dt = \hbar\vec{k}\gamma_p \quad (1)$$

where  $\gamma_p$  is the excitation rate of the atoms. The absorption leaves the atoms in their excited state, and if the light intensity is low enough so that they are much more likely to return to the ground state by spontaneous emission than by stimulated emission, the resulting fluorescent light carries off momentum  $\hbar k$  in a random direction. The momentum exchange from the fluorescence averages zero, so the net total force is given by Eq. (1).

The scattering rate  $\gamma_p$  depends on the laser detuning from atomic resonance  $\delta = \omega_\ell - \omega_a$ , where  $\omega_\ell$  is the laser frequency and  $\omega_a$  is the atomic resonance frequency. This detuning is measured in the atomic reference frame, and it is necessary that the Doppler-shifted laser frequency in the moving atoms' reference frame be used to calculate the absorption and scattering rate. Then  $\gamma_p$  is given by the Lorentzian

$$\gamma_p = \frac{s_0\gamma/2}{1 + s_0 + [2(\delta + \omega_D)/\gamma]^2} \quad (2)$$

where  $\gamma \equiv 1/\tau$  is the angular frequency corresponding to the decay rate of the excited state. Here  $s_0 = I/I_s$  is the ratio of the light intensity  $I$  to the saturation intensity  $I_s \equiv \pi\hbar c/3\lambda^3\tau$ , which is a few mW/cm<sup>2</sup> for typical atomic transitions ( $\lambda$  is the optical wavelength). The Doppler shift seen by the moving atoms is  $\omega_D = -\vec{k} \cdot \vec{v}$  (note that  $\vec{k}$  opposite to  $\vec{v}$  produces a positive Doppler shift). The force is thus velocity-dependent, and the experimenter's task is to exploit this dependence to the desired goal, for example, optical friction for laser cooling.

The spontaneous emission events produce unpredictable changes in atomic momenta so the discussion of atomic motion must also include a “random walk” component. This can be described as a diffusion of the atomic momenta in momentum space, similar to Brownian motion in real space. The evolution of the momentum in such circumstances is described by the Fokker-Planck equation, and it can be used for a more formal treatment of the laser cooling process. Solutions of the Fokker-Planck equation in limiting cases can ultimately be used to relate the velocity distribution of the atoms with their temperature.

The idea of “temperature” in laser cooling requires some careful discussion and disclaimers. In thermodynamics, temperature is carefully defined as a parameter of the state of a closed system in thermal equilibrium with its surroundings. This, of course, requires that there be thermal contact (i.e., heat exchange) with the environment. In laser cooling this is clearly not the case because a sample of atoms is always absorbing and scattering light. Furthermore, there is essentially no heat exchange (the light cannot be considered as heat even though it is indeed a form of energy). Thus the system may very well be in a steady-state situation, but certainly not in thermal equilibrium, so that the assignment of a thermodynamic “temperature” is completely inappropriate.

Nevertheless, it is convenient to use the label of temperature to describe an atomic sample whose average kinetic energy  $\langle E_k \rangle$  in one dimension has been reduced by the laser light, and this is written simply as  $k_B T/2 = \langle E_k \rangle$ , where  $k_B$  is Boltzmann’s constant. It must be remembered that this temperature assignment is absolutely inadequate for atomic samples that do not have a Maxwell-Boltzmann velocity distribution, whether or not they are in thermal equilibrium: there are infinitely many velocity distributions that have the same value of  $\langle E_k \rangle$  but are so different from one another that characterizing them by the same “temperature” is a severe error.

With these ideas in mind, it is useful to define a few rather special values of temperatures associated with laser cooling. The highest of these temperatures corresponds to the energy associated with atoms whose speed and concomitant Doppler shift puts them just at the boundary of absorption of light. This velocity is  $v_c \equiv \gamma/k \sim \text{few m/s}$ , and the corresponding temperature is  $k_B T_c \equiv M\gamma^2/k^2$ , and is typically several mK. (Here  $M$  is the atomic mass.)

The next characteristic temperature corresponds to the energy associated with the natural width of atomic transitions, and is called the *Doppler temperature*. It is given by  $k_B T_D \equiv \hbar\gamma/2$ . Because it corresponds to the limit of certain laser cooling processes, it is often called the *Doppler limit*, and is typically several hundred  $\mu\text{K}$ . Associated with this temperature is the one-dimensional velocity  $v_D = \sqrt{k_B T_D/M} \sim 30 \text{ cm/s}$ .

The last of these three characteristic temperatures corresponds to the energy associated with a single photon recoil. In the absorption or emission process of a single photon, the atoms obtain a recoil velocity  $v_r \equiv \hbar k/M$ . The corresponding energy change can be related to a temperature, the *recoil limit*, defined as  $k_B T_r \equiv \hbar^2 k^2/M$ , and is generally regarded as the lower limit for optical cooling processes (although there are a few clever schemes that cool below it). It is typically a few  $\mu\text{K}$ , and corresponds to speeds of  $v_r \sim 1 \text{ cm/s}$ .

These three temperatures are related to one another through a single dimensionless parameter  $\epsilon \equiv \omega/\gamma$  that is ubiquitous in describing laser cooling. It is the ratio of the recoil frequency  $\omega_r \equiv \hbar k^2/2M$  to the natural width  $\gamma$ , and as such embodies most of the important information that characterize laser cooling on a particular atomic transition. Typically  $\epsilon \sim 10^{-3} - 10^{-2}$ , and clearly  $T_r = 4\epsilon T_D = 4\epsilon^2 T_c$ .

In laser cooling and related aspects of optical control of atomic motion, the forces arise because of the exchange of momentum between the atoms and the laser field. Since the energy and momentum exchange is necessarily in discrete quanta rather than continuous, the interaction is characterized by finite momentum *kicks*. This is often described in terms of *steps* in a fictitious space whose axes are momentum rather than position. These steps in momentum space are of size  $\hbar k$  and thus are generally small compared to the magnitude of the atomic momenta at thermal velocities  $\bar{v}$ . This is easily seen by comparing  $\hbar k$  with  $M\bar{v}$ ,

$$\frac{\hbar k}{M\bar{v}} = \sqrt{\frac{T_r}{T}} \ll 1 \quad (3)$$

Thus the scattering of a single photon has a negligibly small effect on the motion of thermal atoms, but repeated cycles of absorption and emission can cause a large change of the atomic momenta and velocities.

## 20.3 THEORETICAL DESCRIPTION

### Force on a Two-Level Atom

We begin the calculation of the optical force on atoms by considering the simplest schemes, namely, a single-frequency light field interacting with a two-level atom confined to one dimension. It is based on the interaction of two-level atoms with a laser field as discussed in many textbooks.<sup>1</sup>

The philosophy of the correspondence principle requires a smooth transition between quantum and classical mechanics. Thus the force  $F$  on an atom is defined as the expectation value of the quantum mechanical force operator  $\mathcal{F}$ , as defined by  $F = \langle \mathcal{F} \rangle = d\langle p \rangle / dt$ . The time evolution of the expectation value of a time-independent quantum mechanical operator  $\mathcal{A}$  is given by

$$\frac{d}{dt} \langle \mathcal{A} \rangle = \frac{i}{\hbar} \langle [\mathcal{H}, \mathcal{A}] \rangle \quad (4)$$

The commutator of  $\mathcal{H}$  and  $P$  is given by  $[\mathcal{H}, p] = i\hbar(\partial\mathcal{H}/\partial z)$ , where the operator  $p$  has been replaced by  $-i\hbar(\partial/\partial z)$ . The force on an atom is then given by

$$F = - \left\langle \frac{\partial \mathcal{H}}{\partial z} \right\rangle \quad (5)$$

This relation is a specific example of the Ehrenfest theorem and forms the quantum mechanical analog of the classical expression that the force is the negative gradient of the potential.

Discussion of the force on atoms caused by light fields begins with that part of the Hamiltonian that describes the electric dipole interaction between the atom and the light field. The electric field of the light is written as  $\mathcal{E}(\vec{r}, t) = E_0 \hat{e} \cos(kz - \omega t)$  and the interaction Hamiltonian is  $\mathcal{H}' = e \vec{\mathcal{E}}(\vec{r}, t) \cdot \vec{r}$  where  $\vec{r}$  is the electron coordinate. It has only off-diagonal matrix elements given by  $\mathcal{H}'_{eg} = -eE_0 \hat{e} \cdot \langle e | \vec{r} | g \rangle$  where  $e$  and  $g$  represent the excited and ground states respectively. The force depends on the atomic state as determined by its interaction with the light, and is calculated from the expectation value  $\langle \mathcal{A} \rangle = \text{Tr}(\rho \mathcal{A})$  as in Eq. (4), where  $\rho$  is the density matrix found by solving the optical Bloch equations (OBE).<sup>1</sup> Then

$$F = \hbar \left( \frac{\partial \Omega}{\partial z} \rho_{eg}^* + \frac{\partial \Omega^*}{\partial z} \rho_{eg} \right) \quad (6)$$

where the Rabi frequency is defined as  $\hbar\Omega \equiv \mathcal{H}'_{eg}$ . Note that the force depends on the state of the atom, and in particular, on the optical coherence between the ground and excited states,  $\rho_{eg}$ .

Although it may seem a bit artificial, it is instructive to split  $\partial\Omega/\partial z$  into its real and imaginary parts (the matrix element that defines  $\Omega$  can certainly be complex):

$$\frac{\partial \Omega}{\partial z} = (q_r + iq_i) \Omega \quad (7)$$

Here  $q_r + iq_i$  is the logarithmic derivative of  $\Omega$ . In general, for a field  $E(z) = E_0(z) \exp(i\phi(z)) + \text{c.c.}$ , the real part of the logarithmic derivative corresponds to a gradient of the amplitude  $E_0(z)$  and the imaginary part to a gradient of the phase  $\phi(z)$ . Then the expression for the force becomes

$$F = \hbar q_r (\Omega \rho_{eg}^* + \Omega^* \rho_{eg}) + i \hbar q_i (\Omega \rho_{eg}^* - \Omega^* \rho_{eg}) \quad (8)$$

Equation (8) is a very general result that can be used to find the force for any particular situation as long as the OBE for  $\rho_{eg}$  can be solved. In spite of the chosen complex expression for  $\Omega$ , it is important to note that the force itself is real, and that first term of the force is proportional to the real part of  $\Omega\rho_{eg}^*$ , whereas the second term is proportional to the imaginary part.

## A Two-Level Atom at Rest

There are two important special optical arrangements to consider. The first one is a traveling wave whose electric field is  $E(z) = (E_0/2)(e^{i(kz-ot)} + c.c.)$ . In calculating the Rabi frequency from this, the rotating wave approximation (RWA) causes the positive frequency component of  $E(z)$  to drop out. Then the gradient of the Rabi frequency becomes proportional to the gradient of the surviving negative frequency component, so that  $q_r = 0$  and  $q_i = k$ . For such a traveling wave the amplitude is constant but the phase is not, and this leads to the nonzero value of  $q_i$ .

This is in direct contrast to the case of a standing wave, composed of two counterpropagating traveling waves so its amplitude is twice as large, for which the electric field is given by  $E(z) = E_0 \cos(kz)(e^{-iot} + c.c.)$ , so that  $q_r = -k \tan(kz)$  and  $q_i = 0$ . Again, only the negative frequency part survives the RWA, but the gradient does not depend on it. Thus a standing wave has an amplitude gradient, but not a phase gradient.

The steady-state solutions of the OBE for a two-level atom at rest provide simple expressions for  $\rho$ .<sup>1</sup> Substituting the solution for  $\rho_{eg}$  into Eq. (8) gives

$$F = \frac{\hbar s}{1+s} \left( -\delta q_r + \frac{1}{2} \gamma q_i \right) \quad (9)$$

where  $s \equiv s_0/[1 + (2\delta/\gamma)^2]$  is the off-resonance saturation parameter. Note that the first term is proportional to the detuning  $\delta$ , whereas the second term is proportional to the decay rate  $\gamma$ . For zero detuning, the force for a traveling wave becomes  $F = (\hbar k \gamma / 2)[s_0/(s_0 + 1)]$ , a very satisfying result because it is simply the momentum per photon  $\hbar k$ , times the scattering rate  $\gamma$  at resonance of Eq. (2).

It is instructive to identify the origin of both terms in Eq. (9). Absorption of light leads to the transfer of momentum from the optical field to the atoms. If the atoms decay by spontaneous emission, the recoil associated with the spontaneous fluorescence is in a random direction, so its average over many emission events results in zero net effect on the atomic momentum. Thus the force from absorption followed by spontaneous emission can be written as  $F_{sp} = \hbar k \gamma \rho_{ee}$ , where  $\hbar k$  is the momentum transfer for each photon,  $\gamma$  is the rate for the process, and  $\rho_{ee}$  is the probability for the atoms to be in the excited state. Using Eq. (2), the force resulting from absorption followed by spontaneous emission becomes

$$F_{sp} = \frac{\hbar k s_0 \gamma / 2}{1 + s_0 + (2\delta/\gamma)^2} \quad (10)$$

which saturates at large intensity as a result of the term  $s_0$  in the denominator. Increasing the rate of absorption by increasing the intensity does not increase the force without limit, since that would only increase the rate of stimulated emission, where the transfer of momentum is opposite in direction compared to the absorption. Thus the force saturates to a maximum value of  $\hbar k \gamma / 2$ , because  $\rho_{ee}$  has a maximum value of 1/2.

Examination of Eq. (10) shows that it clearly corresponds to the second term of Eq. (8). This term is called the *light pressure force*, *radiation pressure force*, *scattering force*, or *dissipative force*, since it relies on the scattering of light out of the laser beam. It vanishes for an atom at rest in a standing wave where  $q_i = 0$ , and this can be understood because atoms can absorb light from either of the two counterpropagating beams that make up the standing wave, and the average momentum transfer then vanishes. This force is dissipative because the reverse of spontaneous emission is not possible, and therefore the action of the force cannot be reversed. It plays a very important role in the slowing and cooling of atoms.

By contrast, the first term in Eq. (8) derives from the light shifts of the ground and excited states that depend on the strength of the optical electric field. A standing wave is composed of two counter-propagating laser beams, and their interference produces an amplitude gradient that is not present in a traveling wave. The force is proportional to the gradient of the light shift, and the ground-state light shift  $\Delta E_g = \hbar\Omega^2/4\delta$  can be used to find the force on ground-state atoms in low-intensity light:

$$F_{\text{dip}} = -\frac{\partial(\Delta E_g)}{\partial z} = \frac{\hbar\Omega}{2\delta} \frac{\partial\Omega}{\partial z} \quad (11)$$

For an amplitude-gradient light field such as a standing wave,  $\partial\Omega/\partial z = q_r\Omega$ , and this force corresponds to the first term in Eq. (8) in the limit of low saturation ( $s \ll 1$ ).

For the case of a standing wave Eq. (9) becomes

$$F_{\text{dip}} = \frac{2\hbar k \delta s_0 \sin 2kz}{1 + 4s_0 \cos^2 kz + (2\delta/\gamma)^2} \quad (12)$$

where  $s_0$  is the saturation parameter of each of the two beams that form the standing wave. For  $\delta < 0$  the force drives the atoms to positions where the intensity has a maximum, whereas for  $\delta > 0$  the atoms are attracted to the intensity minima. The force is conservative and therefore cannot be used for cooling. This is called the *dipole force*, *reactive force*, *gradient force*, or *redistribution force*. It has the same origin as the force of an inhomogeneous DC electric field on a classical dipole, but relies on the redistribution of photons from one laser beam to the other.

It needs to be emphasized that the forces of Eqs. (10) and (12) are two fundamentally different kinds of forces. For an atom at rest, the scattering force vanishes for a standing wave, whereas the dipole force vanishes for a traveling wave. The scattering force is dissipative, and can be used to cool, whereas the dipole force is conservative, and can be used to trap. Dipole forces can be made large by using high-intensity light because they do not saturate. However, since the forces are conservative, they cannot be used to cool a sample of atoms. Nevertheless, they can be combined with the dissipative scattering force to enhance cooling in several different ways. By contrast, scattering forces are always limited by the rate of spontaneous emission  $\gamma$  and cannot be made arbitrarily strong, but they are dissipative and are required for cooling.

## Atoms in Motion

Laser cooling requires dissipative or velocity-dependent forces that cannot be conservative. The procedure followed here is to treat the velocity of the atoms as a small perturbation, and make first-order corrections to the solutions of the OBE obtained for atoms at rest.<sup>2</sup> It begins by adding drift terms in the expressions for the relevant quantities. Thus the Rabi frequency satisfies

$$\frac{d\Omega}{dt} = \frac{\partial\Omega}{\partial t} + v \frac{\partial\Omega}{\partial z} = \frac{\partial\Omega}{\partial t} + v(q_r + iq_i)\Omega \quad (13)$$

where Eq. (7) has been used to separate the gradient of  $\Omega$  into real and imaginary parts. Differentiating the steadystate density matrix elements found by solving the OBE<sup>1</sup> leads to

$$\frac{dw}{dt} = \frac{\partial w}{\partial t} + v \frac{\partial w}{\partial z} = \frac{\partial w}{\partial t} - \frac{2vq_r s}{(1+s)^2} \quad (14)$$

since  $s_0 = 2|\Omega|^2/\gamma^2$  and  $\Omega$  depends on  $z$ . Here  $w \equiv \rho_{gg} - \rho_{ee}$ . Similarly,

$$\frac{d\rho_{eg}}{dt} = \frac{\partial\rho_{eg}}{\partial t} + v \frac{\partial\rho_{eg}}{\partial z} = \frac{\partial\rho_{eg}}{\partial t} - \frac{iv\Omega}{2(\gamma/2 - i\delta)(1+s)} \left[ q_r \left( \frac{1-s}{1+s} \right) + iq_i \right] \quad (15)$$

Since neither  $w$  nor  $\rho_{eg}$  is explicitly time-dependent, both  $\partial w/\partial t$  and  $\partial \rho_{eg}/\partial t$  vanish. Equations (14) and (15) are still difficult to solve analytically for a general optical field, and the results are not very instructive. However, the solution for the two special cases of the standing and traveling waves provide considerable insight.

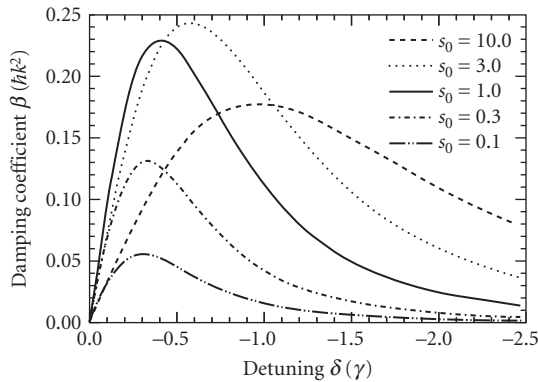
For a traveling wave  $q_i = 0$ , and the velocity-dependent force can be found by combining Eqs. (14) and (15) with the OBE to eliminate the time derivatives. The resulting coupled equations can be separated and substituted into Eq. (8) for the force to find, after considerable algebra,

$$F = \hbar q_i \frac{s\gamma/2}{1+s} \left( 1 + \frac{2\delta v q_i}{(1+s)(\delta^2 + \gamma^2/4)} \right) \equiv F_0 - \beta v \quad (16)$$

The first term is the velocity-independent force  $F_0$  for an atom at rest given by Eq. (9). The second term is velocity-dependent and can lead to compression of the velocity distribution. For a traveling wave  $q_i = k$  and thus the damping coefficient  $\beta$  is given by

$$\beta = -\hbar k^2 \frac{4s_0(\delta/\gamma)}{(1+s_0 + (2\delta/\gamma)^2)^2} \quad (17)$$

Such a force can compress the velocity distribution of an atomic sample for negative values of  $\delta$  (i.e., for red detuned light). For small detuning and low intensity the damping coefficient  $\beta$  is linear in both parameters. However, for detunings much larger than  $\gamma$  and intensities much larger than  $I_s$ ,  $\beta$  saturates and even decreases as a result of the dominance of  $\delta$  in the denominator of Eq. (17). This behavior can be seen in Fig. 1, where the damping coefficient  $\beta$  has been plotted as a function of detuning for different saturation parameters. The decrease of  $\beta$  for large detunings and intensities is caused by saturation of the transition, in which case the absorption rate becomes only weakly dependent on the velocity. The maximum value of  $\beta$  is obtained for  $\delta = -\gamma/2$  and  $s_0 = 2$ , and is given by  $\beta_{\max} = \hbar k^2/4$ . The damping rate  $\Gamma$  is given by  $\Gamma = \beta/M$ , and its maximum value is  $\Gamma_{\max} = \omega_r/2$ , where  $\omega_r$  is the recoil frequency. For the alkalis this rate is of the order of  $10^4$ – $10^5$  s<sup>-1</sup>, indicating that atomic velocity distributions can be compressed in about 10 to 100  $\mu$ s. Furthermore,  $F_0$  in Eq. (16) is always present and so the atoms are *not* damped toward any constant velocity.



**FIGURE 1** The damping coefficient  $\beta$  for an atom in a traveling wave as a function of the detuning for different values of the saturation parameter  $s_0$ . The damping coefficient is maximum for intermediate detunings and intensities.



For a standing wave  $q_i = 0$ , and just as above, the velocity-dependent force can be found by combining Eqs. (14) and (15) with the OBE to eliminate the time derivatives. The resulting coupled equations can again be separated and substituted into Eq. (8) for the force to find

$$F = -\hbar q_r \frac{s\delta}{1+s} \left( 1 - v q_r \frac{(1-s)\gamma^2 - 2s^2(\delta^2 + \gamma^2/4)}{(\delta^2 + \gamma^2/4)(1+s)^2 \gamma} \right) \quad (18)$$

where  $q_r = -k \tan(kz)$ . In the limit of  $s \ll 1$ , this force is

$$F = \hbar k \frac{s_0 \delta \gamma^2}{2(\delta^2 + \gamma^2/4)} \left( \sin 2kz + kv \frac{\gamma}{(\delta^2 + \gamma^2/4)} (1 - \cos 2kz) \right) \quad (19)$$

Here  $s_0$  is the saturation parameter of each of the two beams that compose the standing wave. The first term is the velocity-independent part of Eq. (9) and is sinusoidal in space, with a period of  $\lambda/2$ . Thus its spatial average vanishes. The force remaining after such averaging is  $F_{\text{av}} = -\beta v$ , where the damping coefficient  $\beta$  is given by

$$\beta = -\hbar k^2 \frac{8s_0(\delta/\gamma)}{(1+(2\delta/\gamma)^2)^2} \quad (20)$$

In contrast to the traveling-wave case, this is a true damping force because there is no  $F_0$ , so atoms are slowed toward  $v = 0$  independent of their initial velocities. Note that this expression for  $\beta$  is valid only for  $s \ll 1$  because it depends on spontaneous emission to return atoms to their ground state.

There is an appealing description of the mechanism for this kind of cooling in a standing wave. With light detuned below resonance, atoms traveling toward one laser beam see it Doppler shifted upward, closer to resonance. Since such atoms are traveling away from the other laser beam, they see its light Doppler shifted further downward, hence further out of resonance. Atoms therefore scatter more light from the beam counterpropagating to their velocity, so their velocity is reduced. This damping mechanism is called *optical molasses*, and is one of the most important tools of laser cooling.

Needless to say, such a pure damping force would reduce the atomic velocities, and hence the absolute temperature, to zero. Since this violates thermodynamics, there must be something left out of the description. It is the discreteness of the momentum changes in each case,  $\Delta p = \hbar k$ , that results in a minimum velocity change. The consequences of this discreteness can be described as a diffusion of the atomic momenta in momentum space by finite steps as discussed earlier.

## The Fokker-Planck Equation

The random walk in momentum space associated with spontaneous emission is similar to Brownian motion in coordinate space. There is an analogous momentum diffusion constant  $D$ , and so the atomic motion in momentum space can be described by the Fokker-Planck equation

$$\frac{\partial W(p, t)}{\partial t} = -\frac{\partial [F(p, t)W(p, t)]}{\partial p} + \frac{\partial^2 [D(p, t)W(p, t)]}{\partial p^2} \quad (21)$$

where  $W(p, t)$  is the momentum distribution of the atoms. For the special case when both the force and the diffusion are independent of time, the formal stationary solution is

$$\bar{W}(p) = \frac{C}{D(p)} \exp \left( \int_0^p \frac{F(p')}{D(p')} dp' \right) \quad (22)$$

where  $C$  is an integration constant. Once the force and diffusion are known, the stationary solution of the Fokker-Planck equation emerges easily.

In the simplest and most common case in laser cooling the force is proportional to the velocity and the diffusion is independent of velocity:

$$F(v) = -\beta v \quad \text{and} \quad D(v) = D_0 \quad (23)$$

Then the stationary solution of Eq. (21) for  $\bar{W}(v)$  is

$$\bar{W}(p) \propto e^{-\beta p^2 / 2MD_0} \quad (24)$$

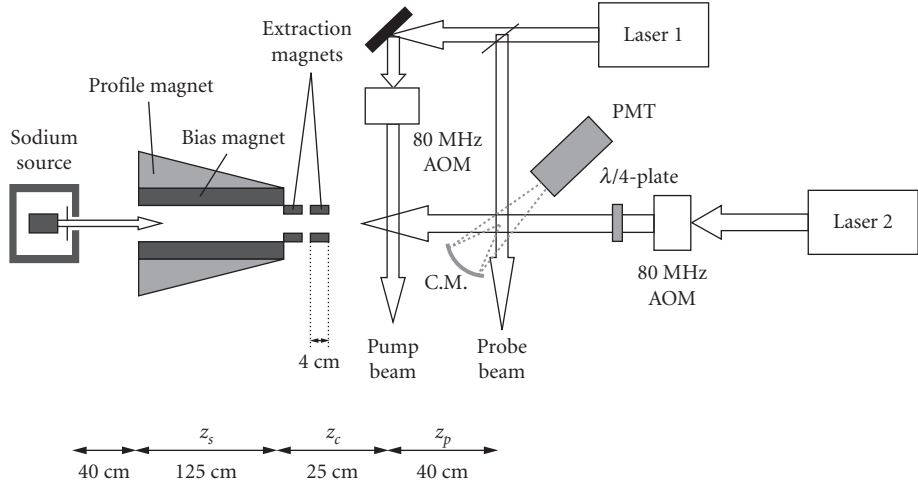
This is indeed a Maxwell-Boltzmann distribution. For low intensity where spontaneous emission dominates,  $D_0 = s\gamma(\hbar k)^2/2$ , so the steady-state temperature is given by  $k_B T = D_0/\beta = \hbar\gamma/2$  for  $\delta = -\gamma/2$ , its optimum value.<sup>1</sup> This is called the *Doppler temperature* because the velocity dependence of the cooling mechanism derives from the Doppler shift. The fact that the conditions of Eq. (23) for the force and diffusion are often approximately correct explains why the notion of temperature often appears as a description of a laser-cooled sample.

One of the most important properties of laser cooling is its ability to change the phase space density of an atomic sample. Changing the phase space density provides a most important distinction between light optics and atom optics. The Hamiltonian description of geometrical optics leads to the brightness theorem, that can be found in many optics books. Thus bundles of light rays obey a similar phase space density conservation. But there is a fundamental difference between light and atom optics. In the first case, the “forces” that determine the behavior of bundles of rays are “conservative” and phase space density is conserved. For instance, a lens can be used to focus a light beam to a small spot; however, at the same time the divergence of the beam must be increased, thus conserving phase space density. By contrast, in atom optics dissipative forces that are velocity-dependent can be used, and thus phase space density is no longer conserved. Optical elements corresponding to such forces cannot exist for light, but in addition to the atom optic elements of lenses, collimators, and others, phase space compressors can also be built. Such compression is essential in a large number of cases, such as atomic beam brightening for collision studies or cooling for the achievement of Bose-Einstein condensation.

## 20.4 SLOWING ATOMIC BEAMS

Among the earliest laser cooling experiments was deceleration of atoms in a beam.<sup>3</sup> The authors exploited the Doppler shift to make the momentum exchange (hence the force) velocity-dependent. It worked by directing a laser beam opposite to an atomic beam so the atoms could absorb light, and hence momentum  $\hbar k$ , very many times along their paths through the apparatus as shown in Fig. 2.<sup>3,4</sup> Of course, excited-state atoms cannot absorb light efficiently from the laser that excited them, so between absorptions they must return to the ground state by spontaneous decay, accompanied by emission of fluorescent light. The spatial symmetry of the emitted fluorescence results in an average of zero net momentum transfer from many such fluorescence events. Thus the net force on the atoms is in the direction of the laser beam, and the maximum deceleration is limited by the spontaneous emission rate  $\gamma$ .

The maximum attainable deceleration is obtained for very high light intensities, and is limited because the atom must then divide its time equally between ground and excited states. High-intensity light can produce faster absorption, but it also causes equally fast stimulated emission; the combination produces neither deceleration nor cooling because the momentum transfer to the atom in emission is then in the opposite direction to what it was in absorption. The force is limited to  $F = \hbar k \gamma_p$ , and so the deceleration therefore saturates at a value  $\bar{a}_{\max} = \hbar k \gamma / 2M$  [see Eq. (2)]. Since the maximum deceleration  $\bar{a}_{\max}$  is fixed by atomic parameters, it is straightforward to calculate the minimum stopping length  $L_{\min}$  and time  $t_{\min}$  for the rms velocity of atoms  $\bar{v} = \sqrt{2k_B T / M}$  at the chosen temperature. The result is  $L_{\min} = \bar{v}^2 / 2\bar{a}_{\max}$  and  $t_{\min} = \bar{v} / \bar{a}_{\max}$ . In Table 1 are some of the parameters for slowing a few atomic species of interest from the peak of the thermal velocity distribution.



**FIGURE 2** Schematic diagram of the apparatus for beam slowing. The tapered magnetic field is produced by layers of varying length on the solenoid, and the bias field is produced by full-length windings. The TOF aspect is implemented with Laser 1 whose beams optically pump the atoms between the hfs states.

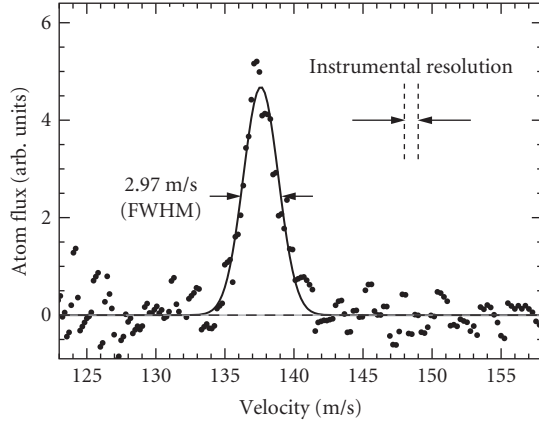
**TABLE 1** Parameters of Interest for Slowing Various Atoms

Atom	$T_{\text{oven}}$ (K)	$\bar{v}$ (m/s)	$L_{\text{min}}$ (m)	$t_{\text{min}}$ (ms)
H	1000	5000	0.012	0.005
He*	4	158	0.03	0.34
He*	650	2013	4.4	4.4
Li	1017	2051	1.15	1.12
Na	712	876	0.42	0.96
K	617	626	0.77	2.45
Rb	568	402	0.75	3.72
Cs	544	319	0.93	5.82

The stopping length  $L_{\text{min}}$  and time  $t_{\text{min}}$  are minimum values. The oven temperature  $T_{\text{oven}}$  that determines the peak velocity is chosen to give a vapor pressure of 1 Torr. Special cases are H at 1000 K and He in the metastable triplet state, for which two rows are shown: one for a 4-K source and another for the typical discharge temperature.

Maximizing the scattering rate  $\gamma_p$  requires  $\delta = -\omega_D$  in Eq. (2). If  $\delta$  is chosen for a particular atomic velocity in the beam, then as the atoms slow down, their changing Doppler shift will take them out of resonance. They will eventually cease deceleration after their Doppler shift has been decreased by a few times the power-broadened width  $\gamma' = \gamma\sqrt{1+s_0}$ , corresponding to  $\Delta v$  of a few times  $\gamma'/k$ . Although this  $\Delta v$  of a few m/s is considerably larger than the typical atomic recoil velocity  $\hbar k/M$  of a few cm/s, it is still only a small fraction of the atoms' average thermal velocity  $\bar{v}$ , so that significant further cooling or deceleration cannot be accomplished.

In order to achieve deceleration that changes the atomic speeds by hundreds of m/s, it is necessary to maintain  $(\delta + \omega_D) \ll \gamma$  by compensating such large changes of the Doppler shift. This can be done by changing  $\omega_D$ , or  $\delta$  via either  $\omega_l$  or  $\omega_a$ . The two most common methods for maintaining this resonance are sweeping the laser frequency  $\omega_l$  along with the changing  $\omega_D$  of the decelerating atoms,<sup>5-7</sup> or by spatially varying the atomic resonance frequency with an inhomogeneous DC magnetic field to keep the decelerating atoms in resonance with the fixed frequency laser.<sup>1,3,8</sup>



**FIGURE 3** The velocity distribution measured with the time-of-flight (TOF) method. The experimental width of approximately  $\frac{1}{6}(\gamma/k)$  is shown by the dashed vertical lines between the arrows. The Gaussian fit through the data yields a FWHM of 2.97 m/s. (Figure from Ref. 78.)

The use of a spatially varying magnetic field to tune the atomic levels along the beam path was the first method to succeed in slowing atoms.<sup>3</sup> It works as long as the Zeeman shifts of the ground and excited states are different so that the resonant frequency is shifted. The field can be tailored to provide the appropriate Doppler shift along the moving atom's path. For uniform deceleration  $a \equiv \eta a_{\max}$  from initial velocity  $v_0$ , the appropriate field profile is  $B(z) = B_0 \sqrt{1 - z/z_0}$ , where  $z_0 \equiv Mv_0^2 / \eta \hbar k \gamma$  is the length of the magnet,  $B_0 = \hbar k v_0 / \mu'$ ,  $\mu' \equiv (g_e M_e - g_g M_g) \mu_B$ , subscripts  $g$  and  $e$  refer to ground and excited states,  $g_{g,e}$  is the Landé  $g$ -factor,  $\mu_B$  is the Bohr magneton, and  $M_{g,e}$  is the magnetic quantum number. The design parameter  $\eta < 1$  determines the length of the magnet  $z_0$ . A solenoid that can produce such a spatially varying field has layers of decreasing lengths as shown schematically in Fig. 2. The technical problem of extracting the beam of slow atoms from the end of the solenoid can be simplified by reversing the field gradient and choosing a transition whose frequency decreases with increasing field.<sup>9</sup>

For alkali atoms such as Na, a time-of-flight (TOF) method can be used to measure the velocity distribution of atoms in the beam. It employs two additional beams labeled *pump* and *probe* from laser 1 as shown in Fig. 2. Because these beams cross the atomic beam at  $90^\circ$ ,  $\omega_D = -\vec{k} \cdot \vec{v} = 0$  and they excite atoms at all velocities. The pump beam is tuned to excite and empty a selected ground hyperfine state (hfs), and it transfers more than 98 percent of the population as the atoms pass through its 0.5 mm width. To measure the velocity distribution of atoms in the selected hfs, this pump laser beam is interrupted for a period  $\Delta t = 10$  to  $50 \mu\text{s}$  with an acoustic optical modulator (AOM). A pulse of atoms in the selected hfs passes the pump region and travels to the probe beam. The time dependence of the fluorescence induced by the probe laser, tuned to excite the selected hfs, gives the time of arrival, and this signal is readily converted to a velocity distribution. Figure 3 shows the measured velocity distribution of the atoms slowed by laser 2.

## 20.5 OPTICAL MOLASSES

### Doppler Cooling

In Sec. 20.3 there was a discussion of the radiative force on atoms moving in a standing wave (counterpropagating laser beams). The slowing force is proportional to velocity for small enough velocities, resulting in viscous damping<sup>10,11</sup> that gives this technique the name *optical molasses* (OM). By

using three intersecting orthogonal pairs of oppositely directed beams, the movement of atoms in the intersection region can be severely restricted in all three dimensions, and many atoms can thereby be collected and cooled in a small volume. OM has been demonstrated at several laboratories,<sup>12</sup> often with the use of low-cost diode lasers.<sup>13</sup>

It is straightforward to estimate the force on atoms in OM from Eq. (10). The discussion here is limited to the case where the light intensity is low enough so that stimulated emission is not important. In this low-intensity case the forces from the two light beams are simply added to give  $\vec{F}_{\text{OM}} = \vec{F}_+ + \vec{F}_-$ , where

$$\vec{F}_{\pm} = \pm \frac{\hbar k \gamma}{2} \frac{s_0}{1 + s_0 + [2(\delta \mp |\omega_D|)/\gamma]^2} \quad (25)$$

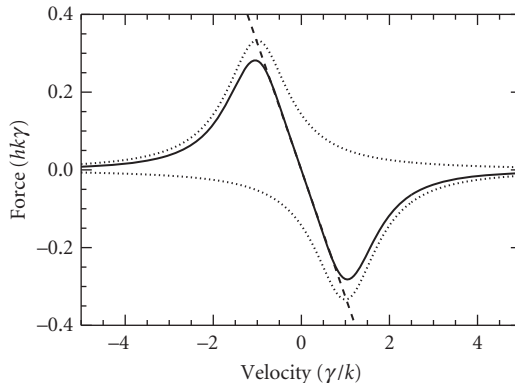
Then the sum of the two forces is

$$\vec{F}_{\text{OM}} \equiv \frac{8\hbar k^2 \delta s_0 \vec{v}}{\gamma(1 + s_0 + (2\delta/\gamma)^2)} \equiv -\beta \vec{v} \quad (26)$$

where terms of order  $(kv/\gamma)^4$  and higher have been neglected [see Eq. (20)].

These forces are plotted in Fig. 4. For  $\delta < 0$ , this force opposes the velocity and therefore viscously damps the atomic motion.  $\vec{F}_{\text{OM}}$  has maxima near  $v \approx \pm \gamma'/2k$  and decreases rapidly for larger velocities.

If there were no other influence on the atomic motion, all atoms would quickly decelerate to  $v = 0$ , and the sample would reach  $T = 0$ , a clearly unphysical result. There is also some heating caused by the light beams that must be considered, and it derives from the discrete size of the momentum steps the atoms undergo with each emission or absorption as previously discussed for Brownian motion (see Sec. 20.3). Since the atomic momentum changes by  $\hbar k$ , their kinetic energy changes on the average by at least the recoil energy  $E_r = \hbar^2 k^2 / 2M = \hbar \omega_r$ . This means that the average frequency of each absorption is  $\omega_{\text{abs}} = \omega_a + \omega_r$  and the average frequency of each emission is  $\omega_{\text{emit}} = \omega_a + \omega_r$ . Thus the light field loses an average energy of  $\hbar(\omega_{\text{abs}} - \omega_{\text{emit}}) = 2\hbar \omega_r$  for each scattering. This loss occurs at a rate  $2\gamma_b$  (two beams), and the energy is converted to atomic kinetic energy because the atoms recoil from each event. The atomic sample is thereby heated because these recoils are in random directions.



**FIGURE 4** Velocity dependence of the optical damping forces for one-dimensional optical molasses. The two dotted traces show the force from each beam, and the solid curve is their sum. The straight line shows how this force mimics a pure damping force over a restricted velocity range. These are calculated for  $s_0 = 2$  and  $\delta = -\gamma$  so there is some power-broadening evident.

The competition between this heating with the damping force of Eq. (26) results in a nonzero kinetic energy in steady state where the rates of heating and cooling are equal. Equating the cooling rate,  $\vec{F} \cdot \vec{v}$ , to the heating rate,  $4\hbar\omega_r\gamma_p$ , the steady-state kinetic energy is  $(\hbar\gamma/8)(2|\delta|/\gamma + \gamma/2|\delta|)$ . This result is dependent on  $|\delta|$ , and it has a minimum at  $2|\delta|/\gamma = 1$ , whence  $\delta = -\gamma/2$ . The temperature found from the kinetic energy is then  $T_D = \hbar\gamma/2k_B$ , where  $T_D$  is called the *Doppler temperature* or the *Doppler cooling limit*. For ordinary atomic transitions,  $T_D$  is typically below 1 mK.

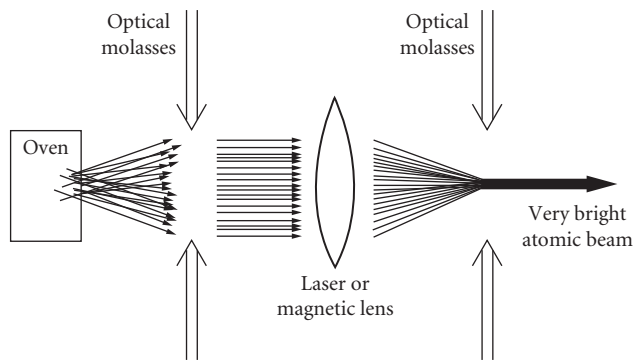
Another instructive way to determine  $T_D$  is to note that the average momentum transfer of many spontaneous emissions is zero, but the rms scatter of these about zero is finite. One can imagine these decays as causing a random walk in momentum space with step size  $\hbar k$  and step frequency  $2\gamma_p$ , where the factor of 2 arises because of the two beams. The random walk results in diffusion in momentum space with diffusion coefficient  $D_0 \equiv 2(\Delta p)^2/\Delta t = 4\gamma_p(\hbar k)^2$  as discussed in Sec. 20.3. Then Brownian motion theory gives the steady-state temperature in terms of the damping coefficient  $\beta$  to be  $k_B T = D_0/\beta$ . This turns out to be  $\hbar\gamma/2$  as above for the case  $s_0 \ll 1$  when  $\delta = -\gamma/2$ . This remarkable result predicts that the final temperature of atoms in OM is independent of the optical wavelength, atomic mass, and laser intensity (as long as it is not too large).

## Atomic Beam Collimation—One-Dimensional Optical Molasses

When an atomic beam crosses a one-dimensional OM as shown in Fig. 5, the transverse motion of the atoms is quickly damped while the longitudinal component is essentially unchanged. This transverse cooling of an atomic beam is an example of a method that can actually increase its brightness (atoms/sec-sr-cm<sup>2</sup>) because such active collimation uses dissipative forces to compress the phase space volume occupied by the atoms. By contrast, the usual realm of beam focusing or collimation techniques for light beams and most particle beams is restricted to selection by apertures or conservative forces that preserve the phase space density of atoms in the beam.

This velocity compression at low intensity in one dimension can be simply estimated for two-level atoms in 1D to be about  $v_c/v_D = \sqrt{\gamma/\omega_r} = \sqrt{1/\epsilon}$ . For Rb,  $v_D = 12$  cm/s,  $v_c = \gamma/k \approx 4.6$  m/s,  $\omega_r \approx 2\pi \times 3.8$  kHz, and  $1/\epsilon \approx 1600$ . Including two transverse directions along with the longitudinal slowing and cooling just discussed, the decrease in phase space volume from the momentum contribution alone for laser cooling of a Rb atomic beam can exceed  $10^6$ .

Clearly optical techniques can create atomic beams enormously more times intense than ordinary thermal beams, and also many orders of magnitude brighter. Furthermore, this number could be increased by several orders of magnitude if the transverse cooling could produce temperatures



**FIGURE 5** Scheme for optical brightening of an atomic beam. First the transverse velocity components of the atoms are damped out by an optical molasses, then the atoms are focused to a spot, and finally the atoms are recollimated in a second optical molasses. (Figure from Ref. 79.)

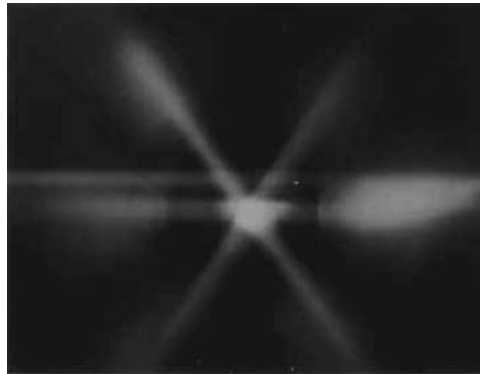
below the Doppler temperature. For atoms cooled to the recoil temperature  $T_r = \hbar\omega_r/k_B$  where  $\Delta p = \hbar k$  and  $\Delta x = \lambda/\pi$ , the brightness increase could be  $10^{17}$ .

## Experiments in Three-Dimensional Optical Molasses

Optical molasses experiments can also work in three dimensions at the intersection of three mutually orthogonal pairs of opposing laser beams (see Fig. 6). Even though atoms can be collected and cooled in the intersection region, it is important to stress again that this is *not* a trap. That is, atoms that wander away from the center experience no force directing them back. They are allowed to diffuse freely and even escape, as long as there is enough time for their very slow diffusive movement to allow them to reach the edge of the region of the intersection of the laser beams. Because the atomic velocities are randomized during the damping time  $M/\beta = 2/\omega_r$ , atoms execute a random walk with a step size of  $2v_D/\omega_r = \lambda/\pi\sqrt{2}\epsilon \cong \text{few } \mu\text{m}$ . To diffuse a distance of 1 cm requires about  $10^7$  steps or about 30 s.<sup>14,15</sup>

Three-dimensional OM was first observed in 1985.<sup>11</sup> Preliminary measurements of the average kinetic energy of the atoms were done by blinking off the laser beams for a fixed interval. Comparison of the brightness of the fluorescence before and after the turnoff was used to calculate the fraction of atoms that left the region while it was in the dark. The dependence of this fraction on the duration of the dark interval was used to estimate the velocity distribution and hence the temperature. The result was not inconsistent with the two-level atom theory previously described.

A few months later a more sensitive ballistic technique was devised at the National Institute of Standards and Technology (NIST) that showed the astounding result that the temperature of the atoms in OM was very much lower than  $T_D$ .<sup>16</sup> These experiments also found that OM was less sensitive to perturbations and more tolerant of alignment errors than was predicted by the 1D, two-level atom theory. For example, if the intensities of the two counter-propagating laser beams forming an OM were unequal, then the force on atoms at rest would not vanish, but the force on atoms with some nonzero drift velocity *would* vanish. This drift velocity can be easily calculated by using Eq. (25) with unequal intensities  $s_{0+}$  and  $s_{0-}$  and following the derivation of Eq. (26). Thus atoms would drift out of an OM, and the calculated rate would be much faster than observed by deliberately unbalancing the beams in the experiments.<sup>12</sup>



**FIGURE 6** Photograph of optical molasses in Na taken under ordinary snapshot conditions in the lab at NIST. The upper horizontal streak is from the slowing laser while the three beams that cross at the center are on mutually orthogonal axes viewed from the (111) direction. Atoms in the optical molasses glow brightly at the center. (Figure from Ref. 19.)

It was an enormous surprise to observe that the ballistically measured temperature of the Na atoms was as much as 10 times *lower* than  $T_D = 240 \mu\text{K}$ ,<sup>16</sup> the temperature minimum calculated from the theory. This breaching of the Doppler limit forced the development of an entirely new picture of OM that accounts for the fact that in three dimensions, a two-level picture of atomic structure is inadequate. The multilevel structure of atomic states, and optical pumping among these sublevels, must be considered in the description of 3D OM, as discussed in the text that follows.

## 20.6 COOLING BELOW THE DOPPLER LIMIT

### Introduction

In response to the surprising measurements of temperatures below  $T_D$ , two groups developed a model of laser cooling that could explain the lower temperatures.<sup>17,18</sup> The key feature of this model that distinguishes it from the earlier picture was the inclusion of the multiplicity of sublevels that make up an atomic state (e.g., Zeeman and hfs). The dynamics of optically pumping atoms among these sublevels provides the new mechanism for producing the ultralow temperatures.<sup>19</sup>

The dominant feature of these models is the nonadiabatic response of moving atoms to the light field. Atoms at rest in a steady state have ground-state orientations caused by optical pumping processes that distribute the populations over the different ground-state sublevels. In the presence of polarization gradients, these orientations reflect the local light field. In the low-light-intensity regime, the orientation of stationary atoms is completely determined by the ground-state distribution: The optical coherences and the excited-state population follow the ground-state distribution adiabatically.

For atoms moving in a light field that varies in space, optical pumping acts to adjust the atomic orientation to the changing conditions of the light field. In a weak pumping process, the orientation of moving atoms always lags behind the orientation that would exist for stationary atoms. It is this phenomenon of nonadiabatic following that is the essential feature of the new cooling process.

Production of spatially dependent optical pumping processes can be achieved in several different ways. As an example, consider two counterpropagating laser beams that have orthogonal polarizations (as will be discussed shortly). The superposition of the two beams results in a light field having a polarization that varies on the wavelength scale along the direction of the laser beams. Laser cooling by such a light field is called *polarization gradient cooling*. In a three-dimensional optical molasses, the transverse wave character of light requires that the light field always has polarization gradients.

### Linear $\perp$ Linear Polarization Gradient Cooling

One of the most instructive models for discussion of sub-Doppler laser cooling was introduced in Ref. 17 and very well described in Ref. 19. If the polarizations of two counterpropagating laser beams are identical, the two beams interfere and produce a standing wave. When the two beams have orthogonal linear polarizations (same frequency  $\omega_l$ ) with their  $\hat{\epsilon}$  vectors perpendicular (e.g.,  $\hat{x}$  and  $\hat{y}$ ), the configuration is called *lin  $\perp$  lin* or *lin-perp-lin*. Then the total field is the sum of the two counterpropagating beams given by

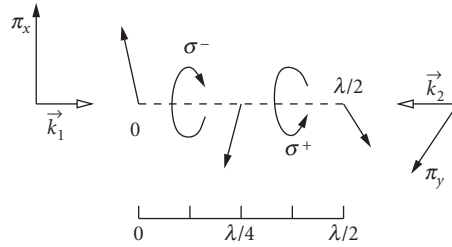
$$\begin{aligned}\vec{E} &= E_0 \hat{x} \cos(\omega_l t - kz) + E_0 \hat{y} \cos(\omega_l t + kz) \\ &= E_0 [(\hat{x} + \hat{y}) \cos \omega_l t \cos kz + (\hat{x} - \hat{y}) \sin \omega_l t \sin kz]\end{aligned}\quad (27)$$

At the origin, where  $z = 0$ , this becomes

$$\vec{E} = E_0 (\hat{x} + \hat{y}) \cos \omega_l t \quad (28)$$

which corresponds to linearly polarized light at an angle  $+\pi/4$  to the  $x$ -axis. The amplitude of this field is  $\sqrt{2}E_0$ . Similarly, for  $z = \lambda/4$ , where  $kz = \pi/2$ , the field is also linearly polarized but at an angle  $-\pi/4$  to the  $x$ -axis.





**FIGURE 7** Polarization gradient field for the lin  $\perp$  lin configuration.

Between these two points, at  $z = \lambda/8$ , where  $kz = \pi/4$ , the total field is

$$\vec{E} = E_0 [\hat{x} \sin(\omega t + \pi/4) - \hat{y} \cos(\omega t + \pi/4)] \quad (29)$$

Since the  $\hat{x}$  and  $\hat{y}$  components have sine and cosine temporal dependence, they are  $\pi/2$  out of phase, and so Eq. (29) represents circularly polarized light rotating about the  $z$ -axis in the negative sense. Similarly, at  $z = 3\lambda/8$  where  $kz = 3\pi/4$ , the polarization is circular but in the positive sense. Thus in this lin  $\perp$  lin scheme the polarization cycles from linear to circular to orthogonal linear to opposite circular in the space of only half a wavelength of light, as shown in Fig. 7. It truly has a very strong polarization gradient.

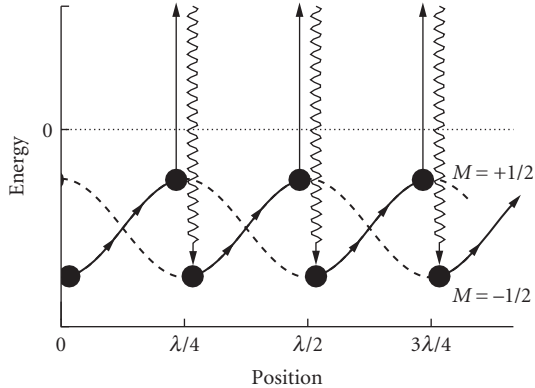
Since the coupling of the different states of multilevel atoms to the light field depends on its polarization, atoms moving in a polarization gradient will be coupled differently at different positions, and this will have important consequences for laser cooling. For the  $J_g = 1/2 \rightarrow J_e = 3/2$  transition (the simplest transition that shows sub-Doppler cooling), the optical pumping process in purely  $\sigma^+$  light drives the ground-state population to the  $M_g = +1/2$  sublevel. This optical pumping occurs because absorption always produces  $\Delta M = +1$  transitions, whereas the subsequent spontaneous emission produces  $\Delta M = \pm 1, 0$ . Thus the average  $\Delta M \geq 0$  for each scattering event. For  $\sigma^-$ -light the population is pumped toward the  $M_g = -1/2$  sublevel. Thus atoms traveling through only a half wavelength in the light field need to readjust their population completely from  $M_g = +1/2$  to  $M_g = -1/2$  and back again.

The interaction between nearly resonant light and atoms not only drives transitions between atomic energy levels, but also shifts their energies. This light shift of the atomic energy levels plays a crucial role in this scheme of sub-Doppler cooling, and the changing polarization has a strong influence on the light shifts. In the low-intensity limit of two laser beams, each of intensity  $s_0 I_s$ , the light shifts  $\Delta E_g$  of the ground magnetic substates are given by<sup>1</sup>

$$\Delta E_g = \frac{\hbar \delta_0 C_{ge}^2}{1 + (2\delta/\gamma)^2} \quad (30)$$

where  $C_{ge}$  is the Clebsch-Gordan coefficient that describes the coupling between the atom and the light field.

In the present case of orthogonal linear polarizations and  $J = 1/2 \rightarrow 3/2$ , the light shift for the magnetic substate  $M_g = 1/2$  is three times larger than that of the  $M_g = -1/2$  substate when the light field is completely  $\sigma^+$ . On the other hand, when an atom moves to a place where the light field is  $\sigma^-$ , the shift of  $M_g = -1/2$  is three times larger. So in this case the optical pumping previously discussed causes there to be a larger population in the state with the larger light shift. This is generally true for any transition  $J_g$  to  $J_e = J_g + 1$ . A schematic diagram showing the populations and light shifts for this particular case of negative detuning is shown in Fig. 8.



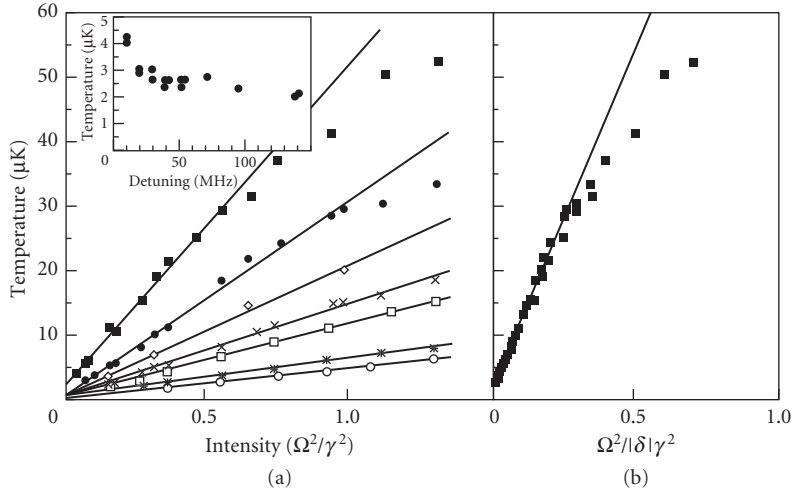
**FIGURE 8** The spatial dependence of the light shifts of the ground-state sublevels of the  $J = 1/2 \leftrightarrow 3/2$  transition for the case of the lin  $\perp$  lin polarization configuration. The arrows show the path followed by atoms being cooled in this arrangement. Atoms starting at  $z = 0$  in the  $M_g = +1/2$  sublevel must climb the potential hill as they approach the  $z = \lambda/4$  point where the light becomes  $\sigma^-$  polarized, and there they are optically pumped to the  $M_g = -1/2$  sublevel. Then they must begin climbing another hill toward the  $z = \lambda/2$  point where the light is  $\sigma^+$  polarized and they are optically pumped back to the  $M_g = +1/2$  sublevel. The process repeats until the atomic kinetic energy is too small to climb the next hill. Each optical pumping event results in absorption of light at a lower frequency than emission, thus dissipating energy to the radiation field.

## Origin of the Damping Force

To discuss the origin of the cooling process in this polarization gradient scheme, consider atoms with a velocity  $v$  at a position where the light is  $\sigma^+$ -polarized, as shown at the lower left of Fig. 8. The light optically pumps such atoms to the strongly negative light-shifted  $M_g = +1/2$  state. In moving through the light field, atoms must increase their potential energy (climb a hill) because the polarization of the light is changing and the state  $M_g = 1/2$  becomes less strongly coupled to the light field. After traveling a distance  $\lambda/4$ , atoms arrive at a position where the light field is  $\sigma^-$ -polarized, and are optically pumped to  $M_g = -1/2$ , which is now lower than the  $M_g = 1/2$  state. Again the moving atoms are at the bottom of a hill and start to climb. In climbing the hills, the kinetic energy is converted to potential energy, and in the optical pumping process, the potential energy is radiated away because the spontaneous emission is at a higher frequency than the absorption (see Fig. 8). Thus atoms seem to be always climbing hills and losing energy in the process. This process brings to mind a Greek myth, and is thus called *Sisyphus laser cooling*.

The cooling process just described is effective over a limited range of atomic velocities. The force is maximum for atoms that undergo one optical pumping process while traveling over a distance  $\lambda/4$ . Slower atoms will not reach the hilltop before the pumping process occurs, and faster atoms will already be descending the hill before being pumped toward the other sublevel. In both cases the energy loss is smaller and therefore the cooling process less efficient. Nevertheless, the damping constant  $\beta$  for this process is much larger than for Doppler cooling, and therefore the final steady-state temperature is lower.<sup>17,19</sup>

In the experiments of Ref. 20, the temperature was measured in a 3D molasses under various configurations of the polarization. Temperatures were measured by a ballistic technique, where



**FIGURE 9** Temperature as a function of laser intensity and detuning for Cs atoms in an optical molasses from Ref. 20. (a) Temperature as a function of the detuning for various intensities. (b) Temperature as a function of the light shift. All the data points are on a universal straight line.

the flight time of the released atoms was measured as they fell through a probe a few cm below the molasses region. Results of their measurements are shown in Fig. 9a, where the measured temperature is plotted for different detunings as a function of the intensity. For each detuning, the data lie on a straight line through the origin. The lowest temperature obtained is 3  $\mu\text{K}$ , which is a factor 40 below the Doppler temperature and a factor 15 above the recoil temperature of Cs. If the temperature is plotted as a function of the light shift (see Fig. 9b), all the data are on a single universal straight line.

## The Limits of Laser Cooling

The lower limit to Doppler laser cooling of two-level atoms arises from the competition with heating. This cooling limit is described as a random walk in momentum space whose steps are of size  $\hbar k$  and whose rate is the scattering rate,  $\gamma_p = s_0 \gamma / 2$  for zero detuning and  $s_0 \ll 1$ . As long as the force can be accurately described as a damping force, then the Fokker-Planck equation is applicable, and the outcome is a lower limit to the temperature of laser cooling given by the Doppler temperature  $k_B T_D \equiv \hbar \gamma / 2$ .

The extension of this kind of thinking to the sub-Doppler processes described in Sec. 20.5 must be done with some care, because a naive application of the consequences of the Fokker-Planck equation would lead to an arbitrarily low final temperature. In the derivation of the Fokker-Planck equation it is explicitly assumed that each scattering event changes the atomic momentum  $p$  by an amount that is a small fraction  $p$  as embodied in Eq. (3), and this clearly fails when the velocity is reduced to the region of  $v_r \equiv \hbar k / M$ .

This limitation of the minimum steady-state value of the average kinetic energy to a few times  $2E_r \equiv k_B T_r = M v_r^2$  is intuitively comforting for two reasons. First, one might expect that the last spontaneous emission in a cooling process would leave atoms with a residual momentum of the order of  $\hbar k$ , since there is no control over its direction. Thus the randomness associated with this would put a lower limit on such cooling of  $v_{\min} \sim v_r$ . Second, the polarization gradient cooling mechanism just described requires that atoms be localizable within the scale of  $\sim \lambda / 2\pi$  in order to

be subject to only a single polarization in the spatially inhomogeneous light field. The uncertainty principle then requires that these atoms have a momentum spread of at least  $\hbar k$ .

The recoil limit discussed here has been surpassed by evaporative cooling of trapped atoms<sup>21</sup> and two different optical cooling methods, neither of which can be based in simple notions. One of these uses optical pumping into a velocity-selective dark state and is described in Ref. 1. The other one uses carefully chosen, counterpropagating laser pulses to induce velocity-selective Raman transitions, and is called *Raman cooling*.<sup>22</sup>

## 20.7 TRAPPING OF NEUTRAL ATOMS

### Introduction

Although ion trapping, laser cooling of trapped ions, and trapped ion spectroscopy were known for many years,<sup>23</sup> it was only in 1985 that neutral atoms were first trapped.<sup>24</sup> Confinement of neutral atoms depends on the interaction between an inhomogeneous electromagnetic field and an atomic multipole moment. Unperturbed atoms do not have electric dipole moments because of their inversion symmetry, and therefore electric (e.g., optical) traps require induced dipole moments. This is often done with nearly resonant optical fields, thus producing the optical traps that will be discussed shortly. On the other hand, many atoms have ground- or metastable-state magnetic dipole moments that may be used for trapping them magnetically.

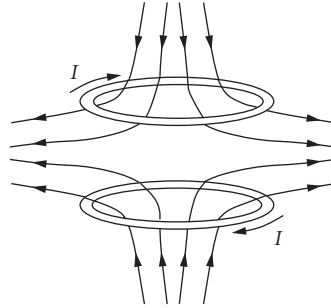
In order to confine any object, it is necessary to exchange kinetic for potential energy in the trapping field, and in neutral atom traps the potential energy must be stored as internal atomic energy. There are two immediate and extremely important consequences of this requirement. First, the atomic energy levels will necessarily shift as the atoms move in the trap, and these shifts will affect the precision of spectroscopic measurements, perhaps severely. Second, practical traps for ground-state neutral atoms are necessarily very shallow compared with thermal energy because the energy level shifts that result from convenient size fields are typically considerably smaller than  $k_B T$  for  $T = 1$  K. Neutral atom trapping therefore depends on substantial cooling of a thermal atomic sample, and is often connected with the cooling process.

The small depth of neutral atom traps also dictates stringent vacuum requirements, because an atom cannot remain trapped after a collision with a thermal energy background gas molecule. Since these atoms are vulnerable targets for thermal energy background gas, the mean free time between collisions must exceed the desired trapping time. The cross section for destructive collisions is quite large because even a gentle collision (i.e., large impact parameter) can impart enough energy to eject an atom from a trap. At pressure  $P$  sufficiently low to be of practical interest, the trapping time is  $\sim(10^{-8}/P)$  s, where  $P$  is in Torr.

### Magnetic Traps

An atom with a magnetic moment  $\vec{\mu}$  can be confined by an inhomogeneous magnetic field because of an interaction between the moment and the field. This produces a force given by  $\vec{F} = \vec{\nabla}(\vec{\mu} \cdot \vec{B})$ . Several different magnetic traps with varying geometries that exploit this force have been studied in some detail, and their general features have been presented.<sup>25</sup> The simplest magnetic trap is a quadrupole comprised of two identical coils carrying opposite currents (see Fig. 10) that has a single center where the field is zero. When the coils are separated by 1.25 times their radius, such a trap has equal depth in the radial ( $x$ - $y$  plane) and longitudinal ( $z$ -axis) directions.<sup>25</sup> Its experimental simplicity makes it most attractive, both because of ease of construction and of optical access to the interior. Such a trap was used in the first neutral atom trapping experiments at NIST.

The magnitude of the field is zero at the center of this trap, and increases in all directions as  $B = A\sqrt{\rho^2 + 4z^2}$ , where  $\rho^2 \equiv x^2 + y^2$ , and the field gradient  $A$  is constant. The field gradient is fixed along any line through the origin, but has different values in different polar directions. Therefore the



**FIGURE 10** Schematic diagram of the coil configuration used in the quadrupole trap and the resultant magnetic field lines. Because the currents in the two coils are in opposite directions, there is a  $|\vec{B}|=0$  point at the center.

force that confines the atoms in the trap is neither harmonic nor central, and angular momentum is not conserved. There are several motivations for studying the motion of atoms in a magnetic trap. Knowing their positions may be important for trapped atom spectroscopy. Moreover, simply studying the motion for its own sake has turned out to be an interesting problem because the distorted conical potential of the quadrupole trap does not have analytic solutions, and its bound states are not well known. For the two-coil quadrupole magnetic trap of Fig. 10, stable circular orbits can be found classically.<sup>1</sup> The fastest trappable atoms in circular orbits have  $v_{\max} \sim 1$  m/s, so the orbital frequency becomes  $\omega_r/2\pi \sim 20$  Hz. Because of the anharmonicity of the potential, the orbital frequencies depend on the orbit size, but in general, atoms in lower energy orbits have higher frequencies.

Because of the dependence of the trapping force on the angle between the field and the atomic moment the orientation of the magnetic moment with respect to the field must be preserved as the atoms move about in the trap. This requires velocities low enough to ensure that the interaction between the atomic moment  $\vec{\mu}$  and the field  $\vec{B}$  is adiabatic, especially when the atom's path passes through a region where the field magnitude is small. This is especially critical at the low temperatures of the Bose condensation experiments. Therefore energy considerations that focus only on the trap depth are not sufficient to determine the stability of a neutral atom trap: orbit and/or quantum state calculations and their consequences must also be considered.

The condition for adiabatic motion can be written as  $\omega_z \gg |dB/dt|/B$ , where  $\omega_z = \mu B/\hbar$  is the Larmor precession rate in the field. The orbital frequency for circular motion is  $\omega_r = v/\rho$ , and since  $v/\rho = |dB/dt|/B$  for a uniform field gradient, the adiabaticity condition is  $\omega_z \gg \omega_r$ . For the two-coil quadrupole trap, the adiabaticity condition can be easily calculated.<sup>1</sup> A practical trap ( $A \sim 1$  T/m) requires  $\rho \gg 1 \mu\text{m}$  as well as  $v \gg 1$  cm/s. Note that violation of these conditions results in the onset of quantum dynamics for the motion (deBroglie wavelength  $\approx$  orbit size). Since the nonadiabatic region of the trap is so small (less than  $10^{-18}$  m<sup>3</sup> compared with typical sizes of  $\sim 2$  cm corresponding to  $10^{-5}$  m<sup>3</sup>), nearly all the orbits of most atoms are restricted to regions where they are adiabatic.

Modern techniques of laser and evaporative cooling have the capability to cool atoms to energies where their deBroglie wavelengths are on the micron scale. Such cold atoms may be readily confined to micron-size regions in magnetic traps with easily achievable field gradients, and in such cases, the notion of classical orbits is inappropriate. The motional dynamics must be described in terms of quantum mechanical variables and suitable wave functions. Furthermore, the distribution of atoms confined in various quantum states of motion in quadrupole as well as other magnetic traps is critical for interpreting the measurements on Bose condensates.

Studying the behavior of extremely slow (cold) atoms in the two-coil quadrupole trap begins with a heuristic quantization of the orbital angular momentum using  $Mr^2\omega_r = n\hbar$  for circular orbits.<sup>1</sup> For velocities of optically cooled atoms of a few cm/s,  $n \sim 10 - 100$ . By contrast, evaporative cooling<sup>21</sup> can produce velocities  $\sim 1$  mm/s resulting in  $n \sim 1$ . It is readily found that  $\omega_z = n\omega_r$ , so that

the adiabatic condition is satisfied only for  $n \gg 1$ . The separation of the rapid precession from the slower orbital motion is reminiscent of the Born-Oppenheimer approximation for molecules, and three-dimensional quantum calculations have also been described.<sup>1</sup>

## Optical Traps

Optical trapping of neutral atoms by electrical interaction must proceed by inducing a dipole moment. For dipole optical traps, the oscillating electric field of a laser induces an oscillating atomic electric dipole moment that interacts with the laser field. If the laser field is spatially inhomogeneous, the interaction and associated energy level shift of the atoms varies in space and therefore produces a potential. When the laser frequency is tuned below atomic resonance ( $\delta < 0$ ), the sign of the interaction is such that atoms are attracted to the maximum of laser field intensity, whereas if  $\delta > 0$ , the attraction is to the minimum of field intensity.

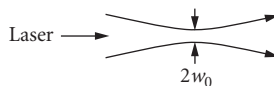
The simplest imaginable trap (see Fig. 11) consists of a single, strongly focused Gaussian laser beam<sup>26,27</sup> whose intensity at the focus varies transversely with  $r$  as  $I(r) = I_0 e^{-2r^2/w_0^2}$ , where  $w_0$  is the beam waist size. Such a trap has a well-studied and important macroscopic classical analog in a phenomenon called *optical tweezers*.<sup>28–30</sup> With the laser light tuned below resonance ( $\delta < 0$ ), the ground-state light shift is everywhere negative, but is largest at the center of the Gaussian beam waist. Ground-state atoms therefore experience a force attracting them toward this center given by the gradient of the light shift. In the longitudinal direction there is also an attractive force that depends on the details of the focusing. Thus this trap produces an attractive force on atoms in three dimensions.

The first optical trap was demonstrated in Na with light detuned below the D-lines.<sup>27</sup> With 220 mW of dye laser light tuned about 650 GHz below the Na transition and focused to a  $\sim 10 \mu\text{m}$  waist, the trap depth was about  $15\hbar\gamma$  corresponding to 7 mK. Single-beam dipole force traps can be made with the light detuned by a significant fraction of its frequency from the atomic transition. Such a far-off-resonance trap (FORT) has been developed for Rb atoms using light detuned by nearly 10 percent to the red of the  $D_1$  transition at  $\lambda = 795 \text{ nm}$ .<sup>31</sup> Between 0.5 and 1 W of power was focused to a spot about  $10 \mu\text{m}$  in size, resulting in a trap 6 mK deep where the light scattering rate was only a few hundred/s. The trap lifetime was more than half a second.

The dipole force for blue light repels atoms from the high-intensity region, and offers the advantage that trapped atoms will be confined where the perturbations of the light field are minimized.<sup>1</sup> On the other hand, it is not as easy to produce hollow light beams compared with Gaussian beams, and special optical techniques need to be employed.

In a standing wave the light intensity varies from zero at a node to a maximum at an antinode in a distance of  $\lambda/4$ . Since the light shift, and thus the optical potential, vary on this same scale, it is possible to confine atoms in wavelength-size regions of space. Of course, such tiny traps are usually very shallow, so loading them requires cooling to the  $\mu\text{K}$  regime. The momentum of such cold atoms is then so small that their deBroglie wavelengths are comparable to the optical wavelength, and hence to the trap size. In fact, the deBroglie wavelength equals the size of the optical traps ( $\lambda/2$ ) when the momentum is  $2\hbar k$ , corresponding to a kinetic energy of a few  $\mu\text{K}$ . Thus the atomic motion in the trapping volume is not classical, but must be described quantum mechanically. Even atoms whose energy exceeds the trap depth must be described as quantum mechanical particles moving in a periodic potential that display energy band structure.<sup>32</sup>

Atoms trapped in wavelength-sized spaces occupy vibrational levels similar to those of molecules. The optical spectrum can show Raman-like sidebands that result from transitions among the



**FIGURE 11** A single focused laser beam produces the simplest type of optical trap.

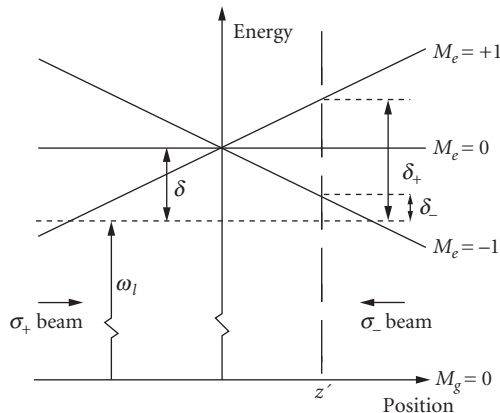
quantized vibrational levels<sup>33,34</sup> as shown in Fig. 19. These quantum states of atomic motion can also be observed by spontaneous or stimulated emission.<sup>33,35</sup> Considerably more detail about atoms in such optical lattices is to be found in Ref. 34.

## Magneto-Optical Traps

The most widely used trap for neutral atoms is a hybrid, employing both optical and magnetic fields. The resultant *magneto-optical trap* (MOT) was first demonstrated in 1987.<sup>36</sup> The operation of an MOT depends on both inhomogeneous magnetic fields and radiative selection rules to exploit both optical pumping and the strong radiative force.<sup>1,36</sup> The radiative interaction provides cooling that helps in loading the trap, and enables very easy operation. The MOT is a very robust trap that does not depend on precise balancing of the counter-propagating laser beams or on a very high degree of polarization. The magnetic field gradients are modest and can readily be achieved with simple, air-cooled coils. The trap is easy to construct because it can be operated with a room-temperature cell where alkali atoms are captured from the vapor. Furthermore, low-cost diode lasers can be used to produce the light appropriate for all the alkalis except Na, so the MOT has become one of the least expensive ways to produce atomic samples with temperatures below 1 mK. For these and other reasons it has become the workhorse of cold atom physics, and has also appeared in dozens of undergraduate laboratories.

Trapping in an MOT works by optical pumping of slowly moving atoms in a linearly inhomogeneous magnetic field  $B = B(z) \equiv Az$ , such as that formed by a magnetic quadrupole field. Atomic transitions with the simple scheme of  $J_g = 0 \rightarrow J_e = 1$  have three Zeeman components in a magnetic field, excited by each of three polarizations, whose frequencies tune with field (and therefore with position) as shown in Fig. 12 for one dimension. Two counter-propagating laser beams of opposite circular polarization, each detuned below the zero field atomic resonance by  $\delta$ , are incident as shown.

Because of the Zeeman shift, the excited state  $M_e = +1$  is shifted up for  $B > 0$ , whereas the state with  $M_e = -1$  is shifted down. At position  $z = z'$  in Fig. 12 the magnetic field therefore tunes the



**FIGURE 12** Arrangement for a magneto-optical trap (MOT) in 1D. The horizontal dashed line represents the laser frequency seen by an atom at rest in the center of the trap. Because of the Zeeman shifts of the atomic transition frequencies in the inhomogeneous magnetic field, atoms at  $z = z'$  are closer to resonance with the  $\sigma^-$  laser beam than with the  $\sigma^+$  beam, and are therefore driven toward the center of the trap.

$\Delta M = -1$  transition closer to resonance and the  $\Delta M = +1$  transition further out of resonance. If the polarization of the laser beam incident from the right is chosen to be  $\sigma^-$  and correspondingly  $\sigma^+$  for the other beam, then more light is scattered from the  $\sigma^-$  beam than from the  $\sigma^+$  beam. Thus the atoms are driven toward the center of the trap, where the magnetic field is zero. On the other side of the center of the trap, the roles of the  $M_e = \pm 1$  states are reversed, and now more light is scattered from the  $\sigma^+$  beam, again driving the atoms toward the center.

The situation is analogous to the velocity damping in an optical molasses from the Doppler effect as previously discussed, but here the effect operates in position space, whereas for molasses it operates in velocity space. Since the laser light is detuned below the atomic resonance in both cases, compression and cooling of the atoms is obtained simultaneously in an MOT.

For a description of the motion of the atoms in an MOT, consider the radiative force in the low-intensity limit [see Eq. (10)]. The total force on the atoms is given by  $\vec{F} = \vec{F}_+ + \vec{F}_-$ , where

$$\vec{F}_{\pm} = \pm \frac{\hbar \vec{k} \gamma}{2} \frac{s_0}{1 + s_0 + (2\delta_{\pm}/\gamma)^2} \quad (31)$$

and the detuning  $\delta_{\pm}$  for each laser beam is given by

$$\delta_{\pm} = \delta \mp \vec{k} \cdot \vec{v} \pm \mu' B / \hbar \quad (32)$$

Here  $\mu' \equiv (g_e M_e - g_g M_g) \mu_B$  is the effective magnetic moment for the transition used. Note that the Doppler shift  $\omega_D \equiv -\vec{k} \cdot \vec{v}$  and the Zeeman shift  $\omega_z = \mu' B / \hbar$  both have opposite signs for opposite beams.

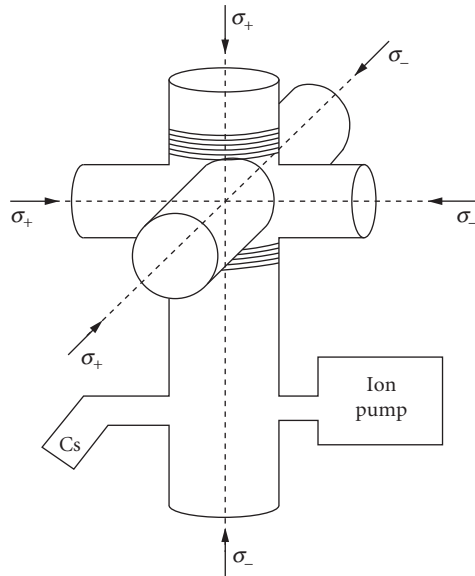
When both the Doppler and Zeeman shifts are small compared to the detuning  $\delta$ , the denominator of the force can be expanded and the result becomes  $\vec{F} = -\beta \vec{v} - \kappa \vec{r}$ , where  $\beta$  is the damping coefficient. The spring constant  $\kappa$  arises from the similar dependence of  $\vec{F}$  on the Doppler and Zeeman shifts, and is given by  $\kappa = \mu' A \beta / \hbar k$ . This force leads to damped harmonic motion of the atoms, where the damping rate is given by  $\Gamma_{\text{MOT}} = \beta / M$  and the oscillation frequency  $\omega_{\text{MOT}} = \sqrt{\kappa / M}$ . For magnetic field gradients  $A \approx 10$  G/cm, the oscillation frequency is typically a few kHz, and this is much smaller than the damping rate that is typically a few hundred kHz. Thus the motion is overdamped, with a characteristic restoring time to the center of the trap of  $2\Gamma_{\text{MOT}} / \omega_{\text{MOT}}^2 \sim$  several ms for typical values of the detuning and intensity of the lasers.

Since the MOT constants  $\beta$  and  $\kappa$  are proportional, the size of the atomic cloud can easily be deduced from the temperature of the sample. The equipartition of the energy of the system over the degrees of freedom requires that the velocity spread and the position spread are related by  $k_B T = m v_{\text{rms}}^2 = \kappa z_{\text{rms}}^2$ . For a temperature in the range of the Doppler temperature, the size of the MOT should be of the order of a few tenths of a mm, which is generally the case in experiments.

So far the discussion has been limited to the motion of atoms in one dimension. However, the MOT scheme can easily be extended to 3D by using six instead of two laser beams (see Fig. 13). Furthermore, even though very few atomic species have transitions as simple as  $J_g = 0 \rightarrow J_e = 1$ , the scheme works for any  $J_g \rightarrow J_e = J_g + 1$  transition. Atoms that scatter mainly from the  $\sigma^+$  laser beam will be optically pumped toward the  $M_g = +J_g$  substate, which forms a closed system with the  $M_e = +J_e$  substate.

The atomic density in an MOT cannot increase without limit as more atoms are added. The density is limited to  $\sim 10^{11}/\text{cm}^3$  because the fluorescent light emitted by some trapped atoms is absorbed by others, and this diffusion of radiation presents a repulsive force between the atoms.<sup>37,38</sup> Another limitation lies in the collisions between the atoms, and the collision rate for excited atoms is much larger than for ground-state atoms. Adding atoms to an MOT thus increases the density up to some point, but adding more atoms then expands the volume of the trapped sample.





**FIGURE 13** The schematic diagram of an MOT shows the coils and the directions of polarization of the six light beams. It has an axial symmetry and various rotational symmetries, so some exchanges would still result in a trap that works, but not all configurations are possible. Atoms are trapped from the background vapor of Cs that arises from a piece of solid Cs in one of the arms of the setup.

## 20.8 APPLICATIONS

### Introduction

The techniques of laser cooling and trapping as described in the previous sections have been used to manipulate the positions and velocities of atoms with unprecedented variety and precision.<sup>1</sup> These techniques are currently used in the laboratories to design new, highly sensitive experiments that move experimental atomic physics research to completely new regimes. In this section only of few of these topics will be discussed. One of the most straightforward of these is the use of laser cooling to increase the brightness of atomic beams, which can subsequently be used for different types of experiments. Since laser cooling produces atoms at very low temperatures, the interaction between these atoms also takes place at such very low energies. The study of these interactions, called *ultra-cold collisions*, has been a very fruitful area of research in the last decade.

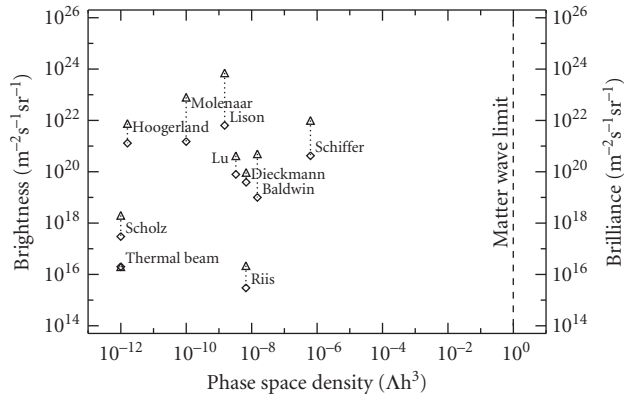
The atom-laser interaction not only produces a viscous environment for cooling the atoms down to very low velocities, but also provides a trapping field for the atoms. In the case of interfering laser beams, the size of such traps can be of the order of a wavelength, thus providing microscopic atomic traps with a periodic structure. These optical lattices described later in this section provide a versatile playground to study the effects of a periodic potential on the motion of atoms and thus simulate the physics of condensed matter. Another topic of considerable interest that will be discussed exists only because laser cooling has paved the way to the observation of Bose-Einstein condensation. This was predicted theoretically more than 80 years ago, but was observed in a dilute gas for the first time in 1996. Finally, the physics of dark states is also discussed in this section. These show a rich variety of effects caused by the coupling of internal and external coordinates of atoms.

## Atomic Beam Brightening

In considering the utility of atomic beams for the purposes of lithography, collision studies, or a host of other applications, maximizing the beam intensity may not be the best option. Laser cooling can be used for increasing the phase space density, and this notion applies to both atomic traps and atomic beams. In the case of atomic beams, other quantities than phase space density have been defined as well, but these are not always consistently used. The geometrical solid angle occupied by atoms in a beam is  $\Delta\Omega = (\Delta v_{\perp} \sqrt{v})^2$ , where  $\bar{v}$  is some measure of the longitudinal velocity of atoms in the beam and  $\Delta v_{\perp}$  is a measure of the width of the transverse velocity distribution of the atoms. The total current or flux of the beam is  $\Phi$ , and the flux density or intensity is  $\Phi/\pi(\Delta x)^2$  where  $\Delta x$  is a measure of the beam's radius. Then the beam brightness or radiance  $R$  is given by  $R = \Phi/\pi(\lambda x_{\perp})^2 \Delta\Omega$ . Optical beams are often characterized by their frequency spread, and, because of the deBroglie relation  $\lambda = h/p$ , the appropriate analogy for atomic beams is the longitudinal velocity spread. Thus the spectral brightness or brilliance  $B$  is given by  $B = R\bar{v}/\Delta v_z$ . Note that both  $R$  and  $B$  have the same dimensions as flux density, and this is often a source of confusion. Finally,  $B$  is simply related to the 6D phase space density. Recently a summary of these beam properties has been presented in the context of phase space (see Fig. 14).

One of the first beam-brightening experiments was performed by Nellesen et al.<sup>39,40</sup> where a thermal beam of Na was slowed with the chirp technique.<sup>1</sup> Then the slow atoms were deflected out of the main atomic beam and transversely cooled. In a later experiment<sup>41</sup> this beam was fed into a two-dimensional MOT where the atoms were cooled and compressed in the transverse direction by an optical molasses of  $\sigma^+ - \sigma^-$  polarized light. Another approach was used by Riis et al. who directed a slowed atomic beam into a hairpin-shaped coil that they called an *atomic funnel*.<sup>42</sup> The wires of this coil generated a two-dimensional quadrupole field that was used as a two-dimensional MOT as described before.

These approaches yield intense beams when the number of atoms in the uncooled beam is already high. However, if the density in the beam is initially low, for example in the case of metastable noble gases or radioactive isotopes, one has to capture more atoms from the source in order



**FIGURE 14** Plot of brightness (diamonds) and brilliance (triangles) versus phase space density for various atomic beams cited in the literature. The lower-left point is for a normal thermal beam, and the progression toward the top and right has been steady since the advent of laser cooling. The experimental results are from Riis et al.,<sup>42</sup> Scholz et al.,<sup>80</sup> Hoogerland et al.,<sup>44</sup> Lu et al.,<sup>81</sup> Baldwin et al.,<sup>82</sup> Molenaar et al.,<sup>78</sup> Schiffer et al.,<sup>83</sup> Lison et al.,<sup>84</sup> and Dieckmann et al.<sup>85</sup> The quantum boundary for Bose-Einstein condensation, where the phase space density is unity, is shown by the dashed line on the right. (Figure adapted from Ref. 84.)

to obtain an intense beam. Aspect et al.<sup>43</sup> have used a quasi-standing wave of converging laser beams whose incidence angle varied from 87° to 90° to the atomic beam direction, so that a larger solid angle of the source could be captured. In this case they used a few mW of laser light over a distance of 75 mm. One of the most sophisticated approaches to this problem has been developed for metastable Ne by Hoogerland et al.<sup>44</sup> They used a three-stage process to provide a large solid angle capture range and produce a high brightness beam.

## Applications to Atomic Clocks

Perhaps one of the most important practical applications of laser cooling is the improvement of atomic clocks. The limitation to both the accuracy and precision of such clocks is imposed by the thermal motion of the atoms, so a sample of laser-cooled atoms could provide a substantial improvement in clocks and in spectroscopic resolution.

The first experiments intended to provide slower atoms for better precision or clocks were attempts at an atomic fountain by Zacharias in the 1950s.<sup>1,45</sup> This failed because collisions depleted the slow atom population, but the advent of laser cooling enabled an atomic fountain because the slow atoms far outnumber the faster ones. The first rf spectroscopy experiments in such a fountain using laser-cooled atoms were reported in 1989 and 1991,<sup>46,47</sup> and soon after that some other laboratories also reported successes.

Some of the early best results were reported by Gibble and Chu.<sup>48,49</sup> They used an MOT with laser beams 6 cm in diameter to capture Cs atoms from a vapor at room temperature. These atoms were launched upward at 2.5 m/s by varying the frequencies of the MOT lasers to form a moving optical molasses as described in Sec. 20.5, and subsequently cooled to below 3  $\mu$ K. The atoms were optically pumped into one hfs sublevel, then passed through a 9.2-GHz microwave cavity on their way up and again later on their way down. The number of atoms that were driven to change their hfs state by the microwaves was measured versus microwave frequency, and the signal showed the familiar Ramsey oscillations. See Chap. 11, "Coherent Optical Transients," for a discussion of Ramsey fringes. The width of the central feature was 1.4 Hz and the S/N was over 50. Thus the ultimate precision was 1.5 mHz corresponding to  $\delta v/v \cong 10^{-12}/\tau^{1/2}$ , where  $\tau$  is the number of seconds for averaging.

The ultimate limitation to the accuracy of this experiment as an atomic clock was collisions between Cs atoms in the beam. Because of the extremely low relative velocities of the atoms, the cross sections are very large (see the next subsection) and there is a measurable frequency shift.<sup>50</sup> By varying the density of Cs atoms in the fountain, the authors found frequency shifts of the order of a few mHz for atomic density of  $10^9/\text{cm}^3$ , depending on the magnetic sublevels connected by the microwaves. Extrapolation of the data to zero density provided a frequency determination of  $\delta v/v \cong 4 \times 10^{-14}$ . More recently the frequency shift has been used to determine a scattering length of  $-400a_0$ <sup>51</sup> so that the expected frequency shift is  $10^4$  times larger than other limitations to the clock at an atomic density of  $n = 10^9/\text{cm}^3$ . Thus the authors suggest possible improvements to atomic timekeeping of a factor of 1000 in the near future. Even more promising are cold atom clocks in orbit (microgravity) where the interaction time can be very much longer than 1 s.<sup>52</sup>

## Ultracold Collisions

Laser-cooling techniques were developed in the early 1980s for a variety of reasons, such as high-resolution spectroscopy.<sup>1</sup> During the development of the techniques to cool and trap atoms, it became apparent that collisions between cold atoms in optical traps was one of the limiting factors in the achievement of high-density samples. Trap loss experiments revealed that the main loss mechanisms were caused by laser-induced collisions. Further cooling and compression could only be achieved by techniques not exploiting laser light, such as evaporative cooling in magnetic traps. Elastic collisions between atoms in the ground state are essential in that case for the rethermalization of the sample, whereas inelastic collisions lead to destruction of the sample. Knowledge about collision physics at these low energies is therefore essential for the development of high-density samples of atoms using either laser or evaporative cooling techniques.

Ground-state collisions play an important role in evaporative cooling. Such elastic collisions are necessary to obtain a thermalization of the gas after the trap depth has been lowered, and a large elastic cross section is essential to obtain a rapid thermalization. Inelastic collisions, on the other hand, can release enough energy to accelerate the atoms to energies too high to remain trapped. Ground-state collisions for evaporative cooling can be described by one parameter, the scattering length  $a$ . At temperatures below  $T_D$ , these collisions are in the s-wave scattering regime where only the phase shift  $\delta_0$  of the lowest partial wave  $\ell=0$  is important. Moreover, for sufficiently low energies, such collisions are governed by the Wigner threshold laws where the phase shift  $\delta_0$  is inversely proportional to the wavevector  $k$  of the particle motion. Taking the limit for low energy gives the proportionality constant, defined as the scattering length  $a = -\lim_{k \rightarrow 0} (\delta_0/k)$ . The scattering length plays an important role not only in ultracold collisions, but also in the formation of Bose-Einstein condensates. In the Wigner threshold regime the cross section approaches a constant,  $\sigma = 8\pi a^2$ .<sup>53</sup>

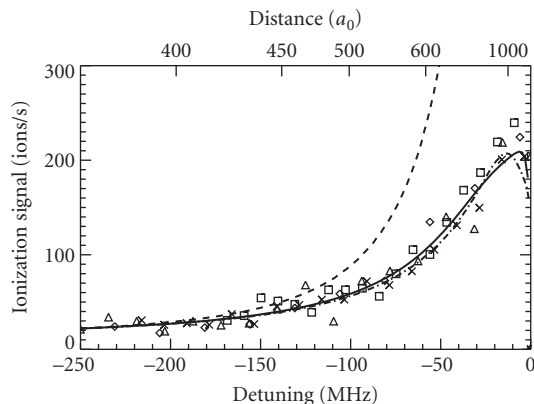
Although ground-state collisions are important for evaporative cooling and BEC, they do *not* provide a very versatile research field from a collision physics point of view. The situation is completely different for the excited-state collisions. For typical temperatures in optical traps, the velocity of the atoms is sufficiently low that atoms excited at long range by laser light decay before the collision takes place. Laser excitation for low-energy collisions has to take place during the collision. By tuning the laser frequency, the collision dynamics can be altered and information on the states formed in the molecular system can be obtained. This is the basis of the new technique of photo-associative spectroscopy, which for the first time has identified purely long-range states in diatomic molecules.<sup>1,54</sup>

For atoms colliding in laser light closely tuned to the S-P transition, the potential is a  $C_3/R^3$  dipole-dipole interaction when one of the atoms is excited. Absorption takes place at the Condon point  $R_C$  given by  $\hbar\delta = -C_3/R_C^3$  or  $R_C = (C_3/\hbar|\delta|)^{1/3}$ . Note that the light has to be tuned below resonance, which is mostly the case for laser cooling. The Condon point for laser light detuned a few  $\gamma$  below resonance is typical 1000 to 2000  $a_0$ .

Once the molecular complex becomes excited, it can evolve to smaller internuclear distances before emission takes place. Two particular cases are important for trap loss: (1) the emission of the molecular complex takes place at much smaller internuclear distance, and the energy gained between absorption and emission of the photon is converted into kinetic energy, or (2) the complex undergoes a transition to another state and the potential energy difference between the two states is converted into kinetic energy. In both cases the energy gain can be sufficient to eject one or both atoms out of the trap. In the case of the alkalis, the second reaction can take place because of the different fine-structure states and the reaction is denoted as a fine-structure changing collision. The first reaction is referred to as *radiative escape*.

Trap loss collisions in MOTs have been studied to great extent, but results of these studies have to be considered with care. In most cases, trap loss is studied by changing either the frequency or the intensity of the trapping laser, which also changes the conditions of the trap. The collision rate is not only changed because of a change in the collision cross section, but also because of changes in both the density and temperature of the atoms in the trap. Since these parameters cannot be determined with high accuracy in a high-density trap, where effects like radiation trapping can play an important role, obtaining accurate results this way is very difficult.

The first description of such processes was given by Gallagher and Pritchard.<sup>55</sup> In their semiclassical model (the GP-model), the laser light is assumed to be weak enough that the excitation rate can be described by a quasi-static excitation probability. Atoms in the excited state are accelerated toward one another by the  $C_3/R^3$  potential. In order to calculate the survival of the atoms in the excited state, the elapsed time between excitation and arrival is calculated. The total number of collisions is then given by the number of atoms at a certain distance, the fraction of atoms in the excited state, and the survival rate, integrated over all distances. For small detunings, corresponding to large internuclear distances, the excitation rate is appreciable over a very large range of internuclear distances. However the excitation occurs at large internuclear distances, so the survival rate of the excited atoms is small. For large detunings the excitation is located in a small region at small internuclear distances, so the total excitation rate is small, but the survival rate is large. As a result of this competition, the collision rate peaks at intermediate detunings.



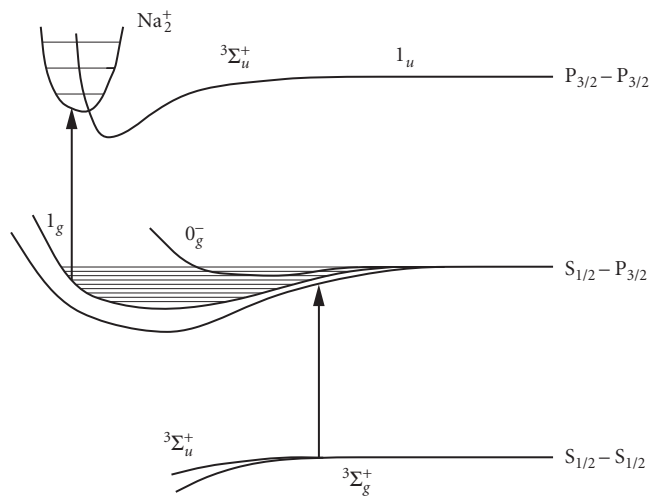
**FIGURE 15** The frequency dependence for the associative ionization rate of cold  $\text{He}^+$  collisions. The experimental results (symbols) are compared with the semiclassical model (solid line), JV-model (dashed line), and modified JV-model (dashed-dotted line). The axis on top of the plot shows the Condon point, where the excitation takes place.

Another description of optical collisions is given by Julienne and Vigue.<sup>56</sup> Their description of optical collisions (JV model) is quantum mechanical for the collision process, where they make a partial wave expansion of the incoming wavefunction. The authors describe the excitation process in the same way as it was done in the GP model. Thus the excitation is localized around the Condon point with a probability given by the quasi-static Lorentz formula.

In still another approach, a completely semiclassical description of optical collisions has been given by Mastwijk et al.<sup>57</sup> These authors start from the GP model, but make several important modifications. First, the Lorentz formula is replaced by the Landau-Zener formula. Second, the authors consider the motion of the atoms in the collision plane. At the Condon point, where the excitation takes place, the trajectory of the atom in the excited state is calculated by integration of the equation of motion. The results for their model are shown in Fig. 15, and are compared with experiment and the JV model. The agreement between the theory and experiment is rather good. For the JV model two curves are shown. The first curve shows the situation for the original JV model. The second curve shows the result of a modified JV model, where the quasi-static excitation rate is replaced by the Landau-Zener formula. The large discrepancies between the results for these two models indicates that it is important to use the correct model for the excitation. The agreement between the modified JV model and the semiclassical model is good, indicating that the dynamics of optical collisions can be described correctly quantum mechanically or semiclassically. Since the number of partial waves in the case of  $\text{He}^+$  is in the order of 10, this is to be expected.

The previous description of optical collisions applies to the situation that the quasi-molecule can be excited for each frequency of the laser light. However, the quasi-molecule has well-defined vibrational and rotational states and the excitation frequency has to match the transition frequency between the ground and excited rovibrational states. Far from the dissociation limit, the rovibrational states are well-resolved and many resonances are observed. This has been the basis of the method of photo-associative spectroscopy (PAS) for alkali-metal atoms, where detailed information on molecular states of alkali dimers have been obtained recently. Here *photo-association* refers to the process where a photon is absorbed to transfer the system from the ground to the excited state where the two atoms are bound by their mutual attraction.

The process of PAS is depicted graphically in Fig. 16. When two atoms collide in the ground state, they can be excited at a certain internuclear distance to the excited molecular state and the two atoms may remain bound after the excitation and form a molecule. This transient molecule lives as long as the system remains excited. The number of rotational states that can contribute to the spectrum is



**FIGURE 16** Photoassociation spectroscopy of Na. By tuning the laser below atomic resonance, molecular systems can be excited to the first excited state in which they are bound. By absorption of a second photon the system can be ionized, providing a high detection efficiency.

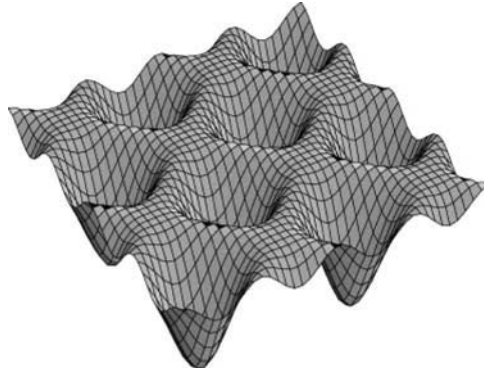
small for low temperature. The resolution is limited only by the linewidth of the transition, which is comparable to the natural linewidth of the atomic transition. With PAS, molecular states can be detected with a resolution of  $\approx 10$  MHz, which is many orders of magnitude better than traditional molecular spectroscopy. The formation of the molecules is probed by absorption of a second photon of the same color, which can ionize the molecule.

PAS has also been discussed in the literature as a technique to produce cold molecules. The methods discussed employ a double resonance technique, where the first color is used to create a well-defined rovibrational state of the molecule and a second color causes stimulated emission of the system to a well-defined vibrational level in the ground state. Although such a technique has not yet been shown to work experimentally, cold molecules have been produced in PAS recently using a simpler method.<sup>58</sup> The  $0_g^-$  state in  $\text{Cs}_2$  has a double-well structure, where the top of the barrier is accidentally close to the asymptotic limit. Thus atoms created in the outer well by PAS can tunnel through the barrier to the inner well, where there is a large overlap of the wavefunction with the vibrational levels in the ground state. These molecules are then stabilized against spontaneous decay and can be observed. The temperature of the cold molecules has been detected and is close to the temperature of the atoms. This technique and similar techniques will be very important for the production and study of cold molecules.

## Optical Lattices

In 1968, Letokhov<sup>59</sup> suggested that it is possible to confine atoms in the wavelength-size regions of a standing wave by means of the dipole force that arises from the light shift. This was first accomplished in 1987 in one dimension with an atomic beam traversing an intense standing wave.<sup>60</sup> Since then, the study of atoms confined in wavelength-size potential wells has become an important topic in optical control of atomic motion because it opens up configurations previously accessible only in condensed matter physics using crystals.

The basic ideas of the quantum mechanical motion of particles in a periodic potential were laid out in the 1930s with the Kronig-Penney model and Bloch's theorem, and optical lattices offer important opportunities for their study. For example, these lattices can be made essentially free of



**FIGURE 17** The “egg-crate” potential of an optical lattice shown in two dimensions. The potential wells are separated by  $\lambda/2$ .

defects with only moderate care in spatially filtering the laser beams to assure a single transverse mode structure. Furthermore, the shape of the potential is exactly known, and doesn't depend on the effect of the crystal field or the ionic energy level scheme. Finally, the laser parameters can be varied to modify the depth of the potential wells without changing the lattice vectors, and the lattice vectors can be changed independently by redirecting the laser beams. The simplest optical lattice to consider is a one-dimensional pair of counter-propagating beams of the same polarization, as was used in the first experiment.<sup>60</sup>

Because of the transverse nature of light, any mixture of beams with different  $\vec{k}$ -vectors necessarily produces a spatially periodic, inhomogeneous light field. The importance of the “egg-crate” array of potential wells arises because the associated atomic light shifts can easily be comparable to the very low average atomic kinetic energy of laser-cooled atoms. A typical example projected against two dimensions is shown in Fig. 17.

The name *optical lattice* is used rather than *optical crystal* because the filling fraction of the lattice sites is typically only a few percent (as of 1999). The limit arises because the loading of atoms into the lattice is typically done from a sample of trapped and cooled atoms, such as an MOT for atom collection, followed by an optical molasses for laser cooling. The atomic density in such experiments is limited to a few times  $10^{11}/\text{cm}^3$  by collisions and multiple light scattering. Since the density of lattice sites of size  $\lambda/2$  is a few times  $10^{13}/\text{cm}^3$ , the filling fraction is necessarily small.

At first thought it would seem that a rectangular 2D or 3D optical lattice could be readily constructed from two or three mutually perpendicular standing waves.<sup>61,62</sup> However, a sub-wavelength movement of a mirror caused by a small vibration could change the relative phase of the standing waves. In 1993 a very clever scheme was described.<sup>63</sup> It was realized that an  $N$ -dimensional lattice could be created by only  $n + 1$  traveling waves rather than  $2n$ . Instead of producing optical wells in 2D with four beams (two standing waves), these authors used only three. The  $\vec{k}$ -vectors of the coplanar beams were separated by  $2\pi/3$ , and they were all linearly polarized in their common plane (not parallel to one another). The same immunity to vibrations was established for a 3D optical lattice by using only four beams arranged in a quasi-tetrahedral configuration. The three linearly polarized beams of the 2D arrangement just described were directed out of the plane toward a common vertex, and a fourth circularly polarized beam was added. All four beams were polarized in the same plane.<sup>63</sup> The authors showed that such a configuration produced the desired potential wells in 3D.

The NIST group studied atoms loaded into an optical lattice using Bragg diffraction of laser light from the spatially ordered array.<sup>64</sup> They cut off the laser beams that formed the lattice, and before the atoms had time to move away from their positions, they pulsed on a probe laser beam at the Bragg angle appropriate for one of the sets of lattice planes. The Bragg diffraction not only enhanced the reflection of the probe beam by a factor of  $10^5$ , but by varying the time between the shut-off of the lattice and turn-on of the probe, they could measure the “temperature” of the atoms

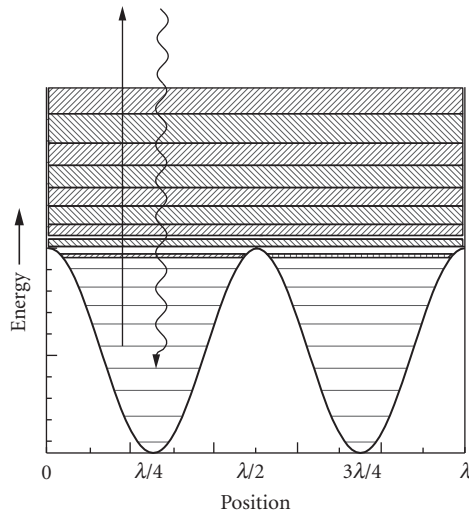
in the lattice. The reduction of the amplitude of the Bragg scattered beam with time provided some measure of the diffusion of the atoms away from the lattice sites, much like the Debye-Waller factor in X-ray diffraction.

Laser cooling has brought the study of the motion of atoms into an entirely new domain where the quantum mechanical nature of their center-of-mass motion must be considered.<sup>1</sup> Such exotic behavior for the motion of whole atoms, as opposed to electrons in the atoms, has not been considered before the advent of laser cooling simply because it is too far out of the range of ordinary experiments. A series of experiments in the early 1990s provided dramatic evidence for these new quantum states of motion of neutral atoms, and led to the debut of de Broglie wave atom optics.

The limits of laser cooling discussed in Sec. 20.6 suggest that atomic momenta can be reduced to a “few” times  $\hbar k$ . This means that their de Broglie wavelengths are equal to the optical wavelengths divided by a “few.” If the depth of the optical potential wells is high enough to contain such very slow atoms, then their motion in potential wells of size  $\lambda/2$  must be described quantum mechanically, since they are confined to a space of size comparable to their de Broglie wavelengths. Thus they do not oscillate in the sinusoidal wells as classical localizable particles, but instead occupy discrete, quantum-mechanical bound states, as shown in the lower part of Fig. 18.

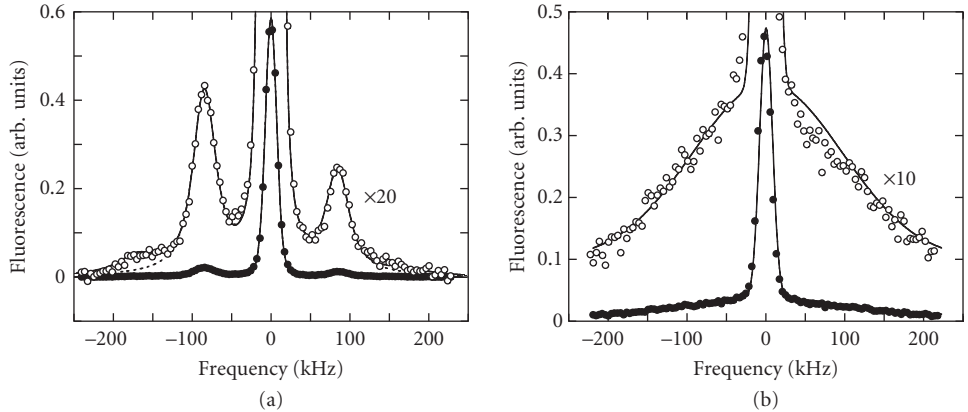
The group at NIST also developed a new method that superposed a weak probe beam of light directly from the laser upon some of the fluorescent light from the atoms in a 3D optical molasses, and directed the light from these combined sources onto a fast photodetector.<sup>65</sup> The resulting beat signal carried information about the Doppler shifts of the atoms in the optical lattices.<sup>34</sup> These Doppler shifts were expected to be in the sub-MHz range for atoms with the previously measured 50  $\mu\text{K}$  temperatures. The observed features confirmed the quantum nature of the motion of atoms in the wavelength-size potential wells (see Fig. 19).<sup>16</sup>

In the 1930s Bloch realized that applying a uniform force to a particle in a periodic potential would not accelerate it beyond a certain speed, but instead would result in Bragg reflection when its



**FIGURE 18** Energy levels of atoms moving in the periodic potential of the light shift in a standing wave. There are discrete bound states deep in the wells that broaden at higher energy, and become bands separated by forbidden energies above the tops of the wells. Under conditions appropriate to laser cooling, optical pumping among these states favors populating the lowest ones as indicated schematically by the arrows.

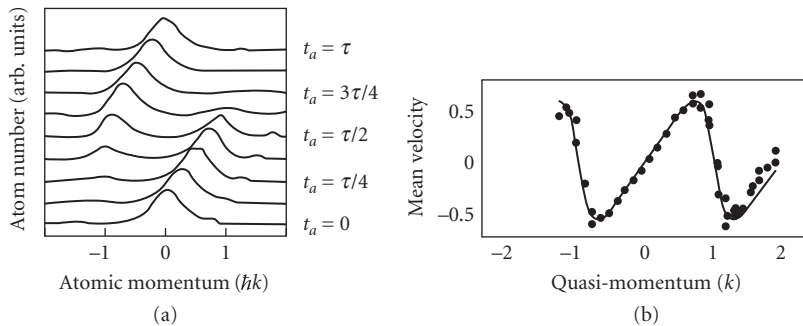




**FIGURE 19** (a) Fluorescence spectrum in a 1D lin  $\perp$  lin optical molasses. Atoms are first captured and cooled in an MOT, then the MOT light beams are switched off leaving a pair of lin  $\perp$  lin beams. Then the measurements are made with  $\delta = -4\gamma$  at low intensity. (b) Same as (a) except the 1D molasses is  $\sigma^+ - \sigma^-$  which has no spatially dependent light shift and hence no vibrational motion. (Figure from Ref. 34.)

de Broglie wavelength became equal to the lattice period. Thus an electric field applied to a conductor could not accelerate electrons to a speed faster than that corresponding to the edge of a Brillouin zone, and that at longer times the particles would execute oscillatory motion. Ever since then, experimentalists have tried to observe these Bloch oscillations in increasingly pure and/or defect-free crystals.

Atoms moving in optical lattices are ideally suited for such an experiment, as was beautifully demonstrated in 1996.<sup>66</sup> The authors loaded a one-dimensional lattice with atoms from a 3D molasses, further narrowed the velocity distribution, and then instead of applying a constant force, simply changed the frequency of one of the beams of the 1D lattice with respect to the other in a controlled way, thereby creating an accelerating lattice. Seen from the atomic reference frame, this was the equivalent of a constant force trying to accelerate them. After a variable time  $t_a$  the 1D lattice beams were shut off and the measured atomic velocity distribution showed beautiful Bloch oscillations as a function of  $t_a$ . The centroid of the very narrow velocity distribution was seen to shift in velocity space at a constant rate until it reached  $v_r = \hbar k/M$ , and then it vanished and reappeared at  $-v_r$  as shown in Fig. 20. The shape of the “dispersion curve” allowed measurement of the “effective mass” of the atoms bound in the lattice.



**FIGURE 20** Plot of the measured velocity distribution versus time in the accelerated 1D lattice. The atoms accelerate only to the edge of the Brillouin zone where the velocity is  $+v_r$  and then the velocity distribution appears at  $-v_r$ . (Figure from Ref. 66.)

## Bose-Einstein Condensation

In 1924 S. Bose found the correct way to evaluate the distribution of identical entities, such as Planck's radiation quanta, that allowed him to calculate the Planck spectrum using the methods of statistical mechanics. Within a year Einstein had seized upon this idea, and generalized it to identical particles with discrete energies. This distribution is

$$N(E) = \frac{1}{e^{\beta(E-\mu)} - 1} \quad (33)$$

where  $\beta \equiv 1/k_B T$  and  $\mu$  is the chemical potential that vanishes for photons: Eq. (33) with  $\mu = 0$  is exactly the Planck distribution. Einstein observed that this distribution has the peculiar property that for sufficiently low average energy (i.e., low temperature), the total energy could be minimized by having a discontinuity in the distribution for the population of the lowest allowed state.

The condition for this Bose-Einstein condensation (BEC) in a gas can be expressed in terms of the de Broglie wavelength  $\lambda_{\text{dB}}$  associated with the thermal motion of the atoms as  $n\lambda_{\text{dB}}^3 \geq 2.612\dots$ , where  $n$  is the spatial density of the atoms. In essence, this means that the atomic wave functions must overlap one another.

The most familiar elementary textbook description of BEC focuses on noninteracting particles. However, particles *do* interact, and the lowest order approximation that is widely used to account for the interaction takes the form of a mean-field repulsive force. It is inserted into the Hamiltonian for the motion of each atom in the trap (*n.b.*, not for the internal structure of the atom) as a term  $V_{\text{int}}$  proportional to the local density of atoms. Since this local density is itself  $|\Psi|^2$ , it makes the Schrödinger equation for the atomic motion nonlinear, and the result bears the name *Gross-Pitaevski equation*. For  $N$  atoms in the condensate it is written

$$\left[ -\frac{\hbar^2}{2M} \nabla_{\vec{R}}^2 + V_{\text{trap}}(\vec{R}) + NV_{\text{int}} |\Psi(\vec{R})|^2 \right] \Psi(\vec{R}) = E_N \Psi(\vec{R}) \quad (34)$$

where  $\vec{R}$  is the coordinate of the atom in the trap,  $V_{\text{trap}}(\vec{R})$  is the potential associated with the trap that confines the atoms in the BEC, and  $V_{\text{int}} \equiv 4\pi\hbar^2 a/M$  is the coefficient associated with strength of the mean field interaction between the atoms. Here  $a$  is the scattering length, and  $M$  is the atomic mass.

For  $a > 0$  the interaction is repulsive so that a BEC would tend to disperse. This is manifest for a BEC confined in a harmonic trap by having its wavefunction somewhat more spread out and flatter than a Gaussian. By contrast, for  $a < 0$  the interaction is attractive and the BEC eventually collapses. However, it has been shown that there is metastability for a sufficiently small number of particles with  $a < 0$  in a harmonic trap, and that a BEC can be observed in vapors of atoms with such negative scattering length as  $^7\text{Li}$ .<sup>67-69</sup> This was initially somewhat controversial.

Solutions to this highly nonlinear Eq. (34), and the ramifications of those solutions, form a major part of the theoretical research into BEC. Note that the condensate atoms all have exactly the same wave function, which means that adding atoms to the condensate does not increase its volume, just like the increase of atoms to the liquid phase of a liquid-gas mixture makes only an infinitesimal volume increase of the sample. The consequences of this predicted condensation are indeed profound. For example, in a harmonic trap, the lowest state's wavefunction is a Gaussian. With so many atoms having *exactly* the same wave function they form a new state of matter, unlike anything in the familiar experience.

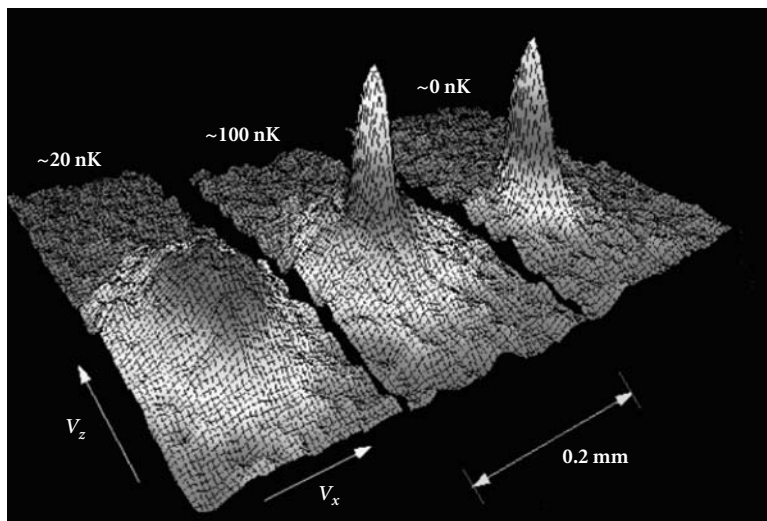
Achieving the conditions required for BEC in a low-density atomic vapor requires a long and difficult series of cooling steps. First, note that an atomic sample cooled to the recoil limit  $T_r$  would need to have a density of a few times  $10^{13}$  atoms/cm<sup>3</sup> in order to satisfy BEC. However, atoms cannot be optically cooled at this density because the resulting vapor would have an

absorption length for on-resonance radiation approximately equal to the optical wavelength. Furthermore, collisions between ground- and excited-state atoms have such a large cross section that at this density the optical cooling would be extremely ineffective. In fact, the practical upper limit to the atomic density for laser cooling in a 3D optical molasses (see Sec. 20.6) or MOT (see Sec. 20.7) corresponds to  $n \sim 10^{10}$  atoms/cm<sup>3</sup>. Thus it is clear that the final stage of cooling toward a BEC must be done in the dark. The process typically begins with an MOT for efficient capture of atoms from a slowed beam or from the low-velocity tail of a Maxwell-Boltzmann distribution of atoms at room temperature. Then a polarization gradient optical molasses stage is initiated that cools the atomic sample from the mK temperatures of the MOT to a few times  $T_c$ . For the final cooling stage, the cold atoms are confined in the dark in a purely magnetic trap and a forced evaporative cooling process is used to cool.<sup>1</sup>

The observation of BEC in trapped alkali atoms in 1995 has been the largest impetus to research in this exciting field. As of this writing (1999), the only atoms that have been condensed are Rb,<sup>70</sup> Na,<sup>71</sup> Li,<sup>72</sup> and H.<sup>73</sup> The case of Cs is special because, although BEC is certainly possible, the presence of a near-zero energy resonance severely hampers its evaporative cooling rate.

The first observations of BEC were in Rb,<sup>70</sup> Li,<sup>72</sup> and Na,<sup>71</sup> and the observation was done using ballistic techniques. The results from one of the first experiments are shown in Fig. 21. The three panels show the spatial distribution of atoms some time after release from the trap. From the ballistic parameters, the size of the BEC sample as well as its shape and the velocity distribution of its atoms could be inferred. For temperatures too high for BEC, the velocity distribution is Gaussian but asymmetrical. For temperatures below the transition to BEC, the distribution is also not symmetrical, but now shows the distinct peak of a disproportionate number of very slow atoms corresponding to the ground state of the trap from which they were released. As the temperature is lowered further, the number of atoms in the narrow feature increases very rapidly, a sure signature that this is truly a BEC and not just very efficient cooling.

The study of this “new form” of matter has spawned innumerable subtopics and has attracted enormous interest. Both theorists and experimentalists are addressing the questions of its behavior



**FIGURE 21** Three panels showing the spatial distribution of atoms after release from the magnetostatic trap following various degrees of evaporative cooling. In the first one, the atoms were cooled to just before the condition for BEC was met, in the second one, to just after this condition, and in the third one to the lowest accessible temperature consistent with leaving some atoms still in the trap. (Figure taken from the JILA Web page.)

in terms of rigidity, acoustics, coherence, and a host of other properties. Extraction of a coherent beam of atoms from a BEC has been labeled an “atom laser” and will surely open the way for new developments in atom optics.<sup>1</sup>

## Dark States

The BEC discussed in the previous subsection is an example of the importance of quantum effects on atomic motion. It occurs when the atomic de Broglie wavelength  $\lambda_{\text{dB}}$  and the interatomic distances are comparable. Other fascinating quantum effects occur when atoms are in the light and  $\lambda_{\text{dB}}$  is comparable to the optical wavelength. Some topics connected with optical lattices have already been discussed, and the *dark states* described here are another important example. These are atomic states that cannot be excited by the light field.

The quantum description of atomic motion requires that the energy of such motion be included in the Hamiltonian. The total Hamiltonian for atoms moving in a light field would then be given by

$$\mathcal{H} = \mathcal{H}_{\text{atom}} + \mathcal{H}_{\text{rad}} + \mathcal{H}_{\text{int}} + \mathcal{H}_{\text{kin}} \quad (35)$$

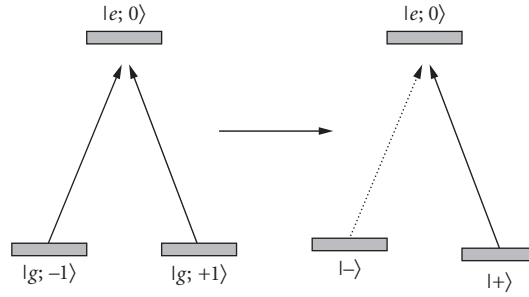
where  $\mathcal{H}_{\text{atom}}$  describes the motion of the atomic electrons and gives the internal atomic energy levels,  $\mathcal{H}_{\text{rad}}$  is the energy of the radiation field and is of no concern here because the field is not quantized,  $\mathcal{H}_{\text{int}}$  describes the excitation of atoms by the light field and the concomitant light shifts, and  $\mathcal{H}_{\text{kin}}$  is the kinetic energy  $E_k$  of the motion of the atoms' center of mass. This Hamiltonian has eigenstates of not only the internal energy levels and the atom-laser interaction that connects them, but also of the kinetic energy operator  $\mathcal{H}_{\text{kin}} \equiv \mathcal{P}^2/2M$ . These eigenstates will therefore be labeled by quantum numbers of the atomic states as well as the center of mass momentum  $p$ . For example, an atom in the ground state,  $|g; p\rangle$ , has energy  $E_g + p^2/2M$  which can take on a continuous range of values.

To see how the quantization of the motion of a two-level atom in a monochromatic field allows the existence of a velocity-selective dark state, consider the states of a two-level atom with single internal ground and excited levels,  $|g; p\rangle$  and  $|e; p'\rangle$ . Two ground eigenstates  $|g; p\rangle$  and  $|g; p''\rangle$  are generally not coupled to one another by an optical field except in certain cases. For example, in oppositely propagating light beams (1D) there can be absorption-stimulated emission cycles that connect  $|g; p\rangle$  to itself or to  $|g; p \pm 2\rangle$  (in this section, momentum is measured in units of  $\hbar k$ ). The initial and final  $E_k$  of the atom differ by  $\pm 2(p \pm 1)/M$  so energy conservation requires  $p = \mp 1$  and is therefore velocity-selective (the energy of the light field is unchanged by the interaction since all the photons in the field have energy  $\hbar\omega_r$ ).

The coupling of these two degenerate states by the light field produces off-diagonal matrix elements of the total Hamiltonian  $\mathcal{H}$  of Eq. (35), and subsequent diagonalization of it results in the new ground eigenstates of  $\mathcal{H}$  given by (see Fig. 22)  $|\pm\rangle \equiv (|g; -1\rangle \pm |g; +1\rangle)/\sqrt{2}$ . The excitation rate of these eigenstates  $|\pm\rangle$  to  $|e; 0\rangle$  is proportional to the square of the electric dipole matrix element  $\bar{\mu}$  given by

$$|\langle e; 0 | \bar{\mu} | \pm \rangle|^2 = |\langle e; 0 | \bar{\mu} | g; -1 \rangle \pm \langle e; 0 | \bar{\mu} | g; +1 \rangle|^2 / 2 \quad (36)$$

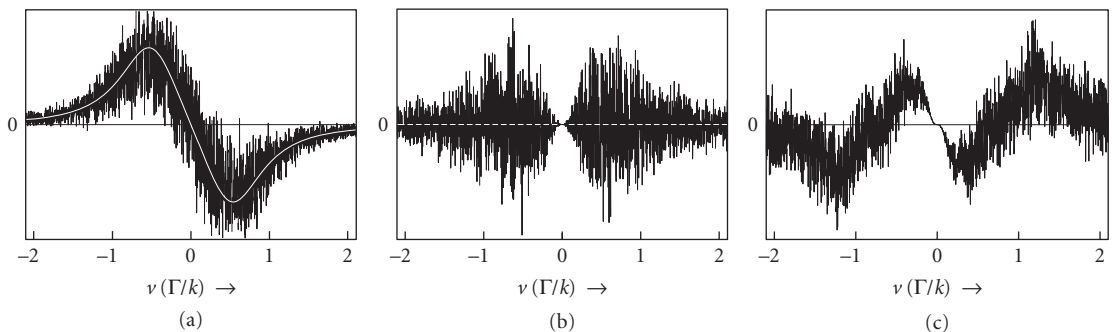
This vanishes for  $|-\rangle$  because the two terms on the right-hand side of Eq. (36) are equal since  $\bar{\mu}$  does not operate on the external momentum of the atom (dotted line of Fig. 22). Excitation of  $|\pm\rangle$  to  $|e; \pm 2\rangle$  is much weaker since it's off resonance because its energy is higher by  $4\hbar\omega_r = 2\hbar^2 k^2 / M$ , so that the required frequency is higher than to  $|e; 0\rangle$ . The resultant detuning is  $4\omega_r = 8\varepsilon(\gamma/2)$ , and for  $\varepsilon \sim 0.5$ , this is large enough so that the excitation rate is small, making  $|-\rangle$  quite dark. Excitation to any state other than  $|e; \pm 2\rangle$  or  $|e; 0\rangle$  is forbidden by momentum conservation. Atoms are therefore optically pumped into the dark state  $|-\rangle$  where they stay trapped, and since their momentum components are fixed, the result is velocity-selective coherent population trapping (VSCPT).



**FIGURE 22** Schematic diagram of the transformation of the eigenfunctions from the internal atomic states  $|g; p\rangle$  to the eigenstates  $|\pm\rangle$ . The coupling between the two states  $|g; p\rangle$  and  $|g; p'\rangle$  by Raman transitions mixes them, and since they are degenerate, the eigenstates of  $\mathcal{H}$  are the nondegenerate states  $|\pm\rangle$ .

A useful view of this dark state can be obtained by considering that its components  $|g; \pm 1\rangle$  have well-defined momenta, and are therefore completely delocalized. Thus they can be viewed as waves traveling in opposite directions but having the same frequency, and therefore they form a standing de Broglie wave. The fixed spatial phase of this standing wave relative to the optical standing wave formed by the counterpropagating light beams results in the vanishing of the spatial integral of the dipole transition matrix element so that the state cannot be excited. This view can also help to explain the consequences of  $p$  not exactly equal  $\pm 1$ , where the de Broglie wave would be slowly drifting in space. It is common to label the average of the momenta of the coupled states as the *family momentum*,  $\mathcal{P}$ , and to say that these states form a *closed family*, having family momentum  $\mathcal{P} = 0$ .<sup>74,75</sup>

In the usual case of laser cooling, atoms are subject to both a damping force and to random impulses arising from the discrete photon momenta  $\hbar k$  of the absorbed and emitted light. These can be combined to make a force versus velocity curve as shown in Fig. 23a. Atoms with  $\mathcal{P} \neq 0$  are always subject to the light field that optically pumps them into the dark state and thus produces random impulses as shown in Fig. 23b. There is no damping force in the most commonly studied case of a real atom, the  $J = 1 \rightarrow 1$  transition in  $\text{He}^*$ , because the Doppler and polarization gradient cooling cancel one another as a result of a numerical “accident” for this particular case.



**FIGURE 23** Calculated force versus velocity curves for different laser configurations showing both the average force and a typical set of simulated fluctuations. Part (a) shows the usual Doppler cooling scheme that produces an atomic sample in steady state whose energy width is  $\hbar\gamma/2$ . Part (b) shows VSCPT as originally studied in Ref. 74 with no damping force. Note that the fluctuations vanish for  $\mathcal{P} = 0$  because the atoms are in the dark state. Part (c) shows the presence of both a damping force and VSCPT. The fluctuations vanish for  $\mathcal{P} = 0$ , and both damping *and* fluctuations are present at  $\mathcal{P} \neq 0$ .

Figures 23a and b should be compared to show the velocity dependence of the sum of the damping and random forces for the two cases of ordinary laser cooling and VSCPT. Note that for VSCPT the momentum diffusion vanishes when the atoms are in the dark state at  $\mathcal{P} = 0$ , so they can collect there. In the best of both worlds, a damping force would be combined with VSCPT as shown in Fig. 23c. Such a force was predicted in Ref. 76 and was first observed in 1996.<sup>77</sup>

## 20.9 REFERENCES

1. H. J. Metcalf and P. van der Straten, *Laser Cooling and Trapping*, Springer-Verlag, New York, 1999.
2. J. Gordon and A. Ashkin, "Motion of Atoms in a Radiation Trap," *Phys. Rev. A* **21**:1606 (1980).
3. W. Phillips and H. Metcalf, "Laser Deceleration of an Atomic Beam," *Phys. Rev. Lett.* **48**:596 (1982).
4. J. Prodan, W. Phillips, and H. Metcalf. "Laser Production of a Very Slow Monoenergetic Atomic Beam," *Phys. Rev. Lett.* **49**:1149 (1982).
5. J. Prodan and W. Phillips, "Chirping the Light Fantastic—Recent NBS Atom Cooling Experiments," *Prog. Quant. Elect.* **8**:231 (1984).
6. W. Ertmer, R. Blatt, J. L. Hall, and M. Zhu, "Laser Manipulation of Atomic Beam Velocities: Demonstration of Stopped Atoms and Velocity Reversal," *Phys. Rev. Lett.* **54**:996 (1985).
7. R. Watts and C. Wieman, "Manipulating Atomic Velocities Using Diode Lasers," *Opt. Lett.* **11**:291 (1986).
8. V. Bagnato, G. Lafyatis, A. Martin, E. Raab, R. Ahmad-Bitar, and D. Pritchard, "Continuous Stopping and Trapping of Neutral Atoms," *Phys. Rev. Lett.* **58**:2194 (1987).
9. T. E. Barrett, S. W. Dapore-Schwartz, M. D. Ray, and G. P. Lafyatis, "Slowing Atoms with ( $\sigma^-$ )-Polarized Light," *Phys. Rev. Lett.* **67**:3483–3487 (1991).
10. J. Dalibard and W. Phillips, "Stability and Damping of Radiation Pressure Traps," *Bull. Am. Phys. Soc.* **30**:748 (1985).
11. S. Chu, L. Hollberg, J. Bjorkholm, A. Cable, and A. Ashkin, "Three-Dimensional Viscous Confinement and Cooling of Atoms by Resonance Radiation Pressure," *Phys. Rev. Lett.* **55**:48 (1985).
12. P. D. Lett, R. N. Watts, C. E. Tanner, S. L. Rolston, W. D. Phillips, and C. I. Westbrook, "Optical Molasses," *J. Opt. Soc. Am. B* **6**:2084–2107 (1989).
13. D. Sesko, C. Fan, and C. Wieman. "Production of a Cold Atomic Vapor Using Diode-Laser Cooling," *J. Opt. Soc. Am. B* **5**:1225 (1988).
14. P. Gould, P. Lett, and W. D. Phillips, "New Measurement with Optical Molasses," in *Laser Spectroscopy VIII*, W. Persson and S. Svanberg, (eds.) Springer, Berlin, 1987.
15. T. Hodapp, C. Gerz, C. Westbrook, C. Furtlehner, and W. Phillips, "Diffusion in Optical Molasses," *Bull. Am. Phys. Soc.* **37**:1139 (1992).
16. P. Lett, R. Watts, C. Westbrook, W. Phillips, P. Gould, and H. Metcalf, "Observation of Atoms Laser Cooled Below the Doppler Limit," *Phys. Rev. Lett.* **61**:169 (1988).
17. J. Dalibard and C. Cohen-Tannoudji, "Laser Cooling below the Doppler Limit by Polarization Gradients—Simple Theoretical-Models," *J. Opt. Soc. Am. B* **6**:2023–2045 (1989).
18. P. J. Ungar, D. S. Weiss, S. Chu, and E. Riis, "Optical Molasses and Multilevel Atoms—Theory," *J. Opt. Soc. Am. B* **6**:2058–2071 (1989).
19. C. Cohen-Tannoudji and W. D. Phillips, "New Mechanisms for Laser Cooling," *Phys. Today* **43**: October, 33–40 (1990).
20. C. Salomon, X Dalibard, W. D. Phillips, A. Clairon, and S. Guellati, "Laser Cooling of Cesium Atoms below 3  $\mu$ K," *Europhys. Lett.* **12**:683–688 (1990).
21. W. Ketterle and N. J. van Druten, "Evaporative Cooling of Trapped Atoms," *Adv. Atom. Mol. Opt. Phys.* **37**:181 (1996).
22. M. Kasevich and S. Chu, "Laser Cooling below a Photon Recoil with 3-Level Atoms," *Phys. Rev. Lett.* **69**:1741–1744 (1992).

23. D. Wineland, W. Itano, J. Bergquist, and J. Bollinger, "Trapped Ions and Laser Cooling," Technical Report 1086, N.I.S.T (1985).
24. A. Migdall, J. Prodan, W. Phillips, T. Bergeman, and H. Metcalf, "First Observation of Magnetically Trapped Neutral Atoms," *Phys. Rev. Lett.* **54**:2596 (1985).
25. T. Bergeman, G. Erez, and H. Metcalf, "Magnetostatic Trapping Fields for Neutral Atoms," *Phys. Rev. A* **35**:1535 (1987).
26. A. Ashkin, "Acceleration and Trapping of Particles by Radiation Pressure," *Phys. Rev. Lett.* **24**:156 (1970).
27. S. Chu, J. Bjorkholm, A. Ashkin, and A. Cable, "Experimental Observation of Optically Trapped Atoms," *Phys. Rev. Lett.* **57**:314 (1986).
28. A. Ashkin, "Application of Laser Radiation Pressure," *Science* **210**:1081–1088 (1980).
29. A. Ashkin and J. M. Dziedzic, "Observation of Radiation-Pressure Trapping of Particles by Alternating Light Beams," *Phys. Rev. Lett.* **54**:1245 (1985).
30. A. Ashkin and J. M. Dziedzic, "Optical Trapping and Manipulation of Viruses and Bacteria," *Science* **235**:1517 (1987).
31. J. D. Miller, R. A. Cline, and D. J. Heinzen, "Far-Off-Resonance Optical Trapping of Atoms," *Phys. Rev. A* **47**:R4567–R4570 (1993).
32. Y. Castin and J. Dalibard, "Quantization of Atomic Motion in Optical Molasses," *Europhys. Lett.* **14**:761–766 (1991).
33. P. Verkerk, B. Lounis, C. Salomon, C. Cohen-Tannoudji, J. Y. Courtois, and G. Grynberg, "Dynamics and Spatial Order of Cold Cesium Atoms in a Periodic Optical-Potential," *Phys. Rev. Lett.* **68**:3861–3864 (1992).
34. P. S. Xessen, C. Gerz, P. D. Lett, W. D. Phillips, S. L. Rolston, R. J. C. Spreeuw, and C. I. Westbrook, "Observation of Quantized Motion of Rb Atoms in an Optical-Field," *Phys. Rev. Lett.* **69**:49–52 (1992).
35. B. Lounis, P. Verkerk, J. Y. Courtois, C. Salomon, and G. Grynberg, "Quantized Atomic Motion in 1D Cesium Molasses with Magnetic-Field," *Europhys. Lett.* **21**:13–17 (1993).
36. E. Raab, M. Prentiss, A. Cable, S. Chu, and D. Pritchard, "Trapping of Neutral-Sodium Atoms with Radiation Pressure," *Phys. Rev. Lett.* **59**:2631 (1987).
37. T. Walker, D. Sesko, and C. Wieman, "Collective Behavior of Optically Trapped Neutral Atoms," *Phys. Rev. Lett.* **64**:408–411 (1990).
38. D. W. Sesko, T. G. Walker, and C. E. Wieman, "Behavior of Neutral Atoms in a Spontaneous Force Trap," *J. Opt. Soc. Am. B* **8**:946–958 (1991).
39. J. Nellessen, J. H. Muller, K. Sengstock, and W. Ertmer, "Laser Preparation of a Monoenergetic Sodium Beam," *Europhys. Lett.* **9**:133–138 (1989).
40. J. Nellessen, J. H. Muller, K. Sengstock, and W. Ertmer, "Large-Angle Beam Deflection of a Laser-Cooled Sodium Beam," *J. Opt. Soc. Am. B* **6**:2149–2154 (1989).
41. J. Nellessen, J. Werner, and W. Ertmer, "Magneto-optical Compression of a Monoenergetic Sodium Atomic-Beam," *Opt. Commun.* **78**:300–308 (1990).
42. E. Riis, D. S. Weiss, K. A. Moler, and S. Chu, "Atom Funnel for the Production of a Slow, High-Density Atomic-Beam," *Phys. Rev. Lett.* **64**:1658–1661 (1990).
43. A. Aspect, N. Vansteenkiste, R. Kaiser, H. Haberland, and M. Karrais, "Preparation of a Pure Intense Beam of Metastable Helium by Laser Cooling," *Chem. Phys.* **145**:307–315 (1990).
44. M. D. Hoogerland, J. P. J. Driessen, E. J. D. Vredenburg, H. J. L. Megens, M. P. Schuwer, H. C. W. Beijerinck, and K. A. H. van Leeuwen, "Bright Thermal Atomic-Beams by Laser Cooling—A 1400-Fold Gain in-Beam Flux," *App. Phys. B* **62**, 323–327 (1996).
45. R. A. Nauman and H. Henry Stroke, "Apparatus Upended: A Short History of the Fountain A-Clock," *Phys. Today* 89 (May 1996).
46. M. A. Kasevich, E. Riis, S. Chu, and R. G. Devoe, "RF Spectroscopy in an Atomic Fountain," *Phys. Rev. Lett.* **63**:612–616 (1989).
47. A. Clairon, C. Salomon, S. Guellati, and W. D. Phillips, "Ramsey Resonance in a Zacharias Fountain," *Europhys. Lett.* **16**:165–170 (1991).

48. K. Gibble and S. Chu, "Future Slow-Atom Frequency Standards," *Metrologia* **29**:201–212 (1992).
49. K. Gibble and S. Chu, "Laser-Cooled Cs Frequency Standard and a Measurement of the Frequency-Shift Due to Ultracold Collisions," *Phys. Rev. Lett.* **70**:1771–1774 (1993).
50. K. Gibble and B. Verhaar, "Eliminating Cold-Collision Frequency Shifts," *Phys. Rev. A* **52**:3370 (1995).
51. R. Legere and K. Gibble, "Quantum Scattering in a Juggling Atomic Fountain," *Phys. Rev. Lett.* **81**:5780 (1998).
52. Ph. Laurent, P. Lemonde, E. Simon, G. Santorelli, A. Clairon, N. Dimarcq, P. Petit, C. Audoin, and C. Salomon, "A Cold Atom Clock in the Absence of Gravity," *Eur. Phys. J. D* **3**:201 (1998).
53. P.S. Julienne and E.H. Mies, "Collisions of Ultracold Trapped Atoms," *J. Opt. Soc. Am.* **B6**:2257–2269 (1989).
54. P. D. Lett, P. S. Julienne, and W. D. Phillips, "Photoassociative Spectroscopy of Laser-Cooled Atoms," *Annual Rev. Phys. Chem.* **46**:423 (1995).
55. A. Gallagher and D. E. Pritchard, "Exoergic Collisions of Cold Na<sup>+</sup>-Na," *Phys. Rev. Lett.* **63**:957–960 (1989).
56. P. S. Julienne and J. Vigue, "Cold Collisions of Ground-State and Excited-State Alkali-Metal Atoms," *Phys. Rev. A* **44**:4464–4485 (1991).
57. H. Mastwijk, J. Thomsen, P. van der Straten, and A. Niehaus, "Optical Collisions of Cold, Metastable Helium Atoms," *Phys. Rev. Lett.* **80**:5516–5519 (1998).
58. A. Fioretti, D. Comparat, A. Crubellier, O. Dulieu, F. Masnou-Seeuws, and P. Pillet, "Formation of Cold Cs<sub>2</sub> Molecules through Photoassociation," *Phys. Rev. Lett.* **80**:4402–4405 (1998).
59. V. S. Lethokov, "Narrowing of the Doppler Width in a Standing Light Wave," *JETP Lett.* **7**:272 (1968).
60. C. Salomon, J. Dalibard, A. Aspect, H. Metcalf, and C. Cohen-Tannoudji, "Channeling Atoms in a Laser Standing Wave," *Phys. Rev. Lett.* **59**:1659 (1987).
61. K. I. Petsas, A. B. Coates, and G. Grynberg, "Crystallography of Optical Lattices," *Phys. Rev. A* **50**:5173–5189 (1994).
62. P. S. Jessen and I. H. Deutsch, "Optical Lattices," *Adv. Atom. Mol. Opt. Phys.* **37**:95–138 (1996).
63. G. Grynberg, B. Lounis, P. Verkerk, J. Y. Courtois, and C. Salomon, "Quantized Motion of Cold Cesium Atoms in 2-Dimensional and 3-Dimensional Optical Potentials," *Phys. Rev. Lett.* **70**:2249–2252 (1993).
64. G. Birkel, M. Gatzke, I. H. Deutsch, S. L. Rolston, and W. D. Phillips, "Bragg Scattering from Atoms in Optical Lattices," *Phys. Rev. Lett.* **75**:2823–2826 (1995).
65. C. I. Westbrook, R. N. Watts, C. E. Tanner, S. L. Rolston, W. D. Phillips, P. D. Lett, and P. L. Gould, "Localization of Atoms in a 3-Dimensional Standing Wave," *Phys. Rev. Lett.* **65**:33–36 (1990).
66. M. Dahan, E. Peik, J. Reichel, Y. Castin, and C. Salomon, "Bloch Oscillations of Atoms in an Optical Potential," *Phys. Rev. Lett.* **76**:4508 (1996).
67. H. T. C. Stoof, "Atomic Bose-Gas with a Negative Scattering Length," *Phys. Rev. A* **49**:3824–3830 (1994).
68. T. Bergeman, "Hartree-Fock Calculations of Bose-Einstein Condensation of <sup>7</sup>Li Atoms in a Harmonic Trap for  $T > 0$ ," *Phys. Rev. A* **55**:3658 (1997).
69. T. Bergeman, "Erratum: Hartree-Fock Calculations of Bose-Einstein Condensation of <sup>7</sup>Li Atoms in a Harmonic Trap for  $T > 0$ ," *Phys. Rev. A* **56**:3310 (1997).
70. M. H. Anderson, J. R. Ensher, M. R. Matthews, C. E. Wieman, and E. A. Cornell, "Observation of Bose-Einstein Condensation in a Dilute Atomic Vapor," *Science* **269**:198–201 (1995).
71. K. Davis, M.-O. Mewes, M. Andrews, M. van Druten, D. Durfee, D. Kurn, and W. Ketterle, "Bose-Einstein Condensation in a Gas of Sodium Atoms," *Phys. Rev. Lett.* **75**:3969 (1995).
72. C. C. Bradley, C. A. Sackett, J. J. Tollett, and R. G. Hulet, "Evidence of Bose-Einstein Condensation in an Atomic Gas with Attractive Interactions," *Phys. Rev. Lett.* **75**:1687–1690 (1995).
73. D. Fried, T. Killian, L. Willmann, D. Landhuis, S. Moss, D. Kleppner, and T. Greytak, "Bose-Einstein Condensation of Atomic Hydrogen," *Phys. Rev. Lett.* **81**:3811 (1998).
74. A. Aspect, E. Arimondo, R. Kaiser, N. Vansteenkiste, and C. Cohen-Tannoudji, "Laser Cooling below the One-Photon Recoil Energy by Velocity-Selective Coherent Population Trapping," *Phys. Rev. Lett.* **61**:826 (1988).



75. A. Aspect, C. Cohen-Tannoudji, E. Arimondo, N. Vansteenkiste, and R. Kaiser, "Laser Cooling Below the One-Photon Recoil Energy by Velocity-Selective Coherent Population Trapping—Theoretical-Analysis," *J. Opt. Soc. Am. B* **6**:2112–2124 (1989).
76. M. S. Shahriar, P. R. Hemmer, M. G. Prentiss, P. Marte, J. Mervis, D. P. Katz, N. P. Bigelow, and T. Cai, "Continuous Polarization-Gradient Precooling-Assisted Velocity-Selective Coherent Population Trapping," *Phys. Rev. A* **48**:R4035–R4038 (1993).
77. M. Widmer, M. J. Bellanca, W. Buell, H. Metcalf, M. Doery, and E. Vredenburg, "Measurement of Force-Assisted Population Accumulation in Dark States," *Opt. Lett.* **21**:606–608 (1996).
78. P. A. Molenaar, P. van der Straten, H. G. M. Heideman, and H. Metcalf, "Diagnostic-Technique for Zeeman-Compensated Atomic-Beam Slowing—Technique and Results," *Phys. Rev. A* **55**:605–614 (1997).
79. B. Sheehy, S. Q. Shang, P. van der Straten, and H. Metcalf, "Collimation of a Rubidium Beam Below the Doppler Limit," *Chem. Phys.* **145**:317–325 (1990).
80. A. Scholz, M. Christ, D. Doll, J. Ludwig, and W. Ertmer, "Magneto-optical Preparation of a Slow, Cold and Bright Ne\* Atomic-Beam," *Opt. Commun.* **111**:155–162 (1994).
81. Z. T. Lu, K. L. Corwin, M. J. Renn, M. H. Anderson, E. A. Cornell, and C. E. Wieman, "Low-Velocity Intense Source of Atoms from a Magneto-optical Trap," *Phys. Rev. Lett.* **77**:3331–3334 (1996).
82. K. G. H. Baldwin, private communication.
83. M. Schiffer, M. Christ, G. Wokurka, and W. Ertmer, "Temperatures Near the Recoil Limit in an Atomic Funnel," *Opt. Commun.* **134**:423–430 (1997).
84. F. Lison, P. Schuh, D. Haubrich, and D. Meschede, "High Brilliance Zeeman Slowed Cesium Atomic Beam," *Phys. Rev.* **A61**:013405 (2000).
85. K. Dieckmann, R. J. C. Spreeuw, M. Weidemuller, and J. T. M. Walraven, "Two-Dimensional Magneto-Optical Trap as a Source of Slow Atoms," *Phys. Rev. A* **58**:3891 (1998).

Todd Ditmire

*Texas Center for High Intensity Laser Science  
Department of Physics  
The University of Texas at Austin  
Austin, Texas*

## 21.1 GLOSSARY

---

$a_0$	normalized peak vector potential of the intense laser pulse
$a_{\text{Bohr}}$	Bohr radius
$b$	confocal parameter
$c$	speed of light
$e$	charge of the electron
$f_p$	relativistic ponderomotive force
$E_a$	atomic field strength
$E_{\text{cr}}$	Schwinger critical electric field
$E_0$	peak electric field amplitude of the intense laser pulse
$f_x$	laser fractional absorption for $x$ process
$k_0$	laser wavenumber
$k_e$	electron wavenumber
$\text{KE}_{e\text{-ATI}}$	kinetic energy of electrons
$I$	laser intensity
$I_{\text{H}}$	ionization potential of hydrogen
$I_p$	ionization potential
$\ell$	plasma scale length
$L_c$	coherence length
$m_e, m_i$	mass of the electron, ion
$n$	refractive index
$n_2$	nonlinear refractive index
$n_{\text{crit}}$	electron critical density
$n_e, n_i$	electron and ion density
$p$	effective harmonic nonlinear order

$P_{  ,\perp}$	polarizability tensor of a molecule parallel and perpendicular to molecular axis
$P_C$	critical power for self-focusing
$q$	harmonic order
$Q_{\text{clust}}$	charge on cluster from outer ionization
$R_0$	initial radius of a cluster
$R_c$	critical ionization distance in molecules
$u_{\text{ion}}$	ion velocity
$U_p$	ponderomotive potential energy
$v_g$	laser group velocity
$v_{\text{osc}}$	electron oscillation velocity
$v_D$	electron drift velocity
$w$	$1/e^2$ focal spot radius of a focused Gaussian laser beam
$W_x$	ionization rate for x process
$z_R$	Rayleigh range of focused laser
$Z$	charge state of ions
$\alpha$	fine structure constant
$\beta_{\text{Rot}}$	molecular rotation constant
$\Delta k$	phase mismatch
$\epsilon_{\text{CE}}$	Coulomb explosion energy
$\epsilon_D$	dielectric function
$\gamma$	relativistic Lorentz factor for electrons
$\gamma_{\text{osc}}$	cycle-averaged relativistic Lorentz factor for electrons in strong field
$\gamma_{\text{SRS}}$	stimulated Raman scattering growth rate
$\Lambda$	Coulomb logarithm
$\lambda_{\text{Debye}}$	plasma Debye length
$\lambda_p$	optical scale length in an overdense plasma
$\nu_{ei}$	electron-ion collision frequency
$\sigma_N$	generalized $N$ -photon cross section for multiphoton ionization
$\sigma_T$	Thomson scattering cross section
$\tau_p$	laser pulse duration
$\omega_a$	atomic unit of frequency
$\omega_{\text{BG}}$	Bohm-Gross frequency
$\omega_0$	angular oscillation frequency of the intense laser pulse
$\omega_p$	plasma frequency
$\omega_{s,A}$	Stokes, anti-Stokes frequency

## 21.2 INTRODUCTION AND HISTORY

---

Strong field physics (or “high field physics” in much of the literature) refers to the phenomena that occur during the interaction of intense electromagnetic waves with matter of various forms. It is characterized by interactions that are often highly nonlinear. While such interactions have been accessed with microwave radiation,<sup>1</sup> traditionally, strong field physics has been studied with intense optical and near-infrared (IR) pulses generated by high-intensity lasers. These interactions occur in a regime in which the electric field of the optical wave dominates the motion and dynamics of electrons subject to these fields. At the highest intensities that are now accessible, the motion of

electrons can become relativistic during each optical cycle, and the magnetic field of the light pulse starts to become important in affecting the motion of electrons in the field.

While it is possible to access strong field effects with what are presently considered rather modest intensities in certain situations, it is customary to consider strong field physics as the regime in which the light intensity is high enough that the peak electric field of the wave  $E_0 = \sqrt{8\pi I/c}$  becomes comparable to the atomic unit of electric field  $E_a = e/a_{\text{Bohr}}^2 = 5.1 \times 10^9$  V/cm, the field felt by an electron in a hydrogen atom. Light acquires this electric field at an intensity of  $3.5 \times 10^{16}$  W/cm<sup>2</sup>, though there are many strong field physics effects which manifest themselves at fields of about 10 percent of  $E_a$  (at intensity  $\sim 10^{14}$  W/cm<sup>2</sup>). At these intensities light interaction with atoms can no longer be described by standard perturbation theory, and light interactions with electrons in a plasma dominate the thermal motion of the free electrons. At higher intensities, beyond  $10^{18}$  W/cm<sup>2</sup>, the field becomes high enough that an electron in an optical frequency wave can be accelerated to relativistic velocity in less than one optical cycle. Such intensities are also characterized by high magnetic fields and optical forces. For example, in a pulse with intensity of  $10^{18}$  W/cm<sup>2</sup>, an intensity quite modest by modern standards, the peak electric field is  $3 \times 10^{10}$  V/cm and the optical magnetic field is 100 MG. The light pressure,  $I/c$ , is  $\sim 0.3$  Gbar. The highest intensity lasers can now reach intensity approaching  $10^{22}$  W/cm<sup>2</sup>.

The theoretical study of high field physics can be said to have started in earnest with a classic paper by L. V. Keldysh in 1964.<sup>2</sup> In this paper, the rate of ionization of an atom or ion in a strong laser field was first derived with a nonperturbative theory. The first real experimental observation of nonperturbative high-field effects occurred in the ground breaking experiment of Agostini et al. in 1979.<sup>3</sup> Their experiment observed, for the first time, truly nonperturbative multiphoton effects in laser-atom interactions by examining photo-electron production from intense 6-photon ionization of Xe atoms at intensity up to  $4 \times 10^{13}$  W/cm<sup>2</sup>. They found that electrons were ejected during ionization with energy higher than that expected from absorption of the minimum number of photons needed for ionization, an effect that came to be known as above threshold ionization.<sup>4</sup> This observation sparked a long campaign of experiments and theoretical work on strong laser field ionization of atoms and ions that continues to this day. These early experiments in strong field multiphoton ionization were followed by the first observation of nonperturbative nonlinear optical phenomena in high order harmonic generation by Rhodes et al. in 1987<sup>5</sup> in which highly nonlinear interactions of an intense laser pulse with a gas of atoms led to emission of a range of high harmonics of the laser frequency. The initial observations of high harmonics were striking in that a range of harmonics extended to very high orders with almost constant intensity, completely at odds with lowest order perturbation theory. In fact, very high nonlinear orders,  $>100$ , have been reported in studies of this effect,<sup>6,7</sup> resulting in the production of coherent light into the soft x-ray region. High harmonic generation with intense laser pulses continues to be studied actively and has led to a revolution in the production of electromagnetic pulses with durations of a few hundred attoseconds.<sup>8,9</sup>

These early nonlinear multiphoton discoveries were followed by the realization that much of these effects could be understood by treating the field classically and the interaction with electrons semiclassically. This simplification in describing strong-field interactions occurred nearly simultaneously by Corkum et al.<sup>10</sup> and Kulander.<sup>11</sup> The semiclassical treatment is now the basis for much of our understanding of strong field ionization, above threshold ionization and high harmonic generation.

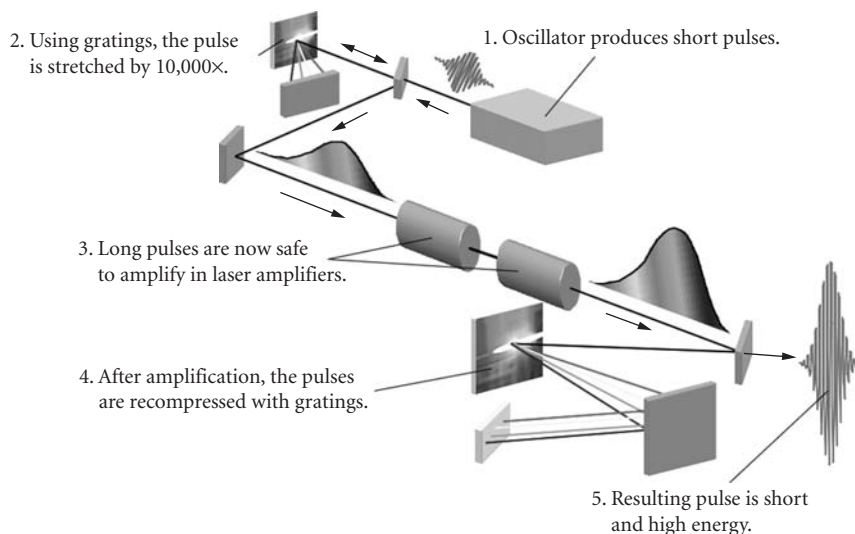
While the study of strong field physics has its origins in the study of atomic ionization, it was also realized early on that strong field interactions with plasmas would manifest unique effects, not only through the ionization of atoms and ions in the plasma but in the collective motion of the plasma electrons driven by the strong forces of an intense laser pulse. The study of intense laser interactions with plasmas has been a very important aspect of strong field physics leading to numerous breakthroughs, such as the development of compact x-ray lasers<sup>12,13</sup> and plasma accelerators.<sup>14</sup> For example, it was realized as early as 1979, in a classic paper by Tajima and Dawson,<sup>15</sup> that an intense laser pulse could be used to drive a plasma wave that could, in turn, accelerate electrons with very high gradient, far above that of traditional accelerators.<sup>16</sup> This has led to a steady advance in understanding intense laser light propagation in underdense plasma. Recent years have seen other important advances in strong field laser interactions. The latest developments in laser technology now enable experiments in plasmas at intensities in which the free electron velocity becomes relativistic.

This has led to new range of nonlinear phenomena created by the relativistic mass increase of the electron in the strong laser field. For example, absorption of light in plasmas becomes much more complicated in the high-field regime, with collective effects playing a much bigger role. This leads to plasma interactions that exhibit large “anomalous absorption” deviating from simple linear kinetic theories of light interactions with plasmas.

This chapter is intended to introduce many of the fundamental concepts underlying the modern strong field physics research. These concepts span descriptions of intense light interactions with single electrons, individual atoms, ensembles of atoms in molecules and clusters, and many charged particles in plasmas. This chapter does not represent a comprehensive review of modern strong field physics research and is not a survey of recent results in the field. No attempt is made to discuss specific experimental results that confirm the phenomena presented (though citations to such work are given). Instead, the basic phenomena underlying the more complex effects observed in strong field physics will be discussed, and the basic equations needed to describe these high-field effects will be presented. (Equations here are presented without proof; the reader is encouraged to seek detailed derivations from the references provided.) If a more detailed review of the various aspects of strong field physics is desired, there have been a number of excellent review articles published in recent years (including a number of older articles which are still relevant). A listing of some of these review articles appears in Sec. 21.12 in Refs. 17 to 41 for the interested reader. (In the remainder of this chapter all units are CGS unless otherwise stated.)

### 21.3 LASER TECHNOLOGY USED IN STRONG FIELD PHYSICS

Before discussing strong field phenomena, it is important to note that advances in this area of physics have been driven by many important leaps in laser technology over the last 20 years. The enabling technology advancement for creating the increasingly higher intensities needed to access strong fields was the invention of chirped pulse amplification (CPA) lasers.<sup>42</sup> The CPA technique, first demonstrated by Strickland and Mourou in 1985,<sup>42</sup> is illustrated in Fig. 1. The goal of CPA is to amplify picosecond to femtosecond duration pulses to high energy in laser gain media, thereby



**FIGURE 1** Architecture used for chirped pulse amplification (CPA) lasers.

reaching the terawatts to petawatts of peak power needed to access strong field phenomena. As illustrated in Fig. 1 a broad bandwidth, mode-locked laser produces a low power, ultrafast pulse of light, usually with duration of 20 to 500 fs. This short pulse is first stretched in time by a factor of around 10 thousand from its original duration using diffraction gratings. This allows the pulses, now of much lower peak power, to be safely amplified in the laser, avoiding the deleterious nonlinear effects which would occur if the pulses had higher peak power.<sup>43</sup> These amplified pulses are, finally, recompressed in time, (again using gratings) in a manner that preserves the phase relationship between the component frequencies in the pulse. The CPA laser pulse output has a duration near that of the original pulse but with an energy greater by the amplification factor of the laser chain. In high-energy CPA systems ( $> \sim 1$  J), severe nonlinearities occurring when the pulse propagates in air can be a major problem, so the pulse must be recompressed in an evacuated chamber. The state of the art in CPA now enables focused intensity of up to  $10^{21}$  W/cm<sup>2</sup> (Ref. 44) with peak intensity up to 1 PW ( $10^{15}$  W).<sup>45</sup> Table top CPA lasers can usually access intensity of  $\sim 10^{19}$  W/cm<sup>2</sup> and high repetition rate ( $\sim 1$  kHz) lasers usually operate with peak intensity of  $\sim 10^{16}$  W/cm<sup>2</sup>.

The first generation of CPA lasers was based primarily on flashlamp pumped Nd:glass amplifiers.<sup>42,46–48</sup> These glass-based lasers, operating at a wavelength near 1  $\mu\text{m}$ , are usually limited to pulse duration of greater than about 400 fs because of gain narrowing in the amplifiers.<sup>49</sup> The most significant scaling of this approach to CPA was demonstrated by the petawatt laser at Lawrence Livermore National Laboratory in the late 1990s.<sup>50</sup> This laser demonstrated the production of 500 J of energy per pulse with duration of under 500 fs, yielding over  $10^{15}$  W of peak power. Since this demonstration, a number of petawatt laser projects have been undertaken around the world.<sup>51</sup>

The second common approach to CPA uses Ti:sapphire as the amplifier material. This material permits amplification of 800 nm wavelength pulses with much shorter pulse durations, often down to  $\sim 30$  fs. However, the short excited state lifetime of Ti:sapphire (3  $\mu\text{s}$ ) requires that the material be pumped by a second laser (usually a frequency doubled Nd:YAG or Nd:glass laser). The inherent inefficiencies of this two-step pumping usually limit the output energy of such a laser to under a few joules of energy per pulse. A number of multiterawatt lasers based on Ti:sapphire now operate in many high-intensity laser labs worldwide.<sup>52–55</sup> These laser typically yield energy of 1 mJ to 1 J (though higher energy examples with energy  $\sim 10$  J do exist), and they typically exhibit repetition rate of 1 kHz at the 1 mJ level or  $\sim 10$  Hz at the 0.1 to 1 J level.<sup>56</sup> To date, the largest scaling of Ti:sapphire technology has been to power levels approaching 1 PW.<sup>54,57</sup>

The third major technology now commonly used in CPA lasers is based on a technique known as optical parametric chirped pulse amplification (OPCPA).<sup>58</sup> In this approach, amplification of the stretched pulses occurs not with an energy storage medium like Nd:glass or Ti:sapphire but via parametric interactions in a nonlinear crystal. This approach is quite attractive because of the very high gain per stage possible (often in excess of  $10^4$  per pass) and the very broad gain bandwidth possible, in principal. To date, a number of CPA lasers based on OPCPA have been demonstrated.<sup>59–61</sup>

## 21.4 STRONG FIELD INTERACTIONS WITH SINGLE ELECTRONS

We begin our discussion of the various strong field phenomena by considering strong field interactions with individual, free electrons (which encompasses the situation in which the electrons are not affected by the electrostatic forces of a collective electron plasma). This discussion will be followed in the next sections by overviews of strong laser field interactions with atoms, molecules, clusters, and then plasmas.

### The Ponderomotive Force

When a strong laser field interacts with a free electron, the field can almost always be treated classically and the trajectory of the electron can be found using classical mechanics. If the intensity is

not too high, below about  $10^{18}$  W/cm<sup>2</sup> for optical and near-infrared frequencies, then motion of the electron can be treated nonrelativistically and the magnetic field of the laser can be ignored. In that case, the electron oscillates at the laser frequency in the direction of the laser polarization. Solution of Newton's equation yields for electron velocity  $v(t) = (eE_0/m_e\omega_0) \sin(\omega_0 t)$ , where  $E_0$  is the laser's peak electric field,  $\omega_0$  is the frequency of the laser light, and  $v_{\text{osc}} = (eE_0/m_e\omega_0)$  is the classical electron oscillation velocity amplitude. While complications arise for very short laser pulses (with envelope comparable to the wavelength) or tightly focused pulses, in a plane wave it is useful to consider the cycle-averaged kinetic energy of this oscillating electron. This energy, called the ponderomotive potential, is

$$U_p = \frac{e^2 E_0^2}{4m_e \omega_0^2} \quad (1)$$

In practical units, the ponderomotive energy is equal to  $9.33 \times 10^{-14} I$  (W/cm<sup>2</sup>)  $\lambda^2$  ( $\mu\text{m}$ ) in eV and is, for example, roughly 10 keV in a Nd:glass laser field at 1.054  $\mu\text{m}$  focused to intensity of  $10^{17}$  W/cm<sup>2</sup>. This ponderomotive energy usually sets the energy scale for most strong field interactions. In a focused laser beam a force  $-\nabla U_p$ , called the ponderomotive force, will act on an electron. The ponderomotive force will tend to accelerate electrons transversely out of the focus from high to low intensity (increasing the electron's energy by  $\sim U_p$ ). In the absence of a strong transverse intensity gradient, a free electron illuminated by a strong laser field will begin to oscillate as the field amplitude increases, but will then come back completely to rest as the intensity falls back to zero, acquiring no net energy from the laser field.

## Relativistic Effects in Strong Field Interactions with Free Electrons

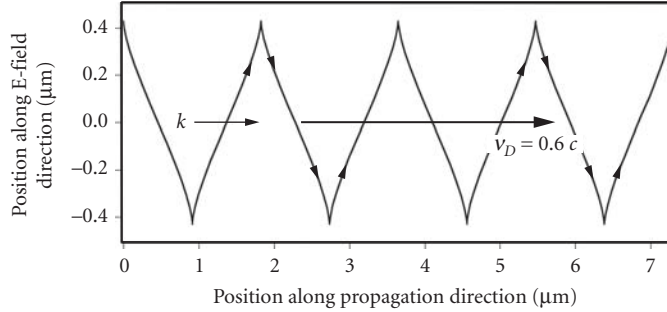
The dynamics of electrons in field strengths at which relativistic effects become important are considerably more complicated. These effects become important when the classical, *nonrelativistic* quantity  $v_{\text{osc}}$  becomes comparable to or greater than  $c$ . At optical and near-IR wavelengths relativistic effects become important at intensity approaching  $10^{18}$  W/cm<sup>2</sup> [where Eq. (1) predicts that the ponderomotive energy exceeds 100 keV in near-IR fields and is, therefore, a large fraction of the 511 keV electron rest mass]. The extent to which the field interaction with the electron is relativistic can be quantified by the dimensionless *normalized vector potential*,  $a_0$ , which is  $v_{\text{osc}}/c$ , and given by

$$a_0 = \frac{eE_0}{m_e c \omega_0} \quad (2)$$

When  $a_0$  approaches 1 (which occurs for 1  $\mu\text{m}$  light at intensity equal to  $1.4 \times 10^{18}$  W/cm<sup>2</sup>), Eq. (1) breaks down. In this regime, the electron motion in the strong field becomes significantly affected by the laser's magnetic field, and, while complex, has been solved analytically by a number of authors.<sup>62-65</sup>

The electron's motion deviates from the simple harmonic oscillation described above because the  $\mathbf{v} \times \mathbf{B}$  force drives the electron forward. The electron now acquires a significant velocity component in the laser's  $k$  direction and, as a result, no longer experiences linearly varying phase and a perfectly sinusoidal oscillation of the electric field. The electron's motion becomes highly anharmonic. Figure 2 illustrates the trajectory of an electron irradiated by a laser field of 1  $\mu\text{m}$  wavelength at intensity of  $10^{19}$  W/cm<sup>2</sup>, ( $a_0 = 2.7$ ). The longitudinal momentum,  $p_z$  can be easily derived from the relativistic equations of motion for the electron in an EM wave. For an electron initially at rest, the field will yield forward momentum such that

$$p_z = \frac{p_x^2}{2m_e c} \quad (3)$$



**FIGURE 2** Trajectory of an electron driven by a relativistic laser field with 1  $\mu\text{m}$  wavelength at an intensity of  $10^{19}$   $\text{W}/\text{cm}^2$ , ( $a_0 = 2.7$  and  $\gamma_{\text{osc}} = 2.1$ ). This illustrates that the electron acquires significant drift velocity along the laser propagation direction and oscillates anharmonically.

if  $p_x$  is the transverse, E-field driven momentum.<sup>66–68</sup> For an electron in a plane wave, a cycle-averaged forward drift velocity  $v_D$  will be acquired in the lab frame, as pictured in Fig. 2. This *average* forward drift velocity is

$$\frac{v_D}{c} = \frac{a_0^2}{4 + a_0^2} \quad (4)$$

This equation indicates that the electron will drift in the forward direction at nearly the speed of light when  $a_0$  is roughly 10, corresponding to a near-IR intensity of about  $10^{20}$   $\text{W}/\text{cm}^2$ .

Finding the transverse oscillation velocity is more complex, but a useful result can be found for weak relativistic fields (when  $a_0$  is between  $\sim 0.3$  and 3 or intensity is in the  $10^{17}$  to  $10^{19}$   $\text{W}/\text{cm}^2$  range for near-IR light). In this regime, one can neglect the longitudinal velocity in the relativistic equations of motion to find an approximate result for the transverse oscillation velocity

$$\frac{v_x}{c} = \frac{a_0}{1 + a_0} \quad (5)$$

which reduces to  $v_{\text{osc}}$  when  $a_0 \ll 1$ .

It is now possible to talk in terms of a relativistic ponderomotive energy which can be written as<sup>22</sup>

$$U_p^{\text{rel}} = (\gamma_{\text{osc}} - 1)mc^2 \quad (6)$$

where  $\gamma_{\text{osc}} = \sqrt{1 + a_0^2/2}$  is the effective cycle-averaged relativistic Lorentz factor (ignoring the contribution from the slower drift of the electron) for linearly polarized light. (Note that in circularly polarized light  $\gamma_{\text{osc}}^{\text{circ}} = \sqrt{1 + a_0^2}$ .) Equation (6) reduces to Eq. (1) when  $a_0 \ll 1$ . Deriving a “ponderomotive force” in a relativistic light beam is a less concrete concept, as the idea of a cycle-averaged force in a weak intensity gradient is of limited utility when, at strongly relativistic intensity, the electron surfs along, almost in phase with the light field at  $c$ . However, a heuristic treatment of the electron dynamics yields a relativistic ponderomotive force that can be written as<sup>69</sup>

$$\mathbf{f}_p = -m_e c^2 \nabla \gamma_{\text{osc}} \quad (7)$$

Finally, we note that this relativistic motion will also eject electrons from the focus of an intense laser. However, unlike the nonrelativistic case in which the ponderomotive force drives the electrons out of the focus at  $90^\circ$  to the laser propagation, the magnetic force causes ejection along an axis folded forward toward the  $k$  direction. This ejection angle can be simply calculated by considering the relativistic kinematics of the absorption of many photons of momentum  $\hbar k$  and the relativistic



relationship between transverse and longitudinal momentum in the EM field, Eq. (3). This yields an ejection angle,  $\theta$ , of electrons with Lorentz factor outside the laser focus of  $\gamma$

$$\theta = \arctan \left[ \frac{2}{\gamma - 1} \right] \quad (8)$$

It should be noted that this equation is only valid for purely plane wave interactions. The field near a real focus will contain longitudinal components which alter the ejection angle of the electrons somewhat.<sup>70</sup> Nonetheless, Eq. (8) correctly indicates that in a strongly relativistic focus, electrons will be ejected with high Lorentz factor and will come out in a cone around the propagation axis of the laser, having surfed along with the field through the laser focus. If electrons are ejected into the field at the peak of an oscillation, a situation that occurs when highly charged ions are ionized by the field (see the next section) the relativistic electrons propagating with small ejection angle  $\theta$  can pick up substantial energy from the laser field. A useful estimate for *maximum* ejected electron energy derived from this relativistic free-wave acceleration mechanism is<sup>71</sup>

$$\gamma_{\max} \approx \frac{eE_0 \theta z_R}{2m_e c^2} \quad (9)$$

where  $z_R = \pi w^2 / \lambda$  is the Rayleigh range of the Gaussian focus. Equation (9) indicates that the ejected electron in the relativistic intensity regime acquire energy proportional to the laser's electric field ( $\sim I^{1/2}$ ) and not its square, as they do in the nonrelativistic case [see Eq. (1)]. When  $a_0 \gg 1$ ,  $\theta$  will be small, and electrons will gain substantial energy from the field. For example, calculations show that an electron produced by ionization at intensity of  $5 \times 10^{21}$  W/cm<sup>2</sup> in a 1- $\mu$ m wavelength laser field focused to a 5- $\mu$ m Gaussian spot can acquire energy up to  $\sim 1$  GeV and are ejected at an angle of  $\sim 3^\circ$ .<sup>71</sup>

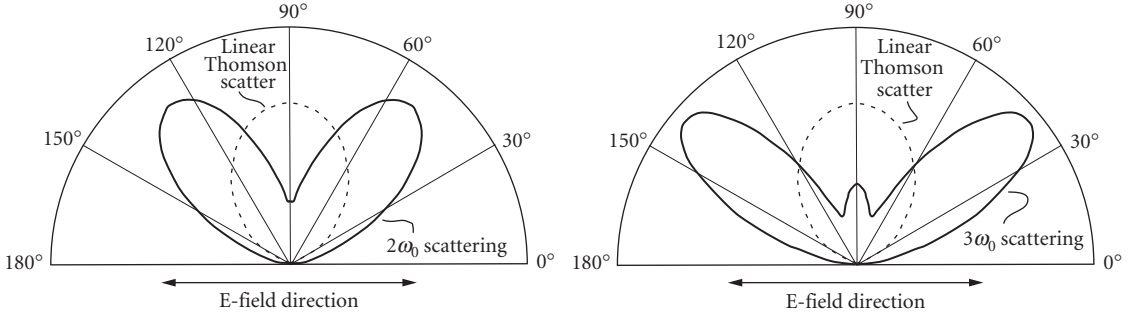
## Nonlinear Thomson Scattering by Electrons in an Intense Laser Field

The acceleration associated with oscillation of a free electron in an electromagnetic wave gives rise to emitted radiation, a process known as Thomson scattering, which has the well-known scattering cross section  $\sigma_T = 8\pi e^2 / 3m_e c^2$ .<sup>72</sup> The *anharmonic* motion of an electron in a strong laser field, as illustrated in Fig. 2, alters the Thomson scattering in an important manner. First, the light scattered from the electron has an emission pattern folded forward toward the laser propagation axis, and second, the radiated light from the electron will contain higher harmonic components.<sup>64,73-77</sup> In a strongly relativistic field ( $a_0 \gg 1$ ), the radiated emission will be forward folded by the effective Lorentz boost, into an angle  $\theta \approx 3/a_0$ . In addition, the anharmonic motion of the electron induced by the magnetic field results in scattered light at even and odd harmonics of the incident light field. It can be shown that the total integrated scattered power into the first three harmonics of the laser field are<sup>74</sup>

$$P_1 \cong \frac{e^2 \omega_0^2 c}{3} a_0^2 \quad P_2 \cong \frac{7e^2 \omega_0^2 c}{20} a_0^4 \quad P_3 \cong \frac{621e^2 \omega_0^2 c}{1792} a_0^6 \quad (10)$$

illustrating the nonlinear intensity dependence of the second and third harmonic. These equations also illustrate that as  $a_0 \rightarrow 1$  the power scattered into harmonics ( $P_2, P_3$ ) will be comparable to the power scattered by linear Thomson scattering,  $P_1$ . The angular distribution of the scattered radiation for linearly polarized light is analytically complex. Figure 3 illustrates the polar distribution of light from the second and third harmonics of nonlinear Thomson scattering at  $a_0 = 1$ . A simple formula for the angular distribution,  $D(\theta)$ , of scattered light from a circularly polarized beam as a function of polar angle  $\theta$  with respect to the laser propagation direction can be derived,<sup>74</sup> where

$$D(a_0, \theta) = \frac{1}{\left( 1 + \frac{a_0^2}{2} \sin^2 \frac{\theta}{2} \right)^4} \quad (11)$$



**FIGURE 3** Azimuthal angular distribution (in the plane perpendicular to the laser propagation direction) of nonlinear relativistic Thomson scattering by an electron in a light field with  $a_0 = 1$ . The dipole distribution from linear Thomson scattering from an electron is shown for comparison. (These plots were adapted from Ref. 75.)

which, of course, reduces to the isotropic polar emission of Thomson scattered light in a weak circularly polarized field.<sup>72</sup>

### High-Field Interactions with Relativistic Electron Beams

The previous discussion considered the interaction of intense light radiation with electrons at rest or nearly at rest initially in the laboratory frame. If the laser collides with electrons that are already relativistic, which occurs when an intense laser pulse interacts with a beam of electrons from a high energy accelerator or synchrotron, the scattered radiation is altered by the fact that the electron sees a laser photon whose energy is upshifted by a factor  $\gamma$ , the Lorentz factor of the relativistic electron beam. If the scattering is linear Thomson scattering, the scattered photon will acquire another factor of  $\gamma$  in its energy when transformed back into the laboratory frame. This  $\gamma^2$  upshift in photon energy can be exploited to produce femtosecond pulses in the x-ray regime by colliding an ultrashort pulse with a relativistic electron beam.<sup>78</sup> The scattered photon will have photon energy given by

$$\hbar\omega_{\text{scat}} = 2\gamma^2\hbar\omega_0 \frac{1 - \cos\phi}{1 + \gamma^2\theta^2} \quad (12)$$

where  $\phi$  is the angle between the laser and the electron beam and  $\theta$  is the angle of the scattered photon with respect to the electron propagation direction. This indicates that if a laser is scattered from the electron beam at a  $180^\circ$  angle, the photons scattered can be upshifted by as much as  $4\gamma^2$ . Furthermore, Eq. (12) indicates that the scattered photons will be emitted in a directed cone with angle  $\sim 1/\gamma$ , with an angular dependence on the upshifted photon energy. This picture must be amended somewhat if the electron beam Lorentz factor is high enough that the laser photon in the electron frame is upshifted in the electron rest frame such that  $\gamma\hbar\omega_0/m_e c^2 \sim 1$ . In this case, the situation becomes that of inverse Compton scattering and the kinematics of the electron recoil from the photon scattering must be considered. This process is, strictly speaking, a linear process; however, practical experimental implementation of this technique has usually been in the high intensity laser regime because of the low scattering cross section of free electrons ( $\sigma_T = 6.6 \times 10^{-25} \text{ cm}^2$ ).

The situation becomes more complex when the laser is intense enough to cause multiphoton Compton scattering, whose scattering efficiency will then scale as  $a_0^{2n}$ , where  $n$  is the multiphoton order.<sup>67</sup> Accessing this regime in the lab is difficult because of the extremely low cross section but is made easier with a very high energy electron beam because an intense laser will have its intensity boosted in the electron frame through relativistic time compression.<sup>79</sup> At relativistic laser intensity

( $a_0 \geq 1$ ) Eq. (12) must be amended, and the maximum scattered photon energy for head on collision and direct backscatter becomes

$$\hbar\omega_{\text{scat}} = \frac{4n\hbar\omega_0\gamma^2}{1 + \frac{4n\hbar\omega_0\gamma^2}{m_e c^2} + a_0^2} \quad (13)$$

The factor of  $a_0^2$  in the denominator arises from the mass shift of the electron in the strong laser field.

## 21.5 STRONG FIELD INTERACTIONS WITH ATOMS

### Keldysh Parameter and Transition from the Multiphoton to the Quasi-Classical Regime

Perhaps the most fundamental process that occurs when a single atom or ion is immersed in a strong laser field is the ionization of the most weakly bound electron. With the exception of recollision double ionization, discussed below, this ionization process is almost always a single electron process, involving the removal of the outermost bound electron by the light field.<sup>18</sup> (This approach to understanding ionization and nonlinear optical dynamics in strong field atomic interactions is termed the “single active electron approximation,” and it underlies most of the theory presented in this section.) High-field interactions with single atoms essentially split into two regimes. The first occurs when the field can be treated quantum mechanically as an ensemble of photons, and the second arises when so many photons participate that the light can be treated as a classical field. In the second case, which occurs at sufficiently long wavelength or high intensity, the motion of electrons in the field can be treated classically. Generally, the second situation arises if the free electron wavepacket is much smaller than its classical oscillation amplitude. In this case a free electron wavepacket is localized to the extent that it can be considered a point particle; in strong field physics this is called the quasi-classical regime. The uncertainty principle implies that this occurs for a free electron when  $U_p/\hbar\omega \gg 1$ .

In the context of atomic ionization, these two pictures of the liberated free electron naturally lead to two regimes of ionization, the multiphoton regime and the semiclassical tunneling regime. These two regimes of ionization can be quantitatively differentiated by the Keldysh parameter<sup>2</sup>

$$\gamma_K = \sqrt{\frac{I_p}{2U_p}} \quad (14)$$

where  $I_p$  is the ionization potential of the atom or ion to be ionized. This quantity can be physically thought of as the ratio of the time it takes for an electron wavepacket to tunnel through the potential barrier of an ion immersed in a uniform electric field (see Fig. 5) to the period of the light oscillation. The Keldysh parameter delineates the barrier between the multiphoton ionization regime, which occurs when  $\gamma_K \gg 1$ , and the tunneling regime, which is the predominant ionization mechanism when  $\gamma_K \ll 1$ . Note that, given the scaling of  $U_p$  from Eq. (1), the latter situation predominates at higher intensity and longer wavelength. In practice,  $\gamma_K$  is a “soft” parameter in which tunneling ionization (described below) can be considered to be a very good approximation, even when  $\gamma_K$  is only slightly less than 1.

### Multiphoton Ionization

When the Keldysh parameter is larger than 1, the ionization of an atom or ion in a strong laser field takes on a predominantly multiphoton character. The atom or ion can be thought of as absorbing a number of discrete photons from the field simultaneously, so that a bound electron acquires enough

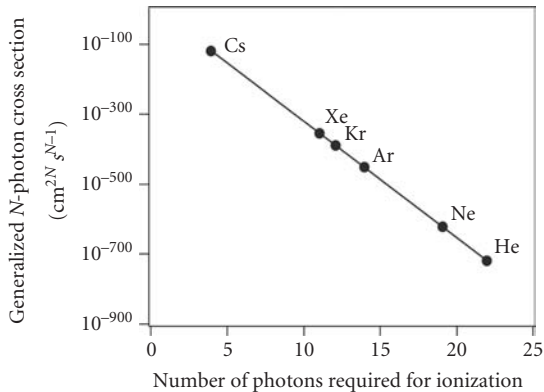
energy to be promoted to the continuum.<sup>80–86</sup> This view tends to predominate practically at modest intensities ( $\sim 10^{13}$  W/cm<sup>2</sup>)<sup>82,85</sup> or with light at wavelengths shorter than optical (UV),<sup>81,84</sup> The most straightforward picture for this process is to say that the ionization rate for  $N$ -photon ionization is given by lowest order perturbation theory<sup>4,87,88</sup> so that the ionization rate can be written as

$$W_N = \sigma_N I^N / (\hbar \omega_0)^N \quad (15)$$

where  $\sigma_N$  is the generalized multiphoton ionization (MPI) cross section. Equation (15) indicates that the ionization rate can be extremely nonlinear with laser intensity. For example,  $N = 22$  when helium is ionized by a 1- $\mu\text{m}$  wavelength laser,<sup>89</sup> though this multiphoton picture turns out to be accurate only for lower ionization potential atoms irradiated at shorter wavelengths. The practical difficulty with this model is in the calculation of  $\sigma_N$ . Lowest order perturbation theory is accurate for a very limited range of intensities and higher order processes soon become important in the calculation of  $\sigma_N$  as intensity is increased. Figure 4 plots the order of magnitude of the generalized cross section as a function of multiphoton order,  $N$ . This plot shows, for example, that the multiphoton ionization cross section for 11 photon ionization of Xe by a 1- $\mu\text{m}$  laser field is about  $10^{-350}$  cm<sup>22</sup> – s<sup>10</sup>. This implies a saturation intensity for multiphoton ionization of atomic Xe by 100 fs pulses of about  $2 \times 10^{14}$  W/cm<sup>2</sup>.

Calculation in the lowest order perturbation theory framework of  $\sigma_N$  is complicated by other factors as well. Resonances with intermediate states complicate the calculation and drastically affect the multiphoton ionization rate. Furthermore, when the field's ponderomotive potential becomes a significant fraction of the ionization potential, the bound state levels can no longer be thought of as unperturbed ion eigenstates; these levels move in energy via the AC Stark shift.<sup>90</sup> Also, as the ponderomotive potential increases, the minimum number of photons needed for ionization may change. Since the ionized electron is “born” into the continuum which has an oscillating field, it must acquire energy equal to  $U_p$  to enter the continuum. As a result, the number of photons needed for ionization is that which overcomes the ionization potential of the unperturbed atom or ion plus the ponderomotive energy, such that  $N\hbar\omega_0 = I_p + U_p$ .

A great number of nonperturbative approaches have been developed to derive more accurate ionization rates in a strong laser field in the multiphoton regime. One of the best known such approaches derives from the original work of Keldysh.<sup>2</sup> This approach has been extensively



**FIGURE 4** Generalized multiphoton cross section for atoms as a function of the multiphoton order,  $N$ . The location of the cross section for ionization of various neutral atoms by a laser at a wavelength of 1  $\mu\text{m}$  are plotted to illustrate the increasing nonlinearity of MPI for more tightly bound atoms. (This plot was adapted from Refs. 80 and 21.)

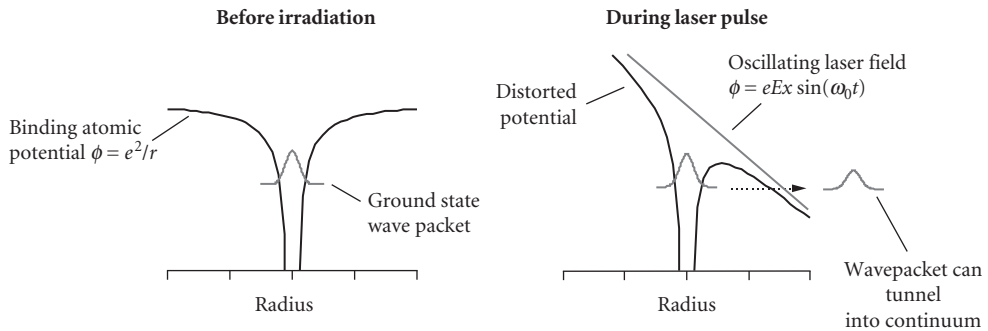
developed by F. Faisal<sup>91</sup> and H. Reiss,<sup>92</sup> ionization calculations based on this approach are usually termed KFR theories or the strong field approximation (SFA). In this approximation, the ionization rate is determined by calculating a quantum mechanical transition probability directly between the ground state of the atom or ion and a continuum state. The ground state is assumed to be the field-free eigenstate unperturbed by the field (accurate for a tightly bound electron) and the final continuum state is assumed to be that of a free electron wavefunction in a plane electromagnetic wave (termed a Volkov state), thereby ignoring the effect of the ion Coulomb field on the outgoing ionized electron. A general equation valid for ionization rate for any Keldysh parameter can be derived in this way. In the multiphoton regime ( $\gamma_K \gg 1$ ) the ionization rate predicted by this theory is<sup>2</sup>

$$W_K = A\omega_0 \left( \frac{I_p}{\hbar\omega_0} \right)^{3/2} \exp \left[ 2N_{\text{eff}} - \frac{I_p^{\text{eff}}}{\hbar\omega} \left( 1 + \frac{2U_p}{I_p} \right) \right] \left( \frac{U_p}{2I_p} \right)^{N_{\text{eff}}} \Phi \left[ \left( 2N_{\text{eff}} - \frac{2I_p^{\text{eff}}}{\hbar\omega_0} \right)^{1/2} \right] \quad (16)$$

where  $I_p^{\text{eff}} = I_p + U_p$  is the effective ionization potential of the atom dressed by the light's ponderomotive potential,  $N_{\text{eff}}$  is the minimum number of photons required to ionize the ion with this  $I_p^{\text{eff}}$ ,  $\Phi[z] = \int \exp[-y^2 - z^2] dy$  is the probability integral and  $A$  is a numerical cofactor of the order of unity that accounts for the weak dependence on the details of the atom. Experiments have illustrated, for example, in 580 nm light that  $A = 24$  for the first ionization of Ar,  $A = 18$  for Kr and  $A = 4$  for Xe.<sup>83</sup> While Eq. (16) is not particularly accurate for most ions and has a rather limited range of applicability, it is useful for estimating the order of magnitude of the ionization rate when  $\gamma_K > 1$ .

## Tunnel Ionization

When the laser field is strong enough and the laser frequency is not too high,  $\gamma_K$  becomes less than 1 and a different picture of strong field ionization emerges. In this regime it is accurate to think of the bound electron wavepacket as evolving in a binding potential that is distorted by the strong light field, a situation known as tunnel ionization, illustrated in Fig. 5. The laser field represents a slowly varying deformation of the ion's confining Coulomb potential which oscillates back and forth. Near the peak of the light field oscillation, the electron can tunnel through the confining potential (pictured at the right in Fig. 5) freeing it and releasing it into the continuum. Because of the exponential nature of the quantum mechanical tunneling rate through a potential barrier, this



**FIGURE 5** Illustration of the potential of an ion distorted by the application of a strong, adiabatically varying electric field. A strong enough field allows tunneling of the bound electron into the continuum thereby ionizing the atom/ion.

method of ionization is strongly nonlinear with increasing electric field. In a Coulomb potential this confining barrier will have a width roughly  $\delta r \approx I_p/eE_0$ , so the electron will tunnel through this barrier with a time

$$\tau_{\text{tun}} \approx \delta r / v \approx \frac{\sqrt{2I_p m_e}}{eE_0} \quad (17)$$

When this time is faster than a laser oscillation cycle, the tunneling picture is valid (equivalent to  $\gamma_k < 1$ ).

The instantaneous ionization rate from tunneling by an electron from a hydrogenlike ion in a quasi-static field is given by<sup>93</sup>

$$W_{\text{H-like}} = 4\omega_a \left( \frac{I_p}{I_H} \right)^{5/2} \frac{E_a}{E(t)} \exp \left[ -\frac{2}{3} \left( \frac{I_p}{I_H} \right)^{3/2} \frac{E_a}{E(t)} \right] \quad (18)$$

where  $I_H$  is the ionization potential of hydrogen (13.6 eV),  $\omega_a = 4.13 \times 10^{16} \text{ s}^{-1}$  is the atomic unit of frequency,  $E_a = 5.14 \times 10^9 \text{ V/cm}$  is the atomic unit of electric field and  $E(t)$  is the instantaneous applied electric field strength. The total ionization rate can be found by integrating Eq. (18) over the entire optical cycle.

There have been many published improvements on this simple tunneling formula.<sup>34,94,95</sup> In fact, the general equation derived by Keldysh retrieves a tunneling rate when it is taken in the limit that  $\gamma_k \ll 1$ .<sup>2</sup> All tunneling models result in an ionization rate with the exponential field dependence  $\sim \exp[-2a/3E(t)]$ , with “ $a$ ” depending on the model. The most sophisticated and most widely accepted model for the tunnel ionization of a complex atom or ion (i.e., multielectron nonhydrogenic ion) was developed by Ammosov, Delone, and Krainov, usually termed the ADK ionization rate.<sup>95</sup> This model predicts that the tunnel ionization rate averaged over one full optical cycle is

$$W_{\text{ADK}} = \omega_a C_{nl} f(l, m) \frac{3^{1/2}}{2\pi^{1/2}} \left( \frac{I_p}{I_H} \right)^{1/4} \left( \frac{E_0}{E_a} \right)^{1/2} \left[ 2 \frac{E_a}{E_0} \left( \frac{I_p}{I_H} \right)^{3/2} \right]^{2n-|m|-1} \exp \left[ -\frac{2}{3} \left( \frac{I_p}{I_H} \right)^{3/2} \frac{E_a}{E_0} \right] \quad (19a)$$

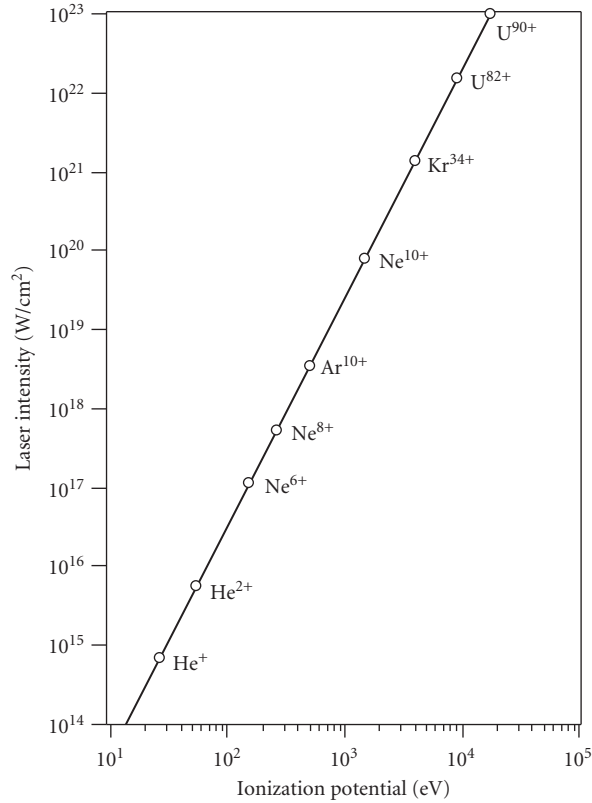
This formula accounts for atomic structure through the principal orbital quantum number  $n$ , the orbital angular momentum  $l$ , and individual magnetic quantum number  $m$ . The atom-dependent cofactors are

$$C_{nl} = (2 \exp[1]/n)^n (2\pi n)^{-1/2} \quad (19b)$$

$$f(l, m) = \frac{(2l+1)(l+|m|)!}{2^{|m|}(|m|)!(l-|m|)!} \quad (19c)$$

The usual method of deriving a net ionization rate is to sum over all  $m$  states of the ionizing ion. The ADK ionization formula has been found experimentally to be quite accurate of over a wide range of intensities and ionic species.<sup>96</sup>

This cycle averaged tunnel ionization rate is very nonlinear. It usually exhibits an intensity dependence that varies as  $I^6$  to  $I^9$ . As a result, strong field ionization tends to exhibit a thresholdlike behavior that quickly saturates once the intensity rises slightly above a threshold value. (Saturation in this context means that  $W \tau_p \approx 1$ , where  $\tau_p$  is the laser pulse duration.) This threshold intensity can be easily estimated by determining when the field becomes high enough to suppress completely the confining Coulomb potential and the electron can freely escape the ion during the peak of the field



**FIGURE 6** Plot of the Barrier Suppression Ionization (BSI) intensity for various ions.

cycle. This simple model, known as the Barrier Suppression Ionization (BSI) model,<sup>96</sup> indicates that the ionization threshold intensity occurs at

$$I_{\text{BSI}} = \frac{cI_p^4}{128\pi Z^2 e^6} \quad (20)$$

where  $Z$  is the charge state of the ion being created by the ionization event. In practical units the BSI intensity is  $I_{\text{BSI}}[\text{W}/\text{cm}^2] = 4.0 \times 10^9 I_p^4 [\text{eV}] Z^{-2}$ . Equation (20) turns out to be remarkably accurate despite its simplicity in predicting the intensity of significant ionization in a strong field. The predicted BSI threshold intensity for a variety of ion species is plotted as a function of ionization potential in Fig. 6, illustrating the extent to which very high charge states can be produced by tunneling with modern high intensity lasers.

### Above Threshold Ionization

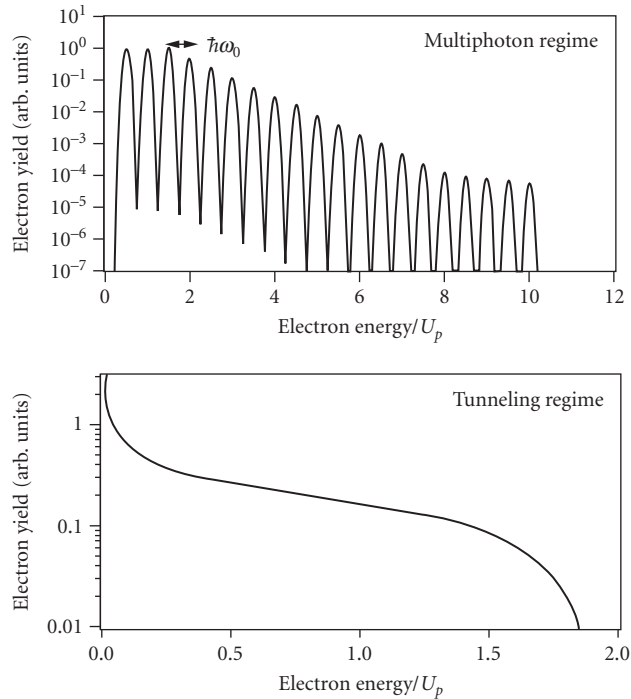
When an atom or ion is subject to a strong ionizing laser field an electron acquires some kinetic energy upon ionization.<sup>3,17,90,97–102</sup> In the weak field regime, the energy acquired by an electron in the light field upon multiphoton ionization can be thought of as a simple extension of the photoelectric effect, in which the electron gains an energy  $\text{KE}_{e^-} = N\hbar\omega_0 - I_p$ , where again,  $N$  is the minimum number of photons needed for ionization.<sup>17</sup> However, as the intensity increases and becomes nonperturbative, the

electron can absorb more than the minimum number of photons needed for ionization, a consequence of the electron remaining in the vicinity of the nucleus long enough during ionization to absorb more than  $N$  photons. The electron now leaves the ion with energy

$$KE_{e^-} = (N+s)\hbar\omega_0 - I_p^{\text{eff}} \quad (21)$$

where the ionization potential is dressed (in other words, shifted in a time-averaged sense) by the ponderomotive potential [as in Eq. (16)], and  $s$  is the number of additional absorbed laser photons. This effect is termed above threshold ionization (ATI) and leads to electron kinetic energy distributions that look qualitatively like those in Fig. 7. These electrons are typically ejected from the focus along the laser polarization direction (at least in the nonrelativistic limit).<sup>103</sup> The absorption of  $s$  additional photons leads to electron energy peaks separated by  $\hbar\omega_0$ , shifted down by an energy  $I_p^{\text{eff}}$  (though ponderomotive acceleration in the focus of a long pulse laser can shift these electron energies back to the undressed energy).

At modest field strengths in the multiphoton regime ( $\sim 10^{13}$  W/cm<sup>2</sup> at IR wavelengths), the yield of electrons in each peak drops off exponentially, as predicted by lowest order perturbation theory. At nonperturbative intensities, however, the yield in each electron ATI peak flattens out and the ATI spectrum develops a plateau over the first few orders, out to an energy of  $\sim U_p$ , (illustrated in Fig. 7).<sup>100</sup> There have been many theories published to explain the quantitative behavior of ATI in



**FIGURE 7** Illustration of the general nature of electron energy spectra resulting from intense ionization of atoms, manifesting the phenomenon known as ATI. At the top the spectrum common for ionization in the multiphoton regime is shown. Here the spectrum is composed of peaks, each corresponding to electrons that have absorbed  $s$  photons above that needed for ionization. On the bottom, a spectrum characteristic of ATI in the tunneling regime is illustrated showing that the spectrum is smooth and extends out to  $2 U_p$ .

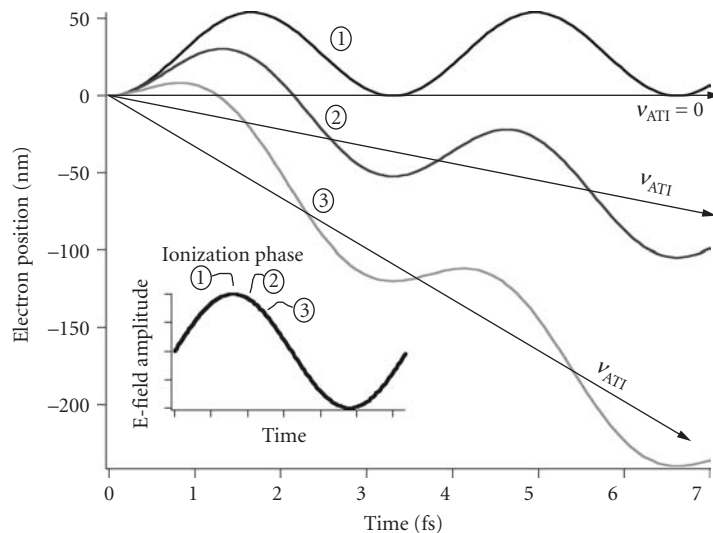


the multiphoton regime. In fact, the strong field approximation of the KFR theories predicts the presence of these multiphoton ATI peaks. Resonances often play an important role in ATI in the multiphoton regime,<sup>104</sup> leading to a rich variety of effects that appear in the ATI energy spectra of optical and near-IR pulses with intensity  $10^{13}$  to  $10^{15}$  W/cm<sup>2</sup>.

As the laser field increases, the character of the electron ATI spectrum takes on a qualitatively different character. At intensities entering the quasi-classical tunneling regime ( $\gamma_K < 1$ ), the spectrum loses its multiphoton character composed of distinct electron energy peaks and becomes a smooth, monotonically decreasing energy distribution, illustrated in Fig. 7. The electron energies have kinetic energy predominantly between 0 and  $2U_p$ , though there is a small component of electrons with energies that reach up to as much as  $10U_p$  through a rescattering process described below.<sup>102</sup> This loss of distinct peaks occurs when the field loses its quantum character and drives the ionization as if it were a classical field.<sup>97,98</sup>

**Quasi-Classical ATI** When ions are ionized in the tunneling regime, which tends to occur in optical and near-IR laser intensities of  $10^{15}$  to  $10^{18}$  W/cm<sup>2</sup>, the shape and energy of electron ATI can be determined by a simple model. As with tunnel and BSI ionization, the field is treated classically and the electron is treated as a compact wavepacket that propagates in the continuum subsequent to tunnel ionization by the classical equations of motion.<sup>105</sup> This so-called quasi-classical model is useful in explaining not only ATI in the strong field, long wavelength regime (i.e., when  $\gamma_K < 1$ ) but also aids in explaining a large number of other strong field phenomena.<sup>10</sup> As such, the quasi-classical model has become one of the major building blocks for understanding modern strong field physics.

In the quasi-classical ATI model, the electron is considered to tunnel into the continuum at a well-defined phase in the oscillating field (see Fig. 8) and propagates in the field as a pointlike charge. When the electron is “born” in to the continuum in this way, it not only oscillates but also acquires some directed drift velocity in the direction of the laser’s polarization, with an energy that is a function of the phase in the field at which it was ionized. (This is true for linear polarized fields; in circularly polarized fields, the electron acquires constant drift velocity.) Solution of



**FIGURE 8** Plot of a calculation showing the classical trajectory of electrons born at three different phases in the laser’s field. These three phase locations are illustrated in the inset. When born at the peak of the field (trajectory 1), the electron oscillates but acquires no net drift velocity. However, when born off the peak, the electron acquires nonzero drift velocity on top of its quiver velocity.

the nonrelativistic equations of motion indicates that the drift component of the kinetic energy acquired by an electron is

$$\text{KE}_{\text{ATI}} = 2U_p \sin^2 \Delta\phi_0 \quad (22)$$

where  $\Delta\phi_0$  is the phase at which the electron is “born” with respect to the peak of the field. Equation (22) indicates that if the electron is born at the peak of the electric field, where the tunnel ionization rate is highest, it will acquire no ATI drift energy. The electron can acquire up to  $2U_p$  of kinetic ATI energy if it is ionized well off of the field peak. If Eq. (22) is combined with a model for static tunnel ionization, an electron energy distribution can be derived. Use of the simple H-like tunnel formula of Eq. (18) leads to an ATI energy spectrum from a linearly polarized field of<sup>105</sup>

$$f(\varepsilon) = \frac{a}{(1 - \varepsilon/2U_p)(\varepsilon/2U_p)^{1/2}} \exp \left[ -\frac{2}{3} \left( \frac{I_p}{I_H} \right)^{3/2} \left( \frac{E_a}{E_0} \right) \left( 1 - \frac{\varepsilon}{2U_p} \right)^{-1/2} \right] \quad (23)$$

where  $a$  is just a normalization constant. The shape of this spectrum for tunnel ionization is illustrated in Fig. 7. This distribution is peaked near zero energy (because the ionization probability is greatest at the peak of the field where  $\Delta\phi_0 = 0$  and  $\text{KE}_{\text{ATI}} = 0$ ) but stretches out to a maximum electron energy of  $2U_p$ . In linearly polarized light, as a rule of thumb, the average electron energy is roughly 10 percent of  $U_p$  at the intensity where the ionization rate saturates.<sup>106</sup>

## Rescattering Effects

The quasi-classical picture of strong field ionization can be extended to explain other observed effects. In this picture once an electron is liberated from its binding potential by tunneling, its motion in the field can be described classically. Once freed into the continuum, the electron can recollide with its parent ion if it is ionized within a certain range of phase of the field,<sup>21,107–116</sup> a process illustrated in Fig. 9. That this happens can be seen by examining the trajectories shown in Fig. 8, in which the electrons return to the  $x = 0$  position in all three cases after ionization at  $t = 0$  (though with different return energy in each case).

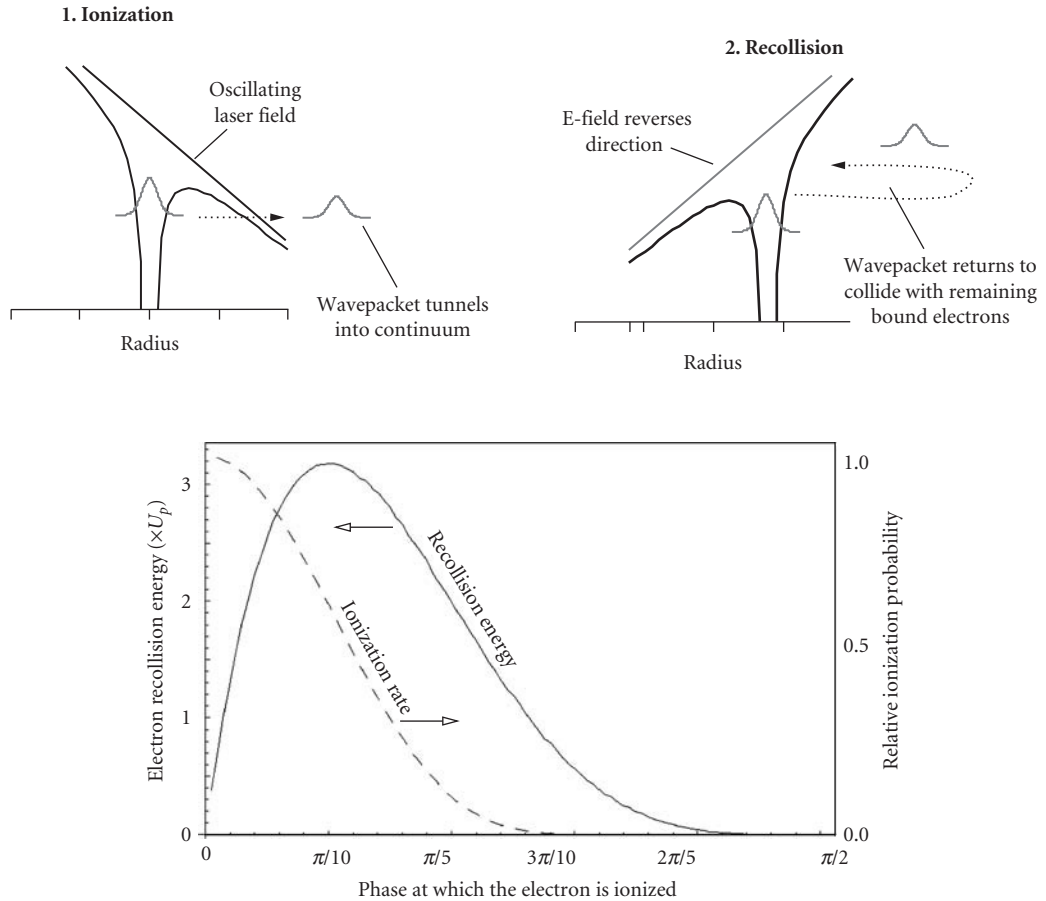
If the field is linearly polarized and the electron is born by tunnel ionization at some time  $t_0$  and  $x = 0$  (the location of the parent ion) in an oscillating electric field  $E_0 \cos \omega_0 t$ , its position as a function of time is

$$x(t) = -\frac{eE_0}{m\omega_0^2} [\cos \omega_0 t + \omega_0 t \sin \omega_0 t_0 - \cos \omega_0 t_0 - \omega_0 t_0 \sin \omega_0 t_0] \quad (24)$$

This classical trajectory will result in the recollision of the tunnel ionized electron with its parent nuclear core for ionization phases of  $\omega_0 t_0 = 0^\circ$  to  $90^\circ$  and  $180^\circ$  to  $270^\circ$ . The highest energy recollisions occur at phases of  $17^\circ$  and  $197^\circ$ . The free electron will have a kinetic energy after it is born by ionization given by

$$\text{KE}(t) = \frac{e^2 E_0^2}{2m_e \omega_0^2} [\sin \omega_0 t - \sin \omega_0 t_0]^2 \quad (25)$$

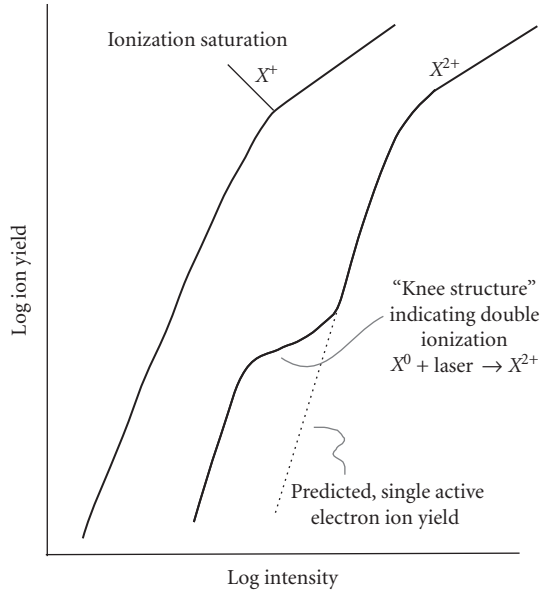
The energy upon return to the nucleus can be found with Eqs. (24) and (25). The maximum energy an electron can have upon returning to its parent nucleus (corresponding to ionization at  $17^\circ$  and  $197^\circ$ ) is  $3.17U_p$ . The recollision energy and tunnel ionization probability as a function of phase in the laser field is illustrated in Fig. 9. This strong field driven electron recollision can manifest itself in a number of important effects. The generation of short wavelength harmonic radiation in this way is discussed in Sec. 21.7, but there are two other consequences of this effect:



**FIGURE 9** The upper illustrations show the process by which a tunnel ionized electron can return to its parent ion and interact with the bound electrons remaining in the ion. The bottom plot shows the energy that such a returning electron will have as a function of the phase in the field at which it was ionized. This shows that the maximum return energy can be  $3.17U_p$ . The relative ionization probability as a function of the field phase is also shown to illustrate how many electrons will return with the energies indicated.

**Strong Field Double Ionization** It has been observed for some time that strong field ionization exhibits a small but significant signature of simultaneous double ionization of ions where two electrons are apparently liberated at the same time in the field.<sup>112,115,117</sup> This effect manifests itself experimentally in the yield of a given ion charge as a function of laser intensity, illustrated in Fig. 10. The “knee” that is seen in the ionization yield of a next higher charge state when the ionization of a lower charge state saturates is clear evidence of double ionization. In addition to rescattering, a number of ideas have been forwarded to explain this strong field behavior.<sup>26</sup> These include:

- *Shake off model*, in which the sudden removal of one electron by tunneling leads to a quantum mechanical relaxation of the second electron into a new set of eigenstates, some of which rest in the continuum and, therefore, lead to ionization.<sup>117,118</sup> This effect is well known and documented in single photon photo-ionization.<sup>119</sup>
- *Collective tunneling*, in which two electrons tunnel out simultaneously from the ion.<sup>120</sup>



**FIGURE 10** Generalized illustration of the ion yield typically measured for ions produced by tunnel ionization, showing the strongly nonlinear increase of ion yield with intensity followed by a roll over at the saturation intensity, where most ions become depleted. The “knee” structure seen in the second ion is the usual experimental signature for nonsequential double ionization.

- *Rescattering*, in which the recolliding electron, described above, collisionally ionizes a second electron. The recolliding electron can acquire sufficient kinetic energy in the field to ionize a second electron through collisional ionization on its return. This is presently the best accepted explanation for strong field double ionization. For example, the double ionization yield is seen to drop dramatically when circularly polarized light is employed.<sup>121</sup> This indicates that the recollision mechanism (at least in the tunneling regime) is likely the dominant mechanism because an electron ionized in circularly polarized light will propagate in such a way that it will not return to the parent ion and cannot ionize a second electron.

**ATI Plateau Extension** A second consequence of the strong field driven recollision is manifested in the electron ATI energy spectrum. As discussed above, ATI electrons in the quasi-classical regime can acquire up to  $2U_p$  of drift energy. However, a laser field-driven recollision can lead to a small number of scattered electrons with energy up to  $10U_p$ .<sup>102</sup> This rescattering leads to the production of an electron ATI spectrum with a large predominance of electrons with energy below  $2U_p$  but with a small fraction of electrons with an energy spectrum plateau that extends out to  $10U_p$ .

## Relativistic Effects

When  $a_0 \rightarrow 1$  strong field ionization dynamics are altered in a number of ways.<sup>40</sup> The most significant effects arise from the forward force exerted by the laser magnetic field, though the relativistic mass increase of the electron does play a role in certain effects.

**Relativistic Tunnel Ionization** It turns out that tunnel ionization rates at relativistic intensity do not deviate significantly from the nonrelativistic rates.<sup>122</sup> The most significant relativistic effects in tunneling occur when the bound state energy  $I_p$  becomes comparable to the rest energy  $m_e c^2$ ; it is the Coulomb correction to the mass of the electron in the ground state that is the principal effect. Therefore, relativistic effects will be important for ions of charge  $Z > \sim 50$ . A relativistic generalization of the Keldysh theory,<sup>34</sup> indicates that the relativistically corrected tunnel ionization rate,  $W_{\text{Rel}}$ , will be higher than the nonrelativistic rate,  $W_{\text{non-Rel}}$  by a factor

$$\frac{W_{\text{Rel}}}{W_{\text{non-Rel}}} \approx \exp\left[-\frac{1}{36}(Z\alpha)^5 \frac{E_{\text{cr}}}{E_0}\right] \quad (26)$$

where  $\alpha$  is the fine structure constant ( $1/137$ ) and  $E_{\text{cr}}$  is the Schwinger critical field from quantum electro-dynamics theory ( $1.3 \times 10^{16}$  V/cm). Using the barrier suppression ionization model to estimate the appropriate  $Z$ , Eq. (26) suggests that the nonrelativistic tunneling rates should be good up to an intensity of  $\sim 10^{26}$  W/cm<sup>2</sup>.

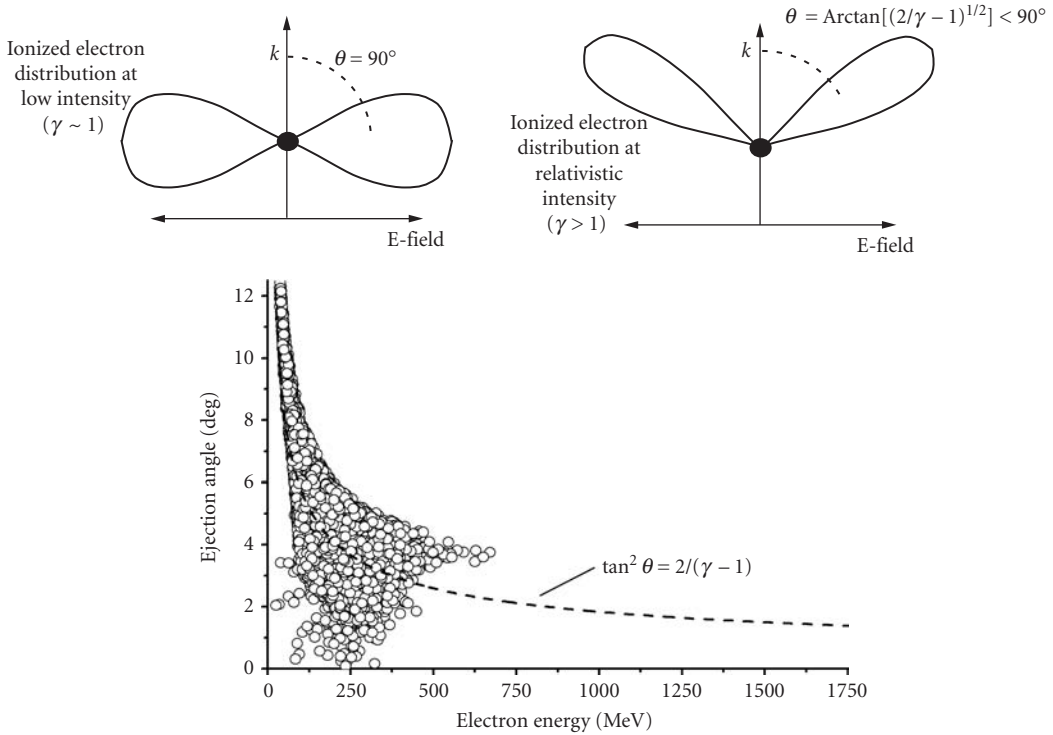
**Relativistic Electron ATI** The ejection of free electrons following tunnel ionization in a relativistic field can be influenced by the laser's magnetic field. At nonrelativistic intensities, electrons are ejected in a rather narrow distribution along the laser polarization axis. As  $a_0$  approaches 1, the magnetic field pushes the electron distribution toward the  $k$  direction of the light propagation, a consequence predicted by Eq. (8).<sup>68</sup> This distribution shift is illustrated in Fig. 11. At highly relativistic intensities (i.e., when  $a_0 \gg 1$ , an intensity of  $> 10^{21}$  W/cm<sup>2</sup> at near-IR wavelengths) tunnel ionized electrons are quickly bent toward the laser propagation axis by the magnetic field. The electron, which will have a velocity near  $c$ , will then “surf” along with the laser pulse acquiring energy from the laser field. Such electrons will be ejected from the laser focus in a narrow cone along the laser direction and will acquire many MeV or even GeV of energy.<sup>71,123</sup> An energy versus angle distribution of electrons ejected in this regime is illustrated in Fig. 11.

**Relativistic Suppression of Rescattering** Another consequence of the forward ejection of electrons in a relativistic light pulse is that the nonsequential double ionization that normally accompanies rescattering of the electrons on their return after ionization is suppressed.<sup>40,124–126</sup> The forward motion of the electron imparted by the magnetic field (see Fig. 2) forces the electron away from the core and prevents the collisional ionization of a second electron. The fall-off of nonsequential ionization yield occurs at intensity as low as  $10^{17}$  W/cm<sup>2</sup> ( $a_0 \approx 0.3$ ). The rescattering plateau in ATI spectra associated with electrons with energy in the  $2U_p$  to  $10U_p$  range also decreases in magnitude because of the rescattering suppression. Furthermore, this phenomenon leads to suppression of single atom high harmonic generation at high intensity.

## Ionization Stabilization

While experimental evidence is scant, there is a strong theoretical basis for believing that, in certain situations, the ionization rate of an atom in a strong field actually declines with increasing intensity.<sup>27</sup> This phenomena has come to be called ionization stabilization. There are usually two manifestations of this stabilization discussed in the literature.

**Adiabatic Stabilization** Quantum mechanical calculations of ionization rates have shown that the ionization rate can be stabilized in ionized atoms at field strengths well above one atomic unit. A simple picture to explain this can be constructed if one considers that the electron wavefunction in the ground state of the atom is considerably altered by the strong oscillating field. The wave function is thought to evolve into a time averaged structure with peaks away

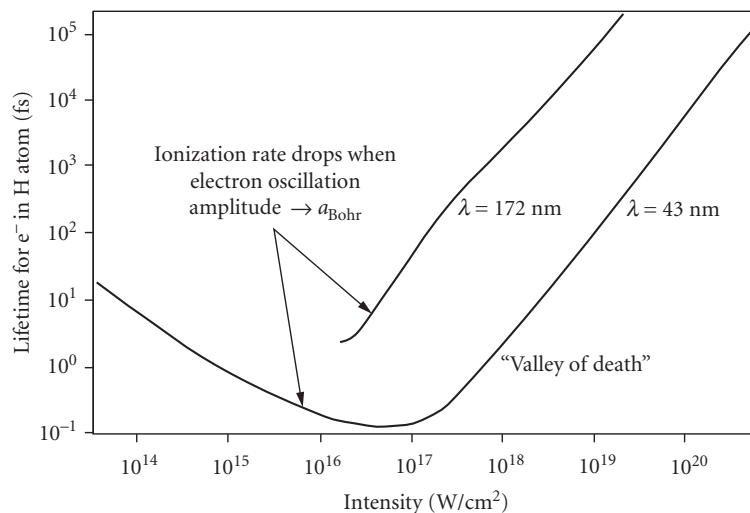


**FIGURE 11** The upper illustrations are a generalized illustration of the angular distribution of electrons produced during ionization with respect to the laser field and propagation directions. In the medium intensity regime, electrons are ejected by tunnel ionization along the E-field direction (left); however, at relativistic intensity, the magnetic field pushes the distribution toward the direction of laser propagation. The latter effect can be understood as the conservation of momentum following the absorption of an extremely large number ( $\sim 10^6$ ) of photons. The bottom plot (*adapted from Ref. 71*) shows the results of a Monte Carlo simulation yielding the ejection angle and energy of electrons produced by irradiation of an Ar ion at intensity of  $5 \times 10^{21}$  W/cm<sup>2</sup>. Here the dashed line is the prediction of Eq. (8); the deviation of the simulation from this equation is a consequence of longitudinal fields at the focus.

from the nuclear center. In a time averaged sense, the bound electron sees *two centers* for the atomic potential.<sup>27,127–129</sup> This deformation of the electron wave function away from the nucleus lowers the ionization rate at higher intensity. Figure 12 illustrates the calculated ionization rates of an electron in an excited state of hydrogen as a function of intensity illustrating the fall of ionization rate at high  $I$ .

**Dynamic Stabilization** This mechanism of ionization stabilization, often termed interference stabilization, arises most prominently in calculations of strong field ionization of Rydberg atoms.<sup>129–131</sup> It is thought to arise from quantum destructive interference of pathways into the continuum. There has been some experimental evidence for this form of stabilization in Rydberg atoms<sup>132</sup> but has yet to be demonstrated in atoms in the ground state.

Numerical simulations have suggested that the magnitude of ionization stabilization decreases at relativistic intensity due to the effects of the magnetic field and the Lorentz force on the electron.<sup>133</sup>



**FIGURE 12** Calculation of the ionization rate of a hydrogen atom in an intense, short wavelength field. (Adapted from Ref. 27.) This calculation shows that at around the intensity at which the electron quiver amplitude is comparable to the size of the hydrogen ground state ( $\sim 1$  Bohr radius) the ionization rate actually decreases (lifetime increases) as the intensity increases from the delocalization of the electron wavefunction.

## 21.6 STRONG FIELD INTERACTIONS WITH MOLECULES

The ionization of small molecules (of less than  $\sim 10$  atoms) by an intense laser field is qualitatively similar to the ionization of single atoms. The two limiting regimes for ionization (multiphoton and tunneling) as discussed in the previous section are still relevant for molecules and the tunnel ionization rate formulas tend to work reasonably well in predicting the ionization rate of electrons in a molecule if appropriately chosen ionization potentials are utilized.<sup>134</sup> Unlike single atoms, however, the motion of the molecule's nuclei during the interaction with the laser pulse can affect the dynamics of the electron ionization and energy gain from the field. Fragmentation of the molecule is one significant consequence of irradiation at high intensity, and the motion of the molecular nuclei has a dynamic impact on the structure of the molecule during its interaction with the intense laser pulse.

### Nuclear Motion and Molecular Alignment in Strong Fields

Because small molecules tend to fragment rapidly in an intense light field, the regime of strong field laser interactions with these molecules is usually limited to rather modest intensity, below about  $10^{15}$  W/cm<sup>2</sup>. Higher intensity pulses tend to destroy a small molecule well before the high intensity can be reached. Much of current research has concentrated on diatomic molecules.

At modest intensity a small molecule will experience a force by the light field which will tend to align it.<sup>135–137</sup> In the absence of the light field, the molecules are randomly oriented and exist in a range of molecular rotation states with energy eigenvalues of  $\epsilon_{\text{Rot}} = \beta_{\text{Rot}} J(J+1)$  and with rotational quantum number  $J$ . Some values of  $\beta_{\text{Rot}}$  are tabulated in Table 1.<sup>138</sup> When a moderately strong light

**TABLE 1** Rotational Constant, and Alignment Well Depth for Three Example Molecules Irradiated at  $10^{15}$  W/cm<sup>2</sup>

Molecule	$\beta_{\text{Rot}}$ (meV)	Max Well Depth (meV)
H <sub>2</sub>	3.89	21.9
N <sub>2</sub>	0.25	96.8
CO <sub>2</sub>	0.048	212

Source: Table Adapted from Ref. 138.

field is applied (below the intensity at which the molecule ionizes), the induced dipole causes the molecule to see a cycle-averaged potential given by<sup>138</sup>

$$V(\theta) = -\frac{I(t)}{2c} [(P_{\parallel} - P_{\perp}) \cos^2(\theta) + P_{\perp}] \quad (27)$$

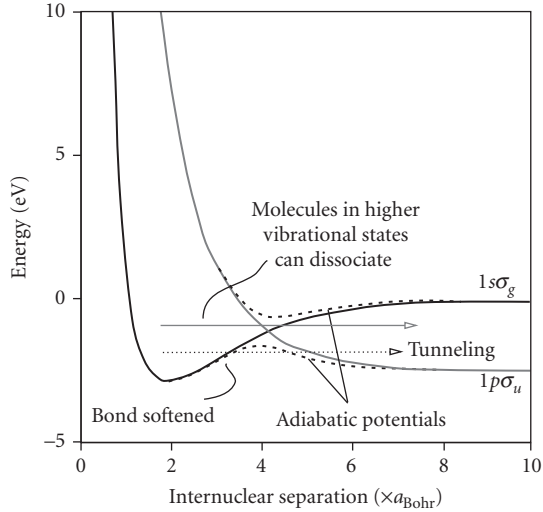
where the  $P$  terms are the parallel and perpendicular components of the polarizability tensor,  $\theta$  is the angle between the molecular axis and the polarization axis and  $I(t)$  is the time dependant intensity. The maximum well depth for some molecules in a field of intensity  $10^{15}$  W/cm<sup>2</sup> is tabulated in Table 1.

The potential of Eq. (27) will tend to align a linear molecule, such as a diatomic along the polarization axis of a linearly polarized field. Because molecules will usually feel a lower intensity field as the pulse of an intense laser ramps up in time, it is usually a good approximation to say that the nuclei of a linear molecule will be (partially) aligned along the laser electric field at subsequent higher intensity. A molecule with nonzero rotational momentum will evolve, classically speaking, in a pendulumlike motion around the laser electric field axis; these states are often called “pendular” states.

Even at modest intensity, the molecule will begin to dissociate via a process known as bond softening.<sup>35,139,140</sup> In a small diatomic molecule, such as H<sub>2</sub> the first electron will be ionized at the equilibrium distance of the two atoms via multiphoton or tunnel ionization. If the molecule is indeed aligned along the light electric field, the molecular nuclei will then begin to separate by bond softening. Molecular dissociation begins to occur when the potential that binds the nuclear wavepackets couples to photons in the strong laser field. This coupling leads to a ladder of potential curves, each shifted by one photon in energy (described by what is known as Floquet theory<sup>141,142</sup>). If the field-dressed states are treated as if they are quasi-static, the Hamiltonian of the molecule can then be diagonalized, distorting the bound potential curves, in a manner illustrated in Fig. 13 (these distorted potentials are termed adiabatic potentials). As can be seen in this figure, the distorted curves allow molecules in excited vibrational states to dissociate, (and some in lower states can tunnel through the distorted potential barrier). This potential distortion is termed bond softening and is the main mechanism by which a molecule begins to fragment as an intense laser is ramped up in intensity. In H<sub>2</sub> this bond softening occurs, for example, at intensity of  $\sim 10^{13}$  W/cm<sup>2</sup>.<sup>35</sup>

There are other means by which molecules can dissociate in midstrength fields ( $I < 10^{14}$  W/cm<sup>2</sup>). In the picture in which the field is treated as a classical, periodically varying alteration to the Hamiltonian of the molecule, the molecule sees states that are shifted down (“dressed”) by an energy equal to the photon energy. The nuclear wavepacket can couple from a bound state to a dissociating state and begin to separate. For example, in H<sub>2</sub><sup>+</sup> immersed in a visible light field of intensity around  $10^{13}$  W/cm<sup>2</sup>, this occurs by coupling first to an unbound state shifted by  $3h\nu$  and then, after some expansion of the internuclear separation, coupling to the continuum of the bound state dressed by two photons. This multiphoton process is often termed above threshold dissociation<sup>143,144</sup> because it results in the absorption of more photons than are energetically required to dissociate the molecule (much like above threshold ionization is absorption of more photons by an electron than needed to ionize).





**FIGURE 13** Nuclear potential energy curves for the first bound and first unbound state of  $\text{H}_2^+$ . The coupling of these states to a strong field leads to mixing and new distorted potentials called “adiabatic states,” which are pictured as dashed curves. The bond softening resulting from these distorted curves permits molecules left in high laying vibrational states to dissociate immediately and those in lower states to tunnel out on a longer time scale.

## Coulomb Explosion

At higher intensity ( $10^{14}$  to  $10^{15}$  W/cm<sup>2</sup>), multiple ionization of the molecular nuclei will lead to a Coulomb repulsion of the ions, a process known as a Coulomb explosion. This explosion happens very quickly and subsequent multiple ionization of the nuclei while in proximity to each other occurs only if the rise time of the laser is comparable or faster than this Coulomb explosion separation time. The characteristic time for explosion of a diatomic is roughly

$$\tau_{\text{CE}} \approx \frac{3}{4} \frac{\mu^{1/2} R_0^{3/2}}{(q_1 q_2)^{1/2} e} \quad (28)$$

where  $\mu = m_1 m_2 / (m_1 + m_2)$  is the reduced mass of the repelling system,  $q_1$  and  $q_2$  are the charge states of the ionized nuclei, and  $R_0$  is the initial separation of the exploding nuclei. Equation (28) indicates that  $\text{H}_2^{2+}$  Coulomb explodes in under 1 fs, while  $\text{N}_2^{2+}$  explodes in about 5 fs.

Upon Coulomb explosion, the ejected ions acquire a kinetic energy just given by their initial Coulomb potential energy. For a diatomic molecule with ions charged by field ionization to  $q_1$  and  $q_2$ , the Coulomb explosion energy is

$$\epsilon_{\text{CE}} = \frac{q_1 q_2 e^2}{R} \quad (29)$$

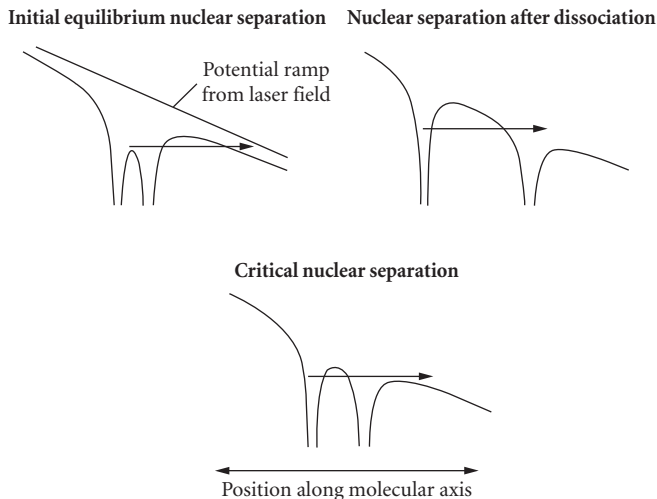
where  $R$  is the separation of the two ions at the point of ionization. In almost all cases, the observed Coulomb explosion energy of an exploding diatomic or other small molecule is less than that expected of an explosion from the molecules equilibrium distance (which is, for example,  $1.4 a_B$  for  $\text{H}_2$ ).<sup>145</sup> This arises because of pre-expansion of the nuclear separation from bond softening and Coulomb repulsion of lower charge states before final ionization. A good rule of thumb is that  $\epsilon_{\text{CE}}$

upon strong field ionization will be about 45 to 55 percent of the energy calculated from equilibrium distances.<sup>138</sup> For example, Coulomb explosion of  $H_2$  usually leads to the ejection of protons with energy between 3 and 5 eV.<sup>146</sup>  $\epsilon_{CE}$  is largely independent of pulse duration and wavelength.<sup>147</sup>

## Molecular Tunnel Ionization and the Critical Ionization Distance

The ionization rate for the first electrons of diatomic molecules in a strong laser field for low charge states in the tunneling regime (i.e.,  $\gamma \ll 1$ ) frequently follows standard atomic tunnel ionization rates, such as the ADK rate of Eq. (19), with the appropriate molecular ionization potential inserted into the formula.<sup>134</sup> Nonsequential recollision double ionization of diatomics also occurs in a manner similar to that of atoms.<sup>148,149</sup> There are, however, some subtleties which manifest in the tunnel ionization rate of certain diatomic species; these deviations from standard tunneling formulas are thought to arise from destructive interference between electrons liberated from the two nuclear centers.<sup>150</sup>

The production of higher charge states in a molecule under higher intensity irradiation and the subsequent Coulomb explosion of the highly charged fragments deviates significantly from the predictions of tunnel ionization of single atoms. In particular, charge states from field ionization of molecular nuclei tend to occur at an intensity much lower than that of the same charge state in an isolated ion. This occurs because of the presence of what is known as the critical ionization radius in the molecule.<sup>151–155</sup> This effect can be explained simply in the quasi-classical tunneling/barrier suppression ionization model described above. It arises because the field-induced tunneling of an electron from the molecule can be aided by the presence of the second charged nucleus of the molecule near the first. This effect is illustrated for a diatomic molecule in Fig. 14, in which a diatomic molecule



**FIGURE 14** Drawing of the electron potential energy curves for a diatomic molecule immersed in a strong slowly varying field for three nuclear spacings. At the initial equilibrium position, pictured in the upper left, ionization by tunneling occurs when the electron tunnels out of the combined Coulomb well into the continuum. On the other hand, if the molecular nuclei have become greatly separated by dissociation, ionization must occur by tunneling from the potential of an isolated ion. However, at an intermediate separation, the electrons from the left-most ion need only tunnel through a narrow barrier formed from the combination of both Coulomb fields. This results in a greatly enhanced ionization rate at this nuclear separation.

is aligned along the axis of the laser electric field. When the nuclei are close together, the electrons are confined in the combined potential of the two nuclei; an applied field then requires an electron to tunnel from the combined potential. At very large nuclear separation, the electron is effectively localized at one of the nuclei and the tunneling rate is just that of an electron tunneling from an isolated Coulomb potential well. However, as the spacing of the diatomic nuclei begins to expand from the close initial position, the outer barrier (on the right in the figure) begins to drop and the central barrier begins to rise. There will occur an optimum distance in which an electron confined to the “uphill” potential need only tunnel through the relatively thin central potential barrier (see Fig. 14 bottom). This separation is the critical ionization distance. A simple analysis of the shape of the potential surrounding two ions each with charge  $q$ , indicates that this critical ionization distance will occur roughly at

$$R_c \approx \frac{4qe^2}{I_p} \quad (30)$$

If we make the approximation that the binding potential of charged ions in a diatomic are roughly given by the unionized molecular ionization potential divided by  $q$ , we find that the critical distance is independent of charge state. For a diatomic such as  $H_2$ , the ionization potential of 15.4 eV suggests a critical ionization distance of about 3.7 Å (about 7 atomic units or 5 times the equilibrium separation). A similar calculation for  $I_2$  suggests a critical ionization distance of 10 a.u. for all of the iodine charge states.<sup>145</sup>

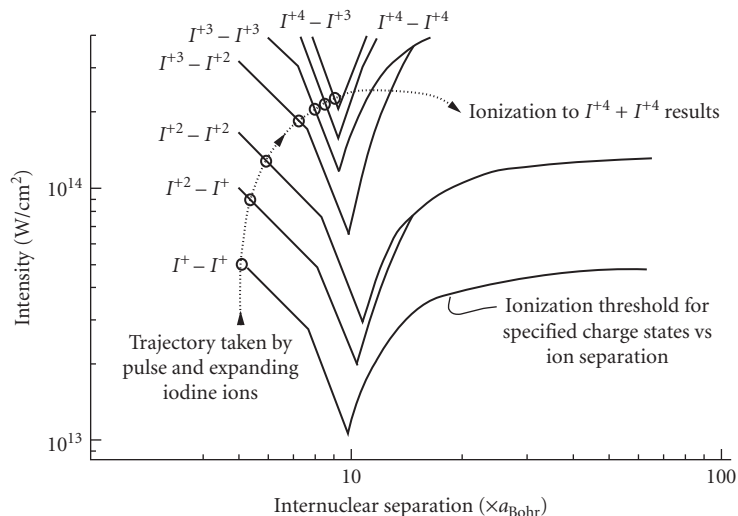
This ionization enhancement at the critical distance explains the appearance of higher charge states in molecular strong field ionization at lower intensity than might be expected.<sup>35</sup> The multiple ionization dynamics follow a multistep process. After some initial ionization of a high  $Z$  molecule, the ions begin to separate. If they come apart to the critical distance on a time scale faster than the laser pulse passes [predicted by Eq. (28) for most small molecules], the nuclei will be rapidly ionized to higher charge states at the critical distance, leading to an energetic Coulomb explosion of the higher charged ions from  $R_c$  separation. This process is described in Fig. 15<sup>156</sup> in which the barrier suppression ionization thresholds are plotted for various charge states of iodine as a function of  $I_2$  separation along with the trajectory of an iodine molecule in a strong field.

There is some theoretical evidence for the presence of a second, more closely spaced critical ionization distance in molecule strong field ionization.<sup>157</sup> This effect, often called charge-resonance enhanced ionization (CREI), is a quantum mechanical effect and results from a localization of part of the electron wavepacket in the upper well at an internuclear separation smaller than  $R_c$  described above. There is presently no experimental evidence for this second critical distance.

## Triatomic and Larger Molecules in Strong Fields

The fragmentation of molecules larger than a diatomic quickly becomes more difficult to describe, though the principles described in the last two subsections apply, particularly if the molecule is linear. However, the ionization dynamics are complicated and many fragmentation channels are usually observed at intensity  $>10^{14}$  W/cm<sup>2</sup>.<sup>138</sup> For example, even in a molecule as simple as  $CO_2$  multiple channels such as  $O^+ + CO^+ + 4.7$  eV and  $O^{2+} + CO^+ + 8.5$  eV are observed with about equal probability when irradiated in near-IR pulses of intensity  $\sim 10^{15}$  W/cm<sup>2</sup>.<sup>138</sup> Many fragmentation channels occur not as a sequence of two independent bond fragmentations but occur as one, nonsequential rupture of both bonds.

Tunnel ionization rates for multinuclear molecules which are linear can often be found by treating the molecule as a single elongated well potential from which the electron can tunnel in the laser field.<sup>158</sup> These so-called structural tunnel ionization models have been employed successfully to explain ionization of more complex molecules, such as benzene,<sup>159</sup> though multielectron effects play a much larger role, and the single active electron approximation implicit in tunnel ionization theory is inaccurate.



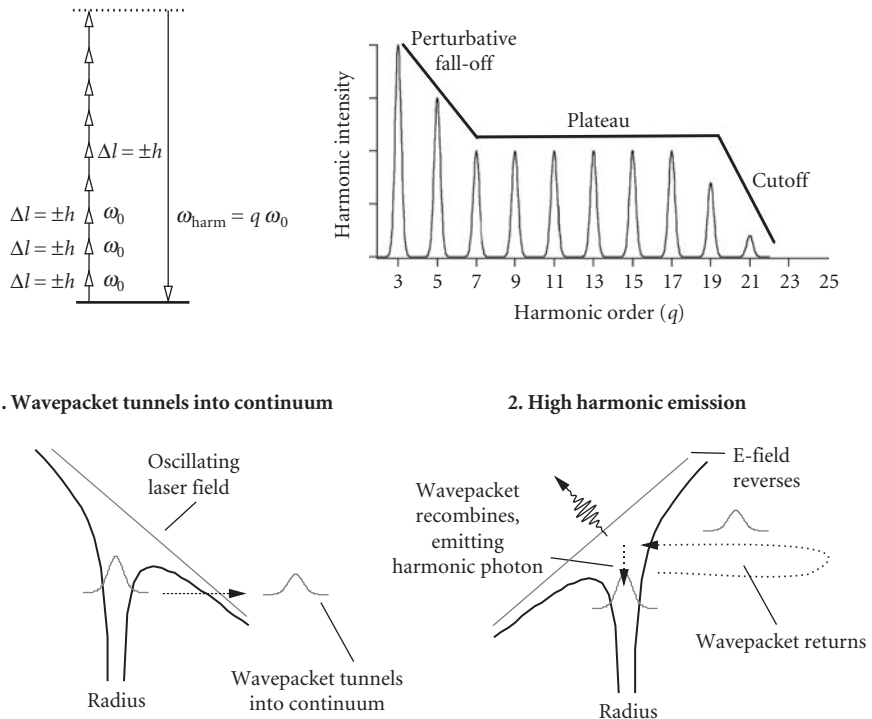
**FIGURE 15** The solid lines in this plot show the BSI ionization threshold for various iodine ion pairs aligned along the laser field as a function of nuclear separation. The large dip in ionization threshold at around  $10a_{\text{Bohr}}$  for all charge state pairs is a consequence of the critical ionization distance described in Fig. 14. The dashed line shows the trajectory in terms of laser intensity and nuclear separation that an iodine molecule undergoes when it is irradiated by a 150-fs pulse at an intensity of  $2.5 \times 10^{14} \text{ W/cm}^2$  showing the various charge states created by BSI ionization in the pulse as the  $\text{I}_2$  molecule Coulomb explodes. The presence of the critical ionization dip results in higher charge state (+4 for both ions) than would be achieved at this intensity by irradiation of a single iodine atom. (Plot adapted from that of Ref. 156.)

## 21.7 STRONG FIELD NONLINEAR OPTICS IN GASES

### High Order Harmonic Generation

When a strong field pulse of light propagates through an extended gas a number of new phenomena occur. These occur when the gas density is high enough that coherent optical and nonlinear optical effects become important, a point that occurs in a practical sense in gases with density above about  $10^{17} \text{ cm}^{-3}$ . The single atom or single molecule interactions described above come into play and often are the seeds to the initiation of other physical effects, the most common of which is strong field ionization leading to plasma formation. However, another important strong field effect which manifests itself at intensity just at or slightly below the intensity threshold for ionization is the generation of radiation at harmonics of the laser field.<sup>7,24,38,160,161</sup> This process, termed high order harmonic generation (HHG), is described in greater detail in other chapters of this volume so only a rudimentary overview is given here.

Harmonic generation in gases subject to strong laser fields arises from the nonlinear oscillations of the bound electrons in the gas's atoms. This is generally performed in gases of rare gas atoms, though HHG from molecular<sup>162</sup> and clustering<sup>163</sup> gases is also possible. At modest intensity ( $<10^{14} \text{ W/cm}^2$ ), HHG can be thought of as a multiphoton process, illustrated in the upper left of Fig. 16. In this picture an atom simultaneously absorbs  $q$  photons from the intense light field and then re-emits a photon with energy  $q\hbar\omega_0$ . Since free atoms in a gas exhibit a centro-symmetric potential, angular momentum must be conserved. This constraint, combined with the fact that the absorption and emission of a



**FIGURE 16** Simple view of the various aspects of high order harmonic generation physics. In the upper left, the multiphoton view of HHG is illustrated showing why only odd harmonics are possible given the need to conserve momentum by the interaction with atoms in a gas. The plot in the upper right is a generalized illustration of the character of a usual HHG spectrum at nonperturbative intensities ( $>10^{14}$  W/cm $^2$ ) showing the presence of an initial fall-off of yield with harmonic order at low orders followed by a long plateau of harmonics at roughly constant yield terminated by a cutoff. The bottom pictures illustrate the quasi-classical picture of HHG in which the generation of harmonic photons can be thought of as a result of a tunnel ionized electron recombining with its parent ion upon return to the nucleus in the field.

photon is accompanied by the change in angular momentum of  $\pm\hbar$ , indicates that only odd harmonics of the light field can be emitted. (It also indicates that harmonics cannot be produced in a gas with circularly or elliptically polarized light.<sup>164,165</sup>) Because all of the atoms in a gas are driven in this way harmonically, their emitted radiation will add coherently and the emitted harmonic radiation will propagate in the same direction as the drive laser and will retain many of the temporal and coherence properties<sup>166</sup> of the driving laser field. More accurately, HHG can be thought of as arising from the nonlinear polarization induced in a medium of density  $n_g$  such that  $\mathbf{P}(t) = n_g \mathbf{d}(t)$ , where  $\mathbf{d}(t)$  is the induced atomic dipole. In the single active electron approximation,  $\mathbf{d}(t) = \langle \psi(t) | \mathbf{er} | \psi(t) \rangle$ , where  $\psi(t)$  is the time-dependent wave function of the laser-driven atom.

This dipole, when driven very nonlinearly by a strong light field, will have Fourier components,  $\mathbf{d}(q\omega_0)$ , at frequencies  $q\omega_0$  out to rather high harmonic orders (where  $q$  is an odd integer). In the weak field regime, where perturbation theory is appropriate,  $\mathbf{d}(q\omega_0)$  varies as the  $q$ th power of the electric field, resulting in a harmonic yields which increase as the  $q$ th power of the incident intensity. Such behavior is indeed observed at intensity below about  $10^{13}$  W/cm $^2$  in gases of noble gas atoms at moderate harmonic number (say  $q = 3$  to  $9$ ). However, in a strong field, at intensity of  $10^{14}$  to  $10^{15}$  W/cm $^2$  the nonperturbative behavior of the laser driven atom leads to an atomic dipole of the  $q$ th harmonic

that will vary with a power law,  $I^p$ , that is usually well below the harmonic order ( $p < q$ ).<sup>167</sup> In most strong field interactions in near-IR pulses at orders of  $q = 11$  to 101,  $p$  will typically rest in the range of 5 to 8.<sup>7</sup>

Harmonic generation in this nonperturbative regime leads to a dramatic spectrum of harmonics that differs markedly from that expected from simple, multiphoton arguments. The emitted harmonic spectrum in this nonperturbative regime usually exhibits behavior illustrated in Fig. 16. The yield of the low order harmonics, out to perhaps the 5th or 7th order, falls exponentially, as expected under perturbation theory. However, the yield of harmonics at higher orders will then remain roughly constant, out to rather high order, a feature usually termed the HHG plateau. This plateau is then followed by an abrupt cutoff in harmonic production. Extremely high orders of harmonics from near-IR lasers have been demonstrated, with  $q > 101$  achievable with sub-100 fs laser pulses. When extremely short ( $< 20$  fs) pulses are used, the gas atoms can survive to an even higher intensity resulting in extremely high order harmonic production. Orders well over  $q \sim 201$  can be produced with such pulses in high ionization potential atoms such as helium,<sup>6,168</sup> though the spectrum loses its distinct harmonic character at these very high orders. Obviously, conversion of a near-IR laser to such high-order results in light with wavelengths in the XUV and soft x-ray region (2 to 30 nm), and as such represents an attractive means for generation coherent pulses in this soft wavelength region.

**Quasi-Classical Model of High Harmonic Generation** In the strong field regime, it is possible to describe HHG with a quasi-classical model, much as strong field ionization and ATI can be described in this regime.<sup>10,11</sup> Again, such a model is appropriate when the light field meets the condition that  $\gamma_k < 1$ . The mechanism for producing harmonic radiation by this model is illustrated in Fig. 16 at the bottom. The strong laser field can induce tunneling of the bound electron wavepacket; this freed electron wavepacket oscillates in the laser electric field. Electrons freed at certain phases of the laser oscillation can return to the vicinity of the nucleus and recombine back down to its initial ground state, emitting a photon of energy  $I_p + \epsilon_{\text{osc}}$ . The periodic return of many wavepackets leads to emission of radiation at well-defined harmonics of the light field.<sup>169</sup>

The energy of the emitted photon depends on the electron's energy upon return to the nucleus. As Eq. (24) illustrates, if the electron is born by tunneling at a phase  $\phi_0$ , then the electron can return to the nucleus to produce a harmonic photon with energy

$$\hbar\omega_{\text{Harm}} = \frac{1}{2}m_e v_{\text{osc}}^2 (\sin\phi - \sin\phi_0)^2 + I_p \quad (31)$$

As mentioned in Sec. 21.5, analysis of Eqs. (24) and (31) indicates that the electron will return with maximum energy at  $\phi_0 = 17^\circ$  and  $197^\circ$  and does so, in that case, with energy  $3.17U_p$ . This analysis leads to a well-known formula for the *maximum* photon energy of the high harmonic spectrum, known commonly as the cutoff harmonic

$$q_{\text{cutoff}} \hbar\omega_0 \approx I_p + 3.2U_p \quad (32)$$

In most experimental situations,  $U_p$  is usually evaluated at the intensity at which ionization starts to saturate. Above this intensity, there are no further atoms to participate in the harmonic generation process so further increase in intensity does not lead to a higher order cutoff harmonic. This cutoff formula was first discovered via numerical simulations<sup>170</sup> and has been well confirmed in many experiments.<sup>6,7,168</sup>

This quasi-classical model for HHG predicts some important features of HHG. Because some time must elapse between the freeing of the electron by tunneling and its return to the nucleus to emit a photon, the emitted harmonic will pick up a phase shift with respect to the laser field.<sup>169,171</sup> This model indicates that this phase shift is intensity dependent and, therefore, has a consequence on the macroscopic phase matching of the harmonics.<sup>172</sup> Also note that Eqs. (24) and (31) indicate that most return energies can be generated by two different electron trajectories, resulting from liberation at two distinct phases in the laser field. The two trajectories, a short and a long trajectory, can

destructively interfere in the harmonic generation because of their differing phases resulting from their different times spent in the continuum before recombining with the parent nucleus.<sup>173,174</sup>

**Harmonic Yield and Phase-Matching Considerations** Because HHG is a parametric process that results from the coherent addition of radiation produced from the nonlinear oscillations of electrons from many atoms in the gas, the harmonic intensity is strongly affected not only by the single atom physics of the atomic dipole, but also by phase-matching processes. As in standard nonlinear optics and usual harmonic generation, the harmonic field will continue to grow along with the propagating laser as long as the HHG field is in phase and newly generated harmonic light can add coherently.<sup>175</sup> If this condition is preserved, the harmonic yield will increase as the square of propagation distance. However, phase shifts associated with differences in refractive index between the fundamental and the harmonic as well as phases intrinsic to a focused laser beam will lead to mismatches that will clamp the harmonic generation.

While there are a number of ways to generate harmonics, one of the most common ways is to focus a Gaussian-shaped beam into a gas medium of length  $L$  with density  $n_0$ . Calculating the harmonic yield is a very difficult problem, however, estimates can be simply made with a few assumptions. A simple model for the harmonic conversion yield can be delineated for a focused Gaussian beam with confocal parameter  $b$  (defined by usual Gaussian optics as  $b = 2\pi w_0^2/\lambda$ , where  $w_0$  is the usual  $1/e^2$  focal radius) and with the induced single atom dipole at the  $q$ th harmonic that varies as  $|d(q\omega)| = \xi_p |E_1|$ . The integrated energy yield of the  $q$ th harmonic generated by a square top pulse of duration  $t_p$  then is given by<sup>167</sup>

$$\text{Energy}_q = \frac{\pi^2 q^2 \omega_0 n_0^2 b \tau_p |d(q\omega)|^2 L^2 \left[ \frac{\sin\{(\Delta k + 2q/b - 2q/pb)L/2\}}{\{(\Delta k + 2q/b - 2q/pb)L/2\}} \right]^2}{p} \quad (33)$$

where  $\Delta k$  is a phase mismatch induced by the medium itself. The final sinc<sup>2</sup> factor is a strong field generalization of the phase-matching factor found in standard nonlinear optics and determines the coherence length

$$L_c = [\pi(\Delta k/2 + q/b - q/pb)]^{-1} \quad (34)$$

over which harmonic generation can build up. A medium length, longer than this coherence length will result in destructive interference and a clamp on the harmonic conversion.

The harmonic yield is determined by a complicated interplay of the laser propagation, the medium density, the atomic response, and loss of media through ionization. As a result, the harmonic conversion efficiency of high harmonics in the plateaus varies broadly and can range from  $10^{-8}$  times the input laser energy for very high harmonics ( $q \sim 31$  to  $101$ ) in tightly bound atoms (such as He or Ne)<sup>176</sup> up to as high as  $\sim 10^{-5}$  for moderate order harmonics ( $q \sim 23$  to  $31$ ).<sup>177</sup> The phase mismatch  $\Delta k$  usually arises at low intensity from the intrinsic dispersion of the gas itself between the fundamental and the harmonic. At higher intensity, as ionization becomes important,  $\Delta k$  will be determined by the dispersion of the plasma itself. In this regime when a plasma density of  $n_e$  is created by ionization

$$\Delta k_{\text{plasma}} \equiv \frac{2\pi n_e e^2}{qc\omega_0 m_e} (q^2 - 1) \quad (35)$$

At higher intensity in weakly focused beams (i.e., when  $b \gg L$ ) this plasma-induced phase mismatch dominates the high harmonic production process. For example, at a plasma density of  $10^{18} \text{ cm}^{-3}$ , the coherence length of the 31st harmonic implied by Eq. (35) is only  $\sim 10 \mu\text{m}$ . Therefore, harmonics are produced only over this length, even if the medium is substantially longer (as is usually the case).

## Attosecond Pulse Generation

The harmonic spectrum schematically illustrated in Fig. 16 in fact has a very broad bandwidth if the entire spectrum is considered as having a coherent phase relationship over the entire spectral window. This implies that such a broad spectrum, when Fourier transformed, results in a pulse, or a train of pulses, with duration well under 1 fs, that is, in the attosecond regime. This situation can indeed be achieved experimentally leading to the production of attosecond pulses with duration approaching 100 as.<sup>9,31,178–180</sup> The physical origin of this can be easily seen within the context of the quasi-classical model. The return of an electron during its HHG generating recollision can be thought of as producing a short burst of bremsstrahlung radiation with duration comparable to the return encounter of the electron. If a laser pulse is short enough, such a bright burst can be made to occur for only one laser cycle and, therefore, produce a single isolated burst of attosecond radiation. This process is described at length in another chapter in this volume.

## 21.8 STRONG FIELD INTERACTIONS WITH CLUSTERS

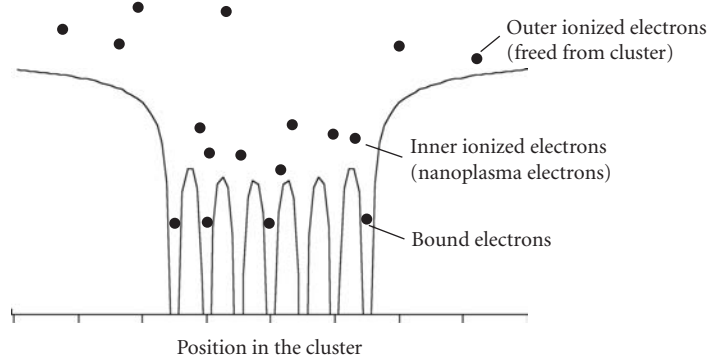
When a strong laser field interacts with a cluster of atoms, collective effects not present in the interaction of strong field pulses with ions or small molecules come into play.<sup>19,39,181–183</sup> Here clusters refer to assemblages of greater than  $\sim 100$  atoms on one hand, but assemblages whose spatial dimension is still well below the laser wavelength, that is, particles with diameter  $< 100$  nm or  $< 10^6$  atoms. Such clusters are usually van der Waals bonded assemblies of atoms or small molecules. Large, easily polarizable atoms such as Xe or Kr form clusters most easily, though even small atoms or molecules, such as  $H_2$  can be made to cluster under the right circumstances.

### Ionization Mechanisms in Clusters

Clusters will ionize in strong laser fields at intensities in which single atoms begin to ionize. In the cluster, however, there are two aspects of the ionization that must be considered, the inner ionization of the constituent atoms and ions and the outer ionization, resulting from the removal of free electrons within the cluster out, away from the cluster.<sup>39</sup> Ionization of the cluster is shaped by the fact that the laser field penetrates completely through the cluster, even when many free electrons are retained in the cluster and act as a plasma. This can be seen by noting that the plasma skin depth  $\lambda_p = c/(\omega_p^2 - \omega_0^2)^{1/2}$  is almost always much smaller than the cluster diameter, even at solid electron density  $n_e$  (note that  $\lambda_p \sim 20$  nm at solid density). Here  $\omega_p = (4\pi e^2 n_e / m_e)^{1/2}$  is the plasma frequency (the resonant frequency at which electron waves in a plasma oscillate).<sup>184)</sup>

**Inner Ionization Processes in the Cluster** When a strong field light pulse begins to interact with the initially unionized cluster the constituent atoms in the cluster undergo ionization. This process is usually termed inner ionization because the electrons liberated from the atoms within the cluster do not necessarily exit the cluster as a whole. If these electrons linger in the cluster, they produce a nanoplasma which has unique collective properties.<sup>181</sup> Inner ionization in the early stages of the laser interaction is usually dominated by quasi-classical tunnel ionization. The tunnel ionization of atoms within the cluster can be enhanced in a manner similar to the enhancement of ionization in diatomic molecules resulting from the suppression of the binding potential from neighboring ions in the molecule (discussed in Sec. 21.6).<sup>185</sup> The presence of nearby ions in the cluster can succeed in lowering the Coulomb binding potential (as illustrated in Fig. 17), and tunnel ionization can be greatly enhanced. This process has been termed “ionization ignition.”<sup>186</sup> A second process can also increase the rate of inner ionization in the cluster. This ionization occurs by collisional ionization by free electrons in the cluster, driven in an oscillatory motion by





**FIGURE 17** Plot of the Coulomb potential of ions arrayed in a cluster. The close proximity of many ions can suppress the barrier of the binding potentials, enhancing the tunnel ionization rate in the cluster. Some ionized electrons, however, will be confined to the cluster potential as a whole, resulting in the formation of a nanoplasma.

the strong laser field. The rate of this laser-driven collisional ionization can be calculated by using the well-known Lotz formula for ionization<sup>187</sup>

$$W_{\text{las}} = n_e \frac{a_i Q_i}{\pi I_p} \sqrt{\frac{1}{m_e U_p}} \int \frac{1}{2K_e} \frac{\ln(K_e/I_p)}{\sqrt{1-K_e/2U_p}} dK_e \quad (36)$$

Here  $a_i \approx 1.1 \times 10^{-37} \text{ cm}^2 - \text{erg}^2$ , and  $Q_i$  is the number of electrons in the outer shell of the ion. This laser driven collisional ionization rate tends to dominate the ionization in the cluster, usually being higher than the tunneling rate for most solid density cluster plasmas.<sup>181</sup> This laser driven collisional ionization in the cluster leads to the production of charges states well above those which are observed in strong field ionization of single atoms at similar intensity.<sup>188–190</sup> For example, Eq. (36) predicts that the ionization rate for  $\text{Ar}^{+15} \rightarrow \text{Ar}^{+16}$  is about  $0.001 \text{ fs}^{-1}$  at an intensity of  $5 \times 10^{17} \text{ W/cm}^2$  in a  $1\text{-}\mu\text{m}$  laser pulse. This would yield approximately 10 percent ionization to He-like Ar during a 100-fs pulse. On the other hand, the BSI theory indicates that an intensity of  $2 \times 10^{21} \text{ W/cm}^2$  would be needed to achieve significant ionization to  $\text{Ar}^{+16}$  by direct field ionization. This laser driven collisional ionization can lead to the production of very high charge states in clusters, even at modest laser intensity.<sup>189,190</sup>

**Outer Ionization of the Cluster** If space charge forces retain the inner ionized electrons in the body of the cluster, the removal of electrons from the cluster sphere, outer ionization, may take much longer than the initial inner ionization (see Fig. 17). There are two regimes for outer ionization in the strong field irradiation of the cluster. First, the laser field itself can extract the electrons from the cluster. In a very strong field (i.e.,  $E_0 \gg Q_{\text{clust}} e/R_0^2$ , where  $Q_{\text{clust}}$  is the number of electrons removed by outer ionization from the cluster, and  $R_0$  is the radius of the cluster), outer ionization occurs almost instantaneously and the cluster enters the Coulomb explosion regime. For laser fields comparable to or smaller than the binding field of the laser, it can be shown that the number of electrons outer ionized by the laser field is<sup>191</sup>

$$Q_{\text{clust}} \approx 12\pi \frac{n_e R_0^2 e E_0}{m_e \omega_p^2} \quad (37)$$

which is proportional to the square root of intensity. Alternatively, outer ionization can occur by electrons that have been heated sufficiently to escape the binding potential of the cluster. In this case, the rate of outer ionization by “free streaming” can be estimated assuming a Maxwellian electron energy distribution with temperature,  $T_e$ <sup>181</sup>

$$W_{fs} = n_e \frac{2\sqrt{2\pi}}{m_e^{1/2}(kT_e)^{1/2}} (K_{esc} + kT_e) \exp\left[-\frac{K_{esc}}{kT_e}\right] \times \begin{cases} \frac{\lambda_e}{4r} (12r^2 - \lambda_e^2) & \lambda_e < 2r \\ 4r^2 & \lambda_e > 2r \end{cases} \quad (38)$$

where  $K_{esc} = Q_{clust}e^2/R_0$  is the energy needed to escape,  $\lambda_e = (k_B T_e)^2 / 4\pi n_e (Z+1)e^4 \ln \Lambda$  is the electron mean free path in the cluster and  $\ln \Lambda$  is the well-known plasma Coulomb logarithm.

## Coulomb Explosion of Small Clusters

If a cluster is stripped of most of its electrons via the outer ionization process very quickly, much faster than the cluster can expand, the cluster will disassemble by a Coulomb explosion. For the cluster to evolve in this limit, two conditions must be met (1) the intensity of the light field must be high enough and (2) the laser pulse must ramp up to the intensity needed for complete outer ionization must faster than the cluster expands.

The first condition is difficult to determine as the intensity needed for complete outer ionization is not easily calculated analytically; it depends on the dynamics of the driven electron cloud in the cluster. This can be estimated by requiring that the laser ponderomotive energy dominates the electron dynamics over the confining potential energy of the cluster,

$$U_p > \frac{Q_{clust}e^2}{R_0} \quad (39)$$

Here  $Q_{clust}$  is the total charge on the cluster sphere from electrons that have previously exited the cluster. The second condition mandates that the rise time of the laser pulse to the stripping ponderomotive potential be faster than the explosion time of the cluster. This characteristic explosion time can be estimated by calculating the time required for a charged cluster to expand from its initial radius,  $a$ , to twice its initial radius. Integration of the motion of a charged deuterium cluster yields for this characteristic explosion time:

$$\tau_{Coul} \approx \sqrt{\frac{m_i}{n_i Z^2 e^2}} \quad (40)$$

where  $m_i$  is the mass of the ions and  $n_i$  is the density of atoms in the cluster. Note that  $\tau_{Coul}$  is independent of cluster radius and equals about 15 fs for fully stripped hydrogen clusters. Equation (40) indicates that the Coulomb explosion limit can usually be accessed in clusters only with intense, sub-100-fs laser pulses.<sup>192</sup>

If a Coulomb explosion is driven and it can be assumed that all electrons are removed prior to any ion movement, the ion energy spectrum from a single exploding cluster, denoted  $f_{sc}(\epsilon)$ , can be stated as<sup>193</sup>

$$f_{sc}(\epsilon) = \begin{cases} \frac{3}{2} \epsilon_{max}^{-3/2} \epsilon^{1/2} & \epsilon \leq \epsilon_{max} \\ =0 & \epsilon > \epsilon_{max} \end{cases} \quad (41)$$

where  $\epsilon_{max}$  is the maximum energy of ions ejected and corresponds to those ions at the surface of the cluster,  $\epsilon_{max} = 4\pi e^2 n_i R_0^2 / 3$ . In hydrogen clusters, for example,  $\epsilon_{max}$  is about 2.5 keV for 5 nm

clusters. This ion spectrum is peaked near  $\varepsilon_{\max}$ . In most experiments, however, the clusters irradiated are composed of a broad size distribution. This tends to broaden the ion energy distribution observed.

## Nanoplasma Description of Large Clusters

In the limit of a Coulomb explosion, the principal absorption mechanism for laser light is in the deposition of the energy needed to expel the electrons from the charged cluster. The other limit of strong field laser cluster interactions occurs when there is little or no outer ionization subsequent to significant inner ionization in the cluster. This tends to occur in larger clusters and clusters composed of higher  $Z$  atoms which can become more highly charged. When outer ionization lags inner ionization, a nanoplasma is formed in the cluster.<sup>181</sup> In this case, the laser interactions with the cluster can be dominated by collective oscillations of the electron cloud.

**Cluster Electron Heating** Because the electrons are confined to the cluster by space charge forces, they can acquire energy from the intense laser field. Because of the collective oscillation of the electron cloud, the electric field inside the cluster will be<sup>72</sup>

$$E = \frac{3}{|\varepsilon_D + 2|} E_0 \quad (42)$$

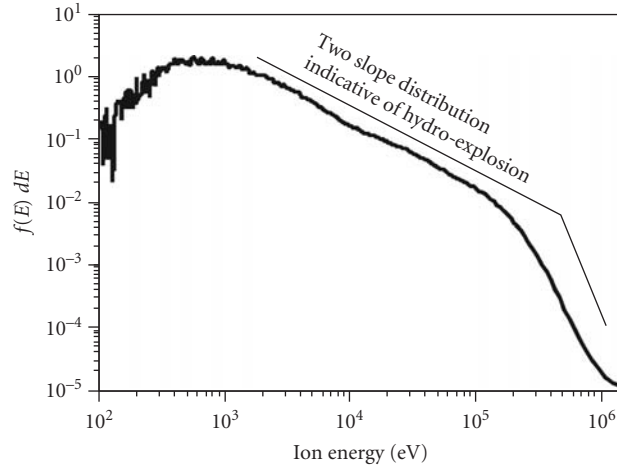
where the dielectric constant can usually be taken to be that from a simple Drude model for a plasma  $\varepsilon_D = 1 - \omega_p^2 / \omega_0(\omega_0 + i\nu)$ .  $\nu$  is the electron-ion collision frequency (discussed below). Equation (42) indicates that the field is enhanced in the cluster when the laser frequency is  $3^{1/2}$  times the plasma frequency, that is, when  $n_e/n_{\text{crit}} = 3$ . ( $n_{\text{crit}} = m_e \omega_0^2 / 4\pi e^2$  is the plasma critical density, at which the laser oscillates at the plasma resonance frequency.) This resonance condition corresponds to a state in which the laser frequency matches the natural collective oscillation frequency of the electron cloud in the spherical cluster. This resonance condition is accompanied not only by an increase of the field in the cluster but also an increase in the electron heating rate and cluster absorption of energy from the laser. The heating rate of electrons in the cluster is then<sup>194</sup>

$$\frac{\partial U}{\partial t} = \frac{9\omega_0^2 \omega_p^2 \nu}{8\pi} \frac{1}{9\omega_0^2(\omega_0^2 + \nu^2) + \omega_p^2(\omega_0^2 - 6\omega_0^2)} |E_0|^2 \quad (43)$$

The choice of collision frequency in this equation is complicated by various aspects of strongly coupled plasma physics, but for most interactions in which the electrons in the cluster are dominated by the driven motion of the laser electric field, we can say that the collision frequency most relevant for strong field cluster interactions is<sup>195</sup>

$$\nu_E = \frac{16Z^2 e n_i m_e \omega_0^3}{E_0^3} \left( \ln \left[ \frac{eE_0}{2m_e \omega_0 \nu_e} \right] + 1 \right) \ln \Lambda \quad (44)$$

where  $Z$  is the average charge state of ions in the cluster and  $\nu_e = (k_B T_e / m_e)^{1/2}$ . The principal consequence of this resonance occurs after the cluster has been initially inner ionized to an electron density near that of a solid ( $\sim 10^{23} \text{ cm}^{-3}$ ). As the cluster expands, its resonance frequency falls and, if the laser pulse is long enough, will come into resonance with the laser. This is accompanied by a violent driving of the cluster nanoplasma cloud with rapid energy deposition in the cluster. Electron temperatures of many tens of keV are possible, even with modest ( $< 10^{16} \text{ W/cm}^2$ ) drive intensities. When such cluster nanoplasmas are irradiated in a dense gas jet, very high (near 100 percent) absorption of the laser occurs<sup>196</sup> and bright x-ray emission, high ion temperatures, and even nuclear fusion can be observed.<sup>182,197-200</sup> Because of this dynamic plasma resonance, there is often an optimum pulse



**FIGURE 18** Example of the ion spectrum resulting from the irradiation of Xe clusters in the nanoplasma regime. These  $\sim 2500$  atom Xe clusters were irradiated by a 100-fs pulse at an intensity of  $\sim 2 \times 10^{16}$  W/cm $^2$ . This illustrates how ions with energies ( $\sim 1$  MeV in these data) much higher than  $U_p$  ( $\sim 1.2$  keV here) can be generated during the interaction with clusters. (Figure adapted from Ref. 189.)

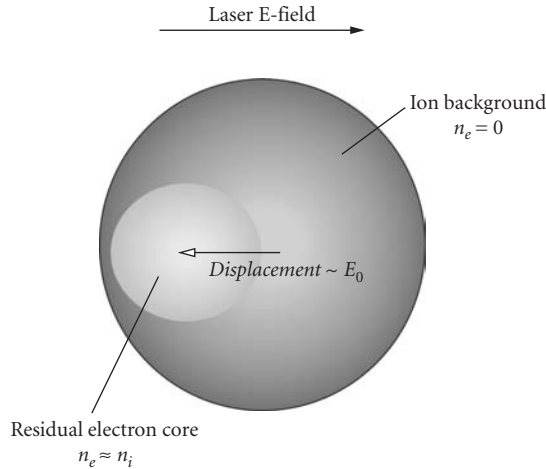
duration for heating clusters in this manner.<sup>201</sup> For example, small Ar clusters can expand into resonance on a 100-fs timescale, while large ( $>10$  nm) Xe clusters can take 1 to 5 ps to reach resonance with a near-IR laser.<sup>202</sup>

**Cluster Expansion Mechanisms** In the nanoplasma regime, the cluster will expand, though not by Coulomb repulsion forces between ions, as it does in the Coulomb explosion regime. Instead, it will expand by the ambipolar potential created by the thermal pressure of the hot electrons in the nanoplasma,  $p_e = n_e k T_e$ . This pressure will lead the cluster to explode on a time scale of  $t_{\text{expl}} \approx R_0 (m_e / Z k T_e)^{1/2}$ . The resulting ion spectrum will be characteristic of that from a hydro-dynamically exploding plasma, as illustrated in Fig. 18. The hot tail that results from such an expansion can lead to the production of ions with hundreds of keV to MeV of energy, even in laser pulses with ponderomotive energies of only  $\sim 1$  keV (an intensity of about  $10^{16}$  W/cm $^2$  in a near-IR field).

It should be noted that the simple model used here to describe the clusters in the nanoplasma regime rely on the assumption that the cluster remains more or less uniform density. During the expansion of the cluster, it will devolve from a uniform density to a plasma with a radial plasma gradient. In this case, the absorption is likely dominated by resonance absorption (described in Sec. 21.10) at the critical density surface around the cluster circumference.<sup>203</sup> In addition to the absorption processes described, various plasma processes can occur, such as electron ion equilibration and electron recombination, affecting the cluster dynamics.

## Intense Laser Pulse Interactions with Clusters in the Nonneutral Regime

The description of the dynamics of a cluster in a strong laser field in a regime intermediate to the Coulomb explosion and the nanoplasma regimes, when outer ionization is only partial, is complicated. Simple electrostatic theory tells us that if some of the electrons have been outer ionized, then



**FIGURE 19** Schematic showing the geometry of the electron cloud within the ion sphere of a partially charged cluster. The electron cloud contracts to create a quasi-neutral core which can be driven from side to side by the strong laser field. When the oscillations are large enough that some of the electron cloud is pulled out away from the ion sphere, outer ionization of these electrons occurs.

the cluster, no longer quasi-neutral will evolve so that the remaining electrons will collapse into an inner, neutral cloud within the cluster, a situation illustrated in Fig. 19.<sup>191</sup> The laser field will then pull the electron cloud over by a distance  $d_0 = 3eE_0/m_e\omega_p^2$ . This extracts electrons through laser field acceleration.

**Electron Stochastic Heating** In the intermediate regime of cluster ionization, there will be a population of electrons that will be driven by the laser in the vacuum surrounding the cluster sphere. These electrons can pass in and out of the cluster a number of times, picking up energy from the laser at each pass, in a manner similar to the vacuum heating described in Sec. 21.10. This heating is called stochastic heating and leads to the generation of a population of very high energy electrons. It can be shown that the maximum energy that can be reached by electrons in this manner is  $\mathcal{E}_{\max} \sim m_e R_0^2 \omega^2$ , an energy which can be well in excess of the ponderomotive energy if the cluster is much larger than a quiver amplitude.<sup>191</sup>

## 21.9 STRONG FIELD PHYSICS IN UNDERDENSE PLASMAS

In this section, we will discuss the physics involved in the interaction of strong field electromagnetic pulses with underdense plasma, namely, plasma in which the plasma frequency  $\omega_p = \sqrt{4\pi e^2 n_e / m_e}$  is smaller than the laser frequency,  $\omega_0$ . In this situation, the refractive index of the plasma  $n = \sqrt{1 - \omega_p^2 / \omega_0^2}$ , is real and the laser field can propagate through the plasma. At high intensity, various field driven coupling mechanisms occur which deposit energy into the plasma fluid through interactions with charged particles individually or through interactions with plasma waves. These interactions tend to heat the plasma electrons as a whole or they directly couple laser energy into a small population of fast electrons.

## Strong Field Inverse Bremsstrahlung Heating

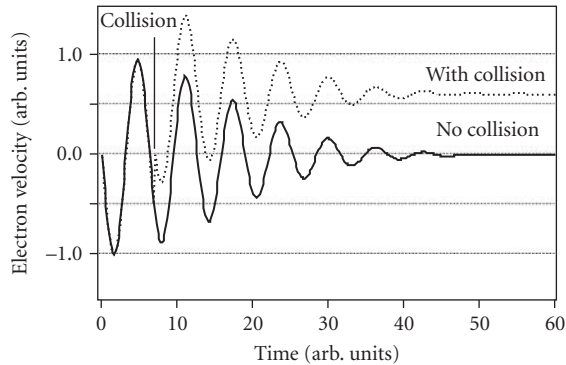
Perhaps the most basic mechanism for an intense light pulse to heat underdense plasma is through inverse bremsstrahlung: collisional heating. In the strong field regime with IR or optical wavelength pulses, the process can be accurately described classically. The nature of the heating is illustrated in Fig. 20. When an oscillating electron in the laser field collides with an ion and scatters from the Coulomb field of the ion, its adiabaticity is broken, acquiring some random, thermal energy from the laser field. The heating rate of electrons is then some appropriate electron-ion collision frequency times the amount of energy gained per collision, which can usually be taken to be the ponderomotive energy. So the heating rate per electron is  $dU/dt|_{IB} \approx \nu_{ei} U_p$ .<sup>184</sup>

At low intensities, the electron-ion collision frequency can be taken to be the usual temperature-dependent plasma electron-ion collision rate.<sup>204</sup> In the strong field regime the picture is a little different. When  $U_p > k_B T_e$  the electron motion is dominated not by thermal motion but instead by the ponderomotive motion of the laser, which means that the standard collision frequencies utilized in normal plasma physics cannot be used. There have been various models published to describe the electron heating and dynamics in this strong field limit.<sup>195,205</sup> A good model for heating of electrons in a strong field leads to a heating rate of<sup>206</sup>

$$\left. \frac{\partial U}{\partial t} \right|_{\text{las}} = \frac{16Z^2 n_i e^3 m_e \omega_0}{3E_0} \ln \left[ \frac{eE_0}{m_e^{1/2} \omega_0 (kT_e)^{1/2}} \right] \ln \Lambda \quad (45)$$

Again,  $\ln \Lambda$  is the usual plasma Coulomb logarithm, which can be taken for the underdense plasmas treated here to be  $\Lambda = (kT_e)^{3/2} / 4\pi^{1/2} Z e^3 n_i^{1/2}$ .

Notice that in this high-intensity regime, the heating rate actually decreases with increasing intensity (as  $I^{-1/2}$ ), which results from the strong decrease of the Coulomb scattering cross section with increasing electron velocity. (The heating rate also decreases with increasing wavelength for the same reason.) It is interesting to note that, when the full kinetic evolution of the electron energy distribution function is solved in the high-field limit, the electron distribution approaches that naturally of a Maxwellian, independent of any electron equilibration.<sup>206</sup>



**FIGURE 20** Calculation of the classical trajectory of an electron in a laser pulse which decays in time adiabatically to zero. The electron velocity falls to zero with the laser field and acquires no net energy when no collision takes place. If, however, an instantaneous  $90^\circ$  collision occurs, this breaks the adiabaticity of the electron's oscillation leaving it with some residual velocity after the pulse field has fallen to zero. This is the origin of inverse bremsstrahlung heating.

## Plasma Instabilities Driven by Intense Laser Pulses

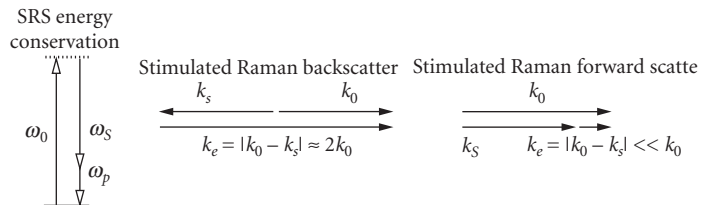
A salient feature of high-intensity laser interactions with plasmas is that plasmas can support collective motion, including coherent waves, which couple to the electromagnetic field of the laser. These plasma waves manifest themselves in various ways, such as in ion acoustic waves, (which are essentially sound waves in the plasma gas<sup>184</sup>). Because a plasma is composed of a positively charged ion fluid and a negatively charged, light electron fluid, it can also support electrostatic and propagating electromagnetic waves, often called Langmuir waves, composed of an oscillating electron density fluctuation.

Because the laser field is an electromagnetic wave, it can couple energy to these plasma waves as the pulse propagates through the plasma. For example, if the pulse drives ion acoustic waves, the process is termed Brillouin scattering. This process is usually not significant in ultrashort pulse, high-intensity interactions because the mass of the ions are so large that the growth rate of such instabilities is too slow for the laser pulse duration. Of greater importance to intense ultrashort laser pulses (with  $I > \sim 10^{16}$  W/cm<sup>2</sup>) is the coupling of laser energy to electron plasma waves. This coupling can occur through a panoply of mechanisms, such as the so-called  $2\omega_p$  mechanism,<sup>207</sup> but the most important process in the strong field regime is electron Raman scattering.<sup>208</sup> The energetics of this process are described in Fig. 21. In Raman scattering, one laser photon is coupled to an electron plasma wave (which naturally oscillates at the plasma frequency) and results in the production (or destruction) of one quanta of the plasma wave with the simultaneous production of a photon at a shifted wavelength. The scattered light has frequency downshifted if energy added to the plasma wave (the Stokes process) or upshifted if energy is absorbed from the plasma (the anti-Stokes process).

In an intense laser pulse this process can undergo positive feedback, resulting in an exponentially growing instability, coupling a significant amount of light energy into the electron plasma wave (which is usually a longitudinal electron density fluctuation). How this happens can be seen if one considers what happens if a Stokes photon is produced in a Raman scattering event at a frequency of  $\omega_s = \omega_0 - \omega_p$ . This new field can add to the fundamental laser oscillation creating a beat frequency of  $\omega_b = \omega_0 - \omega_s = \omega_p$  which can then, in turn, drive the plasma wave resonantly, increasing its amplitude and further driving the production of more Stokes photons. This feedback process leads to exponential growth of the Stokes field and the plasma wave, and is usually referred to as stimulated Raman scattering (or SRS).

The growth rate, defined by noting that the scattered wave amplitude and scattered light field grow as  $\sim e\Gamma t$ , can be found from the coupled nonlinear equations describing the Stokes field (which is the one which will be resonant, growing the fastest) and the plasma wave. In the nonrelativistic limit, this growth rate is<sup>184</sup>

$$\Gamma_{\text{SRS}} = \frac{k_e}{2} \sqrt{\frac{U_p}{m_e} \frac{\omega_p^2}{\omega_{\text{BG}}(\omega_0 - \omega_{\text{BG}})}} \quad (46)$$



**FIGURE 21** On the left, the energetics of Raman scattering in a plasma are demonstrated for the Stokes process in which a laser photon is scattered by a plasma wave creating a lower energy Stokes photon and depositing  $\hbar\omega_p$  of energy into the plasma wave. The right-hand drawing illustrates the conservation of momentum for SRS backscatter and forward scatter, showing that the electron wave k-vector, and hence the growth rate, are maximum for the backscatter case.

here  $\omega_{\text{BG}}$  is the Bohm-Gross plasma frequency  $\omega_{\text{BG}} = \sqrt{\omega_p^2 + 3k_e^2(k_B T_e)^2/m_e}$ , which is simply equal to the plasma frequency for a cold ( $T_e = 0$ ) plasma, and  $k_e = |\mathbf{k}_e|$  is the magnitude of the wave-number of the plasma wave, defined by conservation of momentum by  $\mathbf{k}_e = \mathbf{k}_0 + \mathbf{k}_s$ . Equation (46) illustrates that the growth rate of this instability increases as the square root of the light intensity. In underdense plasma such that  $\omega_0 \gg \omega_p$ ,  $\omega_{\text{BG}}$  the growth rate also scales with the square root of laser drive wavelength. Consequently, high intensity, long wavelength light pulses are much more susceptible to the SRS instability. In practice, an intense light pulse will cause the instability to grow from density fluctuations arising from thermal noise present in any plasma. When the laser pulse has passed, the plasma waves will tend to damp either by collisional processes in the plasma or by noncollisional processes such as Landau damping.<sup>184</sup>

The growth of SRS has two significant consequences: (1) it acts to absorb energy from the intense laser pulse coupling its energy to the plasma electrons and (2) it can drive plasma waves to large amplitude, which, in turn generate high energy, nonthermal electrons. Often the hot electrons generated can have energy many times that of the ponderomotive energy, which means electrons of tens to hundreds of keV even at modest intensity (say  $\sim 10^{16}$  to  $10^{17}$  W/cm<sup>2</sup>). There are two important regimes of SRS.

**Stimulated Raman Backscatter** In a low density plasma ( $\omega_0 \gg \omega_p$ )  $|\mathbf{k}_0| \approx |\mathbf{k}_s|$ . From Eq. (46) it can be seen that for a given plasma density and laser intensity the growth rate is maximum when  $k_e$  is maximum. As Fig. 21 illustrates this occurs when the generated Stokes light is directly backscattered. In this case, when the plasma is cold, the growth rate in the nonrelativistic limit is  $\Gamma_{\text{SRS-bs}} \approx \sqrt{\omega_p \omega_0} U_p / m_e c^2$ . The growth time in this case is just the temporal pulse duration of the main pulse, since the Stokes field propagates backward through the main pulse. If the laser pulse spatial length is comparable to the length of the medium of interaction, a condition satisfied, for example, when an intense picosecond pulse propagates through a gas jet of a few mm in length, SRS backscatter will be the dominant plasma instability.<sup>209</sup> Practically speaking, SRS backscatter will be important—resulting in a significant amount of laser energy backscattered (>1 percent) and significant plasma heating—when  $\Gamma_{\text{SRS}} \tau_{\text{pulse}} \sim 6$  to 7. Equation (46) indicates that this will occur in a 100-fs pulse with wavelength near 1  $\mu\text{m}$  propagating through a plasma of  $n_e \sim 10^{18}$  W/cm<sup>2</sup> when the pulse intensity exceeds  $\sim 2 \times 10^{17}$  W/cm<sup>2</sup>.

**Stimulated Raman Forward Scatter** When the laser pulse is very intense, and the duration is short, so that SRS backscatter has little time to grow, the situation is different. In this case, SRS forward scattering is possible, with geometry illustrated in Fig. 21.<sup>210</sup> Now, though  $k_e$  is small the Stokes or anti-Stokes radiation copropagate with the intense drive laser, (and, in fact, both Stokes and anti-Stokes can be nearly resonant and grow at about the same rate<sup>211</sup>). The scattered radiation growth factor is now determined by the length of the pulse propagation in the plasma. This effect tends to be particularly important for pulses at relativistic intensity (i.e.,  $>10^{18}$  W/cm<sup>2</sup>) so relativistic effects must be included in deriving a growth rate. In this case, the growth rate, in terms of the normalized vector potential  $a_0$ , is<sup>66</sup>

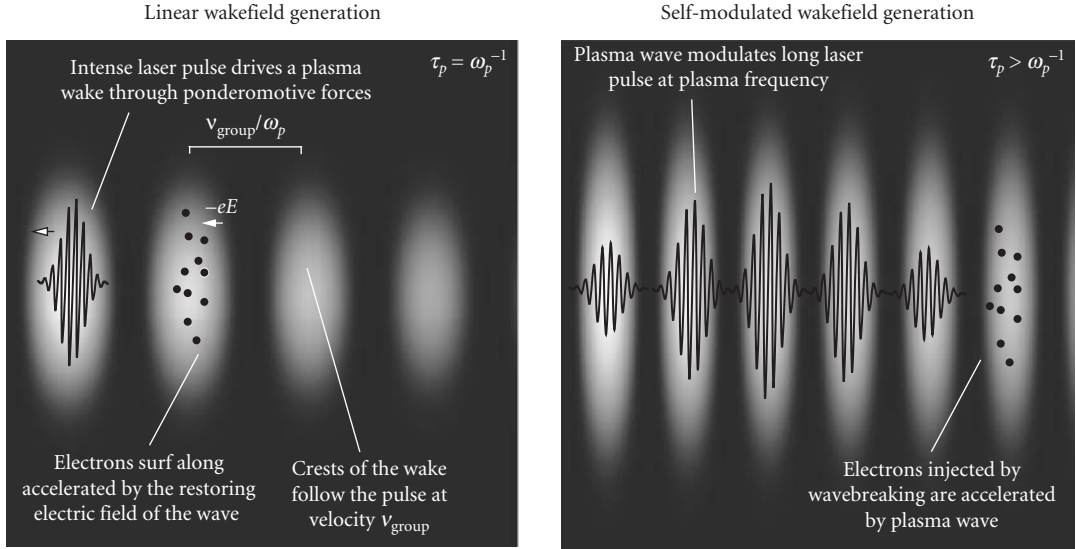
$$\Gamma_{\text{SRS-fs}} = \frac{\omega_p^2 a_0}{\sqrt{8\omega_0(1+a_0^2/2)}} \quad (47)$$

SRS forward scattering becomes important when  $\Gamma_{\text{SRS-fs}} L/c \sim 6$ , where  $L$  is the propagation length through the plasma. Equation (47) yields the surprising result that at strongly relativistic intensity  $\Gamma \sim 1/a_0 \sim 1/I^{1/2}$  so the growth rate actually decreases with increasing intensity. This is a consequence of the increase of the effective mass of the electrons when they are driven at relativistic oscillation velocities. Equation (47) indicates that a 1- $\mu\text{m}$  wavelength pulse traversing 5 mm of plasma at density  $10^{18}$  W/cm<sup>2</sup> will exhibit significant forward scattering when  $a_0 \approx 0.8$ , an intensity of  $\sim 1 \times 10^{19}$  W/cm<sup>2</sup>.

## Wakefield Generation and Electron Acceleration

The plasma instabilities discussed in the section “Plasma Instabilities Driven by Intense Laser Pulses” essentially arise from the fact that electron plasma oscillations can be driven to large amplitude by





**FIGURE 22** Schematic illustration of how wakefield acceleration works in two situations. On the left, the plasma wave is excited by the ponderomotive force of a laser pulse with duration comparable to the plasma oscillation time. On the right is illustrated the case in which the driving laser is longer than a plasma period, but through Raman forward scattering has become modulated at the plasma frequency.

the oscillating ponderomotive force of the strong light field. These plasma oscillations are longitudinal waves, with longitudinal electric fields acting as restoring forces on the oscillating electron density fluctuations. This situation is shown schematically in Fig. 22. The presence of these strong, oscillating electric fields has been investigated for a number of years as a means to accelerate electrons.<sup>14,15,32,212–217</sup> Electrons to be accelerated are either injected externally or get accelerated from the free electrons in the plasma itself, often through a process known as wave breaking (discussed below). Since the acceleration is accomplished through the creation of a plasma wave left in the wake of the ponderomotive force of the laser, this idea is termed plasma wakefield acceleration.

In a general sense, the idea is to expel electrons from a region in the essentially immobile background ions through the ponderomotive force of the laser. The phase velocity of this plasma wave, then, is just that of the group velocity of the laser pulse traveling through the plasma,  $v_g = c\sqrt{1 - \omega_p^2/\omega_0^2}$ . Electrons injected at the right phase of the plasma wave, if traveling at a velocity near this group velocity (i.e.  $\sim c$ ) can surf along with the wave, acquiring energy from it. The laser intensity required is set by the scheme in which the plasma wave is produced (detailed below) but in general the ponderomotive force,  $-\nabla U_p$  at the peak of the pulse should be sufficient to expel a sizable number of electrons from their background neutralizing ions. Practically this means that the required intensity is  $10^{16}$  to  $10^{18}$  W/cm<sup>2</sup> for  $\sim 1$ - $\mu\text{m}$  wavelength pulses in moderate density ( $\sim 10^{18}$  cm<sup>-3</sup>) plasmas. The longitudinal electric field that is produced in such an oscillating plasma wake,  $E_{\text{WF}}$  can be easily estimated using Poisson's equation and the fact that the wave moves at nearly  $c$  with an oscillation frequency of  $\omega_p$ <sup>32</sup>

$$E_{\text{WF}} = \eta\sqrt{4\pi m_e c^2 n_e} \quad (48)$$

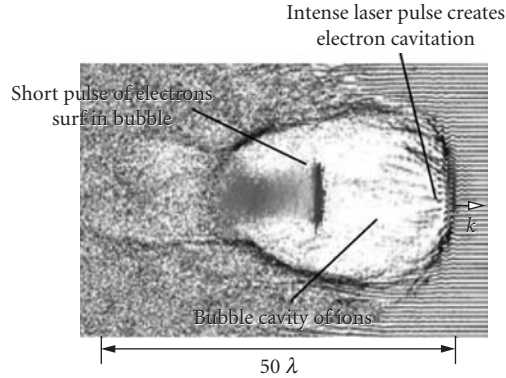
where  $\eta$  is the fractional plasma wave amplitude of the wakefield ( $\Delta n/n$ ). Equation (48) indicates that very large acceleration gradients are possible with plasmas. In a plasma of density  $10^{18}$  cm<sup>-3</sup> nearly 1 GeV/cm acceleration can be achieved if the laser pulse is intense enough to approach  $\eta \sim 1$ .

The accelerating field is limited by the fact that, as one pushes to higher fields, eventually the plasma wave becomes nonlinear. This means that the electron fluid velocity begins to exceed the wave phase velocity and the wave loses its coherence, a situation called wave breaking.<sup>184</sup> This nonlinear behavior can serve to inject electrons out of the coherent wave oscillation into the accelerating gradient of the wakefield.<sup>213</sup> It does, however, set a limit on the maximum electric field attainable. In general this maximum field is very difficult to predict, but a rough estimate can be made using the “cold wave-breaking” limit, which says that the maximum wakefield strength occurs when  $\eta \sim 1$ , that is when  $E_{\max} \approx m_e c \omega_p / e$ .<sup>66</sup>

The limit of acceleration with such laser driven plasma waves, at least in a single plasma stage, arises from the fact that there is a slight mismatch between the electron velocity and phase velocity of the plasma wave, so that electrons eventually move out of the accelerating phase of the wave and catch up to the electric field in the other direction, decelerating the electrons. This dephasing length can be found by assuming that the electrons are relativistic with velocity very near  $c$ , but that the plasma wave has velocity given by that of the laser pulse group velocity. Then the maximum length over which an electron can be accelerated before dephasing is  $L_{\text{dephase}} \approx 2\pi\omega_0^2 c / \omega_p^3$ . For the example just cited, this implies a maximum per-stage acceleration length of 3 cm. Because the acceleration field scales as  $n_e^{1/2}$ , while the dephasing length scales as  $n_e^{-3/2}$  there tends to be an advantage in using lower plasma density (subject to the constraint that it becomes more difficult to propagate an intense focused pulse over longer distances). In general, there are three methods of optical wakefield generation.

1. *Linear wakefield generation.* This method relies on nearly resonantly driving a wakefield in the plasma by matching the laser pulse duration to the plasma oscillation period, such that  $\tau_{\text{pulse}} \approx 2\pi / \omega_p$ .<sup>14,212</sup> This situation is schematically illustrated in Fig. 22 on the left. For the conditions cited in the above examples, the optimum plasma wave amplitude is achieved with a pulse of  $\sim 100$ -fs duration.
2. *Self-modulated wakefield generation.* When the laser pulse is much longer than the plasma oscillation period, it cannot resonantly drive the plasma wave. However, as described in the section “Plasma Instabilities Driven by Intense Laser Pulses,” plasma instabilities can lead to the creation of radiation with frequency shifted by the plasma frequency.<sup>210</sup> This copropagating light, stimulated Raman forward scattering, modulates the laser pulse at the plasma period (illustrated in Fig. 22, right). Consequently, the self-modulated wakefield requires some period of propagation for instability growth and, therefore, typically requires higher intensities than the linear wakefield. In both linear and self-modulated wakefield experiments, the fast electrons that emerge from the plasma typically have a very broad energy spectrum, essentially arising from the fact that if electrons are not externally injected, wavebreaking will tend to inject electrons at ALL phases of the wakefield, leading to a range of accelerated energies.<sup>213,214,216</sup>
3. *Plasma beat wave acceleration.* The third approach to wakefield generation involves copropagating two pulses at slightly different frequencies such that their difference “beat” frequency is resonant with the plasma frequency. This approach usually requires difficult laser technology and is not commonly pursued in the strong field laser regime.<sup>215</sup>

**Bubble Acceleration** A somewhat different regime exists in the plasma when the driving laser pulse is very intense ( $>10^{19}$  W/cm<sup>2</sup>), the pulse duration is shorter than the characteristic plasma oscillation time (about half an oscillation time has been found optimal in simulations<sup>28</sup>), and the pulse is focused to a spot comparable to a plasma oscillation wavelength. In this regime the plasma electron density is driven strongly nonlinearly to an amplitude in which wave breaking occurs over a fraction of a plasma cycle.<sup>218–221</sup> The plasma structure changes and cannot be described as a simple harmonic plasma oscillation like that pictured in Fig. 22. Instead, the plasma electrons are completely expelled by the three-dimensional ponderomotive force of the pulse, leading to a cavity depleted of electrons in the region immediately behind the laser pulse. This “bubble” of electrons filled with the ion background, depicted in Fig. 23, can then accelerate electrons which get trapped in a region just ahead of the closing rear wall of the bubble. The interesting aspect of such a structure is not that the accelerating



**FIGURE 23** Illustration of how a plasma responds and electrons are accelerated when irradiated in the bubble regime. (This figure was adapted from Ref. 28.)

gradient is substantially different than the strongly driven linear wakefield case, but that self-injected electrons tend to get accelerated at one spot in the bubble, leading to electrons accelerated with gradients  $>1$  GeV/cm with a quasi-monoenergetic spectrum, often with energy spread of only a few percent.<sup>219</sup>

### Ponderomotive Channel Formation

The strong ponderomotive forces which lead to the bubble formation described above can also lead to a Coulomb explosion of the ions due to their space charge repulsion while the electron expulsion exists.<sup>222</sup> If the laser pulse is substantially longer than a plasma period (a situation different than the bubble regime just discussed) the laser pulse will pondermotively expel the plasma electrons in a more or less adiabatic manner from the focal region. This electron cavitation is nearly 100 percent if the following cavitation condition is met:  $a_0 > w\omega_p/c$ ,<sup>66</sup> where  $w$  is the spot size radius of the focused laser beam. This ponderomotive cavitation, held during the duration of the laser pulse can then result in an ion radial explosion which will persist even after the pulse has departed because of the inertia imparted to the ions. This ponderomotive channel formation has been observed in experiments with picosecond duration laser pulses (which are long enough to initiate the ion expansion), leading to a channel formed on the laser axis.<sup>223</sup> The radial Coulomb explosion of ions in the channel can lead to the production of radially directed ions with many MeV of kinetic energy.

### Direct Laser Acceleration and Betatron Resonance

The expulsion of electrons by the strong ponderomotive force of a relativistic pulse propagating in an underdense plasma can have other consequences. On a timescale prior to the Coulomb explosion of the heavy ions (often taking many picosecond) the ions do not move significantly, producing a transient radial electric field that will confine a small number of electrons to the pondermotively cleared core, acting as potential well in which electrons can oscillate. As illustrated in Sec. 21.4, electrons in a relativistic intensity laser pulse are actually driven in a forward motion by the combination of the electric and magnetic fields of the laser; this laser driven current in turn creates a toroidal magnetic field. Trapped electrons in the ponderomotive channel will oscillate in this potential well. A relativistic electron trapped in the channel will oscillate at the betatron frequency, which is roughly  $\omega_B = \omega_p/2\gamma^{1/2}$ . If the electron is propagating at relativistic speed along with the laser, the betatron frequency can be in resonance with the oscillations of the laser field. This leads to significant

acceleration of the electron while it remains in resonance with the laser field, a situation termed “direct laser acceleration” (DLA).<sup>224</sup>

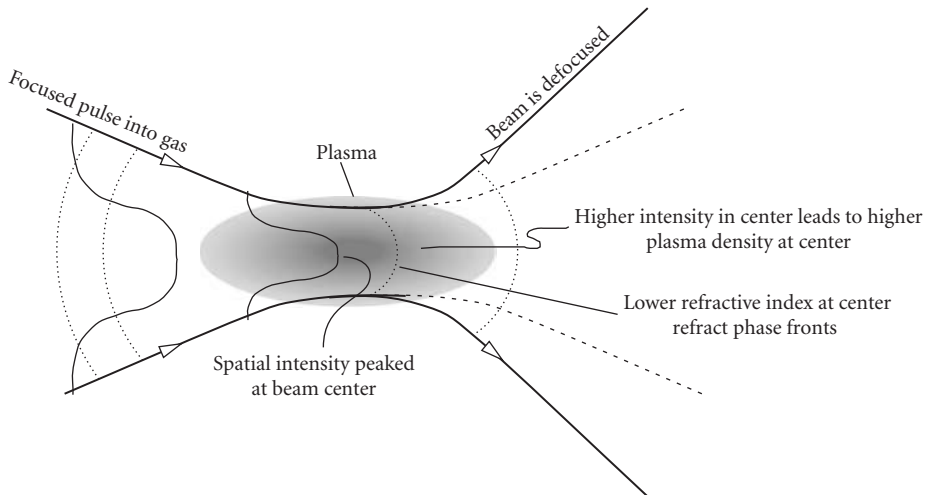
This situation is, in a sense, the inverse to the free electron laser situation. In an FEL energy is coupled from relativistic electrons to an electromagnetic wave in an undulator; in DLA the reverse occurs with the betatron oscillations of the ion channel playing the role of the undulator. The oscillating relativistic electrons will also produce soft x-ray radiation through their interactions with the quasi-static toroidal magnetic field,<sup>28</sup> a situation similar to electrons in a synchrotron.

## Ionization-Induced Defocusing

As an intense focused laser pulse propagates into a gas it will ionize the atoms by tunnel and multiphoton ionization, initiating the creation of a plasma. As this ionization occurs, the electron density of the plasma increases, affecting the propagation of the laser in a process known as plasma-induced defocusing.<sup>225,226</sup> Because the spatial profile of any focused laser pulse is inevitably peaked with higher intensity near the center of the propagation axis, ionization tends to occur in the center of the beam earlier in the pulse, resulting in a higher density plasma on axis than at the edges of the beam. The situation that arises is illustrated in Fig. 24. A plasma has a refractive index less than 1, meaning that the denser plasma yields a *faster* phase velocity. Because of this, the pulse’s phase fronts will advance in the center of the beam, where the ionized plasma has higher electron density, causing a net *defocusing* of the beam. This has the practical experimental consequence of clamping the maximum intensity that can be achieved by a focused laser in a gas target.<sup>226</sup>

The magnitude and specifics of the defocusing effects are difficult to quantify, as they depend on the kind of gas irradiated, the intensity of the laser and the spatial profile of the light beam near the focus (not to mention that the electron density radial profile is transient evolving during the laser pulse itself). However, an estimate for the maximum electron density that can be reached before defocusing clamps the laser intensity can be made by noting that the refractive index near the focus acquires a radially (and time) dependent profile:

$$n(r, t) = \sqrt{1 - \frac{n_e(r, t)}{n_{\text{crit}}}} \approx 1 - \frac{1}{2} \frac{n_e(r)}{n_{\text{crit}}} \quad (49)$$



**FIGURE 24** Description of how plasma formation at the focus of a laser can induce defocusing.

(Assuming that the electron density is well below the critical electron density,  $n_{\text{crit}} = me \omega_0^2 / 4\pi e^2$  which is about  $10^{21} \text{ cm}^{-3}$  for 1- $\mu\text{m}$  wavelength light.) Noting that the higher electron density acts as a negative lens, we can find the focal length of this negative lens by assuming that the laser propagates through the plasma over a length equal to its focused Rayleigh length  $z_R = \pi w^2 / \lambda$ . In this case, ionization-induced defocusing will dominate the propagation of the focused pulse when

$$n_e(r=0) \approx \frac{\lambda}{\pi z_R} n_{\text{crit}} \quad (50)$$

When the on-axis electron density reaches this level, the pulse focusing will be clamped and will begin to defocus. For example, a 1- $\mu\text{m}$  wavelength laser focused to a 10- $\mu\text{m}$  spot will defocus when the on-axis electron density reaches about  $10^{18} \text{ cm}^{-3}$ . Creating any greater electron density will be difficult unless the gas geometry is fashioned so that the beam is focused to its tightest spot outside of the gas.

### Relativistic Interactions in Plasma: Self-Channelling and Self-Phase Modulation

When the light pulse intensity is relativistic ( $a_0 > 1$ ) the electrons oscillating in the strong field of the laser, acquire relativistic velocity during a single cycle. This means that the electron mass changes during the course of the light period affecting the optical properties of the plasma.<sup>25</sup> This can be seen by noting that the refractive index of a plasma,  $n = \sqrt{1 - \omega_p^2 / \omega_0^2}$ , depends on the plasma frequency, which in turn depends on the square root of the electron mass. An increase in the effective mass of the electrons in the plasma through their relativistic oscillation will decrease the instantaneous value of the plasma frequency and, therefore, *increase* the value of the refractive index. Because the relativistic mass increase in the field depends on field amplitude (and hence intensity), the refractive index of the plasma in the relativistic regime is now intensity dependent.

Recalling the field-induced oscillatory gamma  $\gamma_{\text{osc}} = \sqrt{1 + a_0^2 / 2}$  the refractive index in the plasma is now

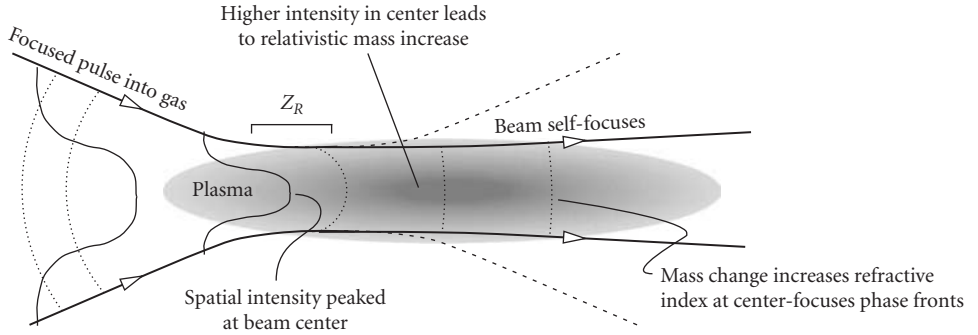
$$n = \sqrt{1 - \frac{\omega_p^2}{\gamma_{\text{osc}} \omega_0^2}} \quad (51)$$

Many of the results of standard nonlinear optics can now be applied to this relativistic underdense plasma. In low-density plasma ( $n_e \ll n_{\text{crit}}$ ) at modest  $a_0$  ( $< 1$ ) Taylor expansion of refractive index allows us to retrieve the refractive index in a standard nonlinear optics format in which  $n = n_0 - n_2 I$ ,<sup>175</sup> where  $n_0$  is the usual, nonrelativistic linear refractive index of the plasma,  $n = \sqrt{1 - \omega_p^2 / \omega_0^2}$  and the nonlinear refractive index is

$$n_2 = \frac{\pi e^2}{m_e^2 \omega_0^2 c^3} \frac{n_e}{n_c} \quad (52)$$

The intensity dependence of the plasma refractive index has two significant consequences, both with analogues in traditional nonlinear optics.

**Relativistic Self-Focusing and Self-Channelling** When a relativistically intense pulse, with a radially dependent intensity profile propagates through the plasma, relativistic effects can cause an increase in the refractive index on the center of the propagation axis, as illustrated in Fig. 25. This causes the phase fronts near the axis to be retarded with respect to those at the pulse's outer edges, resulting in self-focusing of the pulse as it passes through the plasma.<sup>20,227-230</sup> Focusing will occur if the focusing power of the nonlinear refractive index is stronger than the natural defocusing of a pulse from diffraction of the wave (or any ionization-induced defocusing). Because both of these competing



**FIGURE 25** Description of relativistic induced self-focusing and channeling in an underdense plasma.

effects depend on the spot size (a larger spot means lower intensity and less relativistic self-focusing but, at the same time, a larger spot means less defocusing from diffraction). It can be shown that the threshold for self-focusing to occur is independent of intensity and depends only on the power of the light pulse. This critical power is<sup>217</sup>

$$P_c = \frac{2c^5 m_e^2}{e^2} \left( \frac{\omega_0}{\omega_p} \right)^2 \quad (53)$$

or in practical units, (and in a form often quoted in the literature)  $P_c = 17 (\omega_0/\omega_p)^2$  in GW. This means that if a 1- $\mu\text{m}$  wavelength pulse propagates through a plasma at an electron density of  $10^{18} \text{ cm}^{-3}$ , the critical power for the pulse to undergo relativistic self-focusing is  $\sim 20$  TW.

If this power is achieved in the plasma, the pulse can potentially (though not necessarily) undergo relativistic channeling. The power of the laser must exceed  $P_c$ , but, in addition, the self-focal length must be fast enough to force a collapse of the pulse spatially within the experimental extent of the plasma (see Fig. 25). When these conditions are fulfilled, self-channeling occurs, permitting the intense pulse to propagate through the plasma at its focused diameter over a length which is many times that which would be allowed by simple diffraction (i.e.,  $\sim z_R$ ). Self-channeling in underdense plasma of distances up to 100 Rayleigh ranges has been observed.<sup>230</sup> Using these criteria, and Eq. (52) the intensity required for self-channeling in a plasma of length  $l_p$  is  $I > w^2/n_2 l_p^2$ . This relationship implies that a 1- $\mu\text{m}$  wavelength pulse, focused to a radius of 10  $\mu\text{m}$  in a plasma of  $n_e \sim 10^{18} \text{ cm}^{-3}$  with length of 1 mm, will require a peak intensity of about  $10^{18} \text{ W/cm}^2$  to undergo self-channeling.

**Relativistic Self-Phase Modulation** The second nonlinear optical consequence of the relativistic refractive index results from the temporal variation of the intensity of the pulse. This temporal variation leads to a time-dependent refractive index which, in turn, induces a time-varying phase on the pulse, a process known as relativistic self-phase modulation (SPM).<sup>36,231</sup> As in the analogue of SPM in traditional nonlinear optical materials, the relativistic SPM can significantly broaden the spectrum of the pulse. The effects of SPM on a pulse are well treated in the optics literature and the relativistic case is essentially similar to these treatments utilizing Eq. (52). The spectrum of the pulse will be broadened by the SPM through the frequency shift acquired over a propagation distance  $dx$

$$d\omega = -\frac{\omega_0}{c} n_2 \frac{\partial I}{\partial t} dx \quad (54)$$

This relationship shows that a strongly phase modulated pulse (initially transform limited) in a plasma of length,  $L$  will have its initial spectrum broadened significantly when  $I > c/\omega_0 n_2 L$ . This will

be a significant effect, for example, on a 1- $\mu\text{m}$  wavelength pulse in a 1-mm-long plasma of  $10^{18} \text{ cm}^{-3}$  at an intensity of  $> 2 \times 10^{18} \text{ W/cm}^2$  (independent of pulse duration).

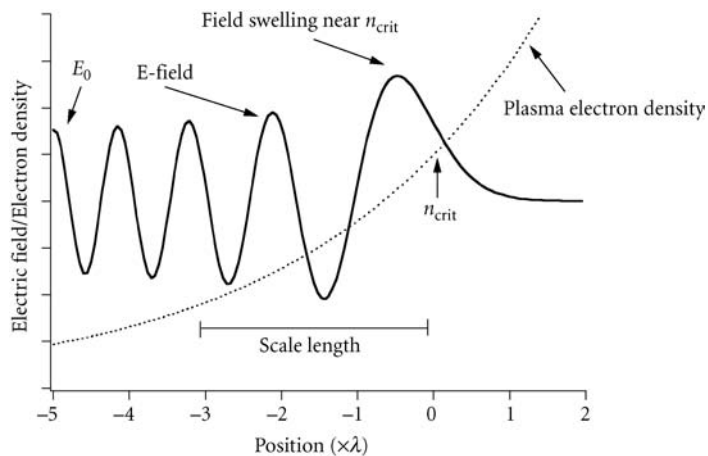
## 21.10 STRONG FIELD PHYSICS AT SURFACES OF OVERDENSE PLASMAS

### Structure of a Solid Target Plasma Irradiated at High Intensity

The irradiation of a solid target with a strong field laser pulse leads to an enormous plethora of effects, far too numerous to detail in this chapter. However, a common aspect of such interactions is that the intense laser pulse deposits energy very quickly into the solid, creating an overdense plasma ( $n_e > n_{\text{crit}}$ ). This plasma expands and, depending on the pulse duration and the temporal structure of the laser pulse, can create an underdense region through which the intense pulse must propagate before reaching the critical density surface (where  $n_e = n_{\text{crit}}$ ) and being reflected. The morphology of such interactions is illustrated in Fig. 26. Solid target interactions are accompanied by a range of mechanisms which serve to absorb laser energy, many of which result in the production of hot electrons. These hot electrons can often have energies in the relativistic range if  $I \lambda^2$  of the laser is greater than  $\sim 10^{17} \text{ W/cm}^2\text{-}\mu\text{m}^2$  (an  $a_0$  of about 0.3).

It is usually convenient to think of strong field laser interactions with solid target plasmas in two regimes.

1. When the laser pulse has very little “prepulse” (i.e., laser energy which precedes the primary, typically Gaussian-shaped pulse, by many picoseconds or nanoseconds), *and* is very fast, the solid target retains a sharp density profile with electron density rising from vacuum to an over critical value within much less than a laser wavelength. This condition can be achieved if the plasma expands much less than a wavelength within the laser pulse duration, a condition which can be estimated by noting that the plasma expands like an ideal gas so a sharp plasma interface is retained if  $\tau_p (k_B T_e / m_e)^{1/2} \ll \lambda$ .
2. If the intense laser pulse is longer or is preceded by significant prepulse (intense enough to preionize the solid before the main pulse arrives), the solid plasma will expand, creating a lower density plasma scale length (as pictured in Fig. 26). In this case, the incoming laser must interact with some region of underdense plasma many wavelengths long, in which effects such as SRS or



**FIGURE 26** Illustration of the laser field as it propagates into a plasma density scale length up to the critical density at the surface of an overdense plasma.

self-channeling as discussed in Sec. 21.9 can take place. The specific profile of the plasma, and the shape of the incoming light field will be complicated, but it is useful to examine the solution when the plasma density profile is linear with position characterized by density scale length  $\ell$ , (the length over which the electron density ramps up from 0 to  $n_{\text{crit}}$ ). In this case, the incoming electric field of the laser is of the form<sup>184</sup>

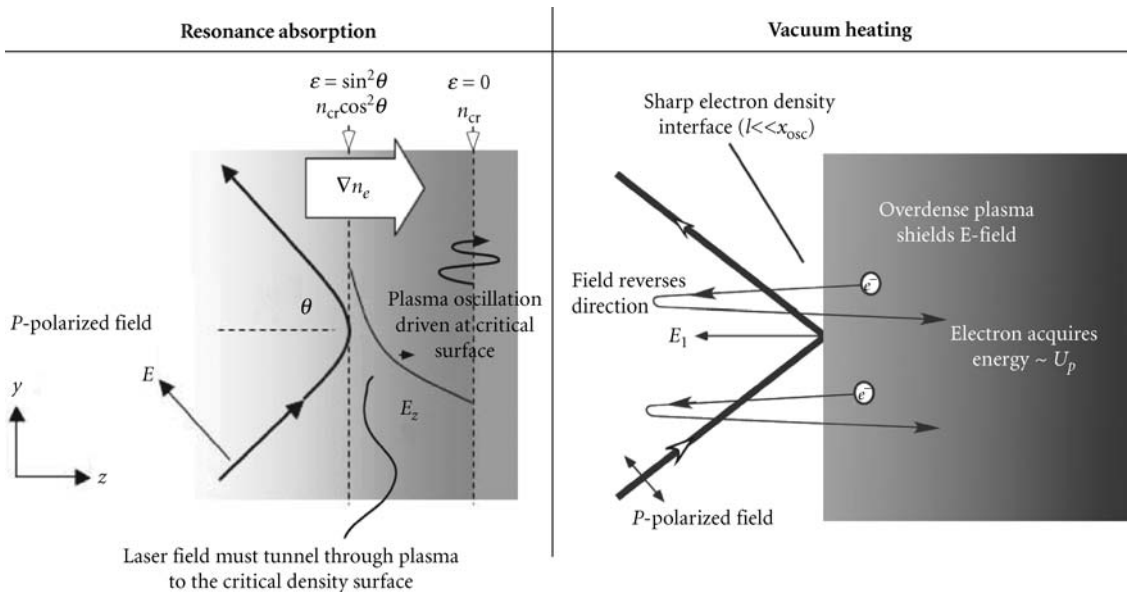
$$E(z) = 2\pi^{1/2}(\omega_0 \ell / c)^{1/6} E_0 \text{Ai}[(\omega_0^2 / c^2 \ell)^{1/3}(z - \ell)] \quad (55)$$

where  $E_0$  is the strength of the incident field in vacuum and  $\text{Ai}[x]$  is the well-known Airy function. The field swells near the critical density reflection point, which has a consequence on many strong field aspects of longer pulse interactions. The extent of this swelling is approximately given as  $E_{\text{MAX}} \approx 1.9(\omega \ell / c)^{1/6} E_0$ .

## Resonance Absorption and Vacuum Heating

When an intense laser creates conditions like those shown in Fig. 26, various absorption mechanisms, almost all of them coupling laser light into plasma electron energy, rise up. Typically, all of these absorption mechanisms will conspire to create a situation in which the absorption of the laser by the solid is in the vicinity of 20 to 60 percent, depending on laser intensity and focal geometry.<sup>232,233</sup> One particularly important absorption mechanism arises when the laser is obliquely incident on the target surface with  $p$ -polarization, a situation with a nonzero component of the laser field oscillating in and out of the target surface, as illustrated in Fig. 27. The component of the laser field perpendicular to the surface of the target  $E_{\perp}$  leads to electrons being driven across a density gradient, depositing energy into those electrons near the critical density surface. The nature of the laser coupling of energy to these electrons depends on whether the plasma interface has a long scale length or is sharp.

**Resonance Absorption** When a plasma scale length greater than the incident laser wavelength exists,  $E_{\perp}$  of the laser can drive resonant plasma oscillations at the critical density surface (where the



**FIGURE 27** Illustration of resonance absorption on the left and vacuum heating on the right.



laser frequency is equal to the plasma oscillation frequency) along a direction parallel to the plasma gradient. These driven plasma oscillations lead to what is known as resonance absorption.<sup>184,234</sup> This process, illustrated on the left in Fig. 26, leads to deposition of laser energy into an electron wave which can be damped by collisions or by other collisionless effects, such as Landau damping or wave breaking, in turn leading to the production of supra-thermal electrons.<sup>235</sup> Because the driving field  $E_{\perp}$  determined two competing effects with incidence angle there is an optimum incidence angle for maximum resonant absorption. Greater incidence angle  $\theta$  produces greater perpendicular component of E-field, however, the laser field reflects further away from the critical density surface at higher incidence angle<sup>184</sup> requiring the field to tunnel further to the resonant electron density at  $n_{\text{crit}}$ . Consequently, the efficiency of resonance absorption peaks at an angle given approximately by

$$\theta_{\text{MAX}} \approx \sin^{-1} \left[ \left( \frac{c}{2\omega_0 \ell} \right)^{1/3} \right] \quad (56)$$

Energy deposited by resonance absorption per unit time in the plasma is linear with laser intensity, and the fraction of laser power absorbed in this manner,  $f_{\text{RA}}$ , can be shown to be equal to<sup>22</sup>  $f_{\text{RA}} \cong 2.6q^2 e^{4q^{2/3}}$ , where  $q = (\omega \ell / c)^{1/3} \sin \theta$ . This absorption mechanism tends to produce a component of hot electrons which travel into the target in a direction normal to the target surface. The electrons usually exhibit an energy distribution much like that of a Maxwellian. Particle-in-cell (PIC) simulations and experiments have shown that, in the strong field, ultrashort pulse regime, temperature of this hot Maxwellian from resonance absorption is roughly, (in terms of indicated units),  $T_{\text{hot}} [\text{keV}] \approx 2 \times 10^{-4} (T_0 [\text{keV}] I [\text{W}/\text{cm}^2] \lambda [\mu\text{m}]^2)^{1/3}$ ,<sup>236</sup> where  $T_0$  is the background plasma temperature. So a 1- $\mu\text{m}$  laser at an intensity of  $10^{18} \text{ W}/\text{cm}^2$  incident on a 1 keV plasma typically produces a distribution of hot electrons with temperature in the vicinity of 200 keV.

**Vacuum Heating** When the plasma density gradient is much smaller than a wavelength (or more accurately, when the plasma density gradient is smaller than the oscillation amplitude of electrons in  $E_{\perp}$ ) a different description of the resonant heating is required. Instead, a situation like that shown on the right side of Fig. 27 exists. Here, an obliquely incident intense laser can pull electrons from the overdense plasma, accelerate them in vacuum and, once the oscillating electric field reverses direction, accelerate them back toward the overdense plasma interface. Once the electrons are propelled back into the overdense plasma, the laser field is shielded and the electrons retain a large fraction of the energy they acquired in their vacuum excursion. This process is commonly called vacuum heating or “Brunel absorption.”<sup>237–239</sup> Like resonance absorption, this process requires  $p$ -polarized light so that  $E_{\perp} \neq 0$ , and results in fast electrons being accelerated in a direction perpendicular to the target surface. The electrons’ average energy will, naturally be roughly equal to  $U_p$  since this is about the energy they gain in their vacuum half-cycle oscillation. When the laser intensity is nonrelativistic, the absorbed power varies as the 3/2 power of intensity (unlike resonance absorption where the power deposition is linear with intensity). The fraction of absorbed laser power in vacuum heating in this case is

$$f_{\text{VH}} = \frac{4eE_0}{\pi m_e \omega_0 c} \left( \frac{\sin^3 \theta}{\cos \theta} \right) \quad (57)$$

where, again,  $\theta$  is the incidence angle of the laser. This absorption is maximum at the highest angles and increases with the square root of the intensity. Note, however, that the *hottest electrons* are created when  $E_{\perp}$  is maximum, a condition which occurs at  $55^\circ$  if we assume nearly 100 percent reflection from the plasma surface. Note that the absorption fraction predicted in Eq. (57) can be  $>1$  at high-intensity and incidence angle. This is because 100 percent reflection was assumed and no relativistic effects are included. Therefore, Eq. (57) is only appropriate for the low-absorption regime. In the strongly relativistic limit (when  $a_0 \gg 1$ ) the dynamics of vacuum heating become

more complicated. It can be shown that in this regime the absorption approaches 100 percent at an optimum angle of  $73^\circ$  and that the fractional absorption is<sup>66</sup>

$$f_{\text{VH}}^{\text{rel}} \approx \frac{4\pi(\sin^2\theta/\cos\theta)}{(\pi + \sin^2\theta/\cos\theta)^2} \quad (58)$$

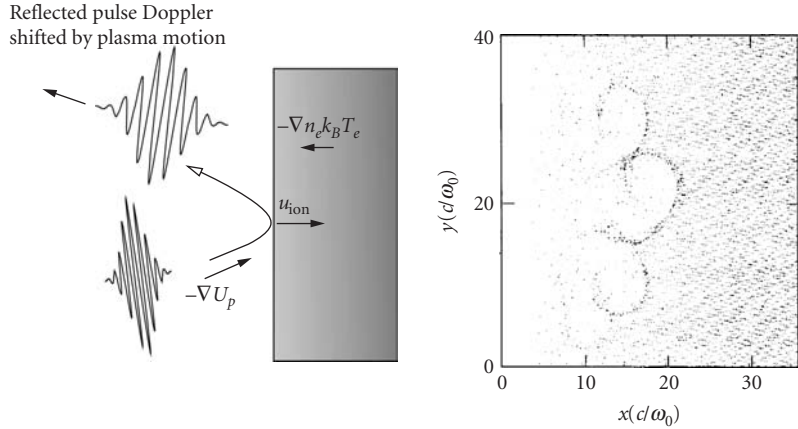
### Other Collisionless Absorption Mechanisms: $\mathbf{j} \times \mathbf{B}$ Heating and Anomalous Skin Effect

Resonance absorption or vacuum heating are usually the most important absorption mechanisms for an intense laser pulse incident on a solid-density plasma (though at near normal incidence, or with  $s$ -polarization, simple collisional absorption is most important when  $\ell \gg \lambda$ ). However, there are other mechanisms which can lead to absorption of an intense light pulse on the surface of an overdense plasma (and the potential for producing hot electrons). In almost all cases these mechanisms rely on the presence of a steep density gradient, just as one finds in the vacuum heating regime discussed above. At modest intensity, defined as the regime in which  $U_p < k_B T_e$ , a phenomena known as the anomalous skin effect takes place.<sup>240</sup> Absorption through this effect essentially results when electrons in the plasma have a large mean free path when compared to the skin depth ( $c/\omega_p$ ) in the plasma. Electrons migrate via their thermal motion into this skin depth region and acquire energy from the electric field's evanescent wave in the plasma. This absorption effect is found to play a minor role in short-pulse laser-plasma interactions (with absorption typically less than 5 percent) and, because of the requirement of low  $U_p$ , is usually not important for laser intensity above about  $10^{15}$  W/cm<sup>2</sup>. Unlike RA or vacuum heating, this absorption mechanism does not require oblique incidence, and therefore, can play a nonnegligible role for moderate intensity, normal incidence situations.

A much more important absorption mechanism at a sharp dense plasma interface occurs in the relativistic intensity regime. In this regime, the magnetic field of the light pulse begins to play a significant role in the trajectory of the driven plasma electrons. Plasma electrons at the surface of the plasma, driven transversely by the E-field with velocity approaching  $c$ , feel an oscillating force in the direction of the laser's  $\mathbf{k}$  vector from the now significant  $\mathbf{V}_{\text{osc}} \times \mathbf{B}$  force.<sup>241,242</sup> The electrons acquire energy in a manner similar to vacuum heating except now the oscillatory driving force is the  $\mathbf{j} \times \mathbf{B}$  term, oscillating at a frequency of  $2\omega_0$ . Oblique incidence is not necessary for this  $\mathbf{j} \times \mathbf{B}$  heating to occur; the heating, in fact, is maximum at normal incidence (where E-field driven vacuum heating vanishes). As a consequence, at relativistic intensity, the relative importance of vacuum heating and  $\mathbf{j} \times \mathbf{B}$  heating depends on incidence angle, polarization ( $s$ - or  $p$ -) and intensity. In general,  $\mathbf{j} \times \mathbf{B}$  heating will dominate when  $v_{\text{osc}} B > 2E_0 \sin\theta$ , even with  $p$ -polarized light, which is equivalent to  $a_0 > 2^{1/2}$  or an intensity greater than  $\sim 4 \times 10^{18}$  W/cm<sup>2</sup> in a 1- $\mu\text{m}$  wavelength field at  $\theta = 45^\circ$ . There are situations when both vacuum heating and  $\mathbf{j} \times \mathbf{B}$  occur, with vacuum heating producing hot electrons normal to the target and  $\mathbf{j} \times \mathbf{B}$  producing electrons parallel to the laser direction. Again, the energy of the accelerated electrons from  $\mathbf{j} \times \mathbf{B}$  heating will roughly equal the relativistic ponderomotive potential,  $(\gamma_{\text{osc}} - 1) m_e c^2$ .<sup>22</sup>

### Ponderomotive Steepening and Hole Boring

An intense pulse incident on a solid density plasma surface will exert a force on that plasma. Because the pulse will have some temporal rise, there is naturally a gradient in the ponderomotive energy  $-\nabla U_p$ , which will drive the plasma inward, as illustrated in Fig. 28.<sup>242</sup> This ponderomotive gradient is really nothing other than the manifestation of the pressure associated with the light pulse  $I/c$ , which can be very high. The light pressure of a pulse at an intensity of  $10^{18}$  W/cm<sup>2</sup> is  $\sim 330$  Mbar, equivalent to the thermal pressure of a plasma at solid density of  $n_e \sim 10^{23}$  cm<sup>-3</sup> when the electron temperature is 2 keV, well above the thermal temperatures of most laser plasmas. At modest intensities, the ponderomotive gradient will simply slow the expansion of the plasma outward. However, when  $I/c > n_e k_B T_e$ , the laser pulse will push the plasma back toward higher density, decreasing the plasma density



**FIGURE 28** On the left is an illustration of how ponderomotive steepening leads to hole boring when intense pulse is focused on a solid target plasma. On the right, a PIC simulation from Ref. 242 is reproduced showing the bubblelike structure that develops in the plasma ions at the surface of a plasma as a result of hole boring by a picosecond duration intense laser.

gradient, a process referred to as ponderomotive steepening. This reversal of the plasma velocity will manifest itself as a red shift in the spectrum of the reflected laser pulse or its harmonics.<sup>243,244</sup>

At very high intensities, such as  $10^{19}$  W/cm<sup>2</sup> or greater, the light pressure can be sufficient to push the plasma, even over the short timescales of laser pulses usually employed, back into the target. The high-intensity limit of ponderomotive steepening is commonly called hole boring, a process pictured in the PIC simulations of Fig. 28. Hole boring drives ions into the plasma at high velocity. This ion velocity can be estimated by balancing the inward ion momentum flux with the light pressure. Accounting for some incidence angle  $\theta$  and some potential fractional absorption,  $f_{\text{abs}}$ , the inward ion velocity is

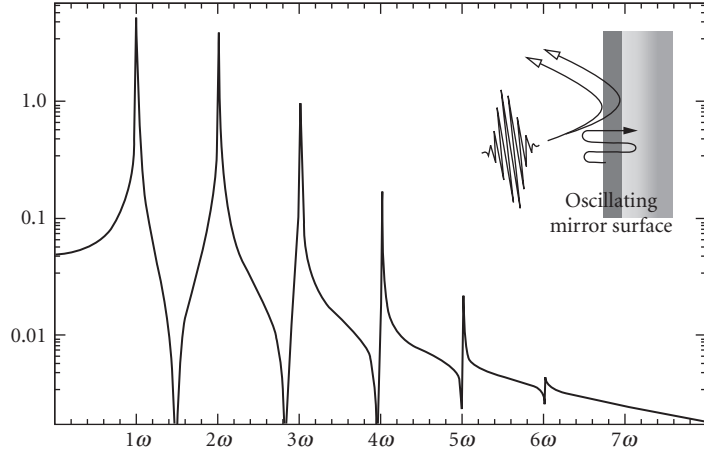
$$u_{\text{ion}} = \sqrt{\frac{(2 - f_{\text{abs}})I \cos\theta}{2n_i m_i c}} \quad (59)$$

Equation (59) predicts, for example, that a solid aluminum plasma irradiated at  $10^{19}$  W/cm<sup>2</sup> can acquire ion velocities during hole boring of  $\sim 4 \times 10^7$  cm/s. It is possible that the high energy ions driven inward at ultrahigh intensities ( $> 10^{20}$  W/cm<sup>2</sup>) can produce a collisionless shock in the underlying overdense plasma.<sup>245</sup> The amount of laser energy absorbed from the laser into these fast ions can be easily estimated and is (for small absorption)  $f_{\text{hole boring}} \approx 2u_{\text{ion}}/c$ . This relation suggests that a few percent of the incident laser energy can be transferred to ions through ponderomotive acceleration.

## High Harmonic Generation from Solid Plasmas

The light reflected from the surface of an overdense plasma at modest intensity will typically retain with good fidelity the spectrum of the incident laser light, though at higher intensity this spectrum can be Doppler shifted from ponderomotive steepening or hole boring. At these high intensities, however, nonlinear interactions can occur at the reflection surface, in such a way that harmonics of the light field are generated.<sup>246–249</sup> At very high intensity ( $> \sim 10^{19}$  W/cm<sup>2</sup>) quite high orders can be generated at the plasma surface, up to orders of  $q \sim 50$  to  $100$ .<sup>248</sup>

The origin of these harmonics can be seen by noting that the ponderomotive pressure at the surface of the plasma is  $\sim \nabla a^2/2$ , which not only has a time averaged term (the force which gives



**FIGURE 29** Plot of the Fourier transform of Eq. (61) with  $kA_{\text{mirror}} = 1$ , showing how harmonics can arise from the oscillating mirror model. The inset shows the geometry of the oscillating mirror.

rise to the hole boring discussed above) but also has a fast time varying component which varies as  $p_{\text{osc}} \sim a_0^2 \sin 2\omega_0 t$ . This rapidly oscillating force will drive the plasma electrons collectively in and out of the plasma. A similar situation occurs for  $p$ -polarized light incident on a solid plasma at an angle, though now the plasma electrons are driven at the laser frequency by the laser's electric field (see the inset to Fig. 29). If the intense light pulse is incident on a sharp-density gradient these driving forces effectively act to create an oscillating critical density surface, or, in other words, an oscillating mirror.<sup>246,247</sup> It is the oscillation of the reflection point in the plasma which yields the nonlinearity leading to high harmonic generation at the plasma surface.

The theory describing this situation is complex, particularly in the relativistic limit, however, a simple analysis of the oscillating mirror amplitude,  $A_{\text{mirror}}$ , in the nonrelativistic limit, shows that<sup>66</sup>

$$A_{\text{mirror}} \cong \frac{\lambda_0}{\pi} \left( \frac{\omega_0}{\omega_p} \right)^3 a_0^2 \quad (60)$$

This equation illustrates that the efficiency of creating these surface high harmonics increases with increasing intensity and with lower surface plasma density (because a lower density plasma is easier to drive by the ponderomotive forces of the laser). Simulations have shown that high harmonic generation from dense plasma surfaces is maximized with the target density in the vicinity of  $4n_{\text{crit}}$ <sup>247</sup> a consequence of an interaction between the second harmonic of the laser and the target surface, leading to violent resonant driving of the plasma surface. Equation (60) also shows that the mirror amplitude begins to approach the scale of one laser wavelength when  $a_0 \rightarrow (n_c/n_{\text{crit}})^{3/4}$ . In the nonrelativistic limit when the mirror oscillates with the laser frequency (the case for obliquely incident  $p$ -polarized light), the reflected light will have an electric field at the plasma surface ( $z = 0$ ) such that

$$E_{\text{refl}}(t) \cong \frac{\omega_p}{2\omega_0} a_0 \sin(\omega_0 t + kA_{\text{mirror}} \sin \omega_0 t) \quad (61)$$

A Fourier transform of this field when  $kA_{\text{mirror}} = 1$  is illustrated in Fig. 29, showing how the nonlinearity introduced by the oscillating mirror amplitude gives rise to numerous harmonics (at both even and odd harmonics of the laser in this case).

In the strongly relativistic limit, the theory becomes much more difficult. PIC simulations have shown, however, that the efficiency of the high orders ( $q \gg 1$ ) can be estimated with the empirical relation  $\eta_q \sim I \lambda^2 (1/q)^{5.249}$ . As this indicates the high harmonic spectrum from solids does not exhibit a plateau and cutoff, but instead, harmonics are created in a spectrum which simply falls off with order as a power law. The yield of the harmonic becomes nearly linear with intensity.

## Relativistic Effects and Induced Transparency

As in underdense plasmas, relativistic effects can affect the optical properties of overdense plasmas as well. Self-induced relativistic transparency is one such effect.<sup>250</sup> At relativistic intensity, the mass change of the electrons leads to an effective shift in the plasma frequency, such that

$$\omega_p^{\text{rel}} = \omega_p / \gamma_{\text{osc}}^{1/2} = \sqrt{\frac{4\pi e^2}{m_e}} \frac{1}{(1+a_0^2/2)^{1/4}} \quad (62)$$

Since  $\omega_p^{\text{rel}}$  drops with the square root of intensity, an overdense, reflecting plasma can be shifted by the relativistic factor in Eq. (62) to one which becomes effectively underdense, with  $\omega_p^{\text{rel}} < \omega_0$ , allowing the high-intensity light to propagate through the plasma. The critical intensity for this to occur, in the strong relativistic limit ( $a_0 \gg 1$ ) is

$$a_0^{\text{trans}} = \sqrt{2} \frac{n_e}{n_{\text{crit}}} \quad (63)$$

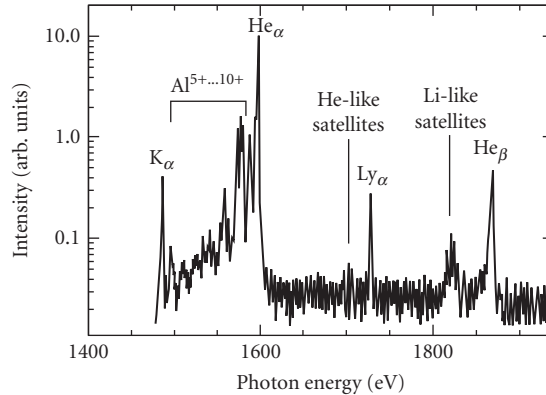
Consequently, a solid density plasma, with  $n_e \sim 10^{23} \text{ cm}^{-3}$ , will become transparent to 1- $\mu\text{m}$  laser light at an  $a_0$  of  $\sim 140$ . This is an intensity near  $3 \times 10^{22} \text{ W/cm}^2$ , just within reach of the highest intensity lasers now available. That this relativistically induced transparency can occur in a plasma was mentioned in the literature many years ago, however, to date there has yet to be a direct experimental observation of this effect.

## 21.11 APPLICATIONS OF STRONG FIELD INTERACTIONS WITH PLASMAS

Modern strong field research now focuses on a range of effects that arise from the basic phenomena that we have described in this chapter. It is impossible to summarize all of these research avenues here, but we conclude in this section with a very brief sampling of some of the applications of high-field research that are among the most active at this writing.

### Femtosecond X-Ray Production

Many of the strong field effects discussed in previous sections result in the production of energetic electrons (through, e.g., plasma or free wave acceleration via wakefield, SRS, resonant absorption, or vacuum and  $\mathbf{j} \times \mathbf{B}$  heating). When electrons are accelerated by these mechanisms at the surface of a cold, solid target, the penetration of these hot electrons will lead to x-ray production. If the laser generating these fast electrons is short, it is possible to produce bright sources of x-rays with femtosecond time duration, which, can, in turn, be used for various pump-probe applications.<sup>38</sup> There are generally three principal ways in which x-rays are generated in these experiments: (1) through the direct interaction with the laser field or other strong fields in and around a plasma; (2) through the ejection of inner shell electrons in the underlying cold solid leading to  $K_\alpha$  line emission; or



**FIGURE 30** An example of an x-ray spectrum produced by irradiation of a solid Al target at intensity of  $\sim 10^{18}$  W/cm<sup>2</sup>. This spectrum shows that not only are H-like and He-like lines emitted from the hot plasma, but also that  $K_\alpha$  x-rays are emitted when the hot electrons produced by the laser penetrate the cold target and knock out K-shell holes in the unionized Al atoms. This x-ray pulse is usually very fast, <1 ps in duration. (*Adapted from Ref. 252.*)

(3) through free-free transitions of the electrons as they pass by highly charged nuclei of the solid, yielding bremsstrahlung radiation. The later process has been shown to yield x-rays with energies well above 1 MeV when intensities of  $>10^{18}$  W/cm<sup>2</sup> are used to irradiate a solid target.<sup>251</sup> A characteristic x-ray spectrum resulting from an example experiment is shown in Fig. 30.

## Fusion Neutron Production

The production of fast ions in strong field interactions, through processes such as ponderomotive acceleration of ions at the surface of a target or through the ejection of ions from the Coulomb explosion of irradiated clusters, can be harnessed to drive nuclear fusion. The production of bursts of 2.45 MeV neutrons when various targets contain deuterium (solid or cluster targets) has been well studied by experiment.<sup>199,253</sup>

## High Magnetic Field Production

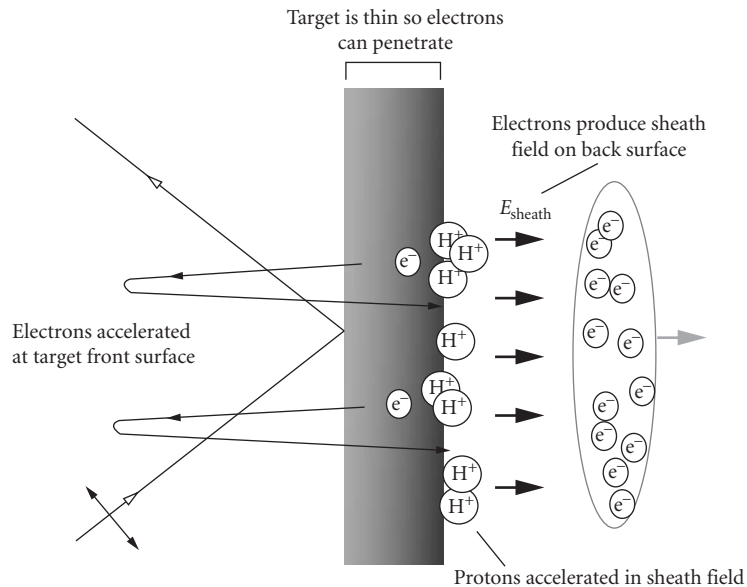
In addition to the very strong magnetic fields associated with high intensity EM waves, the intense irradiation of solid target plasmas can produce strong transient DC magnetic fields. These fields essentially arise from two sources: (1) Thermo-electric magnetic field generation. In the high temperatures and steep density gradients found in intense ultrafast laser irradiation of solids, magnetic fields can be generated by thermal transport effects. In this case the magnetic field is proportional to  $\nabla T_e \times \nabla n_e$  which favors high B-field production in the steep density gradients found in femtosecond laser plasma interactions.<sup>254</sup> (2) Fast electron magnetic field generation. The fast electrons produced by the panoply of mechanisms discussed in previous sections, frequently lead to the production of high peak currents, perhaps exceeding a MA. This leads to enormous B-fields. Fields of upto many 100s of MG are possible with this mechanism.<sup>255</sup>

## MeV Proton Acceleration

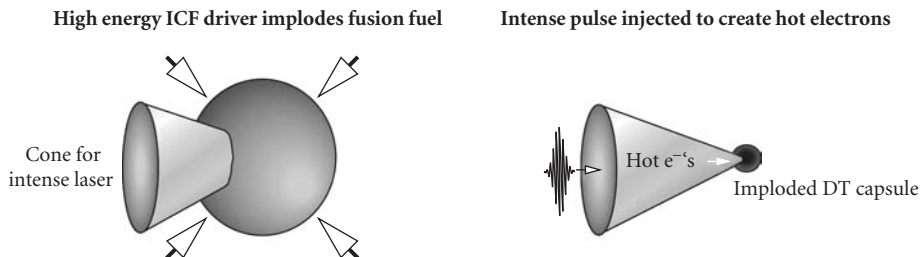
When fast electrons are generated at the surface of a solid target plasma by an intense laser and the target is sufficiently thin such that the electron mean free path is greater than the target thickness, the fast electrons can exit the back surface and set up a strong ambipolar field. This situation is illustrated in Fig. 31. These electrons will set up an electric field which ionizes ions on the back surface (often covered with water and hydrocarbon contamination in vacuum) and accelerate them to high velocity.<sup>256–258</sup> The field created will be of the order of  $eE_{\text{sheath}} \approx k_B T_{\text{hot}} / \lambda_{\text{Debye}}^{\text{hot}}$ , where  $\lambda_{\text{Debye}}^{\text{hot}} = \sqrt{k_B T_{\text{hot}} / 4\pi n_{\text{hot}} e^2}$  is the hot electron Debye radius and  $T_{\text{hot}}$  and  $n_{\text{hot}}$  are the temperature and density of the hot electrons. The sheath field can often be of the order of a few MeV/ $\mu\text{m}$ , so protons can easily acquire many MeV of energy during their acceleration in the direction of the target back surface normal. This ion acceleration mechanism is termed “target normal sheath acceleration” (TNSA). Ion temperatures of a few MeV are often observed when sub-picosecond (200 to 1000 fs) pulses are focused at intensity in the vicinity of  $10^{20}$  W/cm<sup>2</sup>. It has been found that this TNSA mechanism is most effective for higher energy pulses (>1 J) in the >500 fs range since such pulses tend to produce a greater number of hot electrons than sub-100 fs pulses at similar intensities.

## Fast Ignition

The production of fast electrons by an intense short pulse laser has been proposed as a means to ignite a fusion capsule imploded by a large scale laser or Z-pinch, in the so-called inertial confinement approach to fusion (ICF).<sup>259</sup> One variant of ICF, known as fast ignition, is described in Fig. 32. The basic idea is that a separate, high energy driver will assemble at high density (>200 g/cm<sup>3</sup>) a deuterium/tritium fusion fuel, and the short pulse laser will be focused from the side, onto the edge of the fusion fuel, generating a beam of hot electrons with temperature in the range of 1 to 10 MeV which penetrate



**FIGURE 31** Illustration of how protons can be accelerated from the back surface of an intensely irradiated target by the target normal sheath acceleration phenomenon.



**FIGURE 32** Illustration of how fast ignition would utilize an intense pulse to ignite an imploded inertial confinement fusion capsule.

the fuel and heat it to fusion ignition temperature. At present, the most promising method of doing this is to embed a cone in the fusion fuel prior to its compression (see Fig. 32) to permit effective injection of the intense laser at the peak of the fuel's compression. There remain many technical challenges to the ultimate implementation of this idea, with numerous physics issues remaining unsolved (such as understanding how such high peak currents of electrons transport into such a dense plasma or what fraction of short pulse laser energy converts to hot electrons). Nonetheless, there have been experimental studies conducted in Japan in recent years which have yielded promising results on the fast ignition approach at modest laser compression and short pulse laser drive energy.<sup>260</sup>

## Raman Amplification

It has been recently demonstrated that it is possible to amplify ultrashort pulses in a plasma by counterpropagating a long pulse laser with an intense short pulse laser of lower frequency.<sup>261</sup> This superradiant amplification essentially occurs through a parametric process in the plasma closely akin to stimulated Raman scattering. With this high-intensity technique, it may be possible using kJ-class nanosecond lasers to amplify kJ-energy sub-100 fs pulses in a plasma.

## 21.12 REFERENCES

1. T. F. Gallagher, "Rydberg Atoms in Strong Microwave Fields," in *Atoms in Intense Laser Fields*, M. Gavrila, (ed.), Academic Press, San Diego, 1992, pP. 67–108.
2. L. V. Keldysh, "Ionization in the Field of a Strong Electromagnetic Wave," *Soviet Physics JETP* **20**:1307–1314 (1965).
3. P. Agostini, F. Fabre, G. Mainfray, G. Petite, and N. K. Rahman, "Free-Free Transitions Following 6-Photon Ionization of Xenon Atoms," *Physical Review Letters* **42**:1127–1130 (1979).
4. F. Fabre, G. Petite, P. Agostini, and M. Clement, "Multi-Photon above-Threshold Ionization of Xenon at 0.53 and 1.06-Mu-M," *Journal of Physics B-Atomic Molecular and Optical Physics* **15**:1353–1369 (1982).
5. A. McPherson, G. Gibson, H. Jara, U. Johann, T. S. Luk, I. A. McIntyre, K. Boyer, and C. K. Rhodes, "Studies of Multiphoton Production of Vacuum Ultraviolet-Radiation in the Rare-Gases," *Journal of the Optical Society of America B-Optical Physics* **4**:595–601 (1987).
6. Z. H. Chang, A. Rundquist, H. W. Wang, M. M. Murnane, and H. C. Kapteyn, "Generation of Coherent Soft X Rays at 2.7 nm Using High Harmonics," *Physical Review Letters* **79**:2967–2970 (1997).
7. A. L'Huillier and P. Balcou, "High-Order Harmonic-Generation in Rare-Gases with a 1-Ps 1053-Nm Laser," *Physical Review Letters* **70**:774–777 (1993).
8. F. Krausz and P. Corkum, "Research Supports Observation of Attosecond Pulses," *Laser Focus World* **38**:7–7 (2002).
9. M. Hentschel, R. Kienberger, C. Spielmann, G. A. Reider, N. Milosevic, T. Brabec, P. Corkum, U. Heinzmann, M. Drescher, and F. Krausz, "Attosecond Metrology," *Nature* **414**:509–513 (2001).



10. P. B. Corkum, "Plasma Perspective on Strong-Field Multiphoton Ionization," *Physical Review Letters* **71**:1994–1997 (1993).
11. K. C. Kulander, K. J. Schafer, and J. L. Krause, in *Super-Intense Laser Atom Physics*, NATO ASI Ser. , A. L. H. B. Piraux, and K. Rzaewski, (eds.), Plenum Press, New York, 1993.
12. H. Daido, "Review of Soft X-Ray Laser Researches and Developments," *Reports on Progress in Physics* **65**:1513–1576 (2002).
13. J. J. Rocca, "Table-Top Soft X-Ray Lasers," *Review of Scientific Instruments* **70**:3799–3827 (1999).
14. V. Malka, J. Faure, Y. A. Gauduel, E. Lefebvre, A. Rousse, and K. T. Phuoc, "Principles and Applications of Compact Laser-Plasma Accelerators," *Nature Physics* **4**:447–453 (2008).
15. T. Tajima and J. M. Dawson, "Laser Electron-Accelerator," *Physical Review Letters* **43**:267–270 (1979).
16. S. Tazzari and M. Ferrario, "Trends in High Energy Particle Accelerators," *Reports on Progress in Physics* **66**:1045–1094 (2003).
17. J. H. Eberly, J. Javanainen, and K. Rzaewski, "Above-Threshold Ionization," *Physics Reports-Review Section of Physics Letters* **204**:331–383 (1991).
18. K. Burnett, V. C. Reed, and P. L. Knight, "Atoms in Ultra-Intense Laser Fields," *Journal of Physics B-Atomic Molecular and Optical Physics* **26**:561–598 (1993).
19. T. Ditmire, "Atomic Clusters in Ultrahigh Intensity Light Fields," *Contemporary Physics* **38**:315–328 (1997).
20. E. Esarey, P. Sprangle, J. Krall, and A. Ting, "Self-Focusing and Guiding of Short Laser Pulses in Ionizing Gases and Plasmas," *IEEE Journal of Quantum Electronics* **33**:1879–1914 (1997).
21. M. Protopapas, C. H. Keitel, and P. L. Knight, "Atomic Physics with Super-High Intensity Lasers," *Reports on Progress in Physics* **60**:389–486 (1997).
22. S. C. Wilks and W. L. Kruer, "Absorption of Ultrashort, Ultra-Intense Laser Light by Solids and Overdense Plasmas," *IEEE Journal of Quantum Electronics* **33**:1954–1968 (1997).
23. P. Lambropoulos, P. Maragakis, and J. Zhang, "Two-Electron Atoms in Strong Fields," *Physics Reports-Review Section of Physics Letters* **305**:203–293 (1998).
24. T. Brabec and F. Krausz, "Intense Few-Cycle Laser Fields:Frontiers of Nonlinear Optics," *Reviews of Modern Physics* **72**:545–591 (2000).
25. D. Umstadter, "Review of Physics and Applications of Relativistic Plasmas Driven by Ultra-Intense Lasers," *Physics of Plasmas* **8**:1774–1785 (2001).
26. R. Dorner, T. Weber, M. Weckenbrock, A. Staudte, M. Hattass, H. Schmidt-Bocking, R. Moshhammer, and J. Ullrich, "Multiple Ionization in Strong Laser Fields," *Advances in Atomic, Molecular, and Optical Physics* **48**:1–34 (2002).
27. M. Gavrilin, "Atomic Stabilization in Superintense Laser Fields," *Journal of Physics B-Atomic Molecular and Optical Physics* **35**:R147–R193 (2002).
28. A. Pukhov, "Strong Field Interaction of Laser Radiation," *Reports on Progress in Physics* **66**:47–101 (2003).
29. J. Ullrich, R. Moshhammer, A. Dorn, R. Dorner, L. P. H. Schmidt, and H. Schmitt-Bocking, "Recoil-Ion and Electron Momentum Spectroscopy:Reaction-Microscopes," *Reports on Progress in Physics* **66**:1463–1545 (2003).
30. D. Umstadter, "Relativistic Laser-Plasma Interactions," *Journal of Physics D-Applied Physics* **36**:R151–R165 (2003).
31. P. Agostini and L. F. DiMauro, "The Physics of Attosecond Light Pulses," *Reports on Progress in Physics* **67**:813–855 (2004).
32. R. Bingham, J. T. Mendonca, and P. K. Shukla, "Plasma Based Charged-Particle Accelerators," *Plasma Physics and Controlled Fusion* **46**:R1–R23 (2004).
33. T. Ditmire, S. Bless, G. Dyer, A. Edens, W. Grigsby, G. Hays, K. Madison, et al., "Overview of Future Directions in High Energy-Density and High-Field Science Using Ultra-Intense Lasers," *Radiation Physics and Chemistry* **70**:535–552 (2004).
34. V. S. Popov, "Tunnel and Multiphoton Ionization of Atoms and Ions in a Strong Laser Field (Keldysh Theory)," *Physics-Uspekhi* **47**:855–885 (2004).
35. J. H. Posthumus, "The Dynamics of Small Molecules in Intense Laser Fields," *Reports on Progress in Physics* **67**:623–665 (2004).
36. D. Umstadter, S. Sepker, and S. Y. Chen, "Relativistic Nonlinear Optics," *Advance in Atomic, Molecular, and Optical Physics* **52**:331–389 (2005).

37. M. Borghesi, J. Fuchs, S. V. Bulanov, A. J. Mackinnon, P. K. Patel, and M. Roth, "Fast Ion Generation by High-Intensity Laser Irradiation of Solid Targets and Applications," *Fusion Science and Technology* **49**:412–439 (2006).
38. T. Pfeifer, C. Spielmann, and G. Gerber, "Femtosecond X-Ray Science," *Reports on Progress in Physics* **69**:443–505 (2006).
39. U. Saalmann, C. Siedschlag, and J. M. Rost, "Mechanisms of Cluster Ionization in Strong Laser Pulses," *Journal of Physics B-Atomic Molecular and Optical Physics* **39**:R39–R77 (2006).
40. Y. I. Salamin, S. X. Hu, K. Z. Hatsagortsyan, and C. H. Keitel, "Relativistic High-Power Laser-Matter Interactions," *Physics Reports-Review Section of Physics Letters* **427**:41–155 (2006).
41. R. A. Ganeev, "High-Order Harmonic Generation in a Laser Plasma: A Review of Recent Achievements," *Journal of Physics B-Atomic Molecular and Optical Physics* **40**:R213–R253 (2007).
42. D. Strickland and G. Mourou, "Compression of Amplified Chirped Optical Pulses," *Optics Communication* **56**:219–221 (1985).
43. W. Koechner, *Solid-State Laser Engineering*, Springer Verlag, Berlin, 1996.
44. S. W. Bahk, P. Rousseau, T. A. Planchon, V. Chvykov, G. Kalintchenko, A. Maksimchuk, G. A. Mourou, and V. Yanovsky, "Characterization of Focal Field Formed by a Large Numerical Aperture Paraboloidal Mirror and Generation of Ultra-High Intensity ( $10(22)\text{W}/\text{cm}^2$ ) (vol 80, p. 823, 2005)," *Applied Physics B-Lasers and Optics* **81**:727–727 (2005).
45. P. A. Norreys, K. M. Krushelnick, and M. Zepf, "PW Lasers: Matter in Extreme Laser Fields," *Plasma Physics and Controlled Fusion* **46**:B13–B21 (2004).
46. C. N. Danson, J. Collier, D. Neely, L. J. Barzanti, A. Damerell, C. B. Edwards, M. H. R. Hutchinson, et al., "Well Characterized  $10(19)\text{W}/\text{cm}^2$  Operation of VULCAN—An Ultra-High Power Nd: Glass Laser," *Journal of Modern Physics* **45**:1653–1669 (1998).
47. Y. Kitagawa, Y. Sentoku, S. Akamatsu, M. Mori, Y. Tohyama, R. Kodama, K. A. Tanaka, et al., "Progress of Fast Ignitor Studies and Petawatt Laser Construction at Osaka University," *Physics of Plasmas* **9**:2202–2207 (2002).
48. F. G. Patterson and M. D. Perry, "Design and Performance of a Multiterawatt, Subpicosecond Neodymium—Glass-Laser," *Journal of the Optical Society of America B-Optical Physics* **8**:2384–2391 (1991).
49. N. Blanchot, C. Rouyer, C. Sauteret, and A. Migus, "Amplification of Sub-100 TW Femtosecond Pulses by Shifted Amplifying Nd:Glass Amplifiers: Theory and Experiment," *Optics Letter* **20**:395–397 (1995).
50. M. D. Perry, D. Pennington, B. C. Stuart, G. Tietbohl, J. A. Britten, C. Brown, S. Herman, B. et al., "Petawatt Laser Pulses," *Optics Letter* **24**:160–162 (1999).
51. R. F. Service, "Laser Labs Race for the Petawatt," *Science* **301**:154–156 (2003).
52. K. Yamakawa, S. Matsuoka, M. Aoyama, T. Kase, Y. Akahane, H. Takuma, and C. P. J. Barty, "Design and Performance of a 100 TW, Sub-20 fs Ti: Sapphire Laser System," in *X-Ray Lasers 1998*. 1999. pP. 645–648.
53. B. C. Walker, C. Toth, D. N. Fittinghoff, T. Guo, D. E. Kim, C. Rose-Petruck, J. A. Squier, K. Yamakawa, K. R. Wilson, and C. P. J. Barty, "A  $50\text{-EW}/\text{cm}^2$  Ti: Sapphire Laser System for Studying Relativistic Light-Matter Interactions," *Optics Express* **5**:196–202 (1999).
54. F. G. Patterson, J. Bonlie, D. Price, B. W. Hite, and P. Springer, *LLNL Internal Report UCRL-JC-134912*: (1999).
55. V. Yanovsky, V. Chvykov, G. Kalinchenko, P. Rousseau, T. Planchon, T. Matsuoka, A. Maksimchuk, et al., "Ultra-High Intensity-300-TW Laser at 0.1 Hz Repetition Rate," *Optics Express* **16**:2109–2114 (2008).
56. S. Backus, C. G. Durfee, M. M. Murnane, and H. C. Kapteyn, "High Power Ultrafast Lasers," *Review of Scientific Instruments* **69**:1207–1223 (1998).
57. K. Yamakawa and C. P. J. Barty, "Ultrafast, Ultrahigh-Peak, and High-Average Power Ti: Sapphire Laser System and Its Applications," *IEEE Journal of Selected Topics in Quantum Electronics* **6**:658–675 (2000).
58. I. N. Ross, P. Matousik, M. Towrie, A. J. Langley, and J. L. Collier, "The Prospects for Ultrashort Pulse Duration and Ultrahigh Intensity Using Optical Parametric Chirped Pulse Amplifiers," *Optics Communication* **144**:125–133 (1997).
59. I. N. Ross, J. L. Collier, P. Matousek, C. N. Danson, D. Neely, R. M. Allot, D. A. Pepler, C. Hernandez-Gomez, and K. Osvay, "Generation of Terawatt Pulses by Use of Optical Parametric Chirped Pulse Amplification," *Applied Optics* **39**:2422–2427 (2000).
60. I. Jovanovic, C. A. Ebberts, and C. P. J. Barty, "Hybrid Chirped-Pulse Amplification," *Optics Letter* **27**:1622–1624 (2002).

61. Y. X. Leng, L. H. Lin, X. D. Yang, H. H. Lu, Z. Q. Zhang, and Z. Z. Xu, "Regenerative Amplifier with Continuously Variable Pulse Duration Used in an Optical Parametric Chirped-Pulse Amplification Laser System for Synchronous Pumping," *Optical Engineering* **42**:862–866 (2003).
62. J. E. Gunn and J. P. Ostriker, "On the Motion and Radiation of Charged Particles in Strong Electromagnetic WaveS. I. Motion in Plane and Spherical Waves," *The Astrophysical Journal* **165**:523–541 (1971).
63. J. H. Eberly and A. Sleeper, "Trajectory and Mass Shift of a Classical Electron in a Radiation Pulse," *Physical Review* **176**:1570–1573 (1968).
64. F. V. Hartemann, "High-Intensity Scattering Processes of Relativistic Electrons in Vacuum," *Physics of Plasmas* **5**:2037–2047 (1998).
65. J. N. Bardsley, B. M. Penetrante, and M. H. Mittleman, "Relativistic Dynamics of Electrons in Intense Laser Fields," *Physical Review A* **40**:3823–3836 (1989).
66. P. Gibbon, *Short Pulse Laser Interaction with Matter: An Introduction*, Imperial College Press, London, 2005.
67. D. D. Meyerhofer, "High-Intensity-Laser-Electron Scattering," *IEEE Journal of Quantum Electronics* **33**:1935–1941 (1997).
68. C. I. Moore, J. P. Knauer, and D. D. Meyerhofer, "Observation of the Transition from Thomson to Compton-Scattering in Multiphoton Interactions with Low-Energy Electrons," *Physical Review Letters* **74**:2439–2442 (1995).
69. E. A. Startsev and C. J. McKinstrie, "Multiple Scale Derivation of the Relativistic Ponderomotive Force," *Physical Review E* **55**:7527–7535 (1997).
70. B. Quesnel and P. Mora, "Theory and Simulation of the Interaction of Ultraintense Laser Pulses with Electrons in Vacuum," *Physical Review E* **58**:3719–3732 (1998).
71. A. Maltsev and T. Ditmire, "Above Threshold Ionization in Tightly Focused, Strongly Relativistic Laser Fields," *Physical Review Letters* **90**:053002 (2003).
72. J. D. Jackson, *Classical Electrodynamics*, Wiley, New York, 1975.
73. L. S. Brown and T. W. B. Kibble, "Interaction of Intense Laser Beams with Electrons," *Physical Review* **133**:A705–A719 (1964).
74. E. S. Sarachik and G. T. Schappert, "Classical Theory of the Scattering of Intense Laser Radiation by Free Electrons," *Physical Review D* **1**:2738–2753 (1970).
75. S. Y. Chen, A. Maksimchuk, and D. Umstadter, "Experimental Observation of Relativistic Nonlinear Thomson Scattering," *Nature* **396**:653–655 (1998).
76. E. Esarey, S. K. Ride, and P. Sprangle, "Nonlinear Thomson Scattering of Intense Laser-Pulses from Beams and Plasmas," *Physical Review E* **48**:3003–3021 (1993).
77. C. I. Castilloherrera and T. W. Johnston, "Incoherent Harmonic Emission from Strong Electromagnetic-Waves in Plasmas," *IEEE Transactions on Plasma Science* **21**:125–135 (1993).
78. R. W. Schoenlein, W. P. Leemans, A. H. Chin, P. Volfbeyn, T. E. Glover, P. Balling, M. Zolotorev, K. J. Kim, S. Chattopadhyay, and C. V. Shank, "Femtosecond X-Ray Pulses at 0.4 Angstrom Generated by 90 Degrees Thomson Scattering: A Tool for Probing the Structural Dynamics of Materials," *Science* **274**:236–238 (1996).
79. C. Bula, K. T. McDonald, E. J. Prebys, C. Bamber, S. Boege, T. Kotsieroglou, A. C. Melissinos, et al., "Observation of Nonlinear Effects in Compton Scattering," *Physical Review Letters* **76**:3116–3119 (1996).
80. G. Mainfray and C. Manus, "Multiphoton Ionization of Atoms," *Reports on Progress in Physics* **54**:1333–1372 (1991).
81. M. D. Perry and O. L. Landen, "Resonantly Enhanced Multiphoton Ionization of Krypton and Xenon with Intense Ultraviolet-Laser Radiation," *Physical Review A* **38**:2815–2829 (1988).
82. M. D. Perry, A. Szoke, O. L. Landen, and E. M. Campbell, "Nonresonant Multiphoton Ionization of Noble-Gases—Theory and Experiment," *Physical Review Letters* **60**:1270–1273 (1988).
83. M. D. Perry, O. L. Landen, A. Szoke, and E. M. Campbell, "Multiphoton Ionization of the Noble-Gases by an Intense 10(14)-W/Cm<sup>2</sup> Dye-Laser," *Physical Review A* **37**:747–760 (1988).
84. T. S. Luk, H. Pummer, K. Boyer, M. Shahidi, H. Egger, and C. K. Rhodes, "Anomalous Collision-Free Multiple Ionization of Atoms with Intense Picosecond Ultraviolet-Radiation," *Physical Review Letters* **51**:110–113 (1983).
85. A. Lhuillier, L. A. Lompre, G. Mainfray, and C. Manus, "Multiply Charged Ions Induced by Multiphoton Absorption in Rare-Gases at 0.53 Mu-M," *Physical Review A* **27**:2503–2512 (1983).
86. A. Lhuillier, L. A. Lompre, G. Mainfray, and C. Manus, "Multiply Charged Ions Formed by Multi-Photon Absorption Processes in the Continuum," *Physical Review Letters* **48**:1814–1817 (1982).

87. G. Petite, F. Fabre, P. Agostini, M. Crance, and M. Aymar, "Nonresonant Multiphoton Ionization of Cesium in Strong Fields—Angular-Distributions and above-Threshold Ionization," *Physical Review A* **29**:2677–2689 (1984).
88. P. Lambropoulos, "Topics on Multiphoton Processes in Atoms," *Advances in Atomic and Molecular Physics* **12**:87–164 (1976).
89. L. A. Lompre, G. Mainfray, C. Manus, and J. Thebault, "Multiphoton Ionization of Rare-Gases by a Tunable-Wavelength 30-Psec Laser-Pulse at 1.06  $\mu\text{m}$ ," *Physical Review A* **15**:1604–1612 (1977).
90. R. R. Freeman, P. H. Bucksbaum, H. Milchberg, S. Darack, D. Schumacher, and M. E. Geusic, "Above-Threshold Ionization with Subpicosecond Laser-Pulses," *Physical Review Letters* **59**:1092–1095 (1987).
91. F. Faisal, *Theory of Multiphoton Processes*, Plenum, New York, 1987.
92. H. R. Reiss, "Effect of an Intense Electromagnetic-Field on a Weakly Bound System," *Physical Review A* **22**:1786–1813 (1980).
93. L. D. Landau and E. M. Lifshitz, *Quantum Mechanics*, Pergamon, New York, 1965, sec 73.
94. A. M. Perelomov, V. S. Popov, and M. V. Terent'ev, "Ionization of Atoms in an Alternating Electric Field," *Soviet Physics JETP* **23**:924–934 (1966).
95. M. V. Ammosov, N. B. Delone, and V. P. Krainov, "Tunnel Ionization of Complex Atoms and Atomic Ions in a Varying Electromagnetic-Field," *Zhurnal Eksperimentalnoi I Teoreticheskoi Fiziki* **91**:2008–2013 (1986).
96. S. Augst, D. D. Meyerhofer, D. Strickland, and S. L. Chin, "Laser Ionization of Noble-Gases by Coulomb-Barrier Suppression," *Journal of the Optical Society of America B-Optical Physics* **8**:858–867 (1991).
97. U. Mohideen, M. H. Sher, H. W. K. Tom, G. D. Aumiller, O. R. Wood, R. R. Freeman, J. Bokor, and P. H. Bucksbaum, "High-Intensity above-Threshold Ionization of He," *Physical Review Letters* **71**:509–512 (1993).
98. P. B. Corkum, N. H. Burnett, and F. Brunel, "Above-Threshold Ionization in the Long-Wavelength Limit," *Physical Review Letters* **62**:1259–1262 (1989).
99. J. Javanainen, J. H. Eberly, and Q. C. Su, "Numerical Simulations of Multiphoton Ionization and above-Threshold Electron-Spectra," *Physical Review A* **38**:3430–3446 (1988).
100. P. Krut, J. Kimman, H. G. Muller, and M. J. Vanderwielen, "Electron-Spectra from Multiphoton Ionization of Xenon at 1064, 532, and 355  $\text{nm}$ ," *Physical Review A* **28**:248–255 (1983).
101. J. L. Chaloupka, J. Rudati, R. Lafon, P. Agostini, K. C. Kulander, and L. F. DiMauro, "Observation of a Transition in the Dynamics of Strong-Field Double Ionization," *Physical Review Letters* **90**:033002 (2003).
102. B. R. Yang, K. J. Schafer, B. Walker, K. C. Kulander, P. Agostini, and L. F. DiMauro, "Intensity-Dependent Scattering Rings in High-Order above-Threshold Ionization," *Physical Review Letters* **71**:3770–3773 (1993).
103. R. R. Freeman, T. J. McIlrath, P. H. Bucksbaum, and M. Bashkansky, "Ponderomotive Effects on Angular-Distributions of Photoelectrons," *Physical Review Letters* **57**:3156–3159 (1986).
104. G. N. Gibson, R. R. Freeman, and T. J. McIlrath, "Verification of the Dominant Role of Resonant Enhancement in Short-Pulse Multiphoton Ionization," *Physical Review Letters* **69**:1904–1907 (1992).
105. N. H. Burnett and P. B. Corkum, "Cold-Plasma Production for Recombination Extreme-Ultraviolet Lasers by Optical-Field-Induced Ionization," *Journal of the Optical Society of America B-Optical Physics* **6**:1195–1199 (1989).
106. T. Ditmire, "Simulations of Heating and Electron Energy Distributions in Optical Field Ionized Plasmas," *Physical Review E* **54**:6735–6740 (1996).
107. X. Liu, H. Rottke, E. Eremina, W. Sandner, E. Goulielmakis, K. O. Keeffe, M. Lezius, et al., "Nonsequential Double Ionization at the Single-Optical-Cycle Limit," *Physical Review Letters* **93**:263001 (2004).
108. B. Feuerstein, R. Moshhammer, D. Fischer, A. Dorn, C. D. Schroter, J. Deipenwisch, J. R. C. Lopez-Urrutia, et al., "Separation of Recollision Mechanisms in Nonsequential Strong Field Double Ionization of Ar: The Role of Excitation Tunneling," *Physical Review Letters* **87**:043003 (2001).
109. M. Lein, E. K. U. Gross, and V. Engel, "Intense-Field Double Ionization of Helium: Identifying the Mechanism," *Physical Review Letters* **85**:4707–4710 (2000).
110. R. Kopold, W. Becker, H. Rottke, and W. Sandner, "Routes to Nonsequential Double Ionization," *Physical Review Letters* **85**:3781–3784 (2000).
111. H. W. van der Hart, and K. Burnett, "Recollision Model for Double Ionization of Atoms in Strong Laser Fields," *Physical Review A* **62**:013407 (2000).

112. R. Moshhammer, B. Feuerstein, W. Schmitt, A. Dorn, C. D. Schroter, J. Ullrich, H. Rottke, et al., "Momentum Distributions of  $Nen^+$  Ions Created by an Intense Ultrashort Laser Pulse," *Physical Review Letters* **84**:447–450 (2000).
113. B. Sheehy, R. Lafon, M. Widmer, B. Walker, L. F. DiMauro, P. A. Agostini, and K. C. Kulander, "Single- and Multiple-Electron Dynamics in the Strong-Field Tunneling Limit," *Physical Review A* **58**:3942–3952 (1998).
114. B. Walker, B. Sheehy, K. C. Kulander, and L. F. DiMauro, "Elastic Rescattering in the Strong Field Tunneling Limit," *Physical Review Letters* **77**:5031–5034 (1996).
115. B. Walker, B. Sheehy, L. F. DiMauro, P. Agostini, K. J. Schafer, and K. C. Kulander, "Precision-Measurement of Strong-Field Double-Ionization of Helium," *Physical Review Letters* **73**:1227–1230 (1994).
116. W. Becker, A. Lohr, and M. Kleber, "Effects of Rescattering on above-Threshold Ionization," *Journal of Physics B-Atomic Molecular and Optical Physics* **27**:L325–L332 (1994).
117. D. N. Fittinghoff, P. R. Bolton, B. Chang, and K. C. Kulander, "Observation of Nonsequential Double Ionization of Helium with Optical Tunneling," *Physical Review Letters* **69**:2642–2645 (1992).
118. R. Dorner, H. Brauning, J. M. Feagin, V. Mergel, O. Jagutzki, L. Spielberger, T. Vogt, et al., "Photo-Double-Ionization of He: Fully Differential and Absolute Electronic and Ionic Momentum Distributions," *Physical Review A* **57**:1074–1090 (1998).
119. R. Wehlitz, F. Heiser, O. Hemmers, B. Langer, A. Menzel, and U. Becker, "Electron-Energy and Electron-Angular Distributions in the Double Photoionization of Helium," *Physical Review Letters* **67**:3764–3767 (1991).
120. U. Eichmann, M. Dorr, H. Maeda, W. Becker, and W. Sandner, "Collective Multielectron Tunneling Ionization in Strong Fields," *Physical Review Letters* **84**:3550–3553 (2000).
121. D. N. Fittinghoff, P. R. Bolton, B. Chang, and K. C. Kulander, "Polarization Dependence of Tunneling Ionization of Helium and Neon by 120-fs Pulses at 614 nm," *Physical Review A* **49**:2174–2177 (1994).
122. N. Milosevic, V. P. Krainov, and T. Brabec, "Relativistic Theory of Tunnel Ionization," *Journal of Physics B-Atomic Molecular and Optical Physics* **35**:3515–3529 (2002).
123. S. X. Hu and A. F. Starace, "GeV Electrons from Ultraintense Laser Interaction with Highly Charged Ions," *Physical Review Letters* **88**:245003 (2002).
124. S. Palaniyappan, I. Ghebregziabher, A. DiChiara, J. MacDonald, and B. C. Walker, "Emergence from non-relativistic strong-field rescattering to ultrastrong-field laser-atom physics: A semiclassical analysis," *Physical Review A* **74**:033403 (2006).
125. I. Ghebregziabher, S. Palaniyappan, J. MacDonald, and B. C. Walker, "Impact of the Laser Magnetic Field on Recombination and Bremsstrahlung Radiation from Atomic Ionization Rescattering in Ultraintense Fields," *Physical Review A* **73**:033419 (2006).
126. S. Palaniyappan, A. DiChiara, E. Chowdhury, A. Falkowski, G. Ongadi, E. L. Huskins, and B. C. Walker, "Ultrastrong Field Ionization of  $Nen^+$  ( $n \leq 8$ ): Rescattering and the Role of the Magnetic Field," *Physical Review Letters* **94**:243003 (2005).
127. M. Pont and M. Gavrila, "Stabilization of Atomic-Hydrogen in Superintense, High-Frequency Laser Fields of Circular-Polarization," *Physical Review Letters* **65**:2362–2365 (1990).
128. Q. Su, J. H. Eberly, and J. Javanainen, "Dynamics of Atomic Ionization Suppression and Electron Localization in an Intense High-Frequency Radiation-Field," *Physical Review Letters* **64**:862–865 (1990).
129. K. Burnett, P. L. Knight, B. R. M. Piraux, and V. C. Reed, "Suppression of Ionization in Strong Laser Fields," *Physical Review Letters* **66**:301–304 (1991).
130. M. V. Fedorov and O. V. Tikhonova, "Strong-Field Short-Pulse Photoionization of Rydberg Atoms: Interference Stabilization and Distribution of the Photoelectron Density in Space and Time," *Physical Review A* **58**:1322–1334 (1998).
131. O. V. Tikhonova, E. A. Volkova, A. M. Popov, and M. V. Fedorov, "Interference Stabilization of Rydberg Atoms: Analytical Investigation and Numerical Simulations," *Laser Physics* **8**:85–92 (1998).
132. M. P. DeBoer, J. H. Hoogenraad, R. B. Vrijen, L. D. Noordam, and H. G. Muller, "Indications of High-Intensity Adiabatic Stabilization in Neon," *Physical Review Letters* **71**:3263–3266 (1993).
133. L. N. Gaier and C. H. Keitel, "Relativistic Classical Monte Carlo Simulations of Stabilization of Hydrogenlike Ions in Intense Laser Pulses," *Physical Review A* **65**:023406 (2002).
134. A. Talebpour, J. Yang, and S. L. Chin, "Semi-Empirical Model for the Rate of Tunnel Ionization of N-2 and O-2 Molecule in an Intense Ti: Sapphire Laser Pulse," *Optics Communications* **163**:29–32 (1999).

135. J. H. Posthumus, J. Plumridge, L. J. Frasinski, K. Codling, A. J. Langley, and P. F. Taday, "Double-Pulse Measurements of Laser-Induced Alignment of Molecules," *Journal of Physics B-Atomic Molecular and Optical Physics* **31**:L985–L993 (1998).
136. J. H. Posthumus, J. Plumridge, M. K. Thomas, K. Codling, L. J. Frasinski, A. J. Langley, and P. F. Taday, "Dynamic and Geometric Laser-Induced Alignment of Molecules in Intense Laser Fields," *Journal of Physics B-Atomic Molecular and Optical Physics* **31**:L553–L562 (1998).
137. P. Hering and C. Cornaggia, "Coulomb Explosion of N-2 and CO2 Using Linearly and Circularly Polarized Femtosecond Laser Pulses," *Physical Review A* **59**:2836–2843 (1999).
138. C. Cornaggia, "Small Polyatomic Molecules in Intense Laser Fields," in *Molecules and Clusters in Intense Laser Fields*, J. Posthumus, (ed.), Cambridge University Press, Cambridge, 2001, pP. 84–113.
139. P. H. Bucksbaum, A. Zavriyev, H. G. Muller, and D. W. Schumacher, "Softening of the H<sub>2</sub><sup>+</sup> Molecular-Bond in Intense Laser Fields," *Physical Review Letters* **64**:1883–1886 (1990).
140. B. Sheehy and L. F. DiMauro, "Atomic and Molecular Dynamics in Intense Optical Fields," *Annual Review of Physical Chemistry* **47**:463–494 (1996).
141. J. H. Shirley, "Solution of the Schrödinger Equation with a Hamiltonian Periodic in Time," *Physical Review* **138**:B979–B987 (1965).
142. A. D. Bandrauk and M. L. Sink, "Photo-Dissociation in Intense Laser Fields—Predissociation Analogy," *Journal of Chemical Physics* **74**:1110–1117 (1981).
143. A. Giustisuzor, X. He, O. Atabek, and F. H. Mies, "Above-Threshold Dissociation of H<sub>2</sub><sup>+</sup> in Intense Laser Fields," *Physical Review Letters* **64**:515–518 (1990).
144. G. Jolicard and O. Atabek, "Above-Threshold-Dissociation Dynamics of H<sub>2</sub><sup>(+)</sup> with Short Intense Laser-Pulses," *Physical Review A* **46**:5845–5855 (1992).
145. J. H. Posthumus and J. F. McCann, "Diatomic Molecules in Intense Laser Fields," in *Molecules and Clusters in Intense Laser Fields*, J. Posthumus, (ed.), Cambridge University Press, Cambridge, 2001, pP. 27–83.
146. M. R. Thompson, M. K. Thomas, P. F. Taday, J. H. Posthumus, A. J. Langley, L. J. Frasinski, and K. Codling, "One and Two-Colour Studies of the Dissociative Ionization and Coulomb Explosion of H<sub>2</sub> with intense Ti: Sapphire Laser Pulses," *Journal of Physics B-Atomic Molecular and Optical Physics* **30**:5755–5772 (1997).
147. C. Cornaggia, J. Lavancier, D. Normand, J. Morellec, P. Agostini, J. P. Chambaret, and A. Antonetti, "Multielectron Dissociative Ionization of Diatomic-Molecules in an Intense Femtosecond Laser Field," *Physical Review A* **44**:4499–4505 (1991).
148. C. Cornaggia and P. Hering, "Nonsequential Double Ionization of Small Molecules Induced by a Femtosecond Laser Field," *Physical Review A* **6202**:023403 (2000).
149. A. Talebpour, S. Laroche, and S. L. Chin, "Non-Sequential and Sequential Double Ionization of No in an Intense Femtosecond Ti:Sapphire Laser Pulse," *Journal of Physics B-Atomic Molecular and Optical Physics* **30**:L245–L250 (1997).
150. C. Guo, M. Li, J. P. Nibarger, and G. N. Gibson, "Single and Double Ionization of Diatomic Molecules in Strong Laser Fields," *Physical Review A* **58**:R4271–R4274 (1998).
151. S. Chelkowski and A. D. Bandrauk, "Two-Step Coulomb Explosions of Diatoms in Intense Laser Fields," *Journal of Physics B-Atomic Molecular and Optical Physics* **28**:L723–L731 (1995).
152. H. T. Yu, T. Zuo, and A. D. Bandrauk, "Intense Field Ionization of Molecules with Ultra-Short Laser Pulses-Enhanced Ionization and Barrier-Suppression Effects," *Journal of Physics B-Atomic Molecular and Optical Physics* **31**:1533–1551 (1998).
153. M. Schmidt, D. Normand, and C. Cornaggia, "Laser-Induced Trapping of Chlorine Molecules with Picosecond and Femtosecond Pulses," *Physical Review A* **50**:5037–5045 (1994).
154. J. H. Posthumus, L. J. Frasinski, A. J. Giles, and K. Codling, "Dissociative Ionization of Molecules in Intense Laser Fields—a Method of Predicting Ion Kinetic Energies and Appearance Intensities," *Journal of Physics B-Atomic Molecular and Optical Physics* **28**:L349–L353 (1995).
155. E. Constant, H. Stapelfeldt, and P. B. Corkum, "Observation of Enhanced Ionization of Molecular Ions in Intense Laser Fields," *Physical Review Letters* **76**:4140–4143 (1996).
156. J. F. McCann and J. H. Posthumus, "Molecular Dynamics in Intense Laser Fields," *Philosophical Transactions of the Royal Society of London Series a-Mathematical Physical and Engineering Sciences* **357**:1309–1329 (1999).

157. T. Zuo and A. D. Bandrauk, "Charge-Resonance-Enhanced Ionization of Diatomic Molecular-Ions by Intense Lasers," *Physical Review A* **52**:R2511–R2514 (1995).
158. R. J. Levis and M. J. DeWitt, "Photoexcitation, Ionization, and Dissociation of Molecules Using Intense Near-Infrared Radiation of Femtosecond Duration," *Journal of Physical Chemistry A* **103**:6493–6507 (1999).
159. M. J. DeWitt and R. J. Levis, "Concerning the Ionization of Large Polyatomic Molecules with Intense Ultrafast Lasers," *Journal of Chemical Physics* **110**:11368–11375 (1999).
160. J. J. Macklin, J. D. Kmetec, and C. L. Gordon, "High-Order Harmonic-Generation Using Intense Femtosecond Pulses," *Physical Review Letters* **70**:766–769 (1993).
161. M. D. Perry and J. K. Crane, "High-Order Harmonic Emission from Mixed Fields," *Physical Review A* **48**:R4051–R4054 (1993).
162. M. Y. Ivanov and P. B. Corkum, "Generation of High-Order Harmonics from Inertially Confined Molecular-Ions," *Physical Review A* **48**:580–590 (1993).
163. T. D. Donnelly, T. Ditmire, K. Neuman, M. D. Perry and R. W. Falcone, "High-Order Harmonic Generation in Atom Clusters," *Physical Review Letters* **76**:2472–2475 (1996).
164. K. S. Budil, P. Salieres, A. Lhuillier, T. Ditmire, and M. D. Perry, "Influence of Ellipticity on Harmonic-Generation," *Physical Review A* **48**:R3437–R3440 (1993).
165. P. Antoine, A. Lhuillier, M. Lewenstein, P. Salieres, and B. Carre, "Theory of High-Order Harmonic Generation by an Elliptically Polarized Laser Field," *Physical Review A* **53**:1725–1745 (1996).
166. T. Ditmire, E. T. Gumbrell, R. A. Smith, J. W. G. Tisch, D. D. Meyerhofer, and M. H. R. Hutchinson, "Spatial Coherence Measurement of Soft X-Ray Radiation Produced by High Order Harmonic Generation," *Physical Review Letters* **77**:4756–4759 (1996).
167. A. L'Huillier, L. -A. Lompre, G. Mainfray, and C. Manus, "High-Order Harmonic Generation in Rare Gases," in *Atoms in Intense Laser Fields*, M. Gavrilu, (ed.), Academic Press, San Diego, 1992, pP. 139–206.
168. C. Spielmann, N. H. Burnett, S. Sartania, R. Koppitsch, M. Schnurer, C. Kan, M. Lenzner, P. Wobrauschek, and F. Krausz, "Generation of Coherent X-Rays in the Water Window Using 5-Femtosecond Laser Pulses," *Science* **278**:661–664 (1997).
169. M. Lewenstein, P. Balcou, M. Y. Ivanov, A. Lhuillier, and P. B. Corkum, "Theory of High-Harmonic Generation by Low-Frequency Laser Fields," *Physical Review A* **49**:2117–2132 (1994).
170. J. L. Krause, K. J. Schafer, and K. C. Kulander, "High-Order Harmonic-Generation from Atoms and Ions in the High-Intensity Regime," *Physical Review Letters* **68**:3535–3538 (1992).
171. M. Lewenstein, P. Salieres, and A. Lhuillier, "Phase of the Atomic Polarization in High-Order Harmonic-Generation," *Physical Review A* **52**:4747–4754 (1995).
172. P. Salieres, A. Lhuillier, and M. Lewenstein, "Coherence Control of High-Order Harmonics," *Physical Review Letters* **74**:3776–3779 (1995).
173. P. Balcou, A. S. Dederichs, M. B. Gaarde, and A. L'Huillier, "Quantum-Path Analysis and Phase Matching of High-Order Harmonic Generation and High-Order Frequency Mixing Processes in Strong Laser Fields," *Journal of Physics B-Atomic Molecular and Optical Physics* **32**:2973–2989 (1999).
174. M. B. Gaarde, F. Salin, E. Constant, P. Balcou, K. J. Schafer, K. C. Kulander, and A. L'Huillier, "Spatiotemporal Separation of High Harmonic Radiation into Two Quantum Path Components," *Physical Review A* **59**:1367–1373 (1999).
175. R. W. Boyd, *Nonlinear Optics*, Academic Press, Boston, 1992.
176. T. Ditmire, J. K. Crane, H. Nguyen, L. B. Dasilva, and M. D. Perry, "Energy-Yield and Conversion-Efficiency Measurements of High-Order Harmonic Radiation," *Physical Review A* **51**:R902–R905 (1995).
177. E. Takahashi, Y. Nabekawa, M. Nurhuda, and K. Midorikawa, "Generation of High-Energy High-Order Harmonics by Use of a Long Interaction Medium," *Journal of the Optical Society of America B-Optical Physics* **20**:158–165 (2003).
178. M. Drescher, M. Hentschel, R. Kienberger, M. Uiberacker, V. Yakovlev, A. Scrinizi, T. Westerwalbesloh, U. Kleineberg, U. Heinzmann, and F. Krausz, "Time-Resolved Atomic Inner-Shell Spectroscopy," *Nature* **419**:803–807 (2002).
179. A. Baltuska, T. Udem, M. Uiberacker, M. Hentschel, E. Goulielmakis, C. Gohle, R. Holzwarth, et al., "Attosecond Control of Electronic Processes by Intense Light Fields," *Nature* **421**:611–615 (2003).

180. P. Antoine, A. Lhuillier, and M. Lewenstein, "Attosecond Pulse Trains Using High-Order Harmonics," *Physical Review Letters* **77**:1234–1237 (1996).
181. T. Ditmire, T. Donnelly, A. M. Rubenchik, R. W. Falcone, and M. D. Perry, "Interaction of Intense Laser Pulses with Atomic Clusters," *Physical Review A* **53**:3379–3402 (1996).
182. A. McPherson, B. D. Thompson, A. B. Borisov, K. Boye, and C. K. Rhodes, "Multiphoton-Induced X-Ray-Emission at 4–5 keV from Xe Atoms with Multiple Core Vacancies," *Nature* **370**:631–634 (1994).
183. V. P. Krainov and M. B. Smirnov, "Cluster Beams in the Super-Intense Femtosecond Laser Pulse," *Physics Reports-Review Section of Physics Letters* **370**:237–331 (2002).
184. W. L. Kruer, *The Physics of Laser Plasma Interactions*, Addison-Wesley, Redwood City, 1988.
185. C. Siedschlag and J. M. Rost, "Enhanced Ionization in Small Rare-Gas Clusters," *Physical Review A* **67**:013404 (2003).
186. C. Rose-Petruck, K. J. Schafer, K. R. Wilson, and C. P. J. Barty, "Ultrafast Electron Dynamics and Inner-Shell Ionization in Laser Driven Clusters," *Physical Review A* **55**:1182–1190 (1997).
187. W. Lotz, "An Empirical Formula for the Electron-Impact Ionization Cross-Section," *Z. fur Physik* **206**:205–211 (1967).
188. E. M. Snyder, S. A. Buzza, and A. W. Castleman, "Intense Field-Matter Interactions: Multiple Ionization of Clusters," *Physical Review Letters* **77**:3347–3350 (1996).
189. T. Ditmire, J. W. G. Tisch, E. Springate, M. B. Mason, N. Hay, R. A. Smith, J. Marangos, and M. H. R. Hutchinson, "High-Energy Ions Produced in Explosions of Superheated Atomic Clusters," *Nature* **386**:54–56 (1997).
190. M. Lezius, S. Dobosz, D. Normand, and M. Schmidt, "Explosion Dynamics of Rare Gas Clusters in Strong Laser Fields," *Physical Review Letters* **80**:261–264 (1998).
191. B. N. Breizman, A. V. Arefiev, and M. V. Fomyts'kyi, "Nonlinear Physics of Laser-Irradiated Microclusters," *Physics of Plasmas* **12**:056706 (2005).
192. K. W. Madison, P. K. Patel, M. Allen, D. Price, R. Fitzpatrick, and T. Ditmire, "Role of Laser-Pulse Duration in the Neutron Yield of Deuterium Cluster Targets," *Physical Review A* **70**:053201 (2004).
193. K. W. Madison, P. K. Patel, D. Price, A. Edens, M. Allen, T. E. Cowan, J. Zweiback, and T. Ditmire, "Fusion Neutron and Ion Emission from Deuterium and Deuterated Methane Cluster Plasmas," *Physics of Plasmas* **11**:270–277 (2004).
194. L. D. Landau and E. M. Lifshitz, *Electrodynamics of Continuous Media*, Pergamon Press, Oxford, 1984, pp. 272–273.
195. V. P. Silin, "Nonlinear High-Frequency Plasma Conductivity," *Soviet Physics, JETP* **20**:1510 (1965).
196. T. Ditmire, R. A. Smith, J. W. G. Tisch, and M. H. R. Hutchinson, "High Intensity Laser Absorption by Gases of Atomic Clusters," *Physical Review Letters* **78**:3121–3124 (1997).
197. T. Ditmire, T. Donnelly, R. W. Falcone, and M. D. Perry, "Strong X-Ray-Emission from High-Temperature Plasmas Produced by Intense Irradiation of Clusters," *Physical Review Letters* **75**:3122–3125 (1995).
198. T. Ditmire, R. A. Smith, R. S. Marjoribanks, G. Kulcsa, and M. H. R. Hutchinson, "X-Ray Yields from Xe Clusters Heated by Short Pulse High Intensity Lasers," *Applied Physics Letters* **71**:166–168 (1997).
199. T. Ditmire, J. Zweiback, V. P. Yanovsky, T. E. Cowan, G. Hays, and K. B. Wharton, "Nuclear Fusion from Explosions of Femtosecond Laser-Heated Deuterium Clusters," *Nature* **398**:489–492 (1999).
200. G. C. Junkel-Vives, J. Abdallah, F. Blasco, F. Dorchies, T. Caillaud, C. Bonte, C. Stenz, et al., "Evidence of Supercritical Density in 45-fs-Laser-Irradiated Ar-Cluster Plasmas," *Physical Review A* **66**:033204 (2002).
201. U. Saalmann and J. M. Rost, "Ionization of Clusters in Intense Laser Pulses Through Collective Electron Dynamics," *Physical Review Letters* **91**:223401 (2003).
202. J. Zweiback, T. Ditmire, and M. D. Perry, "Femtosecond Time-Resolved Studies of the Dynamics of Noble-Gas Cluster Explosions," *Physical Review A* **59**:R3166–R3169 (1999).
203. H. M. Milchberg, S. J. McNaught, and E. Parra, "Plasma Hydrodynamics of the Intense Laser-Cluster Interaction," *Physical Review E* **64**:056402 (2001).
204. A. B. Langdon, "Non-Linear Inverse Bremsstrahlung and Heated-Electron Distributions," *Physical Review Letters* **44**:575–579 (1980).
205. G. J. Pert, "Inverse Bremsstrahlung Absorption Inlarge Radiation Fields During Binary Collisions—Classical Theory," *Journal of Physics A: General Physics* **5**:506–520 (1972).



206. R. D. Jones and K. Lee, "Kinetic-Theory, Transport, and Hydrodynamics of a High-Z Plasma in the Presence of an Intense Laser Field," *Physics of Fluids* **25**:2307–2323 (1982).
207. C. S. Liu and M. N. Rosenbluth, "Parametric Decay of Electromagnetic-Waves into 2 Plasmons and Its Consequences," *Physics of Fluids* **19**:967–971 (1976).
208. D. W. Forslund, J. M. Kindel, and E. L. Lindman, "Theory of Stimulated Scattering Processes in Laser-Irradiated Plasmas," *Physics of Fluids* **18**:1002–1016 (1975).
209. C. B. Darrow, C. Coverdale, M. D. Perry, W. B. Mori, C. Clayton, K. Marsh, and C. Joshi, "Strongly Coupled Stimulated Raman Backscatter from Subpicosecond Laser-Plasma Interactions," *Physical Review Letters* **69**:442–445 (1992).
210. W. B. Mori, C. D. Decker, D. E. Hinkel, and T. Katsouleas, "Raman Forward Scattering of Short-Pulse High-Intensity Lasers," *Physical Review Letters* **72**:1482–1485 (1994).
211. S. Guerin, G. Laval, P. Mora, J. C. Adam, A. Heron, and A. Bendib, "Modulational and Raman Instabilities in the Relativistic Regime," *Physics of Plasmas* **2**:2807–2814 (1995).
212. V. Malka, S. Fritzler, E. Lefebvre, M. M. Aeonard, F. Burgy, J. P. Chambaret, J. F. Chemin, et al., "Electron Acceleration by a Wake Field Forced by an Intense Ultrashort Laser Pulse," *Science* **298**:1596–1600 (2002).
213. A. Modena, Z. Najmudin, A. E. Dangor, C. E. Clayton, K. A. Marsh, C. Joshi, V. Malka, et al., "Electron Acceleration from the Breaking of Relativistic Plasma-Waves," *Nature* **377**:606–608 (1995).
214. K. Nakajima, D. Fisher, T. Kawakubo, H. Nakanishi, A. Ogata, Y. Kato, Y. Kitagawa, et al., "Observation of Ultrahigh Gradient Electron Acceleration by a Self-Modulated Intense Short Laser-Pulse," *Physical Review Letters* **74**:4428–4431 (1995).
215. M. Everett, A. Lal, D. Gordon, C. E. Clayton, K. A. Marsh, and C. Joshi, "Trapped Electron Acceleration by a Laser-Driven Relativistic Plasma-Wave," *Nature* **368**:527–529 (1994).
216. J. Krall, A. Ting, E. Esarey, and P. Sprangle, "Enhanced Acceleration in a Self-Modulated-Laser Wake-Field Accelerator," *Physical Review E* **48**:2157–2161 (1993).
217. P. Sprangle, E. Esarey, A. Ting, and G. Joyce, "Laser Wakefield Acceleration and Relativistic Optical Guiding," *Applied Physics Letters* **53**:2146–2148 (1988).
218. S. P. D. Mangles, C. D. Murphy, Z. Najmudin, A. G. R. Thomas, J. L. Collier, A. E. Dangor, E. J. Divall, et al., "Monoenergetic Beams of Relativistic Electrons from Intense Laser-Plasma Interactions," *Nature* **431**:535–538 (2004).
219. C. G. R. Geddes, C. Toth, J. van Tilborg, E. Esarey, C. B. Schroeder, D. Bruhwiler, C. Nieter, J. Cary, and W. P. Leemans, "High-Quality Electron Beams from a Laser Wakefield Accelerator Using Plasma-Channel Guiding," *Nature* **431**:538–541 (2004).
220. J. Faure, Y. Glinec, A. Pukhov, S. Kiselev, S. Gordienko, E. Lefebvre, J. P. Rousseau, F. Burgy, and V. Malka, "A Laser-Plasma Accelerator Producing Monoenergetic Electron Beams," *Nature* **431**:541–544 (2004).
221. A. Pukhov and J. Meyer-ter-Vehn, "Laser Wake Field Acceleration: The Highly Non-Linear Broken-Wave Regime," *Applied Physics B-Lasers and Optics* **74**:355–361 (2002).
222. P. Sprangle, E. Esarey, J. Krall, and G. Joyce, "Propagation and Guiding of Intense Laser-Pulses in Plasmas," *Physical Review Letters* **69**:2200–2203 (1992).
223. K. Krushelnick, E. L. Clark, Z. Najmudin, M. Salvati, M. I. K. Santala, M. Tatarakis, A. E. Dangor, et al., "Multi-MeV Ion Production from High-Intensity Laser Interactions with Underdense Plasmas," *Physical Review Letters* **83**:737–740 (1999).
224. A. Pukhov, Z. M. Sheng, and J. Meyer-ter-Vehn, "Particle Acceleration in Relativistic Laser Channels," *Physics of Plasmas* **6**:2847–2854 (1999).
225. S. C. Rae, "Ionization-Induced Defocusing of Intense Laser-Pulses in High-Pressure Gases," *Optics Communications* **97**:25–28 (1993).
226. P. Monot, T. Augustine, L. A. Lompre, G. Mainfray, and C. Manus, "Focusing Limits of a Terawatt Laser in an Underdense Plasma," *Journal of the Optical Society of America B-Optical Physics* **9**:1579–1584 (1992).
227. M. Borghesi, A. J. MacKinnon, L. Barringer, R. Gaillard, L. A. Gizzi, C. Meyer, O. Willi, A. Pukhov, and J. Meyer-ter-Vehn, "Relativistic Channeling of a Picosecond Laser Pulse in a Near-Critical Preformed Plasma," *Physical Review Letters* **78**:879–882 (1997).
228. P. Monot, T. Augustine, P. Gibbon, F. Jakober, and G. Mainfray, "Collimation of an Intense Laser Beam by a Weakly Relativistic Plasma," *Physical Review E* **52**:R5780–R5783 (1995).

229. P. Monot, T. Auguste, P. Gibbon, F. Jakober, G. Mainfray, A. Dulieu, M. Louisjacquet, G. Malka, and J. L. Miquel, "Experimental Demonstration of Relativistic Self-Channeling of a Multiterawatt Laser-Pulse in an Underdense Plasma," *Physical Review Letters* **74**:2953–2956 (1995).
230. A. B. Borisov, A. V. Borovskiy, O. B. Shiryaev, V. V. Korobkin, A. M. Prokhorov, J. C. Solem, T. S. Luk, K. Boyer, and C. K. Rhodes, "Relativistic and Charge-Displacement Self-Channeling of Intense Ultrashort Laser-Pulses in Plasmas," *Physical Review A* **45**:5830–5845 (1992).
231. I. Watts, M. Zepf, E. L. Clark, M. Tatarakis, K. Krushelnick, A. E. Dangor, R. Allott, R. J. Clarke, D. Neely, and P. A. Norreys, "Measurements of Relativistic Self-Phase-Modulation in Plasma," *Physical Review E* **66**:036409 (2002).
232. U. Teubner, I. Uschmann, P. Gibbon, D. Altenbernd, E. Forster, T. Feurer, W. Theobald, et al., "Absorption and Hot Electron Production by High Intensity Femtosecond UV-Laser Pulses In Solid Targets," *Physical Review E* **54**:4167–4177 (1996).
233. D. F. Price, R. M. More, R. S. Walling, G. Guethlein, R. L. Shepherd, R. E. Stewart, and W. E. White, "Absorption of Ultrashort Laser-Pulses by Solid Targets Heated Rapidly to Temperatures 1–1000 eV," *Physical Review Letters* **75**:252–255 (1995).
234. V. L. Ginzberg, *The Properties of Electromagnetic Waves in Plasma*, Pergamon, New York, 1964.
235. D. W. Forslund, J. M. Kindel, and K. Lee, "Theory of Hot-Electron Spectra at High Laser Intensity," *Physical Review Letters* **39**:284–288 (1977).
236. F. N. Beg, A. R. Bell, A. E. Dangor, C. N. Danson, A. P. Fews, M. E. Glinsky, B. A. Hammel, P. Lee, P. A. Norreys, and M. Tatarakis, "A Study of Picosecond Laser-Solid Interactions up to  $10(19) \text{ W cm}^{-2}$ ," *Physics of Plasmas* **4**:447–457 (1997).
237. M. K. Grimes, A. R. Rundquist, Y. S. Lee, and M. C. Downer, "Experimental Identification of 'Vacuum Heating' at Femtosecond-Laser-Irradiated Metal Surfaces," *Physical Review Letters* **82**:4010–4013 (1999).
238. P. Gibbon and A. R. Bell, "Collisionless Absorption in Sharp-Edged Plasmas," *Physical Review Letters* **68**:1535–1538 (1992).
239. F. Brunel, "Not-So-Resonant, Resonant Absorption," *Physical Review Letters* **59**:52–55 (1987).
240. W. Rozmus and V. T. Tikhonchuk, "Skin Effect and Interaction of Short Laser-Pulses with Dense-Plasmas," *Physical Review A* **42**:7401–7412 (1990).
241. W. L. Kruer and K. Estabrook, "J<sub>x</sub> Heating by Very Intense Laser-Light," *Physics of Fluids* **28**:430–432 (1985).
242. S. C. Wilks, W. L. Kruer, M. Tabak, and A. B. Langdon, "Absorption of Ultra-Intense Laser-Pulses," *Physical Review Letters* **69**:1383–1386 (1992).
243. M. Zepf, M. CastroColin, D. Chambers, S. G. Preston, J. S. Wark, J. Zhang, C. N. Danson, et al., "Measurements of the Hole Boring Velocity from Doppler Shifted Harmonic Emission from Solid Targets," *Physics of Plasmas* **3**:3242–3244 (1996).
244. X. Liu and D. Umstadter, "Competition between Ponderomotive and Thermal Forces in Short-Scale-Length Laser Plasmas," *Physical Review Letters* **69**:1935–1938 (1992).
245. L. O. Silva, M. Marti, J. R. Davies, R. A. Fonseca, C. Ren, F. S. Tsung, and W. B. Mori, "Proton Shock Acceleration in Laser-Plasma Interactions," *Physical Review Letters* **92**:015002 (2004).
246. D. vonderLinde and K. Rzazewski, "High-Order Optical Harmonic Generation from Solid Surfaces," *Applied Physics B-Lasers and Optics* **63**:499–506 (1996).
247. R. Lichters, J. MeyerterVehn, and A. Pukhov, "Short-Pulse Laser Harmonics from Oscillating Plasma Surfaces Driven at Relativistic Intensity," *Physics of Plasmas* **3**:3425–3437 (1996).
248. P. A. Norreys, M. Zepf, S. Moustazis, A. P. Fews, J. Zhang, P. Lee, M. Bakarezos, et al., "Efficient Extreme UV Harmonics Generated from Picosecond Laser Pulse Interactions with Solid Targets," *Physical Review Letters* **76**:1832–1835 (1996).
249. P. Gibbon, "Harmonic Generation by Femtosecond Laser-Solid Interaction: A Coherent 'water-window' Light Source?," *Physical Review Letters* **76**:50–53 (1996).
250. P. Kaw and J. Dawson, "Relativistic Nonlinear Propagation of Laser Beams in Cold Overdense Plasma," *Physics of Fluids* **13**:472–481 (1970).
251. J. D. Kmetec, C. L. Gordon, J. J. Macklin, B. E. Lemoff, G. S. Brown, and S. E. Harris, "MeV X-Ray Generation with a Femtosecond Laser," *Physical Review Letters* **68**:1527–1530 (1992).

252. A. Saemann, K. Eidmann, I. E. Golovkin, R. C. Mancini, E. Andersson, E. Forster, and K. Witte, "Isochoric Heating of Solid Aluminum by Ultrashort Laser Pulses Focused on a Tamped Target," *Physical Review Letters* **82**:4843–4846 (1999).
253. D. Hilscher, O. Berndt, M. Enke, U. Jahnke, P. V. Nickles, H. Ruhl, and W. Sandner, "Neutron Energy Spectra from the Laser-Induced D(d,n)He-3 Reaction," *Physical Review E* **64**01:016414 (2001).
254. A. R. Bell, F. N. Beg, Z. Chang, A. E. Dangor, C. N. Danson, C. B. Edwards, A. P. Fews, et al., "Observation of Plasma-Confinement in Picosecond Laser-Plasma Interactions," *Physical Review E* **48**:2087–2093 (1993).
255. M. Tatarakis, A. Gopal, I. Watts, F. N. Beg, A. E. Dangor, K. Krushelnick, U. Wagner, et al., "Measurements of Ultrastrong Magnetic Fields During Relativistic Laser-Plasma Interactions," *Physics of Plasmas* **9**:2244–2250 (2002).
256. R. A. Snavely, M. H. Key, S. P. Hatchett, T. E. Cowan, M. Roth, T. W. Phillips, M. A. Stoyer, et al., "Intense High-Energy Proton Beams from Petawatt-Laser Irradiation of Solids," *Physical Review Letters* **85**:2945–2948 (2000).
257. S. C. Wilks, A. B. Langdon, T. E. Cowan, M. Roth, M. Singh, S. Hatchett, M. H. Key, D. Pennington, A. MacKinnon, and R. A. Snavely, "Energetic Proton Generation in Ultra-Intense Laser-Solid Interactions," *Physics of Plasmas* **8**:542–549 (2001).
258. S. P. Hatchett, C. G. Brown, T. E. Cowan, E. A. Henry, J. S. Johnson, M. H. Key, J. A. Koch, et al., "Electron, Photon, and Ion Beams from the Relativistic Interaction of Petawatt Laser Pulses with Solid Targets," *Physics of Plasmas* **7**:2076–2082 (2000).
259. M. Tabak, J. Hammer, M. E. Glinsky, W. L. Kruer, S. C. Wilks, J. Woodworth, E. M. Campbell, M. D. Perry, and R. J. Mason, "Ignition and High-Gain with Ultrapowerful Lasers," *Physics of Plasmas* **1**:1626–1634 (1994).
260. R. Kodama, P. A. Norreys, K. Mima, A. E. Dangor, R. G. Evans, H. Fujita, Y. Kitagawa, et al., "Fast Heating of Ultrahigh-Density Plasma as a Step Towards Laser Fusion Ignition," *Nature* **412**:798–802 (2001).
261. J. Ren, W. F. Cheng, S. L. Li, and S. Suckewer, "A New Method for Generating Ultraintense and Ultrashort Laser Pulses," *Nature Physics* **3**:732–736 (2007).

---

# SLOW LIGHT PROPAGATION IN ATOMIC AND PHOTONIC MEDIA

---

Jacob B. Khurgin

*Department of Electrical and Computer Engineering  
Johns Hopkins University  
Baltimore, Maryland*

---

## 22.1 GLOSSARY

---

$\omega$	field frequency
$\omega_{12}$	resonant frequency of an atomic transition
$f_{12}$	oscillator strength of an atomic transition
$\gamma_{12}$	damping coefficient (dephasing rate) of the transition
$\epsilon(\omega)$	dielectric constant
$n(\omega)$	refractive index
$e$	electron charge
$m$	free electron mass
$\Omega_p$	plasma frequency
$\Omega$	Rabi frequency
$c$	speed of light in vacuum
$\eta_0$	impedance of vacuum
$\alpha(\omega)$	absorption coefficient
$k(\omega)$	wave vector
$\lambda$	wavelength
$v_g$	group velocity
$S(\omega)$	slow down factor
$\beta_n(\omega)$	$n$ th order dispersion
$B$	bit rate
$N_{st}$	number of bits stored (delayed) in an optical buffer
$\Lambda$	period of Bragg grating or other periodic photonic structure
$\delta n$	refractive index modulation
$\omega_B$	Bragg frequency
$\Delta\omega_{gap}$	Photonic bandgap width

$\kappa$	coupling coefficient
$\tau$	one half of the resonator round trip time
$\Delta V_{\text{pass}}$	width of passband of the photonic structure
$g(\omega)$	gain per unit length of optical amplifier
$\Delta T_d$	delay time

## 22.2 INTRODUCTION

---

While the subject of slow light had become immensely popular in the last decade, the physics of the phenomenon of light propagation in media and structures with reduced group velocity, for which the term “slow light” had been coined, can be traced to the 19th century when the classical theory of dispersion of electromagnetic waves had been first formulated in works of Lorentz<sup>1</sup> and others. Slow wave propagation has also been observed and widely used in the microwave range since as early as the 1940s.<sup>2</sup> Building on this history and following the pioneering works of Refs. 3 and 4, the science and technology of slow light had been transformed from a scientific curiosity to a rapidly evolving field with many potential applications. Slow light propagation had been observed in a wide variety of media and structures ranging from Bose-Einstein condensates and low-pressure metal vapors on one hand, to optical fibers and photonic bandgap structures on the other hand. This makes slow light a truly interdisciplinary field that is not easy to describe in a short review. There exists a body of review work on slow light, starting in 2002 with reviews by Boyd and Gauthier<sup>5</sup> and Milloni<sup>6</sup> who also published a book in 2005 including chapters on slow, fast, and left-handed light.<sup>7</sup> The first comprehensive treatment of diverse slow light schemes has been given in the recent book,<sup>8</sup> which contains contributions from 18 groups that have been actively involved in the slow-light field and have all made significant contributions in recent years.

With all the seeming diversity of slow light schemes, they can be all characterized by a single common feature—the existence of sharp single or multiple resonances. The resonance can be defined by a simple atomic transition, by a Bragg grating or other resonant photonic structure, or by an external laser as in the schemes involving various nonlinear processes—resonant scattering, spectral hole burning, or four-wave mixing. In this chapter, we try to emphasize the commonality of all slow light approaches as well as their distinctive features.

## 22.3 ATOMIC RESONANCE

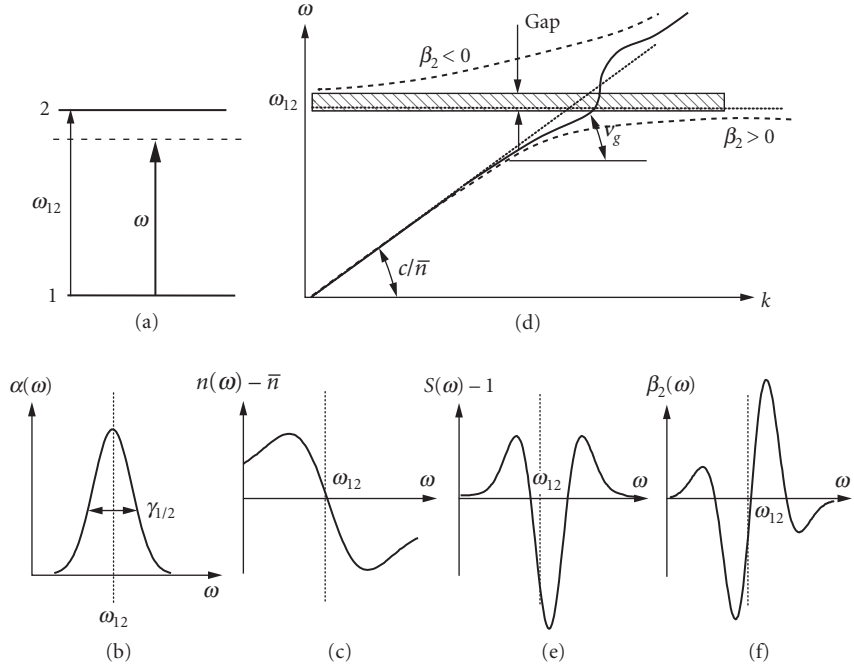
---

Let us consider a simple atomic resonance characterized by the resonant frequency  $\omega_{12}$  and the oscillator strength  $f_{12}$  as shown in Fig. 1a. The dielectric constant in the vicinity of the resonance has a familiar expression

$$\epsilon(\omega) = \bar{\epsilon} + \frac{\Omega_p^2}{\omega_{12}^2 - \omega^2 - j\omega\gamma_{12}} \quad (1)$$

where  $\bar{\epsilon} = \bar{n}^2$  is the nonresonant part or “background” part of the dielectric constant, and  $\gamma_{12}$  is the dephasing rate of the polarization. The expression in the numerator  $\Omega_p$  is the “plasma frequency” that can be found as

$$\Omega_p^2 = \frac{N_a e^2}{\epsilon_0 m_0} f_{12} \quad (2)$$



**FIGURE 1** (a) Two-level atomic resonance; (b) spectrum of absorption coefficient; (c) spectrum of refractive index; (d) dispersion diagram and group velocity in the vicinity of a resonance; (e) spectrum of slowdown factor; and (f) spectrum of group velocity dispersion.

where  $e$  is an electron charge,  $\epsilon_0$  is the dielectric permittivity of vacuum,  $m_0$  is a free electron mass, and  $N_a$  is the concentration of active atoms. From real and imaginary parts of Eq. (1) one immediately obtains the expressions for the absorption coefficient shown in Fig. 1b

$$\alpha(\omega) = \frac{2\omega}{c} \text{Im}(\epsilon^{1/2}) \approx \frac{1}{4\bar{n}c} \frac{\Omega_p^2 \gamma_{12}}{(\omega_{12} - \omega)^2 + \gamma_{12}^2/4} \quad (3)$$

and refractive index (Fig. 1c)

$$n(\omega) = \text{Re}(\epsilon^{1/2}) \approx \bar{n} + \frac{1}{4\bar{n}\omega} \frac{\Omega_p^2 (\omega_{12} - \omega)}{(\omega_{12} - \omega)^2 + \gamma_{12}^2/4} = \bar{n} + \frac{c}{\omega} \alpha(\omega) \frac{\omega_{12} - \omega}{\gamma_{12}} \quad (4)$$

the last relation being a particular form of more general Kramer-Kronig relation. In the vicinity of the resonance the refractive index first increases, then rapidly decreases to the point where  $n(\omega) < \bar{n}$ , and then increases once again to the value of background index. Introducing the wave vector as

$$k(\omega) = n(\omega) \cdot \omega / c \quad (5)$$

One can obtain the dispersion relation between the frequency and wave vector shown in Fig. 1d (solid line) and then introduce group velocity as

$$v_g = \partial\omega / \partial k \quad (6)$$

and slow down factor defined as a relative reduction of group velocity due to resonance

$$S(\omega) = \frac{c}{\bar{n}v_g(\omega)} = 1 + \frac{\Omega_p^2}{4\bar{\epsilon}} \frac{(\omega_{12} - \omega)^2 - \gamma_{12}^2/4}{[(\omega_{12} - \omega)^2 + \gamma_{12}^2/4]^2} = 1 + \frac{c\alpha(\omega)}{\bar{n}\gamma_{12}} \frac{(\omega_{12} - \omega)^2 - \gamma_{12}^2/4}{(\omega_{12} - \omega)^2 + \gamma_{12}^2/4} \quad (7)$$

shown in Fig. 1e. One can now see that there are two regions in which  $S > 0$ , that is, slow light regime, and one region where  $S < 1$ , which can be either the fast light regime ( $0 < S < 1$ ) or negative group velocity regime ( $S < 0$ ) indicating that the light gets reflected. One can get better intuitive picture of the physical phenomena governing slow and fast light propagation by plotting the dispersion curve in the absence of loss (i.e.,  $\gamma_{12} = 0$ ) as dashed line in Fig. 1d. This curve corresponds to a well-known coupled modes model, also known as polariton dispersion curve in solid state physics. The first mode is a photon which in the absence of atomic transition is described by linear dispersion curve  $\omega_p = ck/\bar{n}$ . The second mode is the atomic polarization characterized by a resonance frequency  $\omega_{12}$ . The dispersion curve of atomic polarization is a horizontal line  $\omega_a = \omega_{12}$  indicating the obvious fact that it has zero group velocity as atoms do not move, at least not on the scale of the speed of light. In the vicinity of the resonance, two modes couple into each other and the modified dispersion curve is split into two branches separated by the gap in which the light cannot propagate. Notice that for each wave vector there are two coupled solutions characterized by two different group velocities. The one further away from the resonance has higher group velocity and is usually referred to as a “photonlike,” while the one closer to the resonance has lower group velocity and is usually referred to as “atomlike.” One can then interpret the slow light propagation phenomenon in the following way: The energy gets constantly coupled from the electromagnetic field to the atomic polarization and back. The longer is the time the energy spends in the form of atomic excitation, the slower the coupled mode propagates. Thus the slow light propagation in atomic system can be understood as constant excitation and de-excitation of atoms in which coherence is preserved.

One important implication is related to the strength of the electric field in the electromagnetic wave propagating in a slow light regime caused by an atomic resonance. Since the group velocity is the velocity with which the energy propagates, the local energy density of light beam with power density  $P$  is

$$U = P/v_g = (P\bar{n}/c)S \quad (8)$$

and it gets enhanced by a slowdown factor in the slow light medium. But since the energy density is related to electric field as

$$U = \frac{1}{4}\epsilon_0 \frac{\partial(\omega\epsilon)}{\partial\omega} E^2 + \frac{1}{4}\mu_0 H^2 = S \frac{1}{2}\epsilon_0 \bar{\epsilon} E^2 \quad (9)$$

where the first term corresponds to electric energy and the second term to the magnetic energy. It follows from Eqs. (8) and (9) that  $E^2 = 2\eta_0 P/\bar{n}$ , where  $\eta_0 = \sqrt{\mu_0/\epsilon_0} = 377\Omega$  is the vacuum impedance. Thus the electric field does not get enhanced in the atomic slow light medium. In our intuitive picture this simply means that all the additional energy *compressed* into the medium gets stored in the atomic polarization. This fact has important implications in the nonlinear optics. Also, one can see that without absorption the region of fast light ( $0 < S < 1$ ) is absent in Fig. 1d—and it is important that fast light is associated with the absorption peak, while the slow light is associated only with the off-resonant absorption—hence significant delays of the signal in the slow light are quite possible, while significant advances are difficult to observe due to absorption.

When it comes to practical applications of the slow light, it is important to achieve large delays over significant bandwidth and in a compact device. The obstacles on the way to this goal include the aforementioned loss and the dispersion of group velocity and dispersion of absorption.<sup>9–11</sup> To ascertain the importance of the group velocity dispersion (GVD), one only needs to use the Taylor

series expansion of the dispersion relation  $k(\omega)$  near the signal frequency  $\omega_0$  to obtain the expression for the group velocity

$$v_g^{-1}(\omega) = v_g^{-1}(\omega_0) + \beta_2(\omega_0) \cdot (\omega - \omega_0) + \frac{1}{2} \beta_3(\omega_0) \cdot (\omega - \omega_0)^2 + \dots \quad (10)$$

where  $\beta_n(\omega) = \partial^n k(\omega) / \partial \omega^n$ . One can estimate the limitations imposed by GVD by noticing that the time delay of the signal can be written as

$$T_d(\omega) = v_g^{-1}(\omega)L = v_g^{-1}(\omega_0)L + \beta_2(\omega - \omega_0)L + \frac{1}{2} \beta_3(\omega - \omega_0)^2 L + \dots \quad (11)$$

and then introducing a criterion for the on-off keyed gaussian signal of bit rate  $B$  the difference between the delay times of spectral components at the edges of the signal bandwidth, that is, at  $\omega_0 \pm \Delta\omega_{\text{sig},0}/2$ , should be less than one-half of the bit interval, that is

$$\Delta T_d(L) \approx \beta_2 \Delta\omega_{\text{sig}} L < 1/2B \quad (12)$$

$$|\beta_2| B^2 L < \frac{1}{16 \ln 2} \quad (13)$$

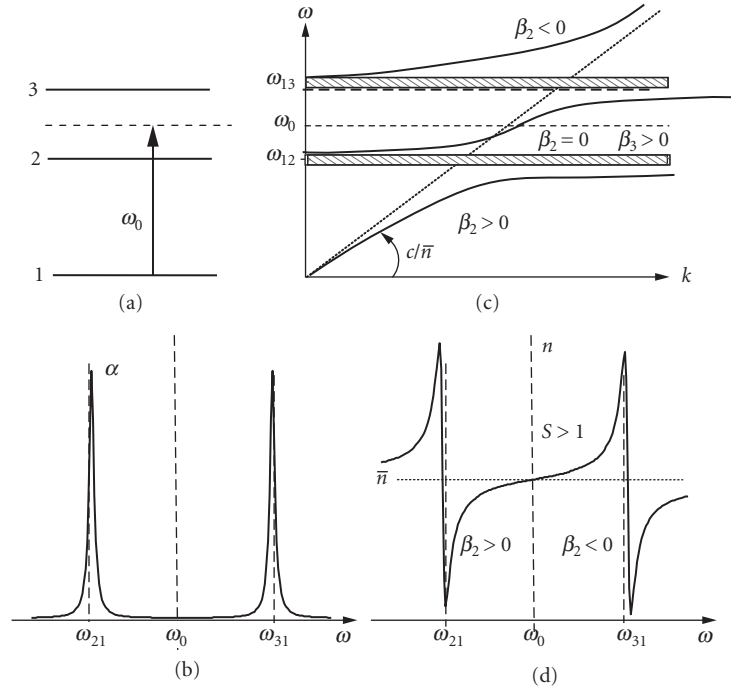
This condition shows the severe limitations imposed by the second order GVD term  $\beta_2$  whose spectrum is plotted in Fig. 1*f*. In addition to GVD, the signal bandwidth is also limited by the dispersion of absorption—the fact that different frequency components of the signal experience different attenuation causes signal distortion, but it is usually GVD that is the main reason that limits slow light scheme performance. Hence, while slow light had been observed in single-atomic resonance schemes as early as 1960s and 1970s<sup>12–16</sup> it was only in 1990s when a double resonance schemes with complete cancellation of  $\beta_2$  had been discovered<sup>17</sup> that the slow light research had really taken off.

## Double Atomic Resonance

Although the first practical slow light results were achieved using phenomenon of electromagnetic transparency (EIT),<sup>17,18</sup> where the double resonance is created by strong pump beam, the main features of the double-resonant atomic schemes can be understood easier if one considers closely spaced narrow resonances do occur naturally in metal vapors, such as, for instance, in Rb<sup>85</sup> Ref. 19 where two D<sup>2</sup> resonances near 780 nm separated by  $\nu_{32} = 3$  GHz have been used most successfully to this date in SL experiments in atomic medium. The rationale for using double resonance can be seen from Fig. 1*d* and *f*, which show that the lowest order GVD term  $\beta_2$  has opposite signs below and above resonance. Then, if one can combine two resonances as in Fig. 2*a*, only the third-order GVD  $\beta_3$  will be a factor for signals centered at frequency  $\omega_0$  in the middle between two transitions where the absorption (Fig. 2*b*) is low, as evident from the dispersion curves Fig. 2*c* and *d*.

A closer look at the dispersion curve Fig. 2*c* reveals the basic trade-off inherent in every slow light scheme—the dispersion curve is split into three branches of which the central one, “squeezed” between two atomic resonances, is the one with a slow group velocity. Clearly, the group velocity, being a slope of the curve is inversely proportional to the splitting between two resonances  $\nu_{32}$ , that is, to the maximum theoretical bandwidth of the scheme. In reality, the





**FIGURE 2** (a) Double atomic resonance and its (b) dispersion and group velocity near it; (c) absorption spectrum; and (d) refractive index spectrum.

practical bandwidth (or bit rate for digital signals) is even smaller than that and is mostly limited by the third-order dispersion<sup>11,20</sup>

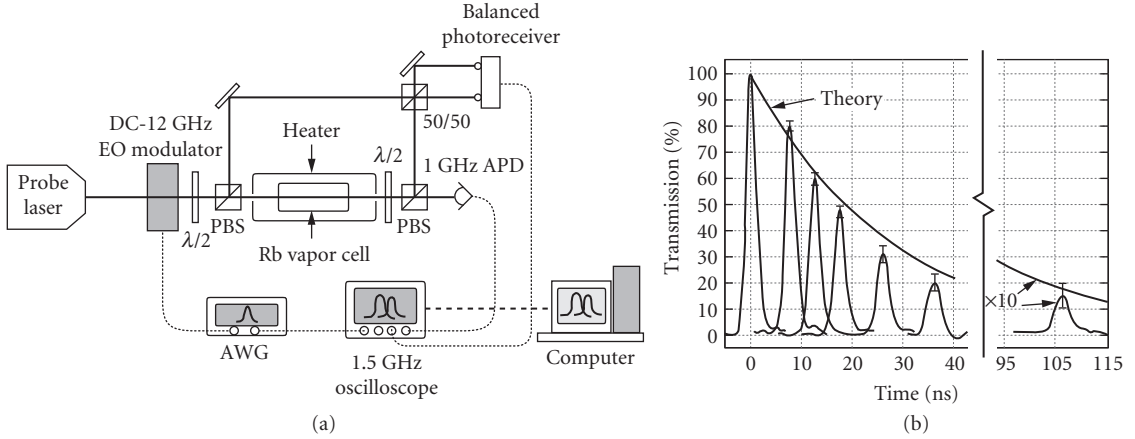
$$|\beta_3|B^3L < 1/16(\ln 2)^2 \quad (14)$$

In the works<sup>19</sup> group delays in excess of 100 ns with 2-ns pulses at 780 nm had been obtained—that correspond to about 50-bit tunable optical buffers. The delay could be tuned by changing concentration of Rb vapor as shown in Fig. 3.

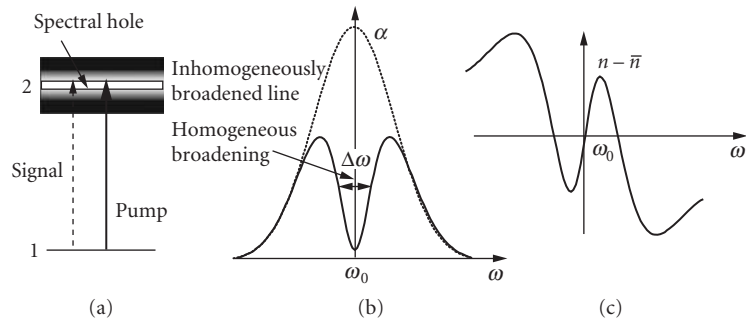
### Tunable Double Resonance—Electromagnetically-Induced Transparency

The double atomic resonant scheme described cannot be adapted to variable bandwidth because the width of passband cannot be changed. To change the passband width, one can consider an alternative of spectral hole burning in the inhomogeneously broadened transition.<sup>21,22</sup> As shown in Fig. 4, a strong pump pulse creates a situation at which the absorption in the frequency range  $\Delta\omega$  becomes depleted. The profile of the absorption spectrum shown in Fig. 4b looks remarkably like the double-resonant profile of Fig. 2. With the refractive index profile shown in Fig. 4c, one can see that a strong reduction of group velocity can be expected near the center of the spectral hole.

By changing the spectrum of the pump, for instance, using intensity or frequency modulation, one can change  $\Delta\omega$  to achieve the maximum delay without distortion for a given bit rate. Delays of 2-bit intervals were achieved in Ref. 23 for a moderate bandwidth of 100 MHz but only in a



**FIGURE 3** Experimental apparatus (a) used in Ref. 19 to obtain variable pulse delays at various optical depths using double resonance in Rb vapor (b).

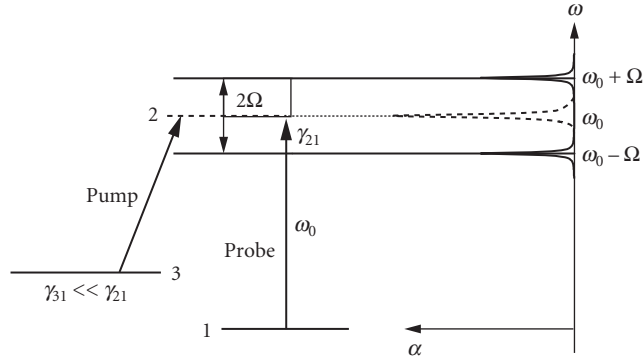


**FIGURE 4** (a) Slow light scheme based on spectral hole burning; (b) absorption spectrum; and (c) refractive index spectrum.

40-cm-long Rb vapor delay line. Since the background absorption in the hole burning is always high, it is the dispersion of loss  $\alpha_2$  that causes the signal distortion and is in fact a limitation in this scheme. The scheme also suffers from the large energy dissipation as the pump gets absorbed.

To avoid large background absorption and to achieve wide passband tunability one uses an entirely different SL scheme based on electromagnetic transparency (EIT), first considered by Harris.<sup>24–26</sup> Without trying to explain all the intricacies of EIT, one can understand the rationale of using it. Since finding two closely spaced atomic resonances is not trivial, one should consider the means for their creation artificially.

Now, the atomic oscillator in the absence of external modulation has just one resonant frequency  $\omega_{12}$  in its response spectrum, just like any harmonic wave whose spectrum contains just one frequency component  $\omega_{12}$ . But if the wave is amplitude modulated with some frequency  $\Omega$ , there will appear two sidebands at frequencies  $\omega_{12} \pm \Omega$  in its spectrum, and when the modulation depth reaches 100 percent the carrier frequency  $\omega_0$ , would get entirely suppressed and the spectrum shows just two sidebands separated by  $2\Omega$ . Now, according to this analogy, if one strongly modulates the strength of atomic oscillator with some external frequency  $\Omega$ , one should expect the absorption spectrum to behave in fashion similar to the spectrum of amplitude modulated wave, that is, it should show two absorption lines separated by  $2\Omega$ . The material should then become more transparent at the resonance frequency  $\omega_0$ —hence the term “EIT.”



**FIGURE 5** Principle of electromagnetic transparency in atomic “Λ” scheme.

To accomplish the EIT transmission modulation there exist numerous schemes, but we shall consider only one—the most widely used three-level “Λ” scheme<sup>1</sup> shown in Fig. 5 in which the ground-to-excited state transition  $\omega_{12}$  is resonant with the frequency of the optical signal carrier  $\omega_0$  and has a dephasing rate of  $\gamma_{21}$ . In the absence of pump, the absorption spectrum (dashed line in Fig. 5) is a normal Lorentzian line. There also exists a strong transition that couples the excited level 2 with the third level 3, but notably, the transition between levels 1 and 3 is forbidden. When a strong resonant pump with intensity  $I_{\text{pump}}$  at frequency  $\omega_{23}$  is turned on, the mixing of states 2 and 3 causes modulation of the absorption of signal. As expected, the Lorentzian peak in the absorption spectrum splits into two smaller peaks at frequencies  $\omega_0 \pm \Omega$ , where the Rabi frequency is

$$\Omega = \left( f_{23} \frac{12\pi\alpha_f I_{\text{pump}}}{m\bar{n}\omega_{23}} \right)^{\frac{1}{2}} \quad (15)$$

where  $\alpha_f = 1/137$  is a fine structure constant. Thus changing pump intensity allows one to achieve full tunability of the group velocity and to achieve very small group velocities.<sup>3,4</sup> But aside from being a convenient technique of implementing the tunable double resonant scheme, EIT has a significant advantage over other schemes because the residual absorption rate at the resonant frequency

$$\alpha(\omega_0) = \frac{1}{\bar{n}c} \frac{\Omega_p^2}{8\Omega^2} \gamma_{31} \quad (16)$$

is proportional to the dephasing rate of the intra-atomic excitation 31, which is not coupled to outside world. Thus typically  $\gamma_{31} \ll \gamma_{21}$  and the residual absorption is much weaker in the EIT than in the case of two independent resonances. It indicates that EIT is a coherent effect and the reduction of absorption occurs because of the destructive interference of the absorption by two sidebands. This effect has a rather simple physical interpretation. While in the simple single, or double-resonant slow light scheme, the energy transferred from the electromagnetic wave to the atomic excitation and back in the EIT scheme the process involves more steps. First, as the signal photon propagates in the EIT medium, it transfers its energy to the excitation of atomic transition between levels 1 and 2. Due to the presence of strong pump wave coupling between levels 2 and 3, the excitation is almost instantly transferred to the long-lived excitation between the levels 1 and 3 and then the process occurs in reverse until the energy is transferred back into the photon. Then the process repeats itself. Overall, most of the time the energy gets stored in the form of 1-3 excitations and thus it propagates with a very slow group velocity. Furthermore, the actual absorption event occurs only when

the excitation 1-3 loses coherence and the energy cannot get back to the photon. Naturally, it is the dephasing rate of this excitation, that is,  $\gamma_{31} \ll \gamma_{21}$ , which determines the residual absorption loss in Eq. (16). We stress here once again that since the energy gets stored in the form of atomic excitation, one cannot expect enhancement in the strength of the optical field.

## 22.4 BANDWIDTH LIMITATIONS IN ATOMIC SCHEMES

The most spectacular results were achieved in slow light experiments of EIT in which the light velocity was slowed down to the pedestrian speed<sup>3</sup> and then even stopped<sup>4</sup> first in metal vapors and then in solid state medium containing rare earth ions.<sup>27</sup> These achievements are of great importance for physics when it comes to manipulating single photons<sup>28</sup> and coherent control.<sup>29</sup> Also important are imaging applications of slow light where indeed impressive results were observed by a number of groups,<sup>30,31</sup> extra high resolution interferometers,<sup>32,33</sup> and rotation sensors.<sup>34</sup> There has also been significant progress on using electrically pumped semiconductor medium to achieve slow light in EIT configuration or using coherent population oscillations.<sup>35–37</sup> But overall the best results in term of the delay-bit rate product were achieved in metal vapors<sup>19,24</sup> at relatively narrow bandwidths. The delays were usually limited by the third-order dispersion. These results follow the basic properties of the lorentzian dispersion—according to Eq. (7) the slowdown factor  $S$  is proportional to  $(\omega_{12} - \omega)^{-2}$ —hence the total delay can be very large in the narrow frequency band near the resonance, but then it changes and becomes much smaller. A number of publications have been devoted to the limits of delay-bit rate product.<sup>9–11,38,39</sup> In fact, it was shown in Ref. 11 and then in Ref. 39 that the most relevant figure of merit for slow light delay line is the minimum length of the delay line  $L$  required to store a number of bits  $N_{st}$  at a given bit rate  $B$ . The required length was found in Ref. 11 to be

$$L \sim cBN_{st}^2[\Omega_p/2\pi]^{-2} \quad (17)$$

indicating that the performance suffers at higher bit rate and also that the required length increases nonlinearly with storage capacity. Indeed, most of the demonstrated and proposed slow light schemes based on atomic transitions do not show spectacular results at bit rates above 1 Gbit/s and for this reason a different class of resonances shall be considered.

## 22.5 PHOTONIC RESONANCE

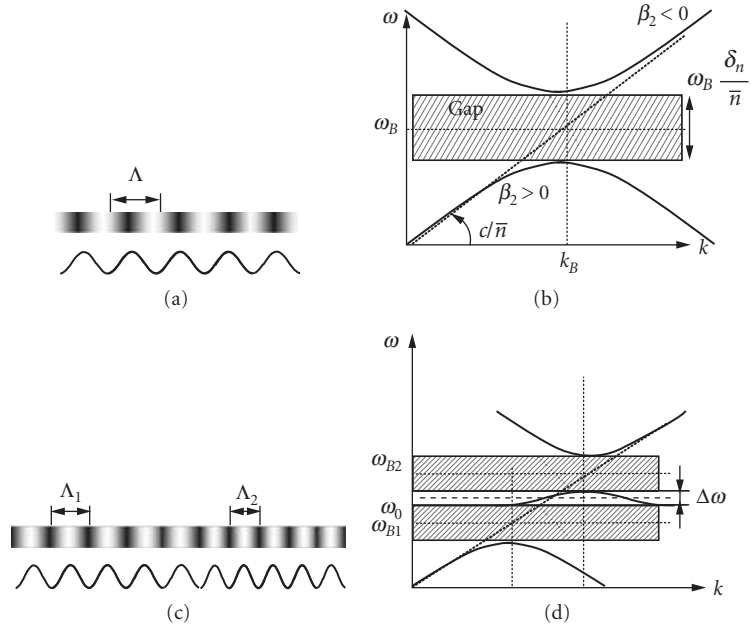
As we have already mentioned, in case of atomic resonance the apparent slow down of light is caused by the resonant energy transfer to and from the excitation of atomic polarization. An entirely different resonance is the photonic resonance in which the energy is resonantly transferred between two or more modes of electromagnetic radiation. When the transfer takes place between forward and backward propagating wave slow light, the group velocity gets reduced and we are once again faced with the slow light phenomenon, albeit of entirely different nature from the slow light in atomic medium.

The most common photonic resonance is the Bragg grating (Fig. 6a)—a structure in which the refractive index is periodically modulated with period  $\Lambda$ ,

$$n = \bar{n} + \delta n \cos\left(\frac{2\pi}{\Lambda}z\right) \quad (18)$$

As a result, a photonic bandgap opens in the vicinity of Bragg frequency<sup>40</sup>

$$\omega_B = \frac{\pi c}{\Lambda \bar{n}} \quad (19)$$



**FIGURE 6** (a) Bragg grating and its index profile; (b) dispersion of Bragg grating; (c) cascaded Bragg grating; and (d) dispersion curve of cascaded grating.

and the dispersion law becomes modified as

$$\frac{k - k_B}{k_B} = \sqrt{\left(\frac{\omega - \omega_B}{\omega_B}\right)^2 - \left(\frac{\delta n}{2\bar{n}}\right)^2} \quad (20)$$

This dispersion law is plotted in Fig. 6b. One can see the similarities between it and the dispersion of a single atomic resonance (Fig. 1d), especially the presence of the gap near the resonance frequency indicating that the light gets reflected from the grating just as it gets reflected from the atomic medium at resonance. Close to the gap, the group velocity indeed gets reduced with the slowdown factor being

$$S = \frac{\left|\frac{\omega - \omega_B}{\omega_B}\right|}{\sqrt{\left(\frac{\omega - \omega_B}{\omega_B}\right)^2 - \left(\frac{\delta n}{2\bar{n}}\right)^2}} \quad (21)$$

Furthermore, the width of forbidden gap is  $\Delta\omega_{\text{gap}} = \omega_B(\delta n/\bar{n})$ , and hence the index contrast  $\delta n/\bar{n}$  can be called the “strength” of the grating. This “grating strength” plays a role equivalent to that played by the oscillator strength of the atomic resonance. But the physics is quite different—the slow down effect in a photonic structure is the result of the transfer of energy between the forward and backward propagating waves—no energy is transferred to the medium. Hence the strength of the electric field in photonic SL structures gets greatly enhanced with important implications for non-linear optics. One can also use simple photonic crystals<sup>41,42</sup> whose dispersion curves are similar to

Bragg gratings but the problem of structures with a single photonic resonance is identical to the single atomic resonance—strong second-order dispersion  $\beta_2$ . Clearly, in order to compensate it one should consider structures with more than one photonic resonance.

## Double Resonant Photonic Structures

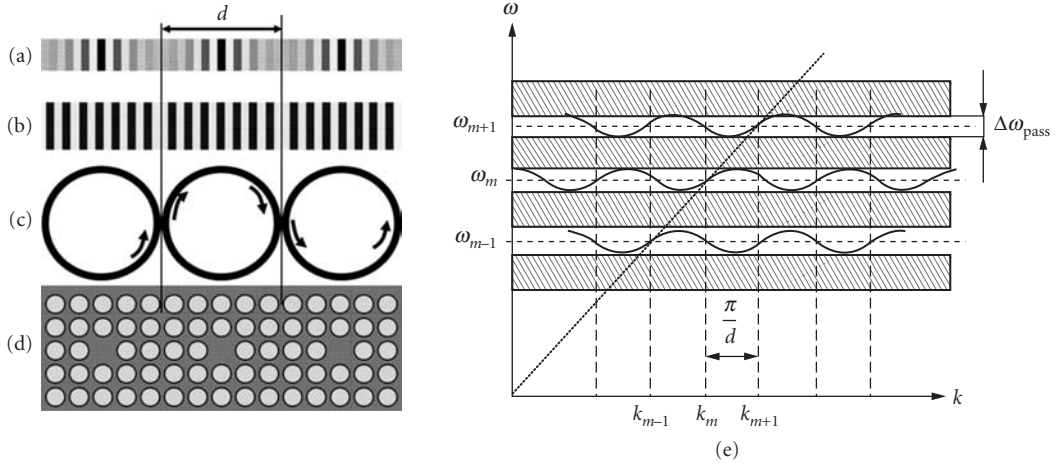
Since any atomic SL scheme requires operation near a particular narrow linewidth absorption resonance, finding such a resonance near a particular wavelength is not an easy task, and, in fact, only a very few absorption lines have been employed in practice, Rb vapors being a “workhorse.” Finding two closely spaced narrow lines is even more difficult, and even if such two lines can be found, the splitting between them  $\nu_{32}$  is fixed—hence the SL delay will be optimized for one particular combination of storage capacity and bit rate.

In contrast, the photonic double resonant can be easily implemented by simply combining two Bragg gratings with slightly different periods  $\Lambda_1$  and  $\Lambda_2$  as shown in Fig. 6c. Such combination was first suggested for dispersion compensation<sup>43,44</sup> and then considered for application in electro-optic modulators.<sup>45</sup> As long as one deals with linear devices, such as delay lines, one can simply cascade two Bragg gratings sequentially and the resulting dispersion curve will be simply the mean of the individual dispersion curves. For the nonlinear and electro-optic devices one can alternate the short segments of Bragg gratings with periods  $\Lambda_1$  and  $\Lambda_2$ . The dispersion curve of Fig. 6d is remarkably similar to the dispersion curve of the atomic double resonance in Fig. 2b. Two gratings engender two photonic bandgaps, centered at  $\omega_{b,i} = \pi c / \Lambda_i \bar{n}$  of almost equal widths  $\Delta\omega_{\text{gap},i} = \omega_{b,i} (\delta n / \bar{n}) \approx \omega_0 (\delta n / \bar{n})$  with a narrow passband  $\Delta\omega$  between them. By choosing the periods  $\Lambda_1$  and  $\Lambda_2$  for a given index modulation  $\delta n$  one can design  $\Delta\omega$  to be arbitrarily narrow or wide. This fact gives the designer true flexibility. In fact, one can show the slowdown factor in this scheme is

$$S(\omega_0) \approx \left[ 1 + \frac{\Delta\omega_{\text{gap}}}{2\Delta\omega} \right]^{1/2} \quad (22)$$

Thus, as one can see, the dispersion curve gets *squeezed* between two gaps and the group velocity decreases with the passband, but the dependence is not as strong as in the case of atomic resonance, thus the photonic structures in general should have far superior performance at large bandwidth when compared to atomic medium. A similar approach can be cascaded photonic crystal waveguides as demonstrated in Refs. 46 to 50.

However, cascaded Bragg gratings have also a number of disadvantages, the first of which is a relatively small index contrast available, and the second is difficulty in fabricating two gratings with a prescribed value of the frequency offset. Furthermore, the cascaded geometry is applicable only to the linear devices that do not incorporate any nonlinear or electro-optic component. For this reason it is preferable to use alternating short segments of gratings with different periods. But a periodic sequence of short Bragg grating segments can be considered a new grating with periodically modulated properties, or Moiré grating (Fig. 7a). In a Moiré grating the segments are not independent but interact coherently—hence its properties are somewhat different from the cascaded grating as shown in Ref. 51, with the main distinction being the fact that the dispersion curve of Moiré grating with period  $d$  is also periodic in wave-vector space with a period  $2\pi/d$ . The ability of a Moiré grating to slow down the light was first predicted in Ref. 51 and demonstrated in Ref. 52. It was also noted that the Moiré grating is only example of periodically structured photonic media in which slow light can be observed. In the periodically structured media, the light energy density is distributed periodically and the periodically spaced regions of high intensity can be thought of as the resonators coupled to each other. Thus we shall refer to them as coupled resonator structures (CRS).<sup>53</sup> Aside from using Moiré gratings, CRS can be fabricated by coupling Fabry-Perot resonators (Fig. 7b), ring resonators (Fig. 7c),<sup>54</sup> or so-called “defect modes” in the photonic crystal (Fig. 7d).<sup>55,56</sup> These and other CRS implementations are discussed at length in the literature<sup>41,57–61</sup> and here we shall only give a short description of their properties and compare them with the EIT-like photonic structures.



**FIGURE 7** Photonic SL structures based on coupled resonators (CRS): (a) Moiré grating; (b) coupled Fabry-Perot resonators; (c) coupled ring resonators; (d) coupled defect modes in photonic crystal; and (e) dispersion in a typical CRS.

A periodic chain of coupled resonators is characterized by three parameters: period  $d$ , the time of one way pass through each resonator  $\tau$ , and the coupling (or transmission) coefficient  $\kappa$ . The dispersion relation in this chain can be written as

$$\sin \omega \tau = \kappa \sin kd \quad (23)$$

The dispersion curves are shown in Fig. 7e and consist of the series of passbands around resonant frequencies  $\omega_m = m/2\tau$  separated by the wide gaps. Presence of multiple resonances indicates that the light propagating through CRS can be considered a superposition of more than one forward and more than one backward propagating wave. Alternatively, one can also think about the resonators as “photonic atoms” analogous to real atoms in EIT. At any rate, the dispersion curve is quite similar to the EIT dispersion curve in sense that it gets *squeezed* into a narrow passband of width

$$\Delta \nu_{\text{pass}} = (\pi \tau)^{-1} \sin^{-1}(\kappa) \quad (24)$$

The three parameters  $d$ ,  $\tau$ , and  $\kappa$  are not independent of each other. First of all  $d$  and  $\tau$  are obviously related to each other. This relation can be obtained from taking a limit of Eq. (23) at  $\kappa = 1$

$$\frac{d}{\tau} = \frac{\omega}{k} = \frac{c}{\bar{n}} \quad (25)$$

which simply indicates that with 100 percent coupling the light simply propagates through medium without reflections. Also related are the size of resonator, that is,  $d$  and the coupling coefficient  $\kappa$ ; to achieve small  $\kappa$ , one needs to confine the light tightly within the resonators which requires large spacing between them. If the index contrast  $\delta n/\bar{n}$  is large, a high degree of confinement can be achieved within a relatively small resonator; otherwise the light will leak from one resonator to another. This issue has been addressed in detail in Ref. 11, but here we simply assume that one uses the smallest resonator size that can be fabricated using a technology with a given index contrast.

Using Taylor expansion of the dispersion relation [Eq. (24)], one obtains the group velocity

$$v_g^{-1} = \frac{\tau}{d\kappa} = \frac{\bar{n}}{c} \kappa^{-1} \quad (26)$$

Hence the slowdown factor is simply

$$S = \kappa^{-1} \quad (27)$$

At the same time the third-order dispersion is

$$\beta_3 = v_g^{-1} \left( \frac{\tau}{\kappa} \right)^2 (1 - \kappa^2) \quad (28)$$

indicating that one can always optimize the performance of CRS delay line by choosing proper coupling coefficient to strike the balance between sufficient delay and low distortion caused by dispersion. As a result one can achieve the following relation between the storage capacity  $N_{st}$  and the required delay line length

$$L \sim cN_{st}^{3/2} \left( \omega \frac{\delta n}{n} \right)^{-1} \quad (29)$$

Comparing Eq. (29) with the results for atomic delay line Eq. (17), one can first notice that the required length of the buffer (essentially the number of coupled resonators) does not increase with the bit rate. Thus the CRS should have much better performance at high bit rates compared to EIT delay lines. This result (and the fact that required length increase only as a power 3/2 of storage capacity) follows the fact that the slowdown factor is not as strong function of passband width in CRS as in EIT. Furthermore, the expression inside the parenthesis can become commensurate with the optical frequency when large index contrast is used. This contrast can be as high as a factor of 2 in Si on SOI ring resonators<sup>61,62</sup> or photonic crystal,<sup>41</sup> which means that one can ultimately store  $N_{st}$  bits of optically encoded information in roughly  $L \sim N_{st}^{3/2} \lambda$  length.<sup>63</sup>

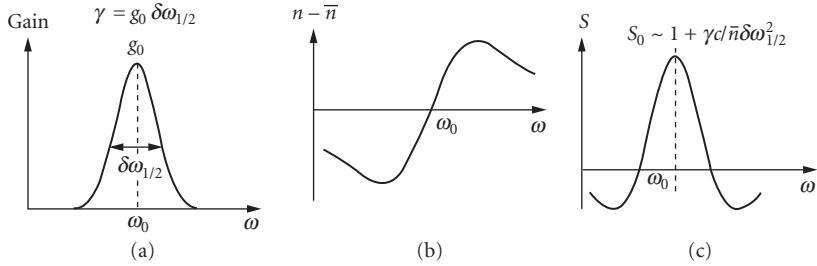
The limitations imposed by high order dispersion can be mitigated by using a combination of CRS with  $\beta_3$ 's of different sign as shown in.<sup>64</sup> Alternatively, one can use the so-called dynamic slow light scheme<sup>65-67</sup> in which the properties of the CRS are adiabatically tuned when the light enters it allowing the compression of spectrum and thus reducing the deleterious effect of dispersion. Similar results can be in principle achieved using semiconductor devices<sup>68,69</sup> combining Bragg grating with quantum wells that are resonant near the Bragg frequency. It should be noted, however, that even dynamic structures have limited storage capacity due to dispersion occurring before the spectral compression, that is, when the light enters the delay line.<sup>70,71</sup>

## 22.6 SLOW LIGHT IN OPTICAL FIBERS

In the prior subsections, we have described the slow light in the vicinity of atomic and photonic resonances that are always associated with loss. In case of atomic resonance, the loss is inherent and can be traced to dephasing of atomic polarization. In case of photonic resonance, the loss occurs simply because the light spends more time inside the delay line (or, in one case, it takes longer effective path by bouncing back and forth or making circles). But it is well known that strong dispersion also takes place in the spectral vicinity of the resonant gain. The advantages of using gain are manifold—first of all one is not faced with attenuation, and second the gain can be changed at will by changing the pump strength and spectrum—hence the delay and the bandwidth can be made tunable.

Consider a gain profile  $g(\omega)$  shown in Fig. 8a and characterized by its peak value  $g_0 = g(\omega_0)$  and the FWHM linewidth  $\delta\omega_{1/2}$ . Usually the peak gain is inversely proportional to the linewidth and therefore it makes sense to introduce the integrated optical gain that is proportional to the total pump power  $\gamma \sim g_0 \delta\omega_{1/2}$ . Applying Kramers-Kronig transform to the gain profile, one can obtain





**FIGURE 8** Slow light in an optical amplifier: (a) gain; (b) index; and (c) slowdown factor.

the refractive index spectrum shown in Fig. 8b. There is a positive slope at the center of the gain and this leads to slowdown factor of

$$S(\omega_0) \sim 1 + g_0 c / \bar{n} \Delta\omega_{1/2} \sim 1 + \gamma c / \bar{n} \Delta\omega_{1/2}^2 \quad (30)$$

shown in Fig. 8c. To achieve tunable gain, most often one uses stimulated Brillouin or stimulated Raman scattering. One unique advantage of these processes is that it can be observed in many media including the ubiquitous silica optical fiber which allows the slow light devices to be easily integrated into communication systems.

In the stimulated Brillouin scattering (SBS) process, a high-frequency acoustic wave is induced in the material via electrostriction for which the density of a material increases in regions of high optical intensity. The process of SBS can be described classically as a nonlinear interaction between the pump (at angular frequency  $\omega_p$ ) and a probe (or Stokes) field  $\omega_s$  through the induced acoustic wave of frequency  $\Omega_A$ .<sup>72</sup> The acoustic wave in turn modulates the refractive index of the medium and scatters pump light into the probe wave when its frequency is downshifted by the acoustic frequency. This process leads to a strong coupling between the three waves when this resonance condition is satisfied, which results in exponential amplification (absorption) of the probe wave. Efficient SBS occurs when both energy and momentum are conserved, which is satisfied when the pump and probe waves counterpropagate. This leads to atypically very narrow gain bandwidth of typically about 30 MHz. With the peak values of Brillouin gain of about  $g_0 \sim 0.02 \text{ m}^{-1}$  one can then expect the slowdown factor to be on the order of only a few percent different from unity—hence the value of this scheme is not in the absolute delay time but in adjustable additional delay

$$\Delta T_d \sim g_0 L / \Delta\omega_{1/2} \quad (31)$$

Since the large value of total gain  $g_0 L$  can lead to Brillouin lasing, it is usually limited to about 10 to 15 meaning that maximum pulse delay of about 2 pulse lengths.<sup>73</sup> It is important that the main limitation for the achievable delay in amplifiers is the dispersion of gain rather than dispersion of group velocity.<sup>73</sup> While this delay of a few pulse lengths is relatively small, it is tunable and as such may be sufficient for many applications.

Tunable slow-light delay via SBS in an optical fiber was first demonstrated independently by Song et al.<sup>74</sup> and Okawachi et al.<sup>75</sup> In the experiment performed in Ref. 74 delay could be tuned continuously by as much as 25 ns by adjusting the intensity of the pump field and the technique can be applied to pulses as short as 15 ns. A fractional slow-light delay of 1.3 was achieved for the 15-ns-long input pulse with a pulse broadening of 1.4.

Following the first demonstrations of SBS slow light in optical fibers, there has been considerable interest in exploiting the method for telecommunication applications. One line of research

has focused on reducing pulse distortion by reducing the distortion caused by the gain dispersion performance<sup>76–81</sup> by essentially trying to shape the Brillouin gain with multiple pumps. In numerous experimental demonstrations of multiple closely spaced SBS gain lines generated by a multi-frequency pump, significant increases in slow-light pulse delay were achieved as compared with the optimum single-SBS-line delay.

Another line of research has focused on broadband SBS slow light.<sup>82–86</sup> The width of the resonance which enables the slow-light effect limits the minimum duration of the optical pulse that can be effectively delayed without much distortion, and therefore limits the maximum data rate of the optical system. Herraes et al.<sup>82</sup> were the first to increase the SBS slow-light bandwidth and achieved a bandwidth of about 325 MHz by broadening the spectrum of the SBS pump field. Zhu et al. extended this work to achieve an SBS slow-light bandwidth as large as 12.6 GHz, thereby supporting a data rate of over 10 Gb/s.<sup>83</sup> The latest results on expanding bandwidth are summarized in the review article.<sup>87</sup>

An alternative way to achieve tunable delays in optical fibers is via stimulated Raman scattering (SRS) can also be achieved in optical fibers. The SRS arises from exciting vibrations in individual molecules also known as optical phonons—as opposed to exciting sound waves (acoustic phonons) as in the SBS process. The optical phonons, unlike acoustic phonons, are localized and have very short lifetimes, measured in picoseconds or fractions of picoseconds. Furthermore, in amorphous materials, such as glass, the frequencies of optical phonons are spread over the large interval (measured in THz)—hence the Raman gain is much broader than Brillouin gain, but is also much smaller in absolute value. Integrated gain  $\gamma \sim g_0 \delta\omega_{1/2}$  is similar for SBS and SRS but in SRS it is spread out over much wider  $\delta\omega_{1/2}$ .

Sharping et al. demonstrated an ultrafast all-optical controllable delay in a fiber Raman amplifier.<sup>88</sup> In this experiment a 430-fs pulse is delayed by 85 percent of its pulse width using SRS in 1-km-long high nonlinearity fiber. The ability to accommodate the bandwidth of pulses shorter than 1 ps in a fiber-based system makes SRS slow light useful for producing controllable delays in ultrahigh bandwidth telecommunication systems.

In addition to optical fibers, SRS slow light has also been demonstrated in a silicon-on-insulator planar waveguide.<sup>89</sup> Since silicon is a single-crystalline material, the Raman gain is concentrated into the narrower bandwidth than in glass, but this bandwidth is still sufficient for delaying short optical pulses of 3 to 4 ps in a very short (8 mm) waveguide. This scheme represents an important step in the development of chip-scale photonics devices for telecommunication and optical signal processing.

Slow light propagation was also demonstrated in erbium-doped fibers<sup>90,91</sup> using coherent population oscillations, but the bandwidth, related to the relaxation time in erbium ion was only on the order of kHz. Other methods included using the parametric gain<sup>92</sup> in the optical fiber as well as taking advantage of EIT in hollow optical fibers.<sup>93</sup>

## 22.7 CONCLUSION

In this chapter, we have only given a very brief overview of the physics involved in the phenomenon of slow (and fast) light propagation. We have shown that while the underlying mechanisms are diverse, they all are characterized by a relatively narrow resonance, whether it is due to an atomic transition, resonance in the photonic structure, or is determined by a pump in an optical amplifier. As a result, the delay bandwidth and physical dimensions of all slow-light media are interdependent and must be optimized for a given set of objectives that depends on application. The applications of slow light, in both linear and nonlinear optics, are so diverse that it is impossible to cover them all even briefly in this chapter. They involve optical communications, optical signal processing, microwave photonics, precise interferometric instruments, and many others, and many new ones appear every year. The multidisciplinary field of slow light experiences rapid growth and this brief survey of the current state of affairs is nothing more than a snapshot intended to provide sufficient background to the newcomers into this field and to suggest a number of sources from which a deeper knowledge can be gained.

## 22.8 REFERENCES

1. H. A. Lorentz, "Über die Beziehung zwischen der Fortpflanzung des Lichtes," *Wiedem. Ann.* **9**:641 (1880).
2. J. R. Pierce, "Traveling-Wave Tubes," *Bell Syst. Tech. J.* **29**:1 (1950).
3. L. V. Hau, S. E. Harris, Z. Dutton, and C. H. Behroozi, "Light Speed Reduction to 17 Metres per Second in an Ultracold Atomic Gas," *Nature* **397**:594–596 (1999).
4. D. F. Philips, A. Fleischhauer, A. Mair, R. L. Walsworth, and M. D. Lukin, "Storage of Light in Atomic Vapor," *Phys. Rev. Lett.* **86**:783–786 (2001).
5. R. W. Boyd and D. J. Gauthier, *Progress in Optics*, Elsevier, Radarweg, Amsterdam, 2002, pp. 497–530.
6. P. W. Milonni, "Controlling the speed of light pulses," *J. Phys. B-At. Mol. Opt. Phys.* **35**:R31 (2002).
7. P. W. Milonni, *Fast Light, Slow Light, and Left-Handed Light*, Institute of Physics, Bristol and Philadelphia, 2005.
8. J. B. Khurgin and R. S. Taylor, *Slow Light: Science and Applications*, Taylor and Francis, New York, 2009.
9. R. W. Boyd, D. J. Gauthier, A. L. Gaeta, and A. E. Willner, "Maximum Time Delay Achievable on Propagation through a Slow-Light Medium," *Phys. Rev. A* **71**:023801 (2005).
10. A. B. Matsko, D. V. Strekalov, and L. Maleki, "On the Dynamic Range of Optical Delay Lines Based on Coherent Atomic Media," *Opt. Exp.* **13**:2210–2223 (2005).
11. J. B. Khurgin, "Optical Buffers Based on Slow Light in EIT Media and Coupled Resonator Structures—Comparative Analysis," *J. Opt. Soc. Am. B*, **22**:1062–1074 (2005).
12. S. L. McCall and E. L. Hahn, "Self-Induced Transparency by Pulsed Coherent Light," *Phys. Rev. Lett.* **18**:908 (1967).
13. D. Grischkowsky, "Adiabatic Following and Slow Optical Pulse Propagation in Rubidium Vapor," *Phys. Rev. A* **7**:2096 (1973).
14. S. Chu and S. Wong, "Linear Pulse Propagation in an Absorbing Medium," *Phys. Rev. Lett.* **48**:738 (1982).
15. S. Chu and S. Wong, "Linear Pulse Propagation in an Absorbing Medium—Response," *Phys. Rev. Lett.* **49**:1293 (1982).
16. B. Segard and B. Macke, "Observation of Negative Velocity Pulse Propagation," *Phys. Lett. A* **109**:213 (1985).
17. S. E. Harris, J. E. Field, and A. Imamoglu, "Nonlinear Optics Using Electromagnetically Induced Transparency," *Phys. Rev. Lett.* **64**:1107 (1990).
18. M. M. Kash, V. A. Sautenkov, A. S. Zibrov, L. Hollberg, G. R. Welch, M. D. Lukin, Y. Rostovtsev, E. S. Fry, and M. O. Scully, "Ultraslow Group Velocity and Enhanced Nonlinear Optical Effects in a Coherently Driven Hot Atomic Gas," *Phys. Rev. Lett.* **82**:5229 (1999).
19. R. M. Camacho, M. V. Pack, and J. C. Howell, "Low-Distortion Slow Light Using Two Absorption Resonances," *Phys. Rev. A* **73**:063812 (2006).
20. R. M. Camacho, M. V. Pack, J. C. Howell, A. Schweinsberg, and R. W. Boyd, "Wide-Bandwidth, Tunable, Multiple-Pulse-Width Optical Delays Using Slow Light in Cesium Vapor," *Phys. Rev. Lett.* **98**:153601 (2007).
21. M. S. Bigelow, N. N. Lepeshkin, and R. W. Boyd, "Observation of Ultraslow Light Propagation in a Ruby Crystal at Room Temperature," *Phys. Rev. Lett.* **88**:023602 (2002).
22. A. V. Turukhin, V. S. Sudarshanam, M. S. Shahriar, and P. R. Hemmer, "Observation of Ultraslow and Stored Light Pulses in a Solid," *Phys. Rev. Lett.* **88**:023602 (2002).
23. R. M. Camacho, M. V. Pack, and J. C. Howell, "Slow Light with Large Fractional Delays by Spectral Hole-Burning in Rubidium Vapor," *Phys. Rev. A* **74**:033801 (2006).
24. K.-J. Boller, A. Imamoglu, and S. E. Harris, "Observation of EIT," *Phys. Rev. Lett.* **66**:2593–2596 (1991).
25. S. E. Harris, J. E. Field, and A. Kasapi, "Dispersive properties of EIT," *Phys. Rev. A* **46**:R39–R32 (1992).
26. A. Kasapi, M. Jain, G. Y. Jin, and S. E. Harris, "EIT: Propagation Dynamics," *Phys. Rev. Lett.* **74**:2447–2450 (1995).
27. A. V. Turukhin, V. S. Sudarshanam, M. S. Shahriar, J. A. Musser, B. S. Ham, and P. R. Hemmer, "Observation of Ultraslow and Stored Light Pulses in a Solid," *Phys. Rev. Lett.* **88**(2):023602 (2002).
28. M. D. Lukin, A. Imamoglu, "Nonlinear Optics and Quantum Entanglement of Ultraslow Single Photons," *Phys. Rev. Lett.* **84**:1419 (2000).

29. F. E. Zimmer, A. Andre, M. D. Lukin, and M. Fleischhauer, "Coherent Control of Stationary Light Pulses," *Opt. Commun.* **264**:441 (2006).
30. R. M. Camacho, C. J. Broadbent, I. Ali-Khan, and J. C. Howell, "All-Optical Delay of Images Using Slow Light," *Phys. Rev. Lett.* **98**:043902 (2007).
31. O. Firstenberg, O. M. Shuker, M. N. Davidson, N. A. Ron, "Elimination of the Diffraction of Arbitrary Images Imprinted on Slow Light," *Phys. Rev. Lett.* **102**:043601 (2009).
32. Z. Shi and R. W. Boyd, "Slow-Light Interferometry: Practical Limitations to Spectroscopic Performance," *J. Opt. Soc. Am.* **25**:136 (2008).
33. Z. Shi, R. W. Boyd, D. J. Gauthier, and C. C. Dudley, "Enhancing the Spectral Sensitivity of Interferometers Using Slow-Light Media," *Opt. Lett.* **32**:915 (2007).
34. M. S. Shakhriar, G. S. Pati, R. Tripathi, V. Gopal, M. Messall, and K. Salit, "Ultrahigh Enhancement in Absolute and Relative Rotation Sensing Using Fast and Slow Light," *Phys. Rev. A* **75**:53807 (2007).
35. P. K. Kondratko, S. W. Chang, H. Su, and S. L. Chuang, "Slow Light with Tunable Bandwidth in p-doped and Intrinsic Quantum Dot Electro-Absorbers," *Appl. Phys. Lett.* **90**:251108 (2007).
36. F. Ohman, K. Yivind, and J. Mork, "Voltage-Controlled Slow Light in an Integrated Semiconductor Structure with Net Gain," *Opt. Express* **14**:9955 (2006).
37. F. G. Sedgwick, B. Pesala, J. Y. Lin, W. S. Ko, X. X. Zhao, and C. J. Chang-Hasnain, "THz-Bandwidth Tunable Slow Light in Semiconductor Optical Amplifiers," *Opt. Express* **15**:747 (2007).
38. R. S. Tucker, P. C. Ku, and C. J. Chang-Hasnain, "Slow-Light Optical Buffers: Capabilities and Fundamental Limitations," *J. Lightwave Technol.* **23**:4046 (2005).
39. D. A. B. Miller, "Fundamental Limit to Linear One-Dimensional Slow Light Structures," *Phys. Rev. Lett.* **99**:203903 (2007).
40. T. Erdogan, "Fiber Grating Spectra," *J. Lightwave Technol.* **15**(8):1277–1294 (1997).
41. T. Baba, "Slow Light in Photonic Crystals," *Nature Photon.* **2**:465 (2008).
42. T. F. Krauss, "Slow Light in Photonic Crystal Waveguides," *J. Phys. D. Appl. Phys.* **40**:2666 (2007).
43. N. M. Litchinitser, B. J. Eggleton, and G. P. Agrawal, "Dispersion of Cascaded Fiber Gratings in WDM Lightwave Systems," *J. Lightwave Technol.* **16**:1523–1529 (1999).
44. S. Wang, H. Erlig, H. R. Fetterman, E. Yablonovitch, V. Grubsky, D. S. Starodubov, and J. Feinberg, "Group Velocity Dispersion Cancellation and Additive Group Delays by Cascaded Fiber Bragg Gratings in Transmission," *Microwave and Guided Wave Letters* **8**:327–329 (1998).
45. Khurgin JB, Kang JU, and Ding YJ, "Ultrabroad-Bandwidth Electro-Optic Modulator Based on a Cascaded Bragg Grating," *Opt. Lett.* **25**:70–72 (2000).
46. D. Mori and T. Baba, "Wideband and Low Dispersion Slow Light by Chirped Photonic Crystal Coupled Waveguide," *Opt. Express* **13**:9398–9408 (2005).
47. M. L. Povinelli, S. G. Johnson, and J. D. Joannopoulos, "Slow-Light, Band-Edge Waveguides for Tunable Time Delays," *Opt. Express* **13**:7145–7159 (2005).
48. D. Mori, S. Kubo, H. Sasaki, and T. Baba, "Experimental Demonstration of Wideband Dispersion-Compensated Slow Light by a Chirped Photonic Crystal Directional Coupler," *Opt. Express* **15**:5264–5270 (2007).
49. S. C. Huang, M. Kato, E. Kuramochi, C. P. Lee, and M. Notomi, "Time-Domain and Spectral-Domain Investigation of Inflection-Point Slow-Light Modes in Photonic Crystal Coupled Waveguides," *Opt. Express* **15**:3543–3549 (2007).
50. T. Kawasaki, D. Mori, and T. Baba, "Experimental Observation of Slow Light in Photonic Crystal Coupled Waveguides," *Opt. Express* **15**:10274–10281 (2007).
51. J. B. Khurgin, "Light Slowing Down in Moire Fiber Gratings and Its Implications for Nonlinear Optics," *Phys. Rev. A* **62**:3821–3824 (2000).
52. S. Longhi, D. Janner, G. Galzerano, G. Della Valle, D. Gatti, and P. Laporta, "Optical Buffering in Phase-Shifted Fibre Gratings," *Electron. Lett.* **41** (2005).
53. A. Yariv, Y. Xu, R. K Lee, and A. Scherer, "Coupled-Resonator Optical Waveguide: A Proposal and Analysis," *Opt. Lett.* **24**:711–713 (1999).
54. C. K. Madsen and G. Lenz, "Optical All-Pass Filters for Phase Response Design with Applications for Dispersion Compensation," *IEEE Photon. Tech. Lett.* **10**:994–996 (1998).

55. A. Melloni, F. Morichetti, and M. Martnelli, "Linear and Nonlinear Pulse Propagation in Coupled Resonator Slow-Wave Optical Structures," *Opt. Quantum Electron.* **35**:365–378 (2003).
56. Z. Wang and S. Fan, "Compact All-Pass Filters in Photonic Crystals as the Building Block for High-Capacity Optical Delay Lines," *Phys. Rev. E* **68**:066616–06661623 (2003).
57. D. D. Smith, C. Hongrok, K. A. Fuller, A. T. Rosenberger, and R.W. Boyd, "Coupled-Resonator-Induced Transparency," *Phys. Rev. A-At. Mol. Opt. Phys.* **69**:63804 (2004).
58. J. E. Heebner and R.W. Boyd, "'Slow' and 'Fast' Light in Resonator-Coupled Waveguides," *J. Mod. Opt.* **49** (2002).
59. S. Mookhejea, "Dispersion Characteristics of Coupled-Resonator Optical Waveguides," *Opt. Lett.* **30**:2406 (2005).
60. M. Notomi, K. Yamada, A. Shinya, J. Takahashi, C. Takahashi, and I. Yokohama, "Extremely Large Group-Velocity Dispersion of line-defect waveguides in Photonic Crystal Slabs," *Phys. Rev. Lett.* **87**(25):253902 (2001).
61. F. Xia, L. Sekaric, and Y. Vlasov, "Ultracompact Optical Buffers on a Silicon Chip," *Nature Photon.* **1**:65 (2007).
62. A. B. Matsko, A. A. Savchenlov, and L. Maleki, "Vertically Coupled Whispering-Gallery-Mode Resonator Waveguide," *Opt. Lett.* 3066 (2005).
63. J. B. Khurgin, "Dispersion and Loss Limitations on the Performance of Optical Delay Lines Based on Coupled Resonant Structures," *Opt. Lett.* **32**:163–165 (2007).
64. J. B. Khurgin, "Expanding the Bandwidth of Slow-Light Photonic Devices Based On Coupled Resonators," *Opt. Lett.* **30**:513 (2005).
65. M. F. Yanik and S. Fan, "Stopping Light All Optically," *Phys. Rev. Lett.* **92**:083901 (2004).
66. M. F. Yanik and S. Fan, "Stopping Light in a Waveguide with an All-Optical Analog of Electromagnetically Induced Transparency," *Phys. Rev. Lett.* **93**:233903 (2004).
67. M. F. Yanik and S. Fan, "Dynamic Photonic Structures: Stopping, Storage, and Time-Reversal of Light," *Stud. Appl. Math.* **115**:233 (2005).
68. Z. S. Yang, N. H. Kwong, R. Binder, and A. L. Smirl, "Distortionless Light Pulse Delay in Quantum-Well Bragg Structures," *Opt. Lett.* **30**:2790–2792 (2005).
69. Z. S. Yang, N. H. Kwong, R. Binder, and A. L. Smirl, "Stopping, Storing, and Releasing Light in Quantum-Well Bragg Structures," *J. Opt. Soc. Am B* **22**:2144 (2005).
70. J. B. Khurgin, "Adiabatically tunable optical delay lines and Their Performance Limitations," *Opt. Lett.* **30**:2778 (2005).
71. R. S. Tucker, "The Role of Optics an Delectroncis in High-Capacity Routers," *J. Lightwave.Technol.* **24**:4655 (2006).
72. R. W. Boyd, *Nonlinear Optics*, 2nd ed. Academic Press, San Diego, 2003.
73. J. B. Khurgin, "Performance Limits of Delay Lines Based on Optical Amplifiers," *Opt. Lett.* **31**(7):948–950 (2006).
74. K. Y. Song, M. G. Herr´aez, and L. Th´evenaz, "Observation of Pulse Delaying and Advancement in Optical Fibers Using Stimulated Brillouin Scattering," *Opt. Express* **13**:82–88 (2005).
75. Y. Okawachi, M. S. Bigelow, J. E. Sharping, Z. Zhu, A. Schweinsberg, D. J. Gauthier, R. W. Boyd, and A. L. Gaeta, "Tunable All-Optical Delays via Brillouin Slow Light in an Optical Fiber," *Phys. Rev. Lett.* **94**:153, 902 (2005).
76. M. D. Stenner, M. A. Neifeld, Z. Zhu, A. M. C. Dawes, and D. J. Gauthier, "Distortion Management in Slow-Light Pulse Delay," *Opt. Express* **13**:9995–10,002 (2005).
77. A. Minardo, R. Bernini, and L. Zeni, "Low Distortion Brillouin Slow Light in Optical Fibers Using AM Modulation," *Opt. Express* **14**:5866–5876 (2006).
78. Z. Shi, R. Pant, Z. Zhu, M. D. Stenner, M. A. Neifeld, D. J. Gauthier, and R. W. Boyd, "Design of a Tunable Time-Delay Element Using Multiple Gain Lines for Increased Fractional Delay with High Data Fidelity," *Opt. Lett.* **32**:1986–1988 (2007).
79. K. Y. Song, K. S. Abedin, K. Hotate, M. G. Herraез, and L. Thevenaz, "Highly Efficient Brillouin Slow And Fast Light Using As<sub>2</sub>Se<sub>3</sub> Chalcogenide Fiber," *Opt. Express* **14**:5860–5865 (2006).
80. A. Zadok, A. Eyal, and M. Tur, "Extended Delay of Broadband Signals in Stimulated Brillouin Scattering Slow Light Using Synthesized Pump Chirp," *Opt. Express* **14**:8498–8505 (2006).

81. T. Schneider, R. Henker, K. U. Lauterbach, and M. Junker, "Comparison of Delay Enhancement Mechanisms for SBS-Based Slow Light Systems," *Opt. Express* **15**:9606–9613 (2007).
82. M. G. Herraiez, K. Y. Song, and L. Thevenaz, "Arbitrary-Bandwidth Brillouin Slow Light in Optical Fibers," *Opt. Express* **14**:1395–1400 (2006).
83. Z. Zhu, A. M. C. Dawes, D. J. Gauthier, L. Zhang, and A. E. Willner, "Broadband SBS Slow Light in an Optical Fiber," *J. Lightwave Technol.* **25**:201–206 (2007).
84. T. Schneider, M. Junker, and K.-U. Lauterbach, "Potential Ultra Wide Slow-Light Bandwidth Enhancement," *Opt. Express* **14**:11082–11087 (2006).
85. K. Y. Song and K. Hotate, "25 GHz Bandwidth Brillouin Slow Light in Optical Fibers," *Opt. Lett.* **32**:217–219 (2007).
86. L. Yi, L. Zhan, W. Hu, and Y. Xia, "Delay of Broadband Signals Using Slow Light In Stimulated Brillouin Scattering with Phase-Modulated Pump," *IEEE Photon. Technol. Lett.* **19**:619–621 (2007).
87. L. Thevenaz, "Slow Light in Optical Fibers," *Nature Photonics* **2**:474–481 (2008).
88. J. E. Sharping, Y. Okawachi, and A. L. Gaeta, "Wide Bandwidth Slow Light Using a Raman Fiber Amplifier," *Opt. Express* **13**:6092–6098 (2005).
89. Y. Okawachi, M. A. Foster, J. E. Sharping, A. L. Gaeta, Q. Xu, and M. Lipson, "All-Optical Slow-Light on a Photonic Chip," *Opt. Express* **14**:2317–2322 (2006).
90. A. Schweinsberg, N. N. Lepeshkin, M. S. Bigelow, R. W. Boyd, and S. Jarabo, "Observation of Superluminal and Slow Light Propagation in Erbium-Doped Optical Fiber," *Europhys. Lett.* **73**:218–224 (2006).
91. H. Shin, A. Schweinsberg, G. Gehring, K. Schwertz, H. J. Chang, R. W. Boyd, Q.-H. Park, and D. J. Gauthier, "Reducing Pulse Distortion in Fast-Light Pulse Propagation Through an Erbium-Doped Fiber Amplifier," *Opt. Lett.* **32**:906–908 (2007).
92. D. Dahan and G. Eisenstein, "Tunable All Optical Delay via Slow and Fast Light Propagation in a Raman Assisted Fiber Optical Parametric Amplifier: A Route to All Optical Buffering," *Opt. Express* **13**:6234–6249 (2005).
93. S. Ghosh, A. R. Bhagwat, C. K. Renshaw, S. Goh, A. L. Gaeta, and B. J. Kirby, "Low-Lightlevel Optical Interactions with Rubidium Vapor in a Photonic Band-Gap Fiber," *Phys. Rev. Lett.* **97**:023, 603 (2006).

*This page intentionally left blank*

---

# QUANTUM ENTANGLEMENT IN OPTICAL INTERFEROMETRY

---

Hwang Lee, Christoph F. Wildfeuer, Sean D. Huver, and  
Jonathan P. Dowling

*Hearne Institute for Theoretical Physics  
Department of Physics and Astronomy  
Louisiana State University  
Baton Rouge, Louisiana*

---

## 23.1 INTRODUCTION

---

The newly emergent fields of quantum sensing and imaging utilize quantum entanglement—the same subtle effects exploited in quantum information processing—to push the capability of precision measurements and image construction using interferometers to the ultimate quantum limit of resolution.<sup>1,2</sup> Alan Migdall at the U.S. National Institute of Standards and Technology, for example, has proposed and implemented a quantum optical technique for calibrating the efficiency of photodetectors using the temporal correlations of entangled photon pairs.<sup>3</sup> It was one of the first practical applications of quantum optics to optical metrology, and has produced a technique to calibrate detectors without the need for an absolute standard.

These quantum effects can also be applied to increase the signal-to-noise ratio in an array of sensors from Laser Interferometer Gravitational Wave Observatory (LIGO) to Laser Light Detection and Ranging (LIDAR) systems, and to synchronized atomic clocks. Quantum imaging exploits similar quantum ideas to beat the Rayleigh diffraction limit in resolution of an imaging system, such as used in optical lithography. We present an introduction to these exciting fields and their recent development.

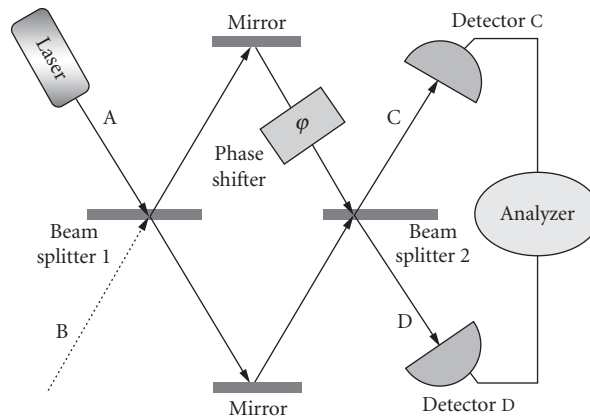
Entanglement is the most profound property of quantum mechanical systems.<sup>4,5</sup> First we need to define entanglement. For simplicity, let us consider a system of two modes A and B only. Modes A and B may describe the two spatial paths of a Mach-Zehnder interferometer or two different polarization modes in an optical cavity. We can put a photon in either of the modes or let them remain empty. Let us suppose a general state of mode A which is a superposition of the two possible states, therefore we obtain  $\alpha|0\rangle_A + \beta|1\rangle_A$ , where  $\alpha$  and  $\beta$  may be complex and  $|\alpha|^2 + |\beta|^2 = 1$  is required for proper normalization of the state. We also write a superposition for a general state for mode B, that is,  $\gamma|0\rangle_B + \delta|1\rangle_B$  and  $|\gamma|^2 + |\delta|^2 = 1$ . Now consider the combined two-mode state  $|\Psi\rangle = (|1\rangle_A |0\rangle_B + |0\rangle_A |1\rangle_B) / \sqrt{2}$ , where either a photon is in mode A or B. It is easy to see that this state cannot be decomposed into a product state for mode A and mode B only, that is, we *cannot* find any coefficients  $\alpha$ ,  $\beta$ ,  $\gamma$ ,  $\delta$  such that the equation  $(\alpha|0\rangle_A + \beta|1\rangle_A)(\gamma|0\rangle_B + \delta|1\rangle_B) = (|1\rangle_A |0\rangle_B + |0\rangle_A |1\rangle_B) / \sqrt{2}$  is satisfied. The state  $|\Psi\rangle$  is an example for a nonseparable state. In general, any nonseparable state of two or more systems is called entangled. Erwin Schrödinger was the first who coined the term entanglement,<sup>6</sup> although he is by far more prominent for his Schrödinger cat. Now we have a proper definition for entangled



*pure* states. But what is the definition for entangled mixed states? Let us suppose two systems A and B that can be in  $n$  different mixed states  $\rho_i^A$  and  $\rho_i^B$  with  $i=1, \dots, n$ . A separable mixed state may be written as  $\rho = \sum_i p_i \rho_i^A \otimes \rho_i^B$ , where the  $p_i$  are probabilities. Mathematicians call this particular sum a convex combination of product states. Now we can define entanglement for mixed states in excluding just these separable states. We say, if the bipartite system *cannot* be written in the above way, we call it entangled.<sup>7</sup>

Entanglement is not necessarily a useful physical quantity. Entanglement is usually discussed together with nonlocal correlations. These nonlocal correlations can be verified by Bell experiments.<sup>8</sup> For a nice review of the current status of Bell experiments see, for example, Ref. 9. The violation of a Bell inequality<sup>10,11</sup> by a specific quantum state is an indication that the state is able to exhibit nonlocal correlations. It is known that for any entangled *pure* state of any number of quantum systems one may violate a generalized Bell inequality.<sup>12,13</sup> An extension of this statement for mixed entangled states has not been found. Furthermore Werner provided in 1989 an example of nonseparable mixed states that do not violate a Bell inequality.<sup>7</sup> This demonstrated that the class of entangled mixed states decomposes into states that are entangled but do not show nonlocal correlations and those that are entangled and are nonlocal. The state  $|\Psi\rangle$  is clearly entangled but only until very recently it has been proven in several experiments that this state violates a Bell inequality.<sup>14-17</sup> Generalizations of this state where the single photon is replaced by  $N$  photons will play an important role in applications described later in this chapter. That also this generalization for  $N$  photons in either of the modes violates a Bell inequality has been proven in Ref. 18 very recently. This shows that the connection of entanglement and nonlocal correlations is still a very hot research topic. Now let us come back to a very practical application, an optical interferometer.

In order to see the role of quantum mechanics in optical interferometers, we first consider a prototype Mach-Zehnder interferometer (MZI).<sup>19</sup> The task is to measure the path-length difference between the two arms of the interferometer. In the standard approach, as shown in Fig. 1, an input laser beam is launched into the first 50-50 beam splitter (BS) on the left in port A, bounced off of the two mirrors in the middle, and recombined at the second 50-50 BS on the right. Light then emerges from the top and bottom ports, C and D, of the second BS, and is then made incident on two photodetectors  $\mathcal{C}$  and  $\mathcal{D}$ , as shown. Typically, the intensities in each port,  $I_C$  and  $I_D$ , are measured at each detector and the result is combined to yield the difference intensity,  $I = I_D - I_C$  which



**FIGURE 1** Schematic of a Mach-Zehnder interferometer. Laser light in port A is split by the first 50-50 beam splitter, acquires a phase difference, and recombines at the second beam splitter and emerges in ports C and D. We take a convention such that, for a balanced interferometer, port C is the dark port. Hence, any light emergent here is indicative of an arm displacement and can be detected by the two detectors and the analyzer.

we shall call the signal. To indicate the phase induced by the path difference between the upper and lower arms, we place an icon for a phase shift  $\varphi$ , which in this example has the value  $\varphi = kx$ . Here  $x$  is the path-length difference between the two arms. The wave number,  $k = 2\pi/\lambda$ , is a predetermined constant, given the optical wavelength  $\lambda$ .

We adopt the convention that the light field always picks up a  $\pi/2$  phase shift upon reflection off of a mirror or off of a BS, and also no phase shift upon transmission through a BS. Then, the two light fields emerging from the second BS out the upper port C are precisely  $\pi$  out of phase with each other, and hence completely cancel out due to destructive interference (the dark port). Consequently, the two light fields recombine completely in phase as they emerge from the lower port D and add up due to constructive interference (the bright port). Hence for a balanced MZI all of the energy that comes in port A emerges out of port D and none out of port C. Clearly, any change in the path difference  $x$  away from the  $x = 0$  balanced condition will cause light to appear in the formerly dark port, and in this way we can measure  $x$  by simply measuring intensities at the detectors.

The question is: How precise a measurement of the path difference  $x$  can we make? If the light intensity incident on port A is  $I_A$ , then in terms of the phase shift  $\varphi$  the output-port intensities can be written as

$$I_C = I_A \sin^2(\varphi/2) \quad (1a)$$

$$I_D = I_A \cos^2(\varphi/2) \quad (1b)$$

It is typical for the analyzer in Fig. 1 to compute the difference intensity  $M = I_D - I_C$  (where  $M$  stands for “minus”) such that

$$M(\varphi) \equiv I_D - I_C = I_A \cos(\varphi) \quad (2)$$

Since  $\varphi/2 = kx/2 = \pi x/\lambda$ , we have that  $I_C = 0$  and  $I_D = I_A$  whenever  $x/\lambda = 0, 1, 2, 3, \dots$ . Hence, our ruler is the light wave itself and the tick marks are spaced the wavelength  $\lambda$  apart. We may start with a balanced interferometer with equal arm lengths,  $x = 0$  (and  $M = I_A$ ), and then slowly move the upper mirror upward increasing  $x$ . As we do we will break the balance and begin to see light emerging from the formally dark port C ( $M$  decreases in the plot).

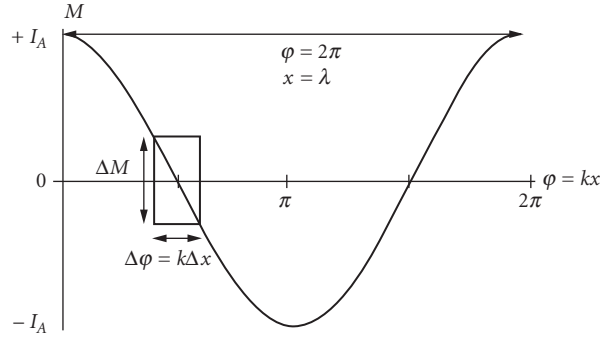
At the point  $\varphi = \pi/2$ , when  $I_C = I_D$ , then  $M = 0$ . Eventually, we will see port C attain maximum brightness and port D will go dark ( $M = -I_A$ ). As we continue the mirror displacement, this process will reverse, as sine and cosine are periodic, and finally port C will go dark again ( $M$  is maximum again with  $M = I_A$ ). At this point, we can stop moving the upper mirror and we are assured that now the path difference  $x$  has gone from 0 to  $\lambda$ . If we take  $\lambda = 1.0 \mu\text{m}$ , then it would seem we have a machine capable of measuring distances to an accuracy of about  $\lambda = 1.0 \mu\text{m}$ . This is consistent with the Rayleigh diffraction limit, typically invoked in classical optics.

Let us now balance the interferometer such that we start at the point  $\varphi = \pi/2$ , when  $I_C = I_D$ , and hence  $M = 0$  in Fig. 2. Note this is where the curve crosses the horizontal axis and the slope of the  $M$ -curve is steepest. If we call the horizontal displacement change  $\Delta\varphi$ , then we can see this is related to the vertical intensity change  $\Delta M$ . For small changes, we may approximate this relation using differentials, that is,  $\Delta M = I_A \Delta\varphi$  or

$$\frac{\Delta M}{\Delta\varphi} = \frac{\partial M}{\partial\varphi} = I_A \sin(\varphi) \quad (3)$$

which may be written as

$$\Delta\varphi = \frac{\Delta M}{\partial M / \partial\varphi} = \frac{\Delta M}{I_A \sin(\varphi)} \quad (4)$$



**FIGURE 2** Typical Mach-Zehnder analyzer. The difference intensity  $M$  is plotted as a function of the phase shift  $\varphi = kx$ , where  $x$  is the arm displacement to be measured. The minimal detectable displacement,  $\Delta x$ , is limited by the fluctuations in the optical intensity,  $\Delta M$ . These fluctuations are quantum mechanical in nature.

The quantity  $\partial M/\partial \varphi$  is the slope of the curve, which is largest at the crossing point, implying our minimum detectable phase  $\Delta \varphi$  is smallest there, via Eq. (4). At the crossing point  $\varphi = \pi/2$  and  $\sin(\pi/2) = 1$ , and so this relation would seem to indicate that *if* we can measure the intensity displacement  $\Delta M$  with infinite precision ( $\Delta M = 0$ ), we can measure the phase (and hence distance) with infinite precision ( $\Delta \varphi = 0$ ). In practice, various technical imperfections tend to set the limit for the finite precision  $\Delta M$ .<sup>20</sup> However, as far as classical electromagnetic waves are concerned, nothing “fundamentally” prevents  $\Delta M$  being zero. Hence, it would appear that *if* we try hard, we could detect any amount of phase shift no matter how small it is.

## 23.2 SHOT-NOISE LIMIT

The problem is that the simple classical arguments we used above do not take into account the effects of quantum mechanics. Specifically it does not take into account the fact that the intensity of the light field is not a constant, which can be measured with infinite precision, but that it fluctuates about some average value, and those fluctuations have their origin in the vacuum fluctuations of the quantized electromagnetic field.<sup>21,22</sup> According to quantum mechanics, optical intensity can never be measured with infinite precision. Hence the uncertainty, in the curve of Fig. 2, always has some finite value, indicated by the box of height  $\Delta M$ . The intensity displacement  $M$  can never be measured with infinite precision and has a fundamental uncertainty  $\Delta M$ , and therefore the consequent phase  $\varphi$  will always have its related uncertainty  $\Delta \varphi$ , which is the width of the box. These fundamental quantum intensity fluctuations suggest that there is a Heisenberg uncertainty principle at work, which in our example implies that the intensity  $I$  and the phase  $\varphi$  cannot both simultaneously be measured with infinite precision.

For a quantum analysis of this phenomenon, we introduce the mean number of photons in the laser field as the dimensionless quantity  $n$ , and note that the intensity  $I$  is then proportional to  $n$  for a steady-state system. If we denote the fluctuation in the phase as  $\Delta \varphi$  and that in the intensity as  $\Delta n$ , we can then write down the Heisenberg number-phase uncertainty relation as<sup>23–25</sup>

$$\Delta n \Delta \varphi \geq 1 \quad (5)$$

This is closely related to the better known energy-time uncertainty principle  $\Delta E \Delta t \geq \hbar$ , where  $\Delta E$  is the uncertainty in the energy,  $\Delta t$  is the uncertainty in the time, and  $\hbar$  is Dirac’s constant (Planck’s constant

divided by  $2\pi$ ). For a standing, monochromatic, electromagnetic wave we have  $E = \hbar n \omega$ , where  $\omega$  is the frequency. This is just the energy per photon multiplied by the average number of photons. Since there is no propagation for a standing wave we have  $\varphi = \omega t$  as the accumulated phase at any point. Approximating both of these expressions with differentials gives  $\Delta E = \hbar \Delta n \omega$  and  $\Delta \varphi = \omega \Delta t$ . Inserting these two expressions into the energy-time uncertainty relation yields the number-phase relation, Eq. (5).

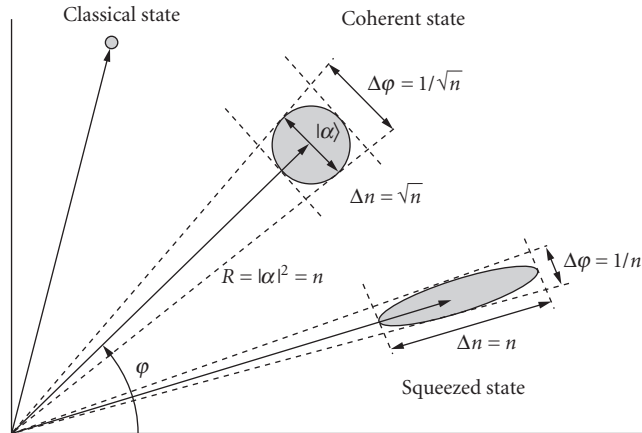
For a laser beam, the quantum light field is well approximated by a coherent state, denoted as  $|\alpha\rangle$ , where the complex number  $\alpha = |\alpha|e^{i\varphi}$  is proportional to the electric field amplitude  $E$  such that  $|\alpha|^2 = n$ , the latter of which we recall is the dimensionless field intensity.<sup>21</sup> This is the dimensionless quantum version of the classical relation  $|E|^2 = I = I_0 n$ . The full dimensional form is  $E = E_0 \sqrt{n}$ , where  $I_0 = |E_0|^2 = \hbar \omega / (\epsilon_0 V)$ , which in SI units,  $\hbar$  is Dirac's constant,  $\epsilon_0$  is the free-space permittivity, and  $V$  is the mode volume for the electromagnetic field. Hence  $I_0$  is the intensity of a single photon. The fluctuations are typically represented in a phasor diagram, as shown in Fig. 3. Here the phase is the polar angle  $\varphi$  measured counterclockwise off the horizontal axis. The radius from the origin to the center of the coherent-state disk is  $R = |\alpha|^2 = n$ . The diameter of the disk  $d$  is on the order of  $d = \Delta n = \sqrt{n}$ . From simple geometry, we can then approximate  $d = R \Delta \varphi$ , where  $\Delta \varphi$  is the uncertainty or fluctuation in the angular  $\varphi$  direction.

Combining all this we arrive at the fundamental relationships between number (intensity) and phase uncertainty for a coherent-state laser beam,

$$\Delta n \Delta \varphi = 1 \quad (6a)$$

$$\Delta n = \sqrt{n} \quad (6b)$$

$$\Delta \varphi_{\text{SNL}} = \frac{1}{\Delta n} = \frac{1}{\sqrt{n}} \quad (6c)$$



**FIGURE 3** Phase-space diagram showing quantum fluctuations. Fluctuations in the radial direction correspond to intensity and those in the angular direction phase. A coherent state is a disk and has fluctuations equal in intensity and phase (a “true” classical state is a point and has no fluctuations). Also shown is a phase squeezed state, which has fluctuations decreased in the angular (phase) direction, at the expense of increase fluctuation in the radial (intensity) direction. Such a phase-squeezed state can be used to beat the shot-noise limit.

The first relation, Eq. (6a), tells us that we have equality in Eq. (5); that is a coherent state in a minimum uncertainty state (MUS). Such a state saturates the Heisenberg number-phase uncertainty relation with equality. This is the best you can do according to the laws of quantum mechanics. The second relation, Eq. (6b), describes the fact that the number fluctuations are poissonian with a mean of  $n$  and a deviation of  $\Delta n = \sqrt{n}$ , a well-known property of the Poisson distribution and the consequent number statistics for coherent-state laser beams.<sup>22</sup> Putting back the dimensions we arrive at

$$\Delta\varphi_{\text{SNL}} = \sqrt{\frac{I_0}{I}} \quad (7)$$

which is called the shot-noise limit (SNL). The term “shot noise” comes from the notion that the photon-number fluctuations arise from the scatter in arrival times of the photons at the beam splitter, much like buckshot from a shotgun ricocheting off a metal plate. We can also import the SNL into our classical analysis above. Consider Eq. (4), where we now take  $I_A = I_0 n$ ,  $\Delta M = \sqrt{I_0 n}$ , and  $\varphi = \pi/2$ . We again recover Eq. (6c) for the phase uncertainty. Hence quantum mechanics puts a quantitative limit on the uncertainty of the optical intensity, and that intensity reflects itself in a consequent quantitative uncertainty of the phase measurement.

In classical electromagnetism, we can also represent a monochromatic plane wave on the phasor diagram of Fig. 3—but instead of a disk the classical field is depicted as a point. The radial vector to the point is proportional to the electric field amplitude  $E$  and the phase angle corresponds to the classical phase of the field. The phase-space point represents the idea that, classically, we can measure number and phase simultaneously and with infinite precision. As we have seen above, quantum mechanically this is not so. The Heisenberg uncertainty principle (HUP) of Eq. (5) tells us that both phase and intensity cannot be measured simultaneously with infinite precision. For a minimum uncertainty state (MUS), such as a coherent state  $|\alpha\rangle$ , we have equality in the HUP, as given in Eq. (6a). Then, combined with the poissonian-statistical distribution of photon number for a coherent state, Eq. (6b), we arrive at the shot-noise limit.

### 23.3 HEISENBERG LIMIT

In 1981, Carlton Caves first proposed the idea of using nonclassical states of light—the so-called squeezed states—to improve the sensitivity of optical interferometers to below even the shot-noise limit.<sup>26</sup> This notion came as somewhat of a surprise to the interferometer community, as it was thought at the time that the shot-noise limit was the ultimate limit on sensitivity as imposed by quantum mechanics. However, there are other minimum uncertainty states besides the coherent state. The easiest way to see this is to look again at the representation of the coherent state as a disk in phase space (Fig. 3). The fact that it is a disk indicates that the fluctuations are the same in all directions, and that the area of the disk is a constant  $\mathcal{A}$ . The pictogram and the HUP then tells us that any quantum state must have an area greater or equal to  $\mathcal{A}$ , and that the MUS has an area equal to  $\mathcal{A}$ . This is, for a coherent state, equivalent to stating the three conditions of Eq. (6). However, we can relax Eq. (6b) and (6c), while still maintaining the HUP of Eq. (6a).

That is, we can decrease  $\Delta\varphi$ , at the expense of increasing  $\Delta n$  at the same time, so that the product  $\Delta\varphi\Delta n = 1$  remains constant and the area of the disk remains the same value  $\mathcal{A}$ . Pictorially this amounts to squeezing the coherent-state disk in the angular direction, while allowing it to expand in the radial direction, as shown in Fig. 3. The important point is that the area  $\mathcal{A}$  of the ellipse remains unchanged so that the HUP is obeyed. However, we can decrease phase uncertainty at the expense of increasing the number uncertainty. Furthermore, it is possible to produce such squeezed states of light in the laboratory, using nonlinear optical devices and ordinary lasers.<sup>27–30</sup>

Now the question is: What is the most uncertainty we can produce in photon number, given that the mean photon number  $n$  is a fixed constant, and that we still want to maintain the MUS condition—that the area of the ellipse remains a constant  $\mathcal{A}$ . Intuitively one cannot easily imagine a scenario where

the fluctuations in the energy,  $\Delta E = \hbar \omega \Delta n$ , exceeds the total energy of the laser beam,  $E = \hbar \omega n$ . Hence the best we can hope to achieve is  $\Delta E = E$  or, canceling out some constants,  $\Delta n = n$ . Inserting this expression in the HUP of Eq. (6a), we obtain what is called the Heisenberg limit:

$$\Delta \phi_{\text{HL}} = \frac{1}{n} \quad (8)$$

Putting back the dimensions we get

$$\Delta \phi_{\text{HL}} = \frac{I_0}{I} \quad (9)$$

This is exactly the limit one gets with a rigorous derivation using squeezed light in the limit of infinite squeezing.<sup>31,32</sup> It is called the Heisenberg limit as it saturates the number-phase HUP, and also because it can be proven that this is the best you can do in a passive interferometer with finite average photon number  $n$ . Converting to minimum detectable displacement we get

$$\Delta x = \frac{\lambda}{n} = \lambda \frac{I_0}{I} \quad (10)$$

where  $I_0$  is the single photon intensity, defined above.

So far, we have considered the situation that we send light in port A and analyzed what came out of ports C and D for the MZI shown in Fig. 1. What about input port B? Classically there is no light coming in port B, and hence it is irrelevant. But, it is not so. In his 1981 paper, Caves showed that no matter what state of the photon field you put in port A, so long as you put nothing (quantum vacuum) in port B, you will always recover the SNL. In quantum electrodynamics, even an interferometer mode with no photons in it experiences electric field fluctuations in that mode.

In the MZI these vacuum fluctuations have another important effect; at the first BS they enter through port B and mix with whatever is coming in port A to give the SNL in overall sensitivity. It becomes clear then, from this result, that the next thing to try would be to plug that unused port B with something besides vacuum. It was Caves' idea to plug the unused port B with squeezed light (squeezed vacuum to be exact). That, with coherent laser light in port A as before—and in the limit of infinite squeezing—then the SNL rolls over into the HL.

In the laboratory, however, infinite squeezing is awfully hard to come by. With current technology,<sup>33–35</sup> the expected situation is to sit somewhere between SNL and HL but a lot closer to the former than the latter. Recent analyses by a Caltech group, on exploiting squeezed light in LIGO, indicates a potential for about a one-order-of-magnitude improvement in a future LIGO upgrade.<sup>36</sup> Not the twelve orders of magnitude that was advertised above, but enough to allow the observatory to sample about 80 times the original volume of space for gravitational-wave sources. That, for LIGO, is a big deal.

## 23.4 “DIGITAL” APPROACHES

Squeezing is an “analog” approach to quantum optical interferometry, in that the average photon number and the degree of squeezing are continuous variables. There is another approach, exploiting discrete photon number and path-entangled optical states, where the photon number is fixed. There is a large body of literature on using entangled particles or photons in a Mach-Zehnder interferometer in order to beat the shot-noise limit. The first such proposal was by Bernard Yurke in the context of neutron interferometry.<sup>37</sup>

In 1986, the use of photon-number eigenstates, the so-called Fock states, to improve the interferometer phase sensitivity by Yurke et al.,<sup>38</sup> and independently by Yuen.<sup>39</sup> They showed that with a

suitably correlated input state the phase sensitivity can be improved to the one proportional to  $1/N$ . The correlated input state—which we call the Yurke state—is given by

$$|\psi\rangle_Y = \left| \frac{N}{2}, \frac{N}{2} \right\rangle + \left| \frac{N}{2} + 1, \frac{N}{2} - 1 \right\rangle \quad (11)$$

where the normalization constant of  $1/\sqrt{2}$  has been dropped for convenience. The two numbers inside the brackets represent the number of photons entering the input ports A and B, respectively. As is the case of the squeezed state, the Fock-state approaches also require the light field incident upon *both* input ports of the MZI. If  $N$  photons entered into each input port of the interferometer in nearly equal numbers, then it is possible to obtain the asymptotic phase sensitivity scaling of order  $1/N$  for large  $N$ , the Heisenberg-limit.<sup>40</sup>

In 1993, Hillery and Mlodinow showed that the SU(2)-squeezed minimum-uncertainty states can also be used for the input state of the Mach-Zehnder interferometer to achieve Heisenberg-limited sensitivity.<sup>41</sup> They called such a state the “intelligent” state. The intelligent state has a fixed number of photons. However, it consists of all the possible combination of the photon number distribution in the input modes such that

$$|\psi\rangle_{INT} = \sum_{k=0}^N C_{N,k} |N-k, k\rangle \quad (12)$$

where the probability amplitude  $C_{N,k}$  varies with  $N$  and  $k$  as well as the degree of squeezing.<sup>42</sup> Although it contains a fixed number of photons, the exact form of the intelligent state depends on the degree of squeezing. Hence, we may put this approach in between the analog and the digital ones.

In 1993, on the other hand, Holland and Burnett proposed the use of the so-called dual-Fock states for the two input ports of the MZI in order to achieve Heisenberg-limited sensitivity.<sup>43</sup> The dual-Fock state has the same number of photons at each input mode such that the quantum state can be written as

$$|\psi\rangle_{DF} = \left| \frac{N}{2}, \frac{N}{2} \right\rangle \quad (13)$$

We see that the dual-Fock state has a much simpler form, compared to the Yurke state of Eq. (11). Why is it that this simple looking dual-Fock state had been overlooked in the earlier investigation? Using the dual-Fock state input, the measurement of the difference intensity does not yield any signal. In other words, the difference between the two output modes is always zero regardless of the amount of phase shift. This prevents the use of dual-Fock state for the interferometer input when the difference signal is measured, and because of that it was discarded, not overlooked. What Holland and Burnett suggested is to construct a probability distribution of the estimated phase, conditioned on the number of photons at each output port. Then, they showed, after sufficient number of trials, the probability distribution becomes narrow such that the phase uncertainty approaches to the  $1/N$  Heisenberg limit. Heisenberg-limited phase measurements have also been proposed for Ramsey-type atom interferometry, where the degenerate Bose-Einstein condensates play the role of atomic dual-Fock states.<sup>44,45</sup>

The conditional probability distributions are generally used for parameter estimation. The phase is not a quantum mechanical observable (that is represented by a self-adjoint operator),<sup>46</sup> and it has to be estimated. Here, instead of direct inversion for the phase shift as performed with the difference-intensity measurement in Eq. (2), the probability distribution is constructed to infer the phase shift given the measurement results (photon counts at C and D ports separately).<sup>47</sup> The error in the phase estimation is then given by the variance of that distribution.

Such phase estimation protocols with conditional probabilities are applied to look for optimal quantum states of the input light field as well as the optimal output measurement schemes.<sup>48–52</sup> Given that the output detection does not have to be the conventional difference intensity measurement,

Sanders and Milburn proposed an ideal canonical measurement based on phase state projection.<sup>48</sup> Using such an ideal measurement strategy, Berry and Wiseman suggested an optimal state that minimizes the so-called Holevo phase variance.<sup>49</sup> They further developed an adaptive measurement scheme that approximates the ideal measurement scheme by Sanders and Milburn. With other measurement strategies such as coincident measurement that exploits the fourth-order correlation, it is also possible to obtain the phase sensitivity beyond the shot-noise limit with the dual-Fock state.<sup>53–57</sup>

## 23.5 NOON STATE

Let us now consider a two-mode, path-entangled, photon-number state, commonly called the N00N state. The idea is that we have a fixed finite number of photons  $N$  that are either all in the upper mode A or all in the lower mode B, but we cannot tell—even in principle—which is which. The state of all up and none down is written  $|\text{up}\rangle = |N\rangle_A |0\rangle_B$  and the state of all down and none up is similarly  $|\text{down}\rangle = |0\rangle_A |N\rangle_B$ . The notation indicates a product state of  $N$  photons either in A or B (but not both) such that

$$|\text{N00N}\rangle \equiv |\text{up}\rangle + |\text{down}\rangle = |N, 0\rangle + |0, N\rangle \quad (14)$$

where a normalization constant of  $1/\sqrt{2}$  has again been dropped for convenience. The N00N state was first discussed in 1989 by Barry Sanders, who was particularly interested in the Schrödinger-cat aspect and how that affected quantum decoherence.<sup>58</sup> It was rediscovered in the context of quantum imaging—particularly for quantum lithography<sup>59</sup>—to circumvent the Rayleigh diffraction limit. The N00N state has the interesting property that it is quantum entangled between the two modes and rigorously violates what is known as a Bell inequality for nonclassical correlations.<sup>18</sup>

To see why a N00N state has the magical properties—super sensitivity and super resolution, in particular—we take a brief look at the difference in behavior between a number state  $|N\rangle$  and a coherent state  $|\alpha\rangle$  in an MZI. When a coherent state passes through a phase shifter  $\varphi$ , such as depicted in Fig. 1, it picks up a phase of  $\varphi$ . This is a property of a classical monochromatic light beam that coherent states inherit quantum mechanically. However, number states are already highly nonclassical states to begin with. Their behavior in the phase shifter is radically different.

When a monochromatic beam of number states passes through a phase shifter, the phase shift is directly proportional to  $N$ , the number of photons. There is no  $n$ -dependence in the phase shift for the coherent state ( $n$  is the average number of photons). In terms of a unitary evolution of the state, the evolution for any photon state passing through a phase shifter  $\varphi$  is governed by

$$\hat{U}(\varphi) \equiv \exp(i\varphi\hat{n}) \quad (15)$$

where  $\hat{n}$  is the photon number operator. The phase shift operator can be shown to have the following two different effects on coherent versus number states,<sup>22</sup>

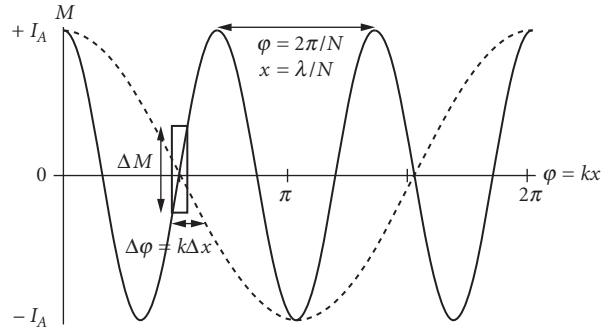
$$\hat{U}_\varphi |\alpha\rangle = |e^{i\varphi}\alpha\rangle \quad (16a)$$

$$\hat{U}_\varphi |N\rangle = e^{iN\varphi} |N\rangle \quad (16b)$$

Notice that the phase shift for the coherent state is independent of number, but that there is an  $N$  dependence in the exponential for the number state. The number state then evolves in phase  $N$  times more rapidly than the coherent state. After the phase shifter the N00N state evolves into

$$|N, 0\rangle + |0, N\rangle \rightarrow e^{iN\varphi} |N, 0\rangle + |0, N\rangle \quad (17)$$





**FIGURE 4** Comparison of the detection signal of a coherent state (dotted) and a N00N state (solid). The N00N state signal oscillates  $N$  times as fast as the coherent state and has maximum slope that is  $N$  times as steep ( $N = 3$ ). The effect is as if the N00N state was composed of photons with an effective wavelength of  $\lambda/N$  instead of  $\lambda$ .

which is the origin of the quantum improvement phase sensitivity. If we now carry out an  $N$ -photon detecting analyzer (still different from the conventional difference intensity measurement), we obtain

$$M_{\text{N00N}}(\phi) = I_A \cos(N\phi) \quad (18)$$

which is the solid curve in Fig. 4. The N00N signal (solid) oscillates  $N$  times as fast as the coherent state (dotted). Two things are immediately clear. The distance between peaks goes from  $\lambda \rightarrow \lambda/N$ , which is the quantum lithography effect—we now beat the Rayleigh diffraction limit of  $\lambda$  by a factor of  $N$ . This sub-Rayleigh-diffraction-limit effect is now commonly called “super resolution.” The slope of the curve at the horizontal axis crossing point gets larger as well, also by a factor of  $N$ . Now the minimal detectable phase, given by Eq. (4), consequently goes down. However, the signal  $M$  for this N00N state is not the same as for the coherent state scheme, as we are now counting photons  $N$  at a time. And it turns out then that  $\Delta M_{\text{N00N}} = 1$  for the new scheme, and then Eq. (4) gives

$$\Delta\phi_{\text{N00N}} = 1/N \quad (19)$$

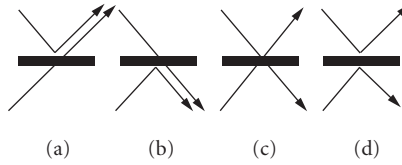
which is precisely the Heisenberg limit of Eq. (8). This Heisenberg limit, or the beating of the shot-noise limit, is now commonly called “super sensitivity.”

For  $N = 1$  and  $N = 2$  (low N00N) it is fairly straightforward to make such states with nonclassical sources of photon number states of either the form  $|1\rangle_A |0\rangle_B$  or  $|1\rangle_A |1\rangle_B$ , that is one photon in mode A and none in B, or one photon in each of modes A and B. The standard approach utilizes spontaneous parametric down-conversion (SPDC), where an ultraviolet (UV) photon is down converted into a pair of number states. The effect of a simple beam splitter transformation on these states<sup>22</sup> is to convert them to low-N00N states, as follows:

$$|1\rangle_A |0\rangle_B \xrightarrow{\text{BS}} |1\rangle_{A'} |0\rangle_{B'} + |0\rangle_{A'} |1\rangle_{B'} \quad (20a)$$

$$|1\rangle_A |1\rangle_B \xrightarrow{\text{BS}} |2\rangle_{A'} |0\rangle_{B'} + |0\rangle_{A'} |2\rangle_{B'} \quad (20b)$$

where Eq. (20a) shows that a single photon cannot be split in two, and Eq. (20b) is illustrative of the more subtle Hong-Ou-Mandel effect—if two single photons are incident on a 50-50 beam splitter they will “stick” and both photons will go one way or both will go the other way, but you never get one photon out each port.<sup>60</sup>

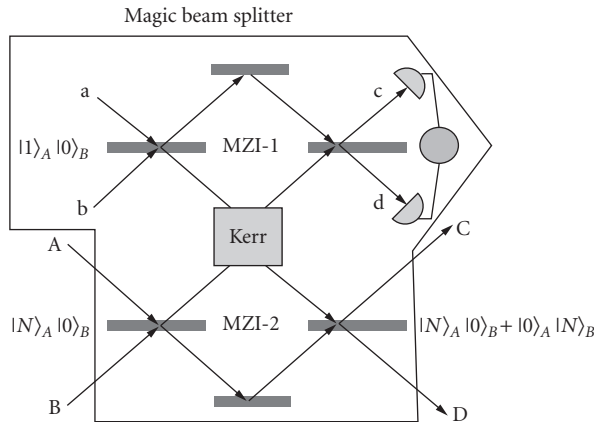


**FIGURE 5** Four possibilities of the output, when sending a  $|1\rangle_A |1\rangle_B$  state through a beam splitter. The diagrams (c) and (d) lead to the same final state, interfering destructively; (c) no phase acquired for transmission-transmission; and (d) a total of  $\pi$  phase shift for reflection-reflection.

As depicted in Fig. 5, it is the probability amplitude for the transition  $|1\rangle_A |1\rangle_B \xrightarrow{\text{BS}} |1\rangle_A |1\rangle_B$  that completely cancels out due to destructive interference. On the other hand, the probability amplitude for the transition indicated by Eq. (20b) adds up, due to constructive interference. So it is relatively easy, once you have a source of single photons, to create low-N00N states. The challenge is then, how to go to high N00N?

One of the first proposals for making high-N00N states was introduced in 2002 by Gerry and Campos, motivated by their applications in lithography and metrology.<sup>61</sup> The idea is to make a kind of quantum computing gate (a Fredkin gate) so that a single photon in the upper MZI-1 controls the phase shift in the lower MZI-2, as shown in Fig. 6.<sup>62</sup> A nonlinear optical material called a cross-Kerr phase shifter couples the two MZIs.

The strength of the cross-Kerr effect, however, is so tiny at the single photon level<sup>63-65</sup> that it comes up 20 orders of magnitude too small for making a good N00N-state generator. There are two



**FIGURE 6** N00N-state generator by Gerry and Campos.<sup>61</sup> In the lower interferometer if  $N$  photons enter upper port A, they will always emerge in lower port D for a balanced Mach-Zehnder. Now if the lower interferometer is coupled to the upper one, via a strong cross-Kerr nonlinearity, a single photon in the lower branch of the upper interferometer causes a  $\pi$  phase shift, directing all  $N$  photons to emerge out port C. If the upper device is also an interferometer, one can arrange a superposition of zero and one photons in the Kerr box, giving rise to a superposition of a 0 and  $\pi$  phase shift. This Kerr superposition results in the N00N state, the number state superposition in the output modes C and D of the lower interferometer.

well-known ways to boost the Kerr effect: put in an optical micro-cavity around the atoms in the Kerr material,<sup>66</sup> or coherently lock the atoms together in an approach known as electromagnetically induced transparency.<sup>67–69</sup> Both roads have their complication and technical challenges. There is, however, a third path.

Here is where the universe of quantum-optical-metrology took some hints from the world of quantum-optical computing. The Gerry-Campos idea is based on an optical Fredkin gate, a sort of a single photon transistor. If such a device could be made easily, it would be a quick and easy road to the all-optical quantum computer. In 2001, Knill, LaFlamme, and Milburn (KLM) proposed an all-optical, digital, scheme for quantum computing that exploited discrete entangled photon states distributed over the modes of an optical interferometer.<sup>70</sup> This discovery ignited a huge international collaborative research and development program on the optical quantum computer. In this scheme, the Kerr nonlinearity is replaced with additional ancillary, mirrors, phase shifters, beam splitters and—most importantly—detectors. The KLM idea is that the detection process in the ancillary devices induces an effective Kerr nonlinearity.<sup>71</sup>

While still not perfect, the effective Kerr produced this way can be much stronger than the usual Kerr materials. So instead of working one time in  $10^{20}$ , our new device works one time in 10, which is a 19-order-of-magnitude improvement. Our group, then at the NASA Jet Propulsion Laboratory, proposed the first high-N00N generation scheme based on all linear-optical devices.<sup>72</sup> The idea is to make the upper and lower mirrors into additional beam splitters and to put detectors just past them. Such a N00N-generating scheme can be stacked to produce N00N states with  $N$  that is arbitrarily high.<sup>73,74</sup> However, at least initially, all such schemes produced N00N states with a probability that scaled exponentially badly as  $N$  increased. The larger and larger you make  $N$ , the far more likely it is that you get only non-N00N states. Recently there has been a great deal of work on the development of schemes that produce N00N “efficiently.”<sup>75–77</sup> So we are well along the digital quantum-computer-paved road to super resolution and super sensitivity—at least in theory.

The demonstration of the doubling of the effective wavelength was made in 1999,<sup>78</sup> and a proof-of-principle demonstration of the super-resolving application to sub-Rayleigh lithography was carried out by the group of Yanhua Shih in 2001.<sup>79</sup> Then in 2004 the  $N = 2$  barrier was breached; the group of Steinberg demonstrated super resolution for  $N = 3$ , and, for  $N = 4$ , the group of Zeilinger demonstrated it as well.<sup>80–82</sup> These 2004 experiments exploited the *effective* Kerr nonlinearities extracted from the photodetection process. While not “optical” metrology, there has been a lot of work on precision frequency measurements with trapped ions. In particular, the so-called maximally entangled states have been exploited to show super resolution and super sensitivity.<sup>83–89</sup>

Then, in 2007, the group of Andrew White demonstrated  $N = 6$  super resolution in a process that used classical photons with a nonlinear  $N$ -photon detection scheme.<sup>86</sup> While interesting, such an approach can never achieve super sensitivity due to its semiclassical nature, as the authors pointed out. The first demonstration of both super sensitivity and super resolution in a single experiment also appeared in late 2007 in a collaborative Japanese and UK experiment.<sup>87</sup> This was the first experiment to beat the shot-noise limit, using N00N states, with  $N > 2$ . However, the results still were not quite at the Heisenberg limit. It lies between the shot-noise limit and the Heisenberg limit.

Another Australian collaboration, of the groups of Geoffrey Pryde and Howard Wiseman, carried out an experiment that produced  $N$  single-photon states of the form of Eq. (20a), and recycled them through the MZI in a feedback-loop implementation of a quantum computing protocol known as the Kitaev phase estimation algorithm<sup>88–90</sup> with the effective  $N = 378$ . The idea is that instead of making such a large N00N state, they make 378 passes through the interferometer, with feedback, using the low  $N = 1$  N00N state. Since all N00N states are equally entangled and violate a Bell inequality for any nonzero value of  $N$ , the trade-off is that of a complicated N00N-state generating scheme with a less complicated single-photon detection scheme with some electronic feedback.<sup>18</sup> Such a protocol is, surprisingly, easier to implement than the high-N00N approach, and arrives at the same performance in sensitivity scaling, the Heisenberg limit. This Australian experiment, once again, illustrates the close connection between quantum optical computing and quantum metrology, as it achieves super sensitivity by running a quantum computational algorithm. A quantum computer is nothing more than a (complicated) quantum sensor, and hence one can design a quantum sensor by exploiting ideas from quantum computing.

## 23.6 QUANTUM IMAGING

Quantum imaging is a new subfield of quantum optics that exploits quantum correlations, such as quantum entanglement of the electromagnetic field, in order to image objects with a resolution (or other imaging criteria) that is beyond what is possible in classical optics. Examples of quantum imaging are quantum ghost imaging, quantum lithography, and sub-Rayleigh imaging.<sup>91,92</sup> In 2000, it was pointed out that N00N states had the capability to beat the Rayleigh diffraction limit by a factor of  $N$ . This super-resolution feature is due to the high-frequency oscillations of the N00N state in the interferometer, as illustrated in Fig. 4. For the quantum lithography application, the idea is to realize that if one has an  $N$ -photon absorbing material, used as a lithographic resist, then these high-frequency oscillations are written onto the material in real space and are not just a trace on an oscilloscope. Mathematically, the  $N$ -photon absorption and the  $N$ -photon detection process have a similar structure, that is,

$$\langle N00N | (\hat{a}^\dagger)^N (\hat{a})^N | N00N \rangle = 1 + \cos(N\varphi) \quad (21)$$

where  $\hat{a}$  and  $\hat{a}^\dagger$  are the mode annihilation and creation operators. From Fig. 4, we see in the solid curve this oscillates  $N$  times faster than if we were using single photons, or coherent light, as in the dotted curve. Recall that, for our MZI, we have  $\varphi = kx = 2\pi x / \lambda$ , where  $x$  is the displacement between the two arms. For lithography  $x$  is also the distance measured on the photographic plate or lithographic resist. If we compare the classical resolution to the N00N resolution we may write,  $\varphi_{N00N} = N\varphi_{\text{classical}}$ , which we can solve for

$$\lambda_{N00N} = \frac{\lambda_{\text{classical}}}{N} \quad (22)$$

Written this way, we can say the effective wavelength of the  $N$  photons bundled together  $N$  at a time into the N00N state is  $N$  times smaller than the classical wavelength. This is another way to understand the super-resolution effect. The  $N$  entangled photons conspire to behave as a single classical photon of a wavelength smaller by a factor of  $N$ .<sup>93</sup> Since the Rayleigh diffraction limit for lithography is couched in terms of the minimal resolvable distance  $\Delta x = \lambda_{\text{classical}}$ , then we have  $\Delta x_{N00N} = \lambda_{N00N} = \lambda_{\text{classical}} / N$ .

Another interesting application is so-called “ghost imaging.” This effect exploits the temporal and spatial correlations of photon pairs, also from spontaneous parametric down conversion, to image an object in one branch of the interferometer by looking at correlations in the coincidence counts of the photons.<sup>94</sup> There is no image in the single-photon counts in either arm, but only in the double photon counts in both arms. The image is in a sense stored nonlocally.

A particular application of this more general idea of quantum imaging has been seen in quantum coherence tomography.<sup>95</sup> In this experiment, they image a phase object placed in one arm of the interferometer, using entangled photons in an  $N = 2$  N00N state. They see not only the factor of two improvement in resolving power, predicted by Eq. (22), but also as a bonus they get a dispersion cancellation in the imaging system due to frequency entanglement between the photons.

Current experiments on N00N states have used rather dim sources of entangled photons, from UV pumped  $\chi^{(2)}$  crystals in a spontaneous parametric down conversion (SPDC) setup.<sup>96</sup> For bright sources of N00N states, one can turn to optical parametric amplifiers (OPA), which is the same setup as SPDC, but in which we crank up the pump power.<sup>97</sup> In this regime of high gain, the creation of entangled photon pairs of the form of Eq. (13) occurs, but we have many, many pairs and the output can be written

$$|\text{OPA}\rangle = \sum_{n=0}^{\infty} a_n |n\rangle_A |n\rangle_B \quad (23)$$

where the probability of a large twin-number state  $|N\rangle_A |N\rangle_B$  is given by  $|a_N|^2$ , which can be quite large in the limit of high pump powers. Passing the OPA state through a 50-50 beam splitter gives the generalized Hong-Ou-Mandel effect term by term, so that we get,

$$|\text{OPA}\rangle \xrightarrow{\text{BS}} \sum_{n=0}^{\infty} \sum_{m=0}^n c_{nm} |2n-2m\rangle |2m\rangle \quad (24)$$

where again the coefficients  $c_{nm}$  can be quite large for high pump powers. Taking the term  $n = 1$  we immediately get the  $N = 2$  N00N state from the regular Hong-Ou-Mandel effect. For larger  $n \geq 1$ , we find that there is always a large N00N component along with the non-N00N. For an  $N = 2$  absorber, the visibility of the  $N = 2$  N00N oscillations was predicted to saturate at a visibility of 20 percent.<sup>98,99</sup> This 20 percent visibility is more than enough to exploit for lithography and imaging, and has recently been measured in a recent experiment in the group of DeMartini in Rome,<sup>100</sup> in collaboration with our activity at Louisiana State University.

Current commercial lithography exploits extreme ultraviolet light of around 100 nm and plans are to go to x-ray in the future. The problem is that the lithography system for x-ray cannot use the same lenses, mirrors, and other imaging devices as did the optical system and so each reduction in wavelength involves a huge cost in technology and hardware investment. But what if we could etch 50-nm-sized features using 500-nm wavelength photons by exploiting quantum entanglement? This is the promise of quantum lithography. However, no real demonstration of quantum lithography has been had, so far, due to the N-photon resist problem.<sup>101</sup>

## 23.7 TOWARD QUANTUM REMOTE SENSING

Improvements in optical metrology and imaging have a natural application in the realm of optical remote sensing, such as in coherent optical laser interferometric radar (LIDAR) or in sensor miniaturization.<sup>102,103</sup> On the other hand, the group of Lloyd at MIT proposed a quantum optical clock synchronization protocol that eliminates the timing jitter of optical pulses that are transmitted through a fluctuating atmosphere.<sup>104</sup> These atmospheric fluctuations are currently the limiting source of noise in the global positioning system. Of course, when the N00N states propagating over distances of kilometers through the atmosphere, then photon scattering and loss and other issues such as atmospheric turbulence become an issue that are not apparent in a table top quantum interferometry demonstration.

The primary issue associated with photon loss is that the visibility of the interference pattern decreases, and that of the N00N state pattern decreases more rapidly than that of the single photon or coherent state interferometer. Hence, when the loss is sufficiently high, the slope of the N00N oscillations in Fig. 4 decreases to the point that, as far as super sensitivity is concerned, we do worse with N00N states than with either single photons or coherent states.<sup>105,106</sup> There are, however, Fock states that offer super resolution and sensitivity better than shot noise that degrade less quickly under loss than N00N states.<sup>107</sup> What we've termed M&M states, of the form

$$|m, m'\rangle \equiv |m, m'\rangle + |m', m\rangle \quad (25)$$

(where a normalization constant of  $1/\sqrt{2}$  has again been dropped for convenience) contain a trade-off of being more resilient to environmental decoherence, but having a greater minimum phase uncertainty of  $1/(m-m')$ .

In quantum optics, the photon loss (as well as the detector inefficiency) is modeled by a series of beam splitters.<sup>25</sup> In doing so, we first need to enlarge the Hilbert space to include the modes that represent the scattered photons and then, after the scattering, trace out those modes.<sup>107</sup> Here, instead of going into details, we use a simple (not necessarily correct) phase-shifter model and give a brief estimation of the loss effect. Consider Eq. (16), describing how coherent states and number states

behave upon passing through a phase shifter. The photon loss might be incorporated in the phase shifter by making the substitution  $\varphi \rightarrow \varphi + i\gamma$ , where  $\gamma$  is the rate at which photons are absorbed. We see then the effect of this loss in Eq. (16) is to produce an exponential loss factor that depends on  $N$ , for number states

$$|\alpha\rangle \xrightarrow{\varphi+i\gamma} |e^{-\gamma} e^{i\varphi} \alpha\rangle \quad (26a)$$

$$|N\rangle \xrightarrow{\varphi+i\gamma} e^{-N\gamma} e^{iN\varphi} |N\rangle \quad (26b)$$

Typically, we have  $\gamma = gL$ , where  $g$  is the loss per unit length and  $L$  the distance traveled through the lossy medium. The exponential dependence of the loss in the coherent (classical) state of Eq. (26a) is called Beer's law for optical absorption. We see that for  $N$ -photon number states, Eq. (26b), we have a super-exponential behavior, or what we call super-Beer's law. It implies that the  $N00N$  states are much more fragile in a lossy environment than a classical coherent state.

Of course, for the number states, such a simple phase-shifter model fails to describe the quantum states of the lesser number of photons, and we need to carry out the detailed analysis mentioned above. Will we then be able to overcome such fragility of the entangled states and achieve super sensitivity in remote sensing? We may have to seek an answer from the field of quantum computing—the tools to fight against decoherence such as quantum error correction or decoherence free subspace.<sup>108,109</sup>

Due to its “digital” nature, the entangled-number-state approach has recently benefited tremendously from an influx of ideas and experimental techniques originally developed in the context of all-optical “digital” quantum computing.<sup>110</sup> The idea is that an optical quantum computer is a giant optical quantum interferometer, where the quantum entanglement between photons is exploited to carry out mathematical calculations, which are impossible on any classical computer. However, in the proposed quantum interferometers the entanglement is exploited to make ultimate precise measurements not possible with any classical optical machine. The optical quantum computer can be turned into an optical quantum interferometric measuring device, and vice versa. Theoretical and experimental tricks, devised for the former, can be exploited in the latter. Since, for over the past 10 years, a lot of efforts have gone into the development of quantum computers, we are now able to leverage this research for quantum optical metrology, imaging, and sensing.

## 23.8 REFERENCES

1. H. Lee, P. Kok, and J. P. Dowling, “A Quantum Rosetta Stone for Interferometry,” *J. Mod. Opt.* **49**:2325 (2002).
2. V. Giovannetti, S. Lloyd, and L. Maccone, “Quantum-Enhanced Measurements: Beating the Standard Quantum Limit,” *Science* **306**:1330 (2004).
3. A. L. Migdall, “Absolute Quantum Efficiency Measurements Using Correlated Photons: Toward a Measurement Protocol,” *IEEE Trans. Instrum. Meas.* **50**:478 (2001).
4. A. Einstein, B. Podolsky, and N. Rosen, “Can Quantum-Mechanical Description of Physical Reality Be Considered Complete?” *Phys. Rev.* **47**:777 (1935).
5. N. Bohr, “Can Quantum-Mechanical Description of Physical Reality Be Considered Complete?” *Phys. Rev.* **48**:696 (1935).
6. E. Schrödinger, “Die gegenwärtige Situation in der Quantenmechanik,” *Die Naturwissenschaften* **2**:827 (1935).
7. R. F. Werner, “Quantum States with Einstein-Podolsky-Rosen Correlations Admitting a Hidden-Variable Model,” *Phys. Rev. A* **40**:4277 (1989).
8. J. S. Bell, “On the Einstein-Podolsky-Rosen Paradox,” *Physics* **1**:195 (1964).
9. M. Genovese, “Research on Hidden Variable Theories: A Review of Recent Progresses,” *Phys. Rep.* **413**:319 (2005).

10. J. S. Bell, "On the Problem of Hidden Variables in Quantum Mechanics," *Rev. Mod. Phys.* **38**:447 (1966).
11. J. F. Clauser, M. A. Horne, A. Shimony, and R. A. Holt, "Proposed Experiment to Test Local Hidden-Variable Theories," *Phys. Rev. Lett.* **23**:880 (1969).
12. N. Gisin and A. Peres, "Maximal Violation of Bell's Inequality for Arbitrary Large Spin," *Phys. Lett. A* **162**:15 (1992).
13. S. Popescu and D. Rohrlich, "Generic Quantum Nonlocality," *Phys. Lett. A* **166**:293 (1992).
14. S. J. van Enk, "Single-Particle Entanglement," *Phys. Rev. A* **72**:064306 (2005).
15. B. Hessmo, P. Usachev, H. Heydari, and G. Björk, "Experimental Demonstration of Single Photon Nonlocality," *Phys. Rev. Lett.* **92**:180401 (2004).
16. S. A. Babichev, J. Appel, and A. I. Lvovsky, "Homodyne Tomography Characterization and Nonlocality of a Dual-Mode Optical Qubit," *Phys. Rev. Lett.* **92**:193601 (2004).
17. M. D'Angelo, A. Zavatta, V. Parigi, and M. Bellini, "Tomographic Test of Bell's Inequality for a Time-Delocalized Single Photon," *Phys. Rev. A* **74**:052114 (2006).
18. C. F. Wildfeuer, A. P. Lund, and J. P. Dowling, "Strong Violations of Bell-Type Inequalities for Path-Entangled Number States," *Phys. Rev. A* **76**:052101 (2007).
19. M. Born and E. Wolf, *Principles of Optics*, 7th ed., Cambridge University Press, Cambridge (2002).
20. J. Fraden, *Handbook of Modern Sensors*, Springer-Verlag, Berlin (1996).
21. M. O. Scully and M. S. Zubairy, *Quantum Optics*, Cambridge University Press, Cambridge (1997).
22. C. C. Gerry and P. L. Knight, *Introductory Quantum Optics*, Cambridge University Press, Cambridge (2005).
23. P. A. M. Dirac, "The Quantum Theory of the Emission and Absorption of Radiation," *Proc. Roy. Soc. A* **114**:243 (1927).
24. W. Heitler, *The Quantum Theory of Radiation*, Oxford University Press, Oxford (1954).
25. R. Loudon, *The Quantum Theory of Light*, Oxford University Press, Oxford (2000).
26. C. M. Caves, "Quantum Mechanical Noise in an Interferometer," *Phys. Rev. D* **23**:1693 (1981).
27. D. Walls, "Squeezed States of Light," *Nature* **306**:141 (1983).
28. M. Xiao, L.-A. Wu, and H. J. Kimble, "Precision Measurement beyond the Shot-Noise Limit," *Phys. Rev. Lett.* **59**:278 (1987).
29. P. Grangier, R. E. Slusher, B. Yurke, and A. La Porta, "Squeezed-Light-Enhanced Polarization Interferometer," *Phys. Rev. Lett.* **59**:2153 (1987).
30. R. Loudon and P. L. Knight, "Squeezed Light," *J. Mod. Opt.* **34**:709 (1987).
31. A. S. Lane, S. L. Braunstein, and C. M. Caves, "Maximum-Likelihood Statistics of Multiple Quantum Phase Measurements," *Phys. Rev. A* **47**:1667 (1993).
32. Z. Y. Ou, "Complementarity and Fundamental Limit in Precision Phase Measurement," *Phys. Rev. Lett.* **77**:2352 (1996).
33. V. V. Dodonov, "Nonclassical States in Quantum Optics: A Squeezed Review of the First 75 Years," *J. Opt. B* **4**:R1 (2002).
34. T. Corbitt and N. Mavalvala, "Quantum Noise in Gravitational-Wave Interferometers," *J. Opt. B* **6**:S675 (2004).
35. H.-A. Bachor and T. C. Ralph, *A Guide to Experiments in Quantum Optics*, 2nd ed., Wiley-VCH, Berlin (2004).
36. H. J. Kimble, Y. Levin, A. B. Matsko, K. S. Thorne, and S. P. Vyatchanin, "Conversion of Conventional Gravitational-Wave Interferometers into Quantum Nondemolition Interferometers by Modifying Their Input and/or Output Optics," *Phys. Rev. D* **65**:022002 (2001).
37. B. Yurke, "Input States for Enhancement of Fermion Interferometer Sensitivity," *Phys. Rev. Lett.* **56**:1515 (1986).
38. B. Yurke, S. L. McCall, and J. R. Klauder, "SU(2) and SU(1,1) Interferometers," *Phys. Rev. A* **33**:4033 (1986).
39. H. P. Yuen, "Generation, Detection, and Application of High-Intensity Photon-Number-Eigenstate Fields," *Phys. Rev. Lett.* **56**:2176 (1986).
40. J. P. Dowling, "Correlated Input-Port, Matter-Wave Interferometer: Quantum-Noise Limits to the Atom-Laser Gyroscope," *Phys. Rev. A* **57**:4736 (1998).

41. M. Hillery and L. Mlodinow, "Interferometers and Minimum-Uncertainty States" *Phys. Rev. A* **48**:1548 (1993).
42. C. Brif and A. Mann, "Nonclassical Interferometry with Intelligent Light," *Phys. Rev. A* **54**:4505 (1996).
43. M. J. Holland and K. Burnett, "Interferometric Detection of Optical Phase Shifts at the Heisenberg Limit," *Phys. Rev. Lett.* **71**:1355 (1993).
44. P. Bouyer and M. A. Kasevich, "Heisenberg-Limited Spectroscopy with Degenerate Bose-Einstein Gases," *Phys. Rev. A* **56**:R1083 (1997).
45. J. A. Dunningham, K. Burnett, and S. M. Barnett, "Interferometry below the Standard Quantum Limit with Bose-Einstein Condensates," *Phys. Rev. Lett.* **89**:150401 (2002).
46. S. M. Barnett and D. T. Pegg, "On Hermitian Optical Phase Operator," *J. Mod. Opt.* **36**:7 (1989).
47. Z. Hradil, "Estimation of Counted Quantum Phase," *Phys. Rev. A* **51**:1870 (1995).
48. B. C. Sanders and G. J. Milburn, "Optimal Quantum Measurements for Phase Estimation," *Phys. Rev. Lett.* **75**:2944 (1995).
49. D. W. Berry and H. M. Wiseman, "Optimal States and Almost Optimal Adaptive Measurements for Quantum Interferometry," *Phys. Rev. Lett.* **85**:5098 (2000).
50. L. Pezze and A. Smerzi, "Phase Sensitivity of a Mach-Zehnder Interferometer," *Phys. Rev. A* **73**:011801(R) (2006).
51. H. Uys and P. Meystre, "Quantum States for Heisenberg-Limited Interferometry," *Phys. Rev. A* **76**:013804 (2007).
52. G. A. Durkin and J. P. Dowling, "Local and Global Distinguishability in Quantum Interferometry," *Phys. Rev. Lett.* **99**:070801 (2007).
53. T. Kim, O. Pfister, M. J. Holland, J. Noh, and O. L. Hall, "Quantum States for Heisenberg-Limited Interferometry," *Phys. Rev. A* **57**:4004 (1998).
54. A. Kuzmich and L. Mandel, "Sub-Shot-Noise Interferometric Measurements with Two-Photon States," *Quantum Semicl. Opt.* **10**:493 (1998).
55. R. A. Campos, C. C. Gerry, and A. Benmoussa, "Optical Interferometry at the Heisenberg Limit with Twin Fock States and Parity Measurements," *Phys. Rev. A* **68**:023810 (2003).
56. R. C. Pooser and O. Pfister, "Particle-Number Scaling of the Phase Sensitivity in Realistic Bayesian Twin-Mode Heisenberg-Limited Interferometry," *Phys. Rev. A* **69**:043616 (2004).
57. F. W. Sun, B. H. Liu, Y. X. Gong, Y. F. Huang, Z. Y. Ou, and G. C. Guo, "Experimental Demonstration of Phase Measurement Precision Beating Standard Quantum Limit by Projection Measurement," *Europhys. Lett.* **82**:24001 (2008).
58. B. C. Sanders, "Quantum Dynamics of the Nonlinear Rotator and the Effects of Continual Spin Measurement," *Phys. Rev. A* **40**:2417 (1989).
59. A. N. Boto, P. Kok, D. S. Abrams, S. L. Braunstein, C. P. Williams, and J. P. Dowling, "Quantum Interferometric Optical Lithography: Exploiting Entanglement to Beat the Diffraction Limit," *Phys. Rev. Lett.* **85**:2733 (2000).
60. C. K. Hong, Z. Y. Ou, and L. Mandel, "Measurement of Subpicosecond Time Intervals between Two Photons by Interference," *Phys. Rev. Lett.* **59**:2044 (1987).
61. C. C. Gerry and R. A. Campos, "Generation of Maximally Entangled Photonic States with a Quantum-Optical Fredkin Gate," *Phys. Rev. A* **64**:063814 (2001).
62. G. J. Milburn, "Quantum Optical Fredkin Gate," *Phys. Rev. Lett.* **62**:2124 (1989).
63. N. Imoto, H. A. Haus, and Y. Yamamoto, "Quantum Nondemolition Measurement of the Photon Number via Optical Kerr Effect," *Phys. Rev. A* **32**:2287 (1985).
64. M. Kitagawa and Y. Yamamoto, "Number-Phase Minimum-Uncertainty States with Reduced Number Uncertainty in a Kerr Nonlinear Interferometer," *Phys. Rev. A* **34**:3974 (1986).
65. P. Kok, H. Lee, and J. P. Dowling, "Single-Photon Quantum Nondemolition Detectors Constructed with Linear Optics and Projective Measurements," *Phys. Rev. A* **66**:063814 (2002).
66. Q. A. Turchette, C. J. Hood, W. Lange, H. Mabuchi, and H. J. Kimble, "Measurement of Conditional Phase-Shifts for Quantum Logic," *Phys. Rev. Lett.* **75**:4710 (1995).
67. H. Schmidt and A. Imamoglu, *Opt. Lett.* **21**:1936 (1996).



68. M. D. Lukin, "Trapping and Manipulating Photon States in Atomic Ensembles," *Rev. Mod. Phys.* **75**:457 (2003).
69. M. Fleischhauer, A. Imamoglu, and J. Marangos, "Electromagnetically Induced Transparency: Optics in Coherent Media," *Rev. Mod. Phys.* **77**:633 (2005).
70. E. Knill, R. Laflamme, and G. J. Milburn, "A Scheme for Efficient Quantum Computation with Linear Optics," *Nature* **409**:46 (2001).
71. H. Lee, P. Kok, and J. P. Dowling, "From Linear Optical Quantum Computing to Heisenberg-Limited Interferometry," *J. Opt. B* **6**:S769 (2004).
72. H. Lee, P. Kok, N. J. Cerf, and J. P. Dowling, "Linear Optics and Projective Measurements Alone Suffice to Create Large-Photon-Number Path Entanglement," *Phys. Rev. A* **65**:030101(R) (2002).
73. P. Kok, H. Lee, and J. P. Dowling, "Creation of Large-Photon-Number Path Entanglement Conditioned on Photodetection," *Phys. Rev. A* **65**:052104 (2002).
74. J. Fiurasek, "Conditional Generation of  $n$ -Photon Entangled States of Light," *Phys. Rev. A* **65**:053818 (2002).
75. H. Cable and J. P. Dowling, "Efficient Generation of Large Number-Path Entanglement Using Only Linear Optics and Feed-Forward," *Phys. Rev. Lett.* **99**:163604 (2007).
76. K. T. Kapale and J. P. Dowling, "Bootstrapping Approach for Generating Maximally Path-Entangled Photon States," *Phys. Rev. Lett.* **99**:053602 (2007).
77. N. M. VanMeter, P. Lougorski, D. B. Uskor, K. Kiding, J. Eisert, and J. P. Dowling, "General Linear-Optical Quantum State Generation Scheme: Applications to Maximally Path-Entangled States," *Phys. Rev. A* **76**:063808 (2007).
78. E. J. S. Fonseca, C. H. Monken, and S. Padua, "Measurement of the de Broglie Wavelength of a Multiphoton Wave Packet," *Phys. Rev. Lett.* **82**:2868 (1999).
79. M. D'Angelo, M. V. Chekhova, and Y. Shih, "Two-Photon Diffraction and Quantum Lithography," *Phys. Rev. Lett.* **87**:013602 (2001).
80. D. Bouwmeester, "High N00N for Photons," *Nature* **429**:139 (2004).
81. P. Walther, J. W. Pan, M. Aspelmeyer, R. Ursin, S. Gasparoni, and A. Zeilinger, "De Broglie Wavelength of a Non-Local Four-Photon State," *Nature* **429**:158 (2004).
82. M. W. Mitchell, J. S. Lundeen, and A. M. Steinberg, "Super-Resolving Phase Measurements with a Multiphoton Entangled State," *Nature* **429**:161 (2004).
83. J. J. Bollinger, W. M. Itano, and D. J. Wineland, "Optimal Frequency Measurements with Maximally Correlated States," *Phys. Rev. A* **54**:R4649 (1996).
84. D. Leibfried, M. D. Barrett, T. Schaetz, J. Britton, J. Chiaverini, W. M. Itano, J. D. Jost, C. Langer, and D. J. Wineland, "Toward Heisenberg-Limited Spectroscopy with Multiparticle Entangled States," *Science* **304**:1476 (2004).
85. D. Leibfried, E. Knill, S. Seidelin, J. Britton, R. B. Blakestad, J. Chiaverini, D. B. Hume, et al., "Creation of a Six-Atom Schrödinger Cat State," *Nature* **438**:639 (2005).
86. K. J. Resch, K. L. Pregnell, R. Prevedel, A. Glichrist, G. J. Pryde, J. L. O'Brien and A. G. White, "Time-Reversal and Super-Resolving Phase Measurements," *Phys. Rev. Lett.* **98**:223601 (2007).
87. T. Nagata, R. Okamoto, J. L. O'Brien, K. Sasaki, and S. Takeuchi, "Beating the Standard Quantum Limit with Four-Entangled Photons," *Science* **316**:726 (2007).
88. J. L. O'Brien, "Precision without Entanglement," *Science* **318**:1393 (2007).
89. J. P. Dowling, "Kittens Catch Phase," *Nature* **450**:362 (2007).
90. B. L. Higgins, D. W. Berry, J. D. Bartlett, H. M. Wiseman, and G. J. Pryde, "Entanglement-Free Heisenberg-Limited Phase Estimation," *Nature* **450**:393 (2007).
91. L. A. Lugiato, A. Gatti, E. Brambilla, "Quantum Imaging," *J. Opt. B* **4**:S176 (2002).
92. J. P. Dowling, A. Gatti, and A. Sergienko, "Special Issue: Quantum Imaging," *J. Mod. Opt.* **53**:(5–6) (2006).
93. J. Jacobson, G. Bjork, I. Chuang, and Y. Yamamoto, "Photonic de Broglie Waves," *Phys. Rev. Lett.* **74**:4835 (1995).
94. Y. Shih, "Quantum Imaging," *IEEE J. Sel. Top. Quantum Electron.* **13**:1016 (2007).
95. M. B. Nasr, B. E. A. Saleh, A. V. Sergienko, and M. C. Teich, "Demonstration of Dispersion-Canceled Quantum-Optical Coherence Tomography," *Phys. Rev. Lett.* **91**:083601 (2003).

96. J. G. Rarity, P. R. Tapster, E. Jakeman, T. Larchuk, R. A. Campos, M. C. Teich, and B. E. A. Saleh, "Two-Photon Interference in a Mach-Zehnder Interferometer," *Phys. Rev. Lett.* **65**:1348 (1990).
97. R. W. Boyd, *Nonlinear Optics*, 2nd ed., Academic Press, San Diego (2003).
98. E. M. Nagasako, S. J. Bently, R. W. Boyd, G. S. Agarwal, "Nonclassical Two-Photon Interferometry and Lithography with High-Gain Parametric Amplifiers," *Phys. Rev. A* **64**:043802 (2001).
99. G. S. Agarwal, K. W. Chan, R. W. Boyd, H. Cable, and J. P. Dowling, "Quantum States of Light Produced by a High-Gain Optical Parametric Amplifier for Use in Quantum Lithography," *J. Opt. Soc. Am. B* **24**:270 (2007).
100. F. Scarrino, C. Vitelli, F. DeMartini, R. Glasser, H. Cable, and J. P. Dowling, "Experimental Sub-Rayleigh Resolution by an Unseeded High-Gain Optical Parametric Amplifier for Quantum Lithography," *Phys. Rev. A* **77**:012324 (2008).
101. H. J. Chang, H. Shin, M. N. O'Sullivan-Hale, and R. W. Boyd, "Implementation of Sub-Rayleigh-Resolution Lithography Using an  $n$ -Photon Absorber," *J. Mod. Opt.* **53**:2271 (2006).
102. K. T. Kapale, L. D. DiDomenico, H. Lee, P. Kok and J. P. Dowling, "Quantum Interferometric Sensors," *Concepts of Physics* **2**:225 (2005).
103. G. Gilbert, M. Hamrick, and Y. S. Weinstein, "Quantum Sensor Miniaturization," *IEEE Photon. Tech. Lett.* **19**:1798 (2007).
104. V. Giovannetti, S. Lloyd, L. Maccone, and F. N. C. Wong, "Clock Synchronization with Dispersion Cancellation," *Phys. Rev. Lett.* **87**:117902 (2001).
105. G. Gilbert, M. Hamrick, and Y. S. Weinstein, "On the Use of Photonic N00N States for Practical Quantum Interferometry," *J. Opt. Soc. Am. B* **25**:1336 (2008).
106. M. A. Rubin and S. Kaushik, "Loss-Induced Limits to Phase Measurement Precision with Maximally Entangled States," *Phys. Rev. A* **75**:053805 (2007).
107. S. D. Huver, C. F. Wildfeuer, and J. P. Dowling, "Entangled Fock States for Robust Quantum Optical Sensors," *Phys. Rev. A* **78**:063828 (2008).
108. P. G. Kwiat, A. J. Berglund, J. B. Altepeter, and A. G. White, "Experimental Verification of Decoherence-Free Subspace," *Science* **290**:498 (2000).
109. M. A. Nielsen and I. L. Chuang, *Quantum Computation and Quantum Information*, Cambridge University Press, Cambridge (2000).
110. P. Kok, W. J. Munro, K. Memoto, T. C. Ralph, J. P. Dowling and G. J. Milburn, "Linear Optical Quantum Computing with Photonic Qubits," *Rev. Mod. Phys.* **79**:135 (2007).

*This page intentionally left blank*

---

# INDEX

---

*Index note:* The *f* after a page number refers to a figure, the *n* to a note, and the *t* to a table.

- Abbe number, 2.23, 2.28, 2.29*f*  
Aberration control, 3.8  
Above threshold ionization (ATI), 21.14–21.17  
  plateau extension of, 21.19  
  quasi-classical, 21.16–21.17, 21.16*f*  
  relativistic electron, 21.20, 21.21*f*  
  strong field interactions with atoms,  
    21.14–21.17, 21.15*f*, 21.16*f*  
Abrasion resistance, of antireflection coatings,  
  7.31–7.32, 7.32*f*  
Abrasive forming, polymer, 3.11–3.12  
Absorbance, water, 1.10  
Absorbers:  
  black, 7.104  
  saturable, 18.5–18.11  
    fast, 18.9–18.10  
    self-amplitude modulation, 18.5–18.7,  
      18.6*f*, 18.7*f*  
    semiconductor saturable absorber mirrors,  
      18.3, 18.10–18.11  
    slow, 18.7–18.9, 18.8*f*  
Absorbing compounds (in black surfaces), 6.15  
Absorbing media:  
  antireflection coatings for, 7.26, 7.27  
  in multilayer reflectors, 7.37–7.38, 7.38*f*  
Absorptance:  
  of metals, 4.6, 4.39, 4.40*f*–4.42*f*, 4.48, 4.49  
  and emittance, 4.49, 4.49*f*, 4.50*t*, 4.51*t*  
  and mass attenuation coefficients for  
    photons, 4.48*t*  
  of optical coatings, 7.12–7.13  
  of water, 1.5*t*, 1.9  
Absorption:  
  bio-optical models for, 1.27–1.29,  
    1.27*f*, 1.28*t*  
  cutoff filters based on, 7.60, 7.60*f*  
  defect-related, 5.37–5.39, 5.38*f*, 5.39*f*  
  by detritus in water, 1.26–1.27  
  in dielectrics, 4.4  
  Absorption (*Cont.*):  
    direct interband, 8.27–8.28  
    by dissolved organic matter, 1.22–1.23, 1.23*t*  
    fundamental edge of (*see* Fundamental  
      absorption edge)  
    impurity-related, 5.37–5.39, 5.38*f*, 5.39*f*,  
      5.51–5.52, 5.51*f*  
    interband (*see* Interband absorption)  
    lattice, 5.13–5.20, 5.15*f*, 5.17*t*, 5.18*f*–5.19*f*,  
      5.20*t*, 5.21*f*  
    of light in laser cooling, 20.4  
    magnetoabsorption, 5.51–5.52, 5.51*f*  
    measurement of, 5.64  
    in multilayer reflectors, 7.40–7.41, 7.41*f*  
    multiphonon, 5.16–5.17, 5.17*t*, 5.18*f*  
    nonlinear, 16.7–16.9  
    by organic detritus, 1.25–1.27, 1.25*t*, 1.26*f*  
    in overdense plasmas, 21.47–21.48, 21.47*f*  
    phonon, 5.13–5.16, 5.15*f*  
    by phytoplankton, 1.23–1.25, 1.24*f*–1.25*f*  
    resonance, 21.47–21.48, 21.47*f*  
    by sea water, 1.21, 1.22*t*  
    in solids, 8.27–8.28  
    spectral, 1.26–1.27, 1.26*f*  
    superlinear, 5.57  
    two-photon, 5.56  
    by water, 1.20–1.29  
  Absorption coefficient(s), 1.23*t*  
    for optical constants, 5.9–5.10  
    spectral  
      of natural waters, 1.27*f*  
      for phytoplankton, 1.24, 1.24*f*,  
        1.25*f*, 1.25*t*  
    of water, 1.5*t*, 1.7*f*, 1.10, 1.17, 1.18*t*  
    natural water, 1.20–1.21  
    sea water, 1.21, 1.22*t*  
  Absorption coefficient dependence, 5.20, 5.21*f*  
  Absorption saturation, 16.21–16.22, 16.21*f*  
  Absorption spectrum, 5.12, 22.6, 22.6*f*, 22.7*f*

- Absorption transitions:  
 direct interband, 5.22–5.23, 5.22f–5.23f, 5.25f  
 indirect, 5.22–5.24, 5.24f–5.25f
- ac Stark effect, 16.3t, 16.7
- Acceleration:  
 bubble, 21.41–21.42, 21.42f  
 direct laser, 21.43  
 electron, 21.39–21.42, 21.40f  
 MeV proton, 21.54, 21.54f  
 plasma beat wave, 21.41  
 target normal sheath, 21.54
- Accordion solutions, 15.28
- Achromatic antireflection coatings, 7.29
- Achromatic beam splitters, 7.62–7.65, 7.62f–7.65f
- Acktar black coatings, 6.55
- Acoustic optical modulators (AOMs), 14.19, 20.13
- Acoustic phonons, 5.14–5.16
- Active nonlinear optical phenomena, 5.54, 5.54t
- Active optical limiting, 13.1–13.3
- Adachi dispersion model, 2.15, 2.22
- Additive pulse modelocking (APM), 18.3, 18.14
- Additives, polymers as, 3.5
- Adiabatic ionization stabilization, 21.20,  
 21.21, 21.22f
- Adiabatic potentials, 21.23, 21.24f
- Aerogels, 6.15
- Aeroglaze Z series, 6.36f, 6.37, 6.37f, 6.39,  
 6.39f–6.42f
- Aeroglaze Z302, 6.14
- Aeroglaze Z306, 6.14, 6.17, 6.29f, 6.35
- Akzo (company), 6.14
- Akzo Nobel paints, 6.39, 6.42f, 6.43f
- All-dielectric color selective (dichroic) beam  
 splitters, 7.65–7.66, 7.67f
- All-dielectric reflectors:  
 broadband, 7.39, 7.40f, 7.45–7.47, 7.45f–7.47f  
 interference filters with, 7.81
- Altaite (PbTe), 2.40t, 2.44t, 2.48t, 2.52t, 2.57t,  
 2.64t, 2.69t
- Alumina (Al<sub>2</sub>O<sub>3</sub>), 2.38t, 2.46t, 2.47t, 2.50t,  
 2.55t, 2.60t, 2.70t, 2.76t
- Aluminum:  
 absorptance of, 4.40f, 4.48t, 4.51t  
 anodized, 6.5f, 6.38f, 6.58f  
 black velvet cloth on, 6.31f  
 commando cloth on, 6.31f  
 flame-sprayed, 6.57  
 grooved and blazed, 6.21, 6.24f, 6.25f  
 optical constants for, 4.11  
 optical properties of, 4.12t, 4.20f, 4.21f
- Aluminum (*Cont.*):  
 penetration depth of, 4.47f  
 physical properties of, 4.52t, 4.54t  
 reflectance of, 4.27t–4.28t, 4.40f, 4.44f, 4.46f  
 roughened, 6.21, 6.22f, 6.30f  
 sandblasted, 6.45f  
 thermal properties of  
 coefficient of linear thermal expansion,  
 4.56t, 4.57f  
 elastic properties, 4.69t  
 at room temperature, 4.55t  
 specific heat, 4.65t, 4.66f  
 strength and fracture properties, 4.70t  
 thermal conductivity, 4.58t, 4.59f–4.60f  
 and UV light, 6.21
- Aluminum alloys:  
 reflectance of, 4.44f  
 thermal conductivity of, 4.59f–4.60f
- Aluminum mirrors, 7.106–7.108, 7.106f–7.108f
- Aluminum oxynitride (Al<sub>23</sub>O<sub>27</sub>N<sub>3</sub>) (ALON),  
 2.38t, 2.44t, 2.47t, 2.50t, 2.55t, 2.60t, 2.76t
- American Society for Testing and Materials  
 (ASTM), 6.17
- Ames 24E, 6.7f, 6.26, 6.26f, 6.27f, 6.34
- Ames 24E2, 6.27f, 6.28f, 6.34
- Ames Perfect Diffuse Reflector, 6.7f
- Ames Research Center, 6.34
- Ammonium phosphate (NH<sub>4</sub>H<sub>2</sub>PO<sub>4</sub>, ADP),  
 2.40t, 2.45t, 2.48t, 2.52t, 2.57t, 2.64t
- Ammosoc-Delone-Krainov (ADK) ionization  
 rate, 21.13
- Amorphous materials, 2.5, 12.26t [*See also*  
 Glass(es)]
- Ampere law, 2.6
- Amplifiers:  
 flashlamp pumped Nd:glass, 21.5  
 lock-in, 5.64  
 optical parametric, 23.13–23.14  
 Raman, 15.4, 15.4f, 22.15  
 Ti:sapphire, 21.5
- Amplifying media, antireflection coatings  
 for, 7.26, 7.27
- AMTIR-1 glass, 2.43t, 2.49t, 2.54t, 2.59t, 2.68t
- AMTIR-3 glass, 2.43t, 2.49t, 2.54t, 2.59t, 2.68t  
 -ance suffix, 4.5
- Angle-of-incidence effects, for cutoff filters,  
 7.56
- Angular distribution, 1.12, 21.8–21.9, 21.9f
- Angular sensitivity, in two-material periodic  
 multilayers theory, 7.37

- Anharmonic oscillator model, of second-order nonlinear optical susceptibility, **10.7–10.9, 10.8f**
- Anisotropic crystals, propagation of light and, **8.8–8.11, 8.9t, 8.10f**
- Anisotropic scattering, **12.7**
- Annealing:  
of glass, **2.28**  
of optical surfaces, **19.3**
- Anodized aluminum surface, **6.5f, 6.38f, 6.58f**
- Anodized surface treatments, **6.44–6.49**  
(See also *specific anodized treatments, e.g.: Martin Black*)
- Anodized surfaces, **6.3t**
- Anomalous (negative) dispersion, **4.4, 18.11**
- Anomalous skin effect, **21.49**
- Antimony flint glass, **2.43t**
- Antireflection (AR) coatings, **7.15–7.32**  
of absorbing and amplifying media, **7.26, 7.27**  
homogeneous-layer, **7.16–7.23, 7.17f–7.19f, 7.20t–7.21t, 7.22f–7.23f**  
inhomogeneous and structured, **7.23–7.26, 7.24f, 7.26f**  
at nonnormal angle of incidence, **7.28–7.31, 7.28f–7.31f**  
nonoptical properties of, **7.31–7.32, 7.32f**  
surface reflections and optical performance, **7.15–7.16, 7.16f**  
of surfaces carrying thin films, **7.27–7.28, 7.28f**  
universal, **7.26, 7.27f**
- Antiresonant Fabry-Perot saturable absorber (A-FPSA), **18.3, 18.11**
- Anti-Stokes four-wave mixing, coherent, **15.2t, 15.3t, 15.4, 15.4f**
- Anti-Stokes scattering, **15.1–15.3, 15.3t**  
coherent Raman, **15.4, 15.4f, 15.34, 15.42, 15.42t, 15.43f**  
multiple, **15.2f**  
Raman, **15.32–15.34, 15.33f, 15.35f**  
shifted Raman, **16.15, 16.15f**  
stimulated Raman, **15.2t**
- Anti-Stokes shift, **15.2, 15.43**
- Anti-Stokes wave, **15.1, 15.43**
- APART (stray light analysis program), **6.19**
- Apparent optical properties (AOPs), of water, **1.4, 1.5t–1.6t, 1.12–1.13**
- Appiqués, black, **6.15**
- Arsenic antisite ( $As_{Ga}$ ), **18.3**
- Arsenic triselenide glass, **2.43t, 2.49t, 2.54t, 2.59t**
- Arsenic trisulfide glass, **2.43t, 2.49t, 2.54t, 2.59t**
- ASP (stray light analysis program), **6.19**
- Aspheric surfaces, **3.8–3.9**
- Assembly of polymers, mechanical, **3.14–3.16, 3.14f, 3.15f**
- Associative memory, optical, **12.34**
- Athermal glasses, **2.26**
- Athermalization, **3.9**
- Atom interferometry, **11.22–11.23, 11.24f**
- Atomic beams:  
brightening of, **20.27–20.28, 20.27f**  
collimation of, **20.15–20.16, 20.15f**  
slowing of, **20.11–20.13, 20.12f, 20.12t, 20.13f**
- Atomic clocks, **20.28**
- Atomic coherence, maximal, **14.28–14.32, 14.29f–14.32f**
- Atomic funnels, **20.27**
- Atomic ionization, **21.3**
- Atomic layer deposition, **7.11**
- Atomic oxygen, black surfaces and, **6.16–6.17**
- Atomic resonance, **22.2–22.9, 22.3f**  
about, **22.2–22.5, 22.3f**  
double, **22.5–22.9**  
features of, **22.5–22.6, 22.6f**  
tunable double resonance, **22.6–22.9, 22.7f, 22.8f**
- Atomic systems, coherence in, **14.4–14.5, 14.4f**
- Atom-laser interactions:  
applications of, **20.26–20.39**  
atomic beam brightening, **20.27–20.28, 20.27f**  
atomic clocks, **20.28**  
Bose-Einstein condensation, **20.35–20.37, 20.36f**  
dark states, **20.37–20.39, 20.38f**  
optical lattices, **20.31–20.34, 20.32f–20.34f**  
ultracold collisions, **20.28–20.31, 20.30f, 20.31f**  
cooling atoms with, **20.3–20.21**  
below Doppler limit, **20.17–20.21, 20.18f–20.20f**  
history of, **20.3–20.4**  
optical molasses, **20.13–20.17, 20.14f–20.16f**  
properties of lasers, **20.4–20.6**  
slowing atomic beams, **20.11–20.13, 20.12f, 20.12t, 20.13f**  
theoretical description, **20.6–20.11, 20.9f**  
trapping atoms with, **20.21–20.39**  
magnetic traps, **20.21–20.23, 20.22f**  
magneto-optical traps, **20.24–20.25, 20.24f, 20.26f**  
optical traps, **20.23–20.24, 20.23f**

- Atoms (generally):  
 in motion, 20.8–20.10, 20.9f  
 trapping of neutral (*see* Trapping atoms)  
 two-level, 20.6–20.8
- Atoms, strong field interactions with, 21.10–21.21  
 above threshold ionization, 21.14–21.17,  
 21.15f, 21.16f  
 ionization stabilization, 21.20–21.21, 21.22f  
 Keldysh parameter, 21.10  
 multiphoton and quasi-classical regimes,  
 21.10  
 multiphoton ionization, 21.10–21.12, 21.11f  
 relativistic effects, 21.19–21.20, 21.21f  
 rescattering effects, 21.18–21.19, 21.18f, 21.19f  
 tunnel ionization, 21.12–21.14, 21.12f, 21.14f
- Attenuation, in water:  
 beam, 1.40–1.41, 1.41f, 1.42f  
 diffuse and Jerlov water types, 1.42–1.46,  
 1.43t–1.45t, 1.44f, 1.45f
- Attenuation functions, of water, 1.13
- Attenuators, neutral, 7.105, 7.105f
- Attosecond pulse generation, 21.31
- Axial thickness, of polymers, 3.10
- Backward Raman amplifiers, 15.4, 15.4f
- Backward Raman generators, 15.4, 15.4f
- Backward Raman scattering, 15.41, 21.38f,  
 21.39
- Bacteria, in water, 1.14
- Baffle surfaces:  
 design of, 6.19  
 in extreme environments, 6.18  
 selection process for black, 6.10–6.12,  
 6.10f–6.11f, 6.12t–6.13t
- Ball Black, 6.5f, 6.6f, 6.50, 6.51f, 6.53f
- Band structures:  
 defined, 9.3  
 of solids, 8.24–8.27, 8.26f
- Bandpass filters, 7.73–7.96  
 about, 7.73, 7.77–7.78, 7.77f–7.78f  
 angular properties of, 7.91–7.94, 7.92f, 7.93f  
 with multiple peaks, 7.90, 7.91f  
 narrow- and medium-, 7.78–7.83, 7.79f,  
 7.80f, 7.82f–7.88f  
 nonpolarizing, 7.66, 7.67f  
 square-top multicavity, 7.82–7.83, 7.82f–7.88f  
 stability and temperature dependence of, 7.94  
 very narrow, 7.83, 7.88–7.89, 7.89f  
 wedge filters, 7.90, 7.91, 7.91f  
 wide, 7.90, 7.90f
- Bandpass filters (*Cont.*):  
 wide-angle, 7.93–7.94, 7.93f  
 for XUV and x-ray regions, 7.94–7.96,  
 7.95f–7.96f
- Bare states, 14.3
- Barium beta borate (BBO), 2.38t, 2.46t, 2.47t,  
 2.50t, 2.55t, 2.60t, 2.75t, 17.1, 18.12
- Barium beta borate (BBO) optical parametric  
 oscillators, 10.18, 10.19f
- Barium crown glass, 2.41t
- Barium dense flint glass, 2.42t
- Barium flint glass, 2.42t
- Barium fluoride (BaF<sub>2</sub>), 2.38t, 2.44t, 2.47t,  
 2.50t, 2.55t, 2.60t, 2.69t, 2.76t
- Barium titanate (BaTiO<sub>3</sub>), 2.38t, 2.44t, 2.47t,  
 2.55t, 2.76t, 12.13t, 12.14–12.16, 12.16f
- Barrier suppression ionization (BSI), 21.14, 21.14f
- Barrier suppression ionization thresholds,  
 21.26, 21.27f
- Beam attenuation, in water, 1.13, 1.40–1.41,  
 1.41f, 1.42f
- Beam attenuation coefficient, 1.7f, 1.10
- Beam cleanup, 12.30
- Beam propagation, split-step, 12.10
- Beam splitters (BSs), 7.61–7.67, 7.62f–7.68f,  
 23.2, 23.2f, 23.14
- Beam walkoff time, 15.30
- Beating (phenomena), 18.19
- Beer's law, 8.7, 8.28
- Beryllium:  
 absorptance of, 4.48t, 4.50t  
 optical constants for, 4.11  
 optical properties of, 4.12t, 4.21f, 4.26f  
 penetration depth of, 4.47f  
 physical properties of, 4.52t, 4.54t  
 reflectance of, 4.28t–4.29t, 4.45f, 4.46f  
 thermal properties of  
 coefficient of linear thermal expansion,  
 4.56t, 4.57f  
 elastic properties, 4.69t  
 at room temperature, 4.55t  
 specific heat, 4.65t, 4.68f  
 strength and fracture properties, 4.70t  
 thermal conductivity, 4.58t, 4.59f–4.60f
- Beryllium surfaces, 6.51, 6.52, 6.53f, 6.58f
- Beta cloth, 6.57, 6.58f
- Betatron resonance, 21.42–21.43
- Biaxial crystals, 8.8, 8.9t, 8.10, 8.10f
- Bidirectional scatter distribution function  
 (BSDF), 6.1, 6.9–6.10, 6.18–6.19

- Bio-optical models, of absorption, 1.27–1.29, 1.27f, 1.28t
- Bird-wing mirror, 12.7, 12.8f
- Birefringence, 8.9, 17.1
- Bismuth germanium oxide ( $\text{Bi}_{12}\text{GeO}_{20}$ ) (BGO), 2.38t, 2.44t, 2.47t, 2.50t, 2.55t, 2.60t
- Bismuth triborate ( $\text{BiB}_3\text{O}_6$ ) (BIBO), 2.38t, 2.46t, 2.47t, 2.50t, 2.55t, 2.60t, 2.75t, 17.14
- Bistable optical switches, 16.31
- Black absorbers, 7.104, 7.105f
- Black chrome, 6.53, 6.54, 6.54f
- Black coatings, 6.13t
- Black cobalt, 6.53, 6.54f
- Black dye, 6.15
- Black felt contact paper, 6.30f, 6.32f
- Black glass, 6.57
- Black Kapton, 6.57, 6.57f
- Black layer system, 6.15
- Black nickel, 6.21, 6.23f
- Black paint, 6.21, 6.24f
- Black surfaces, 6.1–6.59
  - creation of, 6.13–6.16
  - environmental degradation of, 6.16–6.18
    - atomic oxygen effects, 6.16–6.17
    - extreme environments, 6.18
    - outgassing, 6.17
    - particle generation, 6.17–6.18
  - for far-infrared applications, 6.21, 6.26–6.34, 6.28f–6.34f
    - Ames 24E and 24E2, 6.26f, 6.28f, 6.34
    - Cornell Black, 6.26f, 6.27
    - Infrablack, 6.26f, 6.28, 6.28f
    - multiple-layer approach, 6.26, 6.26f–6.27f
    - Teflon overcoat, 6.27
  - optical characterization of, 6.18–6.21, 6.20t
  - paints and surface treatments, 6.35–6.58, 6.37f, 6.43f, 6.53f
    - Acktar black coatings, 6.55
    - Aeroglaze Z series, 6.36f, 6.37, 6.37f, 6.39, 6.39f–6.42f
    - Akzo Nobel paints, 6.39, 6.42f, 6.43f
    - anodized processes, 6.44–6.49, 6.47f, 6.48f, 6.51f, 6.53f
    - black glass, 6.57
    - Black Kapton, 6.57, 6.57f
    - carbon nanotubes and nanostructured materials, 6.55, 6.59f
    - Cardinal Black, 6.36f, 6.39, 6.44f
    - Cat-a-lac Black, 6.39, 6.42f, 6.53f
    - DeSoto Black, 6.37f, 6.39
- Black surfaces, paints and surface treatments (*Cont.*):
- DURACON, 6.55–6.56
- electrically conductive black paint, 6.56
- electrodeposited surfaces, 6.53–6.54, 6.54f, 6.55f
- etching of electroless nickel, 6.49–6.50, 6.50f, 6.51f, 6.53f
- flame-sprayed aluminum, 6.57
- Floquil, 6.44
- gold blacks, 6.57
- high-resistivity coatings, 6.56
- IBM Black (tungsten hexafluoride), 6.56
- ion beam-sputtered surfaces, 6.53
- Parson's Black, 6.44, 6.53f
- plasma-sprayed surfaces, 6.50–6.52, 6.51f–6.53f
- silicon carbide, 6.56
- SolarChem, 6.44, 6.48f, 6.53f
- specular metallic anodized surfaces, 6.57, 6.58f
- sputtered and CVD surfaces, 6.56
- 3M paints and derivatives, 6.35–6.37, 6.36f, 6.38f, 6.53f
- ZO-MOD BLACK, 6.56
- selection process for, 6.10–6.12, 6.10f–6.11f, 6.12t–6.13t
- and substrates, 6.34–6.35
- types and morphologies of, 6.1–6.10, 6.2t–6.4t, 6.5f–6.8f
- for ultraviolet applications, 6.21, 6.22f–6.25f
- Black Tedlar, 6.57f
- Black velvet cloth, 6.31f, 6.33f
- Blazing, gratings and, 5.60
- Blink response (of eye), 13.1
- Bloch equations, optical, 11.3–11.6
- Bloch solution, 8.25
- Bloch sphere, 11.4
- Blooming, thermal, 16.22
- Bombardment, of carbon surface, 6.8f
- Boron, 5.82f, 5.83
- Boron Black, 6.50, 6.51, 6.52f
- Boron carbide, 6.51
- Borosilicate crown glass, 2.41t
- Bose-Einstein condensation (BEC), 14.22, 20.26, 20.35–20.37, 20.36f
- Bose-Einstein distribution of states, 2.16
- Boulder Damage Symposium, 19.1–19.2
- Bound electronic optical Kerr effect, 16.12–16.13, 16.13f



- Bound excitons, 5.26*t*, 5.29, 5.46  
Bound-electronic optical Kerr effect, 16.3*t*  
Bragg grating, 22.9–22.11, 22.10*f*  
Bragg reflection, 20.33  
Breault Research Organization, 6.1  
Bremsstrahlung heating, inverse, 21.37, 21.37*f*  
Brewster's angle, 8.12, 8.23  
Bridge mirror, 12.7, 12.8*f*  
Bright (coupled) state, 14.4  
Brightening, atomic beam, 20.27–20.28, 20.27*f*  
Brillouin gain, 15.48  
Brillouin scattering, 21.38  
    for crystals and glasses, 2.27  
    defined, 2.27  
    in measurement, 5.76, 5.77  
    in nonlinear optics, 16.14, 16.18–16.19  
    Raman vs., 15.1  
    in solids, 8.18  
    stimulated [*see* Stimulated Brillouin scattering (SBS)]  
    in strong-field physics, 21.38  
Brillouin spectroscopy, 5.57–5.58  
Brillouin zone, 8.25, 8.26*f*, 8.27, 8.29, 9.3, 9.4  
Brillouin-enhanced four-wave mixing (BEFWM), 15.53, 15.54, 15.54*f*  
Broadband light sources, 5.58–5.59  
Broadband parametric amplification, 18.12  
Broadband reflectors, all-dielectric, 7.45–7.47, 7.45*f*–7.47*f*  
Broadband SBS slow light, 22.15  
Broadband transient Raman scattering, 15.28–15.32, 15.29*f*  
Broadening, in spectral lines, 14.13, 14.14  
Bromellite (BeO), 2.38*t*, 2.46*t*, 2.47*t*, 2.50*t*, 2.55*t*, 2.60*t*, 2.70*t*  
Bromyrite (AgBr), 2.38*t*, 2.44*t*, 2.47*t*, 2.50*t*, 2.55*t*, 2.60*t*, 2.69*t*, 2.76*t*  
BS-39B glass, 2.43*t*, 2.49*t*, 2.54*t*, 2.59*t*, 2.67*t*  
Bubble acceleration, 21.41–21.42, 21.42*f*  
Bulk (term), 4.3  
Bulk compound semiconductors, 12.20–12.21, 12.20*t*, 12.21*f*  
Bulk modulus, for metals, 4.69*t*
- Cadmium germanium diarsenide (CdGeAs<sub>2</sub>), 2.38*t*, 2.45*t*, 2.47*t*, 2.51*t*, 2.56*t*, 2.61*t*, 2.74*t*  
Cadmium selenide (CdSe), 2.38*t*, 2.46*t*, 2.47*t*, 2.51*t*, 2.56*t*, 2.61*t*, 2.70*t*, 2.77*t*  
Cadmium telluride (CdTe), 2.39*t*, 2.44*t*, 2.47*t*, 2.51*t*, 2.56*t*, 2.69*t*, 2.77*t*
- Calcite (CaCO<sub>3</sub>), 2.38*t*, 2.46*t*, 2.47*t*, 2.50*t*, 2.55*t*, 2.61*t*, 2.74*t*, 2.77*t*  
Calcium molybdate (powelite) (CaMoO<sub>4</sub>), 2.38*t*, 2.45*t*, 2.47*t*, 2.50*t*, 2.55*t*, 2.61*t*, 2.72*t*, 2.77*t*  
Carbamide ((NH<sub>4</sub>)<sub>2</sub>CO), 2.40*t*  
Carbon black particles, 6.15  
Carbon deposition, laser-assisted, 19.5  
Carbon disulfide (CS<sub>2</sub>), 16.13–16.14, 16.14*f*  
Carbon nanotubes, 6.55, 6.59*f*  
Carbon surface bombarded with positive argon ions, 6.8*f*  
Carbon-black suspensions (CBSs), 13.10–13.11, 13.11*f*  
Cardinal Black, 6.36*f*, 6.39, 6.44*f*  
Carrier trapping, 18.21–18.23, 18.22*f*  
Carrier-carrier scattering, 18.20  
Cascaded limiters, 13.6  
Cascaded  $x^{(1)}:x^{(1)}$  processes, of third-order optical nonlinearities, 16.20–16.22, 16.21*f*  
Cascaded  $x^{(2)}:x^{(2)}$  processes, of third-order optical nonlinearities, 16.22–16.24, 16.23*f*, 16.24*f*  
Casting, of polymers, 3.11  
Cat mirror, 12.7, 12.8*f*  
Cat-a-lac Black, 6.39, 6.42*f*, 6.53*f*  
Cauchy dispersion formula, 2.21  
Causality, principle of, 2.8  
Cavities, surface absorption and, 6.15  
Cavity resonance, for cw optical parametric oscillators, 17.2–17.4, 17.3*f*, 17.4*f*  
Cellulose acetate butyrate, 3.4*t*  
Center-of-mass motion of atoms, 20.4  
Ceragyrite (AgCl), 2.38*t*, 2.44*t*, 2.47*t*, 2.50*t*, 2.55*t*, 2.60*t*, 2.69*t*, 2.76*t*  
Cesium chloride (CsCl), 2.68*t*  
Cesium iodide (CsI), 2.39*t*, 2.44*t*, 2.47*t*, 2.51*t*, 2.56*t*, 2.62*t*, 2.68*t*, 2.77*t*  
Cesium lithium borate (CsLiB<sub>6</sub>O<sub>10</sub>) (CLBO), 2.39*t*, 2.45*t*, 2.47*t*, 2.51*t*, 2.56*t*, 2.62*t*  
Chalcopyrite, 2.74*t*  
Charge-coupled devices (CCDs), 5.61  
Charge-resonance enhanced ionization (CREI), 21.26  
Chemglaze Z series (*see* Aeroglaze Z series)  
Chemical vapor deposition (CVD), 6.56, 7.11  
Chirped multilayers, 7.47, 7.48  
Chirped pulse amplification (CPA) lasers, 21.4–21.5, 21.4*f*  
Chirped pulse excitation, 11.25–11.26  
Chirps, in spectroscopy, 11.3

- Chlorophyll:  
 and absorption by phytoplankton, 1.23,  
 1.24, 1.28  
 and beam attenuation, 1.41  
 and diffuse attenuation, 1.44  
 fluorescence by, 1.49  
 and remote sensing, 1.46
- Chloroplasts, 1.23
- Chromatic aberration control, 3.8
- Chromium:  
 absorptance of, 4.48*t*, 4.50*t*  
 optical properties of, 4.13*t*–4.14*t*, 4.22*f*  
 physical properties of, 4.54*t*  
 reflectance in, 4.30*t*–4.31*t*  
 thermal properties of, 4.69*t*
- Clamshell housings, 3.15, 3.15*f*
- Classical electronic polarization theory, 2.14
- Classical harmonic oscillator model, 10.5–10.7,  
 10.6*f*
- Clausius-Mossotti equation, 8.7
- Clausius-Mossotti relationships, 2.24
- Cleaning and cleanliness, of optical surfaces,  
 19.3–19.5
- Clocks, atomic, 20.28
- Closed family, 20.38
- Cluster electron heating, 21.34, 21.35
- Cluster expansion, 21.35, 21.35*f*
- Clusters, strong field interactions with, 21.31–21.36  
 Coulomb explosion, 21.33–21.34  
 intense laser pulse interactions, 21.35–21.36,  
 21.36*f*  
 ionization mechanisms in, 21.31–21.33, 21.32*f*  
 nanoplasma description, 21.34–21.35, 21.35*f*
- Coatings:  
 antireflection, 7.15–7.32  
 of absorbing and amplifying media, 7.26, 7.27  
 homogeneous-layer, 7.16–7.23, 7.17*f*–  
 7.19*f*, 7.20*t*–7.21*t*, 7.22*f*–7.23*f*  
 inhomogeneous and structured, 7.23–7.26,  
 7.24*f*, 7.26*f*  
 at nonnormal angle of incidence, 7.28–7.31,  
 7.28*f*–7.31*f*  
 nonoptical properties of, 7.31–7.32, 7.32*f*  
 surface reflections and optical perfor-  
 mance, 7.15–7.16, 7.16*f*  
 of surfaces carrying thin films, 7.27–7.28,  
 7.28*f*  
 universal, 7.26, 7.27*f*  
 filters with metallic reflecting, 7.80–7.81  
 high performance optical multilayer, 7.96–7.98
- Coatings (*Cont.*):  
 and interference polarizers, 7.70–7.72,  
 7.70*f*–7.72*f*  
 laser-induced damage in, 19.3–19.4  
 measurements on, 7.12–7.14  
 narrowband reflection, 7.43, 7.44*f*  
 phase, 7.101, 7.101*f*–7.104*f*, 7.102  
 reflection, 7.106–7.113, 7.106*f*–7.113*f*  
 thin-film  
 and antireflection coatings, 7.27–7.28,  
 7.28*f*  
 manufacturing of, 7.10–7.12  
 of metal, 7.104, 7.104*f*  
 theory and design of, 7.5–7.10, 7.6*f*, 7.9*f*  
 transmission and reflection of, 7.3  
 types of, 3.17–3.18, 6.13*t*  
 for ultrafast optics, 7.47–7.48, 7.48*f*  
 (*See also specific coatings, e.g.: Ebanol C coating*)
- Coefficient of linear thermal expansion, 4.7,  
 4.56*t*, 4.57*f*–4.58*f*
- Coefficient of thermal expansion (CTE), of  
 metals, 4.6–4.7, 4.10*t*, 4.53, 4.55*t*
- Coherence:  
 in atomic systems, 14.4–14.5, 14.4*f*,  
 14.28–14.32, 14.29*f*–14.32*f*  
 maximal, 14.3, 14.28–14.32, 14.29*f*–14.32*f*
- Coherence length, 10.15
- Coherent anti-Stokes four-wave mixing, 15.2*t*,  
 15.3*t*, 15.4, 15.4*f*
- Coherent anti-Stokes Raman scattering  
 (CARS), 15.4, 15.4*f*, 15.34, 15.42, 15.42*t*,  
 15.43*f*, 16.3*t*, 16.4, 16.5*f*, 16.17–16.18,  
 16.17*f*
- Coherent control, 18.21
- Coherent excitons, 18.19–18.20
- Coherent image amplification, 12.29, 12.30
- Coherent optical transients, 11.1–11.28  
 chirped pulse excitation, 11.25–11.26  
 and cw spectroscopy, 11.2  
 experimental considerations, 11.26–11.28,  
 11.27*f*  
 free polarization decay, 11.7–11.11, 11.8*f*,  
 11.10*f*, 11.11*f*  
 Maxwell-Bloch equations, 11.6–11.7  
 optical Bloch equations, 11.3–11.6  
 phase conjugate geometry and optical  
 Ramsey fringes, 11.19–11.22, 11.20*f*,  
 11.21*f*  
 photon echo, 11.11–11.15, 11.12*f*, 11.13*f*,  
 11.15*f*

- Coherent optical transients (*Cont.*):  
 stimulated photon echo, 11.15–11.19,  
 11.16f–11.19f  
 two-photon transitions and atom  
 interferometry, 11.22–11.23, 11.24f
- Coherent population return (CPR), 14.1, 14.30,  
 14.30f, 14.31f
- Coherent population trapping (CPT), 14.1,  
 14.3–14.5, 14.7, 20.37
- Coherent Raman scattering, 15.3
- Coherent Stokes Raman scattering (CSRS),  
 16.3t, 16.17–16.18, 16.17f
- Cold mirrors, 7.58
- Collected volatile condensable materials  
 (CVCMM), 6.17
- Collective tunneling, 21.18
- Collet-and-cap housings, 3.15, 3.15f
- Colliding pulse modelocking (CPM), 18.3
- Collimation, of atomic beams, 20.15–20.16, 20.15f
- Collisional broadening, spectral-line, 14.13
- Collisional heating, 21.37, 21.37f
- Collisional ionization, 21.31, 21.32
- Collisions, 20.28–20.31, 20.30f, 20.31f  
 excited-state, 20.29  
 ground-state, 20.29  
 trap loss, 20.29
- Colloids, in water, 1.14
- Color, ocean, 1.46
- Color center lasers, 18.10
- Color-selective beam splitters, 7.65–7.66, 7.66f,  
 7.67f
- Commando cloth, 6.31f, 6.33f
- Common glasses, 2.3
- Communications, out-of-plane coupling for, 9.12
- Complex Fresnel relation, 8.15
- Complex refractive index, 1.16–1.17, 2.8
- Compliance tensors, 2.30, 2.31t
- Composites, 12.26t, 12.27t
- Compositional modulation, 5.65, 5.66t, 5.67
- Compression molding, of polymers, 3.12
- Computer numerical control (CNC) lathe  
 turning, 3.12
- Condon point, for laser light, 20.29
- Conduction band (CB), 18.3
- Conductivity:  
 of metals, 4.6  
 of paints, 6.12, 6.12t  
 of polymers, 3.3–3.4  
 of solids, 8.4  
 of water, 1.16
- Conjugate mirrors, phase (*see* Phase conjugate  
 mirrors)
- Connected networks, 3D photonic crystals  
 and, 9.4–9.5
- Constringence, 2.23 (*See also* Abbe number)
- Contamination, of optical surfaces, 19.4–19.5
- Contamination control, 6.16
- Continuous-wave (cw) lasers, 7.14, 14.16–14.18,  
 14.17f
- Continuous-wave optical parametric oscillators  
 (cw OPOs), 17.1–17.31  
 cavity resonance configurations for, 17.2–17.4,  
 17.3f, 17.4f  
 for correlated twin beams of light, 17.28,  
 17.29f, 17.30f  
 for hyperspectral imaging, 17.27–17.28  
 limitations of, 17.30  
 for metrology and optical frequency synthesis,  
 17.28, 17.29  
 multiple-resonant oscillators, 17.16–17.21  
 doubly resonant, 17.16–17.17  
 pump-enhanced singly resonant,  
 17.17–17.20, 17.18f–17.20f  
 triply resonant, 17.20–17.21, 17.21f  
 singly resonant oscillators, 17.4–17.16  
 guided-wave nonlinear structures,  
 17.15–17.16  
 MgO:sPPLT in, 17.14–17.15, 17.15f  
 PPLN crystals in, 17.4–17.13, 17.6f–17.11f  
 QPM nonlinear materials, 17.13–17.14  
 in spectroscopy, 17.21–17.27  
 high-resolution Doppler-free, 17.27  
 photoacoustic, 17.22–17.24, 17.22f–17.24f  
 single-pass absorption, 17.24–17.27,  
 17.25f, 17.26f  
 technological advances in, 17.1–17.2,  
 17.30–17.31
- Continuous-wave (cw) Q-switched modelocking,  
 18.5f
- Continuous-wave (cw) spectroscopy, 11.2
- Continuum excitations, 18.20
- Continuum pulse generation, 18.4
- Controlled grinding, 19.3
- Conventional evaporation, 7.11
- Cooling:  
 of atoms with atom-laser interactions,  
 20.3–20.21  
 below Doppler limit, 20.17–20.21,  
 20.18f–20.20f  
 history of, 20.3–20.4

- Cooling, of atoms with atom-laser interactions (*Cont.*):  
 optical molasses, 20.13–20.17, 20.14f–20.16f  
 properties of lasers, 20.4–20.6  
 slowing atomic beams, 20.11–20.13, 20.12f, 20.12t, 20.13f  
 theoretical description, 20.6–20.11, 20.9f  
 Doppler, 20.13–20.15, 20.14f  
 laser (*see* Laser cooling)  
 polarization gradient, 20.17  
 Raman, 20.21
- Cooling rate, for glasses, 2.5n
- Copper:  
 absorptance of, 4.40f, 4.48t, 4.50t  
 optical properties of, 4.12t–4.13t, 4.22f  
 physical properties of, 4.52t–4.54t  
 reflectance of, 4.29t–4.30t, 4.40f  
 thermal properties of  
 coefficient of linear thermal expansion, 4.56t, 4.57f  
 elastic properties, 4.69t  
 at room temperature, 4.55t  
 specific heat, 4.65t, 4.66f  
 strength and fracture properties, 4.70t  
 thermal conductivity, 4.58t, 4.60f–4.61f
- Copper black, 6.21, 6.23f
- Copper gallium sulfide ( $\text{CuGaS}_2$ ), 2.39t, 2.45t, 2.47t, 2.51t, 2.56t, 2.62t, 2.74t
- Core excitons, 5.26t
- Cornell Black, 6.26f, 6.27
- Cornu equation, for refraction index, 2.22
- Correlated twin beams of light, 17.28, 17.29f, 17.30f
- CORTTRAN glass, 2.43t, 2.49t, 2.54t, 2.59t, 2.67t
- Corundum, 2.70t
- Coulomb attraction, 8.31
- Coulomb explosions:  
 cluster, 21.33–21.34  
 molecular, 21.24–21.25
- Coulomb gauge, for solids, 8.5
- Coulomb potentials, 21.31, 21.32f
- Coupled plasmon-phonon behavior, 5.35, 5.36, 5.36f, 5.37f
- Coupled resonator structures (CRS), 22.11–22.13, 22.12f
- Coupling:  
 in-plane, 9.10–9.11  
 out-of-plane, 9.11–9.12  
 two-beam, 12.4–12.6, 12.4f, 13.8–13.9
- Coupling laser power, 14.14–14.15
- Coupling (tie) layer, of bandpass filters, 7.82
- Coupling schemes, 14.30f (*See also specific coupling schemes, e.g.: Lambda coupling*)
- CR-39 resin (poly-diallylglycol), 3.11
- Craters, surface absorption and, 6.15
- Creep strength, of metals, 4.8
- Cross-Kerr phase shifter, 23.11
- Crown glasses, 2.28, 2.41t, 2.42t
- Crystals:  
 anisotropic, 8.8–8.11, 8.9t, 8.10f  
 biaxial, 8.8, 8.9t, 8.10, 8.10f  
 and dielectric tensor and optical indicatrix, 2.17–2.19, 2.19f  
 and dispersion formulas for refractive index, 2.21–2.22  
 and glasses, 2.1–2.77  
 lattice vibration model parameters for, 2.76t–2.77t  
 material properties of, 2.27–2.36  
 characteristic temperatures, 2.32, 2.33  
 combinations of, 2.36  
 correlations of, 2.36  
 elastic properties, 2.30–2.31, 2.31t  
 hardness and strength, 2.31–2.32, 2.32f, 2.32t  
 heat capacity and Debye temperature, 2.33–2.34  
 material designation and composition, 2.27, 2.29f  
 naming of, 2.27  
 thermal conductivity, 2.35–2.36, 2.35f  
 thermal expansion, 2.34–2.35, 2.34f  
 unit cell parameters, molecular weight, and density, 2.30  
 mechanical properties of, 2.47t–2.48t  
 nonlinear optical, 10.19–10.20, 10.20t–10.22t  
 and nonlinear optical coefficients, 2.26–2.27, 2.27t  
 optical activity of, 8.10–8.11  
 optical applications of, 2.17–2.27  
 as optical materials, 2.4–2.5  
 optical modes of, 2.68t–2.76t  
 with cesium chloride structure, 2.68t  
 with chalcopyrite structure, 2.74t  
 with corundum structure, 2.70t  
 with cubic perovskite structure, 2.73t  
 with diamond structure, 2.68t  
 with fluorite structure, 2.69t  
 other structures, 2.74t–2.76t

- Crystals, optical modes of (*Cont.*):  
 with  $\alpha$ -quartz structure, 2.71*t*  
 with rutile structure, 2.71*t*  
 with scheelite structure, 2.72*t*  
 with sodium chloride structure, 2.69*t*  
 with spinel structure, 2.73*t*  
 with tetragonal perovskite structure, 2.73*t*  
 with trigonal selenium structure, 2.70*t*  
 with wurtzite structure, 2.70*t*  
 with zinblende structure, 2.69*t*  
 optical properties of, 2.6, 2.8–2.9  
 origin and models of, 2.9–2.17, 2.10*f*  
 absorption in transparent region, 2.17  
 electronic transitions, 2.12–2.15, 2.13*f*  
 lattice vibrations, 2.11–2.12  
 multiphoton absorption and refraction,  
 2.15–2.17, 2.16*f*, 2.17*f*  
 and photoelastic coefficients, 2.24  
 physical properties of, 2.37, 2.38*t*–2.43*t*  
 classes and symmetry properties, 2.7*t*  
 composition, structure, and density,  
 2.38*t*–2.41*t*  
 physical constants, 2.8*t*  
 symmetry properties, 2.5, 2.6*t*–2.8*t*  
 Raman scattering in, 8.19*t*–8.20*t*  
 room-temperature dispersion formulas,  
 2.60*t*–2.66*t*  
 room-temperature elastic constants of  
 cubic crystals, 2.44*t*–2.49*t*  
 hexagonal crystals, 2.46*t*  
 monoclinic crystals, 2.47*t*  
 orthorhombic crystals, 2.46*t*  
 tetragonal crystals, 2.44*t*–2.45*t*  
 and scatter, 2.27  
 thermal properties, 2.50*t*–2.53*t*  
 and thermo-optic coefficients, 2.24–2.26  
 and total power law, 2.19–2.20, 2.20*f*  
 uniaxial, 8.8, 8.9*t*, 8.10*f*  
 (*See also Solids*)  
 Cubic crystals, 8.9*t*, 8.20*t*  
 dielectric constants of, 2.18  
 room-temperature elastic constants of,  
 2.44*t*–2.49*t*  
 symmetries of, 2.7*t*  
 Cubic oxides (sillenites), 12.17–12.19, 12.18*t*,  
 12.19*f*  
 Cubic perovskite structure, of crystals and  
 glasses, 2.73*t*  
 Cubic zirconia ( $\text{ZrO}_2 \cdot 0.12\text{Y}_2\text{O}_3$ ), 2.41*t*, 2.44*t*,  
 2.48*t*, 2.69*t*  
 Cumulative size distribution, of particles in  
 water, 1.15  
 Curie temperature, of crystals and glasses, 2.33  
 Cutoff, slope of, 7.56  
 Cutoff filters, 7.53–7.60, 7.54*f*, 7.55*f*, 7.57*f*,  
 7.59*f*–7.61*f*  
 Cw modelocking, 18.5*f*  
 Cyclotron resonance (CR), 5.12, 5.12*f*, 5.40,  
 5.47–5.50, 5.48*f*–5.50*f*  
 Damage, laser-induced [*see Laser-induced*  
 damage (LID)]  
 Damping:  
 in laser cooling, 20.19–20.20, 20.20*f*  
 phonon, 5.14  
 Dark (noncoupled) states, 14.4, 14.6–14.7,  
 20.37–20.39, 20.38*f*  
 Data storage, photorefractive holographic, 12.37  
 De-Broglie wavelengths, 8.4  
 Debye molar heat capacity, 2.33–2.34  
 Debye temperature, for crystals and glasses,  
 2.33–2.34  
 Decay, homogeneous, 11.10, 11.11*f*  
 DEEP SPACE BLACK, 6.49  
 Defect modes (in photonic crystals), 22.11,  
 22.12*f*  
 Defect-related absorption, 5.37–5.39, 5.38*f*,  
 5.39*f*  
 Defocusing:  
 ionization-induced, 21.43–21.44, 21.43*f*  
 self, 13.7, 13.8, 19.9–19.11, 19.10*f*  
 thermal, 13.8  
 Degenerate four-wave mixing (DFWM),  
 16.27–16.28, 16.28*f*, 18.17  
 Dense crown flint glass, 2.42*t*  
 Dense flint glass, 2.43*t*  
 Dense phosphate crown glass, 2.41*t*  
 Density matrix, 16.21, 16.22  
 Dephasing, 11.15, 14.12–14.14  
 Deposition method, of manufacturing  
 thin-films, 7.11–7.12  
 Designer blacks, 6.14  
 DeSoto Black, 6.37*f*, 6.39  
 Detectors, semiconductor, 5.61  
 Detritus, organic:  
 absorption by, 1.25–1.27, 1.25*t*, 1.26*f*  
 in water, 1.14  
 Detuning, 14.11*f*  
 Diamond (crystal), 2.38*t*, 2.44*t*, 2.47*t*, 2.50*t*,  
 2.55*t*, 2.61*t*, 2.68*t*

- Diamond lattice structure, 5.6, 5.16, 5.17*t*  
of air spheres, 9.5  
of crystals and glasses, 2.68*t*  
Diamond-turning process, 3.12  
Dichroic beam splitters, 7.65–7.66, 7.67*f*  
Dicke narrowing, 15.9  
Dielectric broadband reflectors, 7.39, 7.40*f*,  
7.45–7.47, 7.45*f*–7.47*f*  
Dielectric color selective (dichroic) beam  
splitters, 7.65–7.66, 7.67*f*  
Dielectric constant, 2.14, 2.17–2.18  
of crystals and glasses, 2.6*t*  
dispersion of, 8.22*f*  
for solids, 8.15  
Dielectric function, 4.26*f*, 5.8–5.9, 5.12  
Dielectric multiple reflection cutoff filters,  
metal, 7.59–7.60  
Dielectric multiple reflection filters, metal, 7.111  
Dielectric potential, 9.15  
Dielectric reflectors:  
interference filters with, 7.81  
metal, 7.81–7.82, 7.108, 7.109, 7.110*f*  
Dielectric tensor, of crystals and glasses, 2.17–2.18  
Differential reflectivity (DR), 18.1, 18.5, 18.6, 18.6*f*  
Differential transmission (DT), 18.1  
Differential transmission (DT) spectroscopy,  
18.18–18.19  
Diffraction grating, 5.59–5.60  
Diffuse attenuation:  
and Jerlov water types, 1.42–1.46, 1.43*t*–1.45*t*,  
1.44*f*, 1.45*f*  
in water, 1.13  
Diffuse attenuation coefficient, 1.12  
Diffuse Infrared Background Explorer, 6.29*f*  
Diffusely scattering surfaces (*see* Black surfaces)  
Diluted magnetic semiconductors (DMSs), 5.45  
Dipole active modes, infrared, 8.16–8.18, 8.17*f*  
Dipole force, 20.8  
Direct excitons, 5.29  
Direct interband absorption, in solids, 8.27–8.28  
Direct (vertical) interband absorption transitions,  
5.22–5.23, 5.22*f*–5.23*f*, 5.25*f*  
Direct laser acceleration (DLA), 21.43  
Direct pulse generation, 18.4  
Dispersion, 18.11  
Cauchy, 2.21  
for crystals and glasses, 2.21–2.23, 2.60*t*–2.66*t*,  
2.66*t*–2.68*t*  
Drude, 2.21–2.22  
Maxwell-Helmholtz-Drude, 2.12, 2.21–2.22  
Dispersion (*Cont.*):  
in multilayer reflectors, 7.40  
normal vs. anomalous, 4.4  
principle of, 2.23  
range of anomalous, 4.4  
room-temperature, 2.60*t*–2.66*t*, 2.66*t*–2.68*t*  
in solids, 8.14–8.16, 8.22*f*  
Zernike, 2.22  
Dispersion spectrometers, 5.59–5.60  
Displays, out-of-plane coupling and, 9.11–9.12  
Dissipative force, 20.7  
Dissolved substances, in water, 1.13  
Distributed Bragg reflector (DBR) diode laser,  
17.9, 17.10*f*, 17.11*f*  
Distributed feedback (DFB) lasers, 9.6  
Distribution functions, of water, 1.6*t*, 1.12  
Documentation, for polymers, 3.5  
Donor-acceptor pair (DAP) transition, 5.71  
Doppler cooling, 20.13–20.15, 20.14*f*  
Doppler cooling limit, 20.15  
Doppler limit, 20.5  
Doppler shift, 11.19, 20.4  
Doppler temperature, 20.5, 20.11, 20.15  
Double atomic resonance, 22.5–22.9, 22.6*f*–22.8*f*  
Double ionization, strong field, 21.18–21.19,  
21.19*f*  
Double phase conjugate mirrors, 12.7, 12.8*f*  
Double photonic resonance, 22.11–22.13, 22.12*f*  
Double-lambda coupling, 14.24*f*  
Double-sided Feynman diagrams, 11.12–11.13,  
11.13*f*  
Doubly resonant optical parametric oscillators  
(DR OPOs), 10.18  
Doubly resonant oscillators (DROs), 17.2–17.4,  
17.3*f*, 17.4*f*, 17.16–17.17  
Down-conversion, spontaneous parametric,  
23.10, 23.13  
Downdwelling average cosine, of water, 1.6*t*,  
1.7*f*, 1.12  
Downdwelling diffuse attenuation coefficient,  
for sea water, 1.44*t*–1.45*t*  
Downdwelling irradiance, of water, 1.5*t*, 1.7*f*, 1.8  
Downdwelling irradiance diffuse attenuation  
coefficients, for sea water, 1.43*t*  
Downward scalar irradiance, of water, 1.5*t*, 1.7*f*, 1.8  
Dressed states, 14.3  
Drift velocity, 21.7  
Drude approximation, 5.34  
Drude dispersion formula, for crystals and  
glasses, 2.21–2.22

- Drude model, 4.4–4.5, 8.15, 8.21, 8.22*f*, 16.20  
**d**-tensor, 10.11  
 Dual-cavity PE-SROs, 17.18–17.20, 17.19*f*, 17.20*f*  
 Dual-Fock states, 23.8–23.9  
 Ductility, of metals, 4.8, 4.70  
 DURACON, 6.55–6.56  
 Dynamic ionization stabilization, 21.21
- Ebanol C coating, 6.56  
 Echo signal, 11.11–11.12, 11.12*f*  
 ECP-2200, 6.27, 6.29*f*  
 ECP-2200 coating (*see* MH 2200 coating)  
 Edge filters, nonpolarizing, 7.66, 7.67*f*  
 Effective mass, 8.25–8.26, 8.26*f*  
 E-field-dependent electronic polarizability, 19.5  
 “Egg-crate” array, of potential wells, 20.32  
 Ehrenfest theorem, 20.6  
 Einstein-Smoluchowski theory of scattering, 1.30  
 Elastic constants, for crystals:  
   cubic crystals, 2.44*t*–2.49*t*  
   hexagonal crystals, 2.46*t*  
   monoclinic crystals, 2.47*t*  
   orthorhombic crystals, 2.46*t*  
 Elastic properties, of crystals and glasses,  
   2.30–2.31, 2.31*t*  
 Elastic stiffness, of metals, 4.69, 4.69*t*  
 Elasto-optic coefficients, for crystals and  
   glasses, 2.21  
 Electric field amplitude, in multilayer systems,  
   7.9–7.10  
 Electric field reflectance, Fresnel expression  
   for, 4.5  
 Electrically conductive black paint, 6.56  
 Electric-field-modulated reflection spectroscopy,  
   5.66*t*, 5.67  
 Electrodeposited surfaces, 6.8*f*, 6.53–6.54,  
   6.54*f*, 6.55*f*  
 Electroless nickel, etched, 6.5*f*, 6.6*f*, 6.49–6.50,  
   6.50*f*, 6.51*f*, 6.53*f*  
 Electromagnetic spectrum, semiconductor  
   interactions with, 5.3–5.6, 5.4*f*  
 Electromagnetically induced transparency  
   (EIT), 14.1–14.36, 22.5–22.9, 22.7*f*, 22.8*f*  
   coherence in two- and three-level atomic  
     systems, 14.4–14.5, 14.4*f*  
   and cw lasers, 14.16–14.18, 14.17*f*  
   at few photon level, 14.32–14.33  
   gain and lasing without inversion,  
     14.18–14.19  
   as interference effect, 14.2–14.4
- Electromagnetically induced transparency  
   (EIT) (*Cont.*):  
   manipulation of optical properties by,  
     14.10–14.15, 14.11*f*, 14.13*t*  
   coupling laser power, 14.14–14.15  
   dephasing and fluctuations in laser fields,  
     14.13  
   dephasing in gas phase media,  
     14.12–14.13  
   dephasing in solids, 14.13–14.14  
   inhomogeneous broadening, 14.14  
   and maximal atomic coherence,  
     14.28–14.32, 14.29*f*–14.32*f*  
   nonlinear optical frequency conversion,  
     14.24–14.28, 14.24*f*, 14.27*f*  
   physical concept of, 14.5–14.10, 14.6*f*, 14.8*f*,  
     14.9*f*  
   pulse propagation effects, 14.20–14.22  
   and pulsed lasers, 14.15–14.16, 14.16*f*  
   and refraction index in dressed atoms,  
     14.19–14.20  
   in solids, 14.33–14.36, 14.35*f*, 14.36*f*  
   ultraslow light pulses, 14.22–14.23, 14.23*f*
- Electron(s):  
   relativistic, above threshold ionization,  
     21.20, 21.21*f*  
   strong field interactions with single, 21.5–21.10,  
     21.7*f*, 21.9*f*
- Electron acceleration, 21.39–21.42, 21.40*f*  
 Electron beams, strong field interactions with  
   relativistic, 21.9–21.10  
 Electron stochastic heating, 21.36  
 Electron-hole drops, 5.26*t*  
 Electron-hole pairs, 14.34, 16.31  
 Electro-optic coefficients, for crystals and  
   glasses, 2.21  
 Electroreflectance, 5.66*t*, 5.67  
 Electrorefractive photorefractive (ERPR) effect,  
   12.21  
 Electrostriction, 16.18–16.19, 19.5  
 Element wedge, of polymers, 3.10  
 Ellipsometers and ellipsometry, 5.5, 5.57, 5.63,  
   5.66*t*, 5.67–5.69, 5.68*f*, 5.69*f*  
 Elongation, of metals, 4.70, 4.70*t*  
 Embedded polarizers, 7.70–7.71, 7.71*f*, 7.72*f*  
*Emiliana huxleyi*, 1.15  
 Emittance:  
   for crystals and glasses, 2.20  
   of metals, 4.6, 4.49, 4.49*f*, 4.50*t*, 4.51*t*  
   and surface coatings, 6.19, 6.20*t*

- Energy:  
 flow of, in solids, **8.7–8.8**  
 Landau levels of, **5.40, 5.42f**
- Energy bands:  
 magnetic field effects on, **5.40**  
 for solids, **8.25–8.27, 8.26f**
- Energy walk-off angle, **8.9**
- Energy-time uncertainty principle, **23.4**
- Engineering moduli, for crystals and glasses, **2.37**
- Enhanced Martin Black, **6.46, 6.47**
- Enhanced refraction, **14.20**
- Entanglement, quantum (*see* Quantum entanglement, in optical interferometry)
- Entrance damage, laser-induced, **19.3**
- Environmental degradation, of black surfaces, **6.16–6.18**
- Environmentally responsible glass, **2.29–2.30**
- Epner Laser Black, **6.56**
- Etched electroless nickel surface, **6.5f, 6.6f, 6.49–6.50, 6.50f, 6.51f, 6.53f**
- Etching, surface, **6.15**
- Euphotic zone, of water, **1.46, 1.46t**
- Evaporated spacers, **7.83, 7.84f, 7.85f**
- Evaporation method, of manufacturing thin-films, **7.11**
- Excitance, total integrated, **2.19**
- Excitation(s):  
 chirped pulse, **11.25–11.26**  
 continuum, **18.20**  
 excitonic, **18.19–18.20**  
 photoexcitation, **5.70f**  
 single-particle, **5.81, 5.82f**
- Excited state absorption (ESA), **13.5, 16.19**
- Excited state collisions, **20.29**
- Exciton(s):  
 free, luminescence, **5.72, 5.73f**  
 in semiconductors, **5.25–5.29, 5.26t, 5.27f–5.28f, 5.46**  
 and solids, **8.31–8.32**
- Exciton gases, **5.26t**
- Exciton Rydberg, **8.31**
- Excitonic excitations, **18.19–18.20**
- Excitonic magneto-optical effects, **5.46, 5.47f**
- Excitonic molecules, **5.26t**
- Exit damage, laser-induced, **19.3**
- External pulse compression, **18.4, 18.11–18.12**
- External self-action, **16.25**
- Extinction coefficient, of metals, **4.3, 4.11, 4.12t–4.19t, 4.20f–4.26f**
- Extreme environments, black surface degradation in, **6.18**
- Extreme Ultraviolet Explorer, **6.21**
- Extreme ultraviolet (XUV) light:  
 bandpass filters for, **7.94–7.96, 7.95f–7.96f**  
 interference polarizers for, **7.73, 7.76f–7.77f**  
 multilayer reflectors for, **7.42–7.43, 7.53**
- Extrinsic optical properties:  
 of semiconductors, **5.11**  
 of solids, **8.3**
- Fabry-Perot interference filters, **7.78–7.82, 7.79f, 7.80f, 7.92–7.94, 7.93f, 7.96**
- Fabry-Perot interferometers, **7.13, 7.39, 7.39f, 7.40, 7.89**
- Fabry-Perot resonators, **22.11, 22.12f**
- Family momentum, **20.38**
- Fano interferences, **14.2**
- Faraday effect, **5.50–5.51**
- Faraday rotation:  
 free-carrier, **5.50–5.51**  
 interband, **5.44–5.45, 5.45f**
- Faraday's law, **2.6**
- Far-infrared (FIR) lasers, **5.48**
- Far-infrared (FIR) radiation:  
 and black surfaces, **6.21, 6.26–6.34, 6.28f–6.34f**  
 Ames 24E and 24E2, **6.26f, 6.28f, 6.34**  
 Cornell Black, **6.26f, 6.27**  
 Infrablack, **6.26f, 6.28, 6.28f**  
 multiple-layer approach, **6.26, 6.26f–6.27f**  
 Teflon overcoat, **6.27**  
 and EIT, **14.3**
- Far-infrared region, multilayer reflectors for, **7.52, 7.52f**
- Far-infrared (FIR) telescopes, **6.48**
- Far-off-resonance traps (FORTs), **20.23**
- Fast ignition, **21.54–21.55, 21.55f**
- Fast saturable absorbers, **18.8f, 18.9–18.10**
- Fatigue strength, of metals, **4.8**
- Femtosecond, **5.7**
- Femtosecond x-ray production, **21.52–21.53, 21.53f**
- Fermi level, **8.21**
- Fermi's golden rule, **8.25**
- Ferroelectric oxides, **12.13–12.14, 12.13t**
- Ferroelectric photorefractive materials, **12.13–12.17, 12.13t**  
 barium titanate, **12.15–12.16, 12.16f**  
 lithium niobate and lithium tantalate, **12.14**  
 potassium niobate, **12.16–12.17**



- Ferroelectric photorefractive materials (*Cont.*):  
  strontium barium niobate and related compounds, 12.17  
  tin hypothiodiphosphate, 12.17, 12.18*t*  
FF5 glass (593355), 2.49*t*, 2.54*t*, 2.59*t*, 2.66*t*  
Fiber feedback, 17.16  
Fiber pump lasers, 17.7–17.11, 17.9*f*–17.11*f*  
Fiber Raman amplifiers, 22.15  
Fibers:  
  photonic bandgap, 2.23  
  slow light propagation in, 22.13–22.15, 22.14*f*  
Films:  
  and black surfaces, 6.15  
  polymer, 12.23–12.25, 12.26*t*–12.27*t*  
  semiconductor-doped dielectric, 18.11  
  thin (*see* Thin-film coatings)  
Filters and filtering, 7.1–7.114  
  antireflection coatings, 7.15–7.32  
    of absorbing and amplifying media, 7.26, 7.27  
    homogeneous-layer, 7.16–7.23, 7.17*f*–7.19*f*, 7.20*t*–7.21*t*, 7.22*f*–7.23*f*  
    inhomogeneous and structured, 7.23–7.26, 7.24*f*, 7.26*f*  
    at nonnormal angle of incidence, 7.28–7.31, 7.28*f*–7.31*f*  
    nonoptical properties of, 7.31–7.32, 7.32*f*  
    surface reflections and optical performance, 7.15–7.16, 7.16*f*  
    of surfaces carrying thin films, 7.27–7.28, 7.28*f*  
    universal, 7.26, 7.27*f*  
  bandpass, 7.73–7.96  
    about, 7.73, 7.77–7.78, 7.77*f*–7.78*f*  
    angular properties of, 7.91–7.94, 7.92*f*, 7.93*f*  
    with multiple peaks, 7.90, 7.91*f*  
    narrow- and medium-, 7.78–7.83, 7.79*f*, 7.80*f*, 7.82*f*–7.88*f*  
    stability and temperature dependence of, 7.94  
    very narrow, 7.83, 7.88–7.89, 7.89*f*  
    wedge filters, 7.90, 7.91, 7.91*f*  
    wide, 7.90, 7.90*f*  
    for XUV and x-ray regions, 7.94–7.96, 7.95*f*–7.96*f*  
  beam splitters, 7.61–7.67, 7.62*f*–7.68*f*  
    achromatic beam splitters, 7.62–7.65, 7.62*f*–7.65*f*  
    color-selective beam splitters, 7.65–7.66, 7.66*f*, 7.67*f*  
    geometrical considerations for, 7.61–7.62  
  Filters and filtering (*Cont.*):  
    with coatings  
      measurements on, 7.12–7.14  
      transmission and reflection of, 7.3  
    cutoff, heat-control, and solar-cell cover, 7.53–7.60  
    cutoff filters, 7.53–7.60, 7.54*f*, 7.55*f*, 7.57*f*, 7.59*f*–7.61*f*  
    heat reflectors, 7.58  
    solar-cell cover filters, 7.58  
  high performance optical multilayer coatings, 7.96–7.98, 7.97*f*  
  interference polarizers and polarizing beam splitters, 7.69–7.73, 7.70*f*–7.72*f*, 7.76*f*–7.77*f*  
  with low reflection, 7.104–7.106, 7.104*f*–7.105*f*  
  matched, 12.28–12.29, 12.29*f*, 12.30*f*  
  multilayer reflectors, 7.39–7.53  
    all-dielectric broadband reflectors, 7.39, 7.40*f*, 7.45–7.47, 7.45*f*–7.47*f*  
    coatings for ultrafast optics, 7.47–7.48, 7.48*f*  
    for far-infrared region, 7.52, 7.52*f*  
    graded reflectivity mirrors, 7.52  
    imperfections in, 7.40–7.43, 7.41*f*–7.43*f*  
    for interferometers and lasers, 7.39–7.40, 7.39*f*–7.40*f*  
    narrowband reflection coatings, 7.43, 7.44*f*  
    rejection filters, 7.48–7.50, 7.49*f*–7.51*f*  
    resonant reflectors, 7.43–7.45, 7.44*f*  
    for soft x-ray and XUV regions, 7.53  
  neutral filters, 7.67, 7.67*f*–7.68*f*  
  novelty, 12.32, 12.33*f*–12.35*f*  
  phase coatings, 7.101, 7.101*f*–7.104*f*, 7.102  
  reflection, 7.5, 7.5*f*  
  reflection coatings and, 7.106–7.113, 7.106*f*–7.113*f*  
  special purpose coatings, 7.113–7.114, 7.114*f*  
  theory of, 7.1*f*, 7.2  
  thin-film coatings  
    and antireflection coatings, 7.27–7.28, 7.28*f*  
    manufacturing of, 7.10–7.12  
    of metal, 7.104, 7.104*f*  
    theory and design of, 7.5–7.10, 7.6*f*, 7.9*f*  
  transmission, 7.3–7.5, 7.4*f*  
  for two or three spectral regions, 7.98–7.100, 7.98*f*–7.101*f*  
  two-material periodic multilayers theory for, 7.32–7.38, 7.33*f*–7.38*f*

- Filtrate absorption, 1.21
- Finite-difference time-domain (FDTD) solution  
(to Maxwell's equations), 9.3
- Fissures, and surface absorption, 6.15
- Flame-sprayed aluminum, 6.57
- Flashlamp pumped Nd:glass amplifiers, 21.5
- Flexural strength, of metals, 4.70, 4.70*t*
- Flint glasses, 2.28, 2.41*t*–2.43*t*
- Floquet theory, 21.23
- Floquil, 6.44
- Fluor crown glass, 2.41*t*
- Fluorescence, chlorophyll, 1.49
- Fluorite (CaF<sub>2</sub>), 2.38*t*, 2.44*t*, 2.47*t*, 2.50*t*, 2.55*t*,  
2.61*t*, 2.69*t*, 2.77*t*
- Fluoro flint glass, 2.42*t*
- Fock states, 23.8–23.9, 23.14
- Focused beams, 15.41
- Fokker-Planck equation, 20.10–20.11
- Forbidden bands, 9.2
- Forward drift velocity, 21.7
- Forward Raman amplifiers, 15.4, 15.4*f*
- Forward Raman generators, 15.4, 15.4*f*
- Forward-looking infrared (FLIR)  
systems, 6.54
- Fourier-transform spectrometers, 5.60–5.61,  
5.60*f*, 5.72, 7.12
- Four-photon absorption (4PA), 19.10
- Four-wave mixing (FWM), 18.3  
coherent anti-Stokes, 15.2*t*, 15.3*t*, 15.4, 15.4*f*  
degenerate, 18.17  
and EIT, 14.24–14.26, 14.24*f*, 14.27*f*  
resonant, 14.28  
and third-order optical nonlinearities,  
16.27–16.28, 16.28*f*  
transient, 18.17–18.18, 18.17*f*
- Four-wave mixing phase conjugation, 12.6–12.7,  
12.6*f*
- Fracture toughness:  
of crystals and glasses, 2.32, 2.32*t*  
of metals, 4.8, 4.70, 4.70*t*
- Franz-Keldysh effect, 12.22
- Fredkin gate, 23.11
- Free carriers and free-carrier effects, 5.47–5.52  
in crystals, 2.15  
cyclotron resonance, 5.47–5.50, 5.48*f*–5.50*f*  
free-carrier Faraday rotation, 5.50–5.51  
impurity magnetoabsorption, 5.51–5.52,  
5.51*f*  
in semiconductors, 5.33–5.36, 5.35*f*–5.37*f*,  
5.81, 5.82*f*
- Free electron properties, of solids, 8.21–8.24  
Drude model, 8.21, 8.22*f*  
interband transitions in metals, 8.21  
plasmons, 8.23–8.24  
reflectivity, 8.23
- Free polarization decay (FPD), 11.7–11.11,  
11.8*f*, 11.10*f*, 11.11*f*
- Free spectral range, of bandpass filters, 7.77
- Free-carrier Faraday rotation, 5.50–5.51
- Free-exciton (FE) luminescence, 5.72, 5.73*f*
- Frenkel excitons, 5.26, 5.26*t*
- Frequency conversion, nonlinear optical,  
14.24–14.28, 14.24*f*, 14.27*f*
- Frequency mixing, 16.3*t*
- Fresnel reflection coefficient, for metallic  
reflectors, 7.106
- Fresnel relations, 8.11, 8.15
- Fringe power, of polymers, 3.11
- Frogs legs mirror, 12.7, 12.8*f*
- Full width half maximum (FWHM), 18.3
- Fully functional polymers, 12.27*t*
- Fundamental absorption edge, 5.21  
absorption near, 5.21–5.22, 5.21*f*  
high-energy transitions above, 5.29–5.33,  
5.30*f*–5.34*f*
- Fused glass, 2.43*t*, 2.49*t*, 2.54*t*, 2.59*t*, 2.67*t*
- Fusion neutron production, 21.53
- Gain narrowing, in steady-state Stokes  
scattering, 15.21
- Gain saturation, dynamic, 18.8, 18.8*f*
- Gain without inversion, and EIT, 14.18–14.19
- Gallagher-Pritchard (GP) model (of trap-loss  
collisions), 20.29
- Gallium arsenide (GaAs):  
composition, structure, and density of, 2.39*t*  
dispersion formulas for, 2.62*t*  
elastic constants of, 2.44*t*  
lattice vibration model parameters for, 2.77*t*  
linear-chain model calculations for, 5.19*f*  
local vibrational modes for, 5.19*f*  
luminescence in, 5.72, 5.73, 5.74*f*  
mechanical properties of, 2.47*t*  
multiphonon absorption of vacuum-grown,  
5.18*f*  
optical modes of, with zinblende  
structure, 2.69*t*  
optical properties of, 2.56*t*  
Raman scattering of, 5.80, 5.81, 5.81*f*  
thermal properties of, 2.51*t*

- Gallium nitride (GaN), 2.39t, 2.46t, 2.47t, 2.51t, 2.56t, 2.62t, 2.70t, 2.77t
- Gallium phosphide (GaP), 2.39t, 2.44t, 2.47t, 2.51t, 2.56t, 2.62t, 2.69t, 2.77t
- Gap modes (GMs), 5.17
- Gas phase media, dephasing in, 14.12–14.13
- Gases, strong field nonlinear optics in, 21.27–21.31, 21.28f
- Gauss law, 2.6
- Gelbstoff, in water, 1.13 (*See also* Yellow matter)
- Generalized Rabi frequency, 11.4
- Geometrical configuration factor (GCF), 6.12
- Germania glass, fused, 2.43t, 2.49t, 2.54t, 2.59t, 2.67t
- Germanium:
  - absorptance of, 4.48t
  - in crystal form, 2.39t, 2.44t, 2.47t, 2.51t, 2.56t, 2.62t, 2.68t
  - thermal properties of
    - elastic stiffness, 4.69t
    - moduli and Poisson's ratio, 4.69t
    - strength and fracture properties, 4.70t
- Ghost imaging, 23.13
- "Ghosts" (in gratings), 5.60
- Gilvin, 1.13 (*See also* Yellow matter)
- Glass(es):
  - amorphous, 12.26t
  - antireflection coatings for, 7.26–7.28, 7.28f
  - common, 2.3
  - and crystals, 2.1–2.77
  - defined, 2.33
  - hybrid organic-inorganic, 12.27t
  - material properties of, 2.27–2.36
    - characteristic temperatures, 2.32, 2.33
    - combinations of, 2.36
    - correlations of, 2.36
    - elastic properties, 2.30–2.31, 2.31t
    - hardness and strength, 2.31–2.32, 2.32f, 2.32t
    - heat capacity and Debye temperature, 2.33–2.34
    - material designation and composition, 2.28–2.30, 2.29f
    - naming of, 2.27
    - thermal conductivity, 2.35–2.36, 2.35f
    - thermal expansion, 2.34–2.35, 2.34f
    - unit cell parameters, molecular weight, and density, 2.30
  - mechanical properties of, 2.49t
- Glass(es) (*Cont.*):
  - optical applications of, 2.17–2.27
    - dielectric tensor and optical indicatrix, 2.17–2.19, 2.19f
    - dispersion formulas, 2.21–2.23
    - nonlinear optical coefficients, 2.26–2.27, 2.27t
    - scatter, 2.27
    - thermo-optic coefficients, 2.24–2.26, 2.24f
    - total power law, 2.19–2.20, 2.20f
  - as optical materials, 2.4–2.5
  - optical properties of, 2.6, 2.8–2.9
    - lattice vibration model parameters, 2.76t–2.77t
    - origin and models, 2.9–2.17, 2.10f, 2.13f, 2.16f, 2.17f
    - room-temperature dispersion formulas, 2.66t–2.68t
    - summary table, 2.59t
  - physical properties of, 2.37, 2.38t–2.43t
    - optical glass reference table, 2.41t–2.43t
    - physical constants, 2.8t
    - specialty, and substrate materials, 2.43t
    - symmetry properties, 2.5, 2.6t, 2.8t
    - thermal properties of, 2.54t
- Glass scatterers, 13.8
- Glass-based lasers, 21.5
- Glass-ceramics, 2.33
- Goddard Space Flight Center, 6.35, 6.39
- Gold:
  - absorptance of, 4.40f, 4.48t, 4.50t, 4.51t
  - optical properties of, 4.14t, 4.23f
  - physical properties of, 4.52t, 4.54t
  - reflectance of, 4.31t–4.32t, 4.40f
  - thermal properties of
    - coefficient of linear thermal expansion, 4.56t, 4.57f
    - elastic stiffness, 4.69t
    - moduli and Poisson's ratio, 4.69t
    - at room temperature, 4.55t
    - specific heat, 4.65t, 4.66f
    - strength and fracture properties, 4.70t
    - thermal conductivity, 4.58t, 4.60f–4.61f
- Gold black surfaces, 6.57
- Gold iridite, 6.21, 6.22f
- Gordon inequality, 1.21
- Graded reflectivity mirrors, 7.52
- Gradient force, 20.8
- Grain boundaries, of crystals, 2.4

- Gratings:  
 Bragg, 22.9–22.11, 22.10f  
 diffraction, 5.59–5.60  
 formation of, 12.1–12.3, 12.2f  
 Moiré, 22.11, 22.12f  
 transmission, 12.7, 12.8f
- Greenockite (CdS), 2.38t, 2.46t, 2.47t, 2.51t,  
 2.56t, 2.61t, 2.70t, 2.77t
- Grinding, controlled, 19.3
- Gross-Pitaevski equation, 20.34
- Ground-based telescopes, 6.12
- Ground-state collisions, 20.29
- Group Delay Dispersion (GDD), 7.47–7.48, 7.48f
- Group Delay (GD) phase changes, 7.47, 7.48
- Group theory, 5.6
- Group velocity, 22.3–22.5
- Group velocity dispersion (GVD), 11.27, 22.4–22.5
- Grüneisen relationship, 2.34, 2.35
- GUERAP (stray light analysis program), 6.19
- Guided-wave nonlinear structures, 17.15–17.16
- Hafnium dioxide-yttrium oxide ( $\text{HfO}_2:\text{Y}_2\text{O}_3$ ),  
 2.56t, 2.62t, 2.77t
- Halite (NaCl), 2.40t, 2.44t, 2.48t, 2.52t, 2.57t,  
 2.64t, 2.69t
- Hardness:  
 of crystals and glasses, 2.31, 2.32f  
 of metals, 4.8  
 of polymers, 3.2–3.3
- Harmonic generation:  
 high, 21.27–21.30  
 harmonic yield and phase matching, 21.30  
 quasi-classical model, 21.28f, 21.29–21.30  
 from solid plasmas, 21.50–21.52, 21.51f  
 third-order, 16.2, 16.3t  
 in crystals, 16.14  
 energy level diagrams for, 16.5f  
 and semiconductors, 5.56
- Harmonic yield, 21.30
- Hartmann equation, for refraction index, 2.22
- Heat capacity (specific heat):  
 of crystals and glasses, 2.6t, 2.33  
 of metals, 4.7, 4.10t, 4.53, 4.55, 4.55t, 4.65t,  
 4.66f–4.69f
- Heat reflectors, 7.58
- Heat-induced lensing effect, 16.22
- Heating:  
 cluster electron, 21.34, 21.35  
 inverse Bremsstrahlung, 21.37, 21.37f  
 $j \times B$ , 21.49
- Heating (*Cont.*):  
 self-heating, 17.12  
 vacuum, 21.47f, 21.48–21.49
- Heisenberg limit, 23.6–23.7
- Heisenberg number-phase uncertainty  
 relation, 23.4
- Heisenberg uncertainty principle (HUP), 23.6
- Herzberger equation, 2.22
- Hexagonal crystals:  
 anisotropic, 8.9t  
 dielectric constants of, 2.18  
 room-temperature elastic constants, 2.46t  
 symmetries of, 2.7t, 8.20t
- High emittance-low absorptance coatings, 6.16
- High harmonic generation (HHG), 21.27–21.30  
 harmonic yield and phase matching, 21.30  
 quasi-classical model, 21.28f, 21.29–21.30  
 from solid plasmas, 21.50–21.52, 21.51f
- High magnetic field production, 21.53
- High performance optical multilayer coatings,  
 7.96–7.98, 7.97f
- High-energy transitions above fundamental  
 edge, 5.29–5.33, 5.30f–5.34f
- High-Q cavities, 9.12
- High-reflectance zones, of multilayers,  
 7.36–7.37, 7.37f
- High-repetition short-pulse lasers,  
 11.26–11.27, 11.27f
- High-resistivity coatings, 6.56
- High-resolution Doppler-free spectroscopy, 17.27
- Hilbert transforms, 2.8–2.9
- Hole boring, 21.50, 21.50f
- Holographic optical elements (HOEs), 12.31
- Holographic storage:  
 data, 12.37  
 photorefractive, 12.36–12.37
- Holography, real-time, 12.28–12.29,  
 12.29f, 12.30f
- Homogeneity, in polymeric optics, 3.7
- Homogeneous broadening, spectral-line, 14.13
- Homogeneous decay, 11.10, 11.11f
- Homogeneous-layer antireflection coatings,  
 7.16–7.23, 7.17f–7.19f, 7.20t–7.21t,  
 7.22f, 7.23f
- Homogeneously broadened systems, 11.18–11.19,  
 11.19f
- Hong-Ou-Mandel effect, 23.10, 23.14
- Hooke's law, 8.14, 8.21
- Hot mirrors, 7.58
- Housings, lens, 3.15–3.16, 3.15f

- HTF-1 glass, 2.43*t*, 2.49*t*, 2.54*t*, 2.59*t*, 2.68*t*  
 Hughes Airborne Optical Adjunct Coating, 6.49  
 Human eye:  
   active optical limiting by, 13.1  
   damage thresholds for, 13.3, 13.3*f*  
 Hybrid organic-inorganic composites, glasses,  
   and sol-gels, 12.27*t*  
 Hydrologic optics, 1.3 (*See also* Water)  
 Hydrostatic pressure, 5.66*t*  
 Hyperbolic cumulative size distribution, 1.15  
 Hyper-Raman scattering, 15.2*t*, 15.3, 15.3*t*  
 Hyperspectral imaging, 17.27–17.28  
 Hysteresis instability, of metals, 4.10
- IBM Black, 6.56  
 Illinois Institute of Technology, 6.35  
 Imaging:  
   ghost, 23.13  
   hyperspectral, 17.27–17.28  
   quantum, 23.13–23.14  
   time-gated, 15.42, 15.43, 15.44*f*  
 Impurity magnetoabsorption, 5.51–5.52, 5.51*f*  
 Impurity-related absorption, 5.37–5.39,  
   5.38*f*, 5.39*f*  
 Impurity-related vibrational optic effects,  
   5.17–5.20, 5.18*f*–5.19*f*, 5.20*t*, 5.21*f*  
 Index contrast, 3D photonic crystals and, 9.4  
 Index ellipsoid, of crystals and glasses, 2.18–2.19,  
   2.19*f*  
 Index grating, 12.1–12.3, 12.2*f*  
 Index of absorption, 2.8  
 Index of refraction (*see* Refractive index)  
 Indirect (nonvertical) absorption transitions,  
   5.22–5.24, 5.24*f*–5.25*f*  
 Indirect excitons, 5.29  
 Indirect interband transitions, 8.29–8.30, 8.29*f*  
 Indium phosphide (InP), 12.21  
 Induced transparency, 21.52  
 Induced-transmission filters, 7.83, 7.88*f*  
 Inelastic scattering:  
   of light, 5.76–5.83, 5.76*f*, 5.78*f*–5.82*f*  
   and polarization, 1.47–1.49, 1.48*f*, 1.49*f*  
 Inertial confinement fusion (ICF), 21.54, 21.55*f*  
 Infrablack, 6.26, 6.26*f*, 6.28, 6.28*f*, 6.48, 6.48*f*  
 Infrared (IR) dipole active modes, 8.16–8.18,  
   8.17*f*  
 Infrared (IR) region:  
   absorption in, 5.19*f*  
   all-dielectric reflectors for, 7.39, 7.40*f*  
   multilayer reflectors for far-, 7.52, 7.52*f*  
 Infrared (IR) suppressing filters, 7.58, 7.58*f*  
 Inherent optical properties (IOPs), of water,  
   1.4, 1.5*t*, 1.9–1.12, 1.10*f*  
 Inhomogeneous antireflection coatings,  
   7.23–7.26, 7.24*f*–7.26*f*  
 Inhomogeneous broadening, spectral-line,  
   14.14  
 Injection molding, of polymers, 3.2, 3.12–3.13  
 Inner ionization, of cluster, 21.31–21.32, 21.32*f*  
 Inorganic particles, in water, 1.14–1.15  
 In-plane coupling, 9.10–9.11  
 Instantaneous coefficient of linear thermal  
   expansion, 4.7  
 Instrumentation, spectroscopic, 5.58–5.61, 5.59*f*  
   detectors, 5.61  
   and light sources, 5.58–5.59  
   broadband, 5.58–5.59  
   laser, 5.59  
   spectrometers and monochromators,  
     5.59–5.61  
   dispersion spectrometers, 5.59–5.60  
   Fourier-transform spectrometers,  
     5.60–5.61, 5.60*f*, 5.72  
 “Intelligent” state, 23.8  
 Intense laser pulses:  
   cluster interactions with, 21.35–21.36, 21.36*f*  
   plasma instabilities driven by, 21.38–21.39,  
     21.38*f*  
 Interacting beams, propagation of, 16.3  
 Interband absorption, of semiconductors,  
   5.21–5.33  
   absorption near fundamental edge,  
     5.21–5.22, 5.21*f*  
   direct transitions, 5.22–5.23, 5.22*f*–5.23*f*  
   excitons, 5.25–5.29, 5.26*t*, 5.27*f*–5.28*f*  
   high-energy transitions above fundamental  
     edge, 5.29–5.33, 5.30*f*–5.34*f*  
   indirect transitions, 5.23–5.24, 5.24*f*–5.25*f*  
   near fundamental edge, 5.21–5.22, 5.21*f*  
   polaritons, 5.29  
 Interband magneto-optical effects, 5.42–5.46, 5.43*f*  
   excitonic, 5.46, 5.47*f*  
   Faraday rotation, 5.44–5.45, 5.45*f*  
   magnetoreflexion, 5.43, 5.44, 5.44*f*  
 Interband transitions, of solids, 8.27–8.32  
   direct interband absorption, 8.27–8.28  
   excitons, 8.31–8.32  
   indirect transitions, 8.29–8.30, 8.29*f*  
   joint density of states, 8.28, 8.29*f*  
   in metals, 8.21

- Interband transitions, of solids (*Cont.*):  
 multiphoton absorption, 8.30–8.31  
 selection rules and forbidden transitions,  
 8.28, 8.29
- Interference effect, EIT as, 14.2–14.4
- Interference filters, Fabry-Perot, 7.78–7.82,  
 7.79f, 7.80f, 7.92–7.94, 7.93f, 7.96
- Interference polarizers, 7.69–7.73, 7.70f–7.72f,  
 7.76f–7.77f
- Interfering transition pathways, 14.2–14.3
- Interferometers and interferometry:  
 atom, 11.22–11.23, 11.24f  
 Fabry-Perot, 7.13, 7.39, 7.39f, 7.40, 7.89  
 Mach-Zehnder, 23.2–23.4, 23.2f  
 Michelson, 7.42, 7.104f  
 multilayer reflectors for, 7.39, 7.39f  
 phase conjugate, 12.32, 12.33f, 12.34f  
 quantum entanglement in, 23.1–23.15  
   concepts and equations for, 23.1–23.4,  
   23.2f, 23.4f  
   digital approaches, 23.7–23.9  
   Heisenberg limit, 23.6–23.7  
   N00N state, 23.9–23.12, 23.10f, 23.11f  
   and quantum imaging, 23.13–23.14  
   and remote sensing, 23.14–23.15  
   shot-noise limit, 23.4–23.6, 23.5f  
   and third-order optical nonlinearities,  
   16.28–16.29  
   time-domain atom, 11.22–11.24, 11.24f
- Internal self-action, 13.7, 16.25
- International Association for Physical Sciences  
 of the Ocean (IAPSO), 1.4, 1.5t–1.6t
- Intervalley scattering, 18.20
- Intraband magneto-optical effects, 5.47–5.52  
 cyclotron resonance, 5.47–5.50, 5.48f–5.50f  
 free-carrier Faraday rotation, 5.50–5.51  
 impurity magnetoabsorption, 5.51–5.52,  
 5.51f
- Intracavity singly resonant oscillators  
 (IC-SROs), 17.3f
- Intrinsic optical properties:  
 of semiconductors, 5.11  
 of solids, 8.3
- Invar 36, 4.10t, 4.52t, 4.55t, 4.69t, 4.70t
- Inverse Bremsstrahlung heating, 21.37, 21.37f
- Inverse dielectric tensor, 2.6t, 2.19
- Ion beam-sputtered surfaces, 6.53
- Ion-assisted deposition, 7.11
- Ion-beam sputtering, 7.11, 7.14
- Ion-implanted semiconductors, 18.21
- Ionization:  
 above-threshold (*see* Above threshold  
 ionization)  
 atomic, 21.3  
 barrier suppression, 21.14, 21.14f  
 in clusters, 21.31–21.33, 21.32f  
 collisional, 21.31, 21.32  
 double, 21.18–21.19, 21.19f  
 inner, 21.31–21.32, 21.32f  
 molecular tunnel (*see* Molecular tunnel  
 ionization)  
 multiphoton, 21.10–21.12, 21.11f  
 outer, 21.32–21.33  
 stabilization of, 21.20–21.21, 21.22f  
 threshold (*see* Threshold ionization)  
 tunnel (*see* Tunnel ionization)
- Ionization distance, 21.25–21.26, 21.25f, 21.27f
- Ionization ignition, 21.31
- Ionization rate, ADK, 21.13
- Ionization stabilization, 21.20–21.21, 21.22f
- Ionization-induced defocusing, 21.43–21.44,  
 21.43f
- Ionized arsenic antisite (As<sub>Ga</sub><sup>+</sup>), 18.3
- Ion-plating process, 7.11
- IRG 2 glass, 2.43t, 2.49t, 2.54t, 2.59t, 2.67t
- IRG 9 glass, 2.43t, 2.49t, 2.54t, 2.59t, 2.67t
- IRG 11 glass, 2.43t, 2.49t, 2.59t, 2.68t
- IRG 100 glass, 2.43t, 2.49t, 2.54t, 2.59t, 2.68t
- Iris (in eye), 13.1
- Iron:  
 absorptance of, 4.40f, 4.48t, 4.50t  
 optical properties of, 4.15t, 4.23f  
 physical properties of, 4.54t  
 reflectance of, 4.32t–4.33t, 4.40f  
 thermal properties of  
   coefficient of linear thermal expansion,  
   4.56t, 4.57f  
   elastic stiffness, 4.69t  
   moduli and Poisson's ratio, 4.69t  
   at room temperature, 4.55t  
   specific heat, 4.65t, 4.67f  
   thermal conductivity, 4.58t, 4.62f–4.63f
- Irradiance, of water, 1.5t, 1.8–1.9
- Irradiance reflectance (irradiance ratio), of  
 water, 1.6t, 1.7f, 1.12, 1.46–1.47, 1.47f
- Irradiated plasma, 21.46–21.47, 21.46f
- Isotropic crystals:  
 dielectric constants of, 2.18  
 symmetries of, 2.7t
- Isotropic solids, 8.8, 8.9t

- Iturriaga R., 1.25  
*-ivity* suffix, 4.5
- $\mathbf{j} \times \mathbf{B}$  heating, 21.49
- Jerlov water types, 1.42–1.46
- Joint density of states, 8.28, 8.29*f*
- Jumps, electric-field, 9.6
- Junge (hyperbolic) cumulative size distribution, 1.15
- JV model (of trap-loss collisions), 20.30
- $K$  (optical constant of water), 1.17, 1.17*f*
- Kane momentum matrix elements, 8.26
- Keldysh parameter, 21.10
- Keldysh-Faisal-Reiss (KFR) theories, 21.12
- Kerr effect, 18.11–18.15  
 longitudinal, 18.11–18.15, 18.12*f*  
 optical, 16.11–16.14  
 Raman-induced, 16.3*t*, 16.12, 16.17  
 transverse, 18.11, 18.14–18.15
- Kerr lens modelocking (KLM), 16.25, 18.3, 18.14–18.15
- Kerr-lensing (*see* Self-focusing)
- Kerr-type nonlinearity, 14.33
- Kirchhoff's law, 4.6
- Kitaev phase estimation algorithm, 23.12
- Kleinman  $\mathbf{d}$ -tensor, 10.11
- Knill-LaFlamme-Milburn (KLM) scheme, 23.12
- Knoop test, 2.31, 2.32*f*
- Kopelevich model of absorption, 1.28
- Kramers-Kronig (K-K) relations:  
 dielectric-constant, 2.9, 2.12, 2.22  
 dispersion, 5.10–5.11, 16.1, 16.9–16.11  
 for solids, 8.15
- KRS-5 crystals, 2.40*t*, 2.44*t*, 2.48*t*, 2.53*t*, 2.58*t*, 2.65*t*
- KRS-6 crystals, 2.40*t*, 2.44*t*, 2.48*t*, 2.53*t*, 2.58*t*, 2.65*t*
- Ladder coupling, 14.1, 14.6*f*, 14.24*f*
- Lambda coupling, 14.1, 14.6*f*, 14.8*f*, 14.9*f*, 14.26, 14.27
- Lambertian black surface, 6.14
- Landau levels (of energy), 5.40, 5.42*f*
- Langmuir waves, 21.38
- Lanthanum glass, 2.42*t*, 2.43*t*
- Laser:  
 continuous-wave, 7.14, 14.16–14.18, 14.17*f*  
 multilayer reflectors for, 7.39–7.40, 7.39*f*  
 theoretical description of, 20.6–20.11  
 atoms in motion, 20.8–20.10, 20.9*f*  
 Fokker-Planck equation, 20.10–20.11  
 force on two-level atom, 20.6–20.7
- Laser Black, 6.56
- Laser conditioning, 19.4
- Laser cooling, 20.3–20.21, 20.26–20.39  
 about, 20.3–20.4  
 in atomic beam brightening, 20.27–20.28, 20.27*f*  
 in atomic clocks, 20.28  
 below Doppler limit, 20.17–20.21, 20.18*f*–20.20*f*  
 in Bose-Einstein condensation, 20.35–20.37, 20.36*f*  
 in dark states, 20.37–20.39, 20.38*f*  
 defined, 20.3  
 history of, 20.3–20.4  
 in optical lattices, 20.31–20.34, 20.32*f*–20.34*f*  
 by optical molasses, 20.13–20.17, 20.14*f*–20.16*f*  
 properties of, 20.4–20.6  
 Sisyphus, 20.19  
 by slowing of atomic beams, 20.11–20.13, 20.12*f*, 20.12*t*, 20.13*f*  
 in ultracold collisions, 20.28–20.31, 20.30*f*, 20.31*f*
- Laser damage threshold (LDT), of coatings, 7.13–7.14, 7.18
- Laser fields, 14.13
- Laser Interferometer Gravitational Wave Observatory (LIGO), 23.1, 23.7
- Laser Light Detection and Ranging (LIDAR) systems, 23.1
- Laser light sources, 5.59
- Laser power combining, 12.30, 12.31
- Laser pulses, 21.35–21.36, 21.36*f*, 21.38–21.39, 21.38*f*
- Laser technology, for strong field interactions, 21.4–21.5, 21.4*f*
- Laser-induced breakdown (LIB), 19.6–19.9, 19.8*f*
- Laser-induced damage (LID), 19.1–19.11  
 avoidance of, 19.5–19.6  
 and critical NLO parameters, 19.9–19.11, 19.9*f*, 19.10*f*  
 estimates of, 19.2  
 mechanisms of, 19.6–19.9, 19.8*f*  
 and nonlinear optical effects, 19.5  
 package-induced, 19.4–19.5  
 surface damage, 19.2–19.4
- Lasing without inversion (LWI), 14.1, 14.3–14.4, 14.18–14.19

- Lattice absorption, semiconductor, 5.13–5.20  
 impurity-related vibrational optic effects,  
 5.17–5.20, 5.18f–5.19f, 5.20t, 5.21f  
 multiphonon absorption, 5.16–5.17, 5.17t  
 phonons, 5.13–5.16, 5.15f
- Lattice vibrations:  
 of crystals and glasses, 2.11–2.12, 2.76t–2.77t  
 linear-chain model of, 5.8  
 optical, 20.31–20.34, 20.32f–20.34f  
 in solids, 8.16–8.18, 8.17f, 8.19t–8.20t
- Lead titanate (PbTiO<sub>3</sub>), 2.40t, 2.45t, 2.48t,  
 2.52t, 2.57t, 2.64t
- Lead vapor, 14.15, 14.16
- Lens housings, 3.15–3.16, 3.15f
- Lenses:  
 negative, 3.13  
 positive-powered, 3.13
- Lensing, 16.22, 19.5
- LF5 glass (581409), 2.49t, 2.54t, 2.59t, 2.66t
- Li Li polarizing beam splitter, 7.72–7.73, 7.76f
- Light flint glass, 2.42t
- Light modulation, 5.66t
- Light pipe reflectometers, rotating, 5.62, 5.63f
- Light pressure force, 20.7
- Light propagation, in solids, 8.4–8.13  
 anisotropic crystals, 8.8–8.11, 8.9t, 8.10f  
 energy flow, 8.7–8.8  
 interfaces, 8.11–8.13, 8.12f, 8.13f  
 Maxwell's equations, 8.4–8.6  
 wave equations and optical constants, 8.6–8.7
- Light sources, 5.58–5.59
- Limiters:  
 cascaded, 13.6  
 optical, 12.32  
 self-protecting, 13.9  
 tandem, 13.6, 13.6f
- Limiting, optical, 13.2 (*See also* Passive optical limiting)
- Line defects, 9.12–9.13
- Linear electro-optic effect, 12.2–12.3
- Linear optical absorption, 16.18
- Linear optical properties (of semiconductors),  
 5.11–5.39, 5.12f, 5.13t  
 free carriers, 5.33–5.36, 5.35f–5.37f  
 impurity and defect absorption, 5.37–5.39,  
 5.38f, 5.39f  
 interband absorption, 5.21–5.33  
 absorption near fundamental edge,  
 5.21–5.22, 5.21f  
 direct transitions, 5.22–5.23, 5.22f–5.23f
- Linear optical properties (of semiconductors),  
 interband absorption (*Cont.*):  
 excitons, 5.25–5.29, 5.26t, 5.27f–5.28f  
 high-energy transitions above fundamental  
 edge, 5.29–5.33, 5.30f–5.34f  
 indirect transitions, 5.23–5.24, 5.24f–5.25f  
 polaritons, 5.29  
 lattice absorption, 5.13–5.20  
 impurity-related vibrational optic effects,  
 5.17–5.20, 5.18f–5.19f, 5.20t, 5.21f  
 multiphonon absorption, 5.16–5.17,  
 5.17t  
 phonons, 5.13–5.16, 5.15f  
 and models of dielectric function, 5.12
- Linear-chain model, of lattice vibrations, 5.8
- Lin-perp-lin polarization gradient cooling,  
 20.17–20.18, 20.18f, 20.19f
- Lippmann-Bragg holographic mirrors, 7.50
- Liquid crystals, 13.12, 13.12f
- Lithium fluoride (LiF), 2.39t, 2.44t, 2.48t,  
 2.57t, 2.69t
- Lithium iodate ( $\alpha$ -LiIO<sub>3</sub>), 2.39t, 2.46t, 2.48t,  
 2.57t, 2.75t
- Lithium niobate (LiNbO<sub>3</sub>), 2.39t, 2.46t, 2.48t,  
 2.52t, 2.57t, 2.63t, 2.75t, 12.14, 17.1,  
 17.4–17.13, 17.6f–17.11f
- Lithium tantalate (LiTaO<sub>3</sub>), 12.14, 17.14–17.15,  
 17.15f
- Lithium triborate (LiB<sub>3</sub>O<sub>5</sub>) (LBO), 2.39t, 2.46t,  
 2.51t, 2.56t, 2.63t, 2.75t, 17.1
- Lithium-calcium-aluminum fluoride  
 (LiCaAlF<sub>6</sub>) (LiCAF), 2.39t, 2.46t, 2.51t,  
 2.57t, 2.63t
- LLF1 glass (548458), 2.49t, 2.54t, 2.59t, 2.66t
- Local density approximation (LDA), 5.5
- Local vibrational modes (LVM), 5.17, 5.18,  
 5.19f, 5.20, 5.20f
- Localized vibration, 5.82f, 5.83
- Lockheed Martin, 6.46
- Lock-in amplifiers, 5.64
- Long duration exposure facility (LDEF), 6.17
- Longitudinal acoustic (LA) phonons, 5.24,  
 5.25f
- Longitudinal Kerr effect, 18.11–18.15, 18.12f  
 (*See also* Self-phase modulation)
- Longitudinal optic (LO) phonons, 5.24, 5.25f,  
 5.79, 5.79f, 5.80
- Longitudinal relaxation rate and time, 11.5
- Longitudinal-mode (LO) frequencies, for  
 crystals and glasses, 2.11, 2.12



- Lorentz model:  
of absorption, 4.4  
of dispersion, 8.14, 8.21
- Low temperature (LT), 18.3
- Low-Q cavities, 9.12
- Low-temperature (LT) molecular beam epitaxy, 18.21
- LOX8 glass, 6.57
- Luminescence spectroscopy, 5.69–5.75, 5.70f, 5.72f–5.75f
- Lyddane-Sachs-Teller (LST) relation, 2.11, 5.14, 8.17
- Mach-Zehnder interferometer (MZI), 23.2–23.4, 23.2f
- MacNeille polarizers, 7.70–7.72, 7.71f, 7.72f, 7.75f
- Magnesium-oxide doped stoichiometric lithium tantalite (MgO:sPPLT), 17.14–17.15, 17.15f
- Magnetic field modulation, 5.66t
- Magnetic permeability, of water, 1.16
- Magnetic traps, 20.21–20.23, 20.22f
- Magnetoabsorption, impurity, 5.51–5.52, 5.51f
- Magneto-optical (MO) properties  
(of semiconductors), 5.39–5.52, 5.41t  
effect of magnetic field on energy bands, 5.40, 5.42, 5.42f  
interband effects, 5.42–5.46, 5.43f–5.45f, 5.47f  
intraband or free-carrier effects, 5.47–5.52, 5.48f–5.51f  
semiconductor nanostructures, 5.52
- Magneto-optical traps (MOTs), 14.18, 20.24–20.25, 20.24f, 20.26f
- Magnetopolarons, 5.50
- Magnetoreflexion, 5.43, 5.44, 5.44f
- Magnetron sputtering, 7.11
- Mankiewicz Gebr. & Co., 6.35
- Manly Rowe fraction, 15.15
- Manufacturing error budget, for polymeric optics, 3.10
- “Marine snow,” 1.14, 1.29
- Martin Black, 6.3t, 6.12, 6.14, 6.15, 6.26f, 6.28f, 6.46, 6.47f, 6.51f, 6.53f
- Martin Marietta, 6.48, 6.53
- Martin Optical Black, 6.5f
- Mass attenuation coefficients, for photons  
and metals, 4.48, 4.48t, 4.49
- Mass density, of metals, 4.6
- Master oscillator-power amplifier (MOPA) laser, 17.6
- Matched filtering, 12.28–12.29, 12.29f, 12.30f
- Material designation, of crystals and glasses, 2.27–2.30, 2.29f
- Matrix theory for multilayer systems, 7.6–7.10, 7.9f
- Maximal atomic coherence, 14.28–14.32, 14.29f–14.32f
- Maximal coherence, 14.3
- Maximum usable temperature, of metals, 4.7, 4.55t
- Maxwell wave equation, 2.12
- Maxwell-Bloch equations, 11.6–11.7
- Maxwell-Boltzmann distribution, 20.11
- Maxwell-Helmholtz-Drude dispersion formula, 2.12, 2.21–2.22
- Maxwell’s equations:  
for electric and magnetic fields, 1.16, 1.17, 5.52  
methods for solving, 9.2–9.3  
for optical fields, 16.24  
and refractive index, 2.6  
for solids, 8.4–8.6
- Mean coefficient of linear thermal expansion, 4.7
- Measurement techniques, for semiconductors, 5.7, 5.56–5.83  
ellipsometry, 5.67–5.69, 5.68f, 5.69f  
inelastic light scattering, 5.76–5.83, 5.76f, 5.78f–5.82f  
instrumentation, 5.58–5.61, 5.59f, 5.60f, 5.72  
luminescence, 5.69–5.75, 5.70f, 5.72f–5.75f  
modulation spectroscopy, 5.64–5.67, 5.64f–5.65f, 5.66t, 5.68f  
reflection and transmission/absorption, 5.62–5.64, 5.63f  
spectroscopic procedures, 5.56–5.58
- Measurements:  
on coatings, 7.12–7.14  
with surfaces and processes, 6.9–6.10
- Mechanical assembly, of polymers, 3.14–3.16, 3.14f, 3.15f
- Mechanical cycling, of metals, 4.10
- Medium-bandpass filters, 7.78–7.83, 7.79f, 7.80f, 7.82f–7.88f
- Melt data sheets, for glass, 2.29
- Memory, optical, 11.25, 12.34
- Meniscus-shaped elements, 3.13
- Mercury cadmium telluride ( $\text{Hg}_{0.78}\text{Cd}_{0.22}\text{Te}$ )  
narrow-gap alloy, 5.73, 5.74f
- Metal-dielectric multiple reflection cutoff filters, 7.59–7.60

- Metal-dielectric multiple reflection  
filters, 7.111
- Metal-dielectric reflectors, 7.81–7.82,  
7.108–7.109, 7.109f, 7.110f
- Metallic reflecting coatings, 7.80–7.81
- Metallic reflectors, 7.106–7.108, 7.106f–7.109f
- Metal-organic chemical vapor deposition  
(MOCVD), 18.3
- Metals, 4.1–4.70
- absorptance of, 4.39, 4.40f–4.42f, 4.48, 4.49  
and emittance, 4.49, 4.49f, 4.50t, 4.51t  
and mass attenuation coefficients for  
photons, 4.48t
  - aluminum and aluminum alloys  
absorptance, 4.40f, 4.48t, 4.51t  
optical properties, 4.12t, 4.20f, 4.21f  
penetration depth, 4.47f  
physical properties, 4.52t, 4.54t  
reflectance, 4.27t–4.28t, 4.40f, 4.44f, 4.46f  
thermal properties, 4.55t, 4.56t, 4.57f,  
4.58t, 4.59f–4.60f, 4.65t, 4.66f,  
4.69t, 4.70t
  - beryllium  
absorptance, 4.48t, 4.50t  
optical properties, 4.12t, 4.21f, 4.26f  
penetration depth, 4.47f  
physical properties, 4.52t, 4.54t  
reflectance, 4.28t–4.29t, 4.45f, 4.46f  
thermal properties, 4.55t, 4.56t, 4.57f, 4.58t,  
4.59f–4.60f, 4.65t, 4.68f, 4.69t, 4.70t
  - chromium  
absorptance, 4.48t, 4.50t  
optical properties, 4.13t–4.14t, 4.22f  
physical properties, 4.54t  
reflectance, 4.30t–4.31t  
thermal properties, 4.69t
  - copper  
absorptance, 4.40f, 4.48t, 4.50t  
optical properties, 4.12t–4.13t, 4.22f  
physical properties, 4.52t–4.54t  
reflectance, 4.29t–4.30t, 4.40f  
thermal properties, 4.55t, 4.56t, 4.57f, 4.58t,  
4.60f–4.61f, 4.65t, 4.66f, 4.69t, 4.70t
  - germanium  
absorptance, 4.48t  
thermal properties, 4.69t, 4.70t
  - gold  
absorptance, 4.40f, 4.48t, 4.50t, 4.51t  
optical properties, 4.14t, 4.23f  
physical properties, 4.52t, 4.54t
  - Metals, gold (*Cont.*):  
reflectance, 4.31t–4.32t, 4.40f  
thermal properties, 4.55t, 4.56t, 4.57f, 4.58t,  
4.60f–4.61f, 4.65t, 4.66f, 4.69t, 4.70t
  - interband transitions in, 8.21
  - Invar 36, 4.10t, 4.52t, 4.55t, 4.69t, 4.70t
  - iron  
absorptance, 4.40f, 4.48t, 4.50t  
optical properties, 4.15t, 4.23f  
physical properties, 4.54t  
reflectance, 4.32t–4.33t, 4.40f  
thermal properties, 4.55t, 4.56t, 4.57f,  
4.58t, 4.62f–4.63f, 4.65t, 4.67f, 4.69t
  - mechanical properties of, 4.7–4.8  
for mirror design, 4.8–4.10, 4.10t
  - molybdenum  
absorptance, 4.41f, 4.48f, 4.48t, 4.50t, 4.51t  
optical properties, 4.15t–4.16t, 4.24f  
physical properties, 4.52t, 4.54t  
reflectance, 4.33t–4.35t, 4.41f  
thermal properties, 4.55t, 4.56t, 4.58f, 4.58t,  
4.62f–4.63f, 4.65t, 4.67f, 4.69t, 4.70t
  - nickel and nickel alloys  
absorptance, 4.41f, 4.48t, 4.50t, 4.51t  
optical properties, 4.16t–4.17t, 4.24f  
penetration depth, 4.47f  
physical properties, 4.52t, 4.54t  
reflectance, 4.35t–4.36t, 4.41f, 4.47f  
thermal properties, 4.55t, 4.56t, 4.57f,  
4.58f, 4.62f–4.63f, 4.65t, 4.67f,  
4.69t, 4.70t
  - nomenclature for, 4.3
  - optical properties of, 4.3–4.6, 4.4f, 4.11  
dielectric function, 4.26f  
extinction coefficient, 4.11, 4.12t–4.19t,  
4.20f–4.26f  
refraction index, 4.11, 4.12t–4.19t, 4.21f–4.26f
  - penetration depth of, 4.47f
  - physical properties of, 4.6, 4.49, 4.52t–4.54t
  - platinum  
absorptance, 4.41f, 4.48t, 4.50t, 4.51t  
optical properties, 4.17t, 4.25f  
physical properties, 4.54t  
reflectance, 4.36t–4.37t, 4.41f  
thermal properties, 4.69t, 4.70t
  - reflectance of, 4.11, 4.27t–4.39t, 4.40f–4.47f
  - semiconductors and dielectrics vs., 8.4
  - silicon  
absorptance, 4.48t  
physical properties, 4.52t

- Metals, silicon (*Cont.*):  
 reflectance, 4.46f  
 thermal properties, 4.55t, 4.56t, 4.58f, 4.58t,  
 4.63f–4.64f, 4.65t, 4.68f, 4.69t, 4.70t
- silicon carbide  
 absorptance, 4.49f, 4.50f  
 optical properties, 4.19t, 4.25f  
 physical properties, 4.52t  
 reflectance, 4.41f, 4.42f, 4.46f  
 thermal properties, 4.55t, 4.56t, 4.58f, 4.58t,  
 4.63f–4.64f, 4.65t, 4.68f, 4.69t, 4.70t
- silver  
 absorptance, 4.42f, 4.48t, 4.50t, 4.51t  
 optical properties, 4.17t–4.18t, 4.26f  
 physical properties, 4.52t, 4.54t  
 reflectance, 4.37t–4.38t, 4.42f  
 thermal properties, 4.55t, 4.56t, 4.57f, 4.58t,  
 4.60f–4.61f, 4.65t, 4.66f, 4.69t, 4.70t
- stainless steel  
 physical properties, 4.52t  
 thermal properties, 4.55t, 4.56t, 4.57f, 4.58t,  
 4.62f–4.63f, 4.65t, 4.67f, 4.69t, 4.70t
- steel, 4.50t, 4.51t
- tantalum, 4.50t, 4.69t, 4.70t
- thermal properties of, 4.6–4.7, 4.53, 4.55  
 coefficient of linear thermal expansion,  
 4.56t, 4.57f, 4.58f  
 elastic properties, 4.69, 4.69t  
 at room temperature, 4.55t  
 specific heat, 4.65t, 4.66f–4.69f  
 strength and fracture properties, 4.70, 4.70t  
 thermal conductivity, 4.58t, 4.59f–4.63f
- titanium, 4.48t, 4.50t, 4.52t, 4.55t
- tungsten  
 absorptance, 4.42f, 4.48t, 4.50t, 4.51t  
 optical properties, 4.18t–4.19t, 4.26f  
 physical properties, 4.54t  
 reflectance, 4.38t–4.39t, 4.42f  
 thermal properties, 4.69t, 4.70t
- zinc, 4.48t
- Metrology, cw OPOs for, 17.28, 17.29
- MeV proton acceleration, 21.54, 21.54f
- MH 2200 coating, 6.37, 6.38f
- Mica spacers, 7.84f, 7.88–7.89
- Michelson interferometers, 5.60, 7.42, 7.104f
- Microcavities, in 3D photonic crystals, 9.6–9.12,  
 9.7f, 9.8f
- Microcreep strength, of metals, 4.8
- Microstrain, of metals, 4.8
- Microyield strength, of metals, 4.8, 4.70, 4.70t
- Mie scattering, 1.15, 1.32, 2.27
- Mie theory, 1.40
- Miller's rule, 10.9
- Minus filters, 7.43, 7.48, 7.49, 7.50f
- Mirrors:  
 aluminum, 7.106–7.108, 7.106f–7.108f  
 graded reflectivity, 7.52  
 hot and cold, 7.58  
 Lippmann-Bragg holographic, 7.50  
 metals for, 4.8–4.10, 4.10t  
 perfect, 7.47  
 phase conjugate, 12.7, 12.8f–12.9f, 12.33–12.35  
 self-pumped phase conjugate, 12.7,  
 12.8f–12.9f  
 semiconductor saturable absorber, 18.3,  
 18.10–18.11  
 semilinear, 12.7, 12.8f  
 silver, 7.106f–7.108f, 7.107–7.109  
 supermirrors, 7.111  
 (*See also* Reflectors)
- M&M states, 23.14
- Modelocking:  
 additive pulse, 18.3, 18.14  
 colliding pulse, 18.3  
 cw, 18.5f  
 cw Q-switched, 18.5f  
 Kerr lens, 18.3, 18.14–18.15  
 passive, 18.8–18.9, 18.8f, 18.12–18.15  
 Q-switched, 18.4, 18.5, 18.5f  
 soliton, 18.8f, 18.12–18.14
- Modified lambda coupling, 14.24f
- Modulation spectroscopy, 5.64–5.67,  
 5.64f–5.65f, 5.66t, 5.68f
- Mohs scale, 2.31, 2.32f
- Moiré grating, 22.11, 22.12f
- Molasses, optical [*see* Optical molasses (OM)]
- Molding, of polymers, 3.2, 3.12–3.13
- Molecular alignment, in strong fields,  
 21.22–21.23, 21.23t, 21.24f
- Molecular beam epitaxy (MBE), 5.7, 18.3
- Molecular dissociation, 21.23
- Molecular orientational Kerr effect, 16.3t
- Molecular tunnel ionization, 21.25–21.26,  
 21.25f, 21.27f
- Molecular weight, of crystals and glasses, 2.30
- Molecules, strong field interactions with,  
 21.22–21.26  
 Coulomb explosion, 21.24–21.25  
 nuclear motion and alignment in, 21.22–21.23,  
 21.23t, 21.24f

- Molecules, strong field interactions with (*Cont.*):  
 triatomic and larger, 21.26  
 tunnel ionization and ionization distance,  
 21.25–21.26, 21.25f, 21.27f
- Molybdenum:  
 absorptance of, 4.41f, 4.48f, 4.48t, 4.50t, 4.51t  
 optical properties of, 4.15t–4.16t, 4.24f  
 physical properties of, 4.52t, 4.54t  
 reflectance of, 4.33t–4.35t, 4.41f  
 thermal properties of  
 coefficient of linear thermal expansion,  
 4.56t, 4.58f  
 elastic stiffness, 4.69t  
 moduli and Poisson's ratio, 4.69t  
 at room temperature, 4.55t  
 specific heat, 4.65t, 4.67f  
 strength and fracture properties, 4.70t  
 thermal conductivity, 4.58t, 4.62f–4.63f
- Momentum, family, 20.38
- Monochromators, 5.59–5.61
- Monoclinic crystals, 2.7t, 2.18, 2.47t, 8.9t, 8.19t
- Morel model of absorption, 1.24, 1.28
- Morse interatomic potential, 2.16
- Mott-Wannier excitons (*see* Wannier excitons)
- Multicomponent polarizers, 7.69
- Multilayer (ML) coatings, 7.96–7.98, 19.4
- Multilayer reflectors, 7.39–7.53  
 of absorbing materials, 7.37–7.38, 7.38f  
 all-dielectric broadband reflectors, 7.39,  
 7.40f, 7.45–7.47, 7.45f–7.47f  
 coatings for ultrafast optics, 7.47–7.48, 7.48f  
 for far-infrared region, 7.52, 7.52f  
 graded reflectivity mirrors, 7.52  
 imperfections in, 7.40–7.43, 7.41f–7.43f  
 for interferometers and lasers, 7.39–7.40,  
 7.39f–7.40f  
 narrowband reflection coatings, 7.43, 7.44f  
 rejection filters, 7.48–7.50, 7.49f–7.51f  
 for soft x-ray and XUV regions, 7.53  
 in two-material periodic multilayers theory,  
 7.37–7.38, 7.38f
- Multilayers:  
 matrix theory for, 7.6–7.10, 7.9f  
 periodic  
 [(0.5A)B(0.5A)]<sup>N</sup>, 7.35, 7.36f  
 nonabsorbing [AB]<sup>N</sup> and [AB]NA,  
 7.32–7.34, 7.33f–7.35f  
 [xH.(1-x)L]<sup>N</sup>.xH, 7.37
- Multiphonon absorption, 5.16–5.17, 5.17t,  
 5.18f, 19.6
- Multiphoton absorption:  
 of crystals and glasses, 2.15–2.17, 2.16f, 2.17f  
 of solids, 8.30–8.31
- Multiphoton ionization (MPI), 21.10–21.12,  
 21.11f
- Multiphoton refraction, of crystals and glasses,  
 2.15–2.17, 2.16f, 2.17f
- Multiple anti-Stokes scattering, 15.2t
- Multiple bound excitons, 5.26t
- Multiple cavities, in polymeric optics, 3.10
- Multiple quantum wells (MQWs), 12.22–12.23,  
 12.22f
- Multiple Raman scattering, 15.2–15.3, 15.2t
- Multiple Raman Stokes generation, 15.38–15.40,  
 15.40f
- Multiple Stokes scattering, 15.2–15.3, 15.2t,  
 15.3t
- Multiple-layer surfaces, 6.26, 6.26f–6.27f
- Multiple-reflection filters, 7.111–7.113,  
 7.111f–7.113f
- Multiple-resonant oscillators, 17.16–17.21  
 doubly resonant, 17.16–17.17  
 pump-enhanced singly resonant, 17.17–17.20,  
 17.18f–17.20f  
 triply resonant, 17.20–17.21, 17.21f
- Multishot laser-induced damage, 19.4
- Mutually incoherent beam couplers, 12.7, 12.8f
- Mutually pumped phase conjugators  
 (MPPCs), 12.7
- N* (optical constant of water), 1.17, 1.17f
- N* on 1 annealing, 19.3, 19.4
- N<sup>00N</sup> state, 23.9–23.12, 23.10f, 23.11f
- Nanoplasma, in clusters, 21.34–21.35, 21.35f
- Nanostructure semiconductors, 5.52
- Nanostructuring, 6.55, 6.59f
- Nanotubes, 6.55, 6.59f
- Narrowband reflection coatings (narrowband  
 rejection filters), 7.43, 7.44f, 7.49
- Narrow-bandpass filters, 7.78–7.83, 7.79f, 7.80f,  
 7.82f–7.88f, 7.88–7.89, 7.89f
- NAS polymer, 3.4t
- National Institute of Standards and Technology  
 (NIST), 20.16
- Natural waters, 1.3, 1.13–1.15
- N-BaF10 glass (670472), 2.49t, 2.54t, 2.59t, 2.67t
- N-BaK4 glass (569560), 2.49t, 2.54t, 2.59t, 2.66t
- N-BaLF4 glass (580537), 2.49t, 2.54t, 2.59t, 2.66t
- N-BaSF64 glass (704394), 2.49t, 2.54t, 2.59t, 2.67t
- NbF1 glass (743492), 2.49t, 2.54t, 2.59t, 2.67t

- N-BK7 glass (517642), 2.49t, 2.54t, 2.59t, 2.66t  
 NBS Black, 6.49–6.50, 6.50f  
 Near-IR crystals, visible, 10.21t, 10.22t  
 Near-UV spectrum, semiconductor interactions  
 with, 5.4f, 5.5  
 Negative lenses, 3.13  
 Neoprene, 6.32f, 6.34f  
 Net irradiance, of water, 1.5t, 1.7f, 1.9  
 Networks, 3D photonic crystals and, 9.4–9.5  
 Neumann's principle, 2.5  
 Neural networks, 12.33–12.35  
 Neutral arsenic antisite ( $\text{As}_{\text{Ga}0}$ ), 18.3  
 Neutral atoms, trapping of, 20.21–20.39  
 in atomic beam brightening, 20.27–20.28,  
 20.27f  
 in atomic clocks, 20.28  
 in Bose-Einstein condensation, 20.35–20.37,  
 20.36f  
 in dark states, 20.37–20.39, 20.38f  
 with magnetic traps, 20.21–20.23, 20.22f  
 with magneto-optical traps, 20.24–20.25,  
 20.24f, 20.26f  
 in optical lattices, 20.31–20.34, 20.32f–20.34f  
 with optical traps, 20.23–20.24, 20.23f  
 in ultracold collisions, 20.28–20.31, 20.30f,  
 20.31f  
 Neutral attenuators, 7.105, 7.105f  
 Neutral filters, 7.67, 7.67f–7.68f  
 Neutron production, fusion, 21.53  
 Nextel 2010, 6.35, 6.37  
 Nextel Suede Coating Series 3101-C10, 6.37,  
 6.38f, 6.53f  
 N-F2 glass (620364), 2.49t, 2.54t, 2.59t, 2.67t  
 N-FKS glass (487704), 2.49t, 2.54t, 2.59t, 2.66t  
 Nickel:  
 absorptance of, 4.41f, 4.48t, 4.50t, 4.51t  
 optical properties of, 4.16t–4.17t, 4.24f  
 penetration depth, 4.47f  
 physical properties of, 4.52t, 4.54t  
 reflectance of, 4.35t–4.36t, 4.41f, 4.47f  
 thermal properties of  
 coefficient of linear thermal expansion,  
 4.56t, 4.57f  
 elastic stiffness, 4.69t  
 moduli and Poisson's ratio, 4.69t  
 at room temperature, 4.55t  
 specific heat, 4.65t, 4.67f  
 strength and fracture properties, 4.70t  
 thermal conductivity, 4.58f, 4.62f–4.63f  
 Nickel alloys, 4.47f  
 Niobium flint glass, 2.42t  
 N-K5 glass (522595), 2.49t, 2.54t, 2.59t, 2.66t  
 N-KF9 glass (523515), 2.49t, 2.54t, 2.59t, 2.66t  
 N-KzFS4 glass (613443), 2.49t, 2.54t, 2.59t, 2.66t  
 N-LaF2 glass (744447), 2.49t, 2.54t, 2.59t, 2.67t  
 N-LaF33 glass (754523), 2.49t, 2.54t, 2.59t, 2.67t  
 N-LaK10 glass (720504), 2.49t, 2.54t, 2.59t, 2.67t  
 N-LaSF31A glass (883409), 2.49t, 2.54t, 2.59t, 2.67t  
 Noise:  
 shot, 23.4–23.6, 23.5f  
 and stimulated Raman scattering, 15.35–15.38,  
 15.39f  
 Nonabsorbing  $[AB]^N$  and  $[AB]/NA$  multilayers,  
 7.32–7.34, 7.33f–7.35f  
 Noncritical phase matching (NCPM), 17.1  
 Nondegenerate four-wave mixing  
 (NDFWM), 14.28  
 Nonlinear absorption (NLA), 16.29  
 limiters of, 13.6–13.7, 13.6f  
 mechanisms of, 16.12–16.13, 16.13f  
 nondegenerate, 16.27  
 optical limiting by, 13.4–13.7, 13.4f, 13.5f  
 and third-order optical nonlinearities,  
 16.7–16.9  
 Nonlinear atom-field interactions, 11.10  
 Nonlinear optical coefficients, of crystals  
 and glasses, 2.26–2.27, 2.27t  
 Nonlinear optical crystals, 10.19–10.20,  
 10.20t–10.22t  
 Nonlinear optical (NLO) effects, 19.5,  
 19.9–19.11, 19.9f, 19.10f  
 Nonlinear optical frequency conversion,  
 14.24–14.28, 14.24f, 14.27f  
 Nonlinear optical properties (of semiconductors),  
 5.52–5.56  
 Maxwell's equations and polarization power  
 series expansion, 5.52–5.53, 5.54t  
 second-order, 5.53–5.55  
 third-harmonic generation, 5.56  
 third-order, 5.55  
 two-photon absorption, 5.56  
 Nonlinear optics, 10.3–10.23  
 about, 10.4–10.5  
 conversion efficiencies, 10.14–10.16  
 crystals for, 10.19–10.20, 10.20t–10.22t  
 equations for, 10.4–10.5  
 microscopic origin of, 10.5–10.10, 10.6f, 10.8f  
 and MKS systems, 10.21–10.23  
 optical parametric process in, 10.16–10.19,  
 10.17f–10.19f

- Nonlinear optics (*Cont.*):
- phase-matching condition in second-order processes, **10.12–10.14**, **10.12f**, **10.13f**
  - second-order susceptibility tensor in, **10.10–10.11**
  - third-order optical nonlinearities, **16.1–16.31**
    - cascaded  $x^{(1)}:x^{(1)}$  processes, **16.20–16.22**, **16.21f**
    - cascaded  $x^{(2)}:x^{(2)}$  processes, **16.22–16.24**, **16.23f**, **16.24f**
    - four-wave mixing, **16.27–16.28**, **16.28f**
    - interferometry, **16.28–16.29**
    - Kerr effect, **16.11–16.14**, **16.13f**, **16.14f**
    - Kramers-Kronig dispersion relations, **16.9–16.11**
    - nonlinear absorption and nonlinear refraction, **16.7–16.9**
    - propagation effects, **16.24–16.26**
    - and quantum mechanics, **16.4–16.7**, **16.5f**
    - stimulated scattering, **16.14–16.19**, **16.15f**, **16.17f**
    - terms for, **16.1–16.3**, **16.3t**
    - third-harmonic generation, **16.14**
    - time-resolved excite-probe techniques, **16.26–16.27**, **16.26f**
    - two-photon absorption, **16.19–16.20**
    - Z-scan, **16.29–16.30**, **16.30f**
  - ultrashort pulse generation, **18.1–18.23**
    - Kerr effect, **18.11–18.15**, **18.12f**
    - saturable absorbers, **18.5–18.11**, **18.6f–18.8f**
    - semiconductor ultrafast nonlinearities, **18.15–18.23**, **18.16f**, **18.17f**, **18.22f**
    - and ultrafast lasers, **18.3–18.5**, **18.4f**, **18.5f**
- Nonlinear optics in gases, strong field, **21.27–21.31**, **21.28f**
- Nonlinear reflectivity, **18.6–18.7**, **18.7f**
- Nonlinear refraction (NLR), **13.4f**, **13.7–13.8**, **16.7–16.9**, **16.29–16.30**, **16.30f**
- Nonlinear scattering, **13.4f**, **13.8**
- Nonlinear Schrödinger equation (NLSE), **16.25**
- Nonlinear susceptibility, of crystals and glasses, **2.26**
- Nonlinear Thomson scattering, **21.8–21.9**, **21.9f**
- Nonnormal angle of incidence, antireflection coatings at, **7.28–7.31**, **7.28f–7.31f**
- Nonpolarizing beam splitters, **7.63**, **7.64f–7.65f**, **7.65**
- Nonpolarizing edge and bandpass filters, **7.66**, **7.67f**
- Nonreactive evaporation, **7.11**
- Nonresonant degenerate four-wave mixing, **16.27–16.28**, **16.28f**
- No-phonon (NP) photoluminescence, **5.72**, **5.73f**
- Normalized detuning, **14.11f**
- Normalized vector potential, **21.6**
- Normalized water-leaving irradiance, **1.46–1.48**, **1.48f**
- Notch filters, **7.43**
- Novelty filters, **12.32**, **12.33f–12.35f**
- N-PK52A glass (497816), **2.49t**, **2.54t**, **2.59t**, **2.66t**
- N-PSK53A glass (618634), **2.49t**, **2.54t**, **2.59t**, **2.66t**
- N-SF6 (805254), **2.49t**, **2.54t**, **2.59t**, **2.67t**
- N-SK10 glass (623570), **2.49t**, **2.54t**, **2.59t**, **2.67t**
- N-SSK5 glass (658509), **2.49t**, **2.54t**, **2.59t**, **2.67t**
- Nuclear motion, in strong fields, **21.22–21.23**, **21.23t**, **21.24f**
- Null correctors, optical, **3.16**
- Null optics, polymers and, **3.16–3.17**
- N-ZK7 glass (508612), **2.49t**, **2.54t**, **2.59t**, **2.66t**
- Oak Ridge, **6.51**
- Ocean color, **1.46**
- Omnidirectional reflectors, **9.2**
- One-dimensional optical molasses, **20.15–20.16**, **20.15f**
- One-electron transitions, **5.7**
- Open aperture Z-scan, **16.30**
- Open systems, **11.17–11.18**, **11.17f**, **11.18f**
- Optical Bloch equations (OBEs), **11.3–11.6**, **20.3**, **20.6**
- “Optical Characterization in Microelectronics Manufacturing” (S. Perkowitz, D. G. Seiler, W. M. Duncan), **5.61–5.62**
- Optical constants:
- for coatings, **7.13**
  - and dielectric function, **5.8–5.9**
  - of metals, **4.11**, **4.12t–4.19t**, **4.20f–4.26f**
  - of solids, **8.6–8.7**, **8.15**
  - of water, **1.17**, **1.17f**
- Optical frequency synthesis, **17.28**, **17.29**
- Optical indicatrix (index ellipsoid), of crystals and glasses, **2.18–2.19**, **2.19f**
- Optical interconnects, **12.31**, **12.31f**
- Optical Kerr effect (OKE), **16.11–16.14**, **16.13f**, **16.14f**
- Optical lattices, **20.31–20.34**, **20.32f–20.34f**
- Optical limiters, **12.32**

- Optical modes, of crystals and glasses, 2.68t–2.76t  
 with cesium chloride structure, 2.68t  
 with chalcopyrite structure, 2.74t  
 with corundum structure, 2.70t  
 with cubic perovskite structure, 2.73t  
 with diamond structure, 2.68t  
 with fluorite structure, 2.69t  
 other structures, 2.74t–2.76t  
 with  $\alpha$ -quartz structure, 2.71t  
 with rutile structure, 2.71t  
 with scheelite structure, 2.72t  
 with sodium chloride structure, 2.69t  
 with spinel structure, 2.73t  
 with tetragonal perovskite structure, 2.73t  
 with trigonal selenium structure, 2.70t  
 with wurtzite structure, 2.70t  
 with zinblende structure, 2.69t
- Optical molasses (OM), 20.13–20.17  
 defined, 20.3, 20.10  
 Doppler cooling, 20.13–20.15, 20.14f  
 one-dimensional, 20.15–20.16, 20.15f  
 three-dimensional, 20.16–20.17, 20.16f
- Optical monitoring, in thin film manufacturing, 7.11
- Optical parametric amplifiers (OPAs), 23.13–23.14
- Optical parametric chirped pulse amplification (OPCPA), 21.5
- Optical parametric oscillators (OPOs), 10.18–10.19, 10.19f, 14.15 [See also Continuous-wave optical parametric oscillators (cw OPOs)]
- Optical parametric (OP) process, 10.16–10.19, 10.17f–10.19f
- Optical phonons, 5.14
- Optical Ramsey fringes, 11.20–11.22, 11.21f
- Optical responses, classification of, 5.12, 5.13t
- Optical spectroscopy, 11.2
- Optical Stark effect, 16.13
- Optical traps, 20.23–20.24, 20.23f
- Optical tweezers, 20.23
- Optically generated plasmas, 16.20
- Optically polished solid spacers, 7.88–7.89
- Optically induced phase charge, 13.4f, 13.9
- Orange peel, of polymers, 3.11
- Organic black dye, 6.15
- Organic crystals, 12.23–12.25, 12.26t–12.27t
- Organic matter:  
 absorption by, 1.22–1.23, 1.23t, 1.25–1.27, 1.25t, 1.26f  
 passive limiting in, 13.10  
 in water, 1.14
- Organic-inorganic composites, hybrid, 12.27t
- Orlando Black optical coating, 6.54, 6.55f
- Orlando Black surface, 6.8f
- Orthorhombic crystals, 2.7t, 2.18, 2.46t, 8.9t, 8.10, 8.19t
- Oscillator models, of optical nonlinearity, 10.5–10.9, 10.6f, 10.8f
- Oscillators, 12.7–12.9, 12.8f–12.9f (See also specific oscillators, e.g.: Raman oscillators)
- Outer ionization, of cluster, 21.32–21.33
- Outgassing:  
 of black surfaces, 6.17  
 of polymers, 3.4
- Out-of-plane coupling, 9.11–9.12
- Overdense plasmas, strong field interactions  
 with, 21.46–21.52  
 high harmonic generation, 21.50–21.52, 21.51f  
 $j \times B$  heating and anomalous skin effect, 21.49  
 ponderomotive steepening and hole boring, 21.49–21.50, 21.50f  
 relativistic effects and induced transparency, 21.52  
 resonance absorption, 21.47–21.48, 21.47f  
 structure of irradiated plasma, 21.46–21.47, 21.46f  
 vacuum heating, 21.47f, 21.48–21.49
- Oxide layer, aluminum reflectance and, 4.44f
- Package-induced laser-induced damage, 19.4–19.5
- Painted surfaces, 6.2t–6.3t
- Paints and surface treatments, 6.35–6.58, 6.37f, 6.43f, 6.53f  
 Akhtar black coatings, 6.55  
 Aeroglaze Z series, 6.36f, 6.37, 6.37f, 6.39, 6.39f–6.42f  
 Akzo Nobel paints, 6.39, 6.42f, 6.43f  
 anodized processes, 6.44–6.49, 6.47f, 6.48f, 6.51f, 6.53f  
 black glass, 6.57  
 Black Kapton, 6.57, 6.57f  
 carbon nanotubes and nanostructured materials, 6.55, 6.59f  
 Cardinal Black, 6.36f, 6.39, 6.44f  
 Cat-a-lac Black, 6.39, 6.42f, 6.53f  
 conductive/nonconductive, 6.12, 6.12t  
 DeSoto Black, 6.37f, 6.39  
 DURACON, 6.55–6.56  
 electrically conductive black paint, 6.56  
 electrodeposited surfaces, 6.53–6.54, 6.54f, 6.55f

- Paints and surface treatments (*Cont.*):  
 etching of electroless nickel, 6.49–6.50, 6.50f, 6.51f, 6.53f  
 flame-sprayed aluminum, 6.57  
 Floquil, 6.44  
 gold blacks, 6.57  
 high-resistivity coatings, 6.56  
 IBM Black (tungsten hexafluoride), 6.56  
 ion beam-sputtered surfaces, 6.53  
 Parson's Black, 6.44, 6.53f  
 plasma-sprayed surfaces, 6.50–6.52, 6.51f–6.53f  
 silicon carbide, 6.56  
 SolarChem, 6.44, 6.48f, 6.53f  
 sputtered metallic anodized surfaces, 6.57, 6.58f  
 sputtered and CVD surfaces, 6.56  
 3M paints and derivatives, 6.35–6.37, 6.36f, 6.38f, 6.53f  
 ZO-MOD BLACK, 6.56
- Parametric amplification, 10.17–10.18, 16.3t
- Parametric oscillators, 10.18–10.19, 10.18f, 10.19f
- Paratellurite ( $\text{TeO}_2$ ), 2.40t, 2.45t, 2.48t, 2.52t, 2.58t, 2.65t, 2.76t
- Parson's Black, 6.44, 6.53f
- Particles:  
 surface coatings and generation of, 6.17–6.18  
 in water  
 particle size distributions, 1.15–1.16, 1.16f  
 refraction index of, 1.20  
 scattering by, 1.30–1.35, 1.31t, 1.32f, 1.33f, 1.34t–1.35t
- Particulate matter, in water, 1.14–1.15
- Passband region, transmission in, 7.53, 7.54
- Passive modelocking, 18.8–18.9, 18.8f, 18.12–18.15
- Passive nonlinear optical phenomena, 5.54, 5.54t
- Passive optical limiting, 13.1–13.12  
 active vs., 13.1–13.3, 13.2f, 13.3f  
 in materials, 13.9–13.12, 13.10f–13.12f  
 by nonlinear absorption, 13.4–13.7, 13.4f–13.6f  
 by nonlinear refraction, 13.4f, 13.7–13.8  
 by nonlinear scattering, 13.4f, 13.8  
 optically induced phase charge, 13.4f, 13.9  
 by photorefraction, 13.8–13.9
- Pattern recognition, by matched filtering, 12.28–12.29, 12.29f, 12.30f
- Pendular states, 21.23
- Penetration depth, of metals, 4.47f
- Perfect diffuse reflectors (PDRs), 6.7f, 6.27f
- Perfect mirrors, 7.47
- Periclase ( $\text{MgO}$ ), 2.44t, 2.48t, 2.52t, 2.57t, 2.63t, 2.69t
- Periodic multilayers:  
 $[(0.5A)B(0.5A)]^N$ , 7.35, 7.36f  
 nonabsorbing  $[AB]^N$  and  $[AB]NA$ , 7.32–7.34, 7.33f–7.35f  
 $[xH.(1-x)L]^N.xH$ , 7.37
- Periodically poled lithium niobate ( $\text{LiNbO}_3$ ) (PPLN), 17.1, 17.4–17.13, 17.6f–17.11f
- Periodically poled lithium tantalate ( $\text{LiTaO}_3$ ) (PPLT), 17.14–17.15, 17.15f
- Periodically poled potassium titanyl phosphate ( $\text{KTiOPO}_4$ ) (PPKTP), 17.2, 17.28, 17.29f, 17.30f
- Permittivity, of water, 1.16
- Perovskite, 2.73t
- Petawatt lasers, 21.5
- Petzold volume scattering functions, 1.33, 1.33f
- Petzval sums, 3.8
- Phase charge, optically induced, 13.4f, 13.9
- Phase coatings, 7.101, 7.101f–7.104f, 7.102
- Phase conjugate interferometry, 12.32, 12.33f, 12.34f
- Phase conjugate mirrors, 12.7, 12.8f–12.9f, 12.33–12.35
- Phase conjugation:  
 Brillouin, 15.48, 15.52–15.54, 15.52f–15.54f  
 photo echo and geometry of, 11.19–11.22, 11.20f, 11.21f
- Phase dispersion filters, 7.89, 7.89f
- Phase distortion, nonlinearly induced, 16.28–16.29
- Phase matching:  
 and harmonic yield, 21.30  
 and Maxwell-Bloch equations, 11.6  
 noncritical, 17.1  
 QPM materials, 17.1, 17.13–17.14  
 in second-order processes, 10.12–10.14, 10.12f, 10.13f  
 and stimulated Raman scattering, 15.7, 15.34, 15.34f
- Phase pulling, of transient Raman scattering, 15.26–15.27, 15.27f
- Phase retarding reflectors, 7.101–7.102, 7.102f, 7.103f
- Phase shifter, cross-Kerr, 23.11
- Phasesonium, 14.3
- Phase-transition temperatures, of crystals and glasses, 2.32, 2.33



- Phonons, 2.11  
 acoustic, 5.14–5.16  
 coupled plasmon and, 5.35, 5.36, 5.36*f*, 5.37*f*  
 lattice absorption by, 5.13–5.16, 5.15*f*  
 optical, 5.14  
 and Raman scattering, 5.79–5.81, 5.79*f*–5.81*f*  
 transverse optical (TO), 8.16–8.18
- Phosphate crown glass, 2.41*t*
- Photoacoustic spectroscopy (PAS), 17.22–17.26, 17.22*f*–17.24*f*, 17.26*f*
- Photo-associative spectroscopy (PAS), 20.30–20.31, 20.31*f*
- Photoconductors (PCs), 5.61
- Photoelastic coefficients, of crystals and glasses, 2.24
- Photoexcitation, 5.70*f*
- Photoluminescence (PL), 5.70–5.75, 5.70*f*, 5.72*f*–5.75*f*
- Photoluminescence excitation (PLE) spectroscopy, 5.75, 5.75*f*
- Photomultipliers (PMTs), 5.61
- Photon absorption (PA), 19.9, 19.10, 19.10*f*
- Photon echo, 11.11–11.19  
 about, 11.11–11.15, 11.12*f*, 11.13*f*, 11.15*f*  
 stimulated, 11.15–11.19, 11.16*f*–11.19*f*
- Photon echo spectroscopy, 11.26–11.27
- Photon loss, 23.14–23.15
- Photonic bandgaps (PBGs), 9.1–9.17  
 fibers with, 2.23  
 Maxwell's equations, 9.2–9.3  
 in 3D photonic crystals, 9.4–9.12  
 criteria for, 9.4–9.5  
 examples of, 9.5, 9.5*f*  
 microcavities in, 9.6–9.12, 9.7*f*, 9.8*f*  
 2D periodicity in microcavities of, 9.8–9.12, 9.9*f*  
 in-plane coupling, 9.10–9.11  
 out-of-plane coupling, 9.11–9.12  
 and waveguides, 9.12–9.17  
 in photonic crystals with 2D periodicity, 9.13–9.14, 9.13*f*  
 waveguide bends, 9.14–9.16, 9.15*f*, 9.16*f*  
 waveguide intersections, 9.16–9.17, 9.17*f*
- Photonic crystals, 9.3
- Photonic resonance, 22.9–22.13, 22.10*f*, 22.12*f*
- Photon-number eigenstates, 23.7–23.8
- Photons:  
 mass attenuation coefficients for, 4.48, 4.48*t*, 4.49  
 Raman interaction with, 15.21–15.22  
 and water, 1.11
- Photoreactive scattering, 12.9
- Photoreflectance (PR), 5.66*t*, 5.67
- Photorefraction:  
 optical limiting by, 13.8–13.9  
 of third-order optical nonlinearities, 16.22
- Photorefractive effect, 12.1–12.38  
 beam spatial profiles, 12.10  
 devices using, 12.28–12.38  
 associative memories and neural networks, 12.33–12.35  
 gain and two-beam coupling, 12.29–12.32, 12.31*f*  
 holographic data storage, 12.37  
 holographic storage, 12.36–12.37  
 loss and two-beam coupling, 12.31–12.32, 12.33*f*–12.35*f*  
 phase conjugate interferometry, 12.32, 12.33*f*, 12.34*f*  
 real-time holography, 12.28–12.29, 12.29*f*, 12.30*f*  
 solitons, 12.38  
 thresholding, 12.35–12.36, 12.36*f*  
 waveguides, 12.37  
 grating formation, 12.1–12.3, 12.2*f*  
 oscillators and self-pumped mirrors, 12.7–12.9, 12.8*f*–12.9*f*  
 standard rate equation model, 12.3–12.4  
 stimulated photoreactive scattering, 12.9  
 time-dependent effects, 12.10  
 wave interactions, 12.4–12.7  
 anisotropic scattering, 12.7  
 four-wave mixing, 12.6–12.7, 12.6*f*  
 two-beam coupling, 12.4–12.6, 12.4*f*
- Photorefractive materials, 12.10–12.25  
 bulk compound semiconductors, 12.20–12.21, 12.20*t*, 12.21*f*  
 comparison of, 12.13, 12.13*t*  
 cubic oxides (sillenites), 12.17–12.19, 12.18*t*, 12.19*f*  
 features of, 12.10–12.11  
 ferroelectric, 12.13–12.17, 12.13*t*  
 barium titanate, 12.15–12.16, 12.16*f*  
 lithium niobate and lithium tantalate, 12.14  
 potassium niobate, 12.16–12.17  
 strontium barium niobate and related compounds, 12.17  
 tin hypothydiphosphate, 12.17, 12.18*t*  
 figures of merit for, 12.11–12.13  
 steady-state performance, 12.11–12.12  
 transient performance, 12.12, 12.13

- Photorefractive materials (*Cont.*):  
 multiple quantum wells, 12.22–12.23, 12.22f  
 organic crystals and polymer films,  
 12.23–12.25, 12.26t–12.27t  
 passive limiting in, 13.11, 13.12f
- Photorefractive self-oscillation, 12.7, 12.9
- Photorelaxation, 5.70f
- Photosynthetically available radiation (PAR),  
 1.5t, 1.7f, 1.9
- Photovoltage, 5.66t
- Physical constants, for crystals and glasses, 2.8t
- Physical properties:  
 of crystals and glasses, 2.37, 2.38t–2.43t  
 classes and symmetry properties, 2.7t  
 composition, structure, and density,  
 2.38t–2.41t  
 physical constants, 2.8t  
 specialty, and substrate materials, 2.43t  
 symmetry properties, 2.5, 2.6t–2.8t  
 of metals, 4.6, 4.49, 4.52t–4.54t  
 of polymers, 3.2–3.5, 3.4t
- Phytoplankton:  
 absorption by, 1.23–1.25, 1.24f–1.25f, 1.28  
 in water, 1.14
- Picosecond, 5.7
- Picosecond solid-state lasers, 18.10
- Piezo-optic coefficients, for crystals  
 and glasses, 2.21
- Pikhtin-Yas'kov formula, 2.22
- Plasma beat wave acceleration, 21.41
- Plasma frequency, 2.15, 8.21
- Plasma-ion-assisted deposition, 7.11
- Plasmas, 21.3–21.4  
 in fast ignition, 21.54–21.55, 21.54f, 21.55f  
 in femtosecond x-ray production, 21.52–21.53,  
 21.53f  
 in fusion neutron production, 21.53  
 in high magnetic field production, 21.53  
 in MeV proton acceleration, 21.54  
 nano-, 21.34–21.35, 21.35f  
 optically generated, 16.20  
 overdense, 21.46–21.52  
 high harmonic generation, 21.50–21.52,  
 21.51f  
 irradiated plasma, 21.46–21.47, 21.46f  
 $j \times B$  heating and anomalous skin effect, 21.49  
 ponderomotive steepening and hole  
 boring, 21.49–21.50, 21.50f  
 relativistic effects and induced  
 transparency, 21.52
- Plasmas, overdense (*Cont.*):  
 resonance absorption, 21.47–21.48, 21.47f  
 vacuum heating, 21.47f, 21.48–21.49  
 wakefield generation and electron  
 acceleration, 21.39–21.42, 21.40f, 21.42f  
 in Raman amplification, 21.55  
 underdense, 21.36–21.46  
 direct laser acceleration and betatron  
 resonance, 21.42–21.43  
 intense laser pulses, 21.38–21.39, 21.38f  
 inverse Bremsstrahlung heating, 21.37,  
 21.37f  
 ionization-induced defocusing,  
 21.43–21.44, 21.43f  
 ponderomotive channel formation, 21.42  
 self-channeling and self-phase modulation,  
 21.44–21.46, 21.45f
- Plasma-sprayed surfaces, 6.50–6.52, 6.51f–6.52f
- Plasmons, 5.33–5.36, 5.35f–5.37f, 5.58, 8.23–8.24
- Plastic spacers, for bandpass filters, 7.89
- Plate equations, mirror design and, 4.8–4.9
- Plate polarizers, 7.69–7.70, 7.70f
- Platinum:  
 absorptance of, 4.41f, 4.48t, 4.50t, 4.51t  
 optical properties of, 4.17t, 4.25f  
 physical properties of, 4.54t  
 reflectance of, 4.36t–4.37t, 4.41f  
 thermal properties of, 4.69t, 4.70t
- Pockels effect, for crystals and glasses, 2.26
- Point defects, 9.12–9.13
- Poisson's equation, for solids, 8.5
- Poisson's ratio:  
 for crystals, 2.31  
 for metals, 4.7, 4.69t
- Polaritons, 5.29
- Polarization:  
 and inelastic scattering, 1.49  
 at interface of solid, 8.12–8.13, 8.13f  
 and size of electric field, 10.4–10.5
- Polarization dependence, of stimulated Raman  
 scattering, 15.41–15.42, 15.42t
- Polarization gradient cooling, 20.17–20.18,  
 20.18f, 20.19f
- Polarization power series expansion, 5.52–5.53,  
 5.54t
- Polarization splitting, 7.93, 7.93f
- Polarizers:  
 embedded, 7.70–7.71, 7.71f, 7.72f  
 interference, 7.69–7.73, 7.70f–7.72f  
 MacNeille, 7.70–7.72, 7.71f, 7.72f, 7.75f

- Polarizers (*Cont.*):  
  multicomponent, 7.69  
  plate, 7.69–7.70, 7.70f
- Polarizing beam splitters, 7.70–7.73,  
  7.70f–7.72f, 7.74f–7.75f
- Polarons, in magnetic field, 5.50
- Poling process, 12.14
- Polishing, of optical surfaces, 19.3
- Polyallyl diglycol carbonate, 3.4t
- Polyamide (Nylon), 3.4t
- Polyarylate, 3.4t
- Polycarbonate, 3.4t, 3.6, 3.6t, 3.7t, 3.12
- Polychloro-trifluoroethylene, 3.4t
- Polycrystalline materials, 2.3 (*See also* Crystals)
- Polycyclohexyl methacrylate (PCHMA), 3.4t,  
  3.6, 3.6t, 3.7t
- Poly-diallylglycol (CR-39) resin, 3.11
- Polyetherimide (PEI), 3.4t, 3.6, 3.6t, 3.7t
- Polyethersulfone, 3.4t
- Polymer composites, 12.26t
- Polymer films, 12.24
- Polymeric optics, 3.1–3.18  
  coatings on, 3.17–3.18  
  design of, 3.7–3.11  
  aberration control, 3.8  
  aspheric surfaces, 3.8–3.9  
  athermalization, 3.9  
  dimensional variations, 3.10  
  manufacturing error budget, 3.10  
  material selection, 3.8  
  multiple cavities, 3.10  
  optical figure variations, 3.10  
  processing considerations, 3.9  
  specification, 3.10–3.11  
  strategy, 3.7–3.8  
  materials for  
  forms of, 3.2  
  optical properties, 3.5–3.7, 3.6t, 3.7f  
  physical properties, 3.2–3.5, 3.4t  
  selection, 3.1–3.2  
  processing of, 3.11–3.17  
  abrasive forming, 3.11–3.12  
  casting, 3.11  
  compression molding, 3.12  
  geometry considerations, 3.13–3.14  
  injection molding, 3.12–3.13  
  mechanical assembly, 3.14–3.16, 3.14f, 3.15f  
  null optics, 3.16–3.17  
  shrinkage, 3.14  
  single-point turning, 3.12
- Polymeric optics, processing of (*Cont.*):  
  testing and qualification, 3.16  
  vendor selection, 3.13
- Polymers, fully functional, 12.27t
- Polymethyl pentene, 3.4t
- Polymethylmethacrylate (PMMA), 3.4t, 3.6,  
  3.6t, 3.7t, 3.12
- Polymorphs, 2.27
- Polystyrene, 3.4t, 3.6, 3.6t, 3.7t
- Polystyrene co-butadiene, 3.4t
- Polysulfone, 3.4t
- Polytetrafluoroethylene (Teflon), 6.27
- Polyvinylidene fluoride, 3.4t
- Ponderomotive channel formation, 21.42
- Ponderomotive force, 21.5–21.6
- Ponderomotive steepening, 21.49–21.50, 21.50f
- Population trapping, velocity-selective  
  coherent, 20.37
- Positive-powered lenses, 3.13
- Posttreated Martin Black, 6.47
- Potassium bromide (KBr), 2.39t, 2.44t, 2.48t,  
  2.51t, 2.56t, 2.62t, 2.69t, 2.77t
- Potassium dihydrogen phosphate ( $\text{KH}_2\text{PO}_4$ )  
  (KDP), 2.39t, 2.45t, 2.48t, 2.51t, 2.56t,  
  2.62t, 2.75t
- Potassium iodide (KI), 2.39t, 2.44t, 2.48t, 2.51t,  
  2.56t, 2.62t, 2.69t, 2.77t
- Potassium niobate ( $\text{KNbO}_3$ ), 2.39t, 2.46t, 2.48t,  
  2.51t, 2.56t, 2.62t, 2.75t, 12.16–12.17
- Potassium tantalate ( $\text{KTaO}_3$ ), 2.39t, 2.44t, 2.48t,  
  2.51t, 2.56t, 2.62t, 2.73t
- Potassium titanyl arsenate ( $\text{KTiOAsO}_4$ )  
  (KTA), 17.1
- Potassium titanyl phosphate ( $\text{KTiOPO}_4$ )  
  (KTP), 2.39t, 2.46t, 2.51t, 2.56t, 2.63t,  
  2.75t, 17.1, 17.2, 17.28, 17.29f, 17.30f
- Pound-Drever-Hall (PDH) technique, 17.18
- Powelite ( $\text{CaMoO}_4$ ), 2.38t, 2.45t, 2.47t, 2.50t,  
  2.55t, 2.61t, 2.72t, 2.77t
- Power handling capability, of cw lasers, 7.14
- Poynting vector, 8.7
- Praseodymium, 14.34–14.35, 14.35f, 14.36f
- Pressure force, 20.7
- Principle dispersion (term), 2.23
- Prism-based monochromators, 5.59
- Propagation effects, on third-order optical  
  nonlinearities, 16.24–16.26
- Proustite ( $\text{Ag}_3\text{AsS}_3$ ), 2.38t, 2.46t, 2.47t, 2.50t,  
  2.55t, 2.60t
- Pulse area, 11.8

- Pulse excitation, chirped, 11.25–11.26  
Pulse generation, 18.4, 21.31  
Pulse propagation, 14.20–14.22  
Pulsed lasers, 14.15–14.16, 14.16f  
Pulsed transient Raman scattering, 15.22–15.25,  
15.24f–15.26f, 15.24t  
Pump (incident light), 15.1  
Pump depletion, 15.9, 15.10, 15.15,  
15.20, 15.20f  
Pump-enhanced singly resonant oscillators  
(PE-SROs), 17.2–17.4, 17.3f, 17.4f,  
17.17–17.20, 17.18f–17.20f, 17.27–17.28  
Pumping, for cw SROs, 17.2–17.4  
Pump-probe (excite-probe) measurements,  
16.26–16.27, 16.27f  
Pump-probe spectroscopy, 18.18–18.19  
Pump-probe techniques, 18.6, 18.6f  
Pump-resonant singly resonant oscillators,  
17.17–17.20, 17.18f–17.20f  
Purity, of optical materials, 2.5  
Pyrex glass, 2.43t, 2.49t, 2.54t
- Q-switched modelocking, 18.4, 18.5, 18.5f  
Qualification, of polymers, 3.16  
Quality factor (of microcavities), 9.7–9.8, 9.8f  
Quantum coherence tomography, 23.13  
Quantum dots, 12.25  
Quantum entanglement, in optical interferometry,  
23.1–23.15  
  concepts and equations for, 23.1–23.4,  
23.2f, 23.4f  
  digital approaches to, 23.7–23.9  
  Heisenberg limit, 23.6–23.7  
  N00N state, 23.9–23.12, 23.10f, 23.11f  
  and quantum imaging, 23.13–23.14  
  and remote sensing, 23.14–23.15  
  shot-noise limit, 23.4–23.6, 23.5f  
Quantum fluctuations, 15.38, 15.39f,  
23.5, 23.5f  
Quantum imaging, 23.13–23.14  
Quantum interferences, 14.8  
Quantum mechanical model, for solids, 8.4,  
8.24–8.25  
Quantum mechanics, third-order optical  
nonlinearities and, 16.4–16.7, 16.5f  
Quantum remote sensing, 23.14–23.15  
Quantum theory of nonlinear optical  
susceptibility, 10.9–10.10  
Quart-enhanced photoacoustic spectroscopy  
(QEPAS), 17.25–17.26, 17.26f
- $\alpha$ -Quartz (SiO<sub>2</sub>), 2.40t, 2.46t, 2.48t, 2.52t,  
2.57t, 2.64t, 2.71t  
Quasi-phase-matched (QPM) nonlinear  
materials, 17.1, 17.13–17.14  
Quasi-plane-wave solution (to transverse  
profile problem), 12.10
- Rabi frequency, 11.4  
Radiance, of water, 1.5t, 1.6, 1.7f  
Radiation pressure force, 20.7  
Radiation resistance, of polymers, 3.5  
Radiative escape, 20.29  
Radiative transfer theory, 1.4  
Radiometric quantities, of water, 1.4–1.9,  
1.5t, 1.7f  
Raman amplification, 21.55  
Raman amplifiers, 15.4, 15.4f, 22.15  
Raman cooling, 20.21  
Raman cross sections, 15.5  
Raman gain coefficients, 15.16t–15.18t  
Raman generators, 15.4, 15.4f  
Raman induced Kerr effect (RIKE), 16.3t,  
16.12, 16.17  
Raman linewidths, 15.9, 15.10f, 15.11t–15.20t  
Raman modes, of crystals and glasses, 2.11  
Raman oscillators, 15.4, 15.4f  
Raman scattering, 15.1–15.43  
  anti-Stokes, 15.4, 15.4f, 15.32–15.34, 15.33f,  
15.35f, 15.42, 15.42t, 15.43f  
  backward, 15.41, 21.38–21.39, 21.38f  
  Brillouin vs., 15.1  
  coherent, 15.3, 15.4, 15.4f, 15.34, 15.42,  
15.42t, 15.43f  
  for crystals and glasses, 2.27  
  forward, 21.38–21.39, 21.38f  
  measurement with, 5.76–5.83, 5.76f,  
5.78f–5.82f  
  and Raman interactions, 15.2–15.3, 15.3t  
  regimes of, 15.3  
  in solids, 8.16, 8.18, 8.19t–8.20t  
  spontaneous, 15.3, 15.5  
  stimulated (*see* Stimulated Raman  
scattering)  
  transient, 15.22–15.32  
    broadband effects, 15.28–15.32, 15.29f  
    phase pulling, 15.26–15.27, 15.27f  
    pulsed, 15.22–15.25, 15.24f–15.26f, 15.24t  
    solitons, 15.27–15.28, 15.29f  
    spectral properties, 15.32  
  by water, 1.48, 1.49, 1.49f

- Raman shifts, 15.2
- Raman sidebands, generation of, 14.31, 14.32*f*
- Raman spectroscopy, 5.57–5.58, 7.48, 7.66, 7.83, 7.96, 7.97*f*, 7.98
- Raman susceptibility, 15.5–15.6
- Raman threshold, 15.38
- Raman transition frequencies, 15.11*t*–15.15*t*
- Ramsey fringes, 11.20–11.22, 11.21*f*
- Rapid adiabatic passage (RAP), 14.1
- Rayleigh scattering:
  - in crystals and glasses, 2.10, 2.27
  - and scattering by sea water, 1.30
  - in third-order optical nonlinearities, 16.14–16.15
- Rayleigh-wing scattering, 16.13
- Reactive evaporation, 7.11
- Reactive force, 20.8
- Real transitions, 16.4
- Real-time holography, 12.28–12.29, 12.29*f*, 12.30*f*
- Recoil limit, 20.5
- Redistribution force, 20.8
- Redspot Paint and Varnish, 6.35
- Reflectance:
  - at interface of solid, 8.12
  - of metals, 4.5, 4.11, 4.27*t*–4.39*t*, 4.39, 4.40*f*–4.47*f*
  - nonabsorbing  $[AB]^N$  and  $[AB]/NA$  multilayers, 7.32–7.34, 7.33*f*–7.35*f*
  - of optical coatings, 7.12–7.13
  - in solids, 8.22*f*, 8.23
  - specular, of black coatings, 6.26*f*
  - and surface coatings, 6.20*t*
- Reflection(s):
  - from all-dielectric broadband reflectors, 7.47
  - of coatings on substrate, 7.3
  - enhancement of, for filters and coatings, 7.108–7.109, 7.109*f*–7.110*f*
  - filters with low, 7.104–7.106, 7.104*f*–7.105*f*
  - magnetoreflexion, 5.43, 5.44, 5.44*f*
  - magnitude of, 9.2
  - measurement of, 5.62–5.64, 5.63*f*
  - and optical performance, 7.15–7.16, 7.16*f*
  - and phase change of nonabsorbing periodic multilayers, 7.34
  - photoreflexion, 5.66*t*, 5.67
  - total internal, 8.13
- Reflection coatings, 7.106–7.113, 7.106*f*–7.113*f*
  - at angles close to grazing incidence, 7.111
  - enhancement of reflection, 7.108–7.109, 7.109*f*–7.110*f*
  - metallic reflectors, 7.106–7.108, 7.106*f*–7.109*f*
- Reflection coefficient, for optical constants, 5.9–5.10
- Reflection filters, 7.5, 7.5*f*, 7.111–7.113, 7.111*f*–7.113*f*
- Reflectivity:
  - at interface of solid, 8.12
  - nonlinear, 18.6–18.7, 18.7*f*
  - of solids, 8.23
- Reflectivity amplitude, for solids, 8.15
- Reflectometers, 5.62–5.64, 5.63*f*
- Reflectors:
  - heat, 7.58, 7.58*f*
  - metal-dielectric, 7.81–7.82, 7.108, 7.109, 7.110*f*
  - multilayer, 7.39–7.53
    - all-dielectric broadband reflectors, 7.39, 7.40*f*, 7.45–7.47, 7.45*f*–7.47*f*
    - coatings for ultrafast optics, 7.47–7.48, 7.48*f*
    - for far-infrared region, 7.52, 7.52*f*
    - graded reflectivity mirrors, 7.52
    - imperfections in, 7.40–7.43, 7.41*f*–7.43*f*
    - for interferometers and lasers, 7.39–7.40, 7.39*f*–7.40*f*
    - narrowband reflection coatings, 7.43, 7.44*f*
    - rejection filters, 7.48–7.50, 7.49*f*–7.51*f*
    - for soft x-ray and XUV regions, 7.53
    - and two-material periodic multilayers theory, 7.37–7.38, 7.38*f*
  - omnidirectional, 9.2
  - resonant, 7.43–7.45, 7.44*f*
  - very low loss, 7.41–7.42
- Refraction:
  - enhanced, 14.20
  - nonlinear, 16.7–16.9
- Refractive index:
  - of anisotropic crystals, 8.8
  - complex, 1.16–1.17
  - of crystals and glasses, 2.6, 2.8, 8.10
  - dispersion formulas for, 2.21–2.22
  - in dressed atoms, 14.19–14.20
  - of metals, 4.3, 4.11, 4.12*t*–4.19*t*, 4.21*f*–4.26*f*
  - of particles in water, 1.20
  - in polymeric optics, 3.6–3.7, 3.6*t*, 3.7*f*
  - in solids, 8.22*f*, 8.23
  - and temperature, 2.24–2.26
  - uniformity of, 2.5
  - of water, 1.16–1.20, 1.18*f*, 1.19*t*–1.20*t*
- Refractive index spectrum, 22.6, 22.6*f*, 22.7*f*
- Rejection filters, 7.48–7.50, 7.49*f*–7.51*f*
- Rejection ratios, of bandpass filters, 7.77

- Rejection region, for cutoff filters, 7.56
- Relativistic effect(s), in strong field interactions:
  - with atoms, 21.19–21.20
  - with free electrons, 21.6–21.8, 21.7*f*
  - with overdense plasmas, 21.52
  - self-focusing and self-channeling as, 21.44–21.45, 21.45*f*
  - self-phase modulation as, 21.45–21.46, 21.45*f*
- Relativistic electron ATI, 21.20, 21.21*f*
- Relativistic electron beams, strong field interactions with, 21.9–21.10
- Relativistic suppression of rescattering, 21.20
- Relaxation:
  - longitudinal and transverse, 11.5
  - photorelaxation, 5.70*f*
- Remote sensing:
  - quantum, 23.14–23.15
  - in water, 1.46–1.47
- Reorientational Kerr effect, in solids, 16.13–16.14, 16.14*f*
- Rescattering effects:
  - relativistic suppression of, 21.20
  - in strong field interactions with atoms, 21.18–21.19, 21.18*f*, 21.19*f*
- Resins, 3.2, 3.11
- Resistivity:
  - coatings with high, 6.56
  - of metals, 4.54*t*
  - of polymers, 3.5
- Resonance:
  - cyclotron, 5.12, 5.12*f*, 5.40, 5.47–5.50, 5.48*f*–5.50*f*
  - photonic, 22.9–22.13, 22.10*f*, 22.12*f*
  - slow light propagation and atomic, 22.2–22.9, 22.3*f*, 22.6*f*–22.8*f*
- Resonance absorption, in overdense plasmas, 21.47–21.48, 21.47*f*
- Resonant degenerate four-wave mixing, 16.28
- Resonant modes (RMs), 5.17
- Resonant Raman scattering, 16.15
- Resonant reflectors, 7.43–7.45, 7.44*f*
- Retinal damage, 13.3
- Reverse-proton-exchanged (RPE) PPLN, 17.16
- Reverse-saturable absorption (RSA), 13.5, 13.6*f*, 13.7
- Rigidity, of polymers, 3.3
- Ring resonators, 12.7, 12.8*f*, 22.11, 22.12*f*
- Rock-salt lattices, 5.16
- Rotating light pipe reflectometers, 5.62, 5.63*f*
- Rotating wave approximation (RWA), 20.7
- Roughened aluminum, 6.21, 6.22*f*, 6.30*f*
- Roughness, surface, 6.15
- Rubidium, 14.17, 14.17*f*
- Rubidium titanyl arsenate (RbTiOAsO<sub>4</sub>) (RTA), 17.1
- Rubidium titanyl phosphate (RbTiOPO<sub>4</sub>) (RTP), 2.40*t*, 2.46*t*, 2.48*t*, 2.52*t*, 2.57*t*, 2.64*t*
- Rugate filters, 7.49, 7.50
- Rutile (TiO<sub>2</sub>), 2.40*t*, 2.45*t*, 2.48*t*, 2.53*t*, 2.58*t*, 2.65*t*, 2.71*t*
- S on 1 annealing, 19.3, 19.4
- Salt (NaCl), 2.40*t*, 2.44*t*, 2.48*t*, 2.52*t*, 2.57*t*, 2.64*t*, 2.69*t*
- Sandblasted aluminum, 6.45*f*
- Sapphire (Al<sub>2</sub>O<sub>3</sub>):
  - dispersion formulas for, 2.60*t*
  - elastic constants of, 2.46*t*
  - infrared spectrum of, 2.13, 2.13*f*
  - lattice vibration model parameters for, 2.76*t*
  - mechanical properties of, 2.47*t*
  - optical modes of, 2.70*t*
  - optical properties of, 2.55*t*
  - properties of, 2.38*t*
  - thermal properties of, 2.50*t*
  - Ti:sapphire amplifiers, 21.5
  - Ti:sapphire lasers, 18.3
- Saturable absorbers, 18.5–18.11
  - fast, 18.9–18.10
  - self-amplitude modulation, 18.5–18.7, 18.6*f*, 18.7*f*
  - semiconductor saturable absorber mirrors, 18.3, 18.10–18.11
  - slow, 18.7–18.9, 18.8*f*
- Saturable absorption, 13.5
- Saturable Bragg reflectors (SBRs), 18.3, 18.11
- Saturation fluence, 18.5, 18.6
- Scatterance, of water, 1.5*t*, 1.10
- Scattering:
  - angular distribution of, 1.12
  - anisotropic, 12.7
  - in crystals and glasses, 2.27
  - Einstein-Smoluchowski theory of, 1.30
  - nonlinear, 13.4*f*, 13.8
  - rescattering, 21.18–21.20, 21.18*f*, 21.19*f*
  - stimulated, 16.14–16.19
  - from surface, 6.15
  - Thomson, 21.8–21.9, 21.9*f*

- Scattering (*Cont.*):
- by water
    - inelastic and polarization, 1.47–1.49, 1.48f, 1.49f
    - measurement, 1.29–1.30
    - particles, 1.30–1.35, 1.31t, 1.32f, 1.33f, 1.34t–1.35t
    - pure water and pure sea water, 1.30
    - wavelength dependence, 1.35–1.40, 1.35t, 1.36f, 1.37t, 1.38t, 1.39f, 1.40t
  - (*See also specific scattering, e.g.: Anti-Stokes scattering*)
  - Scattering force, 20.7
  - Scattering losses, multilayer reflectors and, 7.41
  - Scattering rate, 20.4
  - Scatterometers, 7.13
  - Scheelite ( $\text{CaWO}_4$ ), 2.38t, 2.45t, 2.47t, 2.51t, 2.56t, 2.61t, 2.72t, 2.77t
  - Schott Glass Technologies, 6.57
  - Schott glasses, 2.22, 2.23, 2.26
  - Schrödinger equation, 2.16, 8.24, 8.25
  - Schrödinger's cat, 23.1, 23.9
  - Sea water, 1.3, 1.18–1.21, 1.18f, 1.19t–1.20t, 1.22t, 1.30
  - Second-harmonic processes, conversion
    - efficiencies for, 10.14–10.16
  - Second-order nonlinear optics:
    - anharmonic oscillator model of
      - susceptibility in, 10.7–10.9, 10.8f
      - phase matching in, 10.12–10.14, 10.12f, 10.13f
      - properties of semiconductors in, 5.53–5.55
  - Second-order susceptibility tensor, 10.10–10.11
  - Selenium, 2.70t
  - Self-action effects, 16.25
  - Self-amplitude modulation (SAM), 18.3, 18.5–18.8, 18.6f, 18.7f
  - Self-channeling, 21.44–21.45, 21.45f
  - Self-defocusing, 13.7, 13.8, 19.9–19.11, 19.10f
  - Self-focusing:
    - and laser-induced damage, 19.5, 19.7
    - as relativistic effect in strong field
      - interactions, 21.44–21.45, 21.45f
    - thermal, 13.7–13.8
    - of third-order optical nonlinearities, 16.25
  - Self-heating, 17.12
  - Self-lensing, 19.5
  - Self-modulated wakefield generation, 21.41
  - Self-oscillation, 12.7–12.9
  - Self-phase modulation (SPM), 21.45–21.46, 21.45f (*See also Longitudinal Kerr effect*)
  - Self-protecting limiters, 13.9
  - Self-pumped phase conjugate mirrors (SPPCMs), 12.7, 12.8f–12.9f
  - Self-trapped excitons, 5.26t
  - Sellaite ( $\text{MgF}_2$ ), 2.40t, 2.45t, 2.48t, 2.52t, 2.57t, 2.63t, 2.71t
  - Sellenite ( $\text{Bi}_{12}\text{SiO}_{20}$ ) BSO, 2.38t, 2.44t, 2.47t, 2.50t, 2.55t, 2.61t, 2.75t
  - Sellmeier dispersion model, for crystals and glasses, 2.14, 2.15, 2.21–2.23, 2.25
  - Sellmeier formula, for refractive index, 8.14
  - Sellmeier model, for crystals and glasses, 2.10, 2.11
  - Semiconductor(s), 5.1–5.83
    - dielectrics and metals vs., 8.4
    - electromagnetic spectrum interactions with, 5.3–5.6, 5.4f
    - ion-implanted, 18.21
    - linear optical properties of, 5.11–5.39, 5.12f, 5.13t, 5.35f–5.37f
      - free carriers, 5.33–5.36
      - impurity and defect absorption, 5.37–5.39, 5.38f, 5.39f
      - interband absorption, 5.21–5.33, 5.21f–5.25f, 5.26t, 5.27f–5.28f, 5.30f–5.34f
      - lattice absorption, 5.13–5.20, 5.15f, 5.17t, 5.18f–5.19f, 5.20t, 5.21f
    - low-temperature, 18.21
    - magneto-optical properties of, 5.39–5.52, 5.41t
      - effect of magnetic field on energy bands, 5.40, 5.42, 5.42f
      - interband effects, 5.42–5.46, 5.43f–5.45f, 5.47f
      - intragand or free-carrier effects, 5.47–5.52, 5.48f–5.51f
      - semiconductor nanostructures, 5.52
    - materials and applications of, 5.84t–5.86t
    - measurement techniques for (*see* Measurement techniques, for semiconductors)
    - nanostructure, 5.52
    - nonlinear, 5.52–5.56, 5.54t
    - optical/dielectric response in, 5.8–5.11
    - passive limiting in, 13.9, 13.10f
    - structure of, 5.6–5.7
  - Semiconductor saturable absorber mirrors (SESAMs), 18.3, 18.10–18.11
  - Semiconductor saturable absorbers, 18.4, 18.5, 18.5f, 18.10

- Semiconductor ultrafast nonlinearities,  
 18.15–18.23  
 applications of, 18.19–18.23  
 and carrier trapping, 18.21–18.23, 18.22*f*  
 in coherent regime, 18.19–18.20  
 and continuum excitations, 18.20  
 and excitonic excitations, 18.19–18.20  
 properties of, 18.16–18.17, 18.16*f*  
 and pump-probe spectroscopy, 18.18–18.19  
 in thermalization regime, 18.20–18.21  
 and transient four-wave mixing, 18.17–18.18,  
 18.17*f*
- Semiconductor-doped dielectric films, 18.11
- Semiconductor-doped glasses, 18.11
- Semilinear mirrors, 12.7, 12.8*f*
- Semiquantum four-parameter model, 2.12
- Service temperature, of polymers, 3.3
- Shake off model (of strong field behavior), 21.18
- Shape factors, of bandpass filters, 7.77
- Shear modulus, for metals, 4.69*t*
- Short flint glass, 2.42*t*
- Short pulse, 11.7
- Shot-noise limit (SNL), 23.4–23.6, 23.5*f*
- Shrinkage, polymer, 3.14
- Sikkens Aerospace Finishes, 6.39
- Silica glass, fused, 2.43*t*, 2.49*t*, 2.54*t*, 2.59*t*, 2.67*t*
- Silicon:  
 absorptance of, 4.48*t*  
 crystals of, 2.40*t*, 2.44*t*, 2.48*t*, 2.52*t*, 2.57*t*,  
 2.64*t*, 2.68*t*  
 IR absorption due to interstitial oxygen in, 5.19*f*  
 multiphonon absorption of vacuum-grown,  
 5.18*f*  
 physical properties, 4.52*t*  
 reflectance, 4.46*f*  
 thermal properties of  
 coefficient of linear thermal expansion,  
 4.56*t*, 4.58*f*  
 elastic stiffness, 4.69*t*  
 moduli and Poisson's ratio, 4.69*t*  
 at room temperature, 4.55*t*  
 specific heat, 4.65*t*, 4.68*f*  
 strength and fracture properties, 4.70*t*  
 thermal conductivity, 4.58*t*, 4.63*f*–4.64*f*
- Silicon carbide (SiC):  
 absorptance of, 4.49*f*, 4.50*f*  
 optical properties of, 4.19*t*, 4.25*f*  
 particles of, 6.15  
 physical properties of, 4.52*t*  
 reflectance of, 4.41*f*, 4.42*f*, 4.46*f*
- Silicon carbide (SiC) (*Cont.*):  
 as surface material, 6.56  
 thermal properties of  
 coefficient of linear thermal expansion,  
 4.56*t*, 4.58*f*  
 elastic stiffness, 4.69*t*  
 moduli and Poisson's ratio, 4.69*t*  
 at room temperature, 4.55*t*  
 specific heat, 4.65*t*, 4.68*f*  
 strength and fracture properties, 4.70*t*  
 thermal conductivity, 4.58*t*, 4.63*f*–4.64*f*
- Silicon-on-insulator planar waveguide, 22.15
- Sillenites (cubic oxides), 12.17–12.19, 12.18*t*,  
 12.19*f*
- Silver:  
 absorptance of, 4.42*f*, 4.48*t*, 4.50*t*, 4.51*t*  
 optical properties of, 4.17*t*–4.18*t*, 4.26*f*  
 physical properties of, 4.52*t*, 4.54*t*  
 reflectance of, 4.37*t*–4.38*t*, 4.42*f*  
 resistivity of, 4.54*t*  
 thermal properties of  
 coefficient of linear thermal expansion,  
 4.56*t*, 4.57*f*  
 elastic stiffness, 4.69*t*  
 moduli and Poisson's ratio, 4.69*t*  
 at room temperature, 4.55*t*  
 specific heat, 4.65*t*, 4.66*f*  
 strength and fracture properties, 4.70*t*  
 thermal conductivity, 4.58*t*, 4.60*f*–4.61*f*
- Silver gallium sulfide (AgGaS<sub>2</sub>) (AGS), 2.38*t*,  
 2.44*t*, 2.47*t*, 2.50*t*, 2.55*t*, 2.60*t*, 2.74*t*, 2.76*t*
- Silver mirrors, 7.106*f*–7.108*f*, 7.107–7.109
- Silver selenogallate (AgGaSe<sub>2</sub>), 2.38*t*, 2.44*t*,  
 2.47*t*, 2.50*t*, 2.55*t*, 2.60*t*, 2.74*t*, 2.76*t*
- Single active electron approximation, 21.10
- Single-particle excitation, 5.81, 5.82*f*
- Single-pass absorption spectroscopy, 17.24–17.27,  
 17.25*f*, 17.26*f*
- Single-point turning, of polymers, 3.12
- Single-scattering albedo, 1.5*t*, 1.7*f*
- Singly resonant optical parametric (SOP)  
 oscillators, 10.18, 10.18*f*
- Singly resonant oscillators (SROs), 17.2–17.16,  
 17.3*f*, 17.4*f*  
 guided-wave nonlinear structures, 17.15–17.16  
 MgO:sPPLT in, 17.14–17.15, 17.15*f*  
 PPLN crystals in, 17.4–17.13, 17.6*f*–17.11*f*  
 QPM nonlinear materials, 17.13–17.14
- Sink, in molding, 3.14
- Sisyphus laser cooling, 20.19



- Skin depth (term), 4.5
- Skin effect, anomalous, 21.49
- Slope of cutoff, 7.56
- Slow light propagation, 22.1–22.15  
 and atomic resonance, 22.2–22.9, 22.3*f*,  
 22.6*f*–22.8*f*  
 in optical fibers, 22.13–22.15, 22.14*f*  
 and photonic resonance, 22.9–22.13, 22.10*f*,  
 22.12*f*
- Slow saturable absorbers, 18.7–18.9, 18.8*f*
- Slowing, of atomic beams, 20.11–20.13, 20.12*f*,  
 20.12*t*, 20.13*f*
- Snell's law, 7.7, 8.11, 8.23
- Sodium chloride (NaCl), 2.69*t*
- Soft x-ray region:  
 bandpass filters for, 7.94–7.96, 7.95*f*–7.96*f*  
 interference polarizers for, 7.73, 7.76*f*–7.77*f*  
 multilayer reflectors for, 7.42, 7.53
- Solar absorptance, 6.19, 6.21
- Solar-cell cover filters, 7.58, 7.59*f*
- SolarChem, 6.44, 6.45*f*, 6.48*f*, 6.53*f*
- Sol-gels, 12.27*t*
- Solid spacers, for bandpass filters, 7.83, 7.88
- Solids:  
 band structures and interband transitions  
 of, 8.24–8.32  
 direct interband absorption, 8.27–8.28  
 energy band structures, 8.25–8.27, 8.26*f*  
 excitons, 8.31–8.32  
 indirect transitions, 8.29–8.30, 8.29*f*  
 joint density of states, 8.28, 8.29*f*  
 multiphoton absorption, 8.30–8.31  
 quantum mechanical model, 8.24–8.25  
 selection rules and forbidden transitions,  
 8.28, 8.29  
 bound electronic optical Kerr effect in,  
 16.12–16.13, 16.13*f*  
 dephasing in, 14.13–14.14  
 dispersion relations in, 8.14–8.16  
 EIT in, 14.33–14.36, 14.35*f*, 14.36*f*  
 extrinsic optical properties of, 8.3  
 free-electron properties of, 8.21–8.24, 8.22*f*  
 intrinsic optical properties of, 8.3  
 lattice interactions in, 8.16–8.18, 8.17*f*,  
 8.19*t*–8.20*t*  
 optical properties of, 8.1–8.32  
 propagation of light in, 8.4–8.13  
 anisotropic crystals, 8.8–8.11, 8.9*t*, 8.10*f*  
 energy flow, 8.7–8.8  
 interfaces, 8.11–8.13, 8.12*f*, 8.13*f*
- Solids, propagation of light in (*Cont.*):  
 Maxwell's equations, 8.4–8.6  
 wave equations and optical constants,  
 8.6–8.7  
 reorientational Kerr effect in, 16.13–16.14,  
 16.14*f*
- Solid-state detectors, 5.61
- Solid-state lasers, 18.3
- Soliton lasers, 18.14
- Soliton modelocking, 18.8*f*, 18.12–18.14
- Solitons:  
 photorefractive, 12.38  
 and third-order optical nonlinearities,  
 16.25–16.26  
 and transient Raman scattering, 15.27–15.28,  
 15.29*f*
- Space groups, of crystals, 2.27–2.28
- Space-based surfaces, 6.17–6.18, 6.20*t*, 6.46
- Spacecraft, 6.12, 6.16–6.17
- Spacers, for bandpass filters, 7.83, 7.88–7.89
- Spatial solitons, 16.26
- Specific heat (*see* Heat capacity)
- Specification, in polymeric optics, 3.10–3.11
- Spectral absorptance, of water, 1.9
- Spectral absorption, by detritus in water,  
 1.26–1.27, 1.26*f*
- Spectral absorption coefficient:  
 for case 1 waters, 1.27–1.28  
 for phytoplankton, 1.24, 1.24*f*, 1.25*f*, 1.25*t*  
 upper bound, in sea water, 1.21, 1.22*t*  
 for waters, 1.10, 1.17, 1.20–1.21, 1.27*f*
- Spectral beam attenuation coefficient, for  
 water, 1.10
- Spectral diffuse attenuation coefficient, for  
 water, 1.12
- Spectral diffusion, 11.15
- Spectral downwelling average cosine,  
 of water, 1.12
- Spectral downwelling irradiance, of water, 1.8
- Spectral downward scalar irradiance, of water, 1.8
- Spectral emittance, of metals, 4.6
- Spectral gain narrowing, in steady-state Stokes  
 scattering, 15.21
- Spectral hole, 18.20
- Spectral hole burning, 22.6, 22.7*f*
- Spectral irradiance reflectance, of water, 1.12,  
 1.46, 1.47*f*
- Spectral net irradiance, of water, 1.9
- Spectral radiance, of water, 1.6
- Spectral scatterance, of water, 1.10

- Spectral scattering coefficient, for water, 1.10
- Spectral transmission, in polymeric optics, 3.6
- Spectral transmittance, 7.3–7.4
- Spectral upward plane irradiance, of water, 1.8
- Spectral upward scalar irradiance, of water, 1.8
- Spectral upwelling irradiance, of water, 1.8
- Spectral volume scattering function (VSFs), 1.37–1.38, 1.38*t*
- Spectrometers, 5.59–5.61, 5.60*f*, 5.72, 7.12
- Spectroscopic ellipsometry, 5.66*t*
- Spectroscopic measurement, 5.56–5.58
- Spectroscopy, 17.21–17.27
  - continuous-wave, 11.2
  - defined, 11.2
  - differential transmission, 18.18–18.19
  - high-resolution Doppler-free, 17.27
  - knowledge derived from, 5.6
  - photoacoustic, 17.22–17.26, 17.22*f*–17.24*f*, 17.26*f*
  - photo-associative, 20.30–20.31, 20.31*f*
  - photon echo, 11.26–11.27
  - pump-probe, 18.18–18.19
  - Raman, 7.48, 7.66, 7.83, 7.96, 7.97*f*, 7.98
  - single-pass absorption, 17.24–17.27, 17.25*f*, 17.26*f*
  - time-dependent, 11.2
- Specular baffles, 6.14
- Specular black surfaces, 6.14
- Specular reflectance, of black coatings, 6.26*f*
- Spherelike Brillouin zone, 9.4
- Spinel ( $\text{MgAl}_2\text{O}_4$ ), 2.39*t*, 2.44*t*, 2.48*t*, 2.52*t*, 2.57*t*, 2.63*t*, 2.73*t*
- Spire Corporation, 6.51
- Split-step beam propagation, 12.10
- Spontaneous emission, 9.8, 20.5
- Spontaneous parametric down-conversion (SPDC), 23.10, 23.13
- Spontaneous parametric process, 10.16–10.17, 10.17*f*
- Spontaneous Raman scattering, 15.3, 15.5
- Sputtered beryllium surface, 6.6*f*
- Sputtered surfaces, 6.56
- Sputtering method, of manufacturing thin films, 7.11, 7.14
- Square-top multicavity bandpass filters, 7.82–7.83, 7.82*f*–7.88*f*
- Squeezing, in quantum optical interferometry, 23.7
- Stability, of bandpass filters, 7.94
- Stainless steel:
  - physical properties of, 4.52*t*
  - thermal properties of, 4.55*t*–4.58*f*, 4.62*f*–4.63*f*, 4.65*t*, 4.67*f*, 4.69*t*, 4.70*t*
- Standard rate equation model, 12.3–12.4
- Standard Test Method (of ASTM), 6.17
- Star Instruments, 6.57
- Stark chirped rapid adiabatic passage (SCRAP), 14.1
- Stationary spectroscopy, 11.2
- Steady-state Stokes scattering, 15.7–15.22
  - gain coefficients in, 15.16*t*–15.18*t*
  - gain narrowing in, 15.21
  - photon description in, 15.21–15.22
  - pump depletion in, 15.9, 15.10, 15.15, 15.20, 15.20*f*
  - Raman linewidths in, 15.9, 15.10*f*, 15.11*t*–15.20*t*
  - spectral gain narrowing in, 15.21
  - steady-state gain in, 15.8–15.9
- Steel, 4.50*t*, 4.51*t*
- Stiffness, in crystals and glass, 2.30, 2.31*t*
- Stimulated Brillouin scattering (SBS), 15.43–15.54
  - equations for, 15.44–15.48, 15.45*f*
  - phase conjugation, 15.48, 15.52–15.54, 15.52*f*–15.54*f*
  - Raman vs., 15.1
  - scattering parameters of materials, 15.48, 15.49*t*–15.51*t*
  - and slow light, 22.14–22.15
  - and stimulated photorefractive scattering, 12.9
  - third-order, 16.18–16.19
- Stimulated parametric process, 10.17–10.18
- Stimulated photon echo, 11.15–11.19, 11.16*f*–11.19*f*
- Stimulated photoreactive scattering (SPS), 12.9
- Stimulated Raman adiabatic passage (STIRAP), 14.1, 14.4, 14.5, 14.7
- Stimulated Raman anti-Stokes scattering, 15.2*t*
- Stimulated Raman scattering (SRS), 15.3–15.43
  - anti-Stokes, 15.2*t*, 15.32–15.34, 15.33*f*, 15.35*f*
  - backward, 15.41
  - coherent spectroscopy, 15.42, 15.42*t*, 15.43*f*
  - equations for, 15.6–15.7
  - focused beams, 15.41
  - formulas for, 15.20*t*
  - geometries for, 15.4, 15.4*f*

- Stimulated Raman scattering (SRS) (*Cont.*):  
 multiple Stokes generation, 15.38–15.40, 15.40f  
 and noise, 15.35–15.38, 15.39f  
 in plasma, 21.38–21.39, 21.38f  
 polarization dependence, 15.41–15.42, 15.42t  
 Raman susceptibility, 15.5–15.6  
 and slow light, 22.15  
 steady-state Stokes, 15.7–15.22  
   gain coefficients, 15.16t–15.18t  
   gain narrowing, 15.21  
   photon description, 15.21–15.22  
   pump depletion, 15.9, 15.10, 15.15, 15.20, 15.20f  
   Raman linewidths, 15.9, 15.10f, 15.11t–15.20t  
   spectral gain narrowing, 15.21  
   steady-state gain, 15.8–15.9  
 Stokes, 15.2t  
 terminology, 16.3t  
 third-order, 16.15–16.18, 16.15f, 16.17f  
 time-gated imaging, 15.42, 15.43, 15.44f  
 transient effects of, 15.22–15.32  
   broadband effects, 15.28–15.32, 15.29f  
   phase pulling, 15.26–15.27, 15.27f  
   pulsed, 15.22–15.25, 15.24f–15.26f, 15.24t  
   solitons, 15.27–15.28, 15.29f  
   spectral properties, 15.32  
 Stimulated Rayleigh-Wing scattering, 16.3t  
 Stimulated scattering, 16.14–16.19 [*See also* Stimulated Brillouin scattering (SBS); Stimulated Raman scattering (SRS)]  
 Stokes scattering, 15.2–15.3, 15.2t, 15.3t (*See also* Anti-Stokes scattering; Steady-state Stokes scattering)  
 Stokes shift, 15.1, 15.43  
 Stokes shifted Raman scattering, 16.15, 16.15f  
 Stokes wave, 15.1, 15.43  
 Strain, in crystals and glasses, 2.6t, 2.30, 2.31t, 2.36  
 Stray light, analysis and issues, 6.10, 6.19  
 Strength:  
   of crystals and glasses, 2.31–2.32, 2.32f, 2.32t  
   of metals, 4.8, 4.70, 4.70t  
   of scattering in water, 1.12  
 Stress:  
   in crystals and glasses, 2.6t, 2.30, 2.31t  
   uniaxial, 5.66t  
 Strong field approximation (SFA), 21.12  
 Strong field double ionization, 21.18–21.19  
 Strong field interactions, 21.1–21.55  
   about, 21.2–21.3  
   with atoms, 21.10–21.21  
     above threshold ionization, 21.14–21.17, 21.15f, 21.16f  
     ionization stabilization, 21.20–21.21, 21.22f  
     Keldysh parameter, 21.10  
     multiphoton and quasi-classical regimes, 21.10  
     multiphoton ionization, 21.10–21.12, 21.11f  
     relativistic effects, 21.19–21.20, 21.21f  
     rescattering effects, 21.18–21.20, 21.18f, 21.19f  
     tunnel ionization, 21.12–21.14, 21.12f, 21.14f  
   with clusters, 21.31–21.36  
     Coulomb explosion, 21.33–21.34  
     intense laser pulse interactions, 21.35–21.36, 21.36f  
     ionization, 21.31–21.33, 21.32f  
     nanoplasma description, 21.34–21.35, 21.35f  
   history of, 21.3–21.4  
   laser technology for, 21.4–21.5, 21.4f  
   with molecules, 21.22–21.26  
     Coulomb explosion, 21.24–21.25  
     nuclear motion and alignment, 21.22–21.23, 21.23t, 21.24f  
     triatomic and larger molecules, 21.26  
     tunnel ionization and ionization distance, 21.25–21.26, 21.25f, 21.27f  
   nonlinear optics in gases, 21.27–21.31  
     attosecond pulse generation, 21.31  
     high order harmonic generation, 21.27–21.30, 21.28f  
   with single electrons, 21.5–21.10  
     interactions with relativistic electron beams, 21.9–21.10  
     nonlinear Thomson scattering, 21.8–21.9, 21.9f  
     ponderomotive force, 21.5–21.6  
     relativistic effects, 21.6–21.8, 21.7f  
   with underdense plasmas, 21.36–21.52  
     applications of, 21.52–21.55, 21.53f–21.55f  
     direct laser acceleration and betatron resonance, 21.42–21.43  
     high harmonic generation, 21.50–21.52, 21.51f  
     intense laser pulses, 21.38–21.39, 21.38f  
     inverse Bremsstrahlung heating, 21.37, 21.37f

- Strong field interactions, with underdense plasmas (*Cont.*):  
 ionization-induced defocusing, 21.43–21.44, 21.43*f*  
 $\mathbf{j} \times \mathbf{B}$  heating and anomalous skin effect, 21.49  
 ponderomotive channel formation, 21.42  
 ponderomotive steepening and hole boring, 21.49–21.50, 21.50*f*  
 relativistic effects and induced transparency, 21.52  
 resonance absorption, 21.47–21.48, 21.47*f*  
 self-channeling and self-phase modulation, 21.44–21.46, 21.45*f*  
 structure of irradiated plasma, 21.46–21.47, 21.46*f*  
 vacuum heating, 21.47*f*, 21.48–21.49  
 wakefield generation and electron acceleration, 21.39–21.42, 21.40*f*, 21.42*f*
- Strontium, 14.15, 14.16*f*
- Strontium barium niobate (SBN), 12.17
- Strontium fluoride ( $\text{SrF}_2$ ), 2.40*t*, 2.44*t*, 2.48*t*, 2.52*t*, 2.57*t*, 2.64*t*, 2.69*t*
- Strontium molybdate ( $\text{SrMoO}_4$ ), 2.40*t*, 2.45*t*, 2.48*t*, 2.52*t*, 2.57*t*, 2.65*t*, 2.72*t*
- Strontium titanate ( $\text{SrTiO}_3$ ), 2.40*t*, 2.44*t*, 2.48*t*, 2.52*t*, 2.57*t*, 2.65*t*, 2.73*t*
- Structured antireflection coatings, 7.25–7.26, 7.25*f*, 7.26*f*
- Styrene acrylonitrile (SAN), 3.4*t*, 3.6, 3.6*t*, 3.7*t*
- Sum frequency generation (SFG), 16.2, 16.3*t*
- Sum rules:  
 for crystals and glasses, 2.9  
 for dispersion in solids, 8.14–8.15  
 for semiconductors, 5.11
- Super resolution, 23.10, 23.12
- Super-Beer's law, 23.15
- Superlinear absorption of light, 5.57
- Supermirrors, 7.111
- Surface coatings, 6.4*t*
- Surface damage, laser-induced, 19.2–19.4
- Surface-tension effects, from polymer molding process, 3.14
- Susceptibility:  
 nonlinear  
 anharmonic oscillator model of  
 second-order, 10.7–10.9, 10.8*f*  
 of crystals and glasses, 2.26  
 quantum theory of, 10.9–10.10  
 Raman, 15.5–15.6
- Swept-carrier time-domain optical memory, 11.25
- Switching, third-order optical nonlinearities and, 16.30–16.31
- Symmetry properties, of crystals and glasses, 2.5, 2.6*t*–2.8*t*
- Tandem limiters, 13.6, 13.6*f*
- Tantalum, 4.50*t*, 4.69*t*, 4.70*t*
- Tantalum crown glass, 2.42*t*
- Target normal sheath acceleration, 21.54
- Teflon overcoat, 6.27
- Teflon Wet Lubricant, 6.27
- Telescopes:  
 and black surfaces, 6.21  
 far-infrared, 6.48  
 ground-based, 6.12
- Temperature(s):  
 of crystals and glasses, 2.32, 2.33  
 in laser cooling, 20.5  
 of metals, 4.7  
 and refractive index of glasses, 2.24–2.26
- Temperature dependence:  
 of bandpass filters, 7.94  
 of line broadening parameters, 15.19*t*  
 of line shift parameters, 15.19*t*
- Temporal instability, of metals, 4.9
- Tensor properties:  
 of crystals and glasses, 2.5, 2.6*t*  
 of third-order optical nonlinearities, 16.2–16.3
- Tensors:  
 compliance, 2.30  
 dielectric, 2.17–2.18  
 $\mathbf{d}$ -tensor, 10.11  
 inverse dielectric, 2.6*t*, 2.19  
 second-order susceptibility, 10.10–10.11
- Tests and testing:  
 Knoop, 2.31, 2.32*f*  
 of polymers, 3.16
- Tetragonal crystals, 8.9*t*, 8.19*t*  
 room-temperature elastic constants, 2.44*t*–2.45*t*  
 symmetries of, 2.7*t*
- Tetragonal perovskite, 2.73*t*
- Tetrahedral lattice site, 5.6
- Textured graphite surface, 6.8*f*
- Thallium bromide (TlBr), 2.40*t*, 2.44*t*, 2.48*t*, 2.53*t*, 2.58*t*, 2.65*t*, 2.68*t*
- Thallium chloride (TlCl), 2.65*t*, 2.68*t*

- The Theory of Coherent Atomic Excitation*  
(B. W. Shore), 14.3
- Thermal blooming, 16.22
- Thermal conductivity:  
of crystals and glasses, 2.6t, 2.35–2.36, 2.35f  
of metals, 4.7, 4.10t, 4.53, 4.55, 4.55t, 4.58t,  
4.60f–4.64f
- Thermal cycling, of metals, 4.10
- Thermal defocusing, 13.8
- Thermal diffusivity, for metals, 4.10t
- Thermal effects, on third-order optical  
nonlinearities, 16.22
- Thermal expansion:  
of crystals and glasses, 2.6t, 2.34–2.35, 2.34f  
for metals, 4.10t  
of metals, 4.6
- Thermal instability, of metals, 4.10
- Thermal properties:  
of crystals and glasses, 2.50t–2.53t, 2.55t  
of metals, 4.6–4.7, 4.53, 4.55  
coefficient of linear thermal expansion,  
4.56t, 4.57f, 4.58f  
elastic properties, 4.69, 4.69t  
at room temperature, 4.55t  
specific heat, 4.65t, 4.66f–4.69f  
strength and fracture properties, 4.70, 4.70t  
thermal conductivity, 4.58t, 4.59f–4.63f
- Thermal self-focusing, 13.7–13.8
- Thermalization, of free electron and hole  
distributions, 18.20–18.21
- Thermomodulation, 5.66t
- Thermo-optic coefficients, of crystals and  
glasses, 2.21, 2.24–2.26, 2.24f
- Thermo-optic effect, 16.22
- Thermoplastic resins, 3.2
- Thermoset resins, 3.2
- Thickness errors, for multilayer reflectors, 7.40
- Thin-film coatings:  
and antireflection coatings, 7.27–7.28, 7.28f  
laser-induced damage to, 19.4  
manufacturing of, 7.10–7.12  
of metal, 7.104, 7.104f  
for multiple reflection filters, 7.111, 7.112,  
7.112f, 7.113f  
theory and design of, 7.5–7.10, 7.6f, 7.9f
- Third-order harmonic generation (THG),  
16.2, 16.3t  
in crystals, 16.14  
energy level diagrams for, 16.5f  
and semiconductors, 5.56
- Third-order optical nonlinearities, 16.1–16.31  
cascaded  $x^{(1)}:x^{(1)}$  processes, 16.20–16.22,  
16.21f  
cascaded  $x^{(2)}:x^{(2)}$  processes, 16.22–16.24,  
16.23f, 16.24f  
and four-wave mixing, 16.27–16.28, 16.28f  
and interferometry, 16.28–16.29  
Kerr effect, 16.11–16.14, 16.13f, 16.14f  
Kramers-Kronig dispersion relations,  
16.9–16.11  
nonlinear absorption and nonlinear  
refraction, 16.7–16.9  
propagation effects, 16.24–16.26  
and quantum mechanics, 16.4–16.7, 16.5f  
and semiconductors, 5.55  
stimulated scattering, 16.14–16.19, 16.15f,  
16.17f  
terms for, 16.1–16.3, 16.3t  
third-harmonic generation, 16.14  
and time-resolved excite-probe techniques,  
16.26–16.27, 16.27f  
two-photon absorption, 16.19–16.20  
and Z-scan, 16.29–16.30, 16.30f
- Thomson scattering, 21.8–21.9, 21.9f
- 3D bandgap materials, 9.2
- 3D optical molasses, 20.16–20.17, 20.16f
- 3D photonic crystals, 9.4–9.8  
criteria for, 9.4–9.5  
examples of, 9.5, 9.5f  
microcavities in, 9.7–9.8, 9.7f, 9.8f
- 3M Black Velvet, 6.14
- 3M Black Velvet 101-C10, 6.12, 6.35
- 3M Nextel Black Velvet, 6.35, 6.36f
- 3M paints, 6.35–6.37, 6.38f, 6.53f  
3M Nextel Black Velvet, 6.35, 6.36f  
MH 2200, 6.37  
Nextel 2010, 6.35, 6.37  
Nextel Suede Coating Series 3101-C10, 6.37,  
6.38f, 6.53f
- Three-level atomic systems, 14.4–14.6, 14.4f, 14.6f
- Three-photon absorption (3PA), 19.9, 19.10,  
19.10f
- Three-wave mixing, 14.26
- Threshold ionization:  
absorbance above, 21.14–21.17, 21.15f, 21.16f  
defined, 21.3
- Thresholding devices, 12.35–12.36, 12.36f
- Time-dependent (transient) spectroscopy, 11.2
- Time-domain atom interferometers,  
11.22–11.24, 11.24f

- Time-gated imaging, 15.42, 15.43, 15.44f
- Time-integrated intensity, 11.18
- Time-of-flight (TOF) measurement of velocity distribution, 20.13, 20.13f
- Time-resolved excite-probe techniques, 16.26–16.27, 16.27f
- Tin hypothiodiphosphate ( $\text{Sn}_2\text{P}_2\text{S}_6$ ), 12.17, 12.18t
- Tiodize V-E17, 6.49
- Titanium, 4.48t, 4.50t, 4.52t, 4.55t
- Titanium dioxide, 6.15
- Titanium sapphire (Ti:sapphire) amplifiers, 21.5
- Titanium sapphire (Ti:sapphire) lasers, 18.3
- Tomography, quantum coherence, 23.13
- Total emittance, of metals, 4.6
- Total integrated excitance, for crystals and glasses, 2.19
- Total internal reflection (TIR), 8.13
- Total mass loss (TML), 6.17
- Total power law, 2.19–2.20, 2.20f
- Total strain, of crystals and glasses, 2.36
- Transfer matrix solution (to Maxwell's equations), 9.3
- Transient four-wave mixing (TFW), 18.17–18.18, 18.17f
- Transient Raman scattering, 15.22–15.32  
broadband effects, 15.28–15.32, 15.29f  
phase pulling, 15.26–15.27, 15.27f  
pulsed, 15.22–15.25, 15.24f–15.26f, 15.24t  
solitons, 15.27–15.28, 15.29f  
spectral properties, 15.32
- Transitions, 16.4 (*See also specific transitions, e.g.: One-electron transitions*)
- Transmission:  
of coatings on substrate, 7.3  
for cutoff filters, 7.54–7.55, 7.55f  
measurement of, 5.64  
in passband region, 7.53, 7.54
- Transmission coefficient, for optical constants, 5.9–5.10
- Transmission filters, 7.3–7.5, 7.83, 7.88f
- Transmission grating, 12.7, 12.8f
- Transmittance:  
at interface of solid, 8.12  
of metals, 4.6  
of optical coatings, 7.12–7.13  
spectral, 7.3–7.4  
of water, 1.5t
- Transparency:  
and absorption, 2.17  
EIT [*see* Electromagnetically induced transparency (EIT)]  
induced, 21.52
- Transparent prisms, 5.59
- Transverse acoustic (TA) phonons, 5.24, 5.25f
- Transverse Kerr effect, 18.11, 18.12f, 18.14–18.15
- Transverse optical (TO) frequencies, for crystals and glasses, 2.11, 2.12
- Transverse optical (TO) phonons, 5.24, 5.25f, 5.80, 5.80f, 8.16–8.18
- Transverse relaxation time, 11.5
- Trap loss collisions, 20.29
- Trapping atoms, 20.21–20.39  
applications of, 20.26–20.39  
and atomic beam brightening, 20.27–20.28, 20.27f  
and atomic clocks, 20.28  
and Bose-Einstein condensation, 20.35–20.37, 20.36f  
and dark states, 20.37–20.39, 20.38f  
magnetic traps, 20.21–20.23, 20.22f  
magneto-optical traps, 20.24–20.25, 20.24f, 20.26f  
and optical lattices, 20.31–20.34, 20.32f–20.34f  
optical traps, 20.23–20.24, 20.23f  
and ultracold collisions, 20.28–20.31, 20.30f, 20.31f
- Triatomic molecules, in strong fields, 21.26
- Triclinic crystals, 2.7t, 2.18, 8.9t, 8.10
- Trigonal crystals, 8.9t, 8.19t
- Trigonal selenium, 2.70t
- Triply resonant oscillators (TROs), 17.2–17.4, 17.3f, 17.4f, 17.20–17.21, 17.21f
- TRU-Color Diffuse Black, 6.49
- Tunable double resonance (electromagnetically induced transparency), 22.6–22.9, 22.7f, 22.8f
- Tunable phase-dispersion filters, 7.89, 7.89f
- Tungsten:  
absorptance of, 4.42f, 4.48t, 4.50t, 4.51t  
elastic properties of, 4.69t  
extinction coefficient for, 4.18t–4.19t, 4.26f  
reflectance of, 4.38t–4.39t, 4.42f  
refraction index for, 4.18t–4.19t, 4.26f  
resistivity of, 4.54t  
strength and fracture properties of, 4.70t
- Tungsten hexafluoride, 6.56

- Tunnel ionization:  
 atomic, 21.12–21.14, 21.12*f*, 21.14*f*  
 molecular, 21.25–21.26, 21.25*f*, 21.27*f*  
 relativistic, 21.20
- Tunneling, collective, 21.18
- Turning, single-point, 3.12
- Tweezers, optical, 20.23
- Twin beams of light, correlated, 17.28, 17.29*f*, 17.30*f*
- Two-beam coupling:  
 optical limiting by, 13.8–13.9  
 photorefractive gain in, 12.29–12.32, 12.31*f*  
 photorefractive loss in, 12.31–12.32, 12.33*f*–12.35*f*  
 and wave interactions, 12.4–12.6, 12.4*f*
- 2D photonic crystals, microcavities of, 9.8–9.12, 9.9*f*  
 in-plane coupling, 9.10–9.11  
 out-of-plane coupling, 9.11–9.12  
 waveguides in, 9.13–9.14, 9.13*f*
- Two-level atoms:  
 coherence in, 14.4–14.5, 14.4*f*  
 force on, 20.6–20.7  
 at rest, 20.7–20.8
- Two-level coupling, 14.30, 14.30*f*
- Two-material periodic multilayers theory, 7.32–7.38  
 $[(0.5A)B(0.5A)]^N$  multilayers, 7.35, 7.36*f*  
 angular sensitivity, 7.37  
 multilayer reflectors of absorbing materials, 7.37–7.38, 7.38*f*  
 nonabsorbing  $[AB]^N$  and  $[AB]NA$  multilayers, 7.32–7.34, 7.33*f*–7.35*f*  
 width of high-reflectance zone, 7.36–7.37, 7.37*f*  
 $[xH.(1-x)L]^N.xH$  multilayers, 7.37
- Two-photon absorption (2PA):  
 energy level diagrams for, 16.5*f*  
 and laser-induced damage, 19.9, 19.10, 19.10*f*  
 and optical limiting, 13.4, 13.5, 13.6*f*  
 of semiconductors, 5.56  
 symbols, 16.8  
 in third-order optical nonlinearities, 16.19–16.20
- Two-photon transitions, 11.22–11.23, 11.24*f*
- ULE glass, 2.43*t*, 2.49*t*, 2.54*t*
- Ultimate strength, of metals, 4.8
- Ultracold collisions, 20.26, 20.28–20.31, 20.30*f*, 20.31*f*
- Ultrafast depletion, of semiconductor band states, 18.21
- Ultrafast lasers, 11.26, 18.3–18.5, 18.4*f*, 18.5*f*
- Ultrafast optics, coatings for, 7.47–7.48, 7.48*f*
- Ultrashort pulse generation, 18.1–18.23  
 Kerr effect, 18.11–18.15  
 longitudinal, 18.11–18.15, 18.12*f*  
 transverse, 18.14–18.15  
 saturable absorbers, 18.5–18.11  
 fast, 18.9–18.10  
 self-amplitude modulation, 18.5–18.7, 18.6*f*, 18.7*f*  
 semiconductor saturable absorber mirrors, 18.3, 18.10–18.11  
 slow, 18.7–18.9, 18.8*f*  
 semiconductor ultrafast nonlinearities, 18.15–18.23  
 carrier trapping, 18.21–18.23, 18.22*f*  
 in coherent regime, 18.19–18.20  
 continuum excitations, 18.20  
 excitonic excitations, 18.19–18.20  
 experimental techniques, 18.17–18.19, 18.17*f*  
 properties, 18.16–18.17, 18.16*f*  
 in thermalization regime, 18.20–18.21  
 and ultrafast lasers, 18.3–18.5, 18.4*f*, 18.5*f*
- Ultralow light pulses, 14.22–14.23, 14.23*f*
- Ultraviolet (UV) crystals, 10.22*t*
- Ultraviolet (UV) light:  
 and black surfaces, 6.21, 6.22*f*–6.25*f*  
 metal-dielectric reflectors for, 7.108–7.109, 7.109*f*  
 semiconductor interactions with, 5.4*f*, 5.5  
 [See also Extreme ultraviolet (XUV) light]
- Uncertainty principle, 23.4, 23.6
- Uncertainty state, 23.6
- Underdense plasmas, strong field interactions  
 with, 21.36–21.46  
 direct laser acceleration and betatron resonance, 21.42–21.43  
 intense laser pulses, 21.38–21.39, 21.38*f*  
 inverse Bremsstrahlung heating, 21.37, 21.37*f*  
 ionization-induced defocusing, 21.43–21.44, 21.43*f*  
 ponderomotive channel formation, 21.42  
 self-channeling and self-phase modulation, 21.44–21.46, 21.45*f*  
 wakefield generation and electron acceleration, 21.39–21.42, 21.40*f*, 21.42*f*

- Uniaxial crystals, **8.8**, **8.9t**, **8.10f**  
 Uniaxial stress, **5.66t**  
 Unit cell, crystal, **2.30**  
 Universal antireflection coatings, **7.26**, **7.27f**  
 Upward plane irradiance, **1.5t**, **1.7f**, **1.8**  
 Upward scalar irradiance, **1.5t**, **1.7f**, **1.8**  
 Upwelling average cosine, **1.6t**, **1.7f**  
 Upwelling irradiance, **1.7f**, **1.8**  
 Urbach tail model, **2.14–2.15**  
 Urbach's rule, **5.23**  
 Urea [(NH<sub>4</sub>)<sub>2</sub>CO], **2.40t**, **2.45t**, **2.48t**, **2.52t**,  
     **2.57t**, **2.64t**  
 Vacuum heating, **21.47f**, **21.48–21.49**  
 Vacuum ultraviolet (VUV) spectrum,  
     **5.4f**, **5.5**  
 Vacuum-metal interfaces, **4.43f**  
 Vacuum-ultraviolet (VUV) radiation, **14.3**  
 Valence band (VB), **18.3**  
 van Hove singularities, **8.28**  
 Vee (V) coupling, **14.1**, **14.6f**  
 Velocity distribution measurement,  
     **20.13**, **20.13f**  
 Velocity-changing collisions, **11.15**  
 Velocity-selective coherent population trapping  
     (VSCPT), **14.5**, **20.37**  
 Very dense crown glass, **2.42t**  
 Very light flint glass, **2.41t**  
 Very low loss reflectors, **7.41–7.42**  
 Vibration(s):  
     lattice, **2.11–2.12**, **2.76t–2.77t**  
     local, **5.17**, **5.18**, **5.19f**, **5.20**, **5.20f**, **5.82f**, **5.83**  
     phonon, **5.14–5.16**  
 Vibrational optic effects, **5.17–5.20**, **5.18f–5.19f**,  
     **5.20t**, **5.21f**  
 Virtual transitions, **16.4**  
 Viruses, in water, **1.14**  
 Visible near-IR nonlinear optical crystals,  
     **10.21t**, **10.22t**  
 Volkov state, **21.12**  
 Volume scattering function (VSFs):  
     for sea water and ocean water, **1.34t–1.35t**  
     spectral, **1.37–1.38**, **1.38t**  
     of water, **1.5t**, **1.7f**, **1.31**, **1.31t**, **1.32f**, **1.33**  
     wavelength dependence of, **1.36f**  
 W point, **9.4**  
 Wakefield generation, **21.39–21.42**, **21.40f**  
 “Walking” backward, by solitons, **15.28**  
 Wannier excitons, **5.26–5.27**, **5.26t**, **8.31**  
 Water, **1.3–1.50**  
     absorption, **1.20–1.29**  
         bio-optical models for, **1.27–1.29**, **1.27f**,  
             **1.28t**  
         by dissolved organic matter, **1.22–1.23**,  
             **1.23t**  
         by organic detritus, **1.25–1.27**, **1.25t**,  
             **1.26f**  
         by phytoplankton, **1.23–1.25**,  
             **1.24f–1.25f**  
         by polymers, **3.4**  
         by sea water, **1.21**, **1.22t**  
     apparent optical properties, **1.12–1.13**  
     attenuation  
         beam, **1.40–1.41**, **1.41f**, **1.42f**  
         diffuse and Jerlov water types, **1.42–1.46**,  
             **1.43t–1.45t**, **1.44f**, **1.45f**  
     constituents of natural waters, **1.13–1.15**  
         dissolved substances, **1.13**  
         particulate substances, **1.14–1.15**  
     electromagnetic properties of, **1.16–1.17**,  
         **1.18t**  
     inherent optical properties, **1.9–1.12**, **1.10f**  
     irradiance reflectance and remote sensing,  
         **1.46–1.47**, **1.47f**  
     particle size distributions, **1.15–1.16**, **1.16f**  
     pure, **1.3**  
     radiometric quantities, **1.4–1.9**, **1.5t–1.6t**,  
         **1.7f**  
     refraction index, **1.18–1.20**  
         particles, **1.20**  
         sea water, **1.18–1.20**, **1.18f**, **1.19t–1.20t**  
     scattering, **1.30**  
         inelastic and polarization, **1.47–1.49**,  
             **1.48f**, **1.49f**  
         measurement of, **1.29–1.30**  
         by particles, **1.30–1.35**, **1.31t**, **1.32f**, **1.33f**,  
             **1.34t–1.35t**  
         by pure water and pure sea water, **1.30**  
         wavelength dependence of, **1.35–1.40**,  
             **1.35t**, **1.36f**, **1.37t**, **1.38t**, **1.39f**,  
             **1.40t**  
         terminology and notation, **1.3–1.4**  
     Water vapor regained (WVR), **6.17**  
     Wave equations, for light propagation in solids,  
         **8.6–8.7**  
     Wave interactions, photorefractive effect and,  
         **12.4–12.7**, **12.4f**, **12.6f**  
     Waveguide bends, **9.14–9.16**, **9.15f**, **9.16f**  
     Waveguide intersections, **9.16–9.17**, **9.17f**



- Waveguides:  
and photonic bandgaps, 9.12–9.17  
in photonic crystals with 2D periodicity,  
9.13–9.14, 9.13f  
waveguide bends, 9.14–9.16, 9.15f, 9.16f  
waveguide intersections, 9.16–9.17, 9.17f  
photorefractive, 12.37  
silicon-on-insulator planar, 22.15
- Wavelength dependence, of scattering, 1.35–1.40,  
1.35t, 1.36f, 1.37t, 1.38t, 1.39f, 1.40t
- Wavelength modulation, 5.66t
- Wavelengths, de-Broglie, 8.4
- Wedge filters, 7.90, 7.91, 7.91f
- Weld-line, in molding, 3.14
- Wide bandpass filters, 7.90, 7.90f
- Wide-angle bandpass filters, 7.93–7.94, 7.93f
- Wulfenite ( $\text{PbMoO}_4$ ), 2.40t, 2.45t, 2.48t, 2.52t,  
2.57t, 2.64t, 2.72t
- Wurtzite ( $\alpha$ -ZnS):  
in crystals and glasses, 2.70t  
lattices of, 5.6  
properties of, 2.41t, 2.44t, 2.46t, 2.48t, 2.53t,  
2.58t, 2.66t, 2.69t, 2.70t
- X-ray region:  
beam splitters for, 7.63  
soft  
bandpass filters for, 7.94–7.96, 7.95f–7.96f  
interference polarizers for, 7.73, 7.76f–7.77f  
multilayer reflectors for, 7.42, 7.53
- Yellow matter, 1.13, 1.21–1.23, 1.28
- Yield strength, of metals, 4.8, 4.70, 4.70t
- Young's modulus:  
for crystals, 2.30, 2.31  
for metals, 4.7, 4.10t, 4.69t  
for polymers, 3.3
- Yttria ( $\text{Y}_2\text{O}_3$ ), 2.40t, 2.44t, 2.48t, 2.53t, 2.58t,  
2.65t, 2.76t
- Yttrium aluminum garnet ( $\text{Y}_3\text{Al}_5\text{O}_{12}$ ) (YAG),  
2.44t, 2.53t, 2.58t, 2.65t, 2.76t
- Yttrium lithium fluoride ( $\text{LiYF}_4$ ) (YLF), 2.45t,  
2.48t, 2.52t, 2.57t, 2.63t, 2.72t
- Yttrium vanadate ( $\text{YVO}_4$ ), 2.40t, 2.45t, 2.48t,  
2.53t, 2.58t, 2.65t, 2.76t
- Yurke state, 23.8
- ZBLAN glass, 2.43t, 2.49t, 2.54t,  
2.59t, 2.68t
- Zernike dispersion formula, 2.22
- Zero dispersion point, for glasses, 2.23
- Zerodur glass, 2.43t, 2.49t, 2.54t
- Zinc, absorptance of, 4.48t
- Zinc crown glass, 2.41t
- Zinc selenide ( $\text{ZnSe}$ ), 2.41t, 2.48t, 2.53t, 2.58t,  
2.66t, 2.69t
- Zinc telluride ( $\text{ZnTe}$ ), 2.41t, 2.48t, 2.53t, 2.58t,  
2.66t, 2.69t
- Zinblende ( $\beta$ -ZnS):  
in crystals and glasses, 2.69t  
lattices of, 5.6, 5.16, 5.17t  
properties of, 2.41t, 2.44t, 2.46t, 2.48t, 2.53t,  
2.58t, 2.65t, 2.69t, 2.70t
- Zinc-germanium diphosphide ( $\text{ZnGeP}_2$ ), 2.41t,  
2.45t, 2.48t, 2.53t, 2.58t, 2.65t
- Zirconia, cubic ( $\text{ZrO}_2 \cdot 0.12\text{Y}_2\text{O}_3$ ), 2.41t, 2.44t,  
2.48t, 2.69t
- ZO-MOD BLACK, 6.56
- Zooplankton, in water, 1.14
- Z-scan:  
for nonlinear optical parameters, 19.9, 19.9f,  
19.10f  
and third-order optical nonlinearities,  
16.29–16.30, 16.30f